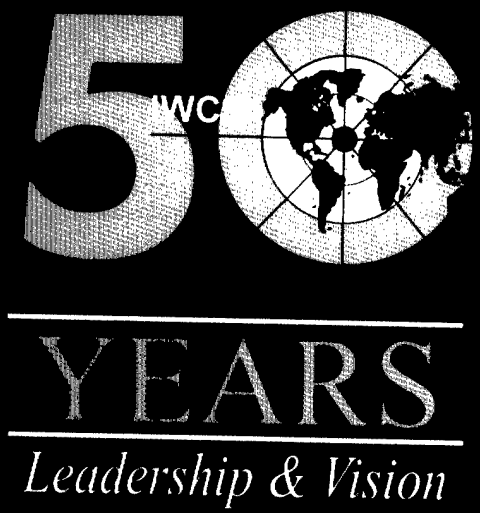
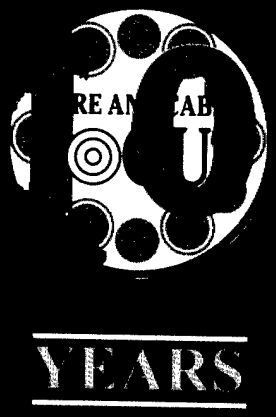
Proceedings of the

50th IWCS/FOCUS

International Wire & Cable Symposium

November 12-15, 2001
Disney's Coronado Springs Resort
Lake Buena Vista, Florida





Sponsored By:
IWCS, Inc. Eatontown, NJ

With Participation By:
US Army CECOM, Fort Monmouth, NJ

Supporting Associates:
Europacable, Brussels, Belgium
WCISA - Wire & Cable Industry Suppliers Association
Wire & Cable Technology International

20020815 166

Proceedings of the

50th IWCS/FOCUS

International Wire & Cable Symposium

November 12-15, 2001
Disney's Coronado Springs Resort
Lake Buena Vista, Florida





Sponsored By:
IWCS, Inc. Eatontown, NJ
Website: www.iwcs.org · Email: admin@iwcs.org

With Participation By:
US Army CECOM, Fort Monmouth, NJ

Supporting Associates:
Europacable, Brussels, Belgium · WCISA - Wire & Cable Industry Suppliers Association
Wire & Cable Technology International

APPROVED FOR PUBLIC RELEASE: DISTRIBUTION UNLIMITED

MISSION

The International Wire and Cable Symposium provides a forum for the exchange of technical information amongst suppliers, manufacturers, and users on technological advancements in materials, processes, and products used for voice, data and video signal transmission systems.

TECHNICAL PRESENTATIONS

		Monday, November 12, 2001
		Special Session
1:00 pm	SESSION	Marketing & Management
		Tuesday, November 13, 2001
9:00 am	PLENARY	The Future of the Cable Industry – A Challenge for the New Century
		Track 1-- Fiber
1:00 pm	SESSION 1	Fiber & Cable Manufacturing/Aerial Cables
1:00 pm	SESSION 2	Splicing & Interconnection
		Track 2 -- Manufacturing, Processing and Materials
1:00 pm	SESSION 3	Thermoplastic Cable Materials
		Track 3 -- Copper
1:00 pm	SESSION 4	Copper Cable Design, Modeling & Testing
		New Products
1:00 pm	EXHIBITORS	Presentations I
		Wednesday, November 14, 2001
		New Products
8:30 am	EXHIBITORS	Presentations II
		Track 1 -- Fiber
1:00 pm	SESSION 5	Premises Cable
1:00 pm	SESSION 6	Fiber Reliability
		Track 2 -- Manufacturing, Processing and Materials
1:00 pm	SESSION 7	Materials Processing & Test Measurement
		Panels
1:00 pm	SESSION 8	Aerospace/Automotive
1:00 pm	SESSION 9	Wireless Alternative To Wired Systems
		Poster
4:00 pm	SESSION 10	Poster Papers
		Thursday, November 15, 2001
		Track 1 -- Fiber
8:00 am	SESSION 11	Fiber Optic Cable Design I
8:00 am	SESSION 12	Fiber Properties I
		Track 2 -- Manufacturing, Processing and Materials
8:00 am	SESSION 13	UV Fiber & Cable Materials
		Track 3 -- Copper
8:00 am	SESSION 14	Electromagnetic Compatibility & Crosstalk
8:00 am	SESSION 15	Applications for Copper Cable Technology
		Track 1 -- Fiber
1:00 pm	SESSION 16	Fiber Optic Cable Design II
1:00 pm	SESSION 17	Fiber Properties II
1:00 pm	SESSION 18	Installation
1:00 pm	SESSION 19	Submarine Cables
		Track 3 -- Copper
1:00 pm	SESSION 20	Copper Materials & Processing

PAPERS

The papers in this volume were printed directly from unedited reproducible copies prepared by the authors. Responsibility for contents rests upon the authors and not the symposium committee or its members. All rights reserved by the International Wire and Cable Symposium, Inc., 174 Main Street, Eatontown, New Jersey 07724.

Proceedings/Publications
INTERNATIONAL WIRE AND CABLE SYMPOSIUM (IWCS)

Proceedings - Bound - Available from IWCS

39th IWCS Proceedings - 1990 - $15.00
40th IWCS Proceedings - 1991 - $25.00
44th IWCS Proceedings - 1995 - $40.00
46th IWCS Proceedings - 1997 - $20.00
47th IWCS Proceedings - 1998 - $15.00
48th IWCS Proceedings - 1999 - $15.00
49th IWCS Proceedings - 2000 - $35.00
50th IWCS Proceedings - 2001 - $50.00

Copies of original proceedings not listed above can be reproduced for $75.00 per copy plus shipping.
CD's 46th, 47th, 48th & 50th IWCS CD - $10.00
Publications - Bound - Available from IWCS
Index of IWCS Papers (1983-1990); PUB #1001RP-1991 - $15.00

Extra Copies of the 2001 Proceedings can be obtained for: 1 - $50; 2 - $100; 3 - $150; 4 - $190; 5 - $230; 6 - $270; 7 - $310; 8 - $350; 9 - $390; 10 - $430; 11 and above - $430 plus $30 for each additional copy.

Shipping/Handling:

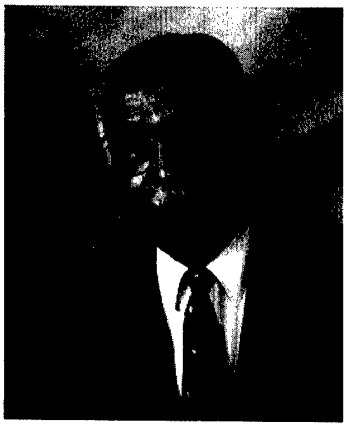
Proceedings	Publications	CDs
$9.00 per copy USA only	$5.00 per copy USA only	$5.00 per copy USA only
$20.00 per copy Canada	$10.00 per copy Canada	$7.00 per copy Canada
$35.00 per copy Airmail (Europe)	$15.00 per copy Airmail	$13.00 per copy Airmail
$40.00 per copy Airmail (Asia)	(Europe and Asia)	(Europe and Asia)

Payment: Make a check or bank draft payable in U.S. Dollars drawn on a U.S. Bank, to the INTERNATIONAL WIRE & CABLE SYMPOSIUM, INC. or use your VISA/MC/AMEX by providing number and expiration date and forward request to: International Wire and Cable Symposium, Inc., 174 Main Street, Eatontown, NJ 07724. Telephone inquiries may be directed to Ms. Pat Hudak +1-732-389-0990. Prices are subject to change.

Photocopies are available for complete sets of papers for 1964 through 2000. Information on prices and shipping charges should be requested from the: US Department of Commerce, National Technical Information Service (NTIS), Springfield, Virginia 22161, Telephone: +1-703-487-4650

Include Title, Year and "AD" Number

13th Annual Wire Cable Symposium (1964) - AD 787164
15th Annual Wire Cable Symposium (1966) - AD A006601
16th International Wire Cable Symposium (1967) - AD 787165
17th International Wire Cable Symposium (1968) - AD 787166
18th International Wire Cable Symposium (1969) - AD 787167
19th International Wire Cable Symposium Proceedings 1970 - AD 714985
20th International Wire Cable Symposium Proceedings 1971 - AD 733399
21st International Wire Cable Symposium Proceedings 1972 - AD 752908
22nd International Wire Cable Symposium Proceedings 1973 - AD 772914
23rd International Wire Cable Symposium Proceedings 1974 - AD A003251
24th International Wire Cable Symposium Proceedings 1975 - AD A017787
25th International Wire Cable Symposium Proceedings 1976 - AD A032801
26th International Wire Cable Symposium Proceedings 1977 - AD A047609
27th International Wire Cable Symposium Proceedings 1978 - AD A062322
28th International Wire Cable Symposium Proceedings 1979 - AD A081428
29th International Wire Cable Symposium Proceedings 1980 - AD A096308
30th International Wire Cable Symposium Proceedings 1981 - AD A110859
31st International Wire Cable Symposium Proceedings 1982 - AD A125662
32nd International Wire Cable Symposium Proceedings 1983 - AD A136749
33rd International Wire Cable Symposium Proceedings 1984 - AD A152119
34th International Wire Cable Symposium Proceedings 1985 - AD A164384
35th International Wire Cable Symposium Proceedings 1986 - AD A180828
36th International Wire Cable Symposium Proceedings 1987 - AD A189610
37th International Wire Cable Symposium Proceedings 1988 - AD A200903
38th International Wire Cable Symposium Proceedings 1989 - AD A216023
39th International Wire Cable Symposium Proceedings 1990 - AD A233634
40th International Wire Cable Symposium Proceedings 1991 - AD A244038
41st International Wire Cable Symposium Proceedings 1992 - AD A259235
42nd International Wire Cable Symposium Proceedings 1993 - AD A279242
43rd International Wire Cable Symposium Proceedings 1994 - AD A293473
44th International Wire Cable Symposium Proceedings 1995 - AD A303506
45th International Wire Cable Symposium Proceedings 1996 - AD A324572
46th International Wire Cable Symposium Proceedings 1997 - AD A338941
47th International Wire Cable Symposium Proceedings 1998 - AD A358377
48th International Wire Cable Symposium Proceedings 1999 - AD A373457
49th International Wire Cable Symposium Proceedings 2000 - AD A393963
Kwic Index of Technical Papers, International Wire Cable Symposium (1952-1982) - AD A027588



MESSAGE FROM THE CEO, DIRECTOR

The symposium this year should be the most exciting symposium to date. During the 50 years since the beginning of IWCS in 1952, the technological changes in the wire and cable industry have been tremendous. Without considering the exceptional changes in electrical and mechanical performances, the changes in cable designs have been outstanding, i.e., from the conventional copper cable (round vs. flat) to fibre optic and now slowly taking its place in the industry is wireless communications. The question is, what changes can we expect to see within the industry during the next 50 years?

The activities planned for this year's 50th anniversary celebration includes something of interest for everyone, both young and old. An expanded plenary session is planned for Tuesday morning along with a continental breakfast. During the session several presentations, pertaining to our 50th anniversary celebration will be included, in addition to the presentation of awards for last year's best technical paper, best presentation and best poster paper. Our keynote speaker Dr. Noritaka Kurauchi's presentation on "The Future of the Cable Industry – A Challenge for the New Century" should provide some insight as to where the industry is going within the next 50 years.

We have taken advantage of the unique location for the symposium by scheduling special activities that will include a visit to Disney's Epcot to witness the spectacular fire works display on Monday Night and to the MGM/Studios on Tuesday for a special New York Street Dinner Party. Also for the first time, golfing is included in our program with a reception scheduled to follow. We have two Disney's courses reserved that are considered outstanding for all golf lovers.

One of the main achievements this year has been the integration of Focus into our 50th anniversary celebration. For the first time a special marketing and management session is scheduled for Monday and on Wednesday a special panel on Aerospace/Automotive Cabling is also included in the program. The numbers of exhibitors are greater this year, resulting in a broader variety of products being displayed as a result of the merger with Focus. The new product presentation sessions that were initiated and quite popular during last year's symposium are being continued again this year.

Committee members Nils Artlöve of Telia Information Carrier in Sweden and John Varachi formerly of Telcordia Technologies, Inc., Morristown, NJ are retiring from the committee this year. On behalf of the Board of Directors and the Symposium Committee, I extend to Nils and John our sincere thanks and appreciation for their dedication and support of the symposium program and objectives.

Dr. Raymond Jaeger, Chairman of the Board of Directors and formerly of Spectran/Lucent Technologies of Sturbridge, MA is also retiring. Ray has been a strong supporter in planning symposium activities for over sixteen years. He is the originator and planner of this year's 50th Anniversary Celebration. The Board of Director's and the Symposium Committee will surely miss his active participation and support. On behalf of the Board and Committee we wish Ray the very best.

On behalf of the Board and Symposium Committee's many thanks and great appreciation is extended to all the companies that contributed to this years 50th Anniversary Celebration. Only through their support have we been able to plan all the special activities that I am sure everyone will enjoy.

Again this should be a great symposium and I am looking forward to seeing and greeting many of you in Orlando, FL.

Elmer F. Godwin

Elmer F. Godwin, *CEO, Director*

HIGHLIGHTS OF THE 49TH IWCS

International Wire and Cable Symposium

November 13, 14, 15 and 16, 2000

Trump Taj Mahal Casino-Resort, Atlantic City, New Jersey

Announcements/Greetings



Elmer F. Godwin
CEO/Director, IWCS
Eatontown, NJ



Dr. Howard Wichansky
US Army CECOM
Fort Monmouth, NJ

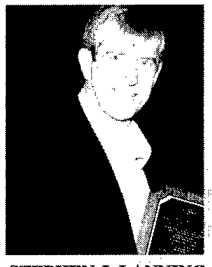
Guest Speakers Plenary Session



JOHN SACH
Chairman, Plenary Session
Pirelli Cables & Systems NA
Lexington, SC



PROFESSOR DAVID N. PAYNE
Director, Optoelectronics Research Center
University of Southampton
Southampton, United Kingdom



STEPHEN J. LANNING
Vice President of Engineering
Aerie Networks Inc.
Denver, CO

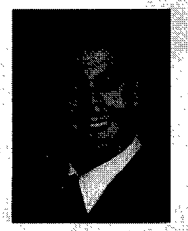
Luncheon Speaker



C.W. METCALF
Fort Collins, CO

Scholarship Recipients

Elmer F. "Ace" Godwin *Christopher Kenneth Eoll Memorial*



Stephen Consenza
Attending
Cornell University



Stephen M. Lopez
Attending
University of NC at Charlotte



Peter Galeotti
Attending
University of NC at Charlotte

Award Winners



Outstanding Technical
Dr. Howard Wichansky of IWCS (on right) making presentation to **Dr. J. Thomas Chapin**, Lucent Technologies, Norcrosss GA and **Dr. Pravin Ghandi,** Underwriters Laboratories, Northbrook, IL (they also accepted for) **Larry L. Bleich**, Lucent Technologies, Omaha, NE and **Thomas Ebert, P.E.,** Underwriters Laboratories, Northbrook, IL



Outstanding Poster Paper
Dr. Howard Wichansky of IWCS (on right) making presentation to **Allen C. Gregory**, Siecor, Hickory, NC (who is also accepting for) **Shami S. Sodhi** and **Gary E. Grogan**, Seicor, Hickory, NC

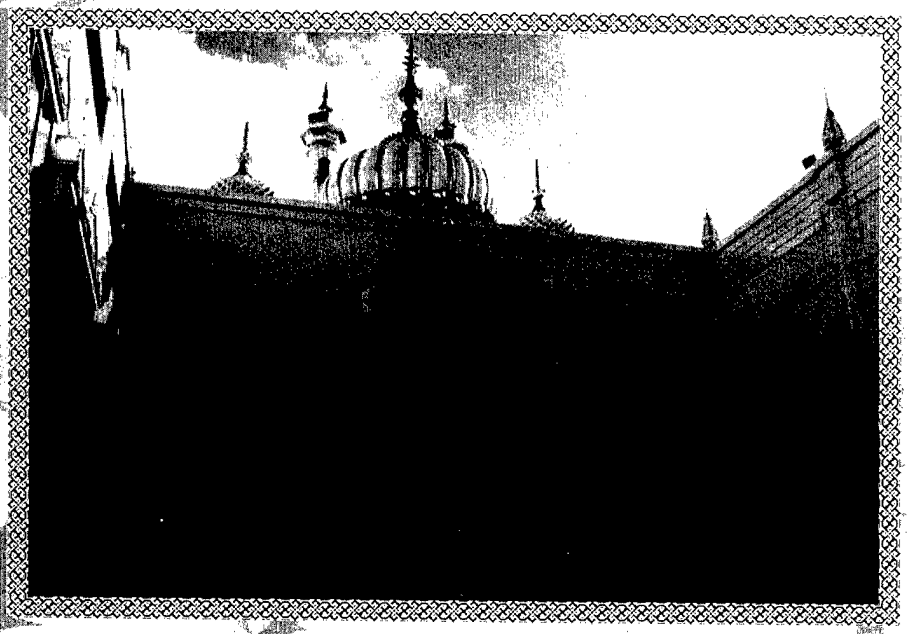


Best Presentation
Dr. Howard Wichansky of IWCS (on right) making presentation to **Eric R. Logan**, Siecor, Hickory, NC

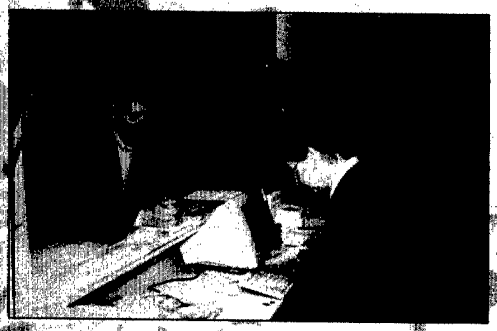
IWCS Retirees

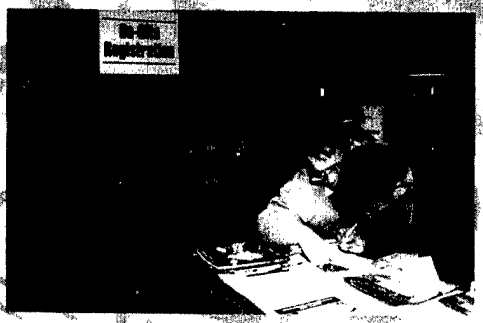


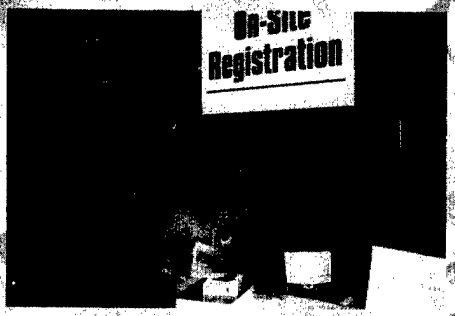
Elmer F. Godwin of IWCS (on left) presenting Retirement Certificates to **Inge B. Kovacs,** consultant for Polycheck Limited, Hackettstown, NJ

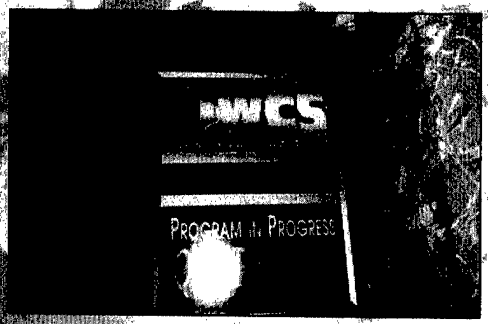


Registration





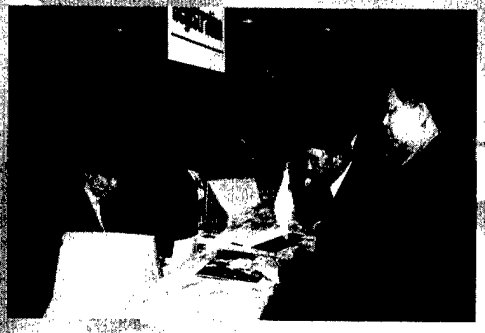














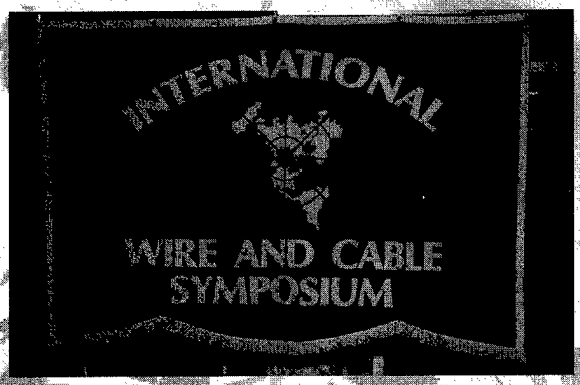









Technical Sessions





















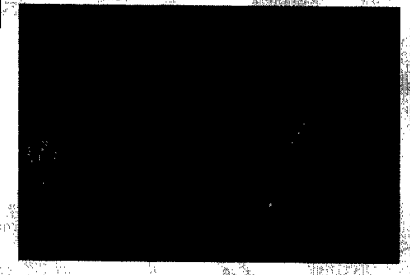




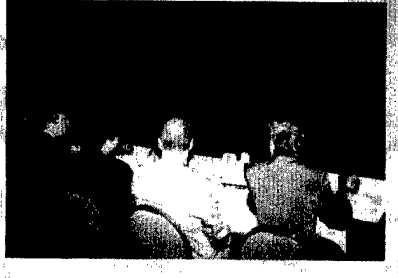
Hospitality





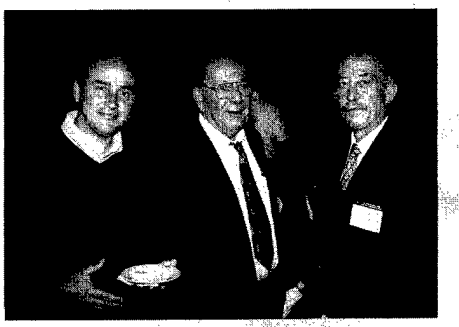





Hospitality









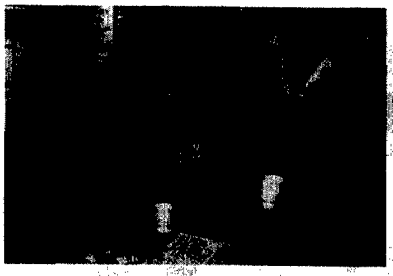


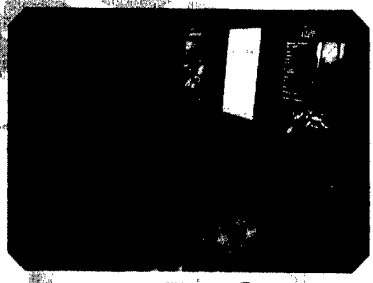




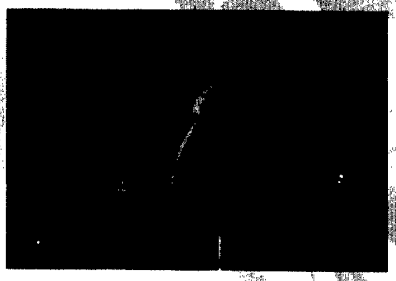
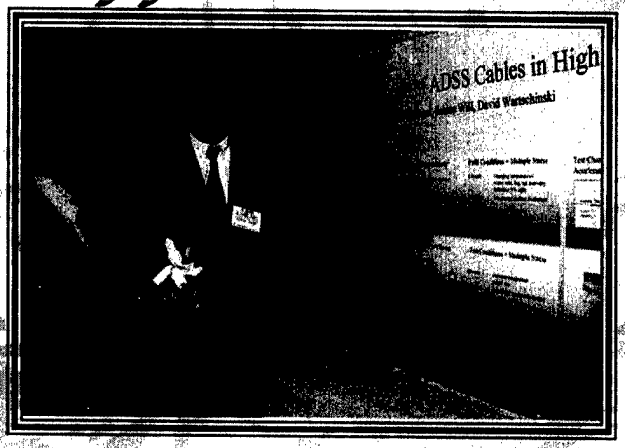
Suppliers Forum







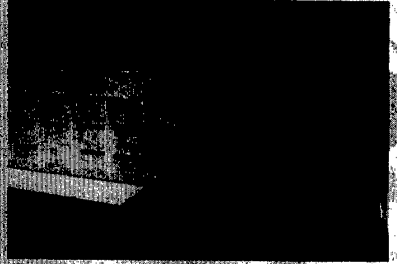
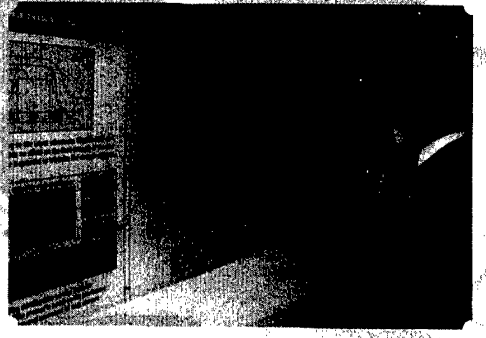








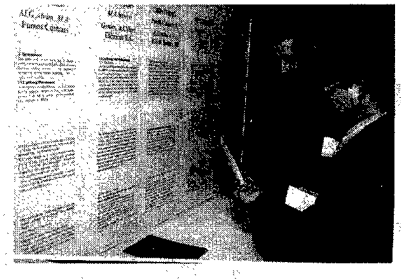


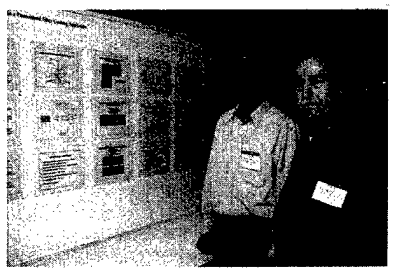


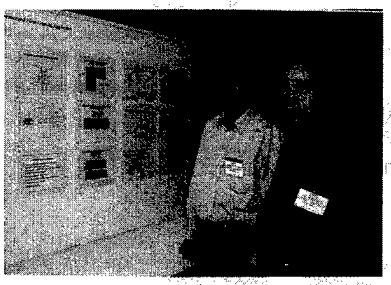




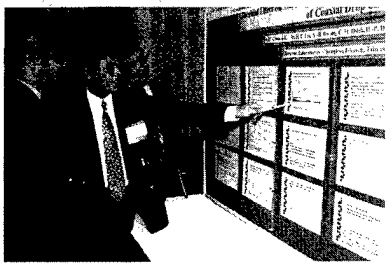




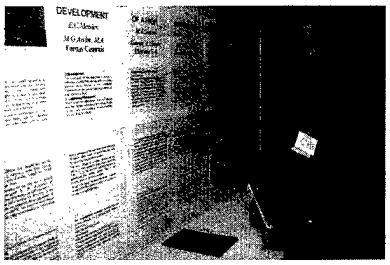


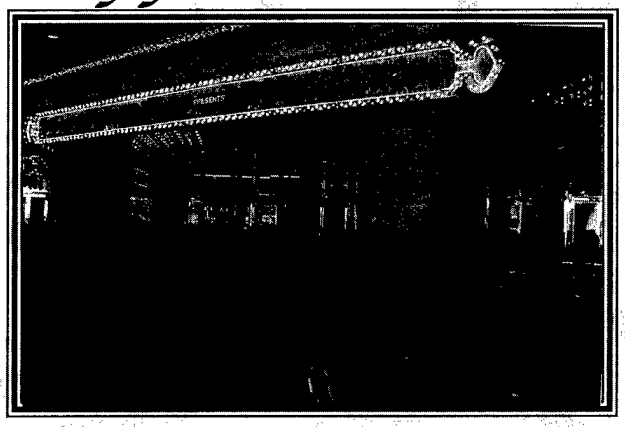


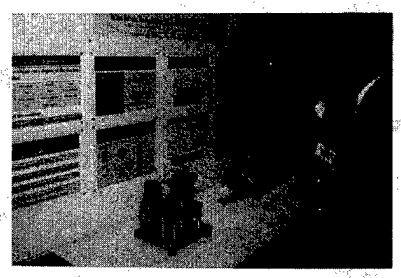


Suppliers Forum

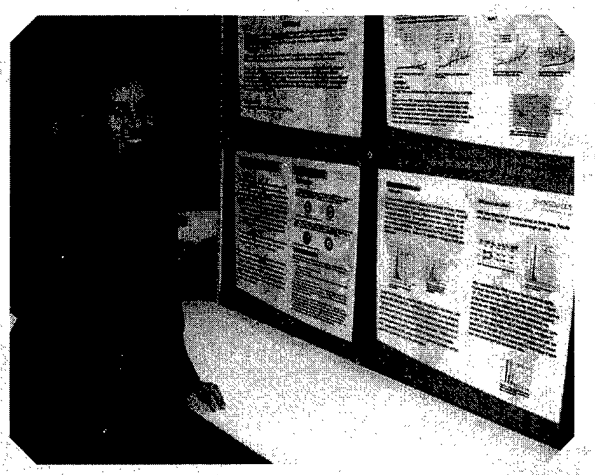


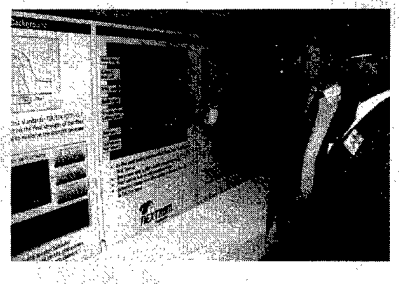












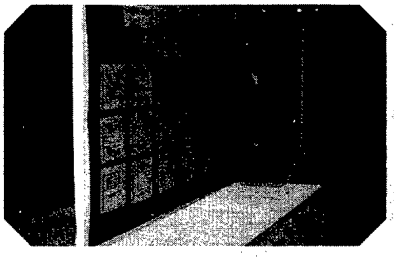








Table of Contents

MISSION ii

PROCEEDING/ PUBLICATIONS iii

MESSAGE FROM THE CEO/DIRECTOR iv

HIGHLIGHTS OF THE 49TH IWCS ..... v-xi

SCHOLARSHIPS xix
Elmer F. "Ace" Godwin Scholarship
& Christopher Kenneth Eoll Memorial Scholarship

AWARDS ..... xx-xxii

50th GOLD SUSTAINING CONTRIBUTORS xxiii

50th ANNIVERSARY SPONSORS xxiv

50th IWCS/FOCUS SYMPOSIUM COMMITTEE xxv

OPENING SPEAKERS xxvi
Dr. Raymond E. Jaeger, Chairman, IWCS Board of Directors, Sturbridge, MA, and *John R. Sach*, Chairman, IWCS Symposium Committee & IWCS Program Committee, Pirelli Communications Cables & Systems NA, Lexington, SC

PLENARY SESSION xxvii
Dr. Noritaka Kurauchi, President, International Cablemakers Federation, Wien, Austria & Chairman, Sumitomo Electric Industries, Ltd., Osaka, Japan

SPECIAL SESSION: Marketing & Management
Monday Afternoon, Nov. 13, 1:00 - 5:00 PM • Fiesta 6
Chairperson: **M. Edward Fenton,** *Wire & Cable Clubs/Fenton Group Inc., Wethersfield, CT*
Moderator: ***William Reichert,*** VP Operations, Madison Cable/Tyco, Worcester, MA

MM-1 **UL Standard Revisions and Proposals, Tri National Standards Harmonization Activities and the 2002 Edition of the National Electrical Code** 1
T. J. Guida, A. D. Wetherell, Underwriters Laboratories Incorporated, Melville, NY

MM-2 **Global Fire Hazard Assessment** 2
S. Galan, Underwriters Laboratories Incorporated, Melville, NY

New Version of the Written Testing Standard NFPA 262/UL 910 2
D. O. Nicholson, ITS ETL SEMKO Testing Laboratories, Cortland, NY

MM-3 **Extending the Limits of Copper Data Cables** 3
P. Kish, NORDX/CDT, Pointe Claire, Quebec, Canada

Lean Enterprise — Walking the Talk 3
P. Murphy, C&M Corporation, Wauregan, CT

MM-4 **Future Developments in Fiberoptic Cable Demand** 4
P. Fay, KMI Corporation, Providence, RI

The World Outlook for Metallic Cables and Fiber Optic Cables 4
J. Barnes, CRU International, London, UK

TRACK 1 – FIBER
SESSION 1: FIBER & CABLE MANUFACTURING/AERIAL CABLES
Tuesday Afternoon, Nov. 13, 1:00 - 5:30 PM • Fiesta 5
Chairperson: ***Dieter S. Nordmann,*** Alcatel Contracting, Hannover, Germany

1-1 **Manufacturing Optimization Using Discrete Event Simulation** 5
T. Goddard, Lucent Technologies, Norcross, GA

1-2 **Nonlinear Modeling of Optical Fiber Drawing with OFC 20** 13
A. Bulsari, AB Nonlinear Solutions Oy, Turku, Finland; *A. Konkarikoski, J. Lahtinen,* Nextrom Oy, Vantaa, Finland

1-3 **Computer-Aided Analysis of Optical Fiber Drawing and Coating: Shape Evolution, Tension-Draw Ratio and Non-Isothermal Coating Effects** 19
J. A. Kulkarni, E. W. Grald, S. Chippada, Fluent Inc., Evanston, IL

1-4 **Study of Cooling Tubes for Fiber Draw using CFD** 28
D. Tschumperle, J.-F. Bourhis, S. Dubois, A. Leon, Alcatel, Conflans-Sainte-Honorine, France

1-5 **Numerical Analysis to Predict Internal Temperatures in Central Core Fiber Optic Cables during Manufacture** 34
L. M. Bocanegra, N. E. Hardwick, III, Lucent Technologies, Norcross, GA

1-6 **Specifying Technical Requirements for Fiber Optic Cables to be Installed on Existing Overhead Transmission Lines** 43
O. I. Bodganova, K. B. Kouftine, OPTEN Limited, Moscow, Russia

1-7 **WITHDRAWN**

1-8 **Novel ADSS Cable Design Technique for a Reduced Weight and Reduced Cable Diameter** 49
M. V. Giacaglia, Lucent Technologies Brazil, Sao Paulo, Brazil

1-9 **Lighting Strike Tests for Mechanically Stressed OPGW Cables** 53
O. I. Bodganova, I. P. Kuzhekin, L. V. Levitova, OPTEN Limited, Moscow, Russia

TRACK 1 – FIBER
SESSION 2: SPLICING & INTERCONNECTION
Tuesday Afternoon, Nov. 13, 1:00 - 5:30 PM • Fiesta 6
Chairperson: ***Bernard J. Cross, II,*** Southwestern Bell Telephone Company, Dallas, TX

2-1 **New Automatic Fusion Time Control System for Core Detection Fusion Splicers Significantly Improves Splice Quality** 56
R. Menegozzi, G. Ruegenberg, Corning Cable Systems, Munich, Germany

2-2 **Investigation of Mass Fusion Splicing between Different Types of Fibers** 61
M. Miura, M. Nakano, Lucent Technologies Yazaki Ltd., Gotemba-city, Japan

2-3 **Development of a New Factory Fusion Splicer** 68
K. Takahashi, S. Yaguchi, N. Kawanishi, T. Ohtani, Fujikura Ltd., Chiba, Japan

Table of Contents

2-4 **Stresses at an Optical-Fiber/Connector-Ferrule Interface**.. 77
J. F. Malluck, W. W. King, B. G. LeFevre, Lucent Technologies, Norcross, GA

2-5 **Analysis of Fiber Breaks in Multimode Connectors**..... 84
O. S. Gebizlioglu, M. R. Özgür, D. Unkel, Telcordia Technologies, Inc., Morristown, NJ

2-6 **Large-Scale Optical Fiber Wiring for 128x128 PLC Switch System with Fiber Physical Contact Connectors and Optical Fiber Circuits**..... 93
Y. Abe, M. Kobayashi, M. Hirayama, R. Nagase, NTT Corporation, Ibaraki-ken, Japan

2-7 **Newly Developed Optical Fiber Distribution System and Cable Management in Central Office** 98
M. Tachikura, K. Mine, H. Izumita, S. Uruno, M. Nakamura, NTT Corporation, Ibaraki, Japan

2-8 **WITHDRAWN**

TRACK 2 – MANUFACTURING PROCESSING & MATERIALS
SESSION 3: THERMOPLASTIC CABLE MATERIALS
Tuesday Afternoon, Nov. 13, 1:00 - 5:30 PM • Yucatan 1-3
Chairperson: ***James R. Leech,*** The Dow Chemical Company, Somerset, NJ

3-1 **The Chemistry of Sulfur Bridged Antioxidants for the Stabilization of Polyolefin Compounds for Wire & Cable Applications** 16
R. E. Lee, K. S. Pearson, Great Lakes Chemical Corporation, West Lafayette, IN; *C. Neri*, Great Lakes Technology Italy, Milan, Italy; *R. M. Riva*, Great Lakes Technology Italy, Pedrengo, Italy; *C. Doumen*, Great Lakes Technology Belgium, Herentals, Belgium; *J. W. Kim*, Asian Stabilizers, Kyonggi-do, Korea

3-2 **A Newly Developed Antioxidant Package Whose Performance is Unaffected by the Presence of Copper or Color** 111
N. Dioh, Equistar Chemicals LP, Cincinnati, OH

3-3 **Next Generation High Performance ADSS Cable Designs with High Modulus Reinforcement Materials**..... 115
S. Neogi, J. Auton, B. G. Risch, D. Rattazzi, Alcatel Fiber Optic Cable R&D, Claremont, NC

3-4 **An Inorganic Optical Fiber Protection System for Premise Cables**..... 122
J. R. Priest, Owens Corning, Granville, OH

3-5 **Development of Optical Fiber Cords with Halogen-Free Jacketing Materials for the Central Offices**..... 129
T. Hayano, O. Kato, Fujikura Ltd., Chiba, Japan; *T. Takemyou*, Nishinippon Electric Wire & Cable Co., Ltd., Oita, *Japan; T. Shimomichi, K. Oohashi, M. Miyamoto*, Fujikura Ltd., Chiba, Japan

3-6 **Creep Behavior of Buffer Tubes** 136
E. Opel, A. Stingl, O. Herrgesell, Corning Cable Systems, Neustadt, Germany

TRACK 3 – COPPER
SESSION 4: COPPER CABLE DESIGN, MODELING & TESTING
Tuesday Afternoon, Nov. 13, 1:00 - 5:30 PM • Monterrey 1-3
Chairperson: ***Hélio J. Durigan,*** Furukawa Industrial S.A., Curitiba, Brazil

4-1 **A Genetic Algorithm Toolkit for Cable Design** 143
H. G. Sasse, B. G. Tunstall, D. E. Coleby, M. M. Al-Asadi, A. P. Duffy, De Montfort University, Leicestershire, UK; *K. G. Hodge, A. J. Willis*, Brand-Rex Limited, Fife, Scotland

4-2 **Mechanical Performance of Different Category 6 Cable Designs** 151
W. Sittinger, Dätwyler Kabel+Systeme GmbH, Neufahrn, Germany; *B. Schmucki, D. Fedier, B. Tresch*, Dätwyler Kabel+Systeme, Altdorf, Switzerland

4-3 **Transmission Parameters of Cascaded Systems** 160
M. M. Al-Asadi, A. P. Duffy, De Montfort University, Leicestershire, UK; *K. G. Hodge, A. J. Willis, D. A. Jackson*, Brand-Rex Limited, Fife, Scotland

4-4 **Testing Between the Specs: Spark Testing for Quality Control** 169
D. Carroll, The Clinton Instrument Company, Clinton, CT

4-5 **New, Versatile Predictive Tool for Structural Return Loss**..... 175
E. Erdas, Beta LaserMike, Dayton, Ohio

TRACK 1 – FIBER
SESSION 5: PREMISES CABLE
Wednesday Afternoon, Nov. 14, 1:00 - 4:30 PM • Fiesta 5
Chairperson: ***Gary Wooddell,*** Equistar Chemicals, LP, Houston, TX

5-1 **New Permanent Access Cable for Economic and Continuously Upgradable LAN** 181
D. Brault, G. le Noane, J.-C. Da Rocha, C. Lagreve, D. Fillatre, Y. Roussel, ACOME, Mortain, France

5-2 **Development of Kink-Resistant Non-Halogen Flame-Retardant Optical Fiber Cord**..... 187
K. Okuno, T. Hosoya, K. Moriuchi, H. Sotome, Sumitomo Electric Industries, Ltd., Yokohama, Japan

5-3 **Manufacturing Method for Flame Retardant Access Cables** 192
A. Harlin, Conex Cables Oy, Vantaa, Finland; *R. Phillips, M. Hirvensalo*, Nextrom Oy, Vantaa, Finland; *M. T. Heino*, NK Cables Ltd., Helsinki, Finland

5-4 **Development of Halogen-Free, Flame-Retardant Miniature Optical Fiber Cord**..... 201
F. Nakamjima, N. Ishii, I. Kobayashi, M. Hara, The Furukawa Electric Co., Ltd., Chiba, Japan; *K. Yamaguchi, H. Ishimaru*, Okano Electric Wire Co., Ltd., Kanagawa, Japan

5-5 **Novel Fire-Resistant Optical Fiber Cables with Simple Structure and Stable Loss Performance**..... 207
M. Kusakari, S. Tanaka, K. Kobayashi, M. Miyamoto, Fujikura Ltd., Chiba, Japan

5-6 **Development of Low Smoke Non-Halogen MiniCord® Cables** 212
J. Wang, K. Chakrabarty, J. T. Chapin, C. G. Wilson, Lucent Technologies Inc., Norcross, GA

Table of Contents

TRACK 1 – FIBER
SESSION 6: FIBER RELIABILITY
Wednesday Afternoon, Nov. 14, 1:00 - 4:30 PM • Yucatan1-3
Chairperson: ***Camille J. Rechel,*** Borden Chemical Incorporated, Cincinnatti, OH

6-1 **Hydrogen Aging Tests for Optical Fibers** 219
M. Shimizu, K. Kuwahara, M. Dazai, Sumitomo Electric Industries, Ltd., Yokohama, Japan

6-2 **Glass Corrosion in Commercial Optical Fibers with Defective Coating** 224
C. E. Tumbill, B. J. Overton, C. Lavallade, Alcatel Cable NA, Claremont, NC

6-3 **Stresses in Optical Fibers: Computation and Impact on Refractive Index** 232
M. Nicolardot, B. Aladenize, Alcatel Cable, Honorine, France; *B. Poumellec,* Université Paris Sud, Cedex, France

6-4 **A Fiber Bragg Grating Measurement System for Monitoring Optical Fiber Strain** 240
S. Capouilliet, J. A. Smith, D. J. Walter, G. S. Glaesemann, G. E. Kohnke, R. D. Irion, Corning Incorporated, Corning, NY

6-5 **Optimization of Loose Tube Optical Cable Manufacture Process Based on Optical Fiber Mechanical Behavior** 249
A. C. da Silva, F. N. Hirose, J. A. M. Neto, J. M. I. Furtado, Furukawa Industrial S. A. Products Eléctricos, Paraná, Brazil

TRACK 2 – MANUFACTURING PROCESSING & MATERIALS
SESSION 7: MATERIALS PROCESSING & TEST MEASUREMENT
Wednesday Afternoon, Nov. 14, 1:00 - 4:30 PM • Fiesta 7-10
Chairperson: ***David B. Kiddoo,*** AlphaGary Corporation, Sparta, NJ

7-1 **The Development of an Improved Reference Cable for the NFPA 262/UL 910 Plenum Fire Test** 253
X. Fang, A. A. Bushelman, Avaya, Inc., Norcross, GA; *P. E. Neveux Jr.,* Lucent Technologies, Norcross, GA; *R. Subramanian,* Avaya, Inc., Norcross, GA; *J. T. Chapin,* Lucent Technologies, Norcross, GA; *P. D. Gandhi,* Underwriters Laboratories, Inc., Northbrook, IL

7-2 **Evaluation of Fiber Coating Stripping Methods by Atomic Force Microscopy of Fiber Surfaces** 257
M. R. Özgür, O. S. Gebizlioglu, Telcordia Technologies, Inc., Morristown, NJ; *C. R. Kurkjian,* Rutgers Univ., Piscataway, NJ

7-3 **Characterization of Coating Systems on Optical Glass Fibers as a Whole by Solid State NMR** 267
V. M. Litvinov, A. A. Dias, DSM Research B.V., Geleen, The Netherlands

7-4 **High-Speed Buffering Process of Compact Loose Tubes for Stranded Cables** 274
M. I. Lahti, Nextrom Oy, Vantaa, Finland; M. T. Heino, J. T. Ravela, NK Cables Ltd., Helsinki, Finland; *P. Lundstrom,* NK Cables Ltd., Oulu, Finland

7-5 **Surface Treatment of Wire and Cable to Improve Adhesion of Overmolded Connectors and Grommets** 280
M. Frey, Champlain Cable Corporation, Colchester, VT

7-6 **In-Line Wall Thickness Measurement for Fiber Optic Applications including Tight Buffer, Loose Tube and Cable Jacketing** 283
S. H. Taylor, Zumbach Electronics Corporation, Mt. Kisco, NY

PANEL
SESSION 8: AEROSPACE/AUTOMOTIVE
Wednesday Afternoon, Nov. 14, 1:00 - 4:30 PM • Fiesta 6
Chairperson: ***M. Edward Fenton,*** Wire & Cable Clubs/Fenton Group, Inc., Wethersfield, CT
Moderators: ***D. Allen,*** DuPont, Wilmington, DE; ***Larry Powell,*** Senior Project Engineer, Delphia Packard Electric, Warren, OH

8-1 **Aerospace Cabling — Aircraft Wiring Aging Effects and Recommendations** 287
K. V. Hollinger, Mitre Coporation, McLean, VA

8-2 **Automotive Cabling — Update on 42 Volt Architecture** 289
N. Traub, SAE Strategic Alliance, Warren, OH

PANEL
SESSION 9: WIRELESS ALTERNATIVES TO WIRED SYSTEMS
Wednesday Afternoon, Nov. 14, 1:00 - 4:30 PM • Monterey 1-3
Chairperson: ***Dr. Howard Wichansky,*** US Army Communications-Electronics Command, Fort Monmouth, NJ

9-1 **Wireless Office and In-Building Solutions-Current and Future** 290
C. Campbell, Cingular Wireless, Atlanta, GA

9-2 **Wireless Mobile Internet: Where It's All Going** 291
M. A. Lapadula, QUALCOMM Incorporated, San Diego, CA

9-3 **Bluetooth Wireless Solutions for Short Range Connectivity** 292
D. Bindbeutel, Trident Systems, Inc., Fairfax, VA

9-4 **Wireless LANs Support Multimedia Applications** 293
L. O. Rodriguez, SRI International, Ft. Monmouth, NJ

SESSION 10: POSTER PAPERS
Wednesday Afternoon, Nov. 14, 4:00 - 6:30 PM • Coronado A-G
Chairpersons: ***James R. Leech,*** The Dow Chemical Company, Somerset, NJ; ***John Kincaid,*** Belden Electronics Division, Richmond, IN; ***Bernard J. Cross, II,*** Southwestern Bell Telephone Company, Dallas, TX

10-1 **Sag-Tension Calculations for Aerial Cable with Linear or Nonlinear Tensile Properties** 297
T. C. Chu, TyCom (US) Inc., Eatontown, NJ

10-2 **Nonlinear Modeling of Secondary Coating from Expensive Experimental Data** 302
A. Bulsari, AB Nonlinear Solutions Oy, Turku, Finland; *M. Lahti,* Nextrom Oy, Vantaa, Finland

10-3 **Weather Ageing of Coloured Polyethylene Jacketing Materials** 306
E. E. R. Persson, PolyOne Sweden AB, Spekeröd, Sweden; *E. J. Cognet,* PolyOne Belgium SA, Assesse, Belgium; *H.-B. Martinsson, H. Larsson,* Borealis AB, Stenungsund, Sweden

10-4 **Shrinkage of Bi- and Unimodal Polyethylene Cable Jacketing Materials — Influence of Molecular Structure and Processing Conditions** 311
M. J. Sandelin, U. W. Gedde, Royal Institute of Technology, Stockholm, Sweden; *H.-B. Martinsson, R. C. Dammert,* Borealis AB, Stenungsund, Sweden

Table of Contents

10-5 **Power Distribution System for Feeding Telecom Objects** .. 316
L. Efraimsson, H. Magnusson, Ericsson Network Technologies AB, Falun, Sweden

10-6 **Analysis of CO Based ADSL Performance Due to Crosstalk from Remote Deployed ADSL Systems** 321
H. Oh, K. Jung, J. Oh, Y. Lee, Korea Telecom Access Network Laboratory, Daejon, Korea

10-7 **Experimental and Calculated Velocity Distributions within a Pressurized Optical Fiber Coating Applicator** 326
S. Ravinutala, G. Finberg, C. Polymeropoulos, Y. Jaluria, G. Elliott, Rutgers Univ., Piscataway, NJ

10-8 **Optical Cable for Multiple Installations with Friction- and Abrasion-Resistant Sheath** 331
Y. Hashimoto, T. Matsuzawa, N. Okada, M. Suematsu, Fujikura Ltd., Chiba, Japan

10-9 **Investigation and Comparison of Various Track Resistant Materials for ADSS Cable** 336
R. Xia, X. Zhong, L. Tang, Chengdu CCS Optical Fiber Cable Co., Ltd., Sichuan, P.R. China

10-10 **A Compact Automated Fiber Cross-Connect Module for a Scalable Optical Cabling System** 341
M. Mizukami, N. Tanaka, K. Sasakura, J. Yamaguchi, K. Kaneko, NTT Corporation, Kanagawa, Japan

10-11 **The AD-Lash System at Overhead Power Lines: The Installation of the AD-Lash System along Railways** .. 346
C. Putz, Corning Cable Systems, Munich, Germany

10-12 **Ribbon Separation Tools & Techniques End and Mid-Span** 351
G. Lochkovic, D. Lockwood, S. Moorjani, J. Richards. S. Torrey, K. Williams, Corning Cable Systems, Hickory, NC

10-13 **WITHDRAWN**

10-14 **Development of Dividing Tool for 4-Fiber Ribbon** 361
K. Ohsono, K. Ohmura, K. Murakami, S. Kikuchi, I. Abe, Hitachi Cable, Ltd., Ibaraki, Japan

10-15 **Correlation of Rheological and Thermal Properties of Waterblocking Gels with Drip Performance** 364
W. P. Cheatle, S. Neogi, J. Auton, B. G. Risch, Alcatel Telecommunications Cable, Claremont, NC

10-16 **Compact Optical Fiber Cable Testing and Maintenance System** 369
A. Ogawa, Y. Hata, H. Yusa, Y. Hishikawa, M. Hamada, H. Maki, Sumitomo Electric Industries, Ltd., Yokohama, Japan

10-17 **Modeling UTP Cabling: Insertion Loss and Bit Errors** 374
J. W. Kincaid, P. Z. Vanderlaan, Belden Electronics Division, Richmond, IN

10-18 **Low-Loss MPO Connectors** 379
M. Tsukamoto, M. Hirao, J. Yamakawa, M. Kamiko, Furukawa Electric Co., Ltd., Chiba, Japan

10-19 **Spectral Flat Attenuators using Co^{2+}-Doped Fiber** 384
K. Nouchi, E. Matsuyama, Y. Morishita, G. Tanimoto, S. Ohneda, Showa Electric Wire & Cable Co., Ltd., Kanagawa, Japan

10-20 **A Field Evaluation of Improved Mechanical Fiber Splice** .. 389
C.-M. Hsiao, H.-j. Chen, T.-C. Chang, H.-P. Hsu, Y.-c. Lin, J. Y. Liu, Chunghwa Telecom Co., Ltd., Taiwan, P.R. China

10-21 **Lay Plate SZ Stranding in Premises Cable Production** 395
J. Nykänen, Nextrom Oy, Vantaa, Finland

10-22 **The Influence of Shotgun Hit Patterns on Damage to Aerial Fiber Optical Cable** 399
K. E. Bow, M. A. Adams, Dow Chemical Company, Midland, MI

10-23 **Time Domain Analysis of Frequency Domain Measurements** 404
M. Lindström, Ericsson Network Technologies AB, Hudiksvall, Sweden

10-24 **The Synergistic Effect of MDH and ATH on Flame Retardation and Smoke Density Suppression** 409
D. H. Park, M. J. Ahn, S. C. Kim, G. J. Lee, LG Cable, Kyungki-do, Korea

TRACK 1 – FIBER
SESSION 11: FIBER OPTIC CABLE DESIGN I
Thursday Morning, Nov. 15, 8:00 AM - 12:00 PM • Coronado H
Chairperson: ***Manuel R. Santana,*** Lucent Technologies, Norcross, GA

11-1 **Crush Investigation of Slotted Core Cables** 415
B. Blazer, A. Stingl, Corning Cable Systems, Hickory, NC

11-2 **Crush and Bending Resistance in Next Generation Cable Designs** 422
L. A. Dixon, P. A. Weimann, R. H. Norris, H. P. Debban, R. D. Small, Lucent Technologies, Norcross, GA

11-3 **Theoretical Analysis about Bending Strain on SZ-slotted Core Cable** 432
M. Yamanaka, N. Okada, A. Yamasaki, M. Miyamoto, Fujikura Ltd., Chiba, Japan

11-4 **Finite Element Analysis — A New Tool for Cable Design** .. 437
S. Das, Structural Solutions, Aiea, Hawaii; *R. H. Knapp,* Structural Solutions, Aiea Hawaii & University of Hawaii at Manoa, Honolulu, Hawaii; *T. A. Shimabukuro,* Structural Solutions, Aiea, Hawaii

11-5 **Influence of Ribbon Stack Twist Laylength and Bending Radius on the Strain Distribution and Attenuation in Optical Fiber Ribbon Cables** 447
N. V. Nechitailo, M. G. Soltis, D. J. Rattazzi, Alcatel Telecommunications Cable, Claremont, NC

11-6 **All Dielectric Optical Cable with Improved Mechanical Resistance** 457
A. Ginocchio, E. Consonni, P. Marelli, Pirelli, Milan, Italy

11-7 **High Density Dry Tube Cable Composing Tightly Stacked Fiber Ribbons** 463
Y. Hashimoto, N. Okada, M. Suematsu, M. Miyamoto, Fujikura Ltd., Chiba, Japan

Table of Contents

TRACK 1 – FIBER
SESSION 12: FIBER PROPERTIES I
Thursday Morning, Nov. 15, 8:00 AM - 12:00 PM • Coronado J
Chairperson: ***John R. Sicotte,*** Corning International K.K., Tokyo, Japan

12-1 **The D-Shaped Optical Fiber as a Platform for Integrated Photonic Devices** 470
M. S. Smith, R. H. Selfridge, G. M. Kraus, Brigham Young University, Provo, Utah

12-2 **Wide Passband WDM (WWDM) Transmission in 1.5 µm Wavelength Region through Optical Fiber Cables installed in Access Networks** 477
H. Nakamura, K. Tsujikawa, Y. Nonoyama, K. Hogari, S. Tetsutani, C. Matsui, F. Yamamoto, T. Sugie, NTT Corporation, Chiba, Japan

12-3 **The Sutdy of Ultra Large Effective Area Fiber & Mating Dispersion Slope Compensating Fiber for Dispersion Flattened Hybrid Optical Fiber DWDM Link** 483
K. Ohsono, K. Kotani, K. Murakami, Y. Bing, T. Yamazaki, H. Shimane, Hitachi Cable, Ltd., Ibaraki, Japan

12-4 **Optical Transmission Characteristics of Optical Fiber Cables and Installed Optical Fiber Cable Networks for WDM Systems** 488
S. Tetsutani, H. Hakozaki, J. Zhou, F. Yamamoto, C. Matsui, K. Hogari, K. Sato, NTT Corporation, Ibaraki, Japan

12-5 **The Influence of Mechanical and Environmental Effects on PMD Coefficient in Loose Tube Optical Cable Design** ... 493
J. Dotto, J. A. M. Neto. L. F. G. Marques, R. F. Cruz, Furukawa Industrial S.A., Paraná, Brazil

12-6 **An Analysis of PMD Variability of Single Slotted Core Cabled Fibers** 499
M. Nakano, M. Miura, Lucent Technologies Yazaki Ltd., Shizuoka, Japan

12-7 **Polarization Mode Dispersion Characteristics of Various High Performance Optical Fibers in Cable** 506
H. Ishikawa, K. Nagayama, N. Akasaka, M. Kaino, M. Shimizu, S. Takaoka, Sumitomo Electric Industries, Ltd., Yokohama, Japan

12-8 **The PMD Prediction for Installed G.652 Cables using Monte Carlo Method** 514
G. Niu, M. Cheng, Yangtze Optical Fibre and Cable Company Ltd., Wuhan, China

TRACK 2 – MANUFACTURING PROCESSING & MATERIALS
SESSION 13: UV FIBER & CABLE MATERIALS
Thursday Morning, Nov. 15, 8:00 AM - 12:00 PM • Yucatan 1-3
Chairperson: ***Dr. Reiner J. Gerdes,*** TransTel Group Incorporated, Norcross, GA

13-1 **Effect of Water Blocking Materials on Moisture Diffusion in Prototype Cable Structures** 518
C. R. Taylor, K. Konstadinidis, R. D. Small, R. Norris, M. R. Santana, R. P. DeFabritis, Lucent Technologies, Norcross, GA

13-2 **Powder Free Super Absorbent Tapes and Yarns for Optical Fibre Cables** 526
M. A. Stradling, BP Global Special Products, Kent, UK; *F. Goene,* Geca-Tapes, Rijen, The Netherlands

13-3 **UV Curve Fiber Optic Buffering Resins** 529
D. Chase, N. Coster, A. Gardiner, K. Unterzuber, E. Murphy, DSM Desotech Inc., Elgin, IL

13-4 **New Generation UV Color Coatings for Optical Fiber** 532
S. Siddiqui, J. R. Szwec, K. Konstadinidis, D. Au, C. R. Taylor, Lucent Technologies, Norcross, GA

13-5 **Improved Curing of UV-Curable Inks for Optical Fibers** ... 540
J. J. Schouten, E. Westfall, DSM Desotech, Elgin, IL

13-6 **Yellowing of Optical Fiber Coatings by Fluorescent Light** 545
H. Sugimoto, Z. Komiya, J. Yoshizawa, T. Ukachi, JSR Corporation, Ibaraki, Japan

13-7 **UV Cure Matrix Resins for Laser Marking of Ribbons** 551
T. Reichert, M. Tilley, E. Murphy, DSM Desotech Inc., Elgin, IL

TRACK 3 – COPPER
SESSION 14: ELECTROMAGNETIC COMPATIBILITY & CROSSTALK
Thursday Morning, Nov. 15, 8:00 AM - 12:00 PM • Monterey 1-3
Chairperson: ***John Kincaid,*** Belden Electronics Division, Richmond, IN

14-1 **EMC Behaviour of Cable Screens** 554
A. R. Coates, A. Gavrilakis, M. M. Al-Asadi, A. P. Duffy, De Montfort University, Leicester, UK; *K. G. Hodge, A. J. Willis,* Brand-Rex Ltd., Fife, Scotland

14-2 **Statistical Analysis of Coaxial Screening Attenuation** 564
C. W. Dole, L. J. Chaote, J. W. Kincaid, Belden Electronics Division, Richmond, IN

14-3 **Crosstalk Coupling between Cable Pairs** 570
M. M. Al-Asadi, A. P. Duffy, De Montfort University, Leicester, UK; *K. G. Hodge, A. J. Willis,* Brand-Rex Ltd., Fife, Scotland

14-4 **Simulation and Measurement of Crosstalk in Twisted Pair Cables** 577
J. Poltz, OptEM Engineering Inc., Calgary, Canada; *D. Gleich, M. Josefsson, M. Lindström,* Ericsson Cables, Hudiksvall, Sweden

14-5 **Noise Tolerance Limits of 1000 Base-T Channels Exposed to Random Noise** 586
J.-H. Walling, Consultant, Quebec, Canada; *M. Bohbot, P. Kish,* Nordx/CDT, Quebec, Canada

TRACK 3 – COPPER
SESSION 15: APPLICATIONS FOR COPPER CABLE TECHNOLOGY
Thursday Morning, Nov. 15, 8:00 AM - 12:00 PM • Coronado K
Chairperson: ***M. Edward Fenton,*** Wire & Cable Clubs/Fenton Group, Inc., Wethersfield, CT

15-1 **The Future of the Copper Cable Access Network** 596
D. L. Waring, Telcordia Technologies, Morristown, NJ; *P. Madon,* Telcordia Technologies, Navesink, NJ

15-2 **From the Physics of Foaming to the Production of High Frequency Cables** 606
T. Reiner, H. Scheid, SIEBE Engineering GmbH, Neustadt/Wied, Germany

15-3 **High Grade Copper/Optical Fibre Hybrid Cable Technology for Investment Safe Broadband Access Networks** 614
P. E. Gregor, H. Büthe, P. E. Zamzow, Nexans Deutschland Industries AG & Co Kg, Moenchngladbach, Germany

Table of Contents

15-4 **Alternate Solutions for Cabling Systems in Both Residential and Business Environments** 621
O. Bouffant, E. Cressan, P. Guillas, H. Le Cozic, P. Mercier, D. Le Bras, Technopole Anticipa, Cedex, France

15-5 **New MDF Terminal Modules for xDSL Application** 629
S. Kim, J. Lee, T. Suh, Korea Telecom, Taejeon, South Korea

TRACK 1 – FIBER
SESSION 16: FIBER OPTIC CABLE DESIGN II
Thursday Afternoon, Nov. 15, 1:00 - 5:00 PM • Coronado H
Chairperson: ***Dr. Peter R. Bark,*** Corning Cable Systems, Hickory, NC

16-1 **Development of an 864-Fiber Ribbon Cable Containing a Novel Ribbon Stack Configuration** 634
J. C. Lail, C. M. Conrad, Corning Cable Systems, Hickory, NC

16-2 **OSP Loose Tube Ribbon Cable — Approaching 2000 Fibers** 643
P. K. Strong, D. S. Hedrick, Corning Cable Systems, Hickory, NC

16-3 **Optimal High Fiber-Counts Microsheath Cables Fitting New Fiber Networks Requirements** 650
P. Jamet, P. Trombert, N. LeCourtier, D. Bernier, M. Delpech, SAGEM Cables Division, Montereau, France

16-4 **Advances in Blown Cable Technology: The Development and Life Cycle Analysis of a High Density Optical Fibre Cable** 658
M. V. Davies, C. J. Esbester, R. Sutehall, Pirelli Cables, South Wales, UK; *P. Barker,* BTexact Technologies, Suffolk, UK; *D. F. Bastin,* BT Wholesale Network Access, Essex, UK

16-5 **Development of High-Density Optical Fiber Cable using Thinner Slotted Rod** 666
M. Hattori, E. Konda, R. Takaoka, D. Iwakura, M. Hara, Furukawa Electric Co., Ltd., Chiba, Japan

16-6 **An Alternate Approach to the Reduction of Cable Weight and Stiffness of High Fiber Count SCR Cables** 672
T. Ottmann, Corning Cable Systems, Hickory, NC

16-7 **Development a Mid-Access Drop Cable with Power Feeder and Ribbon Slotted Core** 680
H. T. Choi, S. C. Park, Y. S. Kim, Y. I. Lee, Taihan Electric Wire Co., Ltd., Kyungki-do, Korea

16-8 **Development of 112-Fiber Optical Cable having Slotted Rod and Stainless Pipes Optimized for Installation into Sewer Pipes** 686
T. Kuwajima, S. Imamura, Y. Suzuki, OCC Corporation, Tochigi, Japan

TRACK 1 – FIBER
SESSION 17: FIBER PROPERTIES II
Thursday Afternoon, Nov. 15, 1:00 - 5:00 PM • Coronado J
Chairperson: ***Xavier Mann,*** Fitel Lucent Technologies, Carrollton, GA

17-1 **Numerical Modeling of Deposition of SiO_2 and GeO_2 in the MCVD Process for the Manufacture of Optical Fiber Preforms** 692
A. Singh, M. Muralidharan, R. O. S. Prasad, A. Dutta, E. W. Grald, Fluent Inc., Lebanon, NH

17-2 **Influences of Profile Variations in PCVD Multimode Fibre on DMD Characteristics of 10 GbE Systems** 698
P. Pleunis, M. Boon, M. van den Heuvel, Draka Comteq, Eindhoven, The Netherlands

17-3 **WITHDRAWN**

17-4 **Validation of Silica Defects Related Attenuation Increase Resistance in S-Band Operation for NZDSF** 703
N. Fujita, S. Hinosihta, T. Sukegawa, T. Yamazaki, O. Kazumasa, K. Kotani, Hitachi Cable, Ltd., Ibaraki, Japan

17-5 **High Performance and High Reliability Dispersion Compensating Fiber Modules using a Novel Packaging Technique** 707
T. Fuji, K. Fukuda, E. Sasaoka, T. Hosoya, Sumitomo Electric Industries, Ltd., Yokohama, Japan

17-6 **Dispersion Managed Fiber Optic Cable** 713
E. Park, S. Park, D. Lee, H. Park, D. Kim, LG Cable, Kumi, Korea; *Y. Chung,* Korea Advanced Institute Science and Technology, Taejon, Korea

17-7 **Attenuation Characterization of a Non Zero Dispersion Shifted Fiber with Negative Dispersion in Slotted Core Cable for Metropolitan Network Applications** 721
D. K. Hall, Corning Cable Systems, Hickory, NC

TRACK 1 – FIBER
SESSION 18: INSTALLATION
Thursday Afternoon, Nov. 15, 1:00 - 5:00 PM • Yucatan 1-3
Chairperson: ***Bernard J. Cross II,*** Southwestern Bell Telephone Company, Dallas, TX

18-1 **Bridging the Last Mile with Fiber Optic Cables in Sewers** 724
J. E. Jeyapalan, Consultant, New Milford, CT

18-2 **New SZ-slotted Core Cable with 4-fiber Ribbons and Single Fibers for Local Network** 732
M. Yamanaka, N. Okada, M. Suematsu, M. Miyamoto, Fujikura Ltd., Chiba, Japan

18-3 **5.5 km Optical Cables Installed in Small Underwater Tubes using Waterflow** 736
W. Griffioen, C. van't Hul, I. Eijpe, W. Greven, F. R. Bakker, Draka Comteq, Gouda, The Netherlands; *B. Wegbrans,* Pirelli Cables, Delft, The Netherlands

18-4 **The Influence of the Optical Cable Surface in Installation by Blowing Method** 742
M. Schneider, M. A. Nunes, R. A. Mazza, Furukawa Industrial S.A., Paraná, Brazil

18-5 **Experience from the Field Installation of Optical Fiber Cables in Metro Gas Pipelines** 747
H.-D. R. Leppert, K. Nothofer, W. Teschner, Alcatel Optical Fiber GmbH, Mönchengladbach, Germany

Table of Contents

TRACK 1 – FIBER
SESSION 19: SUBMARINE CABLES
Thursday Afternoon, Nov. 15, 1:00 - 5:00 PM • Monterey 1-3
Chairperson: ***Nils A. Artöve,*** Telia International Carrier Farsta, Sweden

19-1 **Special Trunk Cable for Deploying Branching Repeaters in Deep Ocean** 753
T. C. Chu, D. Giordano, T. V. Kutt, R. J. Rue, TyCom (US) Inc., Eatontown, NJ; *B. S. Clark,* TyCom (US) Inc., Newington, NH

19-2 **Tight Type Fiber Unit Optical Submarine Cable with DMF to Ultra Long-Haul DWDM Submarine Cable System** 758
K. Yamamoto, J. C. Acquino, O. Nagatomi, R. Kanda, R. Morikawa, OCC Corporation, Kitakyushu, Japan

19-3 **High Count Fibre Submarine Cable Family for Unrepeated Transmission Systems** 764
I. Vintermyr, V. B. Larsen, T. E. Toften, J. Wardeberg, Nexans Norway AS, Oslo, Norway

19-4 **Thermal Modelling Applications in Submarine Cable Development** 770
P. Dupire, Y. Charles, J.-F. Libert, P. Worthington, Alcatel Submarine Networks, Calais, France

19-5 **WITHDRAWN**

19-6 **A Yardstick for the Future Generation of Submarine Unrepeatered Systems** 775
M. Fullenbaum, P. Gaillard, G. Waterworth, Y. Mayolle, P. Le Roux, R. M. Demont, Alcatel Submarine Networks, Cedex, France

TRACK 3 – COPPER
SESSION 20: COPPER MATERIALS & PROCESSING
Thursday Afternoon, Nov. 15, 1:00 - 5:00 PM • Coronado K
Chairperson: ***Hans A. Mayer,*** Engineering Consultant, Melbourne, Australia

20-1 **WITHDRAWN** .....

20-2 **Advanced SZ Stranding Technology for Enhanced Applications** 783
J. Marik, Rosendahl Maschinen GmbH, Pischelsdorf, Austria

20-3 **Increased Scorch Resistance of Medium Voltage Power Cable Insulation by the Use of Liquid Antioxidants** 787
W. A. Voigt, Ciba Specialty Chemicals Inc., Basle, Switzerland

20-4 **Die Lip Build-up in the Filled Low Density Polyethylene Wire and Cable Extrusion** 794
C. D. Lee, Equistar Chemicals, LP, Cincinnati, OH

20-5 **Inverter Surge Resistant Enameled Wire** 799
H. Kikuchi, Hitachi Cable, Ltd., Ibaraki, Japan

20-6 **Benefits of Brominated & Mineral Based Flame Retardants for Wire & Cable** 807
R. Herbiet, D. W. Luther, S. G. Thomas, Jr., Albermarle Corporation, Baton Rouge, LA

AUTHOR INDEX 816

SCHOLARSHIPS

ELMER F. "ACE" GODWIN SCHOLARSHIPS

2000	Stephen Consenza, Cornell University, Freshman — Electrical and Computer Engineering Stephen M. Lopez, The University of North Carolina at Charlotte, Sophomore — Electrical Engineering
1999	Twanaze Mitchell, Auburn University, Freshman — Electrical Engineering Jennifer Gau, University of Pennsylvania, Freshman — Computer Science and Engineering James J. Brown, Georgia Institute of Technology, Sophomore — Computer Engineering
1998	Jothan Bowen, Texas A&M University, Freshman — Digital Communications and Computers John D. Taliaferro, Virginia Tech, Junior — Chemical Engineering
1997	Michael Rich, Georgia Institute of Technology, Freshman — Electrical Engineering Major Billy Oates, Georgia Institute of Technology, Senior — Mechanical Engineering and Math Major Janet Armstrong, Rutgers University, Ph.D. Candidate — Ceramic Engineering Major
1996	Anthony Tindall, Cornell University, Freshman — Mechanical Engineering Major John Belle, North Carolina State University, Sophomore — Electrical Engineering Major
1995	Jason Chang, Princeton University, Freshman — Chemistry Major Fionna Murray, Virginia Tech, Junior — Mechanical Engineering Major
1994	Sara Ransom, Massachusetts Institute of Technology, Freshman — Materials Science Engineering Major Jurron Bradley, Vanderbilt University, Senior — Chemical Engineering Major

CHRISTOPHER KENNETH EOLL MEMORIAL SCHOLARSHIPS

2000	Peter Galeotti, The University of North Carolina at Charlotte, Senior — Computer Science

AWARDS

Year	Outstanding Technical Paper	Outstanding Poster Paper	Best Presentation
2000	H. Paul Debben, Jr., Dr. Luis M. Bocanegra, C. Shawn Davis, Dr. Richard D. Small, Jr., Dr. Peter A. Weimann and Manuel R. Santana – Lucent Technologies - "A New High-Density Central Cable Core Design"	Keiko Shiraishi, Tomotaka Murase and Haruhito Noro - Showa Electric Wire and Cable Company Limited – "Geometric and Mechanical Characteristics of Newly Developed SM-NSP (Single Mode Non-Strippable Primary Coated) Fiber"	Karthik Krishnamurthy - Alcoa Fujikura Limited – "Successful Deployment of ADSS Cables in EHV Environments"
1999	Dr. J. Thomas Chapin and Larry L. Bleich – Lucent Technologies; Dr. Pravin Gandhi and Thomas Ebert – Underwriters Laboratories – "The Development and Performance of a Calibration Cable for the NFPA 262/UL 910 Plenum Cable Fire Test"	Shami S. Sodhi, Allen C. Gregory and Gary E. Grogan – Siecor – "Effect of Temperature, Strain and Installation of PMD in High Fiber Count Ribbon Cables"	Eric R. Logan – Siecor – "The Status and Future of High Fiber Count Cable Designs"
1998	Dr. Bernt-Åke Sultan – Borealis AB; Dr. Thomas Hjertberg and Karin Ericsson – Chalmers University of Technology; and Matti Hirvensalo and Marjo Hänninen – Borealis Polymers Oy – "Novel Halogenfree Flame Retardant Polyolefins Intended for Internal Wiring – Properties and Flame Retardant Mechanism"	Dr. Osman S. Gebizlioglu, Joel D. Mann and C. R. Kurkjian – Bellcore – "The Effect of Preparation Conditions on the Strength of Fusion Splices I: Use of AFM Imaging"	Dr. Priya L. Tabaddor – Lucent Technologies Incorporated – "Mechanics of Delamination Resistance Testing"
1997	Debra A. Simoff, Dr. Mark A. Paczkowski, Dr. Daryl Inniss, Dr. Thomas A. Strasser, J. Renee Pedrazzani, Dr. Rolando P. Espindola, Dr. Robert M. Atkins, Katherine T. Nelson, Valerie J. Kuck, John M. Borick and Jennifer Aspell – Lucent Technologies; and Regina Ragan – California Institute of Technology – "Coatings Having Enhanced UV Transparency for the Fabrication of Optical Fiber Gratings"	Katja Lyytikäinen – Nokia – Maillefer Oy – "Numerical Simulation of Optical Fiber Coating Process"	Dr. Neil R. Haigh – BICC Cables Limited – "Applicability of All – Dielectric Self Supporting Cable Systems to Very High Voltage Overhead Power Lines"
1996	Mitsuru Kamikatano and Matsuhiro Miyamoto – Fujikura Limited; and Osamu Ogawa – Tokyo Electric Power Company – "A Time – Varying Optical Fiber Strain Measurement by Using Brillouin Ring Amplifying System"	Jan Björkman – Telia Network Services; and Dr. Torbjörn Svensson – Telia Research AB – " Aging of Fibres and Ribbon in Water and Filling Compound"'	Dr. Priya L. Tabaddor – Lucent Technologies Incorporated, Bell Laboratories – "An Evaluation of Protective Polymer Coatings for Optical Fiber Applications"'
1995	Jean Luc Lang and Jean-Francois Libert – Alcatel Submarine Network; David I. Curtis and Peter Worthington – STC Submarine Systems Ltd. – "Optical Performance of Submarine Cables in Optically Amplified High Bit Rate Systems"	Richard S. Wagman, Gregory A. Lochkovic and Kevin T. White – Siecor Corporation – "Component Optimization for Slotted Core Cables Using 8 – Fiber Ribbons"	Dr. Dan L. Philen – AT&T Bell Laboratories – "Optical Fiber for Amplified Undersea Systems"
1994	Toshio Kurashima, Kazuo Hogari, Satoshi Matsuhashi, Dr. Tsuneo Horiguchi, Dr. Yahei Koyamada and Yutaka Wakui – NTT Access Network Systems Laboratories; and Hiroshi Hirano – NTT Technical Assistance & Support Center – "Measurement of Distributed Strain in Frozen Cables and Its Potential for Use in Predicting Cable Failure"	Dr. Sverker Forsberg – Swedish University of Agricultural Sciences; and Jan Björkman – Telia AB – "Release of Lead from Lead – Sheathed Telecom Cables in Soil"	Barry J. Keon – Telstra – "The Effects of Optical Fiber Coating and Ink Materials on the Corrosion of the Glass Surface"

Year	Outstanding Technical Paper	Outstanding Poster Paper	Best Presentation
1993	Dr. Yoshinori Namihira and Toshio Kawazawa – KDD R&D Laboratories; and Naoki Norimatsu – KDD Company, Limited – "PMD Reduction of Optical Fiber Cables for Transoceanic Optical Amplifier Submarine Cable Systems"	Willem Griffioen – PTT Research – "Mechanical Lifetime of Optical Fibers"	Timothy S. Dougherty – AT&T Network Cable Systems – "The Temperature of Aerial Plant and Its Effect Upon Foam – Skin Insulation Life" and Wolfgang Wenski – Kabelmetal Electro GmbH – "First Large Scale FITL Installation: Experience From Opal '93"
1992	Nathan E. Hardwick III and Kris Kathiresan – AT&T Bell Laboratories and J. G. Hartley – Georiga Institute of Technology – "Analysis of Fiber Optic Cable Design Conditions in Vicinity of Steam Lines – Ruptured and Pristine"	Svend Hopland and Albert Klykken – Norwegian Telecom – "Installation of Submarine Fiberoptic Cables in Rugged Coastal Terrain"	Peter Latoszynski – Telecom Australia – "Development of Co – Extruded Polyethylene/Polyamide 12 Insect Resistant Telecommunications Cable"
1991	Shigeru Tomita, Michito Matsumoto, Tetsuro Yabuta and Takuya Uenoya – NTT – "Preliminary Research into Ultra High Density and High Count Optical Fiber Cables"	G. Scott Glaesemann – Corning Inc. – "The Effect of Proof Testing on the Minimum Strength of Optical Fiber"	Sue V. Wolfe – STC Submarine Systems – "Structure and High Voltage DC Behaviour of Submarine Cable Mouldings"
1990	Trevor N. Bowmer, Russell J. Miner, Irene M. Plitz, Joseph N. D'Amico and Lal M. Hore – Bellcore – "Thermal Stability Tests for Polyolefin Insulations"	Steve Lischynsky, Helmut Lukas, Robin McIntyre and Grant Pacey – Bell – Northern Research Ltd. – "New Technology for a Single Mode Mechanical Splice"	Harold W. Friesen – AT&T Bell Laboratories – "An Improved Characteristic Impedance Measurement Technique"
1989	Michel Plasse, Lise Desroches and Paul – Andre Guilbert – Northern Telecom Canada Limited – "High Performance Twisted – Pair Cable for LAN Systems"	Werner Bernard and Susan C. Grant – Siecor Corporation – "Fiber Optic Drop Cables in the Subscriber Loop"	Michel de Vecchis – Les Cables de Lyon – "Results on a Large Scale Installation of a Fibre Optic Distribution Network"
1988	Martin C. Light Jr., James A. Moses, Mark A. Sigmon and Christopher A. Story – Siecor Corp. – "Design and Performance of Telecommunication Cable Optimized for Low Fiber Count"	Dr. R. Raman – Contel Laboratories – "Loss at Dissimilar Fiber Splices"	Janice B. Haber – AT&T Laboratories – "Single – Mode Media and Apparatus for Fiber to the Home"
1987	Stephen B. Pierce – Conel Laboratories – "Digital Transmission on Customer Premises Wiring"	William Wood – Bell Communication Research – "Performance Analysis of Optic Fiber Cleavers"	Richard Rossi – General Cable Company – "Cable Sheathing Design and Performance Criteria"

Year	Outstanding Technical Papers	Best Presentations
1986	Simon D. Dadakarides and Bruce B. Lusignam, Stanford University – "Magnetically Loaded Cables"	Dave Fischer, Superior Cable Corp. – "Progress Towards the Development of Lighting Test for Telecommunication Cables" John C. Chamberlain, Siecor Corp. – "Zero Halogen Fire Retardant Fiber Optic Shipboard Cable"
1985	James A. Krabec and John W. Kincaid, Jr., Belden Technical Research Center – "Advances in the Optimization of Multi – Layer Shield Design"	Stephen Hornung, British Telecom Research Laboratories – "Manufacture and Performance of Fibre Units for Installation by The Viscous Drag of Air"
1984	M. Fujise and Y. Iwamoto, KDD Research & Development Laboratories, Tokyo, Japan – "Self-Core-Alignment Arc-Fusion Splicer Based on a Simple Local Monitoring Method"	William E. Dennis, Dow Corning Corporation, Midland, Michigan– "Hydrogen Evolving Tendencies of Cable Fillers and Optical Fiber Coatings"
1983	V. A. Fentress, Raychem Corp. and D. V. Nelson, Stanford University – "Fracture Mechanics Evaluation of the Static Fatigue Life of Optical Fibers in Bending"	J. R. Bury, Standard Telecommunication Laboratories, Ltd., Hailow, England – "Development of Flame Retardant, Low Aggressivity Cables"
1982	R. H. Whiteley, Raychem Ltd. – "A Comprehensive Small Scale Smoke Test"	A. Yoshizawa, The Furukawa Electric Co., Ltd.– "Structure and Characteristics of Cables for Robots"

Year	Outstanding Technical Papers	Best Presentations
1981	C. J. Arroyo, N. J. Cogelia, Bell Laboratories, and B. J. Darsey, Western Electric – "Thermal Behavior of Experimental Plenum Cable Sheaths Determined in a Radiant Heat Chamber"	G. S. Anderson, Belden Corporation – "Installation of Fiber Optic Cable on 457 Meter Tower"
1980	P. Kish and Y. BeBorgne, Northern Telecom Canada Limited, Montreal, Canada – "General Crosstalk Model for Paired Communication Cables"	J. J. Refi, Bell Laboratories – "Mean Power Sum Far – End Crosstalk of PIC Cables as a Function of Average Twist Helix Angle"
1979	S. Masaki, Y. Yamazaki and T. Ideguchi, Nippon Telegraph and Telephone Public Corporation, Japan – "New Aluminum Sheath Cable Used for Electromagnetic Shielding"	I. Wadehra, IBM Corporation – "Performance of Polyvinyl Chloride Communication Cables in Modified Steiner Tunnel Test"
1978	F. Suzuki, S. Sato, A. Mori and Y. Suzuki; Sumitomo Electric Industries, Ltd., Japan – "Microcoaxial Cables Insulated with Highly Expanded Polyethylene By Chemical Blowing Method"	Richard C. Mondello, Bell Labs. – "Design and Manufacture of an Experimental Lightguide Cable for Undersea Transmission Systems"
1977	T. K. McManus, Northern Telecom Canada Ltd. and R. Beveridge, Saskatchewan Telecommunications, Canada – "A New Generation of Filled Core Cable"	William L. Schmacher, AMP Inc. – "Design Considerations for Single Fiber Connector"
1976	N. J. Cogelia, Bell Telephone Laboratories and G. K. Lavoie and J. F. Glahn, US Department of Interior – "Rodent Biting Pressure and Chemical Action and Their Effects on Wire and Cable Sheath"	Michael DeLucia, Naval Ship Research and Development– "Highly Fire – Retardant Navy Shipboard Cable"
1975	T. S. Choo, Dow Chemical U.S.A. – "Corrosion Studies on Shielding Materials for Underground Telephone Cables"	J. E. Wimsey, United States Air Force – "The Bare Base Electrical Systems"
1974	D. Doty, AMP Inc. – "Mass Wire Insulation Displacing Termination of Flat Cable"	G. H. Webster, Bell Laboratories – "Material Savings by Design in Exchange and Trunk Telephone Cable"
1973	Dr. H. Martin, Kabelmetal – "High Power Radio Frequency Coaxial Cables, Their Design and Rating"	R. J. Oakley, Northern Electric Co., Ltd. – "A Study Into Paired Cable Crosstalk"
1972	J. B. Howard, Bell Laboratories – "Stabilization Problems with Low Density Polyethylene Insulations"	S. Kaufman, Bell Laboratories – "Reclamation of Water – Logged Buried PIC Telephone Cable"
1971	R. Lyenger, R. McClean and T. McManus, Bell Northern Research – "An Advanced Multi – Unit Coaxial Cable for Toll PCM Systems"	S. Nordblad, Telefonaktiebolaget L. M. Ericsson – "Multi – Paired Cable of Nonlayer Design for Low Capacitance Unbalance Telecommunications Network" N. Kojima, Nippon Telegraph and Telephone – "New Type Paired Cable for High Speed PCM Transmission"
1970	D. E. Setzer and A. S. Windeler, Bell Laboratories – "A Low Capacitance Cable for the T2 Digital Transmission Line"	Dr. O. Leuchs, Kable and Metalwerke – "A New Self Extinguishing Hydrogen Chloride Binding PVC Jacketing Compound for Cables"
1969	J. P. McCann, R. Sabia and B. Wargotz, Bell Laboratories – "Characterization of Filler and Insulation in Waterproof Cable"	J. D. Kirk, Alberta Government Telephones– "Progress and Pitfalls of Rural Buried Cable"
1968	H. Lubars and J. A. Olszewski, General Cable Corp. – "Analysis of Structural Return Loss in CATV Coaxial Cable"	N. Dean, B.I.C.C.– "The Development of Fully Filled Cables for Distribution Network"

PLENARY SESSION

"The Future of the Cable Industry – A Challenge for the New Century"



Dr. Noritaka Kurauchi
President, International Cablemakers Federation (ICF), Wien, Austria and
Chairman, Sumitomo Electric Industries, Ltd, Osaka, Japan

Dr. Kurauchi was nominated President of International Cable Makers Federation (ICF) this year after Dr. Giuseppe Morchio, former Chairman & CEO of PIRELLI Cavi & Systemi SpA.

The ICF was founded in 1990 as a worldwide platform for the makers of the products within the scope "insulated electric wires and cables, optical fiber cables, and enameled wires." Approximately 70% of the world's manufacturing capability of the products is represented in the ICF by 97 members in 37 countries as of May 2001.

Dr. Kurauchi is currently Chairman of the Board of Sumitomo Electric Industries, LTD. in Japan. He joined Sumitomo Electric in 1958 and worked for R&D and business development of microwave transmission lines for industries, control & communication systems for urban transportation and optical fibers for communication for about thirty years. He stayed at Electrophysics Department of Polytechnic Institute of Brooklyn as a visiting research staff in 1965. From 1984 to 1989 he was stationed in North Carolina, USA, in charge of start-up of operation of optical fiber and cables. In 1991 he was assigned President of Sumitomo Electric and served for eight years.

He was given BE and Dr. Eng. degrees from University of Tokyo in 1958 and 1971 respectively. He is a member of the Institute of Electrical and Electronics Engineers (IEEE) and the Institute of Electronics, Information and Communication Engineers (IEICE) of Japan.

Special Session: Marketing & Management

Chairperson: M. Edward Fenton

Wire & Cable Clubs/Fenton Group, Incorporated, Wethersfield, CT

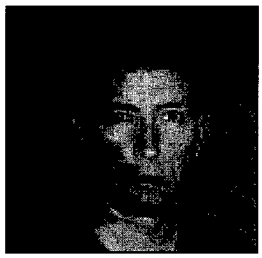
Moderator: William Reichert

Madison Cable/Tyco, Worcester, MA

William Reichert, moderator for this year's Management Session, continues his advisory role for IWCS/Focus after having participated as a session moderator and advisor for Wire & Cable Focus. He also has presented at past IWCS events in 1993 and 1994. Currently Vice President, Operations, for Madison Cable, Worcester, Massachusetts, a part of Tyco Electronics, Reichert has a 17-year career in wire and cable. With Draka USA, he was Vice President, Operations, BIW Cable Systems (1996-1997) and Vice President Operations and later Director, Business Development, Helix HiTemp Cables (1997-2000). With Champlain Cable, he held various management level positions in engineering, marketing, manufacturing, and quality (1989-1996). He started his career at Belden as a quality engineer, later holding manufacturing and quality management positions at plants in Vermont and Louisiana (1985 through 1989).

UL Standard Revisions and Proposals, Tri-National Standards Harmonization Activities and the 2002 Edition of the National Electrical Code





Thomas J. Guida and Austin D. Wetherell

Underwriters Laboratories Incorporated

Melville, NY

+1- 631-271-6200 · austin.d.wetherelljr@us.ul.com & thomas.j.guida@us.ul.com

Abstract

This paper addresses the following wire and cable related topics:

1 - New UL Standards for Safety as well as important proposed and adopted revisions to UL Standards will be discussed.

2 - An overview of the Tri-National standards harmonization activities of Underwriters Laboratories Inc., CSA International and the National Association of Standardization and Certification of the Electrical Sector (ANCE) in Mexico. These projects are being conducted by CANENA Technical Harmonization Subcommittees that are composed of members of industry and standards development organizations from all three countries.

3 – The 2002 National Electrical Code (NEC) will be published in September of 2001. This paper will discuss the impact of any changes on the wire and cable industry.

Keywords: UL Standards, Safety, NEC, ANCE, CSA

Biographies

Thomas J. Guida is a Senior Staff Engineer with Underwriters Laboratories Inc. and has been a member of the Conformity Assessment Services section devoted to wire and cable products for over 28 years.

Austin Wetherell is a Senior Staff Engineer in UL's Conformity Assessment Services Department. He has a B.S.E.E. from Tennessee Tech and an MS from Long Island University.

Austin has been with UL for almost 33 years, most of which dealing with wire and cable products. He is currently UL's alternate member of NEC Code Making Panel 6.

Austin served on the International Wire & Cable Symposium Committee from 1981 to 1984. He has served on various committees and working groups of ASTM, SPE, and IEEE/ICC.

Austin is a member of CSA Subcommittee on C22.2 No. 49 - Flexible Cords and an associate Member of Several CSA Subcommittees, including C22.2 No. 0.3 - Test Methods, and the Technical Committee on Wiring Products. He is a member of the CANENA Technical Harmonization Subcommittee for Trinational Harmonization (USA, Canada, and Mexico) of Flexible Cord Standards.

Special Session: Marketing & Management

Plenum Cable Fire Safety

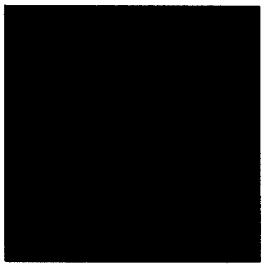
Presentation followed by Panel Discussion

Invited Panel Participants:

Bob Allen, Mohawk/CDT

Dr. J. Thomas Chapin, Lucent Technologies

Global Fire Hazard Assessment



Steven Galan
Underwriters Laboratories Incorporated
Melville, NY
+1- 631-271-6200 · Steven.A.Galan@us.ul.com

Abstract

An update on global fire hazard assessment will be presented. This will include work of IEC 46C/401/NP, a committee formed to investigate fire performance of communications cables installed in buildings.

Keywords: Global, fire hazard, IEC

Biography

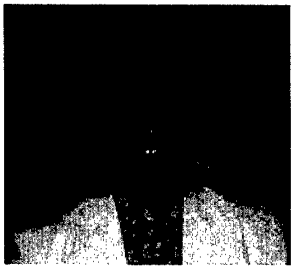
Steve Galan is Underwriters Laboratories Manager for the Wire and Cable Industry. In this capacity, he has corporate responsibilities for UL's global wire and cable initiatives. His primary focus is to provide service to the Wire and Cable Industry where needs and opportunities exist.

Steve has been involved with various activities of UL's TAPCOM (Technical Advisory Panel for Communications Cable). He has also been instrumental in the creation and development of UL's LAN Verification Programs.

Steve has been a member of BICSI, EIA/TIA and represents UL at various NEMA meetings. He currently serves on Code-Making Panel No.6 of the National Electrical Code. He has had articles published in various trade journals, as well as given presentations at trade associations such as EIA/TIA, INTEROP, Wire Association International, ICEA, Interwire, Focus and JEIDA.

Steve joined Underwriters Laboratories in 1977 and holds a BS and MBA from Dowling College.

New Version of the Written Testing Standard NFPA 262/UL 910



Donald O. Nicholson
ITS ETL SEMKO Testing Laboratories
Cortland, NY
+1- 607-758-6375 · dnicholson@itsqs.com

Abstract

A focus on the NFPA RF sub-committee (the players and the roles) that was put together to handle the updates and modifications to the written document. Also the relationship/role between the main NFPA RF NFPA 262 Harmonization Committee and the NFPA 262 Written Standard Update Sub-committee. Nicholson will show the difference in detail and preciseness that now make this fire testing stand one of the most detailed, tested and tried in the industry.

Keywords: NFPA, RF

Biography

Don Nicholson is the General Manager of the Cabling Products Testing Group for ITS ETL SEMKO Testing Laboratories in Cortland, NY. He is a graduate of the State University of New York (SUNY) at Alfred, NY where he majored in Electrical Engineering Technology. He has been employed with ITS ETL SEMKO for over nine years where he has served in such positions as Sales Manager and Industry Manager.

Don participates actively on numerous cabling industry committees such as TIA/EIA, ISO/IEC, NFPA, NEMA, ASTM and ICEA. Prior to working for ITS ETL SEMKO, he worked as a business telephone installer for AT&T and as operations/branch manager for DMC Services. During this period, he oversaw the installation of network infrastructure systems for small to large business. Currently, Don is active with the BICSI Membership and Public Relations Committee where he serves as The Region 1 Representative

Special Session: Marketing & Management

Extending the Limits of Copper Data Cables



Paul Kish
NORDX/CDT, Chairman,
TIA TR-42 Engineering Committee
Pointe Claire, Quebec, Canada
+1-514-822-2345 · paul.kish@nordx.com

Abstract
Delivering the new Category 6 solution. Category 6 cabling is big leap forward from Category 5 / 5e delivering twice the bandwidth while maintaining full backward compatibility and interchangeability with existing applications and hardware.

This presentation will describe the benefits to the end user of better performance cabling as well as the parameters that are important for the wire and cable manufacturer, the designer, and the installer.

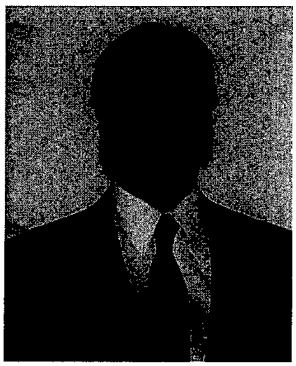
Keywords: Category 6, cabling

Biography
Paul Kish is Director, IBDN Systems and Standards with NORDX/CDT. He is the current chairman of the TIA TR-42 engineering committee responsible for telecommunications cabling standards for commercial and residential installations.

Paul has been active in the development of cabling standards since 1989. In 1991, he initiated the work that led to the publication of additional specifications for Category 3, 4 & 5 cables which, since then, have had a major impact in the cabling industry. Paul Kish is also a member of the BICSI TIM Committee.

Paul Kish graduated with an M.A.Sc. degree in electrical engineering from the University of Waterloo, Ontario, Canada in 1972. He started to work as a cable design engineer with Bell Northern Research in 1972. He joined Northern Electric a year later to work on cable development projects. He has held a number of positions at Northern Telecom including Manager of the Cable Development Laboratories, Manager of Cable Design and Product Manager for IBDN Cabling. Paul Kish is recognised in the industry as an expert in "cable transmission" and for his contribution to the evolution of cabling standards within TIA, CSA, ISO/IEC and IEEE.

Lean Enterprise – Walking the Talk



Paul Murphy
C&M Corporation
Wauregan, CT
+1-860-774-4812
Pmurphy@cmcorporation.com

Abstract
Overview of implementing lean manufacturing principals at a wire and cable company and the lessons learned in the first four years. Relevance to the industry emphasized and the importance as it relates to the difficulties and misconceptions surrounding lean.

Keywords: Lean enterprise

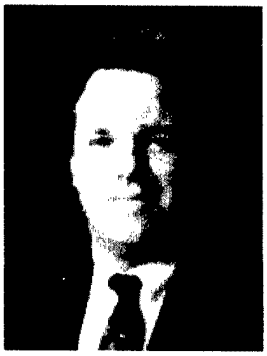
Biography
Paul Murphy is currently the Vice President of Engineering at C&M Corporation a $70M/year manufacturer of bulk cable and cable assemblies for various markets with facilities in Wauregan, CT, Stamford CT, Detroit MI and Hermosillio, Mexico.

Paul has over 13 years of Manufacturing and Engineering experience in the cable assembly Industry, the last 4 with C&M. From the start Paul has been an integral force behind C&M's drive to become a Lean manufacturer. He established C&M's first Lean office and has been responsible for successfully extending the efforts beyond the manufacturing floor and into the enterprise.

Paul holds a Degree in Production Engineering and an MBA in business Management.

Special Session: Marketing & Management

Future Developments in Fiberoptic Cable Demand



Patrick Fay
KMI Corporation
Providence, RI
+1- 401-849-6771 · pfay@kmicorp.com

Abstract
Worldwide demand for cabled fiber has grown dramatically in the last two years. KMI's presentation will look at a forecast of cable demand by application and by region.

Keywords: Fiber

Biography
Patrick Fay directs market research on optical fiber and fiberoptic cable markets. He maintains KMI's FiberGlobeTM database, which includes fiberoptic installation information for more than 50 countries worldwide. He is the author of KMI's "Worldwide Optical Fiber and Fiberoptic Cable Markets," and "Networks of Fiber-based Pan-European Carriers."

Fay also has contributed to many of KMI's custom reports including fiber and cable and gel markets.

Fay has delivered presentations at KMI's Newport Conference on Fiberoptics Markets, KMI's Conference on Europe and the Middle East, and at Lucent Technologies, Norcross, GA. He has appeared on CNBC, and he has been interviewed for articles in Lightwave, Communications Technology, and FibreSystems magazines.

The World Outlook for Metallic Cables and Fiber Optic Cables



Jon Barnes
CRU International
London, United Kingdom
+44-207-903-2116 · jon.barnes@crugroup.com

Abstract
A short overview of recent trends and expected developments in the major regional and world cable markets. This will encompass the outlook in the major product sectors of energy cables, magnet wire, copper telecom cables and fiber optic cables.

Keywords: Metallic cables, copper, magnet

Biography
Jon Barnes (BA Economics) is the Managing Consultant of CRU International's Wire & Cable Research team. In his 10 years with CRU International he has analysed the world-wide insulated wire and cable markets and the copper market.

Jon is the editor of the regular Optical Fiber & Fiber Optic Cable Monitor and the Copper Wirerod, Copper Wire & Cable Monitor. He is also the author of CRU's new Telecoms Cables Service analysing Fibre Optic and Copper Telecom Cable markets.

Manufacturing Optimization Using Discrete Event Simulation

Timothy Goddard
Lucent Technologies Optical Fiber Solutions Inc.
Norcross, Georgia
+1-770-798-5219 · tggoddard@lucent.com

Abstract
Optical cable manufacturing operations consist of tightly coupled, multistage processes. Proper queue management between these processes is critical for the efficient operation of the overall system. While quantitative models have been developed to describe the effect of arrival and service patterns on general systems, they are based on assumptions that cannot usually be applied to manufacturing processes. This problem can be overcome by the use of discrete event simulation (DES). DES methods can be used to determine the optimal queue capacity and prioritization scheme at each stage of a multistage manufacturing process.
In addition, DES can be used to estimate the effect of product mix changes, breakdowns and traffic intensity on the performance of a cable manufacturing operation. "What if" analysis of key system parameters such as line speed and setup time can also be performed in a compressed time frame, showing the best path for overall system improvement.
This paper will start by describing models for optical cable manufacturing operations and their implications for system performance. Next will be a brief review of quantitative models that have been developed in an attempt to predict system performance, along with their limitations. Finally, there will be a more general discussion of DES methods and their applicability to system characterization.

Keywords
Simulation; Queues; Manufacturing; Optimization

1. Introduction
1.1 Optical Fiber Cable Manufacturing
The manufacture of optical fiber cable proceeds in a fairly regular fashion in most cases. First, fibers are color coded to allow explicit identification at each end of a cable. This colored fiber can then be, either singly or in sets, overclad to form buffer tubes in either tight or loose configuration. Alternatively, colored fiber can be formed into flat strip ribbons. A number of these subunit types are then jacketed or sheathed into a cable. Finally, the cable must be tested and packaged to insure customer satisfaction. In a typical cabling facility there will be a number of machines dedicated to each of these operations at every stage of the process.
Two key features of the system described above are fiber batching and operational precedence. In at least one stage, and usually more than one, fibers will be batched together to form a set for a particular cable. All fibers in a specific batch must be present, whether in single or subunit form. At each stage of the manufacturing process described above, all elements of a batch or set must complete processing before the next stage can be completed, leading to a precedence constraint. In some cases, the next operation cannot begin until all units or batches from the previous step are complete.

These two features result in a system that has both parallel and serial attributes, and we will see them become quite important when explicit models are defined later in the work. Obviously it is desirable to optimize this typical fiber optic cabling facility. However, before we proceed, what constitutes "optimal" must be addressed.

1.2 Manufacturing Optimization
At the highest level, optimality equates to minimizing the required investment and ongoing operating expense in plant capacity that must be made to meet a given market demand. This overarching objective is subject to a number of important constraints listed below:

Throughput: The facility must be able to meet production rates required to satisfy customer demand. It is important to note that this demand will usually be both variable as to product mix and uncertain as to volume.

Leadtime: The facility must be able to meet customer demand in a reasonable time frame. A long-running trend, expected to continue, is that customers will desire shorter order/delivery intervals.

WIP and FG: The facility should maintain acceptably low levels of Work in Process (WIP) and Finished Goods (FG) inventories. High levels of WIP usually equate to longer lead times and quality problems. Both WIP and FG inventories represent unrealized ROI and should be avoided.

The challenge for cable manufacturers is to realize the overall objective while meeting these contentious constraints. Ideally, the investment in equipment required to meet a given demand should be minimized. This leads to the goal of maximizing the utilization of installed capacity. On the other hand, as we shall see, this practice can greatly erode lead time performance. Similarly, to insure high throughputs we would like to buffer all operations within a facility from disturbances in the flow of raw materials or product. Therefore general practice might be to hold "safety stock" in front of each operation. Again however, this has a negative impact on both leadtime performance and WIP. The variable nature of product demand and mix over short planning horizons can cause variations in effective system capacity, further complicating the above objective.
To proceed towards an optimal solution we must first develop a model for optical fiber cable manufacturing that addresses these factors along with the variability in both product mix and processing performance inherent in this system. As we shall see, the form of the model will lead to establish analytic techniques for quantification of system performance.

2. Manufacturing Models

2.1 Continuous and Discrete Models

Most manufacturing models tend to fall within two major categories. First, are models that describe what are known as "continuous" processes. A typical continuous process can be represented by a facility such as an oil refinery. Here raw material in the form of crude oil "flows" into the plant, and travels through the various processing steps until it emerges as refined petroleum products. The flow of raw materials at every processing stage is described as a rate, and routings are mostly fixed. The time to complete a quantity of product will be a function of the product flow rate and the dwell time incurred in the system. Often the plant will produce only a few different products, and sometimes only one.

The second type of manufacturing model characterizes discrete lot or piece part production. Here individual items or batches of items move through a "job shop" where they undergo fabrication at numerous processing steps. An example of this type of manufacturing is a contract machine shop producing parts for a number of customers. Such a manufacturer usually produces many different product types or classes, and routings to different process steps can vary greatly by product type or class. The time required to complete a set of products is mostly a function of the batch size and the amount of time spent waiting at the queues in front of the required processing steps.

These two models represent the extremes in terms of how products flow through a manufacturing facility. In fiber optic cable manufacturing we will see below that the best model fits somewhere between.

2.2 Semi-continuous Manufacturing

A model for an optical cable manufacturing facility producing central core ribbon cable is shown in Figure 1 at the right. This model can easily be generalized to other types of optical cable manufacture. In the figure, squares denote processing equipment or servers(s) and circles represent the queues of product waiting to be processed at a server. Lines or arcs represent allowable product routing, and λ and μ represent arrival rate and service rate respectively. This model has elements of both continuous and discrete models described above.

As was described in the first section, cables are produced in discrete batches with product subunits waiting at queues before each processing step. There is also a continuous aspect to this model in that relatively long cables are produced over time on equipment running at a certain speed or rate, and product routings are fixed.

We can characterize this type of manufacturing as "semi-continuous" in that it contains elements of both discrete and continuous manufacturing. As we attempt to optimize a facility characterized by this model it is important that both features be considered. Many times an analysis of system performance is predicated only on the more continuous nature of the system. A good example is the consideration of line speeds and their increase as a method for performance improvement. Although this is an important parameter in the model, failure to include the discrete aspects of the system can result in sub-optimal or even infeasible solutions.

Fiber-optic Cable Manufacturing Model

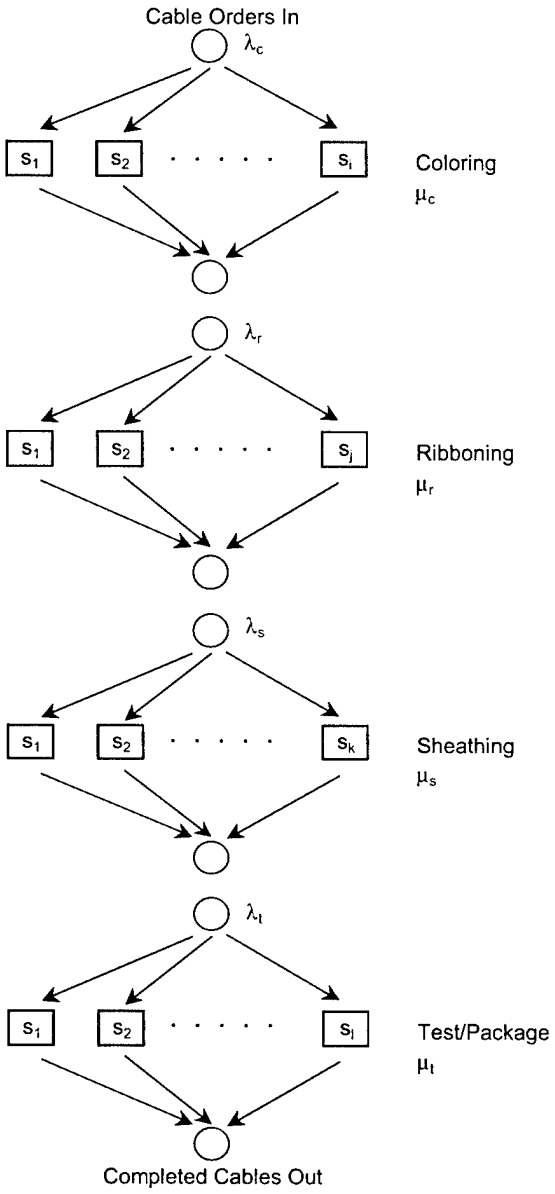


Figure 1. A model for the Manufacture of Ribbon Cable

2.3 Model Specifics

The general model described above can be expanded to include many of the features described in the first section specific to optical cable production. These are listed below along with a brief definition and discussion.

Parallel Servers: At each stage of the production chain there will typically be more than one of any type of machine available to process the order. How these lines are utilized can have a great effect on the overall service rate μ of each process step. For example, coloring lines might be set up to run one of a set of colors only on sequential days, or could be operated so that one of

each line processes a unique color. A batch of ribbons to be produced for a cable could be run all on one line, or split between a number of ribbon lines.

Non-identical Servers: At each processing step individual servers can differ as to speed or product capability. For example, a subset of coloring capacity might be newer generation machines capable of running 25% faster than the older generation. Half of the sheathing lines might be designed to process 12 fiber ribbon cables only, while the other half are capable of producing 24 fiber ribbon cables as well.

Multiple Product Classes: Optical cable manufacturing involves making products of various fiber counts and lengths. This results in a product mix requiring varying processing times and capacity use.

Correlated Processing Times: Since there is a mix of cables fabricated to a certain length at given line speeds, it follows that longer cables can take a greater amount of time to produce at each stage of the process. Hence there is a loose dependence of cable size on processing times at each process step. This assumption will become very problematic to the queuing models that will be discussed later.

Batching: Reiterating the discussion of Section 1, a key feature of optical cable production is the batching together of a number of optical fibers in a sheath. At each stage past the coloring operation fibers will be batched together as sets.

Finite Queues: The waiting area in front of each stage of the process is of finite size, thus blocking in the overall chain can occur if a queue becomes filled to capacity. This problem can be caused not only by a lack of physical space for WIP storage, but also by something as prosaic as a lack of carts in which to store fibers or ribbons.

Queue Discipline: These are the rules that govern in what order jobs are selected from a queue for processing at a server. The most basic rule is FIFO (first-in, first-out), although there are many possible ways to select the next job (first-in, last-out, priority, shortest processing time first). It can even be possible for a job to preempt a job being processed on a server.

Stochastic System: There will be fundamental variability in the operation of an optical cable production facility. In addition to the product mix variability described above, there will be fluctuations in product demand. Machine breakdowns and availability of scarce labor assets will affect the service rate of the different production stages. Finally, defective products will necessitate rework and replacement. Even at small percentages, this can have an enormous effect on the system given the batching discussion above.

The general semi-continuous model described in Section 2.2 along with the specific definitions provided in this section now give us a fairly detailed model for use in optimizing a facility. Having laid out the key features of an optical cable production plant, we will now move towards techniques for quantifying and optimizing the performance of this type of facility.

3. Queuing Theory

A broad class of models similar to the one described in the last section has been the subject of analysis in the field known as queuing theory. These analytic techniques, based on the discrete mathematics of Markov Chains, allows closed-form solutions to an array of service problems based on entities entering a system, waiting in a queue, and then being serviced at a process or processes. Queuing theory has been applied to a broad array of fields, from transportation, communications and service industries, to manufacturing. It allows the performance of a stochastic system to be determined in relation to throughput capability, cycle time and average WIP levels, all parameters we are interested in optimizing in optical cable production.

In this section we will present the fundamentals of the theory, then discuss extensions to more complex systems. Finally we will touch on the limitations of the method relative to the specific model described in Section 2.

3.1 Queuing Fundamentals

3.3.1 Terminology. Queuing models start with a description of an arrival process and a service process. These processes are assumed to be stochastic in nature although we can make inferences about their distribution.

In the system of interest to us, arrivals are seen as jobs that enter the shop to be processed. The rate at which these jobs arrive is defined as λ. Similarly, jobs are processed at a server (a coloring, ribboning or sheathing line) at a rate μ.

An important parameter of a queuing system is ρ, the system traffic intensity, which is defined as the arrival rate divided by the service rate.

$$\rho = \frac{\lambda}{\mu} \tag{1}$$

The average time that a job spends in the shop awaiting and then completing fabrication is defined as W, while the average number of jobs in the shop at any time is defined as L.

Finally, a notation devised by Kendall [1] states that a queuing system can be described completely by a six parameter set, 1/2/3/4/5/6. The 1st parameter denotes the form of the arrival rate to the system. The letter M represents arrival patterns following an exponential distribution. The letter D represents a deterministic arrival rate while the letter G denotes a generally distributed random arrival rate. The 2nd parameter uses an equivalent character set and applies to the service rate of the system. The 3rd parameter is numeric and refers to the number of parallel servers. The 4th parameter describes the queue discipline, while the 5th parameter is numeric, representing the maximum allowable number of customers in the system. The 6th parameter gives the size of the population from which jobs are drawn, usually assumed to be infinite. Putting all these together, an M/M/1/GD/∞/∞ queuing system is one with exponentially distributed arrival and service rates, a single server, general queue discipline, and an infinite capacity for jobs in the system.

3.3.2 Derivation of Little's Law. With definitions in place we now move forward to analytic solutions that have been developed for specific queuing systems.

For the M/M/1/GD/∞/∞ queuing system described above, the steady state probability, π_j, that j (j = 0,1,2...j) jobs exist in the system at any given time is:

$$\pi_j = \rho^j(1-\rho) \quad (0 \le \rho < 1) \tag{2}$$

Note that for a steady state to exist in the system ρ must be less than 1. If not, the increase in jobs in the system will be monotonic with time. Assuming the system is at steady state conditions, the average number of jobs present in the system is:

$$L = \sum_{j=0}^{j=\infty} j\pi_j = \sum_{j=0}^{j=\infty} j\rho^j(1-\rho) = (1-p)\sum_{j=0}^{j=\infty} j\rho^j \tag{3}$$

Defining:

$$S' = \sum_{j=0}^{j=\infty} j\rho^j = \rho + 2\rho^2 + 3\rho^3 + \ldots \tag{4}$$

And noting that:

$$S' - \rho S' = \frac{\rho}{1-\rho} \tag{5}$$

This leads to:

$$S' = \frac{\rho}{(1-\rho)^2} \tag{6}$$

And finally:

$$L = (1-\rho)\frac{\rho}{(1-\rho)^2} = \frac{\rho}{1-\rho} = \frac{\lambda}{\mu-\lambda} \tag{7}$$

Equation (7) shows that the steady state number of jobs for an M/M/1/GD/∞/∞ queuing system can be derived based on knowledge of the arrival and service rate distributions.

Even more useful is a formula first derived by Little [2], which states that the time W a job spends in the system is:

$$L = \lambda W \tag{8}$$

Equations (7) and (8) give us simple yet powerful analytic methods for determining WIP levels and cycletime performance of this queuing system. Additionally, it has been shown that Little's Law is quite robust for any steady state queuing system regardless of arrival rate distributions, the number of servers present, or the queue discipline.

The implications from this analysis are apparent in Figure 2. Here the time a job with μ =1 waits in this queuing system is plotted against traffic intensity. We see that as ρ approaches 1 the time a job spends in the system "blows up" due to a large number of jobs waiting for service. Clearly we want to operate our system at high utilization to minimize capital outlay. The graph in Figure 2 gives us a trade-off curve to determine at what traffic intensity we must operate below to maintain acceptable cycletime performance.

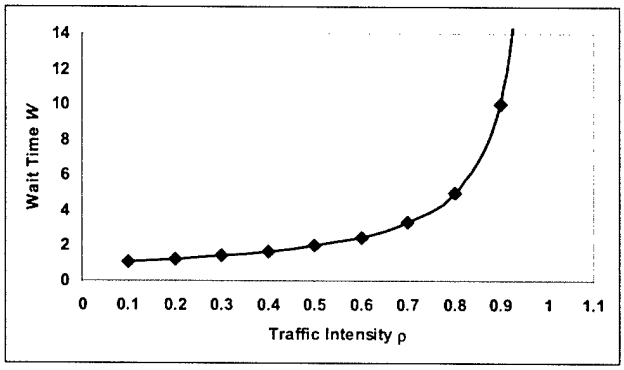


Figure 2. Wait Time vs. Traffic Intensity For an M/M/1/GD/∞/∞ Queuing System

3.2 Extensions of Queuing Theory

A number of researchers have worked to extend the high level results derived in the last section to more specific queuing systems. Among the extensions to the basic theory are derivations based on non-exponential arrival and service rates, finite capacity queues, parallel identical servers and systems where jobs can "balk" or leave the system before completing service. Of these, two are worth noting.

3.2.1 General Service Distributions. When considering the M/G/1/GD/∞/∞ queuing system it is seen that the previous analysis fails given a general service rate distribution. Pollaczek has shown that for such a system with a service time distribution of T where E(T) = $1/\mu$ and V(T) = σ^2 :

$$L_q = \frac{\lambda^2\sigma^2 + \rho^2}{2(1-\rho)} \tag{9}$$

Where L_q is the time a job spends in the queue only, and:

$$L = L_q + \rho \tag{10}$$

Once a value for L has been computed for this case Little's Law can be used as before.

3.2.2 Jacksonian Networks. The second and more important extension to the basic theory is based on a k-stage queuing system. Here a number of servers in series (sometimes known as tandem queues) are considered. In this type of system Jackson [3] showed that if interarrival times for a tandem queuing system are exponential with rate λ, the service times for each stage server(s) are exponential and each stage has infinite queue capacity, then interarrival times to each stage of the queuing system are exponential with rate λ. The validity of this result is dependent on each stage having sufficient capacity so that $\rho < 1$. The usefulness of this result is that each stage can be characterized as an M/M/1/GD/∞/∞ queue, and the cycletime for the overall system can be computed from the sum of the cycletimes of the individual stages. The importance of this lies in the fact that this queuing system more closely resembles that of the optical cable facility shown in Figure 1.

3.3 Limitations of Queuing Theory

The theoretic results presented above, although powerful, falter somewhat when presented with the complexities of real life manufacturing. The results, most notably Little's Law, work well at a high level. They can be applied to our cable manufacturing model and will be reasonably predictive for overall performance.

When we attempt to apply the theory at a detailed level however, it breaks down. Among other problems, this is due mostly to two underlying assumptions in the theory that cannot be applied to cable manufacturing.

First, the queuing analysis presented here assumes that the system being analyzed is stationary. This means that the arrival, and more importantly, the service rates of the system do not change with time or system state. In practically all manufacturing cases we know this not to be true. The service rate of our optical cable manufacturing model is dependent on the product mix, the amount of work waiting to be processed and whether any breakdowns have occurred.

The second assumption for networks of queues is that service rates at each stage are independent. From our cable manufacturing model definitions we see they are correlated.

The net effect is that while queuing theory can predict overall system performance, it cannot show us in detail why the system performs as it does. In the next section we will present a method for accomplishing this.

4. Discrete Event Simulation

An alternate to using theoretical models for characterizing manufacturing system performance is the use of discrete event simulation (DES). In this section we will present an overview of what DES methods are, when they are appropriate to use and how to go about performing a simulation. Then in Section 5 we will present several examples of the use of DES to characterize important optical cable manufacturing parameters.

An excellent definition of a simulation, given by Banks [4], states that; "A simulation is the imitation of the operation of a real-world process or system over time." Such an imitation can be performed manually, or over the past 15 years increasingly by using software on high performance computers. A discrete system is one in which state variables change at discrete, or countable points in time. Hence "discrete event" simulation differs from continuous simulation in that system parameters change at distinct points rather than continuously. This type of simulation makes sense given the form of the model presented in Section 2.

Over the years a number of software products have been developed to make DES projects easier to plan and execute. It must be understood however that even though this methodology can be used to solve problems beyond the reach of theory, it requires the application of time and skill to be successful. The key point to make is that DES can and should be used only when analytic methods prove to be intractable given complex real world systems.

The output of a DES project is a statistical estimate of system performance parameters of interest. Therefore any result generated via DES should be subject to normal goodness criteria for the statistic. As an example, a proper result from a DES would not only be an average cycle time, but should also include upper and lower confidence intervals on this mean.

Given these cautions, DES can be a powerful tool for characterizing the performance of complex manufacturing systems such as our optical cable manufacturing model. Before detailing the procedure for conducting a DES, we will look at some specific advantages and disadvantages of this procedure.

4.1 Advantages and Disadvantages of DES

The advantages of using DES methods for system analysis are many. First, as has been stated, complex models can be studied while relaxing all of the assumptions that limit queuing theory. This is extremely important in that most real world manufacturing processes violate many of the assumptions made in queuing analysis. This is problematic when anything more than general performance characterization is needed. DES, however, is not constrained by these assumptions. Non-exponential service and arrival distributions, non-identical servers or correlated processing times can all be modeled relatively easily. In short, the model does not have to be "assumed away" to obtain tractable solutions.

Second, once a DES model has been constructed, it may be used to answer other questions about the system of interest.

Third, an advantageous feature of creating a virtual model of a manufacturing process is that it can be experimented on without affecting the real process. This can translate to significant cost savings in that procedures that are identified as poor solutions in the virtual system are not attempted on the real system.

Other advantages of DES include a compressed time frame for evaluating long range performance, the ability to model when process data is sketchy or uncertain and the ability to perform "what-if" analysis.

To be objective, there are downsides to using this type of analysis. They include mainly two factors. First, DES is a time consuming endeavor. This is true even when finding solutions to simple problems. Second, it must always be remembered that the virtual model may not accurately reflect the performance of the real system. Although the first concern is to some extent unavoidable, the second is one we can mitigate by using proper modeling procedures. We now turn to a discussion of these.

4.2 Steps for Performing DES

A framework for the successful completion of a DES study is given below in Figure 3. Each step is important and will be discussed separately.

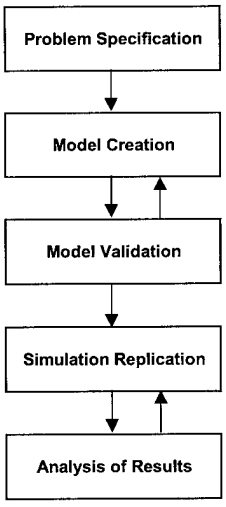


Figure 3. DES Methodology

4.2.1 Problem Specification. This key first step in the DES process should be very specific. If we start with a problem statement such as, "Let's simulate our processes and see where we can improve," we fall prey to the classic mistake of a solution looking for a problem.
The level of detail in the problem statement should include what process is of interest, what processing parameter is being analyzed and what the scope of the solution should be. An example might be, "What effect on throughput does adding additional labor support to a set of ribbon lines have?"
Again, any problem statement must first be evaluated to determine whether analytic methods can be used for a solution. If in fact there are, we save much time and effort.

4.2.2 Model Creation. Once a problem or feature of a system has been identified as a candidate for DES, the next step is to create a model for the simulation. This is usually done using one of a number of available software packages designed specifically for this activity. Current software available contains powerful integrated modeling and runtime environments.
When creating the simulation model it is wise to follow the rule of parsimony. The level of detail in the model should be no more than needed to answer the question at hand. Unneeded complexity will slow the modeling process and can lead to erroneous results. The simplest model will probably also be usable in future simulation projects.
Finally, it is important to gather input on what affects the real system one is modeling from as many domain experts as possible. This will lead to the best imitation of physical system.

4.2.3 Model Validation. This critical modeling step usually receives the least attention, leading to most modeling failures. Once we have developed a predictive DES, we must validate it against the physical system. At its core, the purpose validation is to give the modeler confidence that their model correctly mirrors the performance of a real system.
There are no hard and fast rules for how a validation should proceed, however at least three stages of validation should occur. First inputs that should produce known outputs, usually deterministic in nature, should be applied to the model to check basic logic and calculation. Many basic problems can be first identified here. Second, historic data from the physical system should be applied to the model. The goal is to see that the model mimics what we know actually occurred over time in the real system. Finally the model should be run in parallel with the real system for a period of time to prove agreement with reality.
As one progresses through each of these steps, confidence in the model will increase. If at any point we see that changes need to be made, here is the place to incorporate them.

4.2.4 Simulation Replication. Once we have a DES model in which we have a high degree of confidence, it is time to begin using the model to analyze the system. Remember, as defined, the output of a simulation is a statistical measure of system performance. As simulations are run over time, there is a high degree of correlation between what happens at the beginning of the simulation and the final system state. This can have a large impact on the estimate of the statistic of interest. In different terms, a single run of the simulation is statistically equivalent to a sample size of one.
To develop an estimate of the performance measure of interest with a decent confidence interval, multiple independent replications of the simulation should be run. This is equivalent to obtaining a sample set from which to estimate underlying performance. The exact number of replications needed depends on the tightness of the interval desired and the degree of variability in the system. Note that most commercial simulation software packages are designed to run independent simulation replications.

4.2.5 Analysis of Results. Remembering that simulation results are statistical estimators it is important to apply the usual statistical methods to uncover any significance in the data. Chi-square goodness of fit, t-tests for significance and ANOVA methods must generally be applied to interpret the output of a DES.
On a more fundamental level, one must critically examine all results relative to knowledge of the system being studied. "Do these results make sense based on what we know of our process?" should be an ongoing question. These methods can be powerful in giving a result, but the point is they will always yield some result, whether correct or not.

4.2.6 Other Issues. Looking back at Figure 3, we see two important iteration points. First, if model validation reveals inconsistencies compared to the physical system, stop, and make changes. Proceeding with a model that inaccurately reflects the real system represents wasted time and possibly bad decisions. The second iteration point is the feedback of analysis to further simulation efforts. This can be the most exciting part of the process, as knowledge gleaned from the simulation can be used to explore new ways of optimizing system performance.

5. DES Examples

We will now turn our attention to two examples of the use of discrete event simulation applied to the optical cable model developed in Section 2. In the first example, we will consider the effect of labor availability on the flow of product through this system and it's effect on overall WIP and cycletime. In the second example we will study the effect of service rate distributions in the ribbon fabrication area of our model on WIP and cycletime.
All simulations in this section were done using ARENA [5] simulation modeling software.

5.1 Labor Availability Study

From the model defined in Section 2 we have a plant containing i coloring machines, j ribbon lines, k sheathing lines and l test and packaging stations. For the purposes of this example, let us fix i = j = 12 and k = l = 6. Current practice is to assume an assignment of one operator per line for the coloring and ribboning departments, 3 operators per line for the sheathing department, and 4 operators for the final test and packaging department, for a total of 46 operators. Standard procedure is for the operators to work only at their assigned station. In all cases but sheathing they perform all setup and run-time monitoring. In sheathing the third operator assists with line setup, but is not needed during run-time.
All of these workstations have a rated capacity, but as is most often the case, effective capacity is mainly a function of scarce labor resources. The product demand in this facility is variable, however its distribution is known.
The problem is thus posed: How can we deploy a minimum set of operators such that a given level of demand can be satisfied using the available equipment? Operational considerations that must be addressed include what type of strategy might be used to deploy labor assets. Should operators work alone, or in teams? Should a

dispatch system be used to service lines as jobs need to be loaded? How many operators per line should be deployed to get the best use of the assets?

Other constraints on the system are that WIP levels and overall cycletime remain below a given level.

A simulation was run for this problem based on the methods described in Section 4. The key simulation parameters studied were the overall number of operators used and the strategy for assigning them to machine assets. The proposed operational scheme yielded by the simulation study compared to the original procedure is shown in Table 1 below.

Table 1. Comparison of original and proposed operating procedure

Original Operating Procedure			
Production Area	**Operators per Line**	**Total Operators**	**Average Cycletime**
Coloring	1/1	12	20
Ribbon	1/1	12	45
Sheathing	3/1	18	5
FT&P	4/6	4	10
Overall		46	80
Proposed Operating Procedure			
Production Area	**Operators per Line**	**Total Operators**	**Average Cycletime**
Coloring	3/4	9	22
Ribbon	5/4	15	35
Sheathing	2/1 (+2)	14	6
FT&P	1/1	6	7
Overall		44	70

As we see from the table, the simulation revealed that our labor utilization was out of balance. It was seen that too many labor assets were being used in the coloring and sheathing departments, while ribboning and final test and packaging had too few. In the new scheme, two fewer operators are needed.

Another benefit of this study was to show that by rearrangement of a smaller set of operator resources, we actually reduce the overall average cycletime of the system! By adding more labor assets to the ribbon department, we smoothed the flow of material through the plant by eliminating a bottleneck. Similarly for final test and packaging, having an operator at every available station resulted in every cable that arrived being serviced almost immediately.

5.2 Service Rate Distributions in Ribbon

In the previous example it was seen that the ribbon processing step had a large effect on system cycletime performance. In situations such as this, further study is often warranted to see if other system improvements can be made.

A more detailed model of ribbon production was produced to study the question: What effect does service rate distribution in ribbon production have on cycletime performance during periods of peak demand? Here the system was modeled to include batching, dropouts and machine breakdowns using the operational scheme proposed in the first example.

The result of the simulation revealed that many times, almost complete batches of ribbons sat idle, waiting for the last 1 or 2 ribbons in the batch to be completed. This effectively made the ribbon service time distribution more variable. During peak traffic intensity (> 0.9) the cycletime in ribbon soared as predicted from queuing theory.

Variation of simulation parameters showed that the variability in the time required to complete a batch of ribbons could be greatly reduced by deploying quick response programs for replacements due to drop-outs and designating procedures for keeping batches together by using cellular operating concepts. Given an exponentially distributed arrival rate, what had been a similarly distributed service rate was replaced by a tighter distribution with a standard deviation of around 0.2 for a unit processing time. The net effect on cycletime was quite dramatic and is shown in Figure 4.

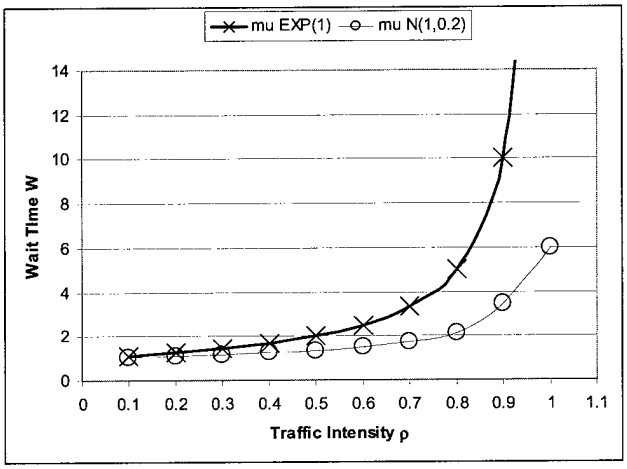


Figure 4: Effect of traffic intensity on cycletime for original and proposed system

Here we see that the original exponentially distributed service rate in ribboning caused great sensitivity to traffic intensity in the shop. The new system, having the more tightly distributed service rate proposed using the simulation results is much less sensitive to peak traffic intensities.

Note that although these results might have been predicted by the queuing theory, we would not have gained insight as to why, or where to address the problem.

6. Conclusions

This work has shown that the characterization of optical cable production must be approached from both a continuous and discrete viewpoint. The optimization of such a model is dependent on properly understanding the multi-stage nature of this system and having a clear understanding of its underlying features.

Methods for quantifying performance include mathematical theory such as queuing models, and more empirical tools such as discrete event simulation. The former can yield quick, closed-form solutions at a high level. The latter is capable of yielding solutions to complex systems often encountered in the real world.

7. References

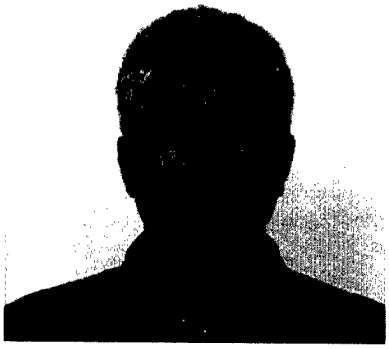
[1] D. Kendall, "Some Problems in the Theory of Queues," *Journal of the Royal Statistical Society*, Series B, 13, p151-185, (1951)

[2] J.D.C. Little, "A Proof of the Queuing Formula L=λW," *Operations Research*, v9, p383, (1961)

[3] J. Jackson, "Networks of Waiting Lines," *Operations Research*, v5, p518-521, (1957)

[4] J. Banks, *Discrete-Event System Simulation*, Prentice-Hall, NJ, p2, (1984)

[5] *ARENA V 3.0*, Rockwell Software, Sewickley, PA, (2001)



Tim Goddard is Technical Manager of the Outside Plant Ribbon Manufacturing Engineering Group at Lucent Technologies Optical Fiber Solutions Inc., Norcross, Georgia. His responsibilities focus on process characterization and optimization in Enhanced AccuRibbon manufacturing. Tim graduated from the Georgia Institute of Technology in 1987 with a BS in Textile Engineering. After 5 years as a process engineer in the industrial textiles industry, he returned to graduate school at Georgia Tech. There he received his MS in Textile Engineering in 1994, and a Ph.D. in 1997.

Nonlinear Modeling of Optical Fiber Drawing with OFC 20

A. Bulsari
AB Nonlinear Solutions Oy, PL 953, 20101 Turku 10, Finland
Tel. +358 2 2154721, E-mail: abulsari @ abo.fi

and

A. Konkarikoski and J. Lahtinen
Nextrom Oy, Ensimmäinen Savu, 01510 Vantaa, Finland
Tel. +358 9 50251, E-mail: Anu.Konkarikoski @ nextrom.com, Jukka.Lahtinen @ nextrom.com

Abstract
Several researchers have modeled various aspects of the fiber drawing process in many different ways. There is also a lot of information on the chemistry of fibers. However, for industrial control purposes, a complete picture of the whole process, taking into account the fiber characteristics, is desirable. In other words, it is not sufficient to accurately control fiber diameter neglecting the strength and attenuation characteristics. Most of the models reported in literature so far are physical models based on first principles with several simplifications and assumptions. Empirical approaches have also been considered in some papers. The empirical models usually resemble reality more closely than the physical models, and such models can be used for control purposes. Figure 1 shows the ideal situation where one or several separate empirical models for several variables would also take into account natural laws such as the conservation of mass, heat and momentum as far as possible.

While dynamic models are useful in the ramp up stages, steady state models are sufficient for the control of fiber characteristics during normal production runs where short term dynamics do not play a significant role. This paper reports only a small subset of the desired set of models as depicted in Figure 1. Two such component models, which are steady state models, and the software incorporating the models are reported in this work. The software has features for the efficient use of the models and for determining optimal process conditions. In the future, the software will also be able to learn these and other component models on its own from production or experimental data.

Keywords
Fiber drawing, nonlinear modeling, neural networks, fiber diameter, fiber characteristics

1. Introduction
The optical fiber draw process is very challenging. Recent development within the fiber industry has changed drastically the requirements for single mode optical fiber draw process, the draw speeds are increased constantly, the general preform diameter has more than doubled during past few years and the tendency is to make even bigger preforms.

Earlier only the fiber draw during a steady state of the process was regarded as quality fiber. Recently the quality ramp, i.e. increasing the draw speed while drawing quality fiber has become very popular. When controlling this kind of process, the short-term dynamics become very important and the modeling becomes very complicated.

New techniques of nonlinear modeling have come up in the last ten to twelve years, and have been successfully used for a variety of purposes, particularly for the prediction and control of material properties of various kinds of materials [1-4].

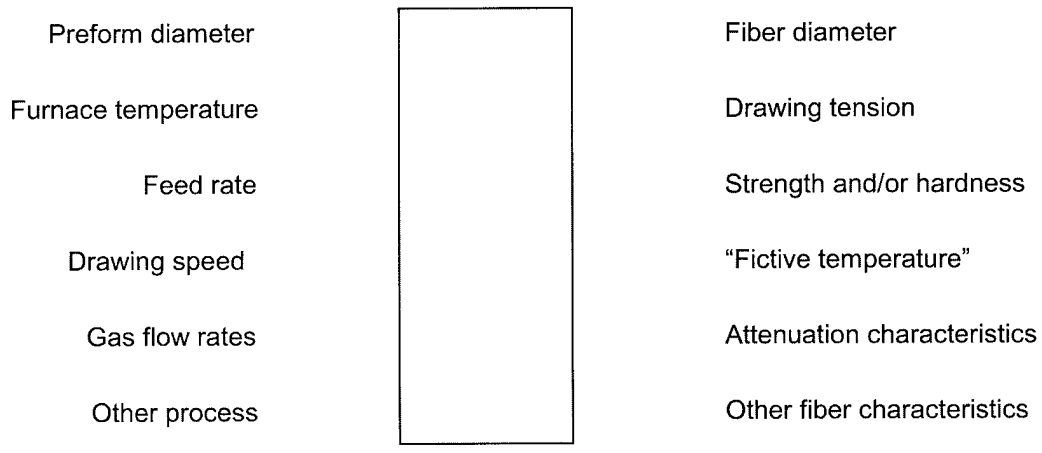


Figure 1. Empirical models of this kind are desirable for industrial control purposes

Several researchers have modeled various aspects of the fiber drawing process in many different ways. Imoto et al. [5] describe the effects of furnace temperature, line speed and fiber diameter on drawing tension.

Even neural network modeling has been attempted in fiber drawing. Shi et al. [6] describe the use of neural networks for identifying furnace decay from patterns of process variables, specifically the normalised tension, the standard deviation of drawing speed, the standard deviation of furnace power, and the frequency of speed fluctuations. Drawing tension is also shown to increase as the furnace decays.

Mulpur and Thompson [7] report the nonlinear aspects of the process dynamics of fiber drawing. Under certain conditions, the dynamics degenerates into a limit cycle, as illustrated by simulation. The simulation model is then used to test model reference control and quasi-nonlinear control, and the authors conclude that the second approach is simpler and effective. They also show the closed loop stability of the scheme.

Kim et al. [8] focus on material properties of fibers through their relations with the fictive temperature. They report valuable observations from experiments carried out under different process conditions. The paper describes even the smaller details of the measurement procedures they followed. The relation of fictive temperature with fiber diameter, drawing tension and aluminium content is given in the paper as a linear equation. Fictive temperature is also quadratically correlated with the dynamic stress corrosion susceptibility.

In this paper we report a small subset of the sets of empirical models for a complete steady-state model. The intention is to continue the work and build a nonlinear dynamic model for Nextrom OFC 20 Fiber Draw Tower.

2. The fiber drawing tower, OFC 20

The fiber drawing tower OFC 20 (Figure 2) is designed for high quality fiber production from a wide range of preforms. The tower modules and the selection of components enable a flexible and upgradable layout for all specific needs.

Produced fiber is of high strength. Its optical and geometrical properties meet all prevailing standards and recommendations.

The optical fiber drawing tower OFC 20 suits a wide range of preform types. Mechanical integrity and solid construction, high quality components such as the advanced drawing furnace and coating system, and an advanced control system NOMOS® result in strong fiber and high yield. The drawing tower also suits the most advanced research applications.

The drawing tower has a frame with a height of up to 30 metres, with alternative component layouts. Several drawing furnace systems are available; several fiber coating systems are possible. The standard measurements include fiber diameters, tensions, flows and temperatures. A process control system with data logging is also included. The experimental and training tower in Vantaa allows experimentation, research and training in realistic atmosphere.

3. Nonlinear modeling

New techniques of nonlinear modeling have come up in the last ten to twelve years, which have made it possible to develop more complicated nonlinear empirical models which take into account the nonlinearities more efficiently. Artificial neural networks are

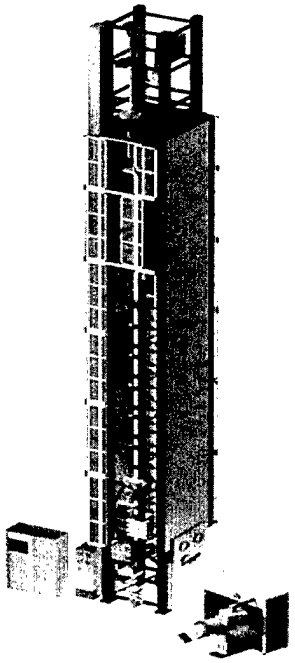


Figure 2. The fiber drawing tower, OFC 20

inspired by the biological neural networks, but have very little in common from our perspective. A large number of different kinds of artificial neural networks are reported in literature, of which about four or five find real world applications. In process engineering, artificial neural networks are more or less synonymous with feed-forward neural networks shown in Figure 3. These networks are said to have universal approximation capability. In other words, they are capable of approximating any continuous, first-order differentiable function to any desired degree of accuracy with a single layer of neurons with sigmoidal activation functions. There is plenty of literature on neural

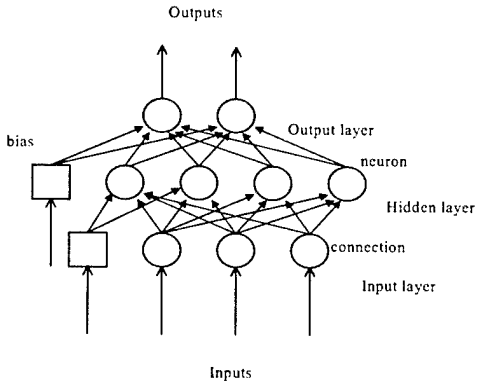


Figure 3. A feed-forward neural network

networks. At least one book on neural networks is designed for chemical engineers [1] which describes several aspects of process modeling and process control.

Artificial neural network models of various configurations were developed and tested for prediction of fiber diameter from limited experimental data. Needless to say, the nonlinear models perform

much better than the linear regression models in terms of accuracy. However, they can also be made more reliable, and thus suitable for process control. This exercise was carried out only for illustration purposes, and the actual models for industrial use cannot be reported for reasons of confidentiality.

Nonlinear models are used for various purposes in process industries. In particular, prediction and control of product properties of various kinds of materials can be performed better with neural networks than with the conventional, linear statistical techniques such as linear regression. Mechanical properties of rolled and drawn steel products such as wire rods [2], paperboard [3], plastics, concrete [4], etc. have been modeled successfully with artificial neural networks. These kinds of models are used for various purposes including process control (determining process variables), for optimising plant operation, for quality control and the reduction of rejects, for estimating variables which are difficult to measure, for product design, for fault detection, etc.

4. Results

Two main components of the relations shown in Figure 1 are fiber diameter and drawing tension. Winding tension is related to drawing tension, and in this case, a nonlinear model of winding tension is reported.

The variables which affect the fiber diameter are shown in Figure 1. The variations in preform diameter and gas flow rates were not considered for the results reported here. That leaves three input variables, furnace temperature, preform feed rate and drawing speed. Figure 4 schematically shows the structure of the nonlinear model for fiber diameter. The same variables determine drawing tension and the winding tension.

The rms errors of prediction of fiber diameter with a nonlinear model were 6.74 μm on the training set and 5.92 μm on the test set. The corresponding rms errors from a linear model were 8.19 μm and 8.87 μm respectively.

The results of the prediction of winding tension with a preliminary model look even better. They would further improve when the process variables of coating are taken into account. The rms errors of prediction of winding tension with a nonlinear model were 2.60 g on the training set and 2.13 g on the test set. The corresponding rms errors of a linear regression model were 5.74 g and 4.67 g respectively. Figure 6 shows the measures of the errors on training set and test set in different colors for linear and nonlinear models.

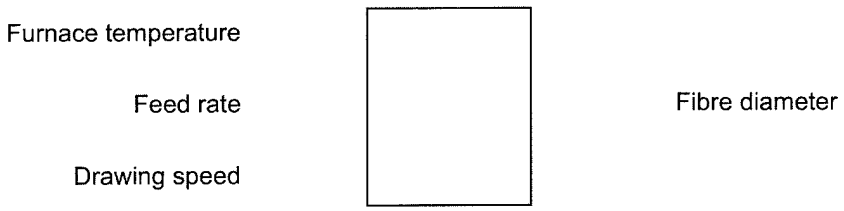


Figure 4. Prediction model for fiber diameter with three inputs

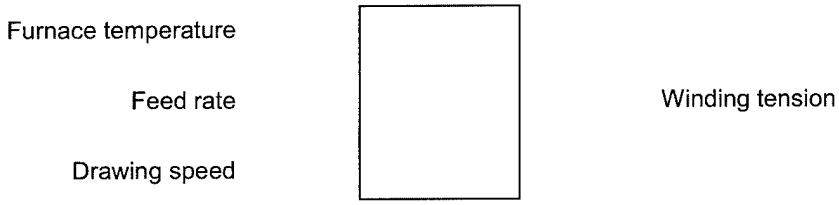


Figure 5. Prediction model for winding tension with the same three inputs

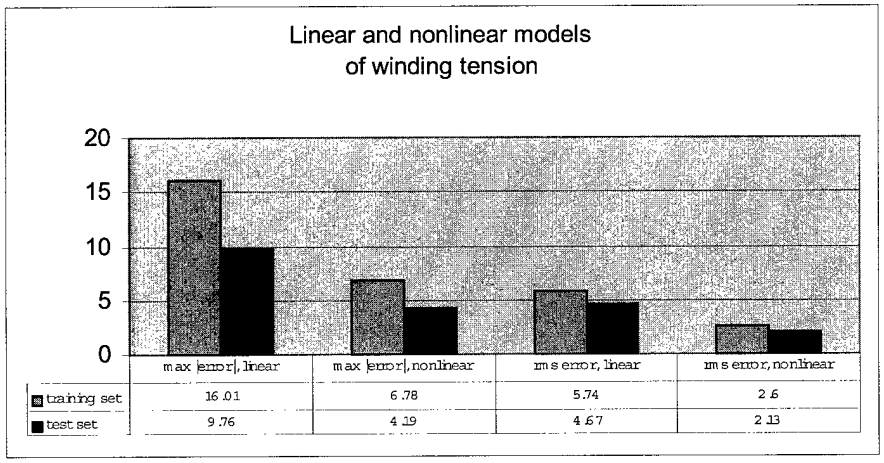


Figure 6. Comparison of linear and nonlinear models for winding tension

Figure 7 shows the results of prediction compared with the measured values of winding tension. The data was taken from an experiment where dynamics was simultaneously being studied. As a result, the actual winding tension varies even when the three input variables are constant, and that is visible in Figure 7.

The model shows an increasing effect on the preform feed rate as well as on the furnace temperature on fiber diameter, which can also be seen from Figure 8. These kinds of curves are also reported by Imoto et al. [5].

5. The software system

The nonlinear models developed for fiber drawing can be complicated for a normal user in the industry. Engineers cannot be expected to be familiar with nonlinear modeling. They cannot be expected to use the raw equations of the models for carrying out predictions or process optimization. However, if the models are available to the engineers in an easily usable form, it could benefit a large number of companies. Therefore, in line with Nextrom's policy of providing a support service, a software system has been developed to be a part of the process knowledge package which will be available in near future not only to Nextrom's customers but also to other companies with optical fiber production.

Today, engineers in industries are overwhelmed by the amount of software that they can use. Almost all of the software require some amount of learning to use, and it can be used efficiently only after some amount of experience with it. We did not want to add to that load, so this software system is designed to be very simple to learn to use. A user without any user training would still be able to use this software conveniently.

The software is highly modular, and each model can be stored in a separate file which the software system reads and uses. The input as well as the output variables can be different for different models. The values of input variables can be fed in manually, or can be picked up from a file. One click of the mouse predicts the output variables. Various features allow the user to see the effects of each input variable on each output variable. Another facility allows the user to determine suitable process conditions in such a way that the output variables stay within desired limits.

The maintenance and recalibration of models is usually necessary. The software also includes algorithms for updating models. This, however, needs some familiarity with nonlinear modeling and requires user training, though the software tries to guide the user with simple messages.

6. Conclusions

This paper illustrates with an example that for industrial control purposes, nonlinear empirical modeling is a practical approach, which does not require assumptions, and is entirely based on observed behaviour of the process and the materials.

Conventional linear statistical techniques of empirical modeling are not suitable because the process is clearly nonlinear. Nonlinear models, perhaps even plain neural network models, or better still, their combination with other models or constraints, can be expected to perform better than the conventional linear techniques, or physical models. The approach has been utilised successfully for a wide range of processes and materials.

The technology has been incorporated in a software system for facile use by OFC producers.

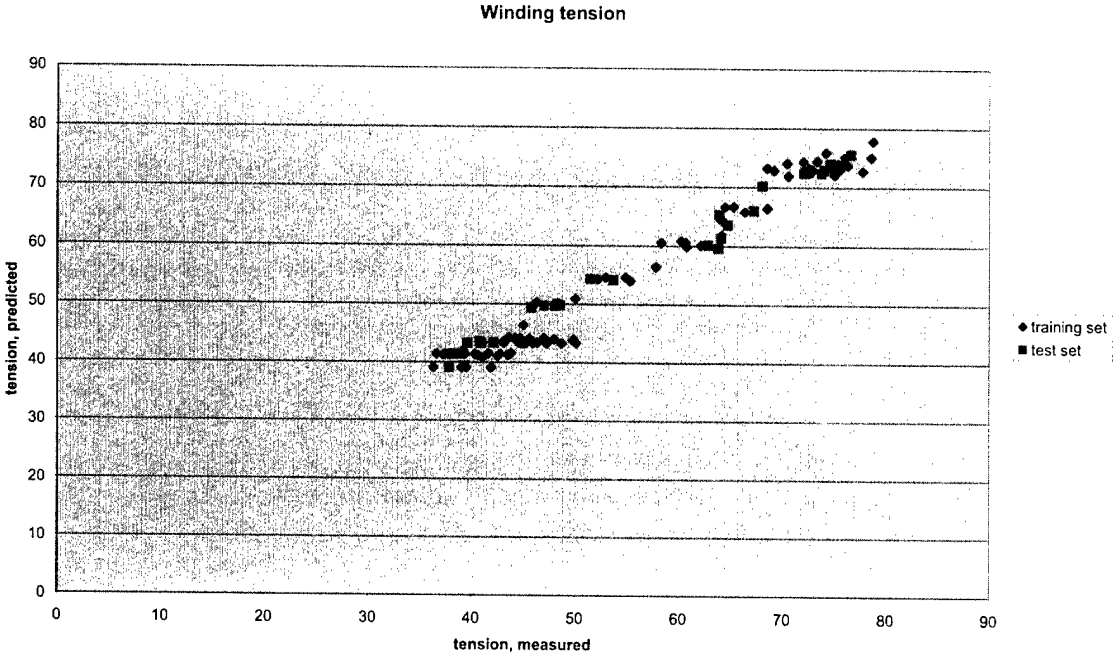


Figure 7. Predicted and measured values of winding tension on training and test sets

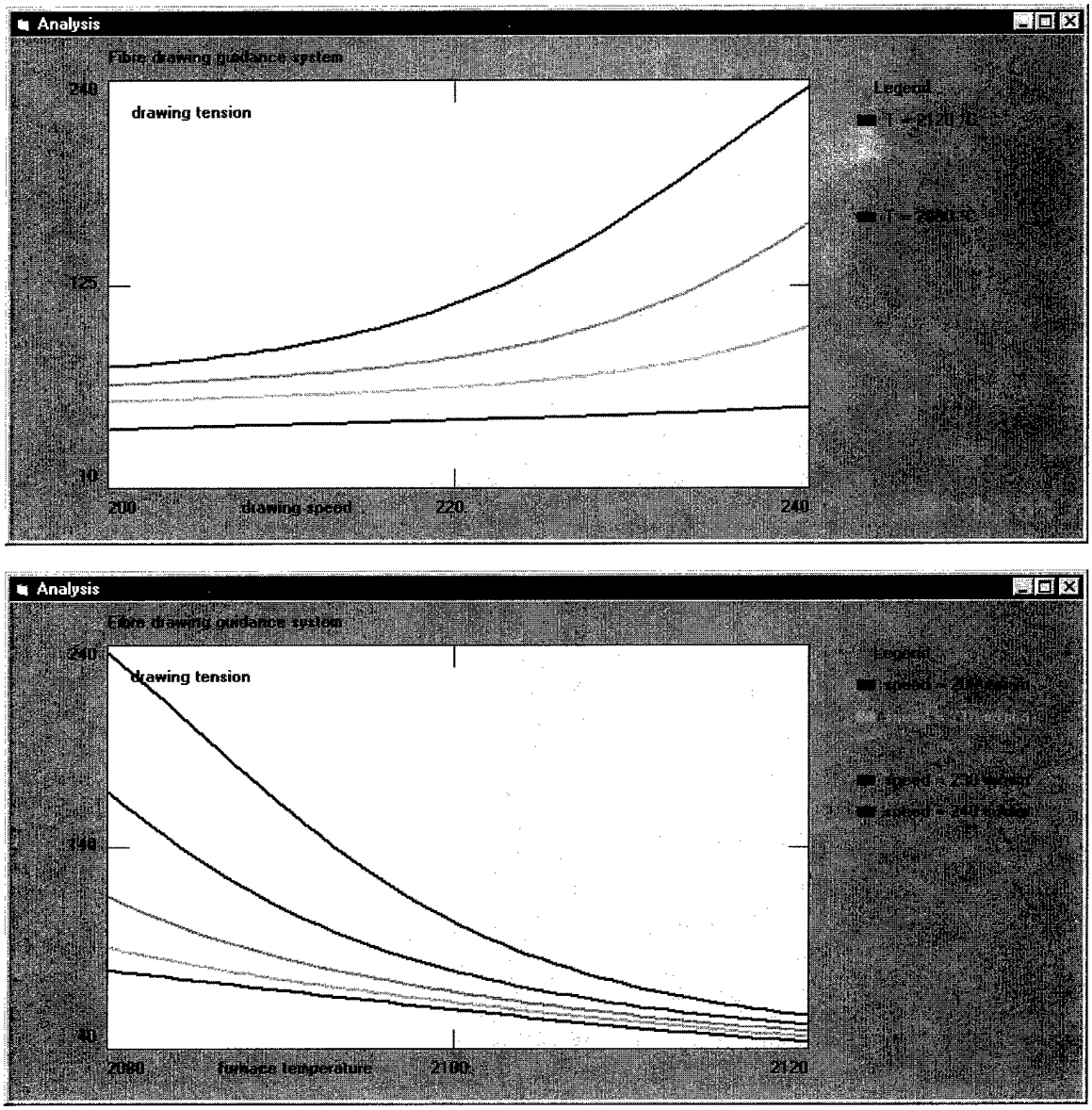


Figure 8. The fiber drawing guidance system also shows the effects of process variables on fiber diameter or other output variables

Acknowledgements

Harri Turunen is gratefully acknowledged for getting this work started. Jouko Berndtson provided the data, and relevant information for this work.

References

[1] A. Bulsari (ed.), *Neural Networks for Chemical Engineers*, Elsevier, Amsterdam, Netherlands, 1995.

[2] A. Bulsari et al., "Neural networks for quality control in the wire rod industry", Wire Industry, Vol. 67 (March 2000) 253-258.

[3] A. Bulsari, "Predicting quality variables of board using neural networks", Internal report NLS/1998/3

[4] A. Bulsari and A. Käppi, "Prediction of compressive strength and compaction degree of concrete", Proceedings of the 1998 EANN Conference, 181-184.

[5] K. Imoto et al., "Optical fiber drawing method with gas flow controlling system", Journal of Lightwave Technology, Vol. 7, No. 1 (January 1989), 115-121.

[6] H. Shi et al., "The Application of Neural Networks to a Condition Monitoring System for the Optical Fiber Drawing Process", Proceedings of ANNIE '96, 915-920.

[7] A. Mulpur and C. Thompson, "Nonlinear Control of Optical Fiber Diameter Variations", IEEE Transactions on Control Systems Technology, Vol. 4, No. 2 (March 1996) 152-162

[8] D.-L. Kim et al., "Relation between the fictive temperature and mechanical strength of optical fibers vs. their drawing conditions", Proceedings of the 49th IWCS, 650-655.

[9] K. Rattan and Y. Jaluria, "Simulation of flow in die and applicator for optical fiber manufacture", IWCS 1999, 700-707

Authors

Mr. Jukka Lahtinen

Nextrom Oy
P.O. Box 44
FIN-01511 Vantaa
FINLAND
Tel. +358-9-50251
jukka.lahtinen @ nextrom.com

Jukka Lahtinen received the degree of B. Sc. in Automation and Mechatronics in 1996. He joined Nextrom in beginning of 1997. Currently he is responsible for Fiber Drawing OFC 20.

Computer-Aided Analysis of Optical Fiber Drawing and Coating: Shape Evolution, Tension-Draw Ratio and Non-Isothermal Coating Effects

Jaydeep A. Kulkarni, Eric W. Grald, and Srinivas Chippada
Fluent Inc.
Evanston, Illinois 60201
+1-847-491-0200 · jak@fluent.com

Abstract
Optical glass fibers are typically formed by heating and drawing under tension a preform of silica glass in a concentric, cylindrical graphite furnace. The primary modes of energy transport are the radiative and the convective heat exchange of the furnace wall with the inert gas inside the heating zone. The first objective of the present work is to simulate the neck-down profile of the fiber as a function of the operating variables such as draw speed and furnace temperature. The governing momentum and energy partial differential equations are solved using the finite element method. The 2-D axi-symmetric, laminar flows of the glass perform/fiber and the inert gas are simulated. The simulation couples heat and momentum transport in the fiber with that in the gas through the boundary conditions on the fiber surface. The diameter of the glass fiber is predicted by employing a deforming mesh free surface approach. Temperature dependence of key material properties of the fiber is taken into account. The variation of the tension in the fiber with changing draw ratios is predicted. The effect of operating variables on the sensitivity of the fiber profile as well as on the flow and temperature fields is studied. Comparisons are made with the results available in the literature.

The second objective of this work is to visualize the flow field within a high pressure coating applicator where a single layer of coating is applied. The 2-D axi-symmetric laminar flow of the coating fluid is simulated. The viscosity of the fluid is assumed to be shear-rate dependent. The effects of heat transfer and viscous heating are also investigated.

The commercial computational fluid dynamics (CFD) program, FIDAP (Fluent Inc., Lebanon, NH), is used to obtain the results presented.

Keywords
Optical fiber; glass fiber; fiber drawing; radiation; FEM; high-speed coating; pressurized coating reservoir; primary coating; biconic die; FIDAP.

1. Introduction
Krishnan and Glicksman [1] were one of the first researchers to perform analytical and experimental studies to study the transport processes in a heated free jet. They used a pre-specified radially lumped temperature distribution and a two-dimensional velocity distribution with an assumed profile to generate the shape of the jet. Kase and Matsuo [2], and Brown [3] performed one-dimensional analyses of the fiber formation from glass flowing through a nozzle rather than from a preform in the furnace. Since these studies were conducted by treating the glass flow as a jet, they have limited applicability in the present day optical fiber production. Paek and Runk [4] experimentally and numerically investigated the fiber drawing process by assuming a heat flux distribution at the furnace and employing a radiation model to determine the radiative heat input at the glass surface. Employing the Rosseland approximation for an optically thick medium, lumped axial velocity and temperature distributions, and a specified heat transfer coefficient at the fiber surface, they studied the thermal transport in the optical fiber drawing process. Myers [5] concentrated specifically on the disturbances that may occur in the fiber drawing process ignoring inertia, gravity, and surface tension. Both Paek and Runk [4] and Myers [5] investigated flow only in the glass region excluding that in the gas. Xiao and Kaminsky [6] were among the first researchers to model the radiative heat transport in the neck-down region without using Rosseland approximation. In their study, they employed the P1 approximation for the radiative transfer in the glass, but their model only considered the upper neck-down region where the diameter is relatively large. In addition, a two-dimensional model was introduced for analyzing the glass and gas flows and radiation. Choudhury, *et al.* [7] have used the zonal method instead of the Rosseland approximation to model radiation and have studied the conjugate problem involving both glass and the gas. In order to solve the resulting transport equations, they used a false transient scheme coupled with an alternating direction implicit (ADI) approach. In this approach, a radial lumping of the axial velocity is employed for the purposes of simplifying the iterative scheme.

The present work extends the applicability of a deforming mesh free surface approach to relatively high draw ratios. Xiao and Kaminsky [6] used this approach to simulate a fiber profile for a draw ratio of 100, whereas in this work results are presented for draw ratios of up to 9216 resulting in the production of fibers of diameter 125 μm starting from 1.2 cm diameter preform. This represents an extension of our earlier work [10] where results with draw ratios of 144 and 576 were presented. The algorithm employed in FIDAP for modeling free surfaces uses an "Arbitrary Lagrangian Eulerian

(ALE)" description where the mesh is moved at a velocity different than that of the material. In this approach, no *ad hoc* assumption/approximation is made while updating the free surface location during the solution phase.

Coating of the optical fiber is performed immediately after drawing to prevent the formation of surface flaws (for example, adhesion of airborne particles), to shield the fiber from surface abrasion and to increase the fiber's tensile strength [11, 12, 13]. Optical fiber coating is usually a "wet" process in which the fiber is drawn through a coating die to apply a thin film of polymeric material. The coating is subsequently cured [11, 12]. A more detailed description of the coating process is available in References 11-14.

It is well known that as the fiber production speed is increased, coating defects can occur such as entrainment of air bubbles between the fiber and the coating layer(s). These bubbles can lead to a variety of problems such as poor signal transmission and inhomogeneous mechanical properties [11]. Gross air entrainment is caused by an instability of the upstream interface between the air and the coating material, which occurs as the fiber speed increases [15].

Fiber production rates (and therefore coating speeds) are now in excess of 20 m/s and will increase in the near future [11, 13]. It is therefore a natural consequence that increasing emphasis has been given to design coating applicators that can be used at high coating speeds without the formation of defects due to instabilities. Pressurized dies are now used in order to achieve higher coating velocities. Operation at high pressure has two main advantages. It helps minimize slip between the coating material and the fiber surface. It also prevents air from entering the coating applicator in the form of bubbles between the fiber and the coating layer(s) [11, 15].

UV-curable acrylates are typically used for optical fiber coating [16.17]. Due to the high shear rates (in excess of 10,000 s^{-1} [16]) experienced by the coating fluid in the die, it is expected that non-Newtonian (shear thinning) effects will be important during the coating process. Because the fiber is coated just after it exits the drawing furnace, it must be adequately cooled first. Filtered gases may be flowed across the fiber to accomplish this. Of course, as the fiber production speed is increased, the distance required to cool the fiber adequately increases. Correlations that relate the fiber temperature with distance, draw speed and cross-flow speed have been developed [18]. The impact of the fiber temperature on the coating process is also important, especially if the material properties of the coating fluid are temperature-sensitive. The temperature of the coating fluid may also be impacted by viscous (shear) heating.

Computational fluid dynamics (CFD) software, which computes the fluid velocities, pressure and temperatures within the coating die and coating bead, can be an effective design tool. The effect of operating conditions, fluid properties and coating die geometry can quickly be evaluated on the computer. By tracking the position of the dynamic contact line, the range of stable operating conditions for a particular die can be determined. In a previous study [14], we used CFD to visualize the flow field within a high-pressure coating applicator where a single layer of coating is applied. That study demonstrated the feasibility of computing the position of the upstream and downstream free surfaces that are formed. Coating speeds between 10 and 20 m/s were studied. The variation of coating thickness with the applied pressure at the die inlet was determined.

In this study, we extend the previous work to include non-Newtonian (shear thinning) viscosity effects and heat transfer. The power-law viscosity model is adopted to represent the variation of the coating viscosity with shear rate. The sensitivity of the coating thickness and dynamic contact line position with power law index, n, is investigated. Finally, the influence of shear heating and heat transfer from the fiber is studied.

The organization of the paper is as follows: the fiber drawing problem is discussed first. The problem description is given in Section 2. Governing equations and boundary conditions are presented in Section 3. The finite element formulation is described briefly in Section 4. Section 5 deals with the solution strategy. Results and discussion are presented in Section 6. The fiber coating problem is then presented. The problem description is given in Section 7. The results and discussion are presented in Section 8. Concluding remarks about both problems are given in Section 9.

2. Problem Description – Fiber Drawing

The schematic of a typical optical fiber drawing process is shown in Figure 1. As the glass preform is drawn vertically through the furnace, its temperature increases as it gains heat due to the radiative transport and, thus, its viscosity decreases. Under the action of tension, the diameter of the fiber decreases as well. An inert gas is introduced either in a concurrent or a countercurrent direction with respect to the motion of the preform. Among the main quantities of interest are the final fiber diameter resulting from the given processing conditions as well as the temperature distribution in the furnace and within the fiber. Conversely, it is also of interest to know the tension in the fiber required to obtain the desired fiber diameter.

As shown in Figure 1, R_{in} is the radius of the preform at the entrance of the furnace and R_{out} is the final radius of the fiber at the exit. The preform enters the furnace with a velocity $u_{in,glass}$ and temperature $T_{in,glass}$. The inert gas enters the furnace at a temperature $T_{in,gas}$ with a velocity $u_{in,gas}$. The furnace is assumed to have a parabolic temperature profile with the maximum temperature, $T_{f,max}$, in the center and minimum temperature, $T_{f,min}$, at the entrance and the exit. R_{out} and $u_{out,glass}$ are the radius and the velocity of the fiber at the exit, respectively. Similarly, $u_{out,gas}$ is the velocity of the inert gas at the exit. The geometrical parameters and the boundary conditions are summarized in Table 1.

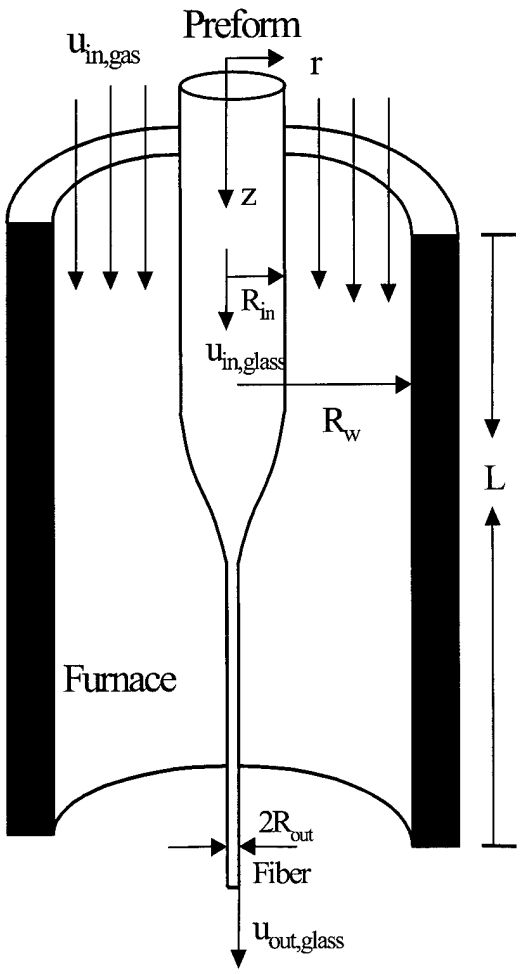


Figure 1. Schematic representation of a typical optical fiber drawing process.

Table 1. Geometric parameters and boundary conditions.

R_w	0.019 m	$T_{in,glass}$	1900 K
R_{in}	0.006 m	$T_{in,gas}$	1900 K
R_{out}	Up to 125 μm	k_{glass}	2.68 W/mK
L	0.0254 m	$C_{P,glass}$	1046 J/KgK
ρ_{glass}	2200 kg/m^3	$C_{P,gas}$	5190 J/KgK
ρ_{gas}	0.022 kg/m^3	ε_w	0.75
$U_{out,glass}$	1,2 and 3 m/s	n	1.5
$U_{in,gas}$	0.1 m/s	$T_{furnace}$	2500, 3000 K
T_{melt}	1900 K	γ	200 /m

3. Theory

3.1 Governing Equations

In the present work, the flow is studied using a 2-D axi-symmetric geometry. Because the Reynolds number is low in both gas and glass, the flow is considered laminar in both the phases. Furthermore, both the phases are treated as Newtonian and incompressible. The stress-divergence form of the momentum equation is used since it results in a natural boundary condition that can be interpreted as the components of the stress acting on the fluid at the boundary. This interpretation is particularly useful for solving free surface problems involving boundary conditions in terms of stress. Thus, the continuity and the momentum equations in either of the phases can be written as:

$$\nabla \cdot \mathbf{u} = 0 \tag{1}$$

$$\rho\left(\frac{\partial \mathbf{u}}{\partial t} + \mathbf{u} \cdot \nabla \mathbf{u}\right) = -\nabla p + \nabla \cdot \left[\mu\left(\nabla \mathbf{u} + \nabla \mathbf{u}^T\right)\right], \tag{2}$$

where ρ and μ are the density and the viscosity of the phase, respectively. Gravity is ignored since its contribution is expected to be small for a thin filament. The viscosity of glass is taken [5] as

$$\mu(T) = 10^7 \exp\left[32\left(\frac{T_{melt}}{T} - 1\right)\right], \tag{3}$$

where T_{melt} is the melting point of glass. The inert gas is assumed to be helium and its viscosity is assumed to be temperature dependent [8,10].

Those material properties that are assumed to be constant are summarized in Table 1. The two phases are considered to be non-participating for the radiative heat transport and hence there is no heat generation in the two phases due to radiation. Since the viscosity of glass is very strongly dependent upon the temperature and as such has strong gradients in the neck-down region, viscous dissipation cannot be neglected. Thus, the energy equation in each phase becomes:

$$\rho C_p\left(\frac{\partial T}{\partial t} + \mathbf{u} \cdot \nabla T\right) = k\nabla^2 T + 2\mu \mathbf{s} : \mathbf{s}, \tag{4}$$

where C_p and k are the specific heat and the conductivity of the phase and **s** is the rate of strain tensor defined as

$$\mathbf{s} = \frac{1}{2}\left(\nabla \mathbf{u} + \nabla \mathbf{u}^T\right). \tag{5}$$

The specific heats of the two phases are assumed to be constant. The Rosseland diffusion approximation is used to model the radiative heat transport within glass. Hence, the effective thermal conductivity of glass can be written as

$$k = k_c + k_r, \tag{6}$$

where k_c is the molecular conductivity and k_r is the radiative conductivity which can be modeled as [4,5]:

$$k_r = \frac{16n^2\sigma T^3}{3\gamma}. \tag{7}$$

Here, n and γ are the refractive index and the absorption coefficient of glass and σ is the Stefan-Boltzmann constant. The

thermal conductivity of helium is assumed to be temperature dependent [8,10].

In order to model the radiative heat transfer between the glass surface and the furnace wall, it is assumed that the fiber surface and the wall furnace are gray and diffuse. A closed enclosure is constructed consisting of four bounding surfaces – the fiber surface, gas inlet, furnace wall and the gas outlet. Each one of these faces is divided into many, constant radiosity zones. In the present study, each zone corresponds with the respective face (i.e., an edge in the axi-symmetric analysis) of a finite element used in the finite element analysis. View factors among all the surface zones are computed by the FACET algorithm [9] employing an area integration technique. It should be noted that, for each zone *i*,

$$\sum_{j=1}^{N} F_{ij} = 1, \tag{8}$$

where F_{ij} is the view factor between zones i and j and N is the total number of zones. The resulting heat exchange between the zone i and the other radiating zones is given by

$$\sum_{j=1}^{N}\left(\frac{\delta_{ij}}{e_j} - F_{ij}\frac{1-e_j}{e_j}\right)\mathbf{q}_r^j = \sum_{j=1}^{N}\left(\delta_{ij} - F_{ij}\right)\sigma T_j^4, \tag{9}$$

where e is the emissivity and $\mathbf{q}_r^j$ is the radiative heat flux. δ_{ij} is the Kronecker delta defined as

$$\delta_{ij} = \begin{cases} 1 \ldots \text{when } i = j \\ 0 \ldots \text{when } i \neq j \end{cases} \tag{10}$$

3.2 Boundary Conditions

The boundary conditions are as follows:

$$u_r = 0, u_z = u_{in,glass}, T = T_{in,glass} \qquad \text{at } z = 0, 0 \le r \le R_{in} \tag{11}$$

$$u_r = 0, u_z = u_{in,gas}, T = T_{in,gas} \qquad \text{at } z = 0, R_{in} < r < R_w \tag{12}$$

$$u_r = u_z = 0, T = T_{furnace} \qquad \text{at } 0 \le z \le L, r = R_w \tag{13}$$

$$\frac{\partial u_z}{\partial r} = 0, u_r = 0, \frac{\partial T}{\partial r} = 0 \qquad \text{at } r = 0, 0 \le z \le L \tag{14}$$

$$u_z = u_{out,glass}, \frac{\partial T}{\partial z} = 0 \qquad \text{at } z = L, 0 \le r \le R_{out} \tag{15}$$

$$\sigma_{zz} = 0, \frac{\partial T}{\partial z} = 0 \qquad \text{at } z = L, R_{out} < r < R_w \tag{16}$$

The following boundary conditions hold at the free surface which is the interface between the fiber and the inert gas:

$$\mathbf{u}\cdot\mathbf{n}\big|_{glass} = \mathbf{u}\cdot\mathbf{n}\big|_{gas}, \mathbf{u}\cdot\mathbf{t}\big|_{glass} = \mathbf{u}\cdot\mathbf{t}\big|_{gas} \tag{17}$$

$$T_{glass} = T_{gas} \tag{18}$$

$$-k\nabla T\cdot\mathbf{n}\big|_{glass} = -k\nabla T\cdot\mathbf{n}\big|_{gas} + \mathbf{q}_r\cdot\mathbf{n} \tag{19}$$

$$\boldsymbol{\sigma}\cdot\mathbf{t}\big|_{glass} = \boldsymbol{\sigma}\cdot\mathbf{t}\big|_{gas} \tag{20}$$

$$\boldsymbol{\sigma}\cdot\mathbf{n}\big|_{glass} - \boldsymbol{\sigma}\cdot\mathbf{n}\big|_{gas} = 2\gamma H\mathbf{n} = \mathbf{0} \ (\because \text{surface tension is neglected}) \tag{21}$$

Surface tension is neglected in the present analysis since its contribution in determining the free surface shape is expected to be small for highly viscous flows.

4. Finite Element Formulation

A structured mesh consisting of linear (4-noded) quadrilateral elements is used for the present analysis. Grading is applied closer to the furnace wall to capture the velocity and thermal gradients and also in the vicinity of the free surface to accurately track its movement.

The governing equations are solved using a commercial CFD code, FIDAP (Fluent Inc., Lebanon, NH), which is based on the Galerkin finite element method. FIDAP has a fully coupled numerical method in which all degrees of freedom are solved simultaneously using the Newton-Raphson method. It also has a segregated method in which each degree of freedom is solved in a sequential manner (including the pressure degree of freedom, which is decoupled from the velocities). The fiber shape is not known *a priori* and is computed using the moving mesh free surface technique. The free surface method is based on the arbitrary Lagrangian-Eulerian (ALE) approach in which the mesh nodes are moved (remeshed) in a manner independent of the material velocity. Several remeshing techniques are available in FIDAP. In the present study, the spines technique, in which the nodes are constrained to move along predefined straight spines, is used.

5. Solution Strategy

The overall problem is severely non-linear and coupled due to the presence of radiation and a free surface, and also due to rapidly changing physical properties. Hence, it is important to provide a good initial guess to ensure stability of the solution. With this objective in mind, the simulation is divided into the following sequential steps: Isothermal run, radiation run and parametric continuation on the draw ratio for steady state free surface runs. The details of these steps can be found in [10]. Parametric continuation alleviated the need to do transient free surface simulations as was done in that work.

6. Results and Discussion

The desired draw ratio is imposed by specifying the inlet velocity, the inlet diameter of the preform and the outlet velocity of the

fiber. Three fiber draw down velocities (exit velocity) of 1, 2 and 3 m/s and two furnace temperatures – 2500 K and 3000 K – were studied. Figure 2 shows the fiber profile for various draw ratios for furnace temperature of 3000 K and draw down velocity of 3 m/s. The initial profile of the fiber was taken to be cosinusoidal.

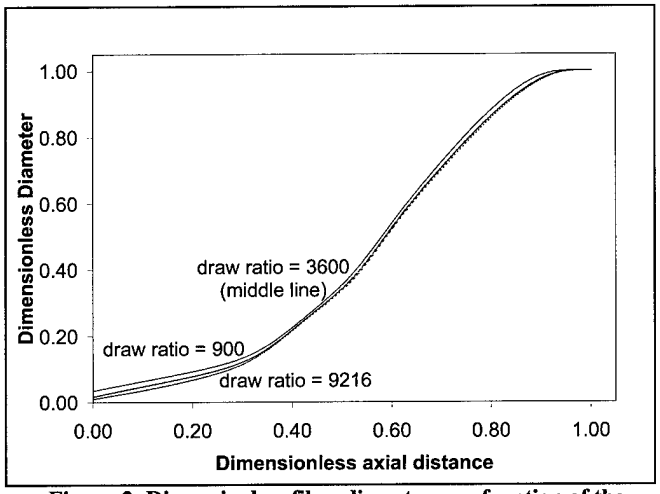


Figure 2. Dimensionless fiber diameter as a function of the dimensionless axial coordinate for various draw ratios. Furnace temperature = 3000 K and draw down velocity = 3 m/s.

The drawing tension as a function of draw ratio is shown in Figures 3 and 4. For a given draw down velocity, the tension decreases as the draw ratio increases, as expected. Also, in the higher draw ratio limit, the tensions are proportional to the draw down velocity. The temperature of the furnace is seen to affect the tension significantly. This is expected since the furnace temperature controls the fiber temperature, which in turn affects the viscosity of the fiber. As shown in our earlier work, the temperature variation in the glass is about 600 K, which leads to variations in the viscosity throughout the fiber of 4 orders of magnitude.

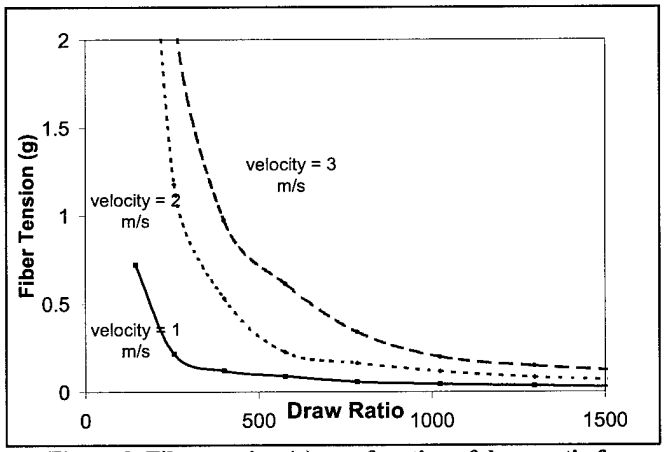


Figure 3. Fiber tension (g) as a function of draw ratio for various draw down velocities. Furnace temperature = 3000 K.

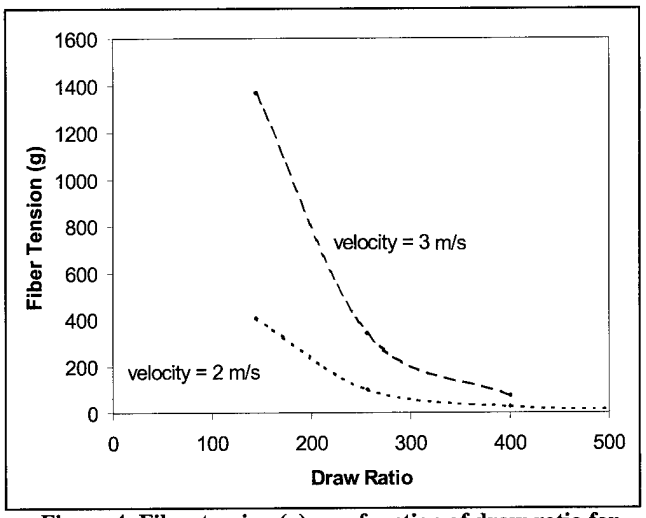


Figure 4. Fiber tension (g) as a function of draw ratio for various draw down velocities. Furnace temperature = 2500 K.

7. Problem Description – Fiber Coating

Figure 5 illustrates the coating die design considered in this study. It corresponds roughly to the biconic die apparatus presented in a recent patent [11]. The dimensions of the die are summarized in Table 2. The geometry is assumed to be axi-symmetric (r is the radial and z is the axial direction). The bulk flow is described by the equations governing the conservation of mass and momentum, as given by Equations 1 and 2. Steady-state conditions are considered – that is, the first term in Equation 2 is dropped. The flow is driven by a normal stress (pressure) at the inlet of the coating reservoir and by the fiber that is moving through the coating die. For a fully developed flow, the normal-stress at the inlet is equal to the pressure, p, of the fluid.

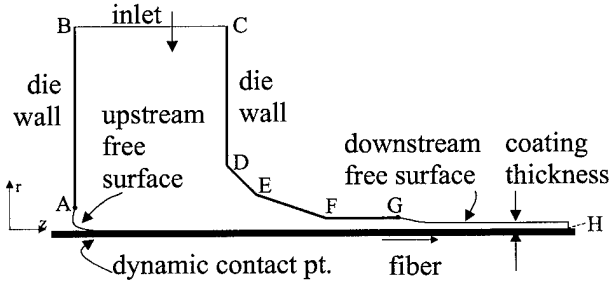


Figure 5. Schematic diagram of biconic optical fiber coating die

The effect of gravity is assumed to be negligible. The fluid viscosity in Equation 2 is replaced by the effective viscosity, η, as described by the power-law model:

$$\eta = \eta_o K D_o^{n-1} \quad \text{if } D < D_o$$
$$\eta = \eta_o K D^{n-1} \quad \text{if } D \geq D_o \qquad (22)$$

Where η_o is the reference viscosity, K is the consistency index, D is the shear rate ($D = \sqrt{0.5(\mathbf{s}:\mathbf{s})}$), D_o is the shear rate cut-off and n is the power law index. Two free surfaces are formed during the coating process, as indicated in Figure 5. At these locations, the

boundary conditions for the normal and tangential stress, as well as the steady-state kinematic condition are applied:

$$\mathbf{n}\cdot\boldsymbol{\sigma} = (2\gamma H - p_a)\mathbf{n} \tag{23}$$

$$\mathbf{u}\cdot\mathbf{n} = 0 \tag{24}$$

where $\boldsymbol{\sigma}$ is the stress tensor, H is the mean curvature of the free surface, γ is the surface tension coefficient and $\mathbf{n}$ is the outward pointing normal vector. The ambient pressure (gauge), p_a, is assumed to be zero (atmospheric). No-slip conditions are applied on the surface of the fiber and on the die walls. At the point of contact between the fiber and the upstream free surface there is need to apply a value for the dynamic contact angle, θ_d. We apply the so-called Navier slip condition near the dynamic contact point in order to remove the non-integrable stress-singularity there. We assume that the upstream free surface is pinned at the top lip of the die entrance (point A) and that the downstream free surface is pinned at the exit of the die (point G). Finally, at the outflow boundary (H), zero normal and tangential stress conditions are imposed.

Table 2. Physical dimensions of coating die

Point	z (μm)	R(μm)
A	0	114.30
B	0	1371.60
C	800	1371.60
D	800	459.57
E	901.70	342.90
F	1988.82	114.30
G	2387.52	114.30
H	3500	63.50

An unstructured mesh consisting of linear (4-noded) quadrilateral elements is used for the coating flow analysis. Care has been taken to construct the grid such that it can capture the deformations that occur as the shape of the upstream free surface is computed.

The FIDAP program described in Section 4 is also used for solving the governing equations for the fiber coating problem. The segregated solver was used for the coating flow solutions. Since the shape and position of both upstream and downstream free surfaces are not known *a priori*, they are computed using the moving mesh free surface technique. Again, as described earlier, the free surface method is based on the arbitrary Lagrangian-Eulerian (ALE) approach in which the mesh nodes are moved (remeshed) in a manner independent of the material velocity. For the coating flow calculations presented here, the mapped technique, in which all nodes in the region below the free surface are remapped (moved) by FIDAP, is used. A typical mesh is shown and further described in [14].

8. Results and Discussion

In our previous work, the problem was solved in dimensionless form. In the current study, however, the problem was formulated and solved using CGS units. For convenience, we adopt SI units here. The baseline solution with constant viscosity was computed first for the following operating conditions:

fiber velocity	20 m/s	
density	1100	kg/m^3
viscosity	1 Pa-s	
surface tension	0.03 N/m	
inlet pressure	59,055.2 N/m^2	

These conditions correspond to the dimensionless inlet pressure of 1.5 from our previous work. A contour plot of the streamlines for this solution is shown in Figure 6. The flow is characterized by a large recirculation in the center of the main body of the die. The flow from the inlet passes on the upstream side of this recirculation, meets the moving fiber and is carried downstream in the resulting film.

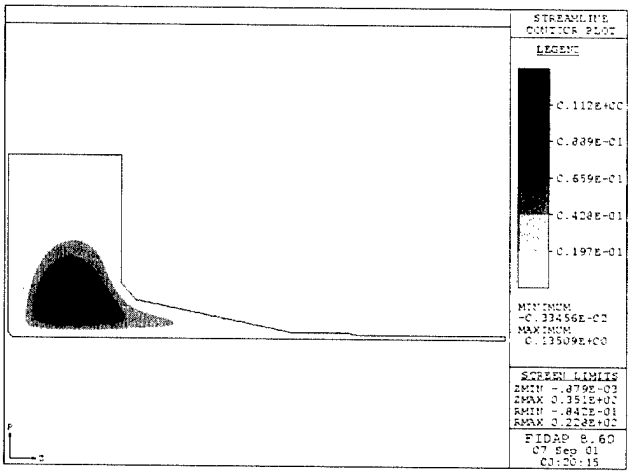


Figure 6. Stream function contours for base case

The velocity vectors near the dynamic contact point are shown in the left image in Figure 7. The flow turns sharply from radially inward (downward in the figure) to the axial direction (to the right in the figure). The dynamic contact line is located slightly downstream (to the right in the figure) of the wall of the die. The formation of the coated film at the exit of the die is shown on the right side of Figure 7.

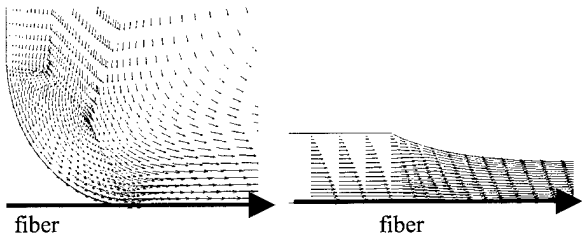


Figure 7. Velocity vectors in the vicinity of the dynamic contact point (left) and the exit from the die (right).

Next, the power law viscosity was introduced. Rather than study any particular coating fluid (since the properties are normally held proprietary), our goal is to characterize the effect of the power law index on the resulting coating flow in terms of: a) coating stability (as dictated by the location of the dynamic contact point), and b) the wet coating thickness. We established the baseline solution for constant viscosity using the following parameters:

η_o	3.3 Pa-s
K	1
n	0.9
D_o	0.1 s^{-1}

The value of η_o was chosen such that the non-Newtonian viscosity in the high shear regions near the fiber is approximately 1 Pa-s (it is actually slightly less than 1).

The plot of the variation of viscosity in the coating die is shown in Figure 8 for n = 0.9 in units of poise. As expected, the viscosity is lowest in the regions of highest shear rate – namely, near the moving fiber and the stationary walls. The viscosity is highest in the regions of low shear near the inlet, in the stagnant area corresponding to the center of the large recirculation, and in the coated film. The viscosity varies between 0.98 and 4.15 Pa-s.

The power law index was then decreased further to 0.85, yielding a more non-Newtonian behavior. The results obtained are summarized in Table 3.

Table 3. Results for different viscosities.

power law index, n	coating thickness	contact line location
1	28.33 μm	42.04 μm
0.9	28.40 μm	50.31 μm
0.85	28.89 μm	30.41 μm

As the power law index is decreased, the wet coating thickness increases slightly. The inlet pressure is kept constant for all runs, but the effective viscosity near the die walls is decreasing as n is decreased. Thus the flow rate through the die increases with smaller n because of the lower frictional losses in the die, causing the coating thickness to increase. The location of the dynamic contact point (DCP) is also listed in Table 3. The DCP location is measured relative to point A on the die wall (see Figure 5). As the power law index is changed from 1 to 0.85, the location of the DCP moves upstream on the fiber from z = 42.04 μm to z = 30.41. This occurs because the viscosity near the fiber is lower, thus the viscous drag is less – the balance of forces at the DCP results in the meniscus being pushed further upstream. The location of the DCP for n = 0.9 is unexpected – as shown in Table 3, the DCP moved *downstream* in this case, counter to the explanation just given.

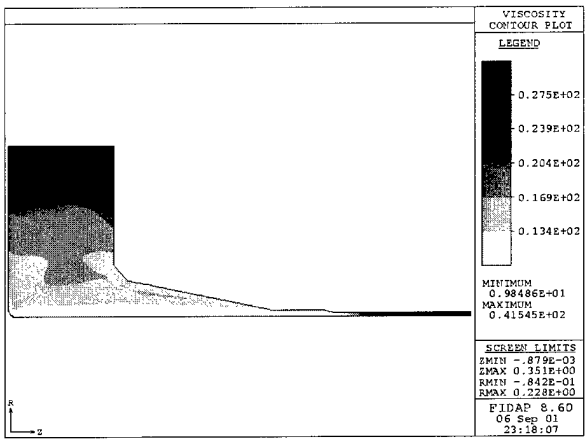


Figure 8. Contours of viscosity for n = 0.9.

The location of the DCP dictates the stability of the coating process. If the DCP moves too far downstream, the coating bead will fail due to air entrainment. If the DCP moves too far upstream, the coating bead can also fail catastrophically. The three coating flow cases described here are thus stable. As shown in our previous work [10], changing the die inlet pressure can effectively control the position of the DCP.

Finally, the effect of heat transfer in the coating die was investigated. Some preliminary results are reported here. To add heat transfer, we solve the energy equation (Equation 4) including the viscous heating term (the last term on the right-hand side). The power law viscosity model was used with a power law index of 0.9. In addition, the following properties were specified:

thermal conductivity	0.195 W/m-K
specific heat	2000 J/kg-K

The temperature of the fluid at the inlet was set to 298 K. The temperature along the fiber was also set to 298 K. The walls of the die were treated as adiabatic. Thus, the only source of thermal energy is through viscous heating. For this case, the solution was calculated on a fixed mesh (i.e., the positions of the free surfaces were not computed). A plot of the temperature contours (in degrees C) is shown in Figure 9. The temperature varies from 298 to 319.2 K – that is, the temperature increase due to viscous heating is about 21.2 K in this case. While there is a slight temperature rise in the main body of the die, most of the temperature increase is experienced in the high shear regions in the narrow section just upstream of the die exit. It should be noted that the viscosity is only a function of shear rate in this calculation. The next logical step in the analysis is to add temperature dependence to the viscosity model, and finally, to

compute the change in coating thickness due to temperature effects (such as the incoming fiber temperature).

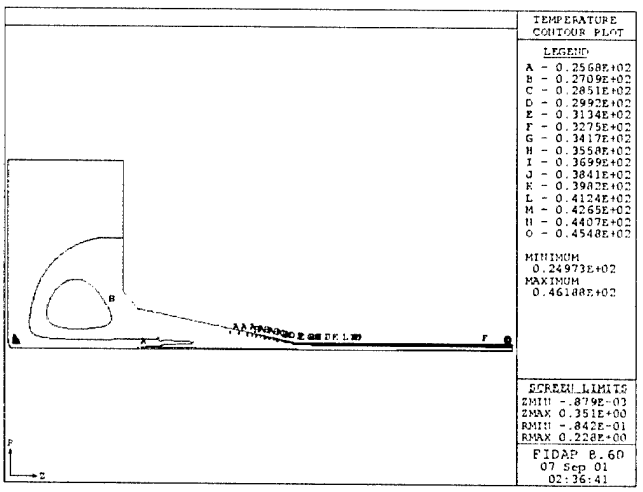


Figure 9. Contours of temperature in coating die

9. Conclusions

A computer modeling of the optical fiber drawing process is presented. The conjugate problem involving flows in both glass and gas are solved using a finite element method. The fiber surface is modeled as a free surface whose location is determined by a deforming mesh approach. It is shown that the temperature and flow fields in the two phases, as well as the shape of the fiber surface, can be accurately predicted. The draw ratios presented here (up to 9216) are comparable to those observed in the real process. It has been verified that the predicted fiber profiles match qualitatively with the numerical results presented elsewhere [7] and quantitative predictions are underway. It is seen that radiation plays an important part and should be properly accounted for. In this model, an enclosure analysis is used to model surface-to-surface radiation in the furnace. The Rosseland approximation is used to model radiation exchange within glass. This model is strictly valid only for optically thick media and could introduce inaccuracy downstream of the draw down region where the fiber diameter is small.

In the second half of our study, the optical fiber coating process is modeled. The velocity, pressure and temperature distribution of the coating fluid in the die calculated. Since two free surfaces are formed, the shape and position of these surfaces is computed using a deforming mesh approach. The effect of non-Newtonian viscosity on the coating flow is demonstrated. As the fluid becomes more non-Newtonian (lower power law index), the coating thickness increases and the dynamic contact point moves upstream. If the dynamic contact point moves too far upstream, the coating bead can become unstable. One way to control the dynamic contact point position is to change the inlet pressure to the die. The effect of heat transfer within the coating die was investigated. In the absence of other energy sources, it was shown that viscous heating alone can increase the temperature of the coating fluid since the shear rates are so high in the die. The effect of temperature dependent fluid properties and the ultimate impact on final coating thickness and stability represent topics for future work.

10. References

[1] S. Krishnan and L. R. Glicksman, "A Two-Dimensional Analysis of a Heated Free Jet at Low Reynolds Numbers," *Journal of Basic Engineering*, 93, 355-364 (1971).

[2] S. Kase and T. Matsuo, "Studies on Melt Spinning: I. Fundamental Equations on the Dynamics of Melt Spinning," *Journal of Polymer Science*, 11, 251-287 (1967).

[3] G. A. Brown (ed. by B. Bendow and S. S. Mitra), *Fiber Optics: Advances in Research and Development*, Plenum Press, p. 55 (1979).

[4] U. C. Paek and R. B. Runk, "Physical Behavior of the Neck-Down Region during Furnace Drawing of Silica Fibers," *Journal of Applied Physics*, 49(8), 4417-4422 (1978).

[5] M. R. Myers, "A Model for Unsteady Analysis of Preform Drawing," *AICHE Journal*, 35(4), 592-602 (1989).

[6] Z. Xiao and D. A. Kaminsky, "Flow, Heat Transfer, and Free Surface Shape During the Optical Fiber Drawing Process," *National Heat Transfer Conference, ASME*, 9, 219-229 (1997).

[7] S. R. Choudhury, Y. Jaluria, and Steve H.-K. Lee, "A computational Method for Generating the Free-Surface Neck-Down Profile for Glass Flow in Optical Fiber Drawing," *Numerical Heat Transfer, Part* A, 35(1), 1-24 (1999).

[8] Y. S. Touloukian et al., *Thermophysical Properties of Matter*, Plenum publishing.

[9] A. B. Shapiro, "FACET- A Radiation View Factor Computer Code for Axi-symmetric, 2-D Planar, and 3-D Geometries with Shadowing," *An Informal Lawrence Livermore Laboratory Report.*

[10] Jaydeep A. Kulkarni, Srinivas Chippada, Ashwini Kumar, and Eric W. Grald, "Computer Modeling of Optical Fiber Drawing Process," *Proceedings of the 49th International Wire and Cable Symposium,* 74-90 (2000).

[11] F.V. DiMarcello, A.C. Hart, R.G. Huff, K.S. Kranz, L.M. Larsen-Moss, "Biconic Coating Die for Making Optical Fibers," *United States Patent,* No. 6,030,664 (2000).

[12] T. Izawa and S. Sudo, *Optical Fibers: Materials and Fabrication*, KTK Scientific Publishers, Tokyo, p. 71 (1987).

[13] K. Rattan and Y. Jaluria, "Simulation of Flow in Die and Applicator for Optical Fiber Manufacture," *Proc. 48th IWCS*, 700-707 (November, 1999).

[14] C. D. Dimitropoulos, S. Chippada, E. W. Grald and J. A. Kulkarni, "CFD Simulation of Optical Fiber Coating Flows," *Proc. 49th IWCS*, 89-96 (November, 2000).

[15] K. N. Christodoulou, S. F. Kistler and P. R. Schunk, "Advances in Computational Methods for Free-Surface Flows", in *Liquid Film Coating* (S. F. Kistler and P. M. Schweizer eds.), Chapman & Hall, London, p. 297 (1997).

[16] U. C. Paek and C. M. Schroeder, "High Speed Coating of Optical Fibers with UV Curable Materials at a Rate of Greater Than 5 m/sec," *Applied Optics*, 20(23), 4028-4034 (December, 1981).

[17] G. Shen, X. Qu, W. She, X. Yu, Q. Sun and H. Chen, "Study of UV-Curable Coatings for Optical Fibers," *J. Coatings Technology*, 71(891), 53-57 (April, 1999).

[18] P. G. Simpkins and P. A. Blythe, "Laws for Fiber Temperature Prediction During Drawing," ASME J. Heat Transfer, 119, 652-655 (August, 1997).

Jaydeep Kulkarni was born in Pune, India. He did his B.S. in Chemical Engineering from the Indian Institute of Technology, Bombay in 1995 and went to the University of Delaware for graduate studies. He finished his Ph.D. in 2000 and since then is working for Fluent Inc.

Study of Cooling Tubes for Fiber Draw using CFD

Denis TSCHUMPERLE, Jean-François BOURHIS, Sophie DUBOIS, Aurélien LEON

Alcatel

Conflans-Sainte-Honorine, France

33 1 39 19 12 00 · denis.tschumperle@alcatel.fr

Abstract

During the draw process, an optical fiber reaches very high temperatures as it exits the draw furnace. Its temperature needs to be quickly lowered to be compatible with coating application. More efficient ways of cooling the fiber are required as natural cooling in ambient air is not able to achieve the desired cooling rate.

An efficient method of lowering the fiber temperature is to pass it through a cooling tube. Cooling is then achieved by maintaining a low tube temperature with cool gas injections. But with increasing draw speeds, traditional cooling tubes have reached their limits. A new design of cooling tubes is a challenging task but also a very time consuming one, as new concepts must be extensively tested before use. Thus, there is a need to efficiently simulate the fiber cooling process without having to build and experimentally test all the proposed designs.

Different concepts of cooling tubes are simulated and compared to define the optimum design of a high efficiency cooling tube. The computed fiber temperature at the tube exit is compared with measurements made on an actual draw tower. The effect of process parameter variation on fiber exit temperature and the heat transfer coefficient between the fiber and the surrounding gas is studied.

Keywords

Optical fiber; cooling; tube; flow; simulation.

1. Introduction

Investigation of the cooling of a moving fiber in an external gas has been made under various hypothesis. Using dimensional analysis, Chida and Katto [1] defined a dimensionless group for the conjugate heat transfer between the fiber and the gas, assuming constant material properties. Pack and Schroeder [2] estimated the forced convective cooling necessary to achieve a given temperature level. Vaskopulos et al. [3] and Choudhury [4] numerically investigated the forced cooling in an enclosure using aiding or opposing gas flow.

In these studies, many simplifications were made in order to numerically solve the resulting equations. Radiative heat transfer was neglected, as well as the effect of variable thermal properties of both the fiber and the gas. In a previous work on fiber cooling in air [5], we have shown the importance of radiative modeling for high fiber temperatures. The effect of property variations with temperature has been emphasized. The same calculation parameters will be used for our current study.

This work presents the numerical simulation of fiber cooling in a tube using Fluent v5.6 software which solves mass and heat transfer including turbulent effects.

The study of two different cooling tube designs will be presented. The first tube (Tube 1) precedes the application of coating in the draw system and the second (Tube 2) is installed after the first coating application.

2. Calculation Setup

Both tubes were studied using the same numerical approach. The turbulence model used is a RNG k-ε with a two-layer zonal model near the walls. This model has been shown as the most accurate model available to describe the turbulent thermal exchange at a fluid-solid interface. The mesh must be refined near the walls within the viscous sublayer with this model.

Due to the presence of heated gases, natural convection must be taken into account using a Boussinesq approximation. The properties of gas, helium, and of the silica fiber are highly temperature dependant and are inserted into the code as piecewise-polynomial functions. More details on the Discrete Ordinate model used to describe the radiative heat transfer and its application to fiber cooling are given in [5].

3. Tube 1 Study

3.1 Model Setup

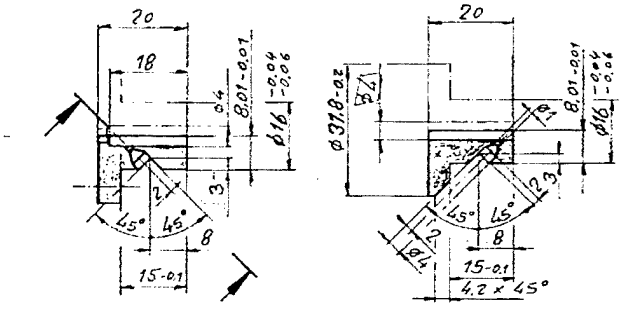


Figure 1. Up and down injector views

Tube 1 is used to cool the fiber before injection of primary coating. This is a cylindrical copper tube with 6 cylindrical helium injections at the top and another 6 at the bottom of the tube each

making a 45° angle with the tube axis (Figure 1). The external tube surface is water cooled and is assumed to be at constant temperature. There is a diameter restriction at the top of the tube.

3.2 Comparison between 2D and 3D model

The first configuration is a tube with an inner diameter of 6 mm and length of 2 m with helium injections of 2 l/min at both the top and the bottom. Draw speeds will be normalized by a reference speed U_{ref}. This test is performed with a draw speed U*=1.2. Due to the configuration symmetry, only $1/6^{th}$ of a tube section is modeled. The external wall is water cooled at 291°K, which is also the temperature of the injected gas. The domain includes a 3 cm large air zone before and after the tube. A no-slip condition is assumed at the walls.

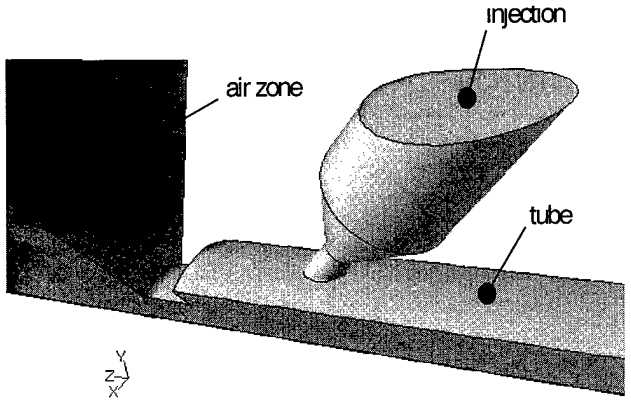


Figure 2. Top domain view, 3D model

The temperature of the fiber is imposed at the domain entry and the fiber temperature is calculated at the exit. Since calculation of 300,000 3D cells requires extensive CPU time, a 2D axi-symmetric model will be used for a parametric study. However, the results of the 2D and 3D models will be compared.

For the 2D model, the 6 injectors are replaced by an annular injection with surface area calculated to result in equivalent flow rates and velocities at the inlet. In this model, the tube wall is meshed and the cooling temperature is applied at the external surface of the tube.

Figure 3 and Figure 4 show the He mole fraction in the tube for the 2D and 3D models, respectively. The mean He mole fraction in the tube is approximately 0.50 in 3D as compared to 0.45 in 2D. It is apparent that there is a high quantity of air entering the tube, despite the 45° orientation of the injectors. This is due to the fiber speed which far exceeds the helium speed near the injectors which has the effect of pulling away helium in the tube.

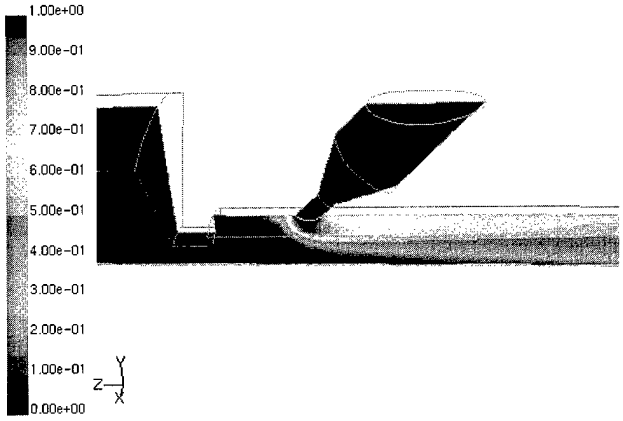


Figure 3. He mole fraction in tube for 3D model

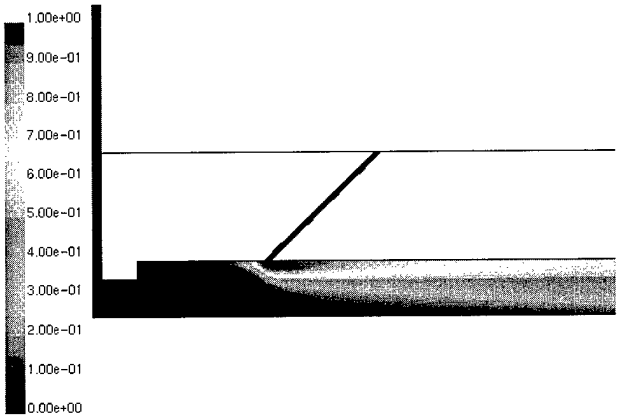


Figure 4. He mole fraction in tube for 2D model

The same situation applies to the bottom injection, but here the helium is more quickly pulled out of the tube due to the large opening at the bottom. There is less than 2°K difference between a flow of 20 l/min of He at the bottom and no flow at all. Thus we can say that the bottom injection has no influence on fiber cooling.

The temperature 3 cm before the tube entry is 758°K and 529°K 3 cm after the tube exit for the 3D case, and 544°K for 2D. There is a 15°K discrepancy between the two models that is likely due to complex 3D flow effects which leads to a greater fraction of He in the tube and thus a better cooling. The agreement is sufficient enough, however, to use the 2D model for our subsequent work.

3.3 Validation

Calculation results are validated by comparison with temperature measurements made on an Alcatel draw tower. The tube studied is 2.5 m long with an inner diameter of 6 mm. He is injected at the top of the tube only. The draw speed is U*=1 and the temperature 2 cm before the tube entry is T_0 = 775°K. An exit temperature is measured 203.5 cm after the tube for various He flow rates. Simulations will be conducted with and without the Discrete

Ordinate radiation model activated. When radiation is taken into account, the fiber emissivity is a function of temperature and the tube's internal emissivity has been imposed at 0.5. The air zone sizes for these calculations are 2 cm long before the tube and 10 cm long after the tube. The temperature 203.5 cm after the tube is extrapolated by using an empirical correlation based on an exponential cooling model $\theta=\exp(-\alpha x)$, where θ is the normalized temperature and α is the cooling coefficient (see ref. [5]).

Figure 5 shows the decrease of the exit temperature with an increasing He flow rate. We can also see that the He flow efficiency stops after 5 l/min which can be directly linked to the He fraction in the tube. For low He flow rates, it can be shown (Figure 4) that He is swept away by the air flow coming along with the fiber and that a large quantity of air enters the tube thus reducing the cooling tube's efficiency. Flow greater than 5 l/min of He insures that less than 5% of ambient air (in moles) will enter the tube.

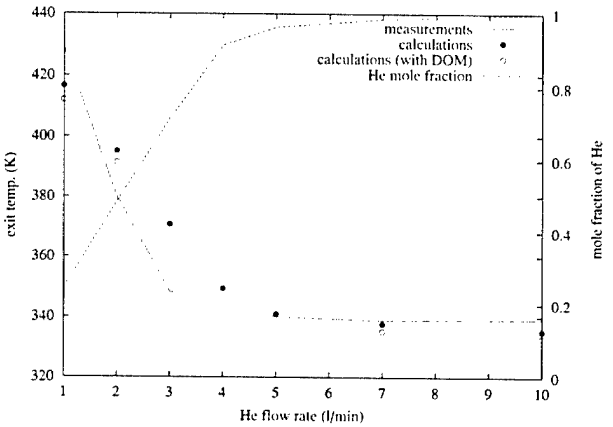


Figure 5. Exit tube temperature and He mole fraction for various He flow rates

Radiation effects lower the fiber temperature less than 5°, hence further calculation will be made without radiative heat transfer which is a time-consuming model.

Computed and measured data exhibit similar general trends, lending confidence in the model for use as a parametric study tool.

3.4 Parametric Study

The parameters of draw speed, He flow rate, and the injector angle of the tube will be changed within the model.

Figure 6 shows the value of the heat transfer coefficient h as a function of longitudinal position x for various draw conditions. It is computed as $h=q/(T-T_\infty)$, where q is the surface heat flux through the fiber surface, T is the temperature of the fiber surface and $T_\infty=293°K$ is the initial temperature of the gas.

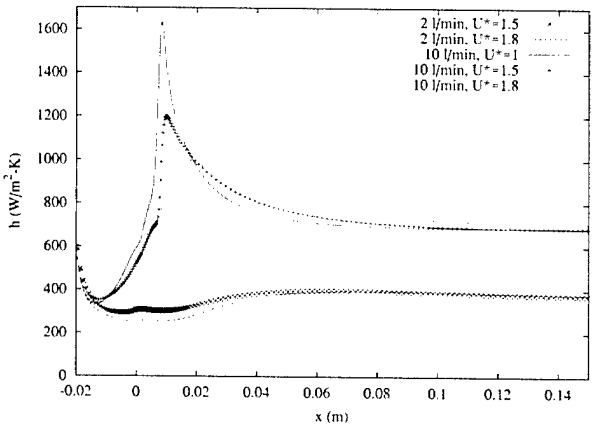


Figure 6. Heat transfer coefficient for various draw conditions

The difference between flowrates of 2 l/min and 10 m/min are here clearly evident. With high He flow, the injected gas effectively impinges the fiber and disturbs the boundary layer around the fiber, which increases the local heat transfer coefficient h. With increasing distance x, the boundary layer gradually returns to a non-perturbed state and h is then driven primarily by the He fraction in the tube. There is then a slight variation of h due to the draw speed. The region where the gas jet has a direct impact on the fiber is approximately 5 cm long.

For the lower He flow injection of 2 l/min, there is an initial slight increase of h due to the diameter restriction near the entry point of the tube, but no direct effect of the gas jet. Afterwards, as He slowly penetrates the fiber boundary layer initially composed of air, h increases to its nominal value. It has a lower value as compared to the case of 10 l/min obviously due to the smaller quantity of He in the tube.

For flows of 10 l/min He, the local maximum of h decreases when U* increases. This is due to the fact that the pertubation flow normal to the fiber is small relative to the fluid going along with the fiber when U* is high. Hence the boundary layer is less perturbed for a high draw speed.

The mean value of the heat transfer coefficient is calculated by $\underline{h} = 1/L\int h(x)dx$, where L is the total length of the tube.

Table 1. Mean value of heat transfer coefficient

U*	1	1.5	1.8	1	1.5	1	1.5
He flow rate (l/min)	10	10	10	2	2	20	20
$\underline{h}$ (W/m²-K)	685.2	683.6	724.0	359.6	355.0	740.4	728.0

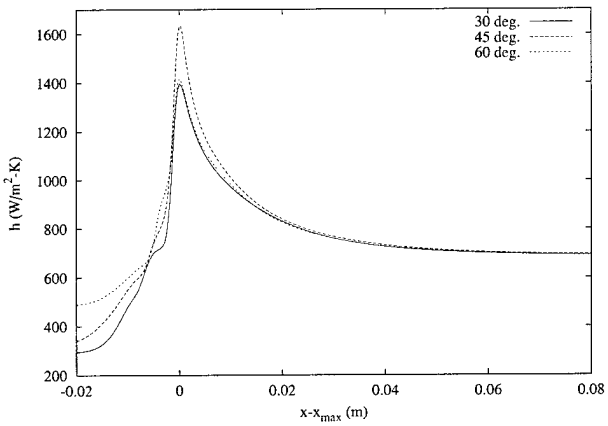


Figure 7. Influence of the injection angle

Figure 7 shows the influence of the injection angle on the heat transfer coefficient h. The curves are shifted such that the maximum value of h occurs at the same position on the x-axis. An injection angle of 45° results in a higher value of the local heat transfer coefficient. The curves are converging towards the same value of h, indicating that the He mole fraction in the tube is independent of the injection angle.

3.5 Conclusion for Tube 1

The calculated and measured results are in agreement thus validating the tool as a means of comparing different cooling tube configurations. This numerical study has highlighted the following points:

- The flow rate of He is critical and must be high enough to not allow too much air inside the tube. However, there is an upper limit after which further He flow rate increases becomes ineffective.
- Results show that the bottom He injection provides no benefit. It may only cool the fiber locally at the injection location for 1 or 2°, but has no long range effect.

4. Tube 2 Study

4.1 Model Setup

Unlike the previously studied tube, the tube 2 design [6] has strong three-dimensional characteristics, meaning that we can not use a 2D axi-symmetric model for such a tube. It is a cylinder of rectangular cross section composed of a copper alloy. Inside lies an injection chamber where helium is injected. Gas is injected only at one side of the inlet chamber, the other being obstructed by a plug. At each side there are two pin-chambers. The pins are intended to perturb the flow and enhance thermal mixing. The fiber moves along the longitudinal axis of the tube.

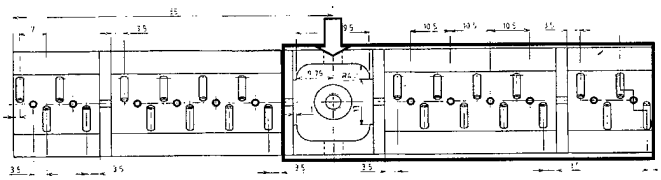


Figure 8. CAD drawing of tube 2 (registered, see [6]), top view

The difficulty in modeling this geometry comes from the numerous pins in the tube. Figure 8 illustrates the lower part of a module. A complete tube is constituted by 3 such modules. It is computationally expensive to model an entire tube, hence, only the region inside the box shown in Figure 8 is included (cf. Figure 9).

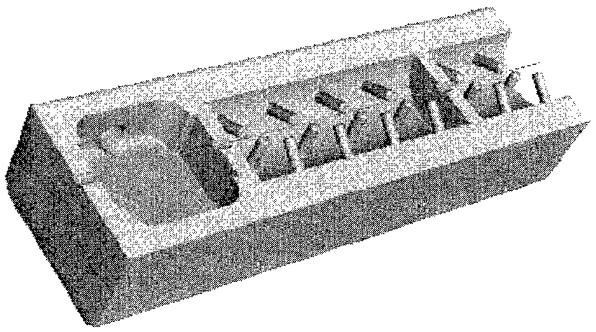


Figure 9. 3D model of tube 2

The mesh has a total of 720 000 elements and is composed of tetrahedral elements except near the fiber surface where structured quad are aligned with the fiber movement.

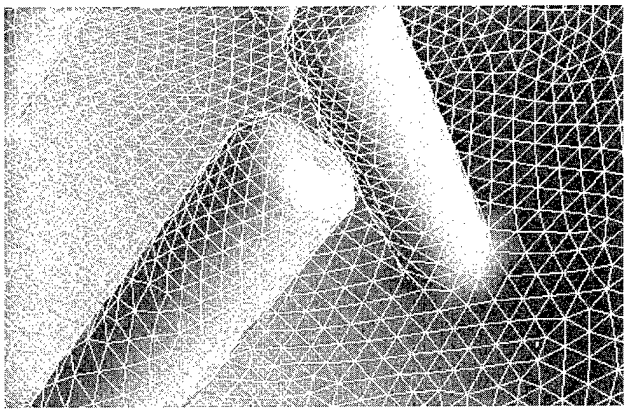


Figure 10. Mesh detail at a pin vicinity

The following boundary conditions (BC) were applied on the middle plane of the tube. For the injection chamber, a symmetry boundary conditions is used both for the solid and the fluid zone. Because of the helicoidal settings of the pins, the fluid zone has a

rotationally periodic condition around the longitudinal axis. In this zone, the solid is assigned a symmetry BC. Helium is injected at 293°K. A pressure inlet is used where the fiber enters the inlet chamber. The pressure imposed is calculated from the opposite side of the injection chamber at the entrance of the first pin-chamber via an User Defined Function (UDF). The fluid exit on the second pin-chamber has a pressure outlet BC and is set at atmospheric pressure. The solid part of the tube is water-cooled on 3 external sides with a temperature set at 288°K. Fiber temperature is imposed at the domain entry (left hand side).

Because this tube is installed after primary coating, fiber temperature is relatively low and radiation can safely be neglected. Unlike tube 1, tube dimensions are small (max chamber length is ~5 cm). The Reynolds number based on the gas inlet velocity and inlet diameter is 36.3 and thus it is assumed that there is no turbulence.

4.2 Validation

The model is validated with temperature measurements made on an Alcatel draw tower. We study the cooling behavior of the fiber between the two coating applicators. The coated fiber has a diameter of 185 µm. One problem is that at this stage the coating is still polymerizing, thus releasing heat. This heat release will be neglected in the following simulations. To minimize the impact of this approximation, the temperature has been measured for a draw speed of U*=0.4. At this low speed, we can more safely assume that the polymerization of coating is complete before the fiber enters the tube.

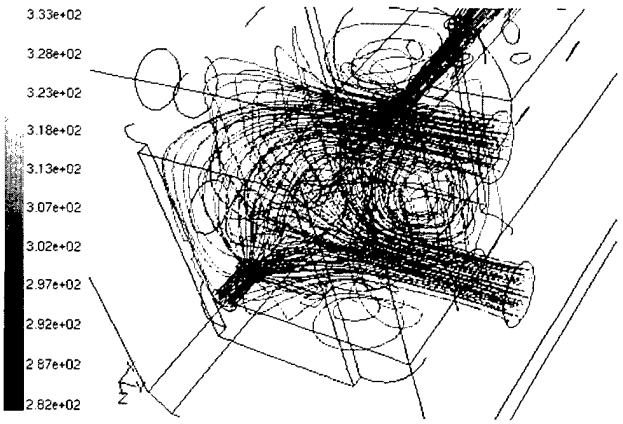


Figure 11. Path lines colored by temperature in the injection chamber, U*=0.4, 10 l/min of He

Figure 11 shows the flow pathlines in the injection chamber where the complex patterns due to the presence of gas entering and leaving the chamber are apparent.

The fiber temperature values at 11 cm before and 9 cm after the complete tube are measured. These data must be interpolated to produce an estimate of the temperature at the beginning of our computational domain. Again, this is done by assuming that the fiber cooling follows an exponential behavior. We can then calculate an exit temperature just at the tube end using Fluent. An empirical correlation for fiber cooling in air reveals the temperature value 9 cm after the tube. The results obtained for various He flows and draw speeds are summarized in Table 2.

Table 2. Comparison between measured and computed temperature values

U*	He flow rate (l/min)	Measured entrance temp. (°C)	Measured exit temp. (°C)	Computed exit temp. (°C)	ΔT (°C)
0.4	2	61.5	49.6	48.7	-0.9
	10		47.7	47.0	-0.7
	40		45.1	44.0	-1.1
1	2	73.4	69.5	66.2	-3.3
	10		64.5	60.9	-3.6
	40		61.9	60.6	-1.3
1.5	10	87.6	85.8	81.7	-4.1

The model is able to accurately predict trends in cooling efficiency, as confirmed by measurement results. The temperature difference, ΔT, between calculation and measurement increases with the draw speed. This is, of course, due to the fact that we have neglected the heat created by the fiber polymerization. At increased speeds, polymerization effects increases the fiber temperature substantially.

4.3 Conclusion for Tube 2

Despite the simplifications in our model's boundary conditions, it accurately estimates the fiber exit temperature for low drawing speeds. Further, the model was able to capture the effects of parameter variation. For higher draw speeds, the calculated values differ from the measured ones due to the polymerization effect.

5. Conclusions

After having studied the fiber cooling in air [5], we validated our modeling tool in the case of cooling tubes. The model is able to predict fiber temperature at the tube exit for various draw speeds and injected gas flow rate.

For tube 1, the model is able to predict an optimal injected gas flow rate that permits good cooling efficiency without using excessive gas. It was also shown that the bottom gas injections were ineffective.

The study of the heat transfer coefficient in the gas inlet area gives us a better understanding of the jet cooling influence and will help in designing a more efficient cooling tube design capable of dealing with ever increasing draw speeds.

6. Acknowledgments

Special thanks to the staff in Conflans who conducted the measurements on the draw tower.

7. References

[1] Chida K., Katto Y., "Conjugate Heat Transfer of Continuously Moving Surfaces", *Int. J. Heat Mass Transfer*, Vol. 19, 461-470 (1976).

[2] Paek U.C., Schroeder C.M., "Forced Convective Cooling of Optical Fibers in High-speed Coating", *J. Appl. Phys.* 50(10), 6144 (1979).

[3] Vaskopulos T., Polymeropoulos C., Zebib A., "Cooling of Optical Fiber in Aiding and Opposing Forced Gas Flow", *Int. J. Heat Mass Transfer*, Vol. 38, 1933-1944 (1995).

[4] Choudhury S.R., "Thermal Transport in the Optical Fiber Drawing Process", Ph. D. Thesis, University of New Jersey (1995).

[5] Tschümperlé D., Nicolardot M., "Fiber Cooling Modelisation During Draw Using CFD" *Proc. Computational Technologies for Fluid/Thermal/Structural/Chemical Systems with Industrial Aplications*, PVP vol. 424-1 (July, 2001).

[6] Lee L. Blyler Jr, Arthur C.Hart Jr, C.Progelhof (American Telephone and Telegraph Bell Laboratories), *US Patent N° 4 761 168* (2/8/1988).

Numerical Analysis to Predict Internal Temperatures in Central Core Fiber Optic Cables during Manufacture

Luis M. Bocanegra
Lucent Technologies, Bell Laboratories
Norcross, Georgia
+1-770-798-4996 ·lbocanegra@lucent.com

Nathan E. Hardwick, III
Lucent Technologies, Bell Laboratories*
Norcross, Georgia
+1-770-394-0640 ·nathanhardwick@mindspring.com
* Retired

Abstract
An easy-to-use thermal simulation model that predicts surface and internal temperatures for central-core fiber optic cables at any time and any discrete position during manufacture has been developed. This model, based on finite control volume analysis, permits variations in central core cable designs and boundary conditions encountered during the cable manufacturing operation. Numerical results from a user-friendly computer program showed a reasonable agreement with experimental data.

Temperature profiles generated from the thermal simulations provide valuable insight when designing central-core fiber optic cable sheathing lines or when varying manufacturing conditions. A quick study of the thermal analysis data vividly reveals the effect of line speed on the temperature profiles. Results also show how significant reductions in core tube temperature can be achieved by (1) merely optimizing water and air cooling lengths prior to jacket extrusion and (2) using two extrusions for the jacket with the first layer being very thin.

Keywords
Thermal modeling; Thermal model for central core fiber optic cables; temperature prediction in fiber optic cable; fiber optic cable

1. Introduction
High manufacturing line speed is a key factor in achieving lower fiber optic cable costs. Increased line speeds can, however, cause excessive internal temperatures within a central core tube cable during subsequent jacket extrusions unless production lines are properly configured. These excessive temperatures during manufacture may adversely affect the mechanical properties of the materials in a fiber optic cable.

A numerical tool that predicts temperatures within a cable during manufacture is highly desirable. Having the capability to perform thermal simulations of instantaneous internal and surface temperatures of a cable sheath during the cabling process is important in identifying the critical temperature regions. Also, such capability provides insights into nonobvious methods for optimizing cabling lines without moving heavy and complicated equipment or performing an excessive number of experiments. This work is a continuation of prior modeling efforts by Hardwick and Liu, and Bocanegra and Hardwick that resulted in a numerical analysis computer program capable of providing valuable insight for variations in cable and line configurations.

2. Description of a Central Core Fiber Optic Cable Manufacturing Line
Central core fiber optic cables are differentiated from other cable designs such as loose tube or slotted core by the position of their optical elements and strength members. Specifically, central core cables have the optical elements located inside a core tube which is placed concentric with the axis of the cable [1]. The construction of the cable outside of the core tube varies with the type of application but in general the sequence of manufacturing operations is described in the following paragraph. Figure 1 shows a simplified schematic for a central core fiber optic cabling line, with only the components pertinent to this paper included.

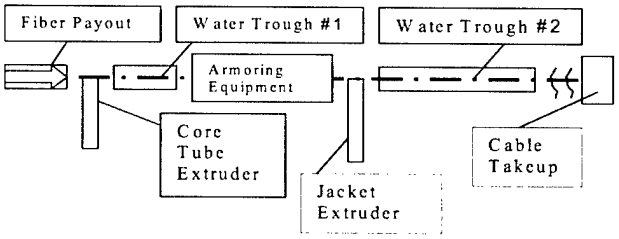


Figure 1 Simplified Schematic for a Central Core Fiber Optic Cabling Line

During the manufacturing process optical elements and filling compound are fed into the tooling of a first extruder where the core tube is formed. Immediately thereafter, the core tube is cooled in water and air and then other components such as water blocking elements and strength members are laid over the core tube. A second extruded layer, and sometimes a third one, follows the previous operations forming a protective jacket that is subsequently cooled in water and air. After a sufficient cooling length the cable is taken onto a reel.

3. Mathematical Model
3.1 Problem Objective
To determine the temperature field within a cable during manufacture at any position in the manufacturing line.

3.2 Assumptions
The problem will be solved under the following assumptions:

- Central core fiber optic cable.

- Filling compound surrounds the optical elements inside the core tube.
- Optical elements are treated as a composite glass rod with cross sectional area equal to that of the optical fibers.
- The cable is axis-symmetric, thus suitable for cylindrical coordinates modeling.
- Negligible thermal contact resistance exists between layers of two different materials.
- Cable components such as a metal armor and water blocking tape or rods and rovings and dielectric tape are treated as a composite material with average properties.
- Cooling water and air temperatures remain constant.
- Heat transfer from the cable to its surroundings is modeled using an effective heat transfer coefficient.
- No internal heat generation sources are present.
- The cable moves at constant speed.
- The extrudate only has axial velocity.
- The manufacturing process is considered steady state from an Eulerian reference frame.

3.3 Mathematical Formulation

Under the previous assumptions, the following governing differential equation [2] and initial and boundary conditions can describe the problem for a length of cable in the manufacturing line. For a justification of equation (5), refer to Section 4.2.

$$\frac{1}{r}\frac{\partial}{\partial r}\left(kr\frac{\partial T}{\partial r}\right)+\frac{\partial}{\partial z}\left(k\frac{\partial T}{\partial z}-u_z\rho cT\right)=0 \quad in$$

$$0 \le r < R_{\max}, \quad 0 < z < Z_{\max}, \quad t > 0 \tag{1}$$

$$T(r,z,t) = Finite, \; for \; t = 0 \; in \; the \; region \tag{2}$$

$$T(r,z,t) = Finite, \; at \; z = 0, \quad t > 0 \tag{3}$$

$$\frac{\partial T}{\partial r} = 0 \; for \; r = 0 \tag{4}$$

$$\frac{\partial T}{\partial z} = Constant, \; at \; z = Z_{\max}, \quad t > 0 \tag{5}$$

$$-k\frac{\partial T}{\partial r} = h(T - T_\infty) \; for \; r = R_{\max}, \quad t > 0 \tag{6}$$

$$u_z(r,z,t) = Constant \tag{7}$$

Because the domain has several materials of unique thermal properties and not all of them are present for all positions along the axial direction of the cable, then the thermal conductivity, density and specific heat become a function of the spatial coordinate. Thus, an exact solution of the mathematical problem is cumbersome. An alternate solution is to use the numerical approach as described below.

4. Numerical Model

A discrete solution can be reached by using a finite-volume energy conservation approach. For this, the cable domain is partitioned into finite volume cells that can be regarded as cylindrical shells of finite length and thickness. The additional assumption that each cell has uniform temperature and thermal properties is made for the sake of simplification. Within a cable, several distinct geometrical regions exist and therefore a particular form of equation will result upon applying the energy conservation equation for each one. Strength members for cable designs with two linear strength members are neglected in the model because of their small relative cross sectional area compared to the cable jacket. Also when several strength members are applied then these are treated as a composite layer of material.

4.1 Discretized Equations

Algebraic equations are derived form energy conservation principles applied to cylindrical finite volumes [3]. Different forms of equations will result depending on where the finite volumes are located. Each finite volume cell or node is identified by its position along the *r*- and *z*-axes. Thus distinct equations for centerline nodes, internal nodes of the same material, internal nodes at the interface of two materials, nodes for outer surfaces and nodes at the start of a new layer of material are generated. For illustration purposes the derivation of the equation for the interface between two different materials is presented below.

4.1.1 Derivation of the Equation at Interface Nodes

This type of node is present at the interface of two different materials (i.e., filling compound and inner surface of core tube). Figure 2 shows this type of cell. All the points within the same cell have the same temperature, however the materials and thermal properties for the upper zone and lower zones of cell **P** are different. Thermal properties for the upper zone of cell **P** and the North cell are the same; similarly, thermal properties for the lower zone of cell **P** and the South cell are equal. Also, in Figure 2,

$$dr_N = \frac{Dr_N}{2} \quad and \quad dr_S = \frac{Dr_S}{2}, \tag{8}$$

$$q_{WPN} = k_{WN} \cdot 2\pi\left(r + \frac{dr_N}{2}\right) \cdot dr_N \cdot \frac{T_W - T_P}{dz} \tag{9}$$

$$q_{WPS} = k_{WS} \cdot 2\pi\left(r - \frac{dr_S}{2}\right) \cdot dr_S \cdot \frac{T_W - T_P}{dz} \tag{10}$$

$$q_{EPN} = k_{W=EN} \cdot 2\pi\left(r + \frac{dr_N}{2}\right) \cdot dr_N \cdot \frac{T_E - T_P}{dz} \tag{11}$$

$$q_{EPS} = k_{ES} \cdot 2\pi\left(r - \frac{dr_S}{2}\right) \cdot dr_S \cdot \frac{T_E - T_P}{dz} \tag{12}$$

$$q_{SP} = k_S \cdot 2\pi(r - dr_S) \cdot dz \cdot \frac{T_S - T_P}{Dr_S} \tag{13}$$

$$q_{NP} = k_N \cdot 2\pi(r + dr_N) \cdot dz \cdot \frac{T_N - T_P}{Dr_N} \quad (14)$$

$$q_{CVN} = (\rho c_p)_{WN} v \cdot \{2\pi(r + \frac{dr_N}{2}) \cdot dr\} \cdot (T_W - T_P) \quad (15)$$

$$q_{CVS} = (\rho c_p)_{WS} v \cdot \{2\pi(r - \frac{dr_S}{2}) \cdot dr\} \cdot (T_W - T_P) \quad (16)$$

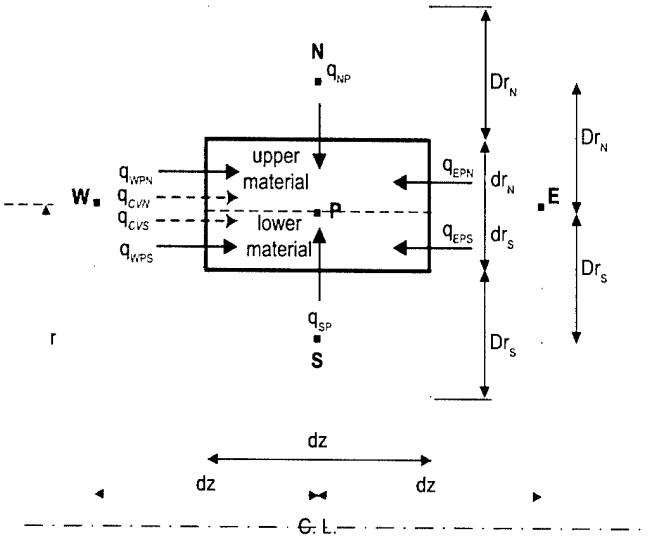


Figure 2. Schematic for the Energy Balance of an Interface Node

Substituting Equations 9 through 16 into Equation 17 that represents the energy balance for cell **P** yields an algebraic expression in Equation 18 to compute the temperature of cell **P**.

$$q_{WPN} + q_{WPS} + q_{EPN} + q_{EPS} + q_{SP} + q_{SN} + q_{CVN} + q_{CVS} = 0 \quad (17)$$

$$T_P = \frac{a_W T_W + a_E T_E + a_S T_S + a_N T_N}{a_W + a_E + a_S + a_N} \quad (18)$$

where,

$$a_W = \{k_{WS} \cdot (r - \frac{dr_S}{2}) \cdot dr_S + k_{WN} \cdot (r + \frac{dr_N}{2}) \cdot dr_N\} \cdot \frac{1}{dz} + (\rho c)_{WS} \cdot v \cdot (r - \frac{dr_S}{2}) \cdot dr_S + (\rho c)_{WN} \cdot v \cdot (r + \frac{dr_N}{2}) \cdot dr_N \quad (19)$$

$$a_E = \{k_{ES} \cdot (r - \frac{dr_S}{2}) \cdot dr_S + k_{EN} \cdot (r + \frac{dr_N}{2}) \cdot dr_N\} \cdot \frac{1}{dz} \quad (20)$$

$$a_S = k_S (r - dr_S) \frac{dz}{Dr_S} \quad (21)$$

$$a_N = k_N (r + dr_N) \frac{dz}{Dr_N} \quad (22)$$

4.2 Boundary Conditions

The following boundary conditions are presented in the same sequence that the different elements that form a cable appear in the manufacturing line. For the initial end of the cable at z = 0, it is assumed that the fibers, filling compound and core tube appear simultaneously:

$$T(r,z) = T_{fibers} \quad for \quad 0 \le r < r_f, and\ z = 0 \quad (23)$$

$$T(r,z) = T_{fill} \quad for \quad r_f \le r < r_g, and\ z = 0 \quad (24)$$

$$T(r,z) = T_{core\ tube\ extrusion} \quad for \quad r_g \le r \le r_c, and\ z = 0 \quad (25)$$

For the start of a metallic armor or layer of strength members or tapes:

$$T(r,z) = T_{armor} \quad for \quad r_{core\ tube\ out} < r \le r_{jacket\ in},\ z = z_{armor} \quad (26)$$

For the jacket extrusion:

$$T(r,z) = T_{jacket\ extrusion} \quad for \quad r_{jacket\ in} < r \le r_{jacket\ out},\ z = z_{jacket\ extrusion} \quad (27)$$

Both core tube and jacket are cooled in water upon leaving the extrusion tooling. The heat is transferred from the cable to the water by forced convection according to the following boundary condition. This condition is present on every external boundary cell.

$$q'' = h_{water\ or\ air}(T_{R_{max}} - T_\infty) \quad for \quad r = R_{max} \quad (28)$$

where

$$T_\infty(r,z) = T_{water} \ or \ T_{air} \quad for \quad r > R_{max} \quad (29)$$

Finally, the temperature for the boundary at the end of the cable where z = z_{max} is unknown since it depends on the convective cooling rates. However, lack of this boundary condition does not hinder from obtaining a numerical solution if a physically feasible condition is imposed. Thus it will be assumed that near the end of the manufacturing line when the cable reaches the take-up, temperature profiles resemble a straight line that satisfies the condition of Equation 5. The outermost nodes in the axial direction reflect this condition, the temperature is computed by using the temperature of the next two upstream nodes.

4.3 Solution Algorithm

The numerical solution for the discrete temperature field is obtained using the Gauss-Seidel iterative method [4]. For the first iteration this method requires an initial temperature field, which is arbitrary, such as the one given below.

$$T(r,z) = T_{fibers} \quad for \quad 0 \le r < r_f, and\ 0 \le z \le z_{max} \quad (30)$$

$$T(r,z) = T_{fill} \quad for \quad r_f \le r < r_g, and\ 0 \le z \le z_{max} \quad (31)$$

$$T(r,z) = T_{core\ tube} \quad for \ r_g \le r \le r_c, \ and \ 0 \le z \le = z_{max} \quad (32)$$

$$T(r,z) = T_{armor} \ for \ r_{armor} < r \le r_{jacket\ in},\ z_{start\ of\ armor} \le z \le z_{max} \quad (33)$$

$$T(r,z) = T_{jacket} \quad for \quad r_{jacketin} < r \le r_{jacketout}, \quad z_{start\ of\ jacket} \le z \le z_{\max} \tag{34}$$

In general, the solution of the equations may be done in any order, but for simplicity the solution algorithm used marches along the z-axis, sweeping all the nodes in the increasing radial direction until the exterior surface is reached. The computation of the temperature for the last axial node of the cable at any radius is obtained from the computed temperatures for the next two upstream nodes.

The convergence of the solution is controlled by adding the absolute value of the difference between the most recent temperature and the one of the previous iteration for each node of the domain. Convergence is achieved when this summation is smaller than an established error tolerance.

The computational algorithm code was written in Visual Fortran [5], with flexibility to allow for different cable designs, manufacturing line configurations and operating conditions. The input data required to execute the program was generated in Visual Basic [6] in which different menus provide options for cable designs, materials, line configurations and line speeds.

4.4 Thermal Properties

Thermal properties were taken as constant from average values provided by material suppliers.

Composite layers of materials such as the combination of a corrugated armor, water blocking tape and air under the armor and polyolefin deposited on top of the armor corrugations were treated as a composite material. For this situation mass averaged density and specific heats were computed. Also, an equivalent thermal conductivity resulted from applying heat conduction principles for multiple layers [7]; this considered variations in thickness for the same material within the composite structure. Layers created by rods and rovings and dielectric tapes and other combinations followed the same treatment.

4.5 Validation of Results

Results were verified by measuring core tube and jacket temperatures at several places as well as fill temperature at the end of the cable. For this verification process, different manufacturing lines and cable designs were used. Although adjustments in the heat transfer coefficients were necessary, predictions for the fill temperature at the end of the cable agreed very well with the measured values.

4.5.1 Heat Transfer Coefficients for Water Cooling.

When a just extruded core tube or jacket enters into a cold-water cooling trough there are quenching effects and turbulence promoters at the start of the cooling trough. The heat transfer coefficient for water was computed from a standard correlation for turbulent external flows on a flat surface [7]. Even for short water troughs the Reynolds number requirement to apply the equation below was satisfied.

$$Nu = (0.037\mathrm{Re}_L^{0.8} - 871)\mathrm{Pr}^{1/3}, \tag{35}$$

for

$$0.6 < \mathrm{Pr} < 60; \quad 5\cdot10^5 < \mathrm{Re}_L < 10^8; \quad \mathrm{Re}_{L,critical} = 5\cdot10^5$$

Cable surface temperature measurements at the exit of core tube water trough resulted in temperatures lower than predicted in part because of its short length and additional cooling effects such as quenching and evaporation. Thus the computed heat transfer coefficient value was adjusted by a factor of two in order to obtain temperature predictions that were within 10% of the measured value. For longer water troughs used to cool the cable once the jacket was extruded, however, adjustments to the heat transfer coefficient were not necessary.

4.5.2 Heat Transfer Coefficients for Air Cooling

For air heat transfer coefficients a fixed value of 35 W/(m^2 K) was used after existing correlations for forced and free convection lead to lower heat transfer coefficient values that over predicted the surface temperature. Predicted temperature values after the heat transfer coefficient was adjusted were within 10% of the measured temperature even for different sizes of cables.

5. Analysis of Results

In this section results for both metallic and dielectric cables are presented. Figure 3 presents a cross section for a metallic cable with the relevant components mentioned in this paper. For the dielectric cable, a dielectric tape that acts as a heat barrier element replaces the armor. In addition, the case of a dielectric cable without a heat barrier tape is analyzed with the purpose of illustrating the effect of core tube reheating at different line speeds. Finally, an analysis of the effect of water trough lengths on the cable temperatures is discussed.

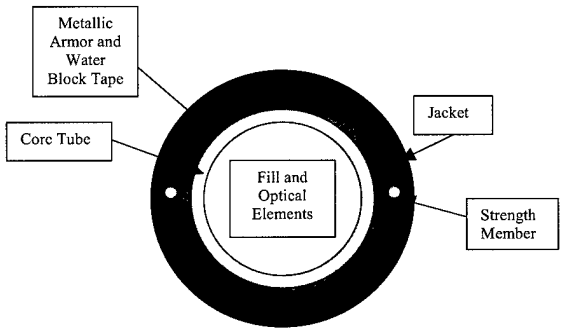


Figure 3. Schematic Representation for the Cross Section of a Central Core Metallic Fiber Optic Cable

5.1 Metallic Cable

The manufacturing processes for metallic cables requires two extrusion processes, the first one for the core tube and second one for the jacket. Each extrusion precedes a cooling water trough as previously described in Section 2. Immediately after the core tube leaves the first water trough and before the second extrusion water block tape, a metallic armor, and strength members are placed over the core tube. Figure 3 shows a cross section for this cable.

Figure 4 presents simulation results for a high fiber count metallic cable. In this figure separate temperature profiles are shown for positions within the cable. Specifically, plots are presented for temperatures of the fill at the interface with the optical fibers as well as for the inside and outside surfaces of both the core tube and jacket. The horizontal axis represents a Normalized Distance along the cabling line; the value of zero corresponds to the location for the core tube extrusion and fill injection. The vertical axis shows the temperature magnitude.

Note that the outer surface of the core tube shows a fast quenching until the surface approaches the water temperature with the implication that the heat transfer rate is greater when the core tube enters the cooling water trough than when it leaves the water. Because the fill in the vicinity of the fibers is initially at a temperature that is lower than that of the core tube, heat transfers from the core tube to the adjacent layer of fill in contact with the core tube. From the fill profile, its temperature is seen to decrease while the core tube is in the water trough. After the core tube leaves the cooling trough the core tube is exposed to air and its outer surface temperature starts to increase while the inner surface and the fill continue transferring heat to the surroundings. Note that the outside surface of the core tube increases its temperature and then remains about constant indicating that it has reached equilibrium with the surrounding air.

For a Normalized Distance equal to 0.12 a sudden temperature decrease at the outer surface of the core tube is observed due to the presence of the metal armor that becomes in contact with the core tube and acts as a heat sink. The jacket extrusion begins at a distance of 0.19 and when completed immediately enters a cooling water trough, referred to as Water Trough #2, where rapid cooling occurs. Thermal energy gets transferred into both the water and the core tube.

This heat transfer from the newly extruded jacket increases the core tube outside surface temperature by about 36 °C. In some cable designs (e.g., without a metallic layer) this re-heating mechanism can increase the temperature of the core tube material to the extent of softening it, thus leading to a loss in stiffness. A close inspection of the plot for the outer surface temperature of the jacket reveals that within the first half of Cooling Trough #2 the cable has reached a temperature close to that of the water and thus the heat transfer rate from the cable to the water decreases with the normalized distance.

Figure 5 shows cable radial temperature distributions in the second water trough for several Normalized Distances, z. At a Normalized Axial Distance z = 0.2, the radial temperature gradient for the jacket is large due to the quenching of the jacket. At the same position the armor and the core tube are being heated. Farther downstream for larger values of z, the radial temperature profiles reveal that all the elements of the cable are transferring heat to the water although at a cooling rate that decreases as z increases. Also, from the plots for z = 0.35 and z = 0.45, it is evident that for the last third of the water trough the cooling rates, which are typically characterized by the slope of the temperature lines, have decreased.

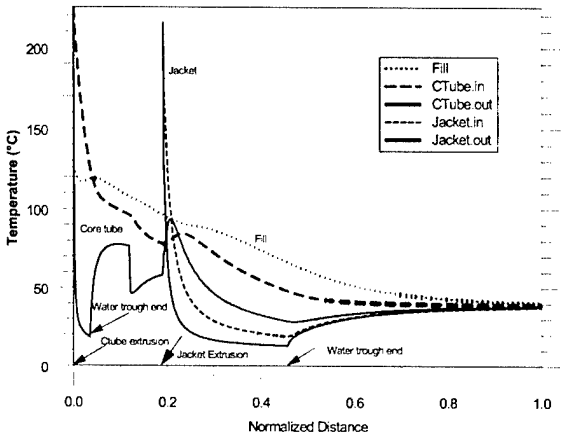


Figure 4. Temperature Variation for a High Fiber Count Metallic Fiber Optic Cable

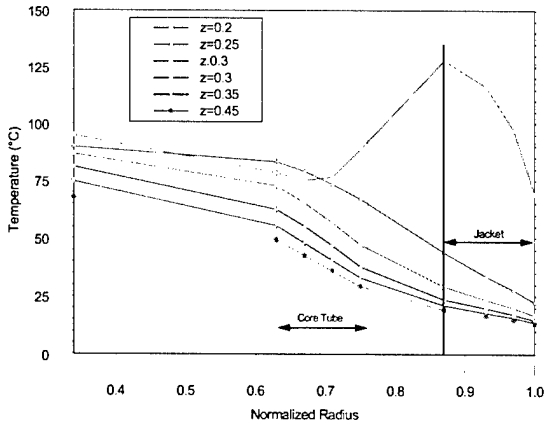


Figure 5. Radial Temperature Profiles for a High Fiber count Cable Metallic Fiber Optic Cable in the Second Cooling Trough Dielectric Cable

5.2 Dielectric Cable

Figure 6 shows characteristic temperature profiles for a dielectric cable. The manufacturing process for this cable is similar to that described in Section 2. Immediately after the core tube has been extruded, however, it enters into cooling Water Trough #1. This figure shows that the outer surface of the core tube undergoes a fast cooling rate until it leaves the cooling trough. Subsequent heat conduction from the core tube material to its outer surface increases the core tube outer surface temperature followed by a small axial temperature gradient while cooling the core tube in air. The jacket is extruded at a normalized distance equal to 0.14, immediately after the dielectric tape is placed around the core tube. Following the jacket extrusion, a sudden temperature decrease in the outer surface of the core tube is observed as a result of the core tube contact with the dielectric tape that initially is at room temperature. Therefore, the thermal barrier prevents an excessive reheat of the core tube by the jacket. Similarly to the case of the metallic cable shown in Figure 4, the outer surface of the jacket undergoes a fast cooling rate in Water Trough #2 thus reaching a temperature close to that of the cooling water at about two thirds of the length of the water trough.

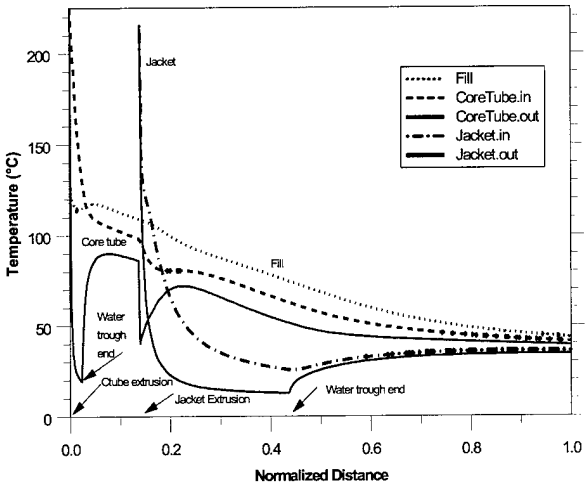


Figure 6. Temperature Profiles for a Dielectric Fiber Optic Cable

5.3 Dielectric Cable without Heat Barrier Tape

Figure 7 presents temperature profiles for the inner and outer surfaces of the core tube and jacket of a dielectric cable when the dielectric tape has been removed. The cable dimensions and manufacturing conditions are the same as those used for the case presented in Figure 6. A close examination of the temperature profile for the outer surface of the core tube reveals that after the jacket has been extruded the core tube experiences a 94% increase in temperature to 167 °C. This reheat of the core tube by the jacket, depending upon the mechanical properties of the core tube material, may result in a detrimental loss of core tube stiffness that translates into core tube deformations at the time the jacket is extruded.

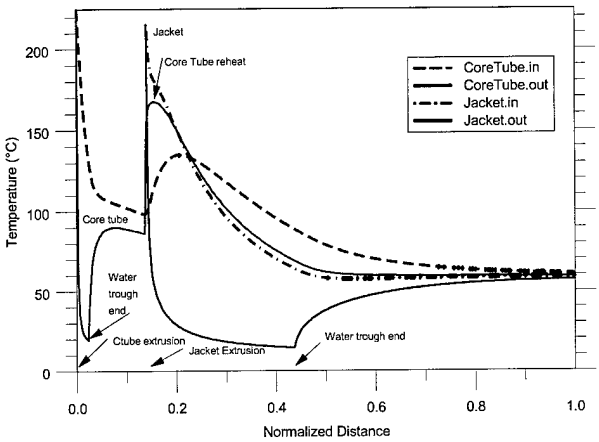


Figure 7. Temperature Profiles for a Dielectric Fiber Optic Cable without Heat Barrier Tape

5.4 Influences of Manufacturing Line Speeds

Figure 8 shows a comparison of temperature profiles for the cable of Figure 7 at several line speeds ranging from 66% of the target speed (TS) to 200% of the target speed. From these profiles two observations are clear. First, at higher line speeds the outer surface of the core tube encounters the jacket extrusion at a higher temperature. Specifically values range from 76 °C at 66% TS to 104 °C at 200% TS. This is attributed to the short residence time of the core tube in the water that does not allow enough time for significant thermal energy diffusion. Relative heat transfer improvements are possible, however, by increasing the length of the first water trough. Also, because of this limited heat transfer capability, as soon as the core tube leaves Water Trough #1, the thermal energy that was not fully transferred to the water reaches the surface of the core tube. Consequently, the core tube temperature increases because of the low convective heat transfer in air.

Second, the net temperature increase for the core tube before and after the jacket extrusion is smaller at higher line speeds. A possible explanation for this phenomenon is that at higher line speeds the convective thermal resistance is smaller, thus favoring the transfer of thermal energy from the jacket to the water than into the core tube.

5.5 Effect of Cooling Trough Lengths

In this section the effect of modifying the lengths of the water cooling troughs are discussed. For illustration purposes three cases for a dielectric cable without heat barrier tape are presented. This situation was chosen because, as discussed in Section 5.3, the absence of a tape will promote the re-heating of the core tube

after the second extrusion. The overall length of the cabling line has been preserved so the differences among the three cases that are presented is in the length of the water troughs used to cool the core tube and the jacket. Also, the distance from the end of the first water trough to the position where the jacket is extruded remains constant for all cases. Finally, because the intention of this section is to discuss the effect of water trough lengths, all the plots show temperatures to the end of water trough #2. For this reason the horizontal axis has been normalized using the distance from the start of Water Trough #1 to the end of Water Trough #2. Thus a "Normalized Length to end of Water Trough #2" of one in the horizontal axis corresponds to the exit end of the cable in Water Trough #2.

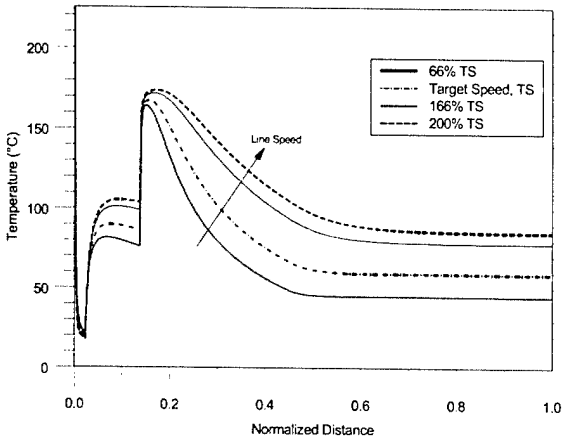


Figure 8. Temperature Profiles for the Outer Surface of a Core Tube at several Line Speeds for a Dielectric Fiber Optic Cable with no Heat Barrier Tape

Figure 9 shows temperature profiles for the inner and outer surfaces of the core tube and jacket for a baseline case. The same description as for Figure 7 applies here except that the cable outside diameter and line speed are different. The cable outside diameter is 70% of that corresponding to Figure 7 and the line speed is 33% larger. For these conditions the outside temperature of the core tube increases 82 °C due to the jacket extrusion. The heat transferred from the jacket into the core tube propagates into it thus increasing its bulk temperature. As the jacket cools, the core tube will start cooling and temperatures increase towards the centerline of the cable for Normalized Lengths greater than 0.54.

Figure 10 presents a comparison of core tube temperatures for modified water troughs lengths with respect to the baseline case. For each case, the lengths for the water troughs in terms of the horizontal axis variable "Normalized Distance to end of Water Trough #2" are shown in Table 1.

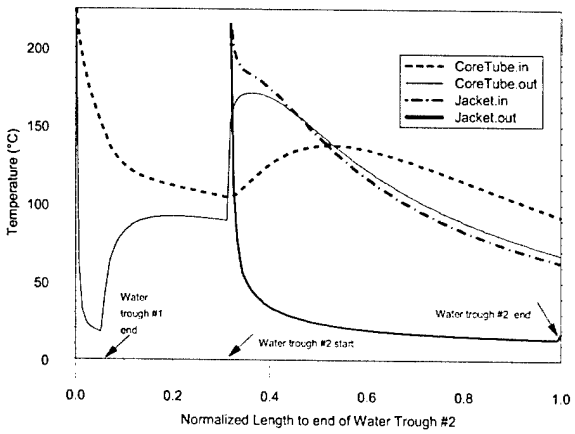


Figure 9. Baseline Case for the Cooling of a Core Tube and Jacket for a Dielectric Cable without Heat Barrier

In Figure 10, the outer surface for the core tube for Cases 1 and 2 when the core tube leaves Water Trough #1 exhibit an additional degree of cooling of 6.3 °C and 7.9 °C, respectively, as opposed to 19.7 °C obtained for the baseline case. The reason for this additional cooling for a longer Water Trough #1 is that more thermal energy has been removed from the core tube prior to the second extrusion. This reduction in thermal energy better positions the core tube to endure any re-heating from the jacket extrusion that otherwise might create softening of the core tube. This core softening, in turn, results in the immediate consequence of loss of its compressive stiffness. Importantly, in this simulation the overall length of the manufacturing line remained unchanged. The length of Water Trough #1 was increased at the expense of decreasing the length of Water Trough #2. Hence, from a heat transfer perspective, it is more effective to remove the heat from the fill and core tube before the jacket is extruded. This is because prior to the hot jacket extrusion, the heat will have less restriction to leave the core tube.

Table 1. Normalized Length of Water Troughs used to Analyze the Effect of Water Trough Length in Cooling

Case	Water Trough #1 Length*	Water Trough #2 Length
Baseline	0.050	0.680
1	0.180	0.550
2	0.375	0.375

- Based on Normalized Length to End of Water Trough #2.

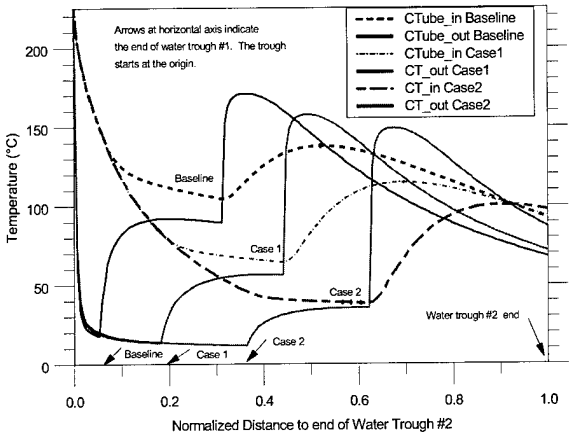


Figure 10. Comparisons for the Effect of Water Trough Lengths on the Cooling of the Core Tube

6. Conclusions

A user-friendly numerical tool, that allows the prediction of interior and surface temperatures of central core fiber-optic cable during manufacture, has been created and experimentally verified. Such a tool is very useful in providing valuable insights for the effects of changes in manufacturing conditions like extrusion temperatures, line speeds and cabling line configurations. In addition, this tool is a good predictor for the temperature profiles when designing cabling lines, introducing new cable designs or changing materials.

This numerical model can be easily adapted to provide the transient internal temperatures for most constant speed extrusion lines that build up a structure (other than cables) having a cylindrical or a flat geometry.

The temperature profiles reveal that either too rapid manufacturing line speeds or absence of an effective heat barrier in the cable can lead to temperatures high enough to cause detrimental core tube softening. From the analysis of water trough lengths it is concluded that the effects of core tube reheating after the second extruder can be attenuated by properly sizing the water troughs without affecting the length of the cabling line. As an alternative, two extrusions for the jacket will also help in decreasing the degree of reheating of the core tube.

Also, the results presented show that during the cooling of a cable, its jacket is quenched rapidly as soon as it enters the water and its outer surface quickly approaches that of the water, thus decreasing the heat convection transfer rate farther downstream. Therefore, the second water trough has to be sized carefully because excessive trough lengths do not improve the cable cooling effectiveness.

The numerical results for any of the cases presented in this paper clearly indicate that as soon as the cable leaves the second water trough and is cooled in air its surface temperature starts increasing due to the propagation of thermal energy towards the outer surface. This suggests that a better way to cool a cable would be to take advantage of the evaporative cooling mechanism by having intermittent cooling in water and air, respectively. The logic behind this is that when a cable leaves a water trough covered by a thin film of water, the evaporation of such film results in a very effective way of heat removal. After the thin film of water evaporates, the outer surface of the cable will increase its temperature while exposed to air. At this point it will be ready for a new immersion in water with a larger temperature differential between its outer surface and the water that in turn translates into a larger heat transfer rate.

7. Acknowledgments

Special thanks to the Materials Department of Optical Fiber Solutions for facilitating thermal properties needed to run the numerical model. Also the authors wish to thank their colleagues in the Outside Plant Cable Development Department for their valuable feedback.

8. References

[1] J. R. Refi, *Fiber Optic Cable – A Light Guide*, abcTeleTraining, Geneva, Illinois (1991).

[2] M. N. Ozisik, *Heat Conduction*, 2nd ed., John Wiley and Sons, New York (1993).

[3] S. V. Patankar, *Numerical Heat Transfer and Fluid Flow*, Taylor and Francis, New York (1980).

[4] M. L. James, G. M. Smith and J. C. Wolford, *Applied Numerical Methods for Digital Computation*, 3rd ed., Harper and Row, New York (1985).

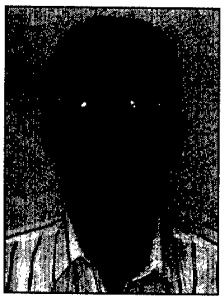
[5] Digital Equipment Corporation, *Digital Visual Fortran*, Version 6.0, Massachusetts (1998).

[6] Microsoft Corporation, *Visual Basic 6.0*, Redmond, Washington (1998).

[7] F. P. Incropera and D. P. DeWitt, *Fundamentals of Heat and Mass Transfer*, 4th ed., John Wiley and Sons (1996).

9. List of Symbols

c	Specific heat	Re	Reynolds number, uL/ν
h	Heat transfer coefficient	T	Temperature
k	Thermal conductivity	t	Time
L	Characteristic length	u	Speed
Nu	Nusselt number , hL/k	z	Axial coordinate
q	Heat transfer rate	ρ	Density
R	Radius	ν	Kinematic viscosity
r	Radial coordinate		



Luis M. Bocanegra
Lucent Technologies
2000 N. E. Expressway
Room 1E-52
Norcross, GA 30071

Luis M. Bocanegra has been a Member of Technical Staff at Lucent Technologies – Bell Laboratories in Norcross, Georgia since 1998. Mr. Bocanegra received his Diploma of Mechanical Engineer from the Catholic University of Peru in 1980, and MSME and Ph.D. degrees from West Virginia University in 1986 and 1988, respectively. He was a Fulbright Scholar from 1984 to 1986 and a United States Pharmacopeia Fellow from 1986 to 1989. During his appointment with Lucent Technologies he has been involved in several Outside Plant Cable Development projects, among them the development of Xpress Tube® cables and a capital expansion project. Prior to joining Lucent Technologies Dr. Bocanegra worked for several years in academia, his field of specialization is Thermo-Fluid Sciences. He also participated in Review Panels for the National Science Foundation and has been peer reviewer for ASME and ASEE.



Nathan E. Hardwick, III
1624 Durrett Way
Dunwoody, GA 30338

Nathan E. Hardwick, III was a Distinguished Member of Technical Staff in the Fiber Optic Cable and Materials Development at Lucent Technologies – Bell Laboratories, Norcross, Georgia. He has received B.S. and M.S. Degrees in Mechanical Engineering form the University of South Carolina and a Ph.D. in Mechanical Engineering from Lehigh University. At Lucent Technologies – Bell Laboratories, Dr. Hardwick served as team leader for (1) design and development of Ultra-High Fiber Ribbon Cable; (2) design and manufacturing processes for all metallic fiber optic cables, underwater cables, and lightning-resistant fiber optic cables; and (3) quality procedures for new product design. He co-invented new fiber optic cable design paradigms and theoretical optimization procedures for more efficient packaging of high fiber count cables. Dr. Hardwick also served as a Bell Laboratories Visiting Professor at North Carolina A&T State University. After retiring in 1999, Dr. Hardwick is consulting in fiber optic cable and communications systems design.

Specifying Technical Requirements for Fiber Optic Cables to be Installed on Existing Overhead Transmission Lines

Olga I. Bogdanova, Konstantin B. Kouftine

OPTEN Limited
15 Semenovsky per, Moscow 105023, Russia
(+7 095) 956-7597, E-mail: opten@opten.ru

Abstract

Deployment of optical cables on existing overhead transmission lines (OHL) that were only designed to bear ACSR conductors and conventional ground wires, encounters, on one hand, the problem of causing additional loads on line structures and ensuring reliable operation of OHL with optical cables, and on the hand the task of developing adequate design of OPGW and ADSS cables with required fibercount to create reliable fiber optic communications line (FOCL). To meet these two tasks a technique is proposed to specify OPGW and ADSS cables, which is based on the following provisions:

1. Creation of 3D model of OHL with actual distances between structures, structure geometry, physical and mechanical parameters of phase conductors and ground wires that can change their spatial position when affected by weather loads.
2. Determining installation conditions to meet applicable national code, in particular, short circuit rating for OPGW and required sag to ensure shield angle. For ADSS cables these conditions include ground clearance (when installing cable below phase conductors) or clearance to phase conductors to avoid inadmissible proximity to phase conductors.
3. Creation of virtual OPGW and ADSS designs using special programs.
4. Virtual stringing of the cables in 3D model of OHL.
5. Check for OHL structures strength margin with the cables installed.
6. Specifying requirements for aerial cables based on the created 3D model of OHL with the optical cable incorporated. Selection of cable drumlengths after splice closure locations were defined.

As a result of the described procedure, cable suppliers would be able to design and offer cables that are as tailor-made for specific conditions as possible. In this case, engineering design of optical cable installation and the installation itself can be implemented within short time with minimum expenditures on OHL reconstruction, and at the same time ensuring reliable operation of aerial cables.

Keywords: Transmission line; structure; optical cables; OPGW; short-circuit rating; ADSS; electric field stress; virtual cable.

1. Introduction

Construction of FOCL on existing OHL requires solving such important problems as selection of optical and mechanical parameters of the cable while ensuring OHL reliability after the cable is installed, and ensuring high reliability and availability of the communications line under design.

Optical cable shall provide reliable optic communications for the lifetime of 25-30 years. Cable lifetime depends both on the cable intrinsic parameters, such as:

For any type of aerial cable:

1. Cable strength members must provide mechanical strength and maximum admissible strain that ensure optical fibers performance for at least 25 years.
2. Cable protective covers and strength members must provide protection of optical fibers from external effects, and optical attenuation in the fibers shall not exceed values required for reliable performance of equipment.

for OPGW

3. Cable outermost strength members must withstand lightning strokes with specified charge.
4. OPGW must withstand short-circuit current that may emerge in the line as a result of asymmetrical operating conditions.

for ADSS cable:

5. Cable outer jacket must withstand electric field strength induced by phase conductors.

and OHL parameters such as:

6. Type, characteristics of structures and phase conductors, span lengths, clearance problems (crossings, etc) to ensure that loads on structures from the optical cable stay within permissible limits.
7. Weather conditions along the FOCL route.

for OPGW

8. For proper protection of OHL from lightning, cable sag at 15°C must not exceed values specified in national code for the span length, over the entire cable liftetime (taking creep into account).
9. Level of short-circuit current in the OHL, considering power grid development..

for ADSS cable

10. Cable sag under the worst weather loads must be selected so that the cable does not clash with phase conductors.
11. Cable attachment point must be selected so that electric field space potential on the cable jacket be within specified limits.

When developing cable design, the following factors guide the process:

1. Determination of strength members cross section area based on its short-circuit rating and dc resistance.
2. Everyday stress and worst-case load that depend on span length, installation conditions and weather loads, must be within set limits.

Everyday stress and maximum admissible load depend on one hand on strength members, and on the other hand, cable admissible strain that depends on cable design and applied loads such wind load, ice load and temperature variations. Regardless of optical core design, 'loose tube' or 'tight unit', optical fiber constantly experiences stress, in loose tube cables due to stranding, and in tight unit cables due to cable strain in the process of installation and during the lifetime. Therefore, when developing cable design, integral effect of all mechanical loads on optical fibers that they experience during cable manufacturing, installation and operation.

Specifying requirements for optical cables shall be based on results of OHL survey that yields the following information:

1. OHL condition
2. Type and condition of structures, ultimate admissible loads on structures.
3. Presence of long crossings and elevation differences.
4. Presence of ground wires on the OHL.
5. Ground wire condition (need for replacement).
6. Exact span lengths and conductor sags.
7. Short-circuit current magnitude in ground wire and its duration are determined.

2. Determining OPGW short-circuit rating

In overhead electrical networks with effectively grounded neutral wire, short circuits to ground are accompanied by current flowing in ground wire, grounded on structures, what results in thermal action upon the wire. In Russia 110 kV OHL have static wires grounded on each structure, above 220 kV OHL have static wires grounded in vicinity of substations (SS) and on some anchor structures. Exception to these practices is OHL with ice melting setup, and static wires used for PLC communications. Flashover of phase conductor insulators to structure results in short-circuit flow in ground wire, if it is a part of the current loop. In case ground wire cannot withstand the short-circuit current, it loses its mechanical strength and, as a consequence, breaks.

When FOCL is built, OPGW is grounded at each structure. Inadequate short-circuit resistance of OPGW leads to additional damage – loss of communication channel. Attempt to use OPGW of increased cross-section area with high short-circuit rating over the entire length of OHL will cause unreasonably high project cost due to more expensive OPGW and increased loads on structures, what requires their reconstruction. Therefore, it is essential to identify OHL sections with considerable thermal action of short-circuit current, then OPGW with smaller metal elements cross section can be used for the most part of the OHL. Besides, additional measures to reduce thermal action may be considered including installation of additional ground wire alongside OPGW, use of all-dielectric optical cable, modification of structure grounding resistance etc.

Thermal action B_{tp} of short-circuit current on ground wire, as well as on other conductors depends on the following factors: current i_{kt} in ground wire and current flow duration t_{trip}, that depend on relay protection parameters.

The highest current in ground wire occurs in case of single-phase-to-ground and double-phase-to-ground short circuit. There is no general criteria to find out what type of short-circuit will cause highest fault current in ground wire, so both types must be considered.

Magnitude of thermal action depends not only on current magnitude, but also on action time, which in its turn is dependent on relay protection of OHL. For that reason the following possible events are considered:

- In case OHL has two protections: primary one with absolute selectivity and zero-sequence current protection (ZSCP) as a backup one - failure of primary protection and actuation of the backup one.
- If OHL has only ZSCP, its failure and short circuit clearing by protections of adjacent line sections - remote backup;
- Unsuccessful auto-reclosing (AR) with repeat short circuit, number of such reclosing is set by ratio of AR;
- Circuit breaker failure with subsequent action of breaker fail protection (BFP), if any;
- Circuit breaker failure when BFP is missing and short circuit clearing by protections of adjacent sections.

In Russia, 330 kV and 500 kV OHL typically have two high-speed relay protections, so action of one the protections is taken into account in calculations. OHL's of this voltage level use towers with two ground wires isolated through the entire length and grounded at approach to substation. Replacement of one ground wire with OPGW, which is to be grounded along the entire line results in growth of short circuit current in OPGW. Current in OPGW considerably depends on resistance of the parallel ground wire. Fig.1 shows change in thermal action on ground wire in event of single-phase-to-ground and double-phase-to-ground faults in one TK-70 (all-steel, 70 sq.mm wire) of 330 kV (line with two ground wires).

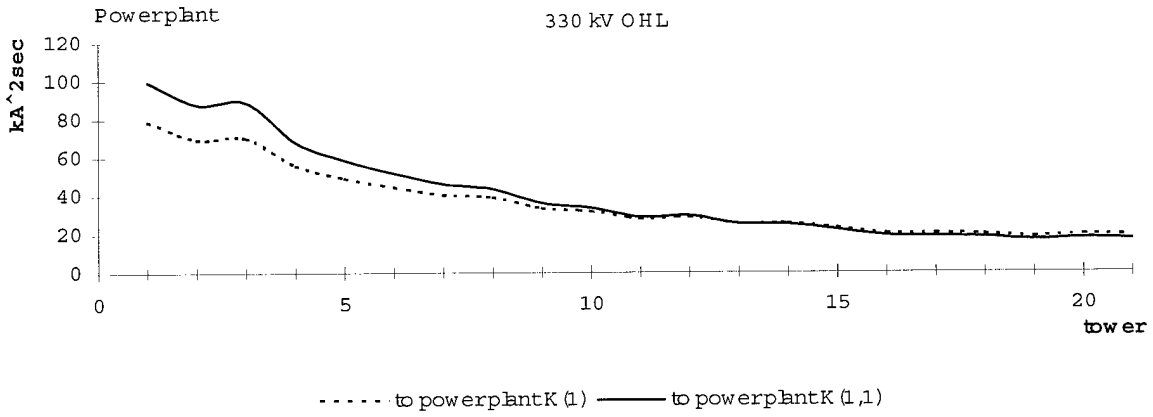


Fig.1. Thermal action on ground wire in case on single-phase-to-ground and double-phase-to-ground short circuit

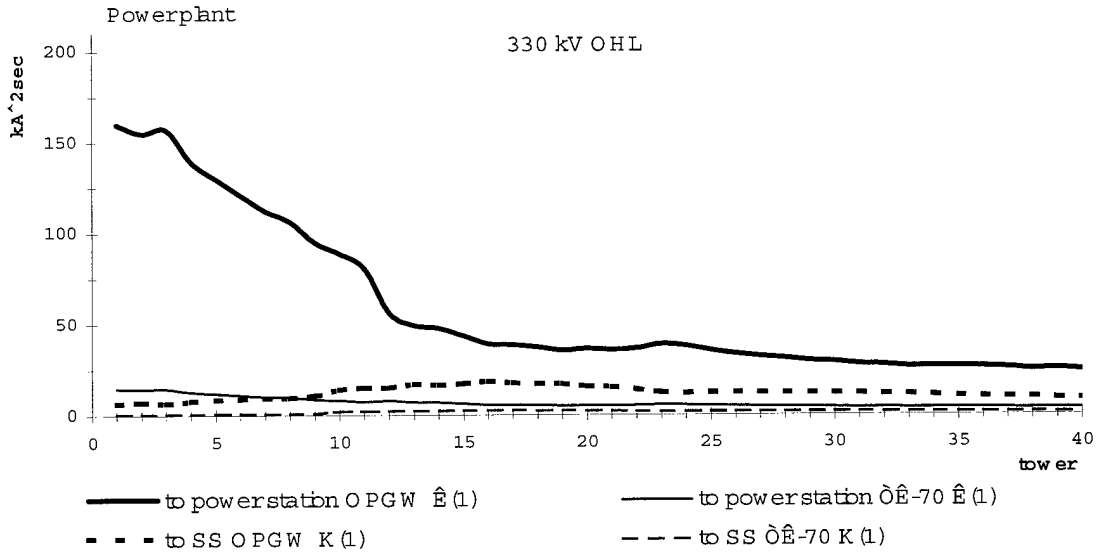


Fig.2. Thermal action on ground wire in case on single-phase-to-ground circuit.

Change in thermal action when one conventional ground wire is replaced with OPGW grounded at each tower of OHL is shown in Fig.2 (single-phase-to-ground faults).

Maximum short circuit currents to ground run at power plants, as well as substations located in areas with high energy consumption. Thermal action on ground wire in event of short circuit in vicinity of such facilities can reach 400 kA^2sec and sometimes even exceed this value. High thermal action can occur in OHL of any voltage, let it be 110-220 kV networks or backbone OHL 330 - 750 kV. As multiple earlier calculations demonstrate, high thermal action on ground wire is most likely in short OHL 110-220 kV at approach to substations, and in the middle of long OHL due to the fact that line may be tripped by stepped current protection, what significantly increases short circuit clearing time. For OHL 330-750 kV maximum magnitude of thermal action can occur only at approach to substation due to using two high-speed protections in such lines. There is a possibility that thermal action on ground wire will be higher in OHL of that voltage range due to using single-phase clearing of short circuit.

In case the problem arises of high short circuit currents at approaches to power plants or SS 330-750 kV, current in OPGW can be reduced by replacing the second parallel ground wire with another wire that has lower specific resistance. This solution is only required if OPGW to be installed alongside an existing ground wire does not meet requirements of short circuit rating.

If OPGW is deployed on OHL 110-220 kV in vicinity of large-capacity power plants and substations, the same technique may be used, provided FOCL runs on towers with two ground wires or there is a possibility to install second ground wire on the towers.

Thermal action at approaches to SS of all voltage ranges can be reduced by way of lowering tower grounding resistance.

Deployment or additional replacement of the second ground wire parallel to OPGW, as well as reduction of tower grounding resistance, is a redesign solution that can be applied to a specific OHL at engineering design stage after all data have been obtained required for calculation of OPGW short circuit rating.

As a result of the calculations of short circuit thermal action, preliminary OPGW diameter and dc resistance@20°C are determined, as well as rough lengths of the sections to receive OPGW with increased short-circuit rating. Preliminary parameters of the bulk OPGW are also defined taking into consideration the required fibercount.

3. Determining OPGW diameter and unit weight

Since OPGW is to be installed on existing OHL by replacing existing static wire, frequently OPGW diameter is limited by mechanical strength of tangent structures. To find out maximum admissible diameter of OPGW, tangent structures must be checked for residual mechanical strength. As far as anchor structures are concerned, it is essential to determined maximum admissible tension of OPGW under the worst weather loading for that area. Mechanical checks on structures involve specific weather cases and conductor and cable parameters; therefore virtual cable parameters are to be determined.

Once OHL survey results are available, cross-section area of virtual OPGW can be found based on stresses in the most heavily loaded components of structures that shall not exceed rated stresses after existing ground wire is replaced with OPGW.

Some software tools allow doing this very easily and fast. For example, based on survey results, OHL model is created in PLS-CADD, parameters of structures, conductors and virtual OPGW are entered. Manufacturer or supplier of OPGW is advised cable weight and tension limitations.

4. OPGW physical and mechanical parameters

Based on electrical design of OPGW and structures strength margin, basic physical and mechanical parameters of OPGW can be defined. However, it should be made certain that OPGW with those parameters can be suspended on OHL with proper shield angle that is with required sag.

When talking about cables sag, it should be kept in mind that tensile load in OPGW results in its creep. The creep phenomenon of ACSR conductors has been extensively discussed by CIGRE, and line designers are recommended to put creep into design, otherwise clearance problems may arise. OPGW creep will lead to sag increase as compared with steel static wire, which practically does not experience any creep, and, as a consequence, infringement of shield angle. Therefore, OPGW designer should be advised OHL span lengths with respective sag limitations, stressing that the said sag is specified for final condition after creep, as well as weather loadings for the OHL. In this case, designer will be able to develop adequate design to fully meet customer's requirements.

5. Specifying requirements for OPGW

In that manner, based on OHL analysis and above-said calculations, requirements for OPGW can be specified that will ensure reliable operation of OHL and FOCL, and at the same time make the project as cost-effective as possible, with minimum, if any, reinforcement of existing structures. Therefore, the following basic factors must guide the process:

- Calculation of currents that may flow in OPGW (with preliminarily defined diameter and dc resistance at 20°C) in case of single-phase-to-ground and double-phase-to-ground short circuits, with fault point changing along the OHL.
- Calculation of thermal action of maximum short-circuit current (single-phase-to-ground or double-phase-to-ground) on OPGW for specific clearing time, with fault point changing along the OHL.
- FOCL route analysis, identification of critical spans (maximum length, maximum elevation difference), structures geometry and their strength margin.
- Calculation of required sags of OPGW at 15°C in the critical spans, taking into consideration cable creep over its lifetime.
- Calculation of OPGW admissible diameter and weight in terms of maximum admissible loads on tangent structures.
- Calculation of maximum admissible tension of OPGW to meet admissible loads on anchor structures.
- Requirement for lightning resistance in Coulombs, which depends on lightning intensity along the OHL and required reliability of the FOCL under design.
- Specifying fibercount and optical parameters of OPGW.

The following requirements for OPGW are provided to cable manufacturer:

- Fibercount according to G...(652, 655)
- OPGW outside diameter, mm - no more than .....
- Weight per unit length, kg/km - no more than .....
- Maximum admissible tension, kg - no more than .....

OPGW shall withstand:

Initial temperature for short-circuit action, °C .....

- Dc resistance at 20°C, Ohm/km .....
- Short-circuit current for 1 sec, kA - at least ....
- Lightning resistance, C .....

- Weather loadings

Radial ice, mm, at the temperature of ...°C.

Wind pressure in icing conditions ... kg/m^2.

Maximum wind pressure at the temperature....°C .... kg/m^2.

Average temperature ...°C.

Operating temperature range from minus ...°C to plus .....°C

Required sags at 15°C are given are the table below.

Table

Span length, m	OPGW sag after creep, m

6. Designing fiber optic communications line using All-Dielectric Self-Supporting (ADSS) cable

When designing FOCL with ADSS cable, one of the main limiting factors to be kept in mind is that installation of ADSS cable will always result in additional loads on structures, as, in contrast to OPGW, presence of this cable had not been originally designed into the OHL. To make decision on possibility and feasibility of using ADSS cable, structures strength margin must be investigated and conclusion made whether cable can be installed without reinforcing the structures. Preliminary mechanical calculations to determine loads on structures can be conducted by way of introducing a virtual cable in OHL model. Before that, cable attachment points at structures should be selected.

The problem of selecting attachment points for ADSS cable arises not only from mechanical strength of structures, but also from electric field stress on the cable jacket. The well-known phenomena of dry band arcing and corona may cause outer jacket damage. Since cable optical core and aramid strength yarns are protected from environmental effects by polymer jackets, it is essential that the outer jacket remained undamaged for the entire lifetime of the cable. Ways to ensure jacket protection from such effects as UV radiation and chemical contamination are well established. The problem of jacket damage due to dry band arcing seems to be solved, for example, by using tracking-resistant materials. However, jackets are not resistant to corona discharges, so if the risk exists that cable jacket can be damaged by corona, special protection devices, such as corona ring or corona coil, are to be used. Full analysis for selection of attachment points and assessment of the risk of corona discharge and dry band arcing can only be carried out after a preliminary survey of OHL, when information is available on mechanical and electrical parameters of OHL, phase conductors and structures, span lengths and clearances.

The best way to go further is to create, based on the acquired data, a computer model of the existing OHL, which can be used to specify requirements for ADSS cable. Besides, this model allows to design installation of actual ADSS cable, determine drumlengths.

Since mechanical properties of ADSS cable differ significantly from those of ACSR conductors, what leads to different sags of the cable and phase conductors, the need arises to model cable behavior in span under varied weather loadings to define admissible cable sag. The sag, in its turn, depends on permissible clearance between cable and phase conductors, or clearance to the ground. With that purpose, we use a program for designing ADSS cable that was specifically developed for customized applications. Cable is designed using real material characteristics as used by cable manufacturers. This cable can be called "virtual", as it is not designed for a specific manufacturer, but is only a makeshift model that predicts suppliers' offers.

An important criterion for selection of ADSS cable attachment point is its clearance to phase conductors under wind and ice loads and their combination. Distance between ADSS cable and phase conductor at structure should be such that a lineman had a safe access to the cable, and in the span a physical contact of the cable and phase conductor must be excluded.

It should be noted that minimum clearance between ADSS cable and phase conductor usually occur not in the midspan, but somewhere between midspan and supports due to their significantly different blowout catenaries and deflection angles. In case check has not been made for the clearance in 3D, blown out cable may get close to a conductor and be subjected to high electric field stress exceeding jacket resistance threshold.

When selecting cable attachment points, minimum admissible clearance to ground objects along the OHL should be considered if the cable is to be installed below phase conductors. When OHL runs in populated area with large number of crossings such as railroads and low-voltage power lines, ADSS cable may have to be installed with small sag, that is with high tension what makes cable considerably more expensive and results in increased loads on structures (as larger diameter cannot be compensated for by lower cable height in terms of resultant loads on structures). In this case preference should be given to installing cable in power space, for example at the level of the middle conductor.

Virtual cable is strung in all spans of the OHL under design with the tension defined at the earlier design stage. After that, clearances are checked between the cable and the ground (objects on the ground), crossings and phase conductors under rated weather loadings for that area. If required, sag in maximum span can be adjusted. If program for designing ADSS cables is not available, computer model of OHL, which is essential for selection of optimum cable design, can be used by line designers to define required sags in various weather cases to meet the above-said criteria.

Thus, specifying requirements for ADSS cable is based on the following steps:

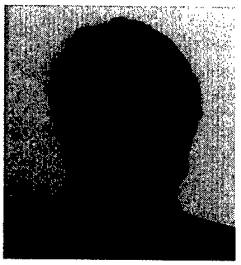
- Determination of fibercount and optical parameters.
- Selection of cable attachment point from calculation electric field space potentials and strength taking into consideration structure design, line voltage, type of phase conductors and phasing (not to forget about phase transposition along the line), design of cable clamps, in case of double-circuit line probability and duration of one circuit being deenergized, contamination in the area (proximity of sea, industrial pollution, etc.)

- Determination of admissible cable sag (in final condition after creep) in the maximum span and span with maximum elevation difference under the rated radial ice for the area.
- Check upon the determined sag in other heavy weather cases for potential clearance problems.

7. Conclusion

The way of specifying requirements for aerial optical cables described above allows power utilities to assess impact the optical cable is going to make on OHL even before offer is received from cable supplier. In Russia where typically steel ground wires of diameters 9 – 11 mm are used, structures have very little strength margin to sustain loads from OPGW and ADSS cables. Therefore, it is essential that customers thoroughly analyzed condition of existing transmission line and how a cable would fit in. In this respect, 3D computer model of transmission line, built using survey data, with virtual optical cable helps simulate varied installation choices and specify precisely requirements for the cable to request an offer from cable manufacturers.

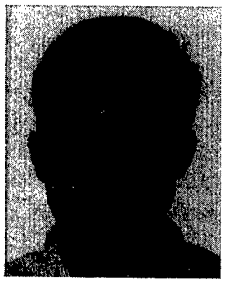
Authors



Olga Bogdanova received her M.S.E.E. from Moscow Power Engineering University in 1973 and Ph.D Degree from the Russian Electrotechnical Institute in 1985.

From 1973 to 1984 she worked with the Research Institute of Electrotechnical Ceramics and investigated radiation impact on ceramics. From 1984 to 1995 she was with Cable Research Institute, where she developed new designs of optical cables and testing techniques. Olga Bogdanova joined OPTEN Limited in 1995 and since then has headed Aerial Optical Cable System Design Group.

E-mail: bog@opten.ru
Mailing Address: OPTEN Limited., 15 Semenovsky per., Moscow, 105023, Russia



Konstantin Kouftine received a Master's Degree in Mechanical Engineering from Moscow Power Engineering University in 1990. He has worked in the Aerial Optical Cable System Design Group with OPTEN Limited as a Senior Applications Engineer for the past 4 years. From 1992 to 1997 he worked with Firm ORGRES of the Ministry of Power of Russian Federation and was responsible for testing aerial optical cables and conductors.

E-mail: kuftin@opten.ru
Mailing Address: OPTEN Limited., 15 Semenovsky per., Moscow, 105023, Russia

Novel ADSS Cable Design Technique for a Reduced Weight and Reduced Cable Diameter

Marcello Valente Giacaglia
Lucent Technologies Brazil – Optical Fiber Solutions
Campinas, Sao Paulo, Brazil
+55-19-3707-7915 · mgiacaglia@lucent.com

Abstract
All Dielectric Self-Supporting (ADSS) cable weight and diameter are very important characteristics as they directly impact the mechanical tension induced on the supporting structure (pole or tower).

The cable diameter itself has to be as small as possible due to its quadratic influence on the tension when ice and/or wind are considered.

Current design techniques use aramid as the cable strength element but they have limitations for very high spans or very adverse environmental conditions.

This paper presents the development and results of a novel technique for designing ADSS cables with reduced weight and diameter, substituting poly-para-phenylene benzobis-oxazole (PBO) fiber for traditional aramid.

Keywords
Optical cable; ADSS; self-supported; aerial cable; PBO; aramid.

1. Introduction
The recent increase in demand for telecommunications services that started with the Internet has been pushing the Telecom Industry to continue deployment of new fiber optic backbones. Deployment in Wide Area Networks (WAN), Metropolitan Area Networks (MAN), Local Area Networks (LAN) and local access, such as Fiber To The Curb (FTTC), Fiber To The Building (FTTB), Fiber To The Home (FTTH) and Fiber To The Desk (FTTD), also is increasing.

One key consideration for building a new long distance network is where the cable will be installed. Possible options are along highways and railways, within gas and oil ducts, and undersea or on overhead lines. Recently, companies who aren't traditionally part of the Telecom Sector have developed new business models resulting in increased revenues as they charge service providers for the use of their Rights Of Way (ROW). Some of these companies are also deploying their own cables and becoming carrier's carriers.

Many of the Utilities Companies that have entered this market are installing ADSS cables on their overhead lines. However, initially the cable industry has faced some issues in designing cables strong enough to support installation over the long spans often found in the field. Stronger cables meant higher weight and diameter. That led to a need for a higher load that the cable and towers should support. Additionally, the cable is submitted to environmental factors such as wind pressure and ice loading. The incremental tension induced on the cable by these factors is also directly correlated with its diameter and weight.

It has long been the goal of the fiber cable industry to design ADSS cables with reduced weight and diameter, with increased maximum installation span capability, and with the ability to use this type of cable on Extra High Voltage (EHV) overhead lines.

2. Cable Strain under Field Conditions
Aerial cable is under continual stress as it is subjected to constant environmental change over its lifespan.

Depending upon where it will be installed, the cable will be exposed to temperature variations in the range of –50 degC up to +50 degC. It will also face sunlight, rain, wind, ice deposition, chemical corrosion and electric stress. The cables must be designed to not only withstand these very aggressive conditions, but also protect the optical fibers during the 30 to 40 years life expectancy.

Regarding mechanical stress, the worst environmental condition the cable has to support is the combination of low temperature, ice loading and wind pressure. The ANSI-C2 National Electric Safety Code (NESC) sets guidelines for designing aerial cable to be installed in USA, dividing the country into three "loading districts", where the conditions are classified as Light, Medium or Heavy loading.

In every installation project, inside or outside the USA, specific local conditions must be considered to define the cable design to be used.

As is well known, the cable strain under loading conditions is directly related to the cable weight and diameter, so the lower these characteristics, the less the cable strain under the same conditions.

As an example, let's compare the effect of weight and diameter on the strain of two cables installed under the same conditions:

Table 1. Comparison of two cables

Characteristic	Cable 1	Cable 2
Diameter (mm)	17	14
Weight (kg/km)	250	180
Modulus (kgf)	250,000	250,000
LEC (10^{-6} 1/°C)	2.2	2.2
Span (m)	500	500
Sag (m)	25	25
NESC condition	Heavy	Heavy
Maximum loaded tension (kgf)*	1,900	1,700

*The maximum loaded tension was calculated using the equation of change of state.

A target for every cable manufacturer is to design cables with diameter and weight as low as possible so a reduction on the maximum loaded tension can be achieved with consequent reduction on the tension at the supporting structure (pole, tower, etc.).

3. Current Technique

Usually, the strength element used in ADSS cables is aramid yarn, a dielectric material with very high modulus and low specific weight that has been demonstrated as an excellent option to achieve the desired results.

Unfortunately, there is a practical limitation on the quantity of aramid yarns that can be used to produce a cable. This limitation is related to the thickness of the aramid layer, because the thicker it is, the more difficult it will be to achieve the desired performance. For the cable to have good tensile performance, the aramid yarns have to be well distributed around the cable core so the tension applied to the cable can be equally divided between each yarn. The consequence of this limitation is a ceiling or maximum working tension value of the cable.

Example: a 72-fiber cable with the following characteristics:

Table 2. Characteristics of a 72-fiber cable

Characteristic	Cable 3
Diameter (mm)	17.7
Weight (kg/km)	278
Maximum working tension (kgf)*	2,700
Modulus (kgf)	444,286
LEC (10^{-6} 1/°C)	1.39

* Without fiber strain.

A cable with the above characteristics can be installed on a 1,500 meter span with 5% EDS sag, supporting the NESC light loading conditions, or it can be installed on a 650 meter span with 5% EDS sag and support the NESC heavy loading condition.

4. Novel Technique

The proposed novel technique is to substitute the aramid yarns with another synthetic fiber with higher modulus. This new material is poly-para-phenylene benzobis-oxazole (PBO).

Table 3 presents a comparison of some characteristics of PBO and aramid; both are high modulus versions:

Table 3. Comparison of PBO and aramid

Characteristic	PBO-HM	Aramid-HM
Density (g/cm³)	1.56	1.44
Tensile strength (g/denier)	42	24
Tensile modulus (g/denier)	2,000	900
Elongation at break (%)	2.5	2.5
Thermal expansion coeff. (10^{-6} 1/°C)	-6	-2

*These values can be found on manufacturers' catalogs.

Looking at the above characteristics, we can point to an express difference in the material modulus: PBO modulus is more than twice as high as the aramid's. This is the most important characteristic of a strength element when designing an ADSS cable.

Using the PBO characteristics to design an alternative to Cable 3 that can support the same environmental conditions described, provides the following results:

Table 4. Characteristics of an alternative 72-fiber cable

Characteristic	Cable 4
Diameter (mm)	15.8
Weight (kg/km)	229
Maximum working tension (kgf)*	2,400
Modulus (kgf)	401,686
LEC (10^{-6} 1/°C)	-1.84

* Without fiber strain.

The most significant result is a more than 11% reduction in the Maximum Working Tension (MWT), which is very good from the point of view of mechanical resistance of the supporting structure.

Another consequence of using PBO is the possibility of producing cables with higher MWT when compared with aramid. Table 5 presents a cable with the same diameter as Cable 3.

Table 5. Characteristics of a high MWT cable

Characteristic	Cable 5
Diameter (mm)	17.7
Weight (kg/km)	278
Maximum working tension (kgf)*	5,500
Modulus (kgf)	924,984
LEC (10^{-6} 1/°C)	-4.11

* Without fiber strain.

This cable can be installed on a 3,000 meter span with 5% EDS sag under NESC light loading conditions or on a 1,400 meter span with 5% EDS sag under NESC heavy loading conditions.

The achievable span for Cable 5 is twice the span for Cable 3!

Tables 6 and 7 compare cables designed with PBO and aramid for various installation spans.

Table 6. Comparison between PBO and Aramid for 72 fibers cable to NESC light loading condition

Span (m)	Cable with Aramid		Cable with PBO	
	Diameter (mm)	MWT (kgf)	Diameter (mm)	MWT (kgf)
200 (2% sag)	14.6	490	14.5	485
400 (4% sag)	14.9	700	14.6	690
600 (5% sag)	15.3	940	14.8	910
800 (5% sag)	15.8	1,300	15.0	1,230
1,000 (5% sag)	16.4	1,690	15.3	1,570
1,500 (5% sag)	17.7	2,700	15.8	2,400
2,000 (5% sag)	19.2	4,000	16.4	3,380
3,000 (5% sag)	22.3	7,060	17.6	5,450

Table 7. Comparison between PBO and Aramid for 72 fibers cable to NESC heavy loading condition

Span (m)	Cable with Aramid		Cable with PBO	
	Diameter (mm)	MWT (kgf)	Diameter (mm)	MWT (kgf)
200 (2% sag)	15.4	1,060	14.9	1,040
400 (4% sag)	16.4	1,700	15.3	1,650
600 (5% sag)	17.2	2,360	15.7	2,240
800 (5% sag)	18.3	3,260	16.2	3,030
1,000 (5% sag)	19.4	4,230	16.7	3,860
1,500 (5% sag)	22.2	6,960	18.0	6,040

Note: Cables 3, 4, 5 and all cables from Tables 6 and 7 are the same design, with the exception of the strength element.

5. Prototype

A prototype was produced to confirm the theoretical calculations.

Table 8. Characteristics of the prototype

Characteristic	Prototype
Diameter (mm)	13.6
Weight (kg/km)	171
Maximum working tension (kgf)*	800
Modulus (kgf)	196,468
LEC (10^{-6} 1/°C)	-0.33

* Without fiber strain.

The prototype was tested to check the real cable modulus.

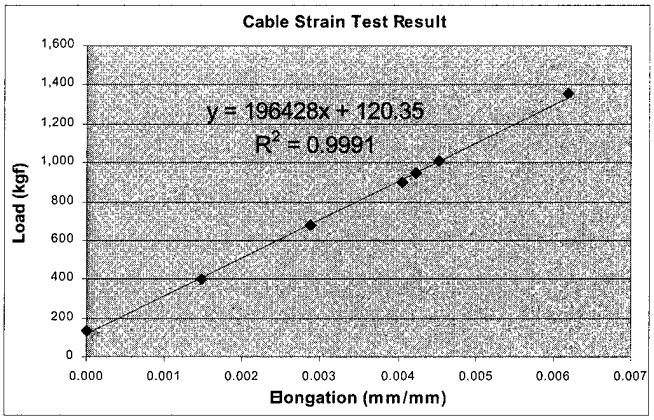


Figure 1. Prototype strain test result

The measured cable modulus is almost equal to the calculated, which is a great result.

A complete set of tests is underway to fully characterize the cable, with special attention to Creep and Vibration tests.

6. Conclusions

As shown in this paper, PBO has already been proven as an effective alternative material to the traditional aramid yarn solution when designing ADSS cables.

The PBO option demonstrates more and more advantages as installation spans and/or the loading conditions increase. We can highlight the 3,000 meters span cable on Table 6 that has 23% lower MWT for PBO than the aramid solution.

Another important advantage of the PBO solution is that its use results in a thinner strength element layer that is more stable with regard to cable production process and cable performance.

7. References

[1] R.C. Gravely III, J.W. Thorton, "Materials, Design and Performance of the Next Generation of All Dielectric Self-Supporting Aerial Loose Tube Fiber Optic Cable" *Proceedings of the 46th IWCS*, p. 191 – 197 (November, 1997).

[2] C. Militaru, "Stress-Strain, Creep and Temperature Dependency of ADSS (All Dielectric Self Supporting) Cable's Sag & Tension Calculation" *Proceedings of the 48th IWCS*, p. 605 – 613 (November, 1999).

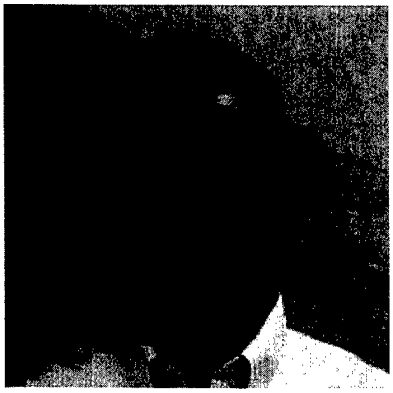
[3] T.-C. Chang et all, "Fiber Strain On Field-Deployed Aerial Optical Cables" *Proceedings of the 49th IWCS*, p. 408 – 411 (November, 2000).

[4] Fu Binlan, "The Development of All Dielectrical Self-Supporting Fiber Optical Cable (ADSS) for Use on Power Lines in China" *Proceedings of the 48th IWCS*, p. 593 – 597 (November, 1999).

[5] ANSI-C2 National Electric Safety Code.

[6] IEEE P1222 Draft, "Standard for All Dielectric Self-Supporting Fiber Optic Cables (ADSS) for Use on Overhead Utility Lines", (1995).

Author



Marcello V. Giacaglia has been engaged in research and development of optical cables since received his degree as an Electrical Engineer from the University of Sao Paulo – Brazil in 1991. He joined Lucent Technologies in 2000 to manage the Technology Department of the brand new Lucent Optical Cables Plant in Campinas – Brazil.

Mailing Address: Lucent Technologies NSB Ltda., Rua Thomas Nielsen Jr. 150, Campinas, 13097-660, Brazil.

Lighting Strike Tests for Mechanically Stressed OPGW Cables

O. I. Bogdanova, I. P. Kuzhekin*, L. V. Levitova*
OPTEN Ltd, 15 Semenovsky per., Moscow, Russia
*Moscow Power Engineering Institute (Technical University),
14 Krasnokazarmennaya str., 111250 Moscow, Russia

Abstract
The problems of resistance of OPGW to the direct lightning strokes are considered. The necessity of lightning strike tests for OPGW is shown and the main test conditions are suggested. One of main condition is the effect of the discharge channel with a normalized current on OPGW what is mechanically stressed, but not less than the everyday stress.

1. Introduction
Application of OPGW for establishing reliable communications is the most optimal way. However, besides communications OPGW should protect the overhead line against lightning strokes.

OPGW have more complex design and lower mechanical strength as compared with conventional ground wires. Direct lightning strokes accompanied by lightning current flow and powerful thermal emission from the lightning channel can result in breakage of a part of strands, thermal effect on optic fibers and reduce OPGW mechanical strength. Ground wire rupture on OHL is prohibitive, as this causes emergency situations and loss of communication. Therefore the issue of OPGW lightning resistance is of high priority.

The effect of lightning stroke on OPGW is poorly studied, both theoretically and experimentally. The available results of simulation of lightning stroke into OPGW testify to low lightning resistance of many types OPGW.

As of now, the thermal effect of the lightning channel on metallic objects, for example, an aircraft hull, is rather well studied. Thus there are computational methods of temperature fields in the vicinity of lightning channel contact point. In particular, the analytical formulas /1,2/ for calculation of temperature fields in metal plates and hemi-space give good concurrence with experimental data. However, when lightning strikes OPGW, there is a more complex situation due to uncertainties of current distribution along the strands and heat transfer from the reference point into the cable. But the main relationships describing the processes in metallic objects can be applied to the case of lightning stroke to OPGW.

One of main criteria for OPGW lightning resistance is retention of its mechanical strength, when operation of optic fibers is warranted for the service life. Therefore, it is necessary to conduct lightning tests for OPGW not only with real currents, but also with mechanical stresses typical for OPGW after installation.

The aim of the paper is to discuss the problems of lightning channel effect on OPGW and lightning tests.

2. Lightning effect on OPGW
If the parameters of OHL (voltage, type and size of supports, number of ground wires, hang angle etc.) and also the lightning activity in the region are known, it is simple to determine a specific number of lightning strokes N onto the ground wire per 100 km per year. The estimations show for OHL in middle latitudes on a plain terrain N~ 20 irrespective of the voltage.

Among the indicated number of strokes approximately 2-3 strokes occur from a positively charged cloud, thus the lightning current is an unidirectional pulse with a front duration of 10^{-5} s and a pulse duration of some hundreds microseconds. The remaining strokes occur from a negatively charged cloud and are multi-component current pulses. The initial high peak current has a front duration of 10^{-5} s and pulse duration of 10^{-4} s. The restrike current has front duration by an order of magnitude less. Between the initial and restrike current pulses there are the intermediate and continuing current components transferring the main charge.

Lightning strokes from a positively charged cloud are characterized by higher amplitudes of a current and charge as compared with these from a negatively charged cloud. In spite of the fact that the number of positive strokes is less, they could be more detrimental for OPGW.

Lightning current flows only through a few strands. Let's estimate thermal effect of a unidirectional current pulse with a normalized specific energy of $2\hat{}10^6$ Joul/ohm (according to IEC 1024). On the assumption that this current flows through 4 aluminum strands 2 mm in diameter in both directions, we shall receive additional heating of these strands by 600 K, that will cause the metal melting. Thus, to a surface heat source from the lightning channel the solid source is added capable of significantly increasing the temperature.
It is necessary to note that this effect will take place on small (about centimeters) distances from the contact point where there isn't leveling of a current density across the

OPGW section. The surface effect at current pulses with high rate of rise will cause an additional energy emission into strands.

3. Thermal effect of a lightning flash at the contact point

A heat flow from the lightning channel enters the object. This flow is developed in a reference zone of the channel, in the region of an anodic/cathodic voltage drop of about 10^{-4}cm in width. At such width the heat flow even at lightning stroke into a strand can be considered plane.

The heat flow is usually given by the equivalent anodic/cathodic voltage drop and the current. As the anodic/cathodic voltage drop is fairly independent of the current and time, the basic parameter defining a heat flow into the object is the transferring charge.

The calorimetric measurements of anodic/cathodic voltage drops gave following values /1/: for aluminum the cathodic voltage drop - 10,2 V, the anodic voltage drop - 8,2 V; for steel - 7,2 V and 6,1 V, respectively.

There is a certain current density at the contact point. On the aluminum cathode it is 18 A/mm^2, on the anode - 25 A/mm^2. Correspondingly, for steel - 22 and 28 A/mm^2. Current densities reach these values fast enough (in time less than 10^{-5}s) and remain practically constant. When changing a current, sizes of contact zone also change: with decrease of a current the spot is reduced, and with increase - extends.

The densities of a heat flow into the object are obtained also. For the aluminum cathode a density of a heat flow is of $1.8\text{^}10^8$ W/m^2, for the anode – $2.1\text{^}10^8$ W/m^2; for steel – $1.6\text{^}10^8$ and $1.8\text{^}10^8$ W/m^2, respectively. These data are also true for OPGW strands, i.e. they can be used for calculation of thermal processes in ÎPGW. The results of calculations are in a good agreement with experimental data for thermo-physical characteristics of a material at room temperature.

The calculations of thermal fields in continuous objects and plates enable to set the trends inherent to OPGW too. Namely:

- Density of a heat flow remains constant; the reference zone area varies with current;
- The main contribution to thermal processes is introduced by a continuing current component, and influence of the initial pulse current components is insignificant;
- The temperature rise of a material in certain depth at the same charge transfer appears to be more, when increasing the amplitude of continuing current and decreasing its duration.

As it was mentioned earlier, for OPGW it is necessary to take into account the energy entering the strands at the expense of Joule heating. Lightning current at the vicinity of the contact point flows primarily through the strands spaced directly nearby the reference zone. The current flowing to adjacent (not struck) strands is hindered because of a contact resistance between strands. At lightning strokes into OPGW nearby the support the pulse current flows during several microseconds in one direction (to a support), as the ground resistance of a support is much less than OPGW wave resistance, what increases heating of strands running towards a support.

4. Lightning tests of OPGW

At present there are publications and regulatory documents for OPGW lightning strike testing. However, test conditions are selected in a rather arbitrary way. In one case [3] tests are conducted at the oscillatory form of the initial current pulse and with OPGW not stressed mechanically. In other cases there isn't a current pulse of necessary amplitude, or just any available current source is used. For that reason, a need has arisen to profoundly substantiate lightning strike test conditions.

As follows from the analysis of thermal processes at an oscillatory pulse current, the heat flow will be pulsating in peripheral areas of reference zone, and the current density will be unequal at different directions of current flow. As a result, the thermal effect appears underestimated, and the tests are not adequate to lightning current effect. Therefore the initial current pulse should be unidirectional. Besides the choice of amplitude of the initial current pulse should be defined by number of lightning strokes into OHL located in the region with known thunderstorm activity. Thus its amplitude should not be less than the average amplitude the initial pulse current component of lightning. Also it is evident that lightning strike tests should be conducted for OPGW mechanically stressed (not less than everyday stress). Our own testing OPGW of different types have shown that at increase of mechanical stress and similar test impulse the number of broken strands increases. The examples of OPGW destruction after lightning strike tests are show in Fig. 1. The tests have been conducted at the Lightning protection laboratory of the Moscow power engineering institute (Technical university) by means of four-component lightning current generator. The test current consists of three components: initial current pulse with average parameters, standard intermediate current component and continuing current component with the varying charge transfer.

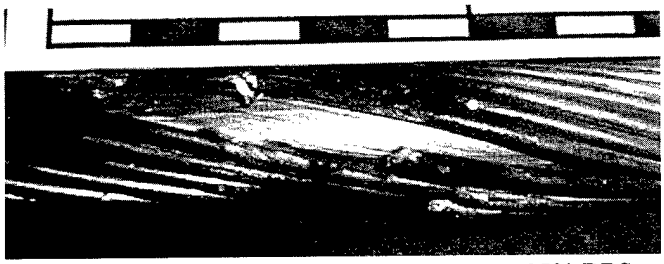


Fig.1. OPGW after lightning test tensioned at 25% RBS (constant component charge 60 C)

5. Conclusions

1. It is necessary to conduct lightning strike tests for OPGW, because today it isn't possible to calculate its heating and degree of failure. The available literature data allow only to formulate the initial conditions of the thermal problem.

2. The test current should include besides a continuing current component, unidirectional pulse current component with parameters typical for lightning

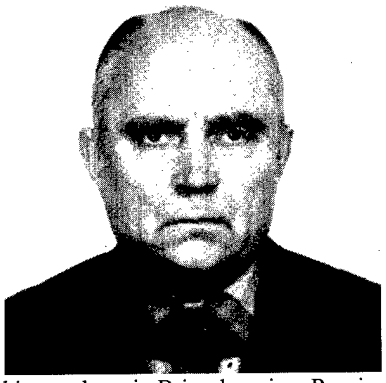
3. OPGW should be mechanically stressed in testing.

6. References

1.N.P. Abramov, I.P. Kuzhekin, V.P. Larionov " The characteristics of melting the walls of metal objects at a lightning stroke ". - *Electricity* 1986, ' 11.

2. N.P. Abramov, I.P Kuzhekin. " Calculation of heating the walls of metal objects at a lightning stroke ". - *Electricity* 1990, ' 5.

3. L. Karpinski, R.Malewski, J.Dabrowsky et all " Lightning current withstand capability of optical overhead ground wires ". - *CIGRE, Session* 2000, 35-302.



Ivan Kuzhekin was born in Brjansk region, Russia, in 1935. He graduated from Moscow Power Engineering Institute as electrical engineer in 1959.In 1969 he defended a thesis « Electrical breakdown and discharge in liquid». His field of work is high voltage impulse technology. He is presently the assistant professor of MPEI.



Ljudmila Levitova was born in Moscow, Russia, in 1955. She graduated from Moscow Power Engineering Institute as electro-physical engineer in 1978. Her field of work is lightning strike and lightning protection of aircrafts, electrical power devices etc. She is presently the head of Lightning protection laboratory of MPEI.

E-mail: lpl @ fee.mpei.ac.ru

New Automatic Fusion Time Control System for Core Detection Fusion Splicers Significantly Improves Splice Quality

Regina Menegozzi, Gervin Ruegenberg
Splice Equipment Development, Corning Cable Systems GmbH & Co. KG
Munich, Germany
+49-89-722-35751 · regina.menegozzi@corning.com

Abstract
Fusion splicers are used to join optical fibers with low splice loss and long-term stability. The loss of each particular splice depends on certain conditions like fiber preparation quality, splicing parameters, the fiber composition itself and especially on variations of the fiber heating. This paper describes a new automatic fusion time control technique for fusion splicers with an image processing core detection system. This new method compensates variations of the fiber heating and reduces the average splice loss by up to 60 percent and the failure rate by up to 70 percent. Furthermore it produces precise attenuation splices.

Keywords
Fiber; fusion splicer; core detection system; profile alignment system; automatic fusion time control; attenuation splice.

1. Introduction
Thermal fusion splicing is the standard method for connecting optical fibers today. For high quality splices, two main techniques have been established.

The bend-coupler based LID-System (Local Injection and Detection) Unit injects light into the fiber in front of the splice position and detects it behind the splice [1], [2]. This method not only gives a reliable splice loss measurement, but also allows monitoring of the actual splice loss during the splice process. So a real time process control is possible, resulting in very low splice losses. The so-called Automatic Fusion time Control (AFC) stops the fusion process exactly when the minimum splice loss is reached.

Another technique is the Core Detection System (CDS), sometimes also called Profile Alignment System (PAS), which uses a special optical system to make the fiber core visible. After the splicing process, the shape of the core can be analyzed to estimate the splice loss [3], [4]. Unfortunately, during the fusion process the light of the arc and of the glowing fiber is so bright that the camera chip is overflowed. Therefore, up to now it was not possible to control the splice process online with the PAS in contrast to the LID-System Unit.

The splice quality depends substantially on the fiber heating during the fusion process. Electrode pollution and wear can cause variations in arc position and temperature. The fiber heating also depends on the position of the fibers within the arc and on the air pressure. One essential mechanism of the fusion process is the self-centering effect due to surface tension of the melted glass. Especially in the case of eccentric fibers, the self-centering effect which aligns the outer contours of the fibers counteracts the core-to-core positioning and causes a misalignment of the cores if the fiber heating and the fusion time are not optimal.

As described above, there are variations in the fiber heating which cannot be completely avoided. These effects can cause high splice losses mainly with eccentric fibers. The same problem occurs if the fusion parameters are not properly adjusted. So it would be very helpful to have an automatic fusion time control system which compensates for all these effects and finds the optimum fusion time for each individual splice. On that score, the LID-System Unit which controls the fusion time automatically according to the LID level seems to be the better solution. Unfortunately there are some special fibers with opaque coatings or very thick coating diameters. In these cases, it is not possible to inject and detect light locally, and so the Automatic Fusion time Control by the LID cannot be used.

The best but high cost solution would be a combination of the LID-System Unit and CDS into one fusion splicer. This paper introduces a more cost efficient solution which allows control of the fusion time with a CDS system. So we are able to remedy one of the major shortcomings of core detection systems.

2. Common Core Detection System
Modern fusion splicers use a couple of techniques to achieve high quality splices. Common core detection fusion splicers have special optical systems included to make the fiber core visible from two lines of sight. With a three axis positioning system, it is possible to align the fiber cores to achieve low splice losses. After the splice process, an image analysis can be done and it is possible to calculate the splice loss from the shape of the fiber core.

But during the fusion process, the fibers are heated up to a temperature in the range from 1700 to 2000 degrees centigrade. At these temperatures, the fibers emit heat radiation and visible light. The visible light is normally bright enough to flood the cameras so that the fibers are neither visible on the screen nor detectable in the image. So the microprocessor has no feedback signal which allows it to draw conclusions on the actual fiber position which would be necessary for an active process control. Figure 1 shows the typical fiber image of a common core detection fusion splicer when the fusing arc is switched on.

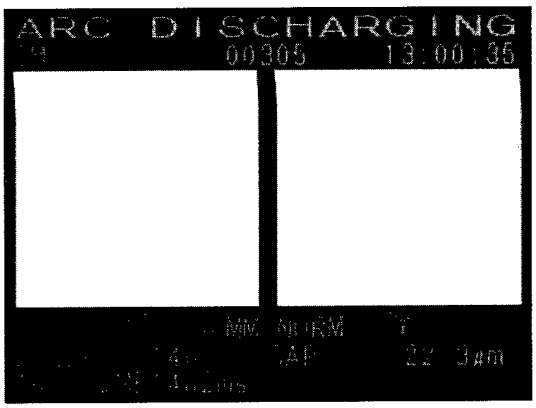


Figure 1. Typical fiber image of a common core detection fusion splicer when the arc is switched on

One effort to overcome this problem uses a temporary reduction of the arc current during the splice process. This allows an image analysis in intervals. But the reduction of the arc current leads to a reduction of fiber heating during these moments, which influences the splice quality. In addition, this method is still not true real-time control.

3. AFCi: Automatic Fusion time Control by image

3.1 Principle of the optical assembly

Our new CDS fusion splicer uses the principle that the spectral width of the light emitted by a glowing fiber is high compared to the spectral width of the light emitting diodes which illuminate the fibers. So we can use a narrow-bandwidth interference filter to block the light emitted by the hot fibers while the light of the illumination LED passes the filter nearly uninfluenced. With this setup, the fibers remain clearly visible during the whole splice process.

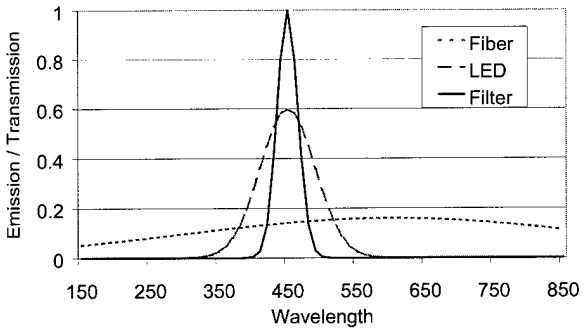


Figure 2. Emission spectra of the hot fiber, the LED and the transmission spectrum of the narrow-band interference filter

In Figure 2, the emission spectra of the hot fiber and the illumination LED are shown in a schematic view. The hot fiber emits a very broad light spectrum from visible to infrared. The LED spectrum is comparatively very narrow. The camera chip is sensitive over the whole visible wavelength range. So the brightness of the fiber image is determined by the spectral integral over the whole visible wavelength range. In our example, the integral of the fiber emission is twice the integral of the LED spectrum although the spectral peak intensity of the LED is higher. The result is that the fiber picture is lit by the fiber glowing.

The spectral curve of a suitable narrow-bandwidth filter is also shown in Figure 2. This filter has a center wavelength similar to that of the illumination LED, but a smaller spectral bandwidth than the LED. Most of the LED spectrum passes through the filter, and so it does not reduce the illumination intensity by much. On the other hand, most of the spectrum of the glowing fiber is blocked by the filter, and so the hot fiber radiation is reduced dramatically. As a result, the fiber emission has little effect on the quality of the fiber image in the camera, and the fiber remains clearly visible during the whole fusion process.

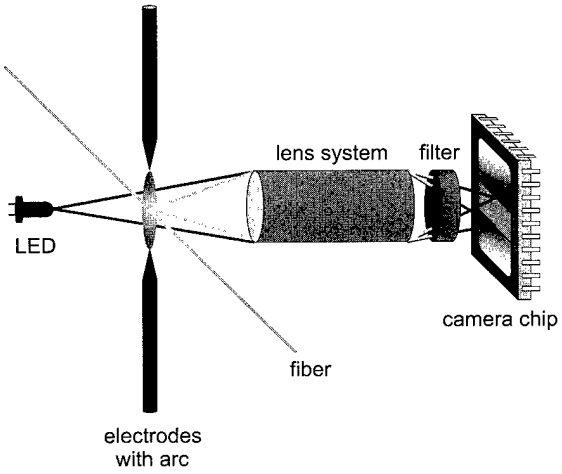


Figure 3. Schematic view of the fiber illustration system with the added narrow-band interference filter

So we are able to block the light emitted from the hot fibers while the light from the illumination passes through. The desired filter characteristic can be achieved with special narrow-band interference filters. These filters can be arranged at any position between the fiber and the cameras. Figure 3 shows the principle of the optical assembly. Actually, two of these systems are used, one for X and one for Y view. Typically a blue LED which leads to a higher optical resolution illuminates the fiber and an optical lens system projects the fiber image onto the camera chip. The fusing arc heats the fiber up and the emitted light of the glowing fibers is blocked by the narrow-band interference filter. So the fibers can be clearly observed during the complete fusion process.

Figure 4 shows a screen shot of the fusion process with our new optical system. The left side of the picture shows the X view, the right side the Y view. This picture has been taken while the arc was on, and the fiber core and the fiber edges are clearly visible. So it is

possible to watch the motion of the two fibers relative to each other and also the flow of the melted glass caused by surface tension.

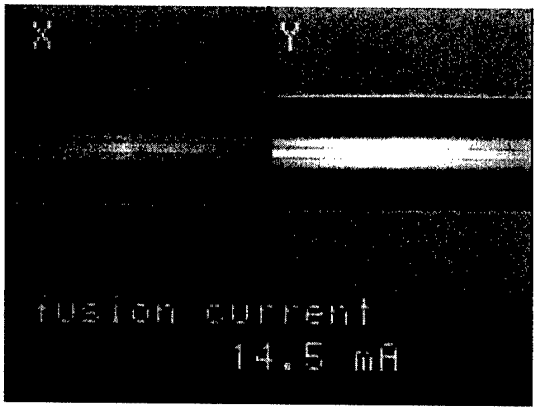


Figure 4. Fiber image during the splice process when the narrow-band interference filter is included

3.2 Process control

To control the fusion process continuously, a very fast processing algorithm is necessary. To achieve true real-time control, the cycle time of the evaluation must be considerably shorter than the minimum fusion time. During such a cycle, an image for each of the optical views must be digitized and analyzed. Typical fusion times are around three seconds. But as mentioned above, the optimal fusion time varies widely depending on variations of the fiber heating. So shorter optimal fusion times (down to half a second) are possible. We were able to reach a cycle time of less than 100 ms, which is reasonable even for fusion times down to half a second. Therefore, our Automatic Fusion time Control by image (AFCi) works for fusion times from 0.5 second up to the maximum fusion time.

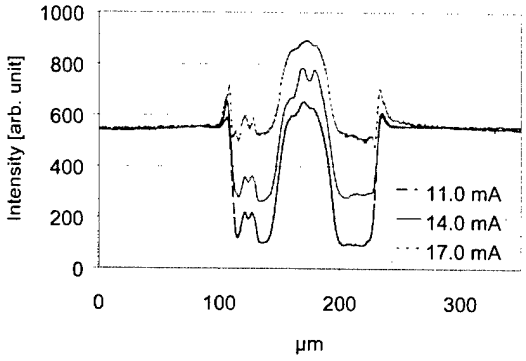


Figure 5. Intensity profile along an image column for different fusion currents

It must also be taken into account that the fiber temperature has an effect on the appearance of the fibers during the fusion process. In principle it is not possible to block all the radiation of the hot fiber with the narrow-bandwidth interference filter. So higher fiber temperatures lead to brighter fiber images. To examine the range of fiber temperature for which the AFCi works we varied the fusion current of the fusion splicer. Figure 5 shows the intensity profiles within one particular image column for different fusion currents. Normal fusion currents are about 14.5 mA. Our AFCi system works in the complete range of fusion currents and is able to compensate the variations in fiber heating even at the worst conditions.

3.3 Splicing eccentric fibers

When splicing eccentric fibers, the fiber geometry changes due to surface tension. So the Automatic Fusion time Control by image is helpful by stopping the fusion process at the optimum time.

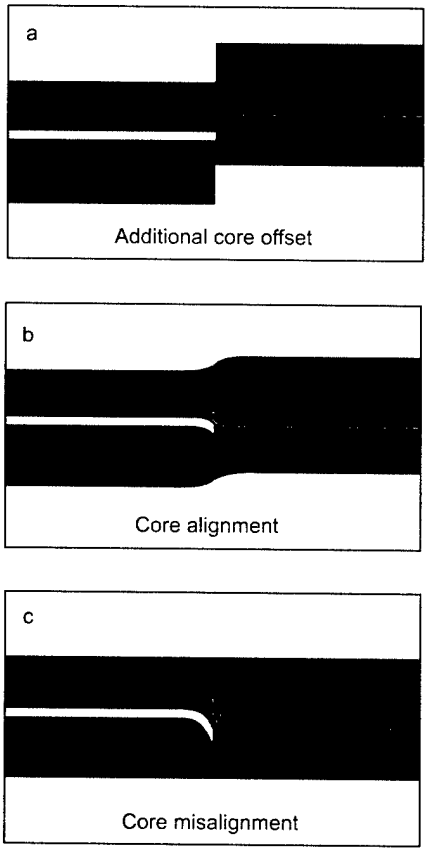


Figure 6. Splicing eccentric fibers

3.3.1 Principle. "Eccentric fiber" means the core is not well centered relative to the cladding. Therefore the cores do not match when the fiber edges are aligned. On the other hand, when the fiber cores are aligned before the fibers are fused together a cladding offset occurs. The melted glass during the fusion process is anxious to minimize this offset on account of the surface tension, which leads to a misalignment of the fiber cores and results in a high splice loss. Therefore, it is necessary to start the fusion process with an additional core offset as illustrated in Figure 6a. During the fusion process, this offset gets continuously reduced until the fiber edges

are aligned (Figure 6c). The Automatic Fusion time Control by image is programmed to stop the fusion process at the time when the cores are aligned and the splice loss is minimized (Figure 6b).

3.3.2 Measurements. To test the improvement of our new AFCi system we have spliced eccentric fibers under worst case conditions. That means the core offset when the fiber edges were aligned was more than one micrometer. The fusion current was varied from –0.5 to +0.5 mA around the optimum value of 14.5 mA. This variance is typical when accounting for electrode wear and other similar effects. Figure 7 shows the results achieved with our new Core Detection System CDS fusion splicer with the Automatic Fusion time Control by image compared to a conventional Profile Alignment System PAS fusion splicer with a fixed fusion time of three seconds. The resulting splice losses were measured with an Optical Time Domain Reflectometer.

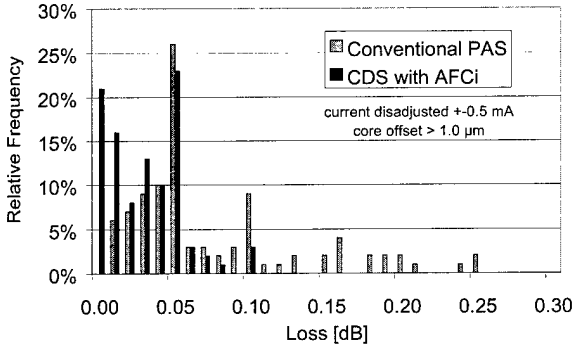


Figure 7. Worst case splicing results with conventional PAS fusion splicer compared to CDS with AFCi system

With the AFCi system, an average splice loss of 0.03 dB on a sample of 100 splices was achieved in contrast to 0.08 dB with the conventional PAS. Therefore, the average splice loss was reduced by up to 60 percent, and the failure rate was reduced by up to 70 percent. The standard deviation was 2% for the AFCi system compared to 6% for the conventional PAS. These results show that our new method is able to compensate for variations in fiber heating even under difficult conditions.

3.4 Attenuation splice

Another application for our new AFCi is creating attenuation splices. These are special splices with a specific predetermined splice loss. The main field of application is analog distribution systems. To avoid an overflow of the receiver, it is necessary to adjust the power of the incoming signal to the receiver's dynamic range. The different losses of the various subscriber lines can be compensated by the loss of a matched attenuation splice.

Figure 8 shows a fiber image of an attenuation splice. The desired splice loss is achieved by a specific fiber core offset in one optical direction. The core bending, which is clearly visible in Figure 8, is caused by the fiber movement due to surface tension of the melted glass as explained above. This core bending also influences the

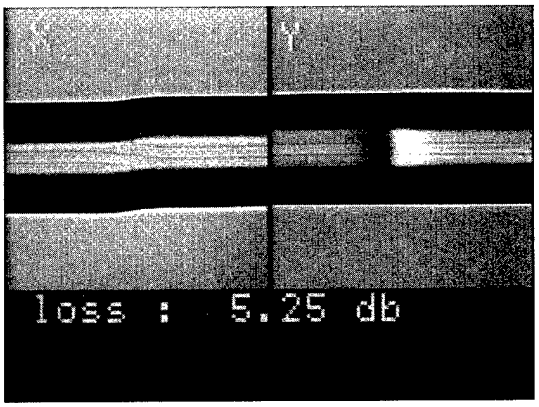


Figure 8. Fiber image of an attenuation splice

splice loss and must be taken into account when calculating the final fiber offset. The splicing process works similar to the eccentric fiber splicing. Before the fusion arc is started, an additional core offset (compared to the final offset) is set. The AFCi stops the fusion process when the final offset is reached. Then the actual splice loss will be determined and corrected if necessary. Attenuation splices in the range from 0.10 dB to 10.0 dB are possible.

4. Conclusions

We have introduced an Automatic Fusion time Control by image (AFCi) for a Core Detection System (CDS) fusion splicer. In the optical path of the imaging system, a narrow-band interference filter is added so that the fiber stays visible during the whole splice process. In combination with a very fast image processing algorithm, it is now possible to control the fusion process in real-time. Measurements show a clear improvement of the splice loss and the failure rate when splicing eccentric fibers. Furthermore, the method can be used to produce precise attenuation splices.

5. References

[1] R. Engel, "Device for coupling light into an optical wave-guide," US Patent 5040866 (August, 1991).

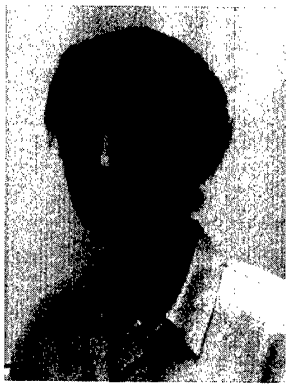
[2] B. Zamzow, G. Ruegenberg, M. Anderson, H. Krupp, "High quality fiber optic splices and significantly improved splice loss measurement accuracy," *Proc. 47th IWCS*, 854-863 (1998).

[3] D. Marcuse, "Loss analysis of single-mode fiber splices," *The Bell Sys. Tech. J.*, 56(5), 703-718 (1977).

[4] B. Zamzow, G. Ruegenberg, M. Anderson, W. Knop, "Numerical simulation of high quality fiber optic splices for high precision loss evaluation," *Proc. 48th IWCS*, 621-628 (1999).

6. Authors

Regina Menegozzi
Corning Cable Systems GmbH & Co. KG
Splice Equipment Development
Zielstattstr. 40
81379 Munich, Germany
regina.menegozzi@corning.com



Regina Menegozzi received her diploma in physics in 1992 at the University of Erlangen. In 1998 she obtained a doctorate degree at the same University working on a simulation of the Ballistic Electron Emission Microscopy, a special method of Scanning Tunneling Microscopy. She joined the department of splice equipment development of Siemens now Corning Cable Systems in 1999. Now she is responsible for the basic research of fusion splicers.

Gervin Ruegenberg
Corning Cable Systems GmbH & Co. KG
Splice Equipment Development
Zielstattstr. 40
81 379 Munich, Germany
gervin.ruegenberg@corning.com



Dipl.-Ing. Gervin Ruegenberg received his diploma of electronics from the University of Kaiserslautern. He joined Siemens in 1984 as a development engineer for optical transmitter and receiver modules. Today he is responsible for development of fusion splicing technique for optical fibers at Corning Cable Systems.

Investigation of Mass Fusion Splicing between Different Types of Fibers

Makiko Miura and Masakazu Nakano
Lucent Technologies Yazaki Ltd.
1157-106 Hotozawa, Gotemba-city, Shizuoka-Pref., 412-0046, Japan
+81-550-89-1428 · miura@lt-y.co.jp

Abstract
In Japan, the increasing use of dense wavelength division multiplexing (DWDM) technologies has led to the increased deployment of Non-zero Dispersion Fiber (G.655 fiber). However much of the network in Japan contains legacy standard single mode fiber (G.652 fiber), or dispersion shifted fiber (G.653 fiber). Therefore, it is common to have to perform fusion splicing between different types of fibers, and there has been concern that the splice loss would be slightly higher than that of splicing between the same types of fibers. The typical cable segments are very short in Japan, which increases the effect of splice loss of the overall network loss. In this report, we have investigated mass fusion splicing between different types of fibers. We have optimized the splice program for G.655 and G.652 fiber splicing and have obtained a splice loss of less than 0.2dB at each wavelength.

Keywords
Mass fusion splicing; G.655 fiber; different types of fiber.

1. Introduction
Recently, Japan has continued to see an increasing use of DWDM transmission technologies by telecommunication companies. This has led to increasing the deployment of G.655 fiber, not only for new routes, but also for extension of existing ones. Therefore, in many cases the cable routes end up containing combinations of legacy G.652 or G.653 fiber and G.655 fiber. Even in the absence of legacy fiber in the network, there are usually at least 2 connections between the NZDF fiber and the terminal equipment. In Japan, almost all fiber optic cable is either 2, 4 or 8 fiber slotted core ribbon cable, and the cables are usually terminated with pre-connectorized fanouts that are mass fusion spliced to the cable ribbon. Although it can be made of any kind of fiber, it is generally recommended that this fanout contain G.652 fiber. Consequently, there has been some concern about the potentially higher splice loss between G.655 fiber and other fiber types.

In this report, we investigated 4-fiber mass fusion splicing between G.655 and G.652 fibers, and between G.655 and G.653 fibers and have developed an optimized splice program for G.655 and G.652 fiber splicing based on a study of the mode field diameter (MFD) analysis after the fusion splicing.

Although optimization of a single splicing in a network might not ordinarily be of much consequence, it needs to be pointed out that in Japan, the typical fiber optic cable segments are very short (i.e. 1km – 1.5km). This means that the contribution of splice loss to the total network attenuation is much greater than in the North American network. Since as previously mentioned almost all cable in Japan is slotted core ribbon cable, a considerable amount of effort is devoted to the optimization of all mass fusion splicing, not only mixed fiber splicing.

2. Fiber characteristics and ribbon geometry
Table 1 shows the optical and geometric characteristics of the fibers used in this study. We chose to study this particular G.655 fiber because it is currently the most commonly deployed NZDF, not only in Japan, but worldwide. Figure 1 shows the geometry of 4-fiber encapsulated ribbon used in Japan.

Table 1. Fiber characteristics using this study

Parameter		G.655	G.653	G.652 *
Mode field diameter (μm)	1550nm	8.4+/-0.6	8.0+/-0.8	10.4 **
	1310nm	7.0 **	6.5 **	9.3+/-0.5
Cladding diameter (μm)		125+/-1.0	125+/-1.0	125+/-1.0
Core/clad concentricity error (μm)		≤0.6	≤0.5	≤0.5
Cladding Non-circularity (%)		≤1.0	≤1.0	≤1.0

*Matched cladding fiber

**Typical value

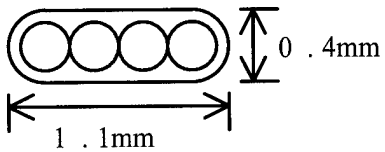


Figure 1. Fiber ribbon geometry

3. Basic splice performance

We investigated the mass fusion splicing between different types of fibers with 4-fiber ribbon using several kinds of splice machines with their standard splice programs. Table 2, Figure 2-1 and 2-2 show the splice loss result between G.655 and G.652 fiber using splice program for dispersion shifted G.653 (DSF) fiber (standard DSF mode). Table 3, Figure 3-1 and 3-2 show the splice loss result between G.655 and G.653 fiber using standard DSF mode. We performed completely random splicing for all combinations. The splice losses were measured using bidirectional OTDR.

As can be seen, the standard splice programs yield lower splice loss between G.655 and G.653 fibers than between G.655 and G.652 fiber. This is caused by the difference of MFD between spliced fibers, as shown in Table 1: the difference in the MFD between G.655 and G.652 fibers is approximately 2 μm, but the difference in MFD between G.655 and G.653 fibers is almost insignificant. Figure 4 shows the correlation between wavelength and typical MFD of each fiber. As shown in this figure, the MFD varies approximately linearly with wavelength, although the slope of MFD vs. wavelength is different for each type of fiber. Therefore the MFD difference between G.655 and G.652 fiber is a wavelength dependent function with shorter wavelengths showing larger differences in MFD. Since MFD difference is one of the major factors affected the splice loss, the wavelength dependence of the MFD difference results in a wavelength dependence in the splice loss.

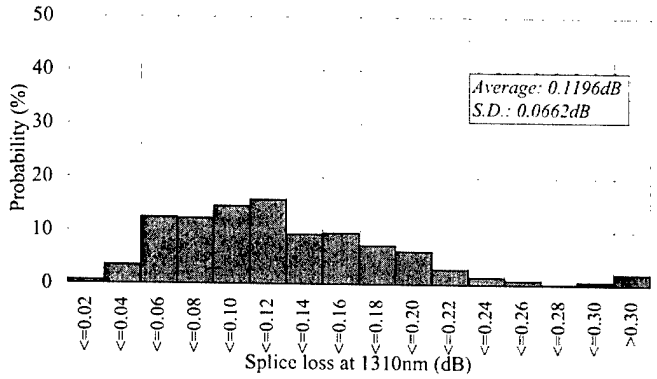


Figure 2-1. Splice performance between G.655 and G.652 fiber at 1310nm

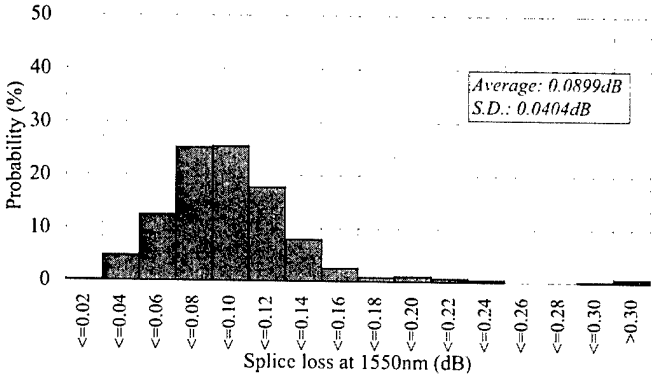


Figure 2-2. Splice performance between G.655 and G.652 fiber at 1550nm

Table 2. Splice performance between G.655 and G.652 fiber (dB)

Items	1310nm	1550nm
Average	0.1196	0.0899
Median	0.1098	0.0860
Standard deviation	0.0662	0.0404
Maximum	0.617	0.449
Minimum	0.010	0.019
N	480	480

Table 3. Splice performance between G.655 and G.653 fiber (dB)

Items	1310nm	1550nm
Average	0.0449	0.0447
Median	0.0323	0.0368
Standard deviation	0.0501	0.0292
Maximum	0.348	0.196
Minimum	0.000	0.005
N	160	160

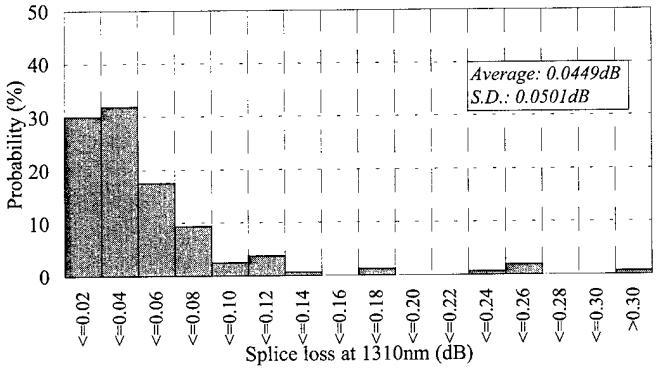


Figure 3-1. Splice performance between G.655 and G.653 fiber at 1310nm

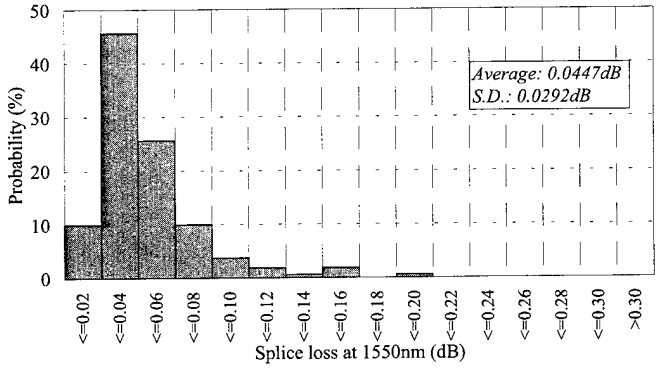
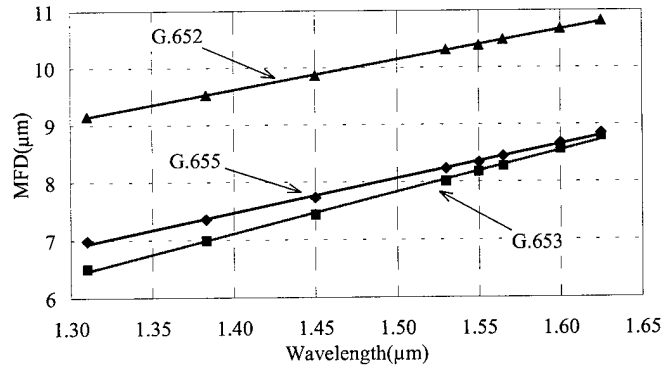


Figure 3-2. Splice performance between G.655 and G.653 fiber at 1550nm



G.655 fiber: $y = 5.935x - 0.836$ (1)

G.653 fiber: $y = 7.197x + 2.962$ (2)

G.652 fiber: $y = 5.274x + 2.234$ (3)

Figure 4. MFD vs. Wavelength

4. Optimization of splicing between different types of fiber

In some respects, the problem of optimizing the splice between G.655 and other fibers is not unique, and there are other fiber splicing that require low loss between fibers with widely different MFD. An example of splicing between fibers with even larger MFD differences is seen in the splicing of some specialty fibers, such as dispersion compensation fiber to G.652 or G.653 fiber. A number of authors have previously reported on the optimization of such splicing in the case of single fusion splicing [1][2][3][4][5][6]. One of the most effective methods of minimizing the loss of such single fiber splicing is to taper the MFD by inducing variable diffusion of the dopant in the core of specialty fiber (which typically has a small MFD). This can be accomplished by moving the electrode during fusion, varying the arc duration or varying the time of post arc.

However, in the case of the mass fusion splicing using current splice machines, we cannot move the electrode during fusion. Also, in mass fusion splicing, it is difficult to control some aspects of the process, such as the end face condition of the individual fibers, the distances between the spliced fibers and the offset between the spliced fibers. Accordingly, we need to take a different approach to optimizing mass fusion splicing between fibers with different MFD. Consequently, we investigated the optimization of the splice program parameters using the matrix method.

Table 4 shows the effective parameters, for splicing between G.655 and G.652 fiber with 4-fiber ribbon. As can be seen, we are able to reduce the splice loss to by i) using a longer arc duration; ii) minimum arc power; iii) increasing the final overlap distance; iv) pulling immediately after forward movement and v) adding a longer post arc. To verify that an improvement in performance could be obtained with the optimized splice program parameters, we performed completely random splicing using the optimized program. Table 5, Figure 5-1, 5-2 and 5-3 show the splice loss results using our optimized program. As can be seen, we have reduced both the actual splice loss and the standard deviation of splice loss for each wavelength. In addition, the splice loss using the optimized program is not highly wavelength dependent.

Table 4. Effective parameter for G.655 and G.652 fiber splicing with 4-fiber ribbon

Parameter	Optimized program	Standard DSF mode
Arc power	Minimum	Center
Arc duration	20 sec	10 sec
Forward	40 μm	30 μm
Pull distance	20 μm	30 μm
Time before pull	1 sec	3 sec
Additional Arc	10 sec	None
Electrode position	Shifted to G.655 fiber side	Center

Table 5. Splice performance between G.655 and G.652 fiber using optimized program (dB)

Wavelength	1310nm	1550nm	1625nm
Average	0.0553	0.0434	0.0482
Median	0.0520	0.0423	0.0445
Standard deviation	0.0207	0.0126	0.0160
Maximum	0.118	0.074	0.084
Minimum	0.023	0.023	0.022
N	80	80	80

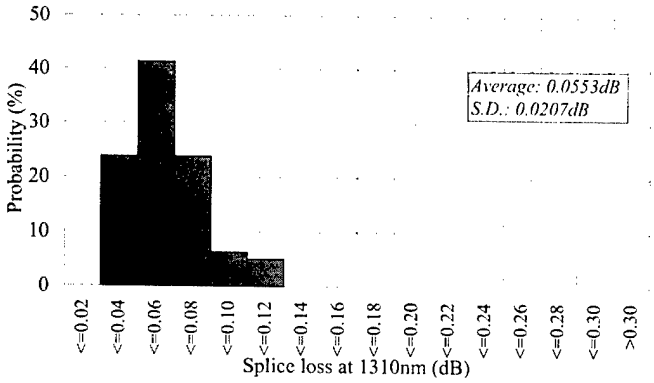


Figure 5-1. Optimized program at 1310nm

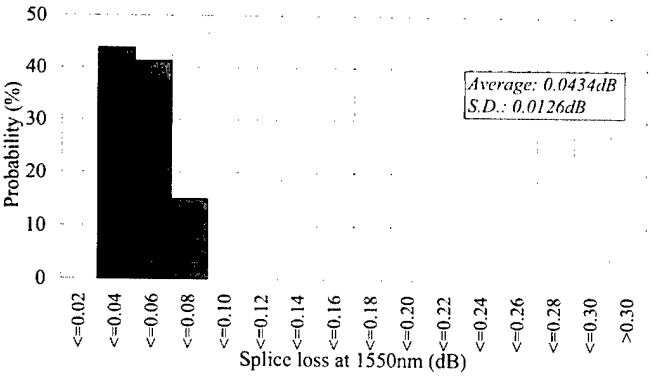


Figure 5-2. Optimized program at 1550nm

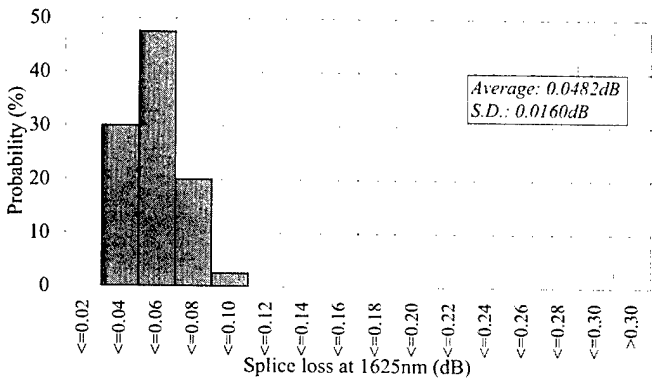


Figure 5-3. Optimized program at 1625nm

5. Analysis of MFD of splice point

The authors have previously reported that splice loss depends strongly on the fiber geometric parameters following fusion splicing [7]. The dependence is particularly strong for the MFD. If this dependence is well understood, an analysis of the MFD at the splice point should provide a method to both minimize the splice loss and the wavelength dependence of the loss. We studied the MFD at the splice point following splicing with both the standard DSF mode and the optimized program and attempted to develop a relationship between loss and MFD.

5.1 Analysis of MFD following fusion splicing between different fibers

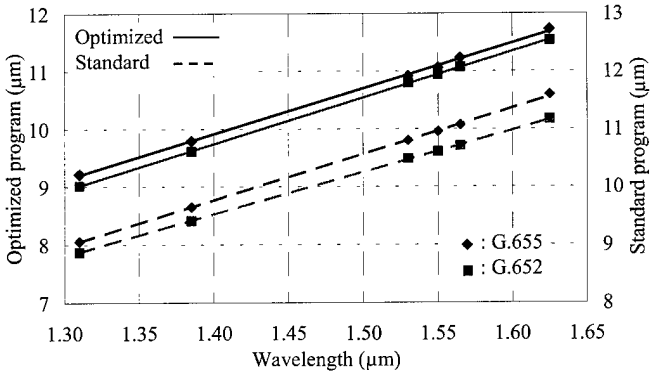
We made a number of G.655/G.653 and G.655/G.652 splices using both the optimized program and the standard DSF mode. We measured the splice loss, using bidirectional OTDR. We then cut the fiber at the splice point and measured the MFD at the fiber end face using the variable aperture method in the far field and calculated the MFD by the Petermann II definition.

Figures 6-1, 6-2, 6-3 and 6-4 show the relationship between wavelength and the mode field characteristics following fusion splicing at the splice point, such as MFD, ΔMFD ratio (ΔMFD_r) and MFD expansion ratio (MFD_e), where,

$$\Delta MFD_r = \frac{MFD_{A\alpha} - MFD_{A\beta}}{MFD_{AAve}} \qquad (4)$$

$$MFD_e = \frac{MFD_A - MFD_B}{MFD_B} \qquad (5)$$

Where α refers to G.655 fiber, β refers to G.652 or G.653 fiber, MFD_A is the MFD following fusion splicing, MFD_{AAve} is the average MFD of fibers α and β following fusion splicing and MFD_B is the MFD before fusion splicing.



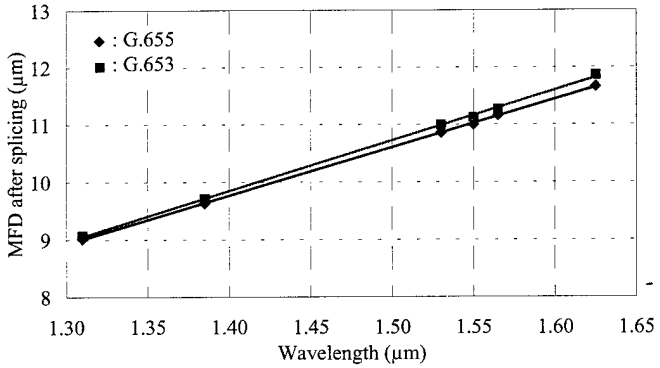
Optimized program G.655: $y = 7.909x - 1.155$ (6)

Optimized program G.652: $y = 8.036x - 1.505$ (7)

Standard DSF mode G.655: $y = 8.011x - 1.444$ (8)

Standard DSF mode G.652: $y = 7.295x - 0.685$ (9)

Figure 6-1. MFD following fusion splicing between G.655 and G.652 fiber



G.655: $y = 8.474x - 2.379$ (10)

G.653: $y = 8.723x - 2.655$ (11)

Figure 6-2. MFD following fusion splicing between G.655 and G.653 Fiber

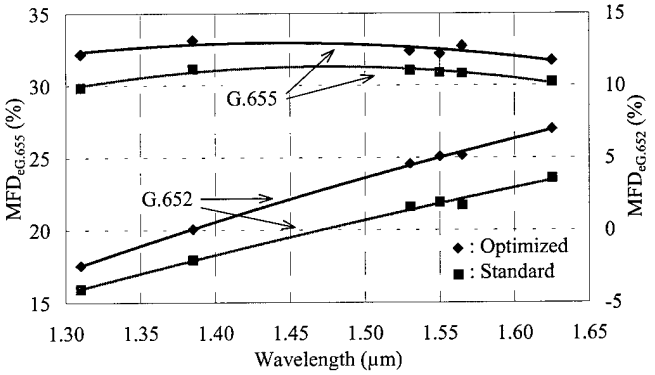


Figure 6-3. Correlation between MFD expansion ratio and wavelength

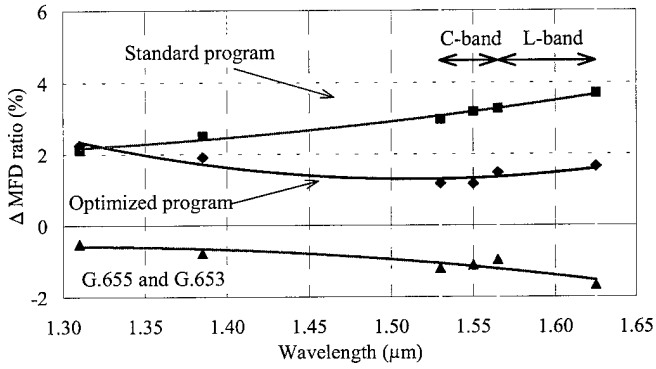


Figure 6-4. Correlation between ΔMFD ratio and wavelength

As a result of this analysis, we see the MFD difference between G.655 and G.652 fiber following fusion splicing using the optimized program tends to be smaller than that resulting from splicing with the standard DSF mode, and there is hardly any MFD difference in the case of splicing between G.655 and G.653 fiber. As shown in Figure 6-1 and 6-2, the MFD following fusion splicing also varies roughly linearly with wavelength. From the approximation formula, the slope gradient following fusion splicing is higher than before fusion splicing. In other words, the MFD at longer wavelength shows a tendency to extend more under the influence of the fusion arc. Figure 6-3 shows the conversion of the increase of MFD following fusion splicing into MFD_e. As can be seen, the MFD_e of G.655 fiber is independent of wavelength, and the MFD_e of the optimized program is larger than that of standard DSF mode. MFD_e of optimized program is larger than that of standard DSF mode, and the splice loss is lower than that of standard DSF mode. At the splice point, the MFD of the G.652 fiber is smaller than it is before splicing due to the pulling distance in the optimized. Again, the ΔMFD ratio is almost same between G.655/G.653 splicing and G.655/G.652 splicing using the optimized program. The value of ΔMFD ratio obtained with

the optimized program is essentially independent of wavelength over the C-Band and L-Band. This is the reason why splice loss is relatively independent of wavelength using the optimized program.

5.2 Effect of splice parameters

We analyzed the effect of each parameter on splice loss and MFD in order to determine the dominant loss mechanism.

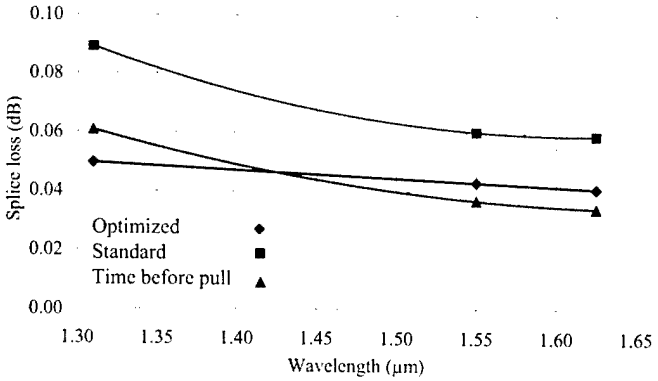


Figure 7-1. Alteration of Time before pull

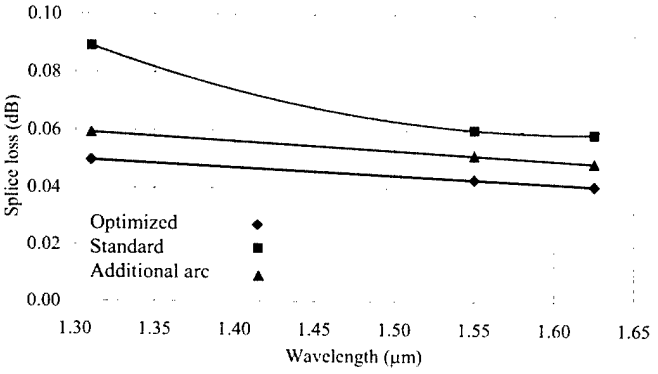


Figure 7-2. Additional arc

On the basis of this analysis, we found that the reduction in overall splice loss is accomplished by the alteration of final overlap, electrode position and time before pull, and the improvement in wavelength dependence is accomplished by arc power reduction, long arc duration and added long post arc. For example, Figure 7-1 and 7-2 show the relationship between splice loss and wavelength for the case in which we varied the time before pull and additional arc.

Again, in the analysis of MFD, MFD expansion of G.652 fiber is smaller than that of G.655 fiber, as figure 6-1 and 6-3. It was studied that G.652 fiber is intended to have larger MFD than that of G.655 fiber under same long arc. Also, MFD of G.652 fiber exceeds that of G.655 at longer wavelength. It becomes apparent at the longer wavelength, as shown is Figure 8-1. Then, to obtain similar slope gradient between G.652 and G.655 fiber, we had the position of electrode shifted to G.655 fiber side from the original arc position as shown in Figure 8-2. By these two factors, MFD difference is small using optimized program.

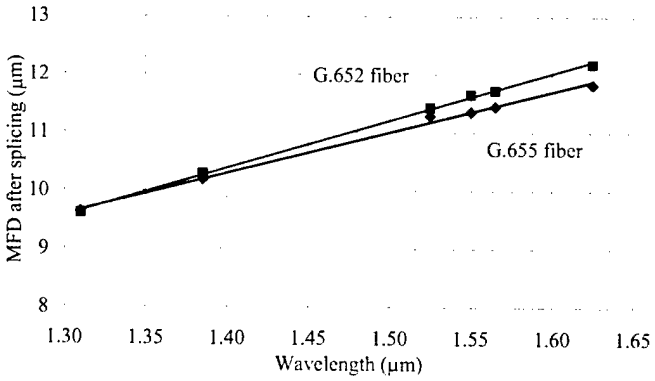


Figure 8-1. Additional arc

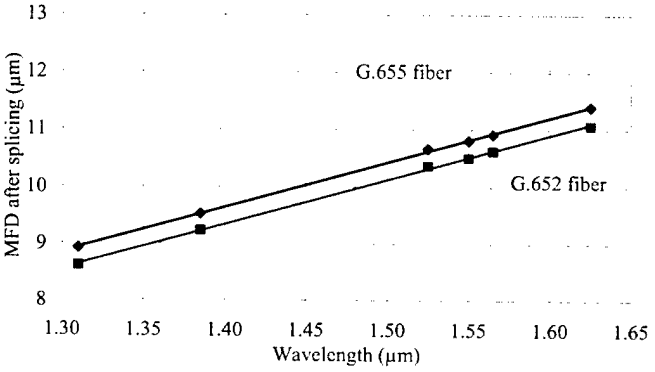


Figure 8-2. Shifted electrode position

6. Conclusions

We investigated 4-fiber ribbon mass fusion splicing between different types of fibers and optimized of the splice program for G.655 and G.652 fiber splicing. We also investigated the effect of the alteration of the parameters on splice loss using the relationship between the wavelength and splice loss or MFD. Analysis of the MFD after fusion splicing is most useful to improve the splice performance. Because power distribution of MFD is three dimensional, we confirm deformation of the core by MFD measurement. If we confirm it using refractive index profile measurement, which is two dimensions, we have to rotate the fiber. Analysis of the MFD after fusion splicing can be simplified and quickly compared with that of the refractive index profile. Accordingly this analysis is more important and the most suitable method for optimized splice performance. In this paper we have

presented results obtained using only one splice machine. However, we believe that the method outlined here, i.e. the analysis of MFD following fusion, would enable us to optimize the splicing conditions for all current splice machines.

7. Acknowledgments

The authors are thankful to Stephan C Mettler of Lucent Technologies, Wayne Lewis and Yosuke Shimozuru of Lucent Technologies Yazaki for discussion and suggestion of technical issue.

8. References

[1] K.Yamada, K.Oosono and Y.Takuma, "Study on Thermally-diffused Expanded Core Er-doped Fiber", IEICE September, B-624 (1992)

[2] M.Hamada, I.Fujita, K.Osaka, Y.Asano and T.Kashiwada, M.Nishimura, "High-strength Splicing of Er^{3+}-Doped Fiber", IEICE September, B-788 (1993)

[3] Y.Akasaka, R.Sugisaki, A.Umeda and K.Kokura, "Investigation for Fusion Splice of Dispersion Compensating Fiber", IEICE March, B-1030 (1995)

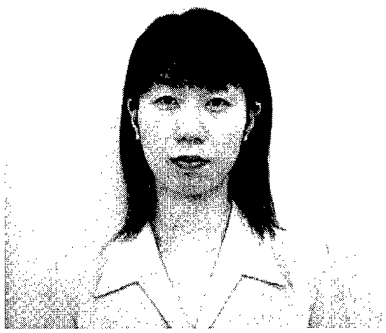
[4] N.Kawanishi, J.Suzuki, K.Ohzawa and S.Yaguchi, "Splice Loss Improvement for Different MFD Optical Fiber Splicing", IEICE September, B-10-25 (1998)

[5] K.Osaka, E.Oki, K.Hattori, T.Sano and M.Shiozaki, "The examination of fusion splicing method among different fiber types", IEICE September, B-10-15 (1999)

[6] M. Cheng, "Optimized Process to Splice Dispersion Compensation Fibers with Standard Single-Mode Fibers", 49th IWCS, 385-388 (2000)

[7] M.Miura, M.Nakano and K.Mitsumori, "An Analysis of Optimization of Mass Fusion Splicing of Non-zero Dispersion Fiber Ribbon", 49th IWCS, 194-202 (2000)

Authors

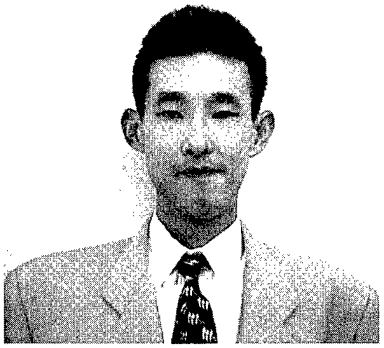


Makiko Miura

Lucent Technologies Yazaki Ltd.

1157-106, Hotozawa, Gotemba-city, Shizuoka-Pref. 412-0046 JAPAN

Makiko Miura received her B.E. degree from Akita University in 1997. She has been engaging in Research & Development Department and her main work is development of evaluation technology with optical fiber, ribbon and cable.



Masakazu Nakano

Lucent Technologies Yazaki Ltd.

1157-106, Hotozawa, Gotemba-city, Shizuoka-Pref. 412-0046 JAPAN

M.Nakano received his B.E. degree from Nihon University in 1991. He has been engaging in Research & Development Department and his main work is development of evaluation technology with optical fiber, ribbon and cable.

Development of a New Factory Fusion Splicer

Kenji Takahashi, Shounosuke Yaguchi, Noriyuki Kawanishi, Taku Ohtani
Precision Instruments R & D Dev. Fujikura Ltd, 1440 Mutsuzaki
Sakura, Chiba, JAPAN
+81-43-484-3962 · ken_taka@opt.fujikura.co.jp

Abstract
A new fusion splicer specifically designed for factory applications has been developed. Although, similar to previous splicers developed for general telecommunication use, this system offers greater splicing process stability when splicing difficult specialty fibers used in optical modules. Also, features were added that provide greater adaptability and flexibility for factory and production use. Examples of these features include high tensile-strength splicing capability, short cleave-length splicing capability, and excellent performance splicing Polarization Maintaining (PM) fiber.

Keywords
Splicing, PM Fiber, Dissimilar Fiber Splicing, DWDM, EDFA, Erbium Fiber, Dispersion Compensation

1. Background
Requirements for optical amplifiers and other complex optical assemblies have increased to meet recent telecommunication technology developments and system deployments. These trends have resulted in a great deal of research and development and more frequent and rapid introduction of a variety of special fibers including new Erbium-doped and Erbium/Ytterbium-doped fibers for amplifiers, special fibers for Bragg gratings, dispersion compensation and inverse dispersion fibers, etc. Furthermore, there are new and more frequent applications for splicing a variety of other existing special fibers, including PM fibers. Hence, there has been a growth in factory splicing demand accompanied by a greater complexity and difficulty in factory splicing, especially with a variety of special fiber combinations. Conventional splicers designed for telecom use in the field cannot satisfy these needs for dissimilar fiber and specialty fiber splicing with the required high quality and repeatability that is essential for stable production line processes. Compounding the difficulties of factory splicing are frequent needs for high tensile strength splicing (with a variety of fiber combinations) to meet requirements for the high splice-point reliability with recoated splices. Accordingly, we undertook the development of a new arc fusion splicer utilizing new technology and features to optimize performance with the variety of factory applications.

2. Pertinent Details
This splicer has many new features to provide effective and high quality splicing capability with various kinds of specialty fibers. Table 1 lists the major specifications of this splicer. In this paper, we introduce some of the unique features of the new splicer.

Table 1. Specifications

Dimensions (W x D x H)	311mm x 218mm x 143mm
Work-Level Height	112mm
Weight	6.0kg
Splicing Time (SM fiber)	25 seconds
Splicing Time (PANDA fiber)	60 seconds (glass clamping)
Heater Time	90 seconds
Monitor	5-Inch LCD
Self Check Functions	Provided
Short Cleave Length	3-5mm
Power Supply	AC-Adapter

2.1 Sweep Arc Discharge Function
Figure1 shows a sample layout of an optical amplifier utilizing a PBC (Polarization Beam Combiner) to couple the power of dual pump lasers. In this example, the amplifier includes 18 splices, and 7 of these splices are combinations of dissimilar fibers. Obviously it is necessary for a factory splicer to provide excellent performance splicing not only homogeneous but also dissimilar fiber combinations.

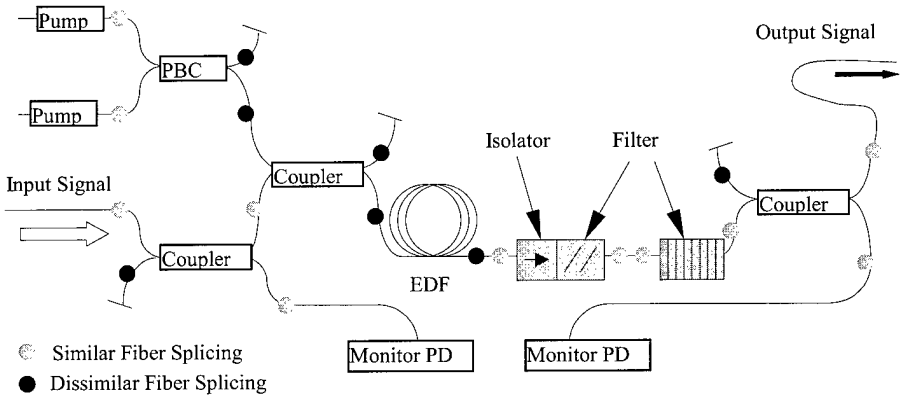


Figure 1. Layout of the Optical Amplifier with PBC

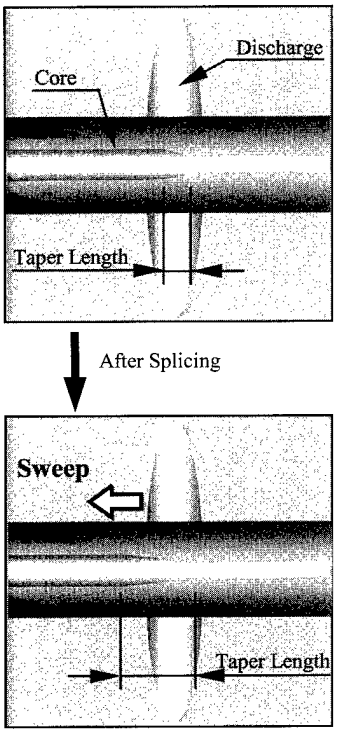


Figure 2. Sweep Arc Discharge Method

For homogeneous fiber splicing, a narrow arc shape and heating area of the fiber is better for producing repeatable low-loss results. The narrow arc helps avoid core distortions (particularly of high NA fibers) at the splice point, and the narrow arc is more stable with little fluctuation of the arc discharge. On the other hand, splice loss with dissimilar fiber combinations may be reduced by use of a wide heating area of the arc discharge. In the case of dissimilar fiber splicing, the wide arc shape can enable a smooth transition from a small mode field diameter (MFD) to a large mode field diameter. In this splicer, new technology has been adopted by use of a sweep arc discharge function that can provide the benefits of both the narrow and wide arc shape.

2.1.1 Logic of the Sweep Arc Discharge. In the case of dissimilar fiber splicing, there is typically a mismatch of MFD between the two fibers. The MFD difference between the fibers results in an abrupt MFD and core transition at the splice point. This has the most pronounced effect on the splice loss for such dissimilar fiber splices. Hence, a method to provide a smooth MFD and core transition is important for low-loss dissimilar fiber splicing.

Figure 2 illustrates the sweep arc discharge method and its benefits. In dissimilar fiber splicing with a MFD mismatch, the splicer initially utilizes a narrow arc. This results in a rather abrupt MFD transition, as previously noted. In the next step, the splicer shifts (sweeps) the splice point relative to the electrodes and simultaneously continuously the arc discharge. This action heats the fiber (with the smaller MFD) down its length in the region adjacent to the splice point. This heating increases the MFD by diffusion of the core dopants. This results in a smoother MFD transition between the small and large MFD fibers (and a smoother core shape) and therefore results in reduced splice loss.

2.1.2 Mechanism of the Sweep Arc Discharge. In order to provide the shift of the splice point, a new sweep function mechanism has been developed. Figure 3 illustrates the sweep function mechanism. Typically, splicers utilize two Z-axis movement mechanisms to advance the right and left fibers towards each other for splicing. The new splicer has a larger Z-axis stage on the right side. The left Z-axis stage is mounted on top of it, and the left Z-axis stage therefore moves relative to the right mechanism.

Both of the Z-axis stages are used to move the fibers forward towards each other to a standard splicing gap set position (typically

aligned with the axis of the electrodes, and therefore also aligned with the arc discharge). Additionally, the Z-axis stage on the right side is used for the movement of the sweep arc discharge. Because the left Z-axis stage is mounted on top of the right Z-axis stage, movement of the right Z-axis stage simultaneously moves both sides, and hence moves the fiber splice relative to the arc. This mechanism therefore provides smooth sweep movement without applying any stress on the fiber splice point.

2.1.3 Result of the Sweep Arc Discharge. Figure4 shows the splice loss results for splicing CS980 fiber to standard SM fiber. This fiber combination is very common in optical amplifiers. In this case, there is a MFD mismatch between the fibers of greater than 3μm. When splicing this fiber combination with splicers utilizing previous splicing technology, it has typically required use of a wide arc shape in order to achieve low loss splicing results.

Unfortunately, the wide arc shape does not provide optimal splicing results in terms of loss and consistency with many homogeneous situations, and the wide arc shape is accompanied with the some fluctuation of the arc discharge.

As can be seen in Figure 4, the average CS980-SMF splice loss using the narrow arc (without sweep) is 0.175dB. Unfortunately, this is higher than the loss that can be achieved with a wide arc. On the other hand, the sweep function provides an improvement in loss of more than 0.05dB. It is remarkable that the sweep arc function can provide such a benefit, while preserving the benefits of the narrow arc shape for homogeneous fiber splicing.

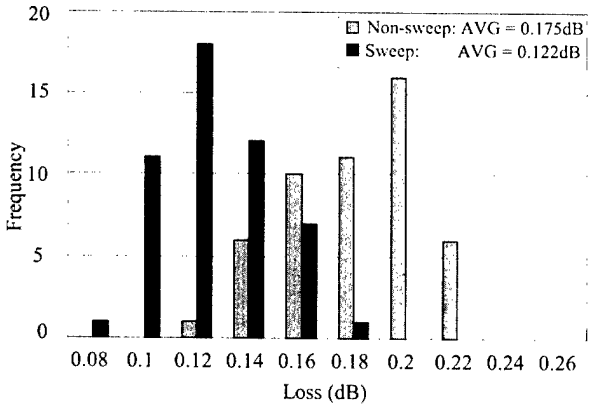


Figure 4. CS980 to SM Fiber Splice Loss

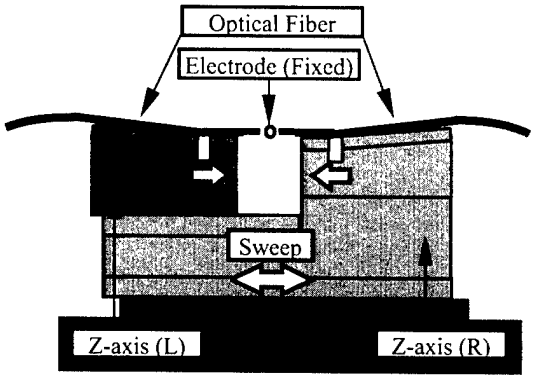


Figure 3. Mechanism of the Sweep Function

2.2 Accurate Estimated Splice Loss

Most fibers used in optical module production have a small MFD, and in some cases a high NA. With such fibers, core deformations at the splice point have a profound effect on splice loss. Core deformations are caused by a small fiber axis offset before the splice, or by bad cleaved fiber ends. These deformations cannot be ignored if accurate loss estimation is to be provided. Hence, detection and analysis of core deformation has been incorporated into the splice loss estimation.

In the case of splicing two fibers that have different MFDs, the splice loss includes loss due to the MFD mismatch. With dissimilar fiber splicing, this loss accounts for much of the total splice loss, so it is necessary to take MFD mismatch into consideration in order to obtain accurate loss estimation. Therefore, the new splicer observes the splice point and measures the amount of MFD mismatch, allowing calculation of the loss due to MFD mismatch.

Figure 5 shows the relationship between measured splice loss and estimated loss for a SM fiber (with MFD of approximately 10um) spliced to an EDF (with MFD of approximately 5um). The loss estimation is greatly improved with the new observation techniques, and accurate estimated loss is realized by including loss due to core deformation and MFD mismatch in the loss estimation algorithms.

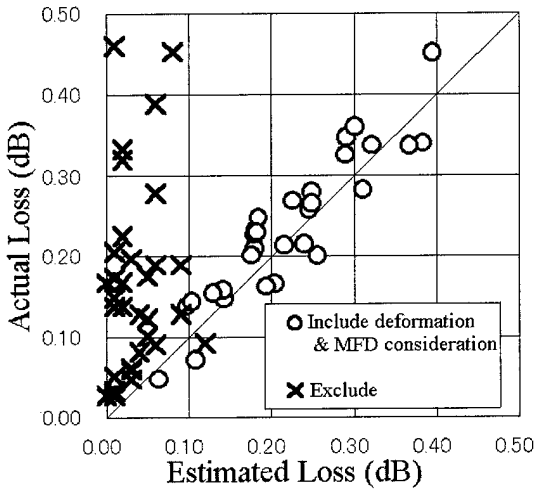


Figure 5. Improvement of Estimated Loss

2.3 PM Fiber Splicing

Recently, several kinds of PM fibers are increasingly used in a variety of optical modules. The new splicer can therefore accurately align and splice a variety of PM fibers automatically. The rotation stages of the new splicer are dramatically improved relative to previous splicer models, and this provides a tremendous reduction in the splicing time of PM fiber. In particular, alignment and splicing time with PANDA fiber has been reduced to one quarter of the time required by former splicers. Moreover, the splicer can recognize the amount of rotational angular offset.

2.3.1 New PM Fiber Image Processing Algorithm. In order to adapt the video analysis system to various kinds of PM fiber, the new splicer utilizes a new video analysis system. PM fibers have some typical characteristics that result in features in the video image profile of each PM fiber type that may be utilized by the video analysis system to detect the rotational position. The most significant and useful features of each kind of PM fiber have been determined and utilized to develop the new video analysis system and alignment algorithms. These new video analysis techniques and methods have been applied to the PM fiber types shown below in Figure 6.

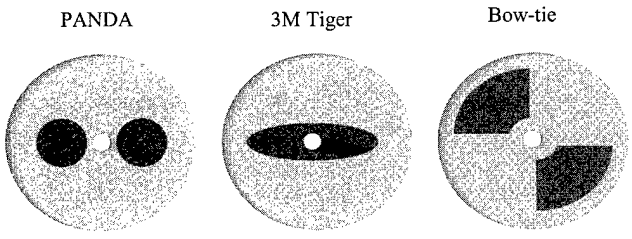


Figure 6. Profiles of PM Fibers

2.3.2 Rapid Splicing with PANDA Fiber. Concerning PM splicing, splicing time has been a serious problem concerning factory splicing productivity. Typically it has required more than 210 seconds to splice PM fiber. This was principally the result of previous video analysis techniques in the observation of PM fiber. The significant and useful video analysis features determined in recent investigations of PM fibers have been utilized to develop new and rapid splicing algorithms for PM fibers.

In the new PM fiber alignment and splicing process, a rough alignment method has been adopted. Initially, the splicer estimates a suitable rotation value and rotational position by preliminary video inspection and analysis of the fibers. This allows the splicer to rotate the PM fiber to a position such that the angular offset is less than 3 degrees. Following that, accurate final alignment is performed by detailed and precise rotary movement and analysis.

Figure 7 shows the splicing time for PANDA fiber. The average time is less than 50 seconds. This high speed splicing of PM fiber will provide greatly improved productivity with PM fiber.

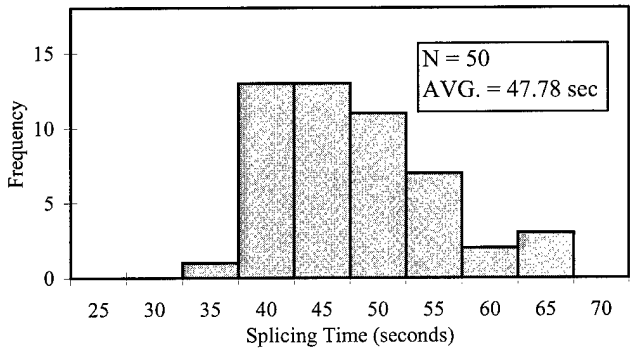


Figure 7. Splicing Time of PANDA Fiber

2.3.3 Polarization Cross-Talk Estimation. The extinction ratio value had been the standard method of evaluation for PM splicing for some time. However, extinction ratio is actually an end-to-end measurement of a PM fiber system, and extinction ratio only partially depends upon the quality of any PM splices included in the system. The extinction ratio depends greatly on the specification and quality of the PM fiber, the polarization cross talk of any PM connector, the rotational accuracy of the alignment of any PM fiber-to-device connection, and also the measurement system and accuracy. In terms of PM fibers for example, there is over a 10dB difference in the extinction ratio between various types of PM fiber of equal length. (As the length of a PM fiber increases, the extinction ratio decreases. The polarization cross-talk specification of a PM fiber should therefore be expressed relative to, or as a function of, fiber length.) In an overall system, the polarization cross talk of the PM splice is typically not the dominant factor in the measured system extinction ratio. Hence, the extinction ratio is not

really a valid measure of the polarization maintaining quality of the splice itself.

On the other hand, the polarization cross-talk value of the splice is a direct result of the PM connection quality of rotation. The splice cross talk depends only on the angle of the two fibers and is therefore a direct result of the accuracy of the splicer's rotational alignment capability.

Since polarization cross talk relates directly to the rotational offset of the polarization axes of the fibers, the splicer can calculate the cross-talk value by analysis of the fibers' rotational offset amount that is observed using the video analysis system. Hence, following completion of the splice, the splicer can calculate and display the polarization cross-talk value of the splice in order to provide indication of the splice quality to the operator. Off course, information of the estimated loss and the angular offset value (measured in degrees) are also available.

2.3.4 Splicing Quality of PM Fibers. Figure 8 shows the polarization cross talk for PANDA fiber splicing. The average cross talk was approximately -41.6dB. Figure 9 shows the polarization cross talk at TIGER fiber splice. The average cross talk was approximately -41.1dB.

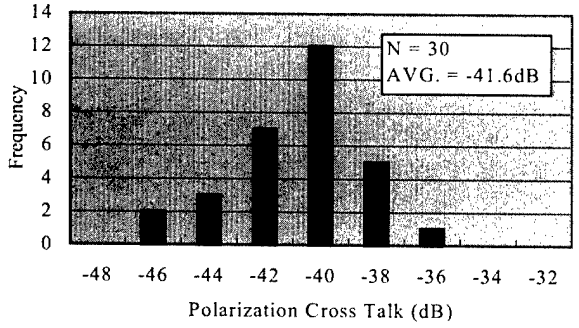


Figure 8. PANDA Fiber Polarization Cross Talk

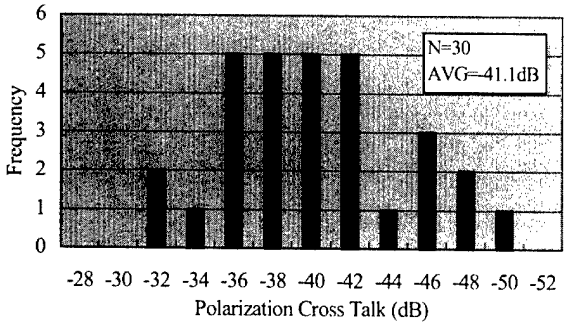


Figure 9. TIGER Fiber Polarization Cross Talk

2.4 Short Cleave Length Splicing for all Fibers

Short cleave length splicing is typically required as part of the solution for high tensile strength splicing. In the case of clamping of the fiber's glass cladding in the splicer alignment V-grooves, micro cracking, scratching, and damage to the surface of the glass fiber results from the V-groove and clamp contact with the fiber surface. As a result, the tensile strength of the splice will be reduced. Therefore, high strength splicing is performed by clamping the fiber on the fiber coating (and not on the glass cladding). This requires use of a short cleave length in order to properly position the fiber in the splicer (and in order to assure accurate alignment). In addition to short cleave length clamping on the fiber coating, achievement of high strength splicing results also depends upon the use of special fiber preparation tools and techniques.

An additional benefit for short-cleave length splicing may be obtained for factory splicing applications even if high strength splicing (and recoated splicing) is not required. Since short-cleave-length-splicing results is a shorter bare-glass spliced region, a shorter splice protection sleeve may be used. Dramatically mini splice protection sleeves are now available with not only reduced length, but also greatly reduced diameter and cross-section. This is of tremendous value in the manufacturing of optical modules with reduced assembly dimensions and tighter internal packaging. An additional benefit is that this allows reduced optical module size without the need for a recoater and proof tester, and without the need for high strength fiber preparation equipment and methods that must be used if the splice is to be recoated. Figure 10 shows the difference between the dimensions of standard splice protection sleeves (formerly the only types available) and the new mini splice protection sleeves.

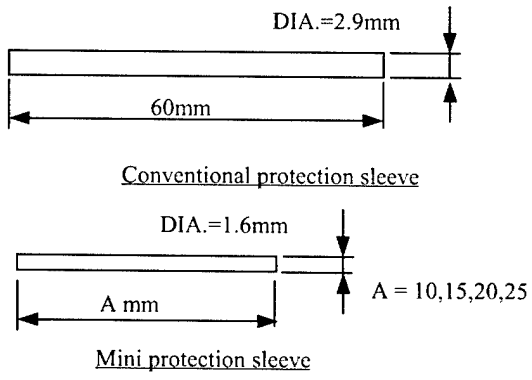


Figure 10. Mini Protection sleeve

Recently, there have been increasing needs high strength and short-cleave-length splicing even in the case of splicing PM fiber. This has been a very difficult problem in the past, especially with some fiber coating types and sizes. Hence, the new splicer incorporates new design features that enable methods for stable

high strength and short-cleave-length splicing even when rotational alignment is required in order to enable PM fiber splicing.

2.4.1 Elimination of V-groove Replacement. When making short cleave length splices in factory applications, a great variety of special fibers may be utilized with many types and diameters of coating. Therefore conventional short cleave splicing has typically required exchange of the V-grooves. This has been required in order to properly locate the center of the fiber with respect to the splicer optical system field of view, and also within the X-Y movable range of the splicer V-groove alignment system. It usually requires over 5 minutes to replace the splicer V-grooves. This operation not only takes time, but also introduces operator skill sensitivity into the production process because it is critical to ensure that the V-grooves are positioned accurately.

In order to eliminate the need for V-groove replacement, the new splicer features an up-down V-groove movement mechanism as shown in Figure 11. This movement of this mechanism ensures that the position of the fiber center is at the proper location regardless of the coating size. This action is taken automatically by the splicer software to compensate for the fiber coating diameter that has been programmed into the splicer for that particular fiber combination. For example, in the case of changing from splicing a fiber with 250μm coating to one with 400μm coating, the V-groove withdraws downward approximately 200μm. Hence, it is easily possible to change the fiber sheath diameter without exchanging the V-grooves.

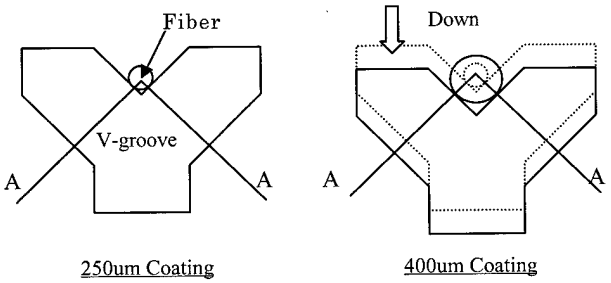


Figure 11. Automated and Accurate V-Groove Up-Down Position Movement

Figure 12 shows a Weibull plot of the tensile strength results for splicing the same fiber combination as in Figure 4 (CS980 spliced to SM fiber). The average strength is approximately 3.0kg (29.7N) and the minimum is approximately 2.1kg (20.5N).

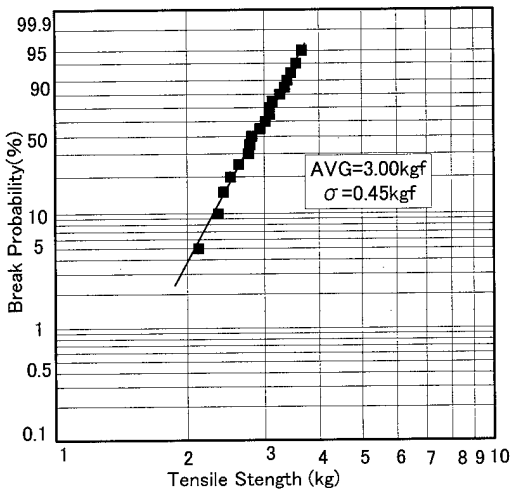


Figure 12. Tensile Strength of Spliced SM Fiber

2.4.2 High Tensile Splicing for PM Fiber. There have been many requests from manufacturers of optical modules for high tensile strength and short cleave length splicing of PM fiber. However, if PM fiber is rotated in the splicer V-grooves while sheath clamping is applied (to hold the fibers in the V-grooves), there will be deformation of the relatively soft fiber coating as well as friction during the rotational motion. This will cause unpredictable and sudden movement and shift of the fiber within the V-groove. As a result, the splicer will be unable to properly observe and analyze the fiber profile. Therefore high strength splicing of PM fiber using the short cleave length method (and coating clamping) has not been reliable or successful.

In the new splicer, a method has been developed to successfully and reliably splice PM fibers with high strength using the coating clamping method. This allows not only high strength, but the same short cleave length capability as with non-PM fiber splicing. In order to achieve this, a V-groove clamp release mechanism has been added to the previously described V-groove up-down movement mechanism.

In the first step, the V-groove clamp is raised to release the clamping pressure on the fiber. Next, the V-groove retracts downward so that it no longer contacts the fiber coating. At this point, the fiber is rotated through a prescribed angle based on previous observation of the fiber orientation by the splicer video analysis system. Next, the V-groove rises back up to the previous position (in contact with the fiber). Finally, the clamp is lowered to secure the fiber in the V-groove. At this time the splicer observation system can once again accurately analyze the fiber rotational orientation. This process is repeated very rapidly until the fiber is accurately aligned.

Using this technique, it is possible to splice PM fiber with high strength, low loss, and (due to the accurate rotational alignment that is achieved) excellent polarization cross talk. Figure 13 shows the Panda fiber polarization cross talk using this high strength method with the clamp release function. The average polarization cross talk with this coating clamping method is almost identical to that achieved using conventional glass clamping of the fiber cladding (as shown previously in Figure 8). Figure 14 shows the Weibull plot of the tensile strength of PANDA fiber splices using this method. The average strength is approximately 3.15kgf (30.9N) and the minimum is approximately 2.2kgf (21.6N). This is essentially the same as that achieved for standard SM fiber high strength splicing (as indicated in Figure 12).

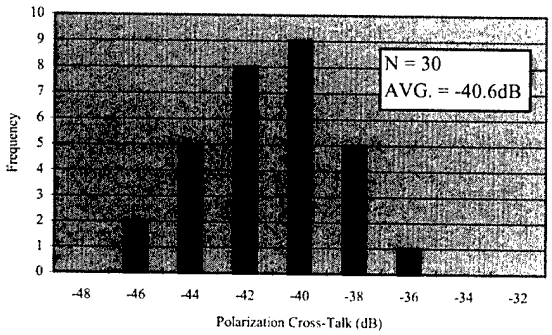


Figure 13. Polarization Cross-Talk of PANDA fiber in splicing with Short cleave length

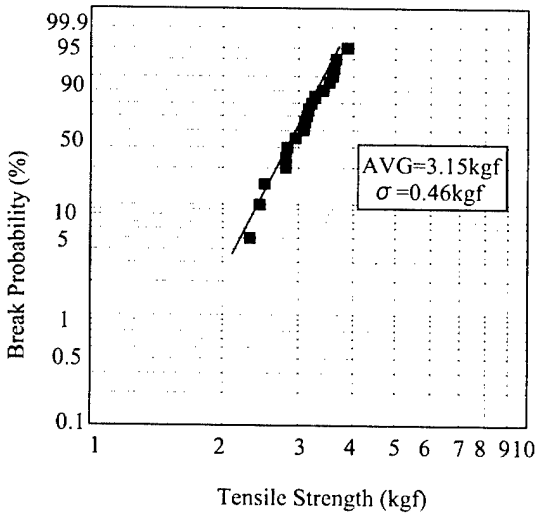


Figure 14. Splice Strength of PM Fiber

In the case of PM splicing with short sleeve length (requiring clamping on the fiber coating), the movement of the V-grooves and clamps to repeatedly release and re-clamp the fiber during the rotational alignment process does result in an increase in the splicing cycle time. Testing shows that the increase is less than 40 seconds. Figure 15 shows the splicing time for (short cleave length) PM fiber splicing.

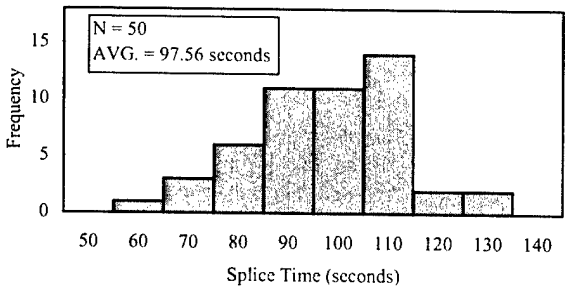


Figure 15. Splicing Time of PANDA Fiber with Short Cleave Length

2.5 Optimized Factory Splicer Design Features

A splicer optimized for use in the factory should have a design optimized for production line applications and needs. Hence, the design requirements are quite different from that of a splicer designed for field use and outside plant cable installation operations. Therefore this splicer has the following features:

2.5.1 Ergonomic Profile & Layout for Production Use. The work level height (top surface) of this splicer is 112mm, which is suitable for production use in the factory. This low profile design even allows bench-top production line use without embedding the splicer into the work surface. With taller splicers, in order to achieve an ergonomic workstation layout, it is frequently necessary to cut a hole in the work surface so the splicer can be recessed downward.

In the new splicer, the tube heater for splice protection sleeves is located at the front of the splicer and the LCD monitor is set to the rear. This layout is ideal for handling even short lengths of fiber extending from the optical module or assembly.

2.5.2 Fiber Holder System. The splicer utilizes a fiber holder system that provides user-friendly operation for each step of the splicing process. The fiber holder system allows easy transfer of the fiber from step to step, and ensures that the fiber is always properly located and positioned for each operation. The fiber holder accurately locates the fiber relative to the stripper blades for high strength splicing, and also properly registers the fiber within the cleaver (and in the optional ultrasonic cleaner, also used for high strength splicing). In addition, another important design feature of the fiber holder system is that it is designed such that the fiber holders are guided and constrained as

the fiber holders are loaded into the splicer. This prevents accidental contamination of the cleaved fiber ends as the fibers are lowered into the splicer V-grooves.

2.5.3 Fiber Preparation Tools. A complete set of fiber preparation tools have been developed for use with the splicer. Included are an exclusive hot jacket stripper, cleaver, and ultrasonic cleaner for high strength operations. Other fiber preparation tools are available for standard strength splicing operations. These standard strength fiber preparation tools offer a lower cost solution. These standard tools may also be adapted for short cleave length splicing (for standard splice strength operations) for use with micro splice protection sleeves. All of these tools have been specifically designed to function in conjunction with the finer holder system. In addition to the fiber preparation tools and micro splice protection sleeves, a new recoater with proof test function has been developed as an adjunct to the splicing system.

2.5.4 PC Communications Function. The splicer has advanced PC communications functions. These include capability for data transfer to and from the splicer, software upgrade from a PC, and direct operation from a PC.

A data transfer software spreadsheet (utilizing Microsoft Excel) allows uploading and downloading of all splicing parameters for every programmable splicing mode and tube heater operating mode, either all at once or selectively (mode by mode). This spreadsheet also allows downloading any splice data in memory from previous splicing operations, and also reprogramming all of the other splicing menus, including setting the splicer operating configuration and supervisory lock-out features (enabling useful production line management control).

The data of the splicing arc conditions, estimated loss, etc., may be output via the serial port for production line SPC data collection. Furthermore, the NTSC video output port may download video images of the fiber.

A complete set of computer command codes is available to allow total customer specific control of the splicer. This allows embedding the splicer into a factory production line PC control system.

2.5.4 User Support Functions. This splicer has a great deal of programmability with a variety of parameters for splicing and loss estimation, which may be used to rapidly establish the best splicing conditions as new specialty fiber combinations are introduced.

Other user support functions include splicer self-diagnostics, and operational configuration control. The configuration control functions include the previously mentioned lock-out features that allow production line supervisors to prevent unauthorized reprogramming of the splicer by production operators, and also a variety of convenience features such as control of the fiber image magnification and display during every stage of the splicing process.

In addition, user help screens and functions provide easy explanation of operation and menu navigation, and boot-up menu & start-up acceleration functions are also available.

3. Conclusions

We developed a new splicer that is optimized for technically challenging factory and production line operations. It has the following significant features:

- The new technology sweep arc discharge function is provided for excellent dissimilar fiber splicing capabilities, while preserving the benefits of the narrow arc profile for homogeneous splicing.
- The splicer is adapted for the variety of PM fibers in use in production applications, with excellent splicing performance.
- Improved loss estimation functions are provided, and also accurate polarization cross talk estimation for verification of PM splice quality.
- Splicing with short cleave length and high strength is available for every fiber type, including PM fibers.
- The splicer features factory-optimized ergonomics, design, fiber preparation equipment, and features

The new splicer has been developed to provide exceptional functionality for factory splicing, laboratory, R&D, and production line use. Excellent performance is provided with the variety of specialty fibers in use or entering optical module production lines.

4. References

[1] K. Ohzawa, et al, "Development of new optical fiber fusion splicer for factory use", Proc. of IWCS '99, pp. 644-649

Authors



Kenji Takahashi

Precision Instruments R&D Dept.

Fujikura Ltd.

1440, Mutsuzaki, Sakura, Chiba, 285-8550,JAPAN

ken_taka@opt.fujikura.co.jp

Kenji Takahashi was born in 1967. He graduated with a mechanical degree from Doshisha University in 1990.

He joined Fujikura Ltd. in 1989 and has been engaged in the research and development of optical fiber fusion splicers.



Noriyuki Kawanishi

Precision Instruments R&D Dept.

Fujikura Ltd.

1440 Mutsuzaki, Sakura, Chiba, 285-8550, JAPAN

nick_k@opt.fujikura.co.jp

Noriyuki Kawanishi was born in 1965. He received his M.E. degree in Electrical Engineering from Toyohashi University of Technology in 1990. He joined Fujikura Ltd. in 1990 and has been engaged in the research and development of optical fiber fusion splicers.



Shonosuke Yaguchi

Precision Instruments R&D Dept.

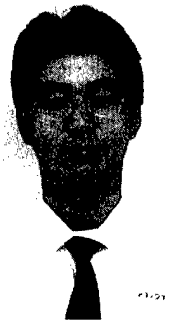
Fujikura Ltd.

1440 Mutsuzaki, Sakura, Chiba, 285-8550, JAPAN

syaguchi@opt.fujikura.co.jp

Shonosuke Yaguchi was born in 1955. He graduated in mechanical engineering from Keio University in 1979.

He joined Fujikura Ltd. in 1979 and has been engaged in the Plant Engineering Section for 12 years and currently is a general manager of the Precision Instruments R&D department.



Taku Ohtani

Precision Instruments R&D Dept.

Fujikura Ltd.

1440, Mutsuzaki, Sakura, Chiba, 285-8550,JAPAN

taku@opt.fujikura.co.jp

Taku Ohtani was born in 1970. He graduated with a mechanical degree from Tokyo University of Agriculture & Tech. in 1994. He joined Fujikura Ltd. in 1994 and has been engaged in the research and development of optical fiber fusion splicers.

Stresses at an Optical-Fiber / Connector-Ferrule Interface

John F. Malluck, Wilton W. King, and Bruce G. LeFevre
Optical Fiber Solutions
Lucent Technologies
Norcross, Georgia
+1-770-798-2680 · jmalluck@lucent.com

Abstract

For the most part, analyses of fiber fractures in connectors have been in the form of postmortem fractography. Typically in these works, characteristics of prefracture stress states have been inferred from fracture surfaces, and plausible qualitative explanations have been advanced about the likely structural mechanics and circumstances leading to fractures. The authors and their colleagues have undertaken a number of investigations of relevant structural mechanics. These have served the useful purpose of elucidating gross mechanisms, but the influence of the fine details of stress distributions have been missing.

Considered here is a cylindrical-ferrule connector for which, typically, the ferrule is ceramic with an outside diameter of 2.5mm or 1.25mm. The fiber to be terminated is bonded into a small-bore axial hole (capillary) in the ferrule by an epoxy or similar adhesive. In addition, fiber insertion into the capillary is facilitated by ferrule designs that provide a conical entrance cavity leading to the capillary. A very high percentage of fiber failures, both in the laboratory and the field, occur at the transition region between the fiber and the capillary; so analysis is focused on that region.

The stress distribution within an optical fiber adhesively bonded to a ceramic ferrule is determined by the finite element method for uniform remote tension acting on the fiber. An axisymmetric model is constructed to represent the fiber, epoxy, and geometry of the ferrule under this particular loading condition. The resulting stress distribution is determined within the fiber and the epoxy layer using the ***ANSYS*** finite element code. Stress concentrations are sought and found at the surface of the fiber, this being the location of damage, which might have been inflicted on the fiber by mechanical stripping of coatings. When the cone-capillary transition is sharp, stress concentration is found there. However, even that is not significant provided there is perfect bonding between the epoxy and the ceramic ferrule. Exploration of several geometries reveals that serious structural weakness is always associated with at least partial epoxy/ceramic debonding. This calls attention to the need to give attention to adhesive characteristics of epoxies and ceramics.

Keywords

Optical Fiber; Connector; Ferrule; Stress Analysis; Finite Element Method; Adhesive Bond

1. Introduction

Connectors and splices are potentially weak links in fiber-optic systems. At these components, degradation of performance or complete loss of function can occur in a variety of ways. One form of catastrophic failure is fracture of a fiber, and in a connector or splice is found bare fiber whose intrinsic local strength may have been substantially reduced by the process of removing protective coatings. But a weakened fiber will only fracture if additionally there is a stress of sufficient magnitude, in particular tensile stress. In this paper we explore such stresses at a critical location in a single-fiber connector typical of current products such as FC, SC, ST, LC, and MU connectors.

As a first step in connectorization, buffer and coating layers are usually stripped off mechanically. "Coating" and "buffer" usually identify polymer layers that protect the fiber, the former is applied in-line with the drawing of the fiber, and the latter is applied in a later operation. Typical outside diameters for fiber, coating, and buffer are 125μm, 250μm and 900μm respectively. The tools used for stripping invariably nick or scratch the bare fiber, and the resulting flaws are sites for amplification of stresses and initiation of cracks. Studies [1,2] have demonstrated that tensile strengths of individual samples of stripped fiber can often be significantly less than 700 MPa (100 ksi). It is the interaction of tensile stress with a flaw that leads to fracture, and so circumstances that place a fiber in longitudinal compression are not dangerous unless that condition can lead to buckling of the fiber. For a fiber in bending, the significance of a flaw will depend upon whether the flaw is on the tension side or the compression side of the bent fiber. Of course, when a fiber is loaded in longitudinal tension that is the nature of the stress throughout.

For the most part, analyses of fiber fractures in connectors have been in the form of postmortem fractography [3,4,5]. Typically in these works, characteristics of prefracture stress states have been inferred from fracture surfaces, and plausible qualitative explanations have then been advanced about the likely structural mechanics and circumstances leading to the fractures. A notable early exception is the work of Kinney [6] in which he reported extensive finite element analyses of thermoelastically induced stresses in biconic connectors.

The present paper focuses on cylindrical ferrule-connector stresses at an optical-fiber/connector-ferrule interface. The fiber is bonded into a small-bore axial hole in the ferrule by an adhesive. A number of investigations of relevant structural mechanics have been undertaken by the authors and their colleagues [7-11] These have served the useful purpose of

elucidating gross mechanisms, but missing have been fine details of stress distributions, one case of which is the subject of the present work. A previous paper of the author's [12] highlighted the stress distributions encountered within connectors. This paper refines the analysis and illustrates a plausible failure mechanism.

Here we consider a cylindrical connector-ferrule for which, typically, the ferrule is ceramic with a diameter of 2.5mm or 1.25mm. The fiber to be terminated is bonded into a small-bore axial hole in the ferrule by an epoxy or similar adhesive. A very high percentage of fiber failures both in the laboratory and in the field occur at the transition to the small hole. So the finite element analysis is here focused on that region for the case of remote tension applied to the fiber.

2. Fiber Optic Connector Description

A single fiber, such as shown in Figure 1, is one of the most common configurations for making optical connections. The heart of the assembly consists of a spring-mounted ceramic ferrule, which guarantees fiber contact between opposing connectors. A mechanically stripped section of fiber is adhesively bonded within a small capillary within the ferrule. The exposed tip of the ferrule-fiber-adhesive assembly is subsequently polished to achieve appropriate optical performance.

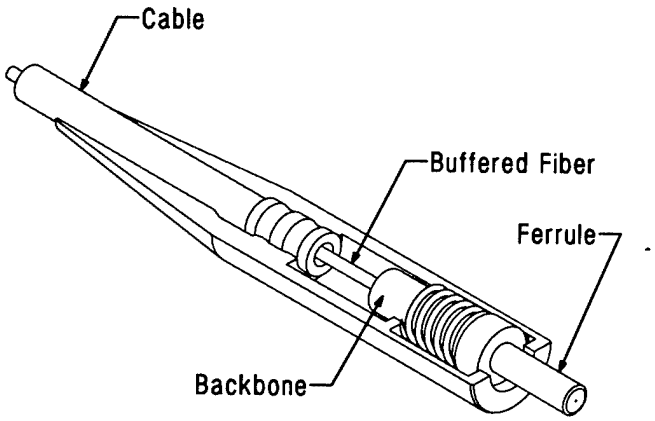


Figure 1. Single Fiber Connector

The specific structural details of the ceramic connector-ferrule assembly are illustrated in Figure 2. Four components of differing material stiffness (stripped fiber, ferrule, backbone, buffered fiber) are bonded together with the epoxy adhesive. A section of unsupported fiber leads into a conical hole, which facilitates fiber insertion into the ferrule capillary. An epoxy cone is formed which partially, or completely, fills the entrance cone to the capillary. Fiber failures are typically observed in the entry cone and capillary transition region.

An element of the buffered fiber is shown in Figure 3. There is continuous bonding of the various layers, so the fiber is indirectly attached to the buffer through the two layers of coating. Thus, one might anticipate that shear rigidities of coating and buffer materials would result in isolation of the fiber in the connector from remotely applied tension, because

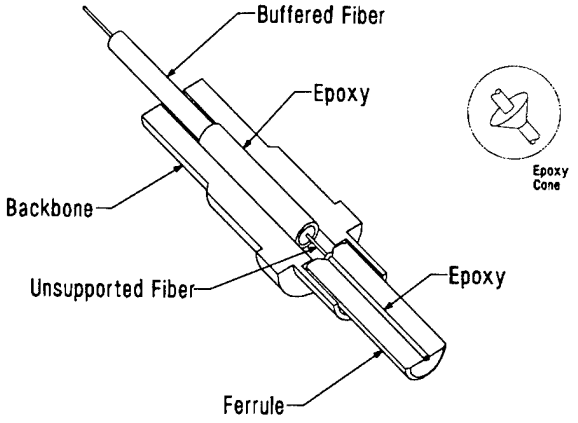


Figure 2. Ceramic Connector-Ferrule Assembly

the buffer itself is adhesively bonded to the connector backbone (Figure 2). However, the inner coating is a very low-stiffness material, so tension applied remotely to the fiber will be transmitted more or less directly to the portion of the fiber at risk. It can be reasonably argued though that tugging on the buffer structure remotely should not load the fiber, because of the very small shear resistance of the inner coating. The fact that significant stresses can be stimulated in the fiber is probably the result of a lengthening zone of shear transfer away from the connector, or perhaps a pinching of the buffer/coating structure so as to unitize it with the fiber where tensile loads are applied [11].

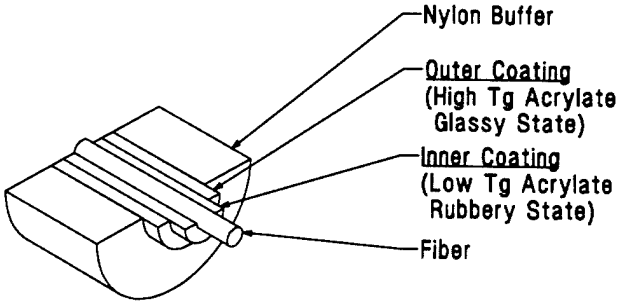


Figure 3. Buffered-Fiber Element

In order for a fiber to separate from the ferrule to which it is bonded, adhesion must be lost either between fiber and epoxy or between epoxy and ceramic ferrule. In load-to-failure tests [11] the two cases shown in Figure 4 have been found in postmortem inspections. Type B is a fairly simple case of fiber fracture accompanying adhesive failure at the fiber-epoxy interface. This shear debonding has been given attention by Etemad [13] and is not treated in the present work. The more common failure mode observed by Sidbury [11] is Type A which is relatively more complex in that the elements are: fiber fracture; shear/tension debonding of the epoxy cone from the ferrule; and epoxy fracture and debonding in the capillary region. An example is shown in Figure 5.

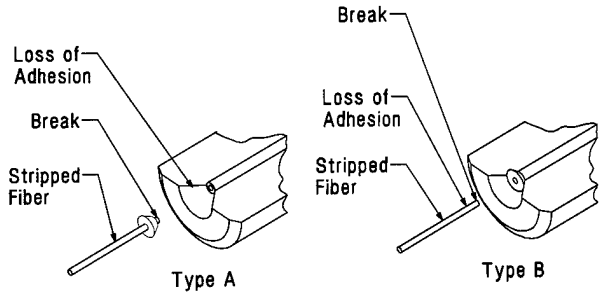


Figure 4. Failure Modes Under Tension

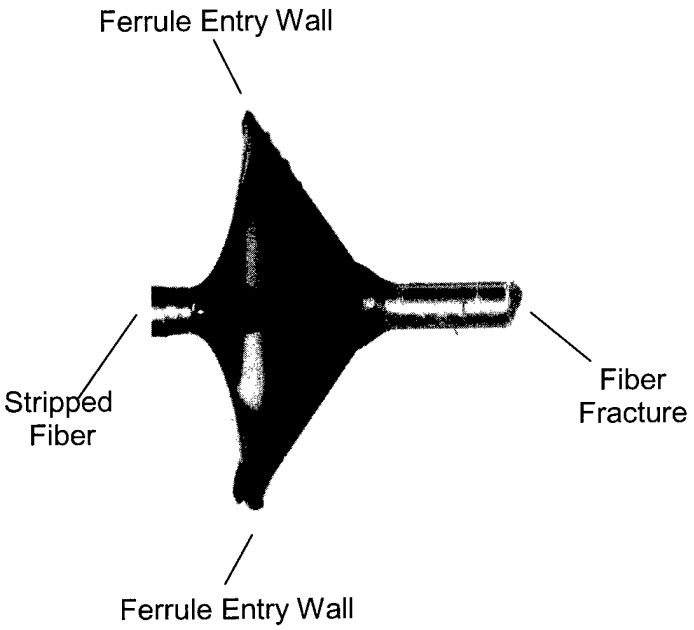


Figure 5. Failure Mode "A"

3. Numerical Modeling

Numerical solutions for stresses within the fiber-ferrule assembly under uniaxial tension were determined by the finite element method using the **ANSYS** finite element code [14]. Figure 6 is a representation of an axisymmetric model representing the fiber, epoxy layer, and epoxy cone. An axisymmetric model is employed as the geometry, loading, and boundary conditions are symmetric about the fiber axis. Since the ferrule ceramic is much stiffer than either epoxy or fiber, the ferrule geometry is simply represented by the rigid boundary conditions surrounding the appropriate portion of the epoxy. Material properties are listed in Table 1.

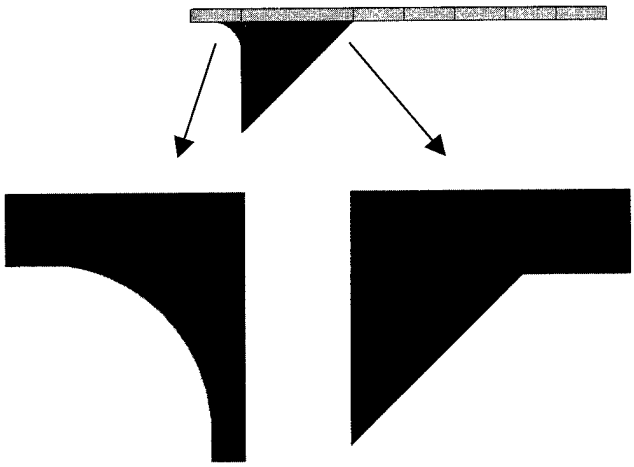


Figure 6. Finite Element Model

Young's Modulus	GPa
Ceramic Ferrule	206
Glass Fiber	76
Epoxy Adhesive	4

Table 1. Material Properties

4. Challenges in Numerical Simulation

The major issues regarding numerical simulation of the fiber-ferrule assembly lie in the disparity of geometric dimensions within the structure and in the presence of stress singularities at sharp corners. The disparity in geometric dimensions occurs because of the difference between the typical 1μm adhesive layer thickness as compared to the 125μm fiber diameter. Fine numerical meshing of the adhesive layer leads to fine meshing of the fiber and these both can lead to large numbers of degrees of freedom in a numerical model. Figure 6 shows a magnified view of a finite element mesh used to represent the epoxy layer and adjacent fiber. As such, the current model consists of over 325,000 elements with in excess of 500,000 degrees of freedom. This issue is however readily addressable by using computers with large amounts of memory, and storage space. The second issue, the presence of stress singularities at sharp corners, is circumvented by the fact that these singularities are kept within the epoxy layer, and do not occur within the glass fiber. Our concern is with stress concentrations within the glass fiber itself, and not with actual stresses in the epoxy layer. These high stresses on the surface of the glass even though localized will interact with surface flaws produced when stripping the fiber.

Figure 7 shows a magnified view of the potential locations of stress singularities within the epoxy layer and stress concentrations within the glass fiber.

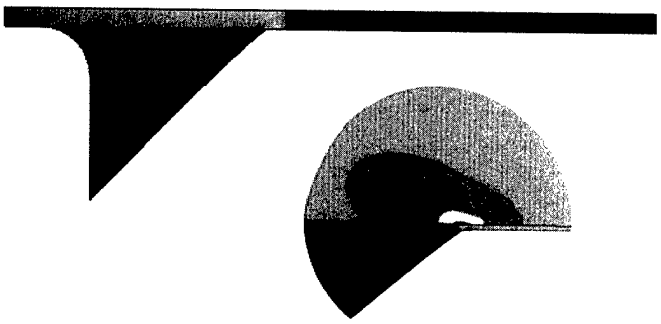


Figure 7. Stress Concentrations and Stress Singularities

5. Numerical Predictions

The stresses within the glass fiber were determined for three specific bonding conditions of the epoxy.

- Epoxy Cone Completely Bonded
- Epoxy Cone Completely Debonded
- Debond Extended Into Capillary

5.1 Epoxy Cone Completely Bonded

The distribution of the maximum principal stress at the fiber surface is shown in Figure 8 for the situation in which the epoxy cone is completely bonded to the ferrule. The surface stress has been normalized to the remotely applied uniform stress, S0. Figure 8 shows that the epoxy effectively isolates the fiber from the applied stress. There is a local stress concentration at the throat of the entry cone, but the peak stress there is less than the applied stress.

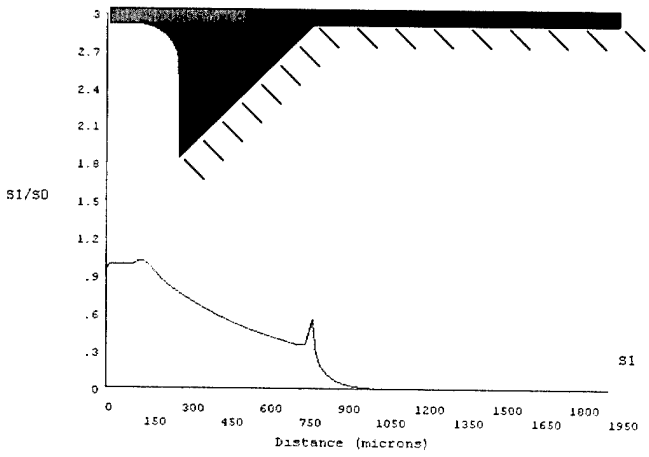


Figure 8. Fiber Surface Stress Distribution – Bonded Cone

5.2 Epoxy Cone Debonded

The distribution of the maximum principal stress at the fiber surface is shown in Figure 9 for the situation in which the epoxy cone is completely debonded. Again, the stress concentration occurs within the glass at the fiber surface. The peak stress concentration of magnitude 2.25, now occurs as the fiber enters the capillary within the ferrule cone. As such when the cone is complete debonded, one would expect fiber failure to occur near the entrance to the capillary.

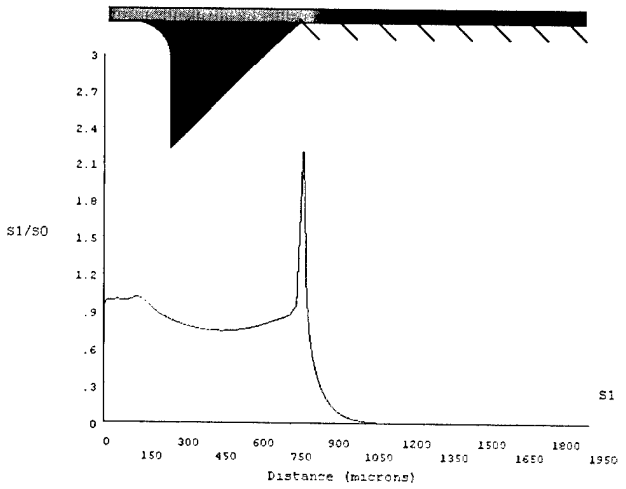


Figure 9. Fiber Surface Stress Distribution – Debonded Cone

When the debond is extended into the capillary, the peak stress concentration remains at about 2.3 but is now located at the end of the adhesive bond, as illustrated in Figure 10. Note that in each case, the critical location always occurs where the debond stops in the capillary.

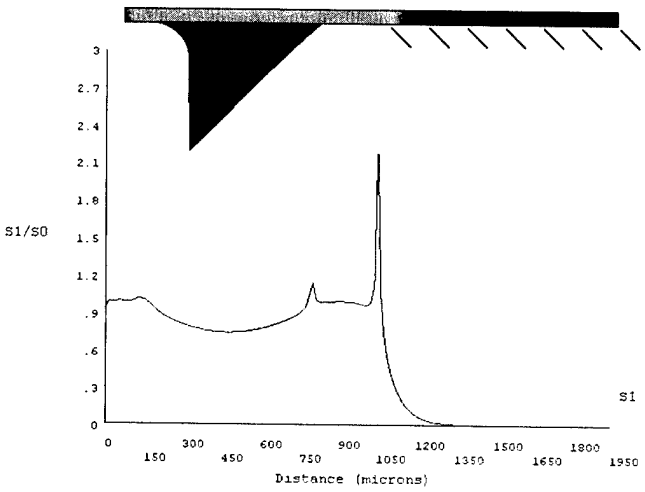


Figure 10. Fiber Surface Stress Distribution – Debond Extended Into Capillary

5.3 Radial Distribution of Stress

The peak stresses we have been describing are highly concentrated at the surface of the fiber. This is illustrated in Figure 11 at the axial location of the peak stress shown in Figure 10. Were the fiber not so brittle, such localized stress would have little bearing on fracture. But, of course, optical fibers are quite flaw sensitive and the most significant flaws are found at the surface.

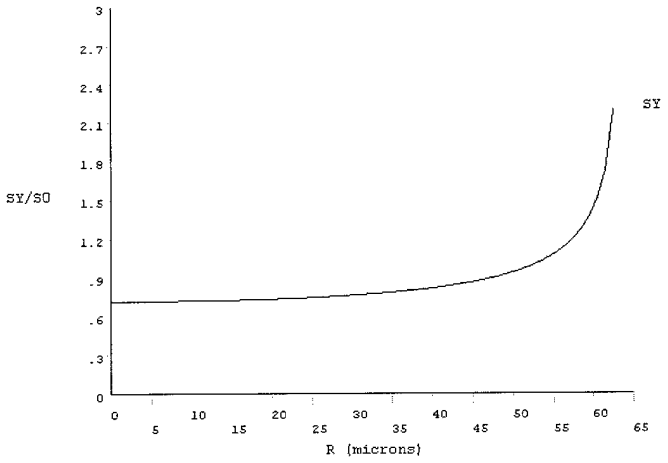


Figure 11. Radial Stress Distribution

5.4 Discussion

The preceding figures illustrate a plausible mechanism for Type A failures occurring at or near the transition of the entry cone to the ferrule capillary. Fiber fracture must be preceded by debonding of the *epoxy/ceramic* interface in the cone area and of the *epoxy/fiber* interface for some distance into the capillary. Fracture then occurs where a flaw encounters the stress concentration. Such flaws may be produced during stripping and insertion of the fiber into the ferrule.

The Type B failure mode is more straightforward in that no plausible mechanism exists without assuming debonding along the *epoxy/fiber* interface from the beginning of the cone to the point where a surface flaw exists. The necessary precursor to both A and B failure modes is prior debonding of the epoxy. The integrity of this adhesive bond can be affected by many things including cleanliness of the interfaces and subsequent environmental exposure to thermal stresses and moisture

Reducing the probability of fiber fracture in connectors requires an understanding of two things (1) the dependence of stress distribution on the geometry of the termination in the ferrule cone area, and (2) the strength and reliability of the adhesive bonding at the epoxy/ceramic and epoxy/fiber interfaces. The first has been the subject of this paper. The second falls within the purview of standards Working Groups TIA/FO 6.3.3 and 6.3.8 that deal (respectively) with adhesives and reliability of passive fiber optic components. These groups has not yet developed standards or informative documents on the subject of adhesive strength of the interfaces in question, but plans to address the subject in its upcoming work program for the following year 2002.

6. Subsequent Investigations

The authors also explored the influence of epoxy layer thickness and the effect of a smooth-radius transition at the capillary entrance.

6.1 Epoxy Layer Thickness

The stress concentration factors corresponding to three epoxy layer thicknesses are shown in Figure 12. These numerical values for stress concentration factor are located at the entry cone to capillary transition. As might be expected, a thinner layer of epoxy causes an increase in stress concentration factor.

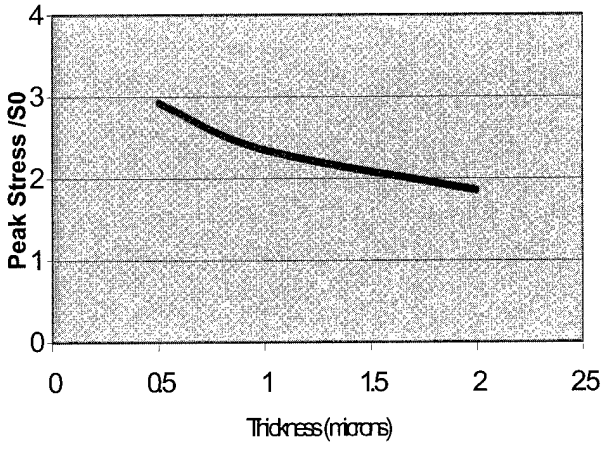


Figure 12. Influence of Epoxy Layer Thickness

6.2 Radius at Capillary Entrance

Stress concentration factors were determined for two values of smooth radii at the entry cone to capillary transition (Figure 13) and are compared with stress concentration for a sharp corner in Figure 14.

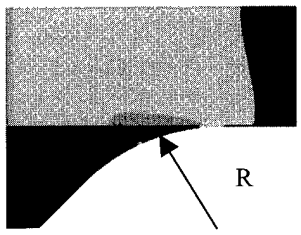


Figure 13. Radius at Cone to Capillary Transition

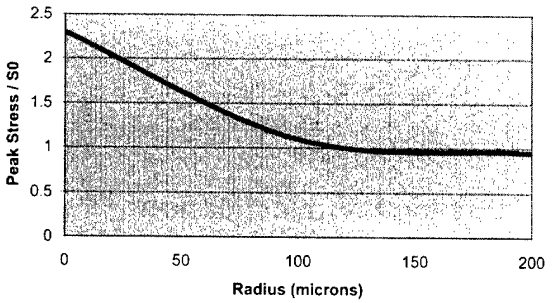


Figure 14. Influence of Radius upon Peak Stress (Only Cone Debonded)

Not surprisingly, a radius greatly reduces the stress concentration at this location. However, while a reduction is peak stress occurs at this location, there is no reduction is peak stress if the debond extends down into the capillary region.

7. Conclusions

The results of the analysis serve to quantify what may be, for most readers, intuitively obvious, at least at a qualitative level. Substantial stress concentrations in the glass fiber are formed at positions where stress singularities in the adhesive are nearby. These high stresses are so localized to the surface of the fiber that one might tend to dismiss their significance. However, the silica fiber is inherently brittle, and flaws are naturally introduced at the surface during the mechanical stripping of polymer coating. So the situation is one of high local stress at a place of high probability for surface flaw.

Even though the axisymmetric modeling of the problem is a great oversimplification of reality, the analysis provides insight to the problem of fiber failure and is consistent with experimental observations. Guidance is provided to the designer with regard to removal of sharp corners.

Finally, the importance of epoxy-ceramic bonding is highlighted.

8. Acknowledgments

The authors wish to express their gratitude to Carmen Sidbury for the use of the experimental observations of fracture within connectors.

9. References

[1] T. Wei, H. H. Yuce, C. H. Hasz and P. L. Key, Degradation of Fiber Strength During Coating Stripping," Proc.38th International Wire and Cable Symposium, pp. 199-204 (1989).

[2] W. R. Wagner, "Extrinsic Fiber Damage and its Effect on the Reliability of Optical Fiber Connectors and Splices," Fiber optic Components and Reliability, Proc. SPIE, Vol. 1580, pp. 168-185 (1991).

[3] W. R. Wagner, "Failure Analysis of Fiber Optic Connectors," Advances in Ceramics 22, Fractography of Glasses , Am. Ceramics Soc., pp. 389-402 (1988).

[4] H. H. Yuce, J. P. Varachl, Jr. and T. Wei, "Analysis of Optical Interconnection Failures by Analytical Techniques," Proc. 9th National Fiber Optic Engineers Conference, pp. 251-256 (1993).

[5] T. Wei, B. T. Devlin, H. H. Yuce and J. P. Varachl, Jr, "Failure Mode Analysis of Fiber Components," Proc. 11th National Fiber Optic Engineers Conference, pp. 1081-1085 (1995).

[6] M. Kinney, "Optical Fiber Stresses within a Biconic Connector," Failure Prevention and Reliability - 1987, ASME DE-19, pp. 75-79 (1987).

[7] J. M. Anderson, A. G. Hardee, W. W. King and B. G. LeFevre, "Design Consideration Relating to Thermally Aggravated Fiber Stress in a Connector Cavity," Proc. ASM Int'l. 4" Electronic-Materials and Processing Congress, pp. 225-228 (1991).

[8] W. W. King, B. G. LeFevre, and A. G. Hardee, "Structural Integrity of Optical Fibers in Connectors"' Structural Analysis in Microelectronics and Fiber Optics: 1997, ASME EEP – Vol. 21, pp. 261-269 (1997).

[9] B. G. LeFevre, W. W. King, A. G. Hardee, A. W. Carlisle and K. B. Bradley, "Failure Analysis of Connector-Terminated Optical Fibers: Two Case Studies," J. of Lightwave Tech.Vol. 11, pp. 537-541 (1993).

[10] B. G. LeFevre, W. W. King, C. K. Sidbury and D. L. Stephenson, " Analysis of Fiber Fracture in Connectors", Proc. National Fiber Optic Engineers Conference, Orlando, pp. 257-268 (September 1998).

[11] C. K. Sidbury, B. G. LeFevre, W. W. King, and D. L. Stephenson, "Fracture of Optical Fibers in Connectors", Proc. 48th Electronic Components and Technology Conf., Seattle, pp. 1450-1454 (May 1998).

[12] J. F. Malluck and W. W. King, "Stress Concentrations in a Connectorized Optical Fiber," Packaging of Electronic and Photonic Devices, ASME EEP-Vol. 28, pp.11-24, (November 2000).

[13] S. Etemad, P. Grimado, F. DeRosa and A. Dori, "A Failure Mechanism for Optical Branching Components: When the Epoxy Lets Go of the Fiber," Proc. 11th National Fiber Optic Engineers Conference, pp. 823-832 (1995).

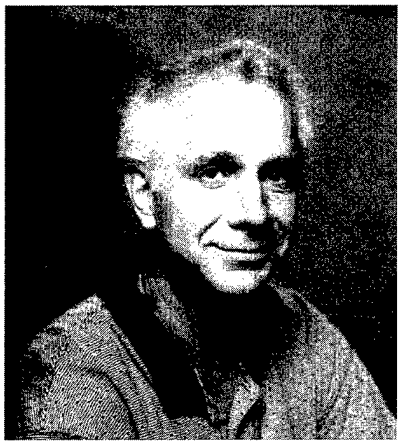
[14] ANSYS User's Manual, Rev 5.6 (November 1999).



John F. Malluck is a Member of Technical Staff in the Optical Fiber Solutions Division of Lucent Technologies. His present duties include numerical simulation of optical component performance. Dr. Malluck received his Ph.D. in Engineering Mechanics from the Georgia Institute of Technology.



Wilton W. King is Emeritus Professor at the Georgia Institute of Technology, Atlanta, where he served on the faculty for 27 years. In 1991, he joined AT&T Bell Laboratories (now Lucent Technologies), Norcross, GA, where he designs and analyzes fiber-optic connector products.



Bruce G.LeFevre is a member of technical staff in Optical Fiber Solutions of Lucent Technologies, Norcross, Ga. He holds a Ph.D. in Materials Science and Engineering from the University of Florida and served on the faculty of the Georgia Institute of Technology prior to joining AT&T Bell Laboratories and moving later to Lucent. His work deals with testing, reliabilty and reliability of fiber optic passive component interconnections. He chairs IEC SC86B and working groups 6.3.8 of TIA.

Analysis of Fiber Breaks in Multimode Connectors

O.S. Gebizlioglu[1*], M.R. Özgür, D. Unkel

[1]Telcordia Technologies, Inc.
445 South Street
Morristown, New Jersey 07960
[1*] 973 829 4956 ogebizli@telcordia.com

Abstract

We present analyses of fiber breaks that were identified to be the root-cause of insertion loss and reflectance failures in connectorized multimode cables. We used precision reflectometry analyses to locate fiber failures within the connectors and special methods developed at Telcordia to gain access to fracture surfaces of fibers broken within the connector body. These methods involved two-stage acid etching with no mechanical intervention to disassemble termini from three sample cables. On the disassembled termini, we used DVM (digital video microscopy) and ESEM (Environmental Scanning Electron Microscopy) analysis to uncover fiber fractures and perform break source analysis (fractography) to determine fracture origin(s) and the state of fracture stress. Disassembly of termini from failed cables by our two-stage acid etching process revealed one or more fiber fractures, all within the adhesive block underneath the metal housing and around large voids near the ferrule entry cone. In all cases presented, fiber fractures were found in regions of connector body where adhesive malformations occurred. Our results represent the first set of experimental data available in the open literature to link fiber failures within connectors to adhesives-related structural discontinuities.

Keywords

Optical fiber; connector; ferrule; adhesive; acid etching; fiber break; fiber fracture; fracture analysis.

1. Introduction

Break source analysis (fractography) of optical fiber failures has been proven to be very important toward improving the reliability of optical fiber, cable, and fiber-based components in modern telecommunications networks. Although optical fiber failures do not occur as frequently as they did during the first decade of the deployment of fiber optic communications systems, they are still encountered in various stages of manufacturing, installation and deployment of fiber-based components and devices. In fiber failures within connectors and splices, a definitive analysis may become impossible due to the inaccessibility of fiber fracture surfaces. There have been numerous attempts[1, 2, 3, 4, 5, 6, 7, 8] to determine the source and mechanical condition of fiber breaks where fiber fracture surfaces were accessible. However, in most fiber failures within connectors, failure analyses have remained inconclusive. In this report, we present results on analyses of fiber failures within multimode connectors. We have used specially developed methods to access fiber fracture surfaces within the connectors and performed definitive break source analyses.

2. Failure Analysis Methods

In this section, we describe a special method[9] of failure analysis that we developed for uncovering the causes of fiber breaks in fiber optic connectors and connectorized cables.

Method Development for Fiber Removal from Connectors

Fiber optic cables and connectors assembled with intrinsically brittle silica glass fiber require special methods and techniques for the root-cause analysis of fiber breaks. The first step in the failure analysis of connectorized fibers involves the removal of connector housing and other material components for access to the fracture surfaces of fibers. However, this removal process has to be carried out to preserve the fracture surface features of broken fibers for subsequent fractography analysis to determine the fracture origin(s) and the state of fracture stress. Therefore, our method consisted of three-step non-mechanical disassembly of connectorized terminations from test cables. Starting from the outside with the metallic housing, we immersed each connectorized termination (terminus) in a mixture of acids with specific affinity to the material of the metallic housing (stainless steel). This first stage of acid etching was followed by extensive DVM (Digital Video Microscopy) analysis of remaining ferrule-adhesive block with attached coated fiber stub. Some connectors, at the end of this first stage, separated to reveal the fiber breaks and allow access to fiber fracture surfaces. For connector samples that remained integral after the first stage, the second stage of acid etching involved the immersion of the ferrule-adhesive block in a medium (such as concentrated sulfuric acid) with affinity to etch the adhesive block. This second stage could be performed either at 25°C or elevated temperature (as high as 200°C). For all connectorized cables investigated to date, this two-stage disassembly has allowed access to fiber fracture surfaces. Thus, the third stage[9] that would involve controlled thermal degradation of the adhesive to remove the fiber from the connector ferrule was not needed in the failure analysis discussed in this report. As described earlier in this section, we used DVM micrographs of termini from the first and second stages of the disassembly process and ESEM (Environmental Scanning Electron Microscopy) micrographs of fracture surface features for broken fiber end(s). On the ESEM micrographs, we note the fracture origin and flaw size based on the regularity or complexity of the fracture surface morphology. As we point it out later in this report, we can make definitive statements about the state of fracture stress (both the mode of fracture and the magnitude of fracture stress) only for low-stress breaks for which fracture surfaces are planar with well delineated fracture features such as fracture origin, mirror, mist, and hackle marks.

3. Results

In this section, we present the results of our failure analyses on three connectorized test cables:

Sample 1 showed one fracture at 5.4 mm from the polished tip of the connector ferrule during the PR (Precision Reflectometry) testing. This particular connector had experienced many matings, cleaning operations and thermal cycles after its fabrication in October 1997.

Sample 2 exhibited two fractures, one at 8.6 mm and another at 12 mm from the polished ferrule tip.

Samples 3a and 3b were subjected to thermal cycling and examined by precision reflectometry. Although both termini passed these first PR tests, the sample 3a failed the second round of PR measurements after inspection by a boroscope. This second PR test indicated fiber fracture at 5.3 mm from the polished tip of the ferrule.

Sample 1

In the first stage of the disassembly process, sample 1 terminus readily separated into two sections: the ferrule and the adhesive block with its fiber as shown in the DVM micrograph of Fig. 1, thereby suggesting that the fiber fracture occurred right at the transition zone (throat) from the ferrule entry cone to the central capillary of the ferrule.

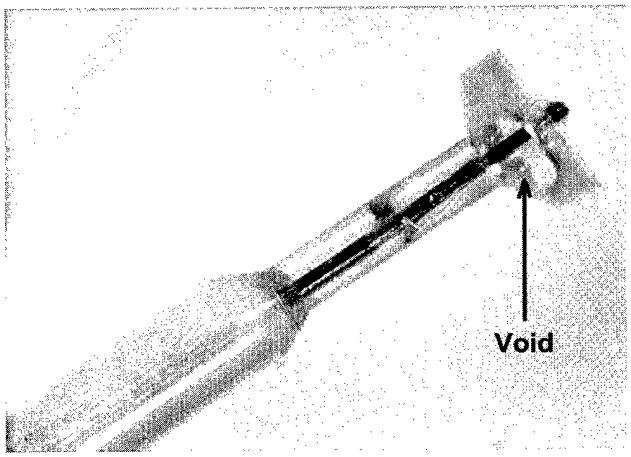


Figure 1. DVM (Digital Video Microscopy) micrograph of sample 1 terminus showing the adhesive block, a large void and the fiber broken at the ferrule throat after removal of the metallic housing.

This micrograph also shows a large void with exposed fiber within the adhesive funnel that was designed to cover the ferrule entry cone. Fig. 2 provides two important details on the adhesive funnel: 1) Internal surface of the funnel is smooth, suggesting low wettability of the ferrule entry cone surface by the adhesive mixture and / or significant shrinkage of the adhesive block following the cure initiation, 2) A planar fracture surface that suggests low-strength break at pre-existing flaws on the fiber surface. Micrograph of Fig. 3 confirms that the large void shown in Fig. 1 went through the thickness of the adhesive funnel side wall. This observation raises the issue of effectiveness in filling the terminus body with adequate quantity of the adhesive mixture prior to the cure process.

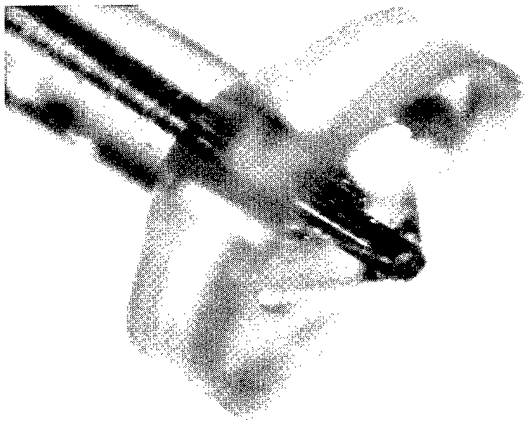


Figure 2. DVM (Digital Video Microscopy) micrograph of sample 1 terminus showing the adhesive block and the adhesive funnel that covers the ferrule entry cone.

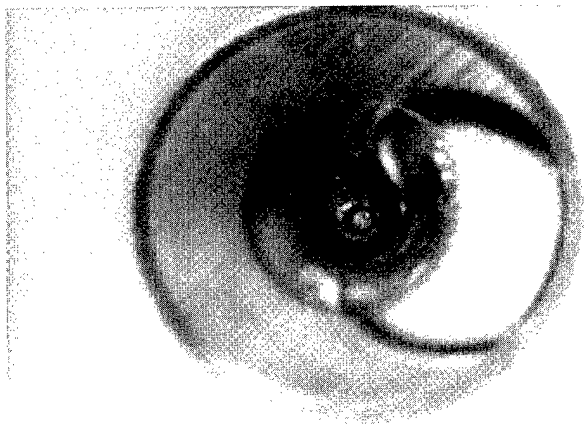


Figure 3. DVM (Digital Video Microscopy) micrograph of sample 1 showing the adhesive funnel with a large void.

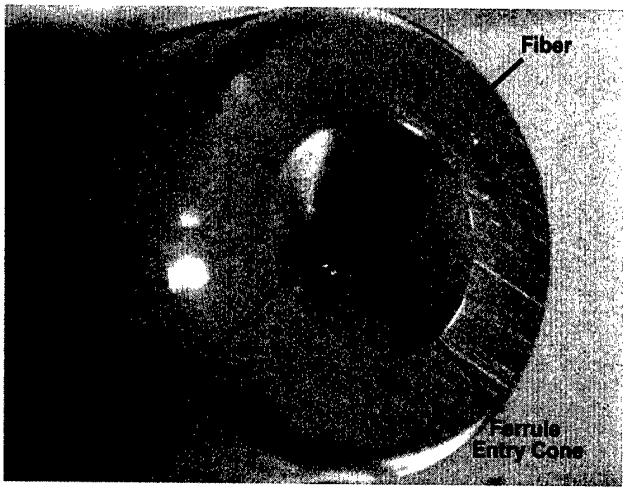


Figure 4. DVM (Digital Video Microscopy) micrograph of sample 1 terminus showing the ferrule entry cone and the broken fiber end at the ferrule throat.

Fig. 4 shows the ferrule entry cone for the sample 1 terminus with no fracture detail on the broken fiber surface at the ferrule throat. A clean ferrule entry cone surface in this micrograph confirms that it was not effectively wetted by the adhesive.

Figs. 5 and 6 present ESEM micrographs of fracture surfaces for the fiber retained in the ferrule and its matching end of the fiber embedded in the adhesive funnel, respectively. These two morphologies suggest clearly a low-strength tensile break with a well defined mirror diameter of 50 μm and flaw size of 5 μm. Based on A.A. Griffith's[10] classic work on the brittle fracture of glass and the well-known relationship between the mirror size and fracture stress[1] for silica glass, we estimated a tensile fracture stress of 345 MPa (50 ksi). This represents a lower bound since bending and torsional effects are known to lead to an enlarged mirror on the fracture surface. This result suggests that a pre-existing flaw on the fiber surface, from various fiber handling operations, is the most likely cause of failure for the sample 1 terminus.

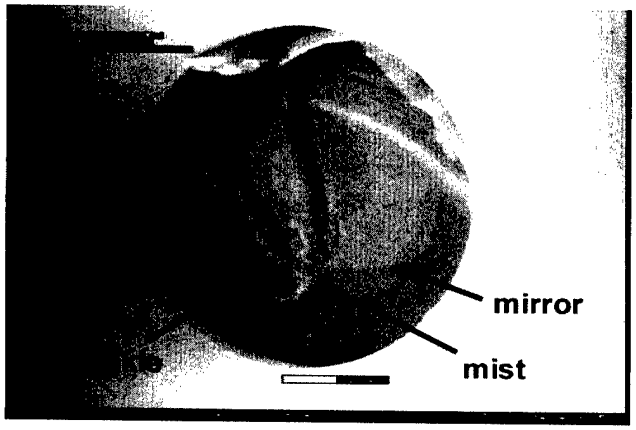


Figure 5. ESEM micrograph of fracture surface morphology of fiber broken at the ferrule throat from sample 1 terminus.

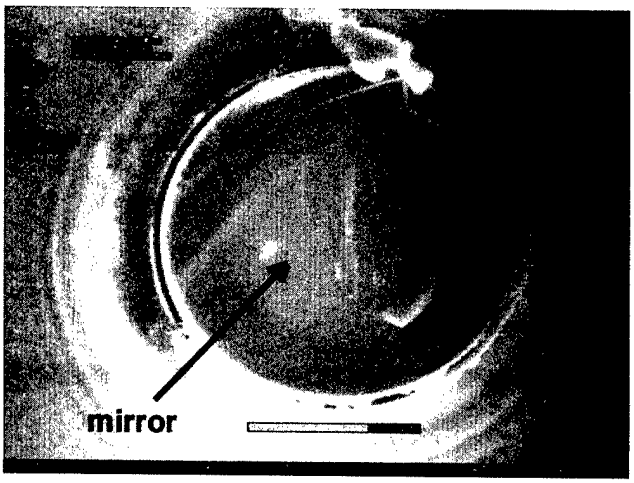


Figure 6. ESEM micrograph of fracture surface morphology of fiber retained within the adhesive funnel from the sample 1 terminus.

Sample 2

As indicated earlier, this sample was used to observe customer's cleaning practices and its potential effects on the integrity of the terminus. By precision reflectometry, two fracture sites were located at 8.6 mm and 12 mm from the polished end of the ferrule. Fig. 7 shows the front piece of the terminus after the first-stage processing and reveals that the fiber fracture occurred within the adhesive block. Micrograph of Fig. 8 shows both the front and rear pieces of the terminus together and indicates that both breaks occurred within the block where it was deficient of the adhesive. It clearly shows that the fiber section within the region of 12-mm fracture site was surrounded only by a thin shell of the adhesive with no mechanical support for the fiber.

Micrographs of Figs. 9 and 10 provide close-up views of the adhesive funnel adjacent to the ferrule entry cone and reveal a large void with exposed and, therefore, unsupported section of the fiber within the ferrule entry cone.

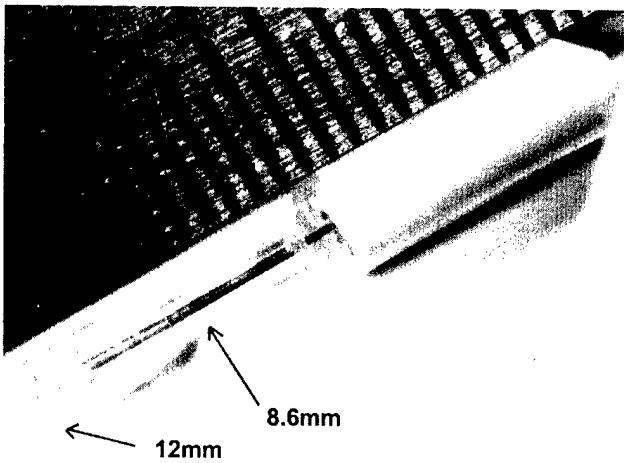


Figure 7. DVM (Digital Video Microscopy) micrograph of sample 2 terminus showing the ferrule and the adhesive block.

ESEM micrograph of Fig. 11 shows the fracture surface morphology for the fiber attached to the lower left-hand piece of the adhesive block, at the 12-mm fracture site, shown in the micrograph of Fig. 8. Although it may suggest a planar surface with no features, Figs. 12 through 14 show the same fracture surface through three clockwise 45° through 90° rotations and suggest fiber fracture in a predominantly torsional deformation.

For the 8.6-mm fracture site, micrograph of Fig. 15 shows the fracture surface morphology of the fiber attached to the ferrule as shown in Fig. 7. Micrographs in Figs. 16 through 19 reveal fracture surface markings with rotations about the fiber axis. The surface morphologies of the pair of fiber ends at the 8.6-mm fracture site show non-planar, complex, and non-matching fracture patterns, and they, therefore, suggest high-strength fracture in a primarily torsional field of deformation.

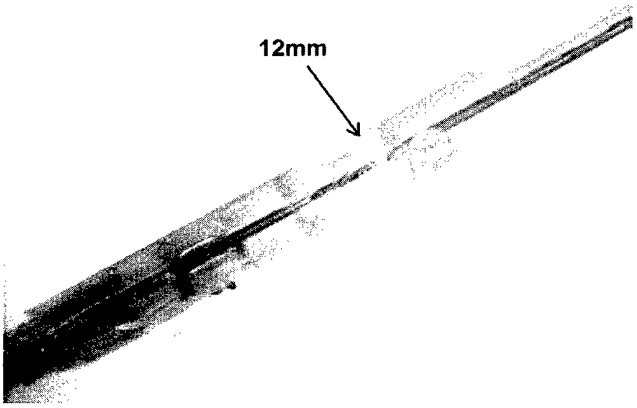


Figure 8. DVM (Digital Video Microscopy) micrograph of sample 2 terminus showing the adhesive block with the broken fiber, at 12 mm from the polished tip of the ferrule.

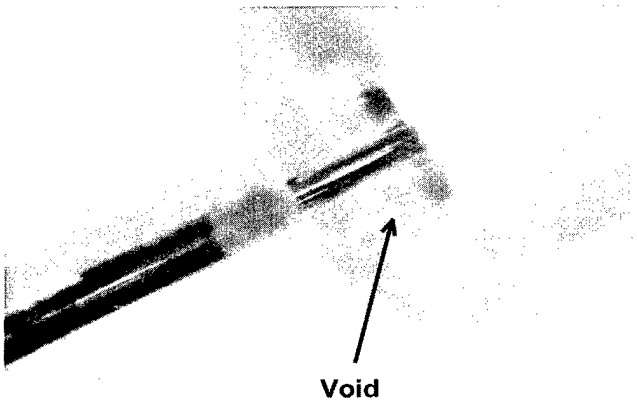


Figure 9. DVM (Digital Video Microscopy) micrograph of sample 2 terminus showing the adhesive funnel with a large void near the ferrule entry cone.

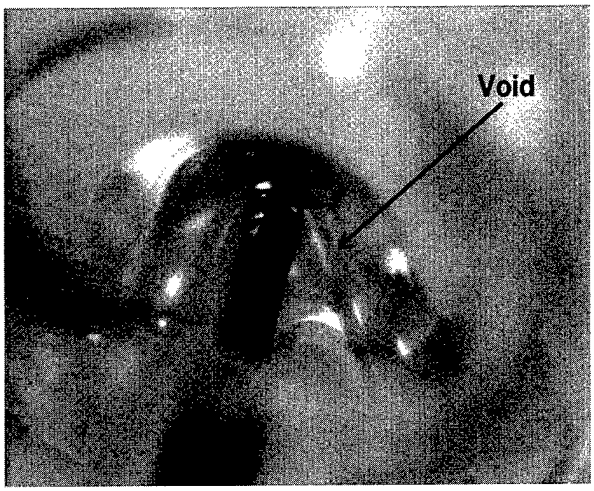


Figure 10. DVM (Digital Video Microscopy) micrograph of sample 2 terminus showing the adhesive funnel with a large void near the ferrule entry cone.

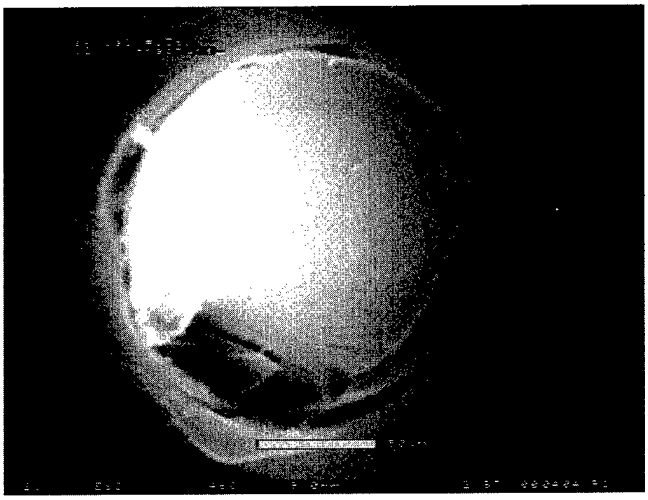


Figure 11. ESEM micrograph of fracture surface morphology of broken fiber at 12 mm for sample 2 terminus.

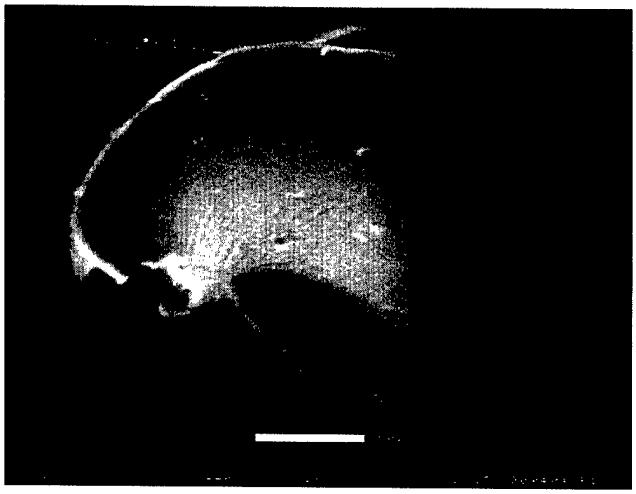


Figure 12. ESEM micrograph of fracture surface morphology of broken fiber at 12 mm for sample 2 terminus.

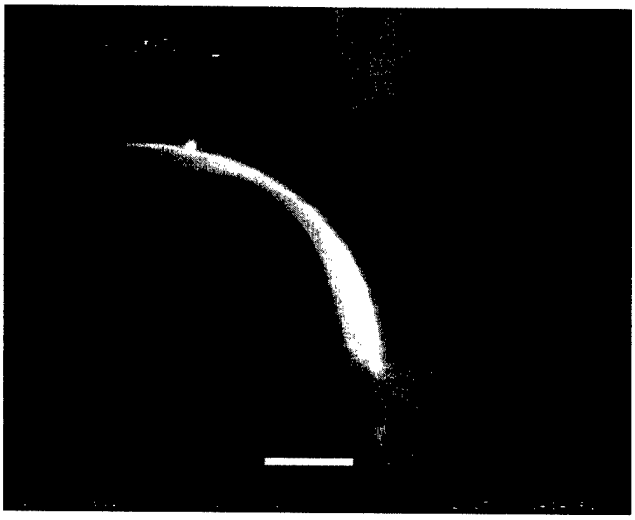


Figure 13. ESEM micrograph of fracture surface morphology of broken fiber at 12 mm for sample 2 terminus.



Figure 14. ESEM micrograph of fracture surface morphology of broken fiber at 12 mm for sample 2 terminus.



Figure 15. ESEM micrograph of fracture surface morphology of broken fiber, ferrule side of the fracture surface at 8.6 mm for sample 2 terminus.

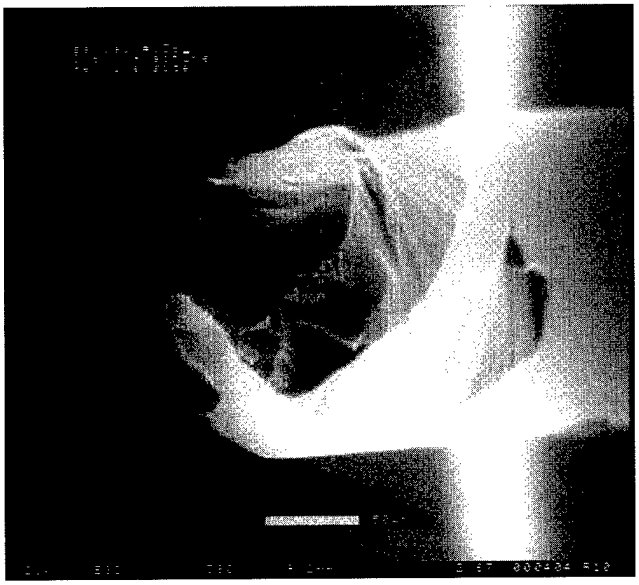


Figure 16. ESEM micrograph of fracture surface morphology of broken fiber, ferrule side of the fracture surface at 8.6 mm for sample 2 terminus.

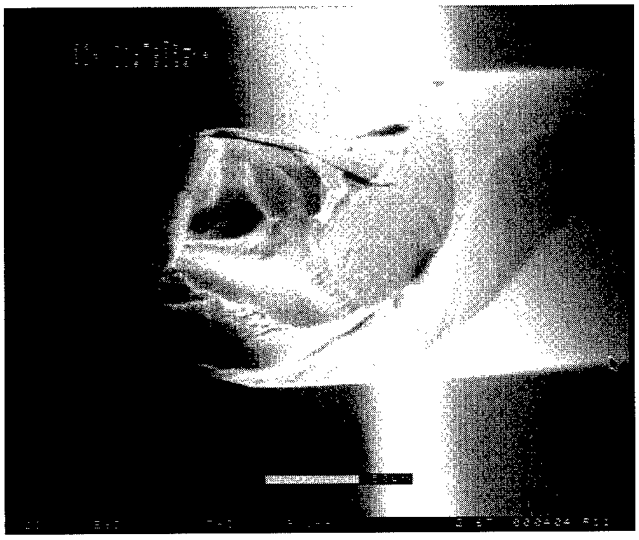


Figure 17. ESEM micrograph of fracture surface morphology of broken fiber, ferrule side of the fracture surface at 8.6 mm for sample 2 terminus.

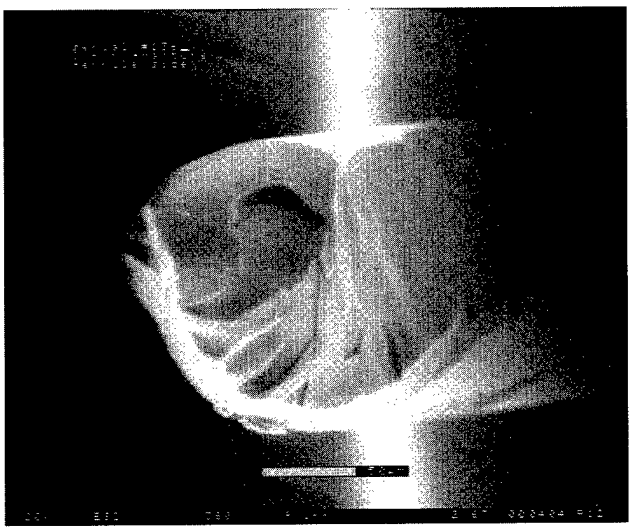


Figure 18. ESEM micrograph of fracture surface morphology of broken fiber, ferrule side of the fracture surface at 8.6 mm for sample 2 terminus.

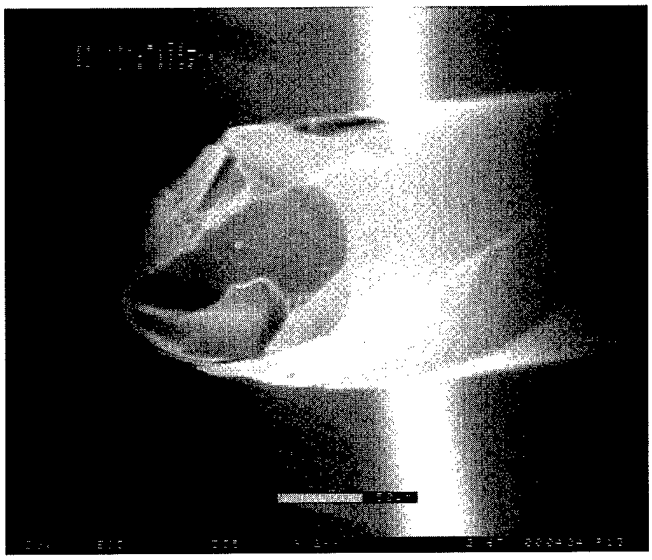


Figure 19. ESEM micrograph of fracture surface morphology of broken fiber, ferrule side of the fracture surface at 8.6 mm for sample 2 terminus.

Sample 3a

The first-stage processing of the sample 3a terminus resulted in a single piece that consisted of ferrule with a thicker adhesive funnel (possibly resulting from a misplaced ferrule in the terminus) and voids within the funnel and the shoulders of the adhesive block as shown in the micrograph of Fig. 20.

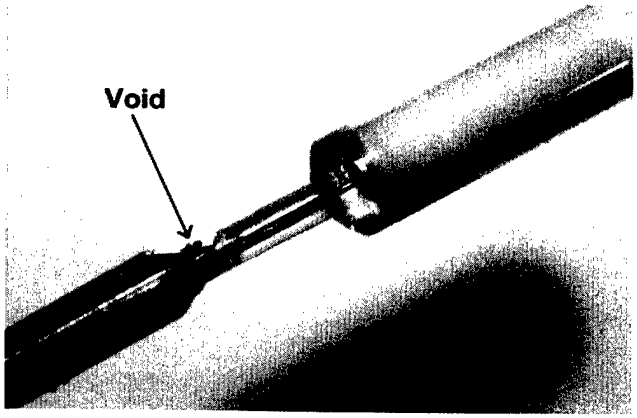


Figure 20. DVM (Digital Video Microscopy) micrograph of sample 3a terminus showing the ferrule and adhesive block after removal of the metallic housing by acid etching.

The second-stage disassembly uncovered the fiber break that occurred at the ferrule throat. ESEM micrographs of Figs. 21 and 22 show two views of the fracture surface for the broken fiber at the ferrule throat. The fracture surface morphologies in these micrographs indicate readily recognizable features of low-strength breaks. Although Figs. 21 and 22 do not show any fracture origins, micrographs of Figs. 23 and 24 show the fracture morphologies of matching fiber ends from the adhesive block and indicate fracture origin as a large flaw at the right-hand edge of the fiber fracture surface. Fig. 24 shows this flaw clearly at the lower right-hand edge of the fracture surface. The flaw is situated at the edge of a large mirror, and its location is indicated by the orientation of the hackle marks shown on the fracture surface of the micrograph of Fig.24.

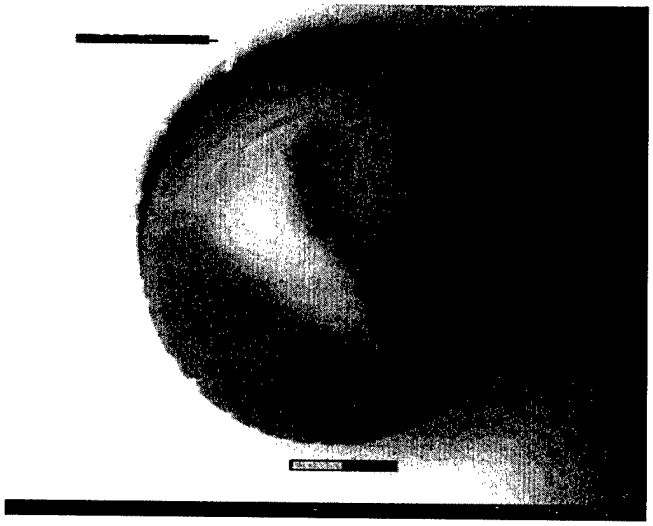


Figure 21. ESEM micrograph of the fracture surface of fiber broken at the ferrule throat from sample 3a terminus.

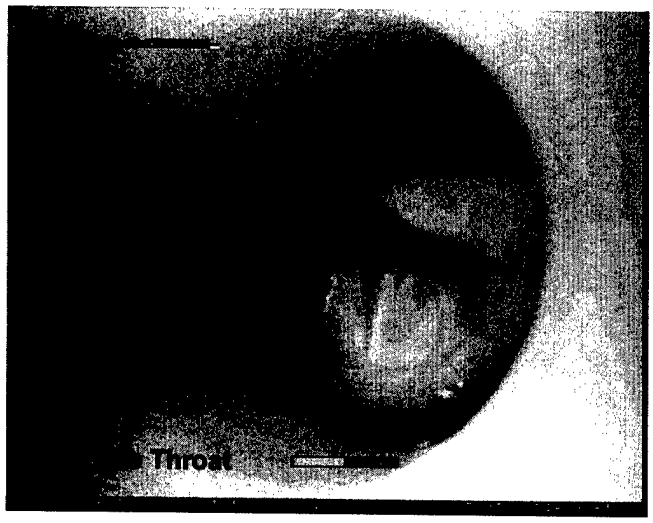


Figure 22. ESEM micrograph of the fracture surface of fiber broken at the ferrule throat from sample 3a terminus showing the ferrule entry cone.

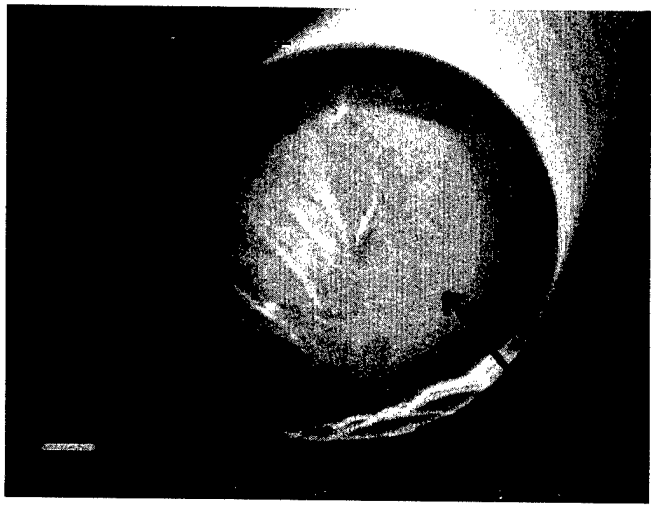


Figure 23. ESEM micrograph of the fracture surface on the adhesive block side for the fiber broken at the ferrule throat from sample 3a terminus.

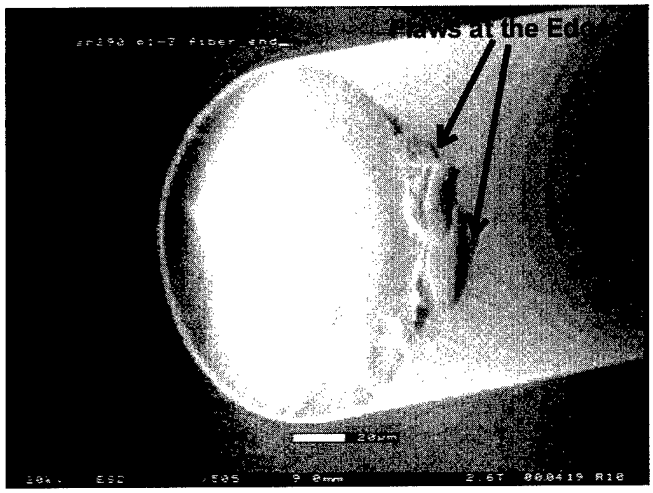


Figure 24. ESEM micrograph of the fracture surface on the adhesive block side for the fiber broken at the ferrule throat from sample 3a terminus.

Moreover, Fig. 24 also shows a bending lip on the left-hand side of the fracture surface. Hence, our analysis reveals that it is a low-strength break with an estimated lower bound fracture stress of 35 ksi.

Sample 3b

Two-stage processing of the sample 3b terminus revealed no fiber breaks. Micrographs of Figs. 25 and 26 show the terminus ferrule with the adhesive block and the ferrule with coated fiber pigtail after removal of the adhesive block by acid etching, respectively. Fig. 26 indicates that fiber in the terminus package retained its integrity as expected from a connectorized cable that exhibited no transmission anomalies. However, as shown in the micrograph, the fiber positioned at an angle to the longitudinal axis of the ferrule suggests heightened risk of bending that may cause transmission loss.

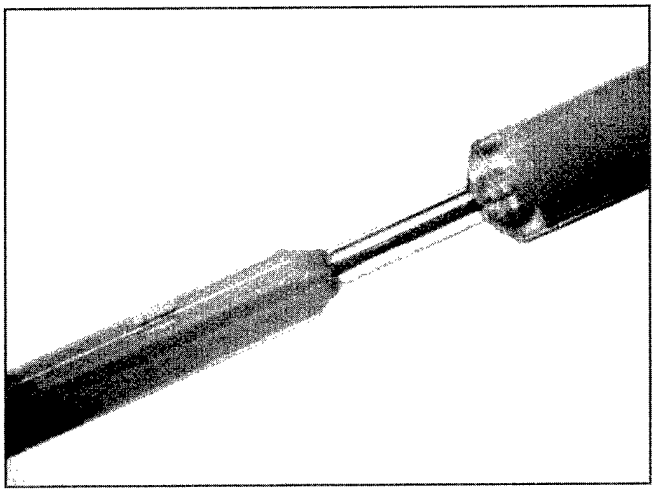


Figure 25. DVM (Digital Video Microscopy) micrograph of sample 3b terminus showing the ferrule and the adhesive block.

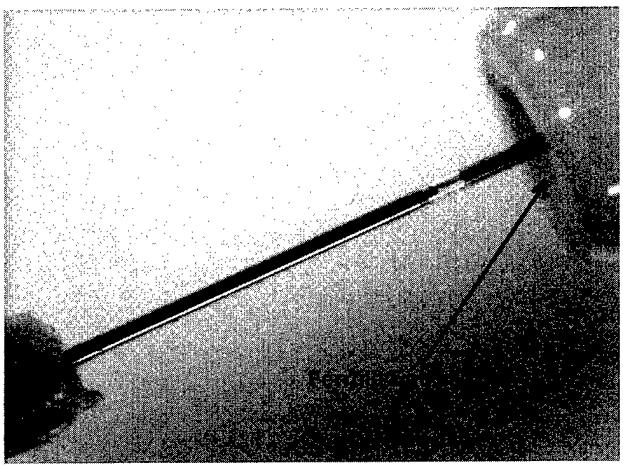


Figure 26. DVM (Digital Video Microscopy) micrograph of sample 3b terminus showing the ferrule, coated fiber, and the jacketed fiber pigtail after the two-stage acid etching.

4. Summary & Conclusions

In this report, we presented the results of failure analyses performed to identify the cause(s) of high insertion loss and reflectance failures of multimode fiber optic cables terminated with fiber optic PC connectors. We used special methods developed at Telcordia[9] to gain access to fracture surfaces of fiber broken within the connector body. These methods involved two-stage acid etching with no mechanical intervention to disassemble termini from three sample cables. On the disassembled termini, we used DVM (digital video microscopy) and ESEM analysis to uncover fiber fractures and perform break source analysis (fractography) to determine fracture origin(s) and estimate the state of fracture stress.

Disassembly of termini from failed cables by our two-stage acid etching process revealed one or more fiber fractures, all within the adhesive block underneath the metal housing and around large voids near the ferrule entry cone. The following table presents a summary of our results from fractography analyses.

Cable Sample	Type of Fractures	Failure Mode
1	Low-Strength	Tensile
2	High-Strength	Complex, Torsional
3a	Low-Strength	Complex @ Ferrule Entry Cone

In all cases presented, fiber fractures were found in regions of connector body where adhesive malformations occurred. Our results represent the first set of experimental data available in the open literature to link fiber failures within connectors to adhesives-related structural discontinuities.

5. REFERENCES

[1] J.J. Mecholsky, R.W. Rice, S.W. Freiman, J. Am. Ceram. Soc., 57(10), 440 (1974).

[2] S.T. Gulati and H.E. Hagy, J.Amer. Ceram. Soc., **65**, 1 (1982).

[3] M. Kinney, "Optical Fiber Stresses within a Biconic Connector," Failure Prevention and Reliability – 1987, ASME DE-19, 75 (1987).

[4] W.R. Wagner, Failure Analysis of Fiber Optic Connectors," Advances in Ceramics 22 – Fractography of Glasses, Am. Ceram. Soc., 389 (1988).

[5] H.H. Yuce, J.P. Varachi, T. Wei, "Analysis of Optical Interconnection Failures by Analytical Techniques," 9th NFOEC Proc., 251 (1993).

[6] B.G. LeFevre, W. W. King, C.K. Sidbury, D.L. Stephenson, "Analysis of Fiber Fracture in Connectors," 14th NFOEC Proc., 257 (1998).

[7] O.S. Gebizlioglu, C.R. Kurkjian, L.A. Reith, "Materials Issues in the Development and Use of Lightguide Fibers, Cables, and Components," in "Reliability of Optical Fibers and Optical Fiber Systems," Ed. D.K. Paul, **CR73**, 68, SPIE Press (1999).

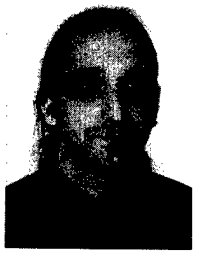
[8] B.G. LeFevre, S.C, Mettler, "Reliability of Fiber Optic Connectors and Splices," in "Reliability of Optical Fibers and Optical Fiber Systems," Ed. D.K. Paul, **CR73**, 115, SPIE Press (1999).

[9] O.S. Gebizlioğlu, M.R. Özgür, "Accessing Fiber Fracture Surfaces in Fiber Optic Connectors," U.S Patent pending.

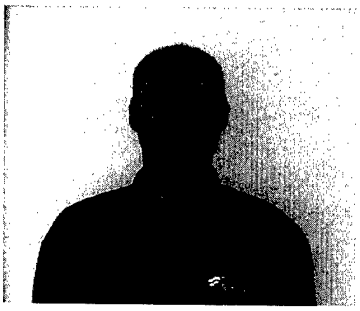
[10] A.A. Griffth, Phil. Trans. 221A, 163 (1920).



Osman S. Gebizlioglu is a Senior Consultant in the Fiber, Transport & Synchronization Technologies Group at Telcordia Technologies. He holds B.Sc and M.Sc degrees in Chemical Engineering from the Middle East Technical University, Ankara, Turkey, and Ph.D from the Polymer Materials Program of the Chemical Engineering Department at Princeton University, Princeton, New Jersey. After a Monsanto Postdoctoral Fellowship appointment in Mechanical Engineering at M.I.T, Cambridge, Massachusetts, he joined Telcordia Technologies in 1987. He has been involved in the investigations of performance / reliability issues in optical fibers, fiber optic cables, components and devices. He chairs the TIA working group on adhesives reliability in interconnecting devices and holds four US patents.



Mustafa R. Özgür is an Associate Consultant in Fiber, Transport & Synchronization Technologies Group at Telcordia Technologies. He holds a B.Sc degree in Mechanical Engineering. Since he joined Telcordia Technologies in 1998, he has been involved in research and testing on fiber optic components.



Dean Unkel is an Associate Consultant in Fiber, Transport & Synchronization Technologies Group at Telcordia Technologies. He joined Telcordia in 1989 while working as a contractor with CDI Telecommunications Corp. He holds a B.S degree from Trenton State College. He has developed expertise in fiber optic fusion splicing, outside plant closures, and automating test procedures for outside plant components.

Large-scale optical fiber wiring for 128 x 128 PLC switch system with fiber physical contact connectors and optical fiber circuits

Yoshiteru Abe, Masaru Kobayashi*, Mamoru Hirayama and Ryo Nagase

NTT Photonics Laboratories, NTT Corporation, * NTT Electronics Corporation
162, Tokai-mura, Naka-gun, Ibaraki-ken, 319-1193, Japan
+81-29-287-7867 · abe-y@iba.iecl.ntt.co.jp

Abstract

The increasing number of channels in DWDM systems has led to the need for large-scale fiber wiring in the system racks. We have developed a novel optical wiring system with a fiber physical contact (FPC) connector for 16 fibers and an optical fiber circuit for 256 x 256 cross wiring. This optical fiber wiring system is designed to install fiber efficiently and without congestion. We used our optical fiber wiring system to construct a 128 x 128 switch system with 1 x 128 planar lightwave circuit (PLC) type thermo-optic switches (TOSW) that had to be capable of handling more than 10000 fibers while offering easy installation and an orderly layout.

Keywords

Optical fiber connector; fiber physical contact (FPC) connector; optical fiber circuit; planar lightwave circuit (PLC); thermo-optic switch (TOSW); optical switch system.

1. Introduction

Dense wavelength division multi/demultiplexing (DWDM) systems are being introduced into commercial communications systems to increase network capacity and flexibility. The increasing number of channels in DWDM systems has led to the problem of fiber congestion and the need for large-scale optical fiber wiring in the system racks. We have already developed a technique for fiber management on a circuit board [1]. This technique provides compact fiber wiring and easy connection for hundreds of fibers on a circuit board with fiber physical contact (FPC) connectors [2] and an optical fiber circuit [3]. To allow this technique to be applied to large-scale optical fiber wiring in system racks, we propose and demonstrate 16-fiber FPC connectors with a push-pull mechanism for ease of connection, and a large-scale optical fiber circuit for connecting units arranged in racks. Moreover, we propose an optical wiring system with the above FPC connector and optical fiber circuit that is capable of installing fiber efficiently and without congestion. We use our optical fiber wiring system to construct a 128 x 128 switch system with 1 x 128 planar lightwave circuit (PLC) [4] type thermo-optic switches (TOSW) [5] . This switch system has to be capable of handling more than 10000 fibers and it is difficult to install fibers efficiently without congestion with the conventional technique. In this paper, we report the usefulness of a large-scale optical fiber wiring system with 16-fiber FPC connectors and optical fiber circuits for constructing systems with many fibers and connections.

2. Component technology

2.1 FPC connector

The structure of the FPC connector is shown in Fig. 1. The FPC connector aligns two fibers in a micro-hole without ferrules and the contact surface is compressed by the elasticity of the fiber without the need for springs. The fiber end protrudes from the connection points and the fiber is buckled when the two fibers are connected. The buckling force realizes physical contact (PC) between the two fibers endfaces. We set the buckling force of the FPC connector between 0.70-0.78 N with buckling and protrusion lengths of 6.8-7.2 mm and 50 m, respectively [6]. The fiber endface is chamfered and polished. The chamfering process is used to remove the ripple found at the edge of the endface when the fiber is cleaved, thus allowing the fiber to be inserted easily into the micro-hole, and to prevent dust from adhering to the endface. Polishing is used to realize PC with excellent optical performance when the contact surface is compressed by the elasticity of the fiber. To prevent the bent fiber from breaking, we use SM-polymer skin coated (PSC) fiber [7], whose glass cladding is covered with a 5 m thick polymer layer.

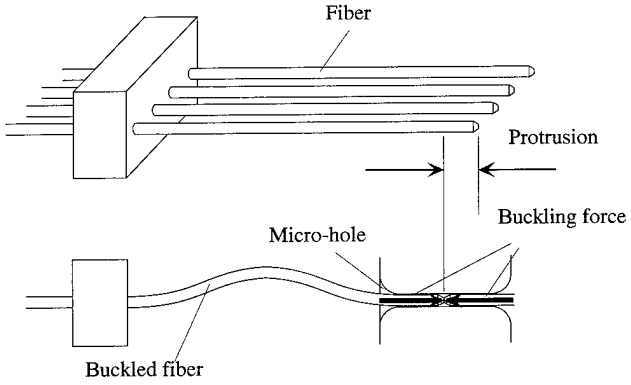


Figure 1. Basic structure of FPC connector

We developed a 16-fiber FPC connector with a push-pull mechanism as shown in Fig. 2. It is designed for 16 fibers with a 0.25 mm pitch. The dimensions of the plug and the adapter are 6 x 11.5 x 32 mm and 8.2 x 13.6 x 26 mm, respectively. The plug and adapter housings are made of an injection-molded plastic. This connector has the same small size as conventional simplex connectors but provides higher density connection. The push-pull mechanism provides ease of operation during connection. The plug has a fiber protector, which protects the fibers fixed to the plug without a ferrule, and prevents dust from adhering to the

fiber endface. The protector opens when it comes into contact with the adapter during connection.

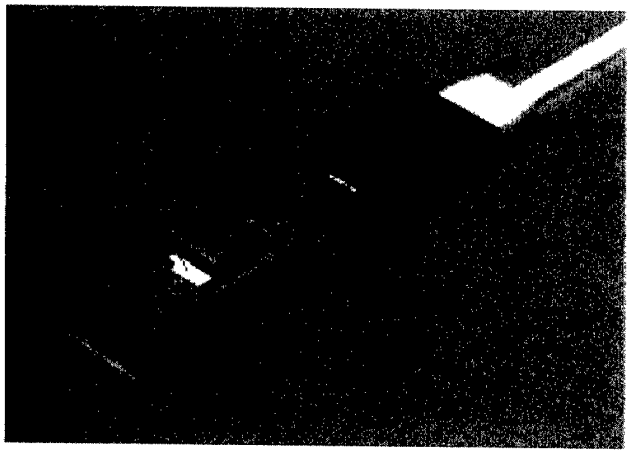


Figure 2. Photograph of 16-fiber FPC connector

2.2 Optical fiber circuit

The optical fiber circuit consists of a pair of adhesive sheets on which fibers are wired with the desired pattern by a wiring machine. In the optical fiber circuit, the fiber is fixed on one adhesive sheet, as shown in Fig. 3. A wiring machine presses the fibers onto the pressure-sensitive adhesive on one sheet. Curved and crossed patterns can easily be obtained with no fiber order errors. After the fibers have been wired, they are sandwiched using the other sheet. The wiring machine has a fiber-head, which can control the x and y coordinates as shown in Fig. 4. The fibers are positioned with an accuracy of 10 m. The wiring machine is designed to let out and cut off the fiber and the wiring speed is more than 100 mm/s. The wiring machine achieves the accurate wiring of many fibers in the correct order.

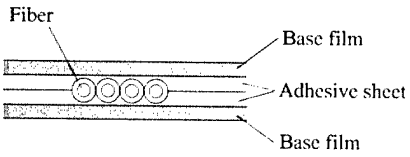


Figure 3. Structure of optical fiber circuit

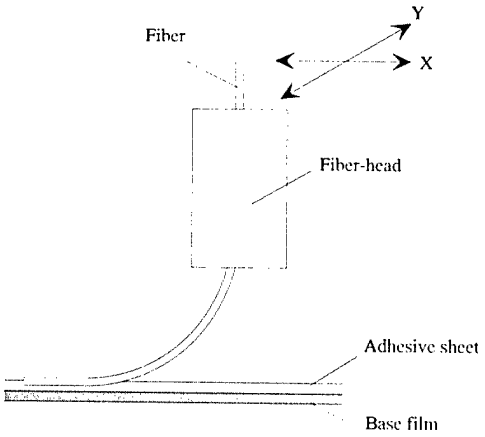


Figure 4. Structure of wiring machine

We developed a 256 x 256 optical fiber circuit with a larger scale than the conventional optical fiber circuit to connect units arranged in a rack, as shown in Fig. 5. This optical fiber circuit has a maximum size of 900 x 1800 mm and 256 managed fibers. These optical fiber circuits are terminated with 32 16-fiber FPC connectors. The pigtail fibers of the optical fiber circuits are covered with protective tubing. This optical fiber circuit is the basic unit of our large-scale optical fiber wiring system.

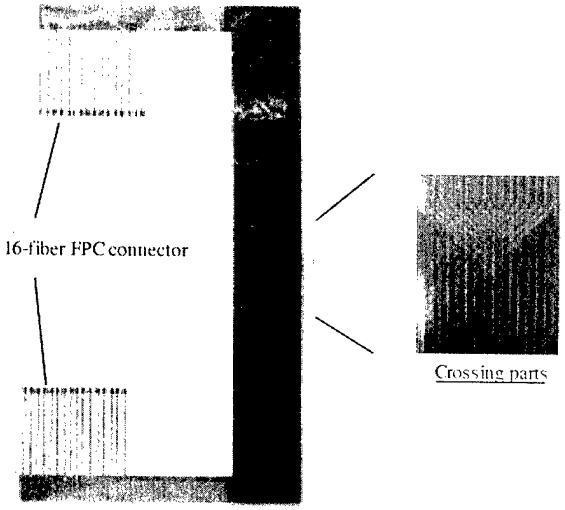


Figure 5. Photograph of 16 x 16 optical fiber circuit

3. Large-scale optical fiber wiring system

3.1 Design

We studied large-scale optical fiber wiring by constructing a 128 x 128 switch system, which requires more than 10,000 fibers to be wired in a complex pattern. The configuration of the 128 x 128 switch system is shown in Fig. 6. This system consists of 1 x 128

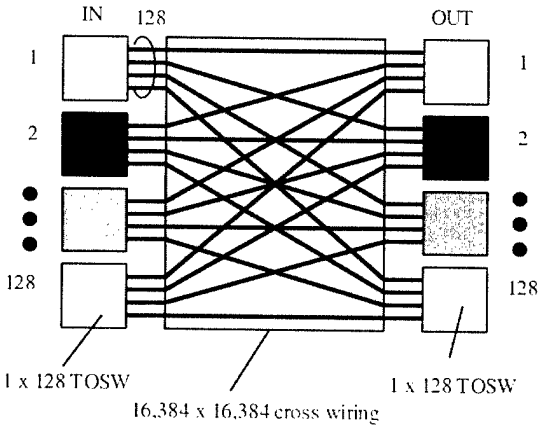


Figure 6. Configuration of 128 x 128 switch system with 16,384 x 16,384 cross wiring

PLC TOSWs and 16,384 x 16,384 cross-wired fibers. It is difficult to realize cross wiring with a 16,384 x 16,384 optical fiber circuit sheet containing 16,384 fibers in terms of fabrication process and size. However, we are able to cross wire 16,384 x 16,384 fibers by using 64 256 x 256 optical fiber circuit sheets, as shown in Fig. 7. We can easily fabricate optical fiber circuits on this scale. We studied the configuration to find a way of installing 64 optical fiber circuit sheets in racks in an orderly layout that avoided fiber congestion, as shown in Fig. 8. Two TOSWs on the IN and OUT sides were mounted on one printed board as one unit, and the shape of the optical fiber circuit is as shown in Fig. 8. In the configuration shown in Fig. 7, it is necessary to wire many pigtail fibers in a crossing pattern and this is its only disadvantage compared with the configuration shown in Fig. 6. However, by employing the configuration shown in Fig. 8, pigtail fibers do not cross and an orderly layout is realized without fiber congestion. The 16-fiber FPC connectors are attached to the pigtail fibers of the optical fiber circuit and connected to the connector interface on the printed board. The optical fiber circuits are installed in storage spaces in the front of the rack, above and below the connector interface. The cross wiring part of the optical fiber circuit is installed in the side of the rack. This configuration means that when we insert/remove a printed board we only have to remove the FPC connectors connected to the printed board interface. We can easily remove an optical fiber circuit in the same way. This wiring system allows easy maintenance.

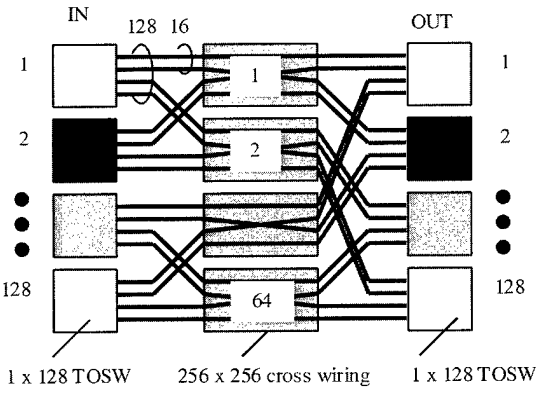


Figure 7. Configuration of 128 x 128 switch system with 256 x 256 cross wiring

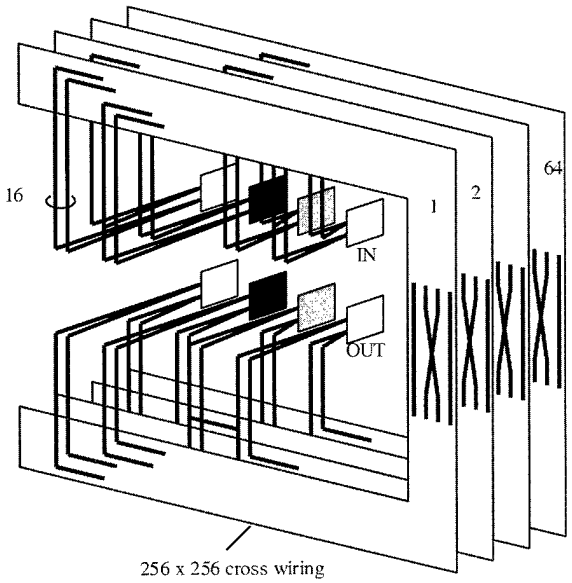


Figure 8. Configuration for installation in racks

3.2 Construction of 128 x 128 PLC switch system

We constructed a 128 x 128 switch system using our proposed large-scale optical wiring system. The appearance is shown in Fig. 9. The specifications of this SW system are given below.

- 19 inch rack x 2: 700 (W) x 700 (D) x 1800 (H) (mm)
- Sub racks x 4 in a rack: 6U, 280 (H) (mm)
- Printed board x 16 in a sub rack: 20 (W) (mm)
- TOSW modules x 2 in a printed board

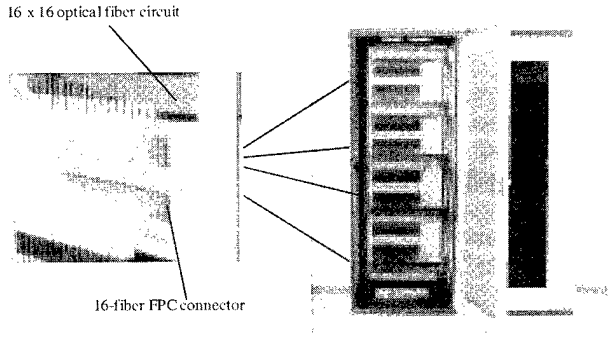


Figure 9. Appearance of 128 x 128 SW system

We were able to realize 16,384 x 16,384 cross wiring, which requires 16,384 fibers, by using 64 256 x 256 optical fiber circuit sheets. These sheets were terminated with 16-fiber FPC connectors and easily installed with an orderly layout in two racks.

We measured the optical performance of a 256 x 256 optical fiber circuit with 16-fiber FPC connectors. Figures 10 and 11,

respectively, show histograms of the insertion loss and return loss at a wavelength of 1.55 m. The average insertion loss for 256 connection points was 0.21 dB, which is sufficiently small for SM connection. The average return loss for 256 connection points was 54 dB, which confirms that all the connection points realized PC connection.

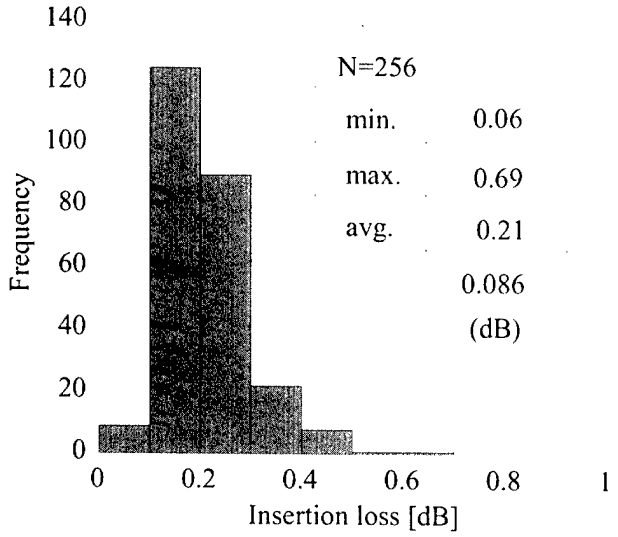


Figure 10. Insertion loss

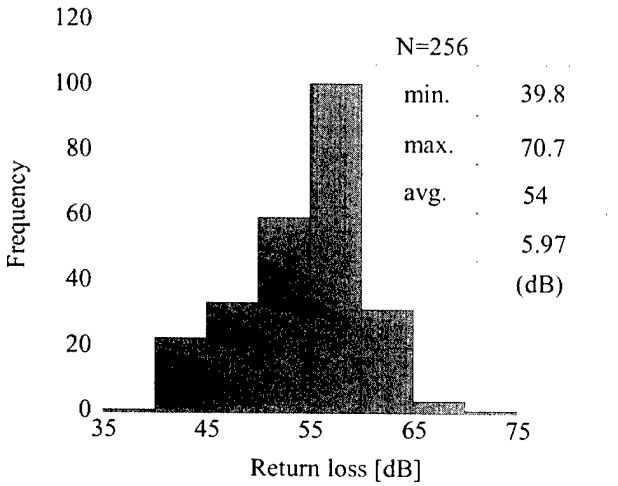


Figure 11. Return loss

4. Conclusions

We proposed and demonstrated a large-scale optical fiber wiring system with an FPC connector and an optical fiber circuit. We confirmed the usefulness of this large-scale optical fiber wiring system by constructing a 128 x 128 switch system, which is required to handle more than 10,000 fibers. We can efficiently construct systems requiring many fibers and connections by employing our large-scale optical fiber wiring system.

5. References

[1] M. Kobayashi, T. Yoshida, S. Asakawa, K. Arishima, M. Hirayama, T. Kominato, T. Goh, Y. Hida, S. Sumida and T. Kawai, "Fibre management technique for optical device integration on circuit board with hundreds of optical connections," *Electron. Lett.*, vol.36, no.17, pp. 1451-1452 (August, 2000).

[2] M. Kobayashi, S. Iwano, R. Nagase, S. Asakawa and S. Mitachi, "Multiple fiber PC connector with 0.2 dB insertion and 60 dB return loss," *OFC'97*, Paper WL 11 (1997).

[3] K. Arishima and M. Hirayama, "Processing and structure of optical wiring for optical circuit board," *Proc. Electronics Society Conf. IEICE*, Paper C-3-11 (1998) in Japanese.

[4] M. Kawachi, "Recent progress in silica-based planar lightwave circuits on silicon," *IEE Proc. Optoelectron.* , vol. 143, no.5, pp. 257-262 (Oct. 2000).

[5] T. Goh, M. Yasu, K. Hattori, A. Himeno, M. Okuno and Y. Ohmori, "Low loss and high extinction ratio strictly nonblocking 16 x 16 thermooptic matrix switch on 6-in wafer using silica-based planar lightwave circuit technology," *J. Ligthwave Technol.*, vol. 19, no. 3, pp. 371-379 (March 2000).

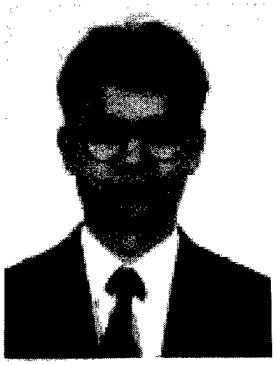
[6] M. Kobayashi, T. Yoshida, S. Asakawa, S. Iwano, R. Nagase, S. Sumida and S. Mitachi, "Injection molded plastic multifiber connector realizing physical contact with fiber elasticity," *IEEE J. Selected Topics in Quantum Electronics*, vol. 5, no. 5, pp. 1271-1277 (Sep. /Oct. 1999).

[7] T. Yoshida, M. Kobayashi and S. Sumida, "FPC optical connector with PSC-SM optical fiber," *Proc. Electronics Society Conf. IEICE*, Paper C-3-58 (1998) in Japanese.



Yoshiteru Abe received the B.E. and M.E. degrees in electronics engineering from Kyushu University, Fukuoka, Japan, in 1996 and 1998, respectively. He joined NTT in 1998. He has engaged in research of optical fiber connectors and optical fiber management.

Mailing address: 162, Tokai-mura, Naka-gun, Ibaraki-ken, 319-1193, Japan



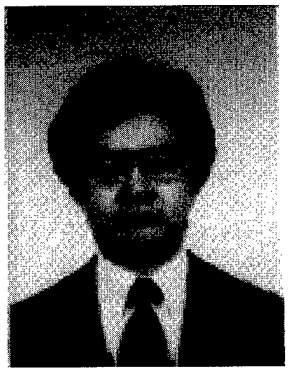
Masaru Kobayashi received the B.E. and M.E. degrees in mechanical engineering from Nagoya University, Nagoya, Japan, in 1986 and 1988, respectively. He joined NTT in 1988. He has been engaged in research on high-resolution optical reflectmetry, optical fiber connectors and optical fiber management.

Mailing address: 162, Tokai-mura, Naka-gun, Ibaraki-ken, 319-1193, Japan



Mamoru Hirayama joined NTT in 1965. He has been engaged in research of optical fiber couplers and optical fiber circuits.

Mailing address: 162, Tokai-mura, Naka-gun, Ibaraki-ken, 319-1193, Japan



Ryo Nagase received the B.E., M.E., and Ph.D. degrees in precision engineering from Tohoku University, Miyagi, Japan, in 1983, 1985, and 1998, respectively. He joined NTT in 1985. He has been engaged in research and development of optical fiber connectors. He is presently a manager in the research and development of optical fiber connection technology.

Mailing address: 162, Tokai-mura, Naka-gun, Ibaraki-ken, 319-1193, Japan

Newly developed optical fiber distribution system and cable management in central office

Masao Tachikura, Koji Mine, Hisashi Izumita, Shigenori Uruno, and Minoru Nakamura
NTT Access Network Service Systems Labolatories, Nippon Telegraph and Telephone Corporation
1-7-1, Hanabatake, Tsukuba-city, Ibaraki, 305-0805 Japan
+81-298-52-4834 · tatikura@ansl.ntt.co.jp

Abstract
We have developed an optical fiber cable distribution system for central offices in order to improve installation, maintenance and operational efficiency. This paper introduces an advanced fiber distribution system for use in central offices in the FTTH era. The system consists of an integrated fiber distribution frame system that we have newly developed, 1.1 mm-diameter miniature optical fiber cords for use as jumpers in the frame, small-diameter optical fiber cables whose size and weight are almost half those of conventional cables, and cable and fiber distribution management techniques for the system. We have simplified fiber identification and fiber distribution management in the system by using a two-dimensional identification code.

Keywords
Central office; fiber distribution; indoor cable; management; splitter; test; FTTH.

1. Introduction
The Japanese government estimates that 10 million customers will subscribe to an ultra broadband Internet service by the year 2005. NTT began to offer an inexpensive FTTH service in 2001. This service provides an access network bandwidth of 10 to 100 Mbps. Moreover, there are many optical access services already available in addition to the FTTH service, e.g. ATM-PON, STM-PON, SONET, and ISDN. To spread the use of these access networks services, we must aggressively reduce the costs of the optical fiber cables and related components that run from optical line terminals (OLT) in NTT central offices to optical network units (ONU) on users' premises. At the same time, we have to reduce the costs of installation, maintenance and operation.

We have been developing an optical fiber cable distribution system for central offices with a view to realizing cost reduction and increased effectiveness, while simultaneously working to improve the efficiency of installation, maintenance and operation. We proposed one type of central office optical fiber distribution system at the 46th IWCS in 1997 [1]. The system consists of FTMs that accommodate 4000 fibers and a test access module, an intermediate-FTM that accommodates splitters, and high count fiber cables. We also proposed a method of cable management for central offices [2]. We have continued to develop the distribution system approach. This paper introduces our new optical fiber distribution and cable management system for the FTTH era.

2. Optical fiber distribution system in central office

2.1 Optical access network architectures for various services
There are many kinds of access network line that depend on the network service being provided. These lines are not discrete in distribution facilities but share such components as cables, cabinets, and closures. Figure 1 shows the optical access network arrangement for existing services. Types (a) to (c) are the arrangements for NTT's FTTH service. All fibers connected to splitters, ONUs, or RTs for the provision of various services are terminated at distribution modules in central offices. The central office distribution system and its management are very important in terms of the complete access network system.

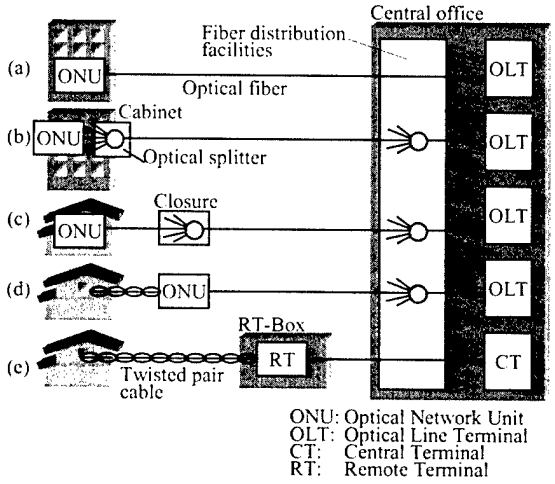


Figure 1. Typical optical access network structures

2.2 Central office optical fiber distribution system
In recent years there has been a demand for central office fiber distribution facilities suitable for various services. The conventional facilities in NTT central offices, namely the optical distribution facilities located between an OLT in a central office and the optical fiber cable for the feeder section, are as follows; a splitter frame designed to split optical signals from the OLT, a fiber termination module (FTM), which terminates and connects the optical fiber cable fed from the feeder section, and a central

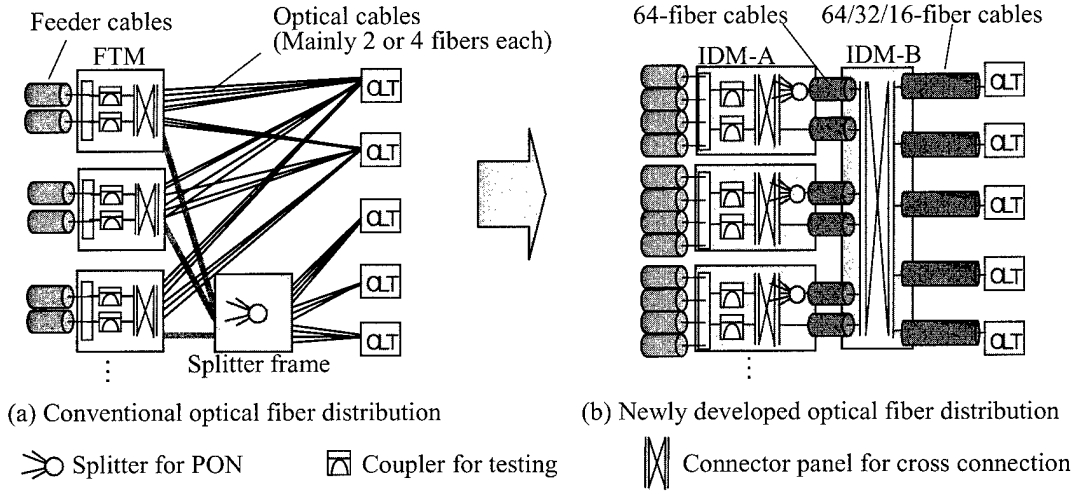


Figure 2. Improvement of optical fiber distribution system

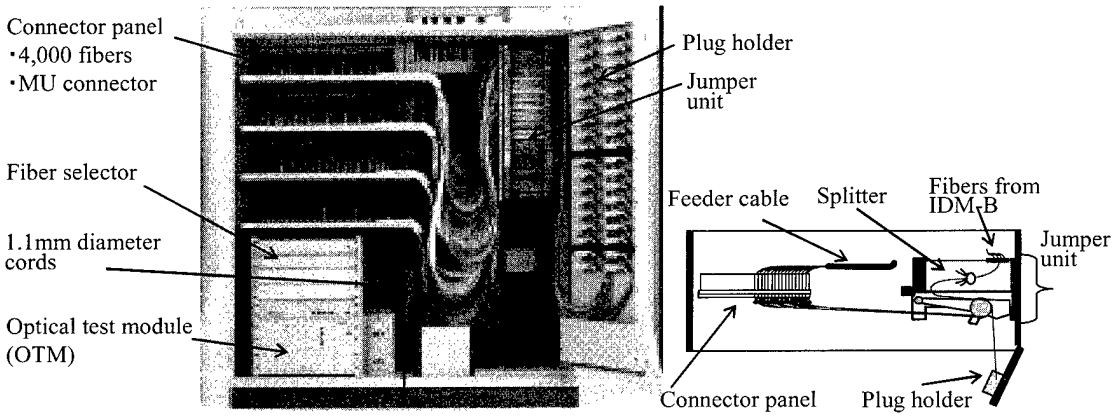


Figure 3. IDM-A (Integrated distribution module)

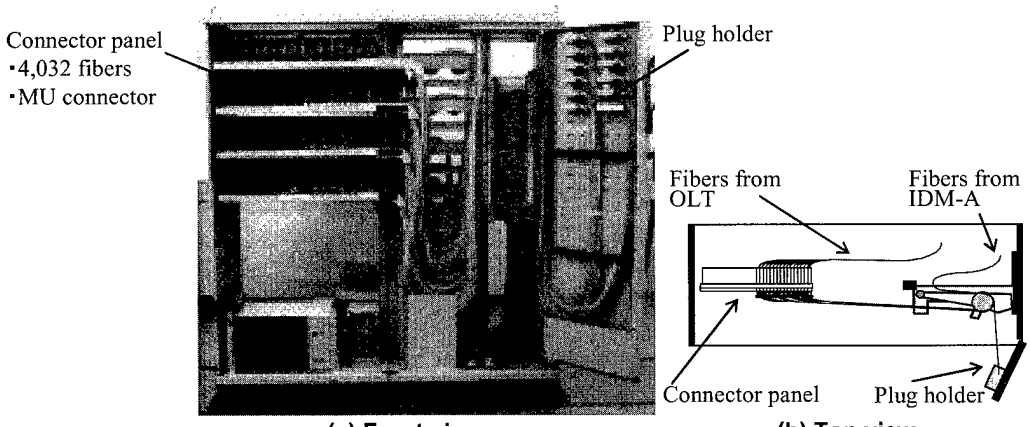


Figure 4. IDM-B (Integrated distribution module)

office optical fiber cable used for optical distribution. Their configuration is shown in Figure 2(a).

The FTM houses optical switches (fiber selectors) that select the optical fiber to be tested, as well as optical couplers that launch the maintenance signal from an optical measurement instrument into optical fibers, making it possible to test optical fiber cables located outside NTT central offices.

Since optical fiber cables have conventionally been distributed independently between multiple OLTs and FTMs, optical fiber cable congestion is likely to occur. In addition, limited space has resulted in a shortage of available floor space for FTM and splitter frame installation. Even worse, since the operators kept facility information records by manually entering the information on data sheets to allow them to control optical office distribution facilities, finding and consulting that information has not been easy. The following section describes the technologies we have developed both to solve these problems and reduce the cost of the central office distribution facilities.

The integrated distribution module (IDM) that we have developed allows the simple optical office distribution scheme shown in Fig. 2(b). It integrates the following functions: a splitter frame function for splitting optical signals, FTM functions for terminating and connecting optical fiber cables, selecting an optical fiber to be tested, and launching a maintenance signal, and a central office optical fiber cable function that implements optical distribution. The IDM consists of IDM-As that terminate and connect the feeder cables from outside the central office, IDM-B that terminates and connects all the optical fiber cables that run from the OLTs, and the central office optical fiber cable that connects the IDM-As and IDM-B. This configuration makes it possible to minimize the additional distribution of optical fiber cables even if an OLT or IDM-A is newly installed. Therefore, the configuration reduces the number of cable threads and relieves cable congestion.

Figure 3 shows a photograph of IDM-A. The connector is more densely packed and more economical than before, since we use an MU connector with a simpler structure than usual with an optical cord sheathed in a material that is stronger than conventional cladding materials despite its diameter being reduced from 1.7 to 1.1 mm. Although the optical cord is temporarily hung in a plug holder, it can be extracted from the holder and connected to the connection panel when needed for service. A distribution tray and guide are attached to the frame to prevent the cord from becoming tangled with other optical cords thus ensuring ease of connection, and the optical cord itself has a degree of rigidity to ensure easy handling.

Figure 4 shows a photograph of IDM-B. IDM-B has almost the same structure as regards optical fiber cord distribution and

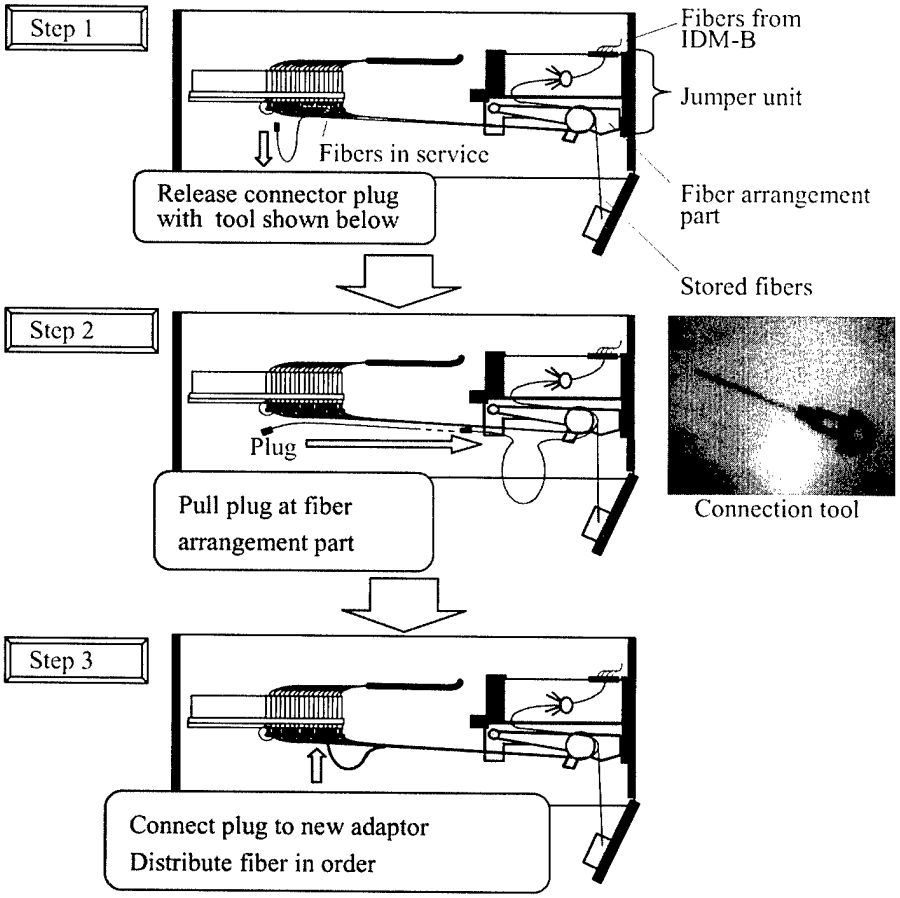


Figure 5. Procedure of plug reset wiring operation (Top view of IDM-A)

manipulation as IDM-A. Both frames can house 4000 optical fibers in a space 160 cm wide; almost double the previous maximum for an FTM with the same width. The advantage of using IDM-A as an FTM arises through the application of planar light-wave circuit (PLC) technology to the optical splitter and optical coupler. This corresponds to the housing density of the distribution frame used with metallic cables. Moreover, the optical measuring equipment used in the optical fiber cable tests was miniaturized, more densely integrated, and housed in IDM-A. The size and weight of optical fiber cables installed inside a central office are almost half those of conventional cables. We achieved this by employing the small diameter optical cord described above. The optical cord uses materials that are both flame resistant and environmentally friendly when ultimately discarded.

The IDM employs a fundamental technique for cross-connect operations. We call this technique the plug reset wiring operation. The technique is a kind of operation rule designed to prevent fiber congestion in the distribution frame IDM. Figure 5 shows the wiring operation procedure viewed from above IDM-A. The jumper unit in IDM-A is a splitter unit package with pigtails (typically 64 optical fiber cords with connector plugs) and has a fiber arrangement part. The way to change a connection at the connection panel is described below and in the figure.

Step 1: Use a connection tool to release the connector plug from a connected adaptor.

Step 2: Pull the plug at the fiber arrangement part. The fiber arrangement part is designed to pull the required fiber. Fiber numbers printed at cord sheath enables us to find the required fiber. This step prevents congestion.

Step 3: Connect the plug to the new adaptor. Finally, rewire the fiber in order in the IDM.

This technique keeps the dense fibers in the IDM in order and prevents congestion.

These technologies have enabled us to reduce the number of optical fiber cables needed for central office optical distribution and produce densely integrated optical components to be housed in the IDM. This has made it possible to reduce the installation and component costs. Table 1 shows the IDM specifications.

Table . Specifications of IDM

Fiber capacity	·IDM-A : 4,000 fibers for both feeder and indoor cables ·IDM-B : 4,032 fibers for both cables from IDM-A and cables from OLT
Dimensions H×W×D[mm]	·1800×1600×600 for both IDM-A and IDM-B
Cord type	·1.1 mm diameter ·Halogen-free materials ·Fire proof
Cable type	·Stranded structure with mono-fiber cords ·64,32, and 16 count fibers cables ·Halogen-free materials ·Fire proof
Connector	·MU connector
Management	·Data registration with two dimensional ID codes ·Database management with IDM-WS and mobile terminal

2.3 Management system for central office

Figure 6 shows the configuration of a system designed to manage central office optical distribution facilities using a two-dimensional identification code. Both the registration and accessing of fiber information are made easy by attaching an information tag with a printed two-dimensional identification code on the optical cord used in the IDM, and reading the two-dimensional identification code on the information tag with an identification code reader. The two-dimensional identification code is also attached to every connector adaptor row on the connection panel. Since the 2-D identification code includes information for facility identification, the connection data can be easily obtained from the code reader. Moreover, outputting the data read by the identification code reader from a mobile terminal to the database server allows us to construct a database automatically. This improves both management efficiency and the

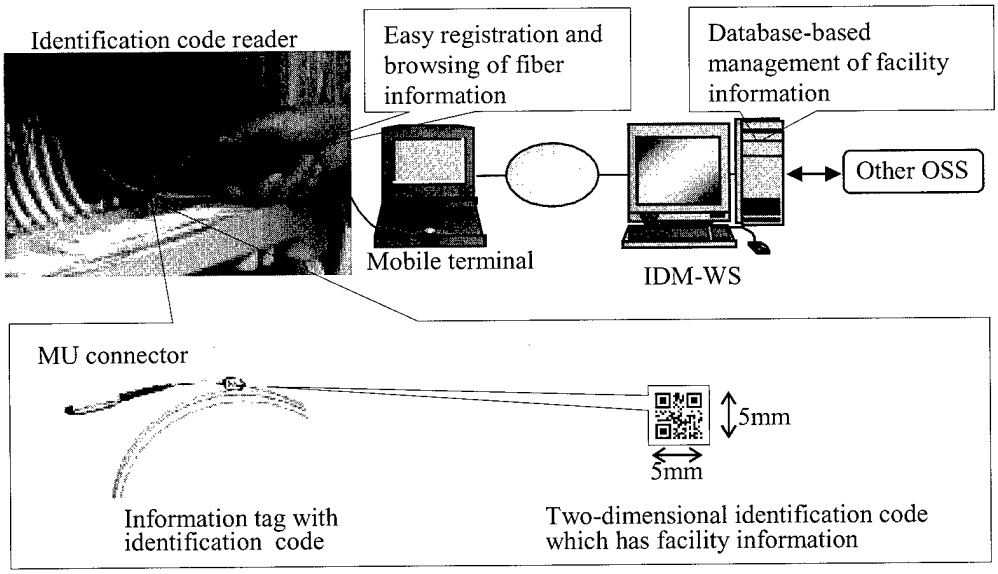


Figure 6. Configuration of IDM management system

operation of the central office optical distribution facilities. We plan to achieve a seamless workflow by linking with the operation systems of external facilities.

2.4 Testing system for access network

Our central office optical fiber distribution system is capable of fiber testing based on the AURORA system [3]. Figure 7 shows the configuration of the fiber testing system. A fiber selector automatically connects test equipment in the OTM to the required fiber in the IDM. The OTM houses devices including an OTDR, an optical power meter, and a light source. The test signal from OTM is input at the coupler. The 1650 nm band test signal of the OTDR and the termination filters for the wavelength, which are installed at both ends of the fiber, enable testing network to be carried out without any service interruption. Table 2 shows the specifications of the testing system we employed.

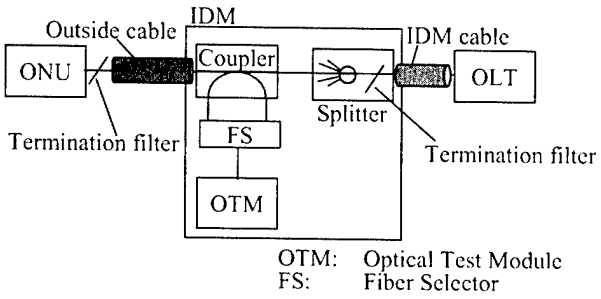


Figure 7. Fiber testing system

Table 2. Specifications of testing system

Network service wavelength	·1310-1550 nm band
Testing wavelength	·1650 nm band
Coupler for testing	·WINC-PLC coupler
Test functions	·OTDR ·Power meter ·Light source
Fiber selector	·1 x 2000 switching structure ·V-groove based mechanical SW

3. Optical fiber cords and cables for IDM

Optical cables in the fiber distribution system must contain a large number of fibers. To realize high fiber-density, the optical cords contained in the cables must be much thinner than the currently-used 1.7-mm diameter cords. Since cords extending from cable ends are installed in the IDM-B frame as fiber jumpers, small diameter cords are also desirable as regards the dense distribution of fibers in the frame. As described the previous section, we have newly developed loose-type 1.1-mm diameter cords and constructed three types of compact cable that contain 16, 32, and 64 optical cords each. The miniature cords are also attached to jumper units as pigtails in IDM-A frames.

3.1 Optical fiber cords

We have studied many types of miniature optical fiber cords [1][4][5], and finally chose a loose-type cord for the distribution system because of its applicability to many types of connectors. Although MU connectors are used as the standard optical connectors in IDM, other types of connector plugs are also needed for connecting the cables to OLTs. The cord structure is shown in Fig. 10 together with the cable structure.

Insufficient flexural rigidity can lead to sudden bending loss as the result of rough handling. Therefore, to provide the miniature optical fiber cord with sufficient flexural rigidity, the cord sheath material must be changed from PVC to some other material with a much higher elastic modulus. Although we used a polyamide sheath for a loose-type cord in a former study [1][5], polyamide has an undesirable characteristic in that it does not recover its straightness after a long period of bending. The thermoplastic elastomer we have chosen for our new cords is good in terms of recovering its shape and also has a high elastic modulus. We have modified the material with flame retardants, while retaining its advantage of being halogen-free.

We have also increased the cord diameter from 1.0 to 1.1 mm so as to reduce the variation in the flexural rigidity, and to make it easy for the fiber's flame retardant property to meet the requirements of the horizontal burning test (Japanese Industrial Standards JIS C 3005).

Figure 8 shows the measurement method we used that employs two-point bend deformation. Reaction force F from the bent cord is measured in a plate separation. We were able to obtain a practical flexural rigidity value in a critically bent condition. The flexural rigidity H can be obtained from precise calculations [5]-[7] as

$$H = 0.3483\, F\, D^2 \qquad (1)$$

We measured the F value just 1 min. after setting the cord at D = 30 mm for 150 mm long samples. This measurement method is comparable to the IEC method (IEC60794-1-2, E17C), but the coefficient 0.3483 in Eq. (1) is rather different from that of the IEC method ($\pi/4$). We assume that this was because of the difference in the approximation degree in the calculation model. We believe that our value is suitable because our experimental result for a thinly coated fiber agreed well with the theoretical values obtained when Eq. (1) was applied.

The typical measured flexural rigidity value for the cords was 25 N mm^2, which is comparable to that of the currently-used 1.7-mm diameter optical fiber cord, and a little smaller than that of the formerly-developed 1.0-mm diameter cord with a polyamide sheath [1][5]. The optical properties under temperature cycle, crush, or bending tests were comparable to those of the other above-mentioned cords.

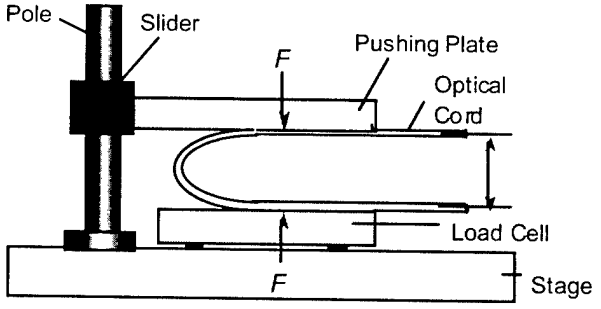


Figure 8. Measurement of flexural rigidity

3.2 Optical fiber cables

Figure 9 shows photographs of newly developed optical fiber cables. They are flame retardant and pass the tilt burning test (JIS C 3005). Cables containing 64, 32, and 16 fibers are 13.7, 10.4, and 8.0 mm in diameter, respectively.

Figure 10 shows the structure of a 64-fiber count cable and of the optical fiber cords it contains. We used a strand type structure for the cable. The strength member of the cable is aramid FRP, rather than the conventionally used steel wire, to make the cable induction free. This is also the case for cables containing 16 or 32 fibers.

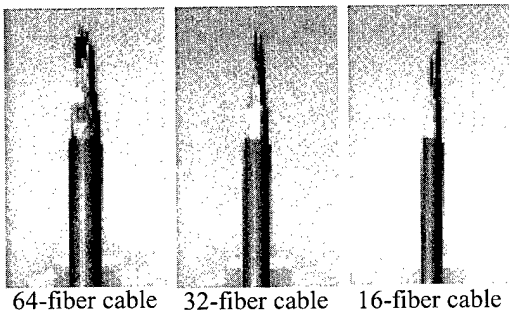
The cable specifications are summarized in Table 3 compared with those of conventional cables. The developed optical fiber cables are almost half the size of conventional cables.

To make it possible to manage the cable and fiber distribution, we have devised a way of providing the cables with an identification code by using length marks. These length marks are incremental numbers printed on the cable sheath by a meter during the cable manufacturing process.

Cables are usually produced in long lengths, and cut into short pieces later to meet specific requirements. So, it is not easy to print different ID codes on each cable piece. But the length mark can be used as a part of the ID code when it is accompanied by a cable lot ID code. The cable lot ID code provides such data as the supplier, production year, cable type, and serial number of the cable lot in a year.

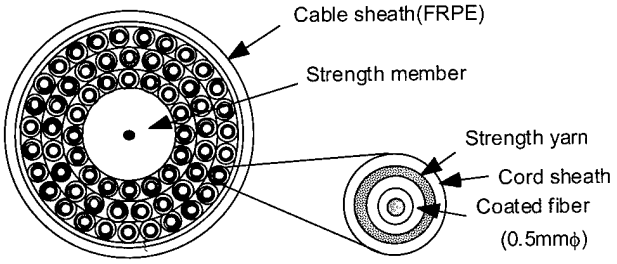
In the database, the length mark numbers at both ends of a cable piece is used for the cable ID code. Since the characters equivalent to the cable lot ID code are printed on the cable sheath with a length mark, we can identify the cable at any point along its length.

The 2-dimensional ID code attached to a fiber cord involves the cable ID code and the number of fibers in the cable. Accordingly, the length mark on the cable plays an important role in relation to fiber distribution management in our system.



64-fiber cable (13.8 mm o.d.) 32-fiber cable (10.4 mm o.d.) 16-fiber cable (8.0 mm o.d.)

Figure 9. Photographs of newly developed optical fiber cables



Developed 64-fiber cable **Optical fiber cord (1.1mmϕ)**

Figure 10. Structures of 64-fiber count cable and miniature optical fiber cord

Table 3. Cable Specifications

	Newly developed	Conventional
Number of fibers (cable diameter)	64-fiber (13.8 mm) 32-fiber (10.4 mm) 16-fiber (8.0 mm)	32-fiber (15.0 mm) 24-fiber (12.5 mm) 16-fiber (12.8 mm) 8-fiber (8.3 mm) etc.
Strength member	Aramid FRP	Ste l wire
Outer diam. of cord	1.1 mm	1.7 mm
Cord sheath	Thermoplastic elastomer	PVC
Diam. of coated fiber	0.5 mm	0.9 mm
Strength yarn	Aramid yarn	Aramid yarn

4. Conclusions

We described our newly developed optical fiber distribution system for use in central offices and related management techniques. The fiber distribution system is based on a frame system called IDM. IDM is composed of two types of frame, IDM-A and IDM-B, and optical cables. Each frame can house 4000 fibers in a 160 cm wide space, almost double the previous maximum for the same width. IDM-A terminates feeder cables from outside the central office. IDM-B is positioned between IDM-As and optical transmission systems (OLTs). This makes it possible to lay optical cables containing a large number of fibers from IDM-B to IDM-As and OLTs in advance of service demands. IDM-A houses densely-integrated optical components such as optical splitters, fiber testing instruments and optical coupler modules. Accordingly, IDM technologies provide us reducing the number of optical fiber cables needed for central office and suitability for various services.

For the IDM, we have also developed loose-type 1.1-mm diameter cords and constructed three types of compact cable that contain 16, 32, or 64 optical cords each. The developed optical fiber cables are almost half the size of conventional cables.

To manage the cable and fiber distribution in the system, we applied a two-dimensional identification code to the fiber distribution facilities.

The IDM and new cables are soon to be installed in central offices. We are expecting the system to play an important role in the forthcoming FTTH era.

5. Acknowledgments

The authors thank Yoshitaka Enomoto and Yutaka Yagi for valuable discussions and assistance. We also thank Nobuo Tomita and Kiminori Sato for their helpful advice and encouragement.

6. References

[1] M. Tachikura, Y. Enomoto, S. Uruno, H. Takemoto, N. Tomita, and H. Takasugi, "Optical fiber distribution system in central offices for the FTTH era", *Proc. of 46th IWCS*, pp.859-866 (November, 1997).

[2] Y. Enomoto, H. Takemoto, M. Tachikura, H. Izumita, and N. Tomita, "A method for managing optical fiber cord in central offices using a two-dimensional identification code", *Technical Digest of 3rd Optoelectronics and Communications Conference (OECC'98)*, pp.166-167 (July, 1998)

[3] N. Tomita, H. Takasugi, N. Atobe, I. Nakamura, F. Takaesu, and S. Takashima, "Design and performance of a novel automatic fiber line testing system with OTDR for optical subscriber loops, *IEEE J. Lightwave Technol.*, 12(5), pp.717-726 (May, 1994).

[4] M. Sato, M. Tachikura, N. Tomita, and S. Iwano, "A 1-mmϕ miniature optical fiber cord adaptable for MU-type connectors", *Proc. of 45th IWCS*, pp.374-780 (November, 1996).

[5] M. Tachikura, H. Takemoto, and N. Tomita, "Miniature optical fiber cords with high flexural rigidity", *Technical Digest of 2nd Optoelectronics and Communications Conference (OECC'97)*, pp.526-527 (July, 1997).

[6] M. Tachikura, "Theoretical analysis on optical fiber strength by bending test", *Electronics and Communications in Japan*, Wiley. Co., part2, 73 (3) pp.73-80 (March, 1990).

[7] M. J. Matthewson, C. R. Kurkjian and S. T. Gulati, "Strength measurement of optical fibers by bending", *J. Am. Ceram. Soc.*, 69(11), pp.815-821 (1986)

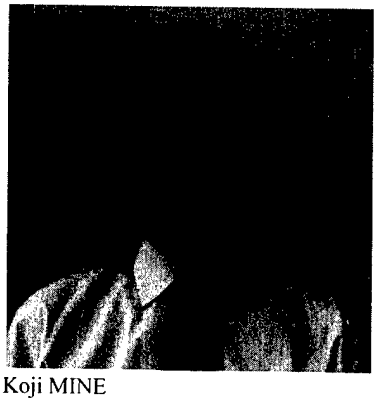
Authors



Masao TACHIKURA

NTT Access Network Service Systems Laboratories, Nippon Telegraph and Telephone Corporation, 1-7-1 Hanabatake, Tsukuba-city, Ibaraki-ken, 305-0805 Japan

Masao Tachikura is a Senior Research Engineer at NTT Access Network Service Systems Laboratories. He joined NTT Electrical Communication Laboratories in 1976. He has been engaged in research on fiber splicing and connection techniques, the mechanical reliability of optical fibers, and fiber switching techniques. He is currently engaged in the research and development of optical cords and a management system for a central office fiber distribution system. He is a member of OSA, IEICE, JSME (The Japan Society of Mechanical Engineers), and JSAP (The Japan Society of Applied Physics).



Koji MINE

NTT Access Network Service Systems Laboratories, Nippon Telegraph and Telephone Corporation, 1-7-1 Hanabatake, Tsukuba-city, Ibaraki-ken, 305-0805 Japan

Koji Mine joined NTT Access Network Systems in 1997. He has been engaged in the research and development of a central office optical fiber distribution management system. He is a member of IEICE.



Hisashi IZUMITA

NTT Access Network Service Systems Laboratories, Nippon Telegraph and Telephone Corporation, 1-7-1 Hanabatake, Tsukuba-city, Ibaraki-ken, 305-0805 Japan

Hisashi Izumita is a Senior Research Engineer at NTT Access Network Service Systems Laboratories. He joined NTT Transmission Systems Laboratories in 1989. He then engaged in research on optical fiber switching techniques and coherent lightwave technology for high performance OTDR and optical fiber distributed sensing. More recently he has been engaged in the development of systems for optical fiber distribution and management, and fiber maintenance. He is a member of IEEE, OSA and IEICE.



Shigenori URUNO

NTT Access Network Service Systems Laboratories, Nippon Telegraph and Telephone Corporation, 1-7-1 Hanabatake, Tsukuba-city, Ibaraki-ken, 305-0805 Japan

Shigenori Uruno is a Research Engineer at NTT Access Network Service Systems Laboratories. Since he joined NTT Electrical Communication Laboratories in 1969, he has been engaged in research on cable jointing, fluoride fiber transmission, the remote control of fiber switches, and in the development of a management system for a central office fiber distribution system. He is a member of IEICE.



Minoru NAKAMURA

NTT Access Network Service Systems Laboratories, Nippon Telegraph and Telephone Corporation, 1-7-1 Hanabatake, Tsukuba-city, Ibaraki-ken, 305-0805 Japan

Minoru Nakamura is an Executive Research Engineer at NTT Access Network Service Systems Laboratories. He joined Nippon Telegraph and Telephone Corporation in 1980. Recently, he has been engaged in the development of an optical access network system.

The Chemistry of Sulfur Bridged Antioxidants for the Stabilization of Polyolefin Compounds for Wire & Cable Applications

Dr. Robert E. Lee[1*], Karen S. Pearson[1], Dr. Carlo Neri[2], Dr. Rosa Maria Riva[3], Cindy Doumen[4], Dr. J. W. Kim[5]

[1]Great Lakes Chemical Corporation, 1801 US Highway 52 West, West Lafayette, IN 47906 USA
[2]Great Lakes Technology Italy, Milan- retired, cneri@glcc.com
[3]Great Lakes Technology Italy, Pedrengo
[4] Great Lakes Technology Belgium, Toekomstlaan 13, 2200 Herentals, Belgium
[5] Asian Stabilizers (Joint venture of Miwon Chemical and Great Lakes Chemical)
542-7 Saegyo-dong, Pyongtaek-shi, Kyonggi-do, Korea

Abstract

This paper is part of a series on antioxidants for polyethylene wire and cable compounds and focuses on the chemistry of sulfur bridged hindered phenolic antioxidants used in peroxide cross linked polyethylene for wire and cable jacketing. Because of their excellent electrical and mechanical properties, polyolefin compounds are used in a variety of wire and cable applications. In applications that require high service temperatures, these compounds are further crosslinked and stabilized with high performance antioxidant systems. Also, select performance data of key phenolic antioxidants in polyethylene wire & cable compounds are discussed.

Keywords

Sulfur Bridged; Antioxidant Chemistry; Peroxide Cross linked HDPE ; Wire & Cable

Stabilization of Polyethylene

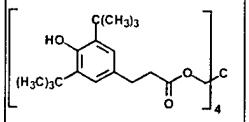
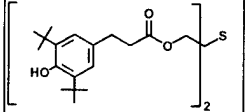
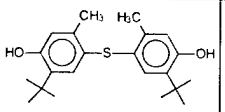
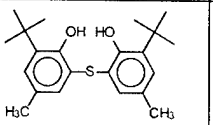
Polyolefins are susceptible to oxidation during processing and use. The radical pathways that lead to the deterioration of physical properties can be controlled by the use of suitable stabilizers. Processing stabilization is usually achieved with combinations of phenolic antioxidants with phosphites or phosphonites. For long-term heat aging (LTHA), high molecular weight phenolic antioxidants are often used[1].

There are three methods for crosslinking polyethylene industrially: 1) using peroxides (CV), 2) using high-energy irradiation (e-beam) and 3) moisture curable (via vinyl siloxanes). Peroxide-mediated crosslinking remains by far the most widely used process. Some of the primary benefits of crosslinking for polyethylene insulation technology are: enhanced mechanical properties to withstand installation and in-service stress conditions, resistance to stress cracking caused by climatic conditions, toughness to withstand possible cut-through from devices supporting the cable and resistance to tracking.[2, 3]

LTHA is of primary importance to high temperature rated wire insulations[4]. To meet such requirements, the antioxidant system has to be very effective. Often to improve LTHA, a high level of antioxidant is used which causes problems in compatibility (migration/bloom), crosslinking mechanisms and high cost. Hindered phenolics that are effective long-term thermal stabilizers invariably interfere with peroxide crosslinking, and to a lesser extent, with irradiation crosslinking[5].

In this study, four structurally different hindered phenolic antioxidants (AO1-AO4) were selected for evaluation in HDPE (Table I). AO2, AO3 and AO4 are characterized by the presence of a sulfur bridge. In fact, AO3 and AO4 are isomeric compounds with a sulfur bridge between the two aromatic rings. Specific chemistry of AO3 was studied to explain the results observed.

Table 1. Phenolic Antioxidants

Product	Structure	Molecular Weight	Diff. Coeff. cm^2/sec
AO1		1178	9.2×10^{-8}
AO2		531	1×10^{-14}
AO3		358	6.9×10^{-5}
AO4		358	n.a.

* Author to whom correspondence should be directed (rlee@glcc.com or ph 765-497-6164)

Evaluation in uncrosslinked HDPE

It is known that AO3 and AO4 have low compatibility with polyolefins below 150°C. AO3 also has a high diffusion coefficient.[6, 7] In spite of these unfavorable characteristics, AO3 appears to be an effective processing stabilizer (Figure 1). Oxidative Induction Time (OIT) experiments performed at 200°C indicate that AO3 provides the best stabilization of the polymer melt. The effectiveness of AO3 is probably due to its relative high molar activity. However, AO3 and AO4 gave materials with high discoloration, arising from quinone moieties formed as the oxidation by-products. The superior performance of AO3 is attributed to the improved solubility and compatibility in HDPE at high temperatures.

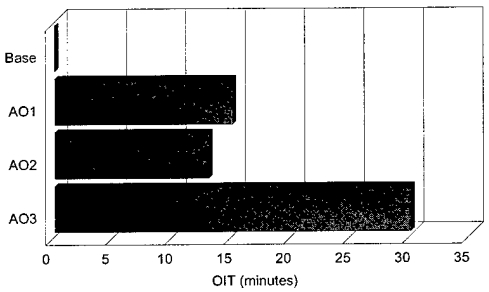


Figure 1. Oxidative Induction Time (OIT) @ 200° C HDPE (0.1% AO)

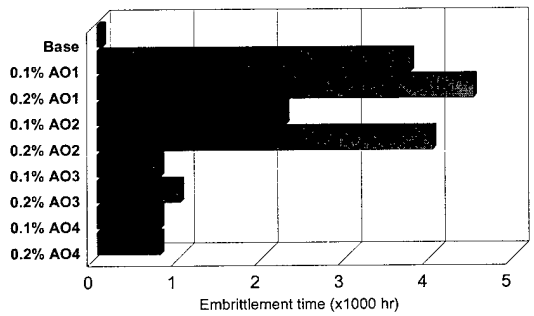


Figure 2. Oven Aging @ 120° C
HDPE PLAQUES (1mm)

The effectiveness of AOs was also evaluated by determining the embrittlement time of plaques after oven aging at 120°C. Under these LTHA conditions, high molecular weight AOs, AO1 and AO2 outperformed the low molecular weight ones, AO3 and AO4 (Figure 2). However, when 2.5% of carbon black is included in the above formulations, the performance of AO3 is comparable to AO2 under LTHA conditions (Figure 3). One plausible explanation is that carbon black offers resistance to migration of AO3.

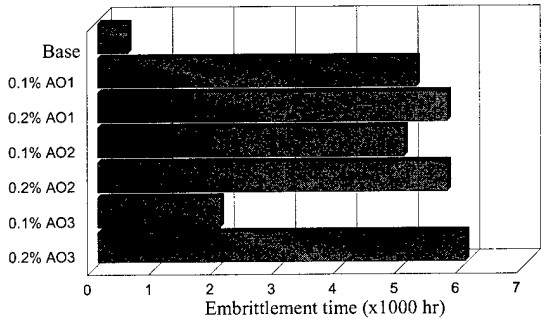


Figure 3. Oven Aging @ 120° C
HDPE PLAQUES (2.5% carbon black, 1mm)

Evaluation in Crosslinked HDPE

All experiments were carried out with 0.5 wt % of peroxide (Trigonox 101) in a Brabender Plasticorder. The additives were first mixed at 130-150°C and the temperature raised to 180°C to promote crosslinking. During this process, the temperature and torque were controlled and recorded. The Δt (in Nm) is the difference between the maximum and the minimum torque value obtained from the rheological curve. In this study the effectiveness of AOs was evaluated by noting the following characteristics during the crosslinking process: Δt, gel & scorch formation (visually inspected) and color (visually inspected after 4 minutes at 180°C).

From the results shown in Table II, the following conclusions can be made: Higher the torque higher the gel and scorch formations, the highest being for the formulation without any AO present. AO3 and AO4 offer the best performance at 0.1 wt %. To achieve a similar performance, 0.6 wt % of AO1 and 0.4% of AO2 is needed. Overall, AO1 and AO2 gave materials with lower discoloration compared to AO3 and AO4.

Table II. Performance of AOs in crosslinked polyethylene

Formulation	Peroxide, %	AO type	AO,%	Color after 4 min	Torque, min (Nm)	Torque max (Nm)	ΔTorque (Nm)	Gellation
1	-	-	-	OW	18	18	0	No
2	0.5	-	-	OW	19	60	41	High
3	0.5	AO1	0.2	OW	19	57	38	Yes
4	0.5		0.4	PY	19	54	36	Yes
5	0.5		0.6	PY	19	51	32	Light
6	0.5	AO2	0.2	OW	19	56	37	Yes
7	0.5		0.4	PY	18	54	36	Light
8	0.5		0.6	PY	18	49	31	No
9	0.5	AO3	0.1	PY	18	54	36	Light
10	0.5		0.2	Y	19	48	29	No
11	0.5	AO4	0.1	Y	18	55	37	Light
12	0.5		0.2	Y	19	50	31	no

OW = off white, PY = pale yellow, Y= yellow

The effectiveness of the AOs was also evaluated by determining the embrittlement time of the crosslinked plaques after oven aging at 120°C as shown in Figure 4. Contrary to the results from the uncrosslinked studies, AO3 was found to be the most effective. One plausible explanation is that the sulfur containing AOs, for example AO3 gets grafted on the polymer backbone during crosslinking and does not volatilize out of the polymer matrix. Figure 5 indicates a possible route to grafting by the sulfur bridged AO3. The same would be true for AO4 as well.

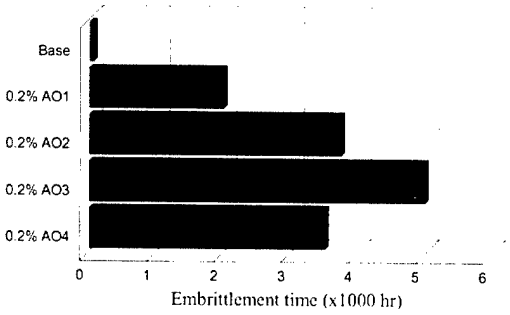


Figure 4. Oven Aging @ 120° C
CROSSLINKED HDPE

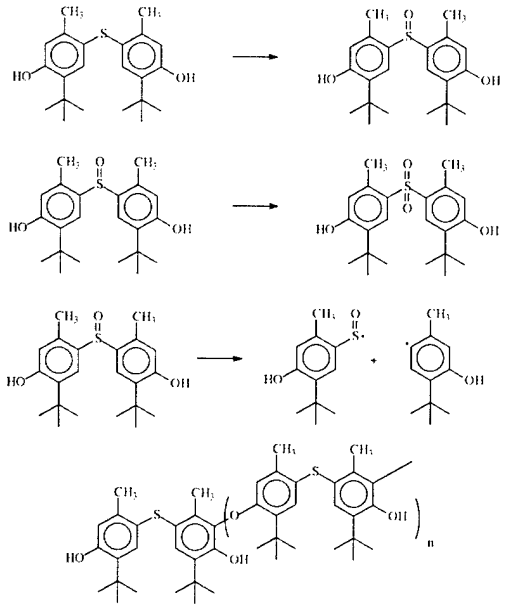


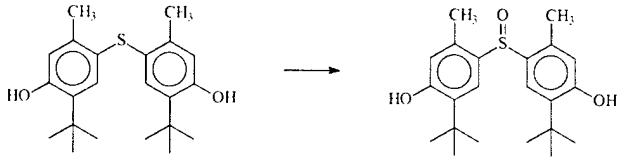
Figure 5. Chemistry of AO3

Peroxide Reactions of Sulfur Bridged Antioxidants

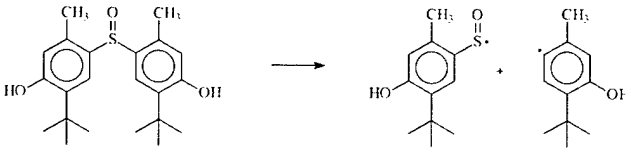
AO3 is a powerful antioxidant widely used in "long lasting" applications like high voltage and ultra-high voltage polyethylene cables, where it guarantees years of lifetime. Nevertheless the outstanding performances are unexpected when considering its physico-chemical characteristics. The melting point for AO3 is 165°C and it tends to sublime just above the melting point. Also, it has low solubility in polyolefins and a significant volatility at room temperature. All of these points would lead to the loss of stabilizer from polyolefin articles during manufacture and use. In fact, AO3 is usually used in PE cross-linked with peroxides. Therefore, its performances could depend on chemical interactions and transformations undergone in presence of peroxides.

To better clarify this hypothesis Great Lakes Technology Italy (R&D) ran a series of model experiments intended to verify the expected reactions and to identify reaction products. Experiments were performed with the most popular peroxides for cross-linking, dicumylperoxide (DICUP) and cumylhydroperoxide (CUHP).

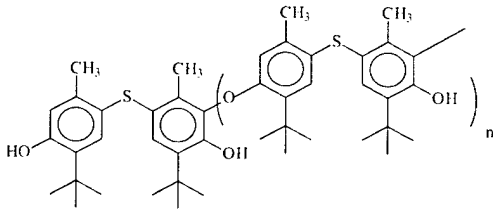
AO3 reacts rapidly at moderate temperature with CUHP giving quantitatively its sulfoxide, as for the following reaction scheme:



When the reaction is performed in chlorobenzene the sulfoxide precipitates as a crystalline white solid , melting at 175°C with decomposition. The decomposition of the sulfoxide gives a long series of by-products and brown tars whose complex composition comes from the first steps reported here below:

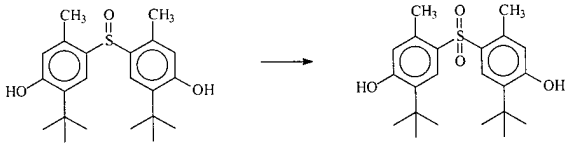


Brown color of tars is then explained by the evolution of the phenoxy-radical to its quinone, as confirmed by thin layer chromatography (TLC) and gas chromatography (GC). Among the tars, over 60 byproducts have been identified by Mass Spectrometry, most of them coming from oligomerization of AO3 radicals and their further oxidation to sulfoxides and sulfones, as represented here below:



Oligomers with "n" from 1 to 4 have been found which, in turn , can have some of the S atoms oxidized to sulfoxide and/or sulfone.

When the reaction with CUHP is performed in a solvent where the AO3-sulfoxide is soluble then the reaction proceed up to the formation of AO3-sulfone , as for the following scheme:



The sulfone can be isolated quantitatively as a white crystalline powder melting at 245°C. It is very thermally stable and highly insoluble in most solvents. No decomposition occurs up to 300°C and it does not dissolves in PE under normal extrusion conditions.

It should be noted that when the oxidation reactions are performed with very pure DICUP in the same conditions the same products are formed but at a much slower rate. However, if just 1% of CUHP is present, then the oxidation proceeds much easier with formation of the same products. This behaviour of AO3 has to be expected if we consider the well known capability of Sulfur based antioxidants to decompose hydroperoxides like CUHP (as the Phosphites do) but to be much less reactive versus the peroxides. The results explain the effectiveness of AO3 as a long lasting antioxidant. In fact, the radicals formed by decomposition of the AO3-sulfoxide can graft to the polymer and their oligomers, regardless of the sulfur oxidation state, can behave as "**High Molecular Weight Antioxidants**", explaining their better compatibility with the polymer and their lower volatility compared with the original AO3.

When these reactions are performed directly on PE plaques, containing 2% of AO3 and immersed respectively into molten DICUP containing some CUHP or pure DICUP, the same chemistry has been verified. The plaques made with pure DICUP remain white even after re-extrusion or compression molding at 200°C whereas those made with DICUP containing CUHP becomes brown and show white particles of the insoluble AO3-sulfone. This confirms the necessity to control the presence of CUHP in DICUP to avoid problems as colored bodies and "discontinuity" by white insoluble particles which have a negative impact on the electrical properties of the cable shield. Migration during processing can also cause buildup of additives on extruder dies surfaces with obvious problems for the producer.

This chemistry of AO3 in peroxide crosslinked cabling helps address a secondary issue related to migration of stabilizers.

Specifically, the extraction of stabilizers in general that led to the decreased protection due to their loss from the polymer. For example, in high voltage cable containing petroleum jelly, extraction of stabilizers from the polyethylene cable jacketing can be particularly critical.[8] AO3 avoids this extraction by being grafted to the polymer.

SUMMARY

For uncrosslinked polyethylene compounds, higher molecular weight antioxidant AO1 provides adequate performance during processing and long term heat aging. However, in compounds containing carbon black, AO3 provides superior performance. In crosslinked compounds, AO3 showed the best performance.
Significant work has shown that the grafting of the stabilizer to the polymer is the likely mechanism and peroxide quality control to avoid hydroperoxides should be utilized to avoid insoluble material arising from these antioxidants.

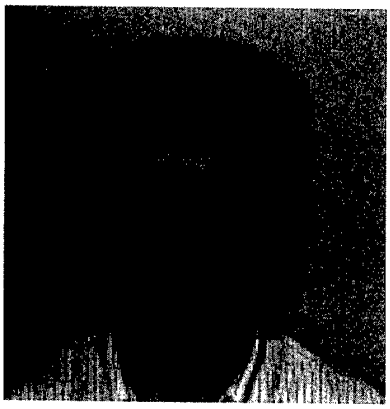
ACKNOWLEDGMENTS

The contributions of Silvestro Costanzi and the laboratories of Great Lakes Chemicals, Italy are gratefully acknowledged. Special appreciation is also extended to Great Lakes Chemical Corporation for permission to use the data presented.

REFERENCES

1. F. Gugumus, 'Antioxidants in Plastics additives', 4th edn, ed. R. Gächter & H. Mueller. Hanser Publishers, Munich, 1993, pp. 1-104.
2. A. Zamore, Wire Journal International, pp. 68-72, September 1996.
3. B. Tot, D. F. Wald, Wire & Cable Asia, pp. 52-57, September 1997.
4. L. Y. Lee, International Wire & Cable Symposium Proceedings, 1997, pp. 744-751.
5. S. K. Dutta, A. K. Bhowmick, P. G. Mukunda, T. K. Chaki, Polymer Degradation and Stabilization, 1992, pp. 75-82.
6. N. C. Billingham, P. D. Calver, A. S. Manke, J. Appl. Poly. Sci, 1981, pp. 3543.
7. R-J. Roe, H. E. Bair, C. Gieniewski, J. Appl. Poly. Sci, 1974, pp. 843.
8. G. D. Brown, J. M. Cogen, M. J. Keogh, International Wire & Symposium, 1996, pp. 167-176.

Dr. Robert E. Lee



Dr. Robert E. Lee is Global Marketing Director for Polymer Stabilizer Applications for Great Lakes Chemical Corporation located in West Lafayette, Indiana. His present focus is new application for existing products and blends of polymer stabilizers.

Dr. Lee received his doctorate in organic chemistry from Purdue University. Later, he worked as a Senior Developmental Chemist for BASF in their OEM automotive coating division. Just prior to joining Great Lakes, he was technical manager for Precision Plastics Inc.

A Newly Developed Antioxidant Package Whose Performance is Unaffected by the Presence of Copper or Color

Ndiba Dioh
Equistar Chemicals LP
Cincinnati, OH
+1-513-530-4313 · ndiba.dioh@equistarchem.com

Abstract
Accelerated heat aging data generated from tensile tests at 165°C indicate that a newly developed antioxidant system for wire and cable compounds results in superior heat aging performance over current commonly used systems. The heat aging performance of Compound A, based on the new antioxidant system; is approximately twice as good as that of Compound B, which is based on a more commonly used system. In addition, data is presented which shows that the heat aging performance of Compound A is unaffected by the presence of copper and a black color concentrate. This may partly explain the superior performance of this new system over those that are currently used.

Keywords: antioxidant; copper poisoning; color concentrates; degradation; heat aging

1. Introduction
Various pigments are commonly added to insulation compounds to make different color wiring. However, it is known that these chemicals can have an adverse effect on heat aging performance. While literature on the effect of color on wire and cable insulation performance exists, these are mostly limited to tele-communications cables and not to automotive wiring which is the subject of this paper [1]. Nonetheless, there is a general perception in the automotive industry that a relationship exists between color and heat aging performance. These relationships are difficult to generalize since the interactions tend to be pigment specific and depend strongly on factors such as the different metals that may be used in their formulation. For this reason, it is advisable to conduct experiments on any given system to accurately determine how a pigment will interact in a given compound.

The physical properties of the aged insulation material can also be greatly diminished in the presence of copper. This phenomenon, commonly known as copper poisoning occurs when the compound is extruded over copper conductors. This premature degradation is often attributed to the fact that copper ions catalyze the decomposition of hydroperoxides which are formed during ageing, thereby supplying new radicals which further promote the ageing process [2]. This effect of copper on the premature degradation of the insulation compound in most cases can be resolved by the use of metal deactivators [2, 3]. The ideal antioxidant system for wire insulation, therefore, will be one which is not susceptible to copper poisoning and is also unaffected by the presence of color concentrates.

In the present work, a newly developed automotive compound, which exhibits heat aging characteristics that are neither influenced by copper poisoning nor the presence of a color concentrate (CC) is discussed. This is achieved by the use of a single antioxidant system as opposed to one that also contains a metal deactivator. The superior heat aging performance of the newly developed compound, A, is demonstrated by comparing its end of life heat aging behavior to that of a more standard compound, B. Both compounds have been developed for 125 °C automotive under the hood wire and cable applications.

2. Experimental
Compounds A and B evaluated in the present work differ only in the antioxidant package used, with all other components such as the base resin and flame retardants being the same. Both are highly filled, non-halogenated, flame retardant peroxide cross linked polyethylene compounds formulated for low voltage 125°C automotive wire and cable under the hood applications. For Compound A, the total additive package consists of a single commercially available primary antioxidant. Compound B contains two hindered phenols. No metal deactivators are used, and the total combined additive levels in both compounds is the same.

Copper powder is added to both compounds in order to simulate insulation performance in the presence of copper conductors. This is done in a Brabender mixer by producing a copper masterbatch (MB) of the compound as described in Table 1. The MB is then let down into the compound in order to efficiently disperse the 100 ppm of copper powder added.

The effect of color is investigated by mixing 1% by weight of a CC into the compound. Based on field observations and customer feedback, a black CC was selected for the present study. This color has been identified as being one of the most likely out of all the standard automotive colors to affect the heat ageing behavior of peroxide crosslinked polyethylene systems. All mixing is carried out in a Brabender at a temperature of 240 F for 3 minutes. No special precautions such as the use of a nitrogen blanket were employed during the production of the blends since the intention was to simulate as closely as possible, standard commercial mixing processes.

A non lead based carbon black filled colorant is used in the present work since the industry trend is a movement away from heavy metal based color systems. The colorant is commercially available from any major color supplier.

Once the compounds are produced as described in Table 1, they are cured at a temperature of 350 F and a pressure of 40,000 psi for twenty minutes into 75 mil thick plaques. The plaques are then cut into Type IV dog bone specimens and heat aged in a circulating oven at a temperature of 165 °C until end of life, with specimens being pulled out for testing at regular intervals. Tensile testing is conducted in accordance with ASTM test method D790 as specified by the J1128 specifications developed for automotive wiring. This procedure was used, in place of the more controlled oxygen uptake methods since it represents the test procedures used in field qualification trials [2].

Table 1. Brabender MB and final compound formulations for incorporating copper and color.

Masterbatch & Components	Weight (%)	Weight (gm)	Cu (gm)	Cu (%)	CC (%)
MB	100	220	2.2	1.0	---
Compound	99	217.8	---	---	---
Cu Powder	1	2.2	2.2	100	---
Final Compound	100	220	0.022	0.01	0.01
Compound	98	215.6	---	---	---
MB made above	1	2.2	0.022	1.0	---
CC	1	2.2	---	---	100

3. Results and Discussion

The effect of copper powder on the heat aging performance of Compound A is shown in Figure 1 where the tensile strength retention is plotted against time. A similar trend is obtained for the retention in elongation shown in Figure 2 for the same compound with and without the use of copper powder. Clearly, from both figures, it can be seen that the heat aging performance of Compound A is not significantly affected by the presence of copper powder.

Similar results are shown in Figures 3 and 4 for Compound B. The tensile strength and elongation results shown indicate that the heat aging performance of this compound is significantly affected by the presence of copper ions. Assuming that the useful life of the insulation is represented by at least an 80 % retention in tensile strength and a 50 % retention in elongation, as specified by the automotive J1128 specifications, the results indicate a 50 % drop in performance due to copper poisoning.

Figures 5 and 6 show the effect of color on the performance of Compound A. As shown, the black CC used in the present study does not adversely affect the heat aging performance of Compound A. The heat aging performance of Compound B on the other hand, is significantly affected by the presence of the black CC as shown in Figures 7 and 8.

The relative effects of color and copper on both compounds is shown in Figures 10 to 12 where the performance of each natural compound is compared to that containing either copper and/or color. From Figures 9 and 10, it is clear that heat aging performance of Compound A is unaffected even when copper and color are both present. However, for Compound B, as shown in Figures 11 and 12, copper and color do have an adverse effect on heat aging performance. In addition, copper appears to have a more profound effect on heat aging than the black CC used. This is shown in Figure 12 where the natural compound with copper performs as poorly as that which contains copper and black. Therefore, the presence of the black CC does not lead to a further drop in heat aging performance in the presence of copper ions.

From all the data presented, the overall performance of Compound A is significantly superior to that of Compound B, especially in the presence of both copper and color. As shown in Figures 10 and 12, failure as defined in the J1128 specifications occurs after approximately 30 days for Compound A as opposed to 12 days for Compound B.

4. Conclusions

Data is presented from accelerated heat aging tests which indicate that a newly developed antioxidant system for wire and cable compounds results in superior heat aging performance over current commonly used systems. In addition, the heat aging performance of the new system is unaffected by the presence of copper or black color concentrate. For the currently used antioxidant system, it is shown that the presence of copper and color, specifically the black colorant used in the present study, adversely affect heat aging behavior. However, the effect of copper is more profound.

5. Acknowledgments

The author would like to thank Mike Richardson and Chris Gulley for their invaluable help in preparing the test samples.

6. References

[1] B.L. Board and H. J. Ruddell, "Investigation of Premature Depletion of Stabilizers from Solid Polyethylene Insulation". International Wire and Cable Symposium Proceedings, 300-312 (1982).

[2] W. Gentzkow and R. Wiedenmann, "Stabilization of Crosslinked Polyethylene against copper-catalyzed thermo-oxidative degradation", J. of Appl. Polymer Scienc: Applied Polymer Symposium 35, 173-182 (1979).

[3] Z. Osawa, "Role of Metals and Metal-Deactivators in Polymer Degradation". Polymer Degradation and Stability 20, 203-236 (1988)

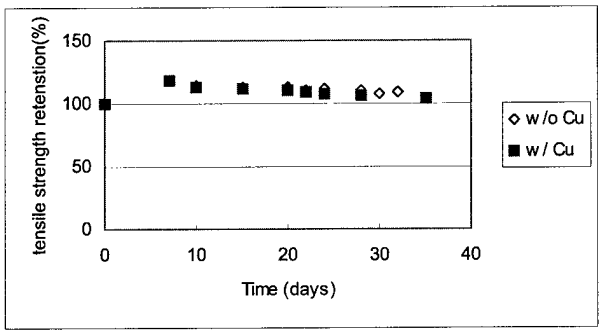


Figure 1. Effect of copper powder on the tensile strength retention of Compound A

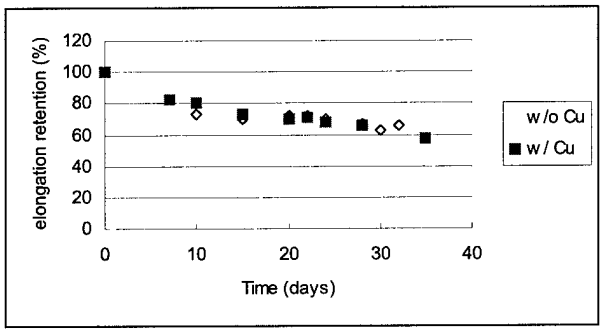


Figure 2. Effect of copper powder on the elongation retention of Compound A

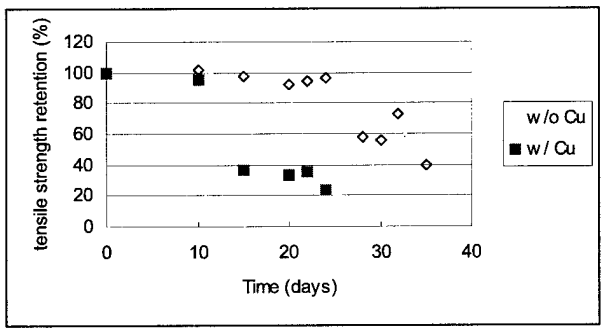


Figure 3. Effect of copper powder on the tensile strength retention of Compound B

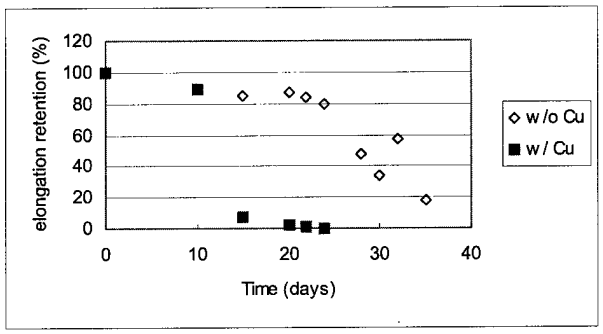


Figure 4. Effect of copper powder on the elongation retention of Compound B

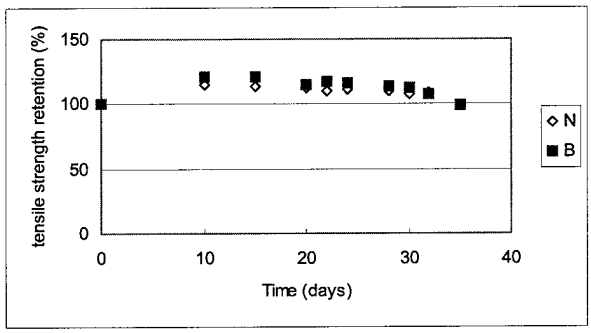


Figure 5. Effect of black color concentrate on the tensile strength retention of Compound A

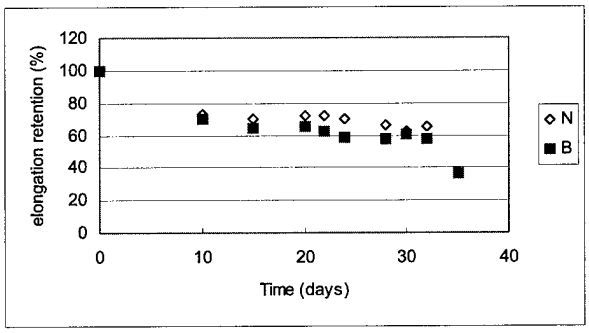


Figure 6. Effect of black color concentrate on the elongation retention of Compound A

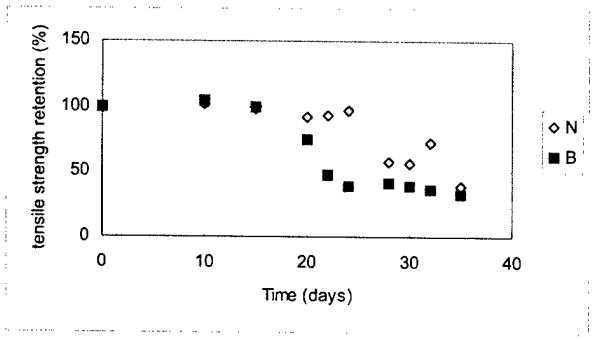


Figure 7. Effect of black color concentrate on the tensile strength retention of Compound B

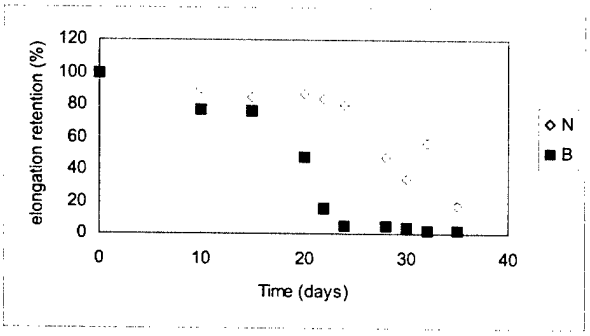


Figure 8. Effect of black color concentrate on the elongation retention of Compound B

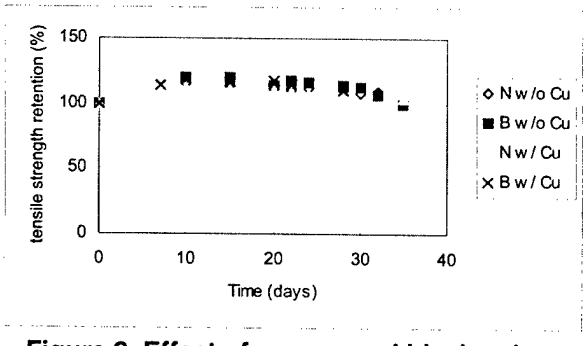


Figure 9. Effect of copper and black color concentrate on the tensile strength retention of Compound A

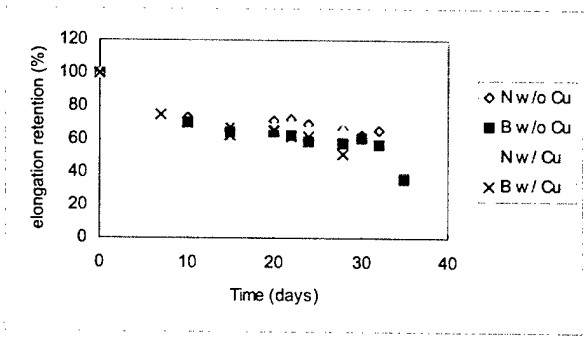


Figure 10. Effect of copper and black color concentrate on the elongation retention of Compound A

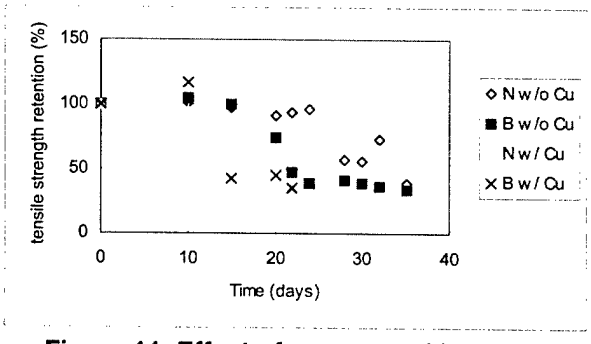


Figure 11. Effect of copper and black color concentrate on the tensile strength retention of Compound B

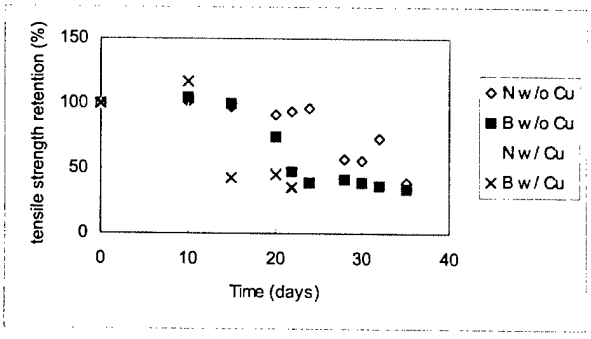


Figure 12. Effect of copper and black color concentrate on the elongation retention of Compound B

Next Generation High Performance ADSS Cable Designs with High Modulus Reinforcement Materials

Swati Neogi, Jeff Auton, Brian G. Risch**, and Dean Rattazzi
Alcatel Fiber Optic Cable R&D, Claremont, NC

**To whom correspondence should be addressed.

ABSTRACT
New ADSS designs are presented that contain PBO fibers with a modulus 220% that of para-aramid. The use of higher modulus PBO materials allows substantial improvements over traditional para-aramid reinforcement in terms of cable MRCL, maximum fiber count, maximum span length, and cable manufacturing lengths. A study of dynamic fatigue lifetime for PBO fiber is also presented that shows that high performance cable designs containing PBO fibers can withstand over 1 000 000 loading and unloading cycles. Although the cost of the PBO material is high relative to aramid, this study shows that this new material is well suited for specialty high load ADSS applications.

KEYWORDS: ADSS; Aramid; Fatigue; Lifetime; PBO; Reinforcement; Reliability

INTRODUCTION
All Dielectric Self-Supporting (ADSS) fiber optic cable offers a rapid and economical solution for utility and telecommunication companies to deploy optical fiber cables along existing electric and telephone utility pole rights of way assets. ADSS cables offer an alternative solution over other aerial application cables such as lashed or Figure-8 cables. All dielectric solutions are preferred and sometimes mandatory for installation in or near electric power lines on utility structures where cables containing metallic elements are not advised.

High modulus reinforcement elements are used in aerial cable reinforcement to minimize cable diameter and weight for a given MRCL and fiber count. Traditionally para-armid fiber has been used due to its excellent combination of high modulus, low density, and high electrical resistivity. Poly(p-phenylene-2,6 benzobisoxazole) (PBO) fiber offers a superior modulus to weight ratio even when compared to para-aramid. Unlike steel and carbon fiber, which also have a high modulus, PBO also has high electrical resistivity making it an interesting candidate material for ADSS cables.

A comparison of properties of cable reinforcing materials is shown in Tables 1,2, & 3.

Table 1a: Comparison of Physical Properties of Various Cable Reinforcing Materials.

Material:	Young's Modulus	Density	Specific Modulus [Gpa(cc/g)]
PBO Yarn	280 GPa	1.56 g/cc	180
Carbon Fiber	255 GPa	1.77g/cc	144
p-Aramid	95-120 GPa	1.44 g/cc	66 - 83
E-Glass	73GPa	2.60 g/cc	28
Steel	200 GPa	7.8 g/cc	25
GRP	50 GPa	2.40 g/cc	21
Polyester	18 GPa	1.38 g/cc	13

Table 1b: Comparison of Strength of Cable Reinforcing Materials.

Material:	Strength (GPa)	Elongation(%)
PBO Yarn	5.6	2%
Carbon Fiber	3.8	1.7%
p-Aramid	3.0	2.5%
E-Glass	3.5	4.8%
GRP	1.5	3%
Steel	4.0	2%

Table 2: Comparison of Electrical Resistivity of Various Cable Reinforcing Materials.[1]

Material:	Resistivity (Ω-cm)
PBO Yarn	7 E 6
Carbon Fiber	1.5 E –3
p-Aramid	7 E 6
E-Glass	5 E 9
Steel	10 E –6

Table 3: Comparison of Coefficient of Thermal Expansion of Cable Reinforcing Materials.[1]

Material:	CTE @ R.T. (per °C)
PBO Yarn	-6.0 E –6
Carbon Fiber	0.6 E –6
p-Aramid	-4.2 E –6
E-Glass	2.8 E –6
GRP	6 E –6
Steel	6.7 E –6

Besides properties such as modulus, tensile strength, density, and coefficient of thermal expansion, the resistance to fatigue under continuous and varying loading conditions is critical for ADSS cable reinforcement materials. If ADSS cable reinforcement materials do not posses adequate fatigue resistance, the

cables can fail under relatively low loads after extended service life.

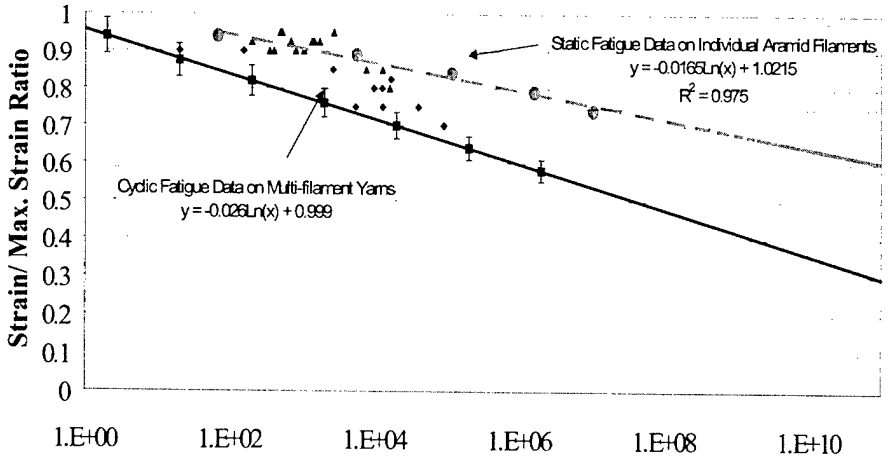
Aramid has been used in load bearing applications such as ADSS cables, composites, ropes, and drive belts for years, and a substantial body of research has been compiled on the long term reliability of various Aramid fibers. However, less data is available for PBO yarn. For continuous load applications various approaches have been used to predict the lifetime of reinforcing fibers depending on the application. For static loading a two parameter Weibull distribution has been used to model both strength and creep rupture of individual aramid fibers.[2,3,4] The Weibull approach to modeling fiber strength is already commonly used to model optical fiber strength and fatigue lifetime.

In ADSS cable applications loading conditions are seldom constant due to ice and wind load variability. Variable loading components from wind and ice are superimposed on a static component contribution from cable weight. For cyclic fatigue alternative lifetime models have been developed. A logarithmic relationship has been established between median fatigue lifetime and applied stress amplitude in cyclic fatigue testing.[5] These cyclic fatigue tests have also produced substantially lower filament lifetimes at equivalent stress levels when compared to static fatigue tests on single aramid filaments. For example, median Weibull fatigue lifetime for single aramid filaments at 70% of break stress (σ_B) under constant loading is 4 orders of magnitude longer than that observed for median cyclic loading lifetime at 5hz. Figure 1 is a comparison of literature data from references 3 and 4 that also includes data collected in the current study in black.

The variation between static fatigue lifetimes of individual aramid filaments and cyclic fatigue lifetimes of aramid yarns is likely due to a combination of: uneven load distribution between individual filaments in yarns, redistribution of load between yarn filaments during testing, and abrasion damage that can occur when individual filaments rub together during cyclic fatigue testing. Due to the fact that ADSS cables experience variability in loading due to vibration as well as changes in wind and ice loading, a cyclic fatigue evaluation has been selected to establish fatigue lifetimes in this study. Additionally, the effects of varying static and dynamic components of load on fatigue lifetime are evaluated which allows an insight on how variations of cable loading conditions can alter fatigue lifetime. The use of actual yarns vs. individual filaments in the testing allows a proper consideration of load distribution and abrasion during fatigue testing. Evaluation of lifetime based on yarn cyclic fatigue testing prevents the risk of underestimating fatigue life that could be possible in static fatigue testing of single filaments.

Figure 1 illustrates that most of the experimental data from this study falls between the two curves obtained in earlier studies. The variation between earlier results and those obtained in the current study can be attributed to variation in loading conditions. The logarithmic slope for the two data sets, however, did not vary substantially from the values obtained in earlier studies.

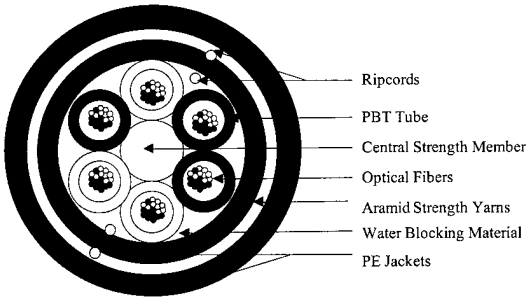
Figure 1: Comparison of Fatigue Life Testing Methods for Aramid



EXPERIMENTAL

ADSS cables were designed with Polybutylene Terapthalate (PBT) tubes containing optical fibers stranded around a central strength member. Superabsorbent waterblocking materials were used to make the interstices between the tubes watertight.[6] The inner core was surrounded by an inner sheath made of Medium Density Polyethylene (MDPE). Between the inner sheath and outer sheath strength yarns were applied. The material of the outer sheath can be either HDPE or a track resistant filled thermoplastic for applications where enhanced resistance to electrical activity is desired.[6, 7,8] A diagram of the cable construction is shown in Figure 2.

Figure 2. Schematic Representation of the Cross Section of Typical ADSS Cable.



Yarn Mechanical Testing:

Cyclic Fatigue Testing:

Mechanical testing was performed using an Instron 5567 tensile tester. A 400-pound load cell was used with Instron's "5kN" pneumatic cord and yarn clamp.

The first segment of the test was performed in tensile extension control at a rate of 50mm/min. The second segment, or cyclic portion of the test, was performed in the load control mode with the upper limit being set for a percentage of the load at rupture and the lower limit set to half the value of the upper limit. Since the 5567 model is an electro-mechanical device the distance between the two limits in the cyclic segment was kept large enough so that there was no danger of burning out the motor or having a large load overshoot. Typical cycle time was about 3.4 seconds, or 17.64 cycles per minute, which corresponds to a frequency of 0.29Hz.

Limits for the cyclic portion of the test were based on the ultimate tensile strength of the various materials. The ratio of maximum load (or stress) to the break load (or stress) of the yarn can be defined by $R_{Max}=\sigma_{Max}/\sigma_B$. For a majority of the tests, the lower load was set to a value that corresponded to one half of the maximum stress value in the loading pattern, and the load was varied between the maximum and minimum values through a linear sawtooth wave pattern. The tensile loading pattern used resulted in a sawtooth load function being superimposed on a static load. This method of setting limits was repeated for various R_{Max} load levels with R_{stress} being kept constant at 50%.

Tensile Testing and LASE Data:

LASE (Load At Specific Elongation) data as well as tensile test data are obtained from the same test method and typically from the same test. Mechanical testing was performed using an Instron 5567 tensile tester. For this test a 6700-pound load cell was used with Instron's "5kN" pneumatic cord and yarn clamp. The gauge length was set for 635mm.

The test was performed in tensile extension control mode at a rate of 320mm/min. A pretension load of 1-3 lbf was applied by hand to the sample to reduce the amount of slack and toe observed during the test. LASE was calculated using the gauge length above over the range of 0.1 - 1.0 % elongation in 0.1% increments such that 0.125 inches of elongation is equal to 1% LASE.

RESULTS AND DISCUSSION

Effect of Load Variability on Fatigue Lifetime:

In the fatigue test method a variable load was superimposed upon a static load. Since the mechanisms between cyclic and static fatigue may vary the effect of varying the dynamic and static contribution was investigated. Initial testing of all yarns was performed to determine maximum tensile stress, σ_B. In the lifetime prediction model the ratio of maximum applied stress to break stress ($R_{Max}=\sigma_{Max}/\sigma_B$) is the dependent variable. Additionally, the loading applied during testing consists of a static load contribution and a dynamic load contribution that is superimposed on the static load contribution in the form of a wave pattern. In this case the wave pattern was a linear sawtooth pattern. The load, therefore, varies and a minimum and maximum load and stress exists within the load profile.

In addition to the maximum stress applied during testing, the ratio of the minimum to maximum load also has an effect on cycles and time to break. As illustrated in the earlier review of literature, completely static loads produce the longest time to failure. As the dynamic contribution of the load increases (i.e. $R_{stress}=\sigma_{min}/\sigma_{Max}$ increases), time to failure decreases dramatically even though average load is reduced by a factor of $[(R_{stress}+1)/2]$. This factor is always less than unity in cyclic load fatigue tests, and in the case where $R_{stress}=1$, we have a simple static fatigue test that can be performed according to the same experimental procedure.

Some examples of the effect of varying R_{stress} while keeping R_{Max} at 93% are illustrated in Table 4.

Table 4: Effect of varying R_{stress} on cycles to failure in aramid cyclic fatigue testing with R_{Max}= 0.93.

R_{stress}	Cycles to Break
0.93	2600
0.50	516
0.10	263

Fatigue Testing:

Cyclic fatigue test data was obtained on a p-aramid, PBO, glass yarn, GRP rod, and carbon fiber; the results are shown in Figure 3. A great deal of variability exists in the fatigue lifetime of these materials. In order to properly interpret the data for an ADSS cable design, a relation to actual loading conditions is needed since both break stress and elongation to break for the materials also varies and the R_{Max} value is normalized according to break stress of each material. An example of relating fatigue data to an actual ADSS application is provided in the cable performance section of this paper.

The fatigue lifetime of the materials can be ranked according to the slope of the plot of stress ratio vs. Log of cycles to failure. Slopes that are smaller in magnitude indicate better fatigue life and less deterioration of properties with time. Table 5 is a comparison of the slopes of the fatigue lifetime curves shown in Figure 3. The fatigue lifetimes of both para-aramid and carbon fiber are superior to Zylon, but the performance of Zylon is very close to that of GRP. GRP has been used in ADSS cables as a central element with a long known performance history in cable reinforcement. The types of glass cable reinforcement yarns tested in this study show poor fatigue performance for continuous load applications. Combined with the obvious weight disadvantage for glass reinforced aerial cables, it is apparent why materials such as aramid or PBO are preferred for ADSS.

Table 5: Slope of Maximum Stress Ratio to Log of Cycle Time Curve for Cyclic Fatigue Testing.

Material:	Log Slope
p-Aramid	-.026
Carbon Fiber	-.030
GRP	-.040
PBO Yarn	-.045
E-Glass	-.066

Figure 3: Fatigue Life of Various Cable Reiforcing Materials

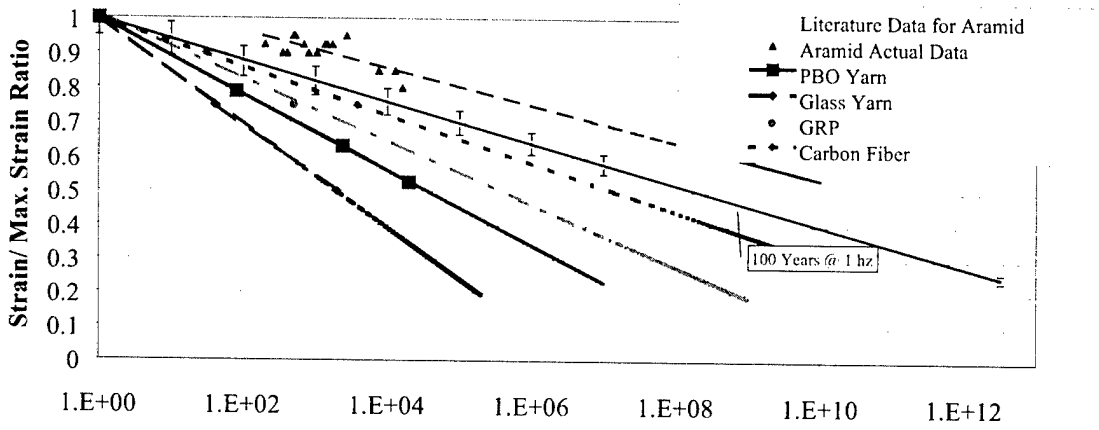


Figure 4 illustrates that, as with aramid fibers, the fatigue life of PBO fibers is reduced when going from static to cyclic loading. As with the cyclic fatigue test results, static load fatigue test results are slightly poorer for PBO relative to aramid yarns. As with the cyclic fatigue data, a logarithmic slope can be obtained to rank the fatigue lifetime of the materials under static loading conditions. The logarithmic slopes for static load fatigue tests are shown in table 6.

Table 6: Slope of Maximum Stress Ratio to Log of Cycle Time Curve for Static Fatigue Testing.

Material:	Log Slope
p-Aramid	-.0165
PBO Yarn	-.0227

Table 7: Comparison of Log Slopes of Static and Cyclic Fatigue Curves for Aramid and PBO Yarns.

Material:	Log Slope		
	Static	Cyclic	Difference
p-Aramid	-.0165	-.026	58%
PBO Yarn	-.0227	-.045	98%

Table 7 illustrates the relative effects of changing load conditions on fatigue life of PBO and aramid yarns. When load conditions were changed from static to cyclic, aramid yarns showed a 58% decrease in the log slope of the fatigue curve whereas PBO yarn showed a 98% decrease. This data indicates that PBO yarn fatigue life is slightly more sensitive to loading conditions than aramid yarns. Based on this data, it is important to properly evaluate cable applications for PBO yarn and compare to fatigue data in order to ensure proper in-service reliability. Evaluation of an actual service application is included in the following section of this paper.

Cable Performance:

Four 144f ADSS Cables were designed to compare performance in ADSS cables of PBO and aramid. Two cables were designed for NESC Medium loading at a span length of approximately 120m (400ft.), and two cables were designed for a cable span of 610m (2000ft.) with 51mm of ice loading and a wind speed of 17.6 m/s. Data is presented for a 2% cable sag installation.

Almost no measurable benefit is seen with the replacement of Aramid with PBO for the lower tensile rated cables although the number of yarn ends and volume of yarn was reduced by approximately 50% in the cable. On the other hand, a dramatic improvement is seen in the data for the long span ADSS cable. Due to the higher modulus of PBO, less PBO is needed to reach an equivalent cable load rating. Additionally, due to a reduction in cable weight per unit length, an iterative effect on cable strength and weight is seen due to the slightly lower cable tensile loading required for the PBO cable.

Table 6: Comparison of PBO and p-Aramid Reinforced Cables.

120m span, NESC Medium loading.

	Aramid	PBO	Improvement
Cable OD	18.9mm	18.4mm	2.5%
Cable Weight	0.331KG/M	0.3418KG/M	3.8%
Cable Modulus	15 KN/%	15 KN%	-

610m Span w. 51mm Ice Loading.

	Aramid	PBO	Improvement
Cable OD	33.8mm	24.5mm	27%
Cable Weight	0.755KG/M	0.424KG/M	43%
Cable Modulus	324 KN/%	277 KN%	-15%
Installation Sag	2%	2%	-
Installation Tension	28 200 N	15 900 N	44%
Max. Loaded Tension	210 000 N	180 000 N	14%
Max. Elongation	0.65%	0.65%	-

Table 6 illustrates the benefit of using high modulus PBO fibers on extremely long span ADSS cables and Figure 5 shows a graphical comparison of cable cross section. A significant reduction is seen on cable OD and cable weight. The reduction in cable weight also leads to a significant reduction in installation and maximum cable tension. Reduced cable weights and tensions are desired to prevent excessive loading on suspension structures and hardware which are considerable concerns for such a long span cable design.

Figure 4: Comparison of Static Load Fatigue Life for Aramid and PBO Fibers

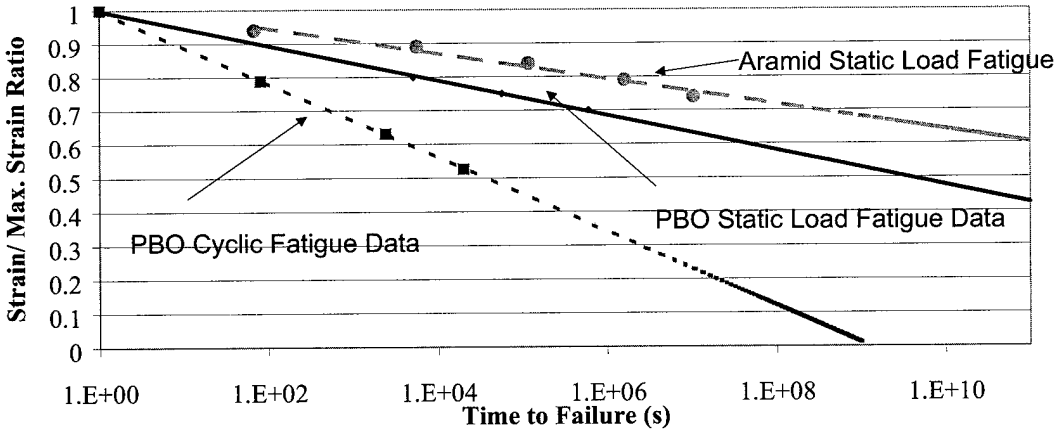
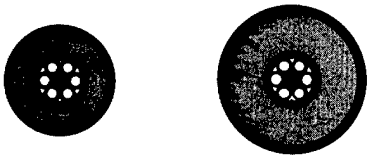


Figure 5: Comparison of PBO and p-Aramid Reinforced Long-span, Heavy Ice Load Cables with Identical Load Ratings and 2% Sag.



PBO Cable
OD = 24.458 mm
Weight =423.79Kg/km

Aramid Cable
OD = 33.834 mm
Weight =755.34Kg/km

With the above design, the installation tension results in only about 0.06% cable elongation, or an R_{Max} value of 0.03. At maximum rated load, the cable elongation would be 0.65%, with an R_{Max} value of 0.325. Static fatigue testing on PBO fiber indicates that the cable would be able to withstand many thousands of years of static loading at the maximum rated cable load. Additionally, dynamic fatigue testing indicates that the cable reinforcing material could withstand approximately 1 000 000 loading and unloading cycles to this load level. Since the conditions that would produce the severe ice loads required to achieve the maximum rated load would occur seasonally, many years of cable life could be expected for the proposed high modulus PBO reinforced long span cable design. Due to variability between fatigue performance in PBO and Aramid cables, it is recommended to do a fatigue loading analysis to correspond to loading conditions for each new cable design. Different loading conditions may have variable contributions from static and dynamic components and therefore give less favorable lifetime estimations.

CONCLUSIONS

Materials test data, cable design data, and reliability data have been provided for use of high modulus PBO fiber in ADSS applications. Because PBO has a modulus substantially higher than Aramid, cable weights and diameters can be substantially reduced for long-span ADSS cables through the use of high modulus PBO fibers. For a 610M (2000ft.) high ice load ADSS design, the reduction in cable weight was 43% and the reduction in cable diameter was 27%. Additionally the reduction in installation tension and maximum service tension was reduced by up to 44%. The reduction in cable tension has the added benefit of reducing loads on suspension hardware and structures.

Reliability testing was performed on PBO yarns and compared to aramid, carbon fiber, glass reinforced composite rod (GRP), and glass yarns. Fatigue resistance of PBO yarns was inferior to that of aramid but comparable to GRP. Due to the fact that PBO and aramid do not have identical fatigue resistance, projected cable loading conditions and cable design specifications should be checked against PBO fatigue data for specific applications. High modulus PBO yarns can withstand approximately 1 000 000 loading and unloading cycles to the maximum rated cable elongation for the long span design presented in this study. When measured fatigue performance of PBO yarns is compared to actual loading conditions for the long span designs presented, many years of reliable service life are predicted.

REFERENCES

[1] Steel was used as a calibration standard for the high resolution DMA used for CTE measurements. Additionally data was checked against vendor product literature. Also see *CRC handbook of Chemistry and Physics 57th Edition,* CRC Press, 1976.

[2] Wagner, H.D., Schwartz, P., Phoenix S. L., "Lifetime studies for single Kevlar 49 filaments in creep-rupture", *Journal of Materials Science* **21** (1986) 1868-78.

[3] Schwartz, P. "Statistics for the Short Term Strength and Creep Rupture of *p*-Aramid Fibers" in *Polymer and Fiber Science: Recent Advences* (1992) VCH Publishers, New York, 77-82.

[4] Wagner, H.D., Phoenix, S.L., and Schwartz, P., "A study of the lifetime of aramid fibers under constant stress", *Proc. Of The Fifth Int.Conf.on Composite Materials* (1985) 245-76.

[5] Qiao, Y. and Farris, R.J. "Lifetime and Property Changes of Kevlar Fiber Yarn under Cyclic Loading", *ACS Polymeric Materials Science and Engineering Fall Meeting Conf. Proc.* **79** (1998) 84-85.

[6] Neogi, S, Risch, B.G., and Soltis, M., "Materials Reliability of Flooded and Dry-Core ADSS Cable", *Proceedings of the 48th International Wire and Cable Symposium,* November 1999, 795-806.

[7] Keller, D.A, D.J. Benzel, J.P. Bonicel, C. Bastide, F. Davidson, "Continued Investigation of ADSS Designs and Reliability Considerations with respect to Field Voltage Tracking and Cable Installation Practices", *Proceedings of the 46th International Wire and Cable Symposium*, November 1997.

[8] DeWitt, W., Neogi, S., Risch, B.G., Coat, P., Ammons, D., Karady, G. and Madrid, J., "High Voltage ADSS Reliability Modeling: Environmental and Climatological Effects on Advanced Jacket Material Selection", *Proceedings of the 49th International Wire and Cable Symposium, November 2000, 337-346.*

AUTHORS



Dean Rattazzi
Alcatel
Fiber Optic Cable R&D
2512 Penny Rd.
P.O. Box 39
Claremont, NC 28610

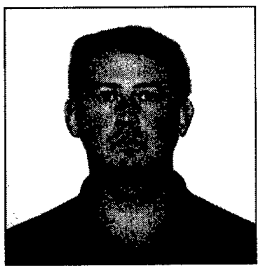
Dean Rattazzi is a Design Engineer at the Alcatel Fiber Optic Cable R&D Center in Claremont, North Carolina. He holds a BA degree in Physics, and a BS degree in Mechanical Engineering from Binghamton University, and an MS degree in Engineering Mechanics from Virginia Tech. His area of research includes the application of finite element modeling to the design and development of fiber optic cables.



Swati NEOGI

Alcatel
Fiber Optic Cable R&D
2512 Penny Rd.
P.O. Box 39
Claremont, NC 28610

Swati Neogi is a Senior Material Scientist and Project Manager at Alcatel's Fiber Optic Cable R&D Center. She received her Ph.D in Chemical Engineering from Ohio University. Before joining Alcatel in 1996, she worked in commissioning a PET plant.



Jeff AUTON

Alcatel
Fiber Optic Cable R&D
2512 Penny Rd.
P.O. Box 39
Claremont, NC 28610

Jeff Auton received his B.S in Biology from Lenoir-Rhyne college in 1984. He worked as a QA Chemist in other industries prior to joining Alcatel in 1989. He has been with Alcatel for 12 years in materials development. Currently Jeff is working at Alcatel's Fiber Optic Cable R&D Center as the Materials Testing Coordinator.



Brian G. RISCH

Alcatel
Fiber Optic Cable R&D
2512 Penny Rd.
P.O. Box 39
Claremont, NC 28610

Brian G. Risch is the Materials Technology Manager at Alcatel Fiber Optic Cable R&D Center. He holds a B.A. degree in physics from Carleton College and a Ph.D. in Materials Science and Engineering from Virginia Polytechnic Institute and State University. His Ph.D. research was in the area of polymer crystallization and structure-property relationships in polymers. Directly after he finished his Ph.D. he worked for ORD laboratories in the area of optical polymers developing new polyurethane and polythiourethanes for high performance opthalmic lens applications. Since 1996 Brian has worked for Alcatel's Optical Fiber Cable R&D center specializing in cable materials.

An Inorganic Optical Fiber Protection System for Premise Cables

James R. Priest
Owens Corning
Granville, Ohio
+1-740-321-7224 · james.priest@owenscorning.com

Abstract

Over the years, the role of reinforcements in premise cable designs has evolved. Current designs rely on the reinforcement to perform tasks far beyond providing tensile strength. It must act as a fire barrier, cushion, optical fiber cover, and more. All of these roles have one central theme, protection of the optical fiber. In addition to this it must have excellent processing characteristics to insure high conversion efficiencies in cable manufacturing. To date this role has been performed quite well by polyaramid fiber tows. In all designs, with the rare exception of a few where smoke generation can be an issue, polyaramid fibers have been acceptably meeting the needs of the cables to the delight of cable designers and manufacturers. Recently demand has arisen for an alternative system. We have developed such a system and have demonstrated its viability with several manufacturers in a multitude of designs.

In this paper, we will discuss our new fiber protection system that has been developed for use in premise cable designs. We will speak to its excellent processing characteristics in cabling equipment. We will also address its craft friendly nature as assessed by outside field installation experts. Examples of how it complies with Telcordia (Bellcore) GR409 specifications and ICEA596 specifications in multiple cable designs will be sighted. However, no information on the designs themselves will be shared to respect the confidentiality of the cable manufacturers who have helped us to evaluate our system. Finally, we will discuss the functional differences between traditional premise reinforcements and our new optical fiber protection system. Among these are fire protection and smoke generation, connectorization and fiber coverage.

Keywords

premise cable; fiberglass; fire and smoke; attenuation; fiber strain; impact; aramid; connectors, furcation

1. Introduction

The premise market being acknowledged as the future of the cable industry, it was interesting to Owens Corning to develop a flexible reinforcement to meet the need of this ever growing market. The role of such reinforcement is vastly different than the outside plant market that we had challenged before. Development of such a product would prove to be both challenging and rewarding. The body of this work and its results will be described in the paragraphs that follow.

2. Key Qualities of a Successful Premise Cable Reinforcement

As we investigated the function of reinforcing fibers in premise cables it immediately became clear that the role was significantly different than in outside plant cables. The critical tasks were manifold and several were unheard of during our development of reinforcements for outside plant cables. To add to the complication the priority of the roles that were shared between the two categories of cable s were different. In order to identify a complete and prioritized list of the qualities of a reinforcement that make it fit for use in premise cables a survey of leading global designers and manufacturers of premise cable was undertaken. The sum result of that survey can be seen in table 1. We will also discuss those points individually in the following paragraphs.

USE CRITERIA	RANK	MEASUREMENT SYSTEM	GOAL
Fibers must be free forming not ribbonized	1	Fiber attenuation and coverage	Meet GR409 or ICEA 596
Meet Tensile Strength Requirement of Cable	2	Tensile test and Fiber attenuation under load	Meet GR409 or ICEA 596
Act as a fire protection layer and not generate smoke	3	Flame and smoke tests	Meet UL flame ans smoke testing, no sticking of opticla fibers to the jacket
Must prevent optical fibers from bonding to jacket	4	Fiber pull out test	No bonding
Must act as a cushion to protect the optical fibers from crush and impact	5	Crush and impact tests	Meet GR409 or ICEA 596
Must Process well in servers and linear over end feeding situations	6	No machine downtime due to reinforcement related issues	No break outs or exploding packages
Must not have issues with stretch or shrink at varying temperatures	7	Cable environmental testing	Meet GR409 or ICEA 596
Must work with a connector	8	Connector tensile testing	Meet GR409 or ICEA 596
Must be craft friendly for manufacturers, assemblers and installers	9	Assessment by Customer's H-E- department	Deemed Craft Friendly by Customer's marketing and field services
Must work on new high speed cable lines	10	Trials on new high speed cable lines	Customer's Engineering Department approval
Must work with furcation systems	11	Tensile test after furcation	Meet GR409 or ICEA 596
Package Lengths in multiples of optical fiber lenghts and below server maximum weight limit	12	Package weight and length	Meet to deliver efficiency to customer
Must work with automated connectorization system	13	Customer Engineering Department approval	Approval
No halogens in coatings	14	No detectable Chlorine, Flourine, Bromine, Astatine or Iodine	Material acceptable globally

Table 1. Ranked Fitness for Use Criteria

The first and most important criteria was that the reinforcing fibers must be free forming and not bound as a ribbon so as to reduce attenuation of the optical fibers. This was the primary problem with traditional reinforcements for optical fiber cables. The best measurement of this quality is found during cable testing. There should be as little attenuation as possible during rest and tensile loaded states. Both common standards have specific allowances for attenuation based on fiber diameter and type but, as a rule of thumb designers tend to strive for zero attenuation.

Our second highest importance criterion was found to be meeting the tensile strength requirements of the cable. This is the primary driving factor in outside plant cables. For, indoor cables it takes precedence over all but attenuation. As expected, the cables have a certain load applied to them during installation and it is the

duty of the reinforcement fibers to bear this load. Again both Telcordia GR409 and ICEA 596 spell out requirements for generic types of cable ratings in tensile properties but cables are also designed for special customer requirements that may go beyond or below these specifications.

The third ranking criterion was that the reinforcement must act as a barrier to fire and reduce the generation of smoke. Standard flame and smoke tests abound for testing conformance to this requirement and are often spelled out specifically by the different specification conventions.

Our fourth ranking quality was that the reinforcement must completely cover the optical fibers and prevent them from bonding to the jacket. Bonding to the jacket leads to increased attenuation as well as poor performance in fire testing. Typically this is evaluated by simply selecting a short section of cable and pulling out the optical fibers through the end of the cable to feel if there is any resistance indicative of bonding.

The reinforcing fiber must also act as a cushion to the optical fibers during crush and impact testing. Again, the requirement for this varies by the standard convention to be followed. It is sufficient to say, however that the reinforcing fibers should bear and disperse any crushing or impact energy and not allow it to be transferred to and thereby damage the optical fiber.

An another criterion is that the reinforcement must process well in many types of cabling operations. It must not effect the overall operating efficiency of a customer's cabling lines by breaking out or fuzzing. It should work well with all types of payoff devices from today's new high technology, high-speed servers to simple over end payoff stands.

It also cannot have issues with expansion or contraction when exposed to different environmental conditions. In this case it must act as a stabilizing member for the cable in extreme conditions. Such conditions are spelled out by the different specification organizations depending upon a cable's intended usage.

An extremely important criterion for acceptance of reinforcement is its ability to work with connector and furcation systems. This is especially important if the reinforcement is intended for use in the broad range of cable that fit into the generic premise category. Generally applying a tensile load with the connector or furcation in place tests the suitability.

Another key item for product acceptance is the acceptance of reinforcement by field craft personnel. If a material is difficult to use, is irritating to the skin or generally hinders their job performance they will reject it and choose not to install cables with that material. Ideally a material will make the installer's job simpler or easier in some way. Typically a cable manufacturer's in house engineers determines the suitability of a material and then sample cables are sent out to installers for their comments.

Of course, the material must be efficient to use in the cable operation. It should be provided in lengths matched to multiples of the optical fiber stock lengths. As splices are not allowed in may designs an ideal package will run out just as the corresponding optical fiber length does. Any material that must be thrown away only adds cost to the total cable.

As halogens are a suspected as a concern for public health, especially in Europe, reinforcement for premise cables should not contain any measurable amounts of halogens. Typically halogens are used as a flame retardant for polymer and composite materials. Debate over their effect on human health continues and other alternatives for fire retardance exist; though they might not be so effective. For the purpose of this product development they should be avoided if possible.

Looking at the sum result of these requirements one may doubt that any one material can perform all of the roles adequately. However, polyaramid fibers perform these roles in common premise cables and one can deduce from that that other materials should be able to be developed to meet the total requirements as well. This was the goal of our research.

3. A New Reinforcement for Premise Cables

Initial trials of reinforcement products for premise cables involved an evaluation of Owens Corning's vast product line. These initial tests included abrasion resistance and physical testing such as tensile and force at specified elongation testing. Results of such testing indicated that two current products were potential candidates for premise cable reinforcements. These products were Owens Corning TS1020 (CR785D) SoftStrand™ and Owens Corning TS1220 (CR785G) InstantDry™. Testing of these products in cables showed that while they were excellent for use in outdoor cables they had major shortcomings for use in premise cables. They tended to produce an unacceptable level of attenuation. They had issues with connectors and furcations and they were not abrasion resistant enough to work with some of the new high speed sever designs used for premise cables. From this work several prototypes were developed to address these issues. One of these prototypes was a radical departure from traditional flexible reinforcement chemistry and manufacturing. This totally new product showed extreme promise and after some adjustments and fine-tuning has been commercialized as Owens Corning's TS3010 Premise Cable Reinforcement.

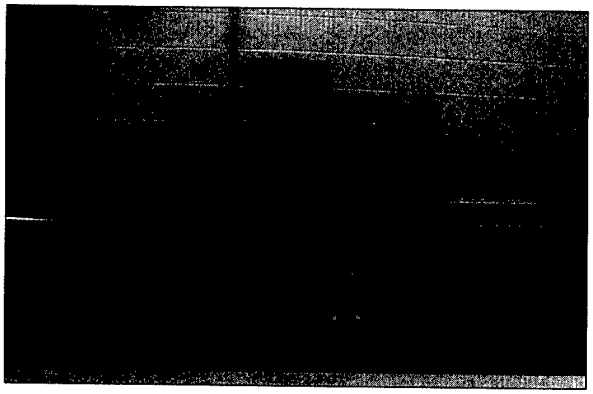
TS3010 from Owens Corning utilizes a unique and patent pending chemistry that is significantly different from those chemistries traditionally used for telecommunications reinforcements. As a result of this chemistry and the unique process necessary to manufacture the glass involved and apply the chemistry, wens Corning TS3010 has some unique properties. It has a nominal tex of 735 grams per kilometer. Its ultimate tensile strength is nominally 488 newtons. At break it has an elongation of 2.49%. At 0.5 and 1.0% strain it has loads of 114 and 231 newtons respectively. The modulus of elasticity for this product was measured to be 84.3 gigapascals nominally. It's coating type is considered proprietary to Owens Corning but is only 0.7% by weight of the material. Its nominal strand width is 2.18 millimeters. The nominal strand thickness for this new product is 0.26 millimeters. It can be

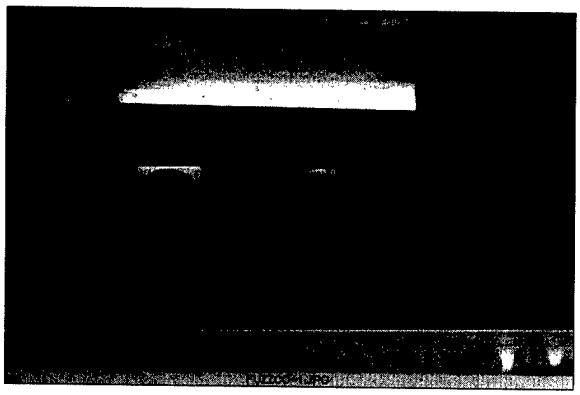
delivered on a variety of server tubes to conform to the needs of customer's equipment and its delivered length is also fit to match multiples of optical fiber length. Package build is such that the product will withstand the highest current server speeds. It's package density of 1.8grams per cubic centimeter and package hardness of 85 as measured by Shore O are good indicators of the sever performance of the product. A product data sheet or additional data necessary for cable design may be obtained by contacting an Owens Corning representative.

4. Processing and Cabling

As processing is a crucial element of any cable reinforcement, we needed a method for evaluating a products processing characteristics without running up large amounts of potentially useless cable and eating up valuable production time on the cable lines of our customers. A suitable test was found in the severe abrasion tests used by the fiberglass industry for evaluating the processing characteristics of its products. Photographs of this testing machine can be seen in Photograph 1 and Photograph 2.

Photograph 1: Severe Abrasion Tester





Photograph 2: Severe Abrasion Tester Vacuum Chamber

This machine works by drawing the reinforcement to be evaluated through a series of guides at a ninety-degree angle. It then passes through a vacuum chamber where abraded filaments are drawn off. Surviving fibers are then collected on the pull roll. A ratio of the weight of the fibers in the vacuum chamber to the fibers on the wrap wheel normalizes for the amount of material run. The contact point composition and fiber pull speed can be varied. For this experiment, blue satin ceramic guides were chosen and the material was pulled at the machine maximum 1000 feet per minute to amplify the results when using such abrasion resistant materials. Chart 1 demonstrates typical results for several materials. We chose to evaluate a typical glass for composite material fabrication, as would have been used when glass first was used to reinforce cables, a typical glass reinforcement for cables commonly available from several manufacturers, Owens Corning TS1020 (CR785D) SoftStrand reinforcement for cables, a typical aramid fiber tow for cable reinforcement, and our new TS3010 premise cable reinforcement.

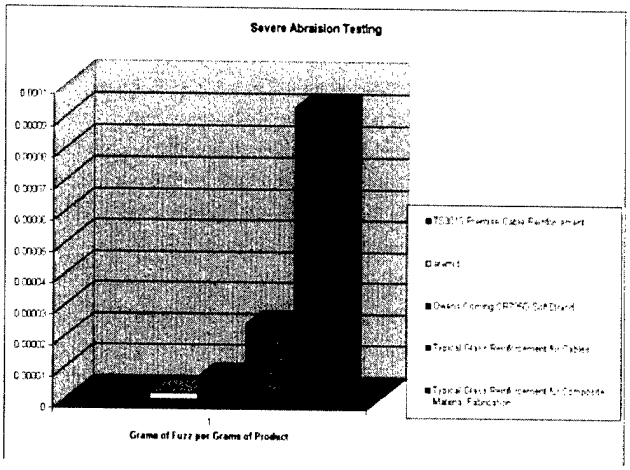


Chart 1: Severe Abrasion Test Results

The results show the fiberglass reinforcement for composites fabrication with a result of $9.3x10^{-5}$grams of fuzz per gram of material, which is shown in blue (far right) on the chart. The typical glass reinforcement for cables is shown second from right in green with a value of $2.4x10^{-5}$grams fuzz per gram of material. The pink bar centered on the chart shows Owens Corning's SoftStrand reinforcement for cables with it's $7.0x10^{-6}$grams per gram result. The yellow bar, second from left is a typical aramid fiber tow used in cables weighing in at $2.0x10^{-6}$grams per gram. The final bar on the far left I red is representative of Owens Corning's new TS3010 premise cable reinforcement and it's $2.0x10^{-6}$grams per gram result. To sum it all up, reinforcements for cables have continually improved their resistance to abrasion. TS3010 has surpassed the performance of all other glass-based products by an order of magnitude and brought the performance of glass equal to that of aramid with respect to processing.

5. Fiber and Cable Coverage

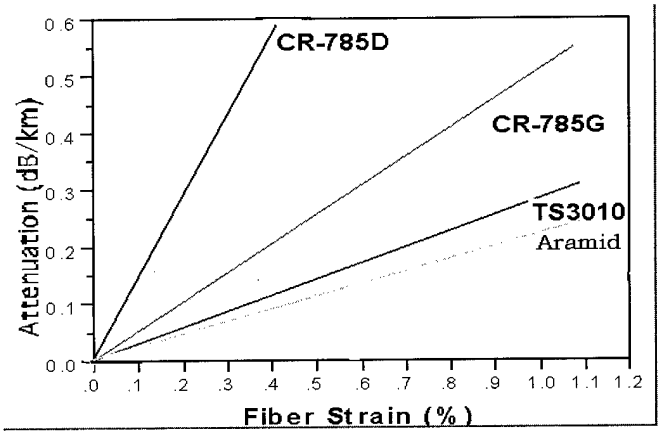
As we investigated the reinforcement fitness for use in premise cables one key factor that always ranked high on the list was coverage. Coverage, it turned out was a many faceted effect. It included the hand of the material. The term hand in this case meant having a particular touch and feel. For a material to be

appropriate for premise cables the hand had to be soft and silky. The fibers had to act individually and be easily separated from the bundle rather than being a tightly bound ribbon or tow. The best way to evaluate the hand of a material is the touch and feel of a person accustomed to handling other materials known to work. It was in this way that we got our first indications that existing glass cable reinforcements would not work. During an early cabling trial using existing Owens Corning products the jacketing line operator made the comment as they were starting the run that the material was not going to work. When asked questions as to why they felt it would not work it was indicated that in past experience, materials that were ribbonized such as traditional cable reinforcements led to unacceptable levels of attenuation and possibly poor coverage where fibers could bond to the jacket. Sure enough this was the result seen in the finished cable. Attenuation was unacceptable with higher levels of reinforcement and at lower levels of reinforcement some fibers were not covered and bonded to the jacketing material. A method to quantify this hand quality of a material needed to be developed. Several methods involving wrapping of mandrels under tension, compression of the strand between two grip points, and differential measurements of a linear strand at rest and under tension were tried. None were found to be repeatable, consistent or applicable to all materials. So, the search for a method to reliably quantify the hand of a material goes on. Until then, the touch of a trained observer remains the best method outside of actual cabling. As we have mentioned, the hand of the material effects fiber and cable coverage and cushioning which leads to one measurable effect, attenuation. Ultimately poor coverage can also lead to poor fire performance as the optical fiber is unacceptably exposed to the fire once it breaches the jacket. Good fillamentation of a reinforcement product is key to acceptable performance in these areas. Some of the effect can be overcome by poor fillamentizing materials by using a high number of a low tex reinforcement but this is usually unacceptable due to limited server spindle availability and the increased cost of lower tex fiber tows. Ultimately a product that fillamentlizes well can cover and suspend the optical fibers in a cable at extremely high tex. For TS3010, which was shown to behave as individual filaments rather than as a bundle we have the ability to tailor to tex based with respect to economics. As a result, we chose to produce a 735 tex product as our first offering.

6. Attenuation Effects

As with all cables attenuation of the optical fibers is a concern. Designs can certainly effect the fiber attenuation at load but the tangible properties of the reinforcement which directly contacts tight buffered fibers can have a dramatic effect. Because of the ribbon like nature of the fiberglass products on the market to date their use in premise cable has been limited to indoor/outdoor cables with a loose tube construction. Some high performance tight buffered cables with 62.5-micron fibers have also been successfully produced. Traditionally the issues with fiberglass reinforcement and attenuation have resided with tight buffered 50-micron fibers. This high attenuation can be attributed to two factors. One is the sensitivity to bend of the optical fiber itself and the other being the stiffness or coarseness of the fiberglass reinforcement. Traditional fiberglass reinforcements have been heavily coated resulting in a stiff bundle of fiberglass. This stiffness resulted in microbending of the optical fiber and hence attenuation. With Owens Corning's new TS3010 and it's loose soft nature this attenuation is not an issue. To demonstrate this a series of cables with from 6 to 24, 50-micron fibers were made. Four different reinforcements, Owens Corning CR785D, CR785G, and TS3010 along with an Aramid standard were chosen. The attenuation was then measured under tensile load. Chart 2 below shows the relationship between fiber strain and type of tension member and attenuation for a cable with 50-micron fibers. The lines depicted on the chart are the moving average of the actual data. When evaluating the scatter involved one can clearly state the advantage that aramid and TS3010 have over traditional fiberglass reinforcements for optical cables but cannot distinguish a real difference between the two premise cable reinforcements. As such, on the basis of fiber attenuation TS3010 is the equal of aramid.

Chart 2: Attenuation versus Fiber Strain for Multiple Reinforcement Types



7. Crush and Impact Effects

As with most required specifications crush and impact resistance can be dramatically effected by cable design. Among the effecting factors are jacket wall thickness and material, cable packing density and the reinforcement materials. The design of the cable is also effected by what cable rating is desired and which convention is to be followed. This varies wildly with impact forces ranging from 0.74 to 23.5 Newton meters. Numbers of impacts can range from 20 impacts in the same location to 2 impacts in each of three different locations. Crushing forces also vary from 3.5 to 10 Newtons per square millimeter. It is well know in the composites industry that different fibers vary on impact resistance based on material and

fiber diameter. E-glass is known to have a lower impact resistance than aramid. E-glass has an impact deformation value of $30x10^8$in.-lb./(lb./sec.) compared to $50x10^8$in.-lb./(lb./sec.) for aramid. On the other hand, E-glass has a fiber toughness of $10x10^3$in.-lb/in.^{3} compared to $8x10^3$in.-lb/in.^{3} for aramid. The other factor coming into play is the diameter of the individual fiber. A larger number of smaller fiber diameter fibers will be able to bend to absorb and better dissipate the energy of and impact or crushing force than a lower number of large fibers. Given the values for fiber diameter and number, and the impact deformation and fiber toughness for the materials to be used in a particular cable design a cable can be developed to meet any of the necessary conventions. Several designers and engineers have done just that and are preparing to launch cables using Owens Corning TS3010 as the reinforcement.

8. Fire and Smoke Information

Perhaps the largest advantage for using a glass-based reinforcement is in meeting fire and smoke tests. Perhaps the most extensive evaluation of composite fabrication materials was undertaken by the United States Navy. Navy studies ranked materials and composites for their performance in fires for use as a guideline for potential manufacturers. Table 2 shows the results of the extensive testing and the resulting ratings.

Table 2: Performance of Reinforcing Fibers in Fires

Parameter	Flame Spread	Burn Through Resistance	Structural Integrity	Smoke Production
Material				
E-glass	Good	Excellent	Good	Excellent
Carbon Fiber	Good	Good	Excellent	Good
Aramid	Fair	Fair	Good	Good

* Flame Spread - The rate that flame travels along the surface of a structure
*Burn Through Resistance - The ability to contain a fire
*Structural Integity - The abilty to support design loads during and after a fire
*Smoke Production - The ammount of smoke produced by a material

Of course from Table 2 Carbon fiber can be ruled out as both common standards conventions require that the cable be dielectric. One cable manufacturer's independent testing of the materials for fuel availability showed Owens Corning TS3010 as having 100 BTU's per pound while a competitive aramid fiber was found to provide 1000 BTU's per pound. Owens Corning's internal testing of flame resistance by ASTM D2863 showed TS3010 to have an Oxygen Index of 99.7%. A comparative sample of aramid fiber was found to have an Oxygen Index of 29%. To be self-extinguishing in air at 1 atmosphere, a material must have an Oxygen Index of 29% minimum. Testing for Loss on Ignition, TS3010 had an average of 0.7% while the comparable aramid sample had an average of 96.7%. From this and the preceding information it can be predicted that cables made with TS3010 will perform superior in fire and smoke testing to their equivalents made with aramid reinforcements. From this one can see the potential system cost savings by using less expensive and less complicated fire retardant polymer jacketing materials.

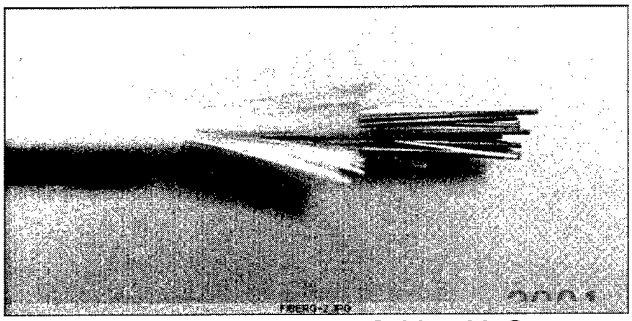
In real world cable testing, several cable manufacturers have submitted their designs using TS3010 to Underwriters Laboratories for fire and smoke testing including UL910 Plenum, UL1581Vertical Tray, UL1651 General Purpose, and UL 1666 Riser fire tests. Results from these tests are specific to cable design and as such are proprietary to the manufacturers involved. We can however tell you that no design using TS3010 has ever failed its intended usage test. Also, several designs have been approved for conversion to TS3010 reinforcement with UL approval.

9. Connector and Furcation Design for Use with Glass Fibers

Connector and furcation compatibility is crucial for any premise cable reinforcement to have real value to the premise industry. By definition a furcation is the break out point where a larger fiber count cables are split out into smaller functional units. A connector is the terminus where a single fiber cable is mated to the device where its signal will be received and either retransmitted or converted. For connectors there are multitudes of designs but for the point at which the reinforcement is engaged to bear the load there are two major design types. These are the glue and crimp types. Glue types by their nature are extremely friendly to fiberglass. However, they are slower and messier to use than their crimp counterparts. As such they do not enjoy the popularity in North America and Europe that they do in Asia and South America. Crimp type connectors involve the bending of the fiber around a base ring and securing it with a crimp ring. Likewise most furcation designs employ a base and crimp ring design. The difficulty for fiberglass lies in this base ring. Typically the base ring is a flat cut piece of metal. The sharp edges of this cut tubing are severely detrimental to fibers. The solution to the problem lies in understanding the critical bend radius for any fiber. This simple calculation holds true for any fiber regardless of material. To complete the calculation one must know three critical elements of the fibers to be used in a connector. First you must know the diameter of the individual fibers in the tow of the material. Second you must know the elastic modulus of the material that the fiber is comprised of and third you need to know the ultimate tensile strength of the material that the fibers are comprised of. From this you can calculate the critical bend radius by using the formula R=ED/2T where R is the critical radius of the fiber, E is the elastic modulus of the fiber and T is the ultimate tensile strength of the fiber. For TS3010 the critical bend radius calculates to be 0.124 millimeters. So long as the radius of the base ring of a furcation or connector is larger than this distance there will be no issues with loading the connection. Given this information some manufacturers of connectors have been able to design connectors and furcations that work with TS3010 as well as its aramid counterparts.

10. Handling and Installation of Glass Reinforced Premise Cables

One important and often overlooked aspect of development of premise or any cables with glass fibers is the acceptance by the production workers and installers. The fiberglass itch, while not an issue for health can be quite a deterrent to the use of such products. Clinical studies have shown that the average human can detect the presence of a 14-micron fiber lodged in their skin. With fibers less than this size the irritation is not an issue. As TS3010 was developed this was taken into consideration to improve acceptance with the workforce. It is also easy to visually detect the difference between cables made with TS3010 and those made with aramid reinforcements, as can be seen in photograph 3 below.



Photograph 3: Optical Fiber Cable with Owens Corning TS3010

As such, it is wise for manufacturers to undertake an education campaign with their customers and installers. In this campaign it is important to discuss the difference between glass and aramid, the advantages of using glass in this design and the differences in handling between the two products. Owens Corning personnel are available to work in together with cable manufacturers on this effort and can provide a wealth of knowledge from their experience with fiberglass.

TS3010 has demonstrated improved knotting strength compared to traditional fiberglass reinforcements. This is due to its improved resistance to abrasion. While not equivalent to aramid in this respect the strength is enough that typical installation techniques can be employed.

One advantage provided by TS3010 as a fiberglass material is its ease of cutting. No longer will installers be required to carry specialized shears, which dull quickly. Any utility scissors or knife can be used to cut the material with ease. Installers who have received advance samples of cable with the new material have seen this as a time saving measure for cable installation.

11. Product Availability

As has been the case with all cabling materials recently, it is understandable that customers may be concerned about taking the risk to qualify TS3010 only to find that its commercial availability is limited. TS3010 is produced using a totally new manufacturing process as well as chemistry. It has been tailored to be rapidly expanded globally as needed. Currently Owens Corning has a new, operational facility manufacturing TS3010 for customers who have qualified it in cables as well as providing samples to those working to qualify. Owens Corning has committed to expand this production to meet the needs of any customer who might purchase TS3010 regardless of consumption levels.

12. Conclusion

To conclude and summarize this paper, Owens Corning has developed a new reinforcement for premise cables. This reinforcement is known as TS3010. Premise cables have been designed and are being qualified using TS3010. One major improvement is fire and smoke performance. Connectors can be designed to work with the new reinforcement. Processing performance of TS 3010 exceeds that of any other glass based reinforcement available on the market today. Customers can realize a total system cost savings by utilizing TS3010 and re-evaluating the total cable design. TS3010 product information, literature and samples are available by contacting an Owens Corning representative.

13. References

[1] E. Greene, "Putting Out The Fire in Marine Composite Construction", Composites Fabrication, 17(7), 20-24 (July 2001)

[2] E. Greene, Marine Composites, Chapters 2,4, (1999)

[3] Owens Corning, Advanced Materials - Solutions for Demanding Applications, (1998)

[4] Bellcore, Generic Requirements for Premises Fiber Optic Cable, GR-409-CORE, Issue 1, May 1994

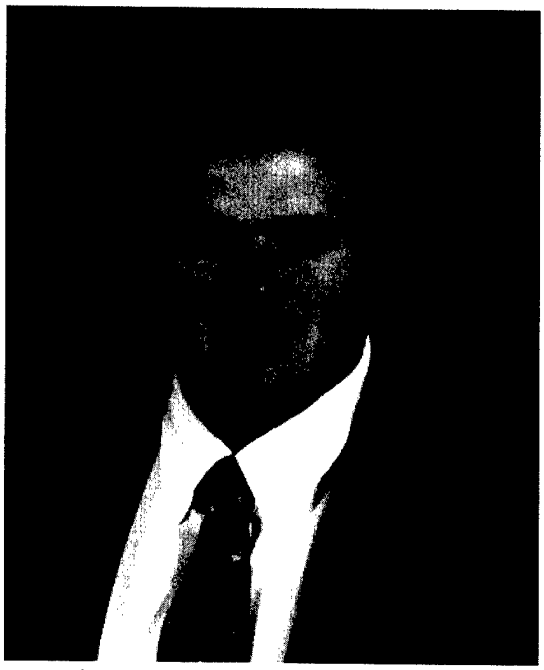
[5] CRC Press, Handbook of Chemistry and Physics, 70th Edition, (1990)

[6] DuPont, Data Manual for Kevlar® 49 aramid

[7] Military Handbook 17A, Part 1. Reinforced Plastics

[8] Owens Corning Science and Technology Data Base

13. Author



James R. Priest

Scientist

Owens Corning Science and Technology Center

2790 Columbus Road

Granville, Ohio 43023

U.S.A.

james.priest@owenscorning.com

James R. Priest is currently a Scientist with Owens Corning, at their Science and Technology Center in Granville, Ohio. He is assigned to Owens Corning's Electrical and Telecommunications Products Laboratory with responsibility to develop products for the telecommunications market segment. He received his Bachelor of Science with a double major in Chemistry and Biology from Ashland University in 1992. From There he joined Clearfield Energy Corporation as an Environmental Specialist with responsibility for pipeline construction and environmental remediation, In 1995, he joined Owens Corning's Resins and Coatings division as an Associate Scientist. While in this role he developed polyester and vinyl ester resins for automotive applications as well as sheet molding compound formulations for automotive and heavy truck applications. In 1998, he joined Owens Corning's Electrical and Telecommunications Products Laboratory in his current role. In this assignment he has developed products such as Owens Corning's InstantDry™ line of superabsorbant tension members.

Development of Optical Fiber Cords with Halogen-Free Jacketing Materials for The Central Offices

Tetsuo Hayano, Osamu Kato, Toshio Takemyou, Tsuyoshi Shimomichi, Keiji Oohashi, Matsuhiro Miyamoto*

Research and Development Dept. Telecommunication Cable Division Fujikura Ltd.
1440,Mutsuzaki,Sakura-shi,Chiba,285-8550,Japan
Phone:+81-43-484-3946 Fax +81-43-484-3976 E-mail:hayano@s.fujikura.co.jp
Telecommunications Engineering Dept. Telecoms & New Media Division
*Nishinippon Electric Wire&Cable Co.Ltd.
Kasugaura,Oita-shi,Oita,870-8632,Japan
Phone:+81-97-537-5568 Fax +81-97-537-5592 E-mail: takemyot@nnd.co.jp

Abstract

Two types of optical-fiber cords for fiber wiring in the central offices have been developed, one of which is a thin optical cord that supports the high-density wiring of systems. It has an outer diameter of 1.1 mm, which represents a reduction of 60% with respect to that of conventional optical cords. Despite its small diameter, the cord provides appropriate flexural rigidity to allow easy handling, and is virtually free of bending curls. The other type of cord is a conventional 1.7-mm optical cord provided with halogen-free flame retardancy. The buffered fiber of 0.9-mm O.D. to be applied to this new cord may be of an UV/PA or UV/TPE structure, in addition to the conventional Si/PA structure. The above two optical cords have passed the horizontal combustion tests under JIS C 3005.

Keywords

Halogen Free; Flame retardant Jacket; Handling Characteristics

1. Introduction

Fiber wiring in the central offices has traditionally been encased in PVC jacketing material and has consisted of Ø1.7-mm cords. However, recent expansion of optical fiber networks has led to the requirement that wiring now be laid out more densely [1]. To achieve even greater wiring density, the authors have been carrying out development aimed at further reducing the diameter and weight of conventional-type optical-fiber cords. In addition, for optical-fiber cords of traditional sizes, which will continue to grow in demand in the future, we have been contemplating the possibility of changing their materials from the conventional PVC to halogen-free materials, as the materials for optical-fiber cables are now required to have lesser ecological impact. This report concerns the results of evaluations conducted on the test-manufactured new optical-fiber cords.

2. Flame Retardant Halogen-Free 1.1-mm Optical Fiber Cord

2.1 Cord Structures and Design Guidelines

Figure 1 represents the structure of the 1.1-mm optical-fiber cord we manufactured for this evaluation. At the outset of the development, the following two points in particular were noted. It was considered likely that, if the conventional optical-fiber cords were further reduced in diameter, their handling characteristics might pose problems in the wiring work for many optical-fiber cords. In view of this possibility, the flexural rigidity, side-pull loss, and bending curls of the new cords were optimized. Furthermore, it was decided that halogen-free materials having flame retardancy would be used in order to provide environmental protection in the event of fire.

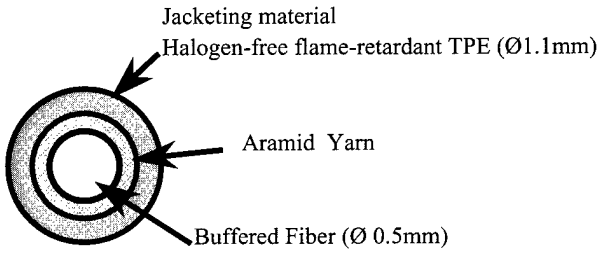


Figure 1. Cross-Sectional Structure of Cord

2.2 Selection of Jacketing Materials

Three types of materials, A, B, and C, were chosen, using the modulus of bending elasticity as the parameter for selection. Table 1 gives their specific values. The three types of materials selected were a polyolefin base resin, a polyester elastmer base resin, and polyamid base resin. These materials were compounded using a flame retardant for the test-manufacture of prototype cords.

Table 1. Modulus of the Bending Elasticity of Base Resins for Sample Jacketing Materials

	Jacketing Material	Modulus of Bending Elasticity (MPa)
A	Polyolefin base	200
B	Polyester Elastmer base	600
C	Polyamid base	1,250

2.3 Prototype Cord Evaluation Methods and Purpose

2.3.1 Flexural rigidity

The flexural-rigidity value is the parameter required for evaluation of the handling characteristics of cords. To measure the parameter value, the two-point bending method was adopted [2]. Figure 2 provides an outline of the measurement method. The sample cord was inserted in a "U" shape between two plates that were positioned in parallel and separated from each other by 30 mm, and the flexural-rigidity value EI was determined by measuring the springback force one minute later and caluculated by equation (1)

$$EI=0.3483 \cdot W \cdot D^2 \qquad (1)$$

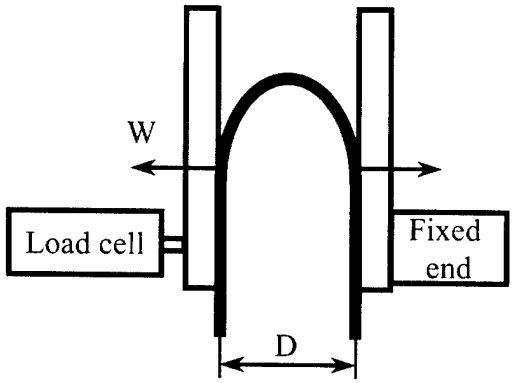


Figure2. Flexural Rigidity Test Method

2.3.2 Side-pull loss

In complex wiring work, a live line may be pulled on by accident. In such an event, concentrated stress would be exerted on the base of the connector, resulting in increased loss due to a bent fiber, which in turn might lead to a communication interruption. In anticipation of this possibility, we measured the transmission loss generated when a cord equipped with an MU connector was bent to a 90-degree angle and pulled.

Figure 3 outlines the test method. The MU connector was fastened horizontally to the base of the tension test machine, and the sample cord was pulled perpendicularly at a speed of 20 mm/min. The maximum value of loss variation produced before the stress reached 5 N was measured.

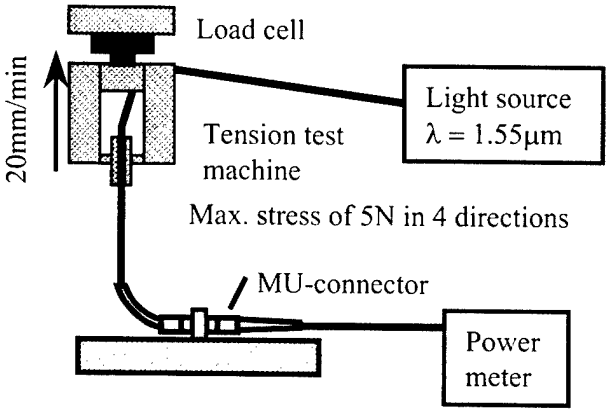


Figure 3. Side Pull Test Method

2.3.3 Bending curls

A wired optical-fiber cord is always provided with a certain amount of extra length, and it is stored bundled into a roll with a diameter of more than Ø60 mm. Therefore, when existing wiring is to be replaced, it will involve the task of unwinding the stored cord. If, in such a case, there are severe bending curls in the cord, it may become tangled, resulting in reduced workability. Figure 4 outlines the bending-curl evaluation method. The bending-curl evaluation procedure is described below.

One meter of cord was wound around a mandrel 60 mm in diameter so as to ensure that the cord was free from twisting and excessive stress, and the cord was then left in a thermostatic oven at 60°C for 15 minutes. After being removed from the oven, the mandrel was allowed to cool at room temperature. Thereafter, the cord was suspended for 6 hours in the standard atmosphere, and the minimum curvature radius was measured when the cord was placed gently on a flat surface.

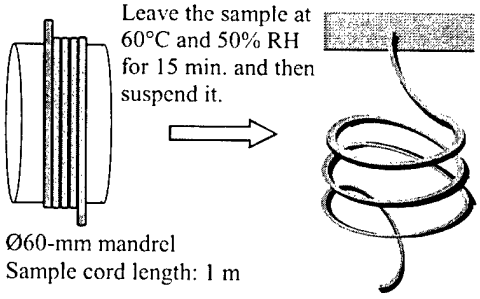


Figure 4. Bending Curl Test Method

2.4 Summary of Evaluation Results

Figure 5 shows the results of the three tests outlined above. The flexural-rigidity value was plotted on the abscissa, while the reciprocal number of the curvature radius of the restored bending curls was plotted on the left ordinate as the bending-curl index. The side-pull loss value was plotted on the right ordinate. These results reveal that a larger flexural rigidity increases bending curls. The graph also indicates that the smaller the flexural-rigidity value, the larger the side-pull loss. In this way, it was determined that there is an optimum range of flexural rigidity for the cords. Based on the balance between those two characteristics, material B was chosen.

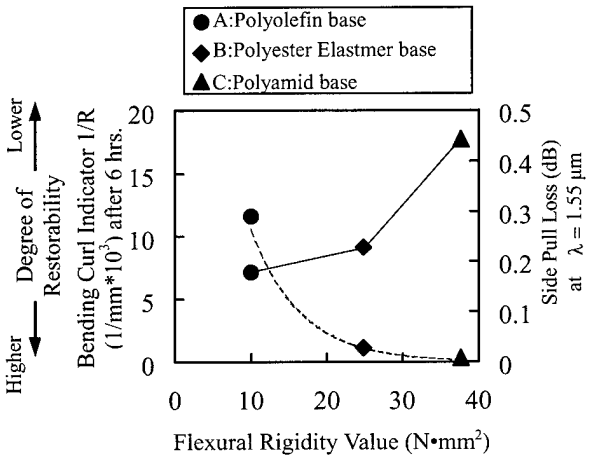


Figure 5. Relationship between Flexural Rigidity Value and Bending Curl / Side Pull

2.5 Various Characteristics of the Selected Cord

Table 2 specifies the combustion characteristics, optical characteristics, and mechanical characteristics of the prototype optical-fiber cord that was test-manufactured using material B, and Figure 6 shows a temperature-characteristic graph of the cord. The prototype cord exhibited excellent results for the various characteristics. As long-term reliability of attenuation, We conducted, low temperature test (-40°C×2,000hr), high temperature test (+85 °C×2,000hr), wet heat test (85 °C×85%RH×2,000hr) , and temperature-cycling test (between -30 °C and +80 °C) by each temperature 12hr maintenance for 10cycles. The cord showed good results. As an example, Figure 7 shows a wet heat characteristic graph of the cord.

Table 2. Table of Evaluation Results

Item	Test Method and Condition	Results
Combustion test	Horizontal combustion under JIS C 3005	Passed
Flexural rigidity	Two-point bending method	25 N•mm²
Wet-heat deterioration of cord sheath	85°C×85%RH ×1 month	Retention of breaking elongation: ≥ 90%
Tensile test	Under tension of 30 N	Elongation: ≤ 1.0 %
Static friction coefficient	R: 60 mm, load: 50 gf	≤ 0.4
Temperature cycling	-10°C to +55°C×3 cyc.	Attenuation increase ≤ 0.01 dB/km
Bending	R15 mm×10 turn.	Attenuation increase ≤ 0.02 dB/turn.
Lateral-pressure	5 N/mm×1 min.	Attenuation increase ≤ 0.02 dB

measurement wavelength: 1.55 μm

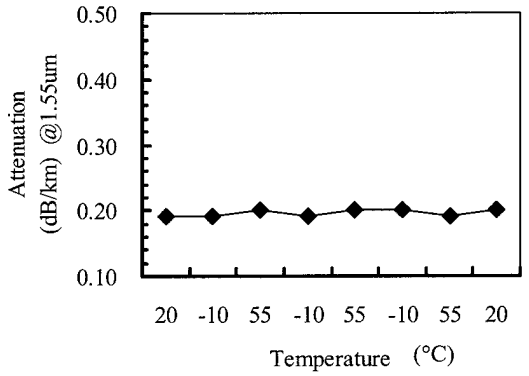


Figure 6. Temperature Characteristics of Ø1.1-mm Cord

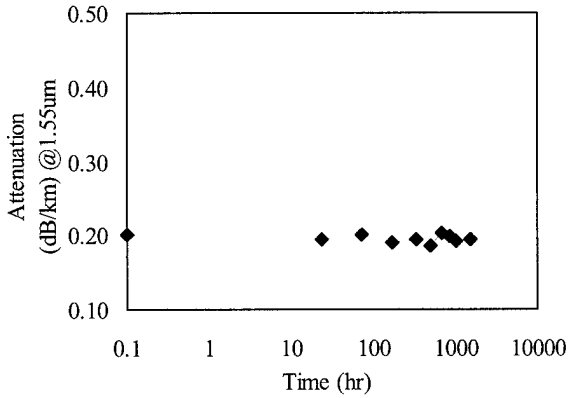


Figure 7. Wet-heat Performance of Ø1.1-mm Cord

3. Flame-Retardant Halogen-Free 1.7-mm Optical-Fiber Cords

The Ø1.1-mm optical-fiber cord discussed above was developed for the purpose of conducting the high-density wiring of 4,000 core of Ø1.1-mm cords. There are also other applications for conventional wiring sizes. The existing Ø1.7-mm optical-fiber cords employ a Ø0.9-mm silicone(Si)/polyamid(PA) buffered fiber. In addition, these cords use PVC as the jacketing material. In light of this, with the aim of alleviating the environmental effects, we sought to save energy in the manufacturing process by employing UV-hardened resins as the structural material of the fiber, and also to get rid of PVC by using halogen-free resins for the jacketing material.

3.1 Structures and Characteristics of Cords

Two different types of Ø0.9-mm buffered fiber were test-manufactured, one of which was a UV-resin(UV)/PA structure. We applied Ø0.4-mm UV-coated optical fiber to the buffer instead of Ø0.25-mm UV-coated optical fiber because of stability of a temperature characteristics. The other structure consisted of a Ø0.25-mmUVcoated/polyester elastomer (TPEE). This Ø0.9-mm buffered fiber was further bound using aramid yarn serving as a strength member, and was then jacketed using a halogen-free resin so as to have a final outer diameter of 1.7 mm. The resin used for the jacketing material had inorganic metal oxides mixed into its polyolefin base as a flame retardant. Figure 8 illustrates the structure of those cords.

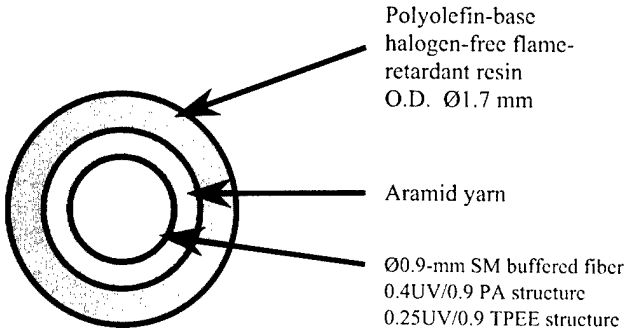


Figure 8. Cross-Sectional View of Prototype Cord

3.2 Comparison of Characteristics Among Different Buffered fibers

3.2.1 Lateral-pressure-resistance characteristics

Figure 9 shows the lateral-pressure characteristics of the individual buffered fibers, and Figure 10 shows those of the cord made of the buffered fibers. In each graph, the imposed load was plotted on the abscissa, and the transmission-loss increase was plotted on the ordinate. A lateral-pressure plate with a loading width of 50 mm was used in the test. While Figure 9 demonstrates that the TPEE buffered fiber is inferior in terms of its lateral-pressure characteristics to conventional buffered fiber and the UV/PA buffered fiber. Figure 10 reveals that, when formed into cords, both types of buffered fibers yield excellent lateral-pressure characteristics, with no significant difference resulting from the

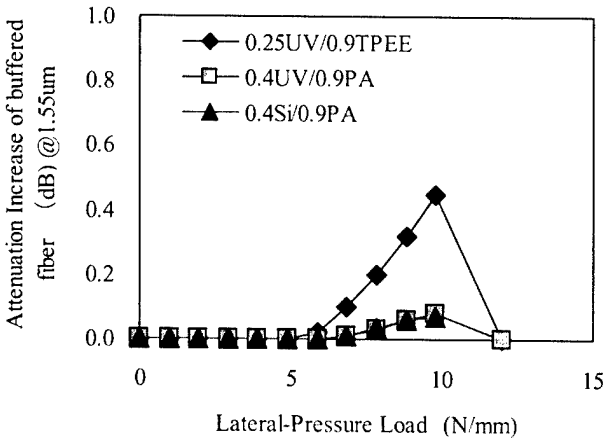


Figure 9. Lateral-Pressure-Resistance Characteristics of Individual Buffered fibers

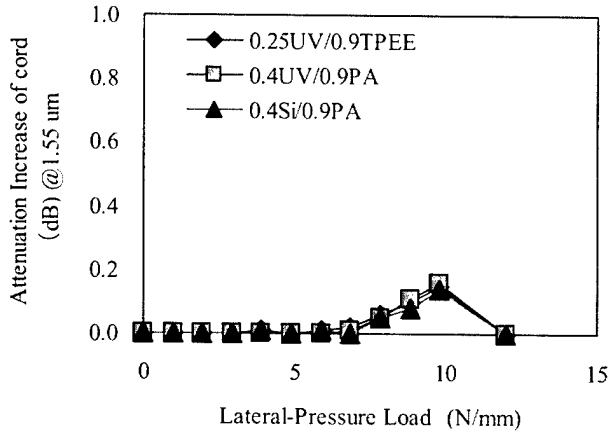


Figure 10. Lateral-Pressure-Resistance Characteristics of Cords

3.2.2 Temperature characteristics

The buffered fibers were exposed to temperatures of -40°C to +85°C, and the cords were exposed to temperatures of -20°C to +60°C, in three cycles, with the temperatures maintained for over 6 hours in each cycle. The measurement wavelength used for the test was 1.55μm. The UV-buffered fibers showed a good characteristics in a wide temperature range. On the other hand, the Si/PA buffered fiber showed high transmission loss at -40°C. The temperature characteristic after jacketing was good in both structure. Figures 11 and 12 show the mesurement results.

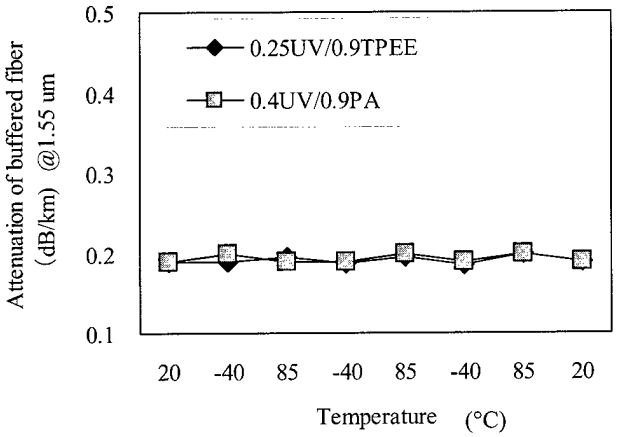


Figure 11. Temperature Characteristics of Buffered fibers

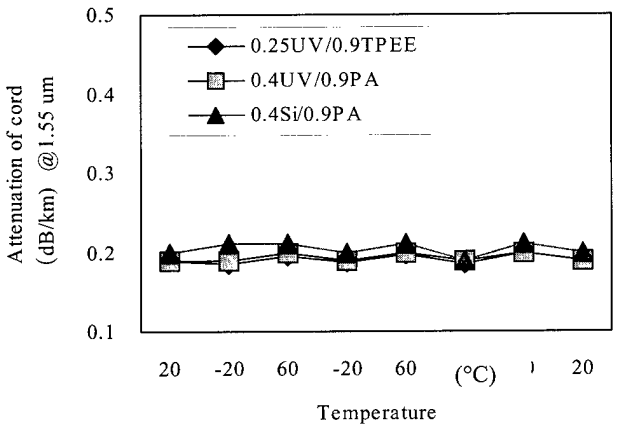


Figure 12. Temperature Characteristics of Cords

3.2.3 Other Characteristics

We also evaluated the sample cords with respect to their inter-process loss variation and tensile and combustion characteristics. Table 3 summarizes the relevant characteristic values. The results were satisfactory, and no difference arising from the structural differences in the Ø0.9-mm buffered fibers was observed. As long-term reliability of attenuation, We conducted, low temperature test (-40 °C×2,000hr), high tenmperature test (+60 °C×2,000hr), wet heat test (60 °C ×95%RH×2,000hr), and a temperature-cycling test (between -20°C and +60°C) by each temperature 12hr maintenance for 10cycles. The cord showed good results. As an example, Figure 13 shows a wet heat characteristic graph of the cords.

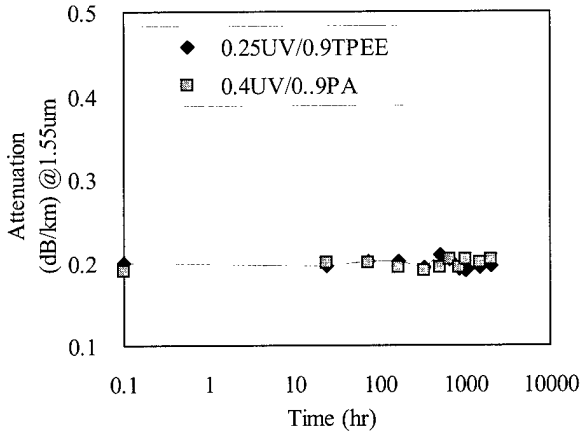


Figure 13. Wet-heat Performance of Ø1.7-mm Cord

4. Conclusions

Flame-retardant halogen-free optical-fiber cords with an outer diameter of Ø1.1mm were successfully developed. In the selection of the materials, the three parameters of flexural rigidity, side pull, and bending curls were taken into account from the viewpoint of handling characteristics.

For optical-fiber cords of the conventional diameter of Ø1.7 mm, the buffering structure was reviewed with the goal of saving energy in the manufacturing process, and their materials were changed to flame-retardant halogen-free materials.

These cords provide excellent features in terms of flame retardancy, various mechanical characteristics, temperature characteristics and long-term reliability.

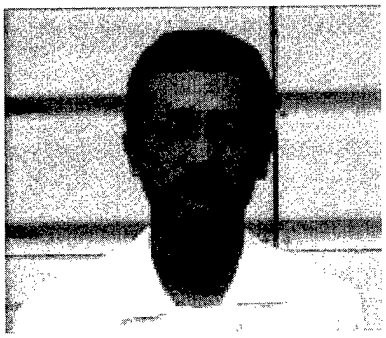
5. References

[1] M.Tachikura et al., IEICE2000, B- 10- 30

[2] M.Tachikura et al., OECC '97, p.526 (1997)

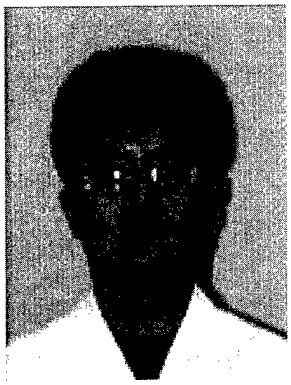
Table 3. Results of the Evaluation of Ø0.9-mm Buffered fibers and Ø1.7-mm Cord

Item	Test Method & Conditions	Unit	Evaluation Results			
			TPEE-Buffered		PA-Buffered	
			Buffered fiber Characteristics	Cord Characteristics	Buffered fiber Characteristics	Cord Characteristics
Inter-process loss	Measured by OTDR (@1.31μm / @1.55 μm)	dB/km	0.32/0.19	0.32/0.19	0.32/0.19	0.32/0.20
Temperature characteristics	Buffered fiber: -40°C to +85°C × 3 cyc. Cord: -20°C to +60°C × 3 cyc. (@1.55 μm)	dB/km	≤0.01	≤0.01	≤0.01	≤0.01
Lateral-pressure characteristics	Load settings Buffered fiber: 9.8 N/mm × 1 min. Cord: 4.9 N/mm × 1 min. (@1.55 μm)	dB	≤0.5	≤0.1	≤0.1	≤0.1
Tensile characteristics	Set stress: 68.6 N × 1 min. Loss increase (dB) (@1.55 μm) Elongation (%)	dB		0.00 0.45		0.00 0.45
Combustion characteristics	Horizontal Combustion Test Specified in JIS C 3005	—		Self-extinction		Self-extinction



Tetseo Hayano
R&D Dept.
Telecommunication
Cable Division
Fujikura LTD.
1440 Mutsuzaki,
Sakura, Chiba,
285-8550, JAPAN

He was born in 1963. He received the B.E. degree in electronic engineering in 1987 from Kyushu University. He joined Fujikura Ltd. after his graduation and has been engaged in research and development of optical fiber , thin cords and cables. He is now a manager of the Research and Development Department Telecommunication Cable Division and a member of the IEICE of Japan.



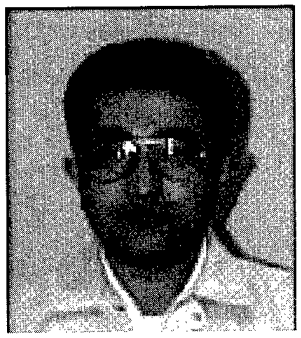
Osamu Kato
R&D Dept. Telecommunication
Cable Division
Fujikura LTD.1440 Mutsuzaki,
Sakura, Chiba,
285-8550, JAPAN

Osamu Kato graduated from Nagoya Institute of Technology with a B.C. degree in 1990. After six years of work as an engineer for material analysis, he has been engaged in research and development of optical fibers. He is now an engineer in the Telecommunication Cable Material Section and a member of the IEICE of Japan..



Toshio Takemyo
Telecommunications
Engineering Dept.
Telecoms & New
Media Division
Nishinippon Electric
Wire&Cable Co.Ltd.
Kasugaura,Oita-
shi,Oita,870-8632,Japan

He was born in 1968.He received the B.C. degree in Department of Applied Chemistry in 1992 from Oita University.
He joined Nishinippon Electric Wire and Cable Ltd. after his graduation and has been engaged in Material Development Group. He is now a Development Engineer of Material Development Group.



Tsuyoshi Shimomichi
R&D Dept.
Telecommunication
Cable Division
Fujikura LTD.
1440 Mutsuzaki,
Sakura, Chiba,
285-8550, JAPAN

He was born in 1960. He joined Fujikura Ltd. after his graduation from Nagasaki University in 1986 with an M.C. degree and has been engaged in research and development of optical fibers and optical fiber coatings. He is now a manager of the Research and Development Department Telecommunication Cable Division and a member of the IEICE of Japan.



Keiji Oohashi
R&D Dept. Telecommunication
Cable Division
Fujikura LTD.
1440 Mutsuzaki,
Sakura, Chiba,
285-8550, JAPAN

He was born in 1956. He graduated from the Tokyo Institute of Technology in 1980 with a B.C. degree in chemistry. After eight years of work as an engineer in the field of materials for motor vehicles, he joined Fujikura LTD. in 1988. He has been engaged in research and development for optical fibers and optical fiber coatings. He is now a general manager of the Research and Development Department Telecommunication Cable Division and a member of the IEICE of Japan.



Matsuhiro Miyamoto
R&D Dept. Telecommunication
Cable Division
Fujikura LTD.
1440 Mutsuzaki,
Sakura, Chiba,
285-8550, JAPAN

He was born in 1953. He graduated from Nagoya Institute of Technology with a B.E. degree of electrical engineering. He joined Fujikura Ltd. after his graduation from Tokyo Institute of Technology with a M.S. degree in 1978 and has been engaged in research and development of optical fiber and optical fiber cables. He is now a general manager of the Research and Development Department Telecommunication Cable Division and a member of IEICE in Japan.

Creep Behavior of Buffer Tubes

Ernst Opel, Andreas Stingl and Oliver Herrgesell
Corning Cable Systems
Neustadt, Germany
+49 9568 932140 · email address: Ernst.Opel@corning.com

Abstract
The cable industry is used to cable tests specified in IEC 60794 - 1-2-E3 (1999), describing especially the crush test of cables under lateral load. Basically, the cable crush performance is defined by the crush performance of the cable design and its components. Considering non-armored cables, the buffer tube lateral stiffness plays a key role with regards to crush resistance. Various papers have been published dealing with the crush performance of tubes. Most of them focus on dimensions and structural stability, neglecting time dependent effects. From our point of view, the time dependent modulus is very important at medium and high crush loads with regards to lifetime and cable stability. Therefore, these investigations were undertaken to get a basic understanding of the crush resistance of buffer tube cables taking into account the phenomenon of nonlinear creep.

A test apparatus for measuring the time dependent material creep as well as the resulting buffer tube creep behavior under lateral load was set up. Furthermore, a finite element model was developed for investigating the evolution of creep strains under load as a function of time. This model was also used for predicting the amount of creep as a function of time.

We found good correlation between the theoretical approach and the measured data.

Keywords
Buffer tube, creep, finite element analysis (FEA),crush test

1. Introduction
Creep is a complex material phenomenon, dependent on a wide range of constraints and parameters such as, stress distribution, polymer orientation, load history, aging and the amount of time elapsed under load, just to mention the most important. Under medium and high loads, the short term creep rate is much higher than the long term values, approaching long term linear creep rates until material deterioration occurs.

Using a measurement setup (see section 3) with high accuracy gave us insight into the creep behavior of the buffer tubes. However, sometimes the results were confusing and not easy to understand. Therefore, we felt the need for a thorough approach on a theoretical basis.

Considering buffer tube crush at medium and high loads, we observed tube deformation to a significant extent. This tube deformation has to be considered as a geometric nonlinearity from the structural point of view, with a stress distribution ranging from compression to strain.

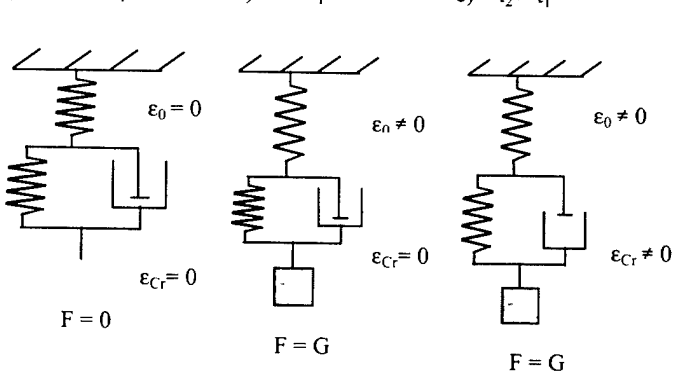
Since creep is a stress- and time dependent phenomenon, we add another time dependent nonlinearity to the geometric and structural nonlinearity of the crush problem coupling structural and time dependent nonlinear effects..

In order to find a good approach to the crush problem, covering all these nonlinearities, we decided to use an implicit finite element model which implemented our measured material data.

2. Basic Theory
2.1 Voigt Kelvin Model
Creep or viscoelastic behavior is typical for many synthetic materials. We can find a very simple definition for the phenomenon of uniaxial creep.

Creep defines the time dependent strains of a uniaxial body under constant axial load.

A more scientific description of this phenomenon can be found in the so-called Voigt Kelvin Model [3].



a) $0 < t < t_1$, $F = 0$, $\sigma = 0$, $\varepsilon = 0$, $\varepsilon_{Cr} = 0$; $\varepsilon_{ges} = \varepsilon_0 + \varepsilon_{Cr} = 0$;

b) $t = t_1$, $F = G$, $\sigma = \sigma_0$, $\varepsilon \neq 0$, $\varepsilon_{Cr} = 0$; $\varepsilon_{ges} = \varepsilon_0 + \varepsilon_{Cr} = \varepsilon_0$;

c) $t_2 > t_1$, $F = G$, $\sigma = \sigma_0$, $\varepsilon \neq 0$, $\varepsilon_{Cr} \neq 0$; $\varepsilon_{ges} = \varepsilon_0 + \varepsilon_{Cr} > \varepsilon_0$;

Figure 1. Voigt Kelvin Model

Figure 1 illustrates the creep behavior of a typical polymer in the Voigt Kelvin model. This theoretical model describes the material behavior by simplifying it to three elements, i.e. two spring elements and a damper. Whereas the spring element represents the linear elastic portion, the damper describes the time dependent behavior of the material. One of the spring elements is connected parallel to the damper.

This spring damper element combination is further serial connected to another single spring element, which represents the instantaneous elastic portion of the polymer. One end of the whole spring-damper element structure is anchored. On the opposite side we apply an imaginary load as described in the load history below.

Figure 1a) shows the initial system configuration, with no load applied, therefore the strains as well as the tensions and creep values are zero.

Figure 1b) represents the moment of material loading, in this case applying an instantaneous constant weight to the spring damper system. This weight generates a constant tension and an elastic strain. Further, as no time has elapsed yet, we don't observe elongation of the damper element representing the creep portion of the system.

Figure 1c) depicts the system with constant load and a certain amount of loading time elapsed. Due to the time dependent damper stiffness, which is a basic property of damper elements, we observe a progressive elongation of the spring damper system as a function of time.

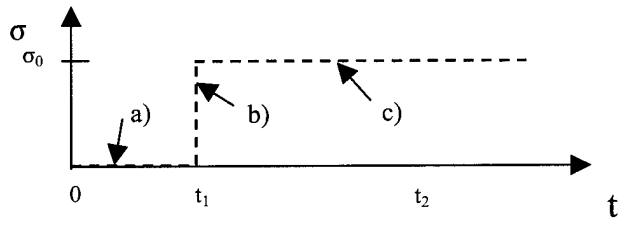


Figure 2. Voigt Kelvin (load history)

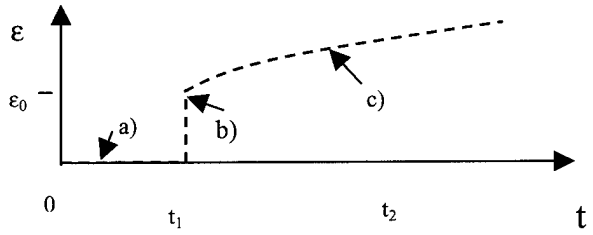


Figure 3. Voigt Kelvin (resultant strain)

The figures above illustrate the loading process as well as the strain response of the Voigt Kelvin model graphically. The loading function is a simple heaviside step function. The response function of the Voigt Kelvin model is similar in shape until the time t_1 is reached.

For times beyond t_1 the trace is totally different due to the damper influence, depicting the typical shape of a uniaxial creep strain curve. The damper can't store energy, but dissipates the energy as a function of time. Therefore we observe nonlinear strains as a function of time.

Based on the ideas of the Voigt Kelvin model we characterized some typical buffer tube materials.

The case of relieving the material after loading is not considered in this paper. Therefore the three element Voigt Kelvin model is sufficient for material description. For considering material behavior in the process of relief with residual strains a four element creep model, as described in [4] is the best choice.

2.2 Material Law

2.2.1 General approach

Creep, even uniaxial creep, is a complex phenomenon dependent on a series of boundary conditions or test parameters, including temperature, amount of load, strain rate and time. Furthermore, it is very important to stay below the material's yield limit in order to avoid material deterioration, especially when considering amorphous polymers, which tend to crazing at high tensile load. Material deterioration, like crazing, further effects like plasticity are different phenomenon, not considered in this paper, as the focus of this paper is buffer tube creep.

Taking into account these thoughts, it makes sense to use a creep differential equation as follows:

$$\frac{\partial \varepsilon(t)}{\partial t} = \dot{\varepsilon}(t) = C_1 \cdot \sigma^{C_2} \cdot \varepsilon(t)^{C_3} \cdot e^{-C_4/T} \qquad \text{f 1)}$$

Where

- C_1, C_2, C_3, C_4 denote constants typical for different materials
- $\varepsilon(t) \xrightarrow{\frac{\partial}{\partial t}} \dot{\varepsilon}(t)$ strain and strain rate
- T: Temperature
- σ: applied stress

Considering a uniaxial creep experiment (Chap. 3), this differential equation provides a reasonable approach for deriving a numerical material description. Under uniaxial load the stress σ is constant in the whole structure under test. Using this fact we transform the differential equation f1) into a simple recursive formula as follows:

$$\frac{\partial \varepsilon(t)}{\partial t} = C_1 \cdot \sigma^{C_2} \cdot \varepsilon(t)^{C_3} \cdot e^{-C_4/T} \xrightarrow{\partial \to \Delta} \frac{\Delta \varepsilon(t)}{\Delta t} = C_1 \cdot \sigma^{C_2} \cdot \varepsilon(t)^{C_3} \cdot e^{-C_4/T}$$

using equidistant time steps and transforming again we get:

$$\Delta \varepsilon = C_1 \cdot \sigma^{C_2} \cdot \varepsilon(t)^{C_3} \cdot e^{-C_4/T} \cdot \Delta t$$

and in a recursive formulation

$$\Delta \varepsilon_{n+1} = C_1 \cdot \sigma^{C_2} \cdot (\varepsilon_n)^{C_3} \cdot e^{-C_4/T} \cdot \Delta t \xrightarrow{with} \varepsilon_n = \varepsilon_{n-1} + \Delta \varepsilon_n$$

Deriving the strains ε from uniaxial measurements with constant stresses, this recursive formulation allows us to fit the strain function ε_n to the measured data by varying the parameters C_1, C_2 to C_4 until optimum coincidence between strain and measurement is reached.
In order to have a reliable basis for this approach, we developed a measurement setup to measure uniaxial creep data. Generating measurement data for a range of constant uniaxial loads (Chap. 3), we got a bundel of creep curves. Fitting our parameters C to these curves and considering σ as a parameter in f1) we derived a reliable material description in the range of material stresses σ expected.

3. Basic Measurement Equipment

3.1 LMG – tensile test apparatus

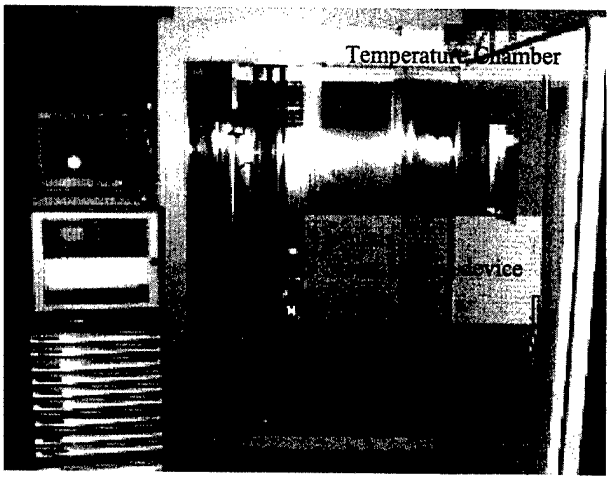


Figure 4. Tensile Test apparatus

Figure 4 depicts a general overview of the tensile test apparatus. As we are considering long term material response, the length measurement unit of the system has to be thermally stabilized, which in our case was done with a temperature chamber. The signal from the sensor is hooked to the computer as well as the elapsed time.

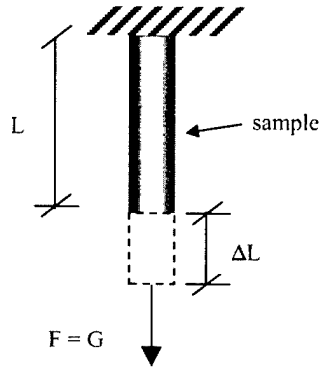


Figure 5. Tensile test (schematic)

The sample, fixed at the upper side, with a sufficient sample length L is charged with the load F at the free end of the sample. The elongation Δl is measured with the apparatus described above and hooked to the computer. Afterwards the time dependent sample strain $\varepsilon(t)$, defined by $\varepsilon(t) = \Delta L/L$ is calculated. Taking into account the cross-section of the sample, the modulus can be calculated with the help of the formula $E(t) = F/(A \cdot \varepsilon(t))$. From the measured time dependent strains, a time dependent modulus was derived. By taking the diameter's tolerance into account, we find an upper and lower limit for the tube cross-section A_t.

3.2 Uniaxial material measurement data.

We measured the creep behavior of several tube and cable materials with our apparatus. In this paper we focus on typical buffer tube materials.

In order to measure the time dependency we charged the materials with different weights, starting with 5 kg up to 10 kg. These are loads which are quite high with regards to modulus loading, but in order to avoid plasticity effects, we made sure not to load more than 70% of the material yield stress limit.

All the values were determined for room temperature, i.e. 23 °C.

Creep test 20 MPa:

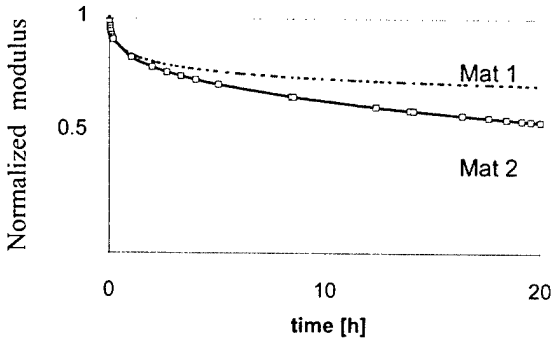


Figure 6. Time dependent modulus for Mat 1 / 2

Figure 6 shows the time dependent modulus exemplary for two of our tested materials, called mat 1 and mat 2, measured and calculated as described in 3.1 for fresh extruded material. For convenient comparison only one trace (one weight) is plotted for each material.

Both traces show the typical creep behavior with decreasing modulus as a function of time, exemplary for one tensile load in each case. Comparing both materials, it can be seen, that Mat 1 has a somewhat higher elastic modulus and a smaller creep rate, causing the small slope of the modulus curve in between 10 to 20 hours. Therefore Mat 1 has a better resistivity against creep.

Taking into account further measurements at different weights, a bundle of traces is derived, representing the material creep behavior over a wide range of constant stresses.

4. Cable Modeling

4.1 Finite Element Solid Model

As described above, the derived material data and the load specific modulus have been used to generate a basic material law as input for a finite element model in order to investigate the tube creep behavior under lateral load.

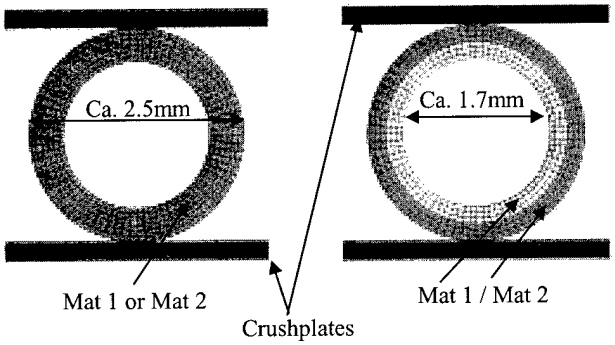


Figure 7. Symmetry expanded 2D FE Models

Figure 7 shows the Finite Element models we developed to investigate the buffer tube creep behavior under crush load. Of course we used the symmetry of the cross-section to reduce CPU time, but for a better illustration the models have been symmetry expanded to the full cross-section size. The tubes have an inner diameter of about 1.7mm and an outer diameter of about 2.5mm. On the left side of Figure 7 we see a standard single layer tube consisting of Mat 1 or Mat 2. On the right side we see a composite Mat 1/ 2 tube. The 2D cross-section model consists of 151 nodes and 121 elements. In order to investigate crush plate edge effects on the buffer tube creep, we also developed a 3D model.

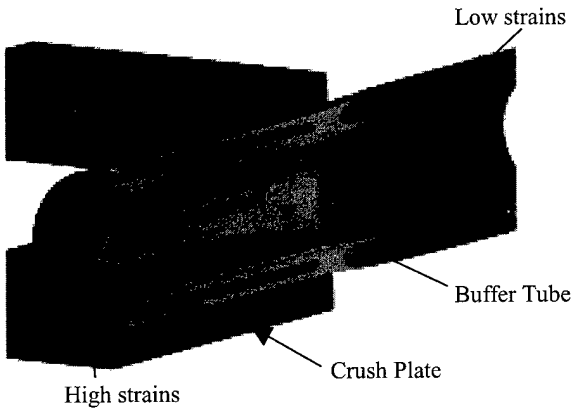


Figure 8. 3D FE Model

Figure 8 shows the 3D model cut axially and vertically with an additional overlay of resultant strains.

For an easier discussion we switch back to a 2D description representing a cross-section axial in the middle of the crush plates.

4.2 Creep under load

In our investigations we used constant lateral pressures $P = F/A_P$ in the range of 0.1 MPa to 1 MPa as crush plate boundary condition. Where A_P denotes the crush plate cross-section.

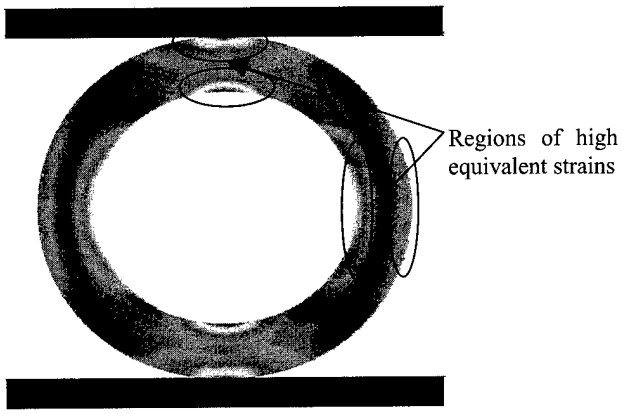


Figure 9. Tube under 0.5 MPa lateral pressure

Figure 9 shows the overall strain distribution in the cross-section under 0.5 MPa lateral pressure after 200 h of constant loading. On the gray scale bright colors depicting high strains, dark colors depicting low strains. We observe maximum strains of up to 2.5%. During the 200 hours of loading we observe a progressive development of ovality.

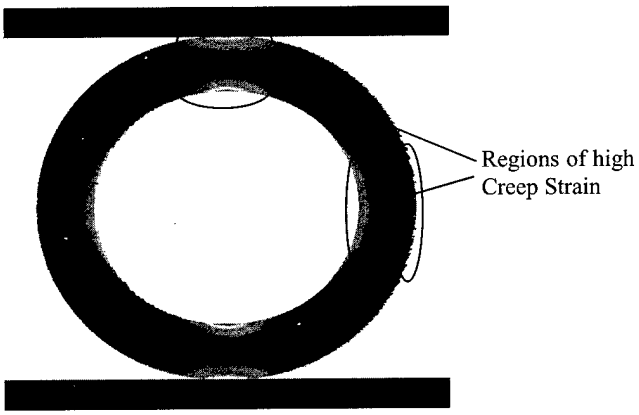


Figure 10. Creep strains(0.5 MPa / 200 hours)

Figure 10 depicts the mere equivalent creep strain portion after 200 hours of constant loading with 0.5 MPa pressure. We observe a maximum of up to 0.5% creep strain occurring in areas of the cross section where high elastic strains occur. (comp. Fig. 10) Another goal of our investigation was to compare the crush behavior of single layer tubes consisting of different material to composite double layer tubes with regards to creep.

5. Measurement of Tube Creep

5.1 Measurement Setup

In order to measure tube creep under lateral load, it was necessary to modify the length measurement unit (compare Section 3) as described below.

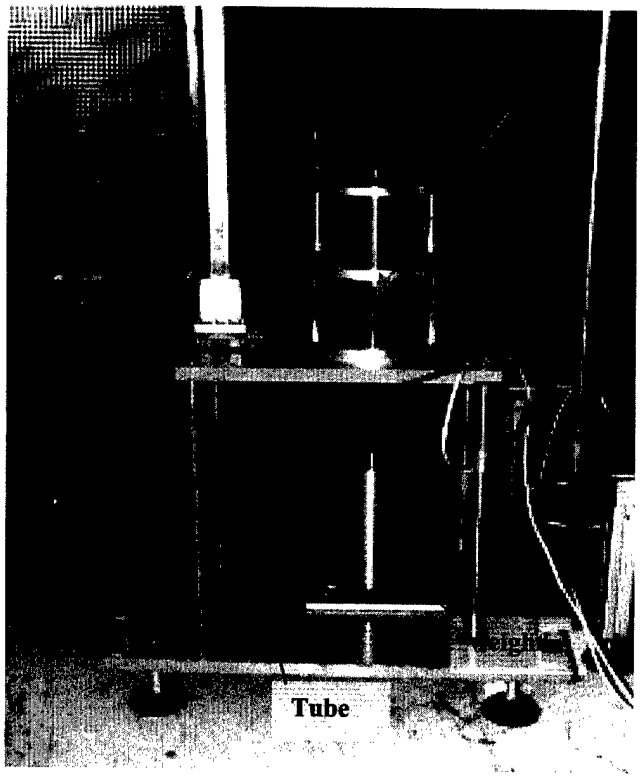


Figure 11. Measurement setup for tube creep

Figure 11 shows the modified length measurement device. The positions of weights, samples and sensors were changed to switch from tensile loading to lateral loading. Again, as described in section 3, the apparatus was temperature stabilized and hooked to the measurement computer.

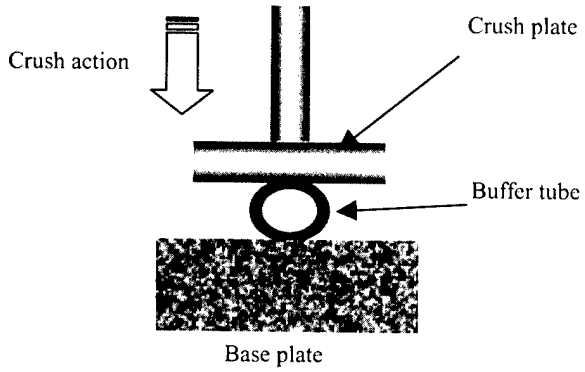


Figure 13. Measurement setup (schematic)

5.2 Reference Calibration

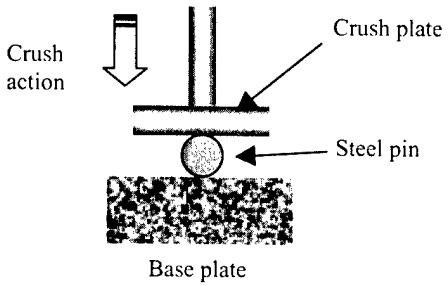


Figure 13. Reference measurement setup

Figure 13 shows the setup to check the systematic error and the measurement accuracy of the length measurement device. For reference, we used a steel pin made of the same material as the basis plate and rack. With ten cycles at test conditions equal to the buffer tube measurement, we found a systematic error of 0.01 mm. For evaluation of all measurement results, this factor has been taken into account.

5.3 Measurement Results

We used the apparatus described in section 5.1 on our different tubes, i.e. single layer Mat 2, single layer Mat 1 and a double layer composite tube of material 1 and 2. "FEA 2" results in max. buffer tube thickness, "FEA 1" results in the the smallest one.

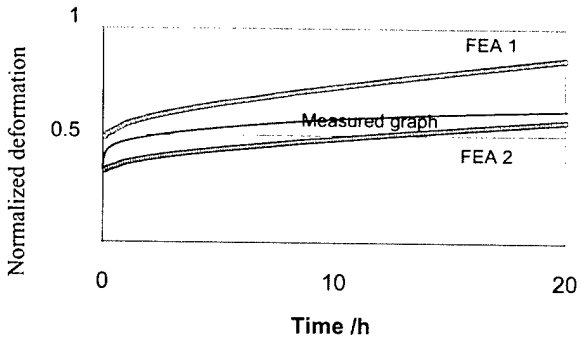


Figure 14. Crush test result of Mat 2

Figure 14 shows the deflection in arbitrary units versus time in hours of a tube consisting of material 2 under 0.5 MPa lateral pressure. The graph depicts three curves defining a span of about 0.15-0.25 digits from lower to upper boundary. The measurement data is well in between these boundaries, which have been calculated using the finite element approach described in section 4. The span in Figure 14, as well as in the graphs below, is caused by the buffer tube wall thickness and diameter tolerances.

As we had no chance to measure the tube dimensions before or after the experiment without cutting the sample, we have to rely on statistics by making several cuts along the buffer tube sample, measuring the tube diameters under a macroscope. We evaluate the worst case, which is actually measured maximum and minimum dimensions, as we don't know the exact diameter of the tube portion under the crush plate.

Alternatively, we could have conducted the crush experiment several times and made a crush test statistic. But due to the amount of time needed, this would have been an impractical solution.

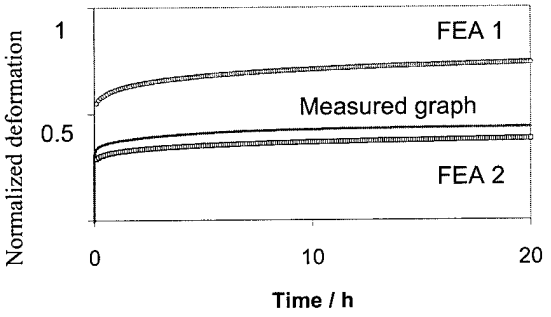


Figure 15. Crush test result of Mat 1

Figure 15 shows the measurement result of a tube consisting of Mat 1. This material has a somewhat better resistance with regards to creep at the used load. This is caused by the somewhat higher elastic modulus, as well as the fact that we are well below the yield limit. Furthermore we are using fresh, unaged material.

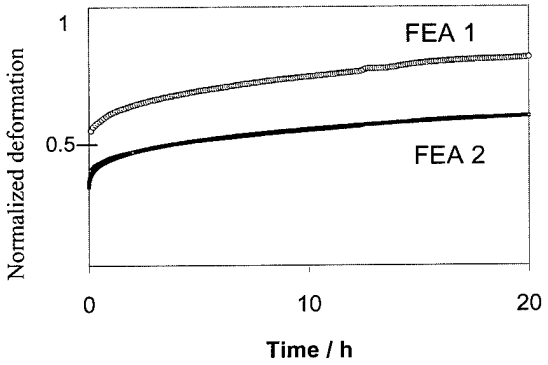


Figure 16. Crush test result of Mat 1 / 2 tube

Figure 16 shows the Crush test result for a double layer tube, consisting of materials 1 and 2, the measured graph and the finite element trace for maximum tube thickness (FEA 2) is nearly the same. Due to the high modulus and good creep properties of Mat 1, the dual layer tube benefits form the presence of this material layer.

6. Conclusion

- The various materials under investigation showed a different creep behavior.
- Buffer Tube Creep under lateral load is a significant factor with regard to medium and long term cable stability under lateral load. This effect could be monitored on cabled fibers, by using the fiber as a sensor.
- The developed method is well apt to determine appropriate materials for applications with long term hydrostatic or lateral loads, like suspensions, pipe or submarine cable applications.
- With the developed recursive numerical creep law approach, it is possible to make reliable predictions of time dependent tube crush, also in the short and medium time range on the basis of a general creep law.
- The tolerance of wall thickness has a significant influence on the resultant tube creep and should be as small as possible.
- Buffer tubes suffer deformation due to long-term creep. This deformation can affect the performance of fibers within the buffer tube, and must be accounted for in cable design.

7. References

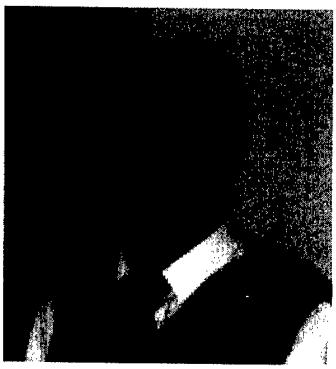
[1] Herrgesell Oliver
Diplomarbeit
Corning 2001

[2] Verein Deutscher Ingenieure
Nichtlineare Berechnungen mit finiten Elementen
VDI-Haus Stuttgart 1997

[3] Hans Batzer
Polymere Werkstoffe
Georg Thieme Verlag
New York 1985

[4] Hasset, Parson, Wagman
"The effect of viscoelastic material properties on optical fiber cable"
46th IWCS, 156pp

Speakers Biography



Ernst A. Opel
Corning Cable Systems
96465 Neustadt Coburg
Germany

Ernst A. Opel was born in Völkenreuth in 1959. He received his Dipl.-Ing.(FH) in Feinwerktechnik from the Georg-Simon-Ohm-FH in Nürnberg in 1987. He joined the RD&E group in Neustadt in 1988 and is presently the manager of the Product Evaluation group. He has authored and co-authored several papers.

Email: Ernst.Opel@corning.com



Dr. Andreas Stingl
Corning Cable Systems
96465 Neustadt Coburg
Germany

Andreas Stingl was born november 1970. He joined Siemens RD&E in 1996, he received his physics degree from the university of Bayreuth in 1997. He worked on his PHD, considering numerical models for cable simulation from June 1997 until February 2000. He is now responsible for FE simulations at RD&E Corning Cable Systems, Neustadt / Coburg.



Oliver Herrgesell
Corning Cable Systems
96465 Neustadt Coburg
Germany

Oliver Herrgesell was born in Kronach in 1973. He received his Dipl. Ing. (FH) in Maschinenbau from the Fachhochschule Coburg 2000. He joined the RD&E group in Neustadt in 2000 for writing his student thesis about creep behavior of buffer tubes.

A Genetic Algorithm Toolkit for Cable Design

Hugh G. Sasse, Benjamin G. Tunstall, Dawn E Coleby, Mohammed M. Al-Asadi, Alistair P. Duffy, Kenneth G Hodge* & Arthur J. Willis*

Dept. Engineering & Technology, De Montfort University
Leicester, Leicestershire, LE1 9BH United Kingdom
+44 (0) 116 250 6157

* Brand-Rex Limited, Viewfield Industrial Estate
Glenrothes, Fife KY6 2RS, Scotland

Principle Contact: E-mail hgs@dmu.ac.uk

Abstract

The multi-variant nature of the design of communications cables magnifies the difficulties in obtaining single 'best' solutions. In fact, there may be many combinations of design factors which give rise to optimal performances but no single optimum. In order to obtain these optima, techniques to avoid testing all combinations of all variables are required to enable finite, convenient, design cycles. This paper extends previous work on Genetic Algorithms (GAs) in cable design by presenting increased flexibility in the design of the GA implementation. The paper also demonstrates how the quantity and quality of parameters included in the problem and solution spaces affect the results obtained. Using analytical, simulation and subjective metrics, the approach is validated using the design of twisted pair cables

Keywords

Optimization; Heuristics; Genetic Algorithms; UTP; TLM; Statistics;

1. Introduction

Modern design problems are, by nature, multi-variant. This leads to their solutions being very difficult to find analytically. To provide a more efficient solution of such problems a number of heuristic algorithms have been developed, which are amenable to computerization. Such techniques provide a 'short-cut' to a solution based on a heuristic ("rule-of-thumb"). Indeed they can be made problem independent by the use of symbols describing the problem (normally one such symbol per dimension, or parameter) so that any of a wide-range of similar problems can be solved by the use of the same symbols. Through the evaluation of this heuristic it is possible to search any multi-variant problem space for a solution that satisfies any number of user requirements. These requirements may be described quantitatively, such as a dimension or weight, or qualitatively and subjectively, such as acceptability of a color. A number of such technique have been developed that can be categorized into two solution methodologies:

- Neighborhood searches
- Global searches

The algorithm of Simulated Annealing [1]that attempts to minimize an objective fitness function (this being the link between the problem space and the specific requirements) typifies the 'Neighborhood' techniques. These techniques depend upon a 'smooth' problem space where a small perturbation in any of the problem descriptors does not produce a sudden change in the result of the function of those descriptors. This can be thought of as being a relatively smooth landscape where steps taken across the landscape do not produce a large step in the height above a reference plane (e.g. sea level). The different neighborhood algorithms describe how the steps should be taken in order to find the lowest (or highest) point in the landscape, without reference to global information about the landscape. An analogy would be trying to walk to the lowest/highest point in a terrain you don't know whilst shrouded in thick fog. However the techniques do have a number of difficulties associated with them in terms of the neighborhood size (the maximum possible step) and the presence of local, sub-optimal, minima. The problem of local minima is reduced by the use of (in Simulated Annealing) a probabilistic movement 'up' the landscape, so that less good solutions will be accepted to allow exit from some local minimum in the hope that a better minimum will be found.

These are contrasted with 'Global' search techniques such as the Genetic Algorithm [2], [3]. This technique permits the searching of the entire problem space (landscape) by starting with a number of potential solutions. Initially, these are simply guesses chosen at random. These guesses are combined and mutated in a manner that is analogous to that of Darwinian evolution in biological systems such that as the process iterates over a number of 'Generations' the population evolves towards the optimal solution within the defined landscape. Such techniques do not therefore depend upon an idea of 'neighborhood' and so can be used for any number of landscapes including those with discontinuities in 'altitude' across a small region; for example, there may be a sharp transition between an acceptable and unacceptable solution.

This paper reviews the operation of Genetic Algorithms and describes the design of a toolkit. Its utility is demonstrated using a model of a cable with varying parameters along its length. The modeling was done using the 1-D Transmission-Line Matrix (TLM) method [4].

2. The Genetic Algorithm

Our earlier work [5] has demonstrated the flexibility presented by the use of Genetic Algorithms (as illustrated in Figure 1) in communication cable design. However, the problem chosen was relatively straightforward in so far as it could be expressed in a few equations and while demonstrating the operation of GAs, lacked the contentious issues present in practical design exercises. In practice, manufactured objects have dimensions, which should fall within specified tolerances, rather than possessing single, absolute, dimensions. For example, the thickness of conductors in a cable will vary a little along its length. Mathematical analysis of such a situation becomes more difficult, and forms of simulation are to be preferred in such cases.

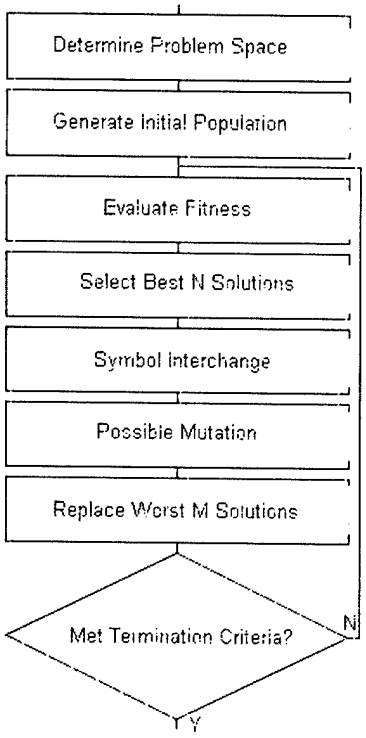


Figure 1. Flow diagram indicating the organization of a generalized Genetic Algorithm

The first step in the implementation of a GA solution is potentially the most important as it determines those parameters (represented as 'Genes') that can be manipulated to provide the optimal solution. For example when choosing parameters for the design of an unshielded twisted pair (UTP) cable; one may include the lay-lengths of each individual pair of wires as parameters that can be manipulated.

An initial population of random solutions (guesses) is then created. If there were sufficient initial guesses, and they were truly random, this set of guesses would reflect the statistical properties of the solution space. This provides the first generation of potential solutions and as such may provide the optimal solution, but subsequent analysis will reveal this.

The fitness' of the current generation members are then evaluated. This provides a measure of the effectiveness of the solutions. The fitness function can be a combination of a wide range of functions including the results from simulations, such as TLM modeling of overall cable performance under any number of conditions.

The better solutions from the current population are then selected for breeding, the worst being replaced by the resulting offspring. This provides for survival of the fittest only, by eliminating the weakest. The breeding is done by exchanging corresponding symbols between pairs of the selected population members. This explores the search space to ensure that all regions of the problem space are investigated for potential solutions. Thus the technique avoids problems such as local minima that hinder neighborhood search techniques. A prerequisite is to ensure randomness of the exchanges and avoid hidden patterns of events.

To enhance the search the newly created population members may be subjected to mutation. This is principally to prevent the population converging on a sub-optimal solution, where the population is "saturated" with one solution type. It also expands coverage of the search space by accessing those parts that cannot be reached by symbol exchange alone.

The fitness determination, selection, breeding and replacement processes are then repeated any number of times so that the population will converge on the best solution available within the problem space. Further checks can be made against the number of generations evaluated as a test for non-convergence.

3. Statistics Overview

In order to have confidence in the results of the GA, some measure is required to indicate that the solution obtained is optimal. The obvious way of finding the best solution is an exhaustive search, examining all points in the solution space in order to ensure that no optima have been missed. This would be slow and computationally intensive, otherwise heuristic techniques would not be of interest.

We know little about the fitness landscape except the fitness results from the first generation (initial guesses). Therefore we are in position of reasoning about a large population (of solutions) when we can only investigate the properties of a small sub-population, i.e. we have a sample of a large population and so, with appropriate reasoning, we are able to assess the probability of an optimal solution.

Let us first assume that the fitness landscape (although complicated) has a Gaussian distribution of fitness values. Thus from any random sample it will be possible to provide an estimate of the mean and standard deviation of the fitness expected from the entire problem space. This can only be provided by the initial population members because the later generations will be skewed towards the fitter solutions and therefore not representative of the whole population of potential

solutions. After the Genetic Algorithm has done its work, and a best fitness is produced, we can see where this fitness lies on the distribution used to model the population as a whole. We can then make assertions from the model about the statistical confidence of the optimality of the solution.

In order to test the validity of the generated designs a confidence interval is required on the mean of the random sample (obtained at Generation 0). This is needed, as we cannot be certain that the sample mean is equal to the mean fitness of the entire population (i.e. the solution space). The worst case would be if the mean of the population is bigger than it first appears, because this would shift the whole Gaussian to the right, meaning that there would be more solutions with the same fitness as our best fitness. To ensure the worst case it was decided to use a 99% confidence interval (giving bounds within which we are 99% certain that the overall mean fitness lies). Using Robson [6]

$$std = \sqrt{\left(\frac{\sum x^2 - \left(\frac{\sum x \times \sum x}{Samples} \right)}{Samples - 1} \right)} \quad (1)$$

and Rees [7]

$$EstimatedMean = \bar{x} + t \times \left(\frac{std}{\sqrt{Samples}} \right) \quad (2)$$

where t is 2.358 (from table D5 in [7], which is the 99% confidence level for a sample size of 120 -- the nearest value in the table to our 100.) So that the best possible fitness is likely to be:

$$BestFitness = EstimatedMean + 2 \times std \quad (3)$$

4. Toolkit Design

In order to maximize the utility of the GA toolkit it was decided to provide a fully modular system that could be used over a wide range of platforms using a command line interface. This maximizes the ability to use the toolkit whilst encouraging the automation of the process using tools such as Expect [8]. In order to achieve a modular design it was necessary to separate as much of the functionality as possible into a number of user-definable files that could be used as required. Such a distribution of functionality reduced the central program (the actual 'toolkit') to the form of an interpreter whose operation is determined by tokens present in the problem specific description files.

In order to describe any problem it was decided to define the toolkits operation in the form of 6 ASCII files. These provide the information necessary to optimize any given heuristic, the files describing:

- The problem space (including any constraints on solution parameters)
- The fitness function(s)
- The selection methodology
- The breeding mechanism
- The mutation rate
- The completion criteria

The exact information stored within each file is dependent upon a number of defined tokens that indicate the user requirements. A typical example of such a file is the completion criteria that has a number of tokens indicating:

- Completion defined by uniform fitness
- Termination due to limited diversity
- Termination of the simulation based on excessive generations

To further permit modularity the population used by the algorithm was stored in a separate database structure. This structure (hidden from the user) permits the creation of dynamic storage structures, as required by the problem under investigation. As well as separating the data storage from the data manipulation the use of ANSI SQL permits the detection of, and recovery from, a wide range of fault conditions (such as connection failures) that may occur when the toolkit is used over a network.

The toolkit has been implemented using GCC 2.95.3 and MySQL 3.23.22 on a Pentium III based machine running Red Hat Linux 7.0. The machine is networked thus centralizing the storage of results and parameter description files whilst permitting the access required by users on other local machines.

5. Preliminary Results

A number of tests were performed to indicate the operation of the toolkit. Each test was carried out using a statistically large population of 100 genomes (guesses). These were selected using the technique of Tournament Selection [9]. In this technique pairs of genomes are selected and their optimality is compared. The more optimal member of each pair being selected for breeding. The technique does not require knowledge of the fitness distribution across the whole population and so is amenable to the use of local sub-populations. The lack of global knowledge furthermore reduces the time required for the selection method. Following selection the genomes were subjected to symbol exchange using Single-point Crossover [3], the simplest of the 'breeding' methods. Newly created population members were then 30% likely to be mutated. This relatively high mutation rate is indicated for when real numbers are used

as alleles [10]. This is doubly true as the symbolic exchange method was prevented from perturbing parameters so as to avoid any possible constraint violations; i.e. a random exchange of bits across two alleles (which are, of course, binary representations) may results in an unacceptable value. Termination was set at 1000 generations, this being arbitrarily selected due to time constraints (see Section 5.5).

The following tests add confidence to the basic operation and then address the issues of which variables should be included in a general design analysis and what effect these are likely to have on the overall result.

5.1 Basic Functionality

Whether or not the system was capable of minimizing the resistance of a unit length piece of material with rectangular cross-section and fixed conductivity (σ) was used as a simple test of the GA's operation. The options used were:

- 0.4 <= Width <= 0.8
- 0.4 <= Height <= 0.8
- Fitness, maximize: width * height * σ

This over-simplified test worked correctly in that the optimal size (0.8 * 0.8mm) was successfully obtained. Any alternative would have been indicative of the algorithm incorrectly processing the fitness function result. Optimization occurred in less than 1 minute for this (1000 generation, 100 genome) case.

5.2 Optimization of Z_o

A more realistic test was then undertaken, the optimization of a multiple-pair cable with the basic configuration of a CAT 5E UTP cable. The draft standard [Willis, personal communication re: prEN50288-3-1] determine that the individual conductors have a diameter of between 0.4 and 0.8mm (inclusive). The overall sizing was preferentially limited at 5mm OD due to manufacturing requirements [Hodge, personal communication]. The cable optimization (fitness) function was a balance between the sizing restrictions (as small as possible) and the characteristic impedance 100 +/-15 Ohms with each being given equal weighting.

5.2.1 No Z_o Preferences.

The initial test for the UTP cable was based on a rectangular fitness function. Here any value of Z_o within the range was deemed to be acceptable. Therefore a value of 100 Ohms was of equal "worth" to that where the impedance was 115 Ohms. This latter being liable (due to handling) to fall outside of the standard when installed.

Using a spot frequency of 100MHz and calculating via the equations for R, L, G, C given in [4] the cable given (with no reference to preferred sizing) was as shown below. Using the statistics given in Section 3 the final cable design was more than 2 (2.3009) standard deviations above the estimated mean.

- Conductor diameter = 0.4 mm
- Dielectric thickness = 0.182 mm
- Z_o = 100.892 Ohms
- Overall Diameter = 3.693 mm

The overall diameter of the cable given is based upon the worst case scenario of non-overlapping cylinders. This assumes that each pair of wires exist within a discrete cylinder, these being placed at the vertices of a square and circumscribed by a cylinder giving the overall diameter, as shown in Figure 2.

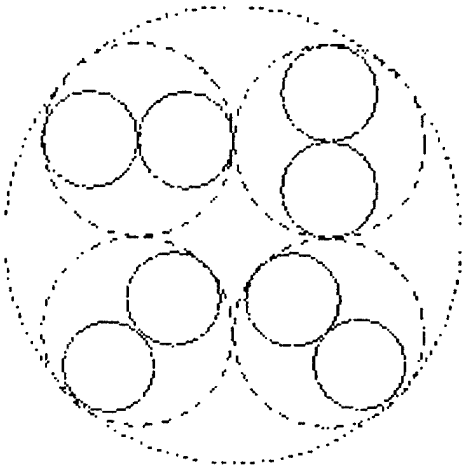


Figure 2. Assumed cable cross-section used to determine the overall diameter of the cabling

5.2.2 Z_o Preferred Towards 100 Ohms.

A further test was carried out using the cabling description given above. However for this simulation the fitness of the characteristic impedance (Z_o) was given by the trapezoid shown in Figure 3. The use of the trapezoidal fitness function provides some measure of 'preference' and indicates that for some values, while a measurement may be acceptable; it is not entirely desirable. This may be used to account for tolerancing issues or simply to encourage an optimum rather than optimal solution.

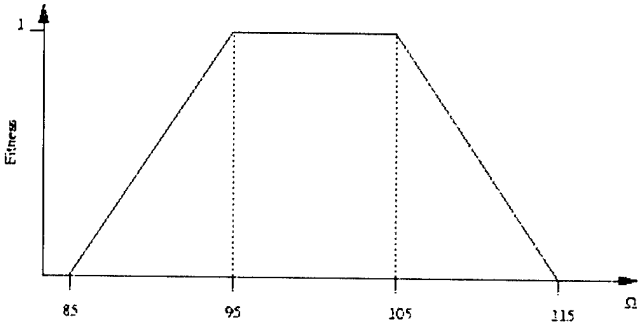


Figure 3. Trapezoid used to determine the fitness based on the characteristic impedance (Z_o)

The final cable design (with a fitness of 3.4444 standard deviations above the estimated mean) was:

- Conductor diameter = 0.475 mm
- Dielectric thickness = 0.217 mm
- Z_o = 100.932 Ohms
- Overall Diameter = 4.384 mm

5.3 Attenuation

This test was an advance on that given in Section 5.2.2. Here an additional measure of the cable attenuation was introduced, this being measured at three frequencies (1MHz, 10MHz, 100MHz). The attenuation fitness was again based on a trapezoidal form, the maximum limit given by [Willis, personal communication re: prEN50288-3-1], the upper right vertex being an arbitrary 2dB lower than the maximum allowed, to encourage a solution that minimizes the likelihood of failure on attenuation once manufactured (and handled).

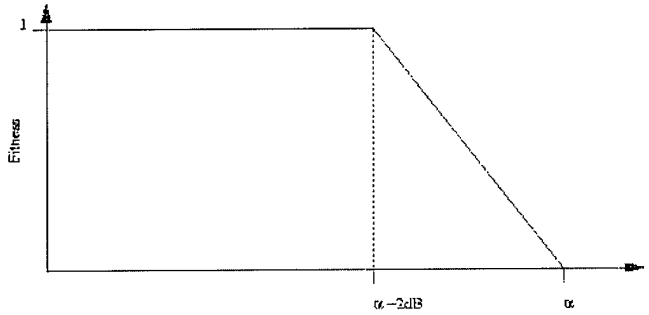


Figure 4. Trapezoid used to determine the fitness of cables based on their attenuation

With the addition of considering the attenuation it was assumed that the diameter of the conductor would increase. This has indeed been found to be the case with the algorithm providing a cable with a fitness of 4.9621 standard deviations above the estimated mean, the overall parameters being:

- Conductor Diameter = 0.8 mm
- Dielectric Thickness = 0.377 mm
- Z_o = 102.369 Ohms
- Overall Diameter = 7.505 mm
- Attenuation @ 1MHz = 1.042 dB / 100m
- Attenuation @ 10MHz = 3.395 dB / 100 m
- Attenuation @ 100MHz = 11.731 dB / 100 m

5.4 Velocity of Propagation

A further criterion of cable design is the velocity of propagation. As this is measured as a Phase delay (D) in [Willis, personal communication re: prEN50288-3-1] the equation required to determine the 'velocity' is the inverse of that given in [11], i.e.

$$v = \frac{\beta}{\omega} \tag{4}$$

Again it was decided to use a trapezoidal form to provide the fitness measure of this parameter (thus moving the final design away from the absolute limits imposed by the standard) so that any changes due to handling would not make the cable non-compliant.

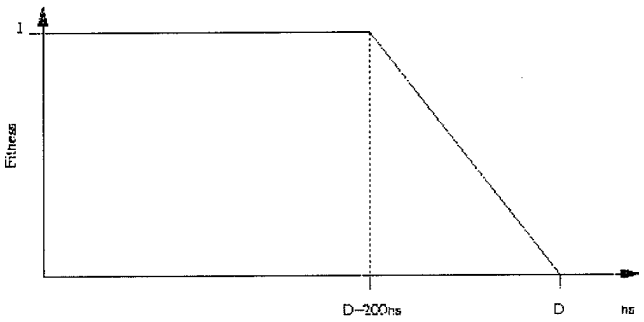


Figure 5. Trapezoid used to determine the fitness of cables based on the velocity of propagation

The cable was, as before tested using three spot frequencies (1MHz, 10MHz, and 100MHz) with the overall fitness being the product of the fitness found for: size (minimal); Z_o (using the trapezoid shown in Section 5.2.2); attenuation (determined as in Section 5.3); and the velocity of propagation trapezoid shown above. The resulting cabling parameters being given as:

- Conductor Diameter = 0.8 mm
- Dielectric Thickness = 0.377 mm
- Z_o = 102.369 Ohms
- Overall Diameter = 7.505 mm
- Attenuation @ 1MHz = 1.042 dB / 100 m
- Attenuation @ 10MHz = 3.395 dB / 100 m
- Attenuation @ 100MHz = 11.631 dB / 100 m
- Velocity of propagation @ 1MHz = 501.442 ns / 100 m
- Velocity of propagation @ 10MHz = 501.448 ns / 100 m
- Velocity of propagation @ 100MHz = 501.451 ns / 100 m

In this instance the cable was 4.9617 standard deviations above the estimated population mean.

5.5 Cable Variations

All of the preceding tests were based upon the cable having a constant size along its length. However this is not a valid assumption due to the inevitable manufacturing tolerances. Therefore a further test was performed for cables where the core diameter (d) varied.

The simulation of this case was for a population of 100 UTP cables. The fitness due to the nominal parameters was calculated as per Section 5.4. However any cables that satisfied all the fitness criteria (i.e. non-zero fitness) were passed to a 1D TLM program [4]. For this program the diameter of the core was randomly perturbed +/- 0.05mm at each node. The nodes are placed at 1mm intervals along a representative 1m length. Following the TLM simulation the resultant time domain voltages were subjected to a Discrete Fourier Transform (DFT) so as to give both the incident and reflected signals at each end of the cable in the frequency domain. From these signals the true attenuation of the cable was calculated (previous results being purely from the nominal sizing). The non-attenuation parameters were given as:

- Conductor Diameter = 0.787 mm
- Dielectric Thickness = 0.377 mm
- Z_o = 103.129 Ohms
- Overall Diameter = 7.440 mm
- Velocity of propagation @ 1MHz = 501.442 ns / 100 m
- Velocity of propagation @ 10MHz = 501.449 ns / 100 m
- Velocity of propagation @ 100MHz = 501.451 ns / 100 m

Figure 6 shows the difference found between the attenuation based on the nominal cable size and that found after calculation when the physical tolerances on the sizes have been accounted for.

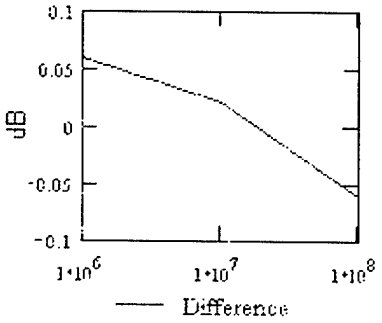


Figure 6. A comparison of the attenuation results from the nominal sizing and that found via TLM

This test took approximately 5 hours to complete. Such a long timescale was the reasoning behind limiting the simulation at 1000 generations. However the final cable fitness was 6.4178 standard deviations above the estimated mean (as given in Equation 2)

5.6 Consideration of Conductor Sizing

It can be noted that the when using attenuation as a fitness criteria the cables tend towards the maximum possible allowed under the standard (see Sections 5.3-5.5). To determine the extent of such effects a further test was undertaken which included an additional cost measure based on the cross-sectional area of the conductors. For this exercise the fitness penalty was proportional to the conductors cross-sectional area. This test was aimed at reducing the diameter of the conductors and hence the overall costing of the cable. The results after 1000 generations being, in this instance:

- Conductor Diameter = 0.519 mm
- Dielectric Thickness = 0.271 mm
- Z_o = 107.082 Ohms
- Overall Diameter = 5.127 mm
- Attenuation @ 1MHz = 1.502 dB / 100 m
- Attenuation @ 10MHz = 4.850 dB / 100 m
- Attenuation @ 100MHz = 16.332 dB / 100 m
- Velocity of propagation @ 1MHz = 501.438 ns / 100 m
- Velocity of propagation @ 10MHz = 501.448 ns / 100 m
- Velocity of propagation @ 100MHz = 501.451 ns / 100 m

For this particular instance the cable was 15.5 standard deviations above the estimated mean (Equation 2).

6. Discussion and Conclusions

The above simulations indicate the applicability of the toolkit. The separation of the user from the underlying techniques provides a user-friendly environment in which no understanding of Genetic Algorithms is required. Indeed the system can be operated knowing only the tokens and the limits imposed by the problem under investigation. In terms of operating speed (normally slow for Genetic Algorithms) the simulations were achieved in the order of 5 minutes, excluding those involving the TLM simulations. This offers the potential for large-scale reductions in the development time of new cabling designs. The toolkit is fully extendible in that it can be applied to any number of problems.

It has been noted that for cables where attenuation is calculated the conductor diameter tends towards the largest dimension allowable under the standard. This has been addressed with the introduction of an additional costing based on the amount of conductor material required to construct the cable. Further measures may also be required to account for the costing of the dielectric material (this having been discounted as negligible in the current implementation).

The initial testing with 1D TLM has shown that the system is capable of optimizing cables with non-constant parameters. This is of importance in that it permits the inclusion of tolerance criteria in the development of cabling. Indeed in a business environment it may be necessary to find the best compromise between the competing requirements of manufacturing and sales. For example, Manufacturing may want the maximum repeatability of the cable parameters. As such they may want

high precision, therefore expensive, cabling. Sales, on the other hand, may want to minimize the cost by accepting a lower precision. However they may want accurate notional parameters. It should therefore be possible to describe an "accuracy vs. precision" problem landscape, with the fitness being a measure of the notional cost of any scrap (non-compliant) cabling. The circumstances of the cabling requirements and other inputs would then allow for an optimization to a preferred "region".

Further work is currently being undertaken to extend the tolerance capabilities of the kit. Special attention is being paid to the statistical implications of their use and the effects on the fitness distribution across the solution space. Other work is being done to provide automatically a fully configurable optimal cabling report based on the data held within the population database (whilst continuing to hide this level of functionality from the user). Furthermore actual manufacturing data, preferences, and tolerances may be included to show the efficacy of the toolkit in a realistic manufacturing environment.

Mention must also be made about the assumption of a Gaussian distribution in fitness prediction. Without being able to derive a distribution from the complex fitness functions (and with the problem space being composed of continuous functions) it is the only possible first assumption, and seems to be standard practice in the statistics field. Though in the light of further evidence the distribution assumed for the fitness landscape could be amended, provided the subsequent statistical reasoning is amended appropriately as well.

7. References

[1] Dowsland, K. A. Simulated Annealing. In: *Modern Heuristic Techniques for Combinatorial Problems*, ed. Reeves, C. R. Great Britain: McGraw-Hill International, 1995.pp. 20-69.

[2] Holland, J. H., Genetic Algorithms *Scientific American*, vol. pp. 44-50, Jul, 1992.

[3] Reeves, C. R. Genetic Algorithms. In: *Modern Heuristic Techniques for Combinatorial Problems*, ed. Reeves, C. R. Great Britain: McGraw-Hill International, 1995.pp. 151-196.

[4] Alasadi, M. M., Duffy, A. P., Hodge, K. G., and Willis, A. J., "Twisted Pair Cable Design Analysis and Simulation," *49th IWCS Symposium,* Atlantic City, pp. pp 111-120, 2000.

[5] Sasse, H. G., Al-Asadi, M. M., Duffy, A. P., Hodge, K. G., and Willis, A. J., "Computer Optimisation of Cable Design," *49th IWCS Symposium,* Atlanic City, pp. pp380-384, 2000.

[6] Robson, C. *Experiment Design and Statistics in Psychology*, Penguin Education, 1983.

[7] Rees, D. G. *Essential Statistics*, Chapman and Hall, 1995.

[8] Libes, D. *Exploring Expect*, O'Reilly, 1994.

[9] Goldberg, D. E. and Deb, K. A Comparative Analysis of Selection Schema used in Genetic Algorithms. In: *Foundations of Genetic Algorithms*, ed. Rawlins, G. J. E. United States: Morgan Kauffman, 1991.pp. 69-93.

[10] Wright, A. H. Genetic Algorithms for Real Parameter Optimisation. In: *Foundations of Genetic Algorithms*, ed. Rawlins, G. J. E. United States: Morgan Kauffman, 1991.

[11] Baden Fuller, A. J. *Microwaves: An Introduction to Microwave Theory and Techniques*, Permagon Press, 1990.

Authors Biographies



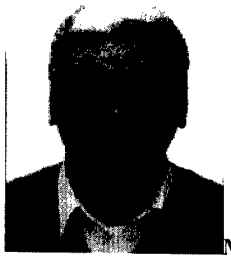
Hugh G. Sasse graduated from The University of York in 1985, and since then has been working in the Machine Vision Group and later the Applied Electromagnetics Group at De Montfort University, Leicester. He embarked on a part-time MPhil/PhD in 1999. His main interests are computer modeling of novel antenna structures and other communication channel components, with an emphasis on optimization of such structures.



Benjamin G. Tunstall obtained a PhD in Biomedical Engineering from De Montfort University in 2001. Joining the Applied Electromagnetics Group in the same year he is investigating the development and application of heuristics to a wide range of Electromagnetic Compatibility issues.

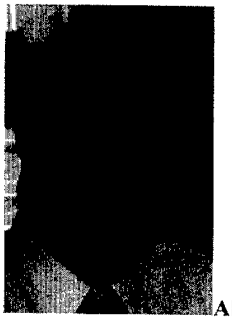


Dawn E. Coleby obtained a 1st class Honours in Medical and Health Statistics from De Montfort University in 2000 and joined the Applied Electromagnetics Group in the same year with the aim of applying statistical techniques to the comparison of complex data.



Mohammed M. Al-Asadi received his BSc. degree from the University of Basra, Iraq and an MPhil degree from the University of Nottingham, UK, both in Electronic and Electrical Engineering in 1988 and 1992 respectively.

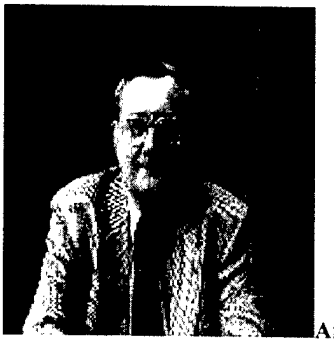
Between 1993 and 1996 he was working on a research project at the University of Nottingham, developing a program to incorporate charge particle motion in electromagnetic fields with transmission line modelling method. In 1996 he joined De Montfort University in Leicester, UK, where he obtained his PhD degree and working as a Research Fellow in communication systems. His research involves the investigation of high frequency performance of structured wire cabling. He is the author and co-author of many journal and conference papers. His research interests include EMC, communication cables, electron beam, field-particle interaction devices, numerical methods and simulation of electromagnetic fields.



Alistair P. Duffy was educated at Conyers School, Yarm; University College, Cardiff, and Nottingham University. He is currently a Principal Lecturer in Communication Engineering at De Montfort University, Leicester. Particular research interests include experimental, numerical and analytical applications for electromagnetics. Particular emphasis for this in recent years has been in communication cable design and analysis. Other aspects of this interest include microwave and rf heating and novel antennas. A substantial interest is in the formal comparison of complex data sets.



Kenneth G. Hodge holds a BEng from Liverpool University and an MSc from Warwick University. He is currently a representative to BSI and CENELEC committees working on LAN cabling. Ken has been working in the cable industry since 1982, he was initially involved with the development of optical and copper data communication and telecommunication cables, then transferred to the R&D facility as Design Manager Optical Cables. He is now Technical Manager at Brand-Rex (Part of Novar plc).



Arthur J. Willis has been involved in the design and development of cables since joining BICC in 1957, and as Chief Engineer was responsible for the early development of communication cables for information technology. He is currently Technical Consultant to Brand-Rex Limited.

Mechanical Performance of Different Category 6 Cable Designs

Werner Sittinger
Dätwyler Kabel+Systeme GmbH
Neufahrn, Germany
+49 8165 9501-190 · w.sittinger@daetwyler.net

Beat Schmucki, Daniel Fedier, Beat Tresch
Dätwyler AG, Kabel+Systeme
Altdorf, Switzerland
+41 41 875-1231 · beat.schmucki@daetwyler.ch

Abstract
In the next edition of the International and European standards for generic cabling a new category 6, defined up to 250 MHz will be included. The balanced cables of this new category 6 will be specified in International and European cable standards which are also in preparation.

This contribution gives an overview about different balanced cable designs. The category 6 performance can be reached with each of these cable designs. But each design yield a certain electrical characteristic for the cable. A comparison shows that the electrical performance of these designs is quite different if the cables are measured under relaxed conditions or under mechanical stress conditions.

Keywords
Balanced cable; category 6; mechanical performance; crush resistance.

1. Introduction
In the International and European standards committees the 2nd editions of the cabling standards ISO/IEC 11801 and CENELEC EN 50173 are currently in preparation. Their publication is expected at the end of the year 2002. The major difference to the 1st edition is the inclusion of new performance classes E, up to 250 MHz, and F, up to 600 MHz.

The class E performance limits are defined on the basis of what is feasible with new state-of-the-art unscreened cabling. The class F performance limits are defined on the basis of screened cabling with individually screened pairs.

The performance classes are defined for installed cabling. For the channel, which is the complete cabling between two active devices and for the permanent link as a subset of the channel.

The installed cabling is built with cables, connecting hardware and cords of a certain performance category. The class E channel performance is based on category 6 components.

Therefore the requirements of the installed cables are defined in the cabling standards by several performance categories. Category 5 cables (specified up to 100 MHz) for the use in class D installations, category 6 cables (specified up to 250 MHz) for the use in class E installations and category 7 cables (specified up to 600 MHz) for the use in class F channels.

For the cable specifications both cabling standards will refer to the corresponding cable standards IEC 61156 and EN 50288, which are also under revision. The cable standards will define the electrical and mechanical performance of screened and unscreened category 5 and 6 cables and of screened category 7 cables.

For the end-user it is very important to know that if he gets a cable according to the draft prEN 50288-5-1 (screened cables up to 250 MHz) or prEN 50288-6-1 (unscreened cables up to 250 MHz), that this cable will fulfill the category 6 requirements after it is installed.

For this reason several mechanical tests are specified in the European draft standards of the EN 50289-3 series. The cable standards of the EN 50288 series refer to these mechanical tests and require that the cables maintain their electrical performance.

The mechanical tests required in EN 50288 are:

- Conductor elongation at break (EN 50289-3-2)
- Shrinkage of insulation (EN 50289-3-4)
- Crush resistance of the cable (EN 50289-3-5)
- Impact resistance of the cable (EN 50289-3-6)
- Abrasion resistance of the sheath markings (EN 50289-3-8)
- Single bend testing of the cable (EN 50289-3-9, clause 4)
- S-bend testing of the cable (EN 50289-3-9, clause 8)
- Tensile performance (EN 50289-3-16)

In the following section 2, six different cable designs are described which provide category 6 performance.

The crush resistance test according to EN 50289-3-5 (draft dated October 2000) is discussed as a typical, representative mechanical test in section 3.

In section 4 the electrical and mechanical performance of the different category 6 cable designs is discussed. The crush resistance test was chosen as a representative mechanical test to compare the different category 6 cable designs. Other mechanical tests, such as the impact resistance test or the bending test, would give the same indication of the mechanical stability of the different cable designs.

2. Category 6 Cable Designs
The performance limits for balanced category 6 cables defined up to 250 MHz can be realized with different cable designs:

Design 1: without any separator

Design 2: with a cross profile as a separator

Design 3: with a chamber profile as a separator

Design 4: a star quad construction with intermediate sheaths

Design 5: with individually screened pairs

Design 6: with individually screened pairs with intermediate sheaths

Design 1 (see Figure 1) is the well known design of UTP cables. Four twisted pairs are covered by a sheath. Optionally, the cable may have an overall screen, either metallic foil or/and braided. Here two cables are tested, unscreened with solid PE insulation (design 1u) and screened with foamed PE insulation and a foil and braid screen (design 1s).

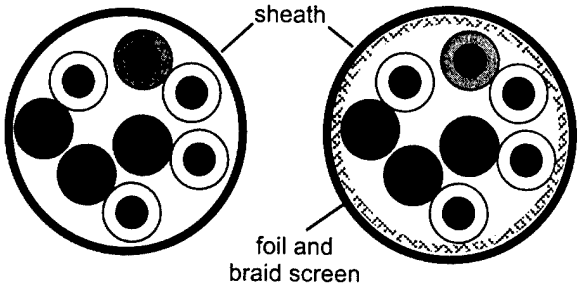


Figure 1. Cable designs without any separator

Design 2 (see Figure 2) has, in addition to design 1, a cross profile to separate the pairs from each other with an overall foil and braid screen.

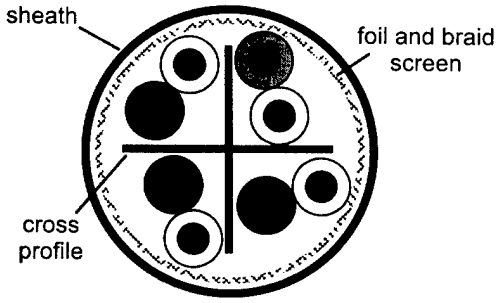


Figure 2. Cable design with a cross profile as a separator

Design 3 (see Figure 3) is similar to design 2. Instead of a simple cross profile the design 3 has a chamber profile. The pairs are laid into closed chambers. (German patent no. 199 47 825). The overall foil screen is bonded to the chamber profile.

Design 4 (see Figure 4) is a star quad construction. The two quads are embedded in intermediate sheaths (HDPE) which are surrounded by foil screens with the conductive side outside. The two screened quads are covered by an overall braid screen and a sheath (European patent no. EP 93 10 43 85.5).

Design 5 (see Figure 5) is a common PiMF category 7 cable. Each pair is separately screened by a metallic foil and all four pairs are covered by an overall braid screen and a sheath.

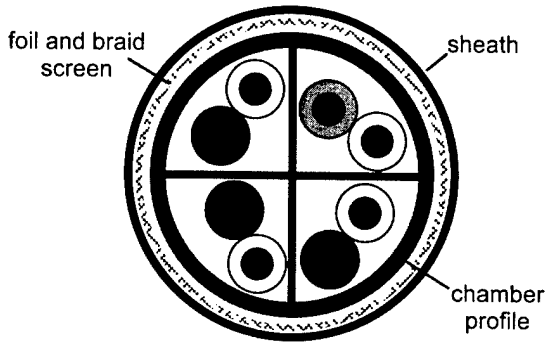


Figure 3. Cable designs with a chamber profile as a separator

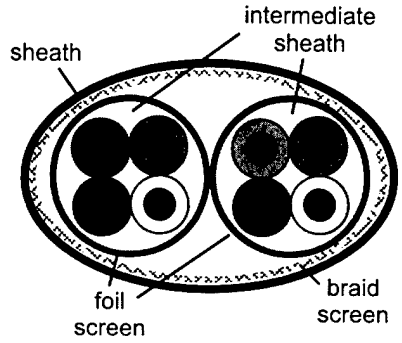


Figure 4. Cable design with a star quad construction with intermediate sheaths

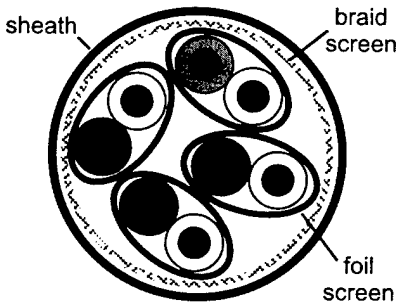


Figure 5. Cable design with individually screened pairs

Design 6 (see Figure 6) is similar to design 5. But each pair is embedded in intermediate sheaths like the quads in design 4. The metallic foil around the pairs is bonded to the intermediate sheaths (European patent pending, no. EP 97 102 913.7-2208).

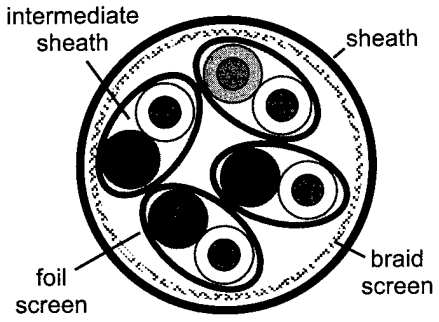


Figure 6. Cable design with individually screened pairs with intermediate sheaths around each pair

3. Crush Resistance Test

The test method for the crush resistance test is specified in the European draft prEN 50289-3-5, dated October 2000. The specification is applicable to coaxial, symmetrical and optical cables used in analogue and digital communication systems.

The test sample is crushed between two steel plates over a 100 mm length of the sample. In addition to the 100 mm the plates shall be rounded at both sides with a radius of about 5 mm. Figure 7 shows a schematic drawing of the test set-up.

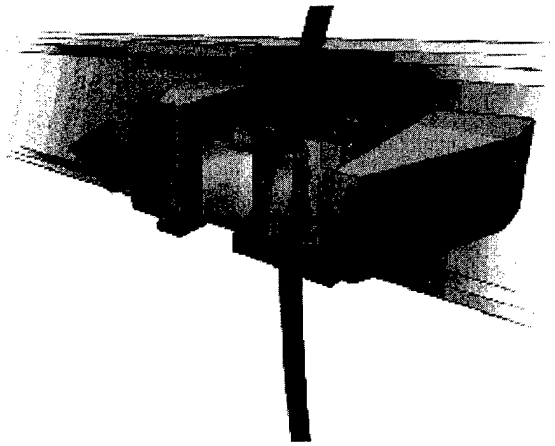


Figure 7. Crush resistance test set-up

For symmetrical cables it is required that after the test, the transmission characteristics shall be within the limiting values specified in the relevant specification.

For symmetrical category 6 cables the relevant specification is the draft European standard prEN 50288-5-1 for screened cables and the prEN 50288-6-1 for unscreened cables.

Both drafts give, for the crush resistance test, the same requirements. The load shall be 1000 N for a duration of 1 minute and a length of 100 mm. The near end crosstalk (NEXT), return loss and characteristic impedance shall remain within the specified limits.

These limits, given in the drafts prEN 50288-5-1 and prEN 50288-6-1, both dated June 2001 are:

$$\text{NEXT} \geq 74{,}3-15\log f,\ 1\ \text{MHz} \leq f \leq 250\ \text{MHz},\ (66\ \text{dB Maximum}) \quad (1)$$

$$\text{Mean impedance: } (100 \pm 5)\ \Omega,\ @\ 100\ \text{MHz, f.f.s.} \quad (2)$$

$$\text{Return loss} \geq 20+5\log f,\ 4\ \text{MHz} \leq f \leq 10\ \text{MHz};\ 25\text{dB},\ 10\ \text{MHz} \leq f < 20\ \text{MHz};\ 25-7\log(f/20),\ 20\ \text{MHz} < f \leq 250\ \text{MHz; f.f.s.} \quad (3)$$

Since the requirements for the mean impedance and the return loss are marked with f.f.s. (for further study), they are given for information only. Conformance with the standard is also given if these limits are not met. The only normative requirement is the requirement for the near end crosstalk (NEXT).

Neither the draft for the test method nor the draft cable specifications define the distance between the crushed cable region and the test equipment. The draft prEN 50289-3-5 for the test method says only that the test report shall state the distance from the test region to one of the ends, normally 1 m maximum.

All the following measurements are carried out at a temperature of 20°C with a network analyzer HP 8753E and 1 GHz Baluns.

The maximum load applied is not only 1000 N, as required by the test standard, because, practically, this seems not high enough.. For example it happened at a building site that a scaffold of 200 kg weight with four wheels was rolled over a data cable which was laid out at the floor for the installation. Each wheel had a width of 2 cm and gives a load of 500 N onto the cable. This is the same pressure as a load of 2500 N on a length of 100 mm. Therefore the load during the tests is incrementally increased to a maximum of 2500 N.

In an installation it can also happen that a cable is exposed to a permanent load during operation. For this reason the measurements are not only taken after the crush resistance test as required by the test standard. The electrical parameters are also measured during the test with a load of 1000 N, 1500 N, 2000 N and 2500 N.

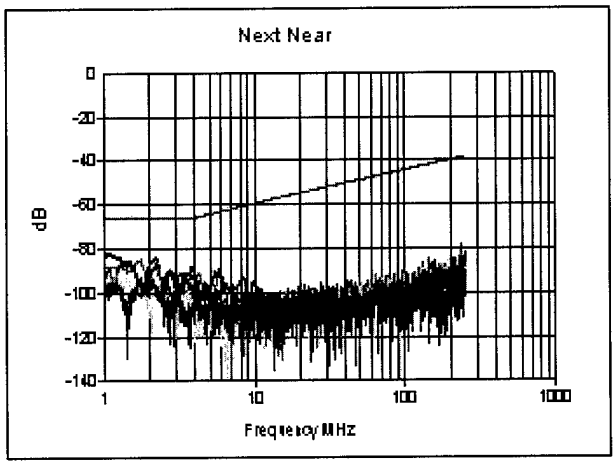


Figure 8. NEXT of cable design 5 before the crush resistance test

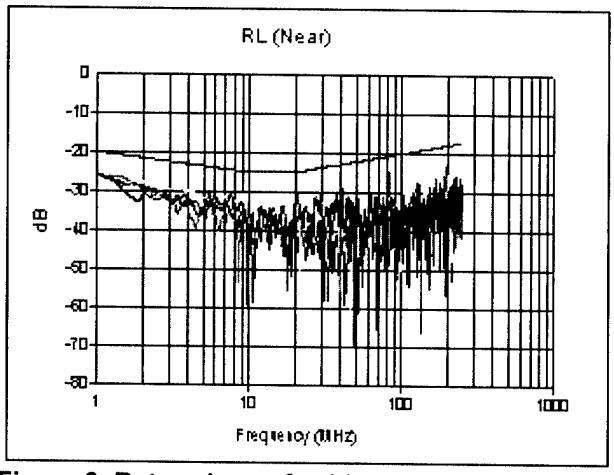


Figure 9. Return loss of cable design 5 before the crush resistance test

Figure 8 shows the NEXT and Figure 9 the return loss of a cable with the design 5 (PiMF) before the crush resistance test.

In Figures 10 and 11 the cable is measured during the crush resistance test with a load of 2500 N at a distance of 1 m.

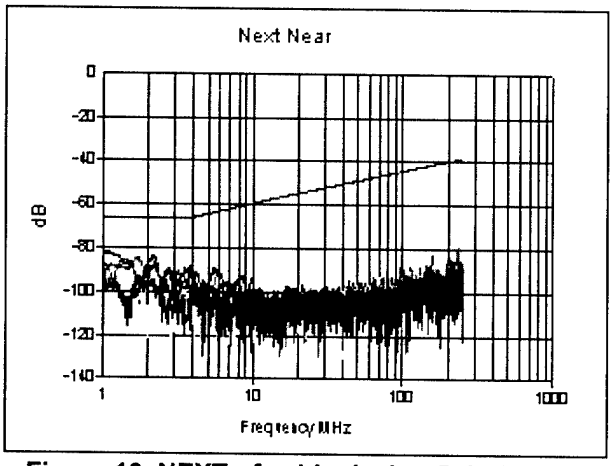


Figure 10. NEXT of cable design 5 during the crush resistance test with a load of 2500 N at 1 m distance

Figure 12 shows the NEXT and Figure 13 the return loss measured after the test, as required by the test standard, i.e. at a distance of 1 m. There is nearly no change in the results for the NEXT, even if the load is 2,5 times higher than required. But the return loss above 10 MHz got worse during the test and also after the test it did not recover completely. The return loss fails the limits above 180 MHz.

In Figures 14 and 15 the NEXT and return loss measurement was performed after the test, but at a distance of 10 m. Compared to Figures 12 it can be seen that the NEXT still has not changed. But the return loss results are different from Figure 13. Now the return loss is better and meets the requirements.

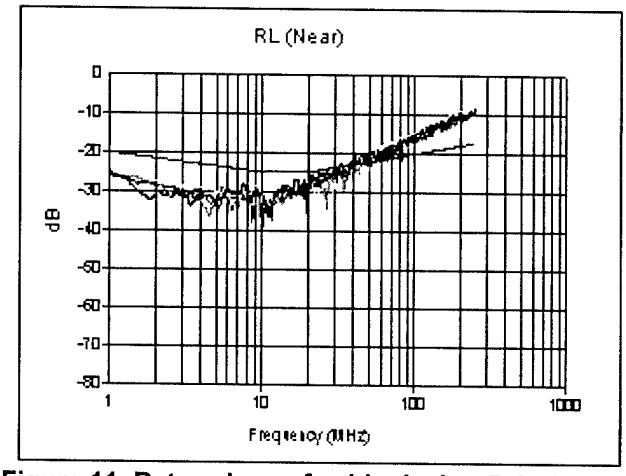


Figure 11. Return loss of cable design 5 during the crush resistance test with a load of 2500 N at 1 m distance

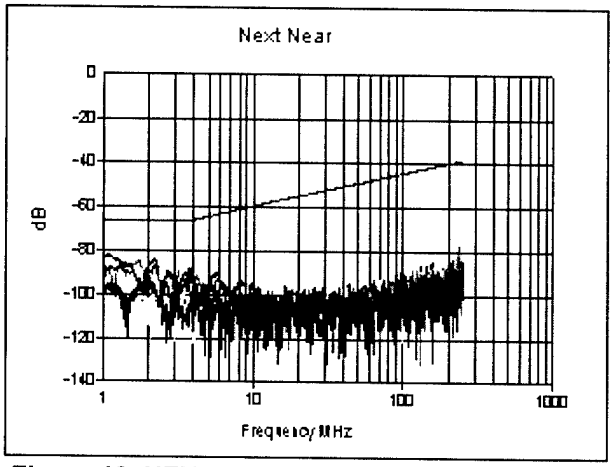


Figure 12. NEXT of cable design 5 after the test with a load of 2500 N at 1 m distance

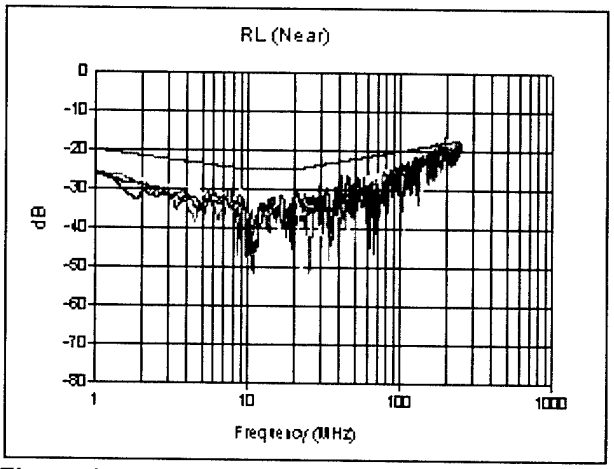


Figure 13. Return loss of cable design 5 after the test with a load of 2500 N at 1 m distance

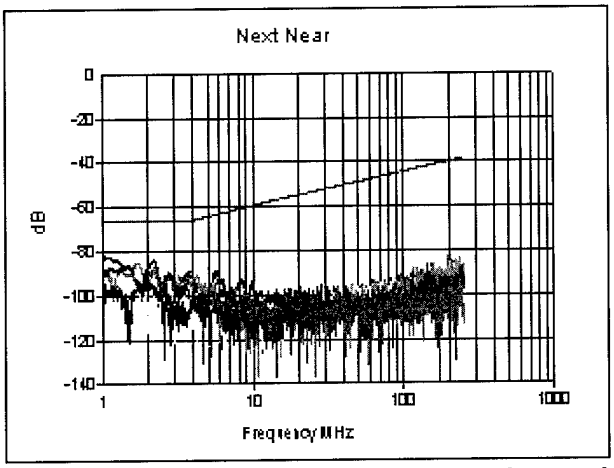


Figure 14. NEXT of cable design 5 after the crush resistance test with a load of 2500 N at 10 m distance

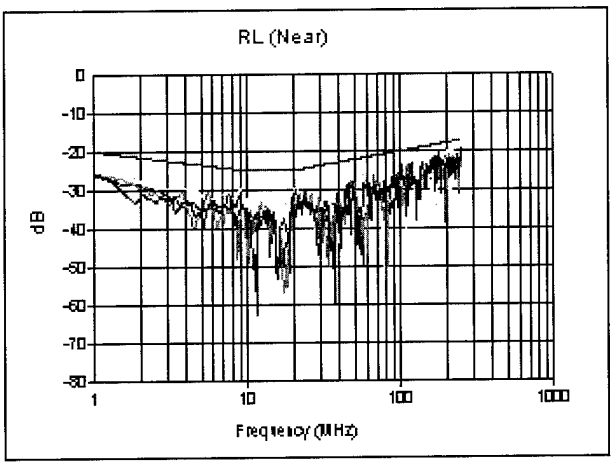


Figure 15. Return loss of cable design 5 after the crush resistance test with a load of 2500 N at 10 m distance

As a conclusion it can be stated that the distance between the crushed cable region and the cable end terminated with the measurement equipment has a significant impact on the test results. In general it was found that a load at a distance of 10 m results in a better performance than a load at a shorter distance of 1 m.

The distance between the load and the cable end terminated with the measurement equipment must be defined by the standard for the test method or by the cable specification. Only measurements performed at the same distance are comparable.

All further measurements are carried out at 1 m distance.

4. Performance of Cat. 6 Cable Designs

4.1 Crush Resistance Test Results

This subsection gives an overview on the results of the crush resistance tests performed at each cable design described in section 2.

Each cable was measured before the crush resistance test, during the test with a load of 1000 N, 1500 N, 2000 N and 2500 N and finally after the load as required by the test standard. At each measurement the parameters NEXT, impedance and return loss were tested against the limits in equations 1 to 3.

Since the impedance and return loss measurements are related to each other, only the NEXT and return loss results are presented in the following.

For a more compact presentation the test results of all cable designs with different loads were evaluated and are combined in two tables and four graphs.

Table 1 and Figure 16 show the minimum margin of the measured NEXT to the limit given in Equation 1.

Figure 8 shows, for example, the NEXT measurement in the frequency range form 1 MHz to 250 MHz of cable design 5 before the load test. The minimum margin to the limit is 18 dB at a frequency of about 1 MHz. The margin is positive because the measured NEXT meets the limit. This minimum margin of 18 dB is given in Table 1 and Figure 16 for the cable design 5 before the load test.

For a better comparison of the mechanical stability of the different cable designs, the NEXT is normalized in Figure 17. For each cable the original NEXT value before the crush resistance test is subtracted from the measured NEXT values during and after the crush resistance test. Cable designs with a high mechanical stability have low variations in the NEXT values.

Table 2 and Figure 18 show the minimum margin of the measured return loss to the limit given in Equation 3.

Figure 11 shows, for example, the return loss measurement in the frequency range from 1 MHz to 250 MHz of cable design 5 during the crush resistance test with a load of 2500 N. The minimum margin to the limit is -10 dB at a frequency of 250 MHz. The margin is negative because the measured return loss exceeds the limit. This minimum margin of -10 dB is given in Table 2 and Figure 18 for the cable design 5 during the crush resistance test with a load of 2500 N.

In Figure 19 the normalized return loss is shown, calculated from the values given in table 2. Again, robust cable designs result in low variations in the return loss during the crush resistance test.

Table 1. NEXT margin to cat.6 limit before, during and after crush resistance test

Force / N	NEXT margin from limit / dB						
	Design 1u	Design 1s	Design 2	Design 3	Design 4	Design 5	Design 6
0	5	-6	3	6	2	18	24
1000	0	-7	2	5	2	18	24
1500	-3	-9	1	4	2	18	24
2000	-4	-11	1	4	2	18	24
2500	-5	-13	1	4	2	18	24
0	3	-6	2	6	2	18	24

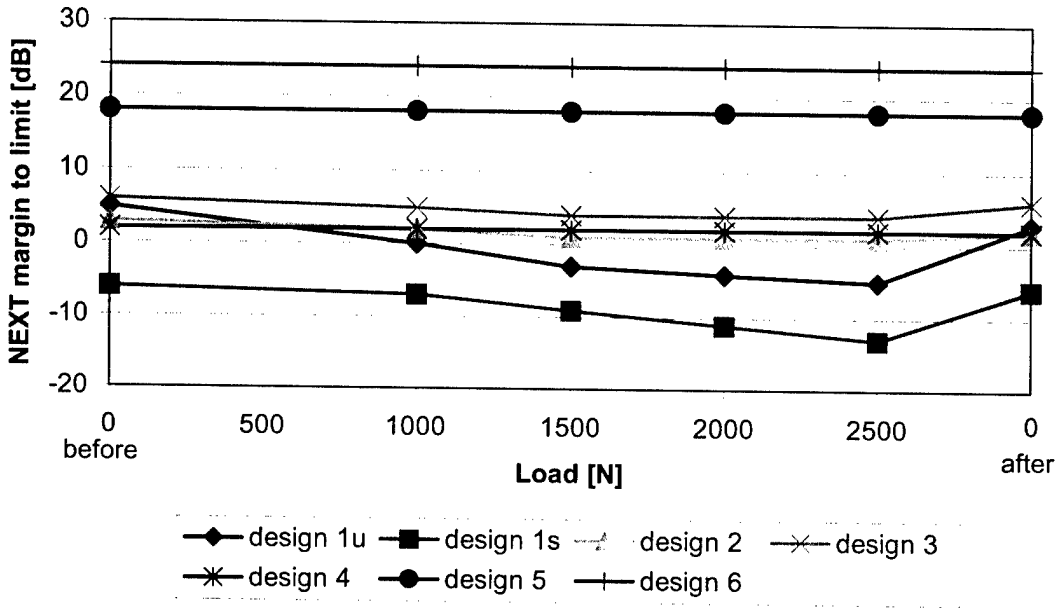


Figure 16. NEXT margin to cat.6 limit before, during and after crush resistance test

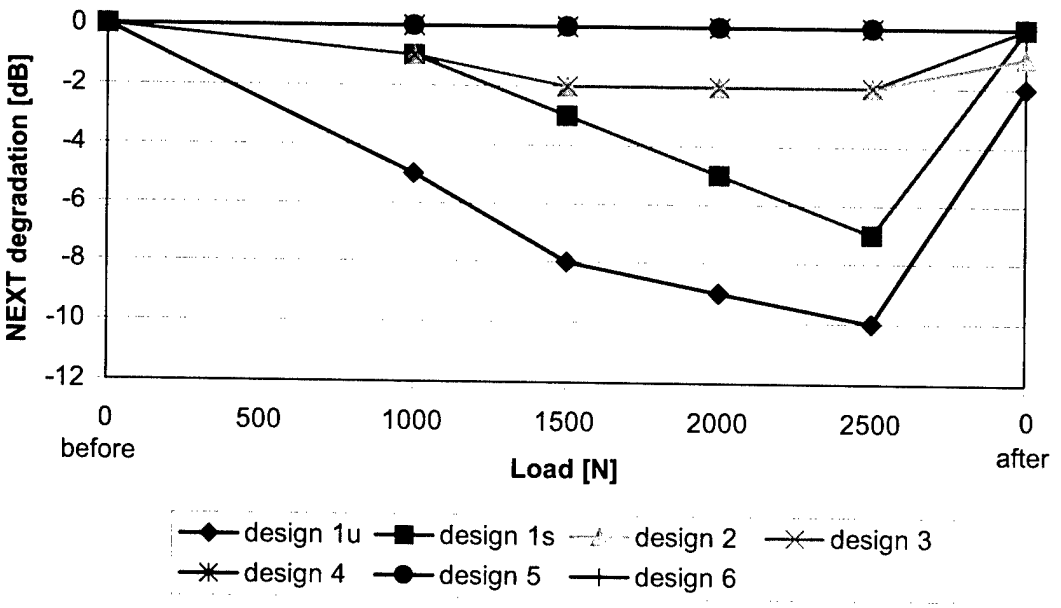


Figure 17. Normalized NEXT as a function of the load

Table 2. Return loss margin to cat.6 limit before, during and after crush resistance test

Force / N	Return loss margin from limit / dB						
	Design 1u	Design 1s	Design 2	Design 3	Design 4	Design 5	Design 6
0	9	2	4	2	6	5	5
1000	2	-5	-2	1	5	-3	5
1500	-1	-9	-5	0	4	-6	5
2000	-2	-9	-7	-3	4	-9	4
2500	-3	-10	-9	-6	3	-10	3
0	8	0	1	1	6	-1	5

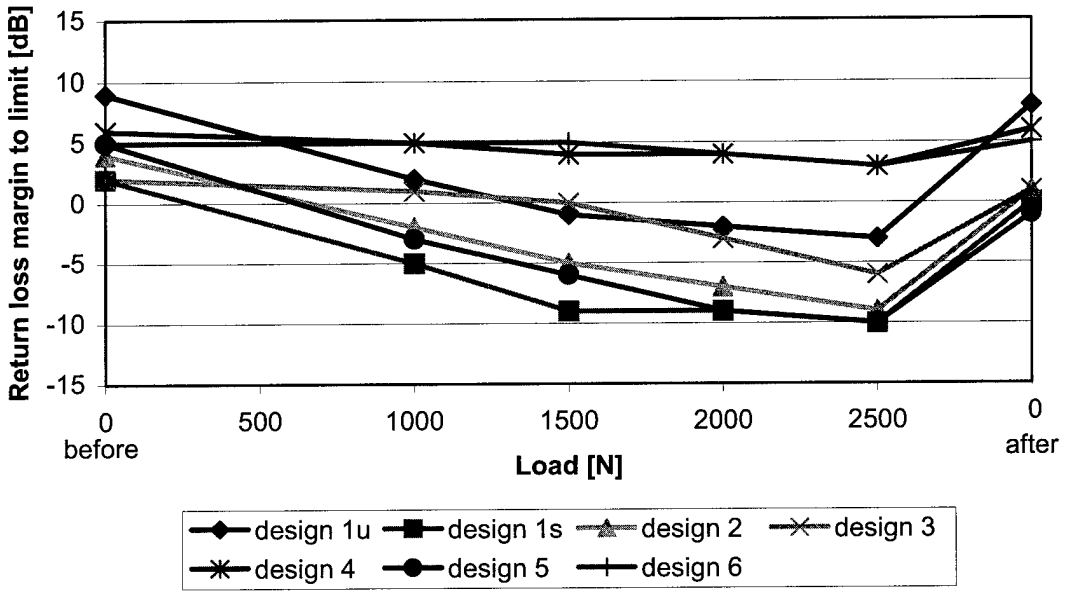


Figure 18. Return loss margin to cat.6 limit before, during and after crush resistance test

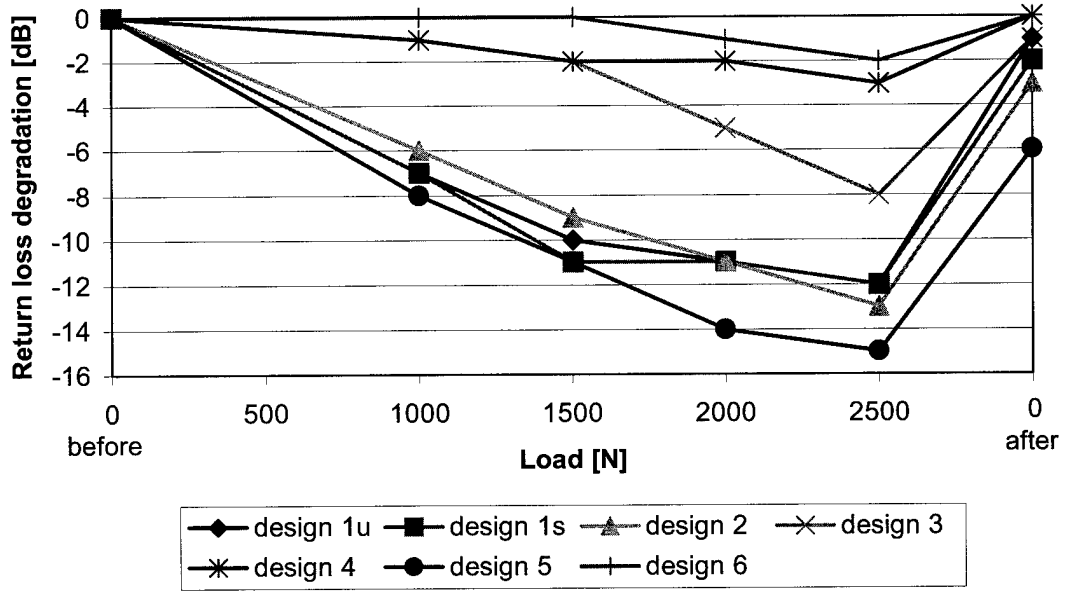


Figure 19. Normalized return loss as a function of the load

4.2 Design 1 – No Separator

The NEXT of the unscreened cable (design 1u) meets the category 6 requirements with a margin of 5 dB. With an increasing load the NEXT fails above a load of 1000 N. After the crush resistance test the cable recovers.

For the return loss the cable fails also above 1000 N and shows a similar behavior, but with a higher margin.

The tested screened version of this cable design (design 1s) is not a category 6 cable. Certainly it is also possible to manufacture category 6 cables with this screened design. But it is more efficient to use the design 2 instead. Already before the crush resistance test the NEXT does not meet the category 6 requirements. But the screened cable shows the same behavior as the unscreened cable. The two curves in Figure 16 for the NEXT and in Figure 18 for the return loss are nearly parallel. Only for the return loss the cable does not recover completely.

4.3 Design 2 – Cross Profile Separator

The NEXT of this cable fulfills the category 6 requirements before, during and after the crush resistance test. With the increasing load the NEXT is much more constant as for cables of design 1. The NEXT after the test is nearly the same as before the test.

Regarding the return loss the cable had already, before the crush resistance test, a lower margin than the unscreened cable with no separator. This lower margin is constant during the whole crush resistance test. The return loss fails already at a load of 1000 N. But after the test the cable recovers and has again a positive margin to the category 6 return loss limits.

4.4 Design 3 – Chamber Profile Separator

The NEXT of this cable is in general better than the NEXT of the design 2 cable. Compared to the cable design 2 the cable recovers completely after the crush resistance test for the NEXT.

For the return loss the cable shows a much more stable behavior like the design 2. It fails the return loss above 1500 N. After the load is removed the cable recovers nearly completely.

4.5 Design 4 – Star Quad with Intermediate Sheath

This cable always meets the category 6 limits for NEXT and return loss before, during and after the test.

For the NEXT the minimum margin is independent of the load up to 2500 N, constant at 2 dB. This small margin is typical for a star quad construction only at low frequencies. For higher frequencies the NEXT margin increases up to 8 dB at 250 MHz.

The return loss margin is also quite constant during the complete crush resistance test. This design has the highest margin for the return loss measured with a load up to 2500 N.

This cable design has the highest mechanical robustness.

4.6 Design 5 – Individually Screened Pairs (PiMF)

This cable is a category 7 cable. Therefore it has a much higher margin to the category 6 NEXT limit, like the cable designs described before. The NEXT margin of 18 dB is absolutely constant during the whole crush resistance test.

For the return loss this cable fails already at a load of 1000 N. With an increased load the return loss gets worse. After the load is removed the return loss recovers, but not above the category 6 limit (which, up to 250 MHz, is identical to the category 7 limit). If the cable would have been tested with a maximum load of 1000 N, as required by the test standard and cable specification, the return loss after the test would meet the limit.

4.7 Design 6 – PiMF with Intermediate Sheath

For the NEXT this cable shows the same behavior as the design 5 cable, but with an even higher margin of 24 dB to the limit.

For the return loss this cable design has a much better performance than the design 5 cable. It does not fail the return loss requirement during the complete crush resistance test up to a tested load of 2500 N. Due to the intermediate sheath around each pair this cable shows for the return loss a similar behavior to the star quad cable (design 4).

This cable design combines the mechanical robustness of the star quad cable with the category 7 performance of a PiMF cable.

5. Conclusions

It was shown that a category 6 cable can be realized with at least six different designs. With each design the current requirements for the crush resistance test can be met. Because only the NEXT, measured after the crush resistance test has to be fulfilled.

The cable designs 2 and 5 show a high mechanical stability for the NEXT parameter, but not for the return loss parameter. Only the cable designs 3, 4 and 6 have a high mechanical stability for both parameters.

The current requirements are just minimum requirements. In some installation situations these requirements might be exceeded. It would be useful to define a second set of requirements for cables with a higher mechanical performance for the use in harsh environments. The higher requirements could be an increased load up to 2500 N and a measurement of the electrical performance during the load. Some of the tested category 6 cable designs meet also this increased requirements for the crush resistance test.

Also, the current definition of the crush resistance test needs to be more detailed. The distance between the crushed cable region and the cable end terminated with the measurement equipment must be defined.

6. References

[1] ISO/IEC JTC 1/SC 25 N696, 2nd CD ISO/IEC 11801 2nd edition: IT- Cabling for customer premises, April 2001.

[2] CLC/TC215(Sec)94, Secretariat's enquiry on Working Draft 13252 „Revision of EN 50173:1995", July 2000.

[3] prEN 50288-5-1, Multi-Element Metallic Cables used in Analogue and Digital Communication and Control, Part 5: Sectional Specification for Screened Cables Characterised up to 250 MHz, Section 1: Horizontal and Building Backbone Cables, June 2001.

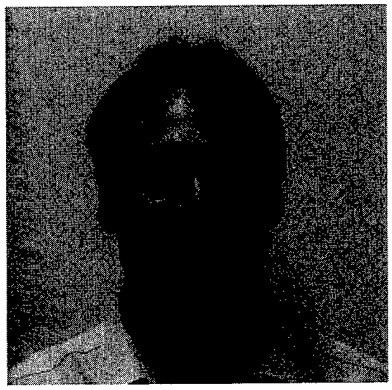
[4] prEN 50288-6-1, Multi-Element Metallic Cables used in Analogue and Digital Communication and Control, Part 5: Sectional Specification for Unscreened Cables Characterised up to 250 MHz, Section 1: Horizontal and Building Backbone Cables, June 2001.

[5] prEN 50289-3-5, Communication Cables – Specifications for Test Methods, Part 3-5: Mechanical Test Methods – Crush Resistance of the Cable, October 2000.

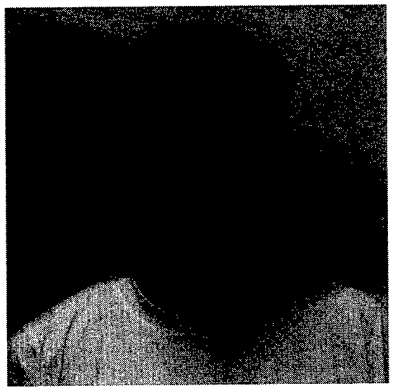
Authors



Werner Sittinger received his diploma in Electrical Engineering in 1991 at the University of Kaiserslautern at the department for optical data transmission. In 1991 he joined Siemens AG in the research and development department for communication cabling. Since 1998, he is working for Dätwyler and his current position is Product Manager for communication cabling.



Beat Schmucki received his diploma in electrical engineering at the Fachhochschule Luzern. He joined Dätwyler in 1984 and was engaged in manufacturing of copper data cables. Since 1990 he is responsible for the development of copper and optical fiber cables.



Daniel Fedier received his degree in electrical engineering in 1991 in Luzern. He joined Dätwyler in 1986 and was engaged in the testing of copper and optical fiber cables and the design of optical fiber systems. Since 1994 he is responsible for the test laboratory and quality manger.



Beat Tresch joined Dätwyler in 2000. He is working in the test laboratory and responsible for the implementation of new test methods and test set-ups.

Transmission Parameters of Cascaded Systems

^[1] *Mohammed M Al-Asadi, [1]Alistair P. Duffy, Kenneth G Hodge, [*]Arthur J Willis & [*]David A Jackson*

[1]EMTERC Center, Faculty of Computing Sciences and Engineering, De Montfort University, The Gateway, Leicester LE1 9BH, UK

[*]Brand-Rex Ltd, Glenrothes, Fife KY6 2RS, Scotland, UK

[^]Principle Author + 44 – 116 - 2506157 · alasadi@dmu.ac.uk

Abstract

An equation for the prediction of the Return Loss of cascaded systems has been previously presented and validated. This paper further validates this equation against experimental data obtained for communication channels containing long copper cables and connectors. The paper also presents an analytical approach to the calculation of the propagation constant and hence the calculation of both attenuation and phase constants for a cascaded system based on knowledge of the impedance and the propagation constants of each element. Both the impedance and the propagation constants used in the proposed analysis of every individual component may be obtained analytically or experimentally and are frequency dependent parameters. The attenuation and phase prediction can account for tolerances in impedance and in length of cables and connectors. The validity of the derived equations is confirmed by comparisons presented with measurements and simulations performed using the Transmission-Line Matrix (TLM) method. Implications for Insertion Loss Deviation (ILD) are also considered.

Keywords

Cable; Connectors; Channels; Cascaded systems; Return Loss; Attenuation; Phase constant; Impedance; Modeling.

1. Introduction

The increase in processor speeds has continued constantly over the last couple of decades. As a result of this increase and higher data volume applications, the pressure to communicate faster has not diminished. While optical fiber provides high bandwidth channels, it is generally only suited to back-bone operation. Coaxial cable, a relatively high bandwidth choice for 'the last mile', is relatively expensive and has greater connectivity problems when compared to twisted-pair. Hence, a constantly improving understanding of the operation of structured wire cabling at higher frequencies is fundamental to the ability of communications systems to meet the challenges faced by pressure from the computing and communications content producing sectors.

Although calculations and modeling of the parameters, e.g. the return loss, for individual transmission channels, such as cables under different termination conditions, have been a increasingly investigated in the last few years [1,2,3], relatively little work has been published on the parameters of an overall cascaded transmission channel. This paper addresses the performance of a complete channel.

A typical configuration of a copper cable transmission channel between the source of the transmitted signal and the receiving end is illustrated in figure 1.

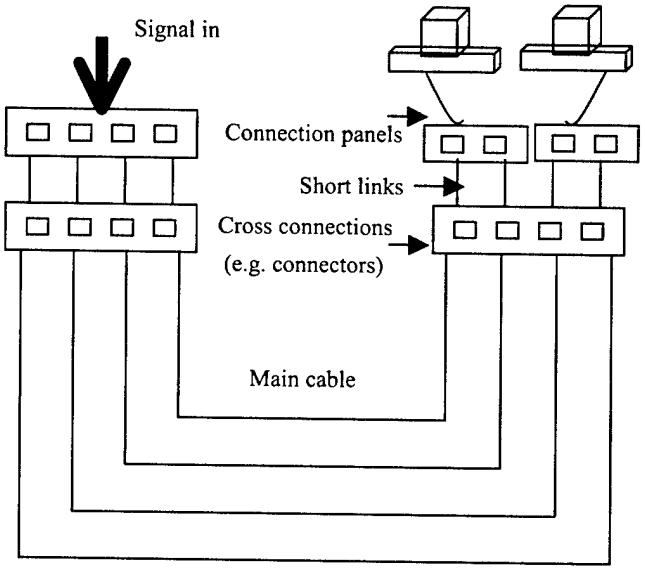


Figure 1. Typical Channel Configuration including short links and connectors

This channel represents a classic cascaded communication system, where each component of the system has its own transmission and reflection parameters. The characteristic impedance of any individual component of such a system may not always perfectly match the characteristic impedance of the neighboring components [4]. This mismatch may result in a significant increase in the return loss value [3]. The impedance mis-matching between system component will also affect the propagation constant measurements[5]. Therefore, the design and development of future facing cabling systems requires a thorough, and detailed, understanding of the secondary transmission characteristics of individual cabling components and their interaction when configured in a system.

This paper presents the development of a general equation for the calculation of the propagation constant and, hence, both attenuation and phase constants of a cascaded system, based on a knowledge of the impedance, the propagation constant and the length of individual parameters of the system. The equation is validated against data obtained by measurements and modeling. In addition to this validation, this paper further validates the return loss equation previously presented against experimental data.

2. Equation Development

2.1 Attenuation and phase constants calculation

A transmission channel containing, for example, four connectors and three cables (two patch links and one horizontal link) can be represented by a two port networks illustrated in figure 2.

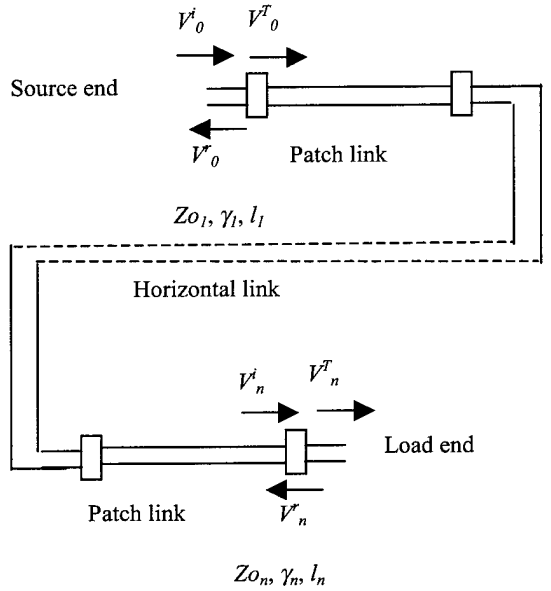


Figure 2. Two-port network representation of a representative channel, illustrating the properties of each component

Taking into account the complex propagation constant, the incident voltage at any part of the system is given as:

$$V_j^i = V_{j+1}^T \cdot e^{-\gamma_j l_j} \tag{1}$$

where j indicates the j th component from the source end, γ is the propagation constant of the jth component and l is the physical length of that component. The superscript T implies a transmitted signal. Similarly, transmitted and reflected voltages at the connection between a channel component and the following one are given respectively as:

$$V_j^T = V_j^i \frac{2 \cdot Z_{oj+1}}{Z_{oj+1} + Z_{oj}} \tag{2}$$

$$V_j^r = V_j^i \frac{Z_{oj+1} - Z_{oj}}{Z_{oj+1} + Z_{oj}} \tag{3}$$

Similarly, incident, reflected and transmitted voltages from, and at, all the channel components can be obtained. Following a similar approach to the approach reported in [3], the relationship between the overall voltage incident into the far end of the channel and the voltage transmitted from the source into the 1st segment of the channel can be obtained as:

$$\frac{V_n^i}{V_0^T} = \left[\prod_{k=1}^{k=n-1} \frac{2 \cdot Z_{ok+1}}{Z_{ok+1} + Z_{ok}} \right] \cdot e^{-\left(\sum_{m=1}^{m=n} \gamma_m \cdot l_m \right)} \tag{4}$$

where n is the number of components cascaded in the channel. To aid visualization and analysis, the channel illustrated in figure 2 can be replaced by one segment of cable having a length that is equivalent to the overall length of the channel as illustrated in figure 3. This can be achieved under the condition that the characteristic impedance of this cable is adjusted so that the relation between the incident voltage reaching the end of the cable and the transmitted voltage from the source is equivalent to that given in equation 4.

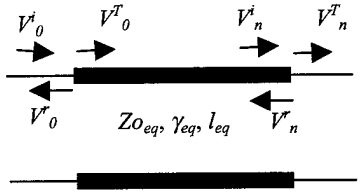


Figure 3. Equivalent circuit to the channel illustrated in figure 2

For the above circuit, the relation between the received voltage at the far end and the incident voltage at the near end of the circuit is given as:

$$\frac{V_n^i}{V_0^T} = e^{-\gamma_{eq} l_{eq}} \tag{5}$$

where γ_{eq} is the desired equivalent propagation constant of the whole channel illustrated in figure 2 and l_{eq} is the equivalent physical length of the equivalent circuit illustrated in figure 3 and given as:

$$l_{eq} = \sum_{k=1}^{k=n} l_k \tag{6}$$

Comparing equations 4 and 5 leads to:

$$e^{-\gamma_{eq} l_{eq}} = \left[\prod_{k=1}^{k=n-1} \frac{2 \cdot Z_{ok+1}}{Z_{ok+1} + Z_{ok}} \right] \cdot e^{-\left(\sum_{m=1}^{m=n} \gamma_m \cdot l_m \right)} \quad (7)$$

Taking the natural logarithm for both sides of the above equation gives:

$$-\gamma_{eq} l_{eq} = \ln \left(\left[\prod_{k=1}^{k=n-1} \frac{2 \cdot Z_{ok+1}}{Z_{ok+1} + Z_{ok}} \right] \cdot e^{-\left(\sum_{m=1}^{m=n} \gamma_m \cdot l_m \right)} \right) \quad (8)$$

Equation (8) can be simplified to the following form:

$$-\gamma_{eq} l_{eq} = \ln \left[\prod_{k=1}^{k=n-1} \frac{2 \cdot Z_{ok+1}}{Z_{ok+1} + Z_{ok}} \right] - \left(\sum_{m=1}^{m=n} \gamma_m \cdot l_m \right) \quad (9)$$

Hence the overall propagation constant of a channel containing n components and having overall length given in equation 6, can be given as:

$$\gamma_{eq} = \frac{-\ln \left[\prod_{k=1}^{k=n-1} \frac{2 \cdot Z_{ok+1}}{Z_{ok+1} + Z_{ok}} \right] + \left(\sum_{m=1}^{m=n} \gamma_m \cdot l_m \right)}{\sum_{i=1}^{i=n} l_i} \quad (10)$$

All the elements of the above equation are known, hence the overall propagation constant can be obtained. Since impedance values of the above equation and propagation constants of all individual elements are complex quantities and are frequency dependent, the obtained overall propagation constant is a complex quantity and is frequency dependent. Given that the propagation constant of any transmission line is [6]:

$$\gamma = \alpha + j\beta \quad (11)$$

where α is the attenuation of that circuit and β is the phase constant, the attenuation constant of the whole channel, per unit length, the insertion loss can be obtained, in dB, from equation 10 as:

$$\alpha_{eq} = \mathrm{Re} \left[\frac{-\ln \left[\prod_{k=1}^{k=n-1} \frac{2 \cdot Z_{ok+1}}{Z_{ok+1} + Z_{ok}} \right] + \left(\sum_{m=1}^{m=n} \gamma_m \cdot l_m \right)}{\sum_{i=1}^{i=n} l_i} \right] \cdot 8.686 \quad (12)$$

and the overall phase constant of the same channel can be obtained from:

$$\beta_{eq} = \mathrm{Im} \left[\frac{-\ln \left[\prod_{k=1}^{k=n-1} \frac{2 \cdot Z_{ok+1}}{Z_{ok+1} + Z_{ok}} \right] + \left(\sum_{m=1}^{m=n} \gamma_m \cdot l_m \right)}{\sum_{i=1}^{i=n} l_i} \right] \quad (13)$$

2.2 Insertion Loss Deviation (ILD) calculation

The total attenuation (insertion loss) of a channel is normally calculated by adding up the attenuation of all the components: this is referred to as the channel insertion loss or the channel attenuation [7]. This is only an approximation, but one which is easy to calculate and relatively accurate if the impedances of the individual channels are close to being matched. In fact, the channel measured insertion loss (overall attenuation) is higher than the result obtained using this approximate method. This difference is due to signal reflection, and re-reflection, between channel components produced as a result of impedance mis-match. Insertion Loss Deviation (ILD) is the difference between the actual insertion loss as measured on a channel and that obtained as a result of adding up the components' attenuation. Hence it can be given as:

$$ILD = \alpha_{eq} - \sum_{k=1}^{k=n} \alpha_k \quad (14)$$

It should be mentioned here that *ILD* is a relatively new term [7] but it is an increasingly important parameter that should be taken into account when assessing channel performance.

Numerical modeling also provides a tool to obtain the overall attenuation constant as well as other operational parameters. This is discussed in the following section.

3. TLM Model

Transmission-Line Matrix (TLM) modeling technique is used for the simulation of twisted pair cables and the mis-matching effects on short link performance [8]. It is a widely used tool for the modeling of microwave devices, circuits and electromagnetic fields simulations. Here, the method reported in [4,8] is again used for the calculation of the attenuation constant of the transmission channel described earlier in this paper. Knowing the incident and reflected voltages at both near and far ends of the transmission channel modeled using the TLM method, the overall attenuation constant of the channel can be obtained. Due to the fact that TLM is a time domain method, Fourier Transformation is used for the calculation of the frequency domain data. The overall attenuation constant is then computed using the following equation:

$$\alpha = -20 \log \left| \frac{V_F^r}{V_N^i} \right| \quad (15)$$

V_F is voltage incident into the load at the far end.

V_N^i is the incident voltage from the source at the near end of the TLM model.

The value obtained using equation 15 can then be used for the validation of the overall attenuation value of the transmission channel obtained using the developed equation 12.

4. Validation

This section deals with the validation of the equations published in reference [4] and those developed and reported in this paper.

4.1 Return Loss Equation Against Measurements

The return loss equation reported in [4] states that:

$$RL = -20\log\left[\frac{Z_1 - Z_S}{Z_1 + Z_S} + \left[\sum_{k=1}^{k=n}\left\{\left(\prod_{i=1}^{i=k}\left(\frac{2\cdot Z_i}{Z_i + Z_{i-1}}\cdot\frac{2\cdot Z_{i-1}}{Z_i + Z_{i-1}}\right)\right)\right\}\right.\right.$$
$$\left.\left.\cdot e^{-2\left\{\sum_{j=1}^{j=k}\gamma_j l_j\right\}}\cdot\frac{Z_{k+1} - Z_k}{Z_{k+1} + Z_k}\right]\right]$$

It was initially compared with data from a common equation obtained from [6], and against data obtained using the TLM approach.

This equation has then been used for the calculation of a transmission channel containing two patch links of 112.7Ω impedance and a horizontal FTP cable (Gigaplus cable) of 99.1Ω impedance. The length of each patch was $2m$ while the length of the horizontal cable was $305m$.

The effects of the connectors have been ignored in these calculations. Results obtained from both measurements and calculations are shown in figure 4.

For a similar transmission channel having the same length as both patches and the horizontal FTP cable, but with an impedance of the patch cable of 105.1Ω while the impedance of the horizontal cable was 98.7Ω, the overall return loss was measured and calculated using equation 26 of reference [4].

Determination of the return loss, generated as a result of different terminations, of a long channel by measurements may include the structural return loss generated as a result of coarseness of the cable geometry due to random manufacturing factors, handling, etc. [9]. While this adds extra features (fine-grain detail) to the results, the analytical solution predicts the performance envelope with excellent precision. This is clear from both figures 4 and 5.

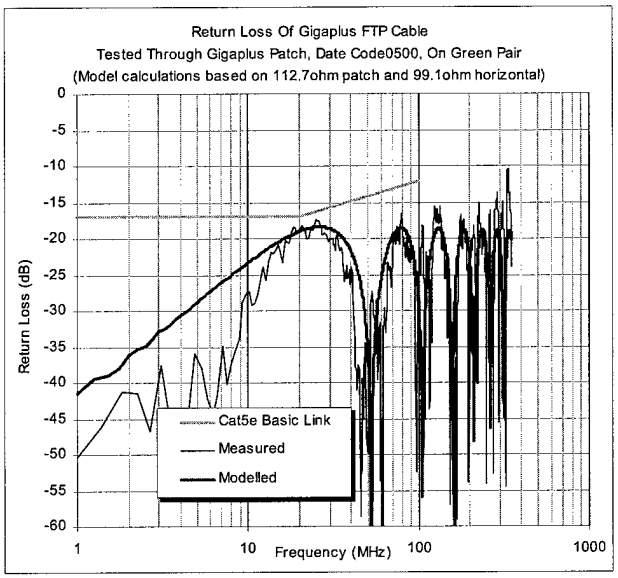


Figure 4. Return loss validation against measurement for a long 7-segment channel.

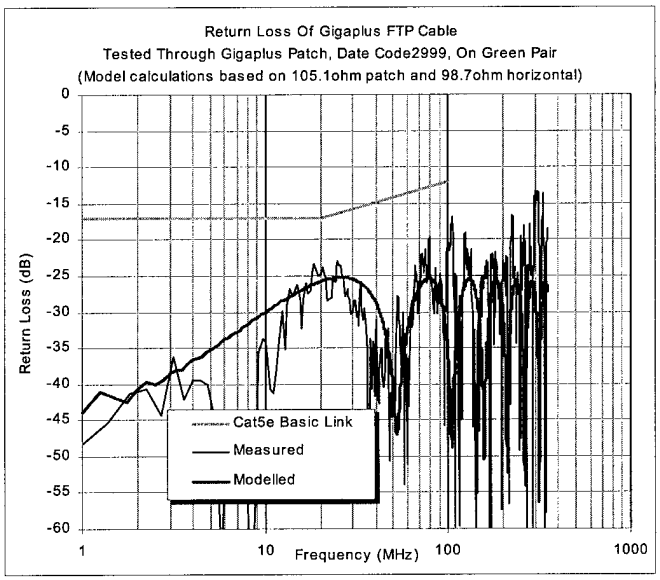


Figure 5. Reproduction of figure 4 using cables with different impedance values

4.2 Attenuation Equation Against TLM

Detailed derivation of the TLM model of a regular and irregular cable is given in both references [8] and [9]. The model developed in these references was then used for the prediction of handling effects, pig-tailing and short link performance under different working conditions. It was also used in reference [4] for the prediction of the overall return loss of a cascaded transmission channel.

TLM model was used for the calculation of the overall attenuation constant of the channel using equation 15 for a 3-segment transmission channel containing a Category 5 cable of 1 meter length connected at both ends via two connectors of 1 cm length. The nominal impedance of both connectors and the cable was 96Ω. Terminating with a matched impedance, the overall attenuation constant was then calculated using equation (12) and plotted along with that obtained using the TLM model for a range of frequencies as illustrated in figure 6.

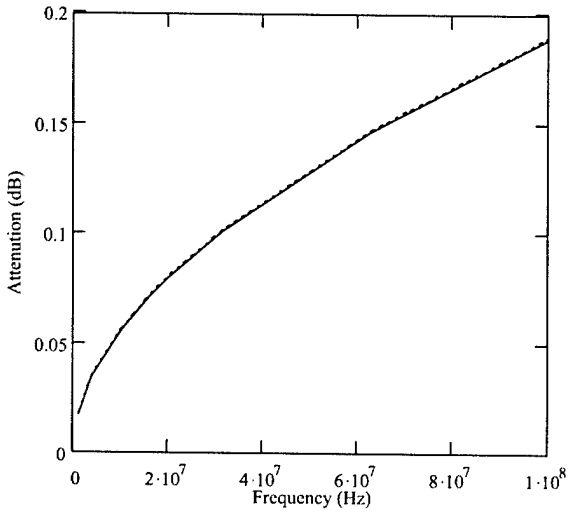


Figure 6. Attenuation constant for a 3-segment channel (1m cable) obtained using the new equation (Solid line) and using the TLM method (Dotted line)

Similarly, the overall attenuation constant of a 7-segment cascaded channel was obtained using both approaches and plotted in figure 7. The length of each patch link is $1m$ and the length of the horizontal cable is $10m$. The impedance of the patch links and the horizontal cables are similar to those used for the production of figure 6. Both figures 6 and 7 show a very good agreement between both sets of results, hence they confirm the validity of the derived equation.

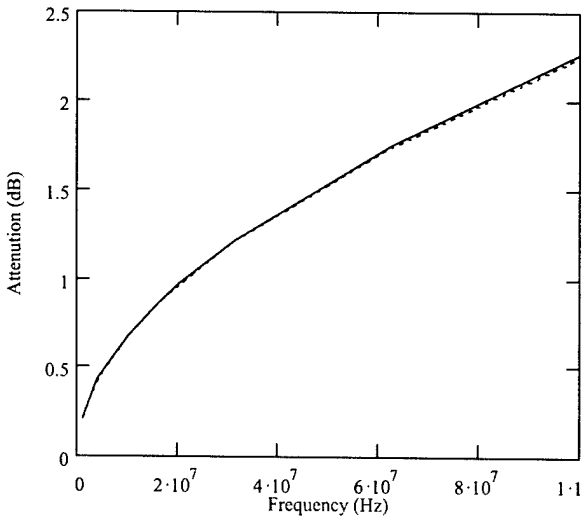


Figure 7. Attenuation constant for a 7 segment channel, using a 10m cable and 1m links, obtained using the new method (Solid line) and the TLM (Dashed line)

To calculate the insertion loss deviation, the overall attenuation of the transmission channel needs to be calculated using the traditional method. Figure 8, shows the overall attenuation constant of the $10m$ channel calculated using both the traditional approach and the new method.

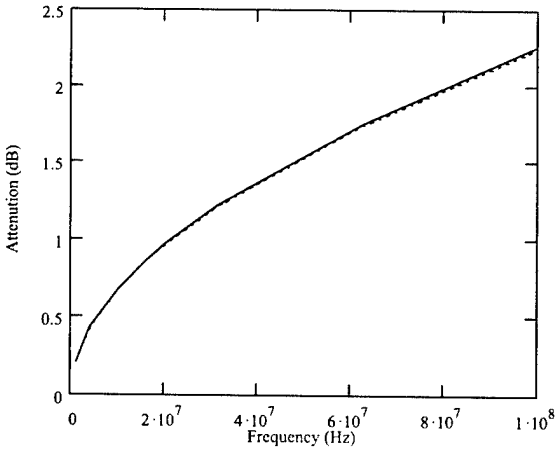


Figure 8. Attenuation constant for a 7 segments channel, using a 10m cable and 1m links, obtained using the new method (Solid line) and the adding up method (Dashed line)

Figure 9 illustrates the Insertion loss deviation calculated from the difference between both values of figure 8 and using equation 14.

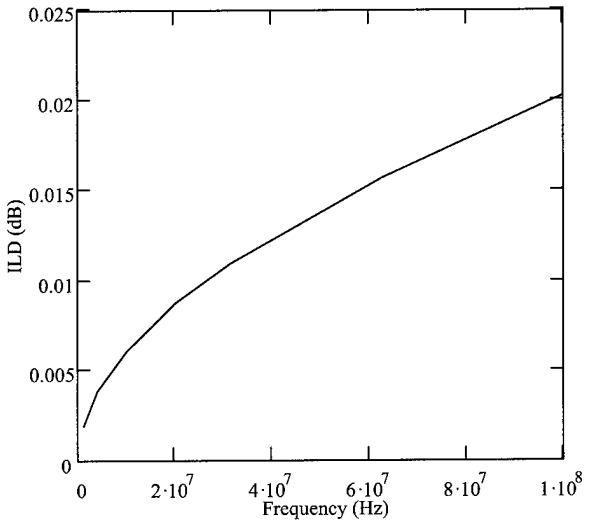


Figure 9. Insertion loss deviation, *ILD*, for the 7-segment 10*m* channel

5. Implementation and Results

After validating the performance of equation (12), it was then used for the calculation of the overall attenuation constant of a practical communication channel containing 7-segments as described earlier and for different termination conditions. The insertion loss deviation *ILD* was also computed.

5.1 Matched conditions

The attenuation was obtained under matching conditions, where the impedance of both patch links illustrated in the 7-segment channel shown in figure 2, match the impedance of the horizontal cable. Connectors were assumed to have the same impedance. Results for a 1*m* patch and a 10*m* cable were reported earlier as plotted as in figures 7 and 8.

For a similar channel having a 2*m* links and a 100*m* cable, the overall attenuation constant is computed using both the new equation and the summation approach. Results are plotted in figure 10.

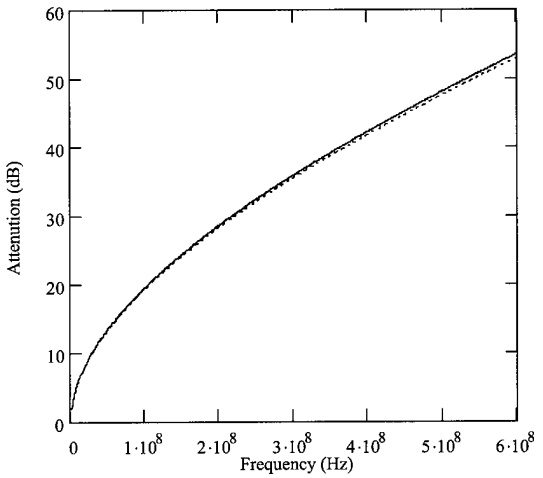


Figure 10. Overall attenuation for a 100*m* channel using the new equation (solid line and the summation method (dotted line).

5.2 Mismatching conditions

For a channel of two patch links and one horizontal cable where the impedance of both patch links mismatches the impedance of the cable, the overall attenuation of the channel and the ILD were also computed using both the new equation and the summation approach. For different lengths of cables and different impedance values, the following tests are carried out, it should be noted that the impedances used are illustrative and not representative of actual channels:

- 2m-10m-2m channel, where the impedance of the 1st link, the cable and the 2nd link are 83,5Ω-96Ω and 74.5Ω respectively, the overall attenuation was calculated using both methods and plotted as in figure 11. The *ILD* was also computed and plotted as in figure 12

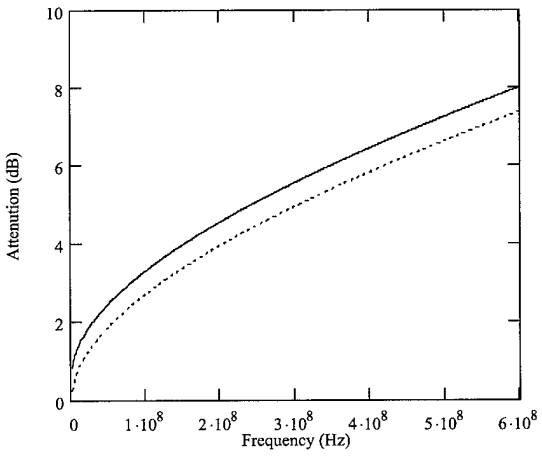


Figure 11. Attenuation for a 14 m channel, new equation (solid line) and summation approach (dotted line)

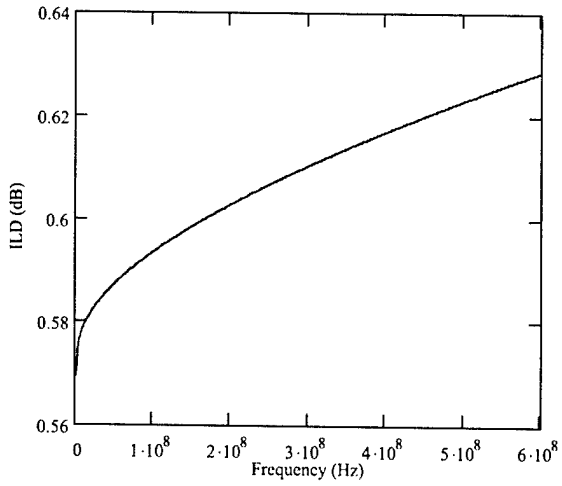


Figure 12. Insertion Loss Deviation of the results presented in figure 11

- For the above channel, where the impedances are 122.5Ω-96Ω and 74.5Ω respectively, the overall attenuation was also calculated using both methods and plotted as in figure 13. The ILD was also computed and plotted as in figure 14

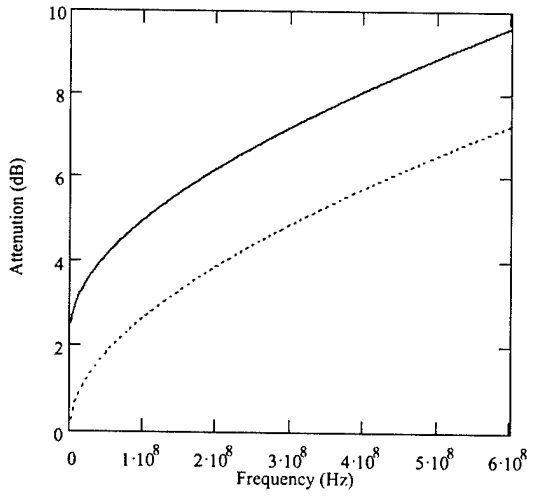


Figure 13. Reproduction of figure 11 for different matching conditions, new equation (solid line) and summation approach (dotted line)

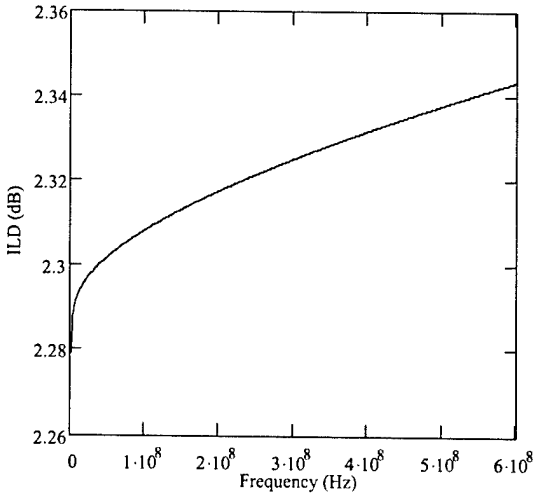


Figure 14. Insertion Loss Deviation, *ILD*, for results presented in figure 13.

- 2m-100m-2m channel, where the impedance of the 1st link, the cable and the 2nd link are 83,5Ω-96Ω and 74.5Ω respectively, the overall attenuation was calculated using both methods and plotted as in figure 15. The *ILD* was also computed and plotted as in figure 16

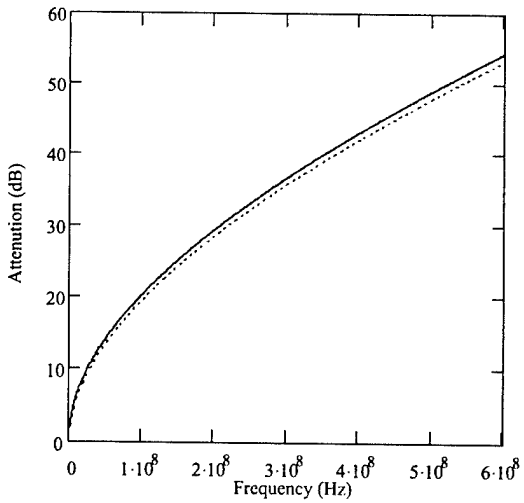


Figure 15. Overall attenuation for a mis-matched 104*m* channel, new equation (solid line) and summation approach (dotted line)

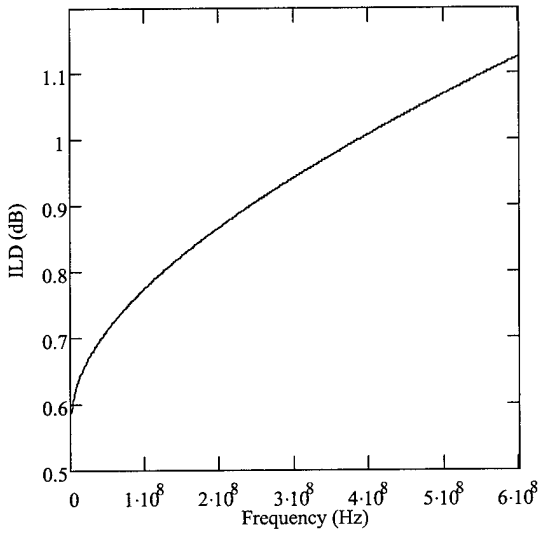


Figure 16. Insertion Loss Deviation of the results presented in figure 15

- For the same long channel, where the impedances are again changed to 122.5Ω-96Ω and 74.5Ω respectively, the overall attenuation was also calculated using both methods and plotted as in figure 17. The ILD was also computed and plotted as in figure 18

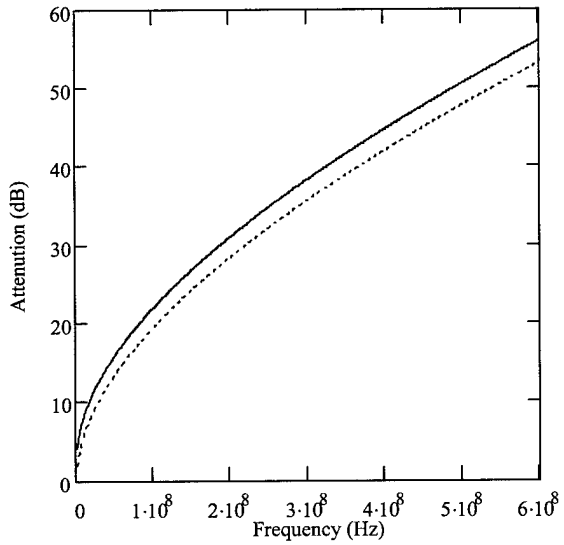


Figure 17. Reproduction of figure 11 for different matching conditions, new equation (solid line) and summation approach (dotted line)

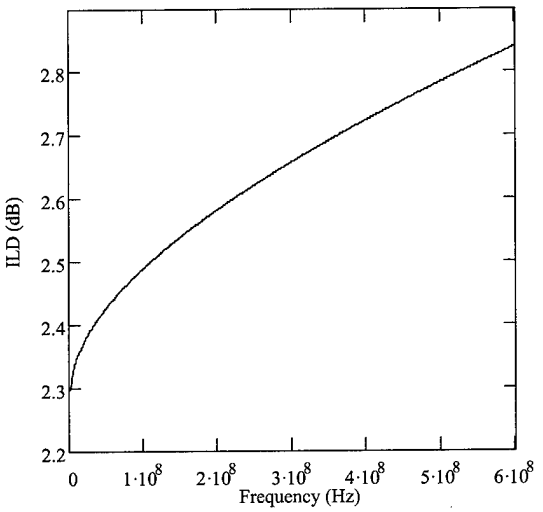


Figure 18. Insertion Loss Deviation of the results presented in figure 17

All the above tests illustrate the need to understand the effects of mismatching in both short and long channel on the channel's overall attenuation constant.

6. Discussion and Conclusion

An equation has been developed for the calculation of the propagation constant of a cascaded system containing many segments, each having different impedance values and different propagation constants. This equation has led to the development of an equation for the calculation of the overall attenuation constant of the system. It has also led to the development of an equation for the calculation of the overall phase constant of the cascaded system as function of the impedance and the propagation constant of each element. The new equation has been validated against the TLM modeling method.

Traditionally, the overall attenuation constant of a communication channel containing many segments of different lengths, different impedance and different propagation constants, was obtained by summing the attenuation constants of all the elements. While this is a simple calculation, it is only approximate. With increasing errors as shorter channels are considered, or where cascaded channels consisting of similar components is being considered. This is clear from results illustrated in section 5. The discussion on Insertion Loss Deviation (ILD) supports the need to treat the system attenuation calculation with care.

Further work is underway to validate and apply the phase constant calculation.

7. References

[1] T. Y. Otoshi, "Maximum and minimum return losses from a passive two-port network terminated with a mismatched load" May 1994, 18 *IEEE Trans on MTT, Vol.42, No. 5,* pp. 787-792.

[2] A. Umek, "Modeling the structural return loss in twisted pair cables", 10th IEEE Mediterranean Electrotechnical conference, MeleCon 2000, Vol.1, pp. 173-176.

[3] I. T. Sylla, M. Slamani, B. Kaminska, F. M. Hossein and P. Vincent, 1998, "Impedance Mismatch and Lumped Capacitance effects in High Frequency Testing" *16th IEEE VLSI Test Symposium Proceedings,* pp. 239-244.

[4] M. M. Al-asadi, A. P. Duffy, K. G. Hodge and A. J. Willis, 2000, "Return loss prediction for cascaded systems", *Proceedings of the 49th IWCS symposium*, pp. 578-585.

[5] D. C. Degroot, D. K. Walker, and R. B. Marks, 1996, "Impedance Mismatch effects on propagation constant measurements" *IEEE 5th Topical meeting, Electrical performance of electronic packaging,* pp. 141-143.

[6] S. Ramo, J. R. Whinnery and T. Van Douzer, *Fields and waves in communication electronics*, 2nd ed., 1984

[7] P. Kish, April 2000 "The effect of network cabling on Bit Error Rate performance", NORDX/CDT, white paper,12 pages.

[8] M. M. Al-asadi, A. P. Duffy, K. G. Hodge and A. J. Willis, 1999, "Analysing link performance in high frequency transmission systems", *Proceedings of the 13th Zurich EMC conference*, pp. 117-120.

[9] M. M. Al-asadi, A. P. Duffy, K. G. Hodge and A. J. Willis, 1997, "Modeling as a tool for analysing handling effects in structured wire cabling", *IEE 10th Int. Conf. On EMC, Warwick, UK,*, pp. 131-136.

Authors Biographies

Mohammed M Al-Asadi, Alistair P Duffy, Kenneth G Hodge and Artuhr J Willis: for photos and biographies, please see paper 04_01 in these proceedings.



David A. Jackson holds a BSc(Hons) in Electrical and Electronic Engineering from Abertay University, Dundee, Scotland. His career has been dominated by the design of test systems, initially as a Research and Development engineer working on test facilities for microprocessor systems. He has spent over 16 years in the cable industry designing and implementing radio frequency test methods.

Testing Between the Specs: Spark Testing for Quality Control

David Carroll
Sales Engineer/The Clinton Instrument Company
Clinton, CT
1-860-669-7548 dcarroll@clintoninstrument.com

Abstract
Spark testing has long been used on the primary insulation line and at packaging, providing first and final insulation quality checks. These tests are often mandatory under agency specifications.

An increasing number of manufacturers are finding that spark testing provides a valuable tool to check for insulation defects prior to or following interim processes including: twinning, bunching, taping, cabling, jacketing and marking.

Spark testers employed at key points of production insure that product damaged by mishandling or faulty prior-processes will not be further processed, which drastically reduces the likelihood that defects will be discovered during final hipot testing or by the customer.

Considerations for spark tester selection and application into interim processes will be discussed.

Keywords
Spark Testing; flaw detection; quality control; proof testing; insulation testing; dielectric testing; interim testing.

1. Introduction
Spark testers provide a clean, reliable, cost-effective in-line method for checking wire and cable insulation quality. The wide range of wire and cable products manufactured require spark test systems of different voltage types and operating frequencies. Systems are commercially available by a number of manufacturers that can test the majority of wire and cable products. These include power mains frequency, DC, Impulse and High Frequency AC spark testers.

Spark testing has long been used on the primary insulation line as the first measure of insulation quality during the production of insulated wire. It is also traditionally used at the packaging line, providing a final insulation quality check prior to shipment. These tests are mandatory under a variety of specifications. The requirements for the major specification agencies such as Underwriters Laboratories (UL) will be described and information necessary to select the appropriate spark test system will be presented.

Aside from these compulsory tests, quality conscious manufacturers are finding that spark testing provides a valuable tool to check for insulation defects prior to or after processes including: twinning, bunching and taping, cabling, jacketing and marking. Spark testers employed at carefully chosen points of production insure that product damaged by mishandling or faulty prior-processes will not find its way into expensive cable assemblies. This can drastically reduce the likelihood that the defects will be discovered during final hipot testing or in the worst-case scenario, discovered by the end user.

These in-process test points are generally not governed by published specifications. The major criterion for the application of a spark test system for these test points are therefore efficacy, reliability and cost-effectiveness. This paper will provide a general overview of the considerations regarding correct selection and application of the various types of spark testing equipment available. These considerations include: selection of test voltage type and level, electrode design and placement, product-grounding strategies, process control, maintenance and operator safety.

In many cases, standard spark testing equipment can be integrated into an existing process on the shop floor. In some instances, due to space considerations, modified or custom designed equipment must be developed for specific applications. When new equipment is to be purchased, spark testers can easily be integrated by the equipment manufacturers.

2. Spark Test Operation and Definitions
While spark testers are used in a number of industries to test a wide range of non-conductive products and coatings, spark testers for insulated wire and cable have evolved through the years into a unique and specialized form. They function by continuously applying a high voltage signal through an electrode to all surfaces of the insulated wire during manufacture. The center conductor is at, or near, ground potential acting as the reference ground or grounded electrode. The polymer under test insulates these electrodes from each other. When a defect or a fault in this coating passes through the high voltage electrode, the electrical resistance of the insulation is lowered to the point where an arc will form, which discharges the electrode, allowing current to flow from the high voltage electrode to the grounded electrode. The spark tester detects this current flow and provides various outputs.

2.1 Voltage Type
Spark testers can be divided into three general types: AC, DC and Impulse.

- AC testers are the most common type of spark test system. They are widely used to test most types of insulated wire products. These vary by frequency and can be further divided into two groups:
- Power mains frequency spark testers, which operate at 50 or 60 Hz. Depending on the Power Mains frequency.
- High frequency spark testers, which operate at frequencies above the power mains frequency. Systems ranging in frequency from 500 Hz. to 4.5 kHz. have been available. These are the single most common type of spark tester.

- DC or direct current testers are used often to test telecommunication wires and foamed products. Due to the more gentle nature of the DC signal, it is preferred for testing very fine wire with delicate insulation that might be damaged by the more aggressive AC type.
- Impulse spark testers operating at 200-250 ips (impulses per second) were adopted early on by the US military. They are still in wide use by military contractors. In the private sector they have been almost entirely replaced by high frequency spark testers.

2.2 System Configuration

Regardless of the manufacturer and the specific configuration, all spark test systems comprise the following components.

- Electrode- The electrode is the "working end" of the spark tester. Product under test travels through the electrode. In the past, there were as many electrode designs as there were manufacturers of spark testers. Agency acceptance of the bead chain electrode accounts for its wide use. Other designs may offer advantages in specific applications.
- High Voltage Power Supply- This is the high voltage Generator, which might be a commercial power supply or a specially designed proprietary transformer. This is typically located within the enclosure that also houses the electrode.
- Control Interface- This provides a means to energize the system, adjust the test voltage and reset the circuitry after a fault has been detected. These controls can be located on the front panel of a separate control unit, operated locally and accessible to the line operator, or it can be interfaced into the centralized, line control system with analog or digital signals.
- Fault Detection Circuitry- This is the heart of the spark tester. The detection circuit analyses the current flow to the electrode. When this current exceeds a predetermined value (that associated with an arc striking ground through faulty insulation) the circuit energizes providing means to actuate alarms, counters and signals for centralized data collection.

3. Spark Testing to Agency Standards

Agency standards ensure that an effective spark test has been applied to wire and cables made to the standard. UL, NEMA, CSA, BSI and other agencies in their published standards for wire & cable products describe the required spark test apparatus as well as the specific test parameters. These include:

Electrode Design

As mentioned above, bead chains are the most common type as they are accepted for the UL, CSA, NEMA and many other published standards.

Test Voltage

The test voltage is specified in every agency specification. Test voltage varies with the insulation thickness or wire gauge (considerations for test voltage selection in the absence of specified voltages will be discussed later in this paper.)

Electrode Length/Dwell time

The dwell time is the amount of time that any point on the wire remains under test in the electrode. Electrodes must be long enough to maintain the specified dwell time at the maximum line speed. Often the dwell time (or electrode length) of an AC spark test is linked to the frequency in Hertz of the spark tester. For example The UL standard for Electrical Wires, Cables and Flexible Cords, UL-1581 requires an electrode length which will allow nine full cycles.

To calculate the maximum allowable line speed for a given electrode length to UL-1581 and all UL standards based on it, the following formula is used:

$$S = (5/9)\,FE$$

Where S is the maximum allowable line speed in feet per minute, F is the test frequency in Hertz and E is the electrode length in inches.

Agency standards generally specify where in the production line the test is to take place. The two most common test points are immediately following primary extrusion and just prior to final packaging.

While these test are often mandatory, there are no limitations imposed by these agencies to the number of spark tests that might be conducted to wire and cable products. Manufacturers are therefore free to employ additional spark tests to monitor the quality of the insulation elsewhere in the production line, between these compulsory tests.

4. Limitations of Agency Standards Testing

Production line spark testers when properly applied in conjunction with agency standards are effective in detecting insulation defects on primary extrusion of single conductor wire. The final spark test at packaging checks the integrity of the cable jacket only when applied over a metallic shield. When there is no shield, this test is ineffective, detecting faults only when damage to the jacket is severe enough to also expose the underlying conductor, which provides the necessary path to ground. No spark tester is able to find defects in component conductors when covered by a jacket.

Expensive engineered cables typically include multiple insulated wires, twisted pairs, bunched and taped groups, fillers, shields and drain wires. A relatively simple finished cable can represent a dozen or more separate processes, each adding to the cost of manufacture. Defects to individual components, if not detected, can be unknowingly manufactured into expensive cable assemblies. Often these defects will be discovered during final hipot testing, but only after a series of expensive value-added operations have been performed to finished goods. While locating these faults is possible, it is a costly, time-consuming process that often results in less profitable short product lengths and high percentages of scrap. In the worst-case scenario defective cables may pass final testing, only to fail in the field and be discovered by the customer with potentially serious consequences.

With continued attention to product quality and minimizing waste in order to increase profitability, spark testing offers a familiar and valuable tool for manufacturers who must tightly control product quality while keeping manufacturing costs low and reducing scrap. It makes sense therefore, from the point of view of both product quality and profitability to have the ability to identify defects in cable components following processes that may introduce damage, and before they are further processed.

5. Interim Spark Testing

Spark testers offer a reliable means by which defective components can be identified. Often the same type of standard equipment already in use for the agency prescribed tests at either end of the production line can be utilized for this "interim" testing.

5.1 Fault Types

The spark test, when properly applied, will detect a wide range of fault types. Defects that can be detected with a spark tester are referred to as "spark faults" and can be divided into two broad categories: Insulation defects and Subsequent defects.

Insulation defects are those flaws that are associated with the extrusion process and are detected during the primary spark test. Faults of this type are caused by a variety of factors including defective raw materials and improper extruder operation. Insulation defects are outside of the scope of this paper and will not be further discussed. A. Hebert and R. Trinklein have recently written a paper that offers a comprehensive discussion of spark fault types associated with the extrusion process in their paper *Troubleshooting colored wire and cable products.* [1]

Subsequent defects are introduced into the product after the primary extrusion of the component conductors. Assuming that an effective spark test has been performed at extrusion and that the product is therefore free of insulation defects, subsequent defects then include anything that compromises the insulation to the point where detection by a spark tester is assured. The causes of these defects are many, careless handling and storage of product, poorly operated or maintained downstream equipment can damage wire. Any process that is out of control can put an insulated wire at risk. The nature of these faults with examples of their causes include:

- Cuts and abrasion. Contact with sharp objects, rough surfaces and impact with objects can cause physical damage to the insulation. Numerous causes have been observed, among the most common are: collision between fork lift trucks and stored process reels, sharp edges on reels that nick the insulation as wire is being paid off, worn or broken twinning bow ferrules that expose sharp edges and moving wire falling off of guide sheaves and being skinned by stationary objects.
- Splices. In continuous cabling operations the spark tester detects splices to individual conductors that have not been identified and removed, in the same way as bare wire.

An analysis of product failure modes is often part of a comprehensive Quality Control Program. Careful observation of the processes involved in a particular cable's manufacture will show the cause for faults of any type. When corrective actions are performed, the spark testers role is then to continuously monitor product quality and alert the operator when control is lost resulting in damage.

6. Application of Interim Spark Testing

Because interim tests are voluntary and not governed by agency specifications, the sole criterion is efficacy. It is important therefore for persons involved in process engineering and quality control to understand what is required in order to effectively apply a spark test system to a process.

Interim tests on single conductors can be performed using the same type of test system employed for the primary insulation test. This is generally a retest after a period of storage or an incoming inspection for product manufactured elsewhere. For these applications, the same test parameters and electrode design used at extrusion can in most cases be repeated with good results.

Interim tests are often performed on conductor pairs, quads or larger groups of conductors. These applications cannot always be successfully tested with standard test equipment. In some cases, modifications to standard equipment are necessary; in other cases custom-made systems must be configured for specific test points.

6.1 Placement of the Spark Test

In order to assure an effective application it is important to consider the location of the test site. The issue is twofold: finding a location that is both effective and practical.

The spark tester must be positioned far enough into the production line so that all of the potential points of damage precede the test, but before the subject wires, due to some later process, become inaccessible. As an example, when twisted pairs are bunched, the test point is best placed just before the closing die, at a lay plate. Or in the case of a bunch being tested for damage, prior to adding a drain wire or shielding.

Having enough physical space to fit the system can be challenging in an existing cabler, for instance. The control unit (when this is a separate component) can usually be located remotely; the electrode and its enclosure pose the bigger problem. In most cases careful consideration, creative thinking and clever design will uncover an adequate location.

6.2 Voltage Type

Each of the three spark tester types (see 2.1 above) has different properties. No single type of spark tester can reliably test all wire applications.

Multiple conductors place a heavy capacitive load on the spark tester. AC spark testers are sensitive to this loading, which can limit the available AC test voltage. If the test voltage is limited to a level that is below the effective test voltage, an effective test cannot be performed.

DC systems are the usual choice for multi conductor testing. These systems are not prone to current losses resulting from high product capacitance the way that AC and Impulse systems are.

6.3 Test Voltage Level

Determining a safe effective test voltage for testing can be difficult. Too high a test voltage and the spark tester can damage the insulation, particularly on the smaller wire sizes. Too low a test voltage and the test will be ineffective, allowing defects to pass through undetected.

In order for the detection circuit to function, an arc (spark) must occur. The design of the electrode is a significant factor in arc generation along with the voltage potential. The voltage level required to generate an arc between two electrodes (one charged and the other grounded) varies with the amount of air gap between them. This is referred to as the "spark gap voltage." Depending on the shape of the electrodes, this voltage can range between 25 and 100 volts (peak) per mil (.001 inches) of air gap.

In practical terms, the center conductor(s) provide the grounded electrode and the spark tester provides the charged electrode. The air gap is the space between the closest bead or bristle to the wire surface plus the insulation thickness, which for the purpose of spark test potentials is treated as additional air gap.

Spark tester test voltages as mentioned earlier are generally specified by agency standards for the primary extrusion test. These voltage levels provide a good starting point for test voltages when testing singles or twisted pairs during interim testing. When a test voltage is not given, it is necessary to experiment to determine adequate test voltage levels. This testing is to determine two key voltages: dielectric breakdown voltage and minimum effective test voltage.

The dielectric breakdown voltage is the voltage level at which good insulation will fail. This value is a function of the dielectric strength of the insulation polymer and the thickness of the insulating layer.

It is difficult to calculate an accurate breakdown voltage of an insulated wire even when the dielectric strength per mil of the insulating polymer thickness is known. It is more accurate to perform a simple test to a wire sample. Place a sample of wire into the spark test electrode and ground one end. Elevate the test voltage until the insulation fails noting the voltage at which failure occurred. Repeat this test on fresh samples several times to arrive at an average value. This is the breakdown voltage for that product.

The minimum effective test voltage is the lowest voltage at which the spark tester will reliably detect a typical fault of the type likely to be encountered in the application. This voltage is also easily determined through testing. Manufacture a fault, which will approximate a fault similar in nature to the actual faults encountered. Set this grounded into the spark tester and elevate the test potential until the fault will reliably be detected. Again repeat this test to arrive at average values. Use fresh samples each time because the carbonized polymer surrounding a previously detected fault site will artificially reduce the fault resistance and will lower the required voltage yielding inaccurate results.

Choosing an effective test voltage is a matter of selecting a voltage between the dielectric breakdown and the minimum effective test voltage levels.

H. Clinton has provided a thorough discussion of this method of determining test voltages in his paper entitled "Selection of 3kHz spark testing potentials for insulating wire." [2]

When a high frequency (AC) tester is used on the primary line for a given wire, but a DC tester is used when testing at twinning or cabling, it is necessary to select the equivalent DC potential to the AC voltage level. To convert an AC potential, which is an RMS (root means squared) measurement, to its DC (Peak) voltage equivalent, multiply the RMS value by 1.414. To convert a Peak voltage to its RMS potential, multiply the Peak Value by .707 (the reciprocal of 1.414)

Testing larger groups after bunching can pose difficulties in the selection of an effective test voltage. It is important to remember that the test voltage for the group cannot exceed the breakdown voltage of any single component conductor. A test voltage that is high enough to find pinhole faults in the middle conductor of the group may well be above the breakdown voltage in each conductor, possibly causing failures.

If detection of anything more than splices and gross physical damage is required, it is preferable to test the individual wires or pairs prior to closing or bunching at safe, effective voltage levels.

6.4 Electrode Type

Although standard electrode designs have been in use for many years, any conductive material that can be electrically connected to the high voltage power supply could conceivably be used as an electrode. The goal in choosing an electrode is to provide good product coverage allowing the test voltage contact with all surfaces of the product under test. Since the electrode is in physical contact with the moving product, it must be made of a material that is both longwearing and not damaging to the insulation. The most common electrode types are: bead chain electrodes, brush electrodes and ring electrodes. Each type has advantages and limitations.

The nearly universal agency acceptance of the bead chain design is an indication of both its effectiveness and its superior wear characteristics, compared with other materials. Bead chain electrodes can be made in different sizes to accommodate different product diameters and to fit different space allocations. Bead chains do not provide perfect coverage on large products, which require higher test voltages. Bead chain electrodes are not suitable for wires running vertically.

Wire Brush Electrodes are widely used to test flat cables, wire running vertically, or very large cables. Brushes typically are spring-loaded and bear directly on the wire surface. This allows for lower effective test voltages, as the air gap between the electrode and the wire surface is essentially eliminated, but wire brushes may abrade more delicate insulation. Brushes wear quickly, and over time will develop a "set" (the bristles bend and loose contact with the product). Bristles may break free from the brush and cling to the product. Due to the rate of wear, brushes must be replaced more frequently than bead chains. Electrodes made of metal rollers are sometimes used in place of brushes; they do not wear quickly, but are suitable only for flat cables

Ring Electrodes encompass many different types. Wire running through charged pigtails, springs, loops and tubes are all examples. Ring electrodes are simple and long wearing. However, ring electrodes are problematic in that adequate clearance must be provided to allow easy wire insertion when stringing up the line at start-up, and to allow variations in the diameter of the product under test. This clearance distance increases the air gap between the charged electrode and the wire surface, which will necessitate a higher test voltage. If the test wire is not guided concentrically through the ring, excessive electrical stress will be applied to the insulation. When the dielectric strength of the insulation is low, damage may result.

6.5 Fault Indication

As with standard production line spark testers, fault indication for interim testing is by front panel fault lights and counters as well as relay contacts, which can initiate process alarms and controls. The testing of single wires, pairs and bunched groups is identical to testing at extrusion or packaging, in terms of fault indication.

When testing multiple conductors, however, testing is often performed on groups of wires, running in parallel, through a common electrode with a single fault detector. This is referred to as "group detection." When the spark tester indicates a fault, it will not be known which conductor of the group tested contained the defect. Often the spark tester is configured to signal the line to halt and the defective conductor is located through visual inspection. In these cases knowing in which wire the fault occurred may not be important to the manufacturer, as that entire portion of the wire will be marked and discarded.

When testing multiple conductors, pairs or quads it is, of course, possible to detect faults in any wire, identifying the specific conductor in which the defect occurred. This is called "individual detection." In this case separate spark testers with individual electrodes are required. Due to the cost and space requirements of separate spark test systems to accommodate cable testing of up to 200 twisted pairs of wires, multi-channel spark test systems comprising separate fault detection, and fault indication circuitry for each channel, all housed into a common enclosure, have been developed. These units offer differentiation between pinholes, and bare wire with separate control outputs for each fault type.

While these custom designed systems are more complex and expensive, some manufacturers have found that having this information available allows for data collection of defect types, and patterns. Data analysis may point out specific processes or equipment that are out of control, leading to high percentages of failure. Corrective action can then be implemented that will justify the cost of the equipment.

6.6 Control Options

Control requirements for spark testers used in interim testing are similar to standard spark testers. Both local and remote control versions are available.

6.7 Grounding of Conductors

There is much confusion within the industry regarding the grounding of conductors during the spark test. In his paper "Grounding of Conductors during the Spark Test," H. Clinton discusses the reasons for grounding in terms of compliance with agency standards, efficacy of test and operator safety. [3] This complex issue will not be discussed in detail here, except to reiterate the importance of providing a secure ground connection to each conductor under test, and to provide a brief overview of the methods by which this grounding can be accomplished.

The grounding of wire on a process reel is relatively easy, requiring only minor modifications to equipment and processes. When the wire is wound onto the reel a tail must be left protruding from the side of the reel at the bottom. This "lead" with the insulation must be stripped from the end will later provide the ground connection during the spark test. The payoff spindle on the cabling machine likely rotates with the reel. It is a small matter then to drill and tap a hole into the spindle, insert a stud and provide some means by which a secure connection can be quickly made during changeover, generally a wing nut or a short lead with an alligator clip, or the like. The payoff rack must then be bonded to earth ground.

When wire is paid-off from a stem or barrel pack, it is also necessary to have the wire at the bottom accessible. When this is the case, a ground lead, bonded to a reliable ground connection can be conveniently made.

Often, prior processes must be altered to ensure that the means for providing the ground will be available. In the case where component wire is purchased off-site, specifying access to both ends of the wire on a reel or barrel, as a condition of sale may be necessary. In cases where this is impossible, there is little choice but to respool the wire, or to make the ground connection at the take-up end of the cable line.

It is equally effective to make the ground connection at take up, however, all of the connections must then be made with each finished reel, which may be cumbersome.

Some agency standards require grounding at both ends. While these tests are not governed by agency standards, the rational for grounding at both ends bears mention. Should there be a break in the conductor (open conductor) when only one end is grounded, the other end of the wire is left ungrounded, or floating. If the break has not opened, an intermittent ground may be present. This can cause false indications by the spark tester. Both cases pose safety concerns for the operator.

6.8 Maintenance

Maintenance on spark testers used for interim testing is the same as for production line spark testers.

The electrodes should be inspected regularly for excessive dirt build up, wear and damage. They should be cleaned or replaced when the condition of the electrode may begin to compromise function, i.e. when the beads or brushes are damaged to the point where they no longer make contact with the product.

Cable connections between spark tester components; power and ground should be inspected periodically for damage and looseness.

The equipment should be calibrated regularly, on the same schedule as the other spark testers in the plant. Since calibration generally only checks the high voltage output against the spark tester's voltmeter, some means of checking detector function and detection sensitivity is also advisable (this is true for all spark testers, regardless of application) this can be accomplished by purposely damaging a wire while it is being tested. If this is not practical, it can be checked offline by use of a grounded probe. Having a probe grounded through an impedance to simulate the load placed on the spark tester when wire is in the electrode will give more accurate results.

7. Conclusions

Mandatory spark tests to agency standards provide adequate in-process and final quality control measures for single conductors and simple cables. These tests are often inadequate, however, in more complex cable constructions that may comprise dozens (if not hundreds) of separate components. These cables involve many

different processes and a considerable amount of handling and storage of component parts. Each added step increases the possibility for damage, caused by many different factors, to individual cable components. This damage, if undetected, can cause failure at final testing, rejected product and lost profit.

Adding spark test systems at logical points of production can identify defects and damage to conductors before they are manufactured into expensive cabled products.

To apply the spark test system to an interim process, an analysis of the process under test, an understanding of spark test function and the elements of a successful spark test are necessary to make certain that product quality is being consistently and accurately monitored.

8. Acknowledgments

Special thanks to Henry Clinton, Marianne Savage and the Engineering Staff of The Clinton Instrument Company for making technical information available and for their assistance in producing this paper.

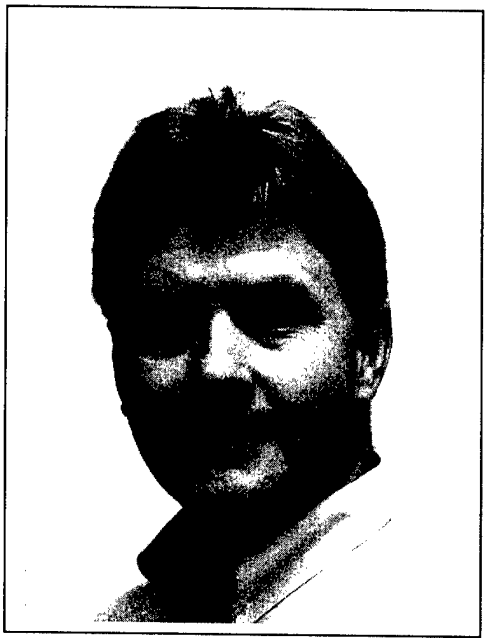
9. References

[1] A. Hebert and R.S. Trinklein, "Troubleshooting colored wire and cable products," *Wire Journal International*, 34(8), 36-37 (August 2001).

[2] H. Clinton, "Selection of 3kHz spark testing potentials for insulated wire," *Wire Journal International*, (1987).

[3] H. Clinton, "Grounding of conductors during the spark test" *Wire Journal International*, (March 1982).

David Carroll did his undergraduate work at Hampshire College in Amherst, Massachusetts. After college he became employed by the Clinton Instrument Company in the Engineering Department. For the past eight years he has been a Sales Engineer specializing in unusual spark testing applications and diversification.



New, Versatile Predictive Tool for Structural Return Loss

Ethem Erdas
Product Marketing Manager, Beta LaserMike,
Dayton, Ohio
+1 937 233 9935; erdase@betalasermike.com

Abstract
This paper describes a novel, versatile predictive analysis tool to assist in the on-line identification and rapid resolution of Structural Return Loss (SRL) faults on a wire or cable production line. An introduction to the problems posed by SRL to data communications products, a definition of SRL, and an explanation of the operation of the proposed predictive system are provided. A case study demonstrates the operation and effectiveness of the system.

Keywords
Structural Return Loss; Fast Fourier Transform; predictive analysis; wire; cable.

1. Introduction
Recent advances in technology and new inventions in the audio, video, and data transfer industries have led to increasing demand for higher data transfer rate requirements in data communications products. Despite the introduction of optical fiber, most data transfer is still carried out by copper cables constructed with decades-old production techniques. However, due to recent improvements in materials and manufacturing processes, it is now possible to manufacture telecommunication cables with data transfer rates many times higher than was attainable just a few years ago.

Meeting these increasing demands for high quality cable products must also be balanced by the need to lower manufacturing costs. Each step in the manufacturing process must be performed with great efficiency and accuracy, requiring the use of sophisticated tools during the various manufacturing stages. Measurement tools can be invaluable in evaluating the quality of the product, but it is important for such tools to be used at the proper time. If it is discovered that a finished cable does not meet the required standards, it may need to be either scrapped or sold as a downgraded product.

One of the parameters used to evaluate the quality of telecommunication cable products is Structural Return Loss (SRL). Until recently, the only way to measure SRL in a cable was to sweep-test the finished product. With a predictive analysis tool such as the one described in this paper, however, it is now possible to monitor various parameters of the cable during manufacturing and to predict its performance as a finished cable. It is also possible to monitor and control several manufacturing process variables and to predict their effect on the performance of finished cable. Early detection of cable failure through this tool makes it possible for manufacturers to realize significant time and material savings, improve productivity, and increase yields.

This paper provides an explanation of the importance of minute variations in the extrusion process, rather than a discussion of the theory and mathematics behind the SRL phenomenon. A case study is presented to demonstrate the effectiveness of the described predictive analysis tool.

2. Definition of SRL
SRL occurs when energy sent from one end of a transmission cable is reflected back to the source of energy due to periodic impedance variations caused by structural imperfections in the cable. More simply, SRL is a loss in transmitted energy. Imperfections causing SRL problems are not necessarily of large magnitude. Typically, these imperfections are impossible to detect using traditional measurement methods. The magnitude of equally spaced reflections caused by seemingly insignificant imperfections add in-phase at certain frequencies. These imperfections result in significant signal loss and cause "dropout". The first destructive SRL spike (resonance) will occur where the period (distance between imperfections) is equal to one-half the wavelength of the signal ($\lambda / 2$) and integral multiples of one-half wavelength. SRL, in decibels (dB), is defined as follows,

$$|SRL| = 20 \log_{10} (V_{returned}/V_{input}) \quad (1)$$

As the signal strength of the reflected wave increases, so does SRL. Therefore, the magnitude of the signal received at the load-end of the cable can be so small that it may appear non-existent. These increased reflections will occur at frequencies determined by the cable's propagation characteristics and by its impedance, which varies due to the presence of periodic physical imperfections. For example, for a coaxial cable in the Very High Frequency (VHF) spectrum, impedance is given as,

$$Z = [138.06 \log (D/d) / \sqrt{\varepsilon}] \ [1] \quad (2)$$

Capacitance is measured using,

$$C = [\, 2 \pi 8.85 \varepsilon / \ln (D/d) \,] \quad (3)$$

where Z is the characteristic impedance of the cable, d is the diameter of the inner conductor, D is the outside diameter of the extruded core, and ε is the dielectric constant of the insulation.

3. SRL Prediction
Equations 2 and 3 indicate that changes in D, d or ε will cause changes in characteristic impedance and capacitance of a cable. These changes can be detected with measurement equipment such as diameter and capacitance gauges. Note that the resolution and measurement rate of this equipment must be sufficient to detect minute variations at high frequencies.

The SRL Prediction system described in this paper was designed to accept analog signals from up to eight on-line measurement gauges. It is capable of processing these signals as individual channels. The first two of the eight possible channels are dedicated to diameter and capacitance gauges. The SRL Predictor uses signals from these two channels to perform Fourier Transform, calculate Impedance, and calculate predicted SRL. To obtain increased sampling frequency, these gauges require higher measurement rates.

Six additional inputs can be used to monitor other process variables. The SRL Predictor processes these signals and calculates all variables except SRL and Impedance. These signals were fed to a filter module that was designed to remove high frequency components to eliminate possibility of aliasing. Aliasing [2] occurs when high frequency components appear as the low frequency where sampling is less than two per cycle of the signal. These signals were then fed to the data acquisition card of the host computer.

The SRL Predictor program uses a Fast Fourier Transform (FFT) algorithm to identify minute, periodic variations in the signal and to transform from the time domain to frequency domain. Using the Fourier Transform (FT), any real signal as a sum of sinusoidal signals of varying frequencies can be expressed. The FT calculates the amplitude and frequency of periodic signals for all frequencies by dissecting the signal into its sine components.

As indicated by Figure 1, the FT of a sine wave with frequency f and amplitude A is a value A at frequency F.

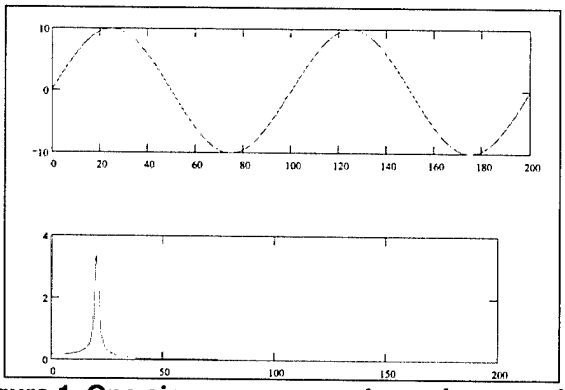


Figure 1. One sine wave generates only one spike

As shown in Figure 2, the sum of two sine waves will generate two spikes, indicating the amplitude and the frequency of each sine wave.

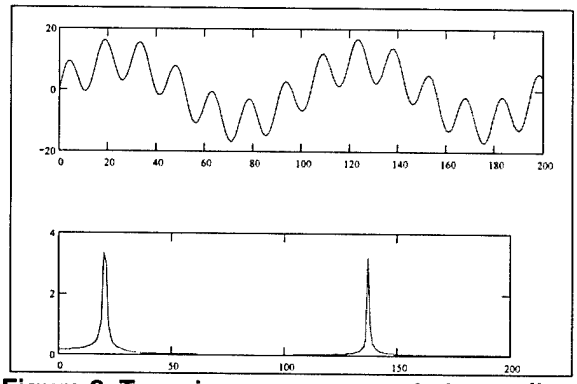


Figure 2. Two sine waves generate two spikes

Figure 3 illustrates that the FT of a square wave generates the spikes representing the sine wave components that make up the square wave.

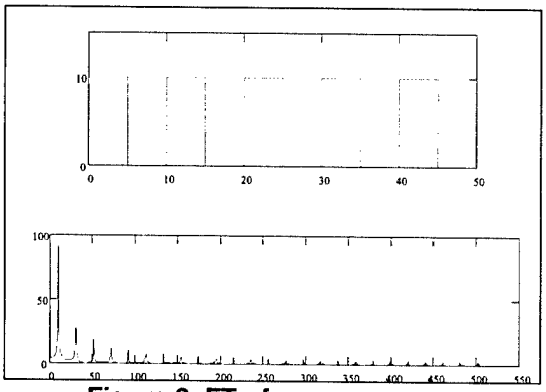


Figure 3. FT of a square wave

Figure 4 shows the sine wave as in Figure 1 with additional noise signal. The noise amplitude was defined to be ten times the amplitude of the sine wave. Even when the sine wave is completely buried in the noise signal, FT is capable of identifying the primary sine wave and the spike representing the amplitude, and the frequency of the sine wave can be seen in the FT graph. This principle allows the identification of cyclical disturbances that may otherwise seem to be merely noise.

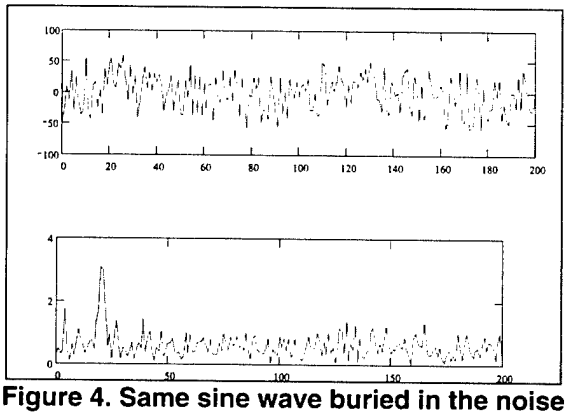


Figure 4. Same sine wave buried in the noise

To use FT in a practical application, the Fast Fourier Transform algorithm can be used on a computer. This algorithm uses a

sampled signal, with 2^N samples (2, 4, 8, 16, 32, 64, 128, 512...). The number of samples must be at least double the maximum frequency being analyzed (Shannon, Nyquist). The Nyquist theorem states that "the sampling rate must be at least twice the frequency of the highest frequency component in the waveform being sampled" [1].

4. Case Study

A case study demonstrates the usefulness of this technique of SRL prediction. In this case, the proposed SRL Predictor system was introduced to a primary extrusion line in a major telecommunication cable manufacturing facility in the USA. A SRL spike was identified on this line, which produced core cable for various types of coaxial cables.

It was reported that three types of coaxial cables failed an SRL sweep-test in a similar manner on this line. In all three cables, dropout occurred at approximately the same frequency (1.1GHz). The cause of this failure was identified as the primary wire extrusion process because the subsequent post-process stages for all three products utilized different machinery. Since the process commonality ended at the completion of primary extrusion, it was determined to be very unlikely that all three post-extrusion processes would have caused a dropout at the same frequency. Figures 5, 6 and 7 show the SRL graphs for each cable from off-line sweep-tests. All tests indicated the presence of a spike at approximately 1.1GHz.

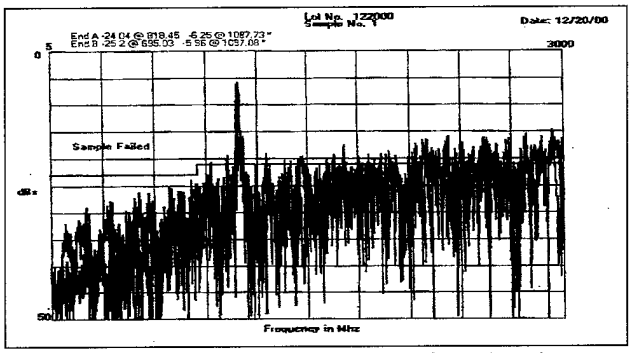


Figure 5: SRL sweep-test of cable #1

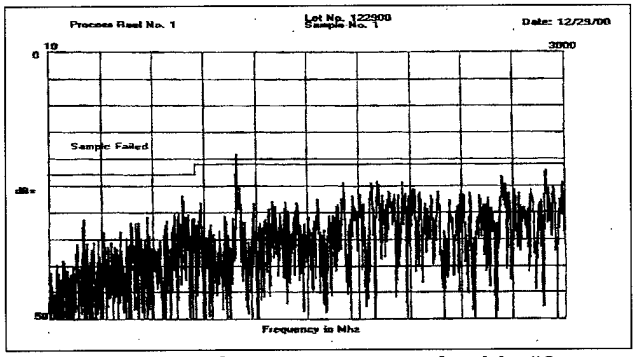


Figure 6: SRL sweep-test of cable #2

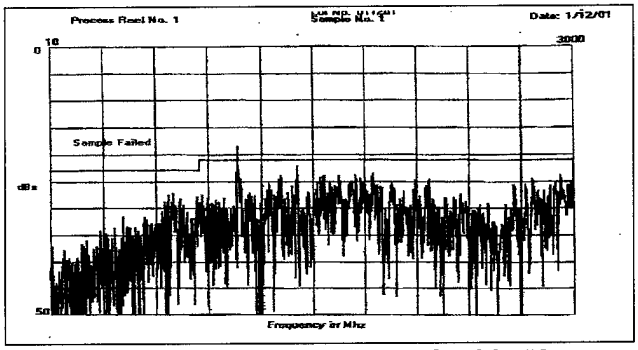


Figure 7: SRL sweep-test of cable #3

Next, it was necessary to determine whether the spike was present at the end of the extrusion process or was introduced during the braiding process. This required that the cable to be tested either during or immediately after the core extrusion process. It was not possible to conduct off-line sweep-tests on the core, so it was necessary to monitor the extrusion process and core parameters while the core was being manufactured.

The diameter gauge used (channel one) was a Multi Function Gauge (MFG1010), which simultaneously utilizes the principles of diameter measurement and fault detection. A unique software algorithm in this gauge combines the two signals to produce fast analog output representation of the cable diameter profile at a sampling rate of 15,000 times per second. The capacitance gauge used (KG1008) was similarly fitted with a short measuring electrode and a fast analog output. Channel three was connected to the tension controller for monitoring line tension variations. Channel four was connected to a hand-held accelerometer for monitoring vibration on various components in the line.

With the MFG diameter gauge, SRL prediction based on diameter variations was performed. As shown in Figure 8, there was a spike (indicating dropout) at approximately 1.1 GHz.

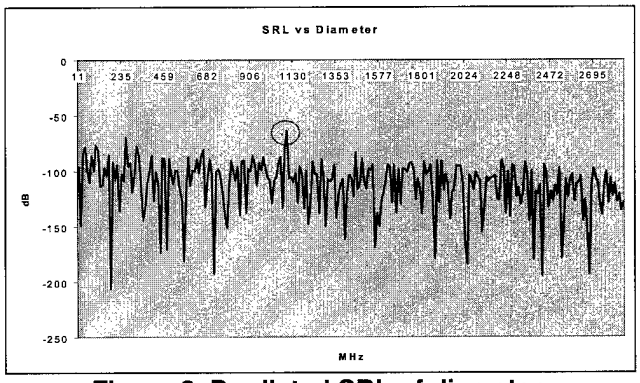


Figure 8. Predicted SRL of diameter, spike at ≅1.1GHz

The same spike was present after SRL measurements were obtained based on capacitance measurements. Figure 9 shows the SRL graph based on capacitance variations, with the spike still present. These tests confirmed that the spike was introduced before the braiding of the cable.

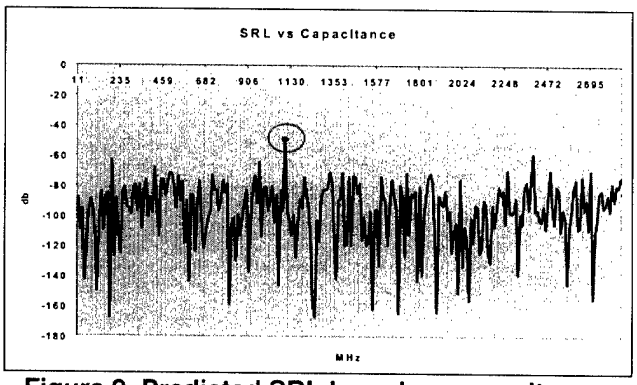


Figure 9. Predicted SRL based on capacitance, spike at ≅1.1GHz

Locating the cause of these variations was the next step. The FFT capability of the SRL Predictor was then used to examine various components of the line and diagnose the problem. Figures 10, 11, 12, 13, and 14 show the results of monitoring various parameters of the cable and extrusion line. A spike at 3.75Hz is visible in all graphs, suggesting the presence of cyclical variations in those parameters.

Figure 10 shows FFT vs. Hz, based on measured capacitance, indicating a 0.0027 pf/ft (.0089 pf/m) spike at 3.75 Hz. With this information and the knowledge that the line speed was 87 ft/min (26.5 m/m), the distance between variations (87ft/min / 60 sec/min / 3.75 Hz) could be calculated as 0.38667 feet (0.1179 meter). Using the "FFT vs. Length" graphing function the same result was found, as shown in Figure 11. It was therefore safe to assume that the process was introducing a variation in capacitance in the cable every (0.38667 ft x 12 inches)=4.64 inches (11.79 cm) of cable length.

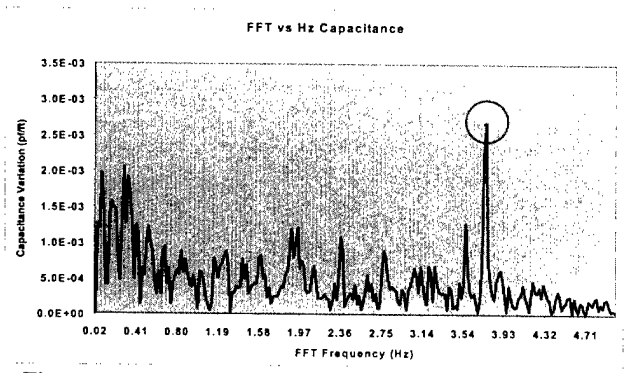


Figure 10. FFT of capacitance, spike at 3.75Hz.

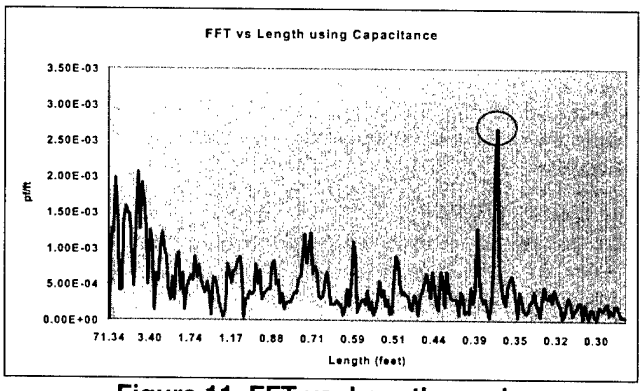


Figure 11. FFT vs. Length graph, spike at 0.387 feet (0.1179 meters)

Figure 12 shows the same 3.75 Hz spike, as ascertained through in diameter measurements.

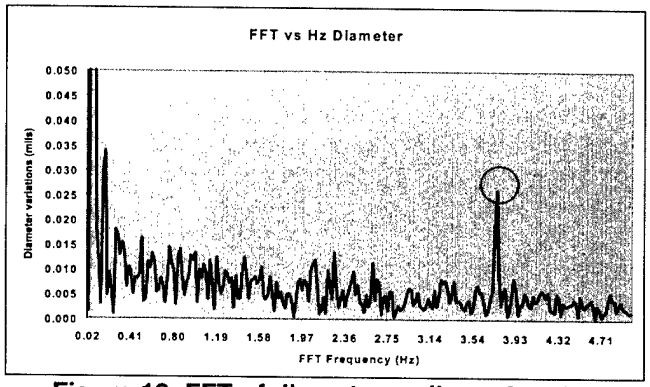


Figure 12. FFT of diameter, spike at 3.75 Hz

Using the multi-channel capability of the SRL Predictor system, the spike was identified in various cable parameters, as part of the attempt to determine possible causes. Since both capacitance and diameter measurements were varying, this problem was clearly a dimensional variation. Possible causes could have been either the mishandling of the conductor or an unstable extruding process. Mishandling of the conductor could have been the result of variations in line speed and/or variations in line tension. On the other hand, unstable extruding processes could have been the result of screw speed variations and/or extruder temperature variations.

Considering the availability of test equipment, access to various test parameters, and the difficulty of troubleshooting these causes, it was decided to focus first on the conductor handling processes. Using the third input channel of the SRL Predictor, FFT analysis was performed based on the line tension, and, as shown in Figure 13, the presence of a 3.75 Hz spike was discovered. This discovery indicated that a variation in line tension was causing the line speed to vary, thus affecting the volume of compound accumulated on the conductor, and resulting in core (insulation) diameter and impedance variations. Thus, conductor handling processes rather than extrusion processes were investigated.

Possible sources for the variation in line tension were considered. These included: out-of-round / damaged sheave or pulley with a

circumference of 4.46 inch (11.38 cm), a worn pulley bearing, a bad gear in one of the gear boxes, a mis-aligned drive mechanism in the capstan(s), an unstable drive-motor due to mechanical / electromechanical imperfection, a cycling motor driver, and oscillation in line speed. This list is clearly only a partial summary of possible causes for such a complex mechanical process.

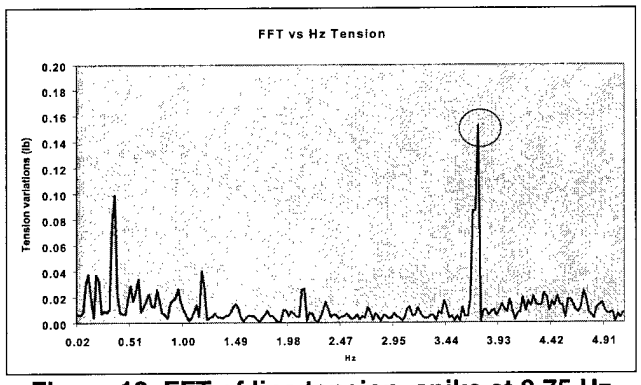


Figure 13. FFT of line tension, spike at 3.75 Hz

After an elimination process to determine most likely causes, a hand-held accelerometer analog output was connected to channel four of the SRL Predictor system. Vibration tests on various components and groups of components were conducted to identify a vibration pattern at 3.75 Hz or its harmonics. Tests conducted on the metering capstan revealed the presence of many vibration patterns, one of them being the 3.75 Hz spike. Figure 14 shows the FFT result of one of these tests, and Figure 15 shows the actual data recorded by the accelerometer itself, showing the 3.75 Hz spike, as well as other spikes.

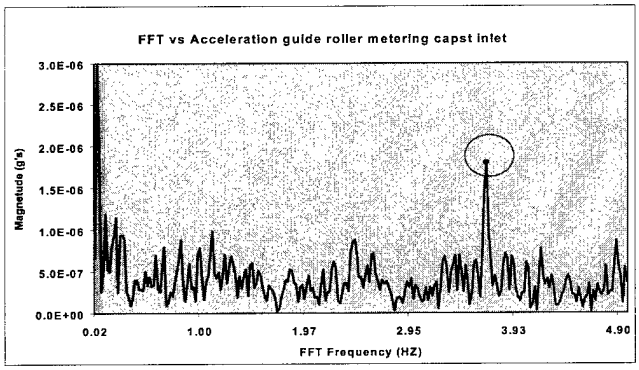


Figure 14. FFT of Accelerometer input, spike at 3.75 Hz

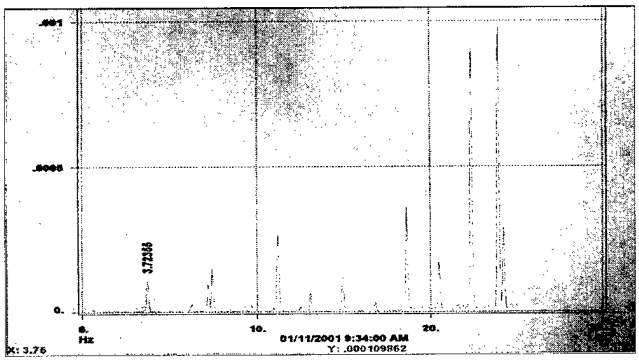


Figure 15. Accelerometer measurement on metering capstan

Having determined that there was a vibration pattern in the metering capstan, the next step was to determine if this was the cause of the spike in the cable. The metering capstan was bypassed by installing guide rollers and running the conductor through these rollers, instead of the capstan sheave. FFT tests on diameter, capacitance, and line tension showed that the spike was no longer present, confirming that the source of the spike was within the metering capstan.

Since the capstan was composed of many components, such as the capstan sheave, sheave drive belt, gearbox, gear drive belt, driver motor, and motor controller, component level troubleshooting and vibration tests were conducted. The following calculations identified the gearbox drive belt as the most likely source.

Motor and Gearbox Pulley Calculations

Pulley diameter: 4.875 in (12.38 cm)
Pulley RPM: 443 rpm/minute
Belt length (measured): 62 inches (157.5 cm)
Belt RPM = (π x pulley rpm x pulley diameter) / (belt length)
= (3.142 x 443 rpm x 4.875 in) / (62 in)
= 111.224 rpm x (1min / 60 sec)
= 1.85373 Hz (4)

Since the drive belt contacted two pulleys per revolution (1.85373 Hz x 2 = 3.707Hz), the resulting frequency was 3.707Hz. While this belt was reported to be new, it was clearly the cause of the failure, as indicated by Figure 16. After this belt was replaced, no spike was present in an off-line sweep-test.

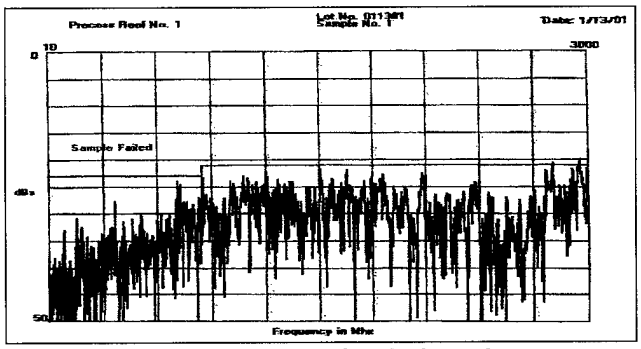


Figure 16. Sweep-test after belt replacement

To determine the magnitude of capacitance and diameter variations causing this spike, a signal generator was used to apply

a sine wave[1] signal to channel one of the SRL Predictor. The signal generator was adjusted to create a spike at 3.75 Hz with the same magnitude as the spike recorded during this case study. The amplitude of the sine wave causing the spike was recorded as 0.00135 volts. Since the KG1008 Capacitance Gauge produces a voltage output of 0 to 10 volts for a capacitance change of 0 to 150 pf/ft (492 pf/meter), the actual capacitance variation was as small as (0.00135 volts x 150 pf/ft / 10 volts)= 0.02 pf/ft (0.0656 pf/m).

The same experiment was conducted for diameter measurements by applying a sine wave signal to channel two of the SRL Predictor. The required amplitude for the sine wave was 0.03 volts. Knowing that the MFG1010 Gauge produces 0 to 10 volts for a diameter change of 0 to 0.04 inches (1.016 mm), the actual diameter change caused by the belt could be calculated as (0.03 volts x 0.04 inches / 10 volts)= 0.00012 inches (0.003mm).

As seen above, it would have been extremely difficult, if not impossible, to detect such variation-patterns using traditional measurement methods. Given the signal amplitude, it would not have been possible to identify the spike causing the SRL dropout at all. While this case study was conducted on a coaxial core line, similar troubleshooting methods can be applied to other types of communication cables.

5. Conclusion

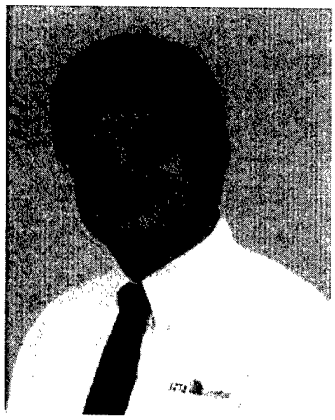
In conclusion, this predictive analysis system demonstrated an ability to troubleshoot potentially costly and complex mechanical problems. The effectiveness of this predictive technique in assisting in the production of high quality telecommunications cables should be highly effective in a competitive marketplace.

6. References

[1] Harold Hughes, "Telecommunications Cables Design, Manufacture and Installation," John Wiley & Sons Ltd. (1997).

[2] Robert W. Ramirez, "The FFT Fundamentals and Concepts" Tektronix, Inc. Englewood Cliffs, New Jersey, (1985).

7. Biography



Ethem Erdas
Beta LaserMike
8001 Technology Blvd.
Dayton, Ohio 45424
Phone: +1 937-233-9935
Fax: +1 937-233-7284
E-mail: erdase@betalasermike.com

Ethem Erdas is Product Marketing Manager for Beta LaserMike of Dayton, Ohio. For the past 11 years, he has held various technical and managerial positions at Beta LaserMike, and he has a B.S. in Electronics and Computer Engineering Technologies from the University of Dayton, of Dayton, Ohio. Prior to Beta LaserMike, he was involved in the development and manufacturing of metal vapor lasers at JC Laser Corp. in Dayton, Ohio. Mr. Erdas was born in Gebze, Turkey.

[1] In this experiment it was assumed that the shape of vibration was a sine wave or was very similar to a sine wave.

New Permanent Access Cable for Economic and Continuously Upgradable LAN

Dominique Brault, Georges le Noane, Jean-Claude Da Rocha,

Christian Lagreve, Daniel Fillatre, Yannick Roussel

ACOME

Usines de Mortain-Romagny – 50140 Mortain -France

+33.2.33.89.31.00 · dob@acome.fr

Abstract

Optical fibers are being increasingly deployed in local area networks, but it many believe that such approaches are still not cost effective. This paper demonstrates that a new LAN optical cable design along with new installation techniques lead to a solution which can be competitive with copper LAN solutions. Moreover this concept allows simpler management and continuously upgradable network such that has never been designed until today. The «anywhere» and « anytime » accessibility concept allows the management of network evolution without modifying the heavy part of network infrastructure.

Keywords

Compact-tube cable; LAN; easy access

1. Introduction

Optical fiber is increasingly used in Local area networks. Some networks still use the same architectures as copper LAN's with the distributed concept, while others use a centralized concept which benefits from the lower attenuation and higher bandwidth of optical fiber. In any case the cost analysis shows that installation and connections generate the main part of network cost. The cost of installation of a distributed copper LAN is 50% of the total cost. So, if an optical fiber network is designed with the same concept, the cost increases very quickly because of the cost installation-connection and optoelectronic components. In centralized solutions the total cost depends on the cable solution and the cost of installation could be a major factor if there is one cable for each terminal or if the passive network is distributed.

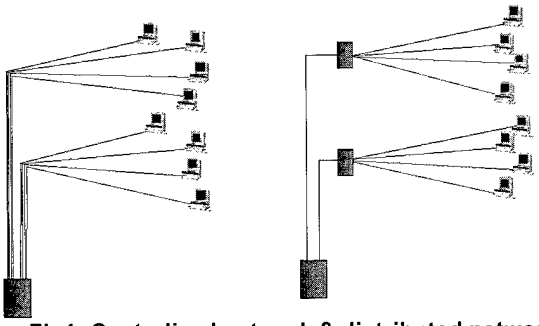


Fig1: Centralized network & distributed network

Moreover installation of new outlets or terminals could represent very high costs.

The goal of this study was to imagine a new cable concept, which could minimize installation costs and allows network evolution in terms of new terminals.

The first stage of this new concept was to imagine a cable which could be laid in the cable trays along the corridors of the building which would allow to pick up some fibers anywhere and anytime. Thus, from each derivation point it would be possible to connect terminal directly in the office.

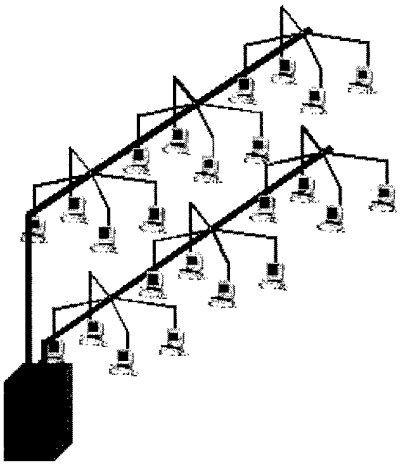


Fig.2 Network architecture using permanent access cable

2. Solution design

2.1 Cable design

The new cable design allows fiber access anywhere and anytime, and even in the case of a high fiber count, fibers could be easily picked up from the cable structure. This means that it is necessary to have direct access to the optical modules.

Most optical cable designs are based on stranded strength members around the optical core of the cable, but this means mid span access to fiber can be difficult.

So the choice has been made for parallel strength members and for a special "flat" shape allowing a direct view of the colored modules. The external position of these strength members and the consequent preferential bending radius of the cable allow the best installation performance.

Easy access to fibers is made by a simple sheath on the optical modules, the optical modules are also easy access themselves (which are of the compact-tube design).The optical modules are not stranded and are consequently easy to remove from the cable.

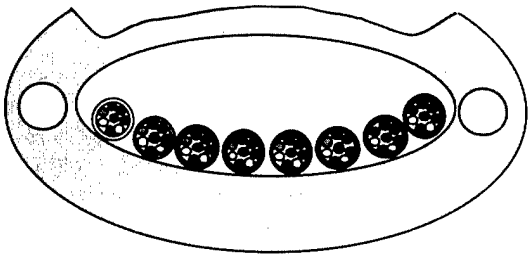


Fig.3: Cross section of a 64 fiber cable containing 8 compact-tubes with 8 fibers each

As shown in fig.3, the cable has a special design with a thinner sheath on the upper side in order to make the cable easier to open and also to control the action of the simple and efficient opening tool.

The method picking up fibers is very simple: Two windows, for example 1 meter apart, are made with the special tool. In the first one, the optical module is cut, then the optical module is pulled out from the second one. The optical module is inserted in a corrugated tube and led to the connection box.

2.2 Performances

This cable has been made and tested and the results are successful. The fiber count could exceed 144 fibers. Optical fibers could be organized in modules containing from 2 fibers to 12 fibers dependant on outlet density in the offices. Individually coloured compact tubes allow easy identification of optical modules.

Outside dimensions for a 64 optical fibers cable are 9.5mm x 15mm.

The cable sheath is made of a halogen free flame-retardant compound in order to give a good compromise between fire retardant properties and low toxicity and smoke generation

The main performance characteristics are detailed in the table below. Thermal characteristics are excellent for this application. The cable structure and the choice of the compact-tube design for optical modules leads to a very good thermal performance from –30°C to + 60°C

The two strength members laid in the outer sheath guarantee the tensile strength of the cable

The crush resistance is excellent due again to the cable design.

Bending radius is totally compatible with installation needs.

Parameter	Value
Temperature cycling	-30; +60°C $\Delta\alpha_{1550nm}$ <0.1dB/km
Tensile performance	600N
Crush resistance	250N/cm
Bending radius Static Dynamic	 50mm 30mm
Impact resistance	>10 N.m

Installation

Cable installation has been tested in a real network, the preferential bending radius allows easy installation, due to the fact that the cable retains its preferential bending radius when the direction changes.

The almost flat shape of the cable and the optical design allow installation in any cable tray. However a better arrangement could be to lay the cable beside the cable tray, leading in this case to easier access.

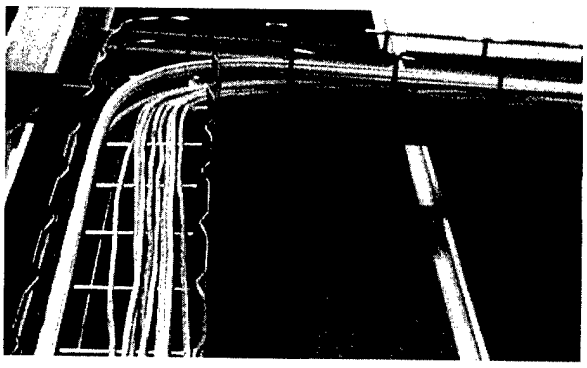


Fig.5: optical cable in cable tray

2.3 Fiber accessibility

Access to the fiber is achieved as follow:

1-Opening the cable with the appropriate tool. Two windows, for example one meter apart, are cut into the upper surface of the cable sheath. The reduced thickness of the upper part of the sheath is designed to facilitate access to the optical fiber modules .

Nevertheless this reduced sheath thickness is not susceptible to tearing due to the special design, and in any case the part of the cable which is exposed to friction has a thicker sheath.

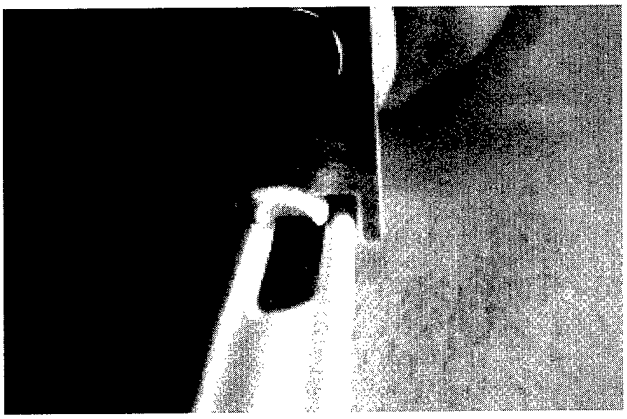


Fig.6 Cable opening

2-After opening the windows the optical module is extracted from the first window, then cut and pulled out from the second one. The fact that the modules are not stranded allows easy access to the required module without disturbing the other modules. As each optical module is individually coloured, identification of the required module is easy.Then the module is ready to be connected to the derivation box.

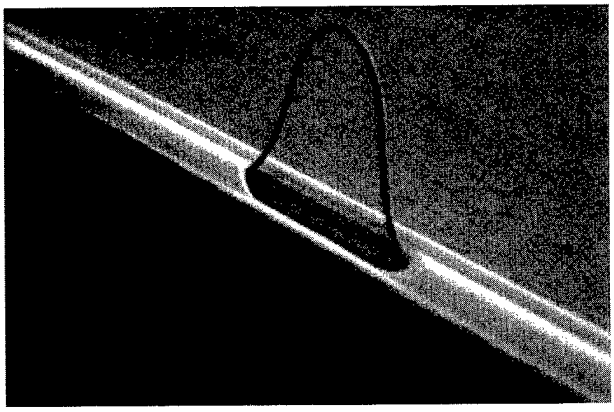


Fig.7 module extraction

3-The selected module can now be inserted in a corrugated tube leading from the cable to the junction box. The box is fixed alongside the cable tray or onto a wall in which case it may be necessary to remove a longer section of compact tube from the cable. Fibres are then ready to be connected to the terminal equipment.

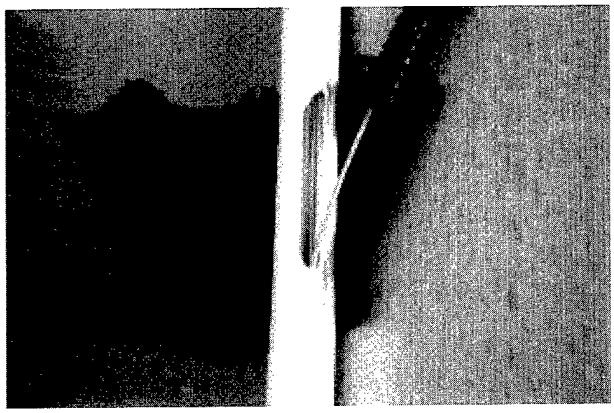


Fig.8 Module extraction

3. System architecture

This concept is designed as a centralized network with a maximum of centralization of both active and passive components.

3.1 Main cabinet

The continuous access cable comes from the office to the main cabinet and where it is split in the bottom of the enclosure. The appropriate optical modules go to the fiber distribution box directly after insertion in corrugated ducts.

Organization of the main cabinet:

Current needs are for bit-rates of 10 or 100Mbps, Switches or hubs are still inexpensive in copper configuration. For this reason it's better to separate optoelectronic conversion from the switching function.

The rack boxes are divided into two spaces: one is dedicated to splicing of optical fiber from the cable to the pigtailed active transceivers. The other is dedicated to the active components (transceivers) themselves. The front panel is equipped with copper RJ45 connectors for 10 or 100Mbps Ethernet protocol. Each "connector" is connected to a port of a copper Ethernet switch.

Main operations can only be made easily on copper interfaces.

3.2 User interface

From the distribution box different solutions are possible:

-The first option is fiber to the desk or fiber to the outlet. Fiber from the distribution box is connected to an optical cable which comes from the office outlet, an optoelectronic device is installed in the outlet or use optical network card is employed in the computer.

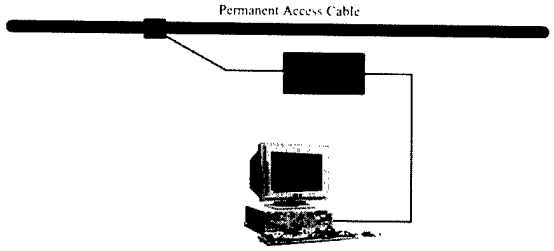


Fig.9 Fiber to the computer

-The second option is to connect fibers from the continuous access cable directly to an optoelectronic device and to connect this equipment to the computer via a copper cable. The system has been designed for 8 or more fibers per module: then from each module it is possible to connect 4 or more computers.

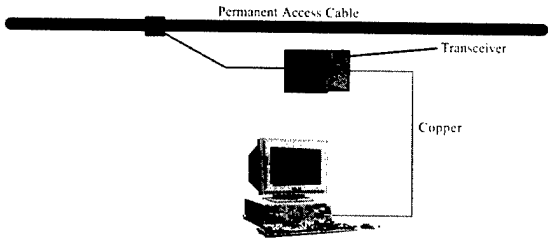


Fig.10 Optoelectronic conversion in the splicing box

-The third option is to connect a component containing an optoelectronic converter and a 4 port miniswitch to the two selected fibers allowing bandwidth sharing between 4 users and to complete the cable system with copper patchcords.

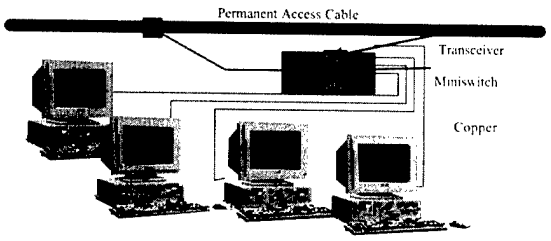


Fig.11 Shared optical fiber with miniswitch

In the last two cases, distances from the optoelectronic device to each user are very short (less than 10 m), the performance of copper patchcords is good enough to support high bandwidth. Moreover the use of copper patchcords is more reliable than optical pigtails because they are more robust, when subjected to frequent connection and disconnection.

3.3 Active components and fibre choice

Today network are still built with multimode fiber, as they allow the use of the cheapest connection solutions and optoelectronic components. For current bitrates and short distances multimode components are cost effective. But for higher bitrate or longer distances it may become viable to use singlemode fiber. Bandwidth is adequate, distance ceases to be an issue. Fiber cost is more effective, but there are two problems to solve with single mode technologies.

The first is connection: one solution is to minimize the use of connectors in the network. The use of pigtailed transceivers allows minimal use of connectors, and mechanical splices have become more cost effective and reliable.

The second one is to use low cost transceivers. At present, for low bitrates (100Mbps) it's possible to use a 780nm LED. Distances are relativly short and coupling attenuation must not be very high, for higher bitrates the use of single mode components such as VCSELs is a solution, but whatever the cost of the transceiver, the problem is a mechanical one, for the coupling of the fiber to the emitter, an innovative solution must be found in order to decrease costs.

3.4 Cost analysis

A cost analysis has been made on existing components and based on a 10/100Mbps Ethernet network. A comparison has been made with a copper distributed network, a standard distributed optical network and a solution with the permanent access concept with 8 fiber modules (4 potential users per splitting point).

In the analysis costs are divided into three parts:

-Installation: the cost of cable laying

-Passive components: cable, cabinet, connectors,

-Active components: switches, optoelectronics (for optic solutions)

The copper distributed LAN has been used as the basis for comparison.

In this kind of network Installation cost represent approximately 60% of total costs. Cost comparison with the same network architecture and optical solutions give a cost, which is twice the copper solution. The cost increase, is due to the cost of active components and connectors.

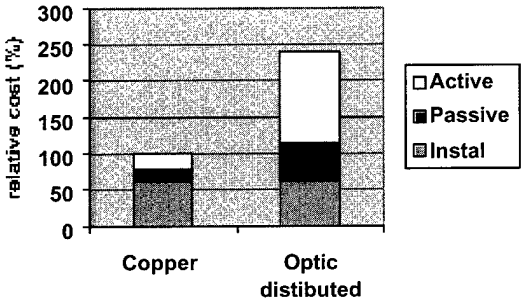


Fig.12 cost comparison copper vs fiber optic

In a centralized architecture installation costs are not reduced because this design requires one cable per user. In the permanent access concept the main part of the network is made with one cable.

The permanent access cable (PAC) is laid from the central cabinet passing close to the users. The cost of installation is decreased by the number of potential users connected per cable.

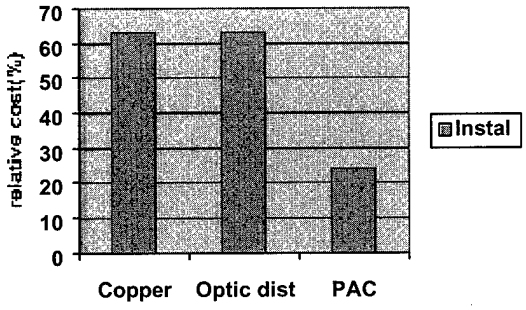


Fig. 13 : relative installation cost comparison

Passive components:

Passive components include cables, connectors, closure, boxes, patchcords....

In the construction of a network all connectors and boxes represent important costs.

The Use of permanent access and the centralized concept minimizes costs.

Optical connectors must be reduced to the minimum necessary and with cross connecting using copper patchcord to minimize the number of connector points.

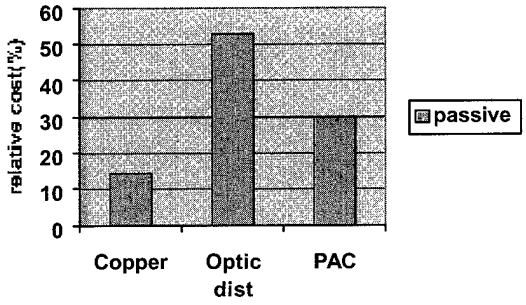


Fig.14: passive cost comparison

Active components

Active components include switches and for optical solutions transceivers.

In both copper and optical network low cost optical transceivers can enable competitive costs to be achieved. If moreover 4 port miniswitches are used to share the bandwidth between users, a cost reduction below that of copper solutions is achievable.

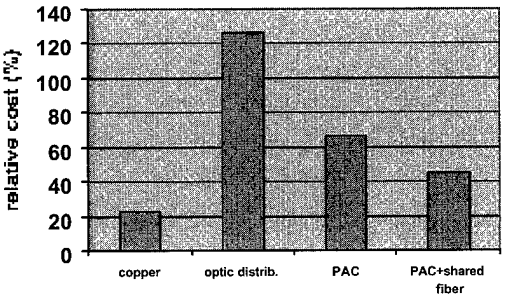


Fig. 15 active cost comparison

A comparison of the different solutions, including all the associated costs shows that an optical solution using a permanent access cable could be competitive with a copper LAN solution and a fiber optic shared solution is cheaper than the copper solution.

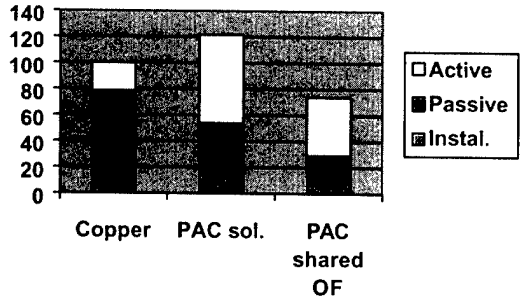


Fig.16: total cost comparison

4. Conclusion

The cost analysis conducted in this study shows that innovative solutions and a new cable design could impact on different parts of total system costs.

The study has demonstrated that a new cable concept based on a centralized network architecture could impact seriously on the total system cost. The permanent access cable allow a reduction in installation and passive component costs.

In the future, the arrival of voice on IP will simplify networks and will allow the rapid deployment of optical networks.

5. Acknowledgments

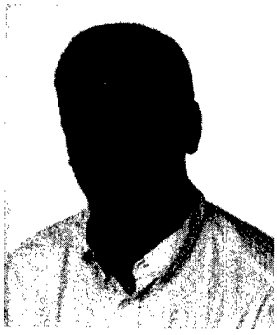
The authors gratefully acknowledge the assistance and support of many individuals who were instrumental in the study and testing of this concept.

References

[1] S. ALBOU, M. LYNCH, "The roads toward convergence" China symposium 3M-Acome.

[2] B. BLELL, "New indoor/outdoor tight buffered fiber LSZH distribution cable", IWCS 1998

Dominique Brault
Acome
50140 Mortain
France



Dominique Brault studies chemistry at the University of Poitiers. He joined Acome in 1982 and began his activities in R&D Materials departement. Then he moved in 1988 to optical activity, being involved in both production team management and new cable projects. Since 1999, he is R&D Product manager for Acome group.

Development of kink-resistant Non-Halogen Flame-Retardant Optical Fiber Cord

Kaoru Okuno, Toshifumi Hosoya, Kiyoaki Moriuchi, Hiroyuki Sotome

Yokohama Research Laboratories, Sumitomo Electric Industries, Ltd.

1, Taya-cho, Sakae-ku, Yokohama, 244-8588 Japan

+81-45-853-7168 · email address: kaoruok@yklab.sei.co.jp

Abstract

Environmental concerns have intensified the demand to stop the use of polyvinyl chlorides (PVC) in recent years, and have fueled the conversion to non-halogen materials. We have developed a Non-Halogen Flame-Retardant (NH-FR) optical fiber cord with excellent kink-resistance in the small 1.5 mm diameter size, which is the anticipated size for equipment interconnection applications. Using NH-FR sheaths on small-diameter optical fiber cords is often accompanied by undesirable kink-resistance degradation. PVC sheaths, on the other hand, have good kink-resistance. This report describes the results of our material characteristics comparison of PVC and non-halogen materials, showing that non-halogen materials can be made with the PVC-like stress-strain (S-S) curve characteristic and can exhibit good kink-resistance.

Keywords

Kink-resistance, Non-Halogen, Flame-Retardant, Optical Fiber Cord

1. Introduction

With the introduction of optical fiber systems into office buildings and residences in recent years, tension-resisting fiber and sheathing reinforced optical fiber cords such as those illustrated in Figure 1 are being used in indoor wiring and for connecting equipment such as optical network units (ONU) and routers. Because of the need for high-density installation, these optical fiber cords must be the narrow gauge 1.5 mm outer diameter type. The optical fiber cords that have been installed often have connectors installed at the ends to allow easy connection to various types of equipment and devices.

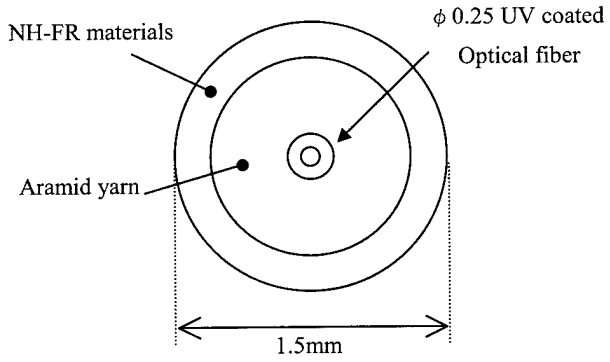


Figure 1. NH-FR Optical fiber cord

Up to now, polyvinyl chloride (PVC) has been used predominantly for the sheathing of optical fiber cords. This is due to PVC's superior mechanical and flame-retardant characteristics, ease of fabrication, and cost performance. However, PVC poses a disposal problem in the incineration of waste because it generates chlorine gas when incinerated and, under certain conditions, dioxins. Furthermore, many PVC materials contain lead-based stabilizers and plasticizers that are suspected of being endocrine inhibitors, causing concerns about their disposal by land-fill as well (Figure 2). Because of these environmental concerns, there is an increasing demand for non-halogen materials in the production of optical fiber cords [1][2].

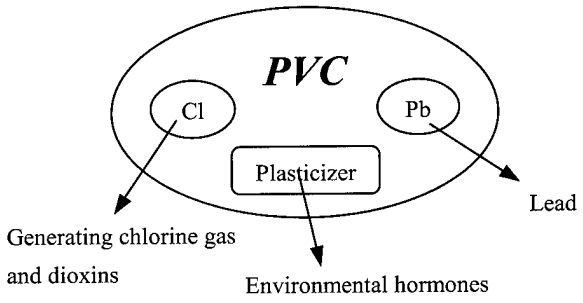


Figure 2. Influence of PVC to environment

In some optical fiber cord interconnection, excess cords are installed although there are no immediate plans to use them in connecting equipment. When left unused, the weight of the connector causes the cords to hang down. The PVC sheathed cords are strong enough to resist buckling, but the non-halogen sheathed cords tend to buckle due to the kinking of the sheathing material. When a cord kinks, the connector's weight is directly transferred to the optical fiber as a stress load, causing increased optical transmission loss due to bending and, in the worst case, the breaking of the optical fiber itself. Because of these problems, it is critically important to consider kink-resistance when using a non-halogen material for optical fiber cord sheathing. Therefore, we examined the characteristics of PVC and various non-halogen materials to determine which characteristics influence the kink-resistance characteristic.

Because chlorine has a combustion reaction suppressing property, PVC is inherently flame-retardant. Non-halogen materials, on the other hand, are not generally flame-retardant, and require flame-

retardant treatment. Furthermore, the physical properties of the material used as the non-halogen base can influence kink-resistance, so the choice of base material is also an important factor. Therefore, in our attempt to develop a 1.5 mm diameter Non-Halogen Flame-Retardant (NH-FR) optical fiber cord with the same level of kink-resistance as a 1.5 mm diameter PVC cord, we chose polyolefin resins whose material characteristics are relatively easy to adjust, as the base material and a metal hydroxide-added system as the flame-retardant treatment process.

2. Production of NH-FR Optical Fiber Cord Samples

As shown in Figure 1, we produced a 1.5 mm outer diameter single-mode optical fiber cord prototype with a 0.25 mm diameter UV coated optical fiber in the center, wrapped with the tension-resisting aramid yarn in the longitudinal orientation and sheathed with a loose-type extrusion-formed sheathing material. We used three types of NH-FR material with two kind of polyolefin resins as the base material and different compounding ratios of metal hydroxide flame retardant as shown in Table 1. NH-FR Samples A and B have different polyolefin resins as the base material but have the same metal hydroxide compounding ratio. NH-FR Samples B and C have the same base polyolefin material but different metal hydroxide compounding ratios, with Sample C having a higher compounding ratio. We also investigated another technique to improve the mechanical properties of the sheathing material, and produced NH-FR Sample D by irradiating NH-FR Sample A with electron beams (EB) of 24 Mrad intensity. Then, we evaluated these four samples along with PVC Sample E.

Table 1. Optical fiber cord Samples

Sample	Base material	Flame-Retardant	Compounding ratio
A	Polyolefin X	Metal hydroxide	α
B	Polyolefin Y	Metal hydroxide	α
C	Polyolefin Y	Metal hydroxide	1.5*α
D	Polyolefin X	Metal hydroxide	α
E	PVC	Non	-

Sample D was Sample A irradiated with EB.

3. Kink-resistance Evaluation Method

Because there is no generally used method for evaluating the kink-resistance of optical fiber cords, we developed our own method. After reviewing a variety of possible methods, we adopted the method illustrated in Figure 3. Specifically, one end of a sample cord is inserted into a hole on a sample holding implement, and a weight is attached and hung from the other end of the cord. The weight weighs 5 g to simulate an actual connector. The cord length between the hole on the sample holding implement and the weight was set at approximately 50 cm to establish uniformity. With the weight on the cord, each sample was left undisturbed at room temperature for 5 minutes and, for acceleration testing, 40°C for 5 minutes. We measured the distance (L) from the top surface of the sample holding implement to the highest point of the bent sample cord as illustrated in Figure 3, and used this measurement as the kink-resistance index. We took the view that larger measurement L, the higher the kink-resistance. We used the 5-minute holding period because our investigation showed that measurement L is almost unchanged after 5 minutes. Figure 4 shows photographs of the actual measurement process. Photograph (a) shows a kinked cord, and photograph (b) shows an unkinked cord. We used this method to test each sample cord to compare the kink-resistance and study correlations to various material characteristics.

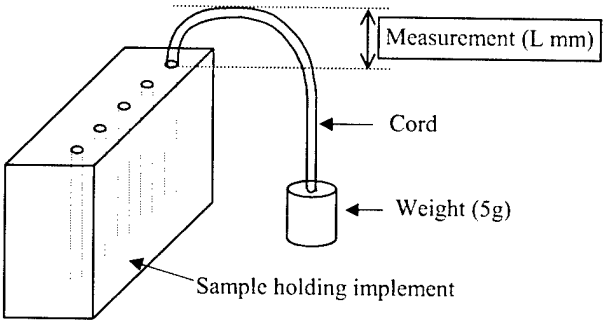
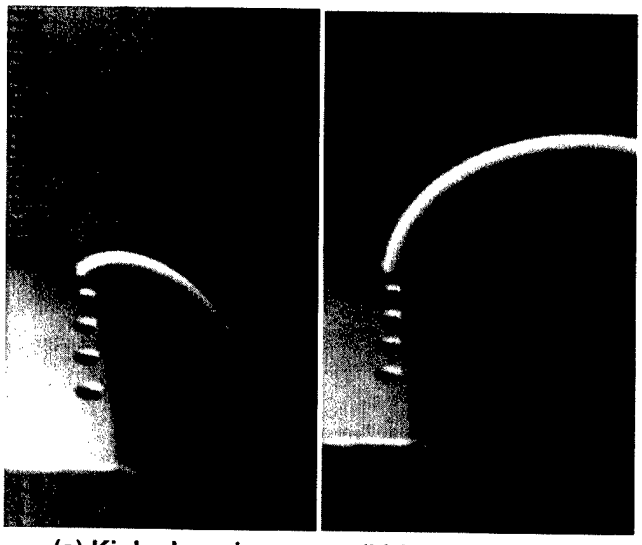


Figure 3. Outline illustration of the evaluation method imitated kink-problem



(a) Kinked cord **(b) Unkinked cord**

Figure 4. Photographs of the measurement process

4. Evaluation Results and Observations

4.1 Results of Kink-resistance Evaluation

Table 2 summarizes the results of our kink-resistance evaluation, performed using the method described above. NH-FR Sample A kinked, but NH-FR Samples B and C appear to have the same or higher kink-resistance than the PVC sheathed Sample E, considering that Samples B and C had L values of 13 and 15 mm, respectively, which are comparable to Sample E's 6 mm. We examined the factors causing these data differences.

Table 2. Results of Kink-resistance evaluation

Condition	Weight 5gf, Holding for 5min.		Young's modulus
Samples	Room temp.	40°C	(MPa)
A	Kink	Kink	212
B	13	8	122
C	15	12	165
D	*	*	*
E	6	3	73

*This sample is under investigation.

4.2 Sheath-thickness and Kink-resistance

Basically, the thickness of the sheath can be seen as factoring into the kink-resistance, and a thicker sheath is probably beneficial in increasing kink-resistance. Therefore, we made NH-FR Sample A with several different sheath thicknesses and evaluated the kink-resistance. Figure 5 summarizes the relationship between the sheath thickness and kink-resistance performance. It clearly shows that thicker sheath cords are more resistant to kinking. The problem, however, is that there is a limit to how thick we can make the sheath, because we must insert a 0.9 mm diameter inner tube inside the cord sheath when attaching a connector to reinforce the connecting part. This evaluation also showed that PVC cords do not kink but NH-FR cords kink when the sheath thickness were the same, indicating that there is a significant difference between these two materials.

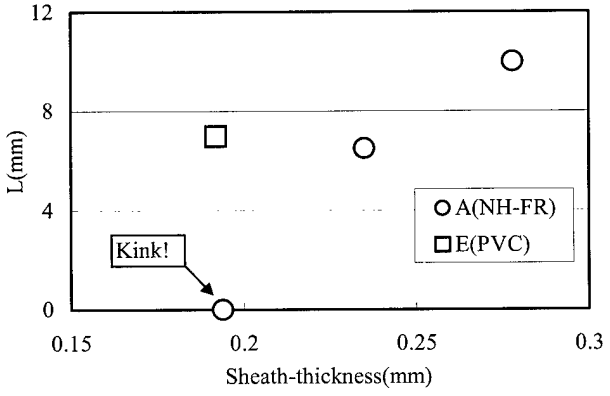


Figure 5. Relationship between the sheath-thickness and Kink-resistance

4.3 Material Characteristics and Kink-resistance

We measured the Young's modulus of each cord sample and investigated the correlation to kink-resistance. Fig. 6 summarizes the results. NH-FR Sample A had a Young's modulus of 212 MPa, which is nearly three times larger than PVC Sample E's 73 MPa, but kinking occurred in Sample A. This suggests that the Young's modulus value alone cannot be used to determine kink-resistance. However, Young's modulus appears to indicate some degree of kink-resistance among cords that are made using the same base material. For example, Samples B and C have same base material, and Sample C with a larger Young's modulus also has a larger L value, indicating that Sample C is more kink-resistant.

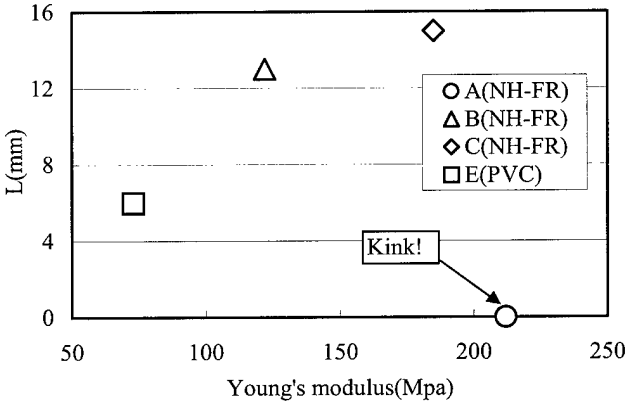


Figure 6. Relationship between the Young's modulus and Kink-resistance

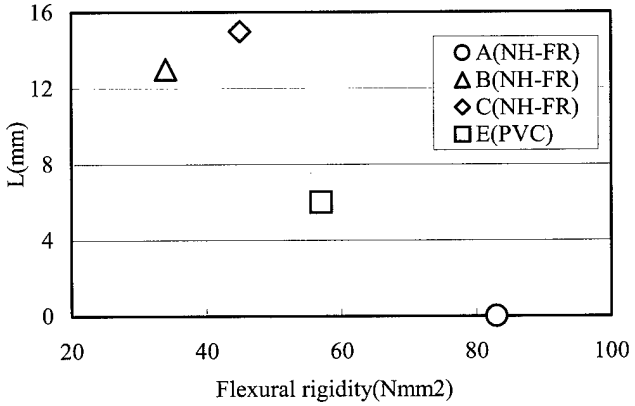
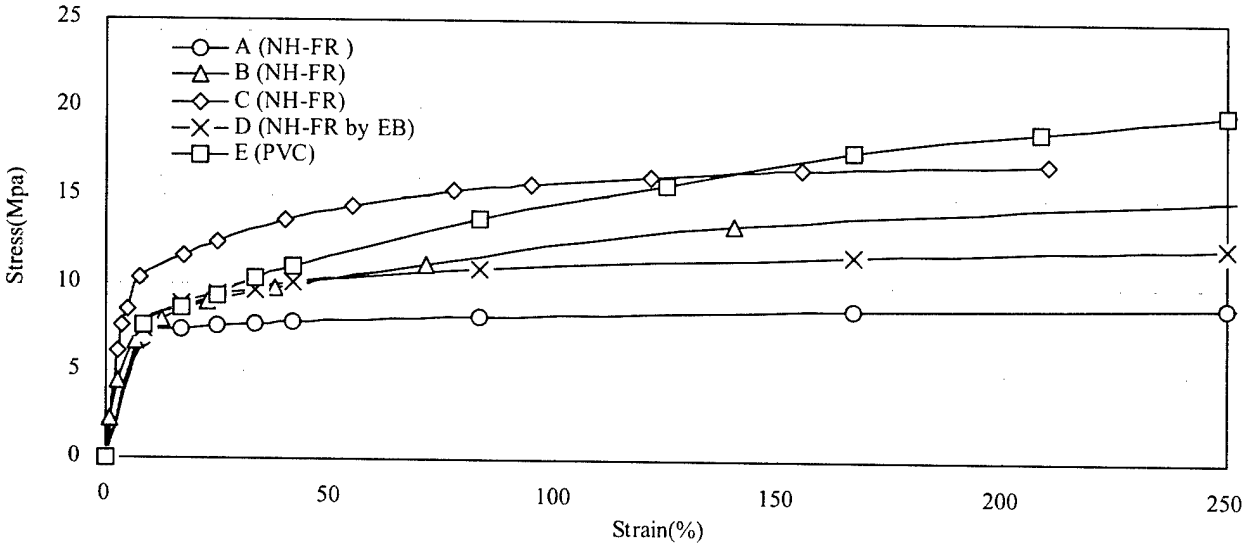


Figure 7. Relationship between the flexural rigidity and Kink-resistance



We also measured the flexural rigidity of each material to investigate its relation to kink-resistance. Figure 7 summarizes the results of this investigation. It shows roughly the same correlation as for Young's modulus.

Figure 8 shows the Stress-Strain (S-S) curve for each sample cord. Measurements were made only on the sheath, after pulling out the 0.25 mm UV resin coated optical fiber and the tension-resisting yarn. The PVC sheathed Sample E demonstrated elasticity until it snapped, and it showed no clear yield point. On the other hand, NH-FR Sample A, which exhibited kink showed a clear yield point near 10% strain. NH-FR Samples B and C, which were found to show similar or higher kink-resistance in the kink-resistance evaluation, have PVC-like S-S curves with no clearly identifiable yield point. Samples A and B use non-halogen materials made using different polyolefin resin base materials, and their crystal characteristics are different, with Sample B having lower crystallinity. It appears that the lowering of the crystallinity expanded the area of elastic deformation, which is affected by the non-crystalline part of the material and caused the yield point to be unclear, resulting in an improved kink-resistance. Sample C's S-S curve is more PVC-like than Sample B. We believe that this is related to the fact that Sample B's kink-resistance index L is larger than Sample C's value.

We also see the suppression of yielding even on the EB cross-linked Sample D. Our opinion is that this improvement is due to the elasticity change caused by the cross-linking of the non-crystalline part by EB irradiation.

5. Characteristics of NH-FR 1.5mm diameter Optical Fiber cord

5.1 Optical Transmission Characteristic

Table 3 shows the optical transmission characteristics of the optical fiber cords made using NH-FR Samples B and C. Both cords show no optical transmission loss between the bare UV resin coated fiber and the cord, indicating that there is no transmission characteristic loss because of the cord making process.

Table 3. Optical transmission properties

Sample	Wavelength (λ) μ m	ϕ 0.25 UV coated SM optical fiber	ϕ 1.5 NH-FR SM optical fiber cord
B	1.5	0.19	0.19
	1.3	0.32	0.32
C	1.5	0.19	0.20
	1.3	0.32	0.32

5.2 Flame Retardant Characteristic

Table 4 shows the results of flame retarding tests on the optical fiber cord made using NH-FR Sample C. Because there is no standardized procedure for the combustion testing of optical fiber cords, we tested our samples to see if they meet the IEC60332, a generally applied standard in Europe where non-halogen optical fiber cord conversion is the most advanced. Table 4 shows the results of this test. Our sample passed the IEC60332-1 test in which a single cord is vertically set up for combustion testing, indicating that our sample has an adequate flame-retardant characteristic.

Table 4. Results of Flame-Retarding tests of NH-FR cord of Sample C

Item	Condition	Specification	Results
JIS 3005 horizontal test	Test on a single horizontal wire or cable	Self-extinguishing	Pass
IEC60332-1	Test on a single vertical insulated wire or cable	Distance between the lower edge of the top support and the onset of charring is greater than 50 mm	Pass
IEC60332-3 category C	Test for vertical flame spread of vertically-mounted bunched wires or cables	Propagation length is less than 250cm	Under investigation

6. Conclusions

We developed an NH-FR optical fiber cord of 1.5 mm outer diameter size, which is likely to be used for interconnecting various types of equipment and devices in the future. This optical fiber cord is small in diameter but has the same level of kink-resistance as PVC sheathed optical fiber cords. Using a newly devised kink-resistance evaluation test, we determined the relative kink-resistance of different materials and investigated the correlations of material characteristics to kink-resistance. This work resulted in the discovery that the kink-resistance of the NH-FR optical fiber cord can be improved by modifying the NH-FR material's S-S curve profile to the PVC-like pattern to eliminate the yield point and increase elasticity.

7. References

[1] K. Okuno, H. Hongo, A. Noguchi, J. Ota and H. Hayami, "Development of Halogen-free Flame-Retardant Optical Fiber Cord", 2000 society conference of IEICE, B-10-11

[2] J. Ota, A. Noguchi, K. Okuno and H. Hayami, Japan Plastics, Vol. 51, No. 11, pp. 37-40, 2000

Authors



Kaoru Okuno

Sumitomo Electric Industries, Ltd.

Yokohama Research Laboratories

1, Taya-cho, Sakae-ku, Yokohama, 244-8588 Japan

Kaoru Okuno received the M.E. degree in Materials Engineering from Iwate University, Japan, in1992. He joined Sumitomo Electric Industries, Ltd. in 1992, and has been engaged in research and development of optical fibers and cables. Mr. Okuno is now a senior engineer of Optical Fibers R&D Dept.

Toshifumi Hosoya

Sumitomo Electric Industries, Ltd.

Yokohama Research Laboratories

1, Taya-cho, Sakae-ku, Yokohama, 244-8588 Japan

Toshifumi Hosoya received the M.S. degree in Reaction Chemistry from Tokyo University, Japan, in1985. He joined Sumitomo Electric Industries, Ltd. in 1985, and has been engaged in research and development of optical fibers and cables. Mr. Hosoya is now a chief research associate of Optical Network R&D Dept. and a member of Chemical Society of Japan and Material Life Society of Japan.

Kiyoaki Moriuchi

Sumitomo Electric Industries, Ltd.

Osaka R&D Laboratory

1-1-3, Shimaya, Konohana-ku, Osaka, 554-0024, Japan

Kiyoaki Moriuchi received the M.S. degree in Applied Chemistry from Osaka University, Japan, in1995. He joined Sumitomo Electric Industries, Ltd. in 1995, and has been engaged in research and development of covering materials on optical fibers and cables. Mr. Moriuchi is a member of New Chemistry R&D Laboratory.

Hiroyuki Sotome

Sumitomo Electric Industries, Ltd.

Yokohama Research Laboratories

1, Taya-cho, Sakae-ku, Yokohama, 244-8588 Japan

Hiroyuki Sotome received the B.S. degree in Applied Physics from Tohoku University, Japan, in1990. He joined Sumitomo Electric Industries, Ltd. in 1990, and has been engaged in research and development of fiber optic cable. Mr. Sotome is now a senior engineer of the Communications Division.

Manufacturing Method for Flame Retardant Access Cables

Ali Harlin[1], Richard Phillips[2], Matti Hirvensalo[2], and Markku T. Heino[3]

1. Conex Cables Oy
   PO Box 44 (Ensimmäinen savu), 01511 Vantaa, FINLAND
   Tel.+358 40 533 2179, ali.harlin@conexcables.com
2. Nextrom Oy, PO Box 44 (Ensimmäinen savu), 01511 Vantaa, FINLAND
3. NK Cables Ltd, PO Box 419, 00101 Helsinki, FINLAND

Abstract

The novel conical extrusion technology offers several advantages for the production of access cables with the HFFR (halogen free, flame retardant) materials.

During recent years, several efficient aerial access and indoor HFFR constructions have been developed. The high fiber count, 8 up to 80, compared to the compact size has been reached by combining the 4-fiber ribbon bundles with a compact core. The drop-down cable designs are often complicated with suspenders, messengers, or Aramid fiber bedding. The aerial conditions may require the use of different layers to improve tracking resistance, moisture barrier, abrasion resistance for installation, or other properties. Altogether the constructions are both efficient but also fairly demanding to manufacture.

The conical extrusion improves production flexibility, which is one of the foremost demands for these applications. Even the whole cable can be produced in one step, which is advantageous from the point of lowering the factory time. Already one conical extruder provides through its flexibility - different multi-layer structures containing from one up to six layers - an effective route for different cables. Between the production steps, the supportive structures and elements can be fed and the production steps can be thus cascaded with high flexibility on the line.

The aerial drop-down and indoor cable designs contain typically HFFR materials. The cone extrusion method has been found to be superior for these shear sensitive materials, and it makes also possible their eventual cross-linking in order to reduce dropping during a fire. We have obtained excellent results with several materials based on different filler/flame retardant systems.

Keywords:

Halogen-free; Flame retardant; Access cable; Aerial drop down; Indoor; Conical extrusion

1. Introduction

The rapid development in the fibre optical communication network has led us to produce more efficient access cables for both indoor and outdoor use. Several efficient designs have been developed recently especially in Japan [1-6].

At the same time, and due to several, often fatal, accidents the safety regulations related to the premises and especially the public buildings have become more strict and hence, several standards in this area have been established.

The discussion about PVC and other halogen-containing materials has led the development in the direction of halogen free, flame-retardant materials and constructions. The final outcome of the debate is still waiting to be seen, and, accordingly, several different material systems depending on application and local requirements are used today.

Nevertheless, the overall performance and cost competitiveness of the cables require the use of lower cost materials and well-optimized designs. This sets also new requirements for the production equipment.

Conical extrusion, as a novel versatile processing method, is in the position to meet the challenge, and to provide the cable producers with a possibility for improving their competence by means of customized products.

In the current paper we focus especially on some aerial access and indoor HFFR constructions and discuss the benefits that conical extrusion can bring to their manufacturing .

2. Structure

A lot of development has been made based on the conventional 4-fiber ribbons, which can be as well of same size but contain only approximately two 0.25 mm coated fibers.

Fiber count 8 up to approximately 24 fibers by combining the 4-fiber ribbon bundles with a compact core can be achieved. Even higher fiber counts are simply achieved by collecting approximately 5 bundles in a SZ slotted core element. This means easily 40 to 80 fibre structures. Different bundle structures for preferred cables are shown by Figure 1 [1-7].

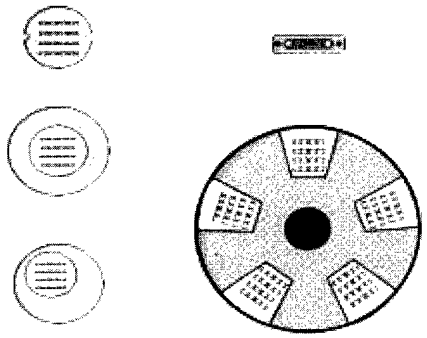


Figure 1. Different bundle structures.

For indoor cables the bundle structures provide an elegant and versatile elementary system, which fulfills the most different and demanding installation requirements. The actual interest is how to manufacture in a flexible and effective way the flame-retardant sheathing layer.

The drop-down cable designs are often more complicated with suspenders, messengers, or Aramid fiber bedding. Also these constructions can meet the flame-retardant requirements, such as the JIS 3005 60 degree inclined combustion test for the drop down cables from pole to housing. Figure 2 shows three examples of drop down cable structures.

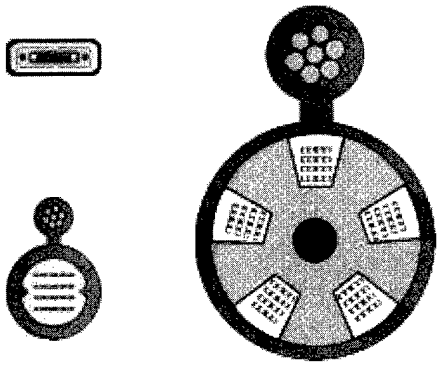


Figure 2. Examples of a drop down cable structures.

3. Design

The indoor requirements are related to different cable surfaces. It can be simply a certain colour, installation specifications or building codes against scratching, ignition or flame spread.

The aerial conditions may require different layers to improve tracking resistance, moisture barrier, abrasion resistance for installation, or other properties depending on the installation environment.

However, the whole sheathing construction has to be economically feasible and contain a sufficient amount of flame-retardant compounds.

The mentioned facts mean that we need a marked flexibility of the production equipment in the fore coming years enabling the manufacture of a variety of customized designs. The key issues are flexibility in making multi-layer constructions and optimal processing conditions for these shear sensitive materials.

4. Materials

The aerial drop-down and indoor cable designs contain typically HFFR materials. The cone extrusion method is found to be superior for these shear sensitive materials, and it provides also a possibility for an eventual cross-linking reaction needed to reduce dropping during a fire.

4.1 Halogen-Free Flame Retardant

In many cases, HFFR materials contain high amounts of mineral fillers, such as magnesium hydroxide (MDH) or aluminum hydroxide (ATH), which make them difficult to extrude. A lot of development work has been carried out during the last decade to improve their poor processing properties [8].

The particle size distribution, coating, and almost every other physical or surface chemical property of these fillers have been influenced. The results have been quite good, but the especially good processability of PVC has not been reached.

There are also other material combinations, of which the calcium carbonate and silane-based char-forming system has shown its competitiveness with PVC compounds as for the extrusion properties. However, in this case, the fire properties are an object of optimization as well. The same is considered to be true for some other systems, where, for example, the char-forming capability of ammonium polyphosphate, melamine, red phosphorus, pentaerythritol, or their combinations are utilized. This latter group will not, however, be further discussed in this presentation.

Extrusion properties of three types of HFFR compounds with different FR agents are compared in Table 1.

Table 1. Different HFFR systems for polyolefins.

FR agent	Extrusion properties
MDH	poor or fair
ATH	poor or fair
$CaCO_3$	good

Filler type and loading, basically determine the fire performance and processability of a compound. High amounts of fillers are usually needed to fulfil the stringent requirements set for indoor cables. Grades with improved extrusion properties are available, but sometimes their fire performance is not good enough. This means that there is a need to utilize several types of HFFR compounds to satisfy the diverse requirements of different applications, which again means that optimization of the processing is needed.

4.2 Cross-Linked Flame Retardant

The dropping of the sheathing and insulation materials is often as destructive as the expanding of fire itself. One way to overcome this problem is simple cross-linking the polymer matrix of the compound. Only the materials based on polyolefins, mentioned above, are simply cross-linkable either with silane or peroxide chemistry. An additional environmental problem is created simultaneously, as the materials are neither recyclable nor easy to combust. However, in demanding environments, such as industrial buildings and installations, offshore, maritime or other vehicle applications, these materials are a possible alternative.

5. Manufacturing

Production of the constructions discussed above is complicated, but not only due to the extrusion properties of the HFFR materials. An additional complication is caused by the supportive structures especially in the drop-down cables. The cables have to be produced thus in processes consisting of several steps.

Also the compact design of the ribbon package limits the forces exerted upon it when it passes the cross-head. Equally important is the lack of residual stresses in the construction, when the cable attenuation is considered.

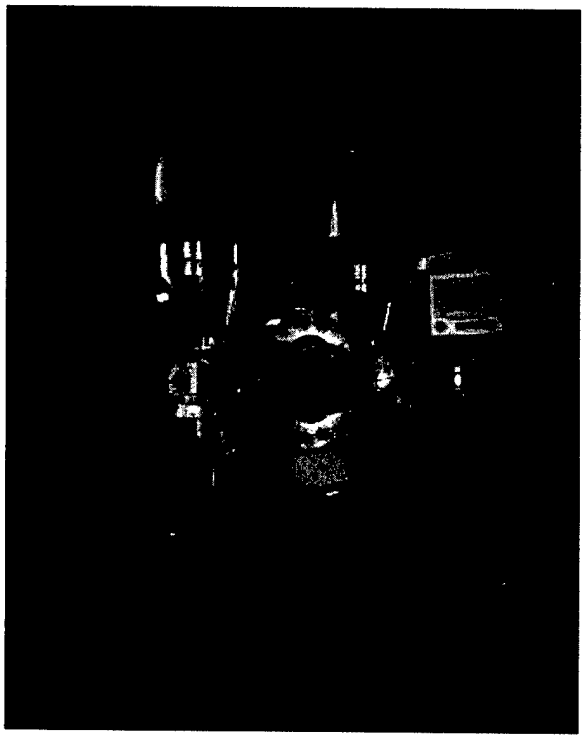


Figure 3. Conical extruder for producing two-layer HFFR sheathing up to 300kg/h (max. cone diameter only 380mm).

NK Cables in co-operation with Nextrom was the first company in the world to combine the novel conical extruder for multi-layer cable jacketing line and use it for commercial production. The line is designed for manufacturing of light fiber optic cables and multi-layer jacketing including e.g. colored skin layers, termite proof jackets and different HFFR constructions. Another installed Nextrom line for FR jacketing and special cables is used mainly for copper data cables (see Figure 3). Actually under pilot phase there is a premises cable line for flame retardant cables (Figure 4).

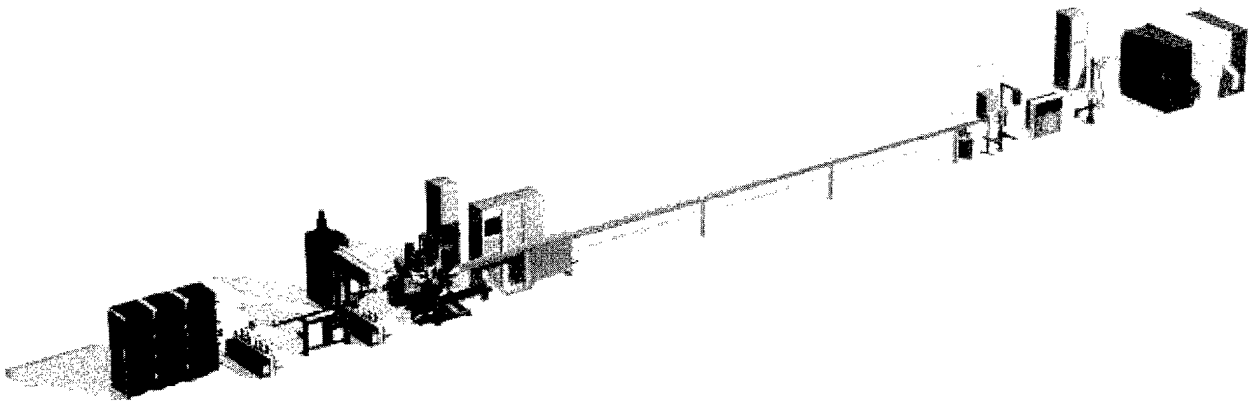


Figure 4. A Conex® line for FR premises cables.

6. Conical Extrusion

The novel conical extrusion has been introduced in the IWCS 99 conference. The paper presented there described the possibilities of conical extrusion in cable applications in general and pointed out its versatility in the production of new fiber optic cables. The examples involved non-metallic lightweight access cables based on four coextruded layers, all made in one step. Another example described indoor/outdoor access cables with two-layer HFFR jacket combining fire retardance with good mechanical properties [9].

A Conical extruder differs a lot from a traditional single-screw extruder both by its construction and extrusion characteristics. The three main components of a conical extruder are rotating conical screws (rotors), stationary conical parts (stators), and a simple die fixed to inner and outer stators (Figure 5). Several helical channels on either side of the rotor serve to transport the material toward the die. Each rotor can coextrude two layers, and any number of additional layers can be achieved by adding further nested stator/rotor/stator combinations.

One to four layers can be obtained with the two-rotor extruder presented in Figure 5. Unlike in screw extrusion, the material flows symmetrically around the cable core resulting in a totally seamless product (no cross-head). In addition, the output of each layer can be varied independently (separate feeding units) on each other and the rotor speed [9-12].

The main advantage of conical extrusion is that it improves the production flexibility, which is one of the most evident demands for the new applications discussed above. Even the whole cable can be produced at once, which is advantageous for lowering the factory times. Already one conical extruder provides through its flexibility - different multi-layer structures with one up to six layers - an effective route for different cables. Between the production steps, the supportive structures and elements can be fed and the production steps can be thus cascaded with high flexibility on the line.

In addition, in the context we would like to point out some of the interesting features of the conical extruder, making it the most interesting and promising new extrusion technology.

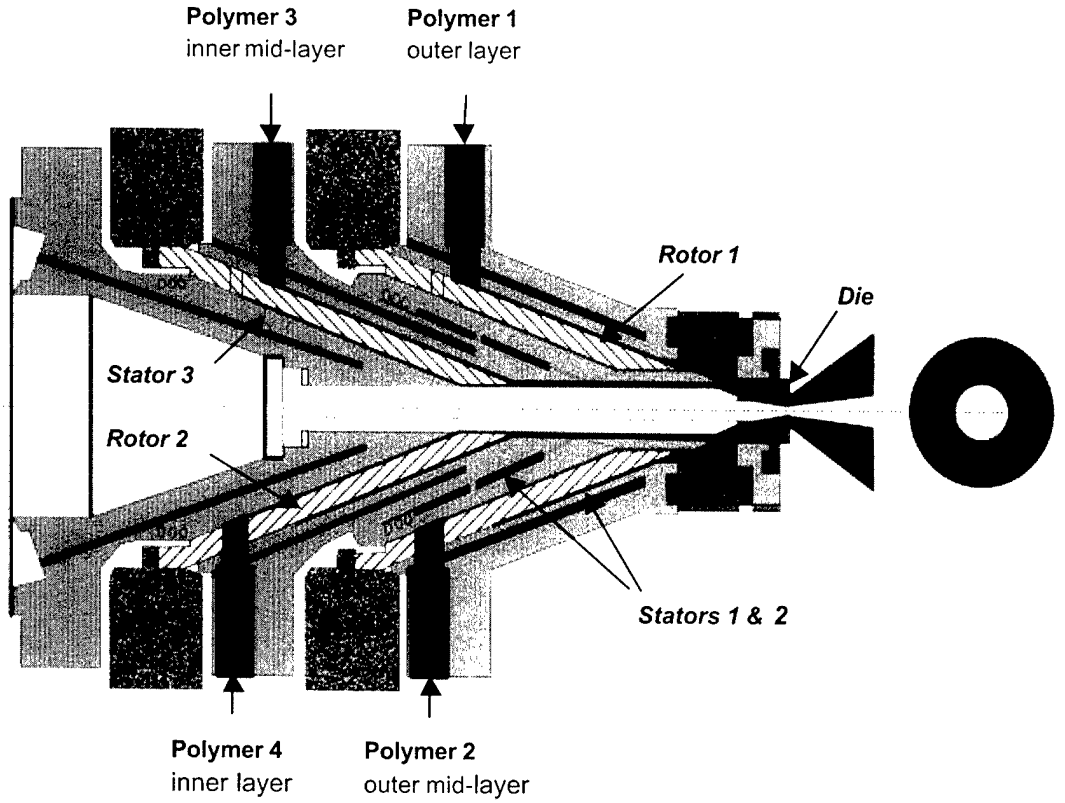


Figure 5. Schematic view of a two-rotor (four-layer) cone extruder [6].

6.1 Short Residence Time

Conical extrusion differs a lot from traditional screw extrusion in many aspects. One important characteristic is the short residence time of the material in the extruder, which is based on the special multi-flight design of the rotors. The conical extruder can have a residence time only about 20-30% of that of a single screw extruder (t_{res} for a single screw extruder ~ 3...5 times t_{res} for a conical extruder).

The short residence time of the conical extruder increases the production efficiency, while the product change over times are short. The production economics is improved as well, while the material needed for purging is little. Especially with the peroxide containing materials the feature provides long run times between cleaning periods of the extruder.

Table 2. Average residence time (t_{res}) of conical vs. traditional extruder at different output levels [9].

Extruder	Output (kg/h)	T_{melt} (°C)	Power (kW)	t_{res} (s)
Model extruder	18.5 35.7 40.2	172 170 167	2.8 6.3 7.0	74 38 34
NMB 60-30D	17.6 34.1 50.5	162 165 171	3.3 7.1 11.4	396 198 132

Table 3. Example of production change over times with conical extruder.

Line speed (m/min)	1st trace	Completed	Scrap (m)
100	2'59"	13'45"	1375
140	2'11"	6'00"	840
160	2'00"	5'10"	827

6.2 Optimal Shear Conditions

Furthermore, due to the conical shape of the rotor, shear stresses are high in the beginning where the melting occurs and then they decrease avoiding thus premature degradation of the polymer. Although the conical extruder is compact, its mixing capacity is still efficient. At the same time the cones contrary to the screws are self- cleaning.

These two fundamental characteristics, short residence time and optimal shearing conditions, make conical extrusion an optimal processing method for all thermoplastics, but in particular for thermally sensitive materials.

6.3 Highly Filled Materials

Highly filled materials are typically difficult to extrude, since they have a tendency to heat up easily through internal friction. Additionally the high loading of fillers markedly reduces the melt strength of the compound.

The conical extruder makes it possible to control the melt temperature very efficiently. The combination of a short residence time and well-controlled shear rates guarantees the best possible conditions for extrusion of the HFFR materials. Table 4 shows some results of basic extrusion experiments with different HFFR compounds.

Table 4. HFFR extrusion on Conex®.

	Conex size	T melt (°C)	P at die (bar)	Q (kg/h/ layer)	d Q (%)
ECCOH 5500	Conex 380-1/2	171	136	107,9	1.7
ECCOH 6600	Conex 280-1/1	171	160	105,2	0.5
Megolon 530S	Conex 280-1/1	172	150	108.7	2.0

ECCOH 6600 is a MDH filled grade from ECC (PolyOne) with a limiting oxygen index (LOI) of 35%. The two other grades are ATH filled: ECCOH 5500 (ECC, PolyOne; LOI 34%) and Megolon S530 from Scapa Polymerics (LOI 40%). As Table 4 indicates they all can be extruded well with a conical extruder.

If the material is over-heated, it droops easily causing tricky handling problems on the wire and in the cooling draft. When the melt temperature of the filled material is controlled, the major part of its melt strength can be benefited as well.

6.4 Seamless Layers

In traditional cable extrusion the seams or weld lines are typical defects in the product caused by all cross-head types. The weld line always tends to be the weak point of the construction. The seamless construction created by conical extrusion improves thus the properties of the sheathing.

The improved properties are evidently observed for the filled materials, which typically have poor welding properties. When the properties are improved we can benefit the development in two ways: we can either utilize even more highly filled materials with improved flame resistance or improve the mechanical performance of the jacket and possible go for thinner layers for material saving.

Also the thin and mechanically more stable layers minimize the need to use expensive materials as skin layer. Alternatively it makes the outer layer more robust against, among others, environmental stresses such as tracking or termite attacks.

6.5 Multi-Layer Structures

Conical extrusion is a versatile processing method for multi-layer constructions. As mentioned above, for example a typical two-rotor extruder can be used for manufacturing of 1 to 4 coextruded layers. In addition, the thickness of individual layers can be easily varied depending on product design. For example thin layers of expensive special materials, combinations of recycled and virgin polymers etc. can be well utilized.

Remembering the seamless high-quality product and optimal processing conditions discussed above, we find that conical extrusion is a useful tool for multi-layer HFFR constructions. The method allows us to combine diverse materials with different functional properties in an efficient and flexible way. It can thus be utilized for improvements in conventional products and design of totally new ones.

7. Cable jacket properties

The prototype cables produced with the novel conical extrusion have a major advantage in the improved mechanical properties of the cable jacket.

7.1 Mechanical properties

The mechanical properties are superior mainly due to the completely different morphology on the jacketing layer. Especially the absence of the seam effect (or weld line) is not present when utilizing the novel conical extrusion process.

In case of classical extrusion it is necessary to utilize a cross-head type of die for jacketing the cable core element. This leads to mass distribution and two separate melt flows to be joined together on butt welding principles forming the seam. Welding is difficult especially in case of highly filled materials and low melt temperatures, both cases being typical for HFFR processing.

The seam is an obvious weak point of the product. It can be observed in particular in bending tests at low temperatures. The area without tie molecules is easily brittle and loose because of poor circular forces on the jacket. Both the impact and loading properties are reduced. The most probable point of failure on the jacket is the sector where there is a seam. The observed weakening in tubular extrusion products is in the range of 10...30% of the nominal values elsewhere.

7.2 Cable performance

The breaking radial forces of the seam and seamless cables, respectively, indicate clearly the weakness of the seam in HFFR materials. Also the cracking properties when the cable is bent especially at low temperatures are better in case of the cone extruded product.

Furthermore, the seam line contains less filler and is thus more sensitive against ESCR and light degradation. The effect might reflect also to other properties.

Finally, controlling orientation is also an interesting feature of conical extrusion. The attenuation values observed remained on the same level as in the case of traditional extrusion process. However the possibility to control orientation provides us new means for the reduction of the shrink back effect.

There is a slight benefit, however observable, at lower thermal expansion for the cone extruded products, which is obviously due to the improved orientation control in the sheathing layers.

8. Conclusions

Conical extrusion is a novel technology, which differs a lot from traditional screw extrusion. Multi-layer extrusion, based on features such as seamless layers, low shearing of the molten material and short residence time, is a superior processing method for plastic materials. For cable manufacturing it gives a lot of possibilities, in particular for tailoring and customizing of designs.

In this paper we focused on some access cables made with HFFR (halogen-free flame retardant) materials showing that conical extrusion offers clear advantages for these applications. First, the gentle processing conditions make it possible to use even highly filled HFFR materials needed to fulfill the most stringent fire safety requirements. We have obtained good results with several materials based on different filler/flame retardant systems Secondly, the versatility of conical extrusion for the manufacturing of different single or multi-layer cable designs, gives significant flexibility for the production of diverse access cables. Based on the cable prototypes produced, the Conex® extrusion process is most suitable for the HFFR access cables.

The technology is marketed through Conex Cables Oy under the trademark of CONEXACT™.

9. References

[1] Akihito Makiyama, et.al., A Study on Strain Characteristics of Fiber Ribbons in a SZ-Grooved Spacer Caused by Cable Bending, *47th International Wire and Cable Symposium,* Philadelphia, Pennsylvania, USA, 147-160, (1998).

[2] Norifumi Kimura, et.al.., Verification by Means of Temperature Characteristic Test and Cable Laying Test on Optimum Design in Fibre Excess Length of Slotted Type Optical Cable, *48th International Wire and Cable Symposium*, Atlantic City, USA, 459-463, (1999).

[3] Seiichirou Takahashi, et.al., Optical Loss Stability of Access Cables in 1600 nm Range, *49th International Wire and Cable Symposium*, Atlantic City, USA, 385-392, (2000).

[4] Tomoyuki Yokokawa, et.al., Downsized Dry and Non-Slotted Core Cable with Ribbons, *49th International Wire and Cable Symposium*, Atlantic City, USA, 403-407, (2000).

[5] Fumiki Hosoi, et.al., Development of Halogen-Free Flame-Retardant Optical Fiber Cables, *49th International Wire and Cable Symposium*, Atlantic City, USA, 427-432, (2000).

[6] Masayoshi Yamanaka, et.al., Development of the New Downsized Aerial Optical Cables with SZ-Slotted Rod and without Slotted Core, *49th International Wire and Cable Symposium*, Atlantic City, USA, 490-495, (2000).

[7] T. Räsänen and J. Ravela, "New Single Loose Tube Cable with Spiralling Channel in Finnish Field Trial", *39th International Wire and Cable Symposium*, Reno, USA, 412-417 (1990).

[8] B. Sultan et al., Novel Halogenfree Flame Retardant Polyolefins Intented for Internal Wiring – Properties and Flame Retardant Mechanism, *47th International Wire and Cable Symposium,* Philadelphia, Pennsylvania, USA, 147-160, (1998).

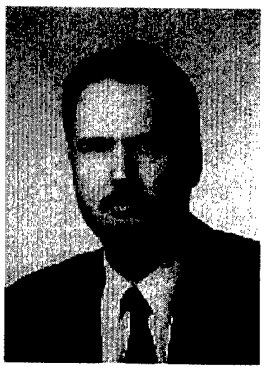
[9] M. Heino, J. Ravela, M. Suvanto, R. Phillips, and T. Vainio, "Novel Non-metallic Multilayer Fiber Optic Cables Based on Cone Extrusion Process", *48th International Wire and Cable Symposium*, Atlantic City, USA, 385-392 (1999).

[10] U. Hochstrasser, R. Phillips, and C. Petit, New Concept for Improved Multi-layer Extrusion, *Wire*, 7, 36-39, (1998).

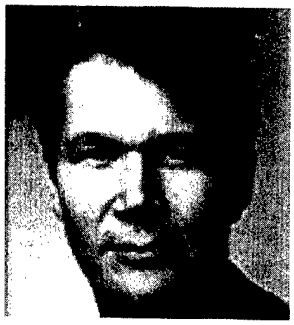
[11] A. Harlin, Conex Extrusion in Cable Production – Application and Advantages, Cables 2001, The AMI International Conference and Exhibition for Plastic Cable Industry, Zurich, Switzerland, (2001).

[12] K. Valta, S. Syrjälä, M. Karttunen, R. Phillips, and K. Kirjavainen, Cone Extruder: Novel Method For Multilayer Extrusions, *Plastics, Rubber and Composites Processing and Applications*, 27 (9), 400-406 (1998).

Authors



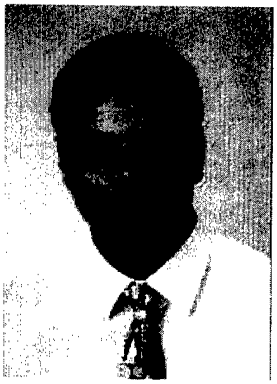
Dr. Ali Harlin
Conex Cables Oy
P.O. Box 44
FIN-01511 Vantaa
Finland



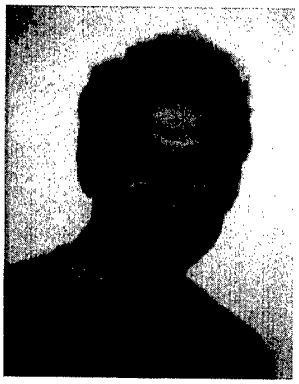
M.Sc. Matti Hirvensalo
Nextrom Ltd.
P.O. Box 44
FIN-01511 Vantaa
Finland

Ali Harlin was born in 1963. He received his M.Sc. degree in Chemical Engineering (Polymer Science) in 1987 and the degree of Dr. Tech. in Polymer Technology (Extrusion technology) in 1996 at Helsinki University of Technology, in Finland. Before joining Nextrom, he worked in Borealis (former Neste Chemicals) as a project manager and development manager. Since 1997 he was with Nextrom as General Manager, Technology & Development. Finally, in 2000 he was nominated Managing Director of Conex Cables Oy.

Matti Hirvensalo was born in 1944. He graduated with a M.Sc. degree in polymer chemistry from the University of Helsinki in 1973. From 1973 to 1991 he worked at Nokia Cables as a researcher, laboratory manager, and research manager. From 1991 till 1998 he worked at Borealis (former Neste Chemicals) on the development of materials for cable applications and managed Borealis' general flame retardant laboratory. Since 1998 he has been flame retardant material expert in Nextrom.



Dr. Richard Phillips
Nextrom Ltd
P.O. Box 44
FIN-01511 Vantaa
Finland



Dr. Markku T. Heino
NK Cables
P.O. Box 419
FIN-00101 Helsinki
Finland

Richard Phillips was born in 1966. He has the degree of Ph.D. (Composite materials) in the EPFL, Lausanne Switzerland. He started in Nextrom 1996 as Technology and Development Manger, Conex®. Since 2001 he has been Technology and Development Manger, Extrusion in Nextrom Oy, Finland and specialized in optical cables technologies.

Markku Heino was born 1963. He received the degree of M.Sc. in Chemical Engineering in 1990 and the degree of Dr. Tech. in Polymer Technology (Blends of Thermotropic Main-Chain Liquid Crystalline Polymers and Thermoplastics) in 1994 at Helsinki University of Technology, Finland. Before joining NK Cables (at that time Nokia Cables) in 1996 he worked as Research Scientist and Project Manager in the Laboratory of Polymer Technology at the HUT. Currently, as R&D Manager at NK Cables (Draka Comteq) he is responsible for the Materials R&D.

Development of Halogen-free, Flame-retardant Miniature Optical Fiber cord

Fuminori Nakamjima, Nobuhisa Ishii, Ichiro Kobayashi, Masami Hara, Kuniaki Yamaguchi, and Hitoshi Ishimaru**

The Furukawa Electric Co., Ltd. *Okano Electric Wire Co., Ltd
Chiba, Japan *Kanagawa Japan
+81-436-1642 f-nakaji@ch.furukawa.co.jp

Abstract

The growing demand for optical communications system in recent years has increased a count of optical fiber cord wirings within equipment and from one equipment to another. So a need for downsizing of optical fiber cords has grown up. The mounting interest in ecology has also raised demand for an optical fiber cord composed of materials that do not produce noxious gases upon combustion after disposal as waste. We designed to develop a small-diameter optical fiber cord which would satisfy these recent requirements and retain the characteristics possessed by conventional optical fiber cords, and successfully developed a halogen-free, flame-retardant miniature optical fiber cord, 1.1 mm in diameter, which offers excellent features. It is expected that use of this optical fiber cord will reduce the wiring space.

Keywords

Optical Fiber Cord; Halogen Free; Flame Retardant; Miniature; Downsizing; Wire; Long-term Reliability; Polyester elastomer

1. Introduction

Optical fiber cords now in common use for wiring within equipment and from one equipment to another generally have PVC sheath and an outside diameter of about 2 mm to satisfy the performance requirements for handling, transmission, mechanical function, flame resistance, etc. The recent growth of demand for optical communications systems, however, has increased an optical cord count of wiring in the equipment and inter-equipment. To meet the growing need for high-density installation of optical fiber cords [1], we fabricated downsized optical fiber cord prototypes and evaluated them few years ago. The result was successful development of a miniature optical fiber cord about 1 mm in outside diameter that has satisfactory characteristics and is protected by a polyamide sheath [2]. We also developed an optical fiber cable using this miniature optical fiber cord [3]. The cord, however, used a polyamide sheath in place of the conventional PVC sheath to provide adequate rigidity at the sacrifice of the flame-retardant property of its conventional counterpart. In response to prevailing awareness of the global environment in recent years, a "green procurement system" has been undertaken by users following the "Law Concerning the Promotion of Procurement of Eco-friendly Goods and Services and Other Entities (Law of Promoting Green Purchasing)", which came into force in April 2001. Because of the desirability of an optical fiber cord free of halogen, we aimed at developing an optical fiber cord having a sheath made of halogen-free flame-retardant resin, and succeeded in developing a halogen-free, small-diameter optical fiber cord having flame-retardation characteristics equivalent to those of the conventional cord. The miniature optical fiber cord thus developed was evaluated for long-term reliability. This paper presents details of the design of covering material for the halogen-free, flame-retardant optical fiber cord, its characteristics, and the results of evaluation of its reliability.

2. Composition of Optical Fiber Cord

Conventional optical fiber cord is generally composed of polyamide-coated 0.9mm buffered fiber and the cord outside diameter is about 2mm. The miniature optical fiber cord we developed is composed of 0.5mm buffered fiber coated with UV resin and the cord outside diameter is 1.1mm. Sheath of the cord is used a flame-retardant, halogen-free resin. A cross sectional view of this cord is shown in fig.1.

2.1 Buffered Fiber

To provide adequate resistance to lateral pressure, 0.25mm UV coated fiber is over coated with UV resin up to 0.5mm in outside diameter. The colored layer, which is 0.25 mm in diameter, and the coated on outside of that both have a low level of adhesion, so the 0.25-mm-diameter colored fiber can easily be pulled out from 0.5-mm-diameter coated fiber using a general-purpose stripper. Because these stripped 0.25-mm-diameter fibers can be arranged and formed fiber ribbon, mass splice can be possible.

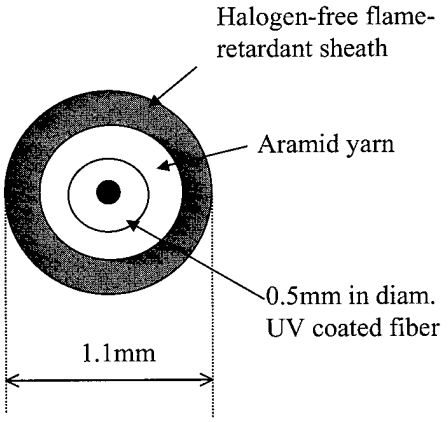


Fig.1 Cross sectional view of 1.1mm diameter optical fiber cord

2.2 Optical Fiber Cord

The miniature optical fiber cord previously developed has an outside diameter of 1 mm [2]. The optical fiber cord discussed in this paper is equivalent to the previous cord in regard to major specifications. The structural specifications are shown in Table 1. The important point in developing this cord was the halogen-free, flame-retardant resin employed for the cord sheath. Its outside diameter of 1.1 mm was chosen for better flame-retardation.

Table 1 Structural Specification of The Optical Fiber

Item	Size, Material
Cord outside diameter	1.1mm
Cord sheath	Flame-retardant, halogen-free plastic
Buffered fiber diameter	0.5mm
Buffered fiber coating	U resin
Type of tensile strength	Aramid yarn
Quantity of tensile strength yarn	1140denier

3. Study of Cord Sheath

3.1 Selection of Base Resin

Downsizing excessively reduces the rigidity of an optical fiber cord if conventional PVC covering is applied to it. Too low a flexural rigidity of the cord tends to produce a small bend near the boot when it is pulled at a right angle to the connector, possibly causing increased losses. To provide the optical fiber cord with an appropriate degree of flexural rigidity, we studied polyester elastomers and polyamide elastomers as thermoplastic resins having relatively high modulus of elasticity. These resins were mixed with a flame-retardant agent to fabricate optical fiber cord prototypes. However when they were bent, held in the bend for a time, then released the prototype cords were found to have a habit of remaining bent. Other cord prototypes, fabricated using each of the resins mixed with the same type and quantity of flame retardant, also were evaluated for this bending habit. For bending evaluation, the prototype cords were wound around a mandrel as shown in Fig .2 and were left in that state of 5 minutes. After their release, they were left as they were for 120 minutes, then their bending radius were measured. The results are shown in Table 2. It was found as a result that the cord using polyester elastomer was more resistant to bends; the polyester elastomer was therefore selected as the base resin for the optical fiber cord.

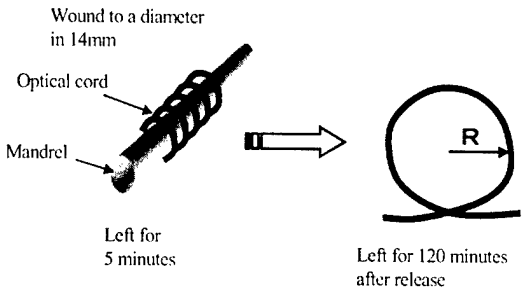


Fig.2 Bending Habit Evaluation Method

Table 2 Bending Habit Evaluaton Results

Material	Flame-retardant polyestr elastomer	Flame-retardant polyamide elastomer
Flexural Modulus	550MPa	500MPa
Radius of curvature	47mm	38mm

3.2 Study of Compounding of Flame-retardant Agent

Flame-retardant agents free of halogen, including metallic hydroxide, nitrogenous material, inorganic phosphoric material, and red phosphorus, were evaluated for flame-retardation. Red phosphorus was found inapplicable to optical fiber cords because it fails to meet the need for colors of a cord. The other three materials (metallic hydroxide, nitrogenous material, and inorganic phosphoric material), therefore, were tested for flame-retardation when compounded with the polyester elastomer resin.

Because most optical fiber cords are laid horizontally, mainly on a floor or a flat space in the equipment, the prototypes were evaluated for their flame-retardation using the horizontal combustion test specified in JIS C 3005 [4]. An optical fiber cord 300 mm long, placed horizontally, was exposed to flames of a burner at the center of the cord, then was examined for the extent of burning after the burner removal. Optical fiber cords that were not, or were inadequately, rendered flame retardant showed that flames spread to both ends after exposure to the burner. The horizontal combustion test method is shown in figure 3. The results of compounding with these flame-retardant agents are shown in figure 4. Test No. 3, of material B, met the flame-retardation target. But flame-retardant agent should be compounded with the base resin in as small as possible to avoid degrading the resin characteristics. We then tried decreasing the quantity of flame-retardant agents and found that the flame-retardation target could be attained by combined use of flame-retardant agents B and C, as test No. 5 shows. Combustion of the optical fiber cord we developed is shown in Fig. 5 (At the flaming) and Fig. 6 (After the burning).

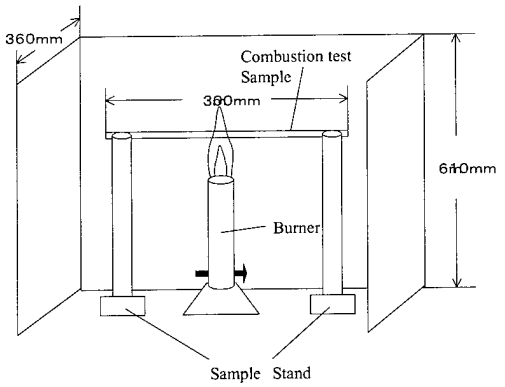
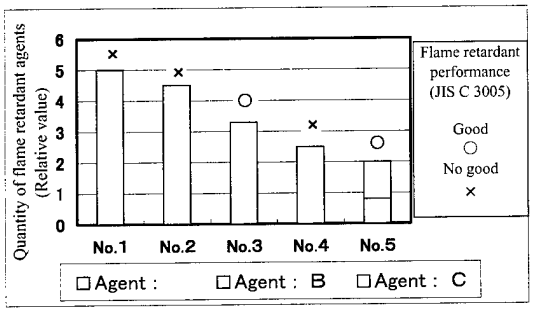


Fig.3 Diagram of Horizontal Combustion Test



A : Metallic hydroxide

B : :Inorganic phosphoric flame retardant agent

C : :Nitrogenous flame retardant agent

Fig.4 Combustion Characteristics of Optical Fiber Cord Versus Quantity of Flame-Retardant Agents

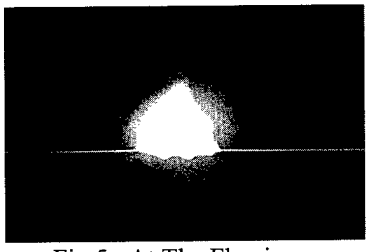


Fig.5 At The Flaming

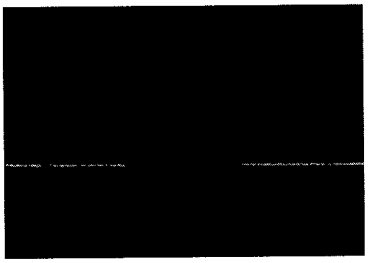


Fig.6 After The Burning

4. Characteristics of Cord 1.1 mm in Diameter

The transmission and mechanical characteristics of the halogen-free, flame-retardant miniature optical fiber cord we developed are shown in Table 3. The cord was evaluated in accordance with IEC60794-1-2.The optical fiber cord, with these characteristics meeting the requirements, was found to have satisfactory performance.

Table 3 Characteristics of Optical Fiber Cord 1.1mm in Diameter

Item and Conditions		Specifications
Transmission loss	1.31μm	0.34 dB/km
	1.55μm	0.20 dB/km
Crush test	500N/100mm	0.00 dB*
Bending loss	r=15mm	<0. 1 dB/turn*
Temperature cycling	-10 ~ +60C	<0.03 dB/km*
Stiffness	r=15mm	56 N·mm² * *
Tensile performance	30N	<0.5%

* Measuring wavelength:1.55μm * * IEC60794-1-2 method E17C

5. Reliability Evaluation

The optical fiber cord we developed was evaluated for reliability in terms of long-term variation in transmission loss through exposure to high temperatures and to high temperature and high humid conditions. The sheaths were also evaluated for durability by measuring rupture elongation after aging in high temperatures and high humid conditions.

5.1 Long-term Transmission Characteristics

The optical fiber cord we developed was exposed to ambient conditions of 85 degrees C and of 85 degrees C at 85% relative humidity. The change in transmission loss was measured at 1.31 um and 1.55 um. Figures 7 and 8 show the results. We confirmed, as a result, that the optical fiber cord was stable in its transmission characteristics even under unfavorable conditions over a long period of time, displaying not much change in transmission loss.

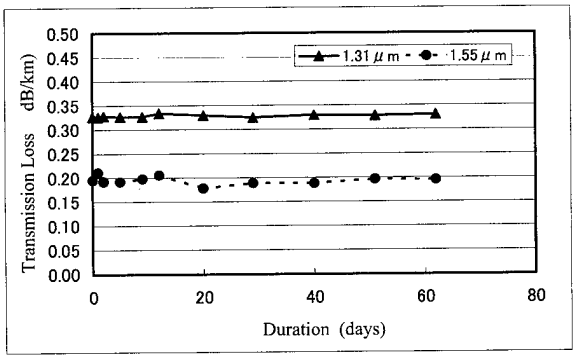


Fig.7 Change in Transmission Loss at 85 Degrees C

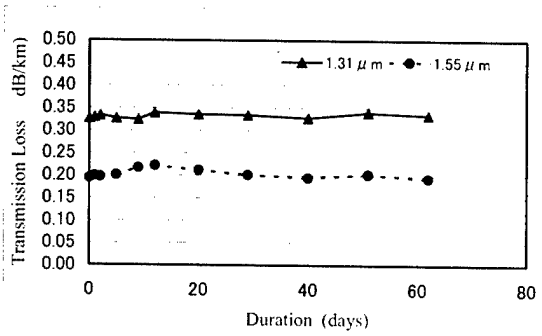


Fig.8 Change in Transmission Loss at 85 Degrees C and 85%R.H.

5.2 The Cord Sheath Characteristics in High Humidity and High Temperature Conditions

Polyester elastomer, the material used in making the sheath, is known from its composition to be subject to hydrolysis, which results in lowering of its physical properties. For this reason, the polyester elastomer was improved to increase its resistance to hydrolysis while ensuring the flame retardation of the cord sheath. Optical fiber cord using the resin before improvement and that using the improved resin were subjected to high temperature and high humid aging to check their degradation from change in rupture elongation. The results are shown in Fig. 9. The sheath made of improved resin was found better than that made of resin that had not yet been improved.

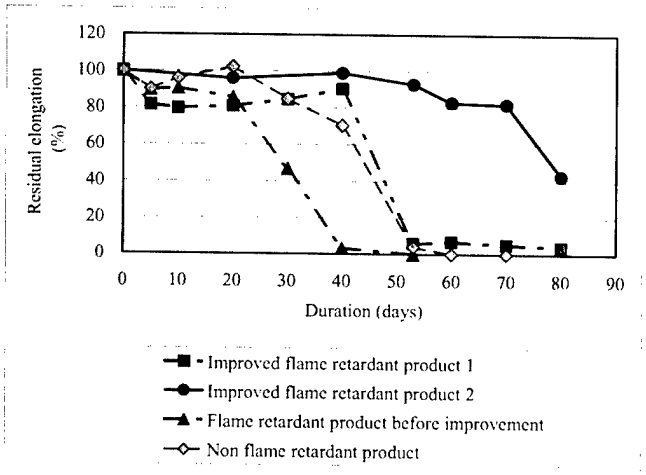


Fig.9 Change in The Sheath Residual Elongation after Aging at 85 degrees C, 85% R.H.

5.3 Predicting Durability of The Sheath

After confirming the increased durability of the resin caused by improvement of its hydrolysis characteristics, as shown in the results of the aging test, we estimated a life time using Arrhenius' equation for practical purposes. Two types of cord sheath using different quantities of some agent are exposed to 60, 70, and 80 degrees C, at 85% relative humidity respectively, and checked for degradation. The time to reach 50% residual elongation was set as the terminal point of degradation. Estimated life slopes based on the test results are shown in figure 10. The following activation energy can be deduced from the results:

Sheath with 20% flame retardant agent : 84.4kJ/mol
Sheath with 30% flame retardant agent : 68.3kJ/mol

The optical fiber cord we developed has flame retardant agent at 20 wt%. From the activation energy of 84.4 kJ/mol for the sheath made of 20wt% pre-improved flame retardant, the sheath is assumed to reach 50% residual elongation at normal temperature (20 degrees C) in 114.5 years. We also confirmed that the lower agent showed increased durability.

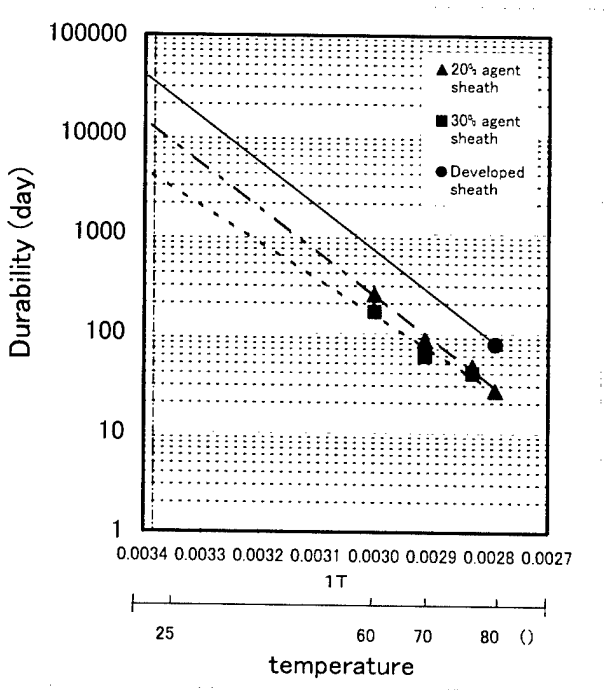


Fig.10 Arrhenius' Plot of Sheath Durability

6. Conclusions

Figure 11 shows an external view of the halogen-free, flame-retardant miniature optical fiber cord we developed, along with a conventional optical fiber cord 1.7 mm in outside diameter and a

polyamide buffered fiber 0.9 mm in diameter. We confirmed that the miniature optical fiber cord we developed possess satisfactory transmission and mechanical characteristics and show a high degree of stability in their characteristics over a long period of time. The optical fiber cord can be effective in saving wiring spaces and in high-density wiring, can be expected to be used widely because they are composed of friendly materials to the environment.

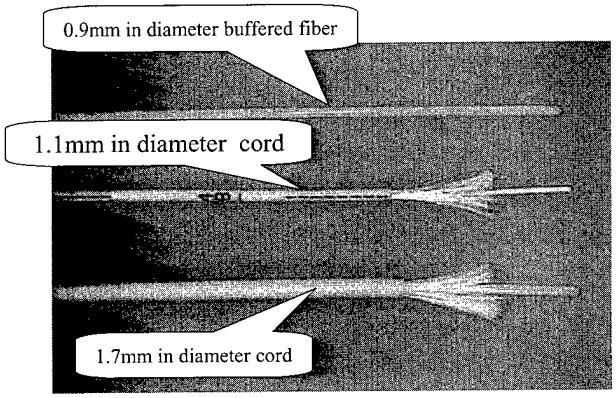


Fig.11 Optical Fiber Cords Photo.

7. REFERENCES

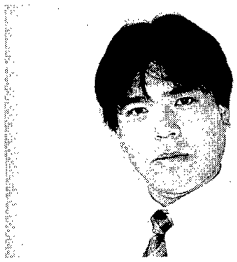
[1] [1]M.Tachikura,Y.Enomoto,S.Uruno,H.Takemoto,N.Tomita and H.Takasugi, "Optical Fiber Distribution System in Central Offices for The FTTH Era" 46th IWCS 1997 pp.859-866.

[2] [2]F.Nakajima, N.Ishii, Y.Watanabe, S.Takagi, "Development of Miniature Optical Fiber Cords" 47th IWCS 1998, pp4-9

[3] [3]I.Kobayashi, K.Yamaguchi, F.Nakajima, H.Ishimaru, K.Ida, F.Hosoi and N.Ishii, "128-fiber cable using downsized optical fiber cord for the central office" EC2000, pp95-101

[4] Japanese Standards Association, "Test methods for rudder or plastic insulated wires and cables JIS C 3005" pp24-25, 1993

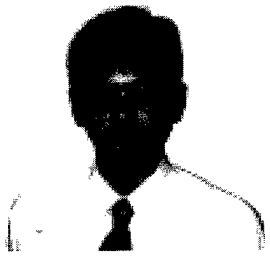
Authors



Fuminori Nakajima

The Furukawa Electric Co., Ltd.
6,Yawata kaigan-dori Ichihara, Chiba, 290-8555 JAPAN
f-nakaji@ch.furukawa.co.jp

He received his M.E. degree in Material Engineering from Nagaoka University of Technology in 1992. He joined The Furukawa Electric Co.,Ltd. in 1992 and has been engaged in research and development of the materials for optical fiber cables. He is now an assistant manager of engineering dep., OPTCOM division.



Nobuhisa Ishii

The Furukawa Electric Co.,Ltd
6,Yawata Kaigan-dori, Ichihara, Chiba, 290-8555 JAPAN
n-ishii@ch.furukawa.co.jp

He received his M.E. degree in Applied Chemistry from Waseda University in 1987. He joined the Furukawa Electric co., Ltd. and has been engaged in the development of the materials for optical fiber cables. He is now a senior research engineer of Fitel Photonics Laboratory.



Ichiro Kobayashi

The Furukawa Electric Co.,Ltd
6-1,Marunouchi 2-Chome,Chiyoda-ku, Tokyo,100-8322 JAPAN
ichiro@ch.furukawa.co.jp

Ichiro Kobayashi received his B.E. degree in Physics from Chuo University in 1986. He joined The Furukawa Electric Co., Ltd and has been engaged in research and development of the optical fiber cable. He is now a manager of engineering dep., OPTCOM division.



Masami Hara

The Furukawa Electric Co., Ltd.
6,Yawatakaigann-dori Ichihara,
Chiba, 290-8555 JAPAN
hara@ch.furukawa.co.jp

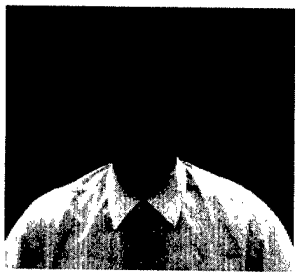
He received his M.E. degree in Physics from Osaka University in 1987. He joined The Furukawa Electric Co., Ltd. and has been engaged in research and development of optical cable. He is now a manager of engineering dep., OPTCOM division



Hitoshi Ishimaru

Okano Electric Wire Co., Ltd
5-28, Fukaminishi, Yamato,
Kanagawa, 242-8501 JAPAN
shimaru@okano-cable.co.jp

He received his B.E. degree in Industrial Chemistry from Kanagawa Institute of Technology in 1988. He joined Okano Electric Wire Co., Ltd.,. He is now a manager of engineering dep.



Kuniaki Yamaguchi

Okano Electric Wire Co., Ltd
5-28, Fukaminishi, Yamato,
Kanagawa, 242-8501 JAPAN
shimaru@okano-cable.co.jp

He received his B.E. degree in Electronic Engineering from Tokai University in 1995. He joined Okano Electric Wire Co., Ltd., and has been engaged in development of the optical fiber cable.

Novel Fire-resistant Optical Fiber Cables with Simple Structure and Stable Loss Performance

Masahiro Kusakari, Shimei Tanaka, Kazunaga Kobayashi, Matsuhiro Miyamoto
Research and development department, Telecommunication cable division, Fujikura Ltd.
1440 Mutsuzaki, Sakura-shi, Chiba-ken, 285 Japan
+81-43-484-3945 · kusakari@s.fujikura.co.jp

Abstract
We have developed two types of fire-resistant optical-fiber cables. The first structure consists of stainless steel tubes, each containing an optical fiber, which is stranded around a tensile strength member and then jacketed with thermoplastic resin. The second structure consists of a stainless steel tube containing optical fibers and two tensile strength members, which are laid parallel to each other and then jacketed with thermoplastic resin (This cable structure allows for single-process manufacture).

We have performed a variety of evaluations (on optical transmission loss characteristics, mechanical characteristics, and fire-resistance characteristics) on the first and second cable structures mentioned above, and have confirmed that these cables possess excellent characteristics.

Keywords
Optical cable, Fire-resistant, Simple structure

1. Introduction
Control and monitoring systems in premise area such as factories, railway stations, banks, and so on should maintain their signal transmission functions even in the event of a fire. To create such systems, optical-fiber cables that can transmit signals even in the event of fire are required. Therefore, we investigated fire-resistant optical-fiber cables. Our target cable is good fire-resistance characteristics with simple and thin structures and low fiber count (1 to 4-fiber).

We conducted fire-resistance tests on the optical-fiber cables, in conformity with the IEC 60331-11 (Apparatus - Fire alone at a flame temperature of at least 750°C) and IEC60331-25 (Procedures and requirements - Optical fiber cables).

2. Fire-Resistance Test
For the studies being reported here, we conducted fire-resistance tests on the optical-fiber cables, in conformity with the IEC 60331-11 (Apparatus - Fire alone at a flame temperature of at least 750°C) and IEC60331-25 (Procedures and requirements - Optical fiber cables). Figure1 shows test apparatus.

The flame temperature shall be measured using two thermocouples. The flow rates of air and propane gas are regulated to ensure that the temperature of two thermocouples shown in Figure 2 will be maintained at 750°C (+50, -0°C).

The combustion time is 90 minutes and the sample is allowed to cool for 15 minutes after fire is extinguished. The optical transmission loss change of the cable is monitored during the entire 105-minute test period.

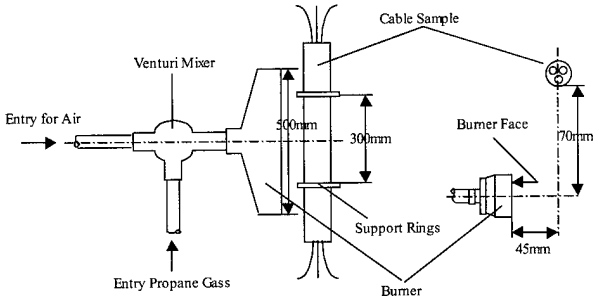


Figure 1. Test apparatus (IEC-60331-11)

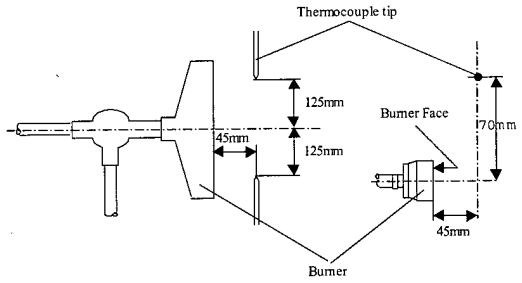


Figure 2. Thermocouple position

3. Cable Design
3.1 Design of Coating Material of Optical Fiber
Two types of materials, Ultra Violet ray curable resin (UV resin) and Silicone are considered for use as the coating material of the optical fibers. It is well known that Silicone exhibits superior characteristics in a high temperature environment. However, it seems possible that, if exposed to a temperature as high as 750°C, either coating material will be burned out. Therefore, we selected to adopt UV resin for the coating material of the fiber, for the productivity of optical fiber.

3.2 Design of Cable Structure
The coating material of optical fibers is burned out when exposed to high temperatures of 750°C or more. Therefore, the cable should desirably have a structure such that no stress is transmitted to the glass.

3.2.1 Basic Study for Cable Design 1 (Fire-resistance characteristics of conventional optical cables)
First, we carried out fire-resistance tests on conventional cables having a variety of structures.

Figure3 shows cross section of test cable. We tested three types of cables, loose tube cable, cord cable and slotted rod cable. Also we tested armor type cable, in order to confirm whether it is possible to protect an optical fiber from a flame by using a steel tape.

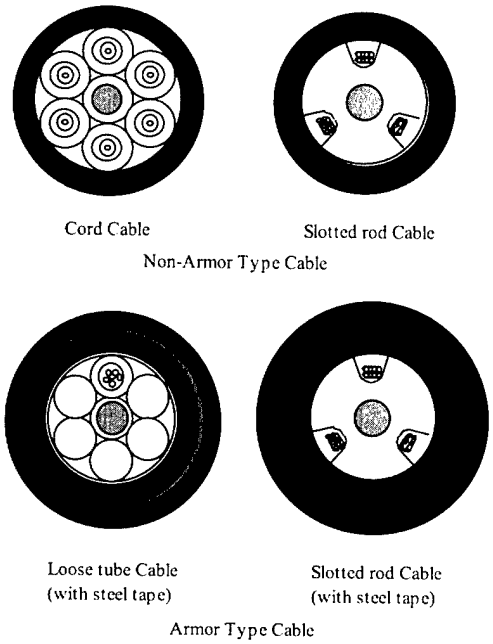
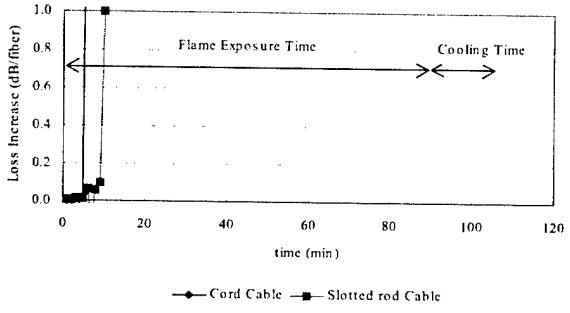


Figure 3. Cross-section of conventional optical cables subjected to a fire-resistance test

Figure 4 shows optical transmission loss changes of conventional non-armor type optical cables at the time of fire-resistance test. For the cord cable and slotted-rod cable, the optical transmission loss increased to 1 dB/fiber ten minutes after the start of the test, and the optical fibers were broken the moment the fire was extinguished.

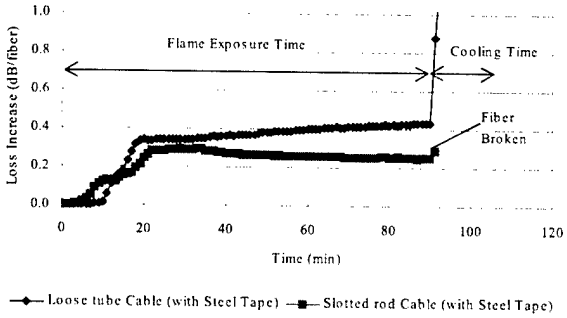


Measuring wavelength: 1550nm

Figure 4. Optical transmission loss changes in the fire-resistance test

(Conventional non-armor type optical cables)

While, figure 5 shows optical transmission loss changes of conventional armor type optical cables at the time of fire-resistance test. The optical transmission loss of loose tube cable using steel tape increased to approximately 0.5dB/fiber during combustion. During cooling time after combustion, the loss increased to a maximum of 2.2dB/fiber. The optical transmission loss of slotted rod cable using steel tape increased to approximately 0.3dB/fiber during combustion, and its optical fibers were broken 2 minutes after the burner was turned off.



Measuring wavelength: 1550nm

Figure 5. Optical transmission loss changes in the fire-resistance test

(Conventional armor type optical cables)

These test results revealed that optical transmission loss hardly increases in the optical fibers of the cables using steel tape when the cables are burned, but that the optical transmission loss in the optical fibers increases or the fibers are broken as the burned cables cool. It can be assumed that, when a burned cable is cooled, TM and other component materials that survived the burning shrink due to the abrupt temperature changes, generating a stress that acts on the optical fibers, with a resultant increase in optical loss and fiber breakage. So, these conventional cables we examined can not be applied for fire-resistant cable.

Therefore, we considered that fire-resistant optical cable should be the structure of protecting each optical fiber.

3.2.2 Basic Study for Cable Design 2 (Fire-resistance characteristics of fiber unit)

We then investigated fiber units with respect to their fire-resistance characteristics.

We tested two types of units, one is stainless steel tube, the other is plastic (PBT) tube wrapped with mica tape, both containing optical fibers. Figure 6 illustrates the structures of the tubes subjected to the test. Figure 7 shows the optical loss changes in the fire-resistance test.

Although neither tube experienced fiber breakage, the plastic tube wrapped with mica tape showed a greater increase in optical transmission loss and lower stability than the stainless steel tube. This led us to consider a cable structure using a stainless steel tube containing optical fibers. We then further examined two types of cable structures through the use of this stainless steel tube containing optical fibers.

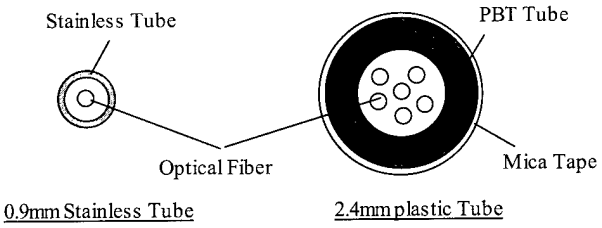
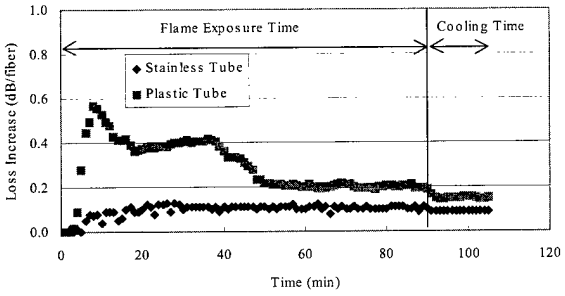


Figure 6. Structures of the tubes studied



Measuring wavelength: 1550nm

Figure 7. Optical transmission loss changes in the fire-resistance test (Fiber units)

4. Prototype Cables

4.1 Design of Prototype Cables

Based on the study results obtained to this point, we designed prototype cables with two different types of structures. The first structure (Type1) consists of stainless steel tubes, each containing an optical fiber (Single-mode fiber), which is stranded around a tensile strength member and then jacketed with thermoplastic resin. The second structure (Type2) consists of a stainless steel tube containing optical fibers (Single-mode fiber) and two tensile strength member, which are laid parallel to each other and then jacketed with thermoplastic resin.

Type 1 is general stranded structure cable, so this cable can be bent in every direction and is excellent in mechanical characteristics. Type 2 is newly developed simple and thin structure cable, that has lower production cost.

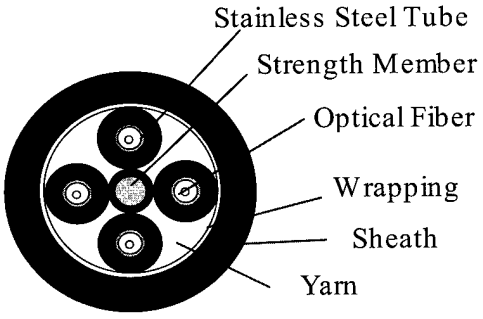


Figure 8. Cross-section of prototype cable (Type1)

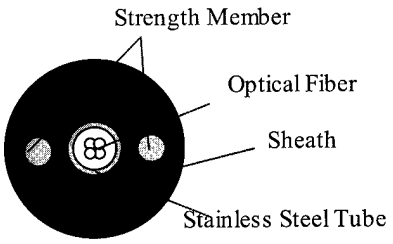


Figure 9. Cross-section of prototype cable (Type 2, 4-fiber)

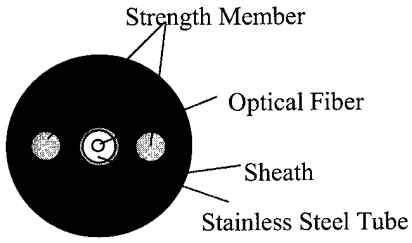


Figure 10. Cross-section of prototype cable (Type 2, 1-fiber)

Table 1. Outer diameter and weight of cables

	Diameter	Weight
Type 1 (4F)	7.5mm	68kg/km
Type 2 (4F)	5.0mm	37kg/km
Type 2 (1F)	4.5mm	30kg/km

4.2 Characteristics of Prototype Cables

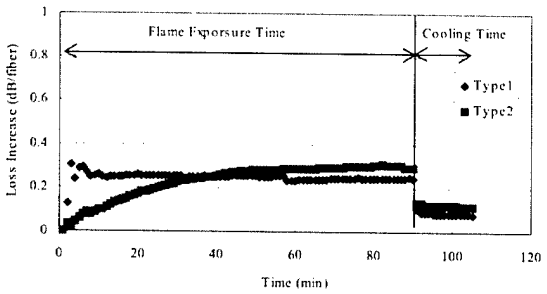
4.2.1 Fire-resistance characteristics of prototype cables

The test results of fire-resistance test are shown in figure 11 and table 2. In each cable, the optical transmission loss increased by approximately 0.3 dB/fiber and stabilized thereafter. When the fire was extinguished after 90 minutes of combustion, the optical transmission loss rapidly fell to 0.1 - 0.15 dB/fiber. No fiber breakage occurred during the subsequent 15 minutes.

Table 2. Test results of fire-resistance test

	After 90min burning	After 90min burning and 15min cooling down
Type1 (4F)	<0.5dB/fiber	<0.2dB/fiber
Type2 (4F)	<0.5dB/fiber	<0.2dB/fiber
Type2 (1F)	<0.5dB/fiber	<0.2dB/fiber

Measuring wavelength: 1550nm



Measuring wavelength: 1550nm

Figure 11. Optical transmission loss changes in the fire-resistant test (Type 1 (4F) and Type 2 (4F))

4.2.2 Other characteristics of prototype cables

Table 3 summarizes the evaluation results for the prototype cables. Both cables satisfied the specifications of Bellcore GR-409 CORE.

Table 3. Characteristics of prototype cables

Item	Unit	Type1	Type2	Type2
		SM 4fiber	SM 4fiber	SM 1fiber
Optical Transmission loss	dB/km	<0.25	<0.25	<0.25
Compressive Strength	dB	<0.1	<0.1	<0.1
Cable Cyclic Flexing	dB	<0.1	<0.1	<0.1
Impact Resistance	dB	<0.1	<0.1	<0.1
Temperature Cycling	dB/km	<0.1	<0.1	<0.1

Measuring wavelength: 1550nm

5. Conclusion

We test-manufactured small-diameter cables of 1 to 4 fibers using stainless steel tubes that contained optical fibers, and then evaluated those cables.

1) When the prototype optical-fiber cables were subjected to a fire-resistance test in accordance with the specifications of IEC60331-11 (Apparatus - Fire alone at a flame temperature of at least 750°C) and IEC60331-25 (Procedures and requirements – Optical-fiber cables). Both cables showed an optical transmission loss increase of 0.5 dB/fiber or less.

2) When the prototype cables were subjected to temperature-characteristic and mechanical-characteristic tests in accordance with Bellcore GR-409 CORE, excellent results were obtained.

Authors



Masahiro Kusakari
Research and development department
Telecommunication cable division
Fujikura Ltd.
1440 Mutsuzaki, Sakura-shi, Chiba-ken, 285 Japan

Masahiro Kusakari was born in 1965. He joined Fujikura Ltd. after his graduation from Nagasaki University with a B.E. degree in 1990 and has been engaged in research and development of optical fiber cables. He is now an engineer in the Telecommunication cable Department and member of the IEICE of Japan.



Shimei Tanaka
Research and development department
Telecommunication cable division
Fujikura Ltd.
1440 Mutsuzaki, Sakura-shi, Chiba-ken, 285 Japan

Shimei Tanaka was born in 1975. He joined Fujikura Ltd. after his graduation from Chiba University with a M.E. degree in 2000 and has been engaged in research and development of optical fiber cables. He is now an engineer in the Telecommunication cable Department and member of the IEICE of Japan.



Kazunaga Kobayashi

Research and development department

Telecommunication cable division

Fujikura Ltd.

1440 Mutsuzaki, Sakura-shi, Chiba-ken, 285 Japan

Kazunaga Kobayashi was born in 1961. He joined Fujikura Ltd. after his graduation from Gunma University with a M.E. degree in 1985 and has been engaged in research and development of optical fiber cables. He is now an engineer in the Telecommunication cable Department and member of the IEICE of Japan.



Matsuhiro Miyamoto

Research and development department

Telecommunication cable division

Fujikura Ltd.

1440 Mutsuzaki, Sakura-shi, Chiba-ken, 285 Japan

Matsuhiro Miyamoto was born in 1953. He joined Fujikura Ltd. after his graduation from Tokyo Institute of Technology with a M.E. degree in 1978 and has been engaged in research and development of optical fiber cables. He is now an engineer in the Telecommunication cable Department and member of the IEICE of Japan.

Development of Low Smoke Non-Halogen MiniCord® Cables

Jianwei Wang, Kaushik Chakrabarty, J. Thomas Chapin and Carla G. Wilson
Fiber Optic Premises Cables, Optical Fiber Solutions, Lucent Technologies Inc.
Norcross, GA 30071

Abstract
Low Smoke Non-Halogen (LSOH) MiniCord® fiber optic cables for interconnect, cross-connect and distribution applications have been developed to meet the stringent optical, mechanical, fire, smoke and environmental requirements typical in Premises applications. The cable designs include single-mode and multi-mode fiber types in simplex and duplex configurations. The cables exceed the optical and mechanical performance requirements of both IEC 60794 and Telcordia GR409. Optical tests include temperature cycling and accelerated aging. Mechanical tests include tensile load, crush, torsion, hot/cold bend, flexing, impact and kink. These cables comply with IEC 60332-1 (fire), IEC 61034-2 (smoke), IEC 60754-2 (acid gas evolution) and NES 713-3 (toxicity). The cable materials are non-halogen and lead-free and meet the European requirements for use in telecommunication equipment. These cables are optimized for Lucent Technologies LC, SC and ST®II+ connectors, but may be used with most commercial connectors. Design and development challenges and performance tests results are presented in this paper.

Keywords
Low smoke, Non-halogen, Premises cable, Cordage

1. Introduction
In just a few years the Internet and Intranet has had a significant effect on network data communications. Accommodating the rapidly changing demands for larger volumes of voice and data has resulted in an increased use of fiber optics. The increased use of fiber optics translates into more electronics, cable, and apparatus being installed into smaller physical spaces. Industry focus on better utilization of this space resulted in the development of "Small Form Factor" (SFF) connectors. SFF provides a means to increase cabling and electronics port densities in less space than required by copper or other fiber connector solutions. Space constraints also facilitated the need for small diameter cordage.

The diameters of most fiber cordage are 2.4 mm and 3.0 mm. These diameters are too large for high-density applications. Hence, cordage products having a diameter less than 2.0 mm are most desirable. In addition, cables used in the Premises environment are required to meet stringent building codes. These codes are specific to the each region, i.e. European, North American, Asia Pacific, etc.

Design and development of MiniCord® Simplex and Duplex optical fiber cordage cables (< 2.0mm) that meets specifications (LSOH) for the European market has been completed. This development was guided by the detailed performance criteria of both IEC 60794 [1] and Telcordia GR409 [2] specifications. The space saving obtained with the developed product increases the port density capacity by 50% and 68% compared to 2.4 mm and 3.0 mm cordage respectively.

The cable design incorporates both single-mode and multi-mode fiber types. However, for simplicity, multi-mode fibers were evaluated for performance during the development because they were considered worst case with regards to micro-bend sensitivity. Design challenges and performance test results are presented in this paper.

2. Cable Design
The LSOH MiniCord® cables have been designed for 62.5/125 µm multi-mode fiber, 50/125 µm LaserWave® multi-mode fiber, 8.3/125 µm depressed clad single-mode fiber, and 8.3/125 µm matched clad single-mode fiber. The fibers are coated with D-LUX 100™ or an equivalent coating. The coated fiber is buffered with a high modulus non-halogen material and that provides rigidity and mechanical protection to the fiber.

The LSOH MiniCord® Simplex has a core that consists of a single buffered fiber, surrounded by aramid yarn strength members, and a rugged jacket (see Figure 1). The cable jacket is made using a fire retardant and low-smoke non-halogen material. The cable has a 1.7 mm diameter and is one of the smallest sized Simplex cables in the industry. The LSOH MiniCord® Duplex has a low-smoke non-halogen over-jacket to provide added protection to the two constituent Simplex parts (see Figure 1). The Duplex cable has a ripcord made from a fire-retardant non-halogen material. The ripcord allows easy removal of the over jacket without bending, deforming or damaging the internal Simplex parts. Table 1 gives the characteristics of the LSOH MiniCord® Simplex and Duplex cables.

Table 1. Characteristics of the LSOH MiniCord® Simplex and Duplex Cable

Fiber Types and Dimensions	
Multi-mode	62.5/125 µm
Multi-mode LaserWave®	50/125 µm
Single-mode - Depressed Clad - Matched Clad	8.3/125 µm
Fiber Coating Dimensions	245 µm
Buffer Outside Diameter	900 µm (0.035 in)
Simplex Dimension	
Nominal outside diameter	1.7 mm (0.067 in)
Duplex Dimension	
Nominal outside diameter	2.3 mm x 4.0 mm (0.156 in x 0.089 in)

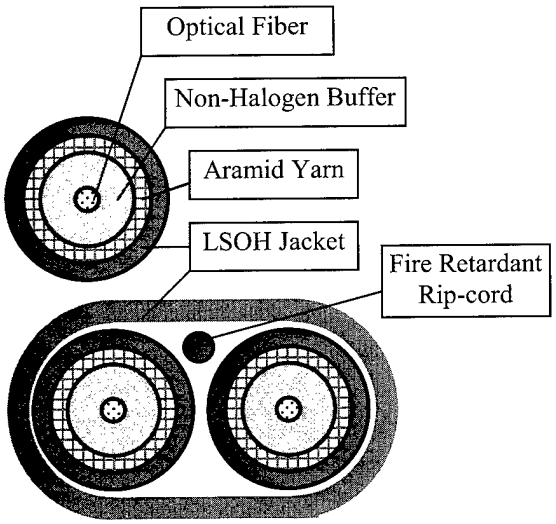


Figure 1. Schematic of Simplex and Duplex Cable

3. Cable Materials

The buffer is made from a high modulus (stiff) Nylon type material. This is a non-halogen thermoplastic and it does not contain any halogenated additives. The rigidity of the buffer material prevents buckling of the buffered fiber when the cables are terminated in a connector. This minimizes optical loss on connectorization. This also minimizes stress concentration at the point where the buffered fiber is attached to the connector, thus ensuring longer life to the assembly.

The cable jacket is made using a LSOH material that is fire retardant, has low smoke and low acid gas evolution on combustion, and has low toxicity. It is an environmentally friendly material – it does not contain halogens, lead, cadmium, sulphur, phosphorus or antimony. These cables meet the European requirements of non-halogen materials for use in telecommunication equipment.

The LSOH cable jacket material has a good balance of strength and flexibility - tensile strength (ASTM D 638) is greater than 2000 psi, and elongation at break (ASTM D 638) is greater than 160%. It is tear resistant, and has excellent cut-through, crush and abrasion resistance. The material is also resistant to various fuels, oils, and cleaners (including isopropyl alcohol) at ambient temperatures. The LSOH material has superior mechanical properties than jacket grade PVC materials at both low and high temperatures. The low temperature brittleness point (LTB, ASTM D 746) is less than –25°C. This is far superior to the LTB point of –10°C to –5°C for most ordinary jacket grade PVC materials. This prevents the LSOH jacket from developing cracks under installation or service loads at sub-zero temperatures. The material is also more resistant than ordinary PVC to be deformed under load at high temperatures above 50°C. In all developmental efforts on MiniCord® cables, we have used superior jacket materials that allow a wider storage temperature range (–40°C to 85°C), and a wider installation temperature range (-30°C to 70°C) than is possible with ordinary PVC based cables.

4. LSOH MiniCord® Cable Performance

4.1 Fire, Smoke and Other Environmental Tests

The LSOH MiniCord® Simplex and Duplex cables passed the IEC 60332-1 fire test [3] when tested at Underwriters Laboratories [4]. According to the IEC 60332-1 standard: "a cable shall pass the test if the distance between the lower edge of the top support and the onset of char shall be greater than 50 mm. In addition, a failure shall be recorded if the burning extends downwards to a point greater than 540 mm from the lower edge of the top support." [3]. The results of the IEC 60332-1 tests performed on the LSOH MiniCord® Simplex and Duplex cables are shown in Table 2. All the samples passed the test with very large margins.

Table 2. Results of IEC 60332-1 Fire Tests. Pass obtained if the distance between the lower edge of the top support and the onset of Char > 50 mm

LSOH MiniCord®	Distance between the lower edge of top support and the Onset of Char (mm)
Simplex	
Sample 1	275
Sample 2	275
Sample 3	315
Sample 4	325
Sample 5	300
Duplex	
Sample 1	350
Sample 2	370
Sample 3	280
Sample 4	230

The LSOH MiniCord® Simplex and Duplex cables passed the IEC 61034-2 smoke test [5], when tested at ITS (Intertek Testing Services, Inc.) [6]. For a test pass, the measured light transmittance must be greater than 60% [5]. The cables passed the test with a very large margin (see Table 3).

Table 3. Results of IEC 61034-2 Smoke Test. Pass requires a minimum light transmittance of 60 %

LSOH MiniCord®	Measured light transmittance	Results
Simplex	95.94%	Pass
Duplex	91.86%	Pass

The LSOH jacket material used in the LSOH MiniCord® Simplex and Duplex cables passed the IEC 60754-2 test for acid gas evolution during combustion [7]. The tests were conducted at Warrington Fire Research, London. The pass criterion for the test is that the measured pH be greater than 4.3 and the measured conductivity be less than 10 µS/mm [7]. The test results gave pH = 4.88 and conductivity = 0.16 µS/mm [8].

The LSOH jacket material has a Toxicity Index of 1.5 and thus complies with the requirements of the NES 713-3 standard. For compliance toxicity index < 5 [9].

4.2 Optical Attenuation, Temperature Cycling and Cable Aging Test

The LSOH MiniCord® Simplex and Duplex cables were tested for attenuation at room temperature, attenuation during temperature cycling, and attenuation after cable aging. The measurements were made at transmission wavelengths of 850 nm and 1300 nm for multi-mode fibers.

The IEC 60794-1-2-F1 temperature cycling test requires that the cable must undergo two cycles consisting of an appropriate low and high temperature for appropriate intervals of time [1]. The low and high temperature limits are to be selected based on end-user requirements. The manufacturer can set the operating temperature to be between the high and low temperature limits of the cycle, if the added optical loss during the temperature cycle is below some value agreed upon with the end-user.

The GR409 temperature cycling test requires interconnect cables to go through temperature cycles between 0°C to 50°C with a constant temperature aging period in between. The maximum allowed added optical loss are: 0.3 dB/km before aging and 0.6 dB/km after aging for single mode fiber cables; 0.6 dB/km before aging and 1.2 dB/km after aging for multi-mode fiber cables [2]. The manufacturer can claim a wider operating temperature range than 0°C to 50°C, if the same added loss requirements are met in the wider temperature range.

Therefore, the temperature cycling test according to Figure 2 was performed on the LSOH MiniCord® Simplex and Duplex Cables. The low and high temperature limits were –20°C and 85°C respectively, and the cable aging was done for seven days at 85°C. Optical loss measurements were made at one-day intervals at the transmission wavelengths of 850 nm and 1300 nm for multi-mode fiber cables.

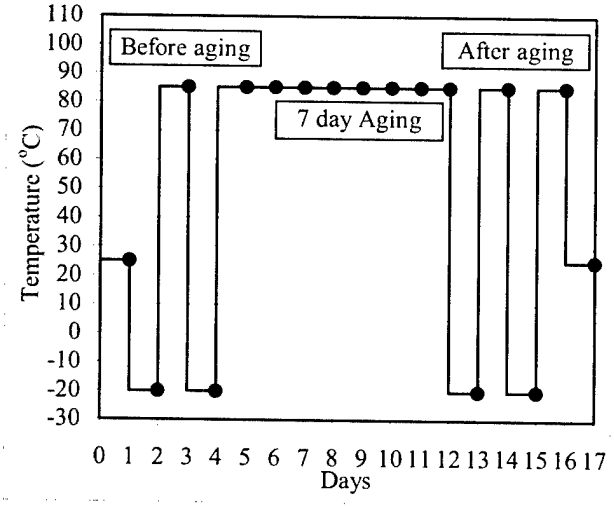


Figure 2. Temperature Cycling and Cable Aging Test for LSOH MiniCord® Cables

The added optical loss of a prototype LSOH MiniCord® Simplex cable (made with 62.5/125 µm multi-mode fiber) is shown in Figure 3. For 1300 nm transmission wavelength, the maximum added loss was 0.31 dB/km before aging and 0.39 dB/km after aging. For 850 nm transmission wavelength, the maximum added loss was 0.33 dB/km before aging and 0.42 dB/km after aging. These maximum added losses occurred at the second exposure to –20°C.

The added optical loss of a prototype LSOH MiniCord® Duplex cable (made with 62.5/125 µm multi-mode fiber) is shown in Figure 4. For 1300 nm transmission wavelength, the maximum added loss was 0.30 dB/km before aging and 0.54 dB/km after aging. For 850 nm transmission wavelength, the maximum added loss was 0.44 dB/km before aging and 0.67 dB/km after aging. Again, these maximum added losses occurred at the second exposure to –20°C.

These added optical loss results are well below the GR409 specified maximum added loss limits of 0.6 dB/km (before aging) and 1.2 dB/km (after aging) for multi-mode fiber interconnect cables. Therefore the LSOH MiniCord® Simplex and Duplex cables easily comply with the IEC 60794 and GR409 temperature cycling and cable aging test requirements in the operating temperature range of –20°C to 85°C. This temperature range is wide enough for most applications in a Premises network.

The added optical loss of a prototype LSOH MiniCord® Duplex cable (made with 50/125 µm LaserWave® multi-mode fiber) is shown in Figure 5. For 1300 nm transmission wavelength, the maximum added loss was 0.74 dB/km before aging and 1.32 dB/km after aging. For 850 nm transmission wavelength, the maximum added loss was 0.71 dB/km before aging and 1.26 dB/km after aging. It is important to note that the added loss is only marginally higher than the GR409 requirements. The cables with 50/125 µm LaserWave® fibers will meet the optical performance requirements of both the IEC 60794 and GR409 standards in operating temperature range of 0°C to 85°C.

The 50/125 µm LaserWave® is a special fiber designed for optimized performance for 10 Gb/s applications at 850 nm transmission wavelengths. The minimum bandwidth is 1500 MHz.km at 850 nm and 500 MHz.km at 1300 nm. These bandwidths are much higher than that available with both 62.5/125 µm multi-mode and the usual 50/125 µm fibers that are optimized for 1 Gb/s applications. The 50/125 µm fiber however is more micro-bend sensitive than 62.5/125 µm fiber. This explains the slightly higher added optical loss observed in the temperature cycling and the cable aging tests for the cables made with the 50/125 µm LaserWave® fiber. Although the added loss is only marginally higher than the GR409 requirements, more importantly, the absolute attenuation at 850 nm and 1300 nm is comparable to cables made with low bandwidth 62.5/125 µm fibers, even at the low temperatures of –20°C (see Table 4). Thus, the cables made with LaserWave® fiber enable a larger bandwidth without sacrificing the optical performance.

The optical transmission and attenuation performance of the LSOH MiniCord® Simplex and Duplex cable prototypes are summarized in Table 4.

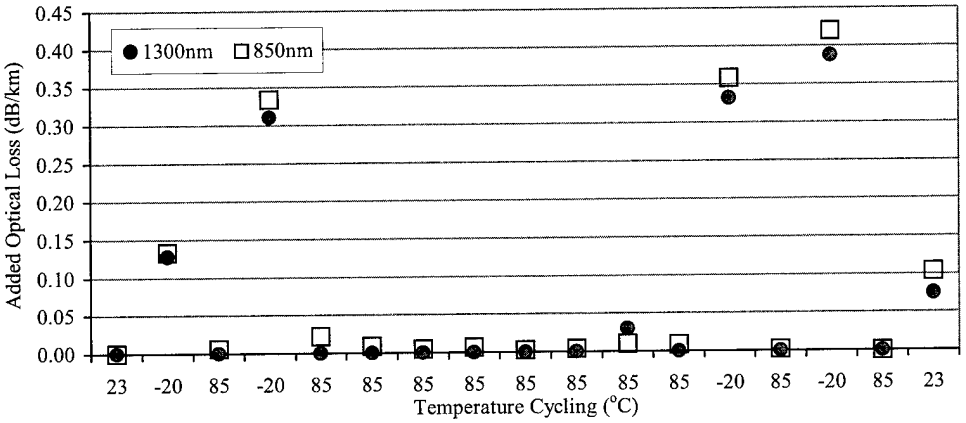


Figure 3. Added Optical Loss for a Prototype LSOH MiniCord® Simplex with 62.5/125 μm Multi-mode Fiber

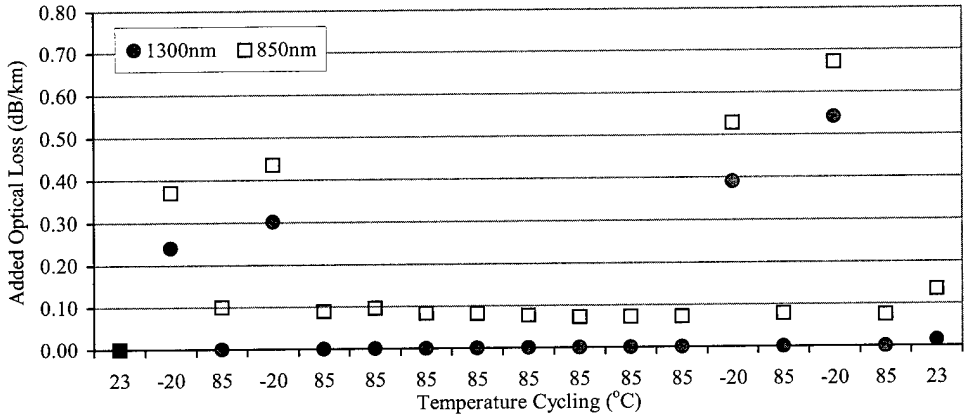


Figure 4. Added Optical Loss for a Prototype LSOH MiniCord® Duplex with 62.5/125 μm Multi-mode Fiber

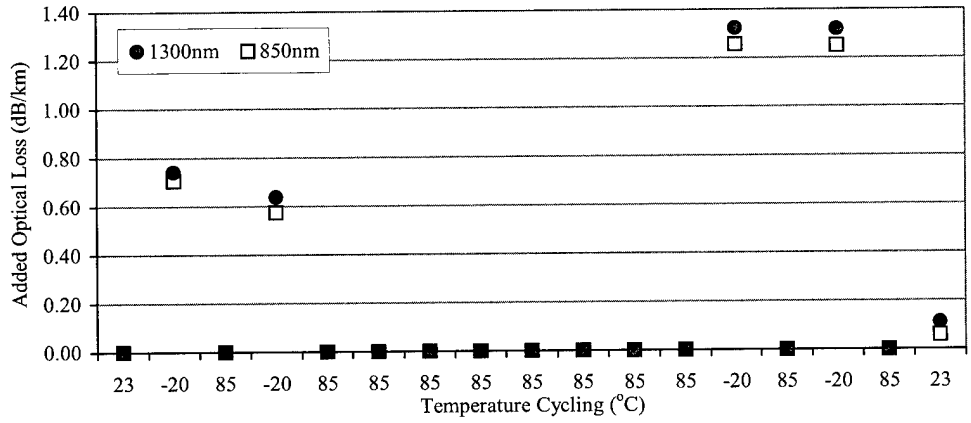


Figure 5. Added Optical Loss for a Prototype LSOH MiniCord® Duplex with 50/125 μm LaserWave® Multi-mode Fiber

Table 4. Optical Performance of LSOH MiniCord® Simplex and Duplex Cables

	Simplex Cable 62.5/125 µm multi-mode (850 nm / 1300 nm)	Duplex Cable 62.5/125 µm multi-mode (850 nm / 1300 nm)	Duplex Cable 50/125 µm LaserWave multi-mode (850 nm / 1300 nm)
Attenuation at 23°C (dB/km)	2.80 / 0.58	3.10 / 0.67	2.45 / 0.54
Attenuation at -20°C, before aging, (dB/km)	3.13 / 0.89	3.53 / 0.97	3.16 / 1.28
Attenuation at -20°C, after aging, (dB/km)	3.22 / 0.97	3.77 / 1.22	3.7 / 1.86
Minimum bandwidth (MHz.km)	160 / 500	160 / 500	1500 / 500

4.3 Mechanical Performance Tests

The LSOH MiniCord® Simplex and Duplex cables were tested for robustness and mechanical performance according to the test procedures specified in the IEC 60794 and GR409 standards. The added optical loss (due to the test loads/deformations) was measured at transmission wavelengths of 850 nm and 1300 nm. The cables easily exceeded the standards requirements.

The IEC 60794 standard requires that there should be no fiber breaks when the cables are subjected to the specified mechanical test [1]. There are no requirements for optical loss. The IEC 60794 mechanical test results are shown in Table 5. There were no fiber breaks and no loss of optical continuity for any sample. The optical losses were extremely low for all the tests.

The GR409 standard requires that there be no damage to the cable jacket when the cables are subjected to the specified mechanical tests. The maximum allowable added loss (due to the test loads/deformations) is 0.30 dB for cables with multi-mode fibers [2]. The results shown in Table 6 indicate that the LSOH MiniCord® Simplex and Duplex cables exceed these requirements in all the tests. There was no damage to the cable jacket of any sample during the tests.

The results indicate that despite their small size, the LSOH MiniCord® cables are very robust. These cables are ideal for installations in confined spaces and for connections that require repeated handling. The excellent mechanical performance is due to the unique cable design features and the appropriate choice of cable materials.

4.4 Shrinkage Tests

The LSOH MiniCord® Simplex and Duplex cables were measured for shrinkage as per EIA-455-86. A 12-inch cable sample was measured prior to and after being placed in an oven at 85°C for four hours. The tests were also done after oven aging at 110°C for two hours. In all the tests, the requirement of shrinkage less than 5% was met.

Table 5. Results from Mechanical Tests according to IEC 60794. Added loss results as shown are the worst-case values that were recorded with the test samples

Test (Standard)	Simplex Cable 62.5/125 µm multi-mode fiber Added Loss (dB)		Duplex Cable 62.5/125 µm multi-mode fiber Added Loss (dB)		Simplex Cable 50/125 µm LaserWave fiber Added Loss (dB)		Duplex Cable 50/125 µm LaserWave fiber Added Loss (dB)	
	850 nm	1300 nm	850 nm	1300 nm	850 nm	1300 nm	850 nm	1300 nm
Tensile Performance (IEC 60794-1-2-E1A)	0.029	0.033	0.001	0.007	0.061	0.047	0.016	0.022
Crush (IEC 60794-1-2-E3)	0.031	0.043	0.000	0.000	0.209	0.298	0.002	0.000
Repeated Bending (IEC 60794-1-2-E6)	0.004	0.003	0.000	0.008	0.004	0.001	0.000	0.006
Torsion (IEC 60794-1-2-E7)	0.003	0.002	0.000	0.001	0.001	0.003	0.001	0.002
Cable Bend (Bend Procedure 1) (IEC 60794-1-2-E11A)	0.003	0.010	0.000	0.002	0.000	0.000	0.000	0.005
Cable Bend at Low Temperature (Bend Procedure 2) (IEC 60794-1-2-E11B)	0.008	0.008	0.152	0.148	0.524	0.599	0.493	0.497
Cable Flexing (IEC 60794-1-2-E8)	--	0.230	--	0.122	--	--	--	0.186
Impact (IEC-60794-1-2-E4)	0.143	0.133	0.009	0.003	0.000	0.004	0.000	0.007
Cable Kink (IEC-60794-1-E10)	No kinks		No kinks		No kinks		No kinks	

Table 6. Results from Mechanical Tests according to GR409. Added loss results as shown are the worst-case values that were recorded with the test samples

Test Standard	Simplex Cable 62.5/125 µm multi-mode fiber Added Loss (dB)		Duplex Cable 62.5/125 µm multi-mode fiber Added Loss (dB)		Simplex Cable 50/125 µm LaserWave fiber Added Loss (dB)		Duplex Cable 50/125 µm LaserWave fiber Added Loss (dB)	
	850 nm	1300 nm	850 nm	1300 nm	850 nm	1300 nm	850 nm	1300 nm
Tensile Strength (EIA 455-33A)	0.113	0.119	0.103	0.102	0.030	0.036	0.000	0.000
Compressive Strength (EIA 455-41A)	0.016	0.015	0.075	0.104	0.002	0.000	0.000	0.000
Cable Cyclic Flexing (EIA 455-104A)	0.000	0.000	0.053	0.045	0.004	0.000	0.000	0.000
Cable Twist (EIA 455-85A)	0.004	0.000	0.003	0.002	0.000	0.000	0.003	0.002
Low Temperature Cable Bend (EIA 455-37A)	0.064	0.068	0.262	0.263	0.045	0.059	0.018	0.016
Cable Impact (EIA 455-25A)	0.017	0.015	0.008	0.009	0.011	0.002	0.000	0.001

5. Connectorization

The LSOH MiniCord® Simplex and Duplex cables can be terminated/connectorized to form jumpers, patchcords, pigtails, and interconnect cables. They are designed specifically for Lucent Technologies LC, SC and ST®II+ connectors and may be used with most commercial connectors. The buffer material is designed for the stiffness that is required for use in non-optical, disconnect-type "pull-proof" connectors. The buffer is easily stripped from the fiber for connectorization. The buffered fibers meet the requirements specified in EIA-455-178 (Coating Removal - Strip Force for Optical Fibers). The cable buffer and jacket materials can withstand exposure to the high temperatures that are often used in the epoxy curing process during connectorization.

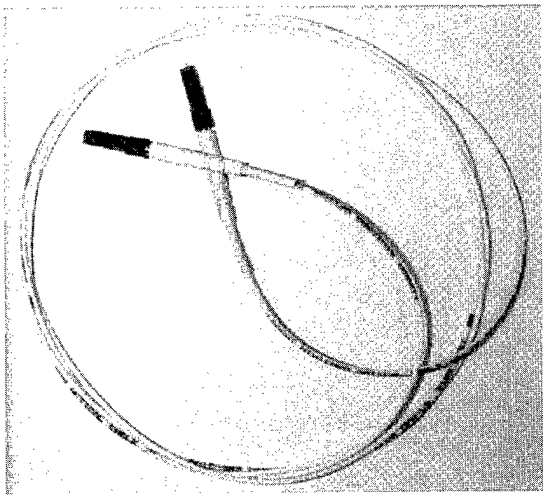


Figure 6. LSOH MiniCord® Simplex with LC Connector

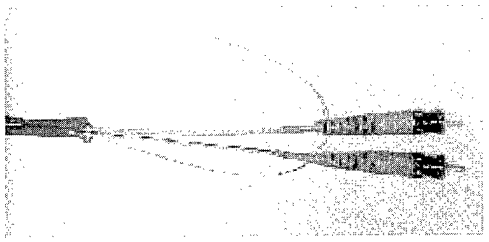


Figure 7. LSOH MiniCord® Duplex with ST®II+ Connectors

6. Conclusions

Fiber optic MiniCord® cables have been developed for interconnect, cross-connect and distribution applications. The single-fiber MiniCord® Simplex is constructed using a Non-Halogen high modulus buffer material and a Low-Smoke Non-Halogen jacket. The two-fiber MiniCord® Duplex has a Low-Smoke Non-Halogen over-jacket to provide added protection to the constituent Simplex parts. These cables meet the European requirements of non-halogen materials for use in telecommunication equipment.

Although optimized for Lucent Technologies LC, SC and ST®II+ connectors, these cables may be used with most commercial connectors. The buffer material is designed for the stiffness that is required for use in non-optical, disconnect-type "pull-proof" connectors. Yet, the cables are flexible for easy handling and installation in high-density applications. The buffer is easily stripped from the fiber. The Duplex has a non-halogen fire-retardant ripcord for easy removal of the over jacket without bending, deforming or damaging the internal Simplex parts.

The cables exceed the optical performance, and the temperature cycling and cable aging test requirements of both IEC 60794 and Telcordia GR409 standards. The cables exhibit minimal added loss in the operating temperature range of –20°C to 85°C. The non-halogen buffer and jacket materials allow a wider storage

temperature range (–40°C to 85°C), and a wider installation temperature range (-30°C to 70°C) than is possible with most ordinary PVC based cables. This is due to the superior mechanical properties of the non-halogen materials at both high and low temperatures.

The rugged design of the MiniCord® ensures superior performance in Telcordia GR409 and IEC 60794 mechanical tests. This includes tensile, crush, torsion, bend, cold bend, flexing, impact and kink tests.

These cables also meet the environmental standards requirements for fire (IEC 60332-1), smoke (IEC 61034-2), acid gas evolution (IEC 60754-2) and toxicity (NES 713-3). The Low Smoke Non-Halogen MiniCord® is attractive for markets and applications where an alternative to PVC micro-assembly cables is desired.

7. Acknowledgements

The authors would like to thank many individuals in the Premises Cable Group, especially Andy Crowley and Martin Stalheim for their support and assistance on this development. Thanks also go to FOCQL for the optical and mechanical tests.

8. References

[1] IEC 60794-2-10 Draft, Fibers and Cables, International Electrotechnical Commission, 2000.

[2] Telcordia GR-409-Core, Generic Requirements for Premises Fiber Optic Cable, 1999.

[3] IEC 60332-1, Tests on Electric Cable under Fire Conditions Part 1: Test on a Single Vertical Insulated Wire or Cable, International Electrotechnical Commission, 1992.

[4] Report from Underwriters Laboratories

[5] IEC 61034-2, Measurement of Smoke Density of Cables Burning under Defined Conditions, 2nd ed., International Electrotechnical Commission, 1997.

[6] Report from Intertek Testing Services

[7] IEC 60754-2, Test on gases evolved during combustion of electric cables - Part 2: Determination of degree of acidity of gases evolved during the combustion of materials taken from electric cables by measuring pH and conductivity, International Electrotechnical Commission, 1997.

[8] Report from Warrington Fire Research.

[9] NES-713, Naval Engineering Standard 713, Issue 3, Determination of the Toxicity Index of the Products of Combustion from small specimens of materials, 1985.

Hydrogen Aging Tests for Optical Fibers

Makoto Shimizu, Kazuya Kuwahara, Masahiko Dazai
Fiber Optics Division, Sumitomo Electric Industries, Ltd.
1, Taya-cho, Sakae-ku, Yokohama, 244-8588 Japan
Phone #: +81 45 853 7147, Fax #: +81 45 851 0935, Email address: makoto-s@sei.co.jp

Abstract
Attenuation increase in fiber due to hydrogen exposure can be divided into two categories. One is reversible attenuation increase caused by hydrogen partial pressure and the other is permanent attenuation increase caused by cumulative hydrogen exposure. As previous studies [1, 2] indicated, accelerated hydrogen aging tests at high temperature could not simulate the actual attenuation increase under ordinary cable deployment conditions. We presumed the mechanisms of the chemical reaction between hydrogen and defects at ambient temperature and observed relative attenuation increases. We also verified the test conditions under 0.01 and 1.0 atmospheres of hydrogen at room temperature, which are being actively discussed now in several international standardization committees, and proposed the test method with 1.0 atmosphere as a new standard for hydrogen aging test. As we have done so far, we contribute this paper to the International Electro-technical Commission (IEC) for further discussion on the improved test method.

Keywords
Hydrogen aging test; Optical fiber; Hydrogen diffusion; Hydrogen reaction; Raman a-mplification

1. Introduction
Technological progress in DWDM requires optical fibers to work with an expanded transmission capacity through use of E-Band (1360 – 1460 nm) in addition to O-Band (1260 – 1360 nm), S-Band (1460 – 1530 nm), C- Band (1530 – 1565 nm) and L-Band (1565 – 1625 nm). IEC 86A/348/CD reports that 4×10^{-4} atmosphere of hydrogen was observed in duct cables several years after the installation. In the presence of hydrogen, attenuation increase is a serious concern particularly at 1383 nm and an introduction of new standards for hydrogen aging tests has been considered necessary to assess fiber properties for the E-band applications.

2. Hydrogen Aging Loss Mechanisms
Hydrogen aging loss is mainly caused by an extreme reaction between hydrogen molecules and defects following on the hydrogen diffusion in optical fiber. We discuss the hydrogen diffusion and the hydrogen reaction below.

2.1 Hydrogen Diffusion
The hydrogen diffusion precedes hydrogen reaction. The equation for the hydrogen diffusion into optical fiber can be expressed as

$$\frac{\partial C}{\partial t} = \frac{1}{r}\frac{\partial}{\partial r}\left(rD\,\frac{\partial C}{\partial r} \right) \qquad (1)$$

where C is hydrogen concentration, t is hydrogen exposure time, D is diffusion coefficient of hydrogen into optical fiber and r is distance in an axis direction from the fiber surface ($0 \le r \le a$).

We see that

$$C = u \times \exp\left(-D\alpha^2 t\right) \qquad (2)$$

If the diffusion coefficient D is constant, u becomes solely a function of r as

$$\frac{d^2u}{dr^2} + \frac{1}{r}\frac{du}{dr} + \alpha^2 u = 0 \qquad (3)$$

The equation 3 covers the Bessel functions $J_0(r\alpha_n)$, and so if they are properly chosen, it satisfies the initial and boundary conditions.

If the initial hydrogen concentration at the surface of the optical fiber is maintained zero, the boundary conditions are satisfied by

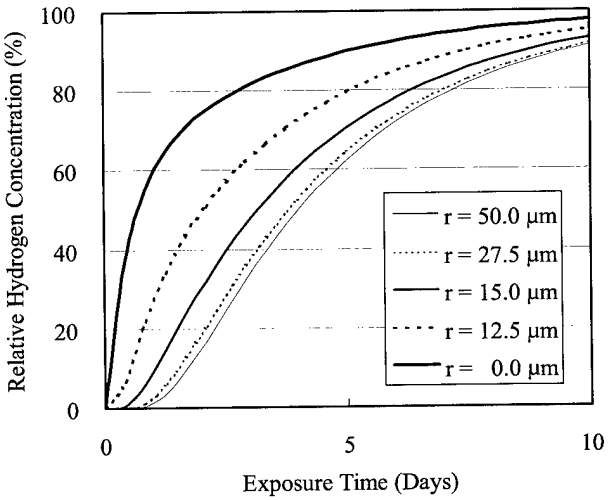
$$C = \sum_{n=1}^{\infty} A_n J_0(\alpha_n r)\exp\left(-D\alpha_n^2 t\right) \qquad (4)$$

and we find

$$\frac{C}{C_0} = 1 - \frac{2}{a}\sum_{n=1}^{\infty}\frac{\exp\left(-D\alpha_n^2 t\right)J_0(r\alpha_n)}{\alpha_n J_1(a\alpha_n)} \qquad (5)$$

where C_0 is exposed hydrogen concentration in the test chamber.

Figure 1 shows the hydrogen diffusions at room temperature calculated by the equation 5. It shows that it takes about 10 days for the hydrogen to diffuse into the core of optical fiber and reach an equilibrium state.



2.2 Hydrogen Reaction

The chemical reactions mentioned below occur subsequent to the hydrogen diffusion under service conditions.

$$Si - O \cdot + H_2 \rightarrow Si - OH + \frac{1}{2} H_2 \quad (6)$$

$$Si \cdot + \frac{1}{2} H_2 \rightarrow Si - H \quad (7)$$

The model of hydrogen reaction between hydrogen molecules and defects can be expressed as

$$[H_2] + [D] \rightarrow [\alpha] \quad (8)$$

where $[H_2]$ is hydrogen concentration, $[D]$ is defect concentration and $[\alpha]$ is concentration of reaction products.

In this case, the equation is

$$\frac{d[\alpha]}{dt} = k[H_2]\cdot[D] = A \cdot \exp\left(-\frac{E_a}{RT}\right)\cdot[\alpha' - \alpha]\cdot P_{H_2} \quad (10)$$

where α' is initial concentration of defects and P_{H2} is hydrogen partial pressure.

We find

$$[\alpha] = \alpha'[1 - \exp(-k \cdot P_{H_2} \cdot t)] \quad (11)$$

$$k = A \cdot \exp\left(-\frac{E_a}{RT}\right) \quad (12)$$

where A is frequency factor, E_a is activation energy, R is gas constant, T is absolute temperature.

The hydrogen aging loss is directly proportional to the concentration of reaction products.

As the activation energy has a certain distribution, the equation 11 and equation 12 become

$$[\alpha] = \sum_{i=1}^{\infty} \alpha_i'[1 - \exp(-k_i \cdot P_{H_2} \cdot t)] \quad (13)$$

$$k_i = A \cdot \exp\left(-\frac{E_i}{RT}\right) \quad (14)$$

These equations indicate that an accelerated hydrogen aging under high hydrogen pressure can simulate the actual reaction in a shorter period of time.

Thus, we proposed the test method with 1.0 atmosphere of hydrogen at room temperature in addition to the one with 0.01 atmosphere of hydrogen to characterize fiber properties under the actual cable deployment conditions of 4×10^{-4} atmosphere of hydrogen.

3. Experiments

3.1 Tested Fibers

The hydrogen aging loss is mainly caused by the hydrogen reaction that follows on hydrogen diffusion. It is considered that the optical fiber with less defects induce lower attenuation increase in hydrogen atmosphere. Inasmuch as the different designs of optical fiber develop varied hydrogen aging loss behavior, we performed hydrogen aging tests for optical fibers with special designs under several different conditions to verify the new test standard. Table 1 shows tested fibers. They were all single-mode fibers produced by several manufactures. Fiber A is Enhanced Pure Silica Core Fiber (E-PSCF). Fiber B and Fiber C are Zero-OH Germanium doped Single-Mode Fibers (Zero-OH Ge doped SMF). Fiber D, Fiber E and Fiber F are Standard Germanium doped Single-Mode Fibers (Standard Ge doped SMF).

Table 1. List of tested fibers

ID	Classification
Fiber A	E-PSCF
Fiber B	Zero-OH Ge doped SMF
Fiber C	
Fiber D	Standard Ge doped SMF
Fiber E	
Fiber F	

3.2 Test Method

A seven (7) km length of each specimen was looped tension free with 280 mm diameter and was exposed to hydrogen in a test chamber. Hydrogen aging loss of each specimen was measured under the test conditions of both 0.01 and 1.0 atmospheres of hydrogen at room temperature.

3.3 Results

Figure 2 and Figure 3 show the spectral attenuation changes of zero-OH Ge doped SMF (Fiber B in Table 1) and standard Ge doped SMF (Fiber F in Table 1) after exposure to 0.01 atmosphere of hydrogen at room temperature. The attenuation increases at 1240 nm as observed in Figure 2 and Figure 3 occur due to the dissolved interstitial hydrogen molecules and are reversible after 14 days in the normal laboratory environment. The attenuation increases between 1380 nm and 1520 nm occur due to the chemical reaction and are permanent. Figure 4 indicates the

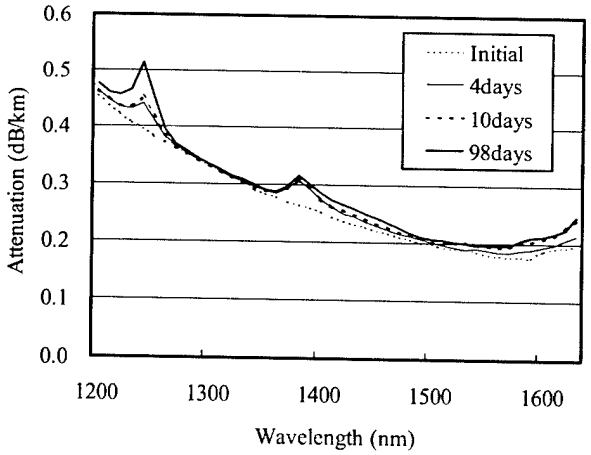


Figure 2. Spectral attenuation changes after exposure to 0.01 atmosphere of hydrogen at room temperature (Fiber B)

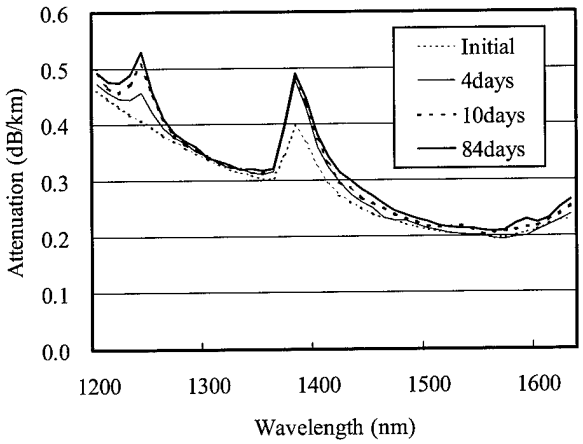


Figure 3. Spectral attenuation changes after exposure to 0.01 atmosphere of hydrogen at room temperature (Fiber F)

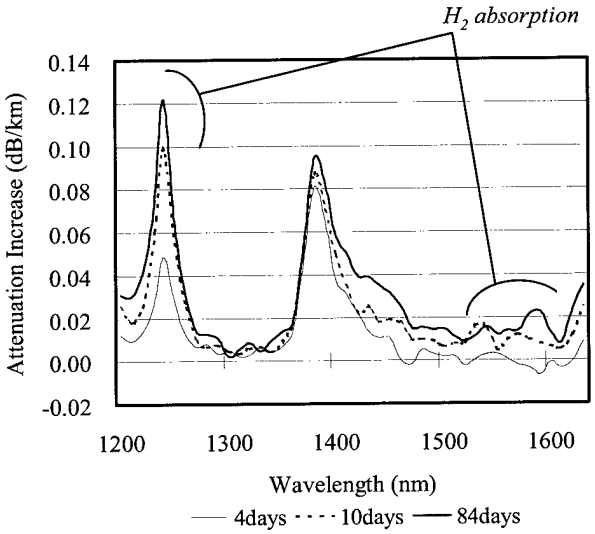


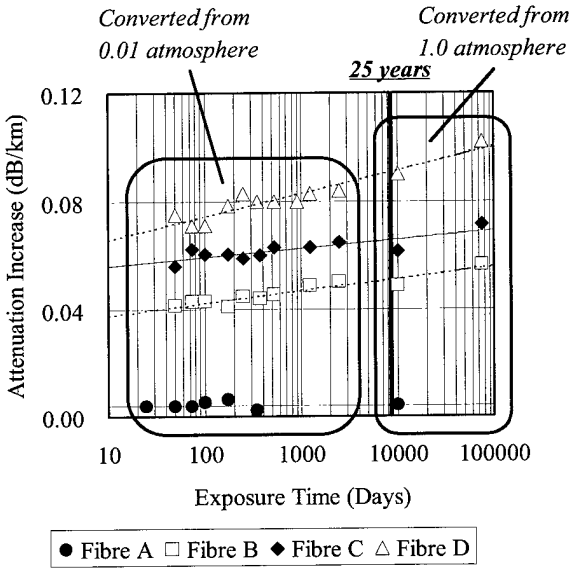
Figure 4. Attenuation Variations after exposure to 0.01 atmosphere of hydrogen at room temperature (Fiber F)

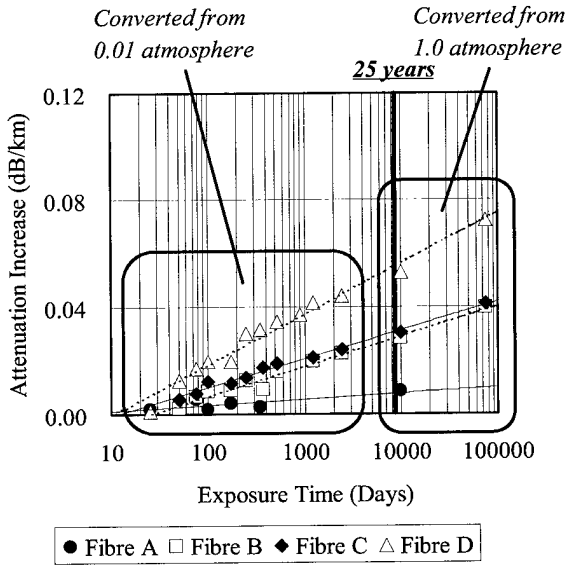
attenuation variations converted from data in Figure 3. The attenuation variation at 1440 nm like at 1383 nm is particularly remarkable. These attenuation increases pose serious problems for the Raman amplification [3]. The principle of the Raman amplification defines that an optical pump signal launched into an optical fiber is to generate a Raman gain along the optical fiber at longer wavelength, and that if you need to have the Raman gain in C-band, the wavelengths of the optical pump signal are required to be around 1440 nm. Hence, we need to address the stability of optical fibers against hydrogen and select appropriate fibers to employ.

4. Analysis

4.1 New Standard for Hydrogen Aging Test

Figure 5 and Figure 6 show the attenuation increases at 1383 nm and 1440 nm after fiber exposure to 4×10^{-4} atmosphere of hydrogen at room temperature converted from the test results after fiber exposure to 0.01 and 1.0 atmospheres of hydrogen respectively. As shown in both Figure 5 and Figure 6, since there





exists a linear relationship for attenuation increases between 0.01 and 1.0 atmospheres, it is considered that not only 0.01 atmosphere test but also 1.0 atmosphere test can simulate the actual hydrogen aging loss induced under ordinary cable deployment conditions. The actual cable deployment condition of 4×10^{-4} atmosphere of hydrogen for the duration of 25 years is equivalent to the 0.01 atmosphere test for 367 days or to the 1.0 atmosphere test for 4 days. Thus, by the exposure to the 1.0 atmosphere, the hydrogen aging loss through the lifetime of optical fiber can be estimated in much shorter period of time than by the 0.01 atmosphere.

4.2 Comparative Study

We estimated the attenuation increases 25 years after deployment (equivalent to 9,125 days in Figure 5 and Figure 6) by the current draft standard method accepted at IEC committee (IEC draft standard method) and by the acceleration test method we proposed (our proposed method). Table 2 summarizes the estimated attenuation increases for each specimen (Fiber A to F) by the IEC draft standard method and by our proposed method. From these results, it is found that the IEC draft standard method tends to underestimate the attenuation increases than our proposed method,

Table 2. The estimated attenuation increase after 25 yeares

1) 1383 nm

ID	Estimated Attenuation Increase at 1383 nm (dB/km)	
	IEC Draft Standard Method	Our Proposed Method
Fiber A	0.005	0.004
Fiber B	0.043	0.052
Fiber C	0.063	0.066
Fiber D	0.071	0.091
Fiber E	0.090	0.119
Fiber F	0.116	0.153

2) 1440 nm

ID	Estimated Attenuation Increase at 1440 nm (dB/km)	
	IEC Draft Standard Method	Our Proposed Method
Fiber A	0.002	0.008
Fiber B	0.007	0.028
Fiber C	0.008	0.030
Fiber D	0.020	0.056
Fiber E	0.021	0.071
Fiber F	0.024	0.071

and at 1383nm the attenuation increase by the IEC draft standard method showed maximum twenty-four percent smaller than by our proposed method, and at 1440 nm maximum seventy-five percent. Thus, even if the IEC draft standard method may be adequate for the evaluation of hydrogen sensitivity of the optical fibers, it may not be adequate for the estimation of hydrogen aging losses.

According to our proposed method, E-PSCF (Fiber A) exhibits excellent stability against hydrogen with 0.004 dB/km attenuation increase at 1383 nm and 0.008 dB/km at 1440 nm. Zero-OH Ge doped SMF (Fiber B and C) shows negligibly small attenuation increase with less than 0.07 dB/km at 1383 nm and less than equal to 0.03 dB/km at 1440 nm. Standard Ge doped SMF manufactured by several sources (Fiber D, E and F) have wider range of attenuation increases with more than 0.09 dB/km at 1383 nm and more than 0.05 dB/km at 1440nm.

4.3 Deciding Factors for Hydrogen Stability

We consider that the number of defects depends strongly on manufacturing process, and type of hydrogen reactions on the kind and quantity of doped materials. These, we presume, are deciding factors on the stability against hydrogen of optical fibers.

4.4 Enhanced Pure Silica Core Fiber

It is well known that optical transmission systems using the Raman amplification demand the optical fiber with less attenuation variation (preferably, less than 0.02 dB/km) at the wavelength of the optical pumps through their entire lifetime of fiber. As shown in Figure 5 and Figure 6, E-PSCF (Fiber A) scarcely induced attenuation increase at both wavelengths under the hydrogen atmosphere compared with other types of fibers, zero-OH Ge doped SMF (Fiber B and C) and standard Ge doped SMF (Fiber D). Hence, E-PSCF (Fiber A) may be said to have greater stability over others for the transmission systems with the Raman amplification.

5. Conclusions

The current standard method accepted at IEC committee requires to "Expose the fiber to 0.01 atmosphere of hydrogen at room temperature and continue hydrogen exposure until the 1240 nm attenuation changes by 0.03 dB/km or more." On the basis of this study we conducted, we concluded that the test method with 1.0 atmosphere of hydrogen at room temperature was proved to be adoptable as the new standard of the hydrogen aging test along with the current standard method with 0.01 atmosphere. While the IEC draft standard method tends to underestimate the hydrogen sensitivity of optical fiber, our proposed method, we believe, ensures more accuracy in a shorter testing time. Hence, we recommend that our proposed method, namely the test under 1.0 atmosphere of hydrogen, be also adopted as the international standard test method.

6. Acknowledgments

Special thanks to the IEC SC86A/WG1 members for their helpful information and discussion.

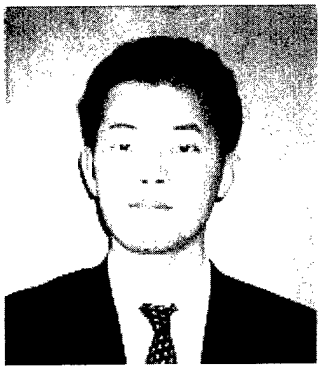
7. References

[1] K. H. Chang, D. Kalish and M. L. Pearsall, "New Hydrogen Aging Loss Mechanism in the 1400 nm Window," *OFC/IOOC '99 Technical Digest*, paper PD22 (February, 1999).

[2] T. Voots , J. Piffaretti, R. Charlton and J. Goudeau, "Hydrogen Aging of Optical Fiber at Low Partial-Pressure," *Proceedings NFOEC 2000*, 473-479 (August, 2000).

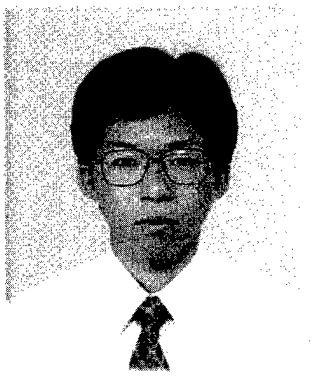
[3] C. Laval, D. Hamoir, "Raman Amplification in Long-haul Submarine Systems," *Proceedings SubOptic 2001*, paper T3.4.5, 286-288 (May, 2001)

Authors



Makoto Shimizu

Makoto Shimizu joined Sumitomo Electric Industries, Ltd. in 1994 as a fiber optics engineer. He holds a B.S. degree in Applied Chemistry and a M.S. degree in Material Science from Keio University. He used to be active in IEC with the standardization of optical fibers and cables.



Kazuya Kuwahara

Kazuya Kuwahara received his B.S. degree in Applied Physics and M.S. degree in Energy Science from Tokyo Institute of Technology in 1991 and 1993, respectively. In 1993, he joined Sumitomo Electric Industries, Ltd. and has worked on the research and development of optical fiber. Currently, he is an engineer of the Optical Fibers R&D Department.



Masahiko Dazai

In 1982, Masahiko Dazai joined Sumitomo Electric Industries, Ltd. as a fiber optics engineer. He holds a B.S. degree in Communication Engineering and a M.S. degree in Electronics Engineering from Tohoku University. He is an assistant manager in Fiber Optics Engineering Department and active in the IEC, ITU-T and JIS with the standardization of optical fibers and cables.

Glass Corrosion in Commercial Optical Fibers with Defective Coating

Charles E. Turnbill, Bob J. Overton, Christelle Lavallade
Alcatel Cable NA
Claremont, North Carolina
+1-828-459-8376 · bob.overton@cable.alcatel.com

Abstract
The strength of optical fibers is highly dependent on the protection afforded by the UV-curable polymeric coatings. Recent studies show that the long-term maintenance of fiber strength can be understood in terms of the coating cure and the nature of the coating chemistry, including adhesion between the coating and the glass and the moieties providing the adhesion. If the cure of the coating materials is not optimized during the manufacture process, the adhesion between coating and glass is adversely affected. This can lead to coating delamination and degradation of the mechanical strength of the fiber over time in harsh environments. Even when the coatings are well-cured, different coating formulations provide different levels of protection against the effects of aging.

Keywords
Coatings; aging; strength; stress corrosion; AFM

1 Introduction
Since the introduction of ultra-violet curing optical fiber coatings in the early 1980's, there has been an evolution of improved formulations. While 10 to 15 years ago it was not uncommon to open flooded manholes and find fiber so degraded in strength that it could not be stripped without fracturing, such is very rarely the case today.

Nevertheless, the long-term strength of optical fibers is still influenced by the choice of coating chemistry, the matching of oligomer(s), monomers and adhesion promoters, and by the quality of the coating cure. In this work, we studied the long-term, stress-free aging behavior of fibers with a number of different coatings, varied in chemistry, and examined fiber with poorly cured primary coating. Two-point bending strength testing was the method of choice for evaluating the evolution of strength and of the stress corrosion factor. As the fibers aged, photo-micrographs were taken to record the visible changes in the coatings, and atomic force microscopy was applied to examine the physical effects on the surface of the fibers.

2 Strength on Aging
2.1 Samples
Eight fiber samples comprising five different optical fiber coating systems are reported on in this paper. Six fiber samples are of standard silica overcladding, and two of them are not pure silica at the glass surface (these are from two different sources). Two of the standard silica fibers have poorly processed coatings. The nomenclature for the fibers is as follows:

- Coating type – 1, 2, 3, 4, and 5
- Glass type – S = standard silica overcladding, and T = silica treated or doped at the surface of the fiber
- Having no additional letter indicates good coating cure and the addition of a P indicates poor coating cure

The list of fiber samples is given below in Table I.

Table 1. Coding for the fiber samples

Code	Coating Type	Glass Type	Coating Cure
1S	1	Standard silica	Good
2S	2	Standard silica	Good
2T	2	Treated silica	Good
3S	3	Standard silica	Good
3T	3	Treated silica	Good
3SP	3	Standard silica	Poor
4S	4	Standard silica	Good
5SP	5	Standard silica	Poor

2.2 Aging
The fiber samples were cut to 15 cm lengths. A number of samples were placed into glass containers of buffered de-ionized water. The containers were sealed and immersed into a silicone oil bath maintained at 60 C. Periodically, samples were removed, allowed to air dry, and equilibrated in the test environment controlled at 50% relative humidity and 23 C for of three days before obtaining the strength and fatigue characteristics.

2.3 Two-Point Bend Testing
The two–point bend dynamic strength testing was executed on single samples per test, 30 samples per set. The two-point bend apparatus was controlled to a constant strain rate of 5 percent per minute. The dynamic fatigue n-values were obtained via the two-point bend apparatus controlling at constant strain rates of 0.025, .25, 2.5 and 25 percent per minute, measuring 12 samples at a time, 24 samples per strain rate. Acoustic sensors detected the break point in all tests.

2.4 Results

Samples 1S, 2S and 2T share some commonalties, in that the glass process is the same for 1S and 2S, and the coatings are the same for 2S and 2T. Draw conditions are similar for all three. Figures 1, 2, and 3 show the evolution of the dynamic fatigue curves with time in 60 C water for these three samples.

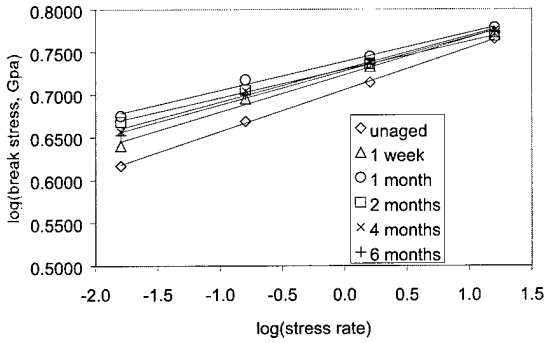


Figure 1. Dynamic fatigue curves for 1S.

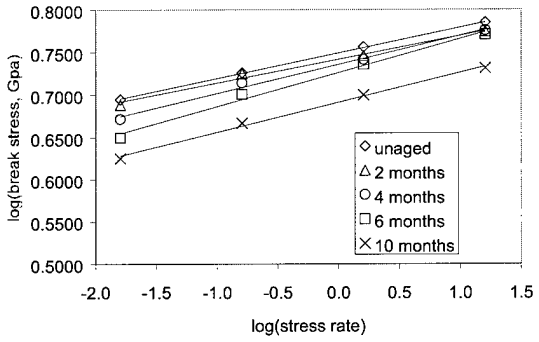


Figure 2. Dynamic fatigue curves for 2S.

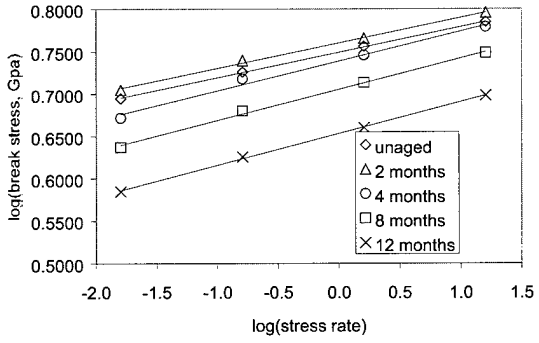


Figure 3. Dynamic fatigue curves for 2T.

These figures show quite different responses to aging. Another way to examine the changes with aging is to look at the Weibull distributions of the 10 percent per minute strain rate results with aging for 1S, 2S and 2T, Figures 4, 5 and 6 below.

In Figures 4, 5 and 6, the change in the strength with aging is better

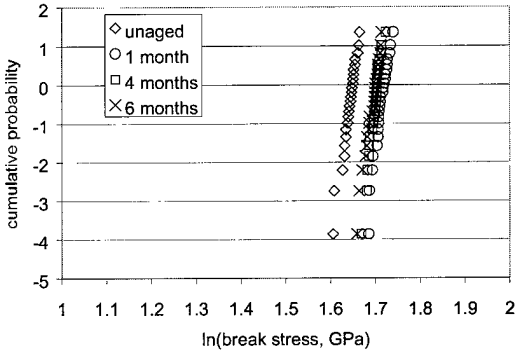


Figure 4. 1S, Weibull distribution, 10%/minute.

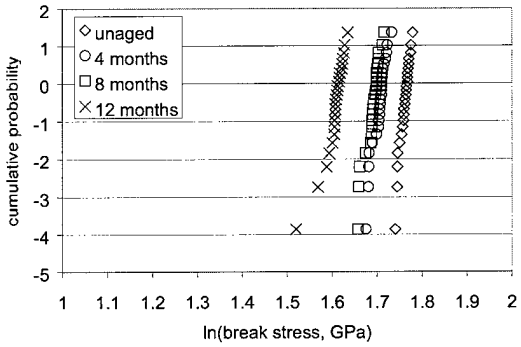


Figure 5. 2S, Weibull distribution, 10%/minute.

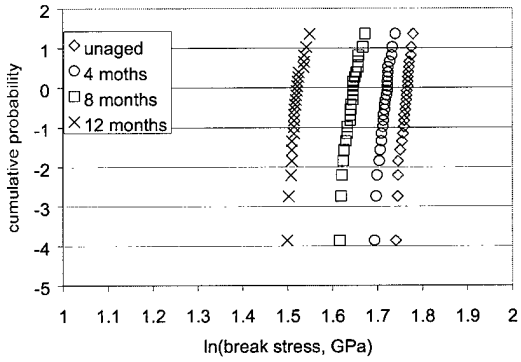


Figure 6. 2T, Weibull distribution, 10%/minute.

seen, where 1S shows an increase in strength maintained up through the 6 months of aging, while 2S and 2T show strength decreasing

with aging time. Note that 2T does show an increase in strength at 2 months, Figure 3. The conclusion based on data represented by the above figures is that the coating system has a profound effect on the behavior of glass strength under long-term, stress-free aging. The limited data on the composition of the glass at the surface of the fiber indicates that some resistance to aging may also be provided by the treatment represented by sample 2T. Work is ongoing in this area.

Next, looking at another coating system, the effects again of a glass composition modification can be examined, as well as the effect of poorly curing the coatings. Figure 7 shows the movement of the dynamic fatigue curves for sample 3S with time aging in 60 C

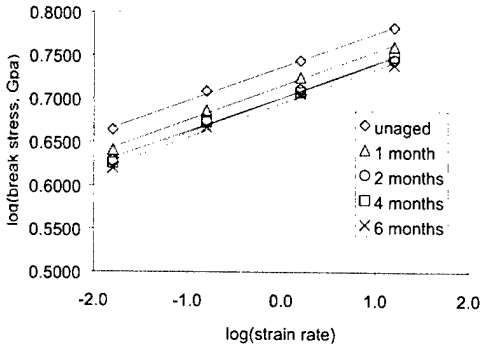


Figure 7. Dynamic fatigue curves for sample 3S.

water.

This coating system, on standard silica-overclad glass and well-cured, exhibits a different response to the effects of aging. There is an initial drop in strength over the range of strain rates during aging, but little change between 2, 4 and 6 months aging. Contrast that

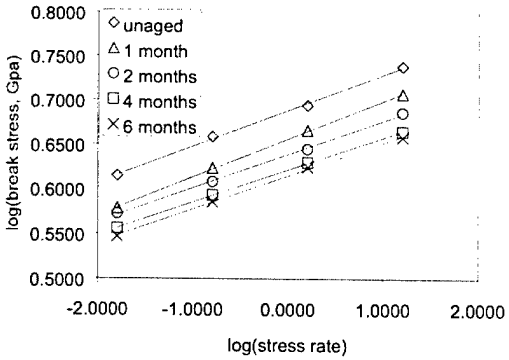


Figure 8. Dynamic fatigue curves for sample 3T.

with 3T, Figure 8.

In Figure 8, the response of the treated silica glass surface is more severe than for sample 3S. The stress corrosion factors for both samples remains excellent, at ~25, during aging.

The largest effect on aging behavior is seen in the poorly-cured analogue 3SP, Figure 9.

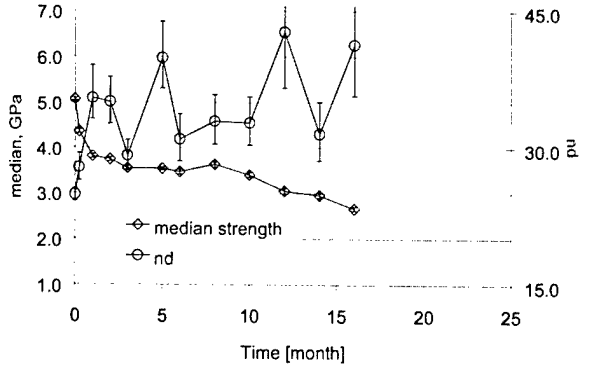


Figure 9. Dynamic fatigue and dynamic strength (TPB) with aging for sample 3SP.

Within one month of aging, the dynamic strength of 3SP fell below 4 GPa, a change of 25 percent. At 14 months the strength was below 3 GPa and falling. AFM micrographs of the surface of this sample are presented in a later section to illustrate the surface damage. The calculated stress corrosion factor rises with aging, but, as the error bars indicate, the broadening of the Weibull distributions of aged samples, even in two-point bending, renders the calculations meaningless.

Another way to compare the coating system 3 series is shown in Figure 10.

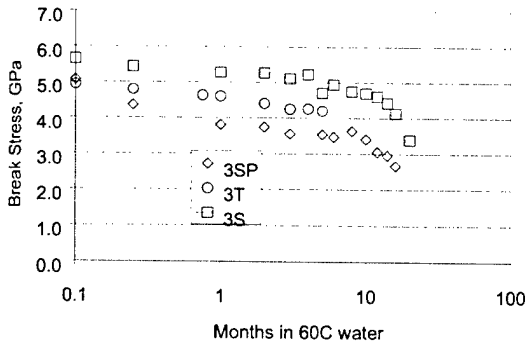


Figure 10. Dynamic strength with aging for 3S, 3T and 3SP.

A good maintenance of strength with aging is represented by 3S, with the glass modification of 3T not showing a benefit, and the poor cure of 3SP resulting in poor aging behavior.

These examples are representative of the results obtained with a far larger set of samples. From the data, it may be generalized that well-cured coatings provide very good resistance to the effects of harsh environments, and poorly cured coatings give very poor resistance for the fiber. Figure 11 shows the dynamic strength for the four representative samples 1S, 2S, 3S, and 4S, given as median strength vs log(aging time). The "knee" in the strength with aging time is still observed with 2S and 4S. 1S and 3S, samples that have aged for only 6 months at this writing, do not yet exhibit the knee, though 3S shows some small loss in median strength.

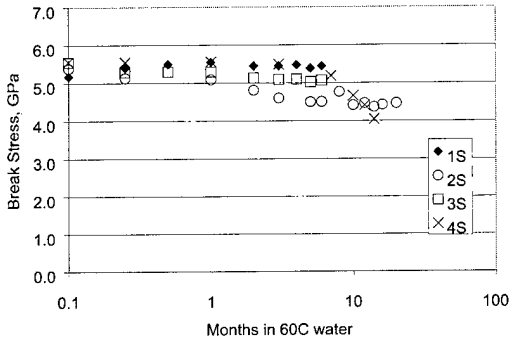


Figure 11. Median strength with aging in 60°C water.

Some differences by coating system are observed, such as the initial increase in median strength for 1S along with the flat trajectory of the data versus aging time. However, for well-cured coatings the aging performance in today's population of fiber is good.

On the other hand, the strength degradation on aging of fiber with poorly-cured coatings remains a hazard, Figure 12.

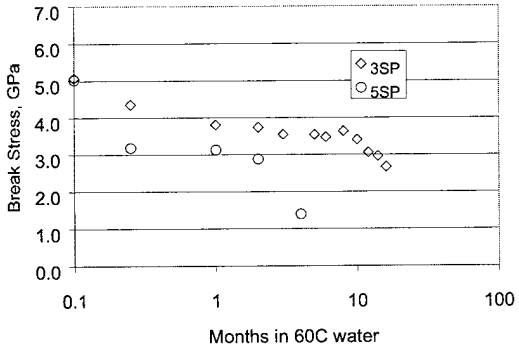


Figure 12. Median strength with aging, poorly cured coatings.

There are, as one might expect, physically detectable features of the fibers that suffer such a degradation of strength on exposure to an accelerated aging environment. Optical microscopy reveals the changes that occur common to all coatings with immersion in 60 C water, with an example in Figure 13.

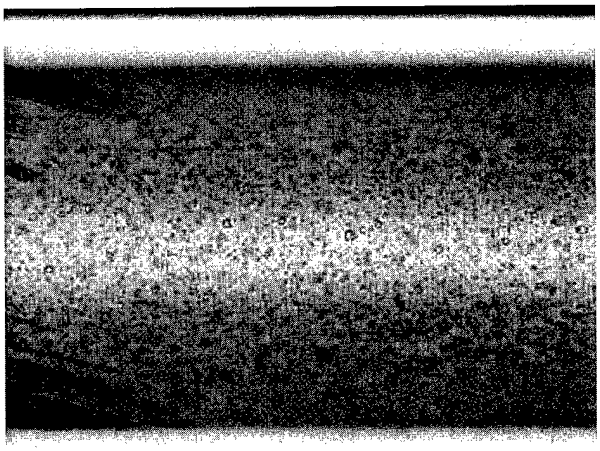


Figure 13. optical micrograph of sample 3S after 6 months aging in 60C water.

All the well-cured coating samples show a similar development of very small bubbles of material within the primary coating. These are believed to be moisture pockets that aggregate around photoinitiator fragments in the bulk of the cured material.

For poorly-cured coatings on sample fibers, there is often severe coating delamination, Figure 14.

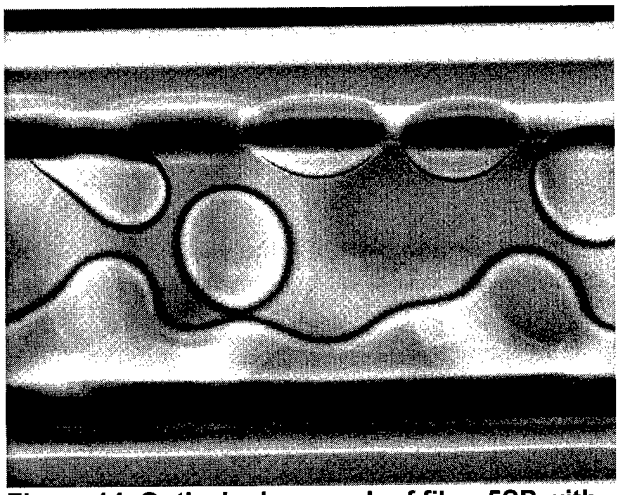


Figure 14. Optical micrograph of fiber 5SP with poorly cured coating, after 1 month in 60C water.

3 Analysis of Glass Surface

3.1 Atomic Force Microscopy

The polymer coating of optical fiber samples must be removed in order to examine the glass surface using an atomic force microscope (AFM). The preferred method in our laboratory, after many trials with different techniques, is hot sulfuric acid [2,3,5-9]. The hot acid technique for removing the coating [1] consists of immersing a portion of fiber to be stripped into ~200 degree C sulfuric acid for 20 seconds. The sample is then rinsed immediately in distilled water with mild ultrasonic agitation for 30 seconds, then moved to a beaker of acetone in the same sonicator for an additional 30 seconds. After drying, the samples are mounted and examined using a Digital Instruments model 3100 AFM operating in the TappingMode™. Glass fibers were obtained from the draw towers prior to any coating application. Particular care was taken not to allow contact with the section of fiber to be examined. Some samples were studied as received, while others were routed through the same hot sulfuric treatment as coated fibers.

3.1.1 Nanoindentation. One meter samples were taken from a spool that had been previously tested and known to have good strength characteristics. The coating was removed from ~4 cm in the middle of each length using the hot sulfuric acid stripping method. Each fiber was very carefully placed on the stage of the AFM fitted with a diamond tipped cantilever purchased from Digital Instruments. The diamond tipped probe was then used to image the fiber and align the area to be indented. Once proper alignment had been achieved, the Z axis of the tip is lowered to move the diamond into the glass surface the desired distance. The diamond tipped cantilever is then replaced with a normal tapping mode tip to image and measure damaged area of the fiber under test. These fibers were then carefully removed from the AFM stage and strung onto a half meter tensile tester set to run at 0.5% per minute strain rate.

3.2 Scanning Electron Microscopy

Break ends from the tensile tester were mounted vertically on an aluminum scanning electron microscope (SEM) specimen stub and coated with a light amount of gold in a vacuum sputter coater. The samples were then viewed in a Philips model XL30 SEM and photographed.

3.3 Results

Use of the AFM reveals little difference between the un-coated fibers taken directly from the draw tower to the microscope and those identical samples that were routed through the hot sulfuric acid treatment. These also compared very well to other samples from different manufacturers prior to water aging (see Figures 15 and 16). Note that the "bent paper" appearance of these and some of the other AFM micrographs is due to computer-flattening of the image for clarity.

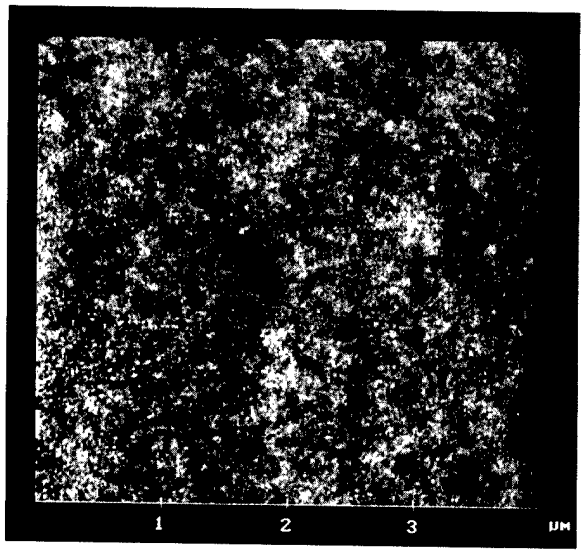


Figure 15. Unaged 2S Acid Stripped

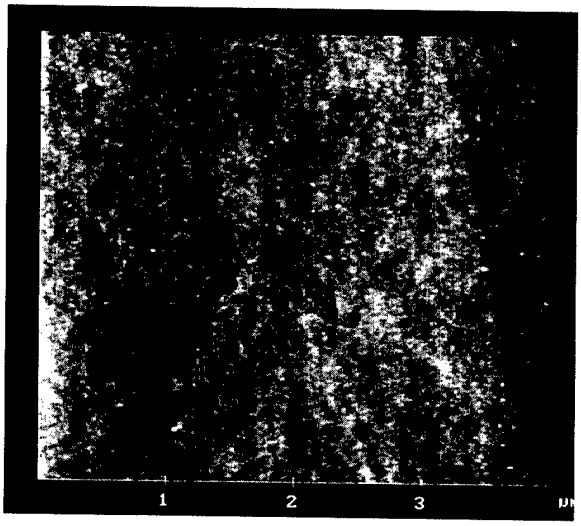


Figure 16. Unaged 3SP Acid Stripped

Aged fibers show considerable difference in physical condition of the surface between the various samples. In order to illustrate the difference clearly in this paper, we present the extreme cases of samples aged 20 months or longer in 60 C water. Another sample of fiber comprising the same coating and glass combination as sample 2S, for which only the dynamic strength was followed by two-point bend, was aged for more than 20 months. The dynamic strength median is shown in Figure 17. Figures 18, 19 and 20 then show the condition of the glass surface obtained by AFM imaging. Two scales are used for sample 3SP in order to illustrate the uniform distribution of the roughness over the entire fiber.

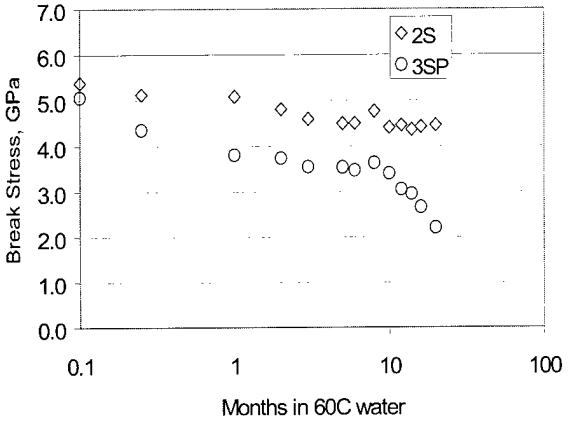


Figure 17. Dynamic strength median on aging in 60°C water.

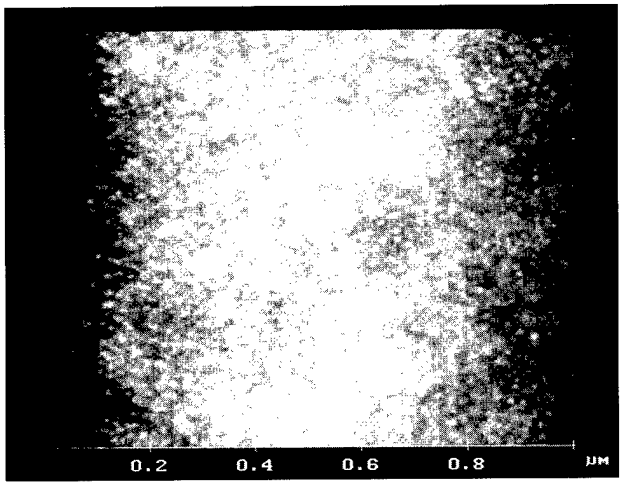


Figure 18. AFM micrograph of 2S after 20 months in 60°C water

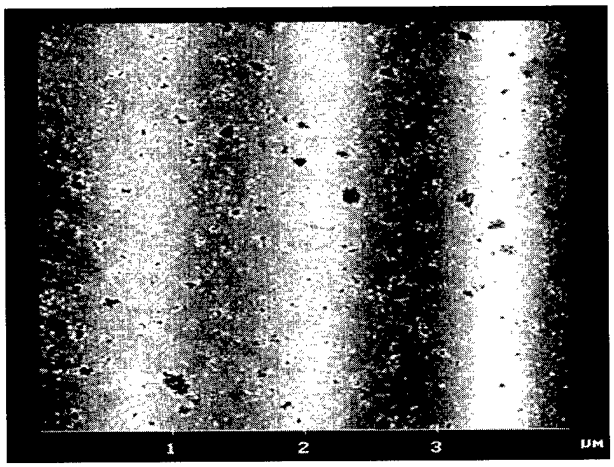


Figure 19. AFM micrograph of 3SP after 20 months in 60°C water.

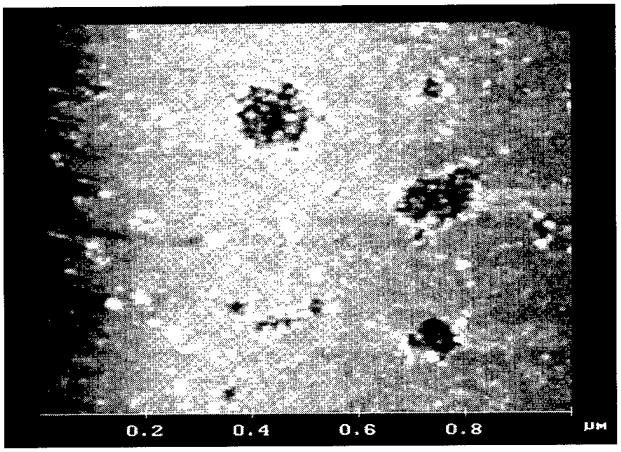


Figure 20. AFM micrograph of 3SP after 20 months aging in 60°C water, same scale as Figure 18.

An AFM section analysis of the pitted areas of sample 3SP shows the depth of the pits ranges from 3 to 4.5 nm, Figure 21.

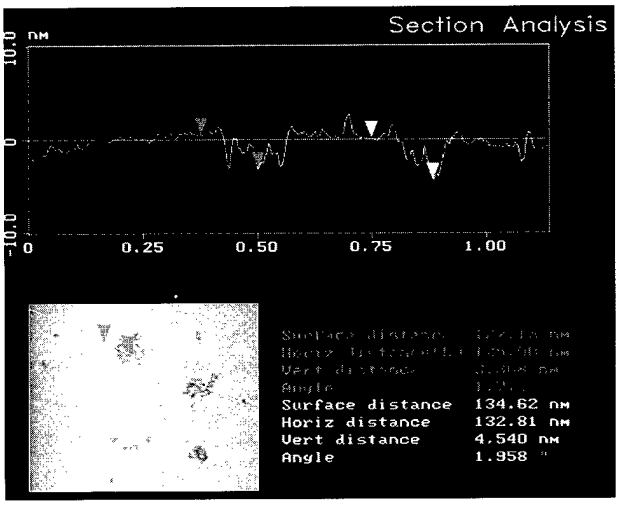


Figure 21. AFM section analysis for sample 3SP.

The AFM, nanoindent attachment and the SEM offer a special combination of investigative tools to create and characterize a flaw at a known location in a fiber, measure stress required to break it, and then match the mirror size at the break source to these data.

The nanoindentor was used to create a scratch-type flaw in the surface of a sample fiber, no aging being involved. Then, the AFM characterization of the flaw depth was obtained, Figure 22. Scratched samples were immediately tested to break in tension and the break ends were preserved. The ends show low-stress breaks indicated by well-defined fracture mirrors, as shown in Figure 23. From the mirror in Figure 23 is calculated a break

stress of 68 KPSI. The break stress recorded by the tensiometer was 68.15 KPSI.

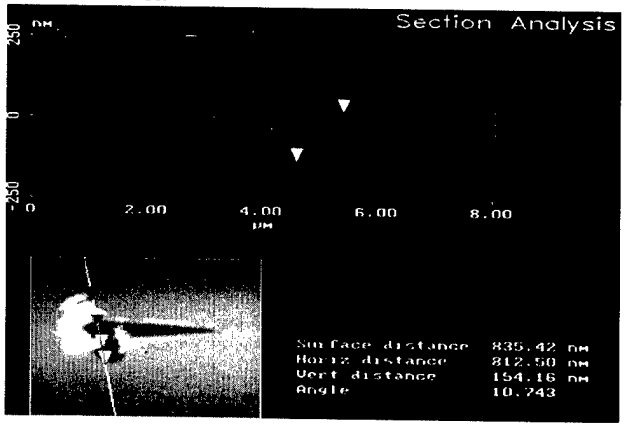


Figure 22. AFM section analysis of a scratched fiber.

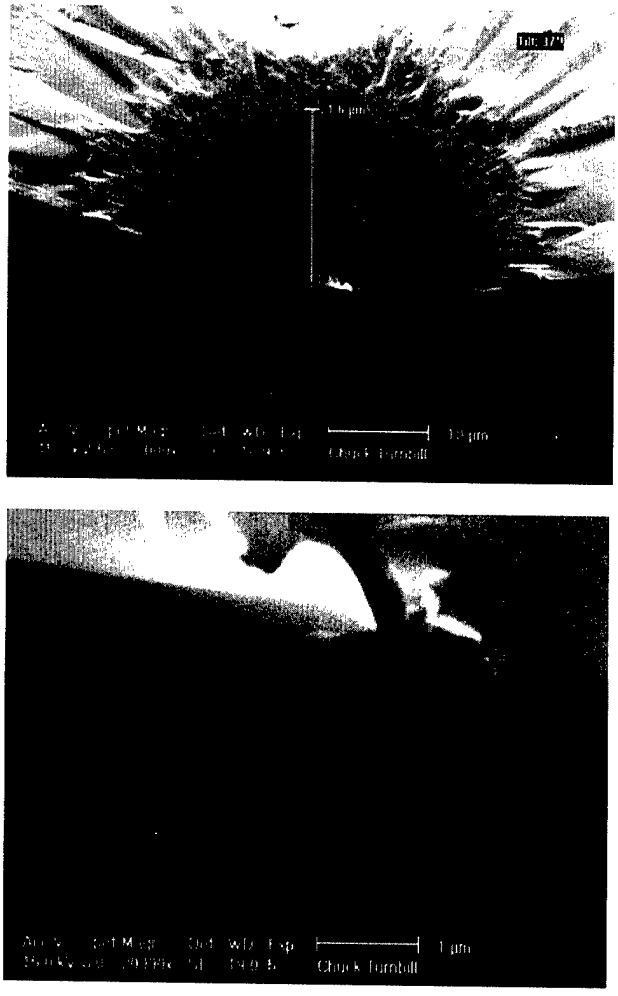


Figure 23. SEM micrographs of the fracture of the scratched fiber.

The depth of flaws required to generate sub-100 KPSI break stress in tension is much greater than the size of the flaws created in sample 3SP and other samples by long-term aging in 60 C water. In general, the lowest values obtained in two-point bending of most fibers with poor coating cure is around 200 KPSI (sample 5SP is an exception, where the lowest strength values in two-point bending approached 100 KPSI). Since two-point bending isolates such a limited area of fiber surface under maximum stress, however, these results raise a serious question about the state of larger flaws in a given fiber sample after aging. This study focused on the so-called "intrinsic" strength of the fiber by using two-point bending to limit the area under maximum stress. A study of larger flaws in aging poses the difficulty that the distribution of flaw size must be narrow and it must be known. This requires that they be artificially created prior to aging.

The nanoindentor scratching technique described above may be a useful tool with which to accomplish this, if recoating is effective. A flaw can be introduced into the glass with a minimum of residual stress, a problem with other indentation techniques. The AFM can precisely characterize the geometry. The correlation between scratched flaw depth and break strength appears to be very good. It is possible then to create a flaw of known strength and then age the fiber to observe the effects on the strength.

4 Summary

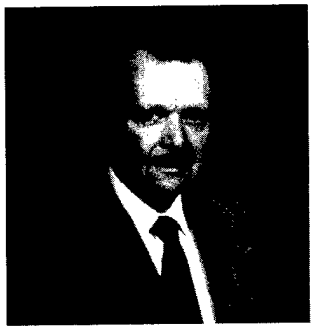
Optical fiber of recent vintage (the past 8 years) shows significant improvement in the resistance to very harsh aging conditions over previous generations. This is attributable to a number of reasons, including better coating formulating that has eliminated the components capable of attacking the glass surface under moist conditions while utilizing better adhesion promoters and surface passivating agents. Coating cure, however, continues to be a major factor, where poor coating cure still results in dramatic decreases in fiber strength. In some cases, such as 5SP, the drop in strength on aging is profound enough to affect handling for splicing. The effects of severe aging and variable coating cure on larger flaws is not yet well-understood, but this study has demonstrated a methodology that appears to be well-suited to generating a family of larger flaws useful for further work in this area.

5 References

[1] J. T. Krause, "Zero Stress Strength Reduction and Transitions in Static Fatigue of Fused Silica Fiber Lightguides," J. Non-Cryst. Solids, 38 & 39 497-502 (1980).

[2] R. S. Robinson and H. H. Yuce, "Scanning Tunneling Microscopy Study of Optical Fiber Corrosion: Surface Roughness Contribution to Zero-Stress Aging," J. Am. Ceram. Soc., 74 [4] 814-818 (1991).

[3] H> H. Yuce, J. P. Varachi Jr. and P. L. Key, "Effect of Zero-stress Aging on Mechanical Characteristics of Optical Fibers," Ceramic Trans.,. 20 191-203 (1991).
[4] M. T. Kennedy, E. Cuellar and D. R. Roberts, "Stress-free aging of optical fibers in liquid water and humid environments, " Proc. SPIE, 1580 152-162 (1991).
[5] H. H. Yuce, J. P. Verachi Jr., J. P. Kilmer, C. R. Kurkjian and M. J. Matthewson, "Optical Fiber Corrosion: Coating Contribution to Zero-Stress Aging," OFC'92 Tech Digest, post deadline paper PD21, OSA, Washington DC, 1992.
[6] M. T. Kennedy, E. Cuellar, D. R. Roberts and M. Stipek, "Stress-free aging of optical fibers in liquid water and humid environments: Part 2," Proc. SPIE, 1791 67-79 (1992).
[7] M. J. Matthewson, V. V. Rondinella and C. R. Kurkjian, "The Influence of Solubility on the Reliability of Optical Fiber," Proc. SPIE, 179 52-60 (1992).
[8] V> V. Rondinella, M. J. Matthewson and C. R. Kurkjian, "Coating Additives for Improved Mechanical Reliability of Optical Fiber," J. Am. Ceram. Soc., in press.
[9] M. J. Matthewson, C. R. Kurkjian and J. R. Hamblin, "Acid Stripping of Fused Silica Fibers Without Strength Degradation," to be submitted, J. Lightwave Tech.



Charles E Turnbill is currently a member of the Coatings Technology group of Alcatel Telecommunications Cable. He is a characterization and microscopy specialists and has worked with RCA Scientific Instruments and NASA's Lunar Research teams. He served as president of the Appalachian Regional Microscopy Society.

Bob J. Overton is the Manager of the Coatings Technology Group with the Alcatel Optical Fiber Division, and a member of the Alcatel Technical Academy as a Distinguished Member of Technical Staff. He has worked in optical fiber and cable for 23 years. He holds a BS degree in Chemistry from Mercer University and a MS in Chemical Engineering from the Georgia Institute of Technology. He has been with Alcatel since 1991, working primarily in optical fiber coatings and ribbon matrix development and processing.

Christelle Lavallade is a Senior Technical Associate with the Coatings Technology Group. She is a graduate of the Lycee Albert Schweitzer de Le Paincy and the AFPA Center of Champs-sur-Marne as a Technicien Superieur Physicien Chemiste. She has worked in glass fabrication development and optical fiber reliability with Alcatel since 1995

Stresses in Optical Fibers : Computation and Impact on Refractive Index

Marc Nicolardot and Bernard Aladenize
Alcatel Câble
53, rue Jean Broutin
78700 Conflans Ste Honorine
France
33 (1)39191200
marc.nicolardot@alcatel.fr
bernard.aladenize@alcatel.fr

Bertrand Poumellec
Labo Physico-chimie de l'état solide
UMR8648 CNRS-UPS
Université Paris Sud
91405 Orsay Cedex
France
Bertrand.Poumellec@lpces.u-psud.fr

Abstract

The stress distribution generated in optical fibers during the drawing process has been modeled considering the deformation of an infinitely small silica slice in a "reverse and forward" process. The component due to the thermal stress and the component due to the drawing force have been evaluated separately. The draw stress is mainly located in the cladding and in the tube, the thermal stress appears in the core.

The effect of these stresses on the refractive index profile is also calculated.

The residual stresses in a preform and in the corresponding fiber are different due to different thermal history and to the absence of drawing stress in the preform, so the profile index in the preform should be different than the profile index in the fiber. This difference has been evaluated.

Key words

Optical fiber, modeling, stress, refractive index, drawing

1. Introduction

The stress distribution in optical fibers impacts mechanical properties and optical properties by affecting attenuation [1-3], refractive index [4] and reliability [5]. For example, the stress difference between the core and the cladding promotes microstructure imperfections, which induces extra-losses [6].

In the manufacturing process of optical fibers, the stresses may come from the drawing force and the cooling process. The drawing force is mainly applied to the more viscous layer. As the temperature decreases, the stress remains stored in this part (mainly the tube) and when the drawing tension is removed, the fiber relaxes and a compressive stress appears in the cladding.

The stress induced from the cooling process comes from step changes in viscosity and thermal expansion coefficients between the different layers of the fiber.

2. Numerical approach for the stress simulation in an optical fiber

This approach is based on mechanical simulations and is aimed to reproduce numerically the drawing process of an optical fiber from a preform. It takes into account the relevant parts of the process concerning the final residual stress in the fiber. The detail of the hypothesis is given below.

2-1 Theory

Large strain-large displacement algorithms are now available for elasto-visco-plastic constitutive laws for materials like molten glass. These algorithms are particularly relevant for the mechanical aspect of optical fiber drawing simulation.

The theory underlying these algorithms is given in [7].

The constitutive law used for the fused silica is a Maxwell model. The strain rate $\dot{\varepsilon}_{ij}$ has two components : a viscoplastic part ($\dot{\varepsilon}_visco_{ij}$) and an elastic part ($\dot{\varepsilon}_elast_{ij}$) :

$$\dot{\varepsilon}_{ij} = \dot{\varepsilon}_visco_{ij} + \dot{\varepsilon}_elast_{ij}$$

The strain rate is related to the stress σ_{ij} and the stress rate $\dot{\sigma}_{ij}$ by :

$$\dot{\varepsilon}_{ij} = (\sigma_{ij} + P\delta_{ij})/2\eta + [(1+\nu)\dot{\sigma}_{ij} + \nu\dot{P}\delta_{ij}]/E$$

where : $P = -(\sigma_{11} + \sigma_{22} + \sigma_{33})/3$ is the hydrostatic pressure,

η is the temperature dependent viscosity of silica,

ν is the Poisson coefficient and

E is Young modulus.

$\delta_{ij} = 1$ if i=j and $\delta_{ij} = 0$ if i≠j.

When large strains have to be treated, the stress rate $\dot{\sigma}_{ij}$ is replaced by the Jaumann stress tensor:

$$\breve{\sigma}_{ij} = \dot{\sigma}_{ij} - \sigma_{jk}\Omega_{ki} - \sigma_{ik}\Omega_{kj}$$

with the spin tensor

$$\Omega_{ik} = (\frac{\partial \dot{u}_k}{\partial x_i} - \frac{\partial \dot{u}_i}{\partial x_k}) / 2$$

An improvement is obtained by using the proper rotation tensor Ω^* instead of Ω leading to the Green-Naghdi stress tensor described in [8]. The application of the principle of virtual displacement with the Green-Naghdi stress tensor and velocity strain tensor leads to a finite element procedure by discretization of the problem.

Thermal expansion is taken into account by a local expansion coefficient.

Systus is the finite element software used (commercialized by ESI Group). The software includes a preprocessor for the mesh, a solver for thermal, mechanical or electromagnetism problems, a postprocessor for the exploitation of the results and a programming language (SIL) which allows one to perform computations with high level instructions that call finite element solver instructions, such that thermal and mechanical resolution can be monitored by a SIL procedure.

Eight node quadratic elements are used in order to obtain a better precision with the elasto-visco-plastic constitutive law.

2-2 Finite element procedure definition

2-2-1 the direct method

This approach consists of directly meshing the preform and the neck-down region that occurs during the drawing process.
The principle is to apply a given displacement at the top of the preform and the drawing speed to the bottom of the drawn « fiber ». A thermal field, obtained by experimental measurement or by thermal simulation, is applied to simulate the drawing furnace. This approach is limited by the large number of elements and by the numerical imprecision, which is crucial when considering a problem that contains both large dimensions (≈ 0.5 m for the neck-down length) and very small dimensions (125µm for the fiber diameter).
Because of the numerical precision issues, the direct application of large strain algorithm is not possible for diameter reductions larger than a factor of 10.

2-2-2- the strain method

A strain approach can be used to avoid problems associated with domains containing both large and very small features. A thin slice of the preform is meshed and followed in its axial displacement during the drawing process. Only the strain of the slice is treated by the finite element procedure. The geometry of an infinitesimal slice is assumed to be a cylinder, although a finite slice is actually conical.

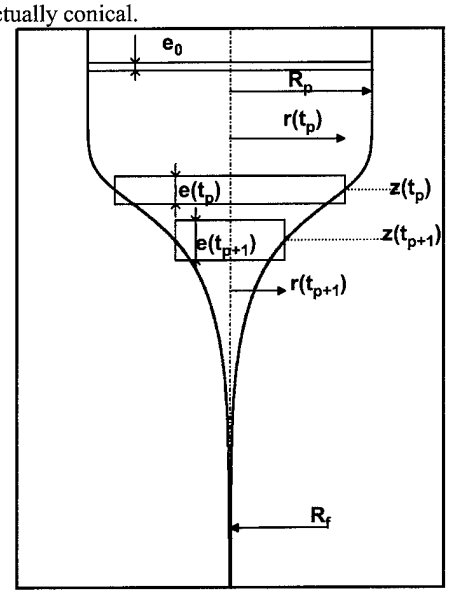


Figure 1: Evolution of the geometry of a slice during the drawing process

This numerical procedure can be used in two ways: Either the temperature map of the neck-down or the neck-down geometry is known. Considering the drawing process, the geometry of the neck-down is easy to obtain experimentally inside the furnace and the temperature of the fiber is easy to obtain below the furnace.

So, both sub-approaches can be used, depending on the part of the process simulated.

- known neck-down temperature method.

The temperature map of the neck-down and the drawing speed are the process input data for the simulation. The neck-down profile, the stress in the fiber and other associated thermo-mechanical results are the outputs of the simulation.

The geometry of the problem can be described as follows.

The problem is assumed to be axi-symmetric, and can be represented in longitudinal section.

The radius of the preform and the fiber is R_p and R_f, respectively. The infinitesimal slice of preform is assumed to have an initial thickness e_0 for the finite element procedure. Although the thickness is finite in the simulation, the computed stress is that of an infinitesimal slice. The number of elements is 1 along the axis and n along the radius to account for the composition profile due to the index profile, and the radial dependence of temperature.

The drawing tension, F, is applied to the slice and inertia effects are neglected.

The radial stress profile during drawing is given by the finite element procedure at time t. In order to obtain the residual stress, the drawing tension is suppressed when the fiber is cooled down to room temperature.

- known neck-down geometry approach

The deformation, e(t), has to be applied to the slice from the knowledge of the neck-down profile, r(z), and the drawing parameters, v_f, R_f and R_p. The output of the simulation is the mean temperature of the slice as a function of its position z, and the stress map in the neck-down region.

This is obtained step by step in the following manner:

Initially, at t=0, the thickness e of the slice is e_0, and the radius r of the slice is R_p,. The initial position of the slice is z(0) and the velocity of the slice is given by:

$$v(0) = R_f^2 \cdot v_f / R_p^2$$

where v_f is the drawing speed.
The recurrence is thus initialized and the finite element procedure can then be applied for the evolution of the slice.
An assumption is made for the temperature and the resulting force necessary to obtain the observed deformation is calculated. An iterative procedure is then used to obtain the temperature for which the deformation leads the actual drawing force. Due to the quasi Arrhenius law for viscosity, the force is very sensitive to the temperature.

2-3- Simulation time for the process :

The objective is to obtain the residual stress in the fiber after drawing, thus only the part of the process for which the stress has not relaxed during the drawing has to be modeled.
Figure 2 represents the diameter and temperature evolution of the glass measured during a typical drawing process of an optical fiber. Position A corresponds to the position relative to the furnace where the geometry of the fiber is stabilized.
At position B, (d = 100 mm under the furnace), the fiber temperature is 1500 °C, thus the viscosity of the glass and its Young modulus are approximately $\eta = 3.\ 10^8$ Pa.s and $E = 73.\ 10^9$ Pa, respectively.

The relaxation time for stress at position B, as given by $\tau = 3\eta/E$ is 0.01s.
So if the simulation begins at $t_2 = 5\tau$ before point B, we are certain that all the relevant history of the fiber is taken into account. This corresponds to a temperature of 1800 °C.
It takes t_1 = 0.05s for the fiber to reach the final diameter (instant A) from the instant B, thus the total time required for the model to obtain the viscous stress in a 125 µm hot fiber at T = 1200°C is t1+t2 = 0.1s.

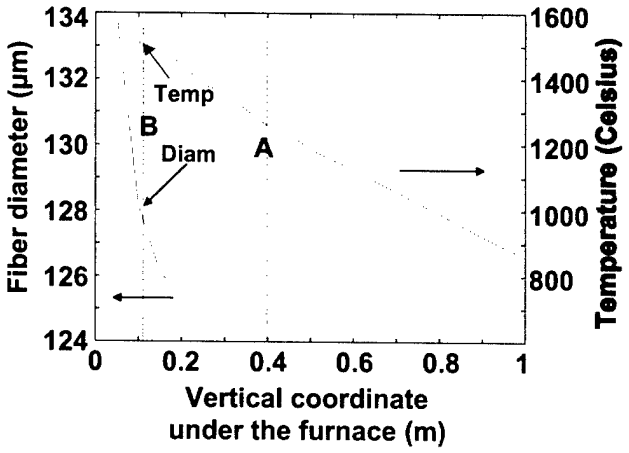


Figure 2: Correspondence between fiber diameter and fiber temperature below the drawing furnace.

At the end of the drawing tower, the fiber is at room temperature, thus the cooling time required to account for the expansion stress is evaluated from the drawing tower height H and the drawing velocity vf :

$t_3 = H / vf$,

of the order of 1s.
In conclusion, only the bottom of the neck-down, including the cooled fiber, has to be modeled with a deformation approach of a slice.

3. Application to the determination of stress distribution in an optical fiber

3-1 Input data for the modeling

3-1-1- Composition of the UPS12 fiber

Calculations have been carried out on UPS 12 mono-mode fiber of step index type made of a core, a cladding and a tube. The core of radius 2,7 µm, is doped with GeO_2 25 mol %, and the cladding, of external radius 15µm, is doped with 0,1 mol % F and 0.07 mol % P_2O_5. The tube, of external radius 62,5µm is made of pure silica.

3-1-2- Physical characteristics of the materials

The thermo-mechanical coefficients have been computed from the chemical composition:

	ν_0	E_0	α_0
Core	0.174	$65.4\ 10^9$ Pa	$23.5\ 10^{-7}\ K^{-1}$
Cladding	0.162	$72.4\ 10^9$ Pa	$5{,}69\ 10^{-7}\ K^{-1}$
Tube	0.162	$73\ 10^9$ Pa	$5.810^{-7}\ K^{-1}$

These values are assumed to be temperature independent. The viscosity of each layer has been measured. The viscosity follows a VFT law:

$$\ln(\eta) = A + \frac{B}{T - C}$$

where T is the temperature in Kelvin and A, B and C are constants.

3- 2 Definition of initial conditions for modeling

The UPS12 fiber is drawn with a tension of 76 g. The cool-down temperature profile during the drawing process has been measured and is exponential with a time constant of τ_0 = 0.25 s. The asymptotic temperature is 20 Celsius.

The simulation must start at a temperature for which the relaxation time for stress is very short. We have shown that an initial fiber temperature of 1800 °C is sufficient. The fiber slice is then elongated and its diameter reduces to 125 µm.

The simulation of elongation must start from the right diameter at this high temperature. The diameter at high temperature is obtained from a compression simulation from a 125 µm diameter slice, compressed with the same force as the draw tension in (76 g) and the temperature profile is reversed for the compression and extension phases (fig. 3).

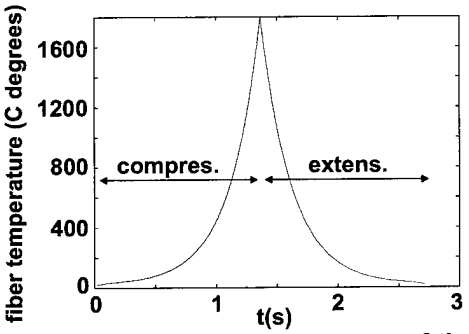


Figure 3: Evolution of the temperature of the slice of fiber during the simulation

The modeling will thus consist of a fictive compression process of a 125µm diameter fiber with force and heating profile corresponding in absolute value to the characteristics of the drawing process and the symmetrical drawing process.

3-3 Results for UPS12 with nominal draw conditions

The stress distribution in the optical fiber has a thermal stress component due to the thermal contraction during cooling, and a stress component due to the viscous elongation.

Hence, each component is evaluated separately.

3-3-1 Thermal stress component

The draw tension is set to 0 g in order to obtain the stress and strain values. Due to the fact that neither tension nor compression force is applied to the fiber slice, the diameter variation is small (pure thermal expansion). The time evolution of the stress σ_z in core, cladding and tube is shown in Fig. 4.

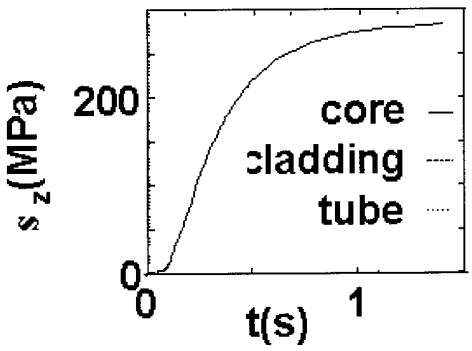


Figure 4: Evolution of the σ_z stress component in the core, cladding and tube

During the cooling phase, the stress in the core increases from 0 to nearly 300 MPa at the end of the cooling phase (t = 1.4 s). The relative stresses in the cladding and in the tube are small due to their large cross section.

Fig. 5 shows the profile for the axial σ_z, orthoradial, σ_t and radial σ_r stresses along the radius of the fiber at the end of the cooling phase.

The stress is mainly located in the core.

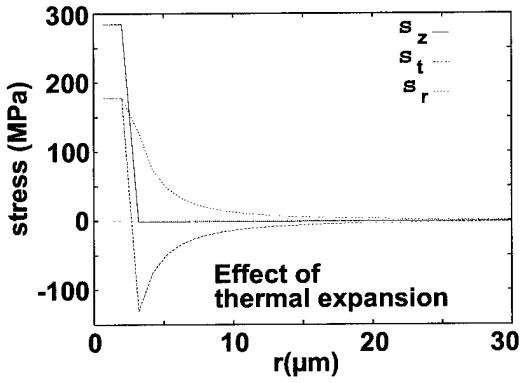


Figure 5: Axial (σ_z), ortho-radial (σ_t) and radial (σ_r) components of stress along the radius of a fiber

3-3-2 Draw stress component.

In this case, the thermal expansion coefficient is set to 0 in the three layers and the draw tension is 76 g. The diameter evolution is shown in Fig. 6. We observe a large variation of the fiber slice diameter at the beginning of the draw when the diameter starts from 133 µm.

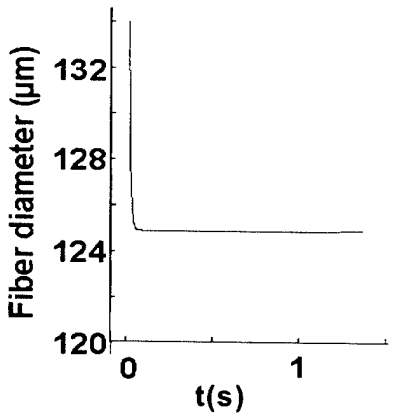


Figure 6: Evolution of the fiber diameter

The time evolution of the axial stress σ_z in the core, cladding and tube is shown Fig.7. During the elongation phase, the tension due to draw is distributed according to viscosity in each of these three layers. When the fiber is at room temperature, the draw tension is removed after passing the capstan, leading to a null integral of stress in the section.

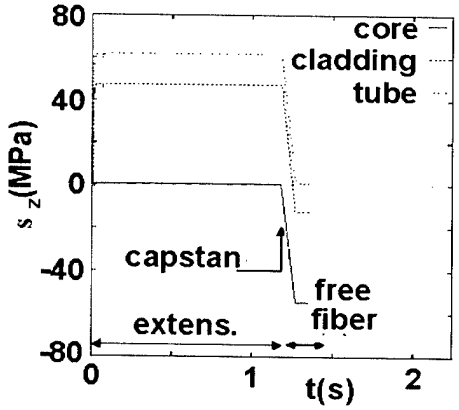


Fig. 7. Evolution of the σ_z stress in the core, the cladding and the tube

The compression of the core and the cladding is compensated for by the small tension in the large cross section of the tube.

The final stress profile in the free fiber is shown in Fig. 8. The radial and ortho-radial components of stress are quasi null.

3.3-3 Total stress.

In this case, the actual thermal expansion coefficient and draw tension are taken into account. The evolution of the diameter is very similar to the case of pure viscous stress (Fig. 6). The time evolution of axial stress, σ_z, in the core, cladding and tube is shown in Fig. 9.

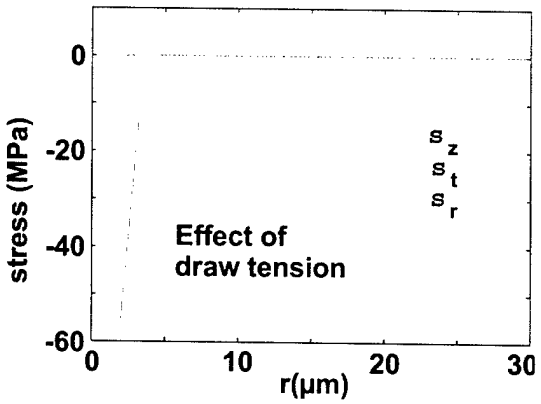


Figure 8: Axial (σ_z), ortho-radial (σ_t) and radial (σ_r) components of stress along the radius of the fiber

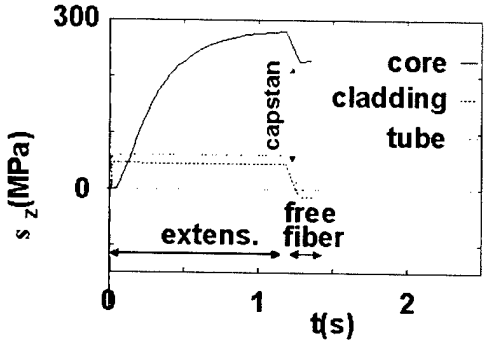


Figure 9: Evolution of the stress component σ_z in the core, the cladding and the tube

The stress σ_z has components due to viscous strain and thermal expansion. Similar to previous, the draw tension (76 g) is removed after passing the capstan. The stress profile (σ_z, σ_t and σ_r) along the radius of the fiber is shown in Fig. 10.

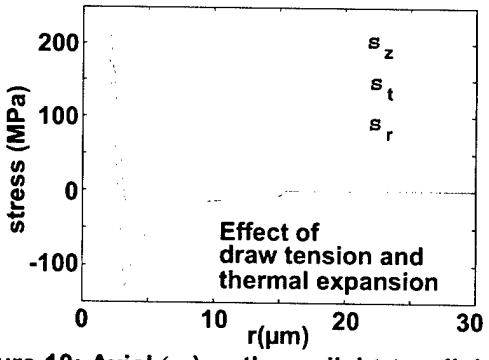


Figure 10: Axial (σ_z), ortho-radial (σ) radial (σ_r) components of stress along the radius

The total stress σz appears as the sum of the thermal expansion stress and the viscous draw stress (Fig. 11). These two components have opposite effects in the core. The expansion

effect leads to an extension stress while the viscous component leads to a compression stress. The expansion effect dominates.
In the cladding and in the tube, the expansion effect is negligible. Hence, the viscous component dominates which leads to a compression stress in the cladding and a small extension stress in the tube.

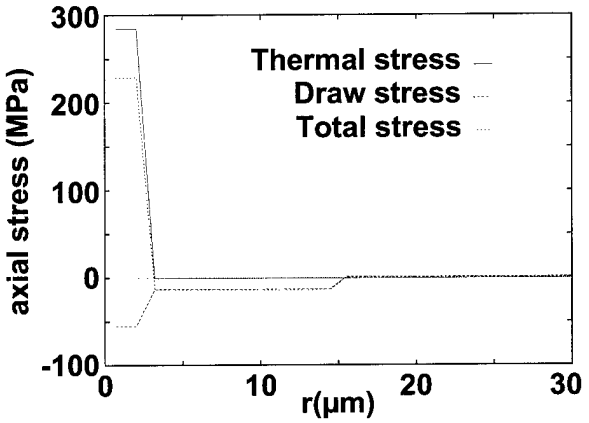


Figure 11: Total axial stress σ_z in the fiber

3-4 Effect of main parameters on stresses

3.4-1 Effect of draw tension

Draw tension of 0g, 76g and 150g were used in the FEM simulation :. Table 1 shows the results.

	core stress (Mpa)	cladding stress (Mpa)	tube stress (Mpa)
150 g drawing tension (F)	+ 175.0	- 26.5	+ 1.2
76 g drawing tension (F)	+ 229.0	- 13.8	+ 0.4
76 g drawing tension (F) no thermal expansion	- 55.0	- 12.9	+ 0.9
0 g drawing tension (F)	+ 284.6	- 1.0	- 0.5

Table 1. Evolution of the stresses with the drawing tension

The stresses follow a linear law as a function of the drawing tension.

3-4-2 Effect of cooling rate.

The nominal time constant for fiber cooling is τ_0=0.25s. Three time constant $\tau = 0.1\ \tau_0$, τ_0 and $10\ \tau_0$. were tested :
Figures 12, 13 and 14 show that while the cooling rate has only a moderate impact on the stress value in the cladding and in the tube, it has a significant effect in the core of the fiber.
As mentioned above, the stresses have two components, the expansion effect and the viscous effect. The cooling rate impacts mainly the expansion component of each stress.

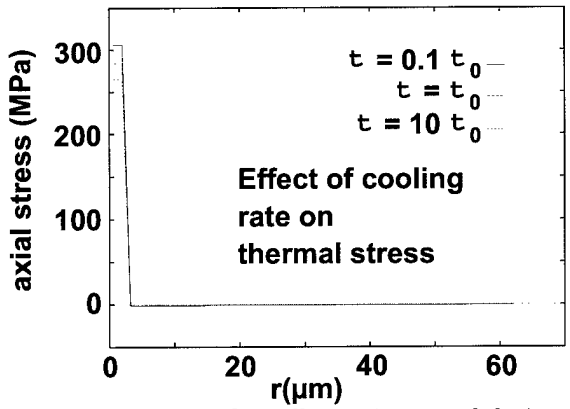


Figure 12: Impact of cooling rate on axial stress

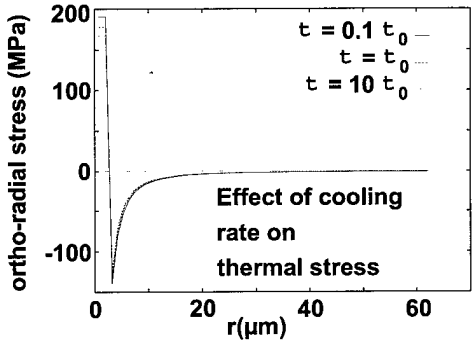


Figure 13: Impact of cooling rate on ortho-radial stress

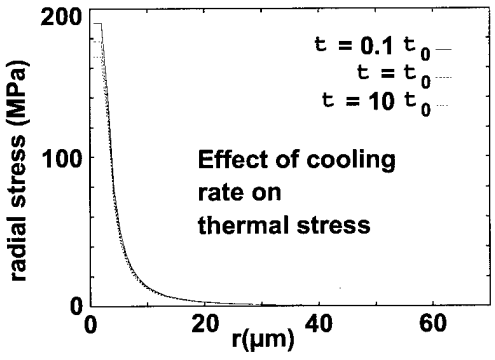


Figure 14: Impact of cooling rate on radial stress

Fig. 15 shows that the cooling rate has no impact on the draw component of σ_z.

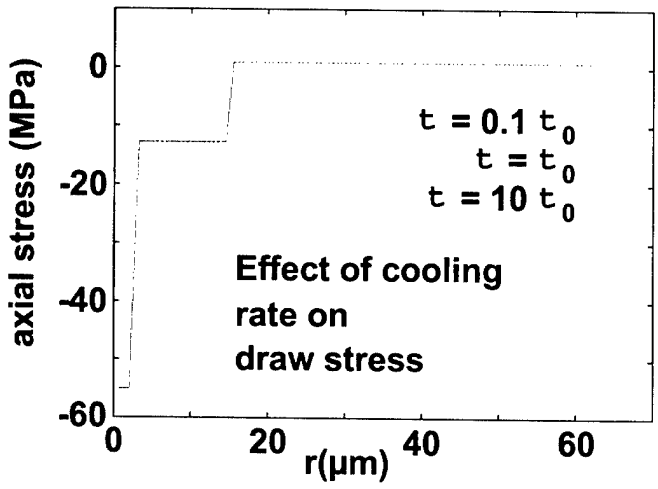


Figure 15: Impact of cooling rate on the draw stress

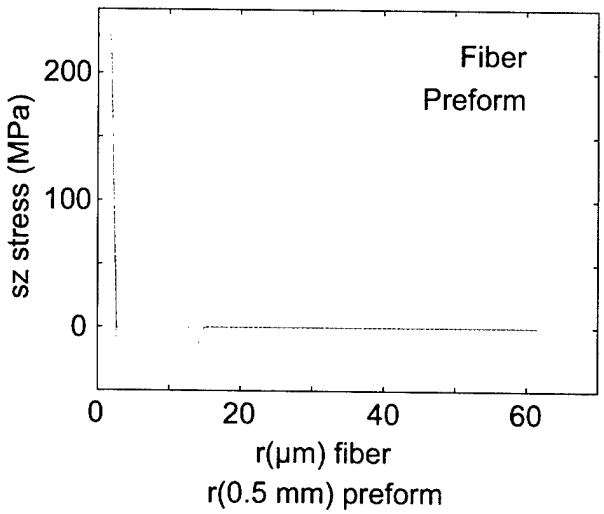


Figure 16 : Comparison of stress profile σz in the fiber and in the preform

4. Evaluation of the impact of stress on the profile index

Photo-elasticity implies that the mechanical stresses modify the refractive index profile of the fiber. Moreover, as far as the mechanical stresses are not the same in the preform and in the resulting fiber, the profile index in the preform will not be the same as the profile index in the resulting fiber. We can now evaluate this effect and model the difference.

4-1 Input data for the modeling

The refractive index of the fiber is determined by the chemical composition and the stress in each layer: for example, GeO_2 and P_2O_5 increase the refractive index of silica and F reduces it. Also, the stresses frozen in the fiber have an impact. For example, a compressive stress leads to an increase of the index.

The refractive index for radial polarization n_r is related to the stress tensor via two photo-elastic coefficients [10]:

$$n_r = n_{mat} - C1\ \sigma_r - C2\ (\sigma_\theta + \sigma_z)$$

For silica, $C1 = 6.626\ 10^{-7}\ MPa^{-1}$ and $C2 = 4.301\ 10^{-6}\ MPa^{-1}$.

The mechanical stresses in the fiber after drawing have been calculated in §3. The same calculations can be performed for the preform. In this case, the drawing force is zero and the cooling rate is about 1500 times lower than during fiber drawing.

4-2 Results

Fig. 16 shows the stress profile σz in the case of UPS12 as compared to that of the preform, with the radial coordinate in the preform scaled to the fiber.

The compressive stress in the cladding of the fiber has a low value (13.8 MPa), thus the stress contribution to dimensionless refractive index in the cladding, $+2.5\ 10^{-4}$ units, is correspondingly low.

A tensile stress of 230 MPa in the core of the fiber leads to a contribution of $-1.9\ 10^{-3}$ units to the refractive index (Table 2).

index_r 10-3	no stress	fiber with stress	Δ1 ws-ns	preform	Δ2 fib-pref
core	30.020	28.152	-1.868	28.317	0.165
cladd.	-0.129	0.118	0.248	0.100	0.018
tube	0	0.002	0.002	0.005	-0.003

Table 2. Impact of stress on the refractive index for radial polarization n_r.

The data reveals that the contribution of stress to the core refractive index must be taken into account.

Fig. 17 gives the refractive index profile in the fiber with stress, in the fiber or in the preform without stress, and in the preform with residual stress.

In the preform, the stresses in the core, in the cladding and in the tube are 228 Mpa, -0.8 Mpa and -0.4 Mpa respectively. In this particular design, the large difference in cooling rates between the fiber and the preform does not induce strong differences in stress and the difference in term of profile index is $1.65.10^{-4}$ units in the core.

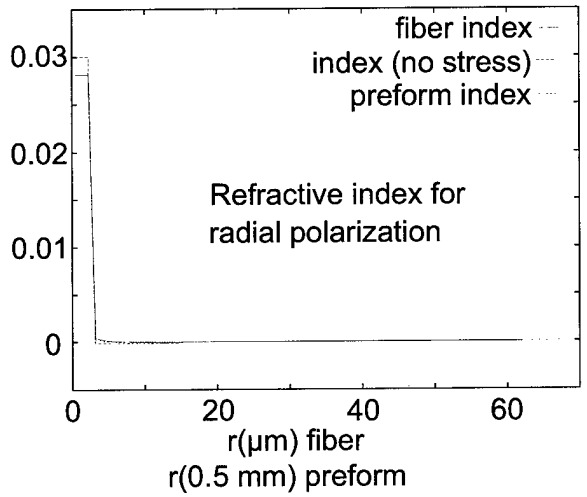


Figure 17 : Comparison of n_r index profile in the fiber and in the preform

5. Conclusion

The various stresses generated during the drawing process in the manufacturing of optical fiber have been computed. In the examples shown, the core is under extension, the cladding under compression while the stress in the tube is found to be negligible.

The stress profile impacts the refractive index profile leading to significant differences from the profile index expected based on the chemical composition.

The stress generated during preform manufacturing can also be computed with the procedure described. The resulting stresses are obviously different than those obtained in the drawing process. Thus, the profile index in the preform is different from the profile index in the resulting fiber. This difference is dependent upon the thermo-mechanical characteristics of each layer and on the processing conditions.

References

[1] K. Nagano, S. Kawasaki and N. Nishida 1978 Applied Optics 16 2080

[2] J.H Hannay 1976 Electronics Letters 12 173

[3] W.S. Bickel, W. Gilliard and B. Bell 1980 Applied Optics 19 3671-3675

[4] W. Scherer 1980 Applied Optics 19 2000-2006

[5] Li, A. Agrawal and M. Tomozawa 1995 J. Americ. Chem. Soc. 78 1393

[6] Y. Hibinio, F. Hanawa and M. Horiguchi J. Appl. Phys. ,1989 65 30 – 34

[7] Klaus-Jürgen Bathe, Finite Element Procedures in engineering analysis, Prentice-Hall, Inc Englewood Cliffs, New Jersey 07632, 1982, IBSN 0-13-317305-4

[8] C. Fressengeas, A. Molinari, Arch. Mech. 36, 4 pp 483-498, 1983

[9] G. W. Scherer : Relaxation in glass and composites, Krieger Publishing Company, 1992.

[10] W. Hermann, Applied Optics, Vol 28, 11, p 1980, 1 june 1980

Authors

Marc Nicolardot graduated from Ecole Centrale Paris in 1986 and received a Ph. D. in semi-conductor physics in 1989. He joined Alcatel Research Center in 1990 and worked on band-gap engineering for opto-electronic devices. Since 1994, he has been working on process modeling for optical fibers.

Bernard Aladenize received an engineering degree in Polymer Engineering from CNAM. France. He joined Alcatel Reseach Center and is now R&D group manager in the Optical Fiber Division at Alcatel Cable, in charge of the process modeling of optical fibers.

A Fiber Bragg Grating Measurement System for Monitoring Optical Fiber Strain

Sylvain Capouilliet, James A. Smith, Donald J. Walter, G. Scott Glaesemann, Glen E. Kohnke and Ronald D. Irion

Corning Incorporated
Corning, NY 14831
607-974-3736 · glaesemags@corning.com

Abstract

A practical method has been developed for deploying an optical fiber containing a strain sensor into fiber and cable processing equipment while simultaneously monitoring the strain sensor. The sensing system employs the use of fiber Bragg gratings and is able to produce an accurate history of dynamic stresses in the optical fiber during processing, cabling, and installation events. The sensing system acquires an optical spectrum with an equivalent stress range of 0.74 GPa and a resolution of 3 MPa at a rate of 7.2 kHz.

Keywords

Fiber, Processing, Cabling, Bragg Grating, Reliability

1. Introduction

The field reliability of cabled optical fiber is determined by the fatigue behavior of the glass fiber, the strength distribution, the in-service stress, and all the process and installation stress events leading up to in-service life. Most lifetime predictions are based on knowledge of proof test stresses and in-service stresses only. Dynamic processing stresses experienced during events like coloring, buffering, ribboning, stranding, jacketing, and installation need to be incorporated as well. However, these processing stresses are often difficult or impossible to quantify by direct means. For example, unloading from the proof test stress is critical to the lifetime of the fiber, but there are no direct means for measuring it. The proof test stress itself is usually measured indirectly using a gauged pulley. Fiber stresses during cabling should be incorporated into reliability models, but direct fiber stress measurements are nearly impossible. Installation stresses can be measured, but only the average stress over meters of fiber. Localized and dynamic fiber stresses during installation are unknown.

The purpose of this paper is to introduce a method for direct measurement of dynamic stresses in optical fiber during processing, deployment, and in-service lifetime. This method employs the well known strain dependence of fiber Bragg gratings.[1] Fiber Bragg gratings have been used to measure static loads in ribbon cables[2,3] and connectors[4]. The novelty of the method presented in this study lies in the simplicity and speed in which the strain of the grating is captured and the ability to actively monitor fiber strain while it's being deployed into processing equipment. Previous studies were able to monitor fiber strain in only stationary fiber.

2. Fiber Stress Measurement System

2.1 Fiber Bragg Grating

Fiber Bragg Grating (FBG) sensors offer significant advantages over more traditional strain sensors such as electromagnetic noise immunity, high sensitivity, compactness, and simplicity of fabrication. Of greater importance for optical fiber is that the sensor can be embedded directly into the material subjected to stress. The FBG is a wavelength selective device created by forming a grating that modulates the index of refraction of an optical fiber. The grating period and the effective index of refraction determine the center wavelength (Bragg wavelength) of the reflected optical spectrum [5, 6]. The gratings used in this study were approximately 1 cm in length.

The shift of Bragg wavelength varies linearly with strain and temperature. The relationship between longitudinal stress and Bragg wavelength at a constant temperature is given by Equation 1 [7].

$$\frac{\Delta\lambda_{bragg}}{\lambda_{bragg}} = \varepsilon_{zz}\left[1-\frac{n_{eff}^2}{2}\left(p_{12}-\nu(p_{11}+p_{12})\right)\right] \quad (1)$$

p_{11} and p_{12} are the strain optic coefficient and ν is poison's coefficient. ε_{zz} is the longitudinal strain.

Assuming silica behaves in a linear elastic fashion one obtains the following dependence of center wavelength on stress;[1]

$$\frac{\Delta\lambda_{bragg}}{\lambda_{bragg}} = \left[1-\frac{n_{eff}^2}{2}\left(p_{12}-\nu(p_{11}+p_{12})\right)\right]*\frac{\sigma_{zz}}{E} \quad (2)$$

E (73 GPa) is the Young's modulus of silica.

It is not possible to separate the effect of the temperature from the effect of the strain with only one grating. To prevent temperature from confounding the strain measurement, one can adjust the reflected optical spectrum using the results of a sister grating, which experiences just the temperature event. Of course, the

[1] Typical fiber process strain levels are less than or equal to 1%; and therefore, the non-linear portion of the stress – strain curve for silica can be ignored.

other option is to control the temperature during the measurement event. This is what was done for this study.

2.2 Measurement System Overview

The measurement system is based on a FBG sensor and a grating spectrometer to measure the optical spectrum. When a fiber experiences stress, the characteristics of the reflected optical spectrum generated by the fiber Bragg grating changes.[1] Figure 1 shows the three major stress phenomena which affect the reflected optical spectrum of a FBG. All three can be observed by a grating spectrometer: Center wavelength, Bandwidth, and Spectrum splitting.

Transverse loading of the FBG causes birefringence and the reflected spectrum is split into two peaks. Two spectral peaks are generated within the Bragg grating because the effective index of refraction for light polarized in the direction of loading is higher than the effective index of refraction for light polarized orthogonal to the transverse loading direction. Complex loading such as bending, torsion, and the onset of transverse stresses may increase the bandwidth of the reflected spectrum.

Figure 2 shows the schematic of the measurement system used in this study. An Amplified Spontaneous Emission (ASE) light source which is broad band, is used to interrogate the FBG as it traverses through a process or handing event that subjects the fiber to tensile stress. The ASE is coupled into the sensing fiber by a fiber optic coupler. A portion of the ASE spectrum is reflected by the grating and coupled into the grating spectrometer by the fiber coupler. The reflected light spectra are then incident on the grating within the spectrometer, which spatially disperses the spectra onto a linear array camera. The linear camera converts the spatially dispersed spectrum into light intensity as a function of wavelength.

A spectrum with a wavelength range of 13 nm and resolution of 0.05 nm is acquired at a rate of 7.2 kHz. This allows for the monitoring of the reflected spectrum as the Bragg grating travels through the stress event. A computer is used to analyze the resulting data and convert it to the stress/time history experienced by the fiber. Critical to this measurement system is the ability to deliver fiber into the process equipment while simultaneously monitoring the grating within the fiber. This will be discussed more in the experiment section.

2.3 Sensor Calibration

For the tensile calibration of the Bragg sensor, a comparison between the center wavelength shift of the FBG and the measured stress obtained from a strain gauge load cell was performed. The results of this comparison are shown in Figure 3.

3. Experiments

3.1 Tensile Testing

A simple tensile test was performed as an initial test of this measurement system. The fiber was attached to a universal-testing machine[1] using the usual dual capstan method and loaded in tension to approximately 0.5 GPa. The resulting change in center wavelength of the grating is shown in Figure 4 to closely match the results of the strain gauge load cell. As expected variations in load with time are easily observed.

3.2 Fiber Processing Simulation

To simulate typical fiber process events, a laboratory apparatus consisting of two belted capstans and a weighted pulley was used. A schematic of this test apparatus is shown in Figure 5. The first capstan pays in the fiber from a payout reel. As the fiber enters the first capstan, it is subjected to near zero tensile load. When the fiber is pulled through the capstan, the fiber is loaded in tension by the weighted pulley and loaded transversely by the pressure from the belt. The tension in the fiber is maintained from the exit of the first capstan, around the pulley to the exit of the second capstan. This fiber processing simulation has the common components (capstan, pulleys, belts and adjustable tension) of a typical fiber manufacturing process; and therefore, the Bragg sensor should experience stress events similar to actual stress events in typical fiber and cabling manufacturing processes.

3.3 Fiber Payout Method

The Bragg grating sensor is spliced into a length of single-mode fiber such that there is 250 m of fiber on either end of the grating. This fiber is then wound onto a payout reel constructed of aluminum. The payout reel has the same dimensions as a typical plastic shipping reel. A fiber pigtail is spliced onto one end of the fiber and is connected to the laser via a fiber optic coupler. Critical to this measurement technique is the ability to deliver fiber into process equipment while maintaining access to a stationary end of the fiber. The reel is placed on its side such that the flanges are oriented in a horizontal fashion as illustrated in Figure 5. The other end of the fiber is threaded through the fiber processing apparatus. When the fiber pays into the fiber processing apparatus it simply winds off the stationary aluminum reel imparting twist into the fiber at a rate of approximately 2 twists per meter. The induced torsional stress is small, less than 28 MPa (4 kpsi).

Once the fiber passes through the fiber handling apparatus it is wound onto a conventional fiber reel. Data collection is initiated just before the grating enters the fiber handling apparatus. Note that the fiber handling apparatus must be stopped before the pigtail portion of the grating fiber is reached. The grating and associated fiber can be reused.

3.4 Experiment Plan for Processing Simulations

Three processing experiments were conducted to examine the ability of the measurement system to capture stress events experienced by the fiber. Two processing parameters were varied, processing speed and the dead weight load as shown in Table 1.

[1] Instron Corp., Canton, MA.

Table 1. Simulated fiber processing events.

	Speed	Load
Test 1	1 m/s	1.083 kg
Test 2	1 m/s	1.389 kg
Test 3	2.5 m/s	1.389 kg

The processing speeds used in this study simulate those used in the cabling of fiber, but are below speeds typically used in coloring and proof testing. The dead weight loads in Table 1 will impart stresses in excess of most fiber processing events and approach those used in proof testing. Note that the configuration of the fiber, i.e., through the pulleys and capstan remained constant.

4. Results and Discussion

Figure 6 shows the stress profile resulting from Test 1. The measurement system was able to capture the gross stress events as well as small variations in stress as the fiber traveled through the process simulation. Initially the stress is low as payoff from the stationary reel is under minimal stress (time segment AB). At roughly point B, the grating experiences what appears to be slight compression just as it enters the first capstan (segment BC). As the grating travels through the capstan (segment CD), it rapidly experiences tension. In approximately 30 milliseconds, a fiber travel distance of 3 cm, the stress rises from near zero to 0.5 GPa as the grating enters the high stress region of the test. After it leaves the first capstan, the stress is essentially constant with rapid oscillations on the order of 7% of the mean tensile load (segment DF). The relatively stable stress event (point E) corresponds with travel over the weighted pulley. As the grating enters the second capstan, the process of fiber stress relief begins. The unloading stress profile for segment FG is symmetric to the loading segment BC. When the grating exits the second capstan the stress in the grating is rapidly unloaded. The unloading rate from the second capstan is approximately 15 GPa/s.

These results are particularly interesting from a fiber reliability point of view. The stress event in Test 1 is similar to the proof testing or coloring of fiber. Proof testing is a critical step in the process history of optical fiber in that it is responsible for establishing the minimum strength of the fiber. Reliability engineers have attempted to incorporate the main stress events of proof stress, loading, and unloading into their models. The unloading event receives particular attention in that it is the last opportunity for a flaw near the proof stress to grow subcritically. With this measurement method it is possible to obtain a direct measure of the actual unloading event. Furthermore, it is possible to quantify the variability in the proof test stress. This could lead to increased accuracy in lifetime predictions and provide valuable input into the design of fiber processing equipment.

Figure 7 shows the results from Test 2 where the load was increased by 300 grams. The stress profile was similar to that in Test 1 with the exception that the stress increased to 0.6 GPa.

Figure 8 shows the results from Test 3 where the speed was increased to 2.5 m/s. The duration of the stress event is reduced by 2.5 times as one would expect; however, the high frequency oscillations have been reduced. Note that the small oscillations in stress after fiber unloading are dampened by the take-up reel at a time near 1500 ms.

The data from Tests 2 and 3 illustrates the necessity for direct information on applied stresses when changing processing speeds. In Test 3 the variability in applied stress decreased as the speed was increased, but the opposite could have easily been true if increased speed introduced vibration into the apparatus.

The application of this dynamic stress measurement technique extends beyond fiber processing. The measurement system demonstrated in this study holds promise for measuring dynamic stresses in fiber during cabling, cable installation, severe weather or other events that produce significant cable strain. Of particular importance is the deployment of cabled fiber in under-sea applications where the consequences of fiber failure are severe.

5. Conclusions

Engineers are constantly redesigning fiber manufacturing and cabling technologies. In doing so they must have accurate knowledge of fiber strain in order to stay within established guidelines. A fiber optic sensing system has been developed that can be deployed in a manufacturing or field environment to measure dynamic stress in optical fiber during processing and deployment events. It uses the well known strain dependence of fiber Bragg gratings and provides a means for high speed data acquisition and real time monitoring as the sensor passes through processing equipment.

Fiber stress histories were obtained on several simulated fiber-processing events. Tensile stresses from loading and unloading, weighted pulleys, and winding were obtained and analyzed.

The data from this strain measurement scheme can be input into existing mechanical reliability models that incorporate multiple stress-time histories. In this way one can accurately evaluate the consequences of design and process changes on long-term reliability of optical fiber in cable. Furthermore, this measurement scheme can be used to monitor long-term stresses in cabled fiber after deployment. Reliability models can be updated with changes in deployed stress states.

6. Acknowledgments

Special thanks to Don Clark, Denise VanZile, and Holly Strzepek, for their assistance in conducting the experiments.

7. References

[1] B. Culshaw, Smart Structures and Materials, (Artech House, Boston, 1996).

[2] Z. Gao, W. Pfandl, R. Engel, and A. Stingl, "A Study of the Fiber Strains in Central Tube Ribbon Cables," *Proceedings of the 48th International Wire and Cable Symposium*, 61-65, Atlantic City, NJ, 1999.

[3] F. Sears et al., "Measurement of Discrete Strain Change in a High-Fiber Count Slotted-Core Ribbon Cable Using Bragg Gratings," Proceedings of the 49th *International Wire and Cable Symposium*, 636-645, Atlantic City, NJ, 2000.

[4] L. Baker, et al., "Fiber Bragg Grating for Stress Field Characterization Inside a Connector," pg. 207-211 in proceedings of SPIE Conference on Optical Fiber Reliability and Testing, Vol. 3848, Boston, MA Sept., 1999.

[5] R. Kashyap, *Fiber Bragg Gratings*, Academic Press, 1999

[6] G. P. Agrawal, *Fiber-Optic_Communication Systems*, John Wiley & Sons, Inc. New York, 1997, Chap 7.

[7] E. Denarie, V.E. Saouma, A. Iocco, and D. Varelas, "*Concrete Fracture Process Zone Characterization with Fiber Optics*" J. Engr. Mech. Vol 127 [5] 2001 494 – 502.

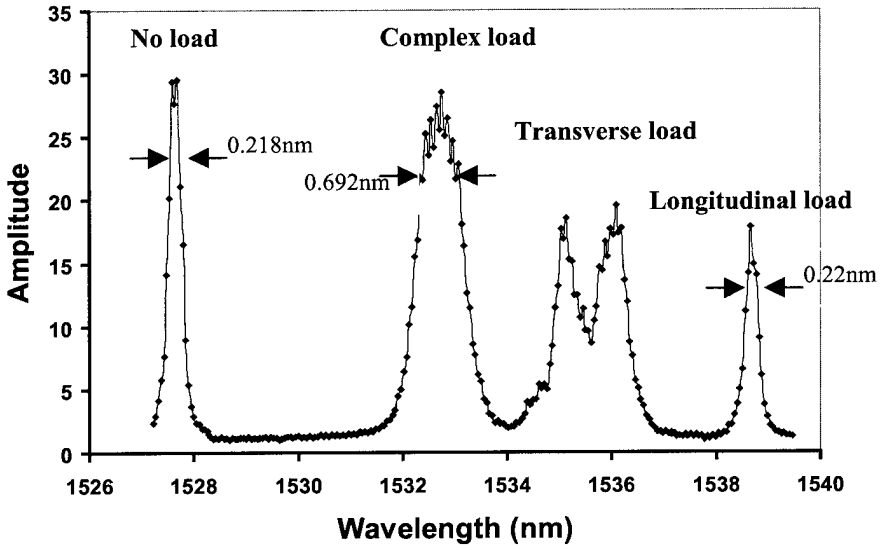


Figure 1. The reflected optical spectrum from a Bragg grating is modified according to the type of loading on the fiber. The phenomena generally monitored are the following: Center wavelength shift, peak bandwidth, spectral splitting.

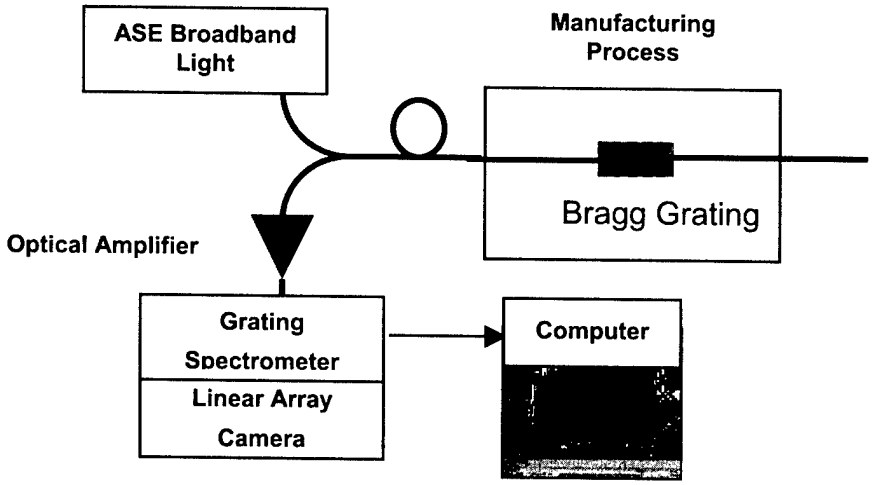


Figure 2. Schematic showing the fiber stress measurement system which is based on dynamically monitoring the return optical spectrum from a fiber Bragg grating.

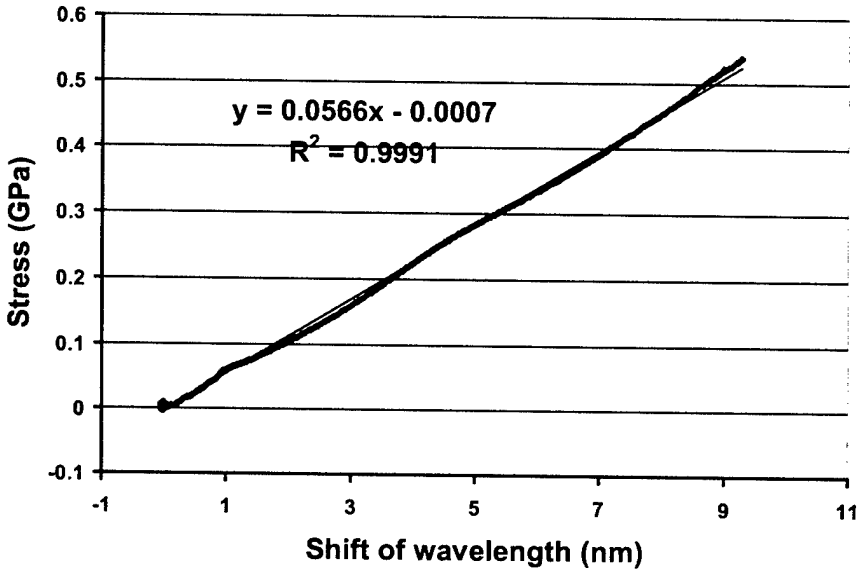


Figure 3. Calibration curve relating center wavelength shift to fiber stress.

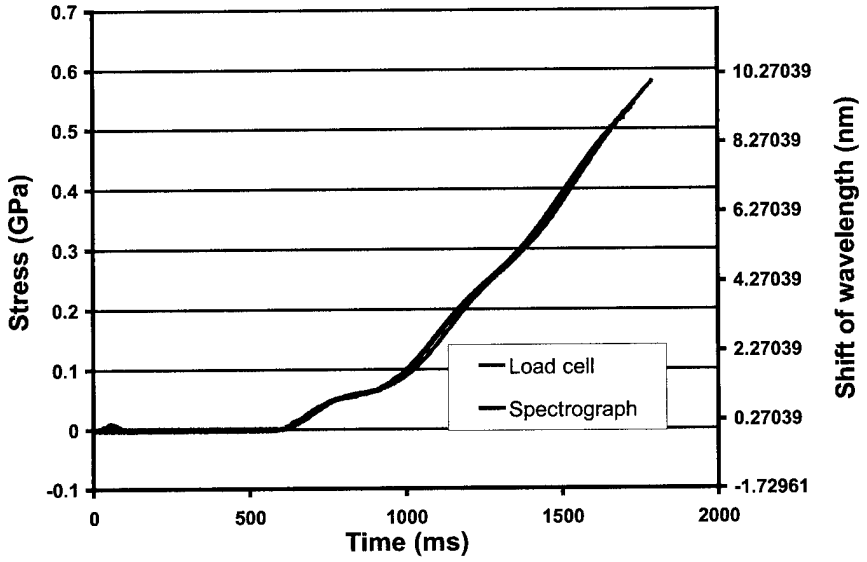


Figure 4. The output from a fiber Bragg grating and load cell obtained by tensile loading the fiber grating in a universal- testing machine.

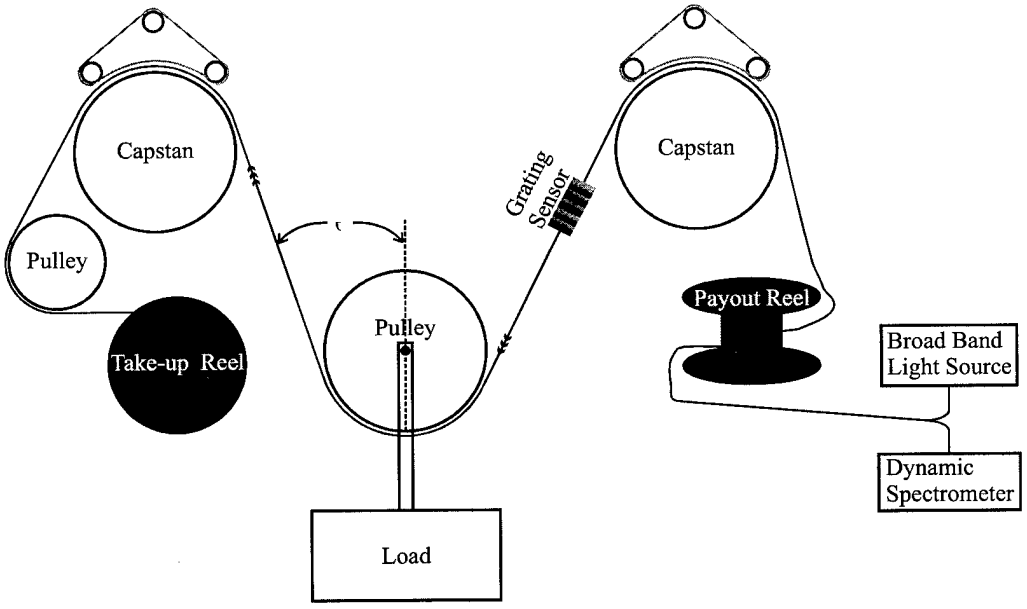


Figure 5. Schematic showing the components of the fiber processing simulator.

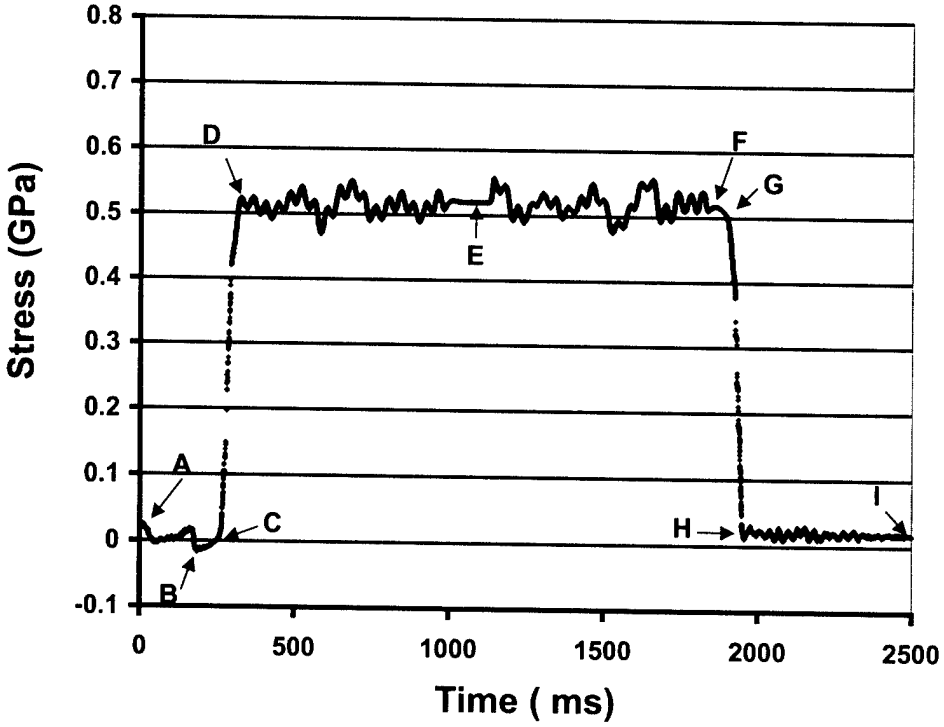


Figure 6. Results from in-process monitoring of the fiber processing simulator under the conditions of Test 1: fiber speed 1 m/s and weight = 1.083 Kg. The labeled points identify specific locations of the Bragg Grating within the fiber processing simulator.

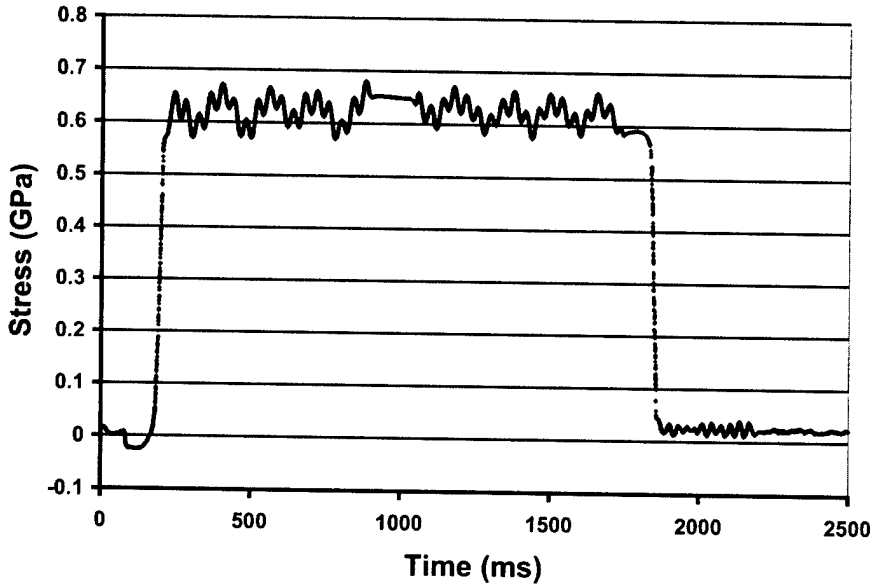


Figure 7. Graph showing the results from in process monitoring of the fiber processing simulator under the conditions of Test 2: fiber speed = 1 m/s and weight = 1.389 Kg.

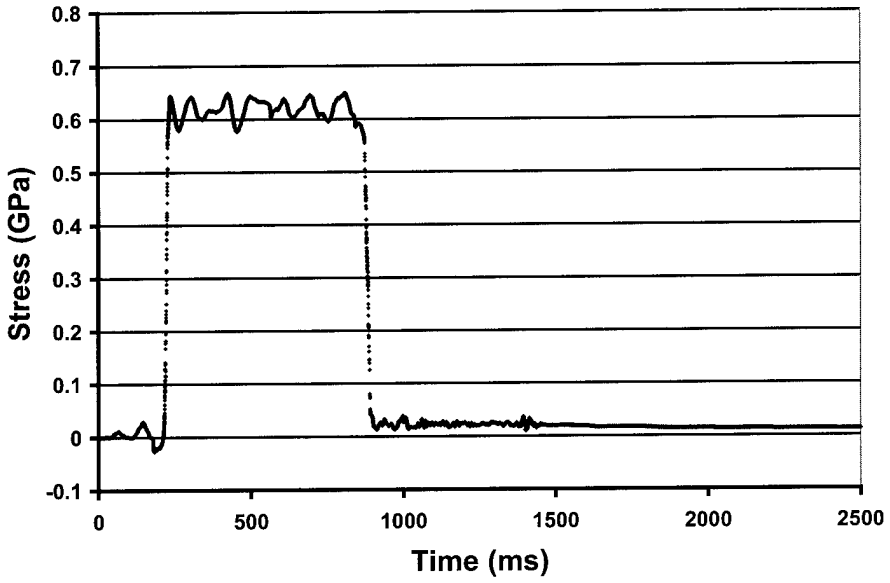
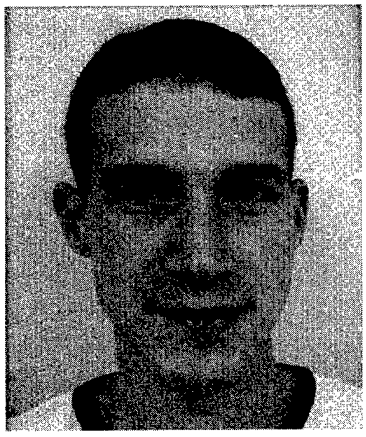


Figure 8. Graph showing the results from in process monitoring of the fiber processing simulator under the conditions of Test 3: fiber speed = 2.5 m/s, weight = 1.389 Kg.



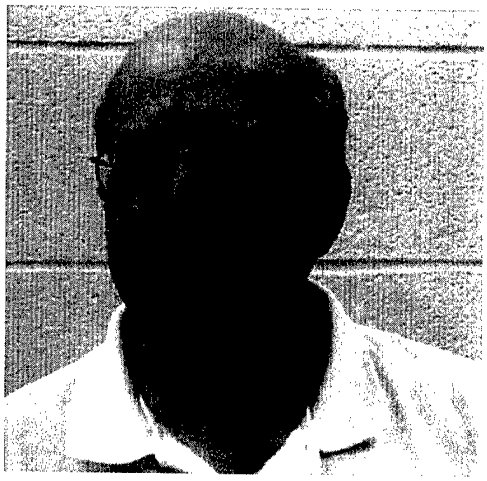
Sylvain Capouilliet
SP-TD-01-1
Corning Incorporated
Corning, NY 14831

Sylvain Capouilliet is originally from Lecelles in the North of France. He graduated from the National Engineering School for Physics of Grenoble and specialized in Physics Instrumentation. The development of this measurement system has been the focus of his internship with Corning Incorporated and is the subject of his Master's thesis.



James A. Smith
SP-TD-01-1
Corning Incorporated
Corning, NY 14831

Jim Smith was born and raised in Charles City, Iowa. He attended Iowa State University and graduated with his B.S. in Engineering Science and Mechanics. He obtained his masters of science in Mechanical Engineering and his Ph.D. in Interdisciplinary Engineering at Texas A&M University. He has consulted at AT&T Bell Laboratories in Murray Hill NJ, worked at the Idaho National Laboratory/EG&G Idaho for three years, and was a research fellow at the Magnetic Resonance Laboratory of the Mayo Clinic. He is currently in the Measurement Systems Design group within the Advance Engineering directorate at Corning Incorporated.



Donald J. Walter
SP-TD-02-1
Corning Incorporated
Corning, NY 14830

Don Walter is a Distinguished Associate in Corning's optical fiber strength laboratory. His responsibilities include developing new strength and fatigue test equipment as well as performing strength and fatigue studies on commercial and developmental fibers. Walter joined Corning in 1977 as a draw technician in the optical fiber development. He also worked as a technician in Corning's Advanced Fiber Products group before assuming his current responsibilities.



G. Scott Glaesemann
SP-TD-02-2
Corning Incorporated
Corning, NY 14831

Scott Glaesemann is a development associate responsible for the optical fiber mechanical testing laboratory at Corning's Sullivan Park technology center and has been employed there for 15 years. He received his Master's degree and doctorate in mechanical engineering from the University of Massachusetts and a bachelor's degree in mechanical engineering from North Dakota State University.



Glenn E. Kohnke
SP-DV-02-6
Corning Incorporated
Corning, NY 14831

Glenn Kohnke is a Senior Research Scientist in Component Technologies Applied Research at Corning Incorporated. He received his B.S., M.S., and Ph.D. degrees from the Institute of Optics at the University of Rochester. He began working on components for optical communications as a post-doctoral scientist at A&T/Lucent Technologies Bell Laboratories. He joined Corning in 1997 and conducts research on fiber Bragg grating devices.



Ronald D. Irion
SP-DV-02-6
Corning Incorporated
Corning, NY 14831

Ron Irion is a Research Technician responsible for fiber Bragg grating fabrication in Component Technologies Applied Research at Corning Incorporated. He began working at Corning in 1992 on Multiclad^{TM} coupler fabrication and joined the gratings group in 1998. He received an associate's degree in 1985 from Alfred State College.

Optimization of Loose Tube Optical Cable Manufacture Process Based on Optical Fiber Mechanical Behavior.

Antonio Carlos da Silva, Flávio N. Hirose, Janúncio A. Medeiros Neto, João Maurício I. Furtado

Furukawa Industrial S.A. Produtos Elétricos, Curitiba, Paraná, Brazil

Phone: +55 41 341-4086, Fax: 55 41 341-4152, E-mail: acsilva@furukawa.com.br

Abstract

Today there is a general industry trend to optimize all steps of cable manufacture process in order to improve the cable performance, reduce the final product cost and get more productivity. The machinery industry is frequently offering new technologies that reach higher speeds and yields. Therefore, with the enhancement of the cable process, the optical fiber has been more exposed to axial and longitudinal stresses. In order to take advantage of these news technologies and optimize cable performance, is specially important to keep the high strength of the fibers during all steps of manufacture process.

Keywords

Optical Fiber Cable; Fiber optic reliability; Reliability of optical fiber in process.

1. Introduction

The optical cable manufacturer industry is continually working to improve the cable processes in order to increase the productivity and performance of optical cables, which is closed related with the fiber strength. During cable process, the fiber is submitted to different effects. Therefore, in the analyze of the fiber mechanical degradation, during all steps of cabling process, these effects must be considered. We take into account all tensions, bending and torsion present in each process stage to determinate the maximum combined stress that may be applied in the fibers without degrade fiber strength. This approach is fundamental, since all events involved in this process can strongly affect the strength distribution of the fiber, which is a key parameter for mechanical reliability model applied to predict optical fiber lifetime. However, the fiber final strength in the installed cable depends on the applied stress and duration of each stress event which the fiber is submitted during cable process and installation. The figure 1 describes the processing steps considered in this paper.

This study allowed us to optimize the optical fiber coloring line speed, define the ideal tensile applied during fiber tubing process, choose the optimum lay length to be applied during stranding and simulate the mechanical reliability during service lifetime.

2. Mechanical Strain for Optical Fiber During Cabling Process

It is well known that to keep the fiber integrity during cabling process is extremely important to maintain the strain level on optical fiber below proof-test level. The total mechanical strain was calculated considering the following mechanical efforts applied to the fiber during the process: tension and bending which are defined as:

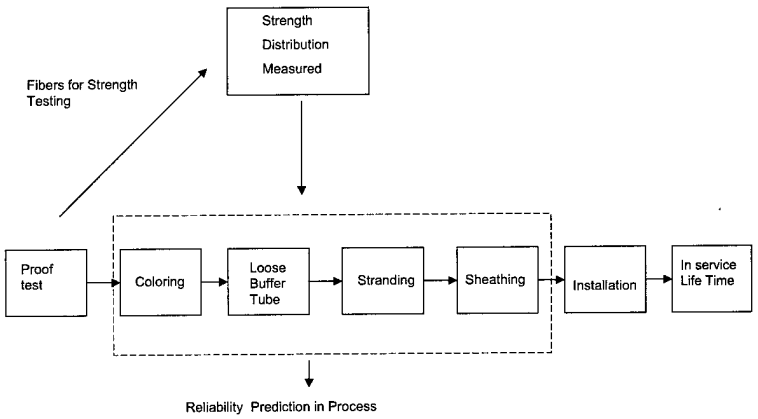


Figure 1. Typical fiber cabling processing steps

a) Tension Loading: For optical fiber with primary and secondary coating the total load supported by the fiber is given by:

$$T_t = T_f + T_p + T_s, \quad \text{or} \tag{1}$$

$$T_t = E_f A_f \varepsilon_f + E_p A_p \varepsilon_p + E_s A_s \varepsilon_s \tag{2}$$

Where: E_f, E_p, E_s = Young modulus of each type of material;
A_f, A_p, A_s = Areas of each material;
$\varepsilon_f, \varepsilon_p, \varepsilon_s$ = Optical fiber elongation strain glass, primary and second coating, respectively.

b) Bending strain: When the fiber is winding in reel or pass through sheaves, bending stress will appear during the manufacturing process. The bending strain depends on material's Young modulus of fiber and reel diameters, as showed in figure 2. From this figure, we can find the bending strain, which is given by:

$$\varepsilon = (D_f/D_b)\,\text{sen}\alpha \tag{3}$$

If we assume that ε can vary from $\varepsilon=0$ until $\varepsilon=\varepsilon_{max}$, the tension on fiber can be written as:

$$\sigma = E(D_f/D_b)\,\text{sen}\alpha \tag{4}$$

Where: σ = Tension on fiber;
E = Equivalent Young modulus;
D_f = Fiber diameter;
D_b = Reel diameter.

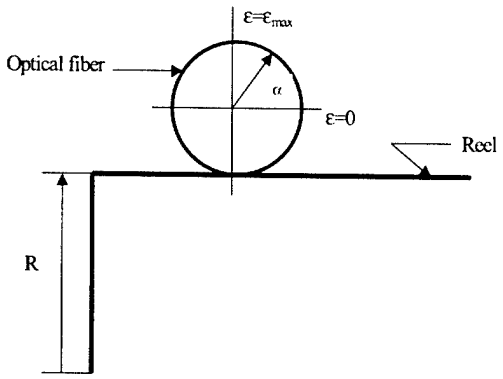


Figure 2. Bending strain on fiber during process

The equivalent strain applied for all process can be obtained using the following equation:

$$\varepsilon_{eq}=\{1/L_o\int_o^{L_o}[1/t_s\int_o^{t_s}\varepsilon_f^n\,dt\,]^b\,dL\,\}^{1/bn} \quad (5)$$

Which can be written as:

$$\varepsilon_{eq}=\left\{\left[(\varepsilon_{ink}^n\frac{t}{t_s})^b\frac{L_s}{L_0}+(\varepsilon_{tube}^n\frac{t}{t_s})^b\frac{L_s}{L_0}+(\varepsilon_{stranding}^n\frac{t}{t_s})^b\frac{L_s}{L_0}+(\varepsilon_{jacket}^n\frac{t}{t_s})^b\frac{L_s}{L_0}\right]^{\frac{1}{bn}}\right\} \quad (6)$$

Where: ε_{eq} = Equivalent strain after processing
ε_{ink} = Strain after coloring
ε_{tube} = Strain after loose buffer tube
$\varepsilon_{stranding}$ = Strain after stranding
ε_{jacket} = Strain after sheathing
t = Fiber time under load
t_s = Time in service
L_s = Fiber length in each manufacture process
L_o = Fiber length which reliability should be assured
t/t_s = normalized time
L_s/L_0 = normalized length
$b = (n_p-2)/(n-2)$

3. Calculus of Strain for Each Process Step

3.1 Coloring Process

The coloring fiber process involves bending and tension stresses. During this process, the fiber is in contact with several sheaves of different diameters for a period of time. Therefore, in order to estimate the contribution associated with this process, we must take into account the total number of sheaves and also the speed of the process. The coloring process contribution for the equivalent strain is given by:

$$\varepsilon_{eq} = \varepsilon_{tr} + \varepsilon_{bend.} \quad (7)$$

where each term can be calculated by:

$$(\varepsilon_{p1}{}^n\, t/t_s)^b\, L_s/L_o = n_1(\varepsilon_1{}^n\, t/t_s)^b\, L_s/L_o + ...+ n_n(\varepsilon_n{}^n\, t/t_s)^b\, L_s/L \quad (8)$$

Where: n= Number of sheaves in coloring machine;
ε = Optical fiber strain;
ε_{tr} = Strain due to tension;
ε_{bend} = Strain due to bending.

2.2 Loose buffer tube process

In the buffer tube process, the total strain is calculated taking into account parameters like extra length and buffer tube dimension. Thermal effects occurred during the tubing process were also considerated. The strain associated with thermal effect is given by:

$$\varepsilon_{th} = \alpha_f\,(T_c - T_0) + \alpha_c\,(T - T_c),\ T > T_c \quad (9)$$

Where: ε_{th} = Thermal strain.
α_c = Tube expansion linear coefficient;
α_f = Fiber expansion linear coefficient;
T_0 = Reference temperature;
T_c = Critical temperature during process;

The critical temperature, T_c, can be calculated by using the following equation:

$$T_c = \{f(2R_h\text{-}f)(2\pi/P)^2/[2(\alpha_c - \alpha_f)]\} + T_0 \quad (10)$$

The equivalent strain for this process is given by:

$$\varepsilon_{eq} = \varepsilon_{tr} + \varepsilon_{bend} + \varepsilon_{th} \quad (11)$$

Where: ε_{eq} = Equivalent strain after loose tube process
ε_{tr} = Strain due to tension;
ε_{bend} = Strain due to bending;
ε_{th} = Thermal strain.

2.3 Stranding Process

Considering the same equation, and all data explained before, strain on the fiber after SZ stranding process was calculated. The strains involved in this process are tension and bending. We used the same equations of coloring and loose buffer tube processes to calculate the strain on fiber. The equivalent strain is given by:

$$\varepsilon_{eq} = \varepsilon_{tr} + \varepsilon_{bend} \quad (12)$$

2.4 Sheathing Process

Also during sheathing process the same equations are used to calculate the fiber strain. Tension, bending and thermal are the strains involved in the process. The equivalent strain in this process was calculated by the following formula:

$$\varepsilon_{eq} = \varepsilon_{tr} + \varepsilon_{bend} + \varepsilon_{th} \quad (13)$$

Finally, the equivalent strain on fiber after all process was calculated using the formula (6). The results is presented in Table1.

Table 1. Strain Results Obtained After All Processes

Process	Tension strain	Bending strain	Total strain
Coloring	3,15 E-51	1,67 E-47	1,67 E-47
Loose Tube	1,01 E-49	6,96 E-47	6,97 E-47
Stranding (SZ)	0	1,39 E-42	1,39 E-42
Sheathing	0	2,026 E-54	2,03 E-54
Total	-	-	1,39 E-42
ε_{eq}(%)	-	-	0,064

4. Results and Discussions

In the calculus, was considered fiber with proof-test 1,0%. The permanent curvature in the fiber occurred during the stranding process is the main contribution to mechanical degradation. The others contributions are not considered. The equivalent tension is ε_{eq}=0,064% due to the stranding process, considering residual effort in the cable.

In order to analyze the effect of cabling process in the fiber strength was manufacture a cable with 48 fibers – 12 fibers in each tube. After the cable process were chosen randomly 12 to make the mechanical test. The parameters 'n', 'm' and 'σ_0' were evaluated, using the Two Point Bending Method, before and after the cabling. The obtained values are showed in the table 2. Note that:

a) There was no changes in the 'm' parameter;
b) There was a slight increase in the 'n' parameter after cabling. This might be influence of the filling compound.
c) The 'σ_0' parameter showed no significative changes.

4.1 Strength Distribution Parameters

The table 2 below shows the results of power constant of fatigue (n) obtained before and after processing. Based in this value it possible to calculate lifetime prediction of fiber in cable.

Table 2. Parameters 'n', 'm' and 'σ_0' before and after cabling

Fiber	Before cabling			After cabling		
	n	m	σ_0	n	m	σ_0
1	13,766	81,930	7,490	13,607	99,574	6,900
2	12,880	69,726	7,008	13,322	89,046	6,823
3	12,557	115,142	7,109	13,793	130,278	6,862
4	13,248	70,397	6,775	13,882	94,819	6,864
5	13,517	114,270	6,930	13,471	76,875	6,884
6	13,255	99,235	6,736	13,250	75,720	6,848
7	12,659	85,497	6,972	13,409	66,895	6,880
8	13,170	78,094	6,858	13,630	93,686	6,739
9	12,727	99,819	6,969	13,323	94,542	6,851
10	13,338	95,011	6,986	13,340	81,391	6,882
11	13,134	79,367	7,109	13,626	93,063	6,667
12	13,046	150,248	6,956	13,952	147,131	6,621
Average	13,108	94,895	6,992	13,550	95,252	6,818
					-2,489%	

4.2 Optical fiber strength after various processes

Several tests based on Bending Fracture Method were made in order to evaluate the fiber strength degradation associated with cabling process. The table 3 shows the values obtained in the tests.

Table 3. Optical fiber strain after various processes

Strain Factor	Strain (%)	L / L_0	t / t_s
Residual strain of manufacturing	0,064	1	1
Installation and stretching (short term)	0,20 (*)	1	3,653E-5
Installation and stretching residual strain	0,05 (*)	1	1
Additional Long Term bending (after installation)	0,014	1/100	1

(*) Maximum strain allowed by various type of underground cable installation.

4.3 Lifetime cable prediction

The lifetime cable prediction was estimated using equation 14.

$$t_s = t_p \left(\frac{\varepsilon_p}{\varepsilon_s} \right)^n \left\{ \left[1 - \left(\ln(1-F)/(N_P L) \right) \right]^{\frac{1}{\alpha}} - 1 \right\} \quad (14)$$

Where: ε_f = Applyed strain in each manufacture process
t_p = Proof-Test Time
F = Optical fiber failure probability
L = Fiber length
N_p = Number of failures by length unit during the proof-test

F = 0,01
α = 0,04256

The equivalent tension strain ε_{eq} is equal to 0,1326% considering the optical fiber failure probability equal to 0,01. With this parameters the lifetime prediction is approximatelly 31 years.

5. Conclusion

According to the experimental values obtained, we concluded that the optical fiber suffered no degradation during the manufacturing cable process. The practical results showed good agreement with the theoretical estimation. The differences between the practical and theoretical results are in the tolerated error margin. This study allowed us to optimize the optical fiber coloring line speed, the ideal tensile applied during fiber tubing process, choose the optimum lay length to be applied during stranding and simulate the mechanical reliability during service lifetime. This study showed that the most significative contribution for the fiber strength distribution is given by the permanent curvature occurred during the stranding process.

6. Acknowledgements

Special thanks to Mr. Fernando Antonio Pinto, and all people that helped to develop this work.

7.References

[1] Mitsunaga,Y.;Katsuyama,Y.;Kobayashi,H.;Ishida,Y. - "Failure Prediction for Long Length Optical Fiber Based on Proof Testing" J.Appl.Phys.53(7),July,1982"

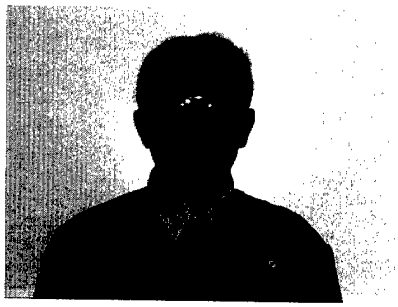
[2] Mitsunaga,Y.;Katsuyama,Y.;Kobayashi,H.;Ishida,Y. - "Strength Assurance of Optical Fiber Based on Screening Test" Electronics and Communication in Japan.66-B(7),July,1983"

[3] Fuchigami,T.;Katsuyama,Y.;Kawase,M. - "Optimum Clearence Design for a Loose Optical Fiber Cable Based on Suppression of Fiber Strain." - Journ.LightWave Tech.,vol.LT-3,n 1.1985",

[4] ."Definition and Test Methods for the Relevant Parameters of Single-Mode Fibres."- ITU-T Recommendation G.650.1993

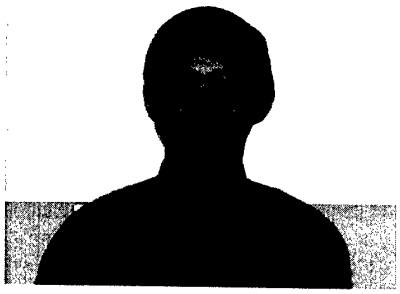
[5] Doremus,R.H. - "Glass Science" John Wiley & Sons.New York.1973

8. Biography



Antonio Carlos da Silva - Furukawa Industrial S.A.
R. Hasdrubal Bellegard, 820 CIC 81450-140
Curitiba – Paraná - Brazil

Antonio Carlos da Silva joined Furukawa Industrial S.A. in 1977 after receiving his B.S. degree as an Mathematics from PUC PR". He has been involved in optical and metallic cables design and installation techniques. He is currently working in Product Engineering.



Flavio N. Hirose – Furukawa Industrial S.A.
R. Hasdrubal Bellegard, 820 CIC 81450-140
Curitiba – Paraná – Brazil

Flávio N. Hirose received joined Furukawa Industrial S. A in 1990 after receiving his B.S. degree as an Electrical Engineer from Federal University of Parana (UFPR). He worked on design and development of optical cables and he is actually responsible for optical fiber drawing process.



Januncio A. M. Neto – Furukawa Industrial S.A.
R. Hasdrubal Bellegard, 820 CIC 81450-140
Curitiba – Paraná – Brazil

Januncio A. Medeiros Neto received his B. S. degree from Federal University of Rio Grande do Norte (UFRN) and M. S. and PhD. In Physics from University of Campinas (UNICAMP) in 1991. After post doctoral appointment at ORC-University of Southhampton – England, he joined UNICAMP as research associated. In 1998, he joined Federal Center of Technological Education (CEFET-PR) as research fellow and Furukawa Industrial S/A. as consultant. He has worked in various areas of glass science such as non-oxide glass for optical fiber and component reliability.

The Development of an Improved Reference Cable for the NFPA 262/UL 910 Plenum Fire Test

Xiaomei Fang[1], Andrew A. Bushelman[1], Paul E. Neveux Jr.[2]
Rajgopal Subramanian[1], J. Thomas Chapin[2], Pravinray D. Gandhi[3]
[1]Avaya, Inc., Norcross, GA
[2]Lucent Technologies, Norcross, GA
[3]Underwriters Laboratories, Inc., Northbrook, IL

Abstract

To improve the intra-laboratory calibration and inter-laboratory harmonization of the NFPA 262/UL 910 plenum cable fire test, continuous efforts have been employed to develop a high-quality reference cable (910ST) with enhanced consistency and reliability. Various prototypes employing a series of vinylidine fluoride - chlorotrifluoroethylene copolymer (PVDF) formulations were produced in order to evaluate the effects of inorganic additives on smoke generation during the plenum cable fire test. Small-scale cone calorimeter tests were also conducted to assess material properties such as, heat of combustion, heat and smoke release rates of the candidate formulations. The correlations between the cone calorimeter results and plenum cable burning characteristics (flame spread, peak smoke optical density and average smoke optical density) were established and evaluated. Using this information, an improved reference cable was produced from the candidate PVDF formulations. These plenum fire test results have strongly demonstrated that the improved reference cable with high-quality control can provide a more reliable and consistent calibration standard in the plenum cable fire test.

Keywords

NFPA 262/UL 910 fire test, cone calorimeter test, flame propagation, smoke generation, plenum cable, 910ST reference cable, color concentrate, PVDF.

Introduction

With increasing demand on network and communication systems, more concerns have been raised concerning the increased amount of cables installed in the plenum spaces and the associated fire and smoke hazards towards life safety and building reliability. Communication cables have been developed for decades to improve fire performance in order to reach a less hazardous condition in case of a fire. Cables with less flame propagation and lower smoke generation have been qualified to meet the strict fire safety requirements in the plenum space.

The NFPA 262/UL 910 test is a well-recognized fire test for plenum cables, which has been issued by the National Fire Protection Association and Underwriters Laboratories. The NFPA 262/UL 910 standard requires the plenum cables tested in the Steiner tunnel to display a flame propagation no greater than 5 feet, a peak smoke optical density (POD) no greater than 0.50 and an average smoke optical density (AOD) no greater than 0.15 to pass the test with a plenum rating, which is designated as CMP for copper, OFNP for optical fiber or MMP for metallic cables as defined in the National Electrical Code (NEC). Those stringent plenum testing criteria in both flame and smoke require consistent and well-controlled tunnel conditions to provide reproducible and reliable testing operations. As specified by the original version of the standard, the natural product, red oak was used as the calibration reference for the Steiner tunnel calibration. However, over the years, red oak has provided limited consistency in fire performance due to the variation of wood structure and moisture content resulting from different supply locations, harvest seasons and age of the trees.

To achieve the desired consistency and reliability that matches the stringent requirements of the NFPA 262/UL 910 test, a reference cable (910ST), consisting of a copper core insulated with a thermoplastic copolymer, was proposed as the calibration reference for the Steiner tunnel.[1] A vinylidine fluoride – chlorotrifluoroethylene (PVDF- based) thermoplastic copolymer, Solef® 32008/0000 from Solvay, was initially chosen as the reference cable material for the calibration.[1] However, it has been observed that small variations in the amount of the white color concentrate in the material has given rise to variations in the smoke generation (POD and AOD) during the NFPA 262/UL 910 tests. To minimize the variation resulting from the thermoplastic material and the reference cable manufacture as well, a continuous effort has been directed to improve the original reference cable to achieve the enhanced consistency and reliability as desired in the fire tests.

In this paper, we give the details of the ongoing effort that has resulted in an improved reference cable for the NFPA 262/UL 910 test. This involves judicious modifications of the thermoplastic material and cable manufacturing details previously described.[1] The new insulate material is a commercially available material named Solef® 32008/0003. This is a natural (uncolored) PVDF-based copolymer with added smoke suppressor.[2-4] Test results from US and UK fire test facilities: Underwriters Laboratories (UL), Intertek Testing Services/ETL Semko (ITS), and Building Research Establishment (BRE), show significant consistency and reproducibility, which strongly demonstrated that the improved 910ST reference cable is qualified to be employed as the calibration standard in the NFPA 262/UL 910 plenum test. The investigation of the material selection process for the improved 910ST reference cable and the color concentrate effect on the smoke behavior of the reference cable in the plenum test is also presented in this paper.

Color Concentrate Effect on the Fire Performance of the Original 910ST Reference Cable

The effect of the color concentrate on the smoke generation in the originally-designed 910ST cables was investigated using the NFPA 262/UL 910 standard. The tests were conducted at UL-Northbrook, IL. The Solef® 32008/0000 PVDF copolymers with and without a small amount of the white color concentrate were employed as the thermoplastic insulation for the 910ST cables. This study included two versions of the white color concentrate, Version I contained a small amount of titanium dioxide (TiO_2) and Version II was a non-TiO_2 formulation. Ten prototypes of 910ST (three prototypes without the color concentrate, three of them with Version I color concentrate, and four of them with Version II color concentrate) were manufactured and tested under the NFPA 262/UL 910 standard.

As illustrated in Figure 1, the 910ST reference cables without white color concentrate generated considerable heat and smoke during the plenum test by showing high values in flame spread, POD and AOD (Prototypes 1-3). The 910ST reference cables with color concentrates (Prototypes 4-10) displayed lower flame propagation and less smoke generation than those without color concentrate. Furthermore, the prototypes containing Version I color concentrate gave even less smoke (40% in POD and 46% in AOD) relative to the prototypes containing Version II color concentrate. During the NFPA 262/UL 910 tests, a significantly larger amount of dripping was observed in the prototypes without color concentrate than the prototypes with the color concentrates. Also the prototypes with Version I color concentrate appeared to drip slightly more than the prototypes with Version II color concentrate.

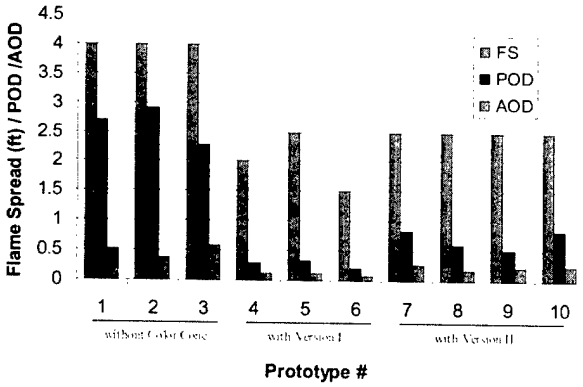


Figure 1. Color Concentrate Effect on the Fire Performance of 910ST Cables

As mentioned earlier, Version I color concentrate contained a small amount of TiO_2 to provide a white appearance, while Version II color concentrate used non-TiO_2 formulation instead. Titanium dioxide is known to react with PVDF at elevated temperatures.[5] Since the amount of smoke evolved in the presence of TiO_2 is much less than without TiO_2, it would appear that the TiO_2 is catalytically breaking down the polymer at elevated temperatures so that the amount of large optically dense particles is significantly reduced. The slightly increased dripping behavior observed in the tests of the prototypes with Version I color concentrate also suggests a higher thermal output generated during the burn in the presence of TiO_2.

Development of the Improved 910ST Reference Cable

1. Material Selection for the Improved 910ST Reference Cable

To ensure the fire performance consistency and manufacturing reproducibility of the 910ST reference cable, the improved prototype was designed to employ a natural PVDF-based copolymer without any color concentrate to achieve the desired fire performance with the target values as follows: POD at 0.3, AOD at 0.1 and FS at 2 ft. A series of PVDF-based resins were studied. The efforts were focused on the smoke generation (POD and AOD) instead of flame propagation since most resins in this study displayed the flame propagation in the desired range. The cone calorimetry (ASTM E1354) and NFPA 262/UL 910 tests were conducted at UL-Northbrook, IL.

In order to select the quality cable material that provided the desired fire performance as a calibration standard, nine PVDF resins (listed in Table 1) from different suppliers were investigated in this study. The three pre-compounded resins (prototypes C, D, and E in Table 2), prepared from the Solvay PVDF containing TiO_2, would not be treated as candidate materials for the improved 910ST cables, but would be included in the dataset to establish a correlation model between the cone calorimetry and the NFPA 262/UL 910 test. The smoke results of six 910ST prototypes using the different PVDF-based resins from the plenum tests are shown in Table 2. Cone calorimetry was used as a small-scale test to determine the fire performance of the resins. The results of this study are given in Table 3. Two smoke parameters in the cone calorimeter test, peak smoke release rate (PSRR) and total smoke (TS), were used in a regression analysis with POD and AOD from the plenum test respectively.

Table 1. Candidate Materials for 910ST Reference Cable

Resin #	Material Description
1	Solef® 32008/0000
2	Solef® 31508/0003
3	Precompound –A
4	Precompound –B
5	Precompound –C
6	Solef® 32008/0009
7	Solef® 32008/0003
8	Solef® 31508/0000
9	Solef® 31008/0000

The main objective of the modeling work is to assess the utility of the small-scale test in predicting the results of a full-scale test such as the NFPA 262/UL 910 test. A three-parameter exponential growth approach was applied to set up a correlation for estimating the plenum test results based on cone calorimeter data. The regression correlation of the peak SRR from the cone calorimetry test and the POD from the NFPA 262/UL 910 test was established using six resins (Resins 1-6 in Table 1) and six corresponding prototypes (Prototypes A-F in Table 2). The results

shown in Figure 2a have a regression coefficient of 0.99 (r^2 = 0.98). The regression correlation of the total smoke from the cone calorimetry test and the AOD from the NFPA 262/UL 910 test is shown in Figure 2b. This has a regression coefficient of 0.95 (r^2 = 0.91). The high value for the correlation coefficient (r^2) indicates that PSRR and TS from the cone calorimeter adequately model POD and AOD of this cable.

Table 2. NFPA 262/UL 910 Results of Six Prototypes

Prototype #	Material	NFPA 262/UL 910 Test	
		POD	AOD
A	Solef® 32008/0000	2.63 ± 0.32	0.49 ± 0.11
B	Solef® 31508/0003	0.11 ± 0.01	0.05 ± 0.00
C	Precompound –A	0.50 ± 0.17	0.17 ± 0.02
D	Precompound –B	0.34 ± 0.06	0.12 ± 0.02
E	Precompound –C	0.26 ± 0.05	0.11 ± 0.01
F	Solef® 32008/0009	0.30	0.06

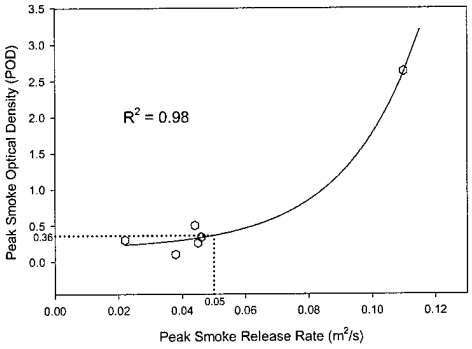
Table 3. Cone Calorimetry Smoke Data of the Candidate Materials

Resin #	Material	Cone Calorimeter Test	
		Peak SSR (m^2/s)	Total Smoke (m^2)
7	Solef® 32008/0003	0.050 ± 0.004	2.54 ± 0.03
8	Solef® 31508/0000	0.097 ± 0.009	7.44 ± 0.85
9	Solef® 31008/0000	0.112 ± 0.036	7.03 ± 0.40

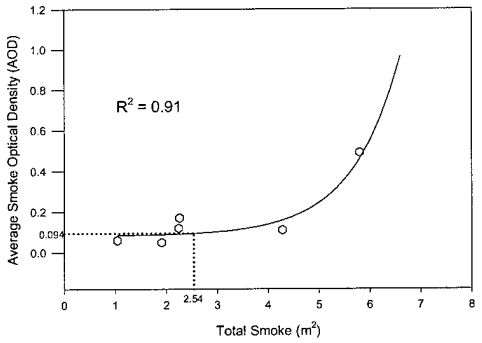
The correlation curves were used to select the insulate materials for the improved 910ST reference cable. Based on the earlier discussions of ruling out pigmented and compounded resins for this product, we were left with just three candidate resins. These resins, numbered 7, 8, and 9 in Table 1 were subjected to the cone calorimeter test. The results are shown in Table 3. Based on the correlation curves in Figures 2a and 2b, the Solef® 32008/0003 resin, with a PSSR at 0.050 and a TS at 2.54, gave an expected POD at 0.36 and an expected AOD at 0.09. This falls in the range of the designed values for the NFPA 262/UL 910 tests. The other two candidate materials gave significantly higher expected POD and AOD values based on their smoke data from the cone calorimetry. Therefore, Solef 32008/0003 was selected as the final candidate material for the improved 910ST reference cable.

2. Improved 910ST Reference Cable Construction

The improved 910ST reference cable was designed and manufactured by Avaya Inc. A 12 AWG copper conductor is insulated using Solef® 32008/0003, with a final cable outside diameter of 0.225 ± 0.004 inches (shown in Figure 3), an eccentricity of 0.030 inches, and an insulate weight of 45.4 lbs/1000ft. As mentioned earlier, the Solef® 32008/0003 resin is produced without any color concentrate. This results in a melting temperature (T_m) at 167°C by DSC, an onset temperature of weight loss at 364°C by TGA under the nitrogen, and a heat of combustion of 6077 Btu/lb by O_2 bomb calorimetry.



(a) Correlation of POD and Peak Smoke Release Rate



(b) Correlation of AOD and Total Smoke

Figure 2. Smoke Correlation between Cone Calorimeter and Plenum Test

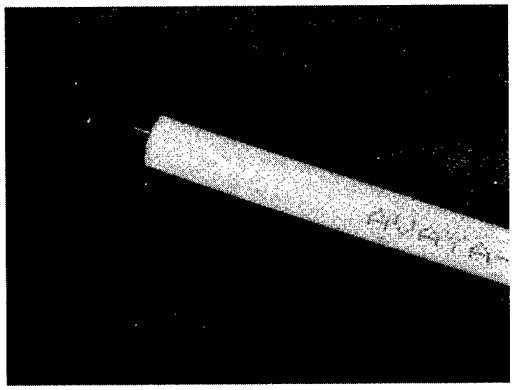


Figure 3. Improved 910ST Reference Cable

3. NFPA 262/UL 910 Fire Results

As a part of the NFPA 262/UL 910 Harmonization Project, the improved 910ST cable was sent to three independent testing laboratories, Underwriters Laboratories (UL) and Intertek Testing Services/ETL Semko (ITS) in the US, and Building Research Establishment (BRE) in UK for testing. The results are summarized in Table 4. From these data, it is clear that the improved 910ST reference cable does give consistent fire performance as is reflected in the low standard deviation on flame spread, POD and AOD. The labs have also commented that the new version of the reference cable was easier to handle, indicating a more pliable insulate. These results demonstrate that the improved 910ST reference cable is qualified to be used as a more reliable calibration standard for the NFPA 262/UL 910 test.

Table 4. Global NFPA 262/UL 910 Test Results of the Improved 910ST Reference Cable

Testing Lab	Test	Flame Spread (ft)	POD	AOD
A	1	1.5	0.26	0.10
	2	1.5	0.34	0.10
	3	1.5	0.22	0.11
	Avg ± Std	1.5 ± 0.0	0.27 ± 0.06	0.10 ± 0.01
B	1	1.0	0.29	0.10
	2	1.0	0.31	0.09
	3	1.0	0.28	0.10
	Avg ± Std	1.0 ± 0.0	0.29 ± 0.02	0.10 ± 0.01
C	1	1.5	0.27	0.13
	2	1.0	0.19	0.10
	3	1.0	---	---
	Avg ± Std	1.2 ± 0.3	0.23 ± 0.06	0.12 ± 0.02

Conclusions

An improved 910ST reference cable using the Solef® 32008/0003 resin has been developed as a reliable calibration standard for the NFPA 262/UL 910 test. Three independent testing laboratories around the world, UL, ITS/ETL and BRE, have conducted plenum fire tests on this cable. The consistent and reproducible results have demonstrated that the improved 910ST reference cable is a reliable calibration standard for the NFPA 262/UL 910 test and will provide a better control to validate the Steiner tunnel performance by eliminating the inconsistency of the previous standard. This is possible only if there is a good control over the raw material that is used in the production of the cable. Specifically, there must be the minimal lot-to-lot variation, especially with respect to ash content, melt viscosity, LOI and heat of combustion.

Acknowledgments

The authors are grateful to Mr. Dennis Biggins of Solvay Advanced Polymers, Inc. for his assistance on the color concentrate issue and materials supply.

References

[1] J. T. Chapin, L.L. Bleich, P. Gandhi, T. Ebert, *International Wire & Cable Symposium Proc.*, 421-426 (1999).

[2] A. Simoens, E. Hannecart, US Patent 5 004 773, 1991.

[3] E. Hannecart, US Patent 4 898 906, 1990.

[4] J. DeBarraly, A. Simoens, US Patent 4 786 662, 1988.

[5] S. Dallek, *Proc. Power Sources Conf.*, 39th, 543-546(2000).

Evaluation of Fiber Coating Stripping Methods by Atomic Force Microscopy of Fiber Surfaces

M.R. Özgür[1], O.S. Gebizlioglu[1], C.R. Kurkjian[2]*

[1]Telcordia Technologies, Inc.
445 South Street
Morristown, New Jersey 07960
[1*] 973 829 4956 ogebizli@telcordia.com

[2] Rutgers University
Piscataway, New Jersey 08855

Abstract

Polymer coatings serve to protect the glass fiber during fiber optic cable production, installation, and maintenance operations. Optical fiber coatings are designed to adhere to the glass fiber for mechanical reliability and satisfactory transmission performance, and they are also required to be easily strippable. The coating removal is most often accomplished by means of mechanical stripping tools that, if not used properly, can mechanically damage the fiber and weaken it. Although a large embedded base (multibillion-dollar) of fiber optic cable exists in modern telecommunications networks as a result of nearly two-decade deployment of telecommunications optical fiber, a reproducible quantitative method for the evaluation of strippability of fiber coatings is still needed. In this report, we present the results of evaluations of mechanically and chemically stripped fiber surfaces by using AFM (Atomic Force Microscopy). For a quantitative assessment of fiber surface cleanliness after mechanical stripping, we examined the surface of hand-drawn silica fiber before and after extended exposure to laboratory air followed by dry wiping/solvent cleaning processes. While freshly hand-drawn fiber exhibited the smoothest surface, acid-stripped fiber that was rinsed with reagent-grade acetone gave a fiber surface that ranked second, thereby quantitatively confirming the effectiveness of solvent cleaning of stripped fiber surfaces. Furthermore, we also show that the fiber surface cleanliness after acid stripping strongly depends on the coating chemistry.

Keywords:

Fiber; coatings; stripping; surface roughness; cleanliness; microscopy; atomic force microscopy.

1. Introduction

Polymer coatings provide mechanical protection to the silica fiber surface and make fiber handling possible during fiber optic cable manufacturing, installation and maintenance operations. In the early years of the fiber optic cable technology, mechanical protection of the fiber surface was the primary function of fiber coatings. More recently, however, protection against fiber microbending has become important as advances in fiber design and manufacturing have led to the development of optical fibers with low attenuation. With these developments, fiber coating contributions to added transmission loss, particularly, at low temperatures have emerged as an essential consideration in long-term performance and reliability of fiber coatings. The need to provide mechanical protection to the fiber surface and to minimize the risk of developing fiber axis perturbations at low temperatures has been met by the design and production of dual-layer coatings. These dual coatings consist of a soft inner layer, or primary coating to support the optical fiber against axis microbends and a tougher outer layer or secondary coating. The purpose of the secondary coating is to provide the necessary mechanical protection to the fiber surface and to mechanically isolate the fiber from its service environment. However, in apparent conflict with mechanical protection function, fiber coatings need to be removable easily and cleanly during installation operations that involve fiber splicing and/or device manufacturing. While good bonding of the coating to the glass surface is required for mechanical protection, particularly, against fatigue and aging of the glass fiber, this requirement might lead to difficulty in stripping the coating from the fiber.[1] Although earlier investigations[2,3] showed no correlation between strip force and coating adhesion to the glass surface, this relationship was re-examined for recent-generation fibers and their coatings in our first report[4]. Secondary coating design has become very challenging since this coating should be tough enough to withstand rough handling while an increase in toughness may, in turn, lead to an appreciable increase in strip force.[5] From a field installer's perspective, it is clear that a low value of strip force is desirable for ease of stripping. However, recent work [6] has shown that increased strip force may lead to significantly increased risk of glass surface damage during stripping. Alternative stripping methods such as thermal stripping have been developed to help control and reduce strip force in coating stripping. In this presentation, we report the results of our investigations on the cleanliness of glass fiber surface from which coatings were removed. We show, by AFM (Atomic Force Microscopy), that ease of coating stripping as indicated by low values of maximum and steady-state strip force, does not guarantee cleanliness of the surface. We also point out that aggressive cleaning may be counterproductive, as shown in the results of Table 1, in generating clean fiber surfaces that are required for fusion splicing and device manufacturing operations.

Table 1. AFM surface roughness measurement results

Sample	RMS 2μ x 2μ	RMS range 500nm x 500nm
As drawn	0.372	0.2-0.4
M.S. 'wipe'	3.305	0.16-0.2
M.S.'2-wipe'	6.4	0.7-2.3
Acetone	0.340	
L.T. acid	0.53	0.14-0.2
H.T. acid	0.744	0.3-0.6

M.S. 'wipe' = mechanical stripping with single alcohol wipe
M.S. '2-wipe' = mechanical stripping with two alcohol wipes
Acetone = chemical stripping with acetone soak
L.T. acid = chemical stripping in sulfuric acid ~170°C
H.T. acid = chemical stripping in sulfuric acid ~ 200°C

2. Experimental Methods and Procedures

In our continuing series of investigations[4,5,7,8,9,10] on the strippability of optical fibers, we have used a broad range of tools such as a computer-controlled stepper motor-driven stripping system*, and a dynamic mechanical analyzer♣ (DMTA, Dynamic Mechanical Thermal Analyzer) for directly characterizing coatings on optical fibers,[5] and a Digital Instruments AFM (Atomic Force Microscope) with a nanoindentation / nanoscratching attachment. In this report, we focus our attention on the cleanliness of fiber surfaces after mechanical or chemical stripping, and, therefore, we present our results in a series of AFM analyses.

We examined surfaces of the stripped fibers by a Digital Instruments Dimension™ 3000 AFM (Atomic Force Microscope). We used nanoindentation / nanoscratching tip and NanoScope™ version 4.32 software in the tapping mode for AFM imaging. The configuration of the diamond tip and cantilever is shown in Fig.1.[11] Indenting, scratching, and subsequent imaging were made with a selected load and scratch length. These indents and scratches were, then, immediately imaged in the tapping mode. As in all AFM imaging, great care must be exercised in the interpretation of the images obtained. Although the diamond tips are quite sharp (the tip radius of curvature of 25 nm), very small features can not be imaged accurately. In addition, while values of hardness (indentation load divided by the contact surface area of the indent) can be calculated, the results can not be used as absolute hardness values. An important factor which affects the size of the indentation produced is the AFM cantilever rotation angle which is labelled as x-rotate parameter.[11] This parameter signifies the cantilever rotation to prevent the cantilever from plowing the surface laterally along the x-direction while the tip indents the fiber surface in the z-direction. Such plowing can result in a much larger indentation. Indents and scratches were made on silica glass surfaces which had never been coated (both drawn fibers and commercially available polished silica plates). In addition, samples of a dual-coated fiber were mechanically stripped and cleaned with two aggressive alcohol wipes, and a fiber which had not been coated was aged in high-purity de-ionized, ultra-filtered water for 6 months. The surface of this fiber was indented and scratched after a nominal drying period of one hour. Finally, surfaces of oxy-hydrogen torch-drawn fiber were examined after exposure to laboratory air followed by repeated cleaning, and surfaces of acid-stripped fibers were examined after dry wiping followed by reagent-grade acetone rinse.

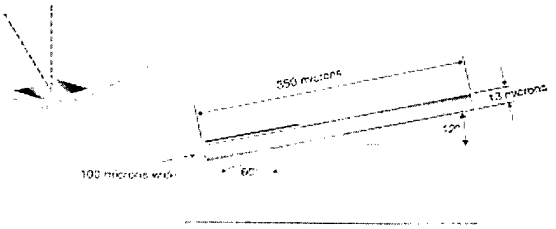


Figure 1. Configuration of the diamond nanoindenting / nanoscratching tip with cantilever.[11]

3. Results and Discussion

In earlier reports,[4,7] we showed that coating dynamic mechanical properties such as storage modulus, coating morphology during stripping, and strip force profiles (maximum strip force and steady-state strip force measured in accordance with FOTP-178) are interrelated. We have also pointed out that strip force profiles when combined with information on the surface cleanliness after stripping provide effective means of evaluating the strippability of optical fibers. In the present report, we briefly review the results of our analyses on the indented/scratched surface of stripped fibers and examine the surface roughness on hand-drawn fiber that was never coated and after exposure to laboratory air followed by cleaning. We also discuss the results of acid stripping followed by dry wiping and solvent rinsing of fibers with specialty coatings.

In an earlier report,[8] we had noted that the surface roughness of fibers which had never been coated and the surface roughness of those fibers from which the coating had been removed with different procedures, varied significantly. A key conclusion from these results was that the nominally clean fiber surface still retained a thin fiber coating film. The presence of this residual film can unfavorably impact fusion splicing productivity and recoating operations. The surface of the fiber which had never been coated had an rms (root-mean-square) roughness of 0.372 nm as shown in Table 1, while a fiber which has been 'cleaned' of its coating by a combination of mechanical stripping and aggressive alcohol wiping, had an rms roughness of 6.4 nm. While this AFM study provided good evidence that such a cleaning procedure did not result in a truly clean surface, a quantitative measurement of the amount of coating remaining on the surface could not be made. Thus, we have recently attempted to use nano-indentation/nano-scratching tips on AFM cantilevers to accurately measure the thickness profile of residual coating film.

* FiberSigma, Bedminster, New Jersey.
♣ Rheometric Scientific, Piscataway, New Jersey.

For establishing a verifiable reference for surface roughness measurements, we first examined a gold reference film. Figure 2 is an image of this gold film which was indented with the diamond tip under a force of 3 x 10^{-5} N. The area of the indent at the surface is approximately 8 x 10^{-15} m^2 and, thus, the calculated hardness (H = F/A) is 3.8 GPa. A second indent under the same conditions gave a calculated hardness of about 4.7 GPa. Both of these indents were produced by using an x-rotate parameter of 20° to minimize the error in the indent size discussed in the experimental section. Even so, the calculated hardness is many times greater than that normally measured. In recent work, Michalske and Houston[12] found that much higher than expected loads were required for the indentation of gold single crystals at similar low loads, and the loads were very dependent on the tip radius. They argued that they were probing very small material regions which were free from dislocations, and, therefore, dislocation nucleation rather than movement was the controlling factor in the response of the material to indentation. Also, as indicated by the instrument manufacturer, hardness measurements should only be used in a comparative way, and only when the measurements are done under identical conditions. Therefore, in this work, the indentation measurements were performed with the same tip and under identical conditions with 20° x-rotate parameter. For the hardness value determined from the image of Fig.5, we estimated a reproducibility of about 20%.

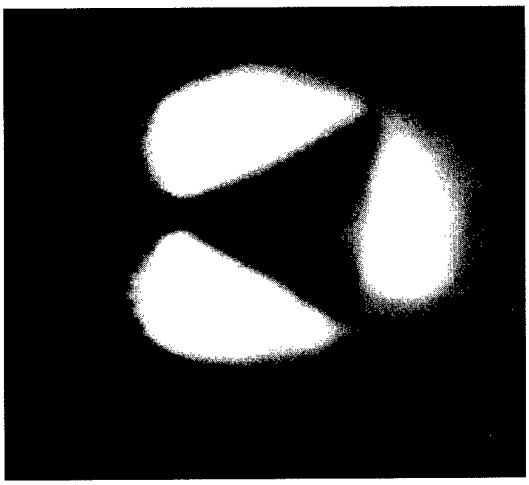


Figure 2. AFM image of a nanoindentation in gold standard sample

Figure 3 is an image of the aged silica fiber which was both indented and scratched. The three vertical lines are the three scratches. They were made with the cantilever moving upward, and, thus, the white (high) material at the top of the scratch resulted from pile-up during scratching. Five indents were made, but unfortunately, four of them were seen to overlap the scratches. The scratch has a width-to-depth ratio of ~3.5:1, while the indent has a ratio of ~9:1. Since the tip has an angle of 60,° this ratio should be 2:1.732 (~1.15:1). The observed discrepancy is due to the imaging of a depression with a tip of comparable radius. Thus, the apparent ratio will be equal to or greater than the real value. The hardness of this aged fiber and the hardness of a 'standard' polished silica plate (F~ 1.5 and 6 x10^{-5} N) were found to be 15.5 and 16.7 GPa, respectively. While these values are about two times greater than those determined by the established hardness measurement methods, they are in line with the high value of hardness found for the gold sample. It is not expected that a dislocation nucleation model would apply in the case of silica glass. However, there continues to be a discussion over the reality and reason for the apparent size (or load) dependence of hardness in silica glass.[13] In any case, these two hardness values are well within the 20% reproducibility of this nanoindentation-based hardness measurement method. Thus, somewhat surprisingly, the 6-month aging in water at 85°C has not affected the hardness. We would expect reduced hardness either due to the formation of silica gel on the surface or the solution of a substantial amount of water in the silica glass.



Figure 3. AFM image of an aged silica fiber indented and scratched

Figure 4 shows an indent made on the polymer surface (the secondary coating) of a dual-coated fiber. The calculated hardness for this material is 517 MPa (3 x 10^{-6} N / 5.8 x 10^{-15} m^2). These indents were found to relax relatively quickly and essentially disappear in the order of a few minutes. Thus, once indented, these polymeric surfaces need to be imaged readily before the relaxations in the sample alter the image of nanoindentations.



Figure 4. AFM image of an indent made on the surface of the secondary coating in a dual-coated fiber.

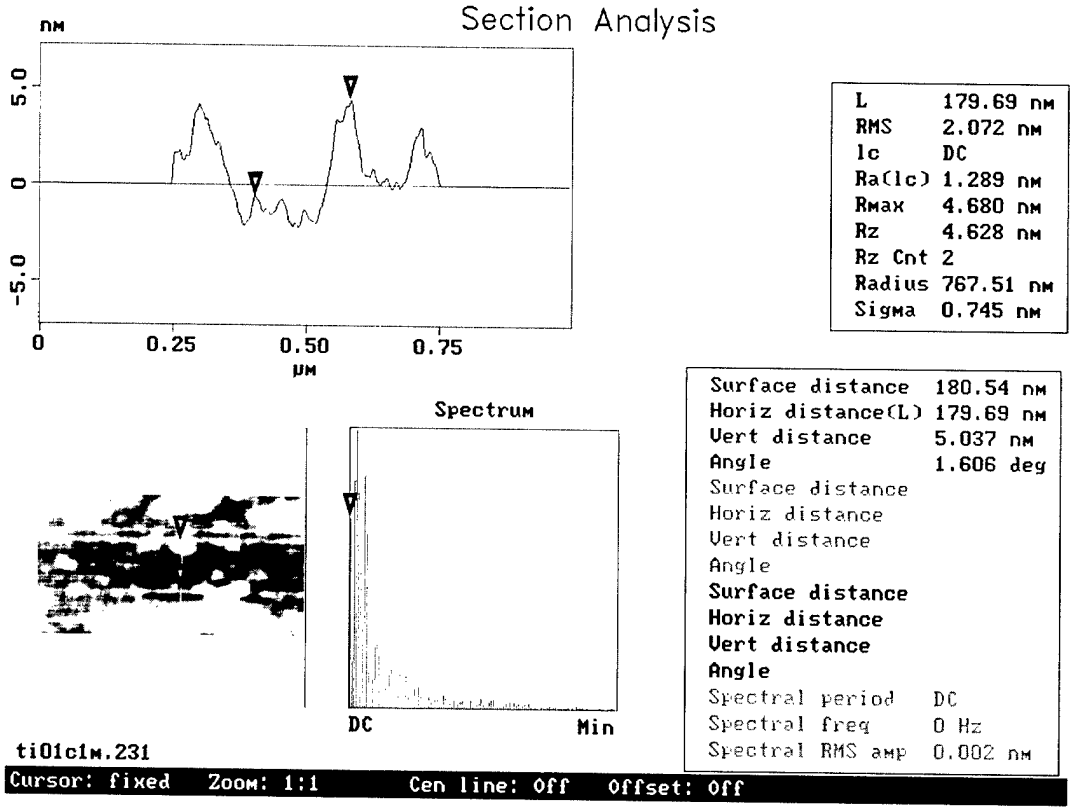


Figure 5. AFM image with section analysis of a mechanically stripped and alcohol-wiped fiber surface.

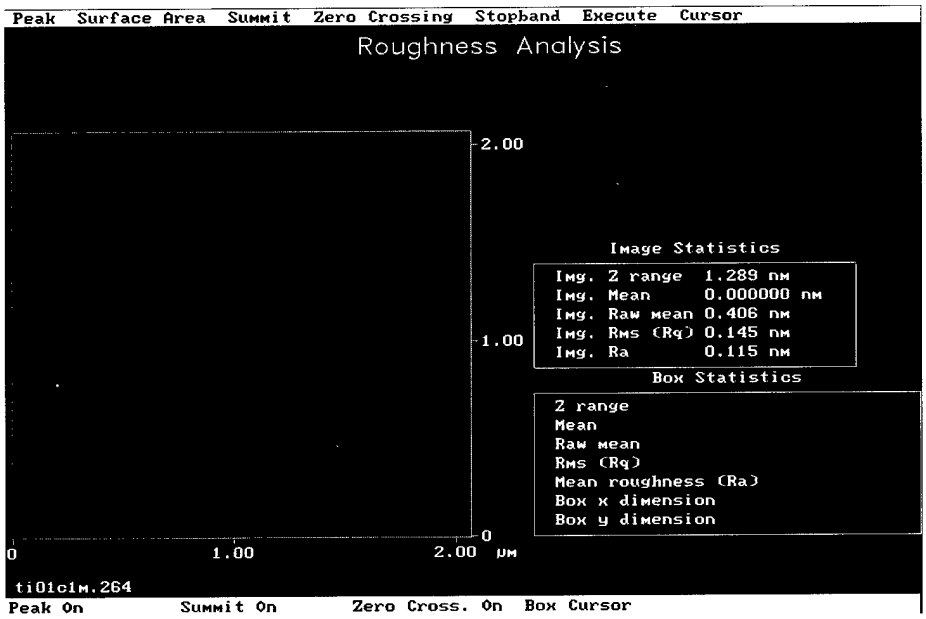


Figure 6. Roughness analysis on the surface of hand-drawn fiber

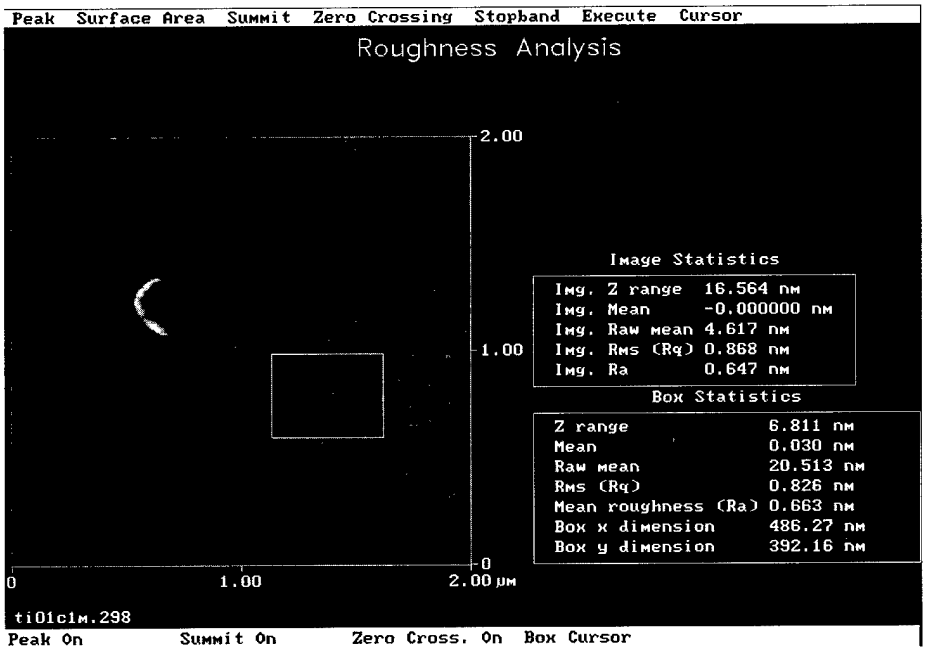


Figure. 7. Roughness analysis on the surface of hand-drawn fiber – three months after drawing

Figure 5 shows a height image (micrograph at the lower left corner) of scratches which were made at very low loads on the silica fiber surface. The surface scratched was that of a fiber which had its polymer coating removed by mechanical stripping and aggressive alcohol wiping. The scratches were made horizontally with the 'auto-indent' feature of the software[11] at progressively higher loads (0.6, 1.2 and 1.8 x 10^{-6} N). It can be seen that the quantity of residual coating varies considerably from point to point on the fiber surface. In fact, although three scratches were made, only one scratch stands out. The lower of the triangular cursors is placed just above the most noticeable scratch. The first scratch to the right of the visible one is barely

visible, while the third scratch on the left, is not seen because of the 'cleanliness' of the surface. The depth of the residual coating as measured is 2.5 nm as seen in the section analysis plot shown at the upper left quarter of Fig.5. However, also seen in this figure is the width of the scratch which is nearly 50 nm. Since the angle of the diamond tip is 60°, the depth should be approximately the same, or ~50(1.732/2) = 43.3 nm. As above, the 25-nm tip can not successfully image such a small impression. Nevertheless, this measurement has shown that stripping with low values of strip force for a fiber coating still leaves a thin residual film on the glass surface. As pointed out earlier, even lower strip force values for silicone rubber-coated fiber result in thicker residual polymer on the glass surface. These results indicate the importance of finding a trade-off between the coating hardness/toughness (and strip force) and interfacial strength (and, therefore, the thickness of residual film).

A key question that has arisen from the discussion presented above is the scale of roughness on the surface of a drawn silica fiber that has never been coated. In order to address this question, we prepared samples of silica fiber (of 250-μm nominal diameter) by hand drawing under an oxy-hydrogen torch from a quarter-inch diameter silica rod. AFM micrograph of Fig. 6 shows a smooth silica surface, within the 4-square micrometer image with a rms (root-mean-square) roughness of 0.145 nm. Fig. 7 reveals that the surface roughness is time-dependent for a sample exposed to the laboratory air for a period of three months. While the 4-sq.μm image area exhibits an rms roughness of 0.868 nm, the boxed region within this area shows an rms roughness of 0.826 nm, thereby indicating substantial roughening of the fiber surface with time.

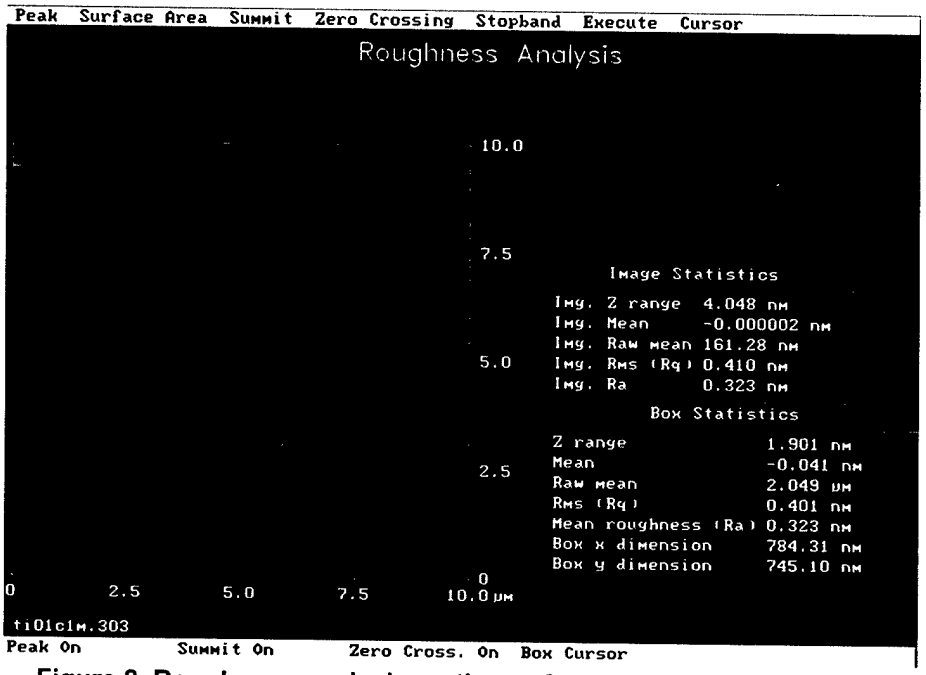


Figure 8. Roughness analysis on the surface of hand-drawn fiber - Alcohol wiped after three months in the laboratory air.

AFM micrograph of Fig. 8 shows the condition of the surface after wiping with an alcohol-soaked piece of optical quality cloth. This cleaning step reduces overall rms roughness to 0.410 nm and local rms roughness as indicated by the boxed region to 0.401 nm. Thus, these results quantitatively confirm the importance of effective cleaning on silica fiber surfaces. However, the cleaning step does not reduce the rms roughness to that of the freshly hand-drawn fiber, thereby raising the question of intrinsic roughening of the silica surface with time. A second alcohol wipe further changes the rms roughness, but it still leaves a surface with features that may have a height of 0.306 μm on a background of 0.150 μm rms roughness as shown in the micrograph of Fig. 9.

At this stage, we attempted to probe the mechanical properties of the surface to compare it with the known properties of the silica glass surface. Fig.10 shows a 3-D view of the silica fiber surface of Fig. 8; it further shows the three indentations made by incrementally changing the indentation force on the diamond tip. From an applied indentation load of 3.5 μN, and the measured area by the section analysis of indentations, we calculated a sample hardness value of 6.4 GPa. This value is in excellent agreement with silica hardness determined by bulk methods. From these results, we conclude that the surface material in the micrographs of hand drawn fiber remains to be silica glass through a series of laboratory exposures followed by alcohol wipes.

Although mechanical stripping has been widely used for cable installation in service provider networks, chemical stripping has found widespread use in device manufacturing. Therefore, we have included acid stripping in our investigations on the strippability of optical fibers. In Fig. 11, we show a 2-D view of a dual-coated fiber surface after a 30-second exposure to fuming sulfuric acid at 200°C followed by dry wiping twice. On the 100-square micrometer area shown in the micrograph, the height scale bar on the right indicates lumps of coating material in excess of 400 nm in height. Fig. 12 shows a one-square micrometer area with height image on the right and phase image on the left, which confirms that the material in the lumps is distinct from the material of the silica glass surface. A 3-D view of this surface in Fig. 13 reveals a broad distribution of residual coating material on the glass surface after dry wiping. We had shown earlier that the effectiveness of acid stripping depends on the temperature and cleanliness of the acid bath as well as the exposure time. In Fig. 14, we show a one-square micrometer area of the sulfuric acid-stripped dual-coated fiber at 200°C after one-minute exposure followed by reagent-grade acetone rinse. Remarkably, we determined a global rms roughness of 0.275 nm and a local mean roughness of 0.192 nm as indicated in the boxed section of the fiber surface. Although the global rms roughness of 0.275 nm is still nearly twice as large as the rms roughness of hand-drawn never-coated fiber surface, it represents the smoothest and cleanest surface of a stripped fiber examined to date in our investigations.

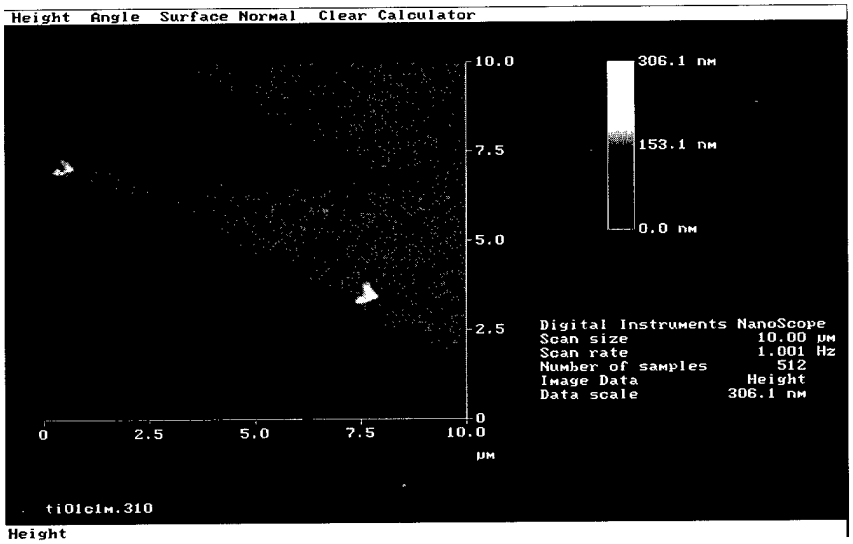


Figure 9. Roughness analysis on the surface of hand-drawn fiber - Two weeks in the laboratory air after second alcohol wipe.

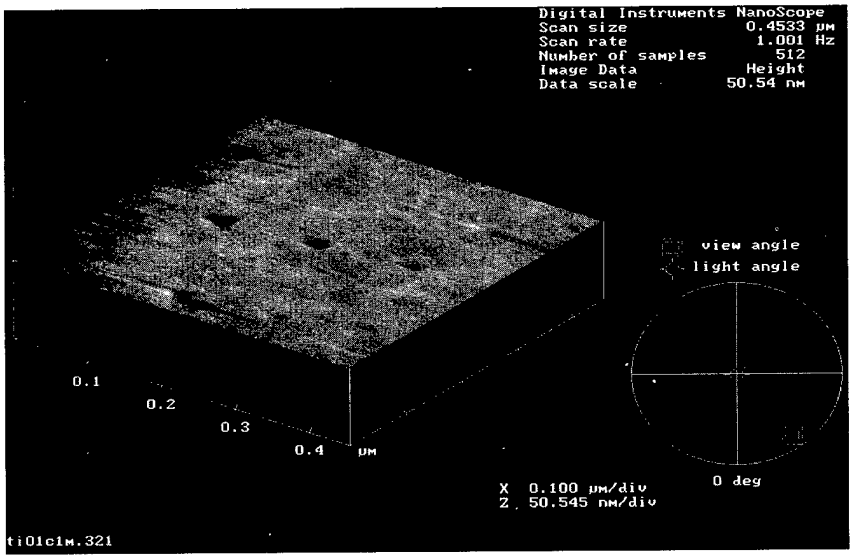


Figure 10. 3-D View of indented surface of hand-drawn fiber - Indented (3.5 µN) after one day in the laboratory air after second alcohol wipe

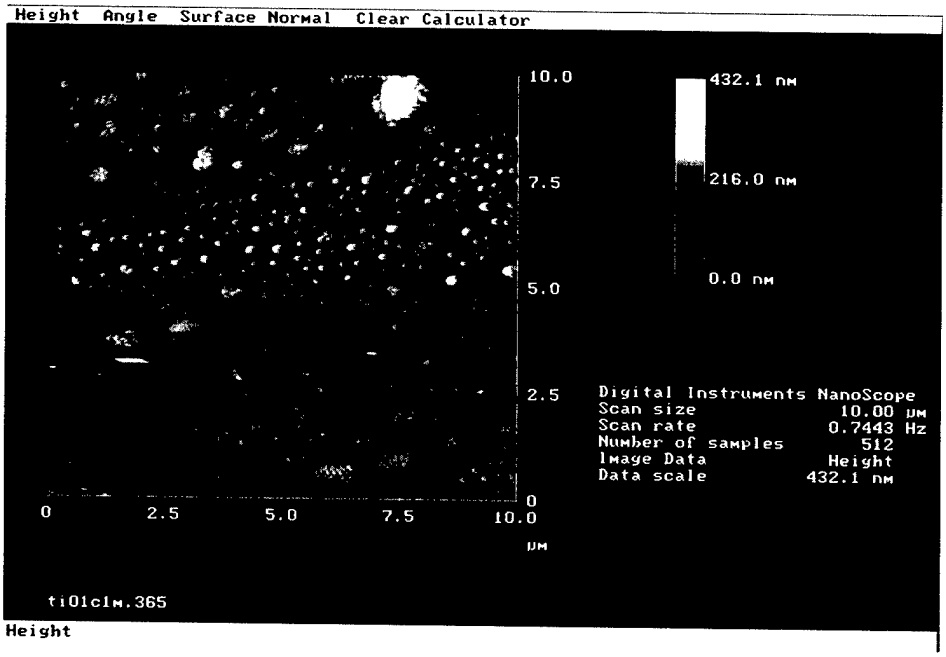


Figure 11. 2-D View of the surface of a dual-coated fiber - fuming sulfuric acid-stripped @ 200°C 30 sec., dry-wiped twice.

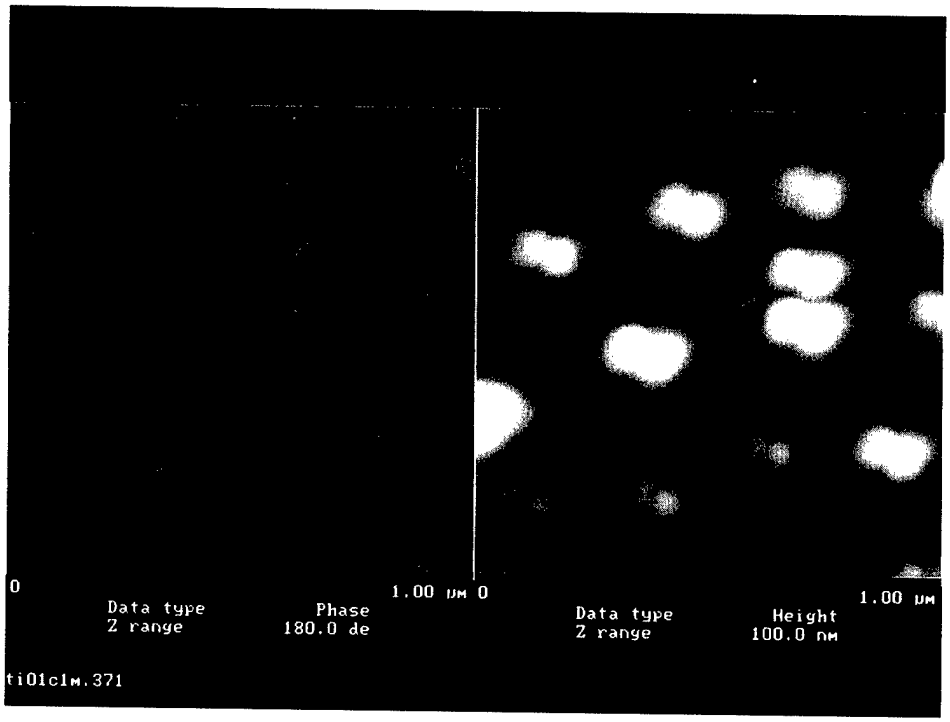


Figure 12. Height (right) and phase (left) images of the surface of dual-coated fiber after fuming sulfuric acid-stripped @ 200°C, 30 sec., dry-wiped twice.

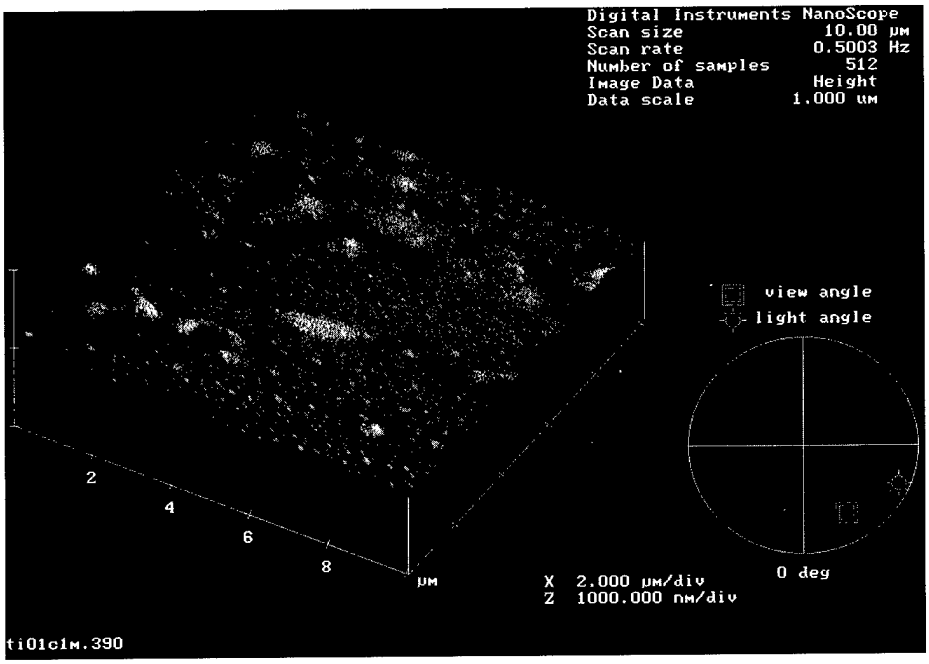


Figure 13. 3-D View of the surface of a standard fiber after acid stripped @ 200°C, 1 minute, dry-wiped twice.

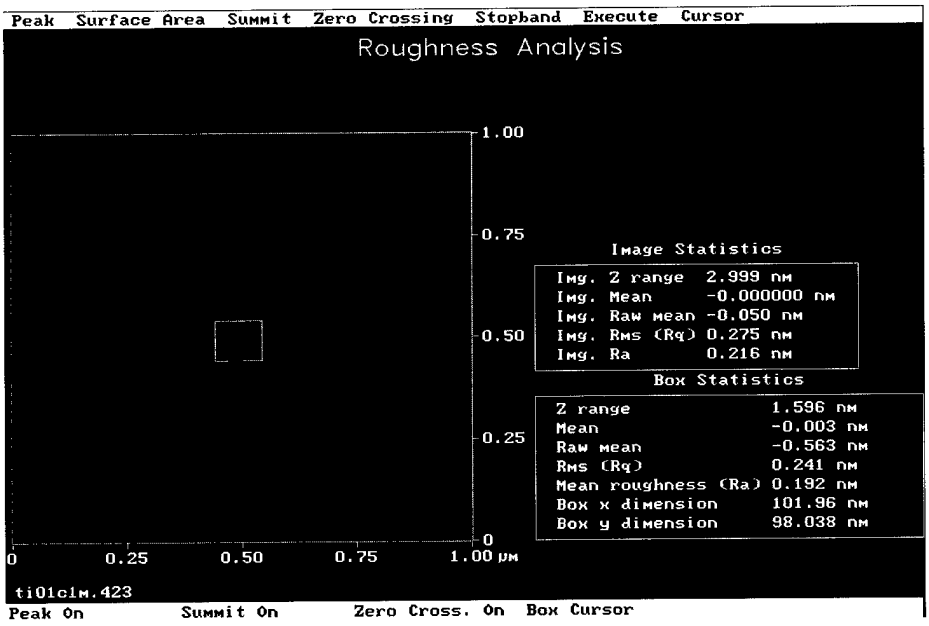


Figure 14. Roughness analysis on the surface of a standard fiber after acid stripped @ 200°C, 1 minute, acetone rinsed.

Finally, we have also examined the surfaces of two high-n value fibers (Fiber A and Fiber B from two different manufacturers) after 1-minute exposure to fuming sulfuric acid at 200°C followed by acetone rinse. Our AFM analyses of these surfaces have revealed a mean roughness of 1.25 nm for Fiber A and 0.19 nm for Fiber B. This nearly six-fold difference in surface cleanliness is under investigation the results of which will be the subject of a future report.

4. Summary

We have been investigating the effectiveness of mechanical and chemical stripping methods for optical fibers. In earlier analyses we found that a nominally clean surface of a stripped fiber still retains a thin coating film. Furthermore, we also uncovered counterproductive aspects of wiping aggressively with an alcohol-soaked optical quality cloth. For a quantitative assessment of fiber surface cleanliness after mechanical stripping, we examined the surface of hand-drawn silica fiber before and after extended exposure to laboratory air followed by dry/solvent cleaning processes. While freshly hand-drawn fiber exhibited the smoothest surface, acid-stripped fiber that was rinsed with reagent grade acetone gave a fiber surface that ranked second in surface roughness to the hand-drawn fiber, thereby quantitatively confirming the effectiveness of solvent cleaning of stripped fiber surfaces.

5. References

[1] H.H. Yuce, P.L. Key and T. Wei, 39th **IWCS Proceedings**, 400 (1990).

[2] H.C.Chandan, J.R. Petisce, J.W Shea, C.R. Taylor, L.L Blyler, D. Inniss and L. Shepherd, **IWCS Proc.**, 239 (1992).

[3] E.H. Urruti, J.W. Botelho and M.A. Botelho, **NFOEC Proc.**, 225 (1995).

[4] O.S. Gebizlioglu, J.D. Mann, C.R. Kurkjian, **NFOEC Proc.**, 42 (1999).

[5] O.S. Gebizlioglu, I.M. Plitz, **NFOEC Proc.**, 113 (1996).

[6] A. Dwivedi and J.L Smith, 45th **IWCS Proc.**, 381 (1996).

[7] J.D. Mann, M.R. Ozgur, O.S. Gebizlioglu, C. R. Kurkjian, **NFOEC Proc., Vol. 1**, 271 (1998).

[8] J.D. Mann, O.S. Gebizlioglu, C.R. Kurkjian, **IWCS Proc.**, 47, 589 (1998).

[9] O.S. Gebizlioğlu, M.R. Özgür, C. R. Kurkjian, **NFOEC Proc., Vol. 1**, 488 (2000).

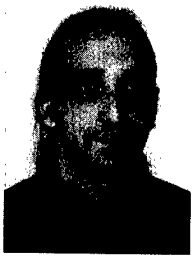
[10] M.R. Özgür, O.S. Gebizlioglu, C.R. Kurkjian, **NFOEC Proc., Vol. 1**, 129 (2001).

[11] Digital Instruments Support Note # 225, Rev.F, Digital Instruments, Inc. Santa Barbara, CA, (1998).

[12] T.M. Michalski and J.E. Houston, **Acta Mater.**, 46, 391 (1998).

[13] K. Hirao and M. Tomozawa, **J. Amer. Ceram. Soc.**, 70, 497 (1987).

BIOGRAPHY



Mustafa R. Özgür is an Associate Consultant in Fiber, Transport & Synchronization Technologies Group at Telcordia Technologies. He holds a B.Sc degree in Mechanical Engineering. Since he joined Telcordia Technologies in 1998, he has been involved in research and testing on fiber optic components.



Osman S. Gebizlioglu is a Senior Consultant in the Fiber, Transport & Synchronization Technologies Group at Telcordia Technologies. He holds B.Sc and M.Sc degrees in Chemical Engineering from the Middle East Technical University, Ankara, Turkey, and Ph.D from the Polymer Materials Program of the Chemical Engineering Department at Princeton University, Princeton, New Jersey. After a Monsanto Postdoctoral Fellowship appointment in Mechanical Engineering at M.I.T, Cambridge, Massachusetts, he joined Telcordia Technologies in 1987. He has been involved in the investigations of performance / reliability issues in optical fibers, fiber optic cables, components and devices. He chairs the TIA working group on adhesives reliability in interconnecting devices and holds four US patents.



Charles R. Kurkjian received his B.Sc. from Rutgers in 1951 and his Sc.D from M.I.T. in 1955. In 1994 he retired as a Distinguished Member of Technical Staff from AT&T Bell Laboratories after 35 years of service and joined Telcordia Technologies as a Member of Technical Staff in Optical Fiber & Components Group. Since 1999, he has been a consultant to Telcordia Technologies.

Characterization of Coating Systems on Optical Glass Fibers as a Whole by Solid State NMR

Victor M. Litvinov, Aylvin A. Dias
DSM Research B.V.
P.O.Box 18, 6160 MD Geleen, The Netherlands
+31-46-4761256 · Victor.Litvinov@DSM.com

Abstract

The functional properties of optical glass fibers are largely determined by molecular structure and network density of UV cured primary (rubbery) coating and secondary (glassy) one. This study explores possibilities of solid state **n**uclear **m**agnetic **r**esonance (NMR) for characterization of primary and secondary coatings on optical fibers as a whole. The advantage of NMR methods is that they do not require extensive sample preparation, direct mechanical or electric contact with a sample and they provide a selective way to study primary and secondary coating systems on optical fibers. It is shown that using this method, mechanical properties of the coatings may be derived without detaching coatings from the fiber. Two different NMR methods are used in this study: *volume average ^1H NMR T_2 relaxation experiments* and *NMR microscopy or imaging. The first method* allows determining the network structure of the primary coating on optical fibers as a whole and to relate it to mechanical properties of the coating. *The second method* determines heterogeneity in the cross-link density in the radial direction. It is shown that some fibers reveal large network heterogeneity that is apparently caused by non-uniform light intensity distribution in the radial direction in draw tower(s).

Keywords

Optical glass fibers; primary and secondary coatings; network structure and its heterogeneity; modulus; NMR microscopy; NMR relaxation.

1. Introduction

Ultraviolet cured coatings on optical fibers fulfill two important functions: (1) to provide mechanical and chemical protection of the silica core and (2) to ensure minimal loss of optical signal. The importance of the mechanical properties of the coatings cannot be understated and has such, there have been extensive efforts to fully characterize these coatings. However, most practical methods of characterizing optical fiber coatings rely on analysis of coatings as sheets cured on a glass substrate.[1,2]

These tests have been used to study the hydrolytic stability of the UV cured coatings,[3] improve the toughness of optical fiber coatings[4] and to examine the effect of branching in the polyether urethane acrylate oligomers on properties for optical fiber coatings.[5] Acknowledging the increasing speed of coating and curing of optical fibers a number of time resolved techniques have also been developed e.g. acrylate conversion can be monitored with real-time Fourier transform infrared (FTIR) spectroscopy with capability for heating and nitrogen inerting was reported by Dias and coworkers[6] while Khan and coworkers developed a dynamic rheological tool to directly measure the development of mechanical properties during UV curing.[7]

As optical fiber coatings lines move to faster speeds there is a growing difficulty with simulating the draw tower conditions in laboratories and this has driven the search for better ways to characterize optical fiber coatings, *in situ,* as it were.

Huy and co-workers acknowledged these limitations and studied optical fiber coatings in situ by using the relationship between degree of polymerization and thermal decomposition behavior. This involved placing optical fibers in a DSC pan and analyzing by thermogravimetry differential thermal analysis.[8]

Yuce and cowokers measured fiber strength and fatigue behavior by performing tensile tests and two point bend tests on coated optical fibers.[9,10]

Chandan and coworkers used fiber strip force measurements and using a modified Instron apparatus as part of a study on the adhesion of coatings on glass optical fiber. Sample preparation involved using adhesive to bind one end onto a flat substrate and after severing the organic coatings pulling at the other end of the optical fiber.[11]

Fiber pull out tests are also used to gain information on the modulus on the primary coatings and have been put to good use to study ageing of optical fiber coatings *in situ.*[12]

Oishi and coworkers developed a 'push in modulus' test, which involved an indentor used to displace the glass core axially while holding the secondary high modulus coating in place. The applied stress and displacement gives data from which the shear modulus of the primary coating is derived.[13]

Chemical analysis of coatings on optical fiber has been performed using attenuated total reflectance FTIR spectroscopy. The extent of acrylate double bond conversion measured at 810 cm^{-1} was used as a measure of the degree of cure.[14] Another measure of cure is to perform extraction studies followed by High Pressure/ Performance Liquid Chromatography on coated optical fibers.[15]

Extraction or gel fraction tests suffer from the problem that it is difficult to obtain cure information about the individual primary or secondary coating in a dually coated optical fiber.[16,17]

Ukachi and co-workers examined the effect of fiber drawing rate on the surface temperature of the coated optical fibers by fitting thermocouple heat sensor just after the primary and secondary coating cups. Experiments revealed that the secondary coating was applied and cured at higher temperatures than the primary coatings and that this temperature was affected by fiber drawing speed and distance between the primary and secondary coating cups.[18]

These techniques testify that there remains a need for a method to determine the mechanical properties of optical fibers in situ with minimal handling. Recently we described the use of solid state nuclear magnetic resonance (NMR) relaxation experiments to analyze UV cured coatings with various amounts of monofunctional monomer. These results indicated good correlation with mechanical tests that were also performed.[19]

It is known that the functional properties of optical glass fibers are largely determined by molecular structure and network density of UV cured primary (rubbery) coating and secondary (glassy) one. Aim of this study is to explore possibilities of solid state NMR for characterization of the coatings on optical fibers as a whole. The advantage of NMR methods is that they do not require extensive sample preparation, direct mechanical or electric contact with a sample and they provide a selective way to study primary and secondary coating systems on optical fibers. Using solid state NMR, mechanical properties of the coatings may be derived without detaching coatings from the fober. Two different NMR methods are used in this study: *volume average ^1H NMR T_2 relaxation experiments* and *NMR microscopy or imaging*.[20-23]

2. NMR Relaxation and NMR Microscopy

The principle of magnetic resonance is based on the magnetic properties of the atomic nuclei. The atomic nuclei (e.g. protons) behave like small bar magnets, and when a sample is placed in a permanent magnetic field, they try to align themselves parallel to the field causing a "bulk magnetization" in the sample. Applying a radio frequency field, the orientation of atomic nuclei is changed and an NMR signal is detected as a function of time. The method does not require direct mechanical or electric contact with a sample. The time/frequency evaluation of the NMR signal contains information about chemical structure, molecular mobility and phase composition. *High-resolution NMR spectroscopy* is used for characterization of chemical structure.[23] *Low-resolution NMR relaxation methods* are used for analysis of phase/ components composition, molecular mobility and network structure.[20,21] Both methods require homogeneous magnetic field and provide *volume average characteristics* of materials.
In order to obtain *spatially resolved information*, *NMR-imaging* (*NMR microscopy*) is used.[22] The technique is widely used for medical diagnostic and in material research. An NMR signal from different positions is detected by applying one or more magnetic field gradients so that the strength of the external magnetic field is varied along certain axes in a controlled way. A typical resolution of NMR microscopy for rubbery materials is about 0.05 mm. NMR microscopy allows one to obtain spatially resolved data on the network density in rubbery materials.[24-26]

Proton NMR T_2 relaxation is established method for analysis of the cross-link density in polymers. Quantitative determination of the crosslink density is usually performed using proton NMR transverse (T_2) relaxation experiments.[19,27,28] The distinguishing feature of T_2 relaxation for viscoelastic networks is the high temperature plateau that is observed at temperatures well above T_g (see Fig. 1). The temperature independence of T_2 is attributed to constraints, which limit the number of possible conformations of a network chain with respect to those of a free chain. A value of T_2 at the plateau, T_2^{pl}, is determined by the asymmetry of random rotations of monomer units and does not depend on the mechanism and frequency of motions of network chains. The theory of the transverse relaxation in elastomeric networks relates T_2^{pl} to the number of statistical segments, Z, between chemical and physical network junctions.[29,30]

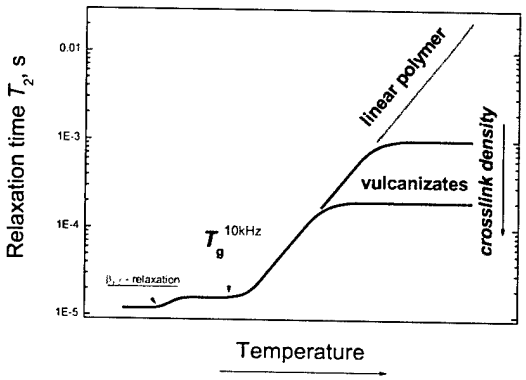


Figure 1. Schematic drawing of T_2 relaxation time against temperature for amorphous polymers

3. NMR T_2 Relaxation in Relation to Mechanical Modulus

A comparison of the cross-link density, as measured by T_2 relaxation experiments, with those obtained by traditional methods for the same samples has proved that the NMR method provides quantitative data on the cross-link density and T_2 is related to mechanical modulus.[27] In order to establish relationship between T_2 relaxation and mechanical properties a series of model UV-cured acrylates was studied by the NMR method and

dynamic mechanical analysis.[19] Mixtures of a *di-* and *mono-*functional acrylate were used as a model system. The *di-* and *mono-*functional acrylates were polyethylene glycol *di-*acrylate (PEGDA) with molar mass M_n of 700 g/mol and 2-ethylhexyl acrylate (EHA), respectively. The mean cross-link density and the fraction of network defects, such as dangling chains, was varied in these networks by changing the content of *mono-*functional acrylate, as can be seen from Fig. 2. The relaxation rate, $1/T_2$, reveals linear dependence against the content of *mono-*functional monomer. (see Fig. 3). Since the relaxation rate at temperatures well above T_g is proportional to the network density, it can be concluded that the cross-link density in cured acrylates is proportional to the content of *mono-*functional monomer.[19]

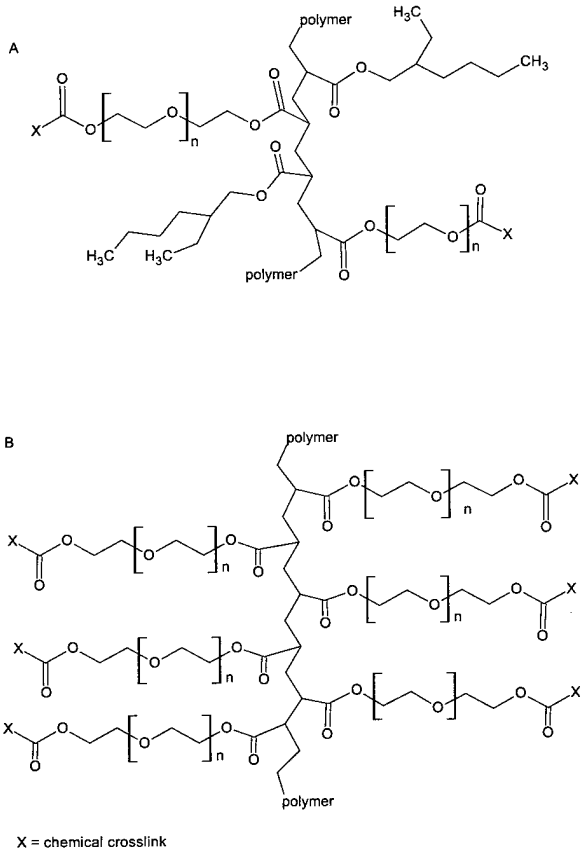


Figure 2. Suggested network structure for compounds PEGDA/EHA (80/20 w/w%) - (A) and PEGDA - (B).[19]

Temperature dependence of modulus (E') reveals a rubber-elastic plateau above –20 °C.[19] A fairly good correlation of the T_2 relaxation rate with the storage modulus (see Fig. 4) proofs that ***the NMR characteristic is directly related to the network structure and mechanical properties.***

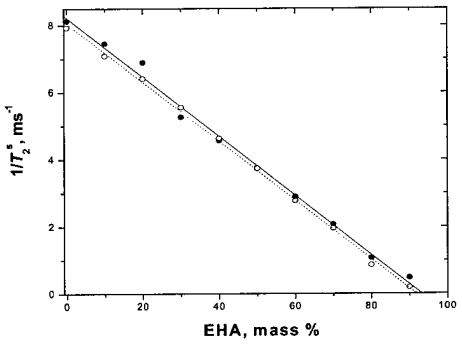


Figure 3. The T_2 relaxation rate at 50°C against the content of EHA for cured acrylates as a whole (closed circles) and swollen samples (open circles).[19]

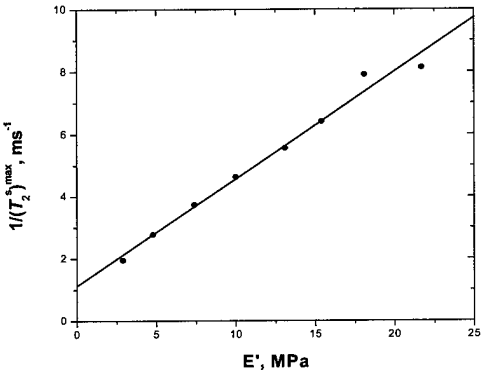


Figure 4. The relaxation rate $1 / T_2^s$ against the storage modulus at 0°C.[19]

4. Experimental Section

Volume average, proton NMR T_2 relaxation experiments were performed on a *Bruker Minispec NMS-120* spectrometer. This spectrometer operates at a proton resonance frequency of 20 MHz. The solid-echo and the Hahn-echo experiments were used to measure the T_2 relaxation decay. The time constants (T_2 relaxation time) that are characteristic of different slopes in the magnetization decay curve were obtained by performing a least-squares fit of the data using a fitting program was written at DSM Research.

NMR images were recorded on a Varian Inova 400 MHz spectrometer, equipped with a shielded imaging probe with a 10 mm insert. A slice thickness was 2 mm. All images have an ***in plane resolution of 0.02x0.02 mm.***

The storage modulus was measured with a Rheometrics solid analyser II at a frequency of 1 Hz.

5. Results and Discussions

5.1 Characterization of Coating Fibers as a Whole by NMR Relaxation

Proton T_2 relaxation experiments are used to obtain volume average data on the structure of primary and secondary coatings on optical fibers as a whole. The T_2 relaxation decay for optical fibers consists of two distinct components with short (T_2^s) and long (T_2^l) decay time (see Fig. 5). *These components originate from rigid secondary and rubbery primary coatings*, respectively. The relative fraction of these components, $\%T_2^s$ and $\%T_2^l$, is proportional to the content of hydrogen in secondary and primary coatings, respectively. For some coatings, a third component with significantly longer decay time is observed. As example, the data for the primary coating that was cured on a glass plate are shown on Fig. 6. Although the relative intensity of this component is very low (below a few per cent) it can be measured with a high accuracy. This component originates from highly mobile small molecules that are low molar mass additives in the formulations and possibly some residual uncured acrylates.

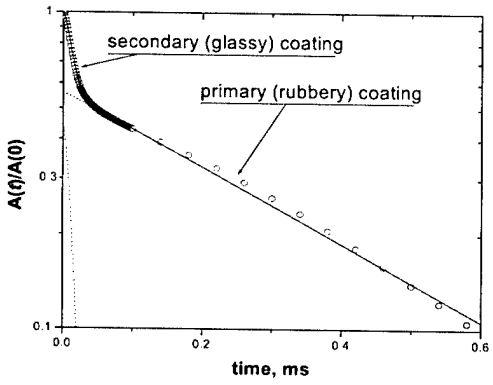


Figure 5. The T_2 relaxation decay for coatings on an optical fiber.[1]

Commercially cured materials often contain a significant fraction of network defects that cause a decrease in the mechanical strength. The following types of network defects could be present: chains that are not chemically attached to the network, dangling chains and chain loops. The T_2 experiment with the swollen samples enhances the differences in mobility of network chains and network defects due to chain disentanglements,[19,27] which allows obtaining more detailed information on the network structure and its heterogeneity (see Fig. 7). The characteristic decay time for optical fibers, T_2^s and T_2^l, is related to rigidity of the secondary coating and the network density in the primary coating, respectively. *The same formulation, which was cured on a glass plate and on glass fiber, reveals significant difference in the network structure, which is apparently caused, by a difference in curing conditions, namely UV-light intensity and the exposure time.* ***The results above show that the NMR method allows determining differences in the network structure of the primary coating on optical fibers as a whole and to relate these differences to their mechanical properties.*** The T_2 experiment with swollen fibers reveals significant volume average heterogeneity of the network structure both for primary and secondary coatings. Molecular (nanometer scale) and macroscopic (micrometers scale) heterogeneity can be present in coating on optical fibers. NMR microscopy data are used below to study macroscopic heterogeneity of the primary coating on optical fibers.

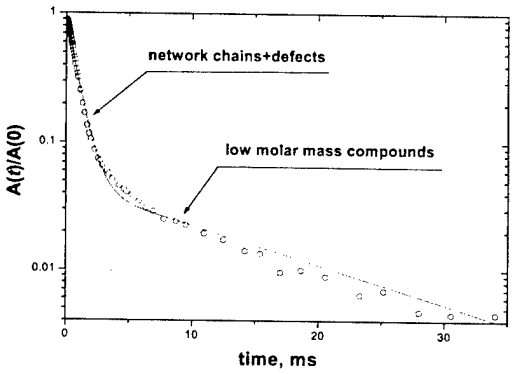


Figure 6. The T_2 relaxation decay for the primary coating cured on a glass plate. The relative fraction of low molar mass molecules is about 4.5 % hydrogen.[1]

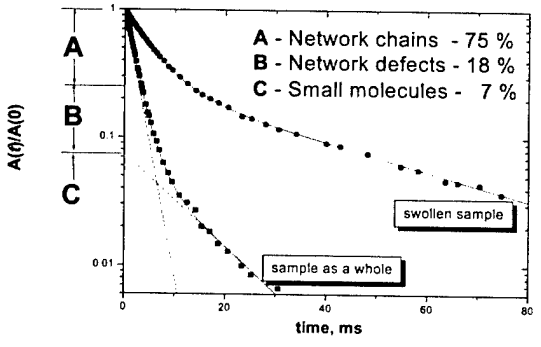


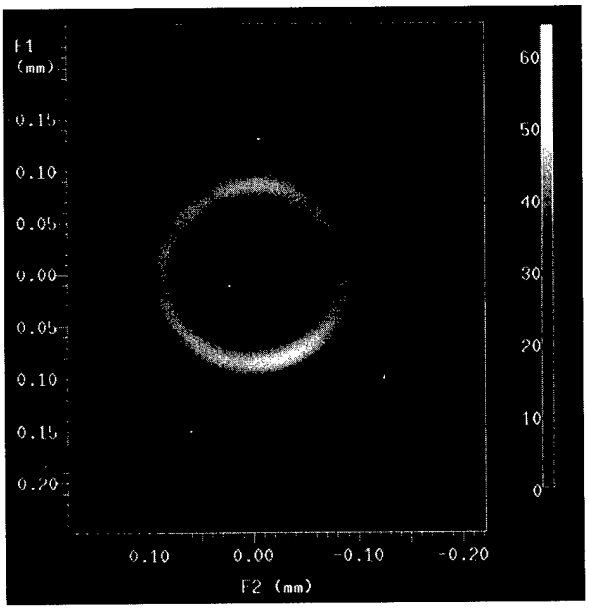
Figure 7. The T_2 relaxation decay for the primary coating as a whole and the swollen one. The coating was cured on a glass plate.[1]

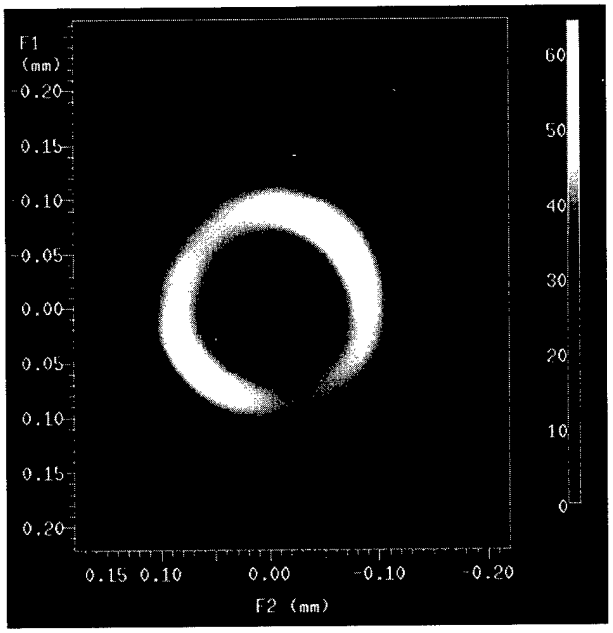
[1] The normalized amplitude of the T_2 relaxation against time (T_2 decay). Points show experimental data points. The sold line represents the result of a least squares adjustment of the decay with a linear combination of two exponential functions. Dotted lines show separate components.

5.2 Heterogeneity of the Primary coating on Optical Fibers as Studied by NMR Microscopy

According to the experiments above, the largest sensitivity to spatial heterogeneity of network structure is achieved for swollen samples. ***An experimental procedure that was used in the present study detects only the primary coating*** because of rather low swelling degree of the secondary coating. NMR images provide (semi)quantitative data on the difference in local swelling degree of the primary coating in the radial direction. Due to low swelling of the secondary coating, it can impose constraints on swelling of the primary coating. Therefore, *the local swelling of the primary coating can be affected by micrometer scale heterogeneity both in the primary and the secondary coatings.*

NMR microscopy pictures for three optical fibbers with different heterogeneity are shown in Fig. 8. The diameter of the glass core is 130 ± 20 μm; the outer diameter of the primary coating for all swollen samples is 220 ± 20 μm. The images are recorded at conditions that enhance the signal of the solvent. Thus, the signal intensity is largely determined by the local concentration of the solvent. *The darker area (low signal intensity), the smaller solvent content is.* In general, differences in the local swelling can be caused by the difference in the cross-link density. *The images reveal* ***large heterogeneity in the cross-link density in the radial direction*** *for two of three samples shown here as well as* ***a significant difference in the overall croslink density*** *between optical fibers.* It is suggested that the network heterogeneity is caused by non-uniform light intensity distribution in the radial direction in draw tower(s).





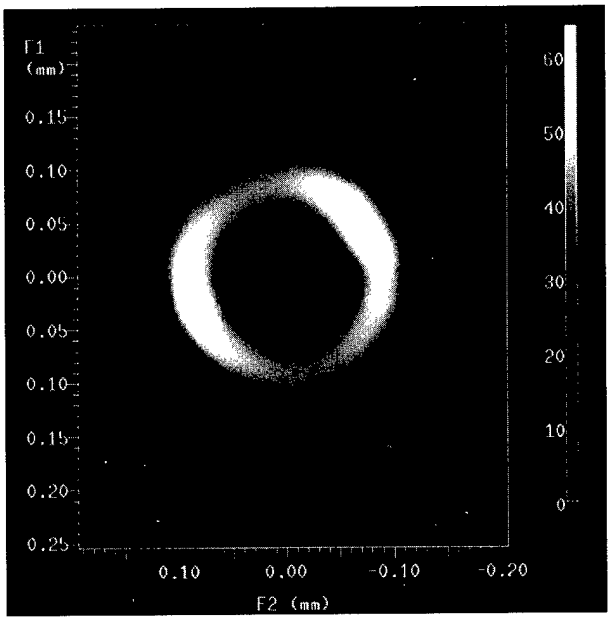


Figure 8. NMR images of the primary coating on optical fibers. The dimensions (in mm) are shown on x- and y - axes. The increase in the darkness corresponds to smaller amount of the solvent absorbed by the coating. The intensity scale is identical for all three figures.

6. Conclusions

These results above demonstrate that volume average NMR T_2 relaxation experiments and NMR microscopy are valuable tools for characterization of coatings on optical fibbers as a whole in relation to the curing conditions. The rubbery primary coating and glassy secondary one can be analyzed selectively by these methods. The NMR methods allow determining differences in the network structure of the primary coating on optical fibers as a whole and to relate these differences to their mechanical properties. It is shown that the same formulation, which was cured on a glass plate and on glass fiber, reveals significant difference in the network structure, which is apparently caused, by a difference in curing conditions, namely UV-light intensity and the exposure time. The NMR experiments reveal significant heterogeneity of the network structure both for primary and secondary coatings, which is caused by molecular (nanometer scale) and macroscopic (micrometers scale) heterogeneity. NMR microscopy reveals large heterogeneity in the cross-link density in the radial direction for some of samples studied. It can be suggested that this heterogeneity is caused by non-uniform light intensity distribution in the radial direction in draw tower(s).

7. Acknowledgments

It is a pleasure to acknowledge the assistance of P.Adriaensens in the acquisition of NMR microscopy pictures.

8. References

[1] J. Mahone, in "*Radiation Curing of Polymers II*," D.R. Randell, ed., RSC publication ISBN 0 85186-377-9, Cambridge, Royal Society of Chemistry, p. 84 (1991).

[2] Z. Komiya, Y. Takasugi, T. Ukachi and G. Pasternak, *Proc. 42nd IWCS*, p.531 (1993).

[3] T.E. Bishop and D.M. Szum, *Proc. Radtec, Europe*, Edinburgh, p.123 (1991).

[4] M. Mori, Z. Komiya and T. Ukachi, *Proc. Radtech 98*, USA, Chicago, p.328 (1998).

[5] H Hintze-Brüning and S. Schunck, *Proc. Radtech, Europe*, Edinburgh, p.705 (1991).

[6] A. A. Dias, H. H. Hartwig and J.F.G.A. Jansen, *Proc. Radtech 98*, USA, Chicago, p.356 (1998).

[7] S.A. Khan, R.A. Frantz and I.M. Plitz, *Proc. Radtech 92*, Vol. II, USA, Boston, p.770 (1992).

[8] S. Huy, M. Chiba, T. Hoshino, O. Shimizu and M. Hani, *Proc. 39th IWCS*, p.691 (1990).

[9] H.H. Yuce, I.M.Plitz, R.A.Front, M.Andrejco, *Proc. 39th IWCS*, p. 715 (1990).

[10] R. A. Frantz, I.M. Plitz, H.H. Yuce and O.S. Gebizlioglu, *Proc. 41st IWCS*, p.279 (1992).

[11] H.C. Chandan, J.R. Petisce, J.W. Shea and C.R.Taylor, *Proc. 41st IWCS*, p.239 (1992).

[12] P.L. Tabaddor, C.J. Aloisio, H.C. Chandan, R.C. Moore, N.W. Sollenberger, C.R. Taylor and J.M. Turnispeed, *Proc. 45th IWCS*, p.303 (1996).

[13] K. Oishi, N. Akasaka, T. Hattori, T. Kakuta and Y. Matsuda, *Proc. 44th IWCS*, p.552 (1995).

[14] A. Mizutani, D. Saitho, S. Endo and N. Yoshioka, *Proc. 41st IWCS*, p.249 (1992).

[15] J.L. Jostan, R.G. Summer and M. Hoffart, *Proc. 41st IWCS*, p.267 (1992).

[16] R.A. Frantz et.al., *Proc. 40th IWCS*, p.134 (1991).

[17] E. Cressan, D. Crespel, O. Fournier, A. Morgand, A. Peraudeau and Y. Ruello, *Proc. 42nd IWCS*, p.843 (1993).

[18] T. Ukachi, A. Aoyama, Y. Naito and K. Igarashi, *Proc. 41st IWCS*, p.261 (1992).

[19] V.M.Litvinov, A.A.Dias, *Macromolecules*, 34 (12), 4051-4060 (2001).

[20] V.J.McBrierty and K.J.Packer, *"NuclearMagnetic Resonance in Solid Polymers"*, Cambridge University Press, Cambridge (1993).

[21] R.Kimmich, *"NMR - Tomography, Diffusometry, Relaxometry"*, Springer-Verlag, Berlin (1997).

[22] P.T.Callaghan, *"Principles of Nuclear Magnetic Resonance Microscopy"*, Oxford Science Publications, Oxford (1991).

[23] R.A.Komoroski, ed., *"High Resolution NMR Spectroscopy of Synthetic Polymers in Bulk"*, VCH Publishers, Florida (1986).

[24] P.Blümler and B.Blümich, in "*NMR. Basic Principles and Progress*" P.Diehl, E.Fluck, H.Günther, R.Kosfeld and J.Seelig, eds. , Springer Verlag, Berlin, p.209 (1994).

[25] W.Kuhn, P.Barth, P.Denner and R.Müller, *Solis State Nuclear Magn. Res.* 6, p.295 (1996).

[26] P.Adriaensens, A.Pollaris, D.Vanderzande, J.Gelan, J.L.White, A.J.Dias and M.Kelchtermans, *Macromolecules*, 32, p.4692 (1999).

[27] V.M.Litvinov, W.Barendswaard and M. van Duin, *Rubber Chem. Technol.* 71, p.105 (1998).

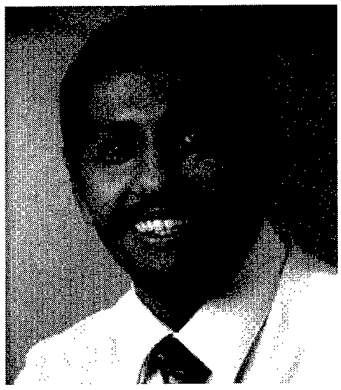
[28] V.M.Litvinov, P.A.M.Steeman, *Macromolecules*, 32, p.8476 (1999).

[29] Yu.Ya.Gotlib, M. I.Lifshits, V.A.Shevelev, I. A.Lishanskii and I. V.Balanina, *Polym. Sci. USSR*, 18, p.2630 (1976).

[30] C. G..Fry and A..C.Lind, *Macromolecules*, 21, p.1292(1988).



Victor M. Litvinov is a senior expert at Department of *Material Properties* at DSM Research in Geleen, The Netherlands. He is responsible for characterization of chemical and physical structures in organic and inorganic materials by solid state NMR techniques, applications of the method for quality control and establishing structure-property relationships. After graduating in 1973 Moscow Academy for Fine Chemical Technology, he worked in Scientific Council on High Performance Polymer Materials at the Presidium Academy of Sciences in Moscow, Russia. In 1978, he received Ph.D in macromolecular chemistry. Since 1985 till 1992, he worked in Institute of Synthetic Polymer Material of Academy of Sciences, Russia. In 1988, 1989-1991, 1992 he received fellowships from A. von Humboldt and German Science Foundations and spent about two years at Max-Planck-Institute for Polymer Research in Mainz, Germany. In 1992, he joined DSM Research in Geleen, The Netherlands.



Aylvin A. Dias is an expert in UV radiation curing of polymers at the department - *Resins, Polycondensates and Coating Technology* at DSM Research, Geleen, The Netherlands. He is responsible for research into new radiation curable materials and applications with emphasis on optical fibre and 3-D stereolithography. His research interests are structure–property relationships and development of time resolved techniques to study photocuring reactions. He obtained his B.Sc in Biological Chemistry at the University of Kent at Canterbury. This was followed by a MSc in synthesis of organic superconductors and PhD where he investigated polymeric and polymerisable photoinitiators. In 1994 after his PhD he joined Coates Lorilleux Research into UV curable inks and coatings. In 1996 he joined DSM Research in the Netherlands. A. Dias is a member of the American Chemical Society and Royal Society of Chemistry.

High-Speed Buffering Process of Compact Loose Tubes for Stranded Cables

Mikko I. Lahti*, Markku T. Heino**, Jussi T. Ravela**, and Paul Lundström***

*Nextrom Oy
P.O Box 44,
Vantaa FIN-01511, FINLAND
+358-9-50251
mikko.lahti@nextrom.com

**NK Cables Ltd.
Draka Comteq
PO Box 419, FIN-00101 Helsinki
FINLAND

***NK Cables Ltd
Draka Comteq
PO Box 269, FIN-90651Oulu
FINLAND

Abstract

Fast growth and continuously expanding needs of information technology set demands of high productivity for telecommunication cable industry. In particular for fiber optic cable production, this means higher line speeds and shorter down times. Since the basic element in fiber optic cables is buffered loose tube, the traditional buffering process is now facing new challenges such as high-speed production and advanced high fiber density cable constructions.

The need for higher fiber density in stranded loose tube cables means that the tube diameters have to be decreased. High line speeds with small tube diameter require new material combinations and optimized process parameters to achieve stable performance in a wide temperature range.

In this study, several PBT and gel types and the main process parameters were investigated for high-speed buffering of compact loose tubes with the aim of a narrow Excess Fiber Length (EFL) range. The optimized loose tubes were stranded to a test cable, which confirmed the good mechanical properties and temperature stability for this compact cable.

Keywords

loose tubes; buffering; high speed; excess fiber length; EFL; stranded; fiber optic cable

1. Introduction

At present the optical cable network is getting closer and closer to the subscribers, both at home and in offices. This means a still growing pressure in building and creating the local and access networks of optical fiber cables. When the environment for such networks is ever growing, varying in nature and complex, a lot of flexibility is required from the network itself and consequently from the cable designs adopted into it. Also, due to the explosive growth of telecommunication needs, e.g. video, internet, other data transfer and even still unknown tele services the fiber counts to be installed are in rapid rise.

One very flexible way to meet these complicated demands is to use duct and especially tube installations. Tubes of different sizes can be installed in advance where network connections are supposed to be needed later. When a need arise, optical waveguides in any form or design, i.e. blown fiber, central loose tube or stranded cable can be blown in. Later on, when the telecommunication environment changes, the fiber count can easily be upgraded by new blown-in cables or by replacing the old ones by new different fiber or cable types.

This paper describes a traditional stranded loose tube cable design intended e.g. for blown-in duct or tube installation. The construction is secure and reliable and adaptable to many applications. Its mechanical and thermal properties can be easily varied and controlled as well as fiber count enhanced if one is not concerned about size increase. Machinery to manufacture this kind of cables exist abundantly around the world. However, the drawbacks of this construction are the need for multiple sensitive operation steps, i.e. bufferings per all colour changes and stranding, and the increase of diameter and weight if fiber count is drastically increased. Further on, if tube count per cable is high, with modern high speed stranding machines capable to strand fast ten to twenty tubes at a time, buffering operation can become a bottleneck leading to heavy investments on extra tubing lines. To lessen these drawbacks a capability was studied to produce extremely minimized tube size (2.3/1.5 mm) with 12 fibers at very high buffering speed (300 m/min) and to strand a cable thereof with proper strain and contraction margins. The work includes an extensive study on materials (PBT and gel types) and optimization of main process parameters.

2. Buffering Process

2.1 Material Selection

Different PBT grades and gel types were studied for high speed buffering in order to achieve controlled EFL. The trials were carried out with a normal loose tube production line [1]. The summary of the results presented in Table 1 points out the importance of the correct material selection on the EFL control. Tooling and process conditions were set out according to the previous tests with similar materials. This preliminary work consisted actually of more than 9 trials. If the EFL value was high then tooling, process parameters and even line speed were changed. With certain material combinations it was almost

impossible to control the EFL of the compact tubes (inner diameter 1.5 mm, 12 fibers) even at low line speeds. All the trials shown in Table 1 would be successful with normal inner diameter sizes (1.8-2.0 mm).

Table 1. Effect of the material selection on the EFL (line speed 300 m/min).

Test	PBT	Gel	EFL (%)
1	A	1	High
2	A	2	High
3	A	3	Low
4	B	1	High
5	B	2	High
6	B	3	Low
7	C	1	Low
8	C	2	Low
9	C	3	Low

PBT C and gel 1 were selected for further studies. Despite the good EFL results of gel 3, gel 1 was chosen for further studies because it has better low temperature characteristics.

2.2 Optimization of Process Parameters

In this part of the study the main process parameters pay-off tension, line speed, cooling water (trough) temperature, gel hose temperature and position of the middle capstan (DWC) were investigated in terms of excess fiber length (EFL). EFL was measured from 5 m samples within 3 hours after each experiment. The aim was to find out, whether the same predictions are valid for the compact tubes as known for loose tubes of traditional size.

Table 2 sets out the different experiments that were carried out during this study. All the trials were made with the same tooling, which was designed to have high draw down ratio (DDR) and high draw ratio balance (DRB) needed with higher line speed. The poor performance of the tooling at line speeds below 200 m/min is clearly shown in Table 2. The set of tooling was not optimized for line speeds under 200 m/min, since it was beyond the scope of this work. Therefore the trials made at 150 m/min had higher EFL values than expected, mainly due to the improper gel feeding with that tooling at low speeds.

A non-linear model was developed based on these trials to describe the relationship of the process conditions and the EFL [2]. The behavior of the buffering process was studied with the model and the effects of the main process parameters on EFL, as predicted by this model, are shown in Figures 1-4 .

Table 2. Effect of the process parameters on the EFL; line tension 6N and take up tension 5N. (L<0.1%, 0.1%<I<0.2%, H>0.2%)

Test	Pay off tension (g)	Gel hose temp. (°C)	Line speed (m/min)	Trough temp. (°C)	Capstan location (m)	EFL (%)
1	60	60	275	42.5	9	I
2	130	60	275	42.5	9	I
3	200	60	275	42.5	9	I
4	60	60	150	42.5	9	I
5	130	60	150	42.5	9	L
6	130	60	233	42.5	9	L
7	130	60	316	42.5	9	I
8*	130	60	400	42.5	9	I
9	130	60	150	42.5	5	I
10	130	60	275	42.5	5	H
11	60	60	275	42.5	5	H
12	130	60	275	42.5	7	I
13	130	60	275	42.5	11	I
14	60	20	275	42.5	9	I
15	130	20	275	42.5	9	I
16	130	20	150	42.5	9	I
17	130	40	275	42.5	9	I
18	130	80	275	42.5	9	I
19	130	100	275	42.5	9	I
20	130	60	275	70	9	H
21	130	60	275	52	9	I
22	130	60	275	33	9	L
23	130	60	275	15	9	L
24	130	60	150	15	9	I
25	60	60	275	15	9	L
26	130	20	275	15	9	L
27	130	60	275	15	5	L
28	130	20	275	42.5	5	H

* increased line tension from 6N to 12N

Figure 1 presents the predictions of the EFL as a function of the cooling trough temperature. Cooling water temperature has a strong effect on EFL (the whole range of variation 0.3%), which increased exponentially with the temperature. The effect slowed

down when the cooling trough temperature reached 60°C. Surprisingly high EFL values were measured in these conditions even though there was not much room for the fibers inside the tube. The line tension (between the middle capstan and exit caterpillar) starts to stretch the tube when it leaves the capstan wheel at elevated temperatures and decreases the EFL.

The relationship of the line speed and EFL is almost linear as shown in Figure 2. Normally, the line speed has even stronger influence on EFL. Here the compact tubes cool down rapidly and therefore it is possible to achieve low EFL at high line speeds. EFL increased only 0.03% when the line speed was raised from 200 m/min to 400 m/min. It might even be possible to increase the line speeds with compact loose tubes in the future.

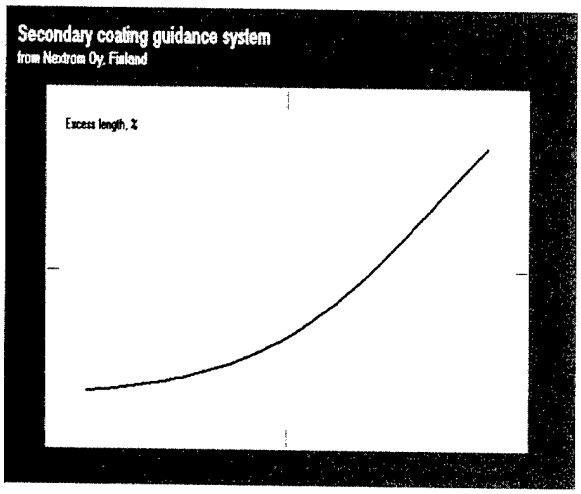


Figure 1. Effect of cooling trough temperature on EFL according to the nonlinear model.

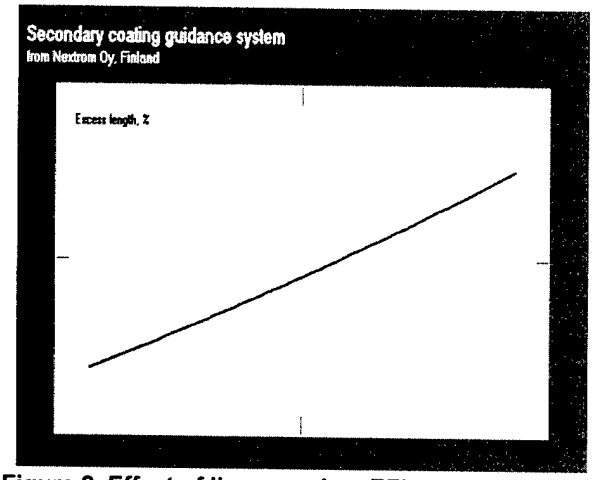


Figure 2. Effect of line speed on EFL according to the nonlinear model.

Figure 3 shows the effect of the pay off tension on the EFL. Initially the increase of the pay off tension decreases the EFL rather linearly which seems to correspond with the theoretical value of the fiber strain at the set tension. When the pay off tension is increased above 120 g, the decrease of the EFL will slow down. The phenomenon is typical also for traditional loose tube production. When the tube leaves the middle capstan, the high strain of the fibers will be released decreasing the EFL. The relaxation of the fiber strain starts to have an effect also on the tube. Therefore the behavior is not completely linear.

The effect of the middle capstan location on the EFL is shown in Figure 4. Efficient cooling and compact size of the tubes reduce the effect of the capstan position on the EFL. The process window which could be adjusted was only 0.1%. With bigger tube sizes normally the process window is in the range of 0.2 to 0.3%.

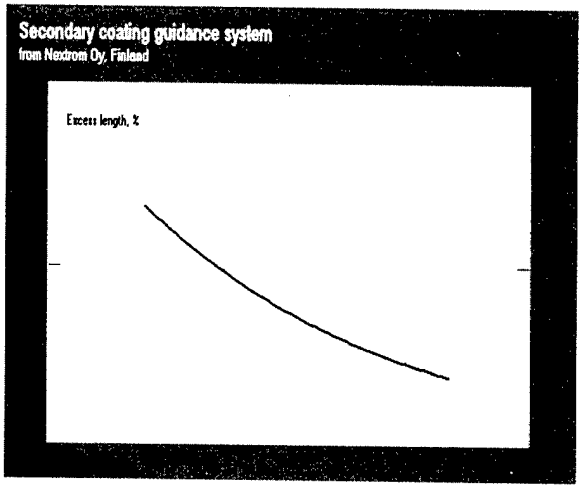


Figure 3. Effect of pay off tension on EFL according to the nonlinear model.

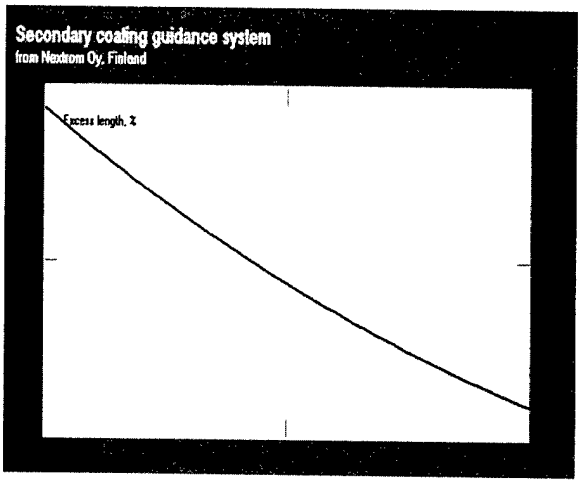


Figure 4. Effect of capstan position on EFL according to the nonlinear model.

With the model it was very easy to validate the compact loose tube process. Changes in process parameters showed similar

effects as with the traditional loose tube process, but the magnitudes of the influences are different and the EFL control is more difficult. Correct material selection and optimized process parameters can however guarantee high-quality buffering process for compact loose tube cables.

2.3 Buffering for the Test Cable

The process conditions for the test cable were selected according to the process model. Description of the buffering conditions for the test cable is shown in Table 3. The main target was to have very narrow EFL range at high speed in order to guarantee perfect cable characteristics at low temperatures.

Table 3. Buffering conditions for the test cable. Line speed 300 m/min

Pay off tension (g)	Gel hose temp. (°C)	Trough temp. (°C)	Capstan location (m)	Line tension (g)	Take up tension (g)
150	20	15	11	600	500

3. Test Cable

3.1 Requirements and Design

To verify the stability and consistency of the process described above a stranded cable was designed, manufactured and tested. The target was to maintain the cable's performance in a wide temperature range and in varying installation conditions. Especially in Northern Europe and Scandinavia –40°C is a normal requirement for this kind of cables to be still operational. In some rare cases even lower temperatures are required. To obtain fair installation properties, even by pulling, a free strain margin of at least 0.5% was considered to be sufficient.

The first, and perhaps the greatest challenge was to create and control reliably and constantly the Excess Fiber Length in a tube with inner diameter only few tens of millimeter larger than the fiber bundle at a speed of several meters per second. Besides, it was known from earlier high speed experience that the tubes tend to relax, shrink on the reels and possibly destroy the carefully adjusted EFL.

The second critical step was to design and perform the stranding so that this carefully set EFL could be maintained and the limited free space around the fiber bundle be utilized for maximum strain and contraction margins. No other requirements for mechanical strength of the cable were set, because they were considered to be outside the focus of this evaluation and more a matter of the outer components of the cable.

The design was based on loose tubes with outer/inner diameter of 2.3/1.5 mm containing 12 fibers and filling gel. A basic six-tube construction was selected for the test purposes (Fig.5).

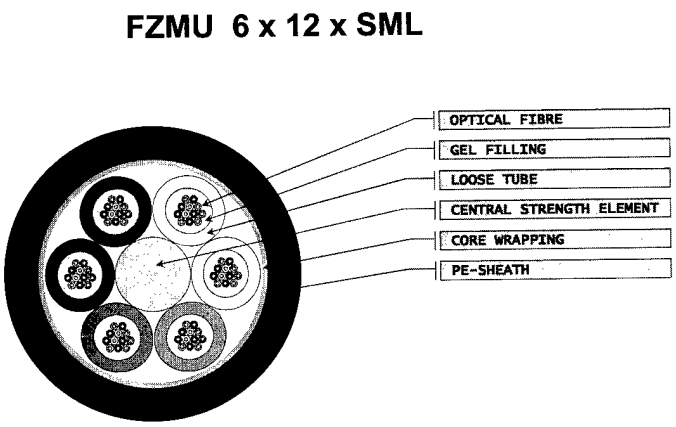


Figure 5: Construction on the test cable.

The core was dry and normal LDPE was selected as the jacketing material for flexibility. This compact cable with outer diameter of 9.5 mm could thus accommodate up to 72 fibers. Two different fiber types (primary coatings) were tested because it was experienced earlier that fibers from varying sources behaved in a different way in extreme conditions. The EFL was targeted to be as close to zero as possible.

3.2 Manufacturing

Buffering of the loose tubes was made as described above (Table 3), and the targeted EFL range was from –0.05% to +0.05%. Negative lower limit was allowed, since inevitable post shrinkage of the tubes was predicted. Based on the earlier studies of material combinations and optimization of process parameters and with the help of experienced operators this goal was reached quite well. In four different tubes the EFL varied from 0.01 to +0.06%.

The stranding was carefully designed so that in the smallest possible space, including the tubes and the cable's overall diameter, the largest possible window for the free movement of the fibers could be obtained. That is, the stranding lay length was calculated as short as the minimum bending radius of fiber bundle allowed. Below this bending radius there was known to be a risk of incremental attenuation at low temperatures. The shortest possible lay length also allowed maximum strain margin for the cable. The cable was estimated to be operational still at –40C° and to tolerate without any fiber strain a tension of 1.6 kN at 0.6% strain without additional reinforcements. With a modern, accurate and high speed Lay-Plate Stranding machine operated by skilled

personnel the lay length could be kept in a tolerance of less than 5%. The reverse points, which normally are problematic in an alternating lay-strander, were easily adjusted to match the same bending radius as in the helical part of the stranding.

3.3 Testing

3.3.1 Temperature Cycles. The cable was temperature cycled between –40 and +70C° for four times and the attenuation was scanned at each step according to IEC 60794-1-2, method F1. In addition, attenuation was measured at room temperature before and after the cycle, for reference. The low temperature attenuation seemed to be very low and stable throughout the cycle and consequently only minor differences could be seen between the two fiber types (Figure 6).

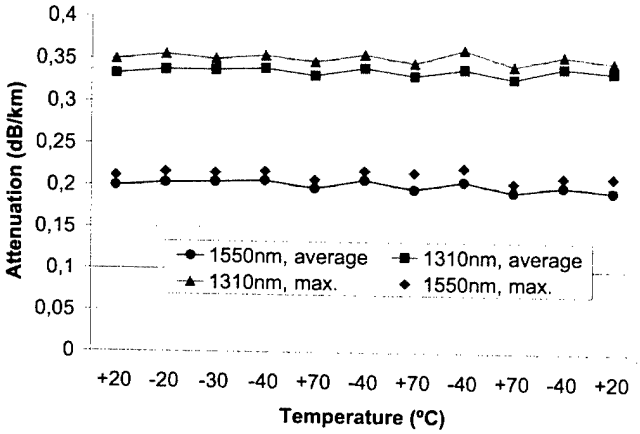


Figure 6. Attenuation vs. temperature during temperature cycling.

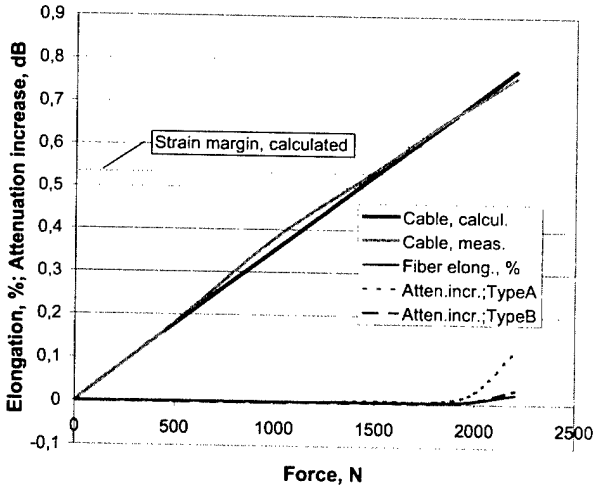


Figure 7. Cable (measured & calculated values) and fiber elongation and attenuation increase for fiber types A and B vs. applied force.

3.3.2 Tensile properties. After the temperature cycles, 200 meters of the cable was subjected to a tensile test to find out the strain margin of the fibers (IEC 60794-1-2, method E1). At a tension of 1500N the Fiber Type A showed a slight increase of attenuation, but the fiber strain was still negligible. The fibers did not start straining until the tension level between 1800 and 2000 N, which indicates slightly bigger strain margin than calculated (Figure 7). Fiber Type A presented higher incremental attenuation than Type B still when the strain was increased. Obviously this type is more sensitive to lateral pressure.

The cable strain was very linear and as predicted, which was obvious since only a single FRP strength member was used as a central element.

As a conclusion, this small compact cable proved to be very stable both under tension and at low temperatures matching very well with the pre-calculated values. This also verifies that both processes, buffering and stranding had been stable and well controlled even though high buffering speed and very small tube size was used.

4. Conclusions

The aim of the work reported here was to produce compact loose tubes for stranded cables at high buffering speed.

An extensive study was first made to find out appropriate material combinations (PBT & gel) and process parameters for the small tube size of 2.3/1.5 mm buffered at a speed of 300 m/min. The aim was to achieve a narrow and controlled Excess Fiber Length (EFL). After optimization of the process parameters a non-linear model was developed to predict the effects of the main process parameters on the EFL.

The compact tubes made with high speed buffering process resulted in controlled Excess Fiber Length (EFL) and their performance was verified also with a test cable. The stranded cable with six compact tubes of 12 fibers showed good mechanical and dimensional stability in a wide temperature range (-40 to +70 °C).

5. Acknowledgments

The authors wish to thank Mr.Heikki Kanninen, at NK Cables, Oulu, Finland for defining the design parameters of the cable and for contributions in result evaluation. Special thanks to Ossi Vuolle, Timo Puhakka and Markku Heino for their valuable assistance during the manufacturing of the test cable.

6. References

[1] M.I. Lahti, "High Speed Polypropylene Buffering", *49th International Wire and Cable Symposium*, Atlantic City, USA, (2000).

[2] A. Bulsari, "Nonlinear Modeling of Secondary Coating of OFCs from Experimental Data",50th *International Wire and Cable Symposium*, Orlando, USA, (2001).

Authors

Dr. Mikko I. Lahti

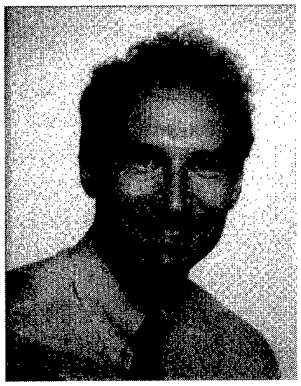
Nextrom Oy
P.O. Box 44
Fin-01511 Vantaa
FINLAND
Tel. +358-9-50251
mikko.lahti@nextrom.com



Mikko Lahti received the degree of M. Sc. in Chemical Engineering in 1991 and the degree of Dr. Tech. in Polymer Technology in 1996. Before joining Nextrom in 1997 he worked as Research Scientist in European Joint Research Center in Milan. Currently, as R&D Manager at Nextrom, he is responsible for the development of the extrusion processes for fiber optic cables.

Dr. Markku T. Heino

NK Cables
Draka Comteq
PO Box 419
FIN-00101 Helsinki
FINLAND
Tel. +358 10 5661
markku.heino@nkcables.fi



Markku Heino received the degree of M.Sc. in Chemical Engineering in 1990 and the degree of Dr. Tech. in Polymer Technology (Blends of Thermotropic Main-Chain Liquid Crystalline Polymers and Thermoplastics) in 1994 at Helsinki University of Technology, Finland. Before joining NK Cables (at that time Nokia Cables) in 1996 he worked as Research Scientist and Project Manager in the Laboratory of Polymer Technology at the HUT. Currently, as R&D Manager at NK Cables (Draka Comteq) his main responsibility is the Materials R&D.

Paul Lundström

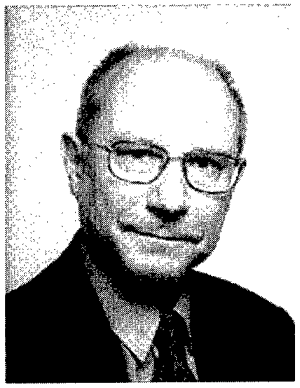
NK Cables
Draka Comteq
PO Box 269
FIN-90651 Oulu
FINLAND
Tel. +358 10 5661
paul.lundstrom@nkcables.fi



Paul Lundström received the degree of Engineer (B.Sc.) in 1972 from the Helsinki Polytechnic in Electrical Engineering. For several years he worked as Production Engineer for the manufacturing of telecommunication cables at Nokia Cables. Since 1982 he worked within the Fiber Optic Cables Department as Quality Manager. From 1997 he has been Product Manager at NK Cables (Draka Comteq) participating in process and cable development.

Jussi T. Ravela

NK Cables
Draka Comteq
PO Box 419
FIN-00101 Helsinki
FINLAND
Tel. +358 10 5661
jussi.ravela@nkcables.fi



Jussi Ravela received the degree of Engineer (B.Sc.) in 1973 from the Helsinki Polytechnic in Mechanical Engineering. He worked as Design Engineer at Nokia Cables, being engaged in the development of cable machinery, e.g. for manufacturing of optical fibers and their further processing. Since 1984 he worked in the area of Optical Fiber Cable Technology, first as a R&D Engineer then as a Design Manager focusing on materials, processing and cable designs. From January 2001 he has been working at NK Cables (Draka Comteq) as Development Manager in Quality Management.

Surface Treatment of Wire and Cable to Improve Adhesion of Overmolded Connectors and Grommets

Margaret Frey, Ph.D.
Champlain Cable Corporation
Colchester, Vermont
+1-802-654-4259 Mfrey@ChampCable.com

Abstract

Although XLPE and XL Polyester type wire insulations have superior performance in many aspects, it is often difficult to get materials typically used in connectors and grommets to adhere satisfactorily. One possible method for improving adhesion between wire insulation/jacket materials and overmolded grommets or connectors is to pre-treat the wire surface with an adhesion aid that is compatible with both materials. This report reviews a systematic study of adhesion between insulation/jacket materials and common overmolding materials.

Overmolding materials included in the study are PVC, TPU, TPE and Nylon. A wide array of adhesion promoters were also investigated including an acrylated urethane, chemically reactive adhesives, an amino functional silane based adhesion promoter, and a water based chlorinated polyolefin adhesion promoter. All experiments were done on injection molded plaques. No single adhesion promoter worked in every case, but for all insulation/overmold combinations at least one successful adhesion promoter was found.

Keywords

Overmolding, connectors, grommets, XLPE, polyester.

1. Introduction

Connectors and grommets are often molded onto wire and cable insulation. Adhesion between two dissimilar plastics, the insulation material and the connector material, is required for a successful end product. One method to improve adhesion is to add a third material between the insulation and the overmold which acts as a compatibilizer. This report reviews a systematic study of adhesion between insulation/jacket materials and common overmolding materials. A wide array of adhesion promoters was also investigated. No single adhesion promoter worked in every case, but for all insulation/overmold combinations at least one successful adhesion promoter was found. Using the appropriate adhesion promoter, energy required to separate the insulation from the overmold material could be increased at least 2 and up to 90 times over the energy required for untreated samples.

2. Materials

Insulation/Jacket Materials:

1. XLPE 150°C rated, halogenated FR (UL3289, VW-1)
2. XLPE 150°C rated, thin wall, halogenated FR (ISO-6722 or SAE J2183 Class D)
3. XLPE 125°C rated, non-halogenated FR (SAE J1128 TXL)
4. XL Polyester 150°C rated, halogenated FR

All materials are proprietary formulations of Champlain Cable Corporation and Huber+Suhner, Inc.

Overmolding Materials:

Overmolding materials were chosen after discussion with molders on the types of materials typically used for connectors and grommets. Recommendations for specific grades were made by the material suppliers.

PVC – GM 8000-95D VW1, Alpha Gary Corporation
TPU – Elastollan® C85A10, BASF
TPE – Santoprene® 251-80, Advanced Elastomer Systems
Nylon 6,12 – Zytel® , DuPont

Adhesion aids:

Adhesion aids were selected based on discussion with suppliers on which types would work best with the insulation/jacket materials and the overmolding materials. These materials represent a broad variety of adhesion chemistries and curing mechanisms.

A – UV curing, acrylated urethane, recommended by manufacturer for PVC
B – chemically reactive adhesive formulation #1
C – chemically reactive adhesive formulation #2
D – amino functional silane based adhesion promoter, (gamma-Aminopropyltriethoxysilane)
E – water based chlorinated polyolefin adhesion promoter
F – Polyurethane conformal coating
G– Acetone cleaning

3. Experimental

3.1 Preparation of Plaques from insulation/jacket materials

Plaques were molded from each of the 4 insulation/jacket materials at the CNRC(Canadian National Research Center) Institute for Materials Research in Boucherville, QE. Plaque dimensions were 7.6 x 16.4 x 0.3 cm. Plaques were irradiated to a total dose of 150kGy, 1.5 MeV; 7.5 mA; 4 physical passes underneath the beam at a traverse speed of 275 cm/min. Irradiation was conducted at H+S (Huber + Suhner, Inc.), Pfäffikon Switzerland and at Champlain Cable, Colchester, VT.

3.2 Treatment with adhesion aids

Adhesion aids were applied according to the manufacturer's instructions on one side of the irradiated plaques. There was a time delay of at least 1 week between the application and curing of the surface treatment and the overmolding.

3.3 Overmolding

Plaques were returned to the CNRC for overmolding. A second plaque was molded onto the treated side of each of the insulation/jacket material plaques. Molding conditions were per the manufacturer's instructions for the overmolded material. A 2mm tab was used at one end of the overmolded plaque to keep the two layers separated for gripping during peel testing.

3.4 Peel Testing

Peel tests were conducted on an Instron Tensile tester with a 90° constant angle peel test fixture and 981N load cell. Three measurements were made for each insulation/overmold/adhesion promoter combination. Peeling tests were conducted at 23°C, 50% RH with a crosshead speed of 152mm/min and a data sampling rate of 10 points per second. The adhesion area was not always completely uniform and this test did not adhere to any ASTM method.

4. Results

In a few cases, adhesion between the insulation/jacket material and the overmold material was so low that no peeling test could be conducted. The samples just fell apart and results were recorded as zeros. In most cases, however, the peeling test was characterized by the total amount of energy (work) required to separate the two layers. This value was determined by calculating the area under the Instron stress – strain curves.

5. Discussion

The degree of adhesion improvement was determined by comparing the bond energy before and after application of an adhesion aid. If the untreated samples had a measurable energy, then the results were normalized based on that energy. Where the energy was zero, the raw values for surface treated samples were used to compare the adhesion aid effectiveness.

5.1 Best Pairs

Data were sorted to determine the most effective adhesion aids for each insulation/overmold pair based on the total energy required to separate the two layers. For all but a few cases, huge improvements in bond strength were achieved.

5.2 Most Effective Adhesion aid for each Overmold material

Data were also analyzed to determine which adhesion aid worked best with each individual material. Results for the overmolding materials are found in Table 2 and results for the insulation/jacket materials are found in Table 3.

The adhesion aids listed with overmolding materials in Table 2 were the most effective on average although they may have actually decreased the bond in specific cases. For example C increased bond energy between PVC and insulation/jacket materials 2,3 and 4, but actually decreased bond energy between PVC and insulation jacket material 1.

Table 1: Adhesion promoters most effective for each jacket/overmold material pair

Insulation Material	Overmold Material	Best Adhesion Aid	Bond Improvement
1	PVC	A	2x
	TPE	B	37x
	TPU	D	19x
	Nylon	B	11x
2	PVC	C	from 0 to 1.1 joules
	TPE	B	6x
	TPU	C	from 0 to 1.5 joules
	Nylon	B	from 0 to 9 joules
3	PVC	C	3x
	TPE	B	32x
	TPU	B	7x
	Nylon	B and C	4x
4	PVC	C	6x
	TPE	E	from 0 to 9 joules
	TPU	D	2x
	Nylon	C	15x

Table 2: Most effective adhesion aid for each overmold material

Overmold material	Best Adhesion Aid	Energy increase factor
PVC	**C**	**3x**
TPE	**B**	**20x**
TPU	**D**	**6x**
Nylon	**B**	**3.5x**

5.3 Most Effective Adhesion aid for each CCC insulation/jacket material

As for the overmold materials, the adhesion aids listed for each insulation/jacket material performed most effectively overall, but may have actually decreased bond energy in specific cases. With

no adhesion aid, insulation/jacket material 2 formed no measurable bond (i.e. plaques fell apart) when overmolded with PVC or TPU. Bond strength increased significantly on the application of surface treatments, but was still was not as high as bonds achieved with other materials. Tests on actual cables will be necessary to assure that the increase in bond is sufficient.

Table 1: Most effective adhesion aids for each insulation/jacket material

CCC Material	Best Adhesion Aid	Energy Increase Factor
1	**B**	**15x**
2	**B**	**3x**
3	**B**	**13x**
4	**E**	**4x**

5.4 Best adhesion aid in the largest range of applications

Adhesion aid B worked in the largest range of insulation/overmold combinations. On average, treatment with B increased the energy required to separate an insulation plaque from an overmold plaque by a factor of 10. In some instances, however, B decreased the energy required to separate the plaques as compared to the untreated plaques: insulation jacket material 3 /PVC and insulation/jacket material 4 /PVC.

Insulation/jacket material 4 formed a strong bond with TPU without any surface treatments. Several surface treatments improved the bond, but are probably not required to achieve an effective bond for this system. In all other combinations, initial bond was low and surface treatment is probably necessary to achieve acceptable bonds.

In general PVC did not bond well with cross-linked polyolefin jacket materials: insulation/jacket materials 1, 2 and 3. This result is not surprising and could be predicted by basic surface chemistry noting that PVC is a polar material while polyolefins tend to be non-polar. Surface treatments did increase the energy required to separate PVC from these polyolefin based insulation/jacket materials. Testing on cable assemblies will be required to demonstrate that the increase is enough to make an acceptable bond.

6. Conclusions

Adhesion aids were found to significantly improve the bond between the insulation/jacket material and common overmolding materials found in connectors and grommets. Since adhesion between materials is determined by the surface chemistry and surface energy of the materials, the results in this study are specific to the materials tested. Geometry of an actual cable and connector assembly, mold design and molding conditions will also impact the bond between insulation/jacket materials and overmold materials. These factors were not investigated here.

For some combinations of insulation/jacket material and overmold material, a sufficient bond may be formed with no adhesion aid. Insulation/jacket material 4 (XL polyester) and TPU stands out at a highly compatible pair. For other combinations, pairs with no adhesion aid had low bond energy and use of the appropriate adhesion aid increased the energy required to separate insulation/jacket materials from overmold materials. The specific choice of adhesion aid is important. In many cases, only one of the adhesion aids tested significantly improved bonding between a specific insulation/jacket material and a specific overmold material. For example only B significantly improved bonding between insulation/jacket material 1 and TPE.

Further experiments will be designed to look at actual cable assemblies and to investigate the effects of mold design and molding conditions. Additional adhesion aids can be investigated for insulation/jacket materials and overmold materials that did not achieve strong bonds with the adhesion aids tested so far. Both the suppliers of overmold materials and the suppliers of adhesion aids demonstrated a depth of knowledge on bonding materials during the course of this study. Their resources will continue to be used as investigation continues

7. Acknowledgments

Special thanks to the CNRC in Boucherville, QE for molding and Instron testing and to Tony Augostino at Champlain Cable for plaque irradiation and surface treatment application.

8. Author

Margaret Frey, Ph.D.
Manager of Material Development
Champlain Cable Corporation
175 Hercules Dr.
Colchester, VT 05465

Margaret Frey earned a B.S. in Chemical Engineering and an M.S. in Textile Science from Cornell University. She earned a Ph.D. in Fiber and Polymer Science from North Carolina State University. She has worked in TS&D at Champlain Cable Corporation since January of 1998.



In-Line Wall Thickness Measurement for Fiber Optic Applications including Tight Buffer, Loose Tube and Cable Jacketing

Scott H. Taylor
Zumbach Electronics Corporation
Mt. Kisco, NY 10549-1412
1-914-241-7080 · staylor@zumbach.com

Abstract
The in-line ultrasonic measurement of wall thickness has become a common quality manufacturing tool for many years in the medical tubing extrusion field, most commonly for medical applications where documented quality is paramount. Recent years have seen the application of this measurement technique to wire and cable jacketing where significant material savings provide for a very attractive investment return. Now this valuable quality tool can be applied to many of the key constructions in the fiber optic arena including tight buffer, loose tube and cable jacketing.

This paper explores the fundamentals of this measurement technique, the benefits available and its application to the extrusion of tight buffer, loose tube and cable jacketing.

Keywords
Ultrasonic; jacketing; wall thickness; tight buffer; loose tube; concentricity.

1. Introduction
Ultrasonic wall thickness measurement provides the unique ability to measure wall thickness at the beginning of the extrusion line which allows for optimum die centering by an operator. A real-time display of the wall about the core immediately shows the results of a centering effort such that subsequent changes can be made as needed to further optimize the wall balance. Without this capability, the manufacturer is dependent on sample checking at the end of the line on start-up. Quite often, a manual change to the die can effect an over correction and begin a process of multiple changes which are time consuming and will still end up with a less than optimum result. Therefore, human nature intervenes and the operator will eventually tend to "leave well enough alone". Beyond optimum die centering, measurement at the die enables a much faster control response when the system is set to control Average or Minimum wall thickness. Continuous wall thickness measurement, of course, enables detailed quality documentation as with other measured parameters.

2. Ultrasonic Measurement Basics
The basics of ultrasonic measurement are quite straightforward. An ultrasonic transducer contains a piezo electric crystal which, when hit with a voltage pulse of very short duration, causes a sound wave to be created at the face of the transducer. Depending on the shape of the transducer lens, a shaped sound wave emanates from the face of the transducer, through water to the surface of the product to be measured. A change in the speed of sound in water occurs when encountering a material with a different acoustic impedance than water. This change causes a reflection back towards the transducer resulting in an interface "echo." A portion of the sound energy continues on into the material and when a subsequent change in speed is encountered, a second echo is reflected back to the transducer.

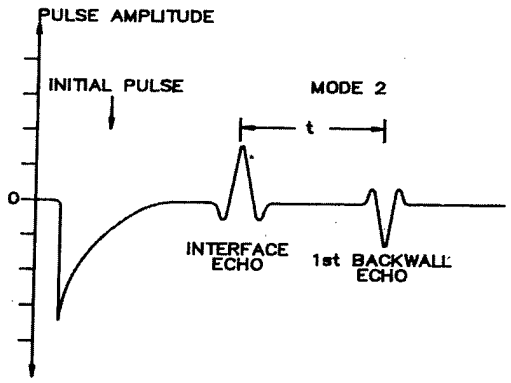


Figure 1. Ultrasonic Measurement Technique

An ultrasonic processor looks for these reflections (echoes) and correlates the distance (t) between them to a wall thickness. The quality or clarity of the echo is a function of the strength of the sound wave to begin with, the degree of difference in acoustic impedance between the two materials and the alignment of the transducer to the reflecting surface. Transducers are generally very rugged devices with long life expectancy and relatively low cost. This low cost facilitates using multiple transducers for applications which require multiple points of wall thickness measurement. A wide range of transducer constructions is readily available to be optimized to the product application depending on wall thickness, resolution required and target (product) size. Use of this technology requires product immersion in water. Unlike the low frequency ultrasonic transducers used for camera distance measurement, these applications require frequencies in the 10 to 30 mhz range which dissipate in air. They therefore require water as a transmission

medium. The range of transducer types routinely used allow measurement of thickness from .0008" (.02 mm) to 2.0" (50 mm) and thicker. Repeatability is on the order of +/- .00004" (.001 mm).

3. Applications

3.1 Tight Buffer

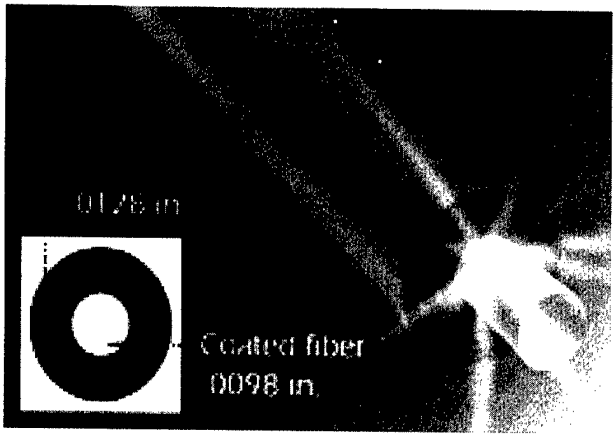


Figure 2. Tight Buffer

Application of ultrasonic wall thickness measurement to a tight buffer product is quite straightforward. The relatively low line speed, line stability and PVC to coated fiber interface make for a very stable installation. Measurement is done as close to the crosshead as mechanically practical as shown in Figure 4. Great precision can be achieved in measurement of the .0128" (.325mm) wall thickness. A small, 4 point sensor assembly, similar to that shown in Figure 3, would be used, oftentimes with guides, to assure product centering within the 4 point measurement field.

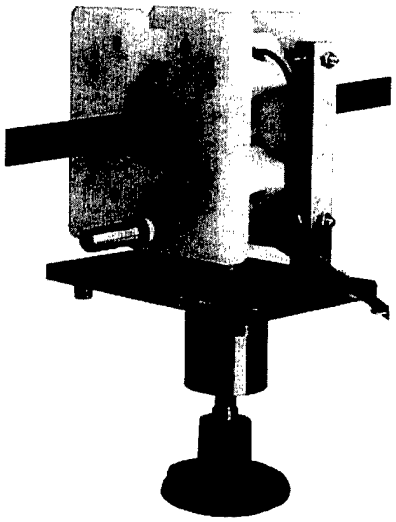


Figure 3. 4 Point Ultrasonic Sensor Assembly

The sensor assembly shown has provision to raise and lower the assembly as needed to facilitate product centering. As with all ultrasonic measurement the sensor requires submersion to a point approximately 1.0" (25.4mm) above the tight buffer.

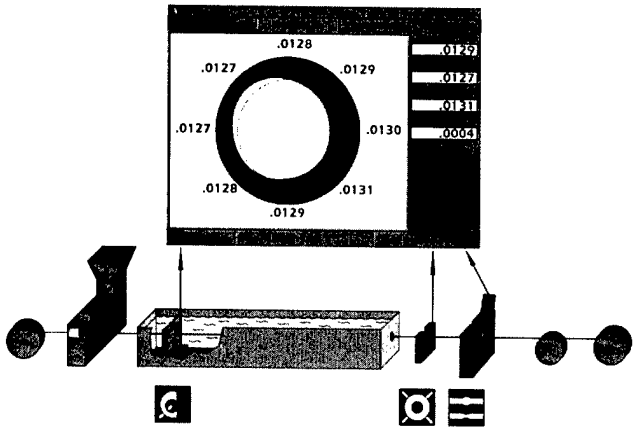


Figure 4. Instrumentation on Tight Buffer Line

3.2 Loose Tube

Loose tube production provides a bit more of a challenge for ultrasonic measurement.



Figure 5. Loose Tube Construction

First, the wall interface between the PBT tube material and the gel filling does not provide as strong an interface as with other materials. This simply necessitates some care being taken initially to assure that the processor is set up appropriately to distinguish this interface. Secondly, it is common for the product to be cooled gradually . The first 10 to 20 ft. of "cooling" trough may in fact have a hot water quench of approximately 135 degrees F (57 degrees C). Subsequent cooling trough sections then have progressively cooler water. Standard ultrasonic transducers are rated at 120 degrees F (49 degrees C) and therefore are not appropriate for continuous submersion in this hotter water. This can be circumvented by positioning the ultrasonic assembly in the second section of cooling trough. While not ideal for operator die centering ease, it is still a reasonable trade-off. Alternatively, high temperature transducers may be used that are suitable for continuous immersion in the hotter water.

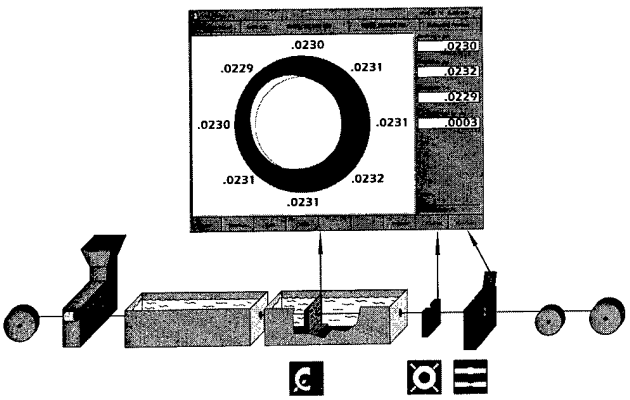


Figure 6. Instrumentation on Loose tube Line

3.3 Jacketing

Fiber optic jacketing covers a broad range of sizes and applications but all generally lend themselves to wall thickness measurement. The outer jacket material may be applied over a host of materials including metal and other blocking materials.

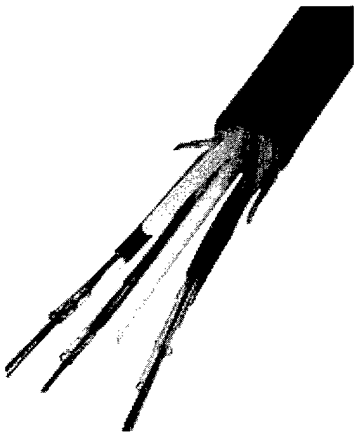


Figure 7. Jacketed Cable

The size range of the cable to be produced will dictate the size of the sensor assembly employed and the number of measurement points from 4 to 6 or 8 points. A fixed sensor assembly as depicted in Figure 5 is positioned just after the crosshead in the first cooling trough.

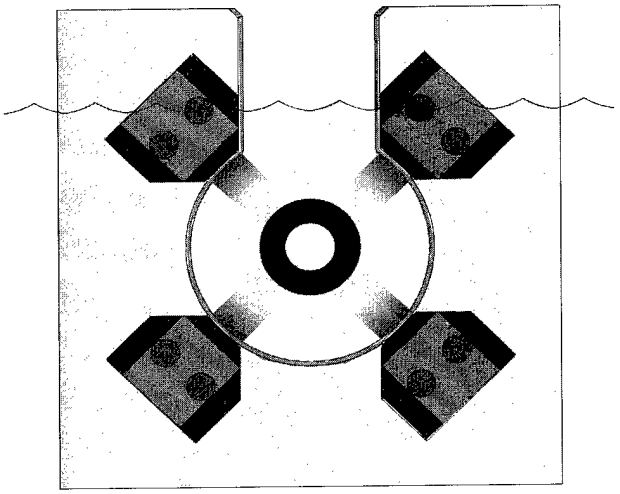


Figure 8. 4 Point Cable Sensor Assembly

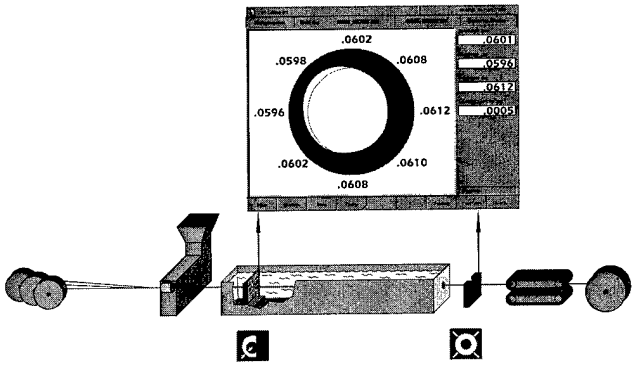


Figure 9. Instrumentation on Jacketing Line

Again, provision needs to be made to assure water submersion to a point just above the face of the lowest transducer. Note that in this application, the measurement field for each transducer is quite wide enabling product position freedom without compromising the measurement. This sensor assembly can be mounted in an existing cooling trough or the trough modified to accommodate it. Alternatively, a custom trough section with sensor assembly may be supplied for positioning at the entry to an existing trough.

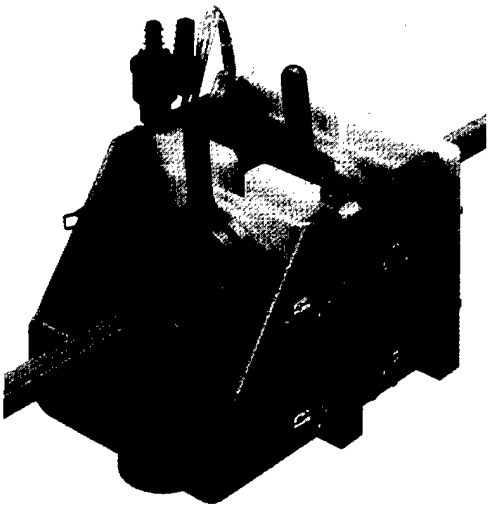


Figure 10. Custom Tank with Sensor Assembly

4.0 Benefits

Once in-line wall thickness measurement is employed in these applications all the traditional benefits of gauging follow. Typically the wall measurement function is added to a more common host processor that provides for the primary instrumentation including diameter measurement and fault detection. The wall measurements and corresponding data collection simply become integrated with these more common measurements. SPC control charts, SQC quality records and data archiving are just a few of the reporting capabilities. Standard trending and tolerance alarms as with other measurements are available to the user. Primary amongst the benefits is more uniform die centering. What was once a tedious chore becomes an almost effortless accomplishment. Thickness control of Average or Minimum wall thickness can be implemented. Significant material savings can readily be achieved for jacketing applications with attractive investment returns.

5.0 Conclusion

Ultrasonic wall thickness measurement has proven itself in hundreds of similar applications in both the tubing extrusion and wire and cable markets. It can contribute equally to the quality production and reporting needs of the fiber optic industry oftentimes while delivering very attractive investment returns.

Author



Scott H. Taylor is Technical Marketing Manger at Zumbach Electronics and has been with the company for 12 years in a number of capacities including Regional Sales Manager. He brings 25 years of ultrasonic application experience to this position and has held product management positions at On Line Controls, Inc. and LFE Corporation.

Aerospace/Automotive Session

Chairperson: M. Edward Fenton

Wire & Cable Clubs/Fenton Group, Incorporated, Wethersfield, CT

Aerospace Segment

Moderator: David Allen

DuPont, Wilmington, DE

David Allen, currently Technical Consultant, Wire & Cable, DuPont Fluoroproducts, continues his advisory role after serving as Aerospace Session moderator at Wire & Cable Focus. During his career at DuPont, Allen has authored several papers on fluoropolymers, fire tests, and other test methods. He represents DuPont on various Code & Technical Committees including: Chairman, SAE/Aerospace Division, AE-8D Subcommittee; Member, ATSRAC (Aging Transportation Systems Rulemaking Advisory Committee); Member, AE-8A Subcommittee on Electrical Installations in Aerospace Vehicles; Technical Consultant, NEMA High Performance Wire & Cable Section; Senior Member, NFPA and IEEE; Charter Member, BICSI; and Member, New England Wire & Cable Club, including its Distinguished Career Award.

Aerospace Cabling – Aircraft Wiring Aging Effects and Recommendations



Kent V. Hollinger
Mitre Corporation
McLean, VA
+1-703-883-6000 · kenth@mitre.org

Abstract

Description of the findings and recommendations of the Aging Transport Systems Rulemaking Advisory Committee (ATSRAC) regarding:

- State of wiring in the current transport category fleet
- Results of intrusive and non-intrusive inspections
- Design practices lessons learned
- Maintenance program improvements
- Training program enhancements

Keywords: UL Standards, Safety, National Electrical Code (NEC), ANCE, CSA

Biography

Kent Hollinger has a very broad and diverse background in aviation maintenance. His OEM experience includes General Electric Aircraft Engines where he led repair development on commercial engines, and Fairchild Dornier as Vice President of Technical Support. His knowledge of third-party repair stations came as a Business Unit General Manager at The NORDAM Group and as Director of Engineering at Chromalloy Compressor Technologies. As Chief Engineer of Northwest Airlines and Vice President of Quality Assurance and Engineering at America West Airlines, Kent gained significant experience in airline maintenance operations.

In addition to these job assignments, Kent has been active in several industry-wide efforts. He is currently the chair of the FAA Aging Transport Systems Rulemaking Advisory Committee, and has previously served as the chair of the ATA Powerplant Subcommittee and as a Working Group chair on the ATA Fuel Systems Safety Leadership Team. Kent has also served on the ATA Engineering, Maintenance & Materiel Council and the ATA Fuel System Safety Leadership Team, and is a licensed Professional Engineer in the State of Ohio.

Aerospace/Automotive Session

Automotive Segment

Presentation followed by Panel Discussion
Co-Hosted by SAE Cable Task Force



Moderator: Larry Powell
Delphi Packard Electric, Warren, OH

Larry Powell is Senior Project Engineer, Delphi Automotive Systems, with 23 years experience in wire and cable design.

In addition to his career at Delphi, Powell holds numerous positions with industry standards organizations and committees including the following:

Chairman, SAE Cable Task Force; Chairman, SAE US Advisory Group for ISO WG4, Low Tension Cable; Chairman, ISO WG4, Low Tension Cable; Chairman, SAE US Advisory Group for ISO SC3; US Delegate, ISO SC3, Electrical & Electronic Devices; Vice Chairman, SAE Electrical Distribution Systems Standards Committee; Member, SAE 42 Volt Advisory Committee; Member, SAE Wiring Systems Task Force; Member, SAE US Advisory Group for ISO WG13, Environmental Conditions.

An original advisor for Wire & Cable Focus, Powell continues his role with IWCS/Focus as aerospace and automotive panel session moderator.

Invited Panel Participants:

David Spires, Alcoa Fujikura
Neng Ku, Yazaki North America
Rob Lassila, Exemplar Mfg.

Automotive Cabling – Update on 42 Volt Architecture



Norm Traub
SAE Cable Task Force, Director of 42V Initiative
SAE Strategic Alliance
Warren, OH
+1-248-273-2463 · ntraub@sae.org

Abstract
All vehicle manufacturers are faced with the task of providing more electrical power to offer increasingly fuel efficient and safer vehicles with additional customer features. This can best be accomplished by raising the system voltage provided by the on-vehicle "utility company." One of the main benefactors associated with a higher voltage electrical system will be the Power and Signal Distribution System. This presentation discusses the potential impact on the wiring system of converting to a single 42V electrical system.

Keywords
Automotive, Cabling, SAE

Biography
Norman L. Traub was named Director of 42 Volt Initiatives for the Society of Automotive Engineers Strategic Alliance (SSA) on February 1, 2001. SSA is an alliance between SAE and its partner companies and government agencies to solve strategic business and technical issues for the automotive, aerospace and off-highway industries.

Traub has made presentations on 42V electrical systems at the SAE World Congress, International Power Electronics Conference, International Society of Automotive Transportation and Technology, IEEE Workshop on Power Electronics in Transportation and the first international congress on "42-V PowerNet: The First Solutions". He was the moderator for the SSA 42-V Executive Panel session entitled, Impact of the Global Economy on the Implementation of 42-Volt Electrical Systems, held during the SAE 2001 World Congress. Global journalists from England, France, Germany and the USA also have interviewed Traub for his technical expertise and insight.

Currently, Traub holds the position of chairman of the 42-V Battery Connection System Specification Workgroup, a multi-national standards workgroup of nine vehicle manufacturers, nine battery suppliers and nineteen connection companies. He is a steering committee member of the MIT/Industry Consortium on Advanced Automotive Electrical/Electronic Components and Systems (52 multi-national companies). He is also the chairman of the SAE 42V Advisory Committee.

Traub began his career at the General Motors Research Laboratories in 1967 as a senior engineer in the electrical engineering department, where he became the holder of four U.S. patents and numerous research reports/publications in the areas of automotive multiplexing, large industrial drive systems, electric cars and automotive safety/security systems.

In 1978, Traub transferred to the former Packard Electric Division of GM in Warren, Ohio. His promotion to senior staff engineer in 1990 resulted in his assignment as head of the Systems Development Center. In 1996, Traub was appointed technology integration manager at Delphi Automotive Systems, Packard Electric Division.

Traub received his bachelor's degree in electrical engineering from Valparaiso University and his master's degree in electrical engineering from Michigan State University.

Wireless Alternatives to Wired Systems Session

Chairperson: Dr. Howard Wichansky
US Army Communications-Electronics Command, Fort Monmouth, NJ

Wireless Office and In-Building Solutions-Current and Future

Clif Campbell
Cingular Wireless
Atlanta, GA
+1-404-236-5900 · clif.Campbell@cingular.com

Abstract
With the development of new high speed wireless data technologies and the push toward standardizing 3rd generation wireless technologies and services, the Wireless Office is fast becoming a reality. The purpose of this talk will be to provide an overview of some of these wireless solutions that is paving the way for the concept of the wireless office.

Keywords
Wireless; Wireless LAN; GPRS; 3GPP, standards.

Biography
Clif Campbell is Director – Technology, in the Strategic Planning organization of Cingular Wireless. In this capacity he is responsible for the development and support of Core network standards and technology strategy within Cingular.

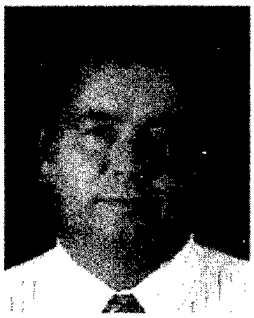
Prior to moving to Cingular at the end of 2000, he was a member of the wireless research and development team within SBC Technology Resources with a focus on wireless data including standards development. He has extensive experience in the areas of wireless and wireline data networks and intelligent networks.

Clif is the chair of the Data Working Group of the GSM North America (NA) organisation, one of the Regional Interest Groups of the GSM Association.

Clif has extensive technology development experience in the areas of data network development, ISDN, and Intelligent Networks and holds a B.Sc. (Eng.) from Imperial College of Science and Technology of the University of London (UK) and an M.Sc. (Eng.) from the same University.

Wireless Alternatives to Wired Systems Session

Wireless Mobile Internet: Where It's All Going



Michael A. Lapadula
QUALCOMM Incorporated, San Diego, CA
(858) 658-2722 · lapadula@qualcomm.com

Abstract
With the rapid development of wireless technology, there is a need for a standard applications and services platform for wireless devices on worldwide networks. Utilizing BREW (Binaray Runtime Environment for Wireless), developers, device manufactures, and wireless carriers can finally offer a hardware independent solution which will combine data and voice capabilities to better suit consumers' needs in a converged wireless Internet world. The percentage of subscribers with internet-ready handsets will quadruple over the next year. Third party software companies may now write windows based applications to allow the sale of such applications to any and all wireless carriers. Imagine navigation and position location, music, multi-player games, information on sporting events in real-time, m-commerce, and potentially hundreds of other applications that can be downloaded directly to your mobile handset when desired from a carrier's catalogue of applications!

Keywords:
Internet, BREW, wireless, wireless applications, mobile

Michael A. Lapadula
5575 Morehouse Drive
San Diego, CA 92121-1714

BIOGRAPHY
Mike Lapadula is Vice President of Government Marketing and Business Development at QUALCOMM in San Diego, CA. In this capacity, Mr. Lapadula is responsible for marketing all QUALCOMM products for government and military customers.

Prior to joining QUALCOMM, Mr. Lapadula was Vice President of Marketing for all business areas for Loral Corporation's Terracom Communications Division. He also worked with Rockwell Collins International Transmission Systems division in Dallas, Texas. Mr. Lapadula has worked on several occasions as a consultant to various US Government groups and has spent over 35 years in the telecommunications business on a worldwide basis.

Wireless Alternatives to Wired Systems Session

Bluetooth Wireless Solutions for Short Range Connectivity



Dan Bindbeutel
Program Manager for Bluetooth Applications, Trident Systems, Inc.
Fairfax, VA
+1-703-691-7780 · dan@tridsys.com

Abstract

Recent years have seen the proliferation of intelligent portable devices such as multifunction cellular phones and personal digital assistants, along with a growth of embedded computing capabilities in all manner of appliances, vehicles, etc. This has led to the desire for a robust method of interconnecting these computing, control, and measurement resources in a way that is both simple to implement and transparent to the user.

One such approach is offered by the Bluetooth specification. Developed by a consortium of electronics manufacturers, the Bluetooth specification defines a wireless network architecture for providing short-range, low-cost voice and data connectivity that can be easily integrated into embedded systems. These Bluetooth network nodes can be implemented using a combination of hardware and software dependent on the capabilities of the host device. Bluetooth not only offers a method for simple, point-to-point cable replacement, but for intelligent management of multiple communication nodes in a dynamic, ad hoc manner, and methods of service discovery that allow nodes to query each other for their capabilities and resources. Bluetooth is targeted at short-range, low- and medium- bandwidth data communication applications such as wireless computer peripherals, PDA connections, and data acquisition devices, and voice applications such as cordless headsets and handsets.

In order to assure the interoperability of Bluetooth links from different manufacturers in a wide variety of applications, the Bluetooth Special Interest Group (SIG) has developed a range of user "profiles" that define the operation of Bluetooth networks in specific applications. These profiles describe what features of the core protocol should be used to support the application. Many of these profiles overlap, and are used as the basis for other profile definitions. As new application areas are defined, new profiles are generated, so that new services can be provided in an ordered, compatible manner. These capabilities allow Bluetooth technology to complement other wired and wireless network mechanisms, providing pervasive connectivity across a broad range of application areas.

This presentation will provide an overview of the Bluetooth specification, its modes of operation, and its capabilities. It will continue by describing how Bluetooth links can be used to eliminate or extend cabled connections while providing additional features. Profile configurations will be discussed, as well as the current state of the emerging Bluetooth product area.

Keywords

Bluetooth; communications; wireless.

1.1 About the Author

Dan Bindbeutel
Trident Systems, Inc.
10201 Lee Highway
Suite 300
Fairfax, VA 22030

Dan Bindbeutel has a thirteen-year background in the development of embedded systems in the areas of wireless voice and data communications and signal and image processing. His recent work has included the applications requiring the sharing of multimedia data over dynamic, ad hoc networks, including Bluetooth. Dan is technical lead on a number of projects in the areas of Bluetooth short-range connectivity and video compression and communications at Trident Systems, Inc., in Fairfax, VA. He resides with his wife and daughter in Annandale, VA.

Wireless Alternatives to Wired Systems Session

Wireless LANs Support Multimedia Applications



Luis O. Rodriguez
SRI International
Fort Monmouth, New Jersey
+1-732-532-6715 · rodriglo@erg.sri.com

Abstract

Wireless LAN products are demonstrating dramatic performance improvements and aggressive pricing, making wireless networking attractive. The use of bandwidth demanding multimedia applications is increasing in mobile user and military markets. In this paper, I describe various wireless LAN products, delve into their state of development, and discuss performance and limitations, as well as the possibilities of commercial and military application. With that as background, I discuss specific WLAN products and how they are being deployed in home and enterprise environments as well as in the commercial public access and military markets. Advances in available bandwidth provide today's business users flexibility, mobility, and performance similar to cabled networks and enable the multimedia and business applications they want access to away from the desktop.

Keywords

Bridge; bandwidth; broadband; cable; wire; wireless; LAN; ISP; mobile networking; multimedia; range; scalability.

1. Introduction

Major wireless LAN (WLAN) manufacturers and researchers are developing wireless networking technologies that are enabling mobile users to operate their multimedia collaboration and business applications in a way that enhances productivity, without being tethered to the desktop. New generation notebook computers and handheld devices continue to be introduced to the American market featuring wireless networking as a ubiquitous feature. Many businesses are investing in wireless access points to connect users with the wired network, installing them in temporary work areas, conference rooms, and lobbies to keep their employees connected to email and other critical business applications. Looking to the future, Internet service providers (ISP) may eventually provision airports, malls, and other public venues with wireless access points for the mobile user. Indeed, mobile IP based networking will be facilitated with introduction of IPv6.

2. About Wireless LANs

Wireless LAN technology is available in several flavors with variations dependent on the manufacturer and the user's intended purpose. What makes WLAN appealing to mobile users today is its convenience, availability of bandwidth (performance), interoperability, and cost. As wireless products were first introduced in schools, healthcare, warehouses and some businesses, devices were relatively slow and rather expensive. Manufacturers even used proprietary technologies. Today's users enjoy the benefits of interoperable technologies from multiple vendors. Employing IEEE 802.11b standards, bandwidth availability and range have significantly improved with the average user now able to access the wired network at near wire rates (~10 mbps), depending, of course, on the number of users connected via an access point or operating peer-to-peer in the same local segment. Wireless LANs can thus be used in combination with cabled LANs to support temporary users, mobile clients, and variety of possible topologies. Users can purchase WLAN products from such vendors as Cisco Systems (formerly Aironet), 3Com, or Lucent (and others), and in many cases be able to use each other's access points. With volume sales and competition come market based pricing so small offices/home office (SOHO) users can afford the flexibility and mobility one can generally equate to wireless telephones.

2.1 Scalability

The number of users in a wireless segment affects bandwidth available to each of them, though many vendors claim support of 65 or more users. One can suppose that in a benign application environment that many users could indeed connect via a single access point. But modeling and laboratory tests conducted at US Army CECOM and by academia tell a more interesting story. A

single user can generate much network traffic and is capable of actually saturating a wireless segment. So users must understand WLAN access is a shared resource and that each device contends for bandwidth, much like Ethernet. WLANs have a finite capacity defined by both waveform and the radio access protocol. known as CSMA/CA (Carrier Sense Multiple Access/Collision Avoidance). Significant overhead is also associated with CSMA's collision avoidance mechanism, which permits multiple users to simultaneously use the wireless segment without 'stepping' on each other's transmissions.

2.2 Bandwidth

What makes users appreciate networking capabilities is the availability of bandwidth. Broadband technologies such as those used in DSL (digital subscriber line) and coaxial cable (cable modem) systems have allowed advanced applications to thrive in both home and office environments. Most will recognize multimedia applications as the most demanding on the network in terms of bandwidth and delay. Mobile users demanded wired performance in wireless products and are now realizing the benefits of advanced technologies. Early deployed wireless systems used RF modems in the ISM band of 915 MHz (902-928 MHz-Mega Hertz). Typical throughput experienced was in the hundreds of kilobits per second with some achieving up to 2 Mbps. Today's market is focused on products operating at 2.4 GHz (Giga Hertz) (2400-2483.5 MHz). Effective use of this frequency range can differ by product. For instance, most vendors claim their product is capable of 11 Mbps (million bits per second). Measurements made at CECOM and by academia clearly show performance may vary from vendor to vendor. Under basic conditions, better products can optimally support individual throughput demands of 6 Mbps, while most will typically support 4.5 Mbps. Clearly, multimedia applications such as voice over IP (VoIP) and video using compression services as MPEG2 (Moving Pictures Experts Group) are readily supported. Carefully engineered networks, using multiple access points with configured users allocated single channel frequencies may achieve up to 14 Mbps of aggregate throughput, but this is not something users will see routinely.

2.3 Range Limitations

Effective radiated power from IEEE 802.11b WLAN devices require conformance with FCC Part 15, otherwise know as ISM Band. Most devices conform by transmitting at 35 to 100 milliwatts and use a 0 dB gain antenna. Because the probability of signal and decoded data error induced by environmental noise or other emissions increase with distance between transmitter and receiver, developers have included bandwidth management algorithms in their devices that will automatically determine the received signal strength and adjust the data mode from 11 Mbps to 5.5 Mbps to 2 Mbps, then to 1 Mbps in the most degraded mode. For example, approximating measurements taken by SRI show a mobile user may locate 50 to 100 feet from an access point and maintain an effective throughput of 4 Mbps. As he moves further to 150 feet, throughput would decrease to about 2.5 Mbps, while at 200 feet throughput would further decrease to about 1.2 Mbps. Changing waveform mode facilitates graceful degradation and reduces the potential for error in data packets that might manifest itself with undesirable applications performance (i.e. blocky or pixilated video). This means a mobile network user should be aware of location relative to access points or peers to prevent being disconnected or disappointing application performance.

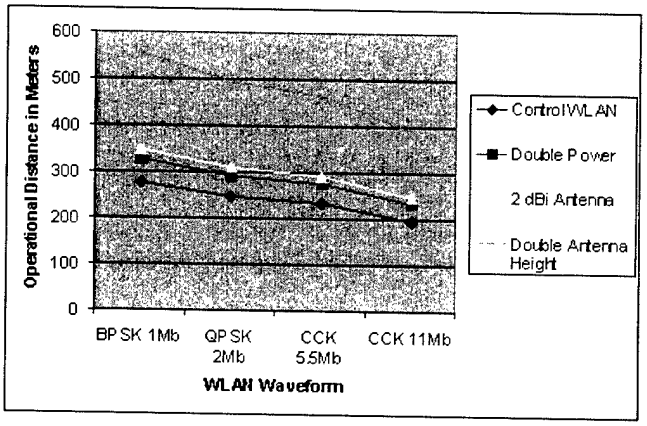
2.4 Extending Range

Though the distance a mobile user may range from an access point or a peer user is limited by radiated transmitter power and receiver sensitivity, several solutions may be applied to mitigate the effects of RF range limitations.

- Positioning of access points
- Use of an external high gain or directional antenna to increase receiver sensitivity and effective transmitted power (FCC restricts ISM band transmissions to 1 watt effective radiated power)
- Use of a mobile ad hoc networking (MANET) protocol

2.4.1 Modeling and Simulation. Studies were performed by SRI of a local network of mobile devices using a baseline of antennas 1 meter in height. The study evaluated the effects of increasing radiated power (2x), using a higher gain antenna (2dBi), and placing an external antenna at 2 meters above ground. The comparisons, shown below, clearly indicate antenna placement significantly affects performance in terms of range and throughput. Many system installers try to place access points as close as possible to ceilings or corners. Considering the effects of multipath fading on low cost radios, installers' plans should include maximizing line of sight to a maximum of potential users as well as minimizing proximity to reflecting surfaces.

Figure 1. Effects of antenna height, gain and power, on wireless LAN performance



2.4.2 Antenna Selection. Selection options are based on intended systems use. Many PC card WLAN products are available with external antenna ports permitting use of small bi-directional, magnetic mount omni-directional, and under certain conditions, parabolic narrow-beam directional antennas. Achievable effective radiated power gains range from 2 dB up to 23 dB, thereby extending range significantly from several hundred meters (under optimal line of sight conditions) to several kilometers.

2.4.3 MANET. Mobile ad hoc networking protocols are beginning to gain the attention of the wireless community. The Internet Engineering Task Force (IETF) MANET working group is working with a dozen draft proposals intended to permit the

routing of datagrams via networked users. Mobile users would remain connected to the wired access point via other connected users with a net effect of having an extended range connection, while sacrificing some bandwidth. This is a field with great potential once standards begin to emerge from the IETF's developers and implemented by manufacturers. For more information on current MANET draft proposals visit http://www.ietf.org/html.charters/manet-charter.html.

2.5 Wireless Bridges

Aside from IEEE 802.11, many WLAN devices function in "bridge" mode, very akin to a wireless Ethernet at the link layer. No Internet Protocol configuration is required for a bridge. Bridges typically operate at 11 Mbps at ranges up to 18 miles and 2 Mbps at ranges to 25 miles with radios emitting 100 to 1000 mw using elevated high-gain directional antennas. They can be used in point to point mode to connect two building's cabled networks, or in point to multipoint mode to connect a group of networks. Wireless bridges provide system architects with much needed flexibility in planning wireless systems deployment and help fill gaps where cabled systems may be costly or take time to install.

2.6 Security

No discussion on WLAN is complete without mention of security. The IEEE 802.11 set of standards did much to gain interoperability, convenience, and reliable performance of WLAN products. It also made wireless networks vulnerable to snooping and unwanted intrusion. IEEE 802.11b defines two basic security mechanisms:

- Service Set ID (SSID)
- Wired Equivalency Privacy (WEP)

2.6.1 Service Set ID. SSID is a string used much like a password to define a common roaming domain among multiple access points. Different SSIDs on access points permit overlapping wireless networks to exist. Several weaknesses affect use of SSID. An access point can be set to broadcast an SSID, allowing any client to associate with the access point. And the user manually configures the SSID, so the string may be widely known. With a small string set, a hacker may scan a set in minutes.

2.6.2 WEP. On the other hand, WEP is an authentication and encryption method that can be used to provide several levels of protection against eavesdropping and intrusion. Advances in encryption algorithms permit use of 40bit, 64bit and 128 bit encryption. To remain usable and interoperable, networks must be pre-configured to ensure all authorized users and access points use the same key. The standard also provides for authentication. Two forms exist; open system and private key. Open system allows any client to associate with an access point. This is obviously not secure. With private key, encrypted challenges and replies are made before network connections are made. WEP only provides for 4 static encryption keys, meaning all clients and access points use the same key, thus a determined hacker could conceivable gain access with enough time and proximity, making it less popular. Commercial products are available to manage network security keys and manage access lists.

2.6.3 Encryptors. Another means of securing a network is to employ an in-line encryption device. In-line high-grade encryptors are potentially expensive. They are gaining use in cabled networks and are readily adapted for use with insecure wireless bridges.

2.6.4 VPN Tunneling. VPN Tunneling is becoming a more common means of communicating securely over insecure links. They are widely used by travelers and remote offices to connect to company networks for email and other applications where privacy is naturally desired. Virtual private network (VPN) tunneling ensures privacy through both authentication and encryption mechanisms. Most importantly, VPN software used in conjunction with IEEE 802.11b products maintain end-to-end interoperability with different vendors' products so long as access to a VPN server is available.

3. Products and Application

A wide variety of WLAN and wireless bridge products have entered the market in the past several years. Depending on user needs, typical products include PC card (PCMCIA) for notebook, laptop, or PDA; PCI cards for PC, and external stand-alone devices for access points and bridges.

3.1 Home Networking

The proliferation of home networks brought on by broadband access and use of WLAN products in the home facilitates simultaneous Internet access by multiple family members on a single ISP account. Whether its for checking up on stock quotes, researching homework assignments or emailing family and friends, WLAN products are rapidly approaching the affordability range of most families and may be beneficial where installing network cables is impractical. As of this writing, for instance, 2Mbps WLAN cards could be purchased for $21 while 11 Mbps devices remain about $80. Access points begin at about $200.

3.2 Enterprise

In the work environment, network planners may employ WLAN products in situations where last mile or even several meters are critical. For example; offices are moving and network configurations do not change; quickly adding a few new users to the network; increased productivity with fast laptop or other mobile device access to the internet from a conference room or waiting area; team members connect while in a temporary location; in an old building difficult to wire; to extend existing cabled LANs; and where mobility is a must.

3.3 ISP/Public Access

Business travelers wanting more accessibility to their corporate email and other business applications are beginning to access the Internet from busy airports, train stations, hotels, and conference centers using the same adapters mobile clients use in the office. Internet service providers are providing promotional or fee for service broadband Internet access for mobile users without having to find a network jack or kiosk, facilitating use of own applications and mobile devices.

3.4 Military

The Armed Services have experimented with use of commercial WLAN and bridge products to meet their needs for mobile broadband access to fixed IP based networks. Though some

applications cannot be readily adopted for use, less sensitive areas are seeing the immediate benefits commercial and business users already experience. Experiments by the Marine Corps and the Army were conducted over the past several years helping them define future requirements for wireless networks. The great benefits of bandwidth have been tempered by the needs for mobility, extended range networking, and traditional military needs for system level privacy, i.e. transmission security and encryption.

4. Multimedia Applications and WLANs

Whether its voice telephony, video conferencing, large email attachments, voice and video clips, satellite imagery, weather maps, data base transactions, or multicast sharing of information transactions by multiple nodes, there is one common denominator for successful networking: *bandwidth!* Wireless LANs and bridges support the necessary throughput demanded by most mobile users and devices. Voice streams may flow at 2.4 or 64 kbps, a fraction of the throughput available. The apparent responsiveness of the network's available bandwidth provides near cabled system performance under typical operating conditions. More demanding video conferencing applications streaming datagrams at 64 or 256 kbps flow at a fraction of the available throughput.

5. Conclusions

Despite significant advances in standards based technology wireless LANs will not replace cabled systems. They are a fit supplement to any cabled infrastructure whether at home, small office, or in the enterprise, meeting last mile requirements, filling temporary requirements, and meeting the needs of business and multimedia applications of mobile users. The military has learned much about the challenges of wireless networking as they seek to supplement their mobile infrastructure.

6. Acknowledgments

Special thanks to Mr. Dave Green and Mr. Joe Kesner, Research Engineers with SRI International, for their assistance in evaluating wireless technologies. Their tireless data collection to validate prediction models helped us visualize propagation variables and to draw conclusions on net performance.

7. References

[1] IEEE-STD-802.11b-1999, "Part 11:Standard for Wireless LAN Medium Access Control (MAC) and Physical Layer (PHY) Specifications: Higher Speed Physical Layer Extension in he 2.4 GHz Band, (1999)

[2] D.B. Green, M.S. Obaidat, "Software Based Tools for Accurately Testing the Performance of Data Networks", Proceedings of the 2001 International Symposium on Performance Evaluation of Computer and Telecommunications Systems, Orlando, FL (July 15-19, 2001)

[3] F. Templin, A. Sastry, "Applications of wireless LANs in Tactical Networks – Architectural issues", SRI Technical Report, (Mar 28, 2000)

[4] W. Stallings, "Local and Metropolitan Area Networks", 6th ed, Prentice Hall Inc., (2000)

[5] J. Conover, "Wireless LANs Work Their Magic, Network Computing, http://www.nwc.com/1113/1113f2.html (Jul 10, 2000)

[6] J.B. Wood, "The Wireless LANs Page", http://www.cis.ohio-state.edu/~jain/cis788-95/wireless_lan /index.html (2/7/2000)

[7] Proxim White Paper, "802.11b Security Issues and Solutions", http://www.proxim.com, (2001)

[8] R. North, D. Bryan, D. Baker, "Wireless Networked Radios: Comparison of Military, Commercial, and R&D Protocols", 2d Annual UCSD Conference on Wireless Communications, San Diego, CA (1999)

[9] Code of Federal Regulations Title 47, Vol 1, Part 15 (Oct 1, 1999) US Government Printing Office

Biography

Mr. Luis O. Rodriguez is a Senior Research Engineer with SRI International, Menlo Park, California. His recent work, in support of the US Army CECOM Research, Development & Engineering Center (CERDEC), Fort Monmouth, New Jersey, includes numerous field exercise deployments, laboratory and field experiments, and research into characterization of mobile ad hoc networking protocols, comparative studies of integrated wireless platforms, adaptive multimedia applications, and next generation Internet protocols (IPv6). Special interest topics include mobile networking, IP mobility, interoperability and transition mechanisms, and bandwidth management under stressed wireless networking conditions. Mr. Rodriguez is a graduate of Rutgers College of Engineering and has over 25 years experience with engineering and employment of military tactical networks.

Sag-Tension Calculations for Aerial Cable with Linear or Nonlinear Tensile Properties

T. C. Chu
TyCom (US) Inc.
250 Industrial Way West
Eatontown, New Jersey 07724

ABSTRACT

A theoretical model to evaluate the tension and sag of aerial cable with linear or nonlinear tensile properties has been formulated. The formulation, which has taken the effects of temperature, permanent residual strain and creep, into consideration, results in a single equation in a single unknown for the cable. The equation can be readily solved by the "Root" function in Mathcad®. The results from this model are in excellent agreement with those evaluated by the graphic method[1] and proprietary software programs. The present model provides a simpler and more flexible method to accurately calculate the sag-tension properties of various aerial cables.

KEYWORDS

Aerial; cable; nonlinear; sag; tension.

1. FORMULATION

Five cases are considered in the formulation:

- Linear cable with negligible residual strain and creep effect, such as high strength steel ropes.
- Linear cable with permanent residual strain after heavy load as a dominating factor, such as ADSS with high content of aramid strength members.
- Linear cable with creep as a dominating factor, such as ADSS with low content of aramid strength members.
- Nonlinear cable with permanent residual strain as a dominating factor, such as ACSR conductors or OPGW with high steel content.
- Nonlinear cable with creep as a dominating factor, such as AAC conductors.

A single equation in single unknown will be derived for each case from the basic catenary equations.

A catenary in a level span with cable weight per unit length, w, the horizontal component of tension H, span length S, cable length L, and the sag of the cable D is illustrated in Fig. 1.

The fundamental equations for the catenary are

$$y(x) = \frac{H}{w}[\cosh(\frac{wx}{H}) - 1] \qquad (1)$$

$$L(x) = \frac{H}{w}\sinh(\frac{wx}{H}) \qquad (2)$$

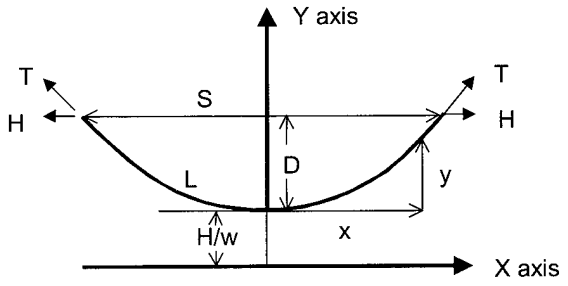


Fig. 1 Catenary Configuration in Level Span

At x = S/2, the half span length, we have the relations for sag D and cable length L

$$D = \frac{H}{w}[\cosh(\frac{wS}{2H}) - 1] \qquad (3)$$

$$L = \frac{2H}{w}\sinh(\frac{wx}{H}) \qquad (4)$$

The sag-tensions of an installed aerial cable are customarily analyzed in three states: a) initial state, b) final state with permanent residual strain a dominating factor, and c) final state with creep a dominating factor. In each state, the sag-tension of the cable is calculated from condition #1 to condition #2 due to changes in ambient temperature and ice/wind loading condition. Normally only one of the final states that gives higher sag values is listed with the initial state in the final sag-tension results.

At condition #1 we have from equation (4)

$$L_1 = \frac{2H_1}{w_1}\sinh(\frac{Sw_1}{2H_1}) \qquad (5)$$

Let L_{10} be the imaginary cable length at zero tension, i.e., the cable is taken from its supports and laid on the ground. Then

$$L_{10} = L_1 - \varepsilon_1 L_1 = L_1(1 - \varepsilon_1) \qquad (6)$$

Where ε_1 is the cable strain under horizontal tensions H_1. Now due to temperature change, ice loading, wind force or all of

three factors the installed cable is changed to a new condition #2.

Then

$$L_2 = \frac{2H_2}{w_2}\sinh(\frac{Sw_2}{2H_2}) \qquad (7)$$

Let L_{20} be the imaginary cable length at zero tension under the new loading condition and the change in length is solely due to the temperature change from T_1 to T_2, then

$$L_{20} = L_{10}[1 + \alpha_c(T_2 - T_1)] \qquad (8)$$

α_c is the thermal expansion coefficient for the cable and is approximated by

$$\alpha_c = \sum_k \frac{\alpha_k E_k A_k}{E_c A_c} \qquad (9)$$

E_c is the modulus of elasticity of the cable and is approximated by

$$E_c = \sum_k \frac{E_k A_k}{A_c} \qquad (10)$$

α_k, E_k, and A_k denote the thermal expansion coefficient, modulus of elasticity, and cross section area of the constituent components in the cable.

The actual cable length under the new loading condition L_2 is related to the imaginary zero tension length L_{20} by

$$L_2 = L_{20}(1 + \varepsilon_2) \qquad (11)$$

ε_2 is the cable strain under horizontal tension H_2. Substituting (5) into (6), (6) into (8), and (8) into (11) yield

$$\frac{2H_2}{w_2}\sinh(\frac{Sw_2}{2H_2}) = \frac{2H_1}{w_1}\sinh(\frac{Sw_1}{2H_1})(1 - \varepsilon_1)(1 + \varepsilon_2)[1 + \alpha_c(T_2 - T_1)] \qquad (12)$$

Equation (12) is the fundamental relation for evaluating the sag-tension of aerial cable. The relationships between the horizontal tensions H_1 and H_2 and cable strains ε_1 and ε_2 depend on the tensile properties of the cable and the effects of residual strain caused by heavy snow load or creep. Finding proper relations between the horizontal tensions and cable strains for each specific cable is the key to solve this equation.

1.1 Linear elastic cable without permanent residual strain and creep effect

In this case the modulus of elasticity E_c is constant. The cable strains ε_1 and ε_2 are related to the horizontal tensions H_1 and H_2 by

$$H_1 = E_c A_c \varepsilon_1 \qquad (13)$$

$$H_2 = E_c A_c \varepsilon_2 \qquad (14)$$

Substitution of (13) and (14) into (12) yields

$$\frac{2H_2}{w_2}\sinh(\frac{Sw_2}{2H_2}) = \frac{2H_1}{w_1}\sinh(\frac{Sw_1}{2H_1})(1 - \frac{H_1}{E_c A_c})(1 + \frac{H_2}{E_c A_c})[1 + \alpha_c(T_2 - T_1)] \qquad (15)$$

With given condition #1, (15) is a single equation in one unknown H_2 and it can be readily solved by using the "root" function in Mathcad®. In this special linear case (15) is valid for all three states.

1.2 Nonlinear cable with permanent residual strain

The stress-strain relations in this case are illustrated in Fig. (2). The stress-strain relation in the initial state is governed by

$$\sigma = E_{c1}\varepsilon \qquad (16)$$

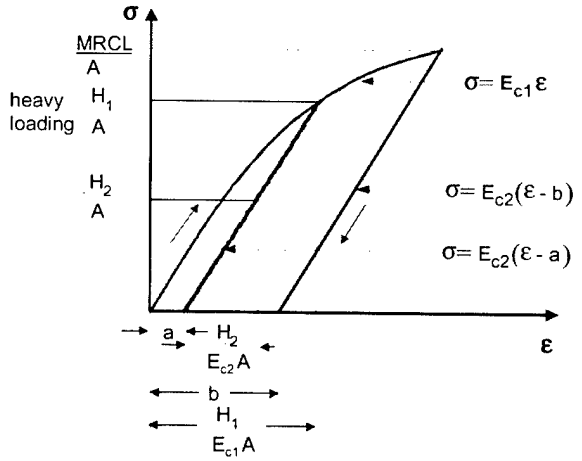


Fig. 2 Stress-strain relations with the effect of permanent residue strain

For cables with linear elastic property E_{c1} is a constant and (16) represents a straight line; for cables with nonlinear property E_{c1} is a function of cable strain or cable tension. This function can usually be approximated by a polynomial

$$E_{c1} = a_0 + a_1\varepsilon + a_2\varepsilon^2 + ... + a_n\varepsilon^n \qquad (17)$$

or

$$E_{c1} = a_0 + a_1(\frac{H_1}{A_c}) + a_2(\frac{H_1}{A_c})^2 + ... + a_n(\frac{H_1}{A_c})^n \qquad (18)$$

The order and coefficients of the polynomial can be determined by curve fitting the cable tensile test data.

The stress-strain relation in the final state after heavy loading is governed by

$$\sigma = E_{c2}(\varepsilon - a) \qquad (19)$$

In which the modulus of elasticity E_{c2} and residue strain "a" are to be determined. E_{c2} can be determined by finding the slope of the de-tensioning straight line from a tensile test of the cable to the Maximum Rated Cable Load (MRCL).

$$\sigma = E_{c2}(\varepsilon - b) \qquad (20)$$

Since the point (H_1/A, $H_1/E_{c1}A$) is the intersection of the curve (16) and the line (19), substitution of $\sigma = H_1/A$ and $\varepsilon = H_1/E_{c1}A$ into (19) yields

$$a = \frac{H_1}{E_{c1}A_c} - \frac{H_1}{E_{c2}A_c} \qquad (21)$$

As shown in Fig. 2 the cable strain ε_2 corresponding to a horizontal tension H_2 in the final state (condition #2) is given by

$$\varepsilon_2 = a + \frac{H_2}{E_{c2}A_c} \qquad (22)$$

and the cable strain ε_1 corresponding to a horizontal tension H_1 at the heavy load (condition #1) is

$$\varepsilon_1 = \frac{H_1}{E_{c1}A_c} \qquad (23)$$

Substitution of (21) into (22) and then substitution of (22) and (23) into (12) yield

$$\frac{2H_2}{w_2}\sinh\left(\frac{Sw_2}{2H_2}\right) = \frac{2H_1}{w_1}\sinh\left(\frac{Sw_1}{2H_1}\right)\left(1 - \frac{H_1}{E_{c1}A}\right)[1 + \alpha_c(T_2 - T_1)]$$
$$\left[1 + \left(\frac{H_1}{E_{c1}A} - \frac{H_1}{E_{c2}A}\right) + \frac{H_2}{E_{c2}A}\right] \qquad (24)$$

This is the equation for evaluating the sag-tension in the final state with the effect of residual strain. Equation (24) is again a single equation in one unknown H_2 and it can be readily solved by using the "root" function in Mathcad®. Note that in this case the horizontal tension H_1 is always from the heavy loading condition (under ice load and wind force). Initial installations are most unlikely happened at this extreme condition. For initial installation at conditions other than the extreme case, Equation (15), together with (16), (17) or (18) if the cable is nonlinear, should be used to find the horizontal tension at the heavy loading condition, and then use (24) to evaluate the horizontal tension H_2 in the final state.

1.3 Nonlinear cable with creep effect

The stress-strain relations in this case are illustrated in Fig. (3). In the initial state, the stress-strain relations also follow (15), (16), (17) and (18).

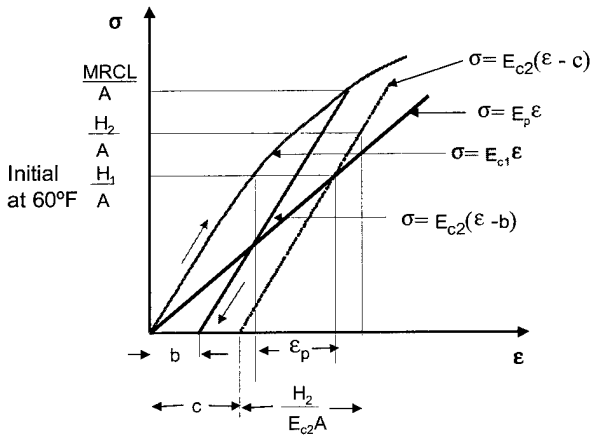


Fig. 3 Stress-strain relations with creep effect

To evaluate the sag-tensions in the final state, a new stress-strain relation involving the creep effect needs to be derived. The creep property of a material is normally tested at 60°F with a constant load for a specific period of time (1000 hours for ADSS). Then the test data is extrapolated to 6 months, a year, or 10 years. The results are plotted as individual linear equations of the form

$$\sigma = E_p\varepsilon \qquad (25)$$

E_p is the modulus or slope of the creep equation and ε_p is the cable strain due to creep at horizontal tension H_1 and 60°F ambient temperature. In a creep dominating case ε_p is greater than "a", the permanent residual strain in Fig. 2. Since the cable is permanently elongated due to the creep effect in the final state the tensile modulus of the cable is changed to E_{c2}, which is again from tensile testing the cable to the Maximum Rated Cable Load (MRCL). The stress-strain relation in the final state including creep effect is thus given by

$$\sigma = E_{c2}(\varepsilon - c) \qquad (26)$$

The constant "c" is determined by using the fact that the point (H_1/A, H_1/E_pA) is the intersection of two lines represented by (25) and (26). Substitution of $\sigma = H_1/A$ and $\varepsilon = H_1/E_pA$ into (26) yields

$$c = \frac{H_1}{E_pA_c} - \frac{H_1}{E_{c2}A_c} \qquad (27)$$

At Condition #2 in the final state, the cable strain ε_2 corresponding to a horizontal tension H_2 is

$$\varepsilon_2 = c + \frac{H_2}{E_{c2}A_c} \qquad (28)$$

Substitution of (27) into (28) and then to (12) yield

$$\frac{2H_2}{w_2}\sinh\left(\frac{Sw_2}{2H_2}\right) = \frac{2H_1}{w_1}\sinh\left(\frac{Sw_1}{2H_1}\right)\left(1 - \frac{H_1}{E_{c1}A}\right)\left[1 + \alpha_c(T_2 - T_1)\right]$$
$$\left[1 + \left(\frac{H_1}{E_pA} - \frac{H_1}{E_{c2}A}\right) + \frac{H_2}{E_{c2}A}\right] \qquad (29)$$

This is the equation for calculating the sag-tension in the final state. It is again a single equation in one unknown H_2 and it can be readily solved by using the "root" function in Mathcad®. Note that in this case the horizontal tension, H_1 in (29), is always evaluated at 60°F ambient temperature. For initial installation at other temperatures, Equation (15), together with (16), (17) or (18) if the cable is nonlinear, should be used to find the horizontal tension at 60°F first, and then use (29) to find horizontal tension H_2 in the final state.

2. RESULTS

The above formulation is applied to two cables: a linear ADSS previously investigated in Ref.1 and a nonlinear AAC (All Aluminum Cable) studied in Ref.2.

Example 1 Linear ADSS Cable

The diameter of the cable is 0.906" and its weight and thermal expansion coefficient are 0.277 lb/ft, and 3.32 x 10^{-6} /F respectively. The span length is 1400 ft. The tensile modulus in the initial state E_{c1} and final state E_{c2} are assumed to be 1.243832 x 10^6 psi and 1.353706 x 10^6 psi. The slope of the creep line E_p is 1.055759 x 10^6 psi. The results from the present method and SAG-10 program are compared in Table 1. They are in good agreement.

Table 1 Comparison of results for ADSS with creep effect

					Final after Creep		Final after Creep		Initial		Initial	
					(present method)		(SAG-10)		(present method		(SAG-10)	
Temp	Ice	Wind	K	Weight	Sag	Tension	Sag	Tension	Sag	Tension	Sag	Tension
F	In	lb/ft^2	lb/ft	lb/ft	ft	lb	ft	lb	ft	lb	ft	lb
0	0.5	4	0.3	1.615	56.26	7048	56.07	7027	54.42	7285	54.10	7285
32	0.5	0	0	1.152	47.80	5910	47.69	5897	45.19	6251	45.17	6229
-20	0	0	0	0.277	18.17	3735	18.16	5735	15.42	4400	15.42	4400
0	0	0	0	0.277	18.40	3687	18.40	3687	15.59	4352	15.59	4352
30	0	0	0	0.277	18.77	3616	18.76	3616	15.85	4280	15.83	4281
60	0	0	0	0.277	19.14	3546	19.13	3546	16.12	4209	16.11	4210
90	0	0	0	0.277	19.52	3476	19.31	3476	16.40	4138	16.39	4139
120	0	0	0	0.277	19.92	3407	19.91	3407	16.69	4067	16.67	4069

Table 2 Comparison of results for ADSS with creep effect

					Final after Creep		Final after Creep		Initial		Initial	
					(present method)		(PLS-CADD)		(present method		(PLS-CADD)	
Temp	Ice	Wind	K	Weight	Sag	Tension	Sag	Tension	Sag	Tension	Sag	Tension
F	In	lb/ft^2	lb/ft	lb/ft	ft	lb	ft	lb	ft	lb	ft	lb
0	0.5	4	0.3	1.615	56.17	7059	56.47	7022	54.22	7284	54.42	7284
32	0.5	0	0	1.152	47.71	5922	47.90	5898	45.14	6257	45.30	6235
-20	0	0	0	0.277	18.08	3753	18.08	3754	15.34	4423	15.34	4423
0	0	0	0	0.277	18.32	3705	18.32	3705	15.51	4376	15.51	4376
30	0	0	0	0.277	18.68	3634	18.68	3634	15.76	4304	15.77	4304
60	0	0	0	0.277	19.05	3563	19.05	3563	16.03	4233	16.04	4233
90	0	0	0	0.277	19.43	3493	19.43	3493	16.30	4162	16.31	4162
120	0	0	0	0.277	19.82	3424	19.82	3425	16.58	4092	16.59	4092

Comparison between the present method and PLC-CADD program also shows good agreement as indicated in Table 2 and Table 3. In this calculation the tensile modulus are assumed to be E_{c1} =1.254946 x 10^6 psi, E_{c2} = 1.353263 x 10^6 psi and E_p = 1.063998 x 10^6 psi.

Table 3 Comparison of results for ADSS with permanent residue strain

					Final after Load		Final after Load		Initial		Initial	
					(present method)		(PLS-CADD)		(present method		(PLS-CADD)	
Temp	Ice	Wind	K	Weight	Sag	Tension	Sag	Tension	Sag	Tension	Sag	Tension
F	In	lb/ft^2	lb/ft	lb/ft	ft	lb	ft	lb	ft	lb	ft	lb
0	0.5	4	0.3	1.615	54.43	7284	54.42	7284	54.22	7284	54.42	7284
32	0.5	0	0	1.152	45.52	6202	45.69	6182	45.14	6257	45.30	6235
-20	0	0	0	0.277	16.16	4201	16.15	4202	15.34	4423	15.34	4423
0	0	0	0	0.277	16.35	4151	16.35	4151	15.51	4376	15.51	4376
30	0	0	0	0.277	16.66	4075	16.66	4075	15.76	4304	15.77	4304
60	0	0	0	0.277	16.97	4000	16.97	4000	16.03	4233	16.04	4233
90	0	0	0	0.277	17.29	3926	17.29	3926	16.30	4162	16.31	4162
120	0	0	0	0.277	17.62	3852	17.62	3852	16.58	4092	16.59	4092

Example 2 Nonlinear AAC Cable

The diameter, weight, and thermal expansion coefficient of this 37 strands AAC "Arbutus" cable are 1.026", 0.746 lb/ft, and 12.3 x 10^{-6} /F respectively. The span length is 1000 ft. The cable has nonlinear tensile property and the tensile modulus in the initial state E_{c1} is characterized by the following function

$$E_{c1} = \frac{100}{\left[1 - 5.31\cdot10^{-3} + (1.74\cdot10^{-5})\left(\frac{H}{A}\right) - (6.17\cdot10^{-10})\left(\frac{H}{A}\right)^2 + (5.05\cdot10^{-14})\left(\frac{H}{A}\right)^3\right]}$$

The tensile modulus in the final state E_{c2} is 8.88 x 10^6 psi and the slope of the creep line E_p is 3.65 x 10^6 psi.

The results from the present method and SAG-10 program in Ref. 2 are in excellent agreement as shown in Table 4.

Table 4 Comparison of results for ACC with creep effect

					Final after Creep		Final after Creep		Initial		Initial	
					(present method)		(SAG-10)		(present method		(SAG-10)	
Temp	Ice	Wind	K	Weight	Sag	Tension	Sag	Tension	Sag	Tension	Sag	Tension
F	In	lb/ft^2	lb/ft	lb/ft	ft	lb	ft	lb	ft	lb	ft	lb
0	0.5	4	0.3	2.125	44.7	5958	45.11	5953	44.15	6032	44.50	6033
32	0.5	0	0	1.696	45.39	4681	45.80	4679	44.3	4796	44.68	4794
-20	0	0	0	0.746	40.68	2298	40.93	2300	38.68	2416	38.89	2413
0	0	0	0	0.746	41.76	2238	42.04	2240	39.79	2349	40.03	2350
30	0	0	0	0.746	43.34	2157	43.66	2158	41.41	2257	41.71	2258
60	0	0	0	0.746	44.87	2084	45.24	2085	42.1	2175	43.32	2175
90	0	0	0	0.746	46.36	2017	46.76	2018	44.5	2101	44.89	2101
120	0	0	0	0.746	47.8	1957	48.24	1958	45.98	2034	46.42	2033
167	0	0	0	0.746	49.99	1872	50.49	1873	48.22	1940	48.72	1939
212	0	0	0	0.746	52.01	1799	52.55	1801	50.29	1861	50.84	1860

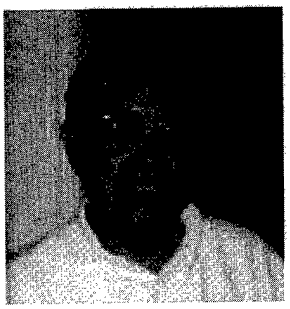
3. CONCLUSION

The model has been demonstrated with a linear ADSS cable and a nonlinear AAC cable. The results from the present are in good agreement with those from the graphic method, SAG-10 and PLS-CADD programs. The present model provides a simpler and more flexible method to evaluate the sag-tension properties of aerial cable with either linear or nonlinear tensile property.

4. REFERENCES

1. Cristian Militaru, "Stress-Strain, Creep, and Temperature Dependency of ADSS (All Dielectric Self Supporting) Cable's Sag & Tension Calculation" Proceedings of 48th International wire & Cable Symposium, 1999, pp. 605-613.
2. Overhead Conductor Manual, Southwire Company, 1994, p. 2.43

BIOGRAPHY



T. C. Chu
TyCom (US) Inc.
Eatontown, NJ

T. C. Chu received his B.S.M.E from Cheng Kung University, Taiwan, 1964, M.S.M.E from Syracuse University, 1967 and Ph.D. Aerospace Engineering from Cornell University, 1971. He joined Bell Laboratories in 1972 and retired in 1997. During his service with AT&T Bell Laboratories, he was responsible for the design and development of AT&T's SL and SL100 fiber optic submarine cables. He is currently with the Advanced Technology Research Group in the Cable Development Division of TyCom (US) Inc., working on new cable design and development.

Nonlinear Modeling of Secondary Coating from Expensive Experimental Data

A. Bulsari
AB Nonlinear Solutions Oy, PL 953, 20101 Turku 10, Finland
Tel. +358 2 2154721, E-mail: NLS @ abo.fi
and
M. Lahti
Nextrom Oy, Ensimmäinen Savu, 01610 Vantaa, Finland
Tel. +358 9 50253134, E-mail: Mikko.Lahti @ nextrom.com

Abstract

New techniques of nonlinear modeling have come up in the last ten twelve years which have opened up new possibilities in empirical process modeling. Secondary coating is a typical process which cannot be modeled adequately by physical modeling. The effects some of the process variables are clearly nonlinear, which makes it imperative for us to take into account the nonlinearities rather than ignore them. Neural network techniques are therefore more suitable for process modeling of secondary coating. Neural networks have been used in various process modeling applications in steel industries, pulp and paper industries, chemical industries, plastics industries, etc.

Keywords

Secondary coating, OFCs, neural networks, nonlinear modeling

1. Introduction

Secondary coating is a plastics extrusion process, followed by controlled cooling and winding under tension (Figure 1). The properties of secondary coatings like excess fiber length depend to a large extent on the process variables and the material properties of the plastic. For a given product, the plastic material, the jelly, the external and internal diameters, and the number of optical fibers in it are fixed. The properties of the secondary coatings, then depend on the process variables, starting from tension on the optical fibers, extrusion variables, jelly temperature, cooling water temperature, line speed, capstan location, winding tension, etc.

In this work, feed-forward neural network models (Figure 2) were developed based on experimental data with process variables as inputs. The nonlinearities are visible in the neural network model (Figure 5). The neural networks used logistic sigmoid activation functions, and were found to be effective. This is a typical situation where the conventional linear statistical techniques are not effective.

2. Nonlinear modeling

There are hardly any processes in this world which are absolutely linear. It is therefore wise to treat the nonlinearities rather than ignore them. To treat the nonlinearities, one can use new techniques of nonlinear modeling, like artificial neural networks. The proponents of linear techniques draw on their simplicity and the possibility of adding nonlinear terms in linear regression. Often this is not done, and is not efficient even if it is done. Nature does not follow the simplicities that we try to fit it in, using common linear techniques.

Neural networks, on the other hand, have the so-called universal approximation capability which make them suitable for most function approximation tasks we come across in process industries. The user does not need to know the type and severity of nonlinearities while developing the models.

Artificial neural networks resemble structurally and to a smaller extent functionally the networks of neurons in biological systems. Like the networks of neurons in the brains, artificial neural networks also consist of neurons in layers directionally connected to others in the adjacent layers (see Figure 2).

There are many different types of neural networks, and some of them have practical uses in process industries [1]. Neural networks have been in use in process industries for about ten years. The multilayer perception, a kind of a feed-forward neural network, is the most common one. Most neural network applications in industries [2-6] are based on them. Nonlinear modeling can also be done in many other ways. The authors are not aware of very many applications of neural networks in plastics industries. Most of the work of the authors is confidential and is therefore not published.

The output of each neuron i in the feed-forward neural network is given by

$$z_i = \sigma\left(\sum_{j=0}^{N} w_{ij} x_j\right)$$

where the activation function is usually the logistic sigmoid, given by

$$\sigma(a)=\frac{1}{1+e^{-a}}$$

The incoming signals to the neuron are x_j, and w_{ij} are the weights for each connection from the incoming signals to the i^{th} neuron. The w_{i0} terms are called biases. This results in a set of algebraic equations which relate the input variables to the output variables. Thus, for each observation (a set of input and output variables), the outputs can be predicted from these equations based on a given set of weights. The training procedure aims at determining the weights which result in the smallest sum of squares of prediction errors.

There are a variety of training methods in use today. Back-propagation used to be the most common training method about ten years back. Today, most people use good optimization methods instead.

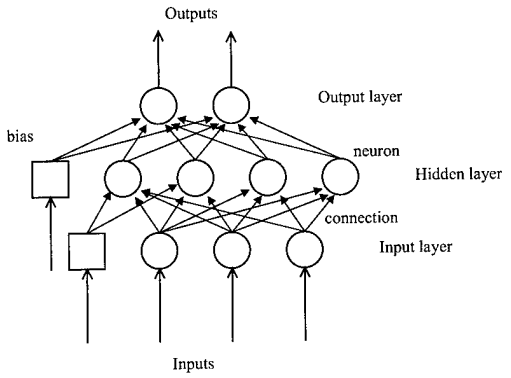


Figure 2. A typical feed-forward neural network

3. Secondary coating line OFC 40

The high-speed secondary coating line OFC 40 (Figure 1) is especially designed for loose tube production but it can be modified for fiber bundle or premises cable production thanks to its modularity. The line comprises multiple new innovations for high productivity and minimized scrap. Secondary coating is the first phase in the manufacturing process of fiber optic cables. The process is important in two ways. Stability and repeatability of the process together with high production speeds and flexibility of operation have been the key criteria in designing this line.

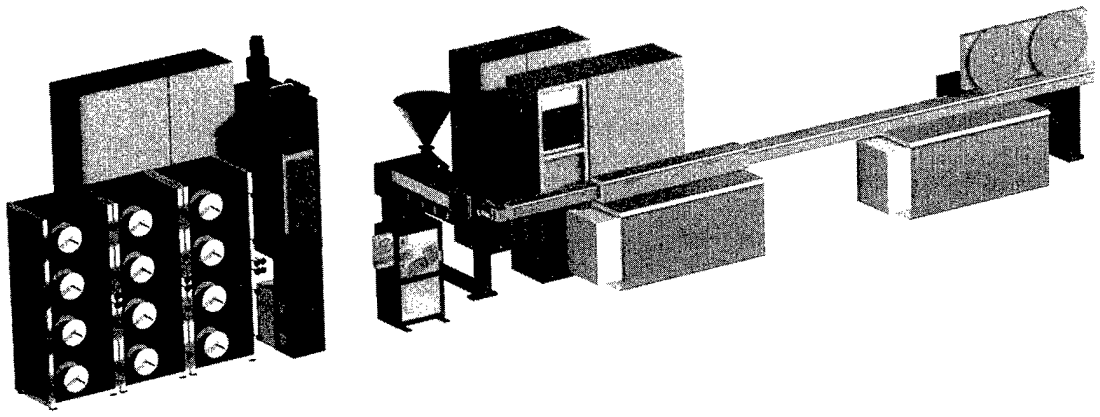


Figure 1. OFC lines are relatively well instrumented, huge amounts of data are logged and left unutilized or underutilized

4. Modeling of product properties

Neural network models have performed well in predicting product properties of various materials [1, 4-6] including material characteristics of pulp, paper, metals, plastics, cement, concrete, etc. These include variables like brightness and freeness of pulp, formation index of paper, mechanical properties of metals like

tensile strength, yield strength, elongation, impact strength of plastics, and compressive strength of concrete.

One interesting example which describes such neural network modeling [5] is about compressive strength and compaction degree of concrete. By upgrading a linear model to a nonlinear model, the uncertainty in compressive strength reduces considerably. This reduction in uncertainty for a medium sized precuts plant which makes 80 000 m^3 concrete can mean a saving of 700 000 mk of cement a year. Since most concrete plants don't even have linear models, the potential for saving is higher.

The rms error (roughly the standard deviation) of prediction of compressive strength with a linear regression model was 4.3 MPa while a neural network model resulted in a rms error of 2.4 MPa. Linear models for this purpose are anyway misleading because they show trends in only one direction implying that the maximum strength can be achieved with 100% water or with 100 % cement. In reality, the strength increases with water content upto a certain extent, and then reduces as concrete is watered down too much. Linear models do not describe this, but it is relatively easy for neural network models to do so.

5. Process guidance system

The nonlinear models can be cumbersome to use in the form of equations. For industrial use, it is important to make them easily accessible. A process guidance system has therefore been developed so that industries can utilize this technology without the need for nonlinear modeling experts. This system also allows us to see the characteristics of the models as described later in this section.

Several product properties of secondary coatings are important for the producers and the users. These properties include excess fiber length (difference between the lengths of the fibers and the tubes), dimensional accuracy (diameter, circularity) of the coatings, elasticity, etc. Excess fibber length was the first product property to be taken into account while developing the guidance system for secondary coating. Excess fiber length depends on several process variables, material characteristics of the coating material, and the dimensions of the coating (inner and outer diameters). Depending on the priorities and the needs of a given production unit, different input vectors can be implemented in the guidance system.

In the examples shown in the successive figures, four input variables are considered: pay-off tension, jelly hose temperature, line speed and cooling water temperature. Figure 3 shows a simple calculation predicting excess fiber length from these four variables.

It is easy to change the models, which may also have a different configuration. The system expects the models to be in files of a certain format. These files can be replaced to change the models. In future, the user will be able to pick the model of his choice at run time also.

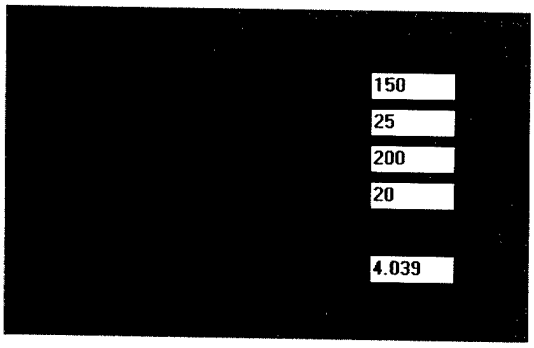


Figure 3. Excess fiber length predicted from four input variables in this model

Another window allows the user to see the effects of the input variables on the product property of interest. These plots also give a hint of how the performance can be improved. Figures 4 and 5 show the effects of line speed and water temperature on excess fiber length.

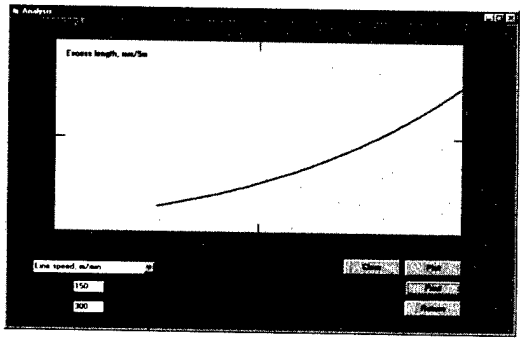


Figure 4. Effect of line speed on excess length according to the nonlinear model

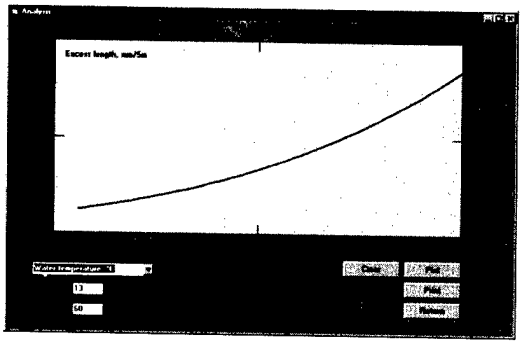


Figure 5. Effect of water temperature on excess length according to model

The guidance system also allows the user to calculate suitable process variables within specified limits with a single click of a mouse, in less than a second.

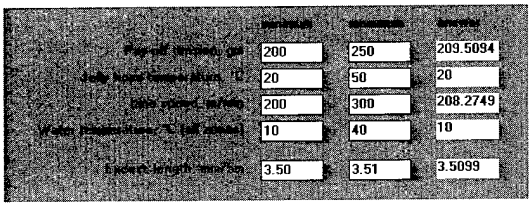


Figure 6. Finding good operating conditions using the nonlinear model

The models for this system were developed from experimental data. Experiments were carried out to measure the variables of interest, in the range of interest. This is, however, expensive, and production units cannot afford to carry out this kind of experiments. Nextrom has the facilities to carry out such experiments for its customers. In future, the requirements for experimentation will be reduced as much as possible. In parallel, model development will be made possible from normal production data. Such models will have a narrower range, but will nevertheless be useful for improving the performance of the secondary coating lines.

References

[1] A. Bulsari (ed.), *Neural Networks for Chemical Engineers*, Elsevier, Amsterdam, Netherlands, 1995.
[2] A. Bulsari and E. Hocksell, "Neural network systems for hardened components", Steel Technology International, 1996/97, 133-138.
[3] A. Bulsari, "Quality of nonlinear modeling in process industries", Internal Report NLS/1998/2
[4] P. Myllykoski and A. Bulsari, "Selection of influential variables for modeling cold rolling of thin sheets", Proceedings of the EANN '97, 155-158
[5] A. Bulsari and A. Käppi, "Prediction of compressive strength and compaction degree of concrete", Proceedings of the EANN '98, 181-184
[6] P. Myllykoski, Prediction of formability of steel sheets, Proceedings of the EANN '98, 221-224

Authors

Authors



Dr. Mikko I. Lahti

Nextrom Oy
P.O. Box 44
Fin-01511 Vantaa
FINLAND
Tel. +358-9-50251
mikko.lahti@nextrom.com

Mikko Lahti received the degree of M. Sc. in Chemical Engineering in 1991 and the degree of Dr. Tech. in Polymer Technology in 1996. Before joining Nextrom in 1997 he worked as Research Scientist in European Joint Research Center in Milan. Currently, as R&D Manager at Nextrom, he is responsible for the development of the extrusion processes for fiber optic cables.

Weather Ageing of Coloured Polyethylene Jacketing Materials

Elisabeth E Ribarits Persson[1], Estelle J Cognet[2], Hans-Bertil Martinsson[3], Håkan Larsson[4]

1) PolyOne Sweden AB, Porsån 8932, S-444 93 Spekeröd, Sweden, +46303778488, elisabeth.ribarits@polyone.com,
2) PolyOne Belgium SA, 2 rue Melville Wilson, B-5330 Assesse, Belgium, +3283660263, estelle.cognet@polyone.com,
3) Borealis AB, S-444 86 Stenungsund, Sweden, hans-bertil.martinsson@borealisgroup.com,

Abstract

In this work PE coloured samples were exposed to accelerated UV light in a weather-O-meter (WOM) in order to study the degradation mechanisms of colour change and mechanical properties as well as chemical degradation using spectrophotometric analysis. The samples were exposed to weather ageing up to 6000 hours or > 7 GJ/m^2 radiation. The most critical colours used in cable jackets, red and orange, have been studied using different pigments and amounts of UV stabilizer. The results of the study show that the degradation of the system: matrix/colorant depends upon pigmentation and the UV stabilization of the polymer matrix. It is also shown that UV light degrades mainly the surface of the jacket, and that the rest of the cross-section is intact, provided that the matrix is stabilized. Inorganic pigments such as lead containing pigments, are stable, but it is also shown that more environmentally friendly pigments are weather resistant. We have also seen examples of pigments that accelerate the degradation of the PE matrix when exposed to UV light.

Keywords

Wire; Cable; Colour; Pigment; Polyethylene; PE; Weatherability; HALS; Weather resistance; Weather stability; Outdoor; Ageing. UV.

1. Introduction

Polyethylene is well suited as a jacketing material in wire & cable applications due to the balance of properties required for the application. Of importance are processing, mechanical and physical properties together with stress crack resistance. To these can be added UV stability for outdoor applications, which most commonly is achieved by the addition of carbon black to prevent UV light penetrating into the jacket. For non-black applications colour pigments are added together with various types of UV stabilizers. In previous years LDPE was used as a jacketing material. However it suffered from limited performance in relation to most of the above mentioned properties. Development lead to the use of LLDPE/MDPE/HDPE and recently to the use of bimodal jacketing materials, with enhanced performance.

There are two types of pigments that can be used to colour cables: inorganic and organic. Most inorganic pigments are extremely weather resistant, heat stable and give excellent opacity. Organic pigments are mainly used for their high tinting strength. Because of increasing environmental concerns about heavy metals, inorganic pigments are being replaced by organic alternatives. The selection of pigments therefore becomes more complex for critical colours like red and orange. It is well known that the inorganic lead pigment has outstanding performance in term of light fastness. In this study, several kinds of pigment were selected, inorganic containing lead, and organic with and without halogen, as this latter criterion is increasingly requested by the Wire & Cable industry.

A coloured polymer material is a complex chemical system comprising a macromolecular matrix with stabilizers, pigments and sometimes mineral or organic fillers. The study of the effect of the UV light is therefore difficult to analyse in such a system. WOM testing is one of the best ways to accelerate the degradation of organic material. The limitation of this technique is in accelerating degradation without creating any mechanism that could not occur in real conditions.

2. Experimental

2.1 Materials

The polymers used are medium density polyethylenes (MDPE) from a unimodal polymerisation process and a high density polyethylene (HDPE) from a bimodal process, see Table 1. Both polymers were base stabilized with 500 ppm stabilizer.

Table 1: Base materials used

MDPE	Unimodal, PE1 (B)	Bimodal, PE2 (C)
Density (kg/m^3)	939	942
MFR (190°C/2.16)	0.2	0.5

The colours used were red and orange in a masterbatch with base resin LLDPE. The colour MB was added at 1% to the matrix.

Table 2 : Colour masterbatches used in the study

Name	Colour	Description
RD1 (E)	Red	Lead free, contains halogens
RD2 (F)	Red	Lead free, halogen free
RD3 (S)	Red	Lead free, halogen free
RD4 (T)	Red	Lead free, contains halogens
OR1 (G)	Orange	Contains lead
OR2 (H)	Orange	Lead free, contains halogens
OR3 (U)	Orange	Lead free, contains halogens

A HALS (Hindered Amine Light Stabilizer) was used in different amounts in the recipes, see Table 3.

Table 3: Recipes. w/o (weight percent)

Sample	PE1	PE2	Colour	HALS
B1	99.95			
C1		99.95		
C2		99.9		0.05
BE1	98.9		RD1	0.05
BF1	98.9		RD2	0.05
BG1	98.9		OR1	0.05
BS1	**98.9**		**RD3**	**0.05**
BT1	**98.9**		**RD4**	**0.05**
BU1	**98.9**		**OR3**	**0.05**
BH1	98.9		OR2	0.05
CE1		98.9	RD1	0.05
CF1		98.9	RD2	0.05
CG1		98.9	OR1	0.05
CS1		**98.9**	**RD3**	**0.05**
CT1		**98.9**	**RD4**	**0.05**
CU1		**98.9**	**OR3**	**0.05**
CH1		98.9	OR2	0.05
BE2	98.85		RD1	0.1
BE3	98.95		RD1	
CF2		98.95	RD2	
CG2		98.95	OR1	
CE2		98.45	RD1	0.5
CF3		**98.45**	**RD2**	**0.5**
CG3		**98.45**	**OR1**	**0.5**
CH2		**98.45**	**OR2**	**0.5**
CS2		**98.45**	**RD3**	**0.5**
CT2		**98.45**	**RD4**	**0.5**
CU2		**98.45**	**OR3**	**0.5**

2.2 Sample preparation

The samples for this study were prepared in a roll mill of 500 gram batches of each formulation, mixed for 10 minutes at 180°C. They were moulded into a plaque at 200°C for 10 minutes (5 minutes at low pressure and 5 minutes at high pressure). Cooling was controlled at 15°C/minute. The thickness of the plaques was 1 mm. From each plaque, dumb-bell shaped specimens according to ISO 527, type A, were punched.

2.3 Weather-O-Meter (WOM) conditions

Dumb-bell specimens of the formulations were placed in the WOM and samples taken out after 1000, 2000, 4000 and 6000 hours. Every 500 hours the samples were removed for cleaning the WOM and for colour testing. The accelerated weather ageing test was performed in an Atlas WOM CI 65 under the following conditions, Table 4:

Table 4: WOM programme

Black panel temperature	63°C
Relative humidity	60%
Water spraying cycle	102 min dry and 18 min wet
Irradiation	0.35 W/m2 at 340 nm
Filter system (interior/exterior)	Borosilicate
Filter exchange interior	1000 hours
Filter exchange exterior	2000 hours
Lamp	Xenon

2.4 Colour measurements

A Color Spectrophotometer datacolor spectraflash SF600 CT+. MC-90 analyzer with dual 128 diode array was used for colour measurements.

The light fastness was evaluated colorimetrically by comparing exposed coloured samples with the original unexposed samples. The colour difference ΔE between the two test specimens is expressed in the CIELAB system.

For the determination of contrast, grey scale (DIN 54001) 1-5 was used. 5 means excellent, with no deviation in contrast and 1 means poor result, with large deviation in contrast, 3 to 4 is acceptable.

2.5 Mechanical properties

Tensile testing was performed using an Alwetron TCT25 tensile testing machine in a constant climate room of 23°C and 50% relative humidity. Testing speed was 50 mm/minute and extensometer was used.

2.6 Chemical analysis

Dumb-bell samples were cut in 100 micron thicknesses using a Leica PolycutE microtome. Analysis was carried out using an FTIR Spectrum 2000 in microscope AutoImage (Perkin Elmer) at distances of 50 and 200 microns from the UV aged surface. The aperture was set to 100x50 microns, meaning analysed from a position between 50-100 and 200-250 microns from the surface. Line scans as well as evaluations of carbonyl growth at 1713cm-1 were performed. Line scans were obtained over the surface by analysis at 21 consecutive positions.

3. Results and Discusion

3.1 Colour measurements

3.1.1 *Effect of the base resin on colour deviation*

All samples based on PE1 and PE2 were compared. There is no clear evidence of the effect of the base resin on colour deviation even at low stabilization ratio. Whatever the polyethylene type used, the deviation is related to the pigment type. However, there are two exceptions. For pigment RD1 and OR1, see figure 1, PE2 has less effect on colour deviation. Here the colour variation between PE1 and PE2 could be more than the double. This is, however, not the case for the other pigments.

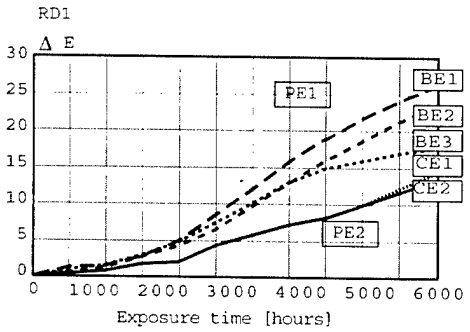


Fig 1: Samples of RD1 as a function of color deviation (ΔE) for PE1 and PE2.

3.1.2 *Effect of stabilization on colour deviation*

The effect on colour deviation depends on the stabilization level and exposure time. After 2000-2500 hours, the more stabilized formulation shows less colour deviation, see fig 2. Thus the degradation of the matrix enhances the colour deviation. If the pigment is not weather resistant, stabilization will not improve the general behaviour. A well stabilized system will not improve the pigment performance, see fig 3.

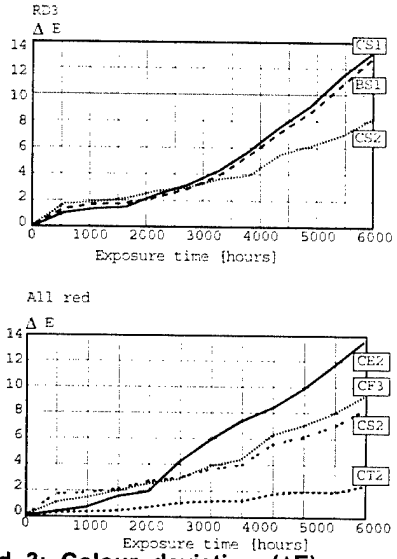


Fig 2 and 3: Colour deviation (ΔE) as a function of exposure time

3.1.1 *Difference between pigments*

All red colour concentrates used in this study are shown in Fig 3. For the comparison, the tested formula contained an extra stabilization in order to not be influenced by matrix degradation.

The RD4 gave the best performance in term of UV resistance after 6000 hours; the colour variation is almost undetectable. In case of halogen free pigment requested , RD2 gave the best compromise in all pigment selections. The colour deviation was acceptable, with a grey scale reading of 4, meaning that the sample was still red after ageing, see Fig 4.

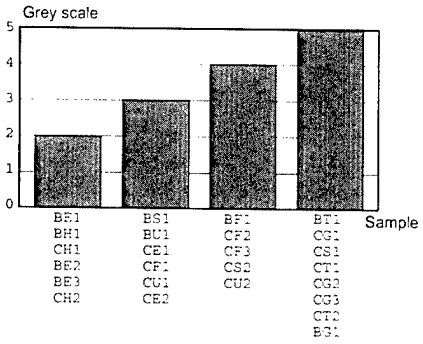


Fig 4: Grey scale evaluation after 6000 hours exposure time

In this study, no halogen free pigments were used in orange concentrates. As expected, the lead pigment, OR1, showed excellent performance during weathering, similar to RD4. The ageing of the pigment OR2 was dramatic. The OR3 performed better, the sample after ageing being a weak orange, with an acceptable grey scale reading of 4.

3.2 Mechanical testing

3.2.1 *Effect of the compound on mechanical testing*

In Fig 5 a and b, elongation at break as a function of exposure time in the WOM is shown for all samples. It should be noted that the stabilization level in this investigation was chosen to obtain the effect on ageing after a limited period of time. The level of stabilization for commercial grades is significant higher.

Regarding this investigation the mechanical properties for unaged unimodal and bimodal polymer is similar, independent of pigment type.

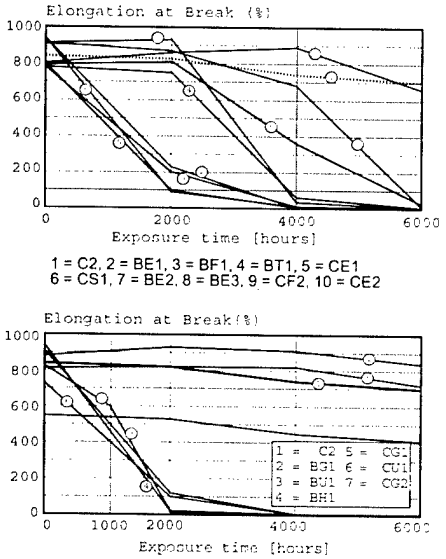


Fig 5 a and b: Elongation at break as a function of exposure time

3.2.2 *Effect of the UV stabilization*

The non-stabilized samples were tested after just 1000 hours. For PE1 and PE2 without pigmentation or UV stabilization, the B1 and C1 was totally destroyed, with no elongation or tensile strength at break remaining. For the samples BE3, CF2 and CG2 without UV stabilization but with 1% colour MB added, the samples retained 10 – 80% elongation after 1000 hours. However, after 2000 hours all non-stabilized samples were destroyed. This is interesting from the perspective that pigmentation of the cable jacket gives a certain protection for a shorter time, even without UV stabilization.

For the C2 samples, which were fully UV stabilized, 90% of the elongation at break is retained after 4000 hours ageing. After 6000 hours, 84% of the initial elongation remains and 46% of the initial tensile strength at break.

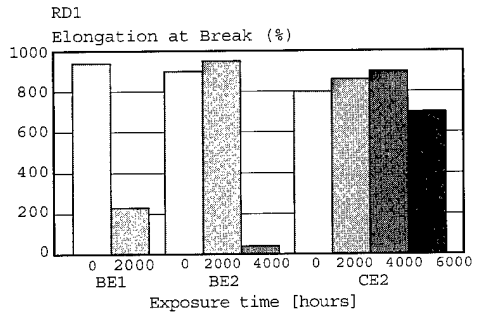


Fig 6: Elongation at break comparison for samples with different UV-stabilisation levels BE1 (0.05%), BE2 (0.1%) and CE2 (0.5%)

In Fig 6, RD1 pigment is represented at three UV stabilization levels. Here it is shown how important is the stabilization of the matrix. At the highest level, represented by sample CE2, the deviation of elongation at break compared with the initial value is only 17% and for the tensile strength at break, it is only 33%.

3.2.3 *Difference between pigments*

In the comparison of pigments for mechanical testing, OR1 is the most stable pigment, and does not interact with the matrix performance. It even protects the matrix compared to the unpigmented sample, C2. For the lead free pigments, RD2 shows the best performance. Unfortunately only one sample BE2 (RD1) with a higher level of UV stabilization was mechanically tested after 6000 hours ageing. This sample showed good performance as discussed above.

As the WOM test is performed at a rather high temperature, 63°C, it should be pointed out that in addition to high UV radiation level, the samples are also exposed to thermal ageing, which naturally also affects the results.

3.3 Chemical analysis

Spectrophotometric analysis was used as a complementary method to colour measurements and mechanical testing. It was clearly seen that samples were degraded depending on the pigment used and the amounts of UV stabilization. In FTIR analysis the degradation of the samples could be seen as an increase of carbonyl at 1713 cm-1 and transvinylene groups at about 909 cm-1. The chemical analyses correlate well with the colour deviation and mechanical testing. Some pigments contributed to the absorption in the FTIR spectra and made the evaluation difficult. In unimodal PE more unsaturated bonds occur in unaged samples. In this study, there was no clear evidence that these affected the further ageing of the samples.

Fig 7 shows line profiles of three samples with base resin PE1 and pigment RD1 with varying amounts of, and without, UV stabilizer. This shows that the degradation process is a surface phenomenon in the UV stabilized materials. The non-exposed surface shows no sign of oxidation, while the exposed surface shows a high level of oxidation. In the non-stabilized sample, the carbonyl level increase occurs deeper into the plaque.

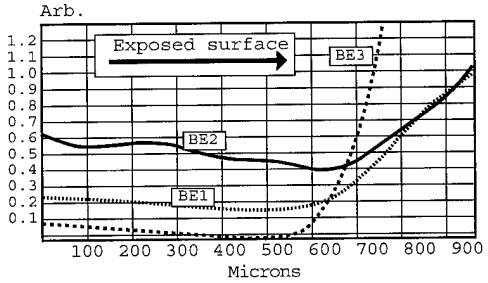


Fig 7: FTIR line profiles for samples with 0% UV-stabilisation BE3 (0%), BE1 (0.05%) and BE2 (0.1%)

It should be noted that the sample thickness is 1 mm.

3.4 Discussion

When used outdoors, a cable is subject to photo-induced oxidation. This lead to mechanical degradation on the surface of the tested sample due to the formation of microfissures. This phenomenon has a whitening effect, while oxidation leads to the formation of yellowish products. Therefore, to analyse the contribution of the pigments in relation to degradation, the matrix must be fully stabilized in order to maintain permeability to oxygen and avoid whitening and yellowing effects (1). The behaviour of a pigment under UV exposure is also important in terms of impact on the photo-degradation of the matrix. If the pigment is photo-transformable, the pigment can lead to premature matrix degradation that would be well stabilized if not coloured.

For the main part of this study a low level of stabilization was used in order to distinguish between samples. The tough WOM conditions chosen, high temperature and radiation, most likely produces a combination of thermal and photo oxidation, which contributes to the results and differentiation of pigment types. In this study we have shown that it is possible to follow the degradation of the samples with mechanical testing, carbonyl increase by FTIR, as well as by colour deviation measurements. With colour deviation it is essential to understand the limitation of the measures when studying PE systems with low stabilization. The measurements in such systems can be influenced by the degradation of the matrix. In this study a limited amount of mechanical tests were accomplished on the high-stabilized samples. In an eventual further study, mechanical tests on high-stabilized samples should be more in focus. To further understand weathering behaviour, different type of stabilization and levels, as well as to broaden the study to other colours, should be

evaluated. Our analyses showed that inorganic pigments are more stable than organic pigments. However, we have seen that more environmentally friendly lead free pigments also perform well in terms of weather resistance. Furthermore this study emphasises the importance of a proper stabilized PE matrix.

4. Conclusion

This study was conducted to enhance understanding of the interaction between polyethylene and colour pigments in Wire & Cable jacketing applications. Various types of red and orange pigments were evaluated as well as unimodal and bimodal polyethylenes.

The main part of the evaluation was made on samples containing a low level of stabilizer to distinguish between the different samples.

There was no significant difference in color measurements as well as mechanical evaluations between unimodal and bimodal PE polymer. Different type of pigment influenced the results more. The orange lead-containing pigment showed the best mechanical performance. The lead and halogen free red pigments showed excellent colour performance and acceptable mechanical properties. Some pigments accelerate brittleness and increase oxidation level. For good mechanical performance as well as colour appearance, proper UV stabilization of the PE matrix is essential.

For stabilized systems the UV degradation of the polymer is a surface phenomenon, which means that even if the surface is affected, the rest of the cross section is intact .

This investigation indicates that the choice of pigment will influence the lifetime of the cable. However, due to the selection of a low level of stabilization, it was not possible to predict the lifetime of a commercial coloured jacket material in this study. Lifetime prediction is difficult, and is also affected by many factors where the cable will be in use, including climate, temperature, temperature fluctuations, radiation level, thickness of jacket etc. For the given conditions in this study, the lifetime of the best samples is well over 3 years. This work will assist efforts regarding choice of pigment, stabilization and PE matrix in order to enhance and to better understand the importance these factors have in the design of a environmentally friendly coloured PE cable jacket for long life performance.

5. Acknowledgement

Many thanks to Magnus Persson, Borealis who performed all the chemical analysis including sample preparation and reporting. And to Pierre Fameree, PolyOne for the entire laboratory work with the WOM and colour measurements.

6. References

1. J. Lemaire, N. Siampiringue, D. Fromageot CNEP, Prévoir le comportement des matériaux colorés, Caoutchoucs & Plastiques N° 793 – Mars 2001).
3. A. Thürmer, Expanding the polymer market through industry focused, innovative developments in light stabilization by Ciba Specialty chemicals, Masterbatch 2000, July 4-6, Geneva, Switzerland.
4. K. Leonas, Pigments and other additives that influence the degradation rate of polyethylene films, Textile Chemist and Colorist, Oct 1992/Vol. 24, No 10.
5. O. Ogbobe, N. Ossal, Effect of colour on the mechanical and chemical properties of naturally photooxidized high density polyethylene, Acta polymer, 43, 173-176, 1992.
6. M.A. Maatoug et al, Role of pigments in the stability of polyethylene systems, Macromol. Mater. Eng., 2000, 282, 30-36.

7. Biography

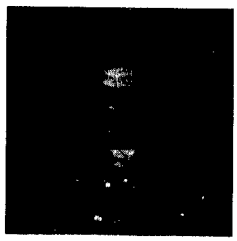
Elisabeth E Ribarits Persson studied Mechanical Engineering and Polymers at Chalmers University of Technology in Sweden, obtaining an M.Sc. in 1987 and later a Licentiate of Technology in Polymer Blends. In 1991 she joined Borealis as a development and technical service engineer and worked also as project manager with market development of polyolefins. In 2000 she was appointed Area Sales Manager for the Nordic countries for PolyOne, business unit Cable Systems.

Estelle J Cognet studied chemistry at Clermont-Ferrand, France and obtained her chemical engineer diploma in 1992. She got a PhD from INSA de Lyon, France in Macromolecular material. She joined PolyOne in 1997 as technical support, Europe. In October 2000, she was appointed Project Manager for colours in the wire & cable business.

Hans-Bertil Martinsson graduated in 1971 and joined Borealis (former Unifos) in 1972. From 1988 to 2000 he was responsible for the development of communication and jacketing grades for wire and cable and is currently project manager in wire & cable applications.

Håkan Larsson graduated 1980 and joined Borealis (former Unifos) the same year. He has been working in various applications area and is currently working within Business Unit Pipe.






Shrinkage of Bi- and Unimodal Polyethylene Cable Jacketing Materials – Influence of Molecular Structure and Processing Conditions

Mikael J. Sandelin
Department of Polymer Technology, Royal Institute of Technology
SE-100 44 Stockholm, Sweden
+46 8 7906763 sandelin@polymer.kth.se

Ulf W. Gedde
Department of Polymer Technology, Royal Institute of Technology
SE-100 44 Stockholm, Sweden
+46 8 7907640 gedde@polymer.kth.se

Hans-Bertil Martinsson
Borealis AB
SE-444 86 Stenungsund, Sweden
+46 303 86433 hans-bertil.martinsson@borealisgroup.com

Ruth C. Dammert
Borealis AB
SE-444 86 Stenungsund, Sweden
+46 303 86701 ruth.dammert@borealisgroup.com

Abstract
Cable jacketing for fibre optical cables should possess low shrinkage. It is shown that bimodal materials exhibit a lower degree of shrinkage than unimodal materials. A high molar mass tail contributes much to the orientation and the absence of a high molar mass tail is believed to be the reason for the lower shrinkage of the bimodal materials. The crystalline orientation was the main factor affecting the shrinkage. The cooling bath temperature was the processing factor which influenced shrinkage the most.

Keywords
Polyethylene; bimodal; unimodal; jacketing; shrinkage; processing conditions; molar mass distribution; chain orientation

1. Introduction
Due to its good mechanical and barrier properties polyethylene (PE) has been used for many years in different cable jacketing applications. Low density polyethylene was previously the most important material in telecommunication cables. During recent years there has been a clear trend towards linear PE. High density polyethylene often suffers from high shrinkage and low environmental stress crack resistance (ESCR). Recent development in polymer synthesis technology has promoted improved materials, i.e. bimodal PE that combines good processability, excellent ESCR and low shrinkage. Demands on the properties of PE jacket compounds have been described by Gau et al [1]. A comparison of uni- and bimodal PE for cable jackets was made by Rogestedt et al [2] and Dammert et al [3].
When PE cable jackets are heated, a marked axial shrinkage can be noted as a result of the recovery of an isotropic state of oriented polymer chains [4]. The material specific shrinkage, which is due to polymer chain structure and crystallinity, is stated to be of minor importance in comparison with the specific processing effect on the shrinkage [4]. Allowing the extruded jacket to crystallise in a rapid but uniform way during extrusion can reduce the post-extrusion shrinkage [5].
The shrinkage is a result of the fact that when a molten polymer is exposed to a stress field, the chain molecules are stretched out to extended chain conformations. The main direction of orientation will be in the direction of the deformation and small entropy elastic forces will act on the chains. In an ideal case these stresses are released during processing. However, for semicrystalline materials, it is in practice not possible to release all stresses, and shrinkage of the jacketing occurs when the molecules are striving towards the non-oriented state. The magnitude of the shrinkage depends on the polymer type, processing conditions and the construction of the cable.
In order to minimise the shrinkage, correct material and cable design and optimised processing conditions are important. This paper describes the influence of processing conditions and the material structure on the shrinkage of bi- and unimodal PE materials.

2. Experimental
2.1 Materials
The Borstar™ PE process consists of a dual reactor system, combining a supercritical propane slurry loop and a gas phase reactor utilising a specially developed proprietary catalyst to produce polyolefins. In the first reactor, the loop reactor, a fraction with little or no comonomer is produced. The melt flow rate of the polymer is high (low molar mass). The material is thereafter transferred to the gas phase reactor without additional catalyst feed. The polymer chains continue to grow from the same catalyst particle, which means that both short and long chains grow from the same particle. This gives products with superior homogeneity, which cannot be obtained by conventional melt mixing. The possibility to tailor-make the molecular structure of the material in the Borstar™ process has been utilised to produce bimodal PE. Two bimodal materials and two unimodal materials, denoted BI, BI-CB, UNI and UNI-CB (CB: carbon black), were studied. Basic data for the materials are presented in Table 1. The split between low molar mass fraction (produced in the loop) and high molar mass fraction (produced in the gas phase reactor) was the same for both bimodal materials. No comonomer was added in the loop, i.e. the low molar mass fraction was linear.

2.2 Mechanical properties
Mechanical properties were measured in a tensile tester, Alwetron TCT 10, at 50 mm/min according to ISO 527-2/5A. Samples were taken from compression moulded plaques. The moulding was performed according to ISO 1827 at 200°C. ESCR was measured according to ASTM D1693.

2.3 Size exclusion chromatography

The molar mass distribution of the materials was determined by size exclusion chromatography on a Waters 150C chromatograph equipped with a refractive index detector and the analyses were carried out at 135°C using 1,2,4-trichlorobenzene as eluent.

2.4 Rheological measurements

Dynamic mechanical measurements were performed on a Rheometrics RDA II at 190°C under nitrogen atmosphere using a plate test fixture with a diameter of 25 mm in the frequency range 0.01 to 500 rad/s. Complex viscosity (η^*) and storage modulus (G') as function of complex modulus (G*) were obtained. From these data, viscosity (complex viscosity at complex modulus 2.7 kPa, $\eta_{2.7\ kPa}$) and shear thinning index ($SHI_{2.7/210}$) were calculated. The shear thinning index $SHI_{2.7/210}$ is defined as the ratio between $\eta_{2.7}$ and η_{210}, where η_{210} is the complex viscosity at a complex modulus of 210 kPa. In addition, two elasticity indices G'_{2kPa} and G'_{5kPa} were determined: G'_{2kPa} = G' at G" of 2 kPa and G'_{5kPa} = G' at G" of 5 kPa. The viscosity $\eta_{2.7kPa}$ is closely related to the average molar mass, whereas SHI is sensitive to the breadth of the molar mass distribution. The elasticity indices, G'_{2kPa} and G'_{5kPa}, are measures of the elasticity of the material and are particularly sensitive to the high molar mass fraction (tail).

2.5 Cable extrusion

A pilot cable line with a 60 mm/24 D extruder was used for extruding a jacket with a thickness of 1 mm directly onto a cold 3 mm single aluminium conductor, using a semi-tube die (cable OD 5 mm). The materials were run with four different line speeds (15, 35, 75 and 140 m/min) at two different extrusion temperatures (180 and 210°C) and two different cooling bath temperatures (23 and 75 °C). The distance between die gap and cooling bath was kept constant.

2.6 Shrinkage

The shrinkage was measured on 400 mm long cable samples according to IEC 60811-1-3. The samples were pre-conditioned at room temperature for 24 h and then kept in an oven at 100°C for 24 h. The total longitudinal shrinkage was determined.

2.7 Molecular draw ratio

The molecular draw ratio, i.e. the extension of the molecules with respect to their unoriented state, was measured by heating samples above the melting point. Samples from the jacketing were axially cut in two pieces and the dimensions prior to heating were: axial (l^0): ~40 mm, thickness (t^0): ~1 mm and outer diameter (d^0): ~5 mm. The samples were immersed in silicone oil and laid on a hot-stage (~180°C) for 2-3 minutes. The dimensions were measured after cooling to room temperature and the molecular draw ratios in the axial and thickness directions calculated as the ratio between the length/thickness before and after melting ($\lambda_a=l_0/l$ and $\lambda_r=t_0/t$). The draw ratio in the tangential direction was calculated assuming constant volume, i.e. $\lambda_a\lambda_r\lambda_{tang.}=1$.

2.8 Differential Scanning Calorimetry

Crystallinities and peak melting temperatures were measured in a Mettler-Toledo 820 Differential Scanning Calorimeter. Thermograms were obtained at a heating rate of 10°C/min. Furthermore, the increase in crystallinity as a result of ageing at 100°C for 24 hours was measured. The samples were heated to 100°C at a heating rate of 10°C/min, maintained at this temperature for 24 hours and then rapidly cooled (150°C/min) to –25 °C. The melting was thereafter recorded during a 10°C/min heating scan. The crystallinities were calculated by converting the recorded heats of fusion into mass crystallinity using the total enthalpy method [6]. Data from Wunderlich and Baur was used [7]. The influence of carbon black as nucleating agent was studied by measuring the onset of crystallisation during a 1°C/min cooling scan.

2.9 Infrared Spectroscopy

Infrared spectroscopy measurements were carried out on a Perkin-Elmer Spectrum 2000 equipped with a Golden Gate Single Reflection accessory. The crystalline orientation was calculated from the absorption peak at 730 cm^{-1}, which is associated to CH_2 rocking in the crystalline phase [8]. This peak overlaps with a peak at 720 cm^{-1} associated to CH_2 rocking in both the crystalline and amorphous phases [8]. The peaks were resolved using Lorenz functions. Both peaks have transition moment vectors perpendicular to the chain axis [9]. The 1078 cm^{-1} peak is associated to skeletal C-C stretching and the 1352 cm^{-1} peak to CH_2 wagging in the amorphous phase [8]. The former has a transition moment vector parallel to the chain axis whereas in the latter case the transition moment vector is perpendicular to the chain axis [9] The orientation was calculated according to the method described by Premnath [10].

3. Results and Discussion

3.1 Mechanical properties

The different materials showed very similar ultimate mechanical properties: fracture stress = 34±1 MPa; fracture strain = 895±45 %; ESCR resistance times over 2000 h.

3.2 Molar mass distribution and rheology

The results from size exclusion chromatography and rheological measurements are shown in Table 1.

Table 1. Data for the materials

	BI	BI-CB	UNI	UNI-CB
M_n [g/mol]	5760	8680	7220	8510
M_w [g/mol]	152500	164000	178000	253500
M_z [g/mol]	823500	910000	1658000	4702500
MFR2 [g/10 min]	0.6	0.5	0.25	0.2
Density [kg/dm^3]	941	954	940	952
T_m [°C]	129.1	128.9	126.1	127.8
w_c [%]	73.5	82.5	74.2	79.4
η_0 [Pas]	33200	41000	386000	672000
$\eta_{2.7}$ [Pas]	17100	21800	60300	71400
G'_{2kPa} [Pa]	680	630	1380	1450
G'_{5kPa} [Pa]	2300	2120	3940	4000
$SHI_{2.7/210}$	37	26	91	88

The unimodal materials have higher $\overline{M}_w$ and $\overline{M}_z$ than the bimodal materials. The molar mass distribution curves presented in Figure 1 show that the unimodal material has a larger high

molar mass tail than the bimodal material. Similar results were obtained for the unfilled materials.

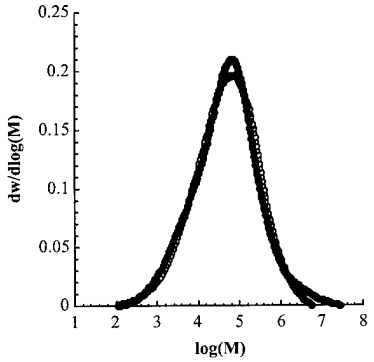


Figure 1. Molar mass distribution for: BI-CB (○) and UNI-CB (●).

Both the bi- and unimodal materials show a pronounced shear thinning behaviour but at low shear rates the bimodal material has considerably lower viscosity (Figure 2).

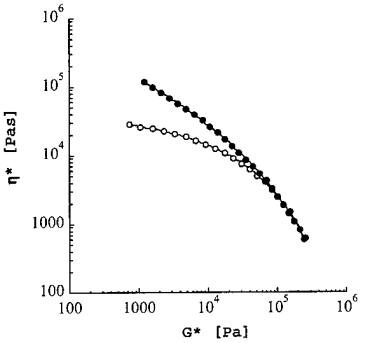


Figure 2. Complex viscosity as a function of complex modulus for: BI-CB (○) and UNI-CB (●).

3.3 Processability

Extrusion performance was evaluated by measuring the extruder pressure at different line speeds and extrusion temperatures. The extruder pressure at 210°C is shown as a function of line speed in Figure 3. The unfilled materials showed the lowest pressures and the bimodal materials showed lower pressures than the unimodal materials.

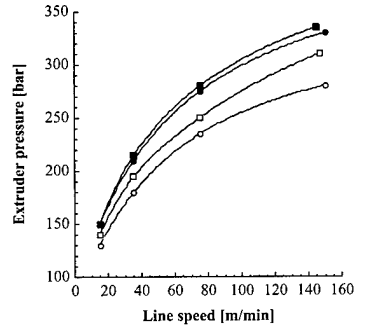


Figure 3. Extruder pressure as a function of line speed for: BI (○), BI-CB (●), UNI (□) and UNI-CB(■).

3.4 Shrinkage measurements, below melting point

The axial shrinkage after ageing for 24 h at 100°C was measured on samples produced at different line speeds and extrusion temperatures. The cooling bath temperature was kept constant at 23°C. The axial shrinkage is shown as a function of line speed in Figure 4 for the two extrusion temperatures; the measurement error is indicated by the bar. The unimodal materials exhibited considerably higher axial shrinkage than the bimodal materials and the axial shrinkage was generally higher after extrusion at the higher temperature. The shrinkage was only moderately affected by the line speed.

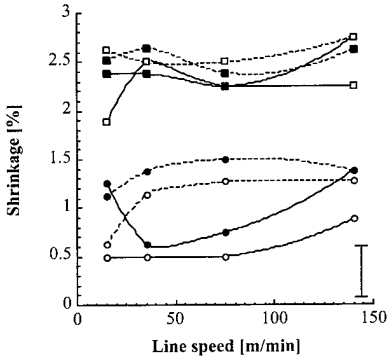


Figure 4. Shrinkage as a function of line speed for: BI (○), BI-CB (●), UNI (□) and UNI-CB(■), continuous line: 180°C extrusion temperature, broken line: 210°C extrusion temperature.

The bimodal material exhibited negligible (0.2%) axial shrinkage after conditioning at 23°C for 24 h prior to ageing in the oven, whereas the unimodal material shrank from 1.0% to 1.5% during conditioning at 23°C. The shrinkage at 23°C must be due to relaxation of the amorphous chains, because no melting of crystallites occurs at this temperature.

The influence of cooling bath temperature was studied for cables extruded at 180°C and at a line speed of 75 m/min (Figure 5; the bar indicates the measurement error). Specimens extruded through a warmer cooling bath showed less axial shrinkage.

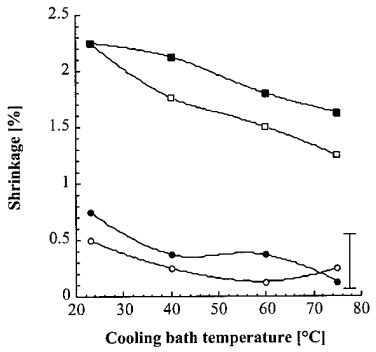


Figure 5. Shrinkage as a function of cooling bath temperature for: BI (○), BI-CB (●), UNI (□) and UNI-CB(■).

3.5 Shrinkage above melting point, molecular draw ratio

Axial molecular draw ratio data for extruded specimens (75 m/min line speed, 23°C cooling bath temperature and both extrusion temperatures) are shown in Figure 6 (the bar indicates the measurement error). The axial draw ratios for the unimodal materials were considerably higher than for the bimodal materials, the difference being approximately a factor of two. The high molar mass tail present in the unimodal materials gives very long relaxation times and hence these materials are more susceptible to crystallise in an oriented state.

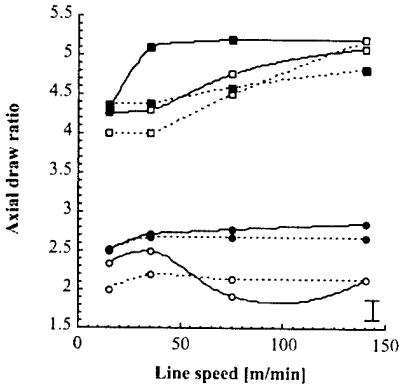


Figure 6. Axial draw ratios as a function of line speed for: BI (○), BI-CB (●), UNI (□) and UNI-CB(■), continuous line: 180°C extrusion temperature, broken line: 210°C extrusion temperature

In the tangential direction the draw ratios were 0.7 to 0.9 and 0.5 to 0.6 for bi- and unimodal materials, respectively. The corresponding values in the radial direction were 0.5 to 0.6 and ~0.4. Since the molecular draw ratios in the radial and tangential direction differed somewhat a low degree of biaxial orientation existed in the materials resulting from biaxial stretching during processing. The axial draw ratio at different temperatures was proportional to the degree of partial melting at temperatures below the peak melting temperature (Figure 7; the bar indicates the measurement error).

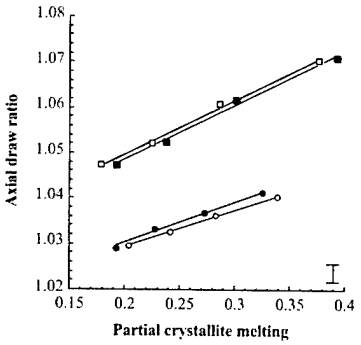


Figure 7. Axial draw ratio as a function of partial melting for BI, 23°C cooling bath (○), BI, 75 °C cooling bath (●), UNI, 23°C cooling bath (□) and UNI, 75°C cooling bath (■).

The axial draw ratios below the melting peak temperature were very low compared to the values obtained for the fully molten polymer. This suggests that the effect on macroscopic shrinkage from the melting of smaller crystallites is small because they are constrained by the presence of larger crystallites, i.e. the crystallites are interconnected in a parallel fashion.

3.6 Infrared Spectroscopy

The Hermans orientation function was obtained from measurement of the dichroic ratio. The Hermans orientation function was used for comparative purposes only, since it is strictly only applicable to systems showing uniaxial orientation. The amorphous orientation was negligible whereas considerable crystalline orientation was detected in specimens extruded at 180°C and a line speed of 75 m/min (Hermans orientation function ~0.8). After ageing at 100°C for 24 h the crystalline orientation decreased to about half the original value, confirming partial melting and relaxation towards an isotropic state of the material.

3.7 Differential Scanning Calorimetry

Crystallinities and peak melting temperatures for the materials (180°C extrusion temperature, 23°C cooling bath and 75 m/min line speed) are shown in Table 1. DSC showed that carbon black had no impact on the onset temperature for crystallisation; the difference between unfilled and filled systems amounted to 0.2-0.4°C only. On ageing at 100°C for 24 h a considerable increase in crystallinity was recorded: 21.0% for the bimodal material and 5.1% for the unimodal material. This finding validates the suggestion that the axial shrinkage is primarily controlled by the relaxation of oriented polymer chains and is not due to recrystallisation [4].

4. Conclusions

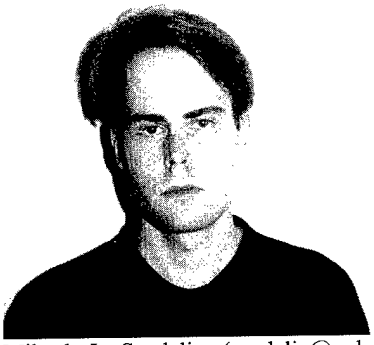
The bimodal materials exhibited a considerably lower degree of shrinkage than the unimodal materials. The line speed had little influence on the shrinkage, but an increase in the cooling bath temperature reduced the shrinkage. An increase in the extrusion temperature generally led to higher shrinkage. The processability of the bimodal materials was better than that of the unimodal materials. The unimodal materials had a high molar mass tail which due to long relaxation times contributes much to orientation. Infrared spectroscopy showed that the crystalline orientation in the materials was high, whereas the amorphous orientation was negligible. The crystalline orientation was decreased on ageing, confirming partial melting and relaxation of the chains in the crystallites. At temperatures below the melting peak, partial melting of the crystalline fraction was found to be proportional to the axial shrinkage. The partial melting data also suggest that the crystallites were interconnected in a parallel fashion.

5. References

[1]. Y. Gau, T. J. Person and C. J. Kmiec, "Advanced Polyethylene Jacketing Compounds for Medium and High Voltage Cable Applications", *Jicable 99*, B10.4, 638-648 (1999)

[2]. L. Rogestedt and H. B. Martinsson, "A new Generation Polyethylene Resins for Cable Jacketing Applications", *46th International Wire & Cable Symposium Proceedings*, 126-131 (1997)

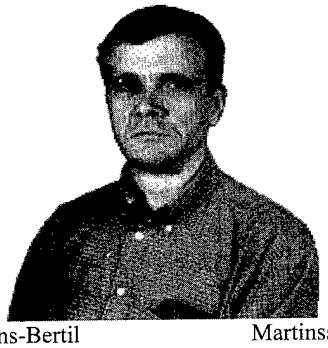
[3]. R. C. Dammert, L. Rogestedt and H. B. Martinsson, "New Polyethylene Manufacturing Process for Improved Cable Products", *Plastics in Telecommunications VIII*, 303-312 (1998)
[4]. H. Stöger, R. Stubbe and M. Ulrich, "Stresses and Behaviour of Polyethylene Sheaths", *CIRED 1985, 8th Int. Conf. on Electricity Distribution (Conf. Publ. No. 250)*, 225-230 (1985)
[5]. T. Chen and J. R. Leech, "Design of Polyethylene Cable Jacket Compounds of Superior Jacketing Performance", *International Wire and Cable Symposium Proceedings*, 807-814 (1999)
[6]. A. P. Gray, "Polymer Crystallinity Determinations by DSC", *Thermochim. Acta*, 1, 563-579 (1970)
[7]. B. Wunderlich and H. Baur, "Heat Capacities of Linear High Polymers", *Adv. Polym. Sci.*, 7, 151-368 (1970)
[8]. S. Krimm, "Infrared Spectra of High Polymers", *Fortschr. Hochpolym.-Forsch.*, 2, 51-172 (1960)
[9]. B. E. Read and R. S. Stein, "Polarized Infrared Studies of Amorphous Orientation in Polyethylene and Some Ethylene Copolymers", *Macromol.*, 1(2), 116-126 (1968)
[10]. V. Premnath, "Determination of Molecular Spatial Orientation on Polymeric Surfaces Using Internal Total Reflection Infrared Dichroism", *Macromol.*, 28, 5139-5143 (1995)



Mikael J. Sandelin (sandelin@polymer.kth.se) received his M.Sc. degree in polymer materials in 2000 from the Royal Institute of Technology, Stockholm, Sweden and is currently a Ph.D. student at the Royal Institute of Technology.



Ulf W. Gedde (gedde@polymer.kth.se) received his M.Sc. Degree in 1977 and his Ph.D. degree in 1980 from the Royal Institute of Technology, Stockholm, Sweden and is currently professor in polymer materials at the Royal Institute of Technology.



Hans-Bertil Martinsson (hans-bertil.martinsson@borealisgroup.com) joined the company (former Unifos) in 1972. From 1988 to 2000 he was responsible for development of communication and jacketing grades for wire and cable and is currently project manager in wire & cable applications.



Ruth Dammert (ruth.dammert@borealisgroup.com) received her M.Sc. degree in organic chemistry from University of Helsinki, Finland, in 1986. After research work at Sandoz A.G., Basle, Switzerland, at University of Zürich, Switzerland and at University of Helsinki, Finland, she joined Borealis (Neste at that time) in 1989 and has since then mainly been involved in the development of materials for cable applications.

Power Distribution System for Feeding Telecom Objects

Lars Efraimsson
+46 23 68530 · lars.efraimsson@eca.ericsson.se
Henric Magnusson
+46 23 68487 · henric.magnusson@eca.ericsson.se
Ericsson Network Technologies AB
Falun, Sweden

Abstract

Distribution of electric energy long distances to small power consumers, i.e. telecom equipment, is becoming more and more common. As of today there has been no commercial solution available for supplying electrical energy long distances to small power consumers. The current alternative to locally produced power is a medium voltage three-phase distribution line or 1 kV, low voltage for shorter distances.
This paper describes a new distribution system that has now been developed and which is simple, reliable and cost effective.
It is also possible to achieve a communication link between telecom sites by using an integrated optical fiber and power cable.
The system is stand-alone and can be fed from a central point using an existing subscription and/or central diesel backup. This way several telecom sites can be powered from one reserve diesel plant.
This would significantly decrease the need for local diesel plants and lead acid batteries and hence the burden on the environment.
The system is fully operational and several systems are in commercial use.

Keywords

XLPE; power; cable; fiber; distribution; supply; backup; MTBF; station; diesel

1. Introduction

The problem is as old as the modern science of electrotechnics i.e. more than a hundred years old. The production and availability of electric energy is located one place, the need in another place. There exist different solutions to this problem, DC transmissions, AC transmissions with transformers, batteries, diesel generators, solar energy, etc.
Demands on the power supply for telecom equipment are high. High reliability and cost effectiveness are vital. Environmental aspects have to be taken into consideration which can cause problems when installing backup systems such as batteries and diesel generators in city areas.
By using remote power feeding the reserve power can be concentrated to one central location using generators that already exist with low maintenance and at an affordable cost for the total network.
The solution presented here gives a better MTBF* at a lower cost in most cases compared with the existing solutions.

*MTBF is defined as medium time between 30 minutes (medium) power failure

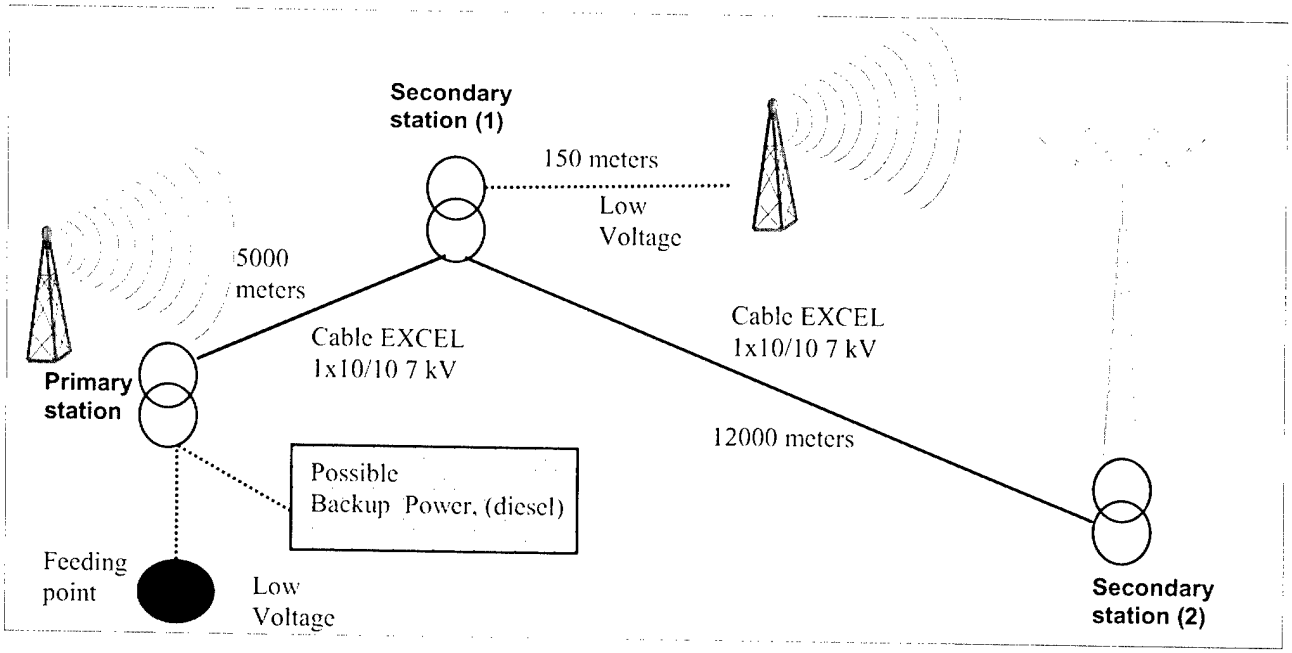


Figure 1. Sample system

2. Existing Solutions

There are different possible solutions to feed remote objects with power:

- Subscription from the local distributor, often combined with some sort of backup.
- Local production using motor and generator, which are powered with some type of fossil fuel.
- Distribution of power from a central feeding point.
- Combinations of above.

Different solutions have advantages and disadvantages regarding reliability, availability and cost. Subscription from a local distributor can be favourable in city areas, even though battery backup will be needed in most cases. In areas without an existing net the local distributor usually has an exclusive right to build a power distribution net. When the distance from an existing feeding point exceeds about 1 km, a 10 kV or 20 kV (three-phase) line will have to be built to fulfill the authorities safety requirements. This is a costly solution that usually requires joint financing by other consumers, i.e. other telecom operators.
Apart from being costly, local production will lead to environmental problems.
Due to safety reasons distribution from a central feeding point also has to be limited to short distances using existing technique.

3. The New Solution

The fundamental idea of the new power supply system is simplicity both in use and in technical solutions. The system is fed from a low voltage supply, usually 110 to 400 volts AC (phase-phase or phase-ground), and the output is also low voltage, usually 110 to 230 volts AC. The technical solution is sturdy and simple and only standard components are used. What is new is the system solution.

The system is fed via the primary station and one or more secondary stations deliver the power to the consuming point(s). The stations work completely autonomously of local control. The only connection between the stations is the high voltage cable, see figure 2.

The system design is as follows; incoming power is transformed to a few kilovolts. The high voltage is transmitted through a coaxially constructed XLPE-insulated cable where the cable screen works as a return conductor. In the secondary receiving station the voltage is stepped down to low voltage.
Several receiving stations can be connected in a chain and the receiving stations can be equipped with battery backup and/or local service power as well as a connection for portable reserve power.
There is also a construction with integrated optical fiber cables and power cable.
Communication between telecom sites is then easy to provide.
The optical fiber is showed in figure 2, below the copper conductor.

Protection and control is achieved mainly on the low voltage side, by the use of primary fuses and thermal over current protection and circuit breakers.
No high voltage fuses are needed. Earth fault protection is a relay monitoring the outer sheath of the cable. It is possible to operate the system with a deficient outer sheath but it should be repaired before corrosion of the cable screen proceeds.

The transmission cable has an outer diameter of only approx. 20 mm and can be laid in the ground, in water or hung in air as self suspending aerial cable, see figure 3. Due to the coaxial design the magnetic field is negligibel and the cable can be placed close to other telecom cables without the risk of magnetic interference.

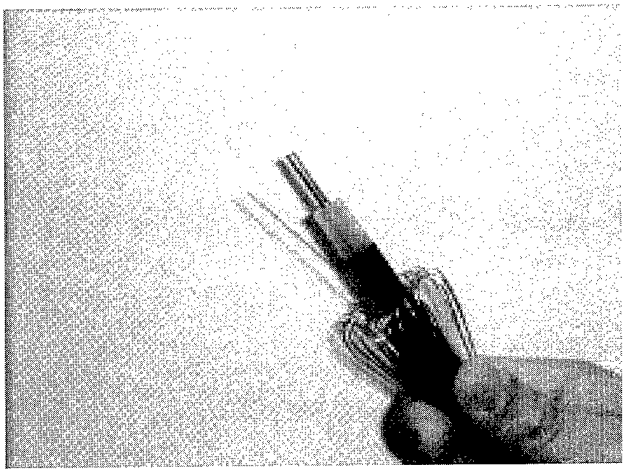


Figure 2. The distribution cable, EXCEL 1x10/10 7 kV with fiber optic cable.

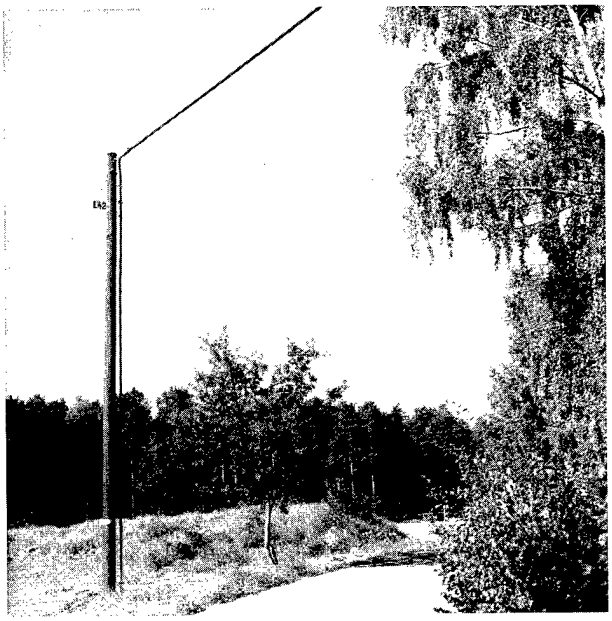


Figure 3. The distribution cable, EXCEL 1x10/10 7 kV

Naturally the cable can be routed together with telecom fiber cables as in figure 4.
The stations can be either free standing or built into existing stations as in figure 5.

3.1 Some key points for the new solution:

- Power transmission over long distances, up to approx. 50 km.
- Transmission of up to approx. 30 kVA.
- High reliability.
- Excellent safety properties.
- Almost free from electromagnetic interference.
- Can be laid together with both copper and optical cables in all environments.
- Power cable can be integrated with fiber optical cables.
- Environment friendly, recyclable cable made of copper and polyethylene (XLPE).
- Several receiving stations can be connected to a single primary station.
- Tree formed network structure.
- Backup power to several receiving stations from one source
- Each station is autonomous and has no need of controlling software.
- More cost effective comparing to existing solutions

4. Existing Solutions vs. the New Solution

When comparing the methods for power feeding of remote objects that are available today with the new method described in this paper there are some properties that need to be stressed.

The cost will usually be considerably lower using remote power feeding than that of conventional alternatives. Cost reductions are possible by reducing the need of batteries at each power consuming station. The need for reserve power installations will also decrease and existing central reserve power can be used. The need for floor space for batteries, rectifiers etc. will also decrease, due to the compact size of the components. See figure 6.

It is possible to achieve a considerable increase in reliability. A statistical calculation has been done which gave the following result.

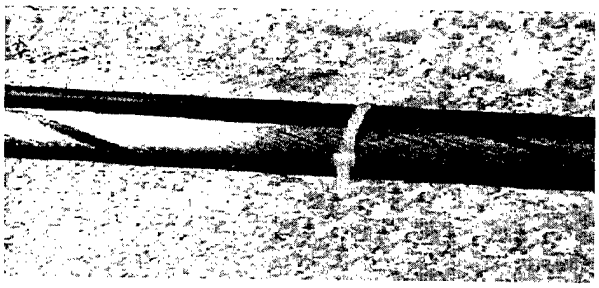


Figure 4. EXCEL cable (black) strapped to submarine optical fiber cable.

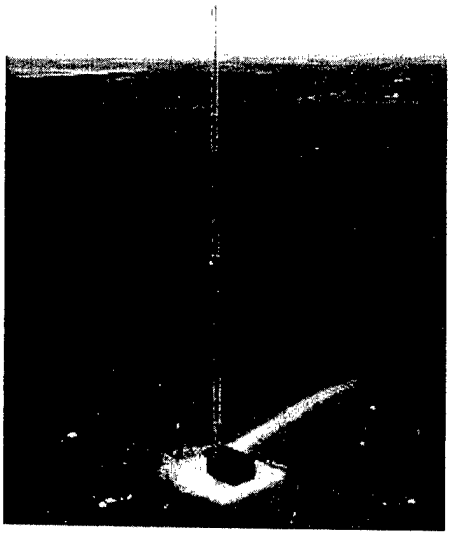


Figure 5. Telecom mast station.

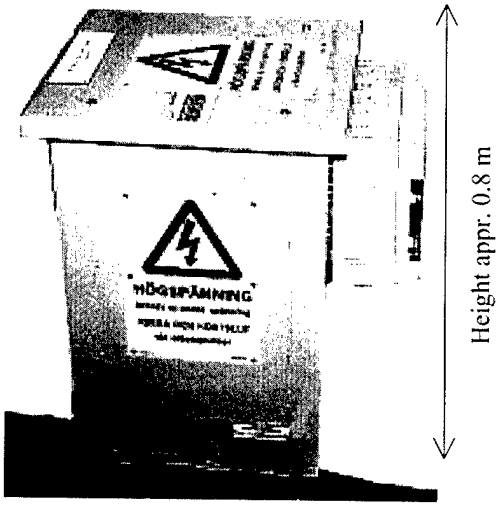


Figure 6. Receiving transformer unit to be built into telecom station.

4.1 Increasing Reliability

Alternative A is a system with a local low voltage feeding. Alternative B is the remote power feeding system fed from low voltage power and diesel backup. MTBF is defined as medium time between 30 minutes (medium) power failure periods.

Alternative	Unavailability	MTBF
A	4×10^{-4}	52 days
B	11×10^{-6}	5 years

There is an obvious need for battery backup in the first case. The conclusion is that it is possible to get a high degree of reliability at a lower cost using remote power feeding. If it is possible to use a local alternative feeding the MTBF will be very high. However this kind of calculation is difficult to do and the result depends highly upon local factors.

There is an advantage having a distribution net of your own since there will not be any other subscribers or power loads on the net that could cause disturbances and give lower reliability.

The remote power feeding system has been in service since spring 1998 [1] and several systems are in commercial use.

5. Power Feeding Telecom in Cities.

In today's society, the increasing demands of availability of reliable communication systems, i.e. high values of MTBF, is important.

In many cases the solution is a separate power system feeding vital telecom equipment.

Often there are existing pipe systems in the cities that can be used for the cable installation.

6. More Power-The 3-phase Solution

If you prefer a 3-phase system, or the power demand is higher than then the 1-phase system can deliver.

The 3-phase cables EXCEL/AXCES can be used for up to 24 kV. Different area sizes enables that several MVA's can be distributed.

These cables work as self-supporting cables, and can also be used as integrated fiber optic cables/power cable.

Several thousand kilometers of the self-supporting cable have been installed in Europe since 1994. Many of these installations have been made in severe environments.

7. Other Applications

When building networks in rural areas without any local power infrastructure the current and most common solution is to use diesel generators with backup batteries. A favourable alternative would be to decrease the number of diesel generators and use remote power feeding for most of the sites.

See figure 7.

In this way the maintenance could be concentrated to the remaining diesel generator(s) and the operating and investment costs would be reduced, at the same time reliability would increase. In such a net the maximum distribution distance can be augmented by modifying the cable design.

To offer reliable power to customer owned terminal equipment is another possibility that should to be taken into consideration.

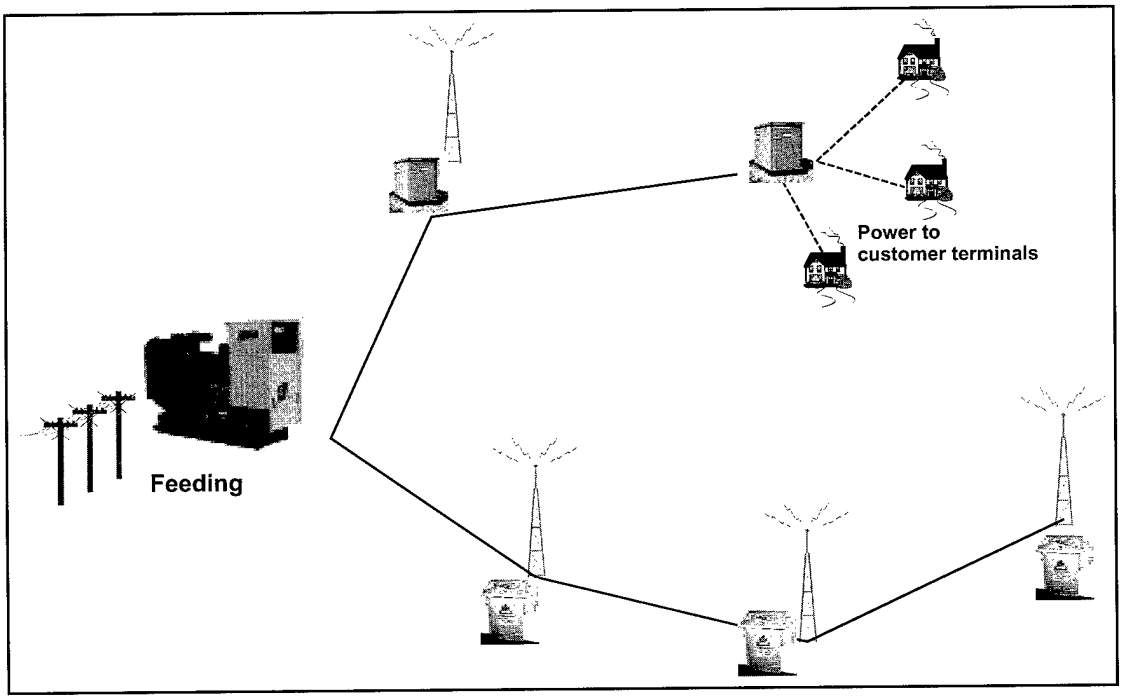


Figure 7. Sample net structure for rural areas.

8. Conclusions

Remote power feeding has the following advantages compared to conventional power feeding methods:

- Lower cost per installed site
- Higher reliability
- Existing reserve power plants can serve many sites
- Integrated power-fiber optic cable for telecom use
- Environment friendly
- Distribution over long distances
- High degree of safety

The service experiences from the installations that are in service are good.
The system is made up from standard components and no communication between the stations is needed.

9. References

[1] Sven-Erik Söderberg, Ericsson Component AB, Sweden
John Åkerlund, Telia AB Network service, Sweden

Remote Power Feeding-Report from a field trial.

Intelec98

10. The Authors



Lars Efraimsson, born 1957
Ericsson Network Technologies AB
Box 731, SE-791 29 Falun, Sweden.
Phone: +46 23 68530
Mail: lars.efraimsson@eca.ericsson.se

Mr. Efraimsson is responsible for technical development.
He has been with the company since 1984.



Henric Magnusson, born 1969
Ericsson Network Technologies AB
Box 731, SE-79129 Falun, Sweden.
Phone: +46 23 68487
Mail: henric.magnusson@eca.ericsson.se

Mr. Magnusson is working in H.V. Laboratory.
He has been with the company since 1990.

Analysis of CO Based ADSL Performance Due to Crosstalk from Remote Deployed ADSL Systems

Hoseok Oh, Kyounghee Jung, Junseok Oh, Youngtark Lee
Korea Telecom Access Network Laboratory
Daejon, Korea
+82-42-870-8533 · ohs@kt.co.kr

Abstract
If the CO based ADSL and the remote deployed ADSL are provided in the same cable, the performance of CO based ADSL system will be degraded due to crosstalk from the remote ADSL systems. We analyzed experimentally that the performance of CO based ADSL with 4km lengths of FS cable is degraded more than 82% compare with normal state. From these results, possible countermeasures such as data rate criteria with cable line loss are proposed.

Keywords
xDSL;ADSL;crosstalk;cable;copper;spectrum management

1. Introduction
With emergence of xDSL using existing copper cables, high-speed data communication on subscriber lines became realized. There are 7 Internet service providers representatively including KT (Korea Telecom) in Korea and the subscribers using high-speed Internet services have exceeded 6,250 thousands peoples on June, 2001. This means that 25% points of subscribers are increase every quarter. Among the various high-speed services, ADSL command an overwhelming majority as 52%(3,500,000 peoples), and cable modems occupy 31% and premise LAN 12.6%. In particular, xDSL technologies have advantages in terms of low investment cost since they use existing copper lines as transmission media. In order to utilize copper lines, which take major portion of existing telecommunication infrastructure, xDSL technologies with transmission bandwidth ranging from some kHz to tens of MHz have been developed and popularized. However, as existing copper lines have been used mainly for voice services with 0-4 kHz frequency band, many problems have emerged such as requirements of line quality for broadband signal in applying xDSL technology, and minimization of crosstalk interference among xDSL services [1]~[4].

When copper cable is only used in overall sections from the CO (Central Office) to the subscriber's premises, there is hardly influence on transmission performance due to crosstalk has been made between the CO based ADSL services. There are cases, however, that the CO based ADSL use the same premises cable with remote deployed ADSL such as FLC (Fiber Loop Carrier) which have ADSL functions, and remote deployed DSLAM (DSL Access Multiplexer). In this case, transmission performance of CO based ADSL is degraded due to the FEXT (far-end crosstalk) interference by the remote ADSL with higher signal power level relatively. In this paper, the effects of crosstalk between ADSL services, which have the properties of DMT line coding and frequency division duplex following G.992.1 or ANSI T1.413 standard, was analyzed, which is the key factor for stable services, for evaluating spectral compatibility between different systems.

2. ADSL Network and Crosstalk
2.1 ADSL Network
High bit rate Internet access services have been competitively offered to homes since 1999. Telecom companies give the Internet access with various xDSL technologies utilizing mainly existing copper access cables, and the xDSL services by remote deployed transmission system are also on the increase for buildings and apartments. Besides, new ISPs (Internet Service Providers) provide various high-speed data services with the transmission system located in premises. The copper cables used in the premises of buildings or apartments accommodate various telecommunication services such as xDSL and POTS at the same time. At this time, if the CO based ADSL using copper cables from CO to home and the remote deployed ADSL using optical fiber cables are provided in the same cable as shown in Figure 1, crosstalk from the remote deployed ADSL systems give rise to performance degradation of CO based ADSL system.

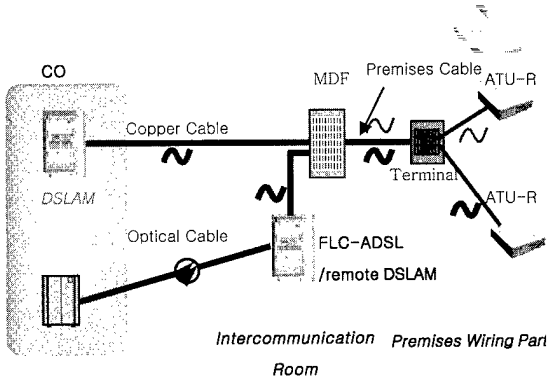
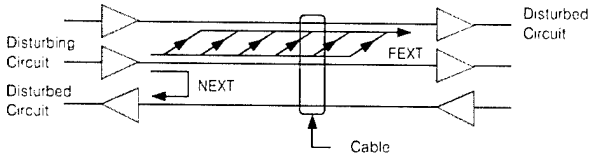


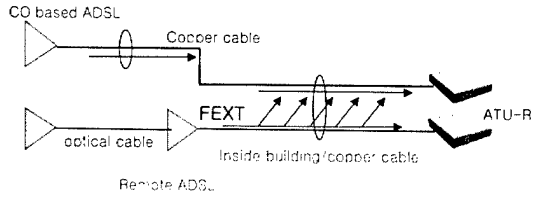
Figure 1. ADSL system deployment

2.2 Crosstalk
The electrical characteristic of copper cable is described with loop resistance, line loss, crosstalk coupling, balance, etc. Here,

crosstalk manifests itself as errors on digital loops. The types of crosstalk are near-end crosstalk (NEXT) and far-end crosstalk (FEXT). With NEXT, shown in figure2(a), the high-level outputs from digital line transmitters are coupled to the inputs of adjacent digital line receivers through nearby coupling paths. A different situation exists for FEXT in which the high-level outputs from a line transmitter are coupled into the same cable section between the two locations. Here the coupling paths are all along the same cable section between the two locations. Figure 2(b) shows a route junction where two digital loops in separate cables converge[5]. If the levels are different at the junctions, one of the line receivers will be subjected to higher and possibly destructive crosstalk. This is the case we have to consider in this paper.



(a)



(b)

Figure 2. Types of crosstalk coupling : (a)NEXT and FEXT in a single cable ; (b) FEXT at a route junction

3. Measurements

3.1 Test setup and Characteristics of Cables

Test setup consists of real 4km lengths of 0.4mm F/S (Foam Skin) cables and 300m lengths of CPEV(City Pair Polyethylene PVC), UTP5(Unshielded Twisted Pair Category 5) cables, DSLAM, ATU-R and test equipment as shown in Figure 3.

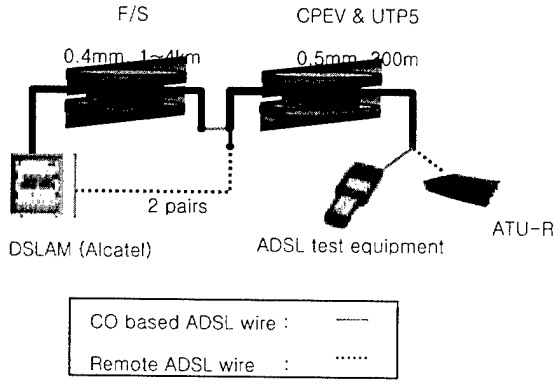


Figure 3. Test setup

First, to evaluate the characteristics of FS cable we measured the line loss and NEXT. Figure 4 shows the line loss of F/S (Foam Skin) cables with 0.4mm and 0.5mm in ADSL transmission frequency range and it is compared with the line loss of PIC cables of ANSI. In this figure, the F/S cable and the PIC cable have very similar characteristics.

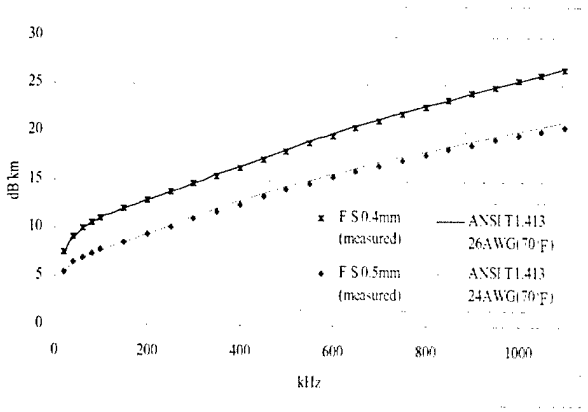


Figure 4. Line loss of F/S and PIC cables

A binder group or a unit of a cable is often consists of 25 twisted pairs. When desired to lay-up, the units are divided into two or more sub-units. Super unit that is assembled with suitable number of units, and sub-units may be used for manufacturing reasons. Figure 5 shows the NEXT power sum loss (PSL) characteristics of all 25 pairs in a binder group when each pair is disturbed by the other 24 pairs in a binder group and also gives the modeled 1% worst case. The 1% worse line is obtained by assuming that each pair's power sum at any given frequency is Gaussian distributed with a mean and standard deviation calculated from 25 measured values. Comparing with K_{NEXT} of ANSI T1.413, NEXT characteristics of F/S cable has very similar to that of ANSI cable as like line loss.

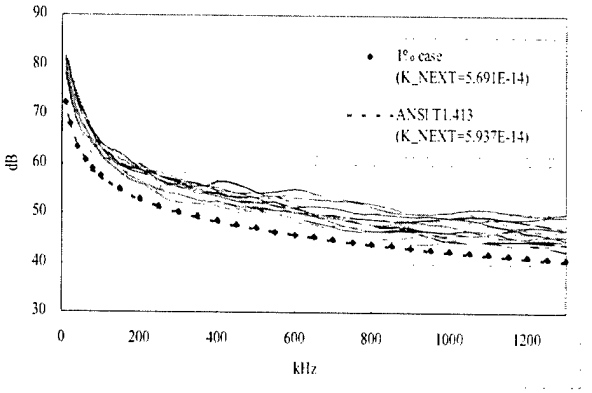


Figure 5. 24 pairs NEXT power sum loss of F/S 0.4mm

Figure 6 is the NEXT power sum when measured at 300kHz as the number of disturber increases. We increase the number of disturbers in order from the most influential disturbing pair to the least one. When interfered by 2 disturbers, the power sum value has about 60% of 24 disturbers' power sum. And in 10 disturbers, it becomes almost 90%. Therefore, this result shows that the corsstalk power sum due to more affecting 10 disturbers almost determines the total crosstalk noise in a binder group. From this result, we used worst 2 pairs as disturbers in this experiment for simplicity because the worst 2 pairs are dominant.

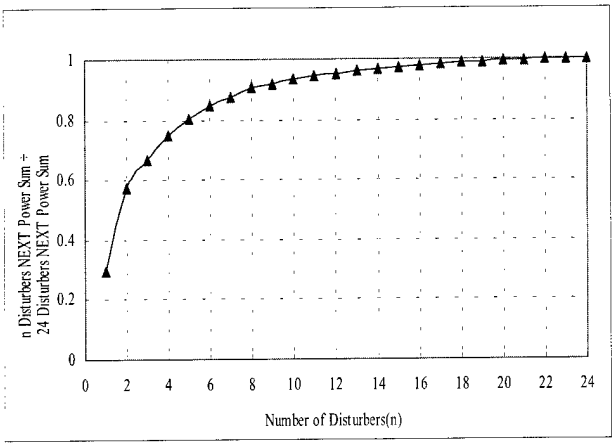


Figure 6. Relation between of disturbers and NEXT power sum

To select 2 pairs with the worst crosstalk among pairs of a cable used in premises, line loss and FEXT for disturber number are measured. Figure 7 shows the line loss and Figure 8 shows the FEXT of 300m lengths of CPEV and UTP5. The difference of line loss between 2 types of cables are small, however the FEXT of UTP5 is better than that of CPEV about 8~10dB. From the FEXT results, the worst 2 pairs were selected as disturbers that affect the CO based ADSL system.

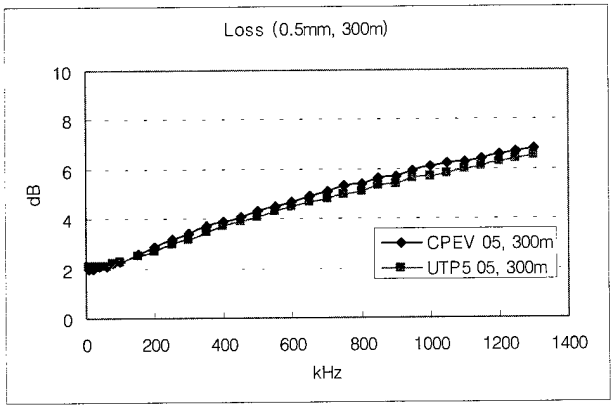
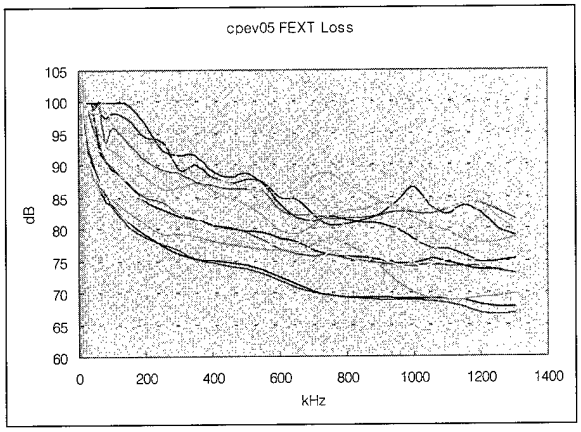


Figure 7. Line loss of CPEV and UTP cat5 cable

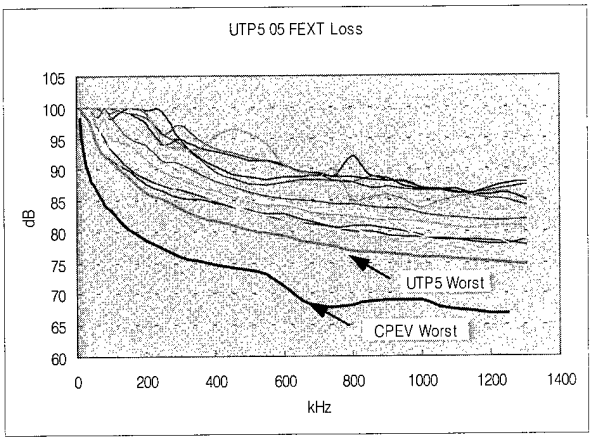
3.3 Performance Test

Under these conditions, the transmission rates of CO based ADSL for FS cable lengths with the lengths of 300m inside cable using test setup were measured.

Figure 9 shows the downstream and upstream rate of CO based ADSL degraded due to FEXT from adjacent 2 pairs of remote deployed ADSL. The figure also shows that the rates of CO based ADSL have 30~80% slowdown for the line length in downstream and the transmission performance of UTP cat5 is better than that of CPEV cable by about 30%. This performance degradation results from the difference between the PSD levels received at ATU-R of each system and the PSD of 3km ADSL system as shown in Figure 10. We could also find that there is no large difference in case 24 disturbers exist.



(a) CPEV cable

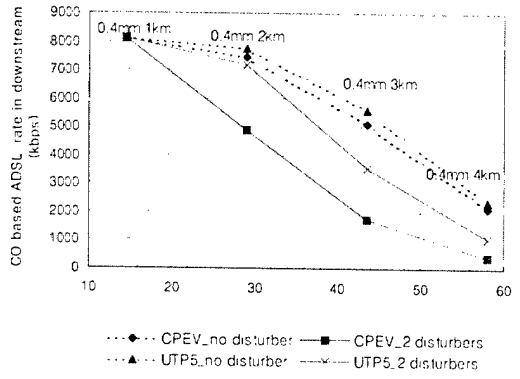


(b) UTP cat5 cables

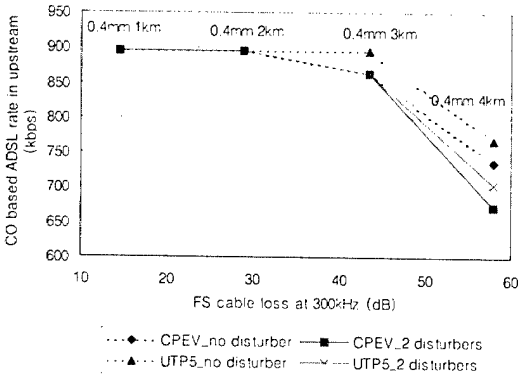
Figure 8. FEXT power loss

This results mean that remote deployed ADSL system is not spectrally compatible with CO based ADSL systems in a same cable. Here, we proposed the limited service performance as

shown in table 1 when it's not impossible to separate 2 types of systems. Table 2 shows the data rate recommended in ITU-T (L.19). The proposed criteria also show that the subscribers located more than 3km lengths could not be provided service.



(a) downstream



(b) upstream

Figure 9. CO based ADSL rate due to FEXT

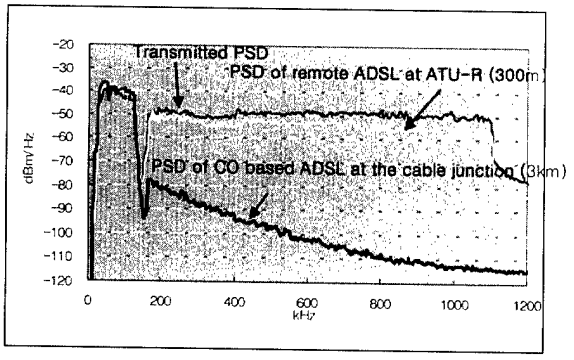


Figure 10. PSD received at ATU-R

Table 1. Service requirement of CO Base ADSL under FEXT environments

Classification	6Mbps or higher	1Mbps or higher
300kHz attenuation	≤ 22dB	≤ 44dB
0.4mm equivalent length	≤ 1.5km	≤ 3km

Table 2. ADSL data rate and loss (ITU-T L.19)

Class		Max. Insertion loss (dB)	Test frequency (kHz)
ADSL/ UADSL	6Mbps	41	300
	4Mbps	47	
	2Mbps	49	
	1.5Mbps	49	

3.4 Case study

Here, we introduce the real case for performance degradation due to crosstalk at a field. The subscribers live in apartment have complained of ADSL performance degradation such as link interruptions and data rate slowdown. The cable configurations of that subscribers are similar as Figure 1 and the length of main cable is 3237m and premise cable 400m. Table 3 shows the data rate measured at node.

Table 3. ADSL data rate at nodes

locations / contents		Premise MDF	Terminal	Degradation Rate
300kHz loss (dB)		50.1	55.4	
Data rate (kbps)	Down	3808	960	75%
	Up	736	704	5%

First, we could suppose that the problems would be in the premises area from the data rate measured as shown in Table 3. Then we measured the PSD (Power Spectral Density) of background noise each location and found out that the crosstalk was the cause of the performance degradation from results as shown in Figure 12.

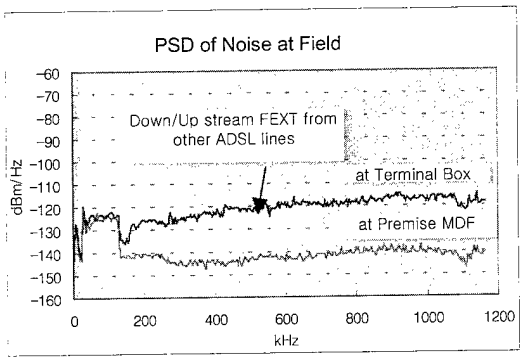


Figure 11. PSD measured at nodes

4. Conclusion

This paper has shown that remote deployed ADSL system is not spectrally compatible with the CO based ADSL systems when the 2 types of systems provide service using the same cable inside buildings or apartments. To measure the transmission performance, 4km cable (JF F/S 0.4mm) for CO based ADSL and 300m lengths of 2 kinds of copper cables (CPEV 0.5mm and UTP Cat5 0.5mm) using in the premises were used. The transmission rates (downstream) of CO based ADSL decrease 30~80% due to crosstalk from adjacent 2 pairs, which have the worst characteristics relatively, used for remote deployed ADSL system. From the results, it is recommended that remote deployed ADSL system should utilize the different cables in the premises when CO based ADSL system provide the service to the same area. If it is impossible to do the thing, criteria of the line attenuation for maximum transmission rate should be prescribed, and if UTP cat 5 is used, 30% data rate could be improved. And also it is not possible to provide ADSL services that have the property of ANSI T1.413 for over 3km of lines length with 0.4mm core diameter. So, it is required to make the rules for spectral management considering that the remote deployed ASDL systems are getting widely used.

5. References

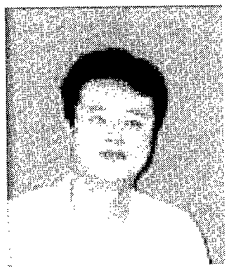
[1] Walter Goralski, "xDSL Loop Qualification and Testing", IEEE Comm. Magazine(May 1999).

[2] Zdzislaw Papir, "Competing for Throughput in the Local Loop", IEEE Comm. Magazine(May 1999).

[3] B. Cerrou, M. Alard, and B. Le Floch, "Coded Orthogonal John W. Cook, "The Noise and Crosstalk Environment for ADSL and VDSL Systems", IEEE Comm. Magazine(May 1999).

[4] Jean-Jacques Werner, "The HDSL Environment", IEEE Journal on Selected Areas in Comm. Vol. 9, No.6 (Aug. 1991).

[5] Whitham D. Reeve, *Subscriber Loop Signaling and Transmission Handbook*, IEEE PRESS (1995)



Hoseok Oh is a senior member of technical staff in Access Network Laboratory, Korea Telecom, Daejeon, Korea. He received the B.S. and M.S. degree in Electronic Engineering from Chungnam National University in Korea in 1991 and 1993, respectively. Since 1993, he has been with the R&D group at Korea Telecom. His research interests include EMI/EMC on telecommunication systems and access network engineering.



Kyounghee Jung is a member of technical staff in Access Network Laboratory, Korea Telecom, Daejeon, Korea. She received B.S. degree in Radio Science and Engineering from Chungnam National University in Korea in 1998. After joined the R&D group at Korea Telecom in 1999, her research interests include the engineering of copper access network for xDSL services and EMI/EMC on telecommunication systems.



Junseok Oh is a member of technical staff in Access Network Laboratory, Korea Telecom, Daejon, Korea. He received the B.S. degree in Physics from Korea Advanced Institute of Science and Technology in 1997. After joined the R&D group at Korea Telecom in 1997, his research interests include the engineering of copper access network for xDSL services and the management of optical access network.



Youngtark Lee received M.S. and Ph.D. degrees in Electronic Engineering from the Sung Kyun Kwan University in Korea, in 1988 and 1999, respectively. Since 1989, he has been with the R&D group at the Korea Telecom, where he is currently a director of Optical Outside Plant Engineering Division. His research interests include optical access network engineering, specialty optical fibers and optical fiber Bragg grating applications.

Experimental and Calculated Velocity Distributions within a Pressurized Optical Fiber Coating Applicator

Sravan Ravinutala[*], *Gunnar Finberg*[*], *Constantine Polymeropoulos*[**], *Yogesh Jaluria*[***] *and Greg Elliott*[***]

Mechanical and Aerospace Engineering Department, Rutgers, The State University of New Jersey
Piscataway, New Jersey
(732) 445-3650 poly@jove.rutgers.edu

Abstract

This work is an experimental and computational investigation of the flow field within a pressurized optical fiber coating applicator. The test apparatus used for the experimentation included an unheated test applicator equipped with two pairs of opposing windows allowing optical access for Particle Image Velocimetry as well as visualization of the axisymmetric flow field. The simulation considered isothermal axisymmetric Newtonian flow. Within the flow regions where the numerical model geometry was similar to that used in the experimentation there was good agreement between the measured and predicted magnitudes of the flow velocities, and the extent of the recirculating region within the applicator.

Keywords

Optical Fiber; coating applicators; flow field

Introduction

The manufacture of optical fibers includes single or multiple stages where protective coatings are applied to the fiber in suitably designed applicators. Upon entering a coating applicator air entrained by the fiber is replaced by the coating liquid in the vicinity of an apparent dynamic contact surface between the air, the liquid and the moving fiber. The flow within the coating chamber is induced by viscous shear due to the moving fiber, and a portion of the fluid is accelerated into the converging portion of a tapered exit die while the remainder is recirculated within the coating chamber. At the coating die exit the coating material is drawn out with the fiber, forming a free surface whose shape is primarily determined by a balance between viscous and inertia forces.

Published experimental work on coating flows with plunging fibers have primarily included measurement of apparent contact angles and of critical fiber speeds for air entrainment [1-4]. A comprehensive discussion of numerical methods used for other coating flows can be found in ref. 5. There are, however, few published studies using numerical simulation of the flow field within an optical fiber applicator. The flow within an optical fiber coating chamber and die was modeled numerically using FIDAP [6], and the results, which included the effect of viscous dissipation, were then used to compute the centering force as a function of the die taper angle. References 7-9 have considered the flow field in an isothermal applicator and the effect of variable temperature, including viscous dissipation, for different applicator geometries and operating conditions, were included in ref. 10. The simulations to date have required an imposition of experimental data, or other ad hoc conditions, for the shape of the upstream meniscus near the moving fiber. Other important aspects of the process that require further detailed consideration include (a) the influence of heat transfer between the applicator walls and the fluid, including effect of thermal conditions and viscous dissipation, (b) non-Newtonian fluid behavior, especially within the exit die region and at high speeds, (c) and the temperature dependence of material properties, particularly its viscosity.

Of particular importance in numerical flow field modeling is the availability of appropriate experimental data so that the predicted results can be validated for at least a set of simplified or limiting conditions. So far, to the authors knowledge, such data have not been available. The present work was therefore undertaken to generate sets of flow field data using a simulated applicator with optical access to the flow field allowing local velocity measurements using Particle Image Velocimetry (PIV), and to compare the results with predictions from ongoing numerical modeling work. Experimental results presented here are for practically isothermal flows with fiber speeds less than 1.67m/sec (100m/min) with negligible viscous dissipation.

Experimental Apparatus

Figures 1(A) and 1(B) are schematic diagrams showing the overall experimental configuration and the PIV setup, respectively. A 245 μm diameter acrylate-coated fiber was used for all the experimentation. The fiber motion was controlled using a commercial optical fiber rewinder and the test applicator used for the present work was equipped with glass windows for optical probing of the flow field. The test liquid (glycerol) was supplied from a pressurized reservoir, and for each fiber speed the liquid flow rate, and pressure, were controlled using a parallel two-valve system. The test applicator was 2 cm x 2 cm in cross-section and the overall effective height was 0.78 cm. Two pairs of 1cm diameter flat glass windows on each wall allowed optical access to the flow from two perpendicular directions. The fiber entrance and exit was through 350 μm and 300 μm diameter coating dies, respectively. The maximum fiber speed used in the present experimentation was 1.67 m/sec, and for all tests the inlet meniscus was located within the entrance die.

---

[*] Graduate Student

[**] Professor, corresponding author

[***] Professor

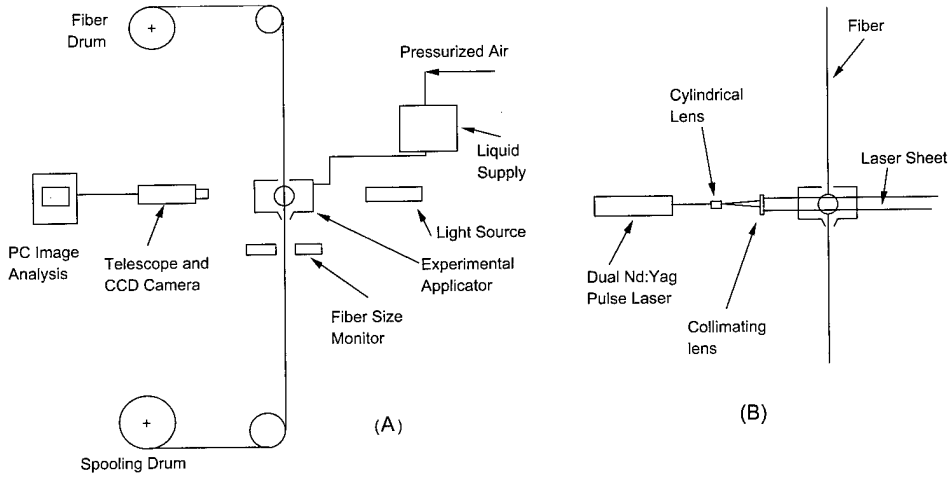


Figure 1. (A) Schematic diagram of experimental apparatus
(B) Normal view of the PIV setup.

Illumination for PIV was provided by a dual head Nd:YAG pulsed laser which had a wavelength of 532 nm, pulse width of 10 ns, repetition rate of 15 Hz and energy of 120 mJ/pulse. The laser produced two independent pulses with a delay time adjusted from 16 μs to 160 μs depending on the field of view and fiber speed. After overlapping the two laser beams, cylindrical and spherical optics were used to form a laser sheet, which was passed transversely through the center of the test applicator and was imaged normal to the sheet. The image pairs were collected using a digital camera, with 1008x1018 pixel resolution and capable of taking two independent images with as little as 1 μs delay between them. Laser and camera timing were controlled by a pulse generator with a better than 1 ns resolution. The glycerol was seeded with reflecting spheres having a diameter of less than 10 μm. The displacement of the particles between the two images was evaluated in pixel subregions of the image using a multi-pass 2-D cross-correlation algorithm. The correlation calculations were based on 32x32 pixel subregions with 50% overlap resulting in 2% expected uncertainty in the measurements. Knowing the magnitude and direction of subregion displacement and the time separation between the two images (i.e. the delay time between the two laser pulses) the velocity could then be calculated. A complete review of PIV and of the processing techniques used in this investigation are given in ref. 11.

Numerical Method

The numerical model considered axisymmetric flow within a cylindrical applicator with an outer radius of 10 cm, and a height of 0.78 cm, equal to the hydraulic diameter and the height of the square sided experimental test section respectively. The entrance meniscus shape was approximated by a third degree polynomial and its outer edge was anchored at the mouth of the 300 μm diameter inlet. The exit was a tapered die with radius changing from 400 μm (which was smaller than that used in the experimentation) to 175 μm over a distance of 2 μm. The flow region was transformed to a rectangular domain and, for the low speed isothermal flows considered in the experimentation, the continuity and momentum equations were solved using a numerical method based on the SIMPLER algorithm. The boundary conditions were no slip at the solid boundaries, previously described prescribed free surface at the entrance, and inlet and outflow using zero second derivatives. For the coating applicator, 102 grid points were used in both the radial and axial directions, and for the die there were 12 grid points in the radial direction and 82 grid points in the axial direction. The inlet for the fluid was located at the bottom of the applicator at the far outer radius. The properties of glycerin were used for all calculations. Typically, convergence was achieved after approximately 3000 iterations.

Results

All of the results are presented as functions of dimensionless variables. The radial distance, r, from the fiber centerline and the axial distance, z, from the exit die inlet were non-dimensionalized by the fiber radius, Rf, and the axial and radial velocity components u and v by the fiber velocity Uf. The stream function was non-dimensionalized by its maximum value. It should be noted that the numerical grid was slightly different from the grid generated by the PIV analysis. Consequently, the closest set of numerical data were selected for comparison with the experimental data points. In addition, because the imposed boundary conditions at the applicator entrance and exit were different than those used during testing, comparisons between experimental and numerical results were expected to be valid away from these regions. Current work is aimed at removing these differences.

Figures 2(a) and (b) are examples of numerical and experimental axial velocity profiles at axial distances from the exit die equal to 10, 32 and 48 fiber radii, and for fiber speeds equal to 0.17 m/s and 1.67 m/s, respectively. Figure 2(c) shows a numerically calculated axial velocity profile for a fiber speed of 15 m/s which is much higher than those tested. The results reflect an increase in boundary layer thickness as the fiber entrained the fluid near the applicator entrance, followed by a region of constant axial velocity near the applicator center, and finally a region where radial components of velocity due to the recirculating flow near the exit resulted in reduced axial velocity.

Figure 3 shows axial velocity profiles at constant radii for the corresponding fiber speeds of fig. 2. Figures 3(a) and 3(b) include the corresponding experimental data and fig. 3(c) shows computed results only for the high fiber speed used in fig. 2(c). The results in figs. 3(a) and 3(b) show that in the region between 20 and 50 radii away from the exit die the axial velocity was independent of axial position. In that region, figs. 3(a) and 3(b), as well as 2(a) and 2(b), show that the experimental and

numerical results were in reasonable agreement. Close to the entrance the increase in axial velocity at constant radius was a consequence of the increase in boundary layer thickness. The decrease in axial velocity at the exit was because of radial velocity components due to flow recirculation. It should be noted that the scatter of the PIV data can be attributed to the large velocity gradients near the fiber which also prevented accurate measurements very close to the moving surface. Current work is aimed at improving the data resolution.

Figure 4 shows numerically calculated streamlines for fiber velocities of 0.17 m/s, 1.67 m/s, and 15 m/s, and fig. 5 shows experimentally measured velocity vectors for fiber velocities of 0.17 m/s and 1.67 m/s. Comparing figs 4(a) and (b) to figs 5(a) and (b), the center of the recirculation region changed only slightly as the speed is increased from 0.17 m/s to 1.67 m/s. In all four figures, the center of the recirculation region was located approximately 22 radii away from the fiber center and 30 radii away from the bottom of the applicator. Figure 4(c) shows that at much greater fiber velocities, the center of the recirculation region moved substantially towards the exit compared to any of the slower velocities. At 15 m/s, the shape of the streamlines was distorted substantially compared to the corresponding shape at lower speeds. The innermost streamlines were quite circular for fiber speeds of 0.17 m/s and 1.67 m/s, but at 15 m/s, the innermost streamline was almost egg shaped.

Conclusions

The flow field within an experimental optical fiber coating applicator was measured using Particle Image Velocimetry and the results were compared with those obtained from numerical solution of the conservation equations. The experimental results, which identified the initial accelerating part of the flow near the entrance of the applicator, a constant velocity flow near the middle, and the recirculating flow near the exit were in good agreement with the computed predictions. The overall measured velocity vector plot within the applicator was also in good agreement with computed streamline plots for the same conditions. This is work in progress and includes improvements in the experimental technique and numerical predictions.

Acknowledgments

The Authors acknowledge the financial support provided by NSF, under grant no CST 96-10102, for this work, and to Professors G. Mungal, E.F. Hasselbrink and Donghee Han for providing the algorithms to process the PIV images used in this study. Mr. Art Henningsen helped with the PIV data analysis.

References

1. Inverarity, G.,"Dynamic Wetting of Glass Fibre and Polymer Fibre," *Br. Polym. J.*, v.1, pp. 245-251, 1969.
2. Ghannam, M., T.,and Esmail, M.N., "Experimental Study of the Wetting of Fibers." *AIChE J.*, v.39, pp. 361-365, 1993.
3. Abraham, A., and Polymeropoulos, C.E., "Dynamic Menisci on Moving Fibers," *Proc. 48th Int. Wire Cable Sym.*, Atlantic City, NJ, 1999.
4. Ravinutala, S., Rattan, K., Polymeropoulos, C. and Jaluria, Y., (2000), "Dynamic Menisci in a Pressurized Fiber Applicator," *Proc. 49th Int. Wire Cable Symp.*, Atlantic City, NJ, 2000.
5. Christodoulou, S.F., Kistler, S.F., and Schunk, P.R., "Advances in Computational Methods for Free Surface Flows", *Liquid Film Coating*, Kistler, S.F., and Schweizer, P.M., eds., Chapman and hal, London, 1997.
6. Abbott, J.S., and Francis, D.C., "Analysis of the Optical Fiber Coating Process Using FIDAP: Flow, Heat Transfer, and 3D Calculation of Centering Forces," Proc. 3rd FIDAP Users Conf., 1989.
7. Lyytikainen, K., "Numerical Modeling of Optical Fiber Coating Process," *CSC News*, Center Sci. Comput., Finland, v. 1, pp. 18-20, 1998.
8. Rattan, K. and Jaluria, Y., "Simulation of Flow in Die and Applicator For Optical Fiber Manufacturing," *Proc. 48th Int. Wire Cable Sym.*, Atlantic City, NJ, 1999.
9. Dimitropoulos, C. D., Chippada, S., Grald, E.W., and Kulkarni, J.A., CFD Simulation of Optical Fiber Coating Flows", *Proc. 49th Int. Wire Cable Sym.*, Atlantic City, NJ, 2000.
10. Zhao, C.Y. and Lee, S.H.K., "Physical Considerations of a Pressurized Optical Fiber Coating Process", *J. Materials Processing and Manufacturing Sciences*, v. 8, pp.53-73, 1999.
11. Raffel, M., Willert, C., and Kompenhans, J., *Particle Image Velocimetry*, Springer-Verlag, New York, 1998.

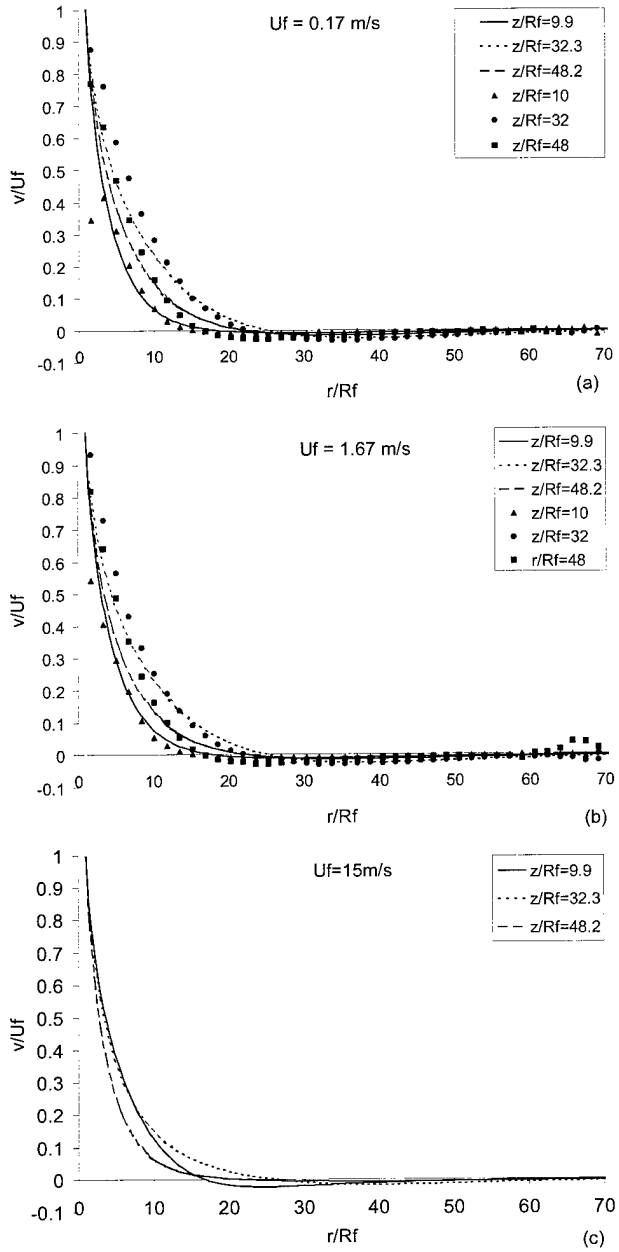


Figure 2. Numerically calculated and experimentally measured axial velocity profiles at different axial positions within the coating applicator.

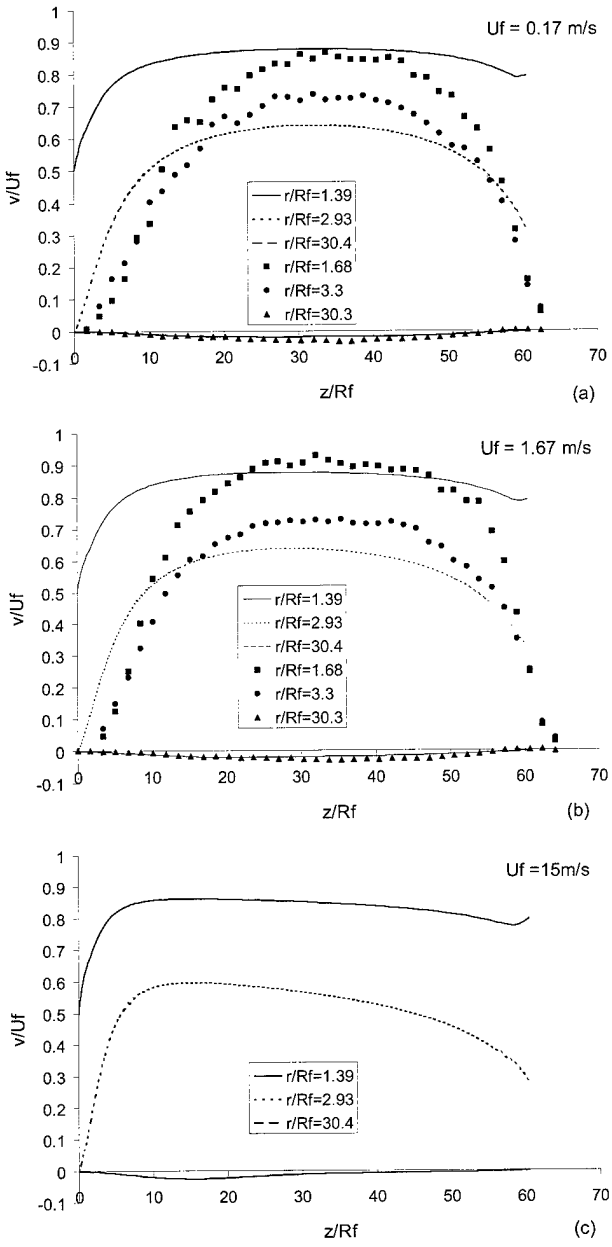
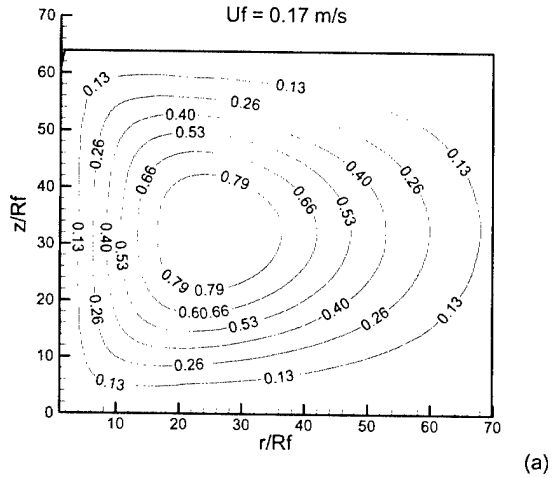
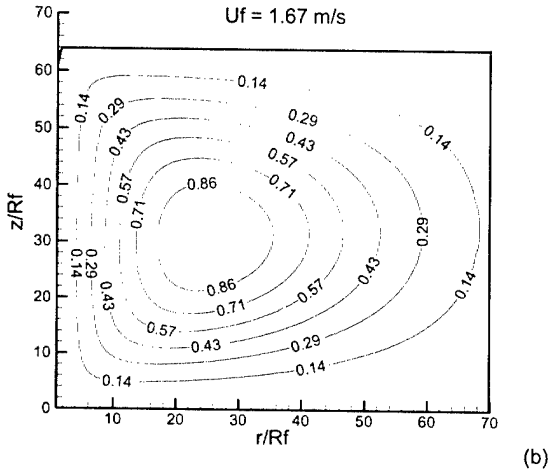


Figure 3. Numerically calculated and experimentally measured axial velocity profiles at different radial positions within the coating applicator.





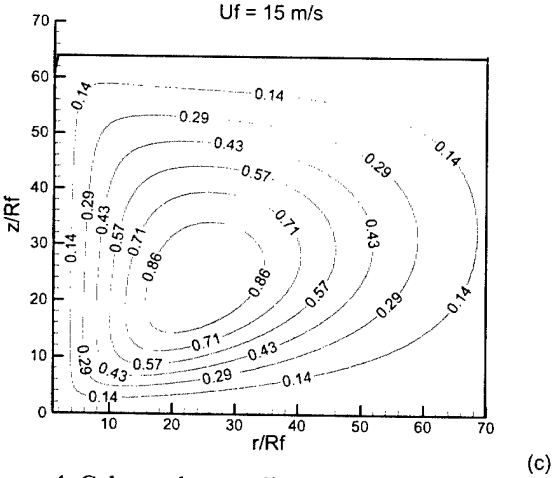
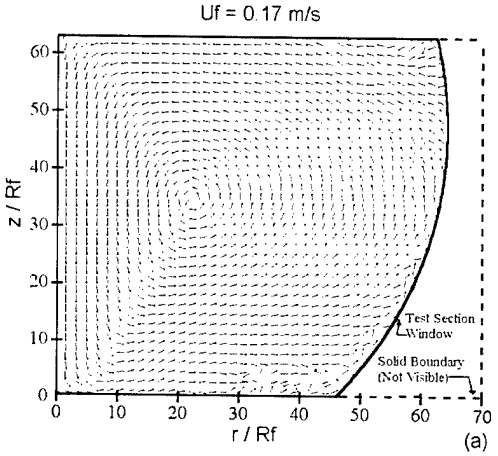


Figure 4. Calcuated streamlines, normalized by the maximum value.



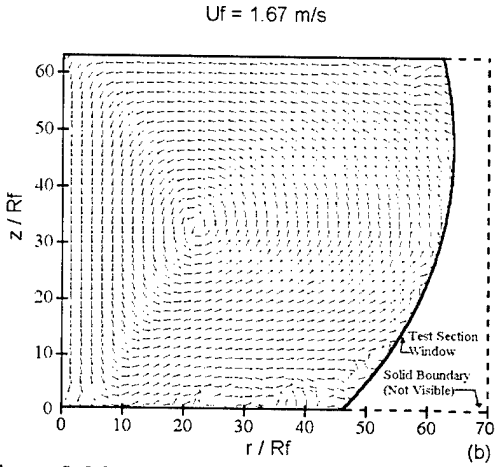
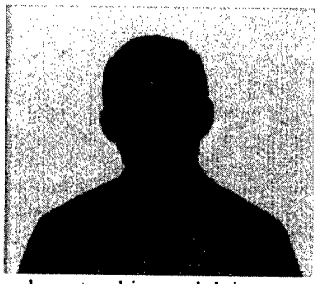


Figure 5. Measured velocity vectors within the coating applicator. Vectors are normalized to the same length.

C.E. Polymeropoulos
Department of Mechanical and Aerospace Engineering
Rutgers University
97 Brett Road, Piscataway, NJ 08854-8058

Dr. Polymeropoulos is a Professor of Mechanical Engineering at



Rutgers and has been teaching and doing research in the general area of thermal processes.

Optical Cable for Multiple Installations with Friction- and Abrasion-Resistant Sheath

Yoshio Hashimoto, Takashi Matsuzawa, Naoki Okada, Michio Suematsu
FUJIKURA Ltd.
1440 Mutsuzaki, Sakura-shi, Chiba-ken, Japan
+81-43-484-3945 · hashimoto@s.fujikura.co.jp

Abstract
We designed and developed a new cable having a special jacketing structure with a friction-resistant outer skin layer. LLDPE with non bread-out alloyed PE is used as a material for the skin layer. LLDPE with non bread-out alloyed PE is excellent in resistance to friction and abrasion. By lowering the friction coefficient of the sheath, it is possible to install additional cables easily in a narrow space. The abrasion-resistant sheath does not damage the existing cables. Use of the new cable makes it possible to accomplish multiple installations safely and efficiently without using any lubricants.

Keywords: Optical fiber cable; multiple installations; friction resistance; abrasion resistance

1. Introduction
In recent years, optical fiber networks have been constructed over a wide area with the dissemination of high-speed transmission networks. In order to construct these networks, it is necessary to install a great number of optical fiber cables. In urban areas, cables have been installed in underground ducts, therefore, additional cables have to be installed in narrow ducts in which ordinary cables are already installed. In Japan, multiple installations with spiral hangers have spread in aerial regions.

For multiple installations mentioned above, attention must be directed to the following points.

1) The installation length is limited because of the friction between the existing cables and duct walls. Additional cables may be difficult to install in a narrow space.

2) Installation of additional cables may cause damage to the existing cables. In order to solve these problems, we attempted to develop a specially designed jacketing structure.

2. Friction- and Abrasion-Resistant Sheath
There are two methods of decreasing the friction coefficient of cable. One is to examine the cable structure, and the other is to devise an installation method.

"Designing a sheath surface of special shape (reducing the contact area)" and "Selecting a sheath material (using a material having a low friction coefficient)" are given as methods of examining the cable structure.

On the other hand, use of a lubricant is given as a measure for installation.

It is necessary to design and use a special closure for "Designing a sheath surface of special shape." This is not simple, however. Installation using a lubricant is not common in Japan.

For these reasons, we selected a new jacket material for examination.

2.1 Sheath material
We investigated the friction coefficients of jacket materials. Fig 1 shows the setup for measuring friction coefficient. A test sample of sheet was prepared by heating press.

New materials such as LLDPE (or FR-PE) with non bread-out alloyed PE and LLDPE with fatty acid amid have the effect of decreasing friction coefficient as shown in Table 1. Especially, the coefficient of friction between same-kind materials is lower as compared with that with PVC. However, the value is not as small as it is possible to disregard it. The surface of LLDPE with fatty acid amid was cleaned with alcohol. As a result, the effect of decreasing friction coefficient was found to diminish.

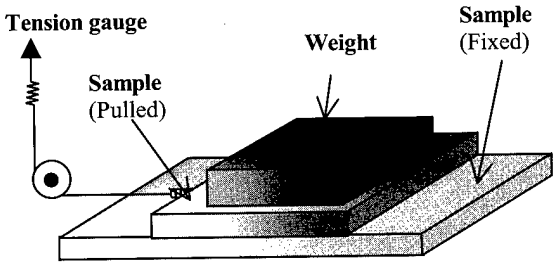


Fig.1 Method of measuring friction coefficient

Table 1 Friction coefficient

Pulled \ Fixed	Friction coefficient: PVC	Friction coefficient: Same material
LLDPE	0.50/0.45	0.36/0.34
FR-PE	0.64/0.61	0.57/0.55
LLDPE with non bread-out alloyed PE	**0.33/0.32**	**0.24/0.23**
FR-PE with non bread-out alloyed PE	0.36/0.34	0.28/0.25
LLDPE with fatty acid amid	0.24/0.20	0.17/0.15
(After cleaning surface with alcohol)	**0.35/0.35**	**0.27/0.25**

Friction coefficient: (dynamic/static)

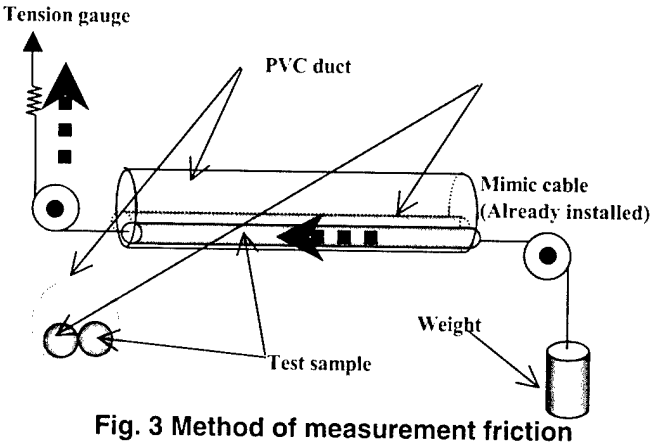
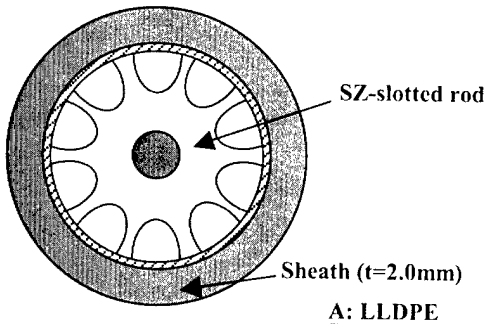


Fig. 3 Method of measurement friction coefficient of multiple installations

2.1 Evaluation with cable sample

We made trial cables shown in Fig 2.



A: LLDPE
B: FR-PE
C: LLDPE with non bread-out PE
D: LLDPE with fatty acid amid

Fig. 2 Cross section of trial cable(s)

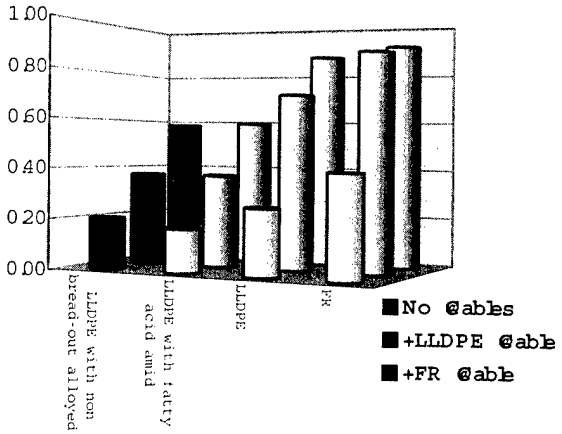


Fig. 4 Relation between cable sheath and measurement result of friction coefficient

2.1.1 Friction coefficient

We made a simulated duct that contains some existing cables, and investigated the friction coefficient of the trial cable. Fig 3 shows the setup for measuring friction coefficient. Two kinds of mimic cables were prepared. The sheath material of one of them is LLDPE, and that of the other is FR-PE.

Fig 4 shows the result of estimation. Type C and D cables have a lower friction coefficient than Type A and B cables. Especially, the effect is remarkable when there is a mimic cable. This result corresponds to the examination result of the sheet sample.

2.1.2 Abrasion resistance

We evaluated abrasion resistance. The test method is shown in Figure 5, and the results are given in Fig 6.

We found out that LLDPE with non bread-out alloyed PE has a high resistance to abrasion.

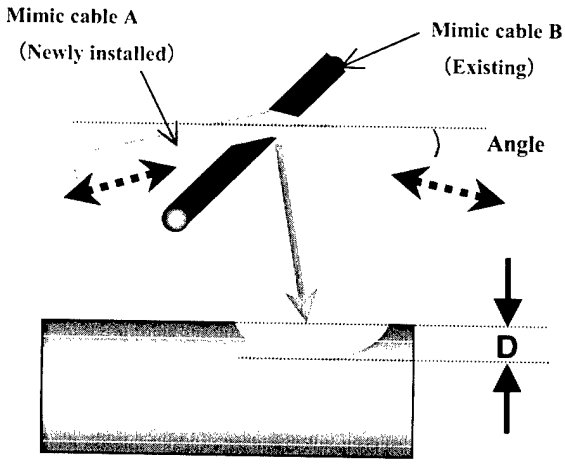


Fig. 5 Measurement method of abrasion resistance experiment

Based on this result, LLDPE with non bread-out alloyed PE was selected as a jacket material.

We investigated the reliability of the LLDPE with non bread-out alloyed PE as shown in Table 2.

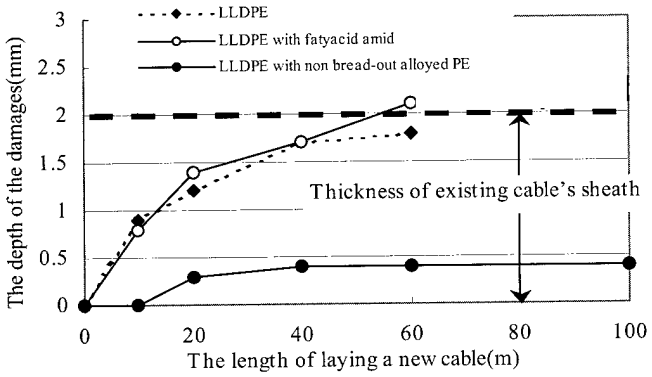


Table 2 Reliability of LLDPE with non bread-out alloyed PE

Test item	Test condition	Time	Result
ESC	50 deg. 10%	48 hours	Good
Heat deterioration	100 deg.	50 days	Good
Chemical resistance	50 deg. 10% sulfuric acid	50 days	Good
	50 deg. 10% hydrochloric acid		Good
	50 deg. 3% NaOH		Good
	50 deg. 10% oil		Good
Friction resistance	70 deg.	30 days	Good
	50 deg. water		Good
	50 deg. alkali-ion water		Good

3. Cable Design

In the case of using non bread-out alloyed PE, material cost becomes higher as compared with the ordinary PE (e.g., LLDPE) sheath, therefore, we investigated the manufacturing technique to form a skin layer with non bread-out alloyed PE on the ordinary sheath by co-extrusion.

Figure 7 shows the cross section of the cable with a formed skin layer. The total thickness of the sheath is 2.0 mm. The thickness of the skin layer is 0.1 mm. This structure allows decreasing the required amount of non bread-out alloyed PE and reducing material cost.

The cable has good transmission characteristics and good cable performances, as well as ordinary PE sheathed cables. The friction coefficient and abrasion resistance are equivalent to those of the LLDPE with non bread-out alloyed PE sheath.

As mentioned above, we succeeded in developing the friction- and abrasion-resistant cable by forming a skin layer of LLDPE with non bread-out PE on the sheath. This cable structure will be effective not only for multiple installations but also for air-assisted cable installation.

The inner layer can also be formed of other materials such flame retardant polyethylene for example. This formed skin layer technology is applicable also to a flame retardant cable.

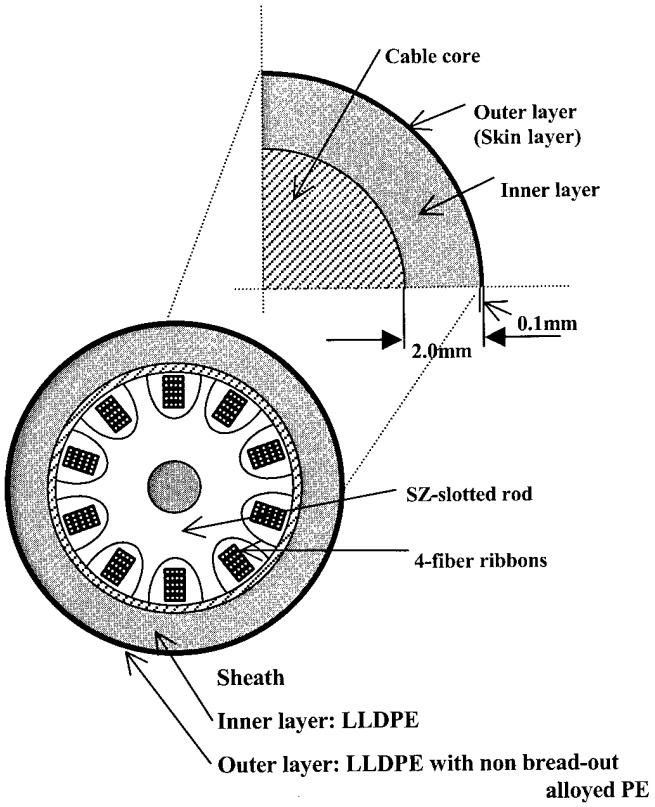


Table 3. Evaluation result of friction-resistant sheath

Sheath	Friction resistance	Abrasion resistance	Cost	**Total**
Ordinary polyethylene (LLDPE)	△ (fair)	△ (fair)	◎ (excellent)	**△ (fair)**
LLDPE with fatty acid amid	◎ (excellent)	△ (fair)	○ (good)	**○ (good)**
LLDPE with non bread-out alloyed polyethylene	◎ (excellent)	◎ (excellent)	△ (fair)	**○ (good)**
LLDPE with non bread-out alloyed polyethylene (formed skin type)	**◎ (excellent)**	**◎ (excellent)**	**○ (good)**	**◎ (excellent)**

4. Conclusions

We successfully developed a cable for multiple installations with friction- and abrasion-resistant sheath by using a special material (non bread-out alloyed PE), and constructed a special structure (formed skin layer).

This type of cable is suitable for multiple installations. Additional cables can be installed easily in a narrow space without using any lubricants, causing no damage to the existing cables.

5. References

[1] Y. Sato et al., "Study of New Slotted Core Cables for Underground Access Networks," Proc. of 47th IWCS 1999

[2] A. Murata et al., "The Investigation for Decreasing Frictional Force of Jacket Materials," IEICE Transmission, Vol.2, J50-B, 1999

[3] A. Sano et al., "The Development of a New Cable Installation Method by Using a New Low-Friction Pulling Rope (New Technology Rope)," ECOC 2000

[4] A. Sano et al., "Development of Low Friction Pulling Rope for Multiple Installation," IEICE Transmission, Vol.2, J50-B, 2000

Authors



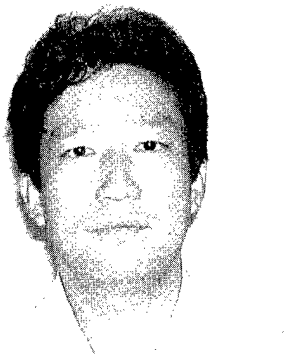
Research and Department Telecommunication Cable Division

Fujikura Ltd.

1440, Mutsuzaki, Sakura-shi, Chiba, Japan

hashimoto@s.fujikura.co.jp

Yoshio Hashimoto was born in 1973. He joined Fujikura Ltd after his graduation from Ibaraki University with a M.E degree in 1998 and has been engaged in research and development of optical fiber cables. He is now an engineer in Research and Department Telecommunication Cable Division and a member of the IEICE of Japan



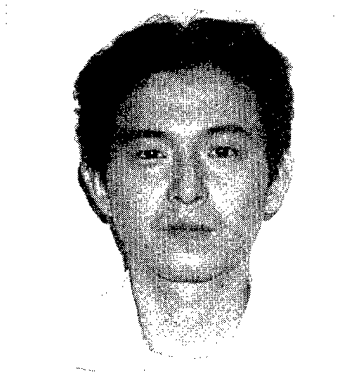
Research and Department Telecommunication Cable Division

Fujikura Ltd.

1440, Mutsuzaki, Sakura-shi, Chiba, Japan

naookada@s.fujikura.co.jp

Naoki Okada was born in 1964. He joined Fujikura Ltd. After his graduation from Chiba University with a B.E. degree in 1986 and has been engaged in research and development of optical fiber cables. He now belongs to optical fiber production engineering department.



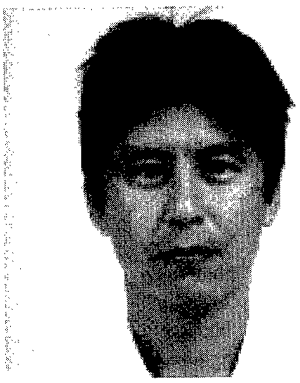
Research and Department Telecommunication Cable Division

Fujikura Ltd.

1440, Mutsuzaki, Sakura-shi, Chiba, Japan

tmatuzaw@fujikura.co.jp

Takashi Matsuzawa was born in 1969. He joined Fujikura Ltd after his graduation from Chiba University with a B.E degree in 1993 and has been engaged in design engineering of optical fiber cables. He is now an engineer in Research and Department Telecommunication Cable Division and a member of the IEICE of Japan.



Research and Department Telecommunication Cable Division

Fujikura Ltd.

1440, Mutsuzaki, Sakura-shi, Chiba, Japan

msuematu@fujikura.co.jp

Michio Suematsu was born in 1963. He joined Fujikura Ltd after his graduation from Nihon University with B.E degree in 1985 and has been engaged in design engineering of optical fiber cables. He is now a manager in Research and Development Telecommunication Cable Division.

Investigation and Comparison of Various Track Resistant Materials for ADSS Cable

Rong Xia, Xingyun Zhong, Liping Tang
Chengdu CCS Optical Fiber Cable Co.,Ltd, An Affiliate of Corning
Chengdu, Sichuan, P.R.China
+86 28 5182968-332, rong.xia@cdccs.com

Abstract
When all dielectric self-support (ADSS) cable is installed under high voltage power line (≥ 110 kV), the outer sheath of the cable will suffer a variety of environmental influence. The heaviest impact onto the cable behavior should be electrical stress, which may result in dry band arcing. In order to protect the core of ADSS and offer the lifetime of at least 20 years, the sheath layer must retain more than 50% of original thickness through its life cycle, therefore the sheath material is required to be well track-resistant.

At present, plentiful commercial sheath materials are claimed to be track resistant. In this paper, the market available track-resistant material is categorized into three main type as: **A**. polyethylene with inorganic filler (density is ca.1.1g/cm^3), **B**. polyethylene with reduced carbon black, and with special UV agent to compensate the function of reduced carbon black (density is ca. 0.95g/cm^3). **C**. flame retardant non-halogen compound (density is ca. 1.5g/cm^3). This paper compares the physical and mechanical properties and processability, and analyzes the mechanism of erosion for these materials. ADSS sample cables have been made with the three types of material, and inspected according to IEEE P1222 [1]. The materials also have been tested based on ASTM D2303 [2]. The results show that type A material is more applicable than the others are.

Keywords
ADSS; High voltage; Dry band arcing; Sheath material; Sheath erosion; Track resistant.

1. Introduction
At present, there are three optic cable structures which are applicable to be laid over high voltage power line: ADSS, AD-Lash and OPGW. OPGW is the best choice for newly built power line while ADSS and AD-Lash are more suitable for telecommunication network over the existing power line. With the advantage of higher reliability, low cost and "live" installation possibility, easily crossing over river, steep slope and high way etc., ADSS has been widely applied over the existing power line to offer or expand telecommunication capacity.

ADSS cable is fixed onto power tower by metal helical clamp and located under high voltage power line. Its lifetime is expected to be at least 20 years. Environmental condition of ADSS is very complicated. It has to undergo mechanical stress (gravity, wind blow, ice load, etc.), electrical stress, weather beat and contamination (dust, chemical pollution, littoral salt fog) rain and contamination (dust, chemical pollution, littoral salt fog). All these factors are harmful to the cable surface. The severest damage is erosion caused by dry band arcing, which might penetrate the jacket and expose the aramid yarn outward. Under UV irradiating, aramid yarn will be quickly aged and lose the function of strength element. This failure will result in degradation of ADSS properties until the fiber breaks in the worst case.

According to the requirements of IEEE P1222 (draft), track resistant jacketing material has to be used when electrical stress on the jacket exceed 12 kV space potential, while normal jacketing material may be used when electrical stress does not exceed 12 kV. The danger of jacket erosion will dramatically increased as ADSS is laid along the extra high voltage power line exceeding 220 kV, therefore cross link jacket material or other valid measures should be considered.

The design, application and experimental research of ADSS have been widely reported, but analysis and discussion of track resistant mechanism are rarely found. This paper categorizes and discusses various commercial anti-tracking materials, and compares their properties through serial experiments.

2. Sheath Erosion Mechanism
Typical design of ADSS is shown on Fig. 1 with jacket thickness of 2 mm.

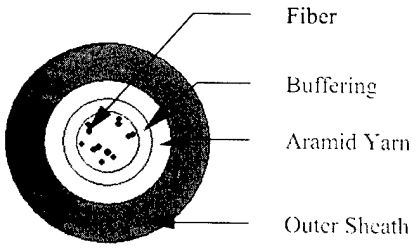
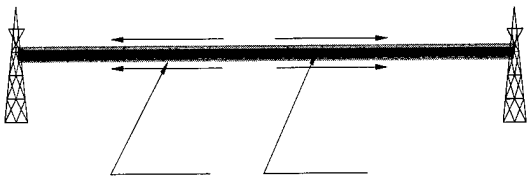


Figure 1. ADSS Cable profile

At the early phase of cable operation, dry band arcing is restrained as jacketing material is hydrophobic and water drop onto jacket surface is easily slide away. As the time goes on, the surface of sheath is gradually degraded due to environmental influence and let the hydrophobic property go down, rain drop and dew water therefore form a layer of conductive film along the cable surface. The surface current in power of mA is driven by space potential and flowed from the middle to the direction of tower [3] as shown in Fig. 2.



Conductive film

Current induced heat can vaporize the water on the cable surface and form a dried area, which blocks off the current. Finally discharge i.e. dry band arcing happens as electrical space potential accumulate to a certain level as shown in Fig. 3.

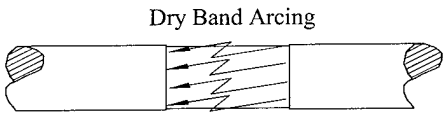


Figure 3. Dry Band Arcing

Electrical arcing will be the most dangerous when dried area reaches around 10 mm wide, and will not happen as dried area broadened further. Electrical arcing will generate high temperature and may cause discharging area reach the temperature of more than 500°C, resulting in degradation and tracking of jacket surface, even Puncturing the jacket in the worst case.

Corona, which normally happens in the position near the metal helical clamps, is also destructive to the cable jacket. It may be eliminated via valid installation measures.

3. Classification and Comparison Track-resistant Materials

3.1 Requirements for Track-resistant Sheath Material

Track resistant jacket material applied onto ADSS cable should be in compliance with following requirements.

- Good anti-tracking property
- Stability against UV degradation
- Good physical and mechanical properties:
    a) Tensile strength and elongation
    b) ESCR
    c) Abrasion resistance
    d) Low temperature properties
- Processability

3.2 Categorization of Track-resistance Material

Material suppliers have been continually developing and marketing a variety of track resistant jacketing materials with their own brand, and occasionally some FRNC material with low smoke, zero halogen properties is also put onto ADSS cable under high voltage power line. This paper categorized the track resistant materials into three types, and their basic composes are:

A. PE + Inorganic filler + Carbon black (2.6%)
-density is approx. 1.1g/cm^3

B. PE + Carbon black (1.0%)
-density is approx. 0.95 g/cm^3

C. EVA / PE + $Mg(OH)_2$/$AL(OH)_3$ + Carbon black (2.6%)
-density is approx. 1.5 g/cm^3

Each commercial anti-tracking material has their unique formula with additives of UV stabilizer and anti-oxidation agent. This paper will compare these three type materials and identify their advantages and disadvantages.

3.3 Mechanisms of Track Resistance

3.3.1 Type A Materials

Type A material is composed of normal PE jacket material and special inorganic filler contents of around 18%, carbon black remains to be 2.6%±0.25.

Carbon black will bring the micro-current into jacket layer under the environment of high electrical stress and accelerate aging process of sheath, induce cracks on the surface of jacket. Suitable inorganic filler contents inside the jacketing material can segregate the carbon black and reduce leak current, improve the property of heat resistance and effectively withstand the thermal destruction caused by dry band arcing.

3.3.2 Type B Materials

Type B material is composed of normal PE jacket material and special UV stabilizing agent, with reduced carbon black content of 1.0% compared with 2.6% in normal jacket material. Track resistance is improved as reduced carbon black content increases the distance between carbon black particles, and the leak current as well as tracking is restrained.

3.3.3 Type C Materials

Type C material is low smoke, halogen free flame-retardant jacketing material (FRNC). It contains inorganic fillers of $Mg(OH)_2$ / $AL(OH)_3$ as high as 50%, and carbon black content of regular 2.6%. Fillers can segregate carbon black particles and reduce the leak current. When dry band arcing happen on the cable surface, the arcing induced heat will dehydrate the flame retardant agent of $Mg(OH)_2$ and $Al(OH)_3$. Process of dehydration will absorb heat, therefore reduce the temperature. Meanwhile decomposed water might be vaporized, which may hold up the electric arcing and reduce the destruction. Another effect of decomposed water is to humidify the dried area and refrain possibility that electric arcing repeatedly happen.

3.4 Comparison of Physical and Mechanical Properties

Each type material of A, B and C is representative of several brands and properties also differ more or less from one brand to another. Major properties of each type material are listed in table 1.

Table 1. Physical & mechanical properties of A, B, C Materials

Item	A kind	B kind	C kind
Density g/cm^3	1.1	0.95	1.5
Melt Index g/10min	0.5	0.5	--
Tensile strength @break, N	16	16	13
Tensile elongation, @break, %	600	700	160
Low temperature °C	<-40	<-76	<-15
OIT @200 °C, min	>50	>30	>50
Shore D	60	60	50
ESCR (50°C,10%Igepal ,F_0) h	>1000	>1000 *	>600

*:ONe brand of toe B material has experienced failure ESCR test at 96 hours/50°C.

Data from table 1 show that sample type A is similar to sample type B except the low temperature property. Low temperature property of sample type A can reach -40°C, and sample type B can only remain -76°C as the same as common jacketing material. All the listed properties of sample type C are apparently worse than that type A and B.

3.4.1 Environmental stress Cracking Resistance (ESCR)

ESCR of sample type C is the shortest among the three type materials. In one case, ADSS cable with one brand of kind C material was even found to become noticeably sticky after temperature cycling test from –40°C to +60°C. One brand form type B has experienced failure on ESCR test.

3.4.2 Stability Against UV Degradation

According to specification of Bellcore GR-20-Core [4], outdoor PE jacketing material must contain evenly distributed carbon black of 2.6%. Type A and C comply with this requirement, but content of carbon black in type B material is lower than this figure and some brand only contain 1.0%, therefore kind B material normally contain some special UV stability agent. Although samples of B material we tested can pass UV stability test of 1000 hours, their UV stability performance under real installation condition are worth further study for a longer duration.

3.4.3 Mechanical Behavior

Tensile strength and elongation of type C material are worse than type A and B. This is because inorganic filler content inside type C material is as high as 50%.

3.4.4 Processability

Processability of type A and B is similar to the common PE jacketing material, and extrusion of type C material need special screw and extrusion parameters,

3.5 Experiments and Discussion

3.5.1 Electrical Erosion Test on Materials

We chosen three samples **a**, **b** and **c** out of track resistant jacketing materials representing type A, B and C respectively to test and compare their anti-tracking properties. Test was performed in accordance with the method of ASTM D2303-96. Specially formulated contaminant solution is flowing down along inclined plane on which two electrodes were hold at fixed position, and the anti-tracking property of the samples under the voltage of 2.5KV and 3.5KV respectively.

Specimen preparation: Moulded specimen with dimensions of 120 x 50 x 6 mm and unpolished surface.

Contaminant solution: 0.1% NH_4Cl + 0.02% wetting agent + distilled water with resistivity of 390 Ω.cm.

Flow speed of contaminant solution: 0.15ml/min. at 2.5kV and 0.30 ml/min. at 3.5kV.

The test apparatus is shown in Fig. 4.

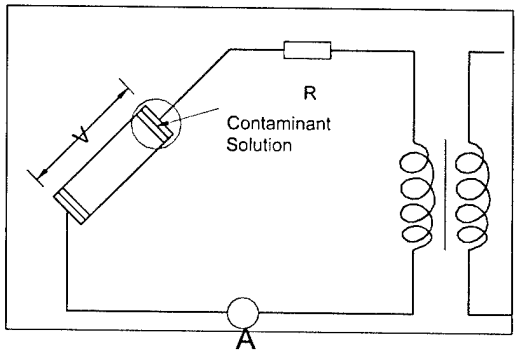


Figure 4. Contaminant and inclined plane test apparatus

Table 2 and Table 3 list the phenomena observed during the test.

Table 2. The erosion results at 2.5kv

	a	b	c
Leak Current (max), mA	10	*	10
Tracking, hour	4	*	6
Track length, mm	10	*	10
Track width, mm	2	*	1
Track depth, max	0.5	*	0.1
Track & erosion area, mm^2	small	*	tiny

Table 3. The erosion test results at 3.5kv

	a	b	c
Leak Current (max) mA	20	*	20
Time to track, hour	3	*	3

Time to fire, hour	5. 5	*	6
Track length, mm	60	*	40
Track depth, mm Max	1. 5	*	2.7
Track width, mm	20	*	10
Track and erosion area, mm2	1200	*	380

* Obvious discharges did not appear around the lower electrode of sample **b**, and electrical erosion was also not observed on the surface of sample **b**. The effect is the same after adjusting flow speed of contaminant solution. Polished the sample surface under water with fine sand paper and observed sample b get burnt after only 5 minutes and 1 minute under voltage of 2.5kV and 3.5kV respectively, so the test was interrupted. The reason might be explained as: 1. Contaminant solution did not wet the surface completely due to good hydrophobic surface of the sample **b**, therefore there was no obvious discharges observed. 2. Sample **b** gets burnt soon after polishing the surface. It indicates that sample **b** is not flame retardant, and this test setup is not effective to evaluate type B material.

The grade of 2.5kV under inclined plane test is enough for ADSS according to the requirement of 25mm/kv in IEEE P1222, and grade of 3.5kV is even more stringent for extra high voltage. It is shown from Table 2 and Table 3 that both sample **a** & **c** are capable to withstand tracking, and sample **c** has slightly better anti-tracking property than that of sample **a**.

3.5.1 Erosion Test on ADSS Cable

ADSS cable samples were made respectively from type A, B and C materials, and put into the electrical test respectively in a salt fog chamber for duration of 1000 hours as specified in IEEE P1222, draft, 1997. The setup of the test apparatus is schemed as Fig. 5.

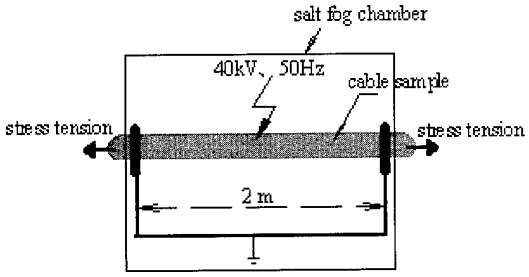


Figure 5. Salt-fog testing apparatus

Experimental condition:

A length of 2m cables was taken from a production reel as specimen and sealed at each end against moisture ingress before being supported horizontally in a salt fog chamber. The center of the specimen was applied with a high voltage at while the two ends of the specimen were kept grounded. Two ends of the specimen were fixed by metal helical clamp, and specimen was tensioned by a spring to exert a force of 9720±972N.

Size of salt fog chamber is around $8m^3$ with a ventilation aperture of 80 cm^2. Three nozzles were evenly distributed inside the salt fog chamber. Each spray cycle include 10 seconds spray and 20 seconds interruption. Spray pressure was 0.33Mpa, and spray volume was 0.4±0.1l/m3.hour. NaCl content in the conductive liquid was 10±0.5kg/m3.

Experimental results are listed in Table 4.

Table 4. ADSS cable salt-fog test result

Item	Sheath of Type A	Sheath of type B	Sheath of type C
Puncturing	No	No	No
Tracking erosion >50% wall thickness	No	No	No
Track depth, mm max	<0.05	<0.05	<0.05

Type A, B and C can all meet the requirements of IEEE P1222, and the test process observation identifies no difference on erosion.

Type A, B and C materials have actually been applying to ADSS cable outer sheath for operating in the high voltage electrical field exceeding 12KV space potential. They are undergoing through the environmental harsh test. We are continuously observing them and in the process of getting more illustrating data.

If the cable experience UV aging tests for 1000 hours before electrical stress test inside salt-fog chamber test, the result will be closer to actual situation condition.

4. Conclusions

All three type materials of A, B and C have the capability of track resistance. Type A material has the best comprehensive performance including track resistance, UV stability, processability etc. among the three type materials, although type B & C have their unique advantage, i.e. type B material with better low temperature behavior and processability, and type C with slightly better anti-track property.

5. Acknowledgments

We thank our colleagues Mr. Wei Zhang and Mr. Chengdong Wei for drawing on the paper, Mr. Jidong Zhong and Mr. Yong He for preparing the tests and last but not the least, the strong support we've been receiving to make it possible from our top management.

6. References

[1] IEEE P1222 Draft, "Standard for ALL Dielectric Self-Supporting Fiber Optic Cables (ADSS) for Use on Overhead Utility Lines", (1997).

[2] ASTM D 2303-96 "Standard Test Methods for Liquid-Contaminant, Inclined Plane Tracking and Erosion of Insulating Materials".

[3] Reinhard Engel and Sabine Will,"Lifetime Predictioin of ADSS-Cables in high Voltage Lines" *Proc. 49th IWCS, proc., pp.. 470~473 (2000).*

[4] Belleore, GR-20-CORE, "Generic Requirements for optical Fiber and Fiber optic cable" Issue 1, September 1994.



Rong Xia received her B.E. degree in chemistry from Sichuan University in 1982. She has been engaged cable material application since 1985 and engaged in optical fiber manufacturing process research from 1989 to 1995. She joined the joint-venture company of Siemens in 1996 and now is a senior engineer in R&D department in Chengdu CCS Optical Fiber Cable Co., Ltd.



Mr. Xingyun Zhong received his B.E. degree in electrical insulation material from Xian Jiao Tong University in 1985 and joined Chengdu Cable Plant as s process engineer at the same year. He has been engaged in design and development of optical fibre cable since 1990 and now is the R&D departmental manager in Chengdu CCS Optical Fiber Cable Co., Ltd.



Ms. Liping Tang, She received her master degree of electrical engineering from Harbin Institute of Electrical Technology in 1991. Now, she is deputy general manager of Chengdu CCS Optical Fiber Cable Co., Ltd., and in charge of production and R&D department.

A Compact Automated Fiber Cross-Connect Module for a Scalable Optical Cabling System

Masato Mizukami, Nobuhide Tanaka, Kunihiko Sasakura, Johji Yamaguchi and Kazumasa Kaneko

NTT Telecommunication Energy Laboratories, NTT Corporation
3-1 Morinosato Wakamiya, Atugi-shi, Kanagawa, 243-0198, Japan
Phone: +81-46-240-2068 e-mail address: mizukami@aecl.ntt.co.jp

Abstract

A new compact automated fiber cross-connect module is proposed for a scalable optical cabling system in intelligent buildings. The module uses a fiber-handling robot, and can connect any of 100 input optical fibers to any of 100 output fibers. By utilizing a micro-optical connector and micro-robot, we can build a module that is about one-fourth the size of conventional automated cross-connect module. We confirmed that the average cross-connection time is about 1 min and insertion loss of the module is less than 1.0 dB.

Keywords

Optical fiber; Optical connector; Robot hand; Cross connect; Automation; Intelligent building; Optical access network;

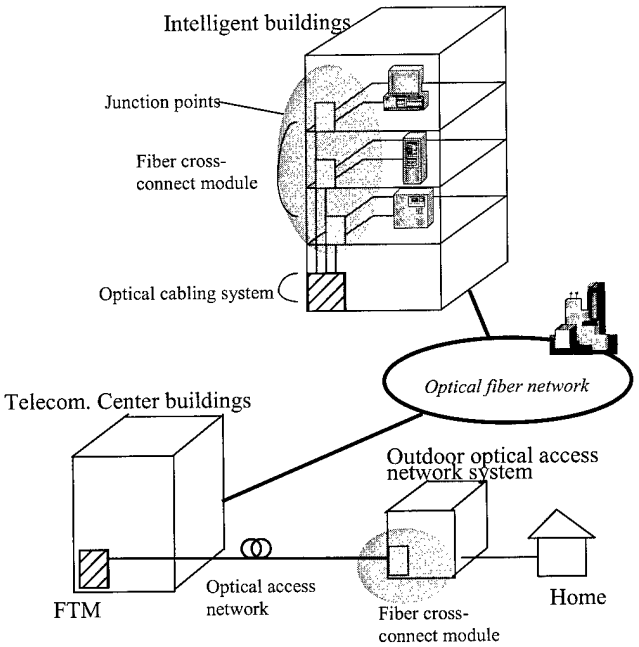
1. Introduction

With the increasing demand for high-speed, broadband communication systems, optical communication networks have become widely installed in intelligent buildings in metropolitan areas. In addition, optical access networks have been constructed to achieve a FTTH system. In intelligent buildings and optical access network systems, many optical fibers must be connected and exchanged at small-scale junction points between floors and at large-scale junction points between access and office networks (Fig. 1).

Much cross-connection work is done manually, which is very complicated and raise network operation costs, and there is a definite possibility of misconnection. In addition, conventional manually operated equipment is large because an optical connected part needs to be handled manually. Besides the problems associated with manual installations, optical cross-connect systems in buildings require high optical performance - a low insertion loss, high return loss, and transparency for optical wavelength. Also, a self-holding optical connection is required even if the power supply is down. To solve these problems and meet these requirements, some automated optical fiber cabling systems have been developed. Two of the major ones are the 4000x4000 automated fiber cross-connecting switch [1], which is for FTM use, and the 100x100 optical fiber cross-connect system [2,3], which is designed for use at connection points in office and access networks in intelligent buildings.

In addition, as the optical access networks continue to spread in the future, it is expected that the need for office-installation types and outdoor-installation types of cross-connection modules will increase. The installation space is generally narrow in an office and in an outdoor optical access network system, and this is one of the obstruction factors of spread of the optical networks in the future. The 4000x4000 automated fiber cross-connecting switch was is 1300 mm x 1800 mm x 600 mm, while 100x100 optical fiber cross-connect system is 530 mm x 440 mm x 380 mm. Both are too large to set up in an office or in an outdoor optical access network system.

In this paper, we propose a compact automated fiber cross-connect module for a scalable optical cabling system. We discuss the possibility of downsizing the fiber cross-connect module by utilizing a micro-optical connector and micro-robot.



FTM: Fiber Termination Module

Figure 1. Application of an optical fiber cross-connect module.

2. System concept

We examined the downsizing and scalability of optical cabling system for small-scale to large-scale connections. Figure 2 shows the concept of the optical cabling system. A cross-connect module can connect any input optical fiber to any output fiber by using a micro-robot and a connection board. An optical cabling system can be controlled by using a remote terminal (PC). Mechanical parts such as the micro-robot of the module are driven by using a controller.

We aimed at the module that is A4 size, which is almost equal to the minimum size of the 8-port premises distribution unit, which is currently used for manual connection in a building. By downsizing such a cross-connect module, we expect that we can achieve scalability by combining modules. A scalable cabling system could be constructed by combining fiber cross-connect modules and optical fiber link board modules, in which a fixed fiber link is cabled. The three-stage link configuration, in which the modules are combined, can be used to construct a large-scale optical cabling system.

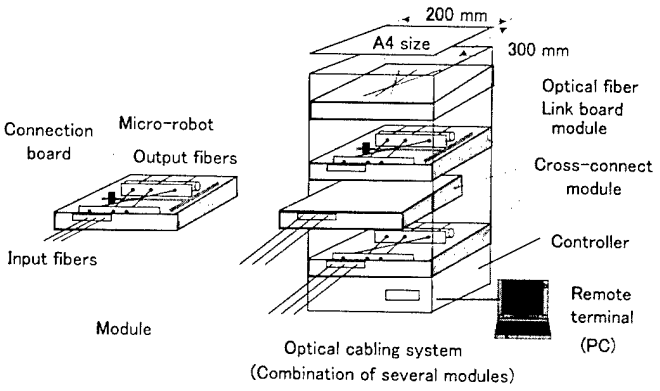


Figure 2. Concept of an optical cabling system.

2.1 Configuration of the cross-connect module

Figure 3 shows the configuration of the fiber cross-connect module. The compact cross-connect module can connect any 100 input optical fibers to any 100 output fibers by exchanging optical fiber cords.

To achieve the downsizing, we proposed a micro-optical connector that uses extra-fine ferrules, a micro-robot for handling the micro-optical connector, a fiber storage space instead of a conventional large fiber storage cartridge and an optical I/O interface by using an 8MPO-type optical connector. In these components, the micro-optical connector and the micro-robot are the key techniques, and the examination is shown in detail in the following chapters. A micro-robot handles the micro-optical connector. The positioning mechanism is used to move the micro-robot in the XYZ directions. Plugs are connected to jacks in the connection board. An optical connector of the optical fiber code rolled up by rewind mechanism lines up in an arrangement board. The input optical interface in the module is the micro-optical connector, which has a diameter of a 0.5 mm ferrule. The output interface is an 8MPO-type optical connector. The jacks are arranged in two lines and those in one line are shifted by a half pitch from those in the other (Fig.4). Further, we use a fiber storage space, which is constructed by using thin plates aligned with a 1.5-mm pitch, instead of a large fiber storage cartridge.

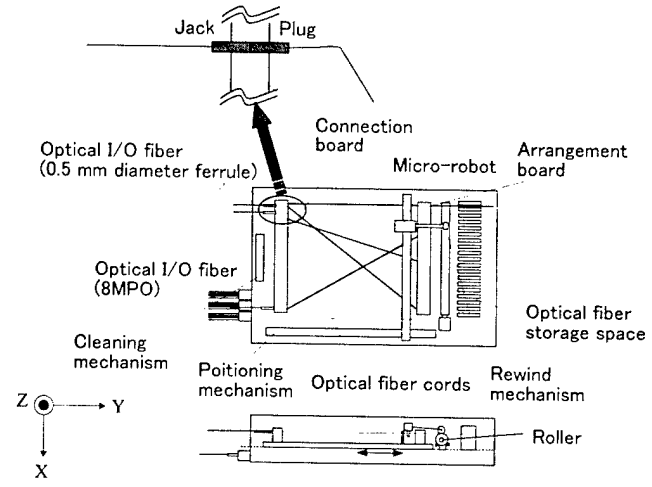


Figure 3. Configuration of the fiber cross-connect module.

2.2 Procedure of cross-connection

Cross-connection is achieved by exchanging one plug for another. Figure 4 shows the main cross-connect operation. In the procedure, the micro-robot first disconnects a pair of target plugs (Pi,Pj) each having an optical fiber cord and arranges them on the arrangement board. The cord is rewound into the fiber storage space to ensure that it does not get entangled with other cords during reconnection. Next, the micro-robot grasps one of the rewound plugs on the arrangement board and connects it to a target jack in the connection board. The second plug is connected in the same way.

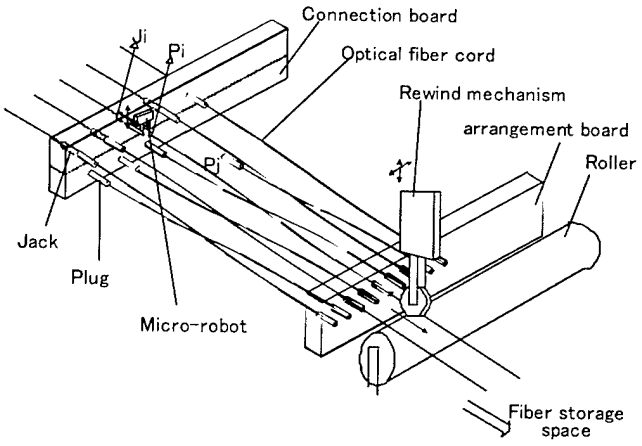


Figure 4. Cross-connect operation.

3. Key techniques

3.1 Micro-optical connector for High-density optical connection

In order to achieve a high-density fiber arrangement, we developed a micro-optical connector that uses extra-fine ferrules with a diameter of 0.5 mm (less than one-half the size of a ferrule of a MU-type connector), and an optical connection board with jacks aligned at a 1.5-mm pitch to connect the micro-optical connector. In order to miniaturize the module, we designed a simple connector structure with leaf springs. Figure 5 shows the basic structure of a micro-optical connector. It consists of a plug and a jack, both which have a ferrule with a diameter of 0.5 mm. The jack consists of a split alignment sleeve, a coil spring and a leaf spring. The coil spring can exert a contact force between the plug and the jack. The removal process of the plug is as follows: The robot hand is inserted, and the spring is pushed and expanded. The plug is returned to the robot hand side by the force from the coil spring. The returning plug is held by the micro-robot hand, and the following process is performed.

3.2 Micro-robot for handling optical connector

We propose the micro-robot mechanism to handle a micro-optical connector. Figure 6 shows the configuration of the micro-robot. To make the cross-connect module compact, we designed the micro-robot as monolithic in the hand and finger part, and a small cam is used for the opening and shutting the finger. We installed a compliance mechanism to absorb errors in Y and Z directions. The compliance mechanism uses gel material and is installed in the hand. The gel mechanism was used instead of the mechanical compliance mechanism, because the gel material is hard in the direction of compression (X) and soft in the direction of the side drift (Y,Z). In addition, it can be miniaturized compared with a mechanical compliance mechanism. As a result, the hand could be miniaturized.

4. Prototype of the module

Figure 7 shows the prototype of the fiber cross-connect module. The prototype is about 290 mm x 400 mm x 110 mm and the length of fiber connection block is about 150 mm for 100 input fibers. The driving mechanisms for X,Y, and Z directions can be removed from the module without influencing on any optical connection. In the X and Y directions, it is driven by a pulse motor through pulleys and timing belt. In the Z direction, it is driven by a pulse motor through a ball screw. An optical fiber cord with a diameter of 0.25 mm is used. The optical I/O interfaces by using an 8MPO-type optical connector and the micro-optical connector are set up in front of the module.

5. Experimental results

5.1 Optical characteristics of the connector

Figure 8 shows the optical characteristics of the micro-optical connector using extra-fine ferrules with a diameter of 0.5 mm. Here, a

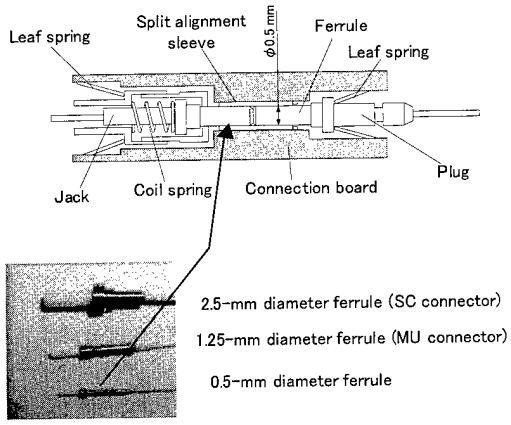


Figure 5. Basic structure of a micro-optical connector.

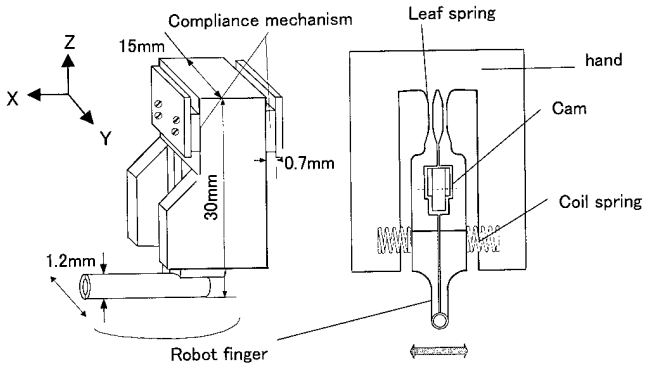


Figure 6. Configuration of the micro-robot hand.

glass-ceramic ferrule was used. The average insertion loss for single mode fibers was 0.22 dB [Fig. 8(a)]. The average return loss was more than 40 dB. Figure 8(b) shows insertion loss changes in a 1000-connections test when insertion loss is 0.5 dB or more and the cleaning is executed. We confirmed intermittent discontinuity was not occurred in the vibration and impact test. This value was quite good for practical use compared with a conventional connector.

5.2 Compliance characteristic of the micro-robot

Figure 9 shows the mechanical characteristics of the micro-optical connector with the glass-ceramic ferrules. This figure shows breaking force when a concentrated load is exerted on the point of a ferrule. We confirmed that the minimum of breaking force is 19 N. Compliance was designed from the product of safety rate multiplied by this breaking force and the positioning error. Figure 10 shows the compliance characteristic of the micro-robot mechanism. The hatched area was designed by the maximum positioning error of the module and the product of safety rate multiplied by this breaking force. In this area, the forces caused by positioning errors are weaker than the forces that can break a plug or a sleeve in the connection or disconnection procedure. The straight line is the measured compliance value for the prototype micro-robot. This line is in the hatched area, which confirms the compliance mechanism functions well enough.

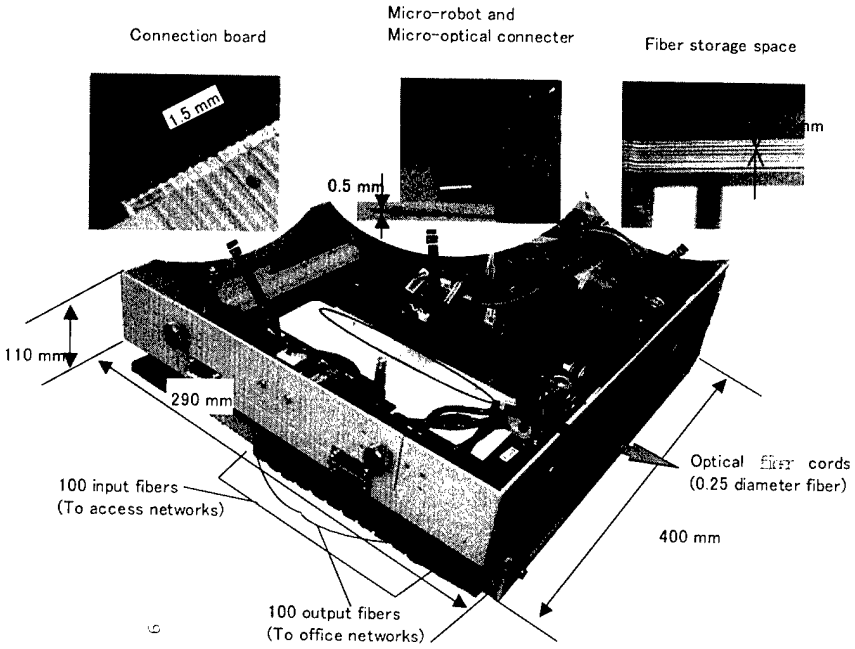


Figure 7. Prototype of the fiber cross-connect module.

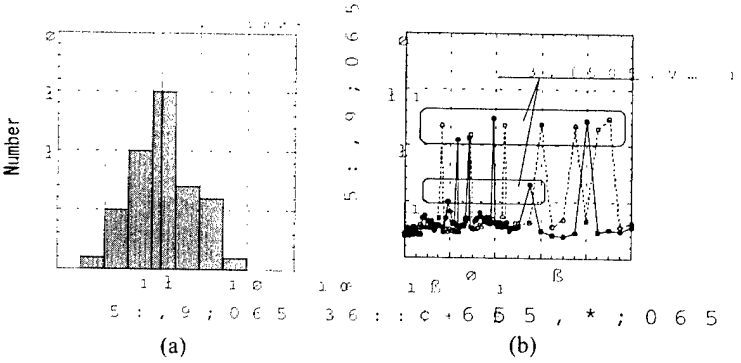


Figure 8. Optical characteristic of the micro-optical connector.

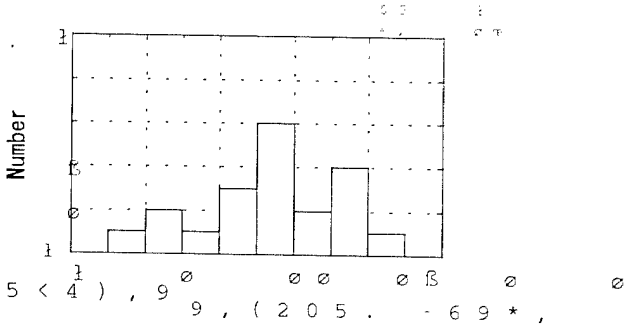


Figure 9. Mechanical characteristic of the micro-optical connector.

5.3 Module performance

The positioning error of the driving mechanism and the assembly error were measured in order to evaluate the relative positioning error. The total amount of errors in X and Y directions was about 100 μm and that of the Z direction was about 50 μm. The errors in Y and Z directions are absorbed by the compliance mechanism. The errors in the X direction are absorbed by the coil spring of the optical connector. We confirmed that the micro-optical connector can be connected and disconnected to target jacks by the micro-robot and that the fiber cord can be rewound into a narrow fiber storage space, which means that the cross connection of optical fibers can be performed by this module.

Figure 11 shows the initial optical characteristics of the cross-connection module. The initial insertion loss between an input and an output fiber was less than 1.0 dB. Table 1 shows the performance comparison between a conventional module and prototype module.

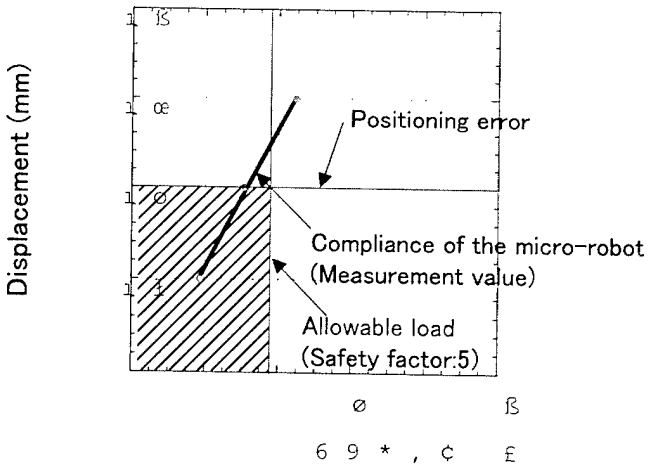


Figure 10. Compliance characteristic.

We confirmed that the average cross-connection time was about 1 min. The module could also be constructed compactly; it was about one-fourth the size and weight of the conventional one. We have confirmed the feasibility of usefulness of the cross-connect module. By optimizing the packaging of the positioning mechanism and performance of the motors, we expect that a module that is in A4 in size can be built.

6. Conclusion

A compact automated fiber cross-connect module that can cross-connect 100 input fibers and 100 output fibers has been developed. We confirmed that the cross connection of optical fibers can be performed by this module. It was shown that the initial insertion loss between an input and an output fiber was less than 1.0 dB. The average cross-connection time for the prototype is about 1 min. We also demonstrated that the module could be constructed compactly; it was about one-fourth the size and weight of conventional one. We confirmed the feasibility of usefulness of the cross-connect module for narrow spaces in intelligent buildings and in outdoor optical access network systems.

References

[1] K. Kaneko, N. Tamaru, J. Yamaguchi, Y. Nishida, H.Izumita, M. Tachikura and N. Tomita, "Automated large-scale fiber cross-connecting switch using a fiber handling method," *Proc. OFC(Optical Ffiber Conference), WK1,170-171(1998)*

[2] J. Yamaguchi, N. Tamaru, T. Shoji, T. Kanai, Y. Nishida,"A 100x100 Optical Fiber Cross-connect System," *Proc. 44th IWCS,232-238 (1995)*

[3] K. Sasakura, J. Yamaguchi, T. Yoshizawa, K. Kobayashi, K. Kaneko, "Automated optical fiber cabling system for intelligent buildings," *Proc. 48th IWCS,364-368(1999)*

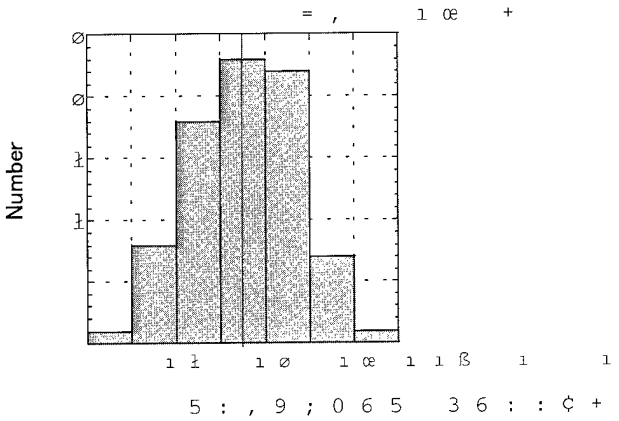


Figure 11. Initial optical characteristic of the cross-connection module .

Table 1. Performance comparison between conventional and prototype module

	8-PT (Manual)	Conventional cross-connect module (Automatic)	Prototype
Number of I/O fibers	8 x 8	100 x 100	100 x 100
Size (mm) W x D x H	215 x 326 x 63	422 x 532 x 207	290 x 400 x 110
Weight (kg) (Excepting controller)		28	10
Closs-connection Time (min)		1	1



Masato Mizukami
NTT Telecommunications Energy Laboratories.
3-1, Morinosato Wakamiya, Atsugishi, Kanagawa, 243-0198 Japan

Masato Mizukami received the B.E, M.E and Dr.Eng degrees in 1988, 1990 and 1997 in Precision Engineering from Kanazawa University, Japan. In 1990, he joined Nippon Telegraph and Telephone Corporation, Tokyo Japan, and has been engaged in research and development on an automatic assembly system of optical modules. He is a member of the Japan Society for Precision Engneering and the Society of Instrument and Control Engineers of Japan.

The AD-Lash System at Overhead Power Lines: The Installation of the AD-Lash System along Railways

Christian Putz

Corning Cable Systems, P&S
D-81303 Munich, Germany
+49 89-5111 3095 • christian.putz@corning.com

Abstract:
In the age of the information society, the annual demand for image, voice and data transmission is rising exponentially. The growing demand for lashed fiber optic cables, allowing rapid installation on overhead power lines, is therefore becoming more and more important throughout the world. An emerging market for this growth is the railroad network. Here an optical cable is installed on a ground wire using the AD-Lash system.

Keywords
ADL-cable, AD-Lash, lashing, ground wire, railway, tunnel

1. Introduction

All Dielectric Lashing is a specially developed technique for attaching a fiber optic cable to the messenger wire of overhead lines. This is carried out using a lashing machine which was developed for most high- and medium-voltage networks. The ADL-cable is secured to the messenger wire with specially developed weather-resistant lashing band (see Fig. 1).

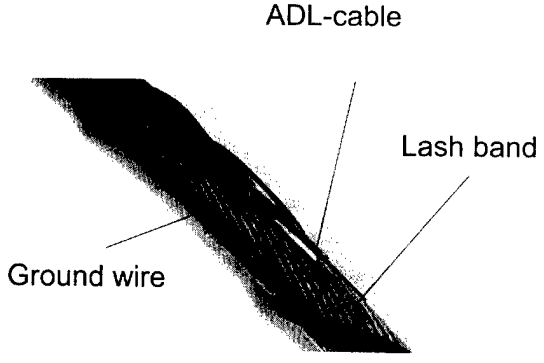


Fig. 1 ADL-Cable System

This paper describes the successful application of this product and technique for the railway environment.

2. AD-Lash System

There are two different methods of installation with the AD-Lash system. The first involves the use of the remote-controlled motorized lashing machine, the second is for manual installation using a manual lashing machine.

2.1 Manual Lashing Machine

The ***manually pulled lashing machine*** (see Fig. 2) is comprised of a chassis with two drive wheels, an idler, a cable guide plate, a spinner with the reel holders and guide rollers for the lashing tape. The ADL-cable is laid out on the ground and runs via the cable guide plate directly under the ground wire. An operator pulls on the pulling rope and thus sets the manual lashing machine in motion. The spinner is driven via the drive wheels and wraps two lashing tapes around the ADL-cable and ground wire approximately twice per meter.

This technique can be used on the ground and phase wires of high voltage lines in smooth terrain. The operators must pull the machine under the ground or phase wire. We have completed succesful installations with the handlash technique in Germany (railway), Austria, China, Polen, Nigeria and Chile.

2.2 Radio Controlled Motor Lashing Machine

The remote-controlled motorized lashing machine (see Fig. 3) is comprised of a drive unit, a spinner and a cable reel. The machine is run by two driven wheels along the ground wire of high voltage-lines. At the same time, the ADL-cable is paid out from the accompanying cable reel and fed via a guide plate below the ground wire.

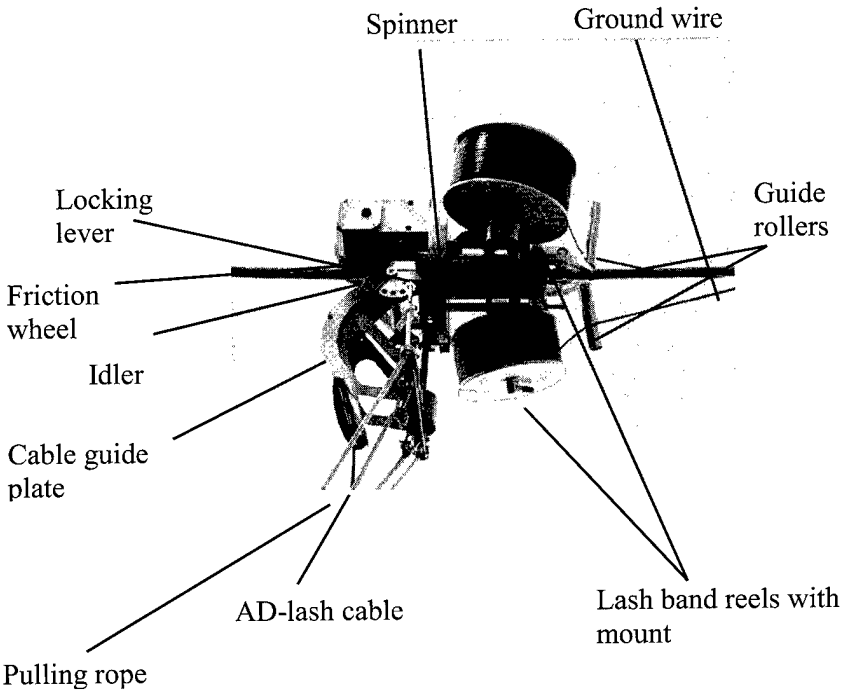


Fig. 2 Manual Lashing Machine

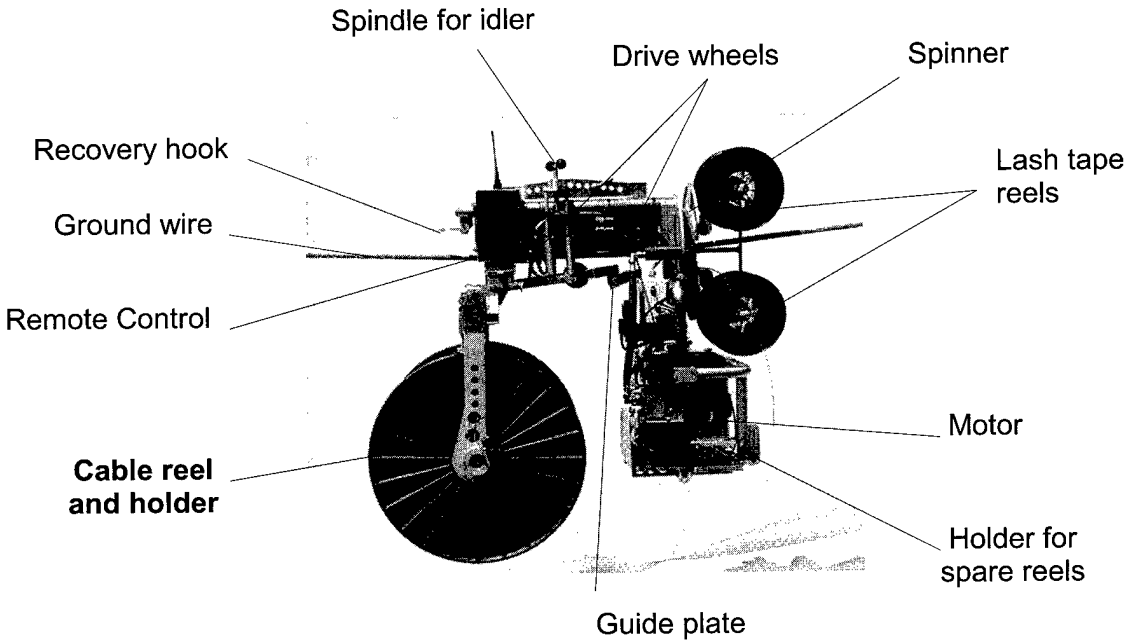


Fig. 3 Motor Lashing Machine

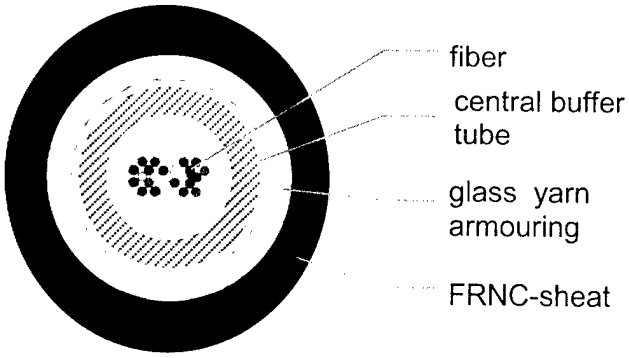
The rotating spinner with the lash tape reels wraps two lash bands around the ground wire with the ADL-cable two times per meter.

The motorized lashing machine is remotely controlled by radio from the ground.

The lashing machine is transferred between overhead wires at the top of the pole with the aid of derricks.

Helicopters have been used and are recommended for high voltage live line installations. This technique allows a 4 times higher rate of installation per day compared with the standard installation technique. It is unaffected by the pole type.

The motorlashing can be used on the ground wire of high voltage lines.



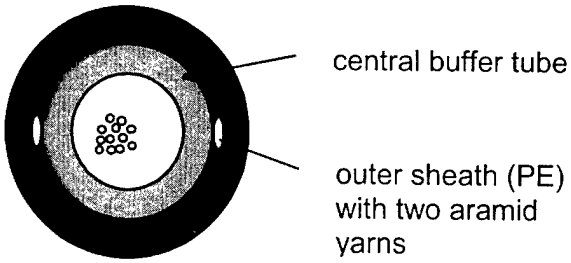


Fig. 4 ADL -cables

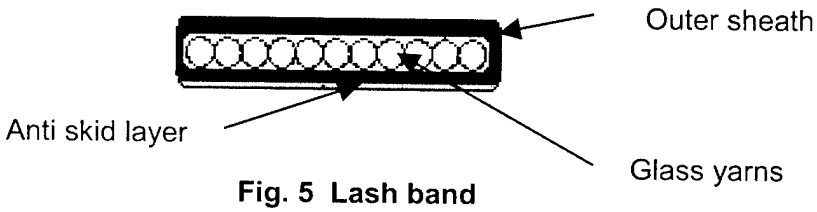


Fig. 5 Lash band

2.3 Cable and Lashband design

Two types of ***ADL-cables*** (see Fig. 4) are used, containing up to 48 fibers. They are a flame-retardant cable for tunnels and our standard ADL-cable. Both cables are of a central buffer tube design. The tunnel cable has a flame resistant sheath and glass yarn armor. The outside diameter is 8.5 mm. The standard ADL cable has a PE sheath and two aramid yarns. The outside diameter is 5.9 mm for up to 24 fibers and 6.5 mm for up to 48 fibers.

Regular lengths are about 2000 m on plastic reels.

Both ADL cables can be supplied in lengths of up to 6000 m on wooden reels in operation with the hand lashing machine.

The special ***lash band*** (see Fig. 5) is weather-resistant and has glass yarn strength members. The jacketing is a special sheathing compound for aerial cables. The shipping length for **handlashing** is usually 600 m. Piece lengths for **motorlashing** of up to 1100 m are possible.

3. Installation on the railway infrastructure

When installing the ADL cable on the ground wire along ***railroad tracks,*** it is necessary to differentiate between installing in the open (see Fig. 6a), in tunnels and on concrete side walls (see Fig. 6b).

The specifications of the German Railway require that the fiber optic cable in the cable troughs be provided with redundancy by installing another fiber optic cable on the ground wire on the opposite side. Two fibers from this cable are required for signal transmission. The remaining fibers are leased out.

The ground wire is routed in the ***open*** along the backs of the poles at traction wire height, 5.30 m above the top of the rail. The span width is usually 70m. The ADL cable is attached to the ground wire with the manually pulled lashing machine. The compression connectors on the ground wire can be passed over by the machine without problems. A bucket car or a cherrypicker is used to place the lashing machine on the ground wire and to transfer it from one side of each pole to the

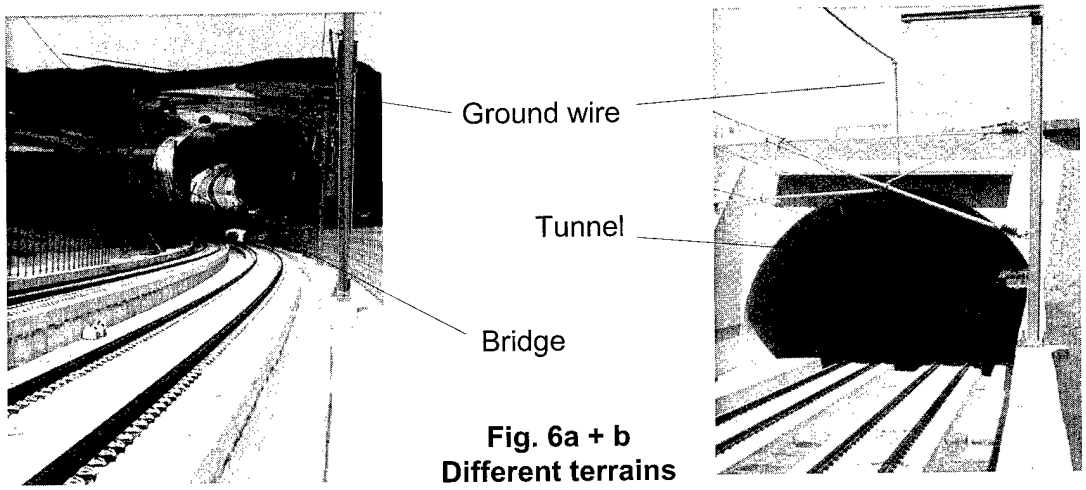


Fig. 6a + b
Different terrains

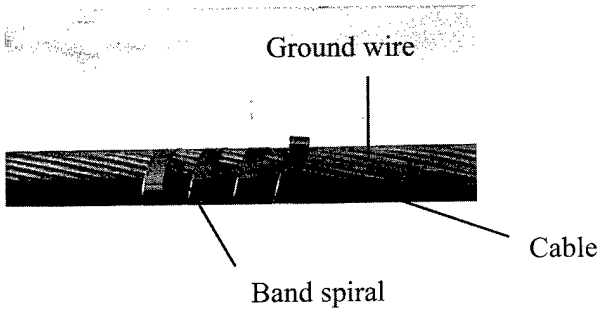


Fig. 7 Band spirals

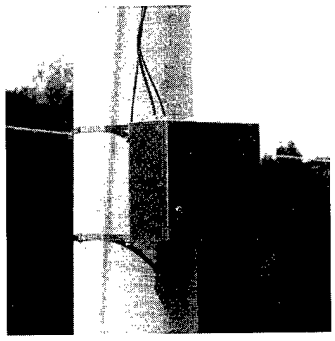


Fig. 10 Splice box

other. On open track, it is possible to install cable at a rate of 2500m / machine per day.

The transition of the overhead ground wire from open track into the ***tunnel*** is made from the pole to the center of the tunnel roof (see Fig. 9). The ground wire is routed at a distance of 150 mm from the tunnel roof or 110 mm from the *concrete wall*. It is not possible to use the lashing machine here. The ADL cable is attached to the ground wire using special high-grade steel ***band spirals*** (see Fig. 7). Using a hydraulic bucket car or a two way vehicle, 1-2 installers fit a band spirals every 80 cm. The installers can thus install up to 150 m of cable in one hour. Tunnels more than 5000 m long are not unknown.

The cable is normally routed around poles and suspension clamps in a bow and secured with RSGU clips (see Fig. 8).

The high-grade steel splice boxes (see Fig. 10) are secured to the poles about 1.5 m below the ground wire. The ADL-cable is inserted

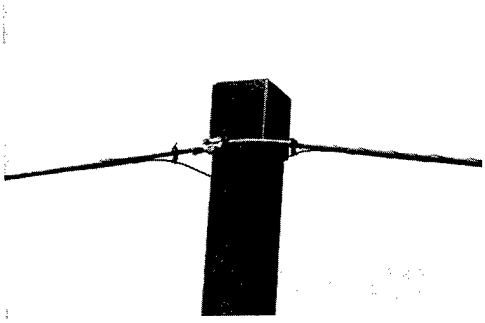


Fig. 8 Tower bypass

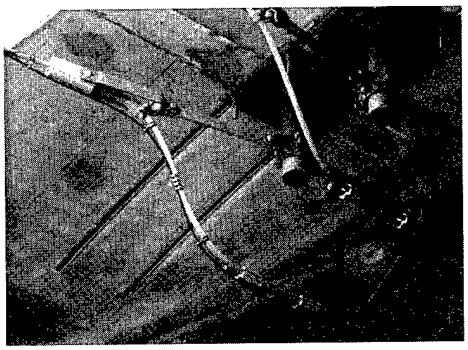


Fig. 9 Crossing from – in the open to the tunnel

in the box and led to the ground. The cables are spliced on the ground and the splice cassettes with cable overlength are installed safely in the box.

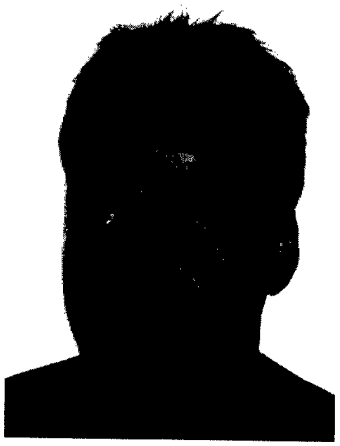
4. Conclusions:

This novel installation technique has successfully been deployed on overhead power lines for 5 years. It has proved to be most reliable even in these difficult conditions. The product and installation process have now been modified and adapted to suit the equally challenging environment of the railways. The technique described in this paper has proven that AD Lash offers the following:

- Easy, rapid and flexible installation of fiber optic cables
- High rate of installation per day (up to 8 km per day)
- Low installed costs

5. Author:

Christian Putz was born in Waldkirchen, Germany in 1965. He received his Dipl.-Ing. (FH) in Feinwerktechnik from Fachhochschule Munich in 1991. He joined Siemens, Communication Cables division, in Munich in 1996. Since 2000 he is engaged in cable installation technology by Project & Services at Corning Cable Systems.



Ribbon Separation Tools & Techniques End and Mid-Span

Greg Lochkovic, Donald Lockwood, Shail Moorjani, John Richards, Scott Torrey, Karen Williams
Corning Cable Systems
Hickory, NC

Abstract
The demand for enhanced alternative ribbon handling techniques is increasing as the US fiber optic network array enters the early stages of mass advancement to the end user. Several optical fiber ribbon separation tools and techniques, ranging from hand separation to the full use of specialized tooling, have been evaluated for efficiency, effectiveness, and propensity to induce optical fiber coating and/or glass, mechanical and optical performance degradations. In this paper, we will discuss the relative merits and issues associated with each ribbon separation tool and technique.

Keywords
Ribbon separation; Sub-unitization; Ribbon separation tool.

Introduction
Many key domestic long haul and metropolitan area fiber optic networks have been well established over the past 20 years. Much of the existing network, particularly the intra-city portion, is composed of cables containing ribbonized fibers due to the associated installation efficiencies relative to other cable types. As mega-bandwidth systems are further realized, new opportunities continue to abound which push optical fiber closer to the end user. Not long from now, tip to tip fiber optic systems will become the standard. As optical fiber penetrates more deeply into the telecommunications network, the need for individual and multi-fiber access is elevated. The ribbon based segments requiring "x"-fiber access, demand interesting handling solutions depending on the ribbon design.

Ribbons have evolved to provide enhanced fiber accessibility through a balance of matrix mechanical characteristics and matrix to ink adhesion. Earlier designs, until the mid-90's, simply sought to ensure a robust and coplanar array of fibers that were tightly bound primarily to provide a suitable geometry for quick and easy connectorization, mainly through mass-fusion splicing. The early UV matrix ribbon designs generally provided hassle free sub-unitization (separation of 2 or more adjacent fibers from the array as a sub-unit) without generating stray fibers; however, the ribbon matrix, in the early designs, tended to cling tightly to single fibers when separated individually. This often created difficulty with single fiber applications. Additionally, single or multi-fiber access without data traffic disruptions, on adjacent fibers, was generally less feasible.

There are 5 key functional handleability attributes associated with multi-fiber ribbons. They are thermal stripabiltiy, peelability, separability, furcatability, and robustness [1]. While this paper deals solely with ribbon separability, we take a brief opportunity to refresh the reader's understanding of each attribute (please see Ref. 1 for a more thorough explanation of each):

1. Ribbon Thermal Stripability - the ability to remove the fiber and ribbon coatings from multi-fiber ribbons using commercially available ribbon stripping tools.
2. Ribbon Peelability - the ability to remove matrix from the fibers in a ribbon, in a continuous fashion, while leaving the individual fiber coatings (including the color layer) intact and free from damage in order to access specific fibers for further re-routing or repair. Various kits are commercially available to assist in this process.
3. Ribbon Separation - the ability to separate sub-units (or groups of one or more coplanar fibers) from a ribbon unit for rerouting or repair. Here again, tools are commercially available to accommodate this process.
4. Ribbon Furcatability - the ability to easily remove the individual fibers (often referred to as "fiber breakout" in the past) from the ribbon structure for further insertion into individual fiber furcation tubes. The preferred ribbon design readily allows subsequent ease of matrix removal from individual fibers (predominantly edge fibers) in order to facilitate fiber insertion into the furcation tubing.
5. Ribbon Robustness - the ability of a ribbon, or a sub-unit from that ribbon, to maintain its structural integrity when subjected to reasonable bending, twisting, and lateral forces once deployed in various enclosures and routing trays.

In contrast to the earlier ribbon designs, most current designs (considered peelable) allow the ribbon matrix to be readily removed from all fibers without matrix adhesion; thus, allowing ease of access to each fiber without data interruptions on adjacent fibers. However, if sub-unitization (as opposed to matrix removal from all ribbon fibers) is desired with the peelable ribbon designs, stray fibers are often generated. Ribbon sub-unitization will

primarily be referred to as "ribbon separation" in the remainder of this paper. For clarity, Figure 1 demonstrates a "separated" –vs- a "peeled" ribbon.

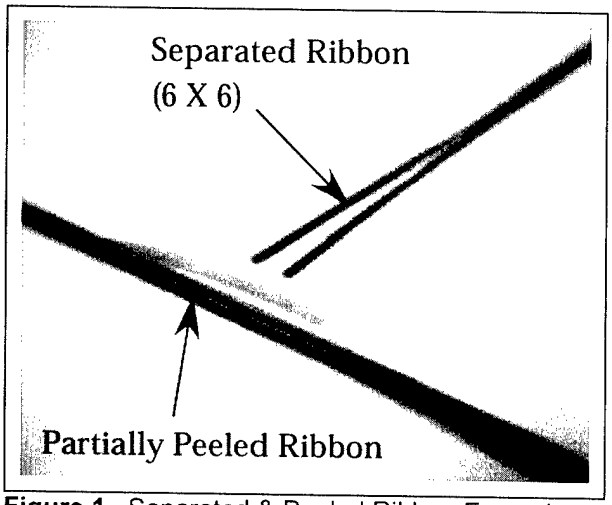


Figure 1. Separated & Peeled Ribbon Example

This paper defines preferred ribbon separation techniques, and reports the testing results for ribbon designs and ribbon separation techniques with respect to:

- Fiber/ribbon damage potential.
- Attenuation during separation.
- Speed and Ease of separation technique.
- Consistency of separation technique.

In addition, we briefly discuss the benefits of "modular" ribbon designs [2, 3, and 4] in fiber optic cable installation. "Modular" is defined as a ribbon design that is constructed in a fashion that readily allows separation at distinct locations in the ribbon as shown in Figure 2.

the trade/industry, was struck upon as an answer to minimization of fiber optic cable size and subsequent manipulation.

Fiber optic ribbon cable designs, initially developed by AT&T in 1975 [6, 7], were used in the first significant optical system studies. Each study employed an adhesive sandwich ribbon design (discussed later in this paper):

- The first fiber optic test system, activated on 1/13/76, was a 650 meter 144 fiber, 12 fiber ribbon cable design tested in ducts buried under the parking lot of an AT&T plant in Atlanta, GA. This cable consisted of multi-mode (MM) fibers from both Corning (62.5 μm MM) and AT&T (50 μm MM) that were operated at 850 nm at a 45 megabits per second (Mb/s) transmission rate. Fiber ends were spliced together to test transmission distances up to 6.8 miles. Single-mode fibers had been developed at the time, but there was initial concern over the ability to couple light in the cores, which were then just 3 – 4 μm in diameter.
- The first commercial fiber optic cable system installation , which involved a total of 10 cables, was performed in Chicago during February, 1977 [10]. The 24 fiber cables contained two 12-fiber 50 μm MM fiber ribbons, and were designed to operate with a transmission rate of 44.7 Mb/s at 850 nm. This installation connected 2 Illinois Bell central offices and a customer location. The first commercial optical traffic was carried on 4/1/77 with a subsequent full cutover by 5/11/77.

Early fiber optic ribbon designs were *primarily* intended to allow ease of connectorization (using both mechanical connectors as well as mass-fusion splicing) from one ribbon to another. Given that this required little more than

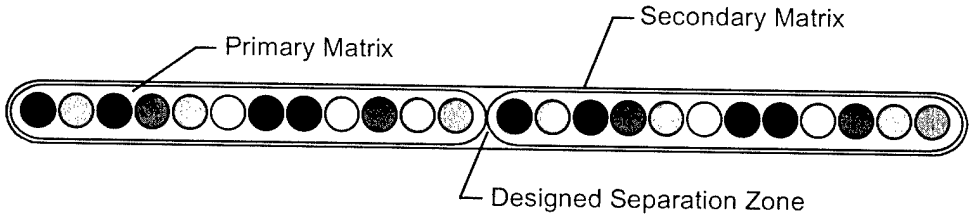


Figure 2. Modular 24 Fiber Ribbon Design

Ribbon Design: a brief history

The need for quick, effective, and efficient handling characteristics (access, splicing, etc.) was identified as a high priority very early in the conception of fiber optic cables, and has continued to evolve since then. Given the high fiber count potential due to the reduced conductor sizing (relative to copper), it was anticipated that splicing and reconfiguration times would be significant without grouped fiber handling techniques [5, 9, 11]. A grouped coplanar assembly of fibers, now referenced as "ribbon" in ensuring that the fibers were bonded together to form a coplanar linear array, some interesting joining techniques were initially employed:

- *Adhesive Sandwich Ribbon (ASR)*
  The fiber array was fixed between layers of adhesive backed tape. This resulted in the widest of the ribbon types (for 12 fiber ribbons, ~ 0.140" –

3.56 mm) due to the tape web left on each side of the ribbon after post assembly trimming. This design was also difficult to strip, using commercially available ribbon thermal strippers, due to the vastly differing properties of the tape backing relative to the fiber coatings.

- *Heat-Welded Ribbon (HWR)*
  Each fiber in the array was pretreated with a protective layer such as ethylene vinyl acetate (EVA). The array was then processed over a heated surface causing a reaction of the EVA resulting in fiber to fiber bonding. This design presented difficulty in cabled attenuation, especially during bending. Due to the uneven ribbon surface (the fiber interstices were not filled to form a flat surface), the ribbons in a stack tended to "lock together"; thereby, creating strain in the ribbon fibers and causing attenuation.
- *Hot Melt Ribbon (HMR)*
  Each fiber in the array was passed through a hot melt adhesive applicator that also formed the ribbon geometry at its exit. The major problem with this ribbon design was the severe line speed limitations associated with the hot melt adhesive application and curing process relative to the other options available at the time.
- *Epoxy-UV Bonded Ribbon (UVBR)*
  This ribbon design is similar to the common ribbon designs used today. The fibers were passed through an uncured bonding material (heat-cured epoxies or UV cured materials), formed into the required linear array, and cured into the final structure. This provided a cohesive unit that could readily be stripped to the glass using commercially available ribbon thermal stripping tools. Cable attenuation performance was also enhanced through the flat surface geometry allowing ease of ribbon movement in the cabled stack.

Today, the UVBR type ribbon has become the design of choice across major fiber optic suppliers due to its inherent capability to meet varying customer needs, higher manufacturing line speed potential, ease of processing, and relatively compact manufacturing equipment.

Ribbon Separation

Ribbon separation techniques have evolved as ribbon designs have advanced over the past 20+ years. Few special tools or chemicals were developed for use in fiber access with the early versions of fiber optic ribbon, namely the adhesive sandwich ribbons. Composed of multiple fibers captured in a tape sandwich, the craftsperson merely had to lift the tape (initiated with a dental pick or similar probing device), and cut it to gain access to the fibers. When ribbon separation was required, the craft would use a razor, or similar sharp cutting tool, to slit the major ribbon structure along the desired ribbon sub-unit plane. Potential fiber damage and attenuation during the access/separation operation was an issue in each attempt. The tape backing materials (typically polyesters) were not designed with a linear crystallinity, which would have allowed continued separation by hand once initiated with a razor; thus, avoiding the potential for fiber damage due to nicking of the inks and other coating materials of the individual fibers.

With the advent of UV curable encapsulants in ribbon designs, which provided significant product and process improvements, the fiber to ribbon geometry also became greatly enhanced. Since similar material properties now comprised the entire glass coating structure, including the ribbon matrix, this design allowed development of new fiber and ribbon separation techniques. Some of the significant developments that resulted from the introduction of the UV-type ribbon structure were the following:

- Ribbon separation tools (the focus of this paper)
- Ribbon thermal stripping tools (initial variants were available for tape ribbons, but were modest, at best, in their intended function)
- More effective mass-fusion splicers
- Kits for end and mid-span fiber access through matrix removal (chemical dissolution and mechanical peel) were developed. These kits were not intended for ribbon separation, and will not be discussed further in this paper.

As high bandwidth end user applications continue to proliferate, it becomes increasingly advantageous for fiber optic network administrators to sub-divide the master (main "x"-fiber structure) ribbons into multiple sub-units as the fiber network builds further toward the end customer. Further, new high fiber count cable designs rely on 24 and even 36 fiber ribbons to achieve the desired packing density. In an effort to minimize handling and processing tool, cable enclosures, and other related inventories, cable system designers have largely made the decision to use the 12 fiber structure as the base unit. As a result, when these types of cables are installed, each 24 or 36 fiber ribbon is sub-unitized into 12 fiber units prior to routing in splice trays and enclosures. In each case, separation to the desired fiber count must be achieved without generating stray fibers. Stray fiber generation not only exacerbates the mass fusion splicing operation, but also introduces the risk of fiber mis-identification, and causes increased fiber breaks upon removal from an enclosure or similar device.

Finally, network administrators prefer to manipulate fibers and ribbons without transmission disruption to neighboring fibers. The ability to generate the desired fiber count sub-units from ribbons without attenuating neighboring fibers is an influential objective.

Ribbon Separation Tool Designs. For our discussion of ribbon separation tools, we have developed a prioritized criterion list of key design features for an effective ribbon separation tool. The first 5 criteria are minimally debatable; however, the user may find reasons that the last 3 criteria are not in order relative to their individual needs and desires:

1. Does not damage ribbon or fibers, and forms robust sub-units without stray fibers or matrix strings.
2. End and mid-span access capability all combined into 1 tool. It is desired that capability exists for a choice of tool advancement or ribbon advancement through the tool as the separation zone is lengthened. Also, tool size can be a factor in the field for mid-span tasks especially in tight field conditions where minimum ribbon excess length is available and where flat working surfaces are not available.
3. Allows any combination of fiber sub-units to be readily separated.
4. Induces minimal attenuation during initiation and during subsequent separation advancement. This has been prioritized as #4 due to the fact that many craftspeople will not manipulate fibers or ribbons with neighboring live fibers.
5. Ease of use. Quick & easy to use with minimal training
6. Allows the advancement of separation, beyond the initial separation zone, to the desired length of the user with minimal induced attenuation. This is prioritized as #6 due to the potential for the user to continue the separation process by hand after initiation by the tool.
7. Resistant to damage and wear (i.e., does not require frequent replacement of components).
8. Easy to clean.

Several alternate separation tools have been proposed, and are discussed, with respect to the top 5 criteria. The relative merits of each tool design are discussed in Table 1 (see Appendix), based on experience and comments by the industry, from 4 recent patents [12, 13, 14, and 15], and 1 older patent originally for copper conductors [16]. The relative patents and associated drawings are readily viewed from most patent databases available on the Internet.

Implicit in all criteria is the handleability of each separation tool design concept. The ease of manipulation for any given tool largely affects its potential use in the field with respect to potential for damage, attenuation, and ease of operation. Again, referring to Table 1 (see Appendix), the tool associated with patent # 4,046,045 would not allow a feasible field mid-span technique due to its size and operability. However, the concept discussed in patent # 6,053,085 can fit in the palm of the hand and requires no set-up; thus, allowing use on ribbons where even minimal excess length is available.

Mechanical Separation Performance. Clearly, attenuation performance means little in a separation tool or procedure if the desired post separation ribbon sub-unit geometry is not robust and readily handled as an individual component. Problem areas often noted with the various tools and procedures used for ribbon separation are:

- Fiber coating damage, which leads to immediate, or worse, delayed fiber breaks in installed systems. *The use of razor blades for ribbon separation has been purposefully avoided in this paper due to the routinely demonstrated high potential in this area.*
- Stray fibers leading to difficulty in mass fusion splicing or connectorization.
- Stringers (strings of loose matrix still attached to the sub-unit) that clog separation tools and also create difficulty in furcation.
- Matrix Overhang (ledges of matrix attached to one sub-unit, but leaving its' opposing counterpart with matrix missing – see Figure 3) which increases the chance for stray fibers during handling.

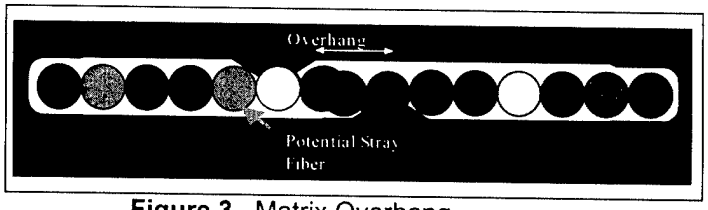


Figure 3. Matrix Overhang

A broad look across several domestic competitive ribbon designs, including Corning Cable Systems', was conducted to evaluate the robustness of each ribbon with one separation tool design (see tool from reference 12), and is presented in Table 2 (see following page). The ribbon codes in the first column of the table are comprised of a letter which represents the ribbon manufacturer, and the fiber count of the ribbon. As a sidenote, the letters used to represent the ribbon manufacturers were selected at random, and were not repeated from one figure , or table, to the next within this paper to ensure professional competitive disclosure. It should also be noted that the 1st "Stray Fibers" column references the strays generated during tool only separation while the second "Stray Fibers" column references the strays generated during application of the tool AND hand separation technique.

Ribbon products from 5 individual domestic manufacturers of 12 fiber ribbons (also referred to as 12 f/r), and from 4 individual domestic manufacturers of 24 fiber ribbons (also referred to as 24 f/r) were evaluated. All 12 f/r's were of a single layer matrix design philosophy while 3 of the 24 f/r's were dual layer leaving only one 24 f/r manufacturer utilizing a single layer matrix approach. All ribbons were tested for a 50/50 separation (i.e., 12 f/r sub-unitized into 2 x 6 f/r's). *It should also be noted that separation using only the hands, in non-modular designs, resulted in stray fibers in most cases across all competitive designs, and is not recommended.* Additionally, we have found that initiation using a separation tool followed by lengthwise propagation using one's hands (referred to, for ease of reference in this paper, as the SUT&H method, translated as Separation Using Tool and Hand method) produced acceptable results. No

Table 2. Mechanical Ribbon Separation Performance

	Tool Separation				Tool click then Hand Separation	
Ribbon	**Overhang**	**Stray Fibers**	**Stringers**	**Matrix Accum. in tool**	**Overhang**	**Stray Fibers**
A12	<1 fiber width	1 in 2/ 3 of samples	1.5-2" stringers	None	2.2 fibers	0.8
B12	<1 fiber. Jagged edges but no overhang	None	Every ribbon up to 3"	Low	3.0	2.3
C12	<1 fiber.	None	> 3" all samples, ink removal in some fibers	High	1.5	0.8
D12	<1 fiber, pulled smoother than others	1 in a sole sample	2" stringer in one sample	Almost None	2.5	1
E12	~0 fiber, smooth, some jagged edges	None	None	None	1.2	0
F24	High (~0.5 fiber wide), jagged edge	None	None	Highest	0.8	0
G24	None	None	None	Lowest	0.8	1
H24	None	None	1"stringers or more	Low	0.5	0
I24	None	None	None	Medium	0.8	0

characterization of hands only separation was performed due to the anticipated low performance.

With respect to overhang generated from "tool only" separation, all 12 f/r manufacturer's designs performed in a similar nature. However, ribbon E12 did show slightly enhanced behavior. This can be attributed to a balance between the "matrix to ink adhesion" and the "matrix tensile characteristics". Generally speaking, the overhang from a separation process should be minimized to less than 0.25 mm (~ 1 fiber width) to ensure stray fiber minimization through sufficient residual matrix to fiber contact. Ribbon A12 proved to be the worst performer with respect to stray fibers. Stray fibers were generated in 66% of the samples for this ribbon using the tool only method. This ribbon was found to possess, by far, the smallest fiber diameters, thickest ribbon cross-section, and worst planarity (average of 52 m where others generally fell below 30 m). Ribbons A12 and B12 benefited the most from a "100% separation tool" technique as evidenced by the overhang performance difference relative to the SUT&H method. Using that method, we actually anticipated a much larger overhang performance in the A12 ribbon than was measured, largely due to the high matrix thickness which increases the cross-sectional strength of the matrix relative to the matrix to ink adhesive power. At this time it is not understood why ribbon A12 did not generate more stray fibers using the SUT&H method relative to the hand only method.

In the past, we have found B12 ribbons to possess a low cured matrix degree of cure, and more importantly, a high degree of cure gradient. Cure gradient refers to the difference between the outer (surface) degree of cure and the inner (matrix to ink) degree of cure. The inner degree of cure is measured after matrix is peeled from the fiber array. A high matrix cure gradient traditionally results in a very low adhesion to the inked fibers or even a low cohesion of the matrix at the micron level thickness near the fibers. Either case results in high overhang during any type of hand separation, which leads to a high frequency of stray fibers as demonstrated in Table 2. Matrix cure gradients are found in a few other manufacturers' ribbon designs as well although not generally to the extent of ribbon B12.

It was further noted, when using the SUT&H method, that overhang increased by an average of 1.3 fiber widths for a total average overhang of 2.1 fiber widths across all manufacturer's ribbon designs. This is significant with respect to stray fibers. Once more, referring to Table 2, there is a correlation between overhang and stray fibers. Note that only the ribbons (again, with the unexplained exception of ribbon A12) with overhang in excess of 1.5 fiber widths (ribbons B12 and D12) exhibited an average stray fiber count per separation greater than 1. An additional observation here is that ribbons B12 and E12 were at opposite ends of the spectrum relative to stray fibers generated using the SUT&H method. Ribbon B12 generated stray fibers in each test while ribbon E12

generated no stray fibers in any of the testing. As earlier stated, ribbon E12 has been optimized with a balance between the "matrix to ink adhesion" and the "matrix tensile characteristics" while achieving a minimum cure gradient in the matrix.

A last observation with the 12 fiber designs is with reference to stringers (3rd bullet under "Mechanical Separation Performance"). All manufacturers' ribbon designs generated stringers during the tool separation testing with the exception of ribbon E12. E12 has been optimized to minimize this trait which is largely a function of matrix to ink adhesion. One mode of stringer generation happens when the matrix to ink adhesion is sufficiently low to allow the matrix to minutely and incrementally slide over the fibers as the ribbon is pulled through the separation tool. In some cases, it is possible for the matrix to slide over the fibers, and at some point, begin to accordion to a level that catches or clogs at the separation tool entrance. When this happens, the matrix ultimately yields, and a stringer is formed. This stringer of matrix material tends to accumulate in the tool, making the problem intensify while also causing the ribbon attenuation, during separation, to increase due to the increased strain on the fibers.

24 f/r separation testing included only a 12/12 separation in the results reported. A noticeable difference was seen in overhang and stray fibers between the 12 fiber ribbon designs and the 24 fiber ribbon designs. In all 24 f/r "tool only" separation testing, no overhang was reported over 1 fiber width, and no stray fibers were generated. Only 1 of the 24 f/r designs was not a dual layer structure as depicted in Figure 2. The dual layer, or modular, ribbon types typically provide enhanced separation unless key design parameters have not been properly chosen. The one ribbon utilizing a single layer 24 f/r design also demonstrated excellent separation character with low overhang; however, an occasional stray fiber was generated. Past IWCS literature indicates that this manufacturer has successfully addressed the separation issue by application of a differential ink to matrix adhesion profile across the ribbon fibers [2]. Referring one last time to Table 3, it is clear that the modular ribbon design provides a distinct advantage in ribbon separation character relative to stray fibers. This becomes clear when noting the lower level of stray fiber generation of the 24 f/r's compared to the 12 f/r's. One further proof of the superiority of the modular concept is in the fact that none of the dual layer 24 f/r designs produced stray fibers; whereas, the sole single layer 24 f/r design did experience an occasional stray. To the extent that a system designer can define an intended sub-unit basis for their system, the modular design may provide enhanced installation and future manipulation activity benefits resulting in lower system management costs.

Separation Attenuation Performance. To date, few installers in the field actually perform ribbon separation with neighboring live fibers; however, as installations trend from long haul and loop projects to fiber to the curb/business/home, this capability will see increasing importance. As fibers are more frequently tapped from dense large fiber count systems, it will not be feasible to shut routing paths down just to accommodate a new customer. Therefore, techniques and separation tools must provide low to no induced attenuation to be considered a successful solution.

Separation attenuation distributions, using a separation tool and measured at 1550 nm, is broken out into its two key components in Figure 4 (see following page): initiation phase (where the tool is clicked for initial separation), and lengthwise advancement phase (where maximum attenuation is noted as the tool is indexed/pulled along the length of the ribbon for 0.5 m). This test was repeated across several manufacturers' ribbons.

Approximately 90% of all ribbon maximum separation attenuations were < 0.05 dB and < 0.5 dB for initiation and lengthwise advancement respectively. Unlike results referenced in Keesee et.al. [17] (where cable access was the focus), the attenuation spikes in ribbon separation tool testing tended to maintain a longer time period of elevated response regardless of ribbon manufacturer or design. In cable access, transient spikes are generally a response to transient and short duration factors such as the snapping of the jacket/buffer material during removal or a subtle nudging of the ribbon stack as the jacket/buffer is removed. With ribbon separation, attenuation effects tend to remain longer due to the inherent nature of the process, which requires the ribbon to be continuously distorted until the separation process is completed.

It is interesting to note that both of the distributions are similar in shape, but that the tail is longer for the "lengthwise advancement" stage. This is primarily a result of the pulling action building on any stresses that were induced during the initiation stage. There is also a greater potential for tool/ribbon misalignment as the tool progresses along the ribbon. The extreme outliers for the "lengthwise advancement" are caused by debris and, in some cases, shaved matrix build-up and stringers as the tool/ribbon advances.

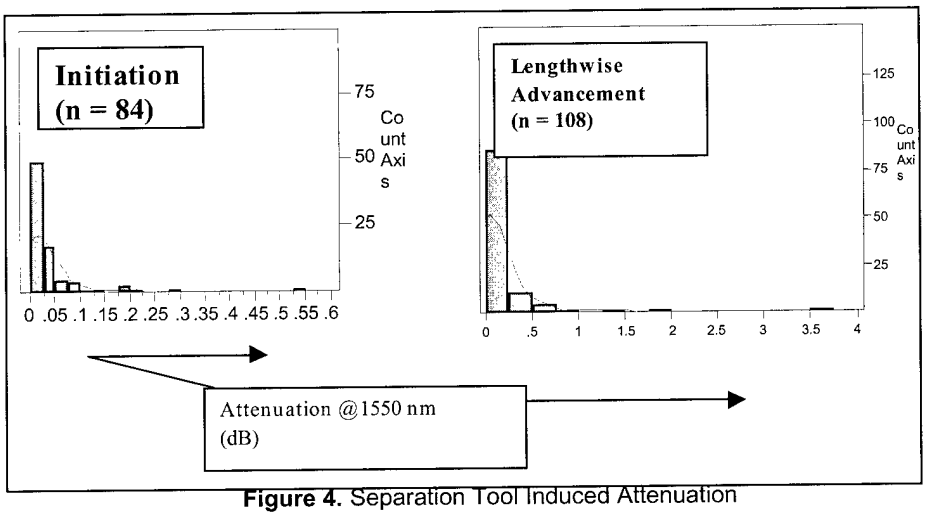


Figure 4. Separation Tool Induced Attenuation

Recent work has shown that localized treatments of the matrix material appear to lower the range of attenuation experienced during initiation. Table 3 shows a trendwise decrease in initiation attenuation (for an outlier ribbon demonstrating higher than normal initiation performance) for various methods of ribbon treatment prior to initiation.

Table 3. Treatment Effect on Initiation Attn

Ribbon Treatment	Avg. Attn. @ 1550, (dB)
N/A (control)	0.230
[1]Edge	0.241
Abrade	0.070
Flame	0.133
[2]Temperature @ 350 F	0.070
[2]Temperature @ 450 F	0.062
[2]Temperature @ 550 F	0.023

Notes: 1. Ribbon Pulled across sharp edge to mechanically stress harden.
2. Soldering iron applied at the indicated temperature.

Note that:

- Edge refers to the process of pulling the ribbon across an edge intended to stress harden the matrix, and allow a more brittle initiation.
- Abrade refers to a subtle abrasion of the matrix surface to weaken it and provide a lower force required during initiation.
- Flame simply references the process of passing the ribbon through a flame to mildly oxidize the surface, and allow a more brittle initiation.
- Temperature is discussed in the following paragraph.

It appears that the effect of a high temperature soldering iron, applied to both sides of the ribbon for ~ 5 seconds each, may be able to diminish the induced initiation attenuation by up to 1 order of magnitude over its untreated counterpart. Remembering that the lengthwise advancement of the tool after initiation is at least partially a function of the induced initiation attenuation, this may provide the installer with an acceptable alternative when forced to deal with live fibers. The concept is still under investigation.

Figure 5 (see following page) shows an additional interesting fact. When comparing D12 to F12fast as well as G24 to I24fast (ribbons from common manufacturers), we see noticeable attenuation performance increases when increasing the rate of pull (again, D12 – see tool to hand for this ribbon – is an anomaly). This was somewhat surprising given that the increase in pull speed was fairly low (from 1 mpm to 2 mpm). *The installer should take special notice of this, and the fact that seemingly very subtle changes in procedure can dramatically affect performance when dealing with live fibers.* The hand separation procedure involved a mid-span initiation with the tool, then lengthwise advancement by hand.

In closing on the topic of separation attenuation, it is important to note that separation with a tool provided consistently enhanced attenuation performance over separation by hand. Figure 5 exhibits the relative attenuation performance of tool –vs- hand separation across the array of manufacturers, designs, and pull rates tested in this program. Referring again to Figure 5, with the exception of ribbon type D12, the tool separation method was superior to separation by hand. When D12 was retested, under the faster pull rate, the tool –vs- hand separation results reversed and were in agreement with the remainder of the ribbons tested. Use of a separation tool tends to minimize the variations in mechanical stresses induced during the lengthwise separation process.

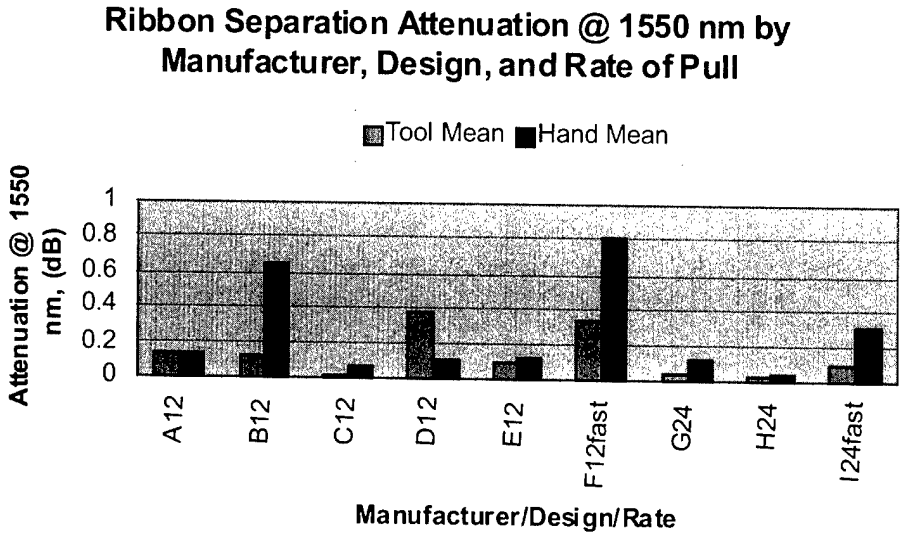


Figure 5. Separation Tool –vs- Hand Attenuation Performance

Conclusion

The need for post installation individual and multiple fiber access is increasing as bandwidth capability moves toward its logical end: individual consumers. A combination of proper ribbon design, ribbon separation tools, and ribbon separation techniques will be required to accommodate this requirement in a statistically consistent and cost effective manner. This paper has demonstrated the potential to accommodate all requirements in parallel. For the system installer, methods and tools provided herein should prove to be invaluable to future efforts.

Acknowledgements

The authors greatly appreciate the "beyond the call of duty" assistance from Cindy Schronce and Jeff Dellinger in taking time from their busy schedules to work with us on separation attenuation measurements. They are awesome!!!

References

1. Lochkovic, G.; Moorjani, S.; Patel, N.; Speights, R.; Stephens, B. "An Overview of Key Ribbon Handleability Attributes", *46th IWCS Proceedings*, November 17, 1997, pp. 260 - 273.
2. Konstadinidis, K., Jackson, K., Sollenberger, N., Siddiqui, S., Taylor, C., Chandraiah, V., DeFabritis, R., Ly, H., Szwec, J., "Optimization of Fiber Ribbon Sub-Unit Robustness by Means of a Lateral Fiber-to-Matrix Adhesion Gradient", *48th IWCS Proceedings*, November 15, 1999, pp. 66 – 71.
3. Punch, N., Moorjani, S., Bissell, S., Williams, K., "Craft-Friendly 24-Fiber Ribbon Design", *48th IWCS Proceedings*, November 15, 1999, pp. 72 - 78.
4. McCreary, S., Beasley, W., Stokes, S., Lindsay, R., "Analysis of a Modular 24-Fiber Ribbon for the Distribution Network", *47th IWCS Proceedings*, November 16, 1998, pp. 432 – 439.
5. Jackson, K., Patel, P., Pearsall, M., Petisce, J., Lochkovic, G., "An Enhanced Ribbon Structure for High Fiber Count Cables In the Loop", *38th IWCS Proceedings*, November14, 1989, pp. 569 – 574.
6. Hecht, J., "Building a Fiber Optic Communication Industry", *Optics and Photonics News*, March, 2001, pp. 22 – 26.
7. Krupa, T., "Putting Fiber to the Test: The Early Days of Lightwave Systems", *Optics and Photonics News*, March, 2001, pp. 28 - 31.
8. Wagman, R., Lochkovic, G., White, K., "Component Optimization for Slotted Core Cables Using 8-Fiber Ribbons", *44th IWCS Proceedings*, November 13, 1995, pp. 472 – 478.
9. Dezelsky, R., Sprow, R., Tolopski, F., "Lightguide Packaging", *The Western Electric Engineer*, Winter 1980, pp. 81 – 85.
10. Schwartz, M., Reenstra, W., Mullins, J., "The Chicago Lightwave Project", *B.S.T.J.*, Vol 57, No. 6, July – August, 1978, pp. 1181 – 1188.
11. Eichenbaum, B., Topolski, F., "Methods of and apparatus for organizing fiber lightguides into a planar array", *United States Patent 4,289,558*, September 15, 1981.
12. Lochkovic, G., Purdue, R., "Ribbon Separation Tool and Method for Separating an Optical Fiber Ribbon", *United States Patent 6,053,085*, April 25, 2000.
13. Mock, G., Kathiresan, K., Lever, J., "Method and Apparatus for Separating One or More Optical Fibers from an Optical Fiber Ribbon", *United States Patent 5,685,945*, November 11, 1997.
14. Osaka, K., Watanabe, T., Kashima, K., "Separating Tool for Multi-core Ribbon Fiber", *United States Patent 5,524,166*, June 4, 1996.

15. Klein, D., "Apparatus for Breaking Out Ribbonized Fiber Optic Cables", *United States Patent 5,926,598,* July 20, 1999.
16. Stevens, C., "Wire Splitter for Round Conductor Flat Ribbon Cable", *United States Patent 4,046,045*, September 6, 1977.
17. Keesee, J., Debban, P., Burcum, L., Santana, M., "Entry and Termination of Central Core Optical Cables Containing Flexible Unit Tubes", *National Fiber Optic Engineers Conference (NFOEC) Technical Proceedings,* July 8, 2001, pp. 162 – 170.

Appendix

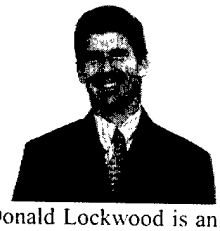
Table 1. Ribbon Separation Tool Characterization

Patent #	Potential Ribbon/Fiber Damage	End & Mid Access Capable	Multiple Sub-unit Combinations	Attenuation during Separation	Ease of Use
4,046,045	**Significant** due to the concave surface of the cutting probes (13). Design requires exact ribbon to tool tolerance which would cause damage from one supplier to the next due to subtle ribbon geometry differences.	Yes, however, bulk of the concept for use in the field is likely prohibitive for either end or mid-span operations.	Yes, but tedious to set-up.	Low during initiation and lengthwise advancement as long as the cutting probe to fiber position is exactly matched. Good handling precision required.	Complicated set-up and difficult field adaptability.
5,524,166	**Moderate** due to double score and shear (62) & (65) design. Also, (65) tends toward sharp fiber bends and potential matrix scraping. The rolling (65) action also can generate fiber tracking, thus allowing coating damage.	Yes. Again, however, significant lengthwise advancement is anticipated to be minimum due to reasons noted in the previous column.	Yes, however, somewhat complicated in set-up with adjustments required in both (62) & (65).	Low to moderate as long as any lengthwise progression is at a slow pace. Matrix damage and build-up during rapid advancement would likely cause high attenuations.	Moderate set-up character, but could reasonably be used in the field.
5,685,945	**Low** during initiation; however, **moderate** during lengthwise advancement. Lack of internal radii on (90) leafs may cause matrix scraping.	Yes, however, bulk of the unit may prove unruly for mid-span applications, esp. where minimum ribbon excess length is available.	Yes, however, field comments have noted some difficulty associated with the dial-type adjustment (esp. in dark areas).	Low during initiation; however, lengthwise advancement would likely cause high attenuation due to matrix scraping as described in the "Potential…Damage" column.	Moderate for end span; however, mid-span may prove difficult due to handling considerations.
5,926,598	**Low** to **moderate** during initiation due to absence of contouring on (40) & (70) in the ribbon contact zone. No separation advancement possible after initiation without significant damage.	Yes. Readily handled and applied.	Yes with readily understood and uncomplicated application. No set-up required.	Low during initiation; however, lengthwise advancement is likely not probable in a live fiber scenario.	Simple; however, lengthwise advancement after initiation is likely not feasible.
6,053,085	**Low** due to contoured surfaces and minimized contact area of (42) & (62) during both initiation and lengthwise advancement.	Yes. Readily handled and applied.	Yes with readily understood and uncomplicated application. No set-up required	Low during initiation and lengthwise advancement (see Figure 4).	Simple for both end and mid-span access.

Biographies



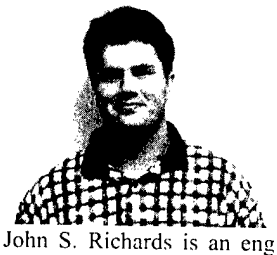
Gregory A. Lochkovic is Manager of the UV Development Group at Corning Cable Systems in Hickory, NC. Key responsibilities include the development of UV related products for both the domestic as well the Japanese markets. He received a B.S.M.E. in 1985 from Purdue University and a M.S. (in Manufacturing Systems) from Clarkson University in 1993. He has worked in various areas of fiber optic cable product and process development since graduation in 1985, and has been with Corning Cable Systems since 1991. He has been awarded 10 patents and has 5 previous publications.



Donald Lockwood is an Applications Engineer, supporting Corning Cable Systems' public network clients. He received a B.S.E.E from the University of Central Florida in 1992. Upon graduation, he served as an officer in the United States Army and joined Corning Cable Systems in May, 2000.



Shail K. Moorjani is a Senior Materials Engineer at Corning Cable Systems in Hickory, NC. His responsibilities include the development of UV-curable materials for optical cable products. He received a B.Tech. in Chemical Engineering from Osmania University, India in 1993 and a M.S. in Chemical Engineering from Michigan State University in 1996. Since he joined Corning Cable Systems in 1996, he has worked on various photocurable materials for loose tube and ribbon cable products for the domestic U.S. and international market.



John S. Richards is an engineer in the UV Development Group at Corning Cable Systems in Hickory, NC. Main responsibilities include the development of UV related products and process improvements for both the domestic and Japanese markets. He graduated with his B.S.M.E from Virginia Tech in 1998 and with a M.S.M.E from Virginia Tech in 2000. He has been with Corning Cable Systems since graduation in 2000.



Scott M. Torrey is the Product Specialist for Ribbon and Ribbon Cable products at Corning Cable Systems in Hickory, NC. Major responsibilities include market strategy, new product development, and training to internal and external customers. He earned his B.S. in Chemistry with University Honors from Carnegie Mellon University in 1993. After serving seven years in the US Navy as a nuclear engineering officer on surface ships, he joined Corning Cable Systems in 2000 in his present role.



Karen E. Williams is Senior Process Technician in the UV Development Group at Corning Cable Systems in Hickory, NC. Her main responsibility includes UV Ribbon development for the domestic market. She received degrees (non-engineering) from Western Carolina University, a B.S. in 1981 and a M.S. in 1985. She has worked with Corning Cables Systems since 1991 in various areas of the fiber optic industry. She has 1 previous publication.

Development of Dividing Tool for 4-fiber Ribbon

Kazumasa Ohsono *Kenji Ohmura* *Kazuya Murakami*
Satoshi Kikuchi *Isao Abe*

Hitachi Cable, Ltd. 5-1-1, Hitaka-cho, Hitachi-shi, Ibaraki-ken, 319-1414, JAPAN
Phone;+81-294-25-3837 · email;ohmura.kenji@hitachi-cable.co.jp

Abstract

In Japan, Slotted rod type optical fiber cables contain many 4-fiber ribbons. When we pull out part of the fibers of the 4-fiber ribbon, we must divide the ribbon into four fibers [1] . When done by hand, this division into four fibers demands skill and time. Moreover, the outer layer of the ribbon around each fiber is difficult in removing. In order to overcome these problems, we have developed a Dividing Tool for 4-fiber ribbons.

With this tool, the work in dividing the 4-fiber ribbon into four fibers takes only about 30 seconds and does not require any skill or experience.

Keywords

Dividing Tool, 4-fiber ribbon, Optical Cable, Optical Network

1 .Introduction

In line with the rapid progress of digital network systems, FTTH systems have been planed to utilize optical cables in all networks from telephone exchanges to subscribers. Some companies are pushing

forward with these plans, hoping to make them a reality by 2010. According to the proposed plans, they require a tool that can easily divide the 4-fiber ribbon into four fibers. At present, we usually use the fan-out technique for the work of mid span access. But it requires a lot of time and labor to use the fan-out. For the purpose of reducing connection costs and providing good handling, we have developed a Dividing Tool for the 4-fiber ribbon into mono-coated fibers.

2.Structure and Procedure of Developed Dividing Tool

The tool is designed to divide a 4-fiber ribbon that is 0.3mm or 0.4mm thick. It has two important parts: dividing edge and cutting edge (Fig. 1).

The dividing mechanism consists of three categories: (1)shearing the 4-fiber ribbon at its end; (2)dividing the 4-fiber ribbon; (3)removal of an outer layer of the ribbon which remains around the fibers. Please look at the details below.

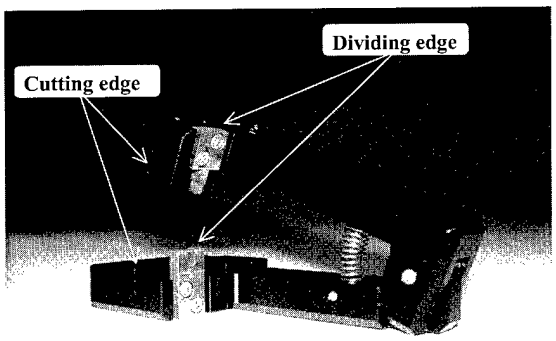


Fig.1 Appearance of Dividing Tool for 4-fiber ribbon

2.1 Shearing at the end of 4-fiber ribbon

By vertically pushing both end-fibers by using the dividing edge, the ribbon is divided into both outside-fibers and two inside-fibers. At the same time, gaps are made by the cutting edge at the surface of the 4-fiber ribbon.

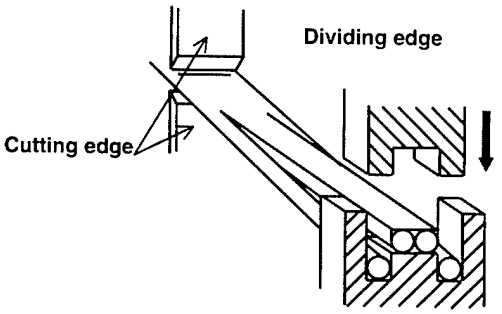


Fig.2 Shearing at the end of 4-fiber ribbon

2.2 Dividing of ribbon

Take each end of both outside-fibers and inside-fibers by hand and divide into optional length.

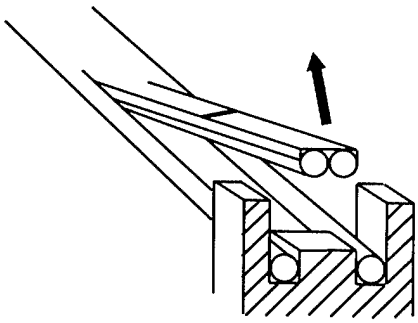


Fig.3 Dividing of ribbon

2.3 Removal of ribbon's outer layer around fibers

By bending each fiber: at the point where there is a gap, the edge of an outer layer comes off the fiber, and then the layer torn off.

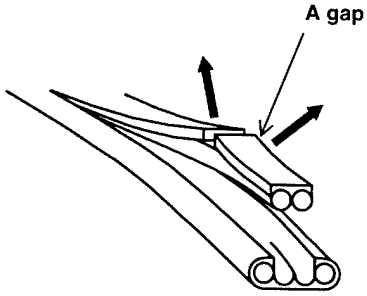


Fig.4 Removal of outer layer of ribbon

3. Performance of Dividing Tool

Performances of the Dividing Tool are shown in Table.1. The tool is small-sized and light weight, therefore it is possible to provide good handling even in a narrow space. The yield of the dividing trial is almost 100% and a waste length from the end of the ribbon is only less than 10 mm.

Table.1 Performance of Dividing Tool for 4-fiber ribbon

	Performance
Size	83(W)x35(D)x25(H) [mm]
Weight	88 [g]
Dividing Time	less than 30 [s] (dividing length:300[mm])
Yield	100 %
Waste Length	less than 10[mm] (from the end of the ribbon)
Tensile Strength of divided fiber	more than 60 [N] (Fig. 5)

4. Working Time for dividing

The working time for dividing the 4-fiber ribbon into four fibers is shown in Table.2.

It takes less than 30 seconds to divide the 4-fiber ribbon of 300mm length without any skill and experience.

Table.2 Working Time for dividing

Categories	Working Time		
	Min. [s]	Max. [s]	Ave. [s]
Shearing divide at the end of 4-fiber ribbon & Dividing along the ribbon	5	10	6.5
Removal of outer layer of the ribbon	10	20	16
Total	15	30	22.5

5. Characteristics of divided fiber

The strength of divided fiber is shown in Fig.5.

The tensile strength of all divided fibers is more than 60 [N]. During the division of the 4-fiber ribbon into four fibers, the degradation in strength was not observed. Fig.6 shows the result

of a Heat Cycle Test. The optical loss changes were measured for temperatures between -30℃ and +70℃ with the divided fiber. The variations of optical loss were less than 0.1dB.

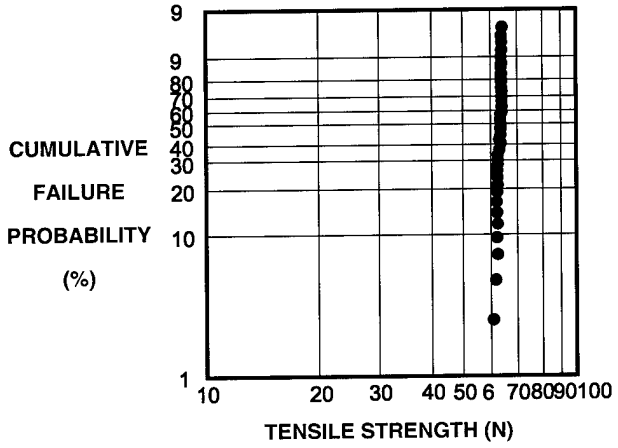
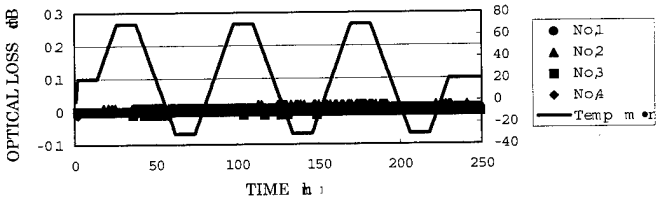


Fig.5 Strength of divided fiber



(at 1.33μ m Wavelength)

Fig.6 Heat Cycle Test results

6.Conclusion

A new Dividing Tool for the 4-fiber ribbon has been developed, which is demonstrated with good performance. Its performance is as follows:

(1) The work time is only about 30 seconds for dividing the 4-fiber ribbon into four fibers.

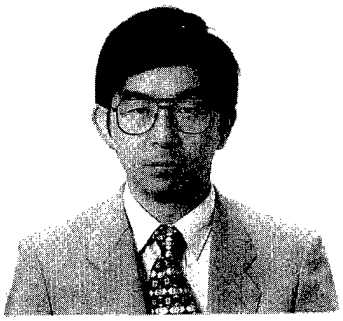
(2) The operation does not require any skill and experience.

(3) The yield of the dividing trial is almost 100% and the tensile strength of divided fibers is more than 60 [N] .

7.References

[1] H.Iwata, et al. "Novel Optical Fiber Cable for Distribution Use in Access Network " 48th IWCS, pp.20-24 (1999).

Author



Kazumasa Ohsono

Hitachi Cable, Ltd.

5-1-1, Hitaka-cho,Hitachi-shi, 319-1414 Japan

Mr. Ohsono received his B.E. degree in Mechanical Engineering from Science University of Tokyo in 1982 before joining Hitachi Cable, Ltd. He has been engaged in research and development of optical fibers and cables. He is now a senior researcher in the 4th Dept., Optroelectronic System Laboratory.

Correlation of Rheological and Thermal Properties of Waterblocking Gels with Drip Performance

Wayne P. Cheatle, Swati Neogi, Jeff Auton, Brian G. Risch
OFCCC, Alcatel Telecommunications Cable
Claremont, NC 28601
828-459-8329 · wayne.cheatle@cable.alcatel.com

Abstract

A study has been performed to correlate the rheological and thermal expansion properties of waterblocking gels used in fiber optic cable with cable drip performance. A model has been developed to estimate the minimum yield stress required to meet the drip performance and the predictions have been compared with experimental data. CTE data for various buffer tube materials and waterblocking gels were measured and tabulated. The effects of the difference in the coefficients of thermal expansion of the gel and tubes have been calculated with respect to the contribution to gel flow.

Keywords

Compound Flow; Rheology; Coefficient of Thermal Expansion; Yield Stress; Waterblocking Gel; Buffer Tubes; Drip Performance; Fiber Optic Cable; Predictive Model

Introduction

Buffer tubes in fiber optic cables are filled with waterblocking gels to prevent moisture ingression into the tubes. This gel serves as a mechanical cushion for the fibers, as well as making cables watertight, and minimizing water contact with fibers that can lead to corrosive effects on glass.[1,2,3] The waterblocking gel should meet many criteria such as viscosity, material compatibility, processability and thermooxidative stability for suitable use in fiber optic cable.[4,5] Along with these criteria, the drip performance of a gel is another important factor in determining suitability of a gel for fiber optic cable. If the drip performance of the gel is poor, it can flow out of the tube and into splice enclosures or other areas where it is not desired. Additionally, too much gel flow from a tube can create a path for moisture ingression within a tube which could render the fiber optic cable susceptible to water permeation. Therefore, Fiber Optic cables are required to have no or minimal flow of water blocking gels at elevated temperatures.

Drip performance is especially important for Aerial cables. Since Aerial cables are suspended high above ground, the potential for flow of large amounts of material exists if gel drip performance is not properly characterized. Aerial cables can also contain a wide range of buffer tube materials ranging from steel or aluminum tubes in OPGW cables to polymeric tubes (PBT or impact polypropylene copolymers) in ADSS cables.

Historically, the only sure way to ensure passing results on buffer tube gel drip testing was to make and test cables. Since this is a costly process, an alternative method of predicting the potential for drip of these gels has been sought. With the aid of newer, more sensitive rheology instrumentation, a correlation of gel drip performance to theoretical zero yield stress is possible via calculations. Yet, this method in itself is not sufficient, as optic cables are of many designs and material compositions. Therefore, the coefficient of thermal expansion (CTE) of the gel and the buffer tube material must also be considered to predict possible drip failures.

A model has been developed to estimate the required minimum value for yield stress for a given buffer tube size. In addition, experimental drip tests have been performed to validate the model. It has been demonstrated that not only the yield stress but also the thermal properties of the gel and tube material affect the drip performance of the tube.

Model

A simple model has been developed for estimating fluid flow in the axial direction in a vertical tube filled with waterblocking gel. It should be noted that these gels behave as non-Newtonian fluids.

The model is based on the following assumptions:

- Laminar, axisymmetric, steady state flow
- Incompressible, homogeneous fluid (no oil separation/single phase)
- No end effect
- No slip condition
- Bingham model is applicable to the Non-Newtonian waterblocking gel [6].

By performing the momentum balance on the controlled volume as shown in Figure 1, and applying the above assumptions, the following equation can be obtained.

$$\frac{d}{dr}(r\tau_{rz}) = \frac{P_0 - P_L - \rho g L}{L} r \qquad (1)$$

Where,

τ_{rz} is the shear stress in z direction at a radius r
ρ is the density of the fluid
L is the length of the tube
P_0 is the pressure at l=0
P_L is the pressure at l=L
Boundary conditions for the above equation are as follows:

At r=0, τ_{rz} = Finite (2)
At r=R, $v_{z=0}$ (no slip condition) (3)

For a fluid , τ_{rz} can be expressed by the following equations using the Bingham model:

$\tau_{rz} = \tau_0 - \mu_0 \, dv_z/dr$ for $r_0 \le r \le R$ (4)
$\tau_{rz} = \tau_0 - \mu_0$ for $0 \le r \le r_0$ (5)

Where $r_0 = 2L\tau_0/(P_0 - P_L + \rho gL)$ (6)

Equation 1 can be solved along with Equations (2)-(6) for the volumetric flowrate, Q. Q is given by

$$Q = \frac{\pi \tau_0}{\mu_0}\left[\frac{1}{4A}\left(R^4 - r_0{}^4\right) - \frac{1}{3}\left(R^3 - r_0{}^3\right)\right] \quad (7)$$

Where $r_0 = 2L\,\iota_0/(P_0 - P_L + \rho gL)$ (8)

To incorporate the effects of thermal expansion differences of the gel and tube materials, it is necessary to calculate the change in volume associated with these differences. The change in volume is given by:

$\Delta V_T = \Delta V_{gel@T} - \Delta V_{tube@T}$ (9)

Where $\Delta V_{gel@T} = Al\beta_{gel}\Delta T$ (10)
$\Delta V_{tube@T} = Al\beta_{tube}\Delta T$ (11)

And,
ΔV_T is the extruded volume of gel at temperature, T
$\Delta V_{gel@T}$ is the volume change of the gel at temperature, T
$\Delta V_{tube@T}$ is the volume change of the tube at temperature, T
A is the area of the inside of the tube
β_{gel} is volumetric coefficient of thermal expansion of the gel
β_{tube} is volumetric coefficient of thermal expansion of the tube
ΔT is the difference between the filling and test temperatures

After substituting and rearranging, the equation becomes

$\Delta V_T = Al_0\Delta T(\beta_{gel} - \beta_{tube})$. (12)

To predict the amount of gel flow to be extruded due to differences in thermal expansion between the gel and tube, one simply rearranges the density equation to obtain:

$Mass(g) = \Delta V_T \rho_{gel@T}$ (13)

Now that the volume and mass of the extruded gel at some temperature, T, is known, it is possible to calculate the yield stress required by the gel material to prevent drip. This can be accomplished by the following relationship assuming that the change in the radius due to thermal expansion is small.

$\tau_0' = F/A = mg/A$ (14)

Where,
τ_0' is the stress associated with the extruded gel
F represents a force
A is the area of the inside of the tube
m is the mass of the extruded gel at temperature, T
g is the acceleration due to gravity which equals 980 cm/s^2

The minimum yield stress value of the gel for a "no flow" condition is the greater of the two values obtained from τ_0 and τ'_0.

Experimental

Yield Stress

Experiments were performed to measure the yield stress of three different waterblocking gels at 80^0C. The yield stress was measured using a controlled stress rheometer, CSL^2 100, manufactured by Carri-Med (TA Instruments). A truncated 3.5°, 2cm-diameter steel cone was used in conjunction with a Peltier (hot) plate supported by a micrometer-pneumatic height adjusting ram. The gap due to truncation was set at 111 micrometers. To minimize shear history, the sample was loaded by raising the ram at a velocity that decays exponentially over distance. After setting the gap, the samples were trimmed and allowed to equilibrate at 23°C for 14 hours to regain structure lost due to loading. After equilibration, the Peltier plate was heated to 80°C and the gap was automatically adjusted for the expansion of the system. The samples were subjected to a stepped ramp experiment between two shear stresses dictated by the viscosity of the gel, which ensured that equilibrium had been reached prior to data collection. Upon completion of the experiments, the curves were analyzed and the yield stresses determined using the Herschel-Bulkley model.

Drip Tests

Drip tests were performed referencing the Bellcore GR-20[7] and FOTP-81[8] methods with modifications allowing the use of laboratory-produced samples instead of production stock samples. The modified experiment requires several 12-inch lengths of tube to be filled with the waterblocking gel of interest. To draw the gel into the tube, one end is submerged in a large container of the gel and the other end is attached to a hose connected to a vacuum pump. In this manner, the tube is filled with the gel with little chance of air entrapment. Filling must be complete throughout the full length of the tube. The presence of an air bubble could give false results in drip performance. Therefore, any occurrence of air bubbles would require the gel to be purged and the tube refilled. After filling, one end of each tube is covered with RTV silicone. The silicone must cover the tube end completely, with no holes. Once cured the RTV silicone can also act as a hanging mechanism for the tube. After applying the silicone, the tube is allowed to set horizontally for a minimum of 24 hours at ambient conditions to allow the gel to recover from any shear stress due to the drawing of the gel into the tube.

In order to pass the drip test, the amount of gel that drips from the tube cannot exceed 0.05 grams in a 24-hour period. A small, glass petri dish or any such similar container is used to catch and weigh any material that may drip. One dish per tube sample must be marked, weighed and the weight recorded prior to placement in the oven. The collection dish must be of sufficient weight that the airflow in the oven does not move the dish away from the tube.

After conditioning, the filled tubes are placed in an oven at 80°C such that each tube hangs vertically with a clearance of 2 to 3 inches between the uncovered end and the oven chamber floor. Tubes should be spaced in such a manner that when the recovery pans are added, no tube will be able to drip into more than one pan. After hanging the tubes, the drip recovery pans are placed in the oven under the respective tube sample. After 24 hours, the collection pans are removed from the oven and allowed to equilibrate at room temperature prior to weighing. The difference in weight is recorded as the drip mass.

Some standards allow the pre-conditioning of the tube prior to measuring drip to take into account the effects of heating, such as thermal expansion differences between the gel and the tube materials. The sample preparation and method described previously are employed with the following modifications. Two collection dishes are marked, weighed and recorded for each tube. After the samples are conditioned in the 80°C oven for one (1) hour, the drip recovery pan is removed and the second pan is placed beneath the tube. Drip evaluation is based on the presence of compound in the second pan after a total time of 24 hours.

Coefficient of Thermal Expansion

Coefficient of Thermal Expansion, CTE, of the gels was determined referencing ASTM D176 and D1903. The method requires the measurement of the specific gravity of the material at different temperatures. To calculate the specific gravity, a water displacement method was employed using a Fisher grease pycnometer made of aluminum and the following calculation:

$$Sp = (Wg - Ww)/(Ww - Wp) \qquad (9)$$

Where,

Sp = Specific gravity,
Wg = Weight of Pycnometer and gel,
Ww = Weight of Pycnometer and distilled water.
Wp = Weight of Pycnometer dry

After calculating the specific gravity at ambient conditions, the pycnometer was placed in an oven at 35°C and allowed to stabilize for 1- 2 hours prior to removal. Any gel that had exuded through the opening in the top of the pycnometer was removed by scraping the casing with a tongue depressor. After allowing the sample to equilibrate at ambient, the pycnometer casing was wiped, weighed and the weight recorded as Wg. The oven temperature was increased by 15°C and the same pycnometer sample was placed in the oven following the above method. This process was repeated to a final temperature of 100°C.

After the specific gravity had been measured at each specified temperature, the Coefficient of Thermal Expansion was calculated using the following formula:

$$E = (SpT_l - SpT_h)/(T_h - T_l)\, SpT_l \qquad (10)$$

Where,

E = Coefficient of Thermal Expansion
SpT_l = Specific gravity lower temperature
SpT_h = Specific gravity higher temperature
T_h = Higher Temperature
T_l = Lower Temperature

Results and Discussions

The drip test and yield stress measurements were performed using the methods described above. Equation (7) has been solved for the 'no flow' condition (Q=0) to determine the yield stress value required for a 'no drip' condition. In addition, equation 14 has been solved to determine the yield stress required by the gel to prohibit exuded gel from dripping from the end of the tube. Table 1 presents the yield stress values predicted by the model for both the 'no drip' and ΔCTE conditions for a number of tube materials as well as measured yield stress values at 80°C for four different gels tested in two tube materials.

A comparison was made between the predicted τ_0 yield stress values and the measured yield stress values at 80°C. The data showed that the measured yield stress values met or exceeded the predicted values. The drip results for the polypropylene tubes in Table 2 showed that no gel had dripped from the tube as predicted by the model. However, for each of the gels studied, the data in Table 2 showed that a measurable amount of gel, exceeding the maximum of 0.05 grams, had dripped from the steel tube.

The contradiction of drip failure of the gels in the steel tubes with the simple model prediction has been investigated to determine the cause of the failure. The model assumes that the tube and the compound always remain at a constant temperature. However, the drip test according to the method FOTP 81 and recommended by Bellcore GR20, requires the filling of the tube at ambient conditions followed by the placing of the tubes in an 80°C oven after conditioning. Therefore, during the drip test the tube and the gel will be subjected to heating until it reaches the steady state temperature of 80^0C. During heating, the tube and the gel will expand unevenly and will cause the extrusion of gel (gel will expand more than the steel). The amount of gel extrusion depends on the difference in CTE values of the tube and gel materials. The CTE values for the various tube materials and gels can be found in Table 3. In addition, the coefficients of thermal expansion of the different gels have been plotted in Figure 2. This data showed an order of magnitude difference between both the steel and aluminum tube material when compared to the gels. The model does not account for this extrusion due to differences in CTE. On the other hand, the polypropylene, PBT and polyamide materials are on the same order as the gels. The data in Table 1 showed that the model holds true in case of the polypropylene tube (PP) where the expansion coefficient of the gel and polypropylene the same order of magnitude. Whereas, the model fails in the case of the steel tubes since the expansion coefficient of the gel is much higher than that of steel.

An attempt has been made to predict the amount of the gel extruded due to differences in thermal expansion between the gel and tube material. Table 4 presents the calculated values for drip based on differences in thermal expansion compared to the measured amount of drip. The expansion was calculated assuming the tube will expand volumetrically. The amount of gel extruded due to the difference in thermal expansion of the gel and tube material was compared to the amount of gel dripped during the drip test in Figure 3. This data showed that the gel extruded due to the difference in CTE of the gel and the tube material constituted the major portion of the measured amount of the gel dripped. This extruded mass data was used in equation 14 to calculate τ'_0 which takes into account the stresses due to the extruded gel hanging from the end of the tube due to CTE differences.

The calculated τ'_0 values are shown in Table 1 for the different tube materials and gels. The data showed that when the tube material has a similar CTE value as the gel, the τ'_0 values are lower than the measured yield stress values for gels A and C. It is uncertain why there was no measurable amount of gel drip for gel B in the polypropylene tube where the τ'_0 value exceeded the measured value. End effects may have some contribution in reducing the yield stress required to prevent extruded gel from dripping. The data also showed that a much higher yield stress is required for the gels when either aluminum or steel is used for the tube material. To support the τ'_0 model, steel tubes were filled with gel D; a higher yield stress compound utilizing the same base oil as gel C. At 80°C, these tubes had gel protrude from the end of the tube due to differential CTE as predicted. Moreover, since the yield stress was higher than the predicted 'no drip' condition, no gel had dripped from the end of the tube which validates the τ'_0 model. To determine whether the model is valid for steady state conditions, a preconditioning step was added to the experiment.

Table 2 presents the amount of compound dripped during one hour of heating (i.e., preconditioning step) and during the remaining 23 hours of heating in the conditioned experiment along with the data collected from the unconditioned experiment. The data showed that the material dripped during the first one hour of heating in the preconditioned experiment is similar to that collected from the unconditioned experiment. This is more evident in Figure 4 which compared the conditioned and unconditioned drip masses. The fact that no gel had dripped after preconditioning validates the model, which simulated the 'no drip' flow at constant temperature.

Conclusions

Flow of waterblocking gel out of a tube in fiber optic cable is not only dependent on the critical yield stress of the gel but on the thermal expansion coefficients of both the gel and buffer tube materials as well. A model has been developed which can be used to predict the minimum gel yield stress required for a given tube inner diameter. If the coefficient of thermal expansion of the gel is lower than or equal to that of the tube material, then rheology alone is sufficient to predict the drip performance. An additional equation has been developed to predict the gel yield stress required for those conditions where differential thermal expansion between gel and tube materials must be considered. The low coefficient of thermal expansion for steel and aluminum tubes has been identified as the principal factor in the greater difficulty that has been seen in achieving acceptable compound flow results with these tubes. However, it has been demonstrated that higher yield stress gels are capable of passing compound flow tests in steel tubes at 80°C.

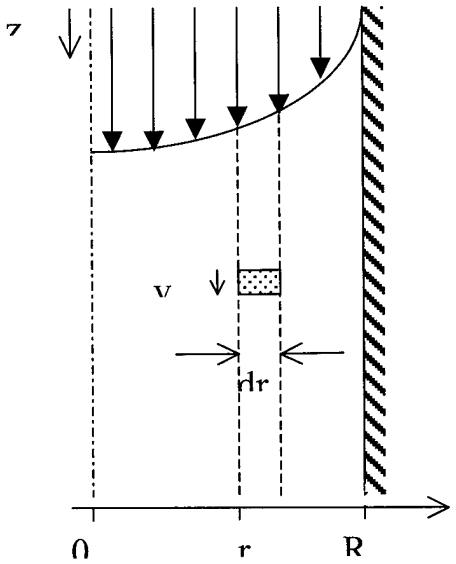


Figure 1. Sketch of the section of tubes.

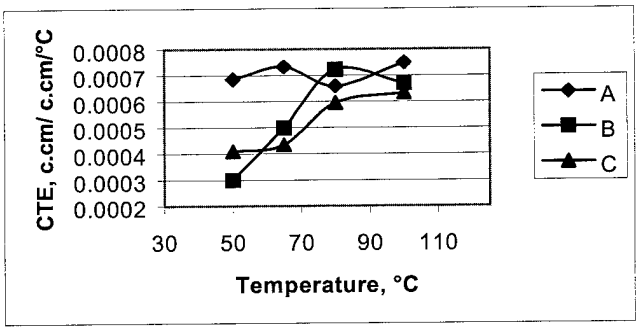


Figure 2. Coefficient of thermal expansion of gel at different temperature.

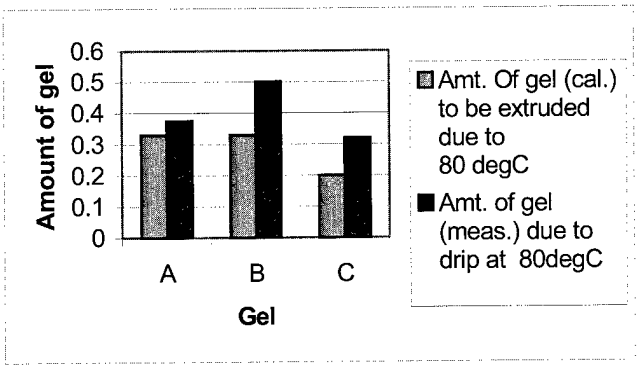


Figure 3. Comparison of the calculated amount of gel extrusion with the measured amount of gel dripped during the test.

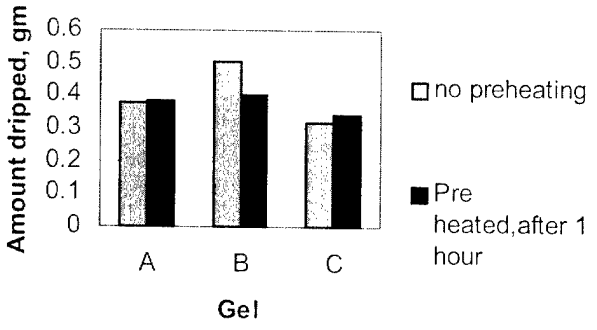


Figure 4. Comparison of unconditioned and preconditioned drip masses.

Table 1. Values of predicted and measured yield stresses at 80 °C for three different gels and various tube materials.

Gel	Tube material	Tube size (ID), mm	Yield stress at 80 °C, Pa		Measured Yield Stress at 80°C, Pa
			Model prediction for no drip, τ_0, Pa	Model prediction for ΔCTE, τ'_0, Pa	
A	Steel	7.8	15	71.30	30±10
A	PP	6.4	13	24.63	30±10
A	Aluminum	7.8	15	69.09	
A	Polyamide	6.4	13	19.10	
A	PBT	6.4	13	27.00	
B	Steel	7.8	16	76.19	14±4
B	PP	6.4	13	28.35	14±4
B	Aluminum	7.8	16	73.92	
B	Polyamide	6.4	13	22.68	
B	PBT	6.4	13	30.78	
C	Steel	7.8	17	61.58	30±3
C	PP	6.4	14	10.52	30±3
C	Aluminum	7.8	17	59.16	
C	Polyamide	6.4	14	4.47	
C	PBT	6.4	14	13.11	
D	Steel	7.8	17	61.58	100±10

Table 2. The amount of compound dripped during unsteady state and steady state heating as a function of tube type.

Tube mat.	Gel	Tube size (ID), mm	Amount dripped with preheating, gm		Amount dripped without preheating, gm
			One hour	After additiona 1 23 hrs	Non heated
Steel	A.	7.8	0.381	0	0.375
PP	A	6.4	0	0	0.0
Steel	B	7.8	.400	0	0.501
PP	B	6.4	0	0	0.0
Steel	C	7.8	.343	0	.320
PP	C	6.4	0	0	0.0

Table 3. CTE values of various materials.

Material	Linear CTE (cm/cm/°C)	Volumetric CTE (cm^3/cm^3/°C)
Steel	0.179E-04	0.537E-04
PP	1.36E-04	4.08E-04
Aluminum	0.235E-04	0.705E-04
Polyamide	1.50E-04	4.50E-04
PBT	1.30E-04	3.90E-04
Gel A	1.98E-04	5.95E-04
Gel B	2.06E-04	6.18E-04
Gel C	1.60E-04	4.81E-04

Table 4. Calculated gel flow due to thermal expansion versus the amount of gel dripped during unsteady state heating.

Gel	Tube mat.	Tube Dia., mm	Amt. Of gel (cal.) to be extruded due to ΔCTE at 80 °C, g	Amt. of gel (meas.) due to drip at 80°C, g
A	Steel	7.8	0.348	0.375
	PP	6.4	0.081	0.0
	Aluminum	7.8	0.337	
	Polyamide	6.4	0.063	
	PBT	6.4	0.089	
B	Steel	7.8	0.372	0.501
	PP	6.4	.093	0.0
	Aluminum	7.8	0.361	
	Polyamide	6.4	0.074	
	PBT	6.4	0.101	
C	Steel	7.8	0.301	0.320
	PP	6.4	0.034	0.0
	Aluminum	7.8	0.289	
	Polyamide	6.4	0.015	
	PBT	6.4	0.043	
D	Steel	7.8	0.301	0.0

[1] M. J. Matthewson and C. R. Kurkjian, "ENVIRONMENTAL EFFECTS ON THE STATIC FATIGUE OF SILICA OPTICAL FIBER", *J. Am. Ceram. Soc.*, 71[3]1988, pp. 177-183.

[2] J. Stone, "INTERACTIONS OF HYDROGEN AND DEUTERIUM WITH SILICA OPTICAL FIBERS", Jour. Of Lightwave Tech. N0. 5, May 1987.

[3] J.T. Krause, "ZERO STRESS STRENGTH REDUCTION AND TRANSITIONS IN STATIC FATIQUE OF FUSED SILICA FIBER LIGHTGUIDES", J. Non-Cryst. Solids, 38&39, 1980, P497

[4] M.T. Costello, "THERMAL ANALYSIS OF BUFFER TUBE GELS IN LOOSE TUBE FIBER OPTIC CABLES", IWCS, 1998, P501.

[5] B.G. Risch, "SWELLING INTERACTION PLASTICIZATION, AND ANTIOXIDANT EXTRACTION BETWEEN FIBER OPTIC CABLE GELS AND POLYOLEFINS", Antec, 1999, P3361.

[6] M. J. Dealy and K.F. Wissbrun, "MELT RHEOLOGY AND ITS ROLE IN PLASTIC PROCESSING", Published by Van Nostrand Reinhold , New York, 1990.

[7] Bellcore GR-20, Issue, Section 6.3.3, July 1998.

[8] EIA/TIA-455-81A, EIA/TIA Standard, FOTP-81, "COMPOUND FLOW (DRIP) TEST FOR FILLED FIBER OPTIC CABLE", 1992

Compact Optical Fiber Cable Testing and Maintenance System

***Atsushi OGAWA*[*1], *Yoichi HATA*[*2], *Hideaki YUSA*[*2],**
***Yoshifumi HISHIKAWA*[*1], *Masahiro HAMADA*[*1], *Hisao MAKI*[*2]**
[*1] Communication Division, [*2] Yokohama R&D Laboratories,
Sumitomo Electric Industries, Ltd.
1, Taya-cho, Sakae-ku, Yokohama, 244-8588, JAPAN
Tel: +81-45-853-7202, Fax: +81-45-852-7922, E-mail: ogawa-atsushi@sei.co.jp

Abstract

We have developed a Compact Optical Fiber Cable Testing and Maintenance System. This system consists of an Optical Testing Equipments (OTE), which integrates a mechanical-type optical switch, an OTDR in one body, and a controller (a personal computer). The optical switch can inject the test light into a specific fiber among up to 200 fibers. The OTE measures characteristics of a large number of fibers automatically. As you apply the OTE to the construction testing system or the Remote Fiber Testing and Maintenance System (RFTMS), the OTE contributes to the big reduction of the time consumption for construction and maintenance of optical network.

Keywords

OTDR; Fiber switch; Maintenance system; Construction System;

1. Introduction

The data traffic in the telecommunication networks is rapidly increasing. The introduction of D-WDM is also increasing and the traffic capacity per fiber is expanded. The optical networks are now required higher credibility as these infrastructures.

On the other hand, we need to reduce the cost of plant investment, management and maintenance. This system meets these demands and supplies the high credibility of the network inexpensively.

Recently the constructions of optical fiber network have been expanding rapidly by the spread of the network. Up to now, we measured characteristics of optical fibers one by one using OTDR when we construct or maintain optical network. It is the most important problems to cut down the construction and maintenance costs.

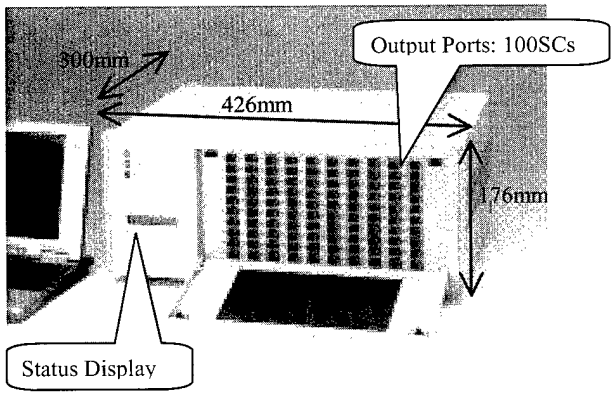


Figure 1. Optical Testing Equipment (OTE)

2. Feature of the OTE

The test unit consists of an OTE, which integrates a mechanical-type optical switch (Fiber Selector: FS) and an OTDR in one body, and a controller. The specifications of the OTE are listed in Table 1, and its appearance is shown in Fig 1. The OTE is handy-sized (426 * 300 * 176 mm) and lightweight (11kg). It is about as compact and light as the usual OTDR. The OTE is developed so as to fit it to 19-inchs racks and the existent fiber termination module and to carry it easily to anywhere.

Table 1. Specifications of OTE

Optical Characteristics		
	Dynamic Range (1us pulse)	1550nm: > 21.9dB typ.25.5dB 1650nm: > 17.4dB typ.20.5dB
	Sampling Resolution	1m
	Dead Zone	Event: 10m (0.02 s pulse) Attenuation: 50m (0.1 s pulse)
Operational Characteristics		
	Power Requirements	100-240VAC, 50-60Hz
	Power Supply Rating	60 watts max.
Physical Characteristics		
	Weight	11kg (50 / 100 fibers type)
	Dimensions	426 * 300 * 176 mm (50 / 100 fibers type)
Environmental Characteristics		
	Temperature	+10 to 40 ˜
	Humidity	20% to 80% no condensing
Fiber Selector		
	Output port	Max. 200 fibers
	Insertion Loss	< 0.7dB typ.0.3dB
	Return Loss	> 40dB
	Switching Time (End to End)	< 3 sec
	Switching Life	> 10,000,000 cycles

The fiber selector is made use of switching fibers. The fiber selector can inject the test light into a specific fiber among up to 200 fibers. Fig 2 and Fig 3 show the structure of fiber selector and the principle of fiber selector [1][2].

The fiber selector connects the mobile fiber and one of fixed fibers on a V-shaped groove. The mobile fiber is connected with OTDR and fixed fibers are connected with output fibers as testing fibers. We achieved low-price and miniaturization of max 200 fibers switching mechanism by high accurate alignment of fixed fibers.

As the test signal wavelength 1310nm, 1550nm, and 1650nm can be used.

3. Operation for Construction

In this chapter, the construction testing system is shown. This system takes full advantage of OTE's merits to support the entire work of construction test.

3.1 System Configuration

Fig.4 shows the structure of construction testing system. Before you start a construction test, you connect all of the fibers with OTE by SC-connector. The fiber selector leads the test light that is sending from OTDR into the test fiber. The fiber selector is able to select up to 200 fibers and the OTE has the OTDR trace analyzing and management function. Once you connect these testing fibers, you can test max 200 fibers automatically.

This system can be remotely controlled through telephone network. Namely in the past workers at the construction site and at the telephone office cooperate to execute the construction test. But if you install this system, you can reduce workers at the telephone office. You can reduce construction period and realize good work. Operating software for construction has only two functions – to control OTE and to make a report of test. We can use it easily like using the general measurement equipments because it has most simple GUI.

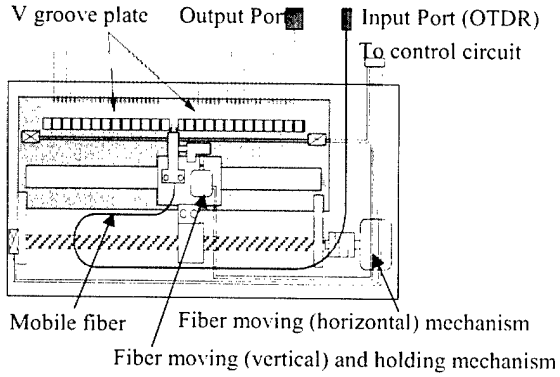


Figure 2. Structure of Fiber Selector

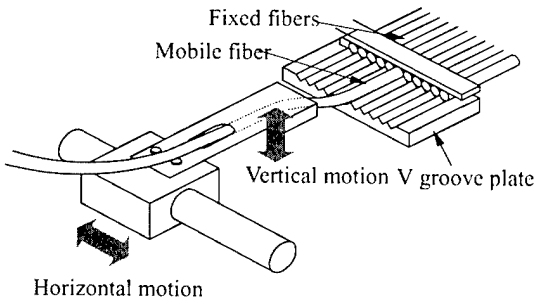


Figure 3. Principle of Fiber Selector

3.2 Remote Control

Preparing for the case that the environment of communication is unstable or inconvenience, the system has the communication functuion by the optical RS232C using the non-service fibers.

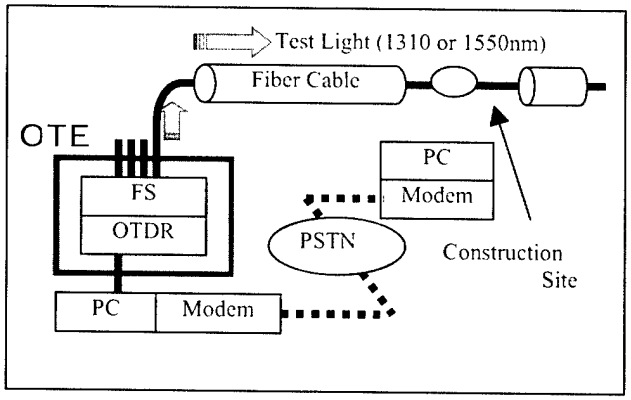


Figure 4. Structure of Dark Fiber Testing

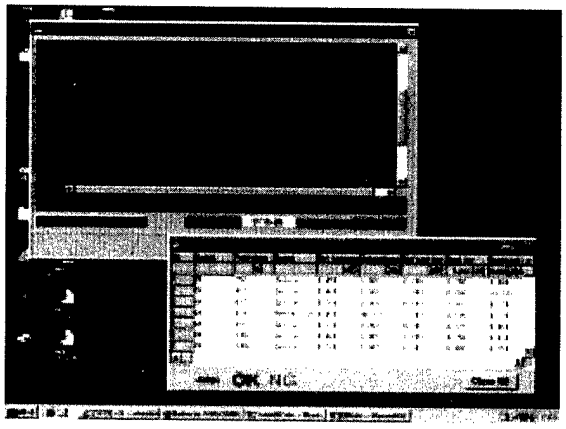


Figure 5. Example display of the Test result by Construction Testing System

3.3 OTDR Test

You can choose one wavelength among 1310nm, 1550nm, and 1650nm. However when you test in-service fibers – for maintenance system -, you should choose the wavelength that is different from in-service wavelength because the test light doesn't influence the service light.

This system has three more functions in addition to the usual OTDR functions. There are the continuous testing function, the analyzing function, and the data management function.

By the continuous testing function the OTE measures all fibers one by one. The analyzing function automatically checks some event point, calculating splice loss and reflection value of each fiber. And it has an analysis function of connections manually. Fig.5 shows the example display of the test results. The data management function is shown in next section.

3.4 Data Management

Test results as the OTDR trace, auto analysis results, and several parameters of each fiber are managed by this function. They are saved in a hard disc. This system has a lot of management functions, for example, to search for the necessary data among these data easily, to reanalyze them as occasion calls, to make a report in various formats.

4. Operation for Maintenance

In this chapter, the Remote Fiber Testing and Maintenance System (RFTMS) is shown. RFTMS is made of OTEs, monitoring centers (MC) and the system server. In this system OTEs and monitoring centers work as each client.

RFTMS has network element management function using electronic map, alarm management function, and test function including functions of the construction testing system [3].

Information such as facilities information, figure information, attribution information and so on, are shared with each client.

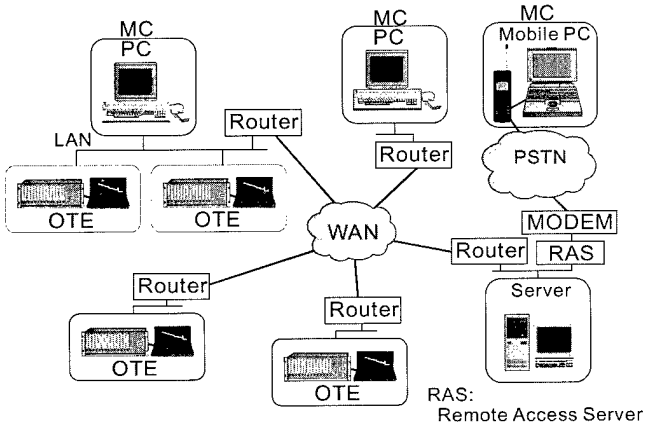


Figure 6. Structure of RFTMS

Alarms that are detected by OTE are informed at once. The details of each alarm can be confirmed with the map on the screen. Therefore RFTMS makes available speedy repair work.

Moreover this system is able to add client later as occasion calls (ex. the spread of the network).

4.1 System Configuration

As occasion calls we can build the simple system using one OTE singly, or the large-scale system using many OTEs and many monitoring centers.

This system of the hardware consists of the test access modules (TAM) that divide / join / cut off the test-light, the OTE that measures optical fibers, some computers that control these equipments, and the network between the OTEs and the remote-control computers.

The diagram of in-service fiber testing is shown in Fig 7.

When you test in-service fibers, you choose the wavelength of test light that is different from the in-service wavelength and use TAM by which test lights are joined to and divided from test fibers. And you use two termination filters in the TAM and at the end of the fiber to cut off the test light [4][5]. Then the service light is not

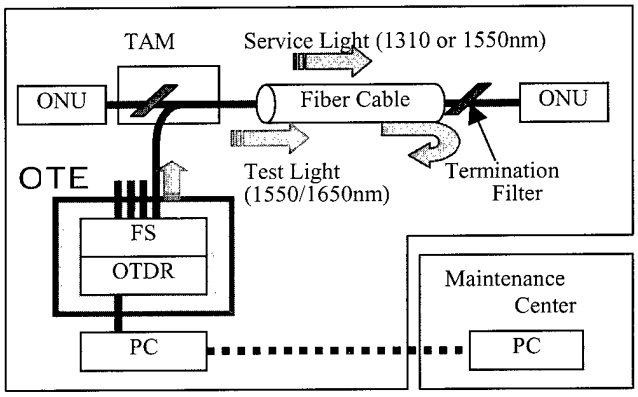


Figure 7. In-Service Fiber Testing

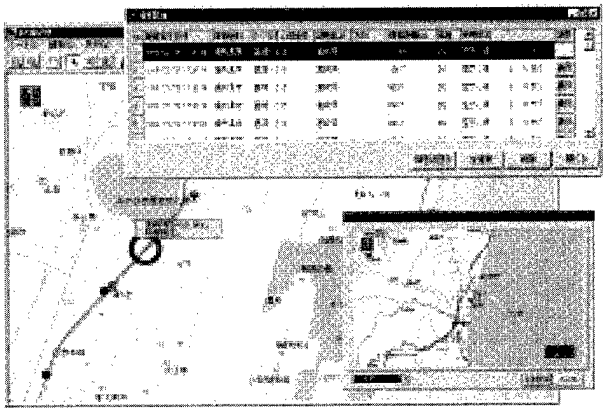


Figure 8. Example display of the fault location by RFTMS

influenced by test light.

We can observe longer fibers by introducing more than one instrument. By test-scheduling function, which controls these OTEs efficiently, we can use these instruments efficiently.

Table 2. Functions of RFTMS

Test Function	Manual Testing
	Continuous Testing
	Test Scheduling
	Periodic Scheduled Testing
	Status Monitoring
	OTDR trace Analysis
	OTDR trace Viewer
	Documentation of Test Results
Alarm Management Function	Alarm Delivery
	Alarm Historic Management
	Fault Location Mapping
	Transmitting SNMPtrap
Network Element Management Function	Network Element Information Management
	Drawing and Photo of each Element Management
	Road Route Search to a fault position

4.2 Test Function

In addition to functions of Construction Testing System the test function of RFTMS has various sub-functions to execute test effectively. For example, the periodic scheduled testing function executes test at an interval of any hours / days / weeks / months, and the status monitoring function checks queue of scheduled testing of each OTE.

Especially Test scheduling function is one of the most important functions because RFTMS needs to control a lot of OTEs. The test function collects test requests from each client and scheduled in order. All requests have each priority levels. The urgent requests are tested prior to the other request. After its requests are finished, the executing test is restarted automatically.

If you install two OTEs at both end of the fiber cable, the test scheduling function schedules so as not to inject test light into same fiber at the same time. So the test scheduling function meets the case of testing long distance cables.

4.3 Alarm Management Function

The alarm management function keeps the property of the fiber and the alarm information to the database when the faults in the fiber network are detected by test function. And this function informs alarms to operators.

The details information of each alarm can be confirmed visually on the screen at each site. Furthermore this system sends these alarms to administrators by e-mail and a phone call.

If you add the transmit SNMPtrap function, the alarm information are send to the manager system. Then RFTMS works as the agent of synthetic network control system.

4.4 Network Element Management Function

Network Element Management Function manages several information of these fiber information and its equipments on a database. By cooperating with the alarm management function we can grasp a location of fault. In addition, a lot of documents, drawing, photo data, and so on related with equipments are saved by pdf format, and you can search and print out these data easily.

5. Expected Efficiency of RFTMS

This system provides you the effect shown table 3. We expect the user of RFTMS to operate repair and restoration works efficiency.

6. Conclusions

RFTMS have been developed as a total maintenance and administration system for the fiber network. Besides RFTMS combine the OTDR and FS, chased handy and easy to use based on high quality and high faculty. We hope that RFTMS is indispensable for maintenance of the optical fiber network.

Table 3. The efficiency of RFTMS

Construction	Remote control	Reduction of cost and period of the construction
Maintenance	Periodic scheduled testing In-service fiber testing	Improvement of the network reliability by the preventive maintenance
	Continuous testing	Immediate detection of the fatal change of the fiber network
	Network Element Management	Improvement of the productivity of the administration and maintenance
Repair and Restoration	Fault location system	Immediate repair work
	Searching for the related Network Element Information	Improvement of the operation of the repair and restoration
	Checking of the fiber optic path	Quick analysis of the cause of the fault

7. References

[1] H.Kohda, Y.Tamura, K.Saito, "Study of opto-mechanical switch using v-groove alignment between mobile fiber and fixed fibers", *in Proc. NFOEC '97,* Vol.2, pp.225-236

[2] T.Shimazu, H.Kohda, T.Komiya, "Development of opt-mechanical switch with rotating v-groove alignment on cylindrical array", *in Proc.EC '99,* pp.324-331

[3] K.Ozawa, Y.Hishikawa, K.Watanabe, H.Maki, "Remote Fiber Test System with Network Element Database and Geographic Information System", *in Proc.OECC '99*

[4] T.Ebihara, N.Nakao, M.Kuroiwa, "Novel Automatic Remote Fiber Line Testing System and New Fiber Termination Module for Expanding Local Subscriber Loops", *in Proc.ECOC '96,* pp.3.39-3.42

[5] N.Tomita, H.Takasugi, N.Atobe, I.Nakamura, F.Takaesu, S.Takashima, "Design and performance of a novel automatic fiber line testing system with OTDR for optical subscriber loops", *IEEE J.Lightwave Tech., Vol.12 No.5,* pp.717-726, May 1994.

Authors

Atsushi OGAWA

Atsushi Ogawa was born in 1970. He received B.E. and M.E. degrees in Information Engineering from Hokkaido University in 1993 and 1995 respectively. He joined Sumitomo Electric Industries, Ltd. in 1995. He has been engaged in research and development of software design engineering. He is now a research engineer of Engineering Department Communications Division. He is a member of the Information Processing Society of Japan.

Youichi HATA

Youichi Hata received B.E. and M.E. degrees in Electronic Engineering from Tokyo Metropolitan University in 1990 and 1992 respectively. He joined Sumitomo Electric Industries, Ltd. the same year and has been engaged in research and development of software design engineering. He is now a senior engineer of optical network R&D Dept. Yokohama R&D Laboratory. He is a member of the Japan Society of Applied Physics.

Hideaki YUSA

Hideaki Yusa was born in 1966 and received his B.S. degree in Electronic Engineering from Tokyo Metropolitan University in 1990. He joined Sumitomo Electric Industries the same year and has been engaged in research and development of optical area network system for data communication technologies and fusion splicing technologies for optical fibers.

Yoshifumi HISHIKAWA

Yoshifumi Hishikawa was born in 1965. He has worked for Sumitomo Electric Industries, Ltd. since 1991 and He joined Sumitomo Electric Industries the same year and has been engaged in research and development of optical area network system for data communication technologies and fusion splicing technologies for optical fibers. He is now a senior engineer of Engineering Department Communications Division.

Masahiro HAMADA

Masahiro Hamada was born in 1962. He received his B.E. and M.E degrees in Electronic Engineering from Shizuoka University in 1985 and 1987 respectively. He joined Sumitomo Electric Industries, Ltd. the same year and has been engaged in development of fusion splicing technologies and remote testing systems for optical fibers. He is now an assistant manager of Optical System Section, Communication Division. He is a member of the institute of Electronics, Information and Communication Engineering of Japan.

Hisao MAKI

Hisao Maki was born in 1958. He received his B.E. and M.E degrees in System Engineering from Kobe University in 1981 and 1983 respectively. He joined Sumitomo Electric Industries, Ltd. the same year and has been engaged in research and development of automatic optical measuring instruments. He is now a chief Research Associate of optical network R&D Dept. Yokohama R&D Laboratory. He is a member of the institute of Electronics, Information and Communication Engineering of Japan.

Modeling UTP Cabling: Insertion Loss and Bit Errors

John W. Kincaid, Paul Z. Vanderlaan
Belden Electronics Division
Richmond, Indiana
+1-765-983-5332 · john.kincaid@belden.com

Abstract
The uniform model for Cat 5 cable and channel is extended from the equation format to a matrix format. Using the chain matrix format (ABCD parameters)the insertion loss and transfer function for a uniform cascade of two port networks is given. Steady state frequency domain transfer function amplitude and phase are plotted for four configurations of cable, terminations and one connector. The transient response performance consisting of impulse response and step response of the network transfer function are presented for each of the configurations.

Keywords
Modeling; utp; step response, impulse response, bit errors.

1. Introduction
This paper is an extension of the work presented at the 1998 International Wire and Cable Symposium [1]. At that time the focus was on return loss of uniform cable, connector and cascade interconnections of these components forming channels. In particular, good agreement was shown between measured and modeled results for a three-connector channel. Since 1998 progress has been made in the standards arena and requirements for return loss of cable and channel have been published as Cat 5E in an addendum to Cat 5 [2]. In the industry at large there is talk of frequencies as high as 1200 MHz for twisted pair cabling. However, work on Cat 6 is maturing and the standard Cat 6 bandwidth will soon be recognized at 250 MHz.

With the exception of requirements for propagation delay and delay skew, the standardization focus has been on performance requirements in the steady state frequency domain. An emphasis has been to provide maximum insertion loss values versus frequency as well as to consider the deviation (ILD) from a smooth insertion loss response. Throughput, real time, transient performance or bit error rate, (BER) performance, have not been explicitly standardized. However, time domain performance, including BER performance, is implicit in the steady state frequency domain characterization provided the noise (crosstalk) environment and encoding techniques are also identified.

The current work has been undertaken as an attempt to begin to identify and model the fundamental performance characteristics of cable and cabling in the time domain.

2. Uniform Cable and Connector System Model

2.1 Equation Format
From [1] the Cat 5 uniform cable model equations are given below. Note the correction to equations (1), (6) and (8) that appeared in [1].

$$\tau = 534 + 36/\sqrt{f} \quad \text{.....(1)}$$

Time delay, nanoseconds per 100 meters.

$$\beta = 2 \cdot \pi \cdot f \cdot \tau / 100000 \quad \text{.....(2)}$$

Phase constant, radians per meter.

$$\alpha = \left(1.967 \cdot \sqrt{f} + 0.023 \cdot f + 0.05/\sqrt{f}\right) \cdot 0.01/8.686 \quad \text{.....(3)}$$

Attenuation constant, Nepers per meter.

$$\gamma = \alpha + j \cdot \beta \quad \text{.....(4)}$$

Propagation constant, radians per meter.

$$Z_o = Z_{hf}/100\left(\left(100 + 5.5/\sqrt{f}\right) - j \cdot 5.5/\sqrt{f}\right) \quad \text{.....(5)}$$

Characteristic impedance, Ohms.

In equation (5) the term Z_{hf} represents the high frequency asymptote of the impedance.
The variable f is frequency in MHz and the operator j is $\sqrt{-1}$.
Also from [1], the connector model is given below.

Time delay, nanoseconds per 100 meters;

$$\tau = 570 \quad \text{.....(6)}$$

Phase constant, radians per meter;

$$\beta = 2 \cdot \pi \cdot f \cdot \tau / 100000 \quad \text{.....(7)}$$

Attenuation constant, Nepers per meter;

$$\alpha = \left(0.4 \cdot \sqrt{f}\right) / 8.686 \quad \text{.....(8)}$$

Propagation constant, radians per meter;

$$\gamma = \alpha + j \cdot \beta \quad \text{.....(9)}$$

Characteristic impedance, Ohms;

$$Z_o = Z_{cx} / 100\left(\left(100 + 5.5/\sqrt{f}\right) - j \cdot 5.5/\sqrt{f}\right) \quad \text{.....(10)}$$

2.2 ABCD (Chain) Matrix Format

This format has been well documented in the literature and may be derived from the theory of two port networks [3]. It has been used to describe cabled interconnections of power lines [4], communication cables [5], microwave components [2] and telephone cable subscriber loops [6].

The ABCD matrix is a 2X2 matrix where the elements are given by,

$$\mathrm{A} = \cosh(\gamma \cdot l) \quad \text{.....(11)}$$

$$\mathrm{B} = Z_o \cdot \sinh(\gamma \cdot l) \quad \text{.....(12)}$$

$$\mathrm{C} = 1/Z_o \cdot \sinh(\gamma \cdot l) \quad \text{.....(13)}$$

$$\mathrm{D} = \cosh(\gamma \cdot l) \quad \text{.....(14)}$$

Thus, using equations (1) through (10) the uniform component model may be compactly expressed as an ABCD matrix, $\mathrm{M_{ABCD}}$ given by equation (15). The parameter l in equations (11) through (14) represents the length of the component expressed in meters.

$$\mathrm{M_{ABCD}} = \begin{pmatrix} \mathrm{A} & \mathrm{B} \\ \mathrm{C} & \mathrm{D} \end{pmatrix} \quad \text{.....(15)}$$

Cascade combinations of components may then be efficiently represented as a system ABCD matrix as indicated in equation (16) where only two components are illustrated.

$$\mathrm{Msystem_{ABCD}} = \mathrm{M1_{ABCD}} \cdot \mathrm{M2_{ABCD}} \quad \text{.....(16)}$$

As the system matrix is written, the sequence of component matrices must follow the physical placement of the components in the system. The system matrix may then be used to solve for the following system parameters:

- insertion loss
- transfer function

3. Insertion Loss

The uniform cable insertion loss magnitude was defined in [1] and results for certain cable and cascaded cable and connector configurations were presented.

Equation (17) gives the insertion loss, $I.L.$, expressed in terms of the ABCD parameters [6].

$$I.L. = -20 \cdot \log\left|\left(Z_L + Z_S\right) / DENOM\right| \quad \text{.....(17)}$$

where $DENOM$ is given in equation (18).

$$DENOM = \mathrm{A} \cdot Z_L + \mathrm{B} + \mathrm{C} \cdot Z_S Z_L + \mathrm{D}\, Z_S \quad \text{.....(18)}$$

Here the source impedance is represented as Z_S and the load impedance as Z_L.

4. Transfer Function

The transfer function equation relating output voltage to input voltage was shown to be a function of load impedance, length and the propagation constant for the uniform line [1]. The corresponding expression for the transfer function, TF, using ABCD parameters [6] is given by equation (19).

$$TF = Z_L / \left(\mathrm{A} \cdot Z_L + \mathrm{B}\right) \quad \text{.....(19)}$$

The transfer functions for the interconnection configurations listed in Table 1 have been computed for the frequency range 0.1-100 MHz. A commercially available mathematical software program was utilized for the calculations as well as preparation of the Figures [7].

Table 1. Component configurations

	Configuration #			
	1	2	3	4
Source Z_S Ohms	100	Z_o	100	100
Cable 1				
Z_{hf} - Ohms	100	100	90	95
Length- m	100	100	100	50
Connector	-	-	-	Cat 5
Cable 2				
Z_{hf} - Ohms	-	-	-	105
Length- m				50
Load Z_L Ohms	100	Z_o	100	100

The transfer function amplitude for each configuration is plotted in Figure 1. Each configuration spans 100 meters in length. Configuration #2, with cable impedance terminations at source and load provides the smoothest response. The most oscillatory is #4 that includes a Cat 5 connector and a cable impedance discontinuity at mid-span. The mid-span discontinuity causes multiple reflections, which are evident as oscillations, between cable and terminations. The oscillations are greatly reduced at frequencies greater than 10 MHz. The drop-off in amplitude as frequency increases leads to signal waveform amplitude distortion, which is a factor in determining the transient performance and BER [8]. The multiple reflections are also a source of amplitude distortion that will affect the transient performance and BER.

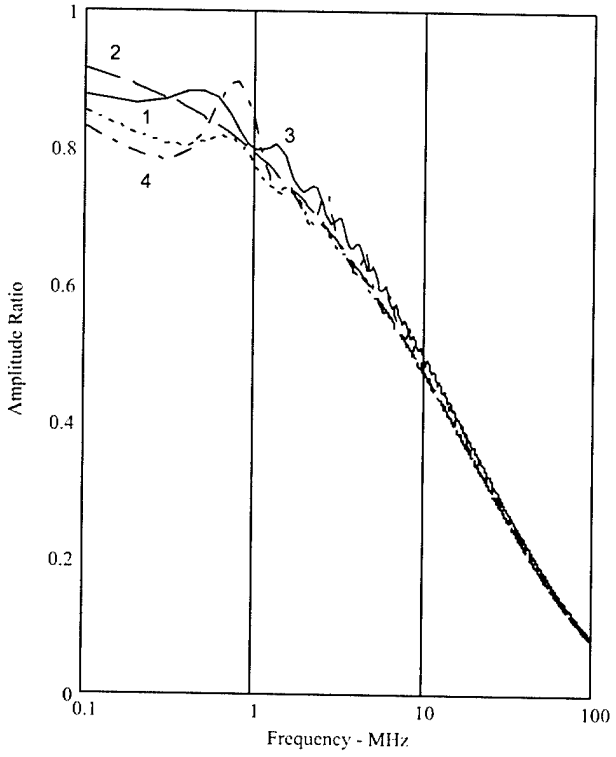


Figure 1. Transfer function amplitude for four configurations

The phase component of the transfer function is plotted in Figure 2. The plot presents the total phase as well as the non-linear component of the phase. Included in the total phase is the linear component that is associated with normal, one direction, propagation delay through the cable. The non-linear component causes signal waveform phase distortion that is a factor in determining the transient performance and BER [8].

Configuration #4 indicates a trend for greater non-linear phase distortion above 100 MHz than for configurations #1-#3. This is due to the connector and cable impedance mismatches that cause multiple reflections and provide an additional non-linear phase distortion component that increases faster with frequency than the inverse square root frequency characteristic from formula (1).

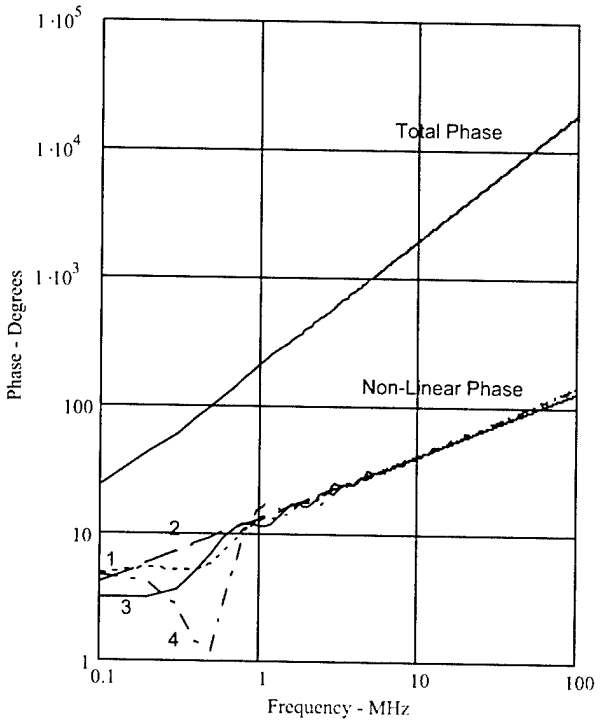


Figure 2. Total phase and non-linear phase components of the transfer function

5. Transient Response

The transfer function indicates amplitude and phase distortion that take place in the steady state frequency domain. The corresponding distortion in the time domain is rise time degradation of the transient response. In addition to rise time degradation there is the possibility of transient waveform modification due to "self interference" with one or more of the reflections that may be present due to impedance mismatches; for example, those exhibited by configuration #4.

The time domain or transient response characteristics may be approximately determined from the transfer function by use of inverse Fourier transform techniques. The results are approximate because the steady state frequency response range is finite between arbitrary lower and upper values and the number of discrete points within the range is typically an integer power of two, 2^N. Furthermore, without an analytical solution, the error or accuracy of the transient solution is not known. A further limitation is the possibility for non-causal response elements to appear in the transient response solution.

The impulse response is approximated by the inverse FFT (Fast Fourier Transform). The step response is approximated by integrating the impulse response over the appropriate time span.

These have been evaluated with standard routines in the math software. The frequency span was 0.1-409.7 MHz with number of points N equal to 4096.

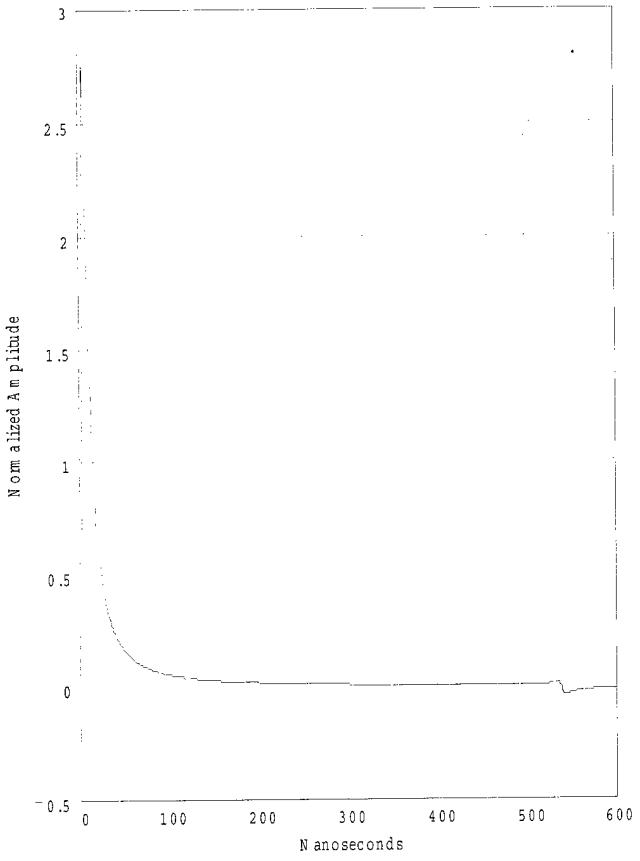


Figure 3. Approximate impulse response for configuration # 4 showing effect of mid-span impedance mismatch

The impulse response for configuration #4 is plotted in Figure 3. The main features are the rapid rise and fall of the response within the first 100 nanoseconds followed by an opposite pulse at around 540 nanoseconds and again at about 1080 nanoseconds which is off-scale. These additional pulses are due to multiple reflections.

The approximate step response for the four configurations is plotted in Figure 4. Configuration #2 with 100-Ohm cable exhibits only rise time degradation because the source and load terminations match the cable impedance. Configuration #3 also has 100-Ohm cable but the source and load terminations are 100 Ohms, which results in an impedance mismatch and causes multiple reflections which cause additional waveform distortion. Reflection effects are also seen in the response for configurations #1 and #4.

Examination of #4 reveals that the reflection effects occur sooner in time because the impedance mismatches are physically closer together than for #1-#3. The reflection pulses alter both the magnitude and time scale of the transient response. The result is a reduction in noise margin and increase in time or phase jitter. In turn, this leads to the possibility of higher BER.

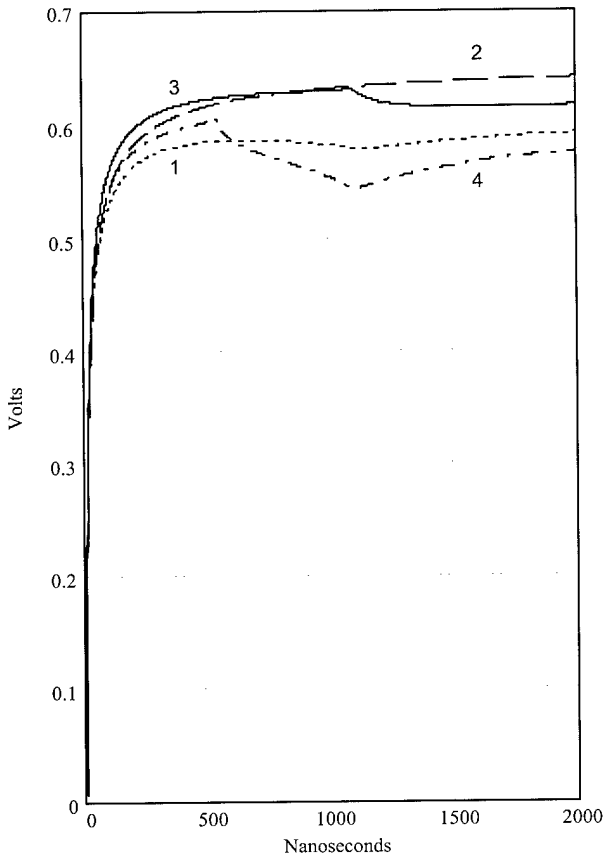


Figure 4. Approximate step response for four configurations

6. Conclusions and Future Work

The Cat 5 uniform cable and channel model have been expressed in chain matrix format and the transfer function has been calculated for four elementary configurations of cable, terminations and one connector. The impedance mismatches were shown to create amplitude and non-linear phase distortion in the steady state frequency domain as well as magnitude and jitter distortions in the transient response, all of which lead to the possibility of increased BER for a given noise (crosstalk) environment and digital data encoding scheme.

Future time domain modeling work will take into account transient response solutions that are determined with a specifiable accuracy.

7. References

[1] J. W. Kincaid and P. Z. Vanderlaan, "Modeling UTP Cabling: Return Loss, Cat 5 and Beyond," *International Wire and Cable Symposium Proceedings* (1998)

[2] *Commercial Building Telecommunications Cabling Standard*, TIA/EIA-568B

[3] D. M. Pozar, *Microwave Engineering*, 2nd ed., John Wiley & Sons, Inc. (1998)

[4] E. L. Harder, "Steady State Performance of Systems Including Methods of Network Solution",,Chapter 10, *Electrical Transmission and Distribution Reference Book*, Westinghouse Electric Corporation (1950)

[5] S. Sammoun, "A New Technique to Evaluate the Transmission Characteristics of Communication Cable Pairs Using Dedicated Mini-Computer," *International Wire and Cable Symposium Proceedings* (1980)

[6] "Spectrum Management for Loop Transmission Systems", *American National Standard* T1.417-2001 (2001)

[7] Mathcad 2001 Professional published by Mathsoft Inc.

[8] John G. Proakis and Masoud Salehi, Communication Systems Engineering, Prentice Hall (1994)



John Kincaid

John is a Senior Product Engineer at the Belden Engineering Center. He holds BSEE and MSEE degrees from the University of Oklahoma and has over 25 years experience with Belden. His experience encompasses engineering management and product development positions in the USA as well as in Europe. He holds nine patents. John is the US Technical Advisor to IEC SC 46A on coaxial cables, and is Convener of IEC SC 46A/WG3 on data and CATV cable. In 2001 he became a member of the IWCS Committee.



Paul Vanderlaan

Paul Vanderlaan is a Senior Product Development Engineer at Belden Electronics Division, Richmond IN and holds a B.S.E.E. degree from Purdue University. He has over 8 years of experience with Belden developing high performance premise cables and holds two patents. Paul actively participates in working groups responsible for the publications of industry standards such as the ANSI/TIA/EIA-568-B documents. He currently co-chairs the TR42.7.2 copper cabling work group and contributes to the continuing research for the development of new telecommunication standards.

Low-loss MPO Connectors

Masayoshi Tsukamoto, Masahiro Hirao, Jun Yamakawa, Michiyasu Kamiko

Fitel Interconnectivity Division, THE FURUKAWA ELECTRIC CO.,LTD.

6, Yawatakaigandori Ichihara, Chiba 290-8555 Japan

Phone: +81-436-42-1674 . E-mail: masat@ch.furukawa.co.jp

Abstract

In recent years, the rapid expansion of optical interconnect network have included the development of high-speed and high-density data-transmission systems. In these systems, the high-density optical connecting techniques with very low insertion loss are required. Under the situation such as this, MPO connector that is suitable for high-density connecting is very promising.

In this paper, we describe a design and characteristics of Low-loss 8-fiber MPO (Multi-fiber Push On) connector utilizing the improved 8-fiber MT ferrule. And we have succeeded in the Low-loss 8-fiber MPO connector that have more excellent characteristics than conventional.

Keywords

MT ferrule; MPO connector; Low-loss

1. Introduction

In recently, with the expansion of optical interconnect network, parallel optical interconnecting technologies have required high speed and high-density data-transmission systems. Such as large fiber optic network and LANs are used to passive optical fiber connectors for easy connecting and disconnecting functions. Therefore, in order to advance the optical network, the low-loss connecting techniques are necessary.

On the other hands, as the MPO connector is easy to connect-disconnect the ribbon fibers, they are widely used data-communication markets [1], [2]. And there are some variations of fiber number up to 24-fiber [3].

In this paper, we describe a design and characteristics for Low-loss MPO connector.

2. Design

2.1 Target characteristic

The target performance for Low-loss MPO connector is established that optical performance in the insertion loss becomes not more than 0.3dB in random mating when alignment pin diameter of 0.6985mm are applied. We use bare ribbon fibers with a diameter of 0.125+/-0.00025mm and a core concentricity error of less than 0.25um to evaluate the Low-loss MPO connector.

2.2 Structure

Low-loss MPO connector is designed on the basis of conventional MPO connector according to JIS F13 type connector (IEC 61754-7) for optical fiber ribbons as shown figure 1. An end-face of MT ferrule is angle polished at 8-degrees with protrusion of fibers. An angled end face of optical fiber prevents reflecting light into the fiber core, so return loss characteristics of angled ferrule get better. Fiber protrusion enables optical fibers to connect directly. This physical contact between fibers realizes low loss connections without index matching material.

MPO connector encloses one MT ferrule. MT ferrule has two alignment holes and fiber holes corresponding to the fiber number. These alignment holes are combined to assure high accuracy alignment in sub-micron range and good optical performance. In a mated pair situation, one connector will have alignment pins while the other one will have alignment holes to accept the alignment pins. The pins are made high precision tolerance, and the close fit of the pins into the holes.

The main cause of connector insertion loss is the position error of fiber core. In general, insertion loss L caused by the position error of fiber core defines as following equation.

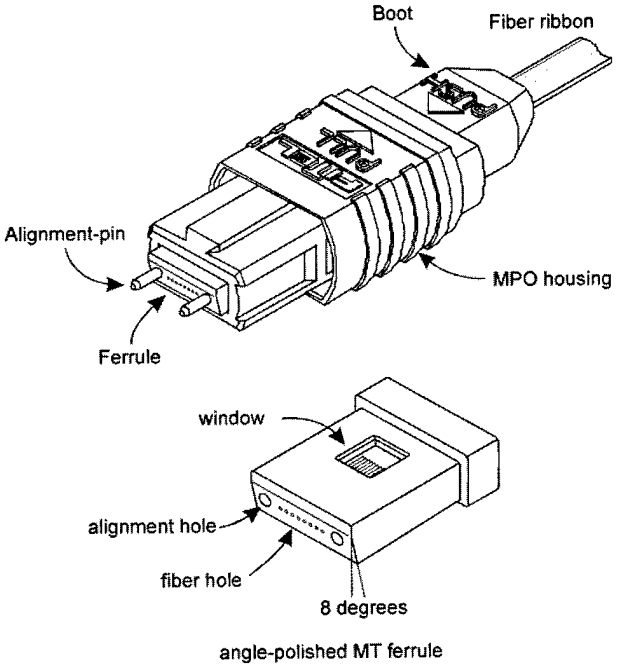


Figure 1. Structure of MPO connector

$$L = 4.34 (R / w)^2 \ [dB] \qquad [4]$$

where R is position error of fiber core [um] and w is mode field radius of single mode fiber [um]. This R happens by following matters:

-Clearance between alignment pins and alignment holes of MT ferrule (E1 in Figure 2)

- Clearance between fibers and fiber holes of MT ferrule (E2 in Figure 2)

- Fiber hole position error (E3 in Figure 2)

- Fiber hole tilt against alignment hole (E4 in Figure 3)

- Bend caused by shrinking the adhesive resin (E5 in Figure 4)

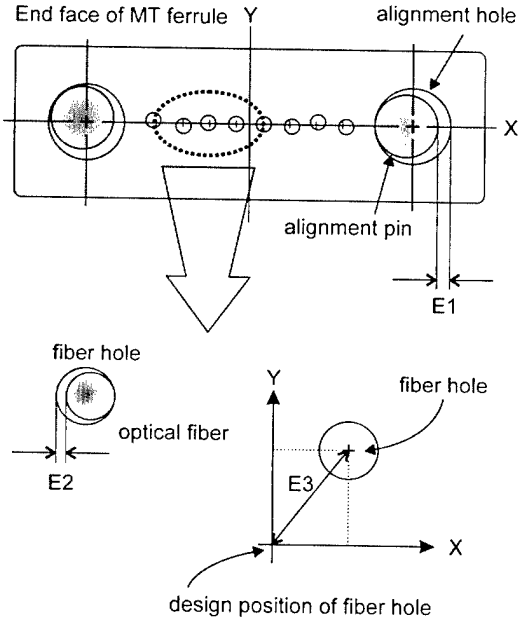
To achieve Low-loss characteristic, we improved the precision of mold pins and V-groove molds to reduce the value of E1, E2, and E3. And we changed the ferrule's window size to reduce the value of E5.

In addition, because of clearance between alignment pins and alignment holes of MT ferrule, two angled MT ferrules are slipped when they are mated each other. This causes position error for center of mated MT ferrules.

Therefore, in order to design the MT ferrule for Low-loss MPO connector, it is necessary to control the position of fiber holes more closely and to consider these causes against y-offset

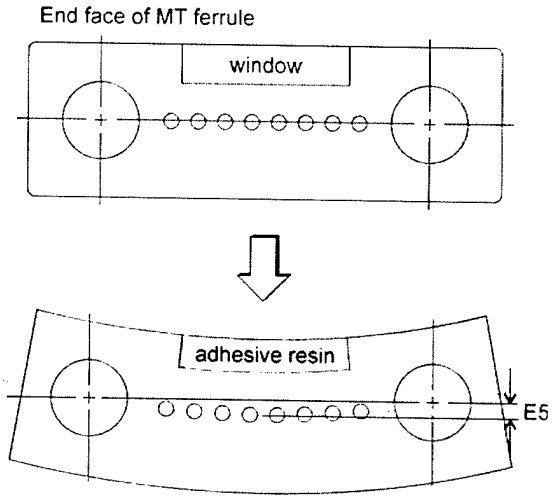
$$\text{y-offset} = E1/2 + E4 + E5$$

We have investigated these values minutely and determined y-offset value.



E1: clearance between alignment pin and alignment hole
E2: clearance between fiber hole and fiber
E3: fiber holle position error

Figure 2. Causes of position error of fiber core



Ferrule's bend caused by shrinking adhesive resin
・Position error of fiber hole is changed

Figure 3. Bend by curing adhesive resin

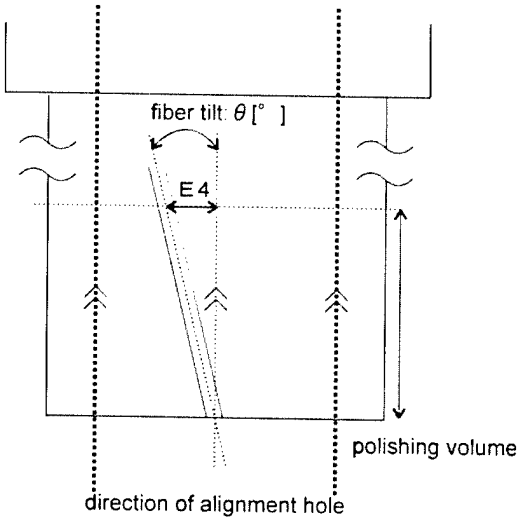


Figure 4. Fiber hole tilt

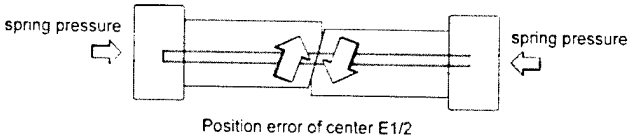


Figure 5. Position error by slipping

2.3 Molding

MT ferrule for Low-loss MPO connector is manufactured by high-accuracy transfer molding technique. In this molding, the thermosetting material is pre-heated hot enough to flow but not to crosslink and then is transported to a hot mold. In a hot mold, crosslinking takes place at higher temperature and pressure. Figure 2 shows the transfer molding operations. First, the clamping device of the molding machine works to clamp tightly the mold. Secondly, the molding resin in tablet form pre-heated at high frequency is charged into the pot (see (1)). In (2), the plunger is inserted into the pot and presses the resin and then the cavity section is filled. After being pressed and heated for a certain time, the mold is open, and the mold product is ejected from the cavity as shown in (3).

In the case of thermosetting plastics, because the curing temperature of the resin is so important factor to consider the characteristics of the molded product, we have optimized some molding conditions that include temperature of a mold, heating time and molding pressure. And we improved some parts of mold to reduce the bend caused by shrinking the adhesive resin and fiber hole tilt.

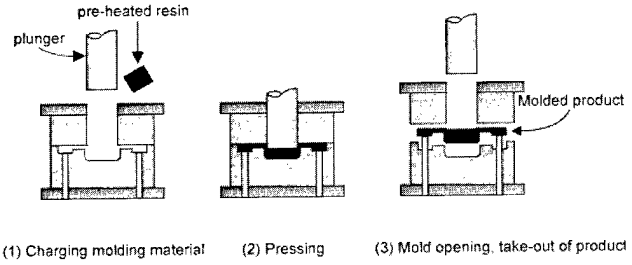


Figure 6. Transfer mold process

1. Characteristics

3.1 Position error of fiber holes

Figure 7 shows the results of position error measurement for Low-loss 8-fiber MPO and standard 8-fiber MPO. Position error value is calculated as y-offset is the origin of the coordinate axis. As the results show, average and deviation of the position error for Low-loss 8-fiber MPO connectors are obviously less than that of standard 8-fiber MPO connectors. And it also shows that over 96% of Low-loss ferrules were less than 0.7[um].

3.2 Optical characteristics

We have evaluated the insertion loss of Low-loss 8-fiber MPO connectors with 1,310nm light source. To evaluate more precisely, we used the single mode optical fiber whose diameter is 0.125+/-0.00025 mm and core concentricity is 0.25um or less and alignment pins whose diameter is 0.6985+/-0.0001mm. Figure 8 shows the insertion loss of Low-loss 8-fiber MPO connector and standard 8-fiber MPO connectors. Newly developed Low-loss 8-fiber MPO connectors were satisfied our target value of 0.3dB or less in random mating. As the results show, the insertion loss for Low-loss 8-fiber MPO connectors is obviously less than that of standard 8-fiber MPO connectors.

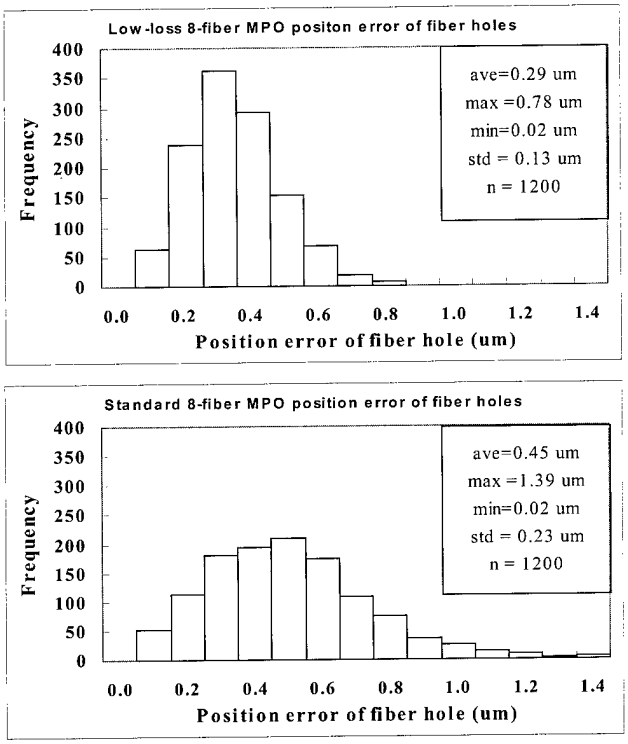


Figure 7. Distribution of Position error of fiber hole

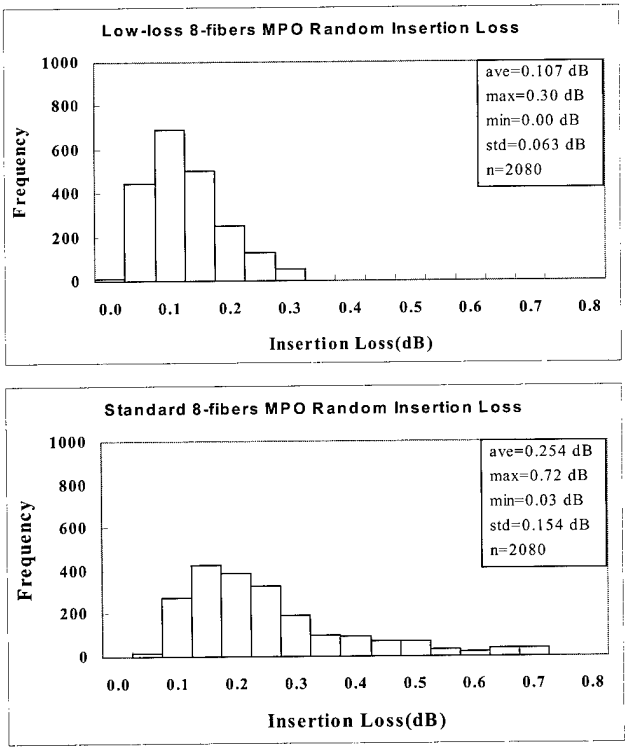


Figure 8. Distribution of insertion loss

3.3 Reliability Test

We have evaluated environmental and mechanical performance for Low-loss MPO connectors in accordance with Telcordia GR-1435-CORE. The test was performed by Low-loss 12-fiber MPO connectors manufactured with fiber ribbon. It is for this reason that we can cover the performance with various fiber number up to 12-fiber. Table 1. shows reliability test results. All the tests were done serially. Insertion-loss variation show very small with less than 0.3dB throughout the tests, it is considered satisfactory results considering tough test condition.

Table 1. Reliability test results

Test	Duration	Test Parameter	Insertion Loss Variation
Thermal Aging	14days	85 °C	< 0.1dB
Humidity	14days	95% at 60 °C	< 0.3dB
Temperature Cycling	42cycles (14days)	-40 °C to 75 °C	< 0.3dB
Vibration	2 hour/axis for 3 axis	10 to 55Hz	< 0.2dB
Twist		2.2N	< 0.1dB
Straight Pull		2.2N	< 0.1dB
Side Pull		2.2N	< 0.2dB
Impact	8 cycles	1.5 m drop	< 0.1dB
Durability	200 cycles	Connect and disconnect	< 0.3dB

1. Conclusions

We have succeeded in developing the Low-loss MPO connectors with MT ferrule manufactured high accuracy molding technique. Then, these Low-loss MPO connectors proved to have extremely low-insertion-loss characteristics not more than 0.3dB. We can apply the results shown in this paper to developing other kinds of MPO connector like the Low-loss 16-fiber MPO or the Low-loss 24-fiber MPO.

2. References

[1] Nagasawa, Yokoyama, Ashiya, and Satake, "A High-Performance Single-Mode Multifiber Connector Using Oblique and Direct Contact Between Multiple Fibers Arranged in Plastic Ferrule", IEEE Photon. Technol. Lett. Vol.3, No.10, p.937-939, 1991.

[2] N. Shimoji, " MPO Optical Backplane C onnector", IEICE Trans. Commun., Vol.E-80B, No.4, p.535-539, 1997.

[3] Suematsu, Shimoji, Iijima, and Hirao, " Development of Two-Dimensional Array 24-Fiber MPO Connector", Euro Cable, A. L. Harmer (Ed.), IOS Press, 2000 © AKM

[4] JIS C 5962:2001,"General rules of connectors for optical fiber cables"



Masayoshi Tsukamoto

The Furukawa Electric

Co.,LTd.

6 Yawatakaigan-dori,
Ichihara, Chiba, Japan

masat@ch.furukawa.co.jp

Masayoshi Tsukamoto was born in Hiroshima, Japan, in 1975. He received the M. E. degree in Yamaguchi University, Japan in 2000. He jointed the Furukawa Electric Company, in 2000.Since then he has been engaged in manufacturing and assembling optical fiber connector components.



Masahiro Hirao

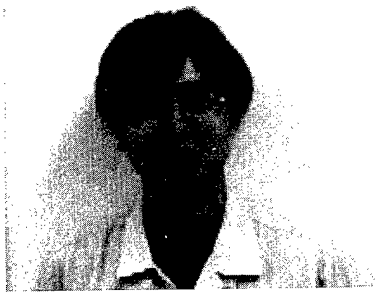
The Furukawa Electric

Co.,LTd.

6 Yawatakaigan-dori,
Ichihara, Chiba, Japan

mhirao@ch.furukawa.co.jp

Masahiro Hirao was specifically selected for this position, based on his educational background and more than six years of experience with FEC in Japan. He earned a Mater degree in Electronics Engineering in 1995 from Nagaoka University of Technology in Japan.



Jun Yamakawa

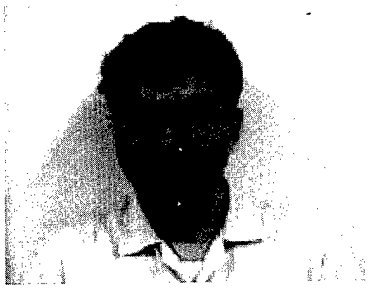
The Furukawa Electric

Co.,LTd.

6 Yawatakaigan-dori,
Ichihara, Chiba, Japan

jun@ch.furukawa.co.jp

Jun Yamakawa was born in Hokkaido, Japan, in 1965. He received the B. E. degree in applied electronic engineering from University of Electro-Communications, Tokyo, Japan, in 1989.He jointed the Furukawa Electric Company, in 1989.Since then he has been engaged in R&D on optical component.



Michiyasu Kamiko

The Furukawa Electric

Co.,LTd.

6 Yawatakaigan-dori,
Ichihara, Chiba, Japan

kamiko@ch.furukawa.co.jp

Michiyasu Kamiko was born in Kanagawa, Japan, in 1960. He received the M. E. degree in applied mechanical engineering from Musashi Institute of Technology , Tokyo, in 1986. He jointed The Furukawa Electric Company, in 1986.

Spectral Flat Attenuators using Co^{2+}-Doped Fiber

Kentaro Nouchi, Eiji Matsuyama, Yuichi Morishita, Gen Tanimoto and Susumu Ohneda

Showa Electric Wire & Cable Co., Ltd.
Optics & Trans. R&D Dept.
4-1-1, Minami-hashimoto, Sagamihara, Kanagawa, 229-1133 Japan
Phone : +81-42-774-8208
Fax : +81-42-773-3967
E-mail address: k940181@snt1.swcc.co.jp

Abstract

We demonstrated that attenuation fibers using a Co^{2+}-doped core have a flat attenuation spectrum in the range of 1520 to 1610 nm. The Co^{2+}-doped fibers have a flat attenuation spectrum with a variation within 3%. The polarization-dependent loss of a 1.5 dB/m ×20 m Co^{2+}-doped fiber was very small, at less than 0.03 dB. In terms of high power endurance, the fluctuation in attenuation of a 40 dB fiber was less than 0.04 dB at 1550 nm with 1 W incident power for 960 hours.

Keywords

Co^{2+} -doped fiber, attenuator, double- core structure

1. Introduction

Optical attenuators have been widely used in single-mode fiber optical networks such as long-distance optical networks and dense-wavelength division multiplexing (DWDM) networks [1]. Recent broadband fiber networks have required optical attenuators that have spectral attenuation flatness, low polarization-dependent loss (PDL), long-term reliability, and high power endurance.

Among the various types of attenuator, such as the metallized film type and the air-gap type, Co^{2+}-doped silica glass fiber (CoDF) type of attenuators have been demonstrated to have many advantages as follows [2]:

(1) Co^{2+}-doped fibers (CoDFs) can be connected to conventional single-mode fibers by fusion splices and optical connectors with low insertion loss (<0.1 dB) and low back reflection (<-55 dB).

(2) CoDFs show high environmental and mechanical reliability.

(3) CoDFs can endure high incident power (< 1 W) without damage.

(4) It is easy to control the attenuation level steps (<0.1 dB) by the length of the CoDF .

Due to these special advantages, CoDF attenuators are expected to be widely utilized in optical equipment such as optical fiber amplifiers and add-drop multiplexers for DWDM networks.

Moreover, a spectral flat response is required for the attenuation spectrum of CoDF attenuators [3]. The attenuation properties of CoDFs are significantly influenced by absorption of Co^{2+}dopant in silica glass. However, the absorption spectrum of Co^{2+}-doped silica glass shows a monotonic increase with an increase in the wavelength range from 1200 to 1700 nm [4]. A second dopant that has decreasing absorption with increasing wavelength could be added to obtain spectral flatness, but it is difficult to control the concentrations of two metal ions [4][5]. It might be possible to prepare spectral flat attenuation fiber from 1520 to 1610 nm employing a double-core structure having doped and undoped regions [6].

In this work, CoDF attenuators with spectral flat response were demonstrated in the range of 1520 to 1610 nm. We also measured the wavelength-dependence of PDL, high power endurance and a temperature cycling test on CoDFs.

2. Experiments

2.1 Samples

CoDFs with a double-structure core were fabricated using the following procedures. (1) A Co^{2+} -doped glass rod for the doped region in a core was fabricated using the vapor-phase axial deposition (VAD) method and the solution doping method. (2) A glass rod for the undoped region of a core was prepared by the rod-in-tube method. The diameter of the Co^{2+}-doped region was designed to be 1/3 of the diameter of the undoped region of the core. (3) A glass cladding was fabricated by the jacketing method. (4) The attenuation fibers were drawn. Figure 1 shows the Co^{2+}-doped region of the CoDFs with a double-core structure and its refractive index profile. The core diameters and the relative refractive-index differences were designed to be 6 to 7 μm and 0.4%, respectively, to minimize mis-alignment loss between a conventional single-mode fiber and the CoDF. The CoDF parameters are shown in Table 1.

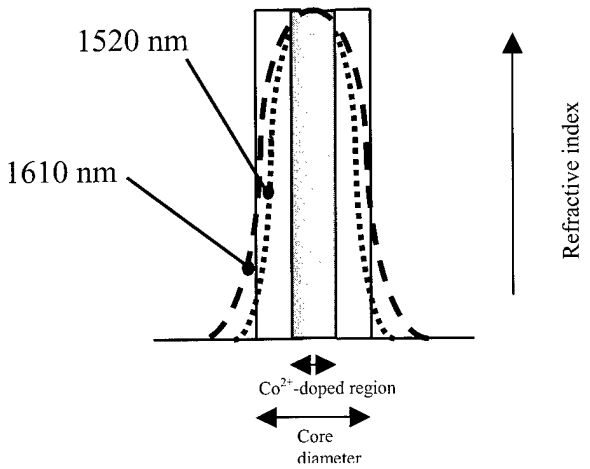


Fig.1 Refractive index profile of double- core structure

..... Mode field pattern at 1520 nm

-------- Mode field pattern at 1610 nm

Table 1 Design of CoDF parameters

Item	Specification
Mode field diameter at 1550nm	9.5 μm ¶1.0μm
Cutoff wavelength	<1300 nm
Cladding diameter	125.0μm ¶1.0 μm
Concentricity between core and cladding	<0.8 μm
Cladding non-circularity	< 2.0%
Coating	UV Curable Resign
Coating diameter	250μm

2.2 Measurements of CoDFs

The properties of the CoDFs fabricated as described the above were measured with the following systems.

Attenuation spectra: The attenuation spectra of the CoDFs were measured with the cutback method using a monochromator connected to a white-light source and a powermeter.

Polarization-dependent loss (PDL): The PDL for CoDFs of various lengths (5 m, 10 m, 20 m) was measured in the wavelength range of 1530 to 1610 nm. The attenuation value of the CoDFs was 1.5 dB/m. The measurement setup was constructed with distributed-feedback laser diodes (DFB-LDs), a polarization scrambler (ADVANTEST: Q8163), an optical sensor (ADVANTEST: Q822232), and an optical powermeter (ADVANTEST:Q8221). Conventional single-mode fibers were connected to the both ends of the CoDFs by fusion splices.

Temperature cycling test: Changes in CoDF attenuation were measured during a temperature cycling test between − 40 and 75 ˘ for 3 cycles. The light sources were Fabry-Perot laser diodes operating at 1550 nm. We measured the variation loss of 3 CoDFs whose attenuations were at 1.5, 4 and 11 dB/m, respectively. Conventional single-mode fibers were joined to the both ends of the CoDFs by fusion splices.

High-power endurance: The high-power endurance of CoDF attenuators was measured *in situ* using a system constructed with a DFB-LD operating at 1550 nm with an Er^{3+}-doped fiber amplifier and a powermeter. The incident power and irradiation time were 1 W and 960 hours, respectively. We also measured the attenuation of CoDF attenuators at various incident power levels from 0.1 to 1 W.

3. Results and discussion

3.1 Attenuation spectra of CoDFs

Figure 2 shows the attenuation spectra of the CoDFs, which were designed to be 1/3 of the diameter of the undoped core (CoDF-1/3) and 1/1 of the diameter of the Co^{2+} fully doped core (CoDF-1/1). The attenuation spectra are normalized to 10 dB at 1550 nm for convenience. The CoDF-1/3 attenuations were 9.8 dB at 1520 nm and 10.1 dB at 1610 nm. On the other hand, in the CoDF-1/1 type, the attenuations were 9.3 dB at 1520 nm and 11.4 dB at 1610 nm. The flat attenuation spectrum of CoDF-1/3 was obtained using the double-core structure technique.

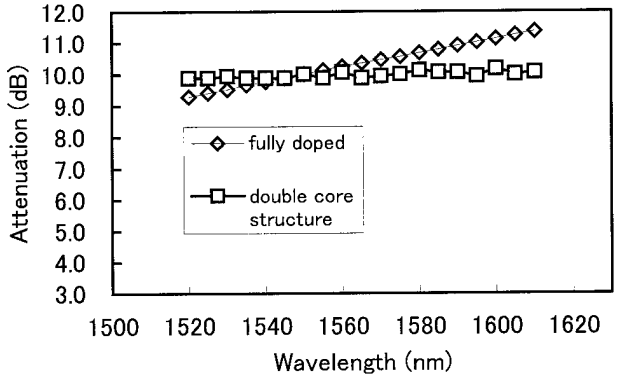


Fig. 2 Attenuation spectra of the CoDF-1/3 (the double- core structure type) and CoDF-1/1 (the fully doped Core type)

These spectral flatness changes can be explained qualitatively. In single-mode fiber with an absorptive dopant, the attenuation is assumed to be determined by three factors: the absorption of the dopant, the region of the dopant and the mode-field pattern. Figure 1

shows the Co^{2+}-doped region and the mode-field pattern at 1520 and 1610 nm. The mode- field pattern changes with the wavelength: the longer wavelength, the more widely mode-field pattern extends [7]. If the absorptive dopant is doped into the central core, the overlap between the mode-field pattern and the doped region becomes smaller at longer wavelength. This smaller overlap leads to smaller attenuation. For compensation of the Co^{2+}-absorption property, we selected the optimal parameters of the above three factors. Figure 3 shows the attenuation spectra of CoDFs with 1.5, 4.0 and 11.0 dB/m attenuation levels at 1550 nm.

The various attenuation values could be controlled by the concentration of Co^{2+}-ion. It was found that the attenuation spectra showed a flat response between 1520 and 1610 nm, and that the spectral variations of the CoDFs were within 3 % of their attenuation. Here, the spectral variation is defined as (αmax - αmin) / α1550, where αmax and αmin are the maximal and minimal attenuations in the wavelength region of 1520 to 1610 nm and α1550 is the attenuation at 1550 nm.

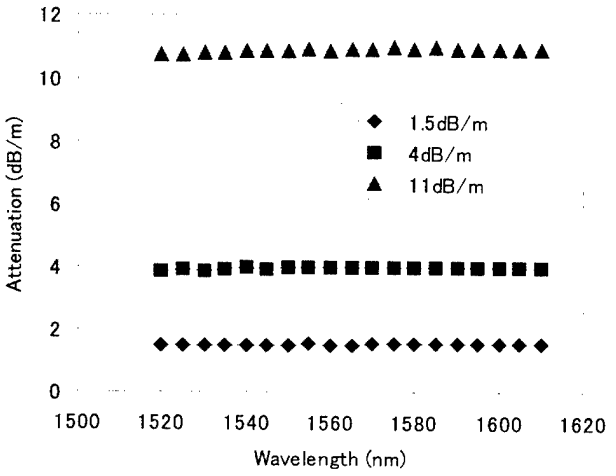


Fig. 3 Attenuation spectra of CoDF 1/3 (double core structure type)

3.2 PDL

Figure 4 shows the PDL of the 1.5 dB/m CoDFs having various lengths of 5, 10 and 20 m. In addition, the PDL of a conventional single-mode fiber is shown in Figure 4. The PDL of all the CoDFs was less than 0.03 dB from 1530 to 1610 nm. It was found that the PDL increased in the longer wavelength region exceeding 1580 nm.

A similar phenomenon was also observed in the single-mode fiber, which usually has no PDL. The increase in PDL at wavelengths exceeding 1580 nm seems to have been caused by the PDL of the polarization scrambler, because the specification of the wavelength range for the polarization scrambler was 1290 to1580 nm. From the results obtained, the PDL of fiber attenuators using CoDFs was found to be similar to that of conventional single-mode fiber.

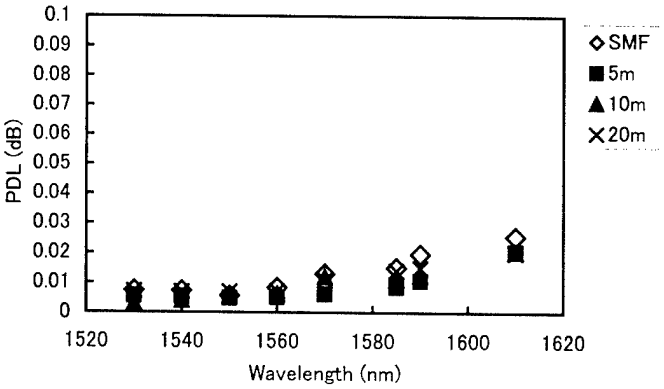


Fig. 4 The PDL of the 1.5 dB/m CoDF 1/3 and conventional single-mode fiber

3.3 Temperature cycling test

The first 3 cycle results of the temperature cycling test of the CoDFs are shown in Figure 5.

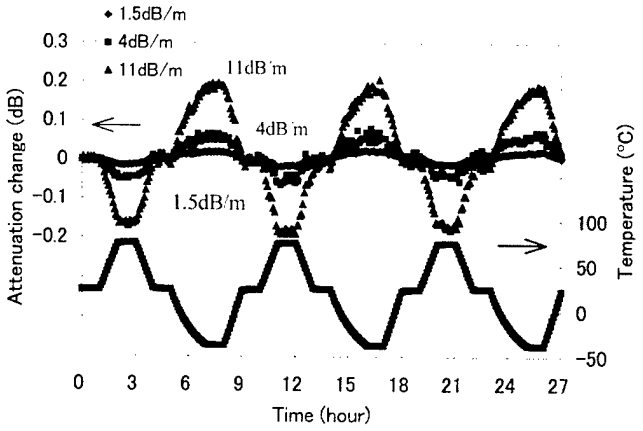


Fig. 5 The temperature cycling test of the CoDFs 1/3

The variations in attenuation were ±0.02 dB/m for the 1.5 dB/m sample, ±0.05 dB/m for the 4.0 dB/m sample and ±0.2 dB/m for the 11 dB/m sample. There were no changes in attenuation before and after the test. Figure 6 shows the relationship between the attenuation variations and the temperature. It was found that the attenuations changed linearly with the temperature, and that the attenuation variation was also dependent on the attenuation level. The temperature dependence for the 1 dB length is shown in Figure 7. Here, the temperature dependence was defined as the angle of the fitted line of Figure 6. The temperature dependence

was proportional to the attenuation levels. It should also be noted that the attenuation variation can be obtained from the total attenuation level, which is independent of the length, and a coefficient of temperature dependence of -2.0 $\cdot 10^{-4}$dB/ ˇ per dB was obtained from the results. Therefore, variation of the attenuation with the temperature is caused by the absorption of Co^{2+} ions [8], because the total attenuation level is determined by the number of Co^{2+} ions.

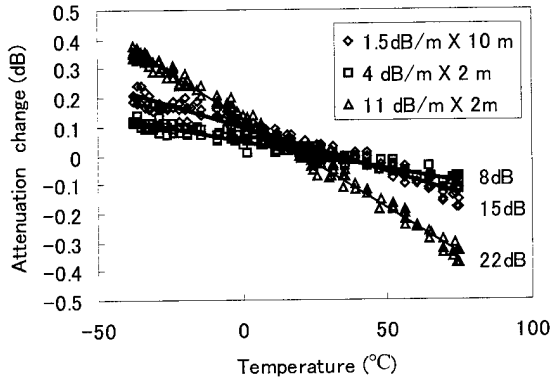


Fig.6 The relationship between the attenuation variations of CoDFs 1/3 and the temperature

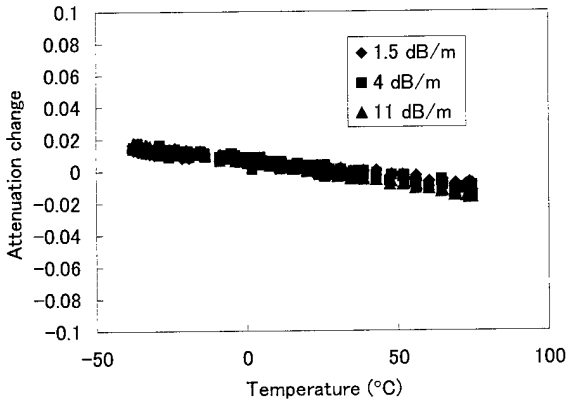


Fig. 7 The relationship between the temperature dependence of CoDFs 1/3 and the temperature

3.4 High- power endurance

The high-power endurance of the CoDFs was verified. The relationship between attenuation and incident power for the 3 CoDFs of 8.6, 20 and 41.8 dB is shown in Figure 8. The attenuation fluctuations of all the CoDFs were below 0.1 dB in the range of 0.1 to 1 W. Figure 9 shows the attenuation fluctuation with an incident power of 1 W for 960 hours. The attenuation fluctuation under light exposure was less than 0.04 dB, which may have been caused by fluctuation of the incident power. From the results obtained, the CoDF attenuator was confirmed to have favorable power endurance.

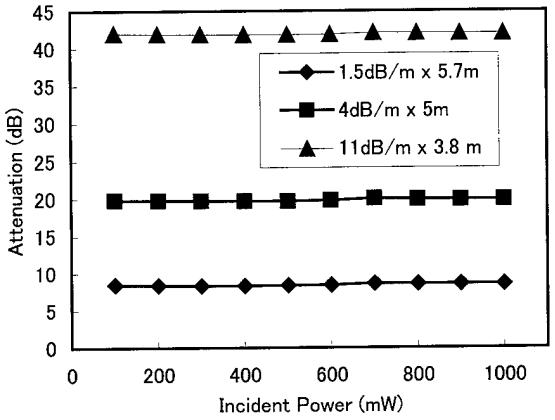


Fig. 8 Relationship between Attenuation and Incident power of CoDF

The results for the high power endurance can be explained by the absorption properties of Co^{2+} ions. The absorption of transition metals containing Co^{2+} ions is caused by transitions of 3d-3d electrons. The energy transitions of 3d electrons, which are in the outermost shell of Co^{2+}ions, are significantly influenced by the phonon. The excitation electrons of the Co^{2+} ions then transfer to heat energy, and the relaxation time is very fast [9].

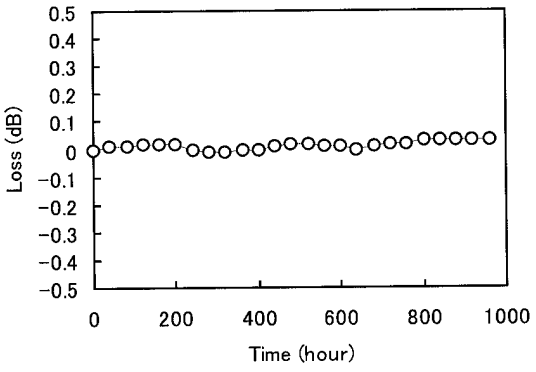


Fig. 9 Power endurance of CoDF

Incident power was 1W

When the Co^{2+} ions of CoDFs absorb high incident power, the Co^{2+} ions may radiate heat, raising the fiber temperature. Then, the attenuation of the CoDF may decrease, as shown by the results

in Figure 7. However, the attenuation of the CoDF did not change at a high incident power of 1 W, because the absorbed energy of the CoDF was effectively radiated outside of the fiber with the distributed fiber length.

4. Conclusions

We have developed spectral flat CoDF attenuators using a double-structure core technique. In the C band (1520-1570 nm) and L band (1570-1610 nm), the CoDFs have flat attenuation spectrum with a variation within 3% and small PDL of <0.03 dB. For the temperature dependence, we demonstrated that the attenuation variations were determined by the total attenuation level, and obtained a temperature dependence coefficient of -2.0×10^{-4}dB/ ˚ per dB. The power endurance was shown to be favorable, with small attenuation variations of <0.1 dB. These results suggest that spectral flat CoDF attenuators can be used in DWDM networks.

5. References

[1] Y. Takeuchi, R. Nagase, and S. Mitachi, in 10th Technical Digest of IOOC'95 (Hong Kong, 1995), Paper WA1-2

[2] M. Saijo,Y. Morishita, Y. Ariga, K. Sugi and K. Muta, in Technical Digest of 46th International Wire and Cable Symposium(International Wire and Cable Symposium, Eatontown, N.J., 1997),p 74

[3] P. Bousselet, M. Bettiati, L. Gasca, M. Goix, F.Boubal, C. Sinet, F. Leplingard and D. Bayart, Technical Digest of Optical Fiber Communication Conference (Optical Society of America, 2000), Paper WG5-1, 2000

[4] P. O. Schultz, J. Am. Ceram. Soc., 57, 309, 1974

[5] K. Kato, Y. Takeuchi, R. Nagase, K. Kanayama, Y. Morishita, A. Kumagai, Y. Ariga, K. Muta, K. Sugi and T. Tabata, Japanese Patent Application No. H8-136736

[6] Y. Morishita, E. Matsuyama, K. Nouchi, and H. Noro, Opt. Lett.26, 783 (2001)

[7] K. Petermann and R. Kuhne, J. Lightwave Technol. 4, 2 (1986)

[8] Digilina, G. A., Trasov, B. V., and Varshal, B. G., Fiz. Khim. Stekla(1985)11(6)672-6.

[9] M. K. Davis, M. J. F. Digonnet, R. H. Pantell, "Thermal effects in doped fibers", J. Lightwav Technol., Vol. 16, No.6, p.1013-1023, 1998

Speaker Biography



K. Nouchi received his M.S. degree from Yamagata University in 1994. He joined Showa Electric Wire & Cable Co., Ltd. in 1994. He is an engineer working with R & D Sec. of Opto-Electronics.

A Field Evaluation of Improved Mechanical Fiber Splice

Chieh-Mei Hsiao, Huei-jen Chen, Ting-Chung Chang, His-Pai Hsu, Y.-c Lin, J.Y. Liu

Network Operation Tech. Lab.,

Telecommunication Labs. Chunghwa Telecom Co., Ltd.

+ 001-886-3-424-5750 hcm_iris@cht.com.tw

Abstract

A field evaluation of improved mechanical fiber splice was conducted to see how reliable these products have become and whether they can be left in the outside plant closures indefinitely. An aerial optic route with a 24-fiber optical cable in a humid and windy area was chosen to test mechanical fiber splice. The trail route is 4.4 km long, with 4 splice points. It turned out that some practices were needed to properly assemble the mechanical fiber splice, but the times spent were acceptable. Products with dedicated tools were able to produce more consistent results than those without tools. Improved mechanical fiber splice does have a more consistent splice characteristic over a long period of time. While a dedicated tool helps craftsman to learn assembly technique more easily and to perform fieldwork more consistently, there is still chances that fiber strain is inadvertently induced inside the splice and causes cable faults later on.

Keywords

Mechanical fiber splice

1. Introduction

Mechanical fiber splices have been in the market for quite some time[1][2]. Our initial experience with them was not favorable. We had observed temperature-dependent splice loss and return loss variations among some of these mechanical fiber splices, fiber breakage inside some of them due to strain induced static fatigue, and drying up of the index matching gel. As more and more improved products of these kinds were available to us, we initiated a field evaluation to see how reliable these improved mechanical fiber splices have become and whether they can be left in the outside plant closures indefinitely.

2. Experiment

2.1 Field test

Figure 1, an aerial optic route with a 24-fiber optical cable in a humid and windy area was chosen to test mechanical fiber splices. The trail route is 4.4 km long, with 4 splice points (point 127-17, 127-35, 127-61, 127-81). At each splice point, fusion splice and mechanical splice from selected products (sample X, Y, Z) were present concurrently and enclosed in the same closure which was mounted on the pole and shown in Figure 2. Optic splice loss and splice return loss of the route were measured periodically (3, 6, 9, 12 months) at both 1310 and 1550 nm using OTDR measured from both directions. All 72 dark fibers were monitored during the field test.

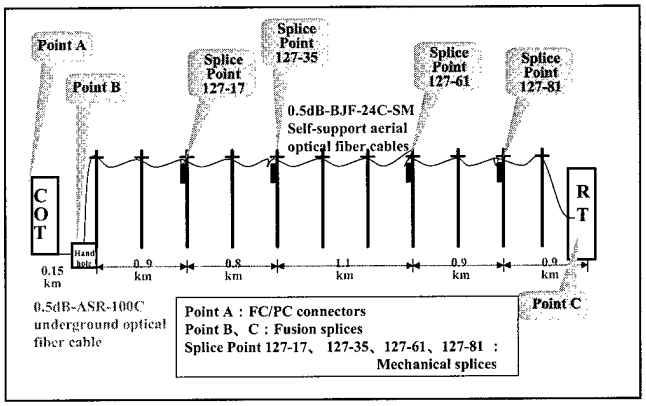


Figure 1. Aerial optical route for field test

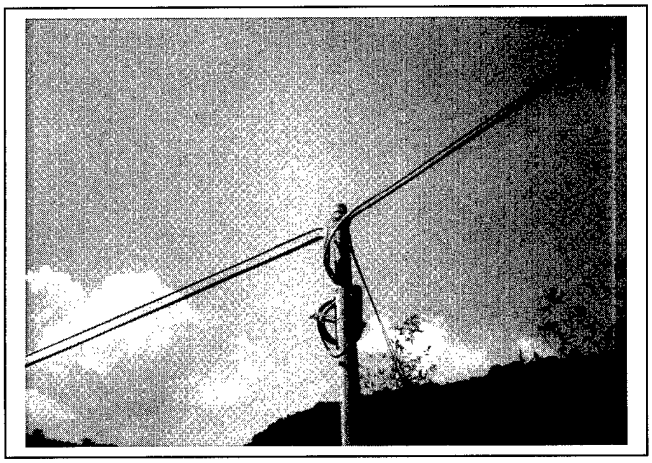


Figure 2. Aerial optical route

2.2 Temperature cycling test in laboratory

Mechanical fiber splice samples were tested according to the temperature curve shown in Figure 3 in an environmental chamber. Splice loss and return loss of each splice point were measured before and after the test as well as during the test at circled point 1 thru 9 in Figure 3.

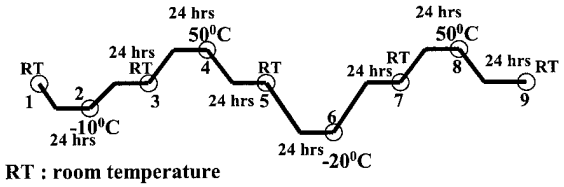


Figure 3. Temperature curve.

3. Result and discussion

3.1 Initial value of splice loss in field test

Initial splice loss of each splice point in the field test route was taken right after the deployment of cable. At 1310 nm all but 6 splices had initial splice loss below 0.1dB, the reminder between 0.11dB and 0.13dB. At 1550 nm while splice points with fusion splice had initial splice loss below 0.05dB except one at 0.09 dB as shown in Figure 4. Splice points with mechanical fiber splice all had somewhat higher initial splice loss. Figure 5 showed the initial splice loss at 1550 nm for splice points using mechanical fiber splice X. Among 16 splices, 12 had splice loss below 0.05 dB but with large variations, the other 4 being 0.52dB, 0.12 dB, 0.13 dB, and 0.22 dB respectively. Figure 6 showed the initial splice loss at 1550 nm for splice points using mechanical fiber splice Y. Among 24 splices, only 2 had splice loss below 0.05 dB, 17 being between 0.05 dB and 0.10 dB, and the other 5 between 0.10 dB and 0.12 dB. Figure 7 showed the initial splice loss at 1550 nm for splice points using mechanical fiber splice Z. It showed 13 splices having splice loss below 0.05 dB, 9 between 0.05 dB and 0.10 dB, and the rest 2 being 0.14 dB and 0.16 dB respectively.

In all, 83% splices with mechanical fiber splices had initial splice loss less than 0.1 dB, and 14% less than 0.2 dB. The only failure was the one with 0.52 dB initial splice loss at 1550nm and 0.071 dB at 1310 nm, which was left uncorrected and found out of order three months after the deployment. It is felt that mechanical fiber splice can do a fairly good job in connecting optical fibers, though its splice loss is larger than fusion splice's. Proper training in assembling mechanical fiber splice is essential, but the time spent is reasonable. Also, products with tools were able to produce more consistent results than that without tools.

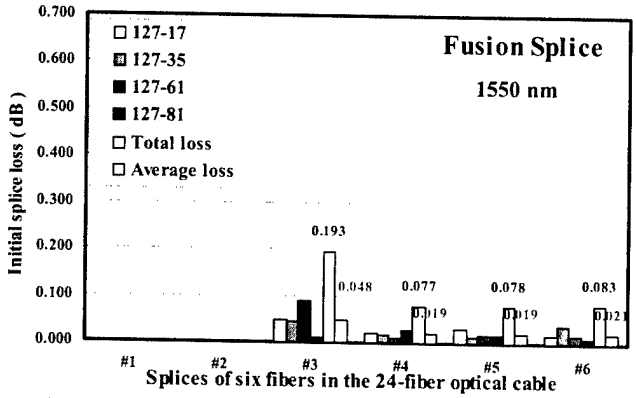


Figure 4. Initial fusion splice loss at 1550 nm

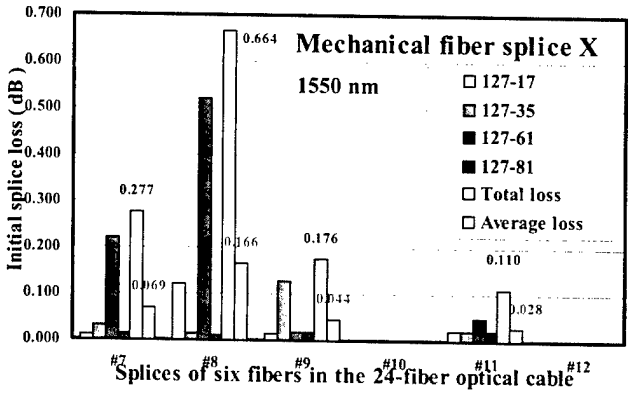


Figure 5. Initial mechanical splice loss at 1550 nm (sample : X)

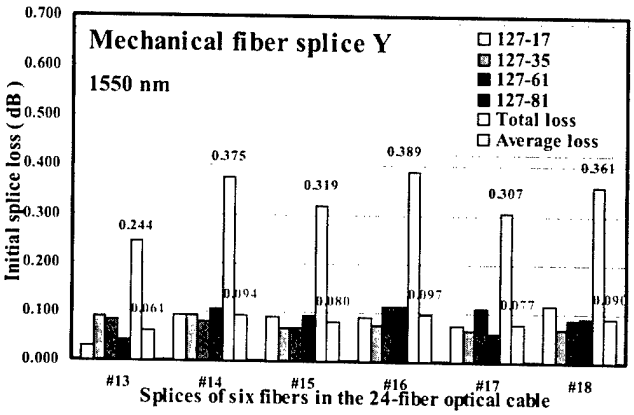


Figure 6. Initial mechanical splice loss at 1550 nm (sample : Y)

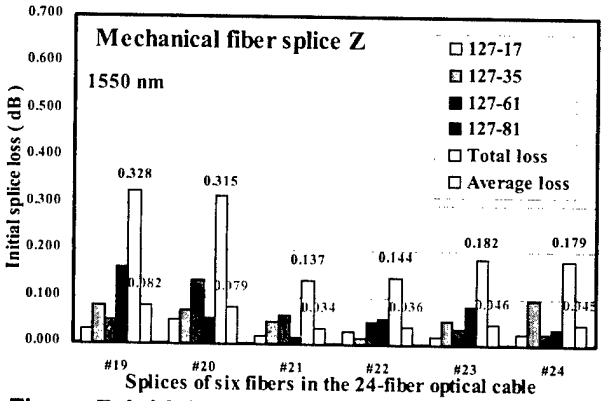


Figure 7. Initial mechanical splice loss at 1550 nm (sample : Z)

3.2 Initial value of return loss in field test

Initial return loss of splice points with mechanical fiber splice was shown in Figure 8 ~ 10 for the three products X, Y, and Z at 1310 nm, and in Figure 11 ~ 13 at 1550 nm. Variations of return loss value for mechanical fiber splice were somewhat larger than that for fusion splice, but all values were below the required -45dB.

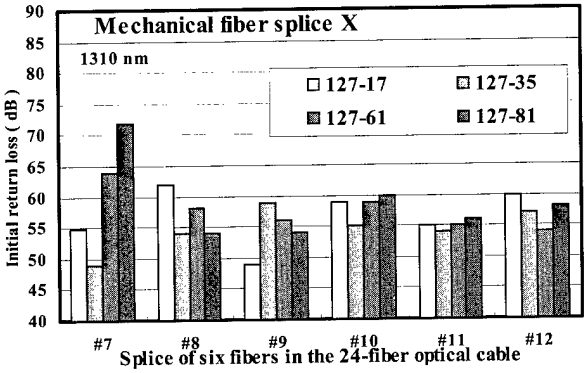


Figure 8. Initial return loss at 1310 nm (sample : X)

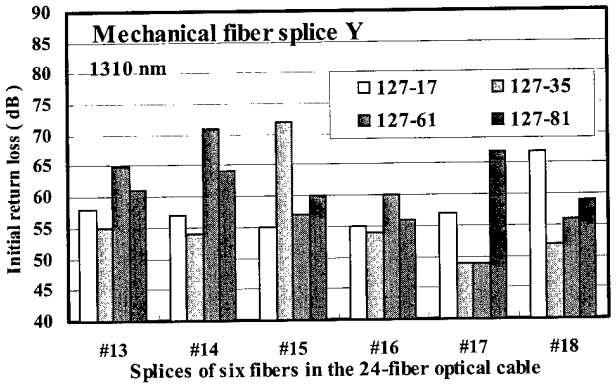


Figure 9. Initial return loss at 1310 nm (sample : Y)

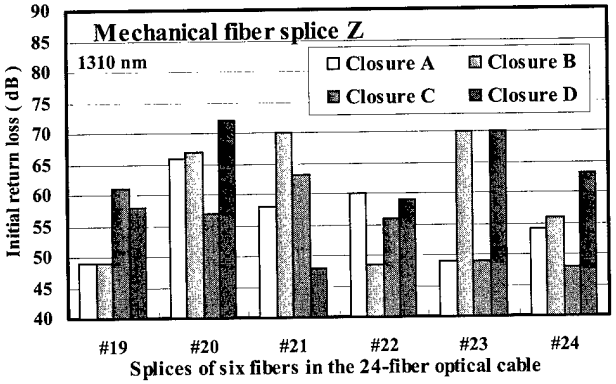


Figure 10. Initial return loss at 1310 nm (sample : Z)

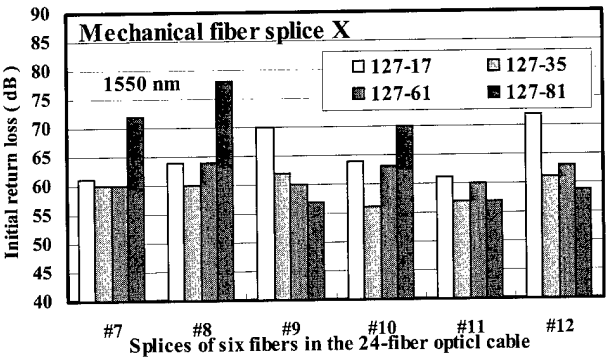


Figure 11. Initial return loss at 1550 nm (sample : X)

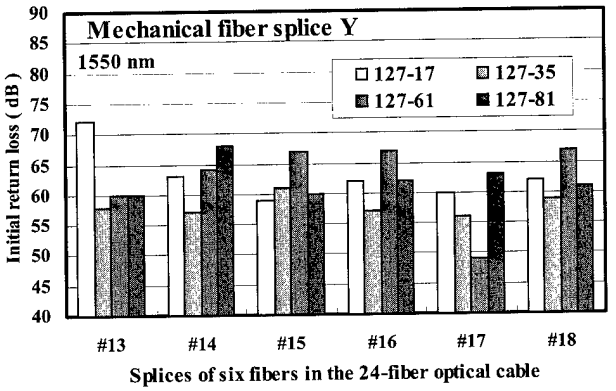


Figure 12. Initial return loss at 1550 nm (sample : Y)

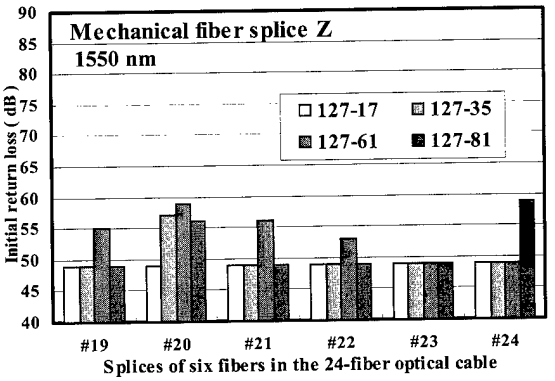


Figure 13. Initial return loss at 1550 nm (sample : Z)

3.3 Variations of splice loss and return loss during field test

3.3.1 Variations of splice loss during field test

Total splice loss of the field test route was measured by an OTDR every three months during the test period. The results were shown in Figure 14 for every dark fiber monitored at 1310 nm and in Figure 15 at 1550 nm. There were no appreciable increases in total splice loss during the one-year period monitored.

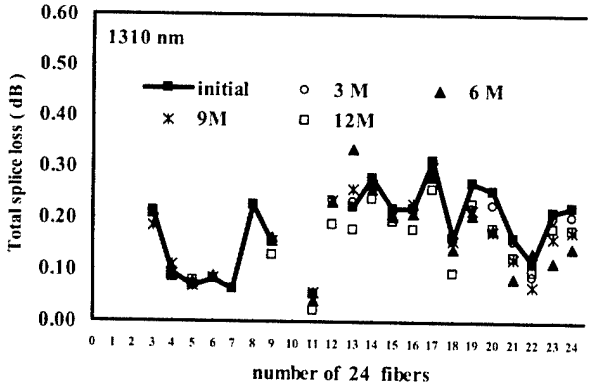


Figure 14. Total splice loss of each fiber at 1310 nm during field test

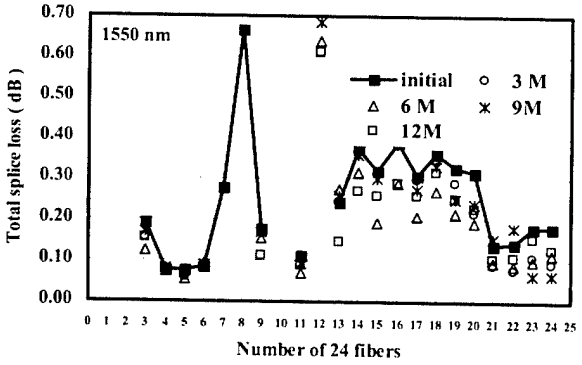


Figure 15. Total splice loss of each fiber at 1550 nm during field test

3.3.2 Variations of return loss during field test

Figure 16 ~ 18 showed the distribution of splice return loss of field test route monitored at 1550 nm for product X, Y, and Z, respectively, during the one-year period. Product Z apparently had larger splice return loss than the other two products. A shift to higher splice return loss during wintertime (the 6th month) was observed in these figures. However, none has been changed to above -45 dB level.

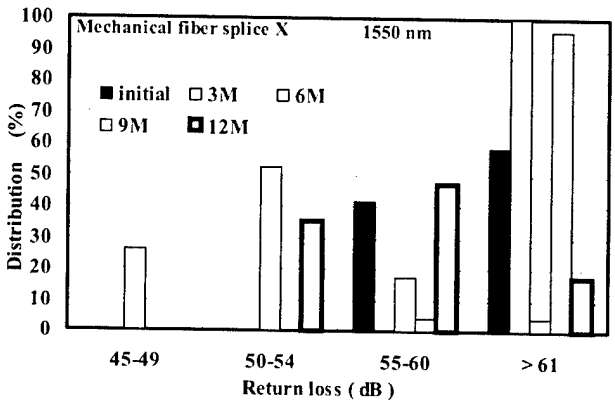


Figure 16. Distribution of Return loss at 1550 nm during field test (sample X)

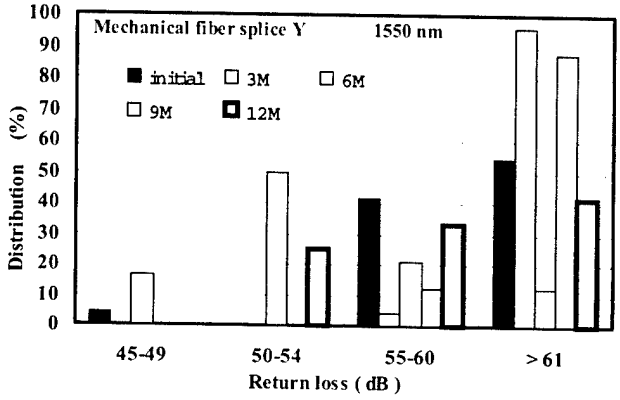


Figure 17. Distribution of Return loss at 1550 nm during field test (sample Y)

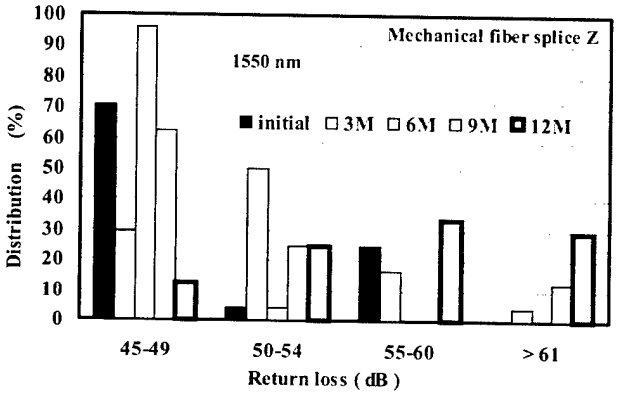


Figure18. Distribution of Return loss at 1550 nm during field test (sample Z)

3.4 Temperature cycling test (in laboratory)

The results of laboratory temperature cycling test were shown in Figures 19 ~ 22. Changes of splice loss as monitored at 1310 nm were shown in Figure 19 for 5 specimens from one of the manufacturers. The changes were minimum and less than 0.01 dB. Figure 20 showed the changes of splice loss at 1550 nm for the same specimens. Here, a specimen changed its splice loss by more than 0.3 dB at higher temperature, and back to around initial value when temperature was below or at ambient. Since fiber loss measurement at 1550 nm is more sensitive to fiber microbending stress than that at 1310 nm, it is felt that the fiber inside this particular specimen is probably strained by micro-bending when temperature is raised. A similar phenomenon was observed in the field test route where a mechanical fiber splice at splice point #127-61 showed splice loss less than 0.1 dB at 1310 nm but 0.52 dB at 1550 nm. That fiber was subsequently found out of order within three months period. Apparently, residue fiber strain around a fiber splice point is still a concern for the deployment of mechanical fiber splice.

Large splice return loss changes were observed during the temperature cycling test for mechanical fiber splice samples. Figure 21 showed the results monitored at 1310 nm and Figure 22 at 1550 nm. The splice return loss increased when temperatures were higher or lower than the ambient, but the values remained below -45 dB in the test range of -10^{0}C to 50^{0}C.

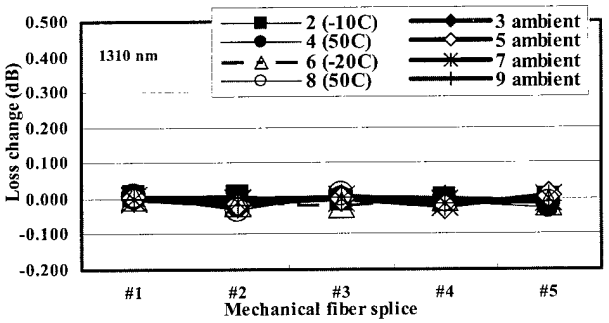


Figure 19. Variations of splice loss at 1310 nm during temperature cycling test

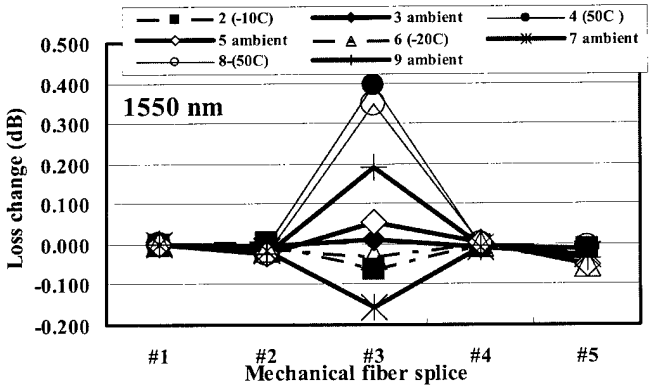


Figure 20. Variations of splice loss at 1550 nm during temperature cycling test

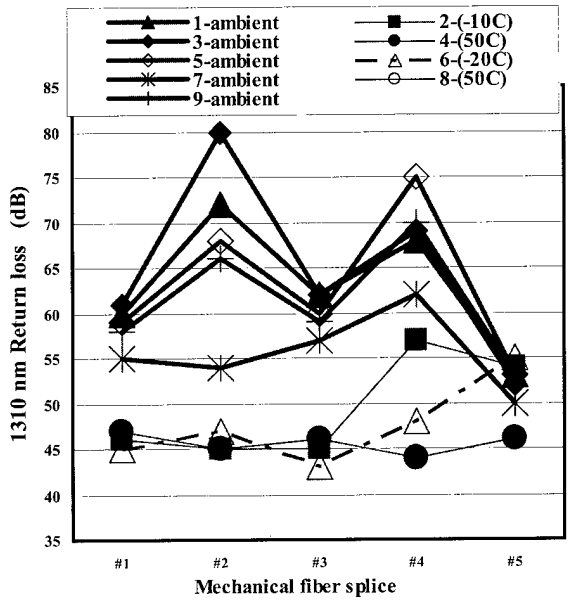


Figure 21. Return loss at 1310 nm during temperature cycling test

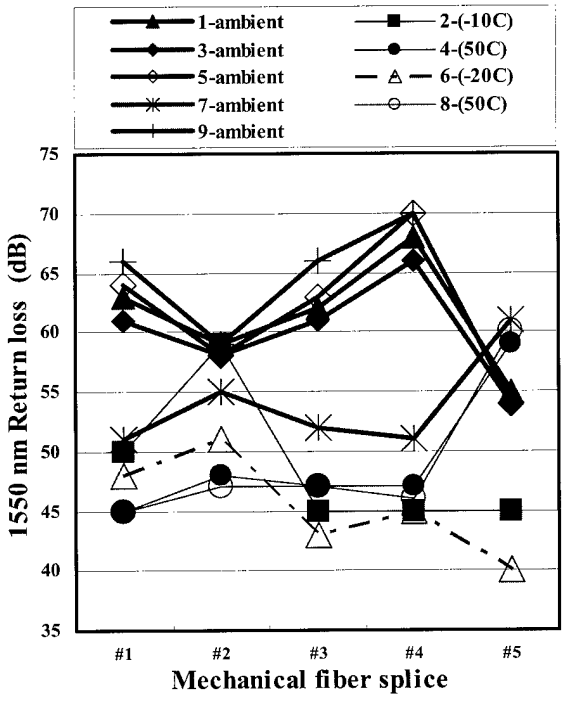


Figure 22. Return loss at 1550 nm during temperature cycling test

Force created by acceleration creates friction force that causes tension to increase. Friction coefficient depends on the material of stranded element and material of lay-plate. In normal cases hardened steel is hard enough to handle stranded elements. Polished surface gives also very low friction co-efficient. With high abrasive materials ceramic might come into consideration. Ceramic eyelets can be inserted in the body of lay-plate. Wear resistance of ceramic is better than steel. Disadvantages are higher price and shock sensitivity. Also ceramic eyelets might limit the minimum radius of the basic circle.

Shape of the hole is designed to minimize tension also with high number of turns. The exact shape is based on experience. Edges are rounded to avoid too small bending radius during production. Also middle section of the hole is shaped according to the wire angles in different production conditions. These angles are functions of number of lay-plates and their distances.

The diameter of the hole is also based on experience. Too large hole size increases diameter of the base circle. If the hole is too small there might be local bending in tube. That causes tension increase. In previous test we have determined optimum diameter of the lay-plate hole for different tube sizes. With very small tubes the relative size of the hole can be little a bit bigger than with large tubes. This is to eliminate problems caused by lumps.

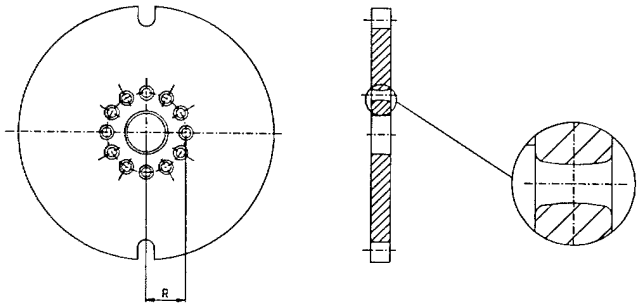


Figure 2. Lay-plate

2. Tests

The tests were made in two steps. First a 12-fiber distribution cable was produced with the jacketing line. Next step was to use that cable as a sub-unit for 72-fiber distribution cable. In both process steps tension variation was measured with different running conditions.

2.1 Test Set Up

Tests were made with two lines. Distribution cable with 12 fibers was run with indoor cable jacketing line (Figure 3).

The main components of the line are integrated lay-plate SZ-strander and aramide server, extruder, cooling trough and take-up.

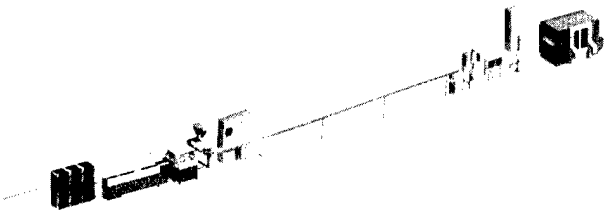


Figure 3. Indoor cable jacketing line

The strander used in this test was a 3m long machine with 13 rotating plates. That kind of a machine is designed for tight buffer and simplex stranding.

Distribution cable with 72 fibers was tested with a SZ stranding line. That line is equipped with a 7m long strander with 19 rotating plates.

This bigger machine is designed for large distribution constructions and ribbons in tube cables.

Tension was measured at both sides of stranding machine with turning wheel and load cell. Tension variation and increase was the difference of those two measurements.

2.2 Test Parameters

Main test parameters are shown in table 1.

Table 1. Test parameters

	Test 1. 12 fiber cable	Test 2. 72 fiber cable
Stranded elements	12x0.9mm tight buffers	6x6.2mm sub-units
Material	PVC	PVC
Line speed	100 m/min	50 m/min
pay-off tension	1N	5N
lay-length	100/250mm	240mm
turns	8	12

In test 1 two different base circle radii were tested. With this test we were able to verify tension variation according to the radius. The specially made plate is shown in figure 4.

Smaller circle diameter is 10.9mm and outer circle 14.4. According to equation 1 the tension difference should be about 50%.

Because the optical fibers with PVC tight buffer are sensitive to surface pressure they were not bind in test 1. One layer of aramide yarn was wrapped around them. Extruder and crosshead were located right after server. The jacket will finally hold the traversing lay.

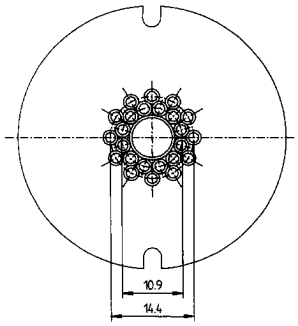


Figure 4. Lay-plate used in tight buffer stranding

That is why it is important to minimize distance between stranding point and crosshead. If distance is too long lay will open because the aramide layer cannot hold it.

In the test number 2, a standard lay-plate for 6 tubes was used. Central strength member was PE buffered FRP. The cable core was cross bound with two dual yarn binding heads. Binding tension was 7.5N/yarn and lay length 35mm.

After the both tests optical performance was measured with OTDR. Fibers used in these tests were single mode fibers. The measurements were made with 1550nm wavelength.

3. Results

3.1 Test 1

Tension variation with two different set ups is shown in table 2.

Table 2. Tension increase in test 1.

	R=10mm	R=14mm
lay 250mm	50%	75%
lay 100mm	45%	70%

Increasing the radius of the basic circle increased tension according to theory.

Speed was not critical. Actually at higher line speeds the tension variation was smaller. This is because tight buffer starts to vibrate just a little bit. That reduces the contact between tight buffer and holes in a stranding plate which makes the friction smaller.

3.2 Test 2

Stranded elements in test 2 are heavier. That causes higher tension increase. Most of the increase is still coming from the heavy cable itself. Stranding creates relatively small variation. That indicates that more turns can easily be used when stranding such cable.

Tension variation in test 2 is shown in figure 5. Turns of stranding tip are shown on X-axis. On Y-axis is tension in grams. Curve 1 is measured before strander. Curve 2 is measured right after strander.

Summary of the tension increases in test 2 is shown in table 3.

Table 3. Tension increase in test 2.

	Tension increase @25m/min	Tension increase @50m/min
Pay-off tension 150g	50%	40%
Pay-off tension 500g	20%	10%

Tension variation was first tested with two different pay-off tensions at two line speeds. After that final test was made at 50m/min and with 5N tension.

Same phenomenon as in test 1 exists also here. The tension variation gets smaller when the line speed is higher. The difference is nevertheless smaller because of the heavier tube.

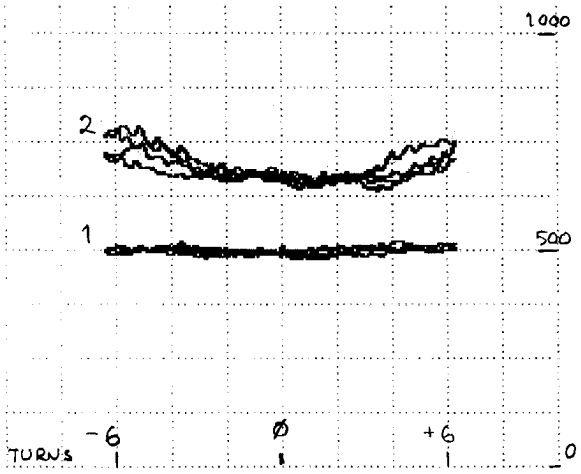


Figure 5. Tension variations in test 2.

Attenuation increase was low in the both tests. The total increase from bare fiber to the final stranded cable core was less than 0.05dB/km. After individual test attenuation increase was less than 0.03dB/km

4. Conclusion

The whole production chain of indoor cable was tested with distribution cable. First step was the stranding and jacketing of 12-fiber sub-unit cable. Next step was stranding and binding 6 times such cables into one 72-fiber distribution cable.

Stranding was studied carefully in both process steps. Tension variation as well as performance of final product was measured.

Design of stranding tools turned out to be very important. Specially when stranding tight buffered fibers the tension variation is higher if tools are not optimized for that product. Because tight buffer is sensitive to a high tension, variations may cause also extra losses in optical performance. High tension might also open the stranding lay by pulling stranded elements. That causes lower performance in mechanical tests. Again that is important in tight buffer stranding because tight buffers are not bound during the process. Only the helical served aramides and cable jacket holds the lay. Tension variation causes uneven lay and longer turning points.

When stranding the 12-fiber sub-units together relative tension variation was the same or even smaller than with tight buffer stranding. Most of the variation is coming from the own weight of the sub-unit. Stranding causes only small increase. Sub-unit with a diameter of 6.2mm and aramide strength member is not that sensitive to the tension. Still high tension peaks might disturb stranding process and reduce mechanical performance. A jacket with thick wall can stand binding that helps to get good results from stranding. There was practically no loss of stranding turns and opening of turning points was small. Our long time experience has also shown that these results are easy to repeat. Once the process is optimized it works reliably.

Further studies will be similar testing with break-out cable.

5. Acknowledgments

I would like to thank my colleagues Markku Heino, Pasi Kauppi and Lauri Louhiluoto for their assistance and help during test runs.

Author

Mr. Jari Nykänen

Nextrom Oy

P.O.Box 44

FIN-01511 Vantaa

Finland



Jari Nykänen received the degree of M.Sc. in mechanical engineering in 1996. Since that he has been working at Nextrom. Today he is product manager of fiber optic indoor cable machinery.

The Influence of Shotgun Hit Patterns on Damage to Aerial Fiber Optical Cable

Kenneth E. Bow / Marc A. Adams
The Dow Chemical Company / Convergent Concepts
Midland, Michigan
+1-989-638-3759 · kebow@dow.com

Abstract
This study employed experimental and theoretical methods to model the patterns of pellet hits produced by a 12-gauge shotgun as a function of pellet size and the distance of the gun from the target. The objective of this study was to produce a statistical model of the pellet hit pattern behavior which can be used to define statistically meaningful tests of fiber optic cable armor performance, to interpret experimental data from cable armor tests and to develop methods for the ballistic testing of armored cable. The study has completed the experimental phase and analysis of the data include the effects of clustering of the pellets. Clusters, or groups of pellets in close proximity to each other, may cause the most damage to cables. The results of the experimental study are applied to the problem of pellet impact patterns on cable to demonstrate the usefulness of the approach. In addition, data on shotgun tests of armored cable are included. It was discovered that the use of coated steel armor can reduce the amount of aramid required for ballistic protection.

Keywords
Shotgun; aerial; fiber optical cable; coated steel; aramid

1. Introduction
A paper was presented in 1999 on the resistance of armored cable to shotgun blasts.[1] Preliminary experimental and theoretical work was reported in that paper on efforts to characterize the stochastic behavior of hit patterns produced by a 12-gauge shotgun. It was also noted in this paper that work would continue on development of a model that gives the probability of damage from a shotgun insult. The results of this work are now complete. This paper will focus on the description and modeling of the statistical properties of hit clusters which occur in any shotgun blast.

The 1999 paper presented a new and effective way of providing ballistic protection to aerial fiber optical cables by combining a coated steel armor with aramid. It was shown that the combination of materials provided a synergy that was more effective than either material separately. The coated steel provided a way to take some of the energy out of the pellet blast while the aramid acted as a safety net to catch the pellet. Less macro- and micro-bending of the buffer tubes in the core of the cable means increased reliability of the fiber optical cable in the aerial environment.

The 1999 paper also introduced a thicker coated steel than the standard product used for underground cables. The steel was 0.25 mm (10 mils) in thickness (excluding coatings) versus the standard product at 0.15 mm (6 mils). Preliminary test data indicated that cable with thicker coated steel could offer higher levels of ballistic protection than previously observed for all-dielectric cables with aramid yarns. For example, test data indicated that combinations of 0.25 mm coated steel, aramid and 0.15 mm steel could stop a #2 pellet which is one of the largest used by small game hunters.

The use of armored cable in aerial applications brings the additional benefits of rodent resistance, moisture barrier and control of jacket shrinkage in addition to the ballistic resistance. Field experience has shown that the armored aerial cable is more robust that unarmored with respect to damage caused by abrasion by trees and other mechanical damage such as that caused by storms. Another benefit is the armored cable can come down a pole into the underground environment without changing sheath designs. The benefit of simpler installation is added to the benefits normally expected for underground fiber optical cable such as rodent resistance and the ability to accurately locate the cable.

2. Variance of the X and Y Pellet Hit Positions
The spatial dispersion of the pellet hits produced by a shotgun blast have been experimentally characterized for American #4, #6 and #7.5 pellet sizes and for distances of 10, 20 and 30 meters from the muzzle of the gun to the target. This was done by shooting 5 to 7 targets made of foam-like material at each distance with each pellet size. Typical shot patterns for a target and the dimensioning of the target to determine the X and Y hit positions are shown in Figures 1 to 3.

Image analysis software was used to measure the geometric properties of the patterns. The distributions of hit positions were determined by counting all pellets with X-hit coordinate less than a given X and all pellets with X-hit coordinate greater than a given X. The number of pellets in each case was divided by the total number of pellets in the load and the cumulative probability associated with each of the given X positions was determined. Using this information and a similar analysis for Y, the cumulative Gaussian distribution function was used to determine the standard deviations of the X and Y hit positions for each pattern. The pattern analysis data (Gaussian distribution parameters and error analysis of the Gaussian distribution) included in Figures 1 to 3 show that the bivariate Gaussian probability distribution function is a good descriptor of the X and Y variation of the pellet hit patterns. Thus the mean and standard deviation (StDev)

parameters of the Gaussian distribution function are adequate to describe the behavior of the patterns.

These data also show that for any given condition of pellet size and distance to the target, the differences between the X and Y standard deviations are statistically insignificant.

3. Clustering of Shotgun Pellets

Knowledge of the dispersion, the variance, of pellet hit positions produced by a shotgun burst is necessary to describe the damaging effects of the burst. Unfortunately, this information, by itself, is insufficient to describe or model the local damage created by pellets hitting in close proximity to other hits. It was discovered in this work that the most damaging effects of shotgun bursts may arise from the impact of pellets in close proximity to each other. This group of pellets is called a cluster and the phenomenon clustering. The frequency of occurrence and the degree of clustering of pellet hits is a principal parameter in determining the damage done by a particular shotgun blast. For identical conditions of gun type, pellet load and distance to the target, not only will the standard deviations of the pellet hit positions vary but also the degree of clustering.

Clustering is a stochastic phenomenon which must be addressed in order to interpret tests for shotgun damage. Clustering is dependent on the dispersion in the hit pattern, the standard deviation of the X,Y hit positions, but also possesses its own statistical behavior, in that, hit patterns with similar X and Y standard deviations can have significantly different degrees of pellet hit clustering. Experimentally measured patterns show that a pattern with larger X and Y standard deviations may have a higher degree of clustering than a pattern with smaller X and Y standard deviations.

The areal density of pellet hits in a cluster, the cluster areal density (CAD), is defined as the number of pellets in the cluster divided by the area of the smallest circle which encloses all the pellets:

Cluster Areal Density (CAD) = (Number of pellets in cluster)/(smallest radius circle that encloses all hits)

CAD is calculated for each pellet hit on the target. To determine the CAD for an N-hit cluster around a given hit, the coordinates of the (N-1) nearest neighbors of the given hit are determined. Using these N positions, a computer minimization routine is used to determine the center and radius of the minimum area circle which encloses all N hits. The number of hits divided by the area of the circle is the N-hit CAD in the pattern at the point of the circle center. By calculating this quantity for every pellet hit position, all cluster areal densities in the pattern are characterized. Sometimes analysis of CAD around two different hits will give the same circle as the solution. These are non-unique clusters, i.e. the clusters have the same hits as members.

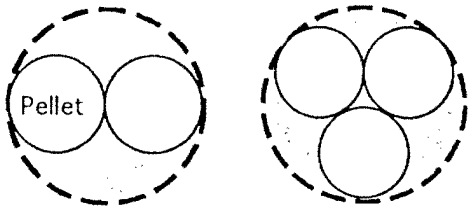
The minimum area circle which "contains" all hits in the cluster encloses each pellet completely; hence the radius of this circle depends on the diameter of the pellets impacting the target. Two benchmark values can be defined for the cluster areal density quantity:

(1) The maximum cluster areal density possible (Dmax) which is simply the density of the cluster when all pellets hit at the same position.

(2) The maximum cluster areal density for which there is still a possibility that the pellet impact footprints do not overlap (Dpno).

Figure 4 shows the geometry involved for a 2 and 3 hit clusters. The same approach is used for 4, 5 and 6 hit clusters.

Figure 4. Minimum Area Circles which Enclose Pellets in Cluster Determine Cluster Areal Density



D_{pno} areal density for N-hit cluster = N/(area of shaded circle)

Using the relationships for the probability of observing cluster areal density as a function of pellet size and distance to the target, we can now define the severity of a particular shotgun test. Remembering that the 90 percentile cluster areal density represents the areal density for which there is only a 0.10 probability of observing a cluster of greater areal density, we can define a pellet hit pattern which will test the armored cable at the 0.90 probability level of surviving a particular kind of shotgun burst.

Table 1 gives the cluster areal densities for various conditions of pellet size and distance to the cable from the gun for a 0.90 probability that the cluster areal density, which will occur in any given shot, will be lower, i. e. less damaging.

Table 1. Percentile Cluster Areal Densities (pellets/in^2) for Various Conditions of Distance to the Target and Pellet Size for Cluster Sizes of 2, 3, 4, 5 and 6 Pellets in the Cluster

Cluster Size (# of pellets in cluster)→ Distance/Pellet Size	2	3	4	5	6
20m / #4	76.9	50.3	26.2	17.4	11.9
20m / #6	104.9	68.7	25.3	16.1	16.8
20m / #7.5	206.0	142.8	55.3	44.4	28.9
30m / #4	46.5	16.3	1.0	0.5	0.2
30m / #6	96.3	6.3	1.3	0.9	0.5
30m / #7.5	88.7	14.2	6.7	2.8	1.3

If we are interested in a worst case condition of a gun shooting #4 size pellets and being no closer to the cable than 20 meters, then

we look in the first row of Table 3. We find that the shotgun blast which hits the cable should contain a maximum areal density, 2-hit cluster of 76.9 pellets/in^2, a maximum areal density, 3-hit cluster of 50.3 pellets/inch^2 (6.45 cm^2), a 4-hit cluster of 26.2 pellets/in^2, a 5-hit cluster of 17.4 and a 6-hit cluster of 11.9. Each of these maximum cluster areal densities for the different cluster sizes are independent, that is, any or all of them can occur in a particular shotgun blast. To have an efficient armor test, all of them should occur in the pellet hit pattern of the test. If it is known that only certain ones are most damaging, then only these need to occur in the pattern.

4. Clustering of Hits on a Cable

A computer program was used to put the pellet hit patterns measured in the tests described above on the image of a 0.75 inch (19 mm) diameter cable. The cable was assumed to have no sag, i.e. a straight cable, and the average Y hit position of the particular hit pattern being studied was positioned on the centerline of the cable. Statistically, this will be the most severe condition for the pellet hits on the cable. The hit pattern which would have been produced on the cable by each target test was analyzed to determine several quantities including the number of pellet hits which would have occurred on the cable, cluster areal density (CAD), and cluster size.

Some selected results are shown in Table 2. These data were gathered by superimposing the image of a cable with a 19 mm (0.75 inch) diameter over the target and noting the number of hits and the clusters in those hits. As expected the number of hits decreased as the target distance increased from 20 to 30 m. Also, as expected, the smaller shot size, with more pellets per shell, had more hits on the cable than the larger sizes. Most interesting, however, is the cluster density which increases dramatically for the smallest pellet size. Note that the #4 and #6 shot at 20 m have about the same CAD while the #7.5 shot has a large CAD across all cluster sizes. At 30 m, there is a significant drop in CAD and cluster size for #4 and #6 shot, while the #7.5 shot has a larger CAD and still shows some cluster sizes as large as 5.

Table 2. Cluster Areal Density (CAD) for a 19 mm (0.75 inch) Cable

Pellet Size, #	Distance m	No. of Pellets		Maximum Cluster Density, Pellets/in^2, per cluster size				
		Target	Cable	2	3	4	5	6
4	20	172	19	43	28	12	9	6
4	30	167	8	14	4	0	0	0
6	20	261	17	49	29	11	6	5
6	30	261	11	8	4	1	0	0
7.5	20	411	29	106	56	25	19	12
7.5	30	397	16	63	7	2	1	0

At the muzzle of the gun, the pellet hit pattern is a step function -zero probability of hit everywhere except over the circle which is the bore diameter of the gun for which there will be some constant value of hits per unit area. With increasing distance from the muzzle, this step distribution function becomes a quasi-normal distribution function. Aerodynamic and, perhaps, other phenomena scatter the flying pellets out of the muzzle column into an expanding cone.

5. Coated Steel for Ballistic Protection

As pointed out in our 1999 IWCS paper, coated steel armor, 0.25 mm thick, can be used as the primary barrier to protect aerial fiber optical cable from damage from shotgun pellets. This steel can be used in combination with aramid and/or 0.15 mm steel. There appears to be synergism between the steel and aramid in stopping the pellets.

Various other sheath constructions have been proposed for ballistic protection. One construction uses a woven aramid tape, applied as two layers, either spirally or longitudinally, for ballistic resistance in the cable.[2] A second design uses a combination of aramid and polyamide inner jacket to provide ballistic resistance.[3] The polyamide is specially modified for this purpose.

The components of the above sheath constructions are shown in Table 3 for cable that is resistant to a #4 pellet at 15 meters. When the 0.25 mm thick coated steel is the primary barrier, the amount of aramid required is significantly reduced over that required for cables protected by aramid layers. Note in Table 3 that for design No. 1 with the 0.25 mm (10 mil) coated steel that only 25 g/m of aramid is needed whereas for design 3 using woven aramid tapes, 68 g/m is needed. For design 4, which uses a combination of aramid and polyamide, 52 g/m is needed.

Table 3. Comparison of Aramid Requirements for Various Cable Designs Resistant to #4 Pellets at 15 m.

	Cable Sheath Construction					
	Outer Jacket	Armor	Aramid	Inner Jacket	Armor	Aramid
1	HDPE	0.25 mm Ctd.Stl.[1]	13 g/m	MDPE	-	12 g/m
2	HDPE	0.25 mm Ctd.Stl.[1]	-	MDPE	0.15 mm Ctd.Stl.[4]	12 g/m
3	PE	-	68 g/m woven[3]	PE	-	-
4	PE	-	52 g/m	PA12[4]	-	-

[1]0.25 mm (10 mil) coated steel

[2]0.15 mm (6 mil) coated steel

[3]2 layers of woven aramid tapes with a weight of 630 g/m^2

[4]Modified polyamide 12, 1 mm (40 mils) thick

By comparing these requirements it can be observed that the coated steel designs need only 18 to 37% as much aramid. This

reduction in aramid requirements can result in a significant cost savings because less aramid is required with the coated steel to provide any given level of ballistic protection. Due to the shortage of aramid for the fiber optical cable manufacturing industry, the combination of coated steel and armaid for ballistic protection may be a very attractive alternative.

If a smaller size pellet is chosen as the threat, the aramid requirements could potentially be reduced further. For a #6 pellet, the aramid requirements in design 1 with coated steel could be reduced to 12 g/m. For design 2, the requirements for woven aramid could be reduced to 59 g/m. For design 3 with polyamide, the requirement could be reduced to 30 g/m. Irrespective, for #6 pellets, the coated steel design still uses 60-70% less aramid.

As reported in the 1999 paper, the 0.25 mm thick coated steel is resistant to #7.5 pellets without the need for aramid. It should also be noted that the armored sheath construction shown in Table 3 (Designs 1 and 2) are also resistant to #3 pellets.

6. Conclusions

Knowledge of the dispersion of pellet hit positions produced by a shotgun blast is necessary to describe the damaging effects of the blast. A significant discovery was made which suggests that the most damaging effects arise from the impact of pellets in close proximity to each other. Previous work has focused on damage from single pellets not the clusters of pellets observed in the experimental work reported in this paper. The frequency of occurrence and the degree of clustering of pellet hits is a principal parameter in determining the degree of damage done be a particlular shotgun blast. Clustering is a stochastic phenomenon which must be addressed in the interpretation of any tests for shotgun blast damage.

Coated steel in combination with aramid can provide protection from #3 shotgun pellets at 15 m. The amount of aramid required is about 60-80% less than that required when woven aramid tapes or a combination of aramid and a polyamide jacket are used. Use of coated steel can result in significant cost savings as well as manufacturing flexibility and can help relieve supply issues associated with the current shortage of aramid fiber.

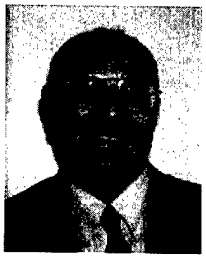
7. References

[1] K. E. Bow, M. D. Luker, Dr. M. A. Adams, "Ballistic Resistant Armored Fiber Optical Cable for Aerial Applications," International Wire and Cable Proceedings, 1999, p. 730-736.

[2] "Twaron® Aramid Tapes as Ballistic Protection for Aerial Optical Fiber Cables," Report IN93/4364, March 1996.

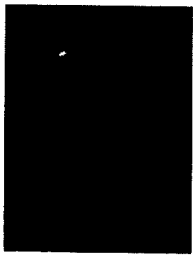
[3] V. Eichorn, "Protection of Fiber Optic Transmission Media in Telecommunication and Data Transfer Cable by Thermoplastic Polymers," Wire Industry, May 1999, p. 298-305

8. Biographies



Kenneth E. Bow
The Dow Chemical Company
200 Larkin Center
1605 Joseph Drive
Midland, MI 48674

Kenneth E. Bow received a B.S. degree in electrical engineering from Michigan State University, East Lansing, MI, in 1962. Following graduation, he joined The Dow Chemical Company, Midland, MI, where he has been involved in the research and development of materials for the wire and cable industry for more than 30 years. He is currently the Chief Scientist for the development of polymer and coated metal products for wire and cable applications. His primary responsibilities are for the global development of applications and cable technology associated with cables using plastic-coated metallic shielding and armoring tapes. Ken is a senior member of the IEEE and the SPE. (E-mail: kebow@dow.com)



Dr. Marc A. Adams
Convergent Concepts
3638 N. Rancho Drive
Las Vegas, NV 89130

Marc A. Adams received the B.S. degree in metallurgy from Case Institute of Technology (now Case Western Reserve University), Cleveland, OH, in 1967. He received a M.S. degree in Material Science and Engineering from the School of Engineering and Applied Science, University of California at Los Angeles in 1972. Continuing his graduate studies at UCLA, he received the Ph.D. degree in Ceramics and Material Science in 1975. He returned to the Jet Propulsion Laboratory in 1976. In 1985, he formed the Impact Physics Group at JPL. Since then he has been the leader of this group which has completed numerous R&D programs, sponsored by several offices of the Department of Defense, on the fundamental and applied aspects of armor mechanics, material behavior under impulsive loading, experimental methods for evaluating armors and the statistics of threat and armor behavior. (E-mail: daisy0303@aol.com)

Target #	1
Pellet Size	4
Distance (m)	20
Mean X (in)	14.024
Mean Y (in	11.269
StDev X (in)	4.178
StDev Y (in)	3.645
No. Pellets on Target	172
Ave. Error/pt-X	0.028
Ave. Error/pt-Y	0.019
Sum X Errors	2.101
Sum Y Errors	-0.312

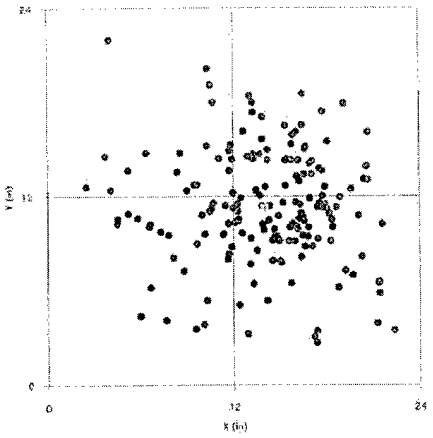


Figure 1. Basic Pattern Analysis

Target #	8
Pellet Size	6
Distance (m)	20
Mean X (in)	11.465
Mean Y (in	11.844
StDev X (in)	3.476
StDev Y (in)	3.646
No. Pellets on Target	263
Ave. Error/pt-X	0.013
Ave. Error/pt-Y	0.008
Sum X Errors	-0.433
Sum Y Errors	-0.776

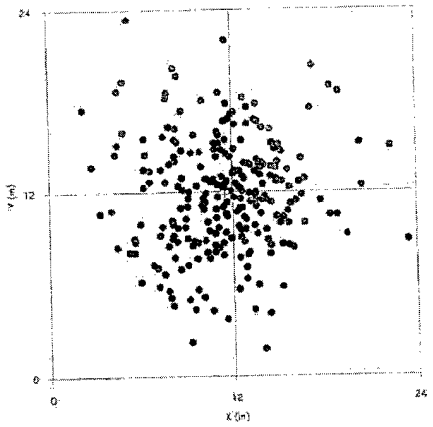


Figure 2. Basic Pattern Analysis

Target #	13
Pellet Size	7.5
Distance (m)	20
Mean X (in)	11.612
Mean Y (in	11.707
StDev X (in)	4.069
StDev Y (in)	3.886
No. Pellets on Target	414
Ave. Error/pt-X	0.012
Ave. Error/pt-Y	0.015
Sum X Errors	-0.424
Sum Y Errors	-3.654

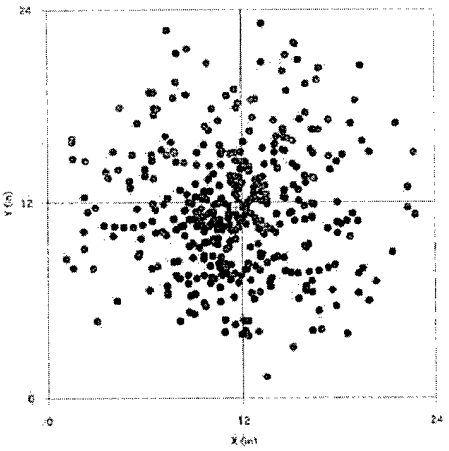


Figure 3. Basic Pattern Analysis

NOTE:
[+] = mean X, Y; X Error and Y Error are Gaussian distribution probability value minus ranked data probability value

Time Domain Analysis of Frequency Domain Measurements

Marcus Lindström
Ericsson Network Technologies AB
Hudiksvall, Sweden
+46-650-36230 · marcus.lindstrom@eca.ericsson.se

Abstract

In some cases it is interesting to study the performance of a transmission channel in time domain. In this paper a method is described for using frequency domain measurements to generate eye pattern diagrams. The transition function is measured using a network analyzer. Even theoretical transmission channels can be used analytically calculated or simulated. The transition function is transformed into an impulse response in time domain using DFT. By convoluting the impulse response with the input signal, the output signal can be studied.

Using these eye pattern diagrams the degeneration of the signal can be studied, it is also possible to study the improvement that can be made using different coding techniques. Crosstalk can be transformed into time domain using the same method. A simplified model to visualize the crosstalk impact on the signal is presented.

Keywords

Eye pattern; Transform; Time domain; Simulation; Transmission; DFT

1. Introduction

Today, when the bit rate is increasing and symmetrical cables are used for higher frequencies, pulse-shaping techniques have been developed to compensate for the poor performance of the cable. To visualize the benefits of the pulse-shaping techniques and as support when developing new algorithms, a simulation tool is being developed to present the signal in an eye pattern diagram when the transmission link is characterized in frequency domain.

2. Preparation of Data For The Transform

2.1 Equal spacing of frequency points

The complex value of the transition function is measured for the cable or transmission link. A network analyzer is very suitable for the work. Another source of frequency domain data can be analytical calculations or simulations of a transmission channel. The DFT algorithm requires equally spaced frequency points including 0 Hz. In network analyzers with a TDR-option it is often possible to set equally spaced frequency points by pressing <Set frequency low pass>. To get the value at 0 Hz an extrapolation is necessary using the two lowest frequency points. If the frequency domain data do not have equally spaced frequency points it is possible to interpolate them. To make this interpolation it is necessary to have a continuous phase. In some network analyzers it is possible to produce it directly, otherwise it has to be calculated afterwards.

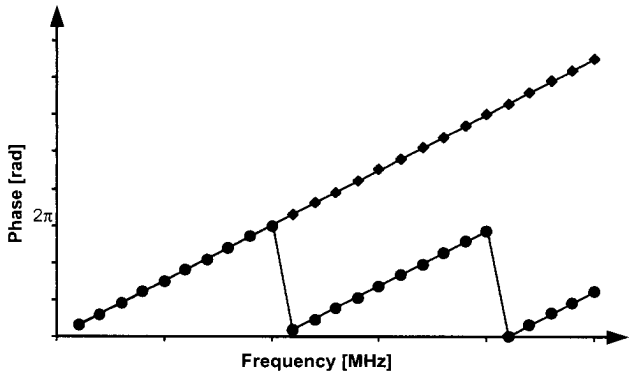


Figure 1 Continuous phase compared to a limited phase.

One easy way to generate a continuous phase, is to estimate the phase for next frequency point just by extrapolating from the latest two values. The estimated value is compared to a measured value adjusted with k·2π and (k+1)·2π. If (k+1)·2π has a closer match to the estimated value, k is increased one step.

2.2 Dividing the cable into smaller parts

If it is of interest to moderate the length of the cable when studying the eye pattern diagram it is possible to divide the cable into smaller parts by taking the nth root of every complex transmission value.

E.g.

$$S21_{1m} = \sqrt[50]{S21_{50m}} = \left|S21_{50m}\right|^{\frac{1}{50}} \cdot e^{j\frac{\varphi}{50}} \quad (1)$$

This operation also requires a linear phase (see 2.1). Before making the transform, the appropriate number of divided parts can be put together by multiplying them by each other.

$$S21_{20m} = S21_{1m}^{20} \quad (2)$$

2.3 Adding the mirror frequencies

To get a time domain signal without imaginary parts, the frequency domain functions real part has to be even and the imaginary part of the function has to be odd. The spectrum is mirrored, conjugated and added as negative frequency components.

$$H_e = H_m^*[N], H_m^*[N-1], \ldots, H_m[0], H_m[1], \ldots, H_m[N]$$

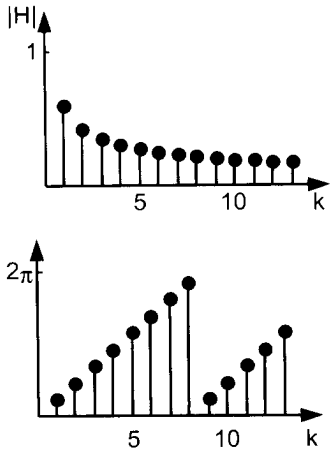


Figure 2 Transition function value and phase

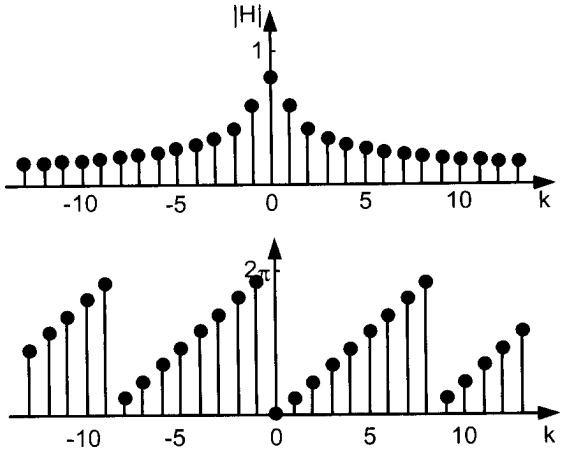


Figure 3 Transition function mirrored and conjugated

3. Stimulus

3.1 Bit pattern generator

An input signal is generated with a PRBS generator and is concatenated with a stated number of 'zeroes' and 'ones' to produce the worst case from an intersymbol interference point of view. The amplitude of the signal is centered on zero to simplify the calculation later.

3.2 Pulse shaping

It is now possible to add the shape of every pulse to the data stream. Rise and fall times can be added or even some kind of pulse shaping like pre-emphasis. The pulse shape is multiplied by every bit in the data stream. There can be different pulse shapes depending on the previous bits. The pulse shape is sampled using a sample frequency twice the highest frequency in the transition function. If there is a mismatch in multiples of sampling intervals and pulse length it will cause an error, in the calculations. No correction has been made for this error.

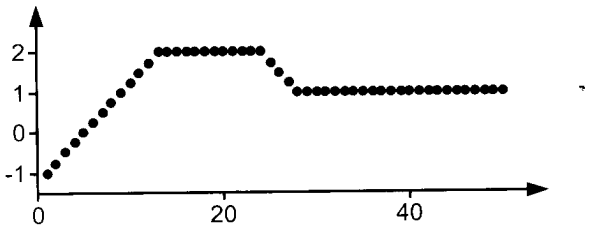


Figure 4 Half-wave pre-emphasis

4. Generating the impulse response

4.1 Transforming into time domain

The impulse response for the system is made by transforming the transition function into time domain using an inverse Fourier transform.

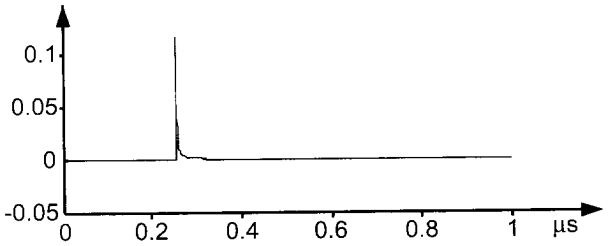


Figure 5 Impulse response

5. The output signal

5.1 Convoluting the output signal with the impulse response

Every sample of the input signal can be considered as an impulse. If the input signal is convoluted with the impulse response the result will be the output signal of the system.

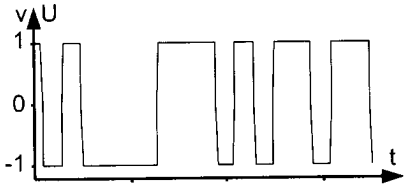


Figure 6 Input signal

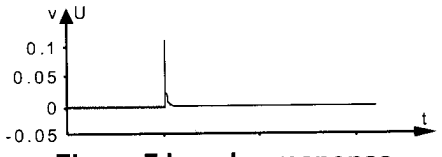


Figure 7 Impulse response

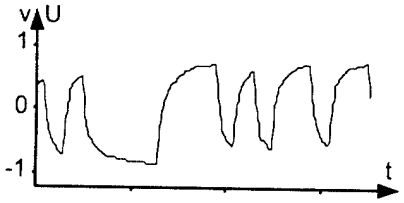


Figure 8 Resulting output signal

5.2 Adding crosstalk to the output signal

If crosstalk is disturbing the communication, the signal from the crosstalk can be added to the main signal. If all combinations between the main signal and the disturbing signal were to be calculated it would take an unreasonable amount of time. Here the approach is to take the highest and lowest voltages from the crosstalked signal and add these to the output. This operation will triple the amount of data in eye pattern diagram.

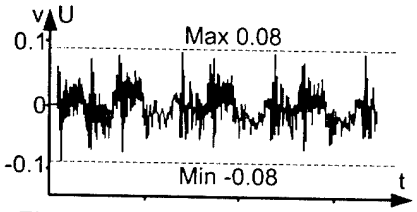


Figure 9 Signal from crosstalk

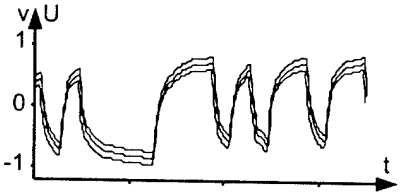


Figure 10 Output signal after crosstalk adding

5.3 Making the eye pattern diagram

The output signal is divided into sections where every section has the same length as one bit. All the sections are plotted on top of each other. This will make the eye pattern diagram. To get a better visualisation, the eyepattern diagram has been repeated twice to get a whole eye in the diagram.

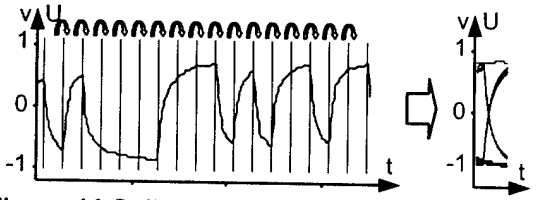


Figure 11 Splitting output signal into slices

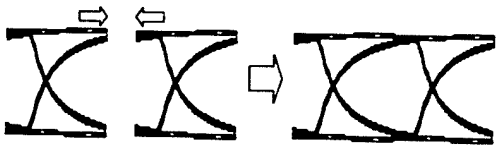


Figure 12 Repeating eye pattern

6. Comparing the results with the measurements

A 10 m length of coaxial cable with capacitive crosstalk coupling at one end is used as test set-up. The transition function for both the normal signal path and the crosstalk coupling is measured with a network analyzer. The measurement is made with different frequency points location and with different frequency spans. The same transmission link is measured in time domain using signal generator and sampling oscilloscope. Different rise times are used both with and without signal causing crosstalk.

6.1 Comparing measured eye pattern with the calculated values

The main transmission path is measured and compared to calculated values. In frequency domain there are 801 equally spaced frequency points up to 3 GHz.

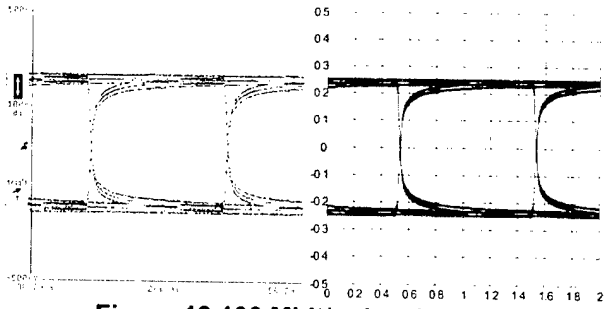


Figure 13 100 Mbit/s rise time 0.3 ns

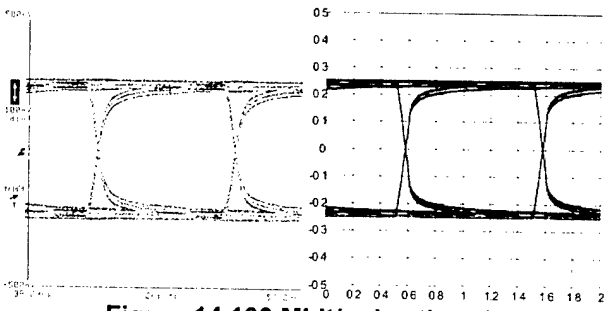


Figure 14 100 Mbit/s rise time 1 ns

6.2 Adding crosstalk to the data stream

As described in 5.2 the worst voltage in the crosstalk-signal is added to the main signal. As shown, crosstalk has more affect on the signal in the calculated case compared to the measured case. An explanation is that worst case is always generated in the simulation.

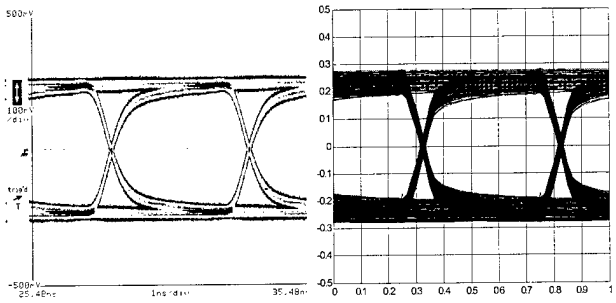


Figure 15 200 Mbit/s rise time 1 ns with crosstalk

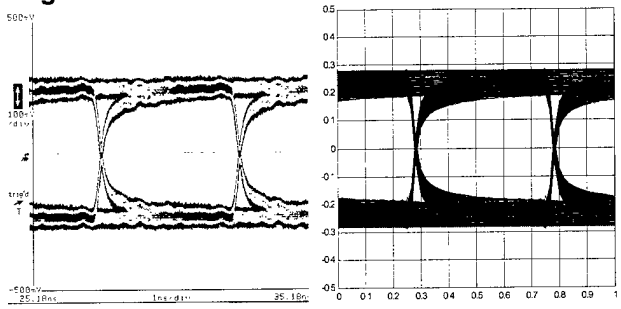


Figure 16 200 Mbit/s rise time 0.3 ns with crosstalk

6.3 Interpolation if frequency points are not equally spaced

If the transition function does not have equally spaced frequency points they can be interpolated as described in 2.1.

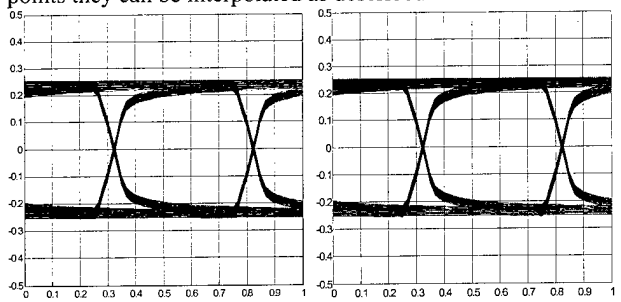


Figure 17 equally spaced frequency points compared to interpolated data

In this example 1601 points are used. In the diagram on the left, equally spaced frequency points are used up to 3 GHz. In the diagram on the right the frequency sweep is from 0.3 MHz to 3 GHz.

6.4 Degeneration from band limited transition function

Degeneration occures when the highest measured frequency is lowered. The highest frequency is in this case 1 GHz. As a result the shortest possible rise time is increased and samples per bit are decreased and will generate a coarser shaped curve. In the example 1 ns rise time is used in the calculation but is ignored due to longer sample time.

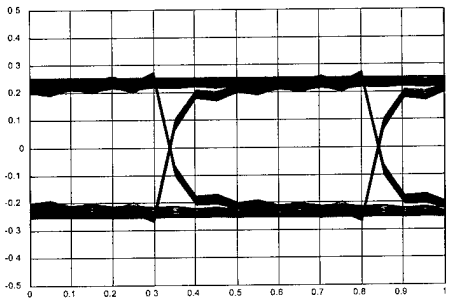


Figure 18 200 Mbit/s rise time 1 ns with limited bandwidth

6.5 Adjusting the length of the cable

A way to adjust the length of the cable is described in 2.2. In this case the cable is divided in 10 lengths of 1 m . It is then possible to combine these into longer cables.

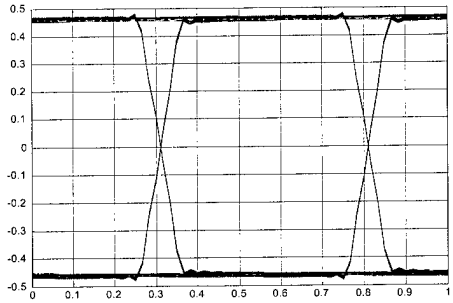


Figure 19 200 Mbit/s rise time 1 ns length 1 m

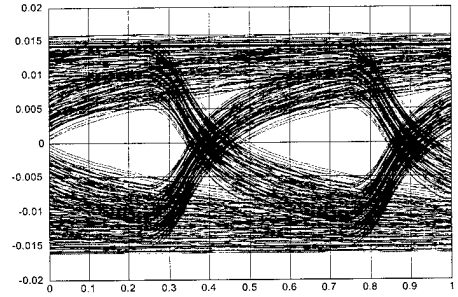


Figure 20 200 Mbit/s rise time 1 ns length 50 m

Notice the different scale in the diagram for the 50 m cable length.

6.6 Using pulse-shaping

To compensate for distortion generated from the non-linearities in the cable, pulse-shaping can be used. These pulse-shaping circuits increase the high frequency parts of the signal. This can cause problem if there is a crosstalk in the system. Crosstalk often increases at higher frequencies. In this case all the crosstalk is near-end crosstalk and generated only in the connector. The improvement due to pulse shaping can be lost in proportion to the rise in crosstalk.

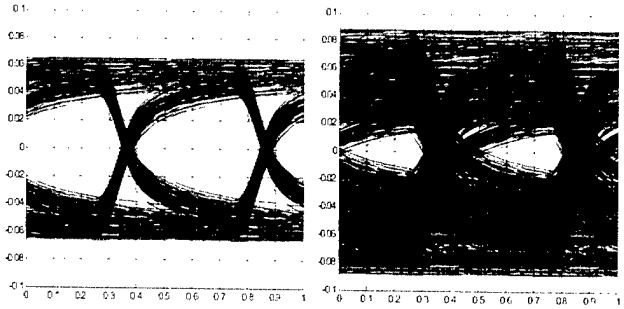


Figure 21 200 Mbit/s with and without crosstalk

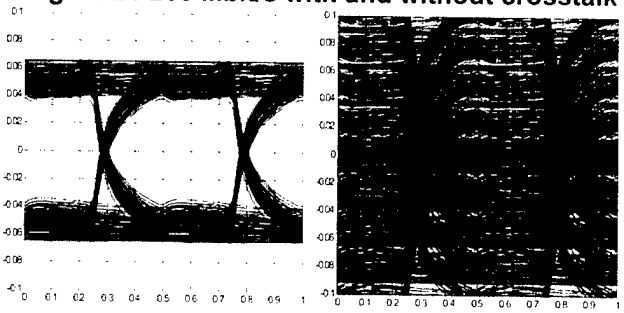


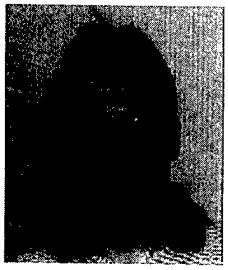
Figure 22 200 Mbit/s with pre-emphasis, with and without crosstalk

7. Conclusions

We made a model of a transmission channel in the frequency domain using data from measurements in the frequency domain. The effect the transmission channel has on the signal can then be simulated in mathematical software such as Mathcad. This is a cheap and quick method to visualize the effects from changes in the transmission channel. An improvement that can be made is to connect different transmission channels in series.

8. References

[1] Sune Söderkvist, *Tidsdiskreta signaler och system*, 2nd ed., Sune Söderkvist, Linköping



Marcus Lindström received his M.Sc.E.E. in 1993 from Linköping Institute of Technology, Linköping , Sweden. He joined Ericsson Network Technologies in 1997 where he is working in the transmission technology department.

The Synergistic Effect of MDH and ATH on Flame Retardation and Smoke Density Suppression

Do Hyun Park, Myeong Jin Ahn, Sang Cheol Kim, Gun Joo Lee

Polymeric materials Technology Group, LG Cable Research & Development Center
555, Hogye-dong, Dongan-gu, Anyang-shi, Kyungki-do, Korea

+82-31-450-8333 · dhpark@cable.lg.co.kr

Abstract

Halogen-free flame retarded polyethylene has been investigated to study the effects of inorganic fillers on the improvement of flame retardation and the suppression of smoke density. Through the analyses on thermal stability and smoke density, it has been revealed that the flame retardation of EVA could be effectively enhanced by incorporation of MDH and ATH. There exist synergistic interactions between MDH and ATH in developing the hard and compact charred layer that increases the resistance to flame stress and reduces the combustion rate.

This argument was verified by the observation of fire performance using cone calorimetry. In addition, morphological study supports that the improvement of flame retardation and the suppression of smoke density are due to hard and compact charred layer developed during the combustion. This compactly charred layer provides a good thermal and flame barrier that prevents jelly filled loose tube from combustion.

Keywords

Wire; cable; Flame-retardant; smoke

1. Introduction

Recently, there have been lots of improvement in cables to make them can be used for both indoor and outdoor application by changing the structure of optical cable or by modifying the materials for cable [1-2]. In order to be used as indoor product, the cable should have the riser level flame retardation. Especially, when the cable is filled with jelly or gel, it is highly required the flame retardant jacket of very high quality to fulfill the requirement of riser level flame retardation. Consequently, there have been a lot of researches on this topic. Until now, halogen compounds have been widely used and exhibited the greatest effect for flame retardation. However, it have been important issues continuously that such problems as the corrosiveness, the smoke emission and the toxicity of combustion products . At last, the use of halogen compounds begins to be limited and the alternative halogen-free flame-retardants such as aluminum or magnesium hydroxides and phosphorous-containing materials have drawn plenty of attention from aerospace, microelectronic, cable and wire manufacturers [3-9]. The inorganic flame-retardants decompose endothermally with the release of water around the temperature at which polymers themselves decompose and do not induce the smoke and corrosive gas problems.

The aim of this work is to study the behavior of flame retardation and smoke evolution of ethylene copolymers such as ethylene-ethyl acrylate (EEA) and ethylene-vinyl acetate (EVA) filled with various combinations of metal hydrates (ATH or MDH). Thermal stability and fire performance are quantitatively analyzed by TGA, oxygen indexer and cone calorimetry. To identify the flame-retardant mechanism of this halogen-free system, the surface morphology after combustion was investigated.

2. Experimental

2.1 Materials

The polymers used in this study are ethylene-ethyl acrylate copolymer (15 wt% ethyl acrylate, EEA), ethylene-vinyl acetate copolymer (28 wt% vinyl acetate, EVA) and maleic anhydride-grafted polyethylene (m-PE). Magnesium hydroxide ($Mg(OH)_2$, MDH) and aluminum trihydrate ($Al(OH)_3$, ATH) are used as the additives to increase the flame retardation and reduce the evolution of smoke during the combustion of materials. The surface of MDH was either treated with stearic acid ($CH_3(CH_2)_{16}COOH$) or untreated. However, the surface of ATH was untreated.

The blend ratio of dual polymer blend (ethylene copolymer/m-PE) that is used as a matrix was fixed at 90/10 by weight. The total content of inorganic fillers is up to 60 wt %. The polymer blends were modified in three ways: (1) 45 wt % MDH and 1 wt % red phosphate (EEA/MDH), (2) 60 wt % MDH (EVA/MDH) and (3) 45 wt % MDH and 15 wt % ATH (EVA/ATH/MDH). The mixtures of polymers and inorganic fillers were processed in a double roll plasticator at 120℃ for 30 minutes. To get sheets (200 x 200 x 1 mm^3), the mixtures were pressed at 185 ℃ for 10 minutes.

2.2 Thermal analysis and mechanical properties

The thermogravimetric analyses were carried out at heating rate of 10 ℃ /min using TGA2950 (Dupont TA instruments Co.). A dumbbell type specimen with the width of 5.6 mm and the gauge length of 20 mm were prepared and tested at 200 mm/min by using Instron 6022 and the number of specimens is at least 5.

2.3 Fire test

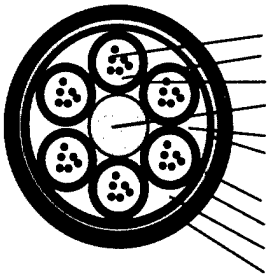
The Limited oxygen indices from burning samples were measured as the oxygen concentration (%) by Oxygen indexer (FTT Co.). Cone calorimeter (FTT Co.) was used to obtain heat release rate (HRR), total smoke release (TSR), according to ASTM 1356-90 under a heat flux of 50 kW/m^2. This heat flux has been chosen because it corresponds to the evolved heat during a fire. The smoke generated from burning samples was measured as the specific optical density (Ds) by Smoke box (Rheometric Scientific Co.). Under flaming mode, the heat flux of furnace was fixed at 2.5 W/cm^2 and then the smoke density caused by the thermal degradation of specimen was measured.

2.4 Morphology

The shape of inorganic fillers and the surface morphology of burned samples were observed using a scanning electron microscopy (Hitachi Co. S-2500C). The samples were coated with gold-palladium and the accelerating voltage was 25 kV.

3. Results and discussion

3.1 Thermal and mechanical properties



Optical fiber (up to 12 per tube)
Filling Compound
Loose Tube
FRP
Filler (if necessary)
Water Blocking Tape
Glass Yarn
Water Blocking Tape
Rip cord
Riser rated Sheath
(LSZH)

Figure 1. The schematic of OFNR Loose Tube 72C

Figure 1 shows the schematic of OFNR Loose tube 72C cable tested with newly developed flame-retardant (FR) materials. In this research, EEA or EVA is blended with m-PE to improve mechanical property and thermal aging property of FR-PE. In the aging experiments (100℃ x 168 hr), the residual tensile strength and elongation is over 85%. As listed in Table 1, the melting temperatures of EEA, EVA and m-PE are 98.0, 70 and 109.4℃ respectively.

Table 1. Thermal properties of polymers

	EEA	EVA	m-PE
T_m(℃)	98.0	70	109.4

EEA/MDH and EVA/MDH have high value of elongation due to the improvement of dispersion by MDH which is surface treated with stearic acid [10]. But in the case of EVA/ATH/MDH, it has low value of elongation due to the addition of inorganic fillers that does not have surface treatment. Comparing with the sample that has EEA, MDH and red phosphate, which is known as having a synergistic effect with MDH on flame retardation, the FR-PE that has EVA with over-filled inorganic filler shows high LOI value. That is, FR-PE with only MDH has high value of LOI [11]. Generally, it can be regarded as the cable that has higher LOI jacket material shows better performance in flame retardation experiment. However, in a real flame retardation test, the result is quite different due to the combustion behavior of flame retardant and the characteristics of char after combustion.

Table 2. Mechanical and flame retardation properties of polymer blends modified with various flame retardants

	EEA/ MDH	EVA/ MDH	EVA/ATH /MDH
Tensile strength (kgf/mm2)	1.23	0.9	1.12
Elongation (%)	458	530	210
Limited Oxygen Index (%)	32	50	42

3.2 Fire performance

3.2.1. Thermogravimetric analysis

According to several studies, magnesium hydroxide ($Mg(OH)_2$, MDH) and aluminum hydrate ($Al(OH)_3$, ATH) are used as halogen-free flame retardant for various plastics. When subjected to elevated temperature, they absorb heat energy that is required to keep burning the specimen before they liberate water vapor. The associated reaction is as follow:

$$\text{HydratePolyolefin} \xrightarrow{\text{Heat \& } O_2} H_2O + \text{Char} + \text{Byproducts}$$

In the course of this reaction, 30 ~ 35 wt% of the substance is released in the form of water vapor. This endothermic dehydration cools the plastic part and the water vapor dilutes evolved combustible gases. The latter is the main mechanism of smoke suppression. In addition to the energy consumption described above, the oxides and other decomposition products of the polymer matrix are deposited as a mineral coating on the surface of the material. This also retards significantly further advancement of the combustion process. This coating and the surface-active magnesium oxides those are formed as intermediate products, adsorb combustion products such as tar and soot particles. Thermogravimetric measurements give some information about the decomposition behavior of a polymer and flame retardant materials (FR-PEs).

Figure 2 shows thermogravimetric analysis of three different FR-PEs. As in Figure 2(c), thermal decomposition of EVA/ATH/MDH

commences earlier around 200• due to the decomposition of ATH. However at later stage, it shows slower decrease of weight than that of EEA/MDH. It is widely known that the decomposition of EVA occurs in two steps. The initiation temperature is about 350•. The first decomposition step is related to the cleavage of acetic acid from the copolymer. Then, as the next step, the decomposition of the polymer backbone is take place.

If the sample has no fillers, the thermal degradation of EEA begins at 400℃ and it proceeds rapidly. Around 500℃, the polymers are completely decomposed without any residues. The thermal degradation temperature of EEA is higher than that of EVA by approximately 40℃. As in Figure 2(c), when the sample is modified with inorganic fillers, the decomposition proceeds in two steps. That is, 200~300 and 330 ~ 500℃. The first step corresponds to the degradation of inorganic fillers including ATH and MDH. The second step is the degradation of polymers, especially polyethylene chains. In summary, even if the onset of degradation of modified polymer blends begins at lower temperature, the weight loss is slowed down in the second step and the amount of residues also becomes large. In other words, over 420℃, the degradation of polymers is effectively retarded by MDH.

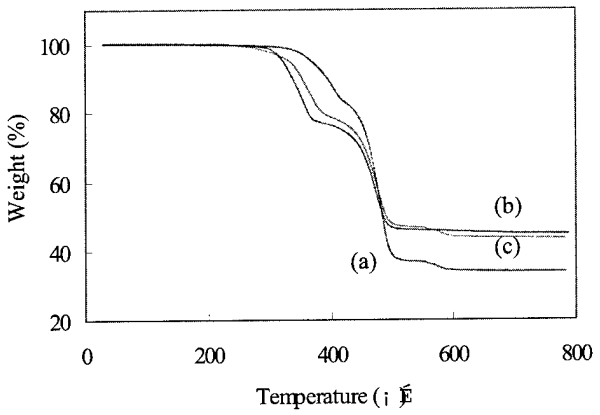


Figure 2. TGA curves of polymer blends modified with various flame-retardants: (a) EEA/MDH, (b) EVA/MDH, (c) EVA/ATH/MDH

3.2.2 Cone calorimeter by oxygen consumption

Figure 3 shows the curves of heat release rate (HRR) that is calculated from the amount of oxygen consumed during the combustion. Polymer blends without inorganic fillers show very high HRR peak over 1,000 kW/m^2. Since thermal degradation proceeds rapidly, all the energy is released within 200 sec. Before ignition, the carbonization of polymeric material and the evolution of gases without oxygen consumption are observed. After ignition, the HRR increase very steeply by the contribution of the external heat source and the combustion of polymer [12].

As shown in Figure 3, by the addition of inorganic fillers such as ATH and MDH, the HRR is dramatically reduced to about 400 kW/m^2 and the second peak is also observed over 250 sec. The curves proceed through three steps: at first stage, after ignition, the degradation of polymeric materials initiates and the values of HRR increases rapidly. However, at second step, the HRR is effectively suppressed by the endothermic reaction of MDH and decreases by the formation of an expanded protective shield, which is induced by inorganic fillers. Thus, over a long time (600 sec) the heat is continuously released. Finally, the HRR increases again which indicates the degradation of heat-protective shield formed on the surface.

Figure 3(a) and (b) show the cases of EEA/MDH and EVA/MDH respectively. In that figure, EEA/MDH exhibit better combustion behavior. This behavior is quite different from the result of oxygen index. The oxygen indices of EVA/MDH and EEA/MDH are 50 % and 32 % respectively. The reason for this discrepancy is that flame retardant system like EVA/MDH is very easy to drip during combustion. Moreover, during combustion, the carbonized layer of that is expanded and cracked. Figure 3(c) is the HRR curve of EVA/ATH/MDH. This is more decreased over an entire range than that of EEA/MDH and the second peak, which is more delayed, is the lowest.

This result comes from the cooperation of ATH and MDH. They effectively prohibit the thermal decomposition of polymer. The reason is that ATH starts to decompose around 60~75℃ lower than decomposition temperature of EVA and MDH begins to decompose between 350℃ and 400℃, that is the maximum temperature of decomposition of polymer. In addition, there is no expansion and crack of carbonized layer because the rigid char is formed. The synergistic effect of ATH and MDH is observed. This behavior is consistent with the results from TGA and smoke density and confirms the synergistic interaction between ATH and MDH as a flame -retardant or smoke suppressant.

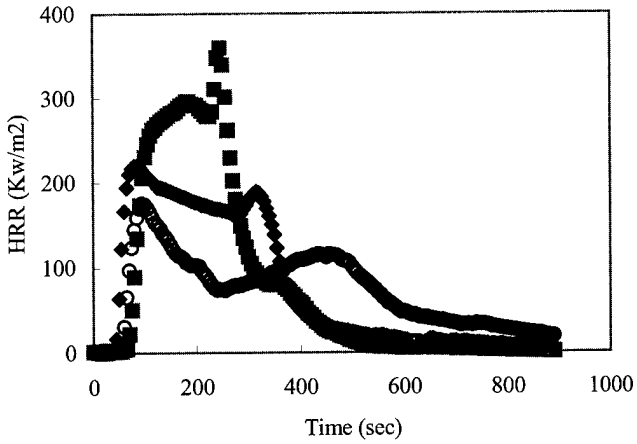


Figure 3. The curves of HRR with time (heat flux of 50 kW/m^2): (a) ◆ -EEA/MDH, (b) ■-EVA/MDH, (c) ○-EVA/ATH/MDH

The total heat evolved (THE) curves confirm the HRR change as shown in Figure 4. Compared with MDH-filled polymer blends, it is found that the surface of blend modified with both MDH and ATH is covered with more compact charred layer. The interaction between MDH and ATH gives a positive contribution to forming the protective shield under flame. For all FR-PEs, the THR has not changed so much, but the time at which THR of EEA modified with MDH reaches the equilibrium value is retarded. This time for EVA is more delayed by the incorporation of ATH and MDH than that of EEA by the addition of only MDH.

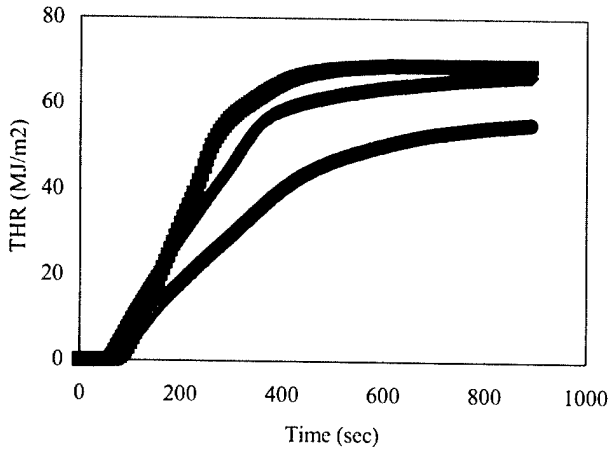


Figure 4. The curves of THE with time (heat flux of 50 kW/m^2): ◆-EEA/MDH, ■-EVA/MDH, ○-EVA/ATH/MDH

Figure 5 depicts total smoke release (TSR). As the figure shows, the combination of MDH and ATH causes a considerable delay in reaching to maximum smoke evolution and significantly lowers the overall level of produced smoke. Therefore, it can be concluded that, as exposed to heat and flame, ATH interacts with MDH and exhibit a synergistic effect on the depression of smoke evolution. In case of EEA/MDH, the addition of flame retardant like phosphorous flame retardant enhances smoke formation because it is acting mainly as the gas phase (by interrupting the radical chain mechanism of the combustion process) and this leads to the production of more soot particles and CO.

Figure 6 shows scanning electron micrographs of the residues after combustion. Compared with only MDH-filled polymer blends, the surface of blend modified with both ATH and MDH is covered with more compact charred layer. The resulting metal oxides form a quasi-ceramic layer on the surface of plastic material inhibiting the further access of flame to fresh polymer. These coating and highly surface-active oxides formed as an intermediate have excellent adsorption abilities for carbon and soot particles as well as for other combustion products. ATH acts as a sintering agent to produce a hard charred layer, which is a good thermal barrier. That is, the interactions between ATH and MDH reinforce the protective shield under flame and thus the evolution of smoke is effectively suppressed. In addition, the effect of flame retardation is also increased.

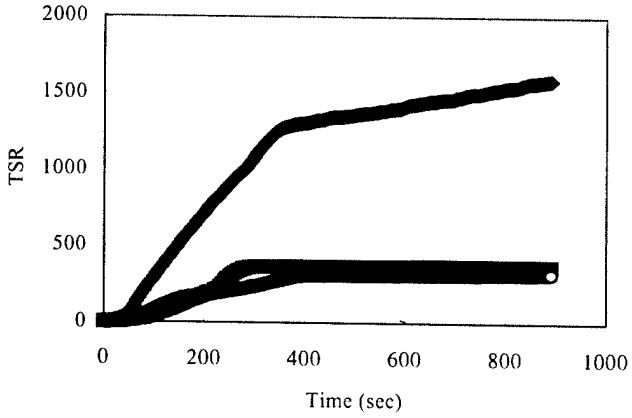


Figure 5. The curves of TSR with time (heat flux of 50 kW/m^2): ◆-EEA/MDH, ■-EVA/MDH, ○-EVA/ATH/MDH

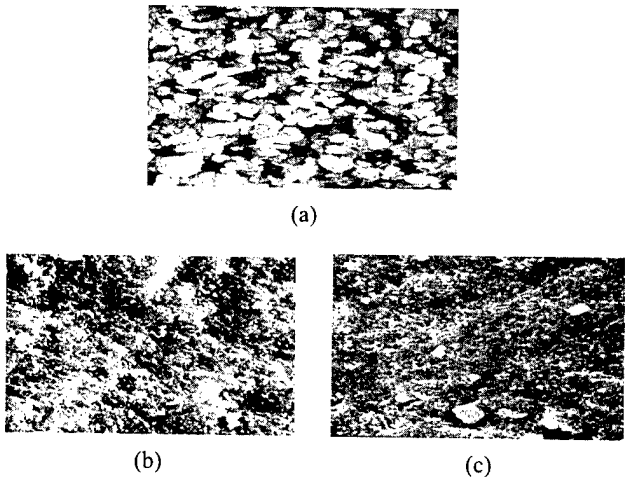


Figure 6. Scanning electron micrographs of the surfaces of polymer blends modified with various flame retardant (after combustion): (a) EEA/MDH, (b) EVA/MDH, and (c) EVA/ATH/MDH

In Figure 7, results of smoke density measurement for EVA/ATH/MDH specimen and the cable that has a jacket of EVA/ATH/MDH are presented. At initial stage, the smoke generation behavior is similar for both cases. However, the smoke continuously evolved for cable because the inside material of cable burns after the jacket material has been burned.

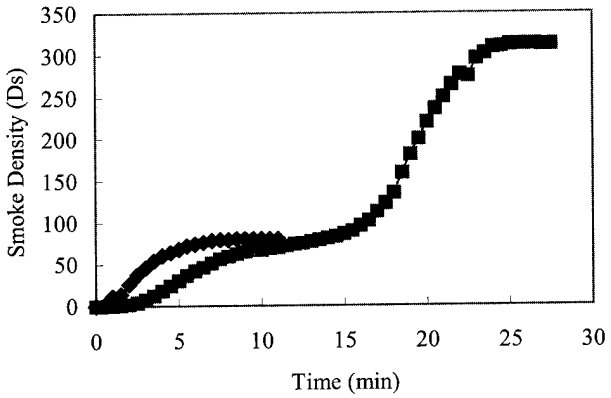


Figure 7. The smoke density versus time ◆-EVA/ATH/MDH, ■-72F L/T cable.

The UL 1666 riser 12ft. vertical shaft flame test has five points of measurement: 1) 12ft maximum temperature of 454 ℃. 12ft maximum height: 2) flame, 3) melting, 4) charring, 5) ash. As shown in Table 3, loose tube 72F cable jacketed with ATH/MDH filled FR-PE passed UL 1666 riser test. If the sheathing material has low flame retardation or less solidification of carbonized layer, it promotes the combustion of flammable material of the cable. This makes the cable shows melt drip phenomena and burn it out. From the result of flame retardation test for cables of various FR-PEs, it can be concluded that the role of jacket in combustion is very critical.

Table 3. Test results of UL 1666 riser

Cable ID	Max Flame Height (ft-in)	Maximum Damage Height (ft-in)			Maximum Temperature (°F)
		Jacket			
		Melt	Char	Ash	
72F L/T	8-6	9-0	8-6	6-0	558

Cable ID	Cable O.D. (in.)	Number of Lengths
72F L/T	0.494	24

4. Conclusions

In this work, we have investigated halogen-free flame retarded polyethylene to study the effect of inorganic fillers on the improvement of flame retardation and the suppression of smoke density. It is revealed that the flame retardation developed by MDH could be effectively enhanced by the additional incorporation of ATH. The interaction between MDH and ATH aids in developing a hard and compact charred layer, which increases the resistance under flame stress and reduces the combustion rate. Thus, due to this additional protective barrier, the flame retardation is improved and the evolution of smoke density is also effectively suppressed.

5. References

[1] Bernard M.B., International Wire and Cable Symposium , 10 (1998).

[2] David A.Keller, Jack Rosko, and Brian Risch., International Wire and Cable Symposium , 17 (1998)

[3] Hirscher M. M., In Fire and Polymers, edited by Nelson, American Chemical Society pp. 462 (1990).

[4] Halloway L. R., Rubber Chem Technol., 61 186 (1988).

[5] Shen K. K., Plastics Compounding, (1988).

[6] Rothon R. N., Paticulate-Filled Polymer Composites, Chap. 6 Paticulate Fillers used as Flam Retarant, edited by Rothon R. N., Harlow Longman, (1995).

[7] Hornsby P. R. and Watson C. L., Polymer Degradation and Stability, 30 74 (1990).

[8] Stinson J. M., J. Vinyl Addit. Tech., 2 94 (1995).

[9] Molesky F., Schultz R., Midgett S., and Green D., J. Vinyl Addit. Tech., 2 159 (1995) (2000)

[10] Pukanszky B., Fekete E. and Tudos F., Makromol Chem Macromol Symp, 28 165 (1989).

[11] Kato H., 工 , 43 6 101 (1995).

[12] Do Hyun Park, Sang Cheol Kim, and Gun Joo Lee., International Wire and Cable Symposium, 422 (2000)

Authors



Do Hyun Park
LG Cable R&D Center
Polymeric materials T/G
Associate Research Engineer



Gun Joo Lee
LG Cable R&D Center
Polymeric materials T/G
Principal Research Engineer



Myeong Jin Ahn
LG Cable R&D Center
Polymeric materials T/G
Senior Research Engineer



Sang Cheol Kim
LG Cable R&D Center
Polymeric materials T/G
Senior Research Engineer

Crush Investigation of Slotted Core Cables

Bradley Blazer and Andreas Stingl
Corning Cable Systems
Hickory, N.C.
email address: Bradley.Blazer@corning.com

Abstract
The crush resistance of fiber optic cable is an important quality-relevant cable property. Cables must have sufficient crush resistance to withstand the rigors of installation and long-term deployment without damage or interruption of service. Crush testing procedures are included in such specifications as IEC 60794, DIN EN 18700 504, and CECC 87 00 M504. This type of testing can provide data such as attenuation change, structural deformation, and mechanical deterioration of the cable structure under lateral load.

The maximum crush force is dependent on the cable design parameters e.g., cable diameter, jacket thickness, structural configuration of the core, and position of the strength members in the jacket or core. Polymer material properties like elastic modulus and yield stress and strain also affect crush performance.

In this paper we focus on slotted core ribbon (SCR) cables to understand the effect of a foamed polymer upjacket over the central strength element. The maximum crush load of such cables is reached when the legs that form the slots buckle or deform to an extent that the fibers begin to receive some of the stress. It is clear that the strength and stability of the legs as well as slot size and shape will significantly affect crush performance. The influence of the foamed layer, the jacket and the lay-length/stranding geometry are not initially so apparent. Therefore the interaction of the structural components of the cable under crush load must be determined. The market driven need to downsize the cable diameter, while simultaneously increasing the fiber density and maintaining tight crush specifications, requires optimization of the cable design.

In order to optimize cable construction, an implicit finite element model has been developed. This model takes into account variables such as cable dimensions, degree of foaming, leg buckling, and material plasticity and has been cross-checked with the actual cable crush behavior with good correlation.

Keywords
Slotted core, foaming, implicit, finite element, crush

1. Introduction
The cable manufacturer is continuously forced to reduce size, weight, and costs. Specifically for non-armored SCR cables, the reduction in size requires thin jackets, small legs and a decreasing ratio of leg size to slot size. Under crush load, the cable jacket and the core legs as well as the solid center portion of the core represent the cable lateral load-bearing elements. If the Jacket thickness is reduced, more load is transferred to the legs. When leg size is also reduced, the cable loses a significant amount of crush performance. It is possible for foaming to have a positive or negative effect, either helping to moderately absorb and distribute some of the load or allowing excessive deformation of the cable structure.

The goal of this investigation is to find an optimum cable construction with small diameter, low weight, and good crush performance.

2. Slotted Core Cables

The SCR cable design is commonly employed in Japan. It features an extruded core profile with a central strength element. In this paper we consider SCR cables with thirteen slots, 1000 fibers and a helical stranding geometry.

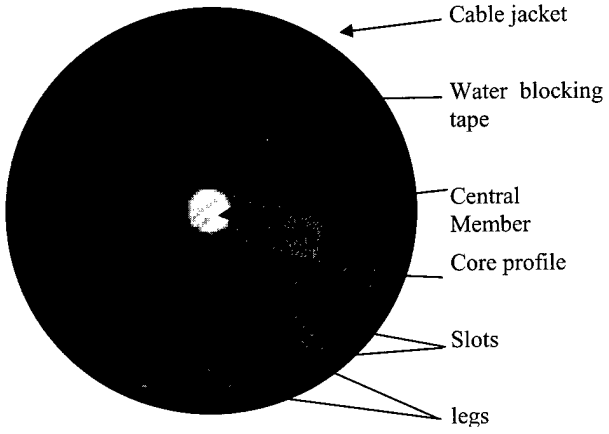


Figure 1. Cross-Section of 1000 F SCR-Cable

Figure 1 shows the unloaded and undeformed cross section of the 1000f SCR cable with fibers removed. Typically 12 slots contain ten 8-fiber ribbons/slot with the thirteenth slot containing 5 ribbons for a total of 125 ribbons or 1000 fibers. The diameter of the cable is approximately 30mm. The picture shows a design with solid polymer upjacket and a steel central member. Core size reduction for this cable design is very limited since the legs are already fairly thin at the root. Weight reduction options include thinner jackets, smaller/lighter central members, or lighter rod materials. The large core upjacket in this particular design is a good candidate for weight reduction. Two methods of upjacket weight reduction are considered in this investigation: Foaming and the introduction of larger cylindrical holes or voids, in a radial arrangement around the central member.

In order to investigate these options we employed an implicit finite element (FE-) model and varied key design parameters.

3. SCR FEA modeling

3.1 2D Cross-Section Modeling

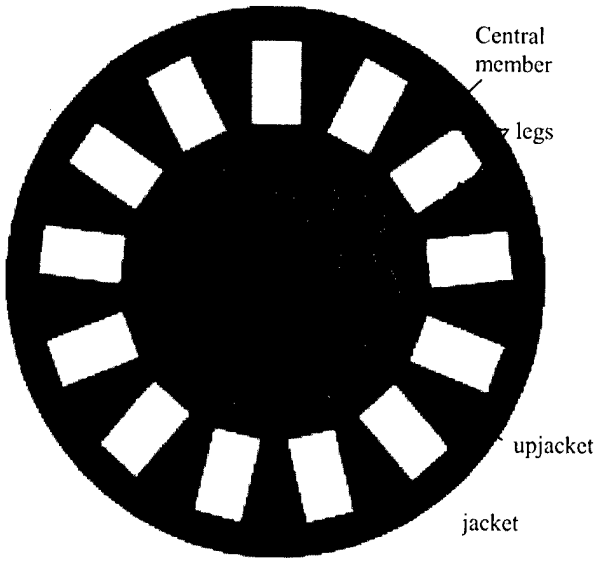


Figure 2. Finite Element Cross-Section of SCR-Cable

Figure 2 shows the initial 2D cable model with an overlaid finite element mesh for structural analysis. In order to save CPU time and to reach maximum flexibility we focused on a rather coarse mesh based on brick elements, accumulating the elements at regions in which high stresses are expected such as the legs and the leg roots. The model represents the major load bearing components of the cable.

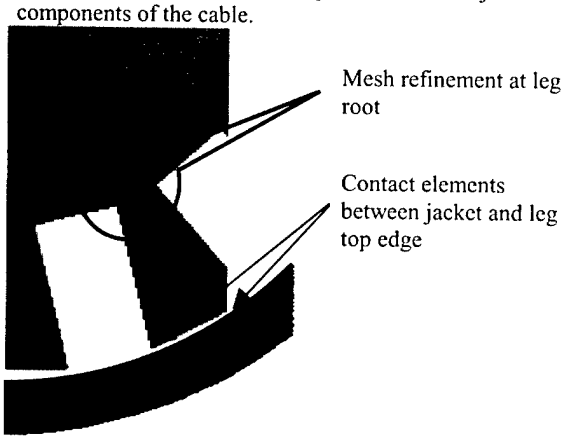


Figure 3. FE Model Sector

Figure 3 shows a zoomed part of the cable model to illustrate the mesh refinement of the legs as well as the contact interface between the core profile and cable jacket. A significant challenge in creating the model was to accurately define the contact elements where various parts of the cable structure interact.

3.2 Modeling of the Leg-Jacket Interface

During the manufacturing process the upjacket is extruded onto the central member, the leg portion is extruded onto the upjacketed central member, ribbons are inserted and the core is wrapped with water blocking tape. Finally the jacket is extruded onto the cable core. The water-blocking layer between cable core and jacket prevents adhesion so the contact element must be defined accordingly.

First trials using the 2D model and neglecting the core water blocking to jacket interface, i.e., assuming the whole cable structure as continuous, led to poor results as illustrated in Figure 4.

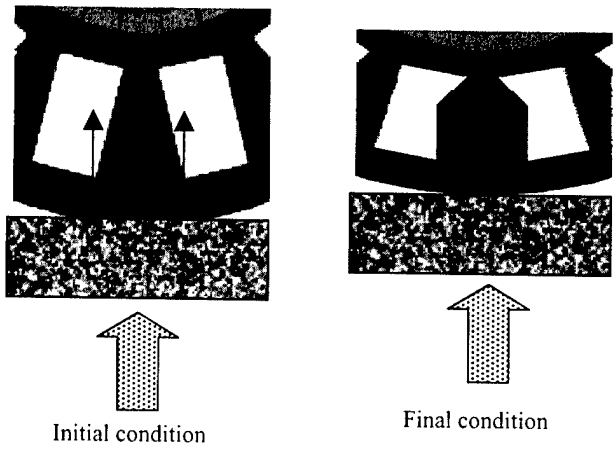


Figure 4. 2D FE Model Sector under Crush Load

Figure 4 shows the leg behavior of the continuous 2D crush model. The cable cross section is symmetrical and the influences of stranding geometry and the discontinuity between jacket and core are neglected. This creates a very symmetric and stable load condition on the bottom leg. As a result, the modeled leg takes the whole normal force, shortening and thickening under the load. Unfortunately, this ideal behavior does not match test observations.

In order to achieve more realism, we felt the need to refine the model of the interface between the jacket and the core. Furthermore we wanted to simulate the effect of shear force on the top edge of the leg caused by the stranding geometry and leg leaning.

To solve the first problem we switched from a continuous model to a discontinuous one. This means that both the cable core and the jacket act separately, without sharing any elements or nodes. Structural interactions between core and jacket are considered via contact and target elements.

To solve the second problem, i.e. to consider the influence of stranding, we had to construct a full 3D model.

3.3 3D Crush Modeling

The 3D model is derived from the 2D model by adding segments or layers of brick elements to the original 2D model until the target model length is reached.

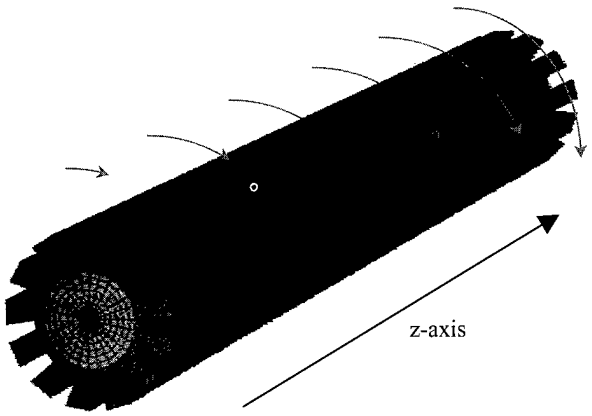


Figure 5. FE Core Profile with Parallel Core Legs

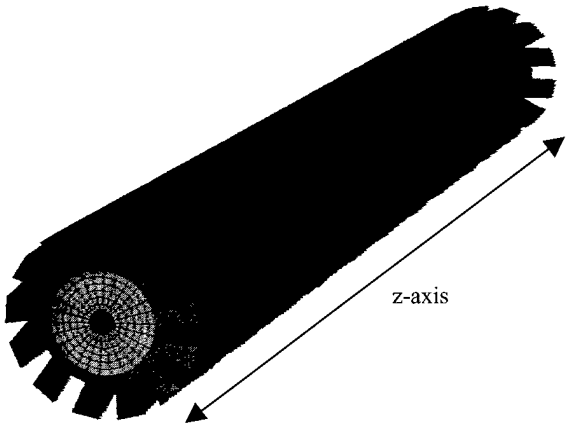


Figure 6. Stranded FE Core Profile

Figures 5 and 6 show the mesh used to simulate the 3D core profile. Due to the element extrusion on the basis of a 2D model, we generated parallel legs (Fig. 5), then added the stranding geometry (Fig. 6).

The model consists of a series of adjacent segments as illustrated in figure 7.

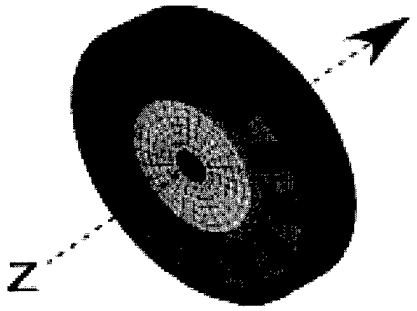


Figure 7. Model Segment in Detail

The stranding geometry is applied to the model by incrementally rotating the segments about the model's longitudinal z-axis.

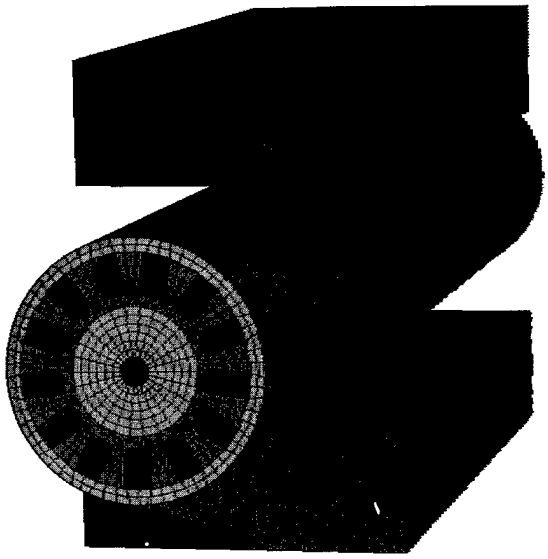


Figure 8. Full 3D Crush Model

Figure 8 shows the complete crush model, including jacket and crush plates.

The crush plate material is high modulus steel, assumed to be structurally rigid under test conditions. Force is transmitted from the plate to the cable using contact elements. Crush plate dimensions are according to IEC 60794.

4. Material Properties and Data

The modulus of the steel central member is assumed to be linear in the range of load applied. Under high crush loads however, the polymer cable components will be strained beyond their yield limits. Therefore it is very important to take nonlinear material behavior into account. Empirical stress – strain data such as that shown in Figure 9 allows this nonlinear behavior to be modeled.

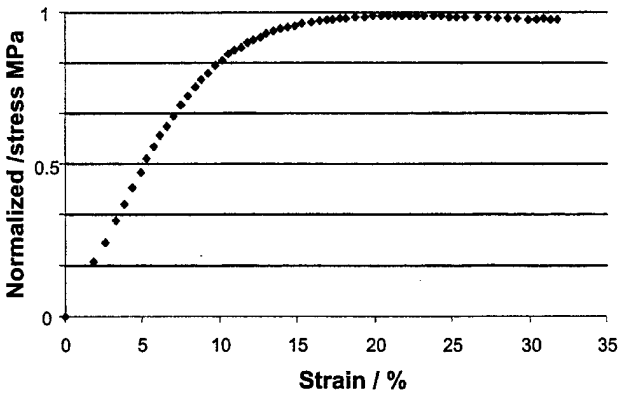


Figure 9. Typical Polymer stress-strain curve

Figure 9 shows a typical stress-strain curve normalized to the maximum stress occurring in the range between 0% and 33% strain.

As mentioned above, one goal of the project was to reduce weight by foaming the upjacket to a degree of up to 70%. The influence of foaming on the polymer properties had to be investigated through material testing. The fortunate result was that the relationship between degree of foaming, modulus and yield was nearly linear in the strain range we were targeting. This helped to simplify the model significantly.

5. Measurement Setup

Crush testing was performed on a load frame using 100mm parallel plates. Samples are typically crushed mid-span on a long sample to eliminate end effects. For the purpose of understanding crush behavior, some samples were prepared with a cleanly cut end that was placed flush with the end of the plates as seen in figure 10.

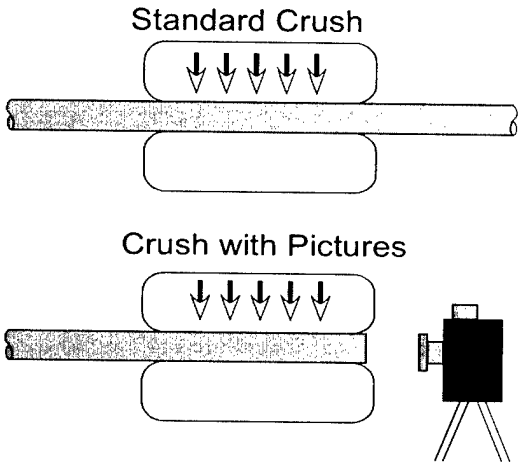


Figure 10. Measurement Setup

A series of pictures taken during the test was then used to observe cable behavior at various load/deflection points. In most cases, the change in boundary conditions due to the presence of the cut cable end adjacent to the crush region has a minimal effect. A comparison of the load vs. deflection curves usually indicates only a slightly lower crush resistance in the cut sample.

The load vs. deflection graph generated by crush testing tends to have distinct features that can be interpreted to provide valuable insight as to mechanical behavior during crush. In figure 11, two similar cables with different degrees of crush resistance are compared. The displacement is separated into 3 regions. In the pre-yield region, very little deformation of the cable geometry occurs. In the slot intrusion region, the slot legs begin to collapse and the fibers begin to feel some of the load. In the collapsed core region all void space is gone and the fibers are fully loaded. Of primary concern is the point at which the fibers begin to feel the effects of the crush load. They are certainly safe in the pre-yield region. The amount of slot intrusion that can be withstood is largely a function of the amount of free space in the slots but the inflection point is a good reference point. For similar designs the deflection at maximum load should be about the same so after evaluating one sample in depth it may be possible to compare other samples based on load vs. deflection data alone.

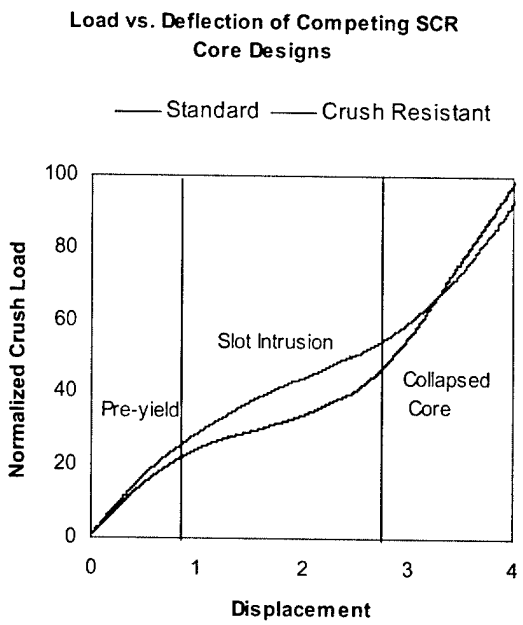


Figure 11. Load vs. Deflection of Experimental SCR Cables with Competing Core Designs

6. Results

6.1 Verification of the Model

The typical force versus deformation behavior of SCR cables features leg buckling under high crush load. It is very important to consider this structural instability in the model, as this effect is the limiting factor for the maximum crush load of the cable. Modeling results were compared to actual test data and photographs to gauge the accuracy of the analysis.

6.1.1 Visual Check

Figure 12 is a visual comparison of the actual crush test vs. the FEA simulation.

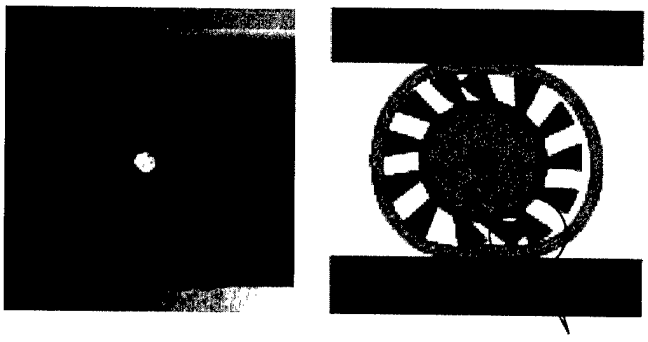


Figure 12. Crushed Cable and Model

Figure 12 shows cable and model cross-sections under a certain crush deformation. Comparing the deformations of the legs we observe an amazing coincidence between cable and model. The

leg overlap at the bottom of the core profile in the model is due to the lack of a contact definition between leg elements. As described above we had to define the contact element between the leg edge and the jacket. Since there is no contact definition between adjacent legs, at high deformations the legs may overlap as seen in figure 12.

6.1.2 Crush Behavior of Cable

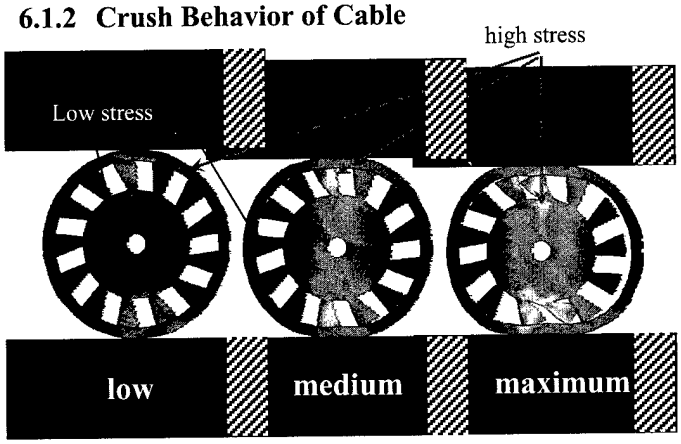


Figure 13. Cable Crush, Different States

Figure 13 shows a 3-state history of the crush simulation, with a color overlay of the stress distribution on the cable cross-section, representing a segment in the middle of the model. On the gray scale, bright depicts high stress, dark depicts low stress. The crush behavior of this cable can be divided roughly into 3 load stages, low, medium and maximum.

a) Low crush load

Under low crush load we observe low tensions in the core, higher tensions in the jacket, i.e. the jacket takes the major part of the load. We observe some transfer of load via the legs into the cable core.

b) Medium crush load

What we call medium crush load in this simulation is the operating limit for the cable, as we observe a noticeable cable ovality, slot cross-section reduction and leg deformation. The legs transfer a considerable amount of load into the core. The legs are loaded close to the maximum of their mechanical stability.

c) Maximum crush load

The stability limit of the core legs is reached. The amount of stress has reached the material yield point. The legs tilt and the structure collapses.

6.1.3 Comparison to Measurement

Several design experiments with different degrees of foaming of the upjacket have been done. Figure 14 shows normalized crush load vs. deflection. The dots depict single measurement points. The dotted trace is fitted to the measurement data. The rest of the traces show the crush forces calculated for different degrees of foaming.

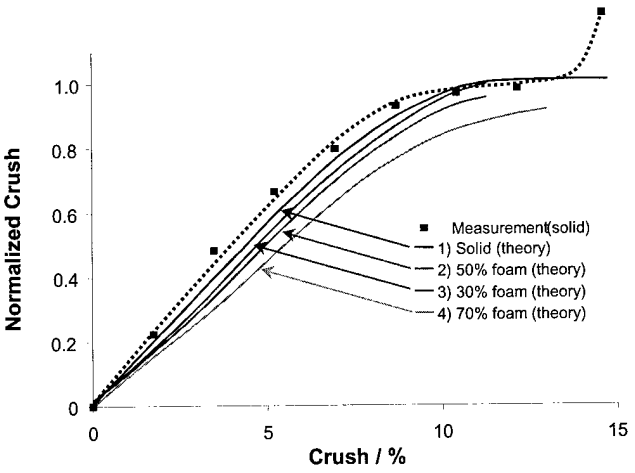


Figure 14. Cable Crush, Load vs. Deflection

The correlation between theory and measurement for the solid cable is very good at low and medium crush loads. At maximum deflection, the measurement indicates a rapid increase in stiffness following leg collapse. Again the lack of a contact definition between legs comes into play and this extreme crush behavior is not modeled.

6.2 Influence of Degree of Foaming on the Cable Crush Performance

Partial foaming of the cable as a means to reduce weight also reduces the lateral stiffness of the cable as seen in figure 14. A positive side effect is that the foamed cable core, by deforming slightly, can relieve the slotted portion from some of the strain. In using our model to investigate this effect, load vs. deflection is no longer the best indicator of crush performance.

As seen in Figure 15, crush deflection deforms the legs and reduces the free slot space. Considering the ribbon stack area as the minimum slot area needed for proper cable operation, monitoring the slot cross-section as a function of crush is a good criterion to characterize the influence of foaming.

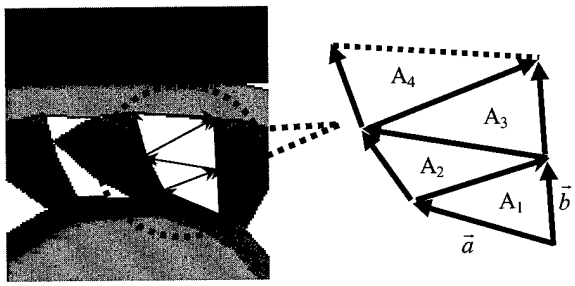


Figure 15. Method to Approximate Deformed Slot Cross-section

Under crush deflection the original rectangular shape of the slot is reduced and deformed to an irregular shape. The cross-section of the deformed slot is approximated using a sub-layer of triangles; each defined by three vectors. The total slot cross-section is calculated as follows.

$$A_{slot} = \sum_i A_i$$

Where A_i is calculated via a simple vector equation:

$$A_i = \frac{\bar{a}_i \times \bar{b}_i}{2}$$

Equation 1. Approximation of Slot Cross-section

We used equation 1 for the calculation of all slot cross-sections during crush.

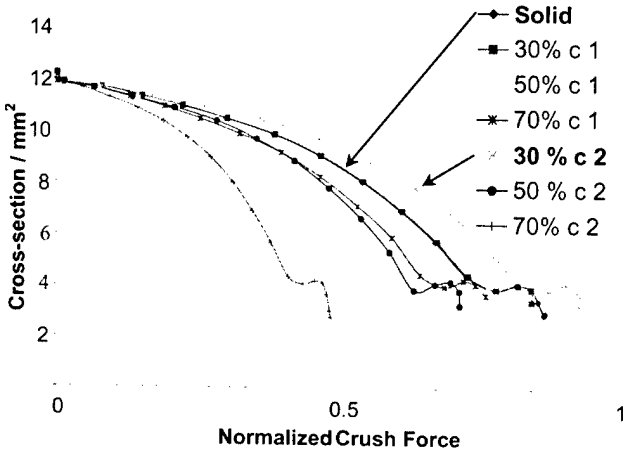


Figure 16. Slot Cross-section vs. Crush of Foam Core

Figure 16 shows the maximum reduction of the slot cross-section as a function of the crush load for different degrees and types of foaming. As expected, the maximum degree of foaming renders the worst crush performance.

The interesting result is that we found one case, with a degree of 30% foaming (c2), which in fact had better crush performance than the solid, i.e. the unfoamed case. This phenomenon can be explained considering the crush deformation and strains.

A very soft upjacket allows substantial deformation and cross-section collapse at low loads. Alternatively with a rigid upjacket all the deformation occurs in the legs and jacket. The result is low overall deformation but significant slot size reduction.

Our design study called 30% c2, on the other hand, provides good stiffness but also buffering benefits for the legs. As a result, the slot cross-section is preserved at higher loads and deflections.

7. Alternative design

As mentioned above the major goal of this study was to reduce weight and costs. An alternative to foaming is to introduce larger scale voids as shown figure 17.

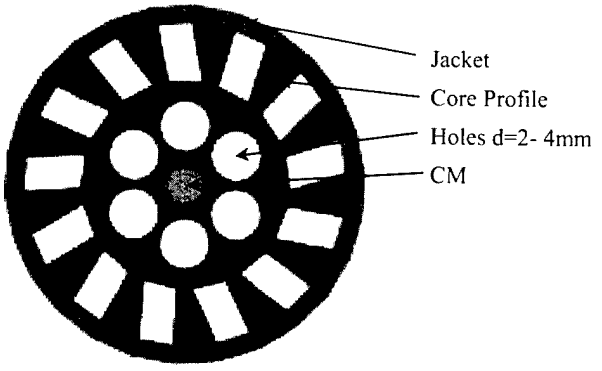
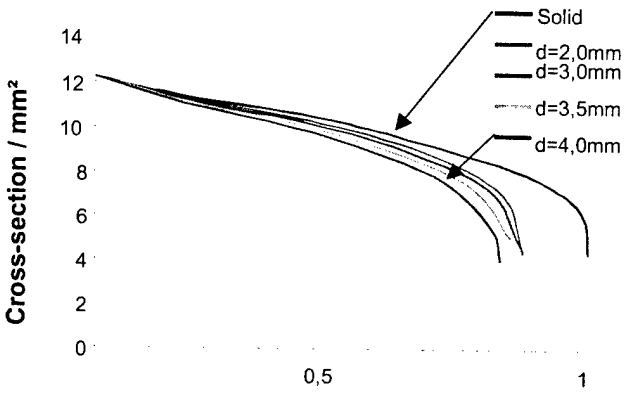


Figure 17. Cable Cross-section with Voids in Upjacket (Void-Core Cable)

The large-scale voids are incorporated in the form of cylindrical holes in the upjacket, parallel to the central member. The diameter of the holes could be 2-4mm.



Normalized Crush-force

Figure 18. Slot Cross-section Vs Crush of Void Core

Figure 18 shows the evolution of slot cross section versus crush force for the void-core cable. The theoretical investigation shows that hole diameters between 2mm and 4mm cause a decrease in crush performance. While we did not focus on that design too much, it may be possible to alter the size, shape and arrangement of the holes to achieve optimal crush performance just as was accomplished with foaming. One point worthy of mention is that by extruding the holes into the upjacket, parallel pipes are generated with a diameter of up to 4mm. These pipes could serve a variety of purposes such as blown fiber applications to extend an installed cable system.

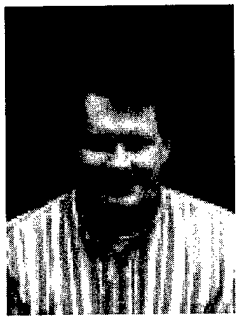
8. Conclusions

- It is possible to model a discontinuous cable with instabilities in an implicit finite element program.
- Foaming is an excellent means to reduce weight.
- Some types of foaming provide an increased crush performance with regard to crush force and attenuation.
- Alternative designs like a void-core cable have been considered theoretically.

References
[1] Klaus-Jürgen Bathe
Finite Elemente Methoden
Springer Verlag
Berlin Heidelber 1990

[2] Dubbel
Handbook of mechanical engineering
Springer Verlag
Berlin Heidelber g1994

Presenting Author



Bradley J. Blazer
Corning Cable Systems RH
P.O. Box 489
Hickory, NC 28603

Bradley Blazer is a Development engineer in the Japan cable group at Corning Cable Systems RD&E in Hickory, NC. His responsibilities include product and process development of slotted core ribbon cables. He received a B.S.M.E. degree from North Carolina State University in 1992 and was an instructor at the US Navy Nuclear Power School from 1992 to 1996. He joined Siecor, now Corning Cable Systems in 1996 as a field engineer and transferred to RD&E in 1999.

Author



Andreas Stingl
Corning Cable Systems
96465 Neustadt Coburg
Germany

Andreas Stingl was born 05.11.1970. He joined Siemens RD&E in 1996; he received his physics degree from the university of Bayreuth in 1997. He has been working on his PHD, considering numerical models for cable simulation from Jun. 1997 until Feb 2000. He is now responsible for FE simulations at RD&E Corning Cable Systems, Neustadt / Coburg.

Crush and Bending Resistance in Next Generation Cable Designs

Lisa A. Dixon, Peter A. Weimann, Richard H. Norris,
H. Paul Debban, Richard D. Small
Lucent Technologies Optical Fiber Solutions
Norcross, GA
+1-770-798-3787 · LAD13@lucent.com

Abstract

Installation costs are an important concern in the deployment of a fiber optic network. The time required to terminate and splice optical cables represents a significant portion of the installation time and costs. Removing waterblocking gels from the cable and fibers during the splice preparation process is a serious nuisance that extends the time, and therefore the cost, of terminating a cable. As a result, the industry trend is to minimize the use of gel, thereby reducing installation costs and improving craft friendliness. However, as incompressible fluids, these gels contribute significantly to the crush resistance of a cable. This functionality is not easily replaced with alternative waterblocking technologies. To understand the overall impact of the design trend to minimize waterblocking gels, this paper evaluates the crush resistance of cables with standard as well as minimized gel content. In addition, this paper will assess both the use of material selection for other cable components (jacket, core tube, etc.) and the effect of cable design to compensate for the removal of these incompressible gels.

Keywords

Fiber optic cable; crush resistance; kink resistance; waterblocking gels.

Introduction

Installation costs are an important concern in the deployment of a fiber optic network. The termination or splicing of optical cables is often the most time consuming installation activity and represents a large portion of the installation costs. In particular, removing waterblocking (WB) gels from the cable and fibers during the splice preparation process is a serious nuisance that extends the time, and therefore the cost, of terminating a cable. As a result, the current industry trend is to minimize the use of gel, to reduce installation costs and improve craft friendliness. Examples of this effort are already on the market, originally in the form of slotted core cables. More recently, cablers have developed "dry core" loose tube [1] and tube-in-tube [2] [3] central core designs, both of which reduce the presence of gel by a substantial amount. These designs use thixotropic gels within the fiber-containing unitizing tubes, which are stranded within an otherwise dry sheath. However, in addition to waterblocking functionality, cable gels also provide a less obvious, but no less critical benefit – resistance to compressive loads caused by crushing and bending. As incompressible fluids, gels can contribute significantly to the compressive resistance of a cable. This functionality is not easily replaced with the alternative waterblocking technologies used to replace the gels.

In order to understand the overall impact of the design trend minimizing waterblocking gels, this paper evaluates the compressive resistance of central core cables with two core designs: standard filled cores, and reduced-gel tube-in-tube cores [3]. As part of this study, selection of the materials of construction for other cable components (e.g. jacket, core tube, etc.) is considered. Finally, the use of sheath design as a tool to compensate for the removal of these incompressible gels is examined.

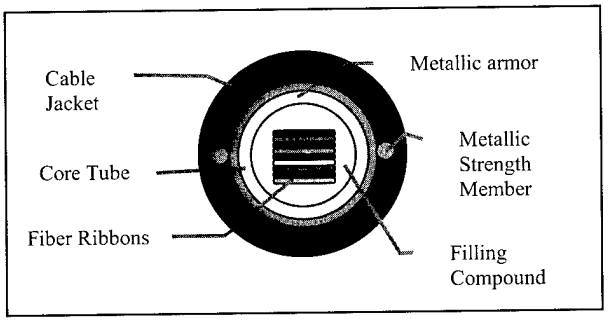
Section 2 presents contemporary cable designs that use waterblocking gels, and the motives for and effects of minimizing the use of gels in new designs. The test used to characterize the compressive resistance of various cable designs analyzed in this paper is described in Section 3. Section 4 presents the initial findings on the effect of reduced gel on compressive resistance of central-core core tubes. Section 5 identifies and reviews the portfolio of options available to the designer to increase the crush resistance of a sheath in the absence of the core gel. In addition, Section 5 presents the results of measurements of the compressive resistance of prototype cables incorporating these design options. Section 6 analyzes the data presented in Section 5, and discusses the most effective design options, as embodied in current cable designs. Section 7 concludes with general comments on designing cables with reduced gel.

2 Background

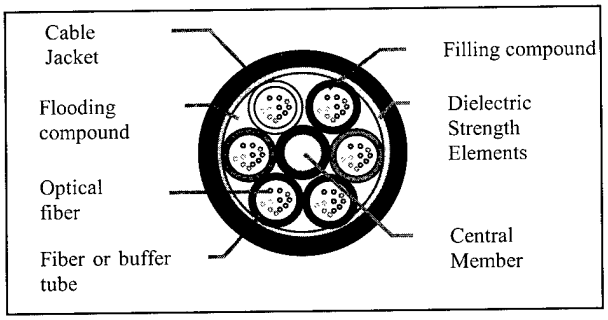
2.1 Use of Waterblocking Gels in Optical Cables

Use of gels to block the ingress of water into and along the length of fiber optic cables dates back to the early generations of optical cables. As shown in Figures 1 a) and b), thixotropic gels are commonly used as "filling compounds" to fill fiber tubes in both central core and loose tube sheath designs. "Flooding compounds" are used to fill the space between fiber tubes and the rest of the sheath, as shown in Figure 1 b). The use of flooding compounds predates optical cables, as this technology was first developed for use in non-pressurized copper cable applications. However, the gels that were eventually developed as *filling* compounds have a combination of key attributes that make them ideal for blocking water in fiber tubes. The filling compounds can be described as follows:

- Highly viscous, to resist displacement by the flow of water, even under pressure.
- Insoluble in water.
- Low viscosity at high temperatures and/or high shear rates, such that the gels are fluid enough to flood all air gaps in the core during fabrication.
- Low yield stress at the full range of cable operating temperatures, to limit mechanical loading (and resulting attenuation) of the optical fibers during temperature cycling and after deformation caused by installation loads.
- No impact on optical performance after environmental aging.



a)



b)

Figure 1: a) A central core cable with WB gel; b) A loose tube cable with WB gels

However, the high viscosity and insolubility that make the gels ideal waterblocking materials also make them a nuisance in the termination and splicing process. Gels must be completely removed from fibers prior to splicing, and solvents are required to fully clean all gel residues. In addition, they have the potential and tendency to drip or smear onto fixtures and surfaces in termination boxes and surrounding areas. These exposed gels are then prone to collecting dust and dirt. For these reasons, eliminating waterblocking gels greatly improves the craft-friendliness of cables during splicing operations and in the handling the ends of cables during installation. [2]

2.2 Reduced Use of Waterblocking Gel in Optical Cables

As mentioned previously, several cable designs currently available on the market have either reduced or eliminated the use of waterblocking gels. The waterblocking function of the gels has been replaced by powders, yarns, tapes, or reinforcing members that incorporate super-absorbent polymer (SAP) particles which swell when in contact with water. These SAP particles are designed to swell fast enough to block all gaps or interstitial spaces between fibers or fiber-containing tubes and the rest of the cable core, blocking the further ingress of water.

However, replacing some or all of the gel with this alternate waterblocking technology reduces the compressive resistance of the overall cable. SAP components leave voids, while the gels fill all voids; as incompressible fluids, the gels resist the deformation of the surrounding sheath. This effect is easily demonstrated using a simple compression test.

3 Comparing Compressive Resistance of Optical Cable Tubes and Sheaths

Adequate resistance to compressive loads is an important attribute for optical cables. Any load that can sufficiently deform the cable sheath such that the load is transferred to the optical fibers can degrade the transmission of the optical signals. The adequacy of a sheath's crush resistance usually is monitored using several Telcordia GR-20 tests: Tensile Load and Bend; Hot Bend: Cold Bend; Impact; and Compression. [4] However, taken together, these GR-20 tests require long lengths of "live" optical cables for testing. To avoid the time and expense of these standard tests, a simple test based on the Telcordia Compression Test has been developed.

3.1 Compressive Test Procedure

The simple compressive test developed to quantify and compare the crush resistance of various cable designs uses 12-inch (30 cm) lengths of cable and a compression test apparatus mounted on an MTS electromechanical materials testing machine. Each sample is clamped firmly at both ends to prevent leakage of gel from the cable, and thus simulates compression of an infinite-length cable. Figure 2 illustrates the test set-up.

In the test, samples are compressed between round platens, which generate an effective gauge length of 4 inches (10 cm). Each sample is compressed to 50% of its original outside diameter at a rate of 2 inches/minute. Measurements of deflection and load are continuously collected in a burst mode for the duration of the test. This data is then used to generate a curve compressive load versus deflection. Figure 3 a) shows a typical deflection curve for a gel-filled metallic central core cable, identical to the cable shown in Figure 1 a), with an outer diameter of 15.5 mm and a core tube diameter of 8 mm. The plot shows an average of five test measurements. Error bars on the plot represent the standard deviation in the compressive load measured at that particular deflection. The error bars are included to provide a feel for the

reproducibility of the measurement. All plots subsequently presented in this paper are averages of multiple measurements, with error bars calculated and plotted as in Figure 3 a).

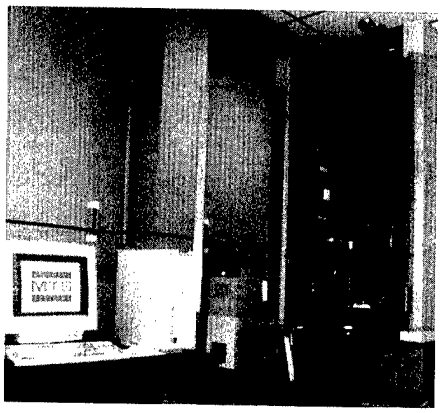
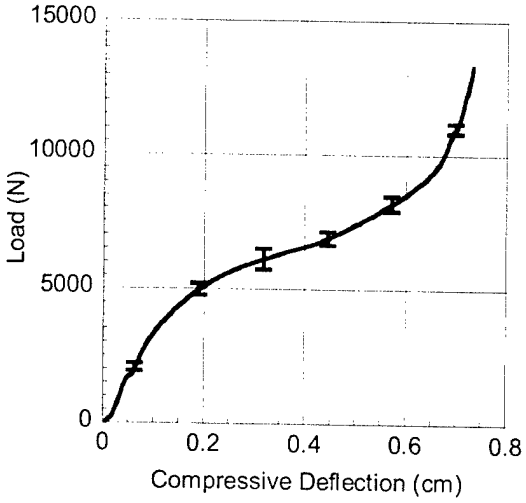


Figure 2: Compression test set-up

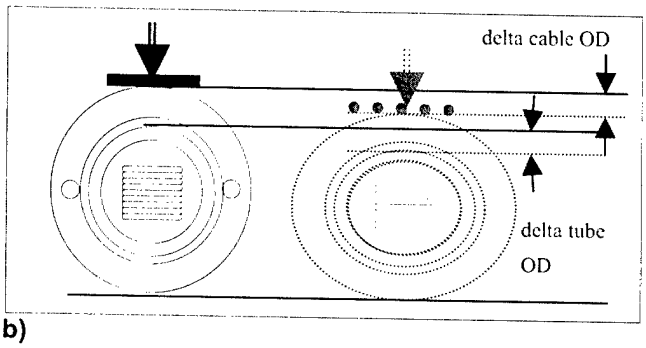
3.2 Deflection Data

When analyzing the compressive resistance of a cable, it is important to identify whether the cable can restrict deflection of the core inner diameter such that loads are not transferred to the optical fiber core. Specifically, the industry standard for compression resistance requires that the fiber core be protected from added loss under loads of up to 2700 N. [4] As a result, different cable designs should be compared based on their deflection at 2700 N. Further, to compare the performance of cables using only plots like the one shown in Figure 3 a), a deflection of a cable's outer diameter must correspond to an equal deformation of the cable core. In the test described above, it is presumed that all compression of the cable is translated to compression of the core diameter, as illustrated in Figure 3 b). For central core designs, this is a safe assumption because: 1) all components can be considered incompressible and 2) the core tube can not shift laterally to avoid being compressed.

Finally, note that the acceptable level of compression for a cable (and, therefore, the core) is dependent on the size of the core, i.e., how much the core tube can be compressed before pinching down on the fibers. Therefore, in order to characterize the compressive resistance of cables using raw deflection data, it is important to compare the behavior of cables with comparable core diameters. In this paper, all data to be presented is for cables or tubes with core tube diameters of 8 mm. For this size core, full scale cable testing following Telcordia standard test procedures confirmed that the maximum fiber-count core was adequately protected at deflections up to 1.8 mm at 2700 N.



a)



b)

Figure 3: a) Typical deflection curve: load vs. compressive deflection for a gel-filled, two-rod metallic cable, 8 mm core tube; b) Deformation of a cable under compressive load where "delta cable OD" is shown to be equivalent to "delta tube OD".

4 Compressive Resistance of Standard Central Core Tubes With and Without Gel

Using the procedure described in Section 3, initial experiments examined the influence of WB gel on the compressive resistance of core tubes used in central-core cables. Figure 4 compares the incremental deflection of a standard polypropylene central core tube (8 mm OD) filled with waterblocking gel to the deflection of the same tube with the cable gel removed (i.e., gel is replaced by air). The "dry" tube is a model of the core tube of a tube-in-tube cable design. Clearly, the incompressible gel significantly improves the compressive resistance of the central core tube.

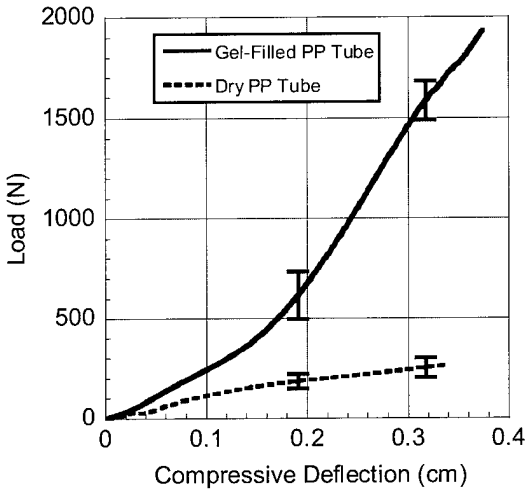


Figure 4: Load vs. compressive deflection curves for impact-modified polypropylene tubes with and without WB gel. Tube outside diameter is 8 mm, and wall thickness is ~0.75 mm.

Having illustrated the effect of the removal of gel on the compressive resistance of standard core tubes used in central-core cables, the next step is to evaluate the effect of filled and dry core tubes on cable compressive resistance.

5 Portfolio of Design Options to Improve the Crush Resistance of a Reduced Gel Sheath

Based on the data presented in Figure 4, it is assumed that the removal of some or all of the gel in a central core cable could degrade its resistance to compressive loads. Relying on basic principles of mechanics, it is possible to identify several options for supplementing or improving the crush resistance of a cable if this type of reduced-gel core is chosen. These options include:

- Selecting a higher modulus core or unit tube material
- Using a thicker walled core or unit tube
- Selecting only the most crush resistant sheath designs for use with reduce-gel cores

Each of these potential design options has been evaluated in this study.

5.1 Alternate Core or Unit Tube Material

To enhance the crush resistance of dry core tubes, multiple options are available. First, alternate core tube materials were examined. All data presented thus far has been for cables made with impact-modified polypropylene copolymer (PP) core tubes. Compared to other engineering plastics used in optical cables, the PP copolymers have relatively low moduli. A higher modulus material would have the potential to improve the crush resistance of the core. Poly(butylene terephtlate) (PBT) is often used in fiber optic cable designs in cases where a higher modulus tube material is needed, as PBT is significantly cheaper than other high-modulus engineering plastics. Table 1 compares the tensile modulus of a standard central core impact-modified PP to the tensile moduli of two standard grades of PBT, measured at 25°C. As shown in the table, PBTs typically have moduli two to three times larger than PP copolymers.

Table 1. Tensile Modulus of Core Tube Materials

Material	Tensile Modulus, 25°C
PP	835 MPa[a]
PBT-1	2600 MPa[b]
PBT-2	2600 MPa[b]

a Measured in laboratory using Instron tensile tester

b Manufacturer's reported data

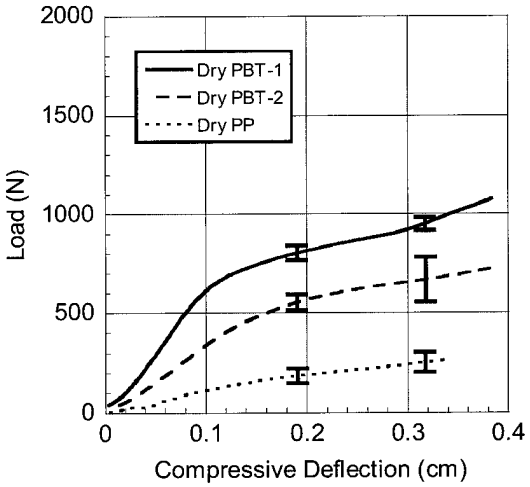


Figure 5: Load vs. compressive deflection for Type 1 and Type 2 poly(butylene terephthalate) (PBT-1 and PBT-2) and impact-modified polypropylene tubes, all without WB gel. Tube outside diameter is 8 mm, and wall thickness is ~0.75 mm.

Figure 5 shows the relative performance of gel-free, dry core tubes made with standard grades of PP and of PBT. The data in Figure 5 clearly shows that, compared to the PP tube, gel-free PBT core tubes provide an incremental improvement in compressive resistance. Figure 6 compares the compressive resistance of three cross-ply dielectric, central core cable prototypes using different core tube materials: PP, PBT-1, and PBT-2. All of these prototypes are gel-free, modeling the sheath

design for a tube in tube cable. Apart from the material used for the core tube, these three prototypes are identical. As shown by the figure, in cabled form, the stiffer core tube material has no effect on the compressive resistance of these dry prototype cables.

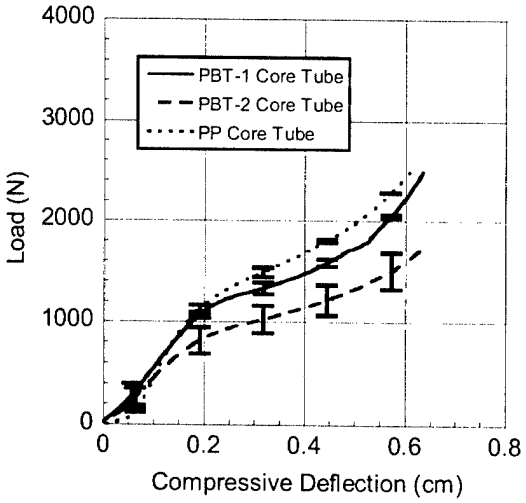


Figure 6: Load vs. compressive deflection curves for dielectric cross-ply cables with 8 mm diameter core tubes, without WB gel. Each of the three cables has a different core: impact-modified polypropylene (PP), Type 1 poly(butylene terephtalate) (PBT-1), and Type 2 poly(butylene terephtalate) (PBT-2).

5.2 Thicker Walled Core or Unit Tube

Another option for improving the crush resistance of the core is to increase the wall thickness of the core tube. Figure 7 shows the deflection curves of two dielectric cross-ply cables, one made with a PP core tube wall thickness of 0.75 mm, and one made with a 50% thicker tube wall (1.1 mm).

The data clearly shows that, at the cable level, the effect of this change is insignificant. In this comparison, relative to the overall diameter of the sheath, the increased wall thickness of the 1.1 mm thick tube is too small to change the compressive behavior of the cable. Increasing the thickness of the core tube is unappealing from the point of view of cable entry and handling. Instead, sheath design options may be leveraged to offer opportunities for significant improvement in crush resistance. These options are discussed in the next section.

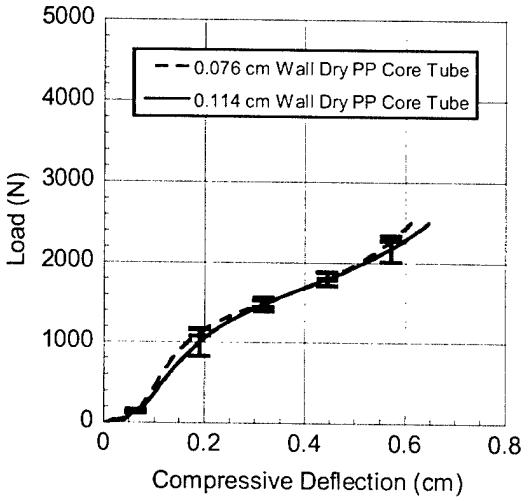


Figure 7: Load vs. compressive deflection curves for two dielectric cross-ply cables: standard PP core tube vs. thicker-walled PP tube.

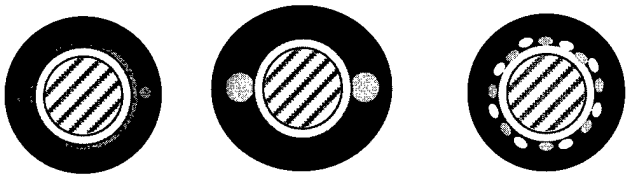
5.3 Crush Resistance of Standard Sheaths

As demonstrated by Figure 6, regardless of the core design, sheath design plays a prominent role in the crush resistance of an optical cable sheath. For example, it is generally expected that armored cables have greater compressive resistance than dielectric cables. While designed to resist intrusion by rodents, armored cables also leverage the presence of the high modulus, corrugated metal armor in resisting crush. A standard armored sheath with linear tensile members is shown in Figure 8 a). Figures 8 b) and c) illustrate two standard dielectric designs, a dielectric linear rod design that uses either two or six linear strength members, and a dielectric cross-ply design that uses two layers of much smaller, helically applied members.

Figure 9 compares the compressive resistance of prototype metallic linear two-rod, dielectric linear two-rod and dielectric cross-ply central-core sheaths with "dry" core tubes. These sheaths model the cable configuration that would be utilized for a "dry core" tube-in-tube design. While the data in Figure 9 clearly shows the metallic linear rod sheath design to be the most robust in the absence of the WB gel, both dielectric linear rod and metallic linear rod designs provide adequate crush performance for a tube-in-tube core.

However, having identified the standard cross-ply sheath as most vulnerable in the absence of WB gel, a final step is to evaluate design options for improving the compressive resistance of this design. One obvious design option to consider is increased jacket thickness. Figure 10 shows the deflection curves of two dielectric cross-ply cables, one made with a jacket thickness of ~1.1 mm, the other made with a 100% thicker jacket (~2.03 mm). The larger thickness was chosen as an attempt to approach the jacket

thickness of a dielectric linear rod cable with a similarly sized core. While the doubling of the jacket thickness improves the crush resistance of the cross-ply design, Figure 10 clearly shows the superiority of the linear rod design in providing crush resistance. In addition, note that the higher crush resistance of the two-rod cable can be achieved at a lower overall materials cost.



a) b) c)

Figure 8: Schematics of: a) metallic linear rod sheath b) dielectric linear rod sheath, and c) dielectric cross-ply sheath

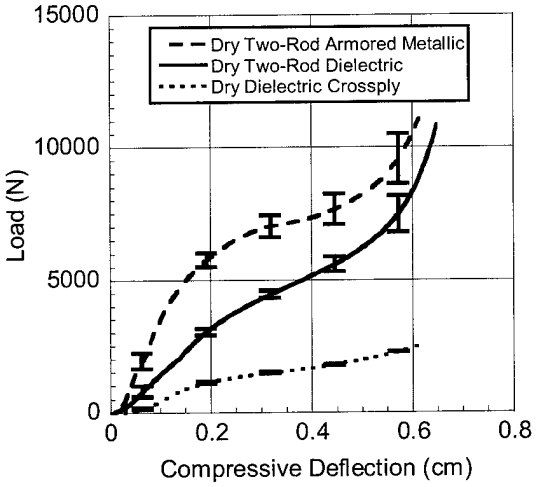


Figure 9: Deflection curves for metallic linear rod, dielectric linear rod, and dielectric cross-ply sheaths, all without WB gel. Schematics of these sheaths are shown in Figure 8.

Figures 11a) and b) reinforce the high inherent compressive resistance of the linear rod design. Figure 11 a) compares the deflection curves measured for the "gel-filled" and "dry" version of the dielectric and metallic linear rod designs, respectively. Clearly, the linear rod design prevents the removal of gel from compromising the crush resistance of the cable. In contrast, Figure 11 b) shows that, even with a PBT core tube, the crush resistance of the dielectric cross-ply design is severely compromised in the absence of core gel.

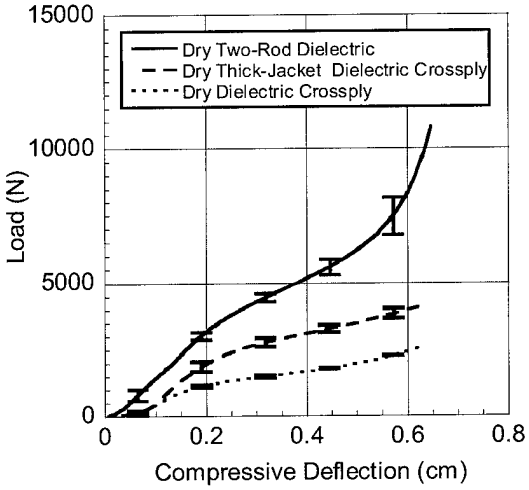
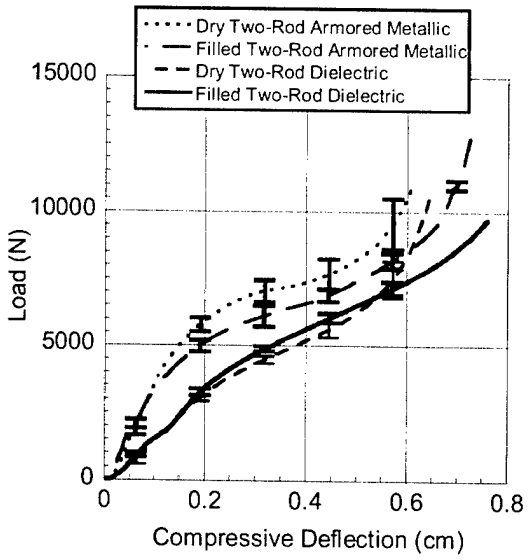


Figure 10: Deflection curves for "dry core" dielectric sheath options: standard dielectric cross-ply, thick-jacketed dielectric cross-ply, and dielectric linear rod sheaths.

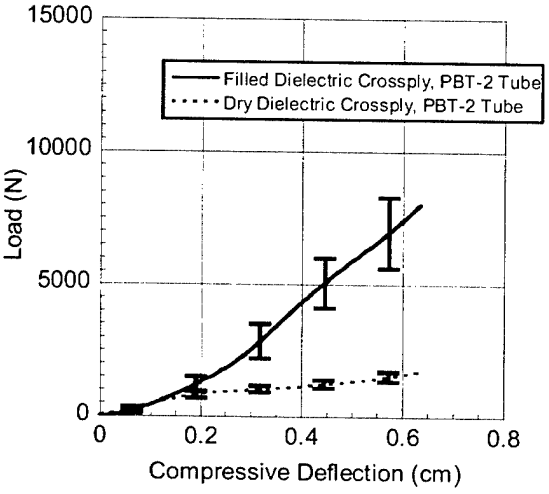
With this collection of data, the next section discusses the most practical design options for providing adequate crush resistance for reduced-gel cores.

6 Design Options

As illustrated by the data presented in the previous section, there are several effective options for improving cable crush resistance. Clearly, with *or* without gel, both metallic and dielectric linear rod sheath designs provide sufficient compressive performance.. In selecting a design that requires minimal changes to manufacturing capabilities, these sheath designs are top contenders. In looking at the more vulnerable cross-ply design, increasing the wall thickness of the core tube is ineffective. On the other hand, increasing the thickness of the jacketing layer provides a significant enhancement in the compressive resistance of the cross-ply design. However, the more substantial improvement provided through use of a linear rod design decreases the attractiveness of pursuing an enhanced cross-ply design in reduced-gel, tube-in-tube cables.



a)



b)

Figure 11: a) Deflection curves for metallic and dielectric linear rod sheaths, with and without WB gel; b) Deflection curves for the dielectric cross-ply sheaths with PBT core tubes, with and without WB gel.

Currently, slotted core, loose tube and central core cables are all offered commercially with reduced amounts of gel. However, in each case, these cable designs all account for the removal of the incompressible gel.

Slotted core designs: The slotted core design uses no waterblocking gel, relying instead on superabsorbent tape or a pressurized duct system to provide sufficient waterblocking protection. Adequate crush resistance is provided by the slotted rod, which is made from a rigid, high modulus plastic. However, these cables tend to have a relatively large diameter, and cables made with this particular design tend to be very difficult to bend.

Loose tube designs: Loose tube designs have minimized the use of gels by replacing the flooding compound between unit tubes with superabsorbent yarns. Crush resistance for loose tube cables can be maintained through use of tubes constructed from relatively high modulus materials (e.g., PBT, nucleated impact-modified PP). Further, the diameter of the unit or buffer tubes is relatively small compared to average central core tube diameters. Following the basic principles of tube mechanics, the small tubes in a loose tube cable will deflect much less than larger tubes in a central core cable under the same load. In addition, the unit tubes are allowed to shift under compressive loads, due to the unitized structure of the loose tube design and the absence of the flooding compound. Therefore, unlike central core cables, the deformation of the sheath or outer jacket is not completely translated into deformation of the tubes. However, the fiber packing density of the cable can be greatly reduced by the encapsulation of fibers in high modulus tubes and the presence of a central strength member. In addition, because of their high stiffness and relatively high wall thickness, the fiber tubes used in loose-tube designs can be unwieldy and difficult to manipulate in installation, e.g. in splice cases.

Central core designs: For central core designs, the recent tube-in-tube designs encapsulate fibers in small flexible tubes, substantially reducing the amount of gel used in the cable. These designs take advantage of the linear rod sheath designs to provide needed crush resistance. Since the sheath provides all of the necessary compressive resistance in these designs, it is possible to design the tubes to be flexible and soft enough to provide for tool-free fiber access and simplified routing and handling in closures. [1] [5]

Based on the discussion above, it is interesting to look at the relative deformation under compressive loads of dry tube-in-tube central core cables versus dry loose tube cables of comparable fiber count. Four "dry core" designs, two armored and two dielectric, have been considered. Schematics of these designs are shown in Figure 12 a) through d).

All of these designs are fully compliant with the Telcordia GR-20 Generic Specification for Fiber Optic Cables. Therefore, they have adequate compressive resistance for low-loss optical performance. As shown in Figures 10 and 11, the linear rod sheaths, both dielectric and metallic, are clearly more crush resistant than other central core options evaluated. However, Figures 13 b) and 14 b) show that, compared to tube-in-tube cables with identical fiber counts, much more compressive deflection occurs in the loose tube constructions. This result is observed for both dielectric and armored cables. As discussed before, the increased deflection of the loose-tube construction is permissible, as the filled unit tubes have substantial crush resistance. In addition, the tubes are able to shift within the

sheath to avoid having the compression of cable be translated directly into the compression of the unit tubes.

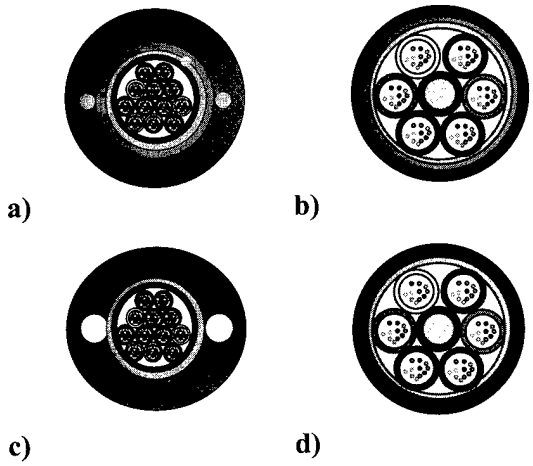


Figure 12: Armored and dielectric cable designs: a) metallic linear rod central core [tube-in-tube], b) light armored loose tube, c) dielectric central core [tube-in-tube], and d) dielectric loose tube.

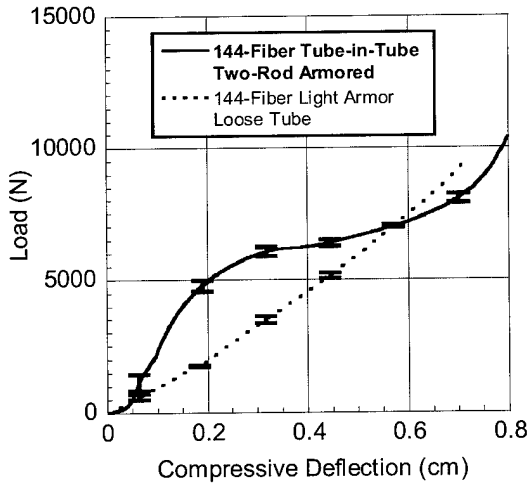


Figure 13: Deflection curves of 144-fiber cables: 1.78 cm diameter metallic linear rod central core tube-in-tube *vs.* 2.31 cm diameter light armored loose tube.

7 Conclusions

The test results presented in this paper clearly indicate that the manufacture of central core cables with either no waterblocking gel or reduced amounts of waterblocking gel is possible without compromising the compressive resistance of the cable. However, the results also identify the current limitations on the types of cable sheath designs that should be used with the reduced gel cores.

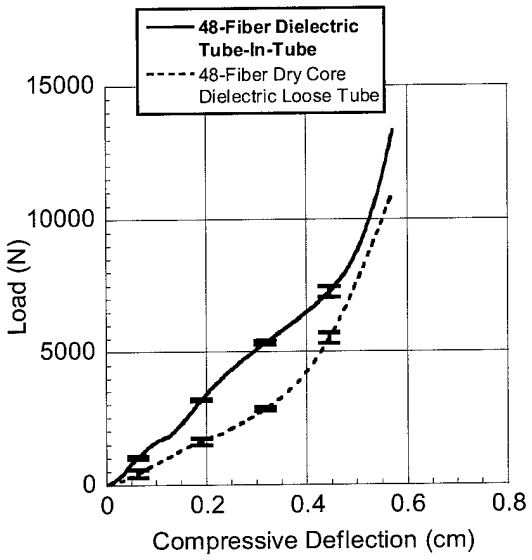


Figure 14: Deflection curves of 48-fiber cables: 1.33 cm diameter dielectric linear rod central core tube-in-tube *vs.* 1.14 cm diameter dielectric loose tube.

8 Acknowledgements

The authors wish to thank Simon Li, a summer intern from Cornell University, for his invaluable assistance with testing and data collection.

9 References

[1] Clyburn III, C.E.; Bringuier, A.G., "A Dry Core Loose Tube Cable for Outside Environments", Proceedings of the Forty-Fourth International Wire and Cable Symposium, 29-36 (1995).

[2] Pastuszka, S., et. al., "A New Type of High Fiber Count, Low Dimension Optical Cable with Simplified Installation Characteristics", Proceedings of the Forty-Eighth International Wire and Cable Symposium, 106-111, (1999).

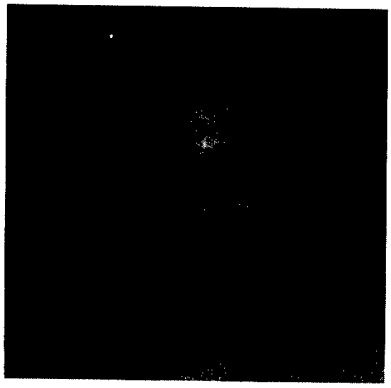
[3] Debban, H.P., et. al., "A New High-Density Central Cable Core Design", Proceedings of the Forty-Ninth International Wire and Cable Symposium, 1-7 (2000).

[4] Telcordia [Bellcore] GR-20-CORE, "Generic Requirements for Optical Fiber and Fiber Optic Cable", Issue 2, July 1998.

[5] Keesee, J.R., et. al., "Entry and Termination of Central Core Optical Cables Containing Flexible Unit Tubes", Proceedings of the National Fiber Optic Engineers Conference, NFOEC 2001, (2001).



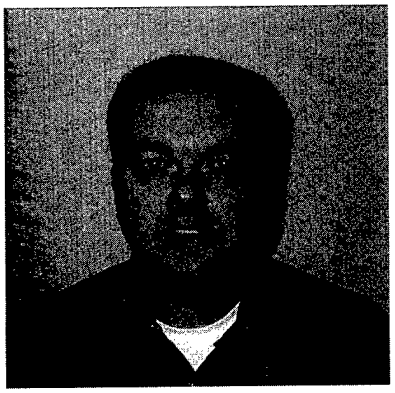
Lisa A. Dixon is a Member of Technical Staff with Lucent Technologies, Inc. Bell Laboratories, Norcross, Georgia. Dr. Dixon joined Lucent Technologies in 1997 in the capacity of Development Engineer. She received her B.S. degree in Engineering Science from Trinity University, an International Diploma from Imperial College, London, UK, and M.S. and Ph.D. degrees in Mechanical Engineering from Georgia Institute of Technology. She is currently working in the area of Outside Plant Cable design and development



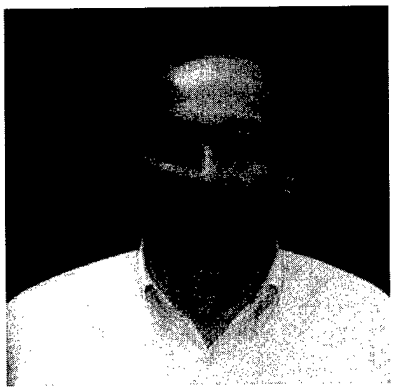
Peter Weimann is a Member of the Technical Staff in the Fiber Optic Materials Technology group at Bell Laboratories, Lucent Technologies, Norcross, GA. His primary focus is materials development for outside plant fiber-optic cable products. Prior to joining Lucent, he received his Ph.D. in Materials Science and Engineering from the University of Minnesota in 1998. His thesis research focused on structure-property relationships in polyolefins. He received a B.S.Eng. in Materials Science and Engineering, as well as a B.S.Econ. in Organizational Management, from the University of Pennsylvania in 1992



Richard H. Norris is a Member of the Technical Staff at Lucent Technologies in Norcross, Georgia. Dr. Norris joined Lucent Technologies in 1997 in the capacity of Development Engineer. He received his B.S. degree in Materials Engineering from North Carolina State University and M.S. and Ph.D. degrees in Metallurgical Engineering from the Georgia Institute of Technology. He is currently working in the area of Outside Plant Cable design and development. His technical affiliations include the Society of Plastics Engineers, ASM International, TMS and he is also a registered Professional Engineer.



H. Paul Debban is a Distinguished Member of Technical Staff with Lucent Technologies – Bell Laboratories in Norcross, Georgia concentrating on Outside Plant Cable Development. He joined Western Electric in 1980 after graduating from the University of Nebraska – Lincoln in 1980 with a BS in Mechanical Engineering. He joined the outside plant optical cable manufacturing engineering group in 1981 and has worked on a broad range of projects including introduction of filled optical cables, the Lightpack® cable core, the AccuRibbon® cable core, armored cables, and others. He has managed several capital expansion projects and has experience in process control. He joined the optical cable design group in 1999.



Richard D. Small is a Member of Technical Staff in the Fiber Optics Materials Technology Group at Bell Laboratories, Lucent Technologies, Norcross, GA. His focus is on both material development of fiber optical cable products and material development of fiber optical ribbon products. He received a Ph.D. in Physical Chemistry from the University of South Florida in 1975. From 1975 until 1978, he was at the University of Notre Dame, doing nanosecond laser flash photolysis organic photochemistry. He joined AT&T in 1978. He has published over 40 outside technical papers in varied technical areas and has 8 patents. He is a member of the American Chemical Society and RadTech.

Theoretical Analysis about Bending Strain of SZ-slotted Core Cable

Masayoshi Yamanaka, Naoki Okada, Akimi Yamasaki, Matsuhiro Miyamoto
Research and development department, Telecommunication cable division
1440, Mutsuzaki, Sakura-shi, Chiba, Japan
+81-43-484-3945 · masayoshi@s.fujikura.co.jp

Abstract

We found out the SZ stranding locus is a very important parameter to get good transmission characteristics for SZ-slotted core cable, and established two analytical methods for SZ-slotted rod. One is to analyze the SZ-stranding locus by Fourier analysis, and the other is to calculate the fiber strain in the SZ-slotted core. The results of these analyses were compared with the transmission characteristics of trial cables. As a result, it became clear that these methods are effective in estimating the cable performance. Use of the new analytical methods has allowed to design and control the quality of SZ-slotted rod, making it possible to achieve stable manufacturing and small drum packaging.

Keywords

SZ-slotted rod; SZ stranding locus; Fourier analysis; distortion ratio; fiber strain.

1. Introduction

Lately in Japan, increasing numbers of ribbon SZ-slotted core cables have been run to construct access networks and FTTH networks [1]. In order to construct these networks economically, it is necessary to design the cables so as to provide easy mid-span access. The SZ-slotted core structure provides an excellent mid-span access capability [2][3]. However, transmission characteristics depend greatly on the SZ-slotted rod structure, therefore the quality control of SZ-slotted rod is very important. Moreover, the demands for smaller diameter of cables, and smaller diameter of storage reel will enhance the precise dimensional and process control of SZ-slotted cabling techniques. For this reason, we studied structural parameters that affect the transmission characteristics.

In order to improve the transmission characteristics, we analyzed the fiber strain in a bent SZ-slotted core cable. So far, it has been reported that the SZ-stranding parameters, e.g., reverse lay length and reverse lay angle, are very important in reducing the fiber strain in the bent cable. However, we found out that the SZ-stranding locus is a critical parameter to achieve good transmission characteristics.

2. SZ-slotted rod

2.1 SZ-slotted Rod Structure

The cross sectional view of the SZ-slotted core cables (100-fiber type, 200-fiber type, and 300-fiber type [3]) is shown in Figure 1. Five 4-fiber ribbons stacked above each other are inserted into the respective slots. The slots rotate by a fixed angle to reverse their direction along length. For compactness, the slot dimension of these cables is reduced as small as possible. The outer diameters of three cables are 12, 16, and 20 mm respectively, which are almost equal to those of the helical slotted rod type cables. The side view of SZ-slotted rod is shown in Figure 2.

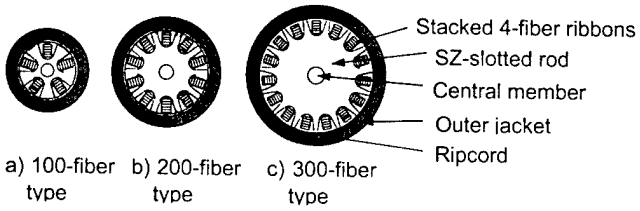


Figure 1. Cross sectional view of SZ-slotted core cables

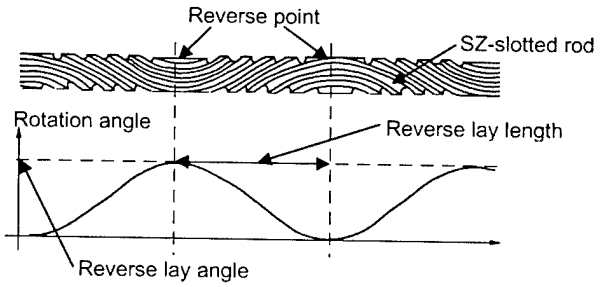


Figure 2. Side view of SZ-slotted rod and structural parameters

2.2 Structural Parameters of SZ-slotted Rod

The reverse lay angle and reverse lay length shown in Figure 2 are very important parameters of SZ-slotted rod. However, the optimum values of these parameters were obtained under the assumption that the SZ stranding locus is sinusoidal wave. Hence, directing attenuation to the SZ-stranding locus, we investigated the ratio of distortion of the SZ-stranding locus relative to the sinusoidal wave, and attempted to calculate the fiber strain in the bent cable using SZ-stranding locus data.

3. Locus Data of SZ-slotted Rod

SZ-stranding locus data were obtained from the encoder moving along the SZ locus shown in Figure 3. The locus data represent angles of rotation per millimeter in the longitudinal direction of the slot. We investigated the following characteristics of the SZ-slotted rod through numerical analysis of these locus data:

1) Reverse lay angle of the SZ-slotted rod

2) Distortion of SZ-stranding form to be determined by Fourier analysis of locus data.

3) Fiber strain in bent cable to be determined by linear integration along the locus of the actual SZ-slotted rod.

4. Evaluation Method

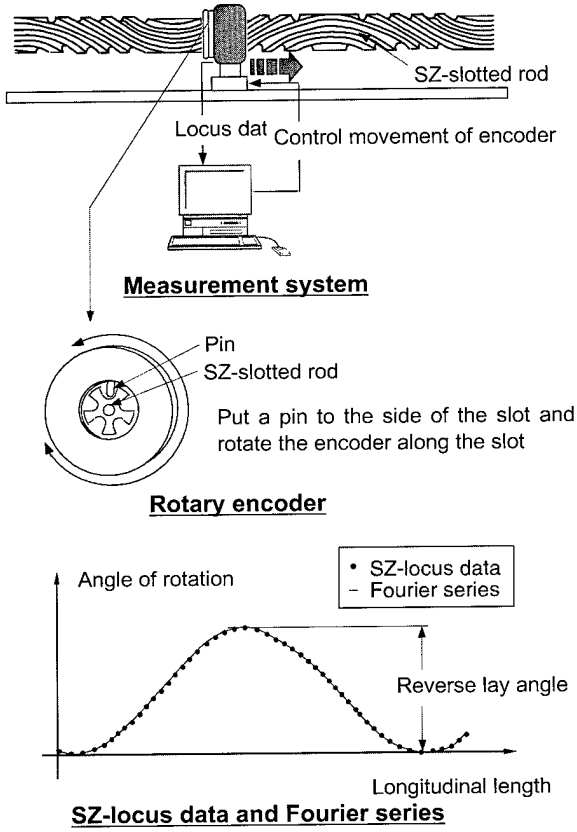


Figure 3. Scheme of SZ-locus measurement system

4.1 Reverse Lay Angle

It is known that the optimum value of reverse lay angle is 275 degrees. In this case, the fiber strain in the bent SZ-slotted core cable is theoretically minimum value [4][5].

The actual reverse lay angle of the SZ-slotted rod can be obtained by analyzing the SZ stranding locus data. The amplifier (peak-to-peak) of the locus indicates the reverse lay angle of the SZ-slotted rod.

4.2 Distortion of SZ-stranding Form

The locus data of SZ-slotted rod were measured by rotary encoder and analyzed by Fourier analysis. Fourier series $F(z)$ is defined as follows:

$$f(z) = A_0 + A_1 \sin(\frac{\pi}{p}z + \varphi_1) + A_2 \sin(2\frac{\pi}{p}z + \varphi_2) + \cdots \quad (1)$$

$$A_n = \sqrt{a_n{}^2 + b_n{}^2}$$

$$\varphi_n = \tan^{-1}\frac{a_n}{b_n}$$

$$A_0 = a_0$$

$$\left.\begin{aligned} a_0 &= \frac{1}{2p}\int_0^{2p} f(z)dt \\ a_n &= \frac{1}{p}\int_0^{2p} f(z)\cos n\frac{\pi}{p}zdz \\ b_n &= \frac{1}{p}\int_0^{2p} f(z)\sin n\frac{\pi}{p}zdz \end{aligned}\right\} \quad (2)$$

Where z is longitudinal distance, p is the reverse lay length of the SZ-slotted rod, and equation (2) is Fourier coefficient.

The Fourier coefficient is obtained by numerical integration of the locus data. Substituting the Fourier coefficient into equation (1), the Fourier series indicating the locus of the SZ-slotted rod can be calculated.

We defined the distortion ratio of the SZ-stranding form as the ratio of higher harmonic waves to fundamental wave in the SZ-stranding locus, which is represented by the ratio of the sum of the effective values of all higher harmonic waves to the effective value of the fundamental wave. Therefore, the distortion ratio of the SZ-stranding form is defined as equation (3)

$$D = \frac{\sum_n E_n}{E_1} \qquad (n = 2,3,4\cdots) \quad (3)$$

where E_n is the effective value of nth harmonic wave, and E_1 is the effective value of the fundamental wave.

4.3 Calculation of Fiber Strain in Bent Cable

The fiber strain in the bent cable was estimated from the locus data of SZ-slotted rod. We investigated an analytical method to calculate the fiber strain. An equation representing the actual SZ-stranding locus was established for the straight cable and bent cable, respectively, and the fiber strain could be calculated as the difference in locus length between the bent and straight cables.

In order to mathematically deal with the locus length, it is necessary to first define the coordinates for SZ-stranding as shown in Figure 4. The longitudinal direction of the cable is taken as z-axis and the plane perpendicular to the longitudinal direction as x-y plane. In Figure 4, a is the pitch circle radius.

Coordinates (x, y, z) of the SZ locus are given as equation (4)

$$\left.\begin{aligned} x &= a\cos\theta \\ y &= a\sin\theta \\ z &= G(\theta) \end{aligned}\right\} \quad (4)$$

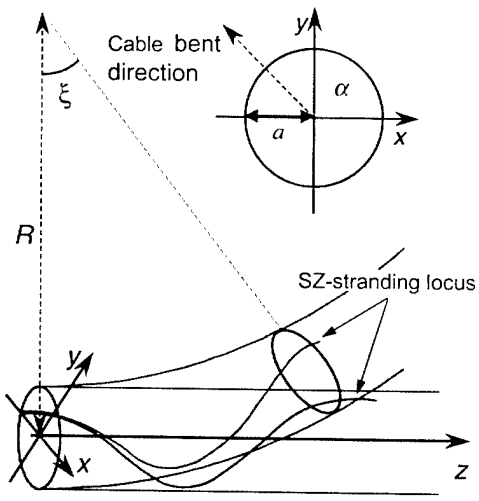


Figure 4. Coordinates for SZ-stranding locus

where $z=G(\theta)$ is the curve approximated to the locus data of the actual SZ-slotted rod.

In case of the cable bent with bending radius R, coordinates (x_b, y_b, z_b) of the SZ locus on the plane at an angle of α with x-axis as shown in Figure 4 are given as equation (5).

$$\left.\begin{aligned} x_b &= B\cos\alpha + a\sin\alpha\sin(\alpha-\theta) \\ y_b &= B\sin\alpha - a\cos\alpha\sin(\alpha-\theta) \\ z_b &= \{R - a\cos(\alpha-\theta)\}\sin\xi \end{aligned}\right\} \quad (5)$$

Then,

$$B = R - \{R - a\cos(\alpha-\theta)\}\cos\xi$$

$$\xi = \frac{G(\theta)}{R}$$

The locus length of the straight cable L and of the bent cable L_b can be calculated by linear integration of equation (4) and equation (5), respectively.

$$\left.\begin{aligned} L &= \int_0^{\phi}\sqrt{\left(\frac{dx}{d\theta}\right)^2+\left(\frac{dy}{d\theta}\right)^2+\left(\frac{dz}{d\theta}\right)^2}\,d\theta \\ L_b &= \int_0^{\phi}\sqrt{\left(\frac{dx_b}{d\theta}\right)^2+\left(\frac{dy_b}{d\theta}\right)^2+\left(\frac{dz_b}{d\theta}\right)^2}\,d\theta \end{aligned}\right\} \quad (6)$$

where ϕ is the reverse lay angle. Then, the fiber strain ε is defined as follows [6]:

$$\varepsilon(\%) = \frac{L_b - L}{L}\times 100 \quad (7)$$

5. Experiments and Discussions

5.1 Dependence of Transmission Characteristics on Distortion Ratio

Three 200-fiber SZ-slotted core cables with 4-fiber ribbons which have different distortion ratios were manufactured and investigated for transmission temperature characteristics in several drum sizes. The form distortion ratios of the samples are given in Table 1.

Table 1. Distortion ratios of samples

Sample No.	1	2	3
Distortion Ratio	1.67	6.03	9.10
Reverse lay angle	273	274	276

The trial cables were fabricated using these samples and investigated for transmission characteristics in several drum sizes at 1550nm. Figure 5 shows the distortion ratio dependence of loss increase under temperature cycling test. The temperature-cycle pattern for this test is from –30 degrees centigrade to +70 degrees centigrade. In this figure, maximum losses under temperature-cycling test are shown. The test result reveals that the loss increase depends greatly on the distortion ratio of the SZ-stranding form.

5.2 Dependence of Transmission Characteristics

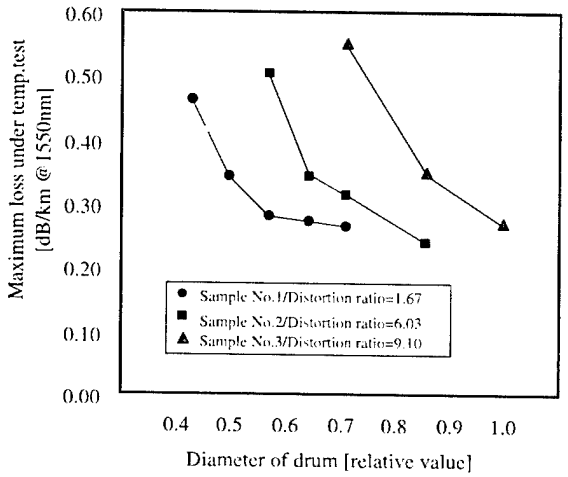


Figure 5. Distortion ratio dependence of loss increase under temperature cycling test

upon Fiber Strain

We investigated the dependence of transmission characteristics on the calculated fiber strain. SZ-slotted core cables of 100-fiber, 200-fiber and 300-fiber types, which have almost the same distortion ratio, were manufactured and evaluated for temperature characteristics. Figure 6 shows the results. The smaller the estimated fiber strain, the better the transmission characteristics become. This result means that the transmission characteristics are affected by the SZ-stranding locus and pitch circle radius.

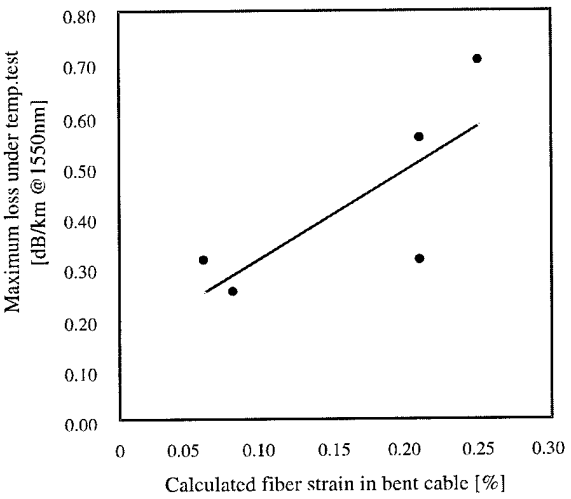


Figure 6. Dependence of transmission characteristics on the calculated fiber strain

6. Conclusions

We have found out the SZ stranding locus was very important parameter to get good transmission characteristics for SZ-slotted core cable. We have investigated the dependence of the characteristics upon the SZ stranding locus.

The locus data of SZ-slotted rod were measured by rotary encoder, and were analyzed by Fourier analysis. We defined the distortion of the SZ stranding form

The fiber strain in bent cable was estimated from the locus data of SZ-slotted rod.

We have manufactured several SZ-slotted core cables with 4-fiber ribbons, which had different distortion ratio and investigated their transmission temperature characteristics. In result, it became clear that the transmission characteristics are affected by the SZ stranding locus.

The quality of SZ-slotted rod can be designed and controlled by the proposed method. As a result, the stable manufacturing and small drum packaging have been achieved.

7. References

[1] J. Kawataka, et al, "Novel Optical Fiber Cable for Feeder and Distoribution Use in Access Networks", *Proc.of 49th IWCS*, 293-297 (2000).

[2] H. Iwata, et al, "Design of Aerial Optical Fiber Cable System Suitable for Easy Branching", *Proc.of 46th IWCS*, 4-11 (1997).

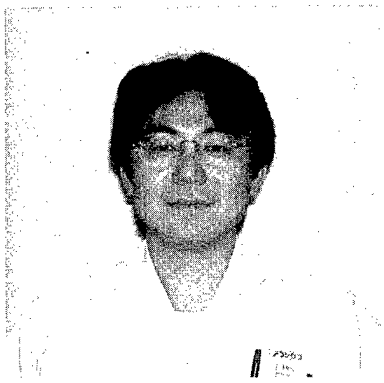
[3] M. Yamanaka, et al, "A new aerial SZ-slotted rod type cable with 4-fiber ribbons", *OECC'97*, p. 518-519 (1997).

[4] M. Yamanaka, et al, "New High Density SZ-stranded Ribbon Slotted Core Cable For Underground Access Networks", *Proc.of 46th IWCS*, 230-239 (1999).

[5] M. Yamanaka, et al, " A Study on Reverse Lay Stranding Loose Tube Cable Containing Ribbon Fibers", *Proc.of 42nd IWCS*, 521-526(1993)

[6] N. Okada, et al, "Study of the SZ-slotted rod type optical cable with 4-fiber ribbons for aerial applications", *Proc.of 46th IWCS*, 785-792 (1997).

Authors



Masayoshi Yamanaka

Fujikura Ltd.

1440, Mutsuzaki, Sakura, Chiba, 285-8550, Japan

Masayoshi Yamanaka was born in 1966. He joined Fujikura Ltd after his graduation from Tohoku University with M.E, degree in 1992 and has been engaged in research and development of optical fiber cables. He is now a chief in the Telecommunication Cable Department.



Naoki Okada

Fujikura Ltd.

1440, Mutsuzaki, Sakura, Chiba, 285-8550, Japan

Naoki Okada was born in 1964. He joined Fujikura Ltd after his graduation from Chiba University with B.E. degree in 1986 and has been engaged in research and development of optical fiber cables. He is now an assistant manager of optical fiber production engineering department.

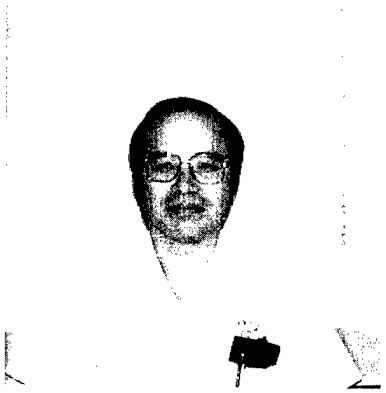


Akimi Yamasaki

Fujikura Ltd.

1440, Mutsuzaki, Sakura, Chiba, 285-8550, Japan

Akimi Yamazaki was born in 1971. He joined Fujikura Ltd after his graduation from Osaka University with M.E. degree in 1997 and has been engaged in research and development of optical fiber cables. He is now an engineer in the Telecommunication Cable Department.



Matsuhiro Miyamoto

Fujikura Ltd.

1440, Mutsuzaki, Sakura, Chiba, 285-8550, Japan

Matsuhiro Miyamoto was born in 1953. He graduated from Nagoya Institute of Technology with B.E. degree of electrical engineering. He joined Fujikura Ltd after his graduation from Tokyo Institute of Technology with M.E. degree in 1978 and had been engaged in research and development of optical fibers and optical cables. He is now belongs to optical fiber production engineering department.

Finite Element Analysis - A New Tool for Cable Design

Suvabrata Das[1], Ronald H. Knapp[1,2] and Terry A. Shimabukuro[1]

[1] Structural Solutions
Aiea, Hawaii
+1-808-488-0655 . sdas@lava.net

[2] University of Hawaii at Manoa
Honolulu, Hawaii
+1-808-956-6592 . knapp@wiliki.eng.hawaii.edu

Abstract
Today, there are numerous cable applications requiring sophisticated designs that satisfy various strength, communication and power transmission functions. These cables often have highly complex structures that require special treatment to model using finite element analysis. The use of general purpose finite element programs for cable design requires a high degree of modeling skill and a significant investment of modeling time. What is needed is a finite element code designed specifically for cable structures. Such a code should simplify model creation and take advantage of known properties of the cable geometry to automatically generate a finite element mesh. Ideally, the creation of the finite element model would be transparent to the cable designer, and the code should facilitate rapid parametric design studies.

Keywords
Cable; design; finite element analysis; pipe; rope.

1. Introduction
In this paper, the development of a new software code for the finite element modeling of many types of cables is discussed. The program makes it easy to generate cable models with an easy-to-use graphical user interface. A finite element mesh of all components is generated automatically. Finite element nodes are created at all component contact points. Upon solving, plots of cable strain, torque or rotation, deformations and stress contours are generated to assess cable performance.

This cable design software is able to model both symmetrical and asymmetrical, axial and compound helical geometries. Nonlinear material behavior and layer locking (circumferential wire contact) also can be modeled. Loads that can be applied to the model simultaneously include tension, twist, bending (including internal friction), cable outer pressure or distributed pressures, component internal or external pressures, clamping, and temperature change. Metallic, polymer and synthetic fiber components can be handled by the code.

This paper summarizes the capabilities of this new design code and reports on its accuracy by modeling simple wire strands and more complex as-built cable constructions. Comparisons with a general purpose finite element program show that the new code developed for cables provides comparable results with significantly less modeling effort.

2. Finite Element Model
The finite element method discretizes structures into multiple elements whose shapes are selected to best match the structural boundaries. Each of these elements is connected to adjacent elements at nodes where nodal displacements and forces are represented by generalized degrees-of-freedom. In the stiffness method, the nodal displacements are the unknowns of the structure. A shape function is assumed for the unknown displacements at any point within an element in terms of the nodal displacements. For each element under static equilibrium, a set of simultaneous linear equations in terms of the unknown displacements can be found by applying the principal of minimum potential energy. These equations for all elements in the structure are systematically assembled into a common set that represents the stiffness equation of the entire structure. Upon implementing the boundary conditions and applying the external loads at nodes, this common system of equations is solved to yield the nodal displacements. Substituting these displacements back into the shape functions for each element provides the distributions of stress and displacement within the element.

Cable structures consist of components with complex helical geometries. The conventional finite element method, though versatile, is not well-suited to analyze such structures. A considerable amount of time must be invested in joining components, discretizing, applying boundary conditions and analyzing the simplest of cables using general purpose finite element programs. Also, a thorough understanding of the finite element method is required.

In the following, a new finite element model developed specifically for cable structures is briefly described. Element generation and other model parameters are controlled internally which makes the finite element method transparent to the cable designer.

2.1 Assumptions
The following assumptions are made in developing the model:

1. Cable components are circular in the transverse cable cross-section, (lay angles of components are sufficiently small);
2. The model is limited to a two-dimensional analysis with radial and circumferential displacements;
3. Cable axial strain is constant over the cable cross-section;
4. Materials are isotropic;
5. The deformations of the components in the transverse cable section are small;
6. All cable components initially in contact with adjacent components remain in contact during loading.

2.2 Finite Element Cable Model
Consider the cross-section of an elementary cable model shown in Figure 1. Contact points (A-F) maintain connectivity in the radial (u) and circumferential (v) directions between adjacent components.

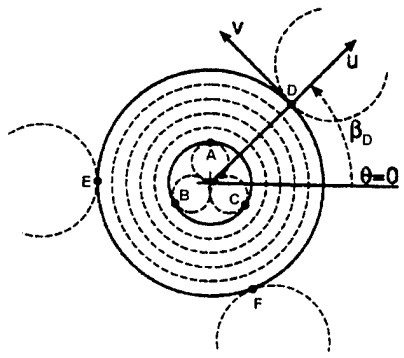


Figure 1. Elementary Cable Model

A macro-ring element model (REM) represents each cable component with nodal degrees-of-freedom at all of its contact points in the radial (u) and circumferential (v) directions. To develop the REM, each component in the cable cross-section is discretized into several circular ring elements shown by concentric dashed circular rings in Figure 1.

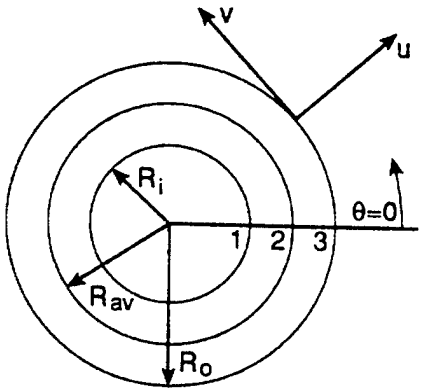


Figure 2. Axisymmetric Ring Element with 3 circular Nodes

Each ring element is an axisymmetric solid element with three nodes that are complete circles at the inner, average and outer element radii (points 1, 2 and 3 in Figure 2). Due to the asymmetrical deformations expected for a typical ring element in a cable component, radial and circumferential displacement functions, u(r,θ) and v(r,θ), respectively, are expressed in polar coordinates according to Fourier series shape functions with quadratic variations in the radial direction [4]:

$$u(r,\theta) = \sum_{k=0}^{N} \left[u_{sk}(r)\cos k\theta + u_{ak}(r)\sin k\theta \right] \qquad (1)$$

$$v(r,\theta) = \sum_{k=0}^{N} \left[v_{sk}(r)\sin k\theta - v_{ak}(r)\cos k\theta \right] \qquad (2)$$

where

$$\begin{aligned} u_{sk}(r) &= b_{1k} + b_{2k}r + b_{3k}r^2 \\ v_{sk}(r) &= b_{4k} + b_{5k}r + b_{6k}r^2 \\ u_{ak}(r) &= b_{7k} + b_{8k}r + b_{9k}r^2 \\ v_{ak}(r) &= b_{10k} + b_{11k}r + b_{12k}r^2 \end{aligned} \qquad (3)$$

In these equations, u_{sk} and v_{sk} are the symmetric components and u_{ak} and v_{ak} are the antisymmetric components of the nodal displacements relative to the θ=0 axis (see Figure 2). From these displacement amplitudes, the displacement at any point within a ring element (r,θ) can be determined from the shape functions (Equations 1 and 2). b_{1k} thru b_{12k} are shape function constants of the harmonic term, k. The upper limit, N, of the summation in Equations (1) and (2) is chosen to satisfy convergence of the series.

For each harmonic term, there are four unknown displacements at each circular nodal point; viz., u_{sk}, u_{ak}, v_{sk} and v_{ak}. The strain-displacement and stress-strain relations [4] are used to determine the stress components in the ring element as a function of these harmonic displacements. The principal of minimum potential energy [10] then is applied to form the stiffness equation of a single ring element.

The next step in the formulation of the REM model is to apply the method of condensation [9] to successive ring elements in a component. This reduces the degrees-of-freedom of the multiple ring elements shown in Figure 1 to only two nodal points that coincide with the inner and outer radii of the component, as shown by the two solid circles. This results in a stiffness equation of the entire component with the unknown harmonic displacements at the component boundaries. The unit displacement method [8] then is applied to obtain the REM stiffness matrix with degrees-of-freedom at each component contact point. Each component contact point is successively displaced by an unit amount at each degree-of-freedom (u and v directions) while the other contact points are held fixed. The elements of the REM stiffness matrix are obtained from the corresponding reaction forces at each component contact point.

Once the stiffness matrices of all REM elements representing all cable components are generated, the usual global coordinate transformations and assembly procedure are applied to form the system equations for the entire cable cross-section. The system loads then are applied to the component contact points. This leads to the following stiffness equation:

$$[K]\{Q\} = \{R\} \qquad (4)$$

In equation (4), {Q} is the unknown displacement vector at component contact points of the cable and {R} is the corresponding load vector. These system of equations are solved to yield the unknown displacements at component nodes. From these displacements, the individual component displacements are isolated and applied as displacement loads to the condensed ring element stiffness model of the component. This yields the distribution of displacements at all points within the component. Strains and stresses then are determined from the strain-displacement and stress-strain relations, and contact forces between components can be found.

In this model, the axial strain is assumed to be constant across each cable component. The component axial strain and any thermal strain, if present, are included in the load vector {R} as an initial strain. The model gives the radial and circumferential displacements at the component nodes as well as the radial, hoop and in-plane shearing stress values across each cable component. The nodal displacements are used iteratively in the tension, torsion and bending kinematic equations [5,6] to determine the overall cable behavior; i.e., axial strain, reaction torque, end rotation, etc. After achieving convergence, the axial, bending and torsional stresses obtained from the kinematic model are superimposed on the radial, hoop and in-plane shearing stresses of the REM solution to obtain the distribution of effective (von Mises) stress across each cable component. This approach has been programed into a computer code [3] for cable design.

3. Verification Examples

In this section, the REM is used to model two different geometries of a wire rope strand and a cable with tubular components. Comparisons of the analysis results for various types of loads applied to these cables is made with those obtained from the general purpose finite element program, ANSYS® [2]. The geometries of the example cables are simple to reveal basic cable behavior and to simplify creation of solid models in ANSYS, which otherwise demand significant skill, effort and time to produce. Further verification of the REM is presented in Section 4 for two as-built cables.

3.1 Strand A

A wire rope strand consisting of seven wires, is modeled with the REM and ANSYS. Three-dimensional solid elements are used to define the wires in the ANSYS model. The geometrical properties of the strand shown in Figure 3 are summarized in Table 1. The wire material is assumed to be linear with an elastic modulus of 200,000 MPa and Poisson's ratio of 0.01. The helical wires are laid at a small lay angle.

A strand length corresponding to three lay lengths of the helical wire Layer 2 is modeled in ANSYS. For an experienced analyst, approximately four hours was required to create the model shown in Figure 4. In contrast, the modeling time for the REM was only several minutes.

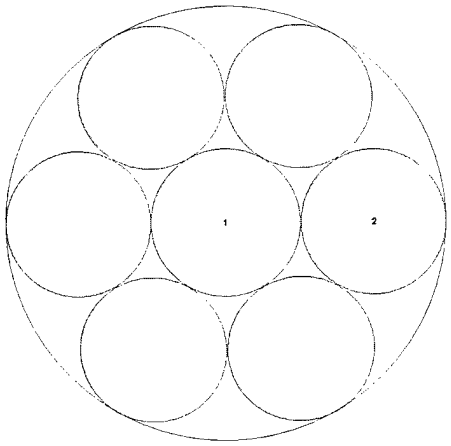


Figure 3. Wire Rope Strand A

Table 1. Geometry of Strand A

	Layer 1	Layer 2
No. of Wires	1	6
Wire Diameter [mm]	4.15	4.00
Layer Inner Diameter [mm]	-	4.15
Lay Length (RHL)* [mm]	-	140
Lay Angle (RHL)	-	10.4°

* RHL = Right Hand Lay

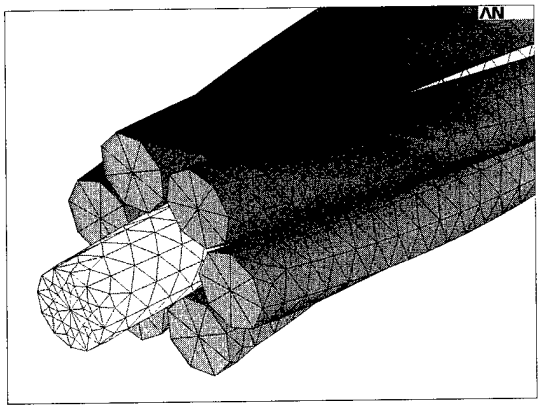


Figure 4. ANSYS Element Mesh

Wire rope Strand A was analyzed for three different boundary conditions. Results are summarized below.

3.1.1 Tension with Both Ends Fixed. Strand A is tensioned to produce a 0.5% axial strain with ends fixed against rotation. Comparative analysis results between the REM and ANSYS models are presented in Table 2.

Table 2. Strand A Tensioned with No Rotation

	REM	ANSYS	Difference
Tension for 0.5% strain [N]	85,160	79,850	6.6 %
Reaction Torque [N-m]	49.9	49.1	1.6 %
Deformed Cable Diameter [mm]	12.147	12.146	0.0 %
Max. Effective Stress [MPa]	1244	1254	0.8 %
Approx. Solution Time* [min]	1	45	-

* Same computer

3.1.2 Tension with One End Free to Rotate. The strand is tensioned at 60,000 N with one end of the strand free to rotate. Analysis results are compared in Table 3. The von Mises effective

stress contour plots from the two analyses models presented in Figures 5 and 6 show close agreement.

Table 3. Strand A Tensioned with Rotation

	REM	ANSYS	Difference
Free End Rotation [deg/m]	-103.7	-102.0	1.7 %
Axial Strain [%]	0.463	0.511	9.4 %
Deformed Cable Diameter [mm]	12.148	12.149	0.0 %
Approx. Solution Time* [min]	1	45	-

*Same computer

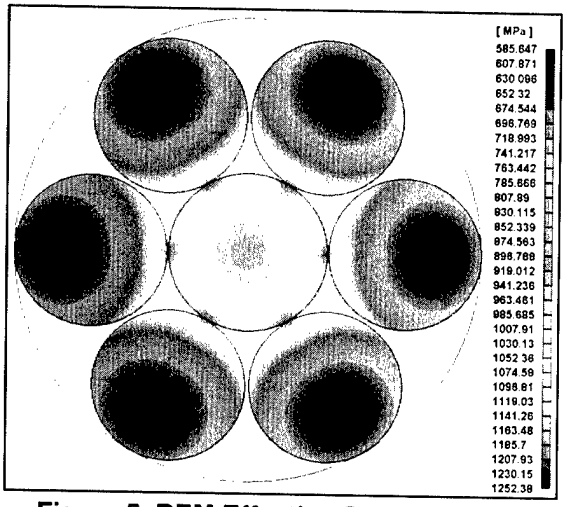


Figure 5. REM Effective Stress Plot for Tension with Rotation

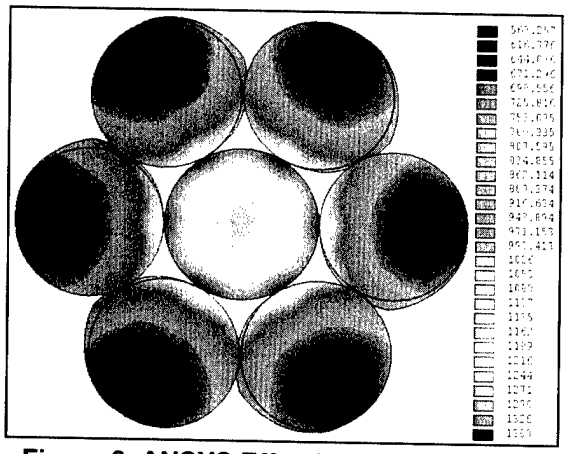


Figure 6. ANSYS Effective Stress Plot for Tension with Rotation

3.1.3 Constant Twist. The strand is subjected to a constant twist of 100 deg/m along its length. Analysis results for the REM and ANSYS models are compared in Table 4. The effective von Mises stress contour plots from the two models presented in Figures 7 and 8 again show close agreement.

Table 4. Strand A with Constant Twist

	REM	ANSYS	Difference
Axial Strain [%]	-0.112	-0.108	3.7 %
Reaction Torque [N-m]	32.9	29.7	10 %
Approx. Solution Time* [min]	1	45	-

* Same computer

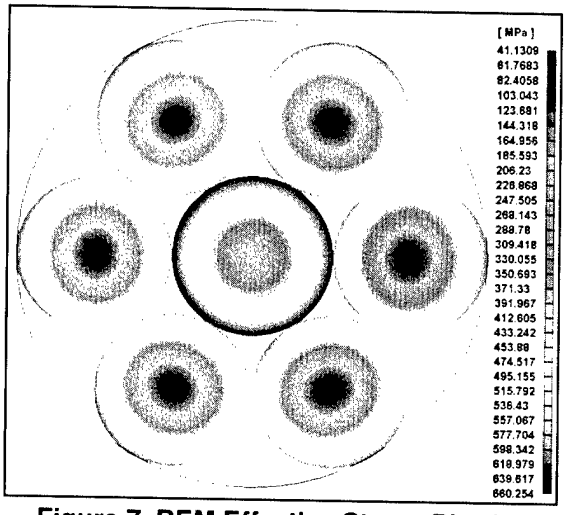


Figure 7. REM Effective Stress Plot for Constant Twist Load

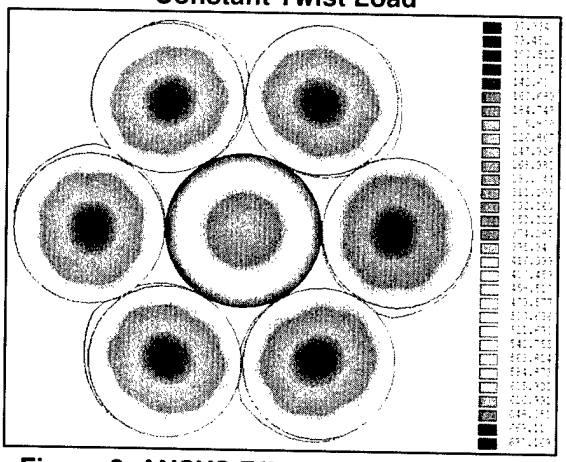


Figure 8. ANSYS Effective Stress Plot for Constant Twist Load

3.2 Strand B

A second wire rope strand consisting of six helical wires around a core wire is modeled by the REM and with ANSYS solid elements. The geometrical properties of this strand, shown in Figure 9, are summarized in Table 5. Strand B has a larger lay angle and a smaller helical wire diameter than Strand A. The larger lay angle was desired for a bending analysis of the cable. Strands A and B have identical material properties.

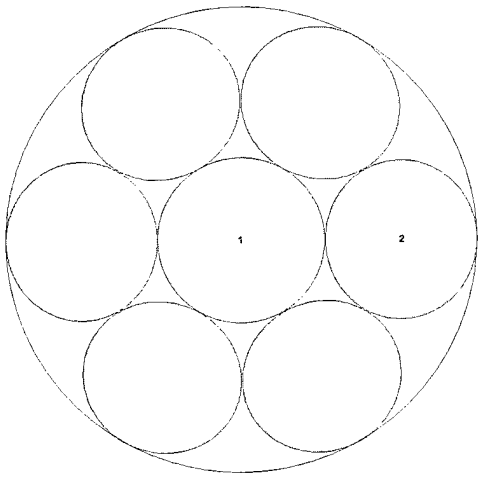


Figure 9. Wire Rope Strand B

Table 5. Geometry of Strand B

	Layer 1	Layer 2
No. of Wires	1	6
Wire Diameter [mm]	4.15	3.75
Layer Inner Diameter [mm]	-	4.15
Lay Length (RHL) [mm]	-	70.0
Lay Angle (RHL)	-	19.5°

A strand length corresponding to five lay lengths of the helical wire Layer 2 is modeled in ANSYS. The modeling time in ANSYS for an experienced analyst was approximately five hours for the mesh shown in Figure 10. Again, the REM required only several minutes to model.

Wire rope Strand B was analyzed for bending and thermal loads. Results are summarized below.

3.2.1 Uniform Bending. This strand was analyzed with the REM and ANSYS codes for bending over a sheave with a diameter of 720 mm. Both ends of the strand are held fixed against rotation. Analyses results are compared in Table 6. Effective stress contour plots for the two models are presented in Figures 11 and 12.

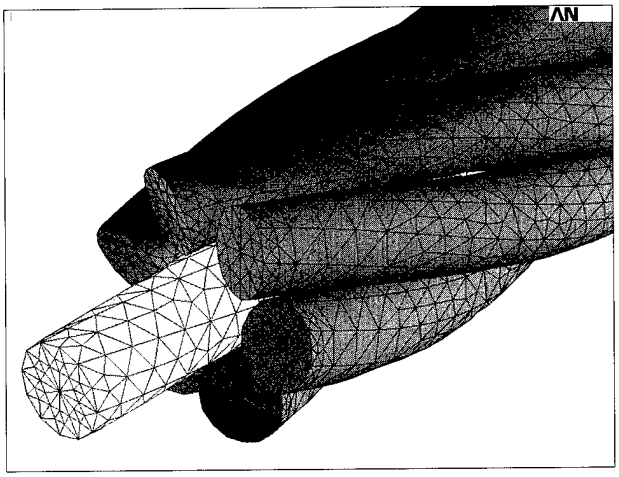


Figure 10. ANSYS Element Mesh

Table 6. Strand B subjected to Uniform Bending

	REM	ANSYS	Difference
Bending Moment [N-m]	37.6	37.0	1.6 %
Max. Effective Stress [MPa]	1153	1211	4.8 %
Approx. Solution Time* [min]	1	60	-

* Same computer

3.2.2 Temperature Change. The temperature of Layer 1 in the strand is increased by 100K, while Layer 2 is held at a constant temperature. The analyses results are compared in Table 7.

Table 7. Wire Rope Strand B under Temp. Change

	REM	ANSYS	Difference
Reaction Torque [N-m]	3.832	3.914	2.1 %
Axial Strain [%]	0.017	0.019	10.5 %
Deformed Cable Diameter [mm]	11.656	11.655	0.0 %
Max. Effective Stress [MPa]	214.4	212.4	0.9 %
Approx. Solution Time* [min]	1	30	-

* Same computer

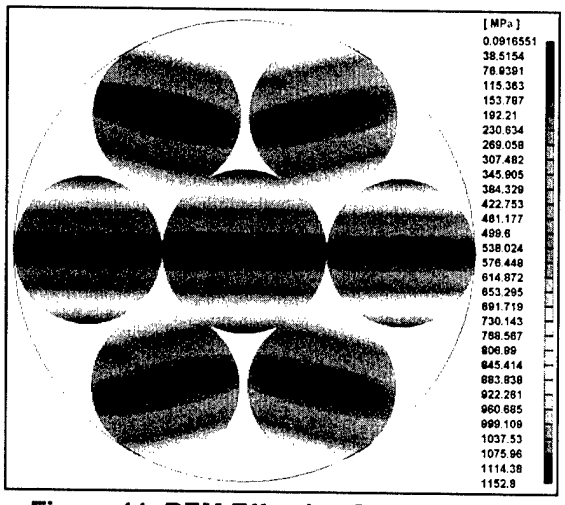


Figure 11. REM Effective Stress Plot for Uniform Bending Load

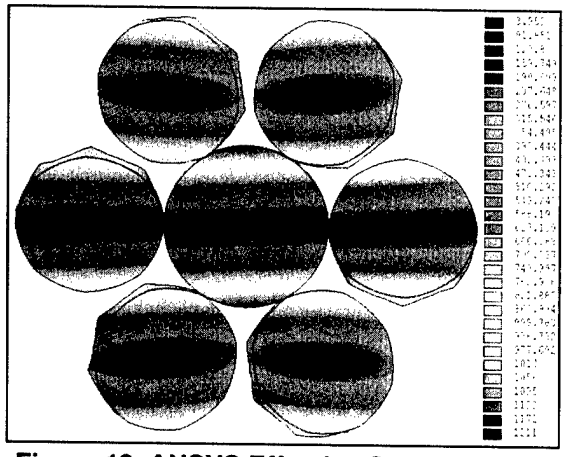


Figure 12. ANSYS Effective Stress Plot for Uniform Bending Load

3.3 Cable with Tubular Components

In this example, the cable shown in Figure 13 is modeled with the REM and ANSYS. The geometry and material properties of the cable are presented in Table 8.

The materials of all cable layers are assumed to be linearly elastic. Layer 1 is a steel wire, Layer 2 consists of six helical polypropylene tubes and Layer 3 is a high density polyethylene jacket.

A cable length corresponding to one lay length of Layer 2 is

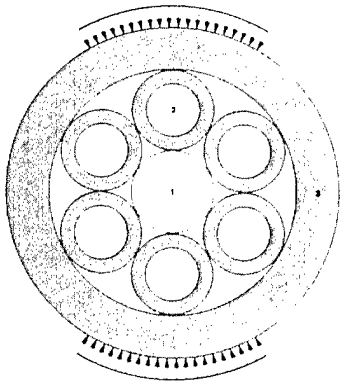


Figure 13. Cable with Tubular Components

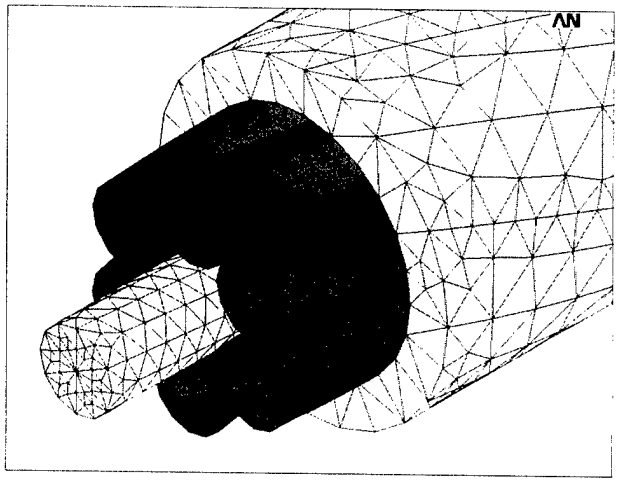


Figure 14. ANSYS Element Mesh

Table 8. Cable Properties

	Layer 1	Layer 2	Layer 3
No. of Wires	1	6	1
Wire Diameter [mm]	4	-	-
Tube Inner Diameter [mm]	-	2.5	11.8
Tube Outer Diameter [mm]	-	3.9	16
Layer Inner Diameter [mm]	-	4	11.8
Lay Length (RHL) [mm]	-	150	-
Lay Angle (RHL)	-	9.6°	-
Elastic Modulus [MPa]	200,000	1,550	883
Poisson's Ratio	0.29	0.46	0.46

modeled with ANSYS solid elements. The time required to create the ANSYS model shown in Figure 14 was approximately ten hours, whereas the REM modeling time was less than ten minutes.

A partial pressure of magnitude 3MPa was applied to the cable outer diameter over an angular span of 60°, centered about the top and bottom of the cross-section to simulate a crushing load (Figure 13). It is assumed that the deflections due to this load are sufficiently small so that the cable materials remain linearly elastic and there is no buckling. The REM and ANSYS results are compared in Table 9. The effective stress contour plots are presented in Figures 15 and 16. Deformation plots using a displacement scaling factor of 2.5 are compared in Figures 17 and 18. These results are all in good agreement.

Table 9. Cable with Tubular Components Under Partial External Pressure of 3MPa

	REM	ANSYS	Difference
Max. Radial Deflection at Cable OD [mm]	-0.166	-0.152	9.2 %
Max. Effective Stress [MPa]	75.8	74.8	1.3 %
Approx. Solution Time* [min]	2	45	-

* Same computer

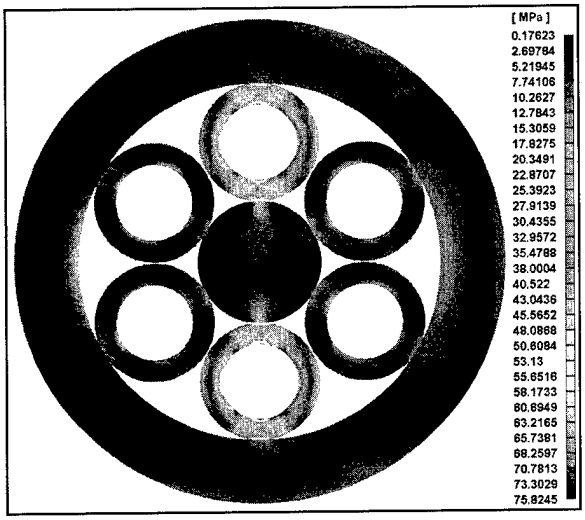


Figure 15. REM Effective Stress Plot for External Partial Pressure

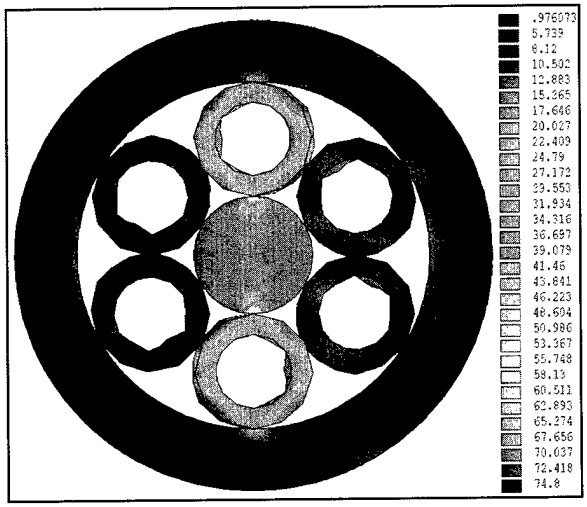


Figure 16. ANSYS Effective Stress Plot for External Partial Pressure

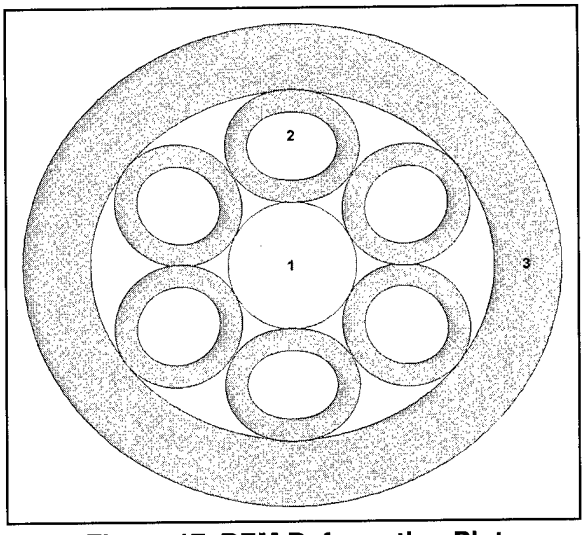


Figure 17. REM Deformation Plot

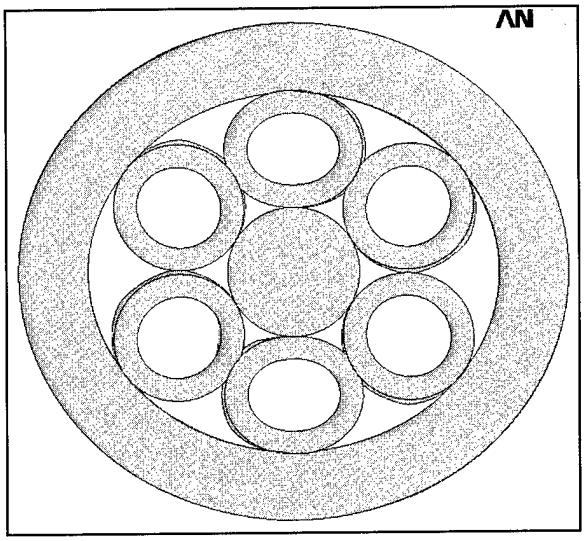


Figure 18. ANSYS Deformation Plot

4. As-Built Cables

In this section, REM analysis results are compared with experimental data of an undersea power cable and a ROV tether cable.

4.1 Self-Contained Oil Filled (SCOF) Power Cable

The cross-section of this power cable is shown in Figure 19. Detailed geometry and properties of this cable are presented in [7]. Layers 1 and 2 are copper keystone conductors that form a center oil duct. Layer 3 is oil-filled Kraft paper insulation. Layer 4 is a non-linearly elastic lead sheath to provide a positive water seal. Layer 5 is a neoprene tape layer and Layer 6 is a jute bedding layer. The geometry of the as-built cable was measured carefully, and stress-strain curves for all materials used in the construction were obtained.

This cable is designed to carry a variety of loads including tension, bending, twist and internal oil pressure. Experimental results for a maximum tension load of 444,800 N with both cable ends fixed against rotation are presented.

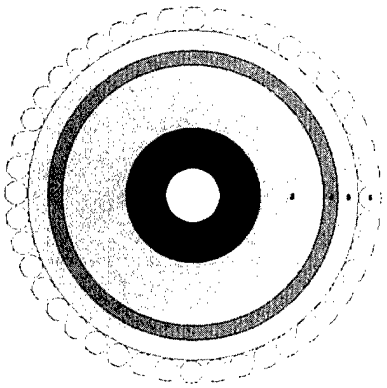


Figure 19. SCOF Cable

Cable axial strain, reaction torque and diameter change obtained with the REM are compared with test data (dots) in Figures 20, 21 and 22 respectively. Agreement is very close.

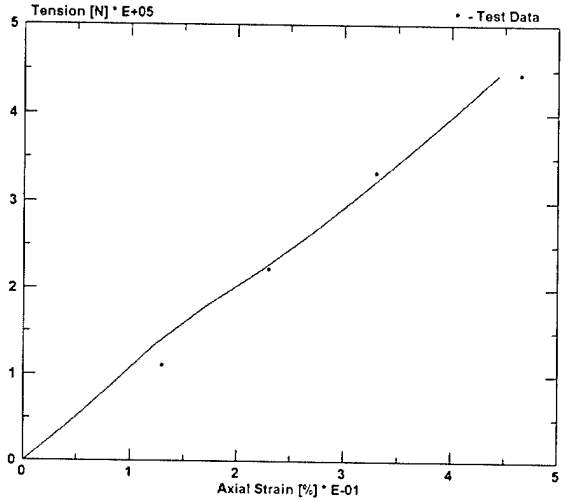


Figure 20. Tension vs. Axial Strain [%]

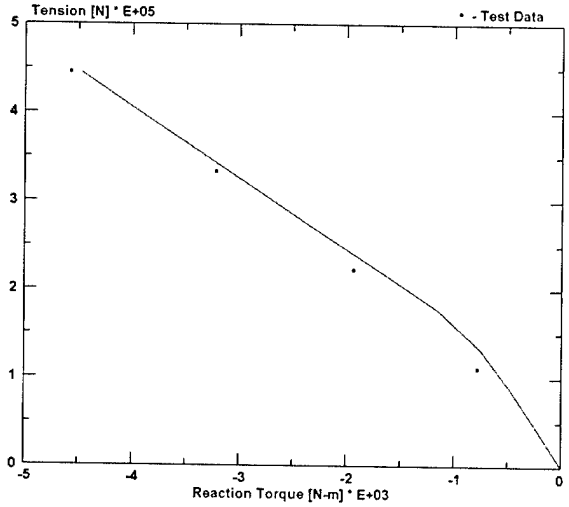


Figure 21. Tension vs. Cable Reaction Torque

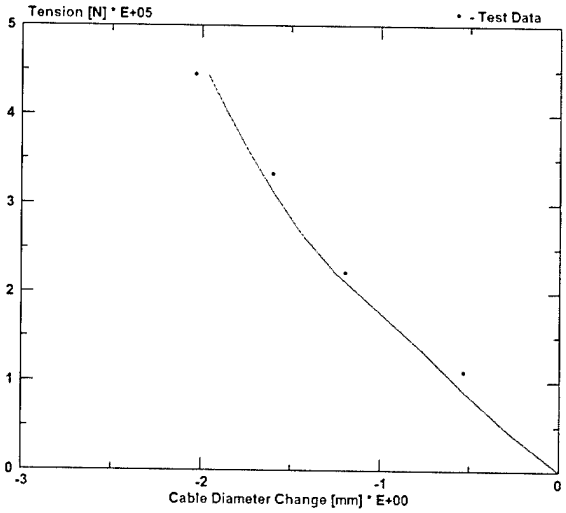


Figure 22. Tension vs. Cable Diameter Change

4.2 Aramid Armored ROV Cable

The cross-section of an as-built ROV cable is shown in Figure 23. The geometry and properties of this cable are given in [1]. The cable core consists of two types of copper conductor strands, a thin-wall stainless steel tube and a high density polyethylene (HDPE) jacket. The copper conductor strands are double helical structures. The strength members are helically-served, unimpregnated aramid yarns represented here by eight layers of keystone wires. There is an intermediate HDPE sheath after the first four aramid layers. Finally, the outer four aramid layers are covered by an HDPE sheath. This cable was analyzed for an axial load of 100,000 N with both ends fixed against rotation. The axial strain from the REM analysis is close to the experimental results shown in Figure 24.

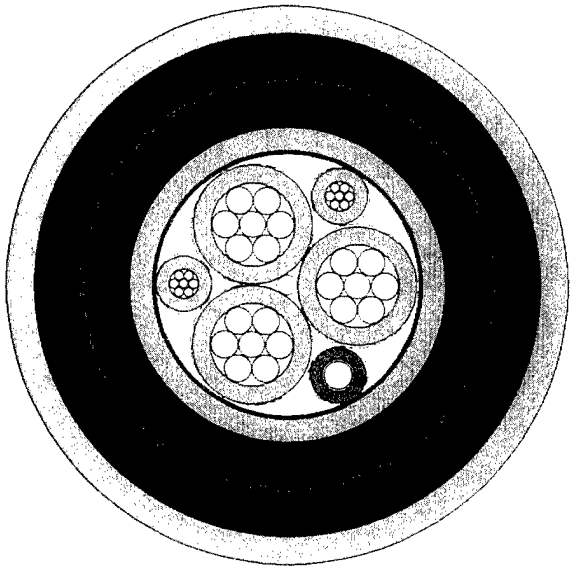


Figure 23. Aramid Armored ROV Cable

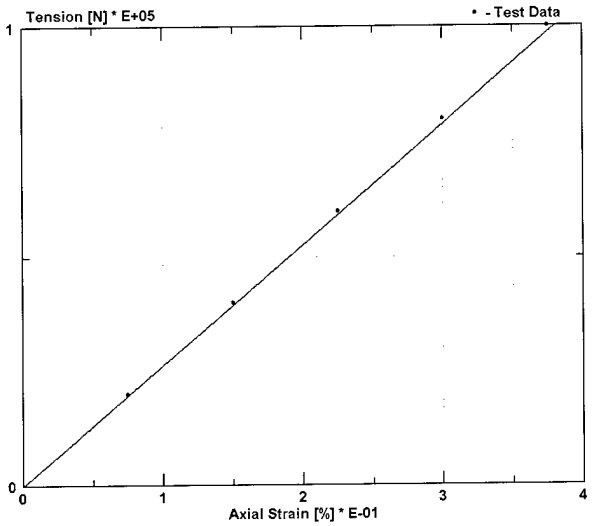


Figure 24. Tension vs. Axial Strain for Aramid ROV Cable

5. Conclusions

In this paper, the basis for the development of a new finite element modeler for cable structures (REM) and its capabilities are presented. A few verification examples also are included. Comparisons have been made with analysis results from the general purpose finite element program, ANSYS.

Analysis results from the REM shows good agreement with those from ANSYS for a variety of load cases and several simple cable constructions. The REM modeling and solution times were significantly lower than those of ANSYS. Also, since the REM is designed to make the finite element method transparent to the user, finite element modeling skills are not required.

The output from the REM model includes overall cable results like axial strain, reaction torque or end rotation, cable diameter change and detailed stress contour plots over the cable cross-section. This provides the designer with better insight into cable performance, and through parametric design studies suggests how a cable design might be improved. Since the REM requires significantly less modeling and solution time than general purpose finite element programs, parametric design studies can be conducted rapidly.

6. Acknowledgment

This work was funded in part by the National Defense Center of Excellence for Research in Ocean Sciences (CEROS). CEROS is a part of the Natural Energy Laboratory of Hawaii Authority (NELHA), an agency of the Department of Business, Economic Development & Tourism, State of Hawaii. CEROS is funded by the Advanced Research Projects Agency (ARPA) through grants to NELHA. This report does not necessarily reflect the position or policy of the Government, and no official endorsement should be inferred.

7. References

[1] J. S. Andreassen, "Aramid Armored ROV Cable for Deep Waters," *Underwater Intervention, Session B, Track 1: Remote Intervention (ROV Tooling and Components).*,(January 2000).

[2] ANSYS® - (Analysis Systems) v5.7, Ansys Inc., 275 Technology Drive, Canonsburg, PA 15317, (2001).

[3] CableCAD® v1.1, Structural Solutions, 98-030 Hekaha St. Suite 20, Aiea, HI 96701, (2001).

[4] R. D. Cook, *Concepts and Applications of Finite Element Analysis*, 2nd ed., John Wiley and Sons, Inc. (1974).

[5] R. H. Knapp, "Derivation of a New Stiffness Matrix for Helically Armored Cables considering Tension and Torsion," *International Journal for Numerical Methods in Engineering.*, 14, 515-529 (1979).

[6] R. H. Knapp, "Helical Wire Stresses in Bent Cables," *Trans. ASME, Journal of Offshore Mechanics and Arctic Engineering.*, 110, 55-61 (February 1988).

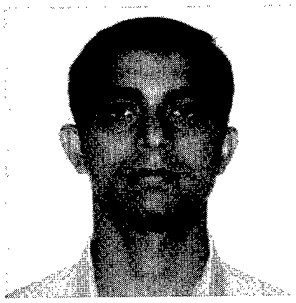
[7] R. H. Knapp, "Structural Modeling of Undersea Cables," *Trans. ASME, Journal of Offshore Mechanics and Arctic Engineering.*, 111, 323-330 (November 1989).

[8] J. S. Przemieniecki, *Theory of Matrix Structural Analysis*, McGraw-Hill, New York. (1968).

[9] E. L. Wilson, "The Static Condensation Algorithm," *International Journal for Numerical Methods in Engineering.*, 8(1), 198-203 (1974).

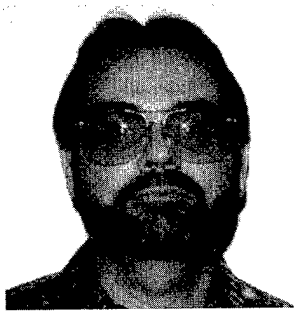
[10] O. C. Zienkiewicz, *The Finite Element Method*, 3rd ed., McGraw-Hill, London. (1977).

Authors



Suvabrata Das
Research Engineer
Structural Solutions
98-030 Hekaha St.
Suite 20
Aiea, HI - 96701

Mr. Das joined Structural Solutions after graduating from the University of Hawaii at Manoa in 1999 with an M.S. in Ocean Engineering. Since then he has been involved in the development of finite element models for the structural analysis of cables. He obtained his undergraduate degree in 1996 from the Indian Institute of Technology at Kharagpur, India.



Ronald H. Knapp
Professor
Dept. of Mechanical Engineering
University of Hawaii
Honolulu, HI - 96822

Dr. Knapp is a professor of Mechanical Engineering at the University of Hawaii and is the founder and President of Structural Solutions. He has been developing numerical models for cables and ropes for nearly 25 years. He obtained his M.S.M.E. degree from the California Institute of Technology in 1969 and his Ph.D. in Ocean Engineering from the University of Hawaii in 1975.



Terry A. Shimabukuro
Application Engineer
Structural Solutions
98-030 Hekaha St.
Suite 20
Aiea, HI - 96701

Mr. Shimabukuro joined Structural Solutions in 1998 and has been responsible for the commercial implementation of computer code for cable design. He has 20 years of mechanical engineering design experience in the defense, medical device and computer industries. He obtained his B.S.M.E. degree from the University of Hawaii in 1980 and his M.S.M.E. degree from Stanford University in 1981.

Influence of Ribbon Stack Twist Laylength and Bending Radius on the Strain Distribution and Attenuation in Optical Fiber Ribbon Cables

Nicholas V. Nechitailo, Matthew G. Soltis and Dean J. Rattazzi

Alcatel Telecommunications Cable R&D
2512 Penny Road
Claremont, NC 28610
+1-828-459-8362 · nicholas.nechitailo@cable.alcatel.com

Abstract

The main goal of this research work is to better understand the influence of ribbon stack twist and cable bending radius on the fiber strain distribution within the ribbons. We also wish to find a correlation between the strain distribution and fiber attenuation. For practical application, it is desirable to find an optimal twist laylength for a wide range of ribbon stack sizes. This paper contains selected results of analytical, finite element and experimental studies. The paper also includes a comparison of the results obtained at Alcatel with the data recently published by Gao *et al.*, [1] of Siemens AG, Germany and by Tabaddor and Aloisio [2] of Lucent, GA, USA.

Keywords

Fiber Ribbon Cable, Attenuation, Strain, Twist, Bending, Buckling, Modeling.

1. Introduction

Optical fibers are small diameter glass strands that are capable of transmitting an optical signal over great distances, at high speeds, and with relatively low signal loss as compared to standard wire or wire cable networks. The use of optical fibers in today's technology has spread into many areas including communications, aviation, and medicine. Most applications of optical fibers require the individual fibers to be placed into groupings, such as in fiber optic cables.

Ribbonizing. There are several ways to manufacture and configure fiber optic cables. One of the common forms is the use of fiber optic ribbons. A fiber optic ribbon is made of several individually coated fibers aligned side-by-side and covered with a protective coating or embedded in a matrix material. This method results in a flat fiber optic ribbon which has the optical fibers held in positions parallel to each other in the same plane, as shown in Figure 1. Domestic and foreign ribbons typically contain from 4 to 36 fibers, and often have fiber counts divisible by four.

The ribbon manufacturing process should provide the following important characteristics of the ribbon product:

1. Stable geometric shape, i.e. low residual twist and bend along the ribbon length with minimum "bowing" in the cross sectional plane.
2. Sufficiently high Young's modulus of the matrix material and good peeling characteristics of the matrix–fiber coating interface.
3. Low residual tension and compression in the fibers.

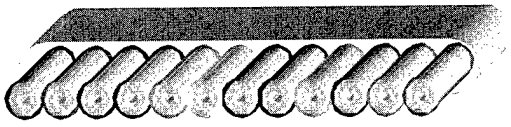


Figure 1. A cross section of a 12-fiber ribbon.

Stacking and Twisting. Ribbon stacks are commonly made of several individual fiber ribbons that are placed on top of each other, and twisted together in a helical or SZ pattern for stack integrity.

Typically the same size ribbons, with the same number of fibers per ribbons, are stacked parallel to each other. As an alternative, ribbon stacks can be composed of ribbons of different widths, forming a rounded stack, to more efficiently accommodate space within a round buffer tube. New design solutions also offer combined parallel and perpendicular positioning of the ribbons in a stack.

In many cases involving square or rectangular ribbon stacks, some or all of the corner fibers may show elevated attenuation in comparison to the rest of the stack. In most cases, high corner-

fiber attenuation is related to the contact of the corner fibers with the tube walls. To solve this, several approaches have been developed: (1) remove corner fibers, (2) select place less bend-sensitive fibers in the corners, (3) put soft cushions around the stack to reduce the contact stress on the corner fiber and to provide centering of the ribbon stack by keeping the stack away from the buffer tube wall.

The role of the twist in the ribbon stack is to provide periodic interchange in the fiber positions and thus to average fiber length and distribution of strain from one fiber to another. Also, twist adds radial compression to hold the stack together as a stable structure, which is important in situations such as sheave loading, loading from caterpillars, or to minimize buckling under thermally induced cable contraction. The stack stability is an important issue in several designs including "tall" stacks as shown in Figure 2.

Too much stack twist (i.e. too short of a twist laylength) will result in undesirably high tensile strain in the corner fibers and high compressive strain in the central fibers. It is known that a short laylength may result in permanent ribbon twist and cause problems during splicing. Also, too much twist can result in reduced mobility of the ribbons to slide with respect to each other to relieve stress in the ribbon stack due to increased contact pressure.

Too little twist, or too long of a twist laylength, may cause more variation in the ribbon excess length and possibly attenuation in the individual ribbons as they buckle under thermally induced cable contraction. Also, stack integrity may be compromised which could result in a collapse during subsequent loading. Stack collapse invites random orientation and unanticipated buckling or fiber-to-fiber stress variation. A long laylength can cause attenuation problems due to bending of the tubes or cables around a mandrel. To avoid attenuation due to bending or winding on a spool, by providing strain averaging through the stack cross section, it is typically recommended to have at least one lay length per mandrel circumference, i.e.

$$\text{Twist Laylength} < \pi D, \qquad (1)$$

where D is the bending diameter.

These opposite trends indicate that the stack twist laylength should have an optimum. The twisted ribbon stack should have a small enough value of radial compression (due to twist) to allow some mobility of the ribbons, yet at the same time should have enough to hold ribbons together as a group to withstand buckling loads during thermal contraction. The optimal twist laylength should provide for sufficient interchange in the fiber positions (strain averaging) to accommodate sheave loading and other mechanical loads.

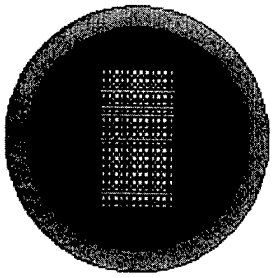


Figure 2. A stack of eighteen 12-fiber ribbons placed in a buffer tube.

Buffering. A stack of ribbons is typically encased in a thermoplastic buffer tube, either gel-filled or dry, as shown in Figure 2. As an alternative, ribbons can be SZ inserted in the grooves of a slotted core.

Stranding and Cabling. The buffered ribbon stacks can be used in the straight shape of the tube with the addition of radial strength members and an outer jacket, as shown in Figure 3a. This will produce a central tube cable configuration. As an alternative, the tubes can be stranded using an SZ path around a central strength member to form a stranded loose tube configuration (Figure 3b).

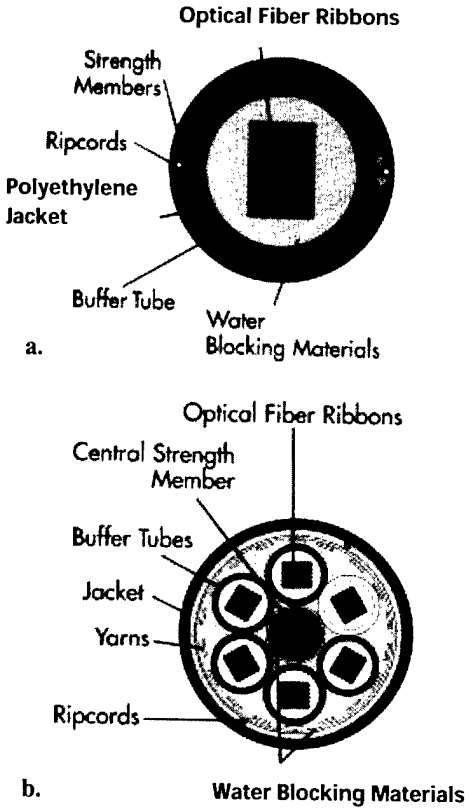


Figure 3. Central tube cable (a) and stranded tube cable (b).

Stranding of the buffered ribbon stacks provides additional interchange in the fiber positions, thus additional strain averaging in the fibers. Figure 4 illustrates the path of the tubes containing ribbons when they are SZ stranded around a central strength member.

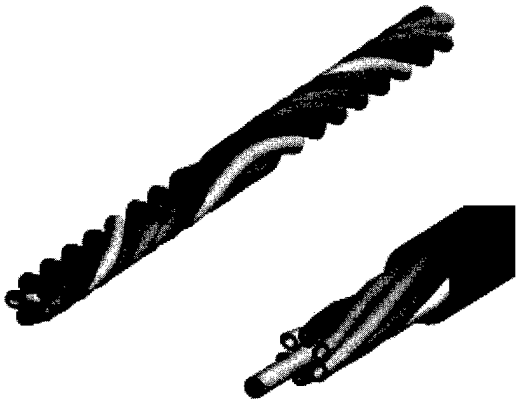


Figure 4. Cable core with buffer tubes SZ stranded around a central strength member.

Final cable configurations are typically obtained by adding strength yarns, ripcords, water swellable tape to fill interstitial gaps, armor tape, and an outer jacket to enclose and protect the cable core structure. Figure 3 shows typical cable components in central tube and stranded tube ribbon cables.

Compared to cables with fiber bundles, ribbon cables offer several attractive advantages. The main customer benefits are mass fusion splicing and, in central tube cables, extremely high fiber-densities. For manufacturers, high fiber-count ribbon cables provide opportunities to use the ribbon stacks as load-bearing elements, providing tensile stiffness and, to some degree, resistance against contraction.

Strain and attenuation. The optical performance of fiber ribbon cables under various thermo-mechanical loads depends on several design and process parameters, as well as choice of materials. The main design parameters influencing strain and attenuation in the fibers are:

- stack size,
- ribbon stack twist laylength and
- bending radius of the cable.

Strain and attenuation in fibers are sensitive to the following process parameters and material characteristics: geometrical imperfections in the ribbon structures, variation in the ribbon matrix stiffness from one ribbon to another, and friction or "tackiness" of the matrix surfaces.

This paper covers only selected aspects of the problem toward the following specific goals:

1. Optimize stack twist laylength to reduce strain variation in the ribbon stack. Ideally, propose a "universal" twist laylength optimal for the ribbon stacks from 6x6f to 36 x 36f.
2. Correlate attenuation distribution with strain distribution.

A description of existing published results and the results obtained by the Alcatel research team follows.

2. Existing Results

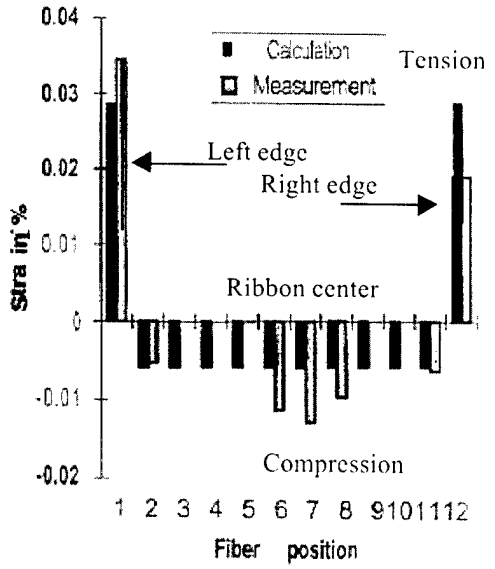
Below is a discussion of two recent publications in the area of ribbon twist.

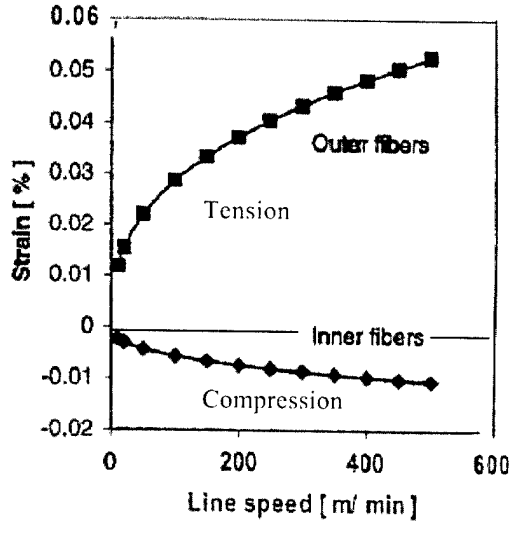
2.1. The strain distribution in individual ribbons and ribbon stacks was analyzed by Gao *et al.,* [1]. The authors presented results of experimental and theoretical studies of the influence of several ribbonizing process parameters, ribbon stranding, and cable bending on the strain distribution in the fibers. Good correlation between the theoretical and experimental results for traditional flat 12-fiber ribbon, as well as for a 216-fiber central tube cable composed of 18 ribbons, was demonstrated (Figure 5a, d). It was shown that the edge fibers in an individual ribbon have residual tensile strain while the rest of the fibers have residual compressive strain (Figure 5a). The strain variation was attributed to the friction in the ribbon die where the edge fibers are subjected to higher friction, and actual tension is induced in the edge fibers. Also, it was shown that the strain variation increased with an increase in line speed (Figure 5b).

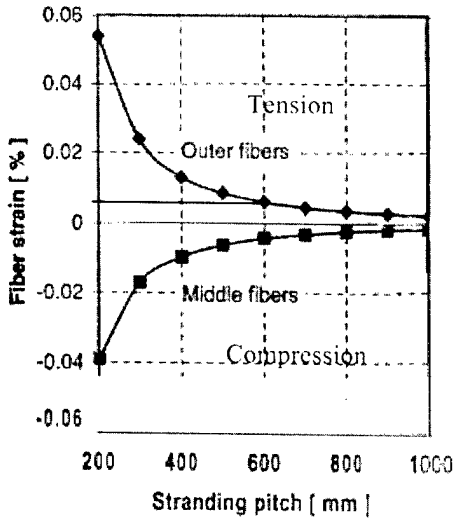
In the ribbon stacking process, an increase in the twist pitch from 200 to 1000mm (i.e. from 7.9" to 39"), caused the tensile strain in the corner fibers to monotonically decrease and the compressive strains in the middle fibers to monotonically increase approaching zero, as shown in Figure 5c.

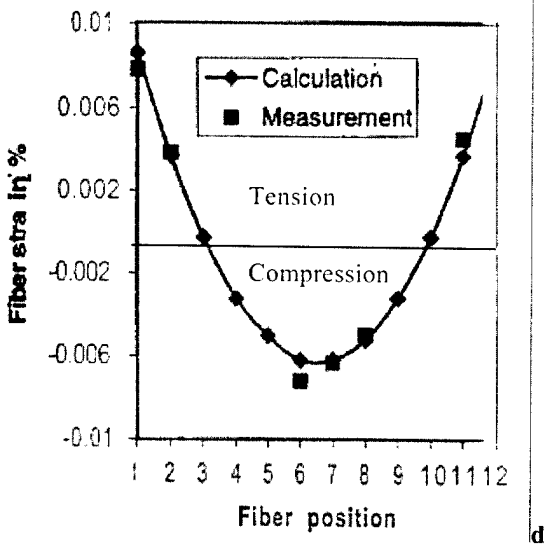
Experimental data using Bragg grating fibers and theoretical results shown in Figure 6a, illustrate a parabolic distribution in the fiber strain in a 12-fiber ribbon. The ribbon is twisted with a 500mm pitch. These results suggest that ribbon twist adds to the tensile strain in the edge fibers and compressive strain in the central fibers.

An increase in the cable bending radius from 200mm to 600mm resulted in a rapid reduction of the level of tensile strain in the corner fibers (Figure 5e). In particular, a cable containing a stack of eighteen 12-fiber ribbons, with a stranding pitch of 400mm and bent at radius of 250mm, produced 0.07% strain in the corner fibers.









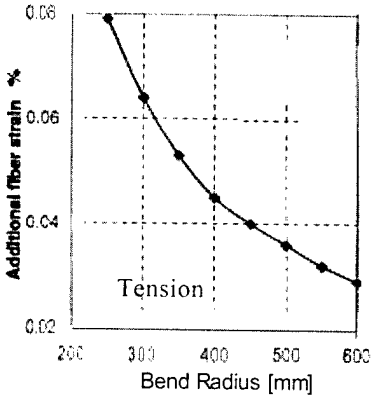


Figure 5. Results of Gao *et al.*, [1] for a flat 12-fiber ribbon and ribbon stack composed of eighteen 12-fiber ribbons:

(a) strain across the ribbon width,
(b) strain in the edge and middle fibers as functions of line speed,
(c) strain in the edge and middle fibers caused by stranding with different pitch,
(d) strain distribution for 500-mm pitch,
(e) maximum strain in the corner fibers of an 18 x 12-fiber ribbon cable as a function of bending radius.

2.2. Tabaddor and Aloisio [2] also performed experimental and analytical studies of the ribbon behavior under twist loading. Samples of 12-fiber and 24-fiber ribbons twisted to an angle of about 80-95° revealed a buckle in the central portion of the ribbon due to compressive stress. At 100-280° rotation, a transition to post-buckling occurred that was accompanied with audible cracking and visible delamination or debonding of fibers from the matrix material. The debonding process was sensitive to the material and geometrical imperfections. Complex global buckling modes were observed for angles of twist above 300°.

Based on these two published works it can be assumed that both the ribbonizing process and stack twist cause an undesirable accumulation of tensile strain in the fibers that are positioned on the edges of the individual ribbons and are in the corners of the stacks. Also, the ribbonizing process and stack twist cause an accumulation of compressive strain in the center of the ribbons and stack, leading to buckling. Subsequent bending of the cable results in additional tensile strain in the corner fibers and may induce additional strain of compression (with the level smaller than the amplitude of added tension) in the fibers close to the center of the ribbon stack.

3. Results of Analytical Solutions

The main goal of this research work is to better understand the influence of the twist laylength of the ribbon stack and bending radius of the ribbon cable on the strain distribution in the ribbon stacks. Also, it is important to correlate the strain distribution with fiber attenuation. It is proposed to optimize the laylength to reduce the level of tensile strain in the corner fibers, and the possibility of fiber buckling in the center of the stack under high longitudinally compressive strain. Other factors and processing parameters such as friction in the ribbon die, ribbon matrix composition and curing process, as well as line speed and ribbon stack size are currently under investigation and the results will be discussed in future papers.

Alcatel analysis tools include: (1) an analytical model based on the fiber position and path and curvature; (2) Alcatel computer-aided design tool; (3) ABAQUS finite element model. Below are the details of the models as well as a description of the results of analytical, finite element, and experimental studies.

3.1. Analytical Model based on the Fiber Path.

The parametric equations of the fiber path can be presented as follows:

$$x = (R + r\cos q)\cos a$$
$$y = r\sin q$$
$$z = (R + r\cos q)\sin a \qquad (2)$$

where $q = a\ 2\ p\ R/L$,

R is the tube bending radius,

r is the distance from a fiber to the ribbon stack center,

q is the stack (fiber) rotation angle,

a is the cable rotation angle,

p is the twist pitch,

L is the stack twist laylength.

The curvature and length of the individual fibers are functions of their position in the ribbon stack. It is believed that an excessive reduction in the radius of fiber curvature would cause attenuation. From this point of view, corner fibers in the stack initially have a small radius of curvature as compared to the fibers close to the stack center. Also, the stack twist induces additional tension in the corner fibers and additional longitudinal compression in the central fibers. Under very high compression, the central fibers can buckle causing a rapid reduction in the fiber radius of curvature and attenuation problems.

Equations (2) were used for the analysis of the strain along the fiber length. Also, the strain averaging or smoothing analysis was performed to model friction between the ribbons. These results suggested that strain reduction or smoothing is limited by the twist laylength. Too short of a twist laylength "locks" the ribbon elements, inhibiting movement even with a significant amount of lubrication.

The fiber curvature will increase with a reduction in the cable bending diameter. This is important for the fiber curvature analysis when the whole tube or cable is spooled, stranded or subjected to installation loads.

3.2. Analytical Model based on the Alcatel Computer-aided Design Tool.

Similar to that of Gao *et al.,* [1] studies were performed at Alcatel R&D. The studies included an analysis of the strain distribution in the 216-fiber composed of eighteen 12-fiber ribbons. The cross section of the 216-fiber cable is shown in Figure 2. The modeling was performed using the Alcatel computer-aided design tool. Analysis of the sensitivity of the principal strain in the central and corner fibers to the cable bending radius and stack lay length was performed.

Influence of the Bending Diameter. Figure 6 shows the change in the strain components in the central and corner fibers under cable bending for the same 24" ≈ 610mm twist lay length. Bending strain (pink color) and principal strain (green and red colors) in the central and corner fibers increased with a decrease in bending radius. Additional fiber bending came from twist (blue color) that is nearly constant due to the stack having the same lay length. The bending component of strain decays as the bending radius approaches 10m (corresponding to reeling the cable on the floor in large loops), but the level of twist strain and principal strain do not reduce significantly with an increasing bending radius.

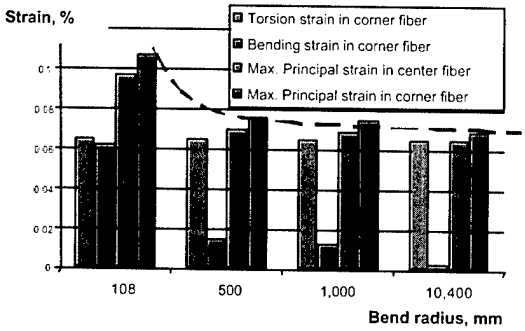


Figure 6. Influence of bending radius on the strain components in the central and corner fibers. Stack lay length 24".

Influence of the Stack Twist Laylength. Figure 7 illustrates the changes in the strain components of the central and corner fibers for the same 108-mm (8.5" OD) reel and various twist lay lengths. The torsional strain component is inversely proportional to the twist laylength. Principal strain (green and red colors) in the central and corner fibers decreased with an increase in the laylength. Additional strain came from bending around the spool (pink color).

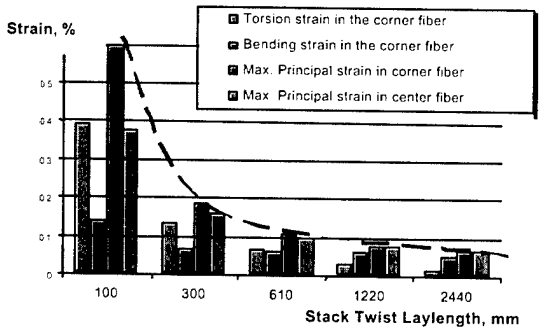


Figure 7. Influence of the lay length on the strain components in the central and corner fibers. Bending diameter is constant 8.5".

Comparison with Published Results. Gao *et al.*, [1] showed that in a central tube 216-fiber cable made of 18 x 12-fiber ribbons with a stranding pitch of 400mm bent at radius of 250mm, the maximum strain in the corner fibers was 0.07%. Computation using the Alcatel computer-aided design tool for the described Alcatel ERK cable of a similar stack configuration gave a maximum principal fiber strain of 0.12%. Considering that the two cables have different properties, - with no information given in Gao *et al.*, [1] about the tube material and size, this is a satisfactory correlation of the strain levels.

Both results, obtained by Gao *et al.*, [1] and at Alcatel, showed that the maximum level of the strains in the corner fiber monotonically decays with an increase in the twist laylength. In particular, an increase in laylength from 200mm to 600mm in both models showed approximately an 8-10 times reduction in the maximum strain level in the corner fibers.

Also, in both cases, the absolute value of strain in the central fibers is smaller than that in the corner fibers (Figures 5c, 6 and 7, where corresponding strains are shown as red and green bars). Additional fiber strain due to the cable bending or tube bending also reduces with an increase in the bending radius as shown in Figures 5d and 7. Higher rates of strain reduction for both models are in the range from 100mm to 500mm for cable bending diameter.

Strain distribution in the ribbon stack cross section. One of the goals of this work is to analyze the strain distribution in the ribbon stack as a function of twist and bending.

Figure 8 depicts the distribution of tensile and compressive strain in the fibers of a selected ribbon of the 216-fiber ribbon stack, when no bending is applied. Figure 9 shows a 3-dimensional view of the principal strain distribution across a ribbon stack when both stack twist and stack bending (8.5" bending diameter) are considered. In both cases, the stack is twisted with a 24" laylength. The longitudinal strain of compression and tension are about 10 times lower than the level of maximum principal strain. The principal strain distribution is a 3-D surface with the lowest strain in the center and highest strain in the corners of the stack. It is important to note that the parabolic distribution of strains (Figure 8) across each ribbon is in agreement with the measurements published by Gao *et al.*, [1] as shown in Figure 5d. A refined analysis of the strain distribution across the ribbon stack was performed using finite element modeling and a discussion is presented below in section 3.3.

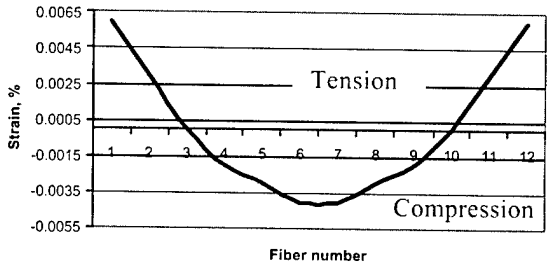


Figure 8. Distribution of tensile and compressive strain in the fibers of a selected ribbon of the 216-fiber ribbon stack when no bending is applied.

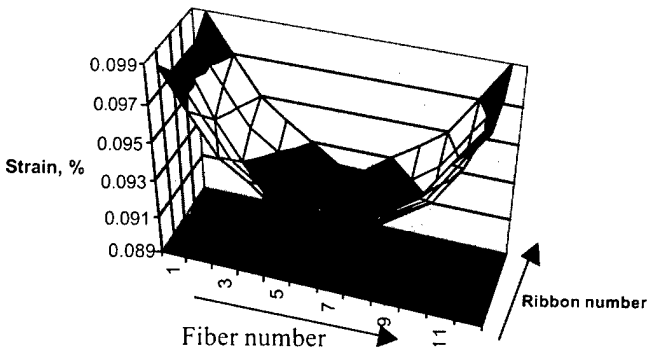


Figure 9. Distribution of the maximum principal strain in the cross section of a bent ribbon stack.

Finding Optimal Twist Laylength

An important goal is to find an optimal stack twist laylength for a wide variety of ribbon stack sizes. Figure 10 shows the influence of the ribbon twist laylength on the level of maximum principal strain in the corner fibers of various ribbon stacks.

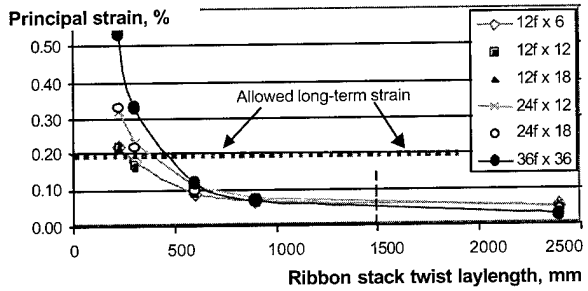


Figure 10. Influence of the ribbon stack twist on the fiber principal strain.

All the stacks considered in the calculations, as described in Figure 11, are placed in the buffer tubes and bent without tension around a mandrel having a diameter 20 times the outer diameter of the buffer tube. Results showed that large stacks (36f x 36), with a twist laylength below 18" and reeled around a mandrel with a diameter 20 times the diameter of the tube, will have high (above 0.19%) principal strain in the fibers. There is a clear trend showing a decrease in strain with a decrease in stack size.

Figure 11 is a 3-D representation of the influence of the ribbon stack size and stack twist laylength on the level of maximum principal strain in the corner fibers when the buffered stack is bent around a mandrel with a diameter that is 20 times the tube outer diameter, and no tension is applied. More fibers per ribbon and more ribbons per stack cause an increse in the principal strain.

Twist Laylength	Strain, %					
	12f x 6	12f x 12	12f x 18	24f x 12	24f x 18	36f x 36
9" = 229mm	0.22	0.22	0.22	0.32	0.33	0.53
12" = 305mm	0.18	0.17	0.16	0.23	0.22	0.33
24" = 610mm	0.09	0.09	0.09	0.11	0.10	0.12
36" = 914mm	0.07	0.07	0.06	0.08	0.07	0.07
96" = 2438mm	0.05	0.05	0.04	0.05	0.04	0.03

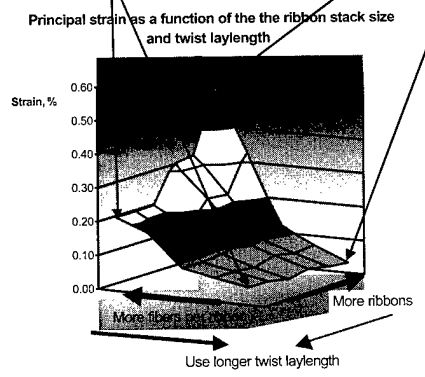


Figure 11. A 3-D representation of the influence of the ribbon stack size and stack twist laylength on the level of principal strain in the corner fibers.

Based on this analysis, it can be suggested that twist laylength should be increased for large ribbon stacks. However, large stacks with increased twist laylength will have longer ribbons on the side of the stack that is subjected to the compressive strain component due to bending. This will result in buckling of the ribbons according to the Euler's equation for a round rod:

$$P_{cr} = \frac{\pi^2 EI}{kL^2} \qquad (3)$$

Where P_{cr} is the critical value corresponding to buckling load, E is the Young's modulus, I is the moment of inertia of the cross section, k is the factor accounting for the end support.



Figure 12. Illustration of the buckling concept.

As can be seen from Equation (3), buckling is sensitive to the length of the ribbon between supports. With the application to the stack twist, this suggests that the laylength should not be too long. Other reasons to keep twist laylength shorter are: (1) radial compression that provides stack stability and integrity of the rectangular ribbon cross section, (2) radial compression and better coupling of the neighbor ribbons should produce enhanced resistance to the buckling load in contrast to buckling of individual loose ribbons.

Overall, we can see two opposite trends with respect to the twist laylength suggesting an existance of an optimal twist laylength corresponding to minimum strain in the stack.

3.3. Finite Element Modeling

Finite element analysis can be used to gain a better understanding of the mechanics of a ribbon and ribbon stack under twist and bending loads. It also allows for an evaluation of design parameters such as ribbon size, stack geometry, and the laylength of the twisted ribbons or tubes that contain them, which greatly helps to produce an optimized ribbon product, and significantly reduces the development cycle time. Finite element models provide the means to investigate the influence of material variations such as differences in the modulus of the matrix from ribbon to ribbon, or the friction characteristics between ribbons on the deformation and strain of the fibers.

Ribbon twist. In order to investigate the influence of ribbon twist on the strain distribution in the fibers, a finite element model of a section of a twelve-fiber ribbon was created using three-dimensional hexahedral elements. Numerical simulations of ribbon twisting were performed using the commercial finite element package ABAQUS. The model of the ribbon and a cross sectional view of the finite element mesh are shown in Figure 13. Since the glass core of the fiber has a modulus that is significantly higher than the coatings and matrix, the coatings were lumped together with the matrix.

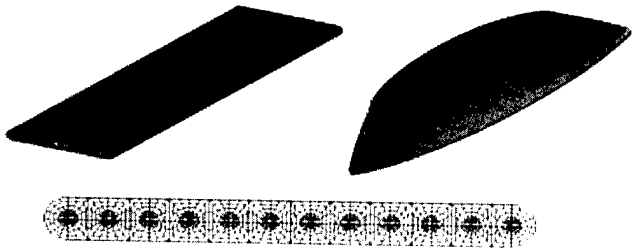


Figure 13. Finite element model of a section of a twelve-fiber ribbon.

The simulations were conducted with one end of the ribbon fixed and the other end twisted through 360 degrees. The length of ribbon modeled is relatively short, so the amount of deformation that the ribbon experiences in this analysis is quite severe. Figure 13 shows the deformed configuration of the ribbon at a twist angle of 134 degrees.

Figure 14 shows the maximum principal strain in the fibers at twist angles of 90 and 180 degrees, respectively. As the ribbon is twisted, tensile strain develops in the outer fibers, and compressive strain develops in the center fibers. Figure 15 shows a plot of the maximum principal and axial strain in the fibers taken at a cross section from the middle of the ribbon.

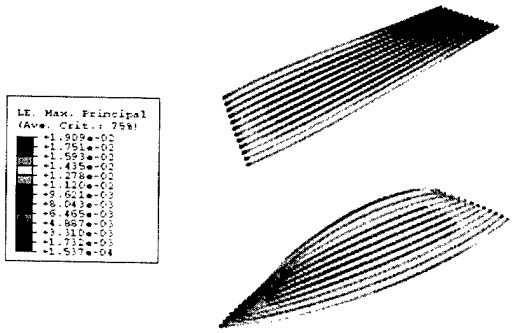


Figure 14. Maximum principal strain in the fibers of a twelve-fiber ribbon twisted at angles of 90 and 180 degrees.

The parabolic shape of the tensile and compressive strain curves agrees with the results obtained by Gao *et al.*, [1] that were discussed above. Both the tensile strain in the outer fibers and the compressive strain in the center fibers increase with increasing twist angles. It is interesting to note that the change in axial strain for all the fibers is quite large for an increasing angle of twist except for fibers four and nine. The distortion of the neighboring fibers could cause buckling of these fibers since they are under a relatively low state of stress. An analysis of the strain induced in the ribbon, coupled with the curvature of the fibers can be used to correlate attenuation with the shape distortion of the fibers.

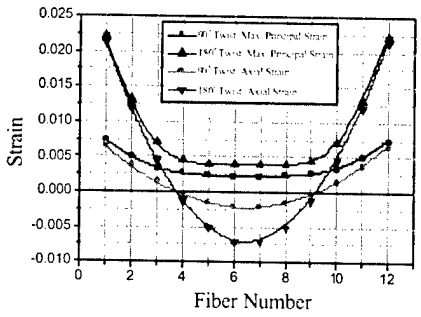


Figure 15. Axial strain distribution in a cross section of a twelve-fiber ribbon twisted at angles of 90 and 180 degrees.

Ribbon stack twist. A finite element model of a stack of ribbons was developed to investigate the strain in the fibers when the entire stack is twisted. Modeling the round fibers in all of the ribbons, as was done for the single ribbon, makes the model extremely large and time consuming to solve. As a simplification, the glass core of each fiber was modeled with a square cross section, with the appropriate dimensions to give the same total area of glass that is in a round fiber. Twelve rectangular fibers were included in each ribbon, and twelve ribbons were taken to comprise the stack. The matrix and fiber coatings were combined as was done for the single ribbon model. Contact surfaces were defined between each of the ribbons to allow for sliding and separation. The contact algorithm allows for the definition of static and kinetic friction coefficients, which provides a means to study effects of any variations in the surface characteristics of the ribbons. Figure 16 shows the initial configuration of the ribbon stack, and the deformed state at a twist angle of 180 degrees.

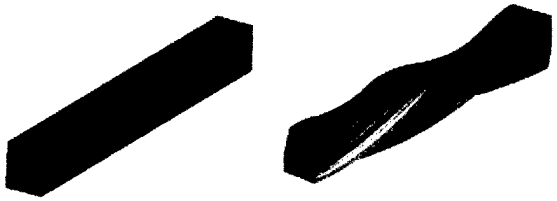


Figure 16. Initial configuration of the ribbon stack, and the deformed state at a twist angle of 180 degrees.

Figure 17 shows the maximum principal strain distribution in the fibers on a cross section taken from the middle section of the ribbon stack, for a ribbon twist angle of 180 degrees. The plot shows a non-uniform variation in the level of strain when transitioning from the outer fibers toward the center of the stack. The results of the finite element analysis revealed three types of 3-D surfaces (Figure 18) for the strain distribution across the ribbon stack. These include: a) a smooth "bowl" shaped surface showing

tensile strain in the outer fibers, and compressive strain in the central fibers, b) a skewed "bowl" shape (shown in Figure 18a) apparently due to transition from a rectangular to skewed cross section of the twisted ribbon stack, when the ribbons have a low coefficient of friction and are sliding with respect to each other, and c) a "bowl" with a concave central part (shown in Figure 18b) suggesting a W-shaped strain distribution across the width of individual ribbons. When correlated to the attenuation, these strain surfaces could explain the non-uniform distribution of attenuation often observed in ribbon stacks (Figures 19 and 20).

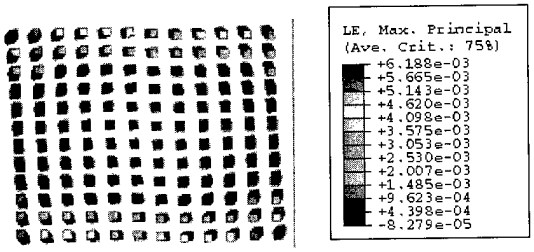


Figure 17. Distribution of maximum principal strain in the fibers on a cross section taken from the middle of the ribbon stack, for a ribbon twist angle of 180 degrees.

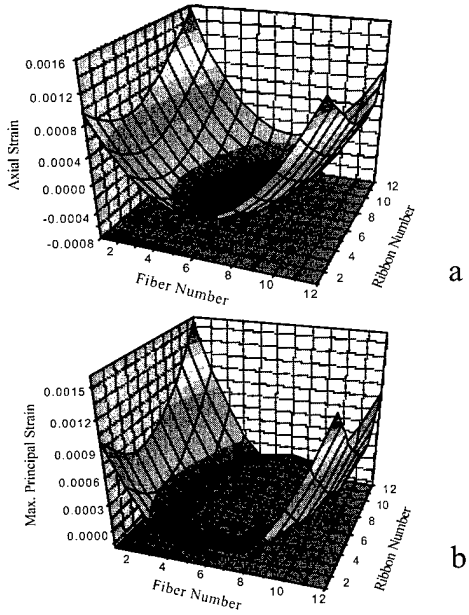


Figure 18. Distribution of (a) axial strain and (b) maximum principal strain in the fibers on a cross section taken from the middle of the ribbon stack, for a stack twist angle of 90 degrees.

Complex deformation modes including ribbon separation and buckling of the ribbons were also observed in the simulations. These deformation states could be attributed to the rate of the applied dynamic twist loading and the large amount of ribbon twist relative the length modeled.

3.6. Experimental Results

Two types of ribbon cables were manufactured: a 216-fiber cable made of eighteen 12-fiber ribbons and a 288-fiber cable made of twelve 24-fiber ribbons. The stack twist laylength in both cables was 24". The 216-f cable was reeled on an 8.5" diameter reel and the 288-f cable on a 14.6" diameter reel. The larger reel for the 288-f cable was used based on the increased ribbon stack size, to reduce the level of strain caused by bending.

As discussed earlier, the distribution of axial strain across the twisted ribbon stack should produce high tension and minimum radius of curvature in the edge fibers of the ribbon stack. These predictions correlated well with the OTDR measurements shown in Figure 19, for the top and bottom ribbons, number 1 and 18. The corner fiber increase in attenuation makes sense from the strain distribution. However, the interesting item is the elevated attenuation in the center ribbon. It is speculated to be due to buckling from the longitudinal compressive stress. Increased friction between the ribbons, a relatively short twist laylength, and low temperature could result in high uniform attenuation in ribbon number 6.

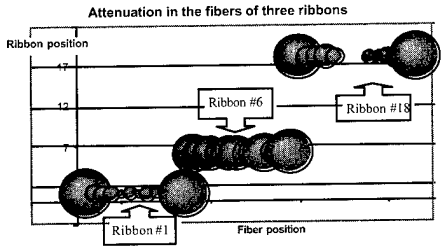


Figure 19. Attenuation in the 216-fiber stack at –40°C. No lubricant was applied between the ribbons. 1550nm wavelength.

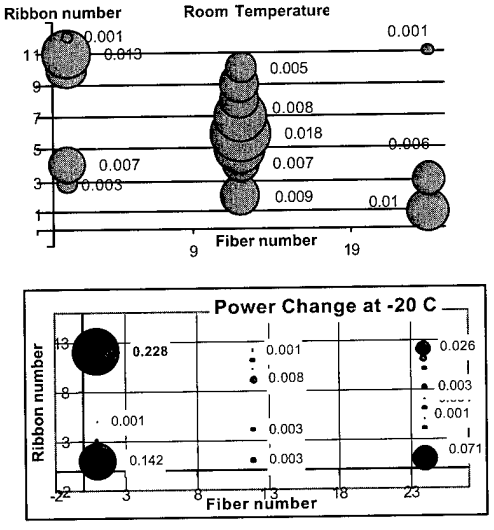


Figure 20. Initial attenuation at room temperature (attenuation after cabling in 700m of cable minus initial fiber attenuation) and power loss at –20°C in the 288-fiber ERK cable. Wavelength is 1550nm.

4. Conclusions and Future Work

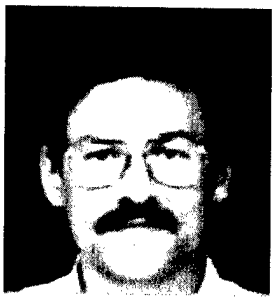
The results of the work can be summarized as follows.

1. Several theoretical models of the ribbon stack have been developed to study the influence of torsion, tension, and bending on the stress-strain in the ribbon stack. The main focus was the contribution from the twist laylength for the worst case when the bending radius is 20 times the diameter of the buffer tube housing the ribbon stack.
2. The parabolic distribution of axial strain across the ribbon width, with tension in the edge fibers and compression in the middle fibers, is more pronounced for higher stack twist and larger stack size. The excessive tension in the corner fibers can cause fiber breakage if a flaw or surface crack exists. Also, the compressive strain can lead to fiber buckling and attenuation problems.
3. The torsion strain component is linearly proportional to the twist laylength. With an increase in the bending radius, the maximum principal strain in the twisted ribbon stacks decays.
4. The results of the finite element analysis revealed three types of 3-D surfaces representing the stress and strain distribution across the ribbon stack. These include: a) a smooth "bowl" shaped surface showing tensile strain in the outer fibers, and compressive strain in the central fibers, b) a skewed "bowl" shape apparently due to transition from a rectangular to skewed cross section of the twisted ribbon stack, when the ribbons have a low coefficient of friction and are sliding with respect to each other, and c) a "bowl" with a concave central part suggesting a W-shaped strain distribution across the width of individual ribbons. Complex deformation modes including ribbon debonding and buckling in the direction of the ribbon width were also observed but can be attributed to the effects of dynamic loading and stack warping.
5. The models helped to correlate the predicted strain distribution in the fibers with the measured fiber attenuation. In particular, the distribution of axial and principal strain across the ribbon stack helped to explain the attenuation in the corner fibers and fibers located in the middle ribbons. Too much twist of the ribbon stack resulted in increased levels of tension in the corner fibers and compression in the central fibers.
6. Future work will involve numerical evaluation of the strain distribution in the stack having "too long" of a twist laylength in order to quantify the upper limit of the stack twist laylength. This will involve analysis of radial strain components responsible for the stack stability as well as increased sliding mobility and the possibility of buckling of individual ribbons.

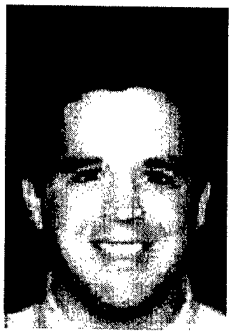
5. References

[1] Zh. Gao, W. Pfandl, R. Engel and A. Stingl "A Study of the Fiber Strains in Central Tube Ribbon Cables," *Proc. IWCS*, 1999, pp. 61-65.

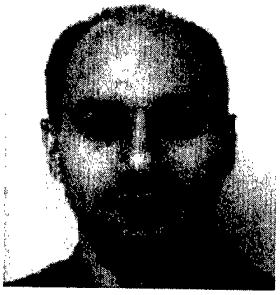
[2] M. Tabaddor and Ch. Aloisio, "Using Twist to Evaluate Fiber Optic Ribbon Properties," *Proc. IWCS*, 2000, pp. 622-627.



Nicholas V. Nechitailo received his Ph.D. degree in Applied Mechanics (Technical Sciences) from the Institute for Problems of Strength, Ukrainian Academy of Sciences (USSR) in 1988 and M.Sc. in Engineering Mechanics from Virginia Polytechnic Institute and State University in 1995. He was a Visiting Scientist at Brown University, Research Associate at Virginia Tech, Research Scientist at American Research Corporation of Virginia, and since 2000 has been working as Design Engineer at Alcatel R&D Center in North Carolina. He performs design of fiber optic cables as well as analytical and experimental studies of the cable structure and materials under various thermo-mechanical loads and environmental conditions toward innovative solutions and improved cable quality.



Matt G. Soltis is the Design Technology Manager for Alcatel's global R&D center for fiber optic cable. He received his B.S. in Aerospace Engineering from the U.S. Naval Academy in 1989. Prior to joining Alcatel in 1997, Matt served as an officer and aviator in the U.S. Marine Corps, specializing in aircraft accident analysis, radar theory, and the kinematics of air-to-air combat.



Dean J. Rattazzi is a Design Engineer at the Alcatel R&D Center for Fiber Optic Cable in Claremont, North Carolina. He holds a BA degree in Physics, and a BS degree in Mechanical Engineering from Binghamton University, and an MS degree in Engineering Mechanics from Virginia Tech. His area of research includes the application of finite element modeling to the design and development of fiber optic cables.

All Dielectric Optical Cable with Improved Mechanical Resistance

Alessandro Ginocchio, Enrico Consonni, Paolo Marelli

Pirelli Cavi e Sistemi SpA
Milan, Italy
+39 02 6442 2798 - alessandro.ginocchio@pirelli.com

Abstract

The use of fully dielectric optical cables for access and trunk networks is rapidly growing. Also the exploitation of existing "right of ways" for installing optical communication cables requires, for specific applications, fully dielectric, light and flexible cables having high mechanical characteristics. The cable mechanical performances are important in order to guarantee a high reliability during installation and service life. In addition, a light and flexible structure can minimize the use of longitudinal reinforcing elements and reduce cable and installation costs.

This paper investigates the mechanism of cable behavior under lateral forces. Different cable samples with different designs have been manufactured and tested at different levels of energy (impact) and applied forces (crush) in order to highlight the contribution of each protective layer. All cable samples have been produced using the same optical core in order to compare effectively the different outer protections.

The results obtained show that the use of a proper multilayer structure manufactured with materials having specific values of Young modulus and energy absorption capacity, can increase significantly the resistance to impact and crush. For some applications it is proved that is possible to replace a metallic protection with a dielectric protection having the same performance in terms of crush and increasing more than twice the performance in terms of impact. The use of additional dielectric protective layers in order to guarantee all the metallic protection functionality (i.e.: rodent protection) are as well investigated.

In conclusion, the newly developed all-dielectric cable, showing also an appreciable bending stiffness and weight reduction, fully complies with the requirements of the most recent network applications.

Keywords

Dielectric optical cable; lightweight; mechanical resistance improvement.

1. Introduction

The use of fully dielectric optical cables is growing mainly in the subscriber loop. At present the challenge for successful penetration of optical fibers into the local distribution network depends on the development of small, flexible, light and cost effective cables. In addition, new installation techniques requiring small and lightweight cables are being introduced also for trunk networks. Another important issue is the exploitation of existing "right of ways". In this case, the use of proper cables having preferably a reduced weight and, at the same time, high mechanical performance, would be very attractive. Moreover, some Telecom operators ask for dielectric cables to be installed in regions characterized by high lightning risk.

For the above reasons, an experimental work has been undertaken to provide a new fully dielectric cable design with improved impact and crush resistance in comparison with standard all dielectric cables or standard metallic cables.

2. Cable design

A whole family of fully dielectric cables have been designed, including different combinations of protective layers, in order to identify the most effective solution for providing cables with a range of physical and mechanical performances suitable for different applications. The original design idea was to consider combinations of relatively "hard" and relatively "soft" layers in order to improve the crush and impact resistance of the cable.

It is well known that the cable resistance to lateral forces is related to the physical characteristics of the optical core and to the physical characteristics of the outer layers. Considering a conventional optical core with loose tube design, once defined the tube dimensions, the number of fibers per tube and the stranding layer geometrical characteristics (number of tubes, lay length and filling factor), the optical core resistance is defined. The use of additional layers allows then to increase the cable resistance to lateral forces. Each additional layer gives its own contribution to the overall cable resistance according to its thickness and its mechanical characteristics.

In order to better highlight the differences, in terms of mechanical performance to lateral forces, a unique optical core design has been considered to manufacture all the different cable samples.

The optical core considered is quite conventional (see figure 1). It is formed by 6 tubes 1.8/2.5 mm stranded around a central dielectric strength member of 2.7 mm. Each tube, jelly filled, includes 12 fiber optics. The core design is dry, without flooding

compound in the interstitial areas, but is equipped with water swellable yarns and a water swellable tape.

The different cable samples, manufactured starting from the same optical core, have been produced using combinations of three materials as protective layers:

- a standard Low-Density polyethylene (used mainly for internal sheath)
- a standard Medium-Density polyethylene (used mainly for the outer sheath)
- a special material with defined density, Young modulus and energy absorption capability

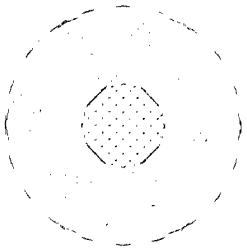


Fig.1 – Optical core cross section

Also a specific metallic armor has been considered in one cable sample for comparison reasons.

All the cable samples have the same dielectric armor, made by 36 aramid yarns 1620 dTex, applied on the inner sheath. The total armor thickness is around 0.1 mm and has been chosen in order to give the same contribution to the lateral resistance of all cable samples.

The cable samples realized are briefly summarized in table 1. A code identifies the type of material, while the layer thickness, expressed in mm, is reported between brackets. The polyethylene grade for the first layer is always low density, while the polyethylene grade for the second or outer layer is medium density.

Table 1 – Cable samples description

Sample	First layer	Second layer	Third layer
1	PE (1.0mm)	-	-
2	PE (1.0mm)	-	PE (1.5mm)
3	PE (1.0mm)	AA (1.5mm)	-
4	PE (1.0mm)	AA (1.5mm)	PE (1.5mm)
5	AA (1.9mm)	-	PE (1.5mm)
6	AB (1.9mm)	-	PE (1.5mm)
7	PE (1.0mm)	PE (1.5mm)	PE (1.5mm)
8	PE (1.0mm)	SPL (0.8mm)	PE (1.5mm)

The codes AA and the code AB refer to a special material with defined characteristics in terms of density, Young Modulus and energy absorbing capacity. Two different "special" materials are considered having different modulation of mechanical characteristics. The material AB has a density 20% greater and a Young modulus 50% greater than material AA. More in detail, this material can be extruded with different density working on compound mix and process parameters. Different values of density correspond to different value of elastic modulus. It is known that the ability of a material to absorb energy, protecting in this way the rest of the structure, is related to its capacity to be properly deformed under stress. An example of stress-strain curve for a material that is very effective in absorbing energy is represented in fig. 2, where the area under the curve up to the critical stress σ_c (the stress where the material begins to be damaged) is maximized.

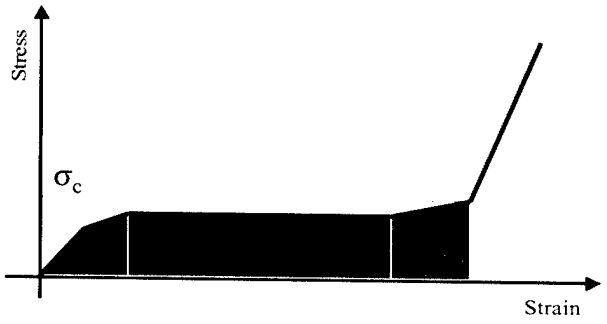


Fig. 2 – Stress-strain curve showing the energy absorption area

The only presence of an effective material for energy absorption does not guarantee, per se, a good performance in terms of impact and crush resistance. The material with absorbing capacity can work effectively only if it is used with a proper combination of other layers with different mechanical characteristics. For this reason, and in order to identify the contribution of the different materials, also some samples that correspond to unfinished cables have been considered and tested (samples 1 and 3).

Outer diameter, weight and bending stiffness for each cable sample are reported in the following table 2.

Table 2 – Data on cable samples

Sample	Outer diam. (mm) (mm)	Weight (kg/km) (kg/km)	Bending stiffness (N m^2)
1	10	70	0.166
2	13	120	1.128
3	13	90	0.333
4	16	155	2.109
5	13.8	115	1.628
6	13.8	120	1.707
7	16	185	2.845
8	15	190	2.315

3. Mechanical tests

In order to characterize the cable samples and to highlight the best combination of layers that maximizes the performance in terms of cable resistance to lateral forces, two standard crush and impact tests have been considered. Nevertheless, different test procedures have been used both in preparing samples and performing the tests in order to really identify the minimum resistance limit of each cable sample.

For this reasons, all the fibers have been monitored during each load application and, for each load or energy level, at least 20 different positions along the cable have been tested.

3.1 Impact test

The impact test has been performed referring to the IEC specification 60794-1-2 with an anvil radius of 10 mm and using different weights falling down from 1 meter height. For each energy level at least 20 different positions along the cable have been tested.

The impact test lay-out is schematized in the following figure 2.

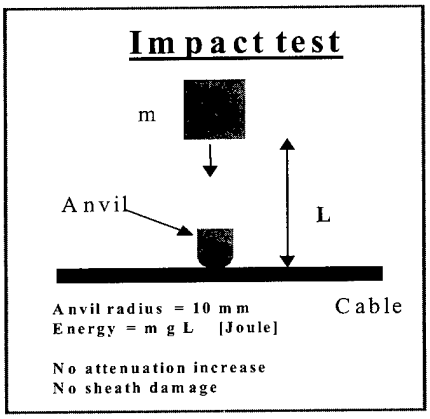


Fig. 2 – Impact test

For each cable sample it is reported, in table 3, the maximum level of energy without having any temporary or permanent attenuation increase (column 2) and the energy at which the first fiber break occurred (column 3).

Table 3 – Impact test results

Sample	Energy (J)	Energy (J) (fiber break)
1	5	10
2	20	25
3	10	25
4	40	45
5	25	30
6	30	35
7	30	35
8	20	25

Let's consider the second column (energy values without attenuation increase). The tests performed on the first two samples show that, for impact resistance, the outer sheath gives the biggest contribution. The cable sample 2, in fact, shows a resistance to impact four times bigger than those of cable sample 1. The use for the cable sample 3 of a softer material instead of the outer material used for the cable sample 2 doesn't give any advantage and the resistance decreases dramatically. But, if we apply an additional outer sheath (sample 4), the cable resistance increases up to a value of 40 joule. The relatively hard outer sheath distributes the energy to a bigger portion of the intermediate softer sheath, increasing the energy absorbing capacity of the cable.

The cable samples 5 and 6, both made with a soft inner sheath, but with two different values of elastic modulus (Young modulus 6 > Young modulus 5), show that a relatively more rigid inner layer (cable sample 6) gives a slightly bigger resistance to impact.

The design of the cable sample 7 is equivalent to the cable sample 4 in terms of dimensions and materials apart the intermediate layer, that is made of standard medium density polyethylene in case of sample 7, and of softer material AA in case of sample 4. It is possible to see that the presence of the special softer material AA in the intermediate position (sample 4) increases significantly the cable impact resistance. The cable sample 8, having a metallic layer (steel polymer laminated), shows a relatively poor performance in term of impact resistance, because the metallic layer has high elastic modulus, but a very low energy absorbing capacity.

The cable sample 4 is the best solution for impact resistance. This solution is also extremely competitive in terms of weight and flexibility to bending, especially in comparison with the cable having the metallic protection (sample 8).

3.2 Crush test

The crush test has been performed referring to the IEC 60794-1-2 specification using a steel plate of 100 mm having edges rounded with 10 mm radius. As for the impact test, for each load, applied for 15 minutes, at least 20 different positions along the cable have been tested. Particular attention has been kept in order to apply the force also in the stranding reversal position where the core is generally weaker. The crush test lay-out is schematized in the following picture (fig.3).

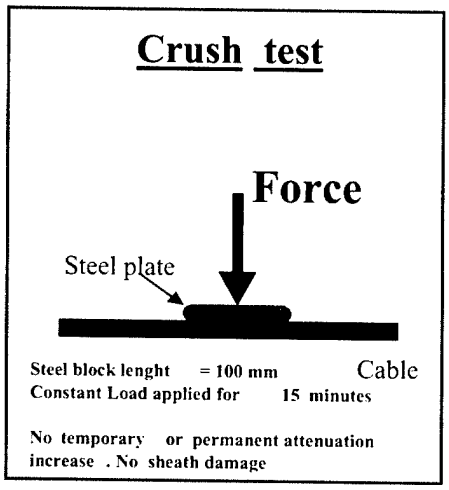


Fig. 3 – Crush test

The crush test results are summarized in table 4, where the second column reports the maximum load without having any temporary or permanent attenuation increase.

Table 4 – Crush test results

Sample	Force (kN)
1	1.50
2	3.00
3	3.25
4	4.00
5	3.00
6	3.00
7	4.00
8	4.25

In case of static load, the cable with metallic armor (sample 8) shows the biggest resistance. Nevertheless, both the dielectric cables 7 and 4 have crush resistance limits very close to the metallic cable. In addition the cable sample 4 has the advantage to be lighter and more flexible.

The analysis of the data related to the cable samples 1, 2 and 4, shows how the crush performance increases adding additional layers to the core structure. The cable sample 1 (just the optical core plus the inner standard sheath), in comparison with the cable sample 2, demonstrates that the optical core gives however a significant contribution to the crush resistance. This is different to what happens in case of the impact test, where the core structure plays a less important part. In the following graph 4 the performances to crush and impact of the cable samples 1, 3 and 4 are summarized. This comparison is interesting because summarizes the different role played by the layers in case of crush or in case of impact stress on the cable. The performance of the sample 4 has been taken as reference (100%) both for crush and impact tests.

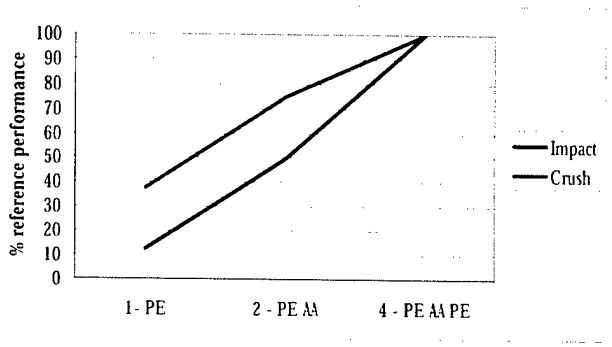


Fig. 4 – Impact and Crush resistance as a function of protective layers

In case of crush test, the cable finished to the first sheath (sample 1) shows a resistance equal to 40% of that of the three layers cable (reference sample 4), while in case of impact test the cable finished to the first inner sheath shows a resistance of only 12% of that of the sample 4. This means that, in case of a static load (crush), the tubes themselves are able to support a significant part of the applied load. On the contrary, in case of a dynamic load (impact), the tubes per se, not having significant energy absorbing capacity, cannot protect efficiently the optical fibers.

3.3 Analysis of the cable deformations

During the crush and impact tests, the cable samples have been subjected to a series of geometrical measurements of the deformations (in terms of outer diameter reduction) as function of the applied energy or load.

The fig. 5 reports the cable diameter reduction, expressed as percentage of the initial diameter measured immediately after the impact application. The samples 4, 5, 7 and 8 have been selected, because most significant.

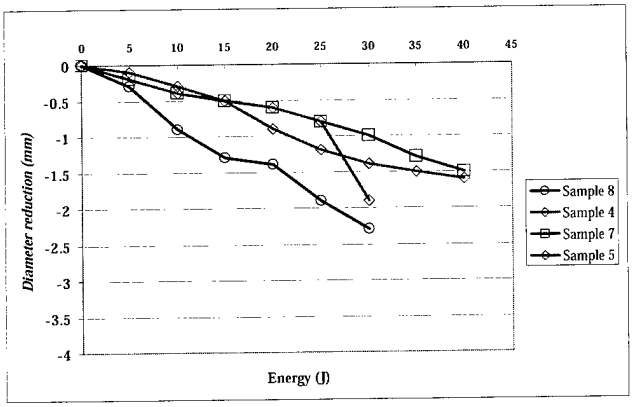


Fig. 5 – Impact test: Cable deformation versus energy

It can be seen how the cable having a metallic armor (sample 8) shows the highest permanent deformation. This, in addition to the fact that such cable showed the lowest energy limit in terms of impact, can also be an additional disadvantage because permanent deformation can cause permanent attenuation increase in case of further load applications. All dielectric cable samples summarized in the graph 5 show a considerable similar behavior up to an energy value of 25 J. For greater values of energy, the cable sample 5 shows a big deformation that justifies the early fiber break (see table 3). The cable samples 4 and 7 present, on the contrary, a quite similar behavior, in term of cable deformation, also for greater values of energy. Nevertheless the cable sample 7 presents attenuation increase over 30 J and fiber break at 35 J, demonstrating that the sample 7 itself has less energy damping capacity in comparison with the sample 4 (40 J and 45 J respectively), which is the best.

Considering the crush test, in the following two graphs the cable deformations during and after the load application are reported for two values of the applied load.

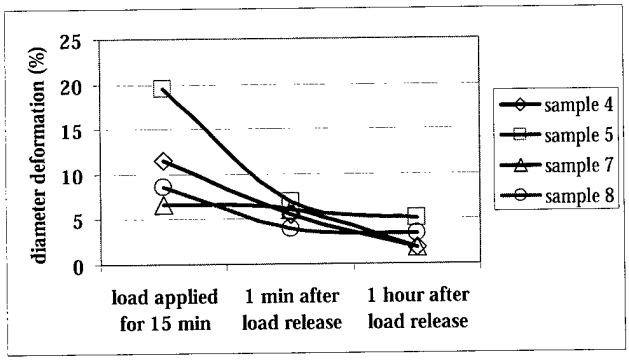


Fig. 6 – Crush test: cable deformation at 3.0kN/100mm versus time

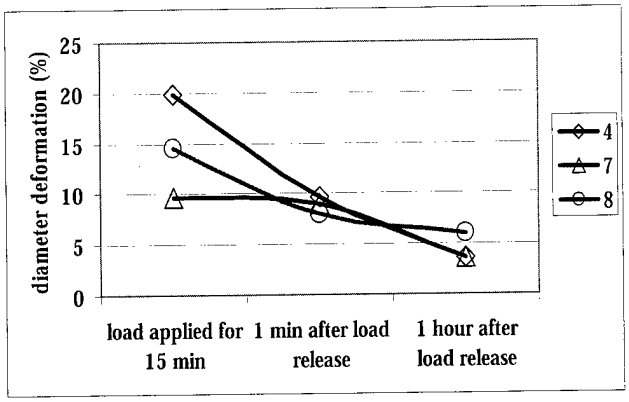


Fig.7– Crush test: cable deformation at 4.0kN/100mm versus time

The cable sample 8, having metallic armor, shows a good resistance to crush force, confirmed also by the attenuation measures, during the load application. The cable 7 shows even a better behavior. Nevertheless, the deformation of the cable 4, also if greater, didn't cause any attenuation increase (see tab. 4). On the contrary, if we consider the deformations after load release, the metallic cable, as easily predictable, shows a poor performance: a significant permanent deformation is present after the test at 4.0 kN. This permanent deformation, in case of further high load applications, could cause permanent attenuation increase, while in case of all dielectric cables, the deformation is quite well recovered, reducing the risk of possible attenuation increase in case of further load applications. The cable sample 5 is the less resistant, because, as just discussed for impact stress, the intermediate relatively soft layer is significantly more effective when it is placed between two conventional "harder" layers, which allows a better distribution of the stresses in the intermediate layer. For this sample 5, the maximum load without attenuation increase was 3.0 kN and thus it was not reported in fig. 7 (4.0 kN crush load).

3.4 Overall comparison of cable features

The four most significant cable samples realized during the present experimentation have been compared in terms of optical and mechanical/physical performances. For each cable sample and for each cable characteristic we assigned a partial score, starting form 1 (the best feature) to 4 (the worst). The total score for each cable sample is the sum of the partial scores relevant to each cable characteristic. Due to the above calculation method, the best overall performance is correspondent to the lowest total sum. In table 5, the ranking of cable samples has been reported.

Table 5 – Ranking of cable samples in terms of optical, mechanical and physical performances

Sample ID number->		4	5	7	8
Impact	Attenuation	1	3	2	4
	Deformation	2	3	1	4
Crush	Attenuation	2	4	2	1
	Deformation after load release	1	4	1	3
Weight		2	1	3	4
Bending stiffness		2	1	4	2
Diameter		4	1	4	2
Total		**14**	**17**	**17**	**21**

The cable design 4 turns out to be the most effective from an overall point of view.

3.5 Dielectric cables and typical metallic protection functionality

The results obtained show that is possible to realize, choosing properly the cable design in terms of multilayer structure, thickness of each layer and selected materials, an all dielectric cable that has better performances (impact, crush, weight, bending stiffness) of traditional metallic cables. Nevertheless, while selecting an all dielectric design, some considerations on other typical metallic protection functionality must be done. The first aspect is related to the "moisture barrier" function performed by the metallic tape. It is known that minimizing the moisture content inside the cable allows to reduce risks of transmission degradation of the fibers during the cable lifetime. On the other hand, the use of an appropriate coating system (fiber coating, ink, filling compound), completely developed in the last years, allows the dielectric cable to have, in terms of mechanical and transmission performance, the same reliability typical of cables with metallic moisture barrier.

Another important feature of metallic cable is their good resistance to the rodent attack. It is very difficult to achieve the same resistance to the rodent attack using an all dielectric design, but we demonstrated that using appropriate dielectric barriers, generally made by glass yarns properly treated, it is possible to manufacture rats-proof optical cables suitable for most installation environments.

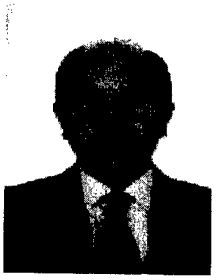
4. Conclusions

A new fully dielectric optical cable family with improved resistance to mechanical side forces has been developed.

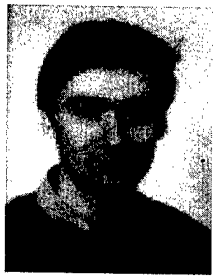
Laboratory tests have been made to verify the mechanical performance of the new cables. Some optical cable samples have been manufactured using respectively the new design and, for comparison, conventional designs. Each cable has been mechanically tested for impact and crush resistance evaluation, using specifically developed procedures.

The final results show that the new cable design allows a superior impact and crush resistance than standard cables. In particular, it is possible to replace a metallic cable with a fully dielectric cable with improved mechanical resistance, lower linear weight, less bending stiffness and, as a consequence, reduced installation costs.

Authors



Alessandro Ginocchio was born in Milano in 1947. He graduated in Electrical Engineering from Politecnico di Milano in 1972 and joined Pirelli in 1974, where he was engaged in the research and development on submarine cables. Since 1987 he has been responsible for the technological development of optical fiber cables.



Enrico Consonni was born in Seregno (Mi) in 1964. He graduated in Aeronautical Engineering from Politecnico di Milano in 1991 and joined Pirelli in 1991, where he has been engaged in research and development of TLC cables, dealing mostly with environmental test, cable design and manufacturing technology.



Paolo Marelli was born in Cantù (Como) in 1954. He graduated in Chemical Engineering from Politecnico di Milano in 1979 and joined Pirelli in 1980. Since 1987 he is involved in the Research and Development on terrestrial and aerial optical cables. He is currently responsible for TLC cables Design in Pirelli Central R&D,E.

High Density Dry Tube Cable Composing Tightly Stacked Fiber Ribbons

Yoshio Hashimoto, Naoki Okada, Michio Suematsu, Matsuhiro Miyamoto
Research and development department, Telecommunication cable division
1440, Mutsuzaki, Sakura-shi, Chiba, Japan
+81-43-484-3945 · hashimoto@s.fujikura.co.jp

Abstract

We designed a new dry tube cable composed of tightly stacked fiber ribbons. The dry tube is an inner tube formed of specially designed water blocking laminated tapes and squared to keep the ribbons arranged in layers. This tight structure provides effective resistance to the fiber movement, thus allowing to achieve complete dryness. Any jelly compounds or special resins that prevent the fiber movement are unnecessary. Consequently, not only the cable diameter but also the cable weight can be reduced drastically.

We manufactured a trial 144-fiber cable with 12-fiber ribbons, and investigated its cable performance. The cable diameter is about 12 mm.

Keyword

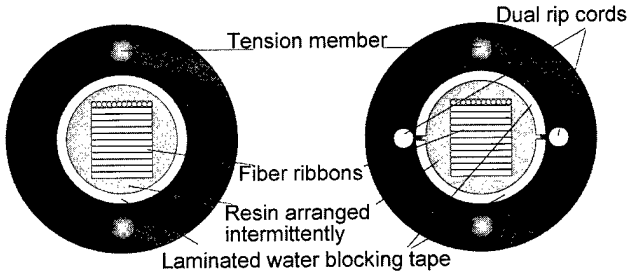
Optical Cable; Fiber ribbon; Dry tube; Mid-span access

Introduction

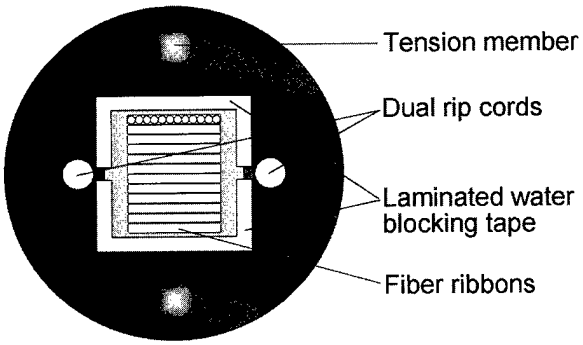
In recent years, a great number of optical cables have been installed to construct access networks and FTTH networks. In order to construct these networks economically, it is necessary to reduce both the cost of components and the construction cost of the networks. From the viewpoint of optical cable design, the cabling cost should be reduced, and the cable structure should be designed so as to allow branching of fibers to other cables or optical drop wires. The number of access points may increase for FTTH networks, therefore, demand for dry structure and easy mid-span access will grow more and more.

1. Cable Design Concept

We have already reported on the dry tube cable with water blocking laminated tapes. This cable provides excellent water blocking performance and ease of sheath removal for mid-span access. In this paper, we discuss the new cable we have evolved further more. The improvement phase (advantages) of the cable is listed in Table 1. Figure 1 (a) shows the conventional structure. This structure provides ease of sheath removal, however, it is not so easy to open the dry tube for picking out the fibers. Figure 1 (b) shows the evolved structure. The inner dry tube is composed of two laminated water blocking tapes, and dual rip cords are arranged at the seams of the tapes. Figure 1 (c) also shows the evolved structure. This structure is optimized for composing stacked fiber ribbons. Higher fiber packing density can be achieved.



(a) Conventional type **(b) Conventional type**



(c) New type

Fig.1 Evolution of cable structure

In this paper, we studied the structure(c) of a 144-fiber cable composed of 12-fiber ribbons. In order to achieve cost reduction, we attempt to manufacture this new cable using simple materials. It is composed of the sheath, two tension members, two rip codes, two laminated tapes, and twelve 12-fiber ribbons. Manufacturing is simple because the cable has a single-layer polyethylene sheath. Twelve ribbons are stacked on top of each other and covered with two laminated tapes as is the case with the structure (b). The laminated tapes are bonded to the sheath and form a kind of tube and play the role of the water blocking. The inner tube is designed as a square to keep the ribbons arranged in layers. This square is twisted. At this time, the seam of laminated tape is arrayed straightly along the cable. We processed in order that the arrangement of dual rip cords and the two laminated tapes does

not follow to twisting ribbons (as shown in Figure 2). Therefore, this structure makes it easy to divide the sheath with use of dual rip cords. The tube is so tight that the fibers are fixed in the cable. It enables the cable structure to be completely dry without any jelly compounds or any special resins. Because of jelly- and resin-free structure, the operation to wipe fibers is unnecessary after picking out them.

Table 1. Cable evolution

	Features of the cable structure	Target
(a)	·Water blocking laminated tape · Intermittent arrangement of resin	· Simple design for easy manufacturing ·Easy removal of sheath
(b)	·Water blocking laminated tape · Intermittent arrangement of resin · Dual rip cords at seam of laminated tape	·Improvement of mid-span access
(c)	·Water blocking laminated tape · Dual rip cords at seam of laminated tape ·Square form of inner tube ·Jelly- and resin- free	·Prevention of disordering of the stacked ribbons

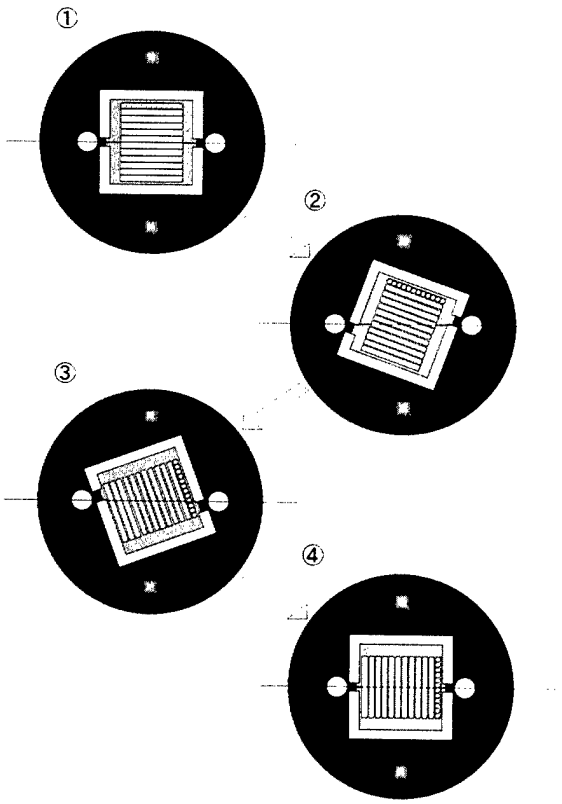


Fig. 2 Arrangement of dual rip cords and two laminated tapes

2. Structural Parameter Design

We manufactured a trial 144-fiber cable with 12-fiber ribbons. The fiber ribbons in the cable are stacked on top of each other and they are twisted at intervals of a fixed angle and a fixed pitch. The array of tapes should not be disordered to obtain excellent transmission characteristics. Moreover, it is demanded that the fiber distortion is as small as possible, which is given when the cable is bent.

2.1 Clearance

The clearance should be designed to be large enough to achieve good transmission characteristics and small enough to prevent disordering of the stacked ribbons. Disordering of the stacked ribbons is classified into two kinds of the following models.

Model (1): Only one ribbon of the uppermost layer or the lowest layer falls away from the stacked array.

Model (2): The state of stacked ribbons is in order, but they rotates loosely independent of the direction of rectangular tube.

Generally, it is known that model (1) may occur when the clearance is smaller [1]. With this model (1), the optimum dimension of the clearance is calculated from the state of stacked ribbons and the cable diameter.

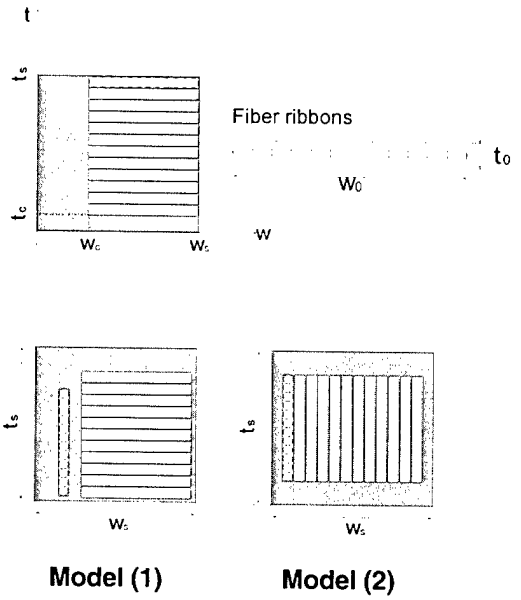


Fig. 3 Array configuration and model of disordering

We assume that the fiber ribbon in the uppermost layer changes the direction from horizontal to vertical. The fiber ribbon moves along the inner wall of the cable. At that time, if the ribbons kept stacked can prevent the movement of the ribbons in the uppermost layer, disordering of the stacked ribbons is not caused. Taking the horizontal space as w_c and the vertical space as t_c as shown in

Figure 3, the relation between $\mathbf{w_c}$ and $\mathbf{t_c}$ that prevent disordering of the stacked ribbons is represented by a curve shown in Figure 4. The lower limit of $\mathbf{w_c}$ and $\mathbf{t_c}$ is decided considering allowable fiber curvature radius in the tube [2]. In addition, the upper limits of $\mathbf{w_c}$ and $\mathbf{t_c}$ are decided considering mechanical strength and cable diameter. The target value of this cable diameter is 12mm or less.

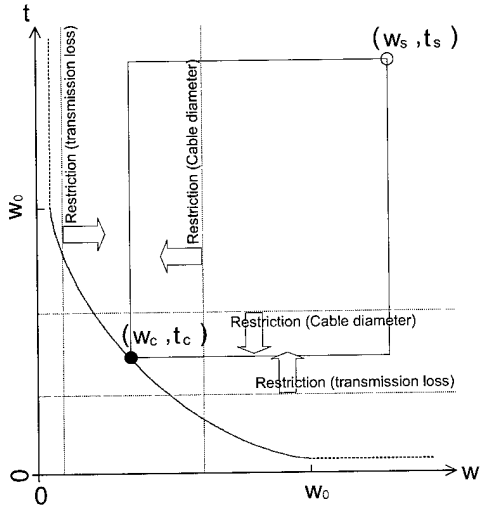


Fig.4 Relation between w_c and t_c that prevent disordering of the stacked ribbons

2.2 Locus of ribbon

The fiber ribbons must be twisted to reduce the fiber strain in the bent cable. Moreover, it may be better to twist SZ-form for easy manufacturing. In case of the SZ-slotted core cable, the fiber strain in the bent cable depends greatly on the bending radius and SZ-reverse lay angle, and fiber ribbons should be stranded around the SZ-slotted rod by back-twisting [3]. On the other hand, the fiber ribbons are SZ-twisted for the studied structure in this paper. Therefore we investigated the optimized SZ-twisting form of the stacked ribbons.

As shown in Figure 5, the x and y axes are taken in the transverse direction of the cable and the z axis in the longitudinal direction. The pitch diameter of the uppermost ribbon which is **w** width is decided as **2a**. When fiber ribbons are helical-stranded by the stranding pitch p, the fiber locus equation can be expressed by Eqs. (1) and (2) (Eq. (1) is the locus of center a fiber in the ribbon, and Eq. (2) is that of the both fibers in the ribbon.). Then θ is the stranded angle of ribbon, ν is the direction of the ribbon and τ is the back twisted angle. In this cable fibers are not back twisted, therefore, τ is always $\pi/2$.

$$\left.\begin{aligned} x_{h0} &= a\cos\theta \\ y_{h0} &= a\sin\theta \\ z_{h0} &= \frac{p}{2\pi}\theta \end{aligned}\right\} (1)$$

$$\left.\begin{aligned} x_{h1,2} &= a\cos\theta \pm A_h\cos(\theta-\tau) \\ y_{h1,2} &= a\sin\theta \pm A_h\sin(\theta-\tau) \\ z_{h1,2} &= \frac{p}{2\pi}\theta + \frac{1}{2}w\sin\nu_h\sin\sigma_h \end{aligned}\right\} (2)$$

where

$$\nu_h = \tan^{-1}(2a\pi/p)$$
$$\sigma_h = \tan^{-1}(\sec\nu_h\tan\tau)$$
$$A_h = w\sqrt{\cos^2\sigma_h + \cos^2\nu_h\sin^2\sigma_h}\,/2$$

When fiber ribbons are SZ-stranded with reverse lay length p and reverse lay angle φ, the fiber locus equations are shown as Eqs. (3) and (4) which give the coordinates of the center(Fiber1-6) and side fibers of a ribbon(Fiber1-1 or Fiber1-12), respectively.

$$\left.\begin{aligned} x_{sz0} &= a\cos\theta \\ y_{sz0} &= a\sin\theta \\ z_{sz0} &= \frac{p}{2} - \frac{p\sin^{-1}(1-2\theta/\varphi)}{\pi} \end{aligned}\right\} (3)$$

$$\left.\begin{aligned} x_{sz1,2} &= a\cos\theta \pm A_{sz}\cos(\theta-\tau) \\ y_{sz1,2} &= a\sin\theta \pm A_{sz}\sin(\theta-\tau) \\ z_{sz1,2} &= \frac{p}{2} - \frac{p\sin^{-1}(1-2\theta/\varphi)}{\pi} + \frac{1}{2}w\sin\nu_{sz}\sin\sigma_{sz} \end{aligned}\right\} (4)$$

where

$$\nu_{sz} = \tan^{-1}\left(a\pi\sqrt{1-(1-2\theta/\varphi)^2\varphi}\,/2p\right)$$
$$\sigma_{sz} = \tan^{-1}(\sec\nu_{sz}\tan\tau)$$
$$A_{sz} = w\sqrt{\cos^2\sigma_{sz} + \cos^2\nu_{sz}\sin^2\sigma_{sz}}\,/2$$

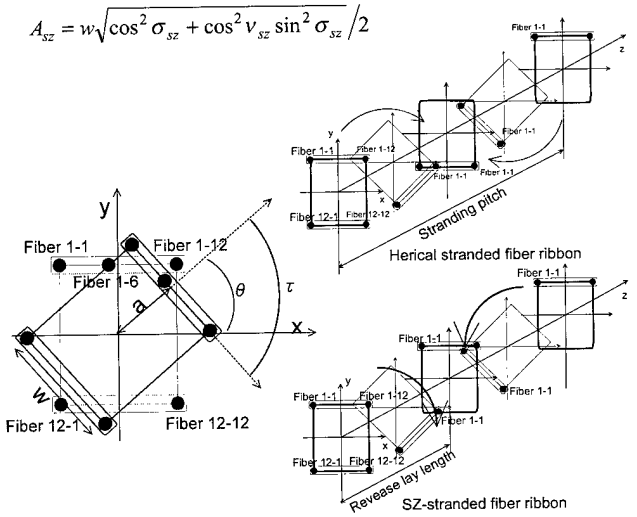


Fig.5 Coordinates of the new cable

The fiber locus equations of bent cable are shown in Eq. (5)~ Eq. (8). Eqs. (5) and (6) are the equations for the helical-stranded ribbon not back twisted, and give the coordinates of the center fiber and two side fibers of the ribbon. Here, r , α and ξ are the bent radius of a cable, bent direction on the x-axis and bending angle of the cable, respectively.

$$\left.\begin{aligned} x_{bh0} &= B_h \cos\alpha + a\sin\alpha\sin(\alpha-\theta) \\ y_{bh0} &= B_h \sin\alpha - a\cos\alpha\sin(\alpha-\theta) \\ z_{bh0} &= \{r - a\cos(\alpha-\theta)\}\sin\left(\frac{p}{2\pi r}\theta\right) \end{aligned}\right\}(5)$$

$$\left.\begin{aligned} x_{bh1,2} &= C_{h1,2}\cos\alpha - D_{h1,2}\sin\alpha \\ y_{bh1,2} &= C_{h1,2}\sin\alpha + D_{h1,2}\cos\alpha \\ z_{bh1,2} &= \{r - a\cos(\alpha-\theta) \mp A_h\cos(\alpha-\theta+\tau)\}\sin\left(\frac{p}{2\pi r}\theta\right) \\ &\quad \pm\frac{1}{2}w\cos\left(\frac{p}{2\pi r}\theta\right)\sin\nu_h\sin\sigma_h \end{aligned}\right\}(6)$$

where

$B_h = r - \{r - a\cos(\alpha-\theta)\}\cos\{p\theta/(2\pi r)\}$

$C_{h1,2} = r - \{r - a\cos(\alpha-\theta) \mp A_h\cos(\alpha-\theta+\tau)\}\cos\{p\theta/(2\pi r)\}$

$D_{h1,2} = -a\sin(\alpha-\theta) \mp A_h\sin(\alpha-\theta+\tau)$

Eqs. (7) and (8) are the fiber locus equations for the SZ-stranded ribbon not back twisted, and give the coordinates of the center fiber and two side fibers of the ribbon in the bent cable, respectively.

$$\left.\begin{aligned} x_{bsz0} &= B_{sz}\cos\alpha + a\sin\alpha\sin(\alpha-\theta) \\ y_{bsz0} &= B_{sz}\sin\alpha - a\cos\alpha\sin(\alpha-\theta) \\ z_{bsz0} &= \{r - a\cos(\alpha-\theta)\}\sin\xi \end{aligned}\right\}(7)$$

$$\left.\begin{aligned} x_{bsz1,2} &= C_{sz1,2}\cos\alpha - D_{sz1,2}\sin\alpha \\ y_{bsz1,2} &= C_{sz1,2}\sin\alpha + D_{sz1,2}\cos\alpha \\ z_{bsz1,2} &= \{r - a\cos(\alpha-\theta) \mp A_{sz}\cos(\alpha-\theta+\tau)\}\sin\xi \\ &\quad \pm\frac{1}{2}w\cos\xi\sin\nu_{sz}\sin\sigma_{sz} \end{aligned}\right\}(8)$$

where

$B_{sz} = r - \{r - a\cos(\alpha-\theta)\}\cos\xi$

$C_{sz1,2} = r - \{r - a\cos(\alpha-\theta) \mp A_{sz}\cos(\alpha-\theta+\tau)\}\cos\xi$

$D_{sz1,2} = -a\sin(\alpha-\theta) \mp \sin A_{sz}(\alpha-\theta+\tau)$

$$\xi = \frac{1}{r}\left\{\frac{p}{2} - \frac{p\sin^{-1}(1-2\theta/\varphi)}{\pi}\right\}$$

The estimated fiber strain (EFS) was determined from the length difference between the center and side fibers of the ribbon in the straight cable, using Eq. (10). In order to obtain good cable characteristic, it is required that EFS be as small as possible. EFS depends on the bending radius of the cable. In this study, we calculated all EFSs, assuming that the bending radius is 500 mm.

$$\left.\begin{aligned} L &= \int_0^{\varphi}\sqrt{\left(\frac{dx}{d\theta}\right)^2 + \left(\frac{dy}{d\theta}\right)^2 + \left(\frac{dz}{d\theta}\right)^2}\,d\theta \\ L_h &= \int_0^{\varphi}\sqrt{\left(\frac{dx_h}{d\theta}\right)^2 + \left(\frac{dy_h}{d\theta}\right)^2 + \left(\frac{dz_h}{d\theta}\right)^2}\,d\theta \end{aligned}\right\}(9)$$

$$\left.\varepsilon(\%) = \frac{L_h - L}{L}\times 100\right\} \qquad (10)$$

The reverse lay angle dependence of EFS was calculated as shown in Figures 6 and 7. The calculated fiber (Fiber1-6) is at the center of an uppermost ribbon (its EFS is the average of those of the fibers in one ribbon). As shown in Figure 6, EFS follows the cable bending direction. The peak of EFS is at $\alpha = \pi + \varphi/2$ or at $\alpha = 2\pi + \varphi/2$, and the peak-to-peak value of it depends on the reverse lay angle. The reverse lay angle dependence of EFS at $\alpha = \pi + \varphi/2$ is shown in Figure 7. When the reverse lay angle is 275deg. ,EFS is about 0.0%

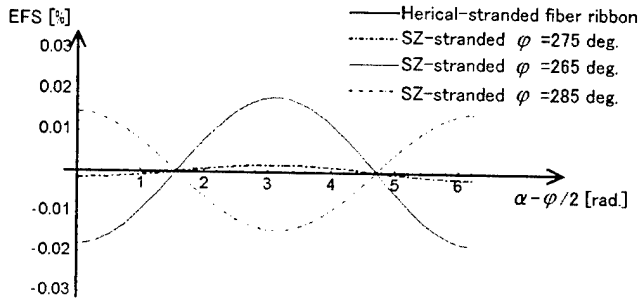


Fig.6 Estimated fiber strains of Fiber1-6

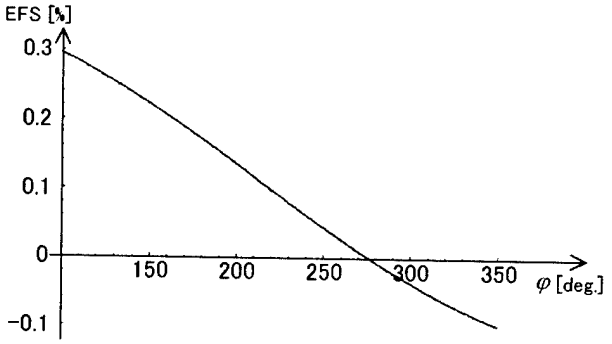


Fig.7 Estimated fiber strain Vs. reverse lay angle at $\alpha = \pi + \varphi/2$

Not only the average of the EFSs in one ribbon, but also the difference of it at both side fibers may influence the cable characteristic. The difference in EFS between Fiber1-1 and Fiber1-12 (the both side fibers of the uppermost ribbon) was calculated. The result is given in Figure 8. The difference in EFS follows the cable bending direction, and the amplitude depends on the reverse lay angle. At $\alpha = \pi + \varphi / 2$ or at $\alpha = 2\pi + \varphi / 2$, however, EFS don't follow the reverse lay angle and remains lower value. It is possible to limit the cable bending direction by arranging tension members opposite to each other in the sheath.

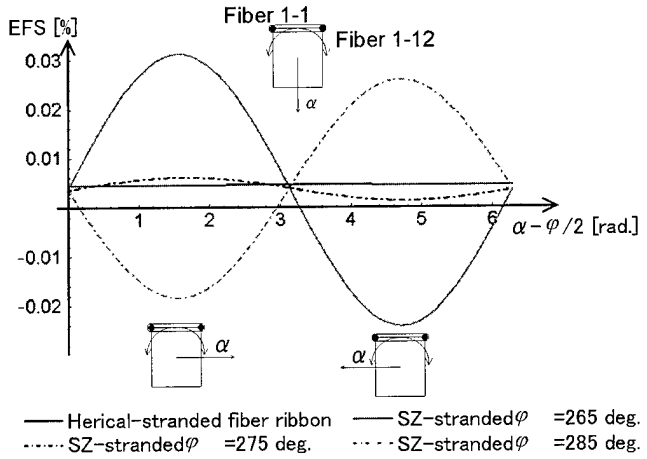


Fig.8 Difference in EFS between Fiber1-1 and Fiber1-12

2. 3 Reverse lay length

It is necessary to fix the fibers in the cable. The force for fixing the fibers in the cable depends on the clearance, reverse lay angle and reverse lay length. The required force is greater the smaller the clearance is. However, the optimum dimension of the clearance is already calculated from the state of stacked ribbons and the cable diameter and cable characteristics. The larger the reverse lay angle, the greater the force becomes. However, the reverse lay angle is already determined from the distortion by bending of the cable. In this chapter, we investigate the required force for fixing the fibers in the cable from the reverse lay length.

We estimate that the force for fixing the fibers increase as the reverse lay length short. To obtain excellent transmission characteristics, the reverse lay length is decided in consideration of EFS. Calculated EFSs in the straight cable are shown in Figure 9. In this calculation, EFS is the difference between the length of center fiber in the uppermost ribbon and length of the edge fiber in the same ribbon. The force is evaluated by measuring the force used to pull the fibers out of a 10 m long cable. The result of trial is shown in Figure 10. The strength of it is compared with ordinary slotted core cable.

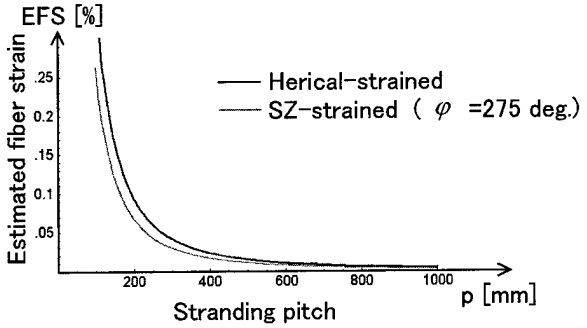


Fig.9 Estimated fiber strain of the straight cable

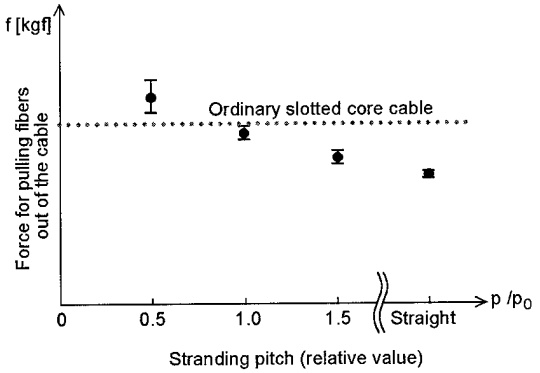


Fig.10 Estimated fiber strain of the straight cable

3. Experimental Result

3.1 Transmission characteristics

We manufactured the helical stranded cable and evaluated its transmission characteristics. The value of transmission loss at –30/70 degrees C are shown as Figure 11. The loss starts increasing at 70 degree. We investigated the reason of loss increase, and found out the fiber length was shorter than the cable length. Therefore the tensile strain may be applied at high temperature. This loss increase could be reduced by the control of the fiber length in a cable.

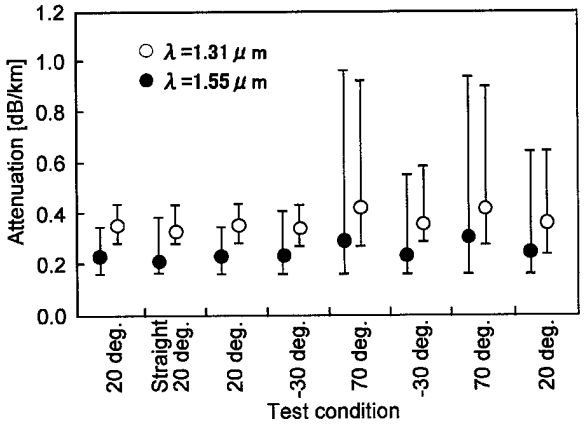


Fig.11 Transmission loss

3.2 Water blocking performance

Excellent water blocking characteristic could be obtained by using water blocking laminated tape. The water leakage after one day is less than 3.0m when the water of the height of 1.0m is poured into the cable from the edge side of it.

3.3 Mid-span access capability

Mid-span access from the installed cables is very important to construct the distributed access networks economically. We introduce the method of mid-span access of a new cable as follows. First of all, a part of dual rip codes where have been inserted in the sheath is taken out. Next, the rip codes are pulled outside. As a result, the sheath is divided. The dual rip cords are arranged at the seam of the two laminated tapes, therefore the cable can be divided in half and we can take the fibers out of the tube easily (the operation to remove the wrapping tape is unnecessary). The operation to wipe fibers is unnecessary after picking out them, because there are no jelly compounds or resins in the tube. In operating of mid-span access there will be few accidents of intermittent discontinuity. The amount of the transmission loss change while operating is 0.1dB@1.55um or less.

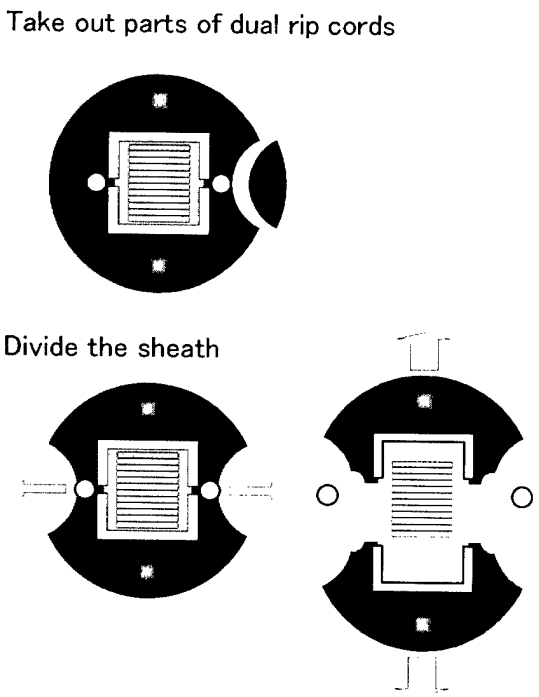


Fig.12 The method of mid-span access operating

3.4 Force for pulling the fibers out of the cable

We can get the sufficient fiber pulling out force by selecting proper reverse lay length, which is important to avoid fiber movement from cable ends. We measured the force when fibers were pulled out from the 10m length of cable. The value was compared with that of ordinary slotted core cable. And the actual reverse lay length was determined.

4. Conclusions

We have designed the new dry tube cable composing tightly stacked fiber ribbons. This tight structure without any fixing material will bring the easy mid-span access operation.

We have clarified the maximum clearance not to allow disordering of the stacked ribbons and also to satisfy an excellent transmission characteristic. Moreover, we optimized the reverse lay angle to make the bend distortion a minimum. In addition, the optimal reverse lay length was experimentally determined from the viewpoint of the sufficient resistance force of fiber movement in the cable. The cable was manufactured based on the parameters such as calculated clearance, calculated reverse lay angle and reverse lay pitch obtained by the experiment.

5. References

[1] M.Yamanaka, "A New Compact Ribbon Cable", 1994 IWCS Proceeding, pp.43-49

[2] N.Okada, "Development of New Dry Cable with Water Blocking Laminated Tape", 2000 IWCS Proceeding, pp.164-167

[3] N.Okada, "Study on bending of SZ slotted core cable with fiber ribbons", 1999 IWCS Proceeding, pp.112-134

Authors



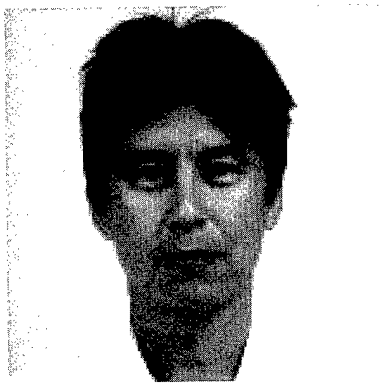
Yoshio Hashimoto

Fujikura Ltd.

1440, Mutsuzaki, Sakura-shi, Chiba, Japan

hashimoto@s.fujikura.co.jp

Yoshio Hashimoto was born in 1973. He joined Fujikura Ltd after his graduation from Ibaraki University with a M.E degree in 1998 and has been engaged in research and development of optical fiber cables. He is now an engineer in Research and Department Telecommunication Cable Division and a member of the IEICE of Japan



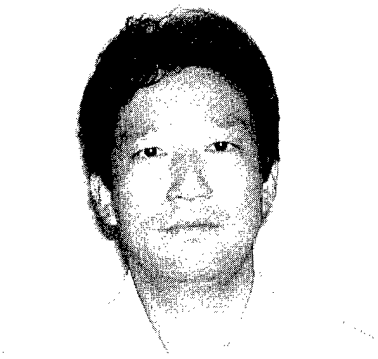
Michio Suematsu

Fujikura Ltd.

1440, Mutsuzaki, Sakura-shi, Chiba, Japan

msuematu@fujikura.co.jp

Michio Suematsu was born in 1963. He joined Fujikura Ltd after his graduation from Nihon University with B.E degree in 1985 and has been engaged in design engineering of optical fiber cables. He is now a manager in Research and Development Telecommunication Cable Division.



Naoki Okada

Fujikura Ltd.

1440, Mutsuzaki, Sakura-shi, Chiba, Japan

naookada@s.fujikura.co.jp

Naoki Okada was born in 1964. He joined Fujikura Ltd. After his graduation from Chiba University with a B.E. degree in 1986 and has been engaged in research and development of optical fiber cables. He now belongs to optical fiber production engineering department.



Matsuhiro Miyamoto

Fujikura Ltd.

1440, Mutsuzaki, Sakura, Chiba, 285-8550, Japan

mmiya@s.fujikura.co.jp

Matsuhiro Miyamoto was born in 1953. He graduated from Nagoya Institute of Technology with B.E. degree of electrical engineering. He joined Fujikura Ltd after his graduation from Tokyo Institute of Technology with M.E. degree in 1978 and had been engaged in research and development of optical fibers and optical cables. He is now belongs to optical fiber production engineering department.

The D-Shaped Optical Fiber as a Platform for Integrated Photonic Devices

Michael S. Smith, Richard H. Selfridge and Garth M. Kraus
Department of Electrical and Computer Engineering, Brigham Young University
Provo, Utah
(801) 378-6313 · selfridge@ee.byu.edu

Abstract

This paper describes the fabrication of an active polymeric waveguide with 5.5 dB of loss in the core region of a D-fiber using a method of centrifugal casting. The integrated waveguide establishes a platform for the development of a variety of fiber-integrated opto-electronic devices that exploit the available bandwidth of optical fibers. We present the fabrication process and introduce the centrifugal casting method as a new means of depositing active polymer into the core region of a D-fiber. This method uses centrifugal forces to form an active polymer waveguide in the core area of a fiber, and represents a unique alternative to standard device-waveguide fabrication processes. We report on the success of this method and discuss its future applications.

Keywords

Fiber optics; photonics; integrated devices.

1. Introduction

In the past few decades, optical fiber has come to dominate the long-haul communications industry. Low loss, low dispersion and immunity to electromagnetic interference are cited as some key characteristics that make fiber superior to metal cable and wire transmission lines [1]. However, the greatest benefit of fiber is the enormous bandwidth it offers. Research indicates that optical fibers are capable of transmitting hundreds of gigabits over hundreds of kilometers [2]. Compare this to gigabit copper links, which are limited to about 30 meters of transmission before the signal is degraded. The potential capacity of fiber-based communication systems makes them ideal for mitigating the traffic of electronic information and handling the demands of high-speed networks. However, to make fiber-based systems that exploit the full transmission bandwidth of fiber, complimentary devices must first be created to send and receive optical signals.

Recent developments in opto-electronic technology have allowed the telecommunications industry to exploit more of the available bandwidth in optical fibers. Major contributions have come from the research of high-speed signal generating devices that use active electro-optic (EO) materials. The optical properties of these materials respond to applied electrical signals, enabling the light that is transmitted through optical fibers to be modulated. Devices using advanced EO polymers and EO crystals such as lithium niobate have already been developed and marketed [3]. Such devices surpass the speed limitations of directly modulated laser diode sources, and are capable of producing light signals with standard bitrates of 10 GHz, with 40 GHz in the near future and 100 GHz on the horizon [4].

Current gigahertz devices using EO materials are made on planar substrates. Optical waveguide structures are patterned into the active material using photolithography and must be carefully aligned with the light-guiding core of optical fibers to achieve efficient device-to-fiber coupling.

This paper introduces a new strategy to simplify the process of fabricating high-speed photonic devices, and to eliminate the need for device-to-fiber coupling. The concept is to create a waveguide from electro-optic polymers within the core of the fiber itself. In this scheme, light from the core launches into the active waveguide and back into the core without ever leaving the fiber. The active properties of the waveguide material can then be exploited to create high-speed modulators or other opto-electronic devices. These devices would be wholly contained within the fiber, or fiber-integrated, and require no alignment or coupling.

This approach is not unprecedented. Products like erbium-doped fiber amplifers (EDFA's) and distributed Raman amplifiers (DRA's), have shown that other active materials can be successfully used in fiber cores to create active fiber-integrated devices [5][6]. However, few efforts have been made that explore the integration of electro-optic materials in the fiber core [7].

Our research has demonstrated that integrated electro-optic waveguides with throughput losses as low as 5.5 dB can be created in the core region of D-shaped fibers. This is accomplished when the glass-core of the fiber is exposed, removed and an electro-optic polymer is deposited in its place using a novel method called centrifugal casting. This method, and the creation of a fiber-integrated waveguide establish a platform for creating high-speed modulators and a host of similar active, fiber-integrated devices.

In the following sections, the fabrication of an integrated, active polymer waveguide is presented. First, D-shaped optical fibers are introduced as the fabrication platform, and the removal of the fiber core using chemical etching is discussed. The centrifugal casting method is next introduced as a means to deposit the EO polymer into the area of the removed core. A report on the results of this method follows, as well as summary describing future work.

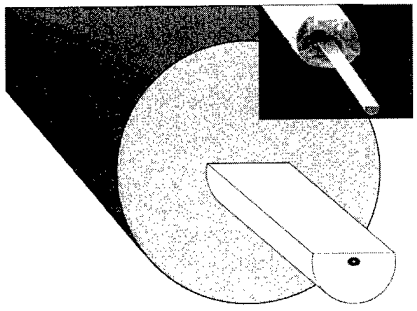


Figure 1. Cross section of a D-fiber

2. Background

2.1 D-Fibers

The fiber-integrated electro-optic waveguide is made using commercially available D-fibers as a platform. The shaped D-fibers, manufactured by KVH Industries, are characterized by a flat surface near the light-guiding core of an optical fiber. The cross section of a D-fiber is shown in Figure 1.

In this research the most important features of D-fibers are their shape and material doping profile. These features are best illustrated by a brief discussion on the manufacture of D-fibers.

D-fibers are made in a process similar to circular fibers. The fiber starts out as a large, hollow silica tube. The cladding and core of the fiber are defined by doping the inner surface of the tube with germanium and fluorine using modified chemical vapor deposition (MCVD). The D shape is created when a flat surface is ground onto the tube's outer surface. The tube, or fiber preform, is then drawn into a thin optical fiber.

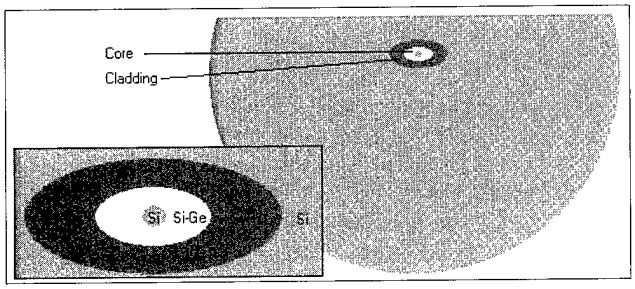


Figure 2. Material doping profile of a D-fiber

The proportional dimensions and doping profile of the preform are preserved in the D-fiber after the drawing process, as shown in Figure 2. The doping profile constitutes the optical waveguide itself within the fiber. Light is guided in the core by the difference of refractive indices in the core/cladding structure. The size of the core is tailored to ensure single-mode propagation along the length of the fiber for a given wavelength [8].

The D-fibers used in this research have elliptic cores and are manufactured to maintain polarization and support single-mode propagation of incident light with wavelengths of 1330 and 1550 nm.

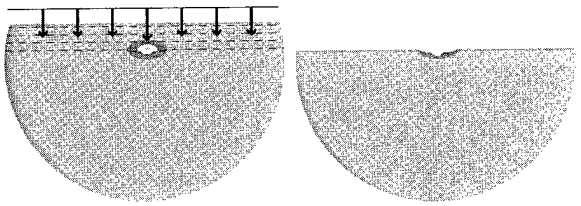


Figure 3. Etching the core of a D-fiber

2.2 Core Removal in D-Fibers

To create the fiber-integrated waveguide, the core of a D-fiber is removed over a short length and replaced by a material with electro-optic properties. The removal of the fiber core is simple. The shape and doping profile of the D-fibers allow the core to be quickly exposed and etched away when the fiber is submerged in a chemical bath, or wet etch. The process is described as follows.

The fiber is prepared by removing a short section of the plastic protective jacket that surrounds the fiber. The bare section is then cleaned and placed in a custom etch boat. The etch boat secures the fiber into a reservoir, which serves as the chemical bath for a wet etch. The etch boats are manufactured with reservoirs of several sizes (2 mm to 2 cm), allowing controlled lengths of the fiber to be etched.

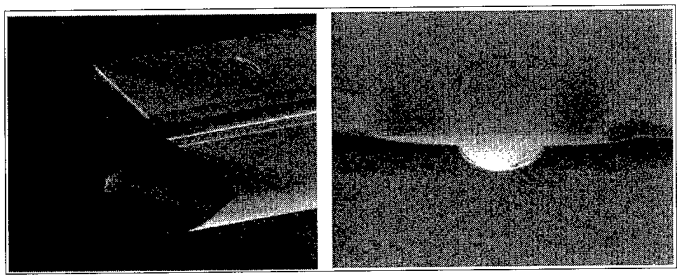


Figure 4. A groove is etched in the core region of D-fibers.

In the etch boat, a solution of 25% hydrofluoric acid (HF) and 75% water removes silica from the outer surface of the fiber. The HF etch is generally isotropic, but the etch rate is sensitive to the presence of trace elements in the silica. When the HF comes in contact with the doped core and cladding regions, it selectively etches the germania-doped core faster than the fluorine-doped cladding and surrounding silica (see Figure 3). The rate of this reaction depends on the concentration of the etchant and is extremely sensitive to temperature.

As a result of the selective etch reaction, a deep, hollow 'groove' is formed into the flat surface of the fiber. The groove runs along the fiber where the core originally existed (Figure 4).

The etch is performed while monitoring the power throughput of a D-fiber from an infrared diode laser source to determine the exact time that the HF breaches and removes the germania-doped core.

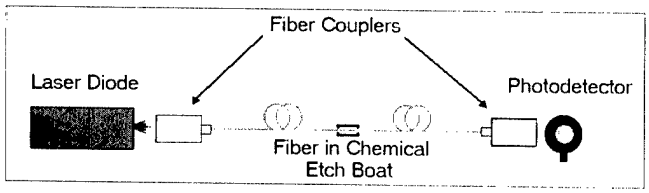


Figure 5. Etching Set-Up

The etch set-up is depicted in Figure 5. When the core is etched away, light ceases to propagate through the fiber. This typically occurs 50 minutes to an hour after the etch begins, at room temperature (20° C). The fiber is left in the etch bath for several minutes after light transmission is extinguished, to ensure that the entire core is etched away. This time is experimentally varied between 2 -12 minutes after extinction. The fiber is removed from the etch and the etchant is cleansed from the fiber with de-ionized water and methanol.

At the etch transitions, interesting structures also develop as a result of the fiber's doping profile. In the center of the core, there is a small region of undoped silica. At the etch transition, this undoped silica is removed more slowly than the germania-doped material and forms into a 'needle' as the surrounding core etches away (see Figure 6).

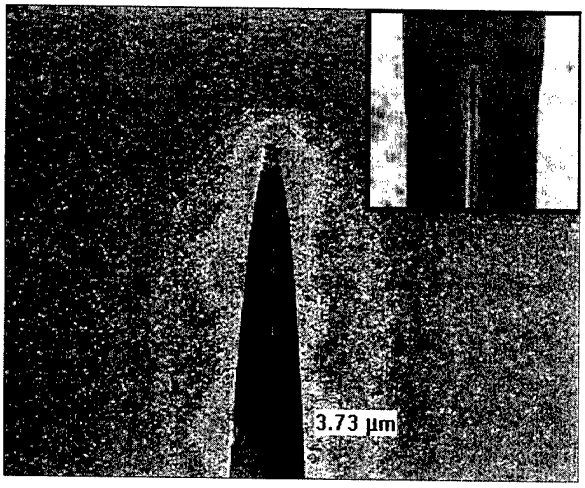


Figure 6. The etch transition and needle

The needles that appear at the etch transitions can be problematic in the construction of a waveguide and may be removed by performing a short secondary wet etch on the fiber. In this case, a buffered oxide etch (BOE) mixture of NH_4F and HF is used as the etchant instead of HF. BOE selectively etches undoped silica faster than germania-doped silica. This etch removes the small amount of silica that forms the needle. Some of the fluorine-doped cladding immediately surrounding the germania-doped core is also etched away by the BOE, which exposes the surface of the core at the transition and makes the groove deeper and wider (see Figure 7).

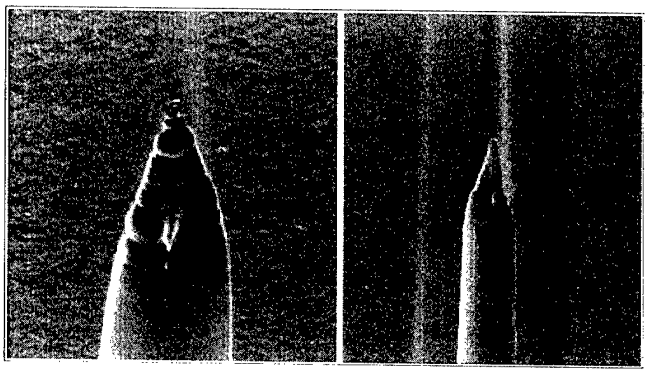


Figure 7. Removal of the needle in a BOE etch

3. Centrifugal Casting

D-fibers can be etched to create a groove in the place of the fiber core. When this groove is filled with an active material, an electro-optic fiber-integrated waveguide can be made. To do this an active electro-optic material is selected that can be applied in liquid form, and is deposited into the groove using a method of centrifugal casting. This method uses centrifugal forces to push the viscous material onto the fiber and into the groove at the surface of the fiber. The fiber contour acts as a mold or form, into which the material is cast. The deposited material serves as the integrated fiber waveguide. This waveguide lies directly in the path of the fiber's core at the etch transitions and has dimensions similar to the original germania-doped silica core.

3.1 Active Polymers

The groove is filled with an active material in liquid form. Many of the active materials used in photonic devices come in solid form, such as crystals like lithium niobate. Fortunately, great advances have been made in the development of active electro-optic organic polymers that can be made in a liquid form [9].[1]

Although more sophisticated materials have been developed, we have chosen to use an inexpensive guest/host active electro-optic polymer to use in our research to develop proof-of-concept devices. The polymer we use is a mixture of a host polymer, poly-methyl-methacrylate (PMMA), and a guest chromophore, Disperse Red-1 Azo Dye (DR-1). To create the polymer in liquid form, 8 grams of PMMA and 0.6 grams of DR-1 are combined with 15 mL of methyl-ethyl-ketone (MEK) and 45 mL of chlorobenzene. Equal proportions can also be used, or more solvent can be added to reduce the viscosity. The solution is mixed at room temperature in a magnetic stirrer for three days to ensure that the polymer and dye are adequately dissolved in the solvents. The liquid polymer is then passed through a 0.2 µm filter to eliminate undissolved polymer and contaminants.

[1] Note the polymer is not actually active in its liquid state. The polymer becomes electro-optic in a separate process known as corona poling. This process is not discussed in this paper.

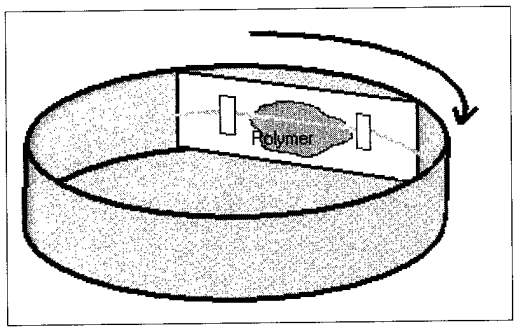


Figure 8. The etched fiber is mounted on a slide and secured in a centrifuge.

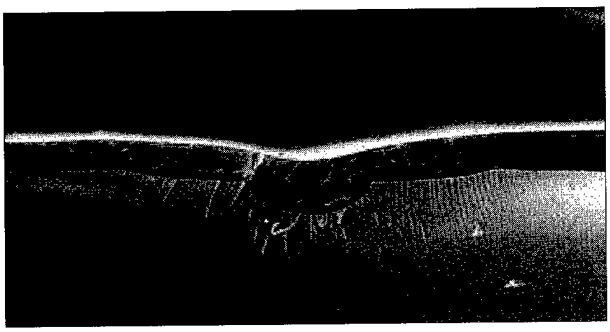


Figure 9. Centrifugal forces create a polymer waveguide in the D-fiber groove.

3.2 Alternative Deposition Methods

The centrifuge method was developed to deposit active materials into the groove of a D-fiber primarily because there was a lack of alternatives. Standard spin coating apparatuses are usually reliable in depositing controlled, uniform layers on planar substrates and may have the ability to fill a groove with a liquid polymer. However, the difficulty in using standard spinners in this case is that they are not very compatible with optical fibers. It is difficult to secure D-fibers so the flat surface is perfectly parallel with the plane of rotation and the fiber is immune to movement from lateral spinning forces. In addition, there are no normal forces in a lateral spin, introducing the possibility of creating air pockets in the groove beneath the liquid polymer in a lateral spin. These bubbles can be destructive to the guiding capability of the waveguide we wish to make. The centrifuge method offers solutions to these problems and has proven to be effective in depositing active materials into the etched groove of a D-fiber to make an integrated waveguide.

3.3 Making the Waveguide

The centrifugal method uses centrifugal forces to cast the liquid polymer into the groove of the D-fiber. In this process, the etched fiber is mounted onto a slide with the etched, flat side facing up, away from the slide. This secures the fiber and makes it possible to mount it into a centrifuge. The slide is then placed in a centrifuge and positioned so that the etched flat side of the D-fiber is facing the axis of rotation, and the length of the fiber is parallel to the rotational plane. The long fiber ends are loosely wrapped around the contour of the centrifuge. Figure 8 shows a fiber mounted to a slide and placed in a centrifuge.

Once the fiber is secured in the centrifuge, the liquid polymer-solvent mixture is applied across the etched section of the fiber using a dropper. The centrifuge is activated and ramps to the desired spin rate. The ramp speed averages 3 seconds, and the spin rate is experimentally varied between 400 and 2000 revolutions per minute. This process spin-casts the polymer onto the fiber and into the etched groove.

After the polymer is spin-cast onto the fiber in the centrifuge, the slide is removed and placed under vacuum in an oven. This step evaporates the remaining solvents from the polymer. The liquid polymer polymerizes and solidifies into a shape that conforms to the fiber's topography. As the polymer hardens, it forms a waveguide in the groove (Figure 9).

Note from the figure that the waveguide is not entirely confined to the geometry of the core groove. The polymer on the surface of the fiber not only fills the groove, but overlaps onto the planar sides of the fiber. These waveguide features are a byproduct of the forces acting on the polymer in the centrifuge.

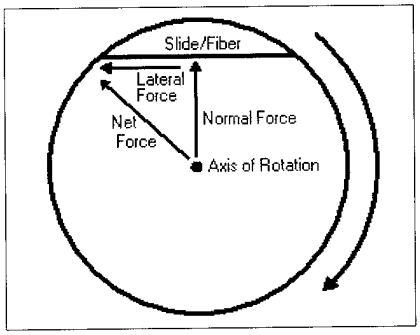


Figure 10. Active forces on a slide in a centrifuge

3.4 Centrifuge Principles

To understand how centrifugal casting operates on the polymer, consider the forces involved in the centrifuge (Figure 10). Here, the polymer is placed in an accelerated frame of reference. Centripetal force acts upon the polymer toward the axis of rotation by the equation:

$$F_{centripetal} = mv^2/r = mw^2r$$

where r is the radius of the circle of rotation, v is the velocity of motion around it and w is the angular velocity. Although centrifugal forces are not physical, they represent the force away from the axis of rotation based on the polymer's inertial frame of reference. Thus it can be said that the polymer mass experiences a "centrifugal" force onto the fiber, which is equal to the centripetal force toward the axis of rotation. Due to the orientation of the fiber in the centrifuge, the net force on the polymer is composed of both forces that are normal to the fiber surface and lateral forces that are parallel to the length of the fiber.

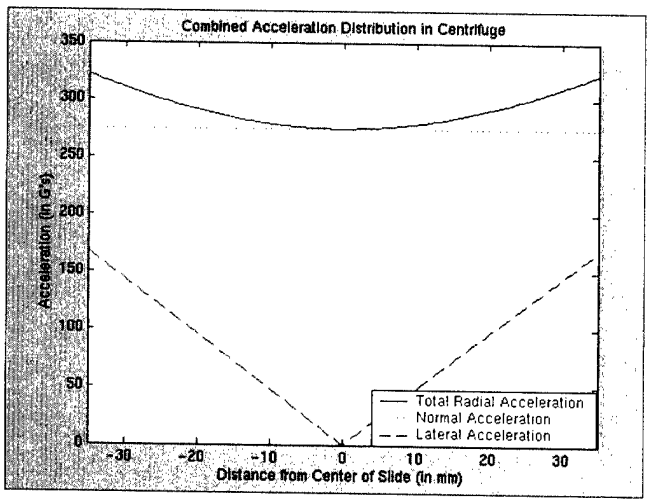


Figure 11. Acceleration distribution on a 7.5 cm slide in a centrifuge (radius 7.2 cm) at 2000 r.p.m.

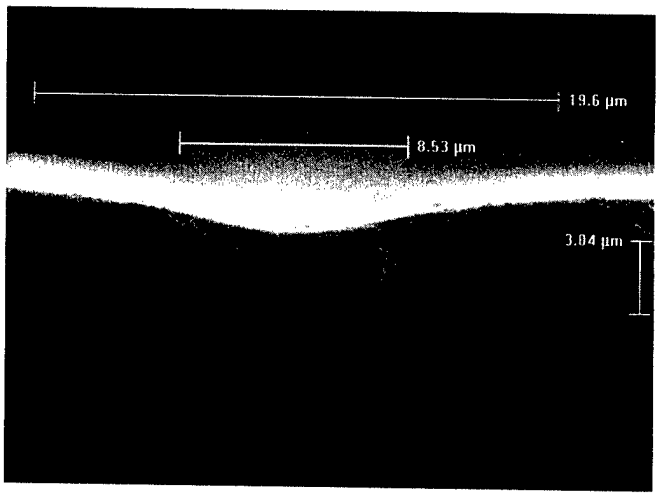


Figure 12. An image of a -7 dB waveguide shows a 3 µm polymer depth over the fiber groove.

Figure 11 shows the normal, lateral and combined spatial acceleration (and equivalent force) distributions that the polymer on the slide experiences at a given centrifuge radius. As a result of the normal forces, the polymer is cast, or pressed into the fiber and fills in the etched groves along the D side where the core previously existed. The lateral forces help to uniformly spread the polymer film across the fiber, much like traditional spin coaters.

Several general factors play the most important roles in the operation of the centrifuge and in determining the polymer's final distribution across the etched D-fiber. The fiber surface contour, the density and viscosity of the applied material, and the spin rate, ramp rate, radius and weight distribution of the centrifuge itself must all be considered in order to characterize operation. These parameters can be explored to tailor a suitable, controlled centrifugal casting process.

4. Results

4.1 Testing Waveguide Loss

To date, we have constructed many fiber-integrated electro-optic waveguides using the centrifugal method with varying degrees of success. After each waveguide has been fabricated, its guiding characteristics are investigated. The principle parameter that is evaluated is the waveguide loss. The power throughput of each waveguide is compared to the throughput of a D-fiber without the integrated device and the power throughput ratio is used to determine the waveguide loss. Some of the fabricated waveguides have also been analyzed visually with light microscopes, an atomic force microscope (AFM) and/or a scanning electron microscope (SEM). The results of loss tests are used in conjunction with SEM images, AFM images and records of process variations to determine which processing parameters have yielded the best results.

Analysis of various waveguides suggests that the initial etch to remove the D-fiber's core should be continued approximately 7 minutes past extinction for best results. Removing the needle at the etch transition in a secondary 15 minute BOE etch also appears to be beneficial. Additionally, cross sectional SEM images indicate that waveguides spun at high rates (1000+ r.p.m.) have thinner polymer layers and exhibit less loss (see Figure 12). This information has been valuable in characterizing and refining the centrifugal method for fabricating fiber-integrated waveguides.

The best fiber-integrated waveguides produced to date have transmitted light with losses as low as 5.5 dB for 2 mm length devices, and 9.3 dB for 2 cm devices.

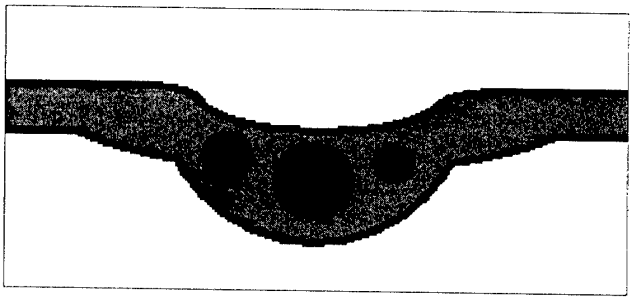


Figure 13. A hybrid ridge waveguide structure showing power in weakly guided modes

4.2 Guiding Characteristics

The cross sectional SEM images of the integrated waveguides also provide insight regarding the general guiding characteristics of the structure. These images show a contoured polymer profile, which is deepest over the fiber's etched groove. This indicates that the device acts as a hybrid ridge waveguide, where the electromagnetic waves are weakly guided by a structurally increased effective index of refraction in this area [10]. Although radiated modes can and do exist in the polymer to the sides of the groove, a significant percentage of the power remains guided in the center region aligned with the fiber core. A depiction of the cross section of this structure is shown in Figure 13.

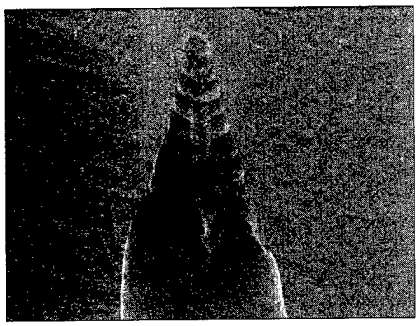


Figure 14. A close-up of the scattering features found at the etch transition

4.3 Loss Mechanisms

Analysis of the information provided by SEM and AFM images lends some understanding of the loss mechanisms that affect the power throughput of the waveguides. The loss mechanisms can be divided into three general categories: material loss, scattering loss and modal loss.

Some losses are naturally expected due to the material absorption of the PMMA/DR-1 waveguide. Research indicates that this material alone can account for 1-2 dB of loss per centimeter. This approximation is verified by the average observed loss differences in 2 mm and 2 cm length waveguides, which is slightly less than 4 dB. These losses can be minimized by the development of active organic polymers with lower absorption in the infrared spectrum.

Scattering from discontinuities in the waveguide also contributes to the loss in the device. A major location of scattering sources is at the etch transition. This is seen when visible 633nm light from a helium-neon laser is launched into the fiber and the transition is observed under a microscope. When a needle is left at the transition, it can be seen to scatter the light. When the needle is removed in a secondary etch, the device loss is generally lower, but scattering can still be seen coming from the edge of the etched core, which is covered with small pits and crags (see Figure 14). Additional scattering can be observed from small particles of contamination along the groove of the fiber and within the polymer.

Radiated modes account for the greatest losses in the waveguides. The transition from the elliptic, low dielectric core to the unusual geometry of the high dielectric waveguide is certainly not ideal for mode matching. Numerical analysis shows that a variety of higher order modes are excited in the groove of the waveguide from the single mode of the fiber core [11]. Power also radiates outward from the transition, coupling into modes in the polymer on the sides of the groove, as seen when 633 nm light is used. The power in these modes is not recovered by the trailing waveguide transition. These radiated mode losses can be minimized by reducing the cross sectional area of the waveguide. This reduces the possibility of exciting higher order modes in the polymer. The higher spin rates that yield thinner polymer layers therefore help reduce the losses due to radiated modes. To reduce these losses in the future, specialized photolithographic techniques can be used to custom-trim the size of the polymer waveguide.

5. Summary

The centrifugal casting method introduced here represents a unique alternative to standard photonic device processing techniques. We have demonstrated that this method can be used to create waveguides from active polymers within the core region of a fiber. These waveguides serve as a platform for the development of integrated active devices that require no aligning or coupling.

The next logical step in this research is to demonstrate the fabrication of such a device. We hope to accomplish this by depositing electrodes on the integrated waveguide that exploit the electro-optic effects in the waveguide polymer. If traveling waves in the electrodes can interact sufficiently with the active waveguide material, a high-speed modulator can be made. The effectiveness of such a device will be determined by improvements in the waveguide losses, the success of electrode deposition, and the development of active polymers with greater electro-optic strength.

6. Acknowledgments

We give special thanks to KVH Industries, Inc. for making this research possible.

7. References

[1] L. D. Green, *Fiber Optic Communications*, CRC Press, Florida, p. 1-13 (1993).

[2] P. E. Green, *Fiber Optic Networks*, Prentice Hall, New Jersey, p.16 (1993).

[3] E. L. Wooten, K. M. Kissa et al., "A Review of Lithium Niobate Modulators for Fiber Optic Communications Systems," IEEE Journal of Selected Topics in Quantum Electronics, 6(1), p.69-82 (January/February, 2000).

[4] D. Chen, H. Fetterman et al., "Demonstration of 110 GHz Electrooptic Polymer Modulators," Appl. Phys. Lett., 70(25), p.3335-3337 (June, 1997).

[5] R. J. Mears et al., "Low Noise Erbium Doped Fiber Amplifiers Operating at 1.54 μm," Electronics, Vol. 23, p. 1026 (1987).

[6] K. Rottwitt et al., "Distributed Raman Amplifiers for Long Haul Transmission Systems," Conf. Proc. IEEE-LEOS (1998).

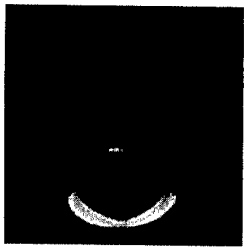
[7] Similar research is reported at Sentel Tech. – Paradigm Optics site: www.senteltech.com/nospecitems.html

[8] R. B. Dyott, *Elliptical Fiber Waveguides*, Artech House, Boston, p. 95-97 (1995).

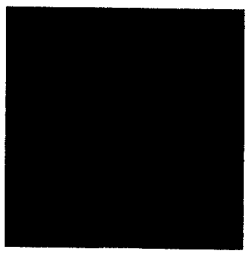
[9] D. M. Burland et al., "Second-Order Nonlinearity in Poled-Polymer Systems," Chem. Rev., Vol. 94, p. 31-75 (1994).

[10] M. M. Liu, *Principles and Applications of Optical Communications*, McGraw Hill, p.94 (1996).

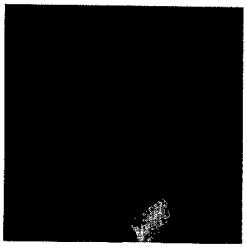
[11] M. V. Pack, "Numerical Analysis of an Electro-Optic Polymer Core Waveguide for High-Speed Optical Modulation," Masters Thesis, BYU (2001).



Michael S. Smith received a B.S. degree in electrical engineering from Brigham Young University, Provo, Utah in 2000. He is currently pursuing an M.S. degree while conducting research on active fiber devices at BYU.



Richard H. Selfridge is an associate professor of electrical and computer engineering at Brigham Young University, Provo, UT. He received a B.S. degree from California State University, Sacramento in Physics in 1978. He was awarded an M.S. and Ph.D. in electrical engineering from the University of California, Davis in 1980 and 1984, respectively. From 1984 through 1987 he was a member of the faculty in the Department of Electrical Engineering at California State University, Sacramento. In 1987 he joined the faculty at Brigham Young University. At that time he established a laboratory dedicated to studying and creating in-fiber active and passive elements. In addition, he collaborates with faculty and students from the mechanical and chemical engineering departments in MEMS research. He teaches classes in electromagnetics, circuits, solid state devices, microwaves and fiber optics.



Garth M. Kraus received the B.S. and M.S. Degree in electrical engineering from Brigham Young University, Provo, Utah in 2001. He has worked on integrated optical components, and is currently employed by IBM where he works with a photonics group developing future optical waveguide devices.

Wide Passband WDM (WWDM) Transmission in 1.5 μm Wavelength Region through Optical Fiber Cables installed in Access Networks

Hirotaka NAKAMURA*, Kyozo TSUJIKAWA*, Yuka NONOYAMA*, Kazuo HOGARI*, Shigekatsu TETSUTANI*, Chikara MATSUI**, Fumihiko YAMAMOTO, and Toshihiko SUGIE****

*Access Network Service Systems Laboratories, NTT
1-6 Nakase, Mihama-ku, Chiba-shi, Chiba 261-0023 Japan
+81-43-211-3299 hirotaka@ansl.ntt.co.jp
**R & D Center, NTT-EAST
***Technical Assistance and Support Center, NTT-EAST

Abstract

In order to meet the rapidly increasing demand for broadband services and to construct cost effective networks in access and metropolitan areas, we have proposed wide passband wavelength division multiplexing (WWDM) technology and newly developed WWDM transponders (TRPs). In this paper, we report the WDM transmission characteristics in the 1.5 μm wavelength region using 1.3 μm zero dispersion single-mode fiber cables installed in access networks and WWDM-TRPs.

Keywords

Wide passband WDM; Gigabit Ethernet; SDH; 1.3 μm zero dispersion single-mode fiber; Access networks.

1. Introduction

Various broadband services are currently being employed and IP traffic is increasing rapidly in access networks. These access networks must meet many requirements, for example, they must have the flexibility to provide various services, the large capacity needed for broadband services, and be cost-effective. WDM technology is a promising solution to the need for a large capacity, and dense WDM (DWDM) technology is now being actively developed. However, DWDM systems are too expensive to be applied to access networks because they require the highly accurate wavelength control of laser diodes (LDs) and MUX/DEMUXs. Therefore, low cost WDM technology has been proposed for access and metropolitan area network applications [1]. We have proposed wide passband WDM (WWDM) technology, which uses 4–8 wavelengths in the 1.5 μm wavelength region, and developed WWDM transponders (TRP) [2][3]. By employing this WWDM technology, we were able to avoid such severe requirements as LD and MUX/DEMUX temperature control, and realize the large capacity and cost effective system required for access networks [4].

In our access networks, we have installed 1.3 μm zero dispersion single-mode fiber (SMF) cables. The cables between central offices and user buildings are usually less than 20 km in length. By contrast, both SMF and dispersion-shifted fiber (DSF) cables have been installed in metropolitan areas and the cables between adjacent central offices in these areas are usually less than 80 km in length.

DSF was originally designed to have the smallest loss and chromatic dispersion values at 1.55 μm so that it could be used for transmission in the 1.5 μm wavelength region. However, nonlinear optical effects, such as four wave mixing, are likely to occur in DSF when it is used in DWDM systems. SMF has been used for 1.31 μm transmission. With SMF, no nonlinear optical effects are generated during 1.5 μm transmission, however the transmission distance is restricted by chromatic dispersion when the bit rate becomes high. In addition, the loss of SMF is increased by fiber bending in the 1.5 μm wavelength region.

In this paper, we describe the WDM transmission characteristics of our transponders. In terms of the optical loss and chromatic dispersion characteristics of installed SMF cables, we clarify the feasibility of WDM transmission in the 1.5 μm wavelength region for the construction of cost effective access and metropolitan networks.

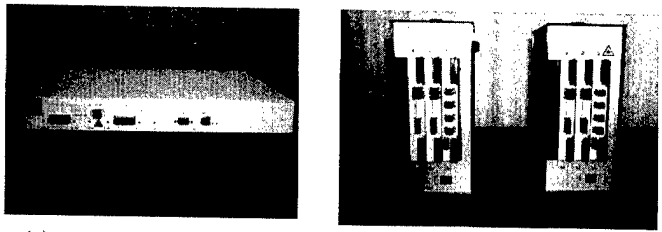
2. Characteristics of WWDM transponder

2.1 WWDM transponder

Figure 1 shows photographs of two types of WWDM transponder (TRP) that we have developed [3]. The WWDM-GbE-TRP has two Gigabit-Ethernet interfaces (Fig.1 (a)), and the WWDM-SDH-TRP has two STM-1 interfaces (Fig.1 (b)). Figure 2 shows their block diagrams and the wavelength allocation. The TRPs consist of interfaces, transmitters, receivers, and MUX/DEMUX, which convert an optical signal from the interface into a WDM optical signal (and vice versa) and transmit two pairs of bi-directional signals over one fiber. The wavelengths of these pairs of signals are 1.53 and 1.55 μm, and 1.57 and 1.59 μm, respectively. 1.5 μm region light sources are easily available because various types have been developed for DWDM. Furthermore, the fiber loss usually has its minimum value in the 1.5 μm region.

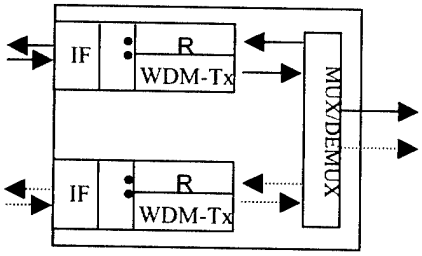
In these transponders, we use a dielectric multi-layer filter, which has a wide passband region (15 nm) and a low insertion loss (< 1dB), as the MUX/DEMUX. We also use four directly modulated

distributed feedback lasers (DFB-LD) for each wavelength, with an isolator and no temperature control. Figure 3 shows the spectrum at 1.59 μm and 25 ℃. The side mode suppression is over 40 dB. This spectrum shifts while maintaining its shape as the temperature shifts. Figure 4 shows the temperature characteristics of the center wavelength. The wavelength shift is 0.1 nm/ ℃, which is normal for a conventional DFB-LD. Therefore, the wavelength shift in our assumed operation temperature range (100℃), is about 10 nm, which is within the MUX/DEMUX passband region. From Fig. 4, the wavelength region of 1.52-1.60 μm is used in these WWDM-TRPs.



(a) (b)

Figure 1. Photographs of WWDM-TRPs developed in this experiment. (a) WWDM-GbE-TRP. (b) WWDM-SDH-TRP.



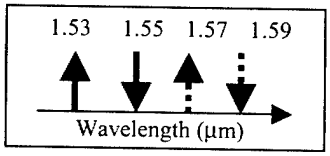


Figure 2. Block diagram and wavelength allocation of WWDM-TRPs.

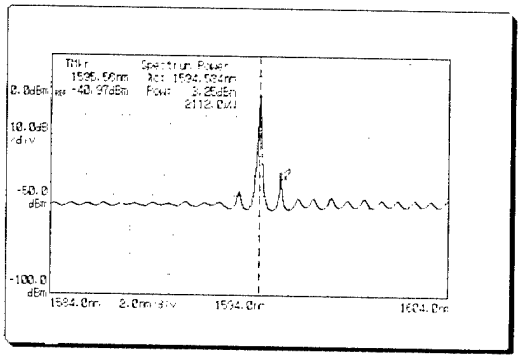


Figure 3. Spectrum of at 1.59 μm at and 25 ℃.

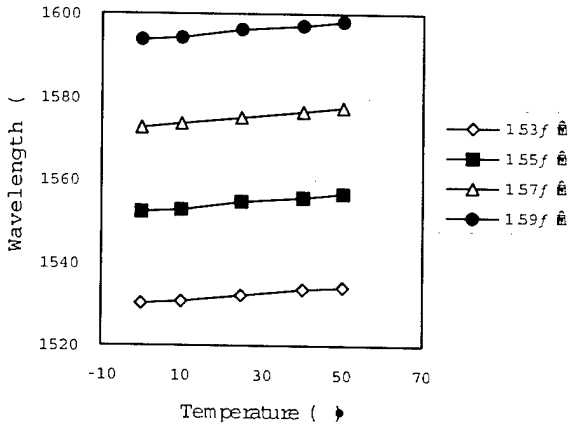


Figure 4. Temperature characteristics of center wavelength of DFB-LD.

2.2 Estimation of transmission characteristics

2.2.1 BER and PLR

In general, the transmission characteristics are evaluated by using the bit error rate (BER) for SDH signal transmission and we measured the BER of the WWDM-SDH-TRP. We estimated the minimum optical received power at a BER of 10^{-10} and also the loss budget, which is the difference between the optical output power and the minimum optical received power.

However, with the WWDM-GbE-TRP, we measured the packet loss rate (PLR) instead of the BER, because Ethernet products are evaluated in terms of their PLRs.

We defined the PLR to be

$$PLR = (N_1 - N_2) / N_1 \quad (1)$$

where N_1 and N_2 denote the total transmitted packet number and the correct received packet number, respectively. The relationship between the PLR and the BER is given by Eq. (2)[5].

$$PLR = 1 - (1 - BER)^{[packetlength(bit)]} \quad (2)$$

Equation (2) is valid under the following conditions; (A) each error packet has only 1 bit error, and (B) packet layer protocol has only an error detection function and has no error recovery function such as forward error correction or retransmission. When the bit error is large, the packet loss is not satisfied by the above conditions and has statistical characteristics and PLR varies by about 0.4 dB.

In Eq. (2), 10^{-8} PLR corresponds to about 10^{-11} BER. Therefore, we estimated the minimum optical received power at 10^{-8} PLR.

2.2.2 Experimental results

Figure 5 shows our experimental setup for laboratory measurements. With this setup, we measured the PLR and BER for back-to-back and, 80 km long SMF and DSF when the optical

received power was attenuated. When measuring the PLR, we used a LAN analyzer to create 64 byte packets of 1000 Base-SX with the smallest possible packet interval of 0.096 μs (IEEE 802.3 standard [6]) and simultaneously transmitted the packets for 4 wavelengths at a maximum throughput of 1488095 packets/sec. When measuring the BER, we used an STM analyzer to generate the $2^{23} - 1$ PRBS signals and simultaneously transmitted signals for 4 wavelengths.

Figure 6 shows the relationships between the optical received power and PLR for a 1.59 μm GbE signal in three different cases. The respective fiber loss and chromatic dispersion values were about 0.20 dB/km and 18.8 ps/nm/km for SMF, and 0.20 dB/km and 2.6 ps/nm/km for DSF. There was no difference between the PLRs for back-to-back and 80 km long SMF and DSF. This means that there is no degradation in the WDM transmission of GbE signals in the 1.5 μm region from a DFB-LD modulated directly at 1.25 Gbps, in terms of chromatic dispersion through the SMF (total dispersion ~1500 ps/nm) and nonlinear optical effects through the DSF. Therefore, the transmission distance of a GbE signal is restricted solely by fiber loss, not by chromatic dispersion or nonlinear optical effects. Figure 7 shows the temperature characteristics of the loss budget for each wavelength. The loss budgets for each wavelength are about 22 dB (< ± 0.5 dB).

Figure 8 shows the relationship between the optical received power and BER for the signal of a 1.59 μm of WWDM-SDH-TRP in two different cases. STM-1 was 155 Mbps and there was no chromatic dispersion induced degradation . The loss budget was about 33 dB.

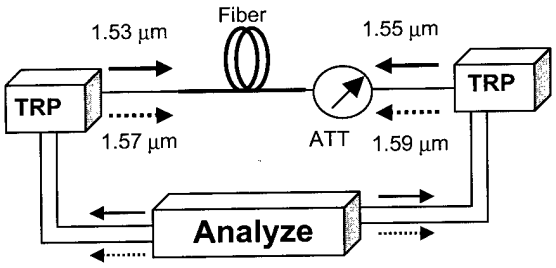


Figure 5. Experimental setup.

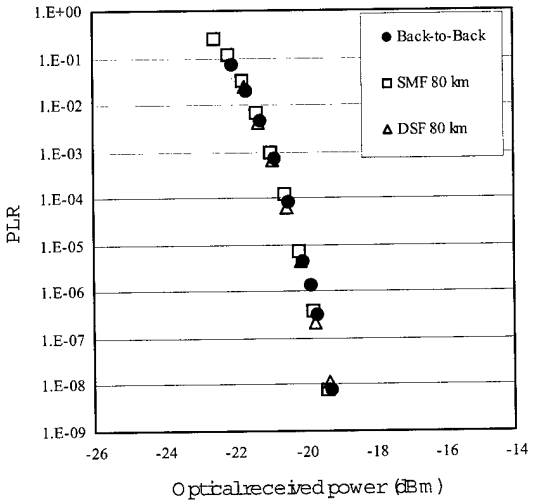


Figure 6. Relationships between optical received power and PLR of a 1.59 μm GbE signal.

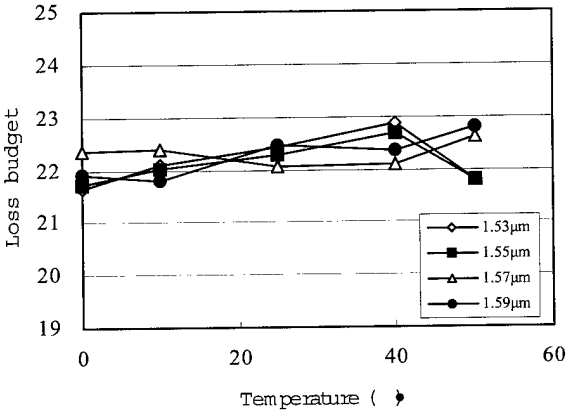


Figure 7. Temperature characteristics of loss budget of WWDM-GbE-TRP.

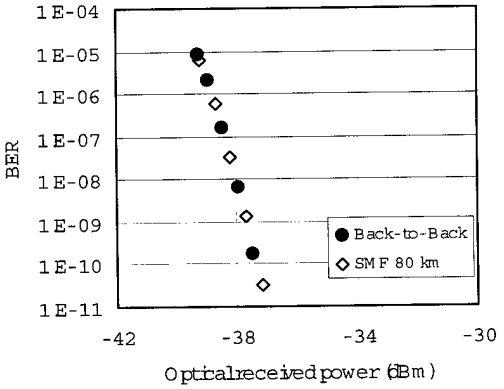


Figure 8. Relationships between optical received power and BER of a 1.59 μm STM-1 signal.

3. Field Measurement

Figure 9 shows the configuration of the optical access networks in which we carried out the field measurement. Routes 1 and 2 were 4.6 and 3.8 km long ring networks, respectively. They consisted of 400-fiber underground cables, and contained 4 MT connectors and 2 fusion splices. Route 3 was a 9.2 km long ring network that consisted of 1000-fiber underground cable and 24-fiber aerial cables and contained 2 SC connectors, 12 MT connectors, and 10 fusion splices. All cables contained 1.3 μm zero dispersion single-mode fibers (SMFs). We measured the loss and chromatic dispersion of several fibers in each route. We also measured the PLR of the WWDM-GbE-TRP for all the routes, and the BER of the WWDM-SDH-TRP for route 3. We observed no extraordinary reflection at the connector in any of the fibers that we measured by OTDR.

3.1 Characteristics of installed SMF cables

The optical losses of SMF cables installed in access and metropolitan areas include the losses at connectors and fusion splices. Connector loss is mainly caused by the offset and depends on the mode field diameter (MFD) of the fibers. Because the MFD decreases as the wavelength shortens, the connector loss increases at shorter wavelengths. By contrast, the bending loss of SMF increases at longer wavelengths. Therefore, the wavelength dependence of the optical loss of SMF cables differs according to the installed conditions (e.g. fiber bends, number of connectors).

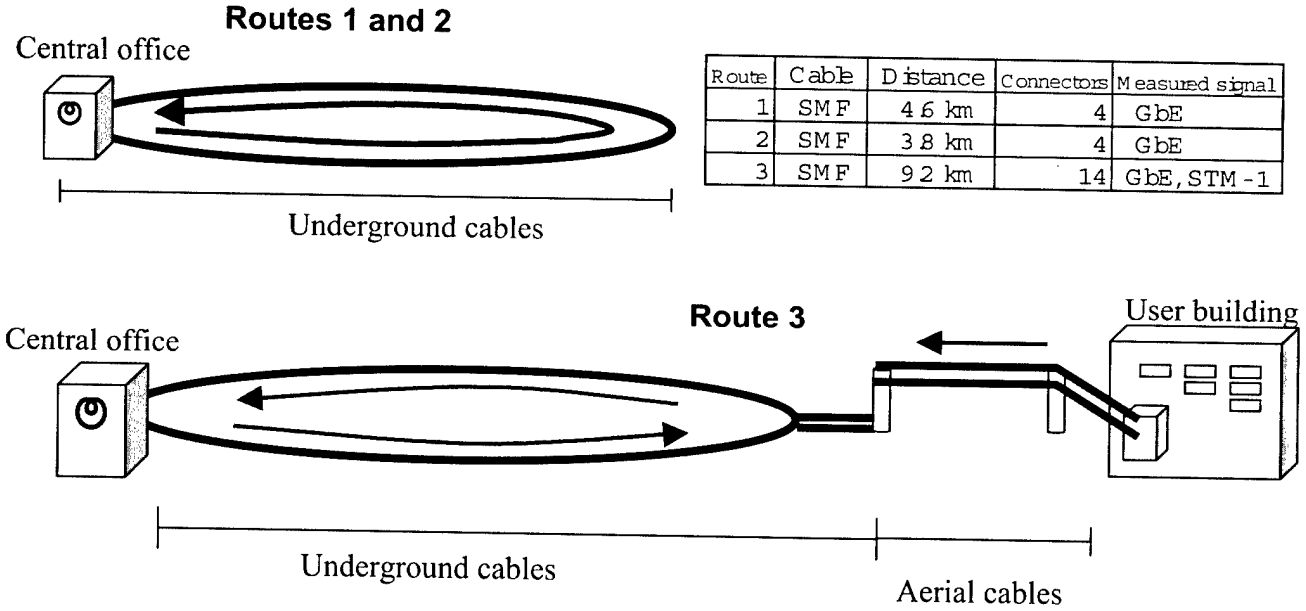
Figure 10 shows a typical optical loss measurement result for installed SMF cable. The loss characteristic of a fiber wound around a bobbin is also shown for comparison. These results indicate that the installed cable loss is increased over the whole wavelength region by the connectors and fusion splices. Figure 11 shows the relationships between the loss at 1.52 μm and at 1.60 μm in all routes. Both values are normalized by the loss at 1.31 μm of each cable. It shows that the loss of installed cables largely differ according to their installed conditions, route 1, 2, and 3. In most fiber, the loss at 1.52 μm was smaller than that of at 1.31 μm, however, the loss of at 1.60 μm was larger than that at 1.52 μm because of the bending loss. Though the bending loss changes corresponding to the bending condition and fiber parameters, in the cases of underground ring networks such as route 1 and 2, the cable loss usually shows largest value at 1.60 μm in the wavelength region of these WWDM-TRPs. Therefore, the total loss at 1.60 μm is required to be within the loss budget of WDM-TRP.

Figure 12 shows the chromatic dispersion of installed SMF cable. Mean value of each route is shown. The curve fitted by the Sellmeier expression is also shown. No extraordinary value was observed for any of the cables. The maximum value was about 19 ps/nm/km at 1.60 μm (total dispersion within 180 ps/nm). Therefore, the transmission distance is not restricted by chromatic dispersion.

3.2 WDM transmission

Figure 13 shows the PLR of a WWDM-GbE-TRP on routes 1, 2, 3, and back-to-back in the laboratory. The measurement method was same as the laboratory test described in section 2.2. In this case, the wavelength of the transmitted signal was only 1.59 μm to eliminate the crosstalk from other wavelengths. These PLRs varied less than 0.5 dB. We obtained the same results for the other three wavelength signals.

When we tested the simultaneous transmission of 4 wavelengths for route 1-1 and 3-1, we observed a power penalty of about 1 dB at 1.59 μm caused by crosstalk from the other wavelength signals, which we also observed in the laboratory measurement.



Route	Cable	Distance	Connectors	Measured signal
1	SMF	4.6 km	4	GbE
2	SMF	3.8 km	4	GbE
3	SMF	9.2 km	14	GbE, STM-1

Figure 9. Configuration of optical access networks.

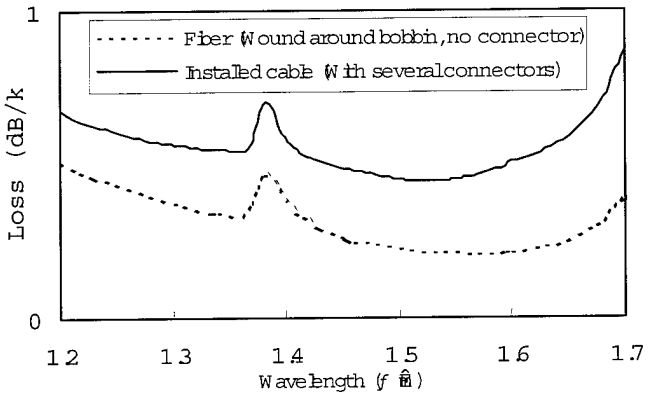


Figure 10. Example of cable loss characteristics.

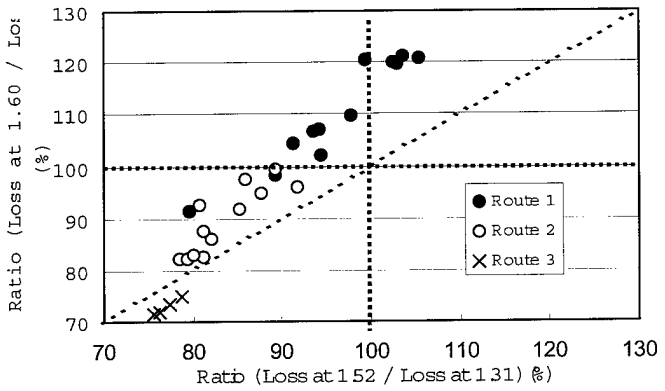


Figure 11. Relationships between cable loss at 1.52 μm and 1.60 μm normalized at 1.31 μm.

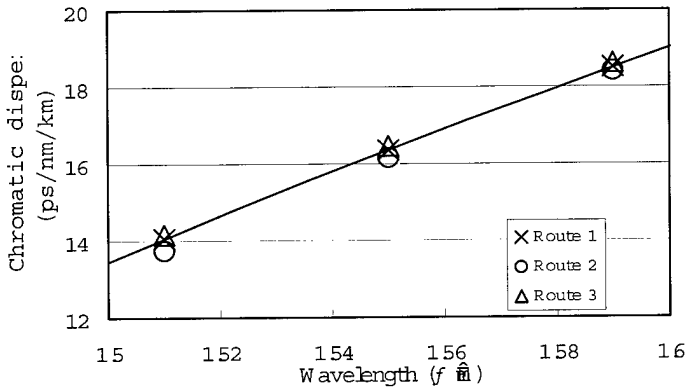


Figure 12. Chromatic dispersion of installed SMF cable.

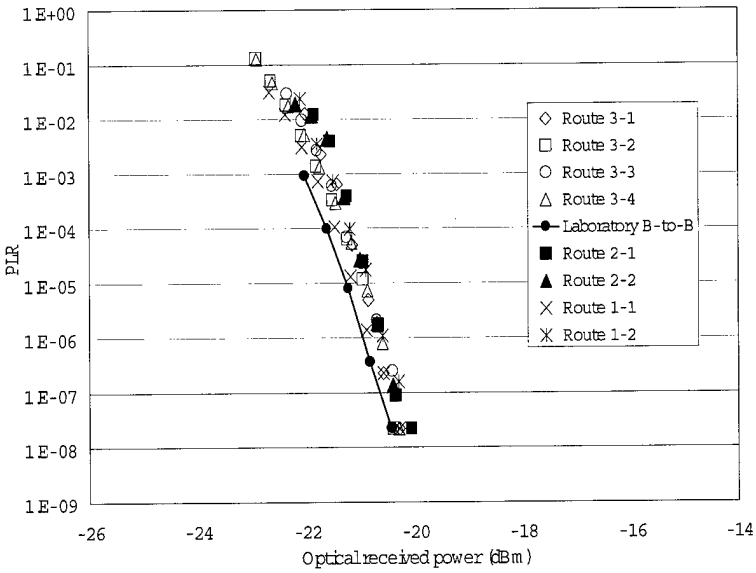


Figure 13. Relationships between optical received power and PLR of a 1.59 μm GbE signal in field measurement.

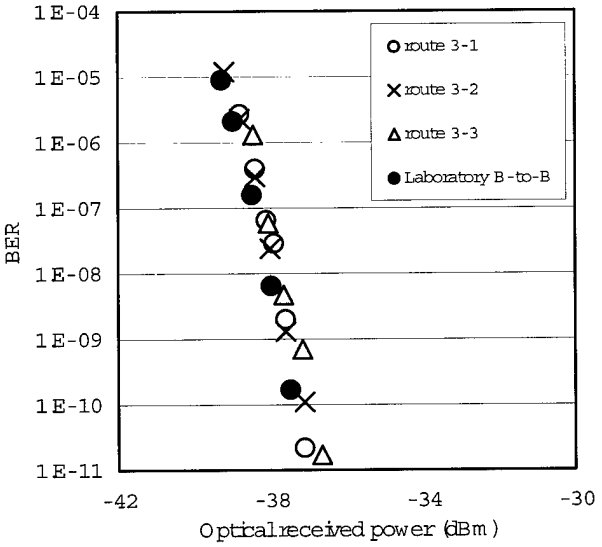


Figure 14. Relationships between optical received power and BER of a 1.59 μm STM-1 signal in field measurement.

Figure 14 shows the BER for a 1.59 μm signal with the WWDM-SDH-TRP through three fibers and back-to-back in the laboratory. The measurement method and conditions were the same as those

used in the laboratory test described in section 2.2. The BER characteristics of all the fibers corresponded with each other. The same results were observed for the other three wavelength signals.

4. Discussion

In the previous section, we mentioned that the cable loss in the ring network usually exhibited its maximum value at 1.60 μm in the wavelength region of these WWDM-TRPs. We also showed that the chromatic dispersion was negligible for 1.5 μm Gigabit Ethernet and STM-1 signals.

With these WWDM-TRPs, the transmission distance is restricted only by cable loss, not by chromatic dispersion because of the 1.25 Gbps and 155 Mbps transmission rates. But, with higher bit rates, the transmission distance is restricted by the chromatic dispersion. In terms of chromatic dispersion, the bit rate of these TRPs is assumed to be up to 2.4 Gbps for SMF [7].

Therefore, by employing WDM in the 1.5 μm wavelength region, we can construct cost effective and large capacity networks for installed SMF cables, namely access and metropolitan area networks using Gigabit Ethernet and Fast Ethernet for broadband IP services, such as content distribution, and large capacity transmission using SDH [4].

5. Conclusions

In this paper, we described a WDM transmission field measurement using a WWDM-GbE-TRP and a WWDM-SDH-TRP developed for access and metropolitan network applications.

In an underground ring networks, the optical loss of most of the fiber cables at 1.60 μm was largest in the wavelength region of 1.52-1.60 μm because of bending loss. The chromatic dispersion values in all the cables were normal and did not restrict the transmission distance. Therefore, we found that the transmission distances of the WWDM-TRPs are mainly decided by the cable loss at 1.6 μm.

We could achieved the WDM transmission of Gigabit Ethernet signals and STM-1 signals in the 1.5 μm wavelength region through 1.3 μm zero dispersion single-mode fiber cable installed in access networks, which were the same as those obtained in laboratory measurements.

Therefore, we believe that inexpensive large capacity access and metropolitan area networks will be constructed using WDM technology.

6. Acknowledgments

The authors thank N. Sato, H. Shinohara, and K. Sato of Access Network Service Systems Laboratories, NTT, and E. Maekawa of NTT-EAST, for support, discussion, and encouragement.

7. References

[1] HEESANG PARK, CHANG JOON CHAE, SEUNG-TAK LEE, and GEUN YOUNG KIM, "Implementation of an optical LAN over an existing PON system by internetworking optical network units," OECC2000, 11D12, (2000).

[2] H. Kawata, H. Nakamura, and T. Sugie, "Service multiplexing systems with wide passband WDM (WWDM) technology for access networks," *Trans. IEICE,* vol. E83-B, No.10, pp.2348-2354, (Oct. 2000).

[3] H. Nakamura, Y. Nonoyama, H. Kawata, and T. Sugie, "A proposal of WDM-Ethernet system in access network for IP service," OHAN/FSAN 2001, P.8, (2001).

[4] T. Sugie, H. Kawata, H. Nakamura, K. Tsujikawa, and Y. Nonoyama, "Wide passband WDM (WWDM) technology and its application to access networks for broadband services," NOC'2001, pp.37-43, (Jun.2001).

[5] M. Ishikawa, Y. Ito, O. Maeshima, and T. Asami, "A traffic measurement tool for IP-based networks," Trans. *IEICE*, vol. E82-D, No.4, pp.756-760, (April 1999).

[6] IEEE, "Carrier sense multiple access with collision detection (CSMA/CD) access method and physical layer specification", IEEE Standard 802.3-1998.

[7] S. Tetsutani, H. Hakozaki, J. ZHOU, F. Yamamoto, C. Matsui, K. Hogari, and K. Sato, "Optical transmission characteristics of optical fiber cables and installed optical fiber cable networks for WDM systems," 50th IWCS, (Nov. 2001).



Hirotaka NAKAMURA received a B.S. degree in applied physics from the University of Tokyo, Tokyo, Japan, in 1999. In 1999, he joined Nippon Telegraph and Telephone Corporation, Tsukuba, Ibaraki, Japan, where he has been engaged in research on the development of WDM access systems.

The Study of Ultra Large Effective Area Fiber & Mating Dispersion Slope Compensating Fiber for Dispersion Flattened Hybrid Optical Fiber DWDM Link

Kazumasa Ohsono[1] *Kengo Kotani*[1] *Kazuya Murakami*[1] *Yao Bing*[1]
Takahiro Yamazaki[2] *Hideki Shimane*[2]

1. The 4th Dept. Optoelectronic System Laboratory, Hitachi Cable,Ltd.
2. Optical Fiber &Communication Cable Dept.,Hitachi Cable Ltd.
Hitaka-cho, Hitachi-shi, Ibaraki-ken, 319-1414 Japan
Phone; +81-294-25-3837· email; ohsono.kazumasa@hitachi-cable.co.jp

Abstract

We have developed new hybrid optical line for the next generation DWDM transmission system. It is using ULF and DSCF for this line. As for ULF, it ascertained that the transmission performance become well in enlarging effective area by using a numerical simulation. We investigated the best design of refractive index profile for ULF, DSCF and fabricated fibers. Using the low loss splicing method by the bridge fiber, we composed a hybrid transmission optical line and confirmed that the attenuation and the dispersion slope was 0.210dB/m and less than 0.01 ps/nm/nm/km respectively.

Keywords

Large core fiber ;low non-linear ; dispersion slope compensating; hybrid transmission line ; bridge fiber splice

1.Introduction

The demand for data communication is growing rapidly due to the increasing popularity of the Internet and other factors. In about 1998 years, the transmission capacity per fiber increased to 10(20) Gbit/s per wavelength by wavelength Division Multiplexing (WDM) technique[1]. Moreover, in recent system, the overall transmission capacity exceeds 1Tbit/s per fiber by the improvement of the WDM techniques [2]. Usually, these techniques are called Dense WDM (DWDM). In order to increase the transmission capacity, increasing the number of wavelengths and the narrowing the channel spacing in the fiber are required. To increase the number of channel increases the optical channel cross-talk and limits the narrowing the channel spacing due to the non-linear interactions. The most practical way to solve a problem of non-linearity is to enlarge effective area. Therefore we challenged to enlarge effective area of the fiber as much as cabling performance allowed while keeping the dispersion slope relatively low level. Further to increase the transmission speed of each channel, e.g. STM-256 (40 Gbit/s per channel system) or more, the edge channel's total dispersion shall keep the allowable DGD of 0.1 - 0.3 bit/pulse. The aid of dispersion & dispersion slope compensation transmission fiber is required to cover the transmission bands, e.g. C-band and L-band. The ultra large effective area low non-linear single-mode fiber (ULF) development is demonstrated by evaluating the combined ULF and mating compensating fiber total performance.

In this paper, we describe a ULF and analyzing the optimum characteristics of the dispersion & dispersion slope compensation fiber as the mate of the ULF. According to this analysis we designed the mate dispersion & dispersion slope compensation fiber (DSCF) profile and fabricated it. The hybrid performance of the ULF and DSCF had demonstrated.

2. Design and simulation of hybrid optical transmission line with ULF & DSCF

2.1 Design of hybrid optical transmission line

In order to increase the transmission capacity, increasing the number of wavelengths and the narrowing the channel spacing in transmission line are required. To realize such a higher transmission capacity, a hybrid optical transmission line has been proposed [3][4]. This line used a single mode fiber with an extra large core (ELF) in the front portion of the span between the inline amplifiers, and dispersion & dispersion slope compensation fiber (DSCF) in the rear portion. Fig.1 shows the configuration of the hybrid optical transmission unit line. A 30km ELF (Aeff=110μm^2) was arranged behind the inline amplifier which put large optical power in the fiber. As for the DSCF, the length was a 15km and the position was arranged behind ELF. The DSCF has a reverse dispersion and dispersion slope of ELF, therefore compensates for the accumulation of dispersion and dispersion slope in ELF.

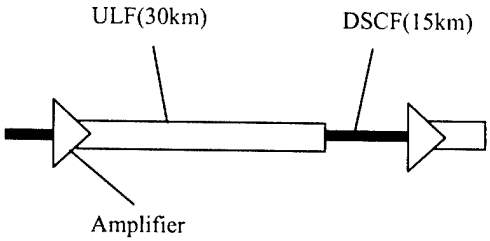


Fig.1 Configuration of the hybrid optical transmission unit line

2.2 Simulation of hybrid optical transmission line

We simulated the transmission of the optical fiber of the DWDM system, using Sprit-Step-Fourier method [5]. Fig.2 shows the block diagram of the DWDM system to have used for a simulation. The transmission parameter of each composition modules and the optical fibers are shown in table 1. We simulated about the case to have used two kinds of optical fiber units which combined ELF, and DSCF, ULF and DSCF. It evaluated a transmission characteristic with eye mask penalty. In this simulation, the influence of the ASE noise of the optical amplifier was not considered. Fig.3 shows relation between the transmission distance and eye mask penalty when the incident peak power is 10 dBm. Also, eye diagram of the ELF system and the ULF system after 10080 km transmission are shown in Fig.3. Above result indicates that the ULF system is more excellent compared with the ELF system regarding the transmission limit in case of the high power input signal.

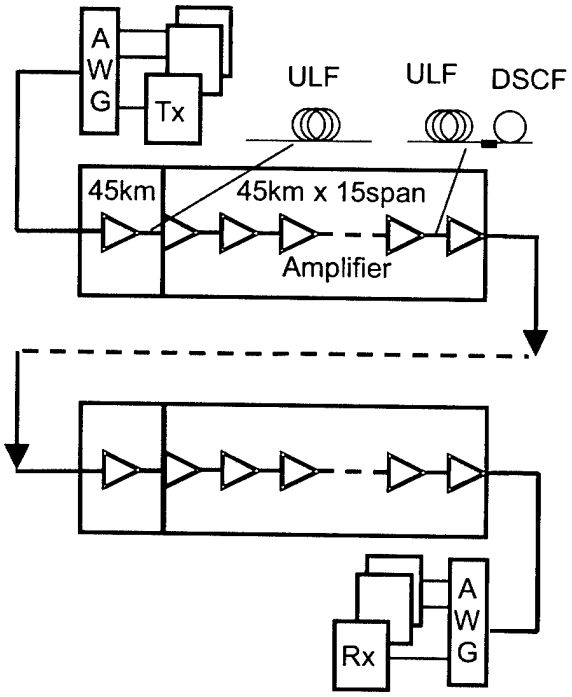


Fig.2 Block diagram of the DWDM system

Table.1 Transmission parameter of each composition modules and optical fibers

Channel spacing [nm]	0.8		
Number of channels	32		
Bit format	RZ-Gaussian		
Number of bits	2^7-1 PRBS		
Bit rate per channel	10Gbit/s/ch		
Pulse width [ps]	8.0		
Transmission distance [km]	10080		
Filter width[nm]	0.25		
Filter factor	1024		
Repeater spacing[km]	45		
EDFA gain[dB]	10.15		
EDFA bandwidth	1530-1560		
EDFA NF	0		
Fiber character @1550nm	ELF	ULF	DSCF
Dispersion [ps/km/nm]	19.8	19.8	-43.55
Dispersion slope [ps/km/nm^2]	0.06	0.06	-0.132
Fiber loss [dB/km]	0.18	0.18	0.27
Joint loss [dB]	0.20	0.20	0.15
Kerr coefficent:n_2 [m^2/W]	2.24	2.24	2.24
A_{eff} [μm^2]	110	180	30
Fiber length [km]	30	30	15

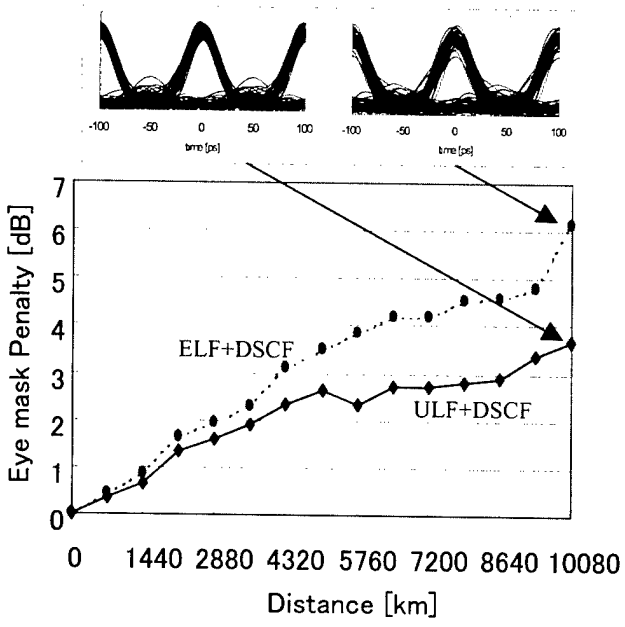


Fig.3 Relation between transmission distance and eye mask penalty

3.ULF design & performance

3.1 Fiber design

There were several kind of refractive index profiles which was proposed for a large Aeff fiber [6]. Considering the cutoff wavelength and macro bending loss, we adopt the depressed clad profile, which had a –0.05% refractive index. We calculated the refractive index of center core to satisfy the Aeff of 180 μm^2, the cutoff wavelength of 1450nm and the macro bending loss (bending diameter, 20mm) of less than 50 dB/m at 1550nm. This bending loss level fiber with a optimized loose type cable realize to transmit at operation wavelength. According to the calculation, we decided that a center core refractive index (Δn) value.

3.2 Fiber fabrication and performance

We used Vapor-phase axial deposition (VAD) method to fabricate ULF because VAD works better in mass production compared with other method. The typical characteristics of the fiber are listed in Table 2. We measured them after loose tube unit cabling. The attenuation was 0.182dB/km at 1550nm. Polarization Mode Dispersion (PMD) was 0.022 ps/root-km.

We obtained good performances, respectively. Furthermore the nonlinear coefficient, n2/Aeff was measured using the cross-phase modulation method: The n2/Aeff was about 50% smaller than that for conventional SMF.

Table2. Typical characteristics of ULF

Dispersion	20.77 ps/nm/km
Dispersion slope	0.062 ps/nm^2 /km
Attenuation	0.182 dB/km
PMD	0.022 ps/$km^{1/2}$
MFD	15.2 μm
Aeff	179.6 μm^2
n2/Aeff	$1.0x10^{-10}$ /w
Macro Bend Loss*	45 dB/m

*Bend diameter=20mm

4.DSCF design & performance

4.1 Fiber design

The tetra cladding structure of the reflective index profile for DSCF is employed. We have calculated the center core diameter to gratify targeting dispersion and slope value under setting the tetra cladding structures. We determined that core radius to achieve the dispersion, -44 ps/nm/km and dispersion slope, –0.13 ps/nm/nm/km. These parameters demonstrate to compensate the positive dispersion and the dispersion slope of ULF when we use ULF and DSCF in the length ratio of two to one.

4.2 Fiber fabrication and performance

We fabricated DSCF using the MCVD method, which can manufacture the very complicated refractive index profile fiber. The characteristics of the trial fiber are shown in Table 3. The compensation ability for ULF is demonstrated because the RDS (Relative Dispersion Slope: Slope/Dispersion) of both ULF and DSCF shows almost the same value, 0.003. The attenuation at 1550nm was 0.256 dB/km, which is substantially low level compared with the other conventional DCF.

Table3. Typical characteristics of DSCF

Dispersion	-43.5 ps/nm/km
Dispersion slope	-0.132 ps/nm^2 /km
Attenuation	0.256 dB/km
PMD	0.06 ps/$km^{1/2}$
MFD	6.3 μm
Aeff	30 μm^2
n2/Aeff	$8.0x10^{-10}$ /w
Macro Bend Loss*	8 dB/m

*Bend diameter=20mm

5.Fiber splice

The MFD of ULF is about 15μm and that of DSCF is about 6μm of which large difference of MFD leads high splice loss. When we connect these optical fibers directly, the splice loss is about over 1 dB, which is a large loss and we can not accept. There are two alternative ways to splice at low loss. One method is to splice directly with TEC* technique, the other method is to use bridge fiber which has middle MFD between ULF and DSCF. We employed bridge fiber method because it enabled us to apply existing splice technique.

*TEC; Thermal Expanded Core

5.1 Selection of suitable bridge fiber

It is required for bridge fiber that the MFD of bridge fiber is easy to expand in splicing with ULF but in splicing with DSCF, the MFD of bridge fiber is hard to expand. After we examined various optical fibers, we concluded Non-zero dispersion fiber who's MFD is 8.5μm was the best.

5.2 splice characteristics

We examined the optimum conditions for fusion with usual fusion splicer. The parameter of discharge power, discharge time and push length is very important. The average loss between ULF and bridge fiber is about 0.17dB and the average loss between DSCF and bridge fiber is about 0.11dB,respectively. The total average loss at 1550nm for ULF / DSCF connection becomes 0.28dB. Fig. 4 shows total splice loss spectrum with bridge fiber at operating wavelength. The uniform spectral loss over the operating wavelength band contributes the easy system design.

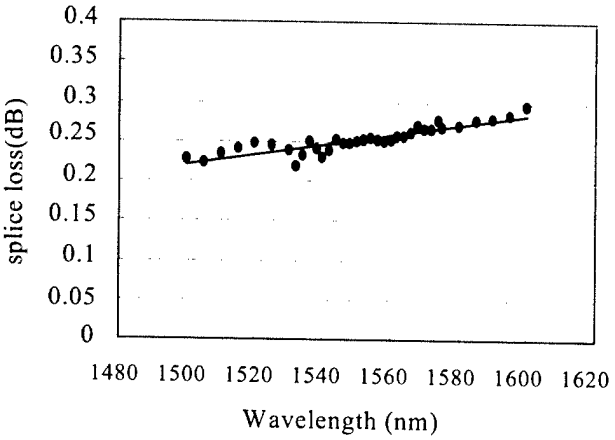


Fig.4 Total splice loss spectrum between ULF and DSCF

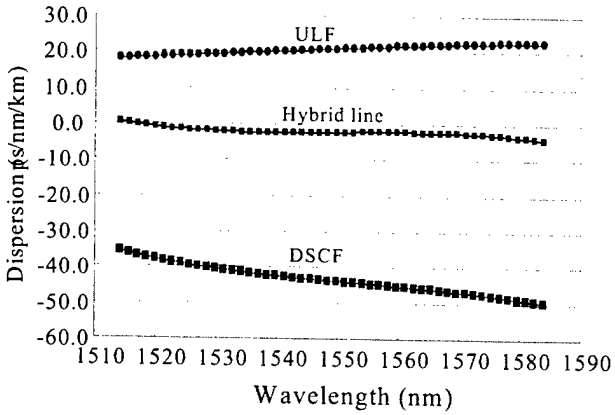


Fig.6 Dispersion spectrum of hybrid line

6.Performances of hybrid line

The spectrum of the attenuation and the dispersion of hybrid fiber 45km(ULF;30km, DSCF;15km) are shown in Fig.5 and Fig.6 respectively. The attenuation at 1550 nm wavelength was a low level of 0.210dB/km. It compensates the dispersion and the dispersion slope in the operation wavelength sufficiently respectively in the cable. As the dispersion slope becomes less than 0.01 ps/nm/nm/km flat characteristics in the wide wavelength, the broad band DWDM for Tera-bit/s transmission system was achieved.

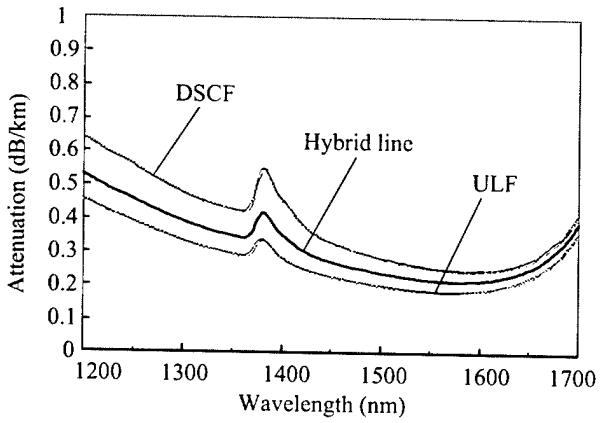


Fig.5 Attenuation spectrum of hybrid line

7.Conclusion

We have developed ULF and DSCF for the next generation DWDM transmission systems. ULF and DSCF optimized a refractive index profile design and distribution design; ULF by VAD method and DSCF by MCVD method. We chose bridge fiber method as the way of splicing between ULF and DSCF and we confirmed low loss. By above investigation, we realized hybrid line with flat dispersion characteristic in the wide wavelength in low attenuation. The performance of the hybrid optical transmission line consisting of these fibers demonstrated the good capabilities for Tera-bit/s DWDM transmission systems. The attenuation of hybrid line was 0.210dB/km, and the hybrid dispersion slope was less than 0.01 ps/nm/nm/km.

8.References

[1] G.E.Keiser, Optical Fiber Technol.,vol5, (1999) pp.3-39

[2] Akiba, "Optical Submarine Cable Network", IEICE 00, March 2000

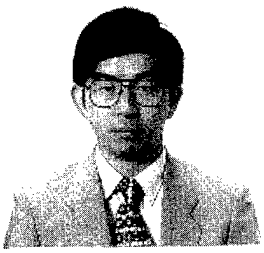
[3] R.Kurebayashi,et al.,OECC 2000,11A1-3 (2000)

[4] T.Tanaka, et al., OECC 2000,11A1-5 (2000)

[5] G.P.Agrawal,"Nonlinear Fiber Optice,2nd.,Academic Press, (1989)

[6] Y.Narita, et al., "Novel Large Effective Area Fiber in a Loose-type Cable",EC 2000,p.67 (2000)

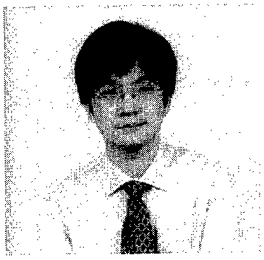
Author



Kazumasa Ohsono

The 4th Dept. Optoelectronic System Laboratory,Hitachi Cable,Ltd.
Hitaka-cho,Hitachi-shi, Ibaraki-ken,319-1414 Japan
Phone;+81-294-25-3837 email: ohsono.kazumasa@hitachi-cable.co.jp

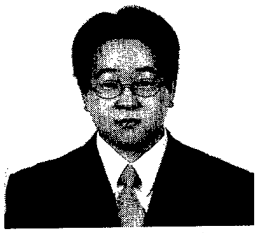
Mr. Ohsono received his B.E. degree in Mechanical Engineering from the Science University of Tokyo in 1982 and joined Hitachi cable, Ltd. He has been engaged in research and development of optical fibers. He is now a senior researcher in Optroelectronic System Laboratory and a member of the IEICE of Japan.



Yoa Bing

The 4th Dept. Optoelectronic System Laboratory,Hitachi Cable,Ltd.
Hitaka-cho,Hitachi-shi, Ibaraki-ken,319-1414 Japan
Phone;+81-294-25-3837 email: yao.bing@hitachi-cable.co.jp

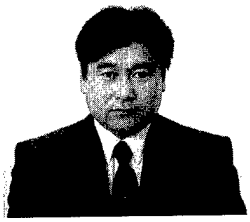
Yamanashi University in 1997. He joined Hitachi Cable, Ltd. in 2001 and he is now engaged in research of an optical fiber communication system. He is now a researcher in research and Optoelectronic System Laboratory and a member of the IEICE of Japan.



Kengo Kotani

The 4th Dept. Optoelectronic System Laboratory,Hitachi Cable,Ltd.
Hitaka-cho,Hitachi-shi, Ibaraki-ken,319-1414 Japan
Phone;+81-294-25-3837 email: kotani.kengo@hitachi-cable.co.jp

Kengo Kotani received B.E. and M.E degrees in mechanical engineering from University of electro-communication in 1997 and 1999, respectively. He joined Hitachi Cable, Ltd. in 1999 and has been engaged in development of optical fiber. He is now a researcher in research and Optoelectronic System Laboratory and a member of the IEICE of Japan.



Takahiro Yamazaki

The Optical Fiber & Communication Cable Department,Hitachi Cable,Ltd.
Hitaka-cho,Hitachi-shi, Ibaraki-ken,319-1414 Japan
Phone;+81-294-25-3804 email: yamazaki.takahiro@hitachi-cable.co.jp

Mr. Yamazaki received his B.E. degree in Electrical Engineering from Ibaraki University o in 1982 and joined Hitachi cable, Ltd. He has been engaged in development of optical fiber cables. He is now a assistant manager in the Telecommunication Department.



Kazuya Murakami

The 4th Dept. Optoelectronic System Laboratory Hitachi Cable,Ltd.
Hitaka-cho,Hitachi-shi, Ibaraki-ken,319-1414 Japan
Phone;+81-294-25-3837 email: murakami.kazuya@hitachi-cable.co.jp

Mr. Murakami received his B.E. degree in Mechanical Engineering from Tohoku University in 1985 and joined Hitachi cable, Ltd. He has been engaged in research and development of optical fibers and optical devices. He is now a senior researcher in Optroelectronic System Laboratory.



Hideki Shimane

The Telecommunications Design Department,Hitachi Cable,Ltd.
Hitaka-cho,Hitachi-shi, Ibaraki-ken,319-1414 Japan
Phone;+81-294-25-3809 email: shimane.hideki@hitachi-cable.co.jp

Mr. Shimane received his B.E. degree in Electrical Engineering from Shibaura Institute of Technology in 1993 and joined Hitachi Cable, Ltd. He has been engaged in the design and development of optical fiber and cables and telecommunications cables. He is now an engineer in the telecommunication Design Department.

Optical Transmission Characteristics of Optical Fiber Cables and Installed Optical Fiber Cable Networks for WDM Systems

Shigekatsu TETSUTANI, *[1]Hiroshi HAKOZAKI, Jian ZHOU, *[2]Fumihiko YAMAMOTO, *[1]Chikara MATSUI, Kazuo HOGARI, and Kiminori SATO

NTT Access Network Service Systems Laboratories, *[1]NTT EAST R&D Center,
*[2]NTT EAST Technical Assistance & Support Center
Hanabatake, Tsukuba, Ibaraki, 305-0805 JAPAN
Phone +81-298-52-2661
Fax +81-298-60-6130
E-mail address: s-tetsu@ansl.ntt.co.jp

Abstract

Many cables containing 1.3-μm zero-dispersion single-mode (SM) optical fibers are installed in trunk and access networks. Recently, there have been a number of studies on wavelength division multiplexing (WDM) systems designed to increase transmission capacity and flexibility. If we can construct WDM systems using SM optical fiber, this will prove very effective in reducing construction costs. Therefore, it is important to examine the wavelength dependence of the transmission characteristics of SM optical fiber cables and networks that have been already installed and joined several optical fibers. In this paper, we describe the optical loss characteristics at various wavelengths. We confirmed that optical transmission was stable up to a wavelength of 1.625 μm (upper wavelength of L-Band).

Keywords

WDM system; SM optical fiber; optical loss characteristics; chromatic dispersion; optical fiber cable networks

1. Introduction

The demand for greater transmission capacity is growing rapidly as a result of the increase in the number of broad-band multimedia services provided by the Internet. Moreover, we must construct a flexible network that responds easily to future customer demands. There have been important developments in WDM technology that have made it possible to improve network capacity and flexibility significantly[1]. If we deploy WDM systems that use SM optical fiber, we can also obtain a cost advantage, because we have already constructed networks using this fiber. First, we investigated the optical loss characteristics of SM optical fiber cables at various wavelengths. Moreover, we measured the optical transmission characteristics of installed SM optical fiber cable networks in a metropolitan area with a view to WDM system applications. This paper describes these measured results.

2. Optical network and cable structure

Figure 1 shows the configuration of an optical fiber network. SM fiber cables are used in both trunk and access networks. A trunk

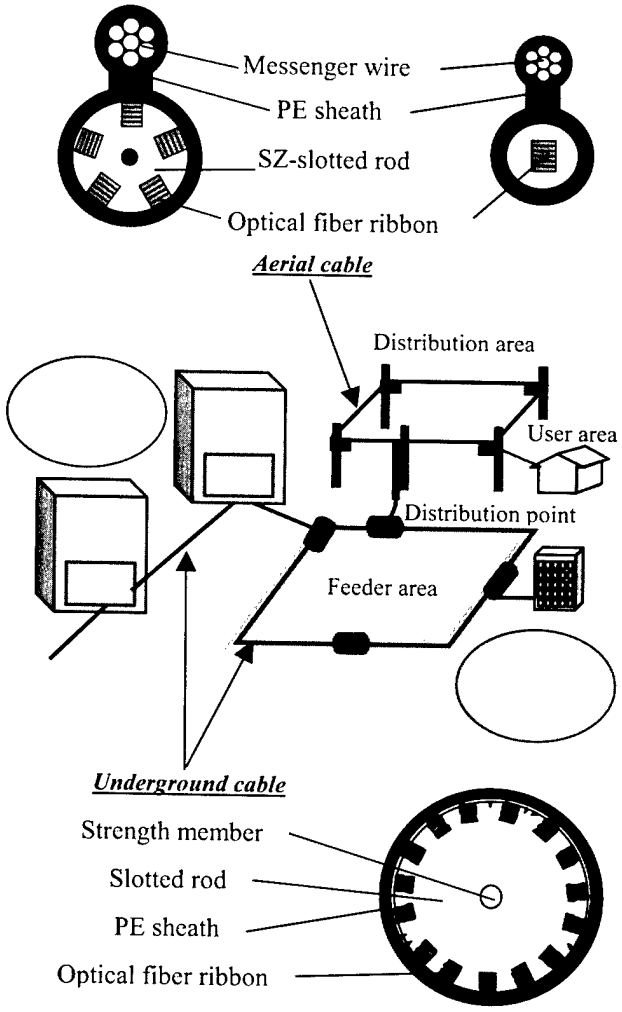


Figure 1. Configuration of optical network and cable structure

network is a line between central offices. An access network consists of 4 areas, the central office area, feeder area, distribution area, and user areas from a central office to residential premises. The feeder area extends from a fiber termination module (FTM) or integrated distribution module (IDM) in a central office[2] to a distribution point. In the distribution area, aerial cable is connected to feeder cable at a distribution point, and led to a customer via telecommunication poles.

We mainly use underground cables for trunk networks and for the feeder areas of access networks. Aerial cables are used for the distribution areas of access networks. The underground cables are composed of fiber ribbons, a slotted rod, strength member water-blocking-tape and polyethylene (PE) sheath[3]. Several fiber ribbons are accommodated tightly in the slots in the rod and stacked closely at the bottom of each slot. We use two kinds of aerial cable. When the cable contains more than 100 fibers, we use SZ slotted-rod type optical fiber cable in which fiber ribbons are stored. This is a self-supporting type structure with excess length[2],[4]. For low-fiber-count regions, we adopt a simple cable structure with no slotted rod, and we stack the fiber ribbons in the cable sheath. This is also a self-supporting type structure with excess length[3]-[5].

3. Cable characteristics

3.1 Loss characteristics of SM optical fiber cable

We measured the mechanical and temperature characteristics of these underground and aerial cables at the following wavelengths; 1.31, 1.35, 1.40, 1.45, 1.50, 1.55, 1.60, 1.625 and 1.65 μm . We incorporated SM optical fibers based on ITU-T G.652[6] in each cable sample, and specifically used a fiber in which optical loss can be induced comparatively easily by bending.

3.2 Underground cable

We investigated 40-, 300-, and 1000-fiber cables.

3.2.1 Mechanical characteristics: Table 1 shows the test conditions and measured results for various mechanical tests. The optical loss increase was 0.06 dB or less at each wavelength indicating very stable levels of performance.

Table 1. Mechanical characteristics

Item	Condition	Underground cable	Aerial cable
Bend	Radius 160-240 mm, 10 cycles	< 0.06 dB (40-,300-1000-fiber cable)	< 0.05 dB (40-,100-fiber cable)
Squeeze	Radius 250-600 mm, 1960-3430 N, 4 cycles		
Twist	±90 degrees		
Impact	1 kg, 1 m		
Crush	1960 N/ 10 cm		

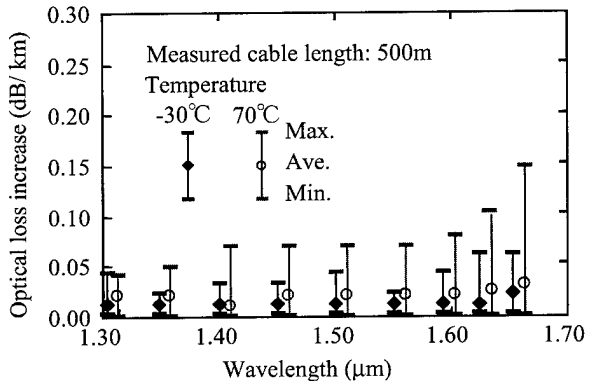
3.2.2 Temperature characteristics: We installed a 500-m optical cable in a thermostatic chamber, and performed a heat cycling test (-30 to +70℃). Figure 2 (a) shows the measured optical loss increase in a 1000-fiber cable. Although optical loss tends to increase at longer wavelengths, we consider this characteristic to be stable up to 1.625 μm, as it was 0.10 dB/ km or less. Other cables produced similar results.

3.3 Aerial cable

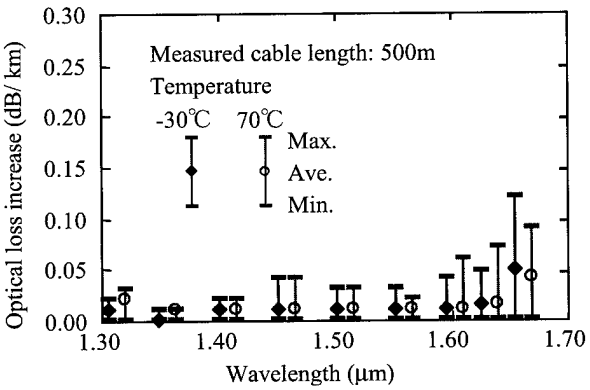
All the tests were performed on 40- and 100-fiber cables.

3.3.1 Mechanical characteristics: Table 1 also shows the test conditions and measured results of our mechanical tests on aerial cable. The optical loss increase was sufficiently small as we found with the underground cable.

3.3.2 Temperature characteristics: A complete cable was suspended between communication poles in a thermostatic chamber. Figure 2 (b) shows the optical loss increase and wavelength of 100-fiber cable. The optical loss increase was less than 0.13 dB/ km over the whole wavelength range. Other cables produced similar results.



(a) 1000-fiber cable (Underground cable)



(b) 100-fiber cable (Aerial cable)

Figure 2. Temperature characteristics

3.3.3 Vibration characteristics: It is necessary to study the effect of wind-induced vibration, especially as regards aerial

cables. We stretched a 35-m aerial cable and vibrated it one million times in a quadratic mode. Figure 3 shows that the optical loss change during the whole test was 0.02 dB/35-m or less at each wavelength, and very stable.

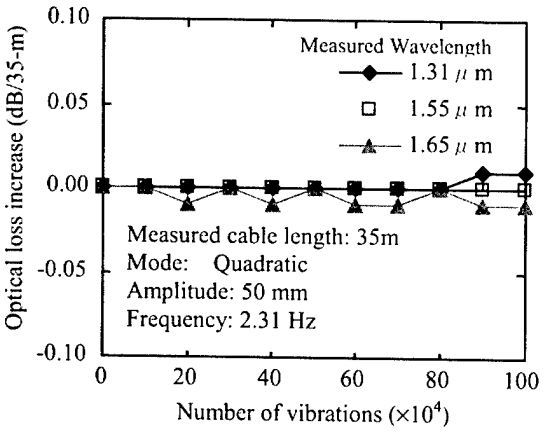


Figure 3. Vibration characteristics (100-fiber cable)

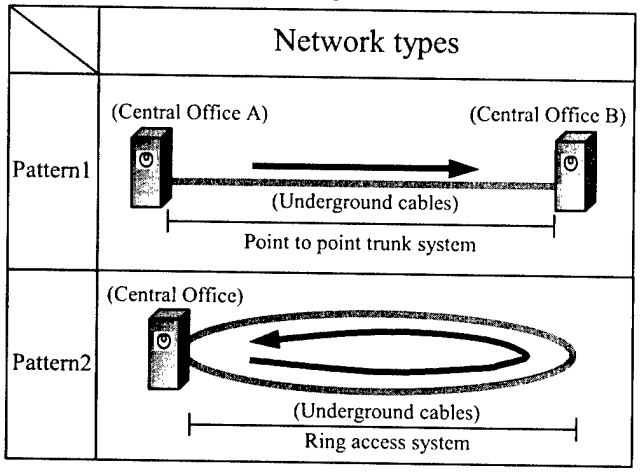
From the above results, we comfirmed that each cable has stable optical loss characteristics up to a wavelength of 1.625μm as regards WDM system applications.

4. Network characteristics

4.1 Transmission characteristics of installed SM optical fiber cable networks

The optical fiber networks that have already been installed and joined several optical fibers can be classified into two network types. These are the point to point (trunk network: pattern 1) and the ring (access network: pattern 2). We use these configurations to investigate the transmission performance in these networks constructed using long distance cable (pattern 1), and underground cable only (pattern 2). We measured the optical loss and chromatic dispersion characteristics of these two types of network in the 1.25 to 1.65 μm wavelength range.

Table 2. Network configurations in the field



4.1.1 Optical loss characteristics: Figure 4 shows the optical loss difference between wavelengths of 1.31 and 1.55 μm with pattern 2. The average optical loss difference is 0.13 dB/km and the optical loss at 1.55 μm is lower than that at 1.31 μm. Other patterns produced similar results. This showed that the network has small wavelength dependence of the optical loss characteristics.

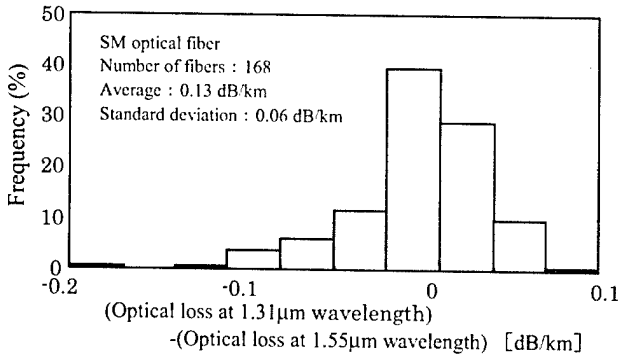


Figure 4. Optical loss difference between 1.31μm and 1.55μm wavelengths

In addition, Figure 5 shows the optical loss difference between wavelengths of 1.55 and 1.625 μm with pattern 2. 1.625 μm is on the edge of the L-band, and the optical loss at this wavelength increases easily when the optical fiber is bent.

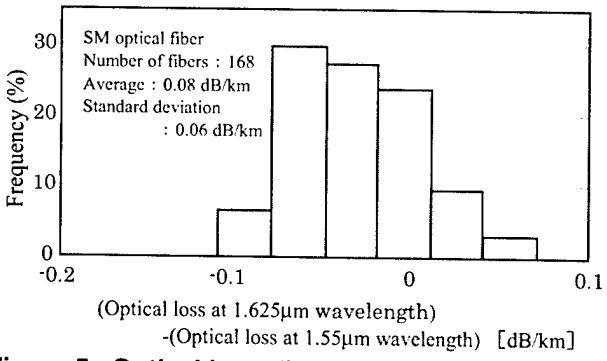


Figure 5. Optical loss difference between 1.55μm and 1.625μm wavelengths

Table 3. Optical loss difference between wavelengths of 1.55 and 1.625 μm

	Average (dB/km)	Standard deviation (dB/km)
Pattern 1	0.02	0.01
Pattern 2	0.08	0.06

Table 3 shows the average and standard deviation of the optical loss difference between wavelengths of 1.55 and 1.625 μm for each pattern.

Based on the above results, we estimated the optical loss difference between wavelengths of 1.55 and 1.625 μm. We used eq. (1) to calculate the optical loss difference with 99.9% probability[9].

$$\text{Optical loss difference} = \text{Ave.} \times \text{transmission distance} + 3.09 \times (\text{Sd}^2 \times \text{transmission distance})^{1/2} \quad (1)$$

Where Ave. is the average optical loss difference and Sd is the standard deviation of the optical loss difference. Table 4 shows the calculated results using eq. (1) and Table 3. This shows that the maximum optical loss difference is less than 2 dB. Thus, we found that the optical loss difference between wavelengths of 1.55 and 1.625 μm is small.

Table 4. Calculated results

	Optical loss difference between wavelengths of 1.55 and 1.625 μm	Transmission distance
Pattern 1	1.0 dB	40 km
Pattern 2	1.9 dB	15 km

4.1.2 Chromatic dispersion characteristics: Figure 6 shows the measured chromatic dispersion characteristics. The chromatic dispersion difference between the maximum and minimum value for each wavelength is less than 2 ps/nm/km. We found that the chromatic dispersion difference for each wavelength is small. Other patterns produced almost same results.

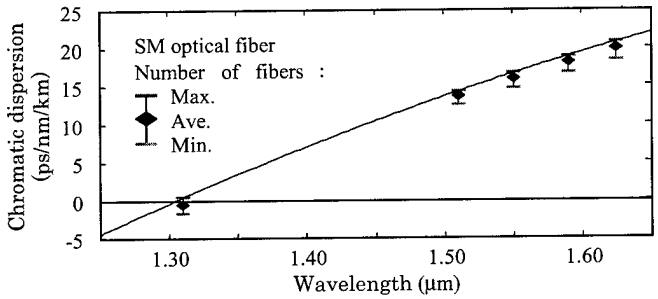


Figure 6. Chromatic dispersion characteristics

Based on the above results, we estimated the chromatic dispersion characteristics using the Sellmeier expression[8]. The maximum value for each wavelength is given by eq.(2)

$$D_{max}(\lambda) = 21.8\,\lambda - 63.1\,\lambda^3 \quad (2)$$

Where $D_{max}(\lambda)$ is maximum chromatic dispersion, and λ is the wavelength. The values calculated using eq.(2) are also shown in Fig. 6.

The relationship between chromatic dispersion, the transmission distance and the transmission rate is expressed in general by eq.(3)[9].

$$B^2 D(\lambda) L \lambda = c \times a \quad (3)$$

With chirp: a=0.061
Without chirp: a=0.5

Where B is the transmission rate, L is the transmission distance and c is the velocity of the light. The relationship between the transmission rate and distance can be calculated using eqs.(2) and (3). The calculation results are shown in Fig. 7.

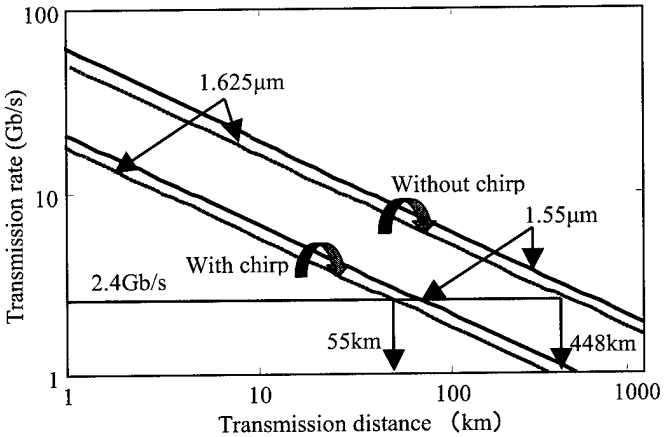


Figure 7. Relationship between transmission rate and distance

A signal can be transmitted 100-km or more at a wavelength of 1.625 μm and a transmission rate of 2.4 Gb/s without chirp. In contrast, the maximum transmission distance is about 50-km at same wavelength and transmission rate with chirp. Thus, we found that the transmission rate and distance depend on the modulation method. Moreover, from Fig. 7, it was also found that the transmission distance at a wavelength of 1.625 μm is about 30% shorter than that at 1.55 μm.

5. Conclusions

This paper described measured SM optical fiber cable characteristics for various wavelengths and the optical transmission characteristics for networks with a view to WDM system applications. The use of SM optical fiber for WDM systems provides a cost advantage, because we have already constructed networks using this fiber. First, we investigated the optical loss characteristics of SM fiber cables at various wavelength. Then, we measured the optical loss and chromatic dispersion characteristics of installed SM optical cable networks.

We confirmed that optical transmission was stable up to a wavelength of 1.625 μm (upper wavelength of L-Band).

6. Acknowledgments

The authors thank K. Nishizawa, H. Shido, E. Maekawa, T. Sugie and N. Sato for their support and encouragement.

7. References

[1] H.Kawata et al, IEICE TRANS. COMMUN., Vol.E83-B, No.10, pp. 2348-2354 (2000).

[2] N. Tomita et al, NTT Review, Vol.12, No.2, pp.90-99 (2000)

[3] H. Iwata et.al, 44th IWCS, pp.627-634 (1995).

[4] H. Iwata et.al, 46th IWCS, pp.4-11 (1997).

[5] J. Kawataka et al, 49th IWCS, pp. 293-297 (2000).

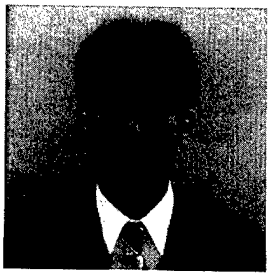
[6] ITU-T Recommendation G.652

[7] ITU-T Recommendation G.982, AppendixIV

[8] ITU-T Recommendation G.651

[9] F. Koyama et.al., IEEE J. Quanum Electronics, Vol.QE-21, No.4, pp292-297 (1985)

Author: Shigekatsu Tetsutani



NTT Access Network Service Systems Laboratories, NTT Corporation

Tsukuba, Ibaraki, 305-0805, JAPAN

E-mail address: s-tetsu@ansl.ntt.co.jp

Shigekatsu Tetsutani is a research engineer. He was born in 1971 and received B.E. and M.E. degrees in electrical and electronic engineering from Shinsyu University in 1994 and 1996, respectively. He joined NTT in1996 and began to undertake research and development on the design of optical fiber networks.

The Influence of Mechanical and Environmental Effects on PMD Coefficient in Loose Tube Optical Cable Design

Jeancarlo Dotto, Janúncio A. M. Neto, Lucio F. G. Marques and Renato F. Cruz

Furukawa Industrial S.A. Produtos Elétricos

R. Hasdrubal Bellegard, 820 CIC ZIP Code:81450-140 Curitiba - Paraná - Brazil

55-41-341-4335 email address dotto@furukawa.com.br

Abstract

In this work we analyze the mechanical and environmental effects on PMD distribution using different cable design. The relationship between PMD parameter, cable design and environmental effects was obtained using two different cable configuration. The cables designs used in this study were an All-dielectric self-supported loose tube cable (AS) and a Single Jacket Loose Tube Cable for duct and lashed aerial installations (IDC), both with standard G652 Single Mode optical fiber. The statistical method uses the concatenate link approach in determining cable PMD. Laboratory tests results presented are showing the effect of the mechanical stress and environmental variation on PMD coefficient behavior. With these results we also show that is possible to specify a PMD statistical upper limit based on cable configuration and to predict the performance of the optical cable link during lifetime.

Keywords

Polarization Mode dispersion; Loose tube cable; Cable design, Mechanical and environmental effects.

1. Introduction

PMD is a fundamental properties of fiber and optical components in which lightwave signals are split into two polarization modes that propagate with slightly different velocities. PMD effect arises in single mode fiber when circular symmetry is broken by the presence of an elliptical core or by non circularly symmetric stresses, which are induced during drawing and packing process. The loss of circular symmetry removes the degeneracy and causes a birefringence resulting in two polarization modes propagating with two different group velocities along two orthogonal axes. Typically, for SM fiber the intrinsic birefringence varies randomly along its length and from fiber to fiber because of the randomness of the underling geometric and stress irregularities over all fiber. Such irregularities can be intrinsic to the waveguide structure, like non-circularity of the fiber core or extrinsic origin associated to cable design and fiber environmental . Therefore, the causes of PMD in single mode fiber are extremely complex since than beside the mechanical effects, the fiber PMD can be strongly influenced by physical surrounding in which the cables are installed[1].

Today, low PMD values is a fundamental requirement for the current optical transmission rates of 10 Gbit/s and beyond. For example, high PMD is a serious issue for WDM network, particularly when the bit rate increase up to more than 40 Gb/s(ref). Actually, high PMD values is emerging as severe constraints on long-haul multi-channel high data-rate systems[2,4]. Therefore, from the practical point of view, it is imperative that cable's manufacturer may guarantee low PMD of cabled fibers. It is well know that this is a complex problem since cabled fibers are submitted to tension, bending and compression during cabling process and after installation, beside that the optical cables are continuously submitted to hash environment and strong temperature variation during lifetime.

In order to guarantee low PMD of Cabled fibers is fundamental optimize all parameters involved in the cable design and understand the effects of cabling process on PMD parameter. In this paper we analyze the influence of mechanical and environmental effects on PMD parameter taking into account the cable design.

2. Cable Design

The relationship between PMD parameter variation , cable design and environmental effects was obtained using two different cable configuration. The cables used in this study were an All-dielectric self-supported loose tube cable and a Single Jacket Loose Tube Cable for duct and lashed aerial installations, both with standard G652 Single Mode optical fiber.

Table 1 describes cables parameters . The main difference in these cables designs are the difference in the lay length, central member diameter exposing the fiber to different bending strain. The theoretical bending strain was estimated considering the fibers inside the loose tube stranded around the strength member and the cable without bending. For the inner duct cable an additional cable was analyzed regarding the number of fiber per tube, since than it has been suggest that the higher fiber packing may lead to a higher PMD value distribution.

Table 1- Summary of Characteristics

	IDC-30 fibers	AS - 36 fibers
Fiber per tube	6	6
Quantity of tubes	5	6
Lay length maximum	4 mm/10m	10mm/10m
Internal diameter of loose tube	1.7mm	1.7mm
External diameter of loose tube	2.5mm	2.5mm
Lay length	80 mm	90 mm
Bending Strain	0.11%	0.20%

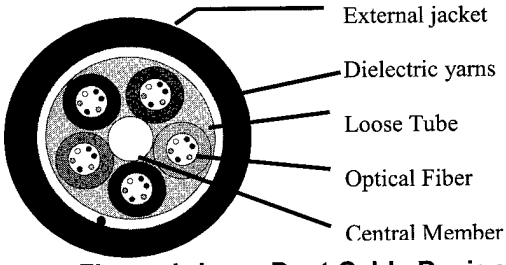


Figure 1- Inner Duct Cable Design

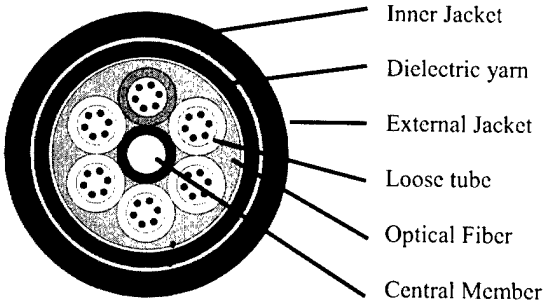


Figure 2 – Self Support cable

These cables were designed with different lay length, tube dimension and central member diameter, the fibers are submitted to different bending strain. However, the fibers are submitted to several degree of stress associated with the cable design type, which can induce a significantly variation on birefringence of the fiber in all length of the cable fiber.

3. Statistical Characterization of PMD

It is well know that PMD is a stochastic attribute on a fundamental level: it varies in magnitude randomly over time and wavelength . The PMD of a long fiber at a given wavelength will change in response to its environment, requiring that it be expressed not a single number, but by means of a probability distribution function [1]. However, cabled fiber PMD shall be characterized on a statistical basis not on an individual fiber basis. A good approach is to consider the statistical properties of the PMD distribution generated from the cabling process. Two method can be used to specify the characteristics of the PMD distribution: The first one is relate with the PMD coefficient variation of concatenated links[5] and the another one is relate to the variation in DGD value of concatenated links. This work apply the first mentioned method , which use the concatenation by quadrature average . In this case, the PMD value of a link is defined as the square root of the sum of squares of PMD values of the cable section that are used to form the link :

$$X_M = \sqrt{\frac{\sum_{i=1}^{M} x_i^2}{M}} \qquad (1)$$

Where:

M number of equal length cable comprising the link

x_i The PMD coefficient of fiber in an individual cable (ps/sqrt(km))

Xm The PMD coefficient of a concatenated link of M cables (ps/sqrt(km))

The Probability distribution of the link coefficients depends on the distribution of the cable PMD coefficients and the M, where the maximum link coefficient for a given distribution (PMD_{max}) is defined in terms of a small probability level , Q, which is the probability that a link PMD coefficient exceeds the maximum PMD. The distribution of the link PMD coefficient can be obtained by using different methods [4,6,7]. All statistical analysis in this work were made using Monte Carlo technique.

4. Experimental and Statistical Analysis of PMD for each cable configuration

The statistical analyses on the PMD coefficients was made using the described cable configuration. Experimental cables were manufactured to assess the effect of the mechanical stress and environmental variation on PMD coefficient behavior . It was performed measurements in one hundred cabled fibers for each configuration, including some high intrinsic PMD coefficient values of the optical fiber (up to 1.0ps/sqrt(km)) just for purpose evaluation. The experimental PMD coefficient was obtained using the interferometric technique with a 1.55 μm light source. All measures were made in a room where a temperature was keep constant at 21 °C. The experimental statistical results for individuals PMD coefficients on cabled fibers are given in table 2, and the characteristic distribution of PMD coefficient is given in figures 3 and 4.

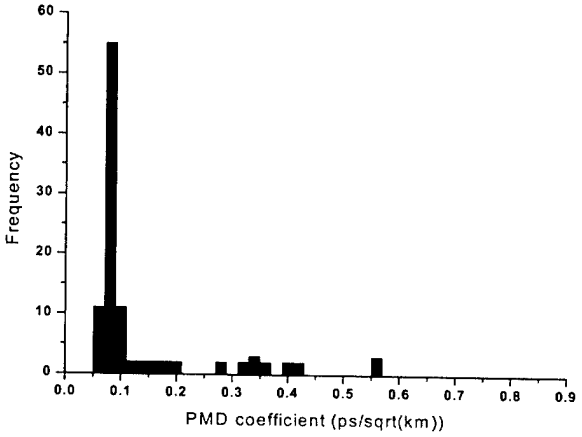


Figure 3 - PMD coefficient distribuition for AS cable

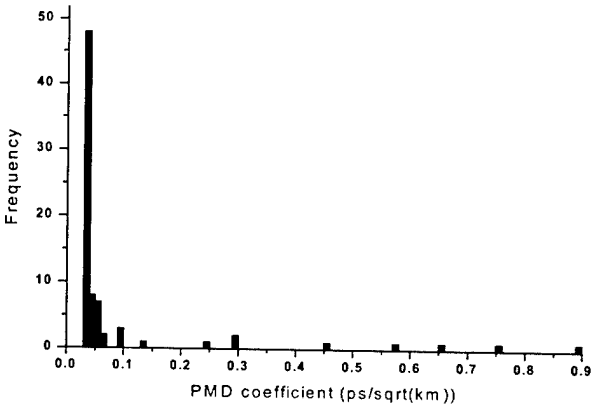


Figure 4 - PMD coefficient distribution for IDC cable

Table 2. PMD coefficient of cabled fibers for each configuration (ps/sqrt(km))

	Cable AS	Cable IDC
Mean	0.137	0.092
Median	0.082	0.036
Maximum	0.568	0.899
Minimum	0.050	0.031

From the practical point of view a real transmission system is made from many spliced section cabled fiber. For example, a typical optical link is build of at least 20 equal length cable sections. However, using the experimental PMD cabled fiber distribution given in figure 3 e 4 was possible to estimate the PMD coefficient for a single fiber path in a hypothetical concatened link of 20 equal lengths in accordance with TIA/EIA TSB 107. The PMD link coefficients for each cable configuration was calculated using Monte Carlo technique by randomly selecting 20 values from the respective distribution, and added in quadrature according equation 1. The process of calculating the PMD link coefficient was repeated until a sufficient number of values has been calculated. In order to obtain probability levels of 10^{-4}, was necessary to take 100,000 of values. The distribution of PMD parameter for each cable configuration is given in figures 5 and 6 respectively.

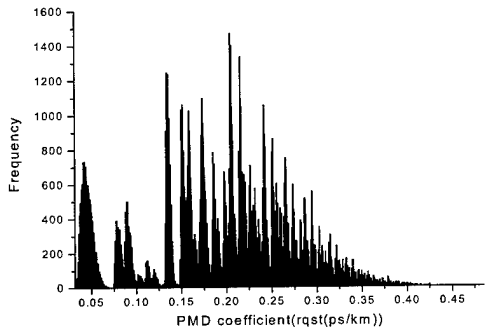


Figure 5. PMD Coefficient Distribution for a hypothetical link build from IDC-30 cable

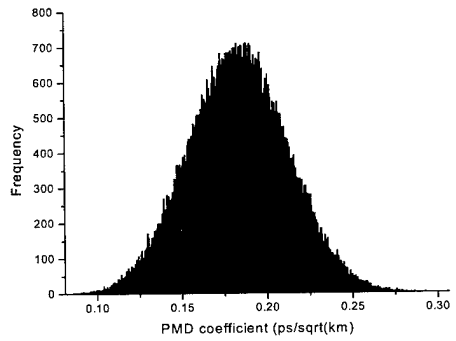


Figure 6. PMD Coefficient Distribution for a hypothetical link of AS cable.

The PMD coefficient distribution obtained given in figure 5 and 6 shows different trends. For the IDC cable design , the maximum PMD coefficient value expected in the link is about 0.47 ps/sqrt (km). For the AS-Cable, the value for a concatenated link was 0. 30 ps/sqrt (km).

5. Mechanical and Environmental Effects on PMD Coefficient

The mechanical and environmental effects on PMD coefficient variation were accessed submitting the cables to the following tests: tensile strength, compression, bending and temperature cycling. Due to the random behavior of the PMD parameters, it is very important that these tests simulate severe mechanical and environmental effects on the cable structure and simulate as near as possible the environment conditions where the cable is installed. The tests were made building two links for each cable configuration. The link for IDC cable was 80 km long splicing 20 fibers together and for AS cable the link was 65 km long splicing 36 fibers together. Both links were built splicing fibers chosen randomly. The total optical loss for the links was respectively 19 and 15 dB.

5.1The environmental evaluation

The environmental effects on PMD coefficient was analyzed submitting both links to the temperature cycle test, where the temperature varies from -40°C to 70°C[8], according to BELLCORE Standard[8] .

During the test, the PMD coefficient variation was monitored at each one hour during the temperature cycle. Table 3 shows the PMD coefficient variation between the reference value measured at 20°C and the average value measured at each temperature cycle.

Table 3 - PMD coefficient variation during thermal cycle in relation to the reference.

	Cable AS	Cable IDC
Maximum variation positive cycles	-30%	-60%
Maximum variation negative cycles	33%	44%

It was observed a strong reduction of PMD Coefficient for IDC cable when compared if AS cable, indicating that the stresses in the IDC cabled fibers are more intense than the AS cable fibers.

5.2 The mechanical evaluation

The effects of fiber strain on PMD coefficient were obtained applying different tension load, taking into account the cable's weight per its length. During the test, the PMD parameter variation was monitored during one hour for each applied load. For each configuration, the maximum load was defined monitoring the total optical power. The tables 4 and 5 show the PMD coefficient variation under different loads for IDC and AS cable respectively.

Tab.4 - PMD coefficient variation under different loads for IDC-Cable

Load	Load(N)	Coef. PMD (ps/sqrt(km))
	No load	0,110
1,0x the weight*	600	0,085
1,5 x the weight	900	0,082
2,0 x the weight	1200	0,075
2,5 x the weight	1500	0,127
3,0 x the weight	1800	0,114
3,5 x the weight	2100	0,111
4,0 x the weight	2400	0,111
	No Load	0,079

Tab.5 - PMD coefficient variation under different loads for AS-Cable

Load	Load(N)	Coef. PMD (ps/sqrt(km))
	No load	0,162
1,0 x the weight	900	0,191
1,5 x the weight*	1350	0,155
2,0 x the weight	1800	0,149
2,5 x the weight	2250	0,159
3,0 x the weight	2700	0,154
3,5 x the weight	3050	0,156
4,0 x the weight	3600	0,154
4,5 x the weight	4050	0,158
5,0 x the weight	4500	0,167
5,5 x the weight	4950	0,18
	No Load	0,191

The macrobending effects were analyzed submitting the cables to different bending radius. The tests were made[9] simulating the bending conforming the cable designs, after that, the bending radios was reduced for simulate a critical situation on the links. The PMD parameter variation under different bending were monitored during one hour. During this period, was made 30 measurements for each 2 minutes. The table 6 and 7 show the PMD parameter average results for IDC and AS cable respectively.

Table 6. The PMD parameter variation due to macrobending for IDC cable design.

Radius (mm)	PMD Coef. (ps/sqroot(km))
Reference	0,079
130 *	0,118
100	0,081
100	0,092
Without Bending	0,080

* Limit defined in the Standards

Table 7. The PMD parameter variation due to macrobending for AS cable design.

Radius (mm)	PMD Coef. (ps/sqroot(km))
Reference	0,167
140	0,133
160*	0,154
180	0,149
Without Bending	0,161

The effects of compression on PMD parameter were obtained submitting the cables to different compressive loading. The compression load was applied taking into account the maximum load defined in Standards[8,9,10]. Which requires loss attenuation increase less than 0.1 dB. The results of the test are given in table 8 and 9 for each cable configuration respectively.

Tab. 8. PMD coefficient variation due to compressive loading for IDC cable design

Load (N)	Coef. PMD (ps/sqrt(km))
Reference	0,080
500	0,080
1000	0,077
1500	0,081
2000	0,081
2500 *	0,096

Tab. 9. PMD coefficient variation due to compressive loading for AS cable design

Load (N)	Coef. PMD (ps/sqrt(km))
Reference	0,140
1000	0,125
1500 *	0,125
Return	0,167

The PMD coefficient for both links associated with mechanical and environmental tests showed that there are some influence of cable design and PMD coefficient. The variation of PMD coefficient under different loading were more significant for the IDC cable. The same behavior was observed for macrobending tests. The effects associated with compressive loading were insignificantly. Regarding temperature test, was observed a strong reduction of PMD coefficient for IDC cable, compare with AS Cable, indicating that the stresses in the fibers on IDC cable is more intense than the AS cable. coefficient when two consecutive temperature cycle is performed.

6. Conclusion

The influence of mechanical and environmental effects on PMD coefficient using two different cable design was studied. The PMD coefficient distribution was obtained using Monte Carlo Method. The maximum value with

probability of 0.0001 was obtained for both cables. The simulation showed lower values than individual fiber cabled values.

The mechanical and environment tests showed that PMD coefficient is more affected under tension effects. The experimental results using the two cable design for PMD coefficient show also lowest value on the link for both cables. The better performance observed on Self Support cable is associated with the cable design since that for this type of cable the fibers are much more mechanically protected than inner duct cable. However, when submitted to different efforts, the stresses induced on cabled fiber is less significant than for IDC cable, which is related with less birefringence variation on the fiber link. The relationship between Monte Carlo analysis and experimental results allowed us to predict a indication of maximum PMD likely to be encountered in a concatenated link, since than the equivalence between the Monte Carlo simulation and the experimental results showed good agreement. was showed that the bending strain defined in cable project influenced the PMD link coefficient.

7. Reference

[1] G.J.Foschini and C.D.Poole, "Statistical theory of polarization dispertion in single mode fiber", Journal of Lightwave Tecnology, Vol. 9, No 11, pp 1439-1456 (1991).

[2] S.A.Jacobs, J.J. Refi and R.E.Fangmann, : Statistical estimation of PMD coefficients for system design", Electronics Letter, Vol 33, No 7, pp 619-621 (1997).

[3] P.A .Andrekson, "High speed soliton transmission on installed finers"OFC 2000, TuP2, altimore, USA, March 2000.

[4] H.Bulow., "Measument of the maximum speed of PMD flutuation in istalled field fiber", Tech. Dig. ECOC 1998, S4.

[5] TIA/EIA TSB 107 , "Guideline for the Statistical Specification of Polarization Mode Dispersion on Optical Fiber Cables", November 1997.

[6] Jscobs, S., "Statistical Estimation of PMD Coefficient of Fiber Paths", National Fiber Optics Engineers Conference, September 1997 USA.

[7] Patel, J. and Read, C., Handbook of the Normal Distribution, Marcel Dekker, Inc., New York, 1982.

[8] BellcoreGR-20

[9} NBR 14103 – Cabos Ópticos Dielétricosubterrâneo

[10] NBR 14160 – Cabos Ópticos Aéreos Auto Sustentados

8. Authors



Jeancarlo DOTTO – Furukawa Industrial S.A.
R. Hasdrubal Bellegard, 820 CIC 81450-140
Curitiba – Paraná – Brazil

Jeancarlo Dotto joined Furukawa Industrial S/A. in 2000 receiving his B.S. degree as an Electrical Engineer from Federal Center of Technological Education (CEFET-PR). He is envolved in the optical fiber and cables evaluation for Quality Department.

Januncio A. M. Neto - – Furukawa Industrial S.A.
R. Hasdrubal Bellegard, 820 CIC 81450-140
Curitiba – Paraná – Brazil



Januncio A. Medeiros Neto received his B. S. degree from Federal University of Rio Grande do Norte (UFRN) and M. S. and PhD. In Physics from University of Campinas (UNICAMP) in 1991. After post doctoral appointment at ORC-University of Southhampton – England, he joined UNICAMP as research associated. In 1998, he joined Federal Center of Technological Education (CEFET-PR) as research fellow and Furukawa Industrial S/A. as consultant. He has worked in various areas of glass science such as non-oxide glass for optical fiber and component reliability.



LUCIO F. G. Marques – Furukawa Industrial S.A.
R. Hasdrubal Bellegard, 820 CIC 81450-140
Curitiba – Paraná – Brazil

Lúcio F. G. Marques joined Furukawa Industrial S/A. in 1997 receiving his B.S. degree as an Electrical Engineer from Federal University of Paraná (UFPr). He has been envolved in the optical fiber and cables evaluation techniques. He is currently Product Engineering.



RENATO Flávio Cruz– Furukawa Industrial S.A.
R. Hasdrubal Bellegard, 820 CIC 81450-140
Curitiba – Paraná – Brazil

Renato Flávio Cruz received his Chemical Engineer degree from Universidade Federal do Paraná (UFPr) in 1988. He joined Furukawa Industrial S/A. in February 1989 since then he has been involved in the development of materials for telecommunication cables. He is currently responsible for the Cable Development Engineer Management.

An Analysis of PMD Variability of Single Slotted Core Cabled Fibers

Masakazu Nakano and Makiko Miura
Lucent Technologies Yazaki Ltd.
1157-106, Hotozawa, Gotemba-city, Shizuoka-Pref., 412-0046, Japan
+81-550-89-1428 nakano@lt-y.co.jp

Abstract
The Japanese service providers have begun installing 10 Gbit/sec DWDM transmission systems. Coinciding with this has been a rapid growth in the rate of deployment of G.655 Non-zero dispersion fiber (NZDF) in new network construction, especially in the Japanese backbone. The target transmission system of that network is 40Gbit/sec, over 250 to 450km in terrestrial lengths. Service providers are concerned with the PMD and chromatic dispersion performance of these cables in the field. The cable is a concatenation legacy network consists of G.655, G.652 and G.653 fibers. In this report, we study the PMD variability of several kinds of fiber commonly used in Japanese terrestrial field. The result of our analysis indicates that the fiber mode field diameter is related to the PMD variation under stressful conditions.

Keywords
PMD variation, MFD, Single slotted core cable, G.655, G.652, G.653

1. Introduction
In the last couple of years, G.655 fiber cable has had the limelight in Japan and there has been rapid growth in the rate of deployment in the backbone optical fiber network. However, for replacement of legacy cable, there is serious difficulty with upgrading the network, since in Japan there are very few available locations for installing brand-new terrestrial optical fiber cables. Depending on the time frame of 40Gbit/sec transmission deployment, service providers may be forced to initially use these mixed fiber networks for 40Gbit/sec. The most common cable type on that network is single slotted core helical stranding cable with encapsulated 4-fiber ribbons. This cable is usually has two or three different fiber types such as NZDF, G.652 matched clad standard single mode fiber (SMF) or G.653 dispersion shifted fiber (DSF).

The authors have previously reported that the cabled fiber PMD performance has some variation under stressful conditions such as mechanical and environmental test condition [1]. That result indicated the possibility that the cabled fiber, which has low PMD performance before installation, may appear higher PMD in the field. We experimentally found differences in PMD performance of NZDF and SMF in the same hybrid cable. This means that the PMD characteristic of cabled fiber is related to fiber characteristics because of the manufacturing process was significantly no difference between each fiber type on that cable.

In this study, we investigated the PMD variation characteristics of 200-fiber count single slotted core helical stranding cable with G.655, G.652 and G.653 fibers. This is a very common cable structure found in the Japanese backbone network. The main purpose of this experiment was investigation of the relationship between PMD performance and MFD differences.

2. The Experimental Cable Structure
Table 1 shows the detail of experiment fibers and cable used in this study. We chose several fiber types that are used in the terrestrial part of the Japanese field. Figures 1 to 3 show the schematic of the experimental cable that has four different fiber types in one slot-rod.

Table 1. Detail of experimental fiber and cable

Fiber parameter				
Parameter	NZDF-S*	NZDF-L*	DSF	SMF Matched clad
MFD (μm)	8.4+/-0.6	9.2+/-0.5	8.0+/-0.8	10.4**
ITU category	G.655	G.655	G.653	G.652
Slot #	#1	#3	#5	#7
Ribbon parameter				
Type	Encapsulated 4-fiber ribbon			
Thickness	0.4 mm			
Width	1.1 mm			
Cable parameter				
Max. fiber count	200 fibers			
Tensile strength member	Metallic (7/ ϕ 1.8mm)			
Slot rod diameter	13 mm			
Jacket thickness	1.7mm (w/ Aluminum laminate)			
Cable outer diameter	17mm			

*NZDF-S as Small effective area, NZDF-L as Large effective area

**Typical value

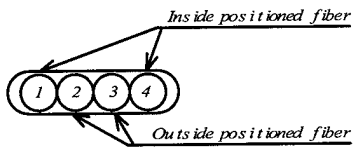


Figure 1. Encapsulated 4-fiber ribbon geometry

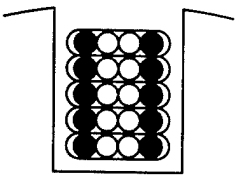


Figure 2. Detail of ribbon position in the slot

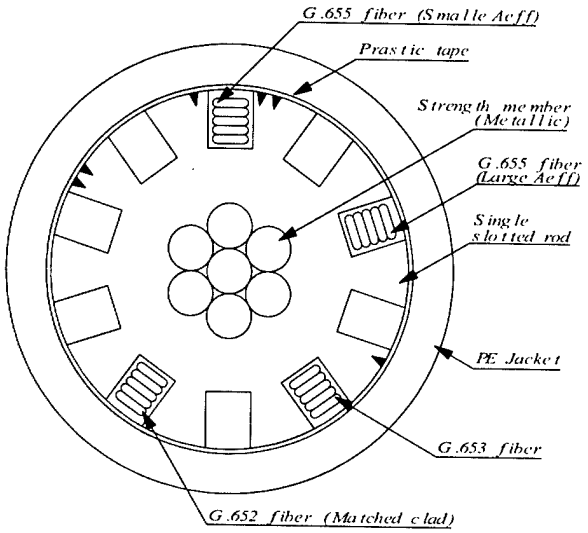


Figure 3. Detail of experimental cable structure

The authors have previously reported that the PMD sensitivity, which was caused by stressful conditions, was dependent on the fiber position in the ribbon. Outside (fiber #1 and #4 on figure 1) and inside positions (fiber #2 and #3) behave differently. Figure 2 shows a schematic of the ribbon layer stacks in the slot. In this study, PMD was measured on the outside positioned fiber (the black paint fibers on figure 2).

3. Relationship between MFD parameter and PMD variation

3.1 MFD parameter

Figure 4 shows the measurement result of MFD on each fiber type that was used in our study. This result was measured by variable aperture method in the far field. The typical MFD at each wavelength was approximated by:

$$MFD(wavelength) = MFD_{slope} \cdot \lambda + MFD_{coef} \qquad (1)$$

where MFD_{slope} is the MFD slope depending on the wavelength range 1310 to 1625 nm, MFD_{coef} is the MFD coefficient of each fiber type. There is strong correlation between MFD_{slope} and MFD_{coef} on a given fiber type that has same refractive index profile. However, this correlation does not apply between the different fiber types. Therefore in this study, we assumed that these parameters are an independent variable.

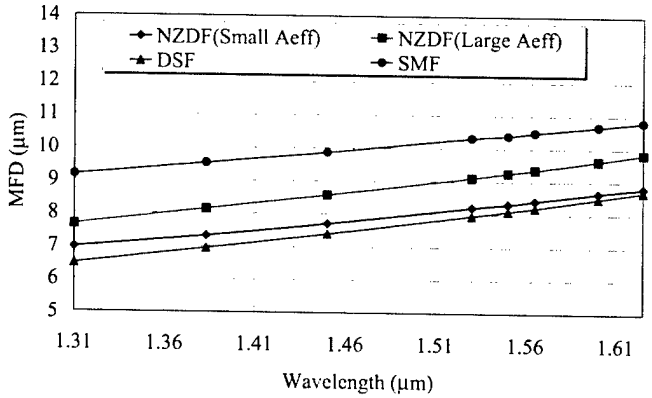
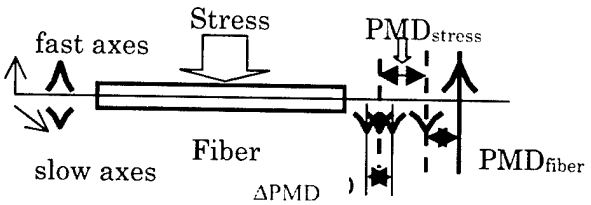


Figure 4. MFD characteristics of experiment fibers

3.2 The model of PMD variation



$$MeasurementPMD = PMD_{fiber} + PMD_{stress} + \Delta PMD \qquad (2)$$

Figure 5. The analysis base model of PMD variation

A number of authors have previously reported on PMD change under stress condition [2][3]. Figure 5 shows our analytical model of the mechanism that varies the PMD under stress conditions. PMD_{fiber} is the intrinsic fiber PMD that is caused by birefringence of initial fiber. PMD_{stess} is basic extrinsic effect (stress, lateral load presser, environmental temperature, manufacturing condition, cable structure etc) and mode coupling. Definition of Δ PMD, which is a standardized Normal distribution, calculated by:

$$\Delta PMD_{average} \pm \quad \Delta PMD$$

might be occur the PMD variation and the $\sigma_{\Delta PMD}$ related to MFD. $\Delta PMD_{average}$ takes zero when the longitudinal distribution of stress is constant. We considered that the PMD_{stress} and Δ PMD might be related to MFD parameter. From this model, the measurement PMD is same as intrinsic PMD when PMD_{stress} is zero.

3.3 Relationship between Δ PMD variation and MFD parameter

We define PMD_{stress} to be the difference in measured PMD of the between any stage in the manufacturing process and the stranding stage (the reference stage). Figure 6 shows the measurement result of $\sigma_{\Delta PMD}$ on each manufacturing process. Theoretically, the best reference for PMD_{stress} is the fiber intrinsic PMD (PMD_{fiber}). However, it is quite difficult to measure intrinsic PMD. The PMD measurement results on individual fibers after stranding was the lowest value on both the average and standard deviation in the

manufacturing process. The largest change of PMD is found after the ribboning process.

The PMD result was measured by Wave-scanning method. Normally, on the coloring and ribboning process, we use many manufacturing machines. During this study, for clear investigation into the effect of MFD differences on PMD performance, we use only one manufacturing machine on both processes for controlling the manufacturing stress on the fiber. The result indicates the $\sigma_{\Delta PMD}$ has a relation to MFD value.

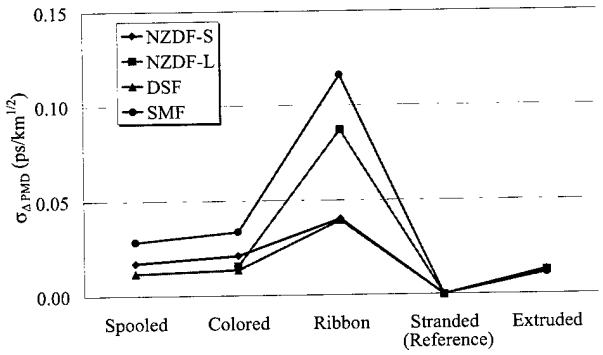


Figure 6. Relationship between PMD change and each manufacturing process

3.4 An analysis result of the PMD variation on manufacturing process

From measurement result of each process, we analyze the relationship between $\sigma_{\Delta PMD}$ and MFD parameter which is shown in formula (1). The $\sigma_{\Delta PMD}$ is related to the MFD parameter by the following empirical formula:

$$\sigma_{\Delta PMD} = \frac{\Delta PMD_{\max(95\%)} - \Delta PMD_{average}}{1.960} \quad (3)$$

$$\Delta PMD_{\max(95\%)} = A \cdot \exp^{B \cdot MFD_{Coef}} \quad (4)$$

$$A = 1.694 \cdot \Delta PMD_{average} + 0.0353 \quad (5)$$

$$B = \frac{6.06e^{-4}}{\Delta PMD_{average}} + 0.1129 \quad (6)$$

where A and B are calculated from $\Delta PMD_{average}$, which is the average differences of measured PMD between each manufacturing stage and stranding stage. $\Delta PMD_{max(95\%)}$ is the maximum ΔPMD on each manufacturing process. We defined that the estimation error ratio was 5% on this analysis.

This analysis indicates that the $\sigma_{\Delta PMD}$ has a relation to MFD parameter and from figure 7, it is shown that the $\sigma_{\Delta PMD}$ becomes large as MFD_{coef}. The result indicates the performance of large MFD fiber has more sensitivity to PMD characteristics than that of small one, which is under stress condition. In this analysis the results take $\Delta PMD_{average}$ because the reference, which was measured PMD of stranding stage, has unknown PMD_{stress}. This means PMD after stranding was not as same as PMD_{fiber}. It is assumed that the longitudinal distribution of stress is the same for each fiber type.

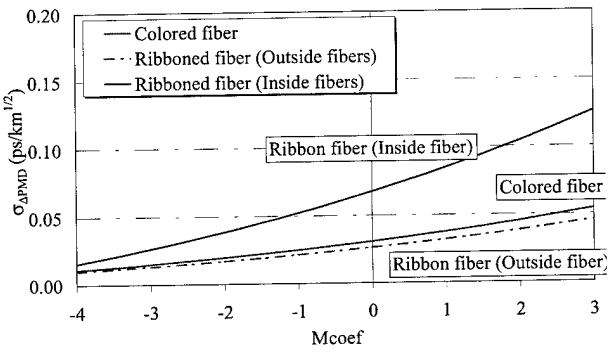


Figure 7. Correlation between MFD_{coef} and $\sigma_{\Delta PMD}$

4. PMD variation of cabled fiber under variable stress condition

4.1 Temperature cycle test condition

This section shows the result of investigation between PMD variation and MFD under temperature cycle test using experimental cable. We tested the 2.16km long cable, which was wound on the 1-meter diameter drum under fixed tensions, with the temperature ranging from -30 to 70 degree Celsius. The temperature was held 3 hour at both -30 and 70 degree Celsius, and changed by 10 degree Celsius per hour. Then the PMD variation was measured with the outside positioned fibers linked (10 fibers of black part in figure2). Measurements were taken on each fiber type at intervals of an hour using Interferometric method.

Table 2. PMD variation under Temperature cycle test condition

Parameter	NZDF-S	NZDF-L	DSF	SMF
σ	0.0134	0.0167	0.0910	0.0109
Average	-0.0067	0.0159	-0.0134	-0.0012
Maximum	0.029	0.053	0.010	0.028
Minimum	-0.028	-0.016	-0.035	-0.029

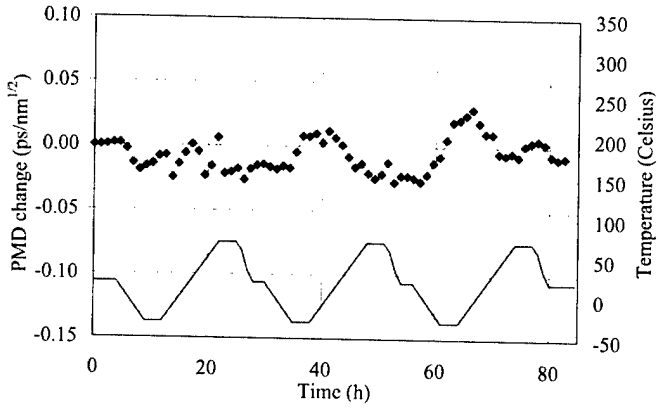


Figure 8-1. Result of Temperature cycle test (NZDF-S; G.655 Small Aeff. fiber)

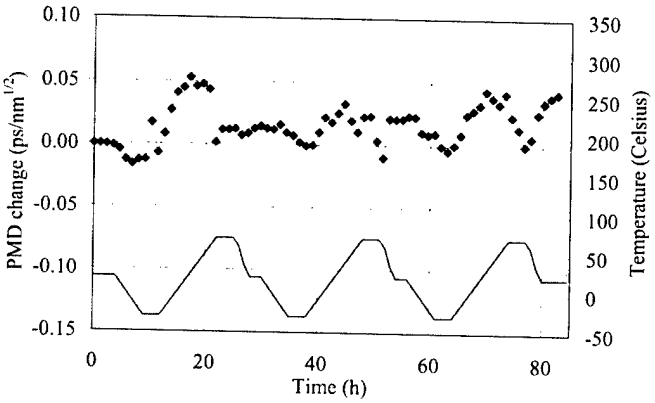


Figure 8-2. Result of Temperature cycle test (NZDF-L; G.655 Large Aeff. fiber)

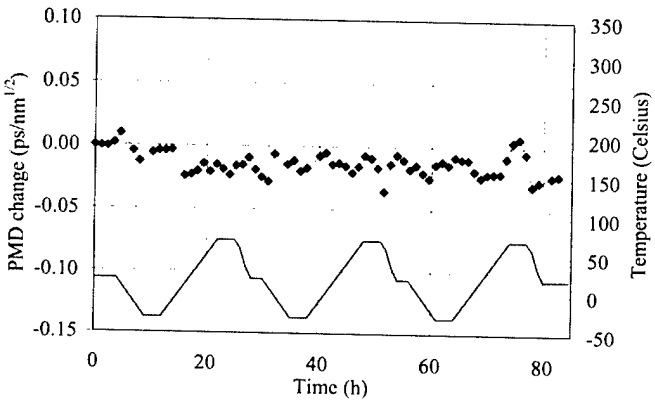


Figure 8-3. Result of Temperature cycle test (DSF; G.653)

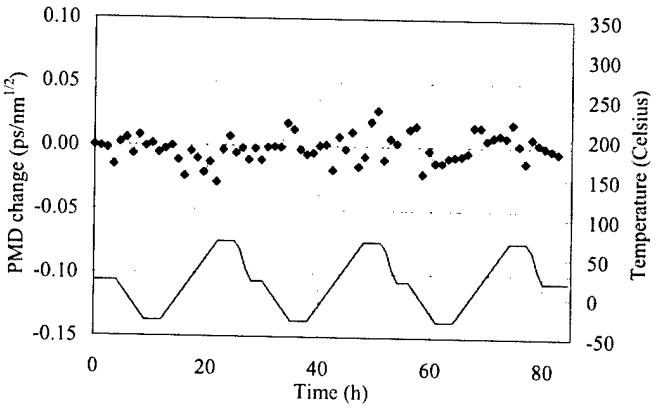


Figure 8-4. Result of Temperature cycle test (SMF; G.652)

Table 2 shows the result summary of PMD variation under temperature cycle test condition and Figures 8-1 to 8-4 show the PMD change of each fiber link. In this analysis, the PMD change was calculated by the difference between each measured PMD and initial PMD (reference).

The result shows that the σ of PMD change (see Table 2) was related to MFD value except SMF result. We assumed that each type of fiber was under same stress conditions by temperature change, because they were in the one cable in the slot and again, manufactured by the same equipment at each process (including a coloring an ribboning process). The test result of SMF shows the better performance than NZDF-S and NZDF-L. However, the results of SMF in figure 8-4 shows more frequent PMD change than that of results of other types of fiber link. The measured fiber link consists of two IDs fiber on NZDF-S, NZDF-L and DSF but SMF link was concatenated by ten IDs fiber. The SMF link has more longitudinal variation of MFD than that of other fiber links. This situation indicates that the wider longitudinal variation of MFD become lower PMD change under the stressful condition. We assumed that this result shows wider longitudinal variation of MFD was caused to PMD_{stress} cancellation but Δ PMD become more wider than small one.

4.2 The relationship between PMD variation and environmental condition

This section reports the PMD variation on similar field condition. During 15 months, the authors were investigating the PMD performance of the cable, which was deployed at the outside of the factory area to simulate an actual field condition. The following result reported the difference of PMD performance between NZDF-S and SMF. The measurement cable type was 600-fiber count helical stranding and the cable length is approximately 0.5km.

Figure 9 shows the measurement result of PMD variation on both of NZDF-S and SMF, which consist of the fiber link from different 20-fiber ID, after 15 months from deployment. Each fiber was concatenated by fusion with link length approximately 10km. The PMD performance of this condition was measured by

Interfelometric test set and it was monitored during 60 hours by 15 minutes interval.

Table 3. PMD variation under similar field condition

Parameter	NZDF-S	SMF
σ	0.0073	0.0189
Maximum	0.017	0.068
Minimum	-0.016	-0.023
Average	0.0018	0.0148

(ps/km$^{1/2}$)

The result, shown in Table 3, reproduces that section 4.1: the PMD variation of SMF was wider than that of NZDF-S. In this experiment, both fiber links, which were concatenated twenty different IDs fiber by random selection, had almost same condition on longitudinal MFD variation. This means that the effect of PMD_{stress} cancellation might be same. Accordingly, the difference of PMD performance was caused by the MFD difference of each fiber types.

From the result of figure 9, the PMD variation was different between Daytime and Nighttime. This experimental cable was deployed at outside of the factory with the straight-line fashion. On daytime, the stress was not applied uniformly in this case since portions of the cable were shaded from sunlight. This situation resulted in wider PMD variation. The longitudinal variation of temperature differences occurred frequent DGD (deferential group delay) change on the output side of fiber link, it generated wider $\sigma_{\Delta PMD}$. On the other hand, nighttime shows a very stable PMD result on both links. In that time, the longitudinal stress level became uniformal and it gave very stable PMD performance. Figures 10-1 and 10-2 show the longitudinal variation of cabled fiber temperature on this experiment cable. The result of this measurement, which was measured by BOTDR, indicates that the above situation. On daytime, the longitudinal cable temperature range was approximately 40 degree Celsius and varied rapidly. At nighttime, the longitudinal variation of temperature was extremely stable than that of daytime.

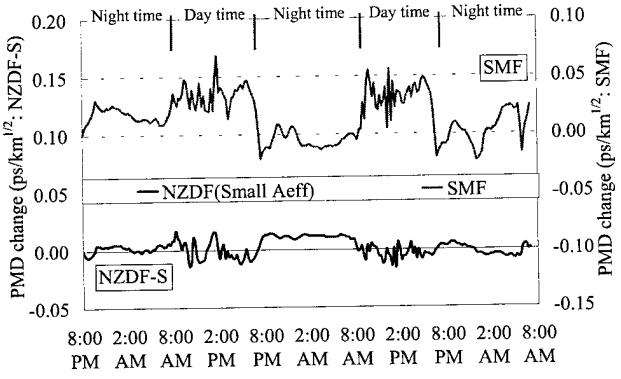


Figure 9. PMD variation of estimation of field condition test result

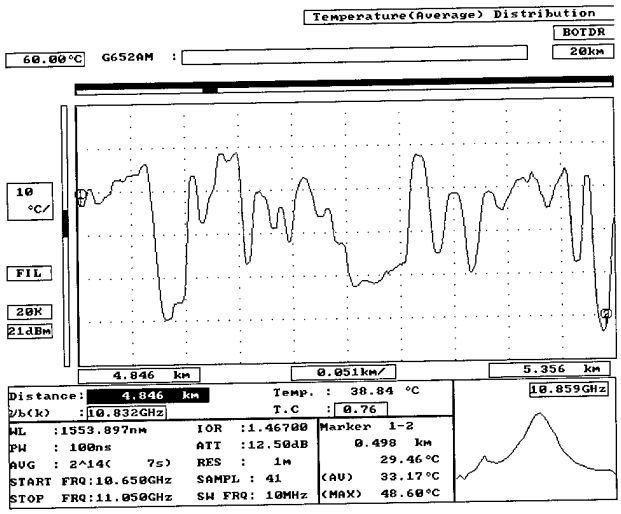


Figure 10-1. Longitudinal variation of cabled fiber temperature on estimation of field condition test cable (daytime)

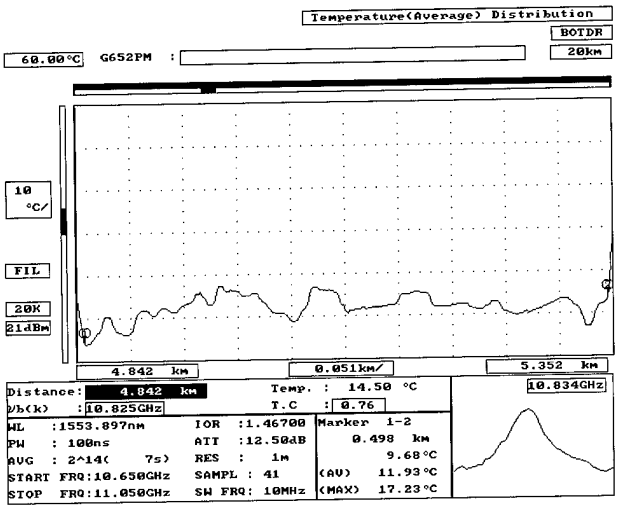


Figure 10-2. Longitudinal variation of cabled fiber temperature on estimation of field condition test cable (nighttime)

Figure 11 shows the PMD variation, which was measured during 15 months, on the same cable condition of above result. The measurement was Wave-scanning method. Again, the link length of each fiber type was approximately 10km. This result shows that the PMD variation over long term was very stable but again, PMD variation of NZDF-S was slightly better than that of SMF. Because of the frequency of measurement, the structure seen in Figure 9 is not presented in Figure 11.

The above experiment result indicates the PMD variation of cabled fiber under stressful condition was related to the measurement time interval. It has some possibility that the faster transmission bit rate system, as the 40 Gbit/sec, might cause the high bit error rate by instantaneous high PMD, which is caused by wider $\sigma_{\Delta PMD}$ element.

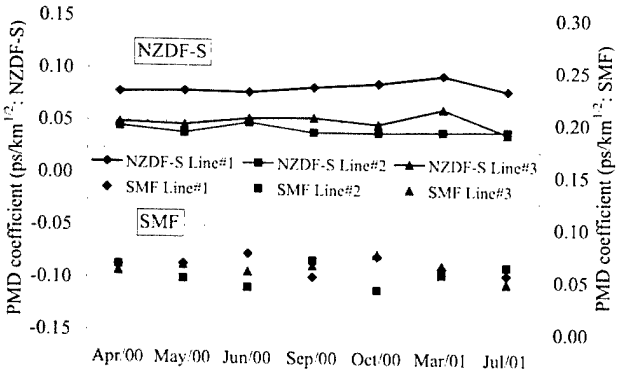


Figure 11. PMD performance of long term monitoring on estimation of field condition cable

5. Conclusions

We investigated the relationship between PMD variation and fiber mode field diameter with 4 different kinds of fibers. The results indicated the following relation to PMD variation characteristic.

- The fiber PMD that was under same stress condition along the fiber length, was depending on the intrinsic fiber PMD (PMD_{fiber}), extrinsic PMD (PMD_{stress}) and ΔPMD variation, which is related to MFD value, and this relation has following formula:

$$PMD_{Total} = PMD_{fiber} + PMD_{stress} \pm \Delta PMD \qquad (2)$$

- When the fiber link has uniform stress along the fiber length and consists of several fiber IDs, the average PMD variation, which is $\Delta PMD_{averagr}$, might indicate lower variation than that if the link consisted of same fiber IDs. However, the instantaneous PMD variation, which is ΔPMD, becomes wider.
- In the case of the fiber link consisting of random MFD fibers and non-random stress, the instantaneous PMD variation, which is ΔPMD, might show extremely wide variation.
- The ΔPMD are related to MFD. Larger MFD fiber show high PMD_{stress} and wider ΔPMD than that of smaller one.

Our result shows that in high-speed transmission networks such as 40Gbit/sec, the instantaneous PMD variation might be considered more important than the average. Finally, small MFD fiber has a possibility to reduce the PMD variation in the stressful environment.

6. Acknowledgments

The authors are thankful to Alan H McCurdy of Lucent Technologies, Yosuke Shimozuru of Lucent Technologies Yazaki for discussion and suggestion of technical issue.

7. References

[1] M. Nakano, M. Miura and T. Sato, "Polarization Mode Dispersion Characteristics of Single Slotted Core, NZD Fiber Ribbon Cable" 49th IWCS, (Nov, 2000)

[2] Franco Cocchini, Antonio Chiantore, Giovanni Carones and Alessandro Ginocenio, "Cable effects on fiber PMD", 45th IWCS, 13 (1996)

[3] M. Artiglia, M. Schiano, T. Tambosso, A. Galtarossa, L. Palmieri and A. Pizzinat, "Reflectometric characterization of distributed birefringence in installed single-mode fibers", 109

Authors



Masakazu Nakano

Lucent Technologies Yazaki Ltd.

1157-106, Hotozawa, Gotemba-city, Shizuoka-Pref. 412-0046 JAPAN

M.Nakano received his B.E. degree from Nihon University in 1991. He has been engaging in Research & Development Department and his main work is development of evaluation technology with optical fiber, ribbon and cable.



Makiko Miura

Lucent Technologies Yazaki Ltd.

1157-106, Hotozawa, Gotemba-city, Shizuoka-Pref. 412-0046
JAPAN

Makiko Miura received her B.E. degree from Akita University in 1997. She has been engaging in Research & Development Department and her main work is development of evaluation technology with optical fiber, ribbon, cable and splicing.

Polarization Mode Dispersion Characteristics of Various High Performance Optical Fibers in Cable

Hiroki Ishikawa[1], Katsuya Nagayama[1], Nobuhiro Akasaka[1], Masaaki Kaino[2], Makoto Shimizu[3], Shinya Takaoka[3]

[1]Yokohama R&D Laboratories, [2]Communication Division, [3]Fiber Optics Division

Sumitomo Electric Industries, Ltd.

1, Taya-cho, Sakae-ku, Yokohama, 244-8588 Japan

Phone: +81-45-853-7164 / Fax: +81-45-851-5300 / E-mail: ishikawa-hiroki@sei.co.jp

Abstract

The polarization mode dispersion characteristics of four types of high performance fibers were measured. The measurement was carried out during loose tube cabling process, under temperature cycling, and after installation.

The tested high performance fibers were non-zero dispersion shifted fiber, effective area enlarged pure silica core fiber, dispersion compensating fiber, and pure silica core fiber. Each fiber has original and specific refractive index profile, so they were expected to have specific PMD characteristics.

The obtained PMD link value of the non-zero dispersion shifted fiber was less than 0.04ps/km$^{1/2}$, during and after cabling process, after installation operation and under temperature cycling. The cabled fibers showed enough low and stable attenuation at 1550nm and 1625nm. These results mean that our original non-zero dispersion shifted fiber is sufficiently applicable for the next generation high bit-rate and ultra long haul optical transmission.

Keywords

Polarization Mode Dispersion; Link-PMD; Non-Zero Dispersion Shifted Fiber; Pure Silica Core Fiber; Dispersion Compensating Fiber; Effective Area Enlarged Fiber; Loose Tube Cable; Wavelength Division Multiplexing.

1. Introduction

In recent years, demands for wide band-width, high bit-rate and ultra long haul transmission systems are significantly increasing with the progress of information technology. In order to meet these demands, we have developed several types of high performance optical fibers. Each high performance fiber has specific advantages respectively, such as low attenuation, low non-linearity, non-zero dispersion over wide wavelength region or dispersion management ability. In high bit-rate DWDM transmission systems, polarization mode dispersion is one of the most considerable properties to use full advantages of these fiber characteristics[1][2]. In this paper, we report measured polarization mode dispersion characteristics of four types of high performance fibers in loose tube cable.

2. High Performance Fibers

We chose four types of high performance optical fibers for our investigation, because of their advantages on long haul transmission, and/or wide band wavelength division multiplexing transmission. In table 1, the refractive index profiles and optical properties of the test fibers are described. The advantages of each fiber are as follows.

(1) Non-Zero Dispersion Shifted Fiber (NZ-DSF) [3].

Our NZ-DSF has positive non-zero dispersion in L-, C- and S-band, in order to prevent FWM generation in these three transmission windows. Therefore the fiber design is optimal especially for future wide band-width WDM systems.

(2) Effective area enlarged Pure Silica Core Fiber (Large A_{eff} PSCF) [4].

Our original large A_{eff} PSCF is low attenuation fiber with pure silica core and it has smaller non-linearity because of its enlarged effective area (approx. 105μm).

(3) Dispersion Compensating Fiber (DCF) [5].

Our DCF has large negative dispersion and high Figure of Merit. Thus it is suitable for dispersion-managed transmission lines. By combining with Large A_{eff} PSCF, low loss and low non-linearity hybrid transmission lines (PureCouple^{TM}) can be realized.

(4) Pure Silica Core Fiber (PSCF)

Pure silica core fiber has extremely low optical attenuation as low as 0.17dB/km because of the highly pure silica in the core portion. This optical fiber is advantageous especially for long haul transmission systems.

3. Experiments

3.1 Test Cable Structure

Loose tube type cable was the trial cable in this analysis to examine PMD behavior of the high performance fibers. We have chosen conventional 144-fiber loose tube cable in which twelve 0.25mm coated fibers were placed in a tube, and twelve tubes were stranded in ROL manner (Fig. 1). The test cable was 19mm in diameter

3.2 PMD Measurement Method

We have used the interferometric technique for PMD measurement in all through the experiment. The measurement system we had chosen was Santec 6000B.

3.3 Original Fiber PMD Measurement

In order to clarify the PMD value of original fibers, we have conducted PMD measurement of fibers before cabling in three different conditions as follows [6].

(a) Spooled condition: The fiber spooled on a bobbin of which the spool diameter was 150mm.

(b) Loose Coil condition: 1,000m of test fiber pieces were loosely coiled and laid flat during the measurement. The coil was 280mm in diameter.

(c) Bare fiber condition: 100m test fiber pieces were loosely coiled in the same diameter as above and immersed in concentrated sulfuric acid to completely remove their fiber coating.

Each condition has advantage and disadvantage respectively. In the spooled condition, the PMD of the same fiber which will be cabled can be measured, though, additional mode coupling and/or birefringence induced by lateral pressure may affect the measured PMD value. In the loose coil condition, the influence of the lateral pressure is much smaller than that of spooled condition, but the measured fiber will not be cabled. The bare fiber condition can eliminate the influence of not only lateral pressure but residual strain caused by fiber coating.

In discussion, we will compare the measured PMD of the fibers in the three conditions with the PMD of cabled fibers and discuss similarity of them.

3.4 Manufacturing Process

In addition to the measurement of fiber PMD, we measured PMD after tube stranding and jacketing, in order to clarify the effect of cabling process on PMD.

3.5 Temperature Cycling

The jacketed cable was subjected to the temperature cycles from –30 to +60 degree C and PMD measurement was made after holding at least eight hours on each temperature. We have conducted three cycles of measurement. During the temperature cycling, the test cable was wound on a wooden reel whose diameter was 1m.

3.6 Cable Installation

In order to examine the stability of PMD and optical attenuation at both 1550nm and 1625nm during the installing operation, we installed the 2km piece of the test cable on the experimental site in Yokohama, and measured the PMD and optical attenuation.

4. Experimental Results

4.1 Optical Attenuation

4.1.1 Manufacturing Process, Figures 2 summarize the measured optical attenuation at 1550nm and 1625nm on original fiber, after tubing, after tube stranding and after jacketing.

As shown by the figures, the fluctuation of attenuation at both 1550nm and 1625nm for each fiber was less than 0.05dB/km. This result means that each high performance fiber is enough stable against manufacturing process.

4.1.2 Temperature Cycling, Figures 3 demonstrates the measured attenuation changes under temperature cycling test at 1550nm and 1625nm.

The attenuation change of each fiber during the temperature cycling was less than 0.06dB/km both at 1550nm and 1625nm. It can be said that each high performance fiber has enough stability against temperature change in loose tube cable.

4.1.3 Cable Installation, In the figures 2, the measured attenuation before and after installation at 1550nm and 1625nm are also demonstrated.

As shown by the figures, the attenuation change of each fiber caused by installing operation was negligibly small both at 1550nm and 1625nm.

4.2 PMD

4.2.1 Original Fiber, Table 2 shows the link-PMD value calculated by central limit method for measured PMD values of each fiber in spool, loose coil and bare fiber condition. As shown in the table, the link-PMD values in spool condition are relatively larger than other conditions. It means that the lateral pressure had affected to enlarge the PMD.

4.2.2 Manufacturing Process, Figures 4 show the PMD measurement results of original fiber in loose coil, after tube stranding and after jacketing. After jacketing, the cable was wound on a wooden drum whose diameter was 1m. The statistical values of

the measured PMD coefficient on jacketed cable are summarized in table 3.

4.2.3 Temperature Cycling, Figures 5 show the PMD measurement results in temperature cycling performed on the cable.

The link-PMD value of each fiber was enough stable against the temperature change.

4.2.4 Cable Installation, Figures 6 show the distribution of PMD values measured before and after the installing operation. The statistical values of the measured PMD coefficient on installed cable are summarized in the table 3

As shown by the figures, the influence of installation operation on PMD was negligibly small.

5. Discussion

5.1 Non-Zero Dispersion Shifted Fiber

As described in section 2, our NZ-DSF has non-zero dispersion regions not only in L- and C-band but in S-band, in order to prevent FWM generation in S-band. Because of this property, the WDM transmission can be expanded into S-band.

The permissible transmission distance for an optical link is roughly given by equation (1) [7].

$$L=[\text{link-PMD } B/100]^{-2} \quad (1)$$

Where B is bit rate [Gbit/s]

link-PMD [ps/km$^{1/2}$]

L is transmission permissible distance [km]

The link-PMD value of NZ-DSF measured after installation was 0.036ps/km$^{-1/2}$. Substituting this value to equation (1), the transmission permissible distance can be derived over 2,000km for 40Gbit/s transmission. As the result of the experiments, it was confirmed that our NZ-DSF was advantageous for future long haul, wide band and high bit rate WDM transmission.

5.2 Large A_{eff} Pure Silica Core Fiber and Dispersion Compensating Fiber

As explained precisely in reference [5], the large A_{eff} PSCF and DCF are designed to use as hybrid line (PureCouple^{TM}). Optimizing the optical characteristics such as chromatic dispersion, dispersion slope, or A_{eff} of each fiber, the hybrid line can realize the transmission with small dispersion and dispersion slope without FWM generation.

Through a theoretical analysis, it was revealed that when the ratio of DCF length to the whole hybrid line was about 30%, the equivalent A_{eff} can be maximized. Thus the effective PMD coefficient of the hybrid line can be estimated by equation (2).

$$L=[\text{link-PMD}_{hybrid} B/100]^{-2} \quad (2)$$

Where

$$\text{link-PMD}_{hybrid}= [0.7 (\text{link-PMD}_{PSCF})^2 + 0.3 (\text{link-PMD}_{DCF})^2]^{1/2}$$

[ps/km$^{1/2}$]

The maximum link-PMD value of large A_{eff} PSCF and DCF measured in all experiments were 0.026ps/km$^{-1/2}$ and 0.039ps/ km$^{-1/2}$ respectively. Substituting these values to equation (2), the transmission permissible length can be estimated over 2,000km for 40Gbit/s transmission.

5.3 Pure Silica Core Fiber

Pure silica core fiber is usually used for long haul line, such as submarine cable, because of its very low optical attenuation. The permissible transmission distance estimated by substituting the maximum Link-PMD value to equation (1) is over 2,000km for 40Gbit/s.

This result means that the PSCF is enough applicable for future high bit rate long haul transmission systems.

5.4 Influence of Fiber Condition

As described by the table 2 in section 4.2.1, the link-PMD value of original fibers varied depending on the fiber condition.

The spool condition showed relatively large link-PMD value. It seems that this result was caused by the lateral pressure and/or macro-bending.

The loose coil and bare fiber condition showed relatively close Link-PMD value to that of jacketed cable. However, the measured link-PMD on both conditions did not coincided to that of jacketed cable. This result suggests that the influence of lateral pressure on loose coil PMD and that of residual stress caused by fiber coating are still remain and the influences are different among the fiber kind.

6. Summary

We have manufactured a loose tube cable with four types of high performance fibers, and measured polarization mode dispersion characteristics of the cabled fibers. The measurement results demonstrated that link-PMD value of each high performance fiber were low enough for the next generation high bit-rate, ultra long haul optical transmission.

7. References

[1] L. Li, C. Wei, "Effect of cabling process and installation on polarization mode dispersion", *Proc. of 49th IWCS*, (2000), pp. 371-375

[2] M. Nakano, M. Miura, T. Sato, "Polarization mode dispersion characteristics of single slotted core cable by NZD fiber ribbon", *Proc. of 49th IWCS*, (2000), pp. 55-64

[3] T. Ooishi, Y. Kubo, Y. Yokoyama, T. Kato, M. Yoshida, M. Onishi, Y. Makio, "Non-zero dispersion shifted fiber for

wide band WDM transmission including S-band", *Proc. of Optoelectronics and Communication Conference*, (2000), pp.136-137

[4] T. Kato, M. Hirano, M. Onishi, M. Nishimura, "Ultra-low nonlinearity low-loss pure silica core fibre for long-haul WDM transmission" *Electronics letters*, (1999), vol. 35, No. 19, pp. 1-2

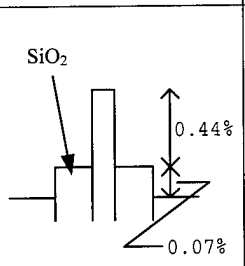
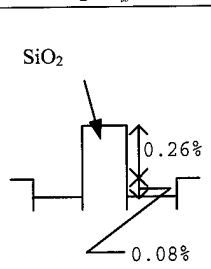
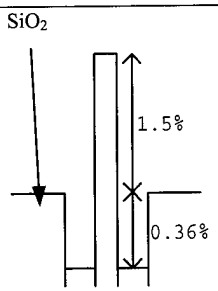
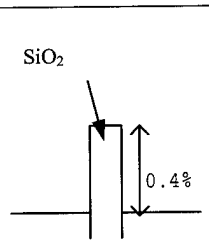
[5] M. Tsukitani, Y. Nagao, E. Yamada, T. Kato, E. Sasaoka, Y. Makio, M. Nishimura, T. Oshima, "High performance nearly dispersion-flattened hybrid optical transmission lines for ultra-large capacity transoceanic systems", *Proc. of 49th IWCS*, (1999), pp. 614-621

[6] T. Sekito, Y. Suetsugu Y. Yamazaki, Y. Saito, "Bending induced polarization mode dispersion with random mode coupling", *Proc. of 43th IWCS*, (1994), pp. 665-671

[7] G. Carones, F. Donazzi, R. Gaspari, A. Ginocchio, "Polarization mode dispersion measurements and relevant theoretical evaluation on optical fiber ribbon cables", *Proc. of 42nd IWCS*, (1993), pp. 639-646

Table 1 Refractive Index Profile and Characteristics of High Performance Fibers

(Typical values)

	NZ-DSF	Large A_{eff} PSCF	DCF	PSCF
Refractive Index Profile				
Attenuation at 1550nm (dB/km)	0.20	0.17	0.26	0.17
A_{eff} at 1550nm (μm^2)	65	105	22	79
Dispersion at 1550nm (ps/nm/km)	+8	+20	-47	+19
Dispersion Slope at 1550nm ($ps/nm^2/km$)	+0.06	+0.06	-0.06	+0.06

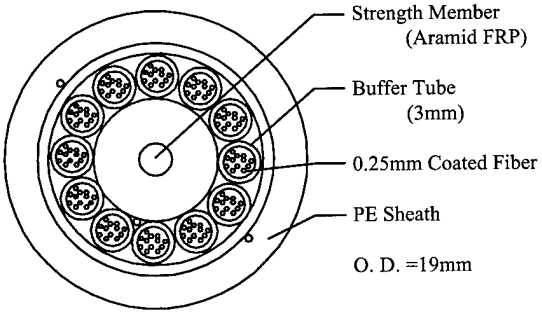
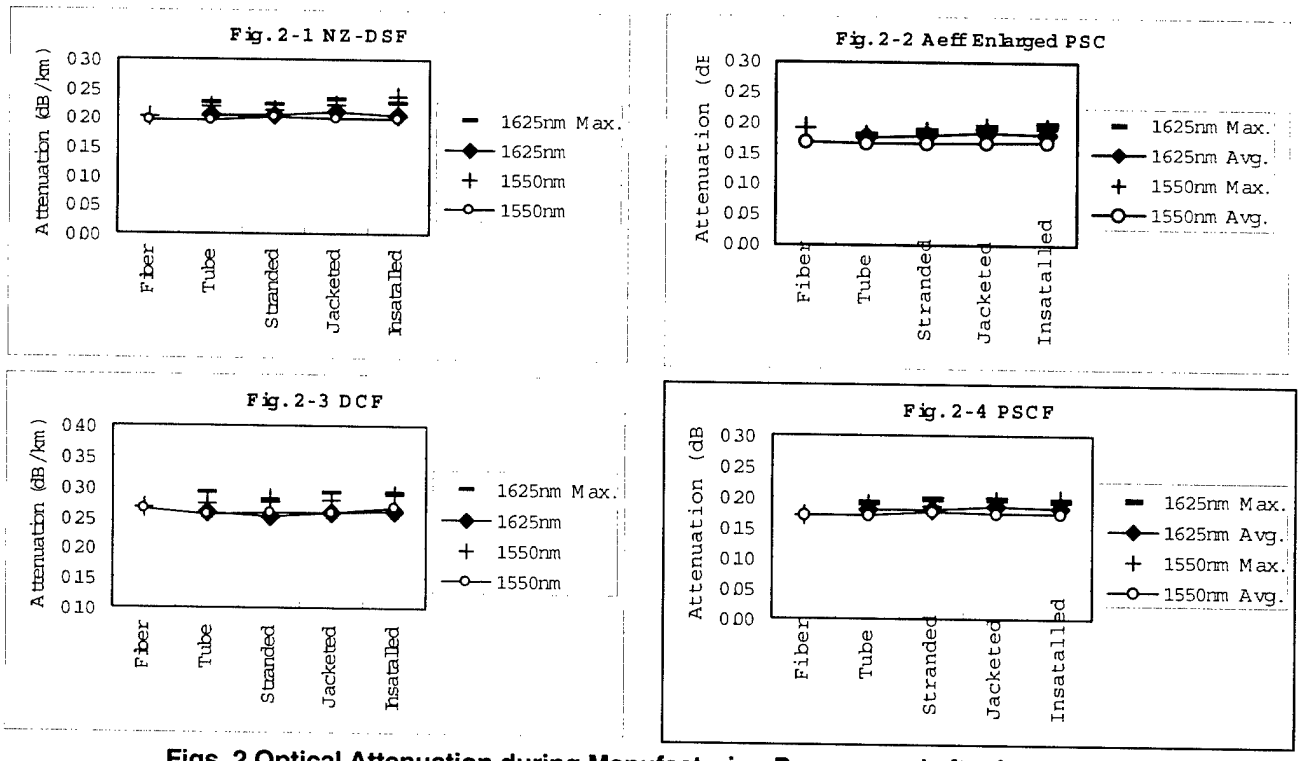


Fig. 1 Test Cable Structure

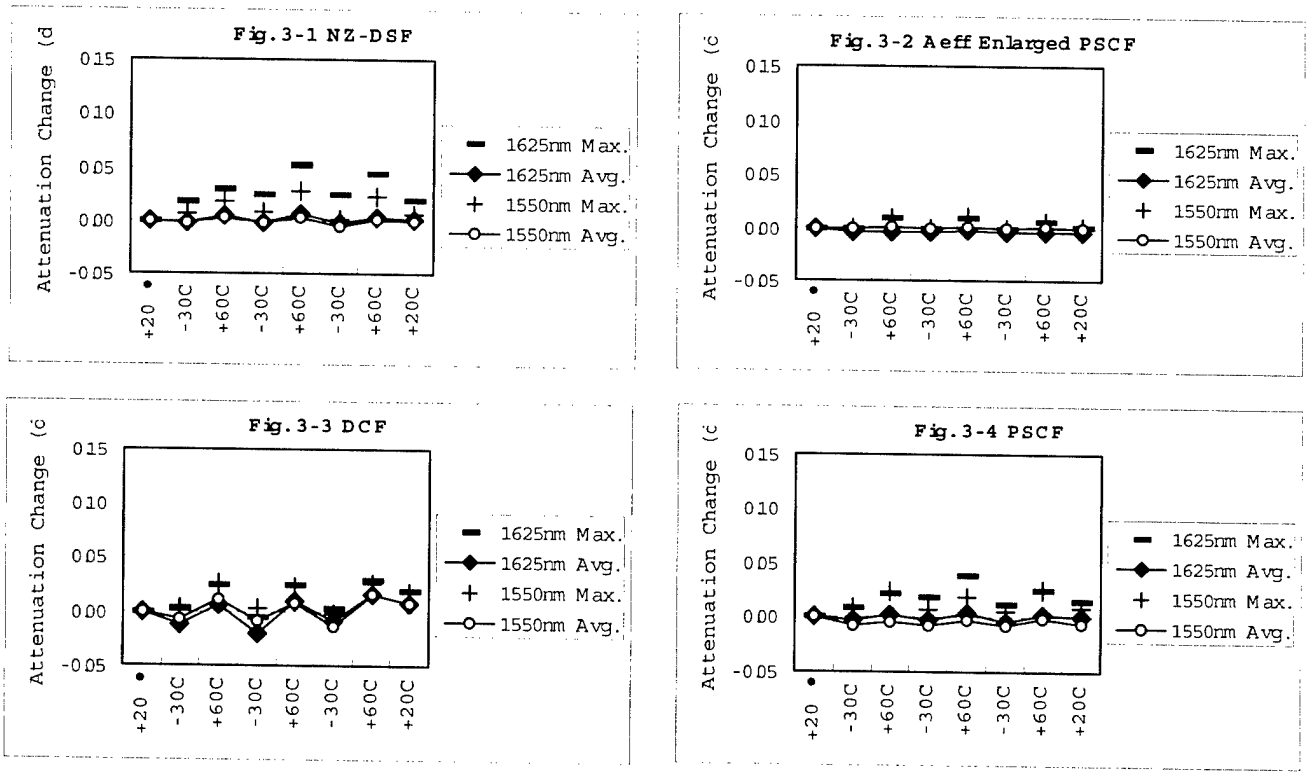
Table 2 Link-PMD of Test Fibers before and after Cabling

(in $ps/km^{1/2}$)

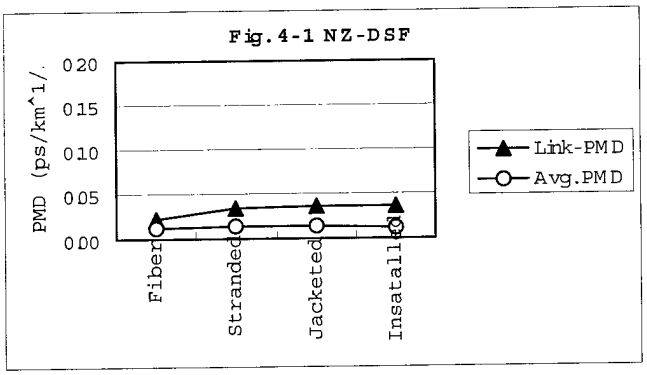
Condition	NZ-DSF	Large A_{eff} PSCF	DCF	PSCF
Spool	0.055	0.073	0.096	0.075
Loose Coil	0.022	0.016	0.018	0.041
Bare Fiber	0.030	0.052	0.035	0.032
Jacketed Cable	0.035	0.026	0.029	0.062

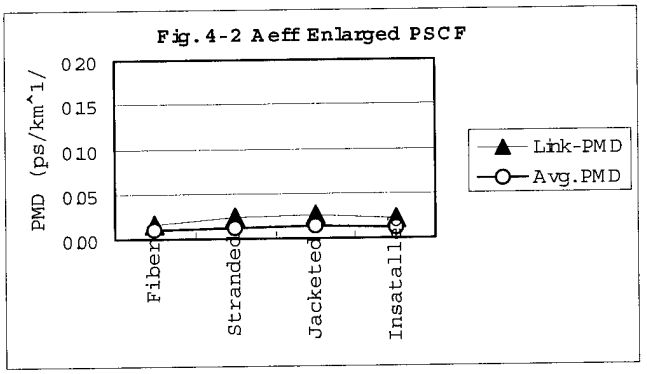


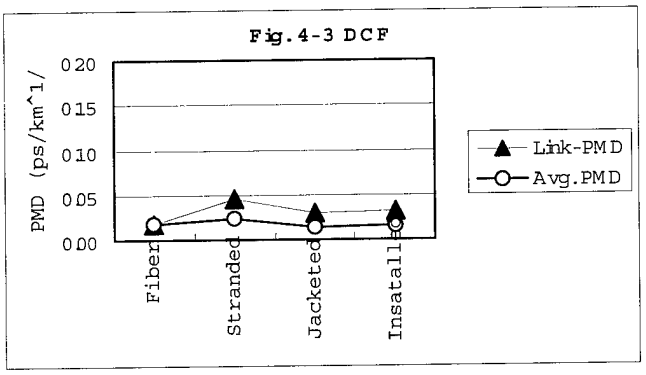
Figs. 2 Optical Attenuation during Manufacturing Process and after Installation

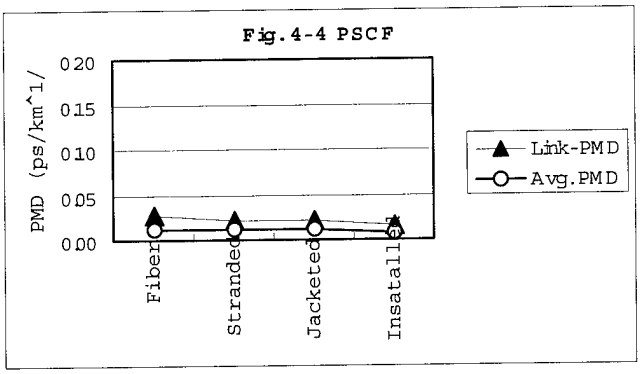


Figs. 3 Optical Attenuation Temperature Cycling Test Results

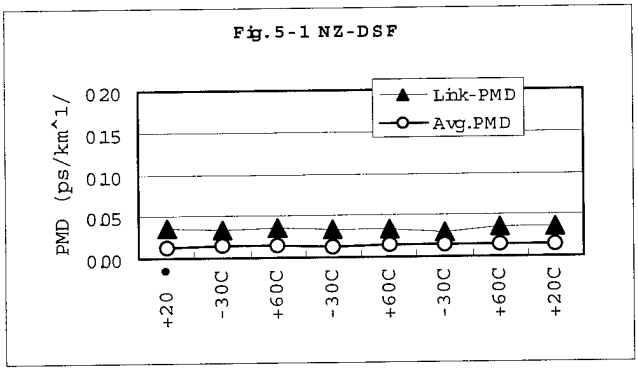


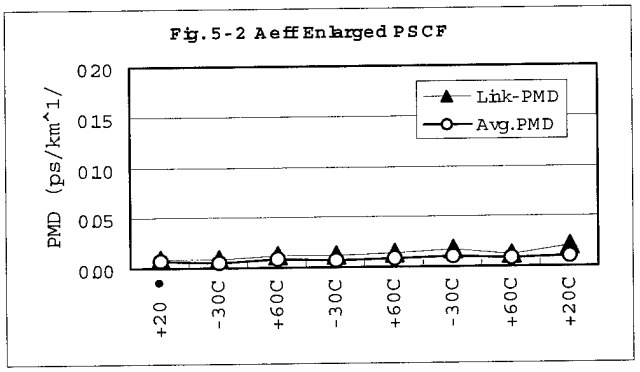


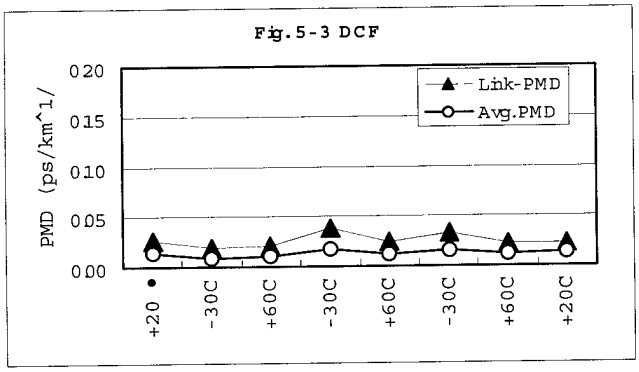


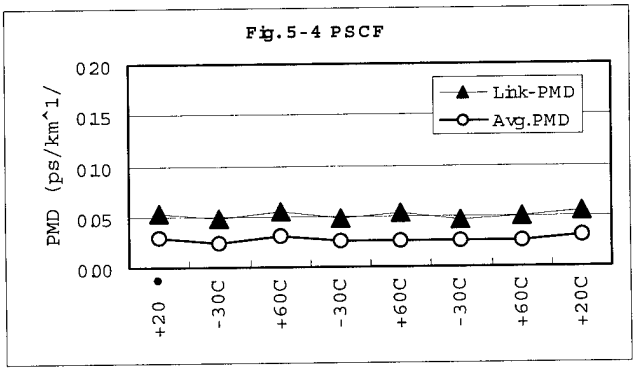


Figs. 4 Measured PMD Coefficient during Manufacturing Process and After Installation

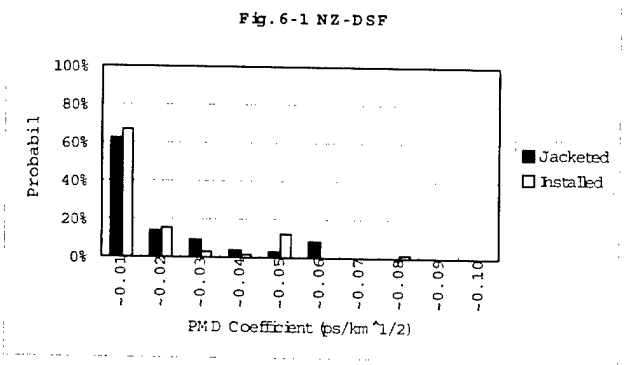


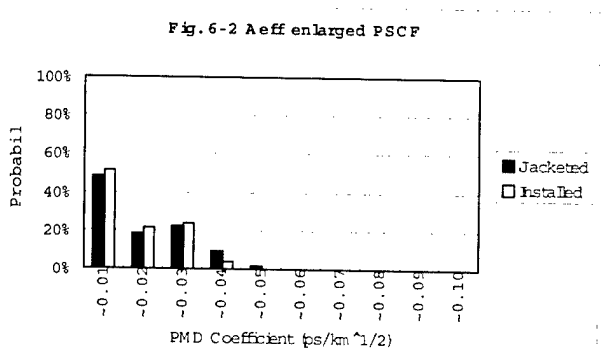


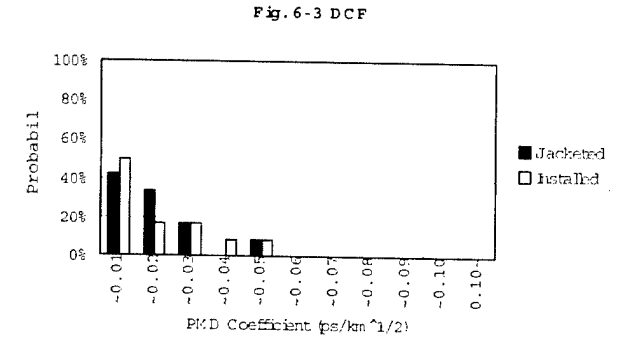


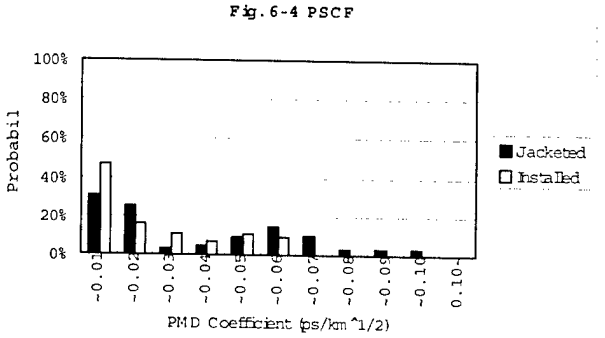


Figs. 5 PMD Temperature Cycling Test Results









Figs. 6 Measured PMD Distribution before and after Installation

Table 3 Statistical Values of PMD

(in ps/km$^{1/2}$)

		NZ-DSF	A_{eff} Enlarged PSCF	DCF	PSCF
After Jacketing	Max.	0.056	0.040	0.044	0.100
	Link-PMD	0.035	0.026	0.029	0.062
	Avg.	0.014	0.014	0.014	0.031
After Installation	Max.	0.075	0.036	0.041	0.056
	Link-PMD	0.036	0.022	0.031	0.039
	Avg.	0.013	0.012	0.015	0.019



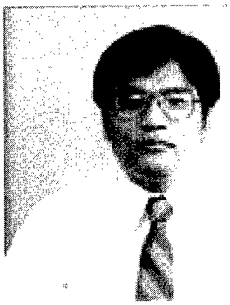
Hiroki Ishikawa
Sumitomo Electric
Industries, Ltd.
1, Taya-cho, Sakae-ku,
Yokohama, 244-8588 Japan

Hiroki Ishikawa received his M. E. degree in applied physics from Tohoku University in 1990. He joined Sumitomo Electric Ind., Ltd. in 1990 and he has been engaged in research and development of fiber optic cables. Mr. Ishikawa is a member of Optical Network R&D department in Yokohama Research Laboratories.



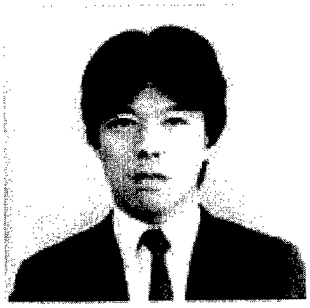
Katsuya Nagayama
Sumitomo Electric
Industries, Ltd.
1, Taya-cho, Sakae-ku,
Yokohama, 244-8588 Japan

Katsuya Nagayama received degrees of M.E from University of Tokyo and Ph.D. from Drexel University. He joined Sumitomo Electric Industries LTD. in 1988, and his current research is optical fiber drawing process. Dr. Nagayama is a member of Optical Fibers R&D department in Yokohama Research Laboratories.



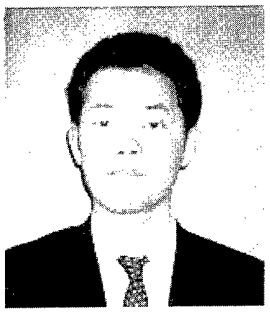
Nobuhiro Akasaka
Sumitomo Electric
Industries, Ltd.
1, Taya-cho, Sakae-ku,
Yokohama, 244-8588 Japan

Nobuhiro Akasaka received his M. E. degree in chemical engineering from Tokyo University in 1983. He joined Sumitomo Electric Ind., Ltd. and he has been engaged in research and development of fiber optic cables. Mr. Akasaka is a Chief Research Associate of Optical Network R&D department in Yokohama Research Laboratories and a member of the IEICE Japan and the Material Life Society of Japan.



Masaaki Kaino
Sumitomo Electric
Industries, Ltd.
1, Taya-cho, Sakae-ku,
Yokohama, 244-8588 Japan

Masaaki Kaino received his B. E. degree in engineering from Kobe University in 1983 and joined Sumitomo Electric Ind., Ltd. He has been engaged in development and design of optical fiber cables. He is an assistant general manager of the Overseas Fiber Optics Engineering section in Communications Division.



Makoto Shimizu
Sumitomo Electric
Industries, Ltd.
1, Taya-cho, Sakae-ku,
Yokohama, 244-8588 Japan

Makoto Shimizu received his B. S. degree in applied chemistry and M. S. degree in material science from Keio University. He joined Sumitomo Electric Ind., Ltd. in 1994, and he has been engaged in design of optical fibers. Mr. Shimizu is a member of Fiber Optics Engineering section in Fiber Optics Division.



Shinya Takaoka
Sumitomo Electric
Industries, Ltd.
1, Taya-cho, Sakae-ku,
Yokohama, 244-8588 Japan

Shinya Takaoka received his M.S. degree in electrical engineering from Shizuoka University in Japan, and M.B.A. degree from Renselaeer Polytechnic Institute in the US. He joined Sumitomo Electric Ind., Ltd. in 1986 and has been engaged in designing, development, and marketing in optical fiber. He is a project manager of Fiber Optics Division.

The PMD Prediction for Installed G.652 Cables Using Monte Carlo Method

Guohui NIU ***Ming CHENG***
Yangtze Optical Fibre and Cable Company Ltd.
Wuhan, CHINA
+86-27-8780-2541 yofcqa@public.wh.hb.cn

Abstract
This paper demonstrates the method to get the linked cable's PMD value upon the practical examples, and this method is accordance with IEC/ITU requirements[1]. IEC recommended three methods to calculate the linked PMD coefficient. The Monte Carlo method for PMD calculation is one of them. The paper uses this method to predict the PMD for installed cables. The determination method of PMD value for cable link is given, and the maximum link length of cables for definite transmission system can also be determined. A statistical calculation program was developed to facilitate the statistical evaluation. By using that program, the probability distribution of the PMD coefficient can be obtained. It can be concluded that the prediction of installed G.652 cables PMD is necessary, feasible, and is convenient for the testing and measuring the actual cables PMD on field.

Keywords
PMD coefficient; statistical evaluation; Monte Carlo Method.

1. Introduction
With the development of optical transmission and dispersion compensation technology, the transmission rate is up to 10Gb/s for G.652 fibre, and the distance for non- relay transmission is over 100km (for G.655 fibre, it is up to 400km). It requires fibre have better Polarization Mode Dispersion (PMD) performance. More and more operators have been trying to upgrade their installed G.652 cables and increase their capacity. The PMD performance has become one of the limitations of the transmission system. It becomes very necessary that accurately predicting the concatenated cable's PMD before they have been installed, or calculating the installed G.652 cable's PMD performance through a reliable way. The requirement for PMD is not based on individual fibre, or individual cable, it is based on linked/concatenated cable. The ITU-T updated G.652 recommendation indicates that when it is required, cabled fibre polarization mode dispersion shall be specified on a statistical basis, not on an individual fibre basis. So it is very necessary for fibre or cable supplier to predict the cable's PMD before installation, or make sure that the cables can meet the customer's demand for increasing the transmission rate before the installed cable being put for higher-bit rate transmission. Here the Monte Carlo Method is one of the ways to evaluate the cable's PMD on the statistical basis.

2. Monte Carlo Method for PMD Evaluation
2.1 Data Collection and Establishment for Probability Function
For the construction of the sampling population, at least 100 cable's PMD coefficients are needed. From the sampling database, randomly select 20 cable PMD data, and calculate the PMD linked value for these 20 cables. According to the requirement of ITU-T, the calculation mentioned above will conduct 100,000 data. From the calculation, the 100,000 linked PMD value establishes the distribution of the probability function.

2.2 Calculation/Evaluation of Linked PMD Value
The formula for the linked fibre in cable's PMD coefficient calculation is as follows (if the length of cables in the link is the same):

$$X_M = \sqrt{\frac{1}{20}\sum_{1}^{20} x_i^2} \qquad (1)$$

Where, x_i refers the measuring value for the i^{th} cable's PMD coefficient. The requirement of ITU-T for the connection is for 20 pieces of cable, so the link is consist of 20 cables, and the summary for the x_i is from 1 to 20.

The linked value for PMD coefficient will be derived from equation (1), and calculated for 100,000 times to get the probability distribution of linked PMD coefficient.

2.3 The Probability Distribution of Linked PMD Coefficient
The distribution for the probability of linked PMD coefficient comes from the algorithm of the Monte Carlo Method, and it is in accordance with the Maxwell Distribution.

2.4 The Designed Linked PMD Coefficient Value, PMD_Q
ITU-T study group 15 (SG 15) indicates that for the concatenated cable's PMD coefficient, there are some requirements should be met. It is that: the link number should not be less than 20 pieces; the probability of the PMD coefficient for concatenated cable (represented by Q) exceeded the design PMD (PMD_Q) is 0.01%, and PMD_Q should not greater than 0.5ps/√km.

The PMD_Q can be achieved with the follows:

$$1 - \int_0^{PMD_Q} f_{link}(X_M)dX_M = Q = 10^{-4} \qquad (2)$$

Where the $f_{link}(X_M)$ is the probability distribution function of PMD coefficient for linked cable.

2.5 The Overall PMD for the Cable Link, PMD_f

The total PMD value for the cable likage, PMD_f, can be derived from the follows:

$$PMD_f = PMD_Q \times \sqrt{L_{link}} \quad (3)$$

Where the L_{link} is the length of the linkage.

3. Case Study: The Example for the Method

3.1 The Input Data

For the purpose of demonstration the influence of individual PMD coefficient on the PMD coefficient of cable link, different groups of cable link were chosen for the calculation. We choose two groups of concatenated cables, one group of cables has relative lower PMD coefficient, and another group has higher PMD coefficient. The other conditions for these two groups of cables, such as cable structure and cable bending strain, are the same. The data of these two groups is given in Table 1 below. The PMD values were taken from the fibre in the cables using interferometric technique.

The main characters of individual fibre's PMD coefficient is in Table 1:

Table 1: The PMD Coefficient of Fibres in Two Groups of Cable

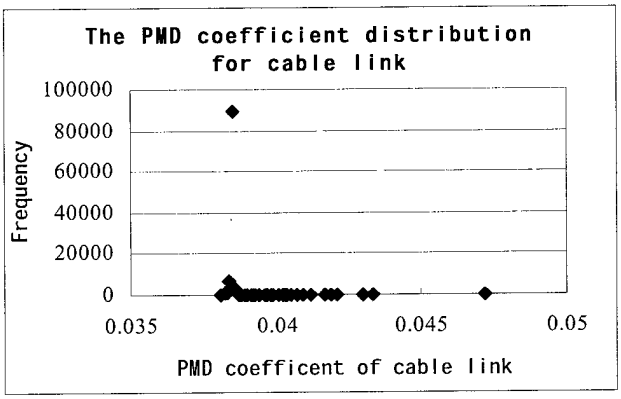
	Group 1	Group 2
MAX	0.128	0.890
MIN	0.014	0.064
AVG	0.043	0.408
STD	0.022	0.168
Note: each group contains 100 cable's data.		

3.2 Evaluate PMD Coefficient of Linked Cable on Statistical Basis: Monte Carlo Method

When the data was ready (100 cable's data for each group), the computer program calculates the data in a specified way. It randomly selects 20 cable's PMD coefficient from given 100 data, and uses formula (1) to get the PMD coefficient of linked cable. 100,000 times of calculation have been conducted automatically, and it results in a probability distribution of PMD coefficient for cable link. From the distribution, the PMD coefficient of cable link vs. frequency is formed.

The PMD coefficient distribution for the cable link was shown in Figure 1.

Group 1



Group 2

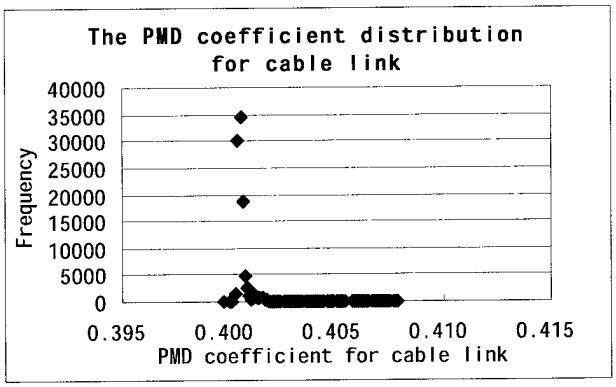


Figure 1: The PMD Coefficient Distribution for Two Groups of Cable Link

3.3 The Main Character of PMD Coefficient for Linked Cable

Besides the PMD coefficient distribution of cable link, the main character of the result, such as the maximum, minimum, average and standard deviation for the PMD coefficient for the linked cable can be obtained. It is useful for us to make a comparison for those PMD coefficients for individual cable and linked cable.

The overall PMD coefficient of cable link is shown in Table 2. It consists the data for Group 1 and 2.

Table 2: The Overall of Cable Link PMD Coefficient for Two Groups of Cable Link

Linked fibre PMD coefficient for two groups		
	Group 1	Group 2
MAX	0.047	0.449
MIN	0.038	0.398
AVG	0.039	0.401
STD	0.0001	0.0004

According to the algorithm of mathematical method used here, the cable PMD coefficient distribution is the probability function of PMD coefficient, and from the distribution, by using the formula (2), it is easy to get the 10^{-4} probability out of it. So the design PMD value (PMD_Q) can be reached. In this example, for Group 1, the

PMD_Q=0.040ps/√km, for Group 2, the PMD_Q=0.409ps/√km. It means that for Group 1, there is 10^{-4} possibility to exceed the PMD coefficient 0.040ps/√km by using the cables in the group; and for Group 2, there is 10^{-4} possibility to exceed the PMD coefficient 0.409ps/√km by using the cables in the group.

3.4 The PMD Value for the Overall Cable Link, PMD_f

As the design PMD (PMD_Q) coefficient is obtained, the total PMD value for the whole cable link can also be reached. According to the equation (3), the cable link PMD, $PMD_f=PMD_Q\times\sqrt{L_{link}}$.

In the example in this paper, we have the cable length for 20 sections, and the length of each section is 5km, so the total length of the link is 100km. Then we can get the overall PMD value for Group 1 cable link is 0.40ps; and the overall PMD value for Group 2 cable link is 4.09ps.

3.5 The Transmission Length for the Certain Transmission Rate

With the PMD value for the entire cable link and the certain transmission rate that required by customer, the designer can make sure that what fibre/cable should be selected for the customer, or, if the installed transmission system can meet the demand of upgrading the transmission rate. It is beneficial for the designers to use this method to consider the configuration of the transmission system. Meanwhile, other factors should also be taken into account, such as the influence of cabling process on the PMD performance, the cable configuration, the bending strain[2, 3, 4], and the instantaneous peak value of the PMD coefficient etc. With all of these factors together, the system designer can work out the construction effectively and accurately.

4. Analysis on the Result

4.1 The Distribution of Individual Fibre PMD and the Cable Link PMD

As it can be obtained from many cases, the fibre's PMD (or PMD coefficient) deviated according to the time and environmental changes. This is due to the statistic characteristics of PMD. So it shows that it is not "stable" from time to time. For the cable link PMD, the performance is much reliable than that of individual fibres. This is because of the balance of the PMD for the linked fibre. From the comparison of the PMD before and after fibre were connected, the standard deviation of them are quite different. For cable link PMD, the standard deviation is much smaller than that of single fibre, which means the PMD of linked cable is much "stable". This is the situation in the practice.

4.2 The Maximum Value of the PMD Coefficient

Comparing the maximum value of the PMD before and after the fibres were connected, the linked value is much smaller than that of single fibre. It is also the effect of PMD attributes. It "smoothen" the PMD differences among the linked fibres. In cable Group 2, the maximum value drops from 0.890ps/√km (the maximum value of individual cables) to 0.449ps/√km (the maximum value of concatenated cables), which is about half of the previous one.

5. Conclusion

According to the PMD_Q, it can be easily derived that the overall PMD for the cable link. And then, the total performance of PMD for the transmission line can be judged.

In the past, due to the limitation of measuring method, the customer prefers to judge the PMD performance based on individual fibre/cable. But according to the character of PMD, it is not accurate to evaluate PMD on the single fibre/cable, because the transmission system performance relies on the PMD of linked cable. From the statistical evaluation in this paper, it can be seen that even some of the individual cable's PMD coefficient is relatively high (0.890ps/√km), the maximum PMD coefficient for the entire cable link can go down dramatically (0.449ps/√km). This is more reasonable for the PMD evaluation, because it is more in accordance with the actual situation of the transmission system.

6. Acknowledgments

Special thanks for the support from Jack Tu, who helped for the development of the computer program in the algorithm. Also many thanks goes to R. Matai, the manager of the Fibre-1 department of YOFC, for his beneficial discussion on the paper.

7. References

[1] STUDY GROUP 15, "Revised G.652-for determination", *ITU-Telecommunication Standardization Sector Temporary Document 051R1 (PLEN)*.

[2] L.F. Marques, A.M. Simiao and R.F. Cruz et al, "Statistical Analysis of PMD using Mote Carlo Method for different configuration of Loose Tube Optical Cable", *OFC' 2001*, WDD12-1-WDD12-3.

[3] Ming CHENG, Guohui NIU, et al, "Bending Performance Study of Large Effective Area G.655 Fibre", *IWCS 1999, Proceedings* pp 516-519.

[4] Dan Gallagher, Marvin Ashby, et al, "Cable and System PMD Prediction", *IWCS 1995, Proceedings* pp 366-371.



Guohui Niu
4 Guan Shan Er road,
Yangtze Optical Fibre and Cable Company Ltd.
Wuhan, 430073
CHINA

Guohui NIU was born in 1957. He is currently the Chief Engineer of Quality Assurance Department and responsible for the statistical analysis and quality control for the fibre and cable production. He worked as an Associate Professor in Mechanical Engineering Department in Wuhan University of Science and Technology for several years until he jointed to YOFC at 1998. He is a graduate of Huazhong University of Science and Technology with a B.E. in Engineering.



Ming Cheng
4 Guan Shan Er road,
Yangtze Optical Fibre and Cable Company Ltd.
Wuhan, 430073
CHINA

Ming CHENG was born in 1962. He received his BSc degree in Physics in 1983 at Wuhan University and MSc degree in Solid-state Physics in 1990 at Huazhong University of Science and Technology in China. Since 1994 he has been with YOFC. He is now a senior R&D engineer and his research interests are fiber optics and fiber manufacturing.

Effect of Water Blocking Materials on Moisture Diffusion in Prototype Cable Structures

Carl R. Taylor, Kariofilis Konstadinidis, Richard D. Small, Richard Norris, Manuel R. Santana, Raymond P. DeFabritis
Bell Laboratories, Lucent Technologies OFS
Norcross, GA
+1-770-798-4685 · crt@lucent.com

Abstract

The environmental integrity of fiber optic cables over the service lifetime of the cable is one of the primary issues that come into consideration during cable design and materials selection. Exposure to liquid water or water vapor, in particular, is a risk factor for outside plant cables either directly buried or placed in ducts within metro areas. In this paper we present results on water diffusion through cable core and jacketing materials in prototype cable structures with and without the presence of water blocking agents such as filling compound or super-absorbent materials. The experiments consist of immersing short, end-sealed tubes in water at various temperatures and measuring the weight change as a function of time. The results show that water blocking materials affect the time-temperature behavior of the system. They significantly affect predicted lifetime of the cable by delaying or preventing saturation and formation of liquid water in the core tube.

Keywords

Fiber optic cable; cable; water blocking; water diffusion; super absorbent powder; polyethylene; polypropylene

1. Introduction

The great demand for bandwidth in the last few years resulted in the installation of thousands of kilometers of fiber optic cable throughout the world. A large percentage of those cables are installed in environments where the presence of water is unavoidable. Direct buried cables, for example, are most likely exposed to a 100% RH environment for the majority of their lifetime. This fact has to be taken into account in cable and materials design in order to protect the fibers from exposure to liquid water or water vapor.

Cable filling compounds have been the materials of choice for protecting optical fibers from direct exposure to water. Their main function is to block water from filling up the cable core in case of catastrophic failure in the cable sheath. In other words they block the rapid propagation of water in the longitudinal direction. Moisture, however, can also diffuse in the radial direction through the cable sheath and core tube. Eventually moisture will reach the optical fibers and ribbons and when the relative humidity in their proximity reaches a critical value, there exists the possibility of water condensation.

It has been shown previously [1] that the presence of a water getter compound in the cable filling compound delays the moisture saturation of the cable core by absorbing the water in the core and keeping the water partial pressure in the core below the saturation vapor pressure for longer times. Cable filling compounds, however, have the disadvantage of adding cost and weight to the cable, in addition to requiring extra time for clean-up during installation. New cable designs have recently been developed that use smaller amounts of filling compound [2]. That was achieved by replacing filling compound in the central core by a water blocking tape. In that design, filling compound is only used in the mini inner tubes of the cable. The use of water blocking tapes within the outer jacket of power cables has also been shown to be beneficial in delaying formation of water trees in power cables [3].

This paper examines the effect of water blocking materials (both filling compounds and water blocking tapes) on the predicted lifetime of the cable.

The first section describes the experimental procedures used to measure the water permeability of polyethylene and polypropylene and the water absorption coefficient of super absorbent powder water blocking tapes. In the second section, the materials' parameters are used in an analytical model to estimate cable lifetimes (in this case, defined as the time for the cable core to reach 95% RH). In the third section, the amount of water absorbed by model cable structures as a function of time and temperature is measured experimentally and the results are used to predict cable lifetimes.

2. Experimental Determination of Materials Parameters

2.1 Super Absorbent Powder (SAP) Tapes

Two SAP tapes were used in this study. Both were commercial grade products. The water absorption coefficient of the tapes (amount of water absorbed per unit length per unit partial pressure) was measured as follows: three 1-meter long samples of each tape were preconditioned at 100°C for 2hrs to drive all the water out. Following the preconditioning the samples were weighed in sealed jars. The samples were then transferred in chambers of varying temperature and humidity for periods of up to seven days. The equilibrium weight of the samples was measured and the water gain was calculated from the difference of the wet and dry samples. The amount of water absorbed increases with increasing water partial pressure as seen in Figure 1. The relationship is approximately linear for the range examined. The slope of the curve provides an estimate of the water absorption coefficient of the tape as seen in Figure 1and Table 1. It is expected that the relationship between the amount absorbed and the relative humidity becomes non-linear as the relative humidity approaches 100%.

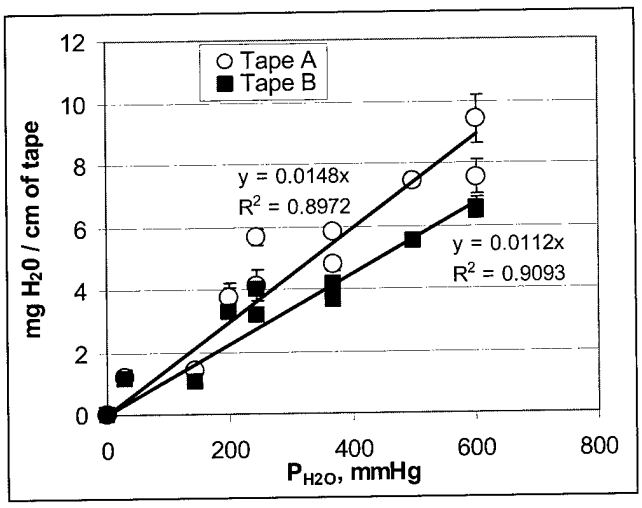


Figure 1. Weight of water absorbed as a function of water partial pressure for two SAP tapes.

Table 1. Absorption coefficient of SAP tapes

Tape	A, g H_2O/cm mmHg
A	1.48×10^{-5}
B	1.12×10^{-5}

2.2 Core Tube and Jacket Materials

The tubes used in these experiments were polypropylene (PP), a typical core tube material, and polyethylene (PE), a typical jacketing material. Both medium and high density PE were examined. The water permeability of these materials was determined experimentally as follows.

Tubes of the materials under consideration were fabricated using a typical cable extrusion process. Samples of fixed length were cut and one end was sealed. The tubes were then filled with water and the other end was subsequently sealed. The samples were weighed and placed in dry ovens of constant temperature. The weight of the tubes was monitored at regular intervals. Four temperatures were used: 21°C, 40°C, 60°C, and 80°C. For the 21°C condition the sample was placed in a desiccator in a controlled temperature lab. The weight loss of the tubes as a function of time and temperature is a straight line as shown in Figure 2 for PP. The slope of the line is equal to the water permeation rate through the tube wall. The values for PP, MDPE, and HDPE are shown in Table 2. These values represent the maximum water flux for the specific geometry since the pressure gradient across the tube wall is equal to the vapor pressure of water ($\Delta P=P_i-P_o=P_s-0=P_s$). The permeability of water, P_e, for the three materials was calculated using the formula for steady state diffusion through a cylindrical wall [4]:

$$W = \frac{2\pi P_e P_s}{\ln(R_2/R_1)} \quad (1)$$

Where W is the rate of water permeation in mg/cm/day, R_1 and R_2 the inside and outside radius of the tube, and P_s the vapor pressure of water in mmHg. The permeability values are shown in Table 3.

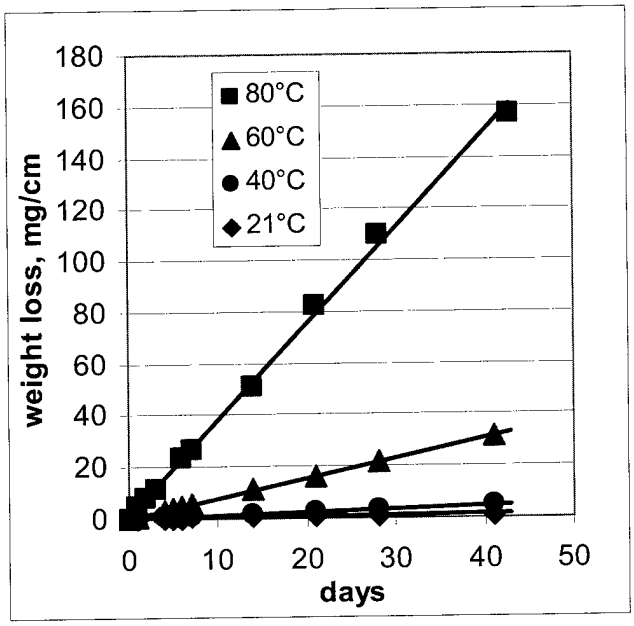


Figure 2. Water loss through a PP tube wall at varying temperatures.

Table 2. Water flux through tube walls for HDPE, MDPE, and PP.

T, °C	W, mg/(cm day)		
	HDPE	MDPE	PP
21	0.0099	0.0135	0.0247
40	0.0380	0.0555	0.1054
60	0.2359	0.3372	0.7104
80	1.3799	2.0557	3.4279

Table 3. Water permeability of PP, MDPE, and HDPE.

T, °C	P_e, g/(cm sec mmHg)		
	HDPE	MDPE	PP
21	2.13E-13	2.90E-13	5.29E-13
40	2.75E-13	4.01E-13	7.62E-13
60	6.32E-13	9.03E-13	1.90E-12
80	1.55E-12	2.31E-12	3.86E-12

3. Analytical Model of Water Diffusion through Cable Walls

It has been shown before [1] that diffusion of water into a cable core can be modeled assuming that the materials inside the core (fibers/ribbon, gel, etc) are characterized by a single water absorption coefficient A, and the materials comprising the cable sheath (core tube, jacket, etc.) are characterized by a single water permeability P_e (Figure 3). If m is the mass of water in the core, p_w the water partial pressure in the core, p_o the external water partial pressure and p_0 the initial water partial pressure inside the core, then the mass balance requires that water accumulation in the core be equal to the rate of water flux through the sheath:

$$\frac{dm}{dt} = \frac{d(Ap_w)}{dt} = P_e(p_o - p_w) \tag{2}$$

The solution to equation 1 is:

$$p_w = (p_o - p_0)(1 - \exp(-P_e t / A)) + p_0 \tag{3}$$

Or in terms of relative humidity:

$$RH = (RH_o - RH_0)(1 - \exp(-P_e t / A)) + RH_0 \tag{4}$$

This model (model A) is valid only in cases where there is simple physical absorption of water by the materials inside the core and the absorption coefficient is a linear function of relative humidity.

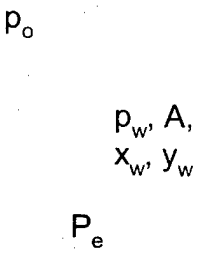


Figure 3. A model cross-section for water diffusion into a cable core.

In the case of super absorbent polymers, however, vapor-liquid equilibrium has to be used to account for non-linearities. A model describing water diffusion in cables containing SAP tapes (model B) has been proposed before [3]. Again referring to Figure 3, vapor-liquid equilibrium exists at all times in the tube and $p_w = y_w P = x_w P_s$, where P is the total pressure in the core, P_s the saturation vapor pressure of water and y_w and x_w the molar fractions of water in the gas and liquid phase, respectively. If n is the total number of moles of water in the core and is distributed between the gas, n_g, and liquid phases, n_l, then:

$$n = n_g + n_l = \frac{p_w V}{RT} + \frac{n_s p_w}{P_s - p_w} \tag{5}$$

Where n_s is the number of moles of the solute (counter ions in the polyelectrolyte powder in this case). If we assume that the number of moles of water in the gas phase is small compared to that of the liquid phase, and convert moles to mass, we get:

$$m \cong \frac{M_w n_s p_w}{P_s - p_w} \tag{6}$$

Where M_w is the molecular weight of water. When $p_w << P_s$, then:

$$m \cong \frac{M_w n_s p_w}{P_s} = A p_w \qquad A = \frac{M_w n_s}{P_s} \tag{7}$$

Which reduces model B to the simple absorption model.

If we substitute equation 6 into 2, and assume $p_o = P_s$ (for tubes immersed in water), we get the following equation for p_w:

$$\frac{dp_w}{dt} = \frac{P_e}{AP_s^2}(P_s - p_w)^3 \tag{8}$$

The solution to equation 6 in terms of %RH is:

$$RH = 100 \times [1 - \sqrt{\frac{(1 - RH_0)^2}{1 + \frac{2P_e}{A}(1 - RH_0)^2 t}}] \tag{9}$$

Figure 4 shows the predictions of the two models for %RH vs. time in the case of a single PP core containing SAP tape. The values for P_e and A were obtained from the previous section. The initial RH in the core was set at 50%. Model B predicts much longer cable lifetimes than model A. The predictions will be compared to experimental results in the following sections.

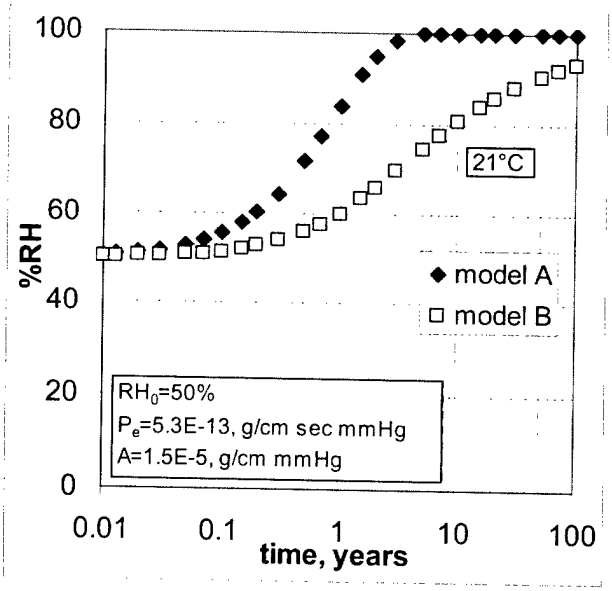


Figure 4. Model prediction for % RH in a PP core containing SAP tape.

4. Experimental

4.1 Water Diffusion in Filled Tubes

The samples consisted of 30-45 cm long tubes filled with either SAP tape or cable filling compound and fiber ribbons. The tube ends were sealed by heating each end until melted, pinching it with a pair of tweezers and quenching it in water. The tubes were weighed and immersed in water baths of constant temperature (21°C, 40°C, 60°C, and 80°C). The samples were removed periodically and their weight was recorded. The following paragraphs describe the results for different combinations of tube and filler materials.

4.1.1 Polypropylene/SAP Tape

A 30 cm long sample of SAP tape was placed in each PP tube (30 cm long, 1.0414 cm OD), the ends were sealed, and the samples were placed in constant temperature water baths. The results for the weight gain per unit length as a function of time are shown in Figure 5. The data can be graphically shifted to a single reference temperature. The resulting master curve and the shift factors, $a_{T,P}$, for a reference temperature of 21°C are shown in Figure 6. The activation energy, E_a/R, for the process can be obtained from the slope of the $\ln a_{T,P}$ vs. 1/T plot and was found to be 3846 K The instantaneous water flux w_i (mg/cm/day) across the tube wall can be calculated from the first derivative of the master curve and was determined numerically. The flux can be converted to %RH inside the tube using the formula:

$$\%RH = 100 \times (1 - \frac{w_i}{w_{\max}}) \qquad (10)$$

Where w_{max} is the maximum water flux. It is achieved when the vapor pressure gradient across the tube wall is equal to the saturation vapor pressure of water and was determined in the water-filled tube experiment. For PP it is 0.0247 mg/cm/day at 21°C. The %RH inside the tube vs. immersion time for the PP/ tape system is shown in Figure 7.

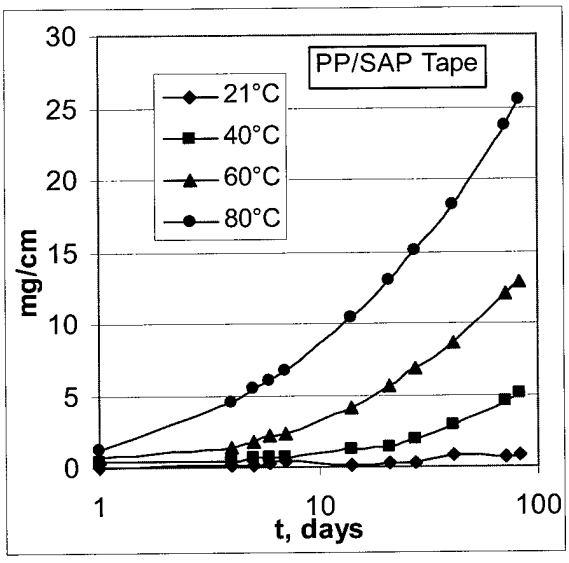


Figure 5. Water gain per unit length vs. time for PP tubes with SAP tape B inside.

The initial rate of 0.0089 mg/cm/day gives an estimated value of ~64% for the initial RH. The projection is that the inside of the tube will reach 95% RH after approximately 25 years of continuous exposure to 21°C water.

For the analytical calculations RH_0 was set at 64% to match the experimental value. The permeability of PP was taken from section 2. The value of A for the particular SAP tape used in this experiment was not measured. The value of the absorption coefficient A that best fit the data at long times was 2.96×10^{-6} g/cm/mmHg, about 5 times less than that of tape A. The model B prediction using those values is also shown in Figure 7.

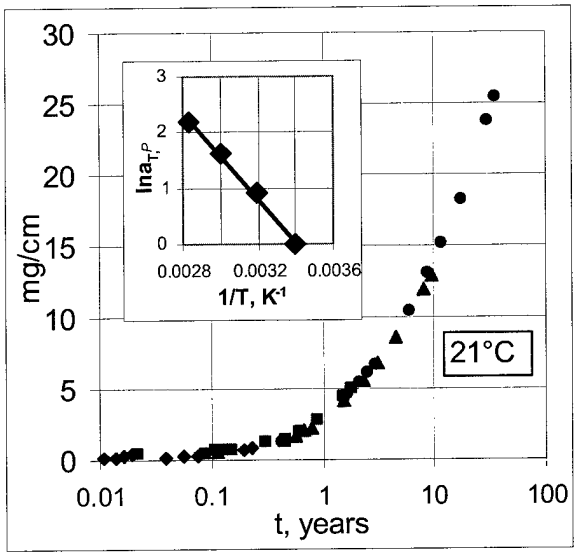


Figure 6. Master curve for water diffusion in PP tubes containing SAP tape.

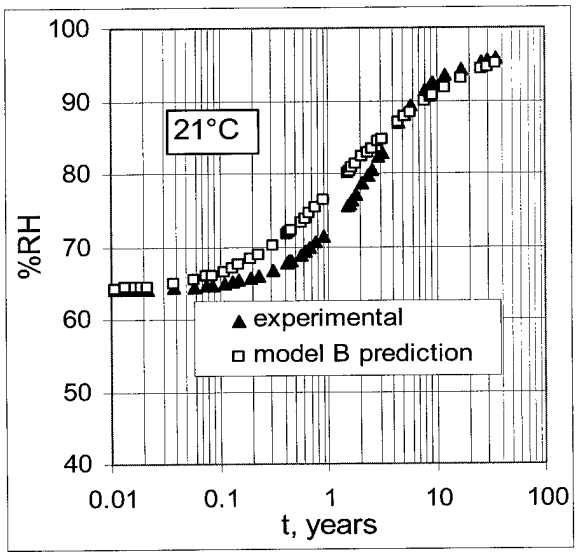


Figure 7. Estimated %RH inside a PP tube containing SAP tape.

4.1.2 *Polypropylene/Cable Gel w/Ribbon Stack*

The same type of experiments and calculations were performed for PP tubes containing a 10-ribbon stack and filled with cable filling compound. The master curve for this system at 21°C is shown in Figure 8. The scatter in the data in this case is due to the small quantities of water involved. The activation energy, E_a/R, is 6175 K. The estimated %RH inside the tube is shown in Figure 9. Saturation inside the tube is reached after a projected time of 2 years. In comparison, the PP tube with SAP tape is still below saturation after more than 30 years. The amount of water absorbed in the PP/tape system is more than ten times that of the PP/gel/ribbon system.

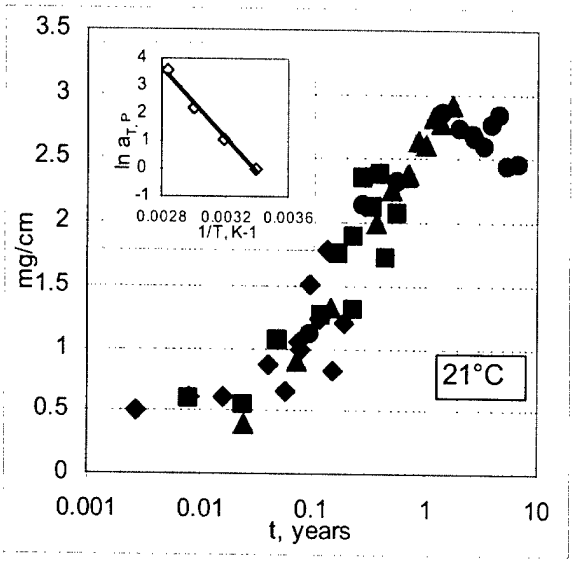


Figure 8. Master curve for water diffusion in PP tubes containing ribbons and cable gel.

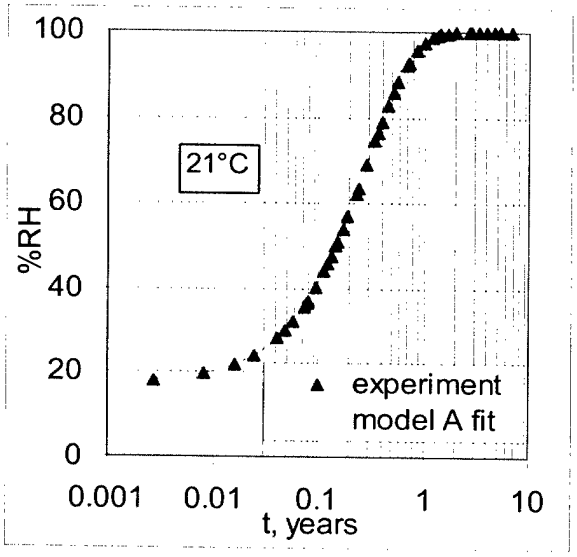


Figure 9. Estimated %RH inside PP tube containing ribbons and cable gel.

Figure 9 also shows the model prediction for this system. The water absorbing capacity of the gel and ribbons is much smaller than the SAP tape of the previous case and the mechanism is most likely simple physical absorption described by model A. The exponential form of the model can be fitted to the data as shown in Figure 9. An estimate of the absorbing capacity of the core can be obtained from the fit.

4.1.3 *Experimental Cable*

The cable construction consisted of PP core tube, SAP tape, dielectric strength members and ripcords, and HDPE jacket. Inside the core tube was a stack of twelve 12-fiber ribbons wrapped in SAP tape. All experiments were done with samples of 20-40 cm long. For the measurement of water permeability through the composite wall of the cable, the ribbons and SAP tape were removed from the core, which was then filled with water and the ends were hermetically sealed with metal caps. The maximum water flux was determined by monitoring the rate of weight loss of the samples at four temperatures. The results are shown in Table 4.

Table 4. Water flux and permeability through cable wall.

T, °C	W_{max}, mg/(cm-day)	P_e, g/(cm-sec-mmHg)
21	7.39E-03	6.1744E-13
40	1.95E-02	5.50017E-13
60	9.99E-02	1.04239E-12
85	5.39E-01	1.93759E-12
	$\ln W_{max}$=-8241/T(K)+25.7	$\ln P_e$=-3133/T(K)-9

Water immersion experiments were performed on samples with and without SAP tape in the core. In both cases there was SAP tape between the core and jacket. The ribbon stack was also present in the core. The master curves for water diffusion into the core and the humidity vs. time curves were determined following the procedures described in previous sections.

Figure 10 shows the master curves and Figure 11 the humidity vs. time curves. The activation energy, E_a/R, was 7550K for both systems. The lifetime of the cable (time required for the core to reach 95% RH) is projected to be well over 20 years. Both systems were below 90% RH at 20 years (measurements were still in progress when this paper was written).

The presence of SAP tape between the core and the jacket appears to provide sufficient protection. When SAP tape is added in the core region, it increases the time required for the core to reach a certain RH by about a factor of one-and-a-half to two. The core tape itself not only provides additional lifetime extension but also is necessary for longitudinal water blocking in case of catastrophic sheath failure.

In this case the cable structure is more complex than a single tube and so it is not possible to describe the system using an analytical model.

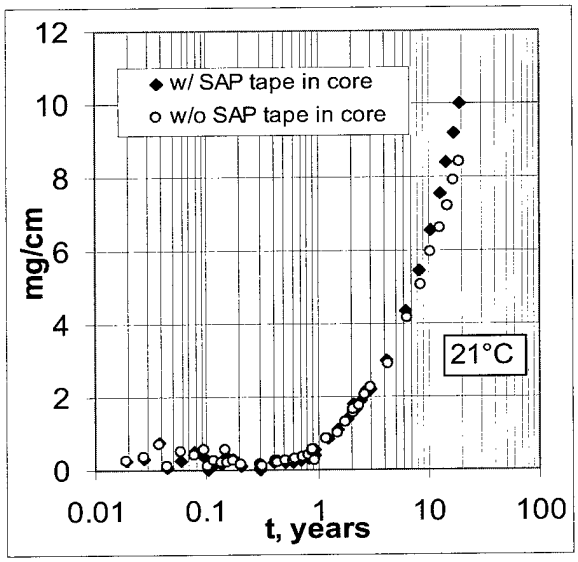


Figure 10. Master curve for water diffusion in an experimental cable containing ribbons with, and without SAP tape in the core.

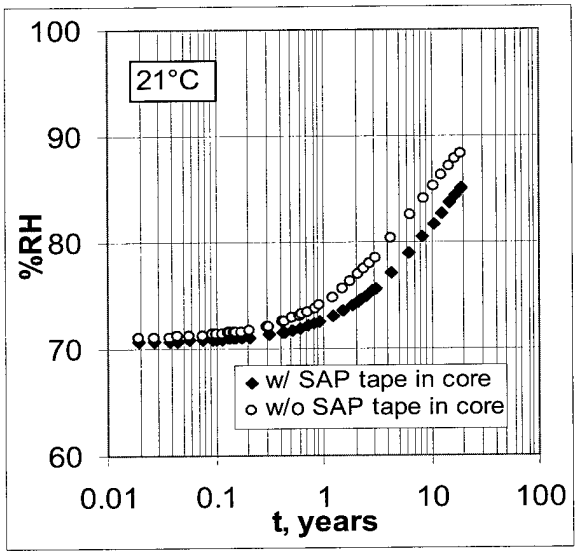


Figure 11. Estimated %RH in the core of experimental cable samples containing ribbons with, and without SAP tape in the core.

5. Conclusions

Three model experimental systems of water diffusion into cable tubes were described in this paper. (A) A polypropylene tube filled with a ribbon stack and cable gel, (B) a polypropylene tube containing SAP water blocking tape, and (C) a cable sample with SAP tape between the core and the jacket and a ribbon stack wrapped in SAP tape in the core region. The estimated %RH inside the core as a function of elapsed time for all three systems is shown in Figure 12. Cable lifetime was defined as the time required for the core to reach 95% RH. It was found that system A would reach it in less than a year of exposure to 100% RH at 21°C. System B would take about 25 years while system C appears to take more than 25 years.

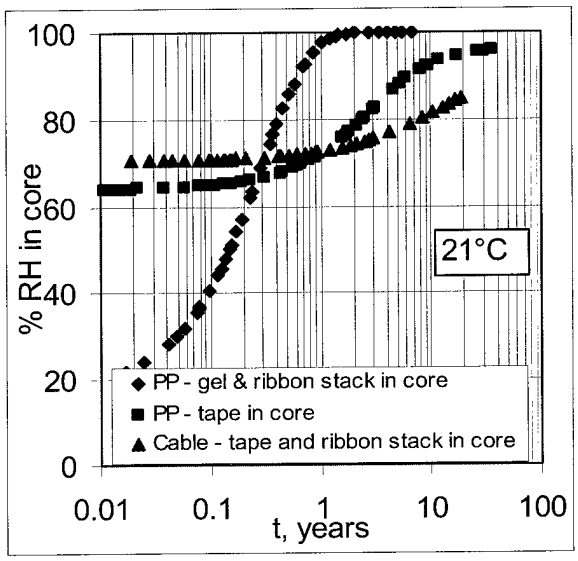


Figure 12. Estimated % RH inside the core of filled tubes immersed in water at 21°C.

The master curves for the same three systems are shown for the condition of 60°C water in Figure 13. This condition represents the worse case scenario where, for example, a cable in a duct is exposed to high temperature steam. Even in the unlikely case of continuous exposure to those conditions, the cable with the SAP tape will take more than a year to reach 85% RH in the core. It should be noted that the cable samples tested had no metal armor, which could further delay any water ingress into the core.

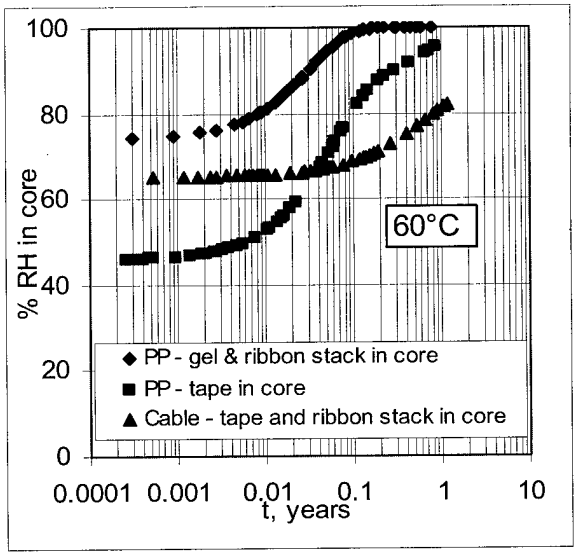


Figure 13. Estimated %RH inside the core of filled tubes immersed in water at 60°C.

The beneficial effect of the water blocking tape is apparent from these results. Even when present only between the core and the jacket, the SAP tape extends the lifetime of the cable beyond the 25-year timeframe for continuous exposure to 100% RH at 21°C. The presence of SAP tape in the central core provides additional water blocking capacity to the system by further delaying the saturation of the core region with water vapor. From these results SAP tapes appear to be viable candidates for replacing cable filling compounds in the cable central core.

The data for systems A and B were also compared to two analytical models. System A agreed best with the simple physical absorption model since no SAP tape was present in the system. System B could be qualitatively described by model B, which takes into account vapor-liquid equilibrium between water vapor in the core and the salt-water solution forming in the tape by the swelling of the polyelectrolyte powder. The polyelectrolyte nature of the powder in the tape causes the system to approach saturation asymptotically. As a result saturation is further delayed (compared to physical absorption) and the lifetime of the cable is extended. System C is too complex to be described by a simple analytical model, however it follows similar behavior to system B as shown by the data.

6. Acknowledgements

Special thanks to Dr. Pete Weimann of OFS for technical assistance and discussions.

7. References

[1] P. Anelli, C. Bosisio, E. Consonni, A. Ginocchio, "Water Getter Flooding Compound for Dielectric Optical Cables," *46th IWCS Proceedings*, p. 756 (1995).

[2] H. Paul Debban, Jr., Luis M. Bocanegra, C. Shawn Davis, Richard D. Small, Jr., Peter A. Weimann, Manuel R. Santana, "A New High-Density Central Cable Core Design", *49th IWCS Proceeding*, p. 1 (2000).

[3] W.S.M. Geurts, R. Ross, M.G.M. Megens, E.F. Steenis, "Moisture Penetration in XLPE and PILC Cables", JiCable '99 Proceedings, p.353 (1999).

[4] R. B. Bird, W. E. Stewart, E. N. Lightfoot, *Transport Phenomena*, Wiley International Edition, New York (1960).



Carl. R. Taylor

2000 NE Expressway, Norcross, GA 30071

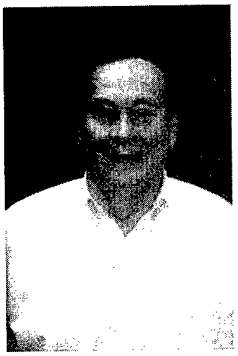
Carl. R. Taylor is currently a Bell Laboratories Technical Manager of the Materials Technology Development and Engineering Group at Lucent Technologies' main Fiber Optic Manufacturing site in Atlanta. The group has responsibility for the design and engineering of materials used in fiber optic cable products as well as responsibility for the quality of all incoming raw materials. He has previously been supervisor of the Plastics Engineering and Characterization Group in Atlanta and Supervisor of the Polymer Materials Research, Engineering, and Applications Group at Bell Laboratories in Murray Hill, NJ. Prior to joining Bell Laboratories in 1977, he earned a B.S. in Chemistry from the College of Wooster in Ohio and a Ph.D. in Physical Chemistry from the University of Wisconsin in Madison. He holds 21 patents and has authored or co-authored more than 50 publications.



Kariofilis Konstadinidis

2000 NE Expressway, Norcross, GA 30071

Kariofilis Konstadinidis is a Member of Technical Staff in the Materials Technology and Quality Engineering group at Bell Laboratories of Lucent Technologies Inc., Norcross, GA. He is involved in the development, qualification, and implementation of UV curable materials for optical fiber applications. He received his Diploma in Chemical Engineering from the Aristotle University of Thessaloniki, Greece, in 1987 and his Ph.D. in Chemical Engineering from the University of Minnesota in 1992. He did his post-doctoral work at Bell Laboratories in Murray Hill, NJ prior to joining Lucent in Norcross in 1995. He has been awarded two patents.



Richard D. Small

2000 NE Expressway, Norcross, GA 30071

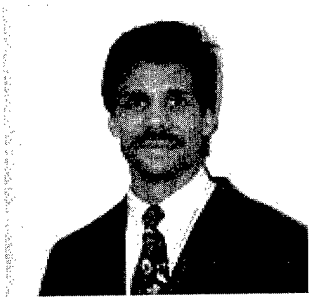
Richard D. Small is a Distinguished Member of Technical Staff in the Fiber Optics Materials Technology Group, Bell Laboratories, Lucent Technologies, Norcross, GA. His focus is on both material development of fiber optical cable products and the evaluation of UV curable fiber optical and ribbon coatings. In 1975 he obtained from the University of South Florida a Ph.D. in Physical Chemistry. From 1975 until 1978 he was at the University of Notre Dame, doing nanosecond laser mechanistic organic photochemistry. He joined AT&T in 1978. He has published over 40 outside technical papers in varied technological areas and has 12 patents. He is a member of the American Chemical Society and RadTech.



Manuel R. Santana

2000 NE Expressway, Norcross, GA 30071

M. R. (Manuel) Santana holds a Bachelor of Science and a Master of Science degree in Electrical Engineering from the University of Hartford and the Georgia Institute of Technology, respectively. Manuel joined Bell Laboratories in 1970 as a cable designer. He has been involved in fiber-optic cable design since the industry's birth in 1974. Manuel is a technology expert in all areas of fiber-optic cable: design, new processes and manufacturing technology. He is a member of various fiber-optic cable standards boards where he has a leadership position in the area of cable specifications. His career in fiber-optics technology has led to the development of the basic cable products that are the heart of the Optical Products SBU. These contributions include the Lightpack® and Accuribbon® core designs, the LXE sheath design, the Tactical military cable and the Duct Saver high-fiber count cable. Manuel was awarded the 1991 Hispanic Engineer of the Year for Outstanding Technical Contribution and the Alexander M. Nicolson trophy by the Lucent Intellectual Property department for patent commercial value. Manuel was appointed Bell Laboratories Fellow in 1994. In addition to his technical contributions, Manuel has made numerous customer presentations to support growing sales in the US and in Puerto Rico, Thailand, Japan, Spain, etc. He is a senior member of the IEEE and he has published thirty technical papers in various external publications. He has been granted twelve patents. Manuel lives in Roswell with his wife. Manuel and his wife have a son and a daughter and are members of The Landmark Church.



Richard H. Norris

2000 NE Expressway, Norcross, GA 30071

Richard H. Norris is a Member of the Technical Staff at Lucent Technologies in Norcross, Georgia. Dr. Norris joined Lucent Technologies in 1997 in the capacity of Development Engineer. He received his B.S. degree in Materials Engineering from North Carolina State University and M.S. and Ph.D. degrees in Metallurgical Engineering from the Georgia Institute of Technology. He is currently working in the area of Outside Plant Cable design and development. His technical affiliations include the Society of Plastics Engineers, ASM International, TMS and he is also a registered Professional Engineer.



Raymond P. DeFabritis

2000 NE Expressway, Norcross, GA 30071

Raymond P. DeFabritis is a Senior Technical Associate in the Materials Technology and Quality Engineering Group at Lucent Technologies inc., Bell Laboratories in Norcross, GA. Starting in 1968 with an AAS degree from the Academy of Aeronautics, his experience has been in microelectronics interconnection circuitry, materials engineering, and UV color codes for optical fiber/ribbon products. He has been awarded two patents.

Powder Free Super Absorbent Tapes and Yarns for Optical Fibre Cables

Michael A. Stradling
BP Global Special Products
Crayford, Kent
+44 1322 526 966

Frank Goene
Geca-Tapes
Rijen, The Netherlands
+31 161 224 108
f.goene@geca-tapes.com

Abstract
Traditionally optical fibre cables are flooded around the loose tubes with petroleum or thixotropic jelly to prevent ingress of water. However there are difficulties associated with the use of this type of water blocking, it is messy and prolongs the jointing process due to cleaning requirements.
Over recent years there has been a move towards 'dry' technologies such as tape or yarn coated with super absorbent polymer.

The use of super absorbent polymer also entails inherent difficulties as the powder can 'dust off' from the tape, possibly leading to health and safety issues such as 'slip' hazards, or particles of powder in the atmosphere.

A method has been developed for producing tape with a continuous non-powder super absorbent coating that addresses these issues. A solution of a pre super absorbent polymer is applied to a non-woven tape and cross-linked in situ. The resultant tape is also thinner than conventional tapes leading to thinner, lighter cables. The coating can be applied by a variety of conventional coating methods such as kiss roll, Meyer bar, flexography, and screen-printing.

Keywords
water blocking, super-absorbent, powder free, tape, yarn, optical fibre cable

1. Introduction
1.1 General
Over recent years there has been a move within the cable industry away from thixotropic gels and petroleum gels towards the use of tapes and yarns that have super absorbent polymers (SAP's) bonded to them. The advantages of these dry technologies are clear; they allow for easier jointing of cables with less messy cleaning regimes, cables can be manufactured that are lighter and thinner, and the process of cable manufacture is simpler as there is no need to ensure complete filling of the interstices within the cable to prevent ingress of water.

The first generation of cable tapes were designed for power cable applications. These materials consisted of two layers of non-woven with in between a blend of polyethylene powder and super absorbent powder as used in diapers. This first generation of tapes were characterized by it's high thickness (typical > 0,35 mm) and a swelling height of more than 5 mm to fill the large voids which were present in these cables.

As cable manufactures start using these water-blocking tapes in dry optical fibre cable there was a demand for thinner material. Another advantage of thinner tapes is that you have more length on a spool at the same outer diameter.

As the fibre density increased, the voids in the cable became smaller and the demand for thinner and low swelling material.

Another issue is dust, and in particular the SAP. As the SAP is not proper bonded to the substrate you can have loose powder in the cable and can cause micro-bending.
Besides this loose powder is more and more becoming an environmental and health issue.

Also the judgement of the performance of the tape itself did change over the years.
As in the beginning swelling height was one of the most important parameter, nowadays swelling speed and gel strength are the most important parameters.

Therefore both companies started to design a new type of water-blocking tape:

- Dust free
- Thin
- High swelling speed (> 80 % of the total swelling height in the first 30 seconds)
- Good gel stability

To achieve this no super absorbent powder could be used. BP special products developed a special super absorbent compound named Sahara what can be coated on any substrate.

During the development of this new generation of water blocking tapes different non-woven were tested to determine the best behaviour in the manufacturing process of the cable and in the cable itself.

It was found out that a spun bonded non-woven did give hardly any slitting debris and was therefore most suitable for this application.

Also with this spun bonded non-woven a thickness of below 0,15 mm can be achieved. These tapes are being used in fibre optic loose tube designs were the tape is applied over the buffer tubes.

1.2 Yarns
Another development what started at the same time was the development of water blocking binder yarns.

The function of these yarns bind is to the PBT tubes together. Due to the method of application (spiral and counter spiral) the binder yarns are capable of blocking the cable against further water ingress.

When using Sahara to make a water blocking binder yarn there are only advantages:

- No loose powder
- No extra thickness of a bonding layer for the SAP
- Low shrinkage
- Flat
- Flexible.
- Strong
- Low weight: long lengths on a spool

This results in a dust free production, no imprint of the yarn in the tube (either due to the high thickness and or shrinkage).

1.3 Coating

Super absorbent polymers of the sodium or potassium poly-acrylate type are usually prepared in the aqueous phase resulting in an alkali soluble polymer that is subsequently cross-linked. To alleviate the problems of SAP based tapes as described above in was thought that it might be possible to coat the alkali soluble poly-acrylate base solution of an SAP directly onto non woven tape and cross-link the material in-situ. The resultant tape would be mono-layer, have no powder therefore would address both the technical and design issues of conventional tapes, and remove the health and safety issues associated with use of super absorbent powders.

2. Polymer selection

One of the difficulties associated with this project was the selection of a polymer suitable for cross-linking in situ. Discussions with a leading manufacturer of SAP's led to the development of a potassium polyacrylate polymer modified with the chemical technology usually used to manufacture self cross-linking styrene acrylate polymers for the production of inks and paints. This technology allows the material to cross-link as it dries, without the use of hazardous cross-linking agents such as polyethylene-imines.

The polymer must be cross-linked as if it is not then it remains simply water soluble and not super absorbent, the degree of cross-linking controls the speed and extent of swelling of the polymer as it absorbs water.

2.1 Acceleration of cross-linking

The cross-linking technology used can be activated by heat or the increase in concentration of the polymer as water evaporates. However both of these processes are relatively slow therefore requiring either high temperatures or extended curing times. In the paint or ink industries a common way of accelerating cross-linking is to use a cross-linking promoter, usually an ammonium carbonate salt of a transition element such as zinc. The cross-linking promoter is activated by changes in pH, that is, when the pH of a solution of polymer drops below about 8.5 the transition metal salt accelerates the cross-linking of the polymer. If the base polymer is solubilised using a volatile alkali material such as ammonia or an ethanolamine then as it dries the volatile material will be driven off, lowering the pH and allowing the cross-linking to occur.

2.2 Control of cross-link density

A balance has to be found in the level of cross-linking used. Very highly cross-linked systems have a very rapid response to the ingress of water, but do not swell by a very large amount. Lightly cross-linked systems will swell by a very large amount, but only relatively slowly. Of primary importance in the water blocking of cables is the prevention of 'water tracking', that is the progress of water along a cable after it has gained entry through a damaged section of sheath. A corollary of this is that the way to prevent water tracking is to block interstices as rapidly as possible, however it is not necessary to 'over-block', that is in cable design it is not necessary to use a tape with a swell height of twenty millimetres to block a two millimetre gap!

2.3 Drying conditions

For optimum water absorption the polymer molecules should be perpendicular to the water interface. Obviously this allows the most rapid penetration of water into the polymer matrix for rapid adsorption; also if the polymer molecules are coherently aligned the matrix will swell more. However the control of polymer alignment is problematic as many factors can affect the polymer orientation. The most significant factor is the evaporation rate; a high rate will tend to align the polymer whereas a low rate will allow the polymer chains to 'relax'. It is at this stage that the selection of the alkaline component is most significant. To achieve optimum performance the cross-linking should take place as the polymer molecules are aligned therefore 'locking' them in place. To a large extent this will depend on the method of application of the polymer solution and the drying system available, for example, if the polymer solution is applied by a kiss roll system it must first be diluted to a suitably low viscosity and will therefore contain a large amount of water. The water must be removed by heat (infrared driers or 'can' driers) but the polymer must not cross-link until the polymer chains are aligned, a slow evaporating alkaline such as tri-ethanolamine should therefore be used so that the solution remains alkali until a high non-volatile content solution has been reached. Conversely, when using a technique such as screen-printing a much higher viscosity and therefore non-volatile content may be used; it is therefore desirable to use a much 'faster' amine such as mono-ethanolamine or ammonia.

2.4 Rapidity of swell

As previously mentioned the primary concern in water blocking a cable is how rapidly the interior spaces within the cable are blocked by the super absorbent polymer. Control of this speed can be achieved in a variety of ways; for instance, the higher the molecular weight of the polymer the more super absorbent it is. Unfortunately, a limitation of the system described in this paper is that there is an upper limit on the molecular weight of the polymer; as the molecular weight of the polymer increases, the viscosity of the solution increases in an exponential fashion and the solution quickly

becomes impossible to handle on conventional printing equipment.
The most obvious way to increase the rapidity of swelling is to increase the surface area to volume ratio of the coating. An obvious way of doing this is to print dots of polymer rather than a continuous film however this option is only available where a printing process is used such as flexography, gravure or screen-printing. Where a coating process such as Meyer bar or kiss roll is used some other way of increasing the surface area must be used; in this case a physio-chemical means. A highly water soluble surface active agent that is incompatible with the polymer is dispersed in the system; when the water borne film is dried this liquid product remains in the film forming 'tunnels' through the polymer matrix. On subsequent exposure to moisture the water will effectively be sucked into these tunnels by the surfactant and more of the polymer will be exposed to the water more rapidly, resulting in more rapid swell.

Also, these tunnels of surfactant have the additional benefit of physically plasticizing the film, making it more flexible.

2.5 Blocking

Once dried and cured the film will obviously absorb moisture from the atmosphere and become tacky which may lead to 'blocking' in the reel. However this problem may be overcome by the addition of a small amount of an anionic emulsion of a Fischer-Tropsch wax. This type of wax emulsion has the advantage of containing only a very small amount of surfactant and the wax itself is very hard and crystalline. During the drying process the wax melts and migrates to the surface of the film; as it subsequently cools it forms small crystals on the surface of the film that prevent blocking and make the material abrasion resistant. Waxes are of course generally water repellent and one would expect that wax on the surface of the film would slow down water uptake; however as the wax crystals in this case are so small and present in such a small amount the water is not repelled and no slow down is observable.

3. Authors

Michael A. Stradling started work with Coates Brothers Inks in 1984 after leaving college with an Ordinary National Diploma in Science. In 1993 he started working for Dussek Campbell (now part of BP Global Special Products) on a variety of projects in the barrier coating and specialised wax field, and more recently, in the cable products area.

Frank Goene

Born 24-03-65

Bachelor degree in Chemical engineering

From 1987 till 1994 Lantor BV dvelopment engineer Firet Cable Wrappings

From 1994 till 2000 BW Industrial Manager R&D

From 2000 Manager R&D Geca Tapes

UV Cure Fiber Optic Buffering Resins

David Chase, Nancy Coster, Andrew Gardiner, Keri Unterzuber, Ed Murphy

DSM Desotech Inc.
1122 St Charles St., Elgin, IL 60120

Abstract

UV cure buffer resins for upjacketing of optical fibers often require good flexibility at low temperatures. Some present acrylate oligomers are based on silicone copolymer polyols. The synthesis of these oligomers is often difficult and the derived compositions tend to be quite costly. Also these materials are not usually suitable for single-coat buffering applications. A new generation of buffering resins is discussed which are not based on silicone polyols. These new buffer resins have demonstrated easy application, improved compatibility, and good performance properties, including greater resistance to water absorption in accelerated environmental testing. They are also suitable for compositions with reduced flammability. The new oligomer chemistry allows the formulation of buffer resins with UL 94 rating of V0 but are halogen-free, and are still durable and clear. These new resins are also suitable for two-coat or one-coat upjacket applications with excellent handling properties and ease of stripping.

Keywords

UV cure, buffer resin, upjacketing, flame retardant, PPG oligomer, silicone oligomer, nonflammable buffer.

Introduction

Due to the rise of the Internet, more and more consumers are demanding higher bandwidth and the need for fiber to the home or desk. Although we may be seeing a slowdown in the long haul market for the up-coming year, the access and premises markets are expected to grow at 30% over the next 4-6 years. Tight buffered fibers are used in these short length cables such as metro rings and access cables for fiber to the home; they are also used in premises applications including the backbone, plenum and riser cables in office systems. Tight buffer constructions are preferred over loose tube because of higher impact resistance and higher flexibility. Loose tube construction can also be more susceptible to water if the tubes become cracked allowing water to fill voids in the gel layer.

Tight buffer fibers are made by taking a standard 250 micron fiber and putting an additional UV coating over the top (up to 400-500 microns) then extruding a thermoplastic layer over top taking the thickness to 900 microns. The UV material is a low-modulus material that protects and cushions the fiber from stress. The thermoplastic (PVC, PP, Polyamide) layer can be replaced by a second UV layer that provides toughness. This two-layer UV system has also been successfully replaced with a single layer of low modulus UV material.

UV cured tight buffer assemblies have several advantages over thermoplastic for cablers. The UV tight buffer can be applied up to 400 or more microns by a standard UV inking line by simply changing the die size. This offers considerable savings compared to installing an extruder and will also reduce the large production floor space required for an extrusion process for the tight buffer. The thermoplastic tight buffer process is characterized by long runs and high scrap rates as the resin color is changed. UV can be turned off and on almost instantly, making short runs a reality and dramatically reducing scrap fiber. The UV tight buffers can be easily controlled to ensure concentricity at every thickness while thermoplastic draws below 600 microns will vary greatly and are prone to fiber breaks. Another considerable advantage for UV is the higher line speeds; extrusion only runs about 200 m/min while UV can reach speeds over 600 m/min.

UV Cure Upjacketing Assemblies

For several years DSM Desotech and its affiliate Japan Fine Coatings, have offered UV cure resins for tight-buffer upjacket assemblies. Most typically these assemblies were composed of two parts; a low modulus inner resin known as Cablelite 950-701, and a higher modulus outer coating Cablelite 3287-9-75. In their usual usage the 950-701 was applied to clear or colored fiber to raise the diameter to about 500 microns. Then the 3287-9-75 outer buffer further raised the diameter to about 900 microns. It is very common for in-tandem application of these coatings in the manner of coat-cure-coat-cure. **Table 1** lists the general characteristics of Cablelite 950-701 and 3287-9-75.

As can be seen from **Table 1**, Cablelite 950-701 is a very low modulus composition with a low Tg as defined by the Tan δ maximum of DMA for a 75 micron film cast and cured on glass plate. This soft inner-buffer provides excellent physical and environmental protection to the individual fiber over a broad range of temperature and exposure conditions.[1] In order to provide UV cure compositions with very low modulus and Tg, it has been the practice to use urethane acrylate oligomers prepared from various polyoxyalkylene polydimethylsiloxane (PDMS) copolymers, which may have hydroxyl functionality on the chain ends or mid-chain pendant.[2]

Our experiences at DSM Desotech, however, are that the preparation of urethane acrylate oligomers from siloxane copolymers is often problematic. Most times the oligomer is clear and homogeneous with good compatibility with other common acrylate components, but sometimes they are

not. It has been demonstrated that the cause of these difficulties is the residual strongly basic catalysts used in the preparation of many PDMS polyols via the alkoxylation with ethylene or propylene oxide. These basic catalysts are known to strongly promote the cyclotrimerization of both aromatic and aliphatic isocyanates.[3] These residual catalysts cause the resultant urethane acrylate oligomer characteristics to be overly sensitive to small variations in the starting raw materials and local reaction conditions. The removal or neutralization of these residual catalysts adds considerable cost the final formulated buffer resin.

A New PPG Based Resin

In order to alleviate the batch-to-batch variability problems of the siloxane based materials, and to provide a more economical inner tight-buffer, we have synthesized a polypropylene glycol based oligomer, and formulated a low modulus buffer resin known as Cablelite 9D7-358. This UV cure composition provides the same superior mechanical and environmental protection as Cablelite 950-701. Its physical characteristics are shown in **Table 2**. This low modulus inner-buffer resin is suitable for tandem application with Cablelite 3287-9-75 or other tough UV cure outer-buffer resins. Or the inner-buffer coated fiber can be spooled and used in other off-line cable construction processes.

One additional benefit of the PPG based buffer resins is a more hydrophobic character. A common characteristic of cured compositions when immersed in water is an initial weight gain followed by a net weight loss upon extended immersion. Keeping these weight changes as small as possible is a desirable trait sought by formulators. It can be seen from the tabulated characteristics of the cited compositions that the new PPG based buffer resin 9D7-358 has less weight change in room temperature water soak, both for the short and long term.

DSM Desotech researchers have also found that 9D7-358 is suited for the incorporation of certain additives for the reduction of flammability such as aluminum trihydroxide (ATH). Although the development of UV cure buffer resins with reduced flammability is in the very early stages, a typical example is also shown in **Table 2** as Cablelite 9D7-369. ATH is a well-known pigment additive to provide reduced flammability in compositions which are translucent to opaque.

Transparent Nonflammable Buffers

While the resins developed to this point were suitable for many applications, collectively there were several deficiencies. In the case of 9D7-358, it is not readily suitable to one-coat upjacket applications, or to off-line two-coat systems. This is because the fully cured buffer resin retains a tendency to adhere to itself on the spool. And the 9D7-358 is a flammable composition. And while the buffer 9D7-369 is nonflammable, and not at all adherent to itself, it is very nearly opaque due to the dispersed flame retardant additive pigment. A further goal of our development efforts then was an optically transparent nonflammable buffer resin with suitability for on-line or off-line two coat applications, and for one-coat upjacketing to 900 microns. A clear and transparent resin allows the tight buffering of colored fiber, while still retaining the ease of individual fiber identification.

The use of PPG based oligomers, with their excellent compatibility with other typical UV cure components, allowed for buffer resin formulation which also utilized various organo-phosphorus and organo-nitrogenous flame retardant additives. The resulting resin 9D7-463 was found to meet all of our present criteria. The typical properties of this nonflammable clear buffer are shown in **Table 3**. And one further benefit of this relatively low modulus resin is that it is very easily stripped from most colored fibers, and especially those colored with Cablelite 751 ink.

Continuing Research

The synthesis and formulation of UV cure inner-buffer resins based on PPG instead of PDMS, represents a significant advance in economy and product reliability. Research and development activities continue at DSM Desotech to expand this chemistry to further enhance its utility in future applications where clear, nonflammable, and durable buffer resins may be required.

Acknowledgements

DSM wishes to thank Nate Rosebrooks of Fluid Coating Technology, Inc. for valuable assistance in preliminary evaluations of a number of buffer resin formulations. And the authors wish to thank Chris Baker and Jack Kelly for all their contributions.

References

1. Ansel, R., et.al., U.S. patent 4496210, (1985)
2. Aoki, H., and Nagasaki, Y., *Current Trends in Pol. Sci.*, **2**, 83-94 (1997).
3. Parodi, F., "Isocyanate-derived Polymers", *Comprehensive Polymer Science*, **5**, 387-412 (1989).

Table 1:
Cablelite UV Cure Buffer Resins

	950-701	3287-9-75
Liquid Coating:		
Viscosity: mPas @ 25°C	2750	9300
Density: g/cc @ 25°C	1.02	1.10
Cured Coating:		
Buffer type:	Inner	Outer
Tensile Strength: MPa	1	30
Elongation: %	22	40
Secant Modulus: MPa	4	730
DMA Tan δ: °C	-116	70
E'=1000 MPa: °C	-118	26
E'=100 MPa: °C	-66	66
H_2O Soak Wt. Change:	2.2%/24 hr	3.0%/24 hr
	-3.0%/336 hr	-----

Table 2:
Cablelite UV Cure Buffer Resins from PPG

	9D7-358	9D7-369
Liquid Coating:		
Viscosity: mPas @ 25°C	2800	3150
Density: g/cc @ 25°C	1.03	1.25
Cured Coating:		
Tensile Strength: MPa	1	7
Elongation: %	32	11
Secant Modulus: MPa	2	108
DMA Tan δ: °C	-42	-51
E'=1000 MPa: °C	-56	-41
E'=100 MPa: °C	-46	80
H_2O Soak Wt. Change:	1.4%/24 hr	-----
	-0.2%/336 hr	-----

Table 3:
Cablelite UV Cure Nonflammable Buffer Resin

	9D7-463
Liquid Coating:	
Viscosity: mPas @ 25°C	2000
Density: g/cc @ 25°C	1.18
Cured Coating:	
Tensile Strength: MPa	7
Elongation: %	26
Secant Modulus: MPa	53
DMA Tan δ: °C	38
E'=1000 MPa: °C	-5
E'=100 MPa: °C	32
H_2O Soak Wt. Change:	-0.9% / 24 hr
	-0.8% / 100 hr
Transmittance: 400-800nm	> 85% @ 250μ
UL 94 Flammability Rating	V-1 to V-0

New Generation UV Color Coatings for Optical Fiber

Shahab Siddiqui, John R. Szwec, Kariofilis Konstadinidis, David (Tat) Au, and Carl R. Taylor

Bell Laboratories, Lucent Technologies, Inc., 2000 Northeast Expressway, Norcross, GA 30071

1-770-798-2871 ss3@lucent.com

Abstract

Optical fibers are colored mainly for identification purposes. The color-coating layer is applied to fully cover the optical fiber all around with a continuous defect-free thin robust polymer film. However, this thin color-coded layer can greatly impact both the glass/fiber transmission characteristics as well as final product performance attributes of finished cables. For that matter, it is highly critical to choose an inking material with well-balanced material properties that is processed optimally to provide acceptable color-coded fibers for downstream packaging into ribbons and cables. The precursor material requirements have become very stringent in recent times with the advent of new fiber and cable product designs. For example, new optical fibers are very sensitive to micro-bends and recent cable designs require higher fiber packing density in the cable. The proper selection of the color coating material plays a key role in delivering these new product design features. This report describes salient material design attributes of three new generation state-of-the-art commercially available UV curable inks from major suppliers. A portfolio of UV ink materials is thus compiled here listing critical ink raw material and colored fiber properties. This comprehensive information package helps to efficiently select a coloring material that is in compliance with the evolving new fiber and/ or cable product designs.

Keywords

Optical Fiber; coatings; UV ink; ribbons; cables; interfacial adhesion; surface friction.

1. Introduction

Today almost all optical fibers used worldwide make use of ultra violet (UV) curable pigmented polymer coatings (inks) for coloring purpose. Even two to three years ago, solvent-based pigmented inks were predominantly used for that purpose. These inks have been alarmingly polluting the environment in recent years by emitting mostly toxic and hazardous air pollutants putting both the environment and human health at great risk. UV curable inks not only provide higher throughput and better quality colored fibers but also promote a safe and healthy working environment by eliminating solvents. In addition to this outstanding health boon, it has been recently realized that the cost of UV colored fiber, by virtue of consistent production of more and more defect-free colored fiber day after day, is approaching the low price tag once associated with solvent ink systems. Despite all these benefits, the UV system of yesterday still lacks some critical features for the rapidly evolving new fiber optic and cable designs of tomorrow. The next-generation ink material is required to have desirable features and it has to be processed properly in order to produce the right end product. New generation optical fibers have provisioned higher bandwidths by intricate design approaches in glass properties and optics; however, in doing so fibers have become more micro-bend sensitive at the same time. Likewise, next generation fiber optic cable designs call for putting more colored fibers into the same size tube for denser packaging. These are just two examples of many innovative design features in the new generation fiber and cable. New product features are continually evolving with seemingly more demanding requirements. Although the color coating is applied externally on a fiber optic as a penultimate step to final product packaging, it seems to impact the glass transmission characteristics quite significantly. Thus, it is highly critical to design and develop next generation inks that will satisfy the new product diversity of tomorrow.

In this paper, we compare three new UV curable inks (Ink A, Ink B and Ink C) from three premium UV ink suppliers to benchmark against our current product as well as scope them out for next generation use. The inks were evaluated as as-received products available commercially with very little or no modification. However, they were required to have state-of-the-art material properties for the evaluation. The suppliers have presumably made these new generation inks by incorporating valuable inputs from their customers in the pursuit of new cutting-edge fiber optic products. It is expected that this evaluation would successfully provide the specific features of the next-generation fiber and/ or cable design. It is to be emphasized here that a set of features of each series of inks is valuable information since each is expected to serve the requirements of a unique product design. Thus, the real benefit of this portfolio development work is in widening the scope of material know-how on a variety of important ink features. So far this approach has been useful to us in meeting challenging design criteria for future fiber optic products.

2. New Generation UV Ink Material Requirements

UV curable color coatings (inks) have found rapid acceptance in the fiber optic industry in the last few years for faster processing speed, better product quality and safer environment. The main constituents of UV curable ink formulations are monomers, oligomers, photo-initiators, some essential additives and certainly pigments. The inks are ~100% solid systems (that is, completely solvent-free). This absence of any volatile solvents made them environmental friendly and highly attractive for processing without exposure to unhealthy VOC (volatile organic compound) emissions. However, the first-generation UV inks, in general, were costlier than solvent-borne inks. The faster processing speed was thought to compensate for it by boosting colored fiber throughput. Certainly the UV ink material quality has always been superior to traditional solvent inks. The viscosity is well controlled and the ink dispersion is very stable. The cure is more predictable and the colored fiber surface properties (friction, adhesion and stiffness) are more amenable to making robust products

consistently. All these features were found to be acceptable initially for earlier generation fiber optic products. More recently, however, these pigment-based coatings have undergone significant improvements in key materials attributes in order to be considered for more challenging future optical fiber product design features. Some key ink material properties for new generation inks are listed below.

- **One resin system for all ink colors**
- **Higher photo-cure speed**
- **Higher pigment loading (thinner color coded layer)**
- **Better ink quality (finer dispersion, longer shelf life, tighter low viscosity range, etc.)**
- **Improved surface properties**
- **Lower cost**

Unlike some original UV systems in the past, the new UV inks are based on a single resin system to formulate the total multi-color package. Because of having more than one resin base to make all colors in the older systems, there was wide variation in viscosity of liquid inks and wide variation in static charge build-up on colored fiber surfaces. This old formulation design made processing of inks quite cumbersome, when more than one set of operation control parameters were used for optimal processing. Also, the different extent of static charge build-up in various colors because of different resin base made ribbon packaging more prone to defects in the product geometry. Thus, this new material formulation with a single clear resin base to make all colors helps in streamlining the color process operation as well as ribbon processing.

The elimination of solvent tends to impart higher viscosity to UV inks compared to traditional solvent-based inks. This makes it somewhat difficult for ink processing specially at high speed. The situation becomes even worse for inks having wide viscosity range across all colors as noted above, which was the case for some older UV ink systems using more than one resin base. In the new generation inks, all ink colors have low and narrow viscosity range to help set up uniform processing across the board (see Table 1). The absence of solvent in UV inks also makes them more prone to building large static charge in the cured polymer film/ coating, which is counter-productive for making defect-free products. The electrostatic charge situation is escalated in older systems using more than one resin base to make the whole spectrum of colored inks, as mentioned above. The new generation UV inks have addressed them with proper formulation and material design strategy to minimize electrical effect to some extent. This is certainly an improvement over old generation UV inks.

Traditionally, there have been 12 industry color standards. Some new design for specific applications requires more color hues, which have to be discernible on a single fiber application. So there is high demand for more than 12 traditional colors for future cable designs. With the new inks available commercially, there are now more than 12 colors to accommodate this new direction in product design.

Undoubtedly, UV inks are cured very efficiently because of their sensitivity to UV light. However, there is continued pressure to even further improve the cure speed to attain much higher productivity. This is a tough requirement considering there is also an increasing demand for thinner color-coded fiber without sacrificing color intensity. In order to have the same or equivalent color vibrancy at reduced thickness, pigment loading in the ink formulation has to be made higher. On the one hand, the photo cure speed can be improved by intricate interplay of the proper selection of the resin system and the right concentration and type of photo-initiator package. On the other hand, higher pigment loading simultaneously poses a threat to the cure since it competes with the photo-initiator for light absorption. The risk of cure impediment by higher pigment loading can have serious consequences on the overall design of a material system for higher photo speed. Thus, alternative design routes to intensify colors are in order. Also, the particle size affects the cure speed. Generally, coarser particles aid in photo curing by allowing efficient light penetration into the bulk due to scattering. However, large particles are also suspected in inducing micro-bending optical loss due to stress build-up in the fiber. So for bend-sensitive fiber designs, there is definite inclination for finely dispersed low particle-count inks without jeopardizing ink cure speed. Some of the new generation inks have been optimized for performance by delicate formulation strategy. They show higher color intensity, higher cure speed and lower particle count (see Table 1).

Surface properties of the cured polymer at the air/solid interface are important for determining critical end-product performances.

Table 1. Material Properties of New Generation UV Curable Inks

Ink	Available Colors	Viscosity @ RT	% Cure @200 mJ/cm^2	Particle Count	Color Vibrancy	Cost
A	18	1700-3000	~85%	Good	Intense for all colors	Medium
B	12	2700-4500	~85%	Marginal	Not Intense	Low
C	12	2400-3300	~90%	Marginal	6 Colors Intense	High

Firstly, the use of one clear resin base in the ink formulation for all colors helps control the surface properties uniformly. Secondly but more importantly, the use of an additive appears critical in balancing surface properties. All new inks seem to have reactive additives/ slip agents added in the formulation in order to modify surface tension of the liquid. Maintaining the surface energy of the solid film quite tightly for a single set of inks across all colors is critical for controlling the surface friction, static electricity and interfacial adhesion of colored fibers.

Finally, the new generation inks have to be priced less than older versions in the fiercely competitive market of today. Although the ultimate criteria for grabbing the market share are its product performance features, still one of the main bottom line drivers is the final cost of making the product. So low cost may turn out to be a critical feature in the final selection of a coloring material. The overall objective is to make a robust product consistently with all the new design features as well as make it cheaply at the same time. The enhanced material properties for the three new generation inks are summarized in Table 1.

Mechanical properties of the clear resin base materials for three inks series were evaluated. The glass transition temperature (T_g) of the ink base is rank ordered below:

Ink A> Ink B> Ink C

3. Colored Fiber Properties

New UV ink materials confer a host of critical physical, mechanical, electrical, and chemical properties on the well-cured colored fiber. The following colored fiber attributes are considered necessary when designing and developing the next generation cutting edge fiber optic products.

- **Low surface friction for all colors**
- **Low electrostatic charge build-up**
- **Optimal degree of cure on fiber**
- **Balanced Interfacial adhesion**
- **Reduced color coding thickness**
- **Acceptable micro-bend resistance**
- **Acceptable fiber aging**
- **Acceptable ribbon/ product performances**

For comparative evaluation purposes, all the inks were processed using a set of pre-determined conditions (high and low cure conditions at two specific speeds: high and low). Compared to older generation inks, the new UV inks processed very well at higher line speed to give nominal colored layer thickness (6-7 μm). The processing parameters were held uniform for all colors because of their comparatively tight viscosity range. Up to a certain coloring line speed (75- 150% increase over the previous line speed) there was no die leaking, color streaking and color skip despite the low viscosity of the inks. It is not to be inferred, however, that using higher coloring speed successfully is only because of material improvement alone but also, this is because of UV process technology improvements at the same time. One of the ink series (ink A) was applied using a smaller die to achieve lower overall colored thickness (30% lower thickness). This was done successfully without any apparent coloring-defect because of higher color vibrancy for the series.

3.1 Surface Friction and Surface Charge of Colored Fibers

The recently made colored fibers showed relatively low surface frictions for all the series of inks evaluated in this study (see Figure 1). In the figure is shown relative surface friction at one cure condition, where all the fibers are known to have cured well. At other cure conditions, the same trend follows for the three series. That is, series C has always demonstrated very low coefficient of friction at all conditions compared against either A or B series. The average relative surface friction for C is below 1 and that for A is below 6. Even the higher value of 6 for ink series A is much below than that for the older generation inks. Generally speaking, lower surface friction represents a much smoother surface condition and is favorable for good packaging loss in the spool especially for new micro-bend sensitive fiber. Actually, ink C showed negligible increase in added loss due to coloring for bend-sensitive products. However, ink C also demonstrated very low ink/matrix adhesion (*vide infra*) presumably due to the same reason, which is presence of the slip agent in larger concentration than that in either ink A or ink B. For some end-product design features, ink C may be desirable. However, for products requiring some level of ink to matrix adhesion as with some specific ribbon designs, either ink A or Ink B is a better choice because of higher interfacial adhesion (*vide infra*). The relative low surface friction across all colors in a series is also a favorable feature in ribbon processing operations. If the surface friction range within a series is wide, it affects ribbon planarity, which in turn affects several key ribbon features. That was generally the case with the older version UV inks.

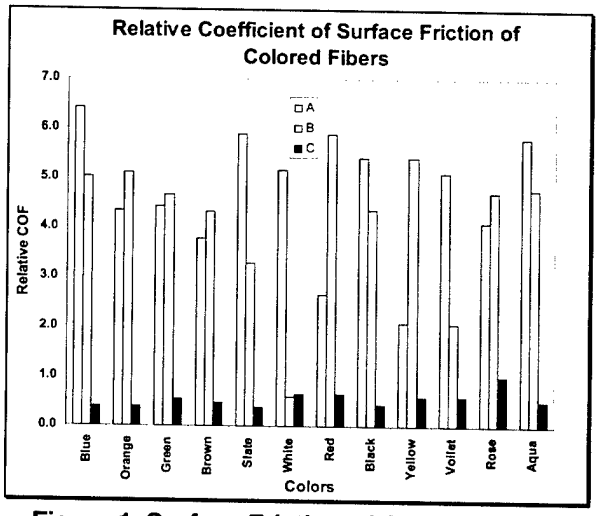


Figure 1. Surface Friction of Colored Fibers

All UV colored fibers (series A, B and C) showed higher electrostatic charge build-up on the surface than the solvent-borne inks used prior to the advent of UV curable inks. Apparently charge dissipation in UV cured film is less efficient than in solvent-based inked film. In downstream applications of all UV colored fibers, extra and more efficient anti-static devices were used to counteract this undesirable effect.

3.2 Optimal Degree of Cure on Fiber

UV cured inks can be processed much faster than solvent-based inks. This is an important attribute of UV inks. However, in recent years there has been a big push towards systems with much faster cure speed than the traditional UV inks used in the first generation. This is mainly for throughput improvement, which

lowers cost and increases productivity by making more defect-free colored fibers in the same given time. The inks were evaluated at various cure conditions by varying line speed and lamp intensity conditions in combination. Both C and B series inks appear to have faster curing characteristics than series A as determined by FTIR (see Figure 2).

All the inks shown in Figure 2 were cured using a particular set of curing condition for comparison purposes. Clearly, ink A seems to have lower % cure than either system B or system C as determined by the disappearance of the >C=C< peak of the acrylate functional group in the FTIR (average cure is 97% for C, 95% for B and 91% for A). Admittedly, this series-to-series comparison is not always very straightforward. Each series has more than likely a different resin base and hence, is likely to show different level of cure anyway (that is, a different % cure number under the same conditions), despite being "fully cured" in each case. However, it certainly shows % unsaturation in the resin, which is potentially available for covalent bonding to other reactive functionality (for example, C=C in ribbon matrix material). That is why, this tool can be useful for comprehending the extent of ink/matrix bonding (hence, interfacial adhesion). The higher the percent cure the lower the unsaturation and hence, lower the ink/matrix adhesion, especially within one ink series. Hence, the knowledge of % cure as a function of cure conditions within a series is more relevant and valuable information in establishing the final coloring line speed for the ink.

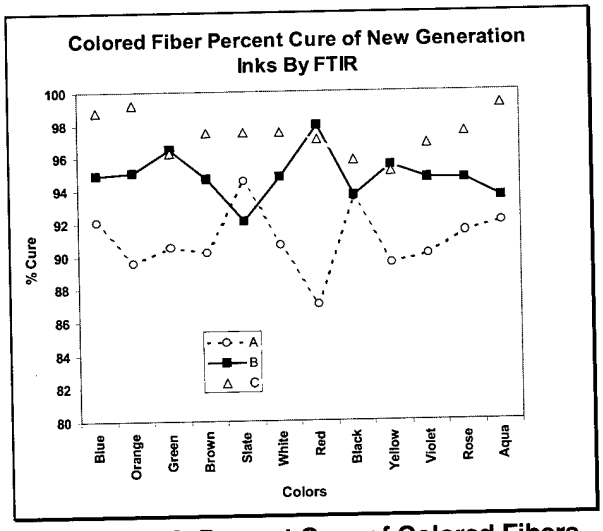


Figure 2. Percent Cure of Colored Fibers

In Figure 3 is shown the percent cure of ink series C, which still maintains a higher percent cure (~95%) at 50% higher coloring line speed.

Similar evaluations were performed for Ink A and Ink B. As opposed to Ink C which showed peak performance at all curing conditions (% cure ~95-97%, see inset of Figure 3), both Ink A and Ink B showed significant drop in cure with higher speed and/ or lower cure conditions. It appears from this work that Ink C can be used to boost up coloring line speed significantly.

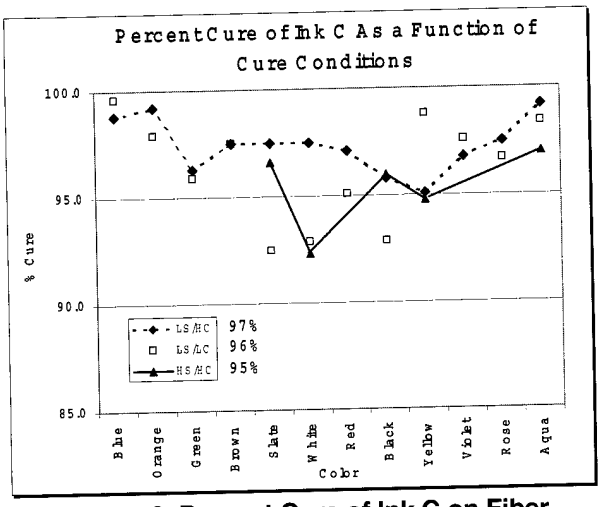


Figure 3. Percent Cure of Ink C on Fiber

LS=Low speed, HC=High cure, HS=High speed and LC= Low cure

3.3 Balanced Interfacial Adhesion

There are three important interfaces in a fiber optic ribbon matrix: (1) glass/primary coating interface, (2) secondary coating/ink interface and (3) ink/matrix interface. All of them are critical in determining its final product performance attributes. Inadvertent loss of adhesion in any one of the interfaces is tantamount to causing havoc in product performances including unnecessary stress in the fiber optic, which affects optical transmission. Ideally, the ink/matrix interface is designed to the weakest of the three linkages since easy matrix removal is a highly desirable design feature in ribbon cables for easier mid-span entry. The fiber coating/ink interface, on the other hand, needs to be robust in order to have excellent color retention. Thus, the state of colored fiber surface is highly crucial in imparting the right interfacial adhesion characteristics.

The three ink series were first evaluated for fiber coating/ink adhesion characteristics by a proprietary test method. They all showed acceptable to very good adhesion at this interface. Most likely, this is attributable to the original fiber used in the first place since adhesion development at this interface is predominantly determined by the surface condition of the substrate fiber.

Next, the inks were evaluated for ink/matrix adhesion by a specially developed in-house test procedure. The results are shown comparatively for six selective colors in Figure 4.

Ink B has the highest adhesion and Ink C has the lowest adhesion when evaluated against a common matrix material under identical experimental conditions (average values for A, B and C are 7.0, 9.1 and 1.4, respectively). Adhesion at this interface is predominantly determined by the state of colored fiber surface. It is known that physical, chemical and mechanical bonding all contribute to the interfacial development between two dissimilar materials including polymers. From chemical point of view, it is expected that Ink C would have the lowest ink/matrix adhesion since it has the lowest degree of C=C (highest percent cure, see Figure 2) available for bonding to the matrix. This is the case, as shown in Figure 4. Following the same logic, however, Ink A

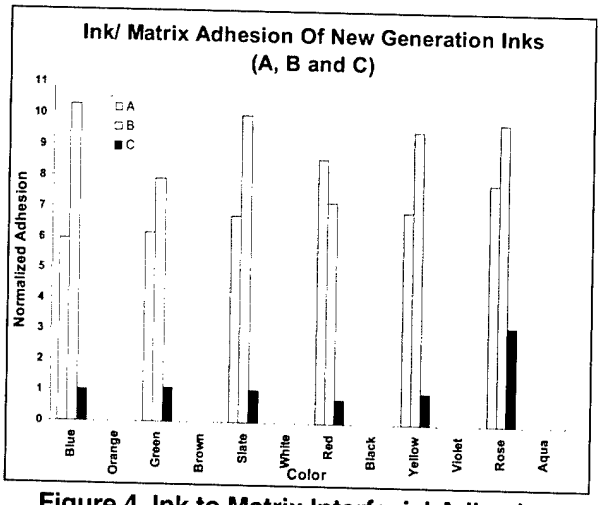


Figure 4. Ink to Matrix Interfacial Adhesion

should have the highest bonding and hence, highest ink/matrix adhesion. As clearly shown in Figure 4, this is not the case. In fact, Ink B has the highest ink/matrix adhesion. Thus, it appears that interfacial adhesion at this boundary is not largely determined by chemical bonding between C=C groups. Rather this phenomenon can be greatly offset by other external factors of largely physical in nature. For example, the extent of adhesion can be greatly impacted by both the content and type of ink additive (slip agent) used to modify the surface energy on the outer-most layer. Apparently, Ink B's highest adhesion is most likely attributable to favorable surface energy formation at the solid Ink B/ liquid polymer matrix due to the slip agent used. By the same token, the level of the slip agent in the ink can also explain the lowest adhesion for Ink C since it also had the lowest surface friction.

It is pertinent to mention here about an important material design dilemma at this time. The slip agent can lower both the surface friction of the colored fiber as well as the ink/matrix adhesion with its increasing concentration in the ink formulation. Low friction is definitely considered a beneficial fiber surface attribute whereas low ink/matrix adhesion is sometimes deemed deleterious to product reliability and handleability. In order to strike a balance in these two diametrically opposing attributes in a product, it is critical to have well balanced ink that satisfies friction as well as adhesion requirements[1,2].

3.4 Reduced Color Coding Thickness

Another important feature of the next generation inks is the expected color vibrancy. This is attractive for two reasons. First and foremost, with higher color intensity it is possible to use lower color coding thickness in order to have the target color outer diameter (C.O.D.) of ≈ 250 μm. The reduced color-coating thickness is critical for future high-fiber count cable designs. Secondly, reduced colored thickness implies reduced material use, which means cost reduction.

The new inks (A, B and C) were all evaluated for color on individual spools containing at least 10 kilometer of colored fiber in each. A hand-held Minolta spectrophotometer was used for the evaluation. The comparative L*, a* and b* color coordinates are respectively shown in Figures 5-7.

As apparent from these figures, only one ink-system that is system A has all the colors that are more intense than regular old generation UV inks. Ink C has about half the colors that are more intense than normal. However, ink B does not appear to have any color vibrancy for any of the colors.

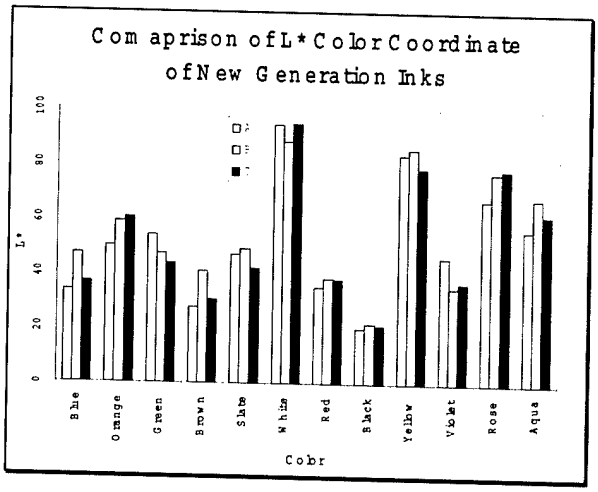


Figure 5. L* Color Attribute of New Inks

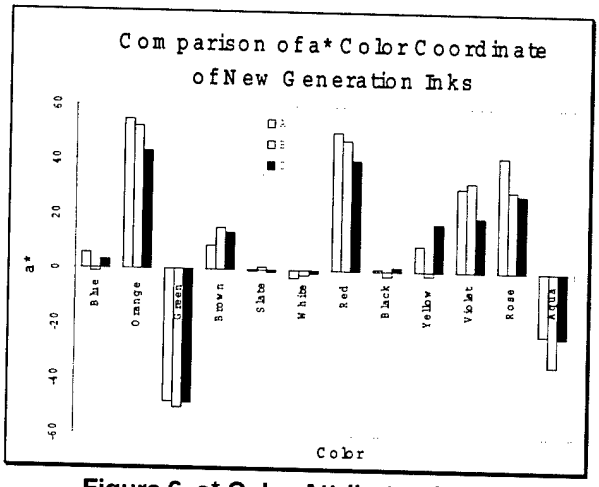


Figure 6. a* Color Attribute of New Inks

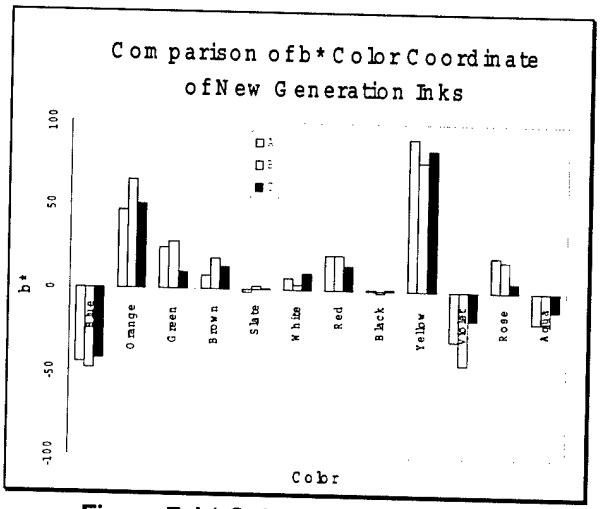


Figure 7. b* Color Attribute of New Inks

Also, Ink A satisfies Munsell color requirements for all standard colors. Both ink B and ink C have several colors that need to be adjusted in order to meet the Munsell color specification.

Ink A was further evaluated to determine if the series could be used for the anticipated colored layer thickness reduction. A smaller die than the nominal was used at coloring, which effectively allowed reduction of the thickness of the color-coating layer by ≈30% without sacrificing any colored fiber performance attributes. All colors of new ink A have successfully produced colored fibers with overall diameter of < 250 μm with no apparent coloring defects. Color measurement on spools revealed very small difference in color attributes (L*, a* and b*) despite big difference in colored layer thickness.

However, color measurement on a single layer of fibers laid flat in tight proximity on a Laneta paper as background showed some difference in the color attributes. Some colors (for example, orange, green, red and rose) appeared lighter in hue, value and chroma on an individual fiber but every color was discernible nevertheless. Also, all colors were within the Munsell color requirement tolerance limits.

3.5 Micro-bend Resistance

Many of the new fiber designs have recently produced highly micro-bend sensitive fiber optic for broadband application. Some old UV inks occasionally showed added sensitivity to micro-bend induced optical loss due to coloring. Apparently the induced stress was due to some extraneous factors. Although not clearly understood, some specific colors of old generation UV inks appeared to have far greater effect than others when applied on sensitive fibers. New generation inks seem to have corrected that problem, especially for the bend sensitive fibers. Notably, the use of one common polymer base resin for making all colors and the use of finer pigment dispersion appear intuitively as features that would help.

All inks, in general, produced colored fibers in accord with optical specification for the uncolored single mode optical fiber. Only Inks A and C were applied on bend-sensitive fibers, however. They both showed compatibility with the new micro-bend sensitive fibers. The attenuation increase due to coloring was relatively low in both cases. Also, no specific color appeared to jump out in loss performance, as experienced earlier with some old ink colors.

3.6 Colored Fiber Aging

The colored fibers made with some of the new inks were aged using Bell core test protocols at 85°C and no humidity in the presence of filling compounds for 30 days. Also, they were aged at more rigorous in-house high temperature/high humidity conditions for up to 30 days. These were done to evaluate long-term reliability and filling compound compatibility issues. Ink A performed acceptably in all tests.

The colored fibers were also tested for color permanence after aging for 30 days at 85°C dry and 85°C/85% relative humidity conditions. The ΔE value was computed for each color in a given series between aged sample and the control (before aging). For comparison purpose, a color having ΔE > 7 was thought to give color identification problem in the long term. Based on this criterion, ink A had all clean passes except two colors that passed marginally. Ink B and Ink C had respectively 5 and 4 colors that failed the test.

3.7 Ribbon and Cable Performances

The new inks were tested for 12- and 24-fiber ribbon product performances. All the ribbons were made using respective inks and a common matrix material keeping all other conditions the same. For example, Ribbon A was made using Ink A and a proprietary matrix material and so on. The results for key ribbon performance attributes are summarized in Table 2. Based on ribbon product performance tests, Ribbon A may appear to be an ideal candidate for a specific ribbon design. Ink/matrix adhesion definitely stands out as a critical performance determinant for ribbons. Ink C has the lowest ink/ matrix adhesion and thus, may be an ideal candidate for the easy peel ribbon.

Ink A was also tested successfully in the loose tube cable configuration. Although not tested at this time, both ink B and ink C are anticipated to work well in the loose tube and buffered fiber products.

Table 2. Ribbon Performance Attributes

Test		Ribbon A	Ribbon B	Ribbon C
Ribbon Strip Yield, %		>80	90	30
Fiber Access	Glue/ Tape	Good	Poor	Good
	EtOH /Gel	Good	Difficult	Good
Sub-units		Good	Good	--
Ink Retention, %		100	90	100
Aging	Ribbon Strip, %	>90	95	10
	Fiber Access Glue/ Tape	Good/ Marginal	Fair	Good

4. Summary

In summary, all these new generation inks show wide variety of attributes that appear highly promising for diverse fiber and cable designs for the future. Although one particular ink series might not demonstrate all the favorable properties at the outright for a specific product design, it is still possible to use it with minor modifications.

Table 3. UV Ink Portfolio At-A-Glance

Features	Ink A	Ink B	Ink C
Particle	👍👍	👎	👎
Viscosity	👍	👎	👍
Color Intensity	👍👍	👎👎	👎
Cost	👎	👍	👎
Fiber Surface Friction	👍	👍	👍👍
Ink/ Fiber Adhesion	👍👍	👎	👍👍
Ink/ Matrix Adhesion	👍👍	👍	👎👎
Percent Cure	👎	👍	👍👍

For exceptional product performance, the material quality of the new inks has also been enhanced in recent times. Better dispersion with improved settling properties, longer shelf-life, tighter low viscosity range across all colors, higher curing rate, availability of new non-traditional colors (beyond the 12 standard colors) for specialty applications are very attractive features of the new generation inks (see Table 3). Most importantly, these inks are much cheaper than old generation inks and have shown better processing characteristics. Table 3 is constructed to distinguish clearly between the inks based on some critical material and fiber parameters. In the table, thumb notation is used to compare the various ink attributes. Two- thumb up is excellent and one thumb up is good in the following table. Likewise two-thumb down is unacceptable and one thumb down is marginal.

5. Conclusions

New generation UV curable inks were recently made available by forward-looking ink companies with deep commitment to serving the industry needs for a slew of innovative fiber optic product designs. The inks evaluated here can certainly be used for new emerging optical fiber design of various types. As demonstrated in this report, there are differences in their performances in the ribbon products because of differences in key ink material properties. Based on a set of critical design criteria, Ink A may appear to be the most promising candidate for a specific product design (see Table 2). However, for some other product designs of the future both Ink B and Ink C certainly appears to be attractive candidates as well.

6. Acknowledgements

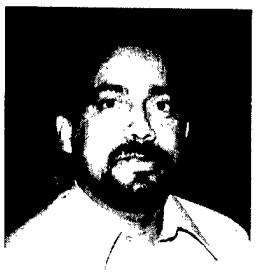
The authors gratefully acknowledge assistance on this project from Mr. Raymond DeFabritis, Ms. Ella Samander, Ms. Theresa Harris, Ms. Gail Weller, and several key production specialists.

7. References

[1] K. Konstadinidis, N. W. Sollenberger, S. Siddiqui, K. W. Jackson, J. M. Turnipseed, T. W. Au, R. P. DeFabritis, C. R. Taylor, *Proceedings of the 46th International Wire and Cable Symposium*, 1997, pp.274-280

[2] K. Konstadinidis, K. W. Jackson, N. W. Sollenberger, S. Siddiqui, C. R. Taylor, V. Chandraiah, R. P. DeFabritis, H. Ly, J. R. Szwec, *Proceedings of the 48th International Wire and Cable Symposium*, 1999, pp.66-71.

8. Biographaphies



Shahab Siddiqui
2000 NE Expressway,
Norcross, GA 30071

Shahab Siddiqui is a Member of Technical Staff in the Materials Technology and Quality Engineering group at Bell Laboratories of Lucent Technologies Inc., in Norcross, GA. He joined AT&T Bell Laboratories in 1984 and worked in many areas of both fundamental and applied polymer chemistry at Bell Labs in Murray Hill, and Princeton, NJ until 1991. Currently he is responsible for the design and development of UV curable inks and related coatings for fiber optic applications at Norcross, GA. He received a Ph.D. degree in Physical Organic Chemistry from the University of Kentucky in 1982. He is the author/co-author of over 35 scientific publications and holds 4 patents.



John R. Szwec
2000 NE Expressway,
Norcross, GA 30071

John R. Szwec graduated from Georgia State University with a B.S. degree in Chemistry in 1994. Currently, he is enrolled for his Master degree in Chemistry. He first joined Lucent Technologies in October of 1994 as a contract employee. John became a permanent employee of Lucent Technologies as Senior Technical Associate in Bell Laboratories in 1996. He is involved in many research and development projects for materials development and has a patent to his credit.



Kariofilis Konstadinidis
2000 NE Expressway,
Norcross, GA 30071

Kariofilis Konstadinidis is a Member of Technical Staff in the Materials Technology and Quality Engineering group at Bell Laboratories of Lucent Technologies Inc., Norcross, GA. He is involved in the development, qualification, and implementation of UV curable materials for optical fiber applications. He received his Diploma in Chemical Engineering from the Aristotle University of Thessaloniki, Greece, in 1987 and his Ph.D. in Chemical

Engineering from the University of Minnesota in 1992. He did his post-doctoral work at Bell Laboratories in Murray Hill, NJ prior to joining Lucent in Norcross in 1995. He has been awarded two patents.



David (Tat) Au
2000 NE Expressway,
Norcross, GA 30071

David T. Au is a Member of Technical Staff in UV coloring process development for optical fiber at Lucent technologies in Norcross, GA. He joined AT&T Bell Laboratories in Whippany, NJ in 1986. His experience includes research and development in semiconductor and printed wiring board technologies. He graduated from Auburn University with Bachelor and Master degrees in Chemical Engineering.



Carl. R. Taylor
2000 NE Expressway,
Norcross, GA 30071

Carl. R. Taylor is currently a Bell Laboratories Technical Manager of the Materials Technology Development and Engineering Group at Lucent Technologies' main Fiber Optic Manufacturing site in Atlanta. The group has responsibility for the design and engineering of materials used in fiber optic cable products as well as responsibility for the quality of all incoming raw materials. He has previously been supervisor of the Plastics Engineering and Characterization Group in Atlanta and Supervisor of the Polymer Materials Research, Engineering, and Applications Group at Bell Laboratories in Murray Hill, NJ. Prior to joining Bell Laboratories in 1977, he earned a B.S. in Chemistry from the College of Wooster in Ohio and a Ph.D. in Physical Chemistry from the University of Wisconsin in Madison. He holds 21 patents and has authored or co-authored more than 50 publications.

Improved Curing of UV-Curable Inks for Optical Fibers

James J. Schouten and Edward Westfall
DSM Desotech
Elgin, IL USA
+1-847-608-0400
James.Schouten@dsm.com; Edward.Westfall@dsm.com

Abstract
As the optical fiber industry has grown by more than 20% each year for the last 10 years, there has been an increasing demand for faster and more efficient fiber manufacturing processes. In one such process—the color coding of optical fibers with UV (ultraviolet light) curable inks—manufacturing speeds have increased by factors of 10 to 20 over the last five years. This has led to increasing problems with ink processing.

This paper compares the effects of three variables on the UV curing of optical fiber inks:

1. The cleanliness of the quartz tubes
2. The amount of nitrogen flow in the lamps.
3. Differences in ink formulations.

The results indicate that the most important variable studied is the quality of the quartz tube surrounding the fiber. The second most important variable is the amount of nitrogen in the curing chamber.

Keywords
Fiber; color coding; inking; UV curing; UV; ultraviolet; optical fiber.

1. Introduction
Ultra-violet (UV) curable inks are used to color individual fibers before they are put into a loose tube or ribbon configuration. Prior to using UV inks, the industry used inks that were 90 to 98% solvents. UV curable inks contain no solvents and are therefore essentially converted from a liquid to a solid with almost no volatile component. There are many variables that contribute to the curing of these environmentally friendly inks. In this paper we will discuss some of the major variables that affect curing.

UV curable inks are a combination of:

acrylate oligomers

acyrlate monomer

photoinitiators

pigments

other additives.

The inks cure with the application of UV light. Free radicals are generated when the photoinitiator is exposed to UV light. It is an extremely fast and efficient process— that is, unless oxygen is present. Oxygen inhibits free radical curing. Simply stated, the more oxygen present the more inhibited the cure.

2. Experimental
As the leading supplier of UV curable coatings for the fiber optics industry, DSM Desotech is very experienced with the curing process. When some of our customers experienced variable results with our UV curable inks, we set out to study, on a commercial inking line, the effects of several important variables that we believed to be affecting the cure process.

2.1 Equipment
The schematic in Fig. 1 shows the various parts of a typical ink. line.

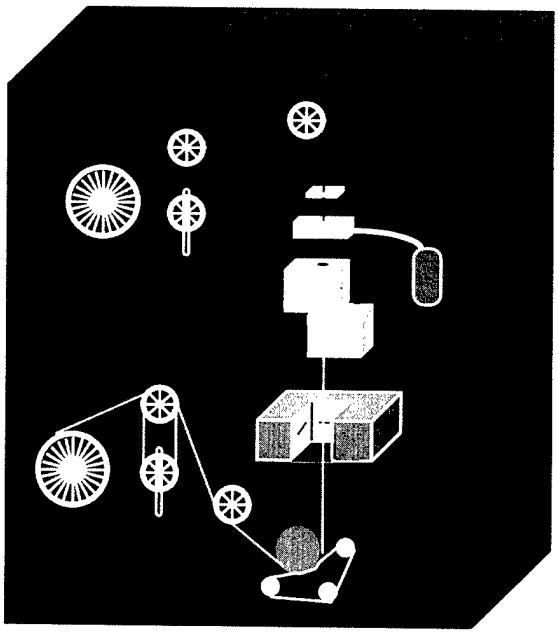


Figure 1.
Schematic of Ink Coloring Line

The major components are the payoff stand, the coating die, the UV lamp for curing the inks, and the rewind stand. This study concentrated on the UV lamp used to cure the ink. The inking line that we used is a commercial ink line, equipped with microwave lamps for the generation of UV light.

The ink is applied in the coating die. The inked fiber proceeds to the curing lamp. The fiber passes through a quartz tube, used because of its excellent transparency to UV light, while passing through the lamp. The quartz tube is necessary to protect the fiber from the strong air current that is needed to cool the UV lamp. The hollow quartz tube is blanketed with nitrogen to speed the curing reaction.

2.2 Variables

At DSM Desotech we tested three variables that we believed would affect the cure of the UV curable inks. These are:

1. The type of ink used (referred to here as Ink A, Ink B and Ink C).
2. The cleanliness of the quartz tubes.
3. The rate of nitrogen flow in the quartz tube surrounding the fiber.

2.3 Constants

The following we held constant throughout the trails:

1. The line speed was constant at 1000 meter/minute.
2. A single 600 watt/inch Fusion "D" lamp was used.
3. Blue inks were used throughout the experiment.

Figure 2 shows three quartz tubes that were used in the experiment. The tubes are labeled as:

Tube # 1 – Clean,

Tube # 2 – Dirty Tube,

Tube # 3 – Very Dirty Quartz Tubes.

The clean Tube #1 was a new tube. The other two tubes were samples given to us by customers. Tube #2 had been used for several days of production. Tube #3 was contaminated (smoked) in 2 minutes because the fiber stalled in the machine.

The nitrogen level was controlled at 40 liters/minute, 10 liters/minute or no nitrogen. The three inks are slight modifications of commercial formulations that were being tested before release for trials.

One of the more interesting results of this experiment is the amount of UV light that is transmitted through the quartz tubes. The light was measure in two ways. The first, shown in Figure 3, measured the light transmission using a Perkin Elmer Lambda 9 UV/VIS/NIR photometer. The entire tube was put into the unit and the transmission was measured in and out of the tube. Figure 3 shows the resultant transmission of the three tubes.

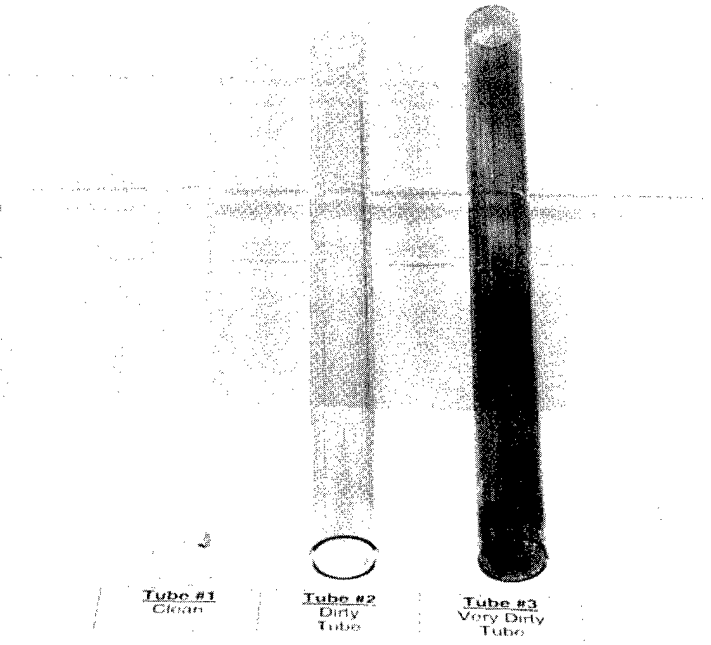


Figure 2.
Quartz Tubes Used for Curing

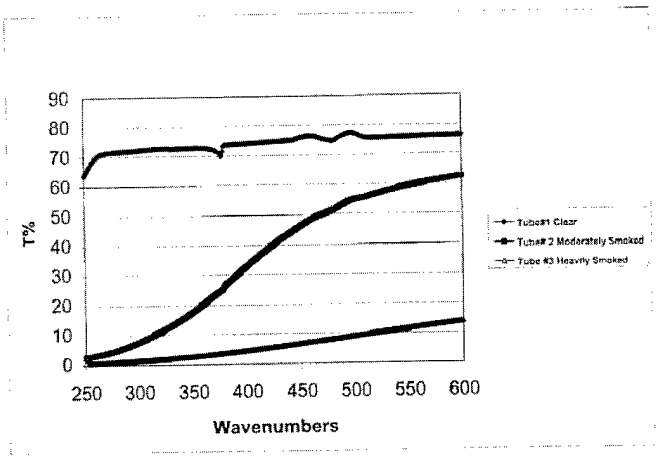


Figure 3
Quartz Tubes (Before Use)

Please note that the entire spectrum is shown in this graph. The UV portion, the main portion needed to cure the inks, is from 250 to about 400 wave numbers.

It is easy to see that about 63% to 78% of the UV light is transmitted through the clean tube. Most of the loss is from reflectance of the tubes surface. The transmittance in Tube #2 is as low as 5% at 250 nanometers and about 35% at 400 nanometers. Please note that 400 nanometers is the top end of the UV portion of the light spectra. The rest of the spectrum is visible light. Tube #3 is allowing from 0 to 5% of the UV light through the quartz tube.

Figure 4 is the UV spectra of the UV light measured on the inking machine. This is a measurement of the actual output of the light from the Fusion 600 Watt/inch lamp. The spectra were measure using a Soletell Sola-Scope. The measurement was taken behind the quartz tube. This spectrum shows only the UV portion of light from 240 to 420 nanometers. The upper curve is the spectra of Tube#1, the lower spectra is Tube #2 and the bottom spectra, which looks almost like the base line, is the spectra of the Tube # 3,Very Dirty Quartz Tube. These measurements confirm the information shown in the previous graph. They also show the importance of keeping the quartz tubes clean for proper curing.

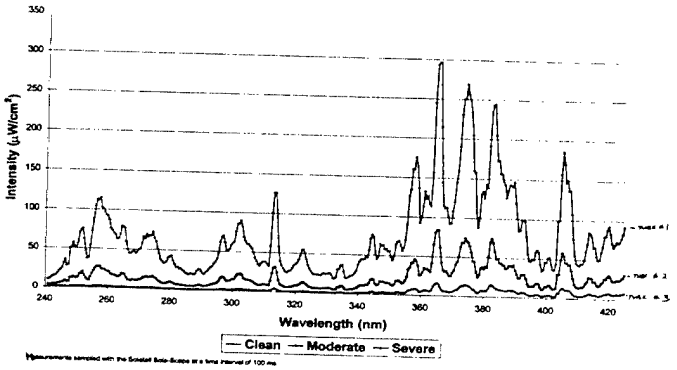


Figure 4

Intensity Comparison of Smoked Quartz Tubes

The three inks were cured using various combinations of quartz tubes and nitrogen flow. The inked fibers were then evaluated after curing. The fibers were tested for: 1. Solvent resistance using methyl ethyl ketone (MEK); 2. Tackiness of the fiber surface; 3. Degree of cure of the inked fiber, and 4. The ability to have breakout when assembled into a ribbon configuration.

3. Results

3.1 MEK Rubs/Rubs to Failure

Table # 1 lists the results of testing the ink using paper wipe saturated with MEK. This test is called the Solvent RUB Test. A back and forth rub with the fiber compressed between the paper wipe is considered a single rub. Looking at the table we can see the effects of both the cleanliness of the quartz tube and the effect of changing the nitrogen level and the two inks. Ink A has excellent MEK resistance at most nitrogen levels until the very dirty tube is used. Actually, there is a failure at the 0 nitrogen level and Tube #2. Ink B passes the MEK rub test at all nitrogen levels until Tube # 3 is used. The MEK resistance is only 20 rubs when Tube #3 was used. Tube #3, The Very Dirty Tube, is not allowing enough UV light through to the fiber to cure the ink.

3.2 Tackiness

Table # 2 lists the tackiness of the fibers made at the different conditions. Tackiness is an arbitrary scale where the fibers were compared directly to each other. The fibers were given a Tackiness value of 1 to 5. A rating of one (1) is a slippery non-tacky surface while a rating of 5 is a very tacky surface. A rating of 1 is very good while a rating of 5 is unacceptable. A very tacky surface will cause high attenuation in the fiber.

Looking at Table # 2, we see that at high nitrogen flow rates the surfaces show very little tack. At zero nitrogen flow, the tack reaches as high as a 5 with Tube # 2 and 3 using ink B. Also, ink A is showing high tack at 10 liter/minute of nitrogen with the very dirty tube. The results are showing that, for best properties, a clean tube is needed with a constant flow of nitrogen.

3.3 % RAU

Table # 3 shows the results of testing of the inks for degree of cure. The degree of cure is measured using a Fourier Transformation Infrared Spectrophotometer (FTIR). The results show good cure using the clean quartz tubes and 40 liter/minute of nitrogen. The results deteriorate with the dirty tube and low nitrogen. Poor cure results when zero nitrogen flow is used and the quartz tube is very dirty.

3.4 Ribbon Breakout

The final Table # 4 shows the results of making ribbons from the samples. Ribbon Breakout is one property used in rating the quality of ribbon. This is the ability of the fiber to release from the matrix. It is a desired feature in that it allows the cable installer to work with the individual fibers. The ribbons were evaluated as either "Okay" or "No" breakout. We can see that for ribbon breakout the nitrogen level is the most important factor. At high nitrogen levels of 40 liter/minute, the breakout is okay for inks B and ink C at with all of the quartz tubes. Ink A has good breakout with the Tubes #1 and #2 and then fails with Tube #3. We did not test (DNT) samples where the previous data predicted a failure.

TABLE 1

MEK Rubs/Rubs to Failure

Tubes	A			B			C		
	40L/M	10L/M	0L/M	40L/M	10L/M	0L/M	40L/M	10L/M	0L/M
#1 Clean	>200	>200	>200	>200	>200	>200	>200	>200	>200
#2 Dirty	>200	>200	10	>200	>200	>200	>200	>200	150
#3 Very Dirty	15	20	30	23	20	20	10	30	16

TABLE 2

Tackiness*

Tubes	A			B			C		
	40L/M	10L/M	0L/M	40L/M	10L/M	0L/M	40L/M	10L/M	0L/M
#1 Clean	1	2	2	1	2	4	1	1	4
#2 Dirty	1	2	3	1	2	5	1	3	5
#3 Very Dirty	2	4	5	1	3	5	1	2	4

Tackiness = Scale 1-5

- 1= Slippery 5 = Very Sticky
- This test indicates surface cure.

TABLE 3

% RAU

Tubes	A			B			C		
	40L/M	10L/M	0L/M	40L/M	10L/M	0L/M	40L/M	10L/M	0L/M
#1 Clean	91	89	86	87	80	75	87	84	77
#2 Dirty	79	79	74	82	80	74	79	74	73
#3 Very Dirty	76	67	69	78	73	74	75	67	66

TABLE 4

Ribbon Breakout

Tubes	A			B			C		
	40L/M	10L/M	0L/M	40L/M	10L/M	0L/M	40L/M	10L/M	0L/M
#1 Clean	Ok	No	DNT	Ok	No	DNT	Ok	No	DNT
#2 Dirty	Ok	DNT	DNT	Ok	DNT	DNT	Ok	DNT	DNT
#3 Very Dirty	No	DNT	DNT	Ok	DNT	DNT	Ok	DNT	DNT

DNT = Did Not Test

Summary

In summary, successful processing of UV curable inks requires tight control of the processing parameters. Today's formulations allow for extremely high processing speeds with consistent results. Understanding those processes helps to attain those speeds. Speeds of 2300 meter/minute using multiple lamps have been routinely used. These speeds are easy to achieve if the right parameters are controlled. Other parameters that also need to be controlled are the reflectors, type of quartz, location of the fiber in the lamp, bulbs, vacuum to remove contaminations, and others. As speed is increased, nitrogen flow will also need to be increased. Table 1

4. Conclusions

There are several conclusions that can be made from this data. They are:

1. The cleanliness of the quartz tube is very important for good curing. The tubes should be replaced with clean tubes on a regular maintenance schedule.
2. Contamination of the tubes can reduce the UV Light Transmission by 50 to 90%.
3. The cleanliness of the quartz tubes affects the bulk curing of the inks as evidenced by the solvent resistance.
4. A nitrogen purge is needed to have the most efficient curing.
5. The nitrogen level affects the surface of the inks. (Tacky or sticky surfaces are know to cause high attenuation).
6. Cure speeds as high as 1000 meter/minute can be attained with one-600 watt lamp.
7. The inks had small changes in response which demonstrates the excellent robustness of these products.

Yellowing of Optical Fiber Coatings by Fluorescent Light

Hideki Sugimoto, Zen Komiya, Junji Yoshizawa, Takashi Ukachi

JSR Corporation, Tsukuba Research Laboratories
25 Miyukigaoka, Tsukuba, Ibaraki, 305-0841 Japan
+81-298-56-1218 · email address: hideki_sugimoto@jsr.co.jp

Abstract

A mechanism of yellowing of optical fiber coatings by exposure to fluorescent light was investigated. The primary coating, which has glass transition temperature (Tg) lower than room temperature, showed yellowing upon exposure to fluorescent light whereas the secondary coating with higher Tg than room temperature exhibited no yellowing. The yellow color reached the maximum around three days and then disappeared after prolonged exposure to fluorescent light. By filtering the fluorescent light at certain wavelength, it revealed that the yellowing behavior was closely correlated to the absorption wavelength of the photoinitiator. It was also demonstrated that the removal of a specific antioxidant resulted in virtually no yellowing. These results suggest that the yellowing of the optical fiber coatings was triggered by the photo-decomposition of the remaining photoinitiators and yellow colored substances were produced by the reaction of the antioxidants with radicals generated from the photoinitiators.

Keywords

Optical fiber coating; yellowing; fluorescent light; photoinitiator; antioxidant;

1. Introduction

UV curable polyurethane acrylates have been favorably used for protective coatings of optical fibers, since the polyurethane acrylates provide wide variety of mechanical properties in addition to good chemical and weathering resistance. The optical fibers are coated by two layers of UV curable coatings, primary and secondary coatings. Recently, yellowing of the optical fibers caused by exposure to fluorescent light has been pointed out, when the coated optical fibers were stored in warehouses. Although, the yellowing of the optical fibers does not always affect their properties, the reduction of the yellowing is required from the standpoint of the quality of commodities. It is known that BHT (2,6-di-*t*-butyl-*p*-cresol), which is included in many polymer materials as an antioxidant, forms a colored stilbene structure in oxidative conditions[1,2]. The possibility of the yellowing caused by the formation of quinone derivatives from hindered phenols is also reported[3]. Optical fiber coatings contain hindered phenols as antioxidants besides BHT, and these additives are considered to cause the yellowing of the optical fibers. However, the mechanism of the yellowing under fluorescent light is hardly revealed. In this study, we carried out detailed experiments with regard to the yellowing of the optical fiber coatings to elucidate the mechanism of the yellowing under fluorescent light and to show guidelines to lead low yellowing coating formulation.

2. Experiments

2.1 Materials

The primary coating, P-1, and the secondary coating, S-1, based on polyurethane acrylate were employed for this study. Table 1 shows Young's modulus and glass transition temperature of cured films of P-1 and S-1.

Table 1. Characteristics of coatings, P-1 and S-1

Cured film	P-1	S-1
Young's modulus (MPa)	1.2	830
Tg (°C)	-8	98

For model experiments, several model coatings derived from P-1 or S-1 were prepared. The formulations of these coatings are listed in Table 2. P-2, P-3 and P-4 are primary coatings based on P-1, S-2 is a secondary coating based on S-1.

Table 2. Formulations of model coatings

Formulation		P-1	P-2	P-3	P-4
Oligomer	A	65	65	65	65
Monomer	A	33	33	33	33
Photoinitiator	A	1.2	...	1.2	1.2
	B	...	1.2	...	...
Hindered Phenol	A	0.3	0.3	...	...
	B	0.3	0.3	0.3	...

Formulation		S-1	S-2
Oligomer	B	57	57
Monomer	B	44	44
Photoinitiator	A	1.2	1.2
Hindered Phenol	A	0.3	...
	B	...	0.3

2.2 Film experiments

A liquid coating was drawn on a glass plate with 200 μm thickness using an applicator bar. The coating was cured by using a UV conveyor at 100 mJ/cm^2 or 500 mJ/cm^2 UV dose under

nitrogen. The resultant films were used for the following experiments.

2.3 Measurement of yellowing behavior

The yellowing behavior of cured films exposed to fluorescent light was followed by the changes of yellowness index (YI) of cured films. The changes in YI of cured films were measured by a color meter (Nihon Densyoku Kogyo Inc. model SZ-Σ80 and MMP-300A) equipped with a halogen lamp in reflection mode. The films cured at 100 mJ/cm^2 under nitrogen were placed in a light box of which inner walls were covered with black paper. It is equipped with 60 cm length; an 18-watt fluorescent lamp set approximately 30 cm from the samples. An emission spectrum of the fluorescent light is shown in Figure 1. The intensity of the fluorescent light was 1300 lux.

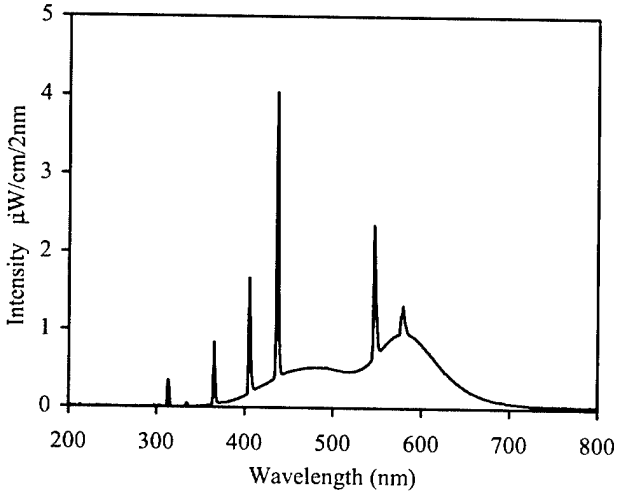


Figure 1. Emission spectrum of fluorescent light

2.4 Effect of wavelength of fluorescent light on yellowing

To evaluate the effect of wavelength of fluorescent light on yellowing, the changes in YI of cured films that were exposed to fluorescent light through wavelength-cut filters were measured. The films cured at 100 mJ/cm^2 under nitrogen were exposed to fluorescent light; without filter, through a 330 nm-cut filter (UV-330), through a 390 nm-cut filter (UV-39) and through a 440 nm-cut filter (Y-44). Transmission spectra of the filters are shown in Figure 2. The intensity of the light before filter was 1300 lux.

2.5 Effect of photoinitiators on yellowing

In order to estimate the effect of photoinitiators on yellowing, the yellowing behavior of two coatings including different kinds of photoinitiator, P-1 and P-2, were compared. These coatings were cured at 100 mJ/cm^2 UV dose under nitrogen and then exposed to fluorescent light without filter or through filters as described above.

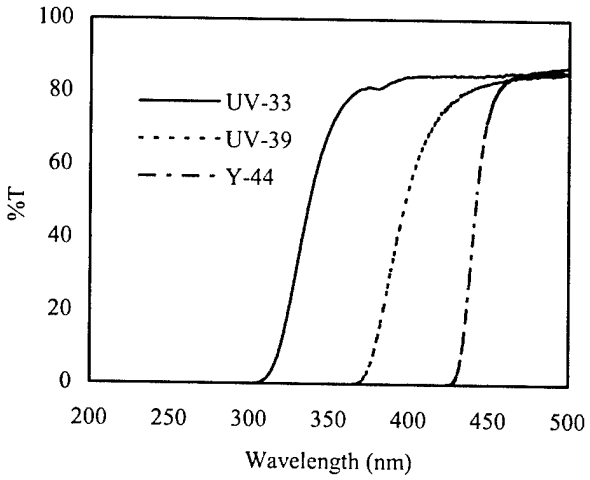


Figure 2. Transmission spectra of wavelength-cut filters, UV-33, UV-39 and Y-44

2.6 Effect of cure dose on yellowing

The yellowing behavior of the films cured at different UV dose was evaluated. The coating, P-1, was cured at 100 mJ/cm^2 and 500 mJ/cm^2 UV dose under nitrogen. These cured films were exposed to fluorescent light without filter.

2.7 Effect of antioxidants on yellowing

To see the effect of antioxidants on yellowing, the yellowing behavior of the coatings with or without antioxidants, P-1, P-3 and P-4, was evaluated. These coatings were cured at 100 mJ/cm^2 UV dose under nitrogen and then exposed to fluorescent light without filter.

2.8 Effect of secondary coatings on yellowing

The effect of the secondary coatings on yellowing was evaluated with doubly coated films. The doubly coated films were prepared as follows; the primary coating without antioxidant, P-4, was cured at 100 mJ/cm^2 UV dose under nitrogen with 130 μm thickness and then the primary film was coated with secondary coating, S-1 or S-2, with 70 μm thickness and irradiated with 100 mJ/cm^2 of UV light under nitrogen. The doubly coated films were heated at 100 °C for 60 minutes and then exposed to fluorescent light without filter. The changes in YI of non-heated doubly coated films were also measured.

3. Results and Discussion

3.1 Yellowing behavior of optical fiber coatings

The changes in YI of the primary coating, P-1, and the secondary coating, S-1, are shown in Figure 3. It is obvious that YI of S-1 just after cure was high, however, it went down in several hours and after that it did not change by exposure to the fluorescent light. On the other hand, YI of P-1 increased as high as 10 in three days and then YI decreased after prolonged exposure to fluorescent light and leveled off at about 4. This fact indicates that the primary coating is the main cause of yellowing of fibers. In the following sections, we mainly investigated yellowing of the primary coatings.

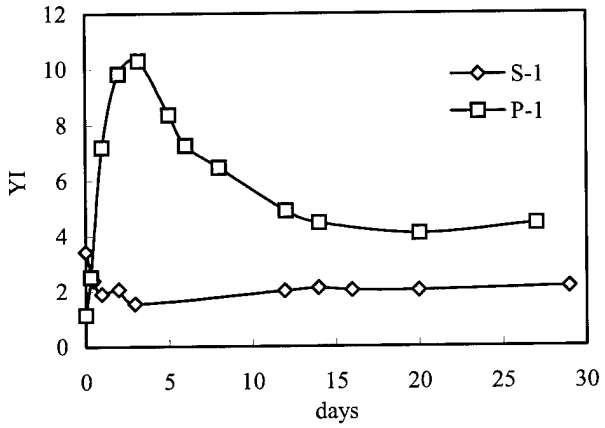


Figure 3. YI changes of P-1 and S-1 upon exposure to fluorescent light

3.2 Effect of antioxidants on yellowing

The yellowing is considered to be caused by the formation of quinone derivatives from hindered phenols[2]. Therefore, the changes in YI of P-1 including both hindered phenol A and hindered phenol B as antioxidants, and P-4 without antioxidants were measured. The results are shown in Figure 4.

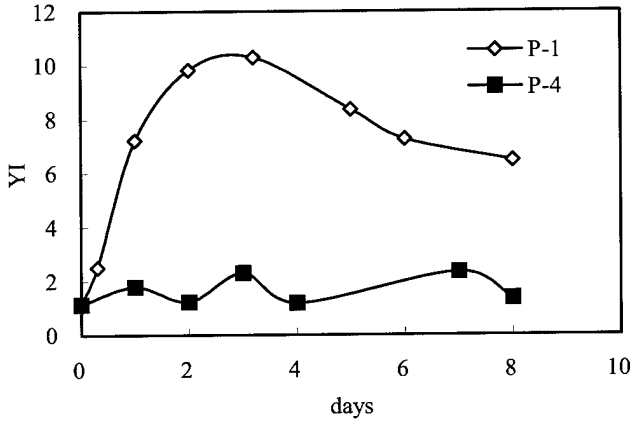


Figure 4. Yellowing of P-1and P-4 under fluorescent light

As can be seen in Figure 4, complete removal of antioxidants resulted in virtually no yellowing by fluorescent light. This observation suggests that hindered phenols are one of the main causes of the yellowing under fluorescent light.

3.3 Effect of wavelength of fluorescent light and cure dose on yellowing

Figure 5 shows the changes in YI of the primary coating, P-1, when cured films of P-1 were exposed to fluorescent light through the wavelength-cut filters, UV-33, UV-39 and Y-44. Figure 5 indicates that the fluorescent light filtered through UV-33 had no effect except for a little delay of reaching maximum YI value. It is interesting that the sample exposed through UV-39 filter showed higher maximum YI value than the samples without filter and with UV-33 filter, although it look longer time to reach the highest YI value than other two samples. The fluorescent light through Y-44 caused little yellowing even after prolonged exposure. These results were summarized as follows.

•UV light with wavelength longer than 440 nm does not yellow the coating.

•UV light with wavelength shorter than 440 nm yellow the coating.

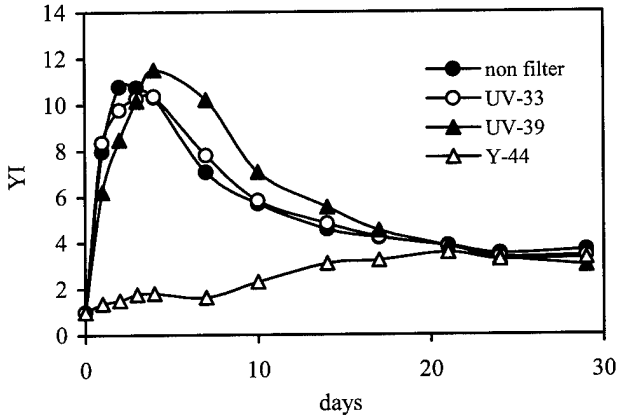


Figure 5. Yellowing of P-1 under fluorescent light without filter or through filters

Figure 6 shows the absorption spectrum of photoinitiator A. Since photoinitiator A has absorption maxima at around 390 nm, the photoinitiator is most likely the compound that triggers the yellowing by absorbing the light shorter than 440 nm[4].

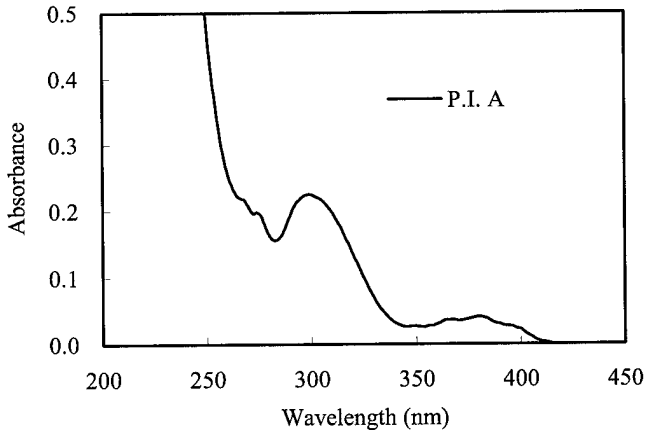


Figure 6. The absorption spectrum of photoinitiator A

Figure 7 shows the changes in YI of P-1 cured at 100 mJ/cm^2 or 500 mJ/cm^2 UV dose. The sample cured at 500 mJ/cm^2 showed

little yellowing upon exposure to the fluorescent light. From these results shown in Figure 5, 6 and 7, the remaining photoinitiators are considered to be another main cause of the yellowing under fluorescent light. The radicals generated by the remaining photoinitiators seem to react with hindered phenols to form conjugated quinone derivatives having yellow color. The sample cured at high UV dose seems to have smaller amount of unreacted photoinitiators, which trigger the yellowing by fluorescent light.

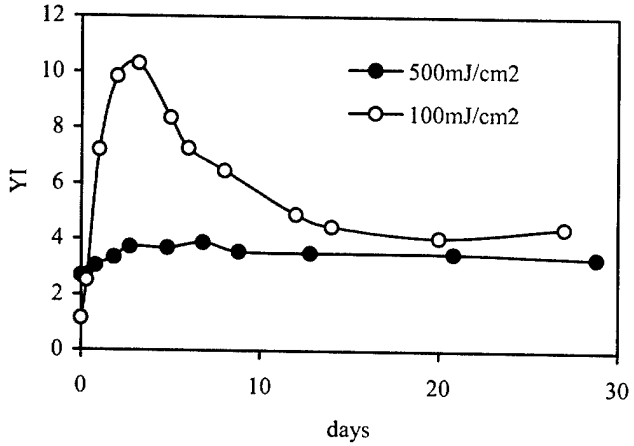


Figure 7. Yellowing of P-1 cured at 100 or 500 mJ/cm² under fluorescent light

3.4 Effect of photoinitiators on yellowing

Since the photoinitiator is considered to be one of the main causes of yellowing under fluorescent light, the wavelength dependence of changes in YI of P-2 was evaluated. P-2 is containing photoinitiator B which has a different absorption maximum from photoinitiator A. The results are shown in Figure 8. The absorption spectrum of photoinitiator B is shown in Figure 9.

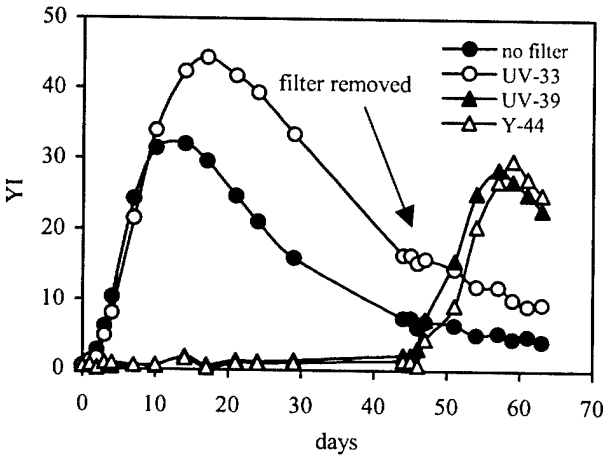


Figure 8. Yellowing of P-2 under fluorescent light without filter or through filters. At 48th day, filters were removed

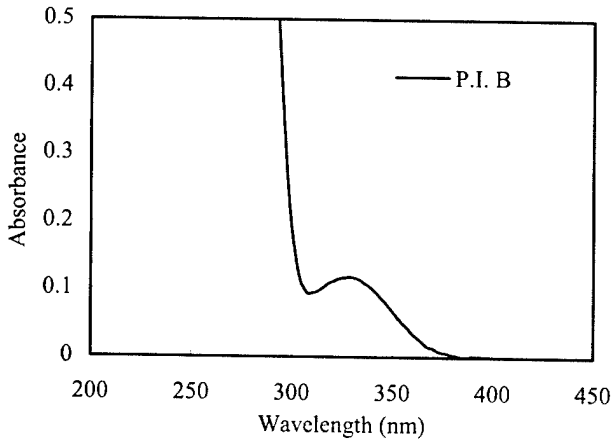


Figure 9. The absorption spectrum of photoinitiator B

Different from the P-1 (see Figure 5), yellowing of P-2 was suppressed by the filter cutting 390 nm or shorter. The yellowing of P-1 was weakened only by the filter cutting 440 nm or shorter. This is in good accordance with the absorption spectrum of photoinitiator B. The photoinitiator included in P-1 absorbs around 390 nm light whereas the one included in P-2 is activated by UV light with shorter wavelengths than 350 nm. These results support that the yellowing under fluorescent light was caused by the reaction of radicals generated from residual photoinitiators and hindered phenols. After the yellowness of the samples exposed to direct light or through 330 nm filter subsided, all the filters were removed. Two samples that had been covered by 390 or 440 nm filter suddenly started to yellow. The maximum YI values of these samples were reached close to the one by the other samples. This behavior also supports that the participation of the remaining unreacted photoinitiators in the yellowing under fluorescent light. The unreacted photoinitiators in the films remained intact while the samples were covered by the filter cutting 390 nm or shorter wavelength light.

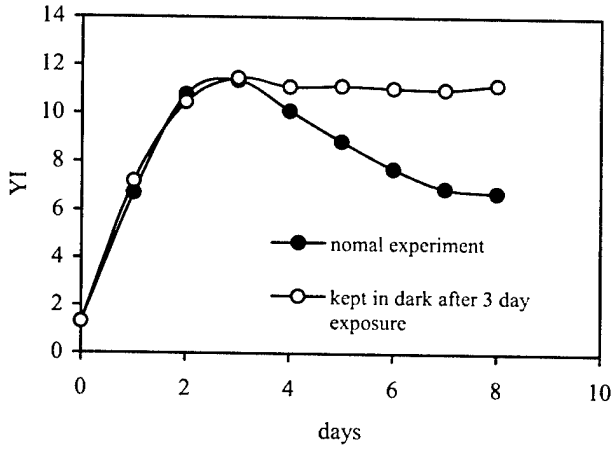
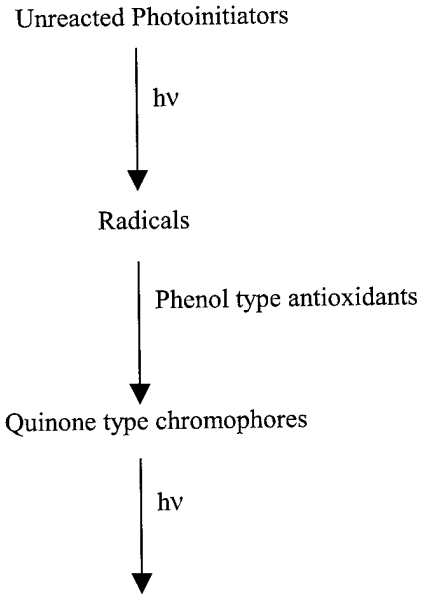


Figure 10. The influence of fluorescent light for disappearance of YI

The influence of fluorescent light against the decrease in YI was evaluated using cured films of P-1. The fluorescent light was cut off when YI reached its maximum. The result is shown in Figure 10. In the dark, the yellow color did not diminished. This result indicates that the disappearance of the yellow color is also a photochemical process.

3.5 Mechanism of yellowing by fluorescent light

The mechanism of yellowing by fluorescent light is illustrated in Scheme 1.



Scheme 1. Mechanism of yellowing induced by fluorescent light

As illustrated above, the remaining photoinitiators in the cured coatings generate radicals by exposure to fluorescent light. These radicals react with hindered phenol type antioxidants and form quinone type derivatives. The yellowing of optical fiber coatings was caused by the formation of quinone type chromopheres. Experimental results suggest that this quinone type chromopheres change into the non-conjugate (non-yellow) compounds by the irradiation of light. The disappearance of yellowness also seems a photochemical process.

According to the mechanism described above, in order to prevent yellowing of primary coating upon fluorescent light exposure, it is necessary to use a specific hindered phenol, which does not easily reacts with radicals derived from the remaining photoinitiators or does not easily form yellow colored substances even if it reacts with radicals. Figure 11 shows the changes in YI of P-1 including both hindered phenol A and hindered phenol B, and P-3 including only hindered phenol B. As can be seen from Figure 11, the yellowing was depressed by the removal of hindered phenol A. Hindered phenol B has little tendency to yellow.

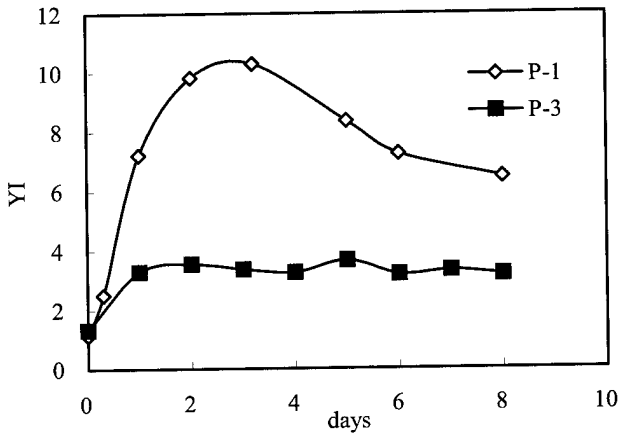
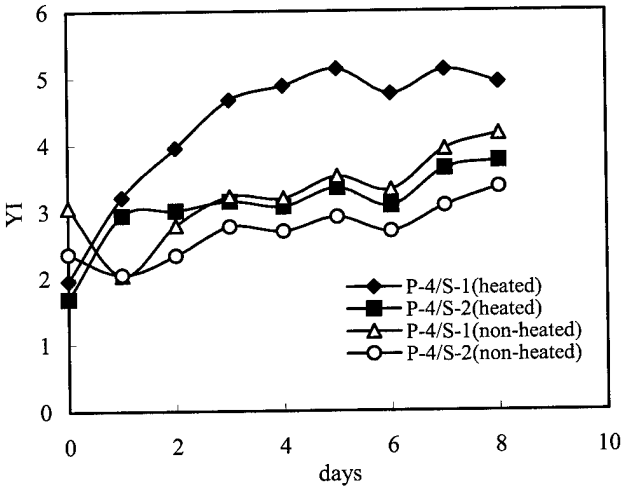


Figure 11. Yellowing of P-1 and P-3 under fluorescent light

3.6 Effect of secondary coatings on yellowing

Since the optical fibers are coated by two layers of primary and secondary coatings in practice, it is necessary to consider the effect of secondary coatings on yellowing. Therefore, as a model of actual optical fiber, the changes in YI of doubly coated films were evaluated. The changes in YI of doubly coated films, P-4/S-1 and P-4/S-2, were shown in Figure 12. P-4 is the primary coating without antioxidants. S-1 and S-2 are the secondary coatings including either hindered phenol A or hindered phenol



B.

Figure 12. Yellowing of doubly coated films, P-4/S-1 and P-4/S-2, under fluorescent light

In the yellowing of non-heated doubly coated films, no significant difference was observed between P-4/S-1 and P-4/S-2. On the

other hand, the doubly coated films heated at 100 °C for 60 minutes behaved differently from non-heated doubly coated films. When the secondary coating contained hindered phenol A, the doubly coated film showed more intense yellowness than that of another one. These observations imply the migration of antioxidants and/or photoinitiators from secondary coating to the primary layer by heating. As shown by singly coated films of primary coating, P-1, existence of hindered phenol A and hindered phenol B gives strong yellowing. When the antioxidants in the secondary coating and the primary coating make this combination, the doubly coated film will show strong yellowing. It is necessary to consider the selection of antioxidants and photoinitiators not only for the primary coating but also for the secondary coating as well for small yellowing under fluorescent light, since the optical fibers are doubly coated and experience high temperature during drawing.

4. Conclusions

The mechanism of the yellowing of optical fiber coatings under fluorescent light was investigated by using model coatings. It is apparent that the primary coating is the main cause of the yellowing of fibers. By using the filtered fluorescent light at certain wavelength, the yellowing of the primary coating was closely correlated to the absorption wavelength of the photoinitiator. Namely, the most rapid yellowing behavior was observed when the light included the wavelengths where the photoinitiator had its maximum absorption. The complete removal of antioxidants prevented the yellowing by exposure to fluorescent light. The use of a specific antioxidant and the irradiation of sufficient UV dose were also effective to decrease the yellowing of optical fiber coatings. The yellowing of optical fiber coatings was triggered by the decomposition of the remaining photoinitiators and yellow colored compounds were formed by the reaction of antioxidants with radicals generated from the remaining photoinitiators. The disappearance of yellow color is also a photochemical process, since the yellow color decreased by prolonged exposure to fluorescent light and extremely slow in the dark. When the secondary coating contained hindered phenol A, the YI of doubly coated film was increased by heating. The antioxidants and/or the photoinitiators seem to migrate from the secondary coating to the primary layer by heating. To prevent the yellowing of optical fibers, the selection and combination of antioxidants for both primary and secondary coatings are important factors.

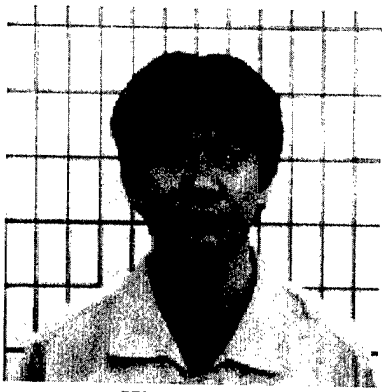
5. References

[1] C. D. Cook, N. G. Nash and H. R. Flanagan, "Oxidation of Hindered Phenol" *J. Am. Chem. Soc.*, 77, 1783 (1955).

[2] O. D. Bangee, V. H. Wilson, G. C. East and I. Holme, "Antioxidant-induced yellowing of textiles" *Polym. Degradation Stab.*, 50(3), 313 (1995).

[3] K. C. Smeltz "Why do White Fabrics and Garments Turn Yellow During Storage in Polyethylene Bags and Wrappings?" *Textile Chemist and Colorist*, 15(4), 52 (1983).

[4] C. Chawla, T. Bishop, E. P. Zahora, and P. Snowwhite, *Proceedings of RadTech '98 North America*, 247 (1998).



Hideki Sugimoto

Tsukuba Research Laboratories, JSR Corp.

25 Miyukigaoka, Tsukuba, Ibaraki, 305-0841 Japan

Hideki Sugimoto received his Ph. D. in Polymer Material Science from Nagoya Institute of Technology and joined JSR Corp. in 1999. He has been engaged in research and development of radiation curable materials for optical fiber coatings.

UV Cure Matrix Resins for Laser Marking of Ribbons

Timothy Reichert, Mark Tilley, Ed Murphy

DSM Desotech Inc.
1122 St. Charles St., Elgin, IL 60120

Abstract

New ribbon matrix compositions have been prepared which are suitable for the marking of ribbons by laser. The authors will discuss the process of laser marking, its potential benefits and limitations. And characteristics of the new compositions will be presented, as well as illustrations of laser marked ribbons. Ribbon marking up to the present has mostly been accomplished with lacquer type inkjet systems. These systems often require substantial maintenance. Also the imprinted images lack permanence. They are susceptible to easy removal from simple abrasion or from exposure to typical cleaning compounds and solvents. The systems to be discussed use titania surface treated pigments, or other specific metal oxides, to achieve a permanent image by combination of thermochromic and photochromic conversion, and by surface ablation of the matrix when irradiated by a focused CO_2 laser. A concern to be further discussed is the possible effect of the surface ablation upon ribbon performance and durability.

Keywords

UV cure, ribbons, marking, laser marking, matrix resin, ink-jet printing.

Introduction

The need for printed information or coding identification on fiber optic ribbon assemblies is rather obvious. There is a present and growing need in the industry to improve the trace ability of optical cable systems and their components. It is advantageous if not only the producer but also the production data of individual ribbons and fibers could be identified. For this purpose a coding on ribbon assemblies representing the manufacturer, coating supplier, lot numbers, and the like is applied during production.

At present the most common method of providing this printed information on ribbons is by ink-jet printing techniques.[1] There are several drawbacks and problems associated with the use of ink-jet printing during production of optical fibers and fiber assemblies. Firstly, optical fiber production speeds are very high and are continuously being improved. For ink-jet printing, drying of the ink, whether it is a solvent-based system or a UV-curable system, may be insufficient, causing running of the ink. Apart from this, the resolution that can be obtained from ink-jet printing is in general insufficient for legible or machine-readable markings to be made on individual fibers. Also the use of additional chemicals and/or curing stages is not favored. In the case of solvent-based inks, solvent may migrate into the coating layers and affect properties, which can result in undesirable optical transmission losses. Finally, ink-jet markings are not permanent, as they show limited scratch and abrasion resistance.

Laser Marking of Ribbons

For the reasons stated, we decided to investigate the laser marking of ribbons as a more facile means to record permanent information upon fiber optic ribbon assemblies. Of course laser marking of organic plastics is well known, and this includes the outer protective layer of optical cables.[2] Laser marking for organic (plastic) materials is usually accomplished by a combination of photochromic and/or thermochromic effects from chemical reduction of metal oxides, and/or physical state changes of surrounding organic binders. A great deal of detailed information is readily available at the websites of laser manufacturers and contrasting agent pigment suppliers.[3]

As a first consideration we examined the possible modes of marking "through" the ribbon matrix onto the colored fibers themselves by a short wavelength photobleaching, or laser marking on, or within, the matrix resin. We decided that marking the individual fibers within a ribbon posed the threat of increasing attenuation or microbend losses due to possible thermally induced changes in the ink and/or the outer primary coating under the ink.

The subsequent considerations about laser marking on, or within, the ribbon matrix were numerous. These related to laser type and light wavelength, the necessary contrasting agents, the mode of actual writing, line speeds, and finally how much change would be needed in current commercial matrix resin composition and performance properties. Chief among these considerations was whether the matrix was to be colored or remain clear and transparent.

It was decided that our efforts would be directed to laser marking of substantially transparent matrix resin with a CO_2 laser at 10.6 micron output using a photomask single exposure mode. This methodology was projected to allow for a nominal line speed of 200 meter/minute while inscribing 15 marks/second or 5 marks/meter of ribbon. These parameters necessitated

only a minimal change in a typical commercial matrix resin of finely dispersing an amount of a contrasting agent pigment. This agent was a TiO_2 surface treated mica-type pigment available from EM Industries, Inc., known commercially as Iriodin LS 800.[4] The dispersed contrast agent concentration was 5% by weight.

Results and Comment

The outcome of these present investigations had both positive and negative aspects. In a positive vein, we were able to show that permanent easily readable inscriptions could be placed on a ribbon surface by short-duration laser exposure through a photomask. Typical exposures were 10μs in duration delivering a radiant dose of about 5 joule. **Figure 1** is an illustration of two such ribbons. The upper ribbon shows a substantially transparent matrix, while the lower ribbon was a matrix also modified with typical ink violet pigment dispersion. The marking of a colored matrix is quite obviously more easily readable. For the transparent ribbon the marking was also easily readable but there was a degree of "reading angle" variability.

However there was a negative outcome to the experiments also. The irradiation of the matrix surface and the thermolysis of the LS 800 pigment caused a rather significant ablation of the matrix. **Figure 2** is an illustration of a surface roughness profile done by means of optical phase-shifting and vertical scanning interferometry.[5] The degree of surface ablation was seen to reach a maximum of about 20μ. This surface damage obviously is cause for concern with relation to water penetration, or stress-induced attenuation.

In closing, it would appear that the easiest and least costly mode of laser ribbon marking is not suited for immediate use. Studies are continuing to investigate less damaging photochromic mechanisms to permanently inscribe fiber optic ribbons.

References

1. Bonicel, J. P., EP 0581680 A1, 1993; EP 0581680 B1, 1993.
2. Kilp, T., Laser Marking of Plastics, Annu. Tech. Conf. Soc. Plast. Eng., 49th, 1901-1903 (1991)
3. See: www.empigments.com, www.controllaser.com, www.lasertechnics.com, www.vektronics.com, and www.domino-printing.com.
4. EM Indusries, Inc., an affiliate of Merk KgaA, Darmstadt, Germany. See: www.empigments.com/Industrial/LaserFlair.cfm.
5. The surface profile examination was done by Michigan Metrology, Livonia, MI, using a WYKO NT2000 instrument. See www.michmet.com.

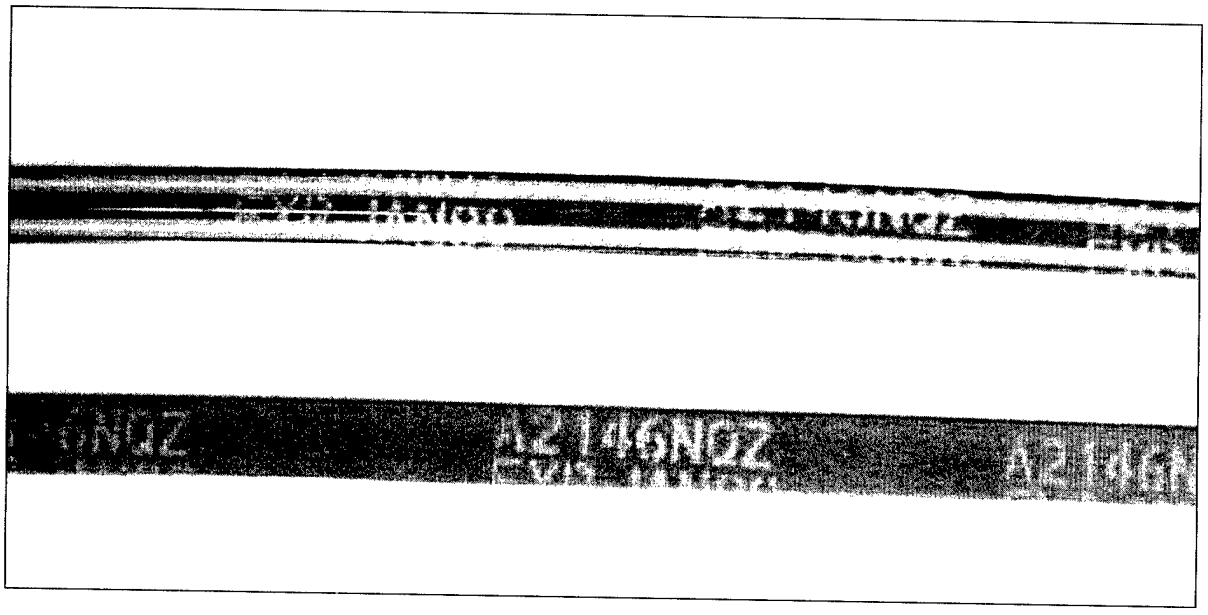


Figure 1: Laser Marked Ribbons.

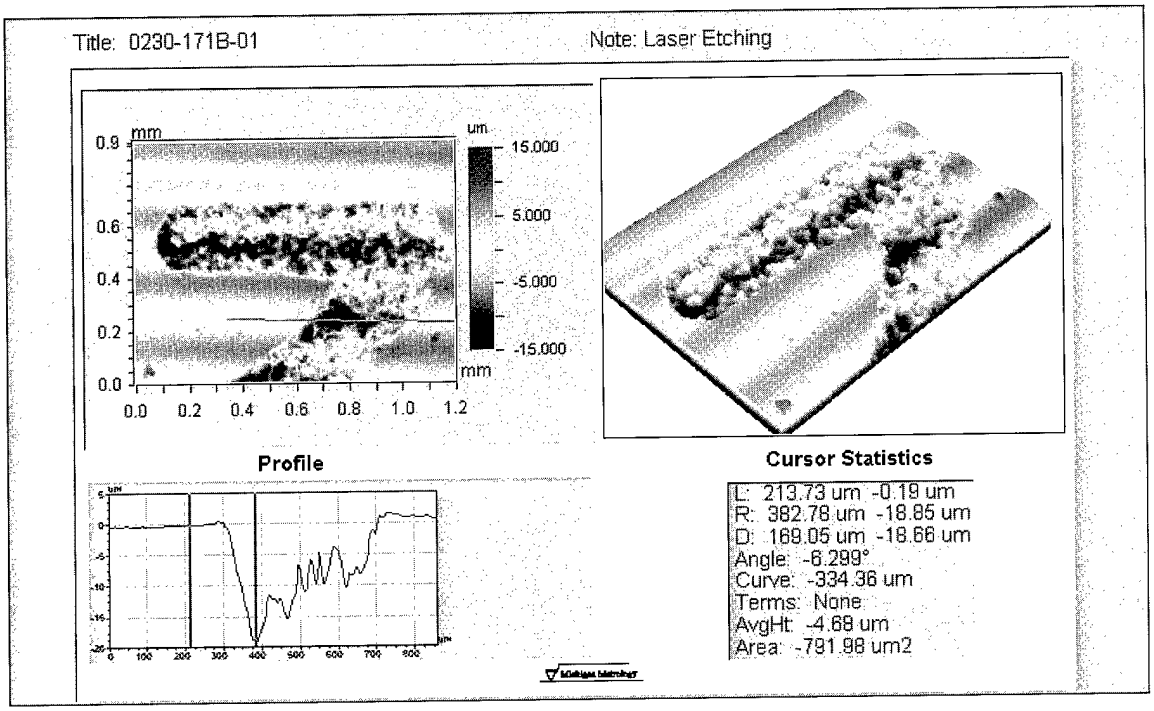


Figure 2: Interferometric Surface Profile of Laser Marked Ribbon

EMC Behaviour of Cable Screens

Alyse R. Coates*, Alexandros Gavrilakis*, Mohammed M. Al-Asadi*, Alistair P. Duffy*
Kenneth G. Hodge+ and Arthur J. Willis+

*De Montfort University, Leicester, LE1 9BH, UK
+Brand-Rex Ltd., Glenrothes, Fife, KY6 2RS, Scotland
Principle Contact: email alyse@dmu.ac.uk

Abstract

As distributed electronic systems become more complex, the Electromagnetic Compatibility (EMC) behaviour of cables becomes more significant. In order to offer protection from electromagnetic interference (EMI) many communication cables are shielded, with only a small fraction of the total current induced on the shield migrating through it. In order to describe this screening performance, the shielding effectiveness, and/or transfer impedance is required, both are closely related. This paper describes two emergent approaches to investigating the EMC behaviour of cables: measurements using a reverberant chamber and simulations using the Transmission-Line Matrix (TLM) method. This paper reviews the use of the reverberant chamber for the shielding effectiveness measurements of cables; three-dimensional numerical modelling is then used to visualise the effectiveness of the stirrer in providing statistically uniform illumination of the cable under test. Results are then presented to show how the positioning and length of the cable effects the shielding effectiveness results obtained. Transmission-Line Matrix (TLM) Modelling is used to extract the surface transfer impedance by hybridising time domain modelling of the cable and theoretical models relating screen primary parameters to its geometric characteristics. Finally the results obtained from TLM modelling are compared with those obtained experimentally.

1. Introduction

Electromagnetic compatibility (EMC) is concerned with designing and operating equipment in such a way that it has an acceptable level of immunity from electromagnetic interference (EMI) from external sources and does not interfere substantially with any other equipment. However, ensuring the EMC of individual systems is compromised if the connecting cables are themselves sources of interference or susceptible to interference. Also it is essential that a signal being transmitted is not unduly modified by an external energy source or by poor design (self inductance). Therefore, it is conjectured that any connecting cables must be rigorously tested to ensure that they are sufficiently shielded to prevent any electromagnetic fields being induced by or interfering with the signal in the cable. Further, requirements of cost, weight and flexibility provide a counter force to excessive and unnecessary shielding. The effectiveness of a shield can be measured in two ways: either by calculating the proportion of an electromagnetic field incident on the shield that is transmitted through it (the 'shielding effectiveness' SE), or by calculating the 'Surface Transfer Impedance' (Z_T) of the cable shield. It is claimed that the shielding effectiveness and Surface Transfer Impedance are proportional [1-6] so the shielding effectiveness can be obtained by first calculating the Surface Transfer Impedance. It is, however, important to be able to obtain SE directly.

The 'shielding effectiveness' of a shield is a ratio (in decibels) of the proportion of an electromagnetic field incident on the shield that is transmitted through it [7]:

$$SE = -20 \cdot \log_{10}\left(\frac{E_t}{E_i}\right) \quad \text{(dB)} \qquad (1)$$

Where: E_t = electric field transmitted through the shield.
E_i = electric field incident on the shield.

Figure 1 shows a diagrammatic definition of the shielding effectiveness of a shield.

The 'Surface Transfer Impedance' (Z_T) of a length 'L' of coaxial cable is illustrated in Figure 2. In the figure 'I' is the current induced by the external (interfering) field on the shield, and 'V' is the potential difference built up between the inner and outer conductors due to the current 'I'. The Surface Transfer Impedance is usually expressed as a per unit length parameter of the cable, and is defined as:

$$Z_T = \frac{V}{I \cdot L} \quad (\Omega m^{-1}) \qquad (2)$$

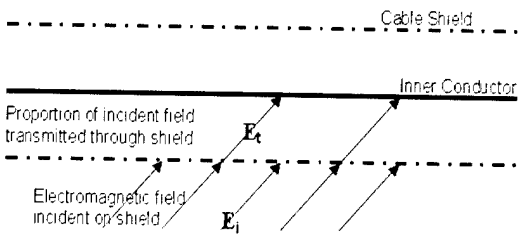


Figure 1. Definition of shielding effectiveness

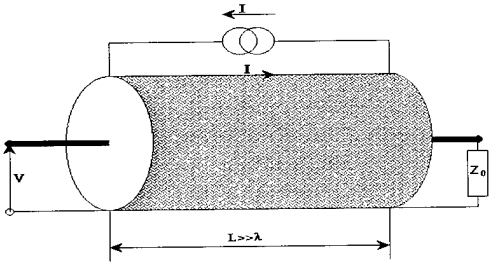


Figure 2. Illustration of Transfer Impedance.

The screening performance of cables is analyzed; by measurements using a reverberant chamber in sections 2-5 and by the TLM method in sections 6 –7.

2. Review of Mode Stirred Chamber Method

It is desirable when conducting EMI tests to isolate the test space from the exterior electromagnetic environment. This is because it is almost impossible to separate the arbitrarily varying ambient electromagnetic signals from the signals of interest produced by the equipment under test, this is one of the main failings of an Open Area Test Site (OATS). To do this the 'test space' can be set up within a Faraday Cage, a metal walled room or chamber which prevents fluctuations in the electromagnetic field outside the chamber from affecting the field inside.

Susceptibility tests can be carried out within the chamber by injecting an electromagnetic field using an antenna then having the equipment under test attached to a detector. However such a chamber contains strong spatial variations in the electromagnetic field, necessitating the rotation of the device under test as this decreases the dependence of the results on the orientation and location of the device under test within the chamber. To eliminate the need for rotating the device under test a rotating reflective surface can be installed in the chamber. This rotating reflective surface (or 'stirrer') alters the 'boundary conditions' within the chamber its purpose is to cause very large changes in the standing wave patterns. This means that the standing waves within the chamber that add together to form the modes (or maximums in the electromagnetic field) are altered with stirrer position. As the modes and nulls move around within the chamber this produces a field within a certain volume that, when averaged over one revolution, is statistically uniform and hence provides uniform illumination to the device under test.

The mode stirred technique is ideal for measuring shielding effectiveness over a wide frequency range and cables of different diameters and sizes can conveniently be measured in the same chamber [8].

The lowest frequency at which the mode stirred chamber can be used is limited by several factors including the stirrer's limited ability to uniformly excite all the modes in the chamber [9] and the number of modes in the chamber [10]. The number of modes in the chamber is a function of chamber geometry. Due to design constraints, the dimensions of the De Montfort University Mode Stirred Reverberation Chamber are 5.00 metres long, 2.95 metres wide and 2.36 metres high. Therefore the lowest operating frequency of the De Montfort University chamber can be estimated as 182.5 MHz [9-11].

The stirrer has to move the position of the modes within the chamber such that when the electromagnetic field is averaged over one revolution of the stirrer it is the same for all points within the working volume. The mode stirrer used here consisted of two, one metre square, 'vanes' set at 45 degrees to the vertical (see Figure 3). The stirrer was positioned as close into one corner as possible thus maximising the volume that had no equipment in it, the 'uncluttered volume' (see Figure 4). Whilst this design is unlikely to provide optimum performance, it is acceptable for the initial tests being undertaken and to provide a basis for comparisons with 3D modelling.

There are two modes of operation within a reverberant chamber. In the 'Mode Stirred Method', 200 measurements are taken during one revolution of the stirrer whilst the stirrer rotates continuously. However, because the stirrer in constantly moving no correcting or averaging is possible. This contrasts with the 'Mode Tuned Method' where the stirrer is stepped at selected, uniform increments (usually 200 per rotation), with the stirrer remaining stationary in its predetermined position whilst the measurements are taken and averaged. The Mode Tuned Method is more repeatable and accurate, however it also takes longer to complete each test run.

In order to use the mode stirred chamber to measure the shielding effectiveness of a cable, the power received at firstly the reference antenna (P_{REF}) and secondly the cable (P_{CAB}) is measured for a range of frequencies for multiple stirrer steps (usually 200). Then the maximum power received for each frequency during one rotation of the stirrer is determined and used in Equation 3. The maximum received power is normally used because it is more stable, easier to detect and control [12] and the result is usually very consistent.

$$SE = -10 \cdot \log_{10}\left(\frac{P_{CAB}}{P_{REF}}\right) \quad \text{(dB)} \qquad (3)$$

For the results to be valid the cable under test must be kept within the 'working volume', the volume within the 'uncluttered volume' in which the electric field is statistically uniform over one rotation of the stirrer. In addition, the cable must not be coiled, as this will increase the self inductance and adversely affect the results.

In order for the cable under test to be located in the centre of the chamber it must be placed on a non-lossy support. One end of the cable was connected to the Network Analyser whilst the other was terminated in the cable's characteristic impedance. Figure 5 shows a basic diagram indicating the connections between the controlling computer, network analyser and the equipment within the chamber.

In such standards as 61000-4-21 [13] the method for using mode stirred chambers for measuring the shielding effectiveness of cables is set out. However, there is an implicit assumption that the cable is straight and horizontal, which limits the length of cable to around one metre under normal circumstances. The purpose of the work reported here is to investigate the electromagnetic susceptibility performance of communication cables, especially for practical lengths for distributed systems (in the order of 10s of metres) which clearly necessitates an alternative or supplementary approach.

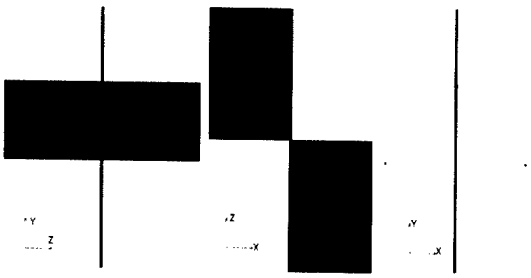


Figure 3. Illustration of the Mode Stirrer.

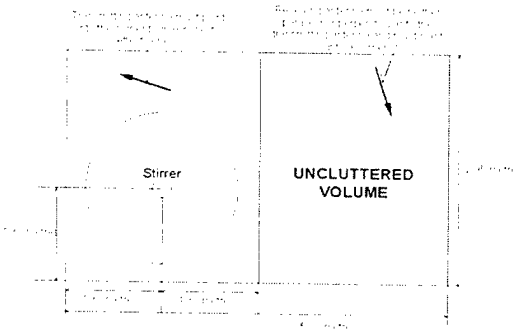


Figure 4. Showing the layout of the chamber.

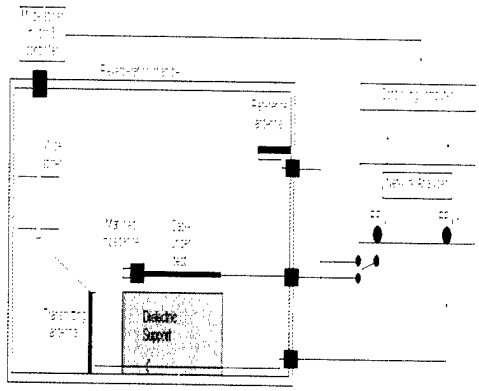


Figure 5. Block diagram of the proposed test set up from [13].

3. Working Volume

In order for the measured shielding effectiveness to be accurate, all points along the cable under test must be subjected to the same (average) electric field. Therefore a volume within the chamber must be defined in which the field is statistically uniform over one revolution of the stirrer. This volume is within the 'uncluttered volume' (see Figure 4) and is known as the 'working volume'. The precise location and extent of the working volume is defined variously as "greater than 0.5 wavelength from the rooms bounding walls, floor and ceiling" [10], "at least λ/3 from the chamber's walls at the lowest test frequency" [9] and "it is recommended that the surfaces bounding the working volume not be located closer than 1 metre from any chamber surface, field generating antenna or tuner assembly" [13].

In order to investigate the working volume of the De Montfort University mode stirred chamber a virtual model was created in a commercial 3-D TLM solver and the electric field was obtained for the verticies of various concentric cuboids whose surfaces were a consistent distance from the surfaces of the uncluttered volume (one such cuboid is shown in Figure 6). The electric field output from each vertex of each cuboid was then examined using the standard deviation method as detailed in 61000-4-21 [13] to determine whether that cuboid was within the working volume for each frequency under scrutiny. The standard deviation response for the electric field in the x, y and z directions and for the maximum of all the electric field measurements of the cuboid whose limits were 0.7 metres from the chamber walls is shown in Figure 7. For each cuboid and each standard deviation the percentage of remaining data points not exceeding 3dB was calculated for each frequency (Figure 8 shows this for the cuboid examined previously). To determine the frequency for which each cuboid contained the working volume a '95% confidence frequency' was used. This frequency was that above which 95% of the standard deviation frequency response was below 3dB (the permitted tolerance). As can be seen, the minimum frequency for which the cuboid in Figure 8 contained the working volume is 183 MHz.

Based on the method presented above the minimum frequency for which each cuboid contained the working volume and the distance of that cuboid's bounding surfaces is shown in Figure 9.

Since the lowest test frequency at which this chamber will be used is 200 MHz (corresponding to the EMC testing frequency range of 200 – 2000 MHz) then the cable under test can be placed anywhere within the uncluttered volume.

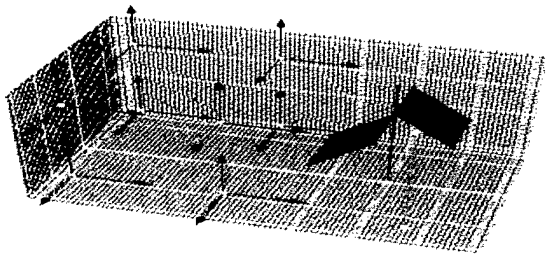


Figure 6. Picture showing the positioning of the output points that formed a cuboid.

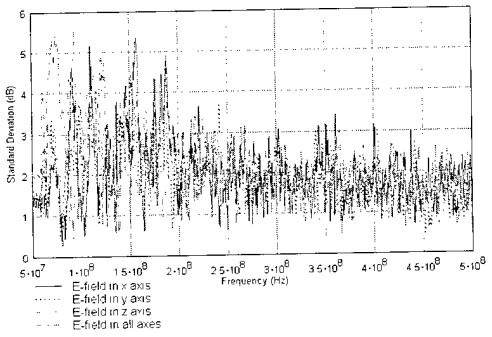


Figure 7. Calculated standard deviation for cuboid whose edges were 0.7 metres from the chamber wall.

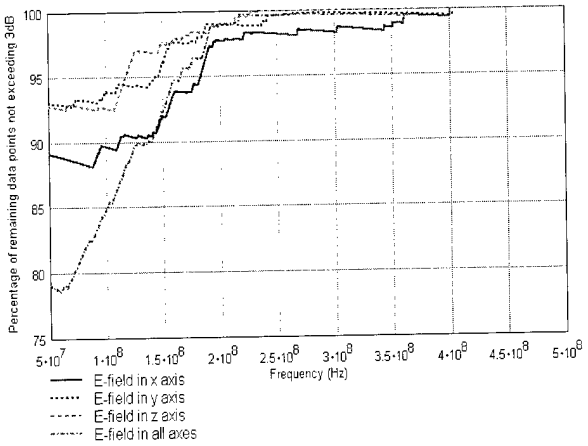


Figure 8. The percentage of remaining data points not exceeding 3dB for each frequency for the cuboid whose edges were 0.7 metres from the chamber wall

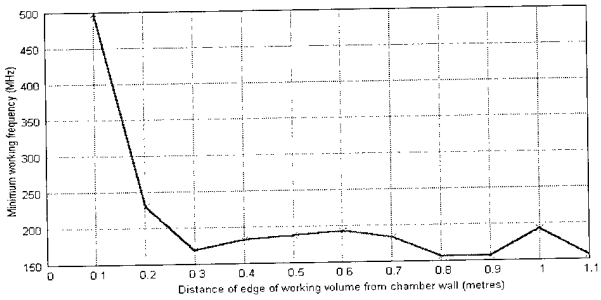


Figure 9. The Minimum Working Frequency For Each Cuboid

4. Cable positioning and orientation

To determine whether the cable under test was subjected to 'uniform illumination' over one revolution of the stirrer, a cable was simulated in a 3-D TLM package. The simulated cable was simply a cylinder 1 metre long with a 0.03 metre radius, with its centre point at the centre of the 'uncluttered volume'. The cable was oriented in the three orthogonal directions (x, y and z) and the surface currents observed for five independent stirrer steps. As can be seen from Figures 10, 11 and 12 as the stirrer rotates the 'hot-spots' of higher surface currents (the darker shades in the figures) move around so that if it were to be averaged over one stirrer rotation it would be seen that the surface currents were statistically uniform.

The cable was then repositioned outside the working volume and the simulation repeated. This cable is not subjected to sufficient surface currents for any shielding effectiveness measurements to be valid.

According to these results the shielding effectiveness of the cable should be the same irrespective of the cable orientation so long as it remains within the working volume as the cable is subjected to an identical field in all three orthogonal directions

To investigate whether the orientation of the cable affected the measured shielding effectiveness a 1 metre length of cable was placed in the centre of the working volume and the shielding effectiveness was measured and calculated using Equation 3. If the orientation of the cable did not affect the results then the measured shielding effectiveness would be identical in each case. As can be seen in Figure 13 the orientation of the cable does not affect the results provided the cable remains in the working volume.

However, when the cable was placed on the chamber floor (see Figure 14) the shielding effectiveness results are dramatically different. This difference is probably because when the cable is next to the ground plane it experiences additional resonances, possibly due to the shield to ground capacitance or transfer admittance. However, whether this is purely due to the cable being on a ground plane or if it is effected by the cable being outside the working volume requires further investigation.

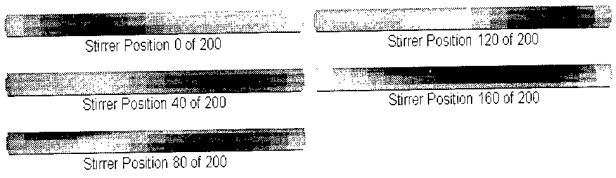


Figure 10. Cable in Centre of Working Volume in Z Orientation

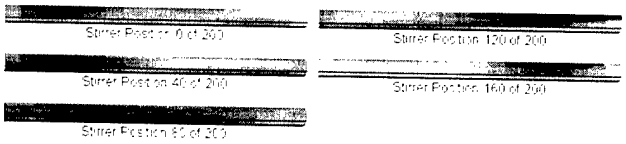


Figure 11. Cable in Centre of Working Volume in Y Orientation

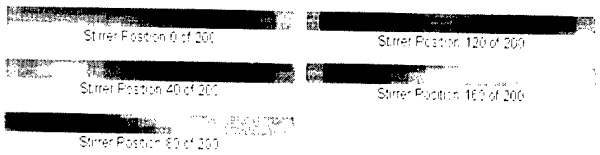


Figure 12. Cable in Centre of Working Volume in Z Orientation

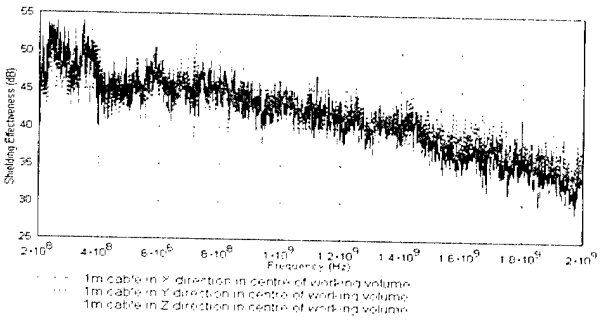


Figure 13. Showing how the orientation of the cable affects the shielding effectiveness

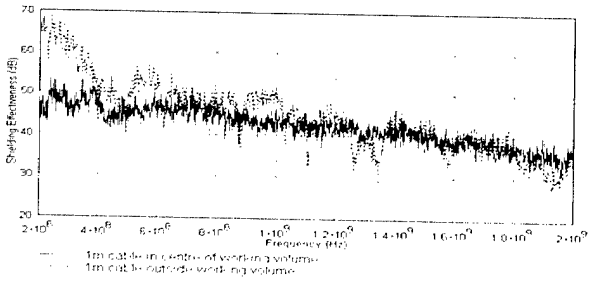


Figure 14. Showing how the positioning of the cable near the ground plane affects the shielding effectiveness.

5. Cable Length

In order for the mode stirred chamber to be of practical use in industry it must be able to be used to test practical cable lengths (in the order of 10 metres). However 61000-4-21 [13] suggests (as previously stated) that the cable should be straight. If this is in fact the case then a rather large mode stirred chamber will be required to perform these tests. The cable however cannot be coiled [2] as this would form an inductor.

In order to determine whether a long cable could be accommodated it was essential to see if the shielding effectiveness results were the same irrespective of whether the cable is straight or bent. To determine this the 1 metre cable was bent in half and its shielding effectiveness was again measured then compared with the straight cable (see Figure 15). These results suggest that a long cable could be accommodated by being placed in a 'zigzag' pattern.

To investigate whether a long cable can be tested within the mode stirred chamber a 10 metre length of RG 58 C/U was attached in a 'zig-zag' pattern to a pegboard (see Figure 16) and held in the three orthogonal directions during separate test runs. The shielding effectiveness results were then compared in Figure 17. As the shielding effectiveness results were the same for each position it was assumed that the cable was subjected to the same electric field and hence it can be inferred that long cables could be tested using the mode stirred chamber.

The definition of shielding effectiveness fails to take account of the fact that the receiving antenna for the cable under test is the cable itself and hence it changes when the cable changes. This may cause the shielding effectiveness of a cable to be length dependent. This suggestion agrees with the results presented by Dole and Kincaid [14] who tested a 30 metre cable and compared the results with those obtained using a 1.5 metre cable. They found that the shielding effectiveness results for their two cables differed by a factor of 20 dB, which would be expected if the shielding effectiveness obtained using their method was length dependant. To investigate whether this conclusion applies to cables tested in the mode stirred chamber a 30 metre cable was tested in the De Montfort University chamber. The shielding effectiveness was then calculated using Equation 3 and the shielding effectiveness results were compared with those obtained using a 1 metre cable, as shown in Figure 18.

The shielding effectiveness results for the 1 metre cable and 30 metre cable are very similar, which is currently being investigated.

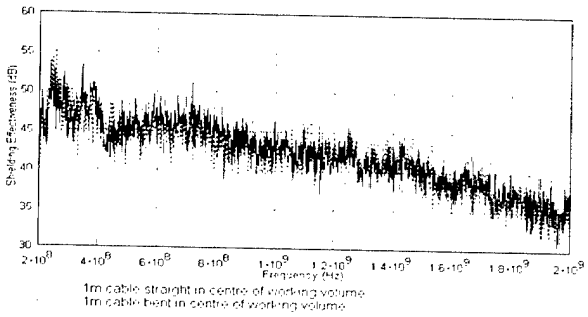


Figure 15. Straight vs. bent

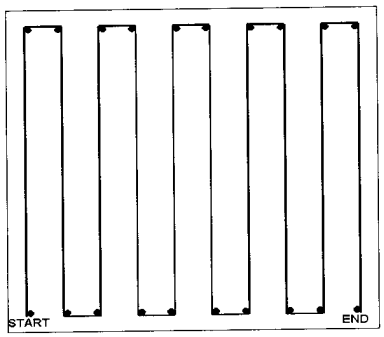


Figure 16. Long Cable configuration

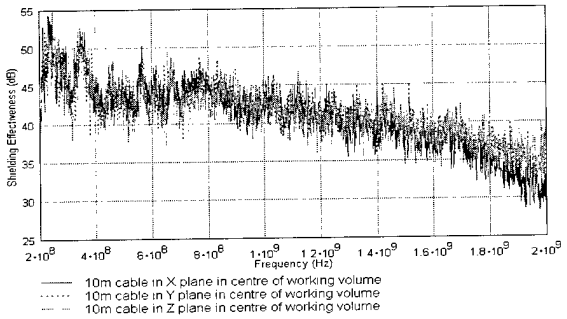


Figure 17. 10 metre Cable on pegboard in 3 orthogonals

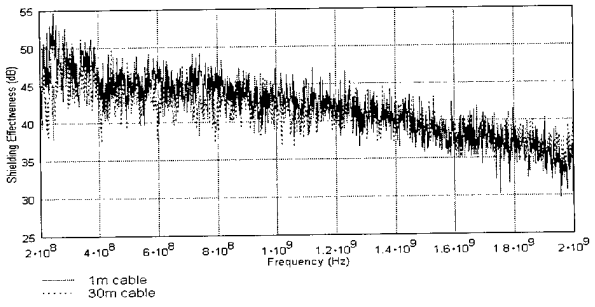


Figure 18. Comparing the Shielding Effectiveness results obtained using a 1 metre cable and a 30 metre cable

6. Theoretical Models for the Transfer Impedance of the Cable.

In order to assess the quality of a shield, the transfer characteristics, predominantly the transfer impedance of the cable have to be tested. A number of existing theoretical models that relate the geometry of the shield to the transfer impedance have been proposed and these are briefly reviewed in this section.

A relatively straightforward model was proposed by Tyni [15]. The two inductances are the braid and the leakage inductances. The braid inductance L_b, which arises from the woven nature of the braid, and the leakage inductance L_a, which is caused by the holes of the braid, are given by,

$$L_b = \frac{-\mu_o h}{4\pi D_m}\left(1 - \tan^2 \alpha\right) \tag{4}$$

$$L_a = \frac{\mu_o 2N}{\pi \cos\alpha}\left(\frac{b}{\pi \cdot D_m}\right)^2 \cdot e^{\left(\frac{-\pi \cdot d}{b} - 2\right)} \tag{5}$$

Where α is the braid angle, D_m is the mean braid diameter, N is the total number of belts (spindles), b is the hole width, d is the braid-wire diameter, h is the radial spindle separation and μ_o is the permeability of free space.

The transfer impedance is then approximated as,

$$Zts \approx j\omega(L_b - L_a) \tag{6}$$

The most significant drawback of this method is that it omits the effect of the shield resistance, which in the low frequencies (LF) region can be quite considerable. On the other hand the parameters required are relatively easy to obtain.

Another model examined, was Katakis' model [16] which is a modified version of Tyni's one. Katakis' major modification was that he added the effect of the radial spindle separation h, in the calculation of D_m,

$$D_m = D_o + 2d + h \tag{7}$$

where D_o is the diameter over the dielectric. Although in most cases [16] this modification improves Tyni's prediction, it also omits the shield resistance.

Another model, proposed by Hoeft [17], approximates the transfer resistance as,

$$R_o = \frac{1}{\pi D\, \sigma T} \tag{8}$$

Where σ is the shield conductivity, D is the diameter of the cable and T is the thickness of the shield. The mutual inductance of the braided shield is given as,

$$M_{12} = \frac{N\mu_0\alpha_m}{(\pi d)^2} \tag{9}$$

given

$$\alpha_m = \frac{4}{3}r^3 \tag{10}$$

Where N is the number of holes per meter, r is the circular hole radius and α_m is the magnetic polarizability. Its main advantage in comparison with the previous models is that it considers the effect of the shield resistance but, on the other hand some of the parameters required (e.g. magnetic polarizability etc.) are more difficult to determine, and subject to approximation errors. Furthermore, this model is very efficient when only the "worst case scenario" for the transfer impedance value is required.

Vance developed a model [18] that relates the transfer characteristics of the shield to braid parameters such as the fill of the braid and the volume of the metal in the braid.

The fill of the braid is given as,

$$F = \frac{N \cdot n \cdot d}{4\pi \cdot a \cdot \cos\alpha} \tag{11}$$

Where n is the number of wires per belt, a is the shield radius and the remaining symbols have their usual meanings.

The optical coverage K of the shield is,

$$K = 2F - F^2 \tag{12}$$

The volume of the braid, U is given as,

$$U = \pi^2 adF \tag{13}$$

and the number of holes per unit length of the shield is,

$$v = \frac{4 \cdot \pi \cdot a \cdot \sin\alpha \cdot \cos\alpha}{N^2 d^2} \cdot F^2 \tag{14}$$

Vance gives the resistance per unit length of the shield approximately as,

$$R_o = \frac{1}{\pi^2 ad\sigma F \cos^2\alpha} \tag{15}$$

By analogy to Kaden [19], the mutual inductance term M_{12} for v (holes/m) is

$$M_{12} = v\frac{\mu_o \cdot m}{4\pi^2 a} \tag{16}$$

where m is the magnetic polarizability of the diamond shaped hole determined experimentally using electrolytic-tank techniques [20].

Additional models have been produced (e.g. Sali [21], Zhou and Gong [22]). As many of these are modifications of the above models, they are not discussed further in this paper.

The transfer admittance, another parameter characterizing the transfer properties of the shield, is defined as,

$$Y_T = \frac{1}{V_o}\frac{dI_{sc}}{dz} \tag{17}$$

where V_0 is the voltage caused by the external field applied on the shield and dI_{sc}/dz is the short circuit current per unit length present on the inner conductor.

Similarly to equation (3) the transfer admittance is usually described by

$$Y_T = j\omega C_{tr} \tag{18}$$

where C_{tr} is the transfer capacitance. In order for the value of the capacitance to be significant, the electric field on the shield should be significant as well. This is only usually significant when the shield is not grounded, but placed close to a conducting structure Moreover the transfer admittance is almost negligible for cables with high optical coverage [23].

The transfer admittance is not an intrinsic property of the shield, as it depends mainly on the external environment of the measurements. A small number of measurements are present on the literature some of them are reviewed in [24].

In the simulations presented in this paper, the model proposed by Tyni is applied, as this is both straightforward and reasonably accurate for the upper frequencies being considered for cable testing.

7. TLM Analysis

The Transmission-Line Matrix (TLM) modeling method is a time domain numerical technique and has been implemented successfully for the simulation of many kind of cables, including Unshielded (UTP) and Shielded (STP) Twisted Pair Cables [25][26]. As described in [27] the TLM approach consists of many transmissions line segments connected together.

In this paper a coaxial cable is examined by simulating the effect of the geometry of the shield on the performance of the inner conductor. The main advantage of the proposed method is that it can be used to examine the behaviour of the system for any form of external field source, either deterministic or random, local or systemic.

The method followed is similar to the one in [25]. Impedance links have replaced the combination of per unit length inductance L and per unit length capacitance C. Two separate circuits have been considered for the shield and the inner conductor of the coaxial as in Figure 19 and they are inter-connected by equation 21.

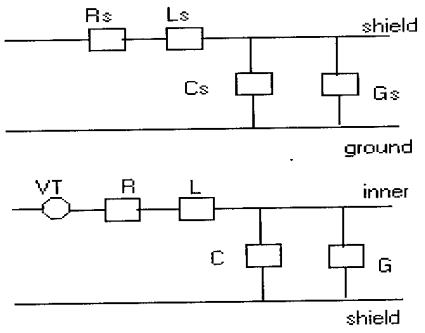


Figure 19. Transmission line segments (top) for the shield, and (bottom) the inner conductor

The L and C combination of the inner conductor is replaced by a link line of impedance ($Z_o=(L/C)^{1/2}$). R and G are time independent so they are left unchanged. The corresponding time step of a wave to propagate a TLM node is ($\Delta t=(L.C)^{1/2}$). Time synchronization between the TLM nodes of the shield and the inner conductor is required, so the shield impedance is calculated as ($Z_{os}=(L_s/\Delta t)$. The shield capacitance is then obtained as ($Cs=(\Delta t)^2/L_s$).
The TLM model of node n and its Thevenin equivalent are shown in Figures 20 and 21,

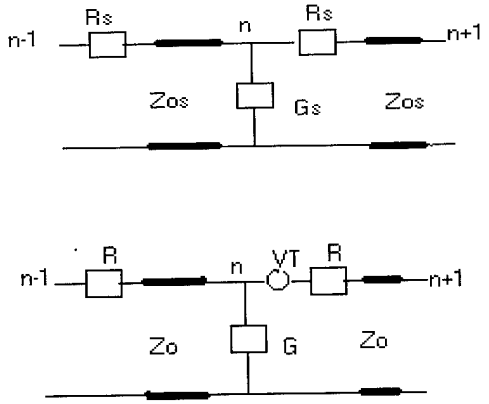


Figure 20. TLM Models for the coaxial system

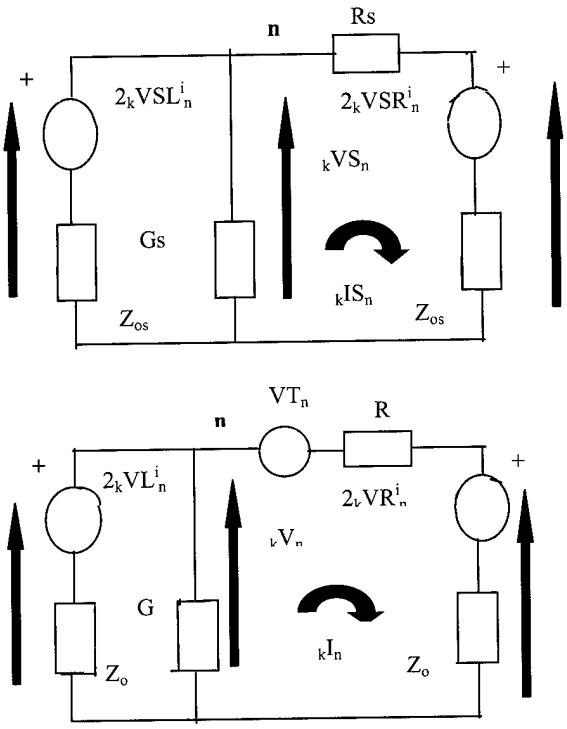


Figure 21. Thevenin equivalent circuits of the coaxial system

Using the parallel generator theorem the nodal voltages of the above circuits are given by,

$$ {}_kVS_n = \frac{\frac{2_kVSL^i{}_n}{Z_{os}} + \frac{2_kVSR^i{}_n}{R_s + Z_{os}}}{\frac{1}{Z_{os}} + \frac{1}{R_s + Z_{os}} + \frac{1}{G_s}} \qquad (19) $$

and

$$ {}_kV_n = \frac{\frac{2_kVL^i{}_n}{Z_o} + \frac{2_kVR^i{}_n - {}_kVT_n}{R + Z_o}}{\frac{1}{Z_0} + \frac{1}{R + Z_o} + \frac{1}{G}} \qquad (20) $$

$$ \text{where } {}_kVT_n = {}_kIs_n \cdot ZT_s \qquad (21) $$

and ${}_kIs_n$ is the shield current of node n, ZT_s is the transfer impedance of the shield and VT is the resulting induced voltage in the inner conductor. Incident and reflected voltages on, and from, the links can be computed and be used in the iterative TLM process [27]. The value for ZT_s can be calculated by using any of the theoretical models (e.g. Tyni, Vance etc.) previously discussed.

8. Validation of TLM against Measurements

The transfer impedance was calculated as the ratio of the load voltage of the inner conductor to the current present on the near end of the shield.

Initially, TLM was compared with measurements, obtained by the authors of this paper, using the Current Probe Method [28,29] for the RG-58 cable. Tyni's model was used for the modeling of the transfer impedance of the shield.

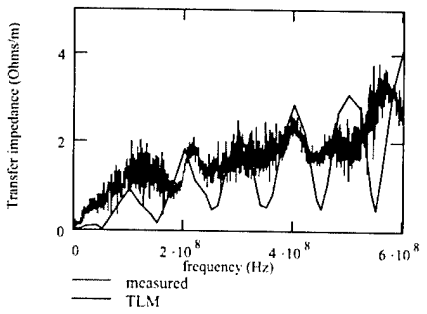


Figure 22. Validation of TLM against measurements for 1m of RG-58 coaxial cable.

Tyni's model in combination with the Vance equation for the transfer resistance, was used to obtain predictions for the measurements of URM76 presented in [23]. Figures 22 and 23 clearly show the very good agreement between the models and the measurements. The position of resonances in the upper frequencies varies with the length of the cable (as discussed in [30]). The modelling of these resonances is the main advantage of the TLM analysis in relation to the pure theoretical analysis of section 6, where only the geometry of the shield is accounted for the calculation of the transfer impedance.

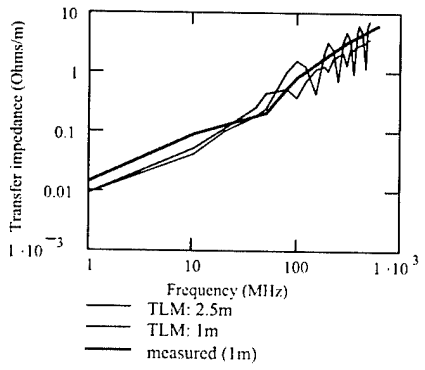


Figure 23. TLM against measurements for URM76 cable

9. Conclusions

The reverberant chamber appears to be a promising method for directly measuring the shielding effectiveness of various cable lengths, provided that several criteria are met. The first of these is that the cable under test is subjected to uniform illumination by the electric field within the chamber. In order for this criteria to be met the cable must be within the working volume, the exact position of which varies with frequency, however for the frequencies of interest in this paper (above 200MHz) the working volume starts a minimum of 0.3 metres from the chamber walls. When the cable is placed within this volume it is subjected to an electric field that varies with stirrer position such that it is 'uniformly illuminated', however when the cable is placed outside this volume it is not subjected to a sufficient field strength for any measurements to be valid. So long as the cable is placed within the defined working volume during the test, its exact position and orientation is irrelevant and, if necessary, the cable can be bent. This finding permits long cables to be tested in any position within the working volume. The slight difference between the shielding effectiveness obtained with the cable in the x direction and those obtained with the cable in the y and z directions is due to the positioning of the connecting cable. If the connecting cable between the test cable and the detector is within the working volume this causes the apparent shielding effectiveness to reduce at high frequencies. To prevent this affecting the results the test cable is usually placed in the z direction when the shielding effectiveness is being measured as in this position an absolute minimum of the connecting cable is within the working volume. Furthermore, when cables of the same type but different lengths were tested, they produced remarkably similar results. Finally, the very good prediction capabilities of TLM were presented and it was verified that the position of the resonances depends on the length of the cable.

10. Acknowledgment

The authors would like to thank Flomerics Ltd., for providing the 3-D Electromagnetic Simulator used in sections 2-5 of this paper.

11. References

[1] J.Goedbloed, *"Electromagnetic Compatibility"*,Prentice Hall, (1990).

[2] Stand.46A/331/CDV, *Cable assemblies, cables, connectors and passive microwave components – Screening attenuation measurement by the reverberation chamber method,*Int. Electrotech. Comission, (1999).

[3] Europ. Stand. BS EN 61726:2000. *Cable assemblies, cables, connectors and passive microwave components – Screening attenuation measurement by the reverberation chamber method,* Europ. Comit. for Electrptechn. Standardization, (2000)

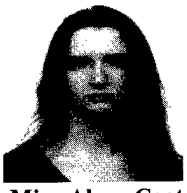
[4] J.R. Peel, "Simple Relations Between shielding effectiveness and Transfer Impedance/Admittance for Cables", Int. Symp. On EMC, Seattle,WA, 134-139,(Aug. 1988).

[5] R.J.Peel, R.Finney, R.M.Lassise, "Relationship of shielding effectiveness to Transfer Impedance/Admittance for Cable Emission and Susceptibility", Nat. Symp. On EMC, San Antonio,TX, 55-62,(Apr. 1984)

[6] G.Dike, R. Wallenberg, J.Birkin, "Electromagnetic Relationships between shielding effectiveness and Transfer

Impedance, Int.Symp.on EMC, IEEE, San Diego,CA, 133-138,(Oct.1979).
[7] C.R.Paul, *"Introduction to Electromagnetic Compatibility"*, John Wiley & Sons, (1992).
[8] R.L. Jesch, "Measurement of shielding effectiveness of Cable and Shielding Configurations by Mode-Stirred Techniques", Trans. on EMC, IEEE, 30,222-228,(Aug.1998).
[9] M.L.Crawford, G.H.Koepke, " Technical Note 1092: Design, Evaluation and Use of a Reverberation Chamber for Performing Electromagnetic Susceptibility/Vulnerability Measurements",US: Nat. Bureau of Standards, (1986)
[10]N.J.Carter, "Mode Stirred Chambers", (Mar 1999), (avail. at http://ourworld.compuserve.com/homepages/Nigel_Carter/modestir.htm.)
[11] M.Petirsch, I.Sotriffer, A. Schwab, "Mode Stirred Chamber as Test Facility for Electromagnetic Susceptibility Measurements", 13th In, Symp.on EMC,Zurich, 679-684, (Feb. 1999).
[12] N.W. Wehling, "Repeatable Low-cost Radiated Susceptibility Tests in a Standard Shielded Enclosure",16-26.
[13] Draft 61000-4-21. "Electromagnetic Compatibility (EMC)-Part 4 : Testing and measurement techniques-Section 21: Reverberation Chamber Test methods" , Int. Electrotechn. Commission,(2000)
[14] C.W. Dole, and J.W.Kincaid, "Screening Attenuation of Long Cables", paper no.04-04, IWCS 49th,(Nov. 2000)
[15] M.Tyni, " The transfer impedance of coaxial cables with braided conductors ", Proc. EMC Symp. Wroclaw, Poland, 410-418, (September 1976)
[16] J.N.Katakis, *"Transfer impedance of wire braided coaxial cables at radio and microwave frequencies"*, MEng Thesis, Univ. of Sheffield, UK, (February 1983).
[17] L.O.Hoeft, " A Model for Predicting the Surface Transfer Impedance of Braided Cables", Rec. Int. Symp. Electromagn. Compat., IEEE ,402-404,(1986)
[18] E.F.Vance, " Shielding Effectiveness of Braided-Wire Shields", Trans. on EMC, 17(2), IEEE, 71-77, (May 1975)
[19] H.Kaden, *"Wirbelstrome und Schirmung in der Nachrichten-technik"*, Springer-Verlag, Berlin, (1959)
[20]S.B.Cohn, "Determination of aperture parameters by electrolytic tank measurements" IRE(39), 1416-1421, (Nov. 1951)
[21] S.Sali "An Improved Model for the Transfer Impedance calculations of braided Coaxial Cables", Trans. on EMC,IEEE, 33(2),139-143,(May 1991)
[22] G.Zhou and L.Gong, "An improved Analytical Model for Braided Cable Shields", Trans. on EMC, 32(2), IEEE, 161-163,(May 1990)
[23] F.A.Benson, P.A.Cudd, J.M.Tealby, "Leakage from coaxial cables", Proc. 139(6),285-303,IEE, (November 1992).
[24] F.Broyde, E.Clavelier, D.Givord, P.Vallet, "Discussion of the Relevance of Transfer Admittance and some Through Elastance Measurement results", Trans. on EMC,IEEE, 35(11),417-422, (November 1993)
[25] M.M.Al-Asadi, A.P.Duffy, A.J.Willis, K.G.Hodge, "Twisted pair Cable Design Analysis and Simulation", paper no. 04-01, IWCS 49th, (November 2000).
[26] M.M.Al-Asadi, A.P.Duffy, K.G.Hodge, A.J.Willis, "Return Loss Prediction for Cascaded Systems", paper no. 17-04,IWCS 49th, (November 2000)
[27] C.Christopoulos, *The Transmission Line Modeling Method TLM*, IEEE Press, New York, (1995)
[28] A. Moriello, T. M. Benson, A. P. Duffy, C. F. Cheng: "Surface Transfer Impedance Measurement: A Comparison Between Current Probe and Pull-on Braid for Coaxial Cables". IEEE Trans - EMC, 40(1), 69-76, (1998)
[29] A.R.Coates, *"The Development of a Simple Method for the Evaluation Of The Surface Transfer Impedance Of Coaxial Cables"*, MEng Thesis, Univ. of Nottingham, UK, (1999)
[30] E.P. Fowler, "Screening of cables and connectors", Electronics and Communications Journal,IEE, 93-102, (April 1994)

Authors Biographies



Miss Alyse Coates studied for a Master of Engineering with Honours Degree in Electrical and Electronic Engineering at Nottingham University, England for four years and graduated in July 1997. Her third and final year projects involved developing a simple method for measuring the surface transfer impedance of co-axial cables. She joined the Applied Electromagnetics Research Group at De Montfort University, Leicester, in September 1999. She is currently involved in developing a mode-stirred chamber to measure the Electromagnetic Susceptibility of communications cables.



Mr Alexandros Gavrilakis holds a BEng (Hons) degree from Staffordshire University, UK and an MSc from the University of Bradford, UK. He joined the Applied Electromagnetics Group at De Montfort University, UK in 2000 where he is reading for a PhD. His research interests involve mathematical and computer modeling of shielded transmission lines and EMC.

For biographies and photos of Mohammed. Al-Asadi, Alistair.P.Duffy Kenneth.K.Hodge, Arthur J.Willis, please refer to paper 04 – 01 " A Genetic Algorithm Toolkit for Cable Design".

Statistical Analysis of Coaxial Screening Attenuation

Carl W. Dole, Lenore J. Choate, and John W. Kincaid
Belden Electronics Division
Richmond, Indiana
765-983-5200 Carl.Dole@Belden.com

Abstract

A statistical evaluation of a measurement system that is used to determine the screening attenuation performance of coaxial cable is presented. The measurement system, which is in accordance with IEC 61196 [1] guidelines, is defined to consist of the test equipment, appropriate personnel to operate the equipment, and samples of coaxial cable that are to be tested. The system measurement error is shown to depend primarily on the test fixture length, the frequency span of the test, and the design of the shield structure under test. The contributions of these components to the measurement error are identified through a series of five measurement system evaluations (MSE's). The MSE's were conducted with two shield designs used on standard 75-ohm coaxial cable. The first is a foil/braid shield design. The second is a single braid shield.

Keywords

Screening attenuation; coaxial cable; statistics; measurement system evaluation; MSE; capability; ANOVA.

1. Introduction

Shield effectiveness of coaxial cable can be measured by several methods such as transfer impedance, absorbing clamp, GTEM, anechoic chamber, and reverberation chamber. The costs involved with these methods can be considerably higher than screening attenuation. Higher costs are incurred for the equipment and for the skilled operator to use the equipment. Absorbing clamp, anechoic chamber, and reverberation chamber may require a highly shielded enclosure. Transfer impedance and GTEM use specially made fixtures. In contrast, screening attenuation uses a low-cost fixture made from commercially available components.

Screening attenuation results of various shield designs of coaxial cable have been presented in past works using appropriate frequency ranges for the fixture length utilized [2,3]. A limited number of samples were tested in these cases and usually only a single typical result of each shield design was presented. Subsequent testing has been performed with multiple samples per shield design in order to obtain a statistically valid picture of the cables and measurement system. The MSE quantifies the variation caused by the sample, by the gage, which consists of the measurement equipment and fixture, and by the operator. Transfer impedance has a generally accepted repeatability of ±6 dB as a rule of thumb. This paper presents the first known statistical analysis of screening attenuation to quantify the repeatability and reproducibility

Measurement system evaluation will be described followed by a brief discussion of capability as it refers to screening attenuation. The results of five MSE's will be presented along with a comparison of them. Suggested areas of further study will be presented along with conclusions drawn from the data presented.

2. Measurement System Evaluation

A measurement system evaluation (MSE) is a statistical tool used to determine the variations in a measurement system. The variation can be categorized as sample, gage, and operator.

Sample variation is the difference in screening attenuation between samples that have the same shield design. This variation can come from the materials, manufacturing process, or effects to the item after manufacture. The first two occur before or during the manufacturing processes whereas the latter occurs subsequent to manufacture. A coaxial cable constructed with a solid tubular shield, such as a semi-rigid coaxial cable, would provide a very stable shield structure. This would permit greater accuracy in determining measurement system error.

Gage variation is from the equipment used to perform the measurement. A perfect gage would give the same result each time one sample is measured, assuming the sample has not changed.

Actual gages always have some variation that must be considered when evaluating data obtained from the gage. Gage variation is not systematic such that the effects could be negated by normalization. The random nature only allows a statistical prediction of the range of variation.

Operator variation is caused by differences between operators in the manner of performing the test. Variations can result from subtle differences in operator technique. Typically three operators test 10 items of a product three times each for a total of 90 measurements. If variations due to different operators are not an issue, one operator can test 16 samples twice for a total of 32 measurements.

Analysis of variance (ANOVA) [4] is applied to the data to determine the total variation and to separate the portions of variation caused by the sample, gage, and operator. Each source of variation is assigned a percentage and decibel value.

In an MSE it is assumed that the screening attenuation of each sample is stable. If it is not, an additional variability component will be added to the total variation. Instability can be as a result of operator handling that causes the shield to change. A coaxial cable constructed with a solid tubular shield would provide a very stable shield structure. A semi-rigid coaxial cable fits this criterion. This would allow a more accurate determination of the gage variation. The MSE is not capable of isolating instability variation from other causes. This became an issue as will be shown in the test results.

3. Capability

Capability refers to the ability of the cable to meet the required specification. The amount of variation can be predicted through statistical analysis of samples taken from one, or preferably multiple, production runs. Maximum, minimum, mean, and standard deviation of screening attenuation characterize the product variation.

A minimum or typical value is usually advertised. Quite often only a single value is given for a broad frequency range. Sometimes no frequency is given.

4. Procedure

4.1 Cable Samples

Two coaxial cable shield designs were evaluated (Table 1). The first, a foil/braid design, was chosen as representative of a common shield design used in the CATV industry. The second, a braid only design, was added because of the variations observed with the first. This will be explained later in this paper.

Table 1. Cable Shield Design

Cable Shield	Inner Foil (bonded to dielectric)	Braid/Angle
Foil/Braid	Al/polyester/Al	60% Al./27°
Braid	N/A	95% b.c./23°

4.2 Screening Attenuation Test Fixture

Two screening attenuation fixtures were used. Both are 76.5mm diameter with the first 1.5m in length and the second 6.7m in length. These have been discussed in detail in a previous publication [5]. The fixture length and the velocities of propagation in the sample and fixture determine the frequencies of the resonant responses. This produces a lower frequency limit of approximately 90 MHz for the 1.5m fixture and 20 MHz for the 6.7m fixture. In addition to providing a lower measurement frequency, the 6.7m fixture allows a longer portion of cable to be under test. The test setup is shown in Figure 1.

4.3 Measurement System Evaluations

Five measurement system evaluations were performed (Table 2). The 1.5m fixture was evaluated first and then the 6.7m fixture. Both shield designs were evaluated in both fixtures.

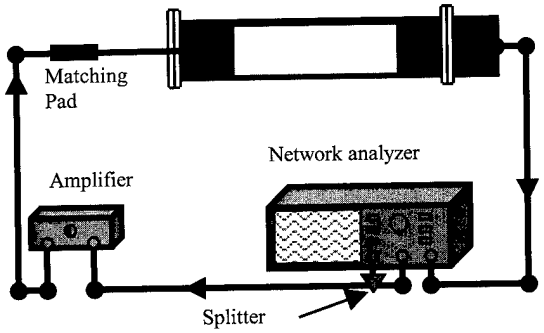


Figure 1. Test Equipment Setup

Table 2. Measurement System Evaluations

MSE	Fixture Length (meters)	Cable Shield	Number of Samples	Number of Operators
1	1.5	Foil/Braid	10	3
2	1.5	Foil/Braid	10	1
3	1.5	Braid	16	1
4	6.7	Foil/Braid	16	1
5	6.7	Braid	16	1

4.3.1 MSE 1 (1.5m, foil/braid)

The initial MSE was performed on the 1.5m length screening attenuation fixture using ten samples of the foil/braid shield. The testing sequence was as shown in Table 3. These samples were rotated through the three operators such that each operator tested each sample three times. Nine measurements per sample and a total of 90 sets of data were produced. The order of testing was randomized during the second and third times each operator tested the ten samples to preclude the possibility that the order of testing would influence the outcome. Figure 2 shows the first data set of screening attenuation for the ten samples.

Table 3. MSE 1 Testing Sequence

Operator	Samples	Sequence
1	1 through 10	In order
2		
3		
1	1 through 10	Random order
2		
3		
1	1 through 10	Random order
2		
3		

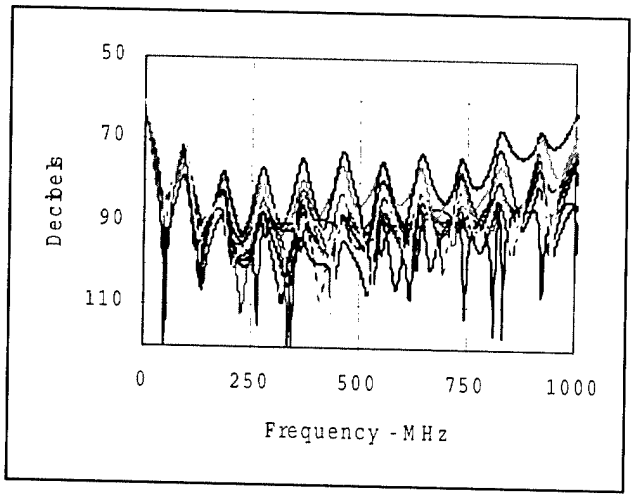


Figure 2. MSE 1 Foil/Braid Screening Attenuation Test Cycle 1, 10 Data Sets

The data derived from the measurements was divided into two frequency ranges for analysis purposes. The first range of 70-500 MHz was chosen to capture the resonance peaks from the first one at the low frequency end to the one just below 500 MHz. The second range was 500-1000 MHz. The worst-case value was extracted for each sample from each frequency range. These values were tabulated and analyzed with commercially available statistics software [6].

The analysis revealed that the operator contributed only a small portion of the variation. The operator contribution was only 2.1% in the 70-500 MHz range and 3.3% in the 500-1000 MHz range. The greatest portion of variation was due to the gage and/or sample.

The number of distinct categories in MSE 1 was only one. When performing an MSE it is desirable to have at least four distinct categories in the data analysis. Distinct categories refer to the number of groups in the data that the measurement system can discern. The number of distinct categories is determined by comparing the sample variation to the gage variation. The smaller the gage variation is in relation to the sample variation, the greater the number of distinct categories. If the number of distinct categories is low, the gage variation is large in comparison to the sample variation.

When the MSE 1 screening attenuation data was examined in its sequence of testing, it was discovered that the screening attenuation of four samples was degraded significantly for the fifth and following tests of those samples. This explained why the number of distinct categories was low. Although the cause was not determined, mishandling of the samples was suspected, because the screening attenuation remained at the degraded level for subsequent tests. This led to MSE 2 using new samples from the same reel of cable.

4.3.2 MSE 2 (1.5m, foil/braid)

Ten new samples of the foil/braid shield were used for a second MSE using the same fixture and setup as MSE 1. These samples came from the same spool of cable as the MSE 1 samples and were interspersed throughout the spool as with the previous set. Only one operator was used because MSE 1 indicated the operator contributed only a small portion of the error. The testing sequence was as shown in Table 3 but with only a single operator.

MSE 2 has a greatly reduced measurement error compared to MSE 1. Measurement error decreased to 4.12 dB in the 70-500 MHz range and 6.41 dB in the 500-1000 MHz range (Table 4). The dramatic drop in measurement error confirmed the suspicion of samples degrading during the first MSE. The number of distinct categories increased, which is desirable. It must be emphasized that the same equipment and samples from the same spool were used in both MSE 1 and MSE 2.

4.3.3 MSE 3 (1.5m, braid)

The third MSE was also with the 1.5m fixture but used 16 samples of the braid shield and one operator. The single braid design was chosen because it was believed that it has a more stable screening attenuation than the foil/braid construction. Since the gage was the same, it would determine if the variation was from the gage or the sample. Table 4 is a comparison summary of MSE 2 and MSE 3.

Table 4. MSE 2 (foil/braid) vs. MSE 3 (braid)

	70-500 MHz		500-1000 MHz	
	MSE 2	MSE 3	MSE 2	MSE 3
Measurement Error (± dB)	4.12	0.26	6.41	0.53
Percent Contribution				
Total Gage (Repeatability)	35.81	14.33	11.97	7.53
Part to Part	64.19	85.67	88.03	92.47
Distinct Categories				
	2	3	4	5

Measurement system errors decreased from 4.12 dB to 0.26 dB in the 70 to 500 MHz range and from 6.41 dB to 0.53 dB in the 500 to 1000 MHz range. Contrasting this MSE 3 measurement error with MSE 2 clearly revealed that the gage introduces only a small amount of variation into the measurements. The large amount of error in MSE 2 is due mainly to the sample variation and not the gage variation.

4.3.4 MSE 4 (6.7m, foil/braid)

A measurement system evaluation was performed on the 6.7m fixture using 16 samples of the foil/braid and one operator. This was

done to see how sample length effects measurement error. The data analysis was divided into frequency sub-bands of approximately 100 MHz, because the longer fixture produces a greater number of resonant points for a given frequency range (Tables 5 and 6). Using the narrower sub-band gave approximately the same number of resonant peaks per sub-band as the 1.5m fixture.

Table 5. MSE 4 (6.7m, foil/braid)

	Frequency (MHz)				
	10-110	110-220	220-320	320-420	420-530
Measurement Error (± dB)	4.54	3.28	9.97	8.39	8.48
Percent Contribution					
Total Gage (Repeatability)	27.39	15.02	48.94	30.77	28.06
Part to Part	72.61	84.98	51.06	69.23	71.94
Distinct Categories					
	2	3	1	2	2

Table 6. MSE 4 (6.7m, foil/braid)

	Frequency (MHz)				
	530-630	630-730	730-850	850-950	950-1050
Measurement Error (± dB)	11.20	8.25	6.59	7.71	9.15
Percent Contribution					
Total Gage (Repeatability)	36.37	25.89	20.46	31.22	27.36
Part to Part	63.63	74.11	79.54	68.78	72.64
Distinct Categories					
	2	2	3	2	2

Measurement error with the 6.7m fixture and the foil/braid shield was similar to, but slightly higher than, the 1.5m fixture with the same cable shield type (MSE 1). In both cases the measurement error increased with frequency.

4.3.5 MSE 5 (6.7m, braid)

A second measurement system evaluation was performed on the 6.7m fixture using 16 samples of the braid shield and one operator. This was done to determine if the sample was causing most of the variation as was the case with the 1.5m fixture. As with MSE 4, the data analysis was divided into frequency sub-bands of approximately 100 MHz (Tables 7 and 8).

Table 7. MSE 5 (6.7m, braid)

	Frequency (MHz)				
	10-110	110-220	220-320	320-430	430-530
Measurement Error (± dB)	0.33	0.74	1.43	1.16	0.85
Percent Contribution					
Total Gage (Repeatability)	31.56	6.74	14.37	7.58	5.23
Part to Part	68.44	93.26	85.63	92.42	94.77
Distinct Categories					
	2	5	3	5	6

Table 8. MSE 5 (6.7m, braid)

	Frequency (MHz)				
	530-630	630-750	750-850	850-950	950-1050
Measurement Error (± dB)	1.69	1.59	1.19	0.98	2.28
Percent Contribution					
Total Gage (Repeatability)	6.74	16.55	5.97	1.54	37.18
Part to Part	93.26	83.45	94.03	98.46	62.82
Distinct Categories					
	5	3	6	11	2

Comparing MSE 4 with MSE 5 shows again that the foid/braid shield design produced more variation than the single braid shield. Again the variation increased with fixture length and frequency.

4.3.6 MSE 1-5 Comparison

The measurement errors for MSE's two through five are shown in Figure 3. MSE 2 and MSE 4 were performed with the foil/braid shield design. MSE 3 and MSE 5 used the single braid design. The general trend is increasing measurement error for increasing frequency and fixture length.

The significantly lower measurement error with single braid compared to the foil/braid designs shows that the gage actually has a small amount of variation. The variation with the foil/braid design is due to sample variation and is more indicative of capability than measurement system error. The variation in contact resistance between the foil and braid could be a cause of this greater variation. Wrinkling of the tape could also be a contribution factor.

5. Areas of Further Investigation

The differences in variation observed between different shield designs suggest that coaxial samples with shield designs other than foil/braid and braid could be evaluated. A coaxial cable constructed with a solid tubular shield would provide a very stable shield structure. A semi-rigid coaxial cable fits this criterion. A four-layer shield of foil/braid/foil/braid would possibly have the greatest variation.

The screening attenuation degradation due to flexing could be investigated in view of observations in MSE 1. The quality of bonding of the tape to the dielectric is another area to consider. The wrinkling of the tape and changes in the overlap could change the screening attenuation.

Capability studies could be performed on additional shield design now that the measurement error has been quantified.

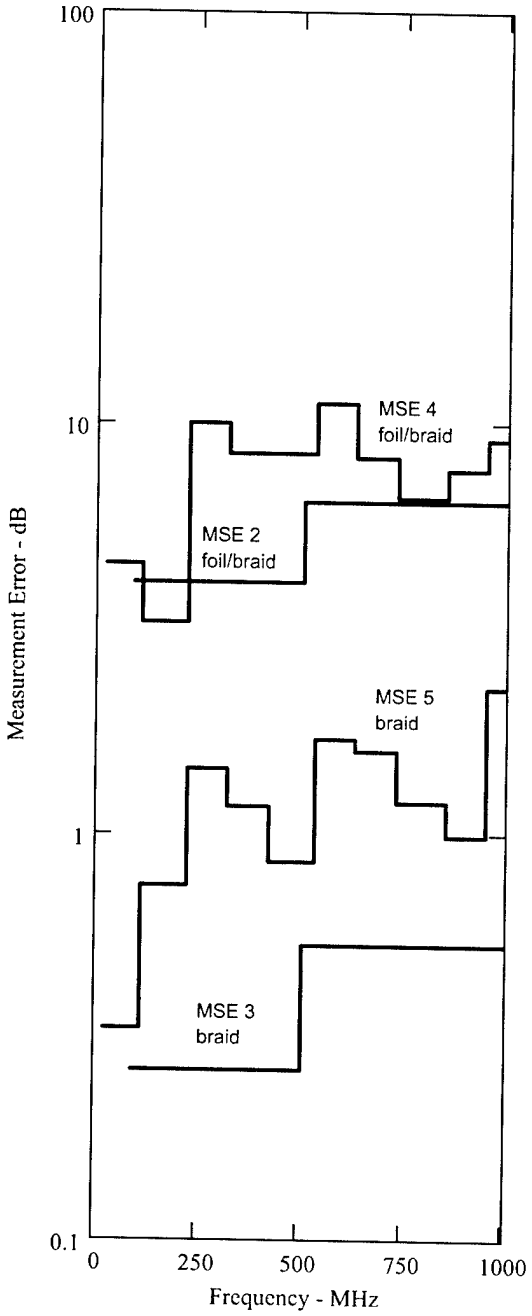


Figure 3 – Measurement Error Comparison

6. Conclusion

It was observed that screening attenuation variations can be a result of sample variation as well as variation in the measurement system. Braid only shield designs have less screening attenuation variation than foil/braid designs. This may be due to changes in contact resistance between the foil and braid. It could also be from wrinkling of the tape and changes in the overlap opening. Variation from the operator is a small percentage of total measurement error.

The screening attenuation test setups evaluated have less than the 6 dB rule-of-thumb measurement error often cited for transfer impedance. The braid only shield design in the 1.5m fixture has less than 1 dB of measurement error. Although the 6.7m fixture with the braid shield has greater than 1 dB measurement error at the higher frequencies, its measurement error at the lowest frequencies, where it extends below the 1.5m fixture, is still less than 1 dB. Measurement error increases as the frequency and fixture length increase.

Screening attenuation provides a cost-effective method for measuring shield effectiveness. It requires a level of skill typical of an electronics laboratory without an elaborate and expensive test setup. Screening attenuation is a tool that can be used for more MSE and capability studies of shield effectiveness.

7. Acknowledgments

The authors are grateful to the Belden Electronics Division for the support extended to develop and evaluate screening attenuation measurement technology. Special thanks go to John Johnson, Belden's resident statistics expert, for his development of the measurement system evaluations and analysis of the data. Thanks to Benjamin Willett, Allen Riek, and Brian Haisley for their work with the laboratory measurements. Thanks also go to Brian Haisley for analyzing data for the measurement system evaluations.



Carl W. Dole

Carl is a Product Engineer and has been with the Belden Engineering Center of Belden Electronics Division for over eleven years. His academic achievements include a B.S. degree in Electrical Engineering Technology ("With Highest Distinction") from Purdue University. Prior to joining Belden, Carl worked 10 years in television broadcast engineering and has a lifetime FCC General Class Radiotelephone License. His areas of responsibility include developing improved electrical test methodologies, writing technical papers, and working on new product development teams. He is a member of SMPTE, IEEE, and SBE.

8. References

[1] 61196-1 Amendment 1 Radio-Frequency Cables – Part 1: Generic Specification – General, definitions, requirements and test methods.

[2] J. Kincaid, and C. Dole, "Test Fixture Design and Shielded Screening Attenuation Performance of CATV Coaxial Cable", *IEE Colloquium on Screening Effectiveness Measurements*, Savoy Place, London (May 6, 1998).

[3] J. Kincaid, and C. Dole, "Implementation of IEC 61196-1 Shielded Screening Attenuation Test Method", *International Wire and Cable Symposium*, Philadelphia, Pennsylvania (November 19, 1998).

[4] R. B. McCall, *Fundamental Statistics for Behavioral Sciences*, 6th ed., Harcourt Brace & Company, Fort Worth (1994).

[5] SCTE (Society of Cable Telecommunications Engineers, Inc.) IPS-TP-403B2 (preliminary-11/11/2000), Test Method for Shield Effectiveness: Screening Attenuation of Coaxial Cable.

[6] Minitab® Reference Manual, Release 11, for Windows™ (June 1996).



Lenore J. Choate

Lenore is a Product Development Engineer at the Belden Engineering Center. She holds a BSE from the University of Tennessee and has over 6 years experience with Belden. Lenore has her EIT and is a member of IEEE and SCTE. She participates in SCTE Interface Practices Subcommittees with working groups 2, 3, and 4.

John W. Kincaid

For biography and photograph please see paper 10-17 "Modeling UTP cabling: Insertion Loss and Bit Errors."

Crosstalk Coupling between Cable Pairs

^[1] **Mohammed M Al-Asadi, [1]Alistair P. Duffy, *Kenneth G Hodge, and *Arthur J Willis**

[1]De Montfort University, The Gateway, Leicester LE1 9BH, UK

*Brand-Rex Ltd, Glenrothes, Fife KY6 2RS, Scotland, UK

^Principle Author + 44 116 2506157 · alasadi@dmu.ac.uk

Abstract

A new approach to the modeling and simulation of electromagnetic coupling between communication channels is presented in this paper. The technique is used for the prediction of cross-talk in cable pairs. It consists of two parts. The first is the use of the Transmission Line Matrix (TLM) method, where both source and victim pairs in a communication channel are modeled and voltages and currents are calculated. The second part treats the twisted wire as a helical antenna and the radiated fields from the source cable impinging on the victim cable are calculated. The induced voltages and currents between the wires of the victim pair are then calculated. Optimization of the method, where windowing is used to reduce the overall-computing burden is also demonstrated. Results obtained for the simulation of a channel of varying lengths are compared to experimental data. The comparison of results shows encouraging agreement.

Keywords

Cable; Channels; Electromagnetic coupling; Cross-talk, TLM

1. Introduction

The next generations of structured wire cables and cabling, such as category 6 (UTP and STP) and category 7 (STP) cables, are now emerging in the open market. Draft performance specifications are pushing traditional design methodology and cable-making processes further than ever before.

There are a number of potential sources of noise in such transmission systems. These range from general EMC issues, like interference generated by lightning [1], to proximity to power transmission lines and railway lines [2]. However, noise is also, and primarily, caused by close proximity of cables and subsequent coupling of radiated electromagnetic fields from adjacent pairs [3], this is the primary focus of this paper.

Near end crosstalk, NEXT, and far end crosstalk, FEXT, are both measures of coupled signal strength between a source pair (the disturbing pair) and a victim pair. One result is gained from analysis of near end energy coupled into the victim pair and the other from the far end coupled energy. The magnitude of the electromagnetic interference varies significantly with a number of factors, including the geometries of the cable pairs [4], the materials used and the energy characteristics of the transmission spectrum. In general, the electromagnetic coupling between external interferers and intra-system issues has attracted some interest [5]. In addition, attention has also focused on the electromagnetic coupling between signals transmitted on pairs of multi-conductor transmission lines [6]. The latter is usually referred to as cross-talk between cable pairs.

Three-dimensional computational methods, such as Finite Element Method (FEM) [7], and Transmission Line Matrix (TLM) method [8] are extensively used for the analysis of electromagnetic coupling. Furthermore, analytical solutions based on field radiation of antenna theory are also used for the prediction of field coupling to transmission-lines [9]. In some cases, two methods such as FEM and TLM are employed in the same model [10], while others have combined both modeling and measurements for the prediction of field coupling [7]. While some approaches have used three-dimensional modeling methods, others have used the calculation of both inductance and capacitance matrices for a multi-conductor transmission lines [11,12]. The objects of this interest have included the investigation of cross-talk between short cables lengths[13], the practical effects of cross-talk [14] and the problems of investigating cross-talk coupling from multiple sources [15].

In this paper, two approaches are combined for the calculation of cross-talk coupling between pairs of a communication cable. These are the one-dimensional TLM approach and the antenna theory [16]. The advantage of such a method is that it allows physical representation of the system but does not incur the memory and run-time overheads of a full 3D solution. For example, it allows the incorporation of such channel specific phenomena as termination changes and handling effects [17]. The development of this method is described in the next section.

2. Method Development

In reference [16], a detailed description of the model, including the capacitive coupling between communication cables was presented. The stages of the operation of the model presented in [16] are illustrated in the calculation of the electromagnetic coupling between two communication channels illustrated in figure 1:

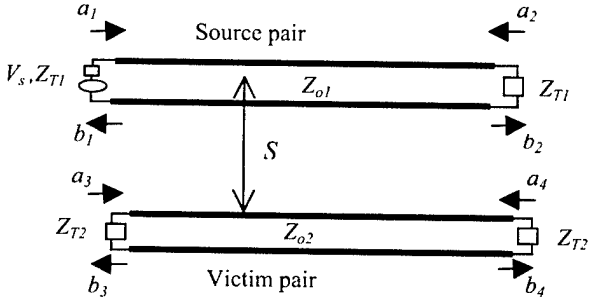


Figure 1. Schematic diagram of two coupled communication channels

where a_1, a_2, a_3 and a_4 are the four incident voltages at the four ports of the two pairs and b_1, b_2, b_3, and b_4 are the reflected voltages at the corresponding ports.

- The cable pair, carrying the interfering signal (the source pair), is modeled using the 1D TLM modeling approach [17], where currents and voltages at all TLM node of the model can be calculated.
- From the currents on the source pair, the radiated electric fields at the center of both wires of the victim pair and the magnetic fields between both wires of the victim channel, are calculated using antenna theory.
- As the capacitive coupling is the only electromagnetic coupling that was investigated in the previous model induced voltage between both wires of victim pair and at any TLM node are then calculated.
- The induced voltages calculated in the previous step, was then injected into the corresponding TLM nodes of the victim channel, from which induced signal on the victim channel can be calculated.

The models progress one iteration and the process starts again.

The next sub-section describes the inclusion of the inductive coupling into the previous model allowing a complete electromagnetic simulation to be achieved.

2.1 Inductive coupling introduction

In this model, the inductive coupling resulting from magnetic field radiation is implemented alongside the electric field coupling. From this, the resultant cross-talk between the pairs can be calculated. As the effects of the E field is already illustrated in reference [16], the inclusion of the H-field is presented here.

The radiated magnetic field, **H**, at any point between the victim pair wires, can be calculated using the following equation:

$$ {}_{\mathbf{k}}\mathbf{H_r} = \sqrt{{}_{\mathbf{k}}\mathbf{Hr_x}^2 + {}_{\mathbf{k}}\mathbf{Hr_y}^2} \qquad (1) $$

where ${}_{\mathbf{k}}\mathbf{Hr_x}$ and ${}_{\mathbf{k}}\mathbf{Hr_y}$ are the resultant fields in both x and y directions calculated at the k^{th} time step and given in equations 8 and 9 of the previous model.. The cables are assumed to be directed along the z direction of the plane.

The induced current at both wires can be calculated as illustrated in figure 2 (where D is the separation between the wires).

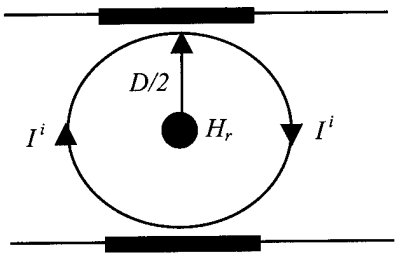


Figure 2. Induced currents on the victim pair

The induced current I^i as a result of the radiated field H_r can be calculated using the following equation:

$$ {}_k I^i = \int \left| {}_k H_r \right| \cdot dl \qquad (2) $$

Using the dimensions of the cable pair, the above equation can then be simplified to:

$$ {}_k I^i = \pi D \left| {}_k H_r \right| \qquad (3) $$

At the connection, (*g*), between any two adjacent TLM nodes, (*n*) and (*n-1*), of the victim pair cable, we have two current values induced as a result of the radiated magnetic fields at both nodes, as illustrated in figure 3.

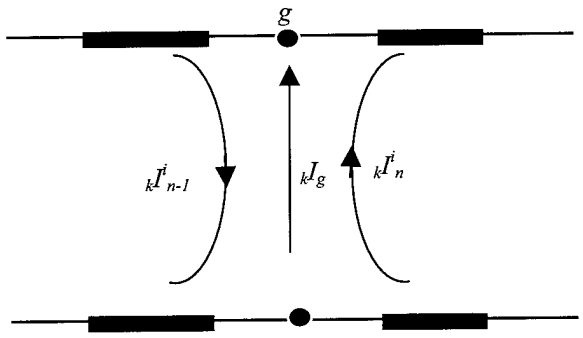


Figure 3. Induced currents on the adjacent nodes of the victim pair TLM model

The induced current between the two wires of the victim pair can be obtained as:

$$ {}_k I_g = {}_k I^i_n - {}_k I^i_{n-1} \qquad (4) $$

The induced current, along with the induced voltage, is illustrated in Figure 4.

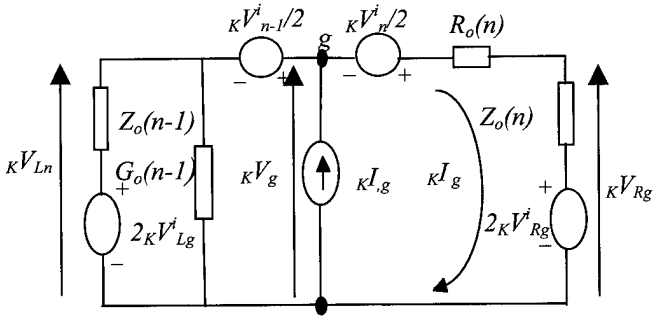


Figure 4. Thevenon equivalent circuit of two adjacent TLM nodes of the victim pair

The voltage at the connection g may then be obtained as:

$$ {}_kV_g = {}_kI_g \frac{Z_o(n)\cdot(Z_o(n-1)+R_o(n))}{Z_o(n)+Z_o(n-1)+R_o(n)} + $$

$$ + \frac{\dfrac{2_kV^i_{Lg}+\left({}_kV^i_{n-1}\right)/2}{Z_o(n-1)} + \dfrac{2_kV^i_{Rg}-\left({}_kV^i_{n}\right)/2}{Z_o(n)+R_o(n)}}{\dfrac{1}{Z_o(n-1)}+\dfrac{1}{Z_o(n)+R_o(n)}+G_o(n)} \qquad (5) $$

The current of the victim pair node can then be obtained as:

$$ {}_kI_g = \frac{{}_kV_g - 2_kV^i_{Rg} + \left({}_kV^i_n/2\right)}{Z_o(n)+R_o(n)} \qquad (6) $$

The incident and reflected voltages of the TLM model of both source and victim pairs can then be calculated as described in references [16] and [17]. At this stage, voltages and currents induced at any TLM node along the victim cable pair, resulting from radiated fields generated from the traveling wave on the source pair, can be calculated. From the TLM model of both the source and the victim cable pairs, both incident and reflected signals at all four ports can be calculated. From those voltages, both Near-End Crosstalk (NEXT) and Far-End Crosstalk (FEXT) can be calculated using the following equations respectively:

$$ NEXT = -20\cdot\log\left|\frac{b_3(f)}{a_1(f)}\right| \qquad (7) $$

$$ FEXT = -20\cdot\log\left|\frac{b_4(f)}{a_1(f)}\right| \qquad (8) $$

Equal-Level Far End Crosstalk (ELFEXT) may also be calculated as:

$$ ELFEXT = -20\cdot\log\left|\frac{b_4(f)}{b_2(f)}\right| \qquad (9) $$

The next section deals with an enhancement to the method which improves the resource requirements of the implementation of the proposed method.

2.2 Windowing of the radiated field calculations

In order to speed up the program, it is assumed that the propagating signals have limited longitudinal effect on the victim pair. In order to both demonstrate this and calculate the cross-talk, a pulse of width of τ *nS* is is associated with a 'coupling window' of w *nS* as illustrated in figure 5.

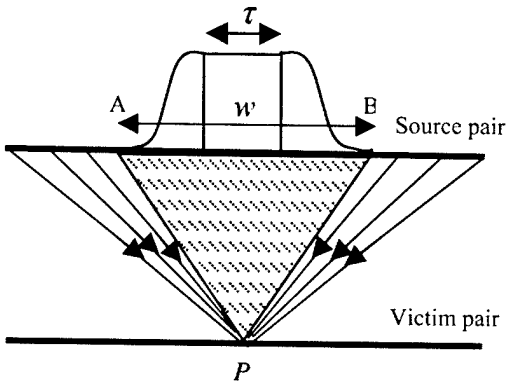


Figure 5. Window calculations of the radiated fields

The values of the currents induced from the nodes before *A* and after *B* are negligible compared to those at any point between *A* and *B*. Therefore, the radiated fields at point p of the victim cable pair are calculated from the summation of those generated by currents travelling between nodes *A* and *B*.

Using the lay length of the source pair, the unit length of the TLM model, and the width of the window, w, the nodes between which the window of the calculation is located can be determined. Tests showed that a window width of 3τ is adequate.

3. Model implementation

For the investigation of both capacitive and inductive coupling, the following steps need to be followed in addition to those stated in section 2.

- Induced voltages and currents at any TLM node of the victim cable pair, as a result of both radiated electric and magnetic fields are calculated.
- The induced voltage is divided into two equal parts at the connection point between the two adjacent TLM nodes of the victim cable pair. The induced current is then represented as a current source and connected between the two wires of the victim pair at the connection between the adjacent TLM nodes.
- Generated voltages and currents at any TLM node of the victim cable pair can then be calculated using equations 5 and 6 respectively. This procedure should be carried at every single iteration of the program.
- The incident and reflected voltages at all the ports of the bundle cable can then be calculated.
- Using the voltages calculated at the above step and implementing equations 7, 8 and 9, NEXT, FEXT and ELFEXT can be determined respectively.

Having described the development of the model and the method of implementation, it is used for the investigation of the crosstalk coupling between communication channels under different working conditions.

4. Validation, Implementation and Results

This section combines the validation of the model and the implementation of the model for the prediction of coupling between two transmission channels spaced at a distance S as in figure 1. The effect of the windowing described in section 2.2 is also investigated. The model is then used for the prediction of electromagnetic coupling between two twisted pair cables in a single cable bundle. Results are compared against those obtained using a 3D TLM model, and measurements and results obtained from reference [13].

4.1 Validation Against 3D TLM

A 3D TLM mesh can represent a volume of free space. Cables and wires can be placed as objects in that volume. This is widely used for the investigation of electromagnetic compatibility problems. Using a commercial 3D TLM solver, a short, $1m$, channel containing two twisted cables was modeled. Figure 6 illustrates the channel

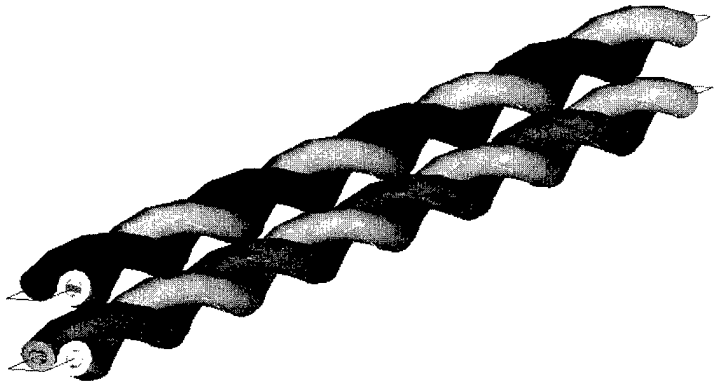


Figure 6. Screen shot of the modeled cable using a 3D TLM solver.

The induced current on the victim pair as a result of sending a short pulse of $2nS$, was determined. The normalized value is plotted against time as illustrated in figure 7.

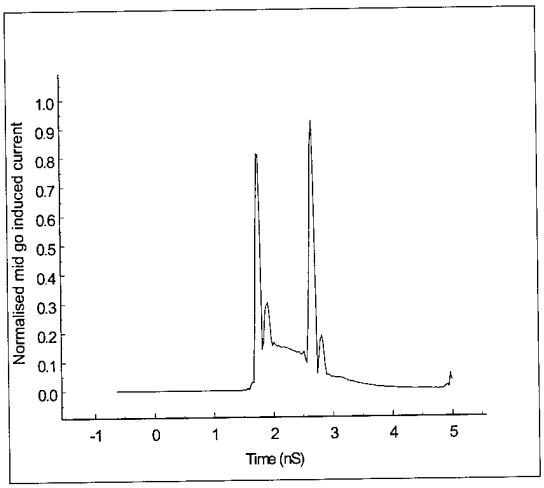


Figure 7. Normalized, time domain, induced current obtained using the 3D TLM model.

Using the same channel, the induced current as a result of radiation generated by the same pulse was calculated using the new method. The normalized value was then plotted as in figure 8. The comparison supports the operation of the proposed method.

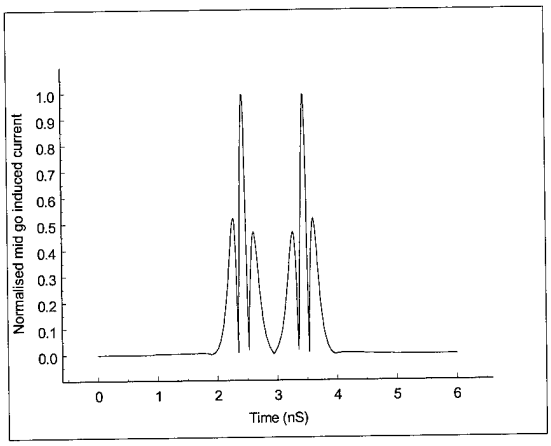


Figure 8. Normalized, time domain, induced current obtained using the new model.

4.2 Implementation for single pair channels

To illustrate the operation of the model, it is used for the calculation of induced voltages on a victim placed at a distance from the channel carrying the signal. The channels consist of parallel pairs of wires, $1m$ in length. All terminating impedances are matched to the nominal impedance of the channel. The separation between both channels is S=5cm. A narrow pulse of $3nS$ is then injected into the source channel. The induced voltage between the wires of the victim channel was calculated at all TLM nodes along the cable and at every time step. The result is plotted in figure 9.

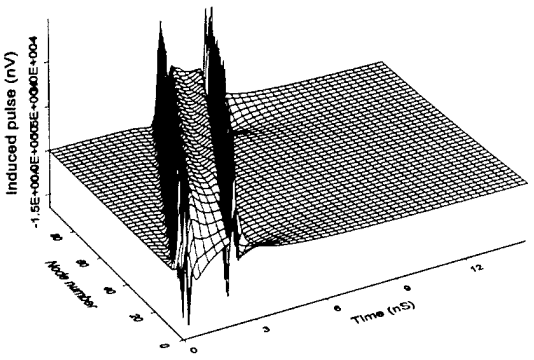


Figure 9. Coupling of pulse of 3*nS* and separation of 5*cm*.

To illustrate the effects of different spacing between neighboring channels on the induced voltage, the response of the same pulse is calculated when the spacing is increased to 25cm. This is illustrated in figure 10.

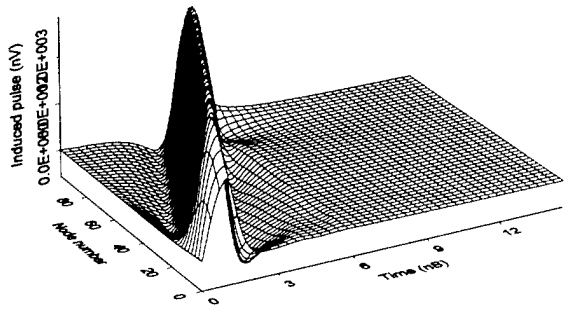


Figure 10. Coupling of pules of *3nS* and separation of 25*cm*.

To illustrate the ability of the new approach the handle any sort of travelling signals the coupled signal on the victim pair was calculated as a result of a double exponential wave travelling on the source channel. The separation is 5 cm. The coupled voltage is plotted as a function of time and along the victim channel as illustrated in figure 11.

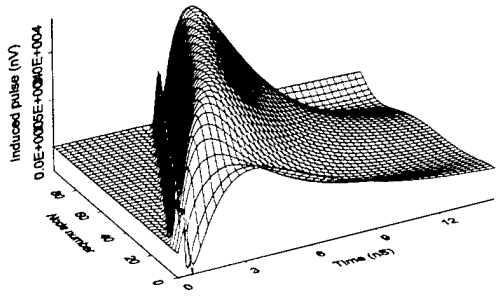


Figure 11. Coupling of double exponential pules of a separation of 5*cm*.

Windowing is further illustrated with a pulse of 2nS injected into the source pair. The termination of both cables were no longer matched (with a 5% difference), thus introducing reflections. The induced voltage distribution along the victim pair was computed without using windowing and illustrated as in figure 12. Using Windowing of $6nS$ width, the induced voltages along the victim pair are also calculated and plotted as in figure 13.

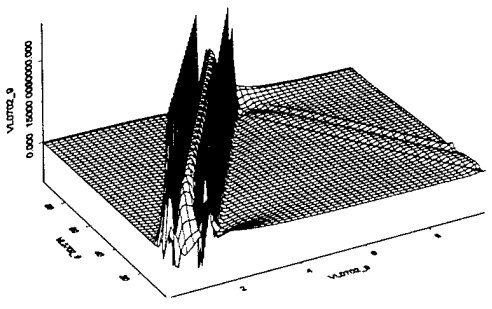


Figure 12. Coupling of a 2*nS* pules of a separation of 5*cm* with mis-matched termination and no windowing.

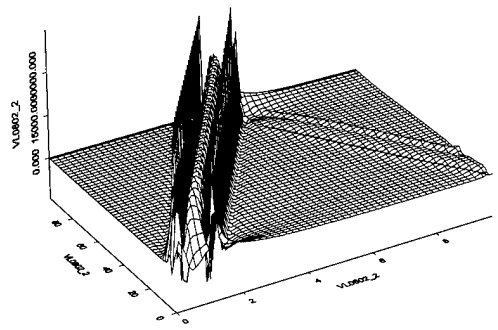


Figure 13. Cross-talk calculation with windowing of $3\tau(6nS)$.

Both figures show excellent agreement. They also show a small reflection generated by the mis-matching at the far end of the cables. The run-time of the program had been reduced dramatically with windowing to around half of the time required for running the program without windowing.

Most of the above results were obtained with a large separation between the coupled channels. To illustrate the calculation of the cross-talk between pairs of the same bundle, a cable of four twisted pairs was modeled. The pair dimensions were: copper diameter $0.53mm$ and distance between centers of the conductors including dielectric of $0.96mm$. The twisting periods of each pair were, $22mm$, $20mm$, $19mm$ and $17mm$. Using a single pulse travelling on the 1st pair of the cable, the near end cross-talk induced on the other pairs was calculated. Table 1 show the calculated values of a $10m$ cable obtained using the new method (between pairs 1 and 2) compared to typical measured values of a $100m$ cable and the standards limits (for reference).

Frequency (MHz)	Near End Crosstalk, NEXT (dB)		
	Standards	Measured (100m)	Calculated (10m)
10	-50	-62	-63.63
20	-45.8	-64.2	-58.39
62.5	-38	-52.5	-51.09
100	-35	-49.2	-48.14

Table 1. Calculated and measured near end cross talk

The calculated NEXT values for channels of different lengths from 1m to 10m length are then plotted as function of the frequency and the channel length as illustrated in figure 14.

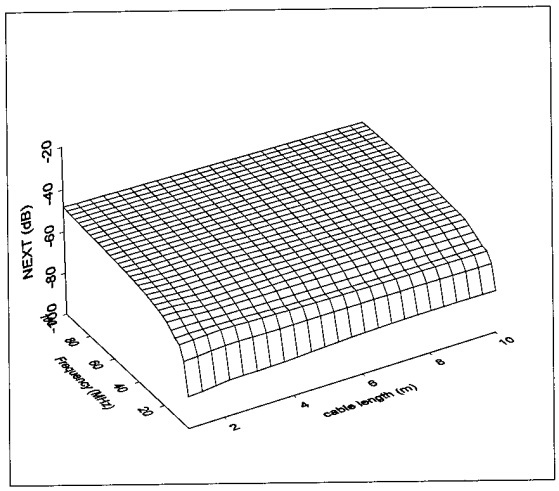


Figure 14. Near End Crosstalk (NEXT), calculated using the new method for different channel lengths and different frequencies

5. Discussion and Conclusion

A method, combining analysis and modeling, for the calculation of crosstalk between communication cable pairs has been presented. This approach was used to calculate the electromagnetic coupling including both electric and magnetic fields between two communication channels. The effects of channel separation, pulse duration and terminations on the coupled pulses were illustrated. The coupling of different pulse shapes was also illustrated using a double exponential pulse transmitted on the source channel. The method then validated against a 3D TLM electromagnetic solver. The mid-go current on the victim channel was calculated using both the 3D solver and the new approach. Both normalized currents illustrate the same shape. This indicates the validity of the method.

While the proposed technique has significant memory and run-time savings over conventional 3D analysis, the simulation of long channels could be time consuming. In order to reduce this, a windowing technique was introduced in order to minimize the time required.

Near End Crosstalk (NEXT) was then calculated between two pairs of a four-pair cable. Results were obtained for different channel length and at different frequency of operation. Although a $100m$ channel was not simulated, the results presented are encouraging. The frequency dependence of the NEXT was also demonstrated.

It can be concluded that a flexible, effective and realistic approach was presented here that can be used for the calculation of crosstalk coupling between communication channels. The approach can also be used for the investigation of the effects of cable irregularities on crosstalk calculations.

6. References

[1] B. Kordi, R. Moini, and F. Rachidi, 2001, "Modeling an inclined lightning return stroke channel using antenna theory", *Proceedings of the 14th Zurich EMC conference*, pp. 331-334.

[2] G. Lucca, A. Bochicchio and M. Moro, 2001, "Electromagnetic interference on telecommunication cable from a railway line: Comparison between calculations and measurements", *Proceedings of the 14th Zurich EMC conference*, pp. 103-108.

[3] C. R. Paul, "Computation of Crosstalk in a Multiconductor Transmission Line", 1981, IEEE trans. On EMC, Vol. EMC-23, No. 4, pp. 352- 358.

[4] Bart Van Thielen and Guy A. E., 2000, "Method for the acceleration of transmission-line coupling calculations", IEEE Trans. On MTT, Vol. 48, No. 9, pp. 1531-1536.

[5] A. P. Duffy, P. Naylor, T. M. Benson and C. Christopoulos, 1993, "Numerical simulation of electromagnetic coupling and comparison with experimental results", IEEE Trans on EMC, Vol. 35, No. 1, pp. 46-54.

[6] C. R. Paul, "Computation of cross-talk in multi-conductor transmission line", 1981, IEEE Trans. EMC, Vol. EMC-23, No. 4, pp. 352-358.

[7] T. Zeeff, C. E. Olsen, T. H. Hubing, J. Drewniak and D. DuBroff, 1999, "Microstrip coupling algorithm validation and modifaction based on measurements and numerical modelling", IEEE Trans. EMC, pp. 323-327.

[8] C. Christopoulos and P. Naylor, 1988, "Coupling between electromagnetic fields and multiconductor transmission systems using TLM", Inter. Jour. Of Numerical modelling: Electroniuc networks, devices and fields, Vol. 1, pp. 31-34.

[9] S. Tkatchenko, F. Rachidi and M. Ianoz, 1995, "Electromagnetic field coupling to a line of finite length: Theory and fast iterative solutions in frequency and time domains", IEEE Trans. EMC, Vol. 37, No. 4, pp. 509-518.

[10] W. P. Carpes, G. S. Ferreira, A. Rizer, L. Pichonand A. Razek, 2000, "TLM and FEM methods applied in the analysis of electromagnetic coupling", IEEE Trans. On Magnetics, Vol. 36, No. 4, pp. 982-985.

[11] D. A. Hill, K. H. Cavcey and R. T. Johnk, 1994, "Crosstalk between microstrip transmission lines", IEEE Trans EMC, Vol. 36, No. 4, pp. 314-321.

[12] C. R. Paul and A. E. Feather, 1976, "Computation of the transmission line inductance and capacitance matrices from the generalized capacitance matrix", IEEE Trans. EMC, Vol. EMC-18, No. 4, pp. 175-183.

[13] J. H. Walling, M. Belenger and V. Le Nir, 1995, "Crosstalk Performance of short length data grade wires", IWCS proceedings, pp. 288-297.

[14] J. R. Sciacero, 1995, "An explanation for unexpected NEXT failures on short UTP links", IWCS proceedings, pp. 119-125.

[15] S. Galli and K. J. Kerpez, 2000, "The problem of summing crosstalk from mixed sources", IEEE communications letters, Vol. 4, No. 11, pp. 325-327.

[16] M. M. Al-Asadi, A. P. Duffy, K. G. Hodge and A. J. Willis, 2001, "A field-circuit approach for predicting electromagnetic coupling between communication channels using TLM and antenna theory", Proceedings of the 14th Zurich EMC conference, pp. 97-102.

[17] M. M. Al-Asadi, A. J. Willis, K. G. Hodge, and A. P. Duffy, 1997, "Modeling as a tool for analyzing handling effects in structured wire", IEE 10th international conference on electromagnetic compatibility, pp. 131-136.

[18] C. R. Paul and M. B. Jolly, 1982, "Sensitivity of crosstalk in twisted pair circuits to line twist", IEEE Trans. EMC, Vol. EMC-24, No. 3, pp. 359-364.

Authors Biographies

For photos and biographies see "A genetic Algorithm Toolkit for Cable Design" paper 04-01 in these proceedings.

Acknowledgement

The support of Flomerics in providing the 3D electromagnetics simulator is gratefully acknowledged.

Simulation and Measurement of Crosstalk in Twisted Pair Cables

Juliusz Poltz
OptEM Engineering Inc.,
453, 3553 - 31st Street N.W.
Calgary, AB Canada T2L 2K7
+1-403-289-0499
jpoltz@optem.com

Dietmar Gleich, Mats Josefsson, Marcus Lindström
Ericsson Cables AB Network Technologies
SE-824 82 Hudiksvall, Sweden
+46-650-360-00
dietmar.gleich@eca.ericsson.se,
mats.josefsson@eca.ericsson.se, marcus.lindstrom@eca.ericsson.se

Abstract
A technique of modeling twisted pair cables and simulating crosstalk is discussed and verified experimentally. A brief description of the cable design environment is provided. This environment is used for entering cable design data including materials, plating, stranding, twisting, and wire naming. The geometrical information is then processed in order to calculate a realistic model of a twisted pair cable. The collapsing of the cable's initial geometry under the pressure of external insulation and shield and in the presence of core twisting is automatically calculated along the cable. The resulting model of the cable is subsequently analyzed numerically using a combination of finite element and boundary element methods. The skin depth value is used for optimizing meshing. Extracted unit parameters are used to build accurate circuit models of the cable. These models are used subsequently in a circuit simulator to calculate S-parameters. Two different set-ups were used to verify simulation results against crosstalk measurement.

Keywords
Cable; cross-talk, simulation, modeling, NEXT, FEXT

1. Introduction
New systems operating at continuously increasing frequencies are rapidly designed and implemented. Since repeated prototyping is too expensive and too slow, computer modeling may offer a cost effective solution. Digital systems utilize frequencies into the GHz range. At these frequencies cable attenuation, dispersion and cross-talk affect the signal quality and system performance in a significant way [1, 2, 3]. Modeling and simulation has proven its ability to predict system behaviour with high accuracy at different design levels (connectors, packages, boards). There is a need to introduce the full benefit of simulation into the cable design activities [4].

A twisted pair cable is difficult to model accurately due to its geometrical extension and frequency dependent characteristics. With the increase in operating frequencies, the secondary effects that were originally neglected in theoretical studies of cables [5] gained importance. It is now necessary to include twisting of wires and pairs, stranding [6] and plating when building cable models. It is impossible to build an accurate model without considering skin and proximity effects in wires, eddy currents in cable shields, and dielectric losses in insulation. The skin effect causes reduction of the interconnect inductance and a rapid increase of the interconnect equivalent resistance. Since conductor and shield losses were analyzed numerically much earlier for power cables [7, 8, 9, 10], a similar technique was adopted in the development of OptEM Cable Designer [11] in order to calculate unit parameters of high frequency cables. Once the current distribution is considered the losses and frequency dependence of unit parameters can be calculated. These values can be then used to assemble circuit models and perform simulation of crosstalk

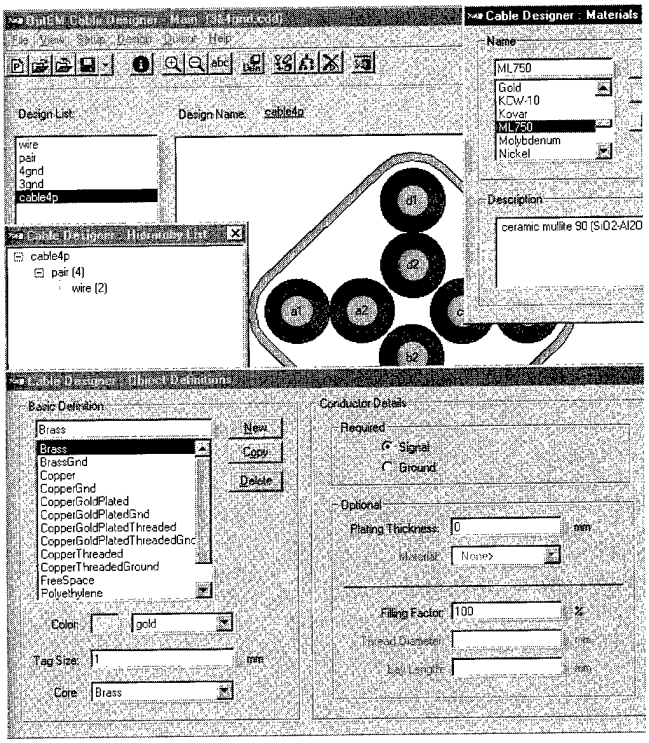


Figure 1. OptEM Cable graphical interface allows the user to select and assign materials and build hierarchical designs from predefined building blocks

2. Computer Aided Cable Design
Twisted pair cable design offers challenges for numerical modeling and electromagnetic simulation. Since results of numerical simulations cannot be more accurate than the geometrical models representing the cable, it is essential to specify the cable geometry as accurately as possible. To achieve this goal we introduced a three stage process: 1) detailed specification of the cable design parameters like wire and

insulation dimensions, materials, stranding, and lay length using a graphical interface as shown in Figure 1; 2) automated shaping of the design based on user experience and material properties and; 3) the generation of models.

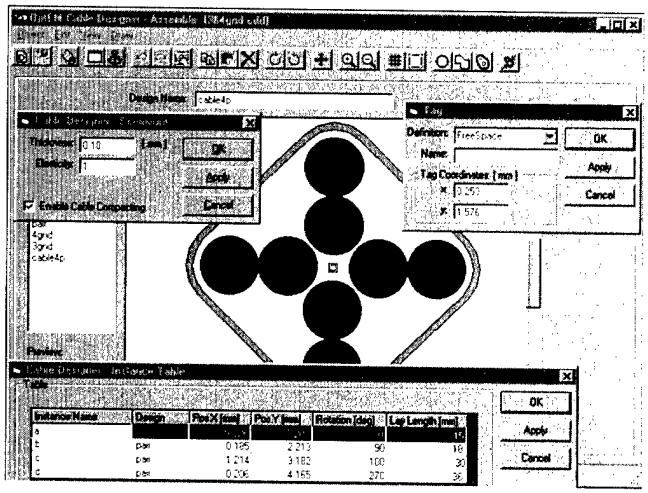


Figure 2. When assembling a new design from components the user selects name, location, rotation and lay length for each new instance.

A graphical environment has been developed to assign different twisting parameters to pairs, bundles and layers. The cable is assembled at a specific location (cross-sectional point). The graphical interface provides a hierarchical environment in which the user can draw a wire, and assign parameters which include conductor details like plating and stranding and its insulation. The wire can be subsequently saved as an independent design which can be used at the next level as a building block for a pair. The pair can then be used a number of times as a building block for a bundle etc. The entire process of assembling a real cable can be replicated in this multistage process of specifying instances and levels. All instances can be individually placed and rotated at any level in order to produce a realistic geometrical structure at a particular location. In addition, each instance carries information related to its lay length which allows the program to automatically generate cross-sectional information at any location of the cable or to assemble a three dimensional model of any section of the cable. Proper assignment of instance names (Figure 2) also allows an automated (hierarchical) naming of wires in the extracted circuit model of the entire cable.

3. Shaping Enclosures and Compacting Wires

The extraction of electrical parameters of a cable cannot be more accurate than the geometrical model of the cable. Therefore it was very important to consider the collapsing of the cable's initial geometry under the pressure of external insulation and shield and in the presence of core twisting. There are two aspects of automated generation of realistic cross-sections along the cable. First is the issue of shaping shields or enclosures to follow the interior of the cable. Second is the issue of resolving conflicts between twisting objects and removing empty space from the interior of the cable.

The deformation of internal and external insulation and shield which is stretched over the concave assembly of wires (Figure 3) is performed hierarchically starting from the interior of the cable towards the outside shield. The deformation is dependent on mechanical properties of the enclosure and must be selected by the user. The user simply specifies an elasticity parameter ($0 \le x \le 1$) which is used to calculate a min and max allowable radius of the enclosure based on the circular radius of the original shape. It is assumed that the non-elastic (x=0) enclosure maintains its original circular shape and that the fully elastic enclosure (x=1) follows a convex path around the core (Figure 3).

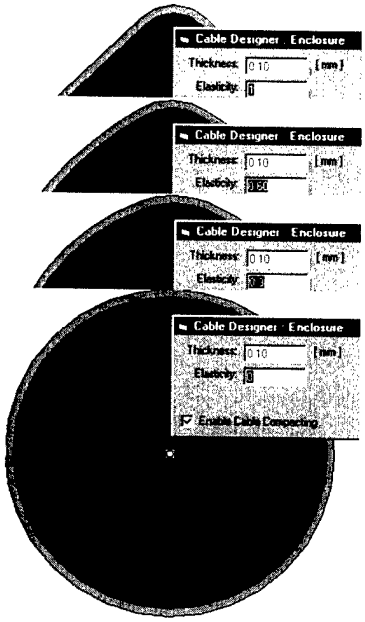


Figure 3. Setting up elasticity of the enclosure for automated formatting

The enclosure can also be used to enable the collapsing algorithm, providing that the user enables it by using the selection box in the Enclosure dialog (Figure 3).

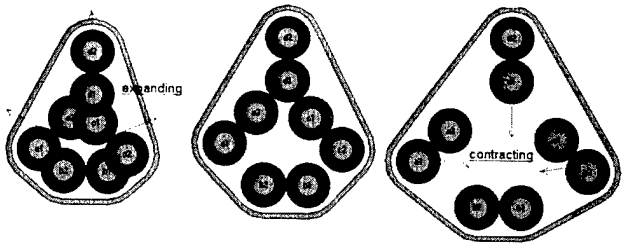


Figure 4. Cable collapsing algorithm maintains integrity of the design by automatically expanding or contracting components

Under normal conditions the wires, pairs and other building blocks of the cable cannot maintain a spatial separation in the presence of the external collapsing force. Therefore initially the

collapsing algorithm was introduced only to remove empty spaces from the interior of the cable (cable contraction). However, we noticed that equally frequent is the need for expanding the core due to conflicts between twisting components that overlap each other. Currently, the collapsing algorithm (Figure 4) performs both – the expanding task (removing conflicts) and contracting task (removing empty space).

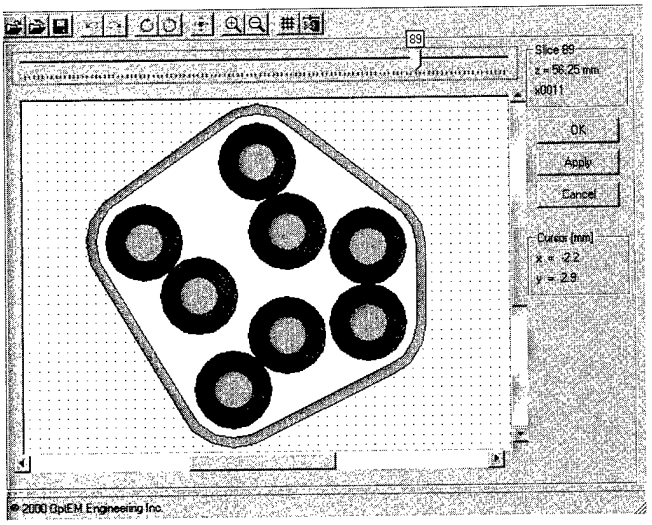


Figure 5. Processing geometry along the cable

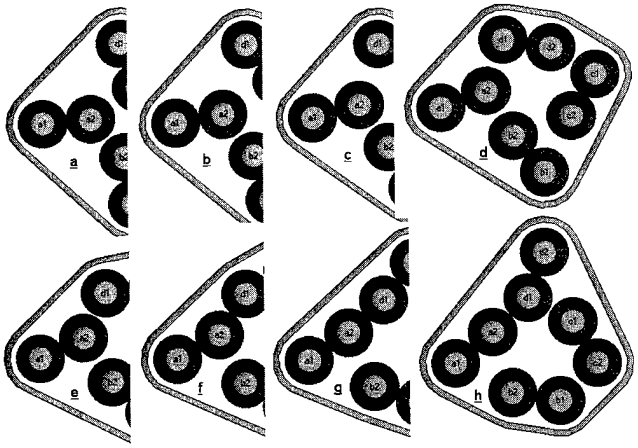


Figure 6. Processing cable before numerical analysis, cross sections a-h are extracted using precalculated segmentation distance

Of course the entire geometry is processed hierarchically. First the cable building blocks are collapsed in the sequence they are assembled, starting from pairs or quads and their insulation. Then the bundles are pressed together followed by the collapsing of the cable enclosure. The contracting and expanding is performed by assigning a tolerance to a helical path of a pair and allowing the pair to deviate from the path only by a certain amount, which is dependent on positions of the pair before and after the cross section that is investigated.

The collapsing of the cable's initial geometry under the pressure of external insulation and shield and in the presence of core twisting is automatically calculated along the cable. This process is performed automatically on all extracted cross sections before the electromagnetic analysis of the cable can start. The effect of multilevel twisting and expanding and contracting can be visually examined in the Process Geometry window (Figure 5). Extracted cross-sections (Figure 6) can be individually edited (if needed) to allow modeling of special effect (cable damage or cable bending).

4. Using BEM for Extracting LRCG Parameters

The skin and proximity effects are well developed and control the current flow in conductors and metal enclosures of high frequency cables. The frequency dependent behaviour of the current density has to be taken into account when calculating electrical characteristics of the cable. Since electromagnetic field distribution and losses in power cables were analyzed numerically much earlier [6-9], a similar technique was adopted in the development of OptEM Cable Designer [11] in order to calculate unit parameters of high frequency cables.

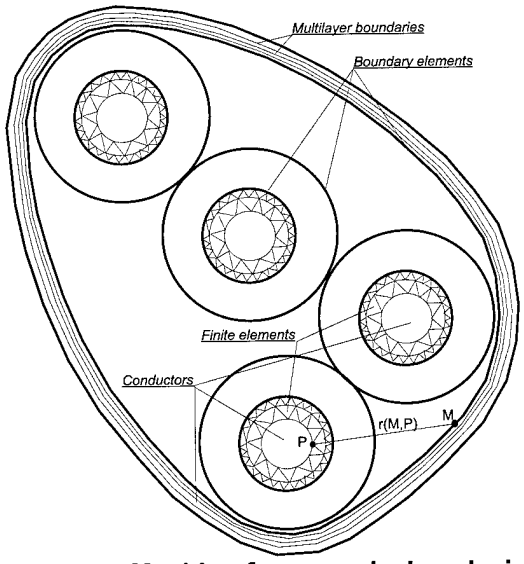


Figure 7. Meshing for numerical analysis combines finite elements and multilayer boundaries

The field solver used in the OptEM Cable Designer software numerically calculates current density (J) in the conductor cross-sections. Theoretically, a second order partial differential equation known as the Helmholtz equation can be used to calculate current distribution in conductors [1, 4, 6, 10]. However, there are some obvious advantages in adopting the equivalent representation of the Helmholtz equation, known as the Fredholm integral equation of the second kind, for calculating unit parameters of cables[6, 7, 10]. In two-dimensional space (cross-section of the transmission system) the longitudinal component of the current density can be calculated from the following integral equation:

$$\underline{J}(M) = -\frac{j\omega\mu\gamma}{2\pi}\int_S \underline{J}(P)\ln\frac{1}{r(M,P)}dS_P - j\omega\gamma\underline{A}(M) \quad (1)$$

where: ω - circular frequency, μ- permeability, γ - conductivity, $\underline{A}(M)$- represents external (source) field, P and M represent points in the cross-section.

OptEM Cable Designer calculates current distribution by solving equation (1) using a combination of Finite Element Method (FEM) and Boundary Element Method (BEM). Bulky conductors are divided into finite elements, whereas ground and power planes are modeled as multilayer boundaries (as shown in Figure 7). Although difficult at the programming stage this method is the most efficient technique of solving the Helmholtz equation for practical interconnect applications. To allow the calculation of unit propagation parameters of cables the complex, frequency-dependent current distribution must be calculated for a set of independent source currents. The inductance and resistance matrices are calculated together as the imaginary and real parts of the impedance matrix. They are both related to the distribution of currents.

Since the current distribution is frequency dependent, the resulting [L] and [R] matrices may be strongly affected by the selection of frequency. By solving the Helmholtz equation, OptEM Cable Designer automatically includes eddy-current and proximity effects when calculating unit parameters (L,R) of the cable.

Losses associated with a conductor include dc loss (due to material resistivity), skin effect loss (due to non-uniform distribution of currents in the conductor cross section), and eddy-current loss in neighbouring wires (due to proximity effect). Eddy-current losses constitute "mutual" resistance values.

Similarly for the current distribution, the charge distribution on the dielectric interface and conductor surface can be calculated. A complex charge distribution in the form of cubic splines is used to represent sources of the electric field for lossy dielectrics. The C and G matrices are calculated from charge distributed on the surface of the conductors.

The numerical method was verified against laboratory testing and analytical formulae available for a simple – single pair configuration. The work was reported in our earlier publication [4].

5. Circuit Models and Crosstalk Simulation

Fast and accurate extraction of L, R, C, and G matrices for selected cross sections allows equivalent circuit models to be built for uniform and non-uniform lossy multiconductor transmission lines. One has to use very efficient modeling and simulation techniques to analyze a substantial portion of a twisted pair cable. A practical approach offering high accuracy and reasonable computational time was selected here. The proposed method uses three-types of modeling: - the two dimensional analysis of uniform, lossy, and coupled multiconductor cross-sections of the cable, an interpolation and extrapolation technique for non-uniform multiconductor sections, and very limited three-dimensional analysis of selected discontinuities like end connectors etc. Segments of wires which are not included in the uniform transmission lines are not ignored but are automatically interpolated between uniform sections or extrapolated to connection points. Before performing analysis, cable twisting parameters are processed in order to calculate repetition distance (the distance along the cable after which the geometry repeats itself). A special data base is used to handle the repetition. Only cross-sections within the first repetition distance are analyzed. If the length of the cable section is longer than the repetition distance the results are reused when the model is constructed. Before circuit analysis can be performed large circuit models are assembled (Figure 8). It is not uncommon that the models contain up to a million of components.

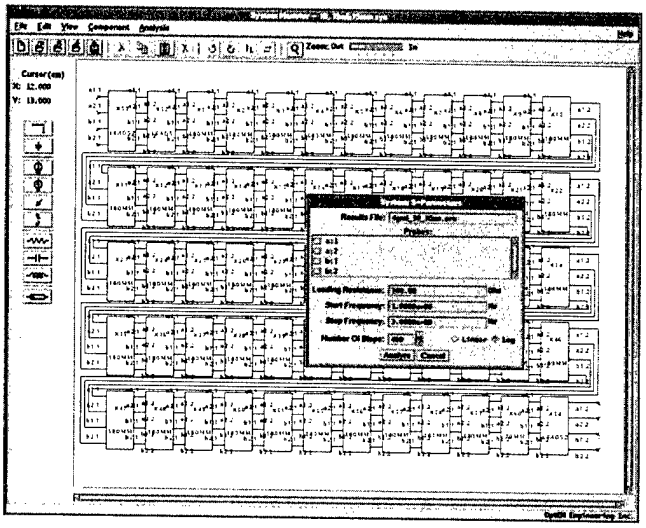


Figure 8. Circuit model of the cable used for S-parameter simulation

Short segments of cables can be modeled very accurately with lumped circuits. Due to twisting of wires the ladder model, which is based on the applied geometrical segmentation, typically consists of LRCG lumped sections with various characteristics. To minimize the number of components one can combine segments by integrating their unit parameters along the wire path. However, the length of a ladder section must be carefully calculated to prevent the filtering effect of higher frequencies which are included in the spectrum of the analyzed signals. The optimal interconnect model consists of lumped sections with a similar cut-off frequency.

The numerical value of the cut-off frequency f_c of a low-pass filter - representing Δx section of the cable - can be calculated from the following formula:

$$f_c < \frac{1}{\pi\sqrt{(L_{max}\Delta x)(C_{max}\Delta x)}} \quad (2)$$

where: $L_{max}C_{max}$ - maximum diagonal terms of the inductance and capacitance matrices.

The highest frequency f_h for which this model is valid is lower than the cut-off frequency. Therefore, the ladder section length for any part of the cable is calculated from the following formula:

$$\Delta x < \frac{1}{\pi f_h \sqrt{L_{\max} C_{\max}}} \qquad (3)$$

This modeling technique may be very expensive numerically for high frequency cables. The number of required components in the model grows proportionally to the increase of the signal frequency and cable length. In addition, even larger circuits are required to model frequency dependent characteristics of the cables. To reduce model size and offer frequency dependent response, a truly frequency-dependent model can be assembled using the concept of modal propagation. This approach offers many advantages for time domain (including TDR) simulation.

For frequency domain simulation (including crosstalk analysis) an alternative approach based on chain parameters can be used [3]. This approach was already investigated by us and produces virtually identical results to circuit simulation. Chain parameter approach is currently implemented in OptEM Cable and allows the calculation of chain parameters of cable sections using precalculated unit parameters. The entire cable is represented by a cascade of uniform sections represented by chain parameters. These chain matrices vary along the cable. However, when connected together (cascaded) they represent in a most general way the non-uniform lossy multiconductor transmission line model of the selected pairs of the cable. In order to calculate crosstalk parameters one has to apply the terminal constrains related to loading conditions and applied current or voltage sources. These terminal conditions must be similar to the S-parameter measurement environment. As a result, backward and forward crosstalk can be calculated for the selected frequency and the entire frequency response can then be assembled by repeating the analysis for other frequency points, each time recalculating unit parameters and chain parameters.

6. Comparison of Crosstalk Simulation and Measurements

Preliminary results of an ongoing investigation are presented in this chapter. To eliminate difficult-to-confirm effects of compacting and enclosure shaping we started from analyzing two simple set-ups (Fig. 9 and 10) which allow accurate and repeatable placement of wires and dimension control. All crosstalk plots in this section represent the absolute value of the S-parameters magnitude in dB.

In all experiments twisted pairs were built from copper wires insulated in polyethylene (PE). The following parameters were used for setting up both the measurements and simulation.

- Diameter over Cu-wire :0.40mm
- Diameter over PE-insulation : 0.80 mm
- Dielectric constant of PE : approx. 2.3
- Lay length of the used pairs : approx. 10 , 20, 30 mm
- PE-board thickness : 20 mm
- Cu-ground plane thickness : > 0.4 mm
- Cable length : 10.15 m

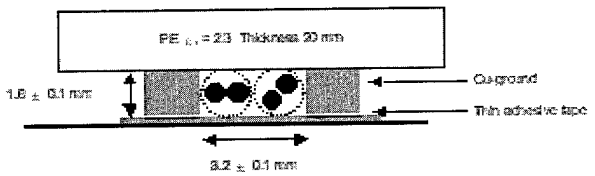


Figure 9. Two twisted pairs surrounded by a set of 3 ground planes

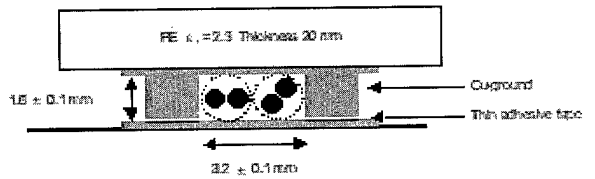


Figure 10. Two twisted pairs surrounded by a set of 4 ground planes

Far-end (FEXT) and Near-end (NEXT) crosstalk with 100 Ohm reference differential impedance was measured and simulated. The results are presented in Figures 11-14.

We started with a set of two pairs with identical twisting of 30 mm. It was reasonable to assume that it should be easier to correlate measurement and simulation when the twisting of both pairs is identical. After all, the crosstalk between pairs with identical twists is very high and the effect of external noise and imperfections of the measurement set up should disappear as marginal in comparison with coupling. This logic proved to be correct as far as the level of the cross talk. However, it was far from being easy to match the simulation and measurement values.

We noticed that consistently simulated FEXT values were much higher than the measured values at high frequencies (Fig 11, 12). Although it still remains to be analyzed in details, we came to the following conclusion. Simulation of cross talk between pairs with identical lay length provides us with the upper limit for cross talk values at higher frequencies. Any random deformations and local oscillation of the twisting will result in reduction of coupling and FEXT which represents the accumulation of coupling along the cable.

Simulated NEXT shows on the other hand characteristic oscillations, which in a way were confirmed by the measurements. If one would average the oscillations in the NEXT simulation and measurement, both plots show a steady level of crosstalk at a very wide range of frequencies. This behaviour is consistent and can be explained using a voltage divider model as an equivalent representation for a long uniform transmission line.

In all captured plots (Figures 11 – 14) the simulation was performed using truly logarithmic scale, whereas the measurement results were collected in a linear scale and show less details at lower frequencies.

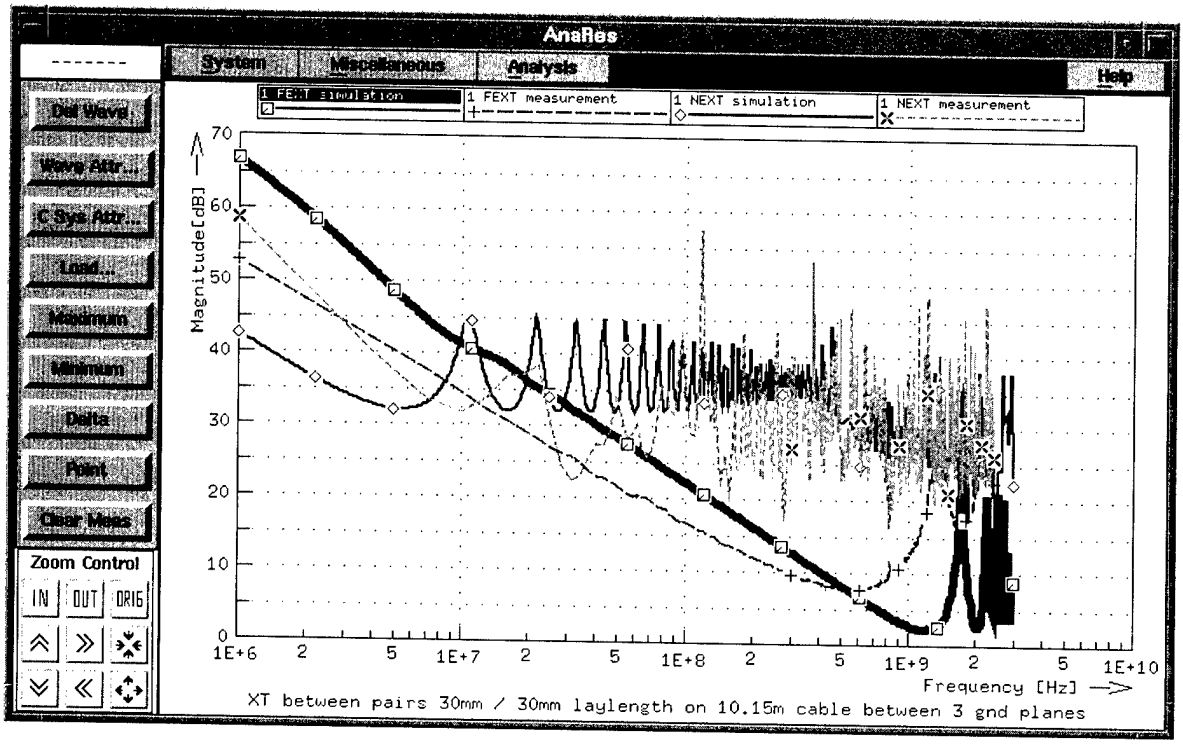


Figure 11. Simulated and measured crosstalk (FEXT, NEXT) between two pairs 10.15m long, both twisted with lay length of 30mm surrounded by 3 ground planes (setup presented in Fig. 9)

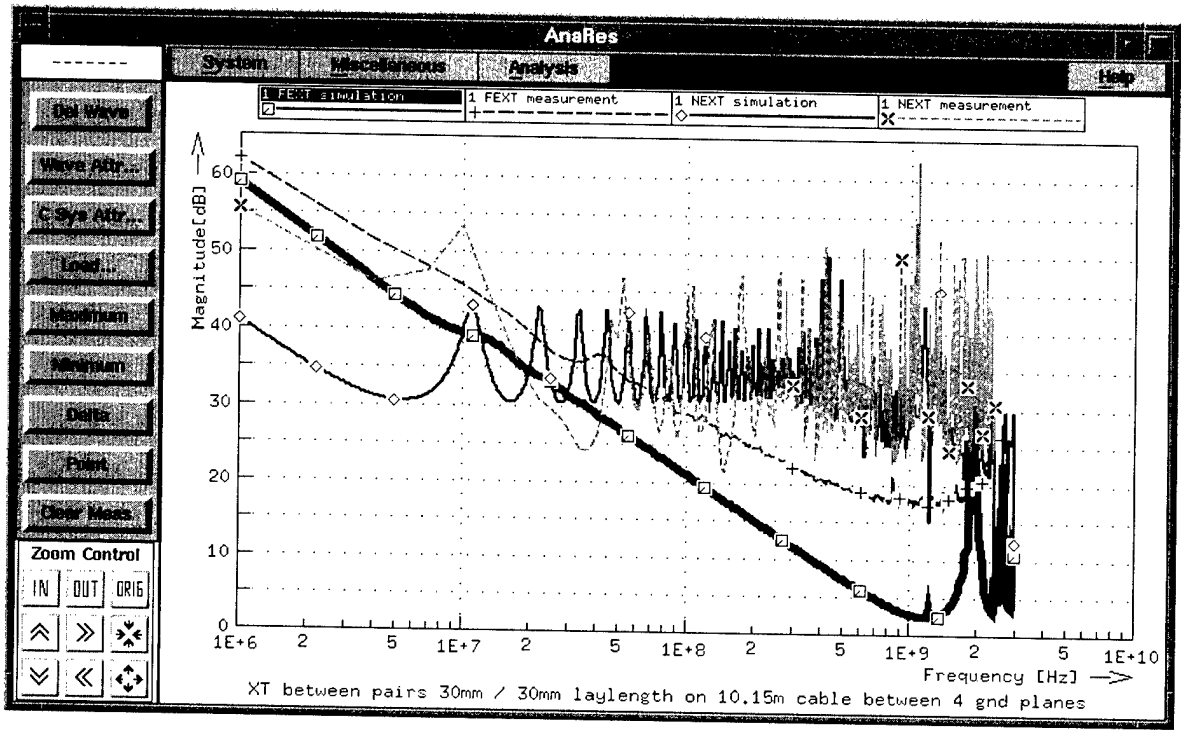


Figure 12. Simulated and measured crosstalk (FEXT, NEXT) between two pairs 10.15m long, both twisted with lay length of 30mm surrounded by 4 ground planes (setup presented in Fig. 10)

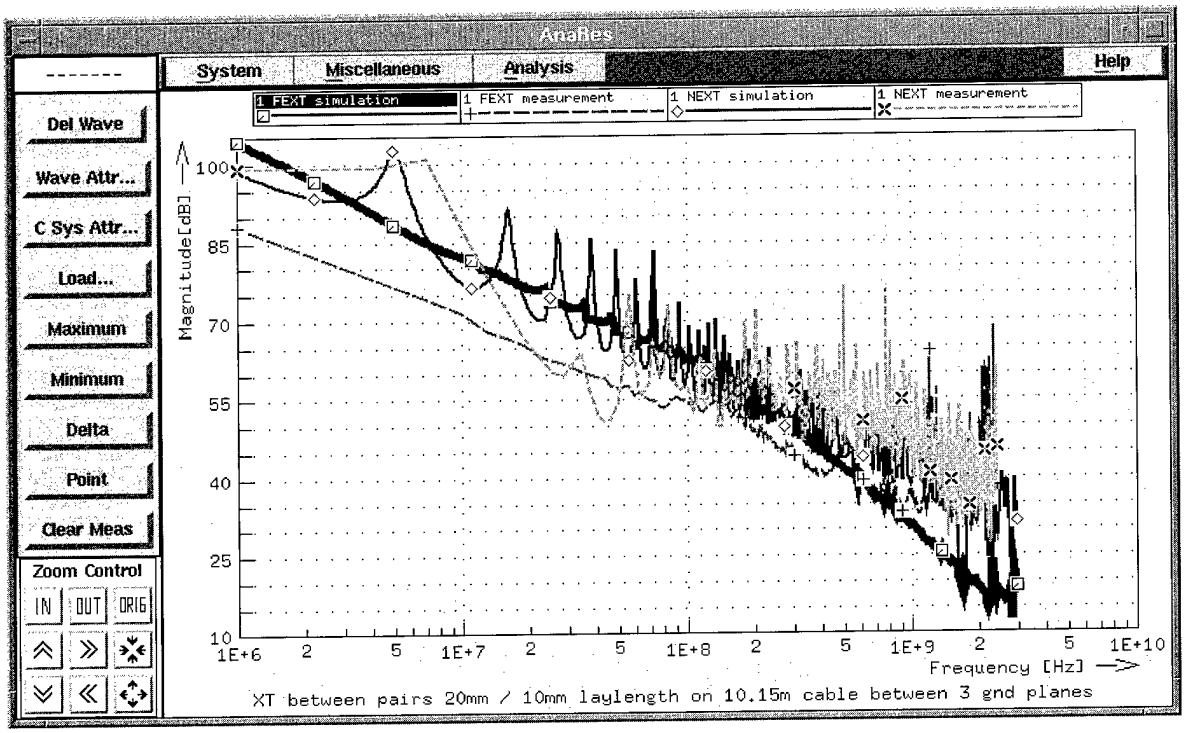


Figure 13. Simulated and measured crosstalk (FEXT, NEXT) between two pairs 10.15m long, twisted with lay length of 20mm and 10mm surrounded by 3 ground planes (setup presented in Fig. 9)

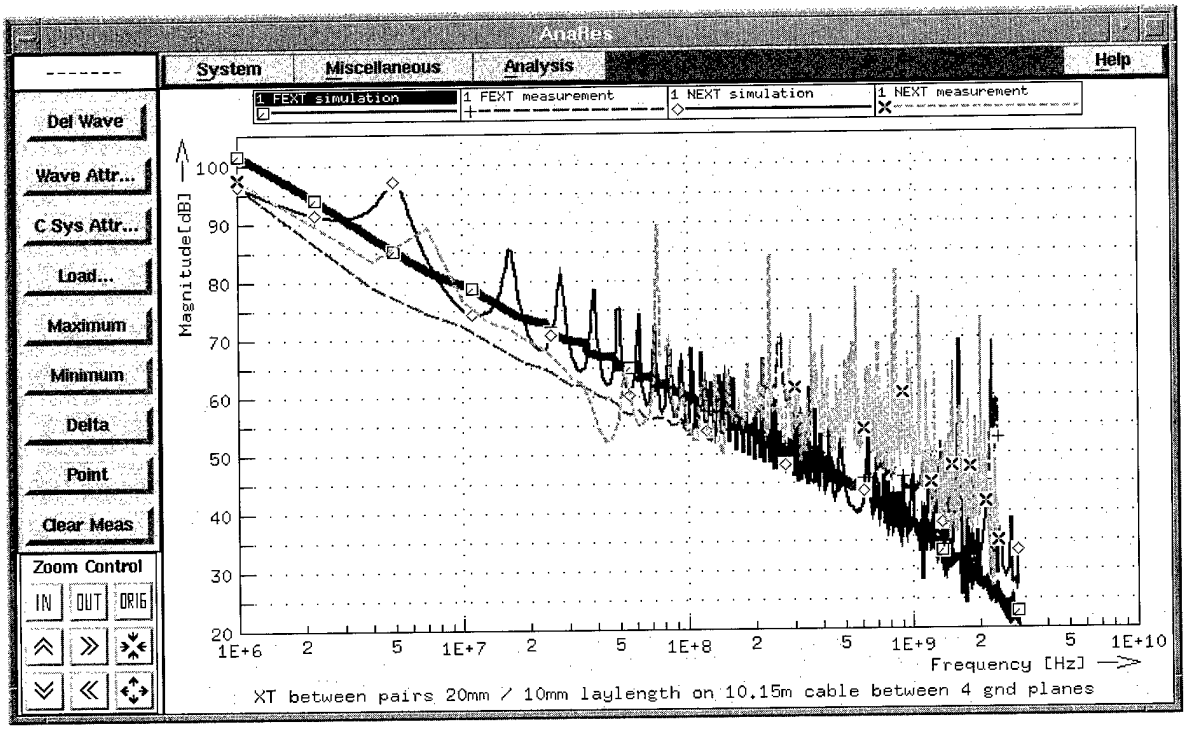


Figure 14. Simulated and measured crosstalk (FEXT, NEXT) between two pairs 10.15m long, twisted with lay length of 20mm and 10mm surrounded by 4 ground planes (Setup presented in Fig. 10)

As expected crosstalk between pairs with different lay length was much smaller. The selected set of pairs with 20mm and 10mm lay length shows drastically different crosstalk pattern (Figure 13 and 14) when compared with the simulation results for pairs with identical twisting. The average crosstalk increases here at a rate 20dB per decade of frequency increase. Although 20mm and 10mm pairs have still very small repetition cycle (of 20mm) both the FEXT and NEXT values are much smaller than those calculated and measured for the 30mm and 30mm set. In fact the values calculated for lower frequencies (less than 80MHz) were so small in the original simulations that we could not match them with the measured values.

Only after including small (together 15mm) connections in our simulation set up we were able to produce cross talk simulation results similar to the measured values. This experiment shows that we are always exposed to the possibility of injecting crosstalk into our system at the connection point. This effect is of course negligible at higher frequencies – when both accumulated FEXT and NEXT are much higher and the "connector effect" can be neglected.

It is also interesting to notice that both cases (30mm/30mm and 20mm/10mm lay length) behave differently in the presence of a complete (4 sided) ground surrounding and a partially open (3 sided) enclosure. As expected in both cases the presence of the full (4 sided) enclosure reduced the crosstalk. However, the impact of the full enclosure on the cable with different twisting is more visible and reaches 10dB.

7. Conclusions and Future Directions

There are seven contributions of the research work described in this paper:

- A tool for hierarchical design of twisted pair cables was built,
- An algorithm for automated generation of cable cross sections including expanding and contracting of the core and enclosure shaping was implemented,
- Using the tool a set of models for twisted pair cables were constructed,
- The models were used in a circuit simulator to calculate crosstalk levels,
- S-parameter environment for simulating twisted pair cables was built,
- A test bench for measuring crosstalk level between pairs of a cable was built,
- Initial simulation and measurement results were correlated.

While working on the project we discovered that:

- Wires and enclosures of high frequency twisted pair cables have cross sectional dimensions within the skin depth range, and an accurate solution of the Helmholtz equation is required. The Helmholtz equation allows for the analysis of eddy-currents, and proximity and skin effects for quasi-TEM propagation.
- Inclusion of twisting in modeling twisted pair cables is essential for prediction of cross talk parameters.
- A combination of Finite Element Method (FEM) and Boundary Element Method (BEM) offer an accurate and efficient method for analyzing twisted pair cables.
- The chain parameter approach and circuit simulation technique offer similar accuracy in modeling crosstalk
- Constructed models of twisted pair cables allow the prediction of NEXT and FEXT and a good correlation with experimental results for a wide frequency range.
- At lower frequencies connecting the wires and measurement set up may inject more crosstalk into our system than a symmetrically built cable with pairs twisting at a different rate. This effect is of course negligible at higher frequencies – when both accumulated FEXT and NEXT are much higher and the "connector effect" can be neglected.

In continuation of this study we plan to:

- Perform additional verification of the simulation procedures against measured results.
- Verify stranding and braiding models.
- Simulate entire measurement set up including connectors and access wires.
- Incorporate chain parameters technique for fast calculation of crosstalk levels.
- Perform statistical analysis of crosstalk levels.

8. References

[1] H. Kaden, *"Wirbelstrome und Schirmung in der Nachrichtentechnik"*, Springer-Verlag, Germany (1959).

[2] H. Hughes, *"Telecommunications Cables Design, Manufacture and Installation ,"* John Wiley & Sons, New York (1997).

[3] C. Paul, *"Analysis of Multiconductor Transmission Lines,"* John Wiley & Sons, New York (1994).

[4] J. Poltz, D. Gleich, M. Josefsson and M. Lindström, "Electromagnetic Modeling of Twisted Pair," *Proceedings of the 49th International Wire and Cable Symposium*, Atlantic City, NJ, Nov. 13-16 2000, pp. 121-128 (2000).

[5] J. Poltz and S. Grzybowski, "Magnetic Field Outside the Three-Core Cable Considering the Cable Stranding", *IEEE Transactions on Power Apparatus and Systems*, Vol. PAS-98, No. 4, p. 1142, (July/August 1979).

[6] E. Kuffel and J. Poltz, "AC Losses in Crossbonded and Bonded at Both Ends High Voltage Cables", *IEEE*

Transactions on Power Apparatus and Systems, Vol. PAS-100, No. 1, pp. 369-374, (January 1981).

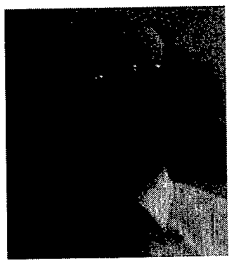
[7] J. Poltz, E. Kuffel, S. Grzybowski, and M.R. Raghuveer, "Models Adopted for the Calculation of Eddy-Current Losses in Pipe-Type Cables", *IEEE Transactions on Magnetics*, Vol. MAG-17, No. 6, P. 2592-2594, (1981).

[8] J. Poltz, E. Kuffel, S. Grzybowski and M.R. Raghuveer, "Eddy-Current Losses in Pipe-Type Cable Systems", *IEEE Transactions on Power Apparatus and Systems*, Vol. PAS-101, No. 4, pp. 825-832, (April 1982).

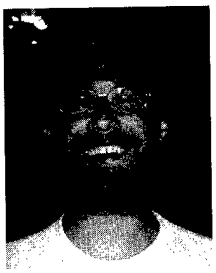
[9] J. Poltz and E. Kuffel, "A Simple and Accurate Evaluation of Eddy-Current Loss in Magnetic Pipe of a Cable", *IEEE Transactions on Power Apparatus and Systems*, Vol. PAS-104, No. 8, pp. 1951-1957, (August 1985).

[10] J. Poltz, "On Eddy Currents in Thin Plates," *Archif fur Electrotechnik*, Springer-Verlag, Germany, Vol. 66 (4), pp. 225-229 (1983).

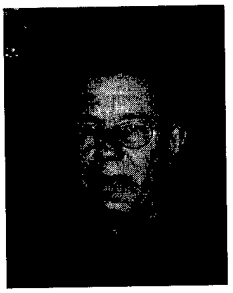
[11] "*OptEM Cable Designer User's Manual*," Version 4.5, OptEM Engineering Inc., Calgary, Alberta, (May 2000).



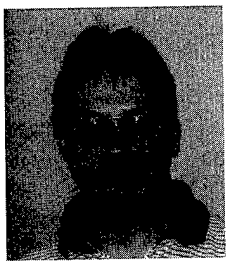
Juliusz Poltz holds M.Sc. and Ph.D. degrees in both mathematics and electrical engineering from Universities in Poznan, Poland. He has published over 70 technical papers related to electromagnetic field analysis. In 1992 Dr. Poltz co-founded OptEM Engineering Inc. located in Calgary Canada. OptEM develops CAE software for interconnect modeling and analysis.



Dietmar Gleich received his Dipl. Ing. (FH) in 1995 from Fachhochschule Ulm, Ulm, Germany and his M.Sc.E.E. from Högskolan i Halmstad, Halmstad, Sweden in 1997. He joined Ericsson Network Technologies in 1997 where he is working in the transmission technology department.



Mats Josefsson received his M.Sc.E.E. in 1980 from Chalmers tekniska högskola, Göteborg, Sweden. He joined Ericsson Network Technologies in 1980 where he is presently leading the transmission technology department.



Marcus Lindström received his M.Sc.E.E. in 1993 from Linköping Institute of Technology, Linköping , Sweden. He joined Ericsson Network Technologies in 1997 where he is working in the transmission technology department.

Noise Tolerance Limits of 1000Base-T Channels Exposed to Random Noise

J.- H. Walling, M. Bohbot**, and P. Kish***

*Consultant, Beaconsfield, Quebec, Canada

1-(514)-695-8220 ; E-mail: jo.walling@sympatico.ca

**Nordx/CDT, Pointe-Claire, Quebec, Canada

Abstract

We have demonstrated the feasibility to measure the sustainable level of alien crosstalk for the 1000Base-T protocol and to determine tolerance limits, which might be used for specification purposes. Towards this purpose we built a differential mode noise injector, capable of injecting noise at different power levels into the four pairs simultaneously, while maintaining the bi-directional transmission of the signal. We characterized this noise injector fully. The noise injector was then installed in the center of a Category 5e channel. This channel, including the noise injector was then re-measured for its transmission performance. We then characterized both sides of the channel, i.e. the side coming from the equipment room towards the injector, and the side from the injector towards the telecommunication outlet. The terminations of the channel were made with patch cords, in order to be able to connect them to a frame error detection system. That means, a patch cord is used at the "equipment room" and at the "telecommunication outlet" and not a pig-tail. Hence, the channel can be characterized as a full "six-connector-configuration", and not as the usual four-connector configuration.

Keywords

Alien crosstalk; alien crosstalk limits; channel; NEXT; FEXT; random noise, noise injector.

1. Background

Last year we presented here an easy method allowing the measurement of alien crosstalk in installed cabling systems [1]. This method is based upon the injection of random white noise into all four pairs of a channel terminated at the other end with 100-Ohm resistors, while measuring the power spectrum on the disturbed cable.

At that time we stated, that there is a lot of discussion about the subject of alien crosstalk, but that most of these discussions remain in a speculative realm without any substantiation.

It is, therefore, our objective here to indicate a way to establish permissible levels for alien crosstalk of installed cabling systems, which then can be used as a basis for the establishment of specification limits. To achieve this we use a random white noise generator to disturb all pairs within one channel simultaneously. One random white noise generator is sufficient, to be used on all four pairs simultaneously, as the noise signals reaching the relatively far distanced transceivers, are sufficiently out of phase, to ensure also a random phase distribution. To this purpose we use a quadruple power splitter. Thus our noise on each individual pair is Gaussian with respect to its amplitude and quasi Gaussian with respect to its phase. However, it is important to mention that the power level of the random noise is nearly constant over the frequency, and does not follow the frequency dependent down slope of coupled noise.

2. Introduction

We limit our reporting to one four-pair channel in a full six-connector configuration (it will be seen later on, that we had to use the connectors at the terminating hardware or for termination purposes). For our test we use a specially designed injector unit, using as a noise source a Noise/Com amplified noise module NC 1109A, which has a flat random noise power output (+10 dBm; -80 dBm/Hz and ?2.0 dB flatness) in the frequency range from 100 Hz to 1 GHz. The output of the random noise generator is attenuated using a step attenuator (0-81.0 dB in steps of 0.1 dB). We use furthermore in the injector unit a passive power splitter M/A-Com DS-4-4, whose four outputs are connected to broadband power amplifiers. We use Mini-Circuits ZFL-1000LN amplifiers, which have reasonable gain flatness within the frequency range considered. In order to increase the crosstalk isolation between the four pairs, the output of each amplifier is additionally attenuated with a 10 dB attenuator.

At the noise injection point, all four pairs of the cable are cut. They are individually fed into low attenuation BH baluns 040-0093. At this point the differential mode signal of the 1000Base-T protocol is converted into a common mode signal. The random noise is then added to the signal stream, using M/A-Com 180? hybrids in a signal summing set-up. The hybrids have a useful frequency range of 2-2000Mhz, though they show deviations in the lower frequency range.

The schematic for a single pair is shown in Fig. 1.

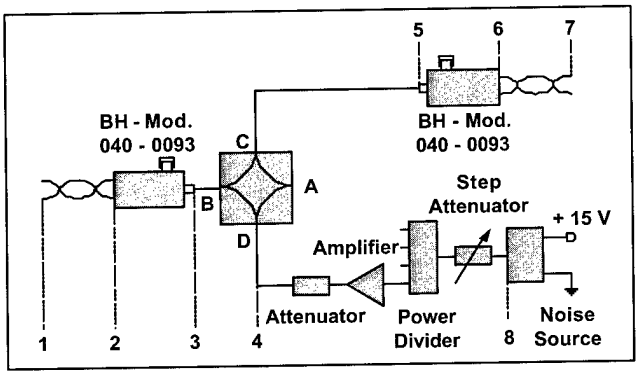


Figure 1: Schematic of the use of a 180-degree hybrid as a summer of signal and an external amplified noise. The difference port A is not terminated.

The schematic of the channel used is shown in Figure 2. It should be noted that the channel is built up with Category 5e components, and that the total channel length is limited to 80 m, in order to take the attenuation in signal path of the injector into account. In Figure 2 is also clearly visible, that the channel is not cut symmetrically, but that the cut is made symmetrically within respect to the horizontal cable.

In the Figure 1 are indicated those points at which measurements are made. These are:

1 – 2 - The channel part from the equipment room (EQ) to the injection point

2-3 + 5-6 - the baluns used for each pair in the injector, measured back-to-back

3-5 or 2-6 - the attenuation in the signal path through the hybrids and/or baluns

4-3 - Attenuation of the hybrid between port D and the summing port B.

4-5 - Attenuation between port D and C.

6-7 - The channel part from the injection point to the telecommunication outlet (TO)

8 - Average output voltage of the random noise source

8-4 - Attenuation of the step attenuator, the power divider, the amplifier and a 10 dB attenuator for different step settings of the step attenuator at the input

At the points 2 ; 6 and 8 are measured the signal voltage levels at both ends and the noise voltage level at the exit of the random noise generator. The measurement of the signal voltage is made without any noise injection, to allow the determination of the S/N ratio. This is done, while the baluns are terminated in the channel and the channel connected to the SmartBits 200, which is switched on, but the traffic is not initiated over the computer.

The determination of the voltage at the points 2; 6 and 8 is done with an oscilloscope using widely varying time-settings and time intervals. The oscilloscope is set, furthermore in an accumulative averaging mode. This allows the determination of the signal and noise voltages sufficiently precise for our purposes, without using a spectrum analyzer.

The terminating patch cords of the channel are connected to the two line cards of a frame error rate detector (SmartBits 200), which establishes also the 1000Base-T traffic. The Fig. 4 shows the entire set-up. In the background are visible the patch cords of the channel (there are actually two channels installed though results are only reported on one of them here).

The frame errors (bit errors) are recorded on both ends of the channel simultaneously. In our trials, the obtained BER levels were on both sides distinctively different, due to the slightly different attenuation of each part of the channel and to the different noise level injected into each direction.

3. Methodology

3.1 Characterization of the noise injector

The noise injector is separated into two parts for characterization, i.e. the hybrid part, including the baluns and the adjustable noise generator itself.

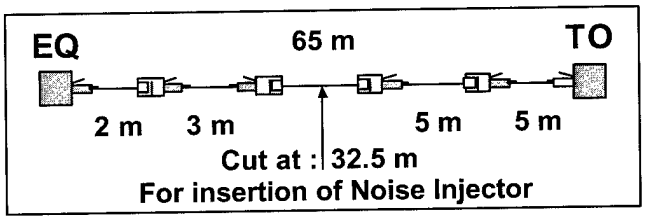


Fig. 2: Category 5e channel used for the measurements. The injection point is 2.5 m off center of the channel, but symmetric within the horizontal cable.

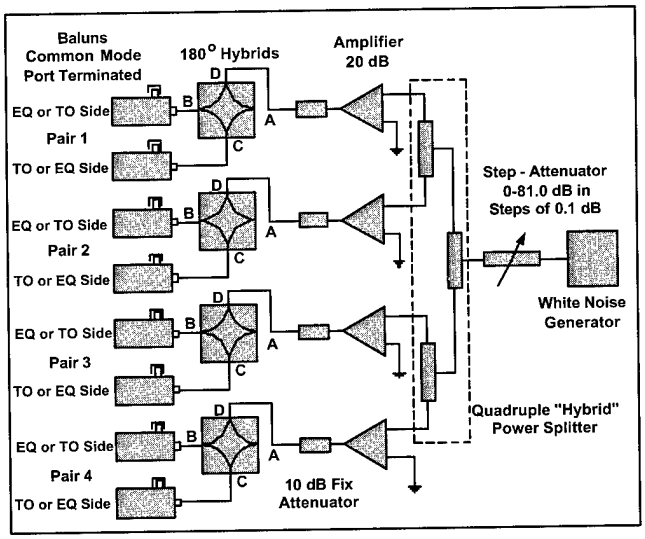


Fig. 3: Complete schematics of the noise injector.

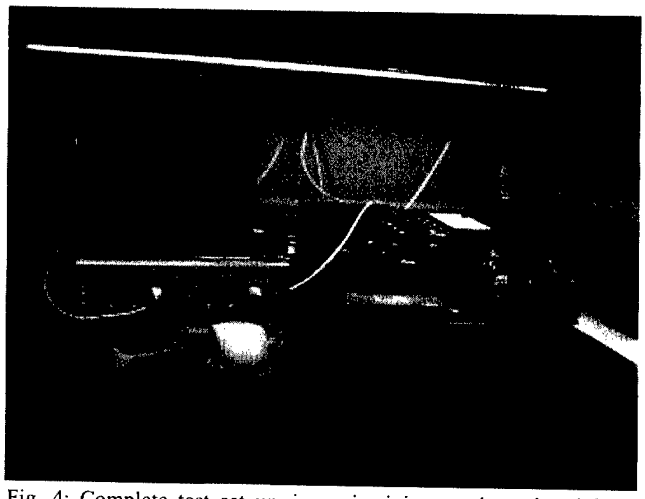


Fig. 4: Complete test set-up, i.e. noise injector, channel and frame error detection system.

We generally measure between 1 and 250 MHz (though Cat. 5e is limited to 100 MHz) with linear frequency division within this interval. We use 1601 points per sweep. For the measurements we also use the BH 040-0093 baluns.

3.1.1 Characterization of the hybrids and the baluns

The noise injector is fully characterized with respect to its attenuation, return loss, crosstalk performance, and balance. These measurements are made between each port.

The performance of the injector with respect to return loss, crosstalk and balance is way beyond specification requirement limits. Therefore they can be ignored here in our further considerations.

A hybrid is a four port device, which, used as a summing device, is not fully reciprocal.

In a 180? hybrid, used as summing device, the A-port has to be left open i.e. it is not terminated. Then the signal at port C and D is summed and available at the port B. The port connection between ports B and C is reciprocal, hence the signal fed into the

D-port is also available, though additionally attenuated, at the port C, and vice versa. These ports are therefore used to pass the signal through the hybrid.

Hybrid are inherently unbalanced devices, hence two baluns have to be used for each pair to convert the 100 Ohm balanced signal into a 50 Ohm unbalanced signal required within the hybrid.

The signal over the path between the B- and C-port is attenuated by the sum the intrinsic attenuation of the baluns at both ends. As in our case the measurements are made also with two baluns, the sum of the port to port attenuation and the intrinsic attenuation is measured.

The noise is generated in an unbalanced mode and is fed into the summing port D. If the signal is zero, the attenuated noise signal is available at both the ports B and C ports. At the B port the noise signal is attenuated by approximately 3 dB, and at the D port by a similar additional amount. The measurement of the path D - B and D - C is made from the unbalanced input port D to one of the balanced output ports. Towards this purpose only one balun is used whose intrinsic loss is known.

3.1.2 Characterization of the noise generator

In order to vary the level of the power of the random noise generator, a variable step attenuator is used whose output is fed into a quadruple hybrid-type power splitter. Each of the four signal paths' is then amplified and fed through a fixed attenuator into the D-Port of the hybrid.

The attenuation of each path up to the D-port is characterized for different step attenuator settings and separately for the combined attenuation/gain of the cascade of power splitter, amplifier, and fixed attenuator. In our case the step attenuator settings are varied in 0.1 dB steps in the range from 27.0 to 46.9 dB. For each frequency point a linear regression is made for all step settings in the interval, mentioned above. This allows the calculation of any interpolated step attenuator setting as a result of acceptable BER limits (see 3.3).

In order to determine the noise at the exit of the noise injector, the generator voltage is measured. This is done, as already mentioned, with an oscilloscope at different frequency settings. The oscilloscope allows also the verification of the randomness of the signal. In fact a FFT transform of time domain measurements indicates clearly the white noise characteristics of the generator.

The Fig. 5 clearly indicates, though subjectively, the randomness of the noise source. For the further calculations the peak-to-peak voltage is used.

The Fig. 6 shows this voltage for different time basis of the oscilloscope. An average value of all measurements is used.

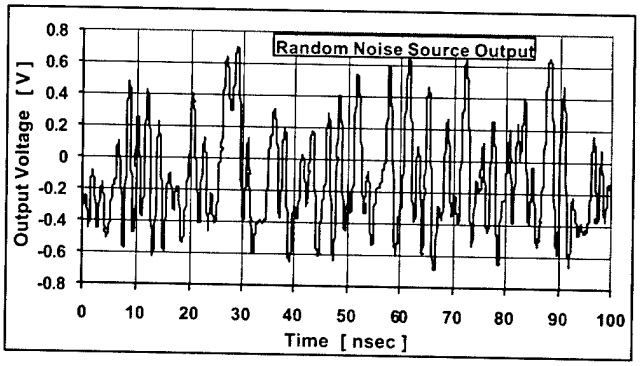


Fig. 5: Random noise source output signal over time.

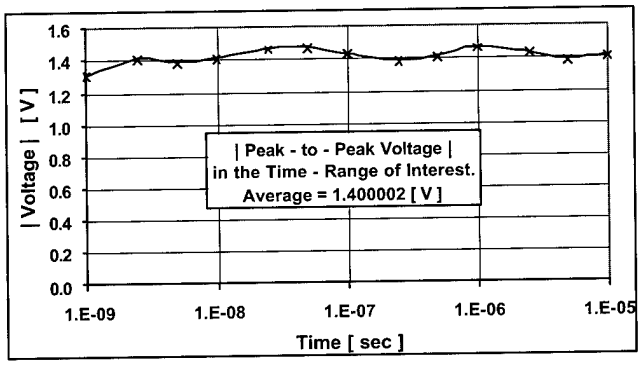


Fig. 6: Average peak-to-peak voltage as a function of time

With this noise voltage level we can determine the noise voltages at the exit of the injector, by summing up all the attenuations in the path from the generator to the exit of the baluns. This can be done also for any step attenuator setting, and using the above determined regressions, also for any intermediate required "step attenuator" setting. If the channel attenuation is determined for each side of the channel, then the noise voltage at the receiver end can be calculated (see 3.2.1).

3.2 The channel

The channel depicted in Fig. 2 has been used for the measurements. The noise injection point is slightly off center of the entire channel however it is centered within the horizontal cable. As a result the attenuation on both sides of the injector are slightly different. This difference is taken into account in our calculations.

3.2.1 Characterization of the channel from the noise injector to the EQ and the TO respectively

Each part of the channel (up to the connection point to the baluns of the noise injector) is characterized with respect to attenuation, NEXT, FEXT, return loss, and balance. The NEXT and FEXT is measured with respect to the EQ and TO respectively.

3.2.2 Characterization of the entire channel

The entire channel, including the noise injector has been characterized with respect to the same parameters. As the noise injector is characterized by itself, an assessment of the added component parameters versus the effectively measured parameters is, therefore, also possible, and may allow an assessment of the impact of forward echo (ILD).

3.3 Measuring the BER as a function of the noise level injected

The BER is measured under the assumption of low frame errors, thus that the frame errors can be equated to bit errors. This is done using different step attenuator settings, in order to determine the interpolated step setting to obtain a BER of 10^{-10}. As already mentioned, the noise, present at the ports B and C of the hybrid, is different. This in turn yields different BER results for the upstream and downstream traffic on the SmartBits 200. To verify the frame error detector for consistency the connections are poled i.e. the ports at the SmartBits 200 are reversed for the EQ and TO side of the channel. The recorded results are, to all practical, purposes identical. This has been also confirmed with a highly asymmetric channel, with a skew of the BER on both sides exceeding 3 decades. For our measurements we kept, therefore, the connection to the EQ-side and the TO-side fixed on the SmartBits 200. The channel is measured twice, with straight and reversed noise injector. In this case the connections coming from the EQ and from the TO are changed between the baluns leading to the hybrid ports B and C, respectively. This yields four measurement series.

For all four cases the required value of the step attenuator setting to obtain a BER of 10^{-10} is determined using a curve fit of the BER values over the step attenuator setting. This allows the interpolation of the required attenuator setting to obtain the targeted BER of 10^{-10}.

3.4 The signal to noise ratio of the channel investigated

To characterize the signal to noise ratio of the entire channel further, we use an earlier defined effective power sum for each pair, i.e. the power sum of added NEXT and FEXT [2]. This is done, as the 1000Base-T protocol is bi-directional on all four pairs. The 1000Base-T protocol can compensate to some extent NEXT, but cannot usually compensate for FEXT. The return loss did not need to be considered here, as the actual results obtained for the components as well as for the entire channel are way beyond the requirements. Thus the echo cancellation of the 1000Base-T protocol can fully compensate any noise resulting from return loss echos.

4. Results

It is impossible to report all data. In fact, our data comprise in excess of 1550 files with over 450 MB. Therefore, this paper will give only an essential excerpt of these data, which will allow the reader to follow the logic sequences of the calculations and will thus permit a repetition and double check of our results.

4.1 The noise injector

The attenuation of the noise injector between the different ports is indicated in Fig. 7 to Fig. 9.

Here the attenuation of the different paths' of the hybrid is shown, not including the balun intrinsic loss. The balun intrinsic loss has to be taken into account in the subsequent calculations. What is clearly evident here is the different noise level at the ports B and C, due to the different attenuation of the hybrid in the corresponding paths'.

The effective power sum of the entire channel, measured with respect to the EQ-side, is indicated together with the attenuation

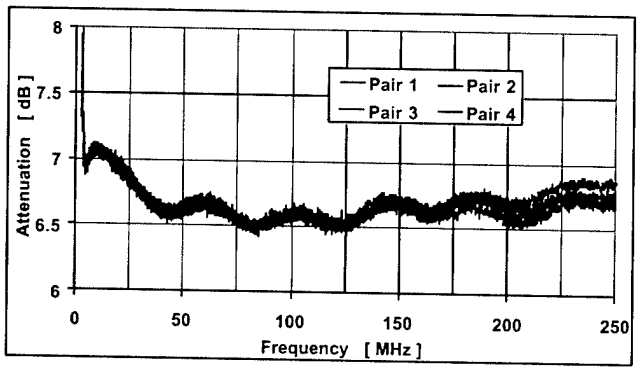


Fig.7: Attenuation of signal path from B-C port

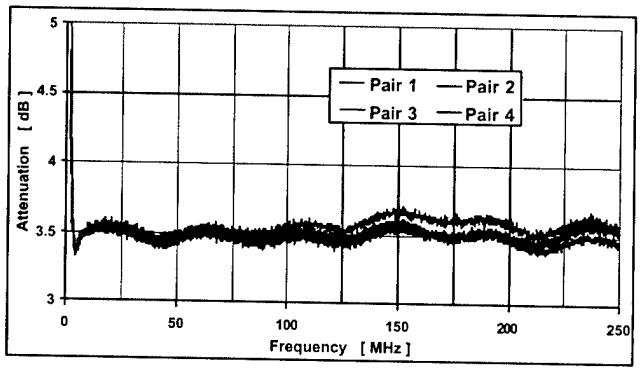


Fig. 8 : Attenuation of noise path from D-B port

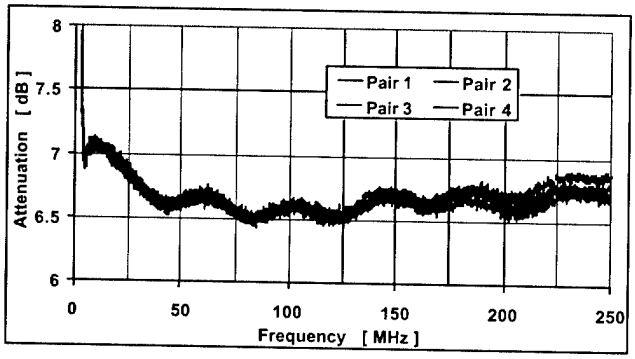


Fig. 9 : Attenuation of noise path from D-C port

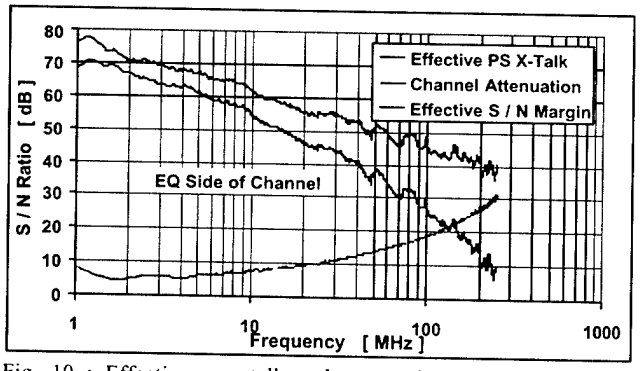


Fig. 10 : Effective crosstalk and attenuation of entire channel, including injector, measured at the Equipment Room (EQ) side

and the resulting effective S/N margin in the Fig. 10. Here the attenuation is averaged, using a quarter of the power summation. The average effective power sum crosstalk has been calculated by the power sum summation of the PS NEXT and PS FEXT values of each pair. The curves for the individual pairs show a pronounced roughness due to reflections, especially at lower frequencies It should be mentioned, that the attenuation of the entire channel is, especially at lower frequencies relatively high. This is due to the attenuation of the noise injector, i.e. the attenuation of the hybrid path and the intrinsic loss of both baluns used for each pair.

4.2 The channel and the parts leading from the injector to the EQ and the TO

Both channel parts, i.e. the section leading to the EQ and to the TO from the injection point, were measured at the EQ and TO, respectively. The effective power sum averages of all four pairs are indicated in the Fig. 11 and 12. In this case the respective effective S / N margins are not indicated.

The Fig. 11 and 12 clearly indicate, that both sections of the channel, i.e. from the equipment room (EQ) to the noise injector and from the telecommunications outlet (TO) to the noise injector, respectively, are nearly identical in their respective margins. The measurements are taken at the EQ and TO side respectively.

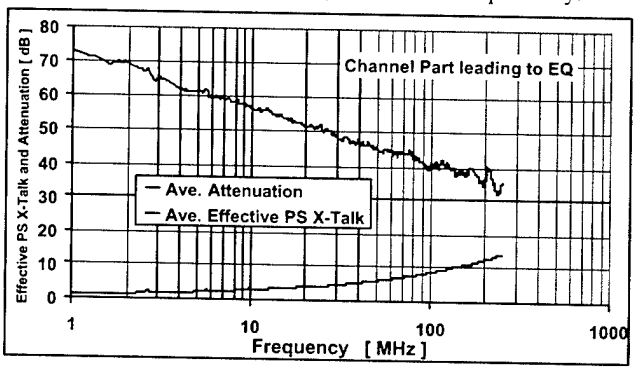


Fig. 11 : Effective crosstalk and attenuation of the part of the channel, leading to the Equipment Room (EQ), measured at the EQ

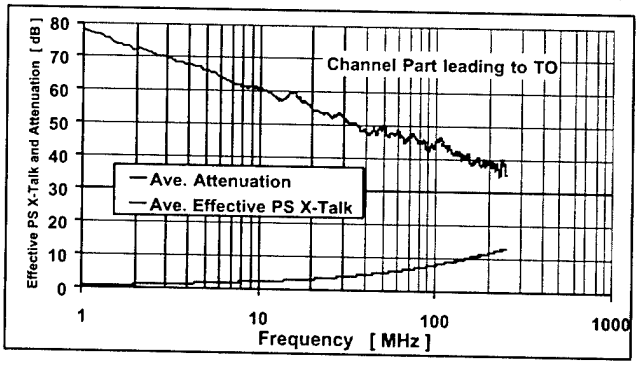


Fig. 12 : Effective power sum crosstalk and attenuation of the part of the channel, leading to the Telecommunications Outlet (TO), measured at the TO. The measurement results at the EQ are comparable.

4.3 The BER measurements

The bit error rate is assessed using differing step attenuator settings. In most cases 0.1 dB steps are used, and for each setting

the bit error rate has been determined over a time of minimum 15 minutes and up to more than 48 hours. After a complete cycle of BER measurements, the noise injector is reversed in direction, and a new series of measurements is taken.

The results are indicated in the Fig. 13 and 14.

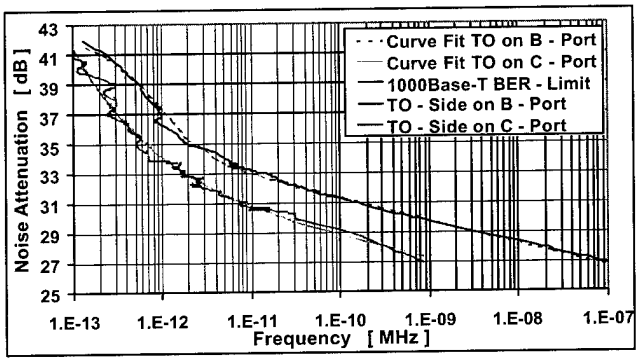


Fig. 13 : Noise attenuation over the step attenuator setting as a function of the obtained BER. Here the channel part leading to the TO is shown, once connected to the B - port and once to the C - port of the injector

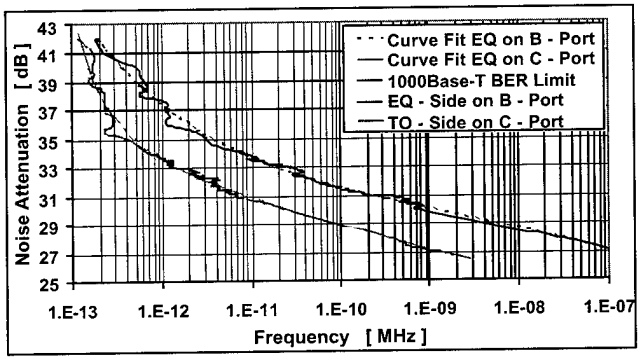


Fig. 14 : Noise attenuation over the step attenuator setting as a function of the obtained BER. Here the channel part leading to the EQ is shown, once connected to the B - port and once to the C - port of the injector

The obtained results are then curve fitted, using a curve-fitting program (SPSS - Table Curve 2D), in order to calculate the interpolated the step attenuator setting, which would be required to yield a BER of 10^{-10}. This noise attenuation is then used to determine the total injected noise signal attenuation up to the equipment room and up to the telecommunications outlet. It is obvious, that the signal path connected to the B-port of the hybrid yields a higher attenuation, and hence requires a higher value of the step attenuator setting to get the same signal to noise ratio, resulting in a comparable BER.

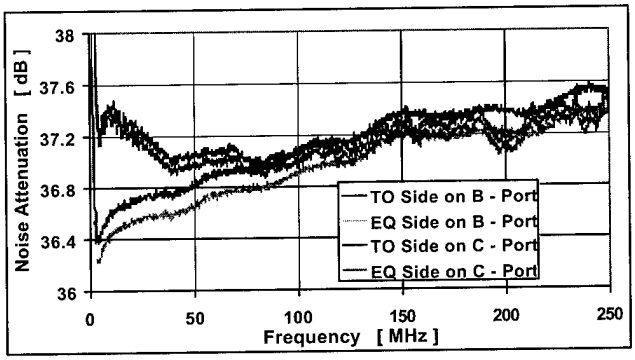


Fig. 15 : Noise attenuation for each side of the channel leading to the EQ and TO, and connected successively to both ports of the noise injector. The values depicted represent the average of the attenuation of each pair path.

The noise voltage is determined at the equipment room and the telecommunications outlet, respectively. This is done, taking into account the slightly different attenuation on each side, as well as the difference of the attenuation of the hybrid ports for each directional orientation of the noise injector within the entire channel from the EQ to the TO.

The Fig. 15 shows the resultant average attenuation over all pairs for the four cases measured. The results are clearly very comparable, especially at higher frequencies. At lower frequencies, there are slight deviations due to the non-linearity of the amplifiers and the low frequency behavior of the hybrids.

4.4 The signal voltage

The signal voltage is determined in the same fashion as the noise peak-to-peak voltage (see 3.1.2 and Fig. 6).

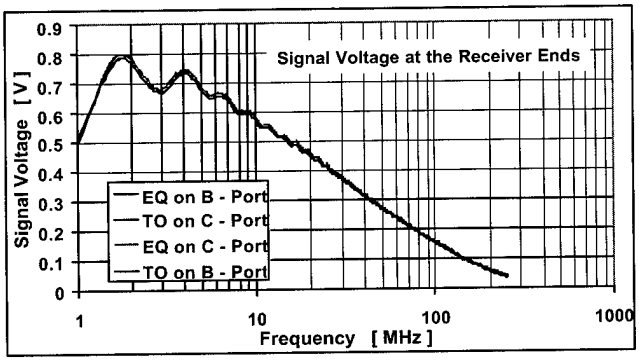


Fig. 16 : Signal voltage at the receiver end for the four configurations of the injector with respect to the channel section leading to the EQ and the TO.

The signal voltage is then calculated for the entire channel end to end, taking the entire channel attenuation in each direction into account. The differences are very minor, and an average is taken for the further calculations. The signal voltage at the receiver ends, thus calculated is shown in Fig. 16.

4.5 The injected noise

The total attenuation for each injected noise path is calculated. The average over all four pair paths' is used and is depicted in the

Fig. 17 and 19. The corresponding noise voltage levels are calculated and are shown in Fig. 18 and 20.

With the values obtained in 4.4 and 4.5 we can now determine the signal to noise ratio at the receiver ends.

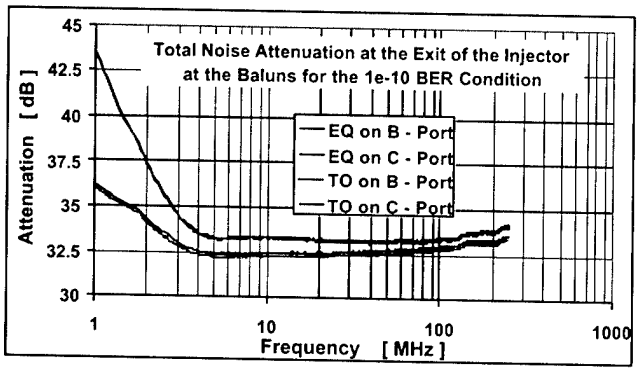


Fig. 17 : Noise attenuation at the exit of the noise injector (at the baluns) for the four configurations of the injector with respect to the channel section leading to the EQ and the TO respectively.

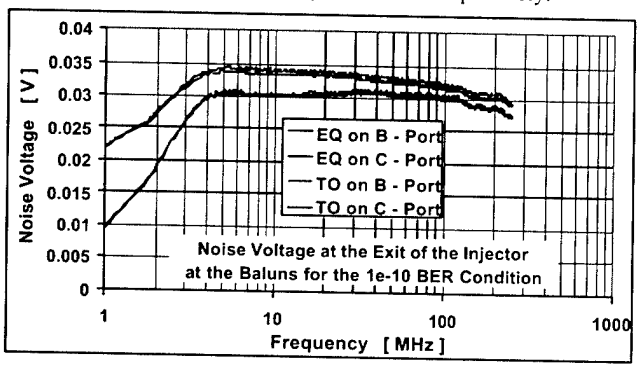


Fig. 18 : Noise voltage at the exit of the noise injector (at the baluns) for the four configurations of the injector with respect to the channel section leading to EQ and TO respectively.

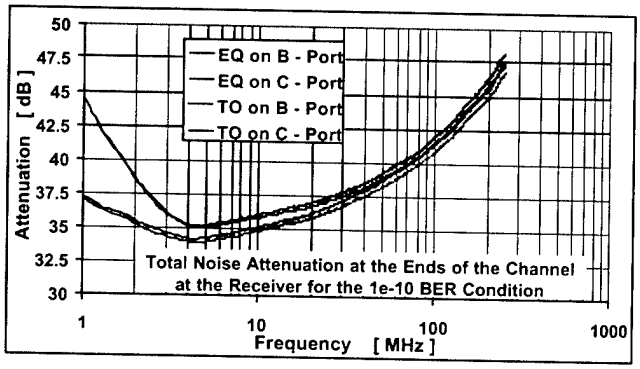


Fig. 19 : Noise attenuation at the receiver ends for the four configurations of the injector with respect to the channel section leading to the EQ and the TO .

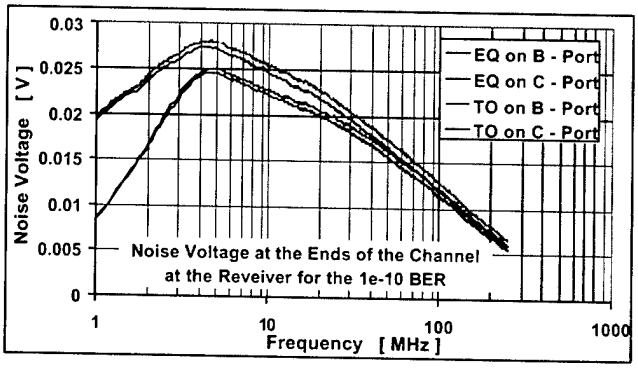


Fig. 20: Noise voltage at the receiver ends for the four configurations of the injector with respect to the channel section leading to EQ and TO respectively

4.5 The sustainable signal to noise ratio

The sustainable signal to noise ratio is shown in Fig. 21. It is calculated from the signal to total noise ratio. That means the noise calculation takes the crosstalk performance of the channel under measurement into account.

The noise voltage generated at the receiver ends due to FEXT and NEXT has been computed and added to the injected noise voltage (voltage sum addition). It is obvious from this figure that the sustainable signal to noise ratio of the 1000Base-T protocol is substantially lower than the channel values specified. Fig. 22 indicatres the curve fit of the obtained values, which is used for the further calculations. In order to obtain reasonably smooth results, also the attenuation of the entire channel has been curve fitted, and the upper envelope will be used. This is shown in Fig. 23.

We can now determine the alien crosstalk, which the system supports, using the Cat. 5e specification requirements.

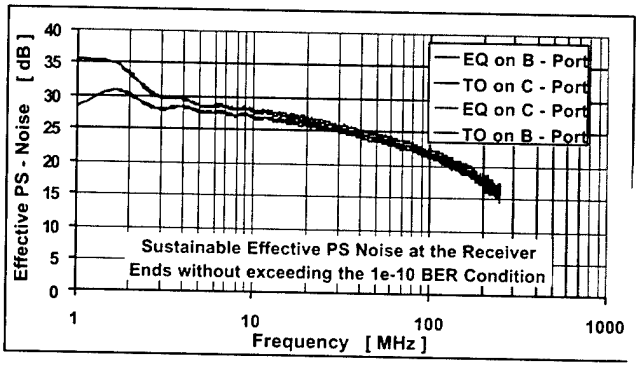


Fig. 21: Calculated sustainable PS Noise, while maintaining a BER o 10^{-10}. The calculation is base upon the voltages shown in Fig.. 1(and Fig. 20.

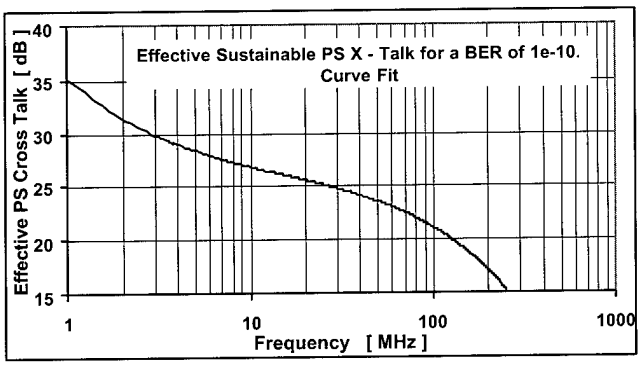


Fig. 22: Curve fit of the results shown in Fig. 21. It is the effective, sustainable PS Noise, while maintaining a BER of 10^{-10}.

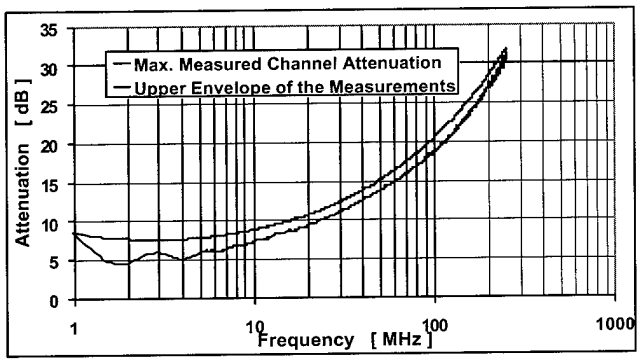


Fig. 23: Curve fit of the attenuation of the entire channel, off-set to obtain the upper envelope.

4.6 The alien crosstalk

To determine the alien crosstalk values from the Cat. 5e performance requirements, we have to use the fact, that the power sum of alien crosstalk and the crosstalk from the specification requirements yields the sustainable power sum crosstalk. Hence, with the specification limits of the Cat. 5e specification, we can now determine the alien crosstalk performance.

The results obtained are shown in the Fig. 24 to Fig. 26. It

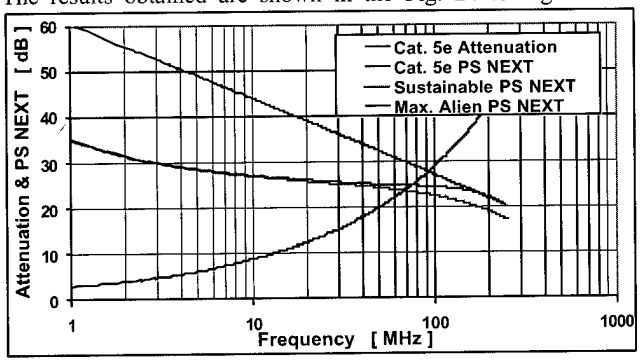


Fig. 24: Cat. 5e attenuation to crosstalk margin and calculated sustainable PS NEXT to maintain a BER level of 10^{-10}.

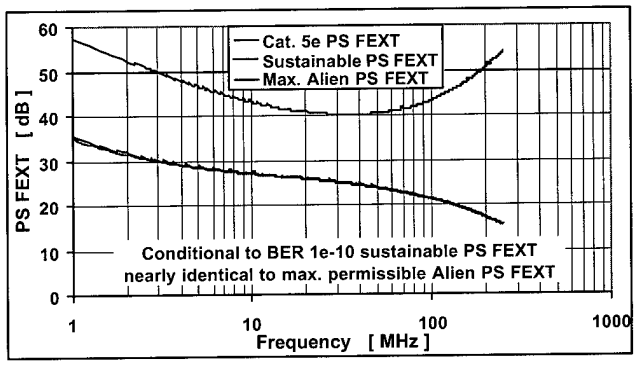


Fig. 25: Cat. 5e PS FEXT and calculated sustainable PS FEXT to maintain a BER level of 10^{-10}

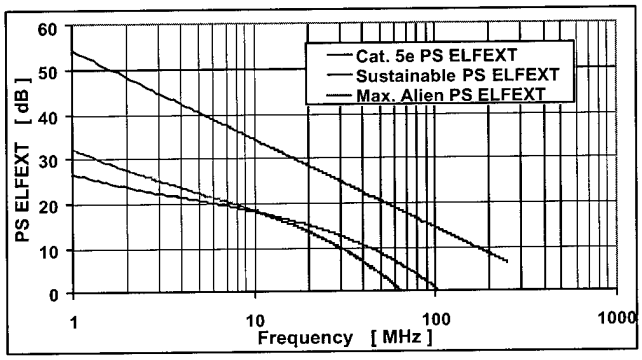


Fig. 26: Cat. 5e PS ELFEXT and calculated sustainable PS ELFEXT to maintain a BER level of 10^{-10}.

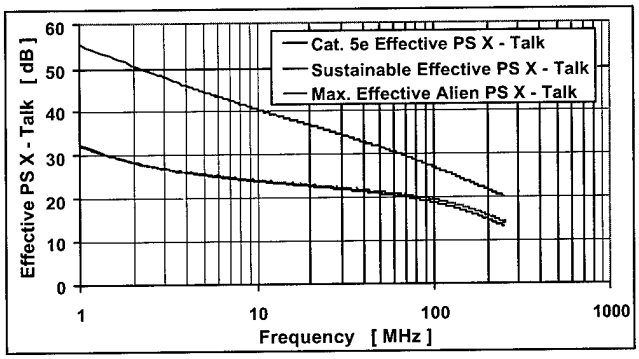


Fig. 27: Cat. 5e effective PS Xtalk and calculated sustainable effective PS ELFEXT to maintain a BER level of 10^{-10}.

should be mentioned, that the PS ELFEXT values are obtained her by subtracting the specified attenuation from the PS FEXT.

5. Discussion of Results

Our results clearly indicate that the internal noise injection into an operating channel is feasible. They indicate furthermore, that the 1000Base-T protocol is a relatively robust system with respect to alien crosstalk. The noise injection unit itself proved to be quite precise in its results, though some improvements with respect to the amplifiers might be helpful.

We attributed the effective measured power sum crosstalk successively to the power sum of the PS NEXT of the channel and the alien PS NEXT and likewise to the power sum of the PS

FEXT of the channel and the alien PS FEXT.

We can do this precisely only for the effective power sum, as the split between PS NEXT and PS FEXT is system dependent and unknown.

We should also like to remind for the reader, that we used for our entire analysis voltage measurements in the time domain. It will be definitely interesting, to verify some results on the noise injector also with a spectrum analyzer in the frequency domain, though we are confident, that our results are on the safe side.

Our results were recorded up to 250 MHz, though the specification requirement limits are at the most 125 MHz, and the peak power spectrum of the 1000Base-T protocol is less than half this frequency. In this frequency range the margins between the alien crosstalk and the specification limit for the crosstalk performance are relatively high.

Therefore, we should like to suggest specifying alien crosstalk performance requirements, which are slightly lower than the crosstalk performance requirements.

Our considerations limit themselves to alien crosstalk performance between telecommunications cables. From a comparison between the injected noise and the internally generated noise in the channel, which is minimum 16 dB, we are also confident, that our statements are holding as well for alien crosstalk with substantially different voltage levels. However, this is not valid anymore for peak power noise spikes induced over power lines. In fact, parallel to our BER measurements, some measurements were made on other channels in the very close vicinity with a 5 kHz 2000 V spike generator. It was necessary to interrupt during these trials our BER measurements.

6. Conclusion

If it is absolutely necessary to determine, as frequently proposed, alien crosstalk performance limits, then these stipulated and/or proposed limits should not be higher than the crosstalk performance requirements of the channel itself.

> Note: Alien crosstalk is dependent on many variables including cable design, cable placement and installation considerations. The actual levels of alien crosstalk obtained in practice are a subject of further study and are beyond the scope of this paper. Our results provide only an indication of the maximum sustainable levels of alien crosstalk for an example Category 5e channel.

The results we obtained indicate clearly, that the alien crosstalk can be substantially below the performance requirement limits, especially at lower frequencies.

7. References

[1] J.-H. Walling and R. Pederian: Cross - talk measurements with random noise sources

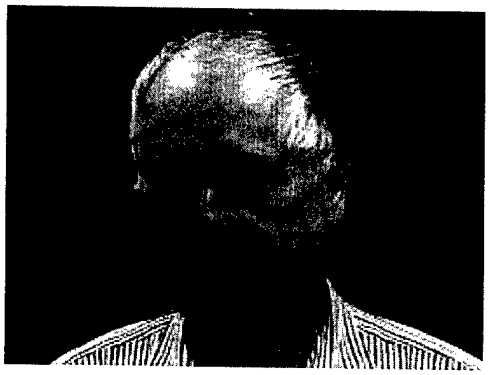
49th IWCS (2000) p. 129-134

[2] J.-H. Walling, M. Belanger and B. Lord: Performance evaluation of multiple pair category 5 backbone cable for high speed data services

43rd IWCS (1994) p. 328-340

8. Authors

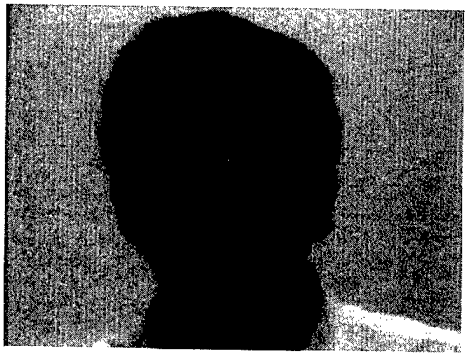
Jörg-Hein **(Jo) Walling** received his diploma in Mechanical Engineering in 1966 at the Technical University of Berlin. In 1974 he obtained a Doctor's degree (Dr.-Ing.) at the same University. In 1974 he joined Northern Electric (later on Northern Telecom and Nortel) in the Research and Development department. Since 1976 he has been senior engineer at the Lachine Cable Plant. He continued to work at the Nordx/CDT facilities, responsible for the design of Outside Plant and Data Grade Wires and Cables. Since 1999 he is an independent consultant for cables, standards and machinery.



Jo is Canadian head of delegation to ISO/IEC JTC1 25C and IEC 46C, and participates actively as an expert in the development of standards in the working groups ISO/IEC JTC1 25C WG3 and IEC 46C WG7. He is also actively involved in the standards writing activities of ICEA and served as a 1st VP of the communications cable section. He is chairman of the UL-CSA Harmonization Committee, the CSA Subcommittee C22.2 No. 214 (Communication Cables).

Jo is curious and always interested in new challenges.

Michel Bohbot is Manager, Strategic Technology Development with NORDX/CDT. He is currently an active member on the IEEE 802.3 standard development committee responsible for the development of high speed Ethernet networking specifications.



Michel Bohbot graduated in electrical engineering from the University of Montreal, Quebec, Canada in 1985. He also graduated in Nuclear engineering from Geneva Engineering School, Switzerland in 1982. He started to work as a design engineer in the development of passive and active networking product in 1985. He joined Northern Telecom in 1989 to work on cabling system testing. He has held a number of positions at Northern Telecom including Product Manager for Networking Equipment and Manager for the IBDN Systems and Applications Laboratories.

Paul Kish is Director, IBDN Systems and Standards with NORDX/CDT. He is the current chairman of the TIA TR-42 engineering committee responsible for telecommunications cabling standards for commercial and residential installations. He has been active in the development of cabling standards since 1989. In 1991, he initiated the work that led to the publication of additional specifications for Category 3, 4 & 5 cables which, since then, have had a major impact in the cabling industry. Paul Kish is also a member of the BICSI TIM Committee.

Paul Kish graduated with an M.A.Sc. degree in electrical engineering from the University of Waterloo, Ontario, Canada in 1972. He started to work as a cable design engineer with Bell.



Northern Research in 1972. He joined Northern Electric a year later to work on cable development projects. He has held a number of positions at Northern Telecom including Manager of the Cable Development Laboratories, Manager of Cable Design and Product Manager for IBDN Cabling. Paul Kish is recognized in the industry as an expert in "cable transmission" and for his contribution to the evolution of cabling standards within TIA, CSA, ISO/IEC and IEEE

The Future of the Copper Cable Access Network

David L. Waring
Telcordia Technologies, Inc.
Morristown, NJ
+1-973-829-4850 · dlw@research.telcordia.com

Phiroz Madon
Telcordia Technologies, Inc.
Navesink, NJ
+1-732-758-2856 · pmadon@telcordia.com

Abstract

The telecommunications industry has long debated the future of the copper access network. Expert opinion ranged from a decline and a replacement by other access networks (wireless, coaxial cable) to the ultimate upgrade via fiber to the home. In the middle of these extremes is an evolutionary scenario which will see the copper access network upgraded by digital subscriber line (DSL) technology to support broadband digital services, accompanied by more gradual displacement of copper cable by fiber optics, initially in the feeder network.

Evidence now supports this gradual copper to fiber evolution, with DSL technology playing a key role. We take a close look at progress, examining both the penetration of fiber feeder, and the projected rollout of DSL. The outlook is optimistic. DSL technology is well proven now. However, the industry must still focus on efficient operations procedures to manage this coming transition. Administration and maintenance of the copper loop must be accurate, automated, and cost effective. The industry needs to focus on its loop facilities and lower layer integrity in the same way it now focuses on upper layer protocol monitoring and service assurance.

Keywords

Local access networks, copper loop plant, subscriber loop, digital subscriber line (DSL)

1. Introduction

Digital subscriber line (DSL) technology is making it possible for users to receive megabits per second over ordinary telephone lines. This has given the copper access network a new "lease on life." A decade ago, pundits were "writing off" the local telephone network as old fashioned, only capable of supporting voice service. But if telephone lines can be upgraded to support reliable always-on broadband digital communications, the local loop can be reused to support an exciting array of new services, including high-performance access to the Internet, flexible voice on packet services, home monitoring and security services, and even downloading of entertainment content such as record albums and movies.

The telephone company twisted pair access network has several notable strengths. First, it is a point-to-point network, meaning that each customer has his or her own dedicated phone line. DSL systems deployed on top of these facilities provide rich upstream as well as downstream bandwidth, particularly important for packet-based applications. The subscriber loop network is one of the most reliable and widely deployed networks in the developed world. In the U.S. the copper access network truly represents a national resource that will play a key role in the Information Age.

There are challenges, however, that must be successfully addressed. The business is undergoing a dramatic change from a regulated monopoly to an unregulated environment, with local competition in which loops can be unbundled and shared. There are critical engineering issues such as loop qualification and spectral compatibility that need to be managed. These subjects will be covered in this paper, focusing on tools and support systems that are needed to ensure successful rollout of DSL.

2. Trends in the Public Access Network

For the first hundred years of the public telephone network, the access network consisted of copper cables serving primarily switched telephone service or Plain Ordinary Telephone Service (POTS). In the 1980s, with advances in transmission technology and continuing advances in integrated electronics, industry researchers and engineers began to plan for the replacement of this network with fiber optics. This evolution began with digital loop carrier (DLC) systems, which started deployment as all-copper pair-gain systems, but quickly evolved to replace feeder network copper with fiber-based facilities. Deployment of DLC represents the beginning of the replacement of the copper access network with fiber.

A natural extension of this architecture led to fiber in the loop (FITL) systems, using two-stages of electronics: fiber in the feeder network, remote electronics, fiber in the distribution network, optical network units (ONUs) located close to the subscriber's premises, and then short (up to several kilofeet) copper distribution cables to the home. This evolution, in which copper is methodically replaced by fiber, and remote electronics increasingly enter the local network, was recognized relatively early on (see for example [1]). What was not as obvious was the *rate* at which this evolution would occur. Many predicted that the access network would convert to all-fiber as quickly as did the long-haul backbone network. This was not the case, however. Although fiber has steadily entered the access network, it has been predominantly in support of DLC, while FITL

penetration has been slower. Figure 1 shows rates of penetration for North America, including traditional all-cooper loops, and DLC, both copper-fed and fiber-fed.

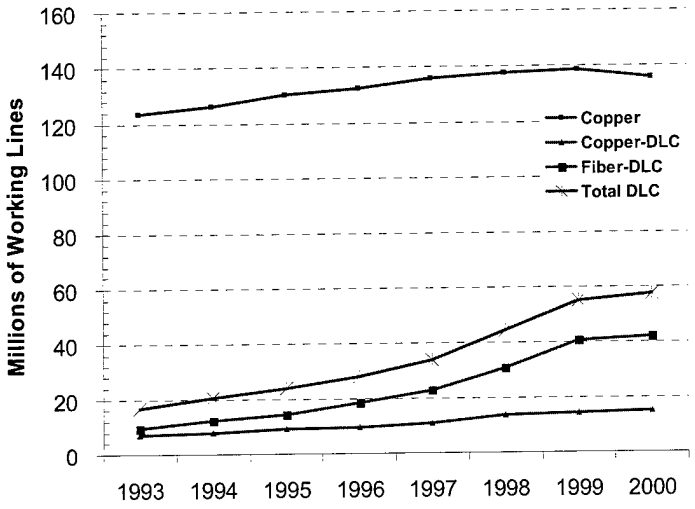


Figure 1. Numbers of working telephone lines in the U.S. [2]

The data shows several interesting trends. First, the deployment of all-copper access lines has been slowing and even declined a bit in 2000. Telephone service, from the customer's point of view, is still metallic and terminated at the customer's premises on a copper pair. But back in the feeder network virtually all the new growth is now being served from fiber-fed DLC. Currently there are about 136 million all-copper working lines, and 42M fiber-fed access lines. So, the evolution to fiber in the feeder network is almost 25% complete.

Demand for wireline telephony service has grown steadily. However, wireless services have also grown tremendously (and, relatively speaking, over a much shorter period of time), leading to the important question of cross-elasticity between traditional wired POTS and wireless services. There almost certainly is significant cross-elasticity between the two offerings, but quantifying the effect is difficult. Figure 2 shows recent *revenues* for the bulk of the U.S. operators. We use revenues, rather than number of subscribers, assuming that revenues will provide a composite reflection of the health of the two types of access architectures.

Note that wireless service is growing significantly, but local wireline revenues continue to grow as well. There is much speculation about whether wireline growth will continue its historical advance. There is some evidence that, as wireless price plans fall, users may for the first time drop their wireline service in favor of a wireless service. Although consistent with Figure 1, this is somewhat at odds with the recent increases in wireline revenues. Some explain recent support for wired service in terms of *second* lines, used increasingly for dial-up access to the Internet. There are some signs that both first line growth is flattening, as wireless becomes a viable primary line option, and that second line growth will saturate in the relatively near future, as demand is satisfied.

The decline in local copper loops has not come as quickly as some predicted, due in part to the recent boost of second lines for modem access. This phenomenon is a precursor to a more significant trend; retrofitting of the copper loop using digital subscriber line (DSL) technology to evolve away from analog POTS service toward sophisticated wideband (100 kb/s up to 1 Mb/s) and broadband (1 Mb/s up to 6 Mb/s) services. As narrowband voice service moves to wireless, demand for wideband and broadband services may emerge just in time to support continued strong use of the local copper loop. One of the (intentional) advantages of Asymmetrical Digital Subscriber Line (ADSL) technology is that it was designed to continue to support analog POTS, while deriving a full-duplex digital channel [4]. This allows the access link to serve both traditional analog service as well as new packet-based services during a transition period to all-digital services.

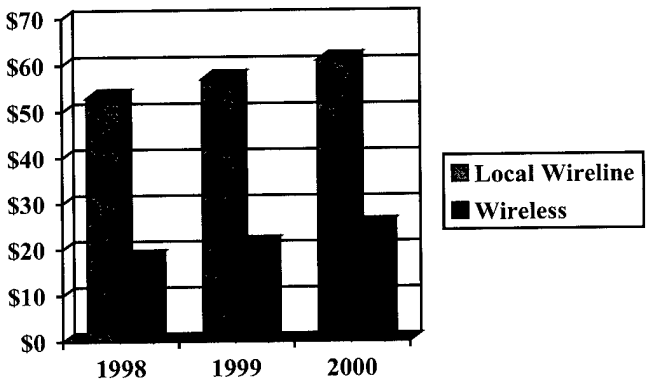


Figure 2. Revenues for the major U.S. operators [3] **in millions of dollars**

Will the need for digital access prove to be the salvation of the copper loop? This will in part depend upon how rapidly and how extensively DSL-based services roll out. Figure 3 shows one projection of subscription rates for new digital packet-based services in the U.S. DSL-based services are projected to grow to 10M households, or approximately 10% of households, by 2003. Recent aggressive rollout of DSL service by large incumbent operators is in keeping with these projections.

A successful deployment of 1 out of 10 households in just a few years represents a major shift in utilization of the local copper loop. Penetration rates beyond 2003 are a bit sketchier, and will depend on the success of new packet-based services being offered over the DSL access link. Clearly high-speed access to the Internet is a compelling service driving much of the current deployment. But ultimately the extent to which the plant is retrofitted may depend on evolution to packet-based *voice* services, along with other new packet-based services.

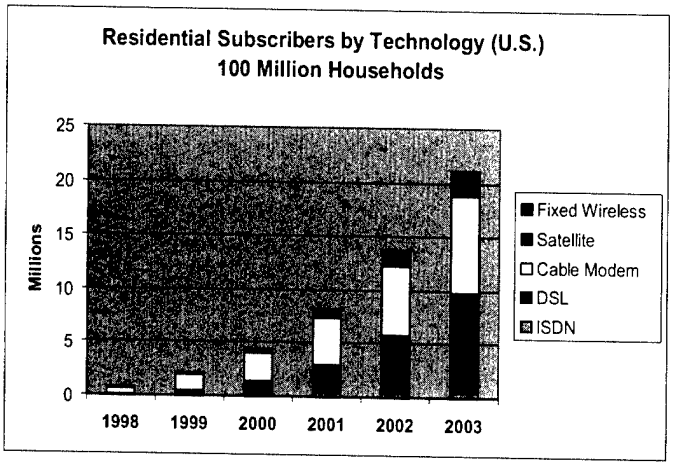


Figure 3. Predicted deployment rates for digital, high-speed access in the U.S. [5]

Contrary to some opinion, we believe that DSL technology will *encourage*, not discourage, the use of fiber in the access network. Fiber will continue to replace twisted pair cable in the feeder network. Copper cable will remain in use over shorter distances and at higher bit rates. To the extent that DSL deployment is successful, it will fuel the use of higher bandwidth by subscribers. For those of us who use a computer and have experienced the steady advances in memory size and dial-up modem speeds, we know how difficult it is to avoid the inevitable pull toward higher performance. Eventually we succumb and obtain a newer, faster machine. Early experience with high-speed access to the Internet has been similar; users become dependent on the performance, and also tend to use the network more. Thus, DSL is really a friend to fiber; it will help create user demand for bandwidth that will ultimately only be satisfied with fiber technology.

We have painted a picture in which the future of the local loop remains vital for many decades to come. The Information Age will see digital communications being delivered to the home by telephone, cable television, satellite, broadcast and wireless access networks. Each of these networks is expected to carve out a niche in the market for service delivery. Table 1 indicates that some platforms may be stronger in certain areas than others, and users will continue to receive services from multiple platforms in a competitive environment. Talk about the public telephone network becoming an irrelevant narrowband platform has subsided as DSL rollout accelerates. So is the future of the copper access network assured? Its future is bright, but only if the access network continues to be *administered and maintained* to its traditional levels of high availability and reliability.

Table 1. Examples of possible network strengths in a competitive environment

Network	Strengths	Possible Limitations
public telephone	Traditional lifeline POTS service. Dedicated Mb/s access using DSL for high-speed packet data.	Not a good video broadcast platform until fiber penetrates deeply into the access network.
cable television	Graceful evolution from analog to digital video. High-speed packet data via cable modems.	Successful offering of voice services will have to overcome engineering challenges.
satellite	Successful launches have introduced consumers to digital video programming.	Inherently one-way; interactive services will not be as effective as those of true two-way networks.
broadcast	The most viable platform for delivery of HDTV.	Inherently one-way; interactive services will not be as effective as those of true two-way networks.
wireless	Mobility, convenience, and pricing competing with that of POTS.	Data access will lag terrestrial systems in bandwidth.

3. Administration and Maintenance of the emerging Digitized Copper Loop

Now that the copper loop is receiving recognition as one of the critical on-ramps to the Information Highway, it needs to be administered and maintained in a fashion consistent with its importance. Any network requires continual upkeep, and the local access network is no exception. The copper access network has historically been highly maintained by a fleet of telephone company repair crews and by automated fault detection and isolation tools. Loop records are maintained in computer databases. Loop testing systems automatically perform short (half a minute) tests on customer lines, either verifying the health of the loop or identifying electrical troubles. This highly mechanized, highly efficient loop testing system is almost universally deployed. Originally developed by the Bell System, one of the most important elements is the Mechanized Loop Testing (MLT) system. This system uses a metallic test bus and full-splitting metallic access relays on line card electronics. A given subscriber loop can be taken out of service and metallically connected to a centralized test head where single-ended measurements are made on the customer's loop. The test head runs a battery of tests aimed at maintaining and diagnosing the customer's narrowband (4 kHz) voice service.

Existing loop record databases along with traditional POTS testing systems will continue to be of significant benefit in the administration and maintenance of the copper loop plant, even as

new DSL-based services are deployed. For example, the most straightforward method of qualifying a loop for DSL service is to pull the loop record from the database and use simulation models to determine the supportable bit rate. If the loop record is accurate, good results can be achieved in this fashion. And with the proper software and interfaces, the process can be all-electronic. If there is some question about the integrity of a loop, traditional MLT tests can be used to validate its health, or, alternatively, identify a range of connectivity problems such as opens, shorts, excessive loss, excessive noise, etc.

To efficiently deploy new DSL systems, however, new levels of detail and accuracy will be required that go well beyond existing capabilities. Since DSL squeezes maximum performance out of the loop, it is not surprising that additional loop detail and precision is needed in order to take maximum advantage of the technology. For example, the loop make-up is needed in very precise terms, in order to obtain a precisely qualified DSL bit-rate.

Often the existing loop information is adequate to roughly qualify some loops, but a "gray" region of loops exists for which more information is needed. For example, shorter loops, associated with customers located closer to a wire center, can be successfully qualified. And long loops, or loops with load coils, can be successfully identified as *not* qualified to support DSL service. This leaves a range of loops in the middle that remain in question. To date the deployment of DSL has been on the order of 1% of access lines. In this early stage operators could provision service to customers whose loops are clearly well-qualified. However, as deployment rates accelerate and move toward 10%, the "gray" region of loops will become more important. Customer subscription rates on the shorter loops will start to saturate, generating more focus on the mid-range loops.

Inaccurate methods for qualifying mid-range loops present a conundrum. If an aggressive approach is taken, a potential customer may be told that he or she can receive service, only to find upon installation that the loop won't support service. We refer to this situation as a "false positive," depicted in Figure 4. A false positive may result in a dispatch by the operator, to check the customer's DSL electronics and wiring, to verify the loop characteristics via two-ended testing, and/or to make a physical rearrangement such as using a different distribution pair or removing a bridged tap. This type of field work is expensive; a rule of thumb is that it costs the operator $150 every time a truck is dispatched to a customer location. As large operators move from 1% to 10% penetration, even a relatively small failure rate, such as 5%, could result in millions of dollars in cost to attend to false positives.

On the other hand, a conservative approach may lead to a potential customer being told that they cannot receive service, when in actuality their loop would support service. We refer to this as a "false negative." False negatives are costly to operators as well, but in a different way. They represent lost revenues. A customer who wants to subscribe to DSL service but is told "no" may simply make do with dial-up service, which typically is not revenue generating for the operator (since local calls are free), or may go to a cable modem competitor. In either case, the local telephone operator stands to lose hundreds of dollars a year in subscription fees. A relatively modest false negative rate, such as 10%, represents millions of dollars in missed revenues for the larger operators.

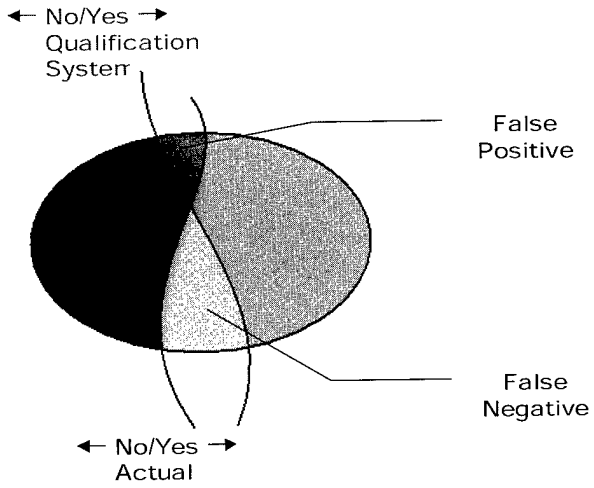


Figure 4. Depiction of "false positive" and "false negative" qualifications

How can operators reduce their false positives and false negatives? There are many ways to attack the problem and several useful tools and solutions are emerging, including:

- Central office (CO)-based testing, for direct and up-to-date validation of loop condition
- Non-intrusive, in-service loop analysis by exploiting capabilities of advanced loop electronics
- An advanced and sophisticated software operations system, to leverage all available information, increase the accuracy of projections, and provide results quickly and efficiently

CO-based testing requires a physical test device in the CO, but direct determination of loop conditions can then be made, and this can be done in an automated fashion for all of the POTS lines currently terminated on the local switch. Thus, the primary target population for DSL services can be qualified. Querying of loop electronics has the advantage of being non-service affecting, and can also be highly automated. However, it pre-supposes that DSL electronics are already in service, and so this approach becomes more relevant as the penetration of DSL increases. Both of these approaches need to be integrated with other related software operations systems (OSs) to create an operations fabric that ties together the various sources of loop information, stores this information in a database, correlates the data, and provide records and qualification results to various users. We will describe each of these approaches in more detail in the following subsections.

3.1 Single-ended testing from the CO

We previously described the MLT system, used extensively in the U.S. to maintain the POTS network. Figure 5 shows how this same test access infrastructure can be upgraded with a broadband test head. The intent is to augment the narrowband test head with a new, broadband testing capability. The broadband test head can probe the loop at frequencies well above the voice band, and thus characterize and qualify the loop for new DSL services that operate in these higher bands. This test head will interface with a switch and connect to a specified loop (by telephone number), apply a set of test pulses to that loop and record the responses. The results are then analyzed using sophisticated signal processing algorithms to qualify the loop.

A major need of operators, particularly the incumbent operators, is to qualify their existing loops for DSL service. In a typical U.S. central office (CO) there may be 10,000 POTS subscribers currently receiving service over their loops. These same subscribers are potential candidates to have their loops upgraded with DSL technology. For example, upgrading with ADSL will allow them to maintain their current POTS service with no changes, while additionally receiving high-speed access to the Internet. Thus, operators would like to know, with high precision, exactly what type of service each of these existing subscribers can receive.

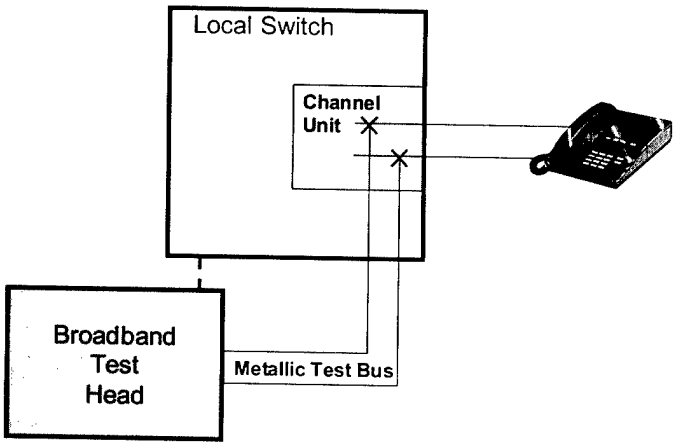


Figure 5. Metallic test access through the local end-office switch

We propose that the process of qualifying a loop for DSL service is more effectively separated into two stages; updating the loop make-up records and storing them in the loop records database, and then qualifying the loops for DSL service based on these electronic records and computer simulation programs. This approach has several advantages. First, it is consistent with the fact that most operators already have an electronic database in which they store their loop make-up records. They may already be using these records as part of an efficient, flow-through loop qualification process. When the broadband test head determines a loop make-up for a given customer line, this information should be compared to the existing record. Any ambiguities need to be resolved via intelligent correlation and decision, yielding a new, more accurate loop make-up. Note that this process is one that can proceed on its own time line. The broadband test head can be programmed to automatically go through the lines in the wire center, determining the loop make-ups. These could be stored in a temporary database and used by a second-tier process that compares the make-ups to the existing database records and intelligently resolves any differences. This second-tier process may use artificial intelligence to resolve differences, and a small number of records may require manual resolution by engineering staff. But the bulk of the process will be automatic and will run in the background over a period of days. Once complete, the accuracy of the loop make-up database is highly improved, and any subsequent DSL qualifications that are performed will in turn be much more accurate, reducing false positives and false negatives.

Qualifying loops in two stages also has the advantage that the DSL qualification can be rerun at a later time with different parameters that may be relevant to current interests. For example, the initial qualification may have been for ADSL service, assuming worst-case crosstalk, but later the operator may wish to qualify the same loop for SDSL service, assuming a more specific crosstalk condition. Although it is possible to initially qualify the line for multiple DSL services under multiple conditions and store away all the results for later use, we believe it is more efficient and fundamental to first obtain the loop make-up, and then run precise qualifications based on specific assumptions about the type of DSL technology and crosstalk. Once the precise loop make-up is stored in the loop database, qualification calculations can be run quickly (seconds). Operators can run "what if" experiments. These can be done on a per-line basis as needed, or in bulk. (E.g., how many customers in a wire center can receive 1.5 Mb/s ADSL service?) If the marketing plans of the operator change, the qualification assumption set can be changed, and the qualifications rerun. If a new DSL system is introduced, the models can be updated and added to the computer simulation programs; the loop make-ups remain the same and there is no need to go back to the broadband test head to physically rerun the tests.

A precise loop make-up is one fundamental set of information in a three-legged model that yields accurate qualifications. The other two "legs" are crosstalk noise, and accurate loop and transmission system models (See Figure 6). The industry has developed highly accurate models for telephone loops and DSL systems in the Alliance for Telecommunications Industry Solutions (ATIS), Standards Committee T1 Telecommunications. In Working Group T1E1.4 industry experts have been working for over a decade to develop precise models for subscriber loops and DSL transmission systems. If these models are given a precise loop make-up and specific crosstalk noise parameters, they yield very accurate predictions of system performance, including bit rate, reach, and performance. (See for example Reference 6 [6].)

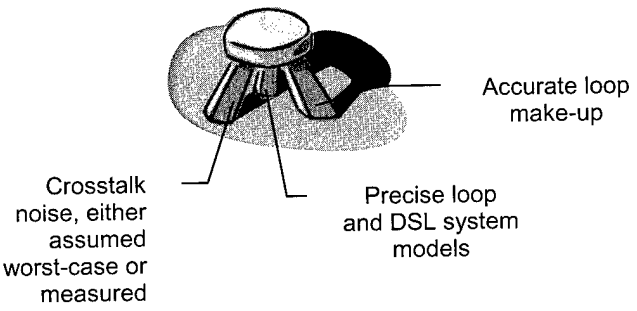


Figure 6. Three legs of accurate loop qualification

An implication of our proposal to separate loop identification from DSL qualification is, of course, that the broadband test head is capable of accurately determining detailed loop make-ups. Several manufacturers of testing solutions are actively pursuing this approach. Telcordia has had good success in accurately identifying loops. Figure 7 below shows several examples, wherein loops were presented to a broadband test head prototype system having no a priori knowledge. The system automatically probed the loops, analyzed the responses and made its best guess as to the loop make-ups, with the results shown.

The ability to determine loop make-ups with high precision in an automated fashion will allow operators to inventory their plant and bring their records up to date, qualify their loops for new services with high accuracy, and lower false positive and false negative rates, all of which will greatly facilitate the deployment of new DSL-based services. But this is only half of the story for effectively utilizing the plant. Once a DSL-based service is successfully installed, it needs to be efficiently maintained.

The broadband test head can support outside plant maintenance as well. A significant portion of outside plant trouble reports are due to problems that occur with the copper facility, for example due to splices which go bad, cables which become waterlogged, work in the field at distribution cross-connect points that may inadvertently disturb working pairs, etc. These problems occur regularly in the POTS world, and the MLT system (or equivalent) has proven very effective in identifying basic connectivity problems of this type. For example, a line fault will disable both POTS and Internet access, and the trouble can likely be identified and cleared with conventional POTS maintenance procedures. However, more subtle failures may occur that only affect the DSL-based service, and a conventional MLT test may not uncover the problem.

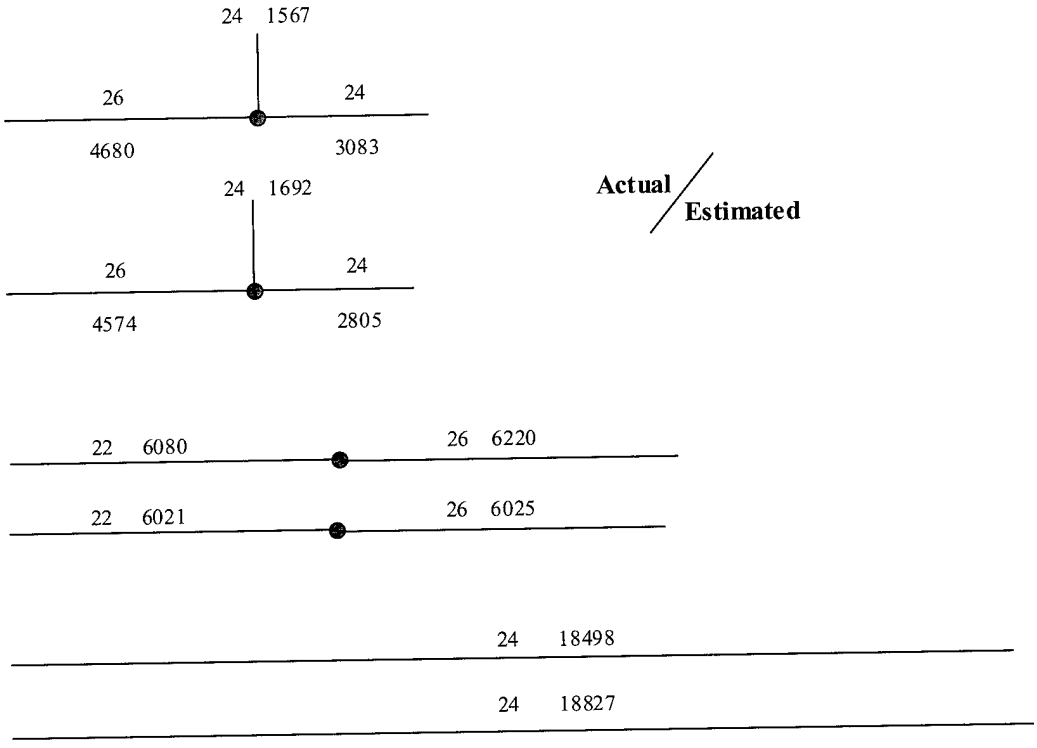


Figure 7. Actual (above) and estimated (below) loop make-ups.

For example, a rearrangement of a section of a customer's line might be made. The craft believes that the section was being replaced with a section of equivalent length and gauge. After the change POTS continues to work, but the DSL service begins to experience high error rates. Unbeknownst to the craft, the new section actually contained an undocumented bridged tap. In this case, the broadband test head can run a loop identification test on the loop in question. Because it can determine loop make-ups, including bridged taps, the correlation software detects that the prior loop make-up record had no bridged taps, and therefore identifies this as a likely source of the problem.

To this point we have described direct testing of the loop facility to determine loop make-up. Additionally, the broadband test head can be used to analyze crosstalk, deriving additional information about the noise environment a particular loop is exposed to. This is again achieved by direct metallic access to a subscriber's loop and wideband measurements. However, unlike the case of loop make-up determination, where the loop is pulsed in a deterministic fashion and other noise on the pair is intentionally processed and removed, in the case of crosstalk analysis it is exactly this loop noise we are interested in. By means of spectrum analysis algorithms, this noise is identified.

There are several approaches that can be used in the noise identification. For example, the composite crosstalk noise profile can be measured and recorded. We believe that a more useful approach is to determine the various *sources* that generate the crosstalk; in other words the "disturbers" that a particular loop is exposed to. In a similar fashion to qualifying loops for DSL service by first identifying the loop make-up, identification of the individual disturbers provides a more fundamental basis for subsequent crosstalk analysis and spectrum management.

Table 2. Correct identifications for the case of DSL single disturbers

BRI	14/14	100%
HDSL	24/24	100%
T1	38/38	100%
ADSL Dn	37/37	100%
ADSL Up	27/27	100%
SDSL 400	26/26	100%
SDSL 1040	27/28	96.4%
SDSL 1552	30/31	96.8%
HDSL2 Dn	29/29	100%
HDSL2 Up	27/27	100%
Totals	**279/281**	**99.3%**

Telcordia has had good success in accurately identifying single disturber crosstalk. Table 2 shows the results of an analysis that takes into consideration only those crosstalkers that have powers greater than or equal to the smallest disturber power used in the classic 1% worst case 49 disturber crosstalk model. An overall accuracy of 99% is obtained in identifying single disturbers.

Current requirements for spectrum management, as embodied in the Spectrum Management Standard, [7] apply relatively rigid rules uniformly across the entire loop plant. These rules do not take into account the individual types of crosstalk sources or crosstalk couplings related to a particular pair in a cable, which may be considerably different than the near worst-case couplings that are assumed in the standard. A system that can characterize crosstalk on a loop-by-loop basis has the potential to yield a much more granular crosstalk characterization of the plant. This data, entered into a new loop spectrum management database, in turn has the potential to be mined, correlated and exploited to provide more optimal performances for individual subscriber loops.

We would be remiss in leaving the subject of single-ended testing without discussing technical hurdles that still need to be overcome. The single-ended testing work is just emerging from research and development laboratories. The results shown here for loop and crosstalk identification are quite impressive, and show the potential for a system that would give operators precise, up-to-date status of their outside plant facilities. Remaining limitations that still need to be overcome, however, include testing through the loss and distortion of the local switch, and the accurate identification of *multiple* crosstalk disturbers.

3.2 Non-intrusive, in-service loop analysis

The process of administering and maintaining the loop plant can be greatly facilitated by the very DSL electronics that are making it possible to support broadband services. Once a DSL is provisioned and operational, much information about the loop channel can be derived from the internals of the DSL adaptive transceivers. Standards for DMT-based ADSL in fact specify Management Information Base (MIB) elements that reflect transmission details of the channel, as shown in Table 3 below.

Upon inspection of Table 3, one can see that these MIBs provide a detailed reflection of the channel, which is closely related to the electrical characteristics of the subscriber loop. This type of information could be stored in a database. In case of service difficulty, the current MIB could be polled and compared to the prior MIB, and any differences will provide insight into the nature of problems on that line. This approach has the advantage of being all-electronic and non-service affecting.

DSL researchers and manufacturers are expanding on this concept to explicitly build lower-layer monitoring and analysis capabilities directly into DSL transceivers. For example, although highly informative the MIBs shown in Table 3 are a *composite* reflection of the channel response and the crosstalk noise. Within the transceiver itself, the crosstalk noise can be easily isolated, thus providing the channel response and noise separately. Going even

further, some are exploring single-ended capabilities that would function even if the link is down, by building test and analysis capabilities right into the front end of the transceivers.[1]

Table 3. Part of DMT Line Code MIB[8]

- adslAturDMTBinBits = $\{a_i\}$
  - number of bits per bin tone downstream (256 tones)
- adslAtucDMTBinBits = $\{b_i\}$
  - number of bits per bin tone upstream (32 tones)
- adslAturDMTBinSNR = $\{SNR_i^r\}$
  - downstream SNR for i^{th} bin tone
- adslAtucDMTBinSNR = $\{SNR_i^c\}$
  - upstream SNR for i^{th} bin tone
- adslAturDMTBinAtn = $\{\alpha_i^r\}$
  - downstream attenuation value for i^{th} bin tone
- adslAtucDMTBinAtn = $\{\alpha_i^c\}$
  - upstream attenuation value for i^{th} bin tone

These non-intrusive approaches are envisioned to be as effective as the CO-based testing described above. They become more relevant as the deployment of DSL matures. Today, with DSL deployment in its infancy, the electronics are simply not in place to provide feedback.

3.3 A Next-generation Broadband Loop OS

We have seen that POTS loop records are available in electronic databases, and new capabilities such as the broadband test head and "smart" DSL electronics will provide additional information on the loop channel and noise. How is all of this information to be exploited?

A new broadband loop OS is needed that will tie together the various sources of loop information, store this information in a database, manage the database and maintain its health, and provide database records to various query processes. Such a system is depicted in Figure 8.

The system needs to be designed to meet the needs of a large operator, where hundreds of thousands to millions of lines of DSL are expected to be provisioned and maintained over the next several years. For example, say the current growth rate of a large operator is 10,000 new DSL provisions a week (half a million lines a year). The successful receipt of 10,000 commitments from subscribers to take up the new service represents the classic output of a sales funnel, where interested customers inquire about price and availability. Typical ratios for sales funnels would say that for every hard sale, there are ten queries. This means that the loop qualification system has to be able to efficiently handle on the order of 100,000 queries a week!

These queries can come from different sources, requiring customized "front ends" to provide data with appropriate format and security. For example, an operator's sales organization can be expected to generate many queries. Competitive Local Exchange Carriers (CLECs) will themselves be marketing and will want to know if individual customers are qualified. Information Service Providers (ISPs) who lease facilities either from the incumbent or competitive local carrier will want to know whether a given potential subscriber can receive service, and at what bit rate. Some operators even provide the general public with access to qualification engines through web interfaces. This is an effective way to reduce the operator burden associated with narrowing the sales funnel; the potential customers self-qualify themselves, and when they are ready to order service the operator becomes more involved.

An important aspect of this architecture is to separate the processing of the different user front ends from the building and maintaining of the underlying database. The database will be built more slowly, for example as nightly results of broadband test head queries are recorded. We discussed how the broadband loop OS must correlate and resolve differences between conflicting loop records. Additionally the system must have knowledge *beyond* the copper loop facilities. For example, in addition to needing a qualified subscriber loop to provide service, electronics need to be available, such as the Digital Subscriber Line Access Multiplexer (DSLAM). Or, the loop may be well qualified based on its make-up, but may already be provisioned with ISDN service or DAML (digital added main line) electronics. Thus the broadband loop OS needs to have access to additional information from other software systems sufficient to form a complete data model of the outside plant. The system may need sub-controllers, to control remote queries and responses of multiple broadband test heads or many DSLAMs across a territory.

The database associated with this next-generation loop OS will require data fields and information significantly beyond current loop records. For example, the identification of the crosstalk disturbers represents new information, not kept today. A proper architecture and database design is needed to make maximum use of existing databases and OSs while ensuring that the new operations architecture is forward-looking, built on a modern software infrastructure, and is scalable.

[1] Note that we otherwise necessarily assume the link is functional enough to allow the DSL transceivers on both ends of the subscriber loop to synchronize. In the case of more severe troubles, this might not be the case, and the information obtainable from the DSL electronics may not be useful.

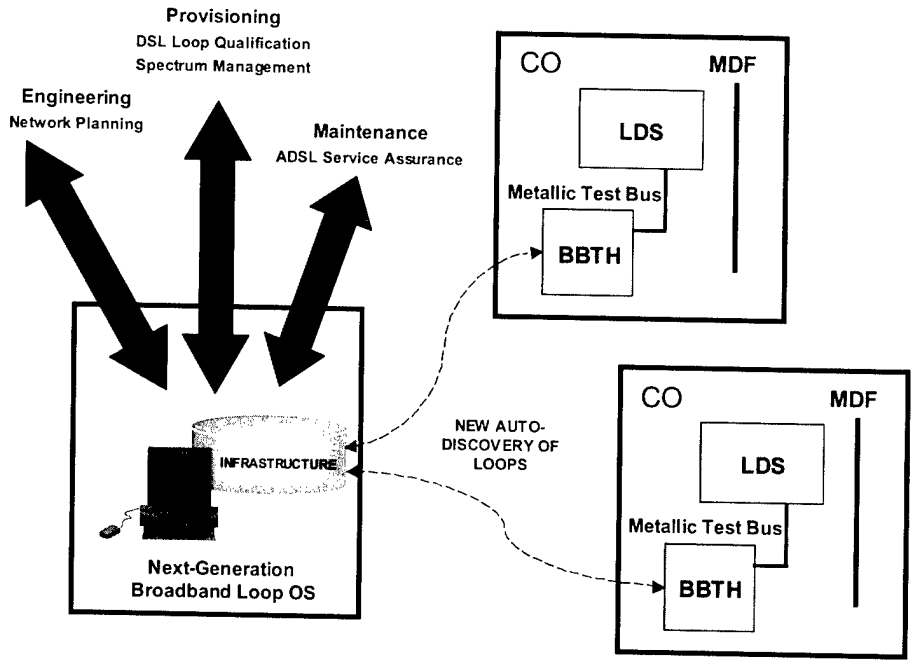


Figure 8. A next-generation broadband loop operations system

4. Conclusions – Evolving a National Resource

We have seen that the copper loop has the potential to support the emerging age of broadband digital connectivity. It is one of several key distribution networks that will propel the Information Age and our national economy. And it will encourage, not hinder, deployment of even more advanced architectures such as fiber in the loop (FITL), by stimulating customer use of broadband connectivity.

It is now clear that telephone operators are in the beginning stages of major deployment of DSL technology. The success of this deployment is critical, if the copper loop plant is to fulfill its important role in this digital revolution. Difficulties in provisioning the technology and maintaining reliable service can threaten the effectiveness of this resource. This comes at a time when competition, unbundling and line sharing complicate the ability of operators to control and monitor their access networks. A comprehensive loop operations support system, based on a next-generation software architecture and receipt of loop data from highly accurate sources, is needed.

Note that the emphasis here is on layers 0 and 1. The authors are well aware that significant work is underway at higher layers to administer and maintain relevant resources (e.g., addresses, paths, packet loss, packet delay). A similar philosophy needs to be extended to the lower layers, where the assets are more physical, e.g., a copper loop. Many successful businesses have analogous needs for managing physical plant, such as fleets of rental cars or inventories of raw materials.

The time to address this need is now. The industry has made tremendous progress in developing digital subscriber line (DSL) technology. DSL has proven to be reliable when properly engineered and installed. Now the industry must capitalize on this technological advance to make sure that general deployment does not get bogged down in issues of provisioning inefficiencies and conflicts due to crosstalk. The low levels of DSL deployment may have masked these issues to date.

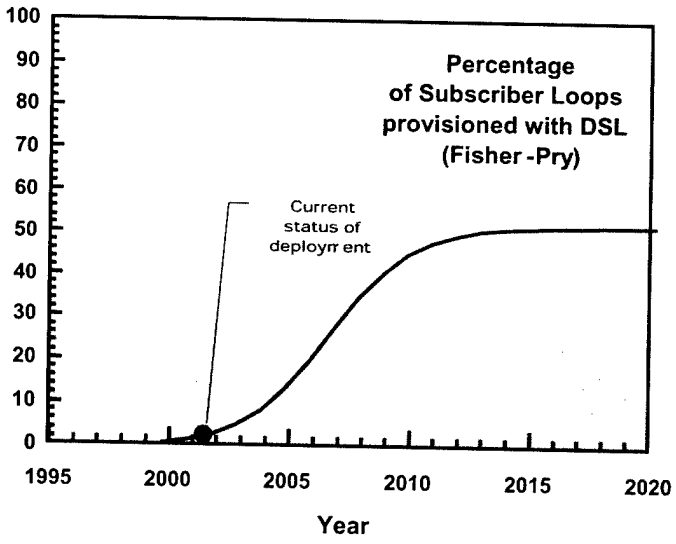


Figure 9. A projection for DSL deployment in the copper loop plant using a conventional Fisher-Pry new technology penetration curve

Most analysts believe DSL deployment will grow rapidly. A conventional Fisher-Pry curve for penetration of new technology is shown in Figure 9. Although there may be much debate about details of this projection, such as the ultimate penetration rate of DSL in the loop plant (assumed here to be 50% of all POTS lines), or how rapidly the deployment will occur, most would not argue that we are on the early portion of the curve and that the curve will ramp-up substantially. It is this steep ramp-up, just ahead of us, which represents a major opportunity for the copper loop plant.

This paper provides a vision for the evolution of the access network in which copper cable will play a critical role for at least the next several decades. If this evolution is properly managed, by applying new technology *and* appropriate operations support capabilities, twisted pair cable may very well prove to be one of the most important "on ramps" to the Information Highway.

5. Acknowledgments

Special thanks to Rob Bond for the FCC data, to Martha Broad for data on wireline and wireless revenues, to Hal Manns for DSL deployment rate data, to Jim Dixon, Stefano Galli and Rob Hausman for the loop make-up identification results, to Ken Kerpez for support on the Telcordia spectral compatibility computer, to Craig Valenti and Ken Kerpez for results on crosstalk identification, and to Craig Valenti for support on ADSL MIBs.

6. References

[1] "Digital Subscriber Line Technology Facilitates a Graceful Transition from Copper to Fiber," D. L. Waring, J. W. Lechleider and T. R. Hsing, IEEE Communications Magazine, Vol. 29, No. 3, March 1991

[2] From 2000 FCC ARMIS Infrastructure Report

[3] From Security and Exchange Commission (SEC) 2000 10-K reports

[4] "The Asymmetrical Digital Subscriber Line (ADSL): A New Transport Technology for Delivering Wideband Capabilities to the Residence," D. L. Waring, Globecom '91 Proceedings, December 2, 1991

[5] IDC, May 2000; "The Need for Speed: Residential High Speed Data Service Market Forecast, 1999-2003

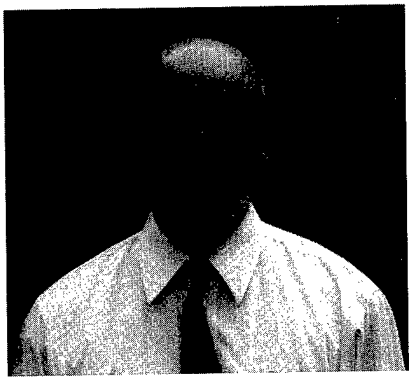
[6] http://net3.argreenhouse.com:8080/dsl-test/index.htm

[7] T1.417-2001, "Spectrum Management for Loop Transmission Systems," January 2001.

[8] ADSL Forum, Working Text WT-036, Revision 2, "DMT Line Code Specific MIB," June 1999



David L. Waring received a Bachelor of Science degree in Electrical Engineering from Drexel University in 1977 and a Master of Science degree in Electrical Engineering from Georgia Tech in 1978. He began his career at Bell Laboratories designing subscriber loop electronics. He moved to Bellcore at its inception in 1984, where he worked on early Metropolitan Area Network field trials and led teams that proposed requirements for HDSL and ADSL. He was project manager of several industry-leading interactive digital video trials. Dave currently leads research into "last mile" broadband local access and customer premises networks. Dave is a Senior Member of the IEEE.



Phiroz Madon received his Bachelors degree in Electrical Engineering from IIT, Bombay in 1977, and his Masters degree in Computer Science from Rutgers University in 1979. He joined Perkin Elmer Data Systems in 1979, where he worked on several systems design and software development projects. In 1985, he joined Bellcore where he was a software development Director on TIRKS, the largest provisioning and configuration management OS in the world. From 1996 to the present, Phiroz has been Senior Scientist in Telcordia Technologies Applied Research organization where he has worked on satellite systems, configuration management and service activation for cable modem systems, and architecture, requirements and software development of service activation, provisioning, and fault management OSs for ADSL. Phiroz has received the Telcordia Software System's Recognition Award for his work on OSMINE, and the Award of Excellence.

From the Physics of Foaming to the Production of High Frequency Cables

Thomas Reiner, Horst Scheid
SIEBE Engineering GmbH
Neustadt/Wied, Germany
+49 2683/3003 0 · siebe@siebe.de

Abstract

Consumer and business desire for high communication increases the market for high frequency cables in computer networks, CATV and GSM-systems. The optimization of electrical and mechanical characteristics of cable insulation by usage of foam techniques requires a perfect understanding of thermodynamical effects and their influence on the production process.

This paper introduces to the physical background of manufacturing foamed cable insulation. Polymer and gas selection is discussed, the technical demands are shown and an explanation of foam growth and stabilization is given.

Using different cable types as example, an efficient way of checking line layout and/or production processes is presented. Therefore, a newly developed software is used, which calculates or simulates thermal and electrical behaviour of the foam with material and processing parameters as input. It is shown that implementing such software into the manufacturing line control gives excellent online quality prediction.

Keywords

foam, RF-cable, high-speed cable, extrusion, blowing agents, gas injection, online control, quality prediction

1. Foaming methods in polymer extrusion

1.1 Chemical blowing agents (CBAs)

These substances are added to the polymer, either as admixture or as powder to mix with the polymer before the extrusion process begins, or it is already contained in the polymer. The amount of the admixed CBAs determines the degree of foaming but also the melt temperature does because the strength of decomposition process depends on the temperature. Organic and anorganic CBAs are used, well known are Azodicarbonic acid diamide and Sodiumbicarbonate. Typical mounts of added substances are between 1% and 5% of the total weight and those mixtures make foaming degrees up to 60 % possible [1].

CBA decomposition may be either endothermic (often producing mostly CO2 while needing energy to react) or exothermic (often producing mostly N2 while setting free energy), which can be measured by DSC methods. In any case, they decompose thermally while giving some chemical by-products that can affect other additives like flame retardants, stabilizers or colorants. By-products act as nucleation particles but can also be a problem for the electrical characteristics, when the polymer is used as insulation layer in cable manufacturing.

The melt temperature and the residence time in the barrel should be chosen so that decomposition rate is well defined and no post foaming effects occur. The decomposition time is a function of particle size because chemical reaction happens on the particle surface. Table 1 shows some typical CBAs with decomposition temperature range and gas yield.

Table. 1. Typical CBAs and some of their properties

Name	Decomposition	Temperature range [°C]	Gas Yield [cm³/g]	Gas
ADC (Azodicarbonic acid diamide)	Exothermic	200-215	150-300	N_2,CO,CO$_2$,NH_3
Sodiumbicarbonate	Endothermic	100-160	140-185	CO_2, H_2O
TSH ((p-Toluenesulfonyl)hydrazide)	Endothermic	110-160	115-140	N_2, H_2O
OBSH ((4,4'-oxybis(benzenesulfonyl)hydrazide)	Endothermic	140-160	120-150	N_2, H_2O
DHT ((2,4,6-Trihydrazino-1,3,5-triazine)	Endothermic	245-285	185-210	N_2, NH_3
TSS ((p-Toluenesulfonyl)semicarbazide)	Endothermic	210-230	120-140	N_2,NH_3,CO,CO_2
DNPT (dinitrosopentamethylenetetramine)	Endothermic	195	190-200	N_2,NH_3,HCHO
BBSH (Benzol-bis-sulfonylhydrazid)	Exothermic	240-250	190-210	N_2
PSCD (Polysulfonylazid)	Exothermic	300-340	80-100	SO_2, CO, CO_2

A problem with CBAs at higher concentrations are deposits on screen and screw, mainly with exothermic powders. This causes from time to time a wash-out with process destabilisation. With CBAs, it is also difficult to foam high temperature polymers like FEP or MFA. In addition, the maximum void ratio is limited to 50-60%. Here, alternatives are physical foam techniques.

1.2 Physical blowing agents

In physical foaming processes liquids or gases are injected into the extruder and dissolve in the plastic material under influence of heat and pressure.

Some important properties of gases used for physical foaming are listed in Table 2 to give a comparison between (H)CFCs, organic and anorganic types.

Table 2. Gases for physical foaming with some relevant properties (n.a. : data not available)

Gas Formula	Tc [°C]	Pc [MPa]	Molar mass [g/mol]	bp [°C, 1013mbar]	Permeation in PE [10^{-12} mol/msPa]	Solubility [x*N_2]
Argon (Ar)	-122	4.91	39.9	-186	220-1100	2
i-Pentane $(CH_3)_2CHCH_2CH_3$	197	3.37	72.2	28.0	n.a.	≈1000
Carbon Dioxide (CO_2)	31	7.38	44.0	-78.4	2900-3800	≈ 10
Nitrogen (N_2)	-147	3.39	28.0	-195.8	30-225	(:=) 1
CFC 11, $CFCl_3$ (Trichlor-fluormethane)	198	4.37	137.4	23.8	n.a.	n.a.
HCFC 22, CHF_2Cl (Chlordifluormethane)	96	4.93	86.5	-40.8	50-60	30
Water (H_2O)	374	22.0	18.0	100.0	n.a.	n.a.
Helium (He)	-268	0.23	4.0	-269.0	1300-2000	0.25

1.2.1 Additive nucleated (heterogeneous) foaming

In most present applications a nucleation substance (sometimes called "kicker") is added to the polymer, in order to start the foaming process. These nucleation substances can work in an active or passive manner. Passive means, that only a matter powder (e. g. Talcum, SiO_2 or TiO_2) is used. Active nucleation substances work equivalently to CBAs, so a small intrinsic foaming ratio (around 5-10%) already exists without adding extra gas to the melt.

1.2.2 Self nucleated (homogeneous) foaming

A relative new kind of foaming procedure needs no nucleation substances. With a characteristic adjustment of production line parameters a fine cell-structured foaming of the melted polymer is obtained. This process is physically described as a self nucleation, that makes an energy transition from a thermodynamic unstable state to a thermodynamic stable region by using the differential energy to create cell sites. A simple self nucleation example is heating up very clean water. Temperature grows up to more than 100°C (at 1013 mbar), resulting in a non-stable state of the liquid. As a little distorsion happens, the water starts boiling while lowering temperature to 100°C.

1.3 Other foaming techniques

Foaming can also be done with adding polymer spheres, which are filled with gas. By heating up, the spheres expand to a predefined size, without chemical decomposition. The additive (called "Expancel" [2]) does not mix with the polymer matrix, so the process has to be selected according to polymer and product demands.

For fluorinated polymers, a method commonly reffered as "free-foaming" is sometimes used. This process produces gases (at excessive temperatures and high shear rates) by thermal decomposition of polymers to create a foam structure. Because of its toxic and hazardous by-products, this method cannot be recommended [3]

2. Description of the foaming process

General requirements to all blowing agents are :

- good solubility (high foaming power)
- rapid diffusibility
- stability and inertness in the applied temperature range
- high evaporation rate of during expansion
- easy handling (no poison, not combustible)
- low electrical attenuation in cable production
- low ODP values (Ozone Deplation Potential bzw. Global Warming Potential according to the agreements of Montreal 1982, Rio de Janeiro 1992 and Kioto 1997).

To understand the foaming process it is helpful to subdivide the total process into single processes and to analyze them :

2.1 Polymer

On principle, almost polymer can be foamed. Criterions for choice are the electrical properties and the rheological characteristics. Considering the molecular structure, foaming poly-crystalline materials is more difficult than amorphous materials like PS. The reason for this fact shows picture 1. For poly-crystalline polymers, the process temperature range is smaller, that means, the production of fine cell-structured foams requires an more exact process control.

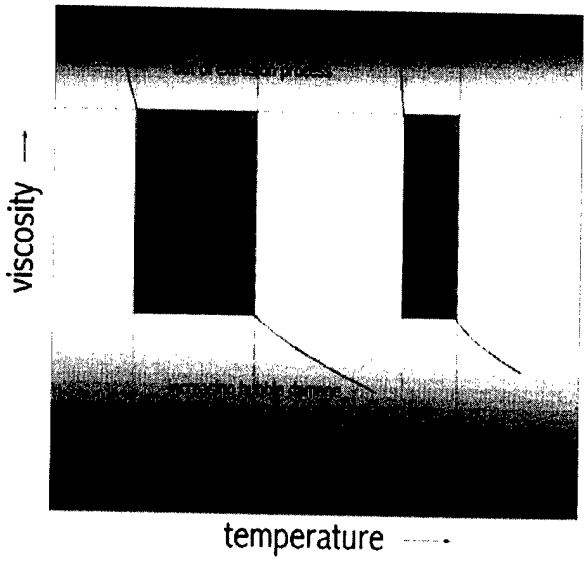


Figure 1. Processing window for foams of amorphous and poly-cristallinic polymer

The relative permittivity is an important electrical parameter. The values are in the range of about 2.1 (PS) to 6.0 (PVDF). Because the communication cable engineering requires smaller values cables are manufactured in bamboo technique or produced with polymer foam. By this means, cables can be produced with relative permittivities to 1.3 (equation 1 for foamed polymer), depending on the void ratio (see picture 2).

$$\varepsilon_{r_r} = \frac{\varepsilon_{r_r}}{2}\left\{\left(1+S_{mf}\cdot\left[\left(1-sg+\frac{sg}{\varepsilon_{r_r}}\right]+\frac{\left(1-S_{mf}\right)}{(1-sg)+\varepsilon_{r_r}\cdot sg}\right\}\right. \quad (1)$$

ε_{rF} : relative permittivity of the polymer foam

ε_{rP} : relative permittivity of the solid polymer

S_{mf} : a foam model factor

sg : the void ratio as volume / $volume_{foam}$

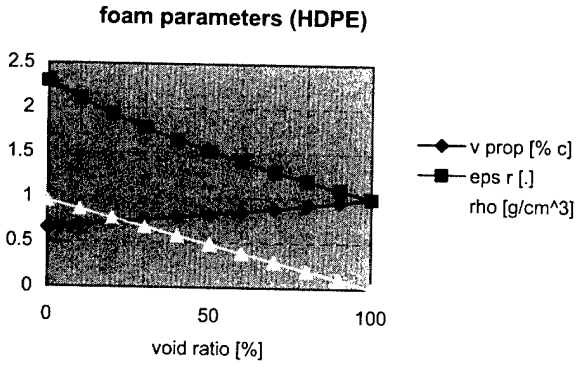


Figure 2. Change of relative permittivity, density and propagation speed, depending on the linear foaming degree (for HD-PE)

The loss factor tan δ consists of a dynamical module (G') and a loss module (G'') of the complex total module

$$|G^*| = \sqrt{G'^2 + G''^2} \quad (2)$$

It gives the relationship between regainable energy and energy dissipation by oscillation processes in alternating electrical fields and should be as small as possible. Typical values are between 10^{-4} for non-polar polymers and 0.06 for polar materials and will be further reduced by the foam (Table 3). The energy loss per second is [3]

$$N = E^2 \cdot 2\pi f \cdot \varepsilon_r \cdot \tan\delta \quad (3)$$

E : field strength [V/cm]

f : frequency of alternating field [Hz]

Because the cable application determines E and f, the term $\varepsilon_r \cdot \tan\delta$ can be chosen depending on the frequency range. For this reason, solid PVC can be used for low-frequency applications without problems (e.g. $f \cdot \varepsilon_r \cdot \tan\delta$= 50 Hz·3.1·0.06 = 9.3), but in high-frequency applications a small loss factor and a foam-reduced small relative permittivity are necessary (e. g. $f \cdot \varepsilon_r \cdot \tan\delta$= 10 MHz·1.4·0.0001 = 1400). However, it must be taken into consideration that ε_r as well as tanδ are depending on temperature and frequency.

Table 3. Some electrical and thermical properties of polymers ([4])

Polymer	ε_r [.]	tanδ [.] at 1MHz	Heat Transfer Capability [W/m·K]	Heat Capacitance [Ws/g·K]
LDPE [illegible]	2.27	$1 \cdot 10^{-4}$	0.22	1.7
W-PVC	3.1	0.06	0.15	0.9
HE1102	2.25	0.005	0.4	1.8
PVDF 11008	5.7	n.a.	0.19	1.4

An additional criterion for the polymer selection are the admixed nucleation substances. If an active nucleation substance is used for direct gassing, the amount is 10 times smaller than by mixes for chemical foaming. Passive kickers are in use much more for high temperature applications. In both of cases about 0.1-0.5 % in weight is sufficient for beginning tests. If the base polymer matrix does not contain nucleation substances, kicker as powder or granules can be added to the polymer before the melt process begins. For high-frequency applications it is important to know, that most additives are polar and reduce electrical quality.

2.2 Gases

According to the above mentioned requirements inert gases have the best properties for physical blowing agents. In most cases nitrogen is in use. The meaning of CFCs decreases in spite of its high solubility because of the ozone layer depletion. Water steam as blowing agents can't be used in the cable manufacturing because of bad electrical properties, Pentan and Butan are combustible. Carbon dioxide is not simple to handle but the

higher solubility in comparison to nitrogen promotes the use of carbon dioxide. Noble gases are inert, but have a lower solubility than N_2 or CO_2 and are more expensive so noble gases are only applied in special applications.

2.3 Foaming agent injection

When using a direct gassed process, gas is injected under high pressure into the barrel, the injection position is typically at 18-20D using a 30-33D screw.

Under typical extrusion conditions (T>120°C, p>10MPa), nearly all inert gases are overcritical (sometimes called "supercritical"). Water, CFCs and organic gases can switch from undercritical to overcritical while changing process temperature or pressure. This phase transition should be avoided because flow measurement at the critical point using parameters like cp or density is not well defined.

Solubility can be described with Henry's law

$$c_A = p_1 S(T) \cdot p_1 S_0 e^{-\frac{\Delta H}{RT}} \qquad (4)$$

c_A : blowing agent mass concentration

p_1 : partial pressure

S_0 : gas solubility coefficient at 0 K

ΔH : molar solubility enthalpy of the gas

R : gas constant (from gas law pV=nRT)

To increase solubility of the blowing agent in the melt, it is necessary to have a minimum barrel pressure at the end of the screw of 100 to 150 bar, a higher pressure level (200-250 bar) gives more spare in process stability and is recommended while using self nucleation techniques.

The polymer system is also influenced by additives such as flame retardants, stabilizers or colorants that can change surface tension and –energy and affects so gas solubility and mixing.

Very important is the dosing and injection equipment, because a constant gas flow is the main condition for stable foam production within small tolerances. (In terms of chemical foaming, this means equipment for exact amount of CBA per mass polymer). This can be demonstrated with a simple calculation : Production of a data cable (inner conductor 0.4 mm, foamed isolation OD 0.9 mm) with a void ratio of 60% at a production speed of 600 m/min needs a gas amount of about 0.12 ln/min (ln is the normalized volume in liters at 1013 mbar and 0°C). Using nitrogen in a direct gassing process at an injection pressure of 300 bar results in a volume of 0.4 cm^3 that has to be dosed linear during one minute. Assuming an equipment with an internal volume of 100 cm^3, in case of a pressure variation of only 1 bar inside the barrel the injection system needs approximately one minute to find a new stable working point ! So the main aspects for the dosing/injection system are

- reproducible gas flow measurement
- constant pressure from the point of flow measurement of 1 bar or better
- short reaction times in case of working point interferences

Siebe developed a new gas injection system, that has in addition a simple user interface, optional automatic parameter changes through the lines process control and a maintenance free gas injector on the barrel that enables foam production as well as solid production without assembling or disassembling any parts.

2.4 Gas dissolution, Mixing

One of the basic steps after the injection is homogenising the gas solution inside the barrel. The efficiency of the mixing process is in first order related to the geometry of the screw and the mixing elements. But it is important not to think in terms of mechanical mixing - the process is not based on a 2-phase (emulsion) system, but on a single-phase (solution) system with a solubility gradient. Too long mixing elements or static mixers with high shear rates can even deteriorate a homogenous solution. Therefore, Siebe designed different screw types with integrated mixing elements to get the fast required dissolution and the constant homogenity needed.

To describe the diffusion process of the blowing agent in the melt, physical gas properties (e.g. solubility, diffusion rate) and extrusion parameters (e.g. melt temperature, barrel residence time) are important, see also Equ. (4)

Diffusion can be described with Fick's law [6]

$$\frac{\partial c_A}{\partial t} = D(T)\frac{\partial^2 c_A}{\partial x^2} \quad D_0 e^{-\frac{E_D}{RT}} \frac{\partial^2 c_A}{\partial x^2} \qquad (5)$$

t : time

D_0 : binary diffusion coefficient of gas in polymer at 0 K

x : diffusion distance

E_D : molar activation energy of the diffusion

Unfortunately, the knowledge about S_0 and D_0 is poor, because permeation measurements give only the product of both. Another problem is, that equations (4) and (5) can only be used, if solubility is low. At high solubility values, the polymer matrix is no longer independent from gas amount and diffusion, even more when gas mixtures are used.

2.5 Melt Transport and Cooling

Once the foaming agent is fully dissolved into the melt, temperature and viscosity must be optimized to have best conditions for cell formation. If temperature is too high and/or viscosity is too low, cell membranes will undergo a minimum thickness and bubbles collapse. With too low temperature and/or too high viscosity, bubbles cannot expand because of a high surface energy (see below).

Using (H)CFCs is normally no problem in respect to saturation level. But with other gases, solubity is much lower and so, melt can be near the critical saturation. This causes an effect that should not be neglected : Even if static system pressure overrides the steam pressure of the blowing agent, local oversaturation and uncontrolled cell growth may happen because of dynamic pressure drops. This is possible on every place, where high shear rates reduce local pressure below critical saturation pressure.

Typical places for high shear rates are all points along the flow channel, where the cross section area has large changes (e.g. screen plate). Siebe makes screw- and flowchannel designs that are highly optimized for reduced differential changes in channel cross section. Measurements have shown that flow field are best with maximum angles below 45°. With higher slopes, uncontrolled local bubbles can establish. These bubbles grow and are transported from a critical size with the melt stream. If in high saturated solutions (for high void applications) pressure loss between screw and die can cause a light oversaturation, bubbles grow and destabilize the melt flow resulting in defects of the finished foam structure.

As the gas acts as a solvent in the polymer, the viscosity of the polymer reduces significantly (not depending on the gas process, e.g. chemical or physical foaming), so the user can either reduce temperature or pressure while maintaining flowability or getting higher throughput at same temperature/pressure level. In most cable extrusion applications, choice is lowering temperature, where up to 10°C per % gas (in weight) is achievable, depending on polymer and gas type.

2.6 Nucleation

As the inner pressure of the dissolved gas gets higher than the outer pressure, the formation of cells can start. Normally, cell growth needs nucleation centres (e.g. solid particles or micro-cracks), where gas molecules collect. Pressure drop can occur as well at the cross head in extrusion as at injection moulding machines by shrinkage or opening the mould.

This pressure drop causes an oversaturation of gas in the melt, that is in physical terms a thermodynamic unstability. As an unstable system tries everytime to stabilize, a certain amount of gas separates from the polymer. The gas molecules collect at certain hot spots, building so called "microbubbles". The physical description of this nucleation and the following step of cell growth is still a point of discussion. So the following short description represents only one possible model :

Nucleation can be separated into homogeneous and heterogeneous. Homogeneous (or spontaneous) nucleation can only happen with extreme oversaturation (see line 3 in picture 3). Heterogeneous nucleation on the other hand needs some boundary surface, where local void creation energy is reduced. This reduction is a function of surface roughness (described with a conicity angle φ) and the angle δ between bubble surface and boundary surface.

The relationship is expressed as [8]

$$\frac{A_{he}}{A_{ho}} = \frac{1}{4}\left[2 \quad 2\cos(\delta \quad \cdot\delta\cos \quad \left(1 \left(c\delta s^2 \right)\varphi \right.\right. \tag{6}$$

A : Number of nucleation sites,

he : heterogeneous,

ho : homogeneous

This formula shows, that heterogeneous cell site creation is much easier then homogeneous. From a view of an operator it means, that the simplest way foam a polymer is to use nucleation particles, that are small in size and have highest possible roughness.

After adding the gas, the melt is oversaturated in terms of normal pressure (picture 3, zone I). Injecting more gas is only possible to a maximum point that depends on material and machine parameters (line 3). When the melt goes through the die, system pressure is lower than the blowing agents steam pressure – a (real) oversaturation occurs and bubbles grow.

At very high gas concentration, nucleation is the main process, at reduced concentration more and more gas separates from the melt by diffusing to existing cells. At the saturation point (line 1) nucleation and diffusion stop. The larger and faster a pressure drop is, the larger the number of cells is, because diffusion time (or diffusion length) is reduced.

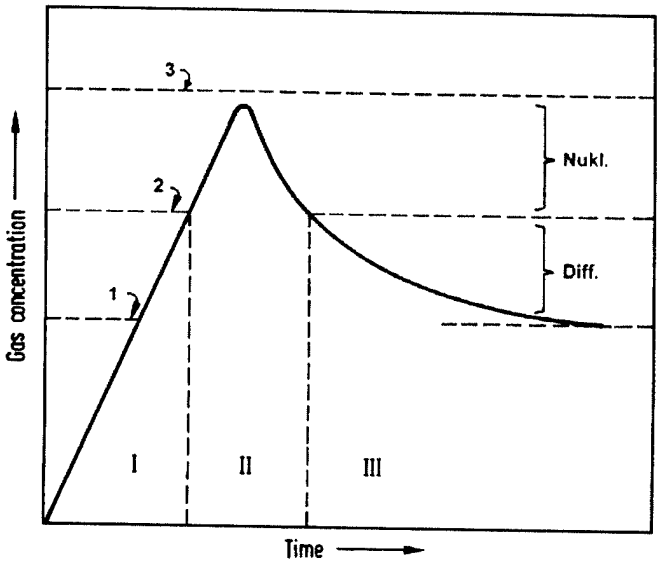


Figure 3. Cell nucleation and growth as a function of gas concentration

2.7 Cell Growth and Stabilization

Existing microbubbles expand, til they reach an equilibrum between pressure inside the cell and steam pressure. In a simplified model of perfect sphercial bubbles, free surface energy ΔF has to be equal to volume creation energy:

$$\Delta F = \sigma dA = pdV$$

$$\Rightarrow \quad 4\pi\sigma d\left(r^2\right. = \frac{4}{3}\pi p d\left(r^3\right) \tag{7}$$

σ : melt surface tension

A,V,r : surface area, volume and radius of the cell

p : inner pressure of cell

Equation (7) shows another fact : at constant surface tension, the inner cell pressure reduces with increasing diameter. If bubbles with very different radius contact, the membrane between can burst and the gas of the small cell (r_a) enters the bigger one (r_b)

$$\Delta p_{a,b} = 3\sigma\left(\frac{1}{r_a} \quad \frac{1}{r_b}\right) \tag{8}$$

Even with stable membrane, there is some diffusion towards the lower pressure. This means, that in high void applications, a too long time between the initial foam growth and lowering temperature below mechanical stability let the foam structure tend to create large cells.

Applications with large cell size and/or low viscosity should also be considered under buoyancy effects [7] :

$$\frac{ds}{dt} = \frac{2r^2 g}{9\eta}(\rho_S - \quad _G) \tag{9}$$

s : way of a cell through the melt

g : gravitational acceleration

ρ_x : density, S : melt, G : gas

η : melt viscosity

By cooling down at the appropriate time, membrane bursts and buoyancy can be suppressed. This time depends on the diffusion speed and can be found in cable or profile extrusion processes as the maximum diameter of the foam cone after the die. The time reduces with cell radius, because diffusion length reduces as well.

If cell size is stabilized below 20 to 50 micrometers, foam is sometimes named "microfoam" or "microcellular foam". Another definition is a minimum number of nucleation centres in the order of 10^{10} per cm^3. The physical background is the same as in larger cell size foam, the difference is the better optical/mechanical structure and the smooth surface feeling because of small cells and typically high nucleation site number.

3 High frequency cable Production

3.1 Plant calculation with CoaxCalc

Regarding to the mentioned facts about physical foaming a complex model for planning a foaming production line has been developed. According to this model numerical calculations by Siebe showed good approximations with real observations. For example, the next lines show a calculation for a coacial cable type RG59.

As base parameters there are the values for cable geometry and the electrical specifications:

Diameter Inner Conductor	: 0.81 mm
Diameter isolation	: 3.65 mm
Capacity	: 54 pF/m
Impedance	: 75 Ω

An HD-PE acts as the base matrix, a inner skin with a wall thickness of 30 µm is assigned for the adhesion. The production speed should be about 100m/min. With these data a lot of production parameters can already be calculated, for example void ratio (around 60%), gas amount (around 0.4 norm liters/min), insulation diameter without gas (around 2.4 mm) or the dimensions of wire guide and die. If the characteristics of the used extruders are known, turn speeds are calculated from mass output (figure 4).

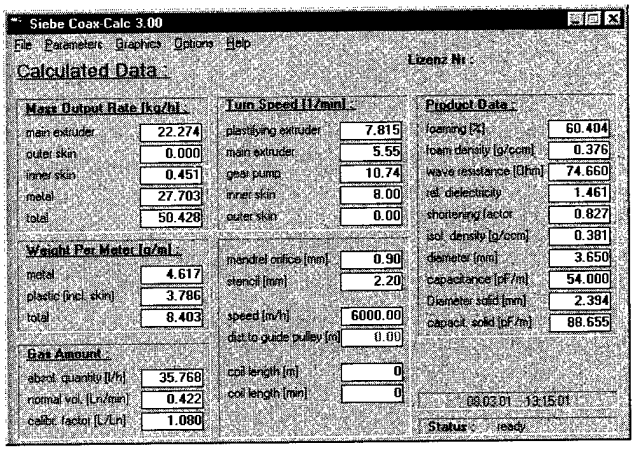


Figure 4. Calculated production data for a RG59 at 100m/min (with a 45mm Siebe gas screw)

If more parameters of the used polymers (like heat capacity, thermal conductivity or damping factors at special frequencies) are available it is possible by choosing the metals for inner and outer conductor to simulate the thermal conditions and to estimate the attenuation of the cable (figure 5 and 6). For example, the thermal simulation figures out minimum lengths for redirecting wheels and for the complete cooling length, the attenuation plot shows the maximum transmitting capability as a function of frequency.

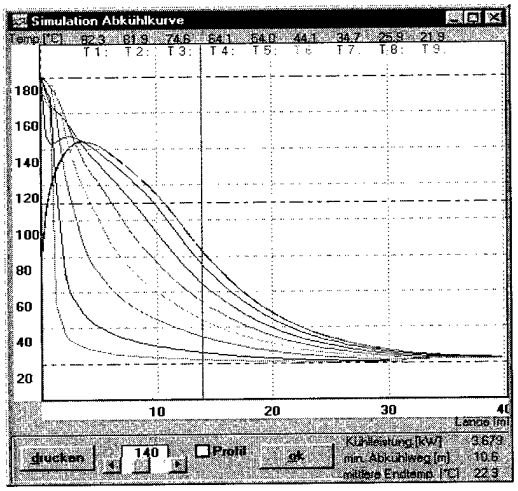


Figure 5. Temperature simulation for laying out the cooling trough for a RG59 (parameters see text)

3.2 Measurement equipment

A foaming line should be equipped with at least one diameter camera (two axes) at the end of the cooling basin and two devices for electrical capacitance (at beginning and end of the cooling basin, called "hot" and "cold" measurement). When inner skin is applied, an additional camera should record the skin wall thickness. Specially for small products spark testers and lump detectors should be installed. In lines for very large cable types (running slowly) as well as very small cable types (running very fast) a measurement device for insulation excentricity is recommended.

Supplementary to the measuring instruments for pressure, temperature and rotational speed in solid production lines there must be measurement devices for gas flow, pressure and temperature in the gas injection area and optionally mass temperature sensors near the cross heads.

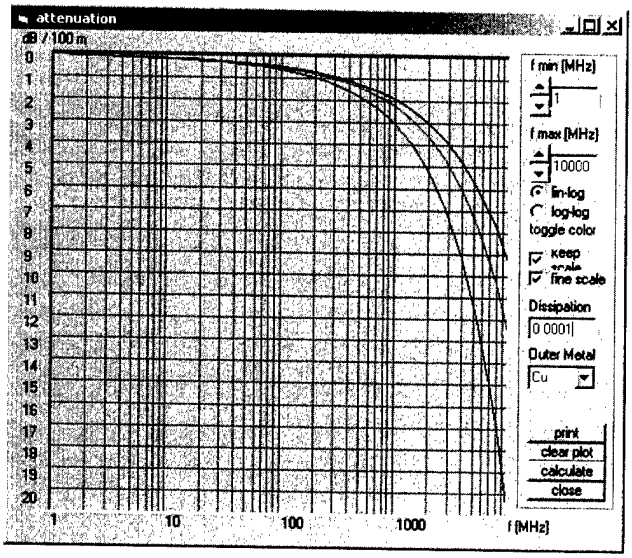


Figure 6. Attenuation plot for different insulation polymers with RG59

There are high standards in the automatic control technology too. A very precise temperature control has to keep the extruder exactly at the setpoint, the accuracy for gas flow control is already mentioned before. Dependent on the line concept the screw turn speed or head pressure must be kept constant by the automatic control system. In the same manner the control for rotational speed must guarantee a no-labile melt flow.

3.3 Online quality management

The manufactures in the cable industry cannot afford that the cable quality is good after the product is totally manufactured in order to improve the foaming production process. For this reason new methods to control the quality during the production are necessary. Here should be shortly presented a solution for this problem.

At many foaming plants the mesurement values for diameter and electrical capacity are recorded by a curve-drawing recorder and than used for the quality control (figure 7). The operator can only see that those measurement values do not exceed the production tolerances.

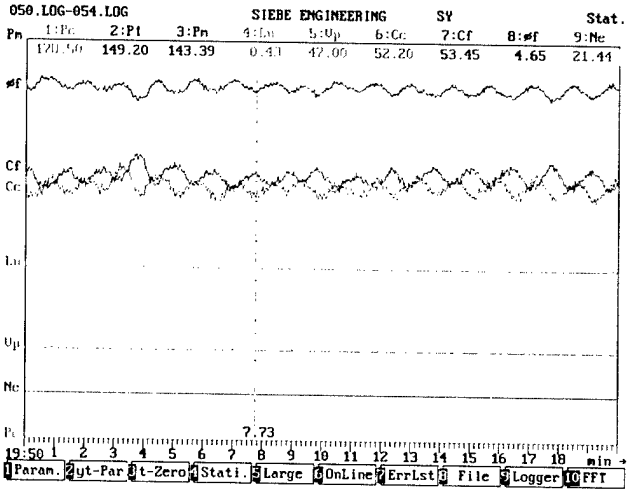


Figure 7. yt-plot of a foaming core production, represented are capacitance (Cc hot capacitance, Cf cold capacitance) and diameter (Øf)

A combined picture with all data in a capacity-diameter-plot with graphs of mass output, foaming degree and gasflow shows much more about critical process parameters because of their special characteristics in the tolerance window. Picture 8 illustrates the same data of the yt-Plot but instabilities in the gas flow control appear on screen because the measurement values accumulate along the ideal position of the mass output and across to the desired value of gas flow.

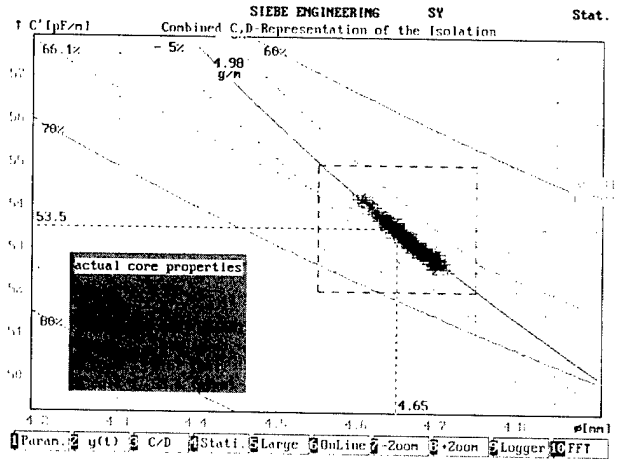


Figure 8. Combined CD-plot, measurement values like ill.. 4.6. line „4.98 g/m" figures constant ideal mass output, in the same manner go desired gas flow (line „0.334 Ln/min") and nominal value for the foaming degree (line „66.1%").

Similar to those preliminary online controls there are concepts like frequency analysis in which time series are transformed in a frequency spectrum (FFT) or cpk-statistics which record the accumulations relative to the production tolerances and are particularly used in the automobile production so.

4. Conclusions

Even if the theoretical description of foam creation is not complete, there is a lot of practical experience, so the application engineer can select the right method and equipment for the foaming process. Chemical foaming is well established since a long time. Since CFCs have to be reduced, research is done to find alternatives in CBAs. Physical foaming with nitrogen and nucleating agents is also well known. A lot of developments made available new processing methods and polymer/gas combinations. Improved foam quality using other gases like CO_2 with simultanously reduced nucleation additives opens new applications to cable insulation production.

Using the above-described results and software, Siebe has developed machinery that combines the advantages of all these processes to one line. Without any changes, the same line permits solid production, chemical foaming and physical foaming in configurations as nitrogen with nucleation additives or carbonic dioxide with self nucleation.

5. References

[1] Helberg,Löw,Riedel, „Chemisches Verschäumen", Kunststoffe 6 (1985)

[2] K. Elfving, "A new grade of expandable microspheres for foaming polypropylene" Blowing agents and foaming processes conference 2001, Frankfurt, paper 5 (2001).

[3] Society of the Plastics Industry, "Safety and Health Hazards Associated with Foaming Fluoropolymers Using Thermal Degradation Processes" http://www.datacable.org/issues/free-foam.htm, (July 2001)

[4] BASF, „Kunststoff im Gespräch", BASF lectures (1981)

[5] Campus 4.0, Plastics Supplier database, http://www.campusplastics.com

[6] Rao, Formeln der Kunststofftechnik, Hanser (1989)

[7] Pahl et al, Praktische Rheologie der Kunststoffe und Elastomere, VDI (1995)

High Grade Copper/Optical Fibre Hybrid Cable Technology for Investment Safe Broadband Access Networks

Paul E. Gregor, Harald Büthe, Peter E. Zamzow
Nexans Deutschland Industries AG & Co Kg
Moenchengladbach, Germany
+49-2166-2229 · paul.gregor@nexans.com

Abstract
In order to take over most modern digital transmission systems, a reliable balanced copper cable design for the transmission of high data rates and broadband signals is necessary for the use in the rapidly growing advanced access networks.

At the same time, the „fibre–to-the-home-philosophy" has to be considered for the cable design. Thus only a combination of copper and fibre stranding elements offers a good compromise between today's system demands and near future challenges in particular with respect to economical aspects.

Generic cabling for the access link section is highly advisable in order to avoid repeated and cost intensive cable network installations, i.e. current and upcoming transmission systems are respected by this new cable plant concept.

Therefore, this paper concentrates on cable delivery lenghts, manufactured regarding the mentioned transmission characteristics.

Due to the strong trend towards high grade digital transmission systems, in particular the development of adequate copper transmission elements for xDSL- circuits are described here.

The performance of the copper cabling for customer application is specified, as there are for long times no international requirements available for the access network cabling using copper technology.

Networks carriers are now about to install copper outdoor cables which guarantee the essential minimum transmission quality, for instance with respect to xDSL-systems.

This paper describes the particular design aspects for outdoor cables, enabling broadband transmission similar to generic cabling for customer premises up to at least 30 MHz.

Transmission parameters like attenuation, crosstalk attenuation, longitudinal conversion loss, return loss, characteristic impedance will be examined.

It will be shown that high grade copper outdoor cables can be used for xDSL-systems if certain design criteria are taken into account.

Finally a few system applications were connected to completed cable links in order to prove correlation between cable properties and channel behavior.

The global concept of copper/hybrid technologies will be described in particular regarding technical and economical aspects.

Keywords
Access network, hybrid cable, copper, optical fibre, xDSL

1. Introduction
The technical development towards higher bandwidths for cabled transmission links is increasing dramatically according to the worldwide market needs. This tendency refers in particular to the components with respect to customer premises on cabling as the final part of a transmission link.

For economical reasons, an access networks is regularly built using copper cable technology. In contradiction, the long distance cable transport networks are completely built with future oriented broadband optical fibre technology.

As shown in figure 1 the so called copper access network bridges the trunk link section and the indoor transmission range normally. Unfortunately this outdoor network section stays still in the infancy. Up to now conventional copper voice frequency cables have been used successfully for lower transmission hierarchies.

In order to meet the requirements for higher bandwidth digital applications however adequate cables and components have to be introduced. Such high grade copper design techniques should consider a minimum frequency range of 30 MHz to meet the demands of current xDSL systems available on market.

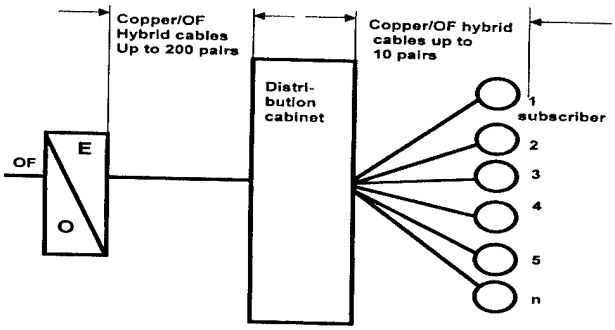


Figure 1. Copper/optical Fibre hybrid concept for an investment save access network

The copper link technology recently offers the most economical solution. But this situation however will change as soon as low cost electronic O/E-devices will be available on a big scale and using pure optical fibre links becomes more economical.

Cable laying cost especially in the access network area are comparatively high and 'fibre-to-the-home-philosophy' will appear in the near future, carriers will be very likely to install both systems at the same time.

2. Solution for investment safe access network

In practice, there are two possible solutions to solve the above described problem, either a custom hybrid copper/optical fibre cable design (model A) or a straight copper cable design with a plastic duct running parallel (model B) which offers the possibility for an immediate or later OF cable installation.

Figure 2 shows a comparison of the estimated installation costs for model A and B. The benefits of the hybrid cable solution are quite obvious. Costs to be considered for a copper/OF-hybrid installation are just slightly above the a plain copper cable installation and are in the range of roughly about half of an installation of two self contained optical and copper cables running parallel.

In addition the special designed copper elements of the custom hybrid solution offer immediate access to high bandwidth operation.

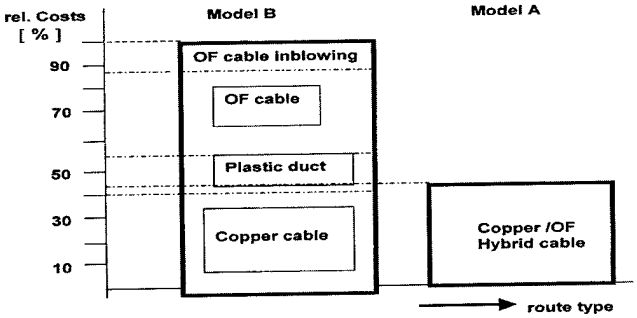


Figure 2. Relative costs of two different cabling models

3. Design criteria for copper/optical fibre hybrid cables

3.1 Core make up and sheath design

Solid copper conductors with diameter of 0,8 mm are insulated with foam skin polyethylene of high grade materials and with highest possible concentricity and homogeneity. These insulated conductors are twisted together to form star quads in a geometrical stable construction with high symmetry. In order to maintain the high quad symmetry special fixing threads are applied helical around the quads.

The quad elements and multiple optical fibre tubes in loose buffer design are stranded together in concentric layers in order to build up the cable core.

The interstices of the cable core are filled with a special compound to achieve reliable longitudinal watertightness. This special compound used has a particular low dielectric pemittivity of 1.6 instead of 2.3 typical for conventional materials.

Different counts of copper stranding elements and multiple fibre tubes have been stranded together based upon users demands. Standard configurations consist of 3 to 4 star quads with 1 to 2 OF tubes containing 6 or 12 singlemode fibres according ITU G652. Special multimode fibres capable of higher data rates and link distances particular for GBit-Ethernet systems are available as an option. In order to meet international provisions regarding fibre- to- the- home performance, 24 fibres can be incorporated.

Figure 3 shows a typical hybrid cable design of type designation: A-02YSOF(L)2Y 8x2x0,8 STVII+6E9/125 0,36 F3,5.

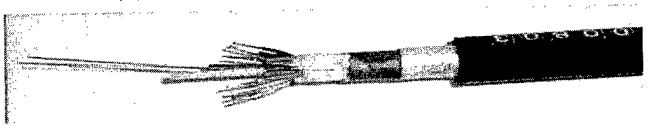


Figure 3. Typical copper/optical fibre cable design consisting of a 4 star quads and 6 SMF

For indoor use, a moisture barrier sheath consisting of an aluminum tape applied longitudinally and a flame retardant halogen free plastic compound have been produced in lower quantities. Swellable threads and tapes are used instead of jelly compound in case that the cables extend into buildings.

4. Transmission characteristics of cable delivery lengths

4.1 DC an VF characteristics

The tests have been carried out on delivery lengths between 100m and 1000m at a temperature of 20°C and at a frequency of 800 Hz employing the MEA/KP5 automatic testing equipment. The results are shown in table 1 and compared to the requirements of specification IEC/PAS 62255-1 Edition 1.0 "Multipair cables used in high bit rate digital access telecommunication networks- Part 1: Outdoor cables"

Table 1. DC an VF properties of copper/OF-delivery lengths

Characteristic @ 20°C	IEC/PAS62255 and customer demands	test result	IEC
DC resistance	≤ 73.2 Ω/Km	≤ 70.0 Ω/Km	189-1 clause 5.1
DC insulation resistance @ 100V, 60 sec.	≥ 1.5 GΩxkm	≥ 10 GΩxkm	
DC resistance unbalance	≤ 3 %	≤ 0.3 %	189-1 clause 5.3.
Mutual capacitance @ 800 Hz	≤ 50 nF/km	≤ 45.4 nF/km	61156-1 clause 3.2.5
Capacitance unbalance quad/quad @ 800 Hz	≤ 440 pF/km	≤ 170 pF/km	61156-1 clause 3.2.6
Capacitance unbalance to earth @ 800 Hz	≤ 1400 pF/km	≤ 530 pF/km	
Dielectric strength cond ./cond cond./screen	500 V, 1 min 2000 V, 1 min	passed passed	61156-1 clause 3.2.3

4.2 High frequency characteristics

4.2.1 Attenuation

The following attenuation results have been collected within a frequency range of 1 MHz and 30 MHz using an automatic driven network analyzer of type HP 4396 A according IEC 61156-1 clause 3.3.2 test method.

A high number of 1200 frequency points have been used in order to detect undesired attenuation peaks.

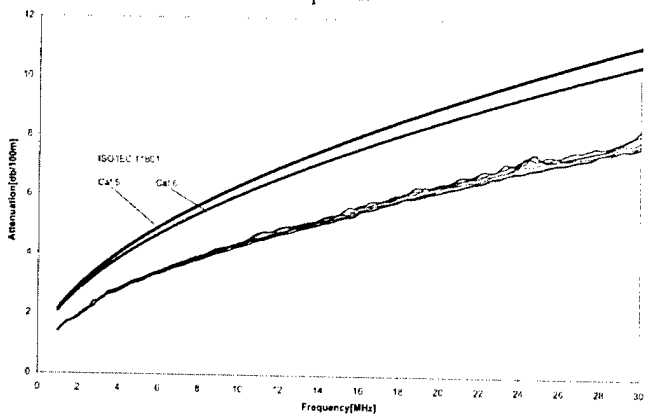


Figure 4. Attenuation level of copper/OF hybrid delivery length

As the IEC-specification does not specify attenuation limits up to now, the international limits of ISO/IEC 11801 have been taken into account as a qualification criteria. As can be seen from figure 4., the recorded values are sufficiently well below the international level and the obtained values almost follow the square root law, as expected.

4.2.2 Longitudinal conversion loss (LCL)

The measurements have been performed according IEC 61156-1 clause 3.3.3 test method within a frequency range from 1 MHz to 30 MHz. The measured values plots are shown in figure 5.

The obtained LCL-level meets the IEC/PAS 62255-1 limit of minimum 40 dB at 1 MHz and proves the high homogeneity of this new access network cable design.

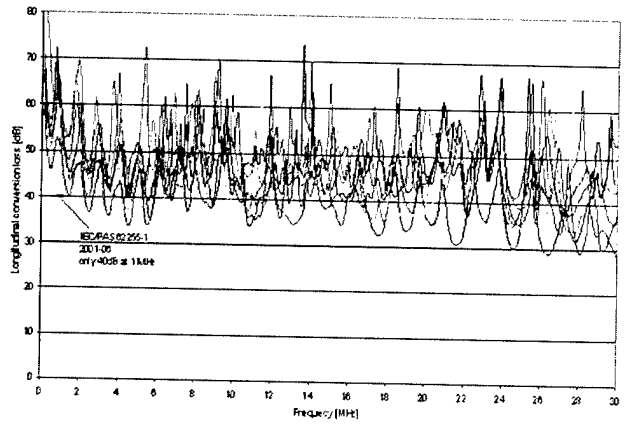


Figure 5. Longitudinal conversion loss of hybrid access network cables

4.2.3 Velocity of propagation

The velocity of propagation has been measured according the test procedure given by IEC 61156-1 clause 3.3.1 concerning a frequency distance between 1MHz and 30 MHz.

As shown in figure 6 the velocity of propagation has been found well above the specified value of at least 60 % at 1 MHz in accordance with IEC/PAS 62255-1..

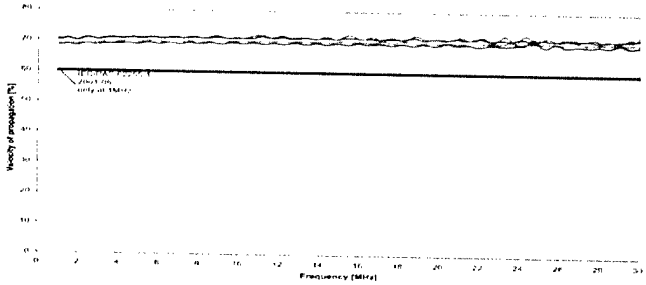


Figure 6. Velocity of propagation of hybrid cables

4.2.4 Near end crosstalk attenuation (NEXT)

The tests have been performed from both sides of the cable within a frequency range from 1 MHz to 30 MHz according IEC 61156-1 clause 3.3.4. Regarding the strong frequency dependency of NEXT a high number of testing points (> 1200) were applied over the selected range. All possible combinations between neighbor quads were measured. The pairs not under test were terminated with a load of the nominal characteristic impedance.

Figure 7 shows the measured NEXT plots in relationship to the requirements of IEC/PAS 62255-1 which are met with remarkable head room.

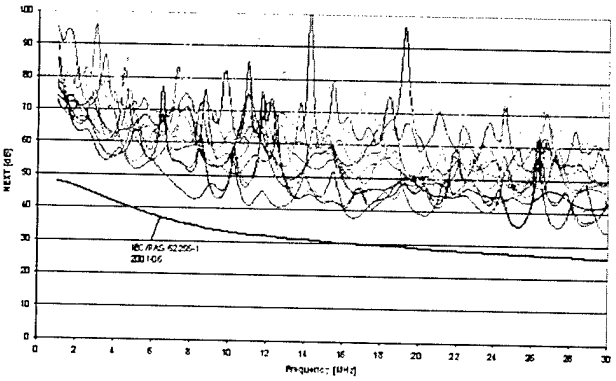


Figure 7. Near end crosstalk attenuation of neighbor quads of hybrid cables

4.2.5 Equal level far end crosstalk attenuation (ELFEXT)

The examinations have been carried within a frequency range from 1MHz to 30 MHz considering the conditions of IEC 61156-1 clause 3.3.5.

Figure 8 shows the plots of all possible combinations and the comparison with the requirements of IEC/PAS 62255-1 again proves the high quality of the stranding element.

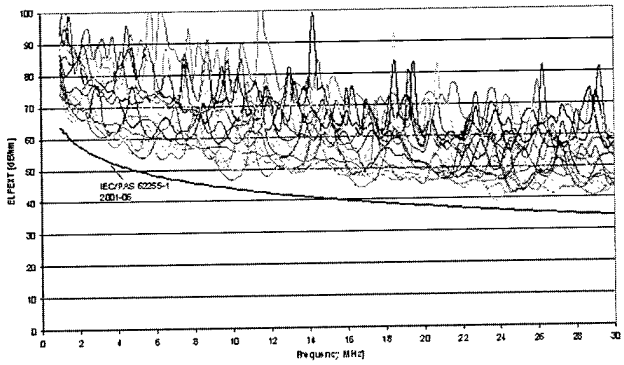


Figure 8. Equal level far end crosstalk attenuation of hybrid cables

4.2.6 Power sum near end crosstalk (PSNEXT)

The results were calculated from the measured value of clause 4.2.4 according the test procedure IEC 61156-1 clause3.3.4.

Figure 9 shows the recorded curves and obviously all measured values meet the specified limit given by IEC/PAS 62255-1.

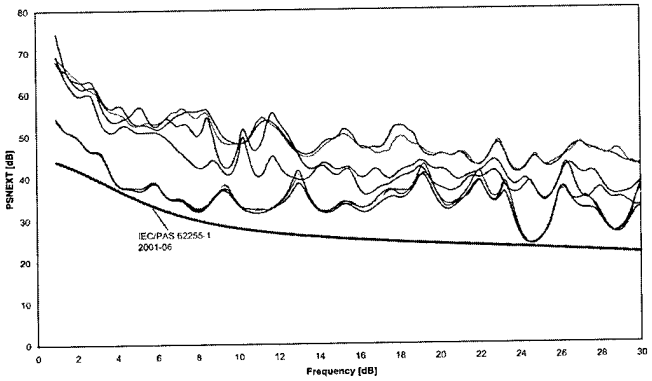


Figure 9. PSNEXT values of hybrid cables

4.2.7 Power sum equal level far end crosstalk (PSELFEXT)

The results of PSELFEXT were calculated from the results of clause 4.2.5 according to IEC 61156-1 clause 3.3.5.

Figure 10 gives the graphical plots in relationship to the requirements given by IEC/PAS 62255-1. A remarkable high quality level has been achieved.

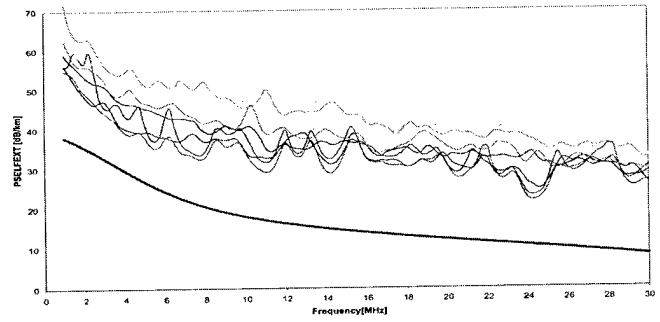


Figure 10. PSELFEXT values of hybrid cables

4.2.8 Characteristic impedance

Examinations have been made in the frequency range from 1 MHz to 30 MHz employing the open/short test method according IEC 61156_1 clause 3.3.6

Figure 11 give the plots of the typical values and the measured values of characteristic impedance meet the requirements of IEC/PAS62255-1

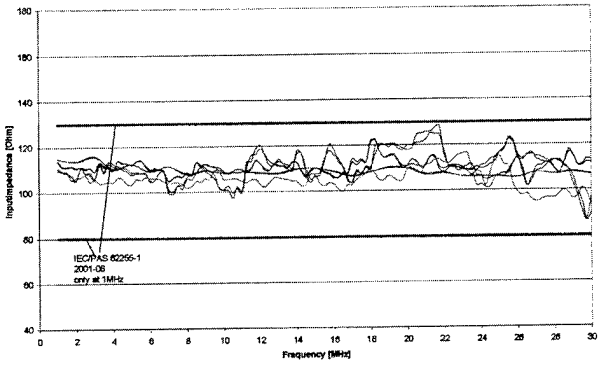


Figure 11. CHI of hybrid cables

5. Maximum possible channel distance

In order to calculate the maximum line spacing the attenuation and near end crosstalk attenuation of delivery length are taken into account. The theoretical results shall be compared to the achieved practical channel distances.

$$L\,max = \frac{NEXT - 0{,}0016\,\sigma 2 - S/N - 20\log N}{a} \quad [km]$$

NEXT= Near End Cross Talk attenuation
σ = Standard deviation respecting NEXT
S/N = Signal to Noise ratio
N = Number of systems operating simultaneously

6. Examination on cable links

These examinations have been performed in order to verify a total link, connecting technique included. It was shown that a total link configuration could be built without unallowed degradation of electrical properties, provided the work is done with certain accuracy and workmanlike.

The cables, 1000 m in length each, were connected together as shown in figure 12.

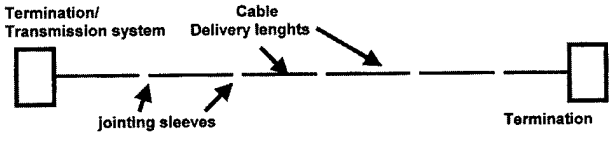


Figure 12. Configuration of cable link in principle

6.1 Technology of jointing sleeves

Connections of quads have been executed conventionally by twisting and soldering of the conductors and trying to maintain the important quad configuration as far as possible.

6.2 Transmission behavior of the cable link

In order to verify the cabling regarding accurate mounting of jointing sleeves the line properties attenuation and NEXT have been tested:

6.2.1 Attenuation

This measurement was performed with a Wandel & Goltermann PSS-19 transmitter and a SPM-19 receiver connected to the link consisting of 8 delivery lengths and a total length of 7763,19m.

Figure 13 shows the attenuation plot for the complete link up to 1,5 MHz. The curve exhibits a favorable smooth performance without undesired peaks.

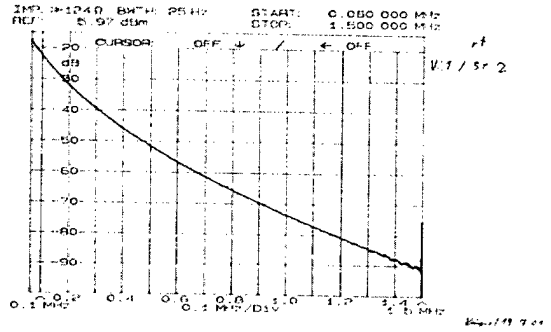


Figure 13. Attenuation of total cable link consisting of connected delivery lenghts

6.2.2 Near end crosstalk attenuation

The NEXT measurements was done with a HP network analyser type 8753C and a HP85046 A S-parameter test set.

The obtained results for the attenuation and NEXT regarding the HDSL frequency 430 kHz are given in table 2:

Table 2. Calculated link distance for a HDSL-System

Line characteristic	Result
Attenuation @ 430 kHz	≤ 64.9 dB/km
NEXT @ 430 kHz	≥ 72.3 dB
Link distance	8.3 km

7. Channel Operation using different transmission applications

7.1 Structure of channel configuration

Various transmission systems have been connected to the above described cable link in order to determine the overall capability of the channel configuration to be used for future access network applications.

As a first step a HDSL-system WWG EST-120 was use consisting of a G 703 interface with HDB3 line coding (Data rate: 2,048 Mbit/s;10 kHz – 430 kHz) together with a E1-service tester was employed in order to detect the correlation between BER and the maximum possible length of a link. The channel structure is shown in figure 14.

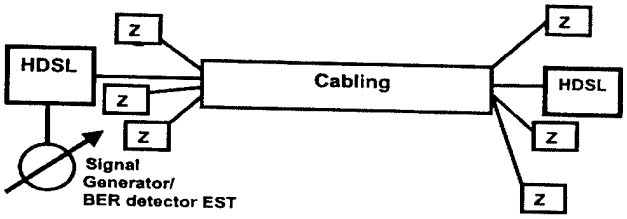


Figure 14. Channel structure for HDSL-transmission system

7.2 Correlation between BER and channel length

The obtained results is shown in figure 15. As the main result of theses measurements, the maximum possible channel length can be stated as 7,5 km, which again proves the high transmission quality of the stranding elements. It must be stated that the measured values are very close the theoretical calculation.

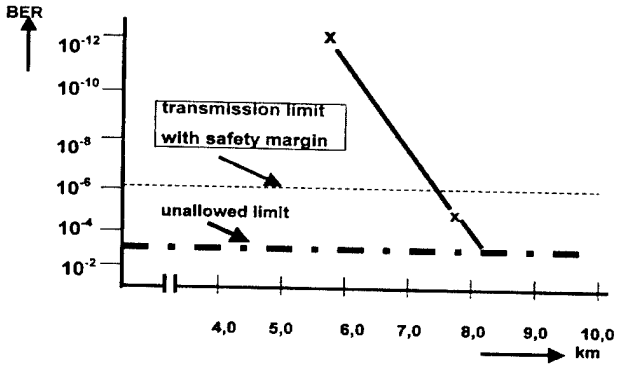


Figure 15. Correlation between BER and channel lenght

7.3 Channel length in correlation to the Ethernet transmission system

A further investigation was made with the above described cabling using 10BaseT-Ethernet systems in relationship to the link distance. Figure 16 shows the determined channel distances in dependence of the to data rate mode.

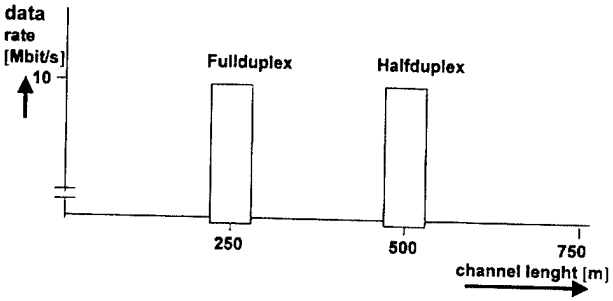


Figure 16. Achieved channel lenghts for 10Base-T-Systems

Since the average access network length is approximately 300m for the final part of the link, this result offers also a very reliable cable and system solution for advanced network technologies.

8. Conclusion

Copper/OF-hybrid cables constitute a highly economical cable solution for the passive cable plant to be installed as an investment safe access network component.

Due to the variable bandwidth and data rate behavior, this cable concept offers a guarantied planning insurance for at least a decade. It is an application independent solution.

The copper quads present remarkable low cost stranding elements for the up-to-date market demands while the integrated optical fibres are ready to immediately go into operation when required.

The described copper/optical hybrid cable design contains star quads which are able to serve as advanced transmission systems demanded by high grade transmission characteristics.

Particular xDSL-technologies shall be supported by this special quad technique in order to realize comparable long channel distances.

The cable design enables installations for outdoor and indoor routing with a sheath construction consisting of a reliable LAP moisture barrier with either regular PE or a flame retardant halogen free jacket compound for in house use.

Most recent jointing sleeves and termination boxes can be applied to the hybrid cable links enabling a rapid standard installation of the hybrid cables.

9. Acknowledgement

The authors would like to express their special thanks to the various members of the team for their support, in particular to Mr. Dietmar Seidel of Nexans Berlin, Mr. Wolfgang Beier Nexans Mönchengladbach, Mr. Rainer Klingner of Company Kellner Telecom Kesselsdorf.

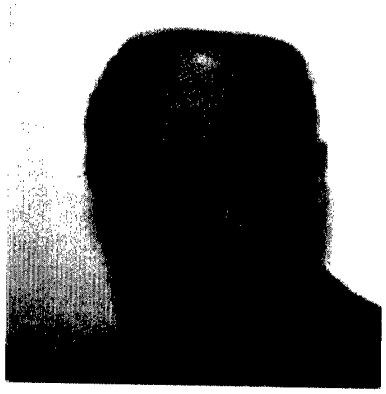
10. References

1. IEC/PAS 62255-1 Multipair cables used in high bit rate digital access telecommunication networks – Part 1:Outdoor cables
2. IEC 60793-1 Optical fibres, Part 1: Generic Specification
3. IEC 60794-1 Optical fibre cables, Part 1: Generic Specification
3. Paul Gregor, Georg Hög, Waldemar Gläsel. Helmut Haag
4. Optical fibre/copper conductor composite LAN cable for Mining application International Wire and Cable Symposium 1985
4. Gregor, Tholen, Knop

   Data cables and system components for the use up to 100 (300)MHz“ International Wire and Cable Symposium Proceedings 1994
5. K. Lehan, G.Hög, P.E.Gregor, P.E. Zamzow, H.G. Haag „Optical fibre/copper hybrid data cable network for LAN-application in large administration buildings

   EFOC LAN, Paris 1992

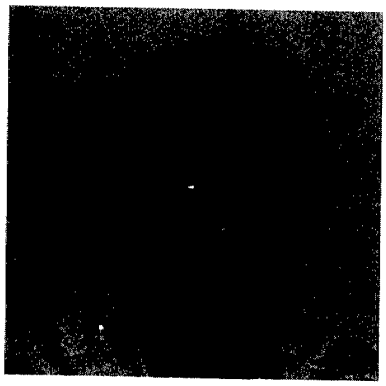
11. Authors



Paul E. Gregor
Nexans Deutschland AG
Mönchengladbach,
Germany

Paul.Gregor@nexans.com

Paul E. Gregor was born in 1941. After study at Ingenieuerschule Duisburg, Germany, he joined AEG Kabel, today Nexans Deutschland Industries, where he had been involved in development projects for special symmetrical and coaxial telecommunication cables. About for a decade he took over the responsibility as head of design department for cable design technology. At present he is responsible for the technical sales department and is acting as a member in national and international standardisation bodies, like DKE resp. ISO/IEC.



Harald Büthe
Nexans Deutschland AG
Mönchengladbach,
Germany

Harald.Buethe@nexans.com

Harald Büthe was born in 1953. He graduated as a Dipl.-Ing. (FH) from FH-Niederrhein Krefeld in 1975 and finished his mathematics and physics studies at Düsseldorf University in 1982 with state examination. He joined AEG Kabel in 1986 as an engineer for optical fibre measurement technique. He was engaged in several different product lines, i.e. OF, OF-cable, CATV-cable and telecommunication cable. His present position with Nexans is product development.



Peter E. Zamzow
Nexans Deutschland AG
Mönchengladbach,
Germany

Peter.Zamzow@nexans.com

Peter E. Zamzow (61) is director of the Nexans company. He completed his post-graduate studies in telecommunications in Munich and Graz as Dipl-Ing. He joined AEG Kabel in 1970 and was engaged in development and production of telecommunication cables. In 1980 he became head of AEG Kabel fibre optic division and in 1982 he was nominated senior engineer and 1995 nominated technical director. From 1992 he was plant manager of the Alcatel Kabel Optical Fibre Cable Plant Mönchengladbach. Since July 1994 he was senior manager of the German CATV- product line. Since 1998 he was responsible for Sales and Marketing in Division Licences and Production Lines world-wide.
Since beginning of 2001 he is head of Research and Development of Nexans Germany.

Alternate Solutions for Cabling Systems in Both Residential and Business Environments

O. Bouffant, E. Cressan, P. Guillas, H. Le Cozic, P. Mercier, D. Le Bras
FRANCE TELECOM - BD/FTR&D/RTA/LLI
Technopole Anticipa
2, avenue Pierre Marzin
22307 LANNION Cedex
France

Abstract

This paper describes the cabling systems defined by France Telecom for offering the high bit rate services such as xDSL (Digital Subscriber Line) in residential and professional environments.

The first part of the document describes the cabling offers proposed to residential and professional customers, ranging from the simplest dedicated for customers wishing the analog phone service only to a cabling offer with optical fibers.
Solutions for ADSL "distributed filters" or "master filter" are proposed as well as solutions for the ISDN. New technologies (such as HomePNA, Powerline or radio) are introduced to enable several terminals in the house to be used, with a simple initial installation. Some more comfortable offers are described to realize a RAN (Residential Area Network) or a LAN (Local Area Network).

The second part of the paper deals with the implementation of these various cabling systems offers in a laboratory and in the field. These experiments can be technical but also commercial.
Some of these experiments are performed in our laboratories or on the test platforms at the Lannion site and others are commercially deployed on customer sites, in the Paris region for example.

Keywords

Customer premises network; home network; cabling system; copper cable; optical cable; xDSL systems;

1. Introduction

France Télécom is currently deploying ADSL technology in several towns in France and testing other technologies (like VDSL) in field trials.
These techniques allow high bit rates (from 500 kbit/s for residential to several Mbit/s for business) for the delivery of broadband services such as high speed Internet access, networking, etc.
The aim of telecommunications operators is to distribute all these services to the Customer Premises Network (CPN), to the home of the residential customer as well as the Local Area Network (LAN) of the business customer.
These cabling system offers in association with service offers are described, as well as the field trials carried out by France Télécom using these cabling system solutions.

2. Cabling system offers

2.1. Introduction

The high bit rate access network is now a reality for residential customers. The most popular networks are cable Television (CATV), xDSL (with ADSL as the most well known) and wireless local loop (WLL).
Concerning ADSL deployment, there are currently about 7.5 million customers, with an increase of 34% since the end of the year 2000 (from TeleChoice for the DSL forum).

The market is becoming very significant and the Residential Area Network (RAN, with reference to the Local Area Network LAN for the business customers) is now a reality within the homes of our customers.
Telcos are building cabling system offers combined with service offers in order to provide their customers with outstanding services in their Residential Area Network.
The killer applications in this field are networked games, music, video, and obviously voice and home automation.

Due to the explosion of Internet services, cabling systems for business buildings must support an increasingly high bit rate. In this context, xDSL techniques have the advantage of meeting demand without any major investment by using the existing network, which generally comprises category 5 copper materials. Many solutions can be deployed to respond to the increase in bit rate: copper cabling systems with category 6 or 7 materials, empty microtubes which can be filled with fibers on request, optical cabling systems with the possibility of using converters at the ends to make the most of existing copper-based equipment.

2.2. "Bottom-of-the-range" cabling system

The cabling system in figure 1 is the minimum technical cabling that is proposed to the customers.
It is defined for customers who initially require POTS services only.

The proposed cabling has a bus or Y (2 branches) topology, with a Network Interface Device (NID) which is the delivery point for France Télécom services. This architecture has 2 or 3 connectors called "T outlets" and a 4-pair cable of category 5 performance.

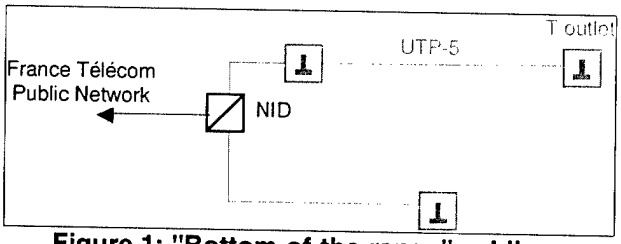


Figure 1: "Bottom-of-the-range" cabling

This cabling system is designed for one or two phone lines and is compatible with ISDN and ADSL "distributed filters" solutions (see figure 2). For ISDN, the services are only available on the Network Termination (NT).

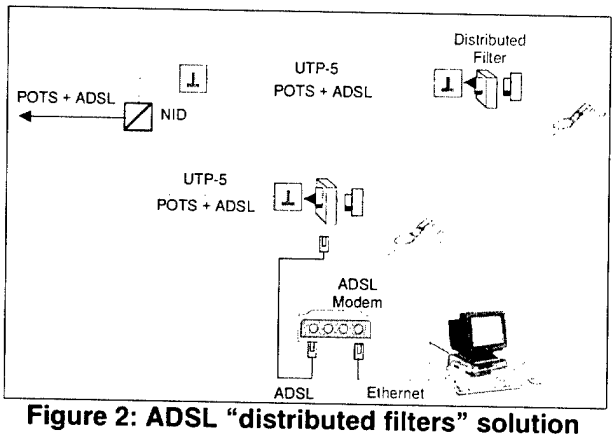


Figure 2: ADSL "distributed filters" solution

With the "distributed filters" solution, no changes to the existing Customer Premises Network (CPN) that comprises "bottom-of-the-range" cabling are required.
Both ADSL and POTS signals are transmitted on the same pair inside the rooms on all outlets. The low-pass filters (LPF) are distributed on the "T" outlets connected to analog phones. On the outlet dedicated to the ADSL signal, the ADSL modem is connected via an adapter. The PC terminal is connected to its ATM or Ethernet interface.

2.3. "Multiservices" cabling system

This cabling system (see figure 3) is defined for customers requiring POTS, ISDN and/or ADSL services.
This "multiservices" cabling has the same topology as "bottom-of-the-range" cabling with a NID associated with a category 5 repartition box, category 5 cable and category 5 RJ45 outlets. This is a class D CPN (according to the IS 11801 standard) allowing the use of frequencies up to 100 MHz.

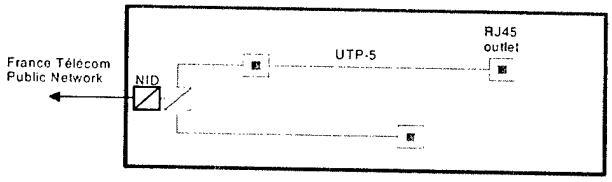


Figure 3: "multiservices" cabling

This cabling system is designed for one or two phone lines and is compatible with ISDN and ADSL "master filter" solutions (see figure 4). For the latter solution, the service is available on all outlets but not simultaneously.
This "multiservices" cabling can use "T outlets" but in this case, it is not a class D cabling system.

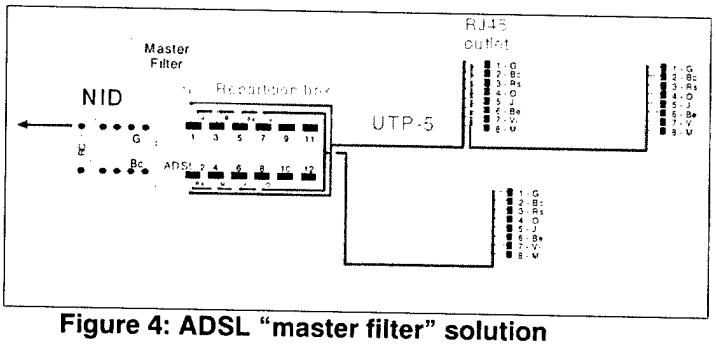


Figure 4: ADSL "master filter" solution

The filter is placed at the input to the NID point (end of public network). The POTS signal is re-injected on pair no.1 of all the CPN branches. The ADSL signal is injected on a free pair. There is a modification of the existing CPN that features "multiservices" cabling.

2.4. "Multi-terminals" options

The two previous cases allow the use of only one PC terminal. The aim now is to give the customer the possibility of installing a RAN (Residential Area Network) for use with several PC terminals and for networking.
Several solutions exist and are described in the following options.
The technologies used are "HomePNA", "Powerline or PLT (Power Line Telecommunications)" and "wireless radio" solutions.
These technologies, similar to the LAN ones, enable resources to be shared on the RAN and infrastructure costs to be reduced.

2.4.1. "Privatize HomePNA" option (figure 5)

The principle is that one pair is re-used on the phone cable to connect 2 PC terminals equipped with Home PNA cards to share high bit rate Internet access such as ADSL for example (see figure 5).
The HomePNA signals are compatible with POTS and ADSL signals.

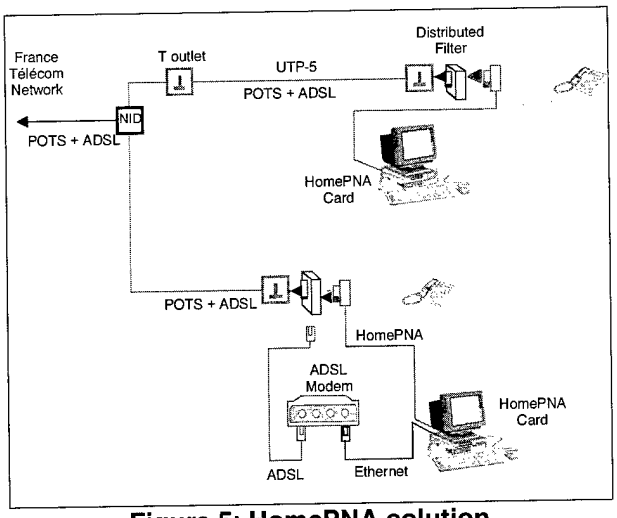


Figure 5: HomePNA solution

The frequency band used for HomePNA is between 1 MHz and 10 MHz, above the ADSL band. The bit rate is about 10 Mbit/s with a future evolution up to 32 Mbit/s with a range of 150 meters to 500 meters between two HomePNA cards.

2.4.2. "PLT" option (figure 6)

The principle of "Powerline" technology[1] is also to share a high bit rate network link between several home devices connected on the same low voltage network via a specific "Powerline" interface (see figure 6).
Several modulations are used by different industrials using a frequency band from 1.6 MHz to 30 MHz.
The bit rates range from 100 kbit/s up to few Mbit/s.

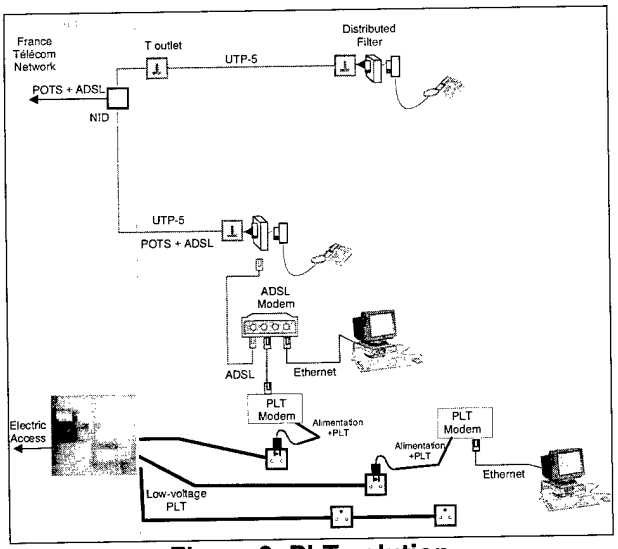


Figure 6: PLT solution

PLT architecture is used behind a high bit rate access such as ADSL. On an Ethernet interface available on the ADSL modem, the connection is made on the low voltage network via the PLT modem. The other terminal is then connected with a PLT modem.

2.4.3. "Wireless Radio" option (figure 7)

The principle of the "Wireless radio" technology is also to share a high bit rate network link between several home devices connected on the RAN.
France Télécom now recognizes three wireless interface standards: HomeRF , IEEE802.11b and Bluetooth.
Bit rates and ranges are dependent on the technology used:

- HomeRF: bit rate from 600 kbit/s to 1.6 Mbit/s on 45 meters maximum,
- IEEE802.11b (Wireless Ethernet): from 1 to 11 Mbit/s on 25 to 100 meters maximum,
- Bluetooth: 800 kbit/s maximum on 5 to 15 meters.

For the "HomeRF" solution, with Internet access sharing software, the PC terminal with the physical connection to Internet (e.g. ADSL modem) uses server software to manage access sharing between the wireless "customers".
For "Bluetooth", each PC terminal connected to the Bluetooth network can be the master. The first terminal connected assumes this role.
For the "IEEE802.11b" wireless Ethernet solution, the wireless access point (radio modem) connected to the ADSL modem manages all the network accesses between terminals equipped with IEEE802.11b cards.

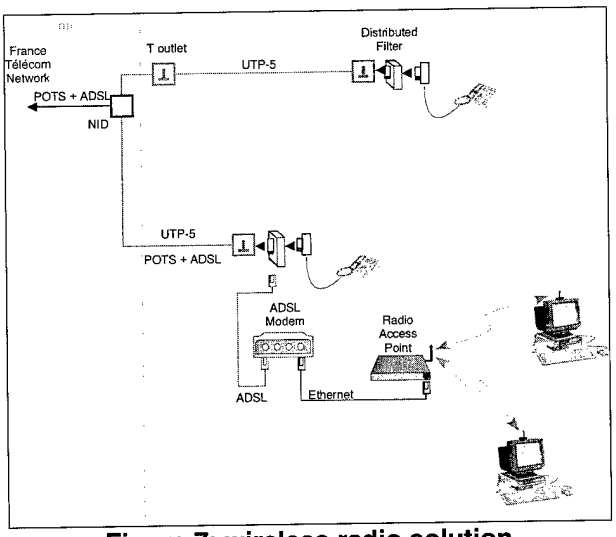


Figure 7: wireless radio solution

2.4.4. Comparison of performances and costs for "no new wire" products

Concerning the products used on the existing CPN ("no new wire" products), performances and costs are summarized in the following table:

	Home PNA	PLT	Radio		
			Home RF	IEEE802.11b	Bluetooth
Bit rate	10 Mb/s	from 100 kb/s to 10 Mb/s	from 600 kb/s to 1,6 Mb/s	from 1 Mb/s to 11 Mb/s	800 kb/s
Range	500 m	100 m minimum	50 m	100 m maximum	5 to 15 m
Estimated cost of materials	60 $ (2 USB cards)	600 $ (2 modems)	300 $ (2 USB boxes)	1200 $ (1 access point + 1 PCMCIA card)	400 $ (2 PCMCIA cards)
Commercial Product	YES	NO	YES	YES	YES

HomePNA products have the best quality/cost ratio, the only constraint is the availability of service at the phone outlet only (average of 2 or 3 in France).
PLT is not cheap at the moment since the products are only prototypes for most of the industrial providers.
Concerning wireless radio products, IEEE802.11b interfaces are business market oriented. This implies that the cost is somewhat too expensive, whereas HomeRF and Bluetooth products have good quality/cost ratio.

2.5. "Multimedia" cabling system

The solution described in figure 8 was defined to provide the customer with many high bit rate services and allowed a RAN to be created: many terminal types can be connected to this cabling system.
The "multimedia" cabling system is based on a star topology from the customer distributor to the category 5 RJ 45 type outlets. The installed cable is also a category 5 type so that the link can be qualified as class D, thus enabling frequencies up to 100 MHz to be used.

The end of the telecom network is located in the customer distributor featuring an RJ 45 panel.
This RAN allows the customer to connect any type of terminal: telephone, PCs, television (via suitable modules), etc.

2.6. Class D Local Area Network cabling system

The solution described in figure 9 is optimized for premises having a population between 50 and 50 000 people. It is defined according to the ISO 11801[12] standard with category 5 elements (cables and ends). This cabling system is usually known as a horizontal cabling subsystem.

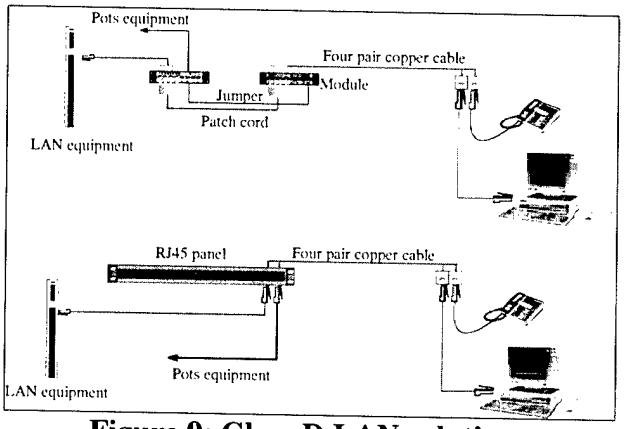


Figure 9: Class D LAN solution

Two types of end equipment can be used to realize this cabling system: management modules or RJ45 panels.

This LAN allows the customer to connect any type of terminal: telephone, PCs, television (via suitable modules), etc.

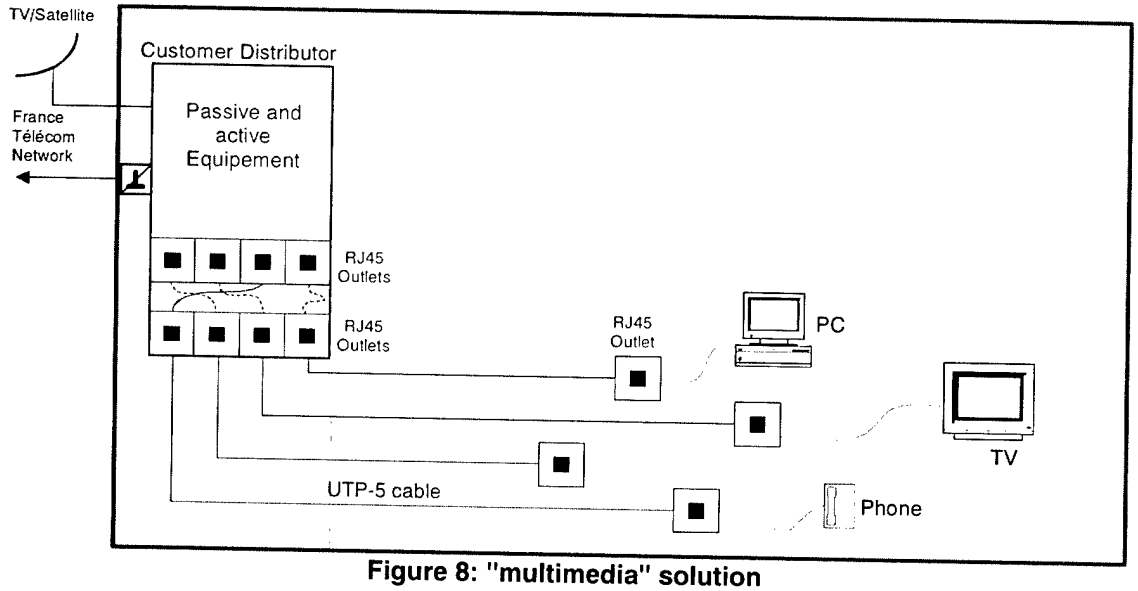


Figure 8: "multimedia" solution

2.7. Optical cabling system

Another solution for delivering higher bit rates is to lay optical fibers up to the outlet. Simultaneously using converters means that existing copper-based equipment can be used to the full (see figure 10).

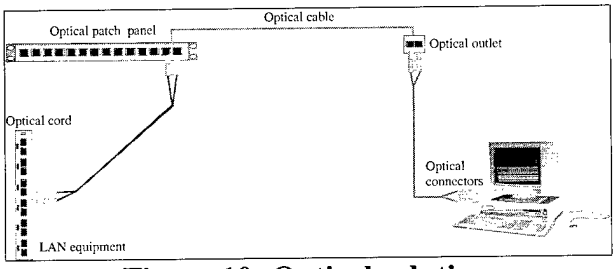


Figure 10: Optical solution

The optical cabling system also allows the use of gigabit Ethernet equipment.
There are many optical connectors available on the market nowadays. The most commonly used are the ST® and the SC, based on ferrules. Two criteria must be taken into account in the choice of a suitable connector: price and the requirements of assembly in the field. This is why other types of connectors can be used: a push-pull connector for the singlemode fibers (e.g. OPTOCLIP®II) and a small factor form connector for the multimode fibers (e.g. VF-45™). One of the advantages of the latter is its duplex configuration that makes cabling management more attractive for the work area.

2.8. Microtubes option

This solution consists in laying microtubes in which microcables are installed subsequently by using the blowing-pulling method. Tubes and cables with specific properties are required. A specifically designed apparatus named microjet® is used and provides additional pushing, thus increasing installation performance.

This technique permits limited investment. In fact, when creating a copper cabling system, empty microtubes can be also laid in parallel. Microtubes are included in the office raceways and an access point is installed when required. The major advantage of this solution is the guarantee of a flexible, upgradeable and easily reconfigurable optical network.

2.9. Conclusion

There are many interesting solutions for the distribution of narrowband and broadband services to both residential and business customers.

The solutions described below are currently being tested in our laboratory and in the field. These experiments (technical or commercial) will be described in the next section.

3. Field trials

3.1. Introduction

All the different cabling solutions described in the previous section, from the "bottom-of-the-range" to the optical cabling system, have been tested in the laboratory and in the field. These experiments can be both technical and also commercial.

This section describes the latest field trials conducted in our laboratories and on actual customer premises.

3.2. In-home showroom

The showroom located in our laboratories in Lannion is common to many FTR&D divisions. Its aim is to present FTR&D innovations concerning services for customers but also new network applications and cabling systems.

The room is designed as a "SOHO (Small Office Home Office)" building with an entrance hall and 4 apartments.

In the entrance hall, the network equipment is located in the floor distributor, which also contains the patch panels and the active equipment common to all the residents of the building (servers, ADSL modem, Home PNA equipment, etc.).

The backbone cabling subsystem of the building that extends from the building distributor to the floor distributor uses copper cable and end equipment that has category 5 specifications. At the entrance to each apartment, there is a passive terminal element, which is called NID (Network Interface Device).
In parallel, a cabling system is produced for the video entrance intercom, from the building distributor to the customer distributor (from the entrance hall to the entrance of the apartments).
The cabling system for 3 of the apartments (no. 2, 3 and 4) is the "bottom-of-the-range" cabling system made of a NID, UTP 4 pair category 5 cable and 1 or 2 "T" outlets.

The larger apartment (no.1) has a "multimedia" cabling system, which is a class D solution made of RJ45 outlets.

A VDSL access is provided to the 2nd apartment and a shared ADSL access to the other apartments via Home PNA interfaces (see "collective Intranet" field trial).
The first apartment has two telecom accesses: one is the traditional POTS and the other is an ADSL access. Figure 11 shows the cabling system from the customer distributor located at the entrance of the apartment to the outlets.

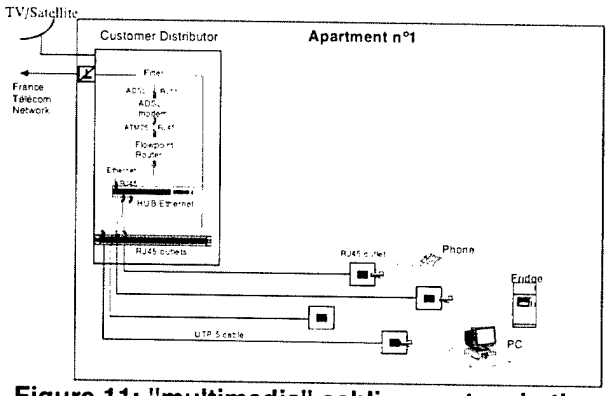


Figure 11: "multimedia" cabling system in the In-home showroom

The "multimedia" cabling solution is also deployed for the experimental house known as "ma m@isonnet" that is described in the next paragraph.

3.3. "Ma M@isonnet" (My H@usenet)

This is a commercial trial conducted with the cooperation of an industrial manufacturer (specializing in network equipment), a property developer and France Telecom.
The property developer's aim is to build a model home in which all the services that can be provided for his customers are exhibited. The future residents can visit this house to choose the services they require: permanent fast Internet connection via ADSL modems, PCs connected via a local network, audio network and also all the "home automation" applications such as remote electronic surveillance via web cam, remote activation of stores, door entrance, alarms, heaters, household devices, etc.

A "multimedia" cabling system is laid in the house with RJ 45 outlets to which any type of terminal can be connected (analog or IP telephone, PCs, household devices, etc.).

An Intranet application has been developed to facilitate the use of all these services: remote electronic services (blinds, door alarms, etc.), personal services (diary, data, etc.), Family shared services (shopping lists, notebook, family diary, etc.), residents shared services (babysitting, local tournament registration, etc.).
These Internet/Intranet services can be accessed from any terminal within the house.
This service offer is now included in the property developer's catalog.

3.4. Collective Intranet

This commercial trial is conducted with the cooperation of a property developer and France Telecom. It is run near Paris and involves a building of approximately 200 customers.

The principle is to share a high bit rate access (ADSL type) between all the residents of a building using the Home PNA equipment (See figure 12).
The ADSL network access is located at the bottom of the building. The Ethernet type interface is connected to an item of equipment (HomePNA switch) which carries out the standard functions of switch, Intranet server, firewall, etc. The Home PNA signals are broadcast on the existing cabling system laid for distributed POTS services. This architecture allows the customer to obtain collective Intranet services and classical POTS services on the same pair and in all outlets via an USB cord.

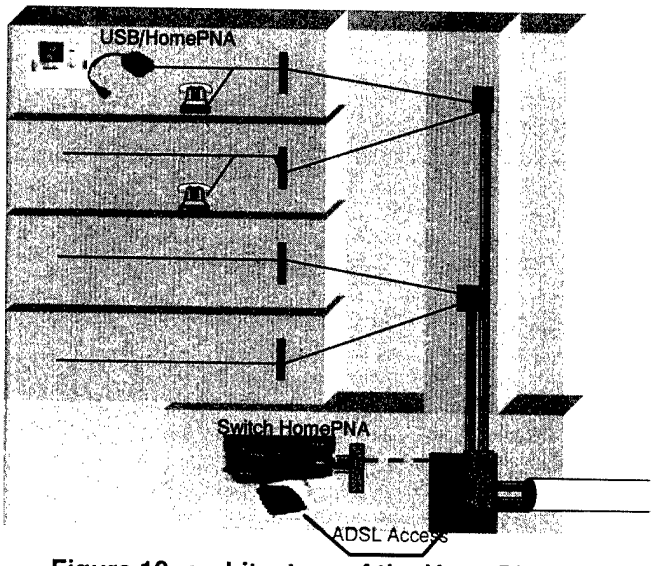


Figure 12: architecture of the HomePNA network in a building

The system range is 500 m for a bit rate of 10 Mbit/s for each of the building's residents.

3.5. VDSL Field Trials

The first technical trials of VDSL systems are currently being conducted in Lannion for 50 customers. Services offered are digital video and fast Internet. The total bit rate is 20 Mbit/s. The customer can simultaneously use internet and watch 3 different programs on his TV. The VDSL modem is also called Residential gateway and is equipped with 3 MPEG decoders and internet interfaces.

The cabling solution deployed is the "master filter" solution (see figure 13). After the filter, the classical telephonic pair (pair 1) is reused. A free pair (pair 4) is used to bring the VDSL signal to the gateway.

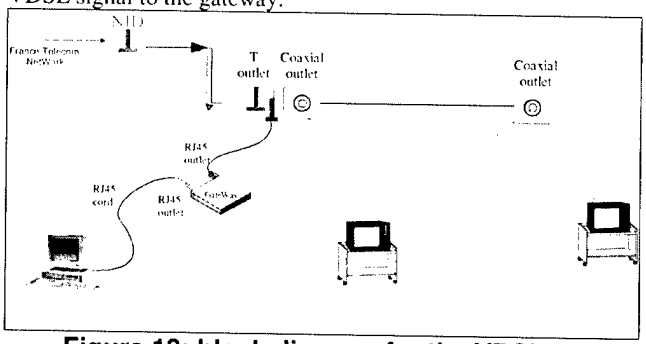


Figure 13: block diagram for the VDSL

This gateway has an Ethernet Interface and 3 coaxial interfaces, in which one PC and 3 TV sets can be connected respectively.
To reuse the existing Televisions, analog TV signals are injected on the coaxial cabling system (as shown in figure 13).

3.6. Optical cabling system field trial

A field trial is currently being conducted inside our company building to study different methods of bringing fibers up to the outlet. The purpose of the trial is to define not only the best technical choice, but also the most economic choice[3].

Three types of optical cabling system are tested:

- Zone 1: "traditional" optical cabling in an existing pathway with 900 µm fiber cables are installed in "dalle marine" raceways partly occupied by copper cables.
- Zone 2: "optimized" optical cabling in a dedicated "steel wire" raceway where compact and light cables (micromodule type) are installed.
- Zone 3: "microtubes" cabling in which tubes with specific characteristics are installed and micro-cables are fitted inside on request with blowing techniques.

For zones 1 and 2, the cabling supplies optical fibers to fifty offices. Each office has two access points that contain four outlets, two multimode (62.5/125 µm) and two singlemode (see figure 14). An outlet comprises two fibers, one for transmission and one for reception. Two cables of eight fibers (four singlemode and four multimode) supply each office: one cable per access point.

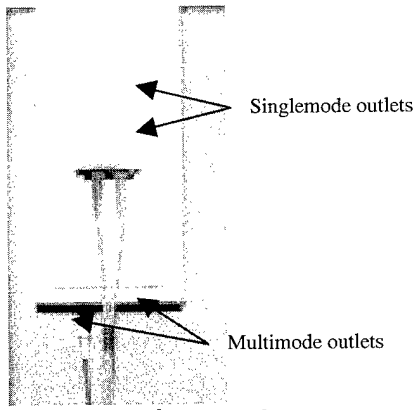


Figure 14: Access point structure

For zone 3, four microtubes tied in a bundle supply the offices. Each office can potentially receive two access points (two microtubes per access point). The microtubes are included in the office raceways and an access point is installed when required.

Different raceways, connectors, cables and racks are installed. The field trial provides information which contributes to determining the most effective way of taking fiber up to the outlet. The "steel wire" raceway seems particularly well adapted for the laying of optical cables or microtubes, where EMC aspects are not to be taken into consideration. The cable, which has a micromodule structure, has a clear economic benefit both for laying and end setting. The OPTOCLIP®II connector has a slightly shorter installation time than the VF-45™ connector, but this depends on the cable used and one of the advantages of the VF-45™ connector is its duplex configuration that makes cabling management more attractive. Two types of rack have been tested and the results show an equivalent installation time. The main advantages of the "wheel concept" system[4] are that its high capacity can reduce the floor space required and that its management is simplified with the use of one length leads. The microtube cabling system benefits in terms of laying and access point installation times but the major advantage of this solution is the guarantee of a flexible, upgradeable and easily reconfigurable optical network.

3.7. Microtube laying system field trial

This solution consists in laying microtubes in which microcables are installed inside later with the blowing-pulling method[5]. Tubes and cables with specific properties are required. A specifically designed device known as Microjet® is used and provides additional pushing, thus increasing installation performance.
An experiment involving horizontal cabling based on the tubing method combined with the blowing-pulling technique has been conducted in FTR&D buildings. Tubes supply about four hundred offices with one tube for each office.
Due to their low weight and small friction coefficient, the tubes are laid twice as fast as conventional building cables. Several tubes are pulled simultaneously through a guide (figure 15).

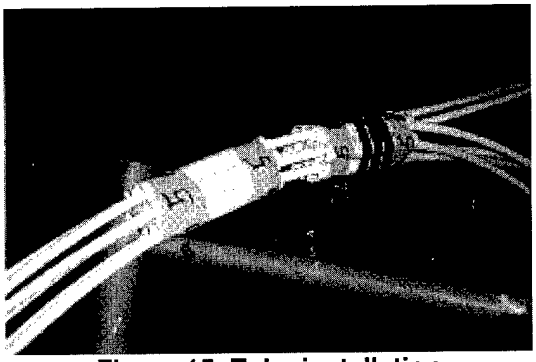


Figure 15: Tube installation

In the distributor, tubes are connected to distribution closures adapted to a 19 inch rack. This is convenient for producing cabling on demand since there is permanent access to the tube and fiber management is easy. In the office, the outlet and connectors are assembled when the cable is blown.
The blowing-pulling performance achieved with the Microjet® tool allows cable installation in a complete horizontal distribution infrastructure. The building has cabling lengths of less than one hundred meters with about 10 or 15 bends of 90°.

Other microtube laying system field trials are planned for the end of this year in Bordeaux and Paris. These trials will be conducted in very high buildings and involve the backbone subsystem (from the building distributor to the customer distributor). In this type of building the backbone cabling is a

difficult operation, mainly due to logistic considerations that mean large delays for access to the building infrastructure. This is why it is highly advantageous to lay microtubes in the passing column so that when a customer (located anywhere in the building) requests an optical fiber, a optical microcable is installed on demand. The access service time is then reduced.

3.8. Conclusion

The various cabling system solutions are tested in our laboratory or in the field. The results of these technical and commercial trials will help France Telecom to define the best technical options but also the most economical ones in order to make the best choices.

4. Conclusion

For the distribution of narrowband and broadband services to both residential and business customers, there are many solutions which are of interest.
For residential users, the re-use of existing cabling systems such as phoneline or powerline is useful for connecting several terminals and for networking.
For new buildings, new cabling systems are created based on LAN cabling systems.
For businesses, different copper and optical cabling system solutions exist to respond to the increased bit rate in the customer LAN. Economically, the advantage of these solutions varies depending on different parameters such as customer type, initial investment, number of outlets needed, etc., but the installation of optical media is becoming an increasing reality.
For both residential and business approaches, solutions are being tested and validation in field trials is in progress to define cabling systems for France Télécom customers.

5. References

[1] IWCS 2000 session 17 track 3 "power line telecommunications for residential home network" O. Bouffant et al., France Télécom R&D / DTD
[2] ISO 11801 standard
[3] Laying Optical Fibers Up to the Outlet - E. Cressan et al - OHAN/FSAN 2001
[4] Density Cross-Connect Mainframe - H. Aoustin et al - EC'99
[5] An economical optical cabling method for building networks - AC. Réau et al - EC'2000

6. Authors



Olivier Bouffant is graduated from the University of Toulon in Electronics in 1992. He joined the France Telecom R&D center in 1994. Working in the Local Loop Infrastructure Laboratory, he is the project manager for in-house Networks for residential and business customers



Emmanuelle Cressan received the title of Docteur of the University of Rennes (Physics and Chemistry of Materials) in 1994. She joined the France Telecom R&D center in 1994 to work on optical cables (writing specifications, performing tests, European standardization, implementation of cables in field trials). In 1998, she joined the Local Loop Infrastructure Laboratory to manage the studies relating to cabling systems for business customers. Since 2001, she is the manager of the ACC (All Cabling Concept) Research and Development Unit working on copper cables and new high bit rate applications on Customer premises Cabling Systems.



Pierrick Guillas began his career with France Telecom R&D in 1976. After six years in Research and development at the Computer Center in Paris, he joined the Local Loop Infrastructure laboratory in 1982. Working on standardization for data cables, he is an expert on copper cables, for outside and inside use, writing specifications and test methods.



Hervé Le Cozic began his career with France Telecom R&D in 1981. After six years in a Physical-Chemical Laboratory, he joined the Local Loop Infrastructure Laboratory in 1987. Working on standardization for data cables, he is in charge of telecom cables, connectors and home wiring tests.

Philippe Mercier began his career with France Telecom R&D in 1980. After five years in the LAN (Physical layer) group, he joined the Access Network Infrastructure Laboratory. Working on business cabling systems, he is in charge of connectors and field trials.



Daniel Le Bras began his career with France Telecom R&D in 1984.
Working in the Access Network Infrastructure Laboratory, he is in charge of residential home network tests, specializing in the powerline infrastructure.

New MDF Terminal Modules for xDSL Application

Sokho Kim, Jaejin Lee,Taesuk Suh
Access Network Laboratory, Korea Telecom
Taejeon, South Korea
+82-42-870-8587 · sokhokim@kt.co.kr

Abstract
This paper introduces the new splitter and connection modules applicable in MDF of central office defined by Korea Telecom for offering xDSL sevices. As a prominent access technology, ADSL services were used by over 4 million users in Korea up to the end of year 2001. Despite of effective reuse of outside plant copper cables, ADSL deployment made central office (MDF Room, Transmission Room) very complicated with new copper cables and jumpers. And installation of several DSLAMs and double cabling of POTS lines (between MDF and Splitter shelf of DSLAMs) provoke serious problems like the floor space & cable duct deficiency and the huge construction expenses. This kind of high speed broadband services demand reconstruction of central office to integrated packet network accommodating Data and Voice transmission.

For the solutions for these problems we have developed 1 pair ADSL splitter jack and terminal block for splitting ADSL signal to voice & data in each other.

We have confirmed that xDSL connectin modules accommodating above products can be applicable to existing MDF and are very economic products to constructing ADSL service infrastructure. Applying 1 pair splitter jack makes maintenances very easy. Also when pulling out splitter jack, feasibility to use ADSL connection modules as a plain MDF connection modules is obtained.

Keywords
ADSL, LPF, ADSL-Splitter, MDF

1. Introduction
Among the access technologies of high speed and broadband service, the DSL technology that deploys the existing copper line has been developed. Korea Telecom had deployed 3 millon ADSL lines in Korea and progressed continuous reduction on construction expenses of ADSL network. However the portions of expenses related with cablings is proximately 20% although the price of DSLAM and ATU-R modem was cut down steeply. The major causes on the huge expenses depends on doubled cabling of POTS line to splitter module in transmission facility at different floor. That also provokes many problems like ambiguous administration range on ADSL line and area shortages in transmission & MDF room of CO.
In this article, new solutions on cabling problems related with ADSL in CO is proposed and evolution plan of MDF facility in era of data + voice packet transmission via copper line will be discussed.

2. Comparison on ADSL cabling schemes in Central Office
As seen in Figure 1, ADSL cabling in CO was composed of DSLAM(including splitter module)in transmission room, separate connection modules in MDF and doubled POTS cablings if no new investment on plain POTS facility. That makes big cabling expenses related with installing inter-floor raceway , cabling 2 lines (ADSL, POTS) to DSLAM. We had discussed 1) special Splitter rack in MDF room and 2) IDC type connection splitter & connection modules suitable to plain MDF rack (Fig 2).

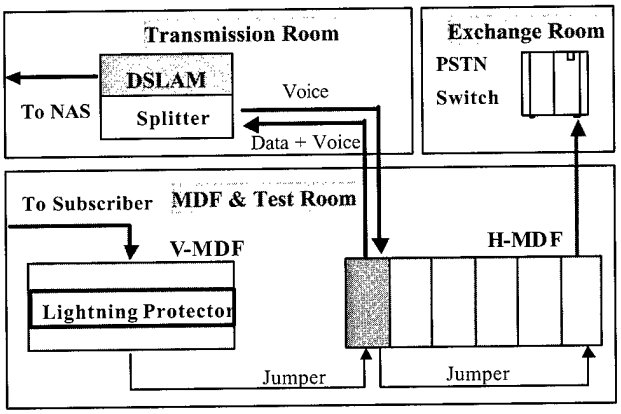
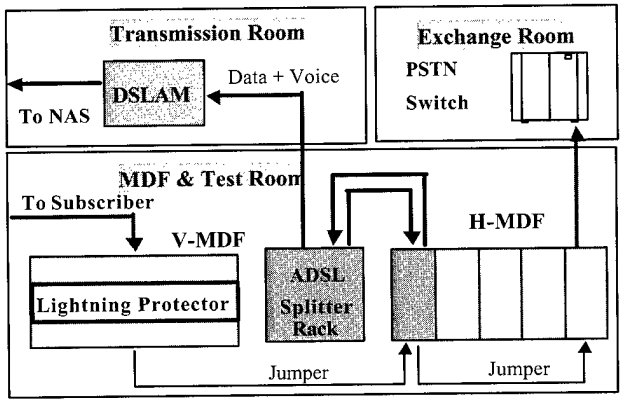
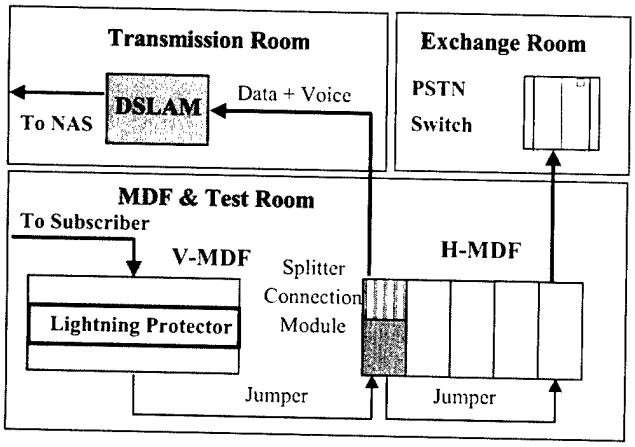


Fig 1 Plain ADSL cabling in CO



Scheme 1. ADSL Splitter rack in MDF room



Scheme 2. IDC type connection splitter & connection modules suitable to plain MDF rack

Fig.2 Improvement schemes for ADSL cablings in CO

3. Design of MDF termination module for ADSL

According to comparision results (Table1), IDC type connection splitter & connection modules suitable to plain MDF rack was selected. New splitter & connection modules was proposed and designed as follows.

Table1. Comparison between two schemes.

Item	Scheme1	Scheme 2
Occupancy	X	O
Cabling	X	O
Time to service	O	X (New Product needed)
Expenses	X (Special Rack, additional cablings)	O (New splitter &- connection module needed)
Adapt to Plain rack	X	O
Maint-enanece	X (replace unit shelf)	O (replace 1pr splitter)
Admin-istration	X (cabling to separate rack)	O (Data+Voice admin. in Plain MDF)

3.1 Design of Plug type 1-pair Splitter

ADSL system need low pass filter(LPF) to split POTS signal and conventional splitter modules have minimum 12 pair splitter circuits in one PCB board to minimize cost reduction. New plug type splitter has the same circuit pattern as conventional splitter module besides surge absorber function(Fig.3). Splitter has 2 layer LPF splitting voice band (200Hz~3.4KHz) from data band(30KHz~) by cutting bands below 8KHz. Surge protection part is moved to outer line interface in DSLAM because horizontal MDF has no earthing bus bar and protector is more effective to protect DSLAM at line interface.

Several splitter & connection modules had developed already for IDC type MDF but those were expensive solutions to replace min.12pair splitter module for one line trouble. New IDC connection module to set splitter on plain MDF rack provoke excessive expenses and installation problems owing to different module size.

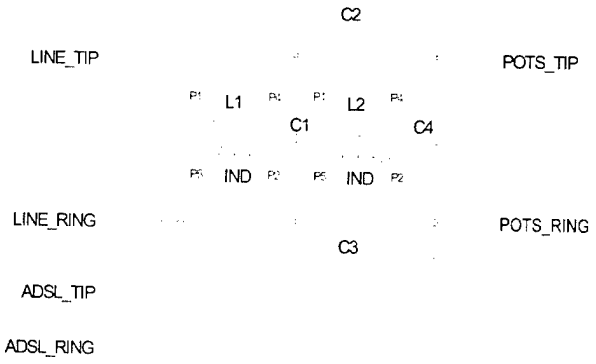


Fig 3. Circuit configuration of 1 pair splitter

Interface part of 1 pair splitter was designed to accept the switching IDC pins connected to each jumpers(ADSL line, POTS line, Data line). The plug shape made easy to handle and replace when that was out of order or when subscriber terminate the service.

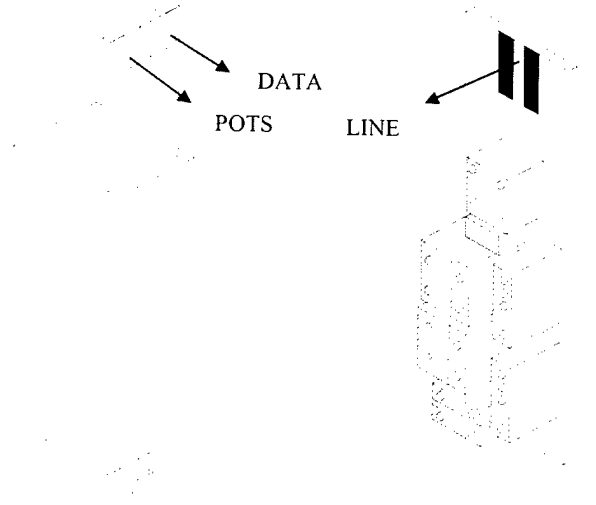


Fig 4. Plug type 1 pair splitter

3.2 Termination Modules for ADSL application

The new termination module which is consist of 8 terminal blocks and one base shelf accommodate 64pairs ADSL lines and can split voice signal to PSTN exchange switch and data

signal to ADSL ATU-C (DSLAM). As shown in Fig 5, the terminal block for 8 pair use accommodate 3 IDC connection points per one subscriber in upper part and one splitter plug in downward part. ADSL line and POTS lines are always swithed in the terminal block and are separated by inserting splitter plug.

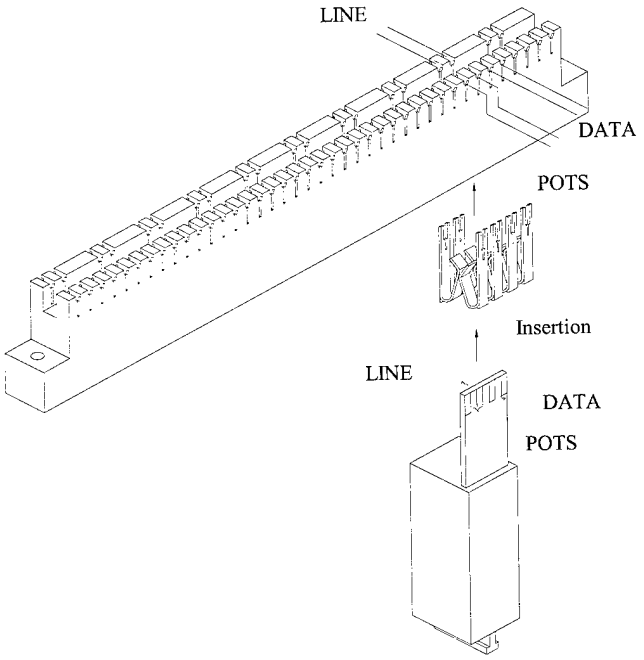


Fig 5. 8 pair Terminal block & splitter for ADSL application

The termination module was designed to replace plain horizontal MDF shelf. (Fig.6) The size is the same as the old but capacity (64pair use) is the half of the old(128pair use) owing to secure easy connection.. But instead of using 2 old shelf (interface of ADSL line and of POTS) one module can be used, and the total capacity is very high as the old shelf.

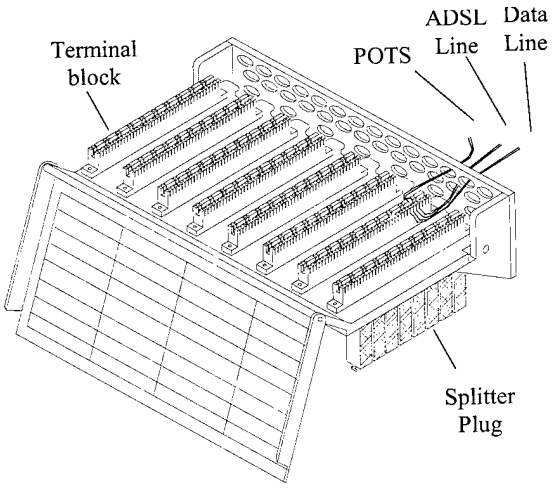


Fig 6. New terminal modules(64Pair) for ADSL

4. Connector & Splitter Characteristics

The performance test of splitter was performed in electrical test on each splitter (Table 2) and in cross test (up/down link speed, up/down attenuation etc) between each spliiter and the other DSLAM (Table 3). And impact & vibration test was performed on splitter plug additionally(Table 4).
The test results was good as the previous shelf type splitter shelf in all the test.

Table 2. Electrical performance of splitter plug

Test Item	Spec.	Freq.(KHz)	Result
Insertion Loss	0.2dB max	1004 Hz	0.1474
Attenuation Distortion (0.2~3.4KHz)	±0.5dB max	0.2	0.1438
		3.4	0.2152
Attenuation Distortion (3.4~4.0KHz)	±1.0dB max	4	0.2456
Delay Distortion (0.6~3.4KHz)	100ms max	0.6	62.66
		3.4	66.48
Delay Distortion (0.2~4.0KHz)	150ms max	4	68.16
Return Loss	20dB min	0.2	37.44
		1	39.12
		2	38.4
		3	33.46
		4	32.44
Longitudinal Balance (0.2~1KHz)	58dB min	0.2	73.48
		0.6	0
		1	0
Longitudinal Balance (1.0~3.0KHz)	53dB min	3	63.304
Attenuation(30KHz)	25dB min	30	74.2
Attenuation (50~1104KHz)	40dB min	300	99
		1104 KHZ	97.4

Table 3. Link test results of splitter plug at 4km cable length

Rate(bps)		SNR		Attenuation		Ping
Down	Up	Atu-c	Atu-r	Atu-c	Atu-r	
2797	2796.8	6.2	6	32	61	12

Table 4. Mechanical performance of splitter plug

Test Item	Condition	Spec.	Result
Impact test	H=10m,10time	No increase	No increase
Vibration	IEC 68-2-6	No increase	No increase

The test specifications on connecting part are conformed to the performance of UTP-5 level in IEC 68 & 512 series and TIA/EIA 568 A. The electrical & reliablilty test was performed on minimum 5 test samples. The reliability tests (twist, durability of IDC pin, repeated insertion of switching pin, impact) on connection pin was decided on the increase values of connection resistance.(Table 5,6)
It is shown that the terminal block has UTP-5 level connection performance.

Table 5. Electrical performance of terminal block

Item	Freq.(MHz)	Spec.	Results
Attenuation	1	0.1	0.017
	4	0.1	0.037
	10	0.1	0.023
	16	0.2	0.011
	20	0.2	0.005
	21.25	0.2	0.02
	65.5	0.3	0.02
	100	0.4	0.03
NEXT	1	>65	93.42
	4	>65	79.22
	10	60	71.4
	16	56	67.14
	20	54	64.912
	21.25	50	64.164
	65.5	44	54.324
	100	40	50.96
FEXT	1<f<100	14	22.9

Table 6. Reliability performance of terminal block

Item	Conditions	Spec	Results
Connection Resistance	0.4mm	5mohm >	0.934
	0.5mm		0.932
	0.65mm		0.76
Insulation Resistance	500Vdc	>100Mohm	Passed
Dielectric Strength	1500Vrms	N B	N B
Tensile strength	0.4mm	>1.6kgf	2.762
Twist	0.4mm,180	5 mohm >	0.11
Durability	100time	5 mohm >	0.1
Repeated Insertion (switching pin)	200time/POTS	20mohm >	4.05
	200time/Data	20mohm >	6.22
Impact	-20 C, 2hrs	N B	N B

* NB : No Breadown or Breakage

5. Conclusion

The application of line splittable terminal module and ADSL splitter plug to construction of ADSL cabling in MDF room of CO was discussed. At first, two schemes about where the splitter is installed was discussed. IDC type connection splitter & connection modules suitable to plain MDF rack have more advanges than separate splitter module in MDF room and hence was developed , tested.

New terminal module for ADSL give good advantages as follows.

- Cost reduction on construction expenses related with doubled cabling
- Secure discrete administration range on ADSL line
- Saving Areas in transmission & MDF room of CO
- Upgrade wrapping type MDF to new IDC type MDF for Voice+data use without rack replacement
- Application as the branch point when unbundling of subscribe lines shall be needed.

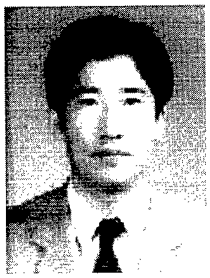
6. References

[1] T1E1-1.4/97-272 Sep,1997. "Location of the Central Office End POTS Splitter"

[2] TIA/EIA-568-A DRAFT 11a May 1999. "Additional Transmission Performance Specification for 4-Pair 100Ω Category 5e Cabling"

[3] ISO/IEC 11801,May 1995. "Information technology –Generic cabling for customer premises"

Authors



Sokho Kim
Korea Telecom Access
Network Laboratory
463-1, Jonmin-dong,
Yusong-gu, Taejon, Korea
305-811

Sokho Kim graduate from HanYang University in 1988 with a M.S. Degree on Material Engineering. After 3yrs developing electronic materials in KIST, he joined in Korea Telecom and is involoved in development of customer promises network devices.



Jaejin Lee
Korea Telecom Access
Network Laboratory
463-1, Jonmin-dong,
Yusong-gu, Taejon, Korea
305-811

Jaejin Lee graduate from KyungBuk University in 1987 with a M.S. Degree on Electronics Engineering and Ph. D on Computer Engineering from Korea University in 1997 Then, now he is a director of xDSL technologies and outside plant devices



Taesuk Suh
Korea Telecom Access
Network Laboratory
463-1, Jonmin-dong,
Yusong-gu, Taejon, Korea
305-811

Taesuk Suh graduate from Ko rea Advanced Institute of Science & Technology in 1986 with a M.S. Degree on Materials Engineering. Then, now he is a director of customer private network section.

Development of an 864-fiber Ribbon Cable Containing a Novel Ribbon Stack Configuration

Jason C. Lail
Corning Cable Systems
Jason.Lail@Corning.com

Craig M. Conrad
Corning Cable Systems
Craig.Conrad@Corning.com

Abstract

Demand for bandwidth in metropolitan rings continues to drive the development of higher fiber count optical cables. This paper focuses on the development process of an 864-fiber single tube ribbon cable designed for 1.25-inch (31.8-mm) duct applications. The process included four development phases. The phases were Determining the Critical Design Limits, Minimizing the Cable Diameter, Developing the 36-fiber Ribbon, and Developing the 864-fiber Cable Design. The new cable design contains a novel ribbon stack configuration. The configuration utilizes a combination of sixteen 36-fiber ribbons and twelve 24-fiber ribbons to maximize the fiber-packing density and minimize cable diameter. Creating a cable design with a diameter less than 26.0 mm was critical for installability in 1.25-inch (31.8-mm) duct applications. The new 864-fiber design, along with the optional fiber counts and sheath types, meets the critical design limits, all relevant industry specifications, and stringent ribbon and cable handling requirements.

**US Patent 6,192, 178 B1 "Fiber Optic Cable with Profiled Group of Optical Fibers" dated February 20, 2001 applies to this work.*

Keywords

1.25-inch duct; Ribbon; 36-fiber; 24-fiber; 864-fiber; Pulling; Air-assisted; Overhang: Metropolitan; Single Tube; Armored; Non-armored; Toneable; Contraction; Attenuation; Kinking; Crush; Installation; Mass-fusion Splicing; Stray

1. Introduction

Telecommunication carriers continue to request higher fiber count optical cables to meet forecasted bandwidth demand, specifically in metropolitan rings. Residential bandwidth demand continues to rise as fiber gets closer to the home and more users get online. In addition, corporate bandwidth demand is rising as high speed networks proliferate. Both residential and corporate bandwidth demand merge at the "bottleneck" of the optical network – the metropolitan ring. In Hecht's article, "Breaking the Metro Bottleneck," he notes, "In the backbone, transmission speeds are measured in trillions of bits per second. On the user end, high-speed networks run at billions of bits per second. But the metro systems that link these two high-speed networks poke along at mere millions of bits per second" [1].

Many existing metropolitan rings contain 4.0-inch (101.6-mm) conduits. The majority of these conduits were installed decades earlier for the installation of steam pipes, power cables, or metallic communication cables. The 4.0-inch (101.6-mm) conduits frequently contain three 1.25-inch (31.8-mm) inner ducts to maximize the efficiency of the conduits for later installations. Some metropolitan networks contain three 1.25-inch (31.8-mm) inner ducts and have two of the three inner ducts filled with previously installed optical cables, leaving one empty duct. Some carriers hope to install the highest fiber count cable available into the empty inner duct. This will allow carriers to remain ahead of the bandwidth demand curve as long as possible.

As bandwidth demand increases into the next decade, merely filling existing empty inner ducts may not suffice. In the next decade, telecommunication carriers may need to replace lower fiber count or slower data rate cables. Five to ten years ago, carriers could install three 216-fiber cables into three 1.25-inch (31.8-mm) inner ducts for a total of 648 fibers. More recently, carriers could purchase and install three 432-fiber cables in the same inner ducts for a total of 1296 fibers. In the future, bandwidth demand could drive the need for three 864-fiber cables or 2592 fibers.

In both 1.25-inch applications, whether it is filling empty inner ducts or replacing older cables, installing only a cable is inexpensive compared to the replacement of existing infrastructure. In the article "Building a Better Backbone," Savage writes, "as much as 40 percent of the cost of a fiber-optic system goes toward purchasing rights-of-way, getting permits, and putting cable in the ground" [2]. The 40% of the cost that Savage refers to can be minimized if telecommunication carriers utilize existing rights-of-way and existing conduit and duct infrastructure. This can be accomplished by installing new cables into empty ducts or by replacing existing cables with new higher fiber count or higher data rate designs.

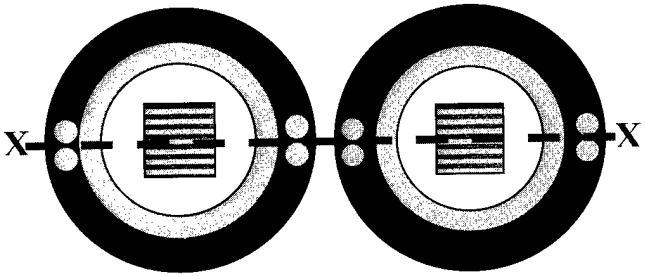
To meet customer demand for higher fiber count cables suited for 1.25-inch (31.8-mm) duct applications, an 864-fiber single tube ribbon cable with a novel ribbon stack configuration was developed. The novel ribbon stack contains optical fiber ribbons of different width to maximize fiber-packing density and minimize cable diameter. This paper will discuss the development phases of the new cable design. The phases included Determining the Critical

Design Limits, Minimizing the Cable Diameter, Developing the 36-fiber Ribbon, and Developing the 864-fiber Cable Design.

2. Determining the Critical Design Limits

The first development objective for the new cable design was determining the design limits for cable diameter, cable flexibility, and installation force based on the installability of the cable designs. The limits were determined by conducting installation experiments in a 1.25-inch (31.8-mm) duct route. Figure 1 shows the two single tube cable designs utilized in the experiment.

The two cables were manufactured with a diameter of 26.0 mm. A diameter of 26.0 mm equates to a 67% fill ratio in a 1.25-inch duct (31.8-mm). The fill ratio was calculated by dividing the area of the cable cross-section by the area contained in the cross-section of the duct inner diameter. The non-armored design had a relative flexibility of 15, and the armored design had a relative flexibiltiy of 10. The relative flexibility was calculated using the equation $B = EI_{XX}$, where B is the relative flexibility, E is the modulus of the cable, and I_{XX} is the moment of inertia about axis XX (shown in Figure 1), the preferential bending plane. A higher value for relative flexibility equates to a more flexible cable design.



Diameter 26.0 mm **Flexibility 15.0** **Type Non-Armored**	**Diameter 26.0 mm** **Flexibility 10.0** **Type Armored**

Figure 1. Installation Cable Designs

The experiment included pulling and air-assisted installation techniques and was performed at Corning Cable Systems' cable installation facility in Winston Salem, North Carolina. The cables were installed in standard 1.25-inch (31.8-mm), smooth-wall, high density polyethylene duct at 0^0C in February of 2001. A cold weather environment was chosen to reduce cable flexibility. Reduced cable flexibility was desired to maximize the differences in installability of the two designs.

The pulling installation was conducted with a standard wheel-pulling capstan. The capstan was equipped with special equipment to monitor the installation force on the cable throughout the installation. For the pulling installations, a moderately difficult 1935-foot (590-meter) route was selected. The route contained six 45^0 turns, three 60^0, and two 90^0 turns with an elevation change of 20 feet (6.1 meters). The configuration of the route was similar to those observed in metropolitan areas.

The air-assisted installation was conducted with standard five-horsepower air-assist installation equipment. For the air-assisted installation, a route of 3700 feet (1128 meters) was selected. The 3700-ft (1128-meter) route was an extension of the same 1935-ft (590-meter) used in the pulling installation. The installation routes are shown in Figure 2. The complete detail of the turns in the route is not shown in the figure. In the figure, the 1935-foot (590-meter) route is represented with the short dashed lines and the complete 3700-foot (1128-meter) route includes the longer dashed lines.

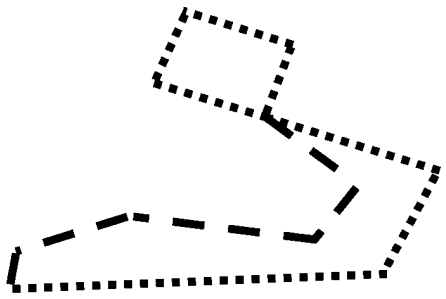


Figure 2. Layout of Installation Routes

After the installations were completed the installability of the two designs was compared. For the pulling installation, the installation forces required to install the cable in the 1935-foot (590-meter) route were compared. However, the measurement of installation forces with air-assisted techniques was difficult and expensive. Therefore, air-assisted installability was based on the installed length achieved with the five-horsepower air-assist equipment.

Table 1 shows a summary of the installation results. With standard pulling techniques, the more flexible non-armored cable required 520 lbs (2314 N) of installation force. The less flexible armored cable required a higher force of 620 lbs (2759 N). The results showed that a more flexible cable required a lower installation force and was, therefore, more easily installed. With air-assisted techniques, the results were similar. The more flexible non-armored design was installed 3700 feet (1128-meters), the complete route, while the less flexible armored design was only installed 3300 feet (1006 meters). Again, the more flexible design was installed more easily [3].

Table 1. Summary of Installation Results

Cable Flexibility	Pulling Load (1935-ft)	Air-Assisted Length
10 	620 lbs	3300 feet
15 	520 lbs	3700 feet

Both the pulling and air-assisted results showed the importance of cable flexibility when installing 26.0-mm single tube cables into 1.25-inch (31.8-mm) ducts. However, the results also showed

that both levels of cable flexibility in this experiment were acceptable for rated installation loads of approximately 600 lbs (2670 N). Since the air-assisted installation lengths exceeded the pulling installation lengths, the air-assisted results were not a limiting factor in determining the critical design limits. For installing single tube cables in 1.25-inch (31.8-mm) ducts, the critical design limits were determined. The design limits were a maximum cable diameter of 26.0 mm, a minimum relative flexibility of 10, and a maximum rated installation load of approximately 600 lbs (2670 N). For cables that are more flexible or that are designed for higher installation loads, 26.0 mm may not be the cable diameter limit.

3. Minimizing the Cable Diameter

After the critical design limits were determined, cable prototype calculations were performed. Calculations focused on maximizing the fiber-packing density of an 864-fiber cable with various ribbon stack configurations. Maximum fiber-packing density was critical to remain below the 26.0-mm diameter design limit for the single tube cable.

Jackson discussed the design of higher fiber count single tube ribbon cables in his IWCS 1999 paper, "Optimal Design Strategies for Central Tube Ribbon Cables Comprising 864 Fibers and Beyond." In the paper he writes, "for very high fiber counts, the number of fibers per ribbon must grow to achieve the highest fiber count for a given ratio of stack to core tube characteristic dimensions". Cable prototypes with traditional (rectangular or square in shape) configurations of 12-fiber and 24-fiber ribbons were considered for this development. However, as Jackson noted, the cable prototypes with even wider 36-fiber and 48-fiber ribbons had higher fiber-packing density than the 12-fiber and 24-fiber ribbon cables [4].

In Figure 3, the cable diameters with traditional ribbon stacks containing 12-fiber, 24-fiber, 36-fiber, and 48-fiber ribbons are plotted for each fiber count. In the figure, cable diameter is on the vertical axis and fiber count is on the horizontal axis. Separate lines are plotted for 12-fiber, 24-fiber, 36-fiber, and 48-fiber traditional ribbon stack cable designs. The figure demonstrates that an 864-fiber cable containing 36-fiber ribbons has a smaller diameter than an 864-fiber cable containing 24-fiber ribbons.

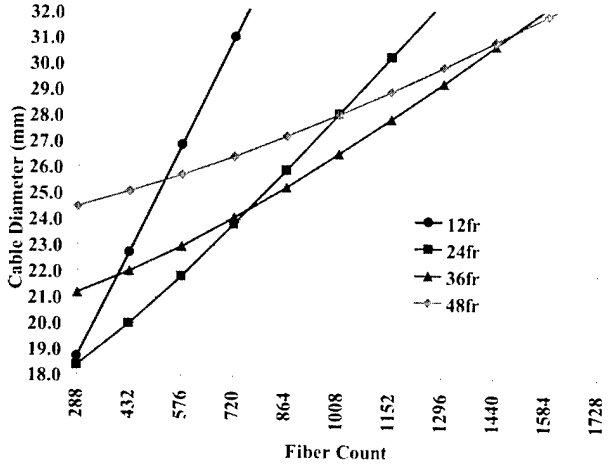


Figure 3. Cables with Traditional Ribbon Stacks

The 864-fiber cable prototype with 12-fiber ribbons had a cable diameter well above 32.0 mm and was not a design option. The 864-fiber cable containing 24-fiber ribbons resulted in a cable diameter of 26.2 mm, while the 864-fiber design containing 36-fiber ribbons produced a cable diameter of 25.2 mm. The 36-fiber ribbon stack provided a 1.0-mm advantage in cable diameter. However, the cable diameter of the 36-fiber ribbon design was only 0.8 mm less than the 26.0-mm limit. It was determined that an increase in fiber-packing density was necessary to insure that the final design would meet the 26.0-mm diameter design limit.

Design methods to improve the fiber-packing density of the 864-fiber design were evaluated. Improved buffer tube and jacket materials were considered to reduce wall thickness and cable diameter. Thinner wall sheaths with various strength element configurations were also considered to reduce cable diameter. However, each method resulted in numerous concerns with regard to industry specifications and internal cable handling requirements. Ultimately, the development team decided to focus on optimizing the ribbon stack configuration to increase fiber-packing density.

The investigation began by considering the optimal method to fill a circular shape with multiple rectangular shapes. Figure 4 shows how to optimally fill a circle with multiple rectangles in a step-like profile. In the example there is no constraint on the difference between W_1 and W_2, the width of consecutive rectangles. With a minute difference between W_1, W_2, etc., numerous rectangles could be used to completely fill the inner diameter of the circle.

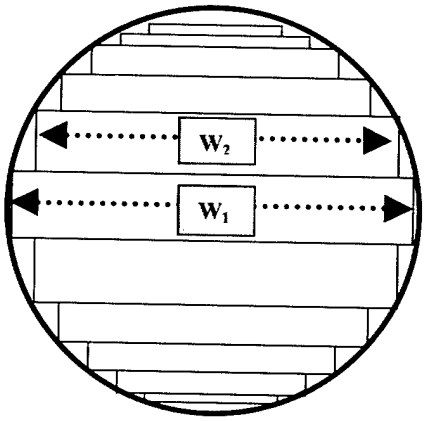


Figure 4. Step-like Structure to Fill a Circle

The step-like structure was then applied to ribbons inside of a buffer tube. However, in the realm of fiber optic cable, the width differences are defined by customer requirements. The customer's desire to mass fusion splice 12-fiber sub-units defines the width differences in the ribbon stack. Therefore, for ribbon stack calculations, only multiples of 12 fibers were incorporated. The novel ribbon stack containing ribbons of multiple widths was termed the "combination ribbon stack."

Design calculations were performed with numerous ribbon stack variations containing 12-fiber, 24-fiber, 36-fiber, and 48-fiber ribbons. The calculations showed that combination ribbon stacks of 12 and 24-fiber ribbons did not create any advantages with

fiber-packing density in the 864-fiber count range. Similarly, the se of 48-fiber ribbons resulted in less than optimum cable diameters in the 864-fiber count range.

Figure 5 shows a closer look at the possible configurations incorporating two different ribbon widths, 36-fiber and 24-fiber. In the figure, the vertical axis is the cable diameter and the horizontal axis shows the various stack configurations. The labels on the horizontal axis are the number of 36-fiber ribbons followed by the number of 24-fiber ribbons. The left-hand portion of the figure shows the 0/36 combination containing zero 24-fiber ribbons and thirty-six 24-fiber ribbons. The right-hand portion of the figure shows the 24/0 combination with twenty-four 36-fiber ribbons and zero 24-fiber ribbons. Notice that with only 24-fiber ribbons the diameter was 26.2 mm, with 36-fiber ribbons the diameter was 25.2 mm, and with the optimized two-ribbon combinations of 16/12 and 18/9 the diameter was around 24.0 mm. The design calculations showed a very significant advantage in cable diameter with the combination ribbon stack configurations.

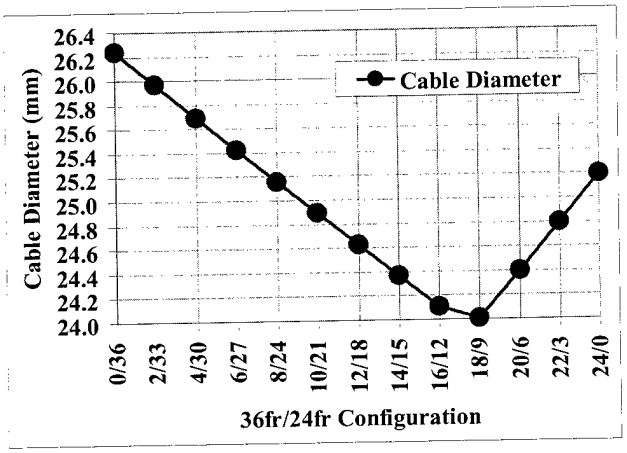


Figure 5. Two-Ribbon Stack Configurations

Several combination ribbon stacks containing three different ribbon widths also had smaller cable diameters. Figure 6 shows two of the three-ribbon configurations combining 36-fiber, 24-fiber, and 12-fiber ribbons. The 14/12/6 configuration contained fourteen 36-fiber, twelve 24-fiber, and six 12-fiber ribbons. Similarly, the 16/10/4 configuration contained sixteen 36-fiber, ten 24-fiber, and four 12-fiber ribbons. In Jackson's design s paper, he found similar results for an 864-fiber design. Jackson stated that, "an optimal solution is to employ fourteen 36-fiber ribbons, twelve 24-fiber ribbons and six 12-fiber ribbons" [4].

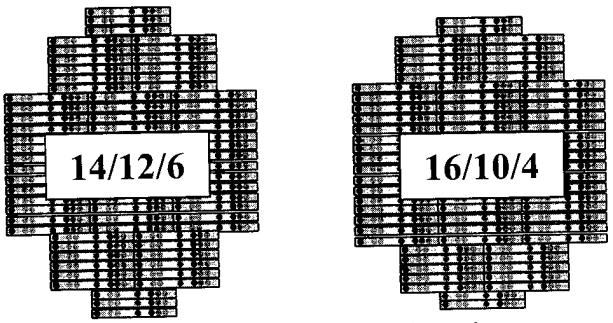


Figure 6. Three-Ribbon Configurations

Both three-ribbon configurations in Figure 6 created slight advantages in cable diameter over the two-ribbon 18/9 and 16/12 configurations. However, slight differences in ribbon geometry and the desire for reduced manufacturing complexity lead to the decision to only consider the two-ribbon configurations. Of the two-ribbon configurations, the 18/9 combination was not selected because it was assymmetrical. The assymmetry was due to the use of nine 24-fiber ribbons, with five above the 36-fiber ribbons and four below the 36-fiber ribbons. Therefore, the 16/12 combination stack was selected for further development.

Because the use of combination stacks was new to Corning Cable Systems, a more traditional stack configuration was also selected for further development. Figure 7 shows the two ribbon stack configurations. The Traditional Stack contained twenty-four 36-fiber ribbons. The Combination Stack contained sixteen 36-fiber ribbons and twelve 24-fiber ribbons.

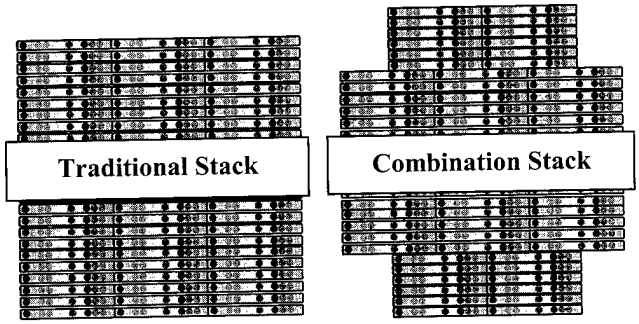


Figure 7. Ribbon Stack Configurations

Both ribbon stack configurations that were considered for further development required the development of a new 36-fiber ribbon.

4. Developing the 36-fiber Ribbon

The most critical aspect of developing the new 36-fiber ribbon was handling. It was important that the handling of the 36-fiber ribbon be as simple as current 24-fiber ribbons on the market. In Thornton's paper on high fiber count cables he states, "For ultra high fiber count cables (or >288), ribbon fiber was the preferred technology due to its mass-fusion splicing ability" [5]. Because mass-fusion splicing creates a critical advantage for ribbon cables, current 24-fiber ribbons on the market can be easily separated into 12-fiber ribbon subunits for mass-fusion splicing. Therefore, it was important to develop a new 36-fiber ribbon with similar manual separation characteristics.

To optimize manual separation, a modular ribbon design was selected. The modular design incorporates a high-modulus inner matrix layer with a low-modulus outer matrix layer to optimize manual separation. The design was similar to Corning Cable Systems' 24-fiber ribbon design discussed by Punch in the proceedings of IWCS 1999. As Punch noted, "Siecor's [now Corning Cable Systems'] previous experience with modular ribbons, coupled with initial 24-fiber feasibility experimentation, indicated the superiority of this design"[6].

A cross-section of the modular ribbon concept is shown in Figure 8. The figure shows the section of a 24-fiber ribbon where the 12-fiber ribbon subunits are joined together. In the figure, two sets of 12 fibers are encapsulated in an inner matrix and the two 12-fiber subunits are then encapsulated together in an outer matrix layer. The chosen 36-fiber ribbon design contained three 12-fiber ribbon subunits and two joining sections.

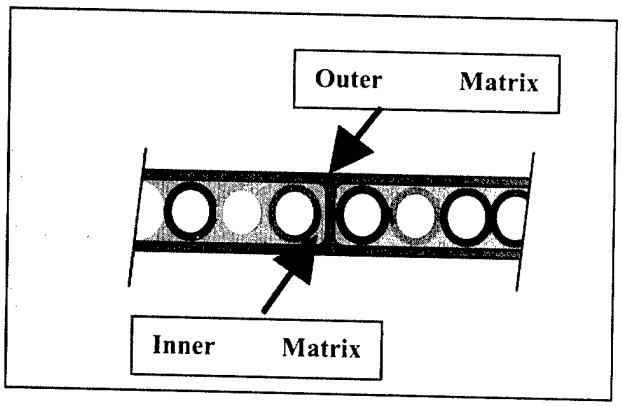


Figure 8. Modular Ribbon Concept

The initial modular 36-fiber ribbon design used different matrix materials for the inner and outer matrices, known for proprietary reasons as B - the inner matrix and C - the outer matrix. With the combination of materials B and C, special processing variables had to be maintained within narrow processing control limits. The narrow process control limits were necessary to maintain acceptable manual separation characteristics.

Control of the processing variable optimized manual separation characteristics by balancing the bond between the inner and outer matrix layers. The two key characteristics for manual separation were stray fibers and outer matrix overhang. During 36-fiber ribbon development, if the bond between the two matrix layers was too high, stray fibers occurred in the 12-fiber subunits during manual separation of the 36-fiber ribbon. The arrow in Figure 9 points to the stray aqua fiber which can occur during separation. The occurrence of stray fibers in the 12-fiber ribbon sub-units makes mass-fusion splicing extremely difficult, if not impossible.

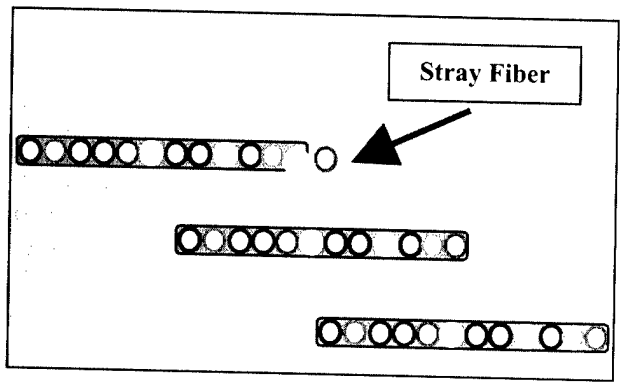


Figure 9. Manual Separation – Stray Fiber

The other key manual separation characteristic was outer matrix overhang. If the bond between the two matrix layers was too low, excessive outer matrix overhang occurred during manual separation, as shown in Figure 10. The thickness of the outer matrix layer is exaggerated in Figure 10 for clarity. The arrows point to the areas where the outer matrix is overhanging from the 12-fiber ribbon subunit.

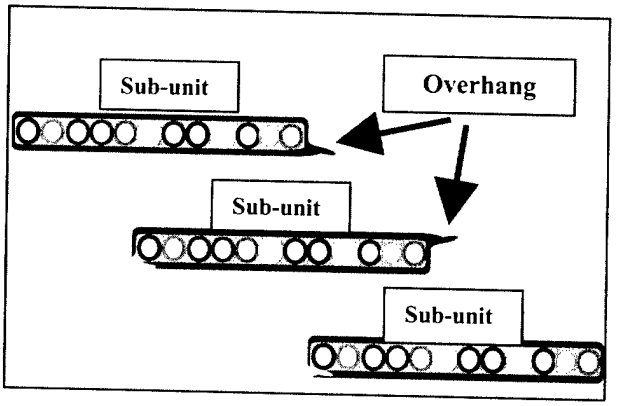


Figure 10. Manual Separation – Matrix Overhang

The excess matrix overhang created two ribbon handling concerns. The first concern was the removal of the ribbon print identification from the adjacent 12-fiber ribbon sub-unit. Since the ribbons were printed on the outer matrix, the removal of the outer matrix from the adjacent 12-fiber ribbon sub-unit could also remove the ribbon print identification. Removal of the ribbon print identification could cause issues with successful execution of the installer's splice plan. Additionally, it was expected that the excess overhang might cause issues with fiber alignment during mass-fusion splicing. However, the relatively soft outer matrix could be easily removed if overhang were to create issues during mass-fusion splicing. Both matrix overhang concerns were less critical than stray fiber occurrences. However, it was expected that the issues could create handling problems in the field.

The desire to further optimize the manual separation characteristics and issues with control of the special processing variable lead to the evaluation of new matrix material combinations for the new 36-fiber ribbon. Several combinations were evaluated and are shown in Table 2, along with the manual separation characteristics of overhang and stray fiber occurrences.

Table 2. Matrix Material Combinations

Inner Matrix Material	Process Variable Setting	Outer Matrix Material	Avg Overhang (mm)	Avg Stray Fibers
B	Low	C	4.80	0.00
B	Med	C	1.60	1.00
B	High	C	2.90	2.40
A	Low	C	1.30	0.00
A	Low	D	2.45	0.20
A	Med	C	2.40	1.60
A	Med	D	2.40	1.20
A	High	C	2.40	2.00
A	High	D	2.80	1.20

Material combination B and C with the process variable at medium (highlighted in gray) was the initial material combination and manufacturing process that was developed. Notice that the average overhang was only 1.60 mm with an average of 1.00 stray fiber per manual separation.

All other material combinations and processing levels produced more overhang than the initial design and/or a higher number of stray fiber occurrences, except the combination of materials A and C with the process variable at low (also in gray). The average overhang was only 1.30 mm with 0.00 stray fibers per manual separation. The results showed that the combination of materials A and C and the process variable at low created the most robust 36-fiber ribbon design with respect to manual separation. In addition, maintaining the processing variable at low was the most robust process for manufacturing the 36-fiber ribbon. Additional production evaluations confirmed that the new material combination with the processing variable at low was a very capable and stable process for manufacturing 36-fiber ribbons.

5. Developing the 864-fiber Cable Design

The final development phase of the 864-fiber cable design consisted of four stages. The first stage focused on evaluating the two ribbon stack configurations in a complex product and process experiment. Once the basic design was determined, stage two focused on developing optional fiber counts and sheath types. Stage three insured that all fiber counts and sheath types met industry specifications. Finally, stage four insured that all fiber counts and sheath types met stringent cable handling requirements.

5.1 The Cable Design Experiment

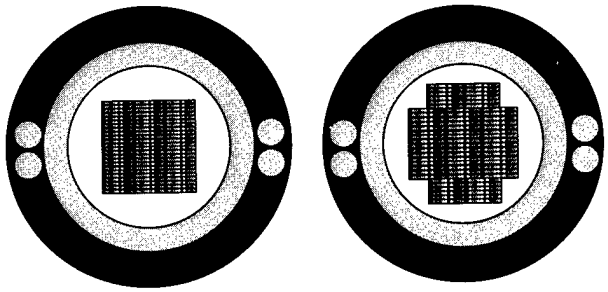
With the new 36-fiber ribbon development complete, the final cable development phase began. The majority of the development for the final 864-fiber design was the result of a complex product and process experiment. The primary variable in the experiment was the ribbon stack configuration. Both the Traditional Stack and Combination Stack (see Figure 9) were evaluated in an eight-cable, two-level, fractional factoral experimental design shown in Table 3.

Four cables were manufactured with the Traditional Stack and are designated with TS in the "Ribbon Stack" column. The other four cables were manufactured with the Combination Stack and are designated with CS in the "Ribbon Stack" column. Additional variables included "Space Ratio," "Ribbon Buffer," "Buffer Setting," "Filling Compound," "Sheath Type," and "Tube Type." Additional description of the variables was not provided for proprietary reasons.

Table 3. Summary of Experimental Design

Cable Name	Space Ratio	Ribbon Buffer	Buffer Setting	Filling Comp	Sheath Type	Tube Type	Cable Diam
1-TS	1.25	A	A	A	B	A	25.2
2-TS	1.25	B	B	B	A	A	24.4
3-TS	1.30	A	B	B	B	B	26.9
4-TS	1.30	B	A	A	A	B	26.1
5-CS	1.25	A	B	A	A	B	23.0
6-CS	1.25	B	A	B	B	B	24.7
7-CS	1.30	A	A	B	A	A	23.9
8-CS	1.30	B	B	A	B	A	25.6

The resulting cable diameters from the experiment are shown in the far right-hand column of Table 3. Notice that the Traditional Stack cables had diameters ranging from 24.4 to 26.9 mm. These cable diameters produced a range of fiber-packing density from 1.85 to 1.52 fibers/mm^2. Fiber-packing density was determined by dividing the number of fibers by the cross-sectional area of the cable. The Combination Stack cables had smaller diameters ranging from 23.0 to 25.6 mm. These cable diameters produced a range of fiber-packing density from 2.09 to 1.69 fibers/mm^2. Figure 11 shows the two typical designs manufactured for the experiment. The Traditional Stack cable contained twenty-four 36-fiber ribbons. The Combination Stack cable contained sixteen 36-fiber ribbons and twelve 24-fiber ribbons.



Traditional Stack **Combination Stack**

Figure 11. Cable Prototype Designs

Numerous cable performance tests were conducted on the eight cables manufactured. Mechanical testing produced similar results for all eight cables in crush, tensile, and bending performance. Field handling test results were also very similar with all eight cables. In addition, the relative flexibility of all of the designs was higher than the minimum of 10 and all of the designs performed well in kink resistance testing. Kink resistance is defined as a cable that kinks at a relatively small bend radius and at a relatively high applied force. Logan correlated good kink resistance to cable robustness in the field [7]. Kink resistance will be discussed further in section 5.4, "Cable Handling Requirements."

The primary responses used for evaluating the cable designs were attenuation performance criteria. The three key criteria were room temperature, temperature cycling, and post-aging temperature cycling attenuation results. Figure 12 summarizes the attenuation results from the experimental cables. In the figure, the horizontal axis shows the respective cable prototypes along with the stack configuration of TS for the Traditional Stack cables or CS for the Combination Stack cables. The vertical axis shows the relative unitless attenuation. Notice that attenuation results with the Combination Stack cables were better than the results with the Traditional Stack cables.

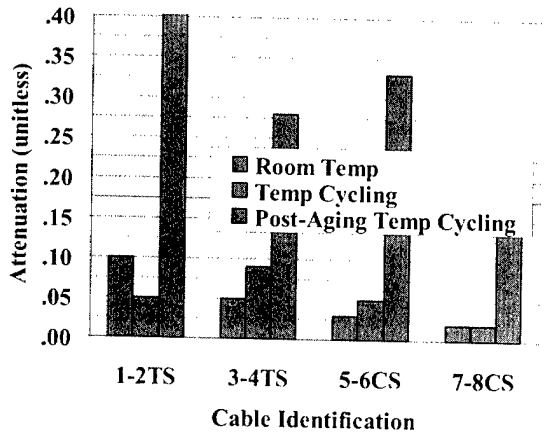


Figure 12. Summary of Attenuation Results

Table 4 summarizes Figure 12 and shows the relative unitless average attenuation of the two stack configurations. The average attenuation of the Combination Stack cables was virtually half that of the Traditional Stack cables. Based on these attenuation performance results, additional development focused on the Combination Stack containing sixteen 36-fiber ribbons and twelve 24-fiber ribbons.

Table 4. Attenuation Comparison of Stack

Ribbon Stack	Room Temp	Temp Cycling	Post-Aging
TS	0.07	0.07	0.36
CS	0.03	0.03	0.22

5.2 Developing Alternative Cable Designs

Subsequent development focused on expanding the available fiber counts to include multiples of 72 fibers from 432 to 864. From the primary 864-fiber design, the product line was expanded to include 504-fiber, 576-fiber, 648-fiber, 720-fiber and 792-fiber designs. Table 5 shows a summary of the available fiber counts and the number of 24-fiber and 36-fiber ribbons contained in each design.

Table 5. Summary of Available Fiber Counts

	Fiber Counts					
	504	576	648	720	792	864
# of 24frs	0	3	3	6	6	6
# of 36frs	14	12	14	12	14	16
# of 24frs	0	3	3	6	6	6

In addition to the planned fiber counts, three sheath types were also developed to meet customer needs. The two standard types were dielectric and armored versions. A third sheath type was added and was termed "toneable." The toneable design contains metallic strength elements for locateability, without the larger cable diameter of the armored design. Table 6 summarizes the available sheath types that were developed, along with the critical design limits of cable diameter, installation load rating, and cable flexibility. The duct fill ratio is also shown for comparison.

Table 6. Summary of Sheath Types

Sheath Type	Cable Diameter mm(in)	1.25-inch (31.8-mm) Fill Ratio	Installation Load Rating lbs(N)	Relative Cable Flexibility
Toneable	23.0(.906)	52%	600(2670)	20
Dielectric	24.0(.945)	57%	600(2670)	20
Armored	25.0(.984)	62%	600(2670)	15

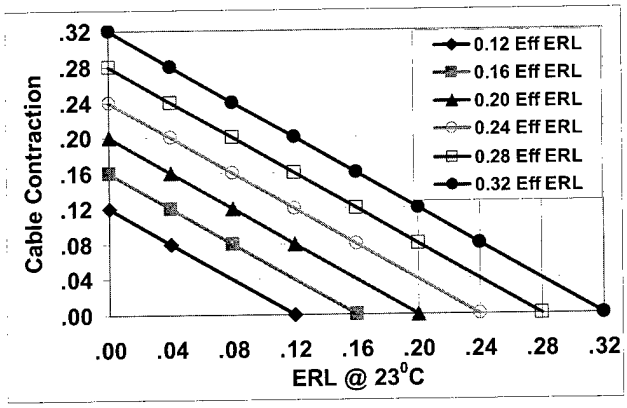
5.3 Meeting Industry Specifications

During development of the alternative cable designs, two industry specifications created key challenges for the product development team. The most difficult requirement to meet was temperature cycling performance. With most optical fiber ribbon cables cold temperature attenuation performance is a critical design criteria. At the industry accepted cold temperature extremes of -40^0 or -30^0C, cable materials shrink and harden creating stresses in the optical fiber ribbons. These stresses create significant attenuation changes when measured at the extreme temperatures as required by most industry specifications.

During the final cable development, two key parameters were identified as critical for meeting industry cold temperature attenuation requirements. Figure 13 shows the correlation of the two key parameters. The two key parameters were cable contraction at the cold temperature extreme and excess ribbon length (ERL) at room temperature. In the figure, cable contraction is on the vertical axis and excess ribbon length is on the horizontal axis. The values within the table represent the sum of the excess ribbon length at room temperature and the cable contraction at the cold temperature extreme. The units are not provided for proprietary reasons.

The sum of the excess ribbon length at room temperature and the cable contraction at the cold temperature extreme equate to the effective excess ribbon length at the cold temperature extreme. The parallel lines represent the effective excess ribbon length (Eff ERL) at the cold temperature extreme. Cables with a high effective excess ribbon length had poor cold temperature attenuation performance. Cables manufactured with low effective excess ribbon length had excellent cold temperature performance.

Figure 13. Cold Temperature Performance Parameters



Two methods for reducing the effective excess ribbon length at the cold temperature extreme were evaluated. The first method was to include additional anti-buckling strength elements into the design to reduce cable contraction at the cold temperature extreme. However, the additional elements reduced cable flexibility, reduced installation lengths, and increased cost. The second method was improved control of excess ribbon length. Several modifications to the manufacturing line were performed to reduce and maintain the excess ribbon length. Reduction and control of the excess ribbon length reduced the effective excess ribbon length at the cold temperature extreme and insured that the design met industry requirements for cold temperature attenuation performance.

The second industry specification that created a challenge for the development team was filling compound flow (drip) performance. Drip testing is performed on a 30-cm (11.8-inch) cable sample. The sample is placed in an oven at a specified high temperature. To meet industry requirements, the filling compound cannot flow from the end of the sample at the specified temperature.

The large inner tube diameter of the higher fiber count designs created a significant problem with meeting industry drip specifications. Numerous variations in filling compound were evaluated. After significant analysis, the key filling compound material characteristic was identified. Cables were then manufactured with the worst-case design. The design exceeded all industry specifications.

5.4 Cable Handling Requirements

Aside from meeting industry specifications, the designs were tested to meet stringent cable handling requirements. The key requirements focused on the robustness of the designs during installation and the preparation time required during mid-span access, end-span access, and closure preparation.

Cable kink performance was the key criteria for evaluating design robustness during installation. Logan's method, which characterizes kink performance by the bend radius and applied load at which kinking occurs, was utilized. Cables were tested across the operating temperature range and compared to other Corning Cable Systems' designs to insure design robustness.

Figure 14 shows the comparison of various cable designs. In the figure, the vertical axis is the applied load, and the horizontal axis is the bend radius. The past cable designs that have been proven in the field are represented with numbers 1 through 10. The only two designs that performed poorly in the field were numbers 5 and 6. The red line represents the point where a good design becomes a bad design based on empirical data from the field. The new higher fiber count designs, represented by number 11, were well above the empirically-determined red line.

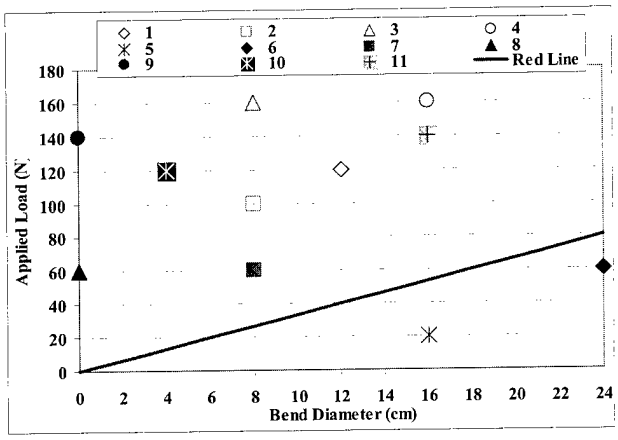


Figure 14. Cable Kink Performance

Cable preparation time was the second key area for meeting stringent handling requirements. Preparation times for an 864-fiber cable were compared with a 432-fiber single tube ribbon cable. For this evaluation, processes for mid-span access, end-span access, and closure preparation were evaluated using appropriate tools. The processes included jacket removal, buffer tube access, ribbon cleaning and identification, ribbon splitting, and ribbon routing inside a closure.

Jacket removal times for the 864-fiber and 432-fiber designs were almost identical, considering the very similar sheath configurations. Buffer tube access was also evaluated. The evaluation showed that with the new Corning Cable Systems' access tool buffer tube access times were comparable. Ribbon cleaning and identification times for the 864-fiber design were approximately double the times for current 432-fiber designs, as expected. This was due to the larger volume of filling compound and the quantity of 12-fiber ribbon sub-units in the 864-fiber design. Ribbon splitting was evaluated with manual separation techniques and with Corning Cable Systems' new 36-fiber ribbon splitting tool. Again, all splitting times were comparable to current ribbon splitting times. Times for ribbon routing in a closure were approximately double routing times for the current 432-fiber ribbon design, as expected.

In summary, the ribbon and cable handling of the new 864-fiber design was very similar to Corning Cable Systems' 432-fiber single tube ribbon design.

6. Conclusion

The development of a novel ribbon stack configuration for the 864-fiber cable was a major technical accomplishment. The new cable design provides a high fiber count cable for metropolitan ring applications, where installability in 1.25-inch inner duct is essential. The design is suitable for increasing bandwidth capacity by filling empty inner ducts or by replacing lower fiber count or slower data rate cables in existing inner ducts. The use of three 864-fiber cables in three 1.25-inch inner ducts allows the customer to utilize 2592 fibers in a single 4.0-inch conduit.

7. Acknowledgments

Special thanks to the key development team members at Corning Cable Systems. The list includes Traci Dobyns, Ron Speights, Steven Flavel, Eddie Hudson, Kitty Tedder, and Ken Temple. Also thanks to support team members from the Telecommunications Cable Plant, R,D&E product evaluation lab, R,D&E materials lab, Hardware and Equipment, and Product Line Management.

8. References

[1] Hecht, "Breaking the Metro Bottleneck," *Technology Review*, June 2001, p. 30-36.

[2] Savage, "Building a Better Backbone," *Technology Review*, June 2001, p. 40-46.

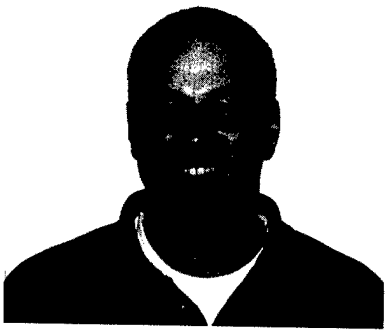
[3] Lail et al, "Maximizing Fiber Count in 1.25-inch Duct Applications ---Defining the Limits---," NFOEC Technical Proceedings (2000): Volume 1, p. 169-180.

[4] Jackson et al, "Optimal Design Strategies for Central Tube Ribbon Cable Comprising 864 Fibers and Beyond," 48th IWCS Proceedings (1999): p. 118-126.

[5] Thornton et al, "Field Proven Ultra High Fiber Count Ribbon Cable Design (864-Fibers in Loose Tube Cable," NFOEC Technical Proceedings (1999): Volume 1, p. 218-229.

[6] Punch et al, "Craft-Friendly 24-fiber Ribbon Design," 48th IWCS Proceedings (1999): p. 72-78.

[7] Logan et al, "Evaluating High Fiber Count Cable Designs for Field Performance," NFOEC Technical Proceedings (1998): Volume 1, p. 385-395.



Jason C. Lail is the supervisor of Ultra-High Fiber Count Ribbon Cable Development at Corning Cable Systems R,D&E facility in Hickory, NC. Jason has a B.S. degree in Mechanical Engineering and a B.A. degree in Business Communication from North Carolina State University. Jason has two previous publications, over 40 internal technical reports, over 40 records of invention, and holds four patents. Jason's focus is on evolutionary high fiber count ribbon cable designs and revolutionary designs to create increased value for the customer.



Craig M. Conrad is the supervisor of Mechanical Engineering Design at Corning Cable Systems R,D&E facility in Hickory, NC. Craig received his M.A. in Physics from the University of South Florida in 1968 and his B.S. in Mechanical Engineering from the University of Florida in 1986. In his current position, Craig supervises mechanical engineering design for the Equipment Development Group.

OSP Loose Tube Ribbon Cable -- Approaching 2000 Fibers --

Parke K. Strong
Corning Cable Systems, Hickory, NC
1-828-323-6088 – parke.strong@corning.com

Douglas S. Hedrick
Corning Cable System, Hickory, NC
1-828-323-6587 – doug.hedrick@corning.com

Abstract

Customers continue to request higher fiber count ribbon cables to meet bandwidth demand in metropolitan areas. Customers desire to minimize installation cost by working within existing infrastructure and by installing a minimum number of cables. This drives the cable designer to increase fiber-packing density, to work within existing infrastructure and to increase fiber count for installing a minimum number of cables.

With increased fiber count, cables inherently become larger and less flexible. Cable diameter and flexibility ultimately limit the installation length of higher fiber count designs. With larger ribbon cable diameters, the loose tube design is more flexible than the traditional single tube design and provides advantages for installation lengths. The loose tube design also provides higher fiber-packing density with existing ribbon sizes and technology.

A 34-mm (1.34-inch) loose tube ribbon cable was evaluated using various installation methods. Cables were installed up to 2300 feet (700 meters). Potential loose tube ribbon cables were then designed for future high fiber count applications. Ongoing evaluations will determine the optimum design.

**US Patent 6,192,178 B1 "Fiber Optic Cable with Profiled Group of Optical Fibers" dated February 20, 2001, applies to this work.*

Keywords

1.25-inch duct; Ribbon; 24-fiber; 12-fiber; Pulling; Air-assisted; Metropolitan; Single Tube; Loose Tube; Installation

1. Introduction

As bandwidth demand increases, cables are becoming larger to accommodate higher fiber counts. Customers typically request higher fiber count cables for large metropolitan areas where telecommunication traffic continues to increase.

As bandwidth demand continues to rise, newer network installations may be installed outside of the existing metro ring infrastructure. These newer networks may consist of two 1.5-inch (38.1-mm) inner ducts in a 4-inch (102-mm) conduit or just direct buried 1.5-inch ducts. These 1.5-inch inner ducts are chosen for higher fiber count cables to minimize the number of cables installed. The outer metro ring application creates demand for the maximum fiber count installable in a 1.5-inch duct.

Existing metro rings typically consist of 4-inch (102-mm) conduit sometimes with three 1.25-inch (31.8-mm) inner ducts already installed. Often, two of the three inner ducts are occupied by older, lower fiber count cables to meet existing bandwidth demand. Customers often request the maximum fiber count that can be installed in the third empty duct. For this paper, the third empty duct is termed the "Third Space Application." This application also creates demand for a higher fiber count cable design.

Currently, there are two ribbon cable designs used in the domestic market for high fiber count applications: single tube and loose tube. As these designs become larger, cable stiffness has become an important issue to installers. Blazer writes, "As installation costs are receiving more scrutiny, stiffness is emerging as an important factor to consider"[1]. The two cable types vary in stiffness and fiber-packing density, thus creating a challenge to determine the optimum design for the 1.5-inch applications and the "Third Space Application." This paper focuses on the most effective ways to maximize metropolitan network fiber count considering cable design, infrastructure, and installation practices.

The first section of the paper evaluates the loose tube and single tube ribbon designs and their effectiveness in high fiber count applications. The second, third, and fourth sections discuss three installation techniques to evaluate the loose tube ribbon design: Pulling, Air-assisted, and the "Third Space Application" or overpulling. The final section presents four loose tube cable designs as potential candidates for a high fiber count cable.

2. Selecting Sheath Design

Single tube and stranded loose tube ribbon cable designs are common in the marketplace. Thus, a comparison was necessary to understand the differences. Figure 1 shows a cross section of Corning Cable Systems' 432-fiber single tube and loose tube ribbon cable designs.

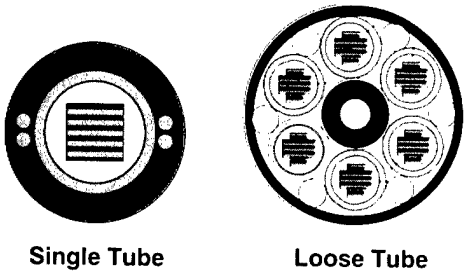


Figure 1. 432-fiber Ribbon Cable

For even higher fiber count applications there are two key areas for comparing the loose tube and single tube designs. The first area is the ability to optimally fill the cable with fiber. With the single tube design and the 1.5-inch (38.1-mm) inner duct constraint, the tube's inner diameter could be as large as 20 mm. With existing ribbon sizes and technology only a stack of thirty-six 36-fiber ribbons could be placed in this design as shown in Figure 2. This results in a fiber count of only 1296 and an inefficient fiber-packing density of 1.70 fibers/mm^2.

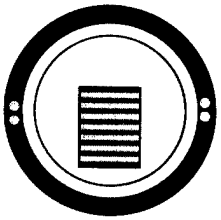


Figure 2. 1296-fiber Single Tube Design

Analysis of the loose tube ribbon design showed, depending on the number of tubes utilized, that the tube inner diameters may range from 8.0-12.0 mm. With existing ribbon sizes and technology, each tube could be optimized for fiber-packing density. Figure 3 shows a prototype 32.5-mm (1.28-inch) design with 1728 fibers and a fiber-packing density of 2.08 fibers/mm^2. The loose tube design provided a critical advantage in fiber-packing density for the higher fiber count applications.

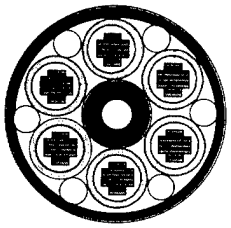


Figure 3. 1728-fiber Loose Tube Design

The second critical area for comparing the loose tube and single tube designs was installation length. For this investigation, duct fill ratios at or above the CCS recommended ratio of 65% were being evaluated. The inside diameter of a 1.5-inch (38.1-mm) duct is approximately 1.45 inches (36.8 mm). The duct fill ratio is determined by dividing the area of the cable outside diameter by the area of the duct inside diameter. Figure 4 shows a 1.34-inch (34-mm) cable inside of a 1.5-inch inner duct. Using a duct inside diameter of 1.45 inches, this 34-mm cable creates an 85% duct fill ratio.

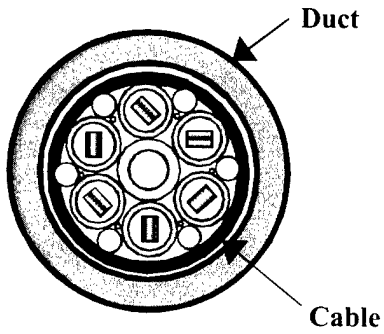


Figure 4. 85% Duct Fill Ratio

With the investigation of duct fill ratios above 65%, it was important to compare the flexibility of loose tube and single tube designs. This was particularly critical with cable diameters above 29.7 mm – the diameter of a cable with a 65% duct fill ratio in a 1.45-inch (36.8-mm) duct. To paraphrase Lail, "In order to install cables with duct fill ratios greater than 65%, one must reduce cable stiffness"[2].

Figure 5 shows the relationship between cable stiffness and cable diameter for the single tube and loose tube cable designs. Because the tube and jacket are concentrated away from the cable center, the stiffness of the single tube design increases faster than that of the loose tube design. Notice at a 30-mm cable diameter, the single tube design is approximately 50% stiffer than the loose tube design.

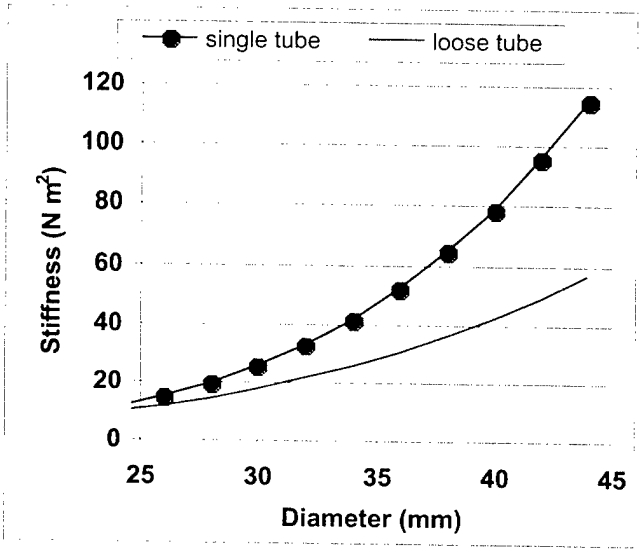


Figure 5. Stiffness vs Diameter

Along with advantages in fiber-packing density, the loose tube design provided installation advantages because it was more flexible than the single tube design. For these reasons, a more detailed analysis was performed on the loose tube ribbon design

with larger cable diameters. The analysis included the manufacture and installation of a six-tube design utilizing three installation techniques: Pulling, Air-assisted, and overpulling in the "Third Space Application."

3. Pulling Installation (1.5-inch Duct)

Corning Cable Systems RD&E used an installation facility to evaluate cable installability. Installability is the level of difficulty associated with placing a cable in a duct. Figure 6 shows a layout of the installation routes utilized for this investigation.

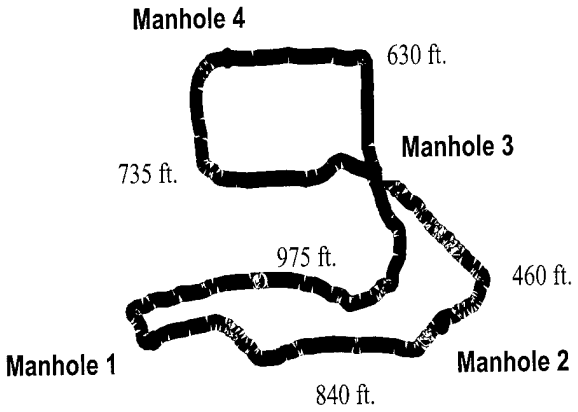


Figure 6. WCP Installation Facility Layout

The first installation application was pulling a 34-mm (1.34-inch) loose tube cable into a new 1.5-inch (38.1-mm) smooth wall, high density polyethylene inner duct. The actual inside diameter of the duct measured 1.45 inches (36.8 mm). This created a fill ratio of 85%.

The 1.5-inch (38.1-mm) inner ducts were installed in a 4.0-inch (101.6-mm) conduit, as shown in Figure 7. In Figure 7, the dashed line represents an inner duct fill ratio of 90%.

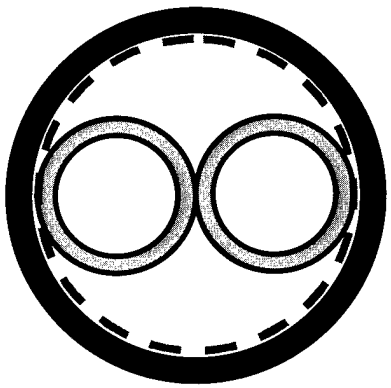


Figure 7. Inner Duct Configuration

The two 1.5-inch (38.1-mm) inner ducts were pulled in the entire 3640-foot (1108-m) route. See Figure 6 for the 3640-foot route layout. For the first cable pulling trial, 1800-pound (454-kg) pulling tape was installed 1930 feet (588 m), from Manhole 1-2-3-4, via the 630-foot route. A standard fiber optic cable pulling grip was attached to the cable central member. Pulling tape was then attached to the pulling grip. The cable was pulled in using a standard wheel-pulling capstan, equipped to monitor the installation load. The cable was installed 1930 feet (588 m) with an installation load of 700 lbs (318 kg). Figure 8 shows a graph of the installation loads during the 1930-foot installation. The total load on the capstan wheel during installation was equal to the sum of the predicted cable and tape loads as shown in Figure 8.

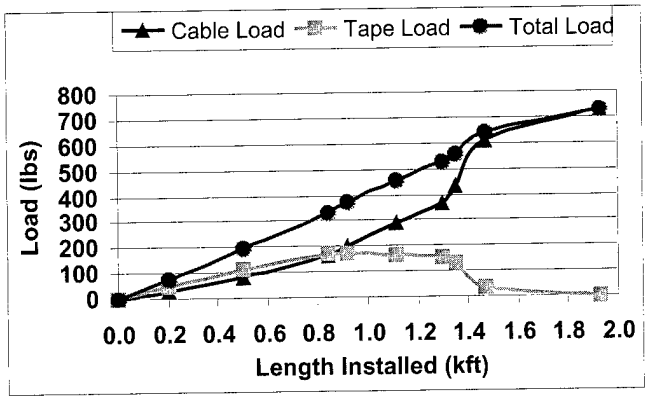


Figure 8. 1940-foot Installation Loads

For the second pulling attempt, pulling tape was installed the entire 3640-foot (1110-m) route. The cable was set up to install from Manhole 1-2-3-4-3-1, via the 630-foot route. During this attempt, the drag force from the pulling tape was considerably higher than in the first attempt. After installing only 600 feet (187 m) of cable, the combined drag from the pulling tape and the cable broke the pulling tape at the pulling grip. Figure 9 shows a graph of the predicted loads during the attempted 3640-foot (1110-m) installation.

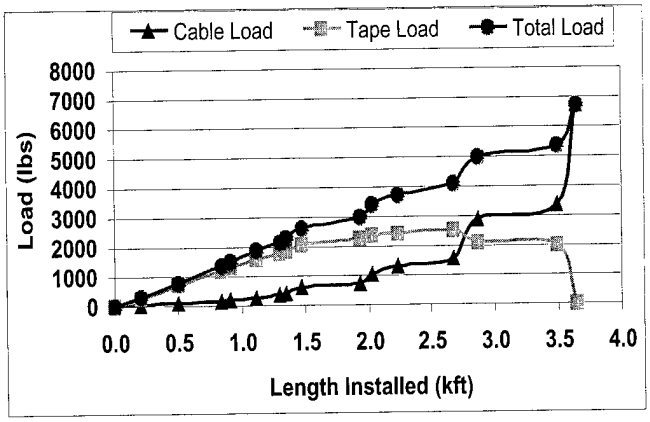


Figure 9. 3640-foot Installation Loads

Unlike the first installation attempt, the 3640 feet of pulling tape in this attempt created a large initial drag force as the cable entered the duct. With a short length of cable in the duct, the drag from the cable quickly increased the pulling tape load. As a result, the pulling tape broke.

Even though the installation in the 3640-foot route was unsuccessful, the success in the 1930-foot route proved that an 85% duct fill ratio was feasible with a loose tube ribbon design and a new smooth-wall inner duct. This provided an excellent benchmark for future development.

4. Air-assisted Installation (1.5-inch Duct)

The second method of installation was air-assisted. As installers target longer installation lengths and become more familiar with air-assist equipment, the method is becoming more popular. Corning Cable Systems purchased equipment for the air-assisted installation trials. The model purchased has a 5.5 hp (4.1 kW) hydraulic pack that provided 250 lbs (1.1 kN) of pushing force.

In order for the air-assist equipment to be effective, air must be blown into the duct at a high velocity. The high velocity air flow creates centering forces that guide the cable in the center of the duct. Once significant cable length is in the duct the air flow also helps to pull the cable. The hydraulic pack is used to run the catepuller, which pushes the cable into the duct. The catepuller and air together create a push-pull system. Typically, air-assisted installations allow longer installation lengths than traditional pulling techniques.

For this second installation application, the cable and equipment were set up for the entire 3640-foot (1109-m), from Manhole 1-2-3-4-3-1. See Figure 6. Once again, the fill ratio with the 34-mm (1.34-inch) cable in the 1.5-inch (38.1 mm) duct was 85%. The cable was successfully installed 2300 feet with the air-assist equipment. This was approximately 370 feet longer than the length installed in the previous pulling installation. Larger hydraulic packs are offered that can provide up to 350 lbs (1.6 kN) of pushing force, which would likely increase installation lengths even further. The results showed that air-assisted installation techniques were feasible for a loose tube ribbon cable with an 85% duct fill ratio in a 1.5-inch inner duct.

5. Third Space Application Installation

As discussed in the introduction, some customers have requested high fiber count cables to fill an existing empty 1.25-inch (31.8 mm) inner duct. In response to these requests, CCS has evaluated an alternate installation technique. This particular application was referred to as the "Third Space Application." The installation technique involves overpulling a cable beside the two previously installed 1.25-inch inner ducts. The unique aspect with the method was that the third empty duct was used to pull in the cable beside the other two inner ducts.

Figure 10 shows a 4.0-inch (101.6-mm) conduit with two 1.25-inch inner ducts and a cable. The outside diameter of a typical 1.25-inch inner duct is 1.66 inches (42.2 mm). When the third inner duct is removed, an area with an approximate diameter of 1.86 inches (47.2 mm) remains. For the "Third Space Application," a 34-mm (1.34-inch) cable was manufactured for installation in the remaining space. This created a fill ratio of 52%.

For the "Third Space Application" trial, Corning Cable Systems purchased two new 1.25-inch (31.8-mm) inner ducts. The two 1.25-inch inner ducts were pulled in along side an existing 1.25-inch inner duct, for a total of three 1.25-inch inner ducts. The completed route went from Manhole 1-2-3-4 via the 630-foot route and totaled 1930 feet (588 m). See Figure 6.

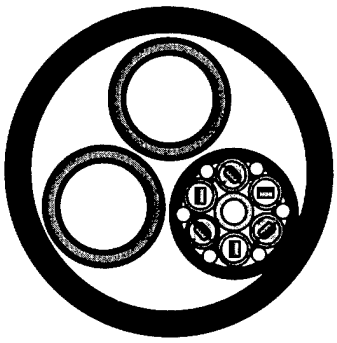


Figure 10. Third Space Application

Refer to Figure 6 while reading this paragraph. A reel payoff cart with the 34-mm (1.34-inch) cable was placed at Manhole 1. The cable was attached to one of the three 1.25-inch inner ducts already installed in the 4.0-inch conduit. A truck with a dynamometer was then used to pull the inner duct out at Manhole 2, as the 34-mm cable was pulled into the inner duct at Manhole 1. The dynamometer was monitored and the installation load recorded. The cable was successfully installed 840 feet (255 m).

For the next pull, the reel cart was left at Manhole 1 and the truck and dynamometer were moved to Manhole 3 and attached to the same 1.25-inch duct. The cable was attached to the 1.25-inch inner duct at Manhole 2. The inner duct was then pulled out at Manhole 3 as the cable was pulled in an additional 460 feet (140 m) from Manhole 2 to Manhole 3. This process was repeated again to Manhole 4, via the 630-foot (192-m) route. After completion of the trial, the cable was installed in the third space of the 4.0-inch conduit a total of 1930 feet.

Table 1 shows the results for the "Third Space Application" trial. Pulling the cable 840 feet (255 m) from Manhole 1 to 2, required an average installation load of 300 lbs (1335 N) and a maximum of 500 lbs (2225 N). Pulling the cable 1297 feet (395 m) required an average of 500 lbs (2225 N) and a maximum of 700 lbs (3115 N). The 1930-foot (588-meter) route from Manhole 1 to 4 required an average load of 700 lbs (3115 N) and a maximum of 1100 lbs (4895 N). The results showed that it was feasible to utilize an existing empty duct to pull in a 34-mm loose tube cable into a 4.0-inch conduit. The results also showed that the installation loads for a 1930-ft route in the "Third Space Application" were similar to the results using traditional pulling techniques in the same 1930-ft route, as noted in Section 3.

Table 1. Third Space Application Results

Route	Length	Average Installation Load	Maximum Installation Load
Manhole 1-2	840 feet	300 lbs	500 lbs
Manhole 1-3	1300 feet	500 lbs	700 lbs
Manhole 1-4	1930 feet	700 lbs	1100 lbs

The two primary design limits for the "Third Space Application" are the short term cable load, or maximum installation load, and the duct breaking strength. To use this method, cables would need to be designed for installation loads above 1000 lbs. In addition, the breaking strength of the duct would also need to be above 1000 lbs. Smooth wall 1.25-inch inner duct is rated for a maximum pulling load of 1800 lbs. The tension needed to install this cable was below the inner duct break strength. However, the type of inner duct and its condition would be a concern at higher installation loads. For example, corrugated inner duct has a breaking strength of 600 lbs and would only be suited for a pull such as from Manhole 1 to 2.

6. Selection of Loose Tube Design

As the installation trials showed, it was feasible to install a 34-mm (1.34-inch) loose tube ribbon cable into a 1.5-inch inner duct and into the third space of a 4.0-inch conduit. With a target diameter of less than 34 mm, it was now necessary to optimize the ribbon stack configuration inside of the buffer tube and then optimize the buffer tube configuration in the cable design.

Various ribbon stack configurations were utilized to maximize the fiber-packing density in several tube sizes. It was determined that using ribbons of various widths in a buffer tube produced a higher fiber-packing density. Fiber-packing density was calculated by dividing the fiber count by the cable area. For example, an 18-mm cable with 216 fibers inside would have a fiber packing density of 0.85 fibers/mm^2. This is a relatively low number because of a rectangular ribbon stack inside of a round tube. Figure 11 shows the buffer tube. Notice the amount of space not filled by ribbon.

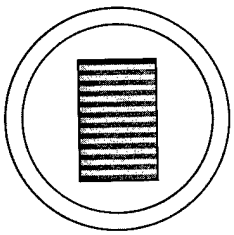


Figure 11. Tube with Rectangular Stack

Figure 12 shows a combination stack, which uses ribbons of different widths inside the same size tube shown in Figure 11. The combination stack contains 288 fibers and has a fiber-packing density 33% higher than the rectangular stack. By utilizing ribbons of different widths, fiber can be placed more efficiently in round tubes. To reference Jackson, "...variable fiber count ribbons can increase the fiber packing density with ribbons in a tube by more than 30% relative to that of constant fiber count ribbons in a square stack"[3].

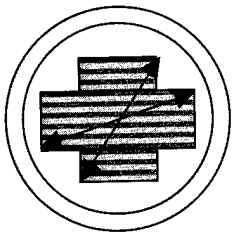


Figure 12. Tube with Combination Stack

Ribbon stacks are characterized by a stack diagonal, which is used to determine the buffer tube inside diameter. Figure 12 shows the stack diagonals for a combination stack. The largest diagonal is used to determine the inside diameter of the buffer tube. For a particular fiber count in a buffer tube with specific ribbon sizes, there is a single combination of different ribbon widths that yields the smallest stack diagonal. Figure 13 demonstrates this with a buffer tube containing 360 fibers.

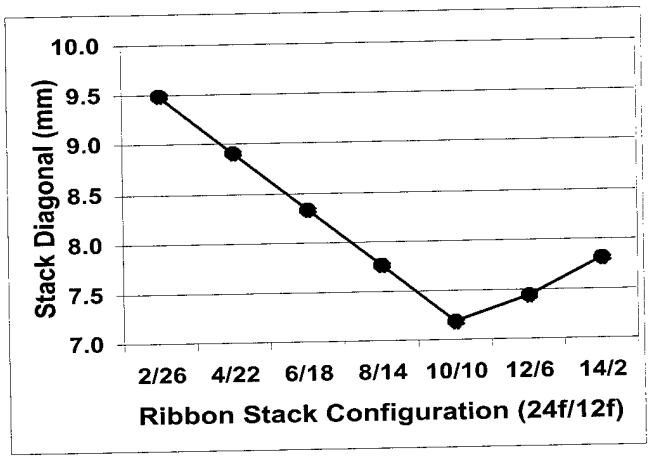


Figure 13. Diagonal vs Stack Configuration

As Figure 13 shows, a combination stack of ten 24-fiber ribbons and ten 12-fiber ribbons yields the smallest stack diagonal, and thus the smallest buffer tube.

After several tube sizes and fiber counts were optimized, various tube layouts were evaluated to determine the most efficient tube configuration for a 1728-fiber cable. Figure 14 shows a 1728-fiber four-position loose tube ribbon cable. The four-position cable contained four buffer tubes with 432 fibers in each tube. Each buffer tube contained fourteen 24-fiber ribbons and eight 12-fiber ribbons. The buffer tubes had an outside diameter of approximately 11.0 mm (0.43 inches). The cable outside diameter for this design

was approximately 32.5 mm (1.25 inches). The fiber packing density was approximately 2.08 fibers/mm^2.

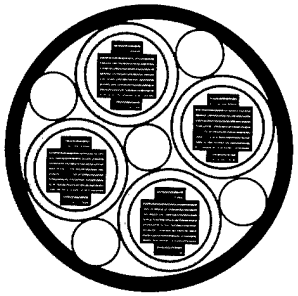


Figure 14. 4-Position Loose Tube Cable

Figure 15 shows an 1800-fiber five-position loose tube cable. The five-position cable contained five buffer tubes with 360 fibers in each tube. Each buffer tube contained ten 24-fiber ribbons and ten 12-fiber ribbons. The buffer tubes had an outside diameter of approximately 10.5 mm (0.41 inches). The cable outside diameter for this design was approximately 32.5 mm (1.25 inches). The fiber packing density was 2.17 fibers/mm^2.

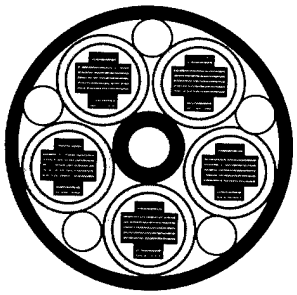


Figure 15. 5-Position Loose Tube Cable

Figure 16 shows a 1728-fiber six-position loose tube cable. The six-position cable contained six buffer tubes with 288 fibers in each tube. Each buffer tube contained six 24-fiber ribbons and twelve 12-fiber ribbons. The buffer tubes had an outside diameter of approximately 10 mm (0.39 inches). The outside diameter for this cable design was approximately 32.5 mm (1.25 inches). The fiber packing density was 2.08 fibers/mm^2.

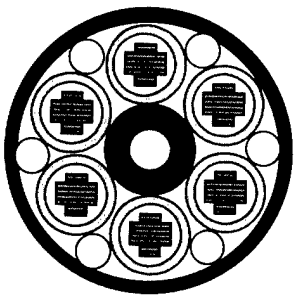


Figure 16. 6-Position Loose Tube Cable

Figure 17 shows a 2304-fiber eight-position loose tube cable. The eight-position cable contained eight buffer tubes with 288 fibers in each tube. Each buffer tube contained six 24-fiber ribbons and twelve 12-fiber ribbons. The buffer tube diameter was approximately 10 mm (0.39 inches). The cable outside diameter for this design was approximately 39 mm (1.54 inches). The fiber packing density was approximately 1.93 fibers/mm^2.

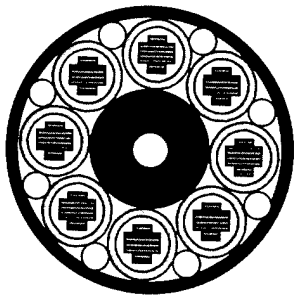


Figure 17. 8-Position Loose Tube Cable

Based on the target cable diameter of 34 mm (1.34 inches), the 8-position design was eliminated as an option. The 4-position, 5-position, and 6-position loose tube designs are being evaluated based on cable and buffer tube access, cable stiffness, fiber count per tube, and cable diameter to determine the optimum cable design for high fiber count applications.

7. Conclusions

With increased fiber count, cables inherently become larger and less flexible. Cable diameter and flexibility ultimately limit the installation length of higher fiber count designs. Two different cable designs, single tube and loose tube, were evaluated to determine the optimum design for existing high fiber count applications. The loose tube design was more flexible than the single tube design and provided advantages for installation. The loose tube design also provided higher fiber-packing density.

A 34-mm (1.34-inch) loose tube cable was used to evaluate three different installation techniques: Pulling, Air-assisted and the "Third Space Application", or overpulling. Table 2 shows the results of the three installation techniques.

Table 2. Summary of Installation Trails

Installation Type	Fill Ratio	Length Attempted	Length Installed	Maximum Installation Load
Pulling	85%	1930 ft	1930 ft	700 lbs
Pulling	85%	3640 ft	600 ft	1000÷
Air-assisted	85%	3640 ft	2300 ft	N/A
Third Space	52%	840 ft	840 ft	500 lbs
Third Space	52%	1300 ft	1300 ft	700 lbs
Third Space	52%	1930 ft	1930 ft	1100 lbs

The results showed that it was feasible to install a 34-mm (1.34-inch) cable into a 1.5-inch (38.1-mm) inner duct, at a fill ratio of 85%. Multiple loose tube cable designs are being evaluated based on cable stiffness, cable and buffer tube access, fiber count per tube, and cable diameter to determine the optimum cable design for high fiber count applications.

8. Acknowledgements

Special thanks to Larry Barrett of Corning Cable Systems for his help with the installation trials.

9. References

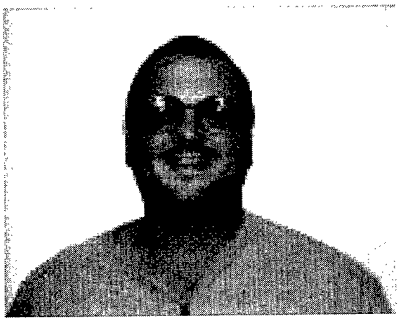
[1] Blazer, "Flexural Rigidity Analysis of Optical Fiber Cable," *49th IWCS Proceedings* (2000): p. 317-322.

[2] Lail et al, "Maximizing Fiber Count in 31.8-mm (1.25-inch) Duct Applications – Defining the Limits," *NFOEC Technical Proceedings* (2000): Volume 1, p. 169-180.

[3] Jackson et al, "Optimal Design Strategies for Central Tube Ribbon Cables Comprising 864 Fibers and Beyond," *48th IWCS Proceedings* (1999): p. 118-126.



Parke Strong received his Bachelor of Science degree in Mechanical Engineering from North Carolina State University. Parke has been with Corning Cable Systems for six years. His first four years were spent as a process engineer in a manufacturing environment. His current position is a product development engineer in the high fiber count development group at the Research, Development and Engineering facility.



Douglas S. Hedrick attended Fairmont State College and Lenoir Rhyne College. Doug has worked with Research, Development and Engineering at Corning Cable Systems for four years in the outdoor cable development group. Doug has an additional 8 years experience in the manufacturing and testing of outdoor cable. Doug also has two patent applications pending.

Optimal High Fiber-Counts Microsheath Cables Fitting New Fiber Networks Requirements

Patrick JAMET, Philippe TROMBERT, Nathalie LECOURTIER, Daniel BERNIER, Maurice DELPECH

SAGEM Cables Division
rue de Varennes Prolongée - 77130 MONTEREAU - FRANCE
+33 1 60 57 31 03 patrick.jamet@sagem.com

Abstract

This paper describes the successful evolution and optimization of the microsheath cable technology up to the high fiber-counts becoming currently required in the new optical fiber networks being rolled-out worldwide

Keywords

High fiber count; microsheath cable; unit; module; mid-span access.

1. Introduction

Since it was first presented [1], the microsheath cable design has been applied to creating a comprehensive family of optical cables suited to the most commonly found applications in this time frame, which typically called for "medium" fiber-counts ranging up to 144 and 288 OF. It is now widely used in this framework, owing to its features to make installation easy and cost-efficient [2]. More generally, the concept of high packing density, micromodules-based cables [3][4][5] has quickly spread, as a favourable alternative to traditional loose tube cables.

Driven by deregulation, IP traffic and broadband services, the building of new fiber networks is surging in most regions, with a marked trend to migrate from long haul backbones towards city-rings or metro applications and closer to end-users, where rights-of-way, duct-space and installation productivity are key factors. This naturally leads to increasing fiber-counts, with needs currently reaching 864 OF. With such high fiber-counts, practical and important features related to cable compactness and handleability on one hand, fiber access, identification and routing on the other, become ever more challenging.

In this evolutionary context, our objectives were to extend, and even to increase the core-benefits of the microsheath design relating to compactness, scalability (modularity), flexibility and versatility, while maintaining a high level of performance.

In particular, this translates into the following target features:

- very high fiber packing density;
- suitability to all types of fibers (standard G652 as well as advanced G655);
- high grade optical, temperature and mechanical performance, adjustable to various installation and environment conditions;
- extremely easy cable entry and fiber access, both end-point and mid-span;
- fast and reliable splicing (both mass or individual) and management of units and fibers inside closures, using existing jointing techniques;
- suitability of the design modular concept to be readily extended to even higher fiber-counts when required by the market.

This has been successfully achieved through the development of 432 and 864 OF cables where fibers are organized in microsheath units (or modules) and "super-units" (or super-modules), as will be described below.

2. Cable design

As a reminder, in the microsheath cable design, the fibers are divided into bundled fiber-modules (containing from 2 to 12 fibers) covered by a thin, easily removable supporting synthetic sheath. The modules are assembled together and enclosed in a protective covering or sheathing including reinforcing members.

The fiber identification is achieved by a user-friendly color-coded scheme applied on fibers and modules.

The level of performance required is achieved by selecting and adjusting the composition, dimensions, and materials used. Furthermore, this structure naturally lends itself to simple, efficient and reliable manufacturing processes, characterized by a minimum number of operations, high running speeds and long production units [6].

In case of high fiber-counts such as 432 and 864-OF, it would not be realistic to pack a great number of modules within a single bundle, with regard to manufacturing, fiber-identification and installation aspects.

On the contrary, the modular concept and production methods of microsheath cables naturally lead to dividing the modules into

several "super-modules", each of them being also covered with a thin, easily removable, coloured sheath, similar to the sheath of the basic modules.

This results in a very limited loss of packing density as compared with the maximum "theoretical" values attainable with a single bundle assembly, the soft super-modules shaping themselves to best occupying the available space inside the outer covering system. On the other hand, this has major advantages regarding:

- the ease and reliability of manufacturing process;
- the ease of fiber identification, based on the same colour scheme at all levels (fibers, modules, super-modules);
- the ease of fiber-access, especially mid-span, and of routing within splice closures, as will be highlighted in a further chapter.

Furthermore, the modularity of super-modules can be chosen and easily adjusted so as to yield an optimal design with regard to various production and/or installation criteria, such as:

- scale of fiber-counts within the family of cables, in order to best organize the production flow of semi-products;
- modularity of network architecture, in order to best meet operator's planning and engineering requirements;
- type and modularity of jointing closures or associated devices, in order to ease and optimize field operations.

On basis of such considerations, and taking into account current market demand in Europe, we have presently opted for super-modules containing 144 fibers divided into 12 basic modules of 12 fibers each.

Figures 1a, 1b and 2 thus illustrate 864 and 432 fibers metal free duct cables, respectively based on 6 and 3 super-modules.

Fig.1a: 864 O.F. µ-SHEATH® cable

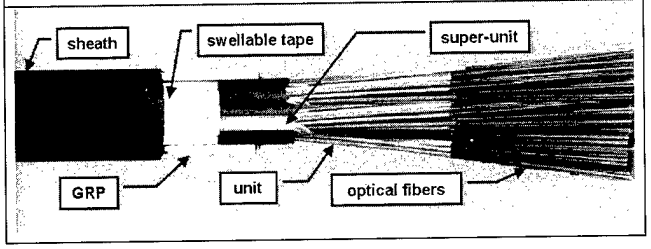
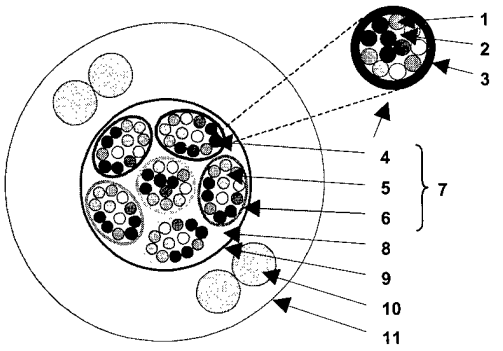
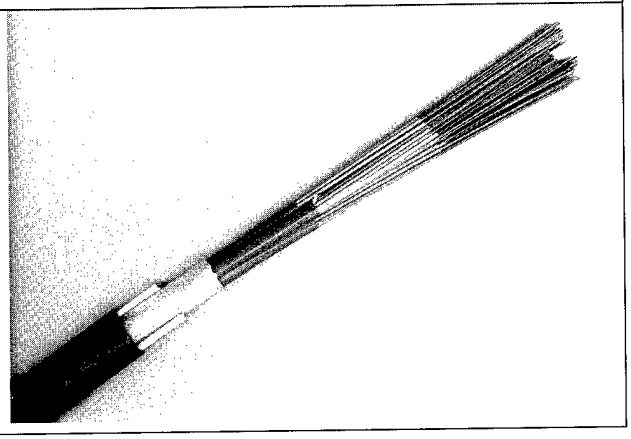


Fig.1b: 864 O.F. µ-SHEATH® cable



1: coloured optical fiber
2: filling compound
3: coloured microsheath
4: 12 O.F. unit (or module)
5: swellable element
6: coloured microsheath
7: 144 O.F. super-unit (or super-module)
8: swellable element
9: tape
10: dielectric strength member
11: HDPE sheath (diameter: 23.5 mm)

Fig.2: 432 O.F. µ-SHEATH® cable



3. Packing density

The microsheath design intrinsically leads to very high fiber packing density all along the range of fiber counts. This results from the minimum empty space allowed within the circular fiber modules as well as within the assembly of units and super-units, and also from the small dimensions of the reinforced covering, which is optimized in relation with the ultra low weight of the cable.

This is all the more significant as the fiber count increases. The packing density reaches values about 1.6 fibers / mm² for 432

O.F. cable and 2.5 fibers / mm² for 864 O.F. cable, which are noticeably higher than the results previously published relating to other high fiber counts cable types [7] [8] [9].

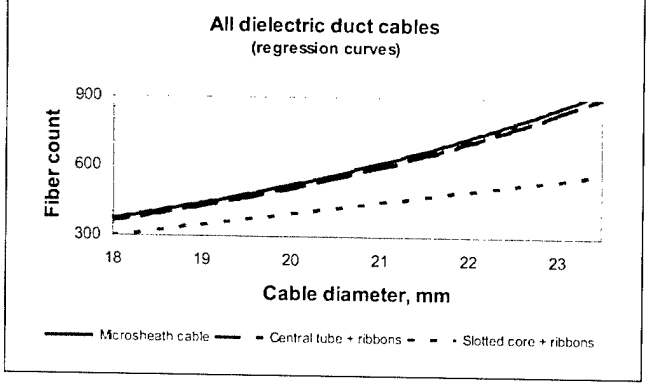
The packing density thus obtained is:

- higher than in the case of cables with stranded loose tubes or with slotted core(s) containing ribbons, which are adversely affected by the sizes of the central strength member and of the tubes or slots designed to accommodate the ribbonized fibers with overlength;

- similar in the case of central tube cables containing ribbons [10] which are however subjected to the constraints associated with the asymmetrical nature of the ribbons.

Figure 3 illustrates this comparison. It is expressed as the fiber counts enabled by the various structures (in the case of metal-free duct cables) as a function of the cable outer diameter.

Fig.3: Comparison of packing density



Furthermore this high packing density translates into very light weight providing high laying ability in spite of the high fiber count.

4. Functional adaptation and performance

A cable design has to be versatile to adapt to the various conditions of installation and environment which can be met in the network infrastructure implementation. Depending on the type of conditions faced, it is necessary to enhance specific characteristics of the cable.

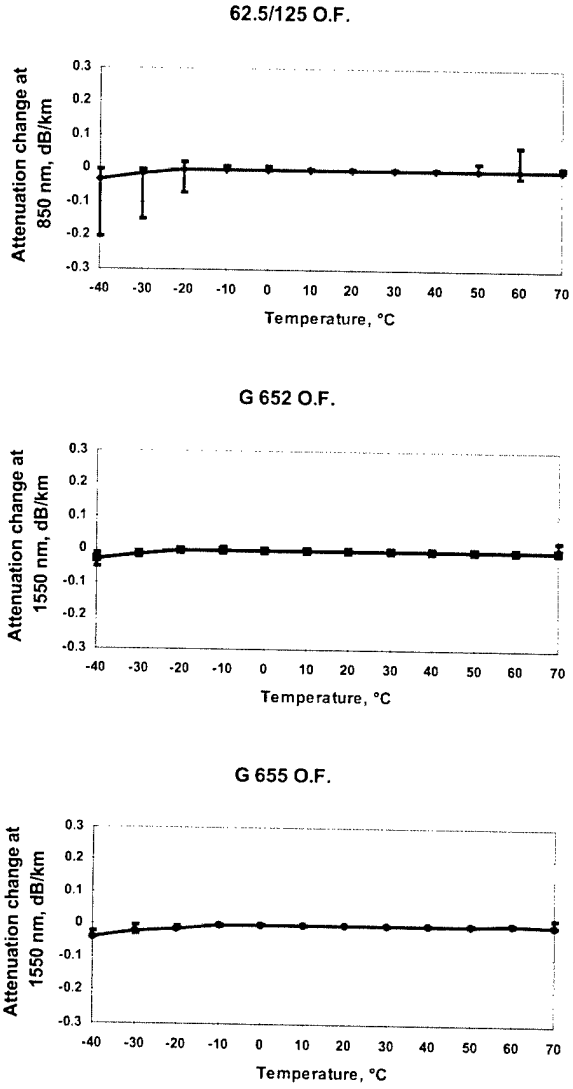
With the microsheath technology, a comprehensive family of cables is easily built on the basis of the central assembly of modules, by varying, in accordance with traditional cable techniques, the design and materials of the protective/reinforcing sheathing system.

For high fiber count cables the same solutions as those currently used on medium fiber count microsheath cables are also applicable as described in table 1.

The main resulting performance for all-dielectric and corrugated steel armoured 432 and 864 OF cables are shown in table 2.

Figure 4 gives the results obtained during temperature cycling with a 432 O.F. cable containing various types of fibers.

Fig.4: Temperature cycling test (432 O.F. cable)



This level of performance fits the functional requirements which are generally associated to the corresponding types of applications according to most international specifications (BELLCORE, IEC, EN, ...).

In particular, taking into consideration the very small weights and diameters displayed, the pulling and bending abilities of the microsheath cables are indeed very high.

5. Installation features

One of the most significant current evolutions of optical networks is the migration from long haul/ backbones applications, which are stabilizing, towards metropolitan/access deployments, which are growing at a fast pace.

This presents operators with new challenges in targeting corporate or residential customers in various situations, ranging from suburban business parks to congested city centers, with some degree of uncertainty as to the location and timeframe of connection. This also involves using alternative and scarce rights-of-way such as subway tunnels and sewer systems.

In this context, operators are seeking solutions to, at the same time, maximize fiber-counts, reduce time and cost of deployment, and preserve flexibility and future-proofing of the cable plant.

To this end, and in addition to their ultra-compactness, scalability and versatility discussed above, microsheath cables offer specific advantages to ease engineering and implementation (laying, jointing, access) at all levels:

- best utilization of existing civil works, or simplification of new civil works: the compactness, pulling and bending abilities of the high fiber-count microsheath cables enable to reduce the volumes of ductings, diggings, troughs or other receiving structures, to increase the lengths between chambers and to follow routes with tight bends.
- simplification of laying process: the small weight and optimally balanced flexibility/stiffness without residual deformation suit all methods, either traditional (pulling, hand laying, ..), or innovative (air or water blowing or jetting). This enables to use, depending on local conditions, the technique most appropriate to reduce installation time, equipment and staff.
- progressive and flexible deployment and allocation of fibers, owing to extremely easy cable entry and fiber access, as illustrated in fig. 5, 6 and 7. This well known feature of the microsheath design is extended at the super-unit level in high fiber-counts cables. This fully meets the need of accessing either mid-span or within closure, either when first installing or when re-entering or upgrading the network. Indeed, access to and tapping of some fibers within live microsheath cables have been field demonstrated.
- fast, reliable, on-demand splicing, which can be performed either individually or taking advantage of existing mass-splicing equipments (fig. 8 & 9) with results comparable to ribbons (fig. 10) [11] [12].
- compactness and simplification of jointing closures (fig. 11) with direct coiling of the modules inside the cassettes, due to high flexibility in all directions, cohesion, small size and identification system of the microsheath units and super-units.

Fig.5: quick cable sheath opening

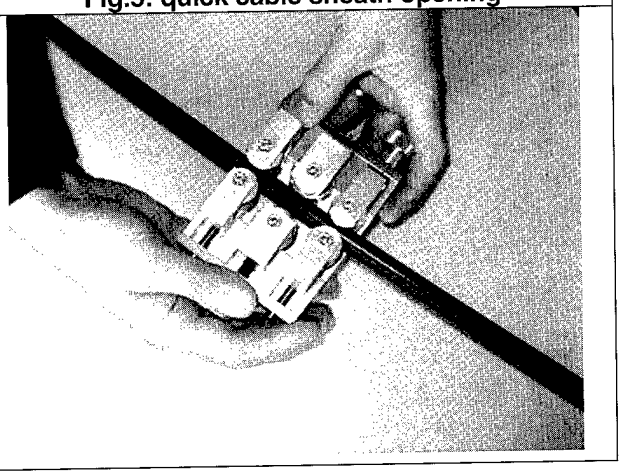


Fig.6: quick super-module opening

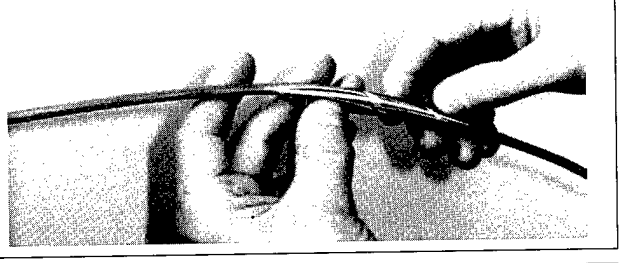


Fig.7: quick module opening

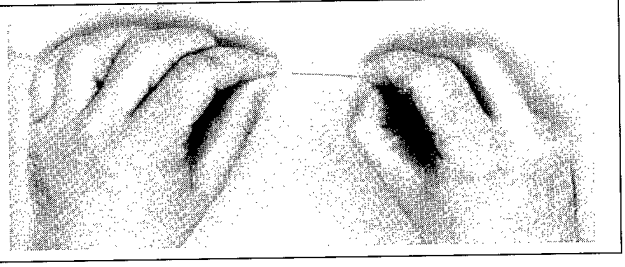


Fig.8: flat arrangement of optical fibers

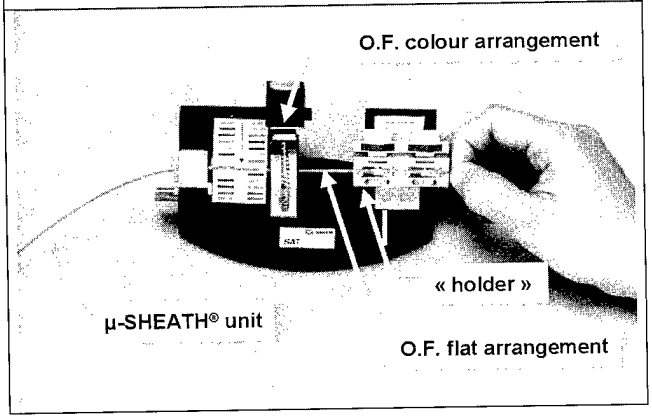


Fig.9: unit mass splicing

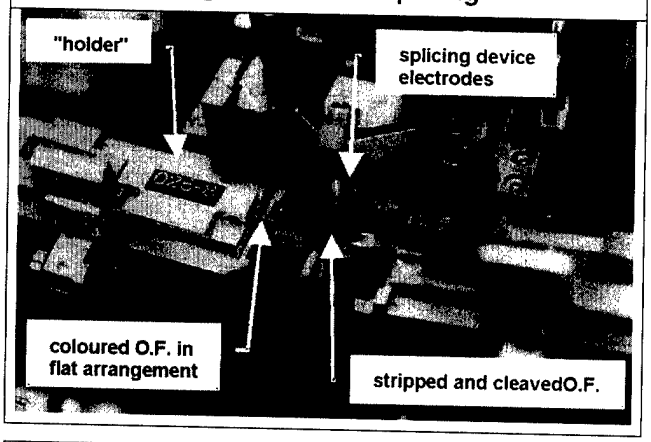


Fig.10: splicing attenuations

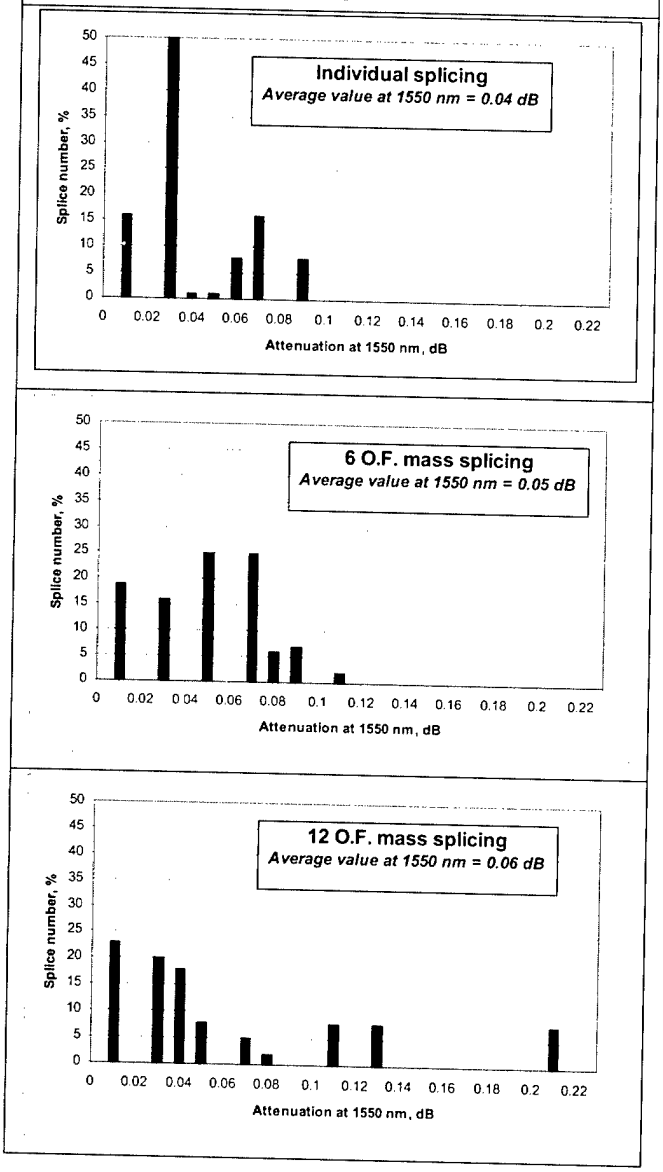
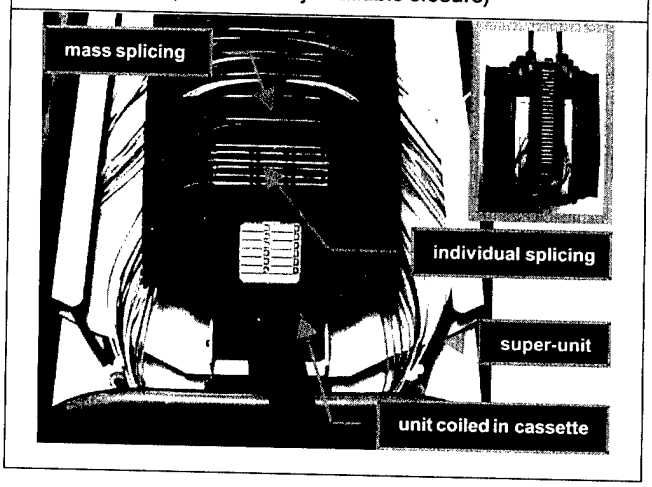


Fig.11: example of jointing
(commercially available closure)



6. Extension to higher fiber counts

The modular design of the 432 and 864 O.F. cables can be readily extended to even higher fiber-counts when required by the market:

- either by increasing the number of super-units (super-modules),
- or by increasing the number of units (modules) inside each super-unit.

Stranding super-units and sheathing assemblies of super-units are indeed easily performed through traditional cablemaking techniques, even on non dedicated manufacturing lines, owing to the cylindrical nature, bending ability and intrinsic strength (resulting from the combination of the individual fibers enclosed), of the super-units.

For instance a super-unit containing 12 units of 12 fibers can accept more than 40 daN (corresponding to 1/3 of the screen test value on each bare fiber) during its stranding operation without any damage. In the same way, an assembly of 12 super-units containing each 12 units of 12 fibers (1728 O.F. cable) would accommodate up to 500 daN during the sheathing process.

7. Conclusion

In conclusion, the microsheath technology and its specific advantages of ultra-compactness and ease of installation (laying, access , routing and splicing) have been successfully extended to high fiber-counts, presently 432 and 864.

Thus, concurring with the evolution of fiber networks towards metro applications and high fiber-counts, microsheath cables provide, over an extended range, an optimal solution to operators and contractors having to plan and deploy fiber cables plants in the most time/cost-effective, flexible and evolutionary manner.

Table 1: µ-SHEATH® cable functional family	
REQUIREMENTS	TYPICAL DESIGN FEATURE
standard requirements (typically for ducts)	basic design: watertight modules, metal free construction, PE sheath. optional: water-blocking, swellable materials in core.
enhanced mechanical protection against crush, impact, rodents (typically direct buried, troughs, sewers, ...)	additional steel corrugated bonded tape optional: additional steel wires armoring.
enhanced protection against fire hazards (typically indoor or tunnel installation)	flame-resistant, LSOH sheath.
enhanced tensile strength	additional dielectric strength members.

Table 2: 432 and 864 O.F. µSHEATH® cables performance (1)				
Fiber count (nominal)	**432 O.F.**		**864 O.F.**	
Cable type	**all dielectric**	**armoured**	**all dielectric**	**armoured**
Maximum O.F. count (2)	468 (432 + 3x12)	468 (432 + 3x12)	936 (864 + 6x12)	936 (864 + 6x12)
Maximum packing density	1.57 O.F./mm²	0.88 O.F./mm²	2.50 O.F./mm²	1.42 O.F./mm²
Outer diameter	19.5 mm	26 mm	23.5 mm	30 mm
Weight	265 kg/km	530 kg/km	400 kg/km	760 kg/km
Construction	Stranded super-modules containing 144 O.F each. Dry (swellable) core waterproofing Polyethylene sheath embedding 4 dielectric strength members	* Corrugated steel armor + PE sheath		* Corrugated steel armor + PE sheath
Optical performance	No change as compared with bare fibers (attenuation, PMD, ...)			
Mechanical characteristics (*)				
- Bending				
Minimum kink radius	95 mm	335 mm	115 mm	390 mm
Minimum static bend radius	195 mm	335 mm	235 mm	390 mm
- Tensile performance				
Maximum installation load	480 daN	600 daN	730 daN	900 daN
Ratio load/weight	> 1.8	> 1,1	> 1.8	> 1,2
- Crush performance				
Maximum load	25 daN/cm	40 daN/cm	25 daN/cm	40 daN/cm
- Impact performance				
Energy	5 N.m	20 N.m	5 N.m	20 N.m
Temperature range				
- Operation (*)	-40 °C / +70 °C		-40 °C / +70 °C	
- Installation (**)	-5 °C / +40 °C		-5 °C / +40 °C	
- Storage / shipping	-40 °C / +70 °C		-40 °C / +70 °C	
Environment				
- Watertightness	Compliant with IEC 794-1-F5			

(1) testing methods according to IEC 60794-1

(2) including an optional spare module in each super-unit

* : Reversible attenuation

** : Between –5 °C and +5 °C, 24 hours storage at +20 °C prior to laying is recommended

References

[1] P.TROMBERT *et al.*, The microsheath cable: a novel design of ultralightweight single mode optical cable for low cost subscriber loop, IWCS, 1991

[2] P.TROMBERT, Joint booming for fiber networks in Europe and Microsheath cables, KMI conference, Paris, may 2001

[3] S. PASTUSZKA *et al.*, A new type of high fiber count, low dimension optical cable with simplified installation characteristics, IWCS, 1999

[4] J.L. ROCHEFORT *et al.*, Nouvelles générations de câbles densifiés, EuroWire, November 2000

[5] H. PAUL DEBBAN *et al.*, A new high density central cable core design, IWCS, 2000

[6] P.JAMET - A.JARLOT, Manufacturing and field experimentation of microsheath cable for low cost subscriber loop, IWCS, 1994

[7] E.R.LOGAN *et al*, The status and future of high fiber count cable designs, IWCS, 1999

[8] F.LEGROS *et al.*, Optical fiber ribbon cable designs for a wide range of applications as the availability of FTTH is realized, IWCS, 1996

[9] SHINSUKE NIIYAMA *et al.*, Down sized fiber optic duct cable, IWCS, 1996

[10] K.W. JACKSON *et al.*, Design and performance of a high capacity, compact, modular ribbon cable comprising 24 fiber ribbons, IWCS, 1996

[11] J.P. BONICEL *et al.*, New concepts in optical cable spliceability versus optical design, IWCS, 1996

[12] P.JAMET *et al.*, Les câbles à microgaine, une technique innovante, une réalité industrielle, OPTO, 1996

µ-SHEATH® is a registered trademark of SAGEM

Authors



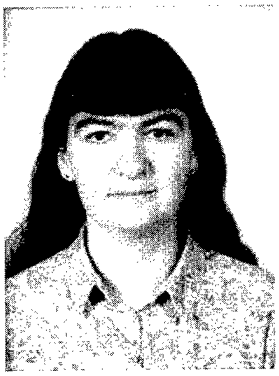
Patrick JAMET
SAGEM, Cables Division
Rue de Varennes Prolongée
77876 MONTEREAU CEDEX
FRANCE
patrick.jamet@sagem.com

Patrick JAMET received his PhD in chemical physics from the DIJON University in 1976. After 11 years in R & D dpt of a telecom cables manufacturer he joined SAGEM in 1989 where he was TELECOM R & D manager. He has 23 years of experience in the optical cable industry and is presently Optical Cables Product Manager. He has been granted more than twenty patents (including microsheath cables).



Philippe TROMBERT
SAGEM, Cables Division
Rue de Varennes Prolongée
77876 MONTEREAU CEDEX
FRANCE
philippe.trombert@sagem.com

Philippe TROMBERT graduated from Institut National Polytechnique de GRENOBLE in 1970. He joined SAGEM in 1973. He has over 25 years of experience in the cable industry including several positions in R&D, marketing and business development of power and telecom cables. He has been granted several patents (including microsheath cables) and is now Product Manager and involved in O.F. cables marketing.



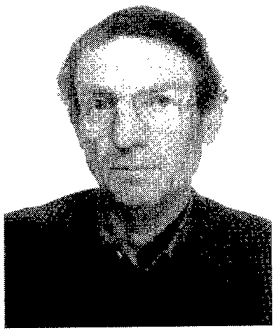
Nathalie LECOURTIER
SAGEM, Cables Division
Rue de Varennes Prolongée
77876 MONTEREAU CEDEX
FRANCE
nathalie.lecourtier@sagem.com

Nathalie graduated from ENSI of CAEN in 1987. She joined SAGEM in 1988. where she was successively involved in quality, testing, R&D and technical contracts for telecom cables. She is now R&D Manager for Optical Cables.



Daniel BERNIER
SAGEM, Cables Division
Rue de Varennes Prolongée
77876 MONTEREAU CEDEX
FRANCE
daniel.bernier@sagem.com

Daniel BERNIER graduated as electronic technician (Lycée Technique Eiffel - DIJON, 1971). He joined SAGEM in 1971 and has been involved in fiber optic cables since 1979.(R&D, processing, testing and production). He has been granted several patents and is presently R & D Engineer for Optical Cables.



Maurice DELPECH
SAGEM, Cables Division
Rue de Varennes Prolongée
77876 MONTEREAU CEDEX
FRANCE
maurice.delpech@sagem.com

Maurice DELPECH joined SAGEM in 1964 where he was a field expert for cables installation and jointing. He has been granted several patents and joined the R&D team in 1997.

Advances in Blown Cable Technology: The Development and Life Cycle Analysis of a High Density Optical Fibre Cable

Martin V Davies, Chris J Esbester, Ralph Sutehall
Pirelli Cables
Newport, South Wales, UK
+44-1633-203400 Martin.Davies@pirelli.com, Chris.Esbester@pirelli.com, Ralph.Sutehall@pirelli.com

Phil Barker
BTexact Technologies, Adastral Park
Martlesham, Suffolk, UK
+44-1473-642649 Phil.A.Barker@bt.com

Dave F Bastin
BT Wholesale Network Access
Brentwood, Essex, UK
+44-1277-322063 Dave.Bastin@bt.com

Abstract
In 1999, a programme of work (the ACTION* programme) was initiated by British Telecommunications plc (BT) aimed at reducing the overall costs of optical cable network expansion, with the goals of at least a 15% reduction in installation time, an increase in installable cable lengths with, therefore, a reduction in the number of cable joints, and the use of smaller sub-duct. At that time, the use of blown cable technology was gaining momentum and the ACTION programme aimed to exploit such techniques with 'miniaturised' cables.

The ACTION programme adopted a system oriented approach, whereby cable, duct, sub-duct and installation were considered as interactive components in order to achieve the cost reduction objectives; part of this approach was to understand the environmental impacts of the component parts. Life cycle assessment was used as a part of the evaluation.

In 1997, Pirelli Cables generated considerable customer interest with the introduction of compact optical fibre cables ("**Rapier**™†" cables) designed for ease and speed of installation. By combining the key attributes of **Rapier** technology and BT network requirements, a range of optimised-for-performance multiple-loose-tube (MLT) cables has been introduced that has the additional advantages of having reduced life-cycle costs and the flexibility for a wide range of fibre counts. This paper considers the development and attributes of these optical fibre cables designed specifically to take advantage of blown cable technology.

Keywords
Optical fibre cable; blown cable; life cycle assessment.

1. Introduction
Optical fibre cables for duct usage take on many formats. The use of a particular technology and cable type depends upon many factors, such as where in an operator's network the cable is to be used, the installation method, the number of fibres required, and the fibre breakout requirements of the route. A network operator will choose a telecommunications cable technology that is appropriate for a particular system in terms of fitness-for-purpose and cost-effectiveness.

The blown cable installation technique is well known for fast installation of long cable lengths, particularly in core/trunk networks and has been widely reported (see, for example, reference [1]). The technique was seen as highly attractive and appropriate for rapid expansion of the BT core and access networks in the response to continuing and increasing customer demand for bandwidth.

At the outset of the integrated ACTION programme it was decided to address several key requirements, as it was realised that simply to design a new cable in isolation from the other plant items used in the network build would limit the savings to be gained by adopting the blown cable approach. These key requirements covered the cable in conjunction with the duct it would occupy, associated network plant, and environmental issues that would be covered by life cycle analysis.

2. BT Network – Optical Cable Evolution
BT has been and continues to be a pioneer in the use of optical technology in its network. Initial (multimode) optical fibre was introduced in the 1970s as proprietary optical line systems (POLS), and in 1981 the Martlesham – Ipswich Monomode Experiment (MIME) was one of the world's first singlemode optical fibre system trials [2]. Thereafter, singlemode fibre quickly

* ACTION is an acronym for Advanced Cabling Techniques In the Optical Network.

† **Rapier** is a trademark of Pirelli Cavi e Sistemi SpA.

supplanted multimode as the telecommunications operator's transmission medium of choice.

Terrestrial optical cable designs evolved through the 1980s and early 1990s as confidence in and understanding of the transmission properties of optical fibre increased. The stabilisation of optical fibre standards/recommendations (e.g. ITU-T G.652) then allowed manufacturers to fully exploit fibre and to provide the most cost-effective cables to system operators. In Europe, multiple loose-tube cable designs predominate, as geography predicates point-to-point route lengths considerably less than those in the US and other continents/countries with lower population density.

With the explosion of bandwidth required by corporate networks and the increasing ubiquity of the Internet, the BT network expanded at an unprecedented rate in the mid 1990s. Also, competition between operators became ferocious and it was necessary to take a fresh look at optical cable deployment as part of the overall cost-optimising approach needed by a modern network operator.

Prior to the ACTION programme, the BT core network comprised conventional high-strength metallic strength member duct cables installed using winching techniques. In the access network, a mix of conventional (duct) cables and Blown Fibre was used, with Blown Fibre being exploited as a means of rapid fibre provision to customer premises.

3. The ACTION Programme

In 1999, as part of a continuing review, BT instigated a radical appraisal of its cable deployment. The outcome was a decision to introduce a phased programme with the objectives of achieving cost-savings through new cables designed to take full advantage of cable blowing installation techniques. It was very quickly realised that cable could not be considered in isolation; cable was part of an overall *system* requirement, the system comprising duct, sub-duct, cable, cable installation and cable joints.

Part of the system approach was to understand the environmental impacts of the different components of the system. Life cycle analysis (LCA) was used, which took much effort from BT, Pirelli and sub-duct suppliers. It was essential that whilst maximising green attributes, the performance and lifetime of the cable was not compromised.

3.1 Objectives

The key objectives of the ACTION programme were to introduce the cost savings and reduced environmental impact realised through using cable blowing as an installation method and to implement the solution within a year – August 2000 was the target launch date. In order to achieve this target, a multi-company and multi-function team was formed to address all the launch requirements. This team comprised BT, Pirelli, sub-duct and installation equipment manufacturers and had to undertake new cable and new sub-duct(s) designs, prove the installation process via pilot trials, define the installation equipment and produce documentation for training. There were also additional inputs from manufacturers of compressors, fleeting equipment and sub-duct connectors to name but a few other contributors.

The interactions and concomitant cost savings are summarised in Figure 1.

An LCA team provided initial feedback on environmental issues (see Section 4).

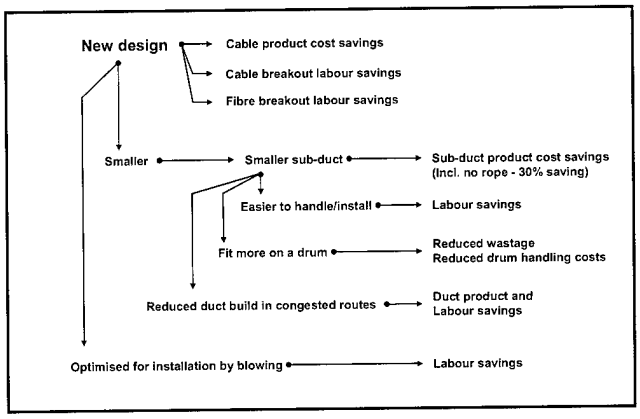


Figure 1: Programme Interactions

3.2 Cable

The rationale for the cable design was not simply to reduce the cable size and weight, but to provide a cable optimised for blowing and, importantly, one that could be detected by conventional RF injection to a copper conductor. From an environmental aspect, a decrease in physical size produces a positive impact; less overall material is used in the cable construction.

The blowing technique allows for a reduction in overall cable tensile strength. As confidence in the strength of optical fibre has grown, BT reduced the tensile requirements of its conventionally installed cable from 3W[‡] to 2W, and a move to blowing reduced this further to 1.5W, which still allows, within defined parameters, conventional installation where required.

In order to benchmark the blown cable installation approach, 20km of Pirelli **Rapier** cable was installed into BT network ducts near Birmingham in the UK. In an 'average' blow length of 1500m, installation speeds greater than 60m/min were attained. However, the trial showed that fleeting was difficult due to the two diametrically opposed peripheral strength members of the **Rapier** cable, which gave an asymmetric bending stiffness leading to inconsistent coiling. In addition, blowing of cable lengths greater than 1-1.5km required installation in both directions from a centre point. Also, the stored kinetic energy of the cable pay-off drum was considered unsafe at installation speeds above 60m/min.

The generic ACTION cable was therefore designed using the requirements ascertained by the initial installation trials (see Section 3.4.1).

[‡] A cable rated at '1W' is able to support 1km of its own weight; 2W can support 2km, etc.

A reduction in cable diameter predicated the use of smaller diameter fibre-containing tubes. Indeed, **Rapier** type cables using fibre bundles had suggested that small tubes that maintained fibre performance during temperature and strain excursions were feasible. The tube size for ACTION cables has been reduced to 1.9mm, with each tube containing 12 fibres. (To put tube size into perspective, a typical 12-fibre tube OD in North America is 2.8mm, and in Europe 2.5mm. Reduction to 1.9mm OD represents a considerable advance.)

The move to a very small tube size required a means to precisely control fibre overfeed and this has been implemented in the production process. Optical performance with the improved process is reliable out to 1650nm with no attenuation increment. This extended wavelength capability allows for the use of long wavelength diagnostic techniques (commonly at wavelengths out to 1620nm) and for extended DWDM as it becomes available.

For extended blowing lengths, a cable requires a bending stiffness within a quite precise window and also minimum memory – ideally the cable should have no set after being wound on a drum.

So, the cable design had to implement many design criteria: -

Fibre count:	12-144 fibres in one design
Diameter:	12-13mm (for 20mm ID sub-duct)
Installation length:	Difficult 1500m route, <45 min
Blow from static start:	500m
Cable detection element:	To be included (copper conductor)
Tensile strength:	1.5W, 0.4% strain
Dynamic bend:	1.5W, 405mm diameter
Temperature performance:	-10C/-40C to +60C/+70C
Mechanical:	Crush, bend, impact, repeated bend and torsion generally to IEC 60794
Water-penetration:	To IEC 60794

The resultant cable design is shown in Figure 2.

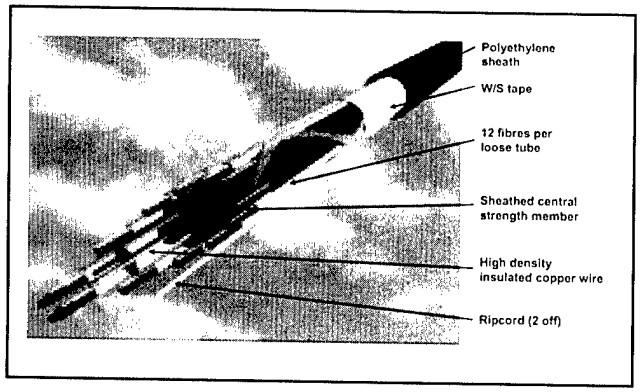


Figure 2: ACTION cable

Extensive cable prototype testing was carried out using an early product management methodology. This process comprised initial prototyping followed by industrialisation using small scale batches, resulting in large scale production. Six complete homologation tests were successfully undertaken in the year 2000 prior to launch.

3.3 Sub-duct

Sub-duct has traditionally been used in order to protect small cables from their larger brethren already in situ. In addition, the blowing installation technique requires an uninterrupted path, which the use of sub-duct provides.

Traditionally, sub-duct has been installed in the following manner: -

- First the duct is proved continuous by using a series of rods.
- Once the duct is proven, a draw rope is attached to the back end of the rods and pulled through.
- The draw rope, once installed, is then used to install a cabling rope.
- The cabling rope is then used to winch the sub-duct into the main duct.
- When the sub-duct is continuous over the cabling section, the cable is winched in using the pre-installed rope present in the sub-duct.

With *small* sub-duct and blowing, this becomes: -

- The sub-duct itself is used as the rod to prove the duct
- Once the sub-duct is installed and continuous over the cable section, the cable is blown into the sub-duct.

So, five processes are reduced to two with the methodology developed during the ACTION programme.

The programme has also allowed a reduction in sub-duct size from 32/26mm (OD/ID) to 25/20mm. It is now possible to install four or more sub-ducts within a 90mm duct instead of three previously – an improvement in duct utilisation of at least 33%.

An incidental reduction in overall cost has been achieved by using the sub-duct rodding process itself. When sub-duct is pulled into place, it generally requires a 24-hour period to allow it to settle. This entailed opening footway boxes and manholes, etc., twice, each operation requiring guarding, gas testing, and in all likelihood removal of contained mud/water. *Pushing* the sub-duct into place allows one operation installation, connection, tying back and labelling, with no settling time.

3.4 Installation

3.4.1 Initial Trials

The initial benchmark trials (see section 3.2) provided the key minimum requirement parameters for a cable in a real-world network installation: -

- To blow 1500m in less than 45 minutes with a pressure of less than 13 bar and an air flow of less than 100 cfm.
- To blow 500m of cable from a 'cold start' – where a cable is static in a sub-duct (i.e. with no air flow).

- To provide a cable with a defined and radially symmetric neutral bend axis.
- To provide a cable with a maximum diameter of 13mm.

3.4.2 *Test Facilities*

From the installation aspect, this initial trial provided several pointers to guide the direction of cable development. In addition, it became obvious that in order to provide rapid feedback to the cable design process, an installation test facility or facilities would be required. This would remove the necessity to prove installation effectiveness in the field and therefore significantly reduce development costs and time.

Pirelli and BT had differing requirements for installation test facilities; Pirelli as a manufacturer required a facility that would provide quick feedback to point to product development direction whereas BT required a facility that gave a sound simulation of actual network blowing performance within sub-duct.

The two team members therefore set up appropriate facilities. Figure 3 shows the Pirelli manufacturing oriented facility, and Figure 4 the BT network simulation sub-duct test route.

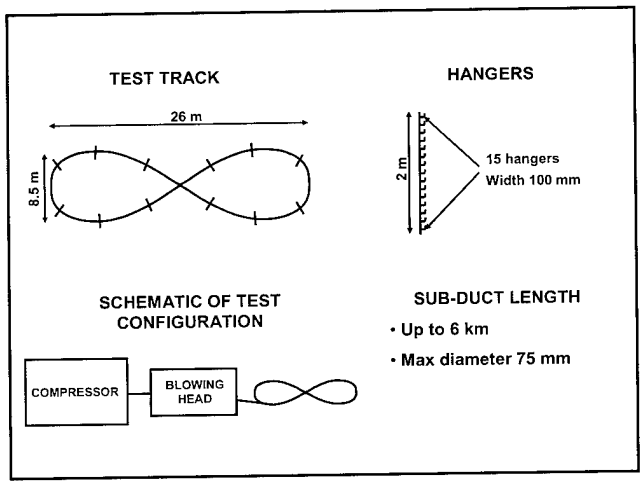


Figure 3: Pirelli test facility

The compact Pirelli test facility allowed for the cable blowing parameters to be optimised. An important feature of the test-bed is the 'reverse bend' facilitated by the figure-of-eight configuration, as this, during blowing trials, revealed any undesirable cable set or memory features.

Building on previous blowing experience, the cable weight, stiffness, diameter (with respect to the sub-duct inner diameter), sheath friction and bending 'memory' were optimised for the desired ACTION cable cross-section. In addition, the sub-duct coefficient of friction was optimised, and the facility aided in the definition of required blowing parameters in terms of working pressure and volumetric throughput.

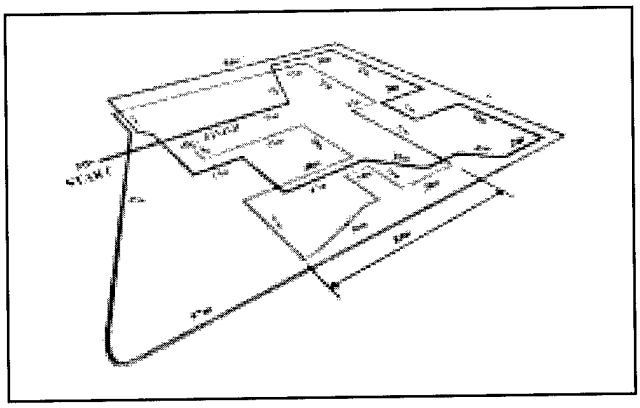


Figure 4: BT test route

In comparison with the Pirelli facility, the BT test route was carefully designed to simulate a 'worst-case' installation within the BT network and is in fact a re-creation of an actual access network route. As can be seen from Figure 4, the route is tortuous – a common feature of the urban network in the UK.

3.4.3 *Test Facilities – Required Blowing Profile*

To provide the requirements defined by the initial blowing trials, a desired 'blowing profile' could be defined with an optimum window. This required a uniform blowing speed defined at approximately 60m/min. 'Too fast' a speed would be unsafe, and 'too slow' a speed would fail to take full advantage of the blowing technique in terms of installation time cost savings.

Figure 5 illustrates the optimum blowing profile window; 1500m achieved in 25 minutes.

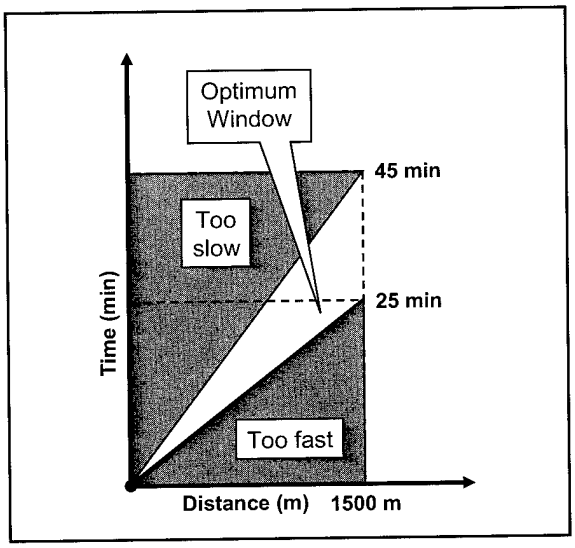


Figure 5: Optimum blowing profile

3.4.4 *Test Facilities – Trials*

Using the combination of the two facilities, several iterations were undertaken to finalise the cable design. The Pirelli compact facility was used for primary design purposes, and potential candidate cables were evaluated at the BT facility; this process realised a fast-track to the final design.

As cable development was in progress, improvements to the sub-duct were undertaken, in particular towards an optimised low-friction liner.

Figure 6 shows a graph of installation time versus distance achieved for the finalised cable and sub-duct designs through the BT facility. Note the following points: -

- 1500m installation length was achieved in less than 25 minutes.
- The time/distance characteristic is essentially linear and route bends have no effect on blowing speed over the distance.
- The blowing characteristic fits the optimum profile almost exactly.

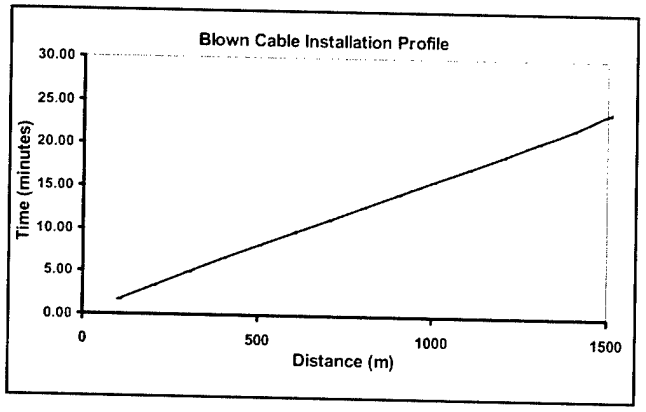


Figure 6: Cable installation

Note also that through cable development, the blowing characteristics of the compact and network simulation routes were continuously compared. Work is in progress to produce a predictive model that will allow the compact test route to effectively simulate a typical network route.

4. Life Cycle Assessment

In developing the new ACTION cable, BT and Pirelli wished to ensure environmental issues were fully considered and this was undertaken as an integral part of the ACTION programme. A full Life Cycle Assessment across the total product's life will take more time, but already significant benefits have been found.

The new cable design has allowed for the use of less quantity and fewer numbers of materials in its manufacturer. The smaller, lighter cable requires fewer processing steps, less processing and less transport. The combination of these factors significantly reduces energy usage in this phase of the life cycle and also has an effect on subsequent stages in the product's life cycle.

The LCA to compare manufacture of the pre-ACTION and ACTION cables has been carried out transparently and in accordance with the ISO14000 series of standards. The functional unit has been defined as 1x144 fibre kilometres.

The initial results of LCA are shown in Figure 7 as a 'spider' diagram.)

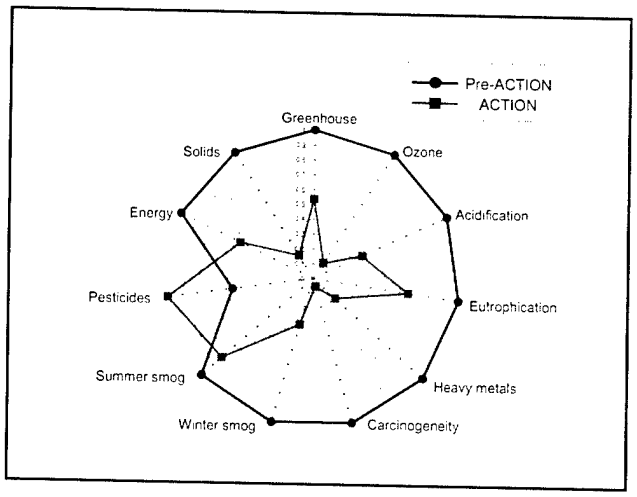


Figure 7: Cable LCA comparison

As always, some approximations have been necessary due to the lack of databases, and data-sensitivity analysis has been carried out. The Sima-Pro methodology [3] has been used, and the Idemat databases supplemented with Boustead [4] and APME databases [5].

The methodology used in the initial LCA was to assess the environmental impact. Ecoindicator 95 was used, preferred to Ecoindicator 99 because it weights more items of generic emissions in the materials inventory such as CxHy aliphatic, CxHy aromatic, etc. In Figure 7, environmental impact figures are presented, related to each impact category considered by Ecoindicator 95 (greenhouse, ozone, acidification, etc.). The cable with the greatest impact is used to normalise the relative readings. The energy impact category quantifies the total energy consumption (the absolute values are expressed in MJ). Energy is also included in each individual category as a contributor to the total impact. The solids category indicates the quantity of solids produced (absolute values in kg) but does not include the impact of their disposal.

4.1 LCA score differences – main influences

If the spider diagram categories are investigated, it is possible to analyse where the new cable design has influenced the results in, generally, a most positive manner: -

- Greenhouse effect: no APL, tube material, copper reduction
- Ozone layer: sheath size reduction
- Acidification: no APL, copper reduction
- Eutrophication: sheath size reduction , tube material, no APL
- Heavy metals: central elements (change from steel to GRP)
- Carcinogeneity: central element (change from steel to GRP)

- Winter smog: copper reduction, no APL
- Summer smog: tube material, sheath size reduction, no APL
- Pesticides: polyester (in ACTION it is mainly contained in the water swellable materials)
- Energy: no APL, sheath size reduction, tube material
- Solids: copper reduction

Clearly, the change to a smaller cable with the same carrying capacity gives many environmental benefits. However, the change from steel to a polyester strength member has resulted in the increase in one adverse environmental impact – generation of chemicals with potential pesticide effects during the manufacture of the material. This points the way to further improvement, and highlights the necessity of evaluating properly changes in materials. In addition, significant environmental benefits have accrued from the change to **Neon**™§ self-coloured fibre in both cables (by eliminating the use of solvents in inks – a pre-coloured coating is applied during fibre manufacture [6]).

In order to put some perspective on the overall environmental improvement, the ACTION cable uses some 40-50% less total mass per unit length of cable when compared with the previous type used in the BT network. This reduction comprises some 40% less PE sheath material, some 50% less tube material, some 80% less copper (as only a single copper element is used), 100% reduction in APL tape and 100% reduction in steel as GRP is used for longitudinal reinforcement. With regard to transport, a reduction of some 40-50% of seasoned pine is achieved per unit length of cable through the use of smaller wooden drums.

The above analysis takes into account the cable alone. Knock-on improvements are realised through the use of smaller sub-duct and the elimination for the need for rope.

This is the beginning of a continuing environmental programme. BT and Pirelli will continue to evaluate properly the environmental impacts of products, and will gradually extend the gates to cover the whole life cycle. The environmental benefits of collaboration across the supply chain are self-evident.

5. Programme results

The following sub-sections summarise in tabular form the considerable number of improvements made by the major moves to a smaller cable design and installation by blowing, in terms of costs and environment.

5.1 Costs

Table 1: Cost savings

Source	Feature	Cost savings
Cable	Radical, small cable with 12 fibres in 1.9 mm tubes	Cable product cost savings
	No interstitial grease or aluminium tape	Weight and cable breakout labour savings
	Fewer tubes	Fibre breakout savings
	Compatible with existing plant and practices	Training savings
Sub-duct	Smaller; no rope	Product cost savings
	Easier to handle and install	Labour savings
	More per drum	Reduced waste and handling costs
	Reduced duct build, smaller cable	Duct product, space and labour savings
Installation	Installation by blowing	Labour savings, no sub-duct lubricant, smaller compressor
	Fewer joints	Material and labour savings

5.2 Environment

Table 2: Environmental factors

Source	Feature	Cost savings
Cable	Radical, small cable	Reductions in cable material, energy usage, storage, transport and waste disposal
	No central steel strength member	Cable material substitution by a lower weight material
	No grease or aluminium tape	Cable material elimination
	Fewer fibre tubes	Reductions in cable material and energy usage
Sub-duct	Smaller duct	Reductions in material, energy usage, storage, transport and disposal
	No rope	Elimination of material
	Easier to handle and install	Reduction in energy usage
	Reduced duct build, smaller cable	product material and energy usage reduction
Installation	Fewer joints	Material, energy usage, storage, transport and disposal reduction
Repair	Less overall plant	Material, energy usage, storage, transport and disposal reduction
Disposal	Less overall plant	Material, energy usage, storage, transport and disposal reduction

§ **Neon** is a trademark of Pirelli Cavi e Sistemi SpA.

5.3 Current and future work

Since August 2000, cable and sub-duct refinement has resulted in enhanced blowing performance over-and-above the initial targets, achieved through understanding the interactions between the various system components. Figure 8 shows the current installation performance.

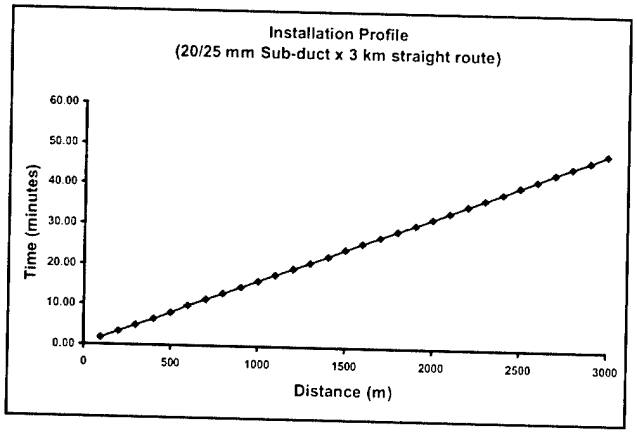


Figure 8: Current performance

The initial targets have been exceeded by a factor of two; the achievable blowing length is now in excess of 3km and installation speed maintained at 60m/min.

In terms of products and installation practice, future work will focus on blowing further with less air (in terms of both required pressure and throughput). This will entail further cable refinement and investigation of the use of ribbed sub-duct and low friction materials – all being considered as an *overall* system. Other options include a 'blow only' variant and modifications in order to exploit the opportunity to install more than one cable into a single sub-duct.

There is also considerable impetus towards in extending the product range by broadening the fibre counts. This involves a range between approximately 60 and 288 fibres per cable in order to meet the demands of metro/access network requirements.

Other activities include the production of a reference test method installation test facility and, of without needing to be said, extension and refinement of life cycle analysis. This last point is a determined objective of both BT and Pirelli.

6. Conclusions

This paper has discussed the benefits achieved by taking an integrated approach to the use of cable within the BT network and has resulted in an optimised cable – sub-duct – installation – repair – disposal system that exceeds initial design targets.

By considering not just the optical fibre cable but also the sub-duct in which it will reside, the installation method and, indeed, the topology of the network itself, it has proved possible to tune the overall system to provide considerable benefits. Such manifold benefits are not restricted simply to cost savings, but also to conservation of resources.

The integrated approach has involved unprecedented co-operation and sharing of information, practices and ideas between multi-function teams within BT, Pirelli and sub-duct manufacturers.

7. Acknowledgments

The success of this development programme is the result of significant contributions from many people at Pirelli and BT, including Elizabeth Ness, Mark Dowling, Glyn Stacey, Phil Wife and Chris Munnings, plus sub-duct and equipment manufacturers, to whom the authors extend their thanks. In addition, we would like to acknowledge the help of Peter Hale in the preparation of this paper.

8. Author Biographies



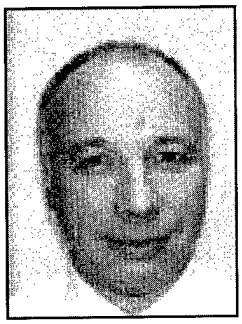
Martin Davies is Chief Engineer with the Communications Cables Division of Pirelli Cables UK, where he is responsible for product design, development, materials and test. He has been an active member of a number of standardisation bodies, including BSI, ETSI and IEC. He is a Chartered Engineer and a Member of the Institute of Electrical Engineers. Recently awarded Pirelli's gold "premio alle invenzioni" for significant patent design.



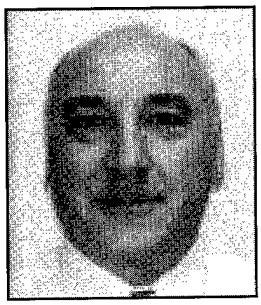
Chris Esbester is the Company Environment Specialist for Pirelli Cables Ltd. in the UK and is responsible for overseeing the environmental management system across all sites to the meet the requirements of ISO 14001. Chris joined Pirelli's Communication Cables plant at Newport, South Wales in 1992, starting in the Quality Assurance Group. He was part of the plant's project team which achieved BS 7750 (Environmental Management Systems) in 1995. In 1999 he took up his present position within the company and completed an MSc in Environmental Management and Technology from the University of Manchester Institute of Science and Technology in 2000.



Ralph Sutehall is Principle Installation Engineer with the Communications Division of Pirelli Cables in the UK, where he is responsible for installation development. He has been working with optical fibre cables for 27 years and is a corresponding member of CIGRE with a special interest in optical cables for use on overhead power lines. Recently awarded Pirelli's gold "premio alle invenzioni" for significant patent design.



Phil Barker is a project engineer in the Access Fibre Systems team at BTexact Technologies, UK – BT's advanced research and technology business centre. He is responsible for the development of fibre products, plant and installation practices for the BT network. For the past twelve years he has been actively involved with development of blown fibre unit and installation equipment. Recently he has been part of BT's ACTION project.



Dave Bastin is BT Lead Project Engineer with recent responsibilities for the national implementation of blown cable installation practices into the BT network, with additional responsibilities for network connectivity and optical fibre commissioning. He has 30 years experience in the communication industry with 14 years in optical fibre and cable disciplines. Dave is the BT representative for major supplier co-operation technical forums.

9. References

[1] M. A. Nunes, A. M. Simião, M. A. Caetano, C. Brunhara, A. C. Silva and L. Silvéro, "Development of a new Optical Fibre Cable to be Installed by Blowing Method," *Proc.49th International Wire and Cable Symposium*, 196-174 (November, 2000).

[2] P. G. Hale, D. Delme Jones, M. M. Ramsay, J. G. Titchmarsh and R. C. Townsend, "A Refined Tight Design Duct Cable for Low Loss Monomode Fibre", *Proc.31st International Wire and Cable Symposium*, (November 1982).

[3] Pré Consultants, the Netherlands.

[4] Boustead Consulting Limited, Black Cottage, West Grinstead, Horsham, West Sussex, United Kingdom.

[5] Association of Plastics Manufacturers in Europe, http://www.apme.org

[6] C. J. Garnham, R. C. Neat and J. W. Rogerson, "A New Concept in Optical Fibre – Self Coloured Coatings," *Proc. EuroCable '97 (Communications Cabling, IOS Press)*, 201-206 (June, 1997).

Development of High-Density Optical Fiber Cable Using Thinner Slotted Rod

Masanori Hattori, Eiji Konda, Ryuji Takaoka, Daisuke Iwakura and Masami Hara
ENGINEERING SEC. OPTOCOM DIV.
THE FURUKAWA ELECTRIC CO., LTD.
Ichihara, Chiba, Japan
+81-436-42-1642 hat@ch.furukawa.co.jp

Abstract
With rapid growth of the Internet accompanied by an increasing volume of communication data traffic, there is a need for an optical access network to be constructed at an economical cost. To meet this requirement, it is necessary to develop the cable suitable for the installation techniques of long-length laying and multi-cable laying. Focusing on outer diameter reduction of optical fiber cables installed in existing duct, we have developed the optical fiber cables of 640 and 1000fibers. These cables have been designed by using thinner slotted rod and thinner cable sheath. The diameter of developed optical fiber cables is thinner by around 3mm compared with conventional optical slotted rod cable. It has been confirmed that optical and mechanical properties of the developed thinner cables are equal to those of conventional slotted rod cable.

Keywords
Thinner slotted rod; Thinner cable sheath; 640fiber cable; 1000fiber cable; inner duct; duct;

1. Introduction
In Japan, Ministry of Land, Infrastructure and Transport is improving the optical fiber network for road management, which includes road condition monitoring and emergency communication network. The optical fiber networks for road management are installed in the information boxes, which are being buried underneath roadways. The diagram of information box is shown in Figure 1.

Each information box has a capacity of a number of ducts. Since telecommunications carriers are allowed to lease surplus ducts, it is possible that they are install cables economically compare to installation in their own underground ducts. Accordingly, it is expected that the nationwide optical fiber network (information highway) will be accelerated in taking shape, to form sophisticated information societies of the 21st century. [1]

With the increase of communication traffic, there is a need for optical access networks to be constructed at an economical cost. To meet this requirement, not only cable cost reduction, but also total cost reduction should be considered including such cable installation and connection techniques of long-length laying and multi-cable laying.

When it comes to the cost reduction of cable installation, both shortening working hours and reducing the amount of installation machinery contribute greatly to this target. One of the most effective measures to achieve this is to decrease the laying tension of optical fiber cables, involving reduction of the friction coefficient of the cable sheath, as well as lightening cable weight and upgrading cable flexibility. Moreover, it seems difficult to allow telecommunications carriers to lease their required number of fibers between major cities, because the number of available installation cables is limited.

Then, it is necessary to develop the cable suitable for the installation and technologies as long-length laying and multi-cable laying.

Furukawa Electric developed the cable laying method, which refers to installing inner ducts in one existing duct, and accommodating one optical fiber cable in each inner duct for joint accommodation.

This program targeted in developing 640 and 1000 fiber cables to be downsized enough to adapt to the piping inserts, with which the conventional counterpart cables do not match, by contriving thinner slotted rod: a considerable number of piping inserts are unable to pass a 640 or 1000 fiber cable.

The results of investigations on these measures will be reported below.

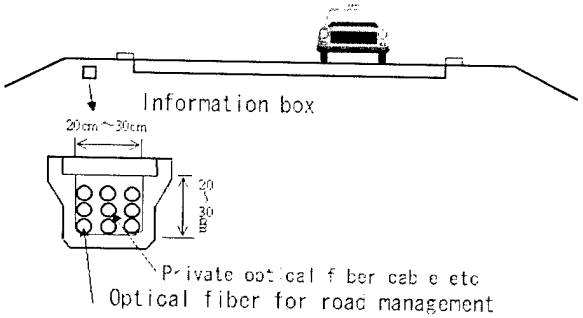


Figure 1 Diagram of information box [1]

2. Technique for thinning cable diameters
A slotted rod cable is comprised of a tension member (T.M.) at the core, a slotted rod as the next component part, a swell tape, and a sheath as the outermost covering. For instance, a cross-sectional view of a 1000 fiber cable is shown in Fig. 2.

The following approaches to downsizing a 640 and 1000 fiber cable are thinkable:

#1 Thinning the thickness of each fiber ribbon,

#2 Reducing each groove dimension on the slotted rod,

#3 Thinning the slotted rod in diameter,

#4 Thinning the sheath in wall thickness.

Approach #1 is sensitive and unrealistic, because of concern with degrading the productivity and the characteristics of the fiber ribbon and difficulty in being spliced with conventional fiber ribbons.

Approach #2 is unrealistic: the conventional groove design has already been optimized.

Approach #3 is possible:, as expansion of the developed slotted rod design technique, and can be materialized with ease.

Approach #4 is possible, by selecting a sheath material with weatherproofing, impact strength, lateral pressure resistance, wear resistance.

Thus, approaches #3, #4 were set under study: thinner slotted rod and thinner sheath.

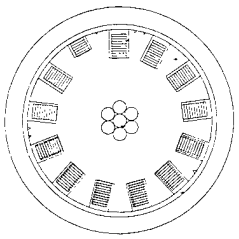


Figure 2 Cross Sectional View of 1000Fiber Cable

2.1 Thinner slotted rod

Reducing the cross-sectional area of a slotted rod leads into not only material decrements in the slotted rod, wrapping tape and sheath but also some saving of cable cost. It is thinkable at first to review the groove dimension of slotted rod, wall thickness between T. M. and bottom of the groove and rib thickness to design thinner slotted rod.

In particular, reducing of the groove dimension of slotted rod and wall thickness between T. M. and bottom of the groove cause to degrade the optical characteristics.

Accordingly, it is necessary to investigate the manufacturing conditions and long-term reliability. As a result, we decided to study reducing the rib thickness.

The rib thickness of conventional slotted rods is around 1.3mm under productivity. It was thinkable that the mechanical properties of thinned ribs would lower. So we investigated that slotted rod materials likely to be suitable for thin-wall manufacturing.

Table 1 shows flexural modulus of the conventional and present trial materials. The slotted rods were made of the trial material with a flexural modulus of 1500MPa. Fig. 3 shows relationship between rib thickness and critical lateral pressures to increase loss. Although the lateral pressure properties depended on the rib thickness, it was confirmed that the lateral pressure properties of thinner rib thickness satisfied safety margins for the required level. [2]

Table 1 Flexural modulus: Conventional & Trial Materials

	Conventional	Trial
Flexural Modulus	1000MPa	1500MPa

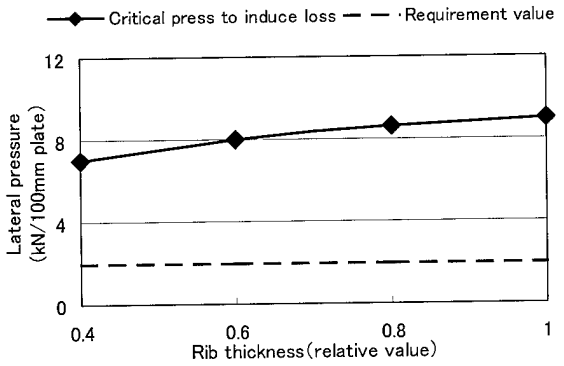


Figure 3 Rib Thickness Vs. Critical Lateral Pressure

2.2 Thinner sheaths

The sheath is designed to protect a fiber cable against external stresses during installation work or as laid; and a fiber cable will be degraded in performance if its sheath is thinned without consideration.

Accordingly, we investigated the following aspects of thinning the sheath.

Table 2 15years weathering

Carbon Concentration (%)	0.5	1.0	1.5	2.6
Cracked Depth(μ m) 0.5mm thickness sheet	20	<10	0	0
Residual Elongation (%) 1.0mm thickness sheet	63	88	93	>93
Residual T.S. (%) 1.0mm thickness sheet	58	99	95	>95

Table 3 Mechanical Properties of Sheath Materials

Item	Standard	Unit	LDPE	L-LDPE
Wear Resistance	ASTM D1630	times /mm	510	1200
Dynamic Coefficient of friction	JIS K 7125	—	0.55	0.36
Tensile Strength	JIS K 6760	MPa	16.2	16.2
Elongation	JIS K 6760	%	600	750
Brittleness Temp.	JIS 7216	℃	<-70	<-70
Hardness Shore D	ASTM D2240	—	45	55

2.2.1 Weatherproof performance

Design parameters for the sheath are carbon-black concentration and sheath thickness. Table 2 shows results of a 15year weathering test. The results showed there were no signs of crack on a 0.5mm thick sheet with 1.5wt% carbon-black.

The trial sheath material was contained with 2.6wt% of carbon black.

Therefore it was found that a thinned sheath thickness using trial material was satisfactory in weatherproof performance.

2.2.2 Mechanical property

External stresses during laying work or as laid are lateral pressure, impact, friction, etc. Table 3 shows a comparison of significant mechanical properties of materials, LDPE and L-LDPE, in current use. They show no difference in tensile strength, elongation or brittleness temperature. However, L-LDPE has a high wear resistance; and a sheath of L-LDPE will scarcely receive any scratch from duct walls or a pulley during installation. That is a superior feature.

In addition, L-LDPE has a low dynamic coefficient of friction, and enables low-tension cable laying work. As a result, the laying length and the working safety can be improved, and total laying cost can be reduced.

Therefore, we decided to apply to L-LDPE for fabricating thinner sheaths.

3. Cable design

It turned out that the rib thickness in a slotted rod and the sheath thickness for an optical fiber cable could be thinned, in technical aspects. Design targets were set up, over against the conventional counterparts.

The target thinner cable needs to be passed through inner ducts. In general laying methods, the maximum tolerable area factor, which was calculated with the bore in a duct and cable outer diameter is recognized at round 60%.

In this context, Fig. 4 shows relationship between cable outer diameter and area factor. The inner ducts for the 1000/640 fibers cables were each 35mm or 27mm in inner diameter.

The area factor is defined as:

Area Factor (%) = Cable Cross Sectional Area /Bore Area of Duct x 100

For instance, according to the above formula, the area factor of an inner duct is found to be 51%, given an inner diameter of 27mm, a content of 400 fibers; similarly, 42% given an inner diameter of 35mm, a content of 640 fibers. The margins for the upper limit (60%) reflect that the bore spaces were not used efficiently.

But it is impracticable for each inner duct to contain the number of fibers for the one-gauge larger cable due to far overshooting limited area factor.

Focusing on an approach to 60% of area factor, given an inner duct with an inner diameter of 27mm, a content of 640 fibers and an inner diameter of 35mm, a content of 1000 fibers, we designed the cables without limits of handling. Table 4 shows relationship between cable series and area factor.

For more concerted design, Figure 5 shows relationship between cable outer diameter and area factor. It was found that a cable outer diameter of round 26mm for 1000 fibers or round 21mm for 640 fibers could calculate up to 60% or less of area factor.

In both cases (640/1000 fibers), each sheath thickness was designed to be 1.5mm; the slotted rod size was set 1mm thinner for 640 fiber cable and 1.8mm thinner for 1000 fiber cable.

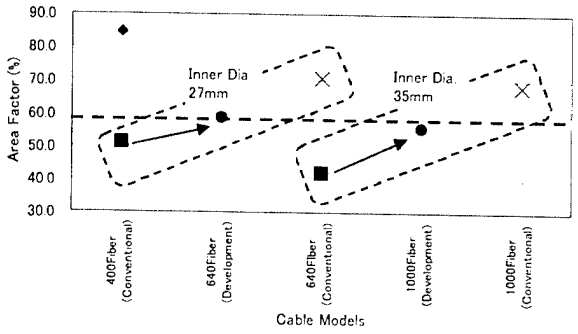


Figure 4 Cable Model Vs. Area Factor

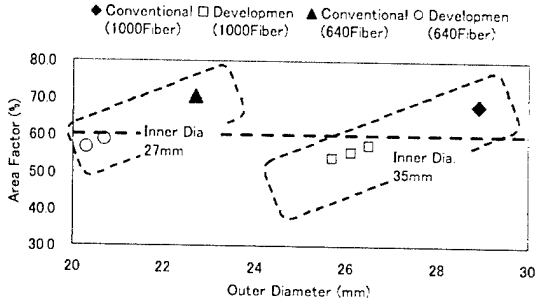


Figure 5 Outer Diameter Vs. Area Factor for 640/1000fiber cables

Table 4 Comparison outer diameter

	640Fiber Cable	1000Fiber Cable
Conventional	22.7mm	28.9mm
Development	20.7mm	26.1mm

4. Results of experiments

The new design cables were produced (fabricated) as described in Chapter 3, and required to perform in an experiment complied with IEC60794. This chapter describes specific results of performance, which are expected to cause more degradation in thinned optical-fiber cables, than in the conventional cables.

4.1 Lateral pressure characteristics

It was concern with degradation of lateral pressure characteristics because of a thinner rib thickness and a thinner sheath thickness than the conventional counterparts. We carried out the test complied with IEC60794-1 Crush, in order to observe variation in fiber loss and cable deformation during examination, given a test wavelength of 1.55 ± 0.02 μm, a load of 1000N, a 50mm flat plate to be held for one minute.

None of the trial cables for 1000/640 fibers observed any variation in fiber loss under the load or any residual loss as unloaded. Then it was found that the component materials incurred no damage.

It was confirmed that the downsized cables have equivalent lateral pressure resistance to conventional cables.

Table 5 Lateral pressure Test

	640Fiber Cable	1000Fiber Cable
Loss change	0.00dB	0.00dB
Residual Loss	0.00dB	0.00dB
Outlook	No damage	No damage

4.2 Impact strength test

It was concerned with degradation of impact strength characteristics because of a thinner rib thickness and a thinner sheath thickness than the conventional counterparts. We carried out the test complying with IEC60794-1 Impact, in order to observe variation in fiber loss and cable deformation during examination, given a test wavelength of 1.55±0.02 μm, a mass of 1kg to be released 1m above, for 15 times.

None of the trial cables for 1000/640 fibers observed any variation in fiber loss as impacted or any residual loss after the test.

Each trial cable was disassembled, and there was no crack or damage for the fiber ribbons. Then it was found that the component materials incurred no damage.

It was confirmed that the downsized cables have equivalent impact properties to conventional cables.

Table 6 Impact strength test

	640Fiber Cable	1000Fiber Cable
Loss change	0.00dB	0.00dB
Residual Loss	0.00dB	0.00dB
Outlook	No damage	No damage
Damage to fiber ribbons	No damage	No damage

4.3 Squeezing test

The trial cables are designed to apply to laying inner duct in an existing duct. The conventional cables were installed with margins for the upper limit area factor (60%) sufficiently, causing no problem when they were being installed. But the trial cables were set close to 60% of area factor, where it was concerned that it would degrade optical characteristics because of melted sheath by friction against curving in a inner duct and squeezing against a inner duct wall.

We carried out a squeezing test against an inner duct wall, which had never been tried out, in the following conditions:

-Laid as 90 degree angled

-With a bending radius of 1700mm for test cable

-In inner duct

-As loaded with 980N

-With 4 reciprocating strokes

-At a test wavelength of 1.55 μm

Squeezing test was carried out according to above condition in order to observe changing of fiber loss during test and surface. In addition, the test load 980N refers to the allowable laying tension for the inner duct. In case, the cable is being laid through an inner duct, assuming that the laying tension increase due to friction against inner duct wall, we recognize that the maximum load of allowing the inner duct to remain unbroken.

Table 7 shows the results.

None of the trial cables for 1000/640 fibers observed residual loss or frictional sheath damage from a duct wall.

Moreover, trial cable was disassembled, and there was no crack or damage for fiber ribbons.

Then it was found that the component materials incurred no damage.

It was confirmed that the downsized cables have sufficient squeezing performance, which undertakes to bear the laying tension increases due to friction against inner duct wall.

Table 7 Squeezing test

	640Fiber Cable	1000Fiber Cable
Loss change	0.00dB	0.00dB
Residual Loss	0.00dB	0.00dB
Sheath surface	No scratch, melt	No scratch, melt
Damage to fiber ribbons	No damage	No damage

4.4 Other properties

The above tests relate to the performance characteristics, which were concerned to degrade due to downsized component of the trial cables. Then it was confirmed that they were not inferior to conventional characteristics.

The other properties were tested complied with IEC60794 for the trial cables.

The results were shown in Table 8.

In conclusion, it was confirmed that the downsized cables have equivalent mechanical properties to conventional cables.

Table 8 Other results (@1.55 μ m)

Item	Method	Results
Loss	OTDR	0.20dB/km
Tensile	0.3% elongation load	<0.01dB
Repeated Bending	R=20d 180° 10times	
Torsion	0.02% elongation load on sheath ±90degree	
Temperature Cycling	-20℃ +60℃ each temp. to be held for 12 H or more	

5.Conclusions

We designed and tried out 640/1000 fiber cables, each equipped with downsized slotted rod and a downsized sheath, which enable more and more telecommunications carriers to join in major trunk routes. These downsized cables are useful for laying work using an inner duct in existing ducts, which will assist in making efficient use of the existing optical communications routes.

As a result, we succeeded in fabricating 2 - 3mm thinner optical fiber cables than the conventional models for 640/1000 fibers, without any cable performance degraded. Those thinned cables can apply to smaller inner ducts, with which the conventional counterparts do not match.

6.References

[1] Ministry of Land, Infrastructure and transport http://www.mlit.go.jp

[2] M.Hattori et al; Development of Optical Fiber Cables for Access Network, FURUKAWA REVIEW P.33No.20 April 2001.

AUTHORS



Masanori Hattori

The Furukawa Electric Co., Ltd.

6,Yawatakaigann-dori Ichihara, Chiba, 290-8555 JAPAN

hat@ch.furukawa.co.jp

He received his M.E. degree in Applied Material Science from Muroran Institute of Technology in 1991. He joined The Furukawa Electric Co., Ltd. in 1991 and has been engaged in research and development of optical fiber cables. He is now an assistant manager of engineering dep., OPTCOM division.



Daisuke Iwakura

The Furukawa Electric Co., Ltd.

6-1,Marunouchi 2-Chome, Chiyoda-ku, TOKYO 100-8322 JAPAN

iwakura@ho.furukawa.co.jp

He received his M.E. degree in Engineering from Electro-Communications University in 1993. He joined The Furukawa Electric Co., Ltd. in 1993 and has been engaged in research and development of optical fiber cables. He is now a production engineer of engineering dep., OPTCOM division.



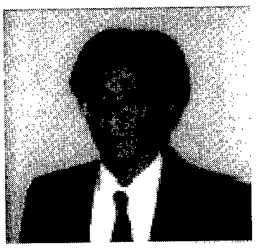
Eiji Konda

The Furukawa Electric Co., Ltd.

6,Yawatakaigann-dori Ichihara, Chiba, 290-8555 JAPAN

konda@ch.furukawa.co.jp

He joined The Furukawa Electric Co., Ltd. in 1977 and has been engaged in research and development of materials and optical fiber cables. He is now an engineer of engineering dep., OPTCOM division.



Masami Hara

The Furukawa Electric Co., Ltd.

6,Yawatakaigann-dori Ichihara, Chiba, 290-8555 JAPAN

hara@ch.furukawa.co.jp

He received his M.E. degree in Physics from Osaka University in 1987. He joined The Furukawa Electric Co., Ltd. and has been engaged in research and development of optical cable. He is now a manager of engineering dep., OPTCOM division.



Ryuji Takaoka

The Furukawa Electric Co., Ltd.

6,Yawatakaigann-dori Ichihara, Chiba, 290-8555 JAPAN

rtakaoka@fiteltech.com

He received his M.E. degree in Mechanical Engineering from Keio University in 1996. He joined The Furukawa Electric Co., Ltd. in 1996 and he has been engaged in research and development of optical fiber cables. He is now an engineer of optical transmission systems Dep., Fitel Photonics Laboratory.

An Alternate Approach to the Reduction of Cable Weight and Stiffness of High Fiber Count SCR Cables

Thomas Ottmann
Corning Cable Systems
Hickory, N.C.
email address: Thomas.Ottmann@corning.com

Abstract

The reduction of weight and stiffness of slotted core high fiber count cables in order to achieve better performance during installation is an important aspect of total cable cost. An innovative approach to achieve these requirements is the use of foamed materials in selected components of the design. The resulting properties of the new cable designs allow for longer installation length between manholes leading to a measurable cost reduction of the overall cable installation.

The overcoat of the central strength member was chosen for the implementation of the foamed material. Solid Polyolefin polymer was replaced by chemically foamed polymer resulting in significant reduction of the cable weight. Furthermore, lower values of cable stiffness were achieved, thus meeting all the customer requirements for this new design.

Foam processing technologies were developed to ensure constant geometrical and density properties. New process control technology was developed to ensure on-line measurability of the product's key properties.

Several prototypes were manufactured and analyzed. The results were used to confirm the behavior of the new cable designs with foamed central member overcoat. Weight reduction was improved by 8-10 % and stiffness reduction 5-10%. The new designs were subjected to a range of environmental and mechanical tests and found to be performing fully within the range of specifications. The introduction of foamed polymer has shown few processing problems and cable properties behaved well within their predicted levels.

Keywords

Slotted Rod Ribbon Cable, Foam Polymers, Weight, Stiffness, Reduction, Central Member Upjacket

1. Introduction

In our technical environment the cost of cable installation is becoming a key element of overall network cost calculation. The reduction of factors that add to higher installation costs of fiber optic cables such as weight and stiffness contributes to the value added of the product. To introduce foam as a replacement for hitherto solid cable parts is an effective way to reduce weight and stiffness. In order to balance the different aspects of requirements for a slotted core ribbon cable the selection of cable part to be replaced, the material used and the process to foam have to be carefully chosen.

2. Theoretical Considerations

The total cable weight is the sum of weight of its single components. Each component contributes to the weight due to its density and volume. The addition is independent of shape. The stiffness that every cable element adds is basically derived from the geometrical shape.

The cables under consideration for this paper generally have a cylindrical shape. This means that every cable element adds to the stiffness of the cable proportionally to the fourth power of the element's distance to the geometrical center of the cable. Therefore one way to reduce the properties in question in a new cable design would be to reduce the diameter of the cable. Another way is to reduce the weight and stiffness generating properties of the materials used to manufacture said cables. A fiber optical cable is mainly a protective sheath and organizer for the information carrying fibers. For a high fiber count slotted core ribbon cable this means that the form of organization oh these fibers is part of the customer requirements. See in Figure 1 the cross-section of a 1000 F slotted core cable. The typical distribution of the ribbon stacks has to be maintained in any new design.

This distribution is the main constraint for a geometry based reduction of the discussed properties.

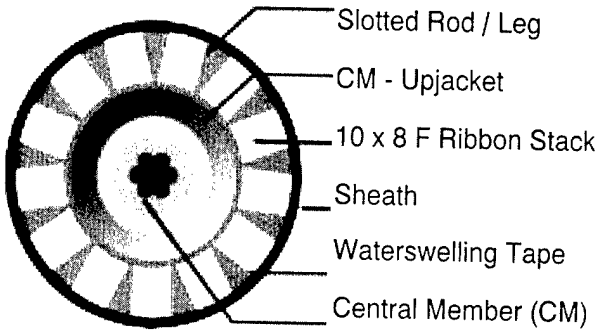


Figure 1: 1000 F Slotted Core Ribbon Cable

2.1 Distribution of Stiffness

The calculation of the theoretical contribution of each cable element to the overall stiffness of a cable design leads to the following distribution in the case of a 1000 F slotted core ribbon cable.



Figure 2: Stiffness Distribution in a 1000 F Slotted Core Ribbon Cable

The slotted rod is contributing a full one third of overall cable stiffness. Therefore, replacing the rod's solid material with a foamed polymer may substantially effect the overall stiffness of the cable.

The distribution of weight by cable component is shown below (Fig.3.).

The cable element's material chosen to be replaced by a foamed polymer was the upjacket over the steel central member. Future reference to foamed cable versus solid cable will always be to the material used for upjacketing the central member.

The manufacturing of a 1000 F SCR cable is divided into the main processes of rod extrusion, stranding and jacketing. The rod extrusion itself is divided into a series of sub-extrusion steps because the cooling properties of the polymers used do not allow for a one step process while maintaining the required tolerances.

The process of upjacketing the central member with polymer to the necessary diameter consists of three steps. Then the slotted rod itself is extruded onto this upjacket. It is only the cylindrical upjacket that will receive foamed polymer replacement.

The distribution of weight shows three major parts: Jacket, slotted rod and CM-Upjacket. While foaming the jacket certainly would greatly reduce stiffness, it's mechanical properties are needed as a protection for the cable. The slotted rod is a major factor for weight but also a sensitive element when it comes to the precision of the extrusion process. The central member upjacket is the only geometrically simple element whose mechanical properties are not fully used for the cable performance.

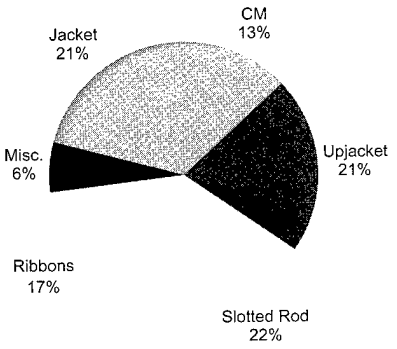


Figure 3: Stiffness Distribution in 1000 F Slotted Core Ribbon Cable

2.2 Central Member Upjacket

Fig. 4 shows the elements that compose the core of an SCR cable. The various layers all require a single extrusion process with its own setup and run time requirements.

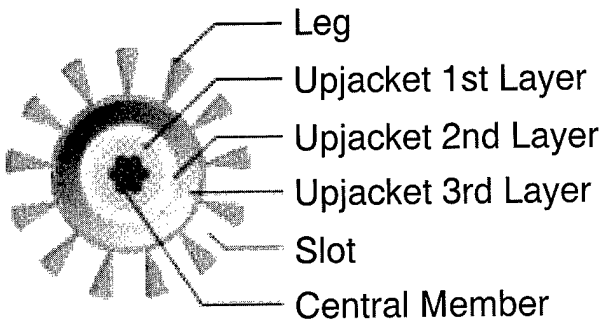


Figure 4: Slotted Rod of 1000 F Cable

The new cable design was chosen in a way such that well tested and proven manufacturing steps i.e. slotted rod extrusion and stranding remained unchanged. This left the three steps of the central member upjacket for further development. While it may seem that the upjacket central member does not provide a direct impact on cable performance, a closer look indicates otherwise.

The requirements to be met under penalty of jeopardizing the cable performance are:

- Eccentricity of the steel in the polymer
- Ovality of the upjacket
- Exact outer diameter
- Bonding of the polymer to the steel

Fig. 5 shows the old elements versus the new introduced foam layer.

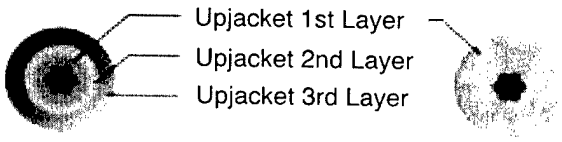


Figure 5: Upjacket of Central Member

The old design was made in three steps of upjacketing while the new design requires only one foam layer. The pros and cons of having three layers in relatively high speed extrusion versus one slow layer of foam will be discussed in section 5.

2.3 Weight Reduction by Material changes

To define the ratio by which a material has been altered by the injection of gas and subsequent forming of foam cells, the term foam rate is used.

The foam rate is defined as follows: If the density of a material is reduced by X%, then it is said the foam rate is X %.

If the density is reduced from 0.945 g/cm^3 to 0.567 g/cm^3 then this equals to a foam rate of 40 % as this same amount of the material has been replaced by gas.

The concept of foam rate is independent of the base resin and gas which compound the foamed material.

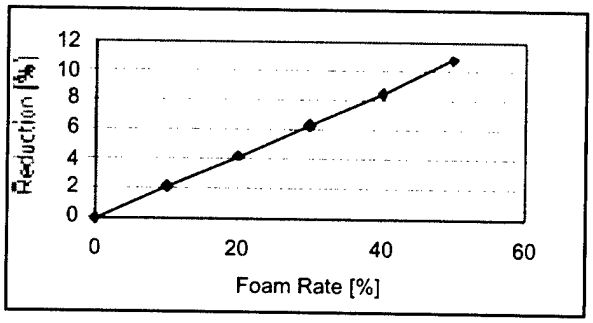


Figure 6: Overall Weight Reduction of a 1000 F Slotted Core Cable due to the Foam Rate of the Central Member Upjacket

Fig. 6 shows the expected weight reduction by foaming the central member upjacket. Please note that the weight reduction is independent of the material and process used to achieve the desired foam rate.

3. Material Selection

3.1 Materials

The materials most widely used in cable construction are polyolefins. This is due to a wide range of advantages such as price, processability and properties like non-toxicity and ground water neutral behavior. The original upjacketed layer as well as the slotted rod consisted of Polyethylene. To maintain this material combination the selection of materials was tightened to the circle of the PE-family. Polyurethanes and other common foamable polymers on the market were ruled out to maintain the overall polyolefinic character of the cable design.

The mechanical properties of foamed polymers are reduced in a linear relationship by the amount of injected gas, the foam rate.

The Young's Modulus of the different PE's vary as follows:

Material	Density [g/cm^3]	Young's Modulus N/mm^2]
LDPE	0.915 - 0.935	200 - 400
MDPE	0.935 - 0.942	600 – 800
HDPE	0.942 - 0.955	1200 - 1400

Table 1: Density and Young's Modulus of PE

As it is expected that mechanical properties drop proportionally with the foam rate, HDPE would substitute MDPE in terms of mechanical stability at a foam rate of 50 %. In order to verify this, a series of tests on foamed samples were performed.

3.2 Property Changes due to Foam Rate

A main concern when replacing solid material with gas filled cells is the compressibility of the material. In order to verify how foamed materials change their properties in the range of the foam rate in question (Goal of overall weight reduction) compression tests were performed. Cylinders of extruded HDPE foam were cut to samples as high as their diameter. These samples were compressed along the longitudinal axis of the cylinders. The load [N] was measured when 10 % deflection relative to the original height was reached. Thus a series of normalized values from samples with different foam rates were obtained.

The results visualized in Fig. 7 show that indeed, a linear relation between foam rate and compressibility can be achieved.

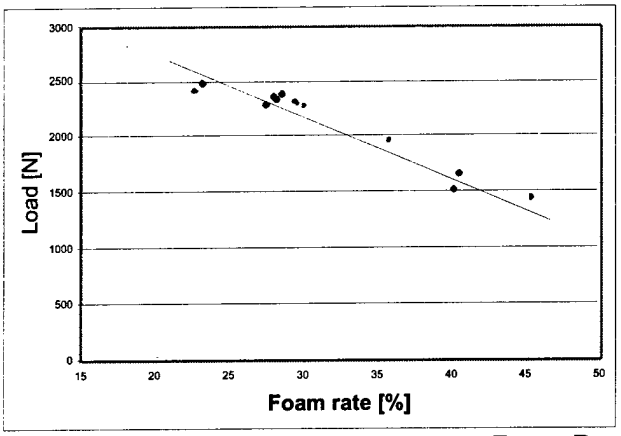


Figure 7: Load for 10 % Deflection vs. Foam Rate (HDPE Samples)

Since the Young's Modulus drops proportionally to the foam rate HDPE was selected as foamable polymer in order to maintain the modulus as high as possible.

3.3 Property Changes due to Temperature

The most critical load applied to a cable with a foamed core is lateral pressure. The results of these tests on the cable will be discussed in section 4.2.

For the purpose of a preliminary assessment of how a foamed core behaves under compression and varying temperature, tests were performed.

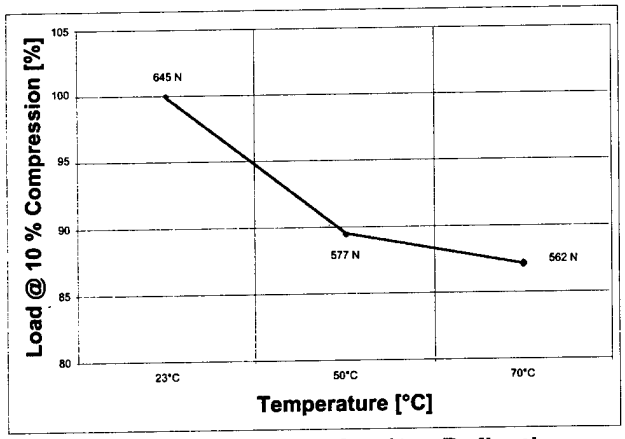


Figure 8: Load for 10 % Deflection vs. Temperature (MDPE Sample 60 % Foamed)

Using the same sample type as in section 3.2 this test was performed by applying a load equivalent to 10 % compression relative to the original sample height. After removing the load, the height-recovery was measured after 5 and 10 minutes. Furthermore the test was performed under three different temperatures 23°C, 50°C and 70°C.

50°C was chosen since it corresponds to the final core cooling temperature while manufacturing the upjacketed central member.

70°C represents the high temperature the cables undergo during environmental testing.

The load needed to compress an MDPE sample by 10 % of its original height dropped by 13 % when the sample was heated to 70°C. (Fig. 8) A similar but lower drop was recorded when using HDPE in these tests.

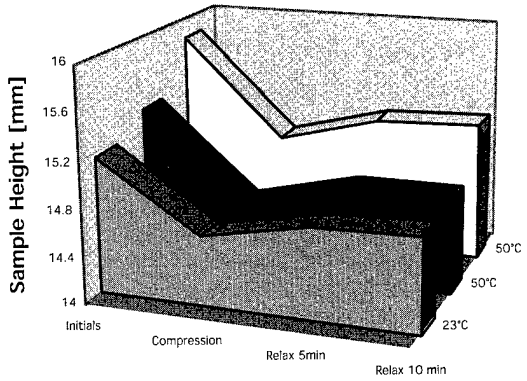


Figure 9: Recovery of Foamed Samples after 10 % Compression under varying Temperature (Samples MDPE 60 % Foamed)

The tests concerning the recovery of sample height after 10 % compression show a temperature independent behavior. The temperatures applied in testing and subsequently expected during cable use in the field do not impact the material properties unfavorably. (Fig. 9)

3.4 Selection of Material and Foam Type

As the previously shown results suggest HDPE is the most suitable material choice out of the PE family for the intended purpose.

Foaming a polymer implies injecting a gaseous agent and distributing this agent evenly throughout the compound. Technologically it is possible to achieve this goal in two ways.

- Chemical Foaming

  This method uses a solid additive containing the gas generating substance and nucleating agent. The batches containing blowing agent and nucleating agent are readily available on the market. The gas generating substance , azodicarbonamide, decomposes at a certain critical temperature. The temperature profile of the extruder is set in a way that this temperature is reached shortly after the beginning of the melting zone in the barrel. The amount of gas generated and consequently the foam rate is controlled

by the processing temperature. This process will be discussed in detail in 5.2.

- Physical Foaming

  Physically foaming uses the same principle as the chemical variant. Gas is dissolved in the melt and expands after leaving the cross head. The difference consists in the way this gas is transported into the melt. Extruders that are equipped for physically foaming polymers utilize a nozzle in the wall of the barrel from where the blowing agent, e.g nitrogenous gas, is injected. The gas is generated outside the extruder by specialized equipment while the nucleating agent is added directly into the extruder hopper or compounded before the foam extrusion. The foam rate is dependent on the gas pressure of the blowing agent during injection. This extrusion variant for generating foams is used when a highly homogenous foam (electrical properties!) is needed with a high foam rate.

  While chemical foaming allows for a good quality foam up to a foam rate of 50 % when using polyolefins, physical foaming allows up to 70 %.

For the new cable design chemically foamed polymer was chosen due to lower investment costs of equipment and the lower requirements to the homogeneity of the obtained product. (No electrical requirements)

4. The New Cable and its Properties

4.1 Weight and Stiffness

The stiffness of the cable with the foamed central member upjacket was reduced by 5 % in comparison to the design with the solid upjacket.

The weight was reduced by 8% at a foam rate of 40 % for the upjacket. Fig. 10 shows the new weight distribution in comparison to a non-foamed design. Further weight reduction would be possible by higher foam rates. This goal competes with processability issues.

4.2 Deflection under Lateral Pressure

A main concern before endeavoring into the design of a cable with a foamed core was the potential behavior under lateral pressure or crush testing.

The standard Crush Test for this cable type specifies a maximum attenuation increase at 1550 nm under a load of 1960 N over a length of 10 cm.

To assess the crush behavior, standard tests as well as modified tests have been performed. The standard test is

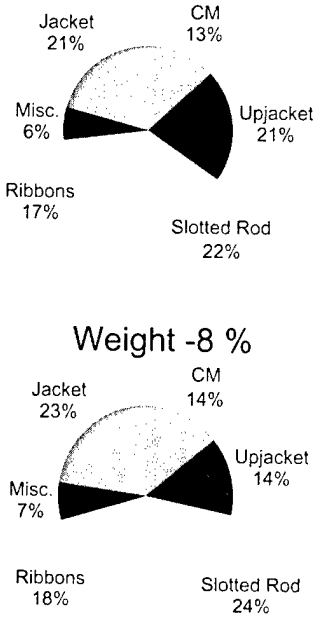


Figure 10: Weight Reduction and Distribution after Foaming the CM Upjacket

performed in the middle of a cable sample to simulate the load as seen in the field. The modified tests were performed at the end of a cable sample while monitoring the deformation of the slotted rod and upjacket visually. In both cases the deflection over the load was recorded.

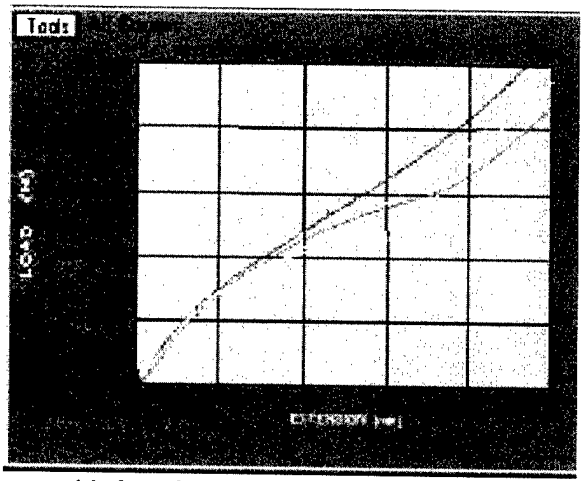


Figure 11: Load vs. Deflection on a Foamed 1000 F SCR Cable

White = cut end, no ribbons. Yellow= cut end, w/ribbons. Green=continuous sample, no ribbons. Red =continuous sample w/ ribbons

The change of slope in the Load vs. Deflection curves in Fig.11 all show that the crush load expected to affect the optical performance of the fibers is far beyond the specified load of this product. (Slope Change at 6000 N).

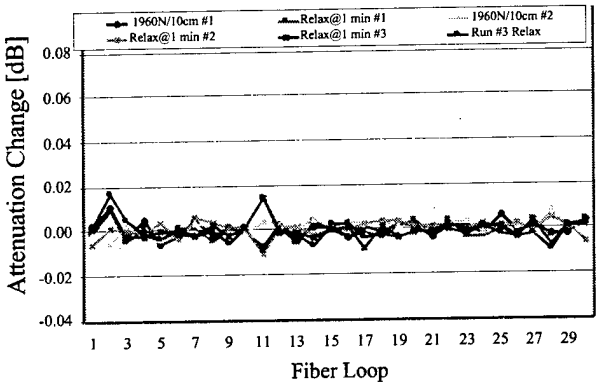


Figure 12: Crush Test on a 1000 F SCR Cable with Foamed Core

As expected the cable showed no evident attenuation increase during spec load. A good correlation between the deflection behavior and the characterization load at which the cable finally showed an attenuation increase was recorded also. (Fig.12)

The same positive results were obtained for the impact test. (Fall height 1m, 25 mm cylinder, Wave length 1550 nm) (Fig.13)

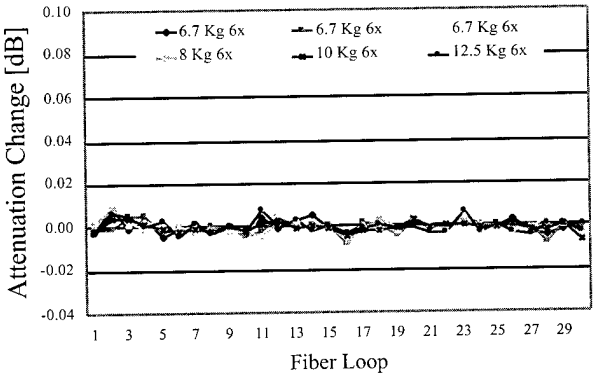


Figure 13: Impact Test on a 1000 F SCR Cable with Foamed Core

An interesting aspect of foamed core SCR cables is the difference in the mechanism by which the cable compensates the load through deformation.(Fig. 14 + Fig. 15)

While a solid SCR core absorbs crush load by rotation of the core and a parallel buckling of the legs, the foamed cores show a tendency to absorb a portion of the load into the foamed part

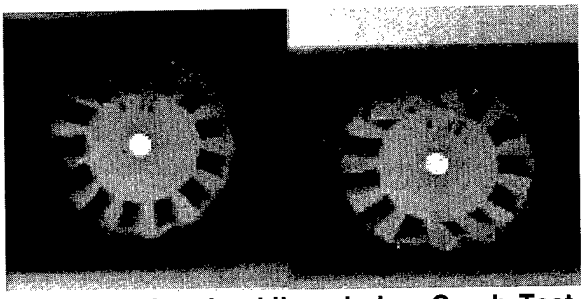


Figure 14: Leg buckling during Crush Test on a 1000 F SCR Cable with Solid Core

of the core. A later onset of the rotary movement is the consequence. The overall performance is the same as for a solid core cable.

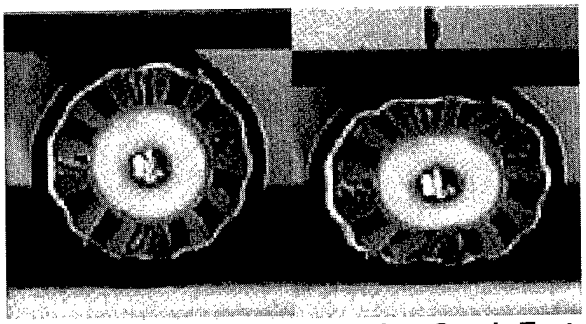


Figure 15: Leg Buckling during Crush Test on a 1000 F SCR Cable with Foamed Core

4.3 Environmental Tests

Temperature cycling testing was performed between –30°C and +70°C. Three cycles were performed with a soak time of 6 hours between temperatures. All 1000 fibers were monitored at a Wavelength of 1550 nm. Fig. 16 shows the results of the TC test.

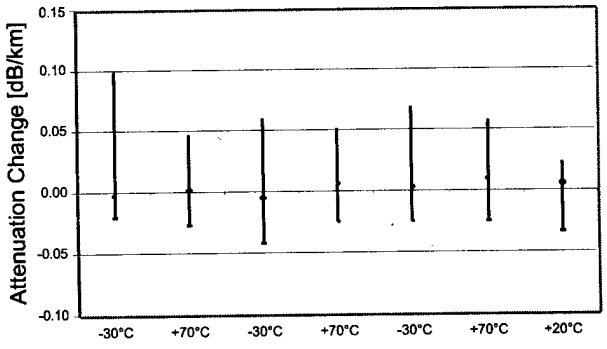


Figure 16: Temperature Cycling Test on 1000 F SCR cable with Foamed Core

5. Manufacturing of Foamed Core

5.1 One Step Process

As already mentioned in 2.2 a solid layer upjacket is made in various passes while a foamed layer can be applied in one step.

Table 2 shows the comparison of area increase between the two processes.

	Area Increase [%]	
Step	Solid Polymer	Foamed Polymer
1	70	176
2	47	25
3	36	-

Table 2: Area Increase on the various steps of Upjacketing

The first step is characterized by the polymer being applied directly onto the steel in both process types, solid and foam extrusion. The second step is different as the solid polymer is applied onto a cold polymer layer while the foam expands over its full cross-sectional area. The foam layer can be applied in one step as the foamed polymeric material to be cooled down is in fact only 60 % of what needs to be cooled in the case of solid extrusion. This avoids lumps and unevenness. The third step is only needed for the solid extrusion process.

The process speeds are in fact very different. While the three steps of the solid extrusion run with an average speed of 40 m/min the foam extrusion is slowed down to 10 m/min. This is due to the intensive cooling needed.

The effective production speed is determined by how quickly the setup processes regarding the solid upjacketing can be performed.

5.2 Important Process Parameters

The foam rate for chemical foaming is determined by the temperature of the polymer in the gas generating area of the extruder barrel. The quantitative decomposition of the blowing agent is due to the applied temperature. Thus the control of the extrusion temperature in a very narrow range is vital for the consistency of the obtained foam rate.

Fig. 17 shows the relationship between extrusion temperature and foam rate for HDPE.

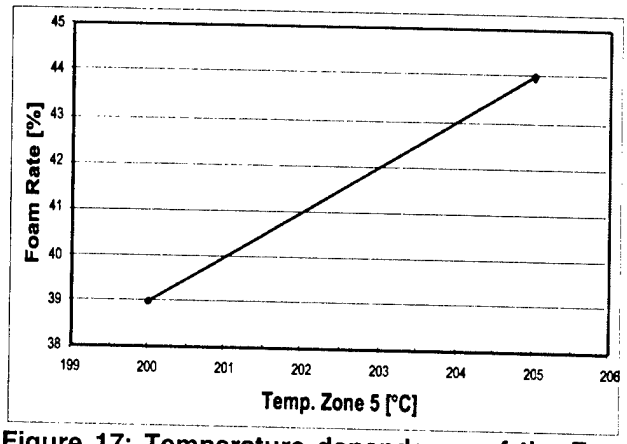


Figure 17: Temperature dependence of the Foam Rate (HDPE) (Azodicarbonamide)

The main factor guiding the process speed of the foamed upjacket is the cooling speed of the foam after the cross head.

Only the surface of the foam is in contact with the cooling water where the extrusion heat can be dissipated into the environment. The heat from the center of the upjacket has to pass through the material by heat flow to the surface as it is valid for every object when cooled by water. Polymer foam is a very efficient insulator so it takes considerably longer than with solid polymer to achieve a cooled product ready to be spooled off.

Figure 18 shows the theoretical cooling behavior of a 1000 F foamed core upjacket. The different lines depict different distances from the central member in direction to the surface of the upjacket. It can be noted that the surface (bottom line) cools very quickly to the environmental temperature while the heat in the core (top line) needs far longer to dissipate the extrusion heat.

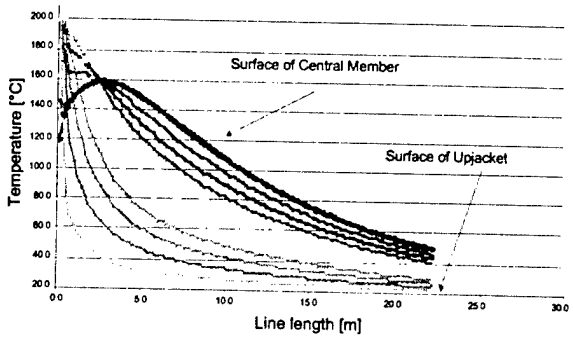


Figure 18: Cooling Behavior of the Foamed Upjacket of a 1000 F SCR Cable

5.3 Process Automatization and Quality Control

The main factor for the quality of the foamed material is the consistency of the foam rate. While this is an important parameter to be monitored it is not easy to be measured.

The measurement itself is not difficult as density measurements by hand pose no difficulty. The difficulty is to obtain a measurable sample without interrupting the manufacturing process. It is standard procedure to cut a sample at startup and end of a production length. These samples determine if the length will be used for further processing or not. But they cannot tell about the consistency of the foaming process during the run.

To solve this problem a new online method of monitoring the foam rate online was devised.

In copper cable applications using foamed materials the capacitance of the product is constantly monitored as a decisive quality factor. The capacitance is measured as the disturbance that the wire plus upjacket causes in a known electrical field applied between the plates of a cylindrical capacitor . The product passes through this cylindrical field.

The foam rate can be expressed as a product of the incoming wire diameter, the capacitance of the product and the final product diameter. By measuring these parameters constantly and processing them online, it was possible to devise a online display of the foam rate and have a parameter for the product quality.

Fig. 19 shows the schematic of the used measuring device.

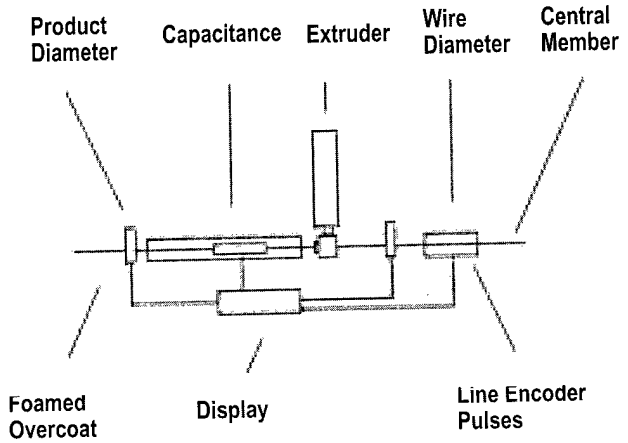


Figure 19: Foam Rate Online Measurement System

6. Conclusions

Foaming the central member upjacket is an efficient way to reduce weight and stiffness of SCR High Fiber Count Cables. It does not require changes to the remaining steps of cable manufacturing, and the resulting products meet all the customer requirements. The expectancy for the future is to substitute more cable elements that hitherto were manufactured of solid polymers with foamed plastics.

7. References

Klempner/Frisch, "Handbook of Polymeric Foams and Foam Technology", Hansa Publishers: Munich, Vienna, New York, Barcelona, 1991

Hrsg. F. Hensen, "Handbuch der Kunststoff-Extrusionstechnik", Hansa Publisher : Munich, Vienna, 1986

Hans Domininghaus, "Die Kunststoffe und Ihre Eigenschaften", VDI-Verlag : Duesseldorf, 1992

Presenting Author

Thomas Ottmann is a Senior Development Engineer in the Japan Cable group at Corning Cable Systems in Hickory , NC. His responsibilities as project leader include the development of process technology and products for slotted core ribbon cables.

He received his degree in Dipl. Ing. Kunststofftechnik (Plastics Engineering) from the Fachhochschule Rosenheim in 1994. He joined Siemens RD & E in 1994.

Before working at Corning Cable Systems RD&E in Hickory, NC as a Development Engineer he worked on the development of Fiber Optic Loose Tube Cables at Siemens RD&E in Neustadt/Coburg.



Thomas Ottmann
Corning Cables Systems RH
P.O. Box 489
Hickory , NC 28603
E-Mail:
thomas.ottmann@corning.com

Development a Mid-Access Drop Cable with Power Feeder and Ribbon Slotted Core

H.T. Choi, S.C. Park, Y.S. Kim, Y.I. Lee
Taihan Electric Wire Co., Ltd.
Anyang-City, Kyungki-do, Korea
+82-31-420-9300
htchoi2@taihan.com, scpark@taihan.com, younsookim@taihan.com, yilee@taihan.com

Abstract
In this paper, we designed a new drop cable of 100-fiber ribbon cable with power feeding unit. The ribbon slotted core is manufactured with sufficient upper and side clearance of groove. In addition, central strength member of slotted core is designed as copper rod for the grounding of power feeder unit. The power-feeding unit is designed for the supply up to 600V electric power. The new cable is conducted to evaluate its performance in accordance with the electrical, mechanical and optical characteristics.

Keywords
Drop cable; SZ slotted rod; mid-access; power feeder.

1. Introduction
The demand of optical fibers is expected to rapidly increase for the IMT-2000 (International Mobile Telecommunication 2000), the next generation of multimedia mobile telecommunication service. It is necessary for the telecommunication service industry to provide a more stable and more economical high bandwidth telecommunication network systems to the subscribers.

Recently subway transport network is considered as useful method of installation of optical cable distribution network systems. With the subway network, telecommunication service companies can distribute the optical fibers economically without additional investment for civil works. To install the optical fiber distribution network in the subway transport system, it is necessary to supply power source for the network equipment as well as optical fiber cable. This is critical point for the telecommunication service provider. It is an undesirable and time consumable solution for them to install the power source and optical fiber cable separately in highly competitive telecommunication market.

Therefore, it is very important to design the cost effective cable structure to supply the power source and optical fibers at the same time. In addition, the optical cable unit should have the suitable structure for the mid-accessibility.

2. Cable Design
2.1 Ribbon Slotted Core
2.1.1 Fiber Excess length in the ribbon slotted core.
Ribbon slotted core design is attractive in order to minimize the cable dimension for the duct installation in the subway network. Moreover, the ribbon fiber in the SZ slotted rod can be easily extracted comparing with helical slotted core for mid accessibility. So the SZ slotted rod design is suitable for drop cable design.

In order to estimate proper mid-accessibility and stable working tension, it is important to control fiber excess length in accordance with SZ reverse lay length and stranded pitches. In addition, in case of SZ slotted core, the fiber strain is the most considerable factor during cable bending.

So it is desirable to establish the correlation between fiber excess length and geometrical properties of slotted core to ensure easy mid accessibility as well as stable working tension. From the above-mentioned problems, we theoretically investigated optimum structure and lay lengths of optical fiber in the SZ slotted rod.

The structural coordination of the SZ stranded ribbon fiber can be defined with cylindrical coordinate system. If we draw a line of a fiber path in the SZ slotted rod, we can say the path of the line will be a sine curve around the center of the SZ slotted rod. The coordinates of the ribbon fiber trace in the SZ slotted rod can be expressed as following equation (1).

$$x = Rs\cos\theta\,,$$

$$y = Rs\sin\theta\,,$$

$$z = \frac{Ps}{2} + \frac{Ps}{2\pi}\sin^{-1}\frac{2\theta}{\phi} \qquad (1)$$

Comparing the radius of ribbon fiber trace and reversing angle with SZ reverse lay length, we can consider an approximation for the fibers excess length in the SZ slotted rod. With this assumption we can drive an equation for the excess length of the ribbon slotted core as following.

$$Fl(l) = \int_C f(x,y,z)dl \approx L\left[1 + (\frac{\pi Rs\phi}{2Ps})^2\right] \qquad (2)$$

Where,

Ps: SZ reverse lay length

Rs: Fiber bending radius

In addition, the SZ slotted rod is stranded with certain lay length with power feeding unit. The induced stranded fiber excess length is estimated by equation (3).

$$F2(l) = \sqrt{\left(\frac{\pi D'}{P}\right)^2 + 1} \quad (3)$$

Where,

P: stranding pitch of slotted core

The total fiber excess length in the drop cable will be the multiplex of the equation $F1(l)$ and equation $F2(l)$.

2.1.2 Mid-accessibility of Ribbon slotted core. The mid-accessibility can be performed when the fiber slack length is enough for the splicing operation at any access point of the drop cable. When the cable jacket is removed at the reverse point, the slack length is simply obtained as equation (4).

$$S(l) = \sqrt{(\frac{F(l)}{2})^2 - (\frac{L}{2})^2} \quad (4)$$

In order to verify this estimation, the ribbon slack length is measured with trial cable. Fig. 1 is shown a schematic representation of relationship between removed jacket length and slack length at the center of the reverse pitch.

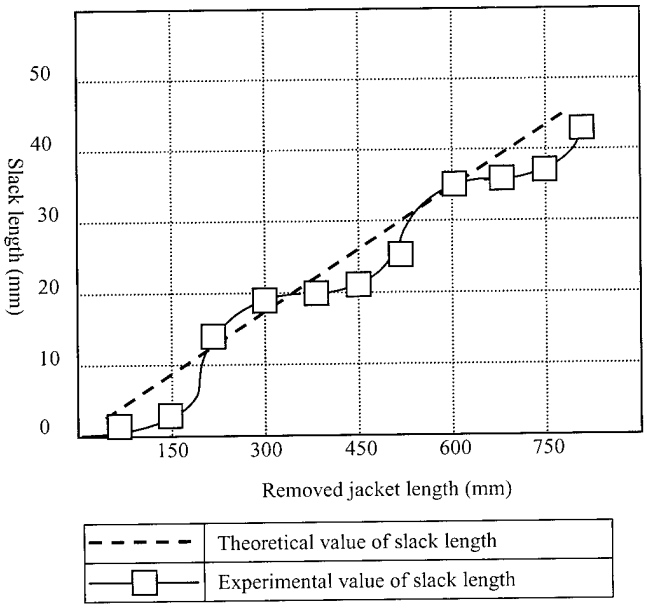


Figure 1. Measurement of Slack length

When the removed jacket length is more than 500mm, the slack length is more than 20mm. In the consideration of the field service, mid-access test is applied on the trial cable. Table 1 shows the results of the mid-accessibility test. The removed jacket length is about 500mm and stranded core lay length is about 200mm and SZ reverse lay length is around 150mm.

With this result, The enough slack length of ribbon fiber can be achieved at any access point. So it is reasonable that the optimal SZ reverse pitch and stranded core lay length can be designed with above approaching method.

Table 1. Fiber slack length for mid-accessibility

Items	Slack length
Maximum	30mm
Minimum	24mm

2.2 Power feeding unit

2.2.1 Function of Copper rod in power feeder. In order to design an optical fiber cable with power feeding unit, it is important to consider optical fiber unit and power feeding unit at the same time to estimate the compatibility both cable units. The copper rod in the power-feeding unit should work as strength member for the optical cable unit as well as conductor for the power supply.

In order to supply the electrical power, it is necessary to select proper copper rod as electrical conductor. For the power cable design this kind of factor is important to provide stable condition in the field. Therefore, it is necessary to determine proper copper conductor diameter, as A.C current resistance of conductor for the power-feeding unit. The proper diameter of the copper conductor of power feeding unit can be derived from the expressions for the voltage drop.

$$\varepsilon = K \cdot \frac{Z \cdot I \cdot L}{1000} \quad (5)$$

Where,

ε: Voltage drop (V)

K: constant for power distribution condition

Z: impedance of the cable (Ω/Km)

I: current (A)

L: cable length (m)

In addition, in the equation (5) the impedance of the cable is obtained from following equation (6)

$$Z = R\cos\theta + X\sin\theta \quad (6)$$

Where,

R: resistance of cable (Ω/Km)

X: reactance of cable (Ω/Km)

$\cos\theta$: Power factor of cable

With the relation between resistance of conductor and the cross sectional area, the diameter for the copper conductor can be calculated according to the BS 6360.

$$R = \frac{4A}{n\pi d^2} K_1 K_2 K_3 \qquad (7)$$

Where,

R: maximum resistance at 20°C

A: volume resistivity at 20 °C of the conductor material

N: number of wires in the conductor

K1: a factor depending on diameter

K2: a factor depending on conductor formation

K3: a factor depending on cross sectional area size

Usually the network system in the subway is used as RAS (Radio access Subsystem) for the mobile communication service. For the conventional RAS equipment, it is estimated around 500W power consumption and the allowable voltage drop is around 15%. So the diameter of the copper rod can be selected with above equations and data. From the results, it is necessary that the power feeder unit is designed as two 8.0 [nominal section copper wire with 1km length in the consideration of the extra equipment for the future.

2.2.2 Function of Copper rod in optical cable unit. In addition, for the optical fiber cable unit, allowable working tension is one of the most important factors to ensure its mechanical and optical properties in the field. The allowable working tension for the optical fiber cable is calculated from the excess length of ribbon fibers in the slotted rod and diameter of copper rod as strength member in the cable.

$$T = E \times A \times F(total) \qquad (8)$$

E: tensile modulus of the strength number

A: area of the strength member

F(total): sum of fiber excess length with maximum allowable fiber strain

With this concept, allowable working tension can be estimated. Theoretical allowable working tension can be calculated with two 8.0 [nominal section copper wires as strength member for the drop cable.

The calculation is resulted in around 4.5kN maximum allowable working tension. This value is considered enough to provide stable pulling tension of the cable in duct for the optical cable installation as well as stable mechanical properties.

2.3 Compatibility of Electric Power and Fiber Optics

When the electric power is applied on the power-feeding unit, the temperature of copper conductor will be increased. This kind of temperature increase has a relation with the current rating of power cable unit. On the standpoint of the power cable design this kind of factor is important to provide stable condition in the field.

In the hybrid cable, the optical cable unit is directly influenced with temperature increase. For the optical fiber cable ambient temperature is important to ensure its mechanical and optical properties all the time.

Therefore, it is necessary to determine proper conductor diameter, A.C current resistance of conductor for the power-feeding unit to estimate proper conductor temperature rise above the ambient temperature.

We consider it is reasonable to analyze the conductor temperature with certain surrounding ambient temperature to ensure the drop cable design. According to the IEC 287, the temperature increase can be estimated with the equation of the permissible current rating of an A.C cable.

When the permissible current rating of power cable is considered as 8A, the temperature increase is calculated with 8.0 [nominal section copper conductor. The temperature increase is calculated with two cases. In the consideration of the duct in the subway, the ambient temperature is assigned as 40°C and 50°C. With these two condition the temperature increase is estimated less than 2°C. Table 2 shows the selection of 8.0 [nominal section copper wire as conductor is also reasonable in the concept of temperature increase as well as electric power supply.

Table 2. Calculation of temperature increase with current rate

Item	Air temperature	Current rate	Conductor temperature
Case 1	40°C	8A	41.3°C
Case 2	50°C	8A	51.5°C

2.4 Cable Construction

The fiber optic unit is 100-fiber SZ slotted rod that has five grooves and each groove contains five 4-fiber ribbons which dimension is 0.35mm×1.10mm. For the consideration of short circuit current during a fault of power feeder, heat resistant glass tape is wrapped around slotted core. A ground wire of power feeder is located a center of the slotted core as strength member to design compact cable structure. In addition, the material of strength member of slotted core is designed as ϕ1.3mm copper rod for the grounding purpose.

The construction of the mid-access drop cable with power feeder and ribbon slotted core is shown in Fig.2. For the proper insulation, XLPE (cross-linked PE) is used as insulation material over the copper conductors. Also for the identification, white and red is used as insulation color for the power-feeding unit respectively. For the circular formation, ϕ3.0mm PE filler is inserted in the stranding process. The SZ slotted rod and power

feeding unit is stranded by reverse lay method for the mid-accessibility.

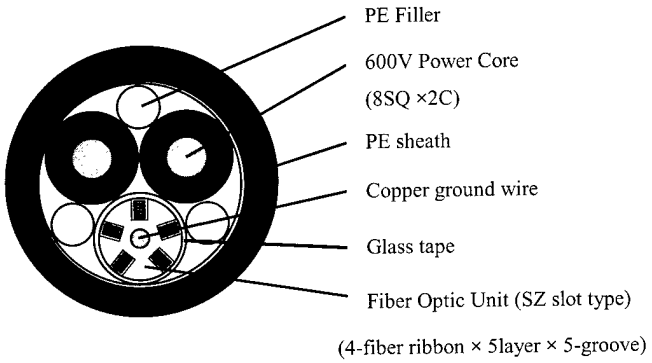


Figure 2. Cable Cross-section

Table 3. Dimension of the new drop cable

Items	Results
Cable diameter	Nom. 17.2mm
Cable weight	Nom. 295kg/km

3. Experimental Analysis

3.1 Heat Shock Test

In order to investigate the characteristics of new cable in response to a simulated short circuit current during a fault, we used a short-current generator to apply an instantaneous large current to the cable. Fig. 3 gives the increased attenuation versus temperature induced current intensity. At that time, the temperature of the cable was increased up to 180°C. and it was shown that the trial cable had a satisfactory heat resistant property.

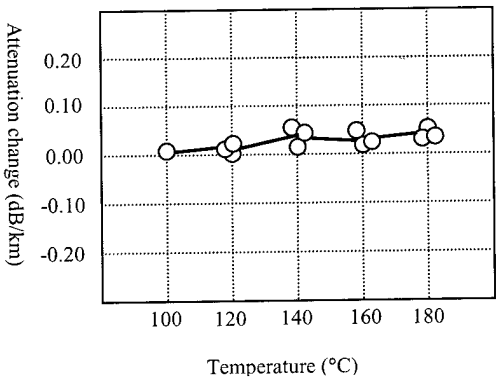


Figure 3. Attenuation against heat shock

3.2 Long Term Heat Aging Test

This test method was chosen by the similar reason as the heat shock aging test and this cable is necessary to have long term high temperature compatibility. The specimens exposed at 20°C to 100°C respectively for 400 hours in chamber and observed transmission loss and the deterioration. The characteristics of attenuation loss in each specimen are shown in Fig. 4. And it is less than 0.05dB/km.

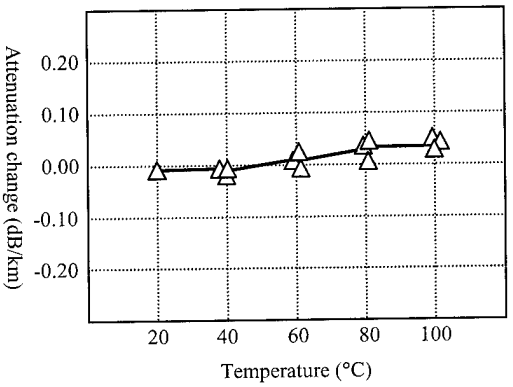


Figure 4. Attenuation against long term heat aging

3.3 Tensile Loading Test

The working tension assumed in the duct environments was applied to the trial cable, and the fiber strain and transmission loss was checked. Fig. 5 shows the relationship between tensile force versus fiber strain of ribbon in slotted rod. There was no change in optical attenuation up to 5kN. At that time, the fiber strain reached up to 0.05%.

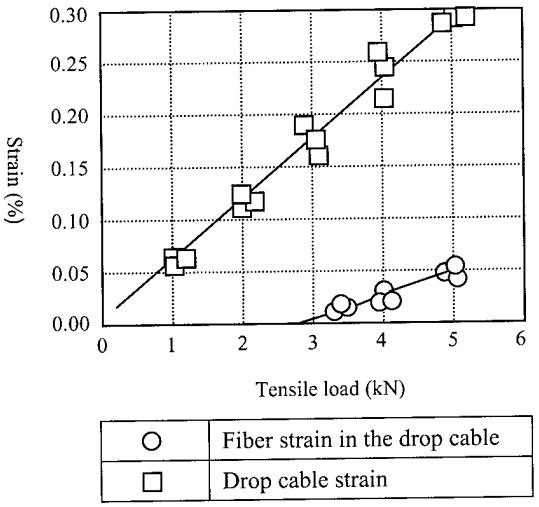


Figure 5. Relationship of strain verse tensile load

3.4 Other Mechanical Test

The new drop cable was evaluated with other mechanical test programs, which was considered as international standards to ensure the quality of cable design. The results that are shown in Table 4 are presented good characteristics of the new drop cable design in several mechanical test programs.

Table 4. Other mechanical test result

Items	Reference standards	Results
Crush	EIA/TIA-455-41 IEC 794- E3	Less than 0.05dB
Impact	EIA/TIA-455-25 IEC 794-1 E4	Less than 0.05dB
Bending	EIA/TIA-455-104 IEC 794-1 E6	Less than 0.05dB
Twisting	EIA/TIA-455-85 IEC 794- E7	Less than 0.05dB
Temperature Cycling	EIA/TIA-455-3 IEC 794-1 F1	Less than 0.05dB/Km

3.5 Electrical Property Test

Power feeding unit is introduced as the solution for the electric power supply of RAS equipment. So the electrical property is also considered as one of the important properties of new drop cable design.

When the nominal section wire area of the conductor is around 8 [. this kinds of electric power cable can be classified as 600V cross linked polyethylene insulated cable according to the Korean Standard C3611. The electrical properties of new drop cable are tested with Korean Standard C3611 as the low voltage power cable. For the reasonable evaluation of the power feeding unit three characteristics, resistance of the conductor, insulation resistance and voltage which is the cable can be resisted within 1 minute are tested with new drop cable. Table 5 shows the electrical properties of drop cable. With these results, we can estimate the power-feeding unit in the drop cable will do a good performance in the filed service.

Table 5. Electrical properties of new drop cable

Items	Results
Conductor Resistance	2.26Ω/Km
Insulation Resistance	2700MΩ.Km
Test Voltage (1500V/ 1min)	No damage

4. Conclusion

The drop cable for the subway network system was investigated to realize a cost effective cable structure. Based on test results, it was confirmed that new developed drop cable with power feeder and ribbon slotted core is satisfied with the requirements for usage of power and conventional drop cable with mid-accessibility.

Slack length for the mid-accessibility is more than 20mm and this length is enough for the identification and jointing operation. Especially, according to the various test programs, we proved that the new developed drop cable for subway network showed excellent mechanical properties. Maximum allowable working tension is estimated around 5kN.

Therefore, it was clarified that the proposed drop cable was enough to ensure reliability of field application. The advantages of new developed drop cable is self -power feeding, excellent mid-accessibility and cost down effect comparing with conventional drop cable. Therefore, the mid-access drop cable with power feeder will be attractive to the telecommunication service companies.

5. Acknowledgments

The authors wish to thank H.S. Ryu and staffs of electric power cable engineering team of TEC for assistance in manufacturing cable including tests and gathering data, and their valuable contributions to this paper.

6. References

[1] Yukihiro Hamada, Fumihiko Shimizu, Hirotaka Tanaka, "A New Optical Cable Attachable to Drop Wires" Proceedings of the 49th International Wire and Cable Symposium, 2000, pp. 8 ~10

[2] Marta Garcia, Carlos G. Cortines, Francisco J.Saez, "Hybrid Cables for Telecommunications and Power Feeding in the Access Network" Proceedings of the 49th International Wire and Cable Symposium, 2000, pp. 16 ~17

[3] Yoshio Ishibashi, Akira Watanabe, Osamu Arai, Kenji Ishii, Yoshinori Kurosawa, "Development of aerial optical fiber cable with greater length of cable compared to supporting wire" Proceedings of the 46th International Wire and Cable Symposium, 1997, pp. 12 ~13

[4] IEC 287 " Calculation of the continuous current rating of cables"

7. Biographies



Hee-tea, Choi

Taihan Electric Wire Co., Ltd. Korea

htchoi2@taihan.com

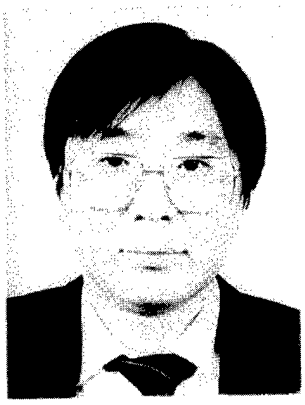
H.T. Choi received his B.A. degree from Hanyang University in 1994. He joined Taihan Electric Wire Co., Ltd. and has been engaged in optical fiber cable manufacturing. Now he is an assistant manager of Communication Cable Engineering Team. He has worked a variety of design and development projects in cables and materials.



Sang-cheol, Park

Taihan Electric Wire
Co., Ltd. Korea
scpark@taihan.com

S.C. Park received his B.A. degree from Ajou University in 1994. He joined Taihan Electric Wire Co., Ltd. and has been engaged in Fiber Optics for ribbon. Now he is an assistant manager of Communication Cable Engineering Team. He has been involved with design of ribbon fiber and slotted rod since 1996. He is now involved in development of slotted rod for high-density ribbon slotted core cable for oversea market.



Young-ik, Lee

Taihan Electric Wire
Co., Ltd. Korea
yilee@taihan.com

Y.I. LEE received his B.A. and M.S. degree from Yonsei University in 1981. He joined Taihan Electric Wire Co., Ltd. and has been engaged in Fiber Optics Engineering Team. Now, he is a general manager and he is a member of SG. 6 CCITT sub-committee of Korea and the Korea Institute of Communication Sciences. His current work focuses on product development and application of fiber optic and cable design.



Youn-soo, Kim

Taihan Electric Wire
Co., Ltd. Korea
younsookim@taihan.com

Y.S. KIM received his B.A. degree from Sungkyunkwan University in 1983. He joined Taihan Electric Wire Co., Ltd. and has been engaged in telecommunication Engineering Team. His current work focuses on development and application of RF and UTP cable with fiber optics.

Development of 112-Fiber Optical Cable having Slotted Rod and Stainless Pipes Optimized for Installation into Sewer Pipes

Takahiro Kuwajima, Satoshi Imamura, Yoji Suzuki
Engineering Department, Kaminokawa Plant, OCC Corporation
Tochigi, Japan
+81-285-56-3314 · email: kuwajima@occ.ne.jp

Abstract
With the rapid spread of the Internet and increase in multi-media information, the construction of FTTH (Fiber To The Home) infrastructures has become an urgent task in many cities. To deal promptly with such needs, it is necessary to develop outstanding cables, which are; usable in existing facilities, economical, and easy to install. Focusing on sewer pipes as inexpensive communication channels, which can be deployed without impairment to the surrounding environment, we have developed an optical cable that integrates the trunk line and branching line. The cable fits the curved surfaces of the inner walls of sewer pipes, and causes little disturbance to the water flowing through the pipes, and is able to control the adherence of pollutants. Also, the cable has a performance of operation of mid-span access and construction to the thin branch pipe. This paper describes the optical characteristic, mechanical characteristic, and installation for the eye-shaped cable into sewer pipe.

Keywords
Optical fiber cable; stainless pipe; sewer pipes.

1. Introduction
To begin with laying an optical fiber cable in a sewer pipe, we developed a cable laying method, a cable fixing robot, and cable laying tools. The cable is usually laid in midair along the street, or in the space along a railway or subway track. When a national or municipal institution such as a public organization lays a new cable, sewer pipes are used because of a land ownership problem. In general, one trunk line has been laid in a conventional pipe. However, there has been an increasing demand for branching. Therefore, we have been required to develop the branchable cable structure and an easy-to-branch method. We have had some problems which should be resolved in order to lay, use, and maintain cables in a narrow space of the sewer pipe originally designed to drain water. In laying a cable, we had to design its shape which does not damage the characteristics of a sewer pipe. First of all, we reviewed the shape of a cable in accordance with that of a sewer pipe and then determined its structure in consideration of ease of cable branching.

2. Cable Structure

2.1 Entire structure
The cable has the shape of an eye and measures 56 mm in width and 20 mm in height (as shown in Figure 1). In the center of the eye, there is a 100-fiber optical cable for the trunk line. On both sides of the 100-fiber optical cable there are three stainless pipes, with an outer diameter of 2.4 mm, incorporating 2-fiber ribbon for the branching line. In total, the cable has 112 optical fibers. This cable can be branched at any point of the cable for the subscribers.

2.2 Trunk line
The trunk line of the structure a 4-fiber ribbon in a grooved slot, allowing the housing of 100 fibers or more.

2.3 Branch line cable
A branch line cable is designed to allow branching from the notch on either side, from any portion of a composite cable. Its stainless tube contains a 2-fiber ribbon and a PE sheath. Figure 2 is a view of the cross section of Figure 1 from the top, which is an example of branch line cable branching treatment.

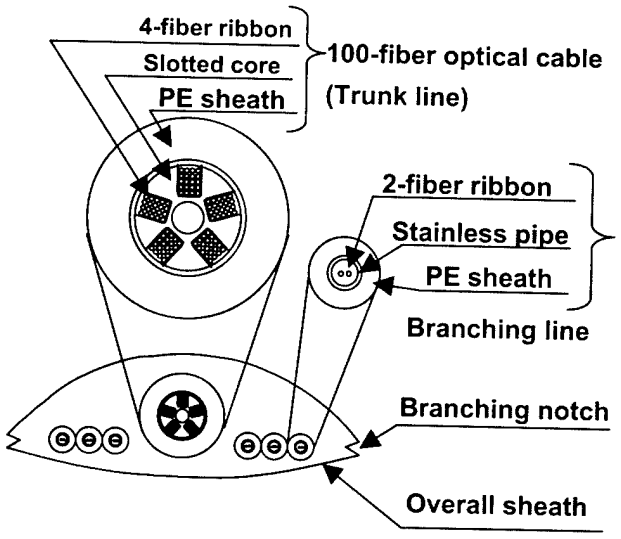


Figure 1. Cross-section of cable

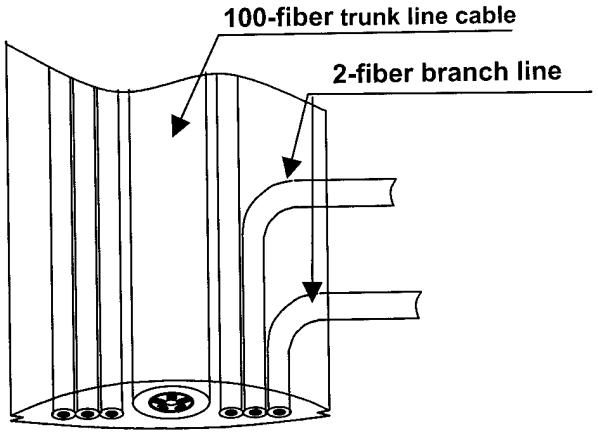


Figure 2-1. Branching treatment example

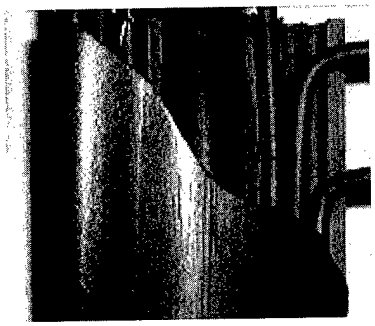


Figure 2-2. Branching treatment example

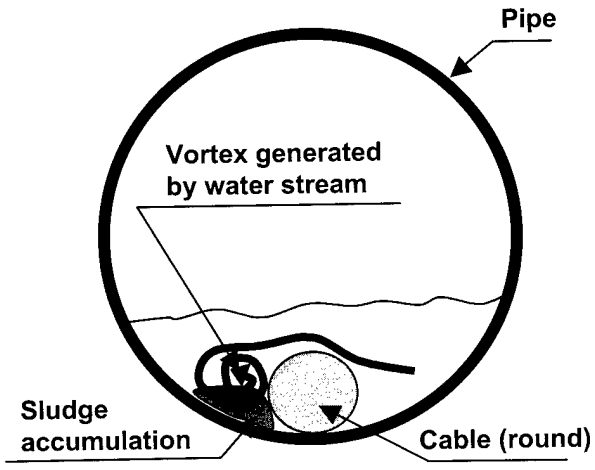


Figure 3. Conventional cable laid in the pipe

3. Advantages of This Cable Structure

3.1 Description of conventional technology

In conventional technology, a vortex occurs on the side of a normal round cable (as shown in Figure 3) when laid in a water stream, and sludge in the water accumulates at that place to prevent the stream. Sometimes, the cable was fixed to the inner top of the pipe to prevent such sludge from accumulating. However, it took a long time to fix the cable at certain intervals using a special robot after it was lain in the pipe. In addition, there was no effective method of collectively fixing a trunk or branch line cable of multiple fibers.

3.2 Description of cable technology

To resolve conventional cable problems, the following two points were mentioned: ① Providing a cable which does not promote sludge accumulation and prevents water stream even if laid in the stream; and ② providing a cable which allows construction of a communication network including a trunk line and branchable lines. Our solutions were: ① to make a convex-shape cable that conforms the inner bottom shape of pipe to prevent a vortex being generated by a water stream; securing the cable, and reducing sludge accumulation in the water (Figure 4). Also, fitting the bottom shape of the cable to the inner surface of the pipe by the contact area of cable and pipe was increased , thus stabilizing the cable position; ② to make a single cable and provide it with multiple functions by bundling multiple independent trunk line and branch line cables and sheathing them; and ③ to place a trunk line cable in the middle and lay branch line cables on both sides of it so that branch line cables can be taken out by cutting the cable side.

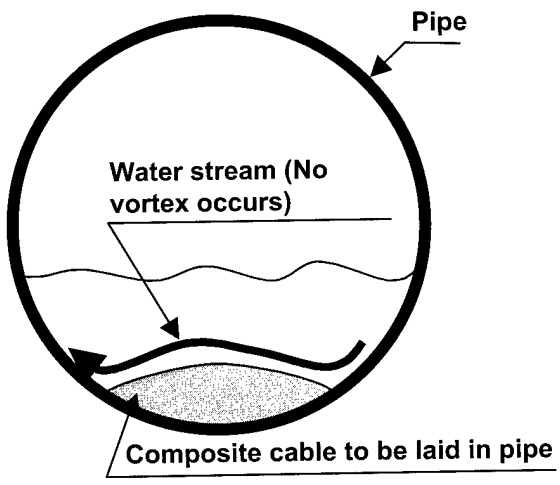


Figure 4. Developed cable laid in the pipe

4. Optical Performance and Mechanical Characteristics

Figure 5 shows the optical transmission losses both during and after manufacturing. Table 1 shows the results of mechanical characteristic tests such as tensile strength, bending, crush, and impact. It was confirmed that there was no problem.

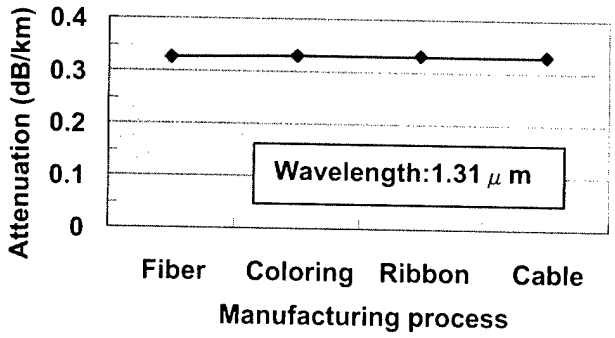


Figure 5. Change in optical attenuation during the manufacturing process

Table 1. Results of mechanical characteristics tests

Test item	Test methods	Result
Tensile strength	2670N	No loss increase
Bending	Bending diameter 10D	No loss increase
Crush	Length:100mm Load:1960N	No loss increase
Impact	Weight:1kg Height:1m	No loss increase

5. Description of Example of Cable Laying Construction

5.1 Preparation and preliminary survey

At the beginning of construction, we washed the pipe to be installed and conducted a high-pressure washing of the main pipe. To stop the water, we installed an anti-sewage net on the upper reaches of the main pipe manhole to provide the condition allowing water only to run. We washed the sewage in the pipe with fresh water before the start of construction. After that, we checked the manhole and public inlet for abnormal oxygen density or toxic gases (Figure 6), and then blew air into the pipe with a blower.



Figure 6. Toxic gas check

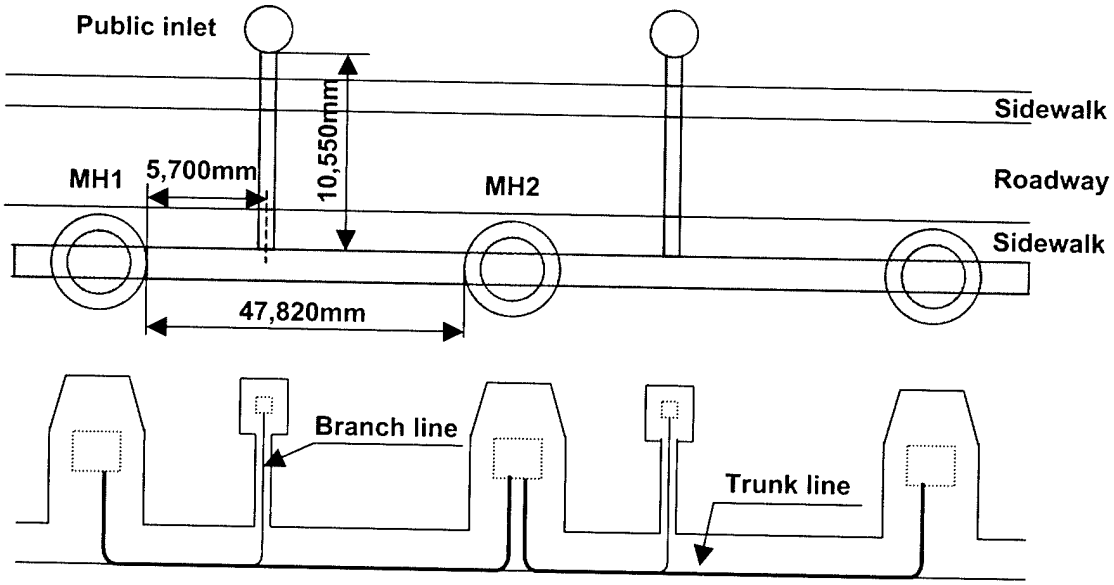


Figure 7. Installation schematic diagram

5.2 Overview of installation

Vehicle Displays Figure 7 shows the installation schematic diagram.

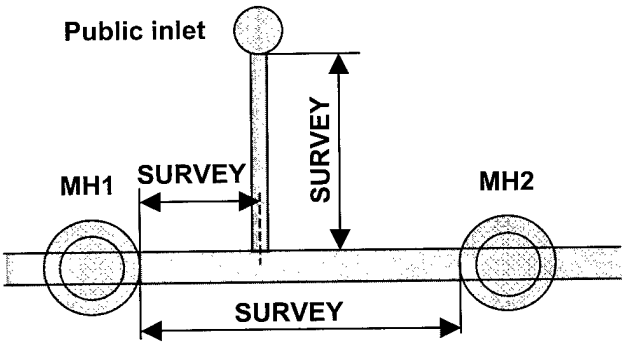
Channel A: Pass the trunk line from MH-1 to MH-2 and lead branch lines to the public inlet. Protect branch lines with a nylon tube and secure with a metal band.

Channel B: Pass the trunk line from MH-1 to MH-2 and lead branch lines to the public inlet. Branch lines are neither protected nor secured.

5.3 Cabling method

Survey a pipe length, a branch position, and a branch length. Pre-harness a composite cable(Figure 8).

- As the cable is laid from upstream, pass a lead-in wire from the downstream manhole of public inlet to a cabling position. Connect the composite cable to the lead-in wire(Figure 9, Figure 12).
- Draw both trunk line cable and branch line cable, which are connected to each lead-in wire, to the pipe simultaneously at a time (Figure 10).
- When each cable is passed to the given position(Figure 11), place a main pipe robot from the manhole and check the branch condition using its robot camera(Figure 13). For handling at the branch, fit the cable to the radius of the pipe from the upstream branch using a balloon robot(Figure 14) for the main pipe. Blow air to reshape the cable.



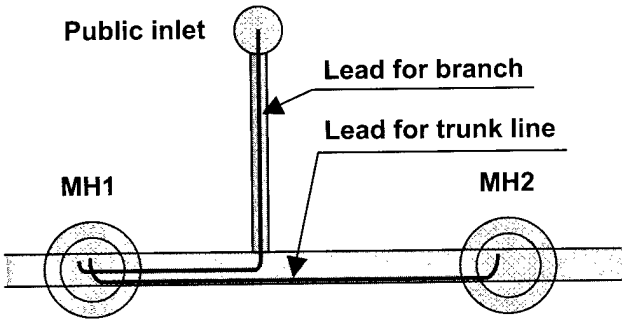


Figure 9. Lead-in wire

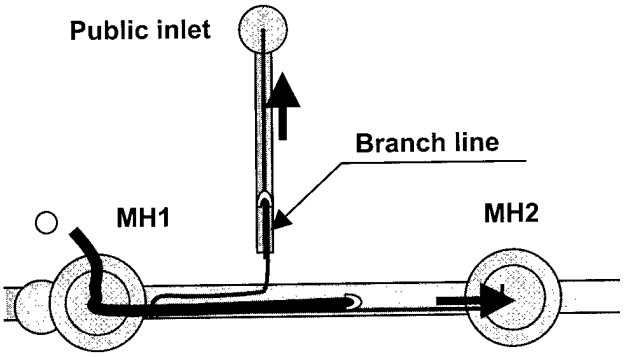


Figure 10. Pull respectively at the same time

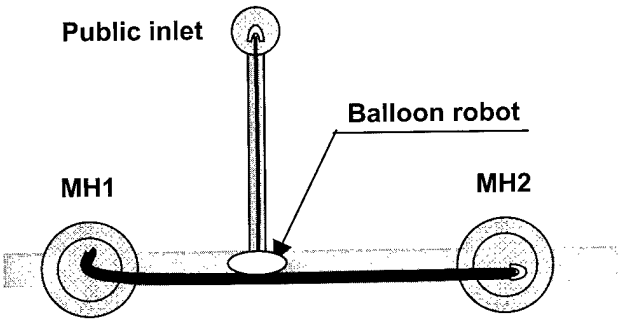




Figure 12. Example of passing a cable

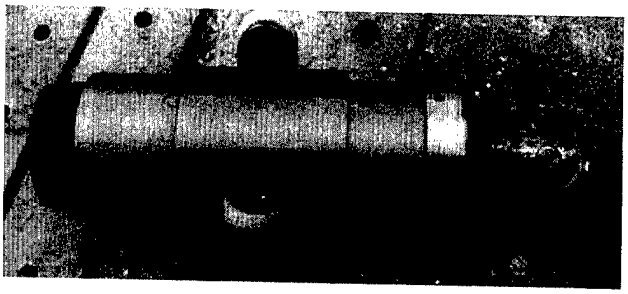


Figure 13. Pipe monitoring camera

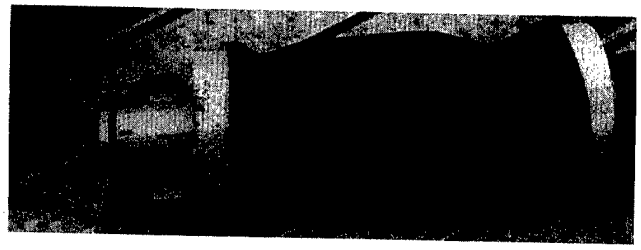
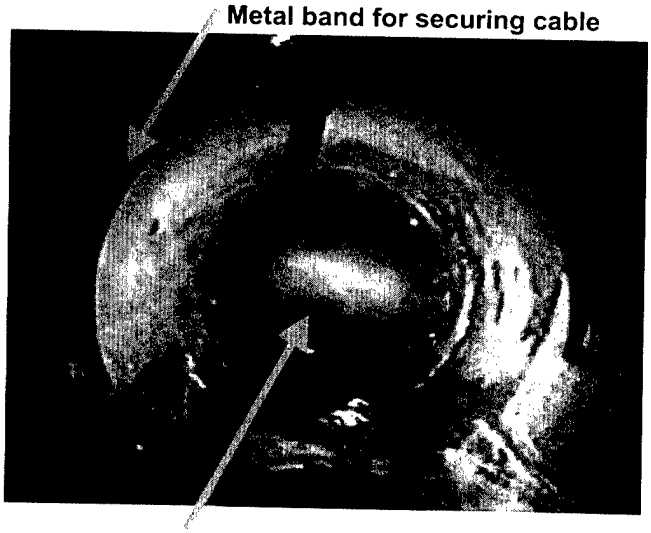


Figure 14. Balloon robot

5.4 Cable securing robot

This robot is equipped with a balloon for fitting the branch section of cable into the pipe. The balloon is inflated at the branch by air and press-fits the cable onto the inner face of pipe. The robot has also been used as a TV camera for viewing the inside of pipe. (Figure 14)

Figure 15 shows a picture of the branching cable taken from the branching side. From the picture we can notice the robot balloon fixing the position of the cable at the branching point.



Balloon robot for securing lead-in wire at branch

Figure 15. Securing cable in service pipe

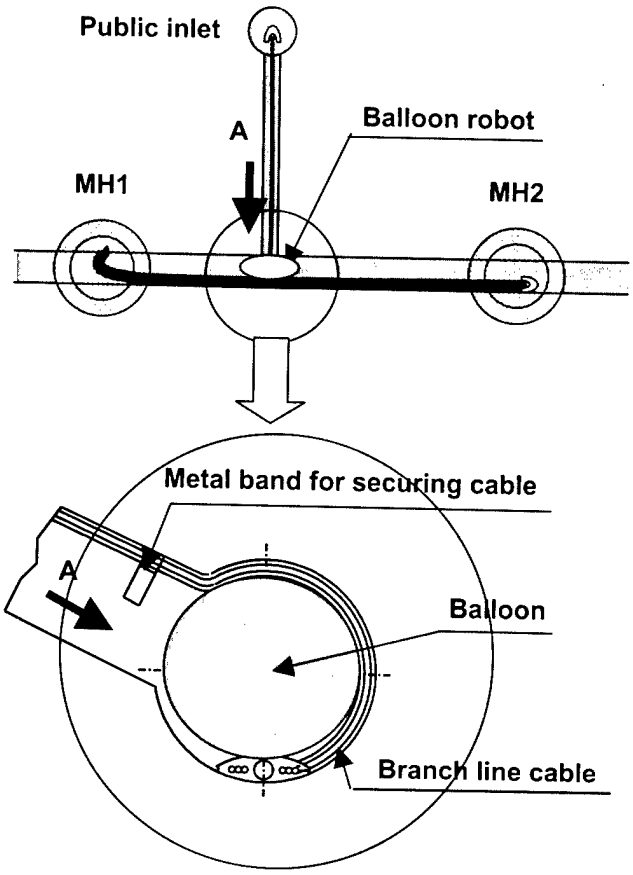


Figure 16. Balloon robot

5.5 Measurement of cable optical loss

The trunk line optical fiber cable of the composite cable is measured in optical loss by loop-connecting two 4-fiber ribbons on one side: The branch line cable is measured in optical loss by loop-connecting 2-fiber ribbons.

5.6 Result of construction

Cabling has been done almost successfully. This method took less time than the method of securing a cable in the pipe. Attention was focused on M-PAC which was suitable for a thin pipe and resistant to rough handling. There was little change in optical loss measurement before and after cabling.

5.7 Future subjects

[1] How to secure a cable at a branch

This experimental site had a condition of fully removing the installed cables from the facilities after the tests. Therefore, we did not use any adhesives, but only one metal band for securing the cable. It was necessary to firmly secure the cable and finish in such a way that no foreign matters adhere to the pipe in actual construction. An adhesive agent that hardens underwater was used for the in-house test but it took several hours for the adhesives to harden completely and the adhesive strength to the

wet pipe was not confirmed. It is necessary to consider another way to secure a cable at a branch section using adhesives.

[2] How to deal with multiple branches

At this time, we have succeeded in laying a cable at only one branch section by human power. In an actual channel, however, it is difficult to lay cables at multiple branch sections. It is, therefore, necessary to develop another cable lying method such as winching up cables in batch.

6. Conclusions

Installation experiments on use of the cable in a pipe with an internal diameter of 200 mm confirmed that the cable had sufficient mechanical characteristics such as tensile strength, installation performance, and suitability for sewer pipes. We carried out the installation experiment in the actual sewer pipe, and obtained good results in all performance characteristics.

However, the following problems on cable development are left and should be resolved in future: [1] the cable is not fully secured. In other words, there is a possibility that a large amount of wastewater may cause the cable to move apart from the pipe side, though it is fit into the inner shape of pipe; [2] Although we actually did not confirm if vortex due to water flow around the installed cable is supressed by the eye shape, theoretically we can suppose that sludge deposits are not likely to occur ; and [3] it is difficult to replace the cable with a new one.

7. Acknowledgments

Special thanks to all people who worked and collaborated on manufacturing and evaluating cables.

8. References

[1] K.Keruma et al, "Development of 48-core Optical Fiber Cable of Stainless Steel Pipe Structure With 4-Fiber Ribbons" OCC corporation., IWCS(2000).

Authors



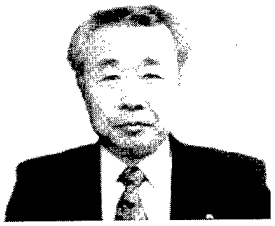
TAKAHIRO KUWAJIMA
OCC Corporation
Engineering Department
Kaminokawa Plant Tochigi,
Japan

Takahiro Kuwajima was born in 1971. He graduated from Utsunomiya University with B.E. degree in Chemistry. He joined OCC Corporation in 1994, and has engaged in engineering department cable division. He is an engineer of the KAMINOKAWA PLANT.



SATOSHI IMAMURA
OCC Corporation
Engineering Department
Kaminokawa Plant Tochigi,
Japan

Satoshi Imamura was born in 1957. He graduated from Utsunomiya University with B.E. degree in Chemistry. He joined OCC Corporation in 1979, and has engaged in engineering department cable division. He is an engineer of the KAMINOKAWA PLANT.



YOJI SUZUKI
OCC Corporation
1st Business Creates Group
Kaminokawa Plant Tochigi,
Japan

Yoji Suzuki was born in 1944. He joined OCC Corporation in 1962, and has engaged in production department cable product. He is a developer of the new product of the KAMINOKAWA PLANT.

Numerical Modeling of Deposition of SiO_2 and GeO_2 in the MCVD Process for the Manufacture of Optical Fiber Preforms

Anugrah Singh, Muralidharan, Ravi O. S. Prasad, Abhijit Dutta, and Eric W. Grald
Fluent Inc.
10 Cavendish Court, Lebanon, NH 03766
+1-603-643-2600 . ewg@fluent.com

Abstract
A numerical simulation of heat and mass transfer during the multicomponent (SiO_2 and GeO_2) modified chemical vapor deposition (MCVD) process with application to the manufacture of optical fiber preforms is performed. The MCVD process is widely used to manufacture glass preforms for high quality optical fiber fabrication. In this process, a silica tube is rotated on a lathe and is heated by a slowly traversing oxy-hydrogen torch. A mixture of gases, such as $SiCl_4$, $GeCl_4$ and O2, flow into the rotating tube and are heated to high temperatures, when SiO_2 and GeO_2 particles are formed and deposited on the tube wall due to thermophoresis. In general, GeO_2 is used as a dopant for increasing the refractive index of the final optical fiber. In this study, the commercial computational fluid dynamics (CFD) package, FLUENT, based on the finite volume method, is used to solve the governing equations for mass, momentum, energy, and species conservation for gases and transport of SiO_2 and GeO_2 particles. The effects of chemical reactions and temperature-dependent fluid properties as well as the localized heating of the moving torch are included. In the MCVD process, the incorporation of GeO_2 is low due to unfavorable equilibrium of $GeCl_4$ oxidation reaction in the presence of $SiCl_4$ at high temperatures. The kinetics of this reversible $GeCl_4$ oxidation reaction is also taken into account in the current model.

Keywords: Optical fiber; deposition; preform; germanium; MCVD; FLUENT.

1. Introduction
The modified chemical vapor deposition (MCVD) process is widely used to manufacture glass preforms for high quality optical fiber fabrication. In this process, a silica tube is rotated on a lathe and is heated by a slowly traversing oxy-hydrogen torch. A mixture of gases, such as $SiCl_4$, $GeCl_4$ and O_2, flow into the rotating tube and are heated to high temperatures, when SiO_2 and GeO_2 particles are formed due to oxidation reactions and are deposited on the tube wall due to thermophoresis (particles experience a net force in the direction of decreasing temperature). The desired refractive index of the preform is achieved by controlling the dopant chemical composition. In general, GeO_2 is used as a dopant for increasing the refractive index of the final optical fiber. Doping of GeO_2 in MCVD is low due to unfavorable equilibrium of $GeCl_4$ oxidation reaction in the presence of $SiCl_4$ at high temperatures. Wood *et al.* (1987) have investigated the chemistry of Germanium incorporation in glass preform in their MCVD experiments. In the MCVD process, it is important to study the effects of various process parameters on the particle deposition rate and efficiency to reduce the production cost. Since GeO_2 is a very costly component in the fiber, experimental studies to optimize the process is often prohibitive. Numerical simulations offer an easy tool to investigate the effects of different parameters in the MCVD process. In a previous study, Muralidharan *et al.* (2000) used the commercial computational fluid dynamics (CFD) package, FLUENT, based on the finite volume method, to study the deposition efficiency of silica particles in the MCVD process.

In this paper, we extend our earlier work to include GeO_2 deposition in the MCVD process. The kinetics of the reversible $GeCl_4$ oxidation reaction is also taken into account in the current model. We have conducted two-dimensional simulations of fully developed flow in a tube and studied the effects of torch temperature and inlet composition of reactant gases on the deposition efficiency of silica and germania particles. The predictions of GeO_2 deposition rate are compared with the results from previous numerical studies and experimental data. Similar study can be used to predict the deposition of GeO_2 in optical fiber preforms which can help in obtaining a better control of the refractive index of optical fibers.

2. Problem Description
Figure 1 shows the sketch of the system used in the present 2D axi-symmetric study. The reactant gases ($SiCl_4$, $GeCl_4$ and O_2) enter the silica tube of radius R as a fully developed laminar flow. The reactant mixture is heated by an external heat source (reaction zone). In the presence of an external heat source at the tube wall, exothermic oxidation of $SiCl_4$ and $GeCl_4$ takes place and SiO_2, GeO_2 and Cl_2 are formed as products.

$$SiCl_4(g) + O_2(g) \Rightarrow SiO_2(s) + 2Cl_2(g) \quad (1)$$

$$GeCl_4(g) + O_2(g) \Leftrightarrow GeO_2(s) + 2Cl_2(g) \quad (2)$$

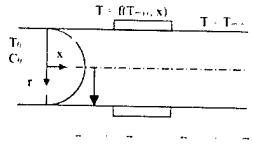


Figure 1 : Schematic of the MCVD reactor

In the above reactions, we see that the oxidation of $SiCl_4$ is irreversible and that of $GeCl_4$ is reversible. The SiO_2 and GeO_2 particles are transported by convection, diffusion, and thermophoresis.
The governing equations for the two dimensional axi-symmetric laminar flow are:

Continuity,

$$\rho v\frac{\partial v}{\partial r}+\rho u\frac{\partial v}{\partial x}=-\frac{dP}{dr}+\frac{\partial \tau_{rx}}{\partial r} \qquad (3)$$

Momentum,

$$\rho v\frac{\partial u}{\partial r}+\rho u\frac{\partial u}{\partial x}=-\frac{dP}{dx}+\frac{\partial \tau_{xr}}{\partial x} \qquad (4a)$$

$$\rho v\frac{\partial v}{\partial r}+\rho u\frac{\partial v}{\partial x}=-\frac{dP}{dr}+\frac{\partial \tau_{rx}}{\partial r} \qquad (4b)$$

Energy,

$$\rho c_p u\frac{\partial T}{\partial x}+\rho c_p v\frac{\partial T}{\partial r}= \frac{1}{r}\frac{\partial}{\partial r}(kr\frac{\partial T}{\partial r})+\frac{\partial}{\partial x}(k\frac{\partial T}{\partial x}) + r_{sc}\Delta H_{sc}+r_{gc}\Delta H_{gc} \qquad (5)$$

In the above equation ΔH_{sc} and ΔH_{gc} are the heat of reaction of $SiCl_4$ and $GeCl_4$ oxidation reaction, respectively.
The $SiCl_4$ oxidation rate is given by,

$$r_{sc} = (k_{sc,0} + k_{sc,1}CX_{o2})\exp(-Esc/RT)CXsc \qquad (6)$$

The reaction rate for the oxidation of $GeCl_4$ is,

$$r_{gc} = k_{gc,0}\exp(-Egc/RT)C^2(X_{gc}X_{o2} - \gamma YgoX_{cl2}/K_{eq}) \qquad (7)$$

The expression for K_{eq} is taken from Kim & Pratsinis (1990) which they obtained by interpolating the experimental data of Wood *et al.* (1987).

$$K_{eq} = \exp(-98.33 - 2.2525e\text{-}3\ T + 19690/T + 12.01\ln T) \qquad (8)$$

In FLUENT, the local mass fraction of each species, m_i is predicted through the solution of a convection-diffusion equation. The conservation equations for different species are

$$\rho v\frac{\partial Y_i}{\partial r}+\rho u\frac{\partial Y_i}{\partial x}= \nabla.(\rho D_i\nabla Y_i)+R_i+S_i \qquad (9)$$

where R_i is the mass rate of creation or depletion by chemical reaction and S_i is the rate of creation by any other source.

Here $D_{i,}$ is the diffusion coefficient for species i in the mixture. In our analysis, we have used dilute approximation theory for the diffusion coefficients. The source terms R_i due to chemical reactions are expressed as,

$$R_{sc} = -r_{sc}M_{sc},\ R_{gc} = -r_{gc}M_{gc},\ R_{cl} = 2\ M_{cl}(r_{sc} + r_{gc})$$

$$R_{so} = r_{sc}M_{so},\quad R_{go} = r_{gc}M_{go} \qquad (10)$$

The source term S_i are nonzero only for SiO_2 and GeO_2 (due to thermophoresis) and are given as,
$S_{so} = -\nabla.(\rho X_{so}V_{th})$

$$S_{go} = -\nabla.(\rho X_{go}V_{th}) \qquad (11)$$

where V_{th} is the thermophoretic velocity defined by,

$$V_{th} = -K(\nu/T)\nabla T \qquad (12)$$

where K is the thermophoretic constant and for the above reactions its value is taken as 0.55 (Kim & Pratsinis, 1990).

3. Boundary Conditions

The reactant gases enter the tube with a parabolic velocity profile. The inlet boundary conditions are given at x = 0 for all r as,

$$T = T_0,\ u = 2U(1 - (r/R)^2),\ v = 0,\ P = P_0,$$

$$X_{sc} = X_{sc,0},\ X_{gc} = X_{gc,0},\ X_{o2} = X_{o2,0},\ X_{cl} = X_{go} = X_{so} = 0 \qquad (13)$$

At the axis (r=0) the symmetry boundary condition is applied for all x.
The preform tube wall temperature profile in the MCVD is a function of axial distance (Morse *et al.*, 1985) and is given by,

$$\begin{aligned} T_w(x) &= T_0 + (T_{max} - T_0)(x/L_1)^2 \quad \text{for } 0 \le x \le L_1 \\ T_w(x) &= T_{max} - (T_{max} - T_{min})(x\text{-}L_1)/(L_2\text{-}L_1) \text{ for } L_1 \le x \le L_2 \\ T_w(x) &= T_{min} \quad \text{for } x \ge L_2 \end{aligned} \qquad (14)$$

The gas properties are calculated for the carrier gas O_2 and are taken as a function of temperature as given in Kim & Pratsinis (1990). The conversion efficiencies of $SiCl_4$ and $GeCl_4$ is calculated from the mixing cup averages as,

$$E_{Rsc} = 1 - \left(\frac{\int_0^R (\rho u Y_{sc})_x r dr}{\int_0^R (\rho u Y_{sc})_{x=0} r dr} \right) \qquad (15)$$

$$E_{Rgc} = 1 - \left(\frac{\int_0^R (\rho u Y_{gc})_x \, r dr}{\int_0^R (\rho u Y_{gc})_{x=0} \, r dr} \right) \qquad (16)$$

The deposition efficiencies of SiO_2 and GeO_2 are,

$$E_{Dgo} = E_{Rgc} - \left(\frac{\int_0^R (\rho u Y_{go})_x (\frac{M_{gc}}{M_{go}}) r dr}{\int_0^R (\rho u Y_{gc})_{x=0} r dr} \right) \qquad (17)$$

$$E_{Dso} = E_{Rsc} - \left(\frac{\int_0^R (\rho u Y_{so})_x (\frac{M_{sc}}{M_{so}}) r dr}{\int_0^R (\rho u Y_{sc})_{x=0} r dr} \right) \qquad (18)$$

4. Solution Procedure

The model equations as described in the previous section were solved using the latest version of the general purpose commercial CFD code FLUENT 5. A detailed description of the numerical method and several validation studies of this software are given by Mathur and Murthy (1997).

A computational grid was set up in two dimensions and the governing equations described earlier were solved in each of the resulting control volumes or cells. All the simulations were carried out for a mesh consisting of 34500 cells; 30 elements in radial direction and 1150 in the axial direction. The grid near the reaction zone was made denser due to steep changes resulting from the chemical reactions.

5. Results and Discussions

Simulations were carried out for a range of process conditions. Table 1 summarizes the various parameters used in the simulations.

Table 1. Simulation conditions used for the MCVD process with $SiCl_4$ and $GeCl_4$

$L_1 = 0.20$ m
$L_2 = 0.22$ m
$R = 0.01$ m
$T_0 = 1073$ K
$P_0 = 101325$ Pa
$T_{min} = 453$ K
$E_{sc} = 4.02 \times 10^8$ J/Kg mole
$E_{gc} = 2.63 \times 10^8$ J/Kg mole
$\Delta H_{sc} = 2.51 \times 10^8$ J/Kg mole
$\Delta H_{gc} = 4.6 \times 10^7$ J/Kg mole
$k_{sc,0} = 1.7 \times 10^{14}$ s^{-1}
$k_{sc,1} = 3.1 \times 10^{16}$ m^3/Kg mole/s
$k_{gc,0} = 2.3 \times 10^{12}$ m^3/Kg mole/s
$C_p = 1090$ J/Kg mole/K
$D_{sc} = D_{sc,0} T^{1.66}$ m^2/s
$D_{gc} = D_{gc,0} T^{1.66}$ m^2/s
$D_{cl} = D_{cl,0} T^{1.66}$ m^2/s
$D_{o2} = D_{o2,0} T^{1.66}$ m^2/s

where,

$D_{sc,0} = 6.32 \times 10^{-6}$, $D_{gc,0} = 6.0 \times 10^{-6}$, $D_{cl,0} = 1.12 \times 10^{-6}$, $D_{o2,0} = 1.76 \times 10^{-6}$ m^2/s

The diffusivity of SiO_2 and GeO_2 particles is assumed to be negligible and their effects on gas properties is neglected. The gas properties are taken as a function of temperature and pressure (Kim & Pratsinis, 1990).

$C = P/R_gT$ J/Kg mole/K, $\mu = \mu_0 T^{1.65}$ Kg/m/s, $k = k_0 + k_1 T + k_2 T^2$ W/mK

where,

$\mu_0 = 1.54 \times 10^{-9}$ Kg/m/s
$k_0 = 4.52 \times 10^{-3}$, $k_1 = 7.62 \times 10^{-5}$, $k_2 = -9.80 \times 10^{-9}$ W/mK

First, we present the results for the process condition of Q = 1.72 lpm, $X_{sc} = 0.23$ and $X_{gc} = 0.18$. The maximum torch temperature for this run was1973 K. The temperature profile at the preform wall is shown in Figure 2.

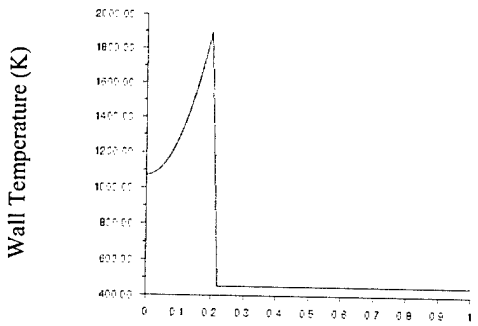


Figure 2: Temperature profile at the tube wall due to the heat source

Figure 3 shows the radial profiles of gas temperature at various axial locations. For $x <= L_1$, the gas temperature is higher near the tube wall than at the tube center. In the deposition zone the gas temperature follows the parabolic profile.

Both $SiCl_4$ and $GeCl_4$ reaction take place first near the tube wall and the mass fraction of SiO_2 and GeO_2 starts to increase in the region near the tube wall (Fig. 4 and Fig. 5). Since the activation energy for $GeCl_4$ oxidation is lower than the $SiCl_4$ oxidation, deposition of GeO_2 starts earlier than

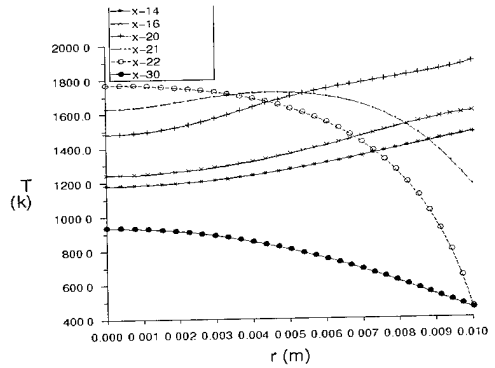


Figure 3: Evolution of radial profiles of gas temperature. The process parameters were, Q = 1.72 lpm, $X_{sc,0}$ = 0.23, $X_{gc,0}$ = 0.18 and T_{max} = 1900 K.

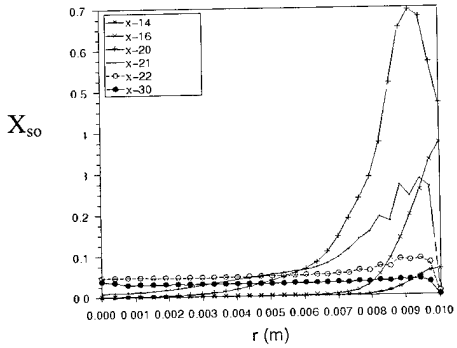


Figure 4: Radial profile of the mass fraction of SiO_2 particles. The inlet conditions were same as in Figure 3.

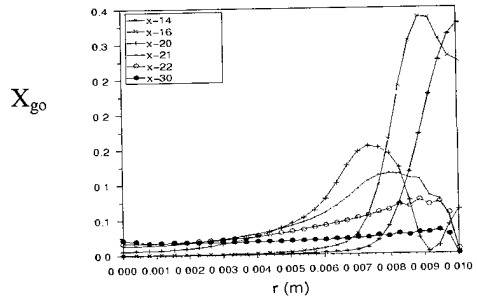


Figure 5: Radial profile of the mass fraction of GeO_2 particles. The inlet conditions were same as in Figure 3.

SiO_2. As we go further down the axis, the temperature increases and the backward reaction of $GeCl_4$ oxidation starts increasing. As a result, the $GeCl_4$ concentration starts increasing. Figure 6 shows the mass fraction of $GeCl_4$ at various axial locations. As it is evident from equation (8), the equilibrium constant for $GeCl_4$ oxidation decreases with temperature, making the backward reaction more favorable. For $16 \leq x \leq 20$ the reaction rates of the forward and backward reaction are equal and the $GeCl_4$ oxidation is in a state of equilibrium. As we go down the tube ($x > 20$), K_{eq} increases and as a result, X_{gc} decreases and X_{cl} increases (Fig. 7). The concentration of GeO_2 decreases along the deposition zone of the preform tube (Fig. 5).

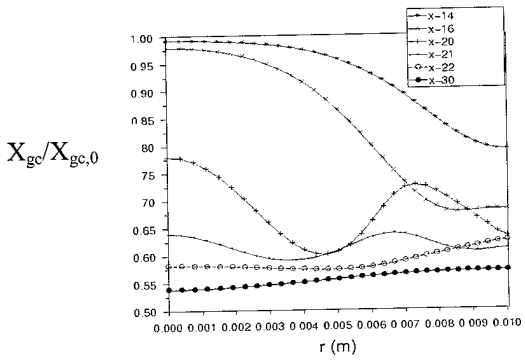


Figure 6: Radial profile of the dimensionless $GeCl_4$ concentration. The inlet conditions were same as in Figure 3.

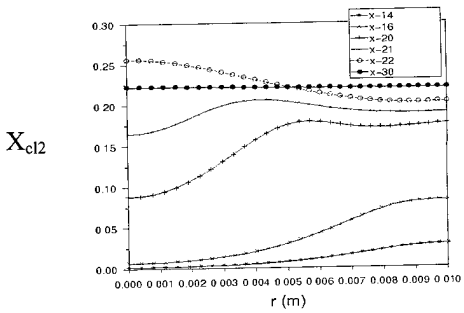


Figure 7: Radial profile of the mass fraction of Cl_2. The inlet conditions were same as in Figure 3.

In the MCVD process, the deposition of SiO2 and GeO2 particles is mainly by the radial velocity. Figure (8a) shows the evolution of radial profiles of the gas stream and thermophoretic velocity of the particles (Fig. 8b). The net particle velocity in the radial direction (Vp) is the sum of radial gas velocity and radial thermophoretic velocity (V_{th}). At the tube center, the radial velocity is zero. At the beginning of the tube, both radial velocity and thermophoretic velocity are small and V_{th} is negative, i.e., particles move towards the tube center due to thermophoresis. As we go down the tube, the temperature gradient (due to the released heat of reaction) in the radial direction increases the thermophoretic velocities. In the reaction zone ($20 \leq x \leq 22$), V_{th} is large and directed towards

the tube wall. Further down the tube, the gas streams starts to cool down and both V_r and V_{th} becomes small. The predicted conversion and deposition efficiencies of $SiCl_4$ and $GeCl_4$ along the axial position is shown in the Figure 9a. The $SiCl_4$ oxidation is complete whereas significant amount of $GeCl_4$ remains unreacted. The deposition efficiencies of both $SiCl_4$ and $GeCl_4$ increase after x = 20 and the deposition efficiency of GeO_2 is smaller than that of SiO_2. Figure 9b shows the thermophoretic flux to the wall, defined as $V_{th,y}\ \rho X_{so}$ for SiO_2 particles and $V_{th,y}\ \rho X_{go}$ for the GeO_2 particles.

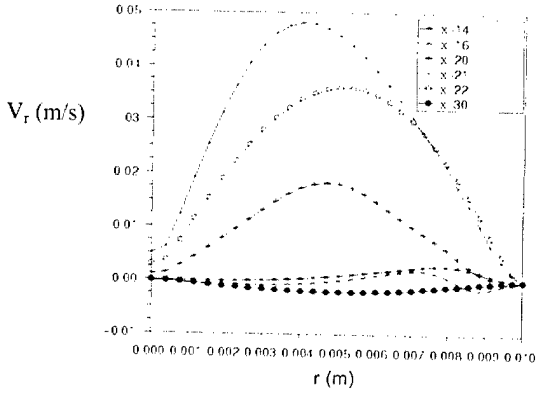


Figure 8a: Evolution of radial profiles of radial velocity of gas stream. The inlet conditions were same as in Figure 3.

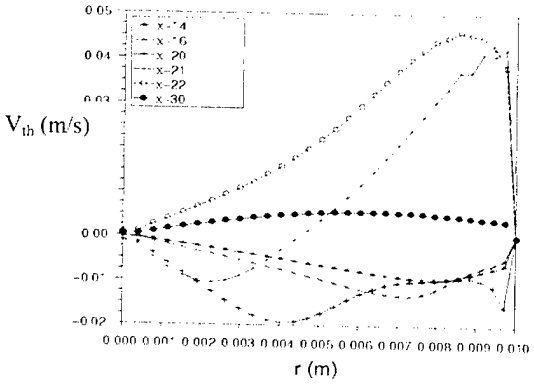


Figure 8b: Evolution of radial profiles of radial thermophoretic velocity of particles. The inlet conditions were same as in Figure 3.

We have carried out a parametric study varying the total gas flow rate at the inlet. In Figure 10 the GeO_2 percentage in the deposited mass is shown as a function of the total gas flow rate. As the gas flow rate increases, the process residence time decreases, and as a result concentration of SiO_2 and GeO_2 both decreases.

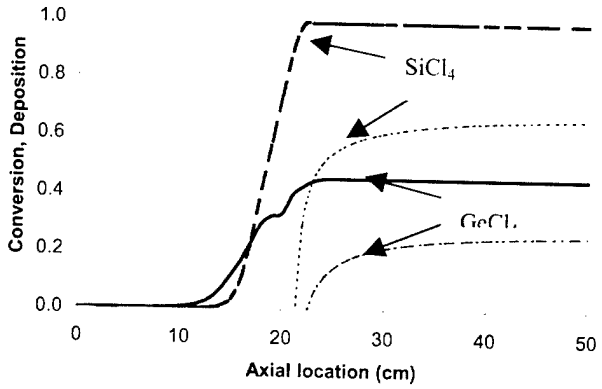


Figure 9a: $SiCl_4$ and $Gecl_4$ conversion (thick lines) and deposition efficiencies (thin lines). The inlet conditions were same as in Figure 3.

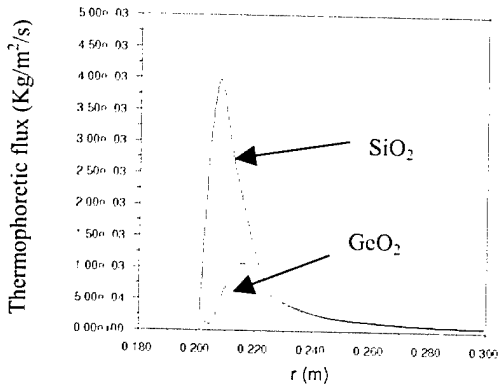


Figure 9b: Thermophoretic fluxes of SiO_2 and GeO_2 to the tube wall for different axial locations. The inlet conditions were same as in Figure 3.

Finally, the $GeCl_4$ conversion efficiency is compared with the experimental results of Wood *et al.* (1987) for various maximum torch temperature (Figure 11). For low T_{max}, the forward reaction rate of $GeCl_4$ oxidation increases, increasing the unreacted $GeCl_4$. The $GeCl_4$ conversion efficiency further increases till the equilibrium is reached. The Gecl4 conversion efficiency is maximum at T_{max} = 1700 K. Our results show a good agreement with the experimental data. At high temperature, the experimentally measured unreacted $GeCl_4$ concentration is higher than the present results.

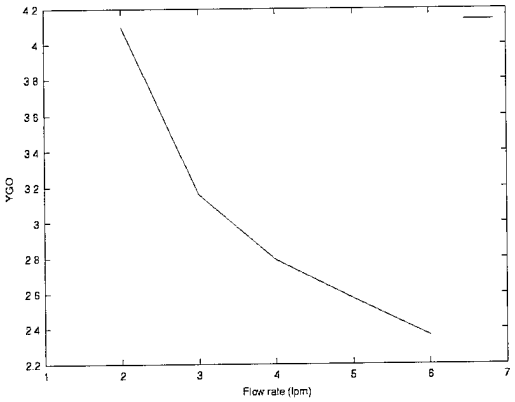


Figure 10. Mole fraction of GeO_2 in the deposited solid as a function of total flow rate, keeping constant the flows of $SiCl_4$ at 1.5g/min, $GeCl_4$ at 1.38 g/min and O_2 at 990 cm^3/min.

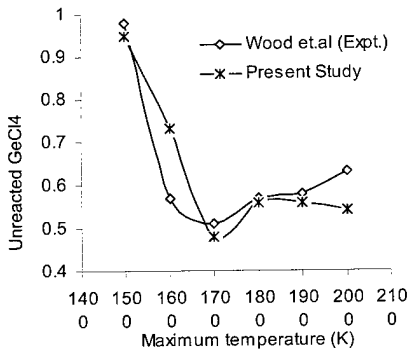


Figure 11. Fraction of unreacted $GeCl_4$ at the outlet for various maximum wall temperatures. The inlet flow rate is 1.72 lpm and the reactant flows were $SiCl_4$ 0.88 g/min; $GeCl_4$ 0.696 g/min; and O_2 1533 cm^3/min.

6. Conclusions

In this paper, the numerical solutions for the velocity, temperature and species concentrations have been obtained including the effect of chemical reactions. Simulations were carried out for a range of parameters, which illustrate the effect of these parameters in GeO_2 incorporation in the preform. At high temperature the reverse reaction is important. At high flow rates, the temperatures are lower and the deposition efficiencies of both SiO_2 and GeO_2 particles decreases. The results also verified the fact that the $GeCl_4$ oxidation is incomplete in the MCVD process and a large fraction of $GeCl_4$ appears in the effluent. This is due to the unfavorable equilibrium between reactants and products. The present study can be used in predicting the values of the MCVD process parameters such as flow rates, torch temperature, gas composition required to control the doping of GeO_2 in the optical fiber manufacturing process.

7. References

1. Kim K. S. and Pratsinis S. E., 1990, "Codeposition of SiO_2 and GeO_2 during production of optical fiber preforms by modified chemical vapor deposition", Int. J. Heat Mass Transfer. 33(9), 1977-1986.

2. Muralidharan, Prasad R. O. and Grald E.W., 2000, "Numerical modeling of the MCVD process for the manufacture of glass preforms", IWCS Symposium.

3. Wood D. L, Walker K. L., MacChesney J. B., Simpson J. R. and Csencsits R., 1987, "Germanium chemistry in the MCVD process for optical fiber fabrication", J. Lightwave Technol. LT-5, 277-285.

4. Mathur, S. R. and Murthy, J. Y., 1997, "A Pressure based method for unstructured meshes", Numerical Heat Transfer, Vol. 31.

5. Morse, T. F., Wang C. W. and Cipolla J. W., 1985, "Laser induced thermophoresis and particulate deposition efficiency", ASME J. Heat Transfer, 107, 155-160.

Influences of Profile Variations in PCVD Multimode Fibre on DMD Characteristics for 10 GbE Systems.

Peter Pleunis, Myrna Boon and Martien van den Heuvel
Product Development, Draka Comteq
Eindhoven, The Netherlands
+31-40-2958620 · p.pleunis@drakafibre.com

Abstract
In this paper, we describe the influences that some specific profile distortions in a multimode fibre can have on the differential mode delay properties of that fibre. We also show that these profile distortions can be controlled to produce a suitable multimode fibre for 10-gigabit Ethernet systems.

Keywords
Fibre; multimode; 10-gigabit Ethernet; Differential Mode Delay; DMD; PCVD; plasma.

1. Introduction
During the last months, the new 10-gigabit Ethernet (10 GbE) standard is under development within IEEE [1]. In parallel with the development of this standard, the TIA (Telecommunications Industries Association) working group FO 2.2.1 has been developing the measurement methods and specifications for the serial multimode solution at 850 nm, which is one of the solutions in the IEEE standard. For the fibre this is based on a differential mode delay (DMD) measurement. This DMD measurement describes very accurate the profile accuracy of the multimode fibre.

2. IEEE 10 Gb/s Standard
Within the IEEE 10 Gb/s standard, the PMD's (Physical Medium Dependent) as indicated in Table 1 are included.

Table 1. PMD's included in the 10 Gb/s standard

Application	Fibre type	Distance
1550 nm serial	SMF	40 km
1310 nm serial	SMF	10 km
1310 nm WWDM	SMF Legacy MMF	10 km 240 m up to 300 m
850 nm serial	Legacy MMF New 50/125 µm MMF	28 m up to 86 m 300 m

From these PMD's we expect that the last one, the 850 nm serial PMD will become the most economic short reach solution in the long term. This solution was one of the firsts for which feasibility was proven in a demonstration experiment with fibres from three different fibre manufacturers in combination with sources from five different source manufacturers. These manufacturers all worked together in workgroup FO 2.2.1 of the TIA to come to a test method and specification for both the sources and the fibres, by which a working system in the field over 300 m is guaranteed with a failure rate less than 1%.

3. Source and Fibre Test Method
3.1 Source Test Method
During the development of the 1-gigabit Ethernet standard, the TIA has already developed a test method characterizing the launch radiation pattern for sources: the encircled flux. This test method is described in Fibre Optic Test Procedure (FOTP) 203 [2]. This test method is also used to define the 10 GbE sources. The specification for these sources to guarantee 300 m for 10 GbE is set as:

Encircled flux requirement:

- ≥ 86% at 19 µm radius
  Eliminates launches too large
- ≤ 30% at 4.5 µm radius
  Eliminates launches too small

3.2 Fibre Test Method
The fibre specification development was mainly supported by three fibre manufacturers: Lucent, Corning and Draka Comteq. Instead of the normally used bandwidth measurement, the fibre test procedure is now based on a DMD measurement. This DMD measurement is already known since 1980 by all multimode fibre manufacturers as a tool for production process fine-tuning, but was never standardized.

The DMD measurement, as now defined in FOTP-220 [3], is a little bit different from the commonly used DMD measurements. The main differences are a smaller spot size (SMF at 850 nm, the mode field diameter is 5 µm instead of approximately 15 µm as used before) and a very short pulse in time domain in combination with a very narrow spectral width of the laser used. This very short pulse is necessary to be able to get a resolution high enough on fibres of 500 m or longer. The very narrow spectral width of the laser is required to eliminate chromatic dispersion in the measurement.

The so-called next generation multimode fibre has to fulfil at least one of the masks as indicated in Table 2 for a DMD measurement according to FOTP-220.

Table 2. Specification for the next generation multimode fibre based on DMD measurement

Mask	Radius 5 to 18 μm	Radius 0 to 23 μm	OFL Bandwidth
1	DMD ≤ 0.23 ps/m	DMD ≤ 0.7 ps/m	≥ 1500 MHz*km
2	DMD ≤ 0.24 ps/m	DMD ≤ 0.6 ps/m	≥ 1500 MHz*km
3	DMD ≤ 0.25 ps/m	DMD ≤ 0.5 ps/m	≥ 1500 MHz*km
4	DMD ≤ 0.26 ps/m	DMD ≤ 0.4 ps/m	≥ 1500 MHz*km
5	DMD ≤ 0.27 ps/m	DMD ≤ 0.35 ps/m	≥ 1500 MHz*km
6	DMD ≤ 0.33 ps/m	DMD ≤ 0.33 ps/m	Not applicable
The fibre should meet any one (or more) of these six masks.			

4. Next generation multimode fibres

4.1 Control of the Profile Shape Parameter (α)

The next generation fibres as defined for these 10 GbE systems are based on the concept of a 50 μm Graded Index Multimode fibre. The main difference with the fibre as it is currently sold in the market, is the alpha, which defines the shape of the refractive index profile. This refractive index profile $n(r)$ as a function of the radius r is given by the α-profile

$$n(r) = n_1 [\, 1 - 2\Delta (r/25)^{\alpha} \,]^{1/2} \qquad (1)$$

where n_1 is the refractive index of the centre of the core and Δ is the refractive index contrast of the fibre.

This results in the profiles shown in Figure 1 for a changing alpha.

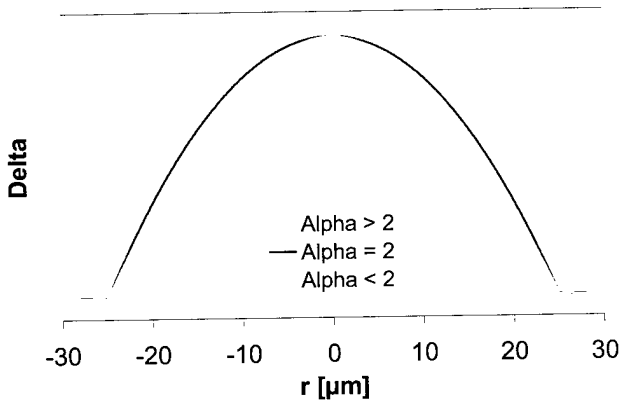


Figure 1. Refractive index profiles for three different profile shape parameters (alpha).

By changing this alpha, we can optimize the bandwidth of a fibre at a certain wavelength. This is shown for two different alphas in Figure 2.

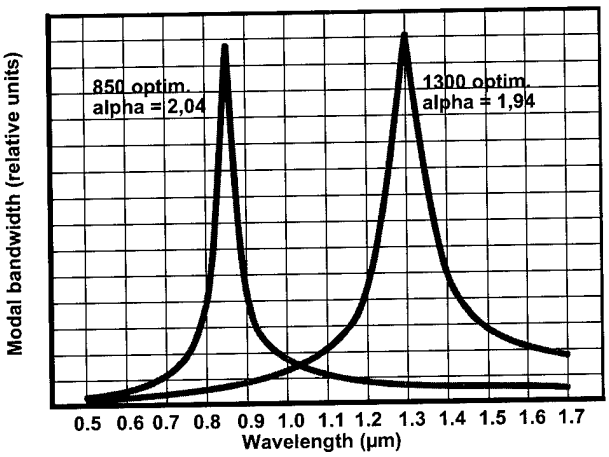


Figure 2. Examples of calculated modal bandwidth, optimized at 850 nm and at 1300 nm, depending on the profile shape parameter (α).

For the next generation fibre this profile parameter alpha is now changed to optimize the bandwidth of the fibre at 850 nm. Due to the proprietary Plasma activated Chemical Vapour Deposition (PCVD) process used in Draka Comteq, we can control this alpha very accurately [4].

4.2 Accurate Control of the Fibre Profile

The PCVD process enables the production of a graded index multimode fibre with a core that is made of several thousands of layers. For each of these layers the refractive index can be changed, resulting in a very accurate α-profile. Fast variations in the centre, the so-called dip, have already been eliminated in the early 80's by the patented etching process [5]. This resulted in multimode fibres where the diameter of the central dip is typically less then 0.1 μm. This very small dip ensures that for the launch conditions now used in actual systems or measurement setups the impact of this central dip is negligible.

During the development of the next generation fibre, we investigated deviations in the area around the central dip. This area had a diameter of approximately 6 μm in the fibre. With the conventional DMD method, this deviation was hardly visible, but by using the new DMD method with the smaller spotsize, this area becomes relevant.

By producing some experimental fibres with different deviations around the central dip, we were able to show the impact of the diameter of the deviation on the DMD measurement. Besides that we demonstrated the effect of changing the deviation from a hump on top of the refractive index into a flattened area of approximately the same size. By solving this deviation around the central dip, we were able to create the close to perfect multimode fibre.

5. Results

First of all, we show you the profiles of the first experimental fibres. In the left-hand-side of Figure 3, 4 and 5 you see half the fibre refractive index profile. In this plot, we also indicated the calculated ideal α-profile and the enlargement of the deviation around the centre of the fibre.

The right-hand-side of the picture shows the resulting DMD measurement result. The x-axis is the time scale, the y-axis shows the several measurements at several positions along the core of the fibre. The lowest pulse is the measurement exactly in the centre of the fibre, the other pulses are measurements with steps of –1 and 1 µm through the core, were the left side and right side from the centre are plotted on the same lines. The top line is the measurement for r = -26 µm and +26 µm.

In Figure 3 you find near the centre of the fiber, the deviation from the ideal α-profile increases, showing a hump in the refractive index profile.

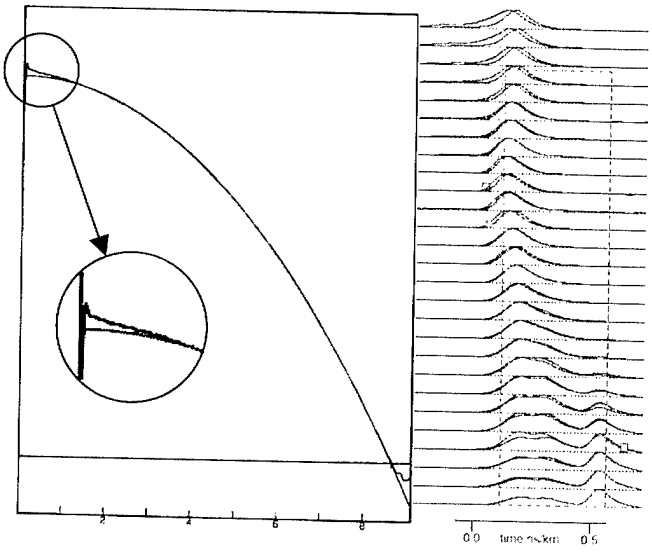


Figure 3. Refractive index profile and DMD measurement of a fibre with an "index hump"

As you can see in the DMD measurement of Figure 3, the profile hump results in severe pulse splitting around the centre of the core. The higher refractive index causes a delay in the light traveling through this part of the fibre.

The DMD width for r = 5 to 18 µm for this fibre is 0.44 ps/m, which is too high to fit any of the masks from Table 2.

If we change the profile hump into a flattened part of the refractive index profile of the fibre with the same size, you can again see the pulse splitting, but now the light travels faster in this area due to the lower refractive index. This is shown in Figure 4.

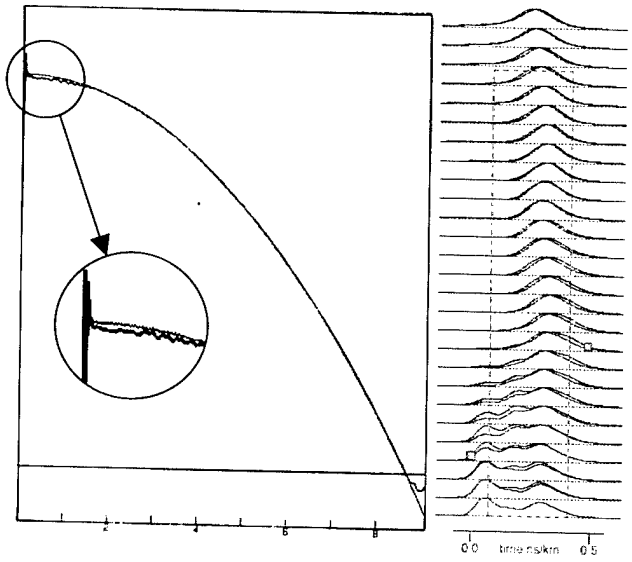


Figure 4. Refractive index profile and DMD measurement of a fibre with an "index flattening"

For the fibre indicated in Figure 4, the DMD width for r = 0 to 23 µm is 0.33 ps/m, fulfilling mask 6 from Table 2. Therefore this fibre is within specification for a 10 GbE system.

Even though the above fibres looked quite nicely if you only saw the refractive index without the calculated ideal α-profile, they still resulted in severe pulse splitting when using very small spot sizes in the centre of the fibre. This was not caused by the central dip which results from the inside tube process, but was caused by the area around it, which can be corrected in the PCVD process to produce the close to perfect fibre. The profile and the DMD measurement of this fibre are shown in Figure 5.

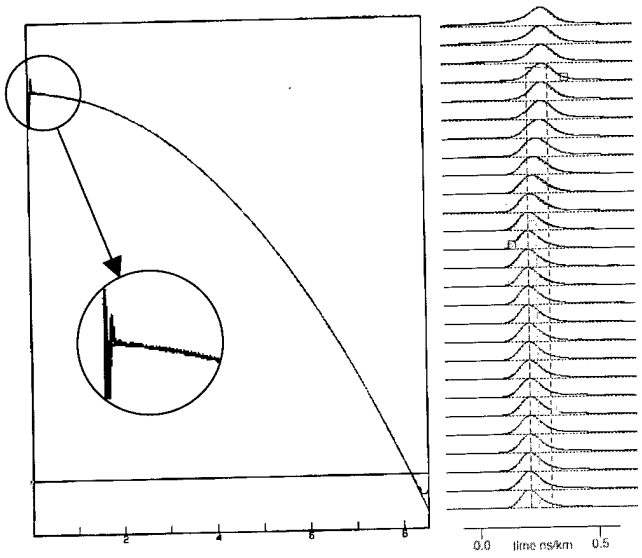


Figure 5. Refractive index profile and DMD measurement of the close to perfect fibre.

The fibre indicated in Figure 5, enables systems far beyond the 300 m at 10 Gb/s. Both the distance and the system speed can be improved significantly. With a similar fibre as the one indicated, we demonstrated in a joined experiment with IBM 15.6 Gb/s transmission over 1 km of this fibre [6].

6. Conclusions

We have been developing the next generation multimode fibres for use in 10 GbE systems. During a validation experiment, feasibility of the system was shown. We indicated the changed bandwidth optimization from 1300 nm towards 850 nm and have shown how this can be done by changing the profile shape parameter alpha.

Based on the newly developed DMD measurement method, we investigated the impact of the central dip and also the profile distortions around this central dip. We showed that the central dip, which is typically less then 0.1 μm diameter in current PCVD multimode fibres, is negligible in the systems and measurement methods used. Around this central dip we indicated an area that should be well controlled to prevent pulse splitting in systems using very small spotsize lasers in the centre of the fibre. In the experiments, we have shown the relation between the pulse splitting in the centre of the fibre and the deviation around the central dip of the fibre. We also showed the close to perfect multimode fibre that can improve system performance significantly. This fibre is made possible due to the very accurate α-profile enabled by PCVD technology.

7. Acknowledgments

The authors would like to thank Gert-Jan Krabshuis for his technical support in producing several preforms for the experiments.

8. References

[1] IEEE std. P802.3ae/D3.1, "Media Access Control (MAC) parameters, Physical Layer, and Management Parameters for 10 Gb/s Operation"

[2] TIA, FOTP-203, "Launched Power Distribution Measurement Procedure for Graded-Index Multimode Fiber transmitters", to be published as TIA/EIA-455-203, PN4669

[3] TIA, FOTP-220, "Differential Mode Delay Measurement of Multimode Fiber in the Time Domain", to be published as TIA/EIA-455-220, PN3-0008

[4] A.H. van Bergen, T. Breuls, "PCVD: The ultimate technology for production of high bandwidth multimode fibres", *47th IWCS proceedings,* p. 66-72 (1998).

[5] US Patent 4.793.843

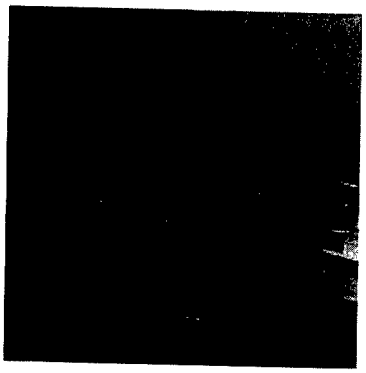
[6] P. Pepeljugoski, D. Kuchta, Y. Kwark, P. Pleunis and G. Kuyt, "15.6 Gb/s Transmission Over 1km of Next Generation Multimode Fiber", *27th European Conference on Optical Communication,* (2001).



Ir. Peter Pleunis
Draka Comteq
Draka fibre Technology
Zwaanstraat 1
5651 CA Eindhoven
The Netherlands
Tel. +31.402958620
e-mail:
p.pleunis@drakafibre.com

Peter Pleunis was born in Nederweert, The Netherlands in 1969. He received his M.Sc. degree in electrical engineering in 1994.

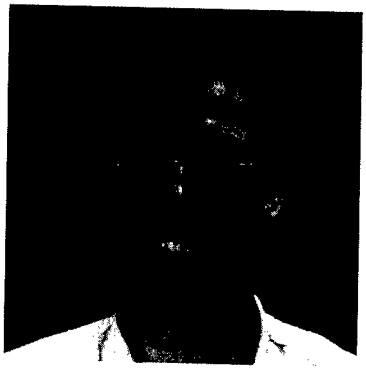
He has been manager of the Test & Measurement group from 1997 until 2000 of Plasma Optical Fibre, which is part of the Draka Holding group. At the moment he is manager of the product development group of Draka Fibre Technology B.V. Since 1997 he is also cooperating in the FO 2.2.1 working group of the TIA.



Ir. Myrna Boon
Draka Comteq
Draka fibre Technology
Zwaanstraat 1
5651 CA Eindhoven
The Netherlands
Tel. +31.402958612
e-mail:
m.boon@drakafibre.com

Myrna Boon graduated from the Technical University Eindhoven in Chemical Engineering. She joined R&D within Draka Fibre Technology in 1999.

Working in the product development group, she is the project manager for optical fibre coating projects.



Ing. Martien van den Heuvel
Draka Comteq
Plasma Optical Fibre
Zwaanstraat 1
5651 CA Eindhoven
The Netherlands
Tel. +31.402923807
e-mail: m.vandenheuvel
@plasma.nl

Martien van den Heuvel was born in 1966, in Eindhoven, The Netherlands. He received his bachelor degree in Chemical Process Engineering in 1990.

Three years later he joined Plasma Optical Fibre. As part of the Process Support group he has always been close related to fabrication. During the period 96-98 he assisted Yangtze Optical Fibre in China as Technical Manager of the fibre production plant. At the moment he is Process Co-ordinator at Plasma Optical Fibre.

Validation of Silica Defects Related Attenuation Increase Resistance in S-Band Operation for NZDSF

Norio Fujita, Shinji Hinosihta, Tetsuya Sukegawa,
Takahiro Yamazaki, Osono Kazumasa, Kengo Kotani
Hitachi Cable, LTD
5-1-1 Hitaka-cho Hitachi-City, Ibaraki-Prefecture, 319-1411, Japan
TEL:+81-294-25-3809/ E-mail: fujita.norio@hitachi-cable.co.jp

Abstract

We validated the attenuation increase resistance in new ITU-T S-Band operation against relatively low hydrogen pressure exposure for a non-zero dispersion-shifted single-mode fiber (NZDSF) (G655). The validation spectrum covers the hydroxyl peak (1383 nm) and the optic signal operational E-Band (1360 - 1460 nm) & S-Band (1460 - 1530 nm). The saturated attenuation increase related hydrogen reactive defects was substantially low and proved the production conditions (VAD preform & Fiber drawing) and the various doping junctions are well synthesized.

We defined the attenuation increase sufficient low with the best optimized structural-relaxation-dopant which allows increasing the efficiency of production.

Keywords

attenuation increase; chlorine (Cl); drawing tension; drawing velocity; fluorine (F); Germanium (Ge); low hydrogen pressure; S-band

1. Introduction

Recent bandwidth widening demand accelerates the use of E-Band and S-Band for not only the conventional SM fiber but also the non-zero dispersion-shifted single-mode fiber (NZDSF) in DWDM systems with optical amplifier. The cable vendor shall validate the stable operation for signal operation and pump operation of Raman-EDFA because these bands include the hydroxyl peak (1383 nm) and silica defects related absorption attenuation unstable region when the both defects and the hydrogen partial pressure exist. Especially, NZDSF fiber has complicated/dopant-riched core-profile to achieve the desired dispersion and dispersion slope, which are enabled by using the various dopants. The silica defects related attenuation increase can validate in very low hydrogen pressure exposure in ambient temperature. The longer-wavelength-shoulder of the OH intravibration spectral attenuation of the high hydrogen pressure, e.g. 1.0 atmospheres, with heat accelerating test [1] shadows the slow reacting silica defects related attenuation increase at 1400 nm wavelength region. TIA/EIA is working for the new standard test method [2] for 1400 nm wavelength operation. We used the same 0.01 atmospheres of hydrogen to examine the attenuation increase at 1400 nm wavelength band.[3] We validated the attenuation increase with Ge-doped-NZDSF by changing the fabrication conditions. We further studied the structural-relaxation-dopant by the allowable high-efficient fabrication condition to find out the optimized co-dopant. The following paragraphs present test equipment / procedure, measurement result of Ge-NZDSF fiber with various fabrication conditions, measurement result of co-dopanted-NZDSF fibers with the allowable high-efficient fabrication condition and conclusion.

2. Low Partial Pressure Hydrogen Test

2.1 Test Fibers

In this test, three types (Type F1, F2 & F3) of Non-Zero Dispersion-Shifted Fibers were used as sample fibers. These were fabricated by the VAD method. Each fiber consists of doped-silica core of 8-9 micro-meters in mode field diameter. Type F1 fiber core was fabricated by using only germanium (Ge) dopant as as a refractive index profile controler. For Type 2F, Chlorine (Cl) was selected as a structural-relaxation-dopant in addition to Ge dopant [4]. Type 3F replaced fluoline (F) instead of Chlorine from Type 2F.

Table 1. Test fibers

Fiber Type	Core Process	Dopant	Fabricated Condition
Type F1	VAD	Ge	DS1-T1, DS1-T2, DS1-T3 DS2-T1, DS3-T1
Type F2	VAD	Ge + Cl	DS1-T1
Type F3	VAD	Ge + F	DS1-T1

(Note);
T: drawing tension (rate) = T1: T2: T3 = 7: 5: 4
DS: drawing speed (rate) = DS1: DS2: DS3 = 4: 2: 1

Cl or F diffused silica glass can be used positively to develop an extreme-low-loss fiber because these dopant enhances structural relaxations which is led by lowering the residual strain thanks to the viscosity matching while fiber drawing. We compare the performance of Cl-codoped NZDSF and F-codoped-NZDSF

2.2 Test Equipment

The schematic experimental setup for the low partial pressure hydrogen test is diagrammed in Fig.1. Each sample fiber was spooled on the bobbin which mounted in a sealed stainless vessel. Both ends of fiber sample were drawn out through a pipe for measurement of the fiber loss change, and the pipe itself was sealed with a epoxy resin adhesive. The gas was premixed gas which

consists of 1.0 percent hydrogen and the balance of nitrogen. The gas was charged into the vessel up to 1.2 atm after it reached to the vacuum of approximately 760 mmHg. The total pressure in the vessel was 1.2 atm because we intend to keep the 0.01 hydrogen-partial-pressure duration of the whole aging test by taking into account of the diffused molecular hydrogen into the silica glass of the test fibers. We confirmed the hydrogen concentration after 13,000 hours (Almost 1.5 years) test by gas chromatography and H2 concentration was with the range of 9600 – 9800 ppm.

The optical loss spectrum of test fibers over 1200-1600 nm range was measured by the cutback method. Measurement wavelength width was 5 nm step except 1350-1450 nm (1350-1450 nm : 1 nm step).

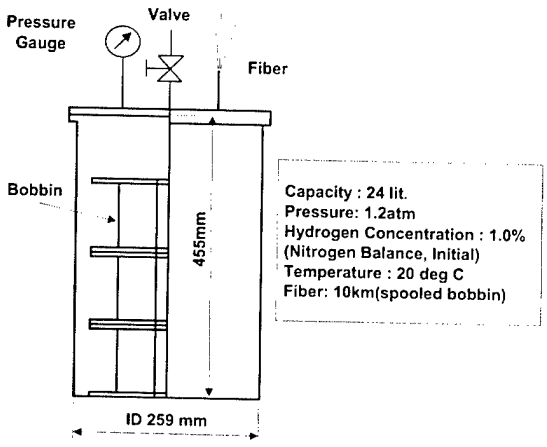


Fig. 1 Configuration of test vessel

2.3 Test Procedure

(1) The optical loss spectrum of the test fibers was measured in the initial time and the subsequent irregular test interval times as shown in the Fig. 2.

(2) The evaluation was done by the loss increase (test stage loss - initial loss) as shown in Fig. 3.

(3) The evaluation wavelengths were decided as follows;

1383 nm: OH peak and representing the pump wavelength band of Raman-EDFA.

1430 nm: Hydrogen reaction with silica intra-vibration peak and representing wavelength of E & S operation band.

(4) The data of the loss increase of each test stage were recorded in order to evaluate the hydrogen reaction loss increase.

(5) The total pressure within the test vessel was monitored during the aging of whole 1.5 year. There were no gas leak because the total pressure was kept at around 1.2 atm.

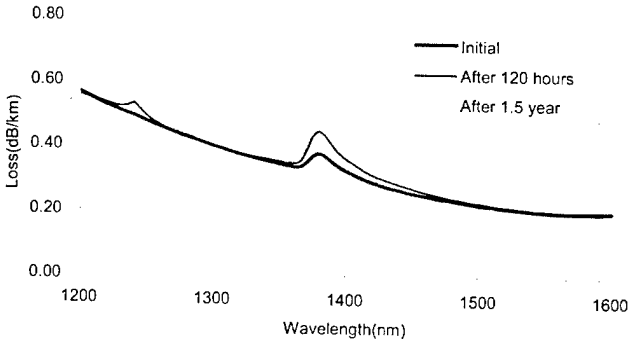


Fig. 2 Spectrum Loss of Initial and Aged Fibers

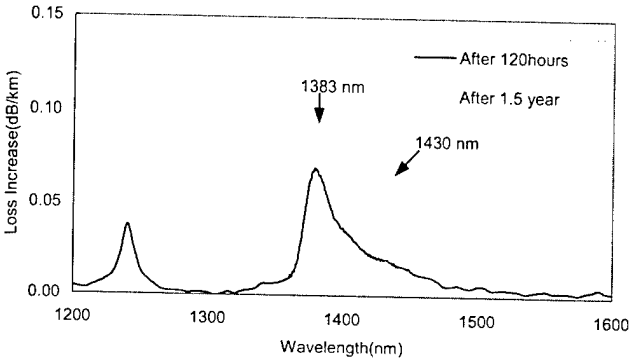


Fig. 3 Spectrum Loss Increase of Fig.2

3. Result of Loss Increase of Type F1

3.1 Loss increase related with drawing tension

(1) Fig. 4 shows the loss increase at 1383 nm & 1430 nm of Type F1 with the parameter of drawing tension.

(2) The higher drawing tension leads the higher loss increase for both wavelengths.

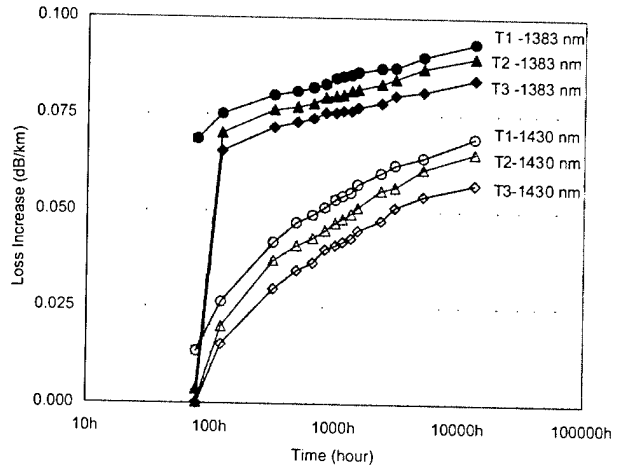


Fig. 4 Loss increase related with drawing tension

3.2 Loss increase related with drawing speed

(1) Fig. 5 shows the loss increase at 1383 nm & 1430 nm of Type F1 with the parameter of drawing speed.

(2) The higher drawing speed leads the higher loss increase for both wavelengths.

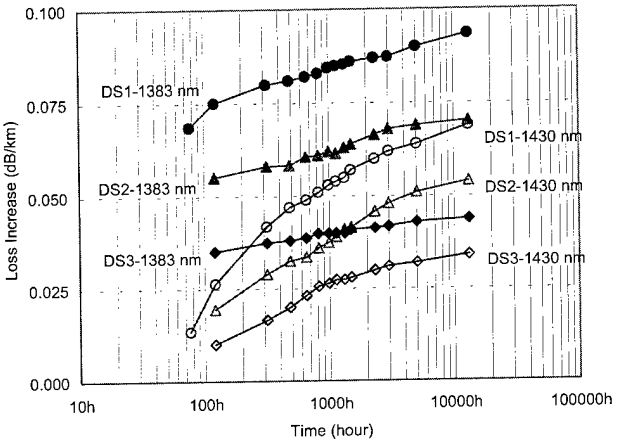


Fig. 5 Loss increase related with drawing speed

4. Result of Loss Increase of Type F2 & F3

(1) Fig. 6 shows the loss increase at 1430 nm of Type F2 and F3 by using the structural-relaxation-dopant, Cl & F respectively. The loss increase of Type F1 shown in Fig. 5 is also plotted for reference.

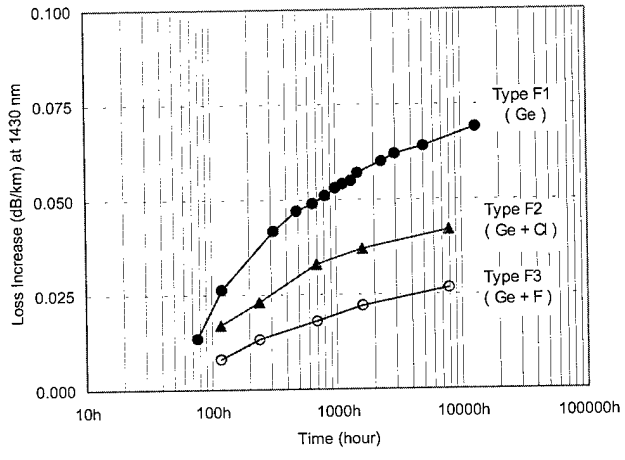


Fig. 6 Loss increase related with Dopant (Cl & F) (Drawing Tension: T1, Drawing Speed: DS1)

(2) Type F2 by Cl doping was improved compared with Type F1.

(3) Further more, Type F3 by F doping proved its sufficient low loss increase compared with Type F2 with the high effective production conditions of T1 & DS1.

5. Conclusions

(1) We have validated the effectiveness of law hydrogen pressure test through the evaluation of the loss increase around 1400 nm wavelength band.

(2) We proved the Type F3 with F-doping had the sufficient loss increase resistance for E & S band operation against the hydrogen aging over the life.

(3) The loss increase at S-operation band is derived from OH peak loss and silica-defect-H2-reaction loss. OH permanent peak loss may be enough saturated after about 200 hours. The measured loss increase at 1430nm after about 200hours and more is dominated by silica-defect-H2-reaction absorption loss which is ruled by the activation energy of the reaction. As a result of above, the loss increase forecast calculation is easy. We could have the conclusion that Type F3 has sufficient low loss increase after 25years by extrapolating calculation ruled by the reaction.

6. References

[1] Kazuhiro Noguchi, Nori Shibata, Naoshi Uesugi, and Yukiyasu Negishi, "Loss Increase for Optical Fibers Exposed to Hydrogen Atmosphere," in Journal of Lightwabe Technology," vol. LT-3, No2, April(1985)

[2] TIA/EIA Working document Ref.PN-4590 (to be publish as TIA/EIA-492CAAB)

[3] K,H Chang, D.Kalish, and M.L. Pearsll, "New Hydrogen Aging Loss Mechanism in the 1400nm Window", OFC, 1999, Post-dead-line paper

[4] A.J. Ikushima et al, "Structural relaxation enhanced by Cl ions in silica glass", Appl. Phys. Lett., Vol.73, No9, 31, Augusut 1998, P1209-1211

Author



Norio Fujita

The Telecommunications Design Department,Hitachi Cable,Ltd.

Hitaka-cho,Hitachi-shi, Ibaraki-ken,319-1414 Japan

Phone;+81-294-25-3837· email; fujita.norio@hitachi-cable.co.jp

Mr. Fujita received B.E. and M.E. degree in Mechanical System Engineering from Yamagata University in 1993 and 1995, respectively. He joined Hitachi Cable, Ltd. in 1995 and has been engaged in the design and development of optical fiber and cables and telecommunications cables. He is now an engineer in the Telecommunication Design Department.



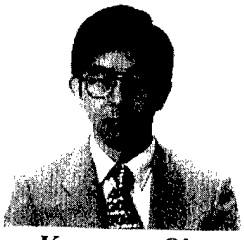
Shinji Hinoshita

The Telecommunications Design Department,Hitachi Cable,Ltd.

Hitaka-cho,Hitachi-shi, Ibaraki-ken,319-1414 Japan

Phone;+81-294-25-3808 email: hinoshita.shinji@hitachi-cable.co.jp

Mr. Hinoshita graduated in Electrical Engineering from Kure National College of Technology in 1970 and joined Hitachi cable, Ltd. He has been engaged in research and development of optical fibers/cables. He is a group manager in the Telecommunication Design Dept. and is a member of IEICE of Japan.



Kazumasa Ohsono

The 4th Dept. Optoelectronic System Laboratory,Hitachi Cable,Ltd.

Hitaka-cho,Hitachi-shi, Ibaraki-ken,319-1414 Japan

Phone:+81-294-25-3837 email: ohsono.kazumasa@hitachi-cable.co.jp

Mr. Ohsono received his B.E. degree in Mechanical Engineering from the Science University of Tokyo in 1982 and joined Hitachi cable, Ltd. He has been engaged in research and development of optical fibers. He is now a senior researcher in Optroelectronic System Laboratory and a member of the IEICE of Japan.



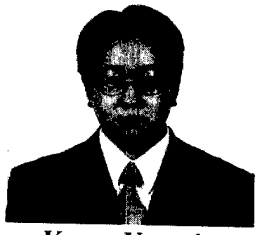
Takahiro Yamazaki

The Optical Fiber & Communication Cable Department,Hitachi Cable,Ltd.

Hitaka-cho,Hitachi-shi, Ibaraki-ken,319-1414 Japan

Phone;+81-294-25-3804 email: yamazaki.takahiro@hitachi-cable.co.jp

Mr. Yamazaki received his B.E. degree in Electrical Engineering from Ibaraki University o in 1982 and joined Hitachi cable, Ltd. He has been engaged in development of optical fiber cables. He is now a assistant manager in the Telecommunication Department.



Kengo Kotani

The 4th Dept. Optoelectronic System Laboratory,Hitachi Cable,Ltd.

Hitaka-cho,Hitachi-shi, Ibaraki-ken,319-1414 Japan

Phone;+81-294-25-3837 email: kotani.kengo@hitachi-cable.co.jp

Mr. Kotani received B.E. and M.E degrees in mechanical engineering from University of electro-communication in 1997 and 1999, respectively. He joined Hitachi Cable, Ltd. in 1999 and has been engaged in development of optical fiber. He is now a researcher in research and Optoelectronic System Laboratory and a member of the IEICE of Japan.



Tetsuya Sukegawa

The Telecommunications Design Department,Hitachi Cable,Ltd.

Hitaka-cho,Hitachi-shi, Ibaraki-ken,319-1414 Japan

Phone;+81-294-25-3837· email; sukegawa.tetsuya@hitachi-cable.co.jp

Mr. Sukegawa received B.E. and M.E. degree in Electronic Information and Engineering from Tokyo University of Agriculture and Technology in 1997 and 1999, respectively. He joined Hitachi Cable, Ltd. in 1999 and has been engaged in the design and development of optical fiber and cables and telecommunications cables. He is now an engineer in the Telecommunication Design Department

High Performance and High Reliability Dispersion Compensating Fiber Modules using a Novel Packaging Technique

Takashi FUJII Keiichiro FUKUDA Eisuke SASAOKA Toshifumi HOSOYA

Sumitomo Electric Industries, Ltd. 1 Taya-cho, Sakae-ku,
Yokohama, 244-8588 Japan
Phone: +81-45-853-7168, Fax: +81-45-851-1565, email address: fujii-takashi@sei.co.jp

Abstract

In order to increase dense wavelength division multiplexing (DWDM) signal channels or each channel bit rate, high-performance dispersion compensating fiber (DCF) modules are required. DCFs which have low nonlinear coefficient or high relative dispersion slope (RDS), however, are sensitive to bending. If it is packaged compactly as a DCF module, the microbend induced loss increases considerably in the long wavelength region. We have developed a suspended in resin coil packaging technique which has no bobbin and ultimately can decrease the stress to fibers. The features of this packaging are low microbending loss, excellent thermal stability, low fiber breakage, and high reliability. Using this technique, high performance bending-susceptible DCFs which have a high RDS for non-zero dispersion shifted fibers (NZ-DSFs) can be packaged as DCF modules.

Keywords

Dispersion compensating fiber; modules; resin; bending loss; non-zero dispersion shifted fiber; packaging

1. Introduction

The huge increase in data communication volumes in recent years have been accompanied by the introduction of long-distance, large-capacity DWDM transmission systems that use optical fiber amplifiers and transmit in the 1550nm wavelength band. There is now a demand for higher DWDM transmission capability, and dispersion compensation technology is one of the keys to increasing the capacity of such systems. While a number of reports have been already published on dispersion compensation methods,[1),2)] but the most widely used method employs DCF. [3)] DCF for module has a large negative dispersion in the 1550nm band, and a type of DCF with a negative dispersion slope has recently been developed (Fig.1). [4)] By incorporating these DCF modules (DCFMs) into a transmission system, it is possible to upgrade a system that uses the widely installed 1310nm band zero-dispersion fiber (SMF: single mode fiber) to a 1550nm band DWDM transmission system which is capable of large transmission capacity. Studies have been also conducted in the U.S. over the last few years on the use of DCFMs in transmission systems that use the increasingly popular NZ-DSF. In this report, we look at a new type of DCFM which has a structure that substantially reduces the strain on the DCF in order to obtain better performance from the DCFM.

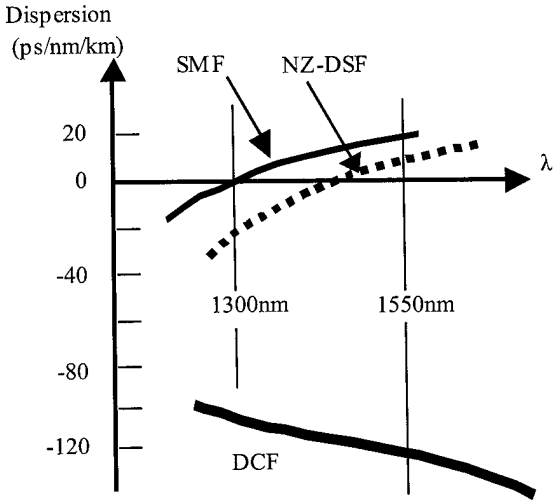


Figure 1. Dispersion management using DCFM

2. Improving DCF Module Performance

For the future increased capacity in DWDM transmissions which have higher bit rates and increased wavelength multiplexing, the transmission line needs to suppress waveform distortion by self phase modulation (SPM), cross phase modulation (XPM), and four wave mixing (FWM). In the case of the DCFM, the key goals are reducing the module insertion loss, optimizing the dispersion slope compensating ratio (DSCR) as defined by (1), and decreasing the non-linearity coefficient of DCFM. [5)]

$$DSCR=(S_{DCF}/D_{DCF})/(S_{SMF\ or\ NZ\text{-}DSF}/D_{SMF\ or\ NZ\text{-}DSF}) \quad (1)$$

These characteristics are influenced in complex ways by the refractive indices of DCF. For example, if we attempt to improve one characteristic while maintaining another, the DCF becomes

further susceptible to the effects of bending and the amount of attenuation caused by even minute amounts of strain tends to increase. In addition, in a DCFM, a DCF from 2 or 3 kilometers up to more than 10 kilometers length is packaged as a module consisting of a box measuring 230 * 230 * 40mm including the pigtail, etc. Because the contents of the box are packed extremely tightly, the environment is highly conducive to increased attenuation in the DCF. This is why bend characteristics are such a key determinant in the design of DCF to be used in modules.

We first conducted analysis of the loss caused by bending. In order to analyze the quantity of a pure bending loss, we tried to definite the bending loss (Fig.2) by (2).

Bending loss = (measured spectrum) – (Rayleigh scattering) – (Absorption by Si-O) – (Absorption by –OH) (2)

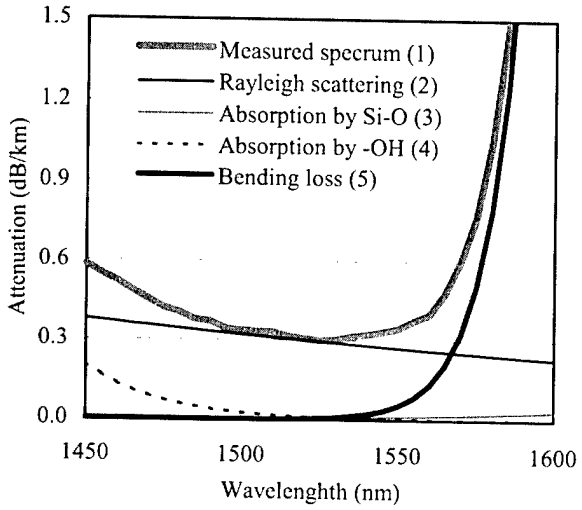


Figure 2. Definition of bending loss

We also studied all the causative factors of bending loss, not just the DCF design. We determined the starting point of our development using experiments of the type described below. The bending loss at longer wavelengths exhibited by fibers with poor bend characteristics (fibers with a large Aeff value) of the type shown in Figure 3 (a) decreases markedly when the fiber is removed from the spool (bobbin) used for winding the fiber (Fig.3 (b)), and falls to levels close to the attenuation values for normal fiber (Fig.3 (c)). While the bending loss in conventional DCFMs is dependent on the bobbin diameter, i.e., on macrobending, we can see that the level of attenuation is also significantly influenced by microbending loss due to the winding tension.

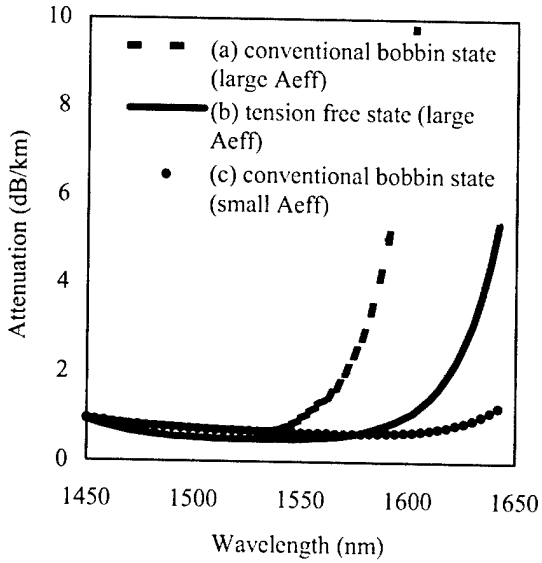


Figure 3. Effect of winding on a bobbin

3. Stress-Free Coil Module Structure

We propose a new DCF module structure (Fig.4) that takes into account the reduction of the strain applied to the fiber to an absolute minimum. In order to reconcile the apparently contradictory requirements of reducing the strain applied to the fiber to an absolute minimum while at the same time using reliable structure that holds the fiber even more firmly and securely, we have adopted the approach of coating the fiber in a flexible resin.

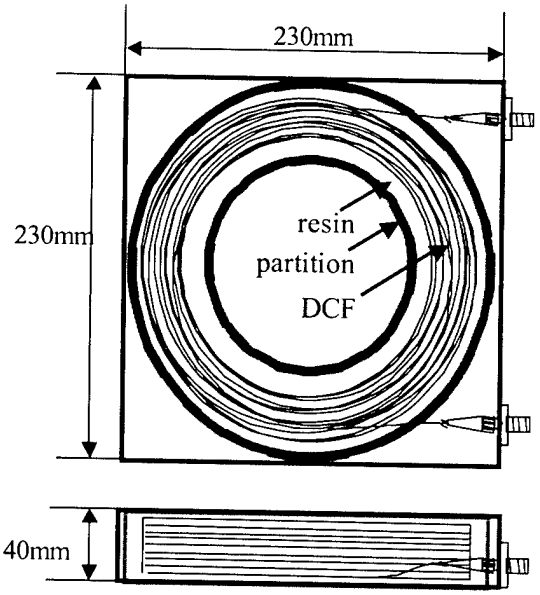


Figure 4. Structure of stress-free coil

One feature of this construction is that, because no spool (bobbin) is used, no winding tension is applied to the fiber. Another feature is the impregnation of the interior of the coil with resin so that the entire fiber is enveloped in the flexible resin. This results in the removal of another source of strain since the fiber no longer needs to support its own weight. And finally, because the spooled fiber is held firmly in place by the resin, it provides excellent reliability. As this structure involves effectively floating the fiber in a bed of resin, we refer to it as a Suspended-In-Resin coil (SIRCOIL).

4. Optical Characteristics of Stress-Free Coil Module

Stress-free coil DCFMs have two strong merits in transmission characteristics. First is their low microbending loss, second is their excellent thermal characteristics. This is because stress-free coil DCFMs can package high performance DCFs. These characteristics are as follows.

4.1 Low microbending loss

Given that minimal stress is applied to the DCF in a stress-free coil module, there should be little increase in attenuation due to fiber bending. To clarify this hypothesis, we conducted the following experiments. We packaged the trial DCF into modules and evaluated their characteristics in the following three situations: (a) a conventional bobbin-wound module (Fig.5 (a)); (b) bundled fibers removed from the bobbin in (a); and (c) the same bundled fibers in (b) molded with resin into stress-free coil module (Fig.5 (c)).

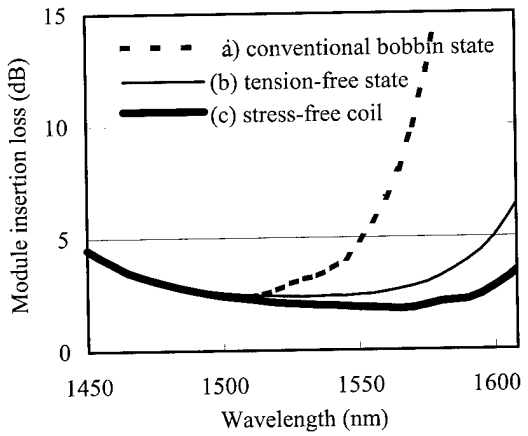


Figure 5. Spectral attenuation of stress-free coil DCFM

As Figure 5 shows, packaging the fiber into the module gives the greatest suppression of attenuation loss as well as improved spectral characteristics than bundled fibers. Presumably that this is related to the fact that the suspension of the fiber in resin alleviates the strain imposed by the fiber's own weight. The figures below also clearly show that using the stress-free coil structure allows the microbending loss to be reduced to an extremely low value. These results indicate that one advantage of the new stress-free coil module is that it provides greater freedom in the design of high-performance DCF.

It is important for DCFMs to be packaged compactly, because of the limited space of the WDM transmission system. Figure 6 shows the relation of bending loss and winding diameter of each state. In the case of conventional bobbin wounded packaging, the smaller the winding diameter, the greater the bending loss. So DCFs cannot be packaged compactly. But in the case of stress-free coil packaging, if winding diameter is small, bending loss increases mainly at the longer wavelength region. As a result, using a stress-free coil packaging technique, a compactly packaged module or long DCF packaged module also can be realized.

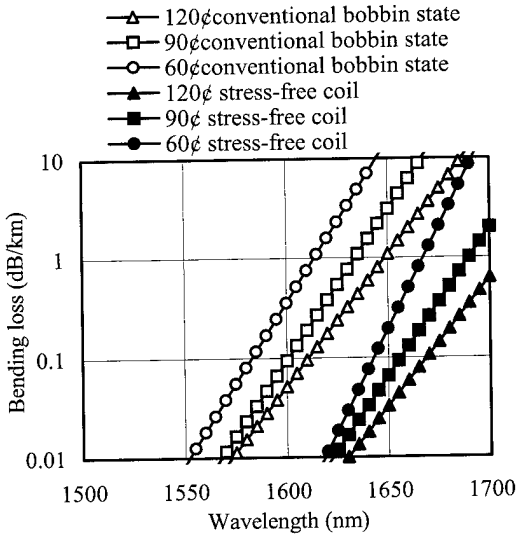


Figure 6. Bending loss characteristics

4.2 Excellent Thermal Characteristics

Due to the low strain applied to the fiber, the thermal characteristics of the new module are significantly improved over those of conventional modules. Figure 7 shows the wavelength dependency of the thermal characteristics of stress-free coil DCFM. In a conventional C-band DCFM, there is a tendency for fluctuations in attenuation to increase from around 1570nm onwards. In the stress-free coil module, the figure shows that there is virtually no variation in attenuation from –20° C through to 70° C.

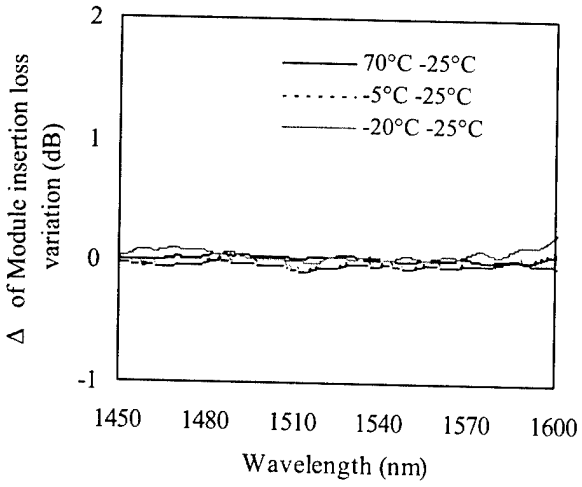


Figure 7. Thermal characteristics of stress-free coil DCFM

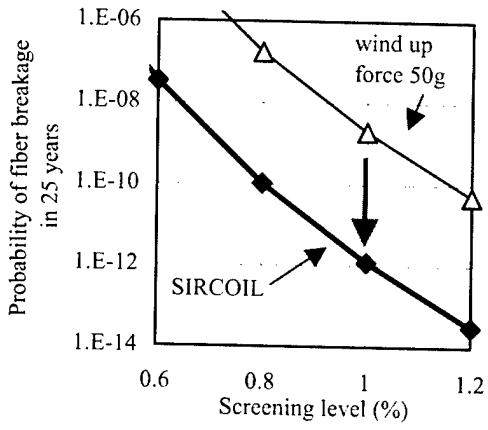


Figure 8. Probability of fiber breakage in 25 years

5. Reliability of Stress-Free Coil Module

Stress-free coil DCFMs have strong advantages not only in transmission characteristics, but also in reliability. These characteristics are as follows.

5.1 Mechanical Reliability

After screening, the probability of fiber breakage *Fs* is given by the following equation.

$$Fs = 1 - \exp\left(- Np \frac{m}{n-2} \frac{\sigma_s^n t_s}{\sigma_p^n t_p} \right)$$

Here, Np is the number of breakages during screening, n is the coefficient of fatigue (value n), m is the Weibull distribution slope (value m), σ p is the strain at the screening test, σ s is the strain during module use, *tp* is the screening time, and *ts* is the time of module use. In the case of a conventional bobbin-wound structure, a winding tension is, for instance 50g, whereas the value of σ s in the stress-free coil structure decreases because there is no winding tension. Consequently, over a 25-year period, the probability of breakage is roughly 1/1000th of that for a conventional structure (Fig.8).

5.2 Optical Reliability

We have focused on reliability tests, because the structure of stress-free coil DCFMs is quite different from the conventional packaging. At first, we confirmed the resin has high reliability by evaluating based on the thermal aging test and dump heat aging test. Now we are going on to evaluate the reliability of stress-free coil DCFMs. Table 1 and Figure 9,10 shows the result of each test (in accordance with Bellcore GR 63[6]). A variation of module insertion loss is less than 0.1dB in every test. The resin was carefully maintained stable state and the stress-free coil structure did not change at all after the dump heat 2000h test, vibration test, and drop test.

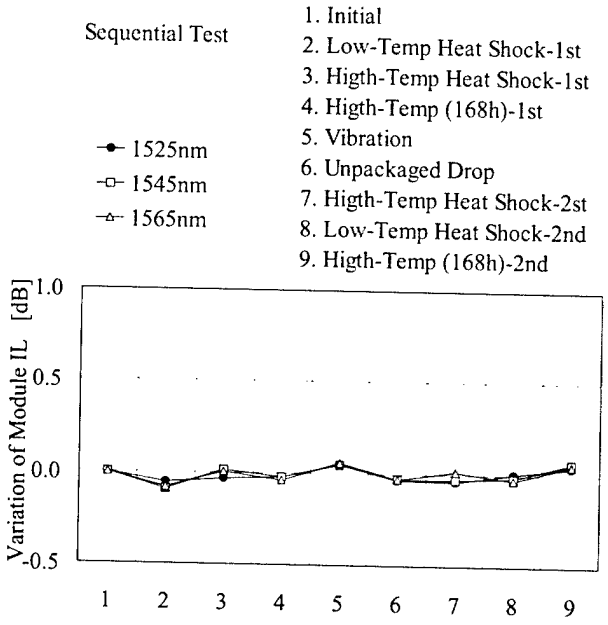


Figure 9. Sequential test result 1(module insertion loss)

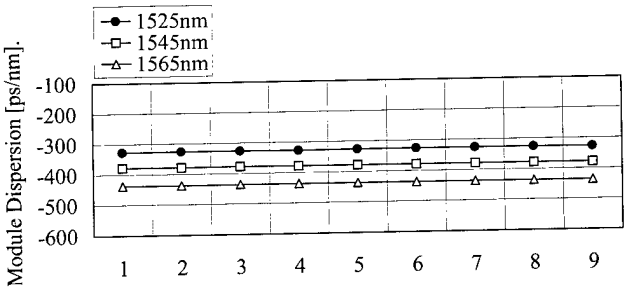


Figure 10. Sequential test result (Dispersion)

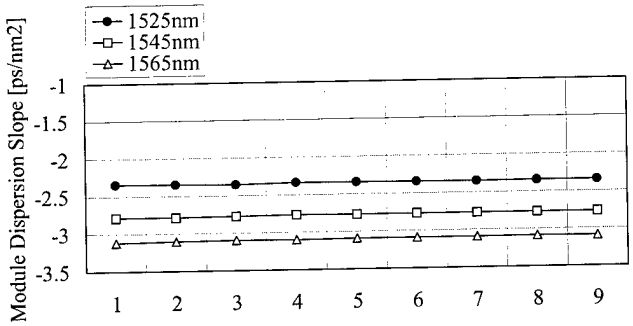


Figure 11. Sequential test result (Dispersion slope)

Table 1. Reliability test result of each packaging

Items	stress-free coil DCM for NZ-DSF	conventional SPOOL DCM80 for SM
	-393ps/nm	-1360ps/nm
	IL variation (OTDR) @ 1550nm	
Vibration	<0.1dB	<0.1dB
Unpackaged Drop	<0.1dB	<0.1dB
Dump Heat	<0.1dB* (1000h)	<0.1dB (2000h)
	* under testing	

6. DCFM Trial Production

New generation NZ-DSFs, such as TeraLight® or PureGuide®, which have a nominal dispersion of +8ps/nm/km at 1.55μm, have recently been introduced (Table 2). In addition to the optimized dispersion in the 1.55μm range (C-band), their zero dispersion wavelengths are designed to be shorter than 1.45μm, enabling the DWDM transmission also in the S-band (1.46μm-1.53μm). In order to effectively utilize wider signal wavelength ranges, in general, lower dispersion slopes are desirable. It is also well known that the effective core area (Aeff) of optical fiber is expected to be as large as possible for suppressing the nonlinear effects in the fiber. There is, however, a trade-off relationship between the dispersion slope and the effective area. The new class of NZ-DSF features an optimal combination of relatively low dispersion slopes (approximately 0.06ps/nm^2/km) and large effective areas (>60μm^2).

Table 2. Characteristics of NZ-DSFs

	PureGuide P-65	NZ-DSF2	NZ-DSF3
Dispersion (ps/nm/km)	8	4.5	4.7
Dispersion Slope (ps/nm^2/km)	0.06	0.045	0.08
RDS (1/nm)	0.0075	0.01	0.017
Aeff (μm^2)	65	52	72

We produced a number of trial DCFMs using the stress-free coil structure as compensators on different types of NZ-DSF. Table 3 shows the characteristics of the trial DCFM, we can optimize DSCR for PureGuide P-65 and NZ-DSF 2 with high FOM. Figure 12 shows the attenuation spectrum of it (including splices), and Fig 13 shows the dispersion spectrum which is concatenated NZ-DSF. In the C-band, the figure shows that the dispersion and dispersion slope adequately can be compensated.

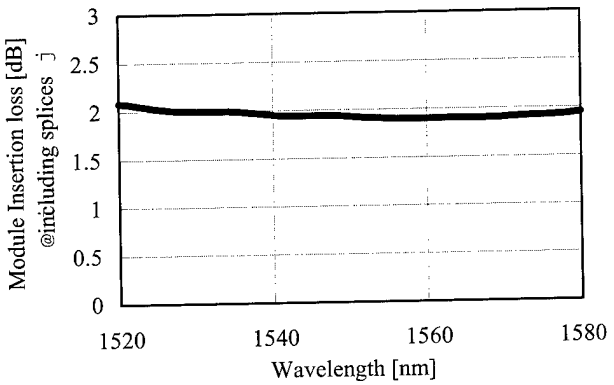


Figure 12. Attenuation spectra of stress-free coil DCFM for NZ-DSF

Table 3. Characteristics of stress-free coil DCFM for NZ-DSFs

Item	Value (@1550nm)
Dispersion	-420 ps/nm
Dispersion slope	-3.9 ps/nm2
FOM (Including splices)	218 ps/nm/dB
PMD	0.29 ps
Module Insertion loss	1.93 dB
DSCR	124% (for PureGuide P-65) 93% (for NZ-DSF2) 55% (for NZ-DSF3)

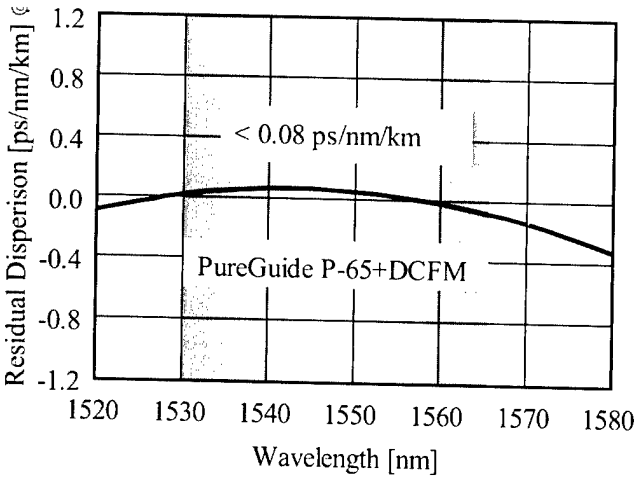


Figure 13. Dispersion spectrum after concatenating PureGuide P-65 with DCFM

7. Conclusions

With the aim of improving the performance of dispersion compensating fiber modules, we developed stress-free coil structure in which the fibers are subjected to minimal strain. Because this new structure reduced microbending loss, it improves DCFM performance, as well as provides excellent reliability. The stress-free coil DCFM structure can be successfully used to compensate for dispersion in NZ-DSF systems. This technology is very useful to increase the capacity of DWDM transmissions.

8. References

[1] M.Shirasaki, Y.Kawahata, S.Cao, H.Ooi, N.Mitamura, H.Isono, G.Ishikawa, G.Barbarossa, C.Yang, C.Lin, : " Variable dispersion compensators realized in high refractive-index contrast technology" Proc. ECOC 2000, PD 2.3, 2000.

[2] S. Ramachandran, B. Mikkelsen, L.C. Cowsar, M.F. Yan, G. Raybon, L. Boivin, M. Fishteyn, W. A. Reed, P. Wisk, D. Brownlow and L. Gruner Nielsen, "All-fiber, grating-based, high-order-mode dispersion compensator for broadband compensation and 1000km transmission at 40 GB/S" Proc. ECOC 2000, PD 2.5, 2000.

[3] M. Onishi et al., "Dispersion Compensating Fiber" Sumitomo Electric Technical Review No. 145, September, 1994.

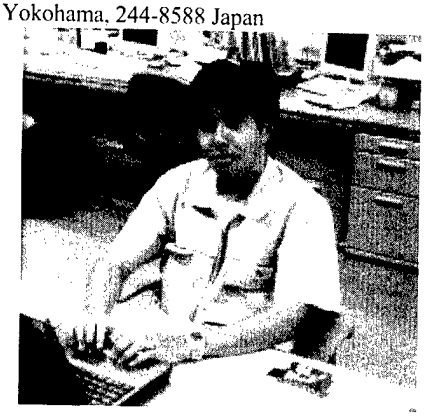
[4] Y. Koyano, M. Onishi, K. Tamano and M. Nishimura, : " Compactly-packaged high performance fiber-based dispersion compensation modules" Proc. ECOC ' 96, 3, pp. 221-224, 1996.

[5] T. Kato, M. Hirano, K. Fukuda, A. Tada, M. Onishi and M. Nishimura " Design optimization of dispersion compensating fiber for NZ-DSF considering nonlinearity and packaging performance" Proc. OFC 2001, TuS6-1, 2001.

[6] " Network Equipment-Building System (NEBS) Requirements" GR-63 BELLCORE October, 1995.

9. Authors

Takashi Fujii, Sumitomo Electric Industries, Ltd, 1 Taya-cho, Sakae-ku, Yokohama, 244-8588 Japan



Takashi Fujii received his B.Sc. and M.Sc. degrees from the Osaka University in 1993 and 1995, respectively. He joined Yokohama research laboratories, Sumitomo Electric Industries, Ltd in 1995 and has been engaged in research and development of optical fibers, cables and components. He is a member of the Institute of Electronics, Information and Communication Engineers.

Keiichiro Fukuda, Sumitomo Electric Industries, Ltd, 1 Taya-cho, Sakae-ku, Yokohama, 244-8588 Japan

Keiichiro Fukuda received his B.Sc. and M.Sc. degrees from Electro Communication University in 1995 and 1997, respectively. He joined Fiber optics division, Sumitomo Electric Industries, Ltd in 1997 and has been engaged in development of speciality fibers.

Eisuke Sasaoka, Sumitomo Electric Industries, Ltd, 1 Taya-cho, Sakae-ku, Yokohama, 244-8588 Japan

Eisuke Sasaoka received his B.Sc. degrees from the Tukuba University in 1986. He joined Yokohama research laboratories, Sumitomo Electric Industries, Ltd in 1986 and has been engaged in research and development of optical fibers.

Toshifumi Hosoya, Sumitomo Electric Industries, Ltd, 1 Taya-cho, Sakae-ku, Yokohama, 244-8588 Japan

Toshifumi Hosoya received his B.Sc. and M.Sc. degrees from the Tokyo University in 1983 and 1985, respectively. He joined Yokohama research laboratories, Sumitomo Electric Industries, Ltd in 1985 and has been engaged in research and development of optical fibers, cables and components.

Dispersion Managed Fiber Optic Cable

Euydon Park[1], Sungyul Park[1], Dongwook Lee[2], Hyeyoung Park[2], Dongyoung Kim[1], Yunchul Chung[3]

[1]Optical production and Technology Development Team, LG Cable, Kumi, Korea
+82-54-941-7020 · edpark@cable.lg.co.kr
[2]Fiber Optics & Telecom. Research Lab., LG Cable, Ahnyang, Korea
+82-31-450-8010 · young2@cable.lg.co.kr
[3]Electrics and Electronics, Korea Advanced Institute Science and Technology, Taejon, Korea
+82-42-869-3456 · ychung@ee.kaist.ac.kr

Abstract

A large dispersion value in optical fiber cable should be maintained to suppress the nonlinear effect induced distortion for the narrow channel spaced DWDM system while small value of dispersion is needed for high bit rate transmission. To meet these two requirements simultaneously, the dispersion distribution control method during the cabling process was exploited. We developed dispersion-distributed cable by the way of designing alternation sections in a single cable piece with standard single mode fiber (SMF) and newly designed negative dispersion fiber (NDF). The dispersions of 17 ps/km/nm of SMF and -15 ps/km/nm of NDF were distributed in the optical cable of 6km length. The average dispersion value of an entire cable length was 1.0 ps/km/nm while the local dispersion was around 17 ps/km/nm as absolute value. Moreover, the developed cable had good optical and mechanical properties and the feasibility of this cable for practical use was confirmed.

Keywords

Chromatic dispersion; Dispersion management; Nonlinear effect; Negative dispersion

1. Introduction

In order to maximize a transmission capacity of a dense wavelength division multiplexing (DWDM) optical transmission system, a method of increasing an optical transmission bandwidth, and a method of increasing a transmission bit rate per channel and making a channel spacing dense for enhancing spectral efficiency have been intensively discussed. As for the optical transmission bandwidth, in the C-band in which the existing erbium doped fiber amplifier (EDFA) has a gain, there is a proposal of expansion of the optical transmission bandwidth up to the L-band of a long wavelength band and the S-band of a short wavelength band, which is probable to be achieved according to the research results on a Raman amplifier, a thulium doped fiber amplifier (TDFA) and the like [1], [2]. In addition, as for the transmission rate per channel, economical commercial application of 40 Gbit/s has been continuously searched from 10 Gbit/s. As for bit rate of carrier wavelength, there have been proposed research results obtained by using the channel spacing from 200 GHz and 100 GHz to 50 GHz and 25 GHz [3]. In order to sufficiently implement various optical transmission loads for such maximized transmission capability, there is a need for an optical cable having optical properties contrary to one another. That is, an optical cable having a small dispersion value is advantageous to enhancement of the transmission bit rate, whereas a large dispersion value is advantageous to narrower channel spacing to suppress nonlinear effects of an optical fiber. A lot of research results obtained by attempting to optimize the dispersion property and the effective area of the optical fiber for simultaneously solving the problems have been published [4]-[6]. However, this method was merely an attempt to select one fixed dispersion coefficient as an optimal value throughout the entire length of the cable, and thus, it was difficult to completely solve both the penalties of high dispersion values and the penalty of low dispersion values at once. We investigated a method of simultaneously solving the penalty of the low dispersion values by allowing the cable to locally have a large absolute dispersion value while reducing the penalty of the high dispersion values, actually fabricated the fiber optical cable, and confirmed the characteristics of the cable.

2. Limit Factor of Optical Transmission System

2.1 Dispersion of Optical Fiber Cable

When modulated signals propagate through the optical fiber at high speed, chromatic dispersion occurs, which is a spreading phenomenon due to the difference in the group velocities of signal wavelength components. The chromatic dispersion has a fatal result in that the signals are overlapped and demodulation thereof cannot be made at a receiving terminal. Generally, if only the effects of the dispersion are taken into consideration, the maximum transmission distance capable of transmitting the signals through the fiber is expressed as the following equation [7]:

$$B^2 L = 7.9 \times 10^5 \frac{c}{\lambda^2 D} \quad (1)$$

Where B is a transmission rate, D is a dispersion value of the fiber, and L is the maximum transmission distance. As for an identical transmission distance, if the transmission rate is quadrupled, the dispersion value is in inverse proportion to the square of 4, so that a small value of one sixteenth of the dispersion value is required. Therefore, in a higher-rate system, the dispersion value must be greatly reduced.

2.2 Nonlinear Effect

In a dense wavelength division multiplexing system, a plurality of signals are transmitted through an identical optical fiber over a long distance, so that when light is incident on the optical fiber, photons and atoms interact with each other, resulting in nonlinear effects. Such nonlinear effects can be largely classified into two types according to generating causes thereof. One type includes Stimulated Raman Scattering (SRS) and Stimulated Brillouin Scattering (SBS) resulting from stimulated scattering of silica molecules. The other type includes Self-Phase Modulation (SPM), Cross Phase Modulation (XPM), and four wave mixing (FWM) resulting from a nonlinear refractive index. The SRS reduces the optical signal-to-noise ratio since signal power of a short wavelength is transmitted as a signal of a long wavelength. The SBS limits maximum applicable power of the optical fiber. The SPM and XPM induce the phase modulation of the optical signal, and the FWM generates a new frequency component due to interference between signals. In case of reducing the channel spacing in a multi-channel transmission system for enlargement of the transmission capacity, the latter, especially FWM, are dominant problems.

In order to reduce power generated by the FWM, the dispersion should be large enough to prevent phase matching. In these ways, since the suppression of the nonlinear signal distortion such as the FWM has a contrary relationship with the enlargement of the transmission capability by means of increase of the transmission rate, there is a need for a special design of dispersion properties in order to simultaneously satisfy two criteria.

3. Cable Design

As a method for suppressing the nonlinear effects while reducing signal distortion due to the dispersion, there has been proposed application of a non-zero dispersion shifted fiber (NZDSF) having a level of about 3 ps/km/nm instead of the conventional SMF having a dispersion value of about 17 ps/km/nm. However, a new problem is brought out in that since such optical cable has optical fibers with small effective areas and thus a relatively small dispersion value, if the channel spacing is narrowed down to a level below 50 GHz, the nonlinear effects such as the FWM are not sufficiently suppressed so that the transmission distance may be very restricted [8], [9]. As a method for solving such a problem, a new-type NZDSF was proposed, which can effectively suppress the nonlinear signal distortion even at the channel spacing of 50 GHz by setting up the dispersion value of the optical cable to a value of about 8 ps/km/nm at an operating central wavelength [6], [8]. However, the method also produces additional costs for compensating the dispersion with respect to the increased dispersion value, causes a dispersion-compensating period to be shortened, and increases complexity of the system. Therefore, the method still has a limitation in that it cannot solve the problems of the dispersion and nonlinear effects simultaneously. Generally, a dispersion compensating fiber (DCF) is used for dispersion compensation. This fiber has a negative dispersion value with a large absolute value and also has relatively large fiber loss. In addition, the nonlinear effects occur due to a small effective area of the fiber. Thus, in the DWDM system, a 2-stage amplifier is constructed and the dispersion compensating fiber is disposed between the stages of the amplifier, thereby deteriorating the optical signal-to-noise ratio. Since the dispersion compensating fiber has a unit cost per length thereof much higher than that of typical fibers, it is preferable to reduce an accumulated amount of dispersion and to minimize use of the dispersion compensating fiber in view of the costs of the system.

Another method is to distribute dispersion values to be variably along the length of the cable so that the cable locally has large dispersion values and, at the same time. In this way, there have been reported methods of varying distribution of the dispersion values of positive values and negative values at a period of tens kilometers by using an optical fiber configured such that its refractive index can be periodically varied in a lengthwise direction thereof by means of fabricating a preform for optical fibers [10]~[13]. These methods to form the lengthwise dispersion distribution by adjusting the outer diameter and a refractive index profile which determine the dispersion values in the preform. The methods merely show a possibility of fabricating a continuous optical fiber having different dispersion values. There is not yet a study on an attempt to actually fabricate a complete product of the cable, in which different dispersions are distributed.

We developed an optical cable having dispersion values distributed in a lengthwise direction to efficiently suppress the nonlinear distortion effects while maintaining the average dispersion value of the optical cable at the value of about 3 ps/km/nm that is a level of the conventional NZDSF. This study overcomes the limitation on the method of fabricating the dispersion-distributed cable by which the dispersion values are varied in the preform for the fiber, and proposes a design concept and a fabricating method concerning a novel dispersion distribution based on a length actually applicable to networks.

Generally, there are no standards for the maximum usable length of the optical cable, which depends on conditions of construction and operation of a line. In a case where a unit cable is long, the number of splicing through the entire network can be reduced and thus it is advantageous in view of optical power loss. However, the maximum usable length of the cable is limited due to factors such as the diameters, routes of ducts and installation methods or technique.

In this paper, the reference length of the dispersion-distributed cable was selected as 6 km that which at present Europe and the like actually apply to a long-distance communications network. In addition, the most widely used SMF is fabricated through a stable process, is most economical and has already been largely installed in the existing communications networks. Thus, as for a newly designed dispersion-distributed cable, it is necessary to improve its compatibility with the SMF. Further, the SMF has a relatively large dispersion value of 17 ps/km/nm and a large effective area of $80\mu m^2$ so that it can effectively suppress the nonlinear effects. From this point of view, we investigated a structure of the dispersion-distributed cable suitable for very high rate and large capacity DWDM communications on the premise of using SMF.

3.1 Dispersion Distribution of the Cable

Figure 1 shows an example of an optical cable in which the cable is divided into n parts and has variations of the dispersion values along the length. Here, β_i and D_i are a propagation constant and a dispersion value of the length of i-th part, respectively. Assuming that β_i and D_i are constant within the length of each part, the magnitude of an optical signal generated by the FWM at an end of the length of the n-th part can be expressed as the following equation [14].

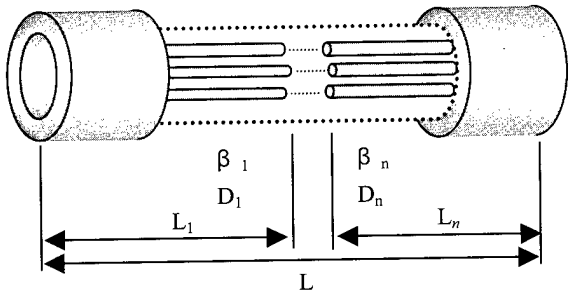


Figure 1. Optical cable divided into *n* parts having different dispersions

$$P_F^{(n)}\left(\sum_{i=1}^{n} L_i\right) = \frac{1024\pi^6 (D\chi)^2}{n_{co}^4 \lambda^2 c^2} \frac{P_i(0)P_j(0)P_k(0)}{A_{eff}^2} \exp\left[-\alpha\left(\sum_{i=1}^{n} L_i\right)\right]\eta \quad (2)$$

where, n_{co} : core refractive index,

c : speed of light,

D : degeneracy factor,

χ: third-order nonlinear susceptibility,

A_{eff} : effective area

$P_q(0)(q=i,j,k)$: q-th input power.

α : fiber loss

η is FWM efficiency and expressed as the following equation:

$$\eta = \sum_{i=1}^{n}\left[\frac{\exp\{(-\alpha + j\Delta\beta_i)L_i\} - 1}{j\Delta\beta_i - \alpha} \prod_{j=1}^{i-1} \exp\{(-\alpha + j\Delta\beta_i)\}L_i\right] \quad (3)$$

Here, $\Delta\beta_n$ represents phase mismatching of the length of the n-th part and can be expressed as the following equation:

$$\Delta\beta_n = -\frac{\lambda^4 \pi}{c^2}\frac{D_n}{d\lambda}[(f_i - f_{on}) + (f_j - f_{on})](f_i - f_k)(f_j - f_k) \quad (4)$$

Where f_i, f_j and f_k are frequencies of the i, j and k-th input light, and D_n and f_{on} represent dispersion and zero dispersion frequency of the length of the n-th part. The equations (2) to (4) show that in case of a cable having a length not more than 6 km, it is effective to lessen the number n of the parts within the length of the cable in order to reduce optical power of a new frequency component due to the FWM appearing over the entire length of the cable. Further, keeping the dispersion value of the length of each part high to increase $\Delta\beta$, i.e. difference in propagation constants for different frequency components, must be taken into consideration. Moreover, it can be seen that it is necessary to reduce power density of input light per unit effective area by enlarging the effective area A_{eff} of the fiber.

In a case where the number n of the parts is set as the minimum value of 2 and the SMF is employed in one part in the predetermined length of the cable, in order to maintain the average dispersion value of the cable at a level of 3 ps/km/nm identical to that of a conventional NZDSF. it is important to optimize the magnitude of a dispersion value of a negative dispersion fiber (NDF) and a ratio between the lengths of the two parts. Further, a figure of merit (FOM) should be large for the effect of suppressing the nonlinear signal distortion of the FWM large. The FOM is an index representing the magnitude of a local dispersion value capable of suppressing the nonlinear effects of the FWM while having a small average dispersion value. Namely, the FOM is a ratio between the sum total of accumulated dispersion of a dispersion-distributed cable and the sum total of accumulated dispersion of a cable having a single fixed dispersion value identical to an average dispersion value of the dispersion-distributed cable. The FOM can be defined as the following equation:

$$FOM = \frac{\sum_{i=1}^{n} |D_i| \cdot l_i}{D_{avg} \cdot L} \quad (5)$$

Where D_{avg} is an average dispersion value, D is the dispersion, l is a distance, and L is a length of a cable. There is a possibility of somewhat changes the ratio between the lengths of the two parts in the length of the cable such as cutting off an end of the cable which may be made in processes of construction, operation and connection of the cable. In considering of that, setting the ratio between the lengths of the two parts in the length of the cable as 1 becomes a condition where a designed average dispersion value is maintained most stably. Figure 2 shows various types of dispersion distributions in the cable. In a case where a dispersion value of the NDF is too small, the dispersion distribution as shown in Figure 2 (c) is obtained and the sum total of accumulated dispersion thereof becomes an area defined by ABEF in Figure 2 (a). In this case, the ratio between the lengths of the two parts drifts away from 1, and the FOM becomes small. In case of a conventional NZDSF, the sum total of accumulated dispersion according to dispersion values is an area defined by AEF in Figure 2 (a) and the FOM is 1, which is a condition where there is no additional effect of local dispersion.

In a case where the dispersion value is too large, the dispersion distribution as shown in Figure 2 (e) is obtained and thus the FOM becomes large. However, the ratio between the lengths of the two parts also drifts away from 1 in the same way as the NDF having the small dispersion value. In this case, since the material dispersion and the waveguide dispersion should be suppressed and increased, respectively, so as to have a large negative dispersion value of the NDF, there are disadvantages in that the structure of the waveguide is complicated and the effective area is reduced [15]. In this paper, we designed the dispersion coefficient of NDF at –15 ps/nm/km and the length ratio between SMF and NDF at 1:1. Therefore the average dispersion coefficient in total 6km length reached 1.0 ps/nm/km that provides more than 3 times of dispersion compensation period than conventional NZDSF, and a very large FOM value, 9.0 was obtained.

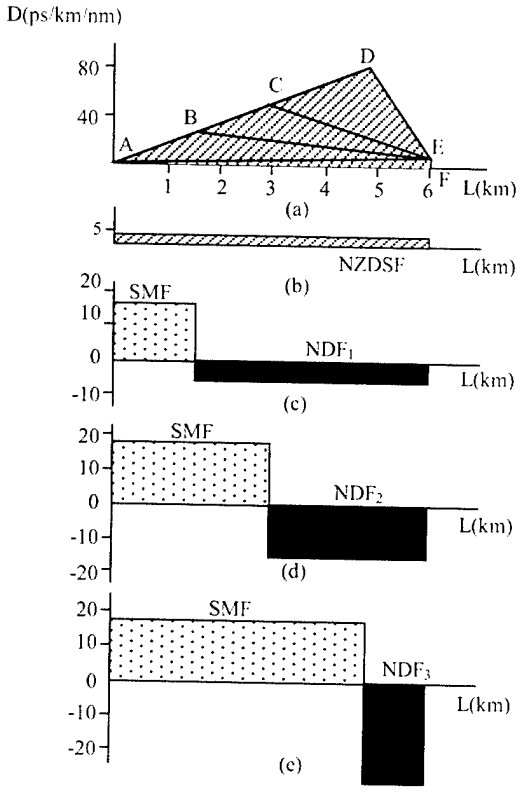


Figure 2. Dispersion distribution and the types of accumulated dispersion

(a) Accumulated dispersion

(b) Dispersion distribution of existing NZDSF cable

(c) Dispersion distribution of cable that has the type of ABEF

(d) Dispersion distribution of cable that has the type of ACEF

(e) Dispersion distribution of cable that has the type of ADEF

4. Fabrication of Cable and The Results

We manufactured two types of optical fibers for the dispersion-distributed cable in advance and then dispersion distribution was formed in the lengthwise direction in a cabling process as calculation to solve the problem of the methods for forming the dispersion distribution in the processes of fabricating the optical fiber.

4.1 Fabrication of Optical Fiber

The SMF employed in the length of a positive dispersion part was designed such that it has a stepped refractive index profile and also a mode field diameter (MFD) of 10.2 μm, loss of 0.20 dB/km and a dispersion value of 17 ps/km/nm at a wavelength of 1550 nm. An optical fiber having negative dispersion that is connected to the above SMF to form a predetermined dispersion distribution should maintain a dispersion value of -15 ps/km/nm and have a large A_{eff}. In addition, this optical fiber should be well compatible with the SMF in view of connection characteristics and the like and represent behavior characteristics similar to those of the SMF under the same cabling condition and loads of construction and operation environment as the SMF. Since such optical fiber has a negative dispersion value at a using wavelength band, the zero dispersion wavelength should be shifted over 1550 nm. A negative dispersion fiber newly designed to have characteristic values shown in Table 1 was fabricated with the MCVD method.

Table 1. Design value of negative dispersion fiber

Characteristic Items	Unit	Design Values
Dispersion @ 1550nm	ps/km/nm	-15
Dispersion slope	ps/km/nm^2	〈0.15
Cut-off wavelength	nm	〈1450
Effective area	μm^2	≥ 60
MFD @ 1550nm	μm	9.0±0.5
Attenuation @ 1550nm	dB/km	〈0.25

4.2 Fabrication of Optical Fiber Cable

The cables were fabricated in such a manner that individual optical fibers are cabled after the optical fibers have been spliced with each other so that a length ratio between the SMF and the NDF can be kept 1:1. In order to overcome breakage of the splicing parts during manufacturing process or reliability reduction of the optical fiber due to degradation of the mechanical strength at the splicing parts, the splicing points should be reinforced properly. A method of reinforcing a splicing point by injecting UV curing resin into the splicing part and irradiating the ultraviolet rays after fusion splicing of glass part of the optical fiber was applied as shown in Figure 3. The cabling process was performed in the same manner as the condition in the SMF cable. The cable structure is a most general loose tube type. The fabricated cable has a structure shown in Figure 4.

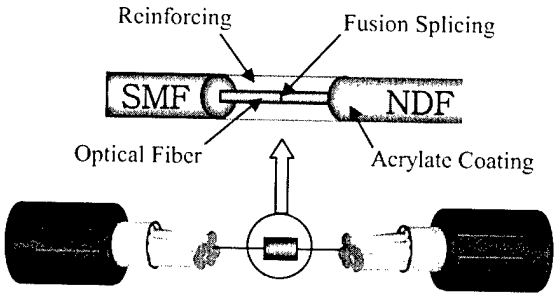


Figure 3. Splicing and reinforcing of two types of optical fibers

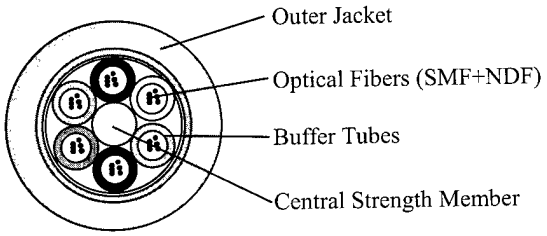


Figure 4. Cable structure for dispersion –distributed cable

4.3 Test Results

The fabricated dispersion-distributed cable was tested as to whether the optical performance calculated at the design stage and the various mechanical/environmental durability and reliability required in its using and operating processes can be maintained.

4.3.1 Optical Properties. The results for measuring the optical properties of the fabricated NDF compared with the SMF are shown in Table 2. It was confirmed that the NDF has dispersion characteristic values, which are approximate to the values confirmed at the design stage. The dispersion values according to the wavelengths are shown in Figure 5. According to the characteristic results confirmed in view of the entire length of the dispersion-distributed cable, the effective area of the fabricated NDF is about 72 μm^2 which is 10% larger than the effective area, 65 μm^2, of the new NZDSF in which a channel spacing of 50 GHz can be used. The average dispersion value of the newly developed cable is near to zero, 1.0ps/km/nm that is 30% lower than the dispersion value of conventional NZDSF, while the local dispersion value is kept at levels of +17 ps/km/nm and -15 ps/km/nm. Since the effective area of the dispersion-distributed cable can be calculated by using the ratio of the lengths of the respective parts of the cable and the following equation [15], an equivalent effective area of the proposed cable calculated as such was compared with those of the conventional cables.

$$\Phi = \int_0^L \frac{n_2(z)}{A_{eff}(z)} \exp(-\alpha z) dz \qquad (6)$$

It is determined that the PMD and loss of the negative dispersion fiber can be improved by additional stability of the manufacturing process.

Table 2. Optical properties of the dispersion-distributed cable

Characteristic Items	SMF	NDF	Dispersion-distributed Cable
Dispersion (ps/km/nm) @1550nm	17.1	-15.1	1.0
Dispersion slope (ps/km/nm^2)	0.055	0.1	0.078
Cut-off wavelength (nm)	1280	1331	-
Effective area (μm^2)	80	65	72
MFD (μm) @1550nm	10.2	9.0	-
Attenuation (dB /km) @1550nm	0.20	0.26	0.25
PMD (ps/km$^{0.5}$)	0.06	0.22	0.16

Table 3. Comparison between the dispersion-distributed cable and NZDSF cable

Characteristic Items	Dispersion-distributed Cable	Conventional NZDSF			New NZDSF
		A	B	C	
Dispersion (ps/km/nm) @1550nm	1.0	~4	~4	~4	~8
Dispersion slope (ps/km/nm^2)@1550nm	0.072	0.07	0.1	0.05	0.058
Effective area (μm^2)	72	53	72	55	65
Attenuation (dB/km) @1550nm	0.25	< 0.22	< 0.25	< 0.22	0.21
PMD (ps/km$^{0.5}$)	0.16	< 0.1	< 0.1	< 0.1	< 0.2

4.3.2 Evaluation of Cabling Characteristics. It was confirmed that the cabling works by which the calculated dispersion distribution is maintained in the cable could be made by using two types of the optical fibers such as the SSMF and NDF. As shown in Figure 6, the dispersion-distributed cable had the same level of cable matching characteristics as the SMF in loss increment during the cabling process.

4.3.3 Evaluation of Cable Reliability. Considering a load produced by the external environment which can be applied to the cable during the operating and installing, it was tested as to whether the optical properties can be maintained under the conditions of temperature changes from -40 to +70°C, 2 cycles and a tensile load of 300 kg as a maximum value. As understood from Figure 7, changes of loss according to the temperature changes were lower than 0.03 dB/km, and the measurable change of loss did not occur at the tensile load lower than 300 kg. Thus, it was confirmed that the fabricated dispersion-distributed cable had the same reliability as the SMF cable.

4.3.4 Mechanical Characteristics. According to the test results of the dispersion-distributed cable based on the Telcordia GR-20 CORE and comparison with the SMF cable, As for the possibility of changes of the characteristics by external mechanical load such as twist, repeated bending, compression and impact, the dispersion-distributed cable showed same properties as SMF cables as shown in Table 4.

Table 4. Mechanical characteristics of the dispersion-distributed cable

Test Items	Test Condition	Attenuation Changes (dB)	
		SMF Cable	Dispersion – distributed Cable
Twist	2m, 180°	0.00	0.00
Repeated bending	20D, ±90°	< 0.01	0.00
Compression	220 N/cm	0.00	< 0.01
Impact	2.0kg, 25times	< 0.01	< 0.01

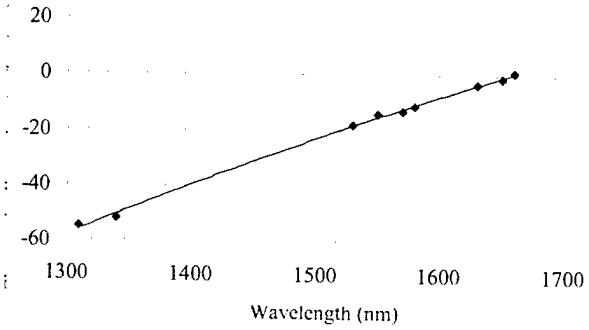


Figure 5. Chromatic dispersion of NDF

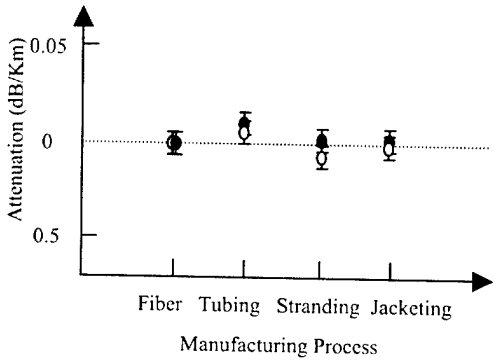
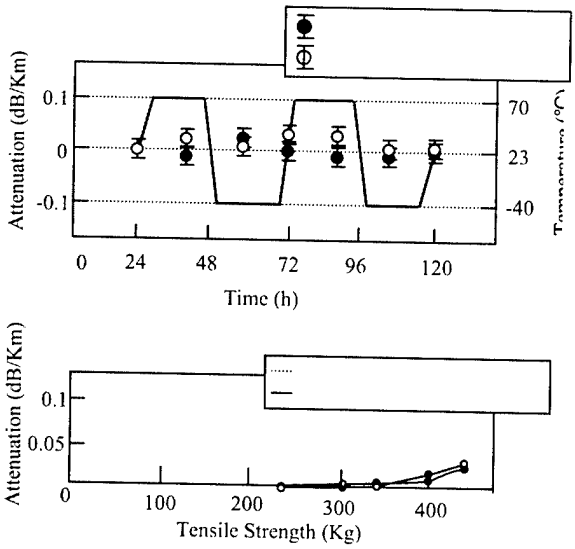


Figure 6. Attenuation change during cabling process



5. Conclusion

In order to increase the transmission rate for ultra high capacity transmission, a cable having a small dispersion value is efficiently used in the DWDM optical transmission system. However, in a case where multiple channels are to be transmitted within a confined bandwidth by narrowing a wavelength interval, a cable having a large dispersion value is advantageous in view of the effects of suppressing the nonlinear effects of the FWM. In order to investigate a degree of meeting these two contrary requirements simultaneously, a figure of merit (FOM) has been newly proposed and employed. We designed and manufactured the negative dispersion fiber (NDF) matching SMF. We fabricated dispersion-distributed cable having both the two types of fibers in 6km length, which NDF of -15 ps/km/nm and SMF of 17 ps/km/nm distributed at same length ratio. The fabricated cable has a high absolute value of local dispersion, 15~ 17 ps/km/nm, which is advantageous over the conventional NZDSF in view of suppressing signal distortion resulting from the nonlinear effects. Further, the average dispersion value is near to zero, 1.0 ps/km/nm that provides more than 3 times of dispersion compensation period than conventional NZDSF, as well as a relatively great effective area, 72 μm^2. Furthermore, it was confirmed that the proposed cable was well compatible even with the same environment for using and operating the cable as the SMF cable.

6. REFERENCE

[1] S. Shen, M. Naftaly, A. Jha and S. J. Wilson, "Thulium-doped Tellurite Glass for S-band Amplification", *Optical Fiber Communication Conference, Technical Digest Series*, TuQ1-2, Mar. 2001

[2] T. Tsuzaki, M. Kakui, M. Hirano, M. Onishi, Y. Nakai and M. Nishimura, "Broadband Discrete Fiber Raman Amplifier with High Differential Gain Operating over 1.65 μm-band", *Optical fiber Communication Conference, Technical Digest Series*, Ma3-1, Mar. 2001

[3] K. Emura, "Multi-Terabit/s DWDM; Technologies and Perspectives", *Optical Fiber Communication Conf., Technical Digest Series*, ML1-1, Mar. 2001

[4] Z. Gills and A. Judy, "New Requirements for Long Haul Optical Transmission", *National fiber Optic Engineers Conference, Technical Proceedings*, PP.20-26, Aug. 2000

[5] A. J. Lucero, S. Tsusa, and V. L. da Silva, "320 Gbit/s WDM transmission over 450km of LEAF Optical Fiber", *Annual Multiplexed Telephony Conference*, 2000

[6] L. de Monotmoriilon, A. Bertaina, P. Sillard, L. Fleury, P. Nouchi, J. Chariot, S. Bigo, J. Hamaide "Optimized Fiber Terabit Transmission", *International Wire and Cable Symposium*, PP.38-44, Nov. 2000

[7] F. Elrefaie, R. E. Wanger, D. A. Atlas, and D. G. Daut, "Chromatic Dispersion Limitations in Coherent Lightwave Transmission Systems", *IEEE J. Lightwave Technol.*, Vol. 6, No. 5, pp. 704-709, May, 1988

[8] S. Bigo, et al., "1.5 Tera bit/s WDM Transmission of 150 Channel at 10 G bit/s over 4×100km of Teralight™", *ECOC '99*, PD2-9, 1999

[9] M. Eiselt, L. D. Garett and R. W. Tkack, Experimental Comparison of WDM Systems Capacity in Conventional and Nonzero Dispersion Shifted Fiber", *IEEE Photon, Technologies Letters*, Vol. 11, No. 2, pp. 281-283, 1999

[10] J. Lee, G. H. Song and U. C. Peak, "Design and Fabrication of Dispersion-Managed Fibers by Periodic Etching during the MCVD Process", *Electronics Letters*, Vol. 37, No. 1, pp. 11-12, Jan. 2001

[11] V. A. Bhagauatula, G. Berkey, D. Chowdhury, A. Evans and M. J. Li, "Novel Fibers for Dispersion-Managed High-Bit-Rate Systems", *Optical Fiber Communication Conference, OSA Technical Digest Series*, pp. 21-22, 1998

[12] Y. Miyajima, M. Ohashi and K. Nakajima, "Novel Dispersion-Managed Fiber for Suppressing FWM and an Evaluation of Its Dispersion Distribution", *In Proc. OFC '96*, Vol. PD7

[13] K. Nakajima, M. Ohashi, T. Horiguchi, K. Kurokawa and Y. Miyajima, "Design of Dispersion Managed Fiber and Its FWM Suppression Performance", *In Proc. OFC*, Vol. Th G3, pp. 87-89, 1999

[14] K. Nakajima, M. Ohasui, K. Shiraki, T. Horiguchi, K. Kurokawa and Y. Miyajima, "Four-Wave Mixing Suppression Effect of Dispersion-distributed Fibers", *Journal of Lightwave Technology*, Vol. 17, No. 10, pp. 1814-1821, Oct. 1999

[15] K. Mukasa and T. Yagi, "Dispersion Flat and Low Non-linear Optical Link with New Type of Reverse Dispersion Fiber(RDF-60)", *Optical Fiber Communication Conference, Technical Digest Series*, TuH7-1, Mar. 2001

Authors



Euydon Park

LG Cable Ltd.

edpark@cable.lg.co.kr

He received B.E. and M.E degrees in Electronics Engineering from Kyungpook University in 1986 and 1991 respectively. He joined LG Cable Ltd. in 1986 and has been engaged in the design and development of optical fiber cable. He is now a general manager of optical product and technology development team.



He received B.E. degree in Electronics Engineering from Kyungpook University in 1996. He joined LG Cable Ltd. in 1996 as a design engineer in the optical fiber cable part. He is responsible for developing optical fiber cable.



Hyeyoung Park

LG Cable Ltd.

young2@cable.lg.co.kr

She graduated Ewha Woman's University in 1988 where She received the B.S. degree in Physics. She joined LG Cable Ltd. in 1998 as a research engineer in the Fiber Optics & Telecom Research Lab. She has been responsible for developing high capacity optical fiber and providing technical support.



He received the B.S. and M.S. degrees in Optics for Optical fiber from the Kyunghee University in 1998 and 2000. Since 2000, he has been a research scientist in Optical Fiber Dept., at LG Cable Ltd.. His main research field is to control the fiber dispersion for developing optical fiber cable.



Dongyoung Kim

LG Cable Ltd.

Kim1267@cable.lg.co.kr

He received B.E. degree in Electronics Engineering from Korea University in 1983. He joined LG Cable Ltd. in 1983 as a research engineer at R&D Center. He worked on the development and test of optical fiber as a manager of Fiber Optics & Telecom Research Lab.. He is now a plant manager of Indong Optical Fiber and Cable Factory in Kumi.



Yunchul Chung

KAIST

ychung@ee.kaist.ac.kr

He received the B.S. degree in electronics engineering from Hanyang University, and received M.S. and Ph.D. degrees in electrical engineering from Utah State university. From 1985 to 1987, he was with Los Alamos National Laboratory under AWU-DOE (Associate Western universities - Department of Energy) graduate fellowship program, where he worked on atomic resonance optical filter for the Navy's blue-green underwater communication. From 1987 to 1994, he was with Lightwave Systems Research Department at AT&T Bell Laboratories where he worked on various aspects of lightwave communication systems including coherent optical communication systems, wavelength-division-multiplexed systems, frequency-stabilized lasers, and multiple quantum-well devices, etc, In 1994, he joined Korea Advanced Instituted of Science and Technology. His current activities include high-capacity WDM transmission system, all-optical network, WDM monitoring techniques, WDM PON, and fiber-optic network for wireless communications, etc.

Attenuation Characterization of a Non Zero Dispersion Shifted Fiber with Negative Dispersion in Slotted Core Cable for Metropolitan Network Applications

Donald K. Hall
Corning Cable Systems
Hickory, North Carolina
+1-828-327-5995 · don.hall@corning.com

Abstract
Three Slotted Core Ribbon cables having design features considered representative of products in commercial use were selected for evaluation of a recently commercialized non zero dispersion shifted fiber with low negative dispersion. Fiber attenuation increases as a result of cable manufacturing and cable temperature cycling were investigated. Results indicated the fiber was compatible with cable designs, materials, and manufacturing processes currently in use.

Keywords
Dispersion compensation, SCR, metro, ring.

Introduction
As traffic demand upon metropolitan fiber networks increases, the need for increased bandwidth is apparent. The C-band (1530-1565 nm) is currently the defacto operating range for higher bandwidth applications due to the usefulness of wavelength division multiplexing (WDM) and erbium doped fiber amplifiers (EDFA) in this range. Standard dispersion unshifted single-mode fiber (SMF), which has a zero dispersion wavelength of 1310 nm, has positive dispersion in the C-band. Short-range applications allow the use of low cost directly modulated distributed feedback (DM-DFB) lasers with SMF. These lasers have a typical positive chirp, which when combined with positive fiber dispersion, limits the dispersion uncompensated range of SMF at 1550 nm to about 80 km at 2.5 Gb/s. Externally modulated distributed feedback (EM-DFB) lasers have greater uncompensated range. Although more expensive, their use is preferable to the high cost associated with dispersion compensation. The use of recently commercialized non zero dispersion shifted fiber (NZ-DSF) with low negative dispersion in the C-band extends the uncompensated range of lower cost DM-DFB lasers to greater than 300 km at 2.5 Gb/s, leading to reduced overall system cost. Such fibers have potential application in slotted core ribbon (SCR) cables used in the Japanese market. The purpose of this investigation was to characterize the attenuation performance of such a fiber in commercial SCR cable designs using standard materials and manufacturing practices. Although the primary test wavelength of interest was 1550 nm, characterization was also conducted at 1310 nm where legacy systems are operated.

Fiber Description
The NZ-DSF used for this investigation were selected to provide attenuation, cutoff wavelength and mode-field diameter measurements across a broad portion of the supplier's product specification range. These values and other optical measurements are indicated in Table 1.

Table 1. Non Zero Dispersion Shifted Fiber Data

	Spec	Actual Range
Attenuation @ 1310 nm (dB/km)	≤ 0.50	0.358–0.443
Attenuation @ 1550 nm (dB/km)	≤ 0.25	0.199–0.231
Mode-Field Dia.@1550 nm (μm)	7.60–8.60	7.70–8.37
Cable Cutoff Wavelength (nm)	≤ 1260	912–1227
Fitted Dispersion (psec/nm•km)		
@ 1530 nm	-10.0– -1.0	-9.4– -6.5
@1605 nm	-10.0– -1.0	-3.8– -1.5

Dispersion unshifted SMF control fibers were also used during this investigation. The SMF initial fiber data is given in Table 2.

Table 2. Standard SMF Fiber Data

	Spec	Actual Range*
Attenuation @ 1310 nm (dB/km)	≤ 0.40	0.328–0.331
Attenuation @ 1550 nm (dB/km)	≤ 0.30	0.187–0.189
Mode-Field Dia.@1310 nm (μm)	8.8 – 9.6	9.07– 9.29
Cable Cutoff Wavelength (nm)	≤ 1260	1186–1197

* NOTE: SMF control fibers were taken from three master lengths.

Selected Cable Designs

Three SCR cable designs having design features considered representative of products in commercial use were selected for evaluation: A non water blocked 128F (2-fiber ribbon/SZ stranded), a dry water blocked 100F (4-fiber ribbon /helically stranded), and a dry water blocked 400F (8-fiber ribbon/helically stranded). One cable of each design was manufactured containing a combination of ribbons of NZ-DSF with low negative dispersion, ribbons of dispersion unshifted SMF for comparison, and mechanical ribbons. Fiber types were mixed within slots, but were not mixed within the same ribbons. Ribbon types were positioned differently in each slot so that each ribbon type had exposure to all locations in the ribbon stack. A construction overview for each of these cables is given in Table 3. Cross-sections of the cables are given in Figures 1 – 3.

Table 3. Construction of Investigative Cables

Fiber Count	128F	100F	400F
...NZ-DSF	48	40	160
...Std. SMF	32	20	80
...Mechanical	48	40	160
Ribbon Type	2f	4f	8f
Cable OD	20.1 mm	12.75 mm	19.5 mm
Jacket Material	PE	PE	PE
Slotted Rod			
...Type	SZ	helical	helical
...No. of slots	8	5	5
...Rod material	PE	PE	PE
...Strength Member	stranded steel	solid steel	solid steel
Water Blocking	none	tape	tape

Testing and Results

All cables were OTDR tested bi-directionally at 1310 nm and 1550 nm before, during, and after temperature cycling. Cables were temperature cycled between –30 °C and 70 °C. Increases in fiber attenuation due to cabling and temperature cycling were chosen as indicators of fiber sensitivity. This data is summarized in Tables 4 - 6. Analysis of the increase in fiber attenuation as a result of cabling indicates that the NZ-DSF experienced no attenuation increases greater than 0.05 dB/km at 1310 nm or 1550 nm for any of the cables. During temperature cycling, attenuation increases of the NZ-DSF were also no greater than 0.05 dB/km at 1310 nm or 1550 nm for any of the cables. Performance of the NZ-DSF was comparable to that of the dispersion unshifted SMF, and is well within the range of values specified in the Japanese telecommunications industry for 1310 nm and 1550 nm.

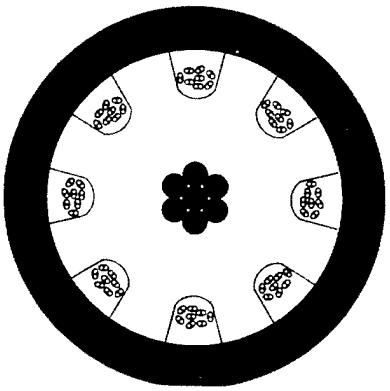


Figure 1. 128F Cable

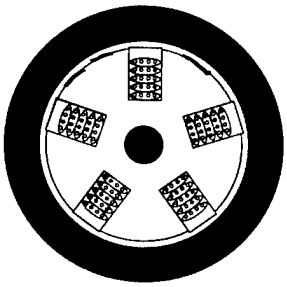


Figure 2. 100F Cable

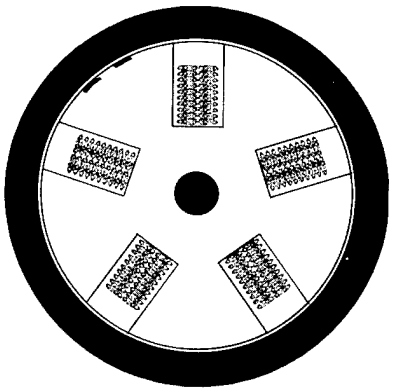


Figure 3. 400F Cable

Table 4. 128F Cable – Attenuation Deltas (dB/km) by Fiber Type

Fiber	Data	1310 nm	1550 nm
NZ-DSF	Cabling Delta	≤ 0.05	≤ 0.05
	70 °C Delta	≤ 0.05	≤ 0.05
	-30 °C Delta	≤ 0.05	≤ 0.05
SMF	Cabling Delta	≤ 0.05	≤ 0.05
	70 °C Delta	≤ 0.05	≤ 0.05
	-30 °C Delta	≤ 0.05	≤ 0.05

Table 5. 100F Cable – Attenuation Deltas (dB/km) by Fiber Type

Fiber	Data	1310 nm	1550 nm
NZ-DSF	Cabling Delta	≤ 0.05	≤ 0.05
	70 °C Delta	≤ 0.05	≤ 0.05
	-30 °C Delta	≤ 0.05	≤ 0.05
SMF	Cabling Delta	≤ 0.05	≤ 0.05
	70 °C Delta	≤ 0.05	≤ 0.05
	-30 °C Delta	≤ 0.05	≤ 0.05

Table 6. 400F Cable – Attenuation Deltas (dB/km) by Fiber Type

Fiber	Data	1310 nm	1550 nm
NZ-DSF	Cabling Delta	≤ 0.05	≤ 0.05
	70 °C Delta	≤ 0.05	≤ 0.05
	-30 °C Delta	≤ 0.05	≤ 0.05
SMF	Cabling Delta	≤ 0.05	≤ 0.05
	70 °C Delta	≤ 0.05	≤ 0.05
	-30 °C Delta	≤ 0.05	≤ 0.10

Conclusions

Based upon the results of this investigation, it is concluded that the NZ-DSF fiber used in this investigation is compatible with SCR cable designs, materials, and manufacturing processes currently in commercial use. Cabled attenuation performance of this fiber at 1310 nm and 1550 nm was well within market expectations.

Acknowledgments

The author would like to thank Neil Abernathy, Doug Coleman, and James Thompson for their technical support during this investigation.



Donald K. Hall
Corning Cable Systems
P.O. Box 489
Hickory, North Carolina 28603

Donald Hall received his B.S. degree in Chemical Engineering in 1983 from The University of Florida. He joined Siecor Corporation, now Corning Cable Systems, in 1996 where he worked for five years as a Senior Materials Engineer at Research, Development, and Engineering in Hickory, North Carolina. He recently assumed a new position as Product Specialist for Flame Retardant Cables.

Bridging the Last Mile With Fiber Optic Cables in Sewers

Dr. Jey K. Jeyapalan, P.E.
Pipeline Engineering Consultant
New Milford, Connecticut, USA
1-860-354-7299 jkjeyapalan@earthlink.net

Abstract
Deployment of metro fiber optic networks requires extensive construction, usually involving excavation of city streets. These excavations cause pollution, traffic hold-ups, economic loss, and unsafe conditions to the inhabitants in every city. Even worse, the repair of the streets after excavation rarely left the streets in acceptable condition once the job was finished that these forced mayors to issue moratoriums on new open cut excavations involved in the last mile work. The novel idea of leasing space inside of existing sewers and house connections by communication companies have a rather interesting appeal in that owners of existing sewers get to generate a new revenue stream and communication companies could install their fiber optic cables at an attractive cost. This paper traces the technological advances to build fiber networks inside of existing sewers, and makes an open invitation to those qualified engineers and scientists in the global market to send in their valuable input toward preparing engineering guidelines with ASCE sponsorship and consensus standards within ASTM.

Keywords
trenchless, rehabilitation, telecommunication, fiber optics, robots, point repair, cleaning, inspection, no-dig, last mile, broadband

1. Introduction
More than 100 million Americans are expected to telecommute to work by 2010. This will increase our productivity and quality of life significantly. This will also save energy, reduce pollution, and re-distribute the wealth and real estate values. For this to happen, we need to turn to existing underground infrastructure to build our communication networks, so that we could avoid additional congestion underground. America already has invested many trillions of dollars in the past century building over 1,400,000 km of sewers in the ground. Civil engineers have been responsible for planning, designing, constructing, operating, and maintaining this vast network of pipes below our feet. Civil engineers will have to start planning now toward working better with telecommunication engineers in making the information age come into full bloom so that any obstacles along the way could be removed with the team approach. This will involve sharing the underground so that the same sewers are used for multiple functions. The high-tech slowdown we have been experiencing due to deflationary monetary policy and excessive regulations that have driven many telecommunication companies into filing for bankruptcy protection have brought internet expansion to a halt. The absence of local fiber optic broadband loops in the last mile also impedes the optical Internet and indeed is a major contributing factor to this slowdown in the telecommunications industry. The Last-Mile is the section of a network that connects from the basement of an end-user building to the metro-area network that surrounds a city. Regulatory atmosphere has to change soon to make this financial arctic winter to thaw. One of such steps in the right direction that came from the American Congress in the past has been the Telecommunications Act of 1996, and almost everything changed in telephony. New entrants entered the market, and the financial markets seeking "the next big thing" facilitated entry with infusions of cash. Long Distance companies, Internet Service Providers, and entrepreneurs who had various levels of familiarity with the telecommunications business promised consumers faster connections, better service and lower rates. Deregulation was working everywhere but in the "last mile." New entrants quickly discovered that while they were experts at designing, marketing and selling services and proficient at installing switching equipment, they were less experienced and significantly disadvantaged when they tried to extend these new and improved services to the customer. The incumbent carriers still had a virtual monopoly on connectivity from the carrier's Point of Presence to the customer premise. Not surprisingly, the rates and the installation intervals offered by the incumbent to their new competitors for connection did little or nothing to facilitate a profit or quality customer service as part of the business plan. Some competitors tried alternate sources. These provided some opportunity for connectivity as well as some economic relief compared to the incumbent, but these resources were limited, and sometimes unavailable. Because of the above, after 5 years of opening up the local telephone access market, CLECs now claim 8% penetration. Those well funded among the new entrants tried to provide their own last-mile connectivity. Aside from the expense involved in such a venture, there was still one problem remained unsolved. Deployment of high-speed metropolitan area fiber optic network rings required extensive construction, usually involving excavation of city streets. These excavations caused pollution, traffic hold-ups, economic loss, and unsafe conditions to the inhabitants in every city. Even worse, the repair of the streets after excavation rarely left the streets in acceptable condition once the job was finished that these forced mayors to shut down most construction on the last mile project. A fiber optic network is fast only as fast as its weakest link. In recent years, and still today even, many companies are laying fiber optic cable between continents, countries and cities. Even building owners have started laying fiber from their rooftop to basement; however, the missing link is still the last mile. While the entire telecosm is in chaos, everyone in this industry should

ask the fundamental question: "where are the on and off ramps to the information superhighway most companies have been building for 2 decades in fiber optic cables?" The answer is " these do not exist to and from more than 97% of the commercial real estate all across of America and the picture is even more dismal for multiple tenant units and single family homes. Naturally these information superhighways with their points of origin permitting no passengers to get on with a similar tale at the other end would remain empty without anyone willing to pay the toll to the owners of such long haul networks, resulting in a mere 10% of the long haul fiber being lit. Given how we humans always take the path of least challenge have avoided bridging the last mile, which would be the hardest and the costliest, without ever realizing that without the ultimate on and off ramps, there would be no use for such long haul routes circling the continents. The so-called fiber glut in the backbone and long haul fiber networks are caused mostly due to the lack of last mile fiber to provide the final link between the premises and the long haul carriers of data, voice, and video. While the world anticipates for long to become a true virtual world, where time and distance could never become factors, the final link has been missing for too long for most of the inhabitants of the world. CityNet telecommunications is a leader in introducing an unprecedented idea, in which it will create true broadband cities all across America and Europe using the sewers as the preferred path for building the last mile fiber network.

The in-sewer deployment system operates without impact to either the sewer operation or to the streets above. In fact, this process most often leaves the sewer in better condition than before the installation. In addition to its non-invasive advantages, preserving transportation infrastructure with no negative impact on the sewer, the in-sewer deployment process is also efficient and cost effective. This deployment technique is less expensive than traditional fiber network construction, but the major advantage with the last-mile network deployment technique is speed.

2. Historical Background

Japanese developed a robot 13 years ago to install glass fibers initially in Tokyo sewers [6]. Tokyo Metro alone has more than 800 km of fiber in the sewer, with over 150 km installed by robots. The original robots had options to either be self-driven or operated by winches. Given most of the sewers in Japan were made of centrifugally cast reinforced concrete pipe, drilling into the pipe wall required significant amount of power through the umbilical cable supplying water, air, electricity, and communication circuits. When the Tokyo Metro discovered that it was better to conserve power, self-driven robots were not the preferred option.

BerliKomm owned by Berlin Water had an ambitious plan in 1997, in that it would provide each customer in Berlin with a broadband connection within 30 days of asking. Berlin water turned to 3 Japanese robots sold by Nippon Hume initially by setting up a new company named Robotic Cabling GmbH Kabelverlegung (RCC) owned with Marubeni and Nippon Hume and installed about 1.5 km of glass fibers in its own combined sewers in Berlin in the winter of 1998. The Japanese robots used by Berlin water came in 3 sizes for pipes of 250-350 mm, 400-450 mm, and 500-1200mm. The robot was steered by a control unit but was not driven by its own power. Instead, they were pulled using winches through the manholes. A special drill was used to cut a hole 6 mm dia. 15 mm deep for the J-hook anchor of the cable with its 2 part resin system that hardens in the hole once deployed after placing the fiber optic cable in the J-hook. Berlin Water as of January 2000 solely owns this business entity and has replaced the Japanese robots with those manufactured in Germany by JT Elektronik GmbH where the same robot could work in pipes of 250 to 1200 mm, provided the right undercarriage is used. Berlin water returned the two units of second generation robots back to Nippon Hume, but kept the third unit of the first generation. A change from the version of the Japanese robots Berlin used is that the 3 units assembled in Berlin could propel it once inside the sewers, in a way no different from the robots Japanese had in their first generation for Tokyo Metro, installing the cable at speeds as high as 200 m/day under optimal conditions as given in [2,3]. Unfortunately, the Berlin drill and dowel anchor robot has eliminated the use of the 2 part resin bonding the Japanese system uses, increasing the likelihood for the anchors to drop out of the holes in which they are inserted along with the fiber optic cable to the floor of the sewer pipe.

Ka-te, Nippon Hume, and RCC Robots together did globally about 50% of the entire 1000 km of sewers carrying fiber optic cables as given in [5]. The robots by Nippon Hume did work primarily in Tokyo, Berlin, and Copenhagen for a total length of over 200 km with some projects going back to 1988. RCC's technology has been used in Berlin in pipes owned by its owner during the past 3 years for a total of about 50 km and another 5 km in Canada on test sections. Ka-te's conduit and clamp technology on the other hand, perhaps due to its non-invasive nature, has built a rather broader track record from installations in Albuquerque, Amsterdam, Atlanta, Bern, Hamburg, Hanau, Hanover, Indianapolis. Landau, Madrid, Munich, Okayama, Regensberg, Soderacra, Vienna, Yokohama, and Zurich. The idea for CityNet was formed in 1999 using Alcatel, Ka-te, CableRunner, and Carter Burgess as partners [4]. CityNet Telecommunications will pay lease revenue to the city to use the sewer pipes for delivering the fiber optic cables directly into buildings. As an additional benefit, CityNet also will monitor the condition of the sewers it uses. CityNet will deliver dark fiber optic networks to telecom carriers and network service providers, who will then activate and provide services to building tenants. CityNet uses a small computer-driven robot shown in Figure 1, called Sewer Access Module (SAM) equipped with CCTV cameras to install alloy rings to support the fiber optic cables inside of the sewer pipes. CityNet has already purchased 53 sets of robots, as part of its agreement with Ka-Te using venture funding in the amount of $ 375 million from 2 rounds of financing. Work is underway in multiple locations in America with contracts in hand with the Cities of Omaha, Indianapolis, St Paul, Scottsdale, Albuquerque, Forth Worth, Pittsburgh, and Vienna, Austria. It is anticipated that by the time this manuscript is in print, several more cities would be under contract with CityNet.

3. Citynet's Technology

The technology used by CityNet telecom is that under the name FAST in Europe as given in [1]. The partnership there is formed among Alcatel, Ka-Te, and IK-T. The work done by this group in Europe amounted to a few small pilot projects totaling about 7 km with the exception of the City of Hamburg, where over 50 km of work has been underway over a period of 3 years. When CityNet approached this European group for large-scale deployment in

America and Europe, it was a perfect match between the two entities. The technology allows point-to-point connections while being able to form backbone connections as either loop networks or mesh networks as well as connections in many different patterns to meet varying customer demands. Up to 9 fiber optic cables in alloy conduits can be installed side by side in a sewer system. These cables are of either 144 fibers, arranged in 6 bundles of 24 each or 72 fibers arranged in 6 bundles with 12 fibers. The outer diameter of these bundled cables in protective conduits measures on the order of 11.5 to 15.5 mm. The speed of installation is 150 m/day in non-man entry pipes and 300 m/day for man entry sewers for anywhere from 1 to 9 cables in the sewers. Work could start rather quickly compared to open-cut work. Most work is done at night when the traffic is low and the flow in the sewer is at its daily minimum. This system can install fiber optic transmission networks in non-man-entry sewage pipes with diameters from 200 to 700mm. The Ka-Te special installation robot has been developed for the laying of protective conduits carrying fiber optic cables in non-man entry sewage pipes as shown in Figure 2. In order to install a clip ring, the spring box on the clip ring is unlocked, so that the ring is snugly pushed against the sewer pipe walls. The cables are tightly fixed to the inside sewer wall without any drilling, cutting or screwing. Depending on the requirements of the communication network, clip rings for sewers with a diameter of 300mm and above can be equipped with up to 9 clips, so that up to 9 protective conduits or 9 fiber optic cables can be mounted. Sewers with a nominal diameter of 200 to 250 mm can be equipped with a maximum of 3 clips. The planning of the work commences with a CCTV inspection of the sewer line. All maintenance work needed are carried out at the onset before installing any cable conduits. In the next step, the clip rings are installed in the sewer by means of the robot. Each ring is fitted with 3 to 9 clips that are used to fasten the steel conduit that will house the single mode fiber optic cable. The clamps are loaded into a magazine that is attached to the robot, which then travels through the sewer, using a laser guide to precisely place each ring in its prescribed location within the sewer – approximately every 1.5 m apart. Once all the rings are placed, SAM crawls back out of the sewer and is fitted with another head, which transports the conduit through the sewer. Once again using the laser guides, SAM fastens the conduit to the clips, locking it securely in place. When this part of the process is completed, the conduit is ready to accept the fiber optics cable. Using a push-pull method, the cable is threaded through the conduit, and then terminated to a patch panel for use by carrier customers. Single mode fiber was selected because it offers the best mix of high bandwidth capability and wide range compatibility with carrier customer systems. Following installation, CityNet then routinely inspects the sewers and provides any necessary cleaning to preserve the integrity of the network and the function of the sewer. Furthermore, the existing sewer pipe structural integrity remains unscathed.

Man- entry sewer pipes are all pipes with a diameter of 800mm and above. By means of expansion bolts and nuts, long channels of fiber optic cable trays are bolted to the inside sewer wall, at a desired center to center distance using a small crew-carrying sled. The small tray could hold 2,200 fibers, while the jumbo tray could handle 5,000. Both trays could be used around curves by cutting and installing shorter lengths. Plastic binders are used at the tray joints. For fixing the expansion bolt, a hole must be drilled into the sewer wall, which poses no major structural problems due to the adequate wall thickness in sewers with a 800mm dia. and above. The cables can be added in the future as demand for the fiber count increases. In Vienna alone, there is over 300 km of installation in the sewers using a fair amount of Corning cables of 8 of 144 fibers and 4 of 288 fibers.

The sewer manholes form an important part of this technology due to them serving as major access ports. Junction boxes and extra cable lengths are stored in the manholes. These manholes also serve as customer connection points. The initial plan for CityNet is to target buildings, which meet certain criteria such as minimum floor area, number of tenants, building owners' needs, type of tenants, existing communication services in the area, etc. A ring topology is used to service the buildings to meet redundancy requirements, optimum bandwidth needs, the tree and branch geometry provided for in the sewer paths, future expansion needs, etc. The splice points on these mini-rings are located off the main traffic to provide a safe zone for access for customer connections and for easy O&M. Some connections from the street sewer fiber optic ring to the premises will be through the laterals in the sewer system, while others will be through pipes installed for carrying the fiber. Often the mini-rings are designed with 2 to 4 aggregation points for the fiber bundles, where most of the fibers in the mini-ring are available for customer connections as shown in Figure 3.

By September 2001, CityNet would have completed the first mini-ring of length 6,000 m in Albuquerque, and would have the fiber lit for paying customers. More than 60% of the pipes forming this ring would be storm sewers and the remainder would be of sanitary sewers with sizes 200 to 1830 mm requiring man-accessible technology for 30% of the total fiber network. Cleaning and mapping of the current condition of the sewer paths have been completed at other sites.

4. Pipe Selection Criteria

Operating a fiber optic network in the sewers poses its own challenges. Proper civil engineering input is essential in the selection of the suitable sewer system for deployment. The factors to consider in selecting the right sewer path are:

Access to the Sewer: The primary access to the sewer for fiber cable installation using a robot is through the manholes at both ends of the reach. It is desirable that the length of the reach is shorter than 135 m, so that the umbilical cable needed by the robot for the supply of air, electricity, and communications circuits could extend from one end of the reach to the other. If man-accessible pipes were chosen, then this limitation would not apply.

Hydraulics of the Sewer: Although engineers intend not to have any leakage of sewage from the sewers, with aging and inadequate maintenance, most sewers have leaking joints during the design life of the sewer. Given this history of performance, the designers have been able to count on only 85% of the actual flow area to convey the flow, due to a loss of some sewage through leaking joints. An estimate of the flow conditions under the worst possible scenario based on past flow records in that sewer needs to be done before the sewer is considered for fiber optic cable installation. Allowance also need to be made for any future plans the sewer owner might have to either add new

discharges or divert some of the existing flows from or to another part of the sewer network. Engineering data used in the evaluation should be based on actual sewer sizes and actual flow conditions rather than those based on original design or as-built drawings.

Structural Capacity of the Sewer: An evaluation of the structural capacity of the sewer to carry the soil load, groundwater load, and live load need to be conducted. This is to ensure that the current condition of the sewer is adequate to house the fiber optic network. The decision whether and when to rehabilitate the sewer if the current condition is found to be questionable need to be carefully taken using all necessary engineering data. If the cost and time duration of rehabilitating the sewer would result in a significant delay and added financial burden to either the sewer owner or the fiber optic network owner, an alternate route for the intended fiber optic mini-ring shall be pursued to ensure that the engineering criteria to be met are not relaxed.

Compatibility of the Sewer Wall: It is not possible to work with certain sewer wall materials depending on the fiber installation technology used. For example, it is not possible to use the drill and dowel method in several pipe wall materials and in old sewers, without having some concern for damage to the pipe wall from structural and hydraulic points of view. The clamp and conduit system on the other hand, can be used in most pipe materials given its non-invasive method of installation.

Presence of Excessive Grease in the Sewer: During the cleaning and inspection process, sufficient grease should be removed to permit inspection of the pipes. Sections of pipe with grease accumulations of over a suitable thickness within one year of cleaning should not be considered candidates for fiber optic system installation until proper remedial action is taken. Remedial action includes tracing source of grease and enacting/enforcing ordnances to require use of grease traps and/or oil separators.

Presence of Excessive Chemical Reagents in the Sewage: Sewage carries many chemical reagents and the longevity of the fiber deployment materials and components in all of such chemicals need to be tested for compatibility before using.

Presence of Excessive Calcium Deposits on the Sewer Walls: Fiber optic systems should not be deployed in sewers with excessive calcium deposition.

Presence of Joint Separations/Offsets: Joint separations/offsets can lead to both infiltration and exfiltration. Structural damage to the sewer may result from pipe bedding material being transported into the pipe.

Presence of Excessive Root Intrusion: Sewers should be free of excessive root intrusion to be eligible for installation of a fiber optic system. Excessive root intrusion is defined as infestation with roots, which will cause 5% blockage of the sewer within the next 10 years, if left untreated.

Condition of the Manholes: Manholes should be in an acceptable physical condition. Additionally, the portions of the manhole that will receive cable supports should be structurally sound.

Condition and Frequency of Lateral Connections: The condition of the lateral connections to the mainline sewer is important both to the hydraulic functioning of the sewer and to the installation and operation of the fiber optic system. The laterals should connect to the intercepting sewer by means of a wye fitting or transition section approved by the municipality. The joint at the intersection should be watertight and should be able to pass a suitable air test. Cracks or offsets can cause infiltration and/or erosion to pipe bedding materials and eventual structural failure. Cracked or offset lateral connections discovered as a result of CCTV inspection should be repaired by suitable techniques to pass an air test. Laterals that protrude into the sewer (i.e. "break-in" laterals) can hinder both normal operations and maintenance of the sewer and deployment of a fiber optic system. Protrusions over 25 mm should be removed and the joint sealed before installation proceeds. Laterals intersecting the same side of the interceptor sewer should be spaced no closer than a desirable distance on center to center. Laterals intersecting from opposite sides of the interceptor should be spaced no closer than a certain distance on center to center.

Sewer Cleaning After Installation of Fiber Optic Cable: Sewers need to be cleaned periodically as part of their maintenance. Once fiber optic cables are installed in the sewer, special precautions must be taken in choosing and applying suitable cleaning methods, which would not cause damage either to the sewer wall or the fiber optic cables.

Sewer Inspection After Installation of Fiber Optic Cable: Periodic maintenance of the sewer will also involve inspection of the internal condition of the sewer system once the fiber optic cables are installed. Special precautions need to be taken in choosing and applying suitable technology for sewer system inspection in order not to cause damage to either the sewer walls or the fiber optic cables.

Sewer Maintenance After Installation of Fiber Optic Cable: Sewers require periodic maintenance involving anything from point repairs, grouting, relining, to total replacement. The current condition of the sewer system and its need for repair or rehabilitation during the design life of the fiber optic network shall be carefully evaluated. The ability of the sewer owner to keep the sewer in serviceable condition and the ability of the sewer owner to be able to do one or more forms of necessary maintenance, repair, or rehabilitation need to be considered in the selection of the suitable components of the sewer system for inclusion in the routes for installing fiber optic networks.

5. Benefits

Detailed engineering studies indicate that the reduction of flow area of the sewer waterway is minimal. The use of 3 to 9 conduits of size 11.5 to 15.5 mm would take up to 3% of the flow area in sewers of sizes in the range of 200 to 700 mm dia. This installation system does not damage the pipe walls made of clay, concrete, and plastics, when properly applied. Pipe inspections by means of CCTV robots can be carried out as before. Sewer cleaning can be done as usual with high-pressure washing and the fiber optic installations are not disturbed. Inspections proved that no grit collected at the deployment components. These installations can be dismantled again without leaving any damage on the sewer pipe walls. Sewer systems with installed fiber cables

can be maintained by a number of appropriate trenchless rehab methods. The operation of the sewer system can be continued in the usual fashion. Leak tests such as smoke testing can be carried out without major problems. The sewer owner is able to generate additional revenue from the lease of the underground sewer network. Cost is minimal due to the use of robots to install the cables.

6. Criteria for Winners

There is more than one player already in this business of installing the fiber optic cables inside of sewers. Here are some barriers for all of them to cross and this list may very well provide the crucial yardsticks that will separate the first mover-winner from the rest in the pack. There are barriers in America toward either a new material or technology in the sewer industry entering the market place. To name a few:

- Has the new material or technology been codified into various engineering task groups at work developing new or updating existing consensus standards?
- Has the new material or technology been used to generate sufficient experience to produce long enough a track record?
- Has the new material or technology been tested by independent laboratories for validation of the vendors' claims?
- Has the material or technology vendor working with qualified installers or contractors who are either licensed or pre-qualified to perform work within the jurisdiction of the sewer agency?
- Will the deployment technology cause damage to the structural or hydraulic integrity of the sewer?
- Does the new material or technology have any resemblance what so ever to another material or technology that had been tried in the prior years or decades and found to be problematic?
- Does the new material or technology vendor aware of the capabilities and limitations of their offering in the market place?
- Does the vendor offer a long-term commitment to the sewer owner and to the customers who lease the fiber networks?
- Most importantly, is the vendor able to deliver materials and methods in line with its representation and does it have the capability to resolve customer complaints in an expeditious fashion?

7. Standardization

Efforts are underway to develop consensus standards within ASTM by bringing industry experts together. ASTM provides a legal, administrative, and publications forum within which producers, users, ultimate consumers, and representatives of government and academia can meet on a common ground to develop standards that best meet the needs of all concerned. The task groups initiate draft standards, which sub and main committees ballot following the Regulations Governing ASTM Technical Committees. The ASTM procedures ensure that the standards produced are technically sound and rest on a solid legal foundation with appropriate concern for legal issues. The group that met during the past 6 months unanimously agreed on the need to establish an ASTM standards development activity and approved the title: "New ASTM Committee on Installing and Operating Fiber Optic Cables in Existing Sewer Systems." The working group has already identified the following types of standards needed to guide this new industry:

1. Standard practice on sewer selection criteria for fiber deployment.
2. Standard test methods on materials, components, longevity.
3. Standard specification on documentation.
4. Standard specification on network topology.
5. Standard specification on safety, access rights, and construction.
6. Standard guideline on decision analysis on economic factors.
7. Standard practice on design, operation, and maintenance.

Similar efforts are underway to develop engineering guidelines within ASCE for this 130,000 member organization of civil engineers to provide their input to the telecommunications industry in this new discipline.

8. Conclusions

1. The installation of fiber optic cables inside of sewers using robots is a major break through in sharing the underground space to form utility corridors. Those in this business should recognize that the trenchless pipeline renovation business in America has matured significantly in the past 10 years. Although more cities are willing to consider this construction option, overall only 30 % of the pipe renovation work needed is done using trench-less methods. The city officials, the engineers, the American public, and the businesses want the least disruption and inconvenience in their daily lives. No doubt that the fiber in the sewer business will renew enthusiasm for using trenchless technology tools in sewer work.
2. CityNet's business plan calls for using the most appropriate sewer rehabilitation technology based on the current condition of the sewer network in which the CityNet's fiber will be deployed. Because most valuable fiber optic network gear are housed in the sewers, laterals, and manholes, it is no longer possible for us to claim "sewers are out of our sight; therefore, they are out of our minds."
3. First mover advantage is always there for certain companies. Once a leader in this field, the odds are in favor for that company to stay as a leader provided the management of that company is nimble, is re-inventing itself with changing times and demands of the clients and is continuing to add the best talent in its work force. Therefore the business of "bridging the last mile divide," by installing fiber optic cables inside of existing sewers will elect a major winner early on based on the overall trenchless technology landscape.
4. The factors which will continue to provide momentum for the market are:
   - Aging underground infrastructure
   - Doing more work with less funds
   - Protecting the environment
   - Increasing congestion in urban and suburban centers
   - Faster rate of technology transfer and information
   - Privatization of utility companies
5. A leading player like CityNet Telecom will initially market to the city major and as more and more of the underground become the managed assets for the city hall by contracts executed by private companies, CityNet would have to be

nimble enough to market to private companies to have entry into existing sewer networks.

6. The present system of licensing of new technology and the relationship of licensor-licensee will turn sour in many cases in America and will go completely out-of-date due to contractors unwilling to pay license fees when they face stiffer competition in price wars.
7. More emphasis will be placed on evaluating the current condition of the entire pipeline network for cost effective maintenance and renovation strategies much along the lines CityNet Telecom is envisioning. More localized repair work would be the preferred option of private companies managing the network for public entities.
8. Not all sewer lines are amenable for installing fiber optic cables and companies which support strong engineering talent on their staff will focus their attention to sewer lines which would satisfy the proper engineering criteria. Others will make costly mistakes and learn as they go and expect someone else to pay for their lessons.
9. The in-sewer deployment offers a win-win situation for all parties involved. For telecom carriers and network service providers, it's a true, end-to-end last-mile fiber optic network, which they control. For cities, it's a unique and powerful economic development tool, added revenue from an existing infrastructure, and of course protection from damage to roads and disruptions to traffic. And for building owners, it provides a major upgrade for their buildings for free, and in turn brings extra value to the buildings
10. Finally the promises of 1996 are coming to pass. Access will be available without disrupting other activities. Carriers, both incumbent and competitive will be able to deliver on their promises of lower rates, higher speeds and better service. The last mile instead of being slow and painful with barriers and potholes will turn to a smooth ride.
11. The author is spearheading a Task Committee within ASCE to develop Engineering Guidelines on Installing and Operating Fiber Optic Cables in Sewers. Likewise, he is leading standardization efforts within ASTM. Anyone with information, data, or case histories that would help these committees carry out its mission to serve the need in this new industry is invited to send along to the author for possible inclusion.

9. Acknowledgements

The author acknowledges the following assistance during the past 15 months. Mr. Michael Hullihan of Gannett Fleming wrote several sections on pipe selection criteria as part of a proposed ASTM standard. Messrs. Drew Azzara and Dan Schultz of ASTM have provided enormous support at ASTM. Messrs. Robert Berger, Steve Merrill, Emilio Pardo, Cyrus Bamji, Ken Rakip, Lee Allentuck, Robert Egan, and Wayne Hackett and Ms. Robin Cary-Pedace provided much inspiration and help. Messrs. Buddy Barnes, and Roger Reich of Carter-Burgess offered many useful discussions. Dr. Hans Bunschi of Ka-te Robotic Systems, Mr. Berthold Roth of CableRunner, Messrs. Curt Hutton, Ray Lovie, Ken Buddington, and Robert Jeyaseelan, Drs Hans-Detlef Leppert and Peter Hermann of Alcatel Optical Fiber provided valuable data on their technologies. Messrs. Patrick Brown, Keith Shaneman, Jorge Serrano, and Lothar Finzel of Corning Cable systems provided useful technical data. Dr. Klaus Beyer of RCC shared the details of the history of RCC, its capabilities, and their record in Berlin sewers. Nippon Hume Corporation, Marubeni Corporation and the Tokyo Metro Government helped the author in understanding the evolution of their robot technology from 1988 to date and shared the track record on the fiber cables in sewers from the projects in Japan, Berlin, and Copenhagen. Mr. Dan Gonos, a telecom consultant, provided timely help and encouragement through the past year. Professor Dietrich Stein from Ruhr University and Professor Jun Tohda from Osaka City University provided valuable technical guidance. CityNet Telecommunications funded the author's work in part.

10. References

[1] Alcatel, Ka-Te, and IK-T (1998) "FAST - Das schneille Modulsystem fur zukunftssichere Telekommunikations-Kabelnetze Informationschricht der Fa. Alcatel Kabel AG, Monchengladbach.

[2] Beyer, Klaus (2000) "Einbau Von Kommunikationskabeln in Abwasserkanalen," Proceedings of the 6th International Pipeline Construction Show with Trade Fair, Hamburg, Germany, June; pp. 370-379.

[3] Beyer, Klaus (2001) "Personal Communications," Berlin, Feb.

[4] CityNet Telecommunications, Inc. (2000) Personal communications, published articles, press releases, and their web site: www.citynettelecom.com

[5] GSTT Nr. 12(1999) "Leitngsverlegung in vorhandenen Netzen Tiel 1: Kabelverlegng in Kanalnetzen, Dec.

[6] Nakazato, T. (1997) "Sewer Optic Fibre Networks in Tokyo," WQI, Feb, pp. 16-18



Dr. Jey K. Jeyapalan, P.E.
9 Sundance Road
New Milford, Connecticut, USA 06776-3840

Dr. Jeyapalan graduated from the University of California at Berkeley and was a civil engineering professor for 10 years. Dr. Jeyapalan has been an international consultant for 30 years on design, engineering, construction, and standardization for a wide range of technology on fiber optic networks in pipelines, trenchless works, pipeline rehabilitation, and failure investigation. He has testified as an expert on numerous disputes, claims, mediations, arbitrations, and lawsuits on failures of pipelines for water, sewage, oil, gas, chemicals, desalination, and hydropower.

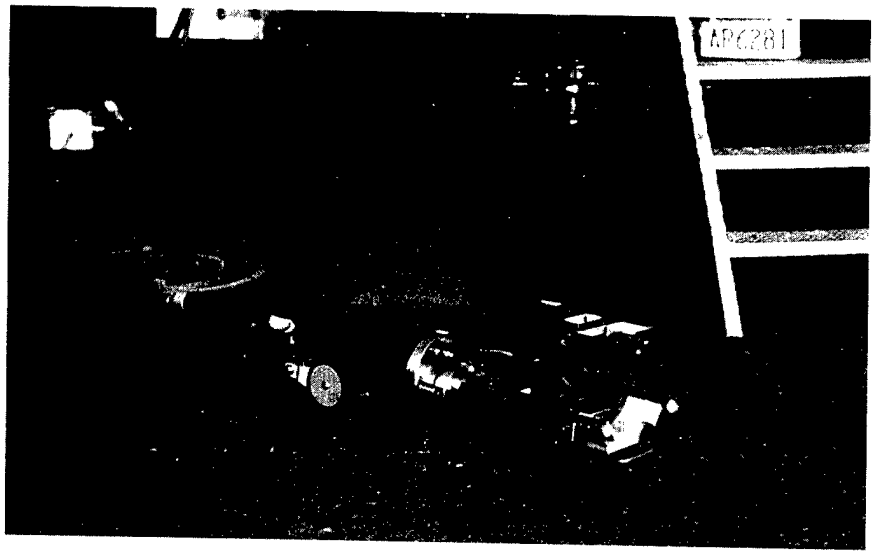


Figure 1. Fiber Optic Cable Robot Before Entering the Sewer System

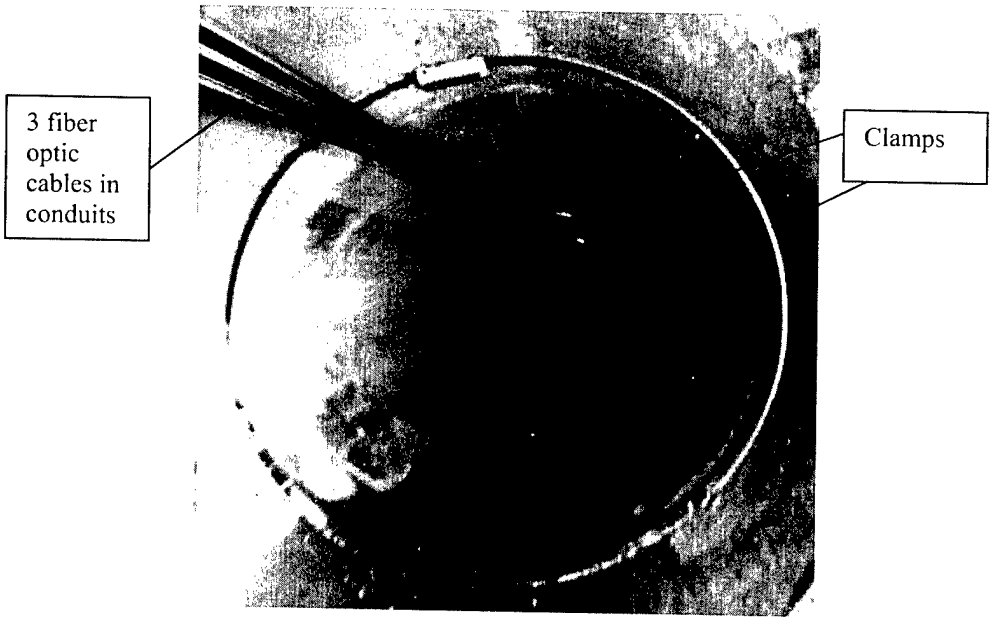


Figure 2. Fiber Optic Cables in a Sewer System

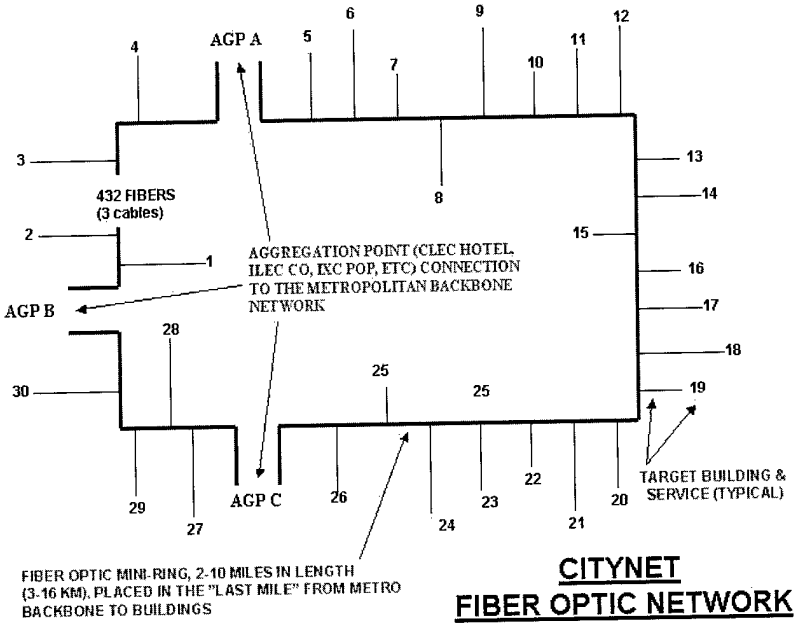


Figure 3. Last Mile Mini-Ring in a Sewer System

New SZ-slotted Core Cable with 4-fiber Ribbons and Single Fibers for Local Network

Masayoshi Yamanaka, Naoki Okada, Michio Suematsu, Matsuhiro Miyamoto
Research and development department, Telecommunication cable division
1440, Mutsuzaki, Sakura-shi, Chiba, Japan
+81-43-484-3945 · masayoshi@s.fujikura.co.jp

Abstract

We developed a new SZ-slotted core cable composed of 4-fiber ribbons and single fibers for local networks. Four-fiber ribbons and bundles of single fibers are accommodated in different slots. A feature of the new cable is the efficient use of fibers for mid-span branching. At a mid-span access point, the 4-fiber ribbon is split into single fibers which are then spliced to a drop wire or a splitter. In case of the cable composed of only 4-fiber ribbons, the fibers not dropped become dark ones. While in case of the cable composed of 4-fiber ribbons and single fibers, the fibers not used for branching are spliced to the single fibers accommodated in the cable. These single fibers are preferentially used for branching downstream of the mid-span access point. This method greatly enhances the efficiency of utilization of fibers. According to this cable design concept, we manufactured a trial cable. The trial cable exhibited excellent performance.

Keywords

Mid-span access; SZ-slotted rod; 4-fiber ribbons; Single fiber.

1. Introduction

In recent years, optical access networks have been constructed to implement FTTH network systems. For economical construction of networks, the mid-span access capability of optical cable is very important. In Japan, SZ-slotted core cables with 4-fiber ribbons are finding applications in access networks because of easy mid-span access and efficient mass splicing of ribbons [1][2]. A schematic view of mid-span branching in the SZ-slotted rod structure is shown in Figure 1.

At a mid-span access point, the 4-fiber ribbon is split into four single fibers which are then spliced to a drop wire or a splitter. All the fibers split from the 4-fiber ribbon are not always used for dropping at the mid-span access point. If only one fiber is used, the three remaining fibers become dark ones, thus decreasing the rate of utilization of fibers to 25% or less.

2. Construction of Access Network

2.1 Network model

In order to compare an SZ-slotted core cable with 4-fiber ribbons and single fibers (hereinafter called "4-fiber ribbon and single-fiber type cable") and an SZ-slotted core cable with 4-fiber ribbons (hereinafter called "4-fiber ribbon type cable") as to the

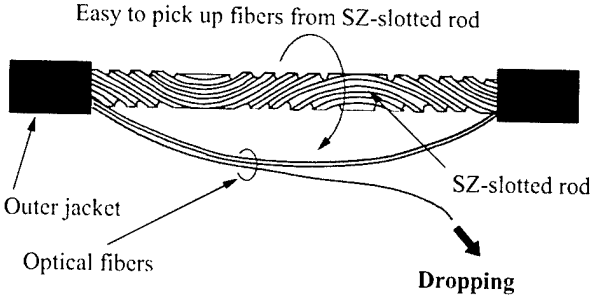


Figure 1. Schematic view of mid-span access operation

efficiency of utilization of fibers, we built a simple network model as shown in Figure 2. In the figure, there are three mid-span access points provided to drop a maximum of four fibers. The number of squares shown by the solid line indicates the number of fibers decided to be dropped. At mid-span access point 1 for example, one fiber is shown dropped. The figure illustrates the

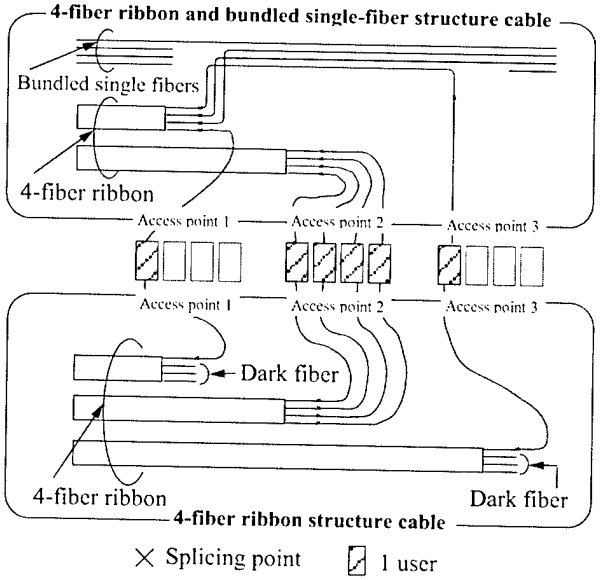


Figure 2. Network model – Comparison of 4-fiber ribbon structure with 4-fiber ribbon structure and bundled single-fiber structure

state of fibers branched for both the 4-fiber ribbon type cable and the 4-fiber ribbon and single-fiber type cable.

2.2 Constructing the network using 4-fiber ribbon structure cable

In the network constructed using the 4-fiber ribbon type cable, only one fiber in the 4-fiber ribbon is dropped at mid-span access point 1. The three remaining fibers become dark ones. At mid-span access point 2, all the four fibers being dropped, there are no dark fibers. At mid-span access point 3, dark fibers are produced as is the case at mid-span access point 1. In this model, six out of the 12 fibers become dark ones.

2.3 Constructing the network using 4-fiber ribbon and single-fiber structure cable

In the network constructed using the 4-fiber ribbon and single-fiber type cable, the three fibers other than the one used for dropping are spliced to the single fibers accommodated in the same cable. One of these single fibers is dropped at mid-span access point 3. At that time, no dark fibers are produced.

The spliced single fibers serve as a bridge linking the fibers left unused at a mid-span access point to somewhere downstream of it. Preferential dropping of the single fibers at the mid-span access point enables efficient use of fibers. The single fibers dropped at a mid-span access point can be reused downstream of it.

So far, there has been information reporting on fiber ribbons able to be branched into single fibers [3] or single-fiber units easy to split [4][5]. Use of the 4-fiber ribbon and single-fiber type cable introduced here enables efficient use of fibers even if it is composed of units unable to be split into single fibers.

3. Cable design

3.1 Cable structure

The SZ-slotted rod structure was applied to provide easy mid-span access. Bundles of single fibers are accommodated together in one of the slots in the 4-fiber ribbon type SZ-slotted core cable put into practical use and field proven. The single fibers are bundled for fiber identification and prevention of fiber movement after cable laying.

3.2 Splicing single fibers to ribbon

In order to construct the network using the cable proposed in this paper, it is necessary to splice plural single fibers together. In this case, there is the method of ribbonizing plural single fibers. Shaping these fibers into a ribbon before splicing makes it possible to reduce the required time for splicing. Figure 3 shows a device for shaping single fibers into a ribbon. This device aligns 0.25UV single fibers with the 4-fiber ribbon and coats the fibers with an adhesive to shape them into a ribbon. Losses due to splicing the obtained ribbon together are shown in Figure 4. Use of this device enables speedy, simple and reliable splicing of the plural single fibers.

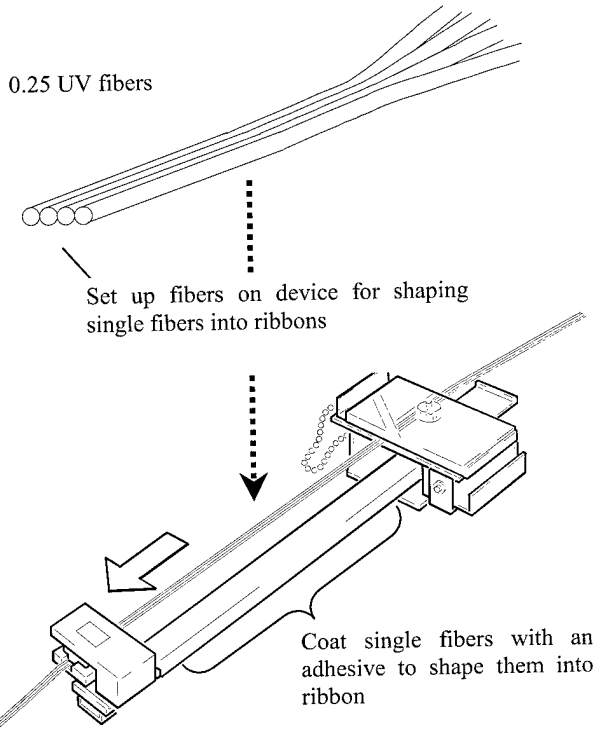


Figure 3. Apparatus transform single-fibers into ribbon fiber

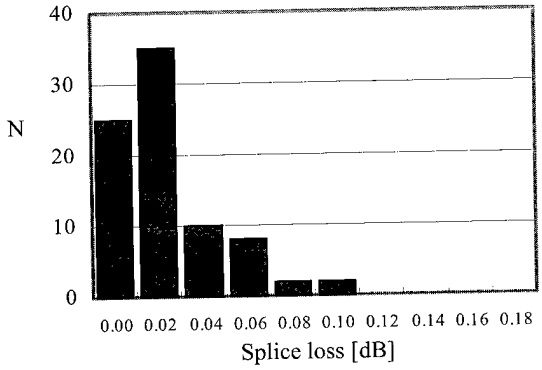


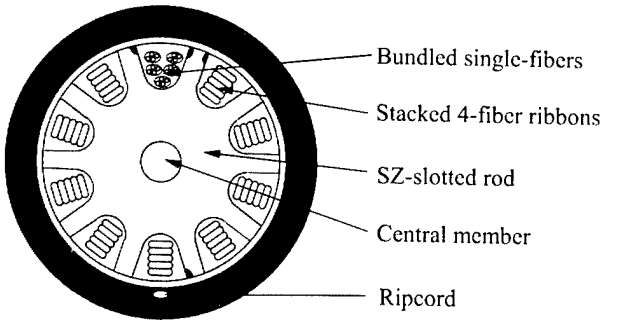
Figure 4. Loss due to splicing obtained ribbon to 4-fiber ribbon

4. Trial cable

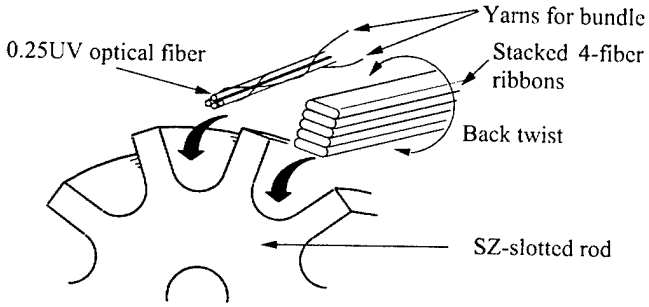
4.1 Trial cable structure

According to the cable design concept, we manufactured a trial 200-fiber type SZ-slotted core cable. The cross sectional view of the trial cable is shown in Figure 6. The 4-fiber ribbon type SZ-slotted rod structure currently in use was applied to provide easy mid-span access [6][7]. Five 4-fiber ribbons stacked on top of each other are accommodated in 9 slots of the rod, and five bundles of single fibers are accommodated together in one slot. Thus the trial cable comprises a total of 200 fibers.

The stacked 4-fiber ribbons are given a back twist to maintain loss performance [8]. In addition, we established the technology of bundling single fibers and accommodating them in the slot simultaneously with accommodating stacked 4-fiber ribbons in the respective slots.



Trial 200-fiber SZ-slotted cable



Insertion of bundled single-fibers and 4-fiber ribbons in SZ-stranding slots

Figure 5. Cross sectional view of trial 200-fiber SZ-slotted core cable with 4-fiber ribbons and bundled single-fibers

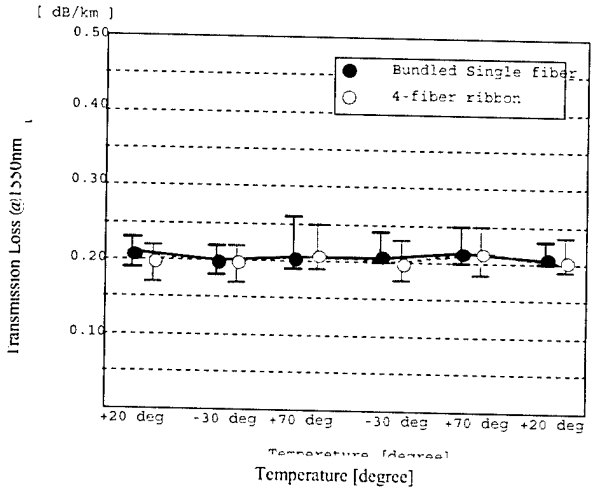
4.2 Cable performance

4.2.1 Mid-span access operation

We tried mid-span access on the trial cable. Changes in optical loss during the mid-span access operation were measured at a wavelength of 1550 nm. As it has been already reported that the cable structure composed of 4-fiber ribbons provides an excellent mid-span access capability [6], we directed special attention to handling of the bundled single fibers. The sampling frequency to measure loss changes was taken as 1 msec. The mid-span access operation comprises the steps: opening the sheath, removing the wrapping tape, picking out the bundles of fibers, cutting the bundling yarns, and selecting the aimed fiber. During the mid-span operation, loss changes were not observed at all. The amount of fiber slack was sufficient for the mid-span access operation. All this proves that the fiber branching operation is easy to perform.

4.2.2 Temperature cycling test

In order to predict the long-term reliability of cable performance, we subjected the trial cable to a heat-cycle test. The temperature-cycle pattern for this test and the obtained results are summarized in Figure 6. During the test, loss changes in both the 4-fiber ribbons and the bundled single fibers were less than 0.06 dB/km at 1550 nm.



4.2.3 Mechanical tests

The new SZ-slotted core cable with 4-fiber ribbons and bundled single fibers was tested to the mechanical test requirements of the international standard IEC 60794-1. The test results are given in Table 1. As seen from the table, the trial cable showed no significant loss changes in all tests.

Table 1. Mechanical tests and results

Cable Test	Test Level	Max loss increase
Impact	9.8N *1m	0.03dB
Crush	1980N/100mm	0.01dB
Torsion	1m * 90 degrees	0.01dB
Repeated bending	R:160mm 90degrees 10 cycle	0.00dB

5. Conclusions

We have a new SZ-slotted core cable composed of 4-fiber ribbons and single fibers for local networks. 4-fiber ribbons and bundles of single fibers are accommodated in different slots. A feature of the new cable is the efficient use of fibers for mid-span branching.

We built a simple network model in order to compare a 4-fiber ribbon and single-fiber type cable as to the efficiency of utilization of fibers. It became clear that the newly developed optical cable enables efficient use of fibers for mid-span branching.

According to this cable design concept, we manufactured a trial 200-fiber SZ-slotted core cable. The trial cable exhibited excellent performance.

6. References

[1] H. Iwata, et al., "Design of Aerial Optical Fiber Cable System Suitable for Easy Branching", *Proc.of 46th IWCS*, 4-11 (1997).

[2] J. Kawataka, et al., "Novel Optical Fiber for Feeder and Distribution Use in Access Networks", *Proc.of 49th IWCS*, 293- 297 (2000).

[3] Kariofilis Konstadinidis, et al., "OPTIMIZATION OF FIBER RIBBON SUB-UNIT ROBUSTNESS BY MEANS OF A LATERAL FIBER-TO-MATRIX ADHESION GRADIENT" , *Proc.of 49th IWCS*, 1-7 (2000).

[4] H. Paul Debban, et al., "A New High-Density Central Cable Core Desin" , *Proc.of 49th IWCS*, 1-7 (2000).

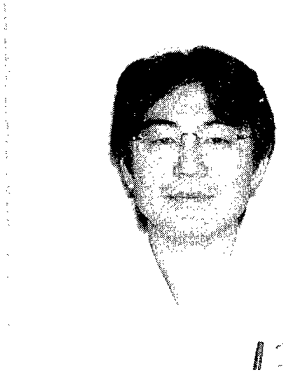
[5] George Dallas PhD., et al., "Thermal and Mechanical Optimization of Easy-Access Flexible Buffering Materials" , *Proc.of 49th IWCS*, 357-361 (2000).

[6] M. Yamanaka, et al., "Development of the New Downsized Aerial Optical Cables with SZ-slotted Rod and without Slotted Core", *Proc.of 49th IWCS*, 490-494 (2000).

[7] M. Yamanaka, et al., "New High Density SZ-stranded Ribbon Slotted Core Cable For Underground Access Networks" , *Proc.of 46th IWCS*, 230-239 (1999).

[8] N. Okada, et al., "Study of the SZ-slotted rod type optical cable with 4-fiber ribbons for aerial applications" , *Proc.of 46th IWCS*, 785-792 (1997).

Authors

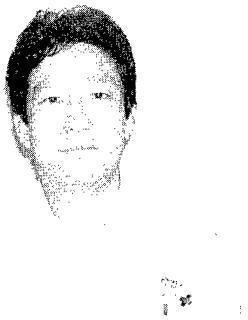


Masayoshi Yamanaka

Fujikura Ltd.

1440, Mutsuzaki, Sakura, Chiba, 285-8550, Japan

Masayoshi Yamanaka was born in 1966. He joined Fujikura Ltd after his graduation from Tohoku University with M.E degree in 1992 and has been engaged in research and development of optical fiber cables. He is now an chief in research and development department telecommunication division.



Naoki Okada

Fujikura Ltd.

1440, Mutsuzaki, Sakura, Chiba, 285-8550, Japan

Naoki Okada was born in 1964. He joined Fujikura Ltd after his graduation from Chiba University with B.E. degree in 1986 and has been engaged in research and develop-ment of optical fiber cables. He is now an assistant manager of optical fiber production engineering department.



Michio Suematsu

Fujikura Ltd.

1440, Mutsuzaki, Sakura, Chiba, 285-8550, Japan

Michio Suematsu was born in 1963. He joined Fujikura Ltd after his graduation from Nihon University with B.E degree in 1985 and has been engaged in design engineering of optical fiber cables. He is now a manager in research and development department telecommunication division.



Matsuhiro Miyamoto

Fujikura Ltd.

1440, Mutsuzaki, Sakura, Chiba, 285-8550, Japan

Matsuhiro Miyamoto was born in 1953. He graduated from Nagoya Institute of Technology with B.E. degree of electrical engineering. He joined Fujikura Ltd after his graduation from Tokyo Institute of Technology with M.E. degree in 1978 and had been engaged in research and development of optical fibers and optical cables. He is now belongs to optical fiber production engineering department.

5.5 km Optical Cables Installed in Small Underwater Tubes using Waterflow

*W. Griffioen, C. van 't Hul, I. Eijpe, W. Greven, F.R. Bakker, B. Wegbrans**
Draka Comteq - NKF Telecom, *Pirelli Cables
Gouda, *Delft, The Netherlands
+31-152605721 · willem.griffioen@nkf.nl

Abstract
A bundle of power cables was installed crossing a 5.5 km sea arm. In this bundle 6 tubes of 25/20 mm are present. In 4 of those tubes compact (6 mm) cables with high fiber density (49 fibers) have been installed without splice, using floating technology (flowing water along the cable). In preparation trials 6 km cables could be installed in one flow.

Keywords
Optical cable; power cable; water crossing; optical fiber; small tubes; installation; jetting; floating.

1. Introduction

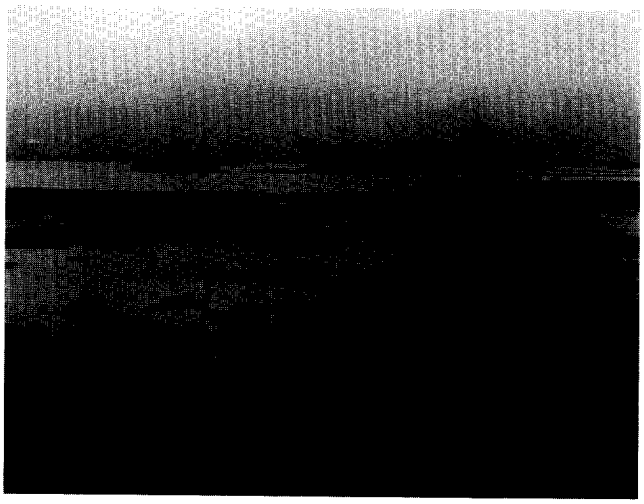


Figure 1. Bundle of power cables and tubes at end of sandbank.

A 150 kV connection, consisting of a bundle of 6 power cables in a star configuration, has been installed. It crosses a 5.5 km wide sea arm, the Westerschelde, located in the southwest of the Netherlands forming the connection of the harbor of Antwerp to the sea. This bundle was ploughed into a 5 m deep slit on the bottom of the sea arm. In the corners of the bundle 6 small tubes of 25 mm outer diameter could be placed. Larger tubes would stick out of the bundle and are easily damaged when the heavy bundle is placed. In these small tubes cables with 49 fibers (1 extra for signaling) were demanded, in a continuous length without splice.

The trajectory is, although passing a 35 m deep crossing, a sandbank (most of the time under water) and a 25 m deep crossing, rather straight assuming that the tubes remain well in position in the corners. But still pulling and even blowing (theoretical maximum installation length of 2500 m) will not do the job. The solution is floating, where water flows along the cable and propels as well as lifts the cable. For this purpose the cable, a laser welded steel tube with fibers, was jacketed with a foamed polyethylene. The density of the 6 mm diameter 49-fiber cable was slightly higher than that of water.

2. Installation Techniques
In the past optical cables were installed in ducts by pulling using a pre-installed winch rope. Today blowing, or jetting, has become a popular technique for this; costing less and increasing the lengths per "pull" [1,2,3]. Here a high-speed airflow is flown along the cable, exerting a drag-force that is distributed over the length of the cable. The duct-length can be chosen such that this drag-force is larger than the friction between cable and duct at every location. In this way tensile stress in the cable is avoided and the "capstan effect", the exponential force built-up in bends and windings of the trajectory, does not occur. By additional pushing of the cable the technique is further improved. Because of the non-linear behavior of the expanding airflow blowing and pushing (= jetting) work in synergy, doubling the installation length.

Instead of airflow also a flow of liquid such as water can be used to install the cable. This floating not only propels the cable but also (partially) lifts it. For a turbulent flow and when the effect of the stiffness of the cable is ignored the installation length l follows with [1]:

$$l = \frac{\pi D_c D_d \Delta p}{4 f (W - \rho_w g \pi D_c^2 / 4)}$$

Here D_c and D_d are the diameters of cable and duct, respectively, Δp the pressure difference over the length l, f the friction coefficient between cable and duct, W the weight of the cable per unit of length, ρ_w the density of water and g the acceleration of gravity. Note that, contrary to jetting, the pressure gradient is linear with floating. This means that synergy with pushing is hardly present.

The stiffness of the cable cannot be ignored with floating. With jetting this stiffness has two effects: A negative because of extra friction in bends and windings of the trajectory and a positive because of a stiffer cable is easier to push. The latter hardly plays a role with floating because the mentioned lack of synergy. So, almost only the negative effect of stiffness remains. In the situation that the density of the cable is close to that of water the negative effect of the stiffness becomes almost the only remaining contribution to friction! Therefore it is important to have as straight as possible trajectories to really benefit from the floating technology.

The biggest advantage of floating is that because of (partial) lifting of the cable much longer installation lengths can be reached, as demonstrated in [4]. Another advantage is that smaller pump capacity is needed because water is more viscous than air. The latter may become a drawback when the tube diameter is small. The speed of the water may drop too much, resulting in even lower installation speed. Also the flow may loose turbulence. Another drawback is the supply and exhaust of water needed and the remaining water in the duct. And extra problems arise with uphill installation: Every 10 m elevation costs 1 bar (hydrostatic) pressure. When begin and end of the duct are located at the same elevation no additional hydrostatic pressure is built up over the total length, but at lower points in between the tube may explode because of too high overall pressure. This is not a problem when the duct is installed under water, because outside the duct the same hydrostatic pressure build-up is present.

3. Mission (Impossible?)

A cross sectional view of the bundle of power cables is shown in Figure 2. It is clear that there is no place for ducts (tubes) with larger diameter without the risk for damaging the ducts. The maximum duct size is 25/20 mm. They are made of HDPE with a special inner liner. In the ducts cables with 49 fibers have to be installed over a length of 5.5 km. A compact cable with high fiber density is needed. Such cables are in use in systems with small-size guide tubes [5,6]. They are made with hermetic laser-welded central steeltubes, with a diameter of 3.5/3.2 mm for 49 fibers, and are jacketed with HDPE with a diameter of 6 mm.

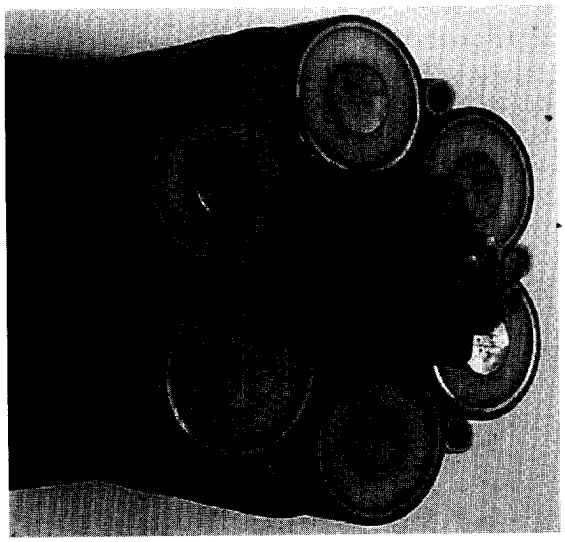


Figure 2. Bundle of power cables and tubes, closer view.

Installation with jetting in very straight trajectories results in about the same lengths per "pull" as with pulling. The jetting distance was calculated to be 2500 m. This is not sufficient when the goal is installation of the 5.5 km in one "pull". Therefore the floating technology was chosen to finish the job. In order to tune the density of the cable to that of water foamed HDPE was used as jacket for the cable. According to calculation installation is possible over more than 8000 m. But then the trajectory must be really as straight as assumed: ducts following the bundle (no short undulations; no twist). In this calculation already a little higher friction coefficient in water was chosen between cable and duct, because the lubricants do not work optimal (if they are not completely washed away), but still some uncertainty remains about its value. When bends are introduced in the trajectory, e.g. to build tandem locations on scaffolds, the installation length further decreases, depending on the sharpness of the bends (a bending radius of 1 m already has a large effect).

4. Equipment

The cables were floated with the same equipment (see Figure 3) as used for blowing cables in small-size guide-tube systems [5,6,7]. Only now a separate head, a part of the equipment used for jetting bundles of said guide-tubes, was used to inject the water.

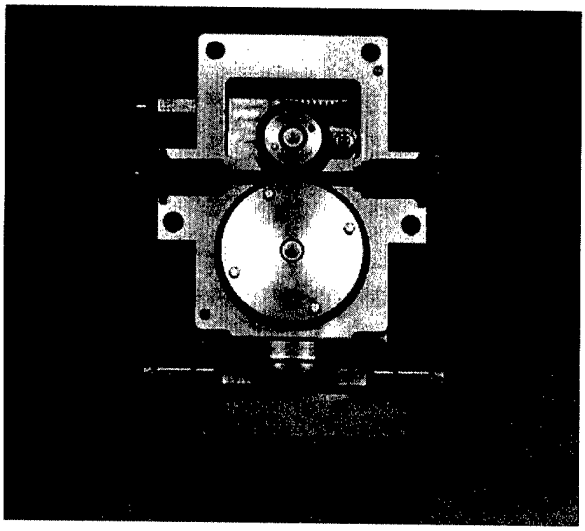


Figure 3. Part of equipment to float cables.

5. Preparation

Before the actual installation, which had to be done in a restricted time schedule (4 cables within 5 days), first field trials were done. The first trial was done in a trajectory with 4 loops of 1566 m around the cable factory, laid on the ground, every time crossing a 20 m high scaffold. After all loops were filled with water a flow of 8 l/min was reached using a pump of 12.8 bar pressure. This flow is enough for turbulence (from 3 l/min) and is equivalent to a water speed of 25 m/min. According to calculation only 75% of the flow is sufficient for the installation, resulting in an expected maximum cable speed of 6 m/min. However, the cable could not be installed at all over the full length. The best result was a length of 3132 m (duct open after 2 loops) with a pump pressure of 15 bars and a flow of 11 l/min through the filled duct. Probably too many bends and undulations were present in the test trajectory (the water crossing is more straight) for which the floating technology is relatively sensitive. But there was more: The flow sometimes suddenly changed, as if a change from turbulent to laminar occurred (theory says that this would happen at much lower flows). A trial at the second day showed even worse results. The cable stopped halfway in a duct open at 3132 m. Later the cable also didn't move when the duct was shortened by 566 m. Are friction properties degrading after a long time filling with water? Note that the water used (from the fire brigade) was dirty.

In another trial 6 km of (fresh) duct was placed in a straight water canal. Two tests were done. In the first test first a winch rope was installed from the end of the duct over a length of 3500 m. This rope was pulled (by rubber boat!) by a nylon wire which was installed by compressed air using a plug. Then the cable was installed, first over 2500 m. Before floating an attempt was done to jet the cable in this duct. It stopped after 680 m, so floating is really the only option. With water 2500 m was reached easily (9 bar, 35 m/min). Then the cable was attached to the winch rope and the second section was pulled "dry". The end (6 km) was reached with a cable speed of 34 m/min, a water pressure of 9,5 bar and a pulling force of less than 500 N.

In a second test a cable (this time with a thin additional nylon jacket) was installed purely by floating. The first 2500 m was installed in the same way as in the first test (no degradation of friction properties this time?). Then the duct was closed and the installation continued. Gradually the pump pressure increased because the rest of the duct was filled with water. When water reached the end of the duct the pressure was 15.5 bar and the flow was 10 l/min. At that time the cable was installed over 4 km and the speed had dropped to 12 m/min. From this moment the speed increased again, gradually, until 15 m/min when the cable length of 5316 m was used. It is expected that, because the flow did not drop further, the end of the duct would have been reached without problems.

6. Water Crossing

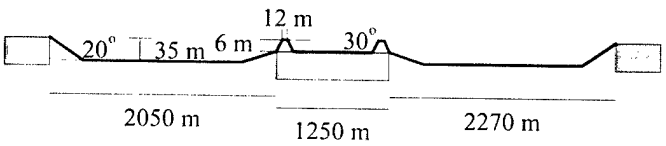


Figure 4. Topology of the water crossing.

The power cable was first installed in 3 portions, the crossings and the sandbank. Then the power cables were spliced together using the scaffolds at the sandbank, at 2050 and 3300 m from the floating starting position. All the time the ducts were kept under pressure, only temporary released when the ducts were coupled together. Unfortunately an anchor damaged the power cable in the 2050 m crossing. This part had to be replaced a few months later. All the time water was able to diffuse through the duct walls in the non-damaged portion (even with higher pressure inside the ducts than outside) filling the ducts with water. Because we were not sure about friction increase after long time exposure to water we blew foam plugs through the ducts a week before the actual installation of the optical cables. Also a flow of dry nitrogen was sent through, repeated 2 days before the actual installation.

The floating could, in principle, be done in tandem operation using the scaffolds. These places were indeed kept standby because the condition of the tubes in the bundle was not 100% sure. Therefore the tubes were laid over the scaffolds, introducing extra bends especially severe at the second scaffold (see Figure 5)

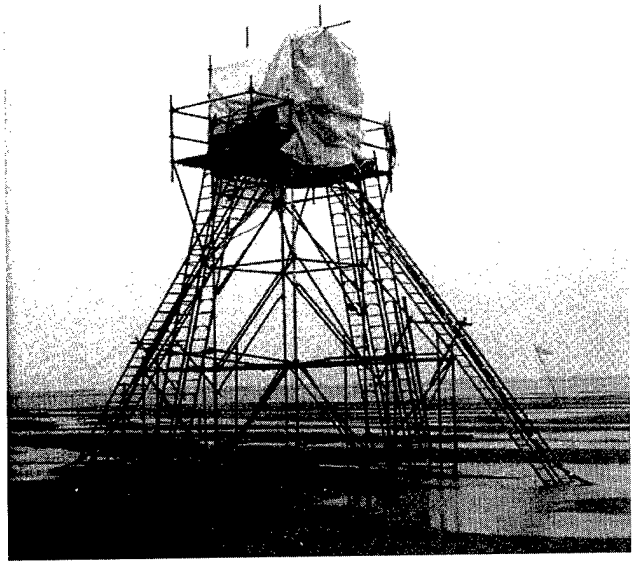


Figure 5. Second scaffold.

7. The Installation

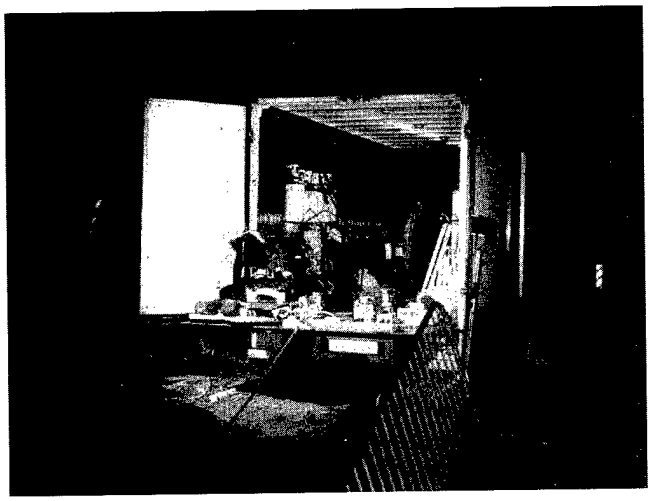


Figure 6. Starting Location.

Water floating was done with water from a tank-lorry (the water in the sea arm is saltish). The first cable stopped halfway in the first crossing (20 bars pressure) and was pulled back. The same cable passed this crossing in another tube, indicating that the tubes were not all as straight as assumed. This cable passed the two scaffolds, considerably loosing speed when passing the second. When the speed dropped below 10 m/min, at 4500 m, a tandem machine was placed at the second scaffold. The waterpump (12 bars) was fed with water from the previous section, using a storage tank (see Figure 7). Now the end (+ 100 m extra tube to create overlength) was reached with a speed of 30 m/min.

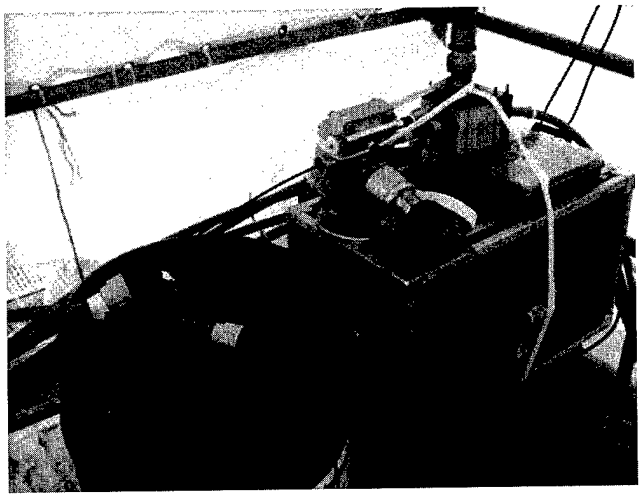


Figure 7. Inside second scaffold.

The second and the third cable reached the second scaffold and after that also here the speed dropped. Just as with the first cable a tandem machine was placed at the second scaffold and the end was reached, this time with speeds of about 20 m/min.

The fourth cable stopped halfway in the first crossing, just as the first cable, and was pulled back. Fortunately the cable reached the first scaffold in another (the last) tube. But now the cable stopped 200 m after this point. With, for the first time, a tandem machine at the first scaffold, the second scaffold was reached with a speed of 22 m/min. After placing a second tandem machine at the second scaffold the installation was continued. After another 800 m the speed of the cable had dropped to below 5 m/min. The next 1000 m was installed with very low speed, dropping even below 3 m/min. Then, at 500 m before the end, the cable stopped. Adding Jetting Lube to the flow of water did not help. Then the waterpump at the second scaffold was boosted with the pump at the first one, using one of the free ducts. This helped and the cable moved again. Later the speed even increased (a late effect from the now well-distributed lube?). The cable reached the end with a speed of 15m/min. It was a long cold and misty night, especially

at the second scaffold (see Figures 5 and 7), then surrounded by water.

8. Conclusions

It has been shown that it is possible to install continuous lengths of 49-fibre cables into 25/20 mm ducts, in corners of a bundle of power cables which was installed at the bottom of a sea arm of 5.5 km. For this it was needed to propel the cable by a flow of water, the floating technique. This technique is very sensitive for bends in the trajectory. In 2 of the 6 tubes no installation was possible, probably because the ducts are not kept as straight in the bundle as was assumed.

9. Acknowledgments

The authors wish to acknowledge Delta Nuts, for which the installation was done, and Visser Smit, for arranging the scaffolds and nautic works. For contributing by valuable input and hard work the following persons are acknowledged: Jack van Oord, Simon Kooiman, Hugo Niesink and other persons from Pirelli Cables, Hennie Rikken, Piet Lock, Pedja Vudjic, Dick van de Dool, Jeroen van 't Heck, Kees van Trigt and other persons from Draka Comteq - NKF Telecom, Captain Jaap (hovercraft), Luc Verlinden (ENI, Belgium), Knut Bungard Jensen (Draka Comteq, Denmark), Gerard Plumettaz (Plumettaz, Switzerland), Herbert Vetter (Vetter, Germany) and John Fee (Polywater, USA).

10. References

[1] W. Griffioen, "*Installation of Optical Cables in Ducts*", Plumettaz, Bex (CH), 1993.

[2] W. Griffioen, "A new installation method for conventional fiber optic cables in conduits", *Proc. 37th IWCS* (1988) 172-178.

[3] W. Griffioen, G. Plumettaz, "Current developments in cable-in-duct blowing techniques", *Proc. 46th IWCS* (1997) 363-367.

[4] P. Mignon, J.L. Campion, J. Le Cam, G. Le Goff, "Floating, a high performance cable laying technique", *Proc. EuroCable Conference* (1999) 200-207.

[5] W. Griffioen, A. van Wingerden, C. van 't Hul, P. Lock, A. van der Tuuk, "Innovative Solutions for Access Networks", *Proc. 49th IWCS* (2000) 538-542.

[6] W. Griffioen, A. van Wingerden, C. van 't Hul, "Versatile outside plant solution for optical access networks", *Proc. 48th IWCS* (1999), 152-156.

[7] G. Plumettaz, "A new universal tool for the placement of microcables in the local and business access network", *Proc. EC'99* (1999) 76-80.

11. Biographies



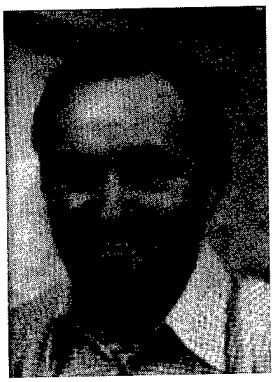
Willem Griffioen received an MS degree in Physics and Mathematics from Leiden University (Netherlands) in 1980 and worked there until 1984. He joined KPN Research, St. Paulusstraat 4, 2264 XZ Leidschendam, The Netherlands. Responsibilities R&D of Outside-Plant and Installation Techniques. He worked at Ericsson Cables, Hudiksvall (Sweden) and at Telia Research, Haninge (Sweden) in the scope of exchange/joint projects with KPN Research. He received his Ph.D. (Reliability of Optical Fibers) in 1995 from the Technical University of Eindhoven (Netherlands). Currently, since 1998, he is product manager at Draka Comteq - NKF Telecom, Zuidelijk Halfrond 11, 2801 DD Gouda, The Netherlands.



Cees van't Hul received a BS degree as Electrical Engineer at Technical High School in Arnhem in 1975. He jointed ELGAWA, a contracting company in Surinam and was responsible for the Medical and Electrical Department. From 1982 he jointed BATCO Surinam as Manager Technical Department until 1985. Since then he jointed Draka Comteq - NKF Telecom, Zuidelijk Halfrond 11, 2801 DD Gouda (Netherlands), first as Project Manager in the contracting of High Voltage systems, later as Manager Quality Department. Since 1995 he is involved in the developing of Telcom Cable systems.



Ignaat Eijpe received a MS degree in Physics from the University of Twente (the Netherlands) in 1989. He joined Draka Comteq - NKF Telecom, Zuidelijk Halfrond 11, 2801 DD Gouda, The Netherlands in 1991. He started in product-development and product-management of optical fibre cable and accessories. He continued his career as manager of the project-department in 1997. Since 2000 he is involved in the development and (project-) implementation of telecommunication cabling systems.



Willem Greven received his degree in advanced technical studies in Delfzijl in 1977. Since then he jointed Draka Comteq - NKF Telecom, IJzerweg 2, 9936 BM Farmsum (Netherlands). He worked at departments of paper-insulated cables, plastics, was quality inspector, co-ordinator final inspection and unit-leader plastics. Since 1996 he joined the team that develops and introduces the JETnet system as senior projects & systems engineer. He made demonstrations and pilot projects of the system all over the world.



Frans Robbert Bakker received his degree in advanced technical studies in Delfzijl in 1989. Since then he jointed Draka Comteq - NKF Telecom, IJzerweg 2, 9936 BM Farmsum (Netherlands). He was co-ordinator first of final inspection and later of plastics. Since 1999 he joined the team that develops and introduces the JETnet system as projects & systems engineer. He made demonstrations and pilot projects of the system all over the world.

Bas Wegbrans received a BS degree as Electrical Engineer at the technical High School in Amsterdam in 1982. He jointed NKF Kabel, Schieweg 9, 2627 AN Delft (Netherlands) in 1982 as developments engineer. He was responsible for the development of cable and cable accessories. Since 1986 he started working in the project department as project engineer. In 1991 he became projects manager and from 1995 until today he worked as a contracts manager. In this job he is responsible for the budget, quality and progress of the execution of special assigned High Voltage contracts and projects. The Power Cable Plant of NKF Kabel in Delft is now a part of Pirelli Cables.

The Influence of the Optical Cable Surface in Installation by Blowing Method

Marcelo Schneider, Marcos Antonio Nunes, Ricardo Augusto Mazza
Furukawa Industrial S.A. Produtos Elétricos
Curitiba, Paraná, Brazil
Phone: +55 41 341-4088, Fax: 55 41 341-4141, E-mail: schneider@furukawa.com.br

Abstract

Recently, the installation of optical fiber cables by blowing method has been largely used in long-haul networks around the world due to its high efficiency. The performance of blowing installation varies significantly depending upon the particular characteristics of a given cable. Factors such as cable weight, external diameter, stiffness and cable surface will make a difference in the installation performance.

In this paper it is presented the study about influence of the cable surface in the blowing installation. Initially it was used a mathematic model to define the drag force in function of the system variables, and through measurements it was verified some relations between cable surfaces and performance in the installations by blowing method.

Keywords

Optical Fiber Cable; Cable Surface; Blow Method; Blowing Installation.

1. Introduction

The constant use of the blowing method for the long distance routes, takes us to improve the techniques to get fast network implementation with high productivity and obviously lower cost. In the same way, it is important to use an optical cable with sufficient performance to attend these necessities.

The performance of blowing installation varies significantly depending upon the particular characteristics of a given cable. Factors such as cable weight, external diameter, stiffness and cable surface will make a difference in the installation performance.

In order to study just the cable surface it was tried to null other variables that could have influence in the results, so it was made a short circuit to insert the cables and to avoid the friction cable-duct influence.

1.1 Formulation

When the airflow goes through between the cable and duct walls it creates a drag force (Fa), showed in Figure 1. This force helps the cable insertion into the duct and can be determined through the shear force (τ), as showed in the Eq.(1):

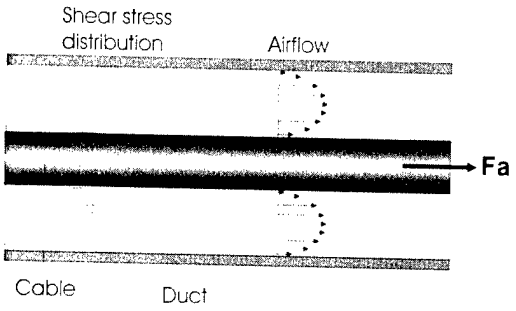


Figure 1. Efforts Distribution

$$\frac{dF_a}{dx} = \tau(x).2\pi.r_c \qquad (1)$$

Where; r_c is the cable radius, τ is the shear stress on the cable surface caused by the airflow into the duct.

The shear force can be determined through the Eq.(2):

$$\tau(x) = \frac{f_c}{2}.\frac{\dot{m}.R.T}{\pi.\left(r_d^2 - r_c^2\right)}.\frac{1}{p(x)} \qquad (2)$$

Where; f_c is the friction coefficient between cable surface and airflow, R = 287 J/kgK is the gases universal constant, T is the airflow temperature, r_d is the duct radius, $\dot{m}$ is the mass flow and $p(x)$ is pressure distribution along the duct. Replacement Eq.(2) in (1), we have:

$$F_a = f_c.K\int_o^L \frac{dx}{p(x)} \qquad (3)$$

Where; K is a constant defined by:

$$K = \frac{\dot{m}^2.R.T}{\pi}.\frac{r_c}{\left(r_d^2 - r_c^2\right)^2} \qquad (4)$$

To calculate the friction coefficient (fc) it used Eq. (5):

$$f_c = \frac{2.\tau}{\rho.u^2}$$

(5)

Where; ρ is the fluid density, u is the airflow speed average and τ is the shear stress.

The shear stress (τ) can be obtained measuring the air pulling force of the cable during its insertion and using the system forces, according to second Newton law.

$$\tau = \frac{\pi r_c^2 (p_L - p_{atm}) + F + f_{mec} wL}{2\pi r_c L} \qquad (6)$$

Where; P_L is the pressure into the duct, L is the length of the cable, f_{mec} is the friction coefficient between cable and duct, w is the cable weight and F is the air pulling force on the cable.

2. Field Tests

2.1 Circuit and Equipment's Characteristics

In order to measure the air pulling force on the cable (F), see expression (6), is necessary to have the friction force (f_{mec}) lower than (F). In this way, we reduced the circuit length to about 240 m, in order to get this condition optimized. Due to the available flat profile area we divided this short circuit in two 105 m segments united by a curve with 5 m radius. The pressure and temperature were measured in six different points along the duct, as showed in the Figure 2.

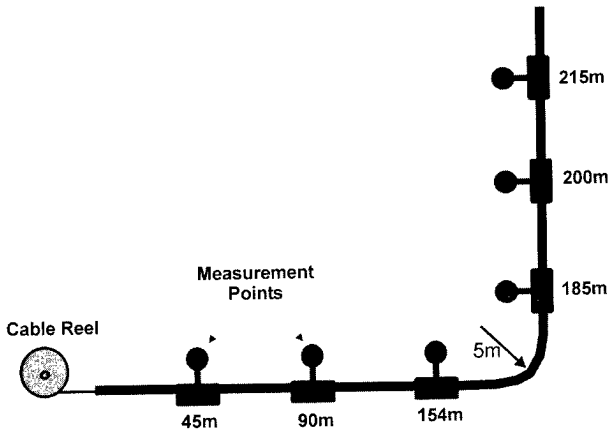


Figure 2

The Figure 3 shows the measure equipments used in each point.The ducts used in these tests were: 40 mm of external diameter, 34 mm of internal diameter and corrugated internal surface. The air compressor used was 10 bar (1 MPa).

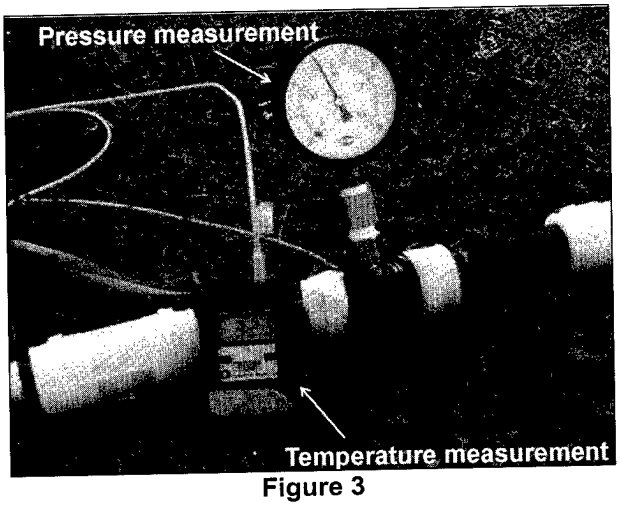


Figure 3

2.2 Cable Characteristics

For these tests were designed three cables to be installed by blowing technique. These cables had their wavy surface in a different intensity with the same inner core, outer sheath material and approximately the same weight. However in the cable design, was respected the maximum variation diameter allowed by blowing equipment manufacturer, (1 mm). The Figure 4 shows the three cables designed to the tests, where the cable 1 presents no waves, the number 2 presents waves with gaps about 50 mm and the number 3 presents with gaps about 10 mm.

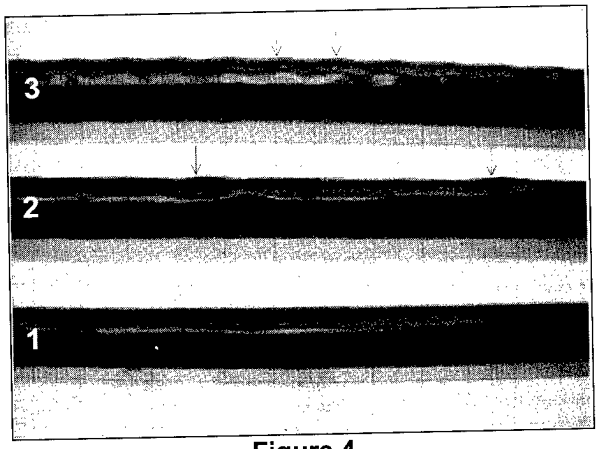


Figure 4

The table 1 shows the characteristics among the test cables.

Table 1. Cables Comparative Analysis

Characteristics \ Cables	Cable 1	Cable 2	Cable 3
Average Distance Peak-Peak (mm)	-	48.46	9.42
Average High Valley-Peak (mm)	-	0.44	0.28
Average Diameter (mm)	12.21	12.03	12.06
Friction Coefficient (cable-duct)	0.051	0.045	0.043

2.3 Air Pulling Force (F) Measurement

In order to measure this force (F), was used a dynamometer as showed in the Figure 5.

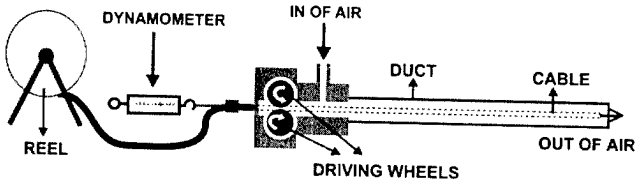


Figure 5

The measurements were made several times along the cable insertion, with this completely loose, without the driving wheels influence.

3. Results and Discussion

3.1 Pressure Measurement

The Figures 6, 7 and 8 present the pressure measurements distribution in the circuit for each cable.

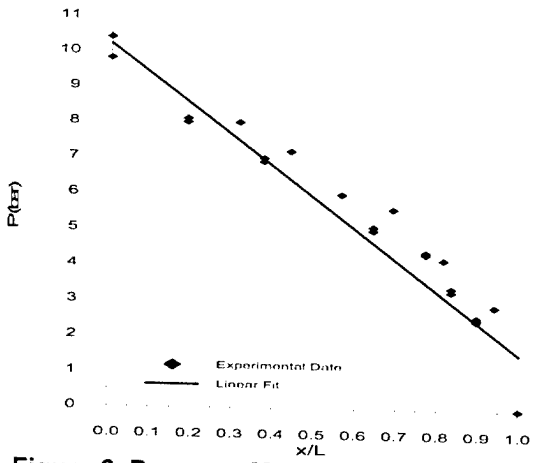


Figure 6. Pressure Measurements Along the Duct During the Cable 1 Inserting

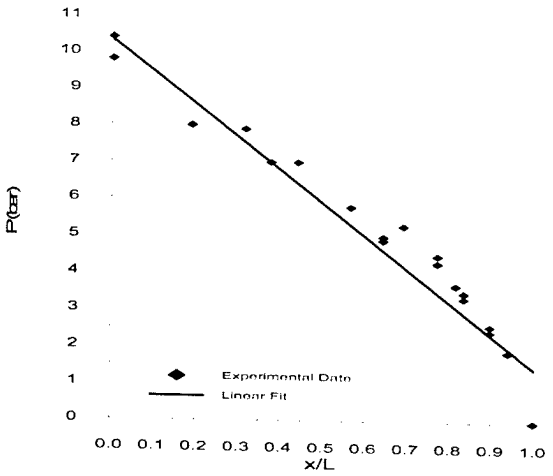
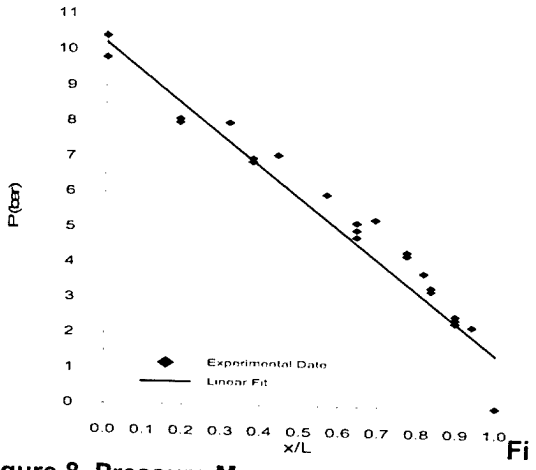


Figure 7. Pressure Measurements Along the Duct During the Cable 2 Inserting



Fi gure 8. Pressure Measurements Along the Duct During the Cable 3 Inserting

The table 2 shows the fitted curves of the cables pressure measurements (P(x/L)) and the drag force (Fa), that it was calculated by integration from (P(x/L)), (see expression 3).

Table 2. Cables Comparative Analysis

Cable	P(x/L)	Fa
1	- 8.9(x/L) + 10.3	$\frac{f_c K.L}{8.9}\ln\left(\frac{10.3}{10.3-8.9(x/L)}\right)$
2	- 8.6(x/L) + 10.2	$\frac{f_c K.L}{8.6}\ln\left(\frac{10.2}{10.2-8.6(x/L)}\right)$
3	- 8.7(x/L) + 10.2	$\frac{f_c K.L}{8.7}\ln\left(\frac{10.2}{10.2-8.7(x/L)}\right)$

Through this table 2, it can be noticed that (Fa) depends on just from the friction coefficient (fc) because (K) is a constant and (x/L) stands for the cable length insertion.

3.2 Friction Coefficient (fc) Values

The friction coefficient (fc) was calculated with the expressions (5), (6) and the measurement explained in the item 2.3,. The table 3 shows the values.

Table 3. Friction Coefficient (fc) Calculated

Cable	f_c
1	0.000361
2	0.000414
3	0.000441

3.3 Cables Performance

The figure 9 shows the drag force by meter inserted (Fa) calculated for the cables. The worst performance was the cable 1, without wavy on its surface. Among those testes we found the cable 3 as the best performance, i.e., the cable 3 had its drag force 18% bigger than cable 1 and 8 % bigger than cable 2.

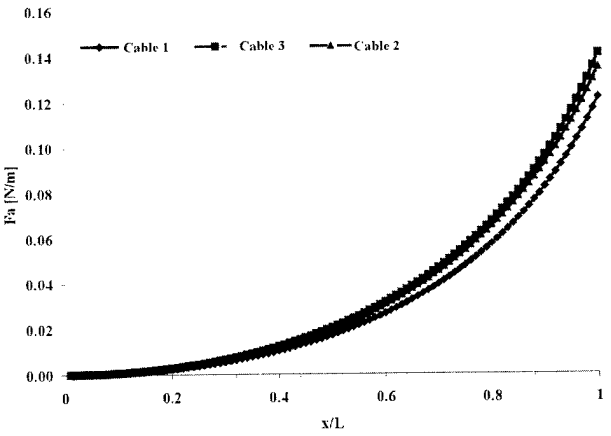


Figure 9. Drag Force (Fa) Calculated

4. Conclusions

In several tests it was observed that cables with wavy surface have presented better performance in the blowing installation, this better performance never was associated to cable surface due to the difficulty to prove it.

This study presented the development of a theoretical model to calculate the drag force (Fa). In this equation there are variables associated to cable surface as shear stress (τ) and friction coefficient (fc). In order to estimate the performance in a blowing installation, it was inserted three similar cables with different surfaces in a circuit especially assembled to decrease the influence of the friction between cable and duct.

It was determined which cable surface would present better performance in the blowing method, through drag force directly influenced by the friction coefficient. Among those tests it was identified the cable 3, the waviest, as the best performance, i.e., the cable 3 had its drag force 18% bigger than cable 1 and 8 % bigger than cable 2. The cable 3 presented a small improvement in the performance in relation to the cable 2, it means that there is a smooth relationship between Distance Peak-Peak and High Valley-Peak that influence the drag force.

The drag force (Fa) equation is exponential in relation to distance of insertion and the differences of the drag forces among cables rise according to insertion distance. It could mean that the cable surface have great influence in long distances installations.

5. Acknowledgments

Special thanks for all people that helped in this work.

6. References

[1] IEC 60794-1-2, "Basic Optical Cable Test Procedures," (1999)

[2] Bellcore GR-356-CORE, "Generic Requirements for Optical Cable Innerduct and Accessories," (October, 1995)

[3] W. Griffioen, "Installation of Optical Cables in Ducts," Plumettaz (1993)

[4] W. Griffioen, "The Installation of conventional Fiber-Optic cables in Conduits Using the viscous Flow of Air," in: *Journal of Ligthwave Technology* (February, 1989)

[5] M. A. Nunes, A. M. Simião, M. A. Caetano, C. Brunhara, A. C. Silva, L Silvério "Development of a new Optical Fiber Cable installed by Blowing Method," IWCS (2000)

7. Biography



Marcelo Schneider - Furukawa Industrial S.A.
R. Hasdrubal Bellegard, 820 CIC 81450-140
Curitiba – Paraná - Brazil

Marcelo Schneider joined Furukawa Industrial S.A. in 1996 after receiving his B.S. degree as an Electrical Engineer from Federal Center of Technological Education (CEFET). He has been involved in the optical fiber cables design and Installation techniques. He is currently Product Development Engineer.



Marcos Antonio Nunes - Furukawa Industrial S.A.
R. Hasdrubal Bellegard, 820 CIC 81450-140
Curitiba – Paraná - Brazil

Marcos Antonio Nunes joined Furukawa Industrial S.A. in 1997 after receiving his B.S. degree as an Electrical Engineer from Federal Center of Technological Education (CEFET). He has been involved in the optical fiber cables design and Installation techniques. He is currently Product Engineering.



Ricardo Augusto Mazza - CEFET
Av. Sete de Setembro, 3165 Centro 80230-901
Curitiba – Paraná - Brazil

Ricardo Augusto Mazza received his B.S degree in 1991 from Universidade Estadual Paulista (UNESP) and in 1994 his M.S degree from Universidade Estadual de Campinas (UNICAMP) in Mechanical Engineering. He is currently a professor at Federal Center of Technological Education (CEFET).

Experience from the Field Installation of Optical Fiber Cables in Metro Gas Pipelines

Hans-Detlef R. Leppert, Klaus Nothofer, Wolfgang Teschner

Alcatel Optical Fiber GmbH, Mönchengladbach, Germany

ABSTRACT

A new and innovative optical network architecture is in the process of being deployed in German and Taiwanese cities by using the gas pipeline system as the right-of-way. The development and principles of this previously untapped right-of-way solution has already been reported by Alcatel in IWCS '99. Gas pipelines are the perfect conduit for deploying optical fiber networks without major disruption and destruction of streets and sidewalks normally caused by conventional cut-and-fill techniques. It is shown that gas pipeline systems provide a cost-effective means to build or expand fiber infrastructure within metropolitan areas.
This paper reports about the experience gained in field installation in different regions of the world, the specific technology and regulation issues, and the corresponding solutions found.
The fiber network is deployed using a specially developed I/O-port to guide the cable into and out of the gas pipe so as to bypass the gas valves. A key part of the system is the sealing kit, together with a specially-designed optical fiber cable. The cable is blown into the gas pipes by means of a stabilized parachute either by using the natural gas flow itself or compressed air, depending on local requirements. The cable bypassing of the valves or additional installed I/O-ports defines fiber access points for networks in an ideal way.
It is demonstrated that this method of deploying optical fiber cables in gas pipelines offers many advantages to the network operator with very little disruption to gas operators, and is environmentally-friendly, as it avoids massive civil engineering in urban areas. Cost, flexibility and speed in deploying the network are the primary advantages for the installer. The gas pipeline system furthermore provides an excellent protection for the optical fiber cable due to it's being situated well below the street surface and other infrastructure. The installation of an optical fiber cable inside the gas pipeline, in addition, offers the possibility of implementing a leakage detection system with high spatial resolution and short response time. Any fiber within the gas pipeline can be used for this application at no additional installation costs.

Keywords

Fiber; gas; metro; access; right-of-way; fiber-in-gas; installation; I/O-port; balloon; sealing.

INTRODUCTION

Optical fiber links have been and are still being installed by new network carriers all over the world, based upon changes within telecommunication laws: predominantly trunk networks. City networks are mostly still traditional copper-based networks, leased by new telecommunication providers from 'older' traditional ones who own them.
Due to the increasing demand for bandwidth and services, optical fiber networks within cities need to be installed, first connecting business customers, then individual premises, based on different FTTH solutions in the access arena.
Due to the fact that 50% of installation costs for conventional cable systems are caused by cable laying, Alcatel sought alternatives[1)] for cable laying, with no or minimal digging, generating the highest profitability compared to conventional methods.
Among various possibilities using existing pipeline networks, fiber-in-gas is one of the superior "carriers" for optical fiber cable links.
Development work had to be done on the necessary components for cable inlet and outlet (I/O-ports), the o.f. cable, itself, and the necessary tools.

Basic considerations for a fiber-in-gas solution

In typical gas pipeline grids (for example, in Germany) the different supply levels are associated with different gas pressures:

? transport network	100 bars	1.45 kpsi
? distribution network	18 bars	261 psi
	4 bars	58 psi
? access network	300 mbars	4,35 psi
	100 mbars	1,45 psi

Transport level pipelines with diameters between DN200 and DN400 are made out of steel (some older lines are of cast iron) with a wall thickness in keeping with pressure design value. They are anticorrosion-coated with polyethylene. Subscriber access networks operate at up to 100 mbars with DN 100 (100 mm diameter) pipe dimensions.
For operational pressures of up to 4 bars, PE-pipes are more frequently used, especially in new networks/access networks.
Natural gas contains approximately:

?	87 %	methane
?	11.0 %	nitrogen
?	1.4 %	ethane
?	0.4 %	carbon dioxide

and some remaining portions of different gases as trace elements. It has a temperature of 11°C (O°C ? 20°C) and a flow rate of 10 ? 15 m/s, depending on actual consumption, gas pressure and pipe diameter.
The inner surface of the pipeline can be corroded significantly and therefore provide an abrasive surface for the installed cable

Safety regulations

Safety regulations exist regardless of country concerning:

- ? I/O-ports to be handled as branch connections
- ? Reinforcement for welded branch connectors in the case of:
  - p > 100 psi
  - thin wall pipes
  - – severe external load
- ? Standards for steel (PE) material
- ? Standards for (steel) gas pipe dimensions
  - DIN EN
  - ASME
  - JIT
- ? Standardization of welding and testing the seam
  - DIN EN
  - ASME

The authorities and therefore also gas companies are looking for:

- ? Certification of the I/O-port/branch connector
  - specified material (to be followed up)
  - certified welders

The I/O-ports, themselves, which are installed within the gas pipes are tested (at least type-tested) by a third body. (In Germany, very often the TÜV).

Components for fiber-in-gas installation

The essential components needed for this solution are:

- ? Optical Fiber Cable
- ? I/O-ports
- ? Balloon-drawn-device
- ? Drilling appliances and single or twin gas-bags — as an example of gas pipe tools not especially for this purpose

Cable

The cable requires protection against natural gas by means of a metal tape, a low friction coefficient and a high filling degree so as to be incompressible during higher gas pressures. The possible high pulling loads have to be compensated for by an equivalent tensile strength. The outer jacket, made out of special HDPE, guarantees a low friction coefficient; the enlarged sheath thickness provides enhanced stability especially for rough (corroded) inner gas pipe surfaces.
In Fig. 1a/1b cross sections of the o.f. cables installed in Taiwan are shown.

In Fig.1 cross section of the o.f. cable typeGaspipe MiniTube TM AJD1 6x24/7x24+1x(22+4) are shown

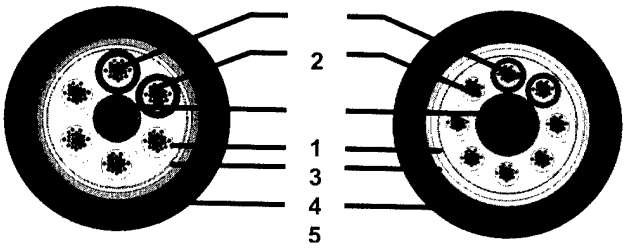


Fig. 1: cross section of optical fiber gas pipe cables

1 = central element (FRP)
2 = buffer tubes with fibers
3 = strain bearing elements
4 = copolymer-coated aluminum tape
5 = high density polyethylene sheath

I/O-port

The I/O-ports have been designed as branching connectors with additional one (two) branches for the inlet and outlet of the o.f. cables. Within these branches (ears) is located the sealing device which seals the outer cable sheath in both radial directions: at the inner wall of the branching leg and at the outer surface of the cable.

Essential design values are:

- Pressure design value of the pipe determines the wall thickness of the I/O-port
- Nominal o.d. of the gas pipe to a suitable standard
  (example: DN 200 (DIN) not equivalent to 200A8 (JIT))
- Standard used for pipeline design

The I/O-ports have have been thoroughly tested together with the sealing device at pressures of up to 100 bars (1.45 kpsi) using helium over a period of >60 weeks resulting in a high safety factor for the tightness of the sealing construction.

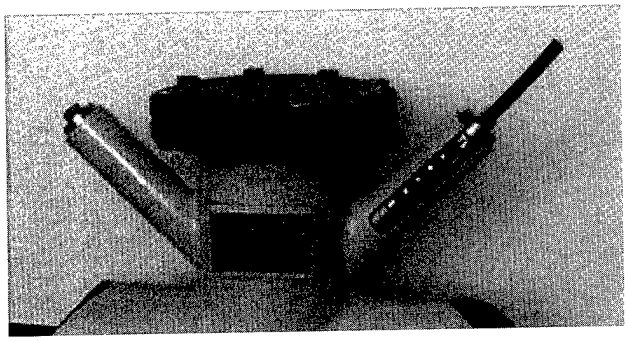


Fig. 2 I/O-port with sealing device

The whole test configuration for long term high pressure tests is shown in figure 3. A test pipeline of 4m in length is fitted with a cable entry and exit component has been operating under 100 bars pressure over a period of >60 weeks, with no gas escape or change of fiber attenuation to date.

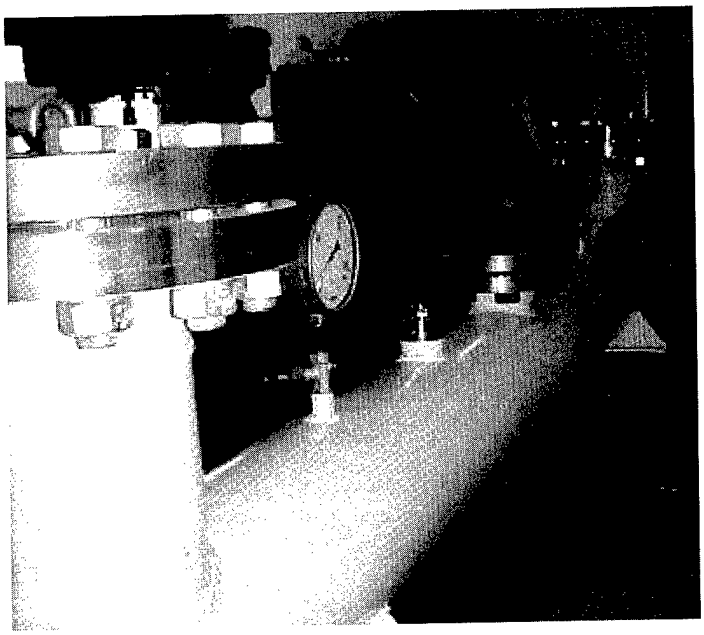


Fig.3: Test configuration of pipeline link with I/O-port components and integrated o.f. cable for 100 bar gas pressure level

Balloon-drawn device

The installation of the cable is done by dragging it in with the help of a special balloon-drawn device ("go-devil"), which can manage the sharp angles in the gas pipeline system – due to geographical topology and existing infrastructures.
The balloon-drawn device consists of a parachute stabilized by a soft ball to prevent the possible collapse of the parachute in tight corners.

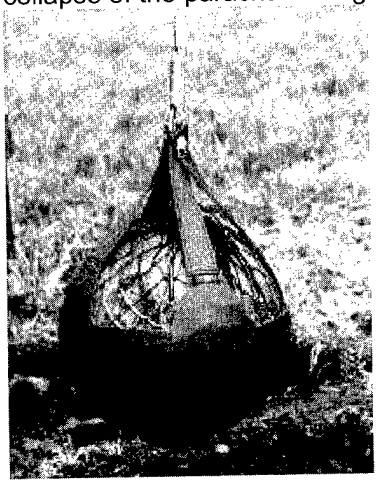


Fig. 4 Balloon-drawn device

Drilling appliance

All preparation work prior to the installation of the o.f. cable itself is done on live gas pipes, i.e.:

- De-coating and cleaning the pipe section
- Welding on of the I/O-port with testing of seams
- Installation of temporary slide valves
- Installation of drilling appliance (driven by cold pressurized air)
- Drilling of hole (the cut piece falling into the pipe)
- Pulling back the drilling appliance
- Closing of valve

The drilling appliance is shown in Fig. 5.

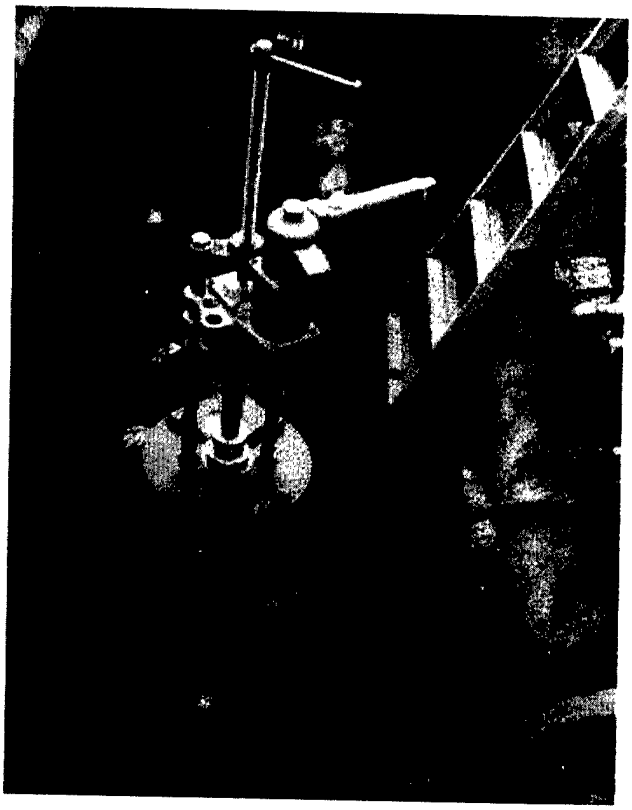


Fig. 5 Completely installed drilling appliance

A similar technique is used for the installation of gasbags (single and/or twin ones) for temporary shut-off of the gas pipe section and/or reduction of gas pressure which is done only during the installation of the o.f. cable.
An installed gas bag system (two single ones) are shown in Fig. 6

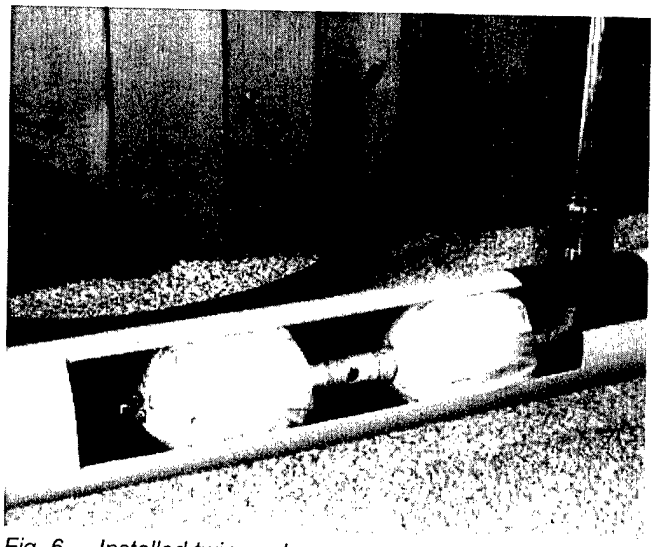


Fig. 6 Installed twin gasbag

Laying procedure

In Fig. 7, a pipeline section is shown in a simplified sketch, including the I/O-ports and demonstrating the by-passing of a valve so as to define one access point for the o.f. cable (point of presence).

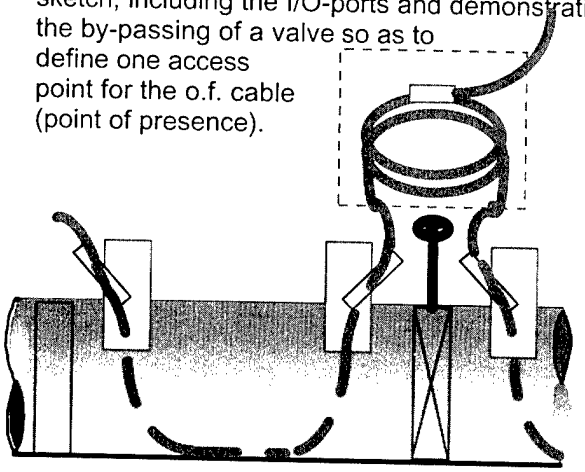


Fig.7 Laying procedure

The laying procedure consists of the following steps:

- Insertion of the balloon-drawn device connected to the o.f. cable
- Insertion of special cable guiding rolls
- Closing of ports and release of gas stream. Depending on the speed of cable laying (typical value up to 100m/min) gas pressure can be adjusted.
- Finishing the laying process by reducing gas pressure below 10 mbars and installation of cable protection/guiding tubes in I/O-ports
- Insertion of sealing packages.

? Mounting of cable bending protection
? Performance of corrosion protection.
? Gas tightness test and quality control of new corrosion cover

Installation experience in major cities

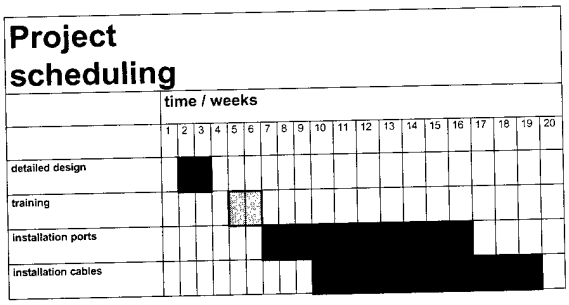
Besides a large number of installations in Germany, always as part of an overall Metro/citynet installation, we acquired a lot of experience during installations in some major Taiwanese cities.
In one of these cities (center and one suburb) the installed network consists of:

? 84 km/56 km 192 O.F. Cable
? 176 / 257 I/O-ports
(2/3 single, 1/3 double)

giving a mean cable length between 2 ports of:

? 477m / 218 m (323 m)

Project scheduling
The scheduling of projects starts with the transfer of skills, followed by the training of customers (gas people) and their sub-contractors in installation technique for I/O-ports. This takes into account the regulations applying in the country and the laying technique. It is based upon the detailed survey/planning of the PON in gas pipes.



Detailed survey/planning
Based on initial general planning which takes into account the desired PON-network design and the actual gas pipeline-network layout, detailed planning is done to verify the documented gas pipeline installations (valves, pressure stations, de-watering, pipe topology including bends, etc.) and consider outside parameters (traffic, gas customers, installed length, accessibility to pipe and/or manholes, etc.).
This 'road-map' documents the planned locations for the I/O-port, direction of blowing, etc.
In this planning procedure, the installation of 5 rings was decided.

Installation
Installation is done by the customers, themselves, after being trained by skilled personnel for at least three reasons

(I) All work on the pipeline should be carried out by the gas company, itself, or with authorized sub-contractors having the necessary certificates for welding work on the gas line.

(II) The responsibility should remain the responsibility of one party: the gas company.

(III) We didn't want to establish a large installation group for this purpose, but rather rely on the ability of our customers and their sub-contractors.

For cable installation, itself, a blowing technique was chosen, using compressed cold air instead of natural gas). For security and safety reasons, there is the additional need of purging the lines with dry nitrogen.
In addition, this direct cable installation work has been done at night in more than 98% of cases.

Reasons:
? safety regulations
? impact on traffic
? impact on gas end-users.

Regulations
The regulations/permission concerning the installation of o.f. cables within gas pipes vary significantly from country to country:

- in Germany, for gas pipes with gas pressure <20 bars, gas companies are allowed to regulate themselves, in keeping with internal safety rules and the I/O-ports manufactured and welded onto the gas pipes in accordance with DIN EN 729 .
- in Taiwan you find some differences between suburbs and city centers: In suburbs, regulations are similar to Germany's, whereas city centers need special clearance from the city council and the Ministry of Energy.

- In Italy – up to now – there exists a general interdiction; no external elements are allowed to be brought/installed within gas pipes.

Conclusions

Reliable knowledge and experience about the implementation of optical fiber networks within gas pipelines have been collected and reported.

The laying procedure, as well as the design of components for the I/O-ports and the o.f. cable which withstands the high mechanical loads during cable laying, have been proven reliable in a large number of metropolitan installations.

The overall costs of this new route technology can drop by about 50% (for one entrance point and one end point).

A further advantage is the short realization time for the total cable system and the less than minor problems regarding right-of-way discussions with owners of the route in question.

Together with realization of high fiber-count broadband telecommunication links, these cables offer a second service concerning the supervision of pipeline damage through a leakage detection system with a high spatial resolution and short response time. Any fiber within the gas pipeline can be used for this application at no additional installation cost.

References

1. Gregor, Haag, Braun. "Optical fiber cable links within drinking water pipes as an alternative telecommunication route technology." International Wire and Cable Symposium, proceedings, 1998
2. Sander, Siever, Kuhn, P Gregor "Lichtwellenleiterkabelstrecken in Gashochdruckleitungen" gwf, Gas . Erdgas 139 (1998) Nr. 10
3. Gregor, Kuhn, Weiss. "Optical fiber cable links within gas pipelines as an alternative telecommunications route technology." International Wire and Cable Symposium, proceedings, 1999
4. DIN VDE 0888: "Optical Fibers for telecommunications and data processing installations." Berlin Offenbach: vde-verlag
5. DIN EN 187000: "Specification of optical fiber cables." Berlin Offenbach: vde- verlag
6. DIN EN 188000: "Specification of optical fibers," Berlin Offenbach: vde- verlag
7. IEC 60793-1: "Optical fibers, Part 1: Generic Specification." Berlin Offenbach : vde- verlag
8. IEC 60794-1: "Optical fiber cables, Part 1 Generic Specification." Berlin Offenbach: vde-verlag

AUTHORS

Hans-Detlef R. Leppert

Alcatel Optical Fiber GmbH
Bonnenbroicher Str. 2-1
D-41238 Mönchengladbach
GERMANY



Hans-Detlef Leppert was born in 1949. After studying physics and obtaining a Ph.D. in experimental plasma physics at Ruhr Universität, Bochum, Germany, he joined AEG Kabel (today Alcatel Optical Fiber GmbH) in 1983, where he has been involved in research & development, as well as quality & engineering in optical fibers and optical fiber cables. He has been responsible for development in optical fibers and the entire R&D planning program. He has also been head of technology, as well as the person responsible for quality & environment in the telecommunication sector. At present, he is responsible for the management system and ROW solutions and is an acting member in national and international standardization bodies, like DKE & EUROTELCAB

Special Trunk Cable for Deploying Branching Repeaters in Deep Ocean

T. C. Chu, David Giordano, Tiiu V. Kutt, R. J. Rue
TyCom Laboratories, TyCom (US) Inc.
Eatontown, New Jersey

Bruce S. Clark
TyCom Integrated Cable Systems, TyCom (US) Inc.
Newington, New Hampshire

Abstract
This paper describes the design and development of an innovative trunk cable for recovering a branching repeater and its two branch cables at water depths up to 6000 meters. The cable utilizes epoxy impregnated aramid rods as strength members; it features high strength, light weight, and balanced torque. A new jointing technique was also developed to terminate the trunk cable in the cable-to-repeater coupling and cable-to-cable joint. Both cable and joint have been tested and qualified; a sea trial has been conducted successfully. Several lengths of the trunk cable have recently been deployed in the South Africa Far East Cable System, SAFE, which is scheduled for service in fourth quarter 2001.

Keywords
Cable; branching; ocean; repeater; trunk.

1. Introduction
A branching repeater is a special repeater that has a trunk cable on one side and two branch cables on the other side as shown in Fig.1, where deepwater cable SL-LW could be replaced with special application cable SL-SPA.

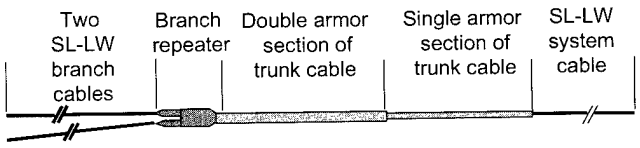


Fig.1 Branching repeater and trunk cable assembled configuration

Early fiberoptic submarine systems deployed branching repeaters at water depth less than 2000 meters where conventional deep water cable has sufficient strength to serve as a trunk cable. Recent submarine cable systems deploy branching repeaters in much deeper water, requiring a new trunk cable with higher tensile strength and properly reduced weight to be developed. The new cable shall meet the following functional requirements:

- The cable shall have sufficient strength to recover the branching repeater and its two branch legs at water depths up to 6000 m.
- The cable itself shall be recoverable by the conventional deep water system cable.
- The cable shall be torque compensated to minimize twisting of the branch cables during recovery.
- The cable shall meet factory and shipboard handling requirements.

System integration of the trunk cable requires the use of cable to repeater couplings and cable to cable joints. These couplings and joints shall meet the following functional requirements:

- The joints and couplings shall transfer the tension and torque of the trunk cable.
- The joints and couplings shall provide optical and electrical continuity.
- The joints and couplings shall withstand the hydrostatic pressure associated with a depth of 6000 m.
- The joints and couplings shall meet factory and shipboard handling requirements.

2. Cable Design
The new trunk cable is composed of two equal lengths, a double armored section (DA) and a single armored section (SA). The cross sections of the two armored lengths are shown in Fig. 2.

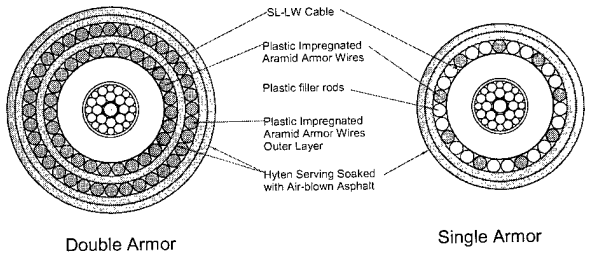
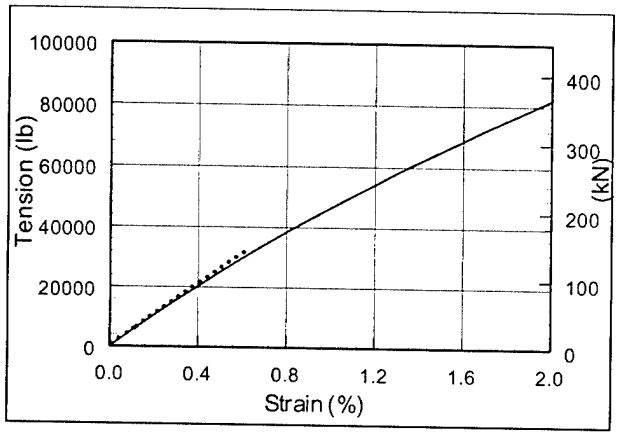


Fig. 2 Cross-sectional views of double and single armored sections

The double armored section consists of an SL-LW core and two layers of plastic impregnated aramid rods. These rods have an excellent strength to weight ratio that provides the required tensile strength with minimum additional cable weight. The two armor

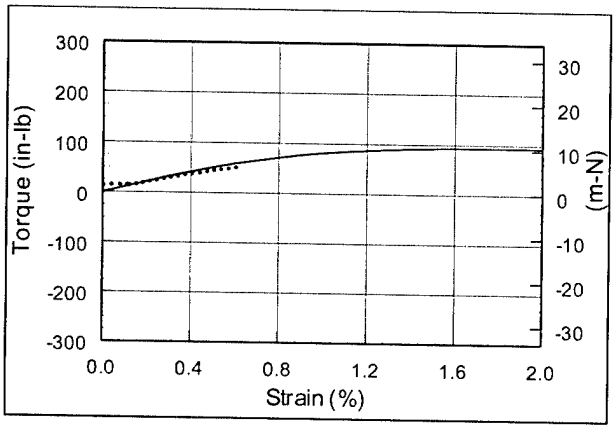
layers are counter laid to minimize the cable torque. The single armor is converted from the double armor at the transition point where the outer armor layer is eliminated and the number of aramid rods in the inner layer is reduced from 27 to 9. The vacated spaces are filled with plastic filler rods to maintain the integrity and positioning of the remaining aramid rods. The lay angle of the armor layer is properly selected to counter-balance the torque from the SL-LW core. The diameters of the double and single armor layers are 33 and 26 mm and the corresponding cable weights in air are 1.24 and 0.9 kg/m, respectively.

Mechanical properties of the trunk cable had been theoretically evaluated with the method previously published[1] before the prototype cable was manufactured. The tensile, torsional and rotational properties of the double armor section are shown in Fig. 3 to Fig. 5. (Note: test data denoted by dots)



Tension vs. Strain with Ends Fixed

Fig. 3 Tensile property of double armor section

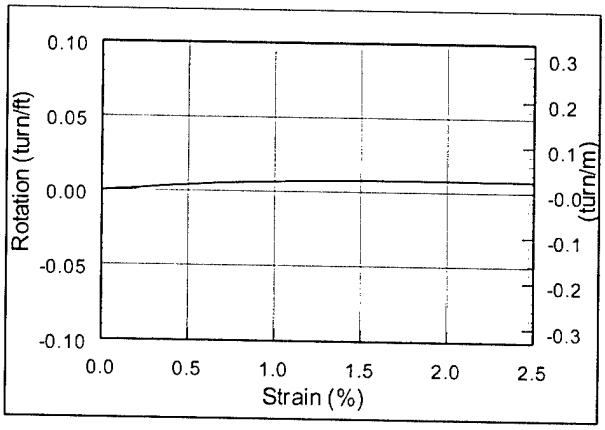


Torque vs. Strain with Ends Fixed

Fig. 4 Torsional property of double armor section

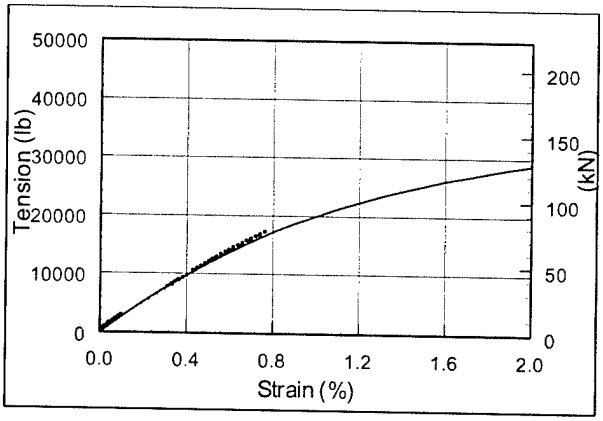
The plots show that the theoretical and test results are in good agreement. The tensile strength of the double armor cable is very high despite its light weight, allowing it to recover the branching repeater at 6000 meters. The torque generated from the double armor cable under applied tension is very low, on the order of the SL-LW core cable. The exceptionally small amount of rotation under high tension ensures that the trunk cable will not tangle the two leg cables during recovery.

Similar plots for the single armor section are shown in Fig. 6 to Fig. 8. Again the predicted theoretical values are in good agreement with the test data.



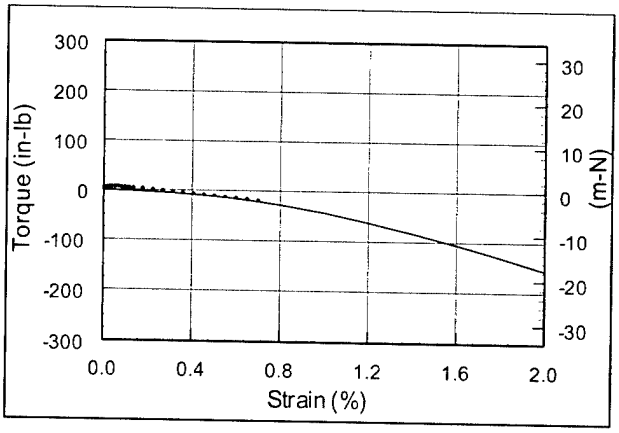
Rotation vs. Strain with One End Free

Fig. 5 Rotational property of the double armor section



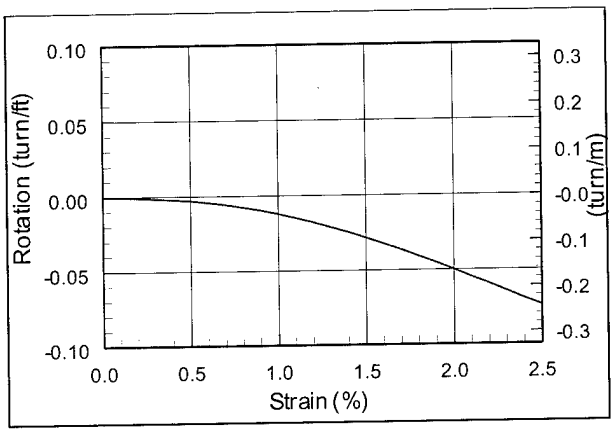
Tension vs. Strain with Ends Fixed

Fig. 6 Tensile property of single armor section



Torque vs. Strain with Ends Fixed

Fig. 7 Torsional property of the single armor section



Rotation vs. Strain with One End Free

Fig. 8 Rotational property of single armor section

The tensile strength of the single armor is sufficient to recover the double armor section at 6000 meters while allowing itself to be recovered by the system deep-water cable due to its lightweight. The rotation of the cable is also small at the operating condition, when the cable strain is normally limited to less than 0.8%.

3. Joint Design

The cable to repeater coupling and cable to cable joint utilizes MJ (Millennia Joint) or UJ (Universal Joint) overmolding technology in conjunction with a unique armor termination method. The new method, which utilizes a combination of mechanical and adhesive techniques, was developed to provide reliable connection between the epoxy impregnated aramid rods contained in the trunk cable and the joint or repeater housings. The cable to repeater coupling is sketched in Fig. 9.

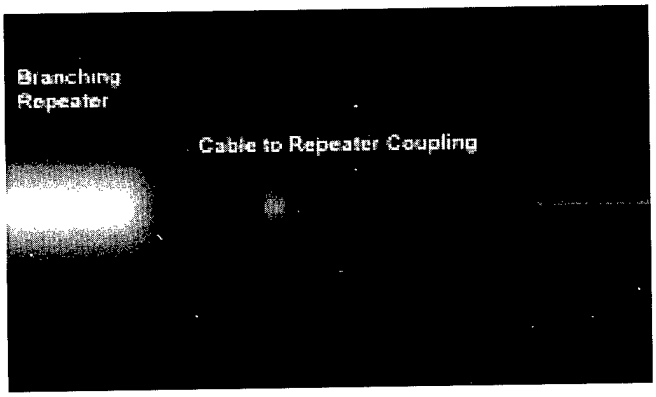


Fig. 9 Trunk cable to branching repeater coupling

Trunk cable segments can also be joined by the new termination method. The cable to cable joint, which is capable of connecting the following cable types, is shown in Fig.10.

- Double Armor Trunk Cable to Double Armor Trunk Cable
- Double Armor Trunk Cable to Single Armor Trunk Cable
- Single Armor Trunk Cable to Single Armor Trunk Cable

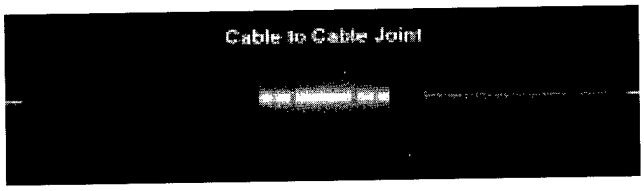


Fig. 10 Trunk cable to cable joint

4. Qualification Tests

A series of qualification tests was conducted which subjected the cable, the cable with coupling, and the cable with joint to the most severe in-service environmental conditions of tension, bending, temperature, and pressure expected in the field. All designs met the requirements. The traditional set of undersea qualification tests demonstrated the performance of the new cable and termination designs. The following table summarizes the mechanical test performance to qualify this product.

Table 1: Mechanical Testing Summary

TEST PERFORMED	PARAMETERS	RESULTS
Tension-Torque-Elongation	NTTS for 1 hr.; fixed end condition	Predicted tension, torque, strain behavior
Tension-Rotation-Elongation	NTTS for 1 hr.; free end condition	Predicted tension, rotation, strain behavior
Tension to Failure	Ramp to failure	>240 kN
Stopper Handling	90 min. at NOTS; 10 min. at NTTS	Successful stopper grip holding
Applied Torsion	1 turn per 10 meters; both directions	Nominal loss change per fiber; No physical damage
Sheave Laying & Recovery	3 passes at 300 kN; 3 meter dia. sheave	Nominal loss change per fiber; No physical damage
Tensile Test without Swivel	NTTS for 1 hr.; fixed end condition	Nominal loss change per fiber; No physical damage
Tensile Test with Swivel	NTTS for 1 hr.; free end condition	Nominal loss change per fiber; No physical damage
Cyclic Tension	30% to 50% NTTS; 26,000 cycles	Nominal loss change per fiber; No physical damage
Storage	-20C to +50C; 10	No physical

TEST PERFORMED	PARAMETERS	RESULTS
Temperature Cycling	cycles	damage
Shock & Vibration	40 g for 500 bumps; three axes 10-150 Hz freq. Sweep at 5 g; 3 axes	No physical damage

Specific emphasis was placed on characterization of the coiling and uncoiling ability of the cable designs to meet factory and shipboard conditions encountered before installation.

5. Sea Trial

The deployment and recovery capability of the special deep ocean trunk cable and trunk cable coupling was successfully demonstrated on a sea trial at an ocean depth of 6000 meters.

The cable configuration used during the sea trial consisted of the SL-LW system cable, a single armor section of trunk cable, a double armor section of trunk cable, a Branching Repeater, and SPA cable branch legs. The double armor section of trunk cable was connected to the Branching Unit with a double armor cable-to-repeater coupling assembly. The shipboard end of the cable segment provided fiber access to enable monitoring of the optical attenuation of the eight fibers during the trials. The optical fibers were connected to a lightwave switch, buffer spool, and optical time domain reflectometer (OTDR). This set-up enabled easy switching between fibers to record the OTDR traces of each fiber.

An actual system Branching Unit deployment was simulated by first deploying one branch leg and connecting the coupling to a ground rope which was paid out while the ship sailed to the beginning location of the second branch leg deployment. The ground rope was recovered while the second branch leg was deployed, allowing the first coupling to be recovered without time-consuming buoy operations. The first coupling was then connected to the Branching Repeater.

The fibers were monitored continuously and OTDR traces were recorded every half-hour. After holding a vertical lead for one hour to collect OTDR traces, the cable was recovered.

In order to achieve maximum recovery tensions, a minimum cable recovery speed of 1 knot (1.85 km/hr) was maintained with a 75 degree lead angle

Very little twisting of trunk cable was observed during deployment, as expected since the cable is torque-balanced. The cable coiled well into the cable tank after recovery. No difference was noticed between the pre-deployment and post-deployment coils.

No significant changes in optical attenuation were observed during the entire deployment/recovery cycle.

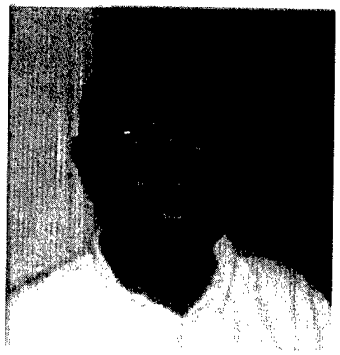
6. Conclusion

A special trunk cable and associated joints and couplings for deep water applications have been developed. The cable and associated joints have passed rigorous qualification tests; and a sea trial has been successfully conducted at 6000 meters water depth. Designed as an integrated part of the system cable, the trunk cable can be handled and deployed conveniently as a normal system cable.

7. References

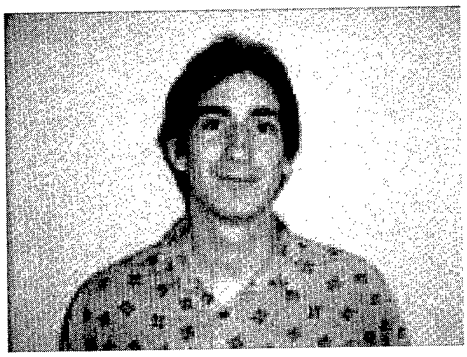
[1] T. C. Chu, "and R. J. Rue, "Evaluation of Mechanical Properties of Various Fiberoptic Submarine Cables in Both Elastic and Plastic Regions," *The Proceedings of the 47th International Wire and Cable Symposium*, 394-403 (1998).

Biography



T. C. Chu, TyCom (US) Inc., Eatontown, NJ 07724

T. C. Chu received his B.S.M.E from Cheng Kung University, Taiwan, 1964, M.S.M.E from Syracuse University, 1967 and Ph.D. Aerospace Engineering from Cornell University, 1971. He joined Bell Laboratories in 1972 and retired in 1997. During his service with AT&T Bell Laboratories, he was responsible for the design and development of AT&T's SL and SL100 fiber optic submarine cables. He is currently with the Advanced Technology Research Group in the Cable Development Division of TyCom (US) Inc, working on new cable design and development.



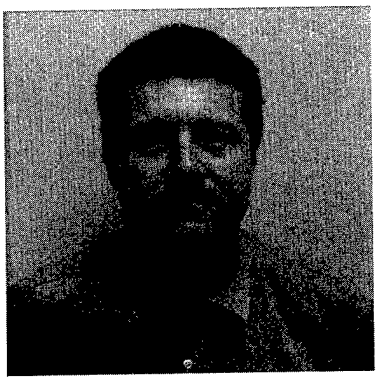
David A. Giordano, TyCom (US) Inc., Eatontown, NJ 07724

David received a B.S.M.E. from Stevens Institute of Technology in 1996 and is completing his M.S.M.E. Since joining AT&T Bell Laboratories in 1997, he has been developing cable joints and couplings for the UQJ, UJ and MJ jointing platforms. Currently David is responsible for developing new cable jointing techniques for the Cable Jointing Technologies Division of TyCom (US) Inc.



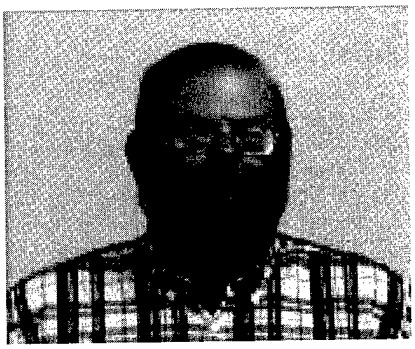
Tiiu V Kutt, TyCom (US) Inc., Eatontown, NJ 07724

Tiiu received her doctorate in civil engineering and engineering mechanics from Columbia University in 1985. Since then, she has worked in several organisations at AT&T on a broad range of problems involving telecommunications cable and repeater installation and recovery as well as tow cables. She is currently with TyCom (US) Inc., a former business unit of AT&T.



R. J. Rue, TyCom (US) Inc., Eatontown, NJ 07724

R.J. Rue received his AAE-MET degree from Vermont Technical College, and his BS-MET degree from Trenton State College. He joined the Undersea Systems Cable Development & Implementation Department at AT&T Bell Laboratories in 1984. His work has been focused on the development testing and analysis of fiber optic undersea cable designs and related hardware. He is currently a Senior Member of Technical Staff with the Cable Development Division of TyCom Laboratories and is responsible for development and qualification testing of new cable, joint, and coupling designs.



Bruce S. Clark, TyCom (US) Inc, Newington NH 03801

Bruce Clark earned his Bachelor of Electronic Engineering Technology from DeVry Institute of Technology and his MBA from the University of New Hampshire. He joined Simplex Wire and Cable (now TyCom Integrated Cable Systems) in 1976 and has performed various functions in the Engineering and Quality departments. He is currently a Senior Product Engineer working on the design, manufacture and qualification of armored submarine telecommunication cables.

Tight Type Fiber Unit Optical Submarine Cable with DMF for Ultra Long-Haul DWDM Submarine Cable System

Kazuto Yamamoto, Juan Carlos Aquino, Osamu Nagatomi, Ryo Kanda, Rokuro Morikawa

Engineering Development Department, Submarine Systems Division
OCC Corporation, Kitakyushu, JAPAN
k-yamamoto@occ.ne.jp

Abstract

We study the possibility of controlling the chromatic dispersion (CD) characteristic of dispersion managed fiber (DMF). Trial manufacturing 2 cable pieces of 45km each, applying DMF is conducted under process control that allows management of chromatic dispersion characteristic. We confirmed that chromatic dispersion of DMF during cabling can be controlled within +/- 0.1[ps/nm/km] of the target and that other optical and mechanical attributes of DMF are not affected by cabling.

Through on-land and sea trial test, optical and mechanical attributes of cable applying DMF in a high-count tight type fiber unit was confirmed to have good performance.

Keywords

High Count, Tight Type Fiber Unit, DWDM, DMF, Submarine Cable.

1.Introduction

DMF have been reported to be one of the suitable solutions to realize DWDM long haul system. Moreover, good performances obtained with submarine cable applying DMF in a tight type fiber unit structure have been reported [1].

However, to realize the application of DMF in actual system, the chromatic dispersion characteristic at each fiber cabled must be controlled. This time, we study the possibility of controlling the chromatic dispersion characteristic of DMF during cabling applying a process optimized for simultaneously managing the attributes of several DMFs deployed in a single cable.

2.Cabling of DMF

DMF, large effective area and large positive dispersion fiber in a hybrid combination with fiber having large negative dispersion and negative dispersion slope characteristics, realizes excellent transmission characteristics with the advantages of low non-linear effects and flat spectral chromatic dispersion characteristic, as shown in Figure 1. And is suitable for DWDM long haul systems.

On the other hand, the individual fibers that constitute DMF have large absolute CD characteristic in comparison with other fibers for WDM applications. Therefore, determining which portion of the fiber is to be cabled is extremely important to maintain its optical attributes.

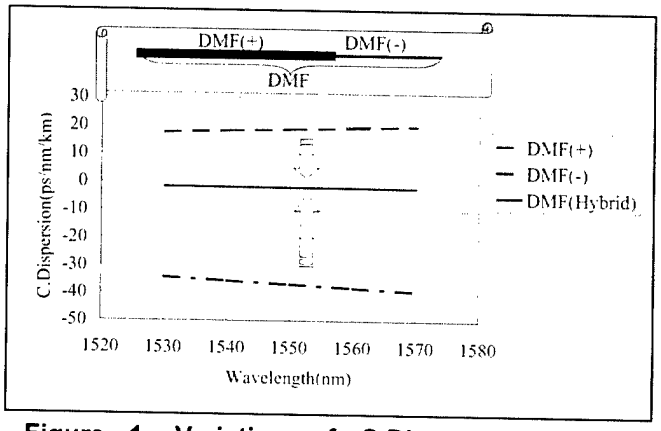


Figure 1. Variation of C.Dispersion spectral characteristic

For example, Figure 2 describes the effect of shifting the optimal position of fiber by around 150m. Having DMF(+)=20[ps/nm/km] and DMF(-)=-40[ps/nm/km] in a 2:1 hybrid combination to form DMF of 45km, the 150m shift on the DMF(+) side results in a shift of the CD characteristic of the span of +0.2[ps/nm/km], when thinking about several spans connected to form a system, this shift can not be neglected.

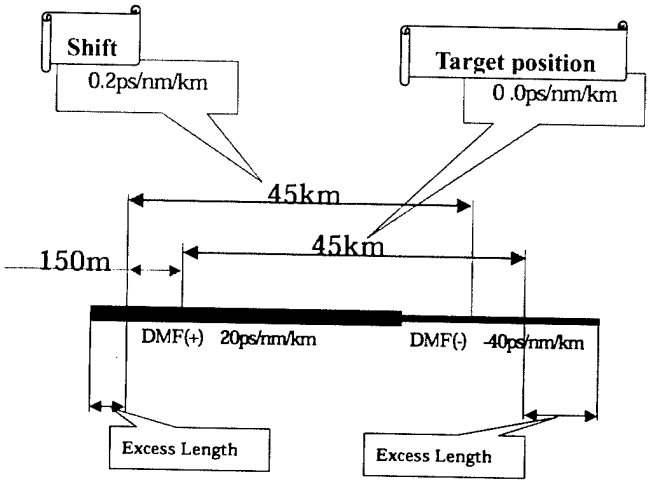


Figure 2. Dispersion Management at fiber

Moreover, in an actual cable several DMFs with different directions and different constituent portions are applied as described in Figure 3, this make controlling cable CD characteristic even more difficult.
On the other hand, if we can manage to control the CD characteristic of each fiber during the cabling process, then we might be able to control the characteristic of the cable for a certain value requested.

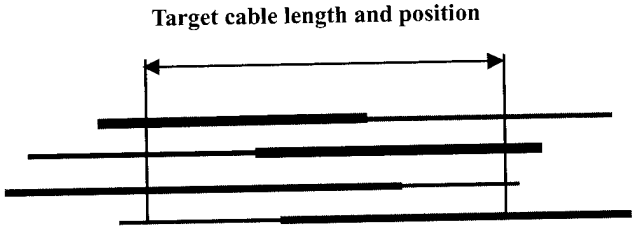


Figure 3. Dispersion Management at Cable

Validation of CD control during cabling Eight DMF 45 km long were applied to trial manufacture two pieces of LW cable, with a total length of 90 km. Each sample was manufactured with 2 pairs of DMF which were arranged in the cable taking into account up-stream and down-stream signals traveling in to actual systems.
Typical characteristic of the constituent DMF(+) and DMF(-) of the DMF applied in the trial manufacturing are shown in Table-1.
Moreover, the structure of the cable manufactured and its main mechanical parameters are shown in Figure-4 and Table-2 respectively.

Table 1. DMF fiber's characteristics

Fiber Type	Clad Diam	Aeff @1550n	Atten. @1550nm	Dispersion @1550nm	Slope @1550nm
	μm	μm^2	dB/km	ps/nm/km	$ps/nm^2/km$
DMF(+)	125	100	0.186	18.7	0.060
DMF(-)	125	25	0.200	-36.8	-0.120

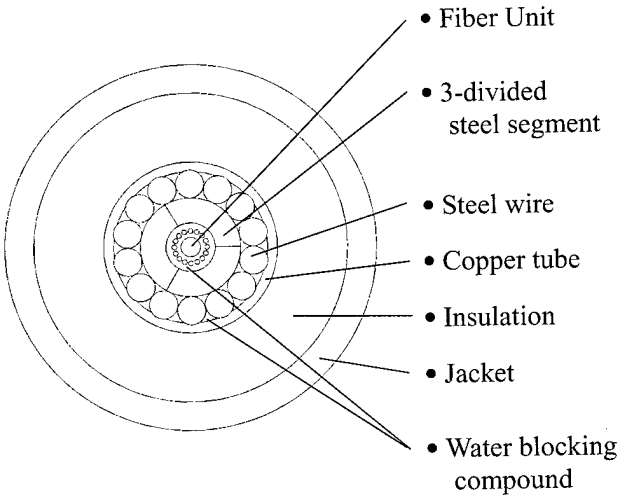


Figure 4. Structure of OCC-22S LW Cable

Table 2. OCC-22SLW Cable's typical characteristics

Cable nominal diameter	22.5 mm
Cable weight in air	8.9kN/km
Cable weight in water	5.0 kN/km
Minimum breaking load	98 kN
Minimum bending radius	900 mm
Maximum deployment depth	8000 m

3. Optical characteristics management

3. 1.Chromatic Dispersion (CD)

Figure 5 and Figure 6 show the chromatic dispersion (CD) characteristic, at 1550nm, of each DMF applied at each step of the cabling process. During the trial manufacturing we targeted a CD value of -1.95 [ps/nm/km].
From the figures we can notice that CD characteristic of each fiber is smoothly controlled to reach a value, after the LW process, that is close to the targeted characteristic. Also deviation between fibers CD values is reduced after cabling. Thus, confirming the viability of the process applied for controlling dispersion of the fibers being cabled.

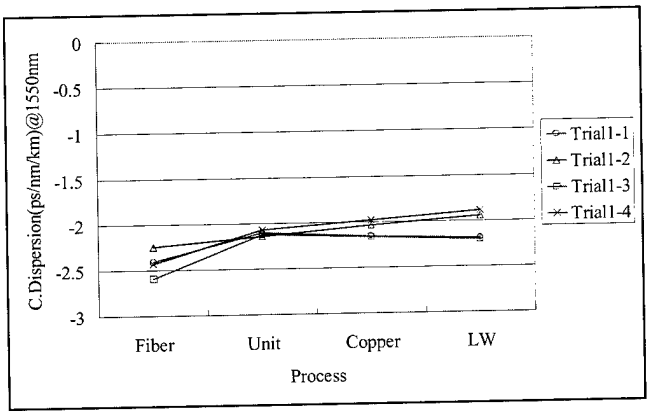


Figure 5. C.D. variation during cabling(Trial 1)

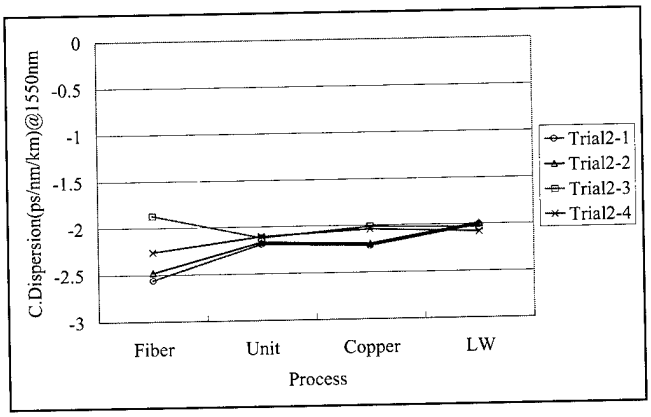


Figure 6 C.D. variation during cabling(Trial 2)

3. 2. CD slope

Figure 7 and Figure 8 show the spectral CD characteristic of each DMF cabled over the C-Band window. It can be noted from the figures that flat spectral CD characteristic on the DMF was obtained with both manufactured cables.

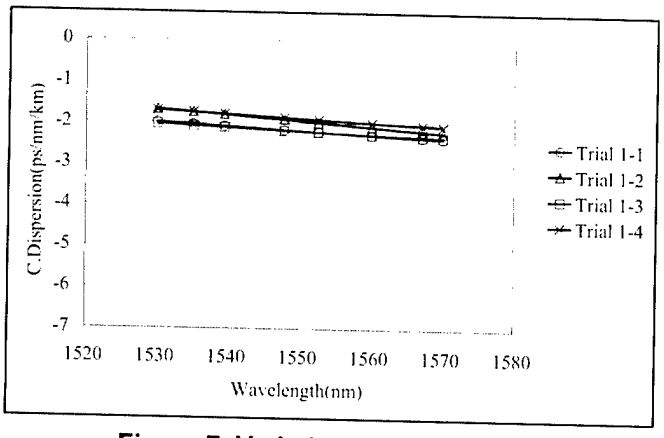


Figure 7. Variation of C.D. spectral characteristic(Trial 1)

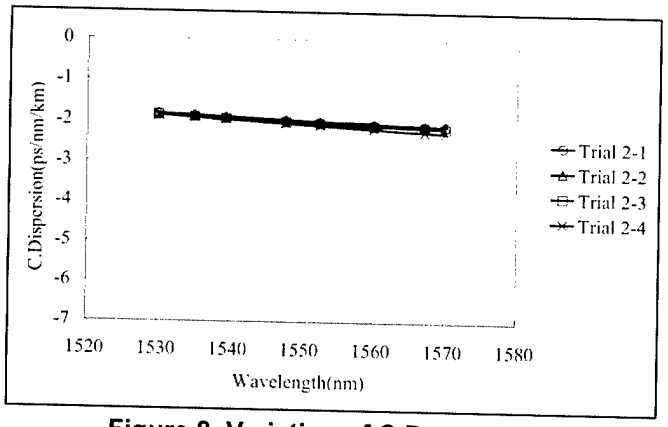


Figure 8. Variation of C.D. spectral characteristic(Trial 2)

After having manufactured 2 cable pieces of 45 km, applying DMF, the CD control process gave us a final CD characteristic on each fiber that was within ±0.1 [ps/nm/km] of the targeted value. These results confirmed that it is possible to control CD characteristic of DMF during the cabling process.

4.Other optical characteristics results

4.1. Optical attenuation

Figure 9 shows the optical attenuation variation after cabling process for 4 DMF cabled during the trial manufacturing. No attenuation increase was observed on each fiber measured. Representative spectral attenuation characteristic of a cabled DMF is shown in Figure-10.

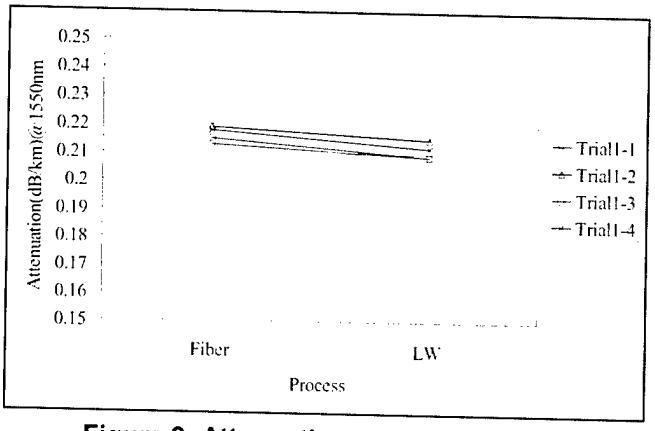


Figure 9. Attenuation variation during

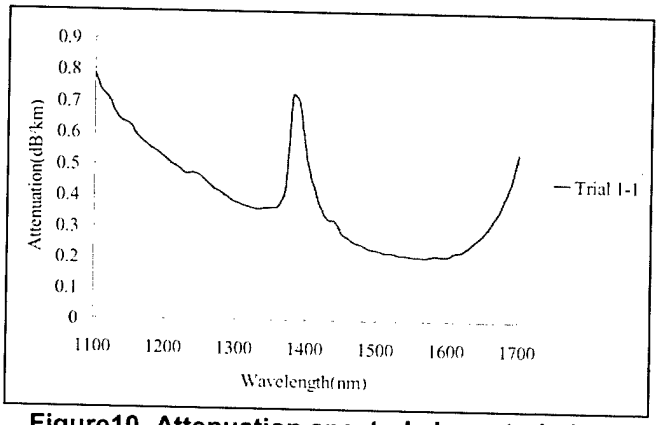


Figure10. Attenuation spectral characteristic

4.2. Polarization Mode Dispersion (PMD)

Figure-11 shows the PMD characteristic of each cabled fiber after LW process. Measured PMD values were under 0.05 [ps/√km], a value good enough for nowadays systems. Also variation from the PMD in fiber to PMD after cabling was at the same level of variations obtained when cabling NZ-DSF for WDM applications.

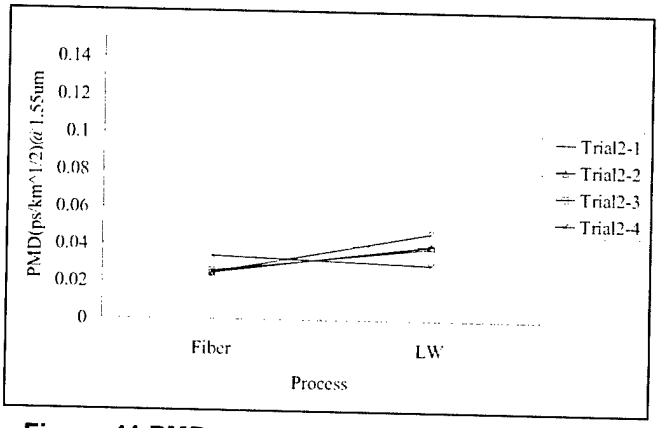


Figure-11 PMD variation during cabling(Trial 2)

From these results, besides being able to control CD characteristic of DMF, we also confirmed that the tight type fiber unit design is suitable for cabling DMF without degrading any of its attributes.

5.Environmental and mechanical test results

5.1.Operational temperature characteristic

Figure 12 shows optical attenuation characteristic per kilometer for 2 measurement loops of 90km, when temperature is cycled from 15 °C to 3 °C and 30 °C. Attenuation variation was confirmed to be less than 0.001 [dB/km]. Which indicates the applicability of DMF in actual systems.

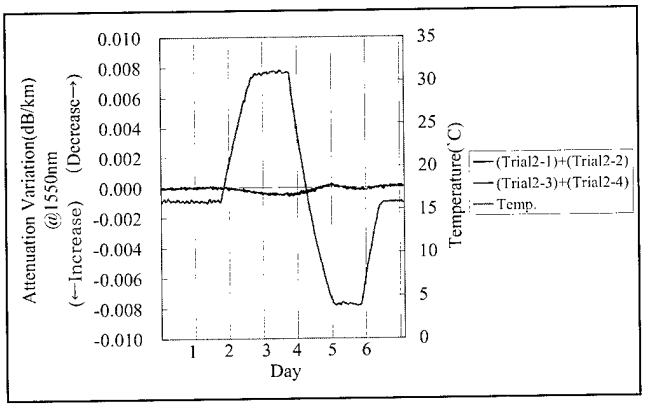


Figure 12. Temperature stability characteristic (Trial 2)

5.2. Sheave test

Figure 13 shows the schematics of the sheave test performed as part of cable's mechanical evaluation program. The cable sample is wound on a R=1.5m sheave and loaded to NOTS(63kN), then the sheave is moved along the cable until completing 50 cycles. Finally load is risen to NTTS(80kN) and 3 additional cycles are performed. Variation and residual attenuation for both DMF(+) and DMF(-) measurement loops were less than 0.001 dB, the minimum detectable variation in the instrument. Confirming the excellent performance that can be obtained with cable applying DMF.

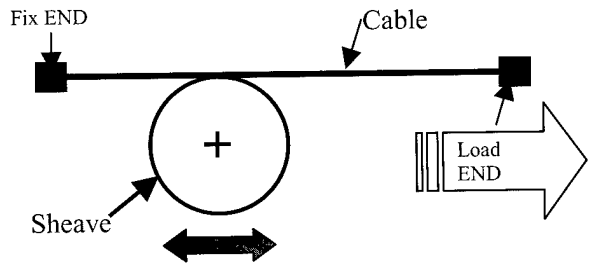


Figure-13 The Sheave test evaluation way

6. Sea Trial

LW cables applying DMF were tested during a sea trial in a sea area where the maximum depth was 8,300m. The cable lay out is described in Figure 14. With a nominal repeater span length of 45 km and a piece of 7.5km were arranged to form 52.5km of cable. Lay, hold and recover operations were conducted.

Also, newly designed Joint Box (JB) and repeater terminations were evaluated during this sea trial. Figure 15 shows a picture of the JB being laid.

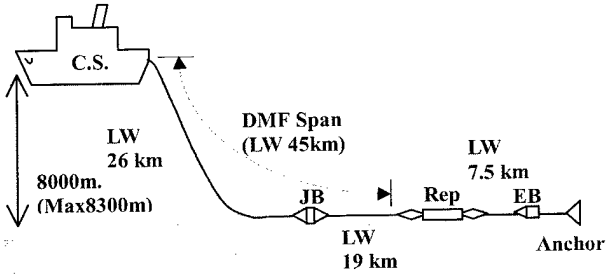


Figure 14. Sea trial lay out

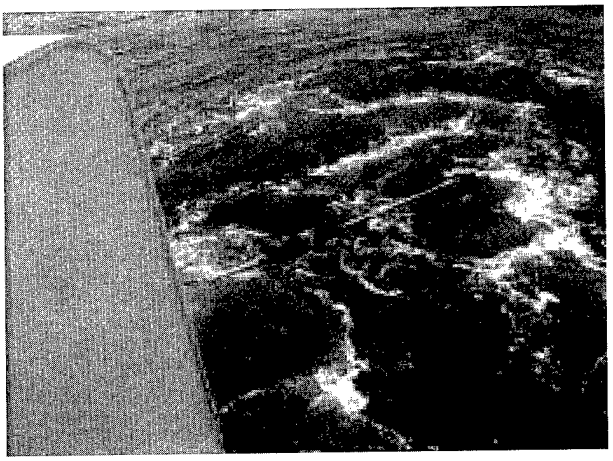


Figure 15. JB being laid during sea trial

Figure 16 shows the optical attenuation continuous monitoring records during each operation of the sea trial. From the figure, variation less than 0.001 dB/km. However the maximum tension experienced by the cable was 64 kN (>NOTS) it was not an effect of the mechanical load on the cable. Referring to Figure 12 this variation can explained as an effect only of the temperature change that the cable undergoes when installed from the ship's tank to the sea bead and back to the tank after recovery.

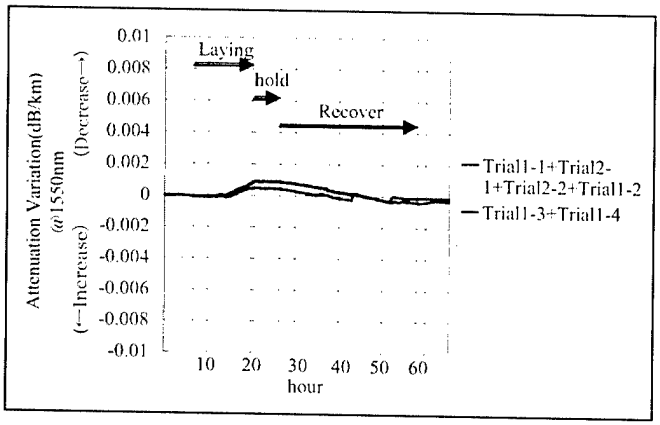


Figure 16. Optical attenuation continuous monitoring results

7. Conclusion

- Control of CD characteristic of each fiber during cabling process was performed and confirmed to be viable. Moreover, CD characteristic of system can be controlled at a level for long haul DWDM submarine systems.
- Through on-land and sea trial test, optical and mechanical attributes of cable applying DMF in a high-count tight type fiber unit was confirmed to have good performance.

8. Acknowledgments

Our special thanks to all the people who worked and collaborated at manufacturing and evaluating the cables.

9. References

[1] Juan C. Aquino, "Development of High-Count Tight Type Fiber Unit for Submarine Cables " 49th IWCS, p.607-612 (2000).

[2] Osamu Nagatomi, "Development of New Tight-Fit-Type Submarine Cable with Large Core Fibers for WDM Systems" 48th IWCS, p.317-323 (1999).

[3] Takato Nishida, "Developtment of Repeaterless Optical Fiber Submarine Cable System for Extensive Application" 45th IWCS, p.527-531 (1996).



KAZUTO
YAMAMOTO
OCC Corporation
1-105-2 Hibiki-Machi
Wakamatsu-ku
Kitakyushu

Kazuto Yamamoto was born in 1967. He graduated from Tokai University with B.E. degree in Mechanics in 1990. Since he joined OCC, he has been engaged in the research and development of optical submarine cables. Actually, he is a Deputy Manager at the Engineering Development Department, Submarine Systems Division.



JUAN CARLOS
AQUINO
OCC Corporation
1-105-2 Hibiki-Machi
Wakamatsu-ku
Kitakyushu

Juan Carlos Aquino was born in 1971. He received his M.E. degree in Electronics from the Kyushu Institute of Technology. He joined OCC in 1999 and has been engaged in the research and development of optical fiber submarine cables. Actually, he is an engineer at the Engineering Development Department, Submarine Systems Division and member of the IEICE of Japan.



OSAMU NAGATOMI
OCC Corporation
1-105-2 Hibiki-Machi
Wakamatsu-ku
Kitakyushu
808-0021 JAPAN

Osamu Nagatomi was born in 1969. He received his B.E. and M.E. degree in Mechanics from the Kyushu University. Since he joined OCC, he has been engaged in the research and development of optical fiber submarine cables. Actually, he is an engineer at the Engineering Development Department, Submarine Systems Division and member of the SNAJ of Japan.



RYO KANDA
OCC Corporation
1-105-2 Hibiki-Machi
Wakamatsu-ku
Kitakyushu
808-0021 JAPAN

Ryo Kanda was born in 1973. He graduated form the Kyushu Institute of Technology with B.E. degree in Electrical Engineering. Since he joined OCC, he has been engaged in the research and development of optical submarine cables. Actually, he is an engineer at the Engineering Development Department, Submarine Systems Division.



ROKURO
MORIKAWA
OCC Corporation
1-105-2 Hibiki-Machi
Wakamatsu-ku
Kitakyushu

Rokuro Morikawa was born in 1957. He graduated form the Housei University with B.E. degree in Mechanical Engineering. Since he joined OCC, he has been engaged in the research and development of optical submarine cables. Actually, he is a Deputy General Manager at the Engineering Development Department, Submarine Systems Division.

High Count Fibre Submarine Cable Family for Unrepeated Transmission Systems

Inge Vintermyr, Vegard Briggar Larsen, Tom Eirik Toften and Jørn Wardeberg
Nexans Norway AS, P.O Box 130 Økern, N-0509 Oslo, Norway
inge.vintermyr@nexans.com

1 ABSTRACT

A high fibre count sea cable family for unrepeated systems is presented, offering maximum 384 fibres. The design is based on stainless steel tubes, offering excellent long term stable mechanical and optical characteristics.

The cable family is accompanied by joint boxes and a branching unit. Likewise, a remote amplifier is presented, which extends the maximum transmission link by typically 80 km. This unit relies on passive optical components, remotely pumped from a land terminal.

Field tests with high G652 fibre bit rates and installation references are also presented.

2 INTRODUCTION

During the recent years there has been an increased demand for high fibre count in both terrestrial and submarine cables, especially in coastal applications as part of a terrestrial network. This requires high fibre count in submarine cables, together with a demand for G655 fibre types to cover future bit rate upgrades.

The submarine cable development has been accompanied by the development of designated cable joints and equipment for remote amplification also presented in this paper.

3 DESIGN OBJECTIVES

The main design objective for the high fibre count sub sea cables has been to provide a family (URC-1 family) of reliable and cost effective cable designs suitable for both present and future fibre types. Hence, the cables developed provide excellent physical protection of the fibres with very low stresses and environmental impacts on the fibre during all service conditions (/1/-/6/).

A branching unit (BU) and cable joint boxes have been developed and qualified for 2000m sea depth. The BU, which splits the fibre count between single and double legs is for example used in transmission links between oil platforms in order to pull in and hang off one submarine cable instead of two.

4 CABLE DESIGN

4.1 Optical Package

The optical package presented in Figure 1 is based on the steel tube technology in which the fibres are protected inside a jelly filled, laser welded stainless steel tube. The cable core consists of up to eight SZ stranded, 3.7 mm OD, steel tubes, each with a capacity of 48 fibres. Thus, up to 384 fibres can be accommodated. The fibres in each tube are uniquely colour coded.
The single tube configuration can also accommodate up to 96 fibres, in a 5.6 mm OD steel tube. Furthermore, the single tube configuration can be fitted with a smaller tube (φ 2.3 mm) for deep sea installations.

Optical testing during manufacturing and qualification have clearly shown that the stainless steel tube provides a stable and reliable environment for the fibres over the whole optical bandwith. This has been demonstrated for standard single mode fibres (G.652) as well as for the new fibre types (G.655) with larger effective areas and reduced chromatic dispersion slope to accommodate higher number of wavelengths for the new submarine "highways"

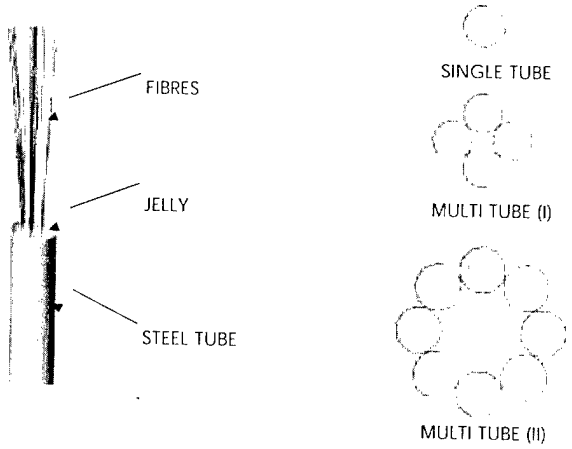


Figure 1. Optical package.

4.2 Cable Core and Armouring

For mechanical protection and electrical insulation a polyethylene sheath is applied over the steel tube(s). For electroding and fault finding purposes, copper conductors are integrated in the interstices between the tubes in the multi tube designs. For the single tube design a copper tape applied over the steel tube ensures electrical continuity.

The overall diameter of the cable core is 10 mm, 16 mm or 20 mm for the single tube, four tubes and eight tube configurations respectively.

The cable core is armoured with galvanized steel wires. All steel wires are preformed in order to provide more uniform coverage, better handling and installation characteristics, and facilitate termination work. A double layer of polypropylene yarn (as shown in Figure 2) or high density polyethylene jacketing is available for outer protection.

A complete range of cables; single armour (SA) and double armour (DA) designs offering tensile strengths from 5 to 400 kN has been qualified. Typical DA designs are shown in Figure 2

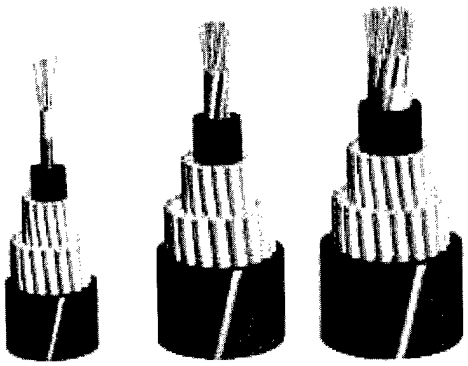


Figure 2. URC-1 cable with 96 to 384 fibres.

The main cable characteristics for the designs are shown in Table 1.

Characteristics	48,96 fibres		192, 384 fibres	
	SA	DA	SA	DA
Cable outer diameter (mm)	20-34	24-42	42	45.5
Cable weight in air (kg/m)	1-2.6	2-5.1	5.1	7
NTTS Load*) (kN)	100-200	150-400	400	400
Min. bend. diam. at NTTS (m)	2.5		3	
Max. water depth (m)	3000/1500		500	
Max fibre count	48/96		192/384	
Operating temp. range (°C)	-20 - +35			

*) Nominal Transient Tensile Strength, 1 hour

Table 1. Cable characteristics. Single armour (SA) and double armour (DA) cable designs

5 CABLE ACCESSORIES

5.1 Joints and Branching Units

The development of high-count fibre cables has been followed by the development and qualification of a family of Joint Boxes and Branching Units (BU). General design and dimensions are shown in Figure 3.

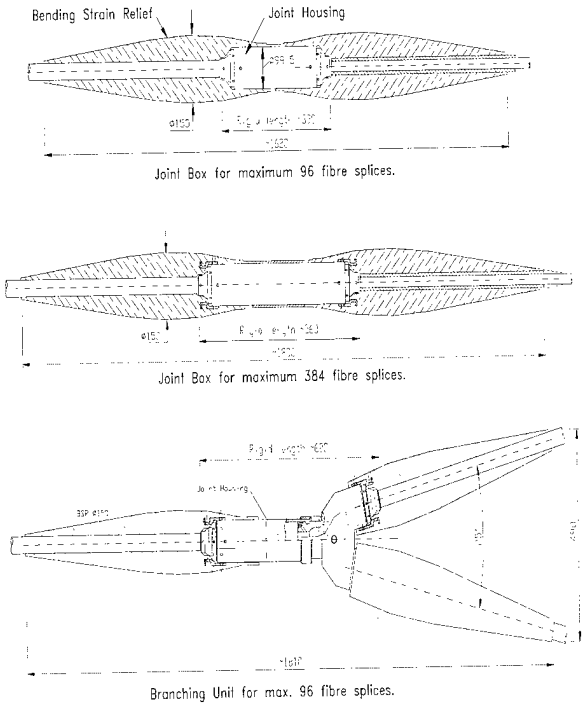


Figure 3. Joint boxes for 96 and 192/384-fibre splices and BU.

The branching unit and the joints are designed and tested for 3 m bending diameter, and can be deployed using standard cable installation procedures and equipment. The units are designed and tested for electrical continuity and insulation from the seawater, which is required for cable electroding and fault finding purposes.

Joints and BU assembly principles are based on mechanical terminating the cable ends followed by fibre jointing before the sea-case closure is installed. (Figure 4 and 5)

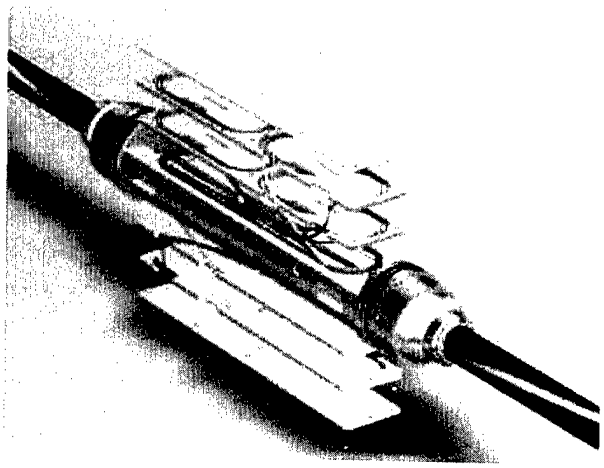


Figure 4. 384 fibres joint box. (Two bend restrictors and outer sea case not shown).

The assembly time for a 384 fibre joint box is shown below.

- Mechanical assembly and fibre splicing: 24 hrs
    - Prepare cable ends and assemble armour termination: 2 x 2 hrs
    - Fibre bracket assembly: 2 hrs
    - Fibre splicing: 16 hrs (24 fibres/hour)
    - Final assembly: 2 hrs
- Optical verification: 16 hrs (24 fibres/hour)

The jointing time is based upon the following manpower:

Cable End A: 2 optical testers
Cable End B: 2 optical testers
Jointing area: 2 jointers.

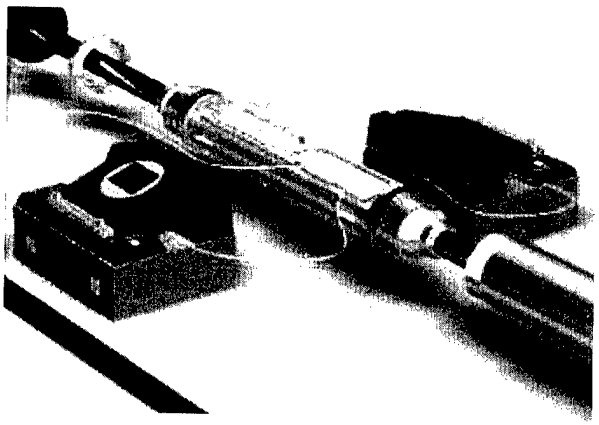


Figure 5. Fibre splicing principles with two jointers working in parallel with fibre splicing.

The jointing time could be further reduced by increasing the manpower, especially during final optical verification.

5.2 Remote Amplifier Box

The Remote Amplifier Box (RAB) amplifies the optical signal in un-repeatered submarine fibre cables. The technology relies on passive optical components, which are optically pumped from a land terminal. The amplification increases the repeaterless transmission link distance from typically 220 km to 300 km.

Figure 6 depicts the optical topography for one fibre pair. An Erbium Doped Fibre (EDF) of typically 25 m length and an optical isolator provide the signal amplification. The unit can presently accommodate up to 96 such fibre pairs, implying up to 192 optical fibres.

The EDF is pumped at 1480 nm from the receiver terminal. One fibre is utilised for both pumping and the amplified signal. For the shown pre-amplification single pumping configuration, a budget improvement of typically 15 dB is feasible. Signal transmission is at typically 1520 nm wavelength.

The RAB relies solely on passive optical components, with pump lasers and control circuitry located in the land station. The system thus maintains the high reliability, low cost and simplicity characterizing un-repeatered systems.

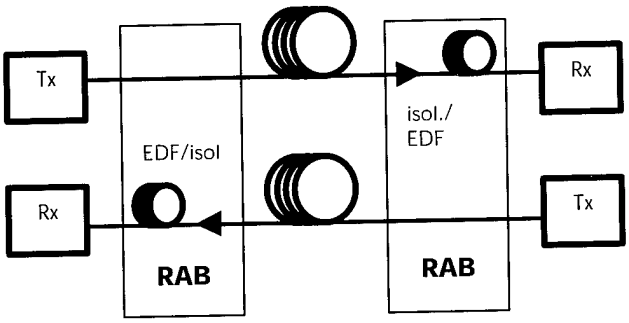


Figure 6. Optical Topography for one transmission channel (one fibre pair shown).

The RAB (Figure 7) is designed to protect the optical components and the fibre splices from the mechanical loads arising in transportation, installation and long term operation. Special attention has been dedicated to hydrogen protection, to which Erbium Doped Fibre is sensitive.

Mechanical termination of the sea cable is accomplished utilising a hydraulically activated cone system. Pressure integrity and minimum hydrogen ingress rely on metal-metal seals and standard compression fittings to the fibre steel tubes. The design permits easy adaptation to all Nexans sea cables.

The optical components (isolators and Erbium Doped Fibre) are secured on aluminium trays, in turn mounted on a central axial bracket. All fusion fibre splices and their protective sleeves, together with fibre service lengths, are secured in dedicated trays.

RAB provides electrical isolation from seawater and continuity through the transmission link, as required for cable electroding purposes.

The 48 fibre pair RAB has overall length 480 mm. Outer diameter is 143 mm. Including bend limiters yields corresponding dimensions 1700 mm by 216 mm. Total weight including bend limiters is approximately 75 kg.

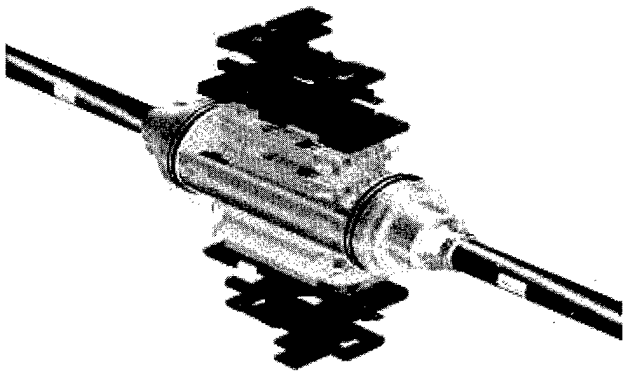


Figure 7. RAB exploded view (48 fibre pairs). Cylindrical outer housing and two bend restrictors have been omitted for clarity

RAB is incorporated within the cable transmission system prior to installation and is deployed using standard cable installation procedures and equipment.

5.3 Sealing of sea casing.

The branching unit , the joint boxes and the Remote Amplifier Box all rely on metal-metal sealing technology. The concept is shown in Figure 8. The primary and secondary seals to the outer sea casing comprise a metal C-ring and an elastomeric O-ring respectively. The materials have been choosen for long term sea water exposure. The cable steel tube is sealed using a standard metal-metal compression fitting, which in turn is mounted in a ceramic insert for electric insulation from the sea water.

The Erbium doped fibre in the RAB is particularly sensitive to hydrogen, which is generated in the sub-sea plant corrosion process. The metal-metal seals offer efficient and reliable hydrogen diffusion barriers.

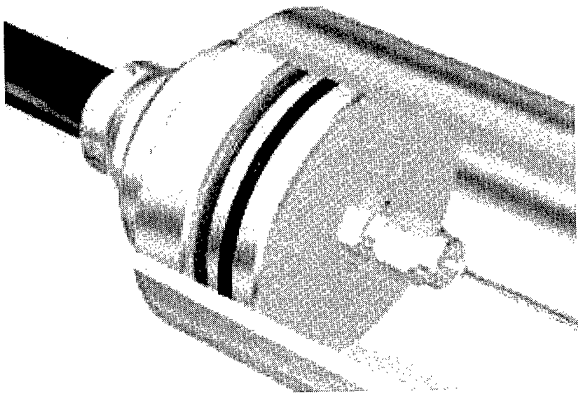


Figure 8. Sealing Principles

6 QUALIFICATION

The family of high count fibre cables, the joint boxes and the BU have been successfully qualified for the loads associated with manufacturing, transportation, installation and operation. The RAB qualification tests are summarised in table 2. The entire cable family up to 384 fibres with associated joint boxes, has been qualified accordingly (Figure 9).

Test	Contents
Sheave passage	200 kN tension, 3 m diameter sheave, three cycles
Torsion	2 kN, 1 turn per 5 m, 5 cycles.
Linear tension	360 kN
Temperature cycling	Temp. range: -20°C-+50°C, 10 cycles.
Hydraulic pressure	450 bar, 24 hours
Vibration	Swept sine 10-150 Hz, 1 g, 3 axis
Shock	Half sine, 20 g, 6 ms, 3 axis
He leak testing	Leak rate better than 10^{-8} cm^3/s. (Room temperature)

Table 2. Qualification Tests.

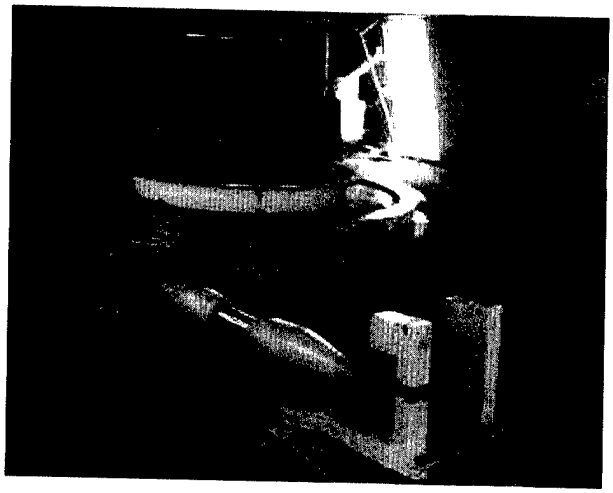


Figure 9: Tensile testing of the 384 fibre cable and joint box at 3 m diameter sheave.

7 INSTALLED SYSTEMS

A high number of sea cables of the described design has been successfully installed and operated. These installations include more than 5000 km cable, with up to 48 fibres. Among the installations are the Ireland-UK Crossing System (245 km and 267 km, 24 fibres) and "Nor Sea Com 1" (740 km total system length, 260 km longest link length, 24 fibres).

To date, about six commercial cable lengths with 192 fibres have been successfully manufactured, tested and installed. Pre- and post installation measurements carried out on 192 fibres cables show only minor differences in optical attenuation, all within 0.195 dB/km as specified by ITU-T for G652 fibres at 1550 nm.

The "Level-3" project (England–Belgium crossing, 121 km, 192 fibres) exhibited average pre- and post installation loss 0.190 dB/km and 0.197 dB/km respectively. The loss variation is attributed to the number of installation joints.

A field trial on the installed Level-3 cable successfully demonstrated 32 channels at 40 Gbit/s /7/. Hence, demonstrating a potential upgrade to 122 Tbit/s for the installed 192 fibre cable.

To date, one commercial cable length (15 km) with 384 fibres have been successfully manufactured, tested and installed across the Oslo fjord in Norway for "Song" as shown in Figure 10 and 11. This length was provided with 288 off G.652 and 96 off G.655 fibres. The length was manufactured and installed without any joint boxes. However, a joint box was qualified and available under the installation.

The 384 fibre cable was installed with the C/V Fjordkabel from Bulk Transport AS in Harstad, Norway. The C/V Fjordkabel is a fairly small vessel; 37.4 metres long, 10.3 metres wide, and has a draft of 2.0 metres. However, this did not cause any problems during the installation as the handling characteristics for the 384 fibre cable turned out to be similar to the cables with lower fibre count.

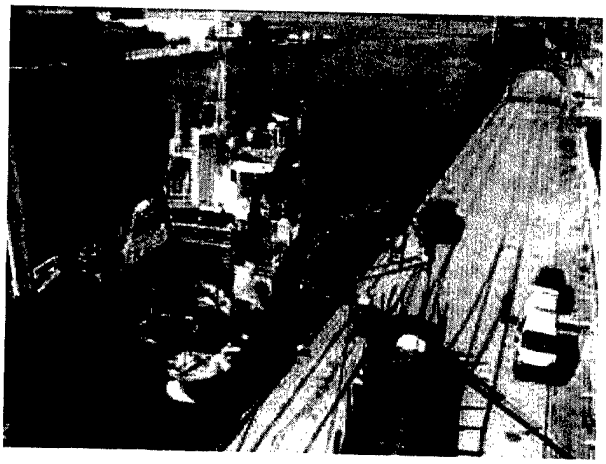


Figure 10. Loading the 384 fibre cable to the installation vessel from rail cars.

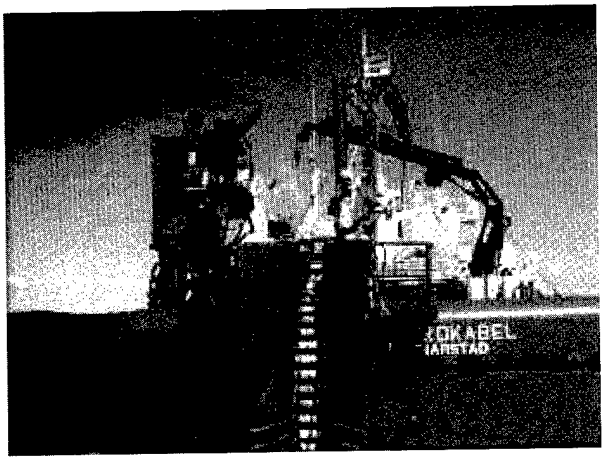


Figure 11. Installation of the 384 fibre cable with the C/V Fjordkabel.

8 CONCLUSION

The URC-1 cable family has been developed, qualified and installed for up to 384 fibres. The design has proved cost effective and reliable.

Tests and experience from installed cables have demonstrated the stability of the optical transmission characteristics of the URC-1 submarine cable under all service environments. More than 5000 km URC-1 sea cable have been successfully installed.

Joints and a branching unit have been developed and qualified for 3000 m sea depth.

A Remote Amplifier Box has been developed and qualified for 3000 m sea depth. The unit is pre-installed on the cable and is deployed with normal cable laying techniques. The unit improves the optical budget in optical transmission links by typically 15 dB, corresponding to typically 80 km. The overall reliability and low cost characteristic to un-repeatered systems is maintained, as the unit is electrically passive.

Acknowledgements

The authors would like to thank previous colleagues at Alcatel Submarine Networks for their kind assistance on providing optical components and input on optical topology and measurements techniques and test facilities.

References

/1/ J.S.Andreassen, I. Vintermyr, "Laser Welded Metallic Tubes in Optical Cables", Proceedings IWCS 1999.

/2/ J.S.Andreassen, "Aramid Armoured ROV Cable for Deep Depths", Underwater Intervention 2000.

/3/ J.S.Andreassen, I.Vintermyr, "Characteristics and Application for Laser Welded Metallic Tubes in Fibre Optical Cable Designs", Eurocable 2000.

/4/ E.Brandon, J.P. Blondel, E. Lefranc, I Vintermyr "Unrepeatered Systems, a High–tech and Cost Effective Solution for High Capacity Transmission"

/5/ G.Berthelsen, I. Vintermyr; "New Low Weight/ Small Diameter Optical Fibre Submarine Cable for Unrepeatered System", Proceedings IWCS 1994.

/6/ I.Vintermyr, R.Vogt, J.S.Andreassen , "192-Fibre count submarine cable for repeaterless systems" Proceedings IWCS 1999.

7/ P.Le Roux et al. "1.28 Tbit/s (32x40 Gbit/s) Field Trial over installed unrepeatered Tangerine 'Cable (121 km of standard fibre). Proceedings Suboptic 2001.

SPEAKER BIOGRAPHY



Dr Inge Vintermyr
Nexans Norway AS
PO Box 130 Økern
N-0509 Oslo, Norway
Inge.vintermyr@nexans.com

Inge Vintermyr graduated from the Norwegian Institute of Technology in 1989 with a Ph.D in Materials Science in 1989, and joined Nexans Norway AS (previous Alcatel Kabel Norge AS) the same year. He has been working with research and development of steel tube based cables and umbilicals since 1991. In 2000 he was appointed Technical Manager for the communications cable division.

Thermal Modelling Applications in Submarine Cable Development

Philippa Dupire, Yves Charles, Jean-François Libert, Peter Worthington
Alcatel Submarine Networks
Calais, France
+33-(0)-321-467-172 · Philippa.dupire@asn.alcatel.co.uk

Abstract
The use of modelling tools is very well adapted to the fast evolution of submarine systems market. Modelling can be used to determine optimal process to maintain product quality and achieve maximum productivity. It also enables to anticipate the behaviour of the new products and processes.

This paper deals more specifically with thermal modelling and describes how it can be used for several practical applications encountered for the cable submarine systems. Theoretical models have been established and validated by practical experiment and are presented and discussed. The first example illustrates the great interest of thermal modelling for cable extrusion manufacturing stage. The second example deals with a test set up for cooling submerged plants. The final example is about cable heating in applications where the cable is used at high current levels for remote powering.

Keywords: Thermal modelling.

1. Introduction
In the last years, the fast evolution of the need of submarine cables has lead to a drastic increase of manufacturing capacities, and to the necessity of a faster release to manufacture of the new products. This can be achieved by different ways like greater risk acceptation, over designed products or increased risks of delay. This paper presents an other way to speed up the release to market by an optimisation of the development and of the industrialisation phases. It shows how a thermal modelling software can contribute to reduce the development phase without increasing the risks of future product non-conformity with regard to the original product requirement. The use of the thermal software is presented hereafter for different stages of the submarine system life. In the first presented situation, the cable manufacturing (insulation stage), opportunity is taken to explain the theory which supports the developed model. Then after a validation exercise of the model by practical experiment, different potential uses of this tool will be described. Other examples of interest of thermal modelling will be also provided for the other stages of the system life like the system assembly (submerged equipment cooling) and the installed system (cable powering).

2. Cable manufacturing stage
2.1 Basic theory of the model
The principle of the first model is to make a heat transfer calculation across a section of the cable, in order to determine the temperature evolution at any point inside the cable cross section, at any time of the insulation process. This can be done by finite element definition of the cable.

The model has been established from a simple geometric shape. The cross section of the cable used for the calculation is shown in figure 1.

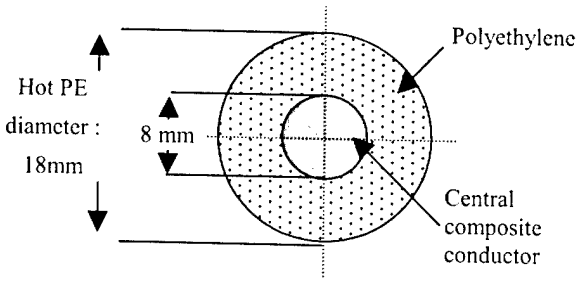


Figure 1 : simplified cable cross section.

The cable cross section is considered as a 2 constituents body : an insulation sheath and a "central conductor". Note that the central composite conductor (i.e. steel tube, vault and copper) is assimilated to one single material which properties have been averaged with the properties from its 3 constitutive materials. This can be done because the global central conductor is a much better heat conductor compared to the polyethylene.

The quad meshing of the simplified cross section of the cable is shown in figure 2. Thanks to the cylindrical symmetry of the cable, the study is performed on one quarter of the cross section.

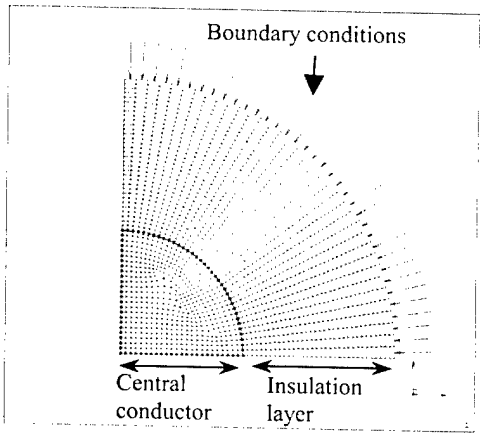


Figure 2 : Meshing of the drawing.

The initial conditions are fixed temperature in each material, typically 210°C for insulation and 20°C for the central conductor.

As shown in figure 2, the effect of what surrounds the cable (water or air) is represented by a convection boundary condition applied on the outer edge of the polyethylene layer. The temperature of this boundary condition can be changed as a function of time in order to simulate the passage of the cable in the different troughs of the cooling path. However the temperature is assumed to be constant all around the cable in each trough.

Heat transfer coefficients have to be defined for the interface between the central conductor and the polyethylene and for the interface between the polyethylene and the surrounding material. They have been calculated from empirical equations [1].

The key advantage of the model is its ability to consider the insulation sheath material density, specific heat and thermal conductivity as being temperature dependent. For that, preliminary bibliographic studies have been done for the materials. As an example, figures 3, 4 and 5 present the obtained data for one insulation sheath material used in submarine cables.

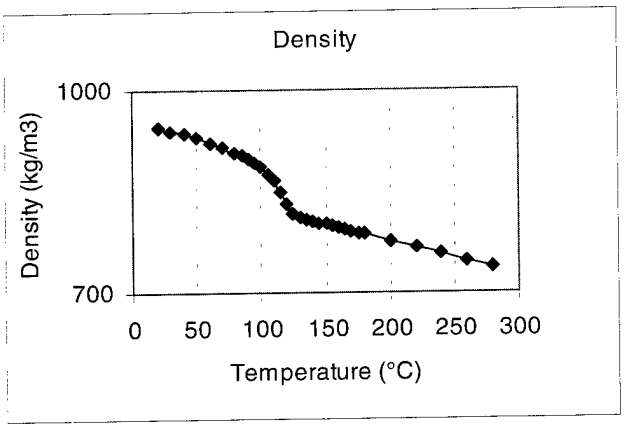


Figure 3 : Polyethylene density as a function of temperature.

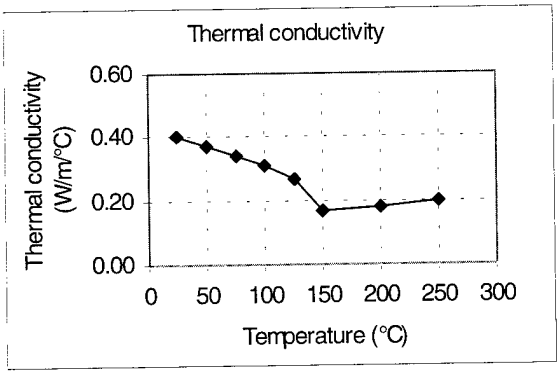


Figure 4 : Polyethylene thermal conductivity as a function of temperature.

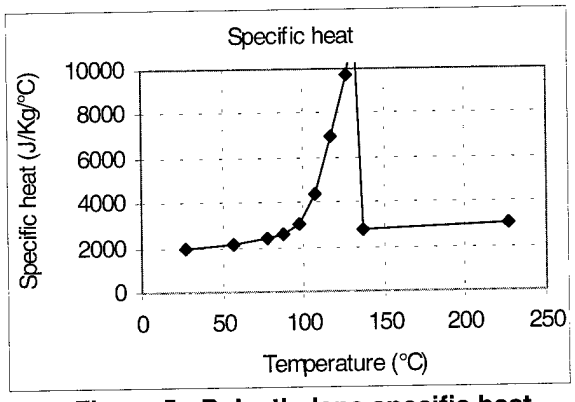


Figure 5 : Polyethylene specific heat as a function of temperature.

These 3 curves illustrate the temperature dependence of the material and they have been integrated in the model.

2.2 Validation exercise

In order to get an estimation of the level of confidence in the developed tool a practical experiment was conducted by processing an actual cable length through the insulation line in which the optical fibres were replaced inside the optical package by thermocouples. Thanks to this test set-up, the cable core temperature was recorded all along the time through the line. The obtained results were in very good agreement with those obtained by the software simulation. (refer to figure 6)

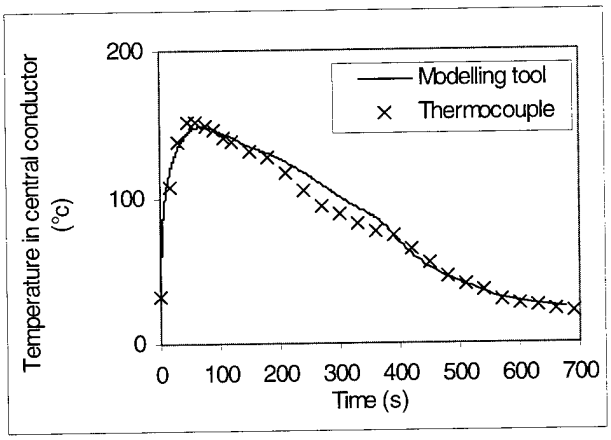


Figure 6 : Comparison between experimental and theoretical results for cable extrusion.

This validation exercise has provided a good confidence in the model allowing its use alone to simulate various process and design conditions.

2.3 Potential uses/Interest

Thanks to this tool, compromise between insulation line capability and requested cooling temperature can be easily found in order to ensure that the insulation material is in solid state prior to cable handling.

As an example, figure 7 shows the temperature profiles close to the centre conductor calculated for a given insulation line with the same water trough temperatures but with 2 different line speeds. The line speed 1 is slower than the line speed 2.

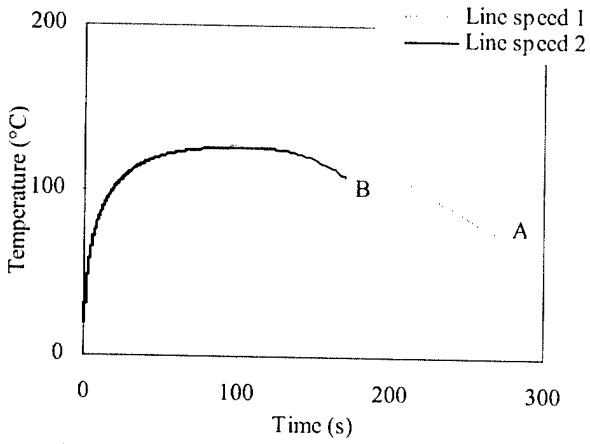


Figure 7 : Temperature profile for 2 different line speeds.

For a material with a solidification point of 100°C, the curve corresponding to line speed 1 shows that the cable can be handled safely at the exit of the trough (reached at point A), since the material is there solidified. This is not the case for line speed 2 (trough exit reached at point B), and that can be an issue in case of passage around pulleys after the trough exit.

In any case, the same modelling can even be used to adjust the water troughs temperatures profile in order to run the line at higher line speed with this material.

An other application can be, in case of change of cable design, to predict its behaviour during insulation process and anticipate possible line setting adjustment.

3. System assembly stage

Submarine systems trend is to carry higher and higher transmission capacities. The optical bandwidth increase is one of the means to achieve it. Capacities have been increased by a factor of 1000 in the last three years thanks to the use of new components like gain equalisers or gain flattening devices. Such equipment are highly temperature dependent and necessitate a very fine tuning to ensure an optimised transmission. One of the issue is that such a tuning has to be realised during system assembly in factory, i.e. under ambient temperature (around 20°C) while the use is under sea bottom temperature typically at 2-4°C. Benefits of cooling the amplifiers by air-flow versus a cooling by water are evident from an industrial point of view. Weight, cost, availability are obviously in favour of air. It can be used, provided that the chosen test conditions in the air represent well enough the sea-water conditions. Thermal modelling tools enable to determine the relationship between the air flow speed and rate and the 2-4°C sea depth temperature, which is typical of transoceanic bottom temperature.

Example of calculation for submerged equipment dissipating a 50 Watts heat energy is shown here after. The equipment body is assumed to have a 1m long and 0.3m diameter cylindrical shape.

The first step is to calculate the surface temperature that the equipment body would have in still water.

The heat transfer in water is made by natural convection. The temperature difference between the surface temperature of the body (Ts) and the water temperature (Tw) is given by the relationship [1] :

$$Ts - Tw = \frac{Q}{A\bar{h}} \qquad (1)$$

where Q is the heat transfer energy rate, A the outer area of the body and $\bar{h}$ the heat transfer coefficient between the body surface and water. This heat transfer coefficient is calculated using the following empirical relationship [1]

$$\frac{\bar{h}D}{k_W} = c(Gr.Pr)^a \qquad (2)$$

where k_W is the thermal conductivity of water, Gr is the Grashof number, Pr the Prandtl number, D the body diameter, and c and a are correction constants depending on the Grashof-Prandtl number product.

Taking k_W = 0.58W/m/°C, the calculation of the heat transfer coefficient gives $\bar{h}$ = 62W/m^2/°C. So with a body area A≅1m^2 and a 50W dissipation, the temperature difference between the surface of the body and the water would be

$$\Delta T = Ts - Tw = 0.81°C,$$

which gives a surface temperature of the body of 4.8°C for a water temperature of 4°C.

The second step is now to consider the submerged equipment in a cross flow of air and to calculate the air temperature required to keep the surface temperature of the equipment body at 4.8°C.

The air is assumed to have a velocity V. The difference between the air temperature (Ta) and the surface temperature of the equipment body (Ts) is given by an equation similar to equation (1)

$$Ts - Ta = \frac{Q}{A\bar{h}} \qquad (3)$$

But as the heat transfer is here governed by forced convection, the heat transfer coefficient between the air and the body has to be calculated using the empirical relationship [1] :

$$\frac{\bar{h}D}{k_a} = cRe^n \qquad (4)$$

where D is the body diameter, k_a is the conductivity of air, Re the Reynolds number, c and n are some constants determined in the reference [1] depending on the Reynolds number.

The Reynolds number is calculated using the equation [1]

$$Re = \frac{VD}{\nu} \quad (5)$$

where ν is the kinematic viscosity of air ($14 \times 10^{-6} m^2/s$ for air temperature close to 0°C).

Taking k_a=0.024 W/m/°C and V=3m/s, the heat transfer coefficient calculated is $\bar{h} = 14$ W/m^2/°C.

Hence, it was derived that the temperature difference calculated between the air and the surface of the body is around 3.5°C and therefore, to maintain the submerged equipment outer surface at 4.8°C, the air temperature should be Ta = 1.3°C when air flow rate is set at 3m/s.

This modelling can be used to assess the influence of air flow rate and air temperature variation on the equipment body surface temperature. Figures 8 illustrates the influence of these 2 parameters.

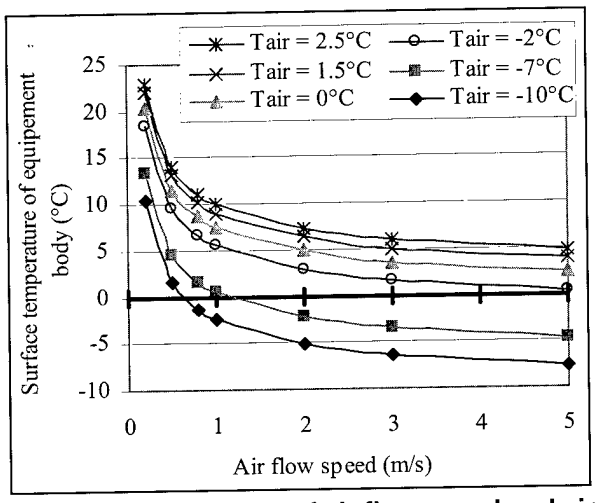


Figure 8 : Influence of air flow speed and air temperature on the equipment body surface temperature.

This graph enables to select a stable working area (air flow speed ≥ 2m/s and air temperature > 0°C) for which the equipment body temperature is independent of air flow fluctuations and where the freezing problems can be avoided.

Thanks to this type of calculation, the final test equipment was drastically lightened when compared to the temperature regulated water tanks, and the system assembly time scale was notably reduced. Figure 9 shows an overview of the cooling room, demonstrating its simplicity over temperature controlled water tanks.

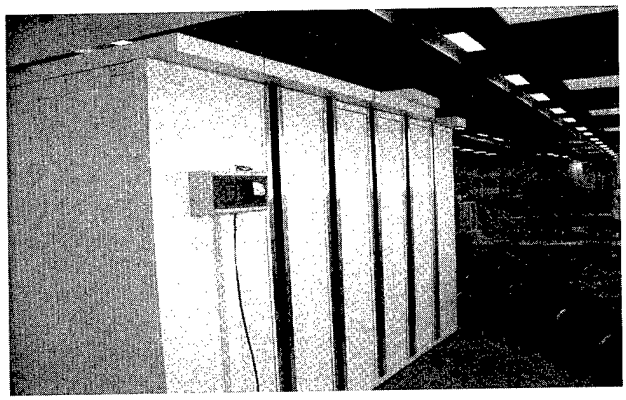


Figure 9 : Final equipment for system assembly test.

4. Installed system (cable powering)

The last example deals with installed cables feeding submerged powered equipment. For normal telecommunications applications, the cable carries only a power feed current of 1 to 2A, and the heating effect is negligible. However, for some applications (as remote powering of offshore sensors) the cable may be required to transmit significant power under much higher current (> 20A). This current is provided from the land station through the line cable, which has an ohmic resistance typically of 1ohm/km. This powering generates heat. The thermal modelling tool enables to calculate the heat transfer through the insulation and the temperature on each component of the cable while the system is in operation. Such an evaluation is conducted to check that the cable does not reach temperatures that can damage the insulation sheath, and to evaluate materials ageing temperature.

A worst case calculation has been done for a cable buried in the sea-bed (see figure 10). The heat loss between the central conductor and the sea-water is assumed to be made by conduction through polyethylene and sea bed.

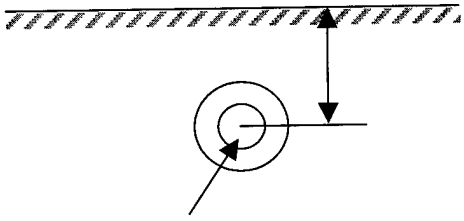


Figure 10 : Scheme of cable buried in the sea bed.

Figures for thermal conductivity are approximately k = 0.4 W/m/°C for the polyethylene, k = 0.3 W/m/°C for the silica (sand)

and k = 0.6 W/m/°C for the sea water, so that it can be assumed that the average thermal conductivity is about k = 0.4W/m/°C.

The heat loss per unit length (in W/m) can be evaluated using the following equation [1] :

$$\frac{q}{L} = \frac{s}{L} k(T_2 - T_1) \qquad (6)$$

where s is a shape factor defined in this case (from reference [1]) by :

$$\frac{s}{L} = \frac{2\pi}{\cosh^{-1}(Z/r)} \qquad (7)$$

where Z is the depth of burial and r the radius of the central conductor.

For a cable with an ohmic resistance of about 1.2 ohm/km and a power feed current of 20A, the heat loss (q/L) is about 0.5 W/m. Then, assuming a 2m burial depth, the difference in temperature between sea water and central conductor (T_2-T_1) can be calculated from equation (6); which gives (T_2-T_1) = 1.3°C.

This is a very small temperature increase, confirming that the use of cable under such conditions will have no effect on the cable reliability.

To further investigate this, the temperature increase in the central conductor has been evaluated for different power feed currents. (see figure 11).

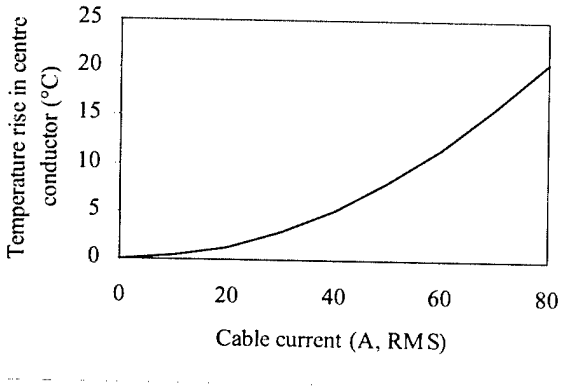


Figure 11 : Temperature rise of centre conductor versus cable current for a cable of 1.2 ohm/km ohmic resistance buried in sea bed (2m).

These results show that the cable is capable of supplying currents of up to 60 A while showing an acceptable increase of its internal temperature (< 10°C).

This type of modelling can be used also at cable design stage. It helps to define the ratio of copper and steel in the composite conductor to optimise the ohmic resistance of cable.

5. Conclusions

Many potential uses of a thermal modelling tool exist. Three examples have been shown in this paper for different applications : process, system assembly and in-field applications. Different types of modelling have been used, as finite element software and analytical calculation. The choice between one or the other depends on the complexity of the problem. They provide very useful tools to anticipate the needs of the cable submarine systems market.

6. Acknowledgments

The authors wish to thank Albert Picavet and Pierre Gaillard for their helpful contribution to this work.

7. References

[1] D. Pitts and L. Sissom, "Heat transfer," *Schaum's Outline Series, Mac Grawhill.*, (1998).

8. Authors

Philippa DUPIRE received her Doctorat of "Sciences for Engineer" from LE MANS (France) in 1996. She is working on cable design modelling for Alcatel since 1997.

Yves CHARLES is graduated from the Ecole Universitaire de LILLE (France). He joined Alcatel in 1993 where he is in charge of submarine cable design and product qualification.

Jean-François LIBERT received his engineering degree from the "Hautes Etudes Industrielles" of LILLE (France). He joined Alcatel in 1984 and he is working as a cable transmission expert.

Peter WORTHINGTON received a BSc in Electronics and Electrical Engineering from the University of Birmingham in 1971. Since 1977 he has been involved in development of optical submarine cables. He is now working for Alcatel as a consultant.

A Yardstick for the Future Generation of Submarine Unrepeatered Systems

M. Fullenbaum, P. Gaillard , G. Waterworth, Y. Mayolle, P. Le Roux, R. M. Demont

Alcatel Submarine Networks

72, Avenue de la Liberté

92723 Nanterre Cedex France

33 (0)1 55 51 63 71, marc.fullenbaum@alcatel.fr

Abstract

A new generation of cable is needed to meet the requirements of the future submarine unrepeatered links:

- Provide added bandwidth flexibility by sheer fibre count increase;
- Provide intrinsic capability to house next generation of large effective area fibre with minimal optical attenuation;
- Enhance network operability by a cost-effective mix of cable optical and mechanical performances
- Reduce network outage with reliable deep plough burial into the seabed.

Therefore a cable design has been optimised for its most efficient packaging of 96 fibres. The goal has been to meet recurring cost targets while setting the performance levels to not only improve the optical link budget, but also to enhance network reliability. This new cable will provide a yardstick against which any submarine unrepeatered cable could be evaluated.

Keywords

Cable; unrepeatered; cost; fibre; protection; performances; business model

1. Introduction

Offshore networks call for more bandwidth flexibility through fibre count, wavelength multiplexing and line data rate for a desired system capability and cable routing. Increasing the number of fibre pairs should ease off this cost, performance and time to delivery trade-off. Cable unavailability has also to be kept to a minimum and this has been paramount in the overall mechanical design and plough-ability of the cable. This has been achieved by an in-house integrated product team endeavour involving system design, terminal design, cable design, marine operations and manufacturing. This integrated product team approach has proven very effective in integrating and validating all the unrepeatered network level needs, especially costs and deployment time frame, into the cable design as to get into the design phase with clear cost and performance objectives.

This paper will describe the new 96 fibre unrepeatered cable and review its associated performances such as the cable cost and the optical, mechanical, plough -ability and attainable protection level performances. The unrepeatered network costs, bandwidth optimisation and service readiness now possible with this new cable is discussed covering, initial costs, upgrade costs and the deployment time frame. A comparison with terrestrial networks in terms of costs, system maintainability and time from inception through to launch is also included.

2. The 96 fibre cable

2.1 Cable description

The main function of a submarine optical cable is to protect the optical fibres. To this end, the URC-4 cable is designed to provide protection over the entire service life of the cable, including laying, burial, and recovery operations for up to 96 optical fibres.

The cable design is based around a 4.6mm laser welded stainless steel tube, which houses the 96 fibres in a stress-free environment to ensure a fault free lifetime. The optical fibres lie freely in a thixotropic jelly, which fills the steel tube blocking water penetration and limiting hydrogen permeation.

This optical package presented in figure 1 is based on a well-known technology widely used in repeatered systems, which has already demonstrated its high efficiency for fibre protection on existing designs. Based on the experience gained in designing a number of submarine optical cables, the URC-4 tube size has been selected to have a fibre density close to already proven cables, in order to accommodate up to 96 fibres.

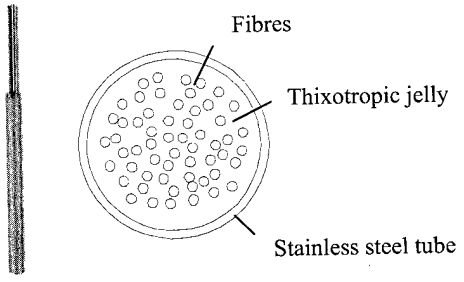


Figure 1: Optical package.

The use of the loose steel tube design to this application allows for precise control of the fibre to tube length ratio (known as fibre

slack) during both manufacture and subsequent operational performance. The high stiffness and low coefficient of thermal expansion of the stainless steel compared to standard polymer tubes ensures that controlled management of the fibre slack to 0.01% is easily and consistently achieved. The steel tube technology has been developed to cater for the new generation of system fibres with higher sensitivity to small changes in fibre slack and micro / macro bending.

Ultra high-strength steel wires are formed around the steel tube optical package to form a pressure-resisting vault. This structure is locked together by a seam welded copper tube which is swaged down on to steel wires providing a stable strength member with a low resistance electrical conductor and hermetic sealing against hydrogen penetration. A polyethylene extrusion bonded to the copper with a co-polymer adhesive provides high voltage insulation and the finished Light-Weight Cable, which can be deployed and recovered from 6500m (See figure 2).

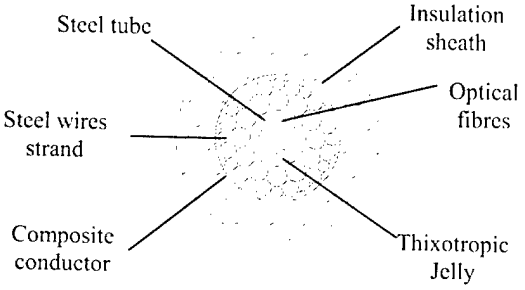


Figure 2: Light Weight cable

In deeper water there are areas of potential abrasion risk where the seabed is rugged or slopes steeply, or where high currents exist. Here as with normal practice, a bonded steel tape is applied to the Light Weight Cable with an additional polyethylene extrusion to form the Light Weight Protected Cable which can be used at depths down to 5500m. In shallow water where other users of the seabed may pose a hazard to the cables, additional external layers of galvanised steel armour wires are added to provide additional protection against crush and mauling. 18 high strength wires of 3.4mm diameter are applied to the Light Weight Cable to form the Single Armoured Cable. This additional protection allows for safe burial operation and surface lay down to 1500m. The addition of a further 21 steel wires of 4.7mm forms the Double Armour Cable which gives further protection for shore ends, cable crossing and areas where burial is not possible in water depths down to 500m.

The cable design ensures that only a very small strain is exerted on the fibres in normal operation. Even if the cable breaks, high strains and seawater ingress are limited to a short length, so that the bulk of the cable will remain serviceable.

These high performances are made possible through a cable structure that isolates fibres from mechanical stresses in normal operations. This is achieved with a unique design where fibres lie freely in a longitudinally welded steel tube. As a result, cable can incorporate any type of optical fibre, as detailed below.

The range of URC-4 cables (Lightweight Protected and Armoured types) is shown in Figure 3.

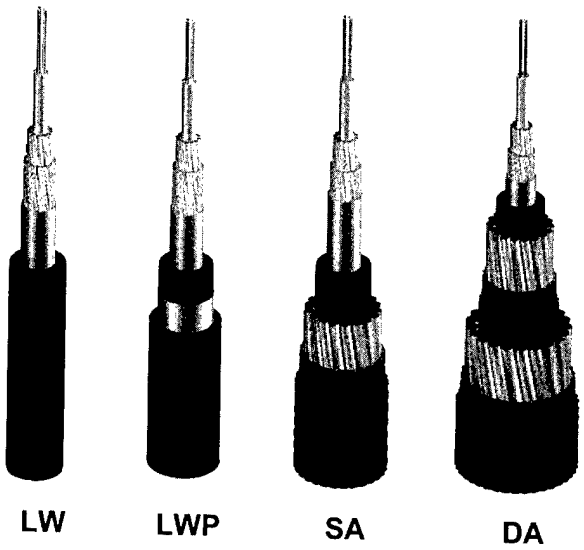


Figure 3: URC-4 cables: Lightweight (LW), Lightweight Protected (LWP), Single Armoured (SA), Double Armoured (DA).

Even in the most adverse conditions (such as cable recovery from deep water), cable parameters are dimensioned so that the amount of stress applied onto the fibres never reaches critical levels.

Moreover, the combination of loose structure and proof-test prevents any fibre break that would be due to ageing stress during the 25 year design life of the system.

The low resistance copper conductor can be used to conduct a low current to monitor on a permanent basis the status of the cable, to localise cable breaks or provide an electroding tone for cable location. The 1.6 Ohm/km resistance and 270nF/km capacitance allow for electroding a complete segment from a single terminal station or beach manhole.

The developed cables main mechanical features are summarised in table 1:

Cable type	LW	LWP	SA	DA
Outer dia. (mm)	17	23	28	43
Weight in air/water	0.68/0.45	0.93/0.50	2.2/1.6	5.4/3.9
NTTS (kN)	70	70	200	400
NPTS (kN)	25	25	60	100
UTS (kN)	100	100	270	600
Crush (kN)	20	20	40	40
Impact (J)	20	20	400	400

Table 1: cables mechanical performances

The URC-4 cable design results from our experience in the use of a steel vault structure surrounding a central stainless steel loose tube.

The advantages of this cable concept are the following:

- The fibres are freely laid in a stainless steel tube, which provides an ultra-stable environment resulting in consistent low levels of attenuation.
- A small but significant fibre slack allows the use of a low proof-test level and prevents excessive fibre stress, even when the cable is under full load.
- The steel vault construction provides a high strength together with an excellent hydrostatic pressure and crush resistance. It can sustain more than 700 bars of pressure.
- The welded copper tube, providing a suitable power conductor and locking together the internal structure.
- The internal steel vault construction provides a high strength to diameter ratio allowing a single armoured cable design with a Nominal Permanent Tensile Strength (NPTS) greater than 50kN, which is the minimum strength necessary to survive deep plough burial.
- The copper barrier, stainless steel tube and a very low permeation coefficient filling jelly offer the fibres three levels of protection against hydrogen.

These advantages which are comparable with long haul repeatered cables, offers high resistance to external aggression and the ability to be reliably deep buried down to 3 meters using standard techniques.

2.2 The cable performances

2.2.1 Optical performances

Unrepeatered transmission systems can require very different types of fibre depending on how the submarine path is integrated in the overall network (part of a terrestrial link, festoon…). As a result, the cable design has to accommodate fibres that can have very different transmission properties and/or cabling sensitivities.

From a transmission standpoint, some of the main features that can be listed to differentiate the fibres are:

- the ITU-T Recommendation the fibre has to comply with (G652, G654, G655),
- effective area (increasing to allow for higher optical power transmission and increased span),
- attenuation level (ultra-low levels required for long spans),
- chromatic dispersion and Polarisation Mode Dispersion (to accommodate higher bit rates and higher numbers of wavelengths).

Table 2 compares some typical data for the various large and non-large effective area bare fibres that can be used in unrepeatered applications.

In addition, the fibre macro/micro bending sensitivity is a key factor in the cable design selection. Even for the fibres that are not bend-sensitive the systems will require that the optical stability over the whole optical bandwidth is ensured. Table 3 shows the compared macrobending and microbending sensitivity of these different fibres.

Fibre type	Effective area (μm^2)	Dispersion @1550nm	Attenuation @1550nm
G652	80	18	0.195
G654	70	20	0.175
Large core	≥100	19 to 20	0.175 to 0.185
G655 (terrestrial)	55 to 72	4 to 8	0.190 to 0.210

Table 2: Fibres for unrepeatered applications

Fibre types	Macrobending sensitivity (dB/m)	Microbending sensitivity (dB/km)
G652	≈ 8	≈ 0.1
G654	≈ 0.5	≈ 0.05
Large core	≈ 2 to 10	≈ 0.4
G655 (terrestrial)	≈ 6	≈ 0.4

Table 3: Macro and microbending sensitivity at 1550nm.

In order to ensure that the benefit of using these various types of fibres is not impaired by any cabling effects, which might result in an optical loss, careful attention has been paid in the design of the optical core as presented above.

The stainless steel tube fibre unit provides a stable and reliable environment for the fibres over the whole optical bandwidth. Figure 4 shows the spectral attenuation of various fibre types after the cable process, demonstrating the capability of the design to house large core fibre as well as traditional "standard" fibre. The very good optical behaviour is achieved thanks to the thixotropic jelly, which acts as a buffer to the fibres, and to the stainless steel tube, which protects the fibres against any potential aggression during manufacturing stages or from cable deployment.

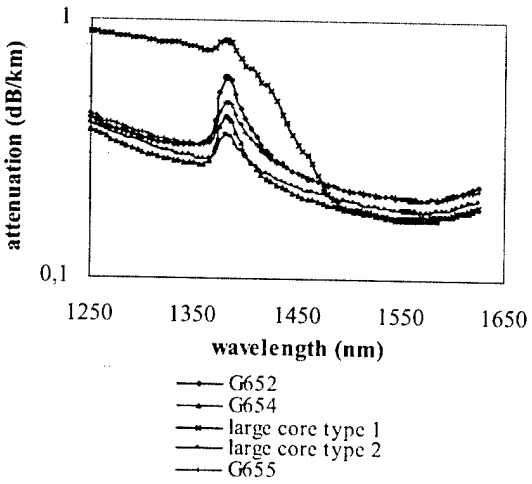


Figure 4: Cabled spectral attenuation for various fibre types.

2.2.2 Mechanical performances

The URC-4 cable benefits from the experience that has been accumulated throughout the years of steel tube based cable design, qualification, manufacture, deployment and in field experience.

The cable and joints are submitted to a full and consistent set of qualification tests in compliance with the ITU G976 recommendation, including: tensile and fatigue, torsion, sheave (bending under tension), crush, impact tests...

As an example of results, the mechanical tensile tests were successfully performed up to the specified cable limits: the NOTS (Nominal Operating Tensile Strength, sustained for 48 hours), the NTTS (Nominal Transient Tensile Strength, sustained for 1 hour) and the UTS (Ultimate Tensile Strength which corresponds to the cable breaking load).

Figure 5 shows an example of qualification tensile test result up to NTTS for URC-4 LW cable, compared with the theoretical curve.

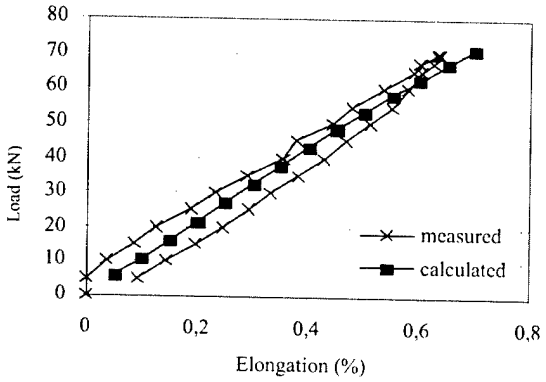


Figure 5: URC-4 Light Weight cable experimental and theoretical load elongation curve up to NTTS.

The URC-4 cables covers the full depth range required for the un-repeatered systems. These cables are fully recoverable and reusable from their maximum depths allowing safe and speedy maintenance at sea. The maximum typical cable recovery depths are given in table 4.

URC-4	Max. recovery depth (m)
LW	6500
LWP	5500
SA	1500
DA	500

Table 4: Maximum recovery depths for URC-4 cables

Figure 6 shows the recovery depth versus recovery speed of the LW URC-4 cable with 4-meter sea swell conditions.

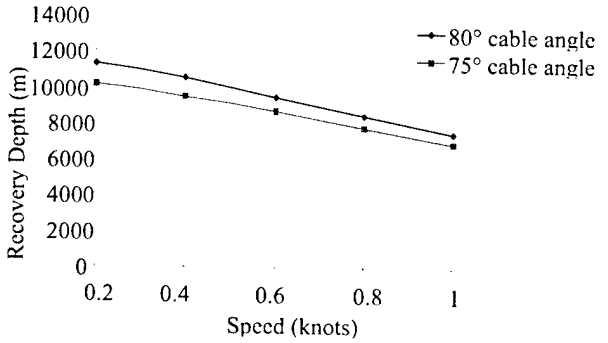


Figure 6: Recovery depth of the URC-4 Lightweight cable.

2.2.3 Cable reliability

Fibre protection against hydrogen is a key factor in long term system reliability. The stainless steel material is very well known not to generate hydrogen. The stainless steel tube also provides good protection against hydrogen, in addition to the conventional hydrogen barrier given by the swaged copper tube over the steel wires strand. Table 5 presents comparative protection against hydrogen ingress for various materials used in the cable core. A stainless steel tube delays the hydrogen ingress by a factor of 10^5 when compared to a plastic tube, and its combination with a copper tube further enhances the fibre protection against Hydrogen.

Material	Permeability to hydrogen (at 10°c)
Plastic	0.75×10^{-8} $cm^3 cm^{-1} atm^{-1/2} s^{-1}$
Stainless steel	$1.8 \times 10^{-13} cm^3 cm^{-1} atm^{-1/2} s^{-1}$
Copper	$1.0 \times 10^{-15} cm^3 cm^{-1} atm^{-1/2} s^{-1}$

Table 5: Permeability to hydrogen of different materials.

The gel-filled steel tube also provides very good pressure resistance for fibres protection. The steel tube can withstand an external hydrostatic pressure of ≥ 100MPa, equivalent to a depth over 10 000m. Furthermore, it is temperature independent compared to a fully non-metallic tube.

As a result, the stainless steel tube is the best in its class for mechanical and thermal fibre protection performance, ensuring the highest degree of reliability available for submarine applications.

2.2.4 Jointing

Given the relatively high number of fibres that the URC-4 cable can contain, jointing and more particularly fibre splicing is an important point to consider.

Standard cable jointing technology has been adapted to develop and qualify the URC-4 joint, using as well fibre mass-fusion splicing technique to reduce the time required to splice the 96 fibres, and to ease fibre placement inside the joint box. As a result, typical jointing times of less than 15 hours for LW cable and 20 hours for SA cable can be achieved under standard conditions, with an average splice attenuation of less than 0.05dB.

This jointing technique can easily be adapted as well to realise connections to Remote Optically Pumped Amplifiers (ROPA), should the link be long enough to require deported optical amplifiers.

In addition and in order to offer more possibilities to maintenance operations, this newly developed cable is compatible with UJ technology.

2.3 A cable design for unrepeatered submarine networks

Unrepeatered submarine networks can be used for several different applications:

- Coastal festoon;
- Island ring;
- to close a transoceanic ring or as a complementary festoon to it;
- to cross submarine sections.

So the main application is clearly coastal city connection which could in many cases be alternatively achieved through a terrestrial network.

Advent of both high power lasers and optical amplification has allowed a rapid technical evolution for unrepeatered systems over the last three years. Unrepeatered systems can now be commercially equipped with a WDM technology scheme while the available channel bit rate can be routinely used at 2.5 Gbit/s or at 10 Gbit/s. System transmission capacity has grown many fold for almost identical transmission distances. Until recently, unrepeatered submarine cables with more than 24 fibres were not common and the final capacity was exclusively expanded through extensive use of wavelength division multiplexing, so as to achieve the required transmission capacities. However cheap bandwidth has become a competitive advantage and dark fibre sales are at the crux of the carriers' carriers strategy, who are often also operating terrestrial networks. Moreover economical models can be very different depending on the customer's business strategy; and a myriad of options are available to allow them to optimise an offshore route according to their specific requirements. The choice being driven mostly by the eventual capacity they want to reach. Altogether this has created a demand for higher fibre counts in unrepeatered submarine cables, sometimes to directly match the land cable. In order to meet the customers' specific requirements and economical constraints, there is a trade-off to make between fibre counts, wavelength count, line rate and network infrastructure costs. Therefore it is paramount to allow for fibre count flexibility which is both practical and sufficient to meet the demand in a specific marketplace.

Increasing the fibre count was the first design parameter. This was the subject of an extensive marketing research taking into account customers' feedback, potential unrepeatered routes, application types and traffic pattern as well as potential line rate. A 96-fibre capability was eventually chosen to achieve the best balance between bandwidth management, WDM technology advances and coastal city fibre connectivity. It is worth pointing out that a 96-fibre cable can offer a 15 Tbit/s full duplex transmission capacity with 32 wavelengths at 10 Gbit/s.

The traditional major incentive for unrepeatered systems over terrestrial systems is their reliability when compared to an alternative terrestrial solution. Figure 7 depicts a sketch of a unrepeatered festoon, an inland terrestrial network and a coastal terrestrial network.

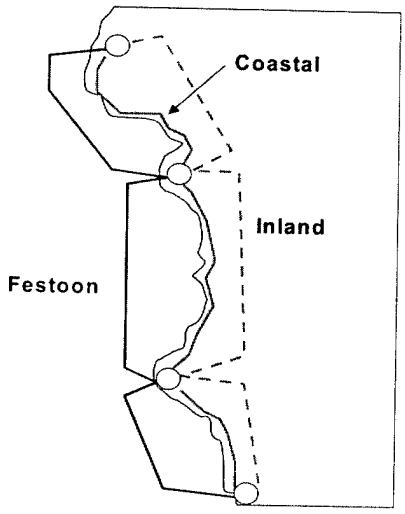


Figure 7: Unrepeatered Festoon versus terrestrial coastal versus inland terrestrial

Indeed the large capacity carried through a single cable is subject to dramatic disruption if the cable is damaged and submarine routes are threatened by rather different failure modes. Overall statistics for terrestrial cable failures world-wide indicate for all causes there is a fault rate of 0.00062 faults/km/year [1]. In contrast, overall statistics for undersea cable failures world-wide indicate a fault rate for all causes of 0.00001 faults/km/year [2].

We have calculated that the failure rate for an unrepeatered cable on the continental shelf would be an order of magnitude less than that of terrestrial cable [3]. Nonetheless a festoon route optimisation is required. Figure 8 shows a block-diagram of the business process to go through in order to find out the best festoon route.

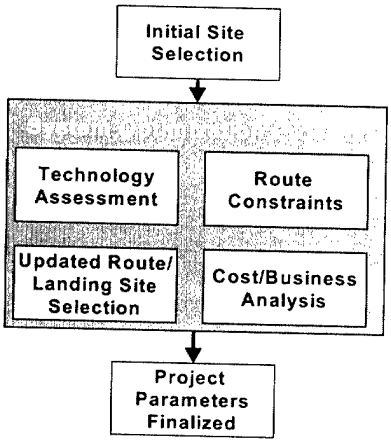


Figure 8: Festoon route optimisation

From a reliability perspective, the main design drivers are the amount and type of other sea bed users (fishing activity, anchoring, dredging etc) as well as the suitability of the sea bottom for cable burial. This may lead to route extension into deeper water to avoid fishing gear aggression or hard sea bed conditions. The cable role in the unrepeatered network reliability is therefore highly significant and great importance is made of the cable's ability to survive accidental damage that might be caused by other sea bed users [5]. Thus setting a water depth capability of at least 4000 m and high crush resistance, as well as a reliable deep burial capability was the second design parameter.

A third important aspect was to keep abreast of all the future technology enhancements in the unrepeatered field. Arrays of different schemes show great promises for both span length and channel count improvement. Many of them revolve around using more signal and pump power, thus putting more demands on the fibre to alleviate the consequent increase in non-linear effects [4]. This has already led to the design of larger effective area fibre and this trend is set to continue; commercially available 150 to 170 square micron fibre are around the corner. This new generation of fibre will tend to exhibit high micro-bending sensitivity, so it is crucial that the cable optical core has the intrinsic capability to house the next generation of fibre especially designed for long haul unrepeatered application.

The URC-4 tube technology has this inherent capability. Diverse fibre mapping scheme, mixing 70 μm^2 effective area with 110 μm^2 (and greater) effective area fibres with different optical transmission characteristics are also of great interest. They can also be best operationally implemented with the tube technology [6]. These design parameters (depth capability, fibre count, large effective area fibre, and burial capability) are simple technical parameters.

The last design parameter was a fixed cable cost that had to be used for each design iteration during the cable design life cycle. An other thorough study was launched to understand the cable work package cost percentage (bare cable, fibre equipped cable, cable installation, cable maintenance) in the overall network cost. This study also entailed an extensive benchmarking analysis to fully comprehend each competitor's product pricing policy, product performances and key messages. At the end, a design to unit cost approach was chosen to encompass all the design parameters previously discussed at once and meet the market price.

It is important to present some cost comparison results for a unrepeatered submarine festoon and an inland terrestrial festoon that would connect the exact same cities with the exact same transmission capacity. An unrepeatered festoon equipped with a 96 fibre cable, loaded with premium submarine standard Non Dispersion Shifted Fibre (NDSF) and a terrestrial network with ducted terrestrial cable, equipped with standard terrestrial G.652 fibre were studied.

Table six shows the comparison that can be drawn between the cable cost percentage of an unrepeatered festoon and the cable cost percentage of a terrestrial network.
A 1.2 Tbit/s capacity system was chosen with 16 fibers out of the 96 fibre cable equipped at 16*10 Gbit/s. These are state of the art configurations that could be commercially implemented today.

	250km unrepeatered link (2 terminals)	250km terrestrial link (2 terminals)
Percentage of installed cable cost in network cost	20 %	29 %
	500km unrepeatered festoon (2 terminals)	500km terrestrial link (2 terminals)
Percentage of installed cable cost In network cost	30 %	42 %
	1000km unrepeatered festoon (4 terminals)	1000km terrestrial link (4 terminals)
Percentage of installed cable cost In network cost	31 %	42 %

Table 6: Cable cost percentage in overall network cost

SDH layer costs and maintenance costs are not included in the overall network cost. Adding the SDH layer cost will only lower the percentage of the installed cable cost while it has been pointed out that the terrestrial maintenance costs are higher than those of the submarine one.

Thus this new 96 fibre cable is in the right cost zone while providing world class performances that outperform all its competitors in the optical and mechanical domain.

The prevalent challenge upon meeting the design to unit cost target was to successfully involve all the stakeholders on the grounds that the cost was the chief built-in parameter. An integrated product team approach was selected with the view to hasten up the design life cycle while, at the same time, ruling out as early as those design options which would have resulted in an expensive cable. It was important that representatives of product marketing, system design, marine operations, cable design, cable manufacture and purchasing were involved up front. Yet again, this team laid great store by abiding to corporate product life cycle policy so that the product quality would meet the necessary standards.
Inasmuch as parallel engineering is not a novel idea, this endeavour arrayed the team towards an emphasis on recurring cost and time to market.

3. Conclusion

This new 96 fibre unrepeatered cable fully meets the present and future unrepeatered systems requirements.

The cable design has taken into account overall system reliability as a key feature.

The system bandwidth management has also been built-in the intrinsic fibre count capability which offers the best potential trade-off between line rate and fibre availability (up to 96 fibre).

It is clearly a best in class product amongst the current high fibre count cables available today in the unrepeatered market place with the best mechanical and optical performances. Just to remind the reader of a few of them: 6500 m depth deployment and reusable recovery, 1500 m plough burial capability, 4 kN/cm crush resistance and the ability to house ultra high effective area fibre.

All of the above has been achieved while retaining the cost level in line with the current market trends and competitor's position.

4. Acknowledgement

The authors would like to acknowledge fruitful discussions with Philippa Dupire, Jean Luc Lang and Eric Brandon as well as their many pieces of advice and good deeds over the course of this paper writing.

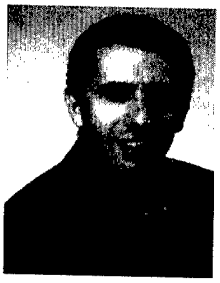
5. References

[1] National Reliability and Interoperability Council, Report to the Nation 1997
[2] International Cable Protection Committee, International Telecommunications Union, "Ten Years of Operating Light Wave Systems," E. Brain, L. Hagadorn, E. Upperco, and Mick Green, SubOptics'97, Conference Proceedings, May 11-16, 1997, pg. 203
[3] "Today's unrepeatered technology yields a viable business alternative to traditional terrestrial systems", Ariane Ducreux, Leigh Frame, John Mariano, Tim Stamnitz
SubOptic 2001

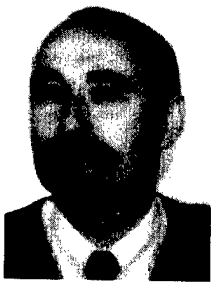
[4] "2.56 Tbis/s Unrepeatered 230 km transmission with 0.8 bits/hz spectral efficiency using low noise fibre Raman amplifier and 170 Aeff fibre", Miyikawa, Morita, Tanake, Sakata and Edagawa, KDD R&D lab Japan, PD-26 Post Deadline paper, OFC 2001
[5]"Enhanced cable protection, an end to end perspective" Gary Waterworth, Jerry Brown, Yves Charles, Jean François Libert, Franck Tortey, SubOptic 2001

[6] " Error-free 100x10 Gbit/s unrepeatered transmission over 350 km", L. Buet, F. Boubal, V. Havard, L. Labrunie, P. Le Roux and E. Brandon, Alcatel Submarine Networks, OFC 2001

6. Pictures of authors



Marc Fullenbaum, Product Marketing



René Marc Demont, Cable Program Manager

Pierre Gaillard, Cable Technical Directorate Manager
Gary Waterworth, Cable Bid Manager
Patrice Le Roux, System Design

Advanced SZ Stranding Technology for Enhanced Applications

Josef Marik
ROSENDAHL Maschinen GmbH
A-8212 Pischelsdorf, Austria
Phone: +43 3113 5100-0; Fax: +43 3113 5100-59 e-mail: office@rosendahl-frisch.com

Abstract

The increasing needs for high-end communication cable of higher transmission rates do have impact on the needs for regular communication cables, too. Future demands on the manufacturing facilities are all the same: Faster, better, and cheaper.

For that reason, the technologies used by producers of copper and fiber communication cables have been reviewed and possibilities for savings were analyzed. One big chance for economizing and improvement has shown up in the cabling process.

Therefore, new equipment has been developed not only to be integrated into new lines but especially to upgrade existing production lines to meet today's and future requirements. Higher efficiency, enhanced range of applications and uncomplicated integration have been the basic design aspects. Using high-tech components and methods for affecting parts and production steps, tests and measuring results showed a significant increase of the quality of the cable compared to common technologies.

The enhanced SZ-Stranding technology improves the cabling process of

- · Sub-units, main-units and cabling of communication cables
- · Tubes, tight buffered and semi-tight buffered fibres of optical fibre cables
- · Control cables, signal cables and cables for electronics
- · Low voltage cables, as installation cables, building wires

To increase the performance of the stranding equipment, modifications and innovations of drive and element guiding systems have been developed and worked out.

Of particular importance for stranding pairs and quads of communication cables with high transmission rates is to keep friction and reversal spots minimal. Best results have been achieved by using one or more duct coated mini-disc accumulator axles, each driven by one high-dynamic frequency controlled AC drive (up to 7000 rpm) supported by a back-spin system. This type of advanced SZ stranders allows an enlarged number of revolutions (up to 20 for telephone cables) at shortest reversal times.

For full utilisation of the stranders features for the entire production process, ancillary units such as inlet capstan, outlet capstan, high-speed concentric binder (binding rate 8000 rpm) with integrated twist-lock or enhanced integrated operating system has been added.

Due to the new system increasing cabling speed and quality, the range of applications for the economic SZ-Stranding and combined SZ-Stranding/Extrusion has become extended significantly. Thus, SZ stranding does not only remain the most efficient technology in the fields of fiber optics but also starts to capture copper at higher levels. The paper shows the way how equipment using the new technology may improve productivity and quality performance of existing and newly built plants for communication cables.

Keywords

SZ-stranding, stranding, oscillator, telephonecable, communicationcable, twinning, pairing, quadding,

1. Introduction

SZ stranding resp. oscillating is a highly economic method of stranding cable elements such as wires, insulated wires, pairs, quads, fibre optic tubes etc. to a strand.

Since mid of the seventies oscillators are used in the cable industry, mainly in Europe later in other areas of the world, too, for manufacturing sub-units of communication cables and building wires. In North America the SZ technology has been applied almost exclusively for the stranding of fiber optic loosetubes.

In the meantime SZ technology has been further developed and today its application in the field of copper communication cables of higher transmission rates over and above the regular communication cables for voice frequencies is already reality. That means copper communication cables for transmission frequencies up to 20 MHz, e.g. LAN cables of catagories 3 and 4, can be manufactured by using advanced SZ technology with all its clear and economic advantages.

In the field of fiber optic cables SZ stranding lines are used for stranding loose tubes, tight buffered and semi-tight buffered fibres with production speeds of above 100 mpm.

2. Basic principle of SZ Stranding

Stranding elements run from stationary pay-off units into the SZ strander. In the SZ stranding unit a preset number of twists in one direction (right-hand lay) will be produced. After a quick reversal of

direction in order to get a short reversal spot a preset number of twists will be generated in the opposite direction (left-hand lay). An adjasent torsion lock in form of a belt-type caterpillar or a single wheel capstan makes sure that a set shape in the strand will be held. Following the strand will be tied up by using a binder in rder to prevent the strand from untwisting. Finally the strand will be wound up on a stationary take-up unit such as a reeler or a barrel coiler.

3. Comparison to other stranding methods

3.1 Conventional stranding

In the case of using conventional stranding methods the stranding elements are paid off from reels and fed into a unidirectional stranding machine producing a cable with either left-hand or right-hand lay. Characteristically the lay direction remains the same throughout the whole length of cable.

Conventional stranding machines are:

- Rigid or Planetary Cage Stranders
- Tubular Stranders
- Bunchers such as single twist and double twist stranders
- Drum Twisters

What are the main disadvantages of conventional stranding ?

Heavy reels loaded with wires and powered by large drives must be rotated. Low production speeds because of high inertia and limited rotational speeds have to be accepted.

The conductor lengths are limited by the reel capacity and loading and unloading of reels result in substantial down time, often equaling production time.

Discontinuous operation has to be accepted and stranding and jacketing cannot be done in a tandem operation process.

These grave disadvantages limit the efficiency and productivity of the stranding process very extremely. SZ stranding enables the cable maker to eliminate above mentioned disadvantages in order to get very economic manufacturing process.

3.2 Twister

Early SZ-stranders for telephonecable were working following the Twister-Principe[1]. This methode was economic, the production ran very stable. Because of the mechanical conception of this machines, only a limited performance of the produced cables could have been achieved.

The main disadvantages where:

- Long reversal length
- High tension and friction on wires
- Insufficient backtwist

Also, the length of the machines often was a problem.

4. Benefits of Advanced SZ-stranding

4.1 Influence of process improvements:

The influence of this advantages on the cable product have been tested and documented in real production conditions. The most significant advantage of the advanced SZ stranding technology is the highly improved performance of the produced cable.

Complete backtwist is achieved because of the reversing stranding head and low friction within the accumulator.

High rotation speeds combined with minimal reversal times allow short laylengths (10 – 200mm) and small reversal spots.

Tension is minimized by using inlet and outlet capstans as well aspoint-to-point guiding elements with special surface treatment at the accumulator.

4.2 General advantages

4.2.1 Continuous production. High-speed stranding lines using advanced SZ stranding technology enable high production speed because of poor inertia and high rotational speeds up to 7000 rpm. They do not have any pay-off limitations because there are no rotating reels. Unlimited wire lengths and continuous operation are given because of the ability to splice wire ends of single conductors utilizing dual flyer pay-off units. Loading and unloading of reels can be done during production which results in minimal down time and high stranding capacity.

4.2.2 Inline Operation. High-speed SZ stranding lines can be connected with a jacketing line in order to make stranding and jacketing in one production process.

4.2.3 Flexibility. The new machines for advanced SZ stranding are small and compact. For line installation there is no foundation required. As well the wide product area offers an enormous flexibility with regard to the different product dimensions to be manufactured. The design of the accumulator disks can be adjusted to the product range in such a way, that retooling will not be required when the product must be changed.

[1] In the double twister SZ machine, two stranding heads rotate in the same direction; the SZ strand is formed as a result of periodic simultaneous changes in the rotation speeds.

6. Equipment for advanced SZ stranding

High-speed stranding machines using advanced SZ stranding technology are equipped with a stretched disk accumulator which is driven by a centrally positioned elastic torsion shaft or a free-wheel counter shaft.

In order to meet the enhanced requirements for copper communication cables extremely short reversal spots on the stranding elements are absolutely necessary. This is particularly important for stranding pairs and quads with high transmission quality. Shortest reversal times of about 30 ms can be achieved by using stranding discs with a minimum rotational diameter of the stranding elements and an elastic torsion shaft instead of a transmission gear. Thus, stored braking energy supports the reversible motor during the acceleration phase.

Minimum friction of the stranding elements in the disk bores, optimal reversed operation, best possible backtwist is necessary for an optimal stranding process and a high cable quality.

A smooth and continuous operation at highest speeds and without vibrations is given by employing individually supported and driven stranding disks. Driving elements of newest technology such as frequency controlled AC servo-motors must be used in order to get undisturbed and continuous operation.

5. Testresults

5.1 Cable: 50 x 2 x AWG24

Insulation: Foam-Skin-PE

Specifications: TR-NWT-421, Issue 3, ICEA S-85-625-1996
ICEA S-84-608-1994

Table 1: Capacitance Unbalance Pair to Pair at 800 Hz, Unit #1 (25 pairs), adjacent pairs

	Specification Value	Measured Value	Meets Specification
	pF/1000 ft	pF/1000 ft	
Minimum Value		0	
Maximum Value	80	43,9	OK
Average		8,6	
Standard Deviation		9,8	
RMS	25	13,1	OK

Table 2: Capacitance Unbalance Pair to Pair at 800 Hz, Unit #2 (25 pairs), adjacent pairs

	Specification Value	Measured Value	Meets Specification
	pF/1000 ft	pF/1000 ft	
Minimum Value		0	
Maximum Value	80	42,9	OK
Average		6,5	
Standard Deviation		8,3	
RMS	25	10,6	OK

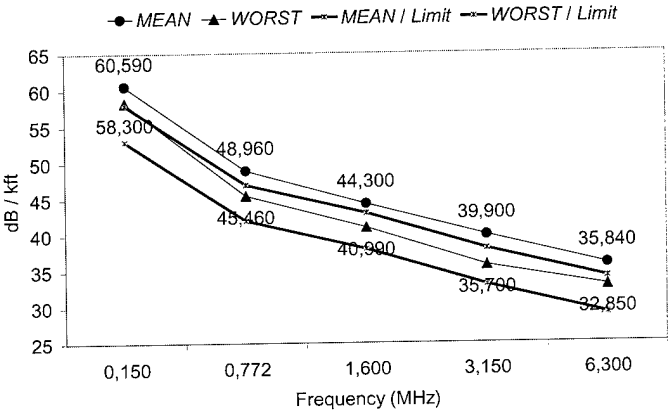


Figure. 1: NEXT Power Sum

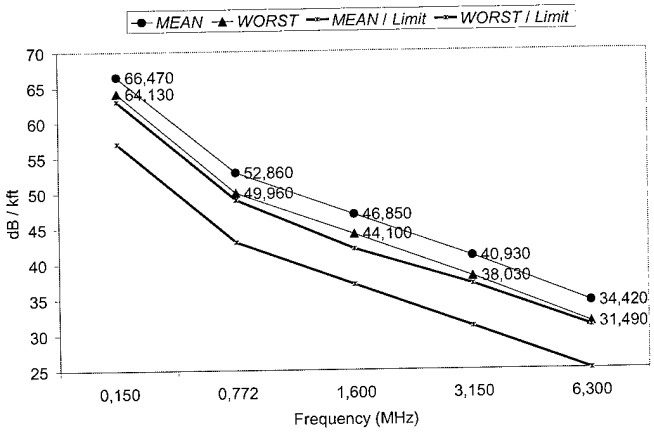


Figure 2: EL FEXT

5.2 Cable: 50 x 2 x 0,6 (5 x 10 pair sub-unit)

Insulation: Foam-Skin-PE

Specification: ROMTELEKOM ST-1-1

Table 3: Cable: 50 x 2 x 0,6 (5 x 10 pair sub-unit)

Parameter	Spec. Limit	Min. Value	Max. Value	Average
Conductor Resistance	66,60 Ohm/km			59,29 Ohm/km
Mutual Capacitance	max. 64 nF/km AVG 55 nF/km			48,9 nF/km
Cap. Unbalance	150 pF/500 m		43 pF/500 m	12 pF/500 m
Attenuation 0,1 MHz	5,55 dB/km	4,11 dB/km	4,72 dB/km	4,32 dB/km
Attenuation 0,3 MHz	8,40 dB/km	7,22 dB/km	7,61 dB/km	7,40 dB/km
Attenuation 1 MHz	15,40 dB/km	13,38 dB/km	13,76 dB/km	13,56 dB/km
Attenuation 3 MHz	26,55 dB/km	22,92 dB/km	23,77 dB/km	23,36 dB/km
NEXT 0,1 MHz	min. 55 dB	63,77 dB	108,32 dB	78,57 dB
NEXT 0,3 MHz	min. 45 dB	60,49 dB	92,74 dB	72,21 dB
NEXT 1 MHz	min. 40 dB	49,39 dB	98,81 dB	63,14 dB
NEXT 3 MHz	min. 33 dB	41,66 dB	75,12 dB	55,85 dB
FEXT 0,1 MHz	min. 60 dB	70,33 dB	101,94 dB	85,50 dB
FEXT 0,3 MHz	min. 50 dB	63,35 dB	98,61 dB	79,35 dB
FEXT 1 MHz	min. 40 dB	55,97 dB	106,50 dB	72,70 dB
FEXT 3 MHz	min. 35 dB	51,03 dB	111,08 dB	68,22 dB

7. Conclusion

New equipment has been developed not only to be integrated into new lines but especially to upgrade existing production lines (using e.g. double twister SZ technology) to meet today's and future requirements.

To increase the performance of the stranding equipment, modifications and innovations of drive and element guiding systems have been developed and worked out.

Of particular importance for stranding pairs and quads of communication cables with high transmission rates is to keep friction and reversal spots minimal.

Best results have been achieved by using one or more duct coated mini-disc accumulator axles, each driven by one high-dynamic frequency controlled AC drive (up to 7000 rpm) supported by a back-spin system (reversal times of about 30 ms).

Thus, short laylengths combined with small reversal spots at high speed production are possible.

Advanced SZ-technology utilized for the production of telephone cables enables to perform at levels suitable for data transmission.

8. Acknowledgments

Special thanks to my fellow engineer Gerhard Seibert who has been my colleague for long time now and who deservedly retired in July of this year. He has been dedicating his entire professional life to the invention and improvement of so many cable manufacturing machines and technologies, especially to the development of the disc accumulator SZ technology, which all the advanced SZ stranding equipment of today is based on.

6. References

[1] D. Vogelsberg and J. Mayer, "Combined Stranding Process in Telephone Cable Manufacture," *Wire Journal International, Vol 19, July 1986, pp36-42*

[2] D.R. Stein, D. Vogelsberg, "In-line pairtwisting and unit stranding with periodically reversed laydirection (SZ) " Wire journal International, April 1995, pp 52-54

[3] K. Bruns "Current Status of SZ Stranding/Cabling of Electrical and Fiberoptic Conductors", Ratingen, 1995

[4] G. Seibert, J. Marik "SZ-Stranding Today" Zotti Kabelseminar, Vienna, 2000.

7. Author:



Josef Marik graduated at the Vienna Engineering College and since has been involved in the wire and cable business for more than 35 years now. He joined ROSENDAHL Maschinen GmbH in 1998 as Business Development Manager. Today, he is Head of the Project Engineering Department.

Increased Scorch Resistance of Medium Voltage Power Cable Insulation by the Use of Liquid Antioxidants

Wolfgang A. Voigt
Ciba Specialty Chemicals Inc., Plastic Additives Segment
Basle, Switzerland, P.O. Box
+41-61-63-62099 • wolfgang.voigt@cibasc.com

Abstract

Scorch resistance of polymeric insulation materials is among the most important quality criteria during the production of LDPE cables crosslinked by organic peroxides. Early peroxide decomposition at elevated temperatures is a major obstacle for both increased line speeds as well as for downsizing the effective insulation thickness. Premature crosslinking and gel formation may be the consequences if inadequate stabilizer systems are applied. High demands in terms of cleanliness within this application led to a focus on liquid stabilizer systems, which may be optionally filtered prior to the mixing. Direct mixing of the stabilizers with the peroxide is facilitated by increased solubility and miscibility of liquid components with the crosslinking agent. Liquid antioxidant systems have been characterized according to resistance to scorch, crosslinking efficiency and retention of mechanical properties after thermal aging. Furthermore, exudation measurements have shown a significant drop in stabilizer blooming when exposing the insulation to elevated temperatures: this potentially translates into less lumping of the stabilized pellets during storage and reduced stickiness and better handling of the stabilized system.

Keywords

liquid; antioxidants; scorch; cleanliness; exudation

1. Introduction

The degrading effects upon the original state and the integrity of polymeric materials, attributable to oxidation, heat and shear, are well known shortcomings of such materials when used in products wherein long-term performance at elevated temperatures is required. The producers of power cables are continuously looking for optimization of current systems as well as into the development of novel solutions. The selection of an appropriate antioxidant system is determined by multiple technical and commercial needs, and in particular the choice of the best stabilization system is very dependent upon the crosslinking technique used [1,2]. The need for reasonably high insulation thickness in medium and high voltage cables represents a significant limitation for organosilane and electron beam crosslinking mechanisms, which makes peroxide crosslinking the preferred domain for Medium and High Voltage power cable insulation. The presence of peroxides, however, may lead to various problems, which have to be carefully considered: extrusion temperatures are usually limited to about 135°C, since peroxides decompose rather rapidly at elevated temperatures; desirable developments in cable production, such as lower insulation thickness and increased throughput, are usually of limited success for the same reasons. The Process Engineer who wants to minimize the risk of premature crosslinking (scorch) has to look for an efficient scorch retarder. On the other hand the crosslinking process taking place immediately after extrusion at temperatures above 180°C should run quickly and smoothly without major interactions between the antioxidant(s) and the crosslinking agent. The term "scorch" is illustrated in Figure 1.

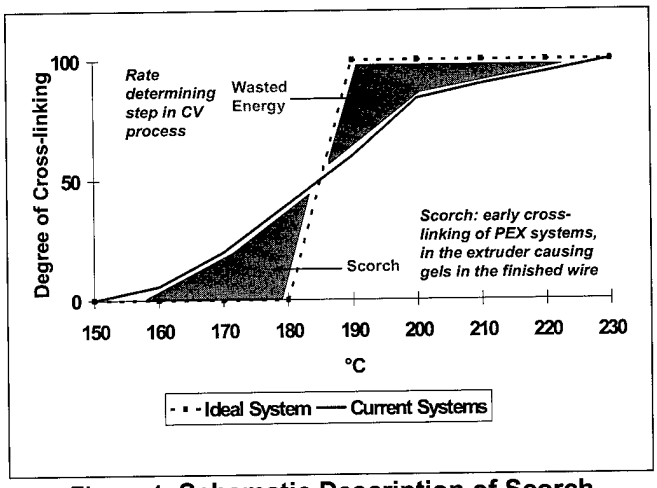


Figure 1. Schematic Description of Scorch

Furthermore, one of the preferred additivation techniques starts with a solution of the additive in the peroxide. While current solid stabilizers systems require a certain period for mixing or are excluded due to poor miscibility, liquid antioxidants can greatly simplify this procedure and enable valuable timesaving. Liquid systems additionally give the option to be filtered from any external impurities before making the additive-peroxide preblend, thus safeguarding the highly desired cleanliness requirements for power cables.

Discussed in this paper are our findings on the impact of different solid and liquid antioxidant systems on the polymer preparation

and processing behavior as well as on the mechanical properties after heat aging.

1.1 Autoxidation Cycle

On their way from the reactor to the final article polymers undergo multiple thermal and mechanical stresses. The combination of heat, shear stress and the presence of oxygen cause the degradation of polymers. Figure 2 is a simplified scheme of the autoxidation cycle, which describes the degradation reactions by radical chain mechanisms, leading to a change of the molecular structure by chain scission or crosslinking. Appropriate stabilizers can efficiently retain the initial properties of the polymer by different mechanisms [3/4/5].

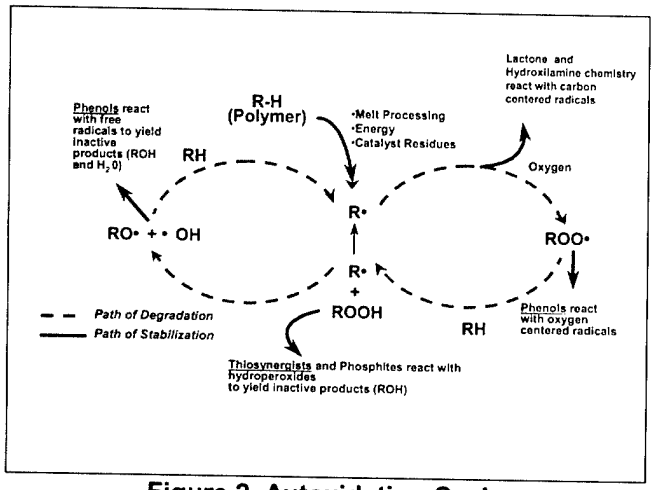


Figure 2. Autoxidation Cycle

1.2 Peroxide Crosslinking

The most widely used process for crosslinking of polyethylene is the incorporation of organic peroxides. In the crosslinking process the peroxide is first decomposed into free radicals, followed by abstraction of the hydrogen atom from the polymer backbone to form PE macroradicals and a variety of products of reactions and rearrangement occurring among the radicals [6]. PE for medium and high voltage power cables is usually crosslinked. The main advantage of crosslinked polyethylene is its enhanced thermal stability above the crystallite melting temperature, enabling both higher voltage and temperature rating on the conductor up to 90°C during continuous service life and even up to 130°C during emergency power operation [7].

1.3 Stabilization of crosslinked Polyolefins

Thermoplastic Materials are usually processed at elevated temperatures and under conditions of high shear stress. Especially in applications such as cable insulation or jacketing these materials additionally have to withstand severe conditions such as continuous exposure to heat during service life. Without suitable antioxidants, i.e. processing and heat stabilizers none of these developments would be possible [8]. Peroxide crosslinked PE is most commonly stabilized by systems comprising phenol derivatives and synergistic organosulphides or stabilizing systems combining both functionalities within one molecule [9].

1.3.1 Phenolic Antioxidants

Phenolic Antioxidants scavenge alkoxy and peroxy radicals; the general mechanism is depicted in Figure 3.

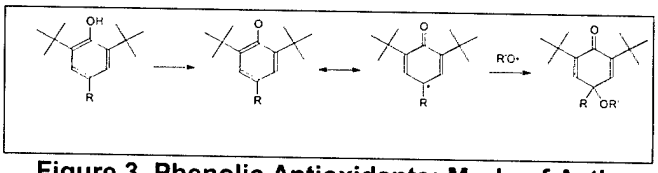


Figure 3. Phenolic Antioxidants: Mode of Action

By donating a hydrogen radical, phenols neutralize these types of radicals being previously formed through severe processing conditions in presence of oxygen or by cleavage of hydroperoxides. Phenolic antioxidants protect polymers during processing as well as in the end application as long-term thermal stabilizers. A huge variety of studies on stabilization with phenols have been carried out in the last decades [10/11/12].

1.3.2 Thiosynergists

Organosulphur compounds such as sulphides, dialkyl-dithiocarbamates or thiodipropionates are well known hydroperoxide decomposers [13]. The general scheme for stabilization can be depicted from Figure 4.

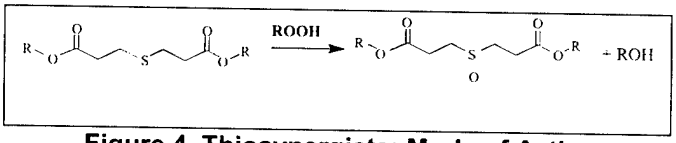


Figure 4. Thiosynergists: Mode of Action

Since hydroperoxides, R-O-O-H, predominantly decompose at higher temperatures to alkoxy and hydroxy radicals, high loadings of e.g. phenolic antioxidants would be needed in order to scavenge reasonable amounts of the so formed radical species. Through a redox reaction, thiosynergists reduce the hydroperoxides to alcohols before the decomposition takes place, i.e. they efficiently reduce the formation of radicals and therefore reduce the necessity for excessive amounts of phenols.

Methodology

By carefully selecting the appropriate formulation for a particular process set-up, it is possible to tailor the desired end properties of the polymer without significantly compromising the crosslinking

efficiency or scorch resistance. The performance data described in the framework of this investigation will compare the behavior of two liquid antioxidant systems AO-L1 and AO-L2 to their traditionally used solid counterparts AO-S1, AO-S2 and AO-S3. Representative test methods for cable insulation have been applied to characterize the different formulations. The product code used in the description can be related to the composition according to Table 1. The antioxidant levels examined during the study are within 0.1 and 0.5%. Use Levels of AO-S1 were usually about 50% higher compared to all the other systems.

Table 1. Product Codes and Trade names

Code	Composition	Trade name
AO-L1	4,6-bis(octylthiomethyl)-o-cresol	IRGASTAB® Cable KV10
AO-L2	Proprietary mixture	EB KV8
AO-S1	1:1 Blend of AO-S4/ AO-S5	IRGANOX® B 835
AO-S2	4,4' thio bis (6-t-butyl-3-methylphenol)	LOWINOX® TBM-6 IRGANOX® 415
AO-S3	6,6'-di-tert-butyl-2-2'-thiodi-p-cresol	IRGANOX® 1081
AO-S4	Thiodiethylene bis [3-(3,5-di-tert-butyl-4-hydroxyphenyl)propionate]	IRGANOX® 1035
AO-S5	Dioctadecyl 3,3' thiodipropionate	IRGANOX® PS 802

2. Experimental

2.1 Miscibility of additives and peroxide

Selected additives were evaluated for their miscibility with the Di-Cup R at 40°C. Of major interest was the absolute solubility/miscibility between both components and the time to obtain a clear solution. Tests were stopped when a clear 1:1 mixture could be obtained within one minute.

2.2 Compound Preparation

The polymer used for the study was a low-density polyethylene, d=0.923 g/cm^3, from ExxonMobil® LD 100 MED; MFI~2.0 dg/min (2.16 kg @ 190°C). The peroxide used was Di-Cup R (98% purity) from Hercules All formulations were prepared by a soaking method: the polymer was heated to 90°C while the stabilizers and the peroxide were heated to 70°C in a water bath, Afterwards the stabilizer/peroxide melt was added to the warm polymer granulate and the whole mixture heated at 90°C for about 60 min. The mixture was agitated every ten minutes, which was repeated until the whole liquid phase was soaked into the polymer.

2.3 Scorch resistance

In order to simulate cable extrusion conditions, 43 g of each compound were weighed and stir melted at 30 rpm in a lab kneader (type Brabender Plasticorder 814 300) at 130°C/2.0 kg load. This temperature was chosen being a typical value for cable extrusion. Scorch time was determined as the time in minutes for a rise of 1Nm of torque over the minimum torque in the kneader.

2.4 Crosslinking procedure

The production of crosslinked PE-LD plaques was carried out in three compression molders at different temperatures: In the first mold a defined weight of material was spread out in a frame and heated up to 120°C for 6 min. During that time the pressure was increased stepwise from 0 to 150 bar. In the next step the frame with the plaques was transferred to a second compression molder and left at 180°C for 15 min at 150 bar for completion of crosslinking. Finally, the plaques were cooled down from 180°C to room temperature within approximately 10 min.

2.5 Gel Content

The amount of insolubles is a measure of the degree of crosslinking obtained. A defined weight of the crosslinked plaques was exposed to boiling decaline for 24h. The soluble parts were filtered through a sieve and both sieve and sample were washed with decaline. Afterwards both were dried in a vacuum dryer until a constant weight was obtained.

The Gel content was determined according to the formula:

$$\text{Gel content (\%)} = 100\ (W_1 - W_2)/W_3$$

W_1=Weight of Sieve and insolubles after vacuum drying

W_2=Weight of the annealed, empty sieve before filtration

W_3=Weight of the polymer sample

2.6 Maximum Torque

5g of each sample were heated to 180°C in a Moving Die Rheometer (Monsanto MDR 2000). The samples were then exposed to an oscillation of ± 3° torsion at 1.66 Hz until the maximum torque was obtained. The maximum torque relates to the degree of crosslinking achieved and is an indication for the interaction between crosslinking agent and antioxidant.

2.7 Thermal Aging and Mechanical Tests

Tensile bars (dimensions according to DIN 53-504-82) were punched from the crosslinked plaques and split into four sets for oven aging at 150°C for 0, 3, 10 and 14 days. The tensile bars were evaluated for retention of tensile strength and elongation (yield; break), which is a measure of the stabilization effectiveness.

2.8 Exudation

Each formulation was kept in the oven at 55°C in order to simulate antioxidant plate out. At the appropriate recall interval, an aliquot was extracted from the oven and measured for surface exudation. The samples were washed with methylene chloride (about 15 seconds contact with polymer) and the solution was then transferred to a flask and evaporated to dryness. The resultant residue was reconstitued with a standard solution and analyzed via liquid or gas chromatography.

3. Results and Discussion

3.1 Miscibility of Additives and Peroxide

Table 2 gives an overview on the ease of miscibility of some stabilizers with DICUP-R. Both the liquid products are easily and quickly miscible in a 1:1 ratio with the peroxide, while the solid systems generally require more time until a homogeneous mixture is obtained. Furthermore the solubility of the solid antioxidant systems is lower compared to the liquid ones.

Table 2. Miscibility of additives with peroxide

Product	Miscibility with 100 phr DI-CUP R (40°C)	Time at 40°C to obtain a homogeneous mixture
AO-L1	100 phr	1 min
AO-L2	100 phr	1 min
AO-S2	3 phr	60 min
AO-S3	50 phr	12 min

3.2 Processing of the Insulation Material

Figure 5 illustrates the resistance of different stabilizer systems to scorch at simulated extrusion temperatures. It can easily be observed that the liquid antioxidant AO-L1 clearly outperforms the solid industry standards AO-S1-3

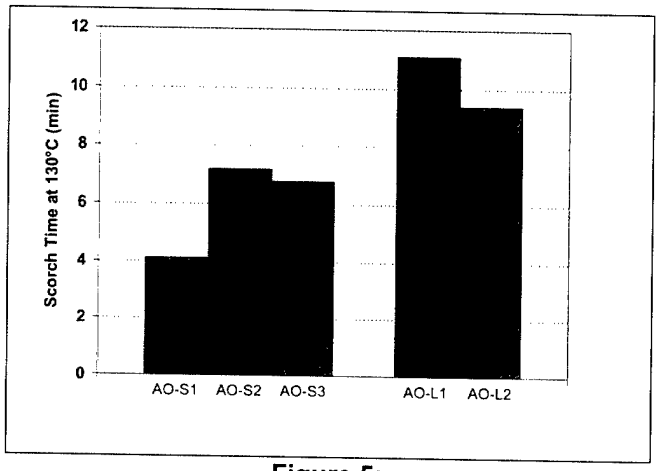


Figure 5:
Antioxidant Contribution to Scorch Resistance

Especially when small insulation layers have to be produced, scorch resistance becomes an important quality issue in manufacturing, since the improved heat flow in a thinner layer will generate an increased decomposition rate of peroxide and subsequent premature crosslinking. In this respect, the second liquid antioxidant AO-L2 is not as efficient as AO-L1, but still meets and slightly improves the standard established by the solid stabilizers. A longer scorch time means higher scorch resistance and fewer problems occur due to premature crosslinking during extrusion. Premature crosslinking in the extruder may result in inhomogenities, which can come loose and get into a cable forming a defect that can jeopardize the performance of the final cable [14, 15]. It is noteworthy to mention that scorch time is not a material constant but heavily depending on the extrusion conditions and amount of processed material. Therefore results for different formulations do always have to be compared for the same conditions.

Figure 6 shows the effect of the stabilizer system on the maximum torque obtained, which is an indicator for the interaction between stabilizer and crosslinking agent. It was expected that a system that provides increased scorch resistance would to a certain extent affect the efficiency of the crosslinking agent. Remarkably, both liquid systems AO-L1 and AO-L2 provide comparable maximum torque to the solid benchmarks AO-S1 and AO-S2, in spite of the solids' inferior results regarding resistance to scorch. However, a slight shift of AO-L1 towards a lower absolute maximum torque compared to AO-S1, AO-S2 and AO-S3 could be observed.

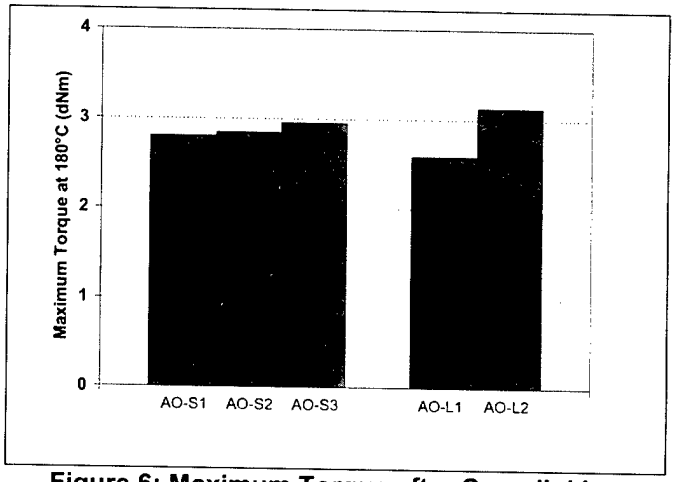


Figure 6: Maximum Torque after Crosslinking

3.3 Gel content and Exudation Behavior

As illustrated in Figure 7 all materials evidenced approximately the same gel content. The degree of crosslinking achieved was at the expected levels for all systems.

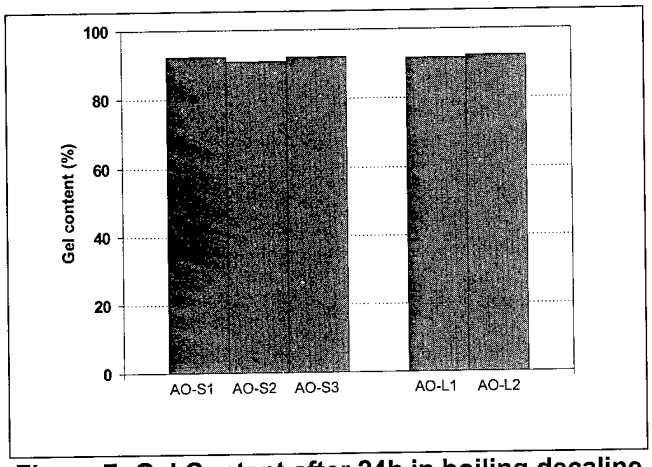


Figure 7: Gel Content after 24h in boiling decaline

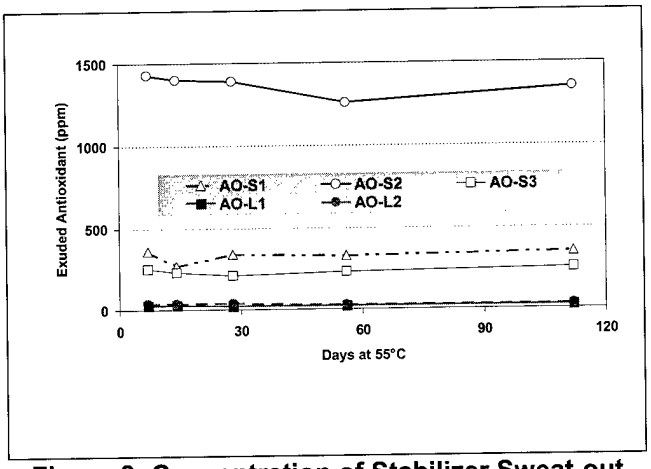


Figure 8: Concentration of Stabilizer Sweat-out after conditioning at 55°C

Since exudation of antioxidants at critical temperatures is of great interest, it was examined how the liquid systems behave in comparison to the solid ones. A high tendency for migration of stabilizers to the polymer surface can cause various problems, such as loss of active radical scavengers and a sticky surface lumping together the granules during storage. Exudation of stabilizers and peroxides is also known to have a negative impact on the extrusion process and the cable product: exudation dust may foul filters and cause slippage and instability in the extrusion process [16]. If poor compatibility is a consequence of a high melting point antioxidant, even more problems are likely to appear: peroxide crosslinkable cable grades are typically extruded at temperatures in the range of 130-140°C in order to minimize early peroxide decomposition. Especially for the high melting AO-S2 ($T_m \approx 160°C$) high exudation in homopolymer XLPE can be observed under critical conditions [17]. After crosslinking, voids may be formed which lead to possible failure sources during electrical testing of cables.

In Figure 8 the sweat out behavior of the different systems was compared after conditioning at 55°C. While AO-S1 and AO-S3 are already an improvement over AO-S2, even in spite of AO-S1's higher loading compared to AO-S2, both the liquid antioxidants AO-L1 and AO-L2 show an impressive improvement in terms of compatibility with the polymer. This offers a further opportunity for the converter to increase the additive loadings were necessary, especially where higher scorch resistance is desired, without expecting severe problems with exudation. However, the increased amount of scorch inhibiting antioxidant has to be examined carefully regarding its influence on the crosslinking process.

3.4 Mechanical Properties after Aging

During its lifetime a power cable is exposed to multiple mechanical and thermal stresses. The polymeric insulation undergoes degradation, which leads to failure if the stabilization package is not properly adapted. In order to safeguard the insulation's mechanical properties, defined mechanical tests have to be passed. The typical assessment for medium voltage power cable insulation allows a deviation of not more than 25% from the initial values after ten days thermal aging at 150°C. As shown in Figure 9 and Figure 10, all stabilizer systems passed the test criteria with the concentrations used in the study. Some of them are even surpassing them for longer aging times, thus leaving the option to further optimize the total amount of stabilizers.

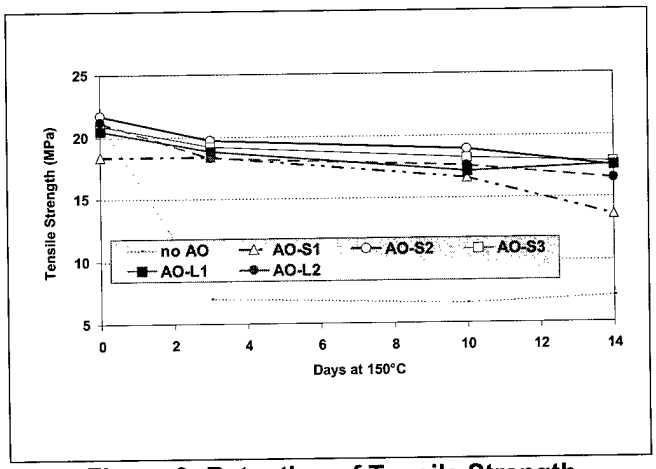


Figure 9: Retention of Tensile Strength

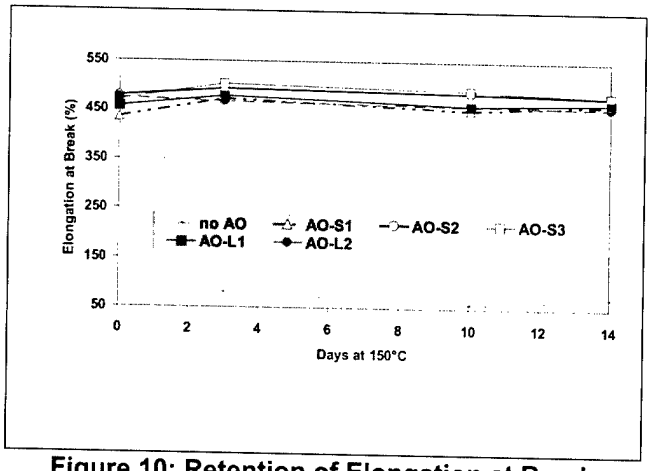


Figure 10: Retention of Elongation at Break

4. Conclusions

Most currently used stabilizers for peroxide-crosslinked polyethylene are supplied as solids. This carries with it the risk of inadequate dispersion in the polymer matrix and creates the potential for the introduction of insulation-destroying contaminants. The use of liquid systems described in this study eliminates the risk of antioxidant being present in the cable as unmelted, poorly distributed particles. High activity as scorch retarders, excellent compatibility with the polymer matrix, high dosing accuracy and the ease with which it can be mixed with the peroxide and the polymer melt result in improved product homogeneity and consequently offer the potential for enhanced insulation performance of the final cable.

5. Acknowledgments

The development of new stabilization chemistries and applications is the result of a lot of hard work by many people. The author wishes to thank all his colleagues for their direct and indirect contributions from the Ciba Specialty Chemical sites around the world. Special thanks to J.Kenny, F.Stricker, T.Bürki, L.Evangelista, M. Gande and D.Müller for all of their work. Sincere appreciation is given to D.Labbé and G.Matey of P&M Ltd., Switzerland, for stimulating discussions.

6. References

[1] Sultan, B.-Å., Palmlöf M., Plastics, Rubber and CompositesProcessing and Applications 21. No. 2, 1994, 65

[2] Stengrevics, E.; King, R.E.; Hofmann, P.; Stabilization of Crosslinked Polyethylene, *RETEC IV*, Houston, Texas, 1989, Conference Proceedings, 331-346

[3] Moss S., Pauquet J.R., Zweifel H., "Degradation and Stabilization of Polyolefins during melt processing", *International Conference on Advances in the Stabilization of Polyolefins and Degradation of Polymers*, Lucerne 1991, Conference Preprints (A.Patsis, Ed.)

[4] Zweifel H., Moss S., "Degradation and Stabilization of High Density Polyethylene during Multiple Extrusion", *Polymer Degradation and Stability*, 25, 1989, 217-245

[5] Drake W.O., Cooper K.D., "Recent Advances in Processing Stabilization of Polyolefins", *SPE Polyolefins VIII International Conference*, February 1993, Houston

[6] Uhniat, M., Kudla S., *Polymer Degradation and Stability*, 71, 2001, 69-74

[7] Vogt, H. in: Mair H.J. (Ed.), "Kunststoffe in der Kabeltechnik, Expert-Verlag, Renningen, 1999

[8] Zweifel H. (Ed.): Plastics Additives Handbook, Hanser, Munich, 2001

[9] Pospisil J., Klemchuk P.P. in: *Oxidation Inhibition in organic materials*, Vol. 1, Boston: CRC Press, 1990, 105

[10] Zweifel H., "Stabilization of Polymeric Materials", Springer, Berlin Heidelberg 1998,

[11] Gächter R. (Ed.), "Plastics Additives", Hanser, Munich, 1990

[12] Gugumus, F.; "Langzeitverhalten von Kunststoffen am Beispiel der Polyolefine", *Thermische Einsatzgrenzen von Kunststoffen in Verarbeitung und Anwendung*, Erlangen 1999

[13] Armstrong et al.: *Eur. Poly. J.* 15, 1979, 241

[14] Gustafsson, B., Dammert R.C., Bostrom, J.O.: Stabilization of peroxide-crosslinked polyethylene, *Angew.Makromol. Chem.*, 261 (2), 1998, 93-99.

[15] Krähenbühl F., Wavre, J.J., *Int.Wire et. Cable Symp. Proceed.*, 556, 1992

[16] US Patent No. 6,127,482, 2000

[17] Matey G.; The Development of a WTR XLPE Insulation, *3rd International Cable Conference*, Budapest, October 1989

Biographical Notes



Wolfgang A. Voigt

Ciba Specialty Chemicals Inc., CH-4002 Basel;

P.O.Box; R-1038.4.21

Wolfgang A. Voigt holds an engineering degree in Material Sciences from Erlangen-Nuremberg's Technical University in Germany. He has been with Ciba Specialty Chemicals since 1995, where he worked as a process engineer within Ciba's former Business Unit Electronic Materials in Italy and Switzerland, dealing with epoxy and epoxy acrylate based solder masks for printed circuit boards. In 1998 he joined the Plastic Additives Segment, where his current work is focused on new Additives and Technologies for Polymer Extrusions, with an emphasis on Wire & Cable Applications. Mr. Voigt is a member of the Wire Association International.

Die Lip Build-up in the Filled Low Density Polyethylene Wire and Cable Extrusion

Chun D. Lee
Equistar Chemicals, LP, Equistar Technology Center
11530 Northlake Drive, Cincinnati, OH 45249
chun.lee@equistarchem.com

Abstract

It is common that a highly filled master batch (MB) contains a low molecular weight (LMw) lubricant as a filler dispersion agent and compounding processing aid. Sometimes, the presence of such a lubricant in the MB creates a die build-up problem in the extrusion process. Several MBs with a laboratory Banbury mixer were produced to investigate the effect of the amount of aluminum stearate (as a lubricant) on dispersion and die build-up. When the MB contains the stearate below the critical amount, die build-up decreases and filler dispersion improves with increased amounts of stearate. At the critical amount of the stearate, the MB shows good dispersion as well as minimum build-up. Above the critical amount, dispersion is still good. But, build-up increases with further increase in the amount of stearate added up to 3.0%. This observation results from the different mechanisms of the die build-up, which depends on whether the stearate level is below or above the critical amount. We confirmed such a mechanism in the commercial extrusion process of the MBs. This observation leads to the conclusion that in the use of the stearate (as a dispersion agent) for highly filled MB, the amount of the stearate need to be optimized to minimize a die build-up of the MB with good filler dispersion.

Keywords

Die build-up, die lifetime, stearate, master batch, LDPE, dispersion agent, stability, filler dispersion

1. Introduction

Die lip build-up, also called plate-out, die drool, die drip, or die peel, refers to the unwanted accumulation of material on the open face of wire and cable extrusion dies. Build-up also creates die streaking onto a surface of an extruded product.

Excessive die lip build-up has been an issue in the wire and cable as well as the plastic industry [1-4]. This is due to the fact that die build-up diminishes both the aesthetic quality and the properties of a product. For an example, a reattached build-up of material in a wire coating extrusion may diminish the dielectric properties of the insulating material [1]. A shorter die lifetime resulting from a quicker die lip build-up requires more frequent downtime. If an extrusion operator observes the die build-up during extrusion, the operation must be stopped for die cleaning. Thus, such an extrusion is not desirable and costly.

Low molecular weight (LMw) materials such as polyolefin wax, silicon oil, or metal stearate have been widely used in the compounding industry to improve filler dispersion as well as the compounding operation [4-5]. Good filler dispersion is critical in the use of a MB for industrial applications. In general, the LMw material used for MB products is incompatible with the base resin of the MB. During extrusion, LMw material can preferentially migrate to the surface of the die. This behavior of LMw material migration appears to be similar to that of fluoroelastomer processing aids. However, the nature of a lubricant layer between LMw and fluoroelastomer is different, leading to the formation of die build-up for the former and elimination of build-up for the latter [6-8].

Several MBs of 50 wt% filler loading were produced using a laboratory Banbury. The laboratory extrusion test has been carried out for the measurement of the die build-up on the MBs. The objective of this work is to investigate the effect of the amount of stearate on the rate of die build-up. The build-up mechanism is proposed as a function of the amount of stearate added. The build-up data of lab scale MBs are in line with those of commercial extrusion with the MBs. The result provides a guideline to optimize the level of lubricant in the production of a MB.

2. Experimental

2-1. Sample preparation

A Farrel ODC Banbury mixer (2400 CC) was used to produce 50% filled MBs with the same components of filler, base LDPE resin, and antioxidants (700 PPM for the primary and 500 PPM for the secondary) but different levels of aluminum stearate. The Banbury drop was pelletized through a 50.8 mm single screw extruder to produce finished pellets products for evaluations.

2-2. Characterization

2-2-1. Rheological measurements

The dynamic rheological measurements were carried out on a Rheometrics RDA-II equipped with parallel plates. The measurements were done at 210°C with a frequency sweep from 398 to 0.0640 rad/sec with 5% of strain. We also used the plots of G' (elastic modulus) vs. G" (loss modulus) for a comparison purpose in the change of melt elasticity.

We obtained the apparent shear viscosity as a function of apparent shear rate for the MBs using a Kayeness capillary rheometer at 210°C.

2-2-2. Filler dispersion test

We used a pressure rise test (PRT) for the filler dispersion of the MBs used in this investigation. The PRT is analogous to the screen pack-plugging test, which is used to determine the quality of MBs. The test uses a Haake 90 single screw extruder (L/D= 23, D= 20 mm). The heated die has a breaker plate followed by the following screen pack arrangement in mesh: 60-60-325-500-60. The extruder screw was run at 150 RPM. The MB was let down to a final 12.5 wt% filler content using the let down resin (LDPE, 7 MI, 0.920 density). The pressure rise (PR) in psi is obtained by subtracting the first 5 minutes reading from the 35 minutes reading: the higher PR means poorer filler dispersion for the MB evaluated due to quicker screen pack plugging.

2-2-3. Stability Test

A thermo-mechanical stability test was carried out using a Haake Rheomix 90 at 60 RPM and 230°C for the MBs. We monitored torque variation as a function of time. The variation represents the extent of thermo-mechanical stability. We also examined the test samples for the rheological change to identify the root cause of the variation.

2-2-4. Die build-up test

A Haake 25 mm single screw extruder at 125 RPM attached with 50 mm slit die with 0.5 mm die opening was used for the laboratory measurements of die build-up. A sheet extrudate was drawn with a take-up device to a 1.5:1draw ratio to minimize a die swell effect. We monitored the percent coverage of the die deposit every 5 minutes during extrusion of the MBs. Average percent coverage was taken from three measurements for each sample.

2-2-5. Infrared (IR) measurements

The die deposit was carefully and quickly collected from the lip of the die as soon as enough build-up was noticed during extrusion. The IR spectra were acquired using a Nicolet 60SX FTIR spectrometer under nitrogen purge. The carbonyl (C=O) stretching band at 1860 – 1610 cm^{-1} was used to measure the extent of degradation. The thickness band at 2107-1976 cm^{-1} was also used for the correction of sample thickness for the spectra.

3. Results and discussion

Table 1 shows the dispersion and rheological data of the experimental MBs containing different amounts of the stearate. As expected, filler dispersion improves with addition of stearate up to 0.5 wt% and remains unchanged with further addition of the stearate up to 1.0%. Further addition of stearate up to 3.0% deteriorates dispersion. The dynamic rheological data indicates little difference in the frequency viscosity at 25 rad/sec for the MBs, A-1, A-2, & A-3 (Table 1) which contain the stearate less that 0.6%. However, we observed a decreased viscosity with further increased level of the stearate, as going from 0.6 to 3.0 %. We confirmed such decreased viscosities in the capillary shear viscosity data (figure 1). A decreased viscosity with further increased amount of the stearate results from a lubricating effect under shear deformation.

Table 1. Basic, dispersion, and rheological data of the experimental MBs with different levels of the stearate.

MB	Level of stearate (%)	PR (psi)	Complex viscosity poise
A-1	0.0	330	5650
A-2	0.3	207	5580
A-3	0.5	110	5520
A-4	0.6	125	5400
A-5	1.0	115	4980
A-6	1.5	140	4440
A-7	3.0	162	4010

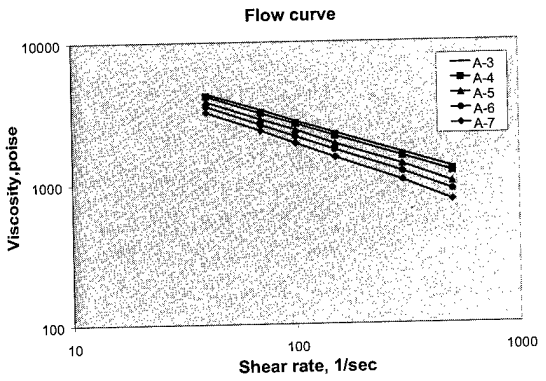


Figure 1. Rheological data for MB, A-3 (0.5%), A-4 (0.6%), A-5 (1.0%), A-6 (1.5%), and A-7 (3.0%).

Figure 2 shows the stability data of experimental MBs. Interestingly, MB A-1 tends to show higher torque build-up with increased mixing time than A-3 during the stability test. The only difference between these two MBs is the amount of stearate. In order to identify the origin of higher torque for A-1, compared to A-3, we examined the rheology of the stability tested samples. As shown in figure 3, the tested A-1 shows much higher G' (elastic modulus) for a given G"(loss modulus) than A-3. Both MB showed very similar G' at a given G" before the test. The higher elasticity for MB A-1, compared to A-3, can be attributed to a presence of chain extension reaction associated with degradation process. MB A-2 showed similar behavior to A-1 (figure 3) whereas MB A-4 through A–7, compared to A-3, shows much less torque with similar elasticity. The reduced torque results from more lubrication effect with higher amount of the stearate addition and subsequently, leads to the reduced degradation under the similar thermo-mechanical treatment.

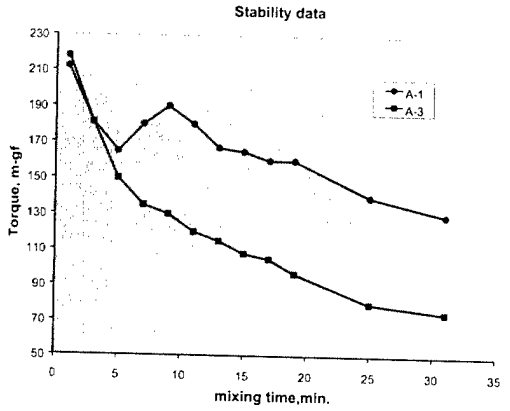


Figure 2. Stability data for MB A-1 (0.0%) and A-3(0.5%)

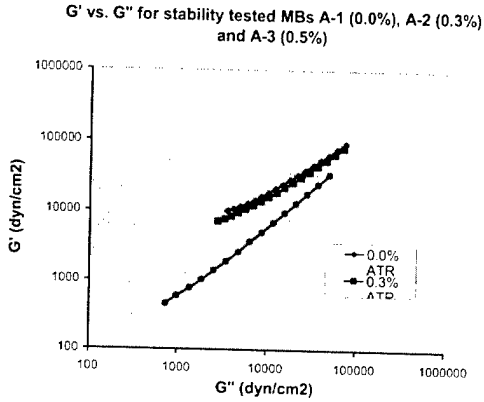


Figure 3. Dynamic rheological data (G' vs. G") for the stability tested MB A-1 (0.0%), A-2 (0.3%) and A-3 (0.5%)

The die build-up test with the lab scale extrusion indicates that the rate of build-up decreases with increased amount of the stearate up to 0.5 % and then increases with further increased amount of the stearate (figure 4).

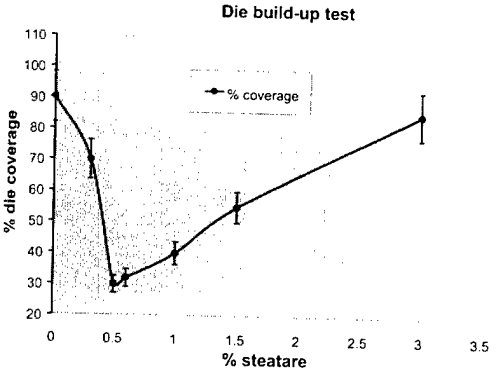


Figure 4. Rate of die build-up as a function of the amounts of stearate.

This result indicates a necessity of optimized amounts of the stearate addition to minimize die build-up with a good dispersion. Coupled with the result of the stability test, the mechanism for the build-up appears to be different, depending on the amount of the stearate. The mechanism will be discussed in a later section....

Figure 5 shows the capillary shear viscosity data of the stability tested MBs A-1 to A-3. A-1 shows lower shear viscosity than A-3. Previously, it has been shown that both MBs showed very similar viscosity data before the test. The lower viscosity for A-1 is indicative of the increased amount of LMw material which was developed by the degradation process during the stability test. It has been indicated that the degradation process develops both melt elasticity and LMw material due to the presence of both reactions; chain extension and chain scission [9]. A similar analogy can be applied to the MB A-1 for more build-up of A-1 with the single screw extrusion process when compared to A-3

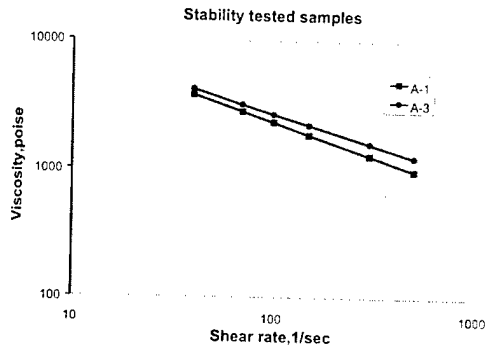


Figure 5. Rheological data for the treated A-1 (0.0%) and A-3 (0.5%)

Figure 6 shows the IR results of the material collected from the die build-up of the MBs. The spectra contain the carbonyl peak at 1725 cm^{-1} along with other major polyethylene peaks. The carbonyl band represents the presence of degraded product in PE [9]. Going from MB A-3 to A-1, we observed an increase in the carbonyl peak height with decreased amounts of the stearate with extrusion. This indicates that A-1 experienced more degradation present during the Haake extrusion than A-3. From A-4 to A-7, it is also shown that the carbonyl peak height increases with further addition of the stearate in the MBs. An increased carbonyl peak height with higher amounts of stearate present in the MBs (A-4 to A-7) originates not from degradation (as discussed previously) but from more stearate in the build-up. For example, more stearate comes along with extrudate for A-7 but not for A-4. The normalized data of the peak with respect to thickness confirms the observation described above (Table 2) where MB C-1 is a commercial product (see Table 3).

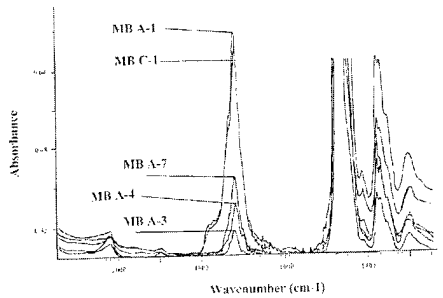


Figure 6. IR data for the die deposits obtained from MB A-1 (0.0%), A-3 (0.5%), A-4 (0.6%), A-7(3.0%), C-1 (0.3%).

Table 2. Normalized carbonyl band with respect to the IR samples of the die deposit collected from extruding the MBs.

MB	% Stearate	Carbonyl band height	Height of thickness band	Normalized ratio
A-1	0.0	30.9	1.4	21.3
A-3	0.5	1.0	1.0	1.0
A-5	1.0	2.2	0.7	3.2
A-7	3.0	4.1	0.7	5.7
C-1	0.3	20.5	1.4	14.8

Table 3 exhibits the basic data and die build-up performance of commercial MBs, C-1 and C-2. Both MBs were produced with identical compositions and compounding conditions but different levels of the stearate: 0.3% for C-1 and 0.5% for C-2. The MBs were letdown to 12.5% filler content for the extrusion evaluation. Both MBs show very similar filler dispersions but much difference in die lifetime. This observation of the die lifetime from the commercial extrusion for the MBs is in line with that of the lab scale build-up measurements (figure 4).

Table 3. Basic, dispersion, and die lifetime data of the commercial MBs.

MB	% stearate level	PR, psi	Die lifetime, hrs
C-1	0.3	178	2
C-2	0.5	108	12 +

4. Proposed mechanism for the die build-up

Based on the results thus far, the critical amounts of stearate were 0.5 wt% for the MB with a minimized build-up and good filler dispersion. It was also found that at amounts of stearate below 0.5%, degradation process promotes build-up. Above that amount, the excess stearate appears to promote the build-up.

Figure 7 describes a proposed model for the origin of die build-up depending on the amount of the stearate. At the amount below 0.5%(figure 7(a)), since there is not enough stearate to cover all filler surfaces, there may be a lot of friction in the interface between the filler and the matrix during mixing/extrusion, leading to a higher extent of degradation. Such degradation promotes both reactions; chain extension and chain scission, leading to enhanced melt elasticity and creating the LMw material. The newly developed LMw is responsible for the build-up during extrusion. At higher amounts of the stearate (>> 0.6%)(figure 7(b)), we can expect good incorporation of the stearate with filler surface which minimizes friction due to the lubricant effects. However, the amount of stearate, which does not incorporate with filler surface, remains in the matrix as excess. Since the amount of filler used for the MBs was fixed, an increased amount of the stearate addition for finished MB represents an increased amount of excess stearate. Such an excess amount of the stearate leads to the formation of die build-up during extrusion.

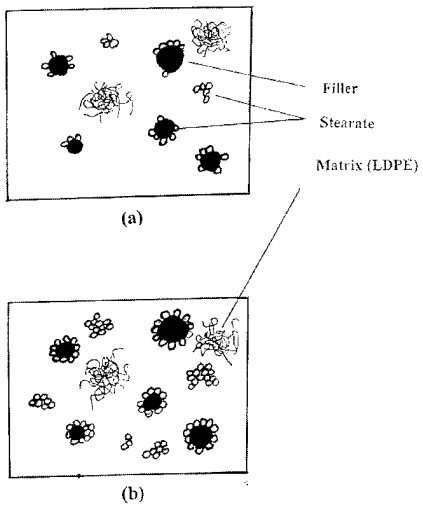


Figure 7. Proposed model for the mechanism o: (a) stearate << critical amount (b) stearate >> critical amount.

5. Conclusions

In the use of the highly filled master batches for extrusion applications, the filler dispersion and extent of die build-up depend on the amount of the stearate. We identified the critical amount of the stearate showing good dispersion as well as minimized die build-up. The critical amount was 0.5 wt% for the MBs investigated for this work. At an amount less than 0.5 wt%, thermo-mechanical degradation promotes die build-up; the build-up increases with decreasing amount of the stearate. The increased die build-up relates to the increased presence of the LMw material developed by the chain scission with the degradation process. At the higher amounts of stearate addition (above 0.6%), the large amounts of stearate create higher rates of die build-up even though the stability increases due to more lubrication: the build-up increases with increased amounts of stearate. This result is in line with the observations from commercial extrusion.

6. References

[1] M.Prober and J.E. Vostovich," Method of Providing Durable, Slick Sliding Surface on Extrusion Forming Apparatus and the Product Thereof", USP 3,942,937, March 9, 1987.

[2] M. Prober and J.E. Vostovich,"Method of Providing Durable R. Gachter and H. Muller. *Plastic Additives Handbook*, 2nd ed., Hansen, New York, 1987. Pp 434-435, 454-455, 646-647.

[3] D.E. Priester and G.R. Chapman,"Reducing Die Build-Up In Extrusion Applications", Polyolefins IX, SPE RETEC, Houston (February, 1995).

[4] S.J.Kurtz and S.R. Szaniszlo," Reduction in Die Drool in Filled Resins and Product Improvement", USP 5,008,056, April 16, 1991.

[5] J.W. Dawes and D.J. Ryan, US Patent, 4,485,062 (1984).

[6] G.R. Chapman, D.E. Priester, and R.D. Souffie,"Advances in the Use of Fluoroelastomer as Processing Aids for Polyolefins", SPE RETEC, Houston (1987).

[7] D.E. Priester and C.W. Stewart, SPE ANTEC, Detroit (May, 1992, pp 2024-2028.

[8] C.M. Chan, A. Nixon, and S. Venkatraman, J Rheology, 36 (5), 1992.

[9] G.R. Rideal and J.C. Padget, "The Thermal-Mechanical Degradation of High Density Polyethylene", J. Polym. Sci. Sym, No 57, 1-15 (1976).

Inverter Surge Resistant Enameled Wire

Hideyuki Kikuchi
Magnet Wire Engineering Dept. Hitachi Cable, Ltd.
Hitachi, Ibaraki, Japan
+81-294-42-5417 kikuchi.hideyuki@hitachi-cable.co.jp

Abstract
Due to growing consciousness of needs for earth environment protection shared by people throughout the world, energy saving is promoted rapidly and inverter-fed motors are now used generally among the industry. Recently, the application of high-speed switching has raised surge voltages and an increasing number of breakdown cases are reported for over 400V inverter-fed motor systems in relatively earlier stages of their life. A product introduced in this report was developed with innovative organic/inorganic nano-composite technology and has succeeded in achieving both inverter surge resistance and mechanical properties, the weakness associated with inorganic materials that the conventional partial discharge resistant enameled wires could not overcome. The newly developed product can maintain more than 1000 times as high voltage endurance as those offered by general enameled wires at a voltage in the neighborhood of the typical inverter surge voltage, even after mechanical stress is applied to it, so it is expected to bring dramatic improvement to the reliability. It may also open the way for performance guarantee of motors in actual operation up to a surge voltage of around 1.38kVp.

Keywords
Inverter; magnet wire; composite; partial discharge.

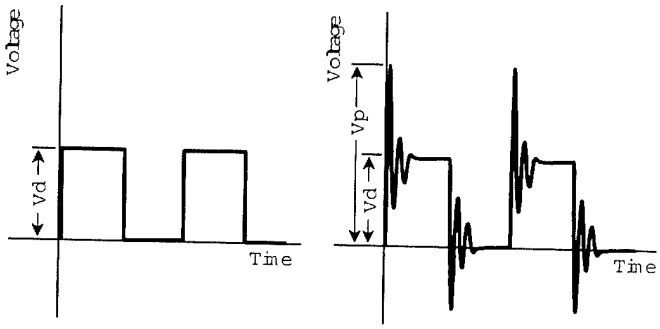
1. Introduction
In response to the global environmental problems, energy saving of electric appliances is pursued today with increasing enthusiasm. In the industrial motor area, an increasing number of motors now have inverters or adjustable speed drives to deliver higher efficiency required of today's industrial motors. Inverter outputs normally have an overlapping high peaking voltage that has a very short rise time generated by a reflected wave (hereinafter referred to as "inverter surge" or simply "surge"), which has been reported to cause a breakdown. [1][2][3] In recent years, elements allowing high-speed switching such as IGBT have been developed as inverter power devices. With the introduction of these devices, an increasing number of breakdown cases are reported in relatively earlier stages of the product life due to a higher surge voltage caused by these devices. Perceived under these circumstances were intensifying demands for development of high inverter surge resistance enameled wires.

The author has suspected that partial discharge is the primary cause in the mechanism of an inverter-surge-induced breakdown. With regard to partial discharge, enameled wires having a multi-layer coating structure containing dispersed metal oxides have been commercialized and released onto the market as a partial discharge resistant enameled wire. Such enameled wires have a three-layer structure, a partial discharge resistant coating film placed between normal enamel coating films to compensate for the weak mechanical properties of the former. Even with such a precaution, their electrical properties are vulnerable to degradation caused by mechanical stress such as elongation, and so far, they have failed to bring remarkable improvement to the useful life of motors in actual operation.

With these in mind, the author has developed a unique organic/inorganic nano-composite insulating material by dispersing an inorganic material at a nano meter-level and successfully achieved satisfactory levels for both partial discharge resistance and coating film flexibility and strength. As a result of application of this material to enameled wires, the electrical life of enameled wires at a voltage in the neighborhood of the typical inverter surge voltage has been successfully improved without sacrificing workability during coil winding such as flexibility to a level more than 1000 times greater than that of general enameled wires, even after they are subjected to mechanical stress.
This report will introduce various advantageous properties of the newly developed inverter surge resistant enameled wire (KMKED-20E).

2. Development Concept
An inverter outputs fast rise time pulse waves by high-speed switching. An inverter is normally coupled to a motor via cables to drive it. Since its outputs have significant voltage steepness, the locations such as a cable starting/terminating end where a change in impedance occurs generate reflected waves, which cause an overlapping surge of about twice as high as the output voltage. An example of the typical output wave shape is shown Figure 1. For a 400V inverter-fed motor system, Vd is typically around 0.55kV and Vp, about 1.1kV, if it is assumed that a surge has a voltage twice as high as an output voltage. Under poor power supply conditions (voltage fluctuations or higher input voltage), however, it is not utterly unlikely to observe Vp as high as 1.6kV. With these in mind, a development concept was formed, which is an enameled wire that can withstand stress normally experienced during coil winding or mechanical stress equivalent to it and yet extend the useful life substantially. It was decided, therefore, that a wire developed should be evaluated for

not only general properties but also voltage endurance after 20% elongation, a test condition exaggerating normal stress experienced during coil winding.



a Voltage at Inverter Terminal b Voltage at motor Terminal

Figure 1. Typical terminal voltage waveforms

3. Inverter-surge-induced Breakdown Mechanism

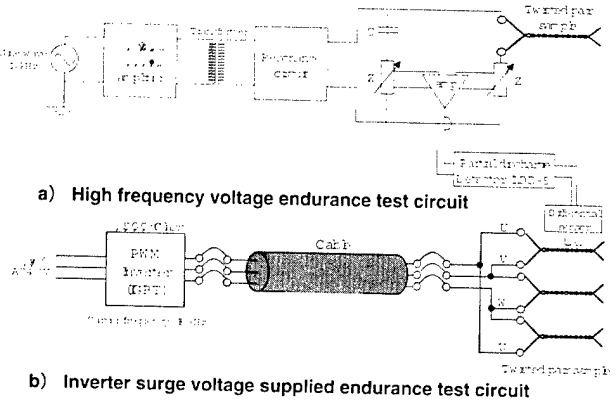
3.1 Inverter Surge and Outbreak of Partial Discharge

When a voltage is applied between two enameled wires, a normally observed DIV (partial discharge inception voltage) is around 0.8kVp for a 30μm-thick coating film, although it depends on the thickness of a coating film. A surge voltage of a 400V inverter-fed system is much higher than this and can cause partial discharge. Accordingly, the author speculated that partial discharge induced by a high surge voltage was mostly responsible for degradation leading to a breakdown and promoted the development depicted below based on this idea.

400V inverter-fed motor systems usually have insulating phase paper inserted at the coil ends, where a potential difference becomes large, to provide better insulation. The process to insert this paper is conducted manually, because it is difficult to automate, thereby posing a problem to motor cost reductions. If something goes wrong with this insulating phase paper insertion process, it can lead to a breakdown case when a surge voltage discussed earlier manifests between coils. In addition, since it is a phenomenon manifesting in a very high frequency range, a surge travels around the motor winding, and if that is the case, a voltage duty ratio will become higher also between wires within a coil. For this reason, reinforcement of insulation between wires has become necessary, which is another reason lying behind a strong need for enameled wires that can offer high inverter surge resistance.

3.2 Evaluation Test Methods and Life Characteristic of General-purpose Enameled Wires

For evaluation tests, both voltage endurance tests, which are high frequency voltage endurance tests using sine wave power supply, and surge voltage endurance tests using an actual inverter were conducted. The actual rise time of inverter surge voltage is 150 nano seconds. Test circuits are shown in Figure 2. Occurrence/nonoccurrence of partial discharge during each test is shown in Table 1. Voltage endurance of each enameled wire in various voltage endurance tests is shown in Figure 3-5. Incidentally, results of the voltage endurance tests are shown in the time elapsed before a breakdown occurs between two twisted pair samples.



a) High frequency voltage endurance test circuit

b) Inverter surge voltage supplied endurance test circuit

Figure 2. Test Circuit

Table 1. Observation of Partial Discharge

Sample	εr	Film thickness (μm)	DIV (Vp)	Occurrence/nonoccurrence of Partial Discharge	
				1.13kVp 10kHz sine wave	1.10kVp Inverter surge
AIW	Approx. 4.2	23	700	Yes	Yes
		34	740	Yes	Yes
		45	849	Yes	Yes
EI/AIW	Approx. 4.0	21	755	Yes	Yes
		34	827	Yes	Yes
		43	862	Yes	Yes
PEW	Approx. 3.8	22	747	Yes	Yes
		34	839	Yes	Yes
		41	880	Yes	Yes
		47	1004	Yes	No (or faint discharge)
Notes			50Hz sine wave	Sensitivity: 10pC	Discharge pulse observation

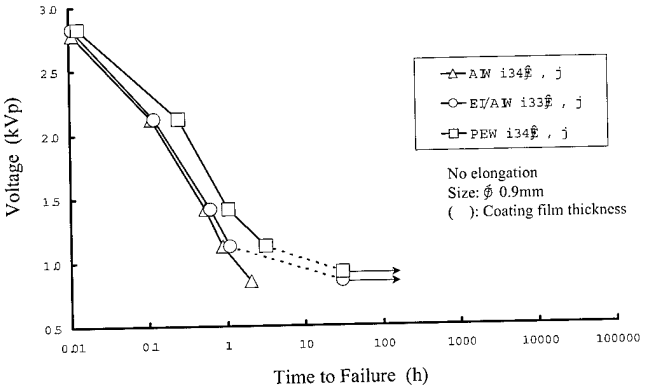


Figure 3. Voltage endurance (10kHz sine wave)

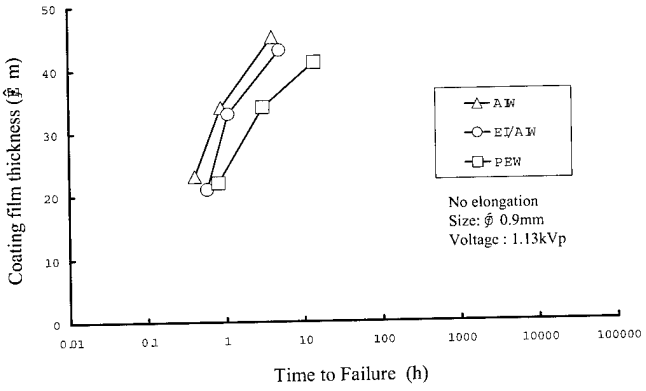


Figure 4. Voltage endurance (10kHz sine wave) **film thickness vs. life**

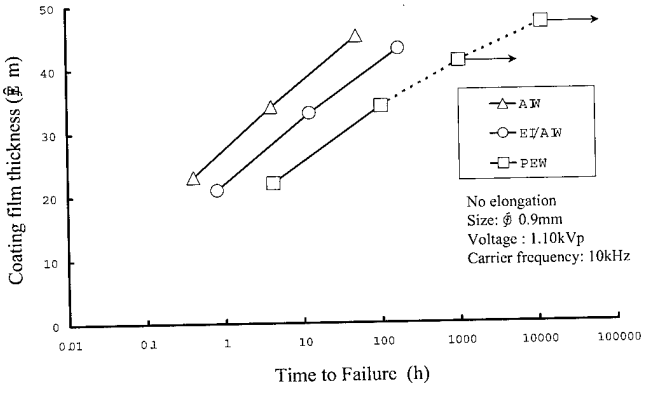


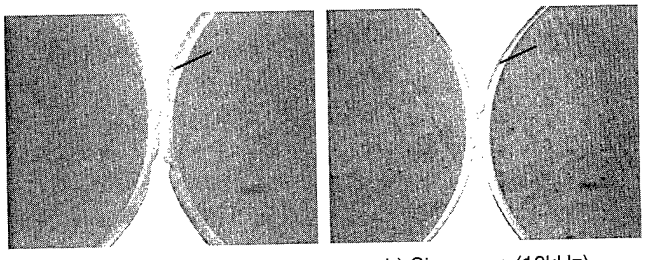
Figure 5. Inverter surge voltage endurance film thickness vs. life

To detect partial discharge, a bridge was used in the high frequency voltage endurance tests and a non-contacting type differential sensor was used in the inverter surge voltage endurance tests to observe partial discharge pulse wave shapes, because the tests were conducted with isolated circuits to measure a potential difference between phases. For evaluation with an actual motor, tests were conducted with a motor with no insulating phase paper inserted between phases so that a potential difference between phases might be applied directly onto wires.

Life was fairly dependent on a coating film thickness in both tests. Correlation with the permittivity of a coating film was also relatively clear, with polyamide-imide enameled wire (AIW), which have higher permittivity, showing a tendency to have a lower partial discharge inception voltage and a shorter life. Polyester enameled wire (PEW) having a 47 μm-thick coating film, with which partial discharge was not observed in the tests, experienced no breakdown for more than 10,000 hours of operation. Accordingly, it may be safe to assume that if no partial discharge occurs, there will be no early inverter-surge-induced breakdown, which takes place during the first several ten to several hundred hours as currently closed up in the market as a problem. In this context, it is true that raising DIV by increasing a coating film thickness is one way of improving the useful life of wires. This approach, however, will lower the space factor of coils, thereby spoiling efforts for improving the efficiency and decreasing the size of motors. It is also possible to raise DIV, if permittivity can be lowered, but this approach is not practical, as it will increase costs substantially.

3.3 Partial Discharge-induced Breakdown Mechanism [4]

Major phenomena named as a cause of degradation of an enamel insulating film includes (1) scission of molecular chains of an organic insulating material by the collision of charged particles, (2) a local temperature rise and (3) degradation caused by oxidization by ozone. To examine which of them contributes most to degradation, cross sections of enameled wires were investigated after the inverter surge voltage endurance tests and the 10kHz sine wave voltage endurance tests. Photos showing their cross sections are shown as Figure 6.



a) Inverter surge b) Sine wave (10kHz)

Figure 6. Cross section of general enameled wire (After voltage endurance test)

Although patterns of erosion are different, cross sections of wires from both inverter surge voltage and 10kHz sine wave voltage endurance tests show equally clear evidences of enamel coating film erosion, which is considered to lead to a breakdown, when it is developed to the extent that the coating film can no longer withstand the electric field. It is possible to explain why coating film erosion takes place where a small gap exists between wires, because discharge is considered to have taken place at the point where there is a gap that is advantageous for discharge to occur according to the Paschen's law. The difference of erosion patterns is considered to be attributable to a difference in the rise time of wave shapes; namely, discharge is considered to have taken place selectively at the points where discharge is most easily induced with inverter surge voltage having a steeper rising edge, hence the tendency of erosion concentrating on limited areas. On the other hand, because of a less steeper rising edge of sine waves, discharge repeats by shifting a point of discharge, hence erosion spreading over a wider area. As can be seen from test results, sine waves can cause a greater degree of erosion than inverter surge does, if voltages applied are same, thereby making wire life shorter.

Next, temperature rises were investigated. Results of the investigation are shown in Figure 7. An input voltage was raised to 550V, a voltage higher than the inverter's rating, so that a higher surge voltage might manifest. Temperature was measured with an ultra-thin thermocouple of a 0.08mm diameter from consideration of heat capacity.

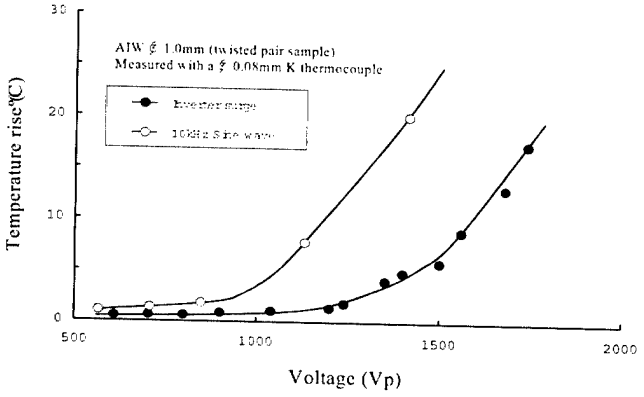


Figure 7. Temperature rise of voltage endurance test

Temperature rose gradually, starting at around 0.9kVp with 10kHz sine waves and around 1.2kVp with surge voltage. In either case, a temperature rise was not observed in the lower voltage range, where partial discharge is not supposed to have taken place. With regard to a temperature rise at around 1.1kVp, sine waves rose temperature by about 8℃ as compared in Figure 3.4, while only a slight rise of about 1℃ was recorded for inverter surge voltage, demonstrating that a larger temperature rise occurred with 10kHz sine waves, which are considered to induce more frequent discharge. It is clear, however, that the temperature rises in both cases are far from a level that can cause degradation of insulating power. Similarly, oxidization by ozone can promote degradation but local coating film erosion cannot be a possible form of phenomena resulting from degradation caused by oxidization by ozone. Accordingly, it is possible to deduce from the phenomenon of coating film erosion that the major cause of a breakdown is scission of molecular chains.

Although temperature rises caused by induction heating, etc. and space charge effects have been reported as observed with breakdowns at voltages below DIV, induction heating pushes temperature up only a little as mentioned earlier, so we can safely conclude that its impacts are minimal. Theoretically, space charge effects can cause a breakdown, but its impacts are considered to be negligible based on the phenomenon considered in this report and the PEW life test that demonstrated over 10,000 hours operation without a breakdown.

For these reasons, we can conclude that an inverter-surge-induced breakdown is nearly equivalent to the phenomenon of degradation caused by partial discharge and that inverter-surge resistance can be improved through improvement of partial discharge resistance.

4. Mechanism to Suppress Erosion by Partial Discharge

As a technique to suppress scission of molecular chains by the collision of charged particles, inorganic materials with higher intermolecular bonding energy are normally used. In the case of enamel coating, sub-micron size metal oxide particles are used. A schematic of the coating film erosion suppression mechanism is depicted in Figure 8.

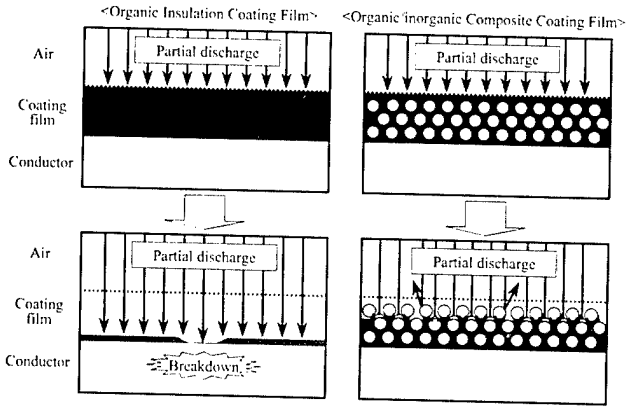


Figure 8. Schematic showing partial discharge erosion suppression mechanism

In an organic/inorganic composite material, charged particles go around the inorganic material, as if to evade it, and collide with the organic material. In this way, a creeping distance is elongated and the collision energy of charged particles are lowered

significantly through reflection and dispersion, hence suppression of erosion. Naturally, partial discharge resistance can be improved by increasing the loading of an inorganic material but this will also weaken mechanical strength. So, if another option, use of an inorganic material of a smaller particle size, is feasible, it is possible to increase surface area per unit weight, which will help increase a creeping distance significantly. Ordinary techniques to reduce a discreet particle size do not guarantee a smaller actual particle size because of aggregation of particles. Therefore, it was recognized as a key to successful development that inorganic particles should be dispersed uniformly over a coating film without causing aggregation.

5. Development of Silica/Polyester-imide Nano-composite Material

The present wire in use is a general self-lubricated heat-resistant wire (EIW-A) having the polyester-imide (EI) basecoat and the self-lubricating type polyamide-imide (AI) topcoat; the author's intention was to develop an improved wire based on this structure and by making the basecoat, which has a thicker film thickness, function as a partial discharge resistant layer. The cross-sectional structure of the improved wire is shown in Figure 9 with that of a partial discharge resistant enameled wire for comparison. As an inorganic material, low permittivity amorphous silica was chosen for the improved wire so as not to lower DIV. Table 2 shows characteristics of dispersion methods. As a method to disperse particles uniformly in a medium, the direct dispersion method is normally used. To improve dispersibility, a coupling agent is often used as aid. It is, however, impossible to eliminate aggregation of particles completely with the direct dispersion method, which also poses a stability problem or frequently observed settlement of particles in the varnish. Furthermore, however small a discreet particle size has been made, aggregation spoils this effort and increases the apparent particle size. Thus, it is expected to produce only a little effect in increasing a creeping distance mentioned above. In other words, as long as the conventional dispersion method is used, it is necessary to improve a partial discharge resistance level by raising a loading rate at the cost of strength against mechanical stress. If a three-layer coating structure is employed to compensate for the loss of mechanical strength, the film thickness of a coating layer to provide partial discharge resistance is limited due to a need for keeping the total thickness of coating layers within an allowable maximum measurement; thus, it will end up in a dilemma of tradeoff between partial discharge resistance and mechanical properties. A special solution mixing method developed newly, on the other hand, can produce varnish with particles dispersed in the colloidal state, which shows excellent stability without causing settlement or a change in the viscosity when left for several months. Particles dispersed in varnish do not aggregate even in a baked coating film, allowing a coating film to maintain clear appearance. This contributes to a substantial increase of the specific surface area of particles, producing the same or higher level of partial discharge resistance even at the loading rate of half the quantity of inorganic material particles used with the conventional method. In addition, due partly to their ultra fine particle sizes, they do not impair the indigenous characteristics of base resin. In this way, the author has successfully developed an organic/inorganic material that warrants sufficiently good properties even when coated singularly.

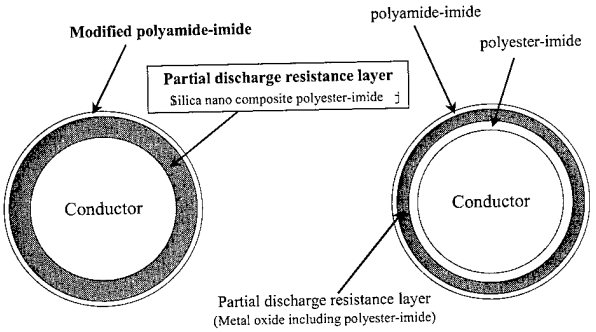


Figure 9. Cross section of development concept

Table 2. Characteristics of Nano-composite Techniques

Items \ Dispersion method	Innovative solution mixing method	Direct dispersion method (conventional method)
Raw material (discreet particle size)	Amorphous Silica (several ten nm, uniform)	Metal oxide particles (several ten nm)
Varnish state and stability	(mono dispersed), clear colloidal solution	~ (aggregation, settlement), whitish slurry
Coating film appearance	(transparency)	¢ (whitish color, rugged surface)
Particle size within a coating film (estimated)	Several ten nm	Sub £ m level
Partial discharge resistance		¢
Mechanical properties (flexibility, strength, etc.)		~
Overall evaluation		¢

6. Properties of Inverter-surge Resistant Enameled Wires

Various properties of a new inverter-surge resistant enameled wire (KMKED-20E), which has a partial discharge resistant EI layer using the innovative nano-composite technology protected by an overcoat of a modified lubricating AI layer superior in scratch resistance, are shown below.

6.1 General Properties

General properties of new product (KMKED-20E) are shown in Table 3. These properties were tested according to JIS C3003 (enameled wire testing methods). Due to effects of the nano-composite material, it shows significant improvement in flexibility, a weakness of the conventional partial discharge resistant enameled wires using the direct dispersion method, making it practically acceptable without any problem, although some deficiencies when compared with general wire (EIW-A) do exist in marginal areas. Its other properties are equivalent to those of general wire. Due to effects of highly scratch resistant modified lubricating AI, it shows values superior to those of general wire in sliding friction and abrasion resistance.

Table 3. General properties

Items \ Samples		Partial discharge resistant enameled wires		General self-lubricated heat-resistant wire (EIW-A)
		New Products (KMKED-20E)	Conventional products (direct dispersion method)	
Flexibility (20% elongation)	Entire layers	2 3d OK	2 3d OK	1 2d OK
	Partial discharge resistant layer	2 3d OK	8d OK	-
Resistance to abrasion	Unidirectional (N)	14.2	13.7	13.7
	Repeated (times)	355	189	205
Coefficient of static friction		0.048	0.072	0.058
Breakdown voltage (kV)		11.5	11.0	11.5
Cut through temperature (°C)		420	366	390
Thermal shock resistance (200°C 1hr)	No elongation	1d OK	2d OK	1d OK
	20% elongation	2 3d OK	6d OK	1 2d OK
Varnish bonding strength (N) (epoxy system varnish)		173	-	125
Thermal index (°C)		200	-	200

6.2 Electrical Properties

The voltage endurance of new product with 10kHz sine waves are shown in Figure 10 through 12, and the life characteristics measured in the inverter-surge voltage endurance tests and evaluation accelerated actual motor with no insulating phase paper inserted between phases are shown in Table 4. The appearance of a wire subjected to 20% elongation of the partial discharge resistant layer surface is compared in Figure 13 for those produced with the newly developed solution mixing method and the conventional direct dispersion method.

With regard to the voltage endurance with 10kHz sine wave at around 1.1kVp, new product showed life more than 1,000 times longer than that of general wire; it maintained useful life even after 20% elongation, a test condition exaggerating normal stress experienced during coil winding, while the same test shortened the useful life of a wire produced with the conventional method significantly, registering life more than 1,000 times longer than that of general wire at around 1.1kVp. After 20% elongation, the conventional wires are found to have many cracks on the surface of its partial discharge resistant layer, which are believed to cause a significant drop of the useful life. In the case of a long wire wound into a coil, defective parts are likely to come close each other, which can make the useful life of such a wire even shorter than that of general wires.

Useful life 300 to 500 times longer than that of the conventional wires has so far been confirmed in the surge voltage endurance tests and accelerated actual motor test with no insulating phase paper, so it is expected to bring dramatic improvement also to almost actual motors.

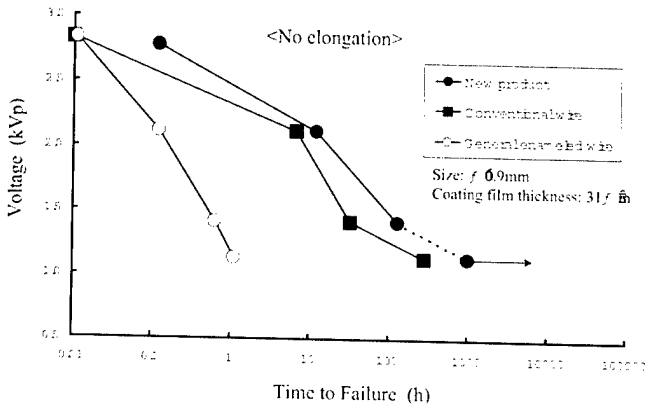


Figure 10. Voltage endurance of new product

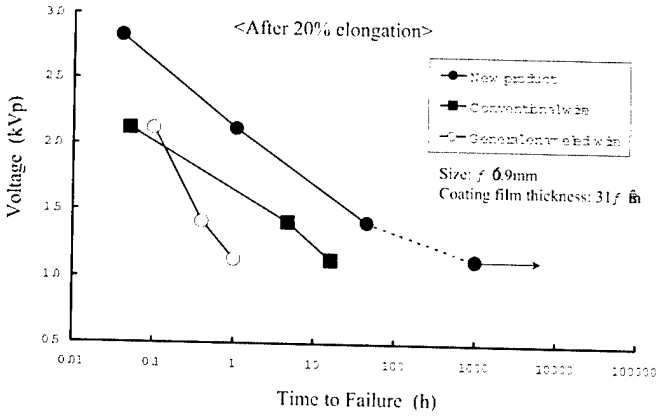


Figure 11. Voltage endurance of new product applied mechanical stress (20% elongation)

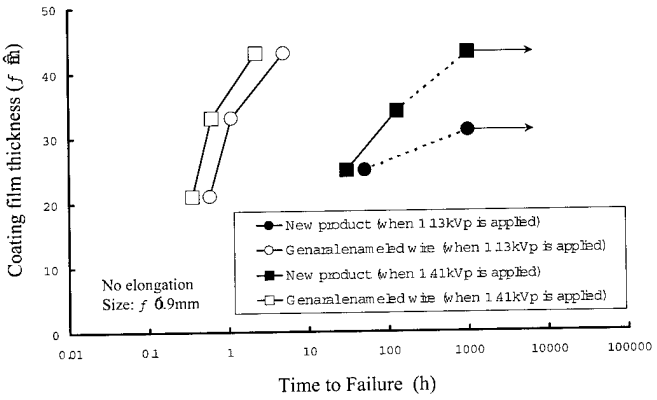
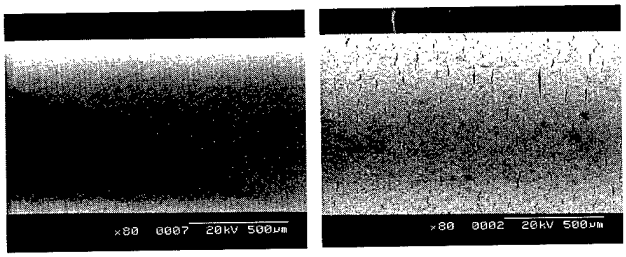


Figure 12. Voltage endurance of new product film thickness vs. life

Table 4. Inverter surge voltage endurance life characteristic

Items \ Samples		New product (KMKED-20E)	General wire (EIW-A)
Enameled wire test	Inverter surge voltage endurance test life Surge voltage: 1.1kVp Temperature: room temperature Mechanical stress: 20% elongation	6500h<	11.2h
Actual motor test	Accelerated motor test life (no insulating phase paper) Surge voltage: 1.5kVp Temperature: 80°C Mechanical stress: coil winding	9000h (still underway)	28h (surge voltage: 1.2kVp)



a) New method b) Conventional method

Figure 13. Partial discharge resistance layer surface

6.3 Life Estimation

Voltage endurance life in the partial discharge degradation range in accordance with the inverse power law and thermal endurance life estimated with Arrhenius plots are shown in Figures 14 and 15 respectively.

The voltage endurance life curve of new product has a steeper inclination than that of General enameled wire because it has a longer life in the lower voltage range, as seen in the measurement using 10kHz sine waves at a variable voltage. When the curve is shifted until it crosses data measured with an actual motor with no insulating phase paper with this inclination maintained, a reading of 1.38kVp is obtained as the voltage corresponding to 20,000 hours. As mentioned earlier, the degree of coating film erosion differs between 10kHz sine waves and inverter surge voltage, while useful life can also vary greatly depending on the model of an inverter, its operation conditions, installation conditions, etc. and the film thickness also has great impacts on the useful life of a wire. Therefore, it must be taken as one example of an estimated life, but its implication is the possibility that an enameled wire, if it has a 31 μ m coating film, can withstand without causing a breakdown a voltage of around 1.38kVp. Sometimes, it may become necessary to assume a maximum voltage of 1.6kVp, if an inverter is to be used under poor power supply conditions. Assuming that a little thick coating film is employed, it may be possible to guarantee a long life even under the 1.6kVp condition, because an increase of a coating film thickness by 10 μ m will extend life by ten times as indicated in Figure 12.

As for thermal endurance life, new product showed a slightly better heat run life than EIW-A in the high temperature zone, but the temperature at which it can endure for 20,000 hours dropped to 221℃, a level almost equivalent to that of EIW-A.

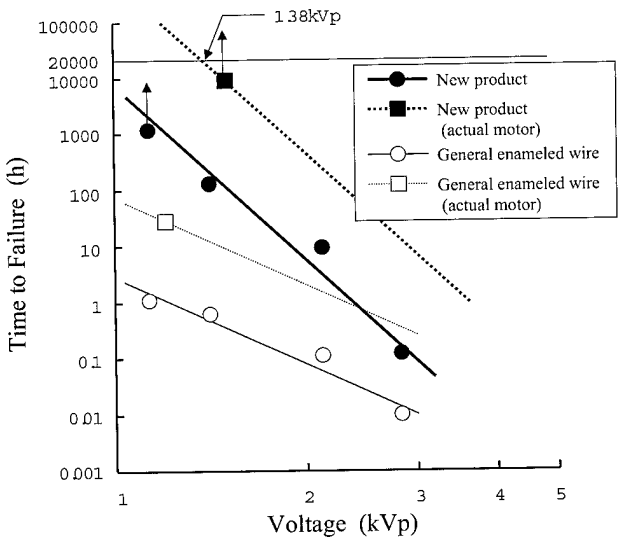


Figure 14. Voltage endurance life

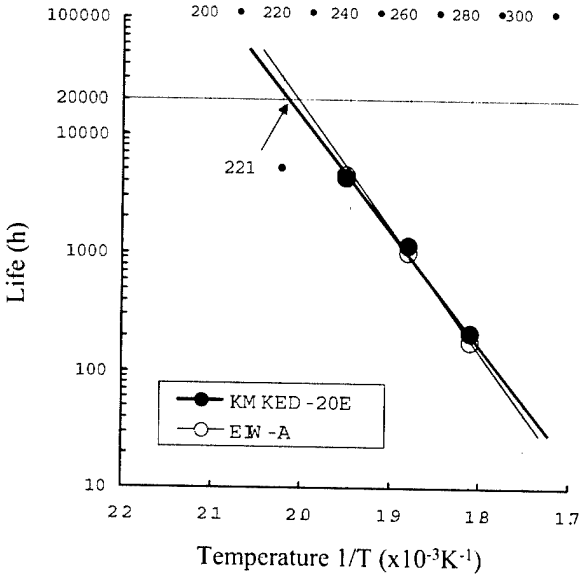


Figure 15. Thermal endurance life

7. Conclusions

The author has developed an organic/inorganic nano-composite insulating material containing silica of a nano-meter-level particle size uniformly dispersed with an innovative solution mixing method and successfully commercialized inverter-surge resistant enameled wires by applying it to enameled wires. The product developed is an enameled wire that has successfully improved mechanical properties, a weakness associated with the conventional partial discharge resistant enameled wires, as well as partial discharge resistance to an unprecedentedly high level and it is believed to contribute to the improvement of reliability of motors. It is also expected to bring favorable effects, when applied to high-voltage equipment coils.

8. References

[1] Moriyama, et al, About inverter surge voltage at a motor terminal, 1996 Annual meeting of Electric Society of Japan. No.911

[2] Japan Electric Machinery Manufacturers Association, Effects on insulation when a 400V-class motor is driven, March 1995

[3] Electric Society of Japan Technical Report No.739

[4] Teikan Hyakutake, Insulating materials, Electricity Insulating Material Manufacturers Association.



Hideyuki Kikuchi is deputy manager magnet wire development dept. of Hitachi Cable, Ltd, Japan. He was majoring in electronics and was doing the research of super-conductor in the Tokyo Denki University. He has worked on new product development of magnet wire based on insulation materials since 1988. Although he developed the nano-composite insulating material this time, he is also the authority of litz wire for deflection yoke coil of color display tube.

Benefits of Brominated & Mineral Based Flame Retardants for Wire & Cable

Rene' Herbiet

Douglas W. Luther

Samuel G. Thomas, Jr.

Albemarle Corporation
451 Florida St.
Baton Rouge, LA 70801-1765
225-388-7840
Fax 225-388-7599
douglas_luther@albemarle.com
sam_thomas_jr@albemarle.com
Martinswerk GmbH
Kölner Str. 110
D-50102 Bergheim
Germany
49-2271-902-523
Fax 49-2271-902-710
rene.herbiet@albemarle.com

Abstract

Flame retardant (FR) plastics play an important role in the fire safety of electrical equipment. One example where fire safety will become increasingly important is in cars, which are being fitted with a greater number of electrical and electronic features. PVC, which is the major resin used in wire & cable today, is inherently flame retarded. However, there is environmental pressure to move from PVC to polyolefins which require additive flame retardants. This paper will highlight the benefits of brominated and mineral based flame retardants in polyolefins to cable manufacturers and compounders in meeting the safety, performance, regulatory and environmental challenges of the future.

Keywords

Electrical; electronic; fire; safety; environmental; recycling; end-of-life; wire; cable; testing; evaluation; flame; retardant; mineral; brominated; bromine; insulation; jacket.

1. Introduction

Cable manufacturers and compounders in the wire and cable industry are facing increasing challenges ranging from more stringent performance requirements to environmental and regulatory pressures. The plastic insulation for wire is subject to a range of requirements depending upon the specific end-use application. The following regulatory and environmental issues will also impact future materials choices [1]:

- Pressure on halogens from Europe
- Pending removal of lead stabilizers from PVC
- End of life issues & recycle

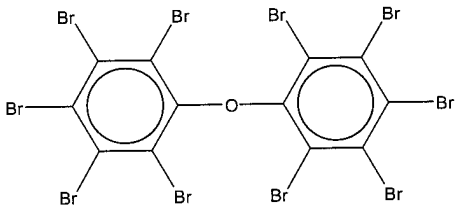
In response to these issues, there is a movement away from PVC, which is inherently flame retardant to polyolefins, which will require flame retardants. Despite the movement from PVC especially, many standard cable applications (e.g., plenum in building and construction) remain major markets for PVC. [2]

The wide variety of wire & cable applications will require a range of material choices to meet cost/performance requirements. Resin choices range from PVC to polyolefins to fluoropolymer (PTFE). PVC is the major resin used globally in wire & cable today, and is the lowest cost resin followed by polyolefins and then PTFE. Flame retardant choices include halogenated (chlorine or bromine), phosphorus types and minerals. As alternatives to PVC, FR/polyolefin systems can provide environmentally acceptable solutions with improved performance.

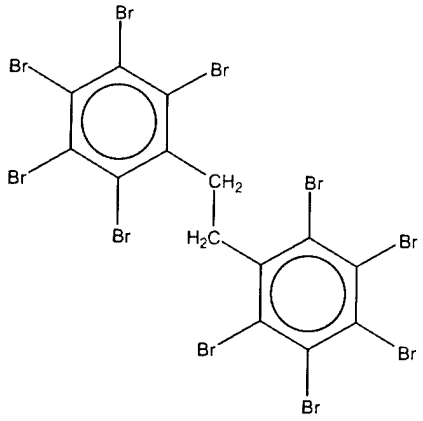
This paper will review the technological and environmental trends impacting flame retardant (FR)/resin choices in the future and offer a range of options for meeting these requirements

This paper will focus on the following FR options for polyolefins:

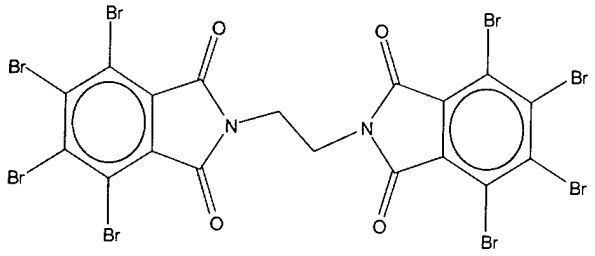
- Decabromodiphenyl oxide (DBDPO)



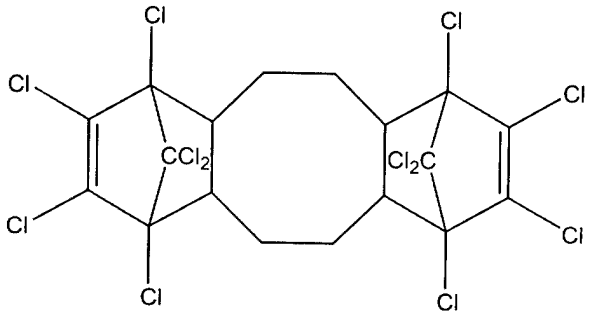
- Ethane 1,2 bis(pentabromophenyl) (EBP)



- Ethylene bis(tetrabromophthalimide) (ETBP)



- Dodecachloro-dodecahydro-dimethanodibenzocyclooctene (DCCO)



- Alumina Trihydrate (ATH)
- Magnesium Dihydroxide (MDH)

In particular the benefits of EBP and ETBP versus DBDPO and DCCO will be highlighted along with the benefits of coated versus uncoated ATH and MDH.

A broad range of FR choices are available today ranging from brominated flame retardants (BrFRs) to minerals. This diverse group of FRs makes it possible to satisfy a challenging set of performance and environmental requirements including low loadings, excellent electrical and mechanical properties, recyclability, low smoke and low corrosion.

2. Fire Safety

The primary reason for using flame retardants in plastics is to inhibit ignition, prevent fire and save property and lives. In 1999, there were 368,500 vehicle fires which accounted for 20.2% of the total number of fires in the U.S. [3] The consequences of these fires were 1850 civilian injuries, 470 civilian deaths and 1.3 billion $ in property damage.

3. Performance Trends

3.1 Flame Retardancy

Increased use of flame retardant is expected due to the introduction of more severe regulations and/or greater government pressure. It is anticipated that pressure will increase with the adoption of a new European classification system that will classify all materials, including cables, based on the risk of fire hazard. Implementation of such a system will help insurers to assess risks and calculate premiums accordingly. [4]

Better flame retardancy (flammability) will be required as insulation/jacket material becomes thinner. The flammability test may switch from a horizontal test to a 45 degree or even to a 90 degree test. Also, good flexibility will be required.

The European commission is working on replacing all national standards for individual countries in Europe with a single flammability test for building wire. The program is called fire performance of electric cable (FIPEC). (5) This new standard, which is pending, would require passing a vertical tray cable flammability test, which is quite severe and most definitely will require flame retardant.

3.2 Electrical Requirements

About 30% of the value of a modern car is accounted for by electronics. [6] In cars, the trend is to replace hydraulic functions by electrical equivalents, which will lead to an increasing number of installed electric motors. The existing 12 Volt batteries will be replaced by 42 Volt batteries. In order to supply systems within car doors with power, large bundles of wire must be threaded through the car body.

3.3 Thermal Stability

Although PVC will continue its general purpose use in automotive, other FR/polymers will be needed to withstand the extreme temperatures under the hood of a car. Flame retardant polyolefin resins are good candidates for meeting these high temperature requirements.[6]

4. Emerging Environmental Initiatives

Two wire and cable market segments in particular are impacted by the environmental initiatives coming from Europe: Cars and Appliances. Cars are impacted by the End-of-Life initiative and appliances by the Waste Electrical and Electronic (WEEE) Directive.

4.1 End-Of-Life

The End-Of-Life (ELV) initiative prevents cars from being placed in landfills at the end of their life. Also, PVC is listed as a restricted material for use in cars in this initiative. (7) Targets for re-use, recycling, and waste disposal are 1-1-2006.

4.2 European Union (EU) Waste Electrical & Electronic Equipment (WEEE) Directive-Draft

WEEE (Article 5.1) requires that plastics containing brominated flame retardants must be separated from other plastics for the purposes of recycling and recovery. (8) This requirement is not necessary because data is available showing that plastics containing brominated flame retardants can be safely and effectively recycled. [9]

Recovery of waste plastics (Article 6.2) is expected to begin in the year 2006.

4.1 EU Restriction of Hazardous Substance (RoHS) Directive-Draft

By January 2008 (Article 4) use of lead and polybrominated biphenyl (PBB) and polybrominated diphenyl ether (PBDE) must be substituted by other substances.

4.2 RoHS

The majority of brominated flame retardants (BFRs) are not an issue for RoHS. As stated above only PBB and PBDE are affected. PDBEs (DBDPO) are currently undergoing risk assessments. The results of the risk assessments will be considered in the decision to substitute for PDBEs. Alternative BFRs which are not on the list and available for substitution of DBDPO are: EBP and ETBP.

5. Recycle Scenarios

The following recycling scenarios have been demonstrated:

5.1 Mechanical Recycling

Physical means are used to reprocess scrap materials into plastics products. Each year about 35,000 MT of PVC are mechanically recycled.(10) However, thermoset plastics cannot be mechanically recycled.

Mechanical recycling consists of sorting and dismantling of the electrical and electronic equipment, shredding and sorting of large parts, and mechanical recycling to produce compounds for for reuse. Work has been carried out to demonstrate that mechanical recycling is feasible for brominated flame retardants (e.g., EBP and ETBP) in high impact polystyrene (HIPS) [11] and polybutyleneterephtalate (PBT). [12]

5.2 Feedstock Recycling

A complementary method to mechanical recycling is feedstock recycling of plastics waste. In feedstock recycling, material is reprocessed into basic chemicals, monomers for plastics or hydrocarbon feedstock.

The European Brominated Flame Retardant Industry Panel (EBFRIP) in cooperation with the Bromine Science and Environmental Forum (BSEF) has carried out a feasibility study on bromine recovery from waste electrical and electronic equipment. [13] The conclusions of the feasibility study are that it is feasible to economically and ecologically perform feedstock recycling, or bromine recovery. It provides bromine producers the opportunity to recycle 10,000 tons/year of bromine in Europe.

5.3 Waste-To-Energy Recovery

Incineration tests, pyrolysis tests, and combustion studies have shown that waste from electrical & electronic equipment can be safely added to today's municipal solid waste. (14)

5.4 Pyrolysis

Pyrolysis as a thermal treatment step is combined with combustion in an experiment done by Berlin Consult Pyrocom. The discarded material is separated into the categories of cables, cathodic tubes, metal housings, plastics casings, printed circuit boards and components containing hazardous materials. The separated cables are passed through a series of steps involving shredding, and metals separation followed by melting and thermally cracking of the plastics. Pyrolysis oils depending on quality may be used for feedstock recycling. The experiment showed that the plastics containing the flame retardants from the scrap equipment being treated contained levels of halogenated dioxins and furans below those specified in the German Hazardous Substance Ordinance. (15)

6. Impact On PVC

When scrap cable is burned, the lead content of PVC poses a problem due to the ash content which contains salts, including lead chloride, which are water soluble. The concern is that these products could end up in the public water supply. Replacement of lead increases the cost of PVC. While lead-free PVC is now available, manufacturers are not actively promoting its use. [16]

EU studies involving the impact of waste on the environment are driving the switch from PVC to polyolefins. Compounds based on polyolefins are expected to overtake PVC as the largest polymer type used in wire and cable by 2006. This switch is based on increasing concerns about what happens to cables during a fire and environmental fears about PVC.[17]

Furthermore, Ricoh Co., Japan's leading comprehensive maker of office equipment (OA), is planning to eliminate using PVC insulated electric wire in 2000. Polyolefin based insulation will be used in its place. [18]

7. German Hazardous Substances Ordinance

The German Hazardous Substances Ordinance (19) prohibits materials containing more than certain amounts of dioxins and furans. The permitted levels are extremely low. Specifically, the Ordinance prohibits any product containing more than 1 ppb of the sum of four congeners:

- 2,3,7,8-tetrabromodibenzo-p-dioxin (TBDD)
- 2,3,7,8-terabromodibenzofuran (TBDF)
- 1,2,3,7,8-pentabromodibenzo-p-dioxin (PeBDD)
- 2,3,4,7,8-pentabromodibenzofuran(PeBDF)

or more than 5 ppb of the sum of eight congeners:

Group 1

- 2,3,7,8 –TBDD
- 2,3,7,8-TBDF
- 1,2,3,7,8-PeBDD
- 2,3,4,7,8-PeBDF

Group 2

- 1,2,3,7,8-PeBDF
- 1,2,3,4,7,8-Hexabromodibenzo-p-dioxin (HxBDD)
- 1,2,3,6,7,8-Hexabromodibenzo-p-dioxin (HxBDD)
- 1,2,3,7,8,9-Hexabromodibenzo-p-dioxin (HxBDD)

7.1 Table 1 shows data confirming that EBP and ETBP in HIPS pass the Ordinance with respect to dioxin and furans:

Table 1. German Hazardous Substance Ordinance Results For EBP and ETBP in HIPS

Flame Retardant	EBP	ETBP
2,3,7,8-TBDD	ND	ND
1,2,3,7,8-PeBDD	ND	ND
2,3,7,8-TBDF	ND	ND
2,3,4,7,8-PeBDF	NA	ND
Sum Group1	0	0
GDO	Pass	Pass
1,2,3,4,7,8-/1,2,3,6,7,8-HxBDD	ND	ND
1,2,3,7,8,9-HxBDD	ND	ND
1,2,3,7,8-PeBDF	ND	ND
Sum Group 2	0	0
Sum Group 1+Group 2	0	0
GDO	Pass	Pass

8. Features of BrFRs and Minerals

Following are the features of BrFRs and minerals which allow them to be effectively used in polyolefins for wire and cable applications:

8.1 BrFRs:

- Efficiency/Low Loadings
- Thermal Stability
- Recyclability
- Excellent Electricals
- Excellent Physical/Mechanical Properties
- Nonblooming/plateout
- Low Density
- Flexible Processing
- Sustainable Resources (Bromine)
- Colorability

8.2 Mineral FRs:

- Low Smoke
- Recyclability
- Low Corrosion
- Improved Electricals
- Nonblooming/plateout
- Good tensile strength and elongation (ductility) with adequate coupling system
- Thermal Stability
- No Synergist Required
- Sustainable Raw Material (Bauxite for ATH and serpentine for MDH)
- Non-volatile

9. Compounded Flame Retardant Materials

9.1 Halogenated Compounds

All halogenated compounds were prepared by mixing in a compounding twin screw extruder. Materials were processed on a Werner and Phleiderer 30mm super compounder with a barrel length to diameter ratio (L/D) of 32/1; at 100-150RPM with a feedrate of 4-6kg/hr. Vacuum degassing was performed near the end of the extruder. All materials were fed gravimetrically at the feedthroat. For polyethylene (PE) resins, barrel temperatures ranged form 160-185°C. Pellets were produced by stranding through a water bath at 25-30°C and fed to a Killion pelletizer. Extruded pellets were injection molded on a Battenfeld 40 ton injection molding press. Using the same melt temperature ranges as were used in the compounding operations, specimens were injection molded using injection pressures of 9.6-11.7 kPa. Samples for electrical testing were prepared by compression molding at 170°C for polyethylene (PE) materials and at 220°C for polypropylene (PP) materials. Property determinations were performed in the laboratories of Albemarle Corporation, except for corrosivity data. Corrosivity measurements were performed by the Department of Fire Technology at Southwest Research Institute, San Antonio, Texas. All data generated are based upon laboratory tests, and should not be used to predict performance in an actual fire situation.

9.2 Mineral Compounds

All mineral flame retardant compounds were prepared by mixing in a 46mm Buss Ko-kneader with an L/D ratio of 11/1. Materials were fed gravimetrically into two feedports. Resin, minor additives and 60% of the flame retardant were fed at the feedthroat, with the balance of the flame retardant added at a down stream feedport approximately halfway down the barrel length. Vacuum degassing was performed near the end of the barrel. For ethylene vinyl acetate (EVA) resins, barrel temperatures ranged from 120-150°C and for polypropylene (PP) resins barrel temperatures ranged from 140-175°C. A directly flanged 70 mm discharge extruder with a hot face wet cut was used to produce pellets. The throughput was 10-15 kg/hr. The EVA pellets were extruded to strips with a thickness of 2mm for further testing, the PP pellets were injection molded on a Boy injection molding press. Property determinations were performed in the laboratories of Martinswerk plc, a company of Albemarle Corporation.

9.3 Materials

Several resins were used in these experiments. LDPE1 is a low density polyethylene commonly used for wire and cable applications, with a melt flow index (190°C/2160g) of 2.8 g/10min and a specific gravity of 0.918. PE1 is a ethylene ethyl-acrylate copolymer commonly used for wire and cable applications, with a melt flow index (190°C/2160g) of 1.5 g/10min and a specific gravity of 0.93. Halogenated flame retardants used in these experiments include decabromodiphenyl oxide (DBDPO), ethylene bis-tetrabromophthalamide (ETBP), ethane 1,2 bis(pentabromophenyl) (EBP) and dodecachloro-dodecahydro-dimethanodibenzocyclooctene (DCCO).

10. Halogenated FR Compounds

10.1 Comparison of Halogenated FR Compounds in LDPE

Three formulations were compared using the materials shown in Table 2.

Table 2. Halogenated LDPE formulations

Component wt%	A	B	C
LDPE1	50.5	46.5	39.5
ETBP	18	-	-
DBDPO	-	21	-
DCCO	-	-	25
Sb_2O_3	6	7	10
Talc	25	25	25
Antioxidant	0.5	0.5	0.5

The mechanical property testing results of these materials is shown in Table 3. Here ETBP shows the highest tensile strength at yield, with DCCO being the lowest. While all formulations have increased viscosity compared to the neat resin, note the increased viscosity of the compound containing DCCO. DCCO produced a much stiffer, less ductile material indicated by the higher flexural modulus values and lower notched izod values. This is appears to be due to the loading levels required for DCCO, since none of these materials are melt blendable in LDPE. All the flame retardants evaluated gave good dielectric and resistance properties. The values in table 1 are within experimental error of each other except for dissipation factor. The dissipation factor of DCCO was slightly improved over the other materials at 0.0036.

Table 3. Mechanical & Electrical Testing Results Halogenated LDPE formulations

Test	A	B	C
Specific Gravity	1.35	1.44	1.48
Melt Flow Index, g/10 min., @190°C/2160g	1.4	1.4	0.9
Tensile Strength @ yield, Mpa	13.7	12.4	11.4
Flexural Modulus, Mpa	593	593	758
Notched Izod Impact Strength, J/m	330	200	60
Dielectric Constant @ 1Mhz	2.53	2.58	2.63
Dissipation Factor @ 1Mhz	0.0052	0.0052	0.0036
Volume Resistivity, ohm-cm	2.1E16	1.0E16	0.4E16
Surface Resistivity, ohms/square	2.8E16	2.8E16	0.6E16

Flammability results are shown in table 4. UL-94, limited oxygen index (LOI), and cone calorimeter results are listed. The formulations were optimized to give V-0 performance at 3.0mm thickness. The UL-94 test severity increases as the thickness of the specimens decreases. Note that at the 1.5mm reduced thickness, ETBP and DBDPO flame retardants both still achieve V-0 performance, while the DCCO drops to a V-1 rating. Cone calorimeter results indicate superior performance of the ETBP flame retardant vs. the other materials. ETBP yields lower peak and average heat release rates, longer time to ignition and greatly reduced smoke generation vs. DBDPO and DCCO based products.

Table 4. Halogenated LDPE formulations – Flammability Results

Test	A	B	C
UL-94 @ 3mm thick	V-0	V-0	V-0
UL-94 @ 1.5mm thick	V-0	V-0	V-1
LOI, % O_2	29.4	30.6	28.6
Cone Calorimeter Peak Heat Release Rate @ 25 kW/ m^2, kW/ m^2	109	148	248
Cone Calorimeter Average Heat Release Rate @ 25 kW/ m^2, kW/ m^2	54	82	93
Cone Calorimeter Time to Ignition @ 25 kW/ m^2, sec	352	361	295
Cone Calorimeter Smoke Factor @ 25 kW/ m^2, MW/ m^2	112	210	177

Corrosion as a result of combustion gasses from cable insulation and jacket materials is of considerable interest and concern. Corrosivity data were generated for the three compounds compared here, and are shown in table 5. These data were generated using the ASTM E-05.21.70 draft standard. Specimens were irradiated for 15 minutes at 25kW/m2 radiant flux in a cone calorimeter. The corrosivity of the smoke generated was measured using Rohrbach 2500 Angstrom probes. For this evaluation duplicate probes were used, one facing up and the other facing down. Corrosion was measured after the 15 minute irradiation and an additional 45 minute exposure to the chamber atmosphere. Probes were measured again after conditioning for 24 hours at 75% relative humidity and 6 days at 35% relative humidity.

Table 5. Halogenated LDPE formulations – Corrosivity Results

Test	A	B	C
Metal Loss Probe Up @ 60 min., Å	183	388	585
Metal Loss Probe Down @ 60 min., Å	197	395	607
Metal Loss Probe Up @ 24 hrs., Å	233	455	720
Metal Loss Probe Down @ 24 hrs., Å	253	485	723
Metal Loss Probe Up @ 6 days., Å	271	571	784
Metal Loss Probe Down @ 6 days., Å	303	571	798

Corrosivity results show ETBP to be the least corrosive followed by DBDPO and DCCO. Smoke from the ETBP based compound exhibits less than half the corrosion of the DCCO based material.

10.2 Bloom/Migration Evaluation in PE

An important consideration when selecting a flame retardant for a wire and cable application is bloom, or migration of the flame retardant of the insulation or jacket material to the surface of the compounded material. Some halogenated flame retardants can migrate to the surface, causing an undesirable chalky appearance. For this evaluation an ethylene ethyl-acrylate copolymer was chosen that is noted for migration propensity. The formulations evaluated are listed in table 6.

Table 6. Halogenated Flame Retardants - Bloom Evaluation Formulations

Component, wt%	D	E	F	G	H
PE1	90.95				
50% carbon black concentrate	1.0	1.0	1.0	1.0	1.0
Antioxidant	0.05	0.05	0.05	0.05	0.05
ETBP	-	20.0	-	-	-
EBP	-	-	20.0	-	-
DBDPO	-	-	-	20.0	-
DCCO	-	-	-	-	25.0
Sb_2O_3	8.0	8.0	8.0	8.0	8.0

All flame retardants were at 20% loading, except for DCCO at 25%. This was done to maintain a UL-94 V-0 rating at 1.5mm thickness. A small amount of carbon black was also added to each formulation to make migration easy to detect. A control formulation without halogenated flame retardant was also included for comparative purposes.

Bloom evaluations were conducted in using 3.0mm thick injection molded specimens. Specimens were aged in a circulating air oven at 70°C for 28 days and removed periodically for examination. Visual examinations were conducted at the end of the aging period. Color change was evaluated with a Hunter spectrophotometer. Results are listed in table 7.

Table 7. Halogenated Flame Retardants - Bloom Evaluation Data

Test	D	E	F	G	H
Aged 1 day @ 70°C, ☐E	0.1	0.1	0.1	3.4	1.5
Aged 2 days @ 70°C, ☐E	0.1	0.1	0.1	3.4	2.2
Aged 3 days @ 70°C, ☐E	0.1	0.05	0.05	3.3	2.5
Aged 4 days @ 70°C, ☐E	0.1	0.05	0.05	3.3	3.0
Aged 7 days @ 70°C, ☐E	0.1	0.1	0.1	3.3	3.3
Aged 14 days @ 70°C, ☐E	0.1	0.1	0.2	3.4	3.5
Aged 21 days @ 70°C, ☐E	0.1	0.1	0.3	3.3	3.4
Aged 28 days @ 70°C, ☐E	0.1	0.15	0.3	3.3	3.6
Visual	None	None	V. Slight	Severe	Severe

The data indicate that ETBP did not bloom after 28 days at 70°C, comparable to the control. EBP began to show very slight indications of migration only at the very end of the test period. Both DBDPO and DCCO showed severe migration. DBDPO showed severe bloom after only 24 hours, while DCCO showed noticeable bloom after one day, but took 14 days to reach equilibrium.

10.3 Halogenated Flame Retardants - Stability

An important feature of any flame retardant system is thermal stablility at elevated temperatures. Thermal stability, or lack of it, serves to limit the utility of a given material. Table 8 shows Thermogravimetric (TGA) data for the halogenenated flame retardants presented. These data indicate that the stability of ETBP and EBP is higher than either DBDPO or DCCO. Also, DBDPO is more stable than DCCO.

Table 8. Halogenated Flame Retardants – Thermal Stability

Material	1% Weight Loss	5% Weight Loss	10% Weight Loss	50% Weight Loss	90% Weight Loss
ETBP	321°C	407°C	424°C	455°C	>600°C
EBP	314°C	344°C	359°C	402°C	423°C
DBDPO	290°C	326°C	344°C	389°C	408°C
DCCO	271°C	300°C	318°C	367°C	382°C

TGA data was generated under nitrogen at 10°C/min.

11. Mineral Flame Retardants

11.1 Comparison of Mineral Flame Retardant Compounds

Alumina trihydrate (ATH) and magnesium dihydroxide (MDH) have been in use for some time as mineral fillers which provide the added benefit of flame retardancy. In terms of processing stability, ATH finds use in polymer systems where the processing temperatures are below 200°C, while MDH is stable at temperatures up to 340°C.

Low ductility and elasticity have been a barrier to the widespread use of ATH and MDH in the wire and cable industry. Due to the poor compatibility between organic polymer materials and the inorganic fillers; compounded products typically had elongation values too low to be suitable for most applications. Retention of elongation and tensile values at elevated temperatures has also been a problem as well as large viscosity increases due to the high loadings typically required. These barriers have now been overcome by improved coating technology.

11.2 Mineral Flame Retardant in Compounded Polypropylene

Table 9 shows test results with compounded polypropylene materials. These compounds were prepared on a Buss Ko-kneader as described previously at a loading level of 65 weight % MDH having a specific surface area of $5m^2/g$; and using a commercially available random copolymer PP extrusion resin containing approximately 4% ethylene.

Table 9. Effect of MDH coating on Compounded PP Properties

Test	Neat Resin	Uncoated MDH	Coated MDH
Tensile Strength (MPa)	23	20.2	12.2
Elongation at break %	280	1	224
Melt Flow Index @ 230°C/5000g, g/10min	7	N/D	6.9
Charpy Impact Strength, kJ/m^2	No break	6.4	No break

Note the increased elongation values, lower viscosity and ductility of the compound containing the surface treated MDH. With ultimate elongation values close to the neat resin, it is possible to develop insulation materials with excellent fitness for use. Ease of processing the compounded material is also observed, primarily due to the lack of melt viscosity increase as indicated by melt flow index. Although tensile strength is reduced with the coated material, it is within the range of an acceptable insulation material for most applications.

11.3 Mineral Flame Retardant in Compounded Ethylene Vinyl Acetate (EVA) Materials

Table 10 shows test results with compounded EVA materials. These compounds were prepared on a Buss Ko-kneader at a loading level of 60 weight % precipitated ATH having a specific surface area of $4m^2/g$; and using a commercially available 19% vinyl acetate EVA extrusion resin. Due to the lower processing temperatures used with EVA, ATH was selected as the mineral flame retardant. ATH grades evaluated include uncoated, amino silane coated, and a new proprietary coating.

Table 10. Effect of ATH coating on Compounded EVA Properties

Test	Uncoated ATH	Amino silane coated	New coating
Tensile Strength (MPa)	9.5	12.4	11.5
Elongation at break %	130	200	510
Melt Flow Index @ 190°C/10kg, g/10min	1.4	1.5	3.0
Volume Resistivity @ 28 days/50°C in water, ohm-cm	1E8	1.6E12	1.5E12

Increased elongation values are shown with the new surface treatment technology, with the elongation values approaching the values of the base resin (although not shown in the table, the base resin values are in the 600% range). Melt viscosity of the compound using the newer coating is significantly reduced vs. untreated and amino silane treated grades. Most notable however are the wet electrical properties. Both surface treated grades of ATH show four decades of improvement in wet volume resistivity vs. untreated material; and are sufficient for many insulation applications and comparable to flexible PVC formulations. Comparable improvements have been demonstrated with crosslinked EVA formulations [20], and similar improvements should extend to polyethylene formulations as well.

Similar improvements are seen in thermoplastic EVA formulation using MDH, shown in table 11. These formulation again use a loading level of 60 weight MDH having a specific surface area of $5m^2/g$; and were prepared using a commercially available 19% vinyl acetate EVA extrusion resin

Table 11. Effect of MDH coating on Compounded thermoplastic EVA Properties

Test	Uncoated MDH	Amino silane coated	New coating
Tensile Strength (MPa)	11.2	13.4	9.3
Elongation at break %	95	180	500
Melt Flow Index @	1.0	1.1	4.5

190°C/10kg, g/10min			
Limited Oxygen Index, $\%O_2$. 50x2mm specimens	41	43.5	81

Using MDH, again the elongation values for both surface treated materials are much improved over the control. Melt viscosity is significantly reduced over the untreated material using the amino silane coating, and significantly further reduced using the new coating. Flame retardancy is also improved by surface treatment, as illustrated by the limited oxygen index (LOI) data. Using this new technology and optimizing formulation and processing, LOI values of up to 80% O_2 are possible.

12. Conclusions

The broad range of choices in flame retardant additive technology creates new possibilities for compounded thermoplastics. Using this technology, it is possible to replace flexible PVC or substances regulated by RoHS without sacrificing performance of wire and cable products. As the regulatory environment and specifications become more challenging, products exist to provide a balance of performance without sacrificing safety, toxicity or effectiveness using bromine chemistry and mineral chemistry.

13. Acknowledgments

The authors would like to thank J.S. Arroyave, D.K. Doucet, T.R. Sapp, and R.W. McConnell for their contributions in compounding, molding and testing materials.

14. Authors



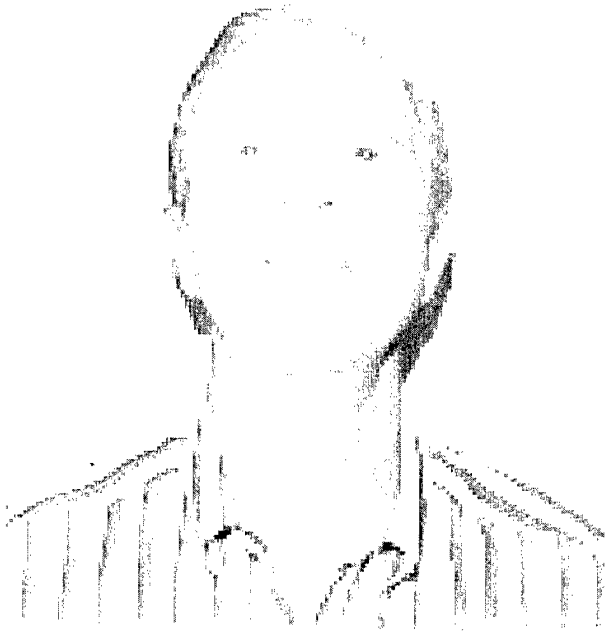
Rene Herbiet

Martinswerk GmbH

Kölner Strasse 110

D-50127 Bergheim, Germany

René Herbiet was born in Eupen/Belgium in 1959 and studied Physics at the Technical University in Aachen/Germany. He then became assistant for two years at the Institute of Materials for Electrotechnical Engineering in Aachen. In 1987, he joined the Continental AG in Germany and was R&D manager for rubber processing technology. He has worked in the areas of rubber compounding, extrusion and vulcanization. In 1995, he received his Ph. D. from the Institute of Plastics Processing in Aachen. In 1996, he joined martinswerk plc in Bergheim/Germany, now a company of Albemarle Corporation, and became head of the R&D department in the plastics division.



Samuel G. Thomas, Jr.

Albemarle Corporation

451 Florida Street

Baton Rouge, LA 70801-1765

Dr. Thomas is a native of Youngstown, Ohio. He has a Ph.D. in chemistry from the University of Cincinnati and an M.B.A. from Michigan State University. He held a series of management positions in R&D over a span of 20 years with Ethyl and Albemarle Corporation. During the past five years, he has held responsibilities in Sales and Marketing in flame retardants. He is currently business manager of flame retardants for Albemarle and currently resides in Baton Rouge, Louisiana with his wife and 15 year old daughter.



Douglas W. Luther

8000 GSRI Ave.

PO Box 14799

Baton Rouge, LA 70898

Doug Luther is a native of Simsbury, Connecticut. He is a journeyman toolmaker and spent 15 years in manufacturing, working in the machine tool and satellite communications industries. After receiving a BS in chemical engineering in 1993 from the University of Connecticut; he worked in the plastics and elastomer industries as a formulation chemist, process engineer, product manager and market development manager. In 2001, he joined Albemarle Corp.'s application development staff, and resides in Baton Rouge, Louisiana with his wife and two sons.

15. References

[1] S. K. Moore and A. Mollet, "PVC Stabilizers Get The Heavy Metals Out", Chemical Week, 161 (20), 41 (May, 1999).

[2] K. Cousins, Polymers for Wire and Cable, RAPRA Technology LTD., 33 (January 2000).

[3] Fire in the United States, June 1999, Federal Emergency Management Agency, United States Fire Administration, National Fire Data Center. National Fire Protection Agency (NFPA) Survey.

[4] K. Cousins, Polymers for Wire and Cable, RAPRA Technology LTD., 57 (January 2000).

[5] Fire Performance of Electric Cable (FIPREC), European Norm EN 50266-2-x.

[6] K. Cousins, Polymers for Wire and Cable, RAPRA Technology LTD, 5 (January 2000).

[7] Directive, 2000/53/EC of European Parliament and the Council on End of Life Vehicles, (September 2000).

[8] Proposal for a Directive of the European Parliament and of the Council on Waste Electrical and Electronic Equipment (2000/C 365 E/12 and E/13) (July 2000).

[9] Bromine Science and Environmental Forum, www.bsef.com.

[10] K. Cousins, Polymers for Wire and Cable, RAPRA Technology LTD, 69 (January 2000).

[11] R. B. Dawson, S. D. Landry, "Environmental Benefits of Flame Retarded High Impact Polystyrene Based on Ethane 1,2 bis(pentabromophenyl)", Int. SAMPE Symp. Exhib. 46 (2001).

[12] R. B. Dawson, S. D. Landry, et. al, "Environmental and Performance Benefits of Brominated Flame Retardants" in Plastics, Engineering Thermoplastics 2001, San Diego, CA, (April, 2001).

[13] Integrated Waste Management From WEEE Containing Brominated Flame Retardants, EBFRIP, 2000.

[14] European Brominated Flame Retardant Industry Panel, Brominated Flame Retardants and Waste from Electrical and Electronic Equipment (WEEE), An Industry Perspective, (June 1999).

[15] K. Cousins, Polymers for Wire and Cable, RAPRA Technology LTD, 73 (January 2000).

[16] K. Cousins, Polymers for Wire and Cable, RAPRA Technology LTD., 3 (January 2000).

[17] Modern Plastics International, "European Wire, Cable Markets Spurred by Telecom Growth", 30 (5), 15 (May 2000).

[18] Japan Chemical Week, "Ricoh Co. Plans To Stop Using PVC-Covered PVC-Covered Wire, 6, (April 30, 1998).

[19] German Chemical Prohibition Ordinance, ChemVerbotsV, Appendix, part 4, No. 4 and 5.

[20] Polymers and Polymer Composites, "New Metal Hydroxides with Improved Performance for Flame Retardancy in Plastics" (8) 8, 551-555 (2000).

Author Index

A

Abe, I. 361
Abe, Y. 93
Adams, M. A. 399
Ahn, M. J. 409
Akasaka, N. 506
Aladenize, B. 232
Al-Asadi, M. M. 143, 160, 554, 570
Aquino, J. C. 758
Au, D. (T.) 532
Auton, J. 115, 364

B

Bakker, F. R. 736
Barker, P. 658
Barnes, J. 4
Bastin, D. F. 658
Bernier, D. 650
Bindbeutel, D. 292
Bing, Y. 483
Blazer, B. 415
Bocanegra, L. M. 34
Bogdanova, O. I. 43, 53
Bohbot, M. 586
Boom, M. 698
Bouffant, O. 621
Bourhis, J.-F. 28
Bow, K. E. 399
Brault, D. 181
Bulsari, A. 13, 302
Bushelman, A. A. 253
Buthe, H. 614

C

Campbell, C. 290
Capouilliet, S. 240
Carroll, D. 169
Chakrabarty, K. 212
Chang, T.-C. 389
Chapin, J. T. 212, 253
Charles, Y. 770
Chase, D. 529
Cheatle, W. P. 364
Cheng, M. 514
Chenm H.-j. 389
Chippada, S. 19
Choate, L. J. 564
Choi, H. T. 680
Chu, T. C. 297, 753
Chung, Y. 713
Clark, B. S. 753
Coates, A. R. 554
Cognet, E. J. 306
Coleby, D. E. 143
Conrad, C. M. 634
Consonni, E. 457
Coster, N. 529
Cressan, E. 621
Cruz, R. F. 493

D

Da Rocha, J.-C. 181
da Silva, A. C. 249
Dammert, R. C. 311
Das, S. 437
Davies, M. V. 658
Dazai, M. 219
Debban, H. P. 422
DeFabritis, R. P. 518
Delpech, M. 650
Demont, R. M. 775
Dias, A. A. 267
Dioh, N. 111
Dixon, L. A. 422
Dole, C. W. 564
Dotto, J. 493
Doumen, C. 106
Dubois, S. 28
Duffy, A. P. 143, 160, 554, 570
Dupire, P. 770
Dutta, A. 692

E

Efraimsson, L. 316
Eijpe, I. 736
Elliott, G. 326
Erdas, E. 175
Esbester, C. J. 658

F

Fang, X. 253
Fay, P. 4
Fedier, D. 151
Fillatre, D. 181
Finberg, G. 326
Frey, M. 280
Fuji, T. 707
Fujita, N. 703
Fukuda, K. 707
Fullenbaum, M. 775
Furtado, J. M. I. 249

Author Index

G

Gaillard, P. 775
Galan, S. 2
Gandhi, P. D. 253
Gardiner, A. 529
Gavrilakis, A. 554
Gebizlioglu, O. S. 84, 257
Gedde, U. W. 311
Giacaglia, M. V. 49
Ginocchio, A. 457
Giordano, D. 753
Glaesemann, G. S. 240
Gleich, D. 577
Goddard, T. 5
Goene, F. 526
Grald, E. W. 19, 692
Gregor, P. E. 614
Greven, W. 736
Griffioen, W. 736
Guida, T. J. 1
Guillas, P. 621

H

Hakozaki, H. 488
Hall, D. K. 721
Hamada, M. 369
Hara, M. 201, 666
Hardwick, III, N. E. 34
Harlin, A. 192
Hashimoto, Y. 331, 463
Hata, Y. 369
Hattori, M. 666
Hayano, T. 129
Hedrick, D. S. 643
Heino, M. T. 192, 274
Herbiet, R. 807
Herrgesell, O. 136
Hinosihta, S. 703
Hirao, M. 379
Hirayama, M. 93
Hirose, F. N. 249
Hirvensalo, M. 192
Hishikawa, Y. 369
Hodge, K. G. 143, 160, 554, 570
Hogari, K. 477, 488
Hollinger, K. V. 287
Hosoya, T. 187, 707
Hsiao, C.-M. 389
Hsu, H.-P. 389

I

Imamura, S. 686
Irion, R. D. 240
Ishii, N. 201
Ishikawa, H. 506
Ishimaru, H. 201
Iwakura, D. 666
Izumita, H. 98

J

Jackson, D. A. 160
Jaluria, Y. 326
Jamet, P. 650
Jeyapalan, J. K. 724
Josefsson, M. 577
Jung, K. 321

K

Kaino, M. 506
Kamiko, M. 379
Kanda, R. 758
Kaneko, K. 341
Kato, O. 129
Kazumasa, O. 703
Kikuchi, H. 799
Kikuchi, S. 361
Kim, D. 713
Kim, J. W. 106
Kim, S. 629
Kim, S. C. 409
Kim, Y. S. 680
Kincaid, J. W. 374, 564
King, W. W. 77
Kish, P. 3, 586
Knapp, R. H. 437
Kobayashi, I. 201
Kobayashi, K. 207
Kobayashi, M. 93
Kohnke, G. E. 240
Komiya, Z. 545
Konda, E. 666
Konkarikoski, A. 13
Konstadinidis, K. 518, 532
Kotani, K. 483, 703
Kouftine, K. B. 43
Kraus, G. M. 470
Kulkarni, J. A. 19
Kurkjian, C. R. 257
Kusakari, M. 207
Kutt, T. V. 753
Kuwahara, K. 219

Kuwajima, T. 686
Kuzhekin, I. P. 53

L

Lagreve, C. 181
Lahti, M. I. 274, 302
Lahtinen, J. 13
Lail, J. C. 634
Lapadula, M. A. 291
Larsen, V. B. 764
Larsson, H. 306
Lavallade, C. 224
Le Bras, D. 621
Le Cozic, H. 621
le Noane, G. 181
Le Roux, P. 775
LeCourtier, N. 650
Lee, C. D. 794
Lee, D. 713
Lee, G. J. 409
Lee, J. 629
Lee, R. E. 106
Lee, Y. 321
Lee, Y. I. 680
LeFevre, B. G. 77
Leon, A. 28
Leppert, H.-D. R. 747
Levitova, L. V. 53
Libert, J.-F. 770
Lin, Y.-c. 389
Lindström, M. 404, 577
Litvinov, V. M. 267
Liu, J. Y. 389
Lochkovic, G. 351
Lockwood, D. 351
Lundström, P. 274
Luther, D. W. 807

M

Madon, P. 596
Magnusson, H. 316
Maki, H. 369
Malluck, J. F. 77
Marelli, P. 457
Marik, J. 783
Marques, L. F. G. 493
Martinsson, H.-B. 306, 311
Matsui, C. 488
Matsui, C.q 477
Matsuyama, E. 384
Matsuzawa, T. 331
Mayolle, Y. 775
Mazza, R. A. 742
Menegozzi, R. 56
Mercier, P. 621
Mine, K. 98
Miura, M. 61, 499
Miyamoto, M. 129, 207, 432, 463, 732
Mizukami, M. 341
Moorjani, S. 351
Morikawa, R. 758
Morishita, Y. 384
Moriuchi, K. 187
Murakami, K. 361, 483
Muralidharan 692
Murphy, E. 529, 551
Murphy, P. 3

N

Nagase, R. 93
Nagatomi, O. 758
Nagayama, K. 506
Nakamjima, F. 201
Nakamura, H. 477
Nakamura, M. 98
Nakano, M. 61, 499
Nechitailo, N. V. 447
Neogi, S. 115, 364
Neri, C. 106
Neto, J. A. M. 249, 493
Neveux Jr., P. E. 253
Nicholson, D. O. 2
Nicolardot, M. 232
Niu, G. 514
Nonoyama, Y. 477
Norris, R. H. 422, 518
Nothofer, K. 747
Nouchi, K. 384
Nunes, M. A. 742
Nykänen, J. 395

O

Ogawa, A. 369
Oh, H. 321
Oh, J. 321
Ohmura, K. 361
Ohneda, S. 384
Ohsono, K. 361, 483
Ohtani, T. 68
Okada, N. 331, 432, 463, 732
Okuno, K. 187
Oohashi, K. 129

Author Index

Opel, E. 136
Ottmann, T. 672
Overton, B. J. 224
Özgür, M. R. 84, 257

P

Park, D. H. 409
Park, E. 713
Park, H. 713
Park, S. 713
Park, S. C. 680
Pearson, K. S. 106
Persson, E. E. R. 306
Phillips, R. 192
Pleunis, P. 698
Poltz, J. 577
Polymeropoulos, C. 326
Poumellec, B. 232
Prasad, R. O. S. 692
Priest, J. R. 122
Putz, C. 346

R

Rattazzi, D. J. 115, 447
Ravela, J. T. 274
Ravinutala, S. 326
Reichert, T. 551
Reiner, T. 606
Richards, J. 351
Risch, B. G. 115, 364
Riva, R. M. 106
Rodriguez, L. O. 293
Roussel, Y. 181
Rue, R. J. 753
Ruegenberg, G. 56

S

Sandelin, M. J. 311
Santana, M. R. 518
Sasakura, K. 341
Sasaoka, E. 707
Sasse, H. G. 143
Sato, K. 488
Scheid, H. 606
Schmucki, B. 151
Schneider, M. 742
Schouten, J. J. 540
Selfridge, R. H. 470
Shimabukuro, T. A. 437
Shimane, H. 483
Shimizu, M. 219, 506
Shimomichi, T. 129
Siddiqui, S. 532
Singh, A. 692
Sittinger, W. 151
Small, R. D. 422, 518
Smith, J. A. 240
Smith, M. S. 470
Soltis, M. G. 447
Sotome, H. 187
Stingl, A. 136, 415
Stradling, M. A. 526
Strong, P. K. 643
Subramanian, R. 253
Suematsu, M. 331, 463, 732
Sugie, T. 477
Sugimoto, H. 545
Suh, T. 629
Sukegawa, T. 703
Sutehall, R. 658
Suzuki, Y. 686
Szwec, J. R. 532

T

Tachikura, M. 98
Takahashi, K. 68
Takaoka, R. 666
Takaoka, S. 506
Takemyou, T. 129
Tanaka, N. 341
Tanaka, S. 207
Tang, L. 336
Tanimoto, G. 384
Tawanishi, N. 68
Taylor, C. R. 518, 532
Taylor, S. H. 283
Teschner, W. 747
Tetsutani, S. 477, 488
Thomas, Jr., S. G. 807
Tilley, M. 551
Toften, T. E. 764
Torrey, S. 351
Traub, N. 289
Tresch, B. 151
Trombert, P. 650
Tschumperle, D. 28
Tsujikawa, K. 477
Tsukamoto, M. 379
Tunstall, B. G. 143
Turnbill, C. E. 224

Author Index

U

Ukachi, T. 545
Unkel, D. 84
Unterzuber, K. 529
Uruno, S. 98

V

van den Heuvel, M. 698
Vanderlaan, P. Z. 374
van't Hul, C. 736
Vintermyr, I. 764
Voigt, W. A. 787

W

Walling, J.-H. 586
Walter, D. J. 240
Wang, J. 212
Wardeberg, J. 764
Waring, D. 596
Waterworth, G. 775
Wegbrans, B. 736
Weimann, P. A. 422
Westfall, E. 540
Wetherell, A. D. 1
Williams, K. 351
Willis, A. J. 143, 160, 554, 570
Wilson, C. G. 212
Worthington, P. 770

X

Xia, R. 336

Y

Yaguchi, S. 68
Yamaguchi, J. 341
Yamaguchi, K. 201
Yamakawa, J. 379
Yamamoto, F. 477, 488
Yamamoto, K. 758
Yamanaka, M. 432, 732
Yamasaki, A. 432
Yamazaki, T. 483, 703
Yoshizawa, J. 545
Yusa, H. 369

Z

Zamzow, P. E. 614
Zhong, X. 336
Zhou, J. 488